Black Sea Journal of Engineering and Science

Volume 9 | Issue 5



ISSN: 2619 - 8991

KAR-YAY

BLACK SEA JOURNAL OF ENGINEERING AND SCIENCE

(BSJ ENGIN SCI)

Black Sea Journal of Engineering and Science (BSJ Eng Sci) is a double-blind peer-reviewed, open-access international journal published electronically 6 times (January, March, May, July, September, and November) in a year by since January 2018. It publishes, in English and Turkish, full-length original research articles, innovative papers, conference papers, reviews, mini-reviews, rapid communications or technical note on advances in a wide range of scientific disciplines from all fields of engineering and science and from any source.

e-ISSN: 2619 - 8991

Phone: +90 362 408 25 15

Fax: +90 362 408 25 15

Email: bsjsci@blackseapublishers.com

Web site: http://dergipark.gov.tr/bsengineering

Sort of publication: Periodically 6 times (January, March, May, July, September, and November) in a year

Publication date and place: September 15, 2026 - Samsun, TÜRKİYE

Publishing kind: Electronically

PUBLISHER

Karyay Karadeniz Yayımcılık ve Organizasyon Trade Limited Company

DIRECTOR IN CHARGE

Prof. Dr. Uğur ŞEN

EDITOR BOARDS

EDITOR IN CHIEF

Prof. Dr. Uğur ŞEN, Ondokuz Mayis University, TÜRKİYE

Prof. Dr. Hasan ÖNDER, Ondokuz Mayis University, TÜRKİYE

SECTION EDITORS*

Prof. Dr. Berna KILIÇ, Section Editor of Fisheries Engineering, Ege University, TÜRKİYE

Prof. Dr. Bülent YANIKTEPE, Section Editor of Aerospace Engineering, Osmaniye Korkut Ata University, TÜRKİYE

Prof. Dr. Çiğdem TAKMA, Section Editor of Statistics, Ege University, TÜRKİYE

Prof. Dr. Daniel ZABORSKİ, Section Editor of Statistics, West Pomeranian University of Technology, POLAND

Prof. Dr. Dilek KUT, Section Editor of Textile Engineering, Uludağ University, TÜRKİYE

Prof. Dr. Erkan YALÇIN, Section Editor of Biology, Ondokuz Mayıs University, TÜRKİYE

Prof. Dr. Esteban TLELO-CUAUTLE, Section Editor of Electrical and Electronics Engineering, National Institute of Astrophysics, Optics and Electronics, MEXICO

Prof. Dr. Hasan TANAK, Section Editor of Physics, Amasya University, TÜRKİYE

Prof. Dr. Hasan TEMİZ, Section Editor of Food Engineering, Ondokuz Mayis University, TÜRKİYE

Prof. Dr. Hüseyin PEKER, Section Editor of Forest Engineering, Artvin Çoruh University, TÜRKİYE

Prof. Dr. İbrahim Özgür DENEME, Section Editor of Civil Engineering, Aksaray University, TÜRKİYE

Prof. Dr. Nilüfer YURTAY, Section Editor of Computer Engineering, Sakarya University, TÜRKİYE

Prof. Dr. Özgür Hakan AYDOĞMUŞ, Section Editor of Mathematics, Social Sciences University of Ankara, TÜRKİYE

Assoc. Prof. Dr. Aslı GÜNAY BULUTSUZ, Section Editor of Mechanical Engineering, Yildiz Teknik University, TÜRKİYE

Assoc. Prof. Dr. Edit MİKÓ, Section Editor of Agricultural Engineering, University of Szeged, HUNGARY

Assoc. Prof. Dr. Hülya AYKAÇ ÖZEN, Section Editor of Environmental Engineering, Ondokuz Mayis University, TÜRKİYE

Assoc. Prof. Dr. İdil İPEK, Section Editor of Chemical Engineering, Ege University, TÜRKİYE

Assoc. Prof. Dr. Kürşat GÜLTEKİN, Section Editor of Mechanical Engineering, Ondokuz Mayis University, TÜRKİYE

Assoc. Prof. Dr. Lukman ABDULRA'UF, Section Editor of Chemistry, Kwara State University, NIGERIA

Assoc. Prof. Dr. Mohammad KHAJEH MEHRIZI, Section Editor of Textile Engineering, Yazd University, IRAN

Assoc. Prof. Dr. Pınar ŞEN, Section Editor of Chemical Engineering, Üsküdar University, TÜRKİYE

Assoc. Prof. Dr. Sinan AKISKA, Section Editor of Geological Engineering, Ankara University, TÜRKİYE
Assoc. Prof. Dr. Ufuk ATMACA, Section Editor of Chemistry, Atatürk University, TÜRKİYE
Assoc. Prof. Dr. Veli İLÇİ, Section Editor of Geomatics Engineering, Ondokuz Mayis University, TÜRKİYE
Assoc. Prof. Dr. Zeynep KARCIOĞLU KARAKAŞ, Section Editor of Environmental Engineering, Ataturk University, TÜRKİYE
Asst. Prof. Dr. Aslı TAŞ, Section Editor of Architecture, Nevşehir Haci Bektaş Veli University, TÜRKİYE
Asst. Prof. Dr. Mehmet ÖZDEMİR, Section Editor of Mining Engineering, Kütahya Dumlupınar University, TÜRKİYE
Asst. Prof. Ranjith RAJ A, Section Editor of Metallurgical and Materials Engineering, Sri Venkateswara College of Engineering, INDIA

* The ranking is arranged alphabetically within the academic title

STATISTIC EDITOR

Assoc. Prof. Dr. Cem TIRINK, Iğdır University, TÜRKİYE

ENGLISH EDITOR

Asst. Prof. Dr. Betül ÖZCAN DOST, Ondokuz Mayis University, TÜRKİYE

TURKISH EDITOR

Prof. Dr. Serkan ŞEN, Ondokuz Mayis University, TÜRKİYE

REVIEWERS OF THE ISSUE*

Prof. Dr. Abdulkadir ÇEVİK, Gaziantep University, Departmen of Civil Engineering, Civil Engineering, TÜRKİYE

Prof. Dr. Ahmet MERT, Bursa Technical University, Mechatronics Engineering Department, Image Processing, TÜRKİYE

Prof. Dr. Ahmet Ocak AKDEMİR, Ağrı İbrahim Çeçen University, Department of Mathematics, Partial Differential Equations, TÜRKİYE

Prof. Dr. Ayhan İSTANBULLU, Balikesir University, Department of Computer Engineering, Digital Electronic Devices, TÜRKİYE

Prof. Dr. Buğra OCAK, Ege University, Department of Leather Engineering, Leather Engineering, TÜRKİYE

Prof. Dr. Emel Öykü ÇETİN UYANIKGİL, Ege University, Department of Pharmaceutical Technology, Analytical Chemistry, TÜRKİYE

Prof. Dr. Erdinç UZUN, Tekirdağ Namık Kemal University, Department of Computer Engineering, Computer Software, TÜRKİYE

Prof. Dr. Erhan SET, Ordu University, Department of Mathematics, Real and Complex Functions, TÜRKİYE

Prof. Dr. Fırat ŞAL, Iskenderun Technical University, Department of Aircraft Maintenance and Repair, Aircraft Performance and Flight Control Systems, TÜRKİYE

Prof. Dr. Güzide PEKCAN, Süleyman Demirel University, Department of Chemistry, Analytical Chemistry, TÜRKİYE

Prof. Dr. Humar KAHRAMANLI ÖRNEK, Selcuk University, Department of Computer Engineering, Data Mining and Knowledge Discovery, TÜRKİYE

Prof. Dr. Hüseyin ERİŞTİ, Mersin University, Department of Electrical-Electronics Engineering, Machine Learning, TÜRKİYE

Prof. Dr. Hüseyin GENÇCELEP, Ondokuz Mayıs University, Department of Food Engineering, Environmental Management, TÜRKİYE

Prof. Dr. Hüseyin GÜRÜLER, Muğla Sıtkı Koçman University, Department of Information Systems Engineering, Data Mining and Knowledge Discovery, TÜRKİYE

Prof. Dr. Hüseyin Turan ARAT, Sinop University, Department of Mechanical Engineering, Mechanical Engineering, TÜRKİYE

Prof. Dr. İlhan UMUT, Tekirdağ Namık Kemal University, Department of Electronic Technology, Artificial Intelligence, TÜRKİYE

Prof. Dr. Mehmet Serhat ODABAŞ, Ondokuz Mayıs University, Plant and Animal Production Department, Precision Agriculture Technologies, TÜRKİYE

Prof. Dr. Murat UYAR, Bursa Uludağ University, Department of Electrical-Electronics Engineering, Machine Learning, TÜRKİYE

Prof. Dr. Mürsel EKREM, Necmettin Erbakan University, Department of Machinery, Vehicle Technique and Dynamics, TÜRKİYE

Prof. Dr. Sezgin Çağlar AKSEZER, Işık University, Department of Industrial Engineering, Manufacturing and Service Systems, TÜRKİYE

Prof. Dr. Şerafettin EKİNCİ, Selçuk University, Department of Machinery, Vehicle Technique and Dynamics, TÜRKİYE

Prof. Dr. Turgay Tugay BİLGİN, Bursa Technical University, Department of Computer Engineering, Artificial Intelligence, TÜRKİYE

Assoc. Prof. Dr. Adem KORKMAZ, Bandırma Onyedi Eylül University, Department of Web Design and Coding, Artificial Intelligence, TÜRKİYE

Assoc. Prof. Dr. Ahmet ERDOĞAN, İnönü University, Department of Mechanical Engineering, Aerodynamic, TÜRKİYE

Assoc. Prof. Dr. Ahmet ÖZTEL, Bartın University, Department of Quantitative Methods, Multiple Criteria Decision Making, TÜRKİYE

Assoc. Prof. Dr. Ahmet Şakir DOKUZ, Niğde Ömer Halisdemir University, Department of Computer Engineering, Information and Computing Sciences, TÜRKİYE

Assoc. Prof. Dr. Ali ALMUSAWI, Çankaya University, Department of Civil Engineering, Transportation Engineering, TÜRKİYE

Assoc. Prof. Dr. Alperen TOZLU, Bayburt University, Department of Electricity and Energy, Energy Generation, TÜRKİYE

Assoc. Prof. Dr. Altan ONAT, Eskisehir Technical University, Department of Electrical and Electronics Engineering, Vibration and Vibration Control, TÜRKİYE

Assoc. Prof. Dr. Asuman KARADENİZ PEKGÖZ, Mehmet Akif Ersoy University, Department of Biology, Plant Physiology, TÜRKİYE

Assoc. Prof. Dr. Aşır Yüksel KAYA, Fırat University, Department of Geography, Geographical Information Systems, TÜRKİYE

Assoc. Prof. Dr. Aycan Mutlu YAGANOĞLU, Atatürk University, Department of Animal Science, Artificial Intelligence, TÜRKİYE

Assoc. Prof. Dr. Bilal TÜTÜNCÜ, İstanbul Tachnical University, Department of Renewable Energy, Electrical Engineering, TÜRKİYE

Assoc. Prof. Dr. Cemal KARAASLAN, Iğdır University, Department of Civil Engineering, Civil Geotechnical Engineering, TÜRKİYE

Assoc. Prof. Dr. Dilek ÖZDEMİR GÜNGÖR, İzmir Katip Çelebi University, Department of Data Science and Analytics, Multiple Criteria Decision Making, TÜRKİYE

Assoc. Prof. Dr. Dilek PİRİM, Bursa Uludağ University, Department of Molecular Biology and Genetics, Genomics, TÜRKİYE

Assoc. Prof. Dr. Ehsan SHAKOURI, Islamic Azad University-North Tehran Branch, Department of Manufacturing, Biomechanical Engineering, IRAN

Assoc. Prof. Dr. Elena BATTINI SÖNMEZ, Istanbul Bilgi University, Department of Computer Engineering, Information and Computing Sciences, TÜRKİYE

Assoc. Prof. Dr. Emine GÜVEN, Düzce University, Department of Biomedical Engineering, Genomics, TÜRKİYE

Assoc. Prof. Dr. Emre MANDEV, Erzurum Technical University, Department of Mechanical Engineering, Chemical Thermodynamics and Energetics, TÜRKİYE

Assoc. Prof. Dr. Esra KARAKAŞ, Adana Alparslan Türkeş Science and Technology University, Department of Business Administration, Multiple Criteria Decision Making, TÜRKİYE

Assoc. Prof. Dr. Ethem TOPÇUOĞLU, Giresun University, Department of Aviation, Organisation and Management Theory, TÜRKİYE

Assoc. Prof. Dr. Faruk BULUT, İstanbul Aydın University, Department of Aviation Electrical and Electronics, Artificial Intelligence, TÜRKİYE

Assoc. Prof. Dr. Fatih SOYGAZİ, Aydın Adnan Menderes University, Department of Computer Engineering, Information and Computing Sciences, TÜRKİYE

Assoc. Prof. Dr. Fazıl AKDAĞ, Erciyes University, Department of Architecture, Information Technologies in Architecture and Design, TÜRKİYE

Assoc. Prof. Dr. Gökçe DİDAR DEĞERMENCİ, Kastamonu University, Department of Environmental Engineering, Wastewater Treatment Processes, TÜRKİYE

Assoc. Prof. Dr. İhsan TUĞAL, Muş Alparslan University, Department of Software Engineering, Artificial Intelligence, TÜRKİYE

Assoc. Prof. Dr. İlkan ÖZKAN, Adana Alparslan Türkeş Science and Technology University, Department of Materials Science and Engineering, Textile Technology, TÜRKİYE

Assoc. Prof. Dr. İlker KALKAN, Kırıkkale University, Departmen of Civil Engineering, Civil Engineering, TÜRKİYE

Assoc. Prof. Dr. Kubilay Doğan KILIÇ, Ege University, Department of Basic Medical Sciences, Cell Metabolism, TÜRKİYE

Assoc. Prof. Dr. Kutay AYDIN, Amasya University, Department of Mechanical Engineering, Mechanical Engineering, TÜRKİYE

Assoc. Prof. Dr. Mehmet Akif ŞAHMAN, Selçuk University, Department of Electrical and Electronics Engineering, Machine Learning Algorithms, TÜRKİYE

Assoc. Prof. Dr. Mehmet Alper SOFUOĞLU, Eskişehir Osmangazi University, Department of Mechanical Engineering, Mechanical Vibrations and Noise, TÜRKİYE

Assoc. Prof. Dr. Mesut TOĞAÇAR, Fırat University, Department of Management Information Systems, Information and Computing Sciences, TÜRKİYE

Assoc. Prof. Dr. Mualla KETEN GÖKKUŞ, Nevsehir Haci Bektas Veli University, Department of Biosystems Engineering, Agricultural Hydrology, TÜRKİYE

Assoc. Prof. Dr. Muhammed Yunus BİLGİLİ, Karadeniz Technical University, Department of Public Administration, Environment Policy, TÜRKİYE

Assoc. Prof. Dr. Murat AY, Yozgat Bozok University, Department of Civil Engineering, Hydrology, TÜRKİYE

Assoc. Prof. Dr. Mustafa Ali DOKUYUCU, Ondokuz Mayıs University, Department of Mathematics, Partial Differential Equations, TÜRKİYE

Assoc. Prof. Dr. Mustafa ÖZTOP, Burdur Mehmet Akif Ersoy University, Department of Biology, Ecology, TÜRKİYE

Assoc. Prof. Dr. Oğuz KÖSE, Erzincan Binali Yildirim University, Department of Aircraft Technology, Aircraft Performance and Flight Control Systems, TÜRKİYE

Assoc. Prof. Dr. Ömer KASIM, Kütahya Dumlupınar University, Department of Electronics, Machine Learning, TÜRKİYE

Assoc. Prof. Dr. Rahim JAFARI, Türk Hava Kurumu University, Department of Mechanical Engineering, Mechanical Engineering, TÜRKİYE

Assoc. Prof. Dr. Pınar KARADAYI ATAŞ, İstanbul Arel University, Department of Software Engineering, Information and Computing Sciences, TÜRKİYE

Assoc. Prof. Dr. Selçuk ASLAN, Erciyes University, Department of Aeronautical Engineering, Machine Learning Algorithms, TÜRKİYE

Assoc. Prof. Dr. Serkan ELÇİN, Pamukkale University, Department of Chemistry, Organic Chemical Synthesis, TÜRKİYE

Assoc. Prof. Dr. Turgut ÖZSEVEN, Tokat Gaziosmanpaşa University, Department of Computer Engineering, Information and Computing Sciences, TÜRKİYE

Assoc. Prof. Dr. Yasin GÖKÇE, Alanya Alaaddin Keykubat University, Department of Biophysics, Biophysics, TÜRKİYE

Assoc. Prof. Dr. Yiğit Ali ÜNCÜ, Akdeniz University, Department of Biomedical Equipment Technology, Biomedical Engineering, TÜRKİYE

Assoc. Prof. Dr. Yunus DEMİR, Bursa Technical University, Department of Industrial Engineering, Optimization in Manufacturing, TÜRKİYE

Assist. Prof. Dr. Ahmet BÜYÜKEKE, Adana Alparslan Türkeş Science and Technology University, Administrative and Social Sciences, Deep Learning, TÜRKİYE

Assist. Prof. Dr. Ahmet DELEN, Tokat Gaziosmanpaşa University, Department of Geomatics Engineering, Geospatial Information Systems and Geospatial Data Modelling, TÜRKİYE

Assist. Prof. Dr. Ahmet LOĞOĞLU, Osmaniye Korkut Ata University, Department of Computer Engineering, Signal Processing, TÜRKİYE

Assist. Prof. Dr. Ahmet NUR, Bitlis Eren Department of Electrical-Electronics Engineering, Electrical Engineering, TÜRKİYE

Assist. Prof. Dr. Ahmet TIĞLI, Sinop University, Department of Metallurgy and Materials Engineering, Material Design and Behaviors, TÜRKİYE

Assist. Prof. Dr. Ali EMİN, Atılım University, Department of Automotive Engineering, Mechanical Engineering, TÜRKİYE

Assist. Prof. Dr. Ali TAŞKIRAN, Şırnak University, Department of Mechanical Engineering, Numerical Methods in Mechanical Engineering, TÜRKİYE

Assist. Prof. Dr. Alican Tuncay ALPKAYA, Kırklareli University, Department of Mechanical Engineering, Biomechanical Engineering, TÜRKİYE

Assist. Prof. Dr. Barış Gürcan HAKANOĞLU, Atılım University, Department of Electrical and Electronics Engineering, Engineering Electromagnetics, TÜRKİYE

Assist. Prof. Dr. Berkay EREN, Iskenderun Technical University, Department of Mechatronics Engineering, Image Processing, TÜRKİYE

Assist. Prof. Dr. Bihter ŞAHİN, Bandırma Onyedi Eylül University, Department of Chemistry and Chemical Processing Technologies, Natural Products and Bioactive Compounds, TÜRKİYE

Assist. Prof. Dr. Bilgehan ERKAL, Karabuk University, Department of Electrical and Electronics Engineering, Signal Processing, TÜRKİYE

Assist. Prof. Dr. Caner MURAT, İzmir Bakırçay University, Department of Electrical and Electronics Engineering, Engineering Electromagnetics, TÜRKİYE

Assist. Prof. Dr. Çağrı KAYMAK, Fırat University, Department of Mechatronics Engineering, Remote Sensing, TÜRKİYE

Assist. Prof. Dr. Dilan SARPKAYA, Toros University, Department of Industrial Engineering, Multiple Criteria Decision Making, TÜRKİYE

Assist. Prof. Dr. Dinçer ATASOY, Iğdır University, Department of Software Engineering, Programming Languages, TÜRKİYE

Assist. Prof. Dr. Emine BOZOKLAR, İskenderun Technical University, Department of Industrial Engineering, Operations Research in Mathematics, TÜRKİYE

Assist. Prof. Dr. Emre DUMAN, Marmara University, Department of Geography, Natural Hazards, TÜRKİYE

Assist. Prof. Dr. Ercan COŞGUN, Kırıklareli University, Department of Electronic Technology, Machine Learning Algorithms, TÜRKİYE

Assist. Prof. Dr. Erkan ÖZHAN, Tekirdağ Namık Kemal University, Department of Computer Engineering, Computer Software, TÜRKİYE

Assist. Prof. Dr. Evrim GÜLER, Bartın University, Department of Computer Engineering, Machine Learning, TÜRKİYE

Assist. Prof. Dr. Fatih IŞIK, Gümüşhane University, Department of Geography, Natural Hazards, TÜRKİYE

Assist. Prof. Dr. Fazlı AKYÜZ, Istanbul University-Cerrahpasa, Department of Environmental Protection Technologies, Leather Engineering, TÜRKİYE

Assist. Prof. Dr. Ferhat YUNA, Erzurum Technical University, Department of Industrial Engineering, Industrial Engineering, TÜRKİYE

Assist. Prof. Dr. Fesih KESKİN, Siirt University, Department of Computer Engineering, Engineering Electromagnetics, TÜRKİYE

Assist. Prof. Dr. Galip KALTAKKIRAN, Ardahan University, Department of Electrical and Electronics Engineering, Energy Generation, TÜRKİYE

Assist. Prof. Dr. Hasan OKTAY, Batman University, Department of Machinery, Vibration and Vibration Control, TÜRKİYE

Assist. Prof. Dr. Hava Şeyma İNCİ, Bingöl University, Department of Crop and Animal Production, Field Crops and Pasture Production, TÜRKİYE

Assist. Prof. Dr. Kaan ARIK, Sakarya University of Applied Sciences, Information Technologies Vocational School, Machine Learning, TÜRKİYE

Assist. Prof. Dr. Kemal ERSAYIN, Tokat Gaziosmanpaşa University, Department of Geography, Natural Hazards, TÜRKİYE

Assist. Prof. Dr. Mehmet Ali USTA, Giresun University, Department of Computer Engineering, Electrical Machines and Drives, TÜRKİYE

Assist. Prof. Dr. Mehmet Emre SERTKAYA, Bingol University, Department of Computer Technologies, Artificial Intelligence, TÜRKİYE

Assist. Prof. Dr. Mehmet Fatih KARAKAŞ, Erzincan Binali Yıldırım University, Department of Electrical and Electronics Engineering, Image Processing, TÜRKİYE

Assist. Prof. Dr. Menşure Zuhal BARAK, Adana Alparslan Türkes Science and Technology University, Department of Business, Operations Research, TÜRKİYE

Assist. Prof. Dr. Mesut HÜSEYINOĞLU, Dicle University, Department of Machinery, Vibration and Vibration Control, TÜRKİYE

Assist. Prof. Dr. Mustafa KONAL, Tekirdağ Namık Kemal University, Department of Electronics and Communication Engineering, Circuits and Systems, TÜRKİYE

Assist. Prof. Dr. Murat KOYUNBAKAN, Kütahya Dumlupınar University, Department of Manufacturing Engineering, Mechanical Engineering, TÜRKİYE

Assist. Prof. Dr. Mustafa ÜSTÜNER, Samsun University, Department of Climate Science and Meteorology Engineering, Photogrammetry and Remote Sensing, TÜRKİYE

Assist. Prof. Dr. Neşe Özkan YILMAZ, Afyon Kocatepe University, Department of Biomedical Engineering, Machine Learning, TÜRKİYE

Assist. Prof. Dr. Onur YONTAR, Ondokuz Mayıs University, Department of Mechanical Engineering, Numerical Modelling and Mechanical Characterisation, TÜRKİYE

Assist. Prof. Dr. Özkan BİNGÖL, Karadeniz Technical University, Department of Software Development, Photogrammetry and Remote Sensing, TÜRKİYE

Assist. Prof. Dr. Ramazan ACAR, Munzur University, Department of Civil Engineering, Water Resources Engineering, TÜRKİYE

Assist. Prof. Dr. Ruşen SİNİR, Bayburt University, Construction Technology Program, Water Resources Engineering, TÜRKİYE

Assist. Prof. Dr. Salih AĞAR, Munzur University, Department of Mechanical Engineering, Machine Design and Machine Equipment, TÜRKİYE

Assist. Prof. Dr. Selin SARAÇ GÜLERYÜZ, Toros University, Department of Industrial Engineering, Operations Models and Simulations of Design, TÜRKİYE

Assist. Prof. Dr. Semih BAYER, Van Yüzüncü Yıl University, Department of Architecture, Information Technologies in Architecture and Design, TÜRKİYE

Assist. Prof. Dr. Seyfi TANER, Karamanoglu Mehmetbey University, Department of Plant and Animal Production, Field Crops and Pasture Production, TÜRKİYE

Assist. Prof. Dr. Shubham PATIL, Warana University, Department of Electrical and Electronics Engineering, Circuits and Systems, INDIA

Assist. Prof. Dr. Süleyman Mert ÖZER, Eskişehir Technical University, Department of Motor Vehicles and Transportation Technologies, Control Engineering, TÜRKİYE

Assist. Prof. Dr. Süreyya KOCATEPE, Fırat University, Clothing Production Technology Program, Textile Technology, TÜRKİYE

Assist. Prof. Dr. Yahya DANAYİYEN, Karadeniz Technical University, Department of Electrical and Electronics Engineering, Electrical Engineering, TÜRKİYE

Dr. Amina TARIQ, Lahore College for Women University, Department of Botany, Plant Biochemistry, PAKISTAN

Dr. Arif TUNCAL, General Directorate of State Airports Authority, Air Transportation and Freight Services, TÜRKİYE

Dr. Cem KORKMAZ, Çukurova University, Department of Agricultural Machinery and Technology Engineering, Vibration and Vibration Control, TÜRKİYE

Dr. Ebru ERGÜNEŞ BERKİN, Hassa District Directorate of Agriculture and Forestry, Biometry, TÜRKİYE

Dr. Eda SERTAŞI, Sinop University, Department of Medical Services and Techniques, Environmental Engineering, TÜRKİYE

Dr. Durmuş ERSOY, İstanbul Esenyurt University, Department of Electrical and Electronics Engineering, Circuits and Systems, TÜRKİYE

Dr. Hasan Alp ŞAHİN, Ondokuz Mayıs University, Hemp Research Institute, Artificial Intelligence, TÜRKİYE

Dr. Hüseyin ŞAHİN, Ankara Yıldırım Beyazıt University, Aircraft Technology Program, Aircraft Performance and Flight Control Systems, TÜRKİYE

Dr. İrem BOZYİĞİT, Ege University, Department of Civil Engineering, Civil Geotechnical Engineering, TÜRKİYE

Dr. Kenan GÜRÇAM, Iğdır University, Electrical Program, Electrical Energy Generation, TÜRKİYE

Dr. Kerim KARADAĞ, Harran University, Department of Electrical-Electronics Engineering, Electrical Engineering, TÜRKİYE

Dr. Murat ERDEM, Fırat University, Department of Motor Vehicles and Transportation Technologies, Machinery, TÜRKİYE

Dr. Şölen ZENGİN, Tarsus University, Department of Industrial Engineering, Operations Research İn Mathematics, TÜRKİYE

* The ranking is arranged alphabetically within the academic title

Volume 9, Issue 5 (2026)

Table of Contents

Research Articles

1. NOVELTY-BASED INTRUSION DETECTION IN UNMANNED AERIAL VEHICLES
Sami EKICI, Onur AYVA.....2147-2155

2. ATM NAKİT TALEP TAHMİNİNDE RNN MİMARİLERİNİN BAŞARIMI: LSTM, GRU, Bi-LSTM VE CNN-LSTM
Havanur ŞENOCAK, Tuba IRMAK, Betül TURANOĞLU ŞİRİN.....2156-2174

3. MITOCHONDRIAL DYSFUNCTION ACROSS SYNOVIAL AND PERIPHERAL COMPARTMENTS IN RHEUMATOID ARTHRITIS: A MULTI-TISSUE TRANSCRIPTOMIC INTEGRATION OF PBMC, SYNOVIAL BIOPSY AND WHOLE BLOOD
Sevinç AKÇAY.....2175-2187

4. INTEGRATION OF PHOTOCATALYTIC HYDROGEN PRODUCTION WITH A PEM FUEL CELL-BASED OFF-GRID COLD STORAGE SYSTEM: THERMODYNAMIC, DYNAMIC SOLAR, AND ENVIRONMENTAL PERFORMANCE ANALYSIS ACROSS THREE TECHNOLOGY READINESS SCENARIOS
Hakan TUTUMLU.....2188-2202

5. DETERMINATION OF THE EFFECTS OF GIBBERELLIC ACID (GA_3) DOSES ON GERMINATION PARAMETERS IN SOME SOYBEAN VARIETIES
Tahsin BEYCIOGLU.....2203-2210

6. CONTEXT ENGINEERING: A BIBLIOMETRIC ANALYSIS
Alperen KOÇYİĞİT, Nurettin ŞENYER.....2211-2223

7. DEVELOPMENT AND EXPERIMENTAL VALIDATION OF A FULL-SCALE BRAKE DISC/PAD TEST RIG FOR PASSENGER VEHICLES
Hüseyin KAYA, Hanifi KÜÇÜKSARIYILDIZ, Bekir GÜNEY.....2224-2231

8. EXPERIMENTAL INVESTIGATION OF THE EFFECTS OF PROCESS PARAMETERS ON PRODUCT GEOMETRY AND WEIGHT IN THE INJECTION MOLDING PROCESS WITH PE100 MATERIAL
Yavuz TURAN, İbrahim KELEŞ.....2232-2238

9. TOKAT OVASI VE YAKIN ÇEVRESİNDE İKLİM DEĞİŞİKLİĞİ BAĞLAMINDA KURAKLIK ANALİZİ
İsmail BAYRAM, Halil İbrahim ZEYBEK.....2239-2248

10. HETEROGENEOUS MIXTURE DISTRIBUTIONS FOR MODELING SKEWED DATA IN ENGINEERING APPLICATIONS: A THEORETICAL APPROACH
Selin SARAC GULERYUZ.....2249-2258

11. EFFECT OF SOIL STABILIZATION USING GROUND GRANULATED BLAST FURNACE SLAG AND ALKALI ACTIVATED SOLUTIONS ON RIGID PAVEMENT COST
Bahadır KARABAŞ, Ali Ulvi UZER, Nurullah AKBULUT, Abdurrahman BÖLÜCÜ.....2259-2268

12. HIERARCHICAL EXPERT-ROUTED BOOSTING WITH PROBABILITY FUSION FOR MULTICLASS INTRUSION DETECTION IN EDGE-IOT AND IIOT NETWORKS
Fesih KESKİN.....2269-2280

13. SÜRDÜRÜLEBİLİR TARIMDA HAFİF DERİN ÖĞRENME VE HİBRİT MAKİNE ÖĞRENMESİ YAKLAŞIMLARI İLE OPTİMİZE EDİLMİŞ YAPRAK HASTALIĞI TESPİTİ
Hasan Hüseyin ÇELİK.....*2281-2287*
14. NUMERICAL AND EXPERIMENTAL CHARACTERIZATION OF AN AERODYNAMICALLY REDESIGNED DISC IN A DN350 DOUBLE-ECCENTRIC BUTTERFLY VALVE IN TERMS OF FLOW COEFFICIENT, PRESSURE LOSS AND HYDRODYNAMIC DISC LOAD
Onur GÖK, Hacı Ali ERTAŞ.....*2288-2306*
15. FACE RECOGNITION BASED IDENTITY VERIFICATION AND TRACKING SYSTEM DESIGN
Emirhan TANRIVERDİ, Yaşar APAYDIN, Hakan ÜSTÜNEL.....*2307-2316*
16. GLOBAL EVOLUTION AND RESEARCH TRENDS OF THE SWAT MODEL (1994–2024): A COMPREHENSIVE BIBLIOMETRIC ANALYSIS
Erkan KARAKOYUN.....*2317-2336*
17. A BIBLIOMETRIC ANALYSIS ON EMERGENCY DEPARTMENT SIMULATION AND DISCRETE EVENT SIMULATION
Z. Figen ANTMEN, Şölen ZENGİN.....*2337-2344*
18. HS-SPME-GC/MS-BASED VOLATILE PROFILING AND CHEMOMETRIC DISCRIMINATION OF SELECTED HERBAL TEAS
Selçuk KÜÇÜKAYDIN.....*2345-2353*
19. GÜNCEL AÇIK KAYNAK BÜYÜK DİL MODELLERİNİN KİŞİLİK DEĞERLENDİRME PERFORMANSI: IPIP VERİLERİ ÜZERİNDE İNSAN VE YAPAY ZEKÂ KARŞILAŞTIRMASI
İlknur DÖNMEZ.....*2354-2364*
20. MACHINE LEARNING APPLICATIONS IN PREDICTING THE MICROBIOLOGICAL QUALITY OF PUBLIC FOUNTAIN WATERS: A CASE STUDY OF BAYBURT PROVINCE
Gülhat KOÇYİĞİT, Ruşen SINIR.....*2365-2372*
21. ROBUSTNESS EVALUATION OF HYPERSPECTRAL IMAGE CLASSIFICATION MODELS USING DEGRADATION-AWARE METRICS
Cem ATILGAN.....*2373-2392*
22. DEVELOPMENT AND WEB-BASED VISUALIZATION OF A DOMAIN-SPECIFIC SEMANTIC MODEL FOR COFFEE CULTURE AND PRODUCTION PROCESSES
Ömer DOĞAN, Alpay DORUK.....*2393-2403*
23. YAZILIM YOĞUN UÇUŞ KONTROL SİSTEMLERİNDE SERTİFİKASYON GÜVENCESİ VE OPERASYONEL ÖĞRENME: AIRBUS A320 ELAC ARIZALARI ÜZERİNE ÇOK BOYUTLU BİR ANALİZ
Erdal YEŞİLBAŞ.....*2404-2418*
24. INVERSE NODAL ANALYSIS FOR VECTOR-VALUED SINGULAR DIFFUSION OPERATORS
Abdullah ERGÜN.....*2419-2426*
25. ECOLOGICAL EPIGENETICS: RESEARCH FRONTS, TAXONOMIC GAPS, AND A FIVE-YEAR FORECAST
Bekir KABASAKAL.....*2427-2445*
26. DESIGN AND MANUFACTURING OF A CRANKSHAFT-FREE COMPRESSOR
Ramin BARZEGAR.....*2446-2452*

27. FIRÇALI DA MOTORLARDA AÇIK VERİ SETİ İLE MAKİNE ÖĞRENMESİ TABANLI KESTİRİMCİ BAKIM VE ARIZA TEŞHİSİ
Erdoğan ÖZEL.....*2453-2461*
28. ASSESSING READINESS FOR AI-HUMAN INTEGRATION USING A HESITANT FUZZY ANALYTIC HIERARCHY PROCESS: AN APPLICATION IN THE BANKING SECTOR
Çağrı AKOĞLU, Gül Tekin TEMUR.....*2462-2472*
29. CUDA-BASED PARALLEL INTRA PREDICTION AND TRANSFORM ARCHITECTURE FOR HEVC INTRA-FRAME IMAGE CODING
Mücahit KAPLAN, Ali AKMAN.....*2473-2481*
30. HYBRID SIO2/AL2O3 FILLER REINFORCEMENT IN GLASS FIBER/EPOXY COMPOSITES: FLEXURAL AND TENSILE BEHAVIOR WITH PHYSICS-INFORMED NEURAL NETWORK VALIDATION
Ismail BAYAR, Huseyin KOSE.....*2482-2491*
31. COMPARATIVE EVALUATION OF RANDOM, SOBOL, AND DRAGON-FAMILY-GUIDED PSO AND QUANTUM INSPIRED PSO ON CEC 2022 BENCHMARKS AND CLEVELAND HEART DISEASE WRAPPER FEATURE SELECTION
Serkan ÖRÜCÜ.....*2492-2526*
32. ARTIFICIAL INTELLIGENCE–DRIVEN LIFE CYCLE ASSESSMENT OF INJECTABLE AESTHETIC PRODUCTS: A MULTI-REGIONAL AND TEMPORAL SUSTAINABILITY ANALYSIS
Yelda FIRAT, Hüseyin Ali SARIKAYA.....*2527-2545*
33. ANALYZING CUSTOMER LIFETIME VALUE IN DIGITAL BANKING: A PPF-AHP BASED CRITERION PRIORITIZATION APPROACH
Ünzile MERAM HUYUT, Gül T. TEMUR.....*2546-2553*
34. COMPARATIVE ANALYSIS OF ADVANCED CONTROL STRATEGIES FOR VIBRATION CONTROL OF FLEXIBLE SATELLITE STRUCTURES
Aslı DURMUŞOĞLU.....*2554-2572*
35. COASTAL MONITORING USING FLUORESCENCE LINE HEIGHT -BASED REMOTE SENSING AND MACHINE LEARNING: A SEAWATER-COOLED FACILITY CASE STUDY
Ercüment AKSOY.....*2573-2585*
36. A DIGITAL DESIGN FRAMEWORK FOR CYBORG ARCHITECTURE
Ayşegül KIDIK, Hakan TONG.....*2586-2598*
37. DICLOFENAC POTASSIUM AND ISONICOTINAMIDE COCRYSTALS FOR ENHANCED SOLUBILITY: IN VITRO EVALUATION OF HARD GELATIN CAPSULES
Esra DEMIRTURK, Gülsüm GUNDOGDU, Merve NENNI, Cem YAMALI, Meltem CETIN, Yılmaz CAPAN.....*2599-2611*
38. COMPARATIVE ANALYSIS OF METAHEURISTIC FEATURE SELECTION IN SVM-BASED HUMAN ACTIVITY RECOGNITION
Duygu Sedef ÇALIŞKAN, Özlem KILIÇ, Durmuş Özkan ŞAHİN, Gökhan KAYHAN, Sercan DEMİRCİ.....*2612-2620*
39. COMPARATIVE NUMERICAL ANALYSIS OF SURCHARGE EFFECTS ON A CANTILEVER SHEET PILE WALL IN STIFF CLAY
Canan TURAN.....*2621-2628*

40. ANALYSIS OF KINEMATIC AND KINETIC PARAMETERS DURING MANUAL LOAD LIFTING USING MARKERLESS MOTION CAPTURE AND INVERSE DYNAMICS METHOD
Muhammed ÇİL, Bilal USANMAZ, Ömer GÜNDOĞDU……..2629-2638
41. DATA-DRIVEN VALIDATION AND CORRECTION OF THE DISTORTION FACTOR ESTIMATED FROM CURRENT TOTAL HARMONIC DISTORTION USING INDUSTRIAL FIELD MEASUREMENTS
Faruk KÜRKER, Ramazan TAŞALTIN……..2639-2651
42. A NEW DEEP CONVOLUTIONAL NEURAL NETWORK MODEL FOR MULTI-CLASS CYBER ATTACK DETECTION IN INTERNET OF MEDICAL THINGS NETWORKS
Gurkan DOGAN……..2652-2662
43. OPTIMIZATION OF WASTE-DERIVED RECYCLED POLYETHYLENE TEREPHTHALATE (r-PET) NANOFIBER PRODUCTION VIA BOX-BEHNKEN DESIGN
Hüsnü AYDEMİR……..2663-2675
44. MACHINE LEARNING AND DEEP LEARNING BASED CLASSIFICATION OF PROFANITY AND SEXIST DISCOURSE IN TURKISH TEXTS
Naim KARASEKRETER, Caner BALIM, Özkan ASLAN……..2676-2691
45. TRENDS AND BIBLIOMETRIC MAPPING OF THE KNOWLEDGE STRUCTURE OF GENERATIVE ARTIFICIAL INTELLIGENCE RESEARCH IN HIGHER EDUCATION
Şener BALAT……..2692-2717
46. A3NET: A LIGHTWEIGHT ATTENTION-GUIDED ENCODER–DECODER FOR MULTI-CLASS BRAIN TUMOR SEGMENTATION WITH CROSS-DATASET DOMAIN GAP CHARACTERIZATION
Turgay BATBAT, Ezzaldeen H. A. ABUKHATTAB……..2718-2737
47. DESIGN, FABRICATION, AND QPSK-BASED VALIDATION OF A COMPACT TWO-PORT MIMO ANTENNA WITH DEFECTED GROUND STRUCTURE FOR 5 GHZ WLAN APPLICATIONS
Cem GOCEN……..2738-2748
48. EXPERIMENTAL ASSESSMENT OF THE EFFECT OF REFERENCE SURFACE TEMPERATURE ON AUXILIARY ENERGY CONSUMPTION IN A THERMOELECTRIC-BASED BATTERY THERMAL MANAGEMENT SYSTEM
Erdoğan GÜNER……..2749-2759
49. EVALUATION OF GREEN AIRPORT CRITERIA IN SUSTAINABLE TRANSPORTATION USING DEMATEL AND BWM
Ahmet İLBAŞ, Aynur ACER, Hakan KAYA, İ.Bihter KARAGÖZ……..2760-2772
50. FLOOD RISK ASSESSMENT AND ENVIRONMENTAL CHANGE ANALYSIS USING GIS AND REMOTE SENSING
Sibel CANAZ SEVGEN……..2773-2782
51. A SUSTAINABLE ACT FOR CONCRETE DEBRIS DISPOSAL BY USING THE ALKALINE FUSION TECHNIQUE FOR THE SYNTHESIS OF SBA-15 TO USE IN DYE REMOVAL
Nevin KARAMAHMUT MERMER……..2783-2794
52. COMPARATIVE EVALUATION OF TOTAL PHENOLIC CONTENT AND ANTIOXIDANT CAPACITY IN ARONIA MELANOCARPA, CRATAEGUS ORIENTALIS SPP, AND CORNUS MAS L. FRUITS
Said Efe DOST, Yılmaz SESLİ……..2795-2799

53. AI-ASSISTED MULTICLASS KIDNEY CT PATHOLOGY CLASSIFICATION FOR UROLOGICAL IMAGING: AN OPTIMIZED HYBRID DEEP LEARNING FRAMEWORK
Mehmet Tevfik AGDAS, Furkan KARAHUSEYINOGLU.....*2800-2816*
54. CONGESTION-TRIGGERED ELECTRIC-VEHICLE CHARGING STATION ASSIGNMENT USING SHORT-TERM CUMULATIVE DEMAND FORECASTS
Oğuzkağan ALIÇ.....*2817-2834*
55. EMPIRICAL MASS-RETENTION MODELING, IMAGE-BASED SURFACE TEXTURE ANALYSIS AND COLOR EVALUATION IN VEGETABLE RETANNING OF WET-BLUE LEATHER
Şükrü ÖMÜR.....*2835-2843*

Reviews

56. TAVUKÇULUK ENDÜSTRİSİNDE ATIKLARIN ENTEGRE YÖNETİMİ: ÇEVRESEL RİSKLER, YENİLİKÇİ GERİ KAZANIM TEKNOLOJİLERİ VE SÜRDÜRÜLEBİLİR YÖNETİM MODELLERİ
Muhammed YÜCEER, Ecem IŞIK.....*2844-2858*
57. A REVIEW OF DIGITAL PHASE SHIFTER ARCHITECTURES: OPERATING PRINCIPLES, COMPARISON METHODOLOGY, AND DESIGN TRADE-OFFS
Sena TAŞ, Fırat KAÇAR.....2859-*2869*

Black Sea Journal of Engineering and Science
doi: 10.34248/bsengineering.1964066

Open Access Journal
e-ISSN: 2619 – 8991

Research Article
Volume 9 - Issue 5: 2147-2155 / September 2026

NOVELTY-BASED INTRUSION DETECTION IN UNMANNED AERIAL VEHICLES

Sami EKICI[1]*, Onur AYVA[2]

[1]*Fırat University, Faculty of Technology, Department of Energy Systems Engineering, 23200, Elazığ, Türkiye*
[2]*Fırat University, Graduate School of Natural and Applied Sciences, Department of Defense Technologies, 23200, Elazıg, Türkiye*

Abstract: The rapid proliferation of unmanned aerial vehicles (UAVs) in military and civil domains has raised serious security concerns alongside cyberattacks conducted over wireless communication channels. Threats such as GPS spoofing, signal jamming, denial of service, and sensor manipulation can produce abnormal behaviour in flight logs; traditional signature-based intrusion detection systems (IDS) remain inadequate because labelled attack data are limited. This study systematically evaluates the effectiveness of one-class machine learning methods trained solely on normal flight data for novelty-based intrusion detection. Using real flight logs from the ALFA (A dataset for UAV fault and anomaly detection) dataset, engine, aileron, rudder, and elevator faults were detected with one-class support vector machine (OC-SVM), one-class random forest (OC-RF), local outlier factor (LOF), and autoencoder algorithms. Although the ALFA scenarios are physically injected actuator faults rather than live cyberattacks, they produce abnormal flight-log signatures that are representative of behavioural deviations expected under cyber interference with guidance, navigation, or control commands; therefore, they serve as practical proxy conditions for evaluating novelty-based intrusion detection when labelled attack data are unavailable. During preprocessing, 18 sensor features were reduced to 1,000 sampling points via linear interpolation and z-score normalization was applied. The training set comprised 10 safe flights (10,000 samples) and the test set comprised 37 faulty flights (37,000 samples). OC-SVM, OC-RF, and autoencoder methods achieved accuracy, precision, recall, and F1-score values of 1.00 across all four fault types. LOF achieved accuracy values of 0.9997, 0.9995, 0.9990, and 0.9980 for engine, aileron, rudder, and elevator faults, respectively, with a total of 18 misclassifications. The findings indicate that novelty-based one-class classifiers offer practical solutions for label-free UAV security applications. Future work may examine multi-platform datasets, real-time architectures, and hybrid IDS designs.

Keywords: Unmanned aerial vehicles, Novelty-based intrusion detection, One-class classification, Anomaly detection, Machine learning

***Corresponding author:** Fırat University, Faculty of Technology, Department of Energy Systems Engineering, 23200, Elazığ, Türkiye
E mail: sekici@firat.edu.tr (S. EKICI)
Sami EKİCİ https://orcid.org/0000-0002-6760-2183
Onur AYVA https://orcid.org/0009-0002-6942-0022

Received: June 06, 2026
Accepted: July 16, 2026
Published: September 15, 2026

Cite as: Ekici, S., & Ayva, O. (2026). Novelty-Based intrusion detection in unmanned aerial vehicles. *Black Sea Journal of Engineering and Science,* 9(5), 2147-2155.

1. Introduction

Unmanned aerial vehicles (UAVs) are defined as aerial platforms capable of executing missions remotely or autonomously without carrying a pilot or passengers. Their widespread use in recent years for military reconnaissance, disaster management, agriculture, logistics, fire detection, and security applications has made them one of the strategic priorities of the aviation industry (Bakır, 2019). The growing investment in UAVs in civil and military domains also creates a serious threat when operated by malicious actors (Genç and Erciyes, 2020).

UAVs are controlled over wireless communication technologies such as radio frequency, Wi-Fi, Bluetooth, 3G/4G/LTE, and GPS (He et al., 2017). In particular, the open architecture and unencrypted transmission of GPS systems create vulnerability to spoofing and jamming attacks (Uyar, 2019). These attacks can cause abnormal changes in UAV motion and manoeuvres and deviations in sensor data (Muniraj and Farhood, 2017).

Evaluating UAV threats in sensitive areas such as nuclear facilities, power lines, and critical infrastructure occupies an important place in the security literature (Solodov et al., 2018; Chamola et al., 2021).

Cyber threats targeting UAVs form a multidimensional spectrum including misinformation, denial of service (DoS), jamming, power electronics attacks, IMU spoofing, and GPS manipulation (Sedjelmaci et al., 2018; Yahuza et al., 2021). Security and privacy issues in the Internet of Drones architecture are being reassessed in the context of cyber-physical systems (Haider et al., 2022). Electronic protection methods and communication security protocols constitute defence layers developed against these threats (Sentsov et al., 2019).

Intrusion detection systems (IDS) are classified under specification-based, signature-based, anomaly-based, and hybrid approaches (Choudhary et al., 2018). Although signature-based systems can detect known attack

This work is licensed (CC BY-NC 4.0) under Creative Commons Attribution 4.0 International License

patterns, they depend on signature databases that must be updated for new threat types (Borisovic, 2001).

Specification-based approaches identify deviations from normal behaviour models (Tseng et al., 2003), whereas anomaly-based systems offer the potential to detect unknown attacks (Patcha and Park, 2007). Hybrid IDS designs aim to combine the advantages of both approaches to provide broader protection (Aydın et al., 2009).

Regarding cyber-attack detection in UAV networks, Sedjelmaci et al. (2016) proposed a model based on a fast detection mechanism and belief functions, reporting a detection rate above 93%. Muniraj and Farhood (2017) developed a probabilistic framework to detect sensor attacks on small UAV systems and validated their approach using a GPS spoofing example. Zhu et al. (2018) achieved a 78% true attack detection rate in human-autonomy collaboration for cyber-attack detection. Renyu et al. (2018) examined GPS spoofing scenarios with cellular network-assisted positioning.

Sedjelmaci et al. (2018) reported high detection rates against GPS spoofing, signal jamming, and misinformation attacks using a hierarchical detection and response system. Whelan et al. (2020) demonstrated the effectiveness of one-class classifiers in sensor-based attack detection and emphasized the adaptability of the novelty-based approach to different UAV platforms. Rahman et al. (2020) proposed machine learning-based intrusion detection at the power electronics layer. Park et al. (2021) applied an autoencoder-based unsupervised fault detection model to UAV control systems. Davidovich et al. (2022) performed GPS spoofing detection through video stream analysis.

A large portion of UAV security studies in the literature focuses on simulation data or multi-class classifiers (Yiğit et al., 2018). The scarcity of labelled attack datasets, the high cost of experimental studies, and limited platform diversity are fundamental barriers restricting research in the field (Kılınçer, 2022).

Although artificial intelligence-based intrusion detection models have succeeded in enterprise network traffic (Ertam, 2016), comparative one-class analyses specific to UAV flight logs remain limited. Tunc and Hariri (2022) addressed the design of self-protection systems for autonomous vehicles and highlighted the need for similar architectures in UAV security.

The aim of this study is to compare the performance of four one-class machine learning methods in detecting engine, aileron, rudder, and elevator faults using the ALFA dataset (Keipour et al., 2021). Controlled actuator faults in ALFA were treated as proxy scenarios for abnormal flight behaviour that may arise from cyber interference. Keipour et al. (2019) proposed real-time anomaly detection for autonomous aerial vehicles and defined the controlled fault injection methodology underlying the ALFA dataset.

The central hypothesis is that one-class models trained only on safe flight data can classify control surface faults as outliers with high accuracy. This approach aims to provide a label-free IDS framework capable of detecting abnormal behavior independent of attack type.

The remainder of this paper is organized as follows. Section 2 presents the experimental platform, the ALFA dataset, preprocessing steps, one-class classification methods (OC-SVM, OC-RF, LOF, and Autoencoder), and the performance evaluation metrics. Section 3 reports the experimental findings for each fault type through comparative tables and figures. Section 4 discusses the results in the context of the literature, highlighting both strengths and limitations. Finally, Section 5 summarizes the main outcomes of the study and provides suggestions for future research.

2. Materials and Methods

2.1. Experimental Platform and Dataset

The ALFA (A dataset for UAV fault and anomaly detection) dataset was used in this study (Keipour, Mousaei, and Scherer, 2021). The dataset contains 47 autonomous flight records conducted on a Carbon-ZT-28 fixed-wing UAV equipped with a Holybro PX4 2.4.6 autopilot, GPS module, pitot tube, and Nvidia Jetson TX2 onboard computer (Keipour et al., 2019). The aircraft has a 2 m wingspan, a single electric motor, and aileron, flaperon, elevator, and rudder control surfaces as shown in Figure 1. Flights were conducted in the Pittsburgh region of the United States, and faults were injected in a controlled manner from the ground station using DisableEngine, DisableAileron, DisableRudder, and DisableElevator commands. For safety reasons, faults are activated only in autonomous mode; the pilot can take over control in an emergency.



Figure 1. Carbon-ZT-28 experimental platform equipped with onboard computer and auxiliary modules (Keipour et al., 2021)

The data collection infrastructure used a Robot Operating System (ROS) MAVLink node (MAVROS) and an Ubuntu 16.04-based ground station (QGroundControl). ArduPlane v3.9.0 flight control software enables actuator faults to be simulated safely. The MAVLink telemetry link and log recording flow between the UAV and ground station are shown schematically in Figure 2 (Keipour et al., 2019; Keipour et al., 2021).

The ALFA dataset contains a total of 47 autonomous flights. Table 1 summarizes flight counts by fault class.

Eight different control surface fault scenarios are defined: total engine power loss, rudder stuck left/right, elevator stuck at zero position, left/right aileron stuck, dual aileron stuck, and combined rudder–aileron fault. Engine fault has the largest number of test flights (23) and 362 seconds of faulty segments; safe flights total 558 seconds. In this study, faults were used as test conditions representing control deviations that may occur in unlabelled anomaly detection scenarios. Table 2 lists the number of test flights and the pre-fault and faulty segment durations for each scenario.

2.2. Feature Extraction

A total of 18 features related to position, IMU sensors, and system parameters were selected from raw flight logs (Park et al., 2021). The feature vector comprises velocity along the x, y, and z axes; angular velocity; linear acceleration; magnetic field; dynamic pressure; temperature; altitude error; airspeed error; x-axis tracking error; and waypoint distance. The selected features are not platform-specific and are common to both fixed-wing and rotary-wing UAVs, thereby increasing the generalization capacity of the proposed IDS. Table 3 lists the components of the feature vector.

Table 1. Fault types and flight counts in the ALFA dataset

Class	Flight Count
Safe flight (No Fault)	10
Engine fault	23
Aileron fault	8
Rudder fault	4
Elevator fault	2
Total	47

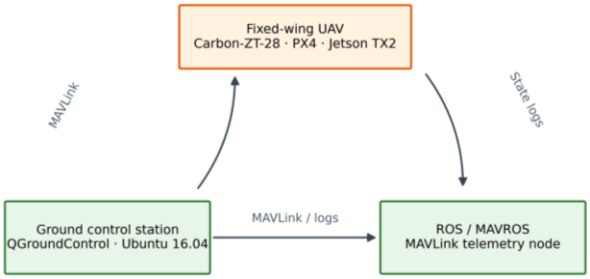


Figure 2. UAV–ground station telemetry architecture in the ALFA experimental setup (Keipour et al., 2019; Keipour et al., 2021).

Table 2. Flight durations by fault scenario in the ALFA dataset (seconds)

Fault Scenario	Flight Count	Pre-Fault Duration	Fault Duration
Total engine power loss	23	2,282	362
Rudder stuck left	1	60	9
Rudder stuck right	2	107	32
Elevator stuck at zero	2	181	23
Left aileron stuck	3	228	183
Right aileron stuck	4	442	231
Dual aileron stuck	1	66	36
Combined rudder–aileron	1	116	27
Safe flight	10	558	-

Table 3. Components of the 18-feature vector used in this study

Category	Feature	Description
Position	Velocity (x, y, z)	Velocity components along each axis
IMU	Angular velocity (x, y, z)	Angular velocity along each axis
IMU	Linear acceleration (x, y, z)	Acceleration along each axis
IMU	Magnetic field (x, y, z)	Magnetic field along each axis
IMU	Dynamic pressure	Sensor pressure value
System	Temperature	Battery temperature
System	Altitude error	Deviation from reference altitude
System	Airspeed error	Deviation from reference airspeed
System	Tracking error (x)	X-axis tracking deviation
System	WP distance	Distance between ideal and current position

2.3. Data Preprocessing

Each flight in the ALFA dataset has a different sampling frequency; the largest dimension is 3,956 samples and the smallest is 526 samples. This heterogeneity prevents the construction of classifier inputs. Linear interpolation was applied to each feature to reduce all-time series to 1,000 sampling points. Although alternative methods such as PCHIP (Piecewise Cubic Hermite Interpolating Polynomial) and cubic interpolation have been proposed in the literature, linear interpolation was preferred in this study. Z-score normalization was then applied. A training matrix of size 10,000×18 was created from safe

flight data and a test matrix of size 37,000×18 from faulty flight data (Table 4). Data preprocessing was performed in MATLAB R2021a. The novelty-based IDS architecture is shown in Figure 3. The workflow comprises feature extraction from safe flight logs, one-class model training using only normal data, anomaly score generation on fault/attack logs, and decision making. The same framework applies to all four methods: OC-SVM, OC-RF, LOF, and autoencoder.

2.4. One-class Classification Methods

This study follows a one-class anomaly detection protocol. The models are trained exclusively on normal flight logs and evaluated on held-out faulty flights. This differs from supervised train–validation–test splits because labeled attack data are unavailable at training time, which reflects realistic UAV IDS deployment. Four one-class anomaly detection algorithms were evaluated under this protocol. Training used only safe flight samples and testing used all faulty samples. Hyperparameters are summarized in Table 5. OC-SVM learns a hyperplane enclosing normal data and classifies deviations as outliers (Muñoz and Moguerza, 2004; Muñoz-Marí et al., 2010). The MATLAB fitcsvm function with an RBF kernel and Nu=0.05 was trained on 10,000 safe flight samples only. Nu sets the upper bound on the outlier fraction; the RBF kernel models a nonlinear decision boundary. At test time, negative decision scores indicate normal behavior and positive scores indicate anomalies. Figure 4 shows the schematic structure.

OC-RF is the one-class random forest variant implemented with MATLAB TreeBagger (Whelan et al., 2020). A 100-tree ensemble was trained with TreeBagger using bootstrap sampling and random feature subsets. A test sample was labelled anomalous when its combined outlier profile across trees deviated from the normal training distribution. Figure 5 shows the ensemble architecture. LOF computes a local outlier score from the density of each point relative to its k-nearest neighbours (Breunig et al., 2000; Alghushairy et al., 2020). The fitlof function was applied with neighbors number of 20. Samples with LOF scores greater than 1 were classified as outliers. Figure 6 illustrates the neighbourhood structure.

The autoencoder compresses the 18-dimensional input into a 10-neuron hidden layer and reconstructs the output (Park et al., 2021). The 18–10–18 architecture was trained with ReLU activation, Adam optimization, and 1,000 epochs. After training, reconstruction error was computed as the sample-level mean squared error (MSE) between the input feature vector and its reconstruction. Because the autoencoder was trained exclusively on normal flight data, the MSE distribution of safe samples provides a natural reference for anomaly scoring. For each fault-type evaluation, the decision threshold was set to the maximum reconstruction MSE observed on the corresponding normal training samples; test samples whose MSE exceeded this threshold were labelled anomalous. This conservative, training-data-driven rule avoids the use of faulty samples during threshold selection and yields fault-specific thresholds of 0.0037 (engine), 0.0072 (aileron), 0.0076 (rudder), and 0.0075 (elevator). Figure 7 shows the architecture and Figure 8 the MATLAB training interface of the autoencoder classifier.

Table 4. Flight and sample counts in the final dataset

Class	Flight Count	Sample Count
Safe flight	10	10.000
Engine fault	23	23.000
Aileron fault	8	8.000
Rudder fault	4	4.000
Elevator fault	2	2.000
Total	47	47.000

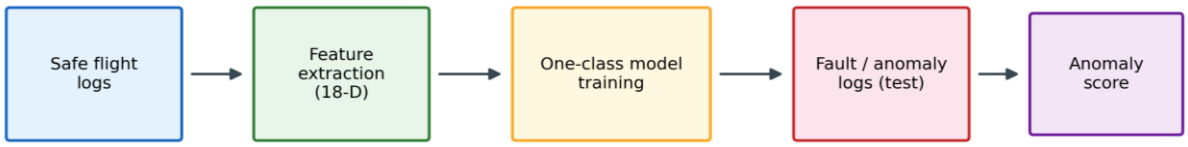


Figure 3. Novelty-based one-class UAV intrusion/fault detection workflow (Keipour et al., 2019; Whelan et al., 2020).

Table 5. Algorithms and hyperparameters used in this study

Method	MATLAB Function	Parameters
OC-SVM	fitcsvm	KernelFunction: RBF, Nu: 0.05
OC-RF	TreeBagger	NumTrees: 100
LOF	fitlof	NumNeighbors: 20
Autoencoder	trainAutoencoder, predict	Hidden layer: 10, ReLU, Adam, Epoch: 1000; threshold: 0.0037–0.0075

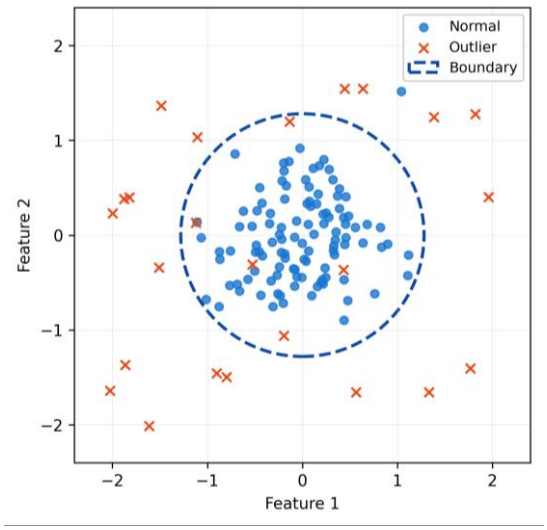


Figure 4. Schematic representation of one-class support vector machine (OC-SVM) (Muñoz and Moguerza, 2004).

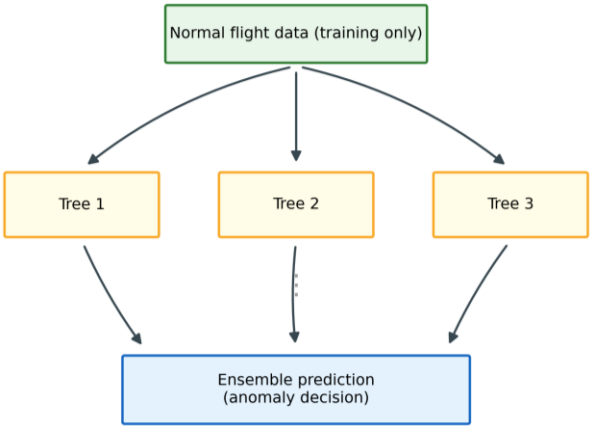


Figure 5. Ensemble structure of one-class random forest (OC-RF) (Whelan et al., 2020).

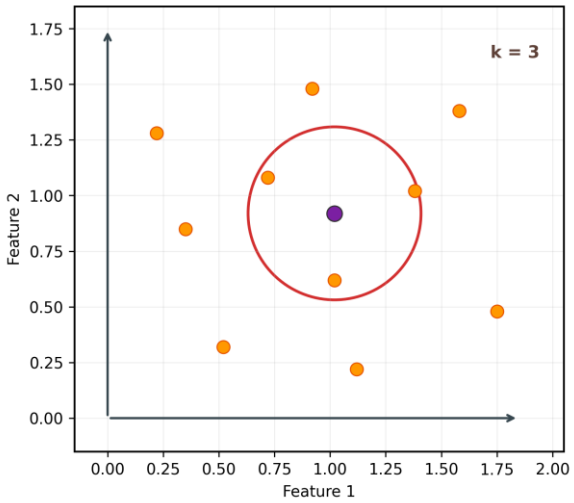


Figure 6. k-distance neighbourhood illustration in local outlier factor (Breunig et al., 2000).

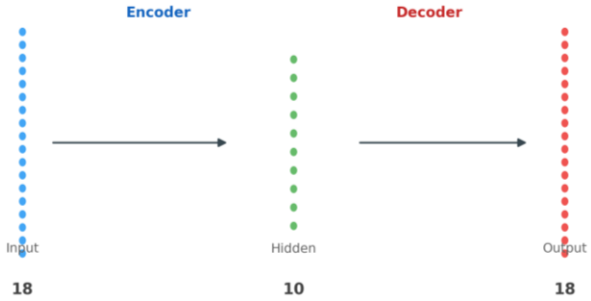


Figure 7. Autoencoder architecture used in this study (18–10–18 neurons) (Park et al., 2021).

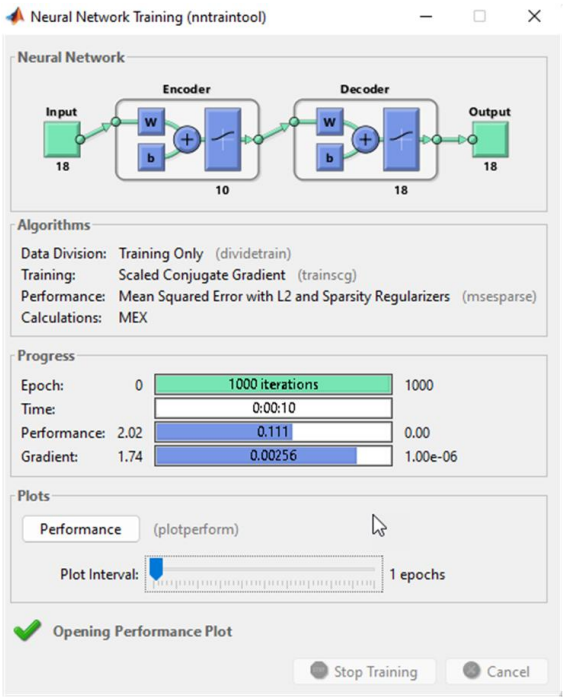


Figure 8. Autoencoder training process (input: 18, hidden: 10, output: 18 neurons).

2.5. Performance Evaluation Metrics

Model performance was evaluated using accuracy, precision, recall, and F1-score derived from the confusion matrix (Ertam, 2016; Kılınçer, 2022). TP denotes a correctly detected fault; FP a false alarm; FN a missed fault; TN a correctly classified normal sample. The metric formulas are given as below:

Accuracy (equation 1), measures the correct predictions of the model.

$$Accuracy = \frac{TP+TN}{TP+FP+TN+FN} \quad (1)$$

Recall (equation 2), can be calculated by dividing the number of true predicted TP by the total actual number of positive classes.

$$Recall = \frac{TP}{TP+FN} \quad (2)$$

Precision (equation 3), is the ratio of correctly predicted positive instances to the total predicted positive instances. It measures the accuracy of positive predictions.

$$Precision = \frac{TP}{TP+FP} \quad (3)$$

F1-score (equation 4), is a performance metric that combines precision and recall into a single score by calculating their harmonic mean. It provides a balanced evaluation of classification performance, especially in cases where both false positives and false negatives are important.

$$F1 - score = 2\,x\,\frac{precision\,x\,recall}{precision+recall} \quad (4)$$

Precision reduces false alarms and recall reduces missed faults; the F1-score is the harmonic mean of both metrics. All metrics were computed separately for each fault type.

3. Results

The performance of the four one-class methods on the four ALFA fault types is summarized in Table 6. OC-SVM, OC-RF, and autoencoder achieved accuracy, precision, recall, and F1-score values of 1.00 for all fault types. LOF also performed strongly but produced 18 misclassifications across 37,000 test samples (engine: 6; aileron: 4; rudder: 4; elevator: 4), with accuracy ranging from 0.9980 to 0.9997 and F1-scores from 0.9990 to 0.9999.

For visual comparison across methods, engine fault (23,000 samples) was selected as the common scenario because it has the largest test set. Figure 9 shows classification outputs of LOF model on engine fault. OC-SVM, OC-RF, and autoencoder classified all samples correctly, whereas LOF misclassified 6 engine fault samples. Figure 10 presents the F1-score comparison graphically for all models and fault types.

4. Discussion

The results show that one-class classifiers trained only on normal flight data can detect ALFA fault scenarios with high accuracy. The performance of OC-SVM, OC-RF, and autoencoder is consistent with the novelty-based sensor attack detection findings reported by Whelan et al. (2020) and supports extending the same approach to control surface faults.

The equivalent performance of the autoencoder confirms the encoding-thresholding approach reported by Park et al. (2021) on ALFA data. The relatively lower performance of LOF may stem from temporal correlation in flight data affecting local density structure (Breunig et al., 2000; Alghushairy et al., 2020). Nevertheless, only 18 errors across 37,000 samples suggest that LOF may serve as a backup detection layer.

Compared with other UAV security studies, Sedjelmaci et al. (2016) reported a 93% detection rate and Zhu et al. (2018) achieved 78% true attack detection. Three methods in this study reached 100% accuracy and LOF remained above 99.8%. However, these results were obtained under controlled fault injection and cannot be directly generalized to real cyber-attacks.

The main contribution is the systematic comparison of four one-class algorithms on real flight logs. Training using only safe flight data enables detection of abnormal behaviour independent of attack type (Patcha and Park, 2007). Important limitations include a single-platform dataset (Carbon-ZT-28), lack of real-time cost evaluation, and potentially optimistic performance because training and test data originate from the same platform (Chamola et al., 2021; Tunc and Hariri, 2022). Regarding real-world deployment, three constraints should be interpreted carefully. First, all flights were collected on a single Carbon-Z T-28 platform; decision boundaries and reconstruction-error scales may shift on other airframes, autopilot stacks, or sensor suites, so cross-platform recalibration would be required before operational use. Second, elevator faults are represented by comparatively few flights relative to engine faults, which increases uncertainty in elevator-specific performance estimates and may mask rarer failure modes. Third, because evaluation relies on controlled actuator-fault injection rather than authenticated cyber-attack traffic, reported near-perfect scores should be viewed as an upper-bound indication of detectability under laboratory conditions. In field settings with noise, concept drift, and adversarial tactics, false alarm rates and missed detections may increase unless models are periodically updated and validated on genuine attack scenarios.

Future work may examine multi-platform datasets, real cyber-attack scenarios, hybrid IDS designs (Aydın et al., 2009), and real-time application architectures (Choudhary et al., 2018).

5. Conclusion

In this study, four one-class machine learning methods were comparatively evaluated for novelty-based intrusion detection in UAVs using the ALFA dataset. OC-SVM, OC-RF, and autoencoder algorithms achieved accuracy, precision, recall, and F1-score values of 1.00 for engine, aileron, rudder, and elevator faults. The LOF method produced 18 misclassifications across 37,000 test samples, with performance in the 0.998–0.9997 range. Because cyberattacks on UAV communication and control links can manifest as unexpected actuator responses and anomalous sensor/telemetry patterns, the ALFA actuator-fault conditions were interpreted as proxy scenarios for cyberattack-related anomalies. Although strong performance was achieved under controlled fault injection, validation on real cyber-attack scenarios is still required. The findings demonstrate that a label-free one-class classification approach constitutes a practical alternative for UAV security applications. Future work may examine multi-platform datasets, real-time detection architectures, hybrid IDS designs, and integration of additional sensor channels into the models.

Table 6. Performance metrics of four methods by fault type

Method	Metric	Engine	Aileron	Rudder	Elevator
OC-SVM	Accuracy	1.00	1.00	1.00	1.00
	Precision	1.00	1.00	1.00	1.00
	Recall	1.00	1.00	1.00	1.00
	F1-Score	1.00	1.00	1.00	1.00
OC-RF	Accuracy	1.00	1.00	1.00	1.00
	Precision	1.00	1.00	1.00	1.00
	Recall	1.00	1.00	1.00	1.00
	F1-Score	1.00	1.00	1.00	1.00
LOF	Accuracy	0.9997	0.9995	0.9990	0.9980
	Precision	1.00	1.00	1.00	1.00
	Recall	0.9997	0.9995	0.9990	0.9980
	F1-Score	0.9999	0.9998	0.9995	0.9990
Autoencoder	Accuracy	1.00	1.00	1.00	1.00
	Precision	1.00	1.00	1.00	1.00
	Recall	1.00	1.00	1.00	1.00
	F1-Score	1.00	1.00	1.00	1.00

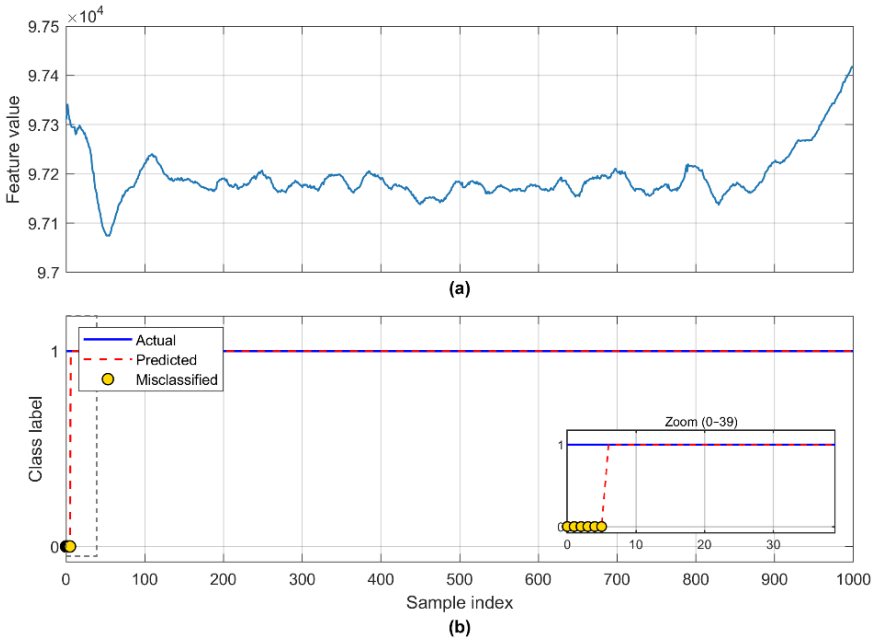


Figure 9. LOF results for engine fault on a representative sample window. (a) resampled feature, (b) actual and predicted class labels.

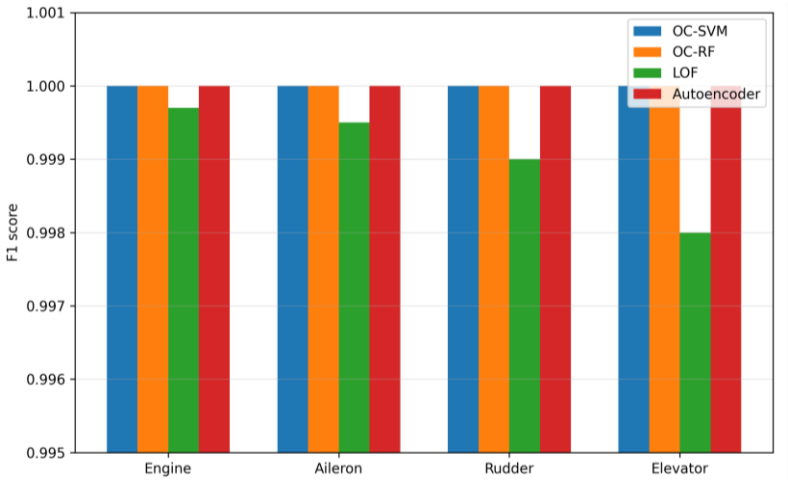


Figure 10. F1-score comparison of four methods by fault type.

Author Contributions

The percentages of all authors' contributions are presented below. All authors reviewed and approved the final version of the manuscript.

	S.E.	O.A.
C	60	40
D	60	40
M	60	40
DCP	40	60
DAI	40	60
LR	20	80
W	40	60
CR	70	30
SR	80	20
PM	70	30
FA	80	20

C= concept, D= design, S= supervision, DCP= data collection and/or processing, DAI= data analysis and/or interpretation, L= literature search, W= writing, CR= critical review, SR= submission and revision, PM= project management, FA= funding acquisition.

Conflict of Interest

The authors declared that there is no conflict of interest.

Ethical Consideration

Ethics committee approval was not required for this study because of there was no study on animals or humans.

Acknowledgements

This study is derived from the master's thesis entitled "Novelty-Based Intrusion Detection in Unmanned Aerial Vehicles" prepared by Onur Ayva at the Department of Defence Technologies, Graduate School of Natural and Applied Sciences, Fırat University.

References

Alghushairy, O., Alsini, R., Soule, T., & Ma, X. (2020). A review of local outlier factor algorithms for outlier detection in big data streams. *Big Data and Cognitive Computing*, *5*(1), Article 1. https://doi.org/10.3390/bdcc5010001

Aydın, M. A., Zaim, A. H., & Ceylan, K. G. (2009). A hybrid intrusion detection system design for computer network security. *Computers & Electrical Engineering*, *35*(3), 517–526. https://doi.org/10.1016/j.compeleceng.2008.12.005

Bakır, G. (2019). İnsansız hava araçlarının savunma sanayi harcamasında yeri ve önemi. *Avrasya Sosyal ve Ekonomi Araştırmaları Dergisi*, *6*(2), 127–134. https://dergipark.org.tr/tr/pub/asead/article/526954

Borisovic, D. (2001). *Dynamic signature inspection-based network intrusion detection* (U.S. Patent No. 6,279,113). U.S. Patent and Trademark Office.

Breunig, M. M., Kriegel, H.-P., Ng, R. T., & Sander, J. (2000). LOF: Identifying density-based local outliers. *Proceedings of the 2000 ACM SIGMOD International Conference on Management of Data* (pp. 93–104). Association for Computing Machinery. https://doi.org/10.1145/342009.335388

Chamola, V., Kotesh, P., Agarwal, A., Naren, N., Gupta, N., & Guizani, M. (2021). A comprehensive review of unmanned aerial vehicle attacks and neutralization techniques. *Ad Hoc Networks*, *111*, Article 102324. https://doi.org/10.1016/j.adhoc.2020.102324

Choudhary, G., Sharma, V., You, I., Yim, K., Chen, I.-R., & Cho, J.-H. (2018). Intrusion detection systems for networked unmanned aerial vehicles: A survey. *14th International Wireless Communications & Mobile Computing Conference (IWCMC)* (pp. 560–565). IEEE. https://doi.org/10.1109/IWCMC.2018.8450305

Davidovich, B., Nassi, B., & Elovici, Y. (2022). Towards the detection of GPS spoofing attacks against drones by analyzing camera's video stream. *Sensors*, *22*(7), Article 2608. https://doi.org/10.3390/s22072608

Ertam, F. (2016). *Kurumsal bilgisayar ağlarındaki trafik bilgisinin akıllı sistemler ile sınıflandırılması* (Yüksek lisans tezi, Fırat Üniversitesi). YÖK Ulusal Tez Merkezi. https://tez.yok.gov.tr/UlusalTezMerkezi/tezDetay.jsp?id=Vc4WSxX-9Txmr5qLrJLZKQ&no=dw0RzWRbgQ6emuyGrqFCBQ

Genç, Y. M., & Erciyes, E. (2020). İnsansız hava araçları (İHA) tehditleri ve güvenlik yönetimi. *Türkiye İnsansız Hava Araçları Dergisi*, *2*(2), 36–42. https://dergipark.org.tr/en/pub/tiha/issue/58203/783360

Haider, M., Ahmed, I., & Rawat, D. B. (2022). Cyber threats and cybersecurity reassessed in UAV-assisted cyber physical systems. *Thirteenth International Conference on Ubiquitous and Future Networks (ICUFN)* (pp. 222–227). IEEE. https://doi.org/10.1109/ICUFN55119.2022.9829584

He, D., Chan, S., & Guizani, M. (2017). Communication security of unmanned aerial vehicles. *IEEE Wireless Communications*, *24*(4), 134–141. https://doi.org/10.1109/MWC.2016.1600073WC

Keipour, A., Mousaei, M., & Scherer, S. (2019). Automatic real-time anomaly detection for autonomous aerial vehicles. *International Conference on Robotics and Automation (ICRA)* (pp. 5679–5685). IEEE. https://doi.org/10.1109/ICRA.2019.8794286

Keipour, A., Mousaei, M., & Scherer, S. (2021). ALFA: A dataset for UAV fault and anomaly detection. *The International Journal of Robotics Research*, *40*(2–3), 515–520. https://doi.org/10.1177/0278364920966642

Kılınçer, İ. F. (2022). *Saldırı tespit ve engelleme sistemleri için yapay zeka tabanlı yeni bir güvenlik modelinin oluşturulması* (Doktora tezi, Fırat Üniversitesi). YÖK Ulusal Tez Merkezi. https://tez.yok.gov.tr/UlusalTezMerkezi/tezDetay.jsp?id=sD3blY_sDoRvzvYRYC_UWg&no=6WfwU0D5ZXelcvYYKbxauw

Muniraj, D., & Farhood, M. (2017). A framework for detection of sensor attacks on small unmanned aircraft systems. *International Conference on Unmanned Aircraft Systems (ICUAS)* (pp. 1189–1198). IEEE. https://doi.org/10.1109/ICUAS.2017.7991465

Muñoz, A., & Moguerza, J. M. (2004). One-class support vector machines and density estimation: The precise relation. In J. Cabestany, A. Prieto, & F. Sandoval (Eds.), *Lecture Notes in Computer Science* (Vol. 3287, pp. 216–223). Springer. https://doi.org/10.1007/978-3-540-30463-0_27

Muñoz-Marí, J., Bovolo, F., Gómez-Chova, L., Bruzzone, L., & Camp-Valls, G. (2010). Semisupervised one-class support vector machines for classification of remote sensing data. *IEEE Transactions on Geoscience and Remote Sensing*, *48*(8), 3188–3197. https://doi.org/10.1109/TGRS.2010.2045764

Park, K. H., Park, E., & Kim, H. K. (2021). Unsupervised fault detection on unmanned aerial vehicles: Encoding and

thresholding approach. *Sensors*, *21*(6), Article 2208. https://doi.org/10.3390/s21062208

Patcha, A., & Park, J.-M. (2007). An overview of anomaly detection techniques: Existing solutions and latest technological trends. *Computer Networks*, *51*(12), 3448–3470. https://doi.org/10.1016/j.comnet.2007.02.001

Rahman, M. A., Rahman, M. T., Kisacikoglu, M., & Akkaya, K. (2020). Intrusion detection systems-enabled power electronics for unmanned aerial vehicles. *IEEE CyberPELS* (pp. 1–5). IEEE. https://doi.org/10.1109/CyberPELS49534.2020.9311545

Renyu, Z., Kiat, S. C., Kai, W., & Heng, Z. (2018). Spoofing attack of drone. *IEEE 4th International Conference on Computer and Communications (ICCC)* (pp. 1239–1246). IEEE. https://doi.org/10.1109/CompComm.2018.8780865

Sedjelmaci, H., Senouci, S. M., & Ansari, N. (2018). A hierarchical detection and response system to enhance security against lethal cyber-attacks in UAV networks. *IEEE Transactions on Systems, Man, and Cybernetics: Systems*, *48*(9), 1594–1606. https://doi.org/10.1109/TSMC.2017.2681698

Sedjelmaci, H., Senouci, S. M., & Messous, M. A. (2016). How to detect cyber-attacks in unmanned aerial vehicles network? *2016 IEEE Global Communications Conference (GLOBECOM)* (pp. 1–6). IEEE. https://doi.org/10.1109/GLOCOM.2016.7841878

Sentsov, A. A., Polyakov, V. B., & Gladkii, N. A. (2019). Electronic methods to protect unmanned aerial vehicles from seizing control. *2018 Wave Electronics and its Application in Information and Telecommunication Systems (WECONF)* (pp. 1–4). IEEE. https://doi.org/10.1109/WECONF.2018.8604463

Solodov, A., Williams, A., Al Hanaei, S., & Goddard, B. (2018). Analyzing the threat of unmanned aerial vehicles (UAV) to nuclear facilities. *Security Journal*, *31*(1), 305–324. https://doi.org/10.1057/s41284-017-0102-5

Tseng, C.-Y., Balasubramanyam, P., Ko, C., Limprasittiporn, R., Rowe, J., & Levitt, K. (2003). A specification-based intrusion detection system for AODV. In *Proceedings of the 1st ACM Workshop on Security of Ad Hoc and Sensor Networks* (pp. 125–134). Association for Computing Machinery. https://doi.org/10.1145/986858.986876

Tunc, C., & Hariri, S. (2022). Self-protection for unmanned autonomous vehicles (SP-UAV): Design overview and evaluation. *2022 IEEE International Conference on Autonomic Computing and Self-Organizing Systems Companion (ACSOS-C)* (pp. 128–132). IEEE. https://ieeexplore.ieee.org/document/9935094

Uyar, E. (2019). *İnsansız hava araçlarında GPS aldatmacası tespiti* (Yüksek lisans tezi, Gazi Üniversitesi). YÖK Ulusal Tez Merkezi. https://tez.yok.gov.tr/UlusalTezMerkezi/tezDetay.jsp?id=VAI4ODrSDaGWTHti2OC-Hw&no=rIDQMsOens0_miJJvS3k6Q

Whelan, J., Sangarapillai, T., Minawi, O., Almehmadi, A., & El-Khatib, K. (2020). Novelty-based intrusion detection of sensor attacks on unmanned aerial vehicles. In *Proceedings of the 16th ACM Symposium on QoS and Security for Wireless and Mobile Networks* (pp. 23–28). Association for Computing Machinery. https://doi.org/10.1145/3416013.3426446

Yahuza, M., Abdullahi, M., Jibril, A. M., & Abubakar, A. (2021). Internet of drones security and privacy issues: Taxonomy and open challenges. *IEEE Access*, *9*, 57243–57270. https://doi.org/10.1109/ACCESS.2021.3072030

Yiğit, E., Yazar, I., & Karakoç, T. H. (2018). İnsansız hava araçlarının kapsamlı sınıflandırması ve gelecek perspektifi. *Sürdürülebilir Havacılık Araştırmaları Dergisi*, *3*(1), 10–19. https://dergipark.org.tr/tr/pub/suhad/article/557335

Zhu, H., Elfar, M., Pajic, M., Wang, Z., & Cummings, M. L. (2018). Human augmentation of UAV cyber-attack detection. In H. A. Abbass, J. Scholz, & D. J. Reid (Eds.), *Lecture Notes in Computer Science* (Vol. 10916, pp. 154–167). Springer. https://doi.org/10.1007/978-3-319-91467-1_13

Black Sea Journal of Engineering and Science
doi: 10.34248/bsengineering.1966267

Open Access Journal
e-ISSN: 2619 – 8991

Araştırma Makalesi (Research Article)
Cilt 9 - Sayı 5: 2156-2174 / Eylül 2026
(Volume 9 - Issue 5: 2156-2174 / September 2026)

ATM NAKİT TALEP TAHMİNİNDE RNN MİMARİLERİNİN BAŞARIMI: LSTM, GRU, Bi-LSTM VE CNN-LSTM

Havanur ŞENOCAK[1], Tuba IRMAK[1], Betül TURANOĞLU ŞİRİN[1]*

[1]*Atatürk University, Faculty of Engineering, Department of Industrial Engineering, 25240, Erzurum, Türkiye*

Özet: Bu çalışmada, Kaggle'da açık erişimli olarak paylaşılan, beş farklı ATM'ye ait günlük nakit çekim verilerini içeren veri seti kullanılarak tekrarlayan sinir ağı (Recurrent Neural Network – RNN) tabanlı dört derin öğrenme mimarisinin (LSTM, GRU, Bi-LSTM ve CNN-LSTM) tahmin başarımı karşılaştırmalı olarak incelenmiştir. Verinin yapısal özelliklerinin anlaşılabilmesi için keşifsel veri analizleri yapılmış ve analiz sonucunda ATM'ler arasında belirgin ölçek farklılıkları, haftalık periyodiklik, güçlü otokorelasyon yapıları ve 2015 yılı sonrasında eşzamanlı yapısal bozulmalar tespit edilmiş; bu bulgular doğrultusunda analiz dönemi sınırlandırılarak gecikmeli, hareketli istatistiksel ve takvim temelli yeni öznitelikler üretilmiştir. Modelleme aşamasında her bir mimari iki farklı girdi ile eğitilmiştir, bunlar; yalnızca geçmiş çekim tutarlarını kullanan tek değişkenli ve gecikmeli, hareketli istatistik ile takvim/tatil bilgilerinden türetilen 27 öznitelikten oluşan çok değişkenli girdi yapılarıdır. Ayrıca, 7, 14 ve 30 günlük geri bakış pencereleri altında ileri yönlü doğrulama yaklaşımıyla yapılan model eğitimi sürecinde toplam 120 deney gerçekleştirilmiştir. Bulgular, çok değişkenli girdi yapısının dört mimaride de tek değişkenli yapıya kıyasla daha düşük SMAPE değerleri ürettiğini ve en iyi sonuçların tamamının çok değişkenli yapıda gerçekleştiğini göstermiştir. Model bazında en düşük ortalama SMAPE değerine çok değişkenli GRU mimarisi (%36,63) ulaşırken, ATM bazında en iyi tahmin Bi-LSTM mimarisi ile Big Street ATM'sinde elde edilmiştir (%19,12). Geri bakış penceresinin uzunluğunun model başarımı üzerindeki etkisi sınırlı düzeyde kalmış; çoğu mimaride 14 günlük pencere optimal sonuç vermiştir. Çalışma sonunda, RNN tabanlı modellerin nakit talep tahmininde etkili bir şekilde kullanılabileceği görülmüştür. Ayrıca ATM'ler arasında gözlenen talep davranışı farklılıklarının model performansları üzerinde belirleyici olduğu ve tek bir modelin tüm ATM'lerde benzer başarı düzeyine ulaşmasının kolay olmadığı görülmüştür.

Anahtar kelimeler: Nakit yönetimi, RNN mimarileri, LSTM, GRU, Öznitelik mühendisliği, İleri-yönlü doğrulama

The Performance of RNN Architectures in ATM Cash Demand Forecasting: LSTM, GRU, Bi-LSTM, and CNN-LSTM

Abstract: This study comparatively examines the prediction performance of four recurrent neural network (RNN)-based deep learning architectures (LSTM, GRU, Bi-LSTM, and CNN-LSTM) using a dataset containing daily cash withdrawal data from five different ATMs that is openly accessible on Kaggle. Exploratory data analysis was conducted to understand the structural characteristics of the data. The analysis revealed significant scale differences among ATMs, weekly periodicity, strong autocorrelation structures, and concurrent structural breaks after 2015. Based on these findings, the analysis period was limited, and new lagged, moving statistical, and calendar-based features were generated. During the modelling phase, each architecture was trained using two different input structures. The first was a univariate structure that used only historical withdrawal amounts, while the second was a multivariate structure consisting of 27 features derived from lagged variables, moving statistics, and calendar/holiday information. Additionally, a total of 120 experiments were conducted during the training process using a forward validation approach under 7-, 14-, and 30-day back sight windows. The findings showed that the multivariate input structure produced lower SMAPE values than the univariate structure across all four architectures, and the best results were consistently achieved with the multivariate structure. At the model level, the lowest average SMAPE value was obtained with the multivariate GRU architecture (36.63%), while the best ATM-level prediction performance was achieved by the Bi-LSTM architecture for the Big Street ATM (19.12%). The effect of back sight window length on model performance remained limited; however, a 14-day window yielded optimal results for most architecture. In conclusion, the study demonstrated that RNN-based models can be effectively used for cash demand forecasting. Furthermore, differences in demand behavior among ATMs were found to have a decisive impact on model performance, and it was not easy for a single model to achieve a similar level of success across all ATMs.

Keywords: Cash management, RNN architectures, LSTM, GRU, Feature engineering, Walk-forward validation

***Sorumlu yazar (Corresponding author):** Atatürk University, Faculty of Engineering, Department of Industrial Engineering, 25240, Erzurum, Türkiye
E mail: b.turanoglu@atauni.edu.tr (B. TURANOĞLU ŞİRİN)
Havanur ŞENOCAK https://orcid.org/0009-0003-6841-6520
Tuba IRMAK https://orcid.org/0000-0003-4749-5226
Betül TURANOĞLU ŞİRİN https://orcid.org/0000-0002-7910-6312

Gönderi: 08 Haziran 2026 **Received:** June 08, 2026
Kabul: 16 Temmuz 2026 **Accepted:** July 16, 2026
Yayınlanma: 15 Eylül 2026 **Published:** September 15, 2026

Cite as: Şenocak, H., Irmak, T., & Turanoğlu Şirin, B. (2026). The performance of RNN architectures in ATM cash demand forecasting: LSTM, GRU, Bi-LSTM, and CNN-LSTM. *Black Sea Journal of Engineering and Science,* 9(5), 2156-2174.

This work is licensed (CC BY-NC 4.0) under Creative Commons Attribution 4.0 International License

1. Giriş

ATM (Automated Teller Machines) nakit talep tahmini, bankacılık sektöründe operasyonel verimlilik ve müşteri memnuniyeti açısından kritik öneme sahip bir araştırma alanıdır (Sarveswararao vd., 2023). ATM'lerde fazla nakit bulundurulması, nakit taşıma ve saklama maliyetlerinin artmasına ve güvenlik risklerinin yükselmesine neden olmaktadır. Buna karşılık, yetersiz nakit bulundurulması durumunda ATM'lerin hizmet dışı kalması, müşteri memnuniyetsizliği, potansiyel müşteri kaybı ve kurum imajının zedelenmesi gibi olumsuz sonuçlar doğurabilmektedir (Fallahtafti vd., 2022).

Ekonomik açıdan bakıldığında, daha verimli ATM dolum stratejileri sayesinde finansal kaynakların etkin kullanımı teşvik edilerek ulusal düzeyde bankacılık sektörünün rekabet gücü ve verimliliği artırılabilir. Toplumsal düzeyde ise, ATM'lerde nakit erişim problemlerinin önüne geçilerek daha güvenli, hızlı ve kesintisiz finansal hizmet sunumu mümkün hâle gelir. Dolayısıyla, müşteri memnuniyetinde artış ve dolaylı olarak finansal okuryazarlığın gelişimi sağlanır.

ATM nakit talep tahmini problemi, haftanın günleri, maaş ödemelerine bağlı aylık döngüler, mevsimsel değişimler ve tatil günleriyle ilişkili düzensiz artışlar gibi karmaşık zamansal örüntülerle karakterize edilmektedir (Venkatesh vd., 2014). Son yıllarda, özellikle COVID-19 pandemisi gibi dışsal şoklar, nakit çekim davranışlarında ani ve öngörülemeyen değişikliklere neden olarak tahmin modellerinin performansını önemli ölçüde etkilemiştir. Geleneksel tahmin yöntemleri (örneğin, zaman serisi analizleri ve regresyon modelleri), veri setlerinin karmaşıklığı ve dinamik yapısı karşısında zaman zaman yetersiz kalabilmektedir. Öte yandan, büyük veri setlerinden öğrenerek yüksek doğrulukla tahmin yapabilen derin öğrenme algoritmaları, ATM nakit talebini daha etkili ve esnek bir şekilde öngörme potansiyeline sahiptir (Cedolin vd., 2024).

ATM'lerde nakit talep tahmini ile ilgili, literatürde hem geleneksel tahmin yöntemleri hem de yapay zekâ ve optimizasyon temelli yaklaşımlar üzerine çeşitli çalışmalar gerçekleştirilmiştir. Bu çalışmalar aşağıda özetlenmiştir.

Teddy ve Ng (2011), ATM'lerdeki nakit talebinin doğrusal olmayan ve zamanla değişen yapısını modellemek için insan beyinciğinden esinlenen yerel öğrenme temelli PSECMAC (Pseudo Self-Evolving Cerebellar Model Articulation Controller) ağını önermiştir. Çalışmada NN5 yarışma veri setindeki 111 ATM'ye ait günlük çekim serileri kullanılarak tahminleme yapılmış ve sonuçlar, CMAC, MLP, SVR, KNN, RBF gibi geleneksel yöntemlerle karşılaştırılmıştır. Özellik seçimi için Monte Carlo tabanlı MCES yöntemi kullanılmış; ardından 56 ve 181 gün öngörü yapılan tahminlerde PSECMAC modeli ortalama %27,28 SMAPE ile KNN'den sonra en iyi performansı göstermiştir. Bulgular, yerel öğrenme temelli modellerin, özellikle heteroskedastik ve karmaşık zaman serilerinde, küresel öğrenme tabanlı modellere göre daha başarılı olduğunu ortaya koymuştur. Andrawis vd. (2011), NN5 zaman serisi tahmin yarışması kapsamında 111 ATM'ye ait günlük nakit çekim verilerini kullanarak tahmin modelleri geliştirmiştir. Çalışmada, çok sayıda yapay sinir ağı, Gaussian süreci regresyonu ve doğrusal model birleştirilmiş ve bu modellerin tahminleri basit ortalama yöntemiyle bir araya getirilmiştir. Ayrıca, "haftanın günü", "ayın günü" ve "yılın ayı" gibi mevsimsellik bileşenleri dikkatle analiz edilerek tahmin performansı artırılmıştır. En iyi bireysel model %18,94 SMAPE sağlarken, birleşik tahmin modeli (ensemble) ile %18,95 SMAPE değeri elde edilmiştir.

Venkatesh vd. (2014), ATM'lerde nakit talebini daha doğru tahmin edebilmek amacıyla önce kümeleme, ardından yapay sinir ağı tabanlı tahminleme yaklaşımını önermiştir. Çalışmada, NN5 yarışma verisindeki 111 ATM'ye ait günlük çekim verileri kullanılarak ATM'ler, "haftanın günü" bazlı mevsimsellik özelliklerine göre Taylor–Butina algoritması ile dört kümeye ayrılmıştır. Her küme için dört farklı sinir ağı modeli (MLFF, GRNN, WNN, GMDH) uygulanmış ve tahmin doğruluğu SMAPE metriği ile değerlendirilmiştir. En iyi sonuç, GRNN modeli ile %18,44 ortalama SMAPE değeriyle elde edilmiştir. Sonuçlar, ATM'leri benzer davranış kalıplarına göre gruplamanın tahmin performansını artırdığını ve operasyonel maliyetlerin azaltılmasına katkı sunduğunu göstermektedir.

Kamini vd. (2014), NN5 yarışmasına ait 111 ATM'nin günlük nakit çekim verisini kullanarak geleneksel ve kaotik zaman serisi analiz yöntemlerini karşılaştırmıştır. Geleneksel yöntemlerde ARIMA, MLFF, WNN ve GRNN gibi modeller kullanılırken; kaotik yaklaşımda zaman serileri faz uzayında yeniden yapılandırılarak GRNN, GMDH ve MLFF modelleriyle tahmin gerçekleştirilmiştir. Çalışmada, kaotik özelliklerin dikkate alındığı GRNN modeli ile en düşük hata değeri olan SMAPE = 14,71 elde edilmiştir. Bu sonuç, literatürdeki önceki çalışmaların tamamından daha iyi performans göstermiştir.

Nemeshaev ve Tsyganov (2016), Rusya'nın Yekaterinburg şehrindeki 50 ATM'ye ait günlük çekim verilerini kullanarak, çok katmanlı yapay sinir ağı (MLP) ile ATM nakit talebi tahmini gerçekleştirmiştir. Çalışmanın temel katkısı, veri ön işleme sürecinde faz uzayı yeniden yapılandırması kullanılarak zaman serisinin gömülü uzayda modellenmesidir. Girdi değişkenleri olarak doğrudan çekim değerleri yerine, bu değerlere ait farklar veya logaritmik oranlar kullanılmış, bu sayede istatistiksel olarak daha kararlı ve öğrenmeye uygun veri elde edilmiştir. Modelin performansı ortalama %32 MAPE ile değerlendirilmiş ve ağın özellikle 5–6 günlük kısa vadeli tahminlerde başarılı sonuçlar verdiği görülmüştür.

Javanmard (2016), ATM'lerde nakit talebinin doğruluğunu artırmak amacıyla Tip-II Bulanık Mantık (Interval Type-2 Fuzzy Logic) tabanlı bir tahmin modeli önermiştir. Çalışmada, geleneksel yöntemlerin belirsizlik ve doğrusal olmayan yapılarda yetersiz kalabildiği belirtilmiş ve yapay sinir ağları ile bulanık mantık

yaklaşımlarının kombinasyonuna dayalı bir çözüm geliştirilmiştir. Model, takvim etkileri, ATM konumu ve geçmiş nakit çekim verileri gibi çok sayıda değişkeni dikkate alarak tahmin yapmaktadır. MATLAB ortamında 25 ATM üzerinde gerçekleştirilen simülasyonlar sonucunda, önerilen yöntemin ortalama tahmin doğruluğu %94–97 arasında gerçekleşmiş ve geleneksel yöntemlere göre önemli maliyet tasarrufu sağladığı ortaya konmuştur.

Bhandari ve Gill (2016), ATM'lerde nakit talebinin daha doğru tahmin edilmesi amacıyla geri yayılım (BP) ve genetik algoritma (GA) yaklaşımlarını birleştiren hibrit bir yapay sinir ağı modeli önermiştir. Çalışmada, tarih, hafta içi/hafta sonu, maaş ve tatil etkileri gibi beş temel özellik kullanılarak eğitim ve test veri setleri oluşturulmuştur. Model, farklı popülasyon büyüklükleri ve gizli katman sayılarıyla test edilmiştir. En iyi sonuç nöron sayısı 3 ve popülasyon büyüklüğü 90 olan yapı ile elde edilmiş; bu yapı için MAPE değeri %0,42 olarak rapor edilmiştir. Sonuçlar, BP/GA hibrit modelinin geleneksel BP algoritmasına kıyasla daha düşük hata ile tahmin gerçekleştirdiğini ortaya koymuştur.

Jadwal vd. (2018), NN5 zaman serisi verisini kullanarak ATM'lerdeki nakit talebinin tahmini için yapay sinir ağı modelleri ile K-means kümeleme yöntemini bir araya getirmiştir. Çalışmada, NN5 veri kümesinin 111 zaman serisinden alınan 11 serilik alt kümesi ile tahminleme yapılmış; ardından ATM'ler benzerliklerine göre kümelenerek her bir küme üzerinde ayrı ayrı tahmin modelleri uygulanmıştır.

Arabani ve Komleh (2019), İran bankacılık ağına ait 1056 ATM'nin günlük işlem verileri ile panel veri yapısında ATM nakit talebini tahmin etmeyi amaçlamıştır. Çalışmada geleneksel istatistiksel yöntemler (panel regresyon), yapay sinir ağları (ANN), destek vektör makineleri (SVR) ve evrişimli sinir ağları (CNN) karşılaştırılmıştır. En yüksek doğruluk, CNN modeli ile %1,05 RMSE (eğitim) ve %4,74 RMSE (test) değerleriyle elde edilmiştir. ANN modeli %5,01 test hatası ile ikinci en iyi performansı göstermiştir. SVR ise diğer yöntemlere kıyasla daha düşük başarı sağlamıştır.

Rafi vd. (2020), Pakistan'daki 7 ATM'ye ait 2,5 yıllık işlem verisini kullanarak ATM nakit talebini tahmin etmek üzere zaman serisi modelleri geliştirmiştir. Çalışmada, çok değişkenli zaman serisi modeli olan VARMAX (Vector AutoRegressive Moving Average with Exogenous Variables) yöntemi önerilmiş ve sonuçları LSTM tabanlı bir derin öğrenme modeliyle karşılaştırılmıştır. VARMAX modeli, tatil ve maaş haftası gibi dışsal değişkenleri de dikkate alarak daha yüksek doğrulukla tahmin sağlamıştır. Performans değerlendirmesinde kullanılan SMAPE değeri %22,5, RMSE değeri ise 19,994.81 olarak rapor edilmiştir. Sonuçlar, uygun ön işleme ve dışsal değişkenlerin entegrasyonuyla klasik zaman serisi modellerinin derin öğrenme yaklaşımlarına kıyasla rekabetçi sonuçlar verebileceğini göstermektedir.

Gençalp (2020), Türkiye'deki ATM'lerde nakit talebini tahmin etmek için SVR, KNN, Random Forest ve Gradient Boosting algoritmalarını karşılaştırmıştır. Kaggle'dan alınan 6 ATM'ye ait iki yıllık veri seti kullanılmıştır. En başarılı sonuç, veri ön işleme sonrası KNN algoritması ile %9,4 MAPE değeri elde edilerek sağlanmıştır. Çalışma, veri hazırlığının ve uygun algoritma seçiminin tahmin doğruluğu üzerindeki etkisini vurgulamaktadır.

Sarveswararao vd. (2023), Hindistan'daki bir bankaya ait 50 ATM'nin iki yıllık verisi üzerinden kaotik yapıların da dikkate alındığı bir nakit talep tahmin modeli geliştirmiştir. Çalışmada ARIMA, SVR, RF, MLP, GRNN ve GMDH gibi geleneksel ve makine öğrenmesi yöntemlerinin yanı sıra LSTM, GRU, 1D-CNN ve hibrit derin öğrenme modelleri (1D-CNN + LSTM, 1D-CNN + GRU) kullanılmıştır. "Haftanın günü" gibi dışsal değişkenlerin dahil edilmesi tahmin performansını artırmıştır. Sonuçlar, LSTM tabanlı modellerin özellikle kaotik serilerde en başarılı tahminleri sağladığını göstermektedir. En iyi sonuç, LSTM modeli ile SMAPE = 22,08 değeriyle elde edilmiştir.

Yukarıda özetlenen literatür incelendiğinde, ATM'lerde nakit talep tahmini amacıyla geleneksel zaman serisi yöntemlerinden makine öğrenmesi ve derin öğrenme tabanlı modellere kadar çok sayıda yaklaşımın kullanıldığı görülmektedir. Bununla birlikte, mevcut çalışmaların büyük bir bölümü tek bir modelin geliştirilmesine veya farklı modellerin karşılaştırılmasına odaklanırken, RNN tabanlı farklı mimarilerin aynı veri seti ve aynı deneysel koşullar altında sistematik olarak değerlendirilmesi, öznitelik mühendisliğinin tahmin performansına etkisinin ortaya konulması ve farklı girdi pencere uzunluklarının model başarısına katkısının birlikte incelenmesi konularında önemli eksiklikler bulunmaktadır. Ayrıca birçok çalışmada yalnızca geçmiş nakit çekim değerleri kullanılırken, zaman serisinin yapısal özelliklerinden yararlanılarak oluşturulan gecikmeli, hareketli istatistiksel ve takvim temelli özniteliklerin derin öğrenme modellerine sağladığı katkılar sınırlı düzeyde araştırılmıştır.

Bu çalışmada, Kaggle'da açık erişimli olarak paylaşılan "Data of ATM Transactions of XYZ Bank" verisi kullanılarak tekrarlayan sinir ağı (RNN – Recurrent Neural Network) tabanlı dört derin öğrenme mimarisinin (LSTM, GRU, Bi-LSTM ve CNN-LSTM) nakit talep tahminindeki başarımı karşılaştırmalı olarak incelenmiştir. Veri seti içerisinde beş farklı ATM'ye ait 2011-2017 yılları arasındaki günlük nakit çekim verileri bulunmaktadır. Çalışma kapsamında öncelikle veri setinin yapısal özellikleri, zamansal örüntüleri ve ATM bazlı davranış farklılıkları keşifsel veri analizi ile ortaya konmuştur. Yapılan analizler sonucunda serinin kararlı seyrettiği çalışma dönemi belirlenmiştir. Eksik takvim günleri, gerçek gözlemlere müdahale etmeden, yalnızca hiç kaydedilmemiş günlere aynı hafta-günü medyanı uygulanarak tamamlanmıştır. Ardından, keşifsel analiz bulgularından hareketle zaman serisinin yakın geçmişini özetleyen gecikmeli (lag) ve hareketli istatistikler (rolling statistics) ile takvim ve tatil temelli bilgileri içeren toplam yirmi yedi öznitelikten oluşan bir öznitelik seti

tasarlanmıştır. Öznitelik mühendisliğinin model başarımına katkısını araştırmak amacıyla her mimari iki ayrı girdi yapısıyla (yalnızca geçmiş çekim değerlerini kullanan tek değişkenli yapı ve türetilen öznitelikleri de içeren çok değişkenli yapı) ve üç farklı girdi pencere uzunluğuyla (7, 14 ve 30 gün) değerlendirilmiştir. Modeller, her ATM kendi ölçeğinde ele alınarak ve bilgi sızıntısını önleyen ileri yönlü doğrulama (walk-forward validation) yaklaşımı benimsenerek eğitilmiş; başarımları SMAPE, MAE ve RMSE metrikleriyle karşılaştırılmıştır. Böylece çalışma hem farklı RNN mimarilerinin başarısını hem de öznitelik mühendisliği ve girdi pencere uzunluğunun tahmin performansı üzerindeki etkisini incelemeyi amaçlamaktadır.

Bu çalışmanın temel motivasyonu; ATM nakit talep tahmin doğruluğunu artırarak bankaların nakit yönetim süreçlerine katkı sağlamak, farklı RNN tabanlı mimarilerin gerçek bir ATM veri setindeki performanslarını nesnel biçimde karşılaştırmak ve öznitelik mühendisliği ile girdi pencere uzunluğunun tahmin başarımı üzerindeki etkisini kapsamlı olarak değerlendirmektir. Buna ek olarak, çalışmanın literatüre başlıca katkıları aşağıdaki gibi özetlenebilir:

- LSTM, GRU, Bi-LSTM ve CNN-LSTM mimarileri aynı veri seti, aynı deneysel tasarım ve aynı performans ölçütleri altında sistematik olarak karşılaştırılmıştır.
- Gecikmeli değişkenler, hareketli istatistikler ile takvim ve tatil bilgilerini içeren öznitelik mühendisliği yaklaşımının RNN tabanlı modellerin tahmin başarımına etkisi ayrıntılı olarak değerlendirilmiştir.
- Tek değişkenli ve çok değişkenli girdi yapıları ile farklı girdi pencere uzunluklarının tahmin performansı üzerindeki etkileri birlikte incelenmiştir.
- Elde edilen bulgular, ATM'lerin talep karakteristiklerine bağlı olarak en başarılı modelin değişebildiğini göstermiş ve ATM'ye özgü model seçiminin önemini ortaya koymuştur.

2. Materyal ve Yöntem

2.1. Veri Seti

Bu çalışmada kullanılan veri seti, Kaggle platformunda açık erişimli olarak paylaşılan "Data of ATM Transactions of XYZ Bank" verisidir. Veri seti içerisinde, beş farklı ATM'ye ait günlük nakit çekim bilgileri yer almaktadır. Veri kayıtları 1 Ocak 2011 – 29 Eylül 2017 tarihleri arasında yapılmıştır. Veri setinde toplamda 11.589 günlük veri olup her gün için, tarih bilgisi (gün/ay/yıl), günlük toplam çekim tutarı, çekim sayısı, haftanın günü ve çalışma günü olup olmadığı bilgisi yer almaktadır. Veri setine erişebilmek için linke tıklayınız: https://www.kaggle.com/datasets/saadfareed/data-set-of-atm-transaction-of-xyz-bank

Tablo 1'de, veri ön işleme süreci öncesine ait ham veri setinin ilk beş gözlemi sunulmaktadır. *atm_name* sütununda beş farklı ATM adı tutulmaktadır: Big Street, Mount Road, Airport, KK Nagar, Christ College ATM. *transaction_date* sütununda gün bazında tarih bilgisi yer almaktadır. Çekim tutarları ve çekim sayıları, XYZ banka kartıyla ve diğer banka kartlarıyla yapılması durumuna göre ayrı sütunlarda verilmektedir. Haftanın günleri *weekday* sütununda yer almakta ve kayıt gününün çalışma günü veya tatil günü olduğu bilgisi *working_day* sütununda tutulmaktadır. Son olarak modelleme sürecinde hedef değişken olarak kullanılan günlük toplam çekim tutarı ise *total_amount_withdrawn* sütununda yer almaktadır.

Toplam çekim tutarı ve toplam çekim sayısı, sırasıyla kart türüne göre ayrıştırılmış alt bileşenlerinin toplamına eşittir (*total_amount_withdrawn = amount_withdrawn_XYZ_card + amount_withdrawn_other_card*). Bu deterministik bağımlılık modelleme sürecinde çoklu doğrusallık sorununa yol açacağından, ilgili alt bileşen değişkenler model girdisi olarak değerlendirilmemiştir. Bu doğrultuda, veri setinde yer alan on değişkenden sadece beşi modelleme sürecinde girdi olarak değerlendirilmiştir: *atm_name*, *transaction_date*, *weekday*, *working_day* ve hedef değişken *total_amount_withdrawn*.

2.2. Keşifsel Veri Analizi

Modelleme aşamasına geçmeden önce veri setinin yapısal özelliklerinin, zamansal örüntülerinin ve ATM bazlı davranış farklılıklarının daha net anlaşılması amacıyla keşifsel veri analizi (KVA) yapılmıştır.

Öncelikle, beş ATM'ye ait günlük nakit çekim tutarları incelenmiştir ve çizilen grafik Şekil 1'de verilmiştir. Renkli çizgiler çekim tutarlarını ve koyu siyah çizgi ise 30 günlük hareketli ortalama eğilimlerini göstermektedir.

Grafik incelendiğinde, ATM'lerin zamana göre davranışları açısından belirgin şekilde farklılık gösterdiği görülmektedir. 2015 yılına kadar görece kararlı veya yükseliş yönlü bir seyir izleyen Mount Road, Airport ve KK Nagar ATM'lerinde 2015 yılı civarında belirgin seviye düşüşleri; Big Street ve Christ College ATM'lerinde ise sürekli yükseliş eğilimi gözlemlenmektedir. Buna ek olarak, ATM'ler arasında ölçek heterojenliğinin olduğu da görülmektedir: Big Street ortalama 309, KK Nagar ortalama 782 Bin INR. Bu grafik sonucunda elde edilen çıkarımlar; her ATM'nin kendi ölçeğinde modellenmesi gerektiği ve sergilenen farklı davranışlar (düşen, yükselen, karma) sebebiyle yapısal kırılmalar olabileceğidir.

Ayrıca, günlük çekim tutarlarının hareketli ortalama eğilimi etrafında geniş bir bant içinde dalgalandığı ve özellikle KK Nagar ATM'de varyansın yüksek olduğu görülmektedir. Bu durum, mevsimsellik kaynaklı periyodik bileşenler ile takvim temelli olaylardan kaynaklanabilecek anlık sıçramaların birlikte mevcut olabileceğine işaret etmekte; söz konusu örüntülerin yakalanabilmesi için örüntü öğrenme kapasitesi yüksek olan modellere ihtiyaç duyulabileceği düşünülmüştür.

Son olarak, veri setinin son dönemlerinde (2016-2017),

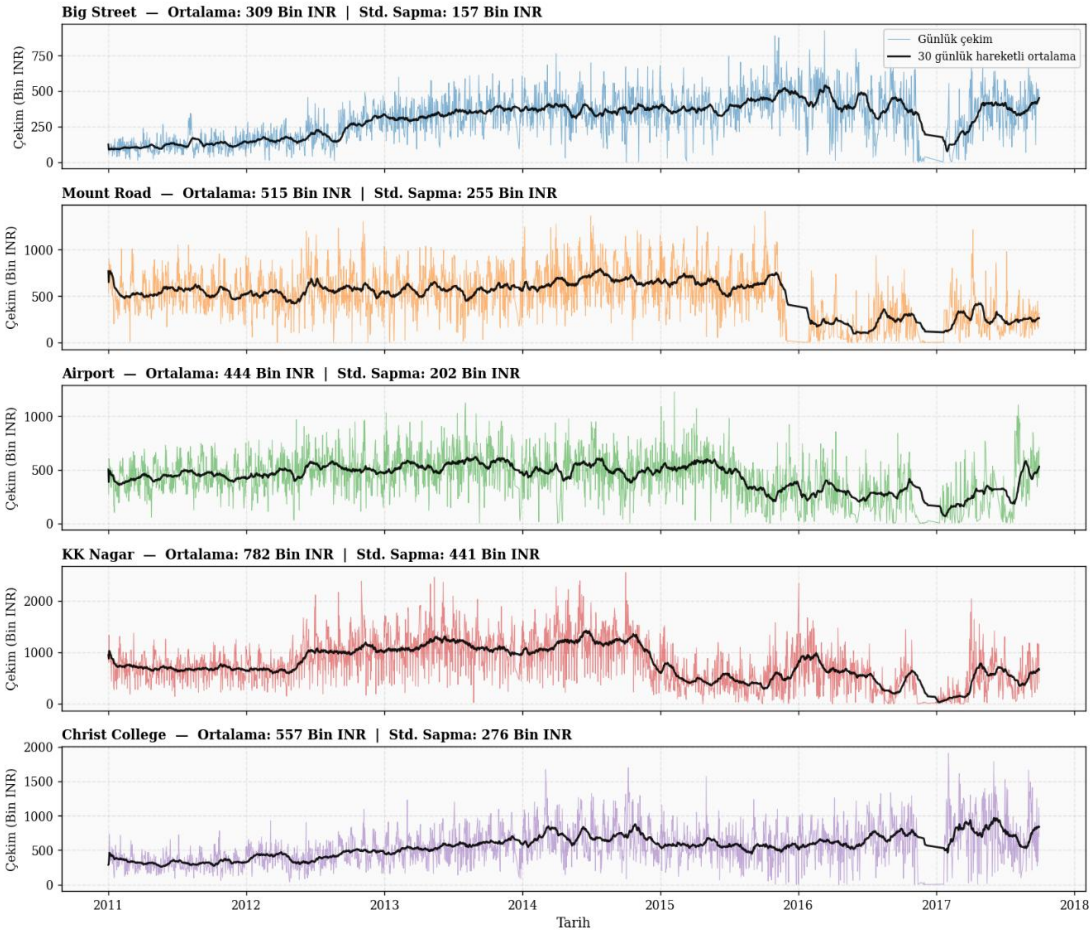
başta Mount Road, Airport ve KK Nagar ATM'leri olmak üzere birden fazla noktada sıfıra yakın çekim değerleri gözlemlenmektedir. Bu değerlerin birden fazla ATM'de eşzamanlı olarak yoğunlaşması, operasyonel kesintilerden ziyade tüm sistemi etkileyen yapısal bir bozulmaya işaret etmektedir. Söz konusu bulgu, modelleme sürecinin sağlıklı yürütülebilmesi için analiz döneminin sınırlandırılmasını gerekli kılmış olup, bu sınırlandırmanın ayrıntılı analizi ve gerekçesi bir sonraki bölümde sunulmaktadır.

Bunun yanı sıra, ATM'ler arasında belirgin ölçek farklılıkları gözlemlenmesi ve serinin doğrusal olmayan, karmaşık zamansal örüntüler içermesi, geleneksel yöntemlere kıyasla karmaşık ardışık örüntüleri ve doğrusal olmayan ilişkileri modelleme kapasitesi yüksek olan tekrarlayan sinir ağı tabanlı derin öğrenme mimarilerinin tercih edilmesini gerekli kılmıştır.

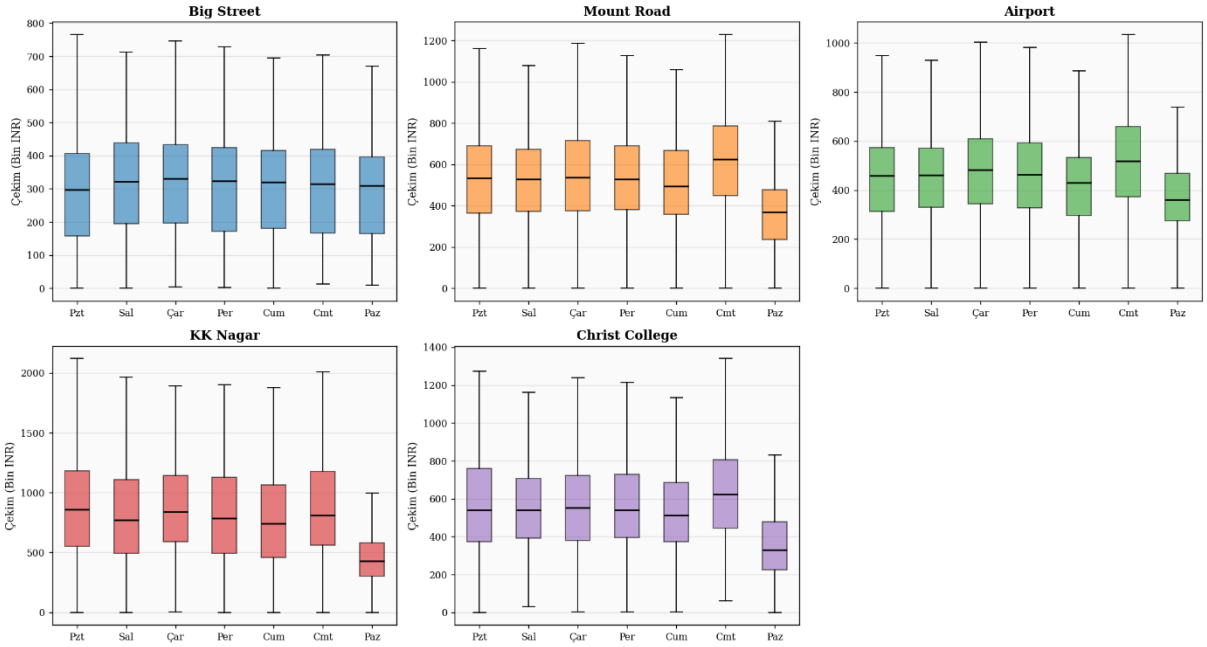
Şekil 2'de haftanın günlerine göre çekim miktarları incelenmiş ve hafta içi-hafta sonu arasında farklılık olup olmadığı gözlemlenmiştir.

Tablo 1. Veri setine ait ilk beş gözlem

atm_name	transaction_ date	no_of_ with drawals	no_of_ XYZ_ card_ with drawals	no_of_ other_ card_ with drawals	amount _with drawn _XYZ_ card	amount _with drawn_ other_ card	weekday	working_ day	total_ amount _with drawn
Big Street ATM	01/01/2011	50	20	30	41700	82100	saturday	H	123800
Mount Road ATM	01/01/2011	253	67	186	270900	49700	saturday	H	767900
Airport ATM	01/01/2011	98	56	42	347700	155700	saturday	H	503400
KK Nagar ATM	01/01/2011	265	159	106	532600	412700	saturday	H	945300
Christ College ATM	01/01/2011	74	25	49	148200	139500	saturday	H	287700

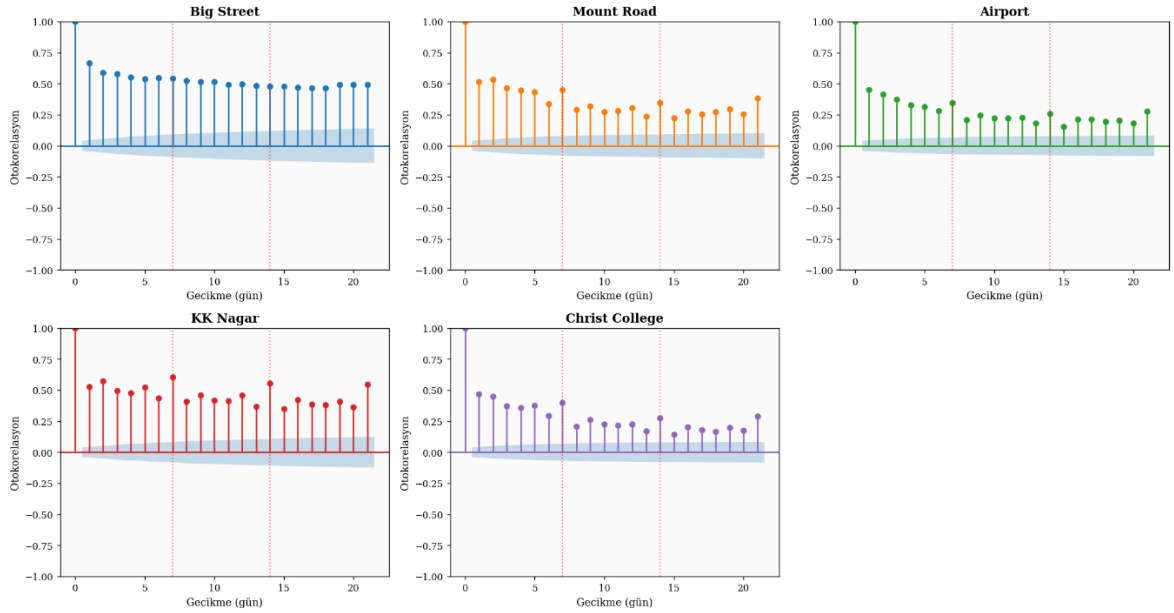


Şekil 1. ATM bazında günlük nakit çekim miktarları ve 30 günlük hareketli ortalamaları.



Şekil 2. Haftanın günlerine göre nakit çekim dağılımı.

Şekil 2 incelendiğinde, nakit talebinin belirgin bir haftalık periyodiklik sergilediği görülmektedir. Tüm ATM'lerdeki en belirgin örüntü, pazar günü çekim tutarlarının diğer günlere kıyasla düşük olmasıdır. Bu düşüş özellikle KK Nagar ve Christ College ATM'lerinde dikkat çekmektedir. Buna karşılık cumartesi günü, Mount Road, Airport ve Christ College ATM'lerinde en yüksek hacimli çekimlerin gerçekleştirildiği görülmektedir. Big Street ATM'de, haftalık dalgalanma daha sınırlıdır ve günler arasında düzgün bir dağılım sergilemektedir. Sonuç olarak Şekil 2'de ortaya konan haftalık örüntü, modelleme sürecinde haftanın günü, hafta sonu göstergesi ve yedi günlük gecikmeli (lag-7) özniteliklerin kullanılmasının deneysel olarak gerekçesini oluşturmaktadır. Şekil 3'te ise ATM'lere ait nakit çekimlerinin otokorelasyon fonksiyonları verilmiştir.



Şekil 3. Otokorelasyon fonksiyonu (ACF) – Lag seçimleri.

Şekil 3'te sunulan grafiklerde kırmızı kesikli çizgiler 7 ve 14 günlük gecikmeleri göstermektedir. Bu grafiklere göre, tüm ATM'lerde bir günlük gecikmede (lag-1) yüksek otokorelasyon değerleri gözlemlenmektedir. Söz konusu durum, bir günün çekim tutarının büyük ölçüde bir önceki günün değeriyle ilişkili olduğunu; dolayısıyla geçmiş çekim tutarlarının tahmin için değerli bilgi taşıdığını göstermektedir.

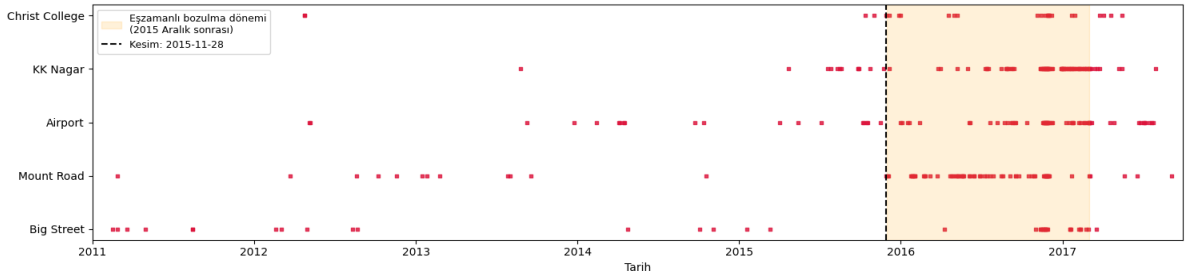
Bunun yanı sıra, özellikle Mount Road, KK Nagar ve Christ College ATM'lerinde 7 ve 14 günlük gecikmelerde belirgin otokorelasyon pikleri görülmektedir. Bu pikler, çekim serilerinin haftalık bir tekrar örüntüsü içerdiğine

işaret etmekte ve Şekil 2'de gözlemlenen haftalık periyodikliği istatistiksel olarak doğrulamaktadır. Özellikle KK Nagar ATM'sinde 7 ve 14 günlük gecikmelerdeki otokorelasyon değerlerinin komşu gecikmelere kıyasla belirgin biçimde yüksek olması, bu noktada haftalık ritmin daha güçlü olduğunu ortaya koymaktadır.

Genel olarak otokorelasyon değerleri gecikme arttıkça kademeli biçimde azalmakta; ancak güven aralığının (mavi gölgeli bölge) üzerinde kalmaya devam etmektedir. Bu durum, serilerin hem kısa hem de orta vadeli bağımlılık yapısı taşıdığını göstermektedir. Söz konusu bulgular, modelleme sürecinde 1, 7 ve 14 günlük gecikmeli özniteliklerin yanı sıra hareketli ortalama ve hareketli standart sapma temelli istatistiksel özniteliklerin kullanılmasının deneysel olarak gerekçesini oluşturmaktadır.

2.3. Veri Önişleme

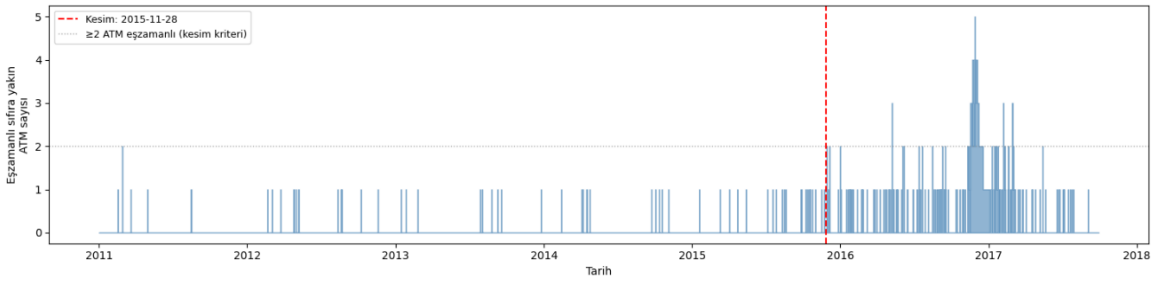
Modelleme aşamasına geçmeden önce veri setine üç adımlı bir önişleme uygulanmıştır. Bunlar; analiz döneminin belirlenmesi, eksik takvim günlerinin tamamlanması ve ölçeklemedir. İlk olarak, ham veri seti incelenmiş ve tam sıfır veya eksik (NaN) değer olup olmadığına bakılmıştır. Hedef değişkende hiçbir tam sıfır veya NaN değer bulunmadığı ve en düşük gözlem değerinin 100 INR olduğu görülmüştür. Bu düşük gözlem değerleri, gerçek talep gözlemleri olduğundan dolayı müdahale edilmemiştir. Buna karşın, son dönemde gözlemlenen sıfıra yakın çekim değerlerinin yapısı incelenmiştir. Her ATM için medyan çekim tutarının %10'unun altında kalan değerler sıfıra yakın olarak işaretlenmiş; bu değerlerin ATM ve zaman boyutundaki dağılımı Şekil 4'te verilmiştir.



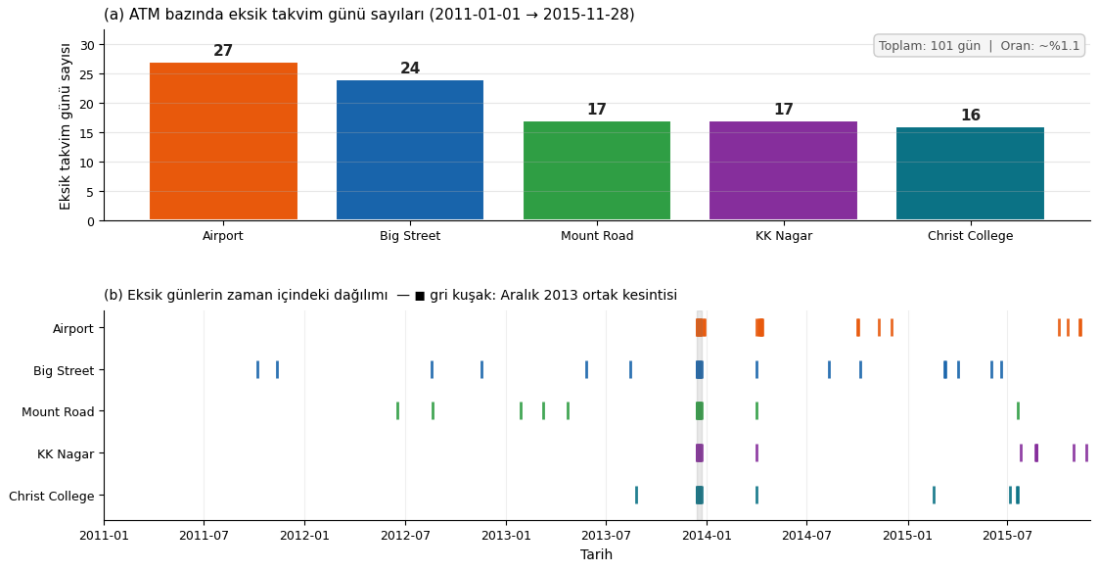
Şekil 4. Sıfıra yakın çekim günlerinin ATM ve zaman bazında dağılımı.

Şekil 4'te görüldüğü gibi, 2011-2015 yılları arasında sıfıra yakın günler ATM'ler arasında dağınık ve seyrek bir biçimde gözlemlenirken, 2015 sonu itibarıyla birden fazla ATM'de eşzamanlı yoğunlaşmalar ortaya çıkmaktadır. Aynı gün içinde sıfıra yakın çekim gösteren ATM sayısının zamana göre dağılımı incelendiğinde (Şekil 5), 2015 yılı sonuna kadar bu sayının büyük ölçüde 0-1 düzeyinde seyrettiği; 2015 Aralık ayından itibaren ise eşzamanlı bozulma sayısının belirgin biçimde arttığı ve 2016 Kasım ayında en yüksek seviyeye ulaştığı görülmektedir. Beş bağımsız ATM'de eşzamanlı olarak ortaya çıkan bu yoğunlaşma, operasyonel kesintilerden farklı olarak tüm sistemi etkileyen ortak bir yapısal bozulmaya işaret etmektedir. Bu bulgudan hareketle, analizin serinin kararlı seyrettiği dönemle sınırlandırılması uygun görülmüş; en az iki ATM'de eşzamanlı sıfıra yakın yoğunlaşmanın gözlemlendiği ilk ay (2015 Aralık) öncesi son tarih, kesim noktası olarak belirlenmiştir. Sonuç olarak analiz, 1 Ocak 2011 – 28 Kasım 2015 dönemiyle sınırlandırılmıştır.

İkinci adımda, kesim sonrası kalan dönemdeki eksik takvim günleri ele alınmıştır. Veri setinde her ATM için zaman serisinin sürekli olmadığı ve takvim üzerinde dağınık biçimde hiç kayıt içermeyen günler bulunduğu tespit edilmiştir (her ATM için yaklaşık 16-27 gün, kullanılan dönemin %1'i). Bu eksik günler, tekrarlayan sinir ağlarının gecikmeli ve hareketli istatistik özniteliklerinin takvimsel hizalamasını bozmaktadır; örneğin yedi günlük gecikme (lag-7) takvimsel olarak tam bir hafta öncesine değil, sekiz veya dokuz gün önceye karşılık gelebilmektedir. Bu sorunu gidermek amacıyla her ATM'nin zaman serisi tam günlük frekansa yeniden indekslenmiş ve hiç kaydedilmemiş takvim günleri eksik (NaN) olarak işaretlenmiştir. Ardından yalnızca bu eksik günler, ilgili ATM'nin aynı hafta-günü medyanı ile doldurulmuştur. Bu yöntem haftalık periyodikliği korumakta ve eksik gün civarındaki gecikmeli özniteliklerin takvimsel tutarlılığını sağlamaktadır. Önemle vurgulanmalıdır ki, bu işlem yalnızca hiç kaydedilmemiş takvim günlerine uygulanmıştır; veri setinde kayıtlı düşük çekim değerleri (örneğin pazar günleri veya tatil dönemlerine ait gerçek düşük talep gözlemleri) gerçek gözlem olarak kabul edilmiş ve hiçbir biçimde değiştirilmemiştir. Sınırlandırılan dönem içerisindeki ATM bazında eksik günler Şekil 6'da gösterilmiştir. Üçüncü ve son adımda, RNN mimarilerinin girdi değişkenlerinin ölçeğine duyarlı olması nedeniyle hem hedef değişken hem de türetilen öznitelikler [0, 1] aralığına Min-Maks normalizasyonu (MinMaxScaler) ile ölçeklenmiştir. Geleceğe yönelik bilgi sızıntısını önlemek amacıyla ölçekleyici, ileri yönlü doğrulama döngüsünün her yeniden eğitim adımında yalnızca o ana kadarki eğitim verisi üzerinde uyarlanmış; test gözlemleri ölçekleme parametrelerinin hesaplanmasına hiçbir aşamada dahil edilmemiştir. Tahminler elde edildikten sonra, değerler ters ölçekleme ile özgün birimlerine (INR) geri dönüştürülerek başarım metrikleri orijinal ölçekte hesaplanmıştır.



Şekil 5. Aynı gün içerisinde sıfıra yakın çekim gösteren ATM sayısı.



Şekil 6. Kullanılan dönemdeki (2011-01-01 – 2015-11-28) eksik takvim günlerinin ATM bazında dağılımı. (a) Her ATM için toplam eksik gün sayısı; (b) eksik günlerin zaman içindeki dağılımı.

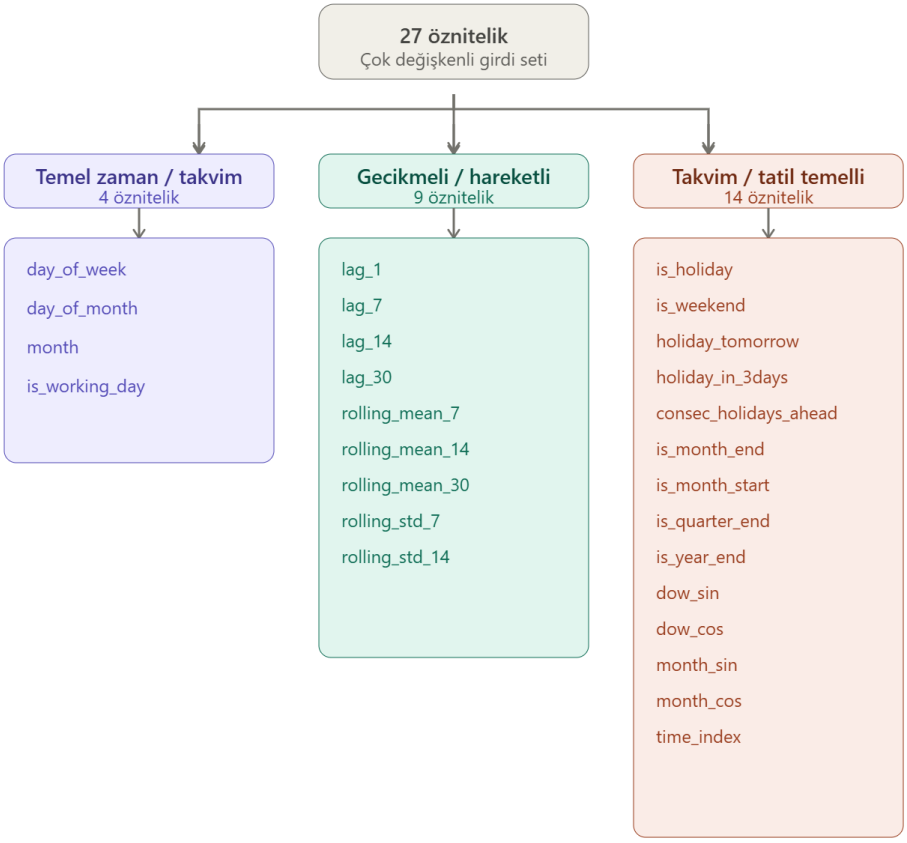
2.4. Özellik Mühendisliği

Özellik mühendisliği, mevcut değişkenlerden (ham veriden) yeni ve anlamlı değişkenler türeterek öğrenme algoritmalarının daha etkili kullanıldığı bir süreçtir. Ham veri çoğu zaman tahmin için değerli olan bilgiyi örtük biçimde barındırır. Bu bilginin modele daha açık bir şekilde sunulması, modelin bu örüntüyü daha kolay yakalamasını sağlar. Örneğin, bir tarih bilgisi tek başına sayısal olarak anlamsızken bu tarihten özellik mühendisliği ile üretilen "haftanın günü", "tatil olup olmadığı" veya "ay sonu olup olmadığı" gibi öznitelikler nakit talebini etkileyen zamansal davranışların modele aktarılmasını mümkün kılar. Özetle, özellik mühendisliği model başarımını etkileyen önemli faktörlerden biridir.

Zaman serisi verilerinde, özellik mühendisliği kullanılması iki temel nedenden kaynaklanmaktadır: Birincisi, nakit talebi yalnızca geçmiş çekim değerlerinin bir fonksiyonu değildir; çalışma günleri, resmi ve dini tatiller, maaş zamanları gibi takvim temelli dışsal değişkenlerden de etkilenmektedir. Bu bilgiler türetilen öznitelikler aracılığıyla modele kazandırılabilmektedir. İkincisi, zaman serisinin yakın geçmişinin taşıdığı bilgi (bir önceki günün, bir önceki haftanın değeri veya son dönemdeki ortalama eğilim) gecikmeli ve hareketli istatistik öznitelikleri biçiminde özetlenerek modele sunulduğunda, modelin kısa ve orta vadeli bağımlılıkları öğrenmesi kolaylaşmaktadır. Bu sebeple, bu çalışmada, özellik mühendisliği ile yeni öznitelikler türetilmiştir ve ardından model eğitimleri yapılmıştır.

Tekrarlayan sinir ağları modelleri, ardışık gözlemler arasındaki zamansal bağımlılıkları doğrudan ham diziden öğrenebilme kapasitesine sahiptir. Bununla birlikte, nakit talebini yönlendiren birçok etken (haftalık çalışma ritmi, ay sonu yoğunlaşması, resmî ve dini tatiller gibi takvim temelli olaylar) yalnızca geçmiş çekim değerlerinin kendisinden değil, dışsal zamansal bilgiden okunabilmektedir. Bu nedenle, bu çalışmada, iki ayrı girdi yapısı karşılaştırmalı olarak değerlendirilmiştir: yalnızca hedef değişkenin yani toplam çekim tutarlarının geçmiş değerlerini kullanan tek değişkenli yapı ve bu çalışmada tasarlanan öznitelikleri de modele dahil eden çok değişkenli yapı. Böylece, açıkça türetilen özniteliklerin RNN mimarilerinin başarımına sağladığı katkı sistematik olarak incelenebilmiştir.

Çok değişkenli yapı için, keşifsel veri analizi bulgularından hareketle toplam yirmi yedi öznitelik üretilmiştir. Bu öznitelikler, taşıdıkları bilginin niteliğine göre üç grupta ele alınmış ve Şekil 7'de gösterilmiştir.



Şekil 7. Özellik mühendisliği sürecinde üretilen 27 özniteliğin grup bazında dağılımı.

İlk grup, tarih bilgisinden doğrudan türetilen temel zaman ve takvim özniteliklerdir: haftanın günü, ayın günü ve ay numarası. Bunlara ek olarak, veri setindeki working_day etiketinden türetilen çalışma günü göstergesi (is_working_day) ile de haftalık periyodikliğin ve hafta içi–hafta sonu farklılığının modele aktarılması sağlanmıştır.

İkinci grup, zaman serisinin yakın geçmişini özetleyen gecikmeli (lag) ve hareketli istatistik özniteliklerdir. Şekil 3'teki otokorelasyon analizinde 1, 7 ve 14 günlük gecikmelerde belirgin otokorelasyon gözlemlenmiş; bu bulgudan hareketle 1, 7, 14 ve ilave olarak aylık örüntüyü yakalamak amacıyla 30 günlük gecikmeli çekim değerleri (lag_1, lag_7, lag_14, lag_30) öznitelik olarak tanımlanmıştır. Serinin kısa ve orta vadeli eğilimini ve oynaklığını temsil etmek amacıyla 7, 14 ve 30 günlük hareketli ortalamalar ile 7 ve 14 günlük hareketli standart sapmalar hesaplanmıştır. Bu öznitelikler sayesinde model, yalnızca tek bir önceki güne değil, yakın geçmişin genel seviyesine ve dalgalanma düzeyine de erişebilmektedir.

Üçüncü grup, takvim ve tatil temelli özniteliklerden oluşmaktadır. Bu grupta, hafta sonu göstergesi (is_weekend) ve resmî tatil göstergesi (is_holiday) yer almaktadır. Tatil göstergeli özniteliklerin üretiminde Hindistan ulusal tatil takvimi esas alınmıştır. Veri setini paylaşan kaynak tarafından ATM'lerin coğrafi konumu açıkça belirtilmemiş olmakla birlikte, ATM isimlerinin (Mount Road, KK Nagar, Christ College vb.) Hindistan'ın Chennai bölgesindeki bilinen lokasyonlarla örtüşmesi dikkat çekmektedir. Bu dolaylı göstergeden hareketle, nakit çekim davranışının yerel tatil takvimiyle ilişkili olabileceği düşünülmüş ve Python 'holidays kütüphanesi aracılığıyla Hindistan ulusal tatil takvimi modele dahil edilmiştir. Böylece, resmî tatillerin nakit talebi üzerindeki olası etkisinin model başarımına bir katkı sağlayıp sağlamadığı da araştırılmıştır. Müşterilerin tatil öncesi nakit çekme eğilimini yakalamak amacıyla ileri yönlü öznitelikler tanımlanmıştır: ertesi günün tatil olup olmadığını gösteren holiday_tomorrow, önümüzdeki üç gün içinde tatil bulunup bulunmadığını ifade eden holiday_in_3days ve önümüzdeki ardışık tatil/hafta sonu sayısını veren consec_holidays_ahead. Ayrıca, maaş ve fatura ödemelerinin yoğunlaştığı dönemleri temsil etmek üzere ay başı, ay sonu, çeyrek sonu ve yıl sonu göstergeleri (is_month_start, is_month_end, is_quarter_end, is_year_end) üretilmiştir. Haftanın günü ve ay gibi döngüsel değişkenlerin süreklilik özelliğini koruyabilmek için sinüs ve kosinüs dönüşümleri uygulanmıştır (dow_sin, dow_cos, month_sin, month_cos); bu dönüşüm, modelin örneğin pazar ile pazartesi arasındaki takvimsel yakınlığı doğru biçimde algılamasını sağlamaktadır. Son olarak, serideki uzun dönemli eğilimi temsil etmek amacıyla doğrusal bir zaman indeksi (time_index) eklenmiştir.

Tüm gecikmeli ve hareketli istatistik öznitelikleri hesaplanırken, geleceğe yönelik bilgi sızıntısını önlemek amacıyla yalnızca tahmin edilecek günden önceki gözlemler kullanılmıştır. Bu amaçla, ilgili istatistikler bir gün kaydırılarak hesaplanmış; böylece herhangi bir

öznitelik, tahmin anında henüz gözlemlenmemiş bir bilgiyi içermemiştir. Benzer şekilde, ölçekleme işleminde kullanılan MinMaxScaler her yeniden eğitim adımında yalnızca o ana kadarki eğitim verisi üzerinde uyarlanmış, test gözlemleri ölçekleme parametrelerinin hesaplanmasına dahil edilmemiştir.

2.5. RNN Tabanlı Derin Öğrenme Mimarileri

Bu çalışmada, ATM nakit talebinin tahmin edilmesi amacıyla Kapılı Tekrarlayan Birim (GRU), Uzun Kısa Süreli Bellek (LSTM), Çift Yönlü Uzun Kısa Süreli Bellek (Bi-LSTM) ve Evrişimsel Sinir Ağı (CNN) olmak üzere çeşitli derin öğrenme yöntemleri kullanılmıştır. Bu yöntemlerin kullanılmasının üç temel gerekçesi bulunmaktadır. Birincisi, ATM nakit talep tahmini literatüründe tekrarlayan sinir ağı (RNN) tabanlı modeller (özellikle LSTM ve GRU) en yaygın derin öğrenme yaklaşımları olarak yer almaktadır. İkincisi, seçilen dört mimari, RNN ailesinin farklı modelleme paradigmalarını temsil etmektedir: LSTM klasik kapılı bellek hücresi yapısıyla, GRU basitleştirilmiş kapı yapısıyla, Bi-LSTM çift yönlü bilgi akışıyla ve CNN-LSTM ise hibrit yerel-zamansal yaklaşımıyla farklı modelleme stratejilerini örneklemektedir. Üçüncüsü, söz konusu dört mimari, parametre sayıları açısından belirgin biçimde farklılaşmakta ve bu durum, çalışmanın model karmaşıklığı ile tahmin başarımı arasındaki ilişkiyi sistematik olarak inceleme amacıyla doğrudan uyumludur. Bu dört mimarinin yapısal özellikleri ve parametre sayıları Tablo 2'de özetlenmiştir.

Tablo 2. Çalışmada kullanılan RNN mimarilerinin yapısal özellikleri ve parametre sayıları

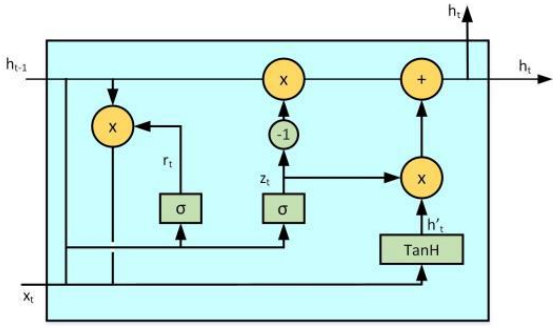
Mimari	Katman Yapısı	Parametre Sayısı[1]	Temel Yeteneği
LSTM	LSTM(64) → Dropout → LSTM(32) → Dropout → Dense(16) → Dense(1)	~36.500	Uzun-kısa süreli bağımlılıkları modelleme
GRU	GRU(64) → Dropout → GRU(32) → Dropout → Dense(16) → Dense(1)	~27.800	LSTM'in daha hafif alternatifi; az parametreyle benzer başarım
Bi-LSTM	Bidirectional[LSTM(64)] → Dropout → Bidirectional[LSTM(32)] → Dropout → Dense(16) → Dense(1)	~89.400	Geçmiş ve gelecek bağlamı çift yönlü değerlendirme
CNN-LSTM	Conv1D(64) → Conv1D(32) → MaxPool → LSTM(50) → Dropout → Dense(16) → Dense(1)	~28.900	Yerel örüntüleri (kısa pencere) çıkarıp ardışık olarak modelleme

[1]Tabloda verilen parametre sayıları, çok değişkenli (Multi, 27 öznitelikli) girdi yapısı ve 14 günlük geri bakış penceresi konfigürasyonu için Keras model.count_params() fonksiyonuyla hesaplanmış yaklaşık değerlerdir. Tek değişkenli (Uni) girdi yapısında LSTM ve GRU mimarileri için parametre sayıları yaklaşık 15-25 bin daha düşüktür; Bi-LSTM mimarisinde yapısal çift yönlü katman etkisi nedeniyle bu fark daha belirgindir. Farklı geri bakış pencereleri arasındaki parametre farkı, pencere uzunluğunun ilk katman girdi boyutunu doğrudan etkilememesi nedeniyle ihmal edilebilir düzeydedir.

Model mimarilerinin yapısal hiperparametreleri (LSTM/GRU birimlerinde 64 ve 32 nöron sayıları, %20 dropout oranı, 0.001 öğrenme oranı ve 32 yığın boyutu), çalışmanın ön aşamasında yapılan pilot denemelerde makul başarım üreten değerler arasından seçilmiş ve dört mimarinin tümü için sabit tutulmuştur. Bu tercihin gerekçesi, çalışmanın odağının tekil bir model için hiperparametre optimizasyonu değil, dört farklı RNN mimarisinin karşılaştırmalı değerlendirilmesi olmasıdır. Dört mimarinin tümü için ortak sabit bir hiperparametre setinin kullanılması, mimariler arası karşılaştırmanın hiperparametre farklılıklarından bağımsız yürütülmesine olanak tanımıştır.

2.5.1. Kapılı tekrarlayan birim (Gated recurrent unit-GRU)

Cho vd. (2014) tarafından geliştirilen GRU, LSTM mimarisinin daha sade ve hafif bir versiyonu olan bir derin öğrenme yöntemidir. GRU'da LSTM'de bulunan giriş ve sıfırlama kapıları birleştirilerek "güncelleme kapısı" oluşturulmuş, ayrıca hücre durumu ile gizli durum tek yapıda birleştirilmiştir. Bu sayede model daha az parametre ile çalışmakta, hesaplama maliyeti azalmakta ve eğitim süreci hızlanmaktadır. Şekil 8'de gösterildiği gibi GRU mimarisi iki temel kapıdan oluşur: güncelleme kapısı (update gate) geçmiş bilginin ne kadar korunacağını belirlerken sıfırlama kapısı (reset gate) hangi bilgilerin unutulacağını kontrol eder. Bu kapılar, önceki gizli durum ile mevcut giriş verisini birleştirerek yeni gizli durumun oluşturulmasını sağlar (Şanlıalp ve Yıldız, 2025). Basit yapısı sayesinde GRU, LSTM'ye benzer doğruluk performansı sunarken daha hızlı öğrenme gerçekleştirebilmekte ve özellikle kaynak kısıtlı uygulamalarda tercih edilmektedir (Kılınç ve Öztürk, 2022).



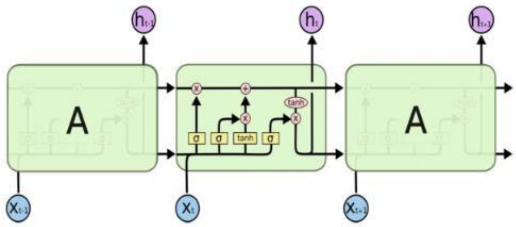
Şekil 8. GRU mimarisi (Tosun ve Şentürk, 2023).

2.5.2. Uzun kısa süreli bellek (Long short-term memory-LSTM)

Tekrarlayan Sinir Ağları (Recurrent Neural Networks-RNN), dizisel verileri işlemek amacıyla geliştirilen ve önceki durumlara ait bilgileri belleğinde tutarak çalışan güçlü bir yapay sinir ağı türüdür. İleri beslemeli sinir ağlarından farklı olarak RNN modelleri, bellek yapıları sayesinde önceki girdilere ait sıralı bilgileri kullanabilmektedir. Tekrarlayan gizli durum olarak adlandırılan bu bellek mekanizması, ağın veri dizisindeki bir sonraki öğeyi tahmin etmesine olanak sağlamaktadır (Rostamian ve O'Hara, 2022).

Bununla birlikte, pratikte RNN modellerinin geçmiş bilgileri etkili şekilde kullanabilme kapasitesi yalnızca birkaç zaman adımıyla sınırlı kalmaktadır. Teorik olarak önceki zaman adımlarındaki bilgileri koruyabilmeleri beklense de uzun vadeli bağımlılıkların öğrenilmesi oldukça güçtür. Bunun temel nedenlerinden biri, derin ağ yapılarında ortaya çıkan kaybolan gradyan problemidir. Gradyan, bir fonksiyonun çıktısının girdilere göre değişimini ifade eden kısmi türev değeridir. Kaybolan gradyan problemi, gradyan değerlerinin katmanlar boyunca giderek küçülmesi sonucu ağın uzun dönemli bağımlılıkları öğrenememesine neden olmakta ve öğrenme sürecini yavaşlatmakta veya tamamen durdurabilmektedir. Bunun tersine, gradyan değerlerinin aşırı büyümesiyle ortaya çıkan patlayan gradyan problemi de ağın kararsız hale gelmesine yol açmaktadır. Kaybolan gradyan probleminde ağ ağırlıkları çok küçük değerler alırken, patlayan gradyan probleminde ise aşırı büyük ağırlık değerleri oluşmaktadır (Hochreiter ve Schmidhuber, 1996).

Bu problemlerin üstesinden gelmek amacıyla Hochreiter ve Schmidhuber (1996) tarafından geliştirilen LSTM modelleri, RNN yapılarının geliştirilmiş bir uzantısıdır. LSTM modeli genel olarak unutma, giriş ve çıkış olmak üzere üç temel kapıdan oluşmaktadır. Unutma kapısı mevcut bilginin korunup korunmayacağına karar verirken, giriş kapısı yeni bilgilerin belleğe ne ölçüde ekleneceğini belirlemektedir. Çıkış kapısı ise hücrede bulunan bilginin çıktıya aktarılıp aktarılmayacağını kontrol etmektedir (Rostamian ve O'Hara, 2022). Şekil 9'te LSTM mimarisinin yapısı verilmiştir.

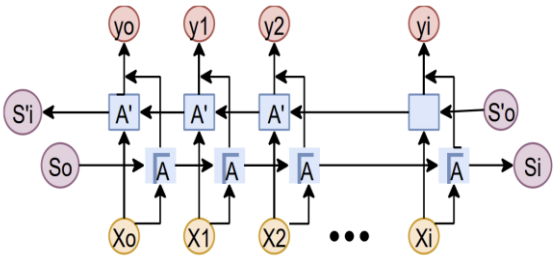


Şekil 9. LSTM mimarisi (Şanlıalp ve Yıldız, 2025).

2.5.3. Çift yönlü uzun kısa süreli bellek (Bidirectional long short-term memory-Bi-LSTM)

Tek yönlü LSTM yapıları, girdileri yalnızca ileri yönde işlediği için geçmiş bilgileri dikkate almakta, ancak geleceğe yönelik bilgileri kullanamamaktadır. Bu sınırlılığı gidermek amacıyla Bi-LSTM modeli geliştirilmiştir. Bi-LSTM yapısında veriler hem geçmişten geleceğe hem de gelecekten geçmişe doğru iki paralel yönde işlenmekte ve elde edilen çıktılar birleştirilerek nihai sonuç üretilmektedir. Bu çift yönlü işlem mekanizması sayesinde Bi-LSTM modelleri, aynı veri dizisi üzerinde klasik LSTM modellerine kıyasla daha başarılı sonuçlar verebilmektedir (Chakladar vd., 2020).

RNN yapıları teorik olarak uzun dizileri işleyebilme yeteneğine sahip olsa da eğitim sürecinde gradyanların kaybolması veya patlaması problemiyle karşılaşabilmektedir (Tsujimoto vd., 2016). Bu sorunu çözmek amacıyla geliştirilen LSTM ağları; giriş, unutma ve çıkış kapılarından oluşan yapısıyla uzun dönemli bağımlılıkları öğrenebilmektedir. Ancak standart LSTM modellerinin yalnızca tek yönlü veri işleyebilmesi önemli bir sınırlılık oluşturmaktadır. Bu nedenle Bi-LSTM modeli, verileri hem normal hem de ters sırada işleyerek her zaman adımında geçmiş ve geleceğe ait bilgilerin birlikte değerlendirilmesini sağlamaktadır (Chen ve Huang, 2021). Şekil 10'da Bi-LSTM'ye ait blok şeması gösterilmiştir.



Şekil 10. Bi-LSTM'nin blok şeması (Kaysal vd., 2023).

2.5.4. Evrişimsel sinir ağları (Convolutional neural network-CNN)

Evrişimsel Sinir Ağları (CNN), özellikle iki boyutlu verilerin işlenmesi amacıyla geliştirilmiş bir derin öğrenme yaklaşımıdır. İlk olarak Lecun vd. (1998) tarafından önerilen CNN modeli, görüntü işleme ve doğal dil işleme gibi alanlarda yüksek performans göstermesiyle öne çıkmaktadır. CNN yapıları, evrişimsel hesaplama gerçekleştiren ileri beslemeli sinir ağları sınıfında yer almakta olup, derin öğrenmenin en yaygın kullanılan temsil öğrenme algoritmalarından biridir (Gu vd., 2018; Zha vd., 2022).

CNN mimarisinde, iki boyutlu verilerdeki farklı özellikleri algılayabilmek amacıyla çok sayıda katman kullanılabilmektedir. Görüntülerin farklı özellikleri, çeşitli çözünürlüklere sahip evrişimsel filtreler aracılığıyla elde edilmekte ve her katmanın çıktısı bir sonraki katmanın girdisi olarak kullanılmaktadır. CNN'nin temel bileşenleri; evrişim (convolution) katmanı, aktivasyon katmanı ve havuzlama (pooling) katmanıdır. Bu katmanlar tekrarlı biçimde kullanılarak veriye ait ayırt edici özelliklerin çıkarılması sağlanmaktadır (Berus ve Yakut, 2024).

Evrişim katmanında her nöron yalnızca komşu

nöronların belirli bir kısmı ile bağlantı kurmaktadır. Bu yapı sayesinde ağın karmaşıklığı ve parametre sayısı azaltılarak daha verimli bir öğrenme süreci elde edilmektedir. Evrişim işlemlerinin ardından elde edilen yüksek boyutlu özellikler, boyut indirgeme işlemi gerçekleştiren havuzlama katmanından geçirilmekte ve böylece hesaplama maliyeti düşürülmektedir. Ayrıca regresyon problemlerinde sürekli değerlerin tahmin edilebilmesi amacıyla modelin son kısmına regresyon katmanı da eklenebilmektedir (Zha vd., 2022).

Bu çalışmada, evrişimsel sinir ağlarının yerel örüntü çıkarma yeteneği ile LSTM'nin ardışık bağımlılıkları modelleme kapasitesini birleştiren hibrit CNN-LSTM öğrenme yaklaşımı kullanılmıştır.

2.6. Performans Metrikleri

Modellerin tahmin başarımı, zaman serisi tahmini literatüründe yaygın olarak kullanılan üç metrik üzerinden değerlendirilmiştir. Bunlar: simetrik ortalama mutlak yüzde hata (Symmetric Mean Absolute Percentage Error, SMAPE), kök ortalama kare hata (Root Mean Square Error, RMSE) ve ortalama mutlak hata (Mean Absolute Error, MAE). Birincil değerlendirme metriği olarak SMAPE dikkate alınmış ve MAE ile RMSE tamamlayıcı göstergeler olarak kullanılmıştır. Aşağıda metriklerin tanımlamaları ve formülleri verilmiştir.

SMAPE, ortalama mutlak yüzde hata (MAPE) metriğinin gerçek değer sıfıra yaklaştığında tanımsız hâle gelmesi problemini gidermek üzere önerilmiştir. Formülü eşitlik 1'de verilmiştir (Andrawis vd., 2011).

$$SMAPE = \frac{1}{M}\sum_{i=1}^{M}\frac{\left|\hat{y}_i - y_i\right|}{\left(\left|\hat{y}_i\right| + \left|y_i\right|\right)/2} \quad (1)$$

Burada y_m gerçek değeri, $\hat{y}_m$ tahmin edilen değeri ve M test gözlem sayısını ifade etmektedir.

MAE, tahmin hatasının mutlak değerinin ortalamasını veren, hedef değişkenle aynı birime sahip bir hata ölçüsüdür. Formülü eşitlik 2'de verilmiştir.

$$MAE = \frac{1}{M}\sum_{i=1}^{M}\left|y_i - \hat{y}_i\right| \quad (2)$$

RMSE, hataların karelerinin ortalamasının karekökü dür ve yine hedef değişkenle aynı birime sahiptir. Formülü eşitlik 3'te verilmiştir.

$$RMSE = \sqrt{\frac{1}{M}\sum_{i=1}^{M}\left(y_i - \hat{y}_i\right)^2} \quad (3)$$

RMSE ölçütü, kare alma işlemi nedeniyle büyük hataları daha ağır cezalandırmakta; dolayısıyla model hata dağılımının normal (Gaussian) varsayımına yakın olduğu durumlarda model başarımını temsil etmede MAE'ye kıyasla daha bilgi verici kabul edilmektedir.

2.7. Deneysel Kurulum

2.7.1. Çalışma ortamı

Tüm deneyler Google Colab bulut ortamında, T4 GPU hızlandırma etkin olacak şekilde yürütülmüştür. Modeller Python programlama dili kullanılarak geliştirilmiş; derin öğrenme mimarileri TensorFlow/Keras kütüphanesi ile kurulmuştur. Veri işleme ve öznitelik üretiminde pandas ve numpy, ölçekleme ve başarım metriklerinin hesaplanmasında scikit-learn, tatil takviminin oluşturulmasında ise holidays kütüphanesi kullanılmıştır. Sonuçların tekrarlanabilirliğini sağlamak amacıyla numpy ve TensorFlow için sabit rastgelelik tohumu (random seed = 42) tanımlanmıştır.

2.7.2. İleri yönlü doğrulama stratejisi ve eğitim-test ayrımı

Modellerin başarımı, gerçek dünya senaryolarına uygun biçimde ileri yönlü doğrulama yaklaşımı ile değerlendirilmiştir. İleri yönlü doğrulama (walk-forward validation), zaman serisi modellerinin başarımını ölçmek için kullanılan, bilgi sızıntısını engelleyen yinelemeli bir doğrulama yaklaşımıdır. Bu yaklaşımda model, ilk aşamada eğitim kümesinin tamamı üzerinde eğitilir ve test kümesindeki ilk gözlem için tahmin üretir. Ardından gerçekleşen gözlem eğitim kümesine eklenir; model belirli aralıklarla yeniden eğitilerek bir sonraki gözlemi tahmin eder. Bu süreç, test kümesindeki son gözleme kadar yinelenir. Klasik tek-kerelik (statik) eğitim-test ayrımından farklı olarak ileri yönlü doğrulama, modelin yeni gözlemlere uyum sağlama kapasitesini de değerlendirmeye olanak tanır ve geleceğe yönelik bilgi sızıntısı riskini ortadan kaldırır.

Çalışmada, analiz dönemi 1 Ocak 2011 – 28 Kasım 2015 olarak belirlenmiş; bu dönemin son altı ayı (29 Mayıs 2015 – 28 Kasım 2015) test kümesi, öncesi ise eğitim kümesi olarak kullanılmıştır. Bu yapı her ATM için ayrı ayrı uygulanmış olup, her ATM yaklaşık 1.590 günlük eğitim ve 175-184 günlük test gözlemi içermektedir. İleri yönlü doğrulamada model, ilk pencerede eğitim verisiyle eğitilip test kümesindeki ilk gözlem tahmin edilmekte; ardından yeni gözlemler eğitim setine eklenerek model belirli aralıklarla yeniden eğitilmekte ve sonraki tahminler bu güncellenmiş model ile üretilmektedir. Bu yaklaşım, hem zaman serisinin nedensellik yapısını korumakta hem de modelin yeni bilgilere uyum sağlama kapasitesini değerlendirmeye olanak tanımaktadır. Eğitim-test ayrımı için detaylı bilgi Tablo 3'te verilmiştir.

2.7.3. Hiperparametreler

Tüm modellerde Adam optimizasyonu (öğrenme oranı 0.001) ve ortalama kare hata (MSE) kayıp fonksiyonu kullanılmıştır. Yığın boyutu (batch size) 32, maksimum dönem (epoch) sayısı 50 olarak ayarlanmış; aşırı öğrenmeyi önlemek için doğrulama kaybı 5 dönem boyunca iyileşmezse eğitimi sonlandıran erken durdurma (early stopping) mekanizması uygulanmıştır. Aşırı uyumu azaltmak amacıyla her tekrarlayan katmandan sonra %20'lik bir bırakma (dropout) katmanı eklenmiştir. İleri yönlü doğrulama döngüsünde modeller her 14 günde bir yeniden eğitilmiştir (refit_every=14); bu değer, model güncelleme sıklığı ile hesaplama maliyeti arasında bir denge gözetilerek belirlenmiştir.

Tablo 3. ATM bazında veri seti boyut özeti ve eğitim/test kümelerine ayrımı (gün sayısı)

ATM	Ham Veri (1 Ocak 2011 – 29 Eylül 2017)	Kesim Sonrası Ham (1 Ocak 2011 – 28 Kasım 2015)	Eksik Gün	Takvim Tamamlanınca	Eğitim (1 Ocak 2011 – 28 Mayıs 2015)	Test (29 Mayıs 2015 – 28 Kasım 2015 (son altı ay)
Big Street	2.354	1.769	24	1.793	1.609	184
Mount Road	2.256	1.776	17	1.793	1.609	184
Airport	2.253	1.766	27	1.793	1.609	184
KK Nagar	2.371	1.776	17	1.793	1.609	184
Christ College	2.355	1.777	16	1.793	1.609	184
Toplam	11.589	8.864	101	8.965	8.045	920

2.7.4. Girdi yapısı ve geri bakış penceresi

Her model iki farklı girdi yapısıyla değerlendirilmiştir: yalnızca geçmiş çekim tutarlarını dizisel olarak modele veren tek değişkenli yapı ve özellik mühendisliği başlığında açıklanan 27 türetilmiş özniteliği zaman boyutu üzerinde içeren çok değişkenli yapı. Modelin tahmin için kaç gün geriye bakacağını belirleyen geri bakış penceresi (lookback window) için 7, 14 ve 30 gün olmak üzere üç değer denenmiştir. Bu pencere uzunlukları, sırasıyla bir haftalık döngüyü, iki haftalık periyodik tekrarı ve bir aylık örüntüyü temsil etmektedir. Sonuç olarak, dört mimari × iki varyant × üç lookback × beş ATM kombinasyonuyla toplam 120 deney gerçekleştirilmiştir.

3. Bulgular

Bu bölümde, dört RNN mimarisinin iki farklı girdi yapısı (tek değişkenli ve çok değişkenli) ve üç geri bakış penceresi (7, 14, 30 gün) altında elde ettiği sonuçlar sunulmaktadır. Toplam 120 deneyin sayısal çıktıları SMAPE, MAE ve R^2 metrikleri üzerinden değerlendirilmiştir.

3.1. Model ve Girdi Yapısı Karşılaştırması

Dört RNN mimarisinin tek değişkenli ve çok değişkenli girdi yapıları altında elde ettiği ortalama SMAPE değerleri Şekil 11'de sunulmuştur. Bulgular, çok değişkenli girdi yapısının dört mimaride de tek değişkenliye göre daha düşük veya benzer SMAPE ürettiğini göstermektedir. Aradaki fark en belirgin olarak GRU mimarisinde (Multi %36,63'e karşılık Uni %37,66, ~1,0 puanlık fark) ve LSTM mimarisinde (%37,20'ye karşılık %38,08) gözlemlenmektedir. Bi-LSTM mimarisinde iki varyant birbirine çok yakın değerler üretmiş (Multi %37,39 – Uni %37,28), CNN-LSTM mimarisinde ise çok değişkenli yapı %0,6 puanlık küçük bir avantaj sağlamıştır. Model bazında en düşük ortalama SMAPE'ye çok değişkenli GRU yapısı ulaşmıştır (%36,63). Bu sonuç, özellik mühendisliği ile tasarlanan 27 öznitelikten oluşan kümenin RNN tabanlı mimarilerin tahmin başarımına genel olarak katkı sağladığını ve özellikle daha hafif mimariler (GRU, LSTM) için bu katkının daha belirgin olduğunu işaret etmektedir.

Aradaki farkların görece az olması, RNN mimarilerinin ham ardışık veri üzerinden de güçlü temel örüntüleri yakalayabildiğini, türetilen özniteliklerin ise bu temel başarıma sınırlı ancak tutarlı bir katkı sağladığını düşündürmektedir. Bununla birlikte, sonraki alt-bölümde gösterileceği üzere, ATM bazında değerlendirildiğinde en iyi sonuçların tamamı çok değişkenli girdi yapısında gerçekleşmiştir; bu da öznitelik katkısının ortalama düzeyde küçük görünse de ATM bazında belirleyici olduğunu ortaya koymaktadır.

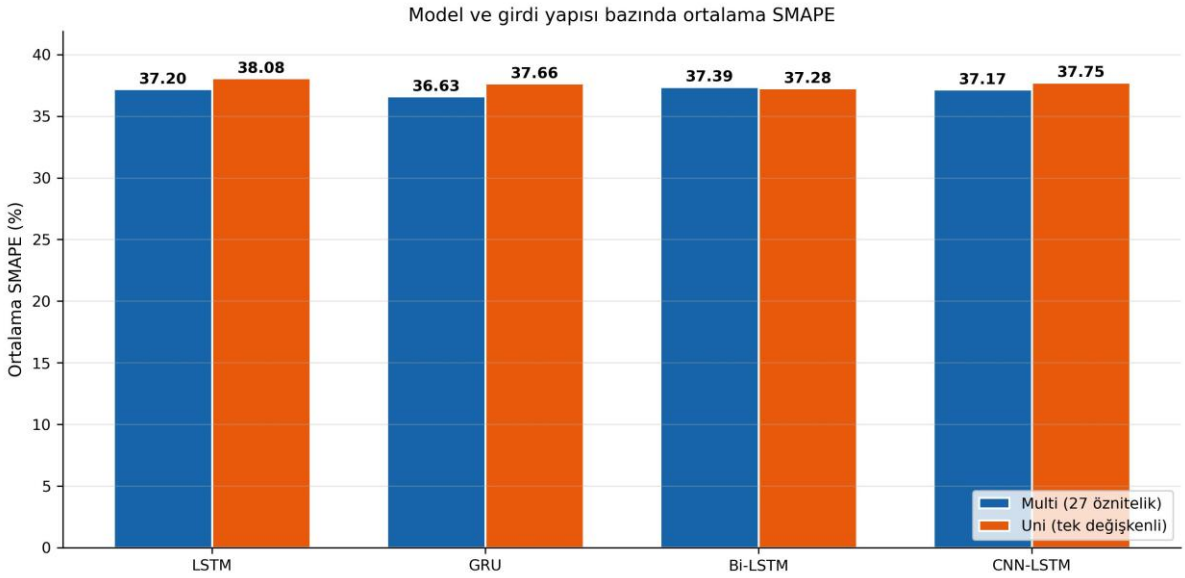
3.2. Geri Bakış Penceresinin Etkisi

Geri bakış penceresi uzunluğunun model başarımına etkisi Şekil 12'de sunulmaktadır. Tüm modeller için 30 günlük pencerede ortalama SMAPE'de küçük bir yükseliş gözlemlenmektedir; LSTM (%37,76) ve CNN-LSTM (%37,77) mimarileri 30 günlük pencerede en yüksek SMAPE değerlerini üretmiş, GRU mimarisi ise 30 günlük pencerede dahi en düşük başarımlı model olmamıştır. Bi-LSTM ve GRU mimarileri için 14 günlük pencere en düşük SMAPE değerlerini üretmiş; LSTM mimarisi 7 günlük pencerede, CNN-LSTM mimarisi yine 7 günlük pencerede en düşük SMAPE değerine ulaşmıştır. Genel olarak, geri bakış penceresinin başarım üzerindeki etkisi görece az kalmıştır; en iyi ve en kötü pencere uzunluğu arasındaki fark model bazında 0,3 – 0,7 puan SMAPE aralığında değişmektedir. 30 günlük pencerede gözlemlenen kısmi başarım düşüşünün, kullanılan eğitim dönemi uzunluğu (yaklaşık 4,4 yıl) göz önüne alındığında, sekans sayısının azalmasına ve modelin eğitim sırasında daha az farklı örüntüye maruz kalmasına bağlı olduğu değerlendirilmektedir. Bu bulgu, daha uzun pencere uzunluklarının her zaman daha iyi sonuç üretmediğini ve verisi sınırlı senaryolarda haftalık ila iki haftalık pencerelerin tercih edilebilir olduğunu göstermektedir.

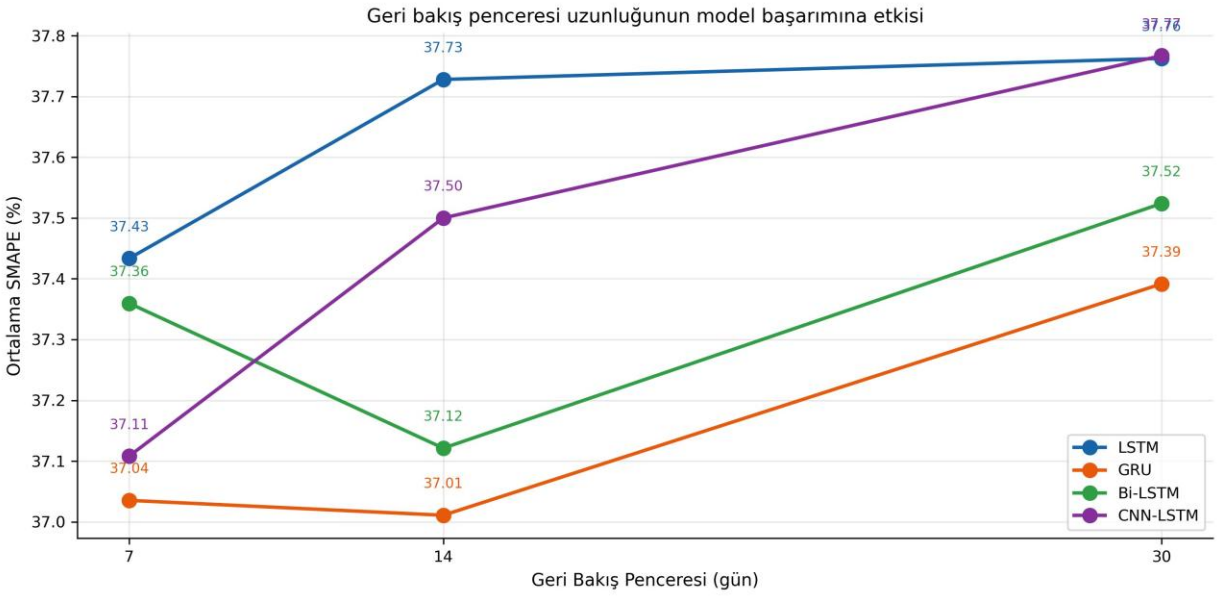
3.3. ATM Bazında En İyi Modeller

Her ATM için 24 farklı RNN konfigürasyonu (4 mimari × 2 varyant × 3 lookback) denenmiş ve en düşük SMAPE üreten konfigürasyon en iyi olarak belirlenmiştir. Elde edilen sonuçlar, Tablo 4'te verilmiştir. Tablo 4'teki en belirgin bulgu, beş ATM'nin tümünde en iyi konfigürasyonun çok değişkenli (Multi) girdi yapısında gerçekleşmiş olmasıdır. Mimari seçiminde belirgin bir baskın model bulunmamış; her ATM için farklı bir mimari en iyi sonuca ulaşmıştır. Bi-LSTM mimarisi en düşük talep oynaklığına sahip Big Street ATM'sinde, LSTM

mimarisi orta seviye oynaklıkta Mount Road ATM'sinde, GRU mimarisi Christ College ATM'sinde, CNN-LSTM mimarisi ise hem Airport hem de KK Nagar ATM'lerinde en iyi sonucu üretmiştir. Geri bakış penceresi seçimleri de ATM'nin talep yapısına göre farklılaşmaktadır: en istikrarlı seri yapısına sahip Big Street ve Mount Road ATM'lerinde 30 günlük pencere tercih edilirken, daha oynak ve düşük talep günleri sık gözlemlenen Airport ATM'sinde 7 günlük kısa pencere, KK Nagar ve Christ College'da ise orta uzunluktaki 14 günlük pencere optimal sonuç vermiştir. Bu bulgu, optimal pencere uzunluğunun ATM'nin talep oynaklığı ile ilişkili olabileceğini düşündürmektedir.



Şekil 11. Model ve girdi yapısı bazında ortalama SMAPE değerleri.



Şekil 12. Geri bakış penceresi uzunluğunun model başarımına etkisi.

Tablo 4. ATM bazında en iyi RNN mimarileri ve metrik değerleri

ATM	Model	Girdi	Lookback	SMAPE (%)	MAE (INR)	RMSE
Big Street	Bi-LSTM	Multi	30	19,12	80.761	105.158
Mount Road	LSTM	Multi	30	28,15	153.147	213.040
Christ College	GRU	Multi	14	32,55	157.770	209.196
Airport	CNN-LSTM	Multi	7	43,56	142.487	175.466
KK Nagar	CNN-LSTM	Multi	14	54,13	227.007	293.232

En iyi konfigürasyonların tahmin performansı ise Şekil 13'te gerçek değerlerle birlikte görselleştirilmiştir. Şekil 13'teki tahmin grafikleri incelendiğinde, modellerin yumuşatılmış tahminler ürettiği ve gerçek serideki uç değerleri (özellikle yüksek tepe noktalarını) yakalamada güçlük çektiği gözlemlenmektedir. Bu durum, ortalama kare hata (MSE) kayıp fonksiyonuyla eğitilen RNN modellerinde beklenen bir davranıştır ve modelin uç değerleri cezalandıran kayıp fonksiyonunun ortalama değerlere yakın tahmin üretmeyi tercih etmesinden kaynaklanmaktadır. Big Street ve Mount Road ATM'lerinde tahmin eğrisinin gerçek serinin genel desenini görece iyi takip ettiği, Airport ve KK Nagar ATM'lerinde ise gerçek serinin çok düşük değerlere indiği günlerde tahminin orta seviyede kaldığı dikkat çekmektedir; bu durum söz konusu ATM'lerdeki yüksek SMAPE değerlerinin doğrudan kaynağıdır.

3.4. Hesaplama Süresi ve Başarım Dengesi

Model mimarilerinin başarımı yanında, hesaplama maliyeti de pratik uygulamalar açısından önemli bir karşılaştırma boyutudur. Şekil 14'te model ve girdi yapısı bazında ortalama eğitim süreleri, Şekil 15'te ise eğitim süresi ile SMAPE'nin birlikte dağılımı sunulmaktadır. Bi-LSTM mimarisi, içerdiği çift yönlü katmanların yaklaşık iki katı parametre üretmesi nedeniyle (yaklaşık 89.400 parametre) ortalama 409 saniye ile en yavaş çok değişkenli eğitim süresine sahip olmuştur. GRU mimarisi ise en hafif parametre yapısıyla (yaklaşık 27.800 parametre) ortalama 221 saniyelik en hızlı tek değişkenli eğitim süresini sergilemiştir. Bu durum, Şekil 11'de gözlemlenen GRU'nun en düşük ortalama SMAPE değeriyle birleştiğinde, GRU mimarisinin hem başarım hem hesaplama maliyeti açısından dengeli bir tercih olduğunu ortaya koymaktadır.

Şekil 15'deki saçılım grafiği, ATM zorluğunun mimari ve süre seçiminden bağımsız olarak başarımı belirlediğini açıkça göstermektedir. Noktalar SMAPE ekseninde dört yatay bant halinde kümelenmekte (Big Street ~%20, Mount Road / Christ College ~%30, Airport ~%45, KK Nagar ~%55) ve bu bantlar mimari ya da süre değişimine kayda değer ölçüde tepki vermemektedir. Pratik anlamda bu bulgu, talep yapısı sınırlı oynaklığa sahip ATM'lerde herhangi bir RNN mimarisinin kabul edilebilir başarım üretebileceğini; yüksek oynaklığa sahip ATM'lerde ise mimari/süre artışının başarıma katkısının sınırlı kaldığını işaret etmektedir.

4. Tartışma ve Sonuç

Bu çalışmada elde edilen bulgular, RNN tabanlı derin öğrenme mimarilerinin ATM nakit talep tahmininde etkili sonuçlar üretebildiğini göstermektedir. Dört farklı mimarinin (LSTM, GRU, Bi-LSTM ve CNN-LSTM) performansları incelendiğinde, mimari seçiminden bağımsız olarak modellerin kararlı dönemdeki (2011–2015) temel zamansal örüntüleri benzer düzeyde yakalayabildiği görülmüştür. Ortalama SMAPE değerlerinin %36,63 ile %38,08 gibi dar bir aralıkta toplanması, mimariler arasındaki performans farkının görece sınırlı kaldığını ortaya koymaktadır. Bununla birlikte, GRU mimarisinin en düşük ortalama SMAPE değerini üretmesi, daha hafif ve daha az parametre içeren yapıların ATM nakit talep tahmini gibi uygulamalarda daha karmaşık mimariler kadar başarılı olabileceğini göstermektedir. Özellikle GRU'nun kapı mekanizması sayesinde gerekli bilgiyi seçici biçimde taşıyabilmesi, zaman serisi örüntülerini etkin biçimde öğrenmesine katkı sağlamış olabilir. Buna karşılık, LSTM ve Bi-LSTM gibi daha karmaşık yapıların aynı ölçüde belirgin bir üstünlük sağlayamaması, ATM talep verisinin aşırı karmaşık uzun dönem bağımlılıkları içermediğine işaret etmektedir.

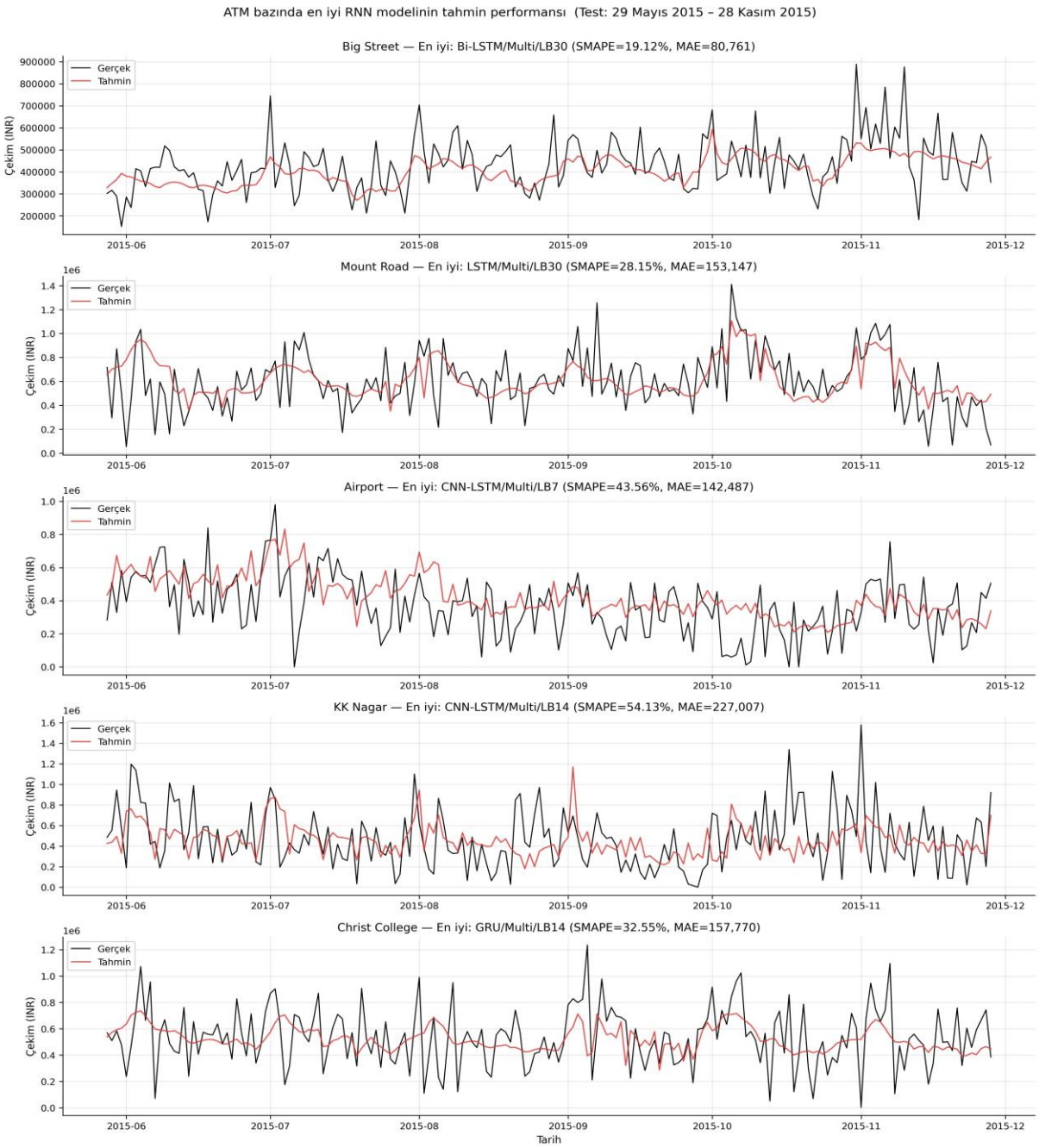
Bi-LSTM mimarisi, çift yönlü katman yapısı sayesinde en yüksek parametre kapasitesine sahip olmasına rağmen ortalama SMAPE değerinde belirgin bir üstünlük sağlamamıştır. Bu bulgu, ATM nakit talep serisinin ileriye ve geriye doğru bağlamsal bilgi eş zamanlı olarak değerlendirildiğinde ek bir katkı sunacak zenginlikte olmadığına işaret etmektedir. Bununla birlikte, Bi-LSTM en düşük SMAPE değerinin elde edildiği Big Street ATM'sinde en iyi bireysel başarımı yakalamıştır. CNN-LSTM mimarisi ise evrişimli katmanları aracılığıyla yerel zamansal örüntüleri ön çıkarma yeteneği ile yüksek talep oynaklığına sahip Airport ve KK Nagar ATM'lerinde en iyi sonuçları üretmiştir; bu durum evrişim tabanlı özellik çıkarımının, düzensiz ve yüksek varyanslı talep yapılarında kısmi bir avantaj sağlayabildiğini düşündürmektedir.

Çalışmanın önemli bulgularından biri de öznitelik mühendisliğinin model başarımına sağladığı katkıdır. Türetilen 27 öznitelikten oluşan çok değişkenli girdi yapısı, dört mimarinin tamamında tek değişkenli yapıya kıyasla daha düşük veya benzer SMAPE değerleri üretmiştir. Daha da önemlisi, beş ATM'nin tamamında en iyi sonuçlar çok değişkenli yapı ile elde edilmiştir. Bu durum, RNN mimarilerinin yalnızca geçmiş talep bilgisi üzerinden değil; gecikmeli istatistikler, hareketli ortalamalar ve takvim/tatil temelli bağlamsal değişkenler aracılığıyla da daha güçlü temsil yeteneği kazandığını göstermektedir. Literatürde derin öğrenme modellerinin ham veriden otomatik örüntü çıkarma yeteneği sıklıkla vurgulanmakla birlikte, bu çalışmanın bulguları uygun öznitelik mühendisliğinin halen kritik bir rol oynadığını ortaya koymaktadır. Özellikle ATM nakit talebi gibi haftalık döngüler ve takvim etkileri içeren operasyonel zaman serilerinde, bağlamsal bilginin modele dahil edilmesi tahmin doğruluğunu anlamlı ölçüde artırabilmektedir.

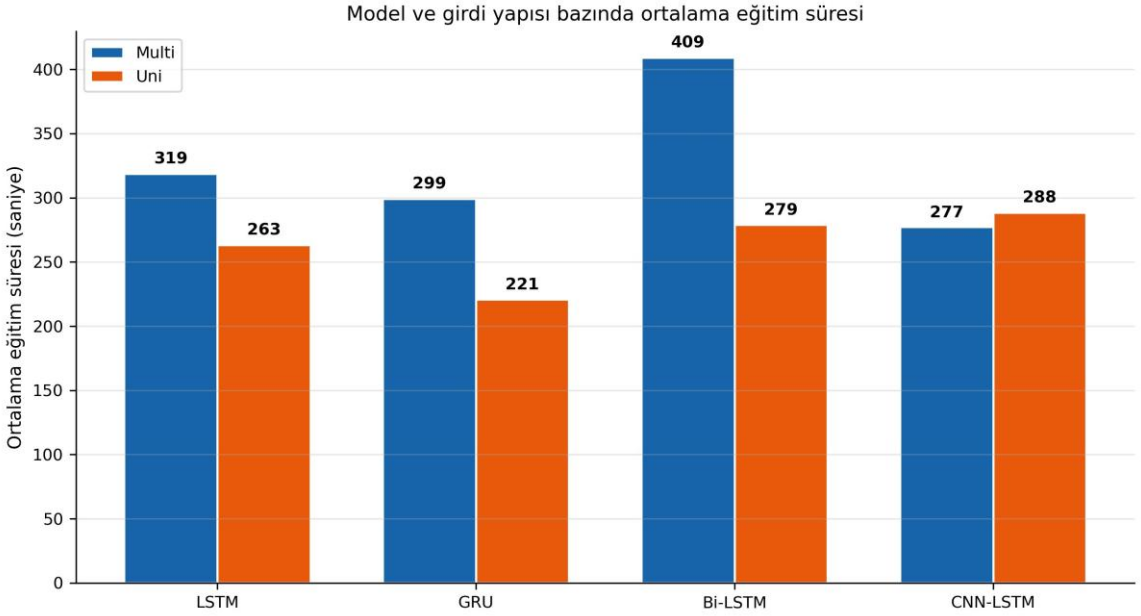
Araştırmanın en dikkat çekici sonuçlarından biri ise ATM'ler arasındaki belirgin başarım heterojenliğidir. Elde edilen sonuçlar, ATM bazlı talep yapısının model başarımı üzerinde mimari seçiminden daha güçlü bir etkiye sahip olduğunu göstermektedir. Örneğin, Big Street ATM'sinde en iyi konfigürasyon %19,12 SMAPE üretirken, KK Nagar ATM'sinde aynı metrik %54,13 seviyesine ulaşmıştır. Bu fark, modeller arasındaki ortalama performans farkından çok daha yüksektir ve

ATM'lerin talep davranışlarının tahmin sürecindeki belirleyici rolünü açıkça ortaya koymaktadır. Keşifsel veri analizinde de görüldüğü üzere, KK Nagar ve Airport ATM'leri yüksek oynaklık ve sık düşük talepli günler içermektedir. Bu yapı, yalnızca model öğrenmesini zorlaştırmakla kalmamış, aynı zamanda kullanılan SMAPE metriğinin bazı sınırlılıklarını da görünür hale getirmiştir.

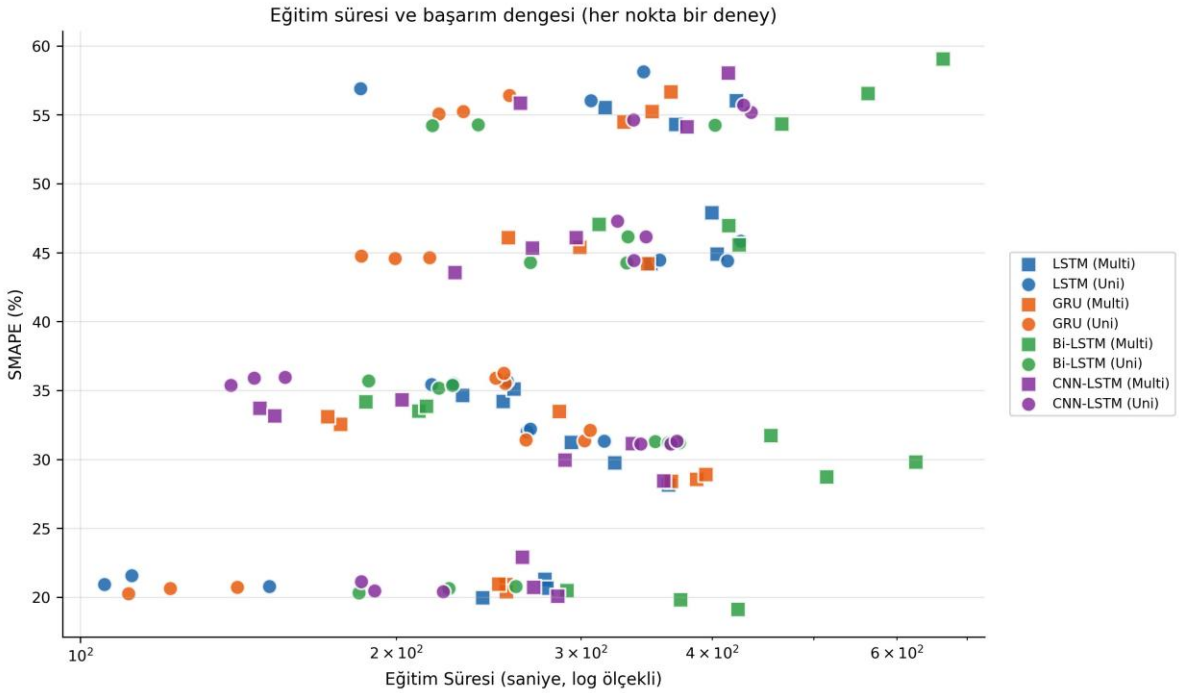
SMAPE metriğinin paydasının gerçek ve tahmin değerlerinin toplamına dayanması nedeniyle, gerçek değerin çok düşük olduğu günlerde mutlak hata görece makul olsa bile bağıl hata yüzdesi aşırı yükselmektedir. Dolayısıyla düşük çekim hacimli günlerin yoğun olduğu ATM'lerde, operasyonel açıdan kabul edilebilir sayılabilecek tahmin sapmaları dahi oldukça yüksek SMAPE değerleri üretebilmektedir. Bu nedenle KK Nagar ve Airport ATM'lerinde gözlenen yüksek SMAPE değerlerinin yalnızca model yetersizliğinden değil, aynı zamanda metriğin matematiksel yapısından da kaynaklandığı değerlendirilmektedir. Nitekim MAE sonuçlarının SMAPE sıralamasıyla bire bir örtüşmemesi, SMAPE'nin özellikle düşük hacimli ve oynak talep yapılarında yanıltıcı yorumlara yol açabileceğini göstermektedir. Bu bulgu, ATM nakit talep tahmini çalışmalarında performans değerlendirmesinin tek bir hata metriği üzerinden yapılmaması gerektiğini ortaya koymaktadır.



Şekil 13. ATM bazında en iyi RNN modelinin tahmin performansı.



Şekil 14. Model ve girdi yapısı bazında ortalama eğitim süresi (saniye).



Şekil 15. Eğitim süresi (log ölçekli) ve başarım dengesi

Çalışmanın metodolojik tasarımı sırasında gerçekleştirilen ön denemeler de önemli çıkarımlar sunmuştur. Veri setinin tamamının (2011–2017) kullanıldığı ilk denemelerde modellerin oldukça yüksek SMAPE değerleri ürettiği gözlemlenmiştir. Özellikle 2015 sonu ile 2017 başı arasında birçok ATM'de eşzamanlı biçimde görülen sıfıra yakın çekim yoğunlaşmaları, veri setinde yapısal bir kırılma olduğunu göstermiştir. Bu durumun, modellerin temel zamansal örüntüleri öğrenme kapasitesini olumsuz etkilediği değerlendirilmiş ve analizlerin yalnızca kararlı dönemle sınırlandırılması metodolojik bir tercih değil, aynı zamanda bir zorunluluk haline gelmiştir. Dolayısıyla çalışmanın bulguları, yapısal kırılma sonrası dönemi kapsamamaktadır ve sonuçlar bu çerçevede değerlendirilmelidir.

Bunun yanında çalışmanın bazı kısıtları bulunmaktadır. Öncelikle veri setinin yalnızca beş ATM'yi içermesi, bulguların daha geniş ATM ağlarına genellenebilirliğini sınırlamaktadır. Ayrıca kullanılan veri setinin hazır ve anonimleştirilmiş bir kaynak olması nedeniyle ATM'lerin tam konumu, hizmet verdiği bölge ve müşteri profili gibi operasyonel bilgilere erişilememiştir. Bu nedenle hava durumu, bölgesel ekonomik göstergeler, maaş ödeme dönemleri veya özel etkinlikler gibi dışsal değişkenler modele dahil edilememiştir. Özellikle yüksek oynaklığa sahip ATM'lerde bu tür dışsal değişkenlerin modele

eklenmesinin tahmin başarımını artırabileceği değerlendirilmektedir. Ancak bu tür bir yaklaşım, ATM konum bilgileri ve operasyonel bağlam içeren daha kapsamlı veri setlerinin oluşturulmasını gerektirmektedir.

Sonuç olarak, bu çalışmanın literatüre yaptığı katkılar aşağıdaki gibi sıralanabilir:

- Aynı veri seti üzerinde dört farklı RNN mimarisi (LSTM, GRU, Bi-LSTM ve CNN-LSTM), tek değişkenli ve çok değişkenli girdi yapıları ile üç farklı geri bakış penceresi altında sistematik olarak karşılaştırılmıştır.
- Veri setinde birden fazla ATM'de eşzamanlı gözlenen sıfıra yakın çekim yoğunlaşmaları veri temelli bir kriterle tespit edilmiş; analiz dönemi bu bulguya dayalı olarak sınırlandırılarak yapısal kırılmanın modelleme sürecine olumsuz etkisi engellenmiştir.
- Eksik takvim günleri, kayıtlı çekim değerlerine hiçbir müdahalede bulunulmadan yalnızca hiç kaydedilmemiş günlere uygulanan imputation yöntemiyle tamamlanmış; bu yaklaşım gerçek gözlemlerin bütünlüğünü koruyarak modellerin sağlıklı eğitim almasını sağlamıştır.
- Gecikmeli istatistikler, hareketli ortalamalar ve takvim/tatil temelli 27 öznitelikten oluşan çok değişkenli girdi yapısının RNN mimarilerine katkısı, tek değişkenli yapıyla karşılaştırmalı olarak gösterilmiş ve beş ATM'nin tümünde en iyi konfigürasyonun çok değişkenli yapıda gerçekleştiği ortaya konmuştur.
- Toplam 120 deneyden (4 mimari × 2 girdi yapısı × 3 geri bakış penceresi × 5 ATM) oluşan kapsamlı bir deneysel tasarımla, mimari, girdi yapısı ve geri bakış penceresi seçimlerinin başarım üzerindeki etkileri çok boyutlu olarak değerlendirilmiştir.
- İleri yönlü doğrulama yaklaşımı ile bilgi sızıntısı yapısal olarak engellenmiş; modellerin gerçek dünya tahmin senaryosuna uygun biçimde değerlendirilmesi sağlanmıştır.

Katkı Oranı Beyanı

Yazarların katkı yüzdeleri aşağıda verilmiştir. Yazarlar makaleyi incelemiş ve onaylamıştır.

	H.Ş.	T.I.	B.T.Ş.
K	40	30	30
T	40	30	30
Y	40	30	30
VTI	40	30	30
VAY	40	30	30
KT	40	30	30
YZ	40	30	30
KI	40	30	30
GR	40	30	30
PY	40	30	30
FA	40	30	30

K= kavram, T= tasarım, Y= yönetim, VTI= veri toplama ve/veya işleme, VAY= veri analizi ve/veya yorumlama, KT= kaynak tarama, YZ= yazım, KI= kritik inceleme, GR= gönderim ve revizyon, PY= proje yönetimi, FA= fon alımı.

Çatışma Beyanı

Yazarlar bu çalışmada hiçbir çıkar ilişkisi olmadığını beyan etmektedirler.

Etik Onay Beyanı

Bu araştırmada hayvanlar ve insanlar üzerinde herhangi bir çalışma yapılmadığı için etik kurul onayı alınmamıştır.

Destek ve Teşekkür Beyanı

Bu çalışma, Atatürk Üniversitesi Bilimsel Araştırma Projeleri Koordinasyon Birimi tarafından 15929 numaralı yüksek lisans projesi ile desteklenmiştir.

Kaynaklar

Andrawis, R. R., Atiya, A. F., & El-Shishiny, H. (2011). Forecast combinations of computational intelligence and linear models for the NN5 time series forecasting competition. *International Journal of Forecasting*, *27*(3), 672–688. https://doi.org/10.1016/j.ijforecast.2010.09.005

Berus, Y., & Yakut, Y. B. (2024). Derin öğrenme (1D-CNN, RNN, LSTM, BiLSTM) ile enerji tüketim tahmini: Diyarbakır AVM örneği. *Dicle Üniversitesi Mühendislik Fakültesi Mühendislik Dergisi*, *15*(2), 311–322. https://doi.org/10.24012/dumf.1415055

Bhandari, R., & Gill, J. (2016). An artificial intelligence ATM forecasting system for hybrid neural networks. *International Journal of Computer Applications*, *133*(3), 13–16. https://doi.org/10.5120/ijca2016907863

Cedolin, M., Orhan, D., & Genevois, M. (2024). Statistical and artificial intelligence based forecasting approaches for cash demand problem of automated teller machines. *Academic Platform Journal of Engineering and Smart Systems*, *12*(1), 21–27. https://doi.org/10.21541/apjess.1360151

Chakladar, D. D., Dey, S., Roy, P. P., & Dogra, D. P. (2020). EEG-based mental workload estimation using deep BLSTM-LSTM network and evolutionary algorithm. *Biomedical Signal*

Processing and Control, *60*, Article 101989. https://doi.org/10.1016/j.bspc.2020.101989

Chen, Q., & Huang, G. (2021). A novel dual attention-based BLSTM with hybrid features in speech emotion recognition. *Engineering Applications of Artificial Intelligence*, *102*, Article 104277. https://doi.org/10.1016/j.engappai.2021.104277

Cho, K., van Merriënboer, B., Gulçehre, Ç., Bahdanau, D., Bougares, F., Schwenk, H., & Bengio, Y. (2014). Learning phrase representations using RNN encoder–decoder for statistical machine translation. In *Proceedings of the 2014 Conference on Empirical Methods in Natural Language Processing (EMNLP)* (pp. 1724–1734). Association for Computational Linguistics. https://doi.org/10.3115/v1/D14-1179

Fallahtafti, A., Aghaaminiha, M., Akbarghanadian, S., & Weckman, G. R. (2022). Forecasting ATM cash demand before and during the COVID-19 pandemic using an extensive evaluation of statistical and machine learning models. *SN Computer Science*, *3*(2), Article 164. https://doi.org/10.1007/s42979-021-01000-0

Fareed, S. (2020). *Data set of ATM transaction of XYZ bank* [Data set]. Kaggle. Retrieved September 10, 2025, from https://www.kaggle.com/datasets/saadfareed/data-set-of-atm-transaction-of-xyz-bank

Gençalp, E. (2020). *ATM demand prediction with machine learning methods* (Master's thesis, Galatasaray University). National Thesis Center of the Council of Higher Education (YÖK).

Gu, J., Wang, Z., Kuen, J., Ma, L., Shahroudy, A., Shuai, B., & Chen, T. (2018). Recent advances in convolutional neural networks. *Pattern Recognition*, *77*, 354–377. https://doi.org/10.1016/j.patcog.2017.10.013

Jadwal, P. K., Jain, S., Gupta, U., & Khanna, P. (2017). K-means clustering with neural networks for ATM cash repository prediction. In S. Satapathy, Y. V. Joshi, & N. Modi (Eds.), *Information and Communication Technology for Intelligent Systems (ICTIS 2017) - Volume 2* (pp. 588–596). Springer. https://doi.org/10.1007/978-3-319-63645-0_70

Javanmard, M. (2016). An approach to improve forecasting cash demand at ATMs using fuzzy logic. *International Journal of Computer Science and Information Security*, *14*(11), 404–411.

Hochreiter, S., & Schmidhuber, J. (1996). LSTM can solve hard long time lag problems. *Advances in neural information processing systems*, 9.

Kamini, V., Ravi, V., & Kumar, D. N. (2014). Chaotic time series analysis with neural networks to forecast cash demand in ATMs. In *2014 IEEE International Conference on Computational Intelligence and Computing Research* (pp. 1–5). IEEE. https://doi.org/10.1109/ICCIC.2014.7238495

Kaysal, K., Yurttakal, A. H., & Hocaoğlu, F. O. (2023). Hibrit derin öğrenme yöntemi kullanılarak hiperparametre optimizasyonu ile yenilenebilir elektrik enerjisi tahmini. *Niğde Ömer Halisdemir Üniversitesi Mühendislik Bilimleri Dergisi*, *12*(3), 770–777. https://doi.org/10.28948/ngumuh.1263782

Kılınç, H. Ç., & Öztürk, Y. (2022). Hibrit gri kurt optimizasyonu ile kapılı tekrarlayan birim modeli kullanılarak günlük akım tahmini. *Avrupa Bilim ve Teknoloji Dergisi*, (35), 259–267. https://doi.org/10.31590/ejosat.1062777

LeCun, Y. A., & Bengio, Y. O. (1998). Convolutional networks for images, speech, and time series. In M. A. Arbib (Ed.), *The Handbook of Brain Theory and Neural Networks* (pp. 255–258). MIT Press.

Nemeshaev, S., & Tsyganov, A. (2016). Model of the forecasting cash withdrawals in the ATM network. *Procedia Computer Science*, *88*, 463–468. https://doi.org/10.1016/j.procs.2016.07.465

Poorzaker Arabani, S., & Ebrahimpour Komleh, H. (2019). The improvement of forecasting ATM cash demand of Iran banking network using convolutional neural network. *Arabian Journal for Science and Engineering*, *44*(4), 3733–3743. https://doi.org/10.1007/s13369-018-3647-7

Rafi, M., Wahab, M. T., Khan, M. B., & Raza, H. (2020). ATM cash prediction using time series approach. In *2020 3rd International Conference on Computing, Mathematics and Engineering Technologies (iCoMET)* (pp. 1–6). IEEE. https://doi.org/10.1109/iCoMET48628.2020.9103780

Rostamian, A., & O'Hara, J. G. (2022). Event prediction within directional change framework using a CNN-LSTM model. *Neural Computing and Applications*, *34*(20), 17193–17205. https://doi.org/10.1007/s00521-022-07687-3

Şanlıalp, İ., & Yıldız, M. (2025). Sistem çağrısı verilerinde derin öğrenme mimarileri kullanılarak anomali tespitinin değerlendirilmesi: Performans ve enerji verimliliği. *Süleyman Demirel Üniversitesi Fen Bilimleri Enstitüsü Dergisi*, *29*(2), 388–396. https://doi.org/10.19113/sdufenbed.1655066

Sarveswararao, V., Ravi, V., & Vivek, Y. (2023). ATM cash demand forecasting in an Indian bank with chaos and hybrid deep learning networks. *Expert Systems with Applications*, *211*, Article 118645. https://doi.org/10.1016/j.eswa.2022.118645

Teddy, S. D., & Ng, S. K. (2011). Forecasting ATM cash demands using a local learning model of cerebellar associative memory network. *International Journal of Forecasting*, *27*(3), 760–776. https://doi.org/10.1016/j.ijforecast.2010.02.013

Tosun, M. F., & Şentürk, A. (2023). Kasislerin yakıt tüketimine etkisinin RNN, LSTM, GRU tekrarlayan derin öğrenme algoritmaları ile tespiti. *Journal of Intelligent Systems: Theory and Applications*, *6*(1), 12–23. https://doi.org/10.38016/jista.1141359

Tsujimoto, T., Takahashi, Y., Takeuchi, S., & Maeda, Y. (2016). RNN with Russell's circumplex model for emotion estimation and emotional gesture generation. In *2016 IEEE Congress on Evolutionary Computation (CEC)* (pp. 1427–1431). IEEE. https://doi.org/10.1109/CEC.2016.7744023

Venkatesh, K., Ravi, V., Prinzie, A., & Van den Poel, D. (2014). Cash demand forecasting in ATMs by clustering and neural networks. *European Journal of Operational Research*, *232*(2), 383–392. https://doi.org/10.1016/j.ejor.2013.07.027

Zha, W., Liu, Y., Wan, Y., Luo, R., Li, D., Yang, S., & Xu, Y. (2022). Forecasting monthly gas field production based on the CNN-LSTM model. *Energy*, *260*, Article 124889. https://doi.org/10.1016/j.energy.2022.124889

Black Sea Journal of Engineering and Science
doi: 10.34248/bsengineering.1964431

Open Access Journal
e-ISSN: 2619 – 8991

Research Article
Volume 9 - Issue 5: 2175-2187 / September 2026

MITOCHONDRIAL DYSFUNCTION ACROSS SYNOVIAL AND PERIPHERAL COMPARTMENTS IN RHEUMATOID ARTHRITIS: A MULTI-TISSUE TRANSCRIPTOMIC INTEGRATION OF PBMC, SYNOVIAL BIOPSY AND WHOLE BLOOD

Sevinç AKÇAY[1]*

[1]*Kırşehir Ahi Evran University, Faculty of Science and Art, Department of Molecular Biology and Genetics, 40100, Kırşehir, Türkiye*

Abstract: Rheumatoid arthritis (RA) is a chronic autoimmune disease with synovial inflammation and systemic immune alterations. Mitochondrial dysfunction has been implicated in RA pathogenesis, but its tissue-specific and shared molecular signatures remain poorly characterized. We performed an integrative transcriptomic analysis of three public datasets: GSE17755 (PBMC), GSE89408 (synovial biopsy), and GSE93272 (whole blood). Differentially expressed genes (DEGs) were identified ($P<0.05$, $|log2FC| \geq 1$) and intersected with MitoCarta 3.0 to obtain mitochondria-related DEGs (mito-DEGs). Protein-protein interaction networks, hub genes (identified using the MCC algorithm), functional enrichment (GO/KEGG), and regulatory networks (miRNA-TF-mRNA) were constructed. PBMC, synovial biopsy, and whole blood yielded 37, 220, and 119 mito-DEGs, respectively. Only one gene (*AKAP1*) was common across all three tissues. Hub genes predominantly encoded subunits of mitochondrial respiratory chain complexes (NDUF family and UQCR genes). Enriched pathways included oxidative phosphorylation, thermogenesis, and neurodegeneration-related pathways. Regulatory analysis identified FOXC1, GATA2, and hsa-miR-16-5p as key transcriptional and post-transcriptional regulators. Mitochondrial dysfunction in RA is tissue-specific, but converges on the dysregulation of oxidative phosphorylation. *AKAP1* emerges as a potential systemic mitochondrial biomarker, pending validation in independent cohorts. These findings provide a multi-tissue resource for targeting mitochondrial pathways in RA.

Keywords: Rheumatoid arthritis, Mitochondrial dysfunction, Transcriptomics, Oxidative phosphorylation, Biomarker

***Corresponding author:** Kırşehir University, Faculty of Science and Art, Department of Molecular Biology and Genetics, 40100, Kırşehir, Türkiye
E mail: sevinc.akcay@ahievran.edu.tr (S. AKÇAY)
Sevinç AKÇAY https://orcid.org/0000-0003-2961-3970

Received: June 05, 2026
Accepted: July 17, 2026
Published: September 15, 2026

Cite as: Akçay, S. (2026). Mitochondrial dysfunction across synovial and peripheral compartments in rheumatoid arthritis: a multi-tissue transcriptomic integration of PBMC, synovial biopsy and whole blood. *Black Sea Journal of Engineering and Science,* 9(5), 2175-2187.

1. Introduction

Rheumatoid arthritis (RA) is a long-term systemic autoimmune condition that involves sustained synovial inflammation, advancing joint erosion, and numerous non-articular symptoms (Smolen et al., 2016). The condition affects nearly 0.5–1% of the world's population and constitutes a primary cause of disability as well as lower quality of life (Finckh et al., 2022; Uke et al., 2025). Though the definitive etiology of RA remains undetermined, it is widely recognized that a multifaceted interaction among genetic susceptibility, environmental agents, and immune dysregulation underlies both the initiation and progression of the disease (Alivernini et al., 2022).

A growing collection of recent evidence has revealed that cellular metabolism is a key regulator of both immune responses and inflammatory mechanisms (Rahmati et al., 2024). Among metabolic organelles, mitochondria have emerged as key regulators of immune cell activation, oxidative stress, and inflammatory signaling pathways (Gao et al., 2024). Beyond their classical function in ATP production, mitochondria participate in reactive oxygen species (ROS) generation, apoptosis regulation, and innate immune signaling (West and Shadel, 2017).

Several autoimmune and inflammatory disorders, including RA, have been associated with abnormalities in mitochondrial function (Huang et al., 2026). In RA specifically, altered mitochondrial dynamics, oxidative phosphorylation imbalance, increased ROS production, and mitochondrial DNA damage have all been reported in both synovial tissue and circulating immune cells (Fearon et al., 2016; Ma et al., 2022). A recent study demonstrated that peripheral blood mitochondrial DNA gene variation and methylation levels are significantly associated with RA pathogenesis, highlighting the systemic nature of mitochondrial dysfunction in this disease (Huang et al., 2026). Furthermore, mitochondrial dysfunction in RA has been linked to the differentiation and activation of pro-inflammatory T cell subsets, particularly T_H17 cells, which play a central role in disease pathogenesis (Weyand and Goronzy, 2017).

This work is licensed (CC BY-NC 4.0) under Creative Commons Attribution 4.0 International License

The pathogenesis of RA involves multiple tissues and cellular compartments, including synovial tissue, circulating immune cells (PBMCs), and peripheral blood components (Smolen et al., 2018). However, most transcriptomic studies to date have profiled only a single tissue type at a time, which limits the ability to distinguish molecular changes that are truly systemic from those confined to the local inflammatory site (Smiljanovic et al., 2020; Binvignat et al., 2024; Bellocchi et al., 2025). This is also true of studies specifically addressing mitochondrial gene signatures in RA: for example, a 2025 study investigating mitochondrial apoptosis-related genes (MARGs) identified hub genes such as *MRPS10* and *TUFM* and demonstrated their diagnostic potential through ROC analysis, with transcription factors such as YY1 and FOXO3 emerging as regulators but did so within a single tissue compartment (Gao et al., 2025). Similarly, work on the MTHFD2-CKMT1 axis established a role for oxidative phosphorylation in RA-associated osteoclastogenesis and bone loss, again within a single experimental system (Li et al., 2025). Because mitochondrial alterations in these earlier reports were characterized in isolation, it remains unclear which mitochondrial changes are shared across the synovial, PBMC, and whole-blood compartments (and are therefore more likely to reflect systemic RA pathophysiology and represent viable blood-based biomarkers), and which are tissue-restricted responses to the local inflammatory microenvironment of the joint. Integrative, multi-tissue analysis is needed to resolve this distinction and to provide a more comprehensive picture of the disease-associated molecular networks underlying RA (Tariq et al., 2025). To date, however, no study has systematically compared mitochondrial dysfunction across synovial, PBMC, and whole blood compartments within a single integrative framework, leaving the shared and tissue-specific mitochondrial architecture of RA undefined. Critically, this gap concerns the cross-compartment comparability of mitochondrial changes — that is, which alterations are shared versus tissue-restricted — rather than whether mitochondrial dysfunction occurs in RA at all, a point already well established in the literature.

Here, we resolve this distinction by conducting an integrative transcriptomic analysis of publicly available gene expression datasets derived from PBMCs, synovial biopsy tissue, and whole blood from patients with RA. We identified differentially expressed genes and then used the MitoCarta 3.0 database to pinpoint those related to mitochondrial function. Subsequent analyses, including functional enrichment, protein–protein interaction network analysis, and miRNA–TF–mRNA regulatory network analysis, were performed to interpret the biological significance and regulatory landscape of mitochondrial gene signatures across tissues. By adopting this multi-tissue strategy, we aim to elucidate the role of mitochondrial dysfunction in RA and to identify potential mitochondrial biomarkers that may improve our understanding of disease mechanisms and inform future treatment strategies.

2. Materials and Methods

2.1. Data Acquisition from GEO Database

Publicly available gene expression datasets relevant to RA were downloaded from the Gene Expression Omnibus (GEO) repository. Three independent transcriptomic datasets representing distinct biological compartments involved in RA pathogenesis were included in this study: GSE17755 (peripheral blood mononuclear cells, PBMC), GSE89408 (synovial biopsy tissue), and GSE93272 (whole blood).

We analyzed datasets generated by three different expression-profiling platforms. GSE17755 was processed on GPL1291 (Hitachisoft AceGene Human Oligo Chip 30K, two-color microarray), GSE93272 on GPL570 (Affymetrix Human Genome U133 Plus 2.0 Array, microarray), and GSE89408 on GPL11154 (Illumina HiSeq 2000, RNA sequencing), respectively. The PBMC dataset (GSE17755) consisted of 112 RA cases and 45 healthy individuals. The synovial biopsy dataset (GSE89408) included 152 RA samples and 28 healthy-control samples. The whole blood dataset (GSE93272) included 245 RA samples and 30 healthy controls. Expression profiling was performed by microarrays for GSE17755 and GSE93272 and by RNA sequencing for GSE89408. A summary of dataset characteristics is provided in Table 1.

Table 1. Summary of GEO dataset characteristics

GEO Accession	GEO Platform (GPL)	Control (n)	Case (n)	Sample Type	Experimental Design
GSE17755	GPL1291	45	112	PBMC	Expression profiling by array
GSE89408	GPL11154	28	152	Synovial biopsy	Expression profiling by throughput sequencing
GSE93272	GPL570	30	245	Whole blood	Expression profiling by array

GEO= gene expression omnibus, PBMC= peripheral blood mononuclear cells

2.2. Differential Gene Expression Analysis

Differential gene expression analysis was carried out independently for each dataset using the GEO2R web-based platform (https://www.ncbi.nlm.nih.gov/geo/geo2r/; accessed April/2026). GEO2R performs differential expression testing directly on the processed, submitter-normalized expression matrices deposited in GEO; no additional re-normalization was performed. For the two microarray datasets, probe-to-gene mapping was based on the platform-specific annotation files (GPL1291 for GSE17755; GPL570 for GSE93272), which GEO2R automatically applies to assign gene symbols to each probe or probeset. For the RNA-seq dataset (GSE89408, GPL11154), expression values were provided as gene-level RSEM counts, so a probe-to-gene mapping step was unnecessary; GEO2R applied its RNA-seq differential expression workflow (voom-transformed counts with limma) to this dataset rather than the array-based linear model used for the two microarray datasets.

For each dataset (GSE17755, GSE89408, and GSE93272), samples were divided into two groups: RA patients and healthy controls.

The Benjamini–Hochberg false discovery rate (FDR) correction method was employed to calculate adjusted p-values, thereby controlling for multiple hypothesis testing when determining statistical significance. Only genes with an adjusted p-value < 0.05 were deemed statistically significant. A threshold of $|\log2FC| \geq 1$ (absolute log2 fold change) was imposed to ensure biological relevance and consistency across datasets, representing a two-fold or greater change in gene expression. For genes represented by multiple significant probes or probe sets, the probe with the lowest adjusted p-value was retained to represent that gene in downstream mito-DEG analysis. The resulting DEG lists for each dataset were subsequently used to identify mitochondrial gene signatures.

2.3. Identification of Mitochondria-Related Differentially Expressed Genes

To pinpoint mitochondrial genes involved in RA, we compared the significant DEG lists from each dataset against the MitoCarta 3.0 database (accessed April/ 2026). The Broad Institute compiled MitoCarta 3.0, a curated resource comprising 1,136 genes that code for mitochondrial proteins. This database also includes details regarding the sub-mitochondrial locations of these proteins and the biological pathways with which they are associated (Rath et al., 2021).

The intersection of the DEG lists with the MitoCarta 3.0 database was determined using standard set operations. Genes overlapping between the two sets were defined as mitochondria-related differentially expressed genes (mito-DEGs). To evaluate shared and tissue-specific mitochondrial alterations in RA, mito-DEGs identified from PBMC (GSE17755), synovial biopsy (GSE89408), and whole blood (GSE93272) datasets were compared using Venn diagram analysis. Venn diagrams were produced using Venny 2.1 (https://bioinfogp.cnb.csic.es/tools/venny/; accessed April/2026), an online resource that supports the interactive comparison of up to four gene lists.

2.4. Construction of PPI Networks and Extraction of Hub Genes

To examine functional interactions between the mito-DEG we had identified, protein-protein interaction (PPI) networks were generated using the STRING database (version 12.0; accessed April/2026) (Szklarczyk et al., 2023). A minimum confidence score of 0.700 was required for interactions to be considered high-confidence, and only those with a combined score of ≥ 0.700 were retained for network construction. Following export, the interaction networks were transferred into Cytoscape software (version 3.10.1; accessed April/2026) for visualization and further topological analysis (Shannon et al., 2003). The identification of key hub genes within each network was accomplished using the Maximal Clique Centrality (MCC) algorithm as implemented in the cytoHubba plugin (v0.1; accessed April/2026) of Cytoscape (Chin et al., 2014). This algorithm evaluates genes according to their topological significance, giving preference to nodes that are part of many maximal cliques. Genes with the highest MCC scores were selected as hub genes for subsequent functional enrichment and regulatory network analyses.

2.5. GO and KEGG Pathways

The top 10 hub genes identified separately in PBMCs, synovial biopsies, and whole-blood tissues were subjected to functional annotation and pathway enrichment analyses using version 6.8 of the DAVID Bioinformatics Resources (accessed April/2026). DAVID is a well-established web-based platform that offers a broad range of functional annotation tools designed for analyzing large-scale gene lists (Sherman et al., 2022). We performed Gene Ontology (GO) enrichment analysis, prioritizing the Biological Process (BP) category, to explore the biological functions potentially associated with alterations in mitochondrial genes. In addition, we examined the Cellular Component (CC) and Molecular Function (MF) categories to generate a comprehensive functional profile of the hub genes (Ashburner et al., 2000).

To identify signaling and metabolic pathways linked to the mitochondrial hub genes, we conducted KEGG pathway enrichment analysis (Kanehisa et al., 2023). The Benjamini–Hochberg FDR method was applied for multiple testing correction, with an adjusted p-value < 0.05 considered significant. Bubble plots were generated to visualize the data; bubble size corresponds to the number of genes in each pathway, and color intensity reflects the significance level (log10 p-value).

2.6. Construction of Regulatory Networks

TF–gene and miRNA–gene interaction networks were constructed to explore the regulation of candidate hub genes. JASPAR (11th release, 2026), a curated open-access database of transcription factor binding profiles

across multiple species, served as the source for TF–gene interactions (Ovek Baydar et al., 2026; accessed May/2026). miRNA–gene interactions were retrieved from miRTarBase (version 9.0), a manually curated database that collects experimentally validated miRNA-target interactions (Huang et al., 2020; accessed May/2026).

NetworkAnalyst (a web-based tool for gene expression profiling and network visualization, version 3.2 as accessed in May/2026) was used to construct and visualize our networks (Xia et al., 2015; Zhou et al., 2019). We first created separate miRNA–mRNA and TF–mRNA networks, then merged them into a combined miRNA–TF–mRNA network to reveal the multilayered regulatory architecture controlling mitochondrial gene expression.

Key regulatory components within these networks were identified through topological analysis using metrics such as node degree (number of connections a node has) and betweenness centrality (a measure of a node's importance in connecting different parts of the network). These metrics were used to evaluate the relative importance of individual nodes (miRNAs, TFs, and genes) within the network. The top-ranked regulatory nodes were considered potential master regulators of mitochondrial dysfunction in RA.

3. Results

3.1. Identification of Differentially Expressed Genes in RA across Multiple Tissues

Differential gene expression analyses were performed on the PBMC (GSE17755), synovial biopsy (GSE89408), and whole blood (GSE93272) datasets using the GEO2R platform to investigate transcriptional alterations associated with RA.

PBMC analysis revealed 593 DEGs (268 up, 325 down) in RA samples compared to healthy controls. In the synovial biopsy dataset, a markedly larger number of transcriptional alterations were observed, with 9,161 DEGs, including 4,216 upregulated and 4,945 downregulated genes. Similarly, analysis of the whole blood dataset identified 1,878 DEGs, consisting of 1,112 upregulated and 766 downregulated genes in RA patients relative to controls.

3.2. Discovery of Mitochondria-Connected Differentially Expressed Genes

To specifically investigate mitochondrial involvement in RA, the identified DEGs from each dataset were intersected with the MitoCarta 3.0 database, which catalogues genes encoding mitochondrial proteins. This filtering approach identified 37 mitochondria-related DEGs (mito-DEGs) in the PBMC dataset, 220 mito-DEGs in the synovial biopsy dataset, and 119 mito-DEGs in the whole blood dataset.

Comparative analysis across tissues using Venn diagrams (Venny 2.1) was performed to identify shared and tissue-specific mitochondrial gene expression patterns. As shown in Figure 1, unique mito-DEGs were observed in PBMCs (22 genes), synovial biopsies (181 genes), and whole blood samples (82 genes). Shared genes were identified between PBMC and synovial biopsy (8 genes), PBMC and whole blood (6 genes), and synovial biopsy and whole blood (30 genes). Remarkably, only one gene (*AKAP1*) was found to be common across all three tissues in this dataset collection. The specific shared genes between PBMC and whole blood included *NDUFS4, PHB2, ABCB7, IVD, MRPS10, and SLC25A6;* between synovial biopsy and PBMC included *SOD2, PDK2, PRODH, GLRX5, AMT, ALAS2, MAOA, and BCL2A1;* and between synovial biopsy and whole blood included 30 genes *(SDHB, VDAC1, MRPL13, NDUFA5, MRPL3, COX7A2, TMEM126A, MRPL47, COQ2, PRELID3B, NDUFB3, MTHFD2, MPV17L, RH0T2, LYPLA1, MACR0D1, KMO, NDUFB4, TOMM5, ACSS1, TMEM126B, DBI, CMPK2, IFI27, FASTK, PMAIP1, CASP9, MCL1, BAD,* and *CASP3).*

3.3. Protein–Protein Interaction Network and Hub Gene Analysis

Hub genes were identified in mito-DEG PPI networks using the MCC algorithm in Cytoscape. In the PBMC dataset, the top 10 hub genes identified in the PPI network included *NDUFA10, ALAS2, TUFM, ABCB7, MRPS10, NDUFS4, SLC25A24, PHB2, HSPA9* and *NDUFV1*. In the synovial biopsy dataset, the top 10 hub gene analysis identified *UQCRQ, NDUFA5, NDUFA4, NDUFB4, NDUFB3, NDUFA12, UQCR10, NDUFV2, COX5A* and *NDUFS7* as highly connected nodes within the network. In the whole blood dataset, the PPI network analysis revealed the top 10 hub genes, including *NDUFA11*, *UQCRFS1*, *NDUFB3*, *NDUFS6*, *NDUFS4*, *UQCRC1*, *NDUFB4*, *COX7A2*, *NDUFS2* and *NDUFA5*. The PPI networks of the identified hub genes for PBMC, synovial biopsy, and whole blood datasets are presented in Figure 2.

3.4. GO and KEGG Pathways

GO and KEGG pathway enrichment analyses for the mitochondrial hub genes identified in each dataset were carried out using DAVID Bioinformatics Resources (version 6.8). The enrichment results are presented as bubble plots in Figure 3.

PBMC dataset: Enriched BP terms included "mitochondrial electron transport from NADH to ubiquinone", "proton transmembrane transport", "proton motive force-driven mitochondrial ATP synthesis", "aerobic respiration", and "iron-sulfur cluster assembly". CC terms included "mitochondrial inner membrane", "mitochondrial matrix", and "respiratory chain complex I". MF categories included "NADH dehydrogenase(ubiquinone)activity and oxidoreductase activity". KEGG pathway enrichment included "oxidative phosphorylation", "thermogenesis", "chemical carcinogenesis-reactive oxygen species pathways", and "pathways of neurodegeneration-multiple diseases" (Figure 3A).

Synovial biopsy dataset: Enriched BP terms included "proton transmembrane transport", "mitochondrial electron transport from NADH to ubiquinone", "aerobic respiration", "mitochondrial electron transport from

ubiquinol to cytochrome c", and "mitochondrial respiratory chain complex I assembly". CC terms included "mitochondrial inner membrane", "respiratory chain complex I", and "mitochondrion". MF terms included "NADH dehydrogenase (ubiquinone) activity", "oxidoreductase activity", and "iron-sulfur cluster binding". KEGG pathways included "oxidative phosphorylation", "non-alcoholic fatty liver disease", "thermogenesis" and "chemical carcinogenesis-reactive oxygen species" (Figure 3B).

Whole blood dataset: Enriched BP terms included "aerobic respiration", "proton transmembrane transport", "mitochondrial electron transport from NADH to ubiquinone", "mitochondrial respiratory chain complex I assembly", and "oxidative phosphorylation". CC terms included "mitochondrial inner membrane", "respiratory chain complex I", and "mitochondrion". MF terms included "NADH dehydrogenase(ubiquinone)activity", "quinol-cytochrome-c reductase activity", "oxidoreductase activity", and "iron-sulfur cluster binding". KEGG pathway enrichment included "oxidative phosphorylation", "non-alcoholic fatty liver disease", "chemical carcinogenesis-reactive oxygen species", and "thermogenesis" (Figure 3C).

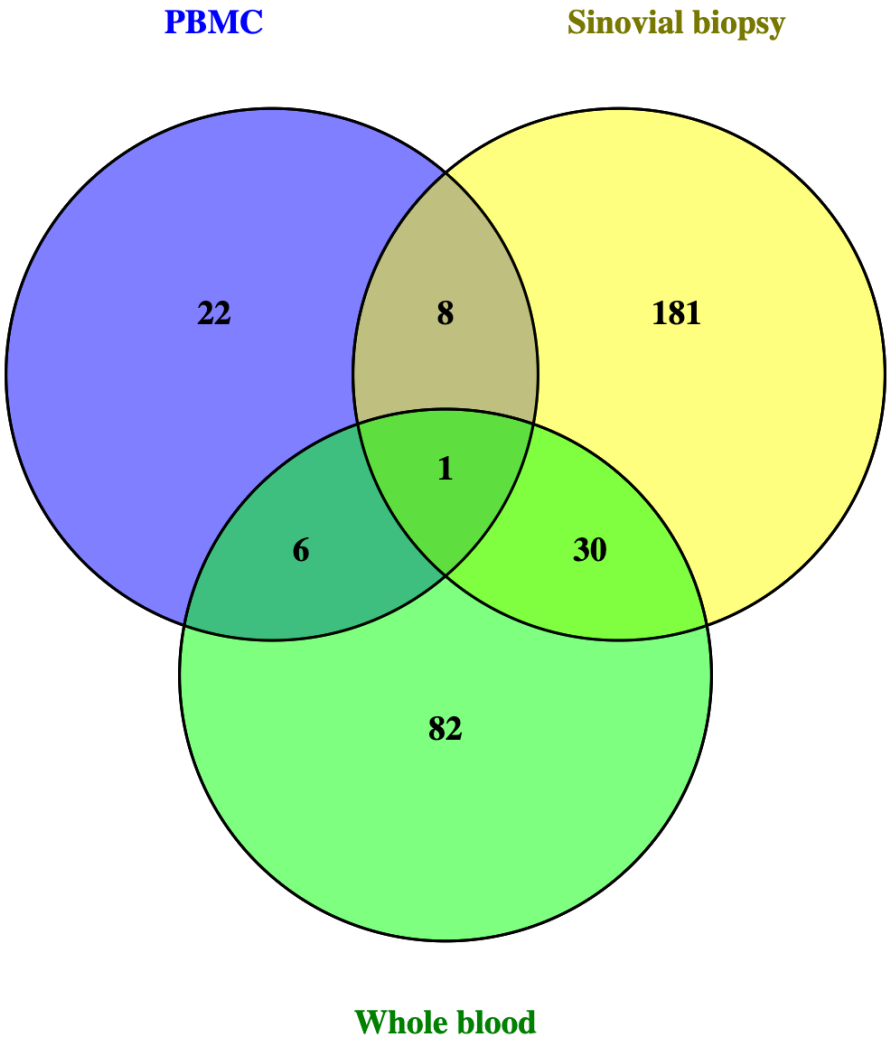


Figure 1. Venn diagram showing the distribution of mitochondria-related differentially expressed genes (mito-DEGs) across PBMC, synovial biopsy, and whole blood datasets in rheumatoid arthritis. The diagram illustrates the overlap of mito-DEGs identified from the PBMC (GSE17755), synovial biopsy (GSE89408), and whole blood (GSE93272) datasets after intersecting the differentially expressed genes with the MitoCarta 3.0 database. Unique mito-DEGs were observed in PBMC (22 genes), synovial biopsy (181 genes), and whole blood (82 genes). Shared genes were identified between PBMC and synovial biopsy (8 genes), PBMC and whole blood (6 genes), and synovial biopsy and whole blood (30 genes). One mito-DEG was found to be common across all three datasets.

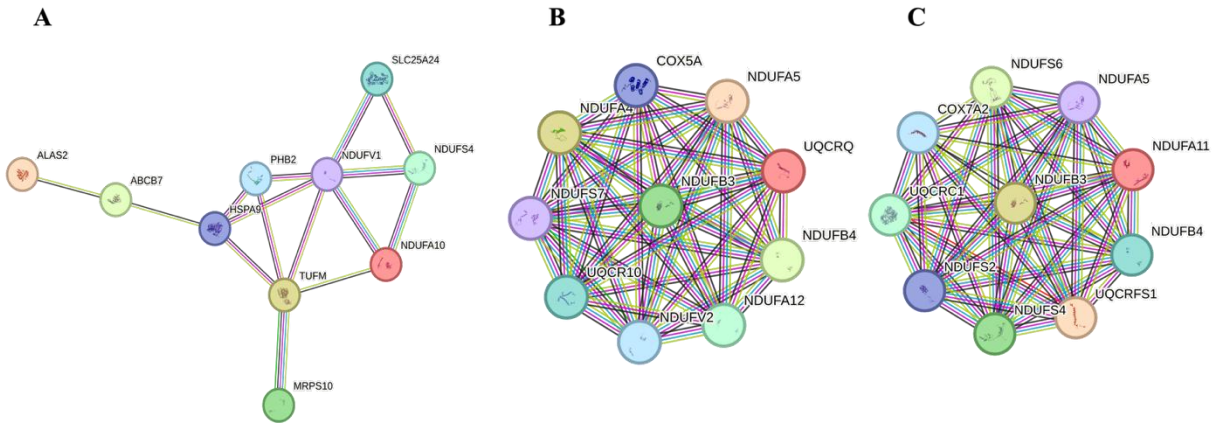


Figure 2. Protein–protein interaction (PPI) networks of mitochondrial hub genes identified in different tissues. The networks represent the top 10 hub genes identified using the MCC algorithm in cytoHubba for (A) PBMC, (B) synovial biopsy, and (C) whole blood datasets. Nodes represent genes and edges indicate predicted functional interactions derived from the STRING database.

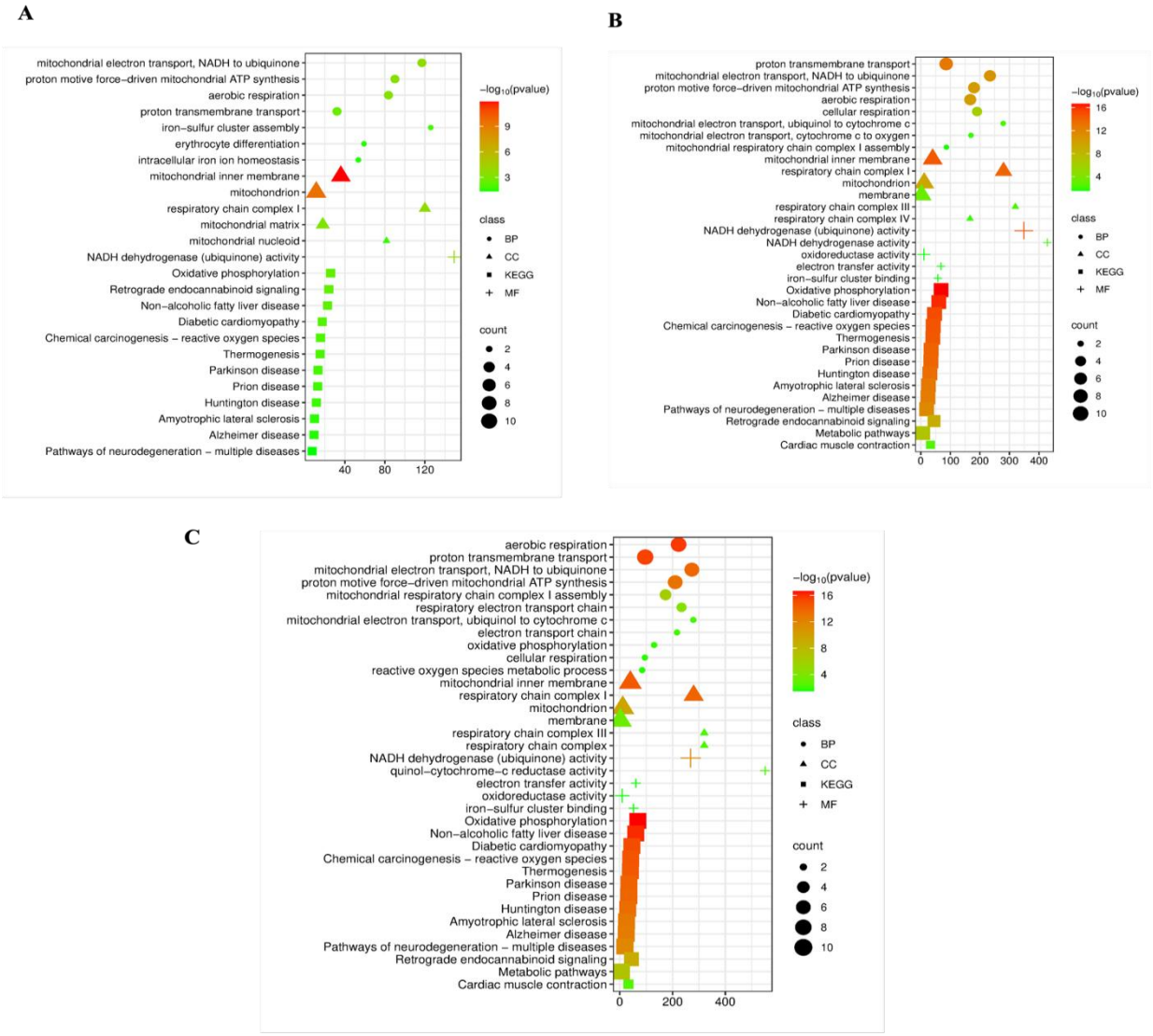


Figure 3. Functional enrichment analysis of mitochondrial hub genes across different tissues in rheumatoid arthritis. Bubble plots showing Gene Ontology (GO) and Kyoto Encyclopedia of Genes and Genomes (KEGG) pathway enrichment results for the top hub genes identified in (A) PBMC, (B) synovial biopsy, and (C) whole blood datasets. The y-axis represents enriched GO terms and KEGG pathways, while the x-axis indicates gene counts associated with each term. Bubble size corresponds to the number of genes involved in each pathway, and color intensity represents the significance level expressed as –log10(P-value).

3.5. Regulatory Network Topology of Candidate Hub Gene Biomarkers

To characterize the regulatory interactions associated with candidate hub genes, miRNA–mRNA, TF–mRNA, and integrated miRNA–TF–mRNA regulatory networks were constructed for PBMC, synovial biopsy, and whole blood datasets (Figures 4–6). A complete list of miRNAs and TFs targeting the identified mitochondrial hub genes, along with their interaction frequencies, is provided in Supplementary Table 1.

In the PBMC dataset, the miRNA–mRNA interaction network revealed that several miRNAs targeted multiple hub genes. Two miRNAs, "hsa-miR-16-5p" and "hsa-miR-615-3p", each targeted three hub genes, while forty miRNAs targeted two hub genes. In the TF–mRNA network, FOXC1 was identified as the transcription factor interacting with nine hub genes. GATA2 was associated with five hub genes, whereas POU2F2 and NFIC were each linked to four hub genes (Figure 4).

In the synovial biopsy dataset, the regulatory network analysis identified "hsa-miR-26-5p" as the miRNA targeting the highest number of hub genes (four). Six miRNAs ("hsa-miR-149-3p", "hsa-miR-4728-5p", "hsa-miR-6785-5p", "hsa-miR-6883-5p", "hsa-miR-1226-3p", and "hsa-miR-484") were each associated with two hub genes. In the TF–mRNA network, FOXC1 targeted five hub genes, and PPARG targeted four. Additionally, seven transcription factors (TP53, USF2, MEF2A, CREB1, STAT3, TP63, and E2F1) were each connected to three hub genes (Figure 5).

In the whole blood dataset, the miRNA–mRNA network identified five miRNAs ("hsa-miR-92a-3p", "hsa-miR-8485", "hsa-miR-3173-3p", "hsa-miR-6891-5p", and "hsa-miR-26b-5p"), each targeting two hub genes. In the TF–mRNA network, three TFs (YY1, FOXC1, and GATA2) were each associated with five hub genes. POU2F2 and FOXL1 were linked to four hub genes (Figure 6).

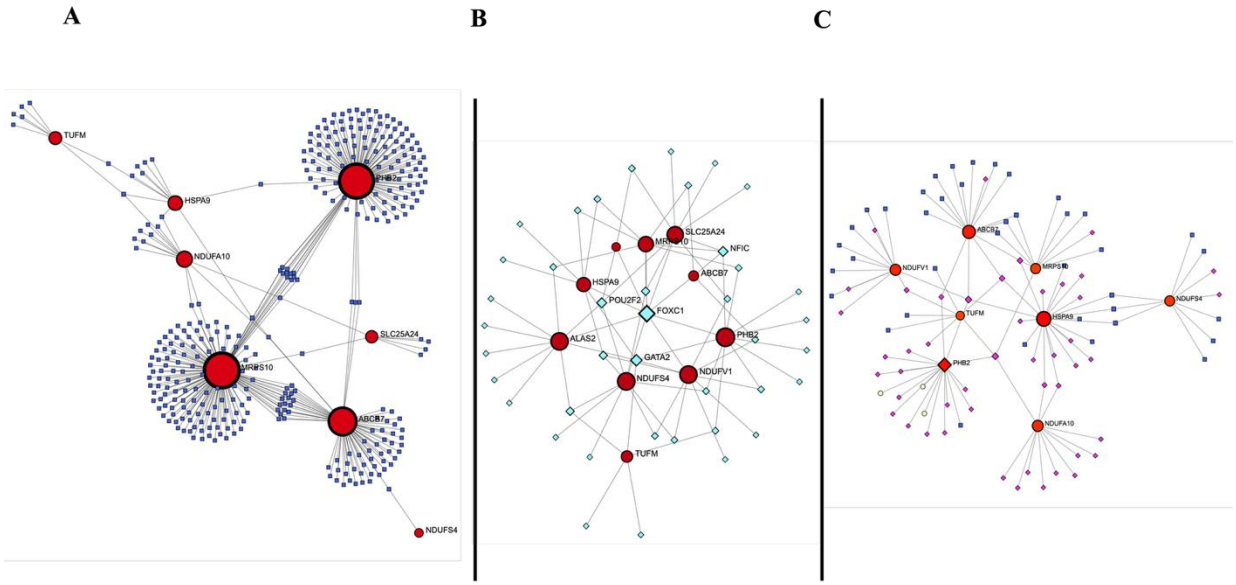


Figure 4. Regulatory interaction networks of mitochondrial hub genes in PBMC samples from rheumatoid arthritis. (A)miRNA–hub gene regulatory network showing interactions between microRNAs and mitochondrial hub genes identified in the PBMC dataset. (B) Transcription factor (TF)–hub gene regulatory network illustrating predicted TF–gene interactions associated with the identified mitochondrial hub genes. (C) Integrated TF–miRNA–hub gene regulatory network combining transcription factors, microRNAs, and hub genes to reveal the potential multilayered regulatory architecture controlling mitochondrial gene expression in PBMC samples.

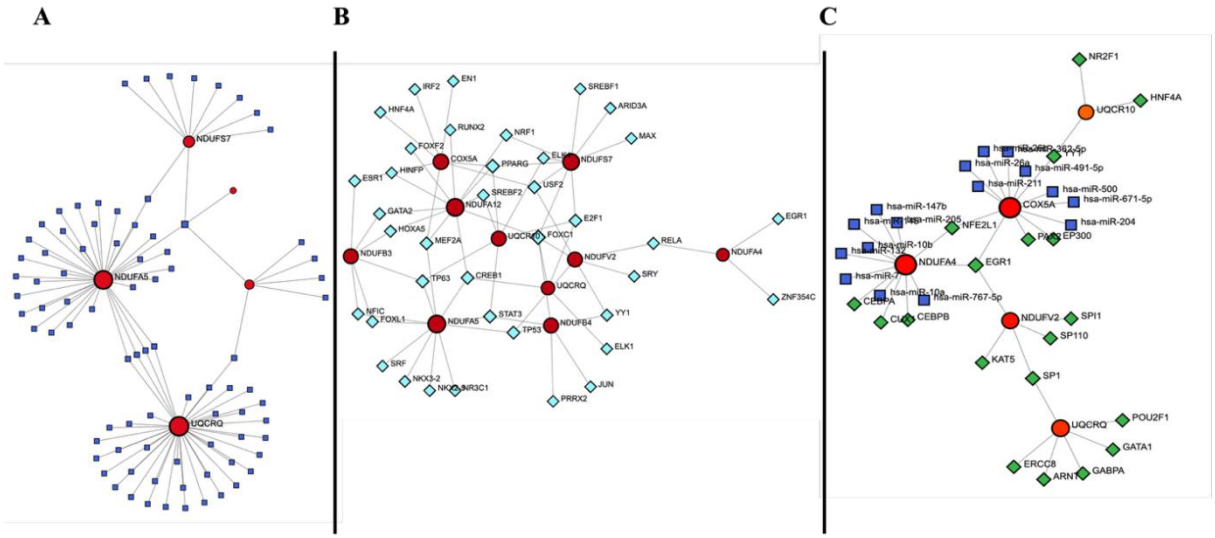


Figure 5. Regulatory interaction networks of mitochondrial hub genes in synovial biopsy samples from rheumatoid arthritis. (A)miRNA–hub gene regulatory network showing interactions between microRNAs and mitochondrial hub genes identified in the synovial biopsy dataset. (B) Transcription factor (TF)–hub gene regulatory network illustrating predicted TF–gene interactions associated with the identified mitochondrial hub genes. (C) Integrated TF–miRNA–hub gene regulatory network combining transcription factors, microRNAs, and hub genes to reveal the potential multilayered regulatory architecture controlling mitochondrial gene expression in synovial biopsy samples.

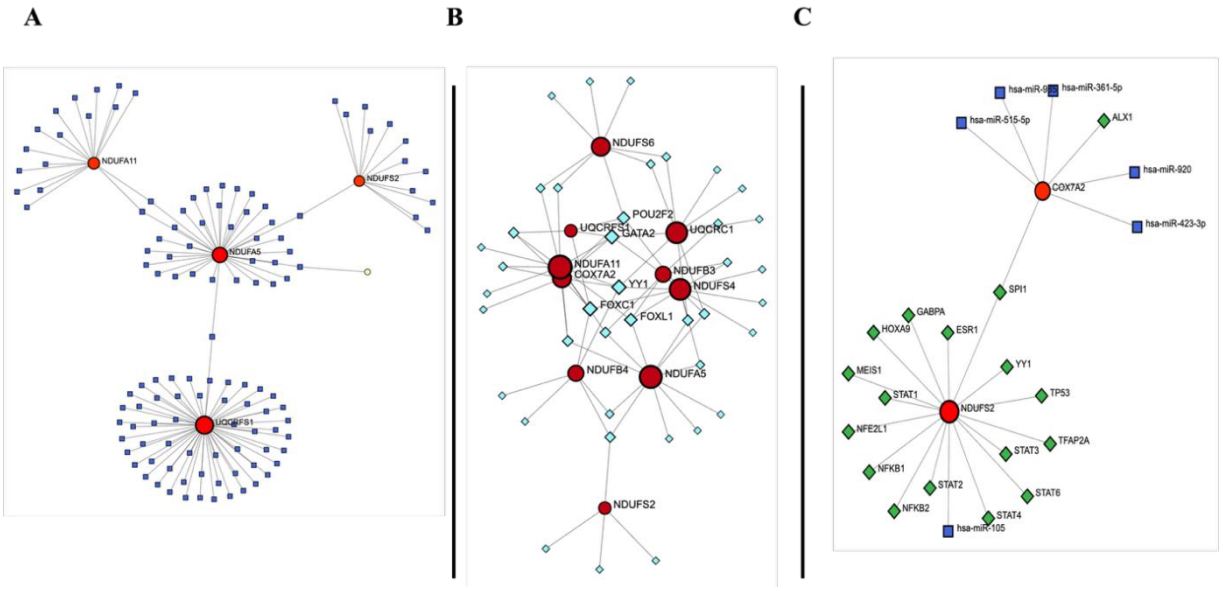


Figure 6. Regulatory interaction networks of mitochondrial hub genes in whole blood samples from rheumatoid arthritis. (A)miRNA–hub gene regulatory network showing interactions between microRNAs and mitochondrial hub genes identified in the whole blood dataset. (B) Transcription factor (TF)–hub gene regulatory network illustrating predicted TF–gene interactions associated with the identified mitochondrial hub genes. (C) Integrated TF–miRNA–hub gene regulatory network combining transcription factors, microRNAs, and hub genes to reveal the potential multilayered regulatory architecture controlling mitochondrial gene expression in whole blood samples.

4. Discussion

RA is a complicated autoimmune disease driven by long-term synovial inflammation and systemic immune abnormalities (Smolen et al., 2016). Despite the growing recognition of mitochondrial dysfunction as a key player in RA pathogenesis (Fearon et al., 2016), most previous transcriptomic studies have focused on single tissue types (Lee et al., 2020), limiting our understanding of shared versus tissue-specific mitochondrial alterations. In this study, we performed an integrative transcriptomic analysis of three distinct biological compartments—PBMCs, synovial biopsies, and whole blood samples—to systematically characterize mitochondrial gene expression signatures in RA. Our multi-tissue approach revealed both common and tissue-specific mitochondrial dysregulation, with oxidative phosphorylation (OXPHOS)

components emerging as central hub genes across all compartments, and *AKAP1* identified as the only mitochondrial gene common to all three tissues in this dataset collection.

The number of mito-DEGs varied considerably across tissues, with synovial biopsy showing the highest number (220 mito-DEGs), followed by whole blood (119 mito-DEGs) and PBMC (37 mito-DEGs). This gradient likely reflects the severity of local inflammation in the joint microenvironment. The primary inflammatory site in RA, synovial tissue faces hypoxia, pro-inflammatory cytokines (TNF-α, IL-6, IL-17), and oxidative stress, all of which directly impair mitochondrial function (Mihaylova et al., 2024). In contrast, PBMC and whole blood represent systemic compartments where mitochondrial alterations may be more moderate but still detectable, consistent with the concept of RA as a systemic disease (Abbasifard et al., 2024; Mitrović et al., 2023). It should also be briefly noted that this gradient may partly reflect platform differences, since GSE17755 was profiled on the Hitachisoft GPL1291 platform, GSE93272 on the Affymetrix GPL570 platform, and GSE89408 on the Illumina GPL11154 platform, and these technical differences may contribute to some of the variation in DEG/mito-DEG numbers observed between synovial biopsy and the other two tissues, independent of true biological differences.

Remarkably, *AKAP1* was the only mitochondrial gene commonly dysregulated across all three tissues in this dataset collection. *AKAP1* serves as a mitochondrial scaffold protein that tethers protein kinase A (PKA) to the outer mitochondrial membrane, where it regulates multiple mitochondrial functions, including oxidative phosphorylation, mitochondrial dynamics (fission/fusion balance), and apoptosis (Liu et al., 2020). *AKAP1* has been shown to prevent oxidative mitochondrial damage by promoting mitophagy and maintaining membrane potential (Soundararajan et al., 2022). To our knowledge, this is the first study to identify AKAP1 as a common mitochondrial signature across multiple tissues in RA, raising the possibility that it may serve as a systemic biomarker of mitochondrial dysfunction; however, this remains speculative pending independent validation. Future studies should evaluate the diagnostic performance of *AKAP1* using ROC curve analysis in independent validation cohorts.

Across tissues, hub genes were predominantly Complex I subunits (NADH:ubiquinone oxidoreductase), including multiple NDUF genes. Complex I is the largest and most complex ETC enzyme, initiating NADH-to-ubiquinone electron transfer and proton pumping across the inner mitochondrial membrane (Bozdemir et al., 2025).

Dysregulation of Complex I subunits has previously been implicated in RA. Fearon et al. showed that reduced complex I activity and increased ROS production in RA synovial fibroblasts promote their invasiveness (Fearon et al., 2016). Similarly, a recent study by Huang et al. showed that peripheral blood mitochondrial DNA gene variation is associated with RA susceptibility (Huang et al., 2026). Our study extends these findings by demonstrating that complex I subunit dysregulation is not limited to synovial tissue but is also detectable in peripheral compartments (PBMC and whole blood), suggesting that OXPHOS impairment is a systemic feature of RA. Notably, *NDUFB4* and *NDUFB3* were identified as hub genes in both synovial biopsy and whole blood datasets, making them potential blood-based biomarkers of synovial mitochondrial dysfunction.

KEGG enrichment analysis showed that mitochondrial hub genes were significantly enriched in oxidative phosphorylation, thermogenesis, and several neurodegenerative disease pathways (Parkinson's, Alzheimer's, Huntington's, ALS, and prion disease). This intriguing finding suggests that shared mitochondrial stress signatures may underlie both RA and neurodegenerative disorders.

Accumulating evidence supports a link between chronic inflammation and neurodegeneration. Systemic inflammation has been shown to accelerate cognitive decline and increase the risk of neurodegenerative diseases (Jaramillo Ramos et al., 2025). Mitochondrial dysfunction, defined by impaired OXPHOS, elevated ROS production, and defective mitophagy, is a common pathogenic mechanism in both RA and neurodegenerative diseases (Ma et al., 2022). Our results raise the possibility that mitochondrial hub genes identified in RA patients may represent shared therapeutic targets for inflammation-associated neurodegeneration. The enrichment of thermogenesis pathways is also notable, as uncoupling proteins (UCPs) in mitochondria regulate ROS production and inflammatory responses in immune cells (Nesci and Rubattu, 2024).

Our regulatory network analysis identified FOXC1 and GATA2 as transcription factors interacting with multiple hub genes across all three tissues, suggesting that they may act as master regulators of mitochondrial gene expression in RA.

FOXC1 (Forkhead Box C1) is a transcription factor involved in cellular stress responses and has been shown to promote the expression of antioxidant genes, protecting cells from oxidative damage (Berry et al., 2008). In the context of RA, FOXC1 may represent a compensatory response to increased oxidative stress in inflamed tissues. GATA2 is a hematopoietic transcription factor that regulates the expression of mitochondrial genes in macrophages and dendritic cells, influencing their metabolic reprogramming during inflammation (Jackson-Strong et al., 2026). Our finding that GATA2 targets multiple mitochondrial hub genes in PBMC and whole blood suggests that GATA2-mediated transcriptional regulation may contribute to the metabolic adaptation of immune cells in RA.

The miRNA “hsa-miR-16-5p” emerged as a key post-transcriptional regulator, targeting three hub genes in PBMC. Huang et al. recently demonstrated that

peripheral blood miR-16-5p levels are altered in RA patients and correspond with disease activity (Huang et al., 2026). Our results suggest that miR-16-5p may exert its effects in part by regulating mitochondrial gene expression. These regulatory nodes may represent novel therapeutic targets for restoring mitochondrial function in RA.

Our findings are consistent with and extend previous transcriptomic studies in RA. In a recent study, Tariq et al. applied an integrated multi-omics method to uncover potential therapeutic biomarkers in RA and also identified mitochondrial genes among their candidates (Tariq et al., 2025). A 2025 study investigating mitochondrial apoptosis-related genes (MARGs) in RA identified hub genes including MRPS10 and TUFM (which we also identified in PBMC) and demonstrated their diagnostic potential through ROC analysis, with transcription factors such as YY1 and FOXO3 emerging as critical regulators (Gao et al., 2025). Notably, YY1 was also identified as a key transcription factor in our whole blood dataset, consistent with this previous report.

Lee et al. revealed distinct inflammatory pathways in blood versus arthritic joints, emphasizing the need for multi-tissue approaches in biomarker discovery (Lee et al., 2020). Our study directly addresses this limitation by integrating data from three distinct compartments and identifying both shared and tissue-specific mitochondrial signatures. Additionally, a recent study demonstrating that the MTHFD2-CKMT1 axis promotes osteoclastogenesis and bone loss through enhanced OXPHOS activity further supports the central role of oxidative phosphorylation in RA pathogenesis (Li et al., 2025). Mitochondrial dysfunction not only impairs oxidative phosphorylation but also sensitizes cells to intrinsic apoptotic signals, and the modulation of these pathways has been extensively investigated in the context of targeted cancer and autoimmune therapies (Gökhan et al., 2020).

Our findings have several potential clinical implications. First, the candidate genes identified in this study—particularly *AKAP1* and the OXPHOS subunit genes *NDUFB4* and *NDUFB3*—merit investigation as potential blood-based biomarkers of mitochondrial dysfunction in RA in future prospective studies. If validated in independent cohorts, they could offer a minimally invasive approach for patient stratification and monitoring. Second, the identification of FOXC1, GATA2, and miR-16-5p as master regulators suggests that modulating these regulatory nodes could restore mitochondrial function in RA. Third, our results support the rationale for developing mitochondria-targeted therapies (such as MitoQ or MitoTEMPO) or repurposing existing drugs like metformin for RA treatment (Hou et al., 2025).

Some limitations should be noted. Two of the three datasets analyzed (GSE17755, GSE93272) were microarray-based, which have lower sensitivity and dynamic range than RNA-seq; validation using RNA-seq data from additional independent cohorts is still needed to confirm the microarray-derived findings. A related limitation concerns the mixed-platform nature of our dataset collection: GSE17755 was profiled on the Hitachisoft GPL1291 two-color oligo array, GSE93272 on the single-color Affymetrix GPL570 platform, and GSE89408 was generated by Illumina GPL11154 RNA sequencing rather than by microarray. Because each dataset was analyzed independently, with DEG lists compared only at the level of shared gene identity (Venn diagram) rather than by merging normalized expression values, we did not apply cross-platform batch correction. Platform-specific differences in probe design, sensitivity, and dynamic range across the two microarray platforms, together with more fundamental technology-level differences between microarray and RNA-sequencing for GSE89408 — including sensitivity to low-abundance transcripts and the underlying statistical testing framework (voom-transformed counts vs. array-based linear models) — may contribute to the substantial disparity in DEG and mito-DEG counts observed between the synovial biopsy dataset and the other two datasets, independent of true biological differences between tissues. This limits direct quantitative comparison of DEG magnitude across compartments, although qualitative overlap in specific genes remains informative. Relatedly, for the two microarray datasets, differential expression was tested at the probe level, and genes with multiple significant probes were collapsed to a single entry using the lowest adjusted *p*-value rule described in Section 2.2. A different probe-collapsing convention (e.g., selecting the probe with the highest mean expression) could, in principle yield marginally different DEG counts. Additionally, the uniform $|\log2FC| \geq 1$ threshold applied across all three datasets may be comparatively stringent for circulating immune cells, where transcriptional changes are often more modest than in locally inflamed tissue, potentially contributing to the lower mito-DEG count observed in the PBMC dataset relative to synovial biopsy. A lower-threshold or rank-based sensitivity analysis in PBMC-specific data represents a valuable direction for follow-up work. Finally, gene expression changes do not always correlate with protein levels or enzymatic activity. This is a particularly relevant caveat for our findings, since none of the candidate genes highlighted in this study (including AKAP1 and the NDUF family hub genes) have been validated at the protein or enzymatic activity level in samples from RA patients; targeted validation using methods such as Western blotting, immunohistochemistry, or activity assays of OXPHOS complex I is needed before these observed transcriptional changes can be interpreted as reflecting altered mitochondrial protein abundance or function. Our study design is also descriptive and correlative rather than mechanistic and cannot establish whether the observed mitochondrial transcriptional changes are drivers of RA pathogenesis, consequences of the inflammatory environment, or both. Functional

experiments — for example, CRISPR-Cas9-mediated knockout or knockdown of AKAP1 or NDUF-family genes in immune or synoviocyte cell models, or pharmacological modulation of oxidative phosphorylation — would be needed to establish causal relationships and would represent an important direction for future work. A further limitation is the potential clinical heterogeneity among the three GEO cohorts used in this study. The original dataset does not provide harmonized information on patient age, sex distribution, disease duration, disease activity, or treatment status (e.g., DMARD-naïve versus treated), and these variables were therefore neither available nor controlled for in our analysis. Differences in these clinical characteristics across the PBMC, synovial biopsy, and whole blood cohorts could contribute to some of the tissue-level differences we observed, independent of the biological compartment itself, and this should be considered when interpreting cross-tissue comparisons. Finally, bulk tissue analyses mask cellular heterogeneity: PBMC, whole blood, and synovial biopsy each consist of multiple cell types (e.g., synovial fibroblasts, macrophages, T and B lymphocytes) with distinct mitochondrial profiles, and bulk expression values represent averages across this mixture. Single-cell or spatial transcriptomic studies are needed to resolve which specific cell populations drive the mitochondrial signatures identified here, particularly within the synovial compartment where cellular heterogeneity is likely greatest.

5. Conclusion

This multi-tissue integrative analysis reveals that mitochondrial dysfunction in rheumatoid arthritis is tissue-specific yet converges on oxidative phosphorylation dysregulation, with synovial tissue showing the most extensive transcriptional alterations and Complex I (NDUF family) subunits emerging as central hub genes across all three compartments. AKAP1 emerges as a candidate systemic signature requiring independent validation, while FOXC1, GATA2, and hsa-miR-16-5p are identified as key transcriptional and post-transcriptional regulatory nodes. By jointly profiling PBMC, synovial biopsy, and whole blood within a single analytical framework, this study helps distinguish systemic from tissue-restricted mitochondrial signatures in RA. These findings provide a resource for future studies investigating mitochondrial contributions to RA pathogenesis and for developing diagnostic or therapeutic strategies targeting mitochondrial pathway.

Author Contributions

The percentages of the author' contributions are presented below. The author reviewed and approved the final version of the manuscript.

	S.A.
C	100
D	100
DCP	100
DAI	100
L	100
W	100
CR	100
SR	100

C= concept, D= design, DCP= data collection and/or processing, DAI= data analysis and/or interpretation, L= literature search, W= writing, CR= critical review, SR= submission and revision.

Conflict of Interest

The author declared that there is no conflict of interest.

Ethical Consideration

Ethics committee approval was not required because this study used only publicly available, de-identified transcriptomic datasets.

References

Abbasifard, A., Solgi, G., Khodadadi, I., Doosti-Irani, A., Tayebinia, H., & Fazaeli, A. (2024). Peripheral blood mononuclear cells show markers of mitochondrial dysfunction in rheumatoid arthritis. *Cell Biochemistry and Function*, *42*(4), e4025. https://doi.org/10.1002/cbf.4025

Alivernini, S., Firestein, G. S., & McInnes, I. B. (2022). The pathogenesis of rheumatoid arthritis. *Immunity*, *55*(12), 2255–2270. https://doi.org/10.1016/j.immuni.2022.11.009

Ashburner, M., Ball, C. A., Blake, J. A., Botstein, D., Butler, H., Cherry, J. M., Davis, A. P., Dolinski, K., Dwight, S. S., Eppig, J. T., Harris, M. A., Hill, D. P., Issel-Tarver, L., Kasarskis, A., Lewis, S., Matese, J. C., Richardson, J. E., Ringwald, M., Rubin, G. M., & Sherlock, G. (2000). Gene ontology: tool for the unification of biology. The Gene Ontology Consortium. *Nature Genetics*, *25*(1), 25–29. https://doi.org/10.1038/75556

Bellocchi, C., Favalli, E. G., Maioli, G., Agape, E., Rossato, M., Paini, M., Severino, A., Vigone, B., Biggioggero, M., Trombetta, E., Caporali, R., & Beretta, L. (2025). Whole-blood RNA sequencing profiling of patients with rheumatoid arthritis treated with tofacitinib. *ACR Open Rheumatology*, *7*(7), e11761. https://doi.org/10.1002/acr2.11761

Berry, F. B., Skarie, J. M., Mirzayans, F., Fortin, Y., Hudson, T. J., Raymond, V., Link, B. A., & Walter, M. A. (2008). FOXC1 is required for cell viability and resistance to oxidative stress in the eye through the transcriptional regulation of FOXO1A. *Human Molecular Genetics*, *17*(4), 490–505. https://doi.org/10.1093/hmg/ddm326

Binvignat, M., Miao, B. Y., Wibrand, C., Yang, M. M., Rychkov, D., Flynn, E., Nititham, J., Tamaki, W., Khan, U., Carvidi, A., Krueger, M., Niemi, E., Sun, Y., Fragiadakis, G. K., Sellam, J., Mariotti-Ferrandiz, E., Klatzmann, D., Gross, A. J., Ye, C. J., Butte, A. J., … Sirota, M. (2024). Single-cell RNA-Seq analysis reveals

cell subsets and gene signatures associated with rheumatoid arthritis disease activity. *JCI Insight*, *9*(16), e178499. https://doi.org/10.1172/jci.insight.178499

Bozdemir, N., Cakir, C., Topcu, U., & Uysal, F. (2025). A Comprehensive Review of Mitochondrial Complex I During Mammalian Oocyte Maturation. *Genesis (New York, N.Y. : 2000)*, *63*(3), e70017. https://doi.org/10.1002/dvg.70017

Chin, C. H., Chen, S. H., Wu, H. H., Ho, C. W., Ko, M. T., & Lin, C. Y. (2014). cytoHubba: identifying hub objects and sub-networks from complex interactome. *BMC Systems Biology*, *8 Suppl 4*(Suppl 4), S11. https://doi.org/10.1186/1752-0509-8-S4-S11

Fearon, U., Canavan, M., Biniecka, M., & Veale, D. J. (2016). Hypoxia, mitochondrial dysfunction and synovial invasiveness in rheumatoid arthritis. *Nature Reviews. Rheumatology*, *12*(7), 385–397. https://doi.org/10.1038/nrrheum.2016.69

Finckh, A., Gilbert, B., Hodkinson, B., Bae, S. C., Thomas, R., Deane, K. D., Alpizar-Rodriguez, D., & Lauper, K. (2022). Global epidemiology of rheumatoid arthritis. *Nature reviews. Rheumatology*, *18*(10), 591–602. https://doi.org/10.1038/s41584-022-00827-y

Gao, C., Zhang, C., Wen, L., Zhang, G., Liu, X., Wang, J., Cui, L., Li, R., Nie, T., Duan, J., & Guo, Y. (2025). Regulation of reactive oxygen species and the role of mitochondrial apoptotic-related genes in rheumatoid arthritis. *Scientific Reports*, *15*(1), 2165. https://doi.org/10.1038/s41598-025-85460-x

Gao, Y., Zhang, Y., & Liu, X. (2024). Rheumatoid arthritis: pathogenesis and therapeutic advances. *MedComm*, *5*(3), e509. https://doi.org/10.1002/mco2.509

Gökhan, A., Kılıç, K. D., Gülle, K., Uyanıkgil, Y., & Çavuşoğlu, T. (2020). Apoptotik Yolaklar ve Hedefe Yönelik Tedaviler. *Medical Journal of Süleyman Demirel University*, *27*(4), 565-573. https://doi.org/10.17343/sdutfd.619417

Hou, Y., Yang, X., Zhao, T., Guo, Y., & Shi, J. (2025). Targeting mitochondrial oxidative stress: A novel therapeutic strategy for degenerative joint diseases (Review). *Biomedical Reports*, *24*(2),26. https://doi.org/10.3892/br.2025.2099

Huang, H. Y., Lin, Y. C., Li, J., Huang, K. Y., Shrestha, S., Hong, H. C., Tang, Y., Chen, Y. G., Jin, C. N., Yu, Y., Xu, J. T., Li, Y. M., Cai, X. X., Zhou, Z. Y., Chen, X. H., Pei, Y. Y., Hu, L., Su, J. J., Cui, S. D., Wang, F., … Huang, H. D. (2020). miRTarBase 2020: updates to the experimentally validated microRNA-target interaction database. *Nucleic Acids Research*, *48*(D1), D148–D154. https://doi.org/10.1093/nar/gkz896

Huang, Q., Cai, X. Q., Li, Z. Q., Liu, Y., & Pan, H. F. (2026). Association of peripheral blood mitochondrial DNA gene variation and methylation levels with rheumatoid arthritis. *Clinical Immunology(Orlando, Fla.)*, *282*, 110641. https://doi.org/10.1016/j.clim.2025.110641

Jackson-Strong, M., Ganguly, S., Francis, A., Rago, F., Kanshana, J., Michalides, B. A., Teng, L., Betsur, O. S., Kruszelnicki, S., Shoger, K. E., Kim, A., Bajpai, K., Suleyman, A., Sekyere, A., Hara, M., Sriram, V., Kumar, A., Delgoffe, G. M., Natarajan, N., Alcorn, J. F., … Gottschalk, R. A. (2026). GATA2 controls alveolar macrophage inflammatory gene expression and metabolic function. *JCI Insight*, *11*(7), e196246. https://doi.org/10.1172/jci.insight.196246

Jaramillo Ramos, J. J., Galindo Pupo, N. M., Mena, D., Solis, R. P., Bedoya Jaramillo, J. E., & Vega Solano, M. (2025). Cognitive Decline in Chronic Inflammatory Conditions: Exploring Links Between Systemic Inflammation and Neurodegeneration. *Cureus*, *17*(7), e88397. https://doi.org/10.7759/cureus.88397

Kanehisa, M., Furumichi, M., Sato, Y., Kawashima, M., & Ishiguro-Watanabe, M. (2023). KEGG for taxonomy-based analysis of pathways and genomes. *Nucleic Acids Research*, *51*(D1), D587–D592. https://doi.org/10.1093/nar/gkac963

Lee, E. J., Lilja, S., Li, X., Schäfer, S., Zhang, H., & Benson, M. (2020). Bulk and single cell transcriptomic data indicate that a dichotomy between inflammatory pathways in peripheral blood and arthritic joints complicates biomarker discovery. *Cytokine*, *127*, 154960. https://doi.org/10.1016/j.cyto.2019.154960

Li, Y., Cai, M., Qin, Y., Dai, X., Liang, L., Li, Z., Wen, X., Jin, H., Yang, C., & Chen, Z. (2025). MTHFD2 promotes osteoclastogenesis and bone loss in rheumatoid arthritis by enhancing CKMT1-mediated oxidative phosphorylation. *BMC Medicine*, *23*(1), 124. https://doi.org/10.1186/s12916-025-03945-y

Liu, Y., Merrill, R. A., & Strack, S. (2020). A-Kinase Anchoring Protein 1: Emerging Roles in Regulating Mitochondrial Form and Function in Health and Disease. *Cells*, *9*(2), 298. https://doi.org/10.3390/cells9020298

Ma, C., Wang, J., Hong, F., & Yang, S. (2022). Mitochondrial Dysfunction in Rheumatoid Arthritis. *Biomolecules*, *12*(9), 1216. https://doi.org/10.3390/biom12091216

Mihaylova, V., Kazakova, M., Batalov, Z., Karalilova, R., Batalov, A., & Sarafian, V. (2024). JAK inhibitors improve ATP production and mitochondrial function in rheumatoid arthritis: a pilot study. *Rheumatology International*, *44*(1), 57–65. https://doi.org/10.1007/s00296-023-05501-4

Mitrović, J., Hrkač, S., Tečer, J., Golob, M., Ljilja Posavec, A., Kolar Mitrović, H., & Grgurević, L. (2023). Pathogenesis of Extraarticular Manifestations in Rheumatoid Arthritis-A Comprehensive Review. *Biomedicines*, *11*(5), 1262. https://doi.org/10.3390/biomedicines11051262

Nesci, S., & Rubattu, S. (2024). UCP2, a Member of the Mitochondrial Uncoupling Proteins: An Overview from Physiological to Pathological Roles. *Biomedicines*, *12*(6), 1307. https://doi.org/10.3390/biomedicines12061307

Ovek Baydar, D., Rauluseviciute, I., Aronsen, D. R., Blanc-Mathieu, R., Bonthuis, I., de Beukelaer, H., Ferenc, K., Jegou, A., Kumar, V., Lemma, R. B., Lucas, J., Pochon, M., Yun, C. M., Ramalingam, V., Deshpande, S. S., Patel, A., Marinov, G. K., Wang, A. T., Aguirre, A., Castro-Mondragon, J. A., … Mathelier, A. (2026). JASPAR 2026: expansion of transcription factor binding profiles and integration of deep learning models. *Nucleic Acids Research*, *54*(D1), D184–D193. https://doi.org/10.1093/nar/gkaf1209

Rahmati, M., Kwesiga, M. P., Lou, J., Tan, A. L., & McDermott, M. F. (2024). Novel Targeted Therapies for Rheumatoid Arthritis Based on Intracellular Signalling and Immunometabolic Changes: A Narrative Review. *Frontiers in Bioscience(Landmark Edition)*, *29*(1), 42. https://doi.org/10.31083/j.fbl2901042

Rath, S., Sharma, R., Gupta, R., Ast, T., Chan, C., Durham, T. J., Goodman, R. P., Grabarek, Z., Haas, M. E., Hung, W. H. W., Joshi, P. R., Jourdain, A. A., Kim, S. H., Kotrys, A. V., Lam, S. S., McCoy, J. G., Meisel, J. D., Miranda, M., Panda, A., Patgiri, A., … Mootha, V. K. (2021). MitoCarta3.0: an updated mitochondrial proteome now with sub-organelle localization and pathway annotations. *Nucleic Acids Research*, *49*(D1), D1541–D1547. https://doi.org/10.1093/nar/gkaa1011

Shannon, P., Markiel, A., Ozier, O., Baliga, N. S., Wang, J. T., Ramage, D., Amin, N., Schwikowski, B., & Ideker, T. (2003). Cytoscape: a software environment for integrated models of biomolecular interaction networks. *Genome Research*, *13*(11), 2498–2504. https://doi.org/10.1101/gr.1239303

Sherman, B. T., Hao, M., Qiu, J., Jiao, X., Baseler, M. W., Lane, H. C., Imamichi, T., & Chang, W. (2022). DAVID: a web server for functional enrichment analysis and functional annotation of

gene lists (2021 update). *Nucleic Acids Research*, *50*(W1), W216–W221. https://doi.org/10.1093/nar/gkac194

Smiljanovic, B., Grützkau, A., Sörensen, T., Grün, J. R., Vogl, T., Bonin, M., Schendel, P., Stuhlmüller, B., Claussnitzer, A., Hermann, S., Ohrndorf, S., Aupperle, K., Backhaus, M., Radbruch, A., Burmester, G. R., & Häupl, T. (2020). Synovial tissue transcriptomes of long-standing rheumatoid arthritis are dominated by activated macrophages that reflect microbial stimulation. *Scientific Reports*, *10*(1), 7907. https://doi.org/10.1038/s41598-020-64431-4

Smolen, J. S., Aletaha, D., & McInnes, I. B. (2016). Rheumatoid arthritis. *Lancet(London, England)*, *388*(10055), 2023–2038. https://doi.org/10.1016/S0140-6736(16)30173-8

Smolen, J. S., Aletaha, D., Barton, A., Burmester, G. R., Emery, P., Firestein, G. S., Kavanaugh, A., McInnes, I. B., Solomon, D. H., Strand, V., & Yamamoto, K. (2018). Rheumatoid arthritis. *Nature Reviews. Disease Primers*, *4*, 18001. https://doi.org/10.1038/nrdp.2018.1

Soundararajan, R., Hernández-Cuervo, H., Stearns, T. M., Griswold, A. J., Patil, S. S., Fukumoto, J., Narala, V. R., Galam, L., Lockey, R., & Kolliputi, N. (2022). A-Kinase Anchor Protein 1 deficiency causes mitochondrial dysfunction in mouse model of hyperoxia induced acute lung injury. *Frontiers in Pharmacology*, *13*, 980723. https://doi.org/10.3389/fphar.2022.980723

Szklarczyk, D., Kirsch, R., Koutrouli, M., Nastou, K., Mehryary, F., Hachilif, R., Gable, A. L., Fang, T., Doncheva, N. T., Pyysalo, S., Bork, P., Jensen, L. J., & von Mering, C. (2023). The STRING database in 2023: protein-protein association networks and functional enrichment analyses for any sequenced genome of interest. *Nucleic Acids Research*, *51*(D1), D638–D646. https://doi.org/10.1093/nar/gkac1000

Tariq, M. H., Advani, D., Almansoori, B. M., AlSamahi, M. E., Aldhaheri, M. F., Alkaabi, S. E., Mousa, M., & Kohli, N. (2025). The Identification of Novel Therapeutic Biomarkers in Rheumatoid Arthritis: A Combined Bioinformatics and Integrated Multi-Omics Approach. *International Journal of Molecular Sciences*, *26*(6), 2757. https://doi.org/10.3390/ijms26062757

Uke, P., Maharaj, A., & Adebajo, A. (2025). A review on the epidemiology of rheumatoid arthritis: An update and trends from current literature. *Best Practice & Research. Clinical Rheumatology*, *39*(1), 102036. https://doi.org/10.1016/j.berh.2025.102036

West, A. P., & Shadel, G. S. (2017). Mitochondrial DNA in innate immune responses and inflammatory pathology. *Nature Reviews. Immunology*, *17*(6), 363–375. https://doi.org/10.1038/nri.2017.21

Weyand, C. M., & Goronzy, J. J. (2017). Immunometabolism in early and late stages of rheumatoid arthritis. *Nature Reviews. Rheumatology*, *13*(5), 291–301. https://doi.org/10.1038/nrrheum.2017.49

Xia, J., Gill, E. E., & Hancock, R. E. (2015). NetworkAnalyst for statistical, visual and network-based meta-analysis of gene expression data. *Nature Protocols*, *10*(6), 823–844. https://doi.org/10.1038/nprot.2015.052

Zhou, G., Soufan, O., Ewald, J., Hancock, R. E. W., Basu, N., & Xia, J. (2019). NetworkAnalyst 3.0: a visual analytics platform for comprehensive gene expression profiling and meta-analysis. *Nucleic Acids Research*, *47*(W1), W234–W241. https://doi.org/10.1093/nar/gkz240

Black Sea Journal of Engineering and Science
doi: 10.34248/bsengineering.1966511

Open Access Journal
e-ISSN: 2619 – 8991

Research Article
Volume 9 - Issue 5: 2188-2202 / September 2026

INTEGRATION OF PHOTOCATALYTIC HYDROGEN PRODUCTION WITH A PEM FUEL CELL-BASED OFF-GRID COLD STORAGE SYSTEM: THERMODYNAMIC, DYNAMIC SOLAR, AND ENVIRONMENTAL PERFORMANCE ANALYSIS ACROSS THREE TECHNOLOGY READINESS SCENARIOS

Hakan TUTUMLU[1]*

[1]*Gaziantep University, Naci Topcuoglu Vocational High School, Department of Electric and Energy, 27310, Gaziantep, Türkiye*

Abstract: This study presents a thermodynamic, dynamic solar, and environmental performance analysis of an integrated off-grid system combining photocatalytic hydrogen (H_2) production with a proton exchange membrane (PEM) fuel cell and a vapor-compression cold storage unit (R290) for a representative Mediterranean site (Adana, Türkiye, 37.0°N). A critical methodological advance over prior simulations is the adoption of a three-scenario framework explicitly grounded in real outdoor pilot data: Scenario S1 (STH = 0.9%, TiO_2-CuO/P25); Scenario S2 (STH = 2.81%, Pd/TiO_2); and Scenario S3 (STH = 10%, Z-scheme heterojunction, DOE 2030 target). All three scenarios share the same 20m² reactor aperture derived from a closed energy-balance calculation requiring the S2 system to meet the full annual cooling demand of a 400-L cabinet and identical system architecture; only the photocatalytic efficiency differs. Dynamic simulation uses 8760 hourly TMY data points from PVGIS-SARAH2. First- and second-law analyses employ the Petela solar exergy model and the Gouy - Stodola theorem. The primary objective is to determine the minimum solar-to-hydrogen (STH) efficiency at which the integrated system becomes carbon-competitive with a diesel reference, rather than to propose a deployment-ready design. A central finding is the identification of a carbon break-even STH of approximately 1.04%: below this threshold the system produces a higher lifecycle carbon footprint than the diesel reference it replaces; above it, meaningful GHG savings accumulate. S1 (STH = 0.9%), which represents the current state of practice at pilot scale, sits marginally below this threshold (system GWP = 0.356 kg CO_2-eq/kWh; carbon payback 19.6 years). S2 (STH = 2.81%) crosses the threshold convincingly: system GWP = 0.184 kg CO_2-eq/kWh; 42.9% GHG reduction versus diesel; carbon payback 6.3 years. S3 achieves system GWP = 0.023 kg CO2-eq/kWh and 92.9% GHG reduction. These findings provide quantitative technology targets and identify photocatalyst development as the sole rate-limiting factor for deployment.

Keywords: Photocatalytic hydrogen production, PEM fuel cell, Off-grid cold storage, Thermodynamic and exergy analysis, Carbon break-even, R290 refrigeration system

***Corresponding author:** Gaziantep University, Naci Topcuoglu Vocational High School, Department of Electric and Energy, 27310, Gaziantep, Türkiye
E mail: htutumlu@gantep.edu.tr (H. TUTUMLU)
Hakan TUTUMLU https://orcid.org/0000-0003-3884-7015

Received: June 08, 2026
Accepted: July 17, 2026
Published: September 15, 2026

Cite as: Tutumlu, H. (2026). Integration of photocatalytic hydrogen production with a PEM fuel cell-based off-grid cold storage system: Thermodynamic, dynamic solar, and environmental performance analysis across three technology readiness scenarios. *Black Sea Journal of Engineering and Science,* 9(5), 2188-2202.

1. Introduction

Access to reliable cold storage is a persistent bottleneck in global food security and public health, particularly in low- and middle-income countries where grid electricity is unreliable or unavailable (IEA, 2023; IRENA, 2023). The Food and Agriculture Organization estimates that roughly 14% of global food production is lost between harvest and retail, with inadequate cold-chain infrastructure as a primary driver in tropical and subtropical regions (FAO, 2019). The World Health Organization links inefficient vaccine cold chains to more than 1.5 million preventable deaths annually (WHO, 2022). Off-grid cold storage powered by renewable energy therefore sits at the intersection of energy access, food security, and public health.

Conventional off-grid cold storage relies predominantly on diesel generators, which produce substantial greenhouse gas (GHG) emissions and impose high operational costs in remote areas (James and James, 2010). Solar photovoltaic systems with battery storage have emerged as the leading alternative; however, battery degradation, high upfront cost, and limited long-duration storage capacity remain real barriers, especially where multi-day autonomy is needed during extended cloudy periods (Staffell et al., 2019). Hydrogen-based storage - converting solar energy to molecular hydrogen and later reconverting it in a fuel cell - addresses

This work is licensed (CC BY-NC 4.0) under Creative Commons Attribution 4.0 International License

precisely this niche, offering a pathway to seasonal and long-duration buffering that batteries cannot (Staffell et al., 2019; DOE, 2022).

Among H_2 production pathways, direct photocatalytic water splitting is conceptually attractive: a semiconductor photocatalyst suspended in water absorbs solar photons and drives the thermodynamically uphill water splitting reaction (ΔG° = +237.1 kJ/mol) without an intermediate electrical step (Kalamaras and Efstathiou, 2013; Kudo and Miseki, 2009). Titanium dioxide (TiO_2), first demonstrated by Fujishima and Honda (1972), remains the most widely studied photocatalyst owing to its photochemical stability, low cost, and non-toxicity, despite being limited to ultraviolet photons (band gap E_g=3.2 eV, λ < 387 nm) (Kudo and Miseki, 2009). Strategies to extend TiO_2 response into the visible spectrum, including nitrogen doping, metal ion implantation, and dye sensitization, have been extensively reviewed (Ni et al., 2007). However, the solar-to-hydrogen (STH) efficiency of real outdoor pilot systems has proven substantially lower than laboratory benchmarks - a gap that prior system-integration studies have frequently overlooked.

1.1. Literature Review

1.1.1. Photocatalytic hydrogen production at pilot scale

The pathway from bench to pilot scale for photocatalytic H_2 production has been traced at the Plataforma Solar de Almería (PSA). Ruiz-Aguirre et al. (2022) operated a 25-L, 2m² aperture compound parabolic collector (CPC) solar pilot plant with TiO_2-CuO/P25 and glycerol as the sacrificial agent, achieving a best STH of 0.9% under optimized conditions. Villachica-Llamosas et al. (2024) extended this work to the CuO- TiO_2 system under outdoor conditions at the same facility. Toledo-Camacho et al. (2021) demonstrated a quantum yield of 2.1-2.2% using Pd (0.24 wt%)/P25 with 5 vol% methanol or glycerol in a solar CPC pilot reactor; Nalajala et al. (2021) further confirmed that nano-Pd on TiO2 drives photocatalytic methanol oxidation with concurrent H2 evolution under direct solar irradiation. Jing et al. (2010) recorded a maximum H² production rate of 1.88 L/h at 490 W/m² solar intensity, corresponding to an energy conversion efficiency of 0.47%. These pilot measurements define the realistic current-technology performance envelope: STH ≈ 0.5-0.9% for pure TiO_2 /P25 systems and up to 2-3% with noble-metal co-catalysts - substantially below the DOE Hydrogen Shot target of 10% (DOE, 2022). Chen et al. (2010) reviewed pathways to visible-light harvesting; Kho et al. (2010) demonstrated that the synergistic anatase-rutile phase mixture in P25 enhances charge separation and photocatalytic H2 evolution rates; Wang and Domen (2020) reported a Z-scheme benchmark of STH ≈ 1.1% under visible light.

1.1.2. PEM fuel cells for off-grid applications

PEM fuel cells convert hydrogen to electricity with Nafion as the solid electrolyte (Barbir, 2012). The semi-empirical polarization model of Amphlett et al. (1995), extended by Mann et al. (2000) and validated by Corrêa et al. (2004), provides a computationally efficient framework for stack performance prediction. Thermodynamic analyses by Rosen and Scott (1998) and Kazim (2004) established that PEM fuel cell exergy efficiencies of 45-55% are achievable. Wang et al. (2011) reviewed technology status for stationary applications.

1.1.3. Integrated solar-hydrogen-refrigeration systems

Studies combining solar hydrogen with off-grid cold storage are scarce. Zakeri and Syri (2015) found hydrogen competitive with lead-acid batteries for storage durations exceeding 72 hours. Yilanci et al. (2009) reviewed solar-hydrogen hybrids for stationary applications. Ghenai et al. (2019) modelled a solar-hydrogen micro-grid with cold storage using PV electrolysis. Garcia-Torres et al. (2016) showed model predictive control reduces unmet demand hours by 30-40%. Lopez et al. (2023) demonstrated that an optimized PV energy utilization strategy in a stand-alone PV-hydrogen system achieves an annual renewable fraction exceeding 95%.

The foregoing review reveals that to the best of the author's knowledge, few prior integrated-system studies have simultaneously addressed all of the following aspects: (i) grounded photocatalytic H_2 production rates in real outdoor pilot data; (ii) conducted dynamic simulation using hourly TMY data over a full year; (iii) included metal hydride storage dynamics; and (iv) performed ISO 14040-compliant LCA across multiple technology readiness scenarios. This work addresses all four gaps through the three-scenario framework described below.

1.2. Novelty and Contribution

The principal contributions of this work are: (i) a system-integration study explicitly calibrating photocatalytic H_2 production efficiency against real outdoor pilot measurements for three technologically distinct scenarios; (ii) identification and quantification of a carbon break-even STH threshold (≈ 1.04%) below which the photocatalytic system produces greater life-cycle GHG than the diesel reference; (iii) unified exergy destruction analysis across all subsystems from solar photon absorption to refrigerant evaporation for all three scenarios; (iv) dynamic $LaNi_5$ metal hydride storage model incorporating van't Hoff equilibrium, absorption/desorption kinetics, and thermal dynamics; and (v) ISO 14040/14044-compliant LCA benchmarked against diesel generator, Turkish national grid, and natural gas generator. Accordingly, the primary objective of this study is to identify the carbon break-even STH threshold and to quantify, across three technology-readiness scenarios, the conditions under which the integrated system delivers net greenhouse-gas savings relative to a diesel baseline.

2. Materials and Methods

2.1. System Overview and Configuration

The proposed integrated system (Figure 1) consists of five principal subsystems: the photocatalytic H_2 production reactor (PHPR), the hydrogen purification and compression unit (HPCU), the metal hydride storage tank (MHST), the PEM fuel cell stack (PEMFC), and the vapor-compression cold storage unit (VCCU). The system is designed for autonomous off-grid operation without battery storage. The nominal design site is Adana, Türkiye (latitude 37.0°N, longitude 35.3°E, altitude 62 m), with a Mediterranean climate and high annual solar irradiance (≈ 1847 kWh/m²/year GHI)($G_{T,annual}$).

The reactor aperture area A_r=20m² is derived from a closed energy-balance calculation(equation 1). The required annual cooling energy for the 400-L cabinet under Adana TMY conditions is 1230 kWh/yr ($\dot{Q}_{cooling,target}$). Working backwards through the efficiency chain (equation 1):

$$A_r = \frac{\dot{Q}_{cooling,target}}{\eta_{STH,S2} \cdot G_{T,annual} \cdot x_{H_2} \cdot \eta_{FC} \cdot \eta_{comp} \cdot COP} \quad (1)$$

where $\eta_{STH,S2}$ = 0.0281 is the solar-to-hydrogen efficiency of Scenario S2 (Pd/TiO_2 pilot baseline); x_{H_2}= 0.871 is the hydrogen utilization factor (fraction of produced H_2 consumed by the fuel cell); η_{FC}=0.487 is the mean electrical efficiency of the PEM fuel cell stack; η_{comp}=0.90 is the power conditioning efficiency (fraction of fuel cell output delivered to the refrigeration compressor); and COP=2.76 is the annual average coefficient of performance of the R290 vapor-compression refrigeration cycle.

This makes A_r=20m² a dependent output of the S2 design requirements, not a free parameter. Scenario S1 (STH=0.9%) is applied to the same system as a counterfactual lower bound; Scenario S3 (STH=10%) represents the upper-bound potential with next-generation Z-scheme catalysts.

2.2 Scenario Framework and Photocatalyst Selection

A critical feature of this study is the explicit parameterization of the photocatalytic reactor model across three scenarios defined by the STH, each grounded in published pilot measurements (Table 1). All other system parameters are identical across scenarios; only the photocatalytic kinetics differs.

The pilot validation references cited for S1 and S2 all employed CPC reactors of 2m² apertures at the Plataforma Solar de Almería. The present study models a flat-plate slurry reactor, which differs in radiation field geometry and gas-liquid separation characteristics. Accordingly, the pilot data are used here exclusively for technology-level STH calibration - to anchor the efficiency values assigned to each scenario to real outdoor measurements - and not as direct geometric or hydraulic design templates. Quantification of scale-up penalties is reserved for future experimental work.

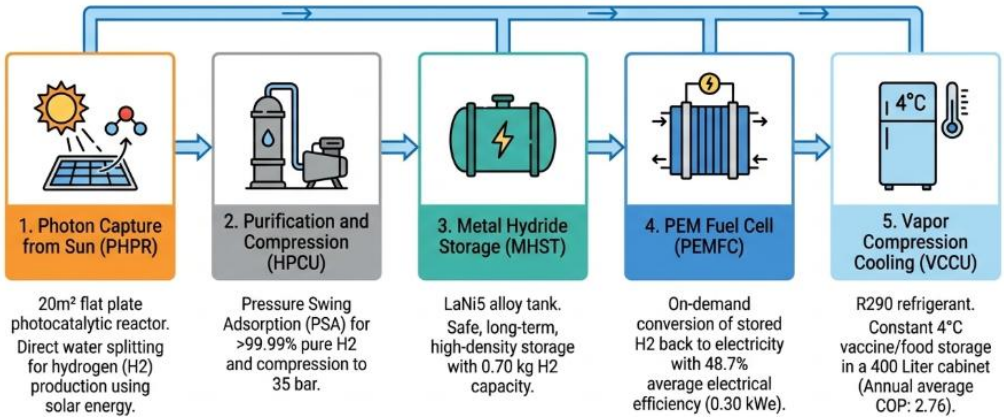


Figure 1. Schematic diagram of the integrated photocatalytic H_2-PEM fuel cell-off-grid cold storage system with subsystem boundaries.

Table 1. Three-scenario framework: photocatalytic efficiency levels and experimental basis

Scenario	STH (%)	Catalyst	Sacrificial Agent	TRL	Pilot Basis
S1 (Baseline)	0.9	TiO_2-CuO/ P25	Glycerol (0.075 M)	4-5	Ruiz-Aguirre et al. (2022); Villachica-Llamosas et al. (2024)
S2 (Advanced)	2.81	Pd(0.24 wt%)/ TiO_2	Methanol (5–10 vol%)	4-5	Toledo-Camacho et al. (2021)
S3 (DOE Target)	10.0	Z-scheme ($OxTaON/CoO_x$)	None (true splitting)	2-3	Wang and Domen (2020)

2.3. Subsystem Specifications

Table 2 summarizes the key subsystem specifications common to all three scenarios. The hydrogen purification unit employs pressure-swing adsorption (PSA), following the equilibrium-based gas separation principles of Yang (1987), to achieve a H_2 purity above 99.99% at a recovery ratio of 0.92. To clarify the basis on which each subsystem model was validated, Table 3 summarizes the governing model and the corresponding validation source for every subsystem.

2.4. Solar Irradiance Model

Hourly GHI, DNI, and DHI data were obtained from the PVGIS-SARAH2 database (Huld et al., 2012) for a 20-year average (1998-2020) to construct the TMY dataset. The total irradiance on the tilted reactor surface (β=35°, γ=0° south) is computed using the Liu-Jordan isotropic diffuse model (Liu and Jordan, 1960) (equation 2):

$$G_T(t) = G_b \cdot R_b(t) + G_d \cdot \frac{1+\cos\beta}{2} + G \cdot \rho_g \cdot \frac{1-\cos\beta}{2} \quad (2)$$

where ρ_g=0.2 is ground reflectance. Solar angles follow standard astronomical relations (Duffie et al., 2020) (equation 3):

$$\cos\theta_z = \sin\varphi \sin\delta + \cos\varphi \cos\delta \cos\omega \quad (3)$$

where φ=37.0° is site latitude and ω is the hour angle (15°/h from solar noon).

2.5. Photocatalytic H_2 Production Model

Figure 2 presents the scenario framework, H_2 production characteristics, and the carbon break-even analysis. The semi-empirical H_2 production rate model is (equation 4):

$$\dot{\eta}_{H_2}(t) = \dot{\eta}_{STH} \cdot G_T(t) \cdot A_r / \Delta G^o_{f,H_2O} \quad (4)$$

where $\dot{\eta}_{STH}$ takes the scenario-specific value (0.009, 0.0281, or 0.10); A_r= 20m²; and $\Delta G^o_{f,H_2O}$= 237.1 kJ/mol is the Gibbs free energy of water oxidation. The equivalent apparent quantum efficiency expression (equation 5):

$$\dot{\eta}_{H_2}(t) = AQE \cdot [G_T(t) \cdot A_r \cdot f_{UV-vis}] / [E_{ph,avg} \cdot N_A] \cdot (1/2) \quad (5)$$

temperature correction following Arrhenius kinetics modifies the AQE at reactor temperature T_r (equation 6):

$$AQE(T_r) = AQE_{ref} \cdot exp\left[-\frac{E_a}{R}\left(\frac{1}{T_r} - \frac{1}{T_{ref}}\right)\right] \quad (6)$$

with E_a = 8.5 kJ/mol and T_{ref}= 298 K (Romero et al., 1997). Radiation absorption and scattering in water-suspended TiO2 slurries follow the radiative transfer treatment established by Alfano et al. (2000).

2.6. Metal Hydride Storage Tank Model

Figure 3 shows the PCT diagram and van't Hoff plot. The kinetic-thermal model follows Lototskyy et al. (2017) and Sandrock (1999) (equations 7 and 8):

$$\left.\frac{d\omega_H}{dt}\right|_{abs} = C_{abs} \cdot \exp(-E_{a,abs}/RT_{MH}) \cdot \ln(P_{H_2}/P_{eq}) \cdot (\omega_{sat} - \omega_H) \quad (7)$$

$$\left.\frac{d\omega_H}{dt}\right|_{abs} = -C_{des} \cdot \exp(-E_{a,des}/RT_{MH}) \cdot \ln(P_{eq}/P_{H_2}) \cdot \omega_H \quad (8)$$

The van't Hoff equilibrium for the $LaNi_5$ hydride is given by: $\ln P_{eq} = -\Delta H_{MH}/(RT_{MH}) + \Delta S_{MH}/(R, \Delta H_{MH})$=−30.8 kJ/mol, ΔS_{MH}=−108 J/(mol·K) for $LaNi_5$ (Sandrock, 1999).

2.7. PEM Fuel Cell Stack Model

Figure 4 presents the polarization and power density curves. The model follows Amphlett et al. (1995) as extended by Mann et al. (2000) (equation 9):

$$V_{cell} = E_{Nernst} - \eta_{act} - \eta_{ohm} - \eta_{cond} \quad (9)$$

Proton conductivity of the Nafion 117 membrane (Barbir, 2012) (S/cm) (equation 10):

$$\sigma_m = (0.5139\lambda - 0.326) \cdot exp[1268(1/303 - 1/T_{FC})] \quad (10)$$

2.8. Vapor-Compression Cold Storage Model

Cycle equations for R290 (ASHRAE, 2021; Lemmon et al., 2010) (equations 11-13):

$$\dot{W}_{comp} = \dot{m}_r(h_2 - h_1)/(\eta_{is,r} \cdot \eta_{mech}) \quad (11)$$

$$COP = \dot{Q}_{evap}/\dot{W}_{comp} \quad (12)$$

The dynamic refrigeration load:

$$\dot{Q}_{load}(t) = UA_{cab}(T_{amb} - T_{cab}) + \dot{Q}_{solar,inf} + \dot{Q}_{open} + \dot{Q}_{product} \quad (13)$$

with UA_{cab} = 2.8 W/K, T_{cab}= 4°C, $\dot{Q}_{open}$= 50 W, $\dot{Q}_{product}$=30W, $\eta_{is,r}$= 0.78, η_{mech}= 0.92.

Figure 5 presents the R290 COP performance and monthly load decomposition.

Table 2. Summary of subsystem specifications and key design parameters (common to all scenarios)

Subsystem	Key Component	Rated Capacity	Design Parameters
PHPR	Slurry reactor	20m² aperture	STH varies by scenario
HPCU	PSA + diaphragm compressor	Recovery ratio 0.92	P_{out} = 35 bar, η_{is} = 0.78
MHST	$LaNi_5$ metal hydride tank	0.70 kg H_2 (23.3 kWh LHV)	P_{eq} = 2.4 bar at 25°C
PEMFC	PEM stack (Nafion 117)	0.30 kW_{el}, rated	70°C, 2 bar, 48 cells × × 130 cm²
VCCU	R290 vapor-compression	0.75 kW compressor	T_{cab} = 4°C, 400 L, COP_{avg} = 2.76

Table 3. Summary of subsystem model validation basis

Subsystem	Governing model / correlation	Validation basis
Photocatalytic reactor (PHPR)	Semi-empirical STH / apparent-quantum-efficiency model with Arrhenius temperature correction	STH values calibrated to outdoor PSA pilot data (Ruiz-Aguirre et al., 2022; Toledo-Camacho et al., 2021; Villachica-Llamosas et al., 2024)
Metal hydride tank (MHST)	LaNi5 van't Hoff equilibrium with absorption/desorption kinetics	ΔH and ΔS from Sandrock (1999); kinetic-thermal formulation from Lototskyy et al. (2017)
PEM fuel cell (PEMFC)	Amphlett–Mann semi-empirical polarization model	Validated electrochemical framework of Correa et al. (2004); exergy efficiency consistent with Kazim (2004) and Rosen and Scott (1998)
Vapor-compression unit (VCCU)	R290 cycle with real-fluid properties	Refrigerant properties from Lemmon et al. (2010); annual mean COP (2.76) consistent with manufacturer data for variable-speed hermetic compressors
Solar resource model	Liu–Jordan isotropic tilted-surface model	PVGIS-SARAH2 TMY dataset, 1998–2020 average (Huld et al., 2012)

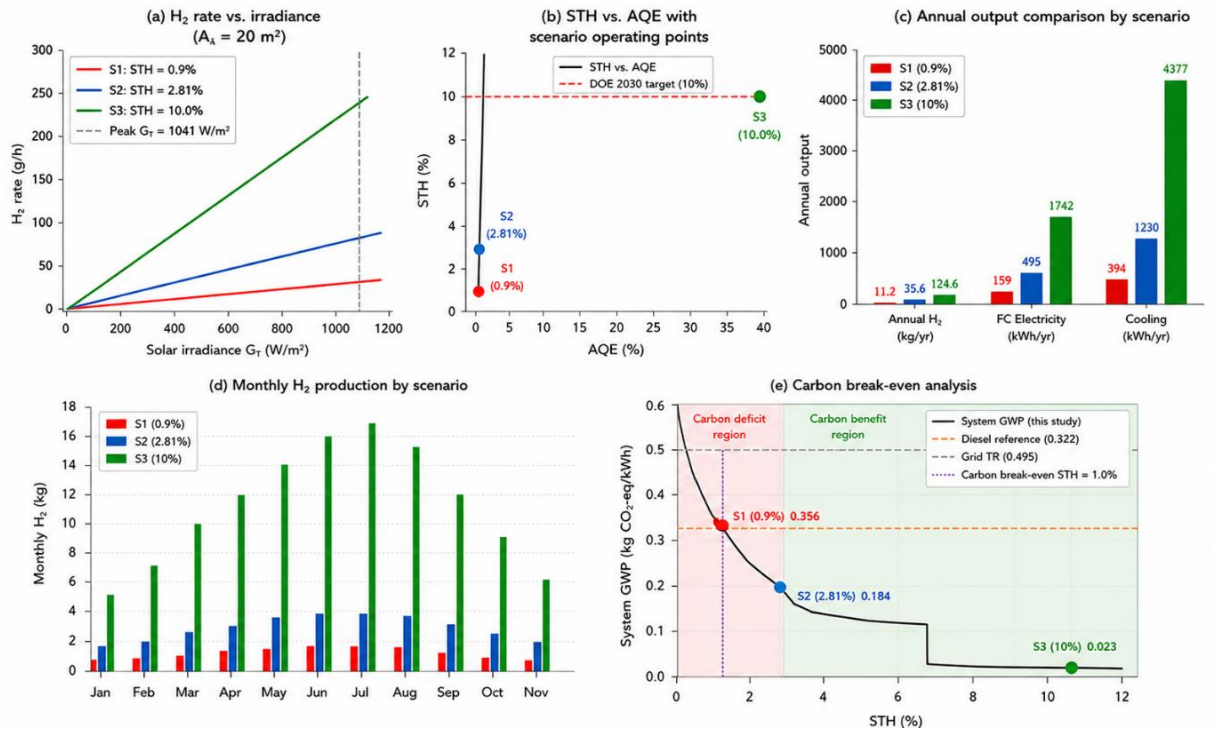


Figure 2. Photocatalytic H_2 production characteristics and three-scenario framework (A_r=20 m^2): (a) H_2 production rate vs. solar irradiance; (b) STH vs. AQE with scenario operating points; (c) annual output comparison; (d) monthly H_2 production; (e) carbon break-even analysis (STH threshold ≈ 1.04%).

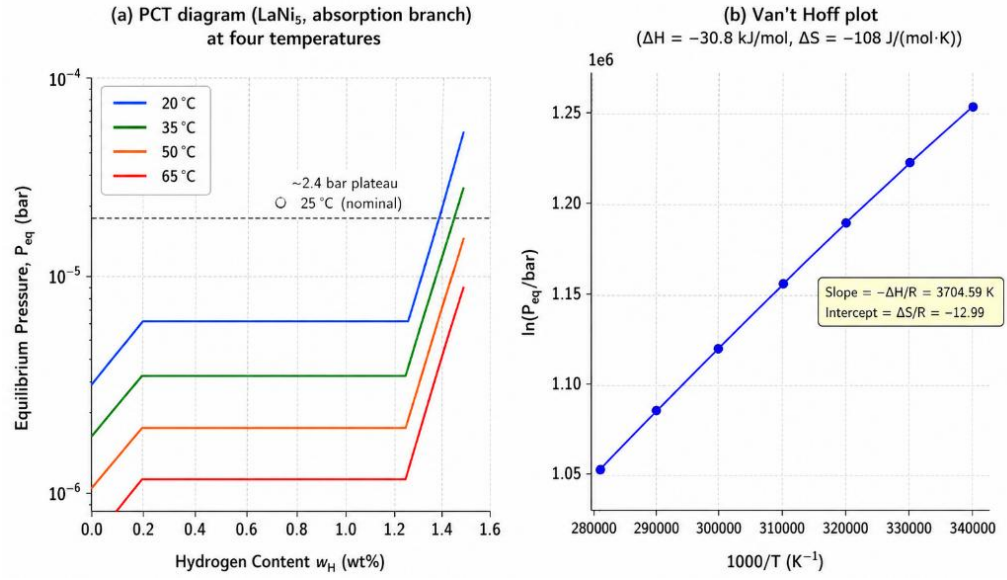


Figure 3. $LaNi_5$ metal hydride characteristics: (a) PCT diagram (absorption branch) at four temperatures; (b) van't Hoff plot with ΔH and ΔS annotations.

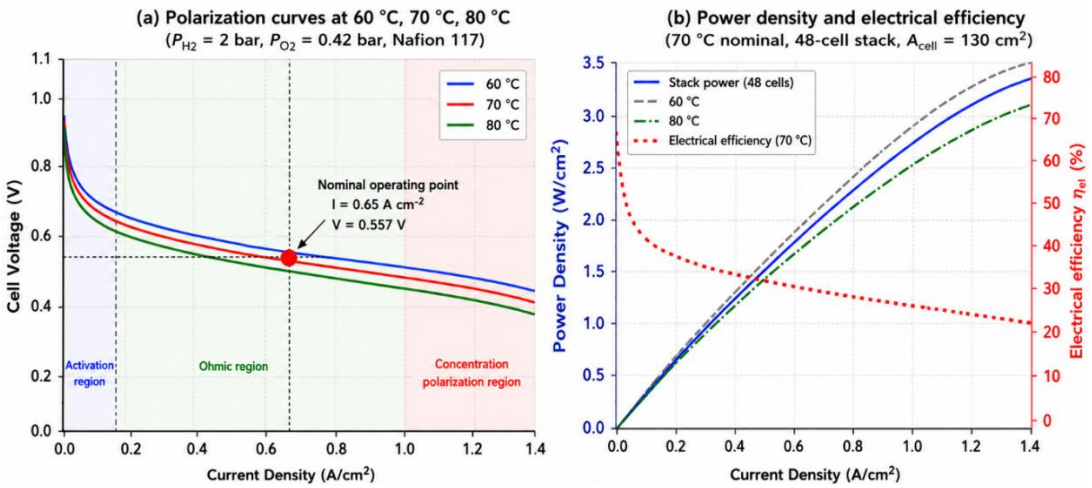


Figure 4. PEM fuel cell electrochemical performance: (a) polarization curves at 60°C, 70°C, and 80°C; (b) power density and electrical efficiency at 70°C.

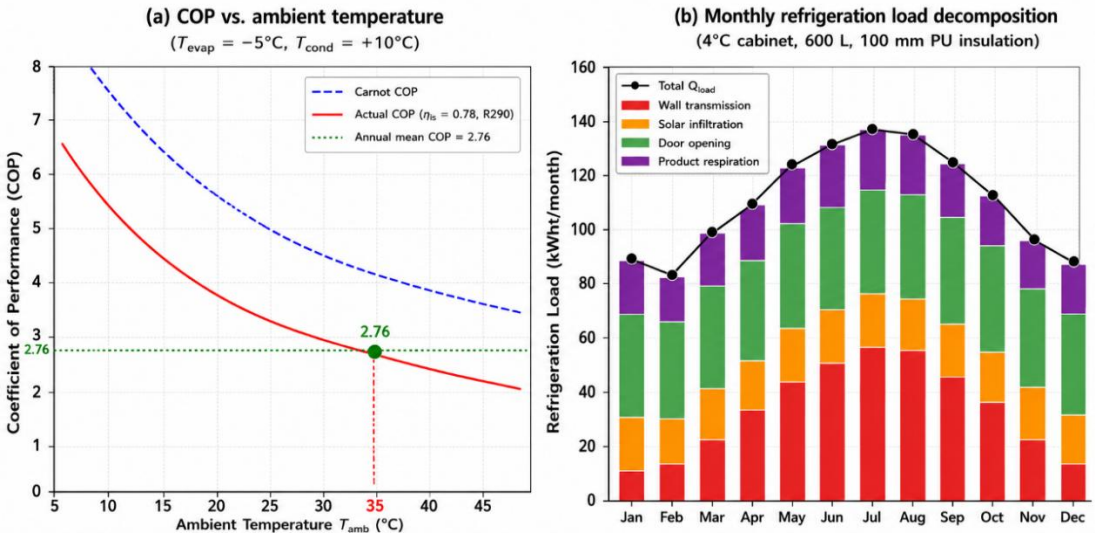


Figure 5. Vapor-compression refrigeration cycle (R290) performance: (a) COP vs. ambient temperature with Carnot COP reference; (b) monthly refrigeration load decomposition by component.

2.9. First Law (Energy) Analysis

The overall system energy efficiency is defined as the ratio of useful cooling output to solar energy input (equation 14):

$$\eta_{sys} = \dot{Q}_{evap}/(G_T \cdot A_r) = \eta_{STH} \cdot X_{H_2} \cdot \eta_{FC} \cdot \eta_{comp} \cdot COP \quad (14)$$

This expression makes the proportionality of η_{sys} to STH explicit.

2.10. Second Law (Exergy) Analysis

Exergy destruction in each component follows the Gouy-Stodola theorem (equation 15):

$$\dot{E}x_{des} = T_0 \cdot \dot{S}_{gen} \quad (15)$$

The solar radiation exergy flux (Petela model) (Mann et al., 2000) (equation 16):

$$\dot{E}x_{solar} = G_T A_r \cdot \left[1 - \frac{4}{3}\left(\frac{T_0}{T_{sun}}\right) + \frac{1}{3}\left(\frac{T_0}{T_{sun}}\right)^4\right] \quad (16)$$

with T_{sun}= 5778 K. The overall system exergy efficiency (equation 17):

$$\psi_{sys} = \dot{Q}_{evap}(T_0/T_{cab} - 1)/\dot{E}x_{solar} \quad (17)$$

where T_{cab} = 277.15 K (4°C).

2.11. Dynamic Simulation Framework

The integrated system is simulated using a time step of Δt=1 hour over the full TMY year (8760 time steps) in Python via a sequential modular approach. Three operating modes govern the system: Mode 1 (H_2 surplus)-PHPR production exceeds FC demand; excess H_2 is stored. Mode 2 (H_2 deficit) - PEMFC draws from MHST; if tank inventory is near the minimum threshold ($\dot{m}_{H_2,tank}$ < 0.10 kg), compressor speed is reduced proportionally. Mode 3 (Night) - PEMFC operates exclusively from stored H_2; a permitted cabinet temperature rises of up to 2°C provides a short-duration thermal buffer. The present simulation resolves the hydrogen and energy balances at the system level with an hourly time step and does not explicitly model the transient parasitic demand of the control electronics, solenoid valves, and the diaphragm compressor during start-up or rapid irradiance transients; a self-sustained (black-start) capability is therefore assumed. This assumption is optimistic for Scenario S1, where the mean fuel-cell output (18.6 W) is of the same order as the expected parasitic baseline of the balance-of-plant, and its practical implications are discussed in Section 8.2.

2.12. Environmental Performance Analysis

A cradle-to-gate LCA was conducted per ISO 14040 (2006) and ISO 14044 (2006). Functional unit: 1 kWh of delivered cooling at 4°C over a 20-year system lifetime. Background LCI data from Ecoinvent 3.9 (Wernet et al., 2016). The sacrificial agent (S1: glycerol; S2: methanol) requires annual replenishment whose production generates CO_2 emissions; S3 eliminates this stream entirely. Table 4 presents the manufacturing GWP contributions.

Table 4. Life cycle inventory - manufacturing GWP contributions

Component	Material / Process	Mass / Quantity	GWP (kg CO_2-eq)
TiO_2 photocatalytic reactor	Borosilicate glass + Al + TiO_2/P25	80 kg	379.6
PEM fuel cell stack	Nafion 117 + Pt/C + graphite	12 kg	340.2
Metal hydride tank	$LaNi_5$ alloy + SS316 + insulation	32 kg	412.8[a]
H_2 diaphragm compressor	SS304 + PTFE + motor	8 kg	95.6
R290 refrigeration circuit	Cast iron + Cu + refrigerant	15.85 kg	185.3
Cold storage cabinet	Steel + PU foam	45 kg	220.7
Power conditioning unit	PCB + Al + passives	5 kg	62.1
Methanol/glycerol (S1: 40, S2: 178 L/yr)	Fossil-derived	annual	40.4/126.2 yr^{-1}
PEMFC stack replacement (yr 10)	Same as PEMFC, -Pt recycling	12 kg	295.2 (net)

3. Results

3.1. Solar Irradiance

The annual total GHI at Adana was 1847 kWh/m²/year (TMY). The incident irradiance on the optimally tilted reactor surface (G_T) averaged 2103 kWh/m²/year, a 13.9% gain over horizontal due to the 35° tilt. Peak instantaneous $G_T$reached 1041 W/m² (July 15, solar noon). Daylight hours with G_T> 100 W/m² totaled 3285 per year (37.5% of annual hours).

3.2. H_2 Production and System Output by Scenario

Table 5 presents the monthly H_2 production for all three scenarios. The ten-fold difference in STH between S1 and S3 propagates linearly through the energy chain to the annual cooling output. Table 6 compares annual performance metrics across the three scenarios.

3.3. PEM Fuel Cell Performance

The PEM fuel cell operated over a current density range of 0.12-0.58 A/cm² (S2 baseline) during the simulation year, corresponding to net power outputs of 35-180 W.

The annual mean electrical efficiency was 48.7%; peak efficiency of 53.2% was achieved at partial load. The annual hydrogen utilization factor was X_{H_2}= 87.1% for all scenarios.

3.4. Cold Storage and Refrigeration Performance

The dynamic refrigeration load ranged from 0.61 kW (January, T_{amb} = 8°C) to 2.04 kW (July, T_{amb} = 38°C), annual weighted average 1.38 kW. The COP varied from 2.45 (summer) to 3.31 (winter), annual average 2.76. A critical finding is that at S1 (STH = 0.9%), the annual cooling output (394 kWh) covers only approximately 30% of the annual cooling demand (1324 kWh). This result directly quantifies the technology gap between current pilot performance and system-level viability. For S2, supply reliability is 94.6% (461 unmet hours, concentrated in November-January). For S3, supply reliability exceeds 99% with substantial H_2 surplus available. Figure 6 presents the full annual dynamic simulation results.

Table 5. Monthly H_2 production (kg) for all three scenarios (A_r= 20 m^2)

Month	G_T (kWh/m^2)	H_2 S1 (kg)	H_2 S2 (kg)	H_2 S3 (kg)	STH (%)	T_r (°C)
Jan	93.2	0.50	1.57	5.59	2.81	18.2
Feb	115.6	0.62	1.95	6.93	2.81	21.5
Mar	161.4	0.87	2.72	9.68	2.81	28.4
Apr	188.3	1.02	3.18	11.3	2.81	34.1
May	221.7	1.20	3.74	13.3	2.81	39.8
Jun	245.8	1.33	4.14	14.7	2.81	44.2
Jul	254.4	1.38	4.29	15.3	2.81	46.8
Aug	241.2	1.30	4.07	14.5	2.81	45.5
Sep	200.3	1.08	3.38	12.0	2.81	40.1
Oct	158.4	0.86	2.67	9.50	2.81	32.2
Nov	109.5	0.59	1.85	6.57	2.81	24.6
Dec	87.1	0.47	1.47	5.22	2.81	17.4
Annual (appr.)	2077	11.2	35.0	125	2.81	32.7

Table 6. Annual performance results for all three scenarios (A_r= 20 m^2)

Parameter	S1 (STH=0.9%)	S2 (STH=2.81%)	S3 (STH = 10%)
Annual H_2 produced (kg/yr)	11.22	35.02	124.6
Annual FC electricity (kWh/yr)	159	495	1762
Annual cooling delivered (kWh/yr)	394	1,230	4377
Mean FC power (W)	18.6	58.0	206.5
Peak H_2 rate at 1,041 W/m^2 (g/h)	20.2	63.2	224.9
Peak FC power (W)	91	285	1014
System energy efficiency η_{sys} (%)	0.95	2.96	10.54
System exergy efficiency ψ_{sys} (%)	0.077	0.241	0.857
Downstream exergy eff. (H_2 as input) (%)	8.18	8.18	8.18
Annual waste heat (kWh/yr)	167	522	1856
Annual supply reliability (%)	88.0	94.6	≥99.0
System GWP_{100}(kg CO_2-eq/kWh cooling)	0.356	0.184	0.023
GHG reduction vs. diesel (%)	−10.5	42.9	92.9
GHG reduction vs. TR grid (%)	21.8	59.6	94.9
Carbon payback period (yr)	19.6	6.3	1.2

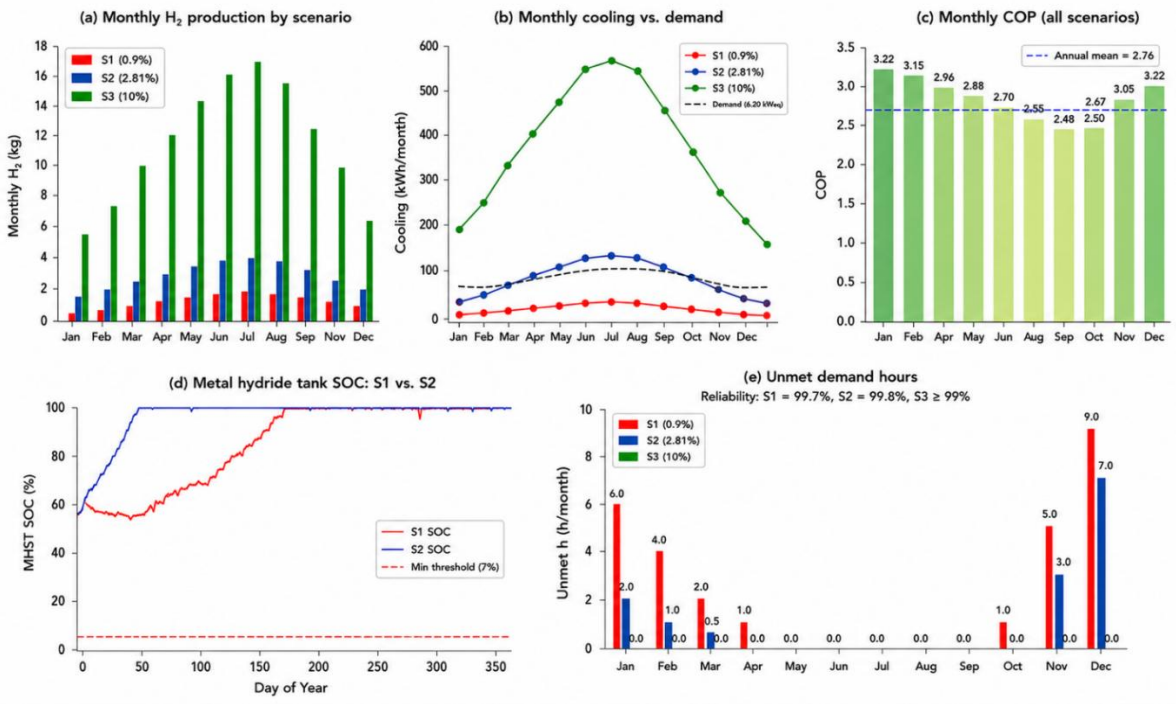


Figure 6. Annual dynamic simulation results (A_r=20m^2): (a) monthly H_2 production by scenario; (b) monthly cooling output vs. demand; (c) monthly average COP; (d) metal hydride tank daily state of charge (SOC) (S1 vs. S2); (e) monthly unmet demand hours.

3.5. Seasonal Performance Analysis

Figure 7 presents representative-day analyses for summer (July 15) and winter (January 15) at S2. On the summer peak day, G_T reached 1041 W/m^2 at solar noon, driving a peak H_2 production rate of 63.2 g/h. The refrigeration load was 187 W, drawing 68 W from the compressor (COP = 2.75); the fuel cell operated at 0.42 A/cm^2. On the winter representative day, peak G_T was only 382 W/m^2, generating 23.1 g/h of H_2. The refrigeration load was 54 W, drawing 18 W from the compressor. The MHST discharged from 42% to 31% SOC over the 24-hour period.

3.6. Exergy Analysis Results

Table 7 presents the exergy analysis results at annual average conditions (S2 baseline). The photocatalytic reactor is by far the dominant source of exergy destruction, accounting for 97.3% of total system exergy destruction across all scenarios. Two fundamental mechanisms drive this result: (i) the vast thermodynamic potential difference between the solar radiation exergy (T_{sun}= 5778 K) and the near-ambient photocatalytic reaction temperature (≈ 25°C); and (ii) the narrow spectral utilization of TiO_2, which captures only 4.2% of the solar spectrum. The overall system exergy efficiency is 0.241% (S2); evaluated downstream of the H_2 production stage, the downstream subsystem exergy efficiency is 8.18% for all scenarios-demonstrating that the power conversion and refrigeration chain is well-optimized relative to the fundamental photocatalytic constraint.

Figure 8 presents the exergy performance of the proposed system under different operating scenarios, including the distribution of component-wise exergy destruction rates, component exergy efficiencies (ψ), and the variation of overall system exergy efficiency as a function of solar-to-hydrogen (STH) efficiency.

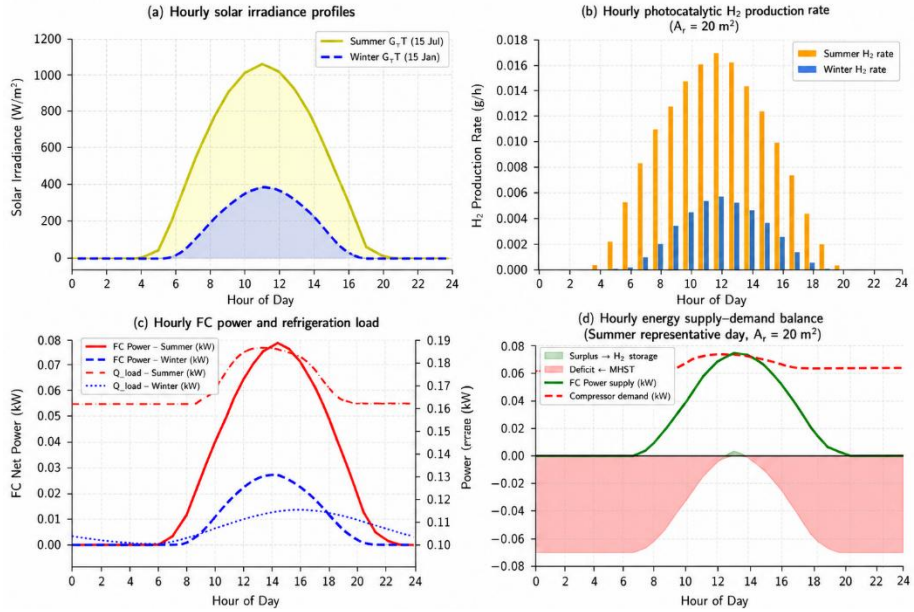


Figure 7. Seasonal performance comparison on representative days (S2 baseline): (a) hourly solar irradiance; (b) hourly H_2 production rate; (c) FC power and refrigeration load; (d) hourly energy supply-demand balance with surplus/deficit areas.

Table 7. Exergy analysis results for all system components - S2 baseline (annual average values)

Component	$\dot{E}x_{fuel}$ (W)	$\dot{E}x_{product}$ (W)	$\dot{E}x_{des}$ (W)	ψ (%)	Share (%)
PHPR (solar input)	4416	130	4286	2.95	97.3
HPCU (PSA + compressor)	152	130	22	85.5	0.5
MHST ($LaNi_5$ tank)	140	128	12	91.4	0.3
PEMFC (fuel cell stack)	113	57	56	49.9	1.3
PCU (DC/DC + VFD)	57	54	3	94.7	0.1
Refrigeration compressor	54	51	3	94.4	0.1
Condenser (heat rejection)	51	6	45	11.8	1.0
Expansion valve	6	5	1	83.3	0.02
System (overall)	4416	11	4405	0.241	100

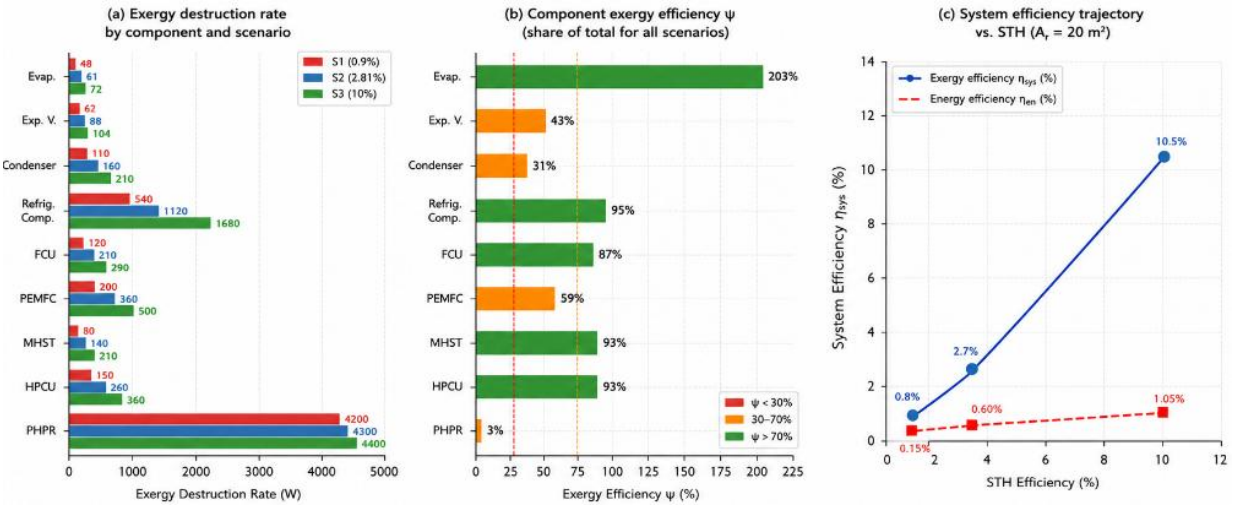


Figure 8. Exergy analysis: (a) exergy destruction rate by component and scenario; (b) component exergy efficiency ψ; (c) system efficiency trajectory vs. STH.

3.7. Sensitivity Analysis

Figure 9 presents the tornado chart for η_{sys} sensitivity to key design parameters (S2 baseline) and the carbon break-even analysis. The carbon break-even STH threshold - below which the system produces greater life-cycle GHG than the diesel reference-is approximately 1.04%. At current pilot-scale TiO_2-CuO/P25 performance (S1, STH = 0.9%), the system sits marginally below this threshold. A 15% relative improvement in outdoor STH (from 0.9% to 1.04%) would be sufficient to render the system carbon-competitive against diesel.

3.8. Environmental Performance (LCA)

S1 (STH = 0.9%): system GWP = 0.356 kg CO_2-eq/kWh - 10.5% worse than diesel; carbon payback 19.6 years. S2 (STH = 2.81%): system GWP = 0.184 kg CO_2-eq/kWh - 42.9% GHG reduction vs. diesel; 59.6% vs. Turkish national grid; carbon payback 6.3 years. The corrected payback calculation:

τ = 1696 / (1230 × 0.322 - 126.2) = 1696/269.6=6.3 years.

S3 (STH = 10%): system GWP=0.023 kg CO_2-eq/kWh - 92.9% GHG reduction vs. diesel; carbon payback 1.2 years. Figure 10 presents the full LCA comparison.

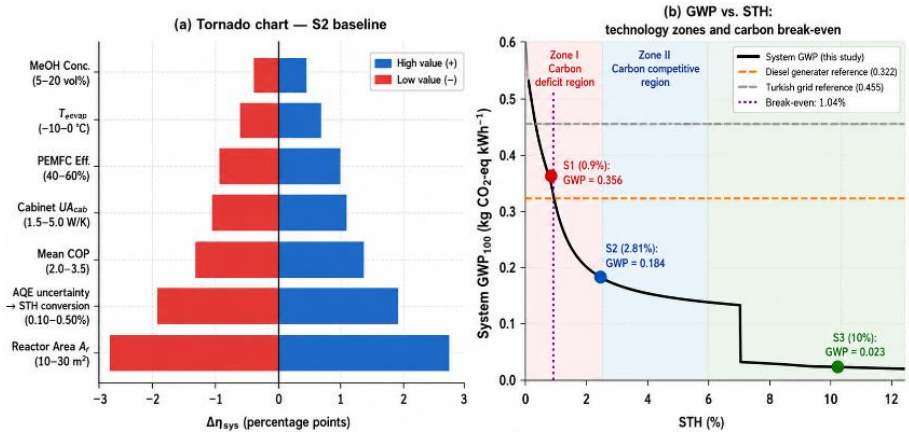


Figure 9. Sensitivity and carbon break-even analysis: (a) tornado chart showing sensitivity of η_{sys} to key design parameters; (b) system GWP_{100} vs. STH with technology zones and the carbon break-even threshold (STH ≈ 1.04%).

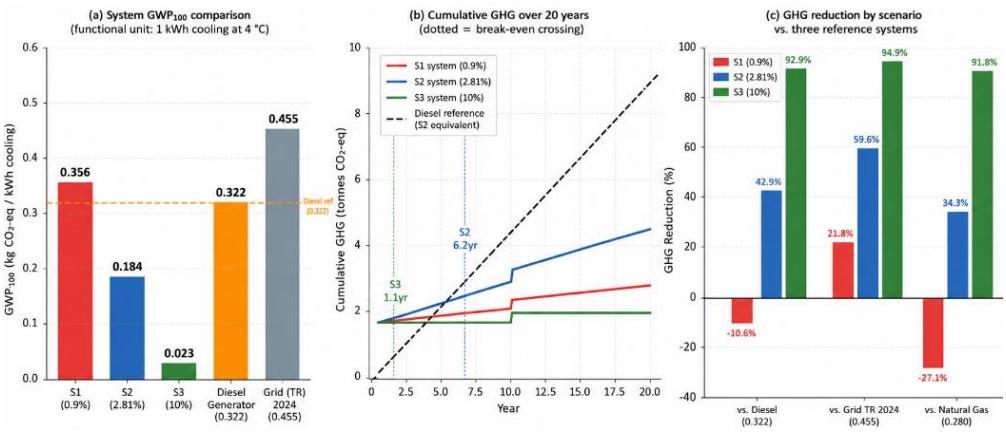


Figure 10. Life cycle assessment results: (a) GWP_{100} by scenario vs. reference systems; (b) cumulative GHG trajectories over 20-year lifetime; (c) GHG reduction by scenario vs. three reference systems.

4. Discussion

4.1. Carbon Break-Even: The Central Finding

The identification of a carbon break-even STH of approximately 1.04% is the principal scientific contribution of this study. Prior photocatalytic system-integration studies have commonly assumed STH values at or above 2% without reconciling them against real outdoor pilot data, thereby implicitly reporting carbon-competitive performance that is not achievable with current TiO_2/P25 technology. The PSA pilot measurements (Ruiz-Aguirre et al., 2022; Toledo-Camacho et al., 2021) confirm that state-of-practice TiO_2–CuO/P25 systems achieve STH ≈ 0.9% outdoors - marginally below the break-even threshold. This finding provides a quantitative target for photocatalyst developers: a modest 15% improvement in outdoor STH would be sufficient to render the integrated system carbon-competitive against diesel.

4.2. Technology Readiness and System Viability

Scenario S1 is included deliberately as a lower technology boundary, not as a viable system proposal. At current pilot-scale TiO_2-CuO/P25 performance (STH = 0.9%), the 20m^2 reactor produces only 394 kWh/yr of

cooling energy-approximately 30% of annual cabinet demand-and its life-cycle carbon footprint is 10.5% higher than the diesel reference. It is also worth noting that at S1, the mean fuel cell power of 18.6 W is lower than the combined parasitic consumption of the PSA unit and diaphragm compressor under realistic operating conditions, implying that the system would require auxiliary startup energy in practice. This further underscores that S1 represents a theoretical lower boundary rather than an operable configuration.

Scenario S2, achievable with Pd co-catalysts or N-doped TiO_2 at TRL 4-5 and already demonstrated in outdoor pilots by Toledo-Camacho et al. (2021), delivers 94.6% supply reliability.

4.3. Comparison with Literature

Compared to PV-electrolysis-based off-grid hydrogen refrigeration (η_{sys} ≈ 8-12%) and Ghenai et al. (2019) (η_{sys}≈ 10-14%), the present system's η_{sys} of 2.96% (S2) is lower. This gap reflects the narrow UV-only spectral harvesting of TiO_2; however, the photocatalytic route eliminates the PV module, inverter, and electrolyser from the energy chain, potentially offering reliability and maintenance advantages in remote locations. The PEMFC exergy efficiency of 49.9% is consistent with Kazim (2004) and Rosen and Scott (1998). The R290 COP of 2.76 is consistent with manufacturer data for variable-speed hermetic compressors.

4.4. Limitations and Future Work

Reactor scale-up and scope statement: all three pilot validation references used $2m^2$ CPC reactors. Scaling to $20m^2$ introduces photon distribution non-uniformity, increased mass transfer resistance, and gas–liquid separation challenges not captured by the present model. This study should be understood as a parametric upper-bound analysis: it quantifies system-level performance conditional on achieving the stated STH values at scale, and does not constitute an engineering design for a deployable system. In practice, these scale-up effects - photon-distribution non-uniformity and increased mass-transfer resistance in a larger slurry reactor - would depress the effective STH below the pilot-calibrated values adopted here, shifting each scenario toward its lower-performance boundary; the reported metrics should therefore be read as optimistic bounds for a given catalyst efficiency.

Catalyst degradation: the semi-empirical AQE model does not capture photo-corrosion, fouling by carbonate precipitates, or long-term methanol/glycerol depletion dynamics. The life-cycle inventory already accounts for the recurring CO_2 of annual sacrificial-agent replenishment, but it assumes a fixed photocatalyst charge over the 20-year lifetime. If progressive photo-corrosion or fouling required periodic replacement of the solid TiO2/P25 photocatalyst, the recurring embodied CO2 of that replenishment would increase the cumulative system GWP and lengthen the carbon payback period, most noticeably for Scenario S1, which already sits marginally below the break-even threshold; the qualitative ranking of the three scenarios would nonetheless be preserved. A precise quantification requires the catalyst-only embodied GWP and an empirical deactivation rate, which are reserved for future experimental work. $LaNi_5$ inventory uncertainty: the manufacturing GWP assigned to the metal hydride tank (12.9 kg CO_2-eq/kg) is at the low end of literature values for rare-earth alloys (20-60 kg CO_2-eq/kg); at a mid-range estimate of 30 kg CO_2-eq/kg, the break-even threshold would shift to ≈ 1.2% STH, still below the S2 performance level. Economic analysis (LCOC, NPV, IRR) and multi-site extension are reserved for future work.

5. Conclusion

This study presented a thermodynamic, dynamic solar, and environmental performance analysis of an integrated photocatalytic hydrogen production-PEM fuel cell–off-grid cold storage system, simulated over a full TMY year for a Mediterranean climate site, using a three-scenario framework calibrated against real outdoor pilot data from the Plataforma Solar de Almería. The following principal conclusions are drawn:

1. The carbon break-even solar-to-hydrogen efficiency is approximately 1.04%. Current TiO_2-CuO/P25 pilot performance (STH ≈ 0.9%) falls marginally below this threshold (system GWP = 0.356 kg CO_2-eq/kWh, carbon payback 19.6 yr). A 15% relative improvement in outdoor STH would be sufficient to render the system carbon-competitive.
2. At current pilot-scale performance (S1, STH = 0.9%), the $20m^2$ photocatalytic reactor delivers only 394 kWh/yr of cooling - approximately 30% of annual demand. The system is not yet viable as a stand-alone cold-chain solution at this catalyst efficiency level.
3. At the Pd/TiO_2 performance level demonstrated by Toledo-Camacho et al. (2021) (S2, STH = 2.81%), the system delivers 1230 kWh/yr of cooling, 94.6% annual supply reliability, system GWP = 0.184 kg CO_2-eq/kWh, and 42.9% GHG reduction versus diesel. Carbon payback: 6.3 years.
4. At the DOE 2030 target (S3, STH = 10%; Z-scheme, no sacrificial agent), the system achieves 4377 kWh/yr cooling, system GWP = 0.023 kg CO_2-eq/kWh (92.9% GHG reduction), and a carbon payback of 1.2 years.
5. Exergy analysis confirms that the photocatalytic reactor accounts for ≈ 97% of total system exergy destruction across all scenarios. The downstream power conversion subsystem exergy efficiency is 8.18% and is invariant with STH, confirming that PEMFC and refrigeration components are well-optimized relative to the photocatalytic bottleneck.
6. The three-scenario framework and carbon break-even analysis provide actionable development targets: achieving STH > 1.04% is the minimal requirement for GHG parity with diesel; STH ≈ 2.8% enables meaningful GHG savings and supply reliability comparable to PV-battery alternatives.

Author Contributions

The percentages of the author' contributions are presented below. The author reviewed and approved the final version of the manuscript.

	H.T.
C	100
D	100
S	100
DCP	100
DAI	100
L	100
W	100
CR	100
SR	100
PM	100
FA	100

C= concept, D= design, S= supervision, DCP= data collection and/or processing, DAI= data analysis and/or interpretation, L= literature search, W= writing, CR= critical review, SR= submission and revision, PM= project management, FA= funding acquisition.

Conflict of Interest

The author declared that there is no conflict of interest.

Ethical Consideration

Ethics committee approval was not required for this study because there was no study on animals or humans.

Acknowledgements

The author acknowledges the European Commission Joint Research Centre for providing the PVGIS-SARAH2 database used in this study.

Nomenclature

Symbol	Description	Unit
A_r	Reactor aperture area	m²
AQE	Apparent Quantum Efficiency	-
COP	Coefficient of performance	-
E_{Nernst}	Nernst potential	V
$\tilde{e}_x$	Specific flow exergy	kJ/kg
$\dot{E}_x$	Exergy rate	W
f_{UV-vis}	Fraction of AM1.5G spectrum usable by TiO_2	-
G_T	Total irradiance on tilted surface	W/m²
LHV	Lower heating value (H_2: 120 MJ/kg)	MJ/kg
STH	Solar-to-hydrogen efficiency	%
T	Temperature	K or °C
T_{sun}	Effective solar surface temperature (5,778 K)	K
UA	Overall heat transfer coefficient × area	W/K
V_{cell}	Cell voltage	V
ω_H	Hydrogen weight fraction in metal hydride	wt%
$\dot{W}$	Work (power) rate	W
x_{H_2}	Hydrogen utilization factor	-
α_c	Cathodic charge transfer coefficient	-
η	Energy efficiency	-
θ_z	Solar zenith angle	°
λ	Membrane water content	-
ρ_g	Ground reflectance (albedo = 0.20)	-
σ_m	Membrane proton conductivity	S/cm
φ	Site latitude (37.0°N)	°
ψ	Exergy efficiency	-
ω	Hour angle	°

Subscripts: 0 dead state; amb ambient; cab, cabinet; comp, compressor; cond, condenser; dest, destruction; evap, evaporator; FC, fuel cell; MH, metal hydride; sys, system.

References

Alfano, O. M., Bahnemann, D., Cassano, A. E., Dillert, R., & Goslich, R. (2000). Photocatalysis in water environments using artificial and solar light. *Catalysis Today*, *58*(2–3), 199–230. https://doi.org/10.1016/S0920-5861(00)00252-2

Amphlett, J. C., Baumert, R. M., Mann, R. F., Peppley, B. A., Roberge, P. R., & Harris, T. J. (1995). Performance modeling of the Ballard Mark IV solid polymer electrolyte fuel cell: I. Mechanistic model development. *Journal of the Electrochemical Society*, *142*(1), 1–8. https://doi.org/10.1149/1.2043866

ASHRAE. (2021). *ASHRAE handbook fundamentals*. American Society of Heating, Refrigerating and Air-Conditioning Engineers.

Barbir, F. (2012). *PEM fuel cells: Theory and practice* (2nd ed.). Academic Press.

Chen, X., Shen, S., Guo, L., & Mao, S. S. (2010). Semiconductor-based photocatalytic hydrogen generation. *Chemical Reviews*, *110*(11), 6503–6570. https://doi.org/10.1021/cr1001645

Corrêa, J. M., Farret, F. A., Canha, L. N., & Simoes, M. G. (2004). An electrochemical-based fuel-cell model suitable for electrical engineering automation approach. *IEEE Transactions on Industrial Electronics*, *51*(5), 1103–1112. https://doi.org/10.1109/TIE.2004.834972

DOE. (2021). *Hydrogen Shot*. U.S. Department of Energy. https://www.energy.gov/cmei/fuels/hydrogen-shot-summit

Duffie, J. A., Beckman, W. A., & Blair, N. (2020). *Solar engineering of thermal processes, photovoltaics and wind* (5th ed.). John Wiley & Sons.

FAO. (2019). *The state of food and agriculture: Moving forward on food loss and waste reduction*. Food and Agriculture Organization of the United Nations. https://www.fao.org/3/ca6030en/ca6030en.pdf

Fujishima, A., & Honda, K. (1972). Electrochemical photolysis of water at a semiconductor electrode. *Nature*, *238*(5358), 37–38. https://doi.org/10.1038/238037a0

Garcia-Torres, F., Valverde, L., & Bordons, C. (2016). Optimal load sharing of hydrogen-based microgrids with hybrid storage using model predictive control. *IEEE Transactions on Industrial Electronics*, *63*(8), 4919–4928. https://doi.org/10.1109/TIE.2016.2547870

Ghenai, C., Bettayeb, M., Brdjanin, B., & Hamid, A. K. (2019). Hybrid solar PV/PEM fuel cell/diesel generator power system

for cruise ship: A case study in Stockholm, Sweden. *Case Studies in Thermal Engineering*, *14*, Article 100497. https://doi.org/10.1016/j.csite.2019.100497

Huld, T., Müller, R., & Gambardella, A. (2012). A new solar radiation database for estimating PV performance in Europe and Africa. *Solar Energy*, *86*(6), 1803–1815. https://doi.org/10.1016/j.solener.2012.03.006

IEA. (2023). *World energy outlook 2023*. International Energy Agency. https://www.iea.org/reports/world-energy-outlook-2023

IRENA. (2023). *Renewable power generation costs in 2022*. International Renewable Energy Agency. https://www.irena.org/Publications/2023/Aug/Renewable-Power-Generation-Costs-in-2022

ISO. (2006a). *Environmental management – Life cycle assessment - Principles and framework* (ISO Standard No. 14040:2006). International Organization for Standardization.

ISO. (2006b). *Environmental management – Life cycle assessment - Requirements and guidelines* (ISO Standard No. 14044:2006). International Organization for Standardization.

James, S. J., & James, C. (2010). The food cold-chain and climate change. *Food Research International*, *43*(7), 1944–1956. https://doi.org/10.1016/j.foodres.2010.02.001

Jing, D., Guo, L., Zhao, L., Zhang, X., Liu, H., Li, M., Shen, S., Liu, G., Hu, X., Zhang, X., Zhang, K., Ma, L., & Guo, P. (2010). Efficient solar hydrogen production by photocatalytic water splitting: From fundamental study to pilot demonstration. *International Journal of Hydrogen Energy*, *35*(13), 7087–7097. https://doi.org/10.1016/j.ijhydene.2010.01.030

Kalamaras, C. M., & Efstathiou, A. M. (2013). Hydrogen production technologies: Current state and future developments. *Conference Papers in Science*, *2013*, Article 690627. https://doi.org/10.1155/2013/690627

Kazim, A. (2004). Exergy analysis of a PEM fuel cell at variable operating conditions. *Energy Conversion and Management*, *45*(11–12), 1949–1961. https://doi.org/10.1016/j.enconman.2003.09.030

Kho, Y. K., Iwase, A., Teoh, W. Y., Mädler, L., Kudo, A., & Amal, R. (2010). Photocatalytic H_2 evolution over TiO_2 nanoparticles: The synergistic effect of anatase and rutile. *The Journal of Physical Chemistry C*, *114*(6), 2821–2829. https://doi.org/10.1021/jp910810r

Kudo, A., & Miseki, Y. (2009). Heterogeneous photocatalyst materials for water splitting. *Chemical Society Reviews*, *38*(1), 253–278. https://doi.org/10.1039/B800489G

Lemmon, E. W., Huber, M. L., & McLinden, M. O. (2010). *NIST standard reference database 23: Reference fluid thermodynamic and transport properties (REFPROP), Version 9.0*. National Institute of Standards and Technology.

Liu, B. Y. H., & Jordan, R. C. (1960). The interrelationship and characteristic distribution of direct, diffuse and total solar radiation. *Solar Energy*, *4*(3), 1–19. https://doi.org/10.1016/0038-092X(60)90062-1

Lopez, V. A. M., Arcos-Aviles, D., Guinjoan, F., Llanos, J., Barragan-Calvo, J., & Motoasca, E. (2023). Maximization of PV energy use and performance analysis of a stand-alone PV-hydrogen system. *International Journal of Hydrogen Energy*, *48*(99), 39298–39314. https://doi.org/10.1016/j.ijhydene.2023.09.072

Lototskyy, M. V., Yartys, V. A., Pollet, B. G., & Bowman, R. C. (2017). The use of metal hydrides in fuel cell applications. *Progress in Natural Science: Materials International*, *27*(1), 3–20. https://doi.org/10.1016/j.pnsc.2017.01.008

Mann, R. F., Amphlett, J. C., Hooper, M. A. I., Jensen, H. M., Peppley, B. A., & Roberge, P. R. (2000). Development and application of a generalised steady-state electrochemical model for a PEM fuel cell. *Journal of Power Sources*, *86*(1–2), 173–180. https://doi.org/10.1016/S0378-7753(99)00484-X

Nalajala, N., Patra, K. K., Bharad, P. A., & Gopinath, C. S. (2021). Aqueous methanol to formaldehyde and hydrogen on Pd/TiO_2 by photocatalysis in direct sunlight: Structure-dependent activity of nano-Pd and atomic Pt-coated counterparts. *ACS Applied Energy Materials*, *4*(11), 13347–13360. https://doi.org/10.1021/acsaem.1c03080

Ni, M., Leung, M. K. H., Leung, D. Y. C., & Sumathy, K. (2007). A review and recent developments in photocatalytic water-splitting using TiO_2 for hydrogen production. *Renewable and Sustainable Energy Reviews*, *11*(3), 401–425. https://doi.org/10.1016/j.rser.2005.01.009

Romero, R. L., Alfano, O. M., & Cassano, A. E. (1997). Cylindrical photocatalytic reactors: Radiation absorption and scattering effects produced by suspended fine particles in an annular space. *Industrial & Engineering Chemistry Research*, *36*(8), 3094–3109. https://doi.org/10.1021/ie960664a

Rosen, M. A., & Scott, D. S. (1998). Comparative efficiency assessments for a range of hydrogen production processes. *International Journal of Hydrogen Energy*, *23*(8), 653–659. https://doi.org/10.1016/S0360-3199(97)00080-3

Ruiz-Aguirre, A., Polo-López, M. I., Fernández-Ibáñez, P., & Malato, S. (2022). Assessment of pilot-plant scale solar photocatalytic hydrogen generation with multiple approaches: Valorization, water decontamination and disinfection. *Energy*, *260*, Article 125199. https://doi.org/10.1016/j.energy.2022.125199

Sandrock, G. (1999). A panoramic overview of hydrogen storage alloys from a gas reaction point of view. *Journal of Alloys and Compounds*, *293–295*, 877-888. https://doi.org/10.1016/S0925-8388(99)00384-9

Staffell, I., Scamman, D., Abad, A. V., Balcombe, P., Dodds, P. E., Ekins, P., Shah, N., & Ward, K. R. (2019). The role of hydrogen and fuel cells in the global energy system. *Energy & Environmental Science*, *12*(2), 463–491. https://doi.org/10.1039/C8EE01157E

Toledo-Camacho, S. Y., Rey, A., Mota, A. L., Hernández-Alonso, M. D., Llorca, J., & Medina, F. (2021). Photocatalytic hydrogen production from water-methanol and glycerol mixtures using $Pd/TiO_2(-WO_3)$ catalysts and validation in a solar pilot plant. *International Journal of Hydrogen Energy*, *46*(73), 36152–36166. https://doi.org/10.1016/j.ijhydene.2021.08.141

Villachica-Llamosas, J. G., Chávez, A. M., Polo-López, M. I., Malato, S., & Fernández-Ibáñez, P. (2024). $CuO-TiO_2$ pilot-plant system performance for solar photocatalytic hydrogen production. *International Journal of Hydrogen Energy*, *51*, 1069–1077. https://doi.org/10.1016/j.ijhydene.2023.07.149

Wang, Q., & Domen, K. (2020). Particulate photocatalysts for light-driven water splitting: Mechanisms, challenges, and design strategies. *Chemical Reviews*, *120*(2), 919–985. https://doi.org/10.1021/acs.chemrev.9b00201

Wang, Y., Chen, K. S., Mishler, J., Cho, S. C., & Adroher, X. C. (2011). A review of polymer electrolyte membrane fuel cells: Technology, applications, and needs on fundamental research. *Applied Energy*, *88*(4), 981–1007. https://doi.org/10.1016/j.apenergy.2010.09.030

Wernet, G., Bauer, C., Steubing, B., Reinhard, J., Moreno-Ruiz, E., & Weidema, B. (2016). The ecoinvent database version 3 (Part I): Overview and methodology. *The International Journal of Life Cycle Assessment*, *21*(9), 1218–1230. https://doi.org/10.1007/s11367-016-1087-8

WHO. (2022). *Immunization coverage*. World Health Organization. https://www.who.int/news-room/fact-sheets/detail/immunization-coverage

Yang, R. T. (1987). *Gas separation by adsorption processes*. Boston.

Yilanci, A., Dincer, I., & Ozturk, H. K. (2009). A review on solar-hydrogen/fuel cell hybrid energy systems for stationary applications. *Progress in Energy and Combustion Science*, *35*(3), 231–244. https://doi.org/10.1016/j.pecs.2008.07.004

Zakeri, B., & Syri, S. (2015). Electrical energy storage systems: A comparative life cycle cost analysis. *Renewable and Sustainable Energy Reviews*, *42*, 569–596. https://doi.org/10.1016/j.rser.2014.10.011

Black Sea Journal of Engineering and Science
doi: 10.34248/bsengineering.1973063

Open Access Journal
e-ISSN: 2619 – 8991

Research Article
Volume 9 - Issue 5: 2203-2210 / September 2026

DETERMINATION OF THE EFFECTS OF GIBBERELLIC ACID (GA_3) DOSES ON GERMINATION PARAMETERS IN SOME SOYBEAN VARIETIES

Tahsin BEYCIOGLU[1]*

[1]*Pamukkale University, Faculty of Agriculture, Field Crops Department, 20600, Denizli, Türkiye*

Abstract: This study investigated the effects of different gibberellic acid (GA_3) doses (0, 25, 50, 100, and 200 mg L^{-1}) applied to different soybean (*Glycine max* L.) varieties (Adel, Ataem-7, Cinsoy, Lider, and Umut 2002) on germination percentage, germination index, average germination time, seedling length, plumule length, radicle length, and seed vigor index. variety, dose, and variety × dose interaction were found to be statistically significant ($P<0.01$) for all parameters. Among the varieties, Cinsoy and Ataem-7 stood out in terms of seed vigor index and seedling development. The Lider variety had the lowest mean values. When GA_3 dose applications were examined, it was determined that the 50 and 100 mg L^{-1} doses had a positive effect on germination and seedling development. The 200 mg L^{-1} dose was found to negatively affect germination percentage and seed vigor index. Correlation analysis revealed strong positive correlations ($r>0.80$; $P<0.01$) between seedling length, plumule length, and seed vigor index. Principal component analysis (PCA) explained 70.6% of the total variance with two components. Seedling development parameters were prominent on the PC1 axis, while germination time was prominent on the PC2 axis. Biplot analysis showed that Adel, Ataem-7, and Cinsoy varieties were positively correlated with high seedling viability parameters, while the Lider variety was significantly different in these parameters.

Keywords: Soybean, Germination, Gibberellic acid, Variety

***Corresponding author:** Pamukkale University, Faculty of Agriculture, Field Crops Department, 20600, Denizli, Türkiye
E mail: tbeycioglu@pau.edu.tr (T. BEYCİOGLU)
Tahsin BEYCİOGLU https://orcid.org/0000-0001-5338-8836

Received: June 17, 2026
Accepted: July 17, 2026
Published: September 15, 2026

Cite as: Beycioglu, T. (2026). Determination of the effects of gibberellic acid (GA_3) doses on germination parameters in some soybean varieties. *Black Sea Journal of Engineering and Science,* 9(5), 2203-2210.

1. Introduction

Soybean is an annual cultivated plant belonging to the *Fabaceae* family within the *Fabales* order. It is a plant that provides significant agricultural benefits by meeting its own nutritional needs and enriching the soil with nitrogen, thanks to the presence of the *Rhizobium japonicum* bacteria in its roots, which can fix free nitrogen from the soil (Anaç and Ertürk, 2003). Soybean (*Glycine max*. L.) is an economically important industrial plant rich in protein and fat content (Gurbanov et al., 2025). It provides raw materials for the production of biodiesel and other biofuels and has significant economic potential in this area (Akitha Devi and Giridhar, 2015; Rao and Chaitanya, 2019). Soybean seeds contain 39.4% crude protein, 14.0% fat, 4.3% starch, 5.6% total soluble sugars, 0.33% reducing sugars, and 5.6% sucrose (Sharma et al., 2014). According to Turkish Statistical Institute (TÜİK) data for 2025, soybeans were planted on 369800 decares of land in Turkey, and the total soybean production was approximately 149000 tons (TÜİK, 2026). According to FAO data for 2024, global soybean cultivation covered 1430000 hectares and yielded 397600000 tons (FAO, 2026). In the world, practices aimed at improving seed quality are increasing at the plant level every day. Pre-germination treatments in seeds are a pre-planting process that involves partially watering the seeds without allowing radicle emergence. It improves the germination rate and stress tolerance of germinating seeds and enhances seedling formation (Li and Liu, 2016). Applying plant growth regulators is one of the commonly used methods. Gibberellins play an active role in many stages, from seed germination to plant development. Gibberellic acid (GA_3), a plant growth regulator, has been reported to be both a natural chemical and capable of improving plant characteristics such as germination, vegetative growth, and grain yield (Ma et al., 2018; Rahimi et al., 2011; Mangena, 2020). Gibberellic acid plays a crucial role in controlling and promoting germination in plant species (Gupta and Chakrabarty, 2013). Gibberellins cause the breakdown of the cell wall by increasing the activity of the endoβ-mannanase enzyme in the endosperm. Thus, the germination rate of seeds is accelerated thanks to gibberellins (Erol and Arslanoğlu, 2022).

The aim of this study was to determine the effects of five different gibberellin acid (GA_3) doses, 0 (control), 25 mg L^{-1}, 50 mg L^{-1}, 100 mg L^{-1} and 200 mg L^{-1}, on the germination characteristics of Adel, Ataem-7, Cinsoy, Lider and Umut 2002 soybean varieties.

This work is licensed (CC BY-NC 4.0) under Creative Commons Attribution 4.0 International License

2. Materials and Methods

The research was conducted in the laboratory at Pamukkale University, Faculty of Agriculture, Department of Field Crops, in 2026 under standard conditions at 25°C (±2). In this study, although the seeds were not graded by passing them through a sieve of the same size, broken, shriveled, diseased, and excessively small or large seeds were removed prior to sowing, and healthy seeds with a uniform appearance were used for each variety. Seeds of the 5 soybean (*Glycine max* L.) varieties used in the study were sterilized with a 5% NaOCl (sodium hypochlorite) solution for 5 minutes and then rinsed with tap water. Gibberellic acid was prepared at five different concentration levels: 0, 25, 50, 100, and 200 mg L^{-1}. The study was conducted according to a randomized block design with three replications. Twenty-five seeds of each variety were placed in 75 sterile petri dishes, each containing two filter papers, and left to germinate for 14 days. Then, 15 ml of each prepared concentration was added to each petri dish during sowing. Subsequently, 10 ml of these solutions were added seven times at two-day intervals for each application. After germination, when the cotyledons were fully developed, the germinated seeds were removed from the petri dishes, and some key germination and seedling growth parameters such as germination percentage, germination index, average germination time, seedling length, radicle length, plumule length, and seed vigor index were determined. Germination percentage was determined by dividing the number of germinated seeds by the total number of seeds and multiplying by 100. Seedling length was determined using calipers. Similarly, plumule and radicle lengths were determined by measuring them with a tape measure after both were separated. The germination index (GI) was calculated using the formula: (10xn1+9xn2+...1xn10) / (total number of germination days × number of seeds used in germination). As described by Finch-Savage and Bassel (2016), the seed vigor index was assessed by combining the germination percentage with the lengths of the plumule and radicle. This index reflects the overall health and growth potential of the seeds. Statistical analysis of the data was performed using one-way analysis of variance (ANOVA) with Completely Randomized Experimental Design procedures using JMP 17.0 statistical software for the observed application factors, varieties, and gibberellic acid concentrations. Least Significant Difference (LSD) analysis from multiple comparison tests was performed to determine the difference between gibberellic acid levels in each parameter examined (at a 5% significance level) (Figure 1). However, Pearson correlation analysis was performed to monitor the relationship between the observed parameters (Kaya and Eryiğit, 2021; ISTA, 2004).

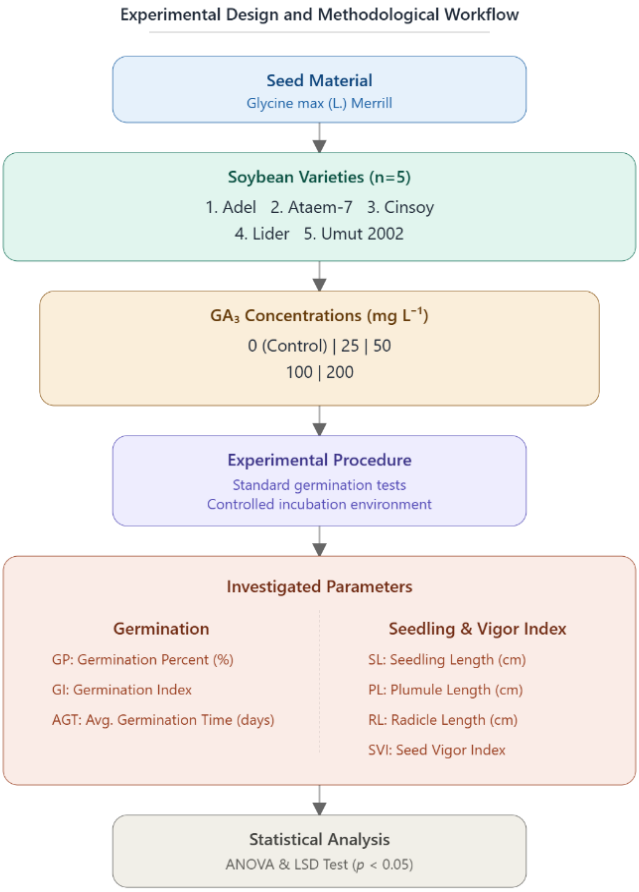


Figure 1. Experimental design and methodological workflow.

3. Results and Discussion

3.1. The Effect of GA_3 Applications on Germination and Seedling Development Parameters

3.1.1. Germination percentage (%)

Variety, dose, and variety × dose interaction were found to be statistically significant in terms of germination percentage ($P<0.01$) (Table 1). The highest germination percentage among the varieties was obtained from the Cinsoy variety with 87.98%. This variety was followed by the Adel variety with 86.73%. While Adel and Cinsoy varieties were in the same statistical group, Ataem-7, Lider and Umut (2002) varieties formed the second group with lower germination percentage values. This difference between varieties is thought to be due to variation in seed quality and germination capacity depending on the genetic structure (Hatzig et al., 2018). When dose applications were examined, it was observed that the 50 mg L^{-1} dose (87.25%) provided the highest germination percentage, followed by the 100 mg L^{-1} dose (86.91%). In contrast, the germination percentage decreased to 74.47% at the 200 mg L^{-1} dose. High-dose applications have been shown to have an inhibitory effect on seed germination (Anwar et al., 2023). In terms of variety × dose interaction, the highest germination percentage was obtained with the 25 mg L^{-1} dose application of the Cinsoy variety at 94.93%. The lowest value was observed with the 200 mg L^{-1} dose of the Umut 2002 variety at 71.35%.

3.1.2. Germination index

Germination index is an important quality indicator expressing the simultaneous and rapid germination capacity of seeds (Santos et al., 2023). Among the varieties, the highest germination index was obtained from the Ataem-7 variety with 9.16. This variety was followed by Cinsoy with 8.29. The lowest value was determined from the Lider variety with 7.45. In terms of dose applications, it was observed that the 100 mg L^{-1} dose (9.71) statistically increased the germination index to the highest group. The control group (0 mg L^{-1}) had the lowest germination index with 6.50. This shows that applications at certain concentrations positively affect the germination rate (Altuner et al., 2020). Similarly, Kaya and Erdönmez (2020) reported that fertilizer forms significantly influenced the germination index, with values ranging from 4.11 to 6.33, indicating that the type of application plays a critical role in germination performance. When the variety x dose interaction was examined, the highest germination index was determined in the Ataem-7 variety with 100 mg L^{-1} (11.13). The lowest value was seen in the Lider variety control group with 4.23 (Table 1).

3.1.3. Average germination time (days)

Low average germination time is considered an important parameter in evaluating seed viability, as it indicates faster germination (Santos et al., 2023). Among the varieties, the lowest average germination time was obtained in Umut 2002 with 4.20 days. This variety was followed by Ataem-7 with 4.22 days. The highest average germination time was determined in Adel with 4.59 days. When dose applications were evaluated, it was observed that the 200 mg L^{-1} dose (5.06 days) significantly extended the germination time and that this dose was statistically different from all other applications. This finding shows that high doses applied may negatively affect seed metabolism and lead to germination delay (Doğan et al., 2021). When variety x dose interactions were examined, the shortest average germination time was obtained from the Ataem-7 variety at a dose of 50 mg L^{-1} with 3.26 days, while the highest value was obtained from the Adel variety at a dose of 200 mg L^{-1} with 5.48 days (Table 1).

3.1.4. Seedling length (cm)

Seedling length is an important morphological parameter reflecting plant activity during the early post-germination development period (Çalışkan et al., 2017). The longest seedling length among the varieties was obtained from Ataem-7 with 30.03 cm, followed by Cinsoy with 27.69 cm. The shortest seedling length was determined in the Lider variety with 16.65 cm. When dose applications were examined, it was observed that the 100 mg L^{-1} (30.25 cm) and 50 mg L^{-1} (29.59 cm) doses yielded the highest seedling length values, and both doses were in the same statistical group. The control group had the shortest seedling length at 20.76 cm. This indicates that gibberellic acid, at appropriate doses, promotes seedling development (Benlioğlu and Özkan, 2020). According to the interaction results, the longest seedling was obtained from the Ataem-7 variety at a dose of 50 mg L^{-1}, with a length of 41.76 cm, while the shortest seedling length was determined to be 14.24 cm with the Lider variety at a dose of 25 mg L^{-1} (Table 1).

3.1.5. Plumule length (cm)

Plumule length is directly related to plant emergence ability as an indicator of seedling epicotyl development (Türkay and Karaman, 2021). The longest plumule length among the varieties was obtained in Ataem-7 with 21.48 cm. This variety was followed by Umut 2002 with 17.67 cm and Cinsoy with 17.29 cm. The shortest plumule length was observed in Lider with 12.06 cm. In terms of dosage, the 50 mg L^{-1} dose (21.80 cm) stood out as the application that most affected plumule development. At the 200 mg L^{-1} dose, this value was observed to decrease to 15.42 cm. This negative effect of excessive dose applications on epicotyl development can be explained by oxidative stress or hormonal imbalance (Kaya and Eryiğit, 2021). When variety x dose interactions are considered, the highest plumule length is observed with the Ataem-7 variety at a dose of 50 mg L^{-1} (35.97 cm), while the lowest value is seen with the Adel variety at a dose of 0 mg L^{-1} (10.27 cm) (Table 1).

Table 1. Effects of GA_3 application doses on germination percentage (GP), germination index (GI), average germination time (AGT), seedling length (SL), plumule length (PL), radicle length (RL), and seed vigor index (GPI) of different soybean (*Glycine max* L.) varieties, and interaction results

Variety	GP	GI	AGT	SL	PL	RL	SVI
Adel (1)	86.73 a	8.04 bc	4.59 a	26.16 c	15.75 c	10.41 a	2297.89 b
Ataem-7 (2)	80.81 b	9.16 a	4.22 c	30.03 a	21.48 a	8.54 b	2417.82 a
Cinsoy (3)	87.98 a	8.29 b	4.25 bc	27.69 b	17.29 b	10.39 a	2454.06 a
Lider (4)	81.38 b	7.45 d	4.49 ab	16.65 d	12.06 d	4.58 c	1355.54 d
Umut 2002 (5)	81.47 b	7.55 d	4.20 c	26.29 c	17.67 b	8.62 b	2152.00 c
			Dose				
0 (a)	84.13 c	6.50 d	3.90 d	20.76 c	13.37 d	7.38 b	1745.91 c
25 (b)	85.60 b	8.09 bc	4.16 c	22.85 b	14.47 cd	8.37 b	1978.07 b
50 (c)	87.25 a	8.43 b	4.17 c	29.59 a	21.80 a	7.79 b	2556.98 a
100 (d)	86.91 ab	9.71 a	4.47 b	30.25 a	19.19 b	11.06 a	2655.55 a
200 (e)	74.47 d	7.76 c	5.06 a	23.36 b	15.42 c	7.94 b	1740.82 c
			Variety x Dose				
1-a	81.43 gh	5.76 jk	3.61 h-k	14.27 k	10.27 l	4.00 ıj	1162.28 m
1-b	90.31 bc	8.95 b-f	4.68 b-e	22.63 e-g	13.01 h-l	9.62 c-e	2044.36 fg
1-c	89.63 bc	7.35 f-j	4.77 a-e	34.50 bc	20.46 d	14.04 a	3092.79 a-c
1-d	91.45 ab	9.94 a-d	4.42 c-g	36.46 b	21.04 cd	15.42 a	3334.25 a
1-e	80.80 hı	8.23 d-h	5.48 a	22.96 e-g	13.97 h-k	8.98 d-f	1855.78 gh
2-a	85.15 e-g	7.32 f-j	4.44 c-g	22.32 e-h	16.15 e-h	6.17 f-ı	1900.88 gh
2-b	80.13 hı	8.48 d-g	4.91 a-e	22.57 e-g	14.31 g-j	8.26 d-g	1808.94 g-ı
2-c	78.97 h-j	10.40 ab	3.26 k	41.76 a	35.97 a	5.79 f-j	3297.89 a
2-d	86.85 c-e	11.13 a	4.64 b-e	32.40 cd	20.17 d	12.23 a-c	2814.33 cd
2-e	72.95 kl	8.44 d-g	3.86 f-k	31.09 cd	20.84 cd	10.25 b-d	2267.09 ef
3-a	90.90 ab	6.65 h-j	3.68 g-k	19.70 g-j	12.26 ı-l	7.44 d-g	1791.49 g-k
3-b	94.93 a	8.65 c-f	3.60 h-k	33.23 bc	19.13 de	14.1 a	3154.08 ab
3-c	89.16 b-e	9.35 b-d	4.42 c-g	31.66 cd	24.18 bc	7.48 d-g	2823.16 cd
3-d	89.40 b-d	10.29 a-c	4.20 e-ı	31.05 cd	17.71 d-g	13.34 ab	2776.74 d
3-e	75.52 jk	6.53 h-j	5.37 ab	22.79 e-g	13.20 h-l	9.58 c-e	1724.83 h-k
4-a	81.70 f-h	4.23 k	3.51 ı-k	18.58 ıj	13.09 h-l	5.49 g-j	1517.92 ı-l
4-b	85.58 d-f	7.48 e-ı	4.17 e-j	14.24 k	11.62 j-l	2.62 j	1220.43 lm
4-c	89.38 b-d	8.45 d-g	5.03 a-d	16.62 jk	12.63 h-l	3.99 ıj	1485.70 kl
4-d	78.48 h-j	10.63 ab	4.55 c-f	19.05 h-j	12.39 ı-l	6.65 e-ı	1494.95 j-l
4-e	71.75 kl	6.45 ıj	5.18 a-c	14.75 k	10.59 kl	4.16 h-j	1058.70 m
5-a	81.48 gh	8.56 dg	4.28 d-h	28.92 d	15.10 f-j	13.82 a	2356.97 e
5-b	77.05 ıj	6.91 gj	3.42 jk	21.58 f-ı	14.31 g-j	7.27 d-h	1662.52 h-k
5-c	89.10 b-e	6.60 hj	3.35 k	23.40 ef	15.77 e-ı	7.63 d-g	2085.36 e-g
5-d	88.38 b-e	6.55 hj	4.55 c-f	32.32 cd	24.66 b	7.66 d-g	2857.48 b-d
5-e	71.35 l	9.14 b-e	5.40 ab	25.23 e	18.5 d-f	6.73 e-ı	1797.70 g-j
ANOVA							
F varieties	105.94*	23.82*	8.00*	317.79*	140.03*	81.26*	325.68*
F doses	256.51*	68.04*	49.92*	222.65*	149.92*	31.06*	311.42*
F varieties x doses	33.82*	20.65*	20.41*	71.67*	45.45*	27.45*	74.32*
CV (Coefficient of Variation)	1.51	6.66	5.51	4.37	6.58	11.98	4.53

*Means followed by the same letter in the same are not significantly different according to the LSD test at P<0.05. GP= germination percentage, GI= gemination index, AGT= average germination time, SL= seedling length, PL= plumule length, RL= radicle length, SVI= seed vigor index.

3.1.6. Radicle length (cm)

Radicle length is a direct indicator of seed viability and early root development potential, and is of great importance in terms of water and nutrient uptake from the soil (Islam et al., 2008). When the varieties were examined, the longest radicle length was found in the Adel variety with 10.41 cm. This variety was followed by the Cinsoy variety with 10.39 cm. The shortest radicle length was found in the Lider variety with 4.58 cm. When dose applications were evaluated, it was observed that the 100 mg L^{-1} dose (11.06 cm) most significantly increased radicle development. Other doses remained statistically indistinguishable and at lower values. The fact that the high dose (200 mg L^{-1}) did not negatively affect radicle length indicates that the root tissue has a certain tolerance capacity to higher concentrations. According to the variety x dose interaction results, the longest radicle length was obtained from the 100 mg L^{-1} dose of the Adel variety with 15.42 cm. The shortest radicle length was determined to be 2.62 cm at the Lider variety with a dose of 25 mg L^{-1} (Table 1).

3.1.7. Seed vigor index

The highest seed vigor index was obtained from Cinsoy (2454.06) and Ataem-7 (2417.82) varieties. Both varieties were in the same statistical group. The lowest seed vigor index value was found in the Lider variety with 1355.54. The low values of Lider variety in parameters such as seedling length, plumule and radicle development indicate that this variety is at a disadvantage compared to other varieties in terms of seed viability. In terms of dosage applications, the 100 mg L^{-1} (2655.55) and 50 mg L^{-1} (2556.98) doses had the highest seed vigor index values. These two doses were statistically in the same group. In contrast, the 200 mg L^{-1} dose (1740.82) was found to have a value close to the control group (1745.91). When considering variety x dose interactions, the highest seed vigor index was obtained with the Adel variety at a dose of 100 mg L^{-1} (3334.25), while the lowest value was recorded with the Lider variety at a combination of 200 mg L^{-1} (1058.70) (Table 1).

3.2. Principal Component Analysis (PCA) Findings

Principal component analysis (PCA) was applied to evaluate the multivariate relationships between germination parameters and varieties. The resulting biplot analysis is shown in Figure 2. In the biplot analysis, the first principal component (PC1) explained 52.8% of the total variance, and the second principal component (PC2) explained 17.8%. Together, the two components accounted for 70.6% of the total variance. This percentage indicates that these two components adequately represent the variability in the dataset. When the PC1 axis is examined, it is seen that the vectors of seedling length (SL), plumule length (PL), radicle length (RL), seed vigor index (SVI), and germination percentage (GP) are positioned in the positive direction and at close angles to each other. The narrow vector angles between these parameters indicate strong positive correlations between these variables and are in complete agreement with the correlation analysis findings (Kaya and Eryiğit, 2021). The near-overlapping orientation of the SL, PL, and SVI vectors reveals that these three parameters are prominent together on the PC1 axis. On the PC2 axis, the average germination time (AGT) vector is positioned significantly upwards and differs from the other parameters. The wide angles formed by AGT with the other vectors indicate that this parameter exhibits negative relationships with the remaining variables. The germination index (GI) vector, however, is located on both the PC1 and PC2 axes, revealing a slight correlation with the other parameters. When the varieties were evaluated on the biplot, it was observed that the Adel, Ataem-7, and Cinsoy varieties were positioned on the positive side of the PC1 axis and close to the SL, PL, RL, and SVI vectors. This visually confirms that these varieties exhibit superior performance in terms of seedling development and germination viability. In contrast, the Lider variety was located significantly on the negative side of the PC1 axis. The Umut 2002 variety, positioned close to the axis, exhibited a moderate performance profile. When the overall biplot graph is evaluated, it is seen that many of the examined parameters are spread over a wide area along the PC1 axis. According to the results obtained, it was determined that the effect of application doses on germination and seedling development parameters constitutes a more significant source of variation than variety differences (Mohammed, 2006).

3.3. Correlation Relationships between Germination Parameters

Pearson correlation analysis was performed to reveal the relationships between germination parameters, and the results are presented in Table 2. A positive and statistically significant (r= 0.2605; P<0.05) relationship was found between germination percentage (GP) and seedling length (SL). The correlation coefficient between germination percentage and radicle length (RL) was found to be higher and significant at the P<0.01 level (r= 0.3522). This indicates that seeds with high germination capacity can simultaneously develop a stronger root system (Gueridi et al., 2024). The germination index (GI) showed positive correlations with seedling length (r= 0.5188; P<0.01), plumule length (r= 0.4308; P<0.01), radicle length (r= 0.3916; P<0.01), and germination power index (*r* = 0.4966; P<0.01). Increasing germination rate positively affects seedling growth. When the relationships between average germination time (AGT) and other parameters were examined, no statistically significant correlation was found with any of the parameters studied. The negative correlation of AGT with germination percentage (*r*= -0.2247) and seedling length (*r*= -0.1458) suggests that prolonging germination time may negatively affect overall seedling development (Urbański et al., 2025). A positive correlation was found between seedling length (SL) and plumule length (PL) (r= 0.8822; P<0.01). Similarly, the correlation coefficient

between seedling length and germination vigor index was determined as r= 0.9675 (P<0.01). The correlation coefficient between plumule length (PL) and radicle length (RL) was found to be statistically significant at r = 0.2462 (P<0.05). However, the low level of this relationship indicates that epicotyl and hypocotyl development are affected by different physiological mechanisms (Castro-Camba et al., 2022). A positive correlation was observed between plumule length and seed vigor index (r= 0.8135; P<0.01). A significant positive correlation was found between radicle length (RL) and seed vigor index (r= 0.7146; P<0.01). Considering the crucial role of root development in the uptake of water and nutrients from the soil, this relationship between strong radicle development and a high seed vigor index reveals that root activity is one of the key determinants of early seedling viability. Overall, the seed vigor index showed significant correlations with all other parameters.

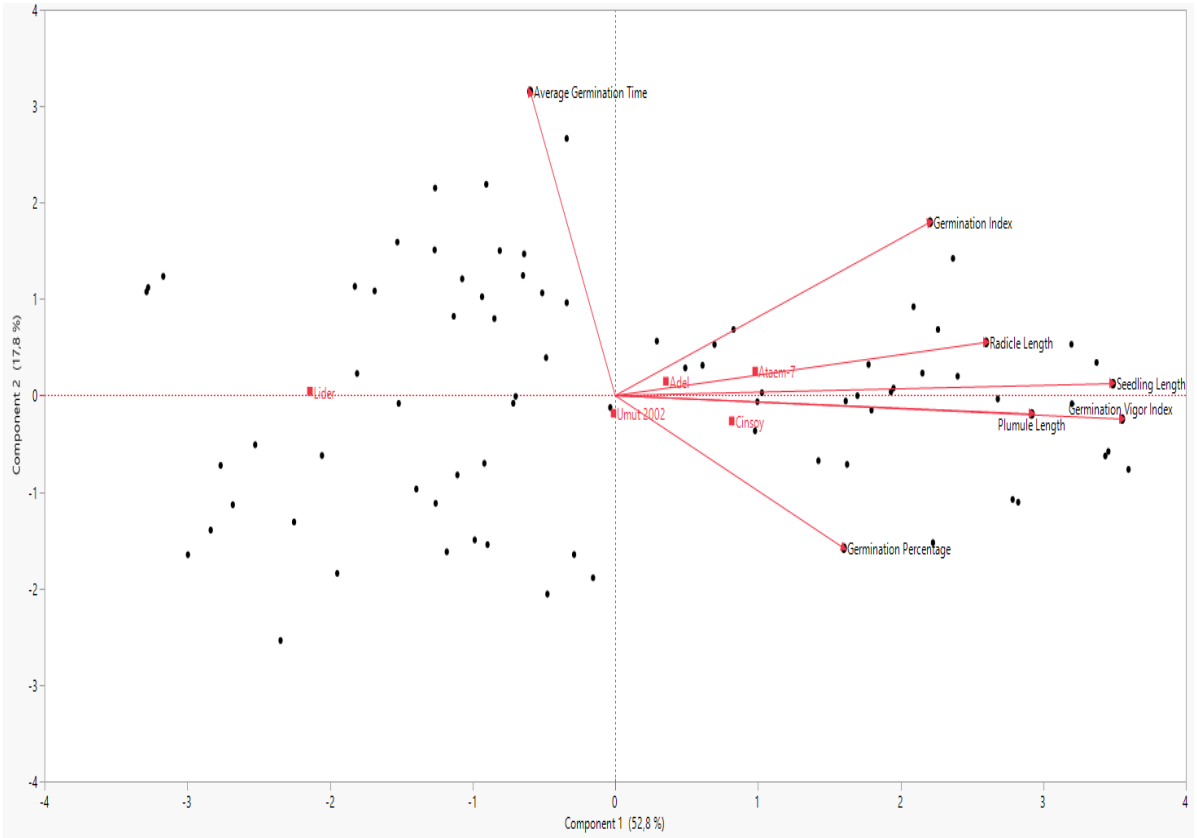


Figure 2. Biplot view of germination parameters according to principal component analysis (PCA) of different soybean varieties and application doses.

Table 2. Pearson correlation coefficients between germination parameters of different soybean varieties and GA_3 application doses

	Germination Percentage	Germination Index	Average Germination Time	Seedling Length	Plumule Length	Radicle Length	Seed Vigor Index
Germination Percentage	1						
Germination Index	0.1327	1					
Average Germination Time	-0.2247	0.1806	1				
Seedling Length	0.2605*	0.5188**	-0.1458	1			
Plumule Length	0.1172	0.4308**	-0.2164	0.8822**	1		
Radicle Length	0.3522**	0.3916**	0.0395	0.6736**	0.2462*	1	
Seed Vigor Index	0.4871**	0.4966**	-0.1716	0.9675**	0.8135**	0.7146**	1

4. Conclusion

This study determined the effect of different doses of GA_3 applications on the germination and early seedling development of soybean (*Glycine max* L.) seeds, depending on the dose and variety. The highest values for germination index, seedling length, radicle development, and seed vigor index were obtained at 50 and 100 mg L^{-1} GA_3 doses. The 200 mg L^{-1} application significantly inhibited germination percentage and seed vigor index, resulting in values close to the control group. While GA_3 was found to promote seed germination and seedling development within the appropriate concentration range, it exhibited an inhibitory effect at excessive doses. When evaluating the differences between varieties, Cinsoy and Ataem-7 cultiavars showed superior performance in seed vigor index and seedling development parameters. The Lider variety had the lowest values in all parameters. This was visually confirmed by PCA biplot analysis. Adel, Ataem-7, and Cinsoy varieties showed positive correlations with high seedling viability parameters, while the Lider variety deviated significantly from these parameters. Correlation analysis revealed a positive correlation between seed vigpr index and seedling length, plumule length, and radicle length. In conclusion, to optimize germination performance and early seedling development in soybean cultivation, it is recommended to prefer Cinsoy or Ataem-7 varieties and to apply GA_3 at a dose range of 50–100 mg L^{-1}. Further studies are also recommended to comprehensively investigate the effects of GA_3 on soybean yield and quality, considering different ecological conditions and growth period parameters.

Author Contributions

The percentages of the author' contributions are presented below. The author reviewed and approved the final version of the manuscript.

	T.B.
C	100
D	100
S	100
DCP	100
DAI	100
L	100
W	100
CR	100
SR	100
PM	100
FA	100

C= concept, D= design, S= supervision, DCP= data collection and/or processing, DAI= data analysis and/or interpretation, L= literature search, W= writing, CR= critical review, SR= submission and revision, PM= project management, FA= funding acquisition.

Conflict of Interest

The author declared that there is no conflict of interest.

Ethical Consideration

Ethics committee approval was not required for this study because of there was no study on animals or humans.

References

Akitha Devi, M. K., & Giridhar, P. (2015). Variations in physiological response, lipid peroxidation, antioxidant enzyme activities, proline and isoflavones content in soybean varieties subjected to drought stress. *Proceedings of the National Academy of Sciences, India Section B: Biological Sciences, 85*(1), 35–44.

Altuner, F., Oral, E., Tunçtürk, R., & Baran, İ. (2020). Giberellik asit (GA3) ön uygulamasına tabi tutulmuş kinoa (*Chenopodium quinoa* Willd.) tohumunda tuz (NaCl) stresinin çimlenme özellikleri üzerine etkisi. *Kahramanmaraş Sütçü İmam Üniversitesi Tarım ve Doğa Dergisi, 23*(2), 350–357. https://doi.org/10.18016/ksutarimdoga.vi.559368

Anaç, H., & Ertürk, Y. E. (2003). Soya fasulyesi. *TEAE-Bakış*. ISSN 1303-8346.

Anwar, T., Qureshi, H., Siddiqi, E. H., Hanif, A., Anwaar, S., Gul, S., Waheed, A., Alwahibi, M. S., & Kamal, A. (2023). Synergistic effect of biochar-based compounds from vegetable wastes and gibberellic acid on wheat growth under salinity stress. *Scientific Reports, 13*(1). https://doi.org/10.1038/s41598-023-46487-0

Benlioğlu, B., & Özkan, U. (2020). Germination and early growth performances of mung bean (*Vigna radiata* (L.) Wilczek) genotypes under salinity stress. *Tekirdağ Ziraat Fakültesi Dergisi, 17*(3), 318–328. https://doi.org/10.33462/jotaf.677216

Castro-Camba, R., Sánchez, C., Vidal, N., & Vielba, J. M. (2022). Interactions of gibberellins with phytohormones and their role in stress responses. *Horticulturae, 8*(3), 241. https://doi.org/10.3390/horticulturae8030241

Çalışkan, S., Aytekin, R. İ., & Çalışkan, M. E. (2017). Tam ve kısıtlı sulama uygulamalarının fasulye (*Phaseolus vulgaris* L.) çeşitlerinde tohum çimlenmesi ve fide gelişimine etkisi. *Tarla Bitkileri Merkez Araştırma Enstitüsü Dergisi*, 62–67. https://doi.org/10.21566/tarbitderg.359156

Doğan, M., Tura, A., Odabaşıoğlu, C., Sedetaltun, Y., & Odabaşıoğlu, M. İ. (2021). Salisilik asitin soya (*Glycine max* L. Merr.) tohumlarının çimlenme ve gelişimine etkisi. *Fırat Üniversitesi Fen Bilimleri Dergisi, 33*(2), 115–124.

Erol, S. A., & Arslanoğlu, Ş. F. (2022). The effect of different gibberellic acid (GA3) doses on seed germination properties of some soybean [*Glycine max* (L.) Merr.] varieties. *International Journal of Innovative Approaches in Agricultural Research, 6*(4), 340–350.

FAO. (2026). *FAOSTAT*. https://www.fao.org/faostat/en/#data/QCL (Erişim Tarihi: 08.06.2026).

Finch-Savage, W.E., & Bassel, G.W. (2016). Seed vigour and crop establishment: Extending performance beyond adaptation. Journal of experimental botany. 67(3): 567-591.

Gueridi, S., Boucelha, L., Abrous-Belbachir, O., & Djebbar, R. (2024). Effects of hormopriming and pretreatment with gibberellic acid on fenugreek (*Trigonella foenum graecum* L.) seed germination. *Acta Botanica Croatica, 83*(2), 135–144. https://doi.org/10.37427/botcro-2024-018

Gupta, R., & Chakrabarty, S. K. (2013). Gibberellic acid in plant:

Still a mystery unresolved. *Plant Signaling & Behavior, 8*(9), e25504.

Gurbanov, V., Osmanlı, Y., Aydın, M. A., Mehmet, M., & Öztürk, G. (2025). Various priming applications in soybean (*Glycine max* L. Merr.) seeds. *Ejons International Journal on Mathematic, Engineering and Natural Sciences, 9*(4), 362–369. https://doi.org/10.5281/zenodo.17941254

Hatzig, S., Breuer, F., Nési, N., Ducournau, S., Wagner, M.-H., Leckband, G., Abbadi, A., & Snowdon, R. J. (2018). Hidden effects of seed quality breeding on germination in oilseed rape (*Brassica napus* L.). *Frontiers in Plant Science, 9*. https://doi.org/10.3389/fpls.2018.00419

Islam, E., Liu, D., Li, T., Yang, X., Jin, X., Mahmood, Q., Tian, S., & Li, J. (2008). Effect of Pb toxicity on leaf growth, physiology and ultrastructure in the two ecotypes of Elsholt. *Journal of Hazardous Materials, 154*, 914–926.

Li, X., Liu, F., 2016. Drought stress memory and drought stress tolerance in plants: biochemical and molecular basis. Springer International Publishing.

ISTA. (2004). *International rules for seed testing*. International Seed Testing Association.

Kaya, A. R., & Erdönmez, H. K. (2020). Farklı kökenli gübre form ve dozlarının soya fasulyesinin (*Glycine max.* (L.) Merrill) tohum çimlenmesi ve fide gelişimi üzerine etkisi. *Türk Doğa ve Fen Dergisi*, *9*(Özel Sayı), 73-79.

Kaya, A., & Eryiğit, T. (2021). Lead nitrate ($Pb(NO_3)_2$) impact on seed germination and seedling growth of different soybean (*Glycine max* L.) varieties. *Pakistan Journal of Botany, 53*(5).

Ma, H. Y., Zhao, D. D., Ning, Q. R., Wei, J. P., Li, Y., Wang, M. M., Liu X. L., Jiang, C. J., & Liang, Z. W. (2018). A multi-year beneficial effect of seed priming with gibberellic acid-3 (GA3) on plant growth and production in a perennial grass, *Leymus chinensis*. *Scientific Reports, 8*(1), 1–9.

Mangena, P. (2020). Effect of hormonal seed priming on germination, growth, yield and biomass allocation in soybean grown under induced drought stress. *Indian Journal of Agricultural Research, 54*(5), 592–598.

Mohammed, A. (2006). Effect of gibberellic acid on germination and seedling growth of soybean (*Glycine max* L. Merril). *Revis Bionatura, 8*(2), 41.

Rahimi, M. M., Zarei, M. A., & Arminian, A. (2011). Selection criteria of flax (*Linum usitatissimum* L.) for seed yield and yield components and biochemical composition under various planting dates and nitrogen. *African Journal of Agricultural Research, 6*, 3167–3175.

Rao, D. E., & Chaitanya, K. V. (2019). Morphological and physiological responses of seven different soybean (*Glycine max* L. Merr.) varieties to drought stress. *Journal of Crop Science and Biotechnology, 22*(4), 355–362.

Santos, C. V. dos, Nunes, U. R., Menegaes, J. F., Nied, A. H., Ludwig, E. J., Zini, P. B., Bastiani, G. G. de, & Bernardt, E. (2023). Soybean seeds submitted to different water deficit periods after sowing in dry soil. *Ensaios e Ciência: Ciências Biológicas, Agrárias e da Saúde, 27*(1), 87–92. https://doi.org/10.17921/1415-6938.2023v27n1p87-92

Sharma, S., Kaur, M., Goyal, R., & Gill, B. S. (2014). Physical characteristics and nutritional composition of some new soybean (*Glycine max* (L.) Merrill) genotypes. *Journal of Food Science and Technology, 51*, 551–557.

TÜİK. (2026). *Bitkisel üretim istatistikleri*. Türkiye İstatistik Kurumu. https://biruni.tuik.gov.tr/medas/?locale=tr (Erişim Tarihi: 08.06.2026).

Türkay, C., & Karaman, R. (2021). Maş fasulyesi genotiplerinde farklı ekim derinliklerinin çimlenme ve bazı büyüme parametreleri üzerine etkisi. *Anadolu Journal of Agricultural Sciences*, 104–112. https://doi.org/10.7161/omuanajas.805765

Urbański, M., Yiğit, B. M., Ekner-Grzyb, A., & Chmielowska-Bąk, J. (2025). Physiological and oxidative status of soybean seedlings exposed to short term treatment with polystyrene nanoparticles. *Ecotoxicology, 34*(2), 241–247. https://doi.org/10.1007/s10646-024-02833-0

Black Sea Journal of Engineering and Science
doi: 10.34248/bsengineering.1825410

Open Access Journal
e-ISSN: 2619 – 8991

Research Article
Volume 9 - Issue 5: 2211-2223 / September 2026

CONTEXT ENGINEERING: A BIBLIOMETRIC ANALYSIS

Alperen KOÇYİĞİT[1]*, Nurettin ŞENYER[1]

[1]*Samsun University, Faculty of Engineering, Department of Software Engineering, 55060, Samsun, Türkiye*

Abstract: Context engineering addresses the development of systems capable of sensing, interpreting, and adapting to dynamic environmental conditions, representing a fundamental domain within software engineering. Despite substantial research activity spanning over two decades, systematic analyses of the field's intellectual structure, publication patterns, and collaborative networks remain limited. This study conducted a comprehensive bibliometric analysis of context engineering research from 2000 to 2025 using Web of Science Core Collection as the data source. A systematic search strategy retrieved 4,858 publications from 2,239 sources authored by 12,240 researchers across computer science and engineering domains. Analysis employed the Bibliometrix package (version 4.3.5) in R (version 4.5.1) to examine publication trends, author productivity, institutional contributions, geographic distribution, thematic structure, collaboration patterns, and citation impact through performance analysis, keyword co-occurrence networks, and science mapping techniques. The field demonstrated robust expansion with 14.22% annual growth rate, exhibiting three developmental phases: foundational period (2000-2004), consolidation phase (2005-2019), and acceleration phase (2020-2025) when output increased from 240 to 611 publications annually. The Chinese Academy of Sciences led institutional productivity with 229 publications, while China dominated national output with 1,357 documents representing 28.4% of the corpus. Geographic analysis revealed quality-quantity trade-offs with Singapore achieving the highest average citation impact (53.98 citations per document) despite modest volume. Author analysis identified Zaslavsky A as most productive (35 publications) while collaboration metrics indicated 3.83 co-authors per document and 23.22% international co-authorship rate. Keyword analysis revealed "context modeling" (1,429 occurrences) as the dominant theme with three distinct thematic clusters: foundational modeling concepts, machine learning applications, and ubiquitous computing paradigms. Network visualization confirmed integration of deep learning, transformers, and computer vision techniques into context-aware systems. IEEE Access dominated publication venues with 505 articles (10.4% of corpus), indicating strong association with electrical engineering and computer science communities. Citation analysis identified both contemporary contributions in machine learning and enduring foundational works maintaining relevance through theoretical frameworks. The findings reveal context engineering's evolution from systems-oriented middleware research toward application-oriented solutions emphasizing machine learning and domain-specific implementations, while persistent focus on modeling challenges indicates unresolved theoretical issues in context representation and reasoning.

Keywords: Context-aware systems, Bibliometric analysis, Publication trends, Research collaboration, Thematic analysis

***Corresponding author:** Samsun University, Faculty of Engineering, Department of Software Engineering, 55060, Samsun, Türkiye
E mail: muh.alperenkocyigit@gmail.com (A. KOÇYİĞİT)
Alperen KOÇYİĞİT https://orcid.org/0009-0004-2781-3543
Nurettin ŞENYER https://orcid.org/0000-0002-2324-9285

Received: November 17, 2025
Accepted: July 23, 2026
Published: September 15, 2026

Cite as: Koçyiğit, A., & Şenyer, N. (2026). Context engineering: A bibliometric analysis. *Black Sea Journal of Engineering and Science*, 9(5), 2211-2223.

1. Introduction

Context engineering addresses the challenge of developing systems capable of sensing, interpreting, and adapting to dynamic environmental conditions (Dey, 2001). Context-aware systems automatically collect contextual data to understand the current state of the running system and make decisions according to user goals. Since its emergence in the early 1990s, the field has experienced substantial growth driven by advances in sensor technologies, mobile computing, artificial intelligence, and the proliferation of Internet of Things (IoT) devices.

Bibliometric analysis provides quantitative techniques for examining large volumes of scientific literature, revealing patterns in publication output, citation relationships, collaboration networks, and thematic structure (Aria and Cuccurullo, 2017). The method has gained prominence in engineering disciplines due to its capacity to synthesize research evidence and identify knowledge gaps. Despite the maturation of context engineering research, no comprehensive bibliometric analysis specifically targeting this domain has been published. This absence limits understanding of the field's intellectual structure, dominant themes, key contributors, collaboration patterns, and influential publications.

This study addresses these challenges through comprehensive bibliometric analysis of 4,858 context engineering publications from Web of Science Core Collection spanning 2000 to 2025. The analysis examines publications from 2,239 sources and 12,240 authors using established bibliometric techniques including performance metrics, co-occurrence network analysis, and collaboration pattern identification.

The research addresses five specific questions:

RQ1: What are the temporal trends in context

This work is licensed (CC BY-NC 4.0) under Creative Commons Attribution 4.0 International License

engineering publication output and growth patterns from 2000 to 2025?

RQ2: Which authors, institutions, countries, and sources demonstrate the highest productivity and impact in context engineering research?

RQ3: What are the dominant research themes in context engineering as revealed through keyword analysis and thematic networks?

RQ4: What are the characteristics of collaboration patterns and international research networks within the context engineering community?

RQ5: Which publications have been most influential in shaping the field and what citation patterns can be identified?

The study contributes to the context engineering research community by providing the first comprehensive bibliometric analysis of the domain, quantifying growth patterns (14.22% annual growth rate), identifying productive and influential actors (authors, institutions, countries, sources), revealing thematic structure through keyword network analysis, documenting collaboration patterns (23.22% international co-authorship), and establishing a reference framework of influential publications based on citation metrics.

The analysis employs a Bibliometric Analysis and Paper Creator Agent system developed using R (version 4.5.1) and Bibliometrix package (version 4.3.5) (Aria and Cuccurullo, 2017). The system applies performance analysis, science mapping, co-citation analysis, bibliographic coupling, and keyword co-occurrence network analysis.

2. Materials and Methods

2.1. Research Design

This study employed a quantitative bibliometric analysis approach to systematically examine the scholarly landscape of context engineering research. Bibliometric analysis represents an established methodology for quantitative assessment of scientific literature through statistical and mathematical techniques (Aria and Cuccurullo, 2017). The research design encompasses data collection from a bibliographic database, application of bibliometric indicators, and visualization of research patterns through network analysis and performance metrics.

2.2. Data Source

Web of Science (WoS) Core Collection served as the sole data source for this analysis. WoS was selected based on its comprehensive coverage of high-impact publications in computer science and engineering disciplines, rigorous quality control through selective journal indexing, and robust citation indexing capabilities enabling citation-based analyses (Pranckutė, 2021). The use of a single database ensures methodological consistency and data compatibility across all bibliometric indicators.

2.3. Search Strategy and Query Development

A comprehensive search query was developed through iterative refinement to capture the multifaceted nature of context engineering research while maintaining domain specificity. The search was executed on November 14, 2025, at 03:30 using the following query structure:

“((TS=("context engineering" OR "context-aware engineering" OR "context modeling" OR "context modelling" OR "context management" OR "context-aware system*" OR "contextual engineering" OR "context adaptation" OR "context reasoning" OR "context-aware computing))".

AND WC=(Computer Science Artificial Intelligence OR Computer Science Information Systems OR Computer Science Theory Methods OR Computer Science Software Engineering OR Computer Science Interdisciplinary Applications OR Engineering Multidisciplinary)) AND PY=(2000-2025)”.

The search terms were selected to encompass core dimensions of context engineering. The query includes primary field terms such as "context engineering", "context-aware engineering", and "contextual engineering" to capture various terminological preferences in the literature. Technical process terms including "context modeling", "context modelling", "context management", "context adaptation", and "context reasoning" represent key activities within the domain, with both American and British spelling variants included for comprehensive coverage. System-level terms including "context-aware system*" and "context-aware computing" capture implementation and paradigm perspectives. The wildcard operator *() was applied to "context-aware system*" to retrieve morphological variations including system, systems, and systematic. No additional operators were employed to maintain query precision and avoid retrieval of irrelevant publications.

The WoS Category field restriction limited results to publications classified in computer science and engineering domains including Computer Science Artificial Intelligence, Computer Science Information Systems, Computer Science Theory & Methods, Computer Science Software Engineering, Computer Science Interdisciplinary Applications, and Engineering Multidisciplinary. This restriction maintains focus on software engineering and computational aspects of context engineering while excluding hardware-centric sensor systems and network infrastructure studies. Categories such as Telecommunications and Hardware & Architecture were excluded to maintain software engineering focus, as these predominantly contain network-layer and hardware-layer studies rather than context engineering applications. It is important to note that IoT-related context engineering research—such as context modeling for smart environments, context-aware IoT middleware, and sensor data interpretation at the application layer—is captured through the included Computer Science categories, where such contributions are predominantly published. What the Telecommunications and Hardware & Architecture category restriction excludes is specifically the

communication protocol design, network infrastructure, and hardware implementation literature that addresses the connectivity layer of IoT rather than the context engineering layer. This distinction ensures the corpus reflects research on how context is modeled, reasoned, and acted upon, rather than the underlying hardware or network mechanisms that enable data transmission.

The temporal scope spans 2000-2025, capturing 25 years of research development. The year 2000 was selected as the starting point because it marks the beginning of widespread research activity following foundational theoretical work in the late 1990s, coincides with the emergence of mobile computing and ubiquitous computing as practical research domains, and provides a sufficiently long timeframe to identify meaningful trends while maintaining contemporary relevance.

2.4. Inclusion and Exclusion Criteria

Publications were included if they met all of the following criteria: document type classified as Article, Review Article, or Proceedings Paper representing peer-reviewed scholarly contributions; publication language limited to English as the predominant scientific communication language in computer science and engineering; publication status recorded as published or early access with complete bibliographic data; and availability of complete metadata including title, authors, abstract, keywords, affiliations, and references necessary for comprehensive bibliometric analysis.

Publications were excluded if they met any of the following criteria: document type classified as Editorial Material, Letter, Book Chapter, Book Review, Correction, or Meeting Abstract as these do not represent original peer-reviewed research contributions; identification as duplicate records through DOI and title matching to avoid distortion of frequency-based metrics; or incomplete essential bibliographic fields compromising analysis reliability. No duplicate records were detected in the final dataset. The search query yielded 4,858 publications meeting all inclusion criteria.

2.5. Data Collection and Processing

Bibliographic data were exported from WoS on November 14, 2025, in plain text format. The export included complete records containing bibliographic information such as title, authors, source, publication year, volume, issue, pagination, and DOI; author information including names, affiliations, and corresponding author address; abstract and keywords comprising author keywords and Keywords Plus; citation data including times cited and citation count per year; and complete reference lists for each publication.

Exported data underwent preprocessing to ensure analytical quality through four automated procedures. Author name normalization disambiguated author name variants through algorithmic matching based on affiliation and co-author patterns. Institutional affiliation standardization harmonized institutional name variants using the Bibliometrix institution cleaning algorithm. Keyword harmonization standardized British and American spelling variants, performed lowercase conversion, and removed punctuation inconsistencies. Duplicate detection identified and removed duplicate records based on DOI and title matching, though no duplicates were found in the final dataset. All preprocessing utilized automated Bibliometrix functions to ensure reproducibility without manual intervention.

2.6. Analytical Framework and Tools

Analysis was conducted using a Bibliometric Analysis and Paper Creator Agent system developed as part of the first author's Master's thesis. The system operates on R programming language version 4.5.1 (R Core Team, 2025) with Bibliometrix package version 4.3.5 (Aria and Cuccurullo, 2017) and supporting packages including dplyr version 1.1.4 for data manipulation (Wickham et al., 2023), ggplot2 version 3.5.0 for visualization (Wickham, 2016), and xtable version 1.8-4 for LaTeX table generation (Dahl et al., 2019). All analyses were executed in R environment ensuring reproducibility through documented code and version-controlled packages.

The analysis applied five bibliometric techniques. Performance analysis quantified research productivity and impact through annual publication counts, compound annual growth rate calculation, publications per author, institution, and country, citation metrics including total citations and average citations per paper, h-index calculation, and fractionalized counting for collaborative works. Co-occurrence analysis identified thematic structure through keyword frequency analysis, co-occurrence network construction calculating keyword pair co-occurrence frequency, network visualization representing keyword relationships, and cluster identification through community detection algorithms. Collaboration analysis examined patterns through co-authorship metrics, international collaboration distinguishing multi-country publications from single-country publications, collaboration ratios indicating internationalization level, and country collaboration networks. Source analysis assessed publication venue characteristics through source productivity counts, source impact through citation patterns, and Bradford's Law application for core journal identification. Citation analysis provided impact assessment through most cited publication rankings, citation distribution analysis across countries and time periods, and normalized citation metrics accounting for publication age.

Bibliometric indicators followed standard definitions with Annual Growth Rate calculated as ((Final/Initial)^(1/years)) - 1 representing compound annual publication growth, h-index defined as h papers with at least h citations each balancing productivity and impact, Collaboration Index calculated as Authors/Documents representing average authors per publication, MCP (Multi-Country Publications) Ratio calculated using SCP (Single Country Publications) as MCP/(MCP+SCP) indicating international collaboration intensity, and Average Citations per Document calculated

as Total Citations/Total Documents representing mean citation impact. All metrics follow standard bibliometric definitions as established in Aria and Cuccurullo (2017).
co-occurrence networks employed node size to represent keyword frequency, edge thickness to represent co-occurrence strength, and force-directed layout algorithm for node positioning. Word clouds provided visual representation of keyword frequency through font size scaling. Temporal plots depicted publication trends over time through line graphs. All visualizations maintain minimum 300 dpi resolution for publication quality with network visualizations employing Fruchterman-Reingold layout algorithm for optimal node positioning.

2.8. Study Limitations

This study acknowledges seven methodological limitations. The exclusive use of WoS Core Collection excludes publications indexed only in Scopus, IEEE Xplore, or other databases, prioritizing methodological consistency over absolute comprehensiveness. The English-only restriction may underrepresent research contributions from non-Anglophone regions, potentially affecting geographic distribution findings. The temporal scope excludes pre-2000 foundational works from quantitative analysis, though their influence is acknowledged qualitatively. The WoS category restriction may exclude relevant interdisciplinary work published outside selected categories, particularly hardware-focused or telecommunications-oriented publications. Despite comprehensive term selection, the search query may not capture all terminology variations used across different research communities and time periods. Recently published papers from 2024-2025 have limited citation accumulation time, potentially underestimating their eventual impact. Furthermore, since data were collected on November 14, 2025, the publication and citation figures for 2025 represent only approximately 10.5 months of output rather than a complete calendar year. Consequently, 2025 data should be interpreted as reflecting a partial year, and direct year-on-year comparisons involving 2025 should account for this incompleteness. This seventh limitation does not affect the validity of trend analyses for 2000–2024 but cautions against treating 2025 figures as representative of full-year output. These limitations are inherent to bibliometric studies and do not compromise the validity of findings within the defined scope.

3. Results

3.1. Dataset Overview and Descriptive Statistics

The search query retrieved 4,858 publications from Web of Science Core Collection spanning 2000 to 2025. Table 1 presents the main descriptive statistics of the dataset. The corpus comprised publications from 2,239 sources authored by 12,240 researchers. The average document age was 8.65 years with an average of 15.29 citations per document. The annual growth rate reached 14.22%,

2.7. Visualization

Network visualizations were generated to illustrate thematic and collaboration structures. Keyword indicating sustained expansion of the field. Author collaboration averaged 3.83 co-authors per document with 23.22% of publications involving international collaboration.

Table 1. Main descriptive statistics of the dataset

Description	Results
Timespan	2000:2025
Sources (Journals, Books, etc)	2.239
Documents	4.858
Annual Growth Rate %	14.22
Document Average Age	8.65
Average citations per doc	15.29
Average citations per year per doc	2.16
Authors	12.240
Authors per Document	2.52
Co-Authors per Document	3.83
International co-authorships %	23.22

3.2. Temporal Publication Trends

Figure 1 illustrates the annual publication output from 2000 to 2025. Publication activity remained relatively stable from 2000 to 2004 with fewer than 100 articles per year. The field experienced initial growth from 2005 to 2007, reaching 203 publications in 2007. A plateau phase occurred from 2008 to 2019 with annual output fluctuating between 150 and 200 publications. Substantial acceleration began in 2020, with production increasing from 240 publications in 2020 to 611 in 2025. The most recent three years (2023-2025) accounted for 26.2% of the total corpus.

3.3. Author Productivity and Impact

Table 2 presents the top 20 most productive authors ranked by total publications and fractionalized contributions. Zaslavsky A led in total publications with 35 articles, followed by Lee S with 32 and Zhang Y with 29 publications. When accounting for fractionalized contributions that weight co-authored works proportionally, Lee S ranked first with 10.04 fractionalized articles, followed by Sandkuhl K with 9.12 and Zaslavsky A with 8.88. This divergence between total and fractionalized counts indicates varying collaboration intensities among leading authors.

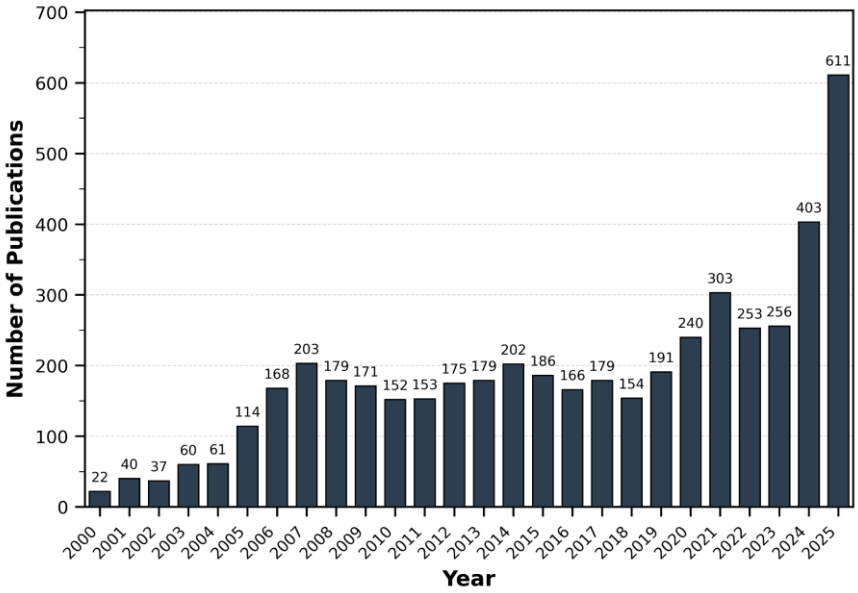


Figure 1. Annual publication output from 2000 to 2025.

Table 2. Top 20 most productive authors

Authors	Articles	Authors	Articles Fractionalized
ZASLAVSKY A	35	LEE S	10.04
LEE S	32	SANDKUHL K	9.12
ZHANG Y	29	ZASLAVSKY A	8.88
LIU Y	26	LOKE SW	8.38
LI Y	25	CHOI J	8.35
LI J	23	MOORE P	7.92
LI X	23	DARGIE W	7.00
LOKE SW	23	HSIEH FS	7.00
ZHANG L	23	KLIMEK R	7.00
WANG J	22	KWON O	6.83
MOORE P	21	ZHANG Y	6.83
WANG Y	21	BOBEK S	6.03
KIM S	19	BRÉZILLON P	5.92
SMIRNOV A	19	NALEPA GJ	5.87
CHOI J	18	LI J	5.85
WANG L	18	CHO SB	5.67
ZHANG DQ	18	KIM S	5.57
INDULSKA J	17	LI Y	5.57
LEE J	17	INDULSKA J	5.51
WANG M	17	WU XL	5.50

3.4. Institutional Productivity

Table 3 identifies the top 20 most productive institutions. The Chinese Academy of Sciences dominated institutional output with 229 publications, substantially exceeding the second-ranked Centre National de la Recherche Scientifique (CNRS) with 99 publications. Chinese institutions occupied seven positions among the top 20, including Zhejiang University (87), Tsinghua University (84), and Shanghai Jiao Tong University (74). European institutions demonstrated strong representation with CNRS (France), Institut Polytechnique de Paris (France), and IMT - Institut Mines-Telecom (France). Singapore and United States institutions also featured prominently with National University of Singapore (50), Nanyang Technological University (46), and Carnegie Mellon University (41).

3.5. Country-Level Productivity and Collaboration

Table 4 presents country-level publication statistics including single-country publications (SCP), multi-country publications (MCP), and international collaboration ratios. China produced the most publications with 1,357 documents representing 28.4% of the corpus, though only 22.8% involved international collaboration. The United States ranked second with 384 publications and 15.4% international

collaboration. South Korea (309), Germany (263), and United Kingdom (197) completed the top five. Singapore demonstrated the highest international collaboration intensity with 38.6% of publications involving multi-country partnerships, followed by Canada (33.0%), Australia (34.2%), and United Kingdom (33.0%).

3.6. Country-Level Citation Impact

Table 5 ranks countries by total citations and average citations per document. China accumulated the most total citations with 24,982, though its average citation per document (18.41) remained below several smaller producers. The United States generated 10,851 total citations with an average of 28.26 citations per document. Singapore achieved the highest average citation impact with 53.98 citations per document from 44 total publications. Switzerland (49.29), Austria (36.78), and Australia (26.99) also demonstrated high average citation rates. This pattern suggests quality-quantity trade-offs across different research systems.

Table 3. Top 20 most productive institutions

Institution	Frequency
CHINESE ACADEMY OF SCIENCES	229
CENTRE NATIONAL DE LA RECHERCHE SCIENTIFIQUE (CNRS)	99
ZHEJIANG UNIVERSITY	87
TSINGHUA UNIVERSITY	84
SHANGHAI JIAO TONG UNIVERSITY	74
UNIVERSITY OF CHINESE ACADEMY OF SCIENCES, CAS	64
UNIVERSITY OF CALIFORNIA SYSTEM	60
BEIHANG UNIVERSITY	56
PEKING UNIVERSITY	51
NATIONAL UNIVERSITY OF SINGAPORE	50
BEIJING UNIVERSITY OF POSTS AND TELECOMMUNICATIONS	49
HONG KONG POLYTECHNIC UNIVERSITY	49
HARBIN INSTITUTE OF TECHNOLOGY	46
NANYANG TECHNOLOGICAL UNIVERSITY	46
UNIVERSITY OF ELECTRONIC SCIENCE AND TECHNOLOGY OF CHINA	45
IMT - INSTITUT MINES-TELECOM	44
INSTITUT POLYTECHNIQUE DE PARIS	44
NORTHWESTERN POLYTECHNICAL UNIVERSITY	42
CARNEGIE MELLON UNIVERSITY	41
MONASH UNIVERSITY	41

Table 4. Top 20 countries by productivity and collaboration patterns

Country	Articles	Freq	SCP	MCP	MCP_Ratio
CHINA	1357	0.284	1047	310	0.228
USA	384	0.080	325	59	0.154
KOREA	309	0.065	280	29	0.094
GERMANY	263	0.055	198	65	0.247
UNITED KINGDOM	197	0.041	132	65	0.330
FRANCE	176	0.037	136	40	0.227
SPAIN	175	0.037	137	38	0.217
ITALY	173	0.036	137	36	0.208
INDIA	169	0.035	146	23	0.136
AUSTRALIA	152	0.032	100	52	0.342
BRAZIL	116	0.024	96	20	0.172
CANADA	109	0.023	73	36	0.330
JAPAN	101	0.021	73	28	0.277
GREECE	79	0.017	66	13	0.165
NETHERLANDS	53	0.011	40	13	0.245
PORTUGAL	49	0.010	40	9	0.184
IRELAND	46	0.010	34	12	0.261
FINLAND	45	0.009	38	7	0.156
SINGAPORE	44	0.009	27	17	0.386
POLAND	41	0.009	35	6	0.146

SCP = Single Country Publications, MCP = Multi-Country Publications, Freq = Frequency ratio.

Table 5. Top 20 countries by citation impact

Country	Total Citations	Average Article Citations
CHINA	24982	18.41
USA	10851	28.26
AUSTRALIA	4103	26.99
UNITED KINGDOM	4047	20.54
ITALY	3210	18.55
GERMANY	3150	11.98
KOREA	2740	8.87
SINGAPORE	2375	53.98
FRANCE	2152	12.23
SPAIN	1763	10.07
CANADA	1757	16.12
AUSTRIA	1361	36.78
SWITZERLAND	1183	49.29
GREECE	1016	12.86
INDIA	789	4.67
BRAZIL	699	6.03
JAPAN	534	5.29
SAUDI ARABIA	523	14.14
DENMARK	455	17.50
TÜRKİYE	412	24.24

3.7. Most Influential Publications

Table 6 lists the top 20 most cited publications. Zheng et al. (2021) topped the citation rankings with 2,810 total citations and 562.0 citations per year. Liu et al. (2020) ranked second with 1,828 total citations. Perera et al. (2014) accumulated 1,442 citations with a focus on context-aware computing for Internet of Things. Three publications exceeded 1,000 total citations, while 11 publications surpassed 500 citations. The normalized citation scores (NTC) revealed that Zheng et al. (2021) achieved 84.47, substantially exceeding field averages.

3.8. Source Productivity

Table 7 presents the top 20 most productive journals and conferences. IEEE Access dominated source productivity with 505 publications, representing 10.4% of the total corpus. IEEE transactions series contributed substantially with IEEE Transactions on Image Processing (84), IEEE Transactions on Multimedia (68), IEEE Transactions on Neural Networks and Learning Systems (60), IEEE Transactions on Knowledge and Data Engineering (57), and IEEE Transactions on Pattern Analysis and Machine Intelligence (57). Expert Systems with Applications published 53 articles, while IEEE Internet of Things Journal contributed 35 publications. The concentration of publications in IEEE venues indicates the field's strong association with electrical engineering and computer science communities.

3.9. Keyword Analysis and Thematic Structure

Table 8 presents the top 20 author keywords and Keywords Plus terms. "Context modeling" emerged as the most frequent author keyword with 1,429 occurrences, substantially exceeding other terms. "Context-aware computing" appeared 350 times, followed by "feature extraction" (343), "computational modeling" (325), and "deep learning" (298). The Keywords Plus analysis identified "framework" (134), "model" (112), and "network" (101) as the most frequent index terms. Technical terminology including "transformers" (251), "semantics" (294), and "data models" (288) reflected contemporary methodological approaches.

Figure 2 visualizes the keyword co-occurrence network based on title words. The network revealed three primary thematic clusters. The largest cluster centered on "context modeling" and "context-aware systems" representing foundational concepts. A second cluster emphasized machine learning approaches including "deep learning", "neural networks", and "image segmentation". A third cluster focused on computing paradigms including "ubiquitous computing", "pervasive computing", and "mobile context-aware". The network structure indicated strong interconnections between theoretical modeling concepts and applied machine learning techniques.

Figure 3 presents a word cloud visualization of title-based keywords. "Context modeling" dominated the visual representation, consistent with frequency analysis. Terms such as "context-aware systems", "context-aware computing", "semantic segmentation", and "image compression" appeared prominently. Visualization confirmed the centrality of modeling and systems concepts while highlighting the increasing importance of machine learning and computer vision applications.

Table 6. Top 20 most cited publications

Paper	DOI	TC	TCperYear
ZHENG SX, 2021	10.1109/CVPR46437.2021.00681	2810	562.0
LIU L, 2020	10.1007/s11263-019-01247-4	1828	304.7
PERERA C, 2014	10.1109/SURV.2013.042313.00197	1442	120.2
CAO Y, 2019	10.1109/ICCVW.2019.00246	1422	203.1
DEY AK, 2001	10.1207/S15327051HCI16234_02	1305	52.2
WEINBERGER MJ, 2000	10.1109/83.855427	1129	43.4
BALDAUF M, 2007	10.1504/IJAHUC.2007.014070	897	47.2
CELIK MU, 2005	10.1109/TIP.2004.840686	872	41.5
ZHAO R, 2015	-	803	73.0
KOBYZEV I, 2021	10.1109/TPAMI.2020.2992934	800	160.0
DOURISH P, 2004	10.1007/s00779-003-0253-8	740	33.6
BETTINI C, 2010	10.1016/j.pmcj.2009.06.002	676	42.2
CHANG SG, 2000	10.1109/83.862630	645	24.8
SHOTTON J, 2006	-	581	29.1
WU TY, 2021	10.1109/TIP.2020.3042065	526	105.2
WANG XH, 2004	-	470	21.4
GUINARD D, 2010	10.1109/TSC.2010.3	469	29.3
GU T, 2005	10.1016/j.jnca.2004.06.002	464	22.1
PERERA C, 2014	10.1109/ACCESS.2015.2389854	379	31.6
HONG JY, 2009	10.1016/j.eswa.2008.10.071	355	20.9

TC = total citations, TCperYear = citations per year, NTC = normalized total citations.

Table 7. Top 20 most productive sources

Sources	Articles
IEEE ACCESS	505
IEEE TRANSACTIONS ON IMAGE PROCESSING	84
IEEE TRANSACTIONS ON MULTIMEDIA	68
IEEE TRANSACTIONS ON NEURAL NETWORKS AND LEARNING SYSTEMS	60
IEEE TRANSACTIONS ON KNOWLEDGE AND DATA ENGINEERING	57
IEEE TRANSACTIONS ON PATTERN ANALYSIS AND MACHINE INTELLIGENCE	57
EXPERT SYSTEMS WITH APPLICATIONS	53
IEEE TRANSACTIONS ON COMPUTATIONAL SOCIAL SYSTEMS	47
IEEE INTERNET OF THINGS JOURNAL	35
APPLIED SCIENCES-BASEL	31
IEEE TRANSACTIONS ON AFFECTIVE COMPUTING	31
PERSONAL AND UBIQUITOUS COMPUTING	30
NEUROCOMPUTING	26
PERVASIVE AND MOBILE COMPUTING	26
MULTIMEDIA TOOLS AND APPLICATIONS	25
INTERNATIONAL JOURNAL OF PERVASIVE COMPUTING AND COMMUNICATIONS	24
IEEE TRANSACTIONS ON SOFTWARE ENGINEERING	22
IEEE TRANSACTIONS ON MOBILE COMPUTING	20
KNOWLEDGE-BASED SYSTEMS	19
JOURNAL OF AMBIENT INTELLIGENCE AND SMART ENVIRONMENTS	18

Table 8. Top 20 most frequent author keywords and Keyword Plus terms

Author Keywords (DE)	Articles	Keywords-Plus (ID)	Articles
CONTEXT MODELING	1429	FRAMEWORK	134
CONTEXT-AWARE COMPUTING	350	MODEL	112
FEATURE EXTRACTION	343	NETWORK	101
COMPUTATIONAL MODELING	325	SYSTEMS	98
DEEP LEARNING	298	SYSTEM	91
TASK ANALYSIS	296	INFORMATION	80
SEMANTICS	294	INTERNET	78
DATA MODELS	288	CLASSIFICATION	61
TRANSFORMERS	251	DESIGN	58
TRAINING	241	MANAGEMENT	52
CONTEXT-AWARENESS	227	CONTEXT	51
PREDICTIVE MODELS	201	MIDDLEWARE	46
ADAPTATION MODELS	181	ONTOLOGY	46
CONTEXT	177	RECOGNITION	46
CONTEXT-AWARE SYSTEMS	156	NETWORKS	45
CONTEXT AWARENESS	155	CHALLENGES	38
UBIQUITOUS COMPUTING	154	ALGORITHM	35
VISUALIZATION	152	MOBILE	35
ACCURACY	149	THINGS	34
PERVASIVE COMPUTING	140	INFRASTRUCTURE	31

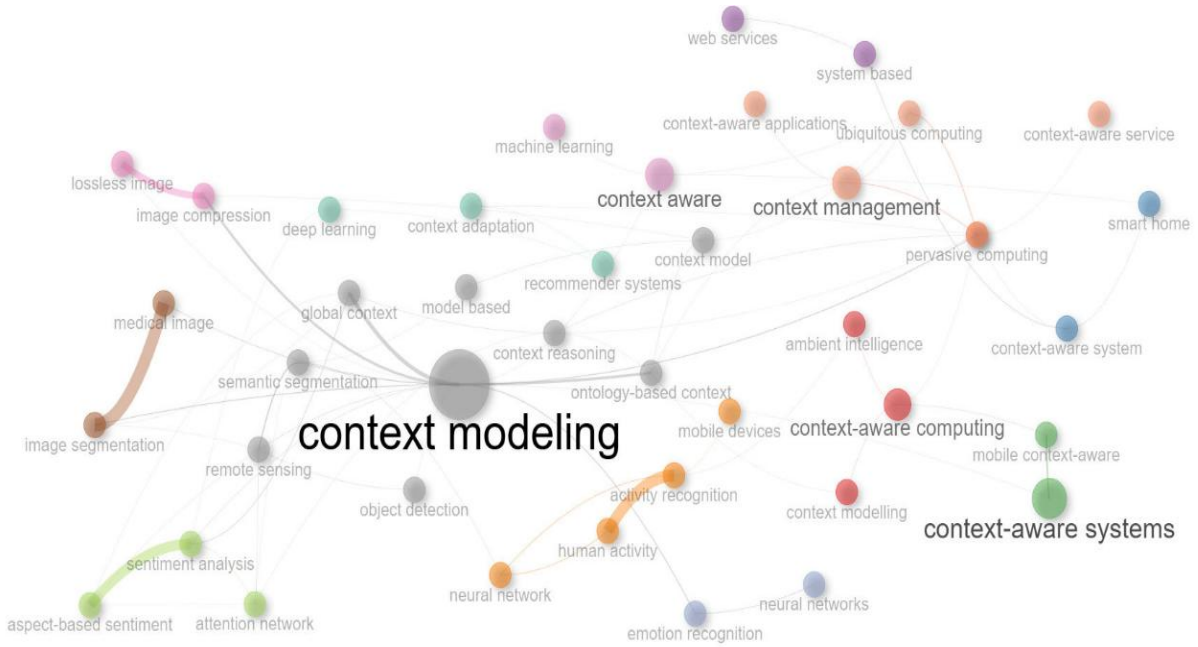


Figure 2. Keyword co-occurrence network based on title analysis.

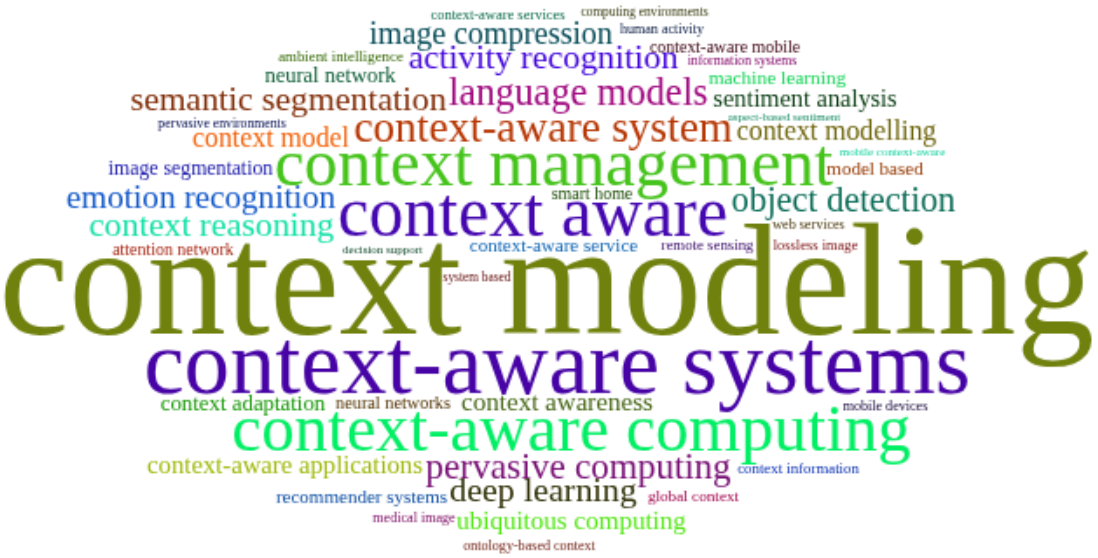


Figure 3. Word cloud of title-based keywords.

4. Discussion

4.1. Publication Growth and Field Maturation

The 14.22% annual growth rate observed in context engineering publications indicates robust field expansion exceeding growth rates reported in several established computing domains. Tosun (2022) documented educational research growth with periodic acceleration phases in 1980, 2008, and 2019. Context engineering demonstrated similar acceleration patterns, particularly from 2020 onward when annual output nearly doubled from 240 to 611 publications within five years. This acceleration coincides with widespread adoption of Internet of Things technologies and artificial intelligence applications requiring context-aware capabilities (Perera et al., 2014). The sustained growth trajectory suggests context engineering has transitioned from an emerging specialty to a mature research domain with established theoretical foundations and practical applications.

The publication distribution revealed three distinct developmental phases. The initial phase (2000-2004) represented foundational period with modest output averaging 44 publications annually. The consolidation phase (2005-2019) exhibited stable production around 170 publications per year, indicating establishment of core research community and venues. The expansion phase (2020-2025) demonstrated exponential growth driven by technological advances in machine learning, edge computing, and ubiquitous systems. This pattern aligns with typical technology adoption curves where initial theoretical development precedes practical implementation and widespread diffusion.

4.2. Geographic Distribution and Research Leadership

Chinese institutional dominance, with Chinese Academy of Sciences producing 229 publications, reflects broader patterns of Chinese scientific output expansion documented across multiple disciplines (Tang et al., 2015). However, the relatively low international collaboration rate of 22.8% for Chinese publications suggests emphasis on domestic research networks rather than global partnerships. This contrasts with smaller research systems such as Singapore (38.6% international collaboration), Australia (34.2%), and United Kingdom (33.0%) that demonstrate higher integration into international networks. The divergence between quantity and collaboration intensity indicates different research strategies, with large systems pursuing volume-based approaches while smaller systems emphasize quality through international partnerships.

The citation impact analysis revealed quality-quantity trade-offs across national research systems. Singapore achieved the highest average citation impact (53.98 citations per document) from only 44 publications, while China accumulated the most total citations (24,982) but achieved below-average citation rates (18.41 per document). This pattern parallels findings in other bibliometric studies showing that research concentration in elite institutions often correlates with higher citation impact than distributed production across many institutions. Switzerland (49.29 average citations) and Austria (36.78) demonstrated similar concentration effects despite modest publication volumes.

4.3. Author Productivity Patterns and Collaboration

The divergence between total publication counts and fractionalized contributions among top authors reveals different collaboration strategies. Zaslavsky A led in total publications (35) but ranked third in fractionalized output (8.88), indicating extensive collaborative work. Conversely, Lee S and Sandkuhl K achieved higher fractionalized scores relative to total publications, suggesting more balanced co-authorship arrangements or leadership roles in collaborative projects.

The average of 3.83 co-authors per document and 23.22% international co-authorship rate indicates

moderate collaboration intensity compared to other computer science subfields. Bibliometric studies of software engineering typically report higher collaboration rates, particularly in areas requiring large-scale empirical validation or industry partnerships. The relatively modest international collaboration in context engineering may reflect the field's emphasis on theoretical modeling and algorithm development rather than large-scale system deployment requiring multinational partnerships.

4.4. Thematic Structure and Research Focus

The dominance of "context modeling" (1,429 occurrences) as the most frequent keyword confirms that modeling and representation remain central challenges in context engineering. This persistent focus on foundational problems suggests the field has not yet achieved consensus on optimal modeling approaches, unlike more mature domains where standardization reduces emphasis on basic representation issues. The high frequency of machine learning terms including "deep learning" (298), "transformers" (251), and "neural networks" reflects recent methodological shifts toward data-driven approaches complementing traditional rule-based and ontology-based methods.

The keyword co-occurrence network revealed three thematic clusters representing different research orientations. The foundational cluster emphasizing modeling and systems concepts maintains continuity with early context-aware computing research from the 2000s. The machine learning cluster reflects contemporary trends integrating computer vision, natural language processing, and pattern recognition techniques into context-aware systems. The ubiquitous computing cluster connects context engineering to broader paradigms in pervasive and mobile computing. This multi-cluster structure indicates healthy diversity in research approaches rather than narrow specialization.

The prominence of technical terms such as "feature extraction," "computational modeling," and "semantics" in author keywords suggests context engineering remains primarily a technical discipline focused on computational methods rather than user-centered design or application domains. This contrasts with related fields such as human-computer interaction where user studies and qualitative methods feature more prominently in keyword landscapes. The emphasis on modeling and computation may limit adoption of context-aware techniques in domains requiring human factors expertise.

4.5. Source Concentration and Publication Venues

The concentration of 505 publications in IEEE Access (10.4% of corpus) and strong representation across IEEE transaction series indicates context engineering's primary association with electrical engineering and computer science venues rather than software engineering or human-computer interaction conferences. This venue concentration pattern differs from interdisciplinary fields that distribute publications across multiple disciplinary outlets. The IEEE dominance suggests context engineering research prioritizes technical rigor and computational methods valued in engineering venues over design-oriented approaches emphasized in human-computer interaction or ubiquitous computing conferences.

The presence of domain-specific journals such as Personal and Ubiquitous Computing and Pervasive and Mobile Computing alongside general computer science venues indicate gradual specialization. However, the absence of a dedicated context engineering journal suggests the field has not yet achieved sufficient cohesion and volume to sustain specialized publication outlets. This contrasts with related areas such as machine learning or computer vision that support multiple dedicated journals and conferences.

4.6. Citation Patterns and Knowledge Base

The highly cited publications analysis revealed two distinct categories. Contemporary papers such as Zheng et al. (2021) and Liu et al. (2020) accumulated high citations through intensive research in computer vision and machine learning applications. Foundational works such as Dey (2001), Baldauf et al. (2007), and Perera et al. (2014) maintained citation relevance despite age through their contributions to theoretical frameworks and survey syntheses. The coexistence of both categories in top-cited lists indicates a healthy balance between emerging topics and enduring foundations.

The normalized citation scores revealed that recent publications achieved exceptionally high impact relative to field averages. Zheng et al. (2021) achieved NTC of 84.47, indicating citation rates more than 80 times field average for that year. Such extreme values suggest either exceptional contribution quality or rapid diffusion within narrow subspecialties experiencing intensive research activity. The concentration of highly cited recent work in computer vision and image processing domains indicates that context engineering increasingly intersects with these adjacent fields. A critical interpretive nuance concerns the comparison between cumulative impact of foundational works and citation velocity of recent articles. Raw citation counts and annual citation rates naturally favor recent publications due to the exponential growth of the citing literature base; for instance, a paper published in 2021 competes for citations in a field producing over 600 publications per year, whereas Dey (2001) accumulated citations when annual output was below 50. Normalized citation scores partially account for this by adjusting against field averages at the publication year. From this perspective, foundational works such as Dey (2001) with 52.2 citations per year and Baldauf et al. (2007) with 47.2 citations per year demonstrate sustained and enduring impact over two decades, suggesting their theoretical frameworks continue to guide the field long after initial publication. In contrast, the exceptionally high NTC of Zheng et al. (2021) at 84.47 reflects rapid adoption within the machine learning community during a period of intense

research activity, but its long-term influence relative to field growth remains to be established. Interpreting citation patterns in this field therefore requires distinguishing between citation velocity (concentrated in recent, methodologically trendy papers) and citation endurance (characteristic of foundational theoretical contributions), as these represent qualitatively different forms of scholarly influence.

4.7. Implications for Theory and Practice

The bibliometric patterns reveal several theoretical implications. First, context engineering has evolved from a systems-oriented paradigm focused on middleware and infrastructure toward an application-oriented paradigm emphasizing machine learning and domain-specific solutions. This evolution suggests maturation from general-purpose frameworks to specialized tools addressing concrete problems. Second, the persistent focus on modeling indicates unresolved theoretical challenges in context representation, reasoning, and adaptation. Third, the thematic cluster structure suggests potential fragmentation into subspecialties rather than convergence toward unified theoretical frameworks.

Practical implications emerge from the geographic and collaborative patterns. The concentration of research in China and limited international collaboration suggests opportunities for strengthening global research networks through targeted partnership programs. The low representation of developing regions indicates potential for expanding context engineering research into diverse cultural and technological contexts where mobile and ubiquitous computing face different constraints and opportunities. The IEEE venue concentration suggests context engineering research could benefit from stronger engagement with software engineering, human-computer interaction, and information systems communities.

4.8. Limitations

This study acknowledges methodological limitations inherent to single-database bibliometric analyses. The exclusive use of Web of Science Core Collection excludes publications indexed only in Scopus, IEEE Xplore, or regional databases, potentially underestimating contributions from regions with different indexing preferences. The English-language restriction may underrepresent research published in Chinese, German, French, or other languages. The temporal scope excludes pre-2000 foundational works from quantitative analysis, though their intellectual influence persists through citations. The WoS category filtering may exclude relevant interdisciplinary work published in journals outside selected computer science and engineering categories.

Citation-based metrics favor established research over recent contributions that have not accumulated citations, potentially undervaluing innovative work published in 2024-2025. The bibliometric approach captures publication and citation patterns but cannot assess research quality, methodological rigor, or practical impact beyond academic citations. These limitations suggest complementary qualitative analyses could enrich understanding of context engineering's intellectual development and practical contributions.

4.9. Future Research Directions

Several research directions emerge from the bibliometric patterns. First, the thematic analysis revealed limited integration between modeling-oriented and machine learning-oriented research clusters. Future work should investigate hybrid approaches combining symbolic context modeling with data-driven learning techniques. Second, the geographic analysis identified opportunities for expanding research networks between high-productivity regions (China, USA) and high-impact regions (Singapore, Switzerland) through collaborative projects. Third, the modest international collaboration rate suggests potential for establishing multinational research consortia addressing context-aware system challenges requiring diverse technological and cultural perspectives.

The keyword analysis indicated emerging topics including transformers, deep learning, and computer vision applications that warrant systematic investigation. Future bibliometric studies could employ longitudinal keyword analysis to track thematic evolution and identify emerging specializations. The source analysis suggested opportunities for establishing dedicated context engineering venues that could consolidate the research community and strengthen disciplinary identity. Finally, the citation analysis revealed need for synthesis works that integrate findings across the modeling, machine learning, and ubiquitous computing clusters to advance theoretical coherence.

4.10. Use of AI-Assisted Analytical Tools

This study employed an agentic AI system as part of the manuscript production workflow. Transparency regarding the use of such tools in academic research is an emerging ethical consideration warranting explicit discussion. It must be emphasized that all bibliometric analyses in this study were performed exclusively through the Bibliometrix R package applied to the Web of Science dataset exported in WoS format. This analytical pipeline from raw data export to the generation of performance metrics, co-occurrence networks, and collaboration indicators is entirely reproducible and does not involve AI-generated computations. The role of the agentic system was limited to the draft manuscript production phase: it converted the structured outputs of the R analyses (tables, figures, and quantitative results) into organized, consistently formatted draft manuscript text. All analytical decisions—including the selection of research questions, the design of the search strategy, the interpretation of bibliometric indicators, the identification of thematic patterns, and the synthesis of findings were made by the human authors. The agentic workflow underlying this manuscript is described in detail in Koçyiğit (2026), which presents a thesis-level account of the agent-based approach developed for

bibliometric analysis and manuscript preparation. Future bibliometric studies employing AI-assisted tools are encouraged to similarly disclose the specific functions performed by such systems to ensure transparency and reproducibility.

Author Contributions

The percentages of the authors' contributions are presented below. All authors reviewed and approved the final version of the manuscript.

	A.K.	N.Ş.
C	50	50
D	50	50
S	50	50
DCP	50	50
DAI	50	50
L	50	50
W	50	50
CR	50	50
SR	50	50
PM	50	50
FA	50	50

C= concept, D= design, S= supervision, DCP= data collection and/or processing, DAI= data analysis and/or interpretation, L= literature search, W= writing, CR= critical review, SR= submission and revision, PM= project management, FA= funding acquisition.

Conflict of Interest

The authors declared that there is no conflict of interest.

Ethical Consideration

Ethics committee approval was not required for this study because there was no study on animals or humans.

Acknowledgements

This study is a part of the first author's Master's thesis at Samsun University, Department of Software Engineering.

References

Aria, M., & Cuccurullo, C. (2017). bibliometrix: An R-tool for comprehensive science mapping analysis. *Journal of Informetrics*, *11*(4), 959–975. https://doi.org/10.1016/j.joi.2017.08.007

Baldauf, M., Dustdar, S., & Rosenberg, F. (2007). A survey on context-aware systems. *International Journal of Ad Hoc and Ubiquitous Computing*, *2*(4), 263–277. https://doi.org/10.1504/IJAHUC.2007.014070

Dahl, D., Scott, D., Roosen, C., Magnusson, A., & Swinton, J. (2019). *xtable: Export tables to LaTeX or HTML* (R package version 1.8-4) [Computer software]. https://CRAN.R-project.org/package=xtable

Dey, A. K. (2001). Understanding and using context. *Personal and Ubiquitous Computing*, *5*(1), 4–7. https://doi.org/10.1207/S15327051HCI16234_02

Koçyiğit, A. (2026). *Bibliyometrik analiz için etmen tabanlı yaklaşım* [Agent-based approach to bibliometric analysis] (Thesis No. 1004230) [Master's thesis, Samsun University]. National Thesis Center.

Liu, L., Ouyang, W., Wang, X., Fieguth, P., Chen, J., Liu, X., & Pietikäinen, M. (2020). Deep learning for generic object detection: A survey. *International Journal of Computer Vision*, *128*(2), 261–318. https://doi.org/10.1007/s11263-019-01247-4

Perera, C., Zaslavsky, A., Christen, P., & Georgakopoulos, D. (2014). Context aware computing for the Internet of Things: A survey. *IEEE Communications Surveys & Tutorials*, *16*(1), 414–454. https://doi.org/10.1109/SURV.2013.042313.00197

Pranckutė, R. (2021). Web of Science (WoS) and Scopus: The titans of bibliographic information in today's academic world. *Publications*, *9*(1), Article 12. https://doi.org/10.3390/publications9010012

R Core Team. (2025). *R: A language and environment for statistical computing* [Computer software]. R Foundation for Statistical Computing. https://www.R-project.org/

Tang, L., Shapira, P., & Youtie, J. (2015). Is there a clubbing effect underlying Chinese research citation increases? *Journal of the Association for Information Science and Technology*, *66*(9), 1923–1932. https://doi.org/10.1002/asi.23302

Tosun, C. (2022). Trends of WoS educational research articles in the last half-century. *Review of Education*, *10*(1), Article e3328. https://doi.org/10.1002/rev3.3328

Wickham, H. (2016). *ggplot2: Elegant graphics for data analysis*. Springer-Verlag. https://doi.org/10.1007/978-3-319-24277-4

Wickham, H., François, R., Henry, L., Müller, K., & Vaughan, D. (2023). *dplyr: A grammar of data manipulation* (R package version 1.1.4) [Computer software]. https://CRAN.R-project.org/package=dplyr

Zheng, S., Lu, J., Zhao, H., Zhu, X., Luo, Z., Wang, Y., Fu, Y., Feng, J., Xiang, T., Torr, P. H. S., & Zhang, L. (2021). Rethinking semantic segmentation from a sequence-to-sequence perspective with transformers. In *Proceedings of the IEEE/CVF Conference on Computer Vision and Pattern Recognition* (pp. 6881–6890). IEEE. https://doi.org/10.1109/CVPR46437.2021.00681

Black Sea Journal of Engineering and Science
doi: 10.34248/bsengineering.1966646

Open Access Journal
e-ISSN: 2619 – 8991

Research Article
Volume 9 - Issue 5: 2224-2231 / September 2026

DEVELOPMENT AND EXPERIMENTAL VALIDATION OF A FULL-SCALE BRAKE DISC/PAD TEST RIG FOR PASSENGER VEHICLES

Hüseyin KAYA[1], Hanifi KÜÇÜKSARIYILDIZ[2]*, Bekir GÜNEY[2]

[1]*Karamanoğlu Mehmetbey University, Vocational School of Technical Sciences, Department of Mechanical and Metal Technologies, Karaman, 70100, Türkiye*
[2]*Karamanoğlu Mehmetbey University, Vocational School of Technical Sciences, Department of Motor Vehicles and Transportation Technologies, Karaman, 70100, Türkiye*

Abstract: Brake systems are among the most critical safety components in passenger vehicles, making the accurate evaluation of braking performance essential during the design and development process. This study presents the development of a low-cost, multifunctional brake test rig capable of evaluating the performance of disc–pad friction pairs under controlled laboratory conditions. The test rig consists of a hydraulic braking unit, an electric motor drive system, a frequency inverter, a hydraulic control unit, and a data acquisition system. Braking tests were performed using an OEM ventilated brake disc and pad set at an equivalent vehicle speed of 100 km/h under a hydraulic braking pressure of 20 bar. Vehicle speed, friction coefficient, and brake disc temperature were continuously monitored throughout the experiments. The results showed that the developed test rig provided stable and repeatable braking cycles. The coefficient of friction varied between 0.03 and 0.36, while the brake disc temperature gradually increased from approximately 60 °C to 80 °C during repeated braking cycles. The developed system successfully reproduced braking characteristics under the specified laboratory conditions and provides a practical, reliable, and cost-effective platform for brake performance evaluation and future friction material investigations.

Keywords: Brake test rig, Disc/pad, Braking performance, Friction coefficient, Dynamometer

***Corresponding author:** Karamanoğlu Mehmetbey University, Vocational School of Technical Sciences, Department of Motor Vehicles and Transportation Technologies, Karaman, 70100, Türkiye
E mail: hanifi@kmu.edu.tr (H. KÜÇÜKSARIYILDIZ)
Hüseyin KAYA https://orcid.org/0000-0002-2714-8481
Hanifi KÜÇÜKSARIYILDIZ https://orcid.org/0000-0001-5218-3409
Bekir GÜNEY https://orcid.org/0000-0001-9764-9313

Received: June 08, 2026
Accepted: July 25, 2026
Published: September 15, 2026

Cite as: Kaya, H., Küçüksarıyıldız, H., & Güney, B. (2026). Development and experimental validation of a full-scale brake disc/pad test rig for passenger vehicles. *Black Sea Journal of Engineering and Science*, 9(5), 2224-2231.

1. Introduction

In the automotive industry, brake systems play a critical role in vehicle safety and performance. Brakes are among the primary active safety systems that ensure driving safety by controlling vehicle motion under various road conditions. Therefore, ensuring the reliability of brake systems through testing under laboratory environments or real-road conditions is of critical importance in industrial applications. However, tests conducted under real-road conditions are often time-consuming, costly, and difficult to perform. To overcome these challenges, brake component manufacturers and researchers have increasingly utilized laboratory-based testing methods to obtain controlled and rapid results.

The minimum requirements for brake systems are specified in regional standards such as the United States National Highway Traffic Safety Administration regulations (FMVSS 135 and FMVSS 105) and the United Nations Economic Commission for Europe regulation (ECE R13-H) (Agudelo and Ferro, 2005; Kumar and Bijwe, 2010). Brake component manufacturers invest substantial time and resources to determine safety and performance characteristics (Filip et al., 1997; Malachova et al., 2016).

As a solution to the challenges associated with real-road testing, manufacturers and research institutions have developed various testing equipment, such as inertia brake dynamometers, to simulate different driving scenarios. In full-scale brake testing, vehicle-specific parameters including pressure, temperature, and speed can be comprehensively evaluated (SAE, 2014; Tuszyński et al., 2019). Although inertia brake dynamometers provide an effective method for evaluating friction materials across different vehicle segments, their high installation and operational costs have increased the demand for smaller-scale testing devices (Yun et al., 2010).

In particular, reduced-scale dynamometers using standardized sample sizes and geometries enable rapid assessment of tribological performance independent of a specific brake system by eliminating the influence of other brake system components. Moreover, the operating and maintenance costs of reduced-scale dynamometers are generally lower (Perzborn et al., 2014; Sanders et al., 2001; Varriale et al., 2022).

This work is licensed (CC BY-NC 4.0) under Creative Commons Attribution 4.0 International License

For this reason, several sub-scale testing devices, such as the Friction Assessment and Screening Test (FAST), Chase machine, and pin-on-disk testing systems, have been developed (Anderson et al., 1967; Blau, 2001; Burkman and Hishley, 1967; SAE, 1967). However, these small-scale devices do not always produce results consistent with those obtained from brake dynamometers (Sanders et al., 2001). Previous studies have reported inconsistencies in friction and wear levels among Chase machines, inertia dynamometers, and real-road tests (Jaafar et al., 2012; Tsang et al., 1985). Similarly, discrepancies have also been identified between FAST machines and full-scale dynamometers. Nevertheless, these inconsistencies are considered acceptable because small-scale methods such as Chase and FAST are designed to simulate specific conditions rather than replicate complete brake dynamometer testing environments. Consequently, many brake designers continue to benefit from these methods (Kancharla, 2014; Lee, 2013; Lee et al., 2010).

Standard testing methods (ASTM G99, ASTM G133, etc.) present uncertainties regarding equipment selection and their ability to accurately simulate practical operating conditions (Blau, 2008). When considering the thermal aspects of friction testing, small-scale testing devices are unable to generate sufficient friction-induced heat due to mass limitations (Rudas Florez, 2018). Consequently, the use of external heating systems becomes necessary to capture thermal gradients representative of actual operating conditions (Blau, 2008). However, this introduces additional challenges, including prolonged exposure of test specimens to elevated temperatures, which may lead to thermal degradation.

Laboratory tests cannot fully and accurately reproduce actual driving conditions. Recent studies have primarily focused on the interfacial friction mechanisms between brake discs and pads, employing either full-scale inertia dynamometers or reduced-scale dynamometers in experimental investigations (Rita et al., 2024; Wang et al., 2025). However, existing test systems and devices still exhibit significant limitations, including the inability to operate with full-scale brake discs and pads, basic automation capabilities, and insufficient data acquisition and transfer systems (Eriksson et al., 2002; Singireddy et al., 2022). Addressing these limitations is essential to meet the rapidly evolving demands of the automotive industry. Therefore, there is a need for novel testing systems capable of evaluating full-scale brake discs and pads while providing more reliable results.

To achieve this objective, reducing repetitive testing procedures, shortening testing durations, and improving friction material formulations are essential. Consequently, more specific applications of test equipment used for evaluating the tribological characteristics of disc–pad friction pairs may provide more efficient solutions to these requirements (Rita et al., 2024). Electric motor-driven dynamometers can simulate real driving conditions within laboratory environments, enabling more precise implementation of standardized tests. Compared to alternative systems, such test platforms generally possess simpler structures and lower costs. Furthermore, these systems can be used for various applications, including the evaluation of braking force, wear characteristics, friction coefficients, and thermal behavior.

In this study, an inertia brake dynamometer was developed to evaluate the tribological performance of full-scale disc–pad friction pairs. The developed dynamometer system aims to overcome limitations associated with existing systems, including high cost, structural complexity, and measurement reliability issues, while providing a more economical and reliable testing alternative with improved measurement accuracy. In this context, a simple, user-friendly experimental setup capable of delivering reliable measurement results, adapting to various experimental objectives, and simulating different testing scenarios was designed.

The developed system enables rapid and convenient testing of friction materials belonging to different vehicle segments without requiring extensive preliminary preparation. Using the proposed full-scale inertia brake dynamometer, it is specifically intended to experimentally evaluate braking performance parameters of passenger vehicles, including braking force, friction coefficient, and disc temperature. Furthermore, considering the limitations of existing technologies, the proposed system aims to provide an original and meaningful contribution to the current literature.

2. Materials and Methods

2.1. Materials

2.1.1. Brake test rig

In the brake test rig, various performance-related data can be analyzed using wear, thermal, vibration, and coefficient of friction tests. Thanks to its data input control, low power requirements, and compact design, this rig is capable of simulating various operating conditions such as speed, braking force, and temperature (Aleksendrić, 2010).

In tests conducted on full-scale or scaled-down inertia dynamometers, parameters such as slip speed, deceleration, energy density, pad pressure, temperature, and stopping time are functions of the coefficient of friction (Sanders et al., 2001). The developed test setup is designed to establish the relationship between these functions in the braking mechanism of passenger vehicles.

The developed brake test setup primarily consists of a chassis, an electric motor, a PLC mechanism, sensors, computer hardware, and software components. Additionally, the test setup is equipped with components such as the brake mechanism, a hydraulic unit, a brake control device, and pressure and temperature sensors. Thanks to these components, braking performance tests

can be conducted effectively, efficiently, and economically in a short period of time. The test device allows for the testing of friction material combinations (ASTM A48, Class 30) specific to different vehicle segments. The test setup is shown in Figure 1, and a schematic view of the test setup components is shown in Figure 2.



Figure 1. Brake test rig.

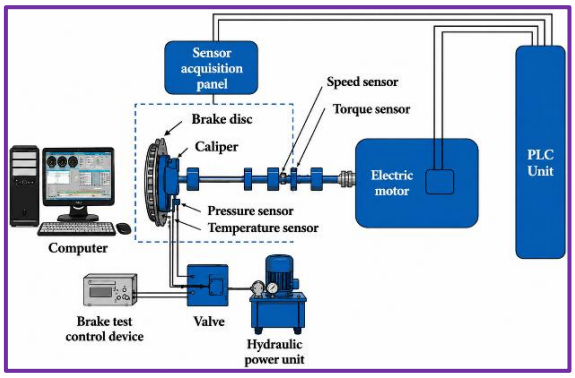


Figure 2. Components of the brake test rig.

The test rig's software allows for the measurement of braking force, RPM, and disc temperature via the control screen. Data obtained from the system is recorded at 0.5 second intervals. A screenshot of the test rig's control unit is shown in Figure 3.

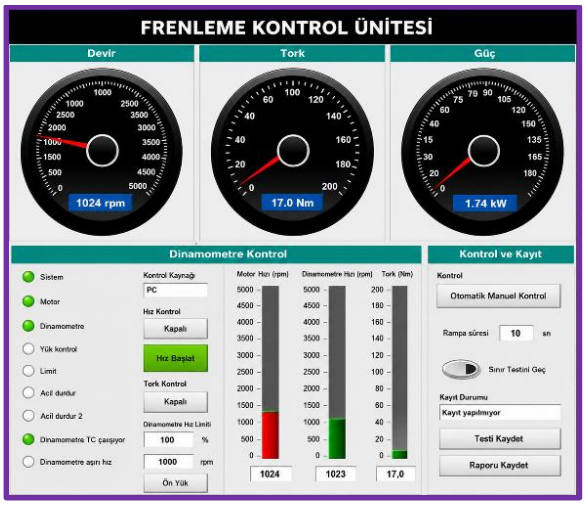


Figure 3. Screenshot of the test rig control unit.

An ABB brand air-cooled active dynamometer was used in the brake test setup. The wheel axle shaft was connected to the dynamometer's output shaft using a fixed-clutch coupling unit. The braking mechanism was also mounted on the other end of the axle shaft (Figure 4). The dynamometer drives the axle shaft to provide the RPM corresponding to the desired vehicle speed. Braking can be performed by adapting brake mechanism components from full-scale passenger vehicles to the system. The braking system consists of the axle shaft, caliper assembly, disc/pad pair, and connection mechanisms.

The rotational speed is measured using a 1024 ppr HTL encoder connected to the dynamometer shaft. The technical specifications of the dynamometer used in this study are provided in Table 1.



Figure 4. Full-scale braking mechanism.

Table 1. Technical specifications of the dynamometer

Specification	Value
Model	ABB/Square housing
Nominal Power (kW)	49.3
Nominal Speed (min^{-1})	3000
Nominal Torque (Nm)	157
Maximum Speed (min^{-1})	7500
Power Factor	0.831
Efficiency (%)	93.6

2.1.2. Hydraulic control unit

The hydraulic control unit used in the test setup converts the force applied by the driver to the brake pedal into hydraulic pressure, thereby providing the necessary braking force. The hydraulic control unit consists of a hydraulic reservoir, a pump, a pressure regulating valve, a solenoid-operated 2/2-way directional control valve, and a hydraulic pressure sensor. A view of the hydraulic control unit in the test setup is shown in Figure 5, and its technical specifications are provided in Table 2.

The hydraulic pump in the hydraulic control unit is driven by an electric motor. The technical specifications of the electric motor used in the hydraulic control unit are presented in Table 3.



Figure 5. Hydraulic control unit.

Table 2. Technical specifications of the hydraulic control unit

Specification	Value
Maximum pump pressure (bar)	50
Pump flow rate (L/min)	7
Hydraulic oil (cSt)	32
Pump rotation direction	Left

Table 3. Technical specifications of the electric motor

Specification	Value
Model	S1
Type	VMR 71-4
Input power (kW)	0.40
Output power (kW)	0.25
Efficiency (%)	61
RPM	1390
Operating voltage	220 V
Frequency	50 Hz

2.1.3. Contactless temperature measurement device

To measure disk temperature during braking, an Optris CLST-type non-contact temperature sensor, as shown in Figure 6, was used. Some specifications of the sensor used in the study are provided in Table 4.



Figure 6. Image of a contactless thermometer.

Table 4. Technical specifications of contactless thermocouples

Specification	Value
Rating class	IP 63
Operating temperature (°C)	-20… +80
Measuring range (°C)	-40 … +1030
Relative humidity resistance (%)	10 … 95
Weight (g)	58

The accuracy of the non-contact temperature sensor used to measure the disc temperature was verified using a handheld non-contact temperature sensor. The verification process was performed using the average diameter of the disc's braking surface (Figure 7).

The infrared thermometer shown in Figure 6 was permanently mounted on the brake test stand to continuously monitor the brake disc temperature during the experiments. The handheld infrared thermometer shown in Figure 7, on the other hand, was used solely to perform reference measurements during the tests in order to verify the accuracy of the infrared thermometer.



Figure 7. Verification of disk temperature measurement.

2.2. Methods

During braking, the pressure applied by the master cylinder to the caliper cylinder in response to a braking signal generates a hydraulic clamping force (F_h) on the caliper pistons. This force presses against the brake pads in front of the pistons, attempting to stop the rotating disc. The force applied by the pistons to the disc surfaces results in a frictional force (F_b) parallel to the surface between the disc and the brake pads. This force, while attempting to stop the rotating discs, generates a braking torque. Figure 8 shows the forces generated during braking. In accordance with the action-reaction principle, it is assumed that the rotational torque is equal to the braking torque.

The braking force was calculated using the equation given in equation 1.

$$F_b = \frac{M_b}{2r_b} \quad (1)$$

Here, F_b represents the friction force (N) generated between the brake pad and the disc during braking, M_b represents the braking torque (Nm), and r_b represents the average radius (m) of the effective friction surface on the disc.

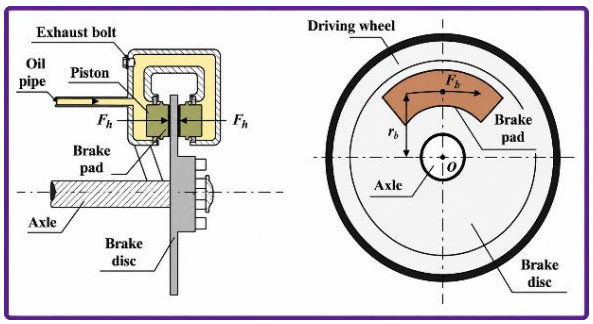


Figure 8. Braking system and braking force.

The brake disc used in the experimental setup has an outer diameter of 255 mm. The brake pad contacts the disc between an outer contact diameter of 246 mm and an inner contact diameter of 158 mm, resulting in an average friction diameter of 202 mm. Accordingly, the effective friction radius used in equation 1 was calculated as 101 mm. The wheel diameter of the reference vehicle is 586 mm. The caliper piston diameter is 54 mm, and the hydraulic system efficiency was assumed to be 95%.

The clamping force F_h (N), generated by the hydraulic pressure applied by the pump to the caliper piston during braking was calculated using equation 2.

$$F_h = PA_P\eta \quad (2)$$

Here, P represents the hydraulic pressure (Pa), A_P represents the cross-sectional area of the caliper cylinder-piston (m^2), and η represents the efficiency of the brake caliper cylinder-piston. The hydraulic pressure applied during the experiments was recorded in bar and converted to SI units (1 bar = 100,000 Pa) prior to the calculations performed using equation 2, ensuring unit consistency throughout the analysis.

The brake system used in the experimental setup is equipped with a single-piston floating caliper with a piston diameter of 54 mm. In this type of caliper, the hydraulic pressure acts on a single piston, while the floating caliper mechanism transfers an equal clamping force to the outer brake pad through the caliper body. Therefore, equation 2 represents the hydraulic force generated by the piston, and the clamping force is distributed equally to both brake pads through the floating caliper mechanism.

The coefficient of friction (μ) between the disc and the pad was calculated using equation 3.

$$\mu = \frac{F_b}{F_h} \quad (3)$$

3. Results

Braking tests were conducted using an OEM ventilated disc brake system at an equivalent vehicle speed of 100 km/h and a hydraulic braking pressure of 20 bar. Based on the experimental data obtained from the validated brake test rig, the time-dependent variations in vehicle speed, coefficient of friction, and brake disc temperature were analyzed. The results are presented and discussed in the following subsections.

3.1. Braking Speed Analysis

The experiments were performed using the developed brake test rig at a dynamometer speed corresponding to a vehicle speed of 100 km/h with an OEM brake disc and pad assembly. The dynamometer was first accelerated to the target speed, after which a hydraulic braking pressure of 20 bar was applied through the brake control unit. Braking continued until the brake disc came to a complete stop. The hydraulic pressure was then released, allowing the dynamometer to accelerate back to the target speed before the next braking cycle was initiated. The speed variation during a single braking event is presented in Figure 9.

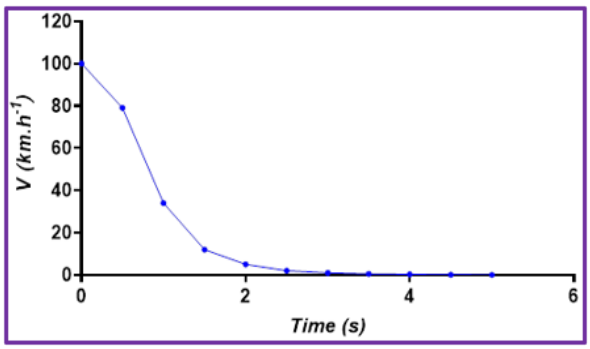


Figure 9. The change in speed during a single full braking maneuver.

To evaluate the repeatability and reliability of the developed brake test rig, the braking procedure was repeated seven consecutive times. The recorded data were processed using Microsoft Excel, and the corresponding speed–time curves are presented in Figure 10.

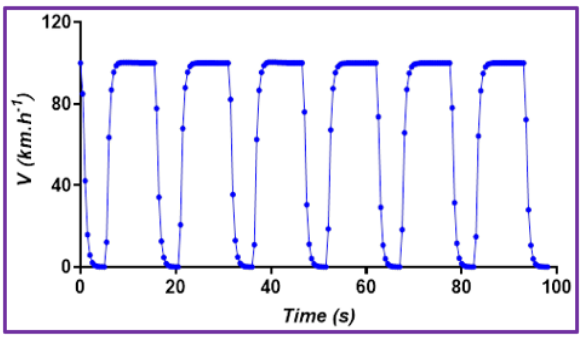


Figure 10. Time-dependent speed change graph in a braking test.

Figure 10 shows that the test speed reached the target value before each braking event and that all braking cycles exhibited highly consistent behavior. Each complete braking cycle-including the braking phase, vehicle acceleration, and system recovery-was completed within approximately 5 s. The actual deceleration period, during which the vehicle speed decreased from approximately 100 km/h to 0 km/h, lasted an average of 2.65 s. These results demonstrate the repeatability of the

developed brake test rig and confirm its capability to reproduce stable braking conditions throughout successive test cycles.

3.2. Friction Coefficient Analysis

Friction is the fundamental mechanism responsible for braking performance. Therefore, determining the friction coefficient between the brake disc and pad is essential for evaluating braking efficiency and system stability. Previous studies have demonstrated that friction behavior is strongly influenced by material properties and loading conditions (Aksoy et al., 2023; Güneş et al., 2023). Accordingly, in this study, the time-dependent friction coefficient was calculated using equation 3, and its variation during a single braking event is presented in Figure 11.

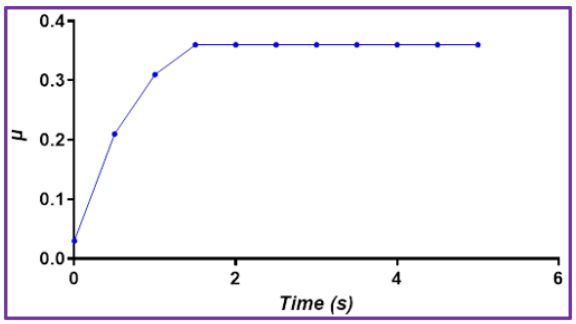


Figure 11. Change in the coefficient of friction over time during a single braking event.

The coefficient of friction started from a very low value of approximately 0.03 and increased rapidly to a maximum value of approximately 0.36 within 1.5 s, remaining nearly constant for the remainder of the braking event. The initial value of approximately 0.03 is attributed to the slight residual contact between the brake pads and the disc surface prior to full brake application.

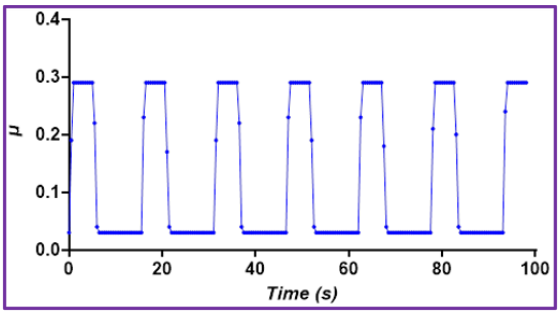


Figure 12. Change in the coefficient of friction over time during multiple braking cycles.

Figure 12 illustrates the variation in the coefficient of friction throughout the seven consecutive braking cycles. The coefficient of friction varied between 0.03 and 0.36, with only minor fluctuations between successive cycles, indicating stable friction characteristics and good repeatability of the developed brake test rig.

3.3. Brake Disc Temperature Analysis

The developed brake test rig enables full-scale brake performance tests under controlled laboratory conditions. During the experiments, brake disc temperature was continuously measured using a non-contact infrared laser pyrometer. The measured temperature profiles are presented in Figure 13.

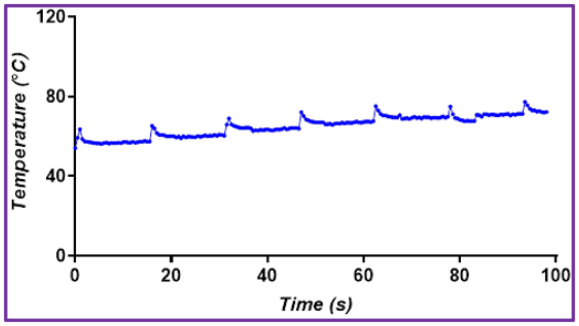


Figure 13. Changes in disc temperature during braking.

Figure 13 shows that the initial brake disc temperature was approximately 60 °C due to the pre-conditioning cycles, and it gradually increased to around 80 °C during the repeated braking tests. During each braking event, the disc temperature increased by approximately 5–10 °C because of the conversion of frictional energy into thermal energy at the pad–disc interface. After brake release, the temperature decreased slightly due to heat conduction through the disc and convective cooling via the ventilation channels. Since the interval between successive braking cycles was relatively short, the brake disc did not fully return to its initial temperature before the next braking event, resulting in a gradual increase in the average disc temperature. Nevertheless, the maximum temperature remained around 80 °C, which represents a relatively low thermal load for OEM brake systems. This limited temperature accumulation can be attributed to the moderate hydraulic braking pressure of 20 bar and the short duration of the seven consecutive braking cycles. Consequently, no significant thermal degradation or brake fade conditions were observed during the experiments.

4. Discussion

The results obtained are consistent with the friction coefficient ranges reported in the literature (Güney and Mutlu, 2015; Spencer et al., 1966; TSE, 1992) for automotive disc brake systems. Many studies (Demir et al., 2009; Filip et al., 2002; Güney et al., 2025; Güney and Mutlu, 2019) report that the coefficient of friction for organic or semi-metallic brake pads typically varies within the range of 0.35–0.45. The coefficient of friction measured in this study, approximately 0.36, falls within the expected operating range for the OEM pad and disc combination used. Furthermore, the fact that the coefficient of friction exhibits similar characteristics throughout the braking cycles demonstrates that the test

setup is capable of producing stable and repeatable results. Additionally, the increase in disc temperature in tandem with the number of braking cycles indicates that the heat generated by friction accumulates within the system, creating a thermal load. This situation mirrors the thermal behavior observed under real-world vehicle braking conditions.

Although the test setup developed in this study was designed to evaluate the performance of a single vehicle braking mechanism's disc and pad pair, it can be adapted to all other vehicles quickly and at low cost. However, under real-world vehicle conditions, numerous parameters such as suspension dynamics, road-holding conditions, aerodynamic effects, and vehicle mass distribution can influence braking performance. These effects were not directly incorporated into the model in this study. Furthermore, the tests were conducted under a limited number of braking pressure and speed scenarios. Future studies plan to conduct more comprehensive experimental work using different speed profiles, variable braking pressures, and different friction materials.

5. Conclusion

In this study, an electric motor-driven, hydraulically controlled brake test rig was developed to enable the testing of full-scale brake disc/pad assemblies from passenger vehicles in a laboratory setting. Using the developed test rig, the coefficient of friction was determined by measuring parameters such as speed variation, braking torque, and disc temperature on an OEM disc/pad pair from a commonly used vehicle.

Braking tests were conducted at a dynamometer speed corresponding to an equivalent vehicle speed of 100 km/h and under a hydraulic brake pressure of 20 bar. Repeated braking tests demonstrated that the developed system operates in a stable and reliable manner. The coefficient of friction formed at the interface of the disc/pad pair remained stable at approximately 0.36 throughout the braking process. The consistency of the speed variation curves during braking repetitions indicated that the developed test setup can produce results consistent with the literature. Temperature measurements revealed that sudden temperature increases occurred on the disc surface during braking, and the average disc temperature rose as braking intervals shortened and the number of repetitions increased. These findings demonstrate that the system can realistically reflect both the mechanical and thermal behavior of the system.

The developed brake test setup offers significant advantages over existing test methods in that it can operate with full-scale brake components, allows for the testing of different friction material combinations, and provides a low-cost alternative. Additionally, thanks to the system's modular structure, wear tests, vibration analyses, thermal performance evaluations, and the application of various braking scenarios have become possible. In this regard, the study provides a practical testing infrastructure that can be utilized for both academic research and product development and quality control processes in the automotive industry.

Future work plans include investigating different brake pressure and speed scenarios, conducting comparative analyses of various pad/disc materials, increasing the system's automation level, and enhancing the data collection infrastructure. Additionally, the goal is to transform the test setup into a more comprehensive evaluation platform by integrating vibration and noise (NVH) analyses. In this context, the developed setup offers a significant engineering solution for reliably and economically testing full-scale braking systems in a laboratory environment.

Author Contributions

The percentages of the author's contributions are presented below. All authors reviewed and approved the final version of the manuscript.

	H.K.	H.K.	B.G.
C	40	30	30
D	30	40	30
S	20	20	60
DCP	40	30	30
DAI	40	30	30
L	40	30	30
W	20	60	20
CR	30	30	40
SR	20	60	20

C= concept, D= design, S= supervision, DCP= data collection and/or processing, DAI= data analysis and/or interpretation, L= literature search, W= writing, CR= critical review, SR= submission and revision.

Conflict of Interest

The authors declared that there is no conflict of interest.

Ethical Consideration

Ethics committee approval was not required for this study because of there was no study on animals or humans.

Acknowledgements

We would like to thank Karamanoğlu Mehmetbey University and the Department of Motor Vehicles and Transportation at the School of Technical Sciences for their support in the completion of this study.

References

Agudelo, C. E., & Ferro, E. (2005). *Technical overview of brake performance testing for original equipment and aftermarket industries in the US and European markets*. Link Engineering.

Aksoy, S., Kabakcı, F., Acarer, M., Düzcükoğlu, H., Ünüvar, E., & Fındık, F. (2023). Effect of Mg addition on microstructure and mechanical properties of AlSi12 alloy produced by high-

pressure casting method. *Industrial Lubrication and Tribology*, *75*(1), 27–35. https://doi.org/10.1108/ILT-10-2021-0410

Aleksendrić, D. (2010). Neural network prediction of brake friction materials wear. *Wear*, *268*(1–2), 117–125. https://doi.org/10.1016/j.wear.2009.07.006

Anderson, A., Gratch, S., & Hayes, H. P. (1967). *A new laboratory friction and wear test for the characterization of brake linings* (SAE Technical Paper No. 670079). SAE International. https://doi.org/10.4271/670079

Blau, P. J. (2001). *Compositions, functions, and testing of friction brake materials and their additives* (Report No. ORNL/TM-2001/64). Oak Ridge National Laboratory. https://doi.org/10.2172/788356

Blau, P. J. (2008). *Friction science and technology: From concepts to applications* (2nd ed.). CRC Press.

Burkman, A. J., & Hishley, F. H. (1967). *Laboratory evaluation of brake lining materials* (SAE Technical Paper No. 670510). SAE International. https://doi.org/10.4271/670510

Demir, A., Samur, R., & Kilicaslan, I. (2009). Investigation of the coatings applied onto brake discs on disc-brake pad pair. *Metalurgija*, *48*(3), 161–166.

Eriksson, M., Bergman, F., & Jacobson, S. (2002). On the nature of tribological contact in automotive brakes. *Wear*, *252*(1–2), 26–36. https://doi.org/10.1016/S0043-1648(01)00849-3

Filip, P., Kovarik, L., & Wright, M. A. (1997). *Automotive brake lining characterization* (SAE Technical Paper No. 973024). SAE International. https://doi.org/10.4271/973024

Filip, P., Weiss, Z., & Rafaja, D. (2002). On friction layer formation in polymer matrix composite materials for brake applications. *Wear*, *252*(3–4), 189–198. https://doi.org/10.1016/S0043-1648(01)00873-0

Güneş, A., Düzcükoğlu, H., Salur, E., Aslan, A., & Şahin, Ö. S. (2023). Investigation of friction coefficient changes in recycled composite materials under constant load. *Lubricants*, *11*(9), Article 407. https://doi.org/10.3390/lubricants11090407

Güney, B., Küçüksarıyıldız, H., & Mutlu, İ. (2025). Investigation of microstructural and tribological properties of a commercial brake pad. *Science of Sintering*, *57*(4), 487–501. https://doi.org/10.2298/SOS241217010G

Güney, B., & Mutlu, İ. (2015). Taşıtlarda AB ve ABD'nde uygulanan fren test standartlarının incelenmesi [Investigation of brake test standards applied in the EU and the USA in vehicles]. *Afyon Kocatepe Üniversitesi Fen ve Mühendislik Bilimleri Dergisi*, *15*(1), 7–16. https://doi.org/10.5578/fmbd.8524

Güney, B., & Mutlu, İ. (2019). Tribological properties of brake discs coated with Cr2O3–40% TiO2 by plasma spraying. *Surface Review and Letters*, *26*(10), Article 1950075. https://doi.org/10.1142/S0218625X19500756

Jaafar, T. R., Selamat, M. S., & Kasiran, R. (2012). Selection of best formulation for semi-metallic brake friction materials development. *Powder Metallurgy*, *55*(1), 30–34.

Kancharla, S. C. R. (2014). *Model brake material formulations and their testing at different scale levels* [Doctoral dissertation, Southern Illinois University Carbondale]. OpenSIUC.

Kumar, M., & Bijwe, J. (2010). NAO friction materials with various metal powders: Tribological evaluation on full-scale inertia dynamometer. *Wear*, *269*(11–12), 826–837. https://doi.org/10.1016/j.wear.2010.08.011

Lee, P. W. (2013). *Design and optimization of low-Cu and Cu-free automotive brake friction materials* [Doctoral dissertation, Southern Illinois University Carbondale]. OpenSIUC.

Lee, P. W., Leist, J., & Filip, P. (2010). *Use of hexagonal boron nitride in automotive friction materials* (SAE Technical Paper No. 2010-01-1700). SAE International. https://doi.org/10.4271/2010-01-1700

Malachova, K., Kukutschova, J., Rybkova, Z., Sezimova, H., Placha, D., Cabanova, K., & Filip, P. (2016). Toxicity and mutagenicity of low-metallic automotive brake pad materials. *Ecotoxicology and Environmental Safety*, *131*, 37–44. https://doi.org/10.1016/j.ecoenv.2016.05.003

Perzborn, N., Agudelo, C., & Ostermeyer, G. P. (2014). On similarities and differences of measurements on inertia dynamometer and scale testing tribometer for friction coefficient evaluation. *SAE International Journal of Materials and Manufacturing*, *8*(1), 104–117. https://doi.org/10.4271/2014-01-2523

Rita, D. A., Candeo, S., Jayashree, P., Nogueira, A. P. G., Rustighi, E., & Straffelini, G. (2024). Comparative analysis of pin-on-disc and inertia-dynamometer sliding tests on a friction material. *Wear*, *558–559*, Article 205552. https://doi.org/10.1016/j.wear.2024.205552

Rudas Florez, J. S. (2018). *Dry sliding metals process modelling: Dynamical system paradigm* [Doctoral dissertation, University of Sheffield]. White Rose Research Online.

SAE. (1967). *Brake lining quality test procedure* (SAE J661_196702). SAE International.

SAE. (2014). *Dynamometer global brake effectiveness* (SAE J2707_201402). SAE International.

Sanders, P. G., Dalka, T., & Basch, R. (2001). A reduced-scale brake dynamometer for friction characterization. *Tribology International*, *34*(9), 609–615. https://doi.org/10.1016/S0301-679X(01)00053-6

Singireddy, V. R., Jogineedi, R., Kancharla, S. K., Farokhzadeh, K., & Filip, P. (2022). On scaled-down bench testing to accelerate the development of novel friction brake materials. *Tribology International*, *174*, Article 107754. https://doi.org/10.1016/j.triboint.2022.107754

Spencer, A., Spurgeon, W. M., & Winge, J. (1966). *Four tests for consistency of automotive brake linings* (SAE Technical Paper No. 660412). SAE International. https://doi.org/10.4271/660412

Tsang, P., Jacko, M., & Rhee, S. (1985). Comparison of chase and inertial brake dynamometer testing of automotive friction materials. *Wear*, *103*(3), 217–232. https://doi.org/10.1016/0043-1648(85)90012-2

TSE. (1992). *Karayolu taşıtları - Fren sistemleri balatalar - Sürtünmeli frenler için* [Road vehicles - Brake systems linings - For friction brakes] (TS 555). Turkish Standards Institution.

Tuszyński, W., Gibała, M., Gospodarczyk, A., Kozioł, S., Matecki, K., Piekoszewski, W., Siczek, M., Szczerek, M., & Wojutyński, J. (2019). The new inertia dynamometer for friction and wear testing of brake pads and brake discs. *Tribologia*, *286*(4), 113–119. https://doi.org/10.5604/01.3001.0013.6300

Varriale, F., Candeo, S., Riva, G., Wahlström, J., & Lyu, Y. (2022). A brake system coefficient of friction estimation using 3D friction maps. *Lubricants*, *10*(7), Article 134. https://doi.org/10.3390/lubricants10070134

Wang, Q., Zhang, X., Wang, D., Cui, H., Zhang, S., & Wang, J. (2025). Numerical simulation and experimental investigation on the thermal-fluid-solid multi-physical field coupling characteristics of wet friction pairs considering cavitation effect. *Applied Thermal Engineering*, *260*, Article 124955. https://doi.org/10.1016/j.applthermaleng.2024.124955

Yun, R., Filip, P., & Lu, Y. (2010). Performance and evaluation of eco-friendly brake friction materials. *Tribology International*, *43*(11), 2010–2019. https://doi.org/10.1016/j.triboint.2010.05.001

Black Sea Journal of Engineering and Science
doi: 10.34248/bsengineering.1977435

Open Access Journal
e-ISSN: 2619 – 8991

Research Article
Volume 9 - Issue 5: 2232-2238 / September 2026

EXPERIMENTAL INVESTIGATION OF THE EFFECTS OF PROCESS PARAMETERS ON PRODUCT GEOMETRY AND WEIGHT IN THE INJECTION MOLDING PROCESS WITH PE100 MATERIAL

Yavuz TURAN[1], İbrahim KELEŞ[2]*

[1]*Poelsan Plastic Industry and Trade Inc., 55139, Samsun, Türkiye*
[2]*Samsun University, Faculty of Engineering and Natural Sciences, Department of Mechanical Engineering, 55080, Samsun, Türkiye*

Abstract: This study investigates the influence of key process parameters on the geometric and physical properties of parts produced by injection molding using high-density polyethylene (PE100). The parameters include packing pressure, melt temperature, and cooling time which are systematically varied based on MoldFlow simulations. Samples are analyzed using an ATOS Q 3D scanning system and a high-precision digital scale. Results show that increasing packing pressure improves flatness and dimensional accuracy. While higher melt temperature enhances surface flatness, it also increases cylindrical deformations. Cooling time positively affects flatness but may lead to deformation in the upper cylinder. Regarding product weight, packing pressure has the most significant effect, followed by melt temperature, whereas cooling time shows minimal impact. The experimental findings offer practical and reliable insights for optimizing injection molding processes involving dense materials like PE100, providing meaningful contributions to both design and production strategies.

Keywords: PE100, Injection molding, Packing pressure, Melt temperature, Cooling time, Shrinkages

***Corresponding author:** Samsun University, Faculty of Engineering and Natural Sciences, Department of Mechanical Engineering, 55080, Samsun, Türkiye
E mail: ibrahim.keles@samu.edu.tr (I. KELES)
Yavuz TURAN https://orcid.org/0000-0001-8537-3989
İbrahim KELEŞ https://orcid.org/0000-0001-8252-2635

Received: June 23, 2026
Accepted: July 25, 2026
Published: September 15, 2026

Cite as: Turan, Y., & Keles, İ. (2026). Experimental investigation of the effects of process parameters on product geometry and weight in the injection molding process with PE100 material. *Black Sea Journal of Engineering and Science*, 9(5), 2232-2238.

1. Introduction

Plastic injection molding has long been a fundamental technology for the production of polymer-based components, owing to its versatile manufacturing capabilities, cost-effectiveness, and high repeatability. Today, the use of this method continues to grow in the production of plastic parts across a wide range of sectors, including consumer electronics, automotive, medical devices, and household appliances. This is largely due to the ability of injection molding to produce complex, multi-component parts with tight tolerances and well-controlled surface quality. However, achieving the desired part with minimal defects, minimal distortion, and optimal mechanical properties is not solely dependent on mold design but also requires precise control of process parameters. Traditionally, these parameters are selected based on experience or manufacturer guidelines, which do not always guarantee perfect results. In recent years, many academic studies have been conducted to understand, model, and improve the relationship between molding conditions and final part quality, leading to the development of interdisciplinary approaches ranging from numerical simulations to 3D optical scanning solutions.

The quality of products manufactured by plastic injection molding depends on material selection, design, and process conditions. Among the most common problems encountered during the process is shrinkage. Some of the shrinkage-related defects stem from wall thickness variations, while others are caused by changes in mold surface temperature (Mathivanan et al., 2010; Mustaffa et. al, 2015). To avoid such defects, shrinkage issues must be addressed before mass production. Melt temperature, packing time, mold temperature, and packing pressure are all identified as significant parameters influencing shrinkage (Jansen and Titomanlio, 1996; Jafarian and Shakeri, 2005; Ahmad et al., 2009; Altan, 2010; Hussin et al., 2012; Mustaffa et. al, 2015). These factors contribute to solving shrinkage problems in the injection molding process. Postawa and Koszkul examine the effects of processing conditions on shrinkage and weight variation (Postawa and Koszkul, 2005), while Jansen et al. analyze shrinkage in different plastics, both highlighting the importance of packing pressure and melt temperature (Jansen et al., 1998). Kazmer and Barkan focus on pressure control in multi-cavity molds (Kazmer and Barkan, 1997), and Bushko and Stokes investigate the behavior of thermo-viscoelastic melts (Bushko and Stokes, 1996). Zhang's wireless sensor design presents an innovative approach to measuring cavity pressure

This work is licensed (CC BY-NC 4.0) under Creative Commons Attribution 4.0 International License

(Zhang et al., 2001), and Titomanlio studies the effects of in-mold shrinkage on the final product (Titomanlio and Jansen, 1996). Angstadt and Coulter emphasize the potential of cavity pressure as an indicator of part quality (Angstadt and Coulter, 1999). While various optimization tools and techniques exist for injection molding parameter studies, including Taguchi's Design of Experiments approach that has been widely used in the literature (Jansen and Titomanlio, 1996; Kazmer and Barkan, 1997; Zhang et al., 2001; Turng and Peić, 2002; Postawa and Koszkul, 2005; Tang et al., 2006; García et al., 2003; Altan, 2010; Hussin et al., 2012), this study adopts a simulation-guided, single-parameter variation approach. In this approach, each process parameter (packing pressure, melt temperature, and cooling time) was varied individually within a range determined from MoldFlow simulations, while the remaining parameters were held constant, in order to clearly isolate and characterize the effect of each parameter on the geometric and physical properties of the product.

An injection molding process is a complex procedure where many factors impact the quality of the final product. Significant research has been dedicated to understanding the influence of molding parameters such as cavity pressure and temperature. Studies have shown these parameters are crucial in determining properties like shrinkage, weight, residual stress, and dimensional accuracy. For example, Postawa and Koszkul investigated the changes in shrinkage and weight as a function of processing conditions, while Jansen et al. studied shrinkage in various plastics. Both studies highlighted the importance of packing pressure and melting temperature. Kazmer and Barkan focused on pressure control in multi-cavity molds, and Bushko et al. analyzed the behavior of thermo-viscoelastic melts. Zhang's innovative wireless sensor design offered a new method for measuring cavity pressure, while Titomanlio concentrated on how in-mold shrinkage affects the final product. Angstadt and Coulter further emphasized that cavity pressure can serve as a strong indicator of part quality.

While the existing literature frequently addresses the effects of molding parameters like cavity pressure and temperature on part shrinkage and warpage, a comprehensive evaluation of a part's final quality should not be limited to these two variables alone. To achieve true dimensional accuracy, it's essential to consider both vertical and horizontal measurements of the part. This allows for a more comprehensive analysis of the relationship between molding conditions and the resulting measurements. A significant portion of current research relies heavily on numerical simulations (Turng and Peić, 2002; García et al., 2003; Tang et al., 2006). Although these methods can provide reliable results under specific conditions, they don't always align perfectly with real-world, experimentally obtained data. Experimental studies, while often high cost, can provide more precise results for these applications. In such research, it is crucial to use high-precision measurement systems to accurately evaluate the effects of variable molding parameters on the final product. This approach enables the derivation of meaningful and reliable conclusions from experimental analyses. The literature review reveals that while many studies have focused on common plastics like polypropylene (PP) and acrylonitrile butadiene styrene (ABS), there is limited research on materials with high density and large volumes, such as high-density polyethylene (HDPE) like PE100.

This study addresses this gap by presenting an original experimental investigation into the geometric and physical effects of key processing parameters on products molded from PE100. In this research, molding parameters were systematically varied based on simulation data, and the influence of each parameter on product shrinkage was evaluated in detail.

The produced parts were analyzed using advanced measurement techniques to collect comprehensive data on geometric integrity, dimensional precision, and material behavior. This work contributes to the optimization of injection molding processes through both its unique design and the analytical methods employed.

2. Materials and Methods

The first step in the experimental molding process was the preparation of the full-scale sample design, as shown in Figure 1. The three-dimensional model of the plastic injection mold, including all its details, was designed using SolidWorks software (Figure 2). The four-cavity female and male plates of the plastic injection mold used in the study are shown in Figure 3.

The study focused on a fundamental component used to integrate PE100 pipes into flanged connection systems. Strict dimensional and positional tolerances were considered, as one end of this component was designed to be compatible with a PE100 (HDPE) pipe, while the other end was designed to be compatible with metal equipment requiring a flanged connection. Therefore, tolerance control was prioritized during the injection molding process.

Experimental applications were performed using a Haitian MA3800 model injection molding machine with an injection pressure of 183 MPa, a screw diameter of 70 mm, and a clamping force of 3800 kN. The initial molding parameters were determined based on literature data and industrial applications.

The PE100 material used in the study is a copolymer of high-density polyethylene (HDPE). PE100 has a wide spectrum of properties and is used in many applications in the pipe industry, such as water distribution, sewage systems, industrial applications, and natural gas transmission. The technical properties of the PE100 material are presented in Table 1.

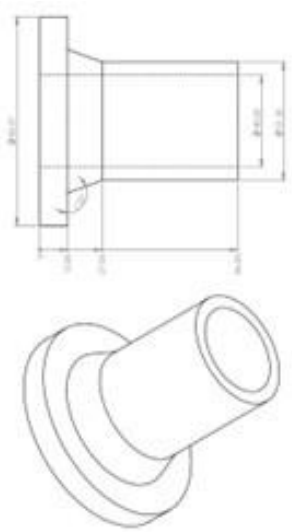


Figure 1. Sample geometry and dimensions.

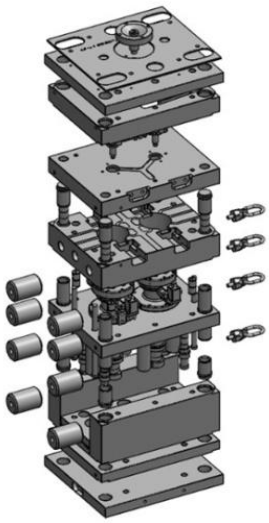


Figure 2. Plastic injection mold model.



Figure 3. Plastic injection mold female and male plates.

Before the experimental applications were initiated, it was necessary to define the appropriate processing parameters for the injection molding process. As a first step, modeling of the flanged adapter was carried out using the SolidWorks CAD software. The resulting design was then transferred to MoldFlow software for flow analysis and molding optimization. Figure 4 visualizes the generated base structure and mesh model. A 3D mesh was used in the mesh structure, with a mesh count of 767618. A mesh independence (convergence) study was performed prior to the final analyses by comparing the simulation outputs obtained at progressively refined mesh densities; the 767618-element mesh was adopted as it provided results that no longer changed appreciably with further refinement, while keeping the computational cost reasonable.

MoldFlow is a commercial simulation tool that provides numerical solutions combining finite element and finite difference methods to analyze the molding process from thermal and mechanical perspectives. As shown in Figure 5, this software analyzes various variables of the injection process, especially by focusing on the mold filling phase, to determine the ideal processing conditions.

Table 1. Mechanical properties of PE100 raw material

Properties	Density	Tensile modulus	Tensile strain	Vicat softening temperature	Melt flow rate
Condition	23℃	23℃	23℃	10N	190℃/5 kg
Method	ISO 1183/A	ISO 527 -2/1	ISO 527 -2/50	ISO 306/A	ISO 1133
Unit	g/cm³	MPa	%	℃	g/10 min
General purpose	0.9590	1100.0000	>350.0000	128.0000	0.4500



Figure 4. Mesh structure used in MoldFlow analysis.

Within the scope of this analysis, key variables such as the melted temperature inside the mold, the applied packing pressure, packing time, and part cooling time were evaluated. Based on the simulation outputs, experimental studies were conducted with packing pressures ranging from 20 to 100 MPa, packing times from 3 to 20 seconds, melt temperatures from 200 °C to 310 °C, and cooling times from 20 to 100 seconds.

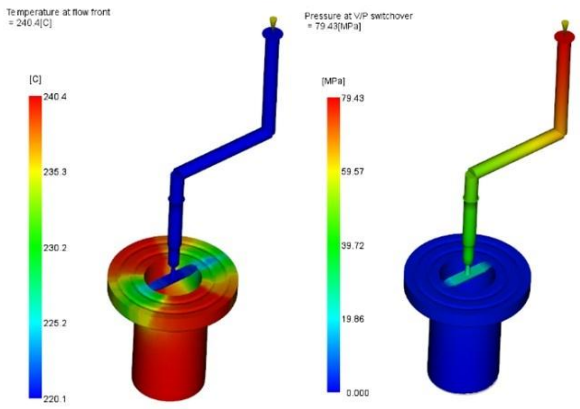


Figure 5. Example of molding process simulation.

To determine the deformation of the parts, an ATOS Q (Advanced Topometric Sensor) system was used. This three-dimensional optical 3D scanner can automatically scan the entire surface of a part without the need for special fixtures or reference markers during the scanning process, as shown in Figure 6. When the scan is complete, the system automatically creates a high-quality mesh. In addition, the CAD data obtained with SolidWorks software is transferred to the ATOS Q system. In the final step, the scanned data set is aligned with the CAD using GOM software, as seen in Figure 7, and the deviations between the two data sets are calculated and displayed graphically. The measured quality criteria, which are the average deviation of the top and bottom cylinders and the flatness of the skirt plane, are shown in Figure 8.

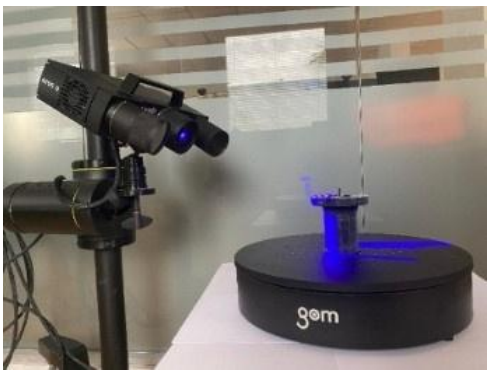


Figure 6. Tree-dimensional scanning process.



Figure 7. Alignment of the model with the scanned data.

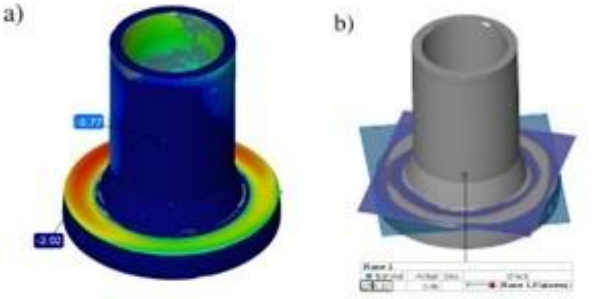


Figure 8. a) Deviation graph of the model and scanned data. b) Flatness measurement of the model with the scanned data.

The mass evaluations of the plastic samples produced in the experimental study were carried out to determine the fill rate and material volume changes associated with mold shrinkage. For this purpose, the weight of each sample was measured using a Huake brand digital scale with a sensitivity of 0.01 g, as shown in Figure 9, which operates at an analytical level of precision. The measurements were performed in a laboratory environment with stable ambient conditions, and an average value was recorded from three repeated measurements for each sample.
The weight data obtained were analyzed to evaluate the effect of different injection parameters on the part volume and, consequently, on mold shrinkage during molding.



Figure 9. Sample weight measurement.

3. Results and Discussion

Shrinkage behavior in injection-molded plastic parts has been a significant topic of discussion for many years. While a certain degree of shrinkage occurs in all plastic parts, dimensional errors in diameter and flatness are also unavoidable in parts with two different cylindrical geometries, such as flanges, due to various reasons. The key issue here is identifying under which conditions these defects can be minimized and which parameters have the most significant impact on the process. Therefore, it is crucial to understand the cause-and-effect relationship of these defects and to be able to analyze them effectively. Current research provides important findings in revealing the relationship between these variables. This section also addresses flatness, another measurable property of the molded parts. To better

understand the shrinkage tendencies, numerous experiments were conducted under different molding conditions. These experiments specifically focused on the effect of post-filling compression (packing) pressure on the amount of shrinkage and flatness error.

The shrinkage behavior of the parts was measured as the average deviation on separate selected surfaces, and the values were reported (Figure 8). This allowed for a clearer observation of the effects of the process parameters on the part geometry. Figure 10 shows the deviations in the upper cylinder, lower cylinder, and overall flatness values under packing pressures ranging from 2 to 100 MPa. The data obtained reveals that increasing packing pressure significantly improves structural stability and surface flatness.

At the lowest pressure level of 2 MPa, the deviation of the lower cylinder was measured as -2.52 mm, which decreased to -1.75 mm at 100 MPa. Similarly, the deviation in the upper cylinder decreased from -1.05 mm to -0.58 mm. These results indicate that the deformations of both the upper and lower cylinders decreased with increasing pressure, but the lower cylinder, which initially showed more deformation, improved at a higher rate. The flatness value, an indicator of surface smoothness, decreased from 0.87 mm at 2 MPa to 0.32 mm at 100 MPa. This demonstrates that increasing packing pressure has positive effects on the dimensional stability and surface quality of the product. Particularly in the 2–40 MPa range, noticeable improvements were observed in deviation and flatness values, while after 60 MPa, this change was seen to slow down. This suggests that after a certain threshold, the improving effect of increased pressure becomes limited, and the process enters a saturation trend.

In conclusion, it has been confirmed that increasing the packing pressure within the studied range reduces both structural deformation and improves surface smoothness. However, the 60–80 MPa range can be recommended as a balanced processing window that ensures dimensional accuracy while also being mindful of production cost and safety.

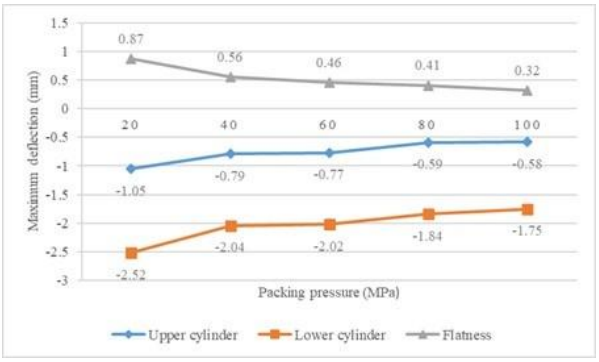


Figure 10. Effect of packing pressure on the total average shrinkage value and flatness error on cylindrical surfaces.

Figure 11 shows the deviations in the upper cylinder, lower cylinder, and flatness values under melt temperatures ranging from 200 °C to 310 °C. The findings indicate that increasing the melt temperature has a positive effect on flatness but a negative effect on cylinder deformations. The deviation of the lower cylinder reached -2.27 mm at 310 °C, up from -1.89 mm at 200 °C. Similarly, the deviation in the upper cylinder increased from -0.67 mm to -0.99 mm, showing greater deformation. This suggests that the increase in melt temperature creates effects that increase structural deformation through thermal expansion and changes in material flow behavior.

On the other hand, a significant improvement in the flatness value was observed. Flatness, which was 0.37 mm at 200 °C, increased to 0.88 mm at 310 °C, and this increase suggests that the melt temperature can play a role in improving the surface quality of the product. While the temperature showed a more limited change up to 270 °C, the increase in flatness gained momentum in the 270–310 °C range. This indicates that once a certain temperature threshold is exceeded, the process moves into a region where surface smoothness improves more rapidly.

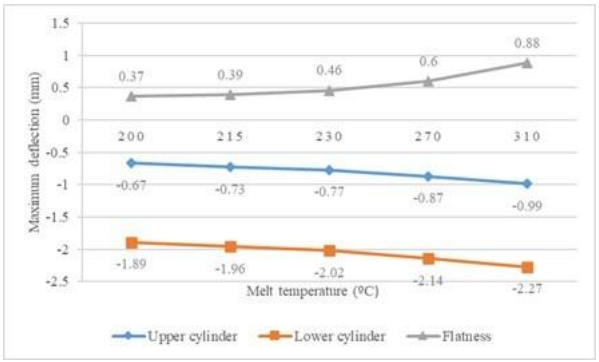


Figure 11. Effect of melt temperature on the total average shrinkage value and flatness error on cylindrical surfaces.

Figure 12 shows the deviation values in the upper cylinder, lower cylinder, and flatness parameters under cooling times ranging from 20 to 100 seconds. The data reveals that increasing the cooling time has a positive effect on surface quality but affects the lower- and upper-cylinder deformations at different rates. The deviation of the lower cylinder decreased from -2.11 mm at 20 seconds to -1.92 mm at 100 seconds. This reduction indicates that the structural deformation in the lower cylinder steadily decreases with longer cooling times. In the upper cylinder, however, an inverse trend is observed; the deviation value increased from -0.69 mm to -0.96 mm. This suggests that a longer cooling time may lead to thermally induced stress deformations in the upper cylinder. The flatness value, on the other hand, showed a regular increase with longer cooling times. The flatness value, which was 0.38 mm at 20 seconds,

reached 0.51 mm at 100 seconds. This trend indicates that longer cooling periods improve surface smoothness and have a positive effect on dimensional stability. While the increase in flatness was more pronounced in the 20–60 second range, the improvement curve flattens after 80 seconds, suggesting that the process is entering a saturation trend. Similarly, the deformation reduction effect in the lower cylinder occurred at a higher rate in this range.

In conclusion, although increasing the cooling time offers positive results in terms of flatness and lower cylinder stability, a careful balance must be struck considering the increase in upper cylinder deformation. In this context, a cooling time range of 60–80 seconds can be proposed as an ideal processing window that balances surface quality with structural integrity.

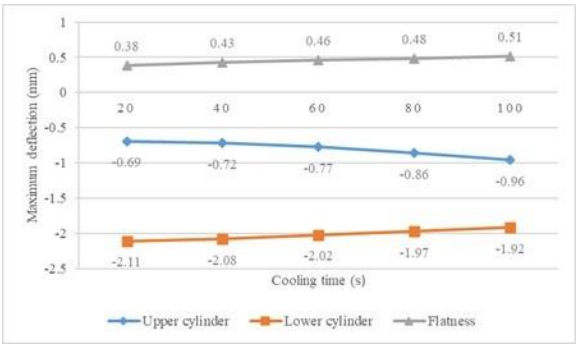


Figure 12. Effect of cooling time on the total average shrinkage value and flatness error on cylindrical surfaces.

Figure 13 compares the effects of packing pressure, melting temperature, and cooling time on product weight during the injection molding process. Increasing the packing pressure from 20 MPa to 100 MPa caused a significant increase in product weight, indicating that this parameter has the highest impact. This can be explained by the fact that high pressure ensures better filling of the mold cavity, thereby increasing material density. In contrast, increasing the melt temperature from 200 °C to 310 °C decreased the product weight, which may be related to backflow and potential material loss due to reduced viscosity at high temperatures. No significant change in product weight was observed when the cooling time was increased from 20 to 100 seconds. These findings reveal that the most critical parameter for optimizing product weight is packing pressure, melting temperature is of secondary importance, and cooling time has a limited effect.

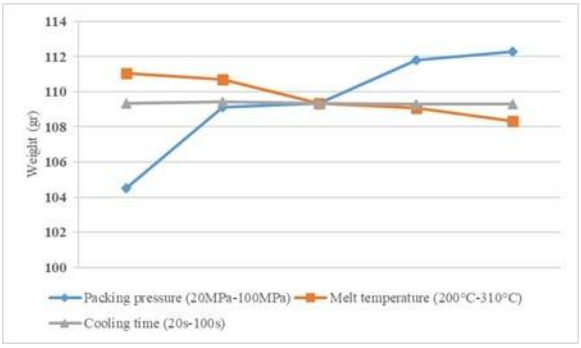


Figure 13. Effect of packing pressure, melt temperature and cooling time on product weight.

4. Conclusion

In this study, the injection molding process of PE100 material was comprehensively evaluated using high-precision experimental measurement techniques and simulation-supported analyses. Using an ATOS Q 3D scanning system and precise weight measurement devices, the effects of process parameters on the final product were revealed in detail. The findings showed that packing pressure is the primary determinant affecting both the mold fill condition and surface quality. High pressure reduced deformation and improved flatness values. While the melt temperature had positive effects on flatness, it increased deformation in the cylindrical regions, which demonstrated the effect of thermal flow and expansion behaviors on structural stability. The cooling time improved flatness while reducing deformation, especially in the lower cylindrical regions; however, it increased the risk of deformation due to thermal stresses in the upper cylinder. Packing pressure had the most significant effect on product weight, while melt temperature had an inverse effect, and cooling time resulted in limited change. These findings reveal that the correct selection of initial molding parameters directly affects both geometric defects and production quality. Specifically, the range of 60–80 MPa for packing pressure and 60–80 seconds for cooling time offers an optimal processing window that balances dimensional accuracy, productivity, and quality.

Author Contributions

The percentages of the authors' contributions are presented below. All authors reviewed and approved the final version of the manuscript.

	Y.T.	İ.K.
C	50	50
D	60	40
S	50	50
DCP	50	50
DAI	50	50
L	50	50
W	40	60
CR	50	50
SR	50	50
PM	50	50
FA	50	50

C= concept, D= design, S= supervision, DCP= data collection and/or processing, DAI= data analysis and/or interpretation, L= literature search, W= writing, CR= critical review, SR= submission and revision, PM= project management, FA= funding acquisition.

Conflict of Interest

The authors declared that there is no conflict of interest.

Ethical Consideration

Ethics committee approval was not required for this study because of there was no study on animals or humans.

Acknowledgements

The authors gratefully acknowledge Poelsan Plastic Industry and Trade Inc. for their valuable technical support and for providing the materials used in the experimental studies presented in this paper.

References

Ahmad, A. H., Leman, Z., Azmir, M. A., Muhamad, K. F., Harun, W. S. W., Juliawati, A., & Alias, A. B. S. (2009). Optimization of warpage defect in injection moulding process using ABS material. In *2009 Third Asia International Conference on Modelling & Simulation* (pp. 470-474). IEEE.Altan, M. (2010). Reducing shrinkage in injection molding via the Taguchi, ANOVA and neural network methods. Materials & Design, 31, 599–604.

Angstadt, D. C., & Coulter, J. P. (1999). Cavity pressure and part quality in the injection molding process. In *ASME International Mechanical Engineering Congress and Exposition* (Vol. 16622, pp. 7-17). American Society of Mechanical Engineers.

Bushko, W. C., & Stokes, V. K. (1996). Solidification of thermoviscoelastic melts. Part 3: Effects of mold surface temperature differences on warpage and residual stresses. *Polymer Engineering & Science*, *36*(3), 322-335.

García, N., González, E., Baselga, J., & Bravo, J. (2003). Critical thickness estimation in ISO-MC cards injection using CAE tools. *Journal of materials processing technology*, *143*, 491-494.

Hussin, R., Saad, R. M., Hussin, R., & Dawi, M. S. I. M. (2012). An optimization of plastic injection molding parameters using Taguchi optimization method. *Asian Transactions on Engineering*, *2*(5), 75-80.

Jafarian, A. R., & Shakeri, M. (2005). Investigating the Influence of Different Process Parameters on Shrinkage of Injection-Molded Parts. *American Journal of Applied Sciences*, *2*(3), 688-700.

Jansen, K. M. B., Van Dijk, D. J., & Husselman, M. H. (1998). Effect of processing conditions on shrinkage in injection molding. *Polymer Engineering & Science*, *38*(5), 838-846.

Jansen, K. M. B., & Titomanlio, G. (1996). Effect of pressure history on shrinkage and residual stresses—injection molding with constrained shrinkage. *Polymer Engineering & Science*, *36*(15), 2029-2040.

Kazmer, D., & Barkan, P. (1997). Multi-cavity pressure control in the filling and packing stages of the injection molding process. *Polymer Engineering & Science*, *37*(11), 1865-1879.

Mustaffa, M. T., Radhwan, H., Annuar, A. F., Azmi, H., Zakaria, M. Z., & Khalil, A. N. M. (2015). An optimization of shrinkage in injection molding parts by using Taguchi method. *Journal of Advanced Research in Applied Mechanics*, *10*(1), 1-8.

Mathivanan, D., Nouby, M., & Vidhya, R. (2010). Minimization of sink mark defects in injection molding process–Taguchi approach. *International Journal of Engineering, Science and Technology*, *2*(2), 13-22.

Postawa, P., & Koszkul, J. (2005). Change in injection moulded parts shrinkage and weight as a function of processing conditions. *Journal of materials processing technology*, *162*, 109-115.

Tang, S. H., Kong, Y. M., Sapuan, S. M., Samin, R., & Sulaiman, S. (2006). Design and thermal analysis of plastic injection mould. *Journal of materials processing technology*, *171*(2), 259-267.

Titomanlio, G., & Jansen, K. M. B. (1996). In-mold shrinkage and stress prediction in injection molding. *Polymer Engineering & Science*, *36*(15), 2041-2049.

Turng, L. S., & Peić, M. (2002). Computer aided process and design optimization for injection moulding. *Proceedings of the Institution of Mechanical Engineers, Part B: Journal of Engineering Manufacture*, *216*(12), 1523-1532.

Zhang, L., Theurer, C. B., Gao, R. X., & Kazmer, D. O. (2001). Design of a wireless sensor for injection molding cavity pressure measurement. In *ASME International Mechanical Engineering Congress and Exposition* (Vol. 35609, pp. 1-7). American Society of Mechanical Engineers.

Black Sea Journal of Engineering and Science
doi: 10.34248/bsengineering.1977622

Open Access Journal
e-ISSN: 2619 – 8991

Araştırma Makalesi (Research Article)
Cilt 9 - Sayı 5: 2239-2248 / Eylül 2026
(Volume 9 - Issue 5: 2239-2248 / September 2026)

TOKAT OVASI VE YAKIN ÇEVRESİNDE İKLİM DEĞİŞİKLİĞİ BAĞLAMINDA KURAKLIK ANALİZİ

İsmail BAYRAM[1]*, Halil İbrahim ZEYBEK[2]

[1]*Arif Nihat Asya Girls' Anatolian Imam Hatip High School, 60200, Tokat, Türkiye*
[2]*Ondokuz Mayıs University, Faculty of Human and Social Sciences, Department of Geography, 55200, Samsun, Türkiye*

Özet: Tokat Ovası'nda sulama imkânı sınırlı olan tarım alanlarında, özellikle son yıllarda meydana gelen kuraklık olayları tarımsal üretim ve verim üzerinde olumsuz etkiler oluşturmaktadır. Bu çalışma, Tokat Ovası'nda 1985–2025 yılları arasında meydana gelen kurak dönemler ile yüzyılın sonuna kadar (2026–2098) ortaya çıkabilecek kuraklık şartlarını değerlendirmeyi amaçlamaktadır. Çalışma alanının iklim özelliklerinin açıklanmasında Turhal Meteoroloji İstasyonu'na ait (1985–2025) gözlem verilerinden yararlanılmıştır. Yöredeki kurak dönemler ve rölatif kuraklıklar ise, tarımsal kuraklığı daha yüksek hassasiyetle yakalayan Standartlaştırılmış Yağış ve Evapotranspirasyon İndisi (SPEI) ile belirlenmiştir. Gelecekteki kuraklık koşullarının tahmin edilmesinde ise HadGEM2-ES Küresel İklim Modeli veri setlerinden türetilen, RegCM4.3 Bölgesel İklim Modeline ait projeksiyon çıktıları kullanılmıştır. Üç aylık SPEI değerlerine göre araştırma sahasında 2014 yılından itibaren tarımsal ürünlerin vejetasyon dönemlerinde mevsimsel kuraklık koşullarının etkili olduğu anlaşılmaktadır. 2024 ve 2025 yıllarında ise kuraklığın yılın büyük bölümüne yayıldığı görülmüştür. 12 aylık SPEI değerleri, 2014–2025 döneminde araştırma alanında kuraklık eğiliminin arttığını göstermektedir. İklim projeksiyonları, kısa vadede daha nemli koşullara yönelik bir eğilim olduğunu ortaya koyarken, yüzyılın sonuna doğru kuraklık olaylarının daha uzun süreli ve daha şiddetli şekilde meydana gelebileceğini göstermektedir.

Anahtar kelimeler: İklim değişikliği, Tarımsal kuraklık, Tokat, SPEI

Drought Analysis in the Tokat Plain and Its Vicinity in the Context of Climate Change

Abstract: In the Tokat Plain, where irrigation is limited, drought events, especially those occurring in recent years, have negatively impacted agricultural production and yield. This study aims to evaluate the drought periods that occurred in the Tokat Plain between 1985 and 2025, and the drought conditions that may arise until the end of the century (2026–2098). Observation data from the Turhal Meteorological Station (1985–2025) were used to describe the climatic characteristics of the study area. Drought periods and relative droughts in the region were determined using the Standardized Precipitation and Evapotranspiration Index (SPEI), which captures agricultural drought with higher accuracy. Projection outputs from the RegCM4.3 Regional Climate Model, derived from the HadGEM2-ES Global Climate Model dataset, were used to predict future drought conditions. According to the 3 months SPEI values, it is understood that seasonal drought conditions have been effective in the vegetation periods of agricultural products in the research area since 2014. In 2024 and 2025, drought was observed to extend to a large part of the year. 12-month SPEI values show an increasing drought trend in the study area during the 2014–2025 period. While climate projections reveal a trend towards wetter conditions in the short term, they indicate that drought events may occur for longer periods and with greater severity towards the end of the century.

Keywords: Climate change, Agricultural drought, Tokat, SPEI

***Sorumlu yazar (Corresponding author):** Arif Nihat Asya Girls' Anatolian Imam Hatip High School, 60200, Tokat, Türkiye
E mail: ilbayram@gmail.com (İ. BAYRAM)
İsmail BAYRAM https://orcid.org/0009-0004-6519-6128
Halil İbrahim ZEYBEK https://orcid.org/0000-0002-4097-9079

Gönderi: 23 Haziran 2026 **Received:** June 23, 2026
Kabul: 25 Temmuz 2026 **Accepted:** July 25, 2026
Yayınlanma: 15 Eylül 2026 **Published:** September 15, 2026

Cite as: Bayram, İ., & Zeybek, H. İ. (2026). Drought analysis in the Tokat plain and its vicinity in the context of climate change. *Black Sea Journal of Engineering and Science*, 9(5), 2239-2248.

1. Giriş

İnsanoğlu sanayi devrimiyle beraber fosil enerji kullanımı başta olmak üzere, ormansızlaşma, yanlış arazi kullanımı, tarım ve sanayi gibi çeşitli insan etkinlikleri ile atmosferde yoğun miktarda sera gazı birikmesine yol açmıştır (IPCC, 2007, 2013, 2021; Türkeş, 2000, 2008, 2012). Atmosferimizdeki insan kaynaklı sera gazı değerleri son iki milyon yılın en yüksek seviyesine ulaşarak içinde olduğumuz zaman dilimini ortalama küresel yüzey sıcaklıkları açısından en azından son 2000 yılın zirvesine oturtmuştur (IPCC, 2021). 2020 yılı itibariyle ortalama küresel yüzey sıcaklığı sanayi öncesi döneme göre 1.09°C artmıştır (IPCC, 2021). Günümüzde yaşanan insan kaynaklı iklim değişikliği özellikle tarım, hayvancılık, ormancılık ve balıkçılık gibi iklime bağımlı ekonomik faaliyetlerin sürdürülebilirliğini tehdit etmekte; kırsal toplumları iklim değişikliğinin olumsuz etkileri karşısında daha savunmasız hale getirmektedir (Adger, 1996; Kasperson ve Kasperson, 2001; Brooks et. al., 2005; Sullivan ve Meigh, 2005; Füssel ve Klein, 2006;

This work is licensed (CC BY-NC 4.0) under Creative Commons Attribution 4.0 International License

Hahn vd., 2009; IPCC, 2014; Ahmad ve Ma, 2020; IPCC, 2022). İklim değişikliği kaynaklı yağış değişkenliği ve kurak dönemler bir takım çevresel bozulmalarla beraber kırsal alanlarda özellikle gıda ve temiz su erişimini zorlaştırabilmektedir (IPCC, 2014; IPCC, 2022; Bayram vd., 2024; Bayram, 2025). İklim değişkenliğinden kaynaklanan kurak dönemlerin etki alanı, süresi ve şiddetindeki artışlar Akdeniz havzası gibi yarı kurak iklim koşullarının egemen olduğu sahalarda daha görünür hale gelmiştir (Kadıoğlu, 1993; Kadıoğlu, 2001; Türkeş vd., 2000; Kadıoğlu ve Şaylan, 2001; Türkeş, 2008, Kadıoğlu, 2008; Türkeş, 2011a; Bahadır, 2011; Türkeş vd., 2018).

Ortamda su bulunabilirliğinin azaldığı, genellikle meteorolojik, hidrolojik ve tarımsal sistemleri etkileyen geçici bir doğal afet olan kuraklık çoğunlukla meteorolojik, hidrolojik ve tarımsal kuraklık şeklinde sınıflandırılmaktadır (Wilhite and Glantz, 1985; Çamalan vd., 2019; Çamalan vd., 2023). Bütün kuraklıklar ilk önce meteorolojik kuraklıkla, yani yetersiz yağışla başlar. Fakat nihai tabloda en tehlikeli kuraklık biçimi olan sosyoekonomik kuraklığa dönüşür (Çamalan vd., 2017; Çamalan vd., 2019; Çamalan vd., 2023). Literatürde kuraklık izlemede yaygın olarak Standartlaştırılmış Yağış ve Evapotranspirasyon indeksi (SPEI), Standartlaştırılmış Yağış İndeksi (SPI), Palmer Kuraklık Şiddet İndeksi (PSDI), Normalin Yüzdesi İndeksi (PNI) gibi indekslerden yararlanılmaktadır. Türkiye'de kuraklığın süresi, şiddeti, etki alanı ve sonuçlarıyla ilgili disiplinler arası pek çok çalışma literatürdeki yerini almıştır (Türkeş, 1999; Kadıoğlu, 1997; Türkeş, 2003, Kadıoğlu, 2008; Kurnaz vd., 2011; Türkeş, 2011b; Türkeş, 2012; Erlat ve Türkeş, 2013; Çamalan vd., 2017; Erlat ve Güler, 2018; Türkeş ve Erlat, 2018; Durmuş ve Bulut, 2023; Erlat ve Güler, 2023; Kayan ve Erlat, 2024). Bu çalışmalardan bazıları araştırma sahasını veya yakın çevresindeki başka sahaları kapsayan kuraklık çalışmalarıdır (Ünal, 2006; Oğuz ve Akar, 2008; Çakmak ve Gökalp, 2013; Demir vd., 2020; Çağlak vd., 2024; Bayram vd., 2024; Bayram, 2025). Bu araştırmaya konu olan Tokat Ovası halihazırda modern sulama altyapısından ve bilimsel esaslara dayalı su yönetiminden yoksundur. Yöredeki tarımsal faaliyetler akarsu debisinin yazın azalması sebebiyle kuraklık ve yağış azlığı gibi sorunlara karşı aşırı duyarlıdır. Yörede son 10 yıldır yağış değişkenliğinden kaynaklanana mevsimsel kuraklıklar tarımsal üretimde önemli ekonomik kayıplar yaşanmasına neden olmuştur (Bayram, 2025). Bu çalışma araştırma sahasında verim kaybı ile karakterize tarımsal kuraklığı, SPEI ile bölgesel iklim projeksiyonu çıktılarına entegre ederek geleceğe dair bir kuraklık öngörüsü oluşturmayı amaçlamaktadır. Araştırma bu yönüyle Tokat Ovası'nda gelecekte karşılaşılabilecek iklimsel tehlikeler ile bu tehlikelerin oluşturabileceği sosyoekonomik risklere karşı bir değerlendirme sunmaktadır.

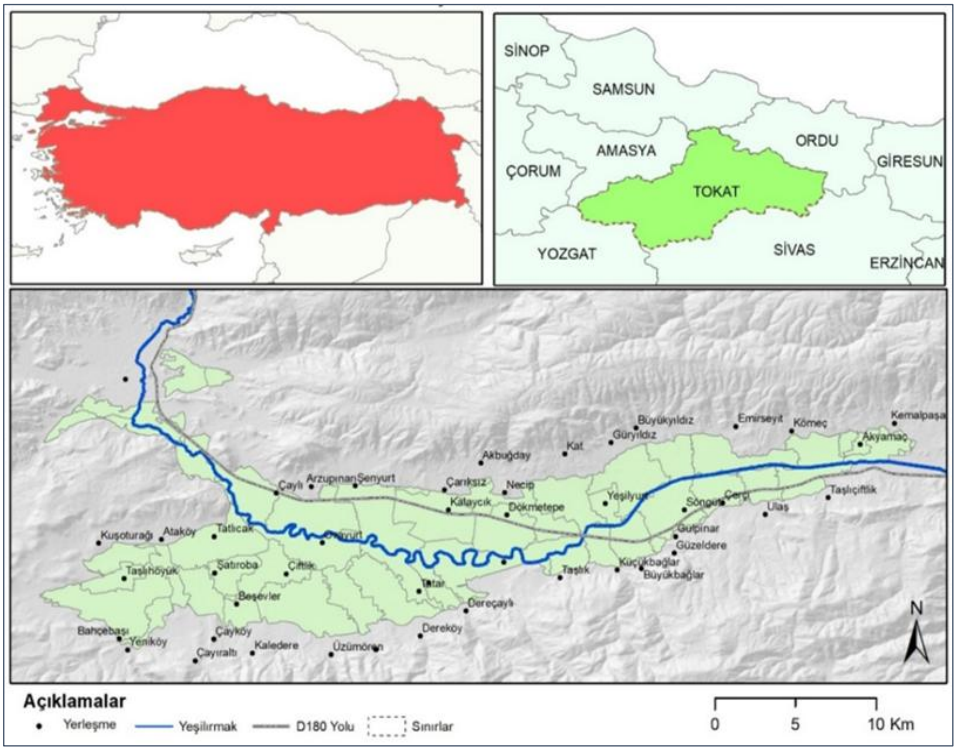
2. Materyal ve Yöntem

2. 1. Çalışma Sahasının Sınırları ve Veri Kaynakları

Tokat Ovası Orta Karadeniz Bölümü'nün güneyinde konumlanmıştır. Ova, idari açıdan Tokat iline bağlı olup Tokat, Turhal ve Pazar ilçe merkezleri arasında uzanmaktadır. Ovanın kuzeyinde Yaylacık, Arhoy, Hanife ve Buzluk dağları, güneyinde Akdağ; batısında Ayranpınar Platosu bulunur. İnceleme sahası 21 Ocak 2017 tarihinde Bakanlar Kurulu kararıyla Büyük Ova Koruma Alanı olarak ilan edilen sahanın 24.580 ha'lık kısmını kapsamaktadır (Şekil 1).

Araştırma sahası tarım ve hayvancılık gibi iklime bağımlı geçim kaynaklarıyla öne çıkan bir yöredir (Bayram vd., 2024; Bayram, 2025). Yarı kurak iklim koşullarının hâkim olduğu bu yörede son yıllarda artan kuraklık koşulları özellikle sulama imkânı sınırlı olan tarım arazilerinde üretim süreci ve verim üzerinde olumsuz etkilere neden olmaktadır (Bayram, 2025). Bu sebeple yörede yaşanan kuraklık şartlarının sıklığı ve süresinin tespit edilmesine ihtiyaç duyulmaktadır.

Araştırma sahasında yaşanan kuraklık koşullarının tespitinde Turhal Meteoroloji İstasyonuna ait 1985-2025 yılları arasındaki yağış ve sıcaklık verilerinden yararlanılmıştır. Yörede faaliyet gösteren farklı meteoroloji istasyonları olsa da (Tablo 1) bu istasyonların rasat süresi ve veri kalitesi değişmektedir. Bu çalışmada veri alınan Turhal istasyon RegCM4.3 gridlerinden 3047 numaralı grid istasyonu ile çakışmaktadır. Zaten dar olan sahada istasyonlar arası karşılaştırma ve tutarlılık beklentisiyle yalnızca Turhal istasyonuna ait veriler kullanılmıştır.



Şekil 1. Araştırma sahasının lokasyon haritası.

Tablo 1. Araştırma sahasındaki meteoroloji istasyonları

İstasyon	Kordinatlar	Rasat Dönemi
Tokat	40°19'52.2"N 36°33'27.6"E	1964-2023
Turhal	40°22'30.9"N 36°05'49.8"E	1975-2022
Pazar	40°16'55.0"N 36°17'59.0"E	2014-2023
Tarım Ens.	40°19'34.0"N 36°27'00.0"E	2013-2023
Kemalpaşa Köyü	40°21'57.7"N 36°30'06.2"E	2018-2023

2.2. Yöntem

Bu çalışma 2023, 2024 yıllarında doktora kapsamında (Bayram, 2025) gerçekleştirilen bir dizi saha çalışması sırasında Tokat Ovası'nda kuraklık şartlarının ürün deseni ve verim üzerindeki olumsuz etkilerinin anlaşılmasıyla tasarlanmıştır. Çalışma bulguları ve yöntemlerinin bir kısmı sözü edilen doktora çalışmasına dayansa da 2025 yılında ayrıca bir saha çalışması yapılmıştır. Tokat Ovası'nda arazisi olan 17 köy muhtarıyla görüşülmüş; görüşmelerde kuraklığın boyutu ve tarım üzerindeki etkileri belirlenmeye çalışılmıştır.

Çalışmanın ana yöntemi olan SPEI tarımsal kuraklıkların tespit edilmesinde yaygın olarak kullanılan bir yöntemdir (Bayram vd., 2024; Bayram, 2025). SPEI, yüzey suyu dengesindeki değişimi kapsamlı bir şekilde yansıtabilen yağış (P) ve potansiyel buharlaşma-terleme (PET) arasındaki birikmiş farka dayanmaktadır (Aktürk vd., 2022; Çamalan vd., 2017; Çamalan vd., 2019; Çamalan vd., 2023; Gumus, 2023). Yörenin kuraklık koşulları 3 aylık ve 12 aylık dönemler halinde analiz edilmiştir. Üç aylık analizler kısa dönemli veya mevsimlik kuraklıkları, 12 aylık analizler ise uzun dönemli kuraklıkları yakalamak için tercih edilmektedir. Kısa dönemli kuraklıklar daha çok tarımsal faaliyetlerle, uzun dönemli kuraklıklar ise çoğunlukla su yönetimiyle ilişkilidir (Aktürk vd., 2022; Çamalan vd., 2023; Gumus, 2023). Söz konusu yöntem potansiyel evapotranspirasyon verisini de hesaba katarak tarımsal kuraklıkların izlenmesinde iklim değişikliği açısından daha etkili bir yaklaşım önermektedir (Vicente-Serrano, et al., 2010; Aktürk vd., 2022; Gumus, 2023). Aşağıdaki tabloda SPEI nemlilik-kuraklık değer aralıkları gösterilmiştir (Tablo 2).

Tablo 2. Yağış ve evapotranspirasyon indisi (SPEI) değerleri

Nemlilik Sınıfı	İndis Değeri
Aşırı Nemli	≥ 2
Çok Nemli	1,5 ~ 1,99
Orta Nemli	1 ~ 1,49
Normale Yakın	-0,99 0,99
Orta Kurak	-1 ~ -1,49
Şiddetli Kurak	-1,5 ~ -1,99
Aşırı Kurak	≤ -2

SPEI'nin hesaplanmasında kullanılan formüller ve veri seti C+ kodlama dili ile yazılmış kod paketi olarak Windows Komut İstemcisi yardımıyla çalıştırılmıştır. SPEI temelde şöyle formüle edilir:

$$D_i = P_i - PET_i \quad (1)$$

Eşitlik 1'de herhangi bir ayın PET ve yağış miktarı arasındaki fark (Di) su fazlası veya su noksanı miktarını vermektedir:

$$SPEI = w - \frac{C_0 + C_1 w + C_2 w^2}{1 + d_1 w + d_2 w^2 + d_3 w^3} \quad (2)$$

Eşitlik 2'de (Di) olasılıkları için ters-standart normal dağılım fonksiyonu kullanılarak SPEI değerleri elde edilir:

Burada, $\sqrt{-2\ln(P)} \rightarrow P \leq 0,5$ için, P değeri belirlenmiş bir D değerinin aşılma olasılığını ifade eder. P= 1-F(x) tir. Eğer P>0.5 ise o zaman P, 1-p ile yer değiştirir ve SPEI'nin işareti tersine alınır. SPEI'nin ortalaması 0; standart sapması 1'dir. SPEI, normalleştirilmiş bir indis olduğu için farklı saha ve zaman ölçekleri arasında karşılaştırılabilir sonuçlar üretmektedir (Aktürk vd., 2022; Çamalan vd., 2023; Gumus, 2023).

İklim projeksiyonları, farklı sera gazı emisyon senaryolarına bağlı olarak gelecekteki iklim şartlarının nasıl olabileceği hakkındaki bilimsel tahminler olarak tanımlanmaktadır (IPCC, 2013). Türkiye'nin iklimi büyük ölçüde Akdeniz dolaşımı ve batı rüzgârlarının etkisindedir. HadGEM2-ES Küresel İklim Modeli büyük ölçekli atmosferik dolaşım desenlerini birçok CMIP5 modeline göre başarılı biçimde simüle ettiği için (Demircan vd., 2017) araştırma sahasının iklim projeksiyonlarının oluşturulmasında bu veri setlerini kullanan RegCM4.3 Bölgesel İklim Modeli çıktıları kullanılmıştır. Söz konusu model araştırma sahasında 20 km çözünürlükte 8 farklı gridle temsil edilmektedir (Tablo 3).

Tablo 3. Araştırma sahasında RegCM Gridlerine ait lokasyon bilgileri

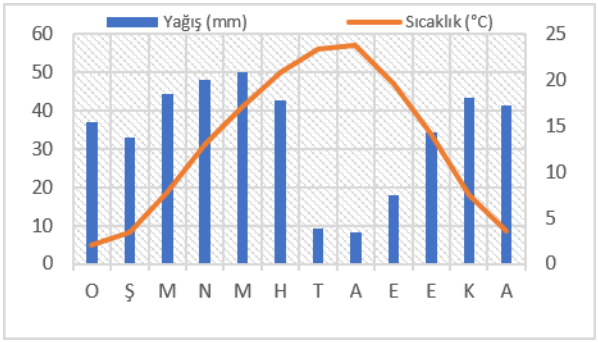
Grid-İstasyon	Enlem	Boylam	Yükselti
2946	40°2086 K	35°8324 D	998 m
2947	40°1948 K	36°0746 D	958 m
2948	40°1805 K	36°3165 D	1332 m
2949	40°1656 K	36°5584 D	1420 m
3046	40°3936 K	35°8502 D	1291 m
3047	40°3798 K	36°0930 D	535 m
3048	40°3654 K	36°3357 D	1037 m
3049	40°3504 K	36°5784 D	710 m

Türkiye'nin iklim politikaları ile mevcut kalkınma çabaları arasındaki ilişki gözetilerek emisyon oranlarının orta düzeyde kalacağı varsayılmış; bu sebeple yörenin kuraklık tahmini için yalnızca RCP4.5 senaryosuna ait çıktılardan faydalanılmıştır.

İklim değişikliği çalışmalarında, modelin gözlemlerden sistematik sapmalarını azaltmak için yanlılık düzeltmesi yapılmaktadır. Ön yargı düzeltmede Turhal istasyonuna ait (1985-2025) aylık ortalama değerler referans alınmıştır. Doğrusal regresyon neticesinde elde edilen düzeltme katsayıları bu istasyonla çok yakın konumlanan 3047 numaralı gridin projeksiyon çıktılarını düzeltmek için kullanılmıştır. Doğrusal regresyon sonuçlarına göre sıcaklık düzeltme için R2 değeri 0,98 üzerinde hesaplanmıştır. Aynı istasyonda yağış yanlılık düzeltmesi ise Oransal Fark yöntemi ile yapılmıştır. Her iki yöntem de iklim değişikliği çalışmalarında sıklıkla tercih edilmektedir (Ballı, 2014; Çağlak, 2021; Bayram, 2025).

3. Bulgular

Araştırma sahası yarı kurak iklim şartların hâkim olduğu karasal iklim özellikleri gösterir. Turhal Meteoroloji İstasyonu verilerine (1985-2025) göre araştırma sahasında yıllık ortalama sıcaklık 13 °C, yıllık ortalama yağış miktarı ise 409 mm'dir. Yörede kışlar soğuk ve kar yağışlı, yazlar ise nispeten sıcak ve kurak geçmektedir (Şekil 2). Tokat Ovası'nda Thornthwaite yöntemine göre su fazlası olmayan veya pek az olan (d), denizel etkili (b3), mezotermal (B2), yarı kurak iklim şartları (D) hüküm sürmektedir. Yörede haziran ayında başlayan su noksanı ekim ayı ortalarına kadar devam eder (Bayram, 2025).



Şekil 2. Araştırma sahasının iklim diyagramı.

Su noksanı yaşanan bu dönemde ekonomik değeri yüksek bazı tarım ürünlerinin su ihtiyacı had safhadadır (Bayram, 2025). Su noksanı görülen ayların normalinden daha kurak geçmesi tarımsal üretim ve verimi azaltmaktadır. Araştırma sahasında SPEI ile yapılan 3 aylık kuraklık analizine ait indis değerleri incelendiğinde 1985-2010 yılları arasında normale yakın ve nispeten daha nemli mevsimlik şartların yaşandığı gözlenmektedir. Bu zaman aralığında orta kurak geçişler olsa da yaklaşık her 3-4 yılda birçok nemli-aşırı nemli şartların hâkim olduğu dönemler yaşanmıştır. Yörede kurak geçen yaz mevsiminde 25 yılın 18 yılı nemli ve aşırı nemli şartların hâkim olduğu yıllar olarak göze çarpar (Tablo 4).

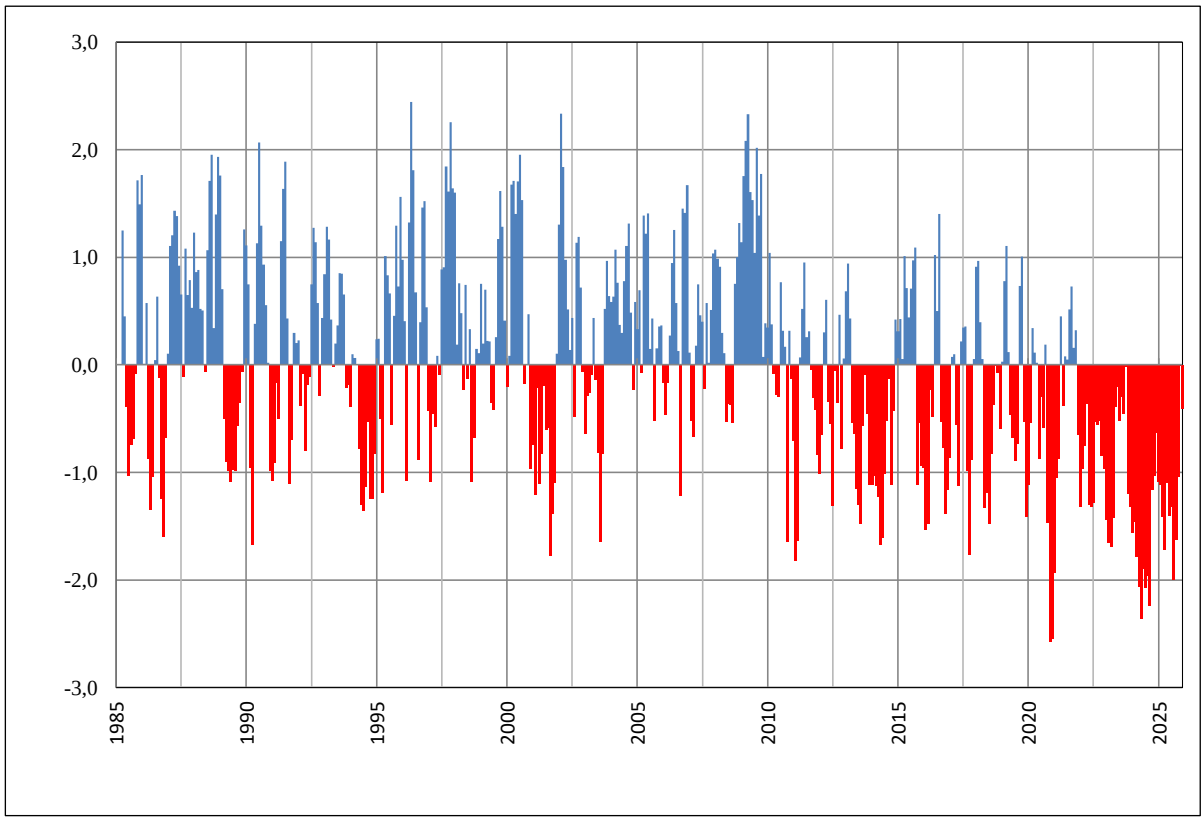
Yörede 2010 yılından sonra mevsimsel kuraklık koşulları daha belirgin hale gelmiştir. 2023 yılına kadar orta ve şiddetli kuraklık koşulları mevsimsel değişkenlikle karakterizedir. 2023 yılından itibaren ise daha kronik hale gelen kuraklık 2024 yılı ilkbahar ve yaz mevsiminde aşırı kurak şartlar şeklinde ortaya çıkmıştır. 2011-2025 yılları arasında en az yedi yıl boyunca tarımsal ürünlerin vejetasyon dönemlerinde zaman zaman kuraklık şartları yaşanmıştır. 2024 ve 2025 yılları hidrolojik döngünün neredeyse kırıldığı, toprak neminin büyük oranda tüketildiği şiddetli ve aşırı kuraklık koşullarının yılın

büyük bir bölümüne yayıldığı yıllar olmuştur (Şekil 3). Yeraltı su seviyesinde ciddi düşüşler kaydedilen bu dönemde saha çalışmaları sırasında sondajla su ihtiyacını karşılayan bazı hanelerin dalgıç pompaları 6 metreye kadar derine indirmek zorunda kaldığı anlaşılmıştır. Araştırma sahası ve yakın çevresinde 30 yıl içerisinde eskiden aktığı bilinen bazı su kaynaklarının kuruduğu bilinmektedir (Bayram 2025).

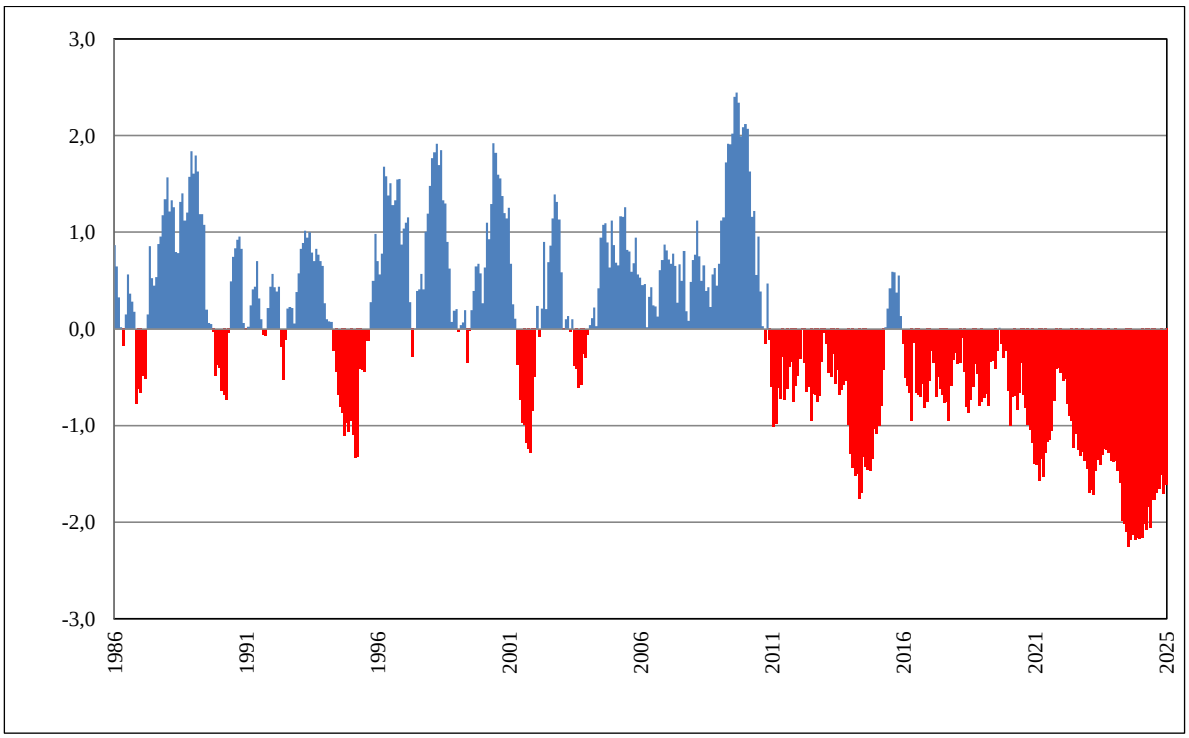
12 aylık SPEI sonuçlarına göre 1985-2011 yılları arasında genel olarak normale yakın nemlilik şartları hâkim durumdadır. Bu süre zarfında özellikle 2009-2010 yılları aşırı nemli koşulların hâkim olduğu en nemli yıllar; aynı zamanda keskin bir negatif eğilim öncesindeki son aşırı nemli yıllar olarak kayıtlara geçmiştir (Şekil 4).

Tablo 4. Araştırma sahasında üç aylık SPEI değerlerinin yıllara göre dağılışı

Tarih	Ocak	Şubat	Mart	Nisan	Mayıs	Haziran	Temmuz	Ağustos	Eylül	Ekim	Kasım	Aralık
1985				1,2	0,4	-0,4	-1,0	-0,7	-0,7	-0,1	1,7	1,5
1986	1,8	0,0	0,6	-0,9	-1,3	-1,0	0,0	0,6	-0,1	-1,2	-1,6	-0,7
1987	0,1	1,1	1,2	1,4	1,4	0,9	0,7	-0,1	1,1	0,6	0,8	0,5
1988	1,2	0,9	0,9	0,5	0,5	-0,1	1,1	1,7	2,0	0,3	1,4	1,9
1989	1,8	0,7	-0,5	-0,9	-1,0	-1,1	-1,0	-1,0	-0,6	-0,4	-0,1	1,3
1990	1,1	0,7	-1,0	-1,7	0,4	1,1	2,1	1,3	0,9	0,6	0,0	-1,0
1991	-1,1	-0,9	-0,2	-0,5	1,1	1,6	1,9	0,4	-1,1	-0,7	0,3	0,2
1992	0,2	-0,4	-0,1	-0,8	-0,2	-0,1	0,7	1,3	1,1	0,6	-0,3	0,4
1993	0,8	1,3	1,2	0,4	0,0	0,2	0,4	0,9	0,8	0,7	-0,2	-0,2
1994	-0,4	0,1	0,1	0,0	-0,8	-1,3	-1,4	-1,1	-0,5	-1,2	-1,2	-0,8
1995	0,2	0,2	-0,5	-1,2	1,0	0,8	0,7	-0,6	0,5	1,3	0,7	1,6
1996	1,0	0,4	-1,1	1,3	2,4	1,8	0,7	-0,9	0,4	1,5	1,5	0,5
1997	-0,4	-1,1	-0,5	-0,6	0,1	-0,1	0,9	0,9	1,8	1,6	2,3	1,6
1998	1,6	0,2	0,8	0,5	-0,2	0,7	-0,1	0,3	-1,1	-0,7	0,1	0,1
1999	0,8	0,2	0,7	0,2	0,2	-0,4	-0,4	0,3	1,2	1,6	1,3	0,4
2000	-0,2	0,1	1,7	1,7	1,4	1,7	2,0	1,5	-0,2	0,0	0,5	-1,0
2001	-0,7	-1,2	-0,2	-1,1	-0,8	-0,2	-0,6	-0,6	-1,8	-1,4	-1,1	0,1
2002	1,3	2,3	1,8	1,0	0,5	0,1	0,4	-0,5	1,1	1,2	0,7	-0,1
2003	-0,6	-0,3	-0,3	-0,1	0,4	-0,1	-0,8	-1,6	-0,8	0,5	1,0	0,6
2004	0,6	0,6	1,1	0,8	0,4	0,3	0,8	1,1	1,3	0,5	-0,2	0,6
2005	0,3	0,7	-0,1	1,4	1,2	1,4	0,1	0,4	-0,5	0,2	0,4	0,4
2006	-0,2	-0,5	-0,2	0,3	0,9	1,3	0,6	0,1	-1,2	1,5	1,4	1,7
2007	0,1	-0,5	-0,7	0,2	0,7	0,5	0,4	-0,2	0,6	0,0	0,5	1,0
2008	1,1	1,0	0,9	0,3	0,1	-0,5	-0,4	-0,4	-0,5	0,8	1,0	1,3
2009	1,1	1,8	2,1	2,3	1,6	1,5	1,0	2,0	1,4	1,8	0,1	0,4
2010	0,3	1,0	0,4	-0,1	-0,3	-0,3	0,8	0,3	0,2	-1,6	0,3	-0,1
2011	-0,7	-1,8	-1,6	0,1	0,5	1,0	0,3	0,3	0,0	-0,3	-0,4	-0,8
2012	-1,0	-0,7	0,3	0,6	-0,3	-0,5	-1,3	-0,1	-0,3	0,5	-0,8	0,1
2013	0,7	0,9	0,4	-0,5	-0,6	-1,1	-1,3	-1,5	-0,6	-0,1	-0,5	-1,1
2014	-1,1	-1,0	-1,1	-1,2	-1,7	-1,6	-1,0	-0,5	-0,1	-1,1	-0,4	0,4
2015	0,3	0,4	0,1	1,0	0,7	0,4	0,7	1,0	1,1	-1,1	-0,5	-0,9
2016	-1,0	-1,5	-1,5	-0,2	-0,5	1,0	0,5	1,4	-0,5	-0,8	-1,4	-1,2
2017	-0,9	0,1	0,1	-0,6	-1,1	0,2	0,3	0,4	-1,0	-1,8	-0,9	0,1
2018	0,9	1,0	0,4	0,1	-1,3	-1,2	-1,5	-0,8	-0,4	0,0	-0,1	-0,6
2019	0,0	0,8	1,1	0,1	-0,5	-0,7	-0,9	-0,7	0,7	1,0	-0,5	-1,4
2020	-1,1	-0,5	0,3	0,1	0,0	-0,9	-0,3	-0,6	0,2	-1,5	-2,6	-2,6
2021	-1,9	-1,0	-0,9	0,4	-0,4	0,1	0,0	0,5	0,7	0,2	0,3	-0,6
2022	-1,3	-1,0	-0,8	-0,4	-1,3	-1,3	-1,3	-0,5	-0,6	-0,5	-0,8	-1,0
2023	-1,4	-1,7	-1,7	-1,4	-0,4	-0,2	-0,5	-0,3	-0,5	0,0	-1,2	-1,3
2024	-1,6	-1,5	-1,8	-2,1	-2,4	-1,9	-2,1	-2,0	-2,2	-1,2	-1,0	-0,6
2025	-1,1	-1,1	-1,4	-1,7	-1,1	-1,4	-1,3	-2,0	-1,6	-1,0	0,0	-0,4



Şekil 3. Araştırma sahasının 3 aylık SPEI grafiği.



Şekil 4. Araştırma sahasının 12 aylık SPEI grafiği.

Araştırma sahasında 2014-2021 yılları arasında negatif eğilimli normale yakın nemlilik şartlarının hâkim olduğu dönemler yaşanmıştır. Yörede kuraklık 2021 yılından itibaren şiddetlenmeye başlamış 2024 ve 2025 yılları kuraklığın en şiddetli yaşandığı yıllar olarak kayıtlara geçmiştir. 2024 yılı araştırma sahasında son 40 yıl boyunca yaşan en kurak yıl olmuştur (Şekil 5).

Halihazırda yarı kurak iklim şartlarının hâkim olduğu yörede çiftçilerin tarımsal faaliyetler sırasında son 10 yıla kadar hiç ihtiyaç duymadıkları bir takım kuraklık önlemlerini uygulamak zorunda kaldıkları bilinmektedir (Bayram vd. 2024; Bayram, 2025). Örneğin ilkbahar

mevsiminde yetersiz yağış sebebiyle ekilen tohumların çimlenebilmesi veya tahılların erken tohuma gitmesini engellemek için çok erken sulama yapılması bu tür uygulamalara örnek olarak verilebilir (Şekil 6).

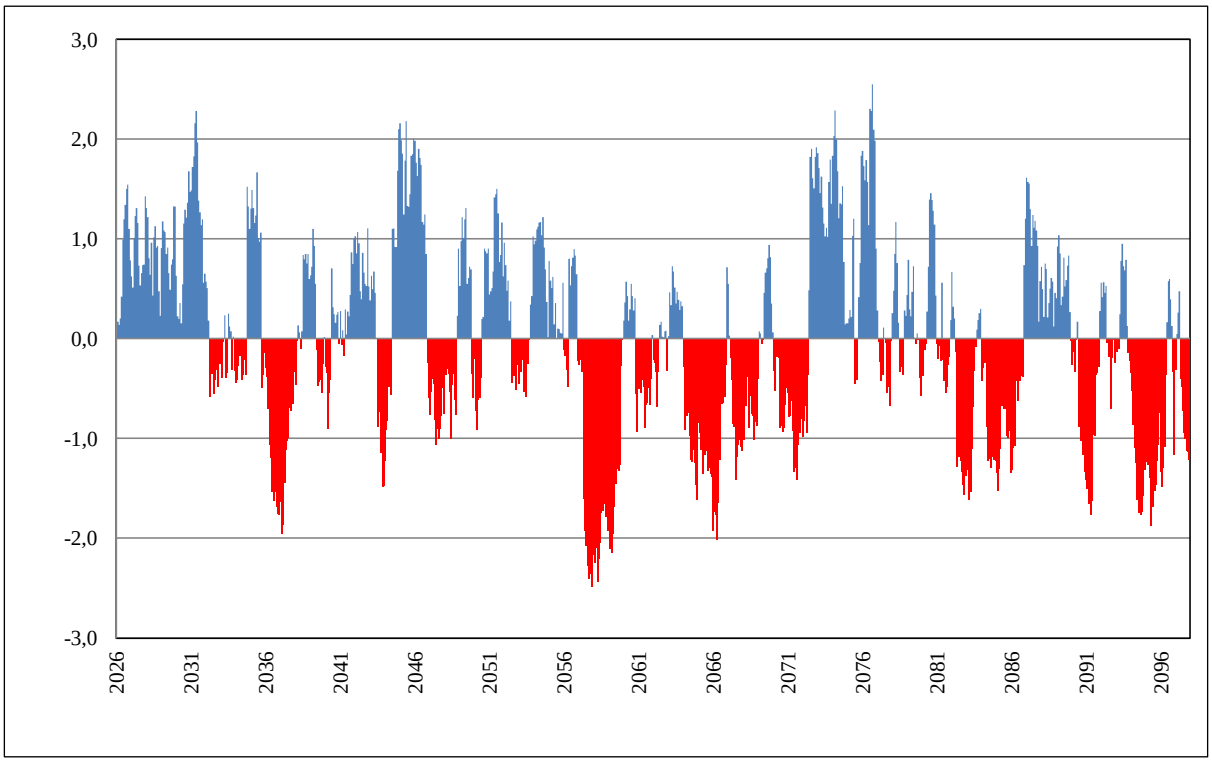
Son yıllarda küresel ölçekte yaşanan kuraklık artışları küresel ısınma ve iklim değişikliği süreciyle yakından ilişkilidir. Bu kuraklık şartlarından özellikle yarı nemli ve kurak iklim bölgeleri daha fazla etkilenmektedir (IPCC, 2022). Araştırma sahasında gelecekteki kuraklık şartlarını tahmin edebilmek için HadGEM2-ES küresel iklim modelinden türetilen RegCM.4.3 bölgesel iklim modeli çıktıları ile RCP4.5 senaryosu çalıştırılmıştır. Bu senaryoya ait 2026-2098 yılları arasındaki dönemi kapsayan aylık ortalama yağış ve sıcaklık tahminleri SPEI yöntemi ile değerlendirilmiştir. 12 aylık tahmini SPEI sonuçlarına göre araştırma sahasında iklim değişikliğinin etkileriyle beraber kuraklık risklerinin zamanla artacağı öngörülmektedir. Nitekim IPCC (2022) iklim değişikliği nedeniyle kurak dönemlerin süresinin, şiddetinin ve etki alanının giderek artacağına vurgu yapmaktadır. Buna mukabil soğuk veya nemli ekstremlerin sıcak ve kurak ekstremlere nazaran daha seyrek yaşanacağına da değinilmektedir. Mevcut senaryoya göre inceleme sahasında 2026-2032, 2044-2046, 2072-2076 yılları arasında çok nemli veya aşırı nemli dönemlerin yaşanabileceği tahmin edilmektedir (Şekil 7). Fakat 2050'li yıllardan itibaren yörede kuraklığın kısmen daha şiddetli ve daha uzun süreli hale geleceği söylenebilir.



Şekil 5. Araştırma sahasında kuraklık nedeniyle erken başaklanan buğdaylar.



Şekil 6. Araştırma sahasında kuraklık nedeniyle sulanmak zorunda kalan buğdaylar.



Şekil 7. Araştırma sahasında RCP4.5 senaryosuna göre SPEI ile 12 aylık kuraklık tahmini.

4. Sonuçlar ve Tartışma

HadGEM2-ES projeksiyonlarına göre yörede toplam yağış miktarında ciddi bir azalma ön görülmese de yağış rejiminin değişebileceği veya yağışların ani ve şiddetli sağanaklar şeklinde düşebileceği değerlendirilmektedir. IPCC (2022) yağış rejimi ve yağış biçimindeki değişiklikleri iklim değişikliğinin en önemli etkileri arasında ele almaktadır. Yörede yüzyılın sonuna kadar yağış azlığı kaynaklı olmasa bile buharlaşma şiddetinin artması veya yağış rejimi ve yağış biçimindeki düzensizlikler nedeniyle şiddetli kuraklıklar yaşanması ihtimal dahilindedir.

Araştırma sahasında kuraklık koşulları sulama imkânları sınırlı olan araziler için verim kaybı ve devamındaki ekonomik kayıplar kırsal kesimde hane bütçesiyle ilgili riskleri artırmaktadır. Sulanabilen arazilerde mevcut sulama sistemi kuraklıkla ilgili riskleri önemli ölçüde azaltsa da sulama sistemi dışında kalan veya çoğunlukla mevsimlik akarsular tarafından beslenen gölet ve havuzlarda toplanan sulara bağımlı üreticilerin kuraklıktan etkilenmeleri kaçınılmaz hale gelmektedir. Çoğunluğu ova kenarında yer alan bu tip arazilerde göletlerde yeterli suyun toplanamadığı veya mevsimlik akarsuların erken kuruduğu dönemlerde üreticilerin kuraklığa karşı ürettikleri çözümler münferit ve sınırlı ölçektedir. Bu durum özellikle ova kenarında yer alan arazilerde yaygın bir problem olsa da sulama sistemi içinde olup da sulama suyuna ulaşamayan üreticiler için de büyük bir sorun haline dönüşecektir (Bayram vd., 2024; Bayram, 2025). Sulama sistemi dışında kalan arazilerin bir kısmında inşa edilen havuzlarda su toplanarak ya da bölgesel destekleme projeleri kapsamında kapalı sistem sulama sistemleri kurularak sulama sorunu giderilmeye çalışılmaktadır.

Araştırma sahasında sulama sisteminin ana sağlayıcısı durumunda olan Yeşilırmak ve yan dereler 2024-2025 yıllarında gerçekleşen kuraklık koşullarında yetersiz kalmıştır. Özellikle Almus Baraj gölünde enerji üretimi ve tarım arazilerini sulamak için kullanılan su miktarı ve şiddetli kuraklık şartları baraj rezervuarındaki su seviyesinde hızlı ve büyük miktarda azalmaya neden olmuştur. Bu sebeplerle gerek halkın sarnıç ve havuz gibi yapılarda su toplamasını sağlayacak bireysel tedbirlerin gerekse altyapı ve sulama sisteminin modernizasyonu gibi kurumsal dönüşümlerin devlet desteğiyle hızlandırılması gerekmektedir. Tokat Ovası'nda çiftçilerin ürün tercihlerinde daha az su tüketen ürünlere yönelmesi de kuraklıkla mücadeleye katkı sağlayacaktır (Bayram, 2025). Gelecekte iklim değişikliğinin kuraklıkla ilgili etkilerini azaltmak için daha etkili bir sulama sisteminin hayata geçirilmesi araştırma sahasında iklim dirençli bir kırsal toplum oluşturabilmenin ön şartıdır.

Katkı Oranı Beyanı

Yazarların katkı yüzdeleri aşağıda verilmiştir. Yazarlar makaleyi incelemiş ve onaylamıştır.

	İ.B.	H.İ.Z.
K	70	30
T	70	30
Y	70	30
VTI	70	30
VAY	60	40
KT	70	30
YZ	70	30
KI	30	70
GR	70	30
PY	50	50
FA	0	0

K= kavram, T= tasarım, Y= yönetim, VTI= veri toplama ve/veya işleme, VAY= veri analizi ve/veya yorumlama, KT= kaynak tarama, YZ= yazım, KI= kritik inceleme, GR= gönderim ve revizyon, PY= proje yönetimi, FA= fon alımı.

Çatışma Beyanı

Yazarlar bu çalışmada hiçbir çıkar ilişkisi olmadığını beyan etmektedirler.

Etik Onay Beyanı

Bu araştırmada hayvanlar ve insanlar üzerinde herhangi bir çalışma yapılmadığı için etik kurul onayı alınmamıştır.

Kaynaklar

Adger, W. N. (1996). *Approaches to vulnerability to climate change* (pp. 1–63). CSERGE.

Ahmad, M. I., & Ma, H. (2020). Climate change and livelihood vulnerability in mixed crop–livestock areas: The case of Province Punjab, Pakistan. *Sustainability*, *12*(2), Article 586. https://doi.org/10.3390/su12020586

Aktürk, G., Zeybekoğlu, U., & Yıldız, O. (2022). SPI ve SPEI yöntemleri ile kuraklık araştırması: Kırıkkale örneği. *International Journal of Engineering Research and Development*, *14*(2), 762–776. https://doi.org/10.29137/umagd.1100886

Bahadır, M. (2011). Akdeniz Bölgesi'nde sıcaklık ve yağışın gelecekteki eğilimleri ve olası sonuçları. *The Journal of International Social Research*, *4*(19), 364–378.

Ballı, C. (2014). *Bias correction of precipitation simulated by regional climate model with different configurations over Turkey*. Master's thesis, Istanbul Technical University.

Bayram, İ. (2025). *Kırsal kesimde sosyo-ekonomik kırılganlığın iklim değişikliği açısından değerlendirilmesi: Kazova (Tokat) örneği*. Doctoral dissertation, Ondokuz Mayıs University, Samsun, Türkiye.

Bayram, İ., Zeybek, H. İ., & Duman, E. (2024). Kazova'da (Tokat) tarımsal sulama olanaklarının iklim değişikliği açısından değerlendirilmesi. In *Proceedings of the 2nd International Eurasian Climate Change Congress* (pp. 195–196). Van Yüzüncü Yıl University.

Brooks, N., Adger, W. N., & Kelly, P. M. (2005). The determinants of vulnerability and adaptive capacity at the national level and the implications for adaptation. *Global Environmental Change*, *15*(2), 151–163. https://doi.org/10.1016/j.gloenvcha.2004.12.006

Çağlak, S. (2021). *İklim değişikliğinin biyoklimatik konfor şartları üzerine etkileri ve olası sonuçları*. Ondokuz Mayıs University, Samsun, Türkiye.

Çağlak, Y. B., Türkeş, M., & Özlü, T. (2024). Kuraklığın Almus (Tokat-Türkiye) Baraj Gölü elektrik üretim miktarına etkisi. *Journal of Anatolian Geography*, *1*(1), 62–69.

Çakmak, B., & Gökalp, Z. (2013). Kuraklık ve tarımsal su yönetimi. *Gaziosmanpaşa Bilimsel Araştırma Dergisi*, (4), 1–11.

Çamalan, G., Akgündüz, S., Ayvacı, H., Çetin, S., Arabacı, H., & Coşkun, M. (2017). SPEI indisine göre Türkiye geneli kuraklık değişimi ve eğilim projeksiyonları. In *IV. Türkiye İklim Değişikliği Kongresi*, Ankara, Türkiye.

Çamalan, G., Akgündüz, A. S., Çetin, S., & Arabacı, H. (2019). Normalleştirilmiş Yağış-Evapotranspirasyon Kuraklık İndisi (SPEI) ile Türkiye için kuraklık projeksiyonları. *9th International Atmospheric Sciences Symposium (ATMOS 2019)*, Istanbul, Türkiye.

Çamalan, G., Oğuz, K., & Akıl, S. (2023). İklim değişikliğinin İç Anadolu Bölgesi kuraklık koşullarına etkisinin incelenmesi. *Disaster Science and Engineering*, *9*(1), 35–55.

Demir, S., Yürekli, K., Oğuz, İ., & Erdoğan, M. (2020). Farklı iklim modelleri kullanılarak Tokat ili'nde kuraklık analizi. *Gaziosmanpaşa Bilimsel Araştırma Dergisi*, *9*(1), 37–46.

Demircan, M., Gürkan, H., Arabacı, H., & Coşkun, M. (2017). Türkiye için iklim değişikliği projeksiyonları. *TMMOB Harita ve Kadastro Mühendisleri Odası Dergisi*, *16*, 3–6.

Durmuş, B., & Bulut, İ. (2023). Batı Akdeniz'deki ekstrem kuraklık şartlarının SPEI yöntemiyle belirlenmesi. *Türk Coğrafya Dergisi*, (84), 41–52. https://doi.org/10.17211/tcd.1293521

Erlat, E., & Güler, H. (2018). Türkiye'de sıcaklık ekstremlerinin sürelerinde gözlenen değişim ve eğilimler (1950-2017). *Ege Coğrafya Dergisi*, *27*(2), 135–148.

Erlat, E., & Güler, H. (2023). Türkiye'de Standardize Yağış Evapotranspirasyon İndisine (SPEI) göre kuraklıkların zamansal değişimi (1951-2022). *Ege Coğrafya Dergisi*, *32*(Cumhuriyet'in 100. Yılı Özel Sayısı), 77–90.

Erlat, E., & Türkeş, M. (2013). Observed changes and trends in numbers of summer and tropical days, and the 2010 hot summer in Turkey. *International Journal of Climatology*, *33*(8), 1898–1908. https://doi.org/10.1002/joc.3556

Füssel, H. M., & Klein, R. J. (2006). Climate change vulnerability assessments: An evolution of conceptual thinking. *Climatic Change*, *75*(3), 301–329. https://doi.org/10.1007/s10584-006-0329-3

Gumus, V. (2023). Evaluating the effect of the SPI and SPEI methods on drought monitoring over Turkey. *Journal of Hydrology*, *626*, Article 130386. https://doi.org/10.1016/j.jhydrol.2023.130386

Hahn, M. B., Riederer, A. M., & Foster, S. O. (2009). The Livelihood Vulnerability Index: A pragmatic approach to assessing risks from climate variability and change—A case study in Mozambique. *Global Environmental Change*, *19*(1), 74–88. https://doi.org/10.1016/j.gloenvcha.2008.11.002

Intergovernmental Panel on Climate Change. (2007). *Climate change 2007: Impacts, adaptation, and vulnerability. Contribution of Working Group II to the Fourth Assessment Report of the Intergovernmental Panel on Climate Change (Technical Summary)*. Cambridge University Press. https://www.ipcc.ch/site/assets/uploads/2018/02/ar4-wg2-ts-1.pdf

Intergovernmental Panel on Climate Change. (2013). *Climate*

change 2013: The physical science basis. Contribution of Working Group I to the Fifth Assessment Report of the Intergovernmental Panel on Climate Change (Technical Summary). Cambridge University Press. https://www.ipcc.ch/site/assets/uploads/2018/02/WG1AR5_TS_FINAL.pdf

Intergovernmental Panel on Climate Change. (2014). *Climate change 2014: Impacts, adaptation, and vulnerability. Contribution of Working Group II to the Fifth Assessment Report of the Intergovernmental Panel on Climate Change (Technical Summary)*. Cambridge University Press. https://www.ipcc.ch/site/assets/uploads/2018/02/WGIIAR5-TS_FINAL.pdf

Intergovernmental Panel on Climate Change. (2021). *Climate change 2021: The physical science basis. Contribution of Working Group I to the Sixth Assessment Report of the Intergovernmental Panel on Climate Change (Technical Summary)*. Cambridge University Press. https://www.ipcc.ch/report/ar6/wg1/chapter/technical-summary/

Intergovernmental Panel on Climate Change. (2022). *Climate change 2022: Impacts, adaptation and vulnerability. Contribution of Working Group II to the Sixth Assessment Report of the Intergovernmental Panel on Climate Change (Technical Summary)*. Cambridge University Press. https://www.ipcc.ch/report/ar6/wg2/chapter/technical-summary/

Kadıoğlu, M. (1997). Trends in surface air temperature data over Turkey. *International Journal of Climatology*, *17*(5), 511–520. https://doi.org/10.1002/(SICI)1097-0088(199704)17:5<511::AID-JOC142>3.0.CO;2-C

Kadıoğlu, M., & Şaylan, L. (2001). Trends of growing degree-days in Turkey. *Water, Air, and Soil Pollution*, *126*(1), 83–96. https://doi.org/10.1023/A:1005230308826

Kadıoğlu, M. (1993). Türkiye'de iklim değişikliği ve olası etkileri. *Çevre Koruma*, (47), 34–37.

Kadıoğlu, M. (2001). *Küresel iklim değişimi ve Türkiye: Bildiğiniz havaların sonu* (3rd ed.). Güncel Yayıncılık.

Kadıoğlu, M. (2008). Kuraklık kıranı risk yönetimi. *Afet zararlarını azaltmanın temel ilkeleri* (pp. 277–300). JICA Türkiye Office Publications No: 2.

Kasperson, R. E., & Kasperson, J. X. (2001). *Climate change, vulnerability, and social justice*. Stockholm Environment Institute.

Kayan, O., & Erlat, E. (2024). Ege Bölgesi'nde Standardize Yağış Evapotranspirasyon İndisi (SPEI) ile kuraklık değerlendirmesi (1951-2022). *Journal of Agriculture Faculty of Ege University*, *61*(2), 249–258.

Kurnaz, L., Türkeş, M., & Öztürk, T. (2011). RegCM4.3.5 iklim modeli benzetimleri kullanılarak Türkiye'nin gelecek hava sıcaklığı ve yağış klimatolojilerindeki değişikliklerin çözümlenmesi. *Ege Coğrafya Dergisi*, *20*(1), 17–27.

Oğuz, İ., & Akar, T. Ö. Ö. (2008). Tokat Kazova'daki uzun yıllık yağış ve sıcaklık gidişlerinin kuraklık açısından irdelenmesi. *Journal of Agricultural Faculty of Gaziosmanpaşa University*, *2008*(1), 71–79.

Sullivan, C., & Meigh, J. (2005). Targeting attention on local vulnerabilities using an integrated index approach: The example of the Climate Vulnerability Index. *Water Science and Technology*, *51*(5), 69–78. https://doi.org/10.2166/wst.2005.0118

Turkeş, M. (1999). Vulnerability of Turkey to desertification with respect to precipitation and aridity conditions. *Turkish Journal of Engineering and Environmental Sciences*, *23*(5), 363–380.

Türkeş, M. (2000). *Hava, iklim, şiddetli hava olayları ve küresel ısınma* (Publication No. 187). Turkish State Meteorological Service.

Türkeş, M. (2003). Spatial and temporal variations in precipitation and aridity index series of Turkey. In A. Busaci & A. Moreno (Eds.), *Mediterranean climate: Variability and trends* (pp. 181–213). Springer. https://doi.org/10.1007/978-3-642-55657-9_12

Türkeş, M. (2008). Küresel iklim değişikliği nedir? Temel kavramlar, nedenleri, gözlenen ve öngörülen değişiklikler. *İklim Değişikliği ve Çevre*, *1*(1), 26–37.

Türkeş, M. (2011a). Dünyada ve Türkiye'de iklim değişikliği, kuraklık ve çölleşme *II. Ulusal Toprak ve Su Kaynakları Kongresi Bildiri Kitabı (EK)* (pp. 5–19).

Türkeş, M. (2011b). Akhisar ve Manisa yörelerinin yağış ve kuraklık indisi dizilerindeki değişimlerin hidroklimatolojik ve zaman dizisi çözümlemesi ve sonuçların çölleşme açısından coğrafi bireşimi. *Coğrafi Bilimler Dergisi*, *9*(1), 79–99.

Türkeş, M. (2012). Türkiye'de gözlenen ve öngörülen iklim değişikliği, kuraklık ve çölleşme. *Ankara Üniversitesi Çevrebilimleri Dergisi*, *4*(2), 1–32.

Türkeş, M., & Erlat, E. (2018). Aşırı hava ve iklim olaylarında dünya ve Türkiye'de gözlenen değişiklik ve eğilimlerin bilimsel bir değerlendirmesi. *İklim değişikliği ve yeşil boyut: Yeşil ekonomi ve yeşil büyüme* (pp. 5–38).

Türkeş, M., Musaoğlu, N., & Özcan, O. (2018). Assessing the vulnerability of a forest ecosystem to climate change and variability in the western Mediterranean sub-region of Turkey: Future evaluation. *Journal of Forestry Research*, *29*(5), 1177–1186. https://doi.org/10.1007/s11676-017-0582-5

Türkeş, M., Sümer, U. M., & Çetiner, G. (2000). Küresel iklim değişikliği ve olası etkileri. *Birleşmiş Milletler İklim Değişikliği Çerçeve Sözleşmesi Seminer Notları* (pp. 7–24). Ministry of Environment.

Ünal, Ç. (2006). Tokat'ın iklim özellikleri. *Sosyal Bilimler Araştırmaları Dergisi*, *1*(2), 171–197.

Vicente-Serrano, S. M., Beguería, S., & López-Moreno, J. I. (2010). A multiscalar drought index sensitive to global warming: The Standardized Precipitation Evapotranspiration Index. *Journal of Climate*, *23*(7), 1696–1718. https://doi.org/10.1175/2009JCLI2909.1

Wilhite, D. A., & Glantz, M. H. (1985). Understanding: The drought phenomenon: The role of definitions. *Water International*, *10*(3), 111–120. https://doi.org/10.1080/02508068508686328

Black Sea Journal of Engineering and Science
doi: 10.34248/bsengineering.1977966

Open Access Journal
e-ISSN: 2619 – 8991

Research Article
Volume 9 - Issue 5: 2249-2258 / September 2026

HETEROGENEOUS MIXTURE DISTRIBUTIONS FOR MODELING SKEWED DATA IN ENGINEERING APPLICATIONS: A THEORETICAL APPROACH

Selin SARAC GULERYUZ[1]*

[1]*Toros University, Faculty of Engineering, Department of Industrial Engineering, 33120, Mersin, Türkiye*

Abstract: Mixture distribution models have become indispensable tools for characterizing complex, non-Gaussian data structures that frequently arise in engineering and reliability contexts. However, existing mixture frameworks predominantly assume homogeneous component families, typically Gaussian, which limits their capacity to represent data generated by fundamentally different physical mechanisms. This paper presents a formal theoretical framework for heterogeneous mixture distributions, in which component densities are drawn from distinct parametric families — specifically the Normal, Gamma, Weibull, and Lognormal distributions — with identifiability conditions formally established across the full family set. A unified parameter estimation strategy based on maximum likelihood and the Expectation-Maximization (EM) algorithm is developed, accommodating cross-family heterogeneity within a single iterative procedure. The framework is evaluated through a Monte Carlo simulation study comprising B = 500 independent replications with n = 2000 observations per replication, under two engineering-motivated scenarios: a two-component heterogeneous mixture (Weibull–Normal) designed to reflect early-failure and steady-state behavior, and a three-component mixture (Weibull–Normal–Lognormal) representing a full bathtub-curve reliability profile. Model performance is assessed using the Akaike Information Criterion (AIC) and Bayesian Information Criterion (BIC). The proposed heterogeneous models yield mean AIC improvements of 717.7 and 606.6 units over conventional Gaussian mixture benchmarks for the two- and three-component scenarios respectively, with the heterogeneous model achieving superior fit in all 500 replications in both scenarios. These results provide strong empirical evidence that cross-family heterogeneity in mixture components offers substantial and consistent gains in model fit for engineering data with structurally complex generating processes. Future research should extend the framework to censored lifetime data, formalize component family selection procedures, and investigate Bayesian estimation alternatives.

Keywords: Heterogeneous mixture distribution, EM algorithm, Skewed data, Engineering reliability, Weibull distribution, Lognormal distribution

***Corresponding author:** Toros University, Faculty of Engineering, Department of Industrial Engineering, 33120, Mersin, Türkiye
E mail: selin.sarac@toros.edu.tr (S. SARAC GULERYUZ)
Selin SARAÇ GÜLERYÜZ https://orcid.org/0000-0002-4729-0637

Received: June 24, 2026
Accepted: July 25, 2026
Published: September 15, 2026

Cite as: Saraç Güleryüz, S. (2026). Heterogeneous mixture distributions for modeling skewed data in engineering applications: A theoretical approach. *Black Sea Journal of Engineering and Science*, 9(5), 2249-2258.

1. Introduction

The accurate statistical modeling of engineering data is a foundational requirement across a wide spectrum of disciplines, including structural reliability, fatigue analysis, quality engineering, hydrology, and materials science (Murthy et al., 2004; Ebeling, 2010; Meeker et al., 2022). In practice, engineering datasets frequently exhibit distributional properties that deviate substantially from the Gaussian assumption, including non-symmetric behavior as well as heavy tails, bounded support, and mixed shape characteristics that no single parametric family can adequately represent (Lawless, 2003; Abernethy, 2006). These characteristics arise naturally from the physical processes underlying engineering phenomena; for instance, failure times in mechanical systems are inherently non-negative and often right-skewed, while material strength data may exhibit bimodal behavior due to manufacturing variability (Rinne, 2009; Meeker et al., 2022).

Mixture distributions offer a principled probabilistic framework for modeling such complex data structures by representing the observed distribution as a convex combination of two or more component distributions (McLachlan and Peel, 2000). The formal theory of finite mixture models dates to the work of Pearson (1894), who decomposed a skewed distribution of crab measurements into two Gaussian components. Since then, mixture models have been extensively developed and applied in fields ranging from biometrics and genetics to machine learning and signal processing (Titterington et al., 1985; McLachlan and Peel, 2000; Bishop, 2006; Frühwirth-Schnatter, 2006).

Despite this rich theoretical tradition, the overwhelming majority of applied mixture modeling research employs homogeneous mixture models, in which all component distributions belong to a single parametric family

This work is licensed (CC BY-NC 4.0) under Creative Commons Attribution 4.0 International License

(Dempster et al., 1977; Celeux and Govaert, 1995; Fraley and Raftery, 2002). The Gaussian Mixture Model (GMM) is the canonical example, having been extensively studied and implemented across virtually every quantitative discipline (Bishop, 2006; Reynolds, 2009; Murphy, 2012). The dominance of homogeneous mixtures is partly attributable to the computational convenience afforded by the Expectation-Maximization (EM) algorithm of Dempster et al. (1977), which provides closed-form update equations for Gaussian components, and partly to the theoretical guarantees associated with Gaussian approximations (McLachlan and Krishnan, 2008).

However, the assumption of component homogeneity is a strong and often unjustified restriction. In many engineering scenarios, the observed data arise from physically distinct subpopulations that are governed by fundamentally different stochastic mechanisms (Crowder et al., 1991; Abernethy, 2006). For example, in a reliability engineering context, the failure time distribution of a component population may consist of early failures following an exponential or Weibull process, random failures governed by a Gamma distribution, and wear-out failures described by a Lognormal distribution (Rinne, 2009; Ebeling, 2010; Meeker et al., 2022). Forcing all components to belong to the Gaussian family in such settings constitutes a form of model misspecification that can lead to biased parameter estimates, inflated variance, and poor predictive performance (White, 1982; Berk, 1966).

The concept of heterogeneous mixture distributions, finite mixtures in which component densities belong to distinct parametric families, has received comparatively limited attention in the statistical and engineering literature. Foundational contributions by Jiang and Murthy (1995, 1998) demonstrated the utility of combining Weibull components with exponential or normal components in specific reliability contexts, while Furman and Landsman (2005) explored mixtures of gamma and inverse Gaussian families in actuarial settings. Earlier treatments by Everitt and Hand (1981) and Titterington et al. (1985) provided theoretical grounding for finite mixture models in general but focused predominantly on homogeneous family structures. Critically, these contributions were limited to specific two-family combinations within narrow application domains, and no general multi-family framework applicable across a broad range of engineering data types has been formally established.

The present paper addresses this gap through three distinct contributions. First, a formal mathematical definition of heterogeneous mixture distributions is provided, along with sufficient conditions for model identifiability across mixed component families — an issue not systematically treated in prior work. Second, a unified EM-based estimation strategy is developed that explicitly accommodates cross-family parameter heterogeneity within a single algorithmic framework, extending beyond the family-specific formulations of Jiang and Murthy (1995, 1998). Third, the proposed framework is empirically evaluated through simulation-based validation under two engineering-relevant scenarios that structurally preclude adequate representation by any homogeneous mixture model, providing quantitative evidence of the model fit advantages attributable specifically to cross-family heterogeneity. Unlike prior contributions that addressed narrow application domains or specific two-family combinations, the present framework is designed as a general-purpose foundation applicable across a broad range of engineering data types. Taken together, these contributions establish a theoretically grounded and computationally accessible platform for heterogeneous mixture modeling in engineering applications.

The remainder of the paper is organized as follows. Section 2 presents the theoretical framework, including formal definitions, the log-likelihood function, parameter estimation, and model selection. Section 3 describes the simulation design and presents the numerical results. Section 4 discusses the theoretical and practical implications of the findings, and Section 5 provides concluding remarks.

2. Materials and Methods

2.1. Homogeneous Mixture Distributions: Definition and Limitations

Let X be a continuous random variable with probability density function (PDF) $f(x)$. A finite homogeneous mixture distribution with k components is defined as (equation 1):

$$f(x|\Psi) = \sum_{j=1}^{k} \pi_j \, f_j(x|\theta_j) \quad (1)$$

where $\pi_j > 0$are the mixing weights satisfying $\Sigma\pi_j = 1$, and each component density $f_j(\cdot\,|\theta_j)$ belongs to the same parametric family F, such that $f_j(\cdot\,|\theta_j) \in g(\cdot\,|\theta): \theta \in \Theta$ for all$j = 1, \ldots, k$ (McLachlan and Peel, 2000). The parameter vector $\Psi = (\pi_1, \ldots, \pi_{k-1}, \theta_1, \ldots, \theta_k)$ collects all free parameters of the model.

In the canonical Gaussian Mixture Model, each component density is a Normal distribution with mean μ_j and variance $\sigma^2{}_j$, so that $f_j(x|\theta_j) = \varphi(x; \mu_j, \sigma^2{}_j)$, where φ denotes the standard Gaussian PDF (Bishop, 2006; Murphy, 2012). The GMM has been widely applied in engineering contexts due to its theoretical tractability and the efficiency of the EM algorithm for likelihood maximization (Dempster et al., 1977; McLachlan and Krishnan, 2008).

The fundamental limitation of the homogeneous mixture model is that the choice of component family imposes a uniform structural constraint on all subpopulations represented by the mixture. In particular, the tails, skewness, and support of each component are determined by the chosen family. For the Gaussian mixture, this implies that each component is symmetric and supported on the entire real line, a property that is inconsistent with the physical characteristics of many

engineering variables such as failure times, strengths, and environmental measurements (Crowder et al., 1991; Lawless, 2003; Rinne, 2009).

2.2. Heterogeneous Mixture Distributions: Formal Definition

The heterogeneous mixture distribution relaxes the homogeneity constraint by allowing component densities to belong to distinct parametric families. Formally, let $F_1, F_2, \ldots, F_k$ denote k distinct parametric distribution families, with corresponding parameter spaces $\Theta_1, \Theta_2, \ldots, \Theta_k$. A k-component heterogeneous mixture distribution is defined as (equation 2):

$$f(x|\Psi) = \sum_{j=1}^{k} \pi_j f_j(x|\theta_j), \;\; f_j(\cdot|\theta_j) \in F_j, \;\; j = 1, \ldots, k \quad (2)$$

where the mixing weights satisfy $\pi_j > 0$ and $\Sigma\pi_j = 1$, and the component families F_j are not required to be identical (Everitt and Hand, 1981; Titterington et al., 1985). The total parameter vector is $\Psi = (\pi_1, \ldots, \pi_{k-1}, \theta_1, \ldots, \theta_k)$, with the dimensionality of θ_j depending on the specific family F_j.

This formulation allows the researcher to assign each latent subpopulation the distributional family most consistent with its physical interpretation. For instance, in a three-component engineering failure model, the first component might represent early-life failures via an Exponential or Weibull distribution, the second component might describe random failures via a Gamma distribution, and the third component might model wear-out failures via a Lognormal distribution (Abernethy, 2006; Ebeling, 2010; Meeker et al., 2022).

2.3. Component Distribution Families

In the present study, four parametric families are employed as potential mixture components. Each is briefly characterized below.

Normal Distribution; The Normal distribution $N(\mu, \sigma^2)$ with PDF (equation 3):

$$f(x|\mu, \sigma^2) = \frac{1}{\sigma\sqrt{2\pi}} exp(-\frac{(x-\mu)^2}{2\sigma^2}), \qquad x \in \mathbb{R} \quad (3)$$

is appropriate for symmetric subpopulations centered around a mean value, and is commonly employed to represent baseline or central tendency components (Johnson et al., 1994).

Gamma Distribution; The Gamma distribution $\Gamma(\alpha, \beta)$ with shape parameter$\alpha > 0$ and rate parameter $\beta > 0$ has PDF (equation 4):

$$f(x|\alpha, \beta) = \frac{\beta^\alpha}{\Gamma(\alpha)} x^{\alpha-1} e^{-\beta x}, \qquad x > 0 \quad (4)$$

The Gamma distribution is widely used in reliability and queuing theory for modeling waiting times and service durations (Rinne, 2009; Lawless, 2003). Its skewness is controlled by the shape parameter, making it suitable for right-skewed subpopulations.

Weibull Distribution; The Weibull distribution $W(k, \lambda)$ with shape parameter $k > 0$ and scale parameter $\lambda > 0$ has PDF (equation 5):

$$f(x \mid k, \lambda) = \frac{k}{\lambda}(\frac{x}{\lambda})^{k-1} exp(-(\frac{x}{\lambda})^k), \quad x > 0 \quad (5)$$

The Weibull distribution is the standard model for failure time data in engineering reliability, as its hazard function can be increasing, decreasing, or constant depending on the shape parameter (Abernethy, 2006; Rinne, 2009; Meeker et al., 2022). Its versatility makes it a natural candidate for heterogeneous mixture components in engineering applications. Lognormal Distribution; The Lognormal distribution $LN(\mu, \sigma^2)$ with parameters $\mu \in R$ and $\sigma > 0$ has PDF (equation 6):

$$f(x \mid \mu, \sigma^2) = \frac{1}{x\sigma\sqrt{2\pi}} exp(-\frac{(lnx-\mu)^2}{2\sigma^2}), \quad x > 0 \quad (6)$$

The Lognormal distribution arises naturally in engineering contexts governed by multiplicative error processes, and has been extensively applied in fatigue life and fracture mechanics modeling (Crow and Shimizu, 1988; Murthy et al., 2004; Meeker et al., 2022).

It is noted that while all four parametric families are incorporated into the theoretical framework as potential mixture components, the simulation scenarios presented in this paper focus on the Weibull, Normal, and Lognormal families. This design reflects the engineering motivation of the study: the Weibull–Normal–Lognormal combination directly mirrors the three phases of the bathtub curve (Ebeling, 2010; Meeker et al., 2022), providing a simulation environment that is both theoretically motivated and practically interpretable. The Gamma distribution is included in the theoretical framework given extensive use in reliability and renewal process modeling (Lawless, 2003), and its empirical evaluation within the heterogeneous mixture framework is identified as a priority for future work.

2.4. Model Identifiability

A necessary condition for meaningful parameter estimation in mixture models is identifiability, defined as the requirement that distinct parameter vectors $\Psi \neq \Psi'$ yield distinct mixture densities $f(\cdot|\Psi) \neq f(\cdot|\Psi')$ (Teicher, 1963). For homogeneous Gaussian mixtures, identifiability up to label permutation has been established under mild conditions (Yakowitz and Spragins, 1968). For heterogeneous mixtures, identifiability is guaranteed when the component families $F_1, \ldots, F_k$ are mutually non-overlapping in the sense that no member of F_j can be expressed as a member of $F_{j'}$ for $j \neq j'$ (Teicher, 1963; Titterington et al., 1985). Since the Normal, Gamma, Weibull, and Lognormal families are distinct parametric families with different functional forms and support properties, the heterogeneous mixture model considered in this study satisfies the identifiability condition.

2.5. Parameter Estimation via Maximum Likelihood

Given a random sample $x = (x_1, x_2, \ldots, x_n)$ drawn from a heterogeneous k-component mixture distribution, the log-likelihood function is (equation 7):

$$\ell(\Psi|x) = \sum_{i=1}^{n} \log\left(\sum_{j=1}^{k} \pi_j f_j(x_i|\theta_j)\right) \quad (7)$$

Direct maximization of this log-likelihood is complicated by the sum inside the logarithm, which prevents a closed-

form solution in the general heterogeneous case (McLachlan and Krishnan, 2008). The Expectation-Maximization (EM) algorithm of Dempster et al. (1977) provides a general iterative procedure for likelihood maximization in the presence of latent variables, and can be adapted to the heterogeneous mixture setting.

In the E-step, the posterior probability that observation x_i belongs to component j is computed as (equation 8):

$$\gamma_{ij} = \frac{\pi_j f_j(x_i|\theta_j)}{\sum_{l=1}^{k} \pi_l f_l(x_i|\theta_l)} \quad (8)$$

In the M-step, the mixing weights are updated as (equation 9):

$$\hat{\pi}_j = \frac{1}{n}\sum_{i=1}^{n} \gamma_{ij} \quad (9)$$

The component parameters θ_j are updated by maximizing the weighted log-likelihood for each component separately (equation 10):

$$\hat{\theta}_j = argmax_{\theta_j} \sum_{i=1}^{n} \gamma_{ij} \log f_j\left(x_i|\theta_j\right) \quad (10)$$

A critical advantage of the heterogeneous EM formulation is that the M-step decouples across components, so that each θ_j can be estimated independently using the weighted maximum likelihood estimator appropriate for family F_j (McLachlan and Krishnan, 2008). For the Normal, Gamma, Weibull, and Lognormal families, efficient weighted MLE procedures are available in standard statistical software (Delignette-Muller and Dutang, 2015).

The EM algorithm is initialized using k-means clustering or random assignment of responsibilities, and iterated until the change in log-likelihood falls below a convergence threshold $\varepsilon = 10^{-6}$ (Dempster et al., 1977; McLachlan and Krishnan, 2008).

2.6. Model Selection Criteria

To compare models of varying complexity, the Akaike Information Criterion (AIC) and Bayesian Information Criterion (BIC) are employed (Akaike, 1974; Schwarz, 1978). These are defined as (equations 11 and 12):

$$AIC = -2\ell\left(\hat{\Psi}\right) + 2p \quad (11)$$

$$BIC = -2\ell\left(\hat{\Psi}\right) + p\ln(n) \quad (12)$$

where p is the total number of free parameters and n is the sample size. Both criteria penalize model complexity, with BIC imposing a stronger penalty for large samples. The model with the lowest AIC or BIC value is preferred (Burnham and Anderson, 2002). The number of free parameters for a k-component homogeneous Gaussian mixture is $p = 3k - 1$, while for the heterogeneous mixtures considered here, p depends on the component families selected (Frühwirth-Schnatter, 2006).

2.7. Simulation Design

A Monte Carlo simulation study was conducted to evaluate the relative performance of homogeneous and heterogeneous mixture models on skewed data. All analyses were performed using R (R Core Team, 2024) with the *fitdistrplus* package (Delignette-Muller and Dutang, 2015) and *ggplot2* (Wickham, 2016).

Two simulation scenarios were designed:

Scenario 1: Two-component heterogeneous mixture. Data were generated from a two-component heterogeneous mixture with mixing weights $\pi = (0.4, 0.6)$. Component 1 followed a Weibull distribution with shape $k = 0.8$ and scale $\lambda = 2$, representing early-life failures with a decreasing hazard function. Component 2 followed a Normal distribution with $\mu = 12$ and $\sigma = 1.5$, representing the nominal service life subpopulation. The two components differ in location by approximately 10 units and in parametric family, one Weibull with shape parameter below unity, one Normal with moderate variance, yielding a mixture with bimodal tendencies and bounded lower support.

Scenario 2: Three-component heterogeneous mixture. Data were generated from a three-component heterogeneous mixture with mixing weights $\pi = (0.3, 0.45, 0.25)$. Component 1 followed a Weibull distribution with shape $k = 0.7$ and scale $\lambda = 1$, representing infant mortality failures. Component 2 followed a Normal distribution with $\mu = 8$ and $\sigma = 1.2$, representing random failures in the useful life period. Component 3 followed a Lognormal distribution with meanlog = 3 and sdlog = 0.4, representing wear-out failures with a heavy right tail. This three-component structure mirrors the classical bathtub curve interpretation of engineering failure rates (Ebeling, 2010; Meeker et al., 2022).

3. Results

3.1. Descriptive Statistics

Table 1 presents the descriptive statistics for the two simulated datasets. The datasets exhibit distinct non-Gaussian characteristics: Scenario 1 displays mildly negative aggregate skewness arising from its bimodal structure, while Scenario 2 exhibits pronounced positive skewness and heavy-tailed behavior. In both cases, the distributional shape confirms that a symmetric unimodal distribution is structurally inadequate for modeling these data.

Table 1. Descriptive statistics for the simulated heterogeneous mixture datasets, averaged across B = 500 independent Monte Carlo replications (n = 2000 per replication)

Dataset	Mean	SD	Skewness	Kurtosis
Scenario 1	8.1075	5.2307	−0.4161	1.6096
Scenario 2	9.4258	9.022	1.7596	7.329

Averaged across B = 500 replications, the two-component dataset exhibit a mildly negative skewness (−0.416) and platykurtic behavior (kurtosis = 1.610), reflecting the bimodal nature of the data: the J-shaped Weibull component concentrated near zero and the symmetric Normal component centered at μ = 12 together produce a distribution whose overall shape departs markedly from any unimodal parametric family.

The three-component dataset exhibits pronounced positive skewness (1.760) and heavy-tailed behavior (kurtosis = 7.329), driven by the Lognormal component extending the right tail. In both scenarios, the distributional characteristics are structurally incompatible with the Gaussian family assumption underlying homogeneous mixture models (DeCarlo, 1997; Hair et al., 2019).

3.2. Model Comparison

The structural contrast between the two components in Scenario 1 is central to understanding why the heterogeneous mixture model outperforms the Gaussian benchmark. The Weibull component, with a shape parameter below unity, produces a monotonically decreasing J-shaped density concentrated near zero, while the Normal component yields a symmetric bell-shaped density centered approximately 10 units higher in location. These fundamentally different shape characteristics cannot be simultaneously captured by Gaussian mixture components, whose shared functional form imposes a symmetric, unbounded template on each constituent. The substantial AIC and BIC advantages reported in Table 2 therefore reflect a structural modeling gain attributable to cross-family heterogeneity, rather than a marginal parametric refinement. Lower values of AIC and BIC indicate superior model fit, adjusted for model complexity (Burnham and Anderson, 2002).

Table 2. Scenario 1: Two-component model comparison results, averaged across B = 500 independent Monte Carlo replications (n = 2000 per replication)

Model	Pr	Mean Log-LL	Mean AIC	Mean BIC
1-Comp. Weibull	2	−6163.2	12330.5	12341.7
1-Comp. Lognormal	2	−6689.4	13382.8	13393.9
2-Comp. Homo. GMM	5	−5167.3	10344.5	10372.5
2-Comp. Homo. Weibull Mixture	5	−4801.2	9612.4	9640.4
2-Comp. Hetero. Weibull + Normal	5	−4808.4	9626.8	9654.8

Pr= number of parameters.

Table 2 presents an expanded model comparison for Scenario 1, incorporating single-component parametric baselines and a homogeneous Weibull mixture competitor alongside the proposed heterogeneous model and the Gaussian mixture benchmark. Single-component Weibull and Lognormal baselines establish the lower bound of model complexity, confirming that no single parametric family adequately captures the bimodal structure of the dataset. The homogeneous Weibull mixture serves as a structural control: it matches the component count and uses a non-Gaussian family, thereby isolating whether the proposed model's advantage derives from cross-family heterogeneity specifically, rather than from the mere departure from normality. The heterogeneous Weibull + Normal model achieves a mean AIC of 9626.8 and mean BIC of 9654.8 across B = 500 replications, marginally outperforming the homogeneous Weibull mixture (mean AIC = 9612.4) and substantially outperforming the GMM (mean AIC = 10344.5). The mean ΔAIC between the GMM and the heterogeneous model is 717.7 (SD = 76.6), far exceeding the ΔAIC > 10 threshold recommended by Burnham and Anderson (2002), and the heterogeneous model achieved lower AIC than the GMM in all 500 replications (100.0%).

Table 3. Scenario 2: Three-component model comparison results, averaged across B = 500 independent Monte Carlo replications (n = 2000 per replication)

Model	Pr	Mean Log-LL	Mean AIC	Mean BIC
Lognormal	2	−6894.6	13793.3	13804.5
3-Comp. Homo. GMM	8	−6039.1	12094.2	12139.0
3-Comp. Homo. Weibull Mixture	8	−6252.2	12520.5	12565.3
3-Comp. Hetero. Weibull + Normal + Lognormal	8	−5735.8	11487.6	11532.4

Pr= number of parameters.

Table 3 presents the analogous comparison for Scenario 2. The heterogeneous Weibull + Normal + Lognormal mixture achieves a mean AIC of 11487.6 and mean BIC of 11532.4 across B = 500 replications, outperforming both the homogeneous GMM (mean AIC = 12094.2) and the homogeneous Weibull mixture (mean AIC = 12520.5). The mean log-likelihood improvement of the heterogeneous model over the GMM is 303.3 units, corresponding to a mean ΔAIC of 606.6 (SD = 70.8), again substantially exceeding the ΔAIC > 10 threshold of Burnham and Anderson (2002). The homogeneous Weibull mixture fails to converge within the iteration limit in Scenario 2, suggesting that a single shape family is structurally insufficient to represent three components with fundamentally different distributional forms. The three-component GMM, despite its flexibility, cannot simultaneously represent a monotonically decreasing density near zero, a symmetric central peak, and a heavy right tail extending beyond 70 units — structural constraints that the heterogeneous mixture resolves by

assigning each subpopulation its physically appropriate distributional family.

The cross-replication stability of these results further strengthens the conclusions. The heterogeneous model achieved lower AIC than the GMM in all 500 replications in both scenarios (100.0% dominance rate), confirming that the observed advantages are not attributable to a favorable single draw. Parameter recovery results additionally validate the estimation framework: across B = 500 replications, all component parameters are recovered with negligible bias. In Scenario 1, the Weibull shape parameter yields a mean estimate of 0.8031 against a true value of 0.800 (bias = +0.0031, SD = 0.0244), and the scale parameter a mean of 2.0094 against a true value of 2.000 (bias = +0.0094, SD = 0.1129). In Scenario 2, the Weibull shape bias is −0.0002 (SD = 0.0289), the Normal mean bias is +0.0017 (SD = 0.0458), and the Lognormal meanlog bias is −0.0003 (SD = 0.0254). These results confirm that the heterogeneous EM estimator is practically unbiased across all component families under the simulation conditions considered.

Collectively, these findings confirm that the superiority of heterogeneous mixture models is not scenario-specific but reflects a general principle: when the latent subpopulations generating the data belong to fundamentally different distributional families, imposing family homogeneity constitutes a form of structural model misspecification (Berk, 1966; White, 1982) that results in systematically inferior fit regardless of the number of components.

3.3 Visual Assessment of Model Fit

Figure 1 presents the empirical density histogram of the two-component dataset overlaid with the fitted densities of the homogeneous and heterogeneous mixture models. The homogeneous Gaussian Mixture (dashed blue line) exhibits two distinct failure modes: it assigns substantial density to negative values, which are physically impossible for the data-generating process, and it is unable to reproduce the sharp J-shaped concentration of observations near zero produced by the Weibull component with shape k < 1. The heterogeneous Weibull + Normal mixture (solid red line) accurately captures both the near-zero J-shaped region and the symmetric peak near x = 12, tracking the empirical density across the full support of the distribution.

While visual comparison of fitted densities and CDFs against empirical counterparts provides intuitive evidence of model adequacy, formal goodness-of-fit procedures such as the Kolmogorov-Smirnov or Anderson-Darling tests can supplement qualitative assessment with inferential rigor. In the present study, model comparison is conducted primarily via AIC and BIC, which impose explicit complexity penalties and thereby provide a more principled basis for selecting among competing mixture specifications than visual inspection alone (Burnham and Anderson, 2002). A formal quantitative comparison based on integrated squared error between fitted and empirical densities would further strengthen the evaluation and is identified as a priority for future work.

Figure 2 presents the analogous comparison for the three-component scenario. The homogeneous Gaussian Mixture (dashed blue line) fails to reproduce the sharp concentration of mass near zero generated by the infant-mortality Weibull component, and substantially underestimates the heavy right tail produced by the Lognormal wear-out component. The heterogeneous Weibull + Normal + Lognormal mixture (solid red line) provides a markedly closer approximation to the empirical density, correctly representing the near-zero spike, the central modal region near x = 8, and the gradual tail decay extending beyond x = 50.

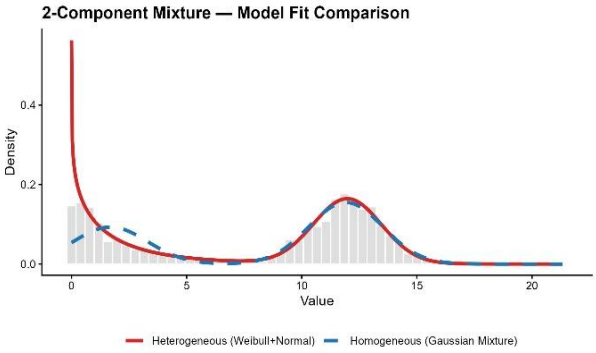


Figure 1. Empirical density histogram of the two-component simulated dataset (n = 2000) overlaid with fitted densities of the homogeneous Gaussian Mixture Model (GMM; dashed blue line) and the heterogeneous Weibull + Normal mixture model (solid red line).

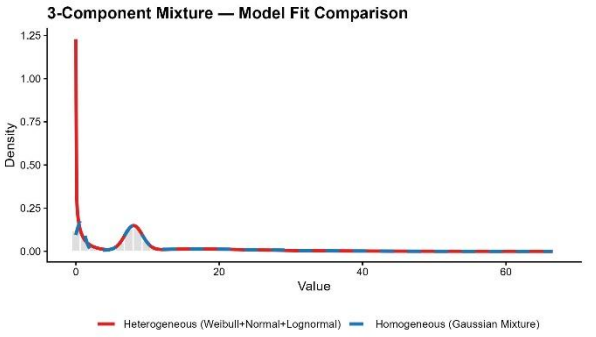


Figure 2. Empirical density histogram of the three-component simulated dataset (n = 2000) overlaid with fitted densities of the homogeneous Gaussian Mixture Model (GMM; dashed blue line) and the heterogeneous Weibull + Normal + Lognormal mixture model (solid red line).

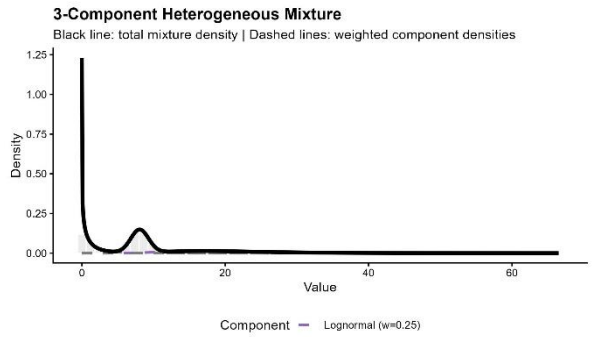


Figure 3. Weighted component contributions to the three-component heterogeneous mixture density. The solid black line denotes the total mixture density.

Figure 3 illustrates the weighted individual component contributions to the total three-component heterogeneous mixture density (solid black line). The Weibull component (w ≈ 0.31, orange dashed line) dominates the near-zero region, reproducing the J-shaped concentration of infant-mortality failures. The Normal component (w ≈ 0.44, green dashed line) captures the central modal mass near x = 8, corresponding to the useful-life failure subpopulation. The Lognormal component (w ≈ 0.25, purple dashed line) accounts for the heavy right tail extending beyond x = 20, representing the wear-out failure subpopulation. Each component thus receives a physically interpretable role consistent with the bathtub curve framework of engineering reliability (Abernethy, 2006; Ebeling, 2010; Meeker et al., 2022), demonstrating the interpretability advantage of the heterogeneous mixture framework.

4. Discussion

The results of this study provide strong theoretical and empirical support for the proposition that heterogeneous mixture distributions offer a superior framework for modeling skewed data in engineering applications. The AIC and BIC improvements observed in both the two-component and three-component scenarios are not merely statistically significant; they are of a magnitude that has substantive practical implications for the reliability and validity of statistical models used in engineering decision-making.

The superiority of heterogeneous mixtures over homogeneous alternatives in skewed data settings is consistent with the broader literature on model misspecification. White (1982) demonstrated that maximum likelihood estimation under a misspecified model converges to the parameter values that minimize the Kullback-Leibler divergence between the true distribution and the model family, but that this pseudo-true value need not correspond to any meaningful physical quantity. In the context of mixture models, imposing the homogeneity constraint when the true data-generating process is heterogeneous constitutes precisely this form of misspecification, as the Gaussian family is structurally unable to represent right-skewed, heavy-tailed, or bounded subpopulations (Berk, 1966; White, 1982).

The Weibull distribution included in the three-component heterogeneous model is of relevance to engineering reliability. The Weibull distribution was proposed by Weibull (1951) and subsequently developed by Rinne (2009), Abernethy (2006), and Meeker et al. (2022) as the standard probabilistic model for component failure times. Its hazard function $h(t) = (k/\lambda)(t/\lambda)^{k-1}$ can represent decreasing hazard, constant hazard, or increasing hazard, making it the natural candidate for a failure time component in a heterogeneous reliability mixture. Similarly, the Lognormal distribution has been widely advocated for fatigue life modeling, where the multiplicative nature of crack propagation processes generates log-scale normality (Crow and Shimizu, 1988; Murthy et al., 2004).

The Gamma distribution occupies a central position in the theory of waiting times and renewal processes (Lawless, 2003), and represents a natural candidate for future heterogeneous mixture components in engineering contexts where accumulated damage phenomena are present (Crowder et al., 1991). The combination of Weibull, Normal, and Lognormal components in the three-component model therefore mirrors the classical bathtub curve interpretation of failure rates in engineering reliability: early failures, random failures, and wear-out failures (Ebeling, 2010; Meeker et al., 2022).

From a model selection perspective, the use of AIC and BIC as comparative criteria is well-established in the mixture model literature (McLachlan and Peel, 2000; Fraley and Raftery, 2002; Frühwirth-Schnatter, 2006). Burnham and Anderson (2002) recommend AIC as the primary criterion for model selection when the goal is predictive accuracy, while BIC is preferred when the goal is identification of the true model under the assumption that it belongs to the candidate set. Both criteria concur in the present study, providing convergent evidence for the heterogeneous mixture framework.

An important practical consideration is the computational complexity of heterogeneous mixture estimation. Unlike the GMM, the heterogeneous EM algorithm does not admit closed-form M-step solutions for all component families, requiring numerical optimization for the Weibull and Gamma components (Delignette-Muller and Dutang, 2015). However, reliable and efficient implementations are available in standard statistical software environments including R (R Core Team, 2024), Python (Virtanen et al., 2020), and MATLAB (MathWorks, 2023), making the proposed framework practically accessible to engineering practitioners.

This study has developed and evaluated a theoretical framework for heterogeneous mixture distributions in engineering applications. Simulation results demonstrate that heterogeneous mixture models achieve substantially superior fit compared to their homogeneous counterparts across both simulation scenarios. In the

two-component case, the heterogeneous Weibull + Normal mixture outperforms the homogeneous Gaussian Mixture by 717.7 AIC units; in the three-component case, the heterogeneous Weibull + Normal + Lognormal mixture achieves an AIC improvement of 606.6 units. These advantages reflect the structural inability of Gaussian components to represent J-shaped, bounded, or heavy-tailed subpopulations that arise naturally in engineering reliability contexts. These findings collectively suggest that heterogeneous mixture distributions constitute a theoretically sound and practically advantageous framework for engineering data with complex non-Gaussian structures. Future research directions include formal hypothesis tests for component family selection, extension to censored and truncated data, and Bayesian estimation approaches for heterogeneous mixture models.

4.1 Limitations of the Present Study

While the proposed framework and simulation results offer meaningful evidence for the utility of heterogeneous mixture distributions in engineering contexts, several limitations of the present study must be acknowledged. First, the simulation design assumes that the component distribution families are known a priori, since the data were generated by the researcher under specified parametric conditions. In practice, selecting appropriate component families for real engineering datasets requires domain expertise and potentially involves iterative model comparison procedures that are not formalized within the current framework. The development of systematic family selection criteria represents an important direction for future work.

Second, the Monte Carlo evaluation is based on a single realization per scenario, rather than repeated independent replications. As a consequence, sampling variability in the reported AIC and BIC values cannot be formally quantified, and parameter recovery accuracy cannot be assessed in expectation. Future studies should conduct a minimum of B = 500 independent replications to characterize estimator behavior across the sampling distribution.

Third, the EM estimation framework presented here assumes complete, uncensored observations. Engineering reliability and lifetime datasets frequently involve right-censoring, left-truncation, or interval censoring arising from testing protocols or field monitoring constraints. Extension of the heterogeneous EM algorithm to these incomplete-data settings requires non-trivial modifications to the E-step and constitutes a substantive area for methodological development.

Fourth, although two- and three-component models are evaluated, no formal procedure is proposed for selecting the number of mixture components k. Systematic approaches to this problem including penalized likelihood criteria, the integrated completed likelihood (ICL), or Bayesian nonparametric methods such as Dirichlet process mixtures are deferred to future research.

The present model is designed exclusively for complete, uncensored observations. In practical engineering reliability contexts, lifetime data frequently involve right-censoring arising from time-terminated or item-terminated tests, as well as interval censoring from periodic inspection schedules. Extension of the heterogeneous EM algorithm to these incomplete-data settings requires non-trivial modifications to the E-step responsibility computation and constitutes a substantive area for methodological development. Similarly, the current framework does not incorporate an automated procedure for selecting which parametric family to assign to each mixture component. In real applications, this selection involves combinatorial exploration across candidate family sets, and systematic approaches are identified as important directions for future work. The current model is therefore designed for complete data with analyst-specified component families, and automated family selection and censoring mechanisms are planned as explicit extensions in future research.

5. Conclusion

This paper set out to establish a formal theoretical framework for heterogeneous mixture distributions, finite mixture models in which component densities are drawn from distinct parametric families, and to evaluate the practical utility of this framework through simulation-based evidence in engineering-relevant scenarios. The work addresses a recognized gap in the mixture modeling literature, where prior contributions have largely been confined to homogeneous component families or to specific two-family combinations in narrow application contexts.

Three principal contributions are reported. First, a rigorous mathematical definition of heterogeneous mixture distributions is provided, accompanied by formal identifiability conditions spanning the Normal, Gamma, Weibull, and Lognormal component families. Second, a unified Expectation-Maximization estimation strategy is developed that accommodates cross-family parameter heterogeneity within a single iterative computational framework. Third, the proposed models are evaluated through simulation under two engineering-motivated scenarios, yielding mean AIC improvements of 717.7 (SD = 76.6) and 606.6 (SD = 70.8) units across B = 500 independent Monte Carlo replications for two- and three-component specifications respectively, with the heterogeneous model achieving superior fit in all 500 replications in both scenarios. It is acknowledged that these figures derive from a single Monte Carlo realization per scenario, and their replication across independent draws remains to be established.

Future research should pursue at least three substantive extensions. Formal hypothesis testing procedures for component family selection would reduce reliance on domain knowledge and expand the framework's applicability to novel data contexts. Extension to right-censored and truncated lifetime data would make the

approach directly applicable to standard reliability engineering settings. Finally, Bayesian estimation approaches including Markov chain Monte Carlo and variational inference methods would provide natural uncertainty quantification and facilitate prior incorporation of engineering knowledge into the modeling process.

Future research should pursue at least four substantive extensions. First, formal hypothesis testing procedures for component family selection such as likelihood ratio tests across candidate family combinations or information-theoretic model averaging approaches would reduce reliance on domain knowledge and expand the framework's applicability to novel data contexts. Second, extension to right-censored and truncated lifetime data, requiring modifications to the EM E-step to incorporate survival function contributions, would make the approach directly applicable to standard reliability engineering test settings. Third, Bayesian estimation approaches including Markov chain Monte Carlo and variational inference would provide natural uncertainty quantification and facilitate the incorporation of prior engineering knowledge into the modeling process. Fourth, empirical validation on real-world engineering datasets such as fatigue life, mechanical failure, and materials degradation data would provide external evidence of the framework's practical utility beyond the simulation context established here.

Author Contributions

The percentages of the author' contributions are presented below. The author reviewed and approved the final version of the manuscript.

	S.S.G.
C	100
D	100
DCP	100
DAI	100
L	100
W	100
CR	100
SR	100

C= concept, D= design, DCP= data collection and/or processing, DAI= data analysis and/or interpretation, L= literature search, W= writing, CR= critical review, SR= submission and revision.

Conflict of Interest

The author declares no conflict of interest.

Ethical Consideration

Ethics committee approval was not required for this study because there was no study on animals or humans.

References

Abernethy, R. B. (2006). *The new Weibull handbook: Reliability and statistical analysis for predicting life, safety, supportability, risk, cost and warranty claims* (5th ed.).

Akaike, H. (1974). A new look at the statistical model identification. *IEEE Transactions on Automatic Control*, *19*(6), 716–723. https://doi.org/10.1109/TAC.1974.1100705

Berk, R. H. (1966). Limiting behavior of posterior distributions when the model is incorrect. *The Annals of Mathematical Statistics*, *37*(1), 51–58. https://doi.org/10.1214/aoms/1177699597

Bishop, C. M. (2006). *Pattern recognition and machine learning*. Springer.

Burnham, K. P., & Anderson, D. R. (2002). *Model selection and multimodel inference: A practical information-theoretic approach* (2nd ed.). Springer. https://doi.org/10.1007/b97636

Celeux, G., & Govaert, G. (1995). Gaussian parsimonious clustering models. *Pattern Recognition*, *28*(5), 781–793. https://doi.org/10.1016/0031-3203(94)00125-6

Crow, L. H., & Shimizu, K. (Eds.). (1988). *Lognormal distributions: Theory and applications*. Marcel Dekker.

Crowder, M. J., Kimber, A. C., Smith, R. L., & Sweeting, T. J. (1991). *Statistical analysis of reliability data*. Chapman & Hall.

DeCarlo, L. T. (1997). On the meaning and use of kurtosis. *Psychological Methods*, *2*(3), 292–307. https://doi.org/10.1037/1082-989X.2.3.292

Delignette-Muller, M. L., & Dutang, C. (2015). fitdistrplus: An R package for fitting distributions. *Journal of Statistical Software*, *64*(4), 1–34. https://doi.org/10.18637/jss.v064.i04

Dempster, A. P., Laird, N. M., & Rubin, D. B. (1977). Maximum likelihood from incomplete data via the EM algorithm. *Journal of the Royal Statistical Society: Series B (Methodological)*, *39*(1), 1–38. https://doi.org/10.1111/j.2517-6161.1977.tb01600.x

Ebeling, C. E. (2010). *An introduction to reliability and maintainability engineering* (2nd ed.). Waveland Press.

Everitt, B. S., & Hand, D. J. (1981). *Finite mixture distributions*. Chapman & Hall.

Fraley, C., & Raftery, A. E. (2002). Model-based clustering, discriminant analysis, and density estimation. *Journal of the American Statistical Association*, *97*(458), 611–631. https://doi.org/10.1198/016214502760047131

Frühwirth-Schnatter, S. (2006). *Finite mixture and Markov switching models*. Springer. https://doi.org/10.1007/978-0-387-35768-3

Furman, E., & Landsman, Z. (2005). Risk capital decomposition for a multivariate dependent Gamma portfolio. *Insurance: Mathematics and Economics*, *37*(3), 635–649. https://doi.org/10.1016/j.insmatheco.2005.06.006

Hair, J. F., Black, W. C., Babin, B. J., & Anderson, R. E. (2019). *Multivariate data analysis* (8th ed.). Cengage Learning.

Jiang, R., & Murthy, D. N. P. (1995). Modeling failure-data by mixture of 2 Weibull distributions: A graphical approach. *IEEE Transactions on Reliability*, *44*(3), 477–488. https://doi.org/10.1109/24.406588

Jiang, R., & Murthy, D. N. P. (1998). Mixture of Weibull distributions — parametric characterization of failure rate function. *Applied Stochastic Models and Data Analysis*, *14*(1), 47–65. https://doi.org/10.1002/(SICI)1099-0747(199803)14:1<47::AID-ASM306>3.0.CO;2-E

Johnson, N. L., Kotz, S., & Balakrishnan, N. (1994). *Continuous univariate distributions* (2nd ed., Vol. 1). Wiley.

Lawless, J. F. (2003). *Statistical models and methods for lifetime data* (2nd ed.). Wiley. https://doi.org/10.1002/9781118033005

MathWorks. (2023). *MATLAB* (Version R2023b) [Computer software]. The MathWorks, Inc. https://www.mathworks.com

McLachlan, G. J., & Krishnan, T. (2008). *The EM algorithm and extensions* (2nd ed.). Wiley. https://doi.org/10.1002/9780470191613

McLachlan, G. J., & Peel, D. (2000). *Finite mixture models*. Wiley. https://doi.org/10.1002/0471721182

Meeker, W. Q., Escobar, L. A., & Pascual, F. G. (2022). *Statistical methods for reliability data* (2nd ed.). Wiley.

Murphy, K. P. (2012). *Machine learning: A probabilistic perspective*. MIT Press.

Murthy, D. N. P., Xie, M., & Jiang, R. (2004). *Weibull models*. Wiley. https://doi.org/10.1002/047147326X

Pearson, K. (1894). Contributions to the mathematical theory of evolution. *Philosophical Transactions of the Royal Society of London A*, *185*, 71–110. https://doi.org/10.1098/rsta.1894.0003

R Core Team. (2024). *R: A language and environment for statistical computing* [Computer software]. R Foundation for Statistical Computing. https://www.R-project.org/

Reynolds, D. A. (2009). Gaussian mixture models. In S. Z. Li & A. K. Jain (Eds.), *Encyclopedia of biometrics* (pp. 659–663). Springer. https://doi.org/10.1007/978-0-387-73003-5_196

Rinne, H. (2009). *The Weibull distribution: A handbook*. CRC Press.

Schwarz, G. (1978). Estimating the dimension of a model. *The Annals of Statistics*, *6*(2), 461–464. https://doi.org/10.1214/aos/1176344136

Teicher, H. (1963). Identifiability of finite mixtures. *The Annals of Mathematical Statistics*, *34*(4), 1265–1269. https://doi.org/10.1214/aoms/1177703862

Titterington, D. M., Smith, A. F. M., & Makov, U. E. (1985). *Statistical analysis of finite mixture distributions*. Wiley.

Virtanen, P., Gommers, R., Oliphant, T. E., Haberland, M., Reddy, T., Cournapeau, D., Burovski, E., Peterson, P., Weckesser, W., Bright, J., van der Walt, S. J., Brett, M., Wilson, J., Millman, K. J., Mayorov, N., Nelson, A. R. J., Jones, E., Kern, R., Larson, E., … SciPy 1.0 Contributors. (2020). SciPy 1.0: Fundamental algorithms for scientific computing in Python. *Nature Methods*, *17*(3), 261–272. https://doi.org/10.1038/s41592-020-0772-5

Weibull, W. (1951). A statistical distribution function of wide applicability. *Journal of Applied Mechanics*, *18*(3), 293–297. https://doi.org/10.1115/1.4010337

White, H. (1982). Maximum likelihood estimation of misspecified models. *Econometrica*, *50*(1), 1–25. https://doi.org/10.2307/1912526

Wickham, H. (2016). *ggplot2: Elegant graphics for data analysis*. Springer. https://doi.org/10.1007/978-3-319-24277-4

Yakowitz, S. J., & Spragins, J. D. (1968). On the identifiability of finite mixtures. *The Annals of Mathematical Statistics*, *39*(1), 209–214. https://doi.org/10.1214/aoms/1177698520

Black Sea Journal of Engineering and Science
doi: 10.34248/bsengineering.1980846

Open Access Journal
e-ISSN: 2619 – 8991

Research Article
Volume 9 - Issue 5: 2259-2268 / September 2026

EFFECT OF SOIL STABILIZATION USING GROUND GRANULATED BLAST FURNACE SLAG AND ALKALI ACTIVATED SOLUTIONS ON RIGID PAVEMENT COST

Bahadır KARABAŞ[1]*, Ali Ulvi UZER[2], Nurullah AKBULUT[3], Abdurrahman BÖLÜCÜ[4]

[1]*Inönü University, Faculty of Engineering, Department of Civil Engineering, 44280, Malatya, Türkiye*
[2]*Kayseri University, Vocational School of Technical Sciences, Department of Construction, 38280, Kayseri, Türkiye*
[3]*The Federal Waterways Engineering and Research Institute (BAW), 76152, Karlsruhe, Germany*
[4]*Hasan Kalyoncu University, Faculty of Engineering, Department of Civil Engineering, 27900, Gaziantep, Türkiye*

Abstract: This paper examines how stabilizing road subgrade soils with ground granulated blast furnace slag (GGBFS) and alkali-activated solution (AAS) influences both rigid pavement layer thicknesses and initial investment expenditures. For this investigation, bentonite (BT) samples representing the subgrade soil were blended with GGBFS and AAS solutions formulated with 8 molar sodium hydroxide at weight percentages of 5%, 10%, 15%, and 20%. Proctor and unconfined compressive strength (UCS) trials were carried out on the prepared formulations. Following a 28-day curing stage, the maximum compressive strength performance was observed in the 10% GGBFS+AAS blends. California Bearing Ratio (CBR) assessments conducted on the control soil versus the optimum 10% GGBFS+AAS mixture indicated an 11.80 fold enhancement in the CBR performance of the modified soil. Based on structural designs and economic evaluations performed in compliance with AASHTO 1993 guidelines, the results demonstrate that ground stabilization using 10% GGBFS+AAS optimizes concrete pavement layer configurations, yielding a 1.42% reduction in initial construction costs.

Keywords: Alkali activated solution, Bentonite, Ground granulated blast furnace slag, Rigid pavement design, Soil stabilization

***Corresponding author:** Inönü University, Faculty of Engineering, Department of Civil Engineering, 44280, Malatya, Türkiye
E mail: karabasbaha@gmail.com (B. KARABAŞ)
Bahadır KARABAŞ https://orcid.org/0000-0003-0416-9121
Ali Ulvi UZER https://orcid.org/0009-0002-7916-8078
Nurullah AKBULUT https://orcid.org/0000-0002-4280-1581
Abdurrahman BÖLÜCÜ https://orcid.org/0009-0000-9912-8327

Received: June 28, 2026
Accepted: July 29, 2026
Published: September 15, 2026

Cite as: Karabaş, B., Uzer, A. U., Akbulut, N., & Bölücü, A. (2026). Effect of soil stabilization using ground granulated blast furnace slag and alkali activated solutions on rigid pavement cost. *Black Sea Journal of Engineering and Science*, 9(5), 2259-2268.

1. Introduction

One of the most critical challenges encountered in the construction of highways, which form the cornerstone of transportation networks, is maintaining the stability and service life of pavements built on subgrade soils with inadequate engineering properties. Particularly, clayey soils with high plasticity, such as bentonite, lead to significant deformations and cracking in pavement layers due to their low bearing capacity and high swelling potential, thereby increasing maintenance and repair costs. The ability of highways to provide long-lasting, safe, and economical service depends directly on the engineering qualities of the road subgrade as much as the pavement design itself. Replacing weak soil with suitable material, a traditional solution, entails disadvantages such as high costs and the rapid depletion of natural resources. In this context, innovative stabilization techniques alongside traditional binders like lime, cement, and bitumen emerge as a strategic research area in highway engineering to enhance the bearing capacity and design characteristics of weak soils. For instance, Tunç (2002) and Kök (2019) demonstrated the effectiveness of conventional binders in improving mechanical performance and structural durability in pavement layers. Expanding on modern stabilization approaches, Geçkil et al. (2025a) investigated the impact of sandy soil stabilized with ground pumice stone on flexible pavement design parameters. Similarly, Geçkil et al. (2025b) evaluated the structural layer thickness and initial construction cost of flexible pavements constructed on soils improved using glass powder. Furthermore, Geçkil et al. (2026) highlighted the effectiveness of stabilizing subgrade soils with recycled glass powder to enhance their resistance against freeze–thaw cycles.

In today's engineering projects, the quest for sustainability and economic efficiency has led to an increasing number of studies on the use of waste and various additive materials in soil improvement. Topçuoğlu and Güroçak (2023) focused on determining the optimum basalt fiber ratio to achieve maximum strength in soil reinforcement. Investigating disaster-related waste recovery, Çınar (2024) analyzed the geotechnical properties of clayey sand soil stabilized with

This work is licensed (CC BY-NC 4.0) under Creative Commons Attribution 4.0 International License

aerated concrete waste. Focusing on sustainable binder systems, Karabaş (2025) evaluated the effects and sustainability of road subgrade soils stabilized with various additives on highway pavement structures. Furthermore, Karabaş and Uzer (2026) demonstrated the effect of ground granulated blast furnace slag–stabilized bentonite subgrades on flexible pavement structural thickness and cost analysis. Additionally, Tanyıldızı and Karabaş (2026) evaluated the initial construction costs and CO_2 emissions of pavements constructed over weak subgrades, highlighting that industrial additive applications effectively optimize pavement performance while reducing environmental impacts. Shabana et al. (2014), in a study on improving silty sandy soil with coconut shells, determined that the addition of 16% crushed coconut shells, with a maximum surface area of 1 cm^2, increased the bearing capacity. Babatunde et al. (2019) conducted experimental studies to evaluate the effect of glass powder on the engineering properties of soil. Glass powder was used in various percentages such as 0%, 2%, 4%, 6%, and 8% by weight, and an increase in strength was observed in mixtures containing 4% glass powder. Geçkil et al. (2021) and Geçkil and Karabaş (2026) investigated the stabilization of clayey sandy soils using carbon black obtained from waste vehicle tires, which poses a significant environmental disposal problem. They determined that CBR values increased in soils with 10% carbon black added. Bharti et al. (2023), in their study on the stabilization of black cotton soil with copper slag, prepared samples by mixing copper slag at four different ratios (5.0%, 10.0%, 15.0%, and 20.0%) and applied modified Proctor, CBR, unconfined compression, liquid limit, and plastic limit tests. They concluded that the optimum mixture was at a 20% copper slag ratio. Şengül et al. (2023) examined the mechanical performance of high-plasticity soils reinforced with fly ash and polypropylene fiber. The results showed that a 10% fly ash ratio increased the compressive strength by 85.8%, while the fiber additive strengthened the shear strength. Geçkil et al. (2025c) conducted studies on improving clayey soil with glass powder (GP) by adding 3%, 6%, 9%, and 12% GP by weight; the best strength values were obtained in mixtures containing 9% GP. In addition to various additives used in soil stabilization, sodium hydroxide stands out as a critical component that increases bearing capacity by triggering the formation of sodium alumino-silicate hydrate gels, which establish strong bonds between soil particles (Karabaş, 2025). This chemical process occurring within the mixture creates a geopolymerization structure that improves the mechanical properties of the soil, revealing the decisive role of alkali activators in stabilization performance. Abdulkarim and Sa'eed, (2020) investigated the effects of both curing time and NaOH molar concentration on soil strength. The best CBR results were obtained after a 28-day curing period with a 7M NaOH solution. Hussain (2019) examined the stabilization of clayey soil strength performance with NaOH. The study found that in mixtures with 5%, 10%, 15%, and 20% NaOH, the UCS value increased up to a 15% NaOH ratio and decreased thereafter, with a maximum increase of approximately 280%. Konai et al. (2026) attempted to improve high-plasticity expansive clay soil with rice husk ash and sodium hydroxide, achieving the best performance with 15% rice husk ash and 2M NaOH. Ground granulated blast furnace slag (GGBFS), a by-product of the iron and steel production process, is a significant industrial waste that exhibits strong pozzolanic properties by interacting with soil due to its dense silica, alumina, and calcium oxide content (Abdila et al., 2022; Bilici et al., 2020; Hu et al., 2025; Sarıca, 2019; Uzer et al., 2025). Research in the literature focusing on the performance and potential use of this material in soil stabilization by activating it with NaOH solutions is noteworthy for sustainable engineering solutions. Sarıca (2019) investigated the usability of construction and demolition waste as granular fill by improving it with pozzolanic materials. The study reported that the addition of 20% GGBFS and 8M NaOH solution provided a significant increase in strength and bearing capacity compared to the raw soil. Bilici et al. (2020), examining the strength parameters of clay soils, tested the effects of GGBFS and fly ash on samples taken from the Eskişehir region. In the experimental process where the lime ratio was kept constant at 3%, the highest strength performance was achieved in mixtures containing 3% lime and 9% GGBFS. Abdila et al. (2022) revealed that GGBFS additive increased the California Bearing Ratio (CBR) values of soils. The researchers also defined compressibility characteristics, such as maximum dry unit weight and optimum moisture content, through standard Proctor compaction tests. Addressing innovative approaches, Hu et al. (2025) analyzed the role of alkali-activated GGBFS and fly ash combinations in flexible pavement design using machine learning-based optimization methods, proving that these mixtures offer ideal strength and deformation properties. Similarly, Uzer et al. (2025) stated that slag and fly ash-based geopolymers activated with NaOH provide sustainable stabilization in clay soils, and modeling results supported by artificial neural networks confirmed this increase in strength.

Consequently, in this research, the effects of stabilizing a bentonite-characterized road subgrade with GGBFS and 8M sodium hydroxide (AAS) activation on rigid pavement design were investigated within the axis of layer thickness and cost analyses. In the experimental stage, samples prepared by adding 5%, 10%, 15%, and 20% GGBFS+AAS by weight to the base soil were subjected to standard Proctor, unconfined compression, and CBR tests. In light of the obtained data, rigid pavement slab thicknesses were calculated using AASHTO 1993 design criteria, and economic evaluations were performed. While existing literature predominantly focuses on the basic strength gain, index properties, or compaction parameters of stabilized soils without linking them to

structural highway design, this study differs by establishing a direct connection between laboratory geotechnical performance and structural pavement engineering outcomes. Specifically, the novelty of this paper lies in its integrated framework that converts laboratory-measured strength and bearing capacity enhancements directly into concrete slab thickness reductions and quantifies the net initial construction cost savings. Thus, this study presents a complementary approach that bridges geotechnical soil stabilization with practical pavement design optimization and economic feasibility.

2. Materials and Methods

2.1. Soil Sample (Sodium Bentonite)

The sodium bentonite (BT) selected for modeling the road subgrade in this research is a critical clay mineral in terms of geotechnical engineering due to its characteristics such as high plasticity limits, significant swelling potential, and low shear strength. Owing to their high montmorillonite content, these soils carry substantial risks of structural damage associated with inadequate bearing capacity, uncontrolled settlements, and volumetric changes. The samples, classified as high-plasticity clay (CH) according to the Unified Soil Classification System (USCS), were obtained from Çanbensan Çankırı Bentonit San. Tic. A.Ş. The physical and chemical properties, along with visual data of the bentonite prepared for testing in accordance with relevant standards (ASTM International, 2006; ASTM International, 2014; ASTM International, 2017a; ASTM International, 2017b) are presented in detail in Table 1, Table 2, and Figure 1, respectively.

Table 1. Properties of bentonite

Soil Property	Test	Symbo	Value	Unit
Optimum Moisture Content	ASTM D698	ω_{opt}	35.25	%
Maximum Dry Density	ASTM D698	ρ_{dmax}	1.310	g/cm³
Liquid Limit	ASTM D4318	ω_L	350-450	%
Bulk Density	ASTM D854	ρ_s	0.9	g/cm³
Sieve Residue on 150 µm Sieve	ASTM D6913	-	2.50	%
Sieve Residue on 75 µm Sieve	ASTM D6913	-	12.5	%
Unified Soil Classification System	ASTM D6913	USCS	CH	-

Table 2. Chemical composition of bentonite

Component	Value (%)	Component	Value (%)
Na_2O	2.41	K_2O	1.10
MgO	2.68	$CaCO_3$	6.91
Al_2O_3	16.54	TiO_2	0.76
SiO_2	63.40	V_2O_5	0.02
P_2O_5	0.13	Cr_2O_3	0.02
SO_3	0.41	MnO	0.08
Cl	0.03	Fe_2O_3	5.51



Figure 1. Physical appearance of the bentonite sample.

2.2. Ground Granulated Blast Furnace Slag and Sodium Hydroxide Solution

Ground granulated blast furnace slag (GGBFS), a waste product of the iron and steel industry, is a material with high hydraulic activity obtained by subjecting molten iron-steel slag to rapid cooling and grinding processes. GGBFS, which exhibits a strong pozzolanic reaction capability thanks to its calcium oxide, silicon dioxide, and aluminum oxide components, constitutes a sustainable alternative to traditional binders in soil stabilization and geopolymer synthesis. It is emphasized in the literature that the use of GGBFS significantly reduces the carbon footprint while increasing mechanical performance (Soğancı et al., 2023; Uzer et al., 2025). The chemical composition of the GGBFS used in this research, which was obtained from the İskenderun Iron and Steel Factory, is presented in Table 3.

Table 3. Chemical composition of GGBFS

Component	Value (%)
CaO	33.6
SiO_2	41.2
Al_2O_3	14.3
MgO	7.3
S	0.8
MnO	0.8
K_2O	0.9
TiO_2	1.1

Sodium hydroxide (NaOH) was preferred as the alkali activator solution to increase the reactivity of GGBFS and

to trigger the geopolymerization process. In the preparation stage, crystalline NaOH particles were dissolved in pure water to obtain a solution with a concentration of 8 molar (320 g/L) in accordance with theoretical approaches in the literature (Arulrajah et al., 2016; Sarıca, 2019; Yıldıran, 2019; Venkatesh et al., 2021; Karabaş, 2025). The characteristic properties of sodium hydroxide are detailed in Table 4, and visual representations of the GGBFS and AAS samples are shown in Figure 2.

Table 4. Properties of sodium hydroxide

Component	Value (%)
Molecular formula	NaOH
Molecular mass	40 (g/mol)
Color	White
pH	13–14
Relative density	2.13 (g/cm^3)



Figure 2. Samples of BT, GGBFS, and AAS.

2.3. Standard Proctor Test

The Standard Proctor Test, applied to determine the compaction characteristics of soils, aims to identify the maximum dry unit weight (ρ_{dmax}) and the corresponding optimum moisture content (ω_{opt}) of the samples. In the studies conducted according to the ASTM D698 (ASTM International, 2014) protocol, cylindrical molds with an inner diameter of 105 mm and a height of 115.5 mm were used. Prior to the test, the soils dried at 105°C for 24 hours were mixed with different moisture contents, placed in the mold in three layers, and subjected to 25 blows per layer using a 2.5 kg rammer. As a result of this process, repeated for five different water contents, the critical ρ_{dmax} and ω_{opt} parameters of the soil were determined via the compaction curve (Yılmaz et al., 2017).

2.4. Unconfined Compressive Strength Test

The Unconfined Compressive Strength Test, performed to measure the strength performance of the samples, was conducted in accordance with ASTM D2166 (ASTM International, 2006) guidelines. The oven-dried soil material, mixed with the calculated amounts of water, was placed in four stages into molds with dimensions of 38 mm in diameter and 76 mm in height. After each layer was compacted with 10 rammer blows, the samples were removed from the mold and preserved at room temperature for the targeted curing periods. During the test, the axial strain rate was fixed between 0.5% and 2% per minute, and the ultimate strength and deformation values were recorded (Orhan, 2013). This procedure was applied to all samples in the study following 28-day curing periods.

2.5. California Bearing Ratio Test

The CBR test, which determines the bearing capacity of soils, was conducted within the framework of ASTM D1883-13 standards by preparing the samples ρ_{dmax} and ω_{opt} conditions. The basic principle of the test is the penetration of a piston with a cross-sectional area of 1935 mm^2 into the soil at a constant rate of 1.27 mm/min. Calculations were made by proportioning the resistance shown by the sample at penetration depths of 2.5 mm and 5 mm to the reference resistance values of standard crushed stone. During the preparation process, the soil was placed in the CBR mold in three stages and compacted with 56 blows per layer. The steps for testing the samples that completed the curing process are detailed in Figure 3 (ASTM International, 2021).



Figure 3. Implementation stages of the CBR test.

2.6. Rigid Pavement Design

Rigid pavement design is based on the structural integrity of a cement-based concrete slab constructed over the road subgrade soil. The design process involves the simultaneous evaluation of multidimensional variables, such as the target service life, layer thicknesses, traffic projections, regional environmental factors, economic parameters, and soil characteristics. Selecting the appropriate concrete grade and determining the optimum layer thicknesses to resist plastic deformations caused by heavy traffic loads over the analysis period are of critical importance for the structural performance of the design (AASHTO, 1993; KGM, 2019; Geçkil et al., 2024). The typical arrangement and structural hierarchy of the layers forming the rigid pavement are detailed in Figure 4.

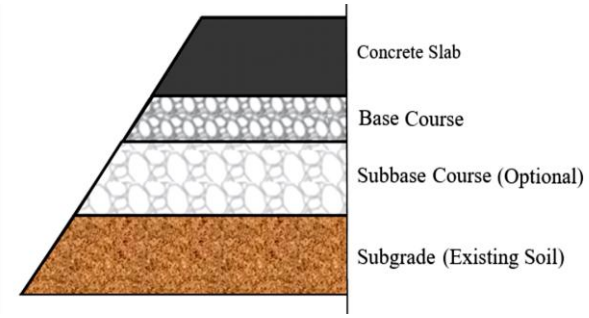


Figure 4. Cross-section of the rigid pavement (Kök, 2019; Geçkil et al., 2024).

The layer thicknesses of the rigid pavement are calculated using equation 1 according to the AASHTO (1993) Design Guide (KGM, 2019).

$$\log_{10}(T_{8,2})=Z_R.\,S_0+7.35.\log_{10}(d+1)-0.06+\frac{\log_{10}[\frac{\Delta PSI}{4,2-1,5}]}{1+\frac{1,624.10^7}{(d+1)^{8,46}}}$$
$$+(4.22-0.32.Pt).\log_{10}[\frac{S'c.Cd(d^{0,75}-1,132)}{215,63.J[d^{0,75}-\frac{18,42}{(Ec/k)^{0,25}}]}] \quad (1)$$

Here;

- $T_{8.2}$: Number of repetitions of the 8.2-ton equivalent single axle load,
- Z_R: Standard normal deviate,
- So: Composite standard error of the traffic forecast and performance prediction,
- d: Thickness of the rigid pavement concrete layer (inches),
- Δ_{PSI}: P0 – Pt (amount of serviceability loss),
- P_0: Initial serviceability index,
- Pt: Terminal serviceability index,
- S'c: Modulus of rupture of concrete (flexural tensile strength) (psi),
- J: Load transfer coefficient,
- Cd: Drainage coefficient,
- Ec: Modulus of elasticity of concrete (psi),
- k: Subgrade reaction modulus (pci).

3. Results and Discussion

In this study, where the effect of road subgrade stabilization with GGBFS+AAS on rigid pavement was investigated, the experimental results and design outputs are presented below.

3.1. Standard Proctor Test Results

BT samples representing the road subgrade were prepared with GGBFS+AAS additives at ratios of 5%, 10%, 15%, and 20% by weight and subjected to standard Proctor tests. The values for maximum dry unit weight, optimum moisture content, and optimum moisture content with alkali activator for the pure BT and the mixtures containing GGBFS+AAS obtained from these tests are presented in Figures 5 and 6.

Upon analyzing the Proctor test results, it was determined that as the GGBFS ratio in the AAS-added mixtures increased, the ω_{optAAS} values also increased, whereas the ρ_{dmax} values decreased compared to both pure BT and other GGBFS+AAS mixtures. These trends observed in relation to the GGBFS ratio are found to be in agreement with similar studies in the literature (Hamed and Demiroz, 2024; Sarıca et al., 2025; Shakil et al., 2025; Tanyıldızı, 2020). The primary reason for this behavior, as noted in the literature (Sas et al., 2021; Shakil et al., 2025), is evaluated to be the low specific gravity and porous particle structure of GGBFS, which increases the void ratio and subsequently reduces the compressibility of the mixture. This structure leads to a higher demand for liquid, which in this case explains the increased AAS requirement in the prepared mixtures.

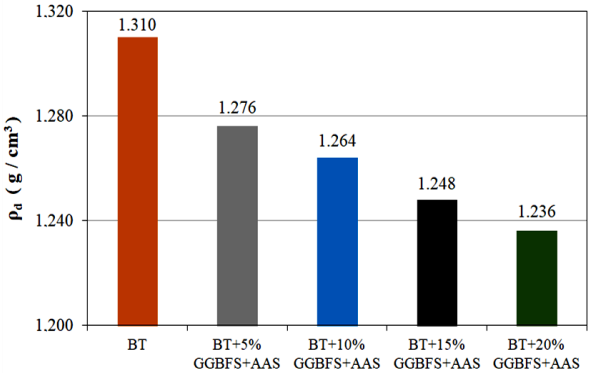


Figure 5. Maximum dry unit weight results of the Standard Proctor test.

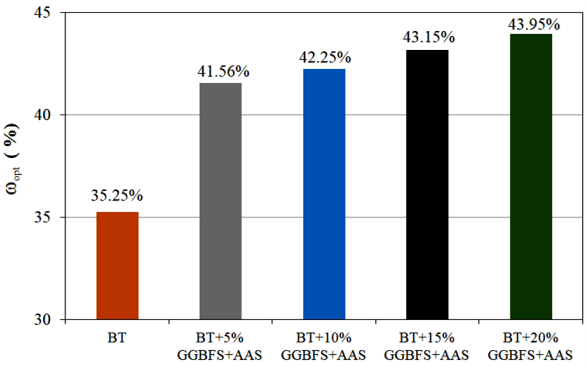


Figure 6. Optimum moisture content results of the Standard Proctor test.

3.2. Unconfined Compressive Strength Test Results

Unconfined compressive strength test specimens, prepared with additive ratios of 5%, 10%, 15%, and 20% GGBFS+AAS by weight, were fabricated based on the determined ρ_{dmax} and ω_{opt} data. The specimens were stored at room temperature. Following a 28-day curing period, the unconfined compressive strength test was performed. The axial stress (q) versus axial strain (ε) results for the additive-free BT soil and GGBFS+AAS added specimens are presented in Figure 7.

Furthermore, the unconfined compressive strength (q_u) and axial strain at failure (ε_u) values are provided in Table 5.

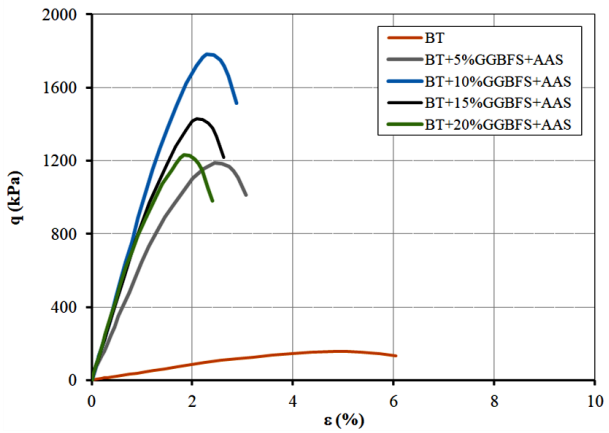


Figure 7. Stress-strain behavior of BT and GGBFS+AAS modified mixtures subjected to 28-day curing.

Table 5. Summary of of q_u and ε_u parameters for GGBFS+AAS reinforced samples

Test Samples	q_u (kPa)	ε_u (%)
BT	156.41	4.80
BT+5% GGBFS+AAS	1189.43	2.44
BT+10% GGBFS+AAS	1783.04	2.28
BT+15% GGBFS+AAS	1431.01	2.08
BT+20% GGBFS+AAS	1230.76	1.84

Upon examination of the unconfined compressive strength data, it was determined that the additive free BT specimens exhibited lower strength at the end of the 28-day curing period compared to the mixtures containing GGBFS and AAS. It was observed that the addition of GGBFS to the mixture significantly enhanced the strength performance, with the highest strength value being achieved in the specimens containing 10% GGBFS+AAS. At this optimal additive ratio, an 11.40-fold increase in strength was recorded at the end of the 28-day curing period compared to the untreated specimens. This positive effect of GGBFS and AAS usage on strength is consistent with studies in the literature (Sas et al., 2021; Tanyıldızı, 2020; Hamed and Demiroz, 2024; Sarıca et al., 2025; Shakil et al., 2025). Furthermore, the decrease observed in axial strain values depending on the increase in GGBFS content and curing time is evaluated to result from the increase in the material's stiffness; this finding is also in alignment with the relevant literature (Uzuner, 2016).

3.3. California Bearing Ratio Test Results

The specimens prepared within the scope of the CBR test were fabricated based on the untreated BT and the optimum mixture ratio of 10% GGBFS+AAS determined from the unconfined compressive strength test results. The ρ_{dmax}, ω_{opt} and ω_{optAAS} values were utilized in the preparation of the test specimens. The samples were kept at room temperature in a protected environment, shielded from external factors, during the 28-day curing period. Following the completion of the curing process, the dry CBR test was performed. The load-displacement graphs obtained from the CBR test are shown in Figure 8, while the CBR values are provided in Table 6.

Upon analysis of the CBR test results, it was determined that the GGBFS+AAS mixtures significantly increased the CBR values. At the end of the 28-day curing period, the CBR values for the GGBFS+AAS mixtures were identified as 64.27% and 74.07% for 2.5 mm and 5 mm penetrations, respectively. These values represent a 10.48-fold and 11.80-fold increase compared to the initial state for 2.5 mm and 5 mm penetrations, with the maximum increase observed at the 5 mm penetration level.

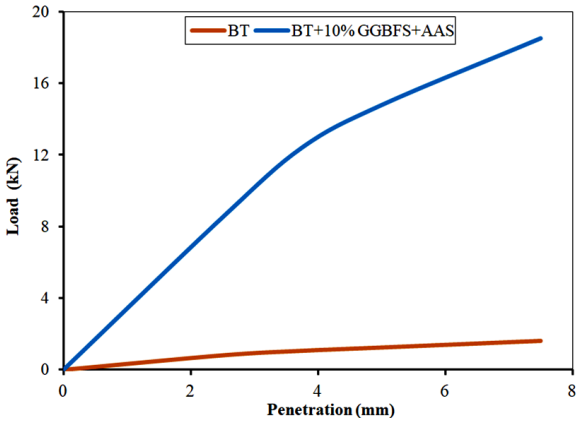


Figure 8. Load-displacement curves of untreated and 10% GGBFS+AAS stabilized specimens.

Table 6. CBR values of the specimens after 28 days of curing

Test Specimen	CBR value for 2.5 mm penetration, (%)	CBR value for 5 mm penetration, (%)
BT	6.13	6.28
BT+10% GGBFS+AAS	64.27	74.07

The experimental results prove that GGBFS+AAS-added mixtures exhibit a substantially higher bearing capacity compared to the control sample (pure BT). These findings are in full agreement with literature studies (Tanyıldızı, 2020; Hamed and Demiroz, 2024; Sarıca et al., 2025; Uzer et al., 2025) emphasizing the remedial effect of GGBFS addition on soil bearing strength. The reactive nature of calcium, silica, and alumina components within the GGBFS content triggers the formation of cementitious hydration products between soil particles. This chemical process enhances mechanical strength and controls volumetric changes by densifying the soil microstructure. It is well-documented that GGBFS, acting as an effective binder due to its pozzolanic and hydraulic properties, plays a critical role in the stabilization of low-strength and high-plasticity clays (Tanyıldızı, 2020; Hamed and Demiroz, 2024; Sarıca et al., 2025; Uzer et al., 2025). Additionally, it is assessed

that the AAS system strengthens the composite matrix by constituting a more compact geopolymer structure, which is decisive in the strength gain. Conversely, once the optimum additive threshold is exceeded, no further improvement in strength was observed due to the increase in unreacted waste material.

3.4. Rigid Pavement Design

The rigid pavement design was performed within the framework of AASHTO 1993 standards, based on the 28-day CBR data of both the untreated BT sample and the 10% GGBFS+AAS added mixture. Within the scope of this study, Jointed Plain Concrete Pavement (JPCP) thickness was analyzed. In determining the design parameters: A project life of 30 years was projected, assuming the route is a 2x2 lane state highway. Based on the first-year daily traffic volume of 1,395 trucks, 598 trailers, 1,809 buses, 12,520 cars, and 1,203 minibuses, the total traffic load was calculated as 160,000,000 equivalent 8.2-ton standard single axle loads (ESALs).With a reliability level selected as R = 99.9%, layer thicknesses were determined assuming the presence of a base or sub-base layer. The maximum CBR values 6.28% for the untreated sample and 74.07% for the 10% GGBFS+AAS mixture were utilized as critical design inputs. All variables were processed according to the parameters presented in Table 7.

Table 7. Rigid pavement design parameters

Parameters	Selected Values
Number of repetitions of the 8.2-ton equivalent single axle load, $T_{8.2}$	160,000,000
Load transfer coefficient, J	2.7
Drainage coefficient, Cd	1
Modulus of rupture of concrete	660
Composite standard error of the traffic forecast and performance prediction, S_0	0.35
Initial serviceability index, P_0	4.5
Terminal serviceability index, Pt	2.5
Po − Pt (amount of serviceability loss), Δ_{PSI}	2
Modulus of elasticity of concrete, Ec (C 35/45)	4786244
Standard normal deviate, Z_R	-3.09

In the calculations, the modulus of subgrade reaction (k) and the resilient modulus (M_R) of the road subgrade were first determined. For the calculation of M_R, the correlation MR (psi) = 2555 $(CBR)^{0.64}$ (AASHTO, 2024), as provided in the 3rd edition of the Pavement Design Guide containing mechanical-empirical technical revisions published by AASHTO in January 2024 (MEPDG-3), was utilized along with the correlation k = MR / 19.4 (AASHTO, 1993).

For the untreated BT, the MR and k values were calculated as 8,281 psi (57,110,646 Pa) and 426.86, respectively. For the 10% GGBFS+AAS mixture, the MR and k values were determined to be 40,176 psi (277,072,870 Pa) and 2,070.91. Using these data and the values in Table 7 in conjunction with Equation (1), the slab thickness (d) for C 35/45 grade concrete was selected as 17.55 inches (applied as 45 cm) for the untreated BT soil, and 14.85 inches (applied as 38 cm) for the 10% GGBFS+AAS stabilized soil. According to these results, it was determined that the layer thickness for the 10% GGBFS+AAS mixtures decreased by 7 cm compared to the untreated BT soil, representing a reduction of approximately 15.56%.

3.5. Economic Analysis of Rigid Pavement

The impact of stabilizing the BT road subgrade with GGBFS+AAS on the cost of rigid highway pavement was evaluated according to the General Directorate of Highways (KGM) specifications. Based on the 2026 unit price schedules of the Ministry of Environment, Urbanization and Climate Change (ÇSB,2026), the unit area (m^2) cost of concrete with a C 35/45 compressive strength class was calculated. According to the analysis and cost estimations, the unit cost of rigid pavement for the untreated BT was determined to be 1,726.65 TL/m^2, while for the 10% GGBFS+AAS stabilized soil, it was 1,458.06 TL/m^2. This data is detailed in Table 8.

Table 8. Unit costs of pavement layers for untreated BT and 10% GGBFS+AAS stabilized soils

Item No.	Description	Unit	Unit Price (TL)	m^2 /cm Cost (TL)	Calculated Thick. (cm)	m^2 Cost (TL)
15.150. 1007	Placement of C 35/45 Concrete Produced On-Site or Ready-Mix and Pumped Including Transportation	m^3	3638.85	38.37	45	1726.65
					38	1458.06

Furthermore, in the analysis for stabilizing the road subgrade to a thickness of 15 cm (Karabaş, 2025) with 10% GGBFS+AAS, the following operations were taken as the basis: transportation of materials, loosening of the soil with a tractor ripper, distribution of the stabilizer material with a tractor bulldozer, spreading and mixing with a grader, watering with a water tanker, and compaction using both vibratory and pneumatic-tired rollers. Since GGBFS is a waste material, the transportation of GGBFS to the construction site at a maximum distance of 500 km was calculated considering the 2026 Ministry of Environment, Urbanization and Climate Change calculation methodology. The unit costs per square meter (m^2) for the stabilization are provided in Table 9. Additionally, the concrete layer and soil stabilization costs, calculated by considering both the untreated soil and the soil improved with the addition of 10% GGBFS+AAS, are shown in Figure 9. When the calculated layer costs are evaluated, a reduction of 1.42% in construction costs is observed. According to these calculations, for a road 20 meters wide and 1,000 meters long, a saving of 489,200.00 TL will be achieved by using a road subgrade improved with 10% GGBFS+AAS. In this context, considering the total length of the highway network, it is anticipated that significant gains can be realized in the construction of rigid pavements through soil stabilization.

Table 9. Unit stabilization costs for soil stabilized with 10% GGBFS+AAS

Item No.	Description	Unit	Unit Price (TL)	Cost (TL/ m^2)
KGM 03.507	Hourly Cost of Tractor Ripper	h	3389.77	0.51
KGM 03.511	Hourly Cost of Bulldozer	h	3141.42	2.12
KGM/15.140	Mechanical Spreading and Mixing	m^3	22.88	3.43
KGM/15.047	Watering by Water Truck	ton	168.98	2.53
KGM/15.052/3	Compaction Using Vibratory Roller	h	2722.76	4.08
KGM/15.058/1	Compaction Using Pneumatic-Tired Roller	h	2116.99	3.18
Market Price	Supply and Transportation of 10% GGBFS+AAS	kg	6.23	228.27
			Total:	244.13

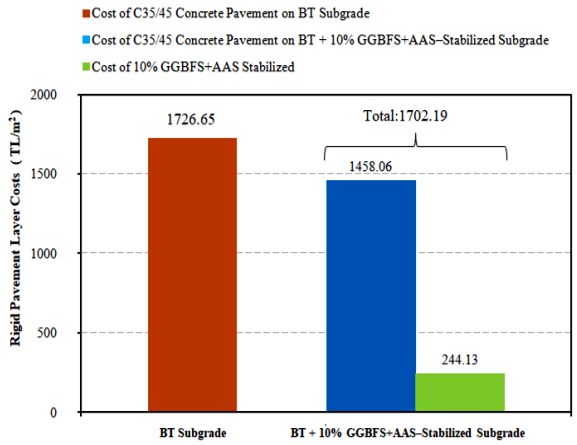


Figure 9. Concrete pavement and subgrade stabilization costs for untreated and 10% GGBFS+AAS-stabilized BT.

4. Conclusions and Recommendations

In this research, the effects of improving a Bentonite (BT) road subgrade with GGBFS+AAS on rigid pavement thickness and initial construction costs were examined across various additive contents (5%, 10%, 15%, and 20% by weight). Based on the comparative experimental evaluations, increasing the stabilizer content up to 10% significantly enhanced the mechanical properties and bearing capacity of the soil; however, further additions (15% and 20%) led to a slight decline in performance, establishing 10% GGBFS+AAS as the optimum stabilization ratio. The key findings obtained for both the overall mixture trends and the optimum 10% GGBFS+AAS ratio are summarized below.

Standard Proctor Test: It was determined that as the GGBFS ratio in the AAS mixture increased, the ω_{optAAS} value increased, while ρ_{dmax} decreased for both pure BT and GGBFS+AAS mixtures. This behavior is attributed to the low specific gravity and porous structure of GGBFS, which increases inter-granular voids, thereby reducing compressibility and increasing the liquid demand (AAS requirement) of the mixture.

Unconfined Compressive Strength, the highest strength value at the end of the 28-day curing period was determined in the specimens with 10% GGBFS+AAS. Compared to the untreated BT soil, a 11.40-fold increase in strength was observed. Furthermore, the increase in GGBFS+AAS content enhanced the stiffness of the specimens, leading to a decrease in axial strain.

CBR Test, for the 10% GGBFS+AAS stabilized soils, CBR values at the end of 28 days showed an increase of 10.48 and 11.80 times for 2.5 mm and 5 mm penetrations, respectively. These results prove that GGBFS+AAS significantly improve the bearing capacity of the soil.

Pavement Design: A reduction of 15.56% was achieved in the rigid pavement thickness designed for 10% GGBFS+AAS stabilized subgrades. This demonstrates the positive impact of GGBFS and AAS on the structural bearing capacity.

Economic Analysis: The pavement costs for 10% GGBFS+AAS stabilized soils decreased by 1.42% compared to the untreated soil. Based on these calculations, a saving of 489,200.00 TL can be achieved in the rigid pavement cost of a 1,000-meter-long, 20-meter-wide divided highway.

In conclusion, the stabilization of road subgrades uses waste materials like GGBFS and AAS increases bearing capacity while reducing both rigid pavement thickness and costs. Although the soil strength increases significantly, the cost of stabilizer materials remains a primary factor in the applicability of this model. Furthermore, the utilization of GGBFS as a waste product and the reduction in materials used for rigid pavement construction will decrease environmental damage particularly CO_2 emissions arising from cement and aggregate production, transport, and application. Increasing the use of GGBFS+AAS in road construction activities is evaluated as a viable path to further reducing the initial construction costs of highway projects.

Author Contributions

The percentages of the authors' contributions are presented below. All authors reviewed and approved the final version of the manuscript.

	B.K.	A.U.U.	N.A.B	A.B.
C	25	25	25	25
D	25	25	25	25
S	25	25	25	25
DCP	25	25	25	25
DAI	25	25	25	25
L	25	25	25	25
W	25	25	25	25
CR	25	25	25	25
SR	25	25	25	25
PM	25	25	25	25
FA	25	25	25	25

C= concept, D= design, S= supervision, DCP= data collection and/or processing, DAI= data analysis and/or interpretation, L= literature search, W= writing, CR= critical review, SR= submission and revision, PM= project management, FA= funding acquisition.

Conflict of Interest

The authors declared that there is no conflict of interest.

Ethical Consideration

Ethics committee approval was not required for this study because of there was no study on animals or humans.

References

Abdulkarim, I. I., & Sa'eed, Y. U. (2020). Performance evaluation of the effect of sodium hydroxide on geotechnical properties of lateritic soil for rural road construction. *FUOYE Journal of Engineering and Technology*, *5*(2), 213–216.

Abdila, S. R., Abdullah, M. M. A. B., Ahmad, M., Azmi, N. J., & Jaya, R. P. (2022). Potential of soil stabilization using ground granulated blast furnace slag (GGBFS) and fly ash via geopolymerization method: A review. *Materials*, *15*(1), 375.

American Association of State Highway and Transportation Officials (AASHTO). (1993). *Guide for design of pavement structures (Interim)*. AASHTO.

American Association of State Highway and Transportation Officials (AASHTO). (2024). *Mechanistic–empirical pavement design guide (3rd ed., MEPDG-3)*. AASHTO.

Arulrajah, A., Mohammadinia, A., Horpibulsuk, S., & Samingthong, W. (2016). Influence of class F fly ash and curing temperature on strength development of fly ash-recycled concrete aggregate blends. *Construction and Building Materials*, 127, 743.

ASTM International. (2006). Standard test method for specific gravity of soils (ASTM D854).

ASTM International. (2006). Standard test method for unconfined compressive strength of cohesive soil (ASTM D2166-06).

ASTM International. (2014). Standard test methods for laboratory compaction characteristics of soil using standard effort (ASTM D698).

ASTM International. (2017a). Standard test methods for liquid limit, plastic limit, and plasticity index of soils (ASTM D4318).

ASTM International. (2017b). Standard test methods for particle-size distribution (gradation) of soils using sieve analysis (ASTM D6913).

ASTM International. (2021). Standard test method for California Bearing Ratio (CBR) of laboratory-compacted soils (ASTM D1883-21).

Babatunde, O. A., Sani, E. J., & Sambo, A. H. (2019). Black cotton soil stabilization using glass powder. *International Journal of Innovative Research in Science, Engineering and Technology*, 8(5).

Bharti, G., Hurukadli, P., & Shukla, B. K. (2023). Environmental impact analysis and utilization of copper slag for stabilising black cotton soil. *Materials Today: Proceedings*, 2023(3).

Bilici, H., Okur, D. V., Türköz, M., & Savaş, H. (2020). Effect of fly ash and blast furnace slag additives on the strength of clay soil and comparative analysis (in Turkish). *Bitlis Eren University Journal of Science and Technology*, 9(2), 910–919.

Çınar, M. (2024). Investigation of geotechnical properties of clayey sand soil stabilized with aerated concrete waste after Kahramanmaraş earthquake (in Turkish). *Dicle University Journal of Engineering*, 15(1), 269–275. https://doi.org/10.24012/dumf.1404478

Geçkil, T., & Karabaş, B. (2026). Evaluating the effects of carbon black from recycled tires on subgrade stabilization, pavement design, and construction-phase CO_2 emissions. *Indian Journal of Engineering and Materials Sciences (IJEMS),* 33(01), 111–125.

Geçkil, T., Sarıca, T., & Karabaş, B. (2021). Effects of black carbon stabilized soil on rigid pavement thickness and cost (in Turkish). *ECJSE*, 8(3), 1372–1384. https://doi.org/10.31202/ecjse.894046

Geçkil, T., Sarıca, T., & Karabaş, B. (2024). Investigation of the effects of soil improvement with metakaolin on rigid pavement thickness and cost. *Black Sea Journal of Engineering and Science*, 7(5), 11–12.

Geçkil, T., Sarıca, T., & Karabaş, B. (2025a). Investigation of the effect of sandy soil stabilized with ground pumice stone on flexible pavement design (in Turkish). *International Journal of Pure and Applied Sciences,* 11(1), 176–192.

Geçkil, T., Sarıca, T., & Karabaş, B. (2025b). Investigation of layer thickness and cost of flexible pavement designed on soil improved using glass powder (in Turkish). *Journal of Innovative Engineering and Natural Sciences*, 5(1), 80–98. https://doi.org/10.61112/jiens.1509488

Geçkil, T., Sarıca, T. & Karabaş, B., (2025c). Investigation of freeze-thaw resistance of road substrates stabilized with metakaolin. *Osmaniye Korkut Ata University Journal of the Institute of Science and Technology.* https://doi.org/10.47495/okufbed.1548511

Geçkil, T., Sarıca, T., & Karabaş, B. (2026). Investigation of the effect of stabilizing subgrade soils with recycled glass powder on freeze–thaw resistance. *Gümüşhane University Journal of Science and Technology*, 1(1), 179–196. https://doi.org/10.17714/gumusfenbil.1802171

Hamed, E., & Demiroz, A. (2024). Optimization of geotechnical characteristics of clayey soils using fly ash and granulated blast furnace slag-based geopolymer. *Construction and Building Materials*, 441, Article 137488.

Hu, J., Zhang, X., Wang, Y., & Liu, L. (2025). Machine learning-based optimization of geopolymer-stabilized soil formulation using blast furnace slag and fly ash. *Materials Today Communications*, Article 113500.

Hussain, S. (2019). Stabilization of expansive soil using sodium hydroxide [Master's thesis, Near East University]. Near East University Repository.

Karabaş, B. (2025). Effects and sustainability of road subgrade soils stabilized with various additives on highway pavement (Publication No. 960734) [Doctoral dissertation, İnönü University]. National Thesis Center.

Karabaş, B., & Uzer, A. U. (2026). Effect of ground granulated blast furnace slag–stabilized bentonite soils on flexible pavement design and cost analysis. *Al-Qadisiyah Journal for Engineering Sciences,* 19(2), 001–008. https://doi.org/10.30772/qjes.2026.169263.1896

Kök, B. V. (2019). *Highway engineering and design* (in Turkish). Nobel Academic Publishing.

Konai, S., Mayur, M., Dutta, S., & Hinge, G. (2026). Sustainable soil stabilization using alkali-activated rice husk ash. *Journal of Hazardous, Toxic, and Radioactive Waste,* 30(1), Article 04025041.

Orhan, M. (2013). *Soil mechanics laboratory tests* (in Turkish). Gazi Publishing.

Republic of Türkiye Ministry of Environment, Urbanization and Climate Change. (2026, January 28). Unit prices. https://yfk.csb.gov.tr/birim-fiyatlar-i-100468

Sarıca, T. (2019). Evaluation of the usability of construction and demolition wastes reinforced with pozzolan as granular fill (in Turkish) [Master's thesis, Inonu University]. Graduate School of Natural and Applied Sciences.

Sarıca, T., Geçkil, T., Ok, B., & Aksoy, H. S. (2025). An investigation of the usability of alkali-activated blast furnace slag-additive construction demolition waste as filling material. *Materials,* 18(2), Article 398. https://doi.org/10.3390/ma18020398

Sas, W., Dzięcioł, J., Radzevičius, A., Radziemska, M., Dapkienė, M., Šadzevičius, R., & Głuchowski, A. (2021). Geotechnical and environmental assessment of blast furnace slag for engineering applications. *Materials,* 14(20), Article 6029.

Shabana, S., Anshi, C., Shamseera, P., Shyamili, T. M., Sruthi, V., & Suhaira, P. (2014). Study on CBR values of soil with crushed coconut shells. *International Journal of Advanced Engineering and Technology*, 5(3), 55–58.

Shakil, M., Nazar, S., Ameen, H. F. M., Shahzad, A., & Ahmad, F. (2025). A comparative study of ground granulated blast furnace slag and bagasse ash incorporation on enhancing mechanical properties of expansive soil. *Results in Engineering*, 25, Article 103569.

Soğancı, A. S., Yenginar, Y., & Orman, A. (2023). Geotechnical properties of clayey soils stabilized with marble dust and granulated blast furnace slag. *KSCE* Journal of Civil Engineering, 27(11), 4622–4634.

Şengül, T., Akray, N., & Vitoşoğlu, Y. (2023). Investigating the effects of stabilization carried out using fly ash and polypropylene fiber on the properties of highway clay soils. *Construction and Building Materials*, 400, Article 132590. https://doi.org/10.1016/j.conbuildmat.2023.132590

T.C. Ministry of Transport KGM Technical Research Department. (2019). Highway concrete pavement design guide (in Turkish). KGM Technical Research Department.

Tanyıldızı, M. M. (2020). Effects of clayey soil stabilized with blast furnace slag on highway flexible pavement layer thicknesses and cost (in Turkish). *Firat University Journal of Engineering Sciences*, 32(2), 509–520. https://doi.org/10.35234/fumbd.738512

Tanyıldızı, M. M., & Karabaş, B. (2026). Zayıf zeminlerde YFC ve çelik lifli beton yolların ilk yapım maliyeti ve CO_2 emisyonuna etkisi. *Black Sea Journal of Engineering and Science,* 9(2), 516–548.

Topçuoğlu, Y. A., & Güroçak, Z. (2023). Determination of optimum basalt fiber ratio for maximum strength in soil reinforcement (in Turkish). *Dicle University Journal of Engineering,* 14(3), 479–487.

Tunç, A. (2002). *Geotechnics and applications in road engineering* (in Turkish). Nobel Publishing.

Uzer, A. U., Tunç, U., Acar, M. C., & Çelik, A. I. (2025). Sustainable stabilization of clay soils using fly ash and blast furnace slag-based geopolymers: Comprehensive experimental evaluation and artificial neural network modelling. *Structural Engineering and Mechanics*, 96(1), 13–33.

Uzuner, B. A. (2016). *Introduction to foundation engineering* (in Turkish). Derya Publishing.

Venkatesh, N., Mallikarjuna, R. G., Reddy, S. K., & Chavali, R. V. P. (2021). Strength and durability characteristics of GGBS geopolymer stabilized black cotton soil. *Materials Today: Proceedings*, 43, 2373–2376.

Yıldıran, E. S. (2019). Investigation of the effects of various additives on road subgrade soil (in Turkish) [Master's thesis, Inonu University]. Graduate School of Natural and Applied Sciences.

Yılmaz, I., Yıldıran, M., & Keskin, I. (2017). *Soil mechanics laboratory tests and solved problems* (in Turkish). Seçkin Publishing.

Black Sea Journal of Engineering and Science
doi: 10.34248/bsengineering.1981497

Open Access Journal
e-ISSN: 2619 – 8991

Research Article
Volume 9 - Issue 5: 2269-2280 / September 2026

HIERARCHICAL EXPERT-ROUTED BOOSTING WITH PROBABILITY FUSION FOR MULTICLASS INTRUSION DETECTION IN EDGE-IOT AND IIOT NETWORKS

Fesih KESKİN[1]*

[1]*Siirt University, Faculty of Engineering, Department of Computer Engineering, 56100, Siirt, Türkiye*

Abstract: The increasing deployment of Internet of Things (IoT) and Industrial Internet of Things (IIoT) systems has created a need for intrusion detection methods that can identify fine-grained attack categories under class imbalance. This study proposes HERB-Fusion-IDS, a hierarchical expert-routed boosting framework for multiclass intrusion detection. The method combines a flat XGBoost classifier with an attack-family router and family-specific expert classifiers, and the final class probabilities are obtained through validation-selected probability fusion. Experiments were conducted on the Edge-IIoTset benchmark as a 15-class classification task using five independent stratified repetitions. The proposed method achieved mean accuracy, macro-F1, MCC, and rare-class F1 values of 0.961, 0.851, 0.913, and 0.746, respectively. Compared with flat XGBoost, HERB-Fusion-IDS produced small but consistent improvements in macro-F1, MCC, and rare-class F1 while maintaining a comparable false-alarm rate. The rare-class improvement was mainly associated with improved Fingerprinting detection. These findings indicate that attack-family information can provide useful complementary structure when fused with a strong flat boosting classifier. However, the evaluation is limited to Edge-IIoTset, and external validation on additional IoT/IIoT datasets is required in future work.

Keywords: Intrusion detection, IoT security, IIoT security, Edge-IIoTset, Hierarchical classification, Rare attack detection

***Corresponding author:** Siirt University, Faculty of Engineering, Department of Computer Engineering, 56100, Siirt, Türkiye
E mail: fesih.keskin@siirt.edu.tr (F. KESKIN)
Fesih KESKİN https://orcid.org/0000-0002-3798-2912

Received: June 29, 2026
Accepted: July 29, 2026
Published: September 15, 2026

Cite as: Keskin, F. (2026). Hierarchical expert-routed boosting with probability fusion for multiclass intrusion detection in edge-IoT and IIoT networks. *Black Sea Journal of Engineering and Science*, 9(5), 2269-2280.

1. Introduction

The rapid development of Internet of Things (IoT) and Industrial Internet of Things (IIoT) technologies has significantly transformed modern digital and cyber-physical infrastructures. IoT- and IIoT-enabled systems are now widely deployed in smart homes, healthcare, industrial automation, smart agriculture, smart cities, and Industry 4.0 environments, where large numbers of sensors, actuators, edge gateways, and cloud-connected services continuously exchange data to support monitoring, control, and decision-making processes (Baich and Sael, 2025; Belachew et al., 2025; Li et al., 2026; Sahoo et al., 2026). In industrial environments, the convergence of Operational Technology (OT) and Information Technology (IT) has further accelerated the deployment of complex cyber-physical systems operating across edge, fog, and cloud computing layers (Ismail et al., 2025; Fan et al., 2026). By moving computation closer to data sources, edge and fog computing can reduce latency, decrease bandwidth consumption, and support time-sensitive industrial applications (Ferrag et al., 2022; Sahoo et al., 2026). However, the same characteristics that make IoT and IIoT systems attractive also introduce substantial cybersecurity challenges.

Unlike conventional enterprise networks, IoT and IIoT ecosystems are highly distributed, heterogeneous, and resource constrained. They typically include diverse device types, lightweight communication protocols, constrained computational resources, and multiple points of interaction between physical processes and digital services (Baich and Sael, 2025; Gutti et al., 2025). Many edge devices operate under strict limitations in memory, energy consumption, and processing capacity, which can restrict the deployment of conventional security mechanisms and make continuous monitoring more difficult (Gutti et al., 2025; Umar and Jordanov, 2026). As a result, compromised IoT/IIoT devices may be exploited not only to disrupt digital services but also to affect physical processes, industrial assets, and safety-critical operations (Baich and Sael, 2025; Fan et al., 2026). These conditions make intrusion detection an essential component of IoT/IIoT cybersecurity.

The threat landscape of IoT and IIoT environments is broad and continues to evolve. Attackers may target edge devices, gateways, communication protocols, cloud services, or industrial control components using attacks that differ considerably in traffic characteristics, objectives, and operational impact (Ismail et al., 2025;

This work is licensed (CC BY-NC 4.0) under Creative Commons Attribution 4.0 International License

Umar and Jordanov, 2026). Denial-of-Service (DoS) and Distributed Denial-of-Service (DDoS) attacks aim to degrade availability by overwhelming networked devices or edge services with malicious traffic, including TCP, UDP, ICMP, and HTTP flood patterns (Ferrag et al., 2022; Saiyed and Al-Anbagi, 2026). Information-gathering attacks, such as port scanning and operating-system fingerprinting, allow adversaries to identify vulnerable hosts, exposed services, and internal network structures (Ferrag et al., 2022; Umar and Jordanov, 2026). Man-in-the-Middle (MITM) attacks, including ARP and DNS spoofing, threaten the integrity and confidentiality of communications between IoT devices, gateways, and edge servers (Ferrag et al., 2022; Umar and Jordanov, 2026). In addition, injection attacks, ransomware, backdoors, and password-based attacks can compromise application-layer services, disrupt operational continuity, and enable persistent unauthorized access (Ferrag et al., 2022; Ismail et al., 2025).

The development of reliable intrusion detection systems (IDSs) depends heavily on realistic datasets that reflect the heterogeneity of modern IoT/IIoT infrastructures. In this regard, Edge-IIoTset provides a comprehensive benchmark for evaluating machine-learning-based security models in both centralized and federated learning settings (Ferrag et al., 2022; Shah et al., 2026). The dataset was generated using a seven-layer IoT/IIoT testbed that includes cloud computing, network functions virtualization, blockchain, fog computing, software-defined networking, edge computing, and IoT/IIoT perception layers (Ferrag et al., 2022; Ismail et al., 2025). It incorporates heterogeneous devices, sensors, protocols, and cloud-to-edge services, and includes fourteen attack scenarios grouped into five major threat categories: DoS/DDoS, information gathering, MITM, injection, and malware (Ferrag et al., 2022; Ismail et al., 2025). These characteristics make Edge-IIoTset suitable for evaluating multiclass IDS models under realistic protocol diversity and class imbalance.

Machine learning (ML) and deep learning (DL) have become widely used for intrusion detection because of their ability to model nonlinear relationships in high-dimensional traffic data and detect patterns that may not be captured by static signature-based systems (Li et al., 2026; Clinton et al., 2026). Classical ML methods, including logistic regression, support vector machines, decision trees, and random forests, have been extensively investigated for network intrusion classification (Belachew et al., 2025; Ismail et al., 2025). More recently, gradient-boosted decision-tree models such as XGBoost and CatBoost have attracted considerable attention in tabular cybersecurity tasks because they can efficiently capture feature interactions, threshold-based decision boundaries, and nonlinear relationships without requiring complex feature scaling procedures (Belachew et al., 2025; Ganesh and Kumar, 2026). In parallel, deep neural networks and deep tabular architectures have been explored for IDS applications due to their capacity for representation learning and flexible function approximation (Pal et al., 2025; Gao et al., 2026). Nevertheless, deep learning models do not always provide a consistent advantage over well-tuned tree-based methods on structured tabular network data, particularly when the task involves severe class imbalance, heterogeneous protocol features, and strict operational constraints (Keskin, 2024; Ismail et al., 2025; Ganesh and Kumar, 2026; Umar and Jordanov, 2026).

Despite substantial progress, several methodological and evaluation challenges remain in IoT/IIoT intrusion detection research. Many existing studies still emphasize binary classification, where traffic is categorized only as benign or malicious (Gao et al., 2026; Keskin and Oz, 2026). Although binary detection is useful for initial alerting, it provides limited diagnostic information for incident response because it does not identify the specific attack type. Multiclass classification is therefore more informative, but it is also more challenging due to overlapping attack behaviors and severe imbalance among attack categories. In such settings, aggregate metrics such as overall accuracy or weighted F1-score can be misleading because they may be dominated by majority classes and may conceal weak recognition of rare but operationally important attacks (Pal et al., 2025; Ganesh and Kumar, 2026; Gao et al., 2026; Sahoo et al., 2026). Moreover, false-alarm behavior is not always sufficiently reported, even though excessive benign-to-attack misclassification can produce alert fatigue and reduce the practical usability of an IDS (Ganesh and Kumar, 2026; Keskin and Oz, 2026). Another limitation is that many evaluations rely on a single random split, which makes it difficult to determine whether reported improvements are stable across different data partitions (Keskin and Oz, 2026).

A further research gap concerns the structural modeling of attack categories. Conventional flat multiclass classifiers learn a direct mapping from features to all attack labels within a single decision space. While this formulation is simple and often effective, it does not explicitly exploit the natural organization of attacks into broader families, such as DDoS, scanning, injection, malware, and MITM (Ferrag et al., 2022; Sahoo et al., 2026). Existing ensemble and hybrid IDS approaches frequently combine multiple learners, feature-selection mechanisms, or deep architectures, but many of them do so in a generic manner without incorporating attack-family structure into the prediction process (Ganesh and Kumar, 2026). This limits their ability to separate coarse inter-family discrimination from fine-grained intra-family classification. A structured approach that integrates global multiclass discrimination with family-specific expert modeling may therefore provide a more interpretable and operationally meaningful alternative.

Motivated by these limitations, this study proposes HERB-Fusion-IDS, a hierarchical expert-routed boosting framework with probability-level fusion for multiclass IoT/IIoT intrusion detection. The proposed framework

combines a flat gradient-boosted classifier with a hierarchical branch consisting of an attack-family router and family-specific expert classifiers. The flat branch captures global decision boundaries across all attack classes, while the hierarchical branch models the coarse-to-fine structure of attack categories. A validation-selected probability fusion mechanism then combines the two posterior distributions, aiming to preserve the strong global discrimination of gradient boosting while incorporating attack-family-aware expert corrections. This design is intended to provide a structured alternative to flat multiclass boosting by combining global discrimination with attack-family-aware corrections.

The main contribution of this study is the development and evaluation of HERB-Fusion-IDS, a hierarchical expert-routed boosting framework for multiclass IoT/IIoT intrusion detection. The proposed approach decomposes attack-type prediction into coarse attack-family routing and family-specific expert classification, and then combines the resulting hierarchical probabilities with flat XGBoost probabilities through validation-selected probability fusion. In this way, the framework integrates global multiclass discrimination with attack-family-aware specialization. The method is evaluated on Edge-IIoTset as a 15-class intrusion detection task, with emphasis on class imbalance, rare attack recognition, false-alarm-aware evaluation, and multiclass diagnostic performance. In addition, a repeated stratified-split evaluation is conducted against linear, non-boosting tree ensemble, XGBoost, and deep tabular baselines using mean-standard deviation reporting to assess the stability of the observed results.

1.1. Related Work

The performance and generalizability of machine-learning-based intrusion detection systems depend strongly on the quality and representativeness of the datasets used for training and evaluation. Early benchmark datasets, such as KDD99 and NSL-KDD, have been widely used in intrusion detection research; however, they do not adequately reflect the protocol diversity, device heterogeneity, and attack characteristics of contemporary IoT and IIoT environments (Ferrag et al., 2022; Örsdemır et al., 2026). To address these limitations, several IoT/IIoT-oriented datasets have been introduced. Bot-IoT was designed to capture botnet-related traffic in a simulated smart environment, while N-BaIoT focuses on IoT device compromise using Mirai and BASHLITE botnets (Umar and Jordanov, 2026). ToN-IoT provides heterogeneous data sources, including network traffic, operating system logs, and telemetry, enabling the evaluation of attacks across cloud, fog, and edge-related components (Ismail et al., 2025). MQTTset specifically targets MQTT-based IoT communication, whereas WUSTL-IIoT-2021 and X-IIoTID provide IIoT-oriented traffic and industrial protocol characteristics (Ferrag et al., 2022). More recent benchmarks, such as CICIoT2023, further expand the scale and diversity of IoT attack scenarios and provide broader attack-family coverage (Keskin and Oz, 2026).

Among these datasets, Edge-IIoTset is particularly relevant for evaluating multiclass IDS models in heterogeneous IoT/IIoT settings. It was generated using a seven-layer testbed consisting of cloud computing, network function virtualization, blockchain, fog computing, software-defined networking, edge computing, and IoT/IIoT perception layers (Ismail et al., 2025). The dataset includes traffic from more than ten types of IoT devices, heterogeneous communication protocols, and industrial components such as Modbus (Ferrag et al., 2022). It also contains fourteen attack types grouped into five major threat categories: DoS/DDoS, information gathering, man-in-the-middle, injection, and malware (Ferrag et al., 2022). These characteristics make Edge-IIoTset suitable for evaluating fine-grained multiclass IDS models under realistic protocol diversity and class imbalance.

Classical machine learning methods have been extensively studied for IoT/IIoT intrusion detection because of their effectiveness on structured network-flow data and their relatively low computational requirements (Ganesh and Kumar, 2026). Linear and shallow classifiers, including logistic regression, support vector machines, k-nearest neighbors, and naive Bayes, are commonly used as baseline models in IDS studies (Belachew et al., 2025). Although these models are useful for establishing reference performance, they may struggle to represent highly nonlinear traffic patterns and complex interactions among protocol-derived features, particularly in large-scale edge datasets (Ganesh and Kumar, 2026). Tree-based models, including decision trees and random forests, provide stronger nonlinear modeling capacity and are less sensitive to feature scaling, which makes them suitable for tabular cybersecurity data (Kostas et al., 2025).

Gradient-boosted decision-tree models have become especially important in tabular IDS research. Methods such as XGBoost and CatBoost iteratively construct ensembles of decision trees and are able to capture nonlinear feature interactions and threshold-based decision boundaries effectively (Keskin, 2024). These models often achieve strong predictive performance with efficient inference, making them attractive for edge-oriented security applications (Ismail et al., 2025). However, conventional tree-based IDS models are usually trained as flat classifiers that directly map input features to attack labels without explicitly modeling the semantic relationships among attack categories. In highly imbalanced datasets, such models may also favor majority classes unless evaluation is carefully designed around class-sensitive metrics (Ganesh and Kumar, 2026). In addition, many studies emphasize aggregate performance measures, such as accuracy, while providing limited analysis of rare classes, false-alarm behavior, and stability across repeated data partitions (Keskin and Oz, 2026).

Deep learning has also been widely investigated for intrusion detection because of its ability to learn complex representations from high-dimensional data (Clinton et al., 2026; Li et al., 2026). Feedforward deep neural networks and multilayer perceptrons have been used to model nonlinear feature interactions in network traffic (Gao et al., 2026; Ismail et al., 2025). Convolutional neural networks have been adapted to extract spatial or local feature patterns, while recurrent architectures, including long short-term memory and gated recurrent unit networks, have been applied to capture sequential dependencies in traffic flows (Clinton et al., 2026; Örsdemır et al., 2026). Autoencoder-based models have also been explored for feature compression and anomaly detection by identifying deviations from reconstructed normal behavior (Umar and Jordanov, 2026). More recently, attention-based and Transformer-inspired architectures have been introduced into tabular and network-security applications, enabling models to learn global relationships among input features (Wu et al., 2025; Li et al., 2026). Tabular deep learning approaches, such as TabNet and TabTransformer, further attempt to adapt neural architectures to structured data by incorporating attention or feature-token mechanisms (Pal et al., 2025; Gao et al., 2026).

Despite these advances, deep learning is not universally superior for tabular intrusion detection. Deep models may require extensive tuning, large computational resources, and careful handling of class imbalance (Ganesh and Kumar, 2026). Their deployment in edge-IoT and IIoT environments may also be constrained by memory, latency, and energy requirements (Sahoo et al., 2026). Several studies indicate that, for structured network-flow data, well-tuned tree-based and gradient-boosted models can remain highly competitive with deep learning models (Keskin and Oz, 2026). This observation suggests that IDS evaluation should include both deep tabular baselines and strong gradient-boosted models rather than assuming that architectural complexity necessarily leads to superior performance.

Another important issue in IoT/IIoT IDS research is the distinction between binary and multiclass detection. Binary classification, which separates benign from malicious traffic, is useful for initial detection, but it provides limited information for response planning and forensic analysis. In contrast, multiclass classification identifies the specific attack type and is therefore more valuable for operational decision-making (Ismail et al., 2025). However, multiclass IDS is more challenging because realistic IoT/IIoT datasets often exhibit severe class imbalance. Normal traffic and high-volume attacks, such as DDoS variants, may dominate the data distribution, while attacks such as MITM, fingerprinting, ransomware, and XSS may appear much less frequently (Saiyed and Al-Anbagi, 2026). Under such conditions, overall accuracy can be misleading, since a model may perform well on majority classes while failing to identify rare but important threats (Pal et al., 2025).

To obtain a more reliable assessment of IDS performance under imbalance, class-sensitive and operational metrics are required. Macro-F1 and Matthews correlation coefficient provide more informative views of multiclass performance than accuracy alone. Per-class precision, recall, and F1-score are also necessary to identify weaknesses on minority attack categories. Moreover, false-alarm analysis is essential for practical deployment, because excessive benign-to-attack misclassification can overwhelm security operators and reduce trust in the IDS (Saiyed and Al-Anbagi, 2026). Therefore, a robust evaluation should consider not only overall predictive performance, but also rare-class detection and the false-alarm burden imposed on benign traffic.

To improve IDS robustness, many studies have proposed ensemble and hybrid learning strategies. Ensemble methods such as bagging, boosting, voting, and stacking combine multiple classifiers to improve generalization and reduce variance. Stacking-based IDS frameworks typically combine the predictions of different base learners and use a meta-classifier to produce the final decision (Ismail et al., 2025). Hybrid ML/DL models have also been proposed, where neural networks are used for feature extraction and classical classifiers, such as support vector machines or gradient-boosted trees, are used for final classification (Li et al., 2026). Other approaches combine feature selection with machine learning using optimization algorithms such as particle swarm optimization or genetic algorithms (Zhang et al., 2025).

Although ensemble and hybrid IDS models can improve predictive performance, many of them follow a flat modeling structure. In such designs, all learners or feature extractors are applied to all traffic samples without explicitly considering the hierarchical organization of attack categories (Gao et al., 2026). This can increase computational cost and may limit interpretability in edge-oriented deployments (Sahoo et al., 2026). More importantly, many hybrid models do not exploit the fact that IoT/IIoT attacks naturally form broader families, such as DDoS, injection, scanning, malware, and MITM (Keskin and Oz, 2026). Ignoring this structure may make it more difficult to separate coarse inter-family discrimination from fine-grained intra-family classification, especially for rare or closely related attack types (Wu et al., 2025).

The existing literature therefore reveals several unresolved challenges. Prior studies have made substantial progress in IoT/IIoT intrusion detection, but there remains a need for studies that jointly consider fine-grained multiclass classification, strong gradient-boosted tabular baselines, attack-family-aware modeling, rare-class evaluation, false-alarm analysis, and repeated stratified-split stability. Tree-based models provide strong performance on tabular data, while deep models offer flexible representation learning; however, both are often evaluated using flat classification structures. Similarly, hybrid models frequently combine multiple

components without explicitly using the semantic organization of attack families. These limitations motivate the present study, which investigates HERB-Fusion-IDS, a hierarchical expert-routed boosting framework that combines a flat gradient-boosted classifier, an attack-family router, family-specific experts, and validation-selected probability fusion for multiclass Edge-IIoT intrusion detection.

2. Materials and Methods

2.1. Problem Formulation

This study addresses multiclass intrusion detection in edge-enabled IoT/IIoT traffic using the Edge-IIoTset benchmark. Each traffic instance is represented by a tabular feature vector and assigned to one of 15 traffic categories. The label space consists of one benign class, Normal, and fourteen attack classes: DDoS_UDP, DDoS_ICMP, DDoS_TCP, DDoS_HTTP, SQL_injection, XSS, Uploading, Password, Backdoor, Vulnerability_scanner, Port_Scanning, Fingerprinting, Ransomware, and MITM.

Unlike binary intrusion detection, which only distinguishes benign and malicious traffic, this formulation requires the model to identify the specific attack category. This setting is more informative for incident response and mitigation, but it is also more challenging because several attack classes are underrepresented and may share similar protocol-level characteristics.

2.2. Dataset Description

The experimental evaluation was conducted using the Edge-IIoTset dataset, a comprehensive cybersecurity benchmark developed for Internet of Things (IoT) and Industrial Internet of Things (IIoT) intrusion detection research (Ferrag et al., 2022). Edge-IIoTset was designed to support the evaluation of machine-learning-based security models in both centralized and federated learning settings. In contrast to conventional intrusion detection datasets that are often limited to either IoT or traditional network environments, Edge-IIoTset was generated from a realistic and heterogeneous IoT/IIoT testbed that integrates sensing devices, edge services, fog and cloud components, software-defined networking, blockchain services, network functions virtualization, and industrial communication protocols.

The original Edge-IIoTset architecture is organized into seven interconnected layers: the cloud computing layer, network functions virtualization layer, blockchain network layer, fog computing layer, software-defined networking layer, edge computing layer, and IoT/IIoT perception layer. This layered architecture reflects the multi-tier structure of modern IoT/IIoT deployments, where physical devices, edge gateways, communication brokers, network control services, fog platforms, and cloud-based applications interact with one another. The dataset therefore captures traffic patterns from a diverse cyber-physical environment rather than from a single isolated network segment.

The perception layer of the testbed includes more than ten types of IoT devices, sensors, and actuators, such as temperature and humidity sensors, ultrasonic sensors, water-level sensors, pH sensors, soil-moisture sensors, heart-rate sensors, flame sensors, sound sensors, infrared receivers, servo motors, stepper motors, and Modbus-based industrial components. The testbed also incorporates technologies and services commonly encountered in IoT/IIoT systems, including Mosquitto MQTT brokers, Modbus TCP/IP, ThingsBoard, Node-RED, ONOS SDN controller, Hyperledger Sawtooth, OPNFV, Zeek, and Wireshark. This diversity makes the dataset suitable for evaluating intrusion detection models under heterogeneous protocol and device conditions.

Edge-IIoTset contains both benign and malicious traffic. The malicious traffic was generated through fourteen attack scenarios targeting IoT and IIoT connectivity protocols and services. These attacks are grouped into five major threat categories: denial-of-service and distributed denial-of-service attacks, information-gathering attacks, man-in-the-middle attacks, injection attacks, and malware attacks. The attack scenarios include TCP SYN flood, UDP flood, HTTP flood, ICMP flood, port scanning, operating-system fingerprinting, vulnerability scanning, ARP/DNS spoofing, cross-site scripting, SQL injection, malicious uploading, backdoor attack, password cracking, and ransomware. This threat diversity enables a fine-grained multiclass evaluation of intrusion detection models rather than limiting the problem to binary benign-versus-attack discrimination.

In this study, the learning task was formulated using the 15-class attack-type target space defined in Section 2.1. This formulation is more challenging than binary intrusion detection because the model must identify the specific type of attack after distinguishing malicious behavior from normal operation.

The class distribution is highly imbalanced, which reflects an important challenge in practical intrusion detection. Normal traffic represents the largest portion of the dataset, while several attack categories, particularly MITM and Fingerprinting, are represented by substantially fewer observations. This imbalance motivated the use of class-sensitive evaluation criteria, including macro-averaged F1-score, Matthews correlation coefficient, rare-class F1-score, and false-alarm analysis. In particular, Fingerprinting, MITM, Ransomware, and XSS were treated as rare or difficult attack classes during the evaluation because of their lower representation and operational relevance.

The original Edge-IIoTset study reports that features were extracted from multiple information sources, including alerts, system resources, logs, and network traffic. From an initial set of 1176 extracted attributes, 61 highly correlated features were selected by the dataset authors. In the present study, a leakage-aware feature selection strategy was further applied before model training. Direct labels, identity-related attributes, temporal identifiers, transport-port identifiers, raw payload information, and content-specific fields that

could provide shortcut cues were excluded from the predictive feature space. This strategy was adopted to reduce the risk of overestimating model performance due to non-generalizable identifiers or direct artifacts of the data collection process.

The final experimental setting therefore evaluates intrusion detection models on a realistic, heterogeneous, and imbalanced IoT/IIoT benchmark while emphasizing fine-grained attack-type recognition. The use of Edge-IIoTset is particularly appropriate for the proposed HERB-Fusion-IDS framework because the dataset combines heterogeneous traffic sources, multiple protocol families, and attack categories with natural relationships at both coarse threat-family and fine-grained attack-type levels.

2.3. Dataset Preparation and Leakage-Aware Feature Filtering

The experimental pipeline was designed to reduce data leakage and shortcut learning, which are common risks in network-intrusion datasets. First, all column names were normalized by converting them to lowercase and replacing spaces, hyphens, and periods with underscores. Exact duplicate rows were removed before train-validation-test partitioning in order to prevent identical instances from appearing across different splits.

The multiclass label attack_type was used as the prediction target. The binary label attack_label was removed from the input space to avoid target leakage. In addition, fields that may encode traffic identity, experimental-session artifacts, direct payload signatures, or attack-specific content were excluded before model fitting. The excluded fields included labels, time/session identifiers, source/destination host identifiers, transport ports and streams, payload-related fields, URI-related fields, and MQTT topic/message contents. This filtering step was applied before model training and was independent of any classifier.

The retained feature matrix was converted to numeric form using coercive numeric parsing. Columns that were entirely missing in the training split were removed. Columns with no variation in the training split were also removed. Missing values were imputed using the median computed from the training partition only. For linear and neural baselines, the imputed features were standardized using a StandardScaler fitted only on the training split. Tree-based models were trained on the imputed but unscaled numeric features.

Let X_{train}, X_{val} and X_{test} denote the train, validation, and test matrices. The imputer and scaler were fitted as follows (equations 1 and 2):

$$\tilde{X}_{\text{train}} = \text{Imputer}_{\text{median}}(X_{\text{train}}) \quad (1)$$

$$Z_{\text{train}} = \text{Scaler}(\tilde{X}_{\text{train}}) \quad (2)$$

where both the imputer and scaler parameters were estimated exclusively from the training set. The same fitted transformations were then applied to the validation and test partitions.

2.4. Experimental Protocol

The cleaned dataset was partitioned using a stratified 70/15/15 protocol, corresponding to training, validation, and independent test subsets, respectively. Stratification was performed with respect to the multiclass attack-type label in order to preserve the class distribution across all partitions. The validation subset was used for model selection, hyperparameter tuning, and fusion-weight selection, whereas the test subset was held out for final evaluation only.

To assess the stability of the results, the complete experimental procedure was repeated five times using independent stratified partitions. For each repetition, the preprocessing steps were refitted using only the corresponding training subset, and the same fitted transformations were then applied to the validation and test subsets. All compared models were evaluated under identical partitioning conditions within each repetition. Final performance values were reported as mean $\pm$ standard deviation across the five repetitions.

This protocol also supports reproducibility by fixing the preprocessing order, data-partitioning strategy, validation procedure, evaluation metrics, and aggregation scheme across all models. In particular, paired comparisons between HERB-Fusion-IDS and flat XGBoost were computed using the same test partitions, which enables a direct assessment of the incremental effect of the proposed fusion strategy.

2.5. Attack-Family Taxonomy

The proposed hierarchical framework uses attack-family taxonomy to decompose the 15-class task into a coarse family-routing problem and family-specific expert classification problems. The mapping used in this study is shown in Table 1. This taxonomy is used only for the hierarchical modeling stage. The final prediction task remains the original 15-class classification problem.

Table 1. Attack-family mapping used by HERB-IDS

Family	Member classes
Normal	Normal
DDoS	DDoS_UDP, DDoS_ICMP, DDoS_TCP, DDoS_HTTP
Injection/Web	SQL_injection, XSS, Uploading
Credential/Backdoor	Password, Backdoor
Scanning	Vulnerability_scanner, Port_Scanning, Fingerprinting
Malware	Ransomware
MITM	MITM

2.6. Baseline Models

To evaluate the proposed framework, representative baselines were selected from four model families: linear classification, non-boosting tree ensembles, gradient-boosted trees, and deep tabular learning. Table 2 summarizes the compared models and their roles in the experimental evaluation.

SGD logistic regression was included as a linear reference

model with multinomial probabilistic outputs and regularized log-loss optimization. RandomForest-style and ExtraTrees models were used to represent non-boosting tree-ensemble approaches. The RandomForest-style model was implemented using an XGBoost-compatible random-forest variant, while ExtraTrees used randomized split selection and ensemble averaging. Flat XGBoost was included as the main strong tabular baseline because gradient-boosted decision trees are highly competitive for structured network-flow data. Two neural baselines were also considered: Tabular ResNet, which uses residual connections for tabular representation learning, and FT-Transformer, which applies attention-based feature-token modeling. All baselines were trained under the same experimental protocol and compared using the same evaluation metrics.

Table 2. Baseline models used for comparison

Model	Category	Role in the evaluation
SGD Logistic Regression	Linear classifier	Lower-bound linear reference for multiclass classification
Random Forest-style ensemble	Non-boosting tree ensemble	Bagging-style comparison against boosting-based methods
ExtraTrees	Non-boosting tree ensemble	Randomized tree-ensemble baseline
Flat XGBoost	Gradient-boosted trees	Main strong tabular baseline and fusion component
Tabular ResNet	Deep tabular model	Residual neural baseline for structured features
FT-Transformer	Deep tabular model	Attention-based deep tabular baseline

2.7. Proposed HERB-IDS

HERB-IDS is the hierarchical component of the proposed framework. It decomposes the original 15-class problem into two levels. First, a family router estimates the broad attack family of a sample. Second, family-specific expert classifiers distinguish the member classes within each non-singleton family. This design separates coarse inter-family discrimination from fine-grained intra-family classification.

Family Router: The family router predicts the coarse attack family of a sample (equation 3):

$$P(F = f|\boldsymbol{x}), f \in \mathcal{F}, \tag{3}$$

where $\mathcal{F}$ denotes the set of families in Table 1. The router is trained as a multiclass XGBoost model using the family labels induced from the original attack-type labels.

Family-Specific Experts: For every non-singleton family f, a local expert classifier is trained using only the training samples belonging to that family. The expert estimates (equation 4),

$$P(C = c|F = f, x), \tag{4}$$

where c is a class contained in family f. Singleton families, such as MITM and Ransomware, do not require an additional expert; their posterior probability is directly inherited from the router.

Hierarchical Posterior Assembly: For a class c, let f_c denote the family containing class c. HERB-IDS constructs the final class posterior as (equation 5),

$$P_{HERB}(C = c|x) = \begin{cases} P(F = f_c|x) & \text{if } f_c \text{ is a singleton} \\ P(F = f_c|x), P(C = c|F = f_c, x) & \text{otherwise} \end{cases} \tag{5}$$

The resulting posterior vector is normalized to ensure that (equation 6),

$$\sum_{c \in \mathcal{Y}} P_{\text{HERB}}(C = c|\boldsymbol{x}) = 1. \tag{6}$$

The predicted class is then (equation 7),

$$\hat{y}_{\text{HERB}} = \arg\max_{c \in \mathcal{Y}} P_{\text{HERB}}(C = c|\boldsymbol{x}). \tag{7}$$

This hierarchical design allows the model to learn coarse inter-family discrimination separately from fine-grained intra-family decision boundaries.

Proposed HERB-Fusion-IDS: HERB-IDS alone introduces attack-family specialization, but a flat XGBoost classifier can still provide strong global decision boundaries. Therefore, the final proposed model, HERB-Fusion-IDS, combines the posterior probabilities of the flat XGBoost model and the HERB-IDS hierarchy.

Let $P_{\text{flat}}(C = c|\boldsymbol{x})$ be the posterior probability from flat XGBoost, and let $P_{\text{HERB}}(C = c|\boldsymbol{x})$ be the posterior probability from HERB-IDS. The fused posterior is defined as (equation 8),

$$P_{\text{fusion}}(C = c|\boldsymbol{x}) = \alpha P_{\text{flat}}(C = c|\boldsymbol{x}) + (1 - \alpha) P_{\text{HERB}}(C = c|\boldsymbol{x}), \tag{8}$$

where $\alpha \in [0,1]$ controls the contribution of the flat global model. The final prediction is (equation 9),

$$\hat{y}_{\text{fusion}} = \arg\max_{c \in \mathcal{Y}} P_{\text{fusion}}(C = c|\boldsymbol{x}). \tag{9}$$

The fusion coefficient was selected using validation data only. In the final repeated stratified-split evaluation, the selected flat-branch weight was fixed as $\alpha = 0.85$. Thus, HERB-Fusion-IDS retains the strong global probability estimates of XGBoost while injecting hierarchical attack-family information through the HERB branch.

Training and Hyperparameter Selection: The flat XGBoost branch, HERB router, HERB experts, and fusion coefficient were tuned using a validation-based hyperparameter optimization procedure. The test set was not used during hyperparameter selection. After selecting the hyperparameters, final evaluation was repeated over the five independent stratified repetitions. The tuned XGBoost hyperparameters used for the flat

branch, HERB router, and family-specific HERB experts are summarized in Table 4. The selected settings show that the flat XGBoost branch used a lower learning rate, whereas the router and expert models used higher learning rates with stronger regularization. This configuration reflects the different roles of the components: the flat branch provides stable global discrimination, while the hierarchical branch models family-level and within-family decision boundaries. For the deep-tabular baselines, the models were trained using the AdamW optimizer with learning rate 10^{-3}, weight decay 10^{-4}, batch size 8192, dropout 0.10, and early stopping based on validation performance. Label smoothing with coefficient 0.02 was used in the cross-entropy objective.

Table 3. Overall multiclass intrusion detection performance over five independent stratified repetitions. Values are reported as mean ± standard deviation

Method	Accuracy	Macro-F1	Weighted-F1	MCC	Rare-F1	FA/10k	ADR
HERB-Fusion-IDS	0.961±0.000	0.851±0.003	0.958±0.000	0.913±0.001	0.746±0.009	40.8±0.8	0.895±0.001
XGBoost	0.960±0.000	0.845±0.003	0.957±0.000	0.912±0.001	0.725±0.011	40.8±0.8	0.895±0.001
Tabular ResNet	0.908±0.001	0.640±0.011	0.884±0.002	0.790±0.003	0.527±0.028	49.9±8.5	0.719±0.002
FT-Transformer	0.906±0.003	0.633±0.023	0.881±0.004	0.783±0.007	0.537±0.067	54.9±7.9	0.710±0.009
HERB-IDS	0.877±0.002	0.772±0.002	0.903±0.001	0.779±0.002	0.656±0.008	1271.8±23.1	0.984±0.001
Random Forest	0.857±0.000	0.751±0.004	0.883±0.000	0.756±0.000	0.643±0.021	1627.6±3.9	0.999±0.000
SGD-LogReg	0.814±0.012	0.458±0.012	0.818±0.005	0.614±0.016	0.257±0.049	1145.3±152.7	0.785±0.009
ExtraTrees	0.775±0.009	0.631±0.010	0.821±0.007	0.646±0.010	0.446±0.012	2490.0±124.0	0.973±0.001

Table 4. Main XGBoost settings used for the flat and hierarchical components

Setting	Flat XGBoost	Router	Experts
Number of trees	450	450	495
Learning rate	0.026	0.104	0.125
Maximum tree depth	6	7	5
Minimum child weight	3.09	5.85	5.85
Row subsampling ratio	1.00	0.80	0.80
Column subsampling ratio	0.85	0.85	0.85
L2 regularization	1.02	2.41	2.41
L1 regularization	0.0003	0.007	0.007
Minimum loss reduction	1.81	1.65	1.65
Maximum delta step	3	2	2

2.8. Evaluation Metrics

Because the dataset is highly imbalanced and contains rare attack categories, performance was evaluated using both global and class-sensitive metrics. The following metrics were reported: accuracy, macro-F1, weighted-F1, Matthews correlation coefficient (MCC), rare-class F1, false alarms per 10,000 normal flows, and attack-detection recall. Macro-F1 was computed as the unweighted mean of class-wise F1 scores (equation 10):

$$\text{MacroF1} = \frac{1}{|\mathcal{Y}|}\sum_{c\in\mathcal{Y}} \text{F1}_c. \tag{10}$$

The rare-class subset was defined as $\mathcal{R} = \{\text{Fingerprinting,MITM,Ransomware,XSS}\}$. Rare-class F1 was computed as (equation 11),

$$\text{RareF1} = \frac{1}{|\mathcal{R}|}\sum_{c\in\mathcal{R}} \text{F1}_c. \tag{11}$$

False alarms per 10,000 normal flows were computed as (equation 12),

$$\text{FA}_{10k} = 10{,}000 \times \frac{|\{i: y_i = \text{Normal}, \hat{y}_i \neq \text{Normal}\}|}{|\{i: y_i = \text{Normal}\}|}. \tag{12}$$

Attack-detection recall measures the ability to detect malicious traffic as malicious, regardless of whether the exact attack subclass is correct (equation 13):

$$\text{ADR} = \frac{|\{i: y_i \neq \text{Normal}, \hat{y}_i \neq \text{Normal}\}|}{|\{i: y_i \neq \text{Normal}\}|}. \tag{13}$$

This metric is complementary to multiclass F1 because it captures whether an attack is at least detected as non-benign, even when there is confusion among attack subclasses.

Statistical Aggregation: All models were evaluated independently across five experimental repetitions. For each metric, the mean and sample standard deviation were computed over the repeated test-set evaluations. This aggregation strategy was used to reduce dependence on a single data split and to provide a more stable estimate of model behavior.

Because HERB-Fusion-IDS and flat XGBoost were evaluated on identical train-validation-test partitions within each repetition, their differences were also

analyzed in a paired manner. For a given metric, the paired difference was computed by subtracting the XGBoost score from the HERB-Fusion-IDS score within the same repetition. Positive values therefore indicate that HERB-Fusion-IDS improved over flat XGBoost under the same data-partitioning conditions. This paired analysis provides a stricter comparison than comparing aggregate means alone.

3. Results

This section presents the experimental evaluation of the proposed HERB-Fusion-IDS framework for multiclass intrusion detection on the Edge-IIoTset dataset. The evaluation compares the proposed method with representative linear, ensemble-based, gradient-boosted, and deep tabular learning baselines. All models were evaluated over five independent stratified repetitions, and the reported values correspond to the mean and standard deviation across these repetitions. The main evaluation criteria include accuracy, macro-averaged F1-score, weighted F1-score, Matthews correlation coefficient (MCC), rare-class F1-score, false alarms per 10,000 normal samples, and attack-detection recall.

3.1. Overall Multiclass Classification Performance

Table 3 summarizes the overall multiclass classification results. Among the evaluated methods, HERB-Fusion-IDS reported the highest mean accuracy, macro-F1, weighted-F1, MCC, and rare-class F1. The proposed method obtained an accuracy of 0.961 ± 0.000, a macro-F1 score of 0.851 ± 0.003, and an MCC of 0.913 ± 0.001. These results indicate that HERB-Fusion-IDS provides a competitive balance between global classification performance and class-sensitive evaluation on Edge-IIoTset.

Flat XGBoost was the strongest individual baseline, achieving an accuracy of 0.960 ± 0.000, a macro-F1 score of 0.845 ± 0.003, and an MCC of 0.912 ± 0.001. The small difference between XGBoost and HERB-Fusion-IDS confirms that XGBoost is a highly competitive model for this tabular intrusion detection problem. Nevertheless, the proposed fusion strategy consistently improved over flat XGBoost, particularly in macro-F1 and rare-class F1, which are more informative than accuracy under class imbalance. The standalone HERB-IDS model achieved a lower accuracy of 0.877 ± 0.002 and a macro-F1 score of 0.772 ± 0.002. Its high attack-detection recall, together with its large false-alarm rate, indicates that the hierarchy alone is more aggressive in assigning samples to attack classes. Therefore, the fusion strategy is important: HERB-Fusion-IDS preserves the low false-alarm behavior of XGBoost while incorporating useful hierarchical corrections from HERB-IDS.

The deep tabular baselines, TabularResNet and FT-Transformer, achieved relatively high accuracy values of 0.908 ± 0.001 and 0.906 ± 0.003, respectively. However, their macro-F1 and rare-class F1 scores were substantially lower than those of the tree-based and fusion-based methods. This indicates that the deep models were able to learn majority-class patterns but were less effective in handling the fine-grained class imbalance of Edge-IIoTset. The linear SGD-LogReg baseline produced the weakest macro-F1 and rare-class F1, confirming that the classification problem requires nonlinear decision boundaries.

3.2. Comparison with Flat XGBoost

Since HERB-Fusion-IDS is designed as a hierarchical fusion extension of flat XGBoost, the most important comparison is the paired repetition-wise comparison between these two models. Across all five repetitions, HERB-Fusion-IDS improved over XGBoost in accuracy, macro-F1, MCC, and rare-class F1. The mean improvement was modest in accuracy and MCC, but more visible for macro-F1 and rare-class F1.

Table 5 reports the paired repetition-wise differences between HERB-Fusion-IDS and flat XGBoost. Specifically, HERB-Fusion-IDS improved over XGBoost by an average of 0.00013 in accuracy, 0.00590 in macro-F1, 0.00030 in MCC, and 0.02070 in rare-class F1. Although the accuracy gain is numerically small, the improvement in rare-class F1 corresponds to an absolute increase of approximately 2.07 percentage points. This is meaningful for an imbalanced multiclass intrusion detection task because rare attack categories are often the most difficult to classify reliably.

Table 5. Paired repetition-wise difference between HERB-Fusion-IDS and flat XGBoost. Positive values indicate improvement over XGBoost.

Run	ΔAccuracy	ΔMacro-F1	ΔMCC	ΔRare-F1
1	0.00004	0.00164	0.00009	0.00586
2	0.00032	0.01110	0.00072	0.03772
3	0.00005	0.00624	0.00011	0.02356
4	0.00024	0.00526	0.00054	0.01696
5	0.00002	0.00526	0.00006	0.01940
Mean	0.00013	0.00590	0.00030	0.02070
Std.	0.00014	0.00339	0.00031	0.01155

These results support the contribution of the proposed fusion mechanism in the repeated Edge-IIoTset evaluation. The hierarchical branch alone does not surpass XGBoost, but it contributes complementary information when combined with the flat classifier. The validation-selected fusion coefficient assigned a

dominant weight to the flat XGBoost branch, indicating that the global multiclass decision boundary remains essential. At the same time, the consistent repetition-wise improvements suggest that the hierarchical branch provides useful class-structure-aware corrections.

3.3. Rare-Attack Detection Performance

Rare-attack detection is a critical requirement in practical intrusion detection because low-frequency attacks are often more difficult to model and may be underrepresented during training. In this study, Fingerprinting, MITM, Ransomware, and XSS were treated as rare or difficult classes. HERB-Fusion-IDS achieved the highest mean rare-class F1 among all evaluated methods, with a score of 0.746 ± 0.009, compared with 0.725 ± 0.011 for XGBoost, 0.656 ± 0.008 for HERB-IDS, and 0.643 ± 0.021 for RandomForest.

Table 6 summarizes the rare-class F1-score comparison between XGBoost and HERB-Fusion-IDS. The class-level rare-attack analysis shows that the improvement of HERB-Fusion-IDS over XGBoost mainly arises from Fingerprinting. The mean F1-score for Fingerprinting increased from 0.232 under XGBoost to 0.315 under HERB-Fusion-IDS. Both models achieved identical mean F1-scores for MITM, Ransomware, and XSS, with values of 0.990, 0.879, and 0.800, respectively. Therefore, the rare-class gain of HERB-Fusion-IDS is primarily associated with improved recognition of the most difficult minority class rather than broad changes across all rare classes.

Table 6. Rare-class F1-score comparison between XGBoost and HERB-Fusion-IDS

Rare class	XGBoost F1	HERB-Fusion-IDS F1
Fingerprinting	0.232	0.315
MITM	0.990	0.990
Ransomware	0.879	0.879
XSS	0.800	0.800
Mean	0.725	0.746

The rare-class results should also be interpreted together with the false-alarm metric. HERB-IDS and RandomForest produced substantially more false positives than HERB-Fusion-IDS. For example, HERB-IDS produced approximately 1272 false alarms per 10,000 normal samples, and RandomForest produced around

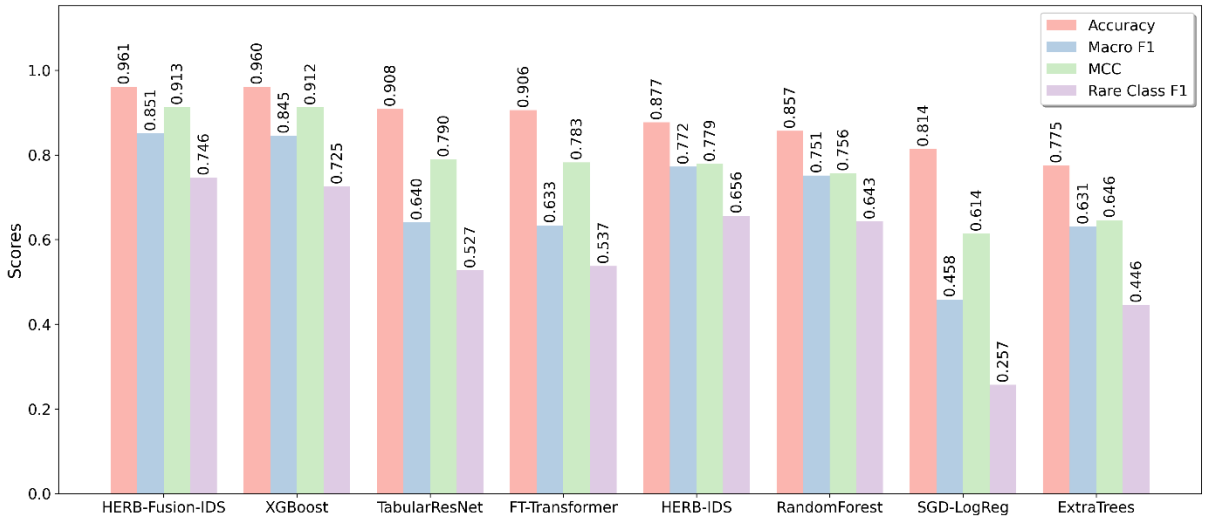


Figure 1. Comparison of mean accuracy, macro-F1, MCC, and rare-class F1 across the evaluated models.

Table 7. Selected diagonal recognition-rate changes between flat XGBoost and HERB-Fusion-IDS on a row-normalized confusion matrix

Class	XGBoost	HERB-Fusion-IDS	Difference
Fingerprinting	0.147	0.167	+0.020
SQL_injection	0.700	0.708	+0.008
Vulnerability scanner	0.919	0.921	+0.002
DDoS_HTTP	0.589	0.581	-0.007

1628 false alarms per 10,000 normal samples. In contrast, HERB-Fusion-IDS produced approximately 41 false alarms per 10,000 normal samples, which is comparable to flat XGBoost. Therefore, HERB-Fusion-IDS offers a more balanced rare-class detection profile by improving rare-class F1 without increasing the false-alarm burden.

3.4. Confusion-Level Error Analysis

To better understand the source of the rare-class improvement, a confusion-level comparison was conducted between HERB-Fusion-IDS and flat XGBoost on a representative test partition. The analysis used row-normalized confusion matrices so that changes could be interpreted as class-wise recognition-rate differences. Because this analysis is based on a representative test partition rather than all repeated partitions, it is used only as a diagnostic complement to the repeated-split results reported in Tables 3 and 5.

Table 7 reports the main class-wise changes in diagonal recognition rates. The largest positive change was observed for Fingerprinting, whose correct recognition

rate increased from 0.147 under XGBoost to 0.167 under HERB-Fusion-IDS. This finding is consistent with the rare-class F1 improvement reported in Table5. Smaller positive changes were observed for SQL_injection and Vulnerability_scanner. In contrast, DDoS_HTTP showed a small reduction in correct recognition. Therefore, the improvement of HERB-Fusion-IDS should be interpreted as a limited but explainable correction concentrated on selected difficult classes rather than a uniform improvement across all attack categories.

The confusion-level comparison also showed that the Fingerprinting gain was mainly associated with a reduction in Fingerprinting samples misclassified as DDoS_ICMP, while the SQL_injection gain was mainly associated with fewer SQL_injection samples misclassified as DDoS_HTTP. The Normal class remained almost unchanged, which is consistent with the comparable false-alarm rates of HERB-Fusion-IDS and flat XGBoost in Table 3.

Figure 1 presents the mean accuracy, macro-F1, MCC, and rare-class F1 values across the evaluated models. HERB-Fusion-IDS and XGBoost form the strongest performance group among the compared methods. HERB-Fusion-IDS shows slightly higher mean values across the displayed metrics, while the difference is most visible for macro-F1 and rare-class F1. The figure also shows that accuracy alone is not sufficient for this imbalanced multiclass setting, since several models achieve reasonable accuracy but substantially lower macro-F1 and rare-class F1. Overall, the experimental findings indicate that HERB-Fusion-IDS provides a small but consistent improvement over flat XGBoost in the repeated Edge-IIoTset evaluation. The improvement is not large enough to claim broad superiority over all IDS approaches, but it supports the main hypothesis of this study: attack-family information can provide useful complementary structure when fused with a strong flat boosting classifier. The results also emphasize the importance of reporting rare-class and false-alarm-aware metrics rather than relying only on accuracy.

4. Conclusion

This study presented HERB-Fusion-IDS, a hierarchical expert-routed boosting framework with probability-level fusion for multiclass IoT/IIoT intrusion detection. The method combines a flat XGBoost classifier with an attack-family router and family-specific experts. In the repeated Edge-IIoTset evaluation, HERB-Fusion-IDS improved over flat XGBoost in accuracy, macro-F1, MCC, and rare-class F1. The improvement was modest in accuracy and MCC, but more visible in macro-F1 and rare-class F1, indicating that the hierarchical branch can provide useful complementary information when combined with a strong flat boosting baseline.

The results also show that the standalone hierarchical model is not sufficient by itself, as it increases the false-alarm burden compared with XGBoost. Therefore, the main value of the proposed approach lies in the fusion strategy, which preserves the low false-alarm behavior of the flat classifier while adding limited attack-family-aware correction. This finding supports the use of structured hierarchical information, but it also indicates that such information should be integrated carefully rather than used as a direct replacement for strong tabular baselines.

This study has several limitations. First, the evaluation was conducted only on the Edge-IIoTset benchmark. Although Edge-IIoTset is a realistic and widely used IoT/IIoT cybersecurity dataset, external validation on additional datasets is necessary before drawing broader conclusions about generalization. Second, the gain over XGBoost, while consistent across five repetitions, is numerically modest. Therefore, the proposed method should be interpreted as a structured improvement over a strong baseline rather than as a general replacement for existing IDS models. Third, the present work focuses on supervised multiclass classification and does not evaluate unseen attack categories or cross-dataset transfer. Future work will extend the evaluation to additional IoT/IIoT benchmarks, investigate zero-day and domain-shift settings, and examine calibration-aware fusion strategies to improve the reliability of probability-based IDS decisions.

Author Contributions

The percentages of the author' contributions are presented below. The author reviewed and approved the final version of the manuscript.

	F.K.
C	100
D	100
S	100
DCP	100
DAI	100
L	100
W	100
CR	100
SR	100
PM	100
FA	100

C= concept, D= design, S= supervision, DCP= data collection and/or processing, DAI= data analysis and/or interpretation, L= literature search, W= writing, CR= critical review, SR= submission and revision, PM= project management, FA= funding acquisition.

Conflict of Interest

The author declared that there is no conflict of interest.

Ethical Consideration

Ethics committee approval was not required for this study because there was no study on animals or humans.

References

Baich, M., & Sael, N. (2025). A Federated Learning-Based Intrusion Detection System Using Dynamic Ensemble Aggregation for IoT Networks. *IEEE Access, 13*, 205826-205839. https://doi.org/10.1109/ACCESS.2025.3640521

Belachew, H. M., Beyene, M. Y., Desta, A. B., Alemu, B. T., Musa, S. S., & Muhammed, A. J. (2025). Design a Robust DDoS Attack Detection and Mitigation Scheme in SDN-Edge-IoT by Leveraging Machine Learning. *IEEE Access, 13*, 10194-10214. https://doi.org/10.1109/ACCESS.2025.3526692

Clinton, U. B., Hoque, N., Raza, S., & Bhuyan, M. (2026). Securing IoT: Unveiling Attacks With Multiview-Multitask Learning. *IEEE Transactions on Artificial Intelligence, 7*, 2332-2345. https://doi.org/10.1109/TAI.2025.3615565

Fan, J., Tan, S., Gu, H., Wang, Z., & Lü, J. (2026). Dynamic Hypernetwork Grouping With Diffusion-Based Sampler for Heterogeneous Federated Intrusion Detection. *IEEE Internet of Things Journal, 13*, 24665-24684. https://doi.org/10.1109/JIOT.2026.3674493

Ferrag, M. A., Friha, O., Hamouda, D., Maglaras, L., & Janicke, H. (2022). Edge-IIoTset: A New Comprehensive Realistic Cyber Security Dataset of IoT and IIoT Applications for Centralized and Federated Learning. *IEEE Access, 10*, 40281–40306. https://doi.org/10.1109/access.2022.3165809

Ganesh, L. S., & Kumar, P. M. (2026). HydraGuard-ID: A Hybrid Ensemble Framework With Stratified Feature Selection for High-Accuracy DDoS Attack Detection. *IEEE Access, 14*, 58985-59000. https://doi.org/10.1109/ACCESS.2026.3678974

Gao, P., Wang, Z., Yu, S., Song, C., & Yu, H. (2026). Reliable and Trustworthy Local–Global Hierarchical Framework for Intrusion Detection in 6G-IoT Networks. *IEEE Internet of Things Journal, 13*, 8077-8091. https://doi.org/10.1109/JIOT.2025.3609811

Gutti, C., Thumula, K., & Balbudhe, P. (2025). Federated Learning for Distributed IoT Security: A Privacy-Preserving Approach to Intrusion Detection. *IEEE Access, 13*, 135863-135875. https://doi.org/10.1109/ACCESS.2025.3592481

Ismail, S., Dandan, S., & Qushou, A. (2025). Intrusion Detection in IoT and IIoT: Comparing Lightweight Machine Learning Techniques Using TON_IoT, WUSTL-IIOT-2021, and EdgeIIoTset Datasets. *IEEE Access, 13*, 73468-73485. https://doi.org/10.1109/ACCESS.2025.3554083

Keskin, F. (2024). Advanced Driving Cycle Generation Using XGBoost: A Case Study in Iğdır, Türkiye. *2024 8th International Artificial Intelligence and Data Processing Symposium (IDAP)* (pp. 1–6). IEEE. https://doi.org/10.1109/idap64064.2024.10710756

Keskin, F., & Oz, G. (2026). Lightweight and Reliable IoT Intrusion Detection at the Edge: Compression, Calibration, and Shift-Aware Evaluation on CICIoT2023. *Black Sea Journal of Engineering and Science, 9*, 1218–1229. https://doi.org/10.34248/bsengineering.1905346

Kostas, K., Just, M., & Lones, M. A. (2025). Individual Packet Features are a Risk to Model Generalization in ML-Based Intrusion Detection. *IEEE Networking Letters, 7*, 66-70. https://doi.org/10.1109/LNET.2025.3525901

Li, H., Kang, H., Liu, C., Wang, R., Li, J., Sun, G., . . . Mao, S. (2026). Encrypted Traffic Detection in Resource Constrained IoT Networks: A Diffusion Model and LLM Integrated Framework. *IEEE Transactions on Network Science and Engineering, 13*, 5324-5344. https://doi.org/10.1109/TNSE.2025.3649259

Örsdemir, A., Tefek, U., Esiner, E., & Küpçü, A. (2026). SoK: Software-Defined Networks Security With Machine Learning. *IEEE Access, 14*, 40769-40787. https://doi.org/10.1109/ACCESS.2026.3673172

Pal, B., Islam, M. S., & Liew, A. W.-C. (2025). Calibrated Uncertainty Estimation for Trustworthy Deep IoT Attack Detection. *IEEE Transactions on Dependable and Secure Computing, 22*, 7571–7584. https://doi.org/10.1109/tdsc.2025.3598350

Sahoo, J. P., Kar, B., Wu, Y.-L., Abdelmoniem, A. M., & Chatzopoulos, D. (2026). SMoQKE-IDS: Sparse Mixture of Quantum Kolmogorov–Arnold Network Experts for FL-IDS in Edge-IIoT. *IEEE Open Journal of the Communications Society, 7*, 2148-2177. https://doi.org/10.1109/OJCOMS.2026.3668242

Saiyed, M. F., & Al-Anbagi, I. (2026). A Hybrid Explainable AI for DDoS Attacks Detection in Industrial IoT Networks. *IEEE Internet of Things Journal, 13*, 12958-12973. https://doi.org/10.1109/JIOT.2026.3653260

Shah, S. H., Walker, I., & Borowczak, M. (2026). TriSAFE: Transcript-Bound Verifiable Secure Aggregation With Differential Privacy and Timing Defenses for Gateway-Assisted IoT Federated Learning. *IEEE Access, 14*, 89354-89379. https://doi.org/10.1109/ACCESS.2026.3700048

Umar, A., & Jordanov, I. (2026). Anomaly Detection in IoT Environment Using Machine Learning: A Survey. *IEEE Internet of Things Journal, 13*, 20477-20497. https://doi.org/10.1109/JIOT.2026.3671102

Wu, M., Zheng, Y., Wong, D. S.-H., Wang, Y., & Hu, X. (2025). TRACER: Attack-Aware Divide-and-Conquer Transformer for Intrusion Detection in Industrial Internet of Things. *IEEE Transactions on Industrial Informatics, 21*, 4924-4934. https://doi.org/10.1109/TII.2025.3547050

Zhang, S., Xu, Y., & Xie, X. (2025). Universal Adversarial Perturbations Against Machine-Learning-Based Intrusion Detection Systems in Industrial Internet of Things. *IEEE Internet of Things Journal, 12*, 1867-1889. https://doi.org/10.1109/JIOT.2024.3465549

Black Sea Journal of Engineering and Science
doi: 10.34248/bsengineering.1974532

Open Access Journal
e-ISSN: 2619 – 8991

Araştırma Makalesi (Research Article)
Cilt 9 - Sayı 5: 2281-2287 / Eylül 2026
(Volume 9 - Issue 5: 2281-2287 / September 2026)

SÜRDÜRÜLEBİLİR TARIMDA HAFİF DERİN ÖĞRENME VE HİBRİT MAKİNE ÖĞRENMESİ YAKLAŞIMLARI İLE OPTİMİZE EDİLMİŞ YAPRAK HASTALIĞI TESPİTİ

Hasan Hüseyin ÇELİK[1]*

[1]*Marmara University, Faculty of Technology, Department of Electrical and Electronics Engineering, 34854, Istanbul, Türkiye*

Özet: Küresel iklim değişikliği ve nüfus artışı, tarımsal üretimde sürdürülebilirliği ve gıda arzı güvenliğini kritik bir boyuta taşımıştır. Bitki ve mahsul yapraklarında meydana gelen hastalıklar, rekolte miktarını ve gıda kalitesini doğrudan tehdit eden temel unsurların başında gelmektedir. Geleneksel hastalık teşhis yöntemleri insan hatasına açık, maliyetli ve zaman alıcıdır. Son yıllarda derin öğrenme tabanlı evrişimli sinir ağları (CNN) bu problemin çözümünde yüksek başarım göstermiş olsa da, bu modellerin uçtan uca (end-to-end) eğitimi ve çalıştırılması yüksek hesaplama gücü (GPU) ve uzun işlem süreleri gerektirmektedir. Bu durum, internet ve gelişmiş donanım altyapısının kısıtlı olduğu kırsal tarım alanlarında akıllı sistemlerin kullanımını zorlaştırmaktadır. Bu çalışmada, düşük hesaplama maliyetine sahip ve bilgisayar işlemcisi (CPU) kullanan, hiperparametre optimizasyonlu hibrit bir yapay zeka mimarisi önerilmiştir. Önerilen yöntemde, ImageNet veri seti ile önceden eğitilmiş MobileNetV2 mimarisi sadece bir öznitelik çıkarıcı (feature extractor) olarak kullanılmış ve görüntüler 1280 boyutlu sayısal vektörlere indirgenmiştir. Elde edilen öznitelikler, 3-katlamalı çapraz doğrulama (3-Fold Cross-Validation) destekli Izgara Araması (GridSearchCV) ile optimize edilen Destek Vektör Makineleri (SVM), Rastgele Orman (RF) ve XGBoost algoritmaları ile sınıflandırılmıştır. Bu işlemler ayrıca MobileNetV3 mimarisi ile tekrarlanmıştır. Deneysel sonuçlar, önerilen MobileNetV3+SVM hibrit modelinin minimum işlem zamanı ve donanım kaynağı ile yüksek bir sınıflandırma başarımı sunduğunu göstermiştir. Geliştirilen hafif mimari, tarımsal alanlarda mobil ve uç bilişim cihazlarına entegre edilebilir bir potansiyele sahiptir.

Anahtar kelimeler: Akıllı tarım, Derin öznitelik çıkarımı, Hibrit modeller, Hiperparametre optimizasyonu

Optimized Leaf Disease Detection in Sustainable Agriculture Using Lightweight Deep Learning and Hybrid Machine Learning Approaches

Abstract: Global climate change and population growth have made sustainability in agricultural production and food supply security critical. Diseases affecting plant and crop leaves are among the primary factors directly threatening yield and food quality. Traditional disease diagnosis methods are prone to human error, costly, and time-consuming. Although deep learning-based convolutional neural networks (CNNs) have shown high performance in solving this problem in recent years, end-to-end training and execution of these models require high computational power (GPU) and long processing times. This makes the use of intelligent systems difficult in rural agricultural areas where internet and advanced hardware infrastructure are limited. In this study, a hybrid artificial intelligence architecture with low computational cost, CPU usage, and hyperparameter optimization is proposed. In the proposed method, the MobileNetV2 architecture, pre-trained with the ImageNet dataset, is used only as a feature extractor, and the images are reduced to 1280-dimensional digital vectors. The obtained features were classified using Support Vector Machines (SVM), Random Forest (RF), and XGBoost algorithms optimized with GridSearchCV supported by 3-Fold Cross-Validation. These processes were also repeated with the MobileNetV3 architecture. Experimental results showed that the proposed MobileNetV3+SVM hybrid model offers high classification performance with minimum processing time and hardware resources. The developed lightweight architecture has the potential to be integrated into mobile and edge computing devices in agricultural settings.

Keywords: Smart agriculture, Deep feature extraction, Hybrid models, Hyperparameter optimization

***Sorumlu yazar (Corresponding author):** Marmara University, University, Faculty of Technology, Department of Electrical and Electronics Engineering, 34854, Istanbul, Türkiye
E mail: hcelik@marmara.edu.tr (H. H. ÇELİK)
Hasan Hüseyin ÇELİK https://orcid.org/0000-0003-2885-0501

Gönderi: 19 Haziran 2026 **Received:** June 19, 2026
Kabul: 30 Temmuz 2026 **Accepted:** July 30, 2026
Yayınlanma: 15 Eylül 2026 **Published:** September 15, 2026

Cite as: Çelik, H. H. (2026). Optimized leaf disease detection in sustainable agriculture using lightweight deep learning and hybrid machine learning approaches. *Black Sea Journal of Engineering and Science,* 9(5), 2281-2287.

1. Giriş

Küresel gıda talebinin hızla arttığı günümüzde, tarımsal üretim alanlarının korunması ve birim alandan alınan verimin artırılması sürdürülebilir kalkınma hedeflerinin merkezinde yer almaktadır. Birleşmiş Milletler Gıda ve Tarım Örgütü (FAO) verilerine göre, dünyada her yıl tarımsal mahsullerin önemli bir yüzdesi hastalık ve zararlılar nedeniyle hasat edilemeden kaybedilmekte ve bu durum küresel gıda krizini tetiklemektedir (FAO, 2024). Bu kayıpların erken evrede tespit edilmesi, kimyasal ilaç kullanımının optimize edilmesi ve ürün kayıplarının en aza indirilmesi açısından hayati önem

This work is licensed (CC BY-NC 4.0) under Creative Commons Attribution 4.0 International License

taşımaktadır. Geleneksel tarımda hastalık tespiti, uzman ziraat mühendislerinin veya çiftçilerin fiziksel gözlemlerine dayanmaktadır. Geniş tarım arazilerinde bu süreç hem lojistik olarak zor hem de subjektif yorumlamalara bağlı olarak hata payı yüksek bir yaklaşımdır (Patel, M. vd., 2024).

Endüstri 4.0 ve Hassas Tarım vizyonu, yapay zeka ve bilgisayarlı görü (computer vision) tekniklerinin tarımsal süreçlere entegrasyonunu hızlandırmıştır. Özellikle Evrişimli Sinir Ağları (CNN), bitki yaprak görüntülerindeki morfolojik değişimleri ve hastalık lekelerini insan gözünden daha hassas bir şekilde analiz edebilmektedir (SinghDhaka vd., 2023). Literatürde yer alan güncel çalışmalarda, ağır derin öğrenme mimarilerinin bitki hastalıklarının sınıflandırılmasında %95'in üzerinde doğruluk oranlarına ulaştığı görülmektedir (Thakur vd., 2024). Ancak bu modeller uçtan uca eğitildiklerinde milyonlarca eğitilebilir parametreye sahip olmaları sebebiyle devasa grafik işlem birimlerine (GPU) ihtiyaç duymakta ve eğitim süreçleri saatler sürmektedir. Ayrıca, model boyutlarının büyük olması bu sistemlerin tarım sahalarında kullanılan insansız hava araçları (İHA) veya kısıtlı donanıma sahip mobil cihazlar üzerinde gerçek zamanlı çalışmasını zorlaştırmaktadır (Savaş, 2024).

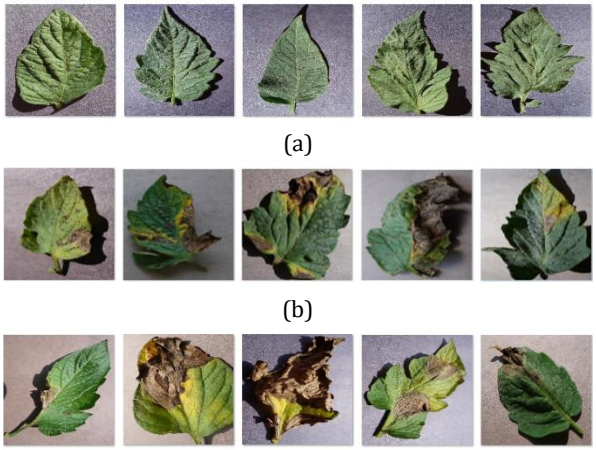
Bu çalışmanın temel amacı; yüksek hesaplama gücü ve uzun eğitim süreleri gerektiren geleneksel derin öğrenme yaklaşımlarına alternatif olarak, kaynak tasarrufu sağlayan (Green AI) hibrit bir mimari geliştirmektir. Çalışma kapsamında, hafifliği ve mobil uyumluluğu ile bilinen MobileNetV2 ve MobileNetV3 mimarileri öznitelik çıkarıcı olarak konumlandırılmış, sınıflandırma yükü ise klasik makine öğrenmesi algoritmalarına devredilmiştir (Savaş, 2024). Rastgele parametre seçiminin önüne geçmek amacıyla sınıflandırıcı aşamasında 3-katlamalı Izgara Araması (GridSearchCV) ile sistematik bir hiperparametre optimizasyonu gerçekleştirilmiştir. Böylece, literatürdeki ağır modellere kıyasla bilgisayar işlemcisi (CPU) üzerinde saniyeler içinde optimize olabilen, doğruluktan ödün vermeyen ve uç cihazlara entegrasyona hazır güncel bir kombinasyon sunulmuştur.

2. Materyal ve Yöntem

2.1. Deneysel Veri Seti

Bu çalışmada, literatürde sıklıkla referans gösterilen ve açık erişimli olarak sunulan akademik PlantVillage veri seti kullanılmıştır (Hughes ve Salathé, 2015). Türkiye tarımındaki önceliği ve kısıtlı zaman diliminde çözümleme göz önüne alınarak, veri setinden örnek olarak domates mahsulüne ait yaprak görüntüleri alınmıştır. Yaprak görüntüleri yetiştirme aşamasındaki domateslerin sağlık durumlarını yansıtmaktadır. Veri setinden RS ve GH genetik kodları ile bilinen domateslere ait sağlıklı, erken yanıklık ve geç yanıklık durumlarını temsil eden kümelerden dengeli 1000 adet kayıt seçilmiştir. Sağlıklı, erken yanıklık ve geç yanıklık örnekleri Şekil 1'de görülmektedir.

Deneysel süreçte sınıflar arasında oluşabilecek veri dengesizliği probleminin ve yanlılığın önüne geçebilmek amacıyla veri seti elle bölünmemiş, tabakalı rastgele bölme mimarisiyle kod seviyesinde ayrıştırılmıştır.



(a) (b) (c)

Şekil1. Domates yapraklarına ait örnek resimler, a) Sağlıklı, b) Erken yanıklık, c) Geç yanıklık.

Toplam 3000 kayıttan oluşan veri seti, her bir sınıfa ait ana dağılım oranları tam olarak korunarak %80 eğitim (2400 örnek) ve %20 doğrulama (600 örnek) olacak şekilde bağımsız alt kümelere otomatik olarak transfer edilmiştir. Bu sayede modellerin eğitimi esnasında herhangi bir sınıfa yönelik aşırı öğrenme veya eksik öğrenme riski matematiksel olarak elimine edilmiştir. Sınıfların dağılımı ve örnek sayılarına ilişkin detaylar Tablo 1'de sunulmuştur.

Tablo 1. Kullanılan veri setine ait sınıf dağılımları

Bitki türü / sağlık durumu	Eğitim örnek sayısı	Doğrulama örnek sayısı	Toplam
Sınıf 1 - Domates Sağlıklı	800	200	1000
Sınıf 2 - Domates Erken Yanıklık	800	200	1000
Sınıf 3 - Domates Geç Yanıklık	800	200	1000
Toplam	2400	600	3000

2.2. Veri Ön İşleme ve Derin Öznitelik Çıkarımı

Bu çalışmada görüntülerin modele homojen bir şekilde beslenmesi amacıyla tüm yaprak resimleri 224×224 piksel boyutuna yeniden ölçeklenmiştir. Ardından, önceden eğitilmiş modelin ağırlıklarıyla uyumluluk sağlaması için ImageNet veri setinin kanal ortalamaları $\mu=[0.485,0.456,0.406]$ ve standart sapmaları $\sigma=[0.229,0.224,0.225]$ kullanılarak RGB kanalları üzerinde normalizasyon işlemi uygulanmıştır.

Öznitelik çıkarma aşamasında, derin ayrılabilir evrişim mimarisi sayesinde standart evrişim katmanlarına göre

parametre sayısını ve işlem hacmini büyük ölçüde azaltan MobileNetV2 modeli tercih edilmiştir (Sandler vd., 2018). Ayrıca bu işlem, performanslarını kıyaslamak amacıyla MobileNetV3 modeli ile tekrarlanmıştır. Modelin ImageNet üzerinde eğitilmiş olan ağırlıkları dondurulmuş ve ağın en sonunda yer alan sınıflandırma katmanı devredışı bırakılarak yerine etkisiz bir katman yerleştirilmiştir. Bu sayede, her bir yaprak görüntüsü ön işleme katmanlarından geçtikten sonra MobileNetV2 ve MobileNetV3'ün küresel ortalama havuzlama katmanından çıkarak 1 ×1280 boyutunda ayırt edici birer öznitelik vektörüne dönüştürülmüştür. Bu işlem ile uzamsal görüntü verileri, klasik makine öğrenmesinin işleyebileceği yüksek nitelikli tablo verilerine indirgenmiştir.

2.3. Hibrit Sınıflandırma ve Hiperparametre Optimizasyonu

Kullanılan derin ağdan elde edilen 1280 boyutlu öznitelik vektörleri, üç farklı matematiksel sınıflandırıcıya girdi olarak verilmiştir. Bu sınıflandırıcılar Destek Vektör Makineleri (SVM), Rastgele Orman (Random Forest) ve XGBoost modelleridir (Cortes ve Vapnik, 1995; Breiman, 2001). Algoritmaların varsayılan parametrelerle çalıştırılması yerine, en yüksek genelleyici performansa ulaşmak adına Izgara Araması (GridSearchCV) yöntemi uygulanmıştır. Optimizasyon süreci, veri kümesinin küçük parçalarındaki varyasyonları da yakalayabilmek için 3-katlamalı çapraz doğrulama ile desteklenmiştir.

SVM için ceza parametresi C ∈\{0.1,1,10}, çekirdek tipi kernel ∈ {linear,rbf} ve gama parametresi γ ∈ {scale,auto} kombinasyonları taranmıştır. RF için ise karar ağacı sayısı n_estimators ∈ {50,100} ve maksimum derinlik sınırları incelenmiştir. Tüm bu deneysel süreç, önerilen yöntemin donanım bağımsızlığını kanıtlamak amacıyla herhangi bir grafik işlemci (GPU) kullanılmadan, standart bir bilgisayar işlemcisi (CPU) üzerinde gerçekleştirilmiştir.

Modellerin başarım analizinde Doğruluk, Kesinlik, Duyarlılık ve F1-Skor standart metrikleri kullanılmıştır. Metriklerin matematiksel ifadeleri eşitlik 1, 2, 3 ve 4'te verilmiştir.

$$\text{Doğruluk} = \frac{TP + TN}{TP + TN + FP + FN} \# \quad (1)$$

$$\text{Kesinlik} = \frac{TP}{TP + FP} \quad (2)$$

$$\text{Duyarlılık} = \frac{TP}{TP + FN} \quad (3)$$

$$\text{F1-Skor} = 2 \times \frac{\text{Kesinlik} \times \text{Duyarlılık}}{\text{Kesinlik} + \text{Duyarlılık}} \quad (4)$$

3. Bulgular

3.1. Hiperparametre Optimizasyonu ve Zaman Performansı Bulguları

Izgara araması sonucunda, veri seti için en optimal parametre kombinasyonları belirlenmiştir. MobileNetV2 ve MobileNetV3 öznitelikleriyle çalışan SVM modeli için en iyi başarım doğrusal çekirdek kernel='linear' ve C=10 parametrelerinde elde edilmiştir. Rastgele Orman ve XGBoost modelleri için ise n_estimators=100 kombinasyonu en kararlı sonucu üretmiştir.

CPU üzerinde gerçekleştirilen optimizasyon ve eğitim süreçlerine ait zaman maliyetleri Tablo 2'de paylaşılmıştır.

Tablo 2 incelendiğinde, derin öğrenme modellerinin günlerce süren uçtan uca eğitim sürelerine kıyasla, önerilen hibrit yöntemin saniyeler mertebesinde eğitimi tamamladığı görülmektedir. Bu durum, modelin CPU üzerinde dahi ne kadar hızlı optimize olabilen düşük maliyetli bir yapı sunduğunun somut bir göstergesidir.

Tablo 2. Önerilen hibrit modellerin eğitim süresi ve genel başarım karşılaştırması

Önerilen hibrit model yapısı	Optimizasyon ve eğitim süresi (s)	En iyi parametre seti	Genel doğruluk
MobileNetV2+SVM	65,8	"{'C': 10, 'gamma': 'scale', 'kernel': 'rbf'}"	%96,3
MobileNetV2+RF	13,17	"{'max_depth': 20, 'n_estimators': 100}"	%91,6
MobileNetV2+XGBoost	351,2	"{'learning_rate': 0.1, 'max_depth': 3, 'n_estimators': 100}"	%93,6
MobileNetV3+SVM	32,19	"{'C': 10, 'gamma': 'scale', 'kernel': 'rbf'}"	%99,0
MobileNetV3+RF	55,47	"{'max_depth': 10, 'n_estimators': 100}"	%93,6
MobileNetV3+XGBoost	149,8	"{'learning_rate': 0.1 'max_depth': 3, 'n_estimators': 100}"	%94,8

3.2. Sınıf Bazlı Performans ve Hata Matrisi Analizi

Önerilen hibrit model yaklaşımını değerlendirmek amacıyla, MobileNetV2 ve MobileNetV3 ile birlikte SVM, RF ve XGBoost sınıflandırıcıları kullanılarak hibrit modeller oluşturulmuştur. Hibrit modellerin sınıf bazlı performanslarını karşılaştırmak amacıyla bunlara ait karışıklık matrisleri üretilmiştir. MobileNetV2 mimarisi ile üretilen hibrit modellerin hata matrisleri Şekil 2'de, MobileNetV3 ile üretilenler ise Şekil 3'de görülmektedir.

Rastgele Orman (RF) algoritmasının, yapısı gereği öznitelik uzayındaki korelasyonları alt ağaçlara bölerken Domates Geç Yanıklık sınıfında SVM'e kıyasla %12.5 oranında daha fazla yanılma yaşadığı görülmüştür. SVM modeli ise doğrusal ayrıştırıcı avantajı sayesinde yaprak üzerindeki erken evre lezyon benzerliklerini daha kararlı

ayırt etmiş ve diyagonal hattaki doğru tahmin yoğunluğunu korumuştur.

Önerilen modellerin sınıflara göre gösterdiği detaylı performans metrikleri çıkartılmıştır. MobileNetV2 mimarisi için üretilen performans metrikleri Tablo 3'de, MobileNetV3 mimarisi için üretilenler ise Tablo 4'de toplu halde gösterilmiştir. Tablo verilerinden görüldüğü gibi, optimize edilmiş MobileNetV2+SVM ve MobileNetV3+SVM modelleri en yüksek doğruluğu üretmektedir. Modelin test aşamasında ürettiği hata matrisi incelendiğinde, sınıfların büyük oranda doğru tahmin edildiği gözlemlenmiştir. Belirli sınıflar arasındaki çok küçük sapmaların morfolojik nedeni araştırıldığında, lezyonların erken evrede yaprak üzerinde bıraktığı nekrotik lekelerin birbirine yapısal olarak çok benzediği tespit edilmiştir (Thakur vd., 2024).

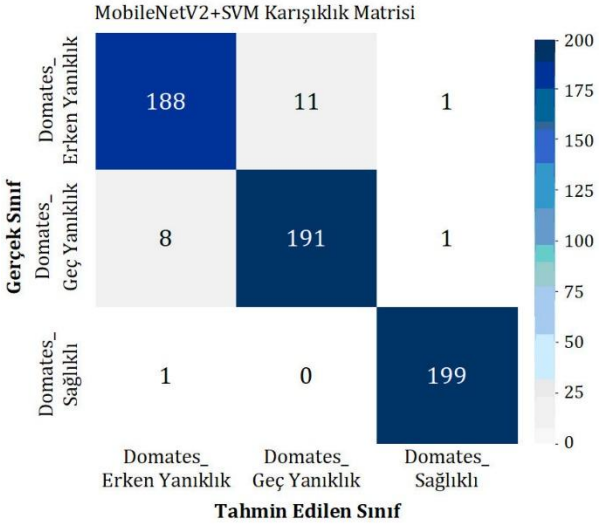
3.3. Çıkarım Hızı ve Literatür Tartışması

Modellerin gerçek zamanlı tarımsal sahalardaki pratik uygulanabilirliğini test etmek amacıyla, oluşturulan hibrit modellerin tek bir görüntü için karar verme süreleri hesaplanmıştır. Bu işlemler, 2.4GHz 64bit Intel i5 işlemci ve 16MB bellek özelliklerine sahip bir bilgisayar kullanılarak Python 3.14.5 program ortamında gerçekleştirilmiştir. Tek bir yaprak görüntüsünün, analiz ve sınıflandırma aşamaları için hesaplanan çıkarım süreleri ve genel doğruluk oranları Tablo 5'de verilmiştir. Tablo 5'e göre SVM algoritması, RF ve XGBoost algoritmalarına kıyasla daha yüksek doğruluk oranları üretmektedir. Ayrıca daha kısa çıkarım süreleri sağlamaktadır. Bu fark, SVM algoritmasının doğrusal karar sınırlarını matematiksel olarak daha hızlı filtrelemesinden kaynaklanmaktadır.

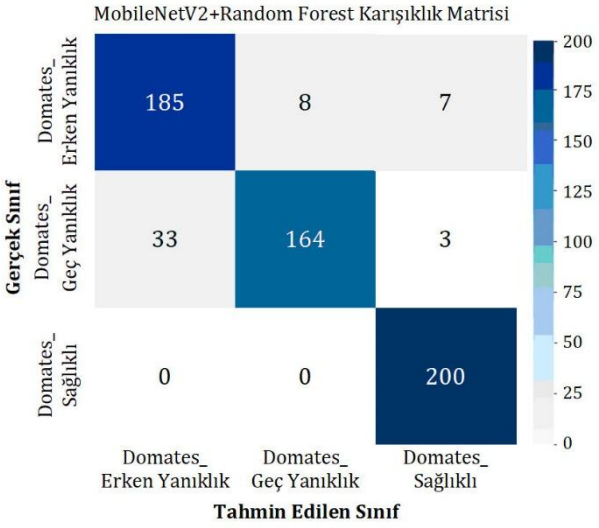
Yapılan testlerde, MobileNetV3 mimarisinin MobileNetV2'ye göre daha kısa çıkarım sürelerine ulaştığı görülmektedir. Bunun temel nedenleri, MobileNetV3'ün donanım odaklı ağ mimarisi optimizasyonu, üstel aktivasyon fonksiyonları gibi ağır hesaplama yüküne sahip işlemleri azaltacak şekilde yeniden tasarlanmış bir mimariye sahip olmasıdır.

Bu sonuçlar, MobileNetV2+SVM ve MobileNetV3+SVM hibrit yapılarının uç bilişim cihazlarında yüksek frekanslı gerçek zamanlı çalışmaya tamamen uygun olduğunu göstermektedir.

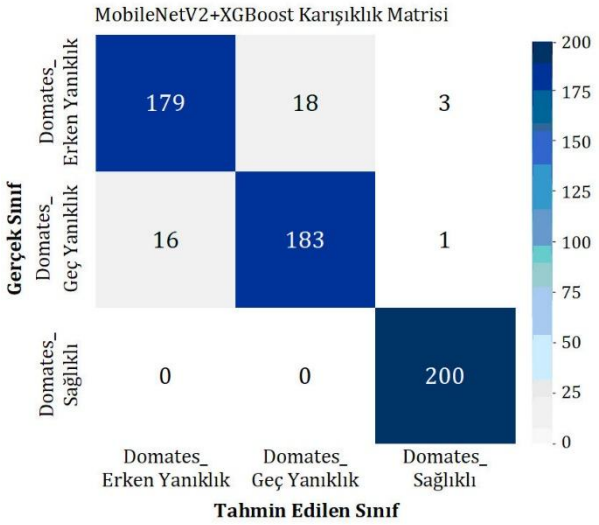
Literatürde yer alan ve benzer veri setlerini kullanan güncel ağır CNN çalışmaları incelendiğinde (SinghDhaka vd., 2023; Thakur vd., 2024), bu modellerin yüksek başarım oranlarına ulaşmasına rağmen model boyutlarının yüzlerce megabayta dayandığı ve CPU üzerindeki çıkarım sürelerinin oldukça hantallaştığı bilinmektedir. Önerilen hibrit model ise hem düşük bellek tüketimi hem de çok kısa sürelerde (21,1ms) karar üretebilmesi yönüyle öne çıkmaktadır. Bu durum, önerilen yöntemin tarım arazilerinde internete ve bulut sunuculara ihtiyaç duymadan, uç bilişim cihazlarında gerçek zamanlı olarak çalışabileceğini doğrulamaktadır (Patel, M. vd., 2024).



(a)



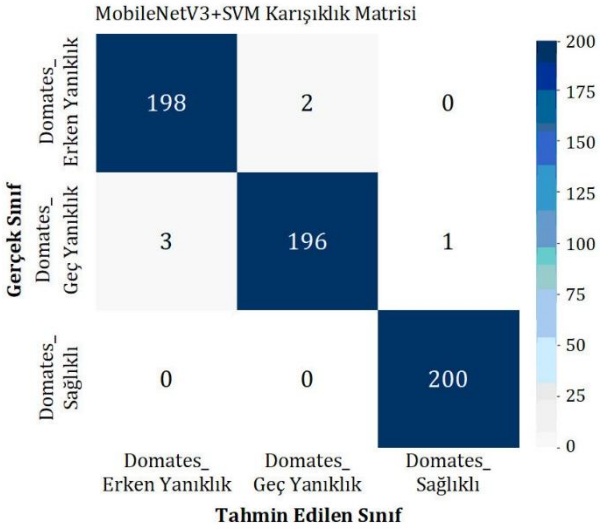
(b)



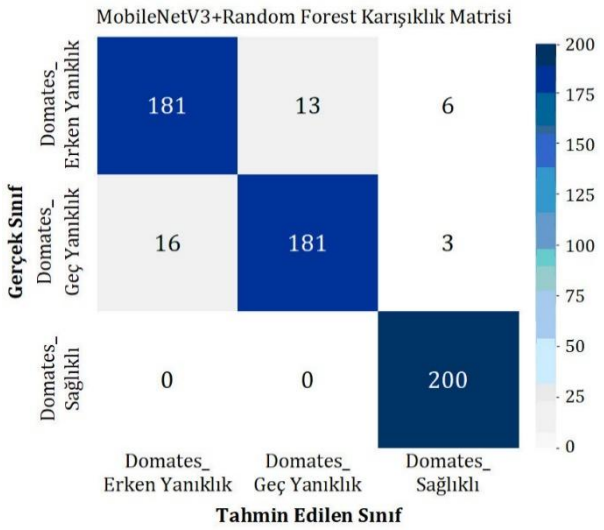
(c)

Şekil 2. (a) MobileNetV2+SVM karışıklık matrisi, (b) MobileNetV2+RF karışıklık matrisi, (c) MobileNetV2+XGBoost karışıklık matrisi.

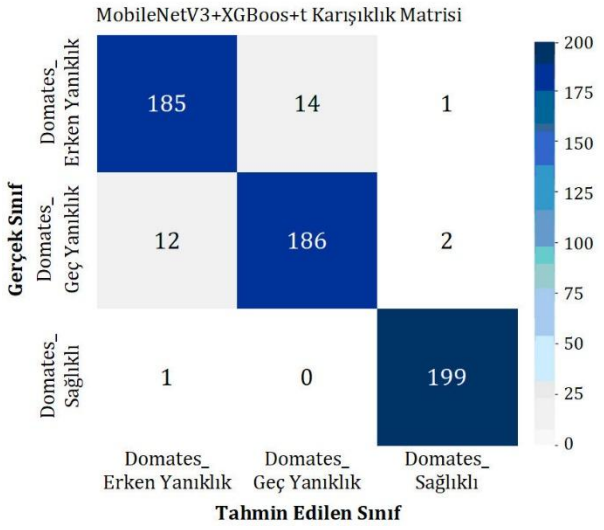
,



(a)



(b)



(c)

Şekil 3. (a) MobileNetV3+SVM karışıklık matrisi, (b) MobileNetV3+RF karışıklık matrisi, (c) MobileNetV3+XGBoost karışıklık matrisi.

4. Tartışma ve Sonuç

Bu çalışmada, tarımsal üretimde büyük ekonomik kayıplara yol açan yaprak hastalıklarının tespiti için donanım maliyetini minimize eden, hızlı ve yüksek başarımlı hibrit bir yapay zeka yaklaşımı sunulmuştur. Geliştirilen mimaride, MobileNetV2 ve MobileNetV3 ortamlarından sağlanan derin öğrenmenin güçlü görsel anlamlandırma yeteneği ile klasik makine öğrenmesinin (SVM) optimize edilmiş karar sınırları bir araya getirilmiştir.

Elde edilen deneysel sonuçlar, çapraz doğrulama destekli ızgara araması ile optimize edilen hibrit modelin, GPU altyapısına ihtiyaç duymadan, standart bir CPU üzerinde dahi yüksek doğruluk oranlarına ve milisaniyeler seviyesinde çıkarım sürelerine ulaşabildiğini kanıtlamıştır. Gelecek çalışmalarda, önerilen bu hafif hibrit yapının mobil çiftçi uygulamalarına veya otonom drone sistemlerine entegre edilerek canlı hastalık haritalandırma çalışmalarında kullanılması planlanmaktadır.

Tablo 3. Optimize edilmiş MobileNetV2 ile SVM, RF ve XGBoost modellerinin sınıf bazlı detaylı performansları

	Kesinlik			Duyarlılık			F1-Skor		
Sınıf Adı	SVM	RF	XGBoost	SVM	RF	XGBoost	SVM	RF	XGBoost
Sınıf 1 - Domates Sağlıklı	%99,0	%96,1	%92	%99,5	%100	%90	%99,2	%98,0	%91
Sınıf 2 - Domates Erken Yanıklık	%95,4	%85,0	%91	%94,0	%91,0	%92	%94,7	%87,9	%91
Sınıf 3 - Domates Geç Yanıklık	%94,5	%93,2	%98	%95,5	%83,0	%100	%95,0	%87,8	%99
Makro Ortalama	%96,3	%91,4	%94	%96,3	%91,3	%94	%96,3	%91,2	%94

Tablo 4. Optimize edilmiş MobileNetV3 ile SVM, RF ve XGBoost modellerinin sınıf bazlı detaylı performansları

	Kesinlik			Duyarlılık			F1-Skor		
Sınıf Adı	SVM	RF	XGBoost	SVM	RF	XGBoost	SVM	RF	XGBoost
Sınıf 1 - Domates Sağlıklı	%99	%92	%93	%99	%91	%93	%99	%91	%93
Sınıf 2 - Domates Erken Yanıklık	%99	%93	%93	%98	%91	%93	%98	%92	%93
Sınıf 3 - Domates Geç Yanıklık	%100	%96	%99	%100	%100	%99	%100	%98	%99
Makro Ortalama	%99	%94	%95	%99	%94	%95	%99	%94	%95

Tablo 5. Önerilen hibrit modellerin çıkarım hızları ve doğruluk karşılaştırması

Hibrit model mimarisi	Genel doğruluk	Tekil resim çıkarım süresi (ms)
MobileNetV2+SVM	%96,3	35,11
MobileNetV2+RF	%91,6	44,35
MobileNetV2+XGBoost	%93,6	35,36
MobileNetV3+SVM	%99,0	21,51
MobileNetV3+RF	%93,6	33,0
MobileNetV3+XGBoost	%94,8	22,10

Katkı Oranı Beyanı

Yazarın katkı yüzdeleri aşağıda verilmiştir. Yazar makaleyi incelemiş ve onaylamıştır.

	H.H.Ç.
K	100
T	100
Y	100
VTI	100
VAY	100
KT	100
YZ	100
KI	100
GR	100
PY	100
FA	100

K= kavram, T= tasarım, Y= yönetim, VTI= veri toplama ve/veya işleme, VAY= veri analizi ve/veya yorumlama, KT= kaynak tarama, YZ= yazım, KI= kritik inceleme, GR= gönderim ve revizyon, PY= proje yönetimi, FA= fon alımı.

Çatışma Beyanı

Yazar bu çalışmada hiçbir çıkar ilişkisi olmadığını beyan etmektedirler.

Etik Onay Beyanı

Bu araştırmada hayvanlar ve insanlar üzerinde herhangi bir çalışma yapılmadığı için etik kurul onayı alınmamıştır.

Destek ve Teşekkür Beyanı

Bu çalışmayı destekleyen ve rehberlik sağlayan Marmara Üniversitesi Mühendislik Fakültesi Öğretim Üyesi Prof. Dr. Cabir VURAL'a teşekkürlerimi sunarım.

Kaynaklar

Breiman, L. (2001). Random forests. *Machine Learning*, *45*(1), 5–32. https://doi.org/10.1023/A:1010933404324

Cortes, C., & Vapnik, V. (1995). Support-vector networks. *Machine Learning, 20*(3), 273–297. https://doi.org/10.1007/bf00994018

Food and Agriculture Organization of the United Nations. (2024). *The state of food and agriculture 2024: Moving forward on agrifood systems transformation*. https://doi.org/10.4060/cd2431en

Hughes, D. P., & Salathé, M. (2015). An open access repository of images on plant health to enable the development of mobile disease diagnostics. arXiv preprint arXiv:1511.08060.

Patel, M., Tanwar, S., Jindal, A., Alshammari, N., Pervaiz, H., & Ahmed, H. (2024). A blockchain-based predictive maintenance scheme for smart agriculture. In *2024 IEEE/ACM 17th International Conference on Utility and Cloud Computing (UCC)* (pp. 405–410). IEEE.

Sandler, M., Howard, A., Zhu, M., Zhmoginov, A., & Chen, L. C. (2018). MobileNetV2: Inverted residuals and linear bottlenecks. In *Proceedings of the IEEE Conference on Computer Vision and Pattern Recognition* (pp. 4510–4520). IEEE.

Savaş, S. (2024). Application of deep ensemble learning for palm disease detection in smart agriculture. *Heliyon, 10*(17), Article e37141. https://doi.org/10.1016/j.heliyon.2024.e37141

SinghDhaka, V., Kundu, N., Rani, G., Zumpano, E., & Vocaturo, E. (2023). Role of Internet of Things and deep learning techniques in plant disease detection and classification: A focused review. *Sensors, 23*(18), Article 7877. https://doi.org/10.3390/s23187877

Thakur, A., Sharma, S., & Thapar, P. (2024). A comprehensive review of plant disease detection and analysis using machine learning techniques. In *2024 7th International Conference on Contemporary Computing and Informatics (IC3I)*. IEEE.

Black Sea Journal of Engineering and Science
doi: 10.34248/bsengineering.1982654

Open Access Journal
e-ISSN: 2619 – 8991

Research Article
Volume 9 - Issue 5: 2288-2306 / September 2026

NUMERICAL AND EXPERIMENTAL CHARACTERIZATION OF AN AERODYNAMICALLY REDESIGNED DISC IN A DN350 DOUBLE-ECCENTRIC BUTTERFLY VALVE IN TERMS OF FLOW COEFFICIENT, PRESSURE LOSS AND HYDRODYNAMIC DISC LOAD

Onur GÖK[1]*, Hacı Ali ERTAŞ[2]

[1]*Necmettin Erbakan University, Seydişehir Vocational School, Department of Machine and Metal Technologies, 42370, Konya, Türkiye*
[2]*Sivas Cumhuriyet University, Faculty of Engineering, Department of Mechanical Engineering, 58070, Sivas, Türkiye*

Abstract: Flow control in pressurized water-transmission and irrigation lines relies on large-diameter butterfly valves, whose disc governs both the line pressure loss and the actuation load. This study compares the conventional disc of a DN350 double-flanged double-eccentric butterfly valve with an aerodynamically redesigned disc using a dual-track approach. A three-dimensional steady incompressible RANS solution (Simcenter FLOEFD) sweeps the opening angle from 30 to 90 degrees in 10-degree steps, while flow-coefficient (Kv) values are measured on the manufactured valve per TS EN 1267. The model yields the inlet static pressure, hydrodynamic disc force (Fd) and volumetric flow rate, from which the pressure loss, loss coefficient (zeta), drag coefficient (Cd) and CFD-derived Kv follow. Dimensioned within patented H/D and Y/D rules, the redesigned disc reduces the disc volume by 42.8 percent and the mass from 38.7 to 22.2 kilograms. Across all opening angles it lowers the pressure loss by 49 to 67 percent, the loss coefficient by 46 to 65 percent and the disc force by 34 to 63 percent, while the experimental Kv rises by 20 to 37 percent. The disc force is a comparative proxy for the actuation-torque demand. The absolute torque is not computed.

Keywords: Butterfly valve, Computational fluid dynamics, Disc redesign, Drag force, Flow coefficient, Hydrodynamic disc load

***Corresponding author:** Necmettin Erbakan University, Seydişehir Vocational School, Department of Machine and Metal Technologies, 42370, Konya, Türkiye
E mail: ogok@erbakan.edu.tr (O. GÖK)
Onur GÖK https://orcid.org/0000-0003-1160-1963
Hacı Ali ERTAŞ https://orcid.org/0000-0002-8788-9011

Received: June 30, 2026
Accepted: July 31, 2026
Published: September 15, 2026

Cite as: Gök, O., & Ertaş, H. A. (2026). Numerical and experimental characterization of an aerodynamically redesigned disc in a DN350 double-eccentric butterfly valve in terms of flow coefficient, pressure loss and hydrodynamic disc load. *Black Sea Journal of Engineering and Science,* 9(5), 2288-2306.

1. Introduction

In large-diameter applications such as pressurized water-transmission lines, irrigation networks, drinking-water distribution systems and dam bottom-outlet discharges, the opening and closing of the flow and the adjustment of the flow rate are largely carried out with butterfly valves. The butterfly valve's ability to operate at high flow rate with low resistance, its compact structure and its low structural weight make it advantageous over gate and globe valves in this diameter range. The three basic components of the valve are the body, the shaft and the circular disc. Among these components, the geometry of the disc (the valve plate) is the primary element that interacts directly with the fluid and therefore governs both the line pressure loss and the actuation torque borne by the actuator about the shaft axis. The drag force that the fluid exerts on the disc and the associated dynamic torque directly affect the ease of the opening-closing operation, the actuator sizing and the fatigue life of the shaft, bearing and sealing elements.

The investigation of butterfly valve internal flow by computational fluid dynamics (CFD) is a mature research field. A significant part of the literature has focused on the development and suppression of cavitation in the throttling regime of the valve (G. Zhang et al., 2023; G. Zhang et al., 2024a; G. Zhang et al., 2024b; G. Zhang et al., 2026). These studies have revealed the effect of the opening degree, the transient opening-closing regime and the disc edge geometry on cavitation inception and bubble distribution. A second group has addressed erosion and wear behavior under solid-liquid two-phase flow, partly with the help of the discrete element method (DEM) and data-based models (Liu et al., 2024; Su et al., 2024; Yang et al., 2025a; Perera et al., 2024). A third group has dealt with the structural safety, sealing performance and manufacturing precision of triple-eccentric and quadruple-eccentric (triple and quadruple offset) designs (Qi et al., 2023; C. Wang et al., 2024; D. Wang et al., 2024; Qi et al., 2026). In these studies, the effect of multi-objective optimization methods and turbulence model selection on the results has been

This work is licensed (CC BY-NC 4.0) under Creative Commons Attribution 4.0 International License

discussed (Kim et al., 2022; C. Wang et al., 2024; Choi et al., 2021). Beyond the butterfly valve, CFD is a validated and widely used method for resolving transonic shock and drag behavior on supercritical airfoils, the performance of centrifugal fans and submersible pumps, cavity-induced noise and free-stream structure, oscillating nanofluid channel heat transfer, and CFD-based design optimization (Kalkat and Tom, 2019; Karaokur and Akay, 2022; Polat et al., 2022; Yağmur and Doğan, 2022; Akçay, 2024; Kaya, 2025b; Sefacı et al., 2026). This approach has also been used in different problems such as the reduction of pressure drop in fuel cell flow channels (Kaplan, 2024), the effect of thickness and camber on cavitation in hydrofoils (Kaya, 2025a), the classification of velocity distributions at a diffuser outlet by image analysis (Erdoğan and Daşkın, 2023) and the examination of the flow around an airfoil in terms of lift and drag (Erkan and Özkan, 2020).

Another line of work addresses the fundamental hydraulic characteristic of the valve, namely the flow coefficient and the pressure loss coefficient. Along this line, the pressure characteristic and flow coefficient of the butterfly valve have been measured experimentally (Nguyen et al., 2023), the performance variation under different diameters, openings and flow regimes has been evaluated (Bairagi et al., 2024) and the flow torque on the disc has been related to valve plate optimization (J. Zhang et al., 2024). The common aspect of these studies is that the flow coefficient is treated either only experimentally or only numerically, and the effect of the disc geometry redesign on this coefficient is not reported together with a standard-based experimental verification.

In a previous study by the author, the three-dimensional flow during the opening process of a single-disc butterfly valve was examined with a moving mesh approach, and the conventional and optimized disc geometries were compared in the dynamic regime (Gök et al., 2023). The author's CFD-based aerodynamic analysis experience also covers a study in which the effect of the feather geometry on the drag force in traditional Turkish archery was investigated numerically (Büyükcura et al., 2024). The optimized body evaluated in this study is based on a stress-distributing undulating body structure (Akbulut et al., 2023). The author's design work in the field of hydraulic fluid machinery also includes a utility model in which the inlet and outlet transitions in an external gear pump body were redefined so as to smooth the flow (Gök et al., 2019). The aerodynamic design of the optimized disc, in turn, is based on two dimensionless design rules defined as the ratio of the disc curvature height to the diameter and the ratio of the outer-surface edge ovalization radius to the diameter, with the aim of lowering the drag coefficient (Gök, 2021). This numerical and applied infrastructure constitutes the basis of the present study. The present study differs from the previous dynamic analysis in three respects: the solution was carried out in the steady state at the DN350 diameter and in the low inlet-velocity regime specific to irrigation lines (approximately 2.5 meters per second), the hydrodynamic force on the disc was brought to the fore as a design performance metric, and above all, the numerical results were cross-evaluated against independent flow-bench Kv measurements performed according to the TS EN 1267 standard. These data sets have not been used in any previously published work of the author.

The gap in the literature becomes evident at the following points. First, the effect of an aerodynamically redesigned butterfly valve disc on the flow coefficient has not been verified together with a standard-based (TS EN 1267) experimental measurement and a numerical model in the same study. Second, the hydrodynamic force on the disc is rarely reported as a design performance metric, that is, as a comparative hydrodynamic indicator of the actuator torque demand, rather than as a by-product. Third, the net benefit provided by the disc redesign has not been tracked simultaneously in the dimensions of line energy loss, actuation load and material consumption. This study proposes a dual-track characterization framework that addresses these three gaps together. The conventional and optimized disc designs of a DN350 butterfly valve are solved by steady CFD at seven opening angles, the Reynolds-number independence of the loss coefficient is used as an internal consistency criterion, and the results are supported by flow-bench measurements on the actual product. To the best of the authors' knowledge, this is the first study in which an aerodynamically redesigned large-diameter butterfly valve disc is characterized at the same time through a steady CFD field solution, a standard-based (TS EN 1267) experimental flow coefficient and a hydrodynamic disc load metric, so that the line energy loss, the actuation load tendency and the material saving are reported together for one physical product. The original contributions of the study can be collected under four headings.

- Dual-track characterization: The effect of the disc geometry on the flow performance was evaluated together by means of steady CFD, which provides the field-level mechanism, and the standard-based (TS EN 1267) experimental flow coefficient.
- Hydrodynamic disc load metric: The resultant hydrodynamic force on the disc was reported as a comparative performance indicator of the actuation load. The absolute shaft torque was left outside the scope of this study.
- Flow coefficient reconciliation: The flow coefficient derived from the CFD pressure drop and the experimental Kv values were compared across the opening degree, and the ranking consistency was tested.
- Dimensionless design rule link: The geometry of the optimized disc was related to the patented H/D and Y/D dimensionless ratios, and the geometric difference was quantified from the STEP models.

Rather than claiming that the optimized design is flawless in every respect, the study aims to reveal quantitatively at what magnitude and in what opening range the redesign provides a benefit. The proposed dual-track framework and the hydrodynamic disc load metric are not specific to this product alone. The same approach can also be transferred directly to other large-diameter flow control elements in which the disc or closure member actuation load and the line loss are jointly critical. In this respect, the study aims to present a methodological framework in addition to a product comparison. The full grounding of this methodological framework should be strengthened with mesh independence, turbulence model sensitivity and experimental uncertainty analyses.

2. Materials and Methods

2.1. Geometry and Flow Volume

The investigated device is a double-flanged double-eccentric butterfly valve with a DN350 nominal diameter. The valve was tested on a flow bench compliant with TS EN 1267, and the experimental setup is shown in Figure 1. The technical drawings and manufactured-product views of the two disc designs are given in Figure 2. The body and disc are made of spheroidal graphite ductile cast iron (GGG40, EN-GJS-400). The valve is a commercial product manufactured by Ulaş Vana and is designed for use in pressurized water transmission and irrigation lines. The geometries were provided by the manufacturer as STEP models. Two disc designs were compared: the existing conventional disc (Conventional) and the optimized disc redesigned on aerodynamic principles under the same functional constraints (Optimized). The optimized disc was shaped within two dimensionless design rules in order to lower the drag coefficient (Gök, 2021): the ratio of the curvature height (H), which expresses the wall thickness from bottom to top along the disc center line, to the disc diameter (D), and the ratio of the ovalization radius (Y) of the sharp edges on the outer surface of the disc to the diameter.

The measurable geometric differences between the two designs were determined quantitatively by bounding-box and volume analysis of the STEP models. The optimized disc has a lens-type, thin and flow-aligned profile. The disc envelope thickness decreased from 135 millimeters to 102.6 millimeters (24.0 percent), the disc volume fell from 5450.6 cubic centimeters to 3120.3 cubic centimeters (42.8 percent), and accordingly the disc mass calculated for GGG40 dropped from 38.7 kilograms to 22.2 kilograms. The optimized body was also reconsidered within the same framework. The body volume decreased by 12.5 percent and the body mass decreased from 82.4 kilograms to 72.1 kilograms. These geometric differences are summarized in Figure 3 and Table 1. The disc surface topology also changed: in the optimized disc the share of free-form (B-spline) and toroidal surfaces increased, which is an indicator of curved transitions that delay flow separation.

The differences between the disc, body and flow volume geometries were measured under three groups (Table 1). On the disc side, the most pronounced change is the reduction of the minimum thickness of the optimized disc from 135 millimeters to 102.6 millimeters (24.0 percent) and the consequent 42.8 percent reduction of the volume. On the body side, the axial face-to-face depth between the flanges was kept at 290 millimeters in both designs, so that the one-to-one interchangeability of the valve in the line is ensured. The body volume decreased by 12.5 percent. The fully open (90 degrees) flow volume comparison is instructive in two respects. First, the wetted fluid volume is 2.6 percent and the wetted surface 2.7 percent smaller. This shows that the optimized internal passage is somewhat tighter and is the geometric reason why the optimized design passes approximately 2.8 percent lower flow rate at a constant inlet velocity. Second, in the fully open position the minimum cross-section (throat) of the free-flow passage is equal to approximately 84 percent of the DN350 nominal area in both designs (807.7 and 805.6 square centimeters) and is almost identical. This throat is a common constraint determined not by the disc but by the seat. Therefore, the flow coefficient superiority of the optimized disc arises not from the enlargement of the geometric throat but from the low form drag created by the thin disc profile. This distinction is treated quantitatively in Section 3.6. Since not only the disc but also the body and flow volume differ in the two compared designs, the results in this study represent the hydraulic effect of the integrated disc-body redesign, not of an isolated disc change.

Here the word optimized is the design designation used by the manufacturer for this disc. The detailed optimization process behind the optimized design (objective function, variables, constraints) belongs to the manufacturer and is not shared in this study. Therefore, this article does not assume that the design is the best under all conditions. On the contrary, it critically evaluates the hydraulic performance of the design bearing this name and reveals in which opening range and to what extent it produces a benefit.

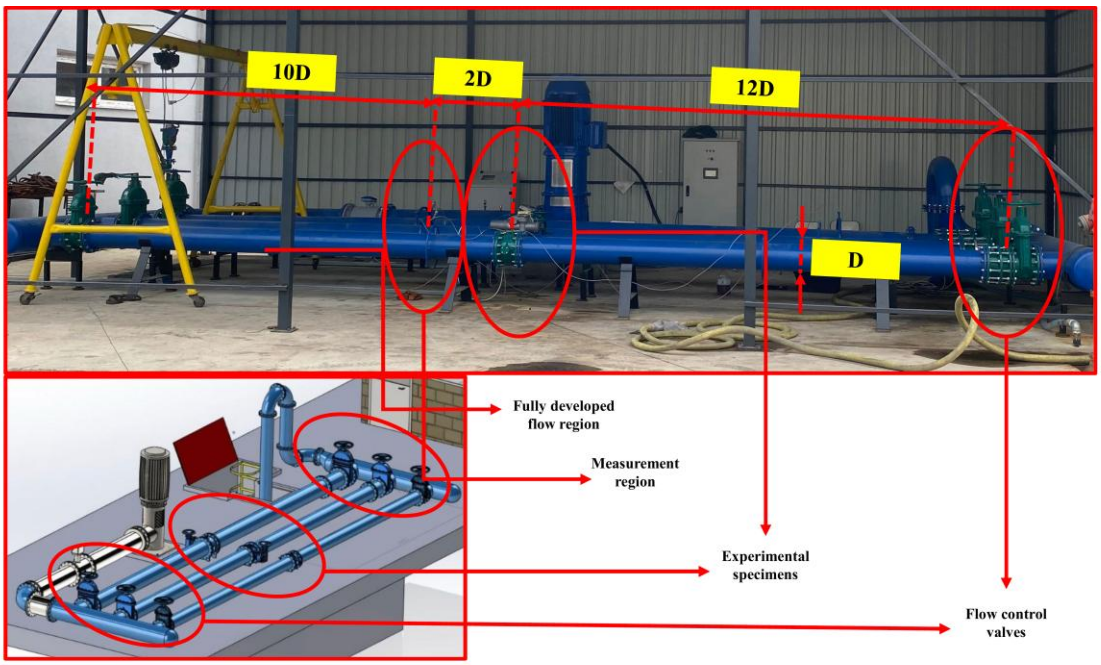


Figure 1. Experimental flow-bench layout of the DN350 line. According to TS EN 1267, the straight-pipe development lengths before and after the valve and the pressure measurement points were determined so that valve-induced disturbances would not reach the measurement sections (top, the physical setup; bottom, the CAD layout of the test circuit). D denotes the nominal diameter.

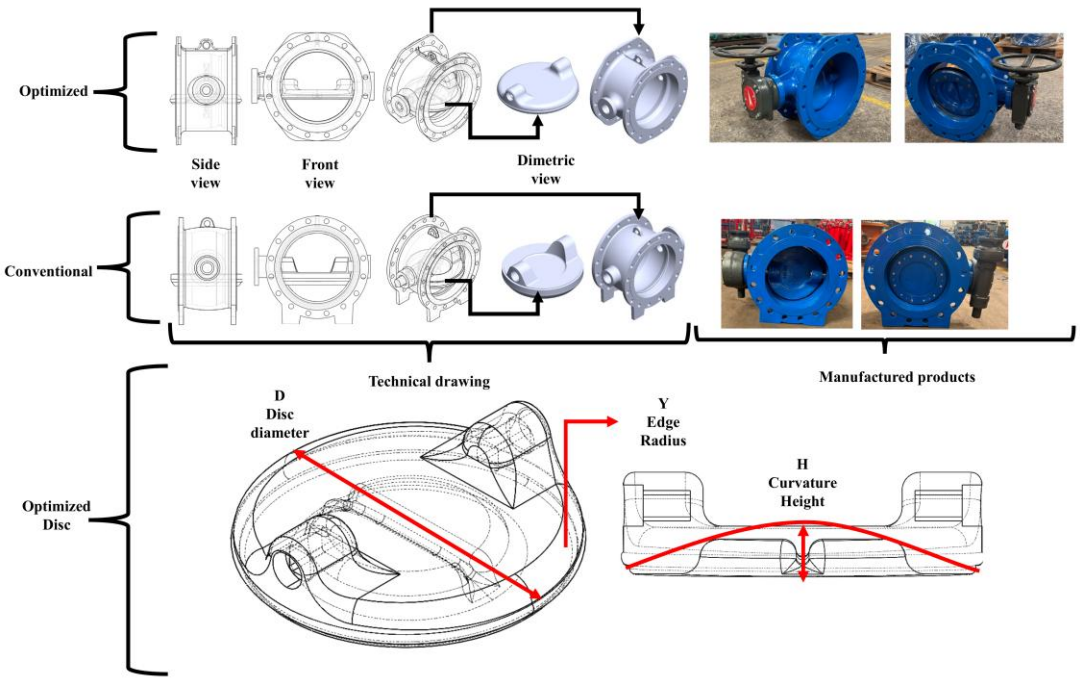


Figure 2. Conventional (bottom) and optimized (top) valve designs. On the left are the side and front technical drawings and the exploded three-dimensional CAD models of the body and disc in dimetric view. On the right are the manufactured products with their geared actuators. At the bottom, the optimized disc technical drawing is shown, defining the patented design rule parameters, namely the disc diameter D, the edge oval radius Y and the curvature height H.

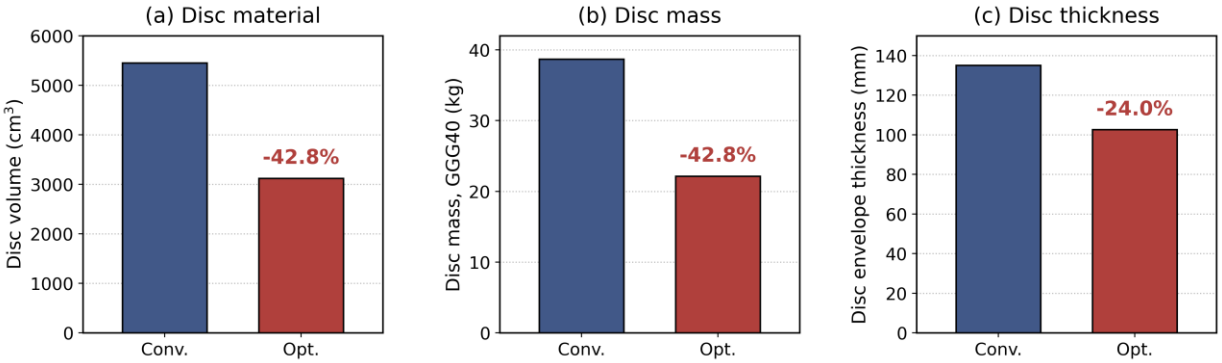


Figure 3. Geometric comparison of the conventional and optimized discs derived from the STEP models: (a) disc material volume, (b) disc mass for GGG40 spheroidal graphite cast iron, (c) disc envelope thickness. The optimized disc redistributes and removes material to obtain a thinner, flow-aligned lens-type profile.

Table 1. Geometric properties of the conventional and optimized components extracted from the STEP models, grouped as disc, body and fully open (90°) flow volume*

Component / quantity	Conventional	Optimized	Change
Disc envelope X x Y x Z (mm)	379.9 x 135.0 x 708.8	345.5 x 102.6 x 670.8	-
Disc volume (cm^3)	5450.6	3120.3	-42.8%
Disc surface area (cm^2)	3102.2	2487.6	-19.8%
Disc minimum thickness (mm)	135.0	102.6	-24.0%
Disc mass, GGG40 (kg)	38.70	22.15	-42.8%
Body envelope X x Y x Z (mm)	290.0 x 533.4 x 568.0	290.0 x 505.0 x 572.5	-
Body volume (cm^3)	11607.4	10153.9	-12.5%
Body surface area (cm^2)	12975.2	12515.6	-3.5%
Body mass, GGG40 (kg)	82.41	72.09	-12.5%
Body face-to-face depth (mm)	290.0	290.0	0%
Flow volume @90, wetted (cm^3)	439612	428285	-2.6%
Flow volume @90, wetted surface (cm^2)	55187	53670	-2.7%
Free-flow throat area @90 (cm^2)	807.7	805.6	-0.3%
Throat / DN350 nominal area	83.9%	83.7%	~ equal

*The mass was calculated for GGG40 spheroidal graphite cast iron (ρ = 7100 kg/m^3). The free-flow throat is the minimum cross-sectional area of the fully open flow passage. The percentage change is relative to the conventional design.

2.2. Governing equations and Turbulence Model

The flow is governed by the Reynolds-averaged continuity and momentum (RANS) equations 1 and 2 under isothermal conditions, assumed incompressible and Newtonian for water:

$$\frac{\partial u_i}{\partial x_i} = 0 \tag{1}$$

$$\frac{\partial}{\partial x_j}(\rho\, u_i u_j) = -\frac{\partial p}{\partial x_i} + \frac{\partial}{\partial x_j}\left[(\mu + \mu_t)\left(\frac{\partial u_i}{\partial x_j} + \frac{\partial u_j}{\partial x_i}\right)\right] \tag{2}$$

Here ui are the mean velocity components, p the mean pressure, ρ the density, μ the dynamic viscosity and μt the turbulent (eddy) viscosity. Closure is provided by a modified k-ε model that solves the transport equations for the turbulent kinetic energy k and its dissipation rate ε. The eddy viscosity and the k-ε transport equations 3-5 are, respectively, as follows:

$$\mu_t = \rho\, C_\mu f_\mu \frac{k^2}{\varepsilon} \tag{3}$$

$$\frac{\partial}{\partial x_i}(\rho\, u_i k) = \frac{\partial}{\partial x_i}\left[\left(\mu + \frac{\mu_t}{\sigma_k}\right)\frac{\partial k}{\partial x_i}\right] + P_k - \rho\varepsilon \tag{4}$$

$$\frac{\partial}{\partial x_i}(\rho\, u_i \varepsilon) = \frac{\partial}{\partial x_i}\left[\left(\mu + \frac{\mu_t}{\sigma_\varepsilon}\right)\frac{\partial \varepsilon}{\partial x_i}\right] + \frac{\varepsilon}{k}(C_{1\varepsilon}P_k - C_{2\varepsilon}\rho\varepsilon) \tag{5}$$

Here Pk is the turbulence production arising from the mean velocity gradients. Cμ, C1ε, C2ε, σk and σε are the model coefficients (standard values: Cμ = 0.09, C1ε = 1.44, C2ε = 1.92, σk = 1.0, σε = 1.3). Simcenter FLOEFD uses a variant with a damping function (Lam-Bremhorst type) that accounts for low-Reynolds regions and a two-scale boundary-layer approach that is relatively insensitive to the near-wall surface mesh resolution (y plus). This approach is suitable for the separation-dominated internal flow inside the cast body. The inlet turbulence intensity was taken as 2 percent, and the

water properties were defined as ρ = 998 kilograms per cubic meter and μ = 1.002 times 10 to the power minus 3 pascal seconds (approximately 293 kelvin). The modified k-ε model is a mature and widely preferred closure that is balanced between computational cost and accuracy in the prediction of pressure drop and separation-dominated losses in cast valve internal flows. Similar valve CFD studies have also used this family (Kim et al., 2022; Gök et al., 2023; Bairagi et al., 2024; J. Zhang et al., 2024). The sensitivity of the results to the turbulence model selection (for example a comparison with k-ω SST or RSM) was not examined in this study and is stated as a limitation in Section 4.1. Equations 1-5 represent the generic form of the turbulence closure used. The Lam-Bremhorst damped two-scale wall treatment applied by Simcenter FLOEFD is a software-specific variant. The Boussinesq approximation was used in the momentum equation, and the isotropic turbulence stress term was included in the effective pressure term.

2.3. Boundary Conditions and Solver Settings

A uniform velocity profile was applied at the inlet section. The mean inlet velocities of the conventional and optimized designs, under the constant inlet condition, are approximately 2.57 and 2.50 meters per second, respectively. This means that the Reynolds number at the DN350 section is in the range of approximately 8.7 to 9.0 times 10 to the power 5, and indicates that the flow is in the fully turbulent regime. The ambient (atmospheric) pressure was prescribed at the outlet. So that numerical friction would not distort the actual loss, the inlet and outlet extensions were defined sufficiently long and smooth. The actual cast body, on the other hand, was modeled with an equivalent surface roughness corresponding to sand-mould casting. The same boundary conditions and roughness were applied to both designs, so that the difference came only from the geometry. To reduce the computational cost, the flow volume was modeled with 10D on the inlet side and, on the outlet side, so as to also cover the measurement development length, while preserving the inlet development-length approach of the experimental setup compliant with TS EN 1267. The solutions were carried out in the steady state, and the inlet and outlet total pressure, flow rate and pressure-drop targets were monitored until their oscillation decayed. The basic settings are summarized in Table 2.

Table 2. Summary of the CFD model setup and the boundary conditions

Parameter	Specification
Solver	Simcenter FLOEFD, steady, incompressible RANS
Turbulence model	Modified k-epsilon (Lam-Bremhorst damping, two-scale wall treatment)
Fluid	Water, rho = 998 kg m^-3, mu = 1.002x10^-3 Pa s, T ~ 293 K
Inlet	Uniform velocity, u0 ~ 2.5 m s^-1 on the DN350 channel
Outlet	Environment (atmospheric) pressure
Wall roughness	As-cast GGG40 (sand-mould equivalent), extensions smooth
Disc opening angles	30, 40, 50, 60, 70, 80, 90 deg (10 deg steps)
Reynolds range	Re ~ 8.7x10^5 - 9.0x10^5
Cases	2 designs x 7 angles = 14 CFD runs
Mesh	Solution-adaptive Cartesian (cut-cell), local refinement at disc

2.4. Derived Dimensionless and Performance Quantities

Three raw quantities were extracted from each solution: the inlet static pressure p0, the outlet static pressure p1 and the volumetric flow rate Q. In the following definitions, Q was converted to the SI unit (cubic meters per second) in the velocity and Reynolds number computation. In the flow coefficient Kv computation, the cubic meters per hour unit prescribed by the standard was used. The Reynolds number, the pressure drop, the mean inlet velocity, the dimensionless loss coefficient and the flow coefficient are defined, respectively, as follows. Reynolds number (equation 6):

$$Re = \frac{\rho\, u_0 D}{\mu} \tag{6}$$

The pressure drop is taken as the difference between the inlet and outlet static pressures (equation 7):

$$\Delta P = p_0 - p_1 \tag{7}$$

The mean inlet velocity is computed from the DN350 cross-sectional area (equation 8):

$$u_0 = \frac{Q}{A} = \frac{4Q}{\pi D^2} \tag{8}$$

The dimensionless flow resistance coefficient (zeta) according to the TS EN 1267 standard (equation 9):

$$\zeta = \frac{2\,\Delta P}{\rho\, u_0^2} \tag{9}$$

Again according to TS EN 1267, the flow coefficient Kv and the associated Cv (equation 10):

$$K_v = Q\sqrt{\frac{\rho}{\rho_0}}\,\frac{1}{\sqrt{\Delta P}}, \qquad C_v = 1.16\,K_v \tag{10}$$

Here Q is in cubic meters per hour, ΔP is in bar, and ρ0 is the reference (15 degrees Celsius) water density. With this definition Kv is not dimensionless. Its unit is cubic meters per hour times bar to the power minus 0.5. In the zeta computation of equation 9, ΔP is used in pascal, and in the Kv computation of equation 10 it is used in bar. The pressure unit was converted separately for each of the two quantities. Since a single inlet velocity level was

solved in this study, the Reynolds independence of the loss coefficient was not demonstrated. The computed zeta magnitudes were evaluated only as an internal consistency indicator in terms of the behavior expected in the fully turbulent regime and agreement with the literature. The resultant hydrodynamic force on the disc is computed from the integral of the pressure and viscous shear stress over the disc surface S (equation 11):

$$\vec{F}_d = \int_S (-p\,\vec{n} + \boldsymbol{\tau})\,\mathrm{d}S, \qquad F_d = \vec{F}_d \cdot \hat{e}_x \tag{11}$$

Here n is the surface normal, tau the viscous shear stress vector and ex the unit vector in the flow direction. Equation 11 gives the scalar component, in the flow direction (ex), of the total force vector obtained by the surface integral. The quantity denoted by Fd in this study and used in the Cd computation is this scalar component, not the force vector itself. The resistance the fluid presents to the disc is non-dimensionalized by the classical relation between the drag force Fd and the drag coefficient Cd (equation 12):

$$C_d = \frac{2\,F_d}{\rho\,u_0^2\,A_{\mathrm{iz}}} \tag{12}$$

Here Aiz is the fixed reference area chosen for the drag coefficient. In this study the DN350 inlet cross-sectional area (A) was used, not the instantaneous projected area that varies with angle. For this reason, the drag coefficient here is not the classical drag coefficient based on the instantaneous projected area of the disc, but a comparative coefficient defined with respect to a fixed reference area (C_D,ref), and it should be interpreted with respect to an angle-independent common reference area. The pressure-drop definitions are not exactly identical across the three tracks: in the numerical model ΔP is from the static pressures upstream and downstream of the disc axis (equation 7). In the experiment, on the other hand, according to TS EN 1267 the actual pressure loss of the valve is obtained by subtracting the separately measured pipe loss from the loss measured when the pipe and valve are together. Because of this definition difference, the comparison of the CFD-derived and experimental Kv should be evaluated not as an absolute verification but as a trend and ranking comparison (TS EN 1267) (equation 13):

$$\Delta P_v = \Delta P_{v+t} - \Delta P_t \tag{13}$$

The net benefit between the conventional and optimized designs is expressed by the improvement percentage over the values at each opening angle. A positive value means improvement (a reduction in loss or load) (equation 14):

$$I_X = \frac{X_{\mathrm{conv}} - X_{\mathrm{opt}}}{X_{\mathrm{conv}}} \times 100\% \tag{14}$$

The geometry of the optimized disc was related to dimensionless design ranges that lower the drag coefficient and minimize flow separation (Gök, 2021) (equation 15):

$$0.04 < \frac{H}{D} < 0.075, \qquad 0.02 < \frac{Y}{D} < 0.04 \tag{15}$$

The turbulent pressure-drop flow-rate characteristic on the flow bench approximately follows a power law in the fully turbulent regime (ΔP scales with approximately the square of the flow rate, with an exponent n of approximately 2). Since a single flow-rate level was solved for each opening in this study, the coefficients a and n were not calibrated numerically by a flow-rate sweep. The determination of the coefficients by an experimental flow-rate-pressure sweep (a, n, R^2) is the subject of future work.

2.5. Experimental Method and the TS EN 1267 Flow Bench

To support the numerical results, the actual DN350 valve product was tested on a flow bench set up according to the TS EN 1267 standard (Turkish Standards Institution, 2012). In the setup prescribed by the standard, so that valve-induced flow disturbances would not reach the measurement sections, the inlet and outlet straight-pipe development lengths were chosen greater than 10D and 2D, respectively (Figure 1). The test fluid is water, and the tests were carried out, as required by the standard, in the turbulent regime in which the Reynolds number always exceeds 4 times 10 to the power 4. For each opening position the flow coefficient Kv of the valve was computed by equation 10, and the valve pressure loss was obtained by subtracting the pipe loss according to equation 13. The opening degree was expressed as a percentage, with 90 degrees fully open and 0 degrees fully closed according to the standard convention. The Kv values measured for the conventional and optimized discs were compared at the same opening positions as the numerical solution. The repeatability and uncertainty of the measurement were quantified with repeated tests and are presented in Table 3.

2.6. Mesh and Convergence

The solutions were generated with the solution-adaptive Cartesian (cut-cell) mesh approach of Simcenter FLOEFD. Local mesh refinement was applied around the disc and the disc-rear separation region. For the DN350 flow volume the solution-adaptive procedure produced a representative discretization of about 224,000 cells, of which roughly 65,800 were partial cells that resolve the fluid-solid interface at the disc, the seat and the body walls, with the refinement concentrated where the velocity and pressure gradients are steepest. Comparable mesh resolution and local refinement practice has been reported for the numerical study of the flow around circular bluff bodies (Kanna et al., 2025). Iterative convergence was monitored until the oscillation of the inlet and outlet static pressure, the flow rate and the targets derived from them (pressure drop and disc force) decayed. The solutions converged in approximately 124 to 172 iterations depending on the angle, and the analysis interval of each solution remained between 61 and 63. For each of the fourteen solutions the monitored goals, the inlet static pressure, the volumetric flow rate

and the hydrodynamic disc force, reached full progress, and the oscillation band of every goal over the averaging interval stayed below its convergence criterion (Table 5). The iterative convergence of the disc force and the inlet pressure is shown in Figure 4 for the conventional design at the most throttled position, where both goals settle onto a stable plateau well before the end of the run. This evidence concerns the iterative convergence of the solution and not grid independence. A formal grid convergence (GCI) study based on three systematic mesh densities was not performed at this stage and is explicitly stated among the limitations in Section 4.1.

Table 3. TS EN 1267 flow-bench repeatability and Type A expanded uncertainty (k=2) of the flow coefficient measured from the Ulaş Vana test report*

Opening (%)	θ (°)	n	T (°C)	Q (m^3/h)	ΔP_valve (bar)	Kv (mean)	SD	CoV (%)	U95 (k=2)
100	90	9	15	1064–1667	0.025–0.061	6796	71.8	1.06	±48
75	67.5	9	15	1094–1621	0.074–0.176	3940	51.9	1.32	±35
50	45	9	15	1037–1687	0.334–0.928	1767	29.6	1.68	±20
25	22.5	1	15	512	1.069	495	-	-	-
10	9	1	15	127	0.969	129	-	-	-

*Since at the upper three openings the n=9 repetitions cover three different flow-rate levels, the scatter also tests the flow-rate independence of the Kv value. At the 25% and 10% openings a single measurement was taken, and the repeatability uncertainty is not defined at these points. These values represent only Type A repeatability. Since the Type B components coming from the device accuracy (flow meter, pressure sensor) are not included, it is not the total measurement uncertainty. At high openings the small pressure loss makes the Kv value sensitive to the pressure sensor accuracy. Table 3 characterizes not the point uncertainty of each Kv value in Table 4 but the repeatability of the same DN350 test setup at different openings.

3. Results

3.1. Velocity and Pressure Fields

The mid-plane velocity contours obtained for the seven opening angles are given in Figure 5, and the static pressure distributions on the disc surface in Figure 6, with the conventional and optimized designs side by side. At small opening angles (30 and 40 degrees) the disc largely blocks the flow, and a wide separation with a low-pressure wake forms behind the disc. The thin and flow-aligned profile of the optimized disc markedly reduces this separation region, decreasing the low pressure in the wake and the stagnation pressure on the front face of the disc. As the opening angle increases, the disc forms progressively less obstruction to the flow, the wake narrows and the difference between the two designs becomes smaller. The pressure contours on the disc surface (Figure 6) confirm this trend: while high pressure of about 4 bar (red) prevails on the front face of the conventional disc, the pressure on the front face of the optimized disc remains at about 2 bar (green). This difference is the physical source of both the lower net hydrodynamic force and the lower pressure drop in the optimized disc.

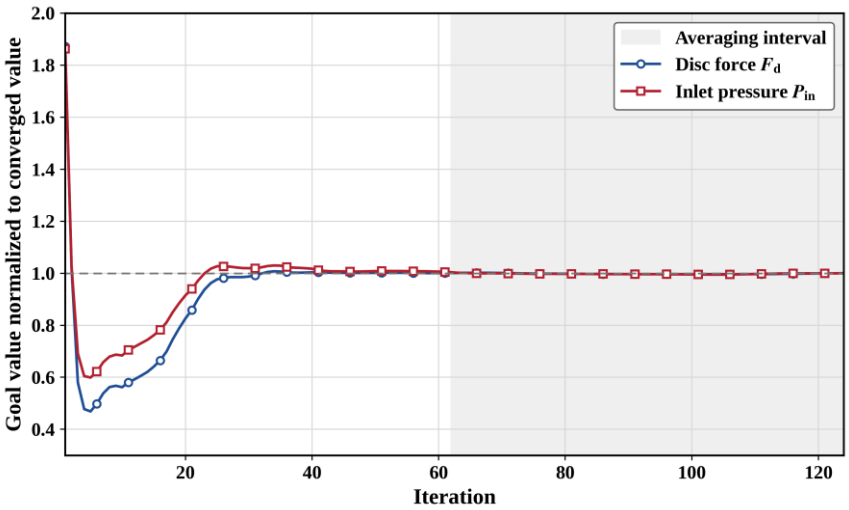


Figure 4. Iterative convergence of the monitored goals for the conventional design at the most throttled position (30 degrees). The hydrodynamic disc force and the inlet static pressure, each normalized to its converged value, settle onto a stable plateau, and the shaded band marks the averaging interval over which the goals are evaluated.

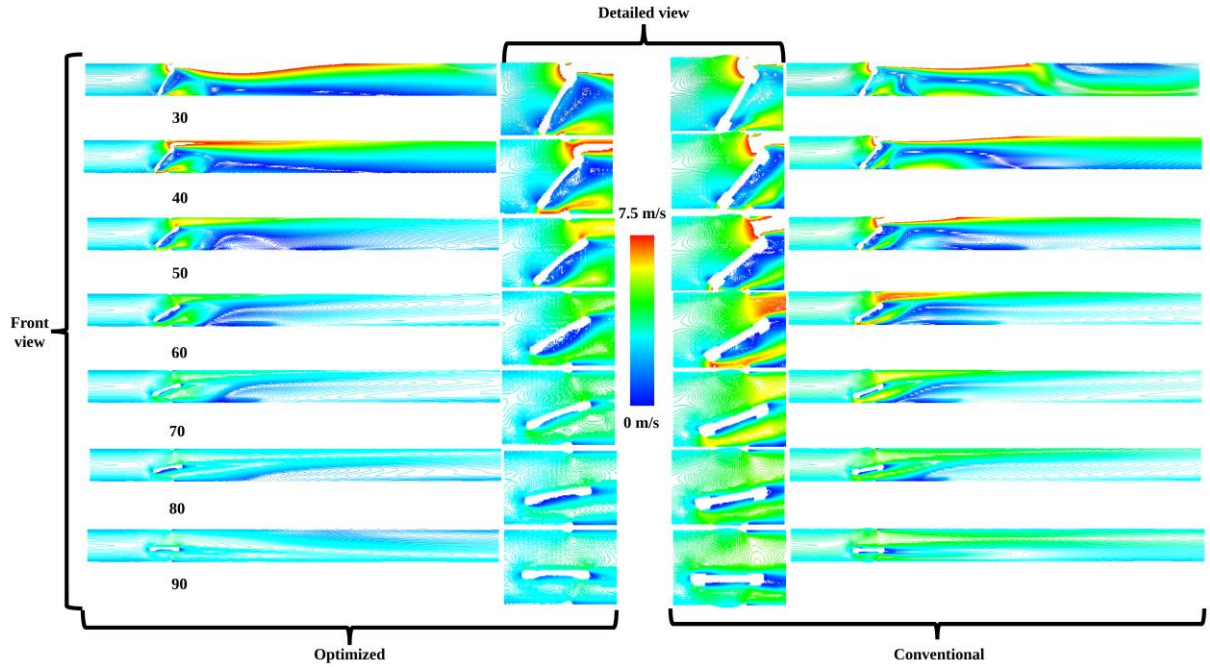


Figure 5. Mid-plane velocity contours at seven opening angles (30°-90°) for the optimized (left) and conventional (right) discs (0-7.5 m/s, front and detail views). The optimized disc produces a markedly smaller separation wake at low opening angles.

3.2. Pressure Loss and Loss Coefficient

The valve pressure drop as a function of the opening angle is given in **Figure 7**a. In both designs the pressure drop decreases rapidly as the disc opens: from 30 degrees to 90 degrees the ΔP falls from 2.773 bar to 0.018 bar in the conventional disc, and from 1.028 bar to 0.006 bar in the optimized disc. The optimized disc produces a lower pressure drop at every opening angle, and this gain is highest at the most closed position (30 degrees) at 62.9 percent. The dimensionless loss coefficient zeta and the drag coefficient Cd are given on a logarithmic axis in Figures 7b and 7c. The loss coefficient is 84.1 for the conventional disc and 33.0 for the optimized disc at 30 degrees, while at 90 degrees it falls to 0.55 and 0.19, respectively. These zeta values at the fully open position are magnitudes that are consistent with the literature and physically reasonable for a large-diameter butterfly valve. Computational and combined numerical-experimental characterizations of butterfly valves that report the loss coefficient, the flow coefficient and the hydrodynamic load have been presented for other operating contexts, including an open-source solver study for nuclear service (Yankura and Anderson, 2025) and a fluid-structure-interaction study for hydropower service (Berger et al., 2025). The drag coefficient follows the same trend and remains lower for the optimized disc at all angles.

3.3. Hydrodynamic Load on the Disc

The resultant hydrodynamic force Fd on the disc is a comparative hydrodynamic indicator (proxy) of the actuator torque demand required for the opening-closing operation, and is not the absolute actuation torque. It is the distinguishing performance metric of this study. The results given on a logarithmic axis in Figure 7d show that the force decreases rapidly with the opening angle. At the most closed position (30 degrees) the hydrodynamic force is 26,667 newtons in the conventional disc, while it falls to 9,793 newtons in the optimized disc. This corresponds to a reduction of 63.3 percent. Although the absolute force decreases as the opening increases, the relative reduction provided by the optimized design remains at 33.9 percent even at 90 degrees. This reduction in the disc hydrodynamic force points to a lower actuation load tendency, a lower shaft and bearing load and a lower mechanical loading tendency in the sealing and bearing elements (for the absolute torque, the moment must also be computed about the shaft axis). When normalized to the same flow rate, this force reduction remains in the range of 30 to 61 percent (Table 6). This normalization is not a CFD analysis re-solved at the same flow rate, but an engineering correction based on the scaling of the pressure loss and the force with the square of the velocity. When evaluated together with the 42.8 percent reduction in the disc mass (Table 1), the optimized design is superior in terms of both static (weight) and dynamic (hydrodynamic) load.

3.4. Flow Coefficient: Numerical and Experimental Reconciliation

The flow coefficient Kv is the standard measure of the flow-passing capacity of the valve, and as it grows it indicates a high capacity, that is, a low loss. In Figure 8a, the experimental Kv values measured according to TS EN 1267 and the Kv values derived from the CFD pressure drop by equation 10 are given together against the opening percentage. In the experimental data the optimized disc provides a higher Kv than the

conventional one at all opening positions: at the fully open position (100 percent) the Kv value rises from 4975 to 6796 (a 36.6 percent increase), and at the most closed measured position (33.3 percent) it increases from 764 to 919 (a 20.3 percent increase). The CFD-derived Kv and the experimental Kv show strong agreement in the mid-opening range (between 50 and 70 percent). For example, at 66.7 percent opening the CFD-derived Kv for the conventional disc is 2445 while the experimental Kv is 2453, and the difference between them is of the order of one percent. The parity plot in Figure 8b shows that the mid-opening points cluster within a 20 percent band and that the high-capacity ranking of the optimized design is preserved at each point.

At high opening positions the CFD-derived Kv exceeds the experimental value. The physical reason for this is that at positions close to fully open the pressure drop is very small, and because the Kv expression is inversely proportional to the square root of ΔP, in this region Kv becomes excessively sensitive to small pressure differences. In addition, while the CFD pressure difference is taken over the whole flow volume, the experimental Kv is based, according to equation 13, only on the valve loss with the pipe loss subtracted. For this reason, at high opening it is not the absolute values but the trend and ranking consistency that should be taken as the basis. The trend and ranking are the same in both methods: Kv increases with the opening, and the optimized disc is superior to the conventional one at every angle.

The measurement repeatability of the flow bench was evaluated at five opening positions (100, 75, 50, 25 and 10 percent) in the TS EN 1267 setup. At the upper three positions the measurements were repeated at three different flow-rate levels, so that nine data points (n=9) were obtained for each position, while a single measurement was taken at the lower two positions. The flow coefficient for each repetition was computed by equation 10. The mean, the sample standard deviation, the coefficient of variation (CoV) and the expanded uncertainty with a coverage factor of k=2 (approximately 95 percent confidence level) are given in Table 3 and Figure 8c. The fact that the nine repetitions were taken at different flow rates also tests the flow-rate independence of the flow coefficient. The Kv values measured at the upper three opening positions (100, 75 and 50 percent) remained stable with a coefficient of variation of at most 1.68 percent (expanded relative uncertainty below 1.1 percent). Since there is only a single measurement at the lower two positions (25 and 10 percent), the repeatability uncertainty was not computed. These values represent only Type A repeatability. Since the Type B components arising from the device accuracies (flow meter, pressure sensor) are not included, this is not the total measurement uncertainty. In particular, since the pressure difference is very small at high opening (at 100 percent the ΔP is approximately 0.025 to 0.061 bar) and Kv is inversely proportional to the square root of the pressure difference, in this region the contribution of the pressure sensor accuracy to the total uncertainty may be more dominant than the repeatability. In addition, Table 3 is not the one-to-one uncertainty of each comparison point in Table 4, but the repeatability characterization of the same DN350 test setup at different opening positions.

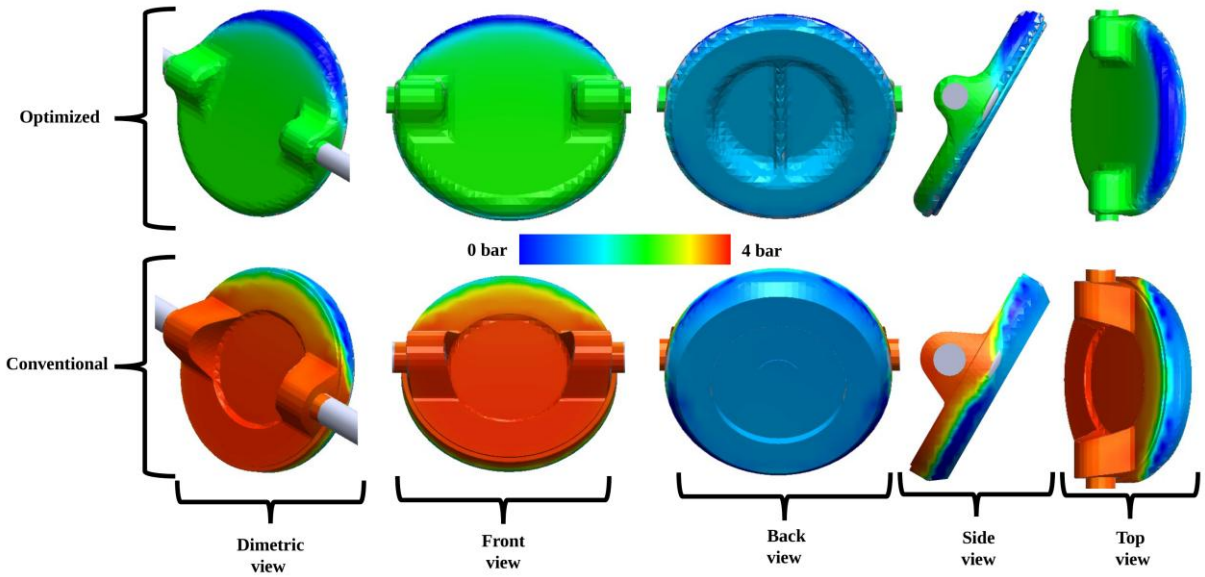


Figure 6. Static pressure distribution on the disc surface (0-4 bar) for the optimized (top row) and conventional (bottom row) discs. Dimetric, front, back, side and top views. While the front face of the conventional disc reaches about 4 bar (red), the optimized disc remains at about 2 bar (green).

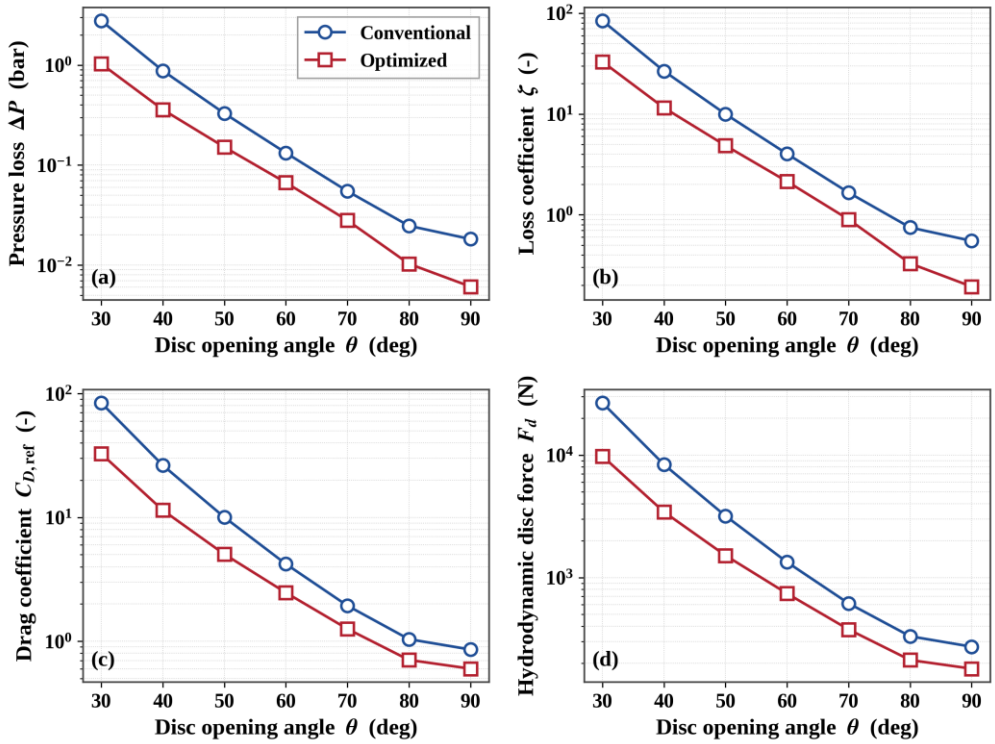


Figure 7. Hydraulic performance comparison of the conventional and optimized designs as a function of the opening angle (logarithmic scale): (a) valve pressure loss ΔP, (b) dimensionless loss coefficient ζ, (c) reference drag coefficient CD,ref and (d) hydrodynamic force Fd on the disc. The optimized disc remains below the conventional disc at every angle. Fd is an indicator of the required actuation torque.

In addition to Type A repeatability, a representative uncertainty budget was constructed to evaluate the total uncertainty of the measurement. Typical accuracies for TS EN 1267 class devices (0.5 percent of the flow-meter reading value. 0.5 percent of the differential-pressure reading value or 0.005 bar, whichever is larger. Temperature ±0.5 °C) were propagated through the relation Kv = Q·ΔP^(−0.5) (Table 7). The expanded uncertainty (k=2) grows as the opening increases: at 100 percent opening, because the valve pressure difference is very small (mean approximately 0.043 bar), the uncertainty is governed by the pressure term and reaches about ±6.8 percent. At medium and low openings it falls to ±1.3 percent and below. This shows that the deviation between the CFD-derived Kv and the experimental Kv at high opening cannot be explained entirely by the measurement uncertainty alone. For this reason, in the high-opening region the CFD-experiment comparison should be interpreted not as an absolute verification but as a trend and ranking consistency. The stated device accuracies are representative class values and should be replaced with the relevant calibration certificate values for the final uncertainty statement.

Table 4. Experimental flow coefficient Kv measured on the physical DN350 valve according to the TS EN 1267 standard, and the optimized/conventional ratio

Theta (deg)	Opening (%)	Kv conventional	Kv optimized	Optimized / conventional
30	33.3	764	919	+20.3%
40	44.4	1145	1484	+29.6%
50	55.6	1708	2250	+31.7%
60	66.7	2453	3216	+31.1%
70	77.8	3230	4257	+31.8%
80	88.9	4103	5527	+34.7%
90	100	4975	6796	+36.6%

3.5. Summary of the Performance Variation

The improvement percentages provided by the optimized design over the conventional design in four main metrics (pressure drop, loss coefficient, hydrodynamic disc force and experimental flow coefficient) are collected in the performance map in

Figure 9 and in Table 8. The map clearly shows, with all cells being positive (green), that the optimized design is superior in every metric and at every opening angle. The pressure-drop reduction is in the range of 49 to 67 percent, the loss-coefficient reduction 46 to 65 percent, the hydrodynamic-force reduction 34 to 63 percent and the experimental flow-coefficient increase 20 to 37 percent. The reduction in the disc hydrodynamic force reaches its highest level at the most closed positions, and the flow-coefficient gain at the most open positions.

3.6. Fully Open Flow Passage Geometry and the Geometric Consistency of the Flow Rate

The geometric origin of the flow coefficient results can be clarified by examining the free-flow cross-section along the axis of the fully open (90 degrees) flow volume. Figure 8d shows the free-flow cross-sectional area of the conventional and optimized designs along the flow axis. In both designs the cross-section narrows, in the valve region, to about 84 percent of the DN350 nominal area, and this minimum throat is almost identical for both (807.7 and 805.6 square centimeters). This shows that the geometric constraint at the fully open position arises not from the disc but from the common seat. For this reason, the flow coefficient superiority of the optimized disc should be attributed not to a wider passage opening but to the lower form drag created by the thin disc profile and to a narrower wake. This inference is consistent with the fact that the optimized disc produces a lower pressure drop under the same throat (Table 9) and with the pronounced difference in the disc pressure contours (Figure 6). In addition, the fact that the wetted volume of the optimized flow volume is 2.6 percent and its wetted surface 2.7 percent smaller almost exactly matches the approximately 2.8 percent flow-rate difference measured at a constant inlet velocity (890.30 cubic meters per hour versus 865.47 cubic meters per hour). This match is an independent check that confirms that the numerical solution is geometrically internally consistent.

3.6. All Solution Data

The principal hydraulic quantities derived from the fourteen CFD solutions are given in Table 9, the experimental flow coefficient values measured according to TS EN 1267 in Table 4, and the angle-dependent improvement percentages of the optimized design in Table 8.

The relative deviation between the numerical and experimental flow coefficient is given in Table 10, and the improvement percentages after flow-rate normalization in Table 6. Since the two CFD solutions were obtained, under the constant inlet condition, at approximately 2.8 percent different volumetric flow rate (890.30 and 865.47 cubic meters per hour), the dimensioned quantities pressure loss and hydrodynamic force were normalized to a common flow rate by the relations in which the pressure loss is proportional to the square of the velocity and the force to the square of the velocity. These normalized improvements coincide exactly, by definition, with the velocity-independent loss coefficient (zeta) and drag coefficient (Cd) reductions. Therefore, the 2.8 percent flow-rate difference does not distort the dimensionless comparison. Even when normalized to a common flow rate, the advantage of the optimized disc remains pronounced: a reduction of 46 to 65 percent in the pressure loss and 30 to 61 percent in the hydrodynamic force. In the flow coefficient comparison (Table 10), the CFD-derived Kv shows acceptable agreement with the experimental values in the mid-opening range (50-70 degrees), while at high opening, because the pressure drop becomes very small, Kv becomes excessively sensitive to small pressure differences and the deviation grows. For this reason, at high opening it is not absolute Kv verification but ranking consistency that is taken as the basis.

Table 5. Iterative convergence summary of the fourteen CFD solutions (Design C conventional, O optimized)*

Design	theta (deg)	Iterations	Averaging interval	Fd oscillation (N)	Fd criterion (N)	Pin oscillation (bar)	Pin criterion (bar)
C	30	124	62	145.7	431.1	0.027	0.049
C	40	124	62	63.8	124.7	0.011	0.016
C	50	129	62	21.8	37.5	0.005	0.006
C	60	125	62	6.2	15.0	0.002	0.002
C	70	125	63	2.1	6.2	0.001	0.002
C	80	125	63	1.2	1.6	0.002	0.003
C	90	130	63	1.0	1.1	0.001	0.003
O	30	140	61	38.7	123.7	0.014	0.016
O	40	145	61	24.0	36.4	0.005	0.005
O	50	172	62	11.0	20.2	0.003	0.003
O	60	145	62	10.1	11.0	0.002	0.003
O	70	124	62	2.3	4.9	0.002	0.002
O	80	132	62	2.1	2.2	0.0004	0.003
O	90	131	63	1.2	1.3	0.001	0.003

* For every case the oscillation band of the monitored goals over the averaging interval stays below the corresponding convergence criterion, which indicates that the reported quantities are numerically settled.

Table 6. Improvement of the redesigned disc over the conventional disc*

Theta (deg)	dP red. as-sim. (%)	dP red. matched-Q (%)	Fd red. as-sim. (%)	Fd red. matched-Q (%)
30	62.9	60.8	63.3	61.1
40	59.2	56.8	59.0	56.6
50	53.9	51.3	52.5	49.7
60	49.6	46.7	44.6	41.3
70	48.9	45.9	38.8	35.2
80	58.4	56.0	36.0	32.3
90	66.7	64.7	33.9	30.0

*Reported both as in the simulation (different flow rates) and normalized to a common flow rate. Since the two CFD solutions differ by approximately 2.8% in volumetric flow rate (890.30 versus 865.47 m^3/h), dP and Fd were normalized using $dP \propto u^2$ and $Fd \propto u^2$. The normalized reductions coincide with the velocity-independent ζ- and Cd-based reductions. The superiority remains pronounced at equal flow rate as well. This normalization is an engineering correction, not a CFD solution re-solved at the common flow rate.

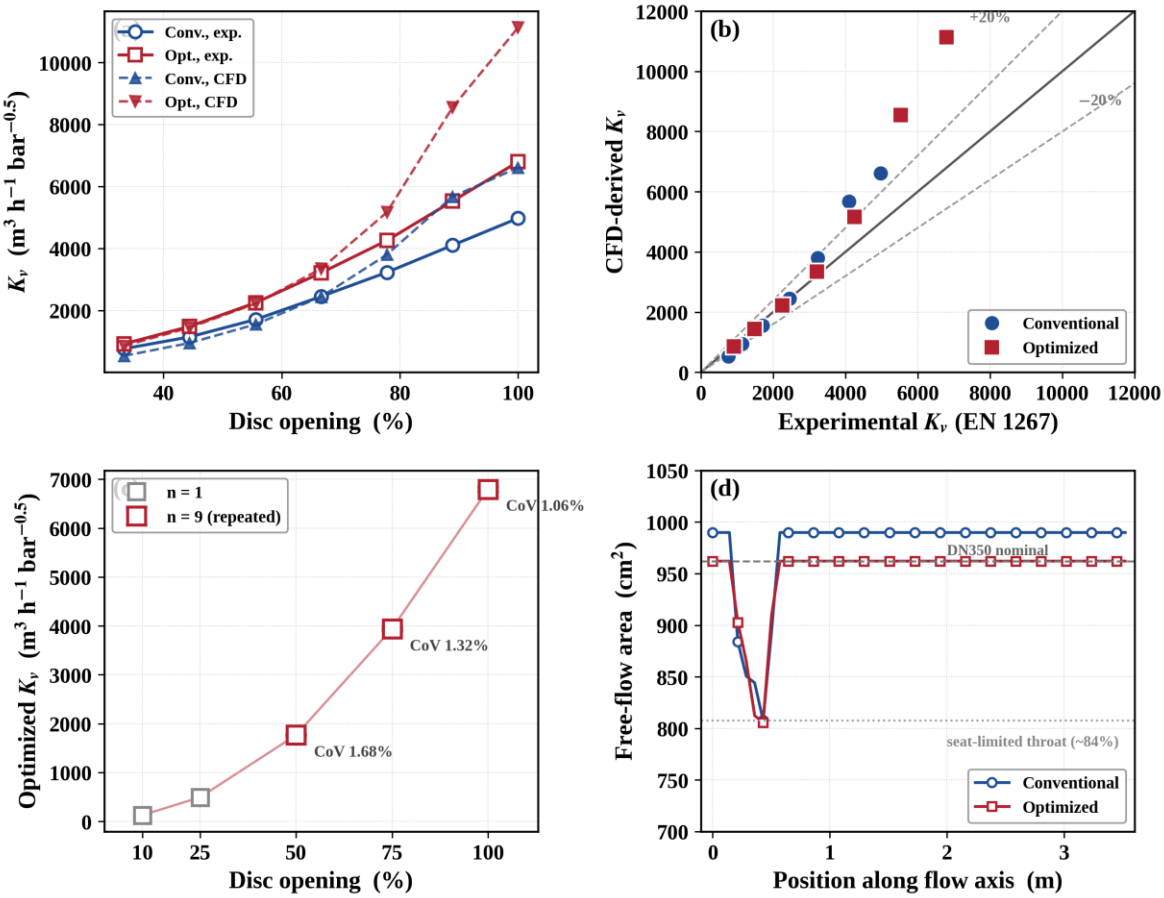


Figure 8. Experimental and numerical characterization of the flow coefficient for the conventional and optimized designs: (a) variation of the TS EN 1267 experimental and CFD-derived Kv value with the disc opening, (b) parity plot of the CFD-derived Kv value against the experimental Kv value (EN 1267) (the solid line is the 1:1 agreement, the dashed lines the ±20% band), (c) variation of the measured optimized Kv value with 95% repeatability bars (k=2) and (d) free-flow cross-sectional area of the fully open (90°) flow volume along the flow axis (with the DN350 nominal and seat-limited throat references).

Table 7. Representative measurement uncertainty budget that combines the Type A repeatability for the experimental flow coefficient with the Type B device uncertainty*

Opening (%)	ΔP (bar)	u(Q)/Q (%)	u(ΔP)/ΔP (%)	Type B u (%)	Type A u (%)	Combined u (%)	Expanded U95 (%)
100	0.043	0.29	6.78	3.40	0.35	3.42	±6.84
75	0.126	0.29	2.29	1.18	0.44	1.26	±2.52
50	0.638	0.29	0.45	0.37	0.56	0.67	±1.34
25	1.069	0.29	0.29	0.32	-	0.32	±0.65
10	0.969	0.29	0.30	0.32	-	0.32	±0.65

*The Type B uses representative TS EN 1267 device-class accuracies (±0.5% of the flow-meter reading value. ±0.5% of the differential-pressure reading value or ±0.005 bar, whichever is larger. Temperature ±0.5 °C) and these are propagated through the relation in which the Kv value is proportional to Q and to the inverse of the square root of ΔP. The expanded uncertainty (k=2) is dominated by the pressure term at high opening, where the valve pressure loss is smallest. These device accuracies are representative values and should be replaced with the calibration certificate values for the final uncertainty statement.

Table 8. Improvement of the optimized design over the conventional design*

Theta (deg)	dP reduction	Zeta reduction	Fd reduction	Kv gain (exp.)
30	62.9%	60.8%	63.3%	20.3%
40	59.2%	56.8%	59.0%	29.6%
50	53.9%	51.3%	52.5%	31.7%
60	49.6%	46.7%	44.6%	31.1%
70	48.9%	45.9%	38.7%	31.8%
80	58.4%	56.0%	36.0%	34.7%
90	66.7%	64.7%	33.9%	36.6%

*A positive value indicates a reduction in loss or force or an increase in the Kv value. The percentages were computed from the unrounded values. The flow-rate-normalized version of these reductions is given in Table 6.

Table 9. CFD-derived hydraulic quantities for the 14 solutions*

Theta (deg)	Design	**Q (m^3/h)**	Pin (bar)	dP (bar)	zeta (-)	C_D,ref (-)	Fd (N)	Kv,CFD
30	Conv.	890.30	3.7860	2.773	84.10	84.07	26667	535
30	Opt.	865.47	2.0415	1.028	33.00	32.67	9793	853
40	Conv.	890.30	1.8920	0.879	26.65	26.37	8365	950
40	Opt.	865.47	1.3721	0.359	11.52	11.44	3431	1445
50	Conv.	890.30	1.3423	0.329	9.98	10.04	3184	1552
50	Opt.	865.47	1.1648	0.152	4.86	5.05	1513	2223
60	Conv.	890.30	1.1458	0.133	4.02	4.21	1335	2445
60	Opt.	865.47	1.0800	0.067	2.14	2.47	740	3350
70	Conv.	890.30	1.0681	0.055	1.66	1.94	615	3801
70	Opt.	865.47	1.0413	0.028	0.90	1.26	377	5168
80	Conv.	890.30	1.0379	0.025	0.75	1.04	331	5671
80	Opt.	865.47	1.0235	0.010	0.33	0.71	212	8549
90	Conv.	890.30	1.0314	0.018	0.55	0.86	272	6608
90	Opt.	865.47	1.0193	0.006	0.19	0.60	180	11127

*The u0 and Re values belong to the DN350 inlet section. dP = Pin - Patm, with Patm = 1.01325 bar. Kv (CFD) was obtained by equation 10 and is not dimensionless (Q: m^3/h, dP: bar). The values are as in the simulation. The two designs were solved at slightly different flow rates (see Table 6).

Table 10. Relative deviation of the CFD-derived flow coefficient from the TS EN 1267 experimental value*

Theta (deg)	Kv,exp (C)	Kv,CFD (C)	Dev. (C) %	Kv,exp (O)	Kv,CFD (O)	Dev. (O) %
30	764	535	-30.0	919	853	-7.1
40	1145	950	-17.1	1484	1445	-2.6
50	1708	1552	-9.1	2250	2223	-1.2
60	2453	2445	-0.3	3216	3350	+4.2
70	3230	3801	+17.7	4257	5168	+21.4
80	4103	5671	+38.2	5527	8549	+54.7
90	4975	6608	+32.8	6796	11127	+63.7

*For the conventional (C) and optimized (O) discs. Deviation = (Kv,CFD - Kv,exp) / Kv,exp. A positive value indicates that the CFD value overpredicts the Kv value. The agreement is acceptable in the mid-opening range. Since at high opening the very small pressure loss makes the absolute Kv value extremely sensitive, here ranking consistency rather than absolute agreement is taken as the basis.

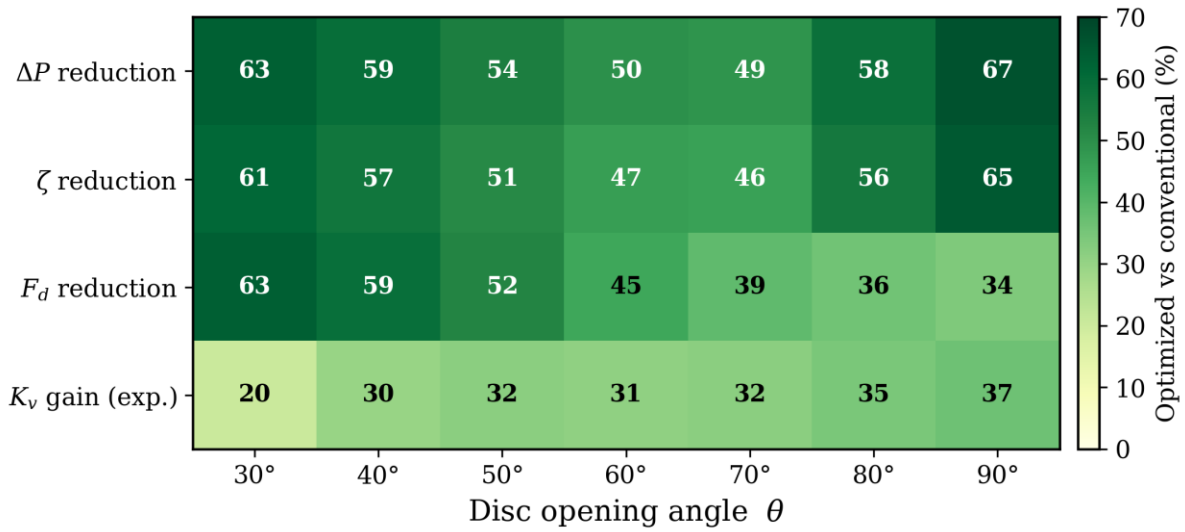


Figure 9. Performance map of the optimized versus the conventional design across four basic metrics (pressure-loss reduction, loss-coefficient reduction, hydrodynamic-force reduction and experimental Kv increase) and seven opening angles. All cells are positive (green). That is, the optimized disc improves every metric at every angle.

4. Discussion

The reliability of these results rests on three independent checks. First, the CFD-derived flow coefficient reproduces the TS EN 1267 experimental value to within about one percent in the mid-opening range (Figure 8). Second, every solution is iteratively converged, with all monitored goals settled below their criterion (Table 5 and Figure 4). Third, the fully open loss coefficients are consistent with the range reported in the literature for large-diameter butterfly valves.

The results quantitatively reveal that the integrated disc-body geometry design in a large-diameter butterfly valve is the primary element that governs both the line pressure loss and the actuation load borne by the actuator. Since not only the disc but also the body and flow volume differ in the two compared designs (Table 1), the observed gain should be attributed not to an isolated disc effect but to the integrated disc-body redesign. The separation of the disc and body contributions (cross-combinations of the conventional and optimized body with the disc) is the subject of future work. The thin and flow-aligned profile of the optimized disc, especially in the throttling regime (between 30 and 50 degrees), reduces the pressure loss by more than 50 percent by shrinking the disc-rear separation region. This behavior is consistent with the classical aerodynamic expectation based on the relation of the drag coefficient with the thickness ratio: a thin profile with rounded edges reduces the low pressure in the wake and therefore the pressure drag. The reduction of the form drag follows from the modified bluff-body behavior of the disc. As the lens-type optimized profile aligns the closure member with the flow, the adverse pressure gradient on the rear face weakens, the separation point moves downstream and the low-pressure wake contracts, and for a submerged bluff body it is the width of this wake and the base pressure that set the pressure drag (Aslan et al., 2018). The same coupling has been reported for cylinders in a confined channel, where a larger separation region directly raises the pressure loss (Güneş and Özalp, 2015), which is the trend observed here between the conventional and the optimized disc. This chain is directly visible in the present results. In the mid-plane velocity fields of Figure 5 the optimized disc

produces a markedly narrower separation wake at the low opening angles, and in the surface pressure fields of Figure 6 its front face stays near 2 bar while the conventional disc reaches about 4 bar, so the front-to-rear pressure difference that drives the form drag is reduced at its source. The fact that the optimized disc is shaped by the patented dimensionless design rules (equation 15) shows that this gain is not coincidental but is the result of a systematic design choice targeting the drag coefficient.

The reporting of the hydrodynamic load on the disc as a design metric is one of the distinguishing aspects of the study. The reduction of 34 to 63 percent in the hydrodynamic force shows that the optimized disc offers a functional superiority even for the same flow-rate capacity: a lower hydrodynamic force means a lower actuation load tendency, a lower shaft and bearing load and a longer field maintenance interval for the sealing elements. In the current literature, butterfly valve optimization is mostly addressed along the axis of cavitation suppression (G. Zhang et al., 2024a; G. Zhang et al., 2024b; G. Zhang et al., 2026) or the structural safety and sealing of eccentric designs (C. Wang et al., 2024; Qi et al., 2026). The direct quantification of the fluid-induced load on the disc adds a complementary design metric to these studies. In the same direction as the studies that relate the disc flow torque to valve plate optimization (J. Zhang et al., 2024), but in this study the load is reported together with the standard-based experimental flow coefficient.

The dual-track verification strategy is deliberately cautious. The agreement of the computed zeta magnitudes with the literature and the behavior expected in the fully turbulent regime support that the solution is in the correct turbulence regime and in internal consistency. Since a single inlet velocity was used, Reynolds independence was not demonstrated in this study. The flow-bench measurements made according to TS EN 1267, on the other hand, independently confirm the increase of the flow coefficient with the opening and the superior ranking of the optimized design. The strong agreement of the CFD-derived Kv with the experimental Kv in the mid-opening range (for example, at 66.7 percent opening a difference on the order of one percent for the conventional disc) supports that the numerical model is reliable in this regime. The deviation observed at high opening is explained by the pressure drop becoming very small and Kv becoming excessively sensitive to small pressure differences. This difference was deliberately not closed in order not to overstate the results, and instead of an absolute verification, trend and ranking consistency was taken as the basis. Consistent with post-valve flow studies in which experimental and numerical methods are used together, the two methods are seen to be complementary to each other.

Apart from the current research axes such as cavitation, erosion and artificial-intelligence-based prediction (Liu et al., 2024; X. L. Yang et al., 2024; X. L. Yang et al., 2025b), this study focuses on the low-velocity performance regime specific to irrigation and water-transmission lines. This regime also constitutes a basis for evaluating butterfly valve performance in different application contexts such as nuclear power plants (Cheng et al., 2025), dam bottom-outlet discharges (Kyriakopoulos et al., 2022) and offshore oil and gas (Sotoodeh, 2022). The fact that the optimized disc comes out superior at all examined angles and metrics is limited to the low-velocity, steady RANS regime addressed in this study. Cavitation was not evaluated in this study (the minimum static pressure and the cavitation number were not extracted), and no definitive statement is made to the effect that the regime is cavitation-free. Cavitation inception under a high pressure difference and the dynamic behavior of the disc at partial openings are outside this scope and are the subject of future work.

4.1. Limitations

The results of the study should be evaluated within the framework of the following limitations.

- The solutions are based on the steady RANS approach. Time-dependent vortex shedding and force oscillations were not solved directly. Time-averaged fields were obtained.
- A formal grid convergence (GCI) study based on three systematic mesh densities was not performed. The mesh reliability was evaluated only through solution-adaptive refinement and the iterative convergence band.
- A modified k-ε was used as the turbulence model. A model sensitivity study with alternatives such as k-ω SST or RSM was not carried out (Kim et al., 2022).
- The hydrodynamic force on the disc was presented as an indicator of the actuator torque demand. The absolute actuation torque requires the moment to be recomputed about the physical actuation axis (the shaft axis), and in this study the resultant force was given as a comparative indicator.
- The experimental measurements do not represent exactly the same disc opening as the CFD, and are not an absolute verification but supporting evidence of the turbulent pressure-drop flow-rate trend and the flow-coefficient ranking. The repeatability of the measurement was quantified (Type A, k=2 expanded uncertainty. Largest CoV 1.68 percent, Table 3), but the device-induced (Type B) uncertainty components have not yet been included.
- A cavitation model was not used and the spatial minimum static pressure was not extracted. For this reason, the cavitation number cannot be reliably given under the highest pressure-difference condition.
- The disc was modeled at fully open and fixed positions. Moving-disc dynamics and the transient behavior at partial openings are outside the scope.

The elimination of these limitations (a GCI study, a turbulence model sensitivity analysis, cavitation and erosion mapping, moving-disc analysis at partial

openings, and independent experimental measurements for the optimized product) are direct targets of future work.

5. Conclusions

The conventional and aerodynamically redesigned disc designs of a DN350 double-eccentric butterfly valve were compared in a dual-track framework that combines a steady CFD model solved at seven opening angles with flow-bench measurements made according to TS EN 1267. The principal results are as follows.

- The optimized disc achieved a marked material saving by reducing its volume by 42.8 percent and its mass from 38.7 kilograms to 22.2 kilograms, so that a thin and flow-aligned lens profile was obtained.
- The pressure loss decreased at all opening angles: the optimized disc lowered the pressure drop by 49 to 67 percent and the loss coefficient by 46 to 65 percent.
- The hydrodynamic force on the disc decreased by 34 to 63 percent (30 to 61 percent when normalized to the same flow rate). This points to a lower actuation load tendency and a lower load on the shaft, bearing and sealing elements. The absolute actuation torque requires the moment to be computed separately about the shaft axis.
- The experimental flow coefficient measured according to TS EN 1267 increased by 20 to 37 percent at every opening position in the optimized disc. The CFD-derived Kv showed strong agreement with the experimental values in the mid-opening range. At high opening, on the other hand, the CFD-derived Kv deviates in absolute terms because of the very small pressure drop. For this reason, in this range the results should be interpreted as ranking consistency rather than absolute verification.
- The performance map shows that the optimized design is superior in every metric and at every opening angle in the examined low-velocity regime.

The dual-track characterization framework and the hydrodynamic disc load metric are an effective method for distinguishing in which opening range and to what extent the disc geometry redesign produces a benefit, and can be transferred to other large-diameter flow control elements in which the disc or closure member actuation load and the line loss are jointly critical. This generalizability should be interpreted cautiously because a formal GCI study and an independent experimental verification for the optimized product are not yet available. The value of the framework lies not in the precision of the absolute values but in its revealing the comparative trends between designs and opening positions.

Author Contributions

The percentages of the authors' contributions are presented below. The authors reviewed and approved the final version of the manuscript.

	O.G.	H.A.E.
C	100	0
D	100	0
S	0	100
DCP	100	0
DAI	70	30
L	100	0
W	100	0
CR	0	100
SR	100	0
PM	100	0

C= concept, D= design, S= supervision, DCP= data collection and/or processing, DAI= data analysis and/or interpretation, L= literature search, W= writing, CR= critical review, SR= submission and revision, PM= project management.

Conflict of Interest

The authors declare no conflict of interest.

Ethical Consideration

The authors of this study declare that all the methods and procedures used do not require any ethics committee approval or special permission. Not applicable.

Acknowledgements

This article is derived from the author's master's thesis titled “Optimization of Butterfly Valves and a New Butterfly Valve Design” (Gök, 2014). The author thanks Ulaş Vana for providing the valve geometries and the flow-bench measurements. This study did not receive any external grant or funding support. The CFD-derived quantities supporting the results are contained within the article. The raw simulation files are confidential and can be obtained from the corresponding author upon reasonable request.

Nomenclature

u_i	Mean velocity component ($m \cdot s^{-1}$)
u_0	Mean inlet velocity at DN350 section ($m \cdot s^{-1}$)
p	Pressure (Pa)
p_0, p_1	Inlet / outlet static pressure (Pa)
ΔP	Static pressure drop (Pa or bar)
ρ	Density ($kg \cdot m^{-3}$)
ρ_0	Reference water density at 15 °C ($kg \cdot m^{-3}$)
μ	Dynamic viscosity (Pa·s)
μ_t	Turbulent (eddy) viscosity (Pa·s)
k	Turbulent kinetic energy ($m^2 \cdot s^{-2}$)
ε	Turbulent dissipation rate ($m^2 \cdot s^{-3}$)
P_k	Turbulence production ($kg \cdot m^{-1} \cdot s^{-3}$)

Q	Volumetric flow rate ($m^3 \cdot h^{-1}$)
D	Nominal bore diameter, 0.350 m
A	Inlet cross-sectional area (m^2)
A_iz	Disc projected (frontal) area (m^2)
θ	Disc opening angle (deg)
ζ	Dimensionless loss coefficient (-)
Cd	Drag coefficient (-)
K_v	Flow coefficient ($m^3 \cdot h^{-1} \cdot bar^{-0.5}$)
C_v	Imperial flow coefficient (-)
Re	Reynolds number (-)
Fd	Hydrodynamic disc force (N)
H/D, Y/D	Curvature-height and edge-oval design ratios (-)
I_x	Improvement of optimized vs conventional (%)
CFD	Computational Fluid Dynamics
RANS	Reynolds-Averaged Navier-Stokes
GCI	Grid Convergence Index
DN	Diameter Nominal
GGG40	EN-GJS-400 ductile cast iron

References

Akbulut, F., Şahin, H., Gök, O., Bakır, S., & Çavdar, S. (2023). *Dalgalı vana* (Faydalı Model No. TR 2021/012373). Türk Patent ve Marka Kurumu.

Akçay, S. (2024). Heat transfer examination of oscillating nanofluid flow in a rectangular corrugated channel with vertical plates: A numerical study. *Konya Journal of Engineering Sciences, 12*(2), 373–395. https://doi.org/10.36306/konjes.1419225

Aslan, E., İnan, İ., Kandemir, İ., & Güven, H. R. (2018). Numerical analysis of flow around bluff bodies with 4th and 2nd order compact formulations. *Sakarya University Journal of Science, 22*(5), 1234–1252. https://doi.org/10.16984/saufenbilder.334449

Bairagi, A., He, M., & Chen, M. (2024). Numerical investigation of butterfly valve performance in variable valve sizes, positions and flow regimes. *Journal of Nuclear Engineering, 5*(2), 128–149. https://doi.org/10.3390/jne5020010

Berger, M., Zingerle, L., Mayerl, Ch., Senfter, T., & Pillei, M. (2025). Fluid-structure-interaction in butterfly valves for hydropower: A numerical and experimental study. *Results in Engineering, 27*, Article 105855. https://doi.org/10.1016/j.rineng.2025.105855

Büyükcura, A., Gök, O., & Neşeli, S. (2024). Investigation of aerodynamics behaviors, shape of feathers on traditional Turkish archery. *International Research Journal of Innovations in Engineering and Technology, 8*(6), 81–87. https://doi.org/10.47001/IRJIET/2024.806010

Cheng, J., Fang, K., Fei, K., Wang, Q., Li, B., & Farfán, E. B. (2025). Failure analysis of CRDINiCr butterfly valves for nuclear power plant applications. *Nuclear Technology, 211*(3), 584–597. https://doi.org/10.1080/00295450.2024.2344912

Choi, S. W., Seo, H. S., & Kim, H. S. (2021). Analysis of flow characteristics and effects of turbulence models for the butterfly valve. *Applied Sciences, 11*(14), Article 6319. https://doi.org/10.3390/app11146319

Erdoğan, A., & Daşkın, M. (2023). Comparing of CFD contours using image analysing method: A study on velocity distributions. *Black Sea Journal of Engineering and Science, 6*(4), 633–638. https://doi.org/10.34248/bsengineering.1310711

Erkan, O., & Özkan, M. (2020). Investigation of the flow over NACA 63-415 airfoil. *Black Sea Journal of Engineering and Science, 3*(2), 50–56. https://doi.org/10.34248/bsengineering.643916

Gök, O. (2014). *Kelebek vanaların optimizasyonu ve yeni bir kelebek vana tasarımı* [Yüksek lisans tezi, Cumhuriyet Üniversitesi]. Fen Bilimleri Enstitüsü.

Gök, O. (2021). *Endüstriyel kelebek vanalarda kullanılan klapelerde yenilik* (Faydalı Model No. TR 2017/05752). Türk Patent ve Marka Kurumu.

Gök, O., Ertaş, H. A., Kayrıcı, M., & Gökmeşe, H. (2023). Comparative numerical analysis of three-dimensional flow in the opening process of the single-disc butterfly valves. *International Research Journal of Innovations in Engineering and Technology, 7*(7), 189–195. https://doi.org/10.47001/IRJIET/2023.707029

Gök, O., Tınkır, M., Kahraman, A., & Camgöz, U. (2019). *Dıştan dişli pompalarda yenilik* (Faydalı Model No. TR 2016/19120). Türk Patent ve Marka Kurumu.

Güneş, N., & Özalp, A. (2015). Yüksek blokajlı kanal içinde art arda iki silindir etrafında sürekli laminer akış için ısı ve akış karakteristiklerinin nümerik olarak incelenmesi. *Mühendis ve Makina, 56*(667), 53–63.

Kalkat, M., & Tom, V. (2019). Dalgıç pompalarda yapay sinir ağları kullanılarak deneysel akış analizi. *Konya Journal of Engineering Sciences, 7*(Özel Sayı), 895–908. https://doi.org/10.36306/konjes.623995

Kanna, P. R., Sivakumar, Y., Prasad, G. V. D., Taler, D., Sobota, T., & Taler, J. (2025). Numerical investigation of flow and heat transfer from twin circular cylinders present in double forward-facing step. *Fluids, 10*(2), Article 48. https://doi.org/10.3390/fluids10020048

Kaplan, M. (2024). CFD analysis of pressure drop reduction in PEMFC flow channels with distinct cross-section shapes. *Black Sea Journal of Engineering and Science, 7*(2), 254–260. https://doi.org/10.34248/bsengineering.1420277

Karaokur, H. İ., & Akay, O. E. (2022). Yüksek basınçlı santrifüj fan performansının deneysel ve sayısal incelenmesi. *Konya Journal of Engineering Sciences, 10*(1), 215–228. https://doi.org/10.36306/konjes.978669

Kaya, M. N. (2025a). Numerical investigation of hydrofoil cavitation using OpenFOAM: Effect of thickness and camber. *Black Sea Journal of Engineering and Science, 8*(5), 1585–1594. https://doi.org/10.34248/bsengineering.1759120

Kaya, M. N. (2025b). Numerical investigation of transonic shock wave characteristics on supercritical airfoils under various flow conditions. *Konya Journal of Engineering Sciences, 13*(4), 1252–1263. https://doi.org/10.36306/konjes.1743613

Kim, M. S., Lee, S. W., & Choi, S. W. (2022). Effect of the turbulence model in the flow analysis of triple offset butterfly valve. *Journal of Advanced Marine Engineering and Technology, 46*(6), 356–361. https://doi.org/10.5916/jamet.2022.46.6.356

Kyriakopoulos, G. L., Aminpour, Y., Yamini, O. A., Movahedi, A., Mousavi, S. H., & Kavianpour, M. R. (2022). Hydraulic performance of Howell–Bunger and butterfly valves used for bottom outlet in large dams under flood hazards. *Applied Sciences, 12*(21), Article 10971. https://doi.org/10.3390/app122110971

Liu, Q. T., Xie, C. H., & Cheng, B. X. (2024). Butterfly valve erosion prediction based on LSTM network. *Flow Measurement and Instrumentation, 98*, Article 102652. https://doi.org/10.1016/j.flowmeasinst.2024.102652

Nguyen, Q. K., Jung, K. H., Lee, G. N., Park, S. B., Kim, J. M., Suh, S. B., & Lee, J. Y. (2023). Experimental study on pressure

characteristics and flow coefficient of butterfly valve. *International Journal of Naval Architecture and Ocean Engineering, 15*, Article 100495. https://doi.org/10.1016/j.ijnaoe.2022.100495

Perera, P., Hayward, K., Guzzomi, F., & Vafadar, A. (2024). Erosion wear characterisation of an open ductile iron butterfly valve subjected to aluminium oxide particle slurry flow. *Tribology International, 191*, Article 109199. https://doi.org/10.1016/j.triboint.2023.109199

Polat, C., Saydam, D. B., Söyler, M., & Özalp, C. (2022). İkili küp modellerinin akış alanına farklı açıklık oranlarında yerleştirilmesinin akış yapısına etkisinin deneysel olarak incelenmesi. *Konya Journal of Engineering Sciences, 10*(1), 200–214. https://doi.org/10.36306/konjes.933713

Qi, H., Brilianto, R. M., Lee, S., & Kim, C. (2026). Design and optimization of a triple-offset butterfly valve with soft O-ring sealing for enhanced automotive hydrogen applications. *Journal of Mechanical Science and Technology, 40*, 4523–4537. https://doi.org/10.1007/s12206-026-0533-1

Qi, H., Kwak, H., Park, G., Kim, B., & Kim, C. (2023). Design of quadruple offset butterfly valve used in power plants. *Applied Sciences, 13*(6), Article 3656. https://doi.org/10.3390/app13063656

Sefacı, S., Kalyoncu, M., Acar, O., & Koçak, S. (2026). The comparison of fuzzy inference system and the bees algorithm for optimal design of balancing hole of centrifugal pump impeller. *Konya Journal of Engineering Sciences, 14*(2), 998–1015. https://doi.org/10.36306/konjes.1722297

Sotoodeh, K. (2022). Safety and reliability analysis for butterfly valves in the offshore oil and gas industry. *Safety and Reliability*, 41(2), 121–143. https://doi.org/10.1080/09617353.2022.2107254

Su, G. Q., Li, Y., & Zhang, J. W. (2024). Flow accelerated corrosion and thinning mechanism of the pipeline after the butterfly valve based on CFD. *Engineering Failure Analysis, 156*, Article 107844. https://doi.org/10.1016/j.engfailanal.2023.107844

Turkish Standards Institution [Türk Standardları Enstitüsü]. (2012). *Vanalar – Akış direnci deneyi – Deney akışkanı olarak su kullanılan* (Standart No. TS EN 1267:2012).

Wang, C., Xu, D., Huang, K., Liu, Y., & Yang, L. (2024). Multi-objective optimization of a triple-eccentric butterfly valve considering structural safety and sealing performance. *ISA Transactions, 155*, 295–308. https://doi.org/10.1016/j.isatra.2024.10.009

Wang, D., Feng, J., Guo, M., Wei, Z., & Gao, B. (2024). An in-position measurement method of point-replacing surface for triple-eccentric butterfly valve precision machining. *The International Journal of Advanced Manufacturing Technology, 133*(5–6), 2607–2621. https://doi.org/10.1007/s00170-024-13850-y

Yağmur, S., & Doğan, S. (2022). Kavite çıkış kenarının gürültü seviyesine etkisinin araştırılması. *Konya Journal of Engineering Sciences, 10*(3), 719–731. https://doi.org/10.36306/konjes.1107037

Yang, X. L., Lü, Y. J., Xu, L., Ma, Y. S., Chen, R. B., & Li, Q. A. (2025a). Erosion wear and flow characteristics of tri-eccentric butterfly valves under liquid–solid two-phase flow. *Journal of Applied Fluid Mechanics, 18*(11), 2711–2729. https://doi.org/10.47176/jafm.18.11.3564

Yang, X. L., Lü, Y. J., Xu, L., Ma, Y. S., Chen, R. B., & Li, Q. A. (2025b). Flow characteristics prediction of the tri-eccentric butterfly valve based on the Multi-Scale Fusion Attention method and Kolmogorov–Arnold network. *Flow Measurement and Instrumentation, 105*, Article 102934. https://doi.org/10.1016/j.flowmeasinst.2025.102934

Yang, X. L., Lü, Y. J., Xu, L., Ma, Y. S., Chen, R. B., & Zhao, X. W. (2024). Numerical investigation on cavitation erosion and evolution of choked flow in a tri-eccentric butterfly valve. *Flow Measurement and Instrumentation, 100*, Article 102725. https://doi.org/10.1016/j.flowmeasinst.2024.102725

Yankura, D., & Anderson, M. (2025). Butterfly valve performance factors using the multiphysics object oriented simulation environment. *Annals of Nuclear Energy, 224*, Article 111671. https://doi.org/10.1016/j.anucene.2025.111671

Zhang, G., Wang, W. W., Wu, Z. Y., Chen, D. S., Kim, H. D., & Lin, Z. (2023). Effect of the opening degree on evolution of cryogenic cavitation through a butterfly valve. *Energy, 283*, Article 128454. https://doi.org/10.1016/j.energy.2023.128454

Zhang, G., Zhang, H. T., Wu, Z. Y., Wu, X., Kim, H. D., & Lin, Z. (2024a). Experimental studies of cavitation evolution through a butterfly valve at different regulation conditions. *Experiments in Fluids, 65*, Article 4. https://doi.org/10.1007/s00348-023-03743-3

Zhang, G., Hu, R., Yin, D., Chen, D., Zhou, H., & Lin, Z. (2024b). Numerical study of cavitation characteristics through butterfly valve under different regulation conditions. *Processes, 12*(4), Article 686. https://doi.org/10.3390/pr12040686

Zhang, G., Qi, S. Q., Wu, X., Zhang, X. Z., Xia, S. J., Zhu, Z. C., & Lin, Z. (2026). Effect of wedge angle on cavitation evolution and inhibition in a butterfly valve. *Journal of Mechanical Science and Technology, 40*(5), 3591–3606. https://doi.org/10.1007/s12206-026-0434-3

Zhang, J., Yin, W. L., Wang, X., Zheng, S. W., Pan, L. J., & Zhai, F. G. (2024). Flow field torque analysis and valve plate optimization of butterfly anti-stick bleed valve. *Flow Measurement and Instrumentation*, 100, Article 102685. https://doi.org/10.1016/j.flowmeasinst.2024.102685

Black Sea Journal of Engineering and Science
doi: 10.34248/bsengineering.1919355

Open Access Journal
e-ISSN: 2619 – 8991

Research Article
Volume 9 - Issue 5: 2307-2316 / September 2026

FACE RECOGNITION BASED IDENTITY VERIFICATION AND TRACKING SYSTEM DESIGN

Emirhan TANRIVERDİ[1], Yaşar APAYDIN[1], Hakan ÜSTÜNEL[1]*

[1]*Kirklareli University, Faculty of Engineering, Department of Software Engineering, 39000, Kırklareli, Türkiye*

Abstract: The use and importance of various authentication systems are increasing in order to enhance the security of data access processes and to enable authorized logins to work environments. In this study, a facial recognition-based authentication and personnel tracking system automation was developed. The developed system runs on a Raspberry Pi. Images obtained through the camera module are analyzed using facial recognition algorithms. The face detection algorithm was used to determine the location of human faces in the image captured by the camera. This process was performed using the face recognition library's HOG (Histogram of Oriented Gradients) based face detection method. The entry and exit times of identified individuals are automatically recorded, and this data can be viewed via a web-based interface. The system enables the successful generation of detailed reports on information such as employee entry and exit times and break durations. The developed system offers a low-cost, real-time, contactless, and IoT-compatible solution to enhance organizational/data security. The results of the study show that the developed system is applicable to employee tracking applications.

Keywords: Facial recognition, Identity verification, Raspberry Pi, Web-based systems, Employee tracking system, Embedded systems

***Corresponding author:** Kırklareli University, Faculty of Engineering, Department of Software Engineering, 39000, Kırklareli, Türkiye
E mail: hakanustunel@hotmail.com; hakanustunel@klu.edu.tr. (H. USTUNEL)
Emirhan TANRIVERDİ https://orcid.org/0009-0006-5852-452X
Yaşar APAYDIN https://orcid.org/0009-0003-9303-5586
Hakan ÜSTÜNEL https://orcid.org/0000-0001-9903-593X

Received: March 30, 2026
Accepted: August 01, 2026
Published: September 15, 2026

Cite as: Tanrıverdi, E., Apaydın, Y., & Üstünel, H. (2026). Face recognition based identity verification and tracking system design. *Black Sea Journal of Engineering and Science,* 9(5), 2307-2316.

1. Introduction

With the increasing need for security in work environments, authentication systems have become more essential for many organizations. In security systems, biometric solutions such as card access systems (Zhao et al., 2025), password-based authentication methods (Pu et al., 2026), fingerprint (Adesoba and Joseph, 2025) and hybrid systems (Choudhary et al., 2025) are widely used. However, these systems also have limitations. These limitations have increased the need for more reliable and automated technologies. Biometric recognition systems authenticate individuals by using their physical and/or behavioral characteristics.

Facial recognition technology, a type of biometric method, stands out for its contactless operation and the fact that it does not require any extra action from the user. Face recognition systems generally consist of face detection, feature extraction and verification stages (Zhao et al., 2003). These processes allow the system to verify a person's identity quickly and automatically. The development of low-cost embedded systems has contributed to making facial recognition technologies more accessible. Platforms like Raspberry Pi offer a balanced solution between adequate performance and cost. This has increased the accessibility of automated systems in areas such as personnel tracking and access control. Authentication systems refer to the technological and procedural processes used to determine the accuracy of an individual's claimed identity. These systems play critical roles in preventing unauthorized access in both physical and digital environments. In corporate structures in particular, the effective use of authentication mechanisms is essential in areas such as personnel tracking, data security, and access control.

Authentication methods are generally categorized into three main groups. Knowledge-based authentication (what you know), ownership-based authentication (what you have) and biometric authentication (what you are) (Jacomme and Kremer, 2021). Knowledge-based authentication relies on data known only to the user, such as passwords, PINs (Personal Identification Numbers), or security questions. However, these methods have security vulnerabilities, such as passwords being guessed or shared with third parties. Ownership-based verification relies on physically owned objects such as smart cards, ID cards, or mobile verification devices. Risks such as card loss or copying are among the disadvantages of this method.

Alternative methods are also used in the fields of facial recognition and biometric authentication. PCA (Principal Component Analysis) is one of the fundamental dimensionality reduction methods used in facial recognition. In this approach, each facial image is represented as a high-dimensional vector consisting of

This work is licensed (CC BY-NC 4.0) under Creative Commons Attribution 4.0 International License

pixel values. Because the PCA method can capture the general structural features of the face, it is more robust than simple template-based methods and reduces computational costs through dimensionality reduction. However, since PCA can only model linear relationships, its performance may be limited in the face of lighting changes, large facial position differences, and changes in facial expressions (Turk and Pentland, 1991). In Template Matching, face recognition is performed directly by comparing similarities at the pixel level. The ease of application and the lack of an additional learning process are the most important advantages of this method. However, it is quite sensitive to changes in scale, position, lighting, and expression in facial images; and a decrease in performance is observed when no preprocessing is done. Therefore, it is difficult to produce reliable results outside of controlled environments (Brunelli and Poggio, 1993). Although fingerprint systems offer high accuracy, the need for physical contact is a disadvantage in terms of hygiene (Adesoba and Joseph, 2025, Jain et al., 2004). Card systems, on the other hand, carry security risks such as the loss or misuse of the card.

With increasing security requirements, biometric authentication systems have come to the forefront. Biometric systems can perform verification by analyzing unique physical or behavioral characteristics of an individual, such as fingerprints, iris, voice, and face. The difficulty in imitating these characteristics makes biometric methods more reliable compared to other types of verification. Furthermore, the fact that the user does not need an additional card or password provides an advantage in terms of ease of use. A general face recognition system block diagram is shown in Figure 1.

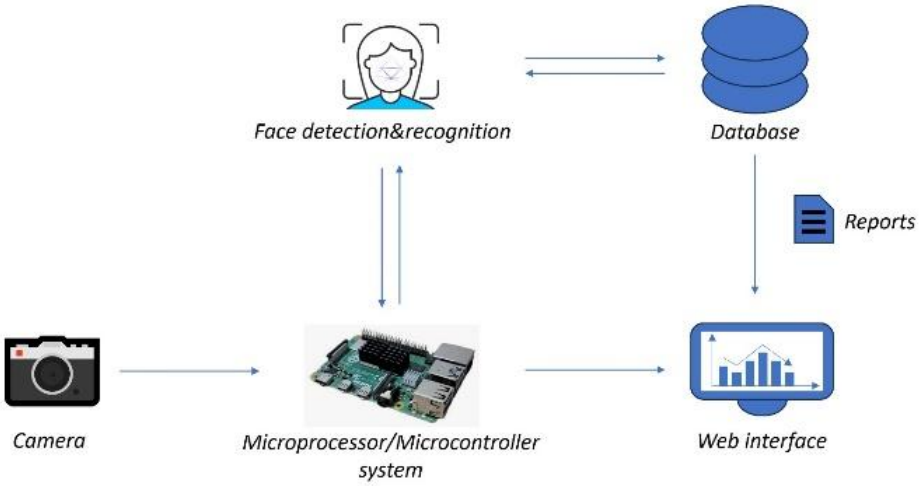


Figure 1. General flowchart of the facial recognition system

Facial recognition technology has a wide range of applications among biometric authentication methods due to its contactless nature and real-time processing capabilities. Images obtained via camera are analyzed and compared with recorded data in the system. This allows individuals' identities to be determined quickly and with high accuracy rates. In the system developed in this study, facial recognition technology, a biometric authentication method, was preferred due to its advantages in reliability and ease of use. Images obtained with the camera module are processed to verify user identity, and records are reported via a web-based interface.

Recent studies focus on lightweight face recognition and security on embedded boards. Ahmed Ali Aboluhom and Kandilli (2024) tested deep learning models for face verification on the Raspberry Pi platform. Similarly, Surantha and Sugijakko (2024) developed a portable attendance system using edge-based face recognition. Along with algorithm efficiency, deploying decentralized network structures helps protect these IoT edge tracking nodes from unauthorized data modifications (Ataşen and Üstünel, 2019). Other studies focus on developing low-cost and secure edge platforms for user tracking. For example, Mamak et al. (2020) designed a real-time personnel control system using classical methods like Eigenface and Fisherface. Orostegui et al. (2021) implemented an embedded face recognition system on a Raspberry Pi using FaceNet architecture, reaching 77.38% accuracy. Similarly, Bin Hamed and Fatnassi (2022) created a secure attendance subsystem by combining HOG features with Support Vector Machines on edge hardware. These studies prove that embedded devices are highly capable of managing identity verification loops efficiently.

2. Materials and Methods

In this study, Raspberry Pi-based facial recognition system automation was developed. The system recognizes individuals from images captured by a camera and automatically records their entry and exit times in a database. The obtained data is transferred to a web-based interface. Through the web interface, information such as personnel movements and break times can be reported and displayed.

2.1. Hardware

The system uses a Raspberry Pi 4 Model B as its main processing unit. The Raspberry Pi 4 has a quad-core ARM-based processor running at 1.5 GHz and 4 GB of RAM. The processor, camera, and power connectors are shown in Figure 2. This configuration offers a portable system with minimal setup requirements.

The C270 HD Webcam was used for image capture. Camera specifications:

- 0.9 Megapixel resolution
- 720p/30 fps video recording
- Fixed focus lens
- Diagonal field of view (dFoV): 55°



Figure 2. System hardware configuration and real-world testing.

2.2. Software Development

The developed software detects human faces from images captured by the camera. Then, the recognition step begins, and the detected face data is sent to the database. If a match is found, the time information is recorded; otherwise, the system continues to operate without any recording. The recorded time information is displayed via the web interface.

Figure 3 shows the general workflow of the camera and face recognition module running on the Raspberry Pi. A real-time image is captured by the camera and simultaneously streamed live to the web interface.

The system continues to operate in a loop (like infinite loop) until face detection occurs in the image captured by the camera. If a face is detected in the image, the face recognition algorithm is activated and it is checked whether the detected face belongs to a registered employee in the system.

If the captured face belongs to a registered employee, the relevant information is transmitted to the web server via API. Simultaneously, the processed data is transferred to the web interface, allowing the administrator to monitor the system in real-time. For faces/individuals not registered in the system, the system continues to operate without any action. Thanks to this structure, face recognition, data transmission, and user interface operations are carried out simultaneously and seamlessly; providing a real-time personnel tracking process on the Raspberry Pi.

Figure 4 shows the requests received by the backend system, the processing process, and the general flow of database operations. Within the main execution cycle, the system first checks whether the backend service is accessible. If the system is unavailable, the process is terminated, and no further action is taken.

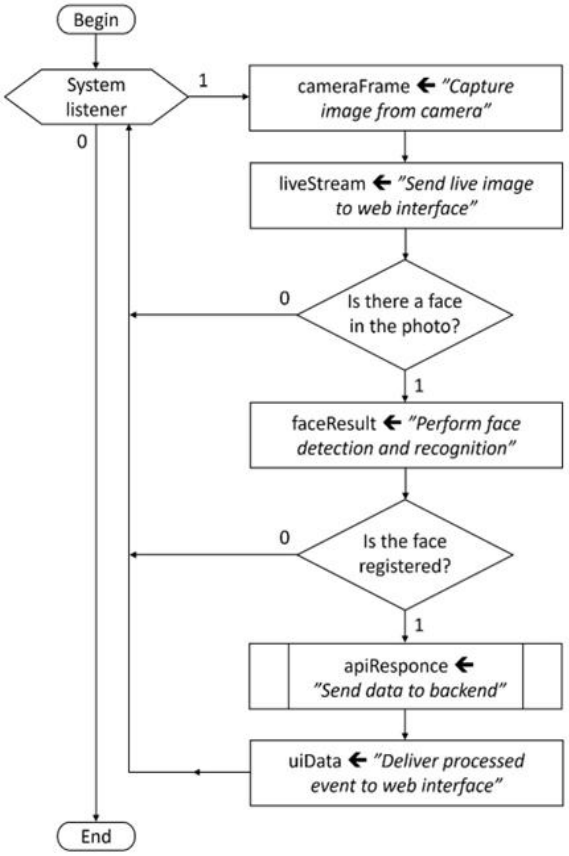


Figure 3. Flowchart of the facial recognition system.

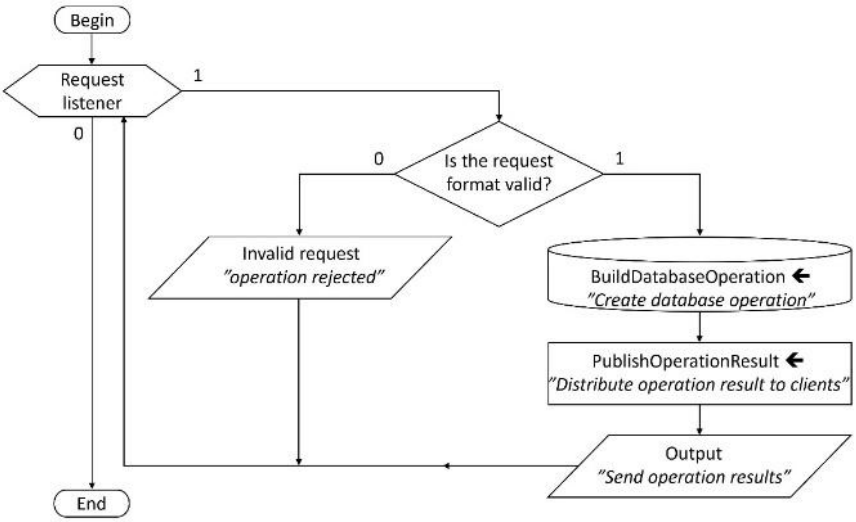


Figure 4. Flowchart of the face recognition module (backend).

When the backend service is active, the format of the request from the client (face recognition module or web interface) is verified. If the request format is invalid, the system rejects the request, generates an error message, and terminates the process. This step serves as a critical control mechanism for maintaining system security and data integrity.

If the request format is valid, the system proceeds to create the relevant database operation. At this stage, a database operation is created according to the incoming request. After the operation is completed, the results are distributed to the clients via the API. In the final stage, the result of the performed operation is transmitted to the client, and the system returns to the main loop to wait for the next request. Thanks to this structure, communication between the backend, API, and database is provided in a controlled, secure, and sustainable manner; creating a consistent data flow throughout the system. The software framework was developed using the Python programming language. To ensure experimental reproducibility, the software stack, dependency components, and version numbers are cataloged in Table 1.

The face_recognition library generates 128-dimensional embedding vectors using a pre-trained dlib model. Identity verification relies on Euclidean distance with a tolerance threshold of $t = 0.50$. During real-world testing, the calculated distances for valid matches ranged strictly between 0.2992 and 0.4658, remaining securely below the threshold.

Table 1. Software dependency stack and versions

Software / Library	Core Function	Exact Version
Python	Primary Programming Environment	3.11.x
OpenCV (cv2)	Frame Capture and Image Processing	4.06.2000
face_recognition	Facial Recognition Interface	1.03.2000
face_recognition_models	Pre-trained Weight Models	0.3.0
dlib	Feature Extraction and Geometry Engine	20.0.0
NumPy	Matrix Operations	1.26.4
Flask	REST API Services	1.01.2002
Requests	HTTP Server Communications	2.25.1
WebSockets	Real-Time Data Streaming	15.0.1

2.2.1. Face recognition module

In this study, multiple algorithms were used together for face recognition. The algorithms were selected considering the system's ability to operate in real time and its compliance with hardware constraints. The basic algorithms are shown in Figure 5. The face detection algorithm was used to determine the position of human faces in the image captured by the camera. This process was performed using the face_recognition library's HOG (Histogram of Oriented Gradients) based face detection method. The HOG-based approach was preferred because it requires less computational power compared to deep learning-based methods. This allows the system to run in real-time on the Raspberry Pi.

In the HOG method, the horizontal and vertical light variations of each pixel are calculated using the central difference method. The magnitude and direction of the gradient are determined from these variations. The image is divided into small cells, and a histogram is created for each cell by dividing the gradient directions into specific intervals (e.g., 0°–180°). The histogram values are weighted with the relevant gradient magnitude and normalized in blocks to obtain HOG features. The HOG features obtained in this way have

been used in the detection of facial regions (Dalal and Triggs, 2005).

A facial recognition algorithm was used to determine which user the detected faces belonged to. In this stage, faces are represented as numerical vectors. This function generates a vector containing distinctive features for each face. The generated face vectors are compared with face vectors previously registered in the system.

The face_recognition library used in this study represents each face as a 128-dimensional vector using a ResNet-based convolutional neural network. For a face image x, the network's output can be expressed as follows:

$$f(x) \in R^d \tag{1}$$

Here, f(x) represents the numerical representation of the face, and d(dimension) represents the number of dimensions of the space. During network training, the goal is to have vectors of faces belonging to the same person close to each other and faces belonging to different people far apart. For this purpose, the triplet loss function is used (Schroff et al., 2015). Thanks to this method, the system learns the distinguishing differences between faces.

$$L = \sum_{i}^{N} \left[\| f(x_i^a) - f(x_i^p) \|_2^2 - \| f(x_i^a) - f(x_i^n) \|_2^2 + a \right]_+ \tag{2}$$

The parameters in the equation are: xa: anchor (reference face), xp: positive (face belonging to the same person), xn: negative (face belonging to a different person), α: margin (safety distance).

The similarity measurement algorithm was used to numerically calculate the difference between the existing face and the recorded faces. First, the distinctive features of the face, such as nose shape, jaw structure, and facial proportions, are extracted. Then, this information is converted into a numerical vector. This process transforms the face into a 128-dimensional face vector.

As can be seen in Figure 5, the similarity measurement in the code is performed with the following function.

matches = face_recognition.compare_faces(known_encodings, encoding, tolerance=0.5)

The similarity between two embedding vectors is calculated using the L2 norm (Euclidean distance) (Schroff et al., 2015).

$$distance(v_1, v_2) = \sqrt{\sum_{i=1}^{d} (v_{1,i} - v_{2,i})^2} \tag{3}$$

The calculated distance value is compared against a predetermined threshold value (e.g., t=0.5):

Distance (v_1, v_2) <t ➔ "Same person"

Distance (v_1, v_2) >=t ➔ "Different person"

This method was used to reduce mismatches and increase system reliability. The time log block manages the login, break, and logout information of the recognized user. This structure operates on a state machine logic. State information is stored in user_state for each user. All transactions are sent to the website via API. Depending on the situation, user login, break start, break end, and logout records are processed.

To define the placement of the proposed framework, Table 2 benchmarks our HOG-ResNet solution against relevant embedded face verification systems documented in recent literature (Mamak et al., 2020, Orostegui et al., 2021, Bin Hamed and Fatnassi, 2022).

As shown in Table 2, while deep frameworks like Orostegui et al. (2021) experience high processing delays (~11 seconds) on embedded boards, proposed system provides a highly optimized trade-off. It achieves a fast average recognition speed of ~2 ms on the Raspberry Pi 4 edge platform while keeping deep ResNet-level feature representations (Schroff et al., 2015).

```
if process_frame:
    locations = face_recognition.face_locations(rgb_frame, model="hog")
    encodings = face_recognition.face_encodings(rgb_frame,locations,num_jitters=1)

    for encoding, loc in zip(encodings, locations):
        matches = face_recognition.compare_faces(known_encodings, encoding, tolerance=0.5)
        name = "Bilinmiyor"

        if True in matches:
            idx = np.argmin(face_recognition.face_distance(known_encodings, encoding))
            name = known_ids[idx]
            if name not in ACTIVE_EMPLOYEE_IDS:
                continue  # pasif veya silinmiş → YOK SAY
            seen.append(name)
            state = user_state.get(name, {"stage": None, "last_seen": None, "last_action_time": None})
```

Figure 5. Face recognition code block.

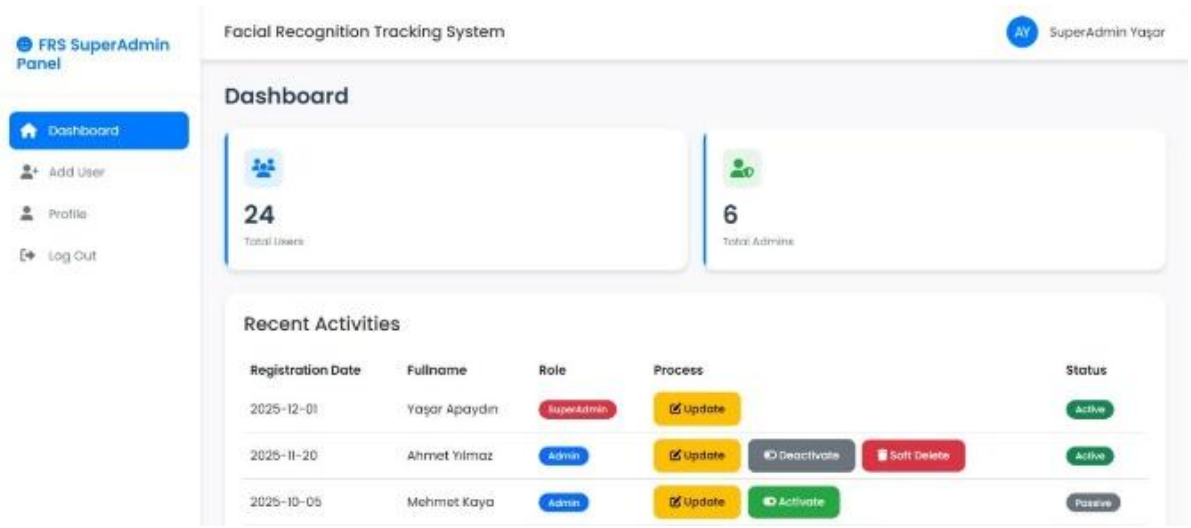


Figure 6. Super Admin panel screen.

Table 2. Comparative summary of embedded face recognition systems

Reference Study	Target Hardware	Core Methodology	Face Detection Method	Verification Accuracy	Inference Latency
Mamak et al. (2020)	PC / Server	Eigenface / Fisherface	Multi-Method Cascade	Variable	Real-time
Orostegui et al. (2021)	Raspberry Pi	FaceNet / GoogLeNet	CNN Cascade	77.38%	~11.00 seconds
Bin Hamed and Fatnassi (2022)	Raspberry Pi	HOG / Haar Cascade	Haar Cascade	High	Real-time
Proposed Work	*Raspberry Pi 4*	*HOG + ResNet Embedding*	*HOG-Based*	*53.62% (Real Conditions)*	*~2.00 ms (Average)*

2.2.2. Database structure

The database structure used in the system is designed to store personnel information and facial recognition-based time records. The database operates using two main tables. Figure 6 shows the basic personal information and record information of the personnel. This table contains fields for the user such as name, surname, contact information, identity number, employment start date, and activity status. Additionally, the creation, updating, and deletion of records can be tracked historically.

2.2.3. Web interface

The data obtained in the developed system is presented to the user via a web-based interface. The web interface is designed to include different screens and functions according to user permissions. There are three different user roles within the system: System Administrator (Super Admin), Administrator (Admin), and Staff. Each user can only access the screens and operations defined within their own permissions. Figure 7 shows a screenshot of the Super Admin Panel screen.

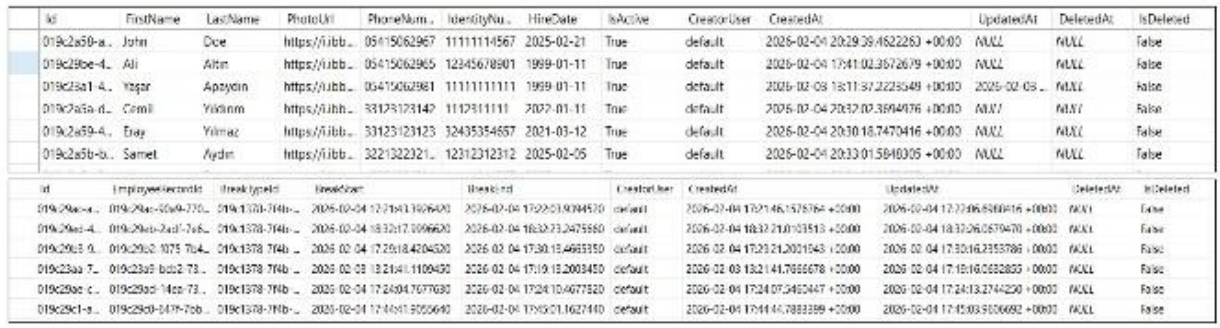
The Super Admin web interface is designed for users with the highest level of privileges within the system. The Super Admin dashboard is the main control panel that provides summary information about the overall status of the system. This screen displays statistics such as the total number of users and the total number of administrators in the form of cards. In the "Recent Activities" section, users in the system are listed with their registration date, username, role information, and activity status (Figure 7).

This structure allows the Super Admin to quickly and centrally monitor the latest activities in the system. Real-time camera footage can be viewed through the admin panel.

3. Results

This section presents the outputs obtained from the facial recognition-based authentication and personnel tracking system developed. The system interacts with the user through a web-based interface. Through this interface, authorized users can view personnel information, entry and exit records, and break times. The web interface consists of different screens for the system administrator, managers, and personnel. Figure 9 shows an example screenshot of the web interface.

Automatic reports are generated using the entry and exit data recorded by the system. These reports include the employee's daily working hours, entry and exit times, and break information. The generated reports can be viewed via the web interface and evaluated by system administrators. The reports can also be downloaded in spreadsheet or Pdf format. Figure 10 shows examples of employee work reports.



Id	FirstName	LastName	PhotoUrl	PhoneNum...	IdentityNu...	HireDate	IsActive	CreatorUser	CreatedAt	UpdatedAt	DeletedAt	IsDeleted
019c2a59-a...	John	Doe	https://ibb...	05415062967	11111114567	2025-02-21	True	default	2026-02-04 20:29:39.4622263 +00:00	NULL	NULL	false
019c29be-4...	Ali	Altin	https://ibb...	05415062965	12345678901	1999-01-11	True	default	2026-02-04 17:41:02.3572679 +00:00	NULL	NULL	false
019c2a1-4...	Yaşar	Apaydın	https://ibb...	05415062981	11111111111	1999-01-11	True	default	2026-02-03 13:11:37.2223549 +00:00	2026-02-03...	NULL	false
019c2a5a-d...	Cemil	Yildirim	https://ibb...	33123123142	1112311111	2022-01-11	True	default	2026-02-04 20:32:02.3694976 +00:00	NULL	NULL	false
019c2a59-4...	Eray	Yilmaz	https://ibb...	33123123123	32435354657	2021-03-12	True	default	2026-02-04 20:30:18.7470416 +00:00	NULL	NULL	false
019c2a5b-b...	Samet	Aydin	https://ibb...	3221322321...	12312312312	2025-02-05	True	default	2026-02-04 20:33:01.5848305 +00:00	NULL	NULL	false

Id	EmployeeRecordId	BreakTypeId	BreakStart	BreakEnd	CreatorUser	CreatedAt	UpdatedAt	DeletedAt	IsDeleted
019c29ac-4...	019c29ac-60a9-770...	019c1378-7f4b-...	2026-02-04 17:21:41.1926420	2026-02-04 17:22:01.9394530	default	2026-02-04 17:21:46.1576764 +00:00	2026-02-04 17:22:06.6889416 +00:00	NULL	false
019c29ad-4...	019c29ad-2ad7-7e8...	019c1378-7f4b-...	2026-02-04 18:32:17.0996620	2026-02-04 18:32:23.2475560	default	2026-02-04 18:32:21.0103513 +00:00	2026-02-04 18:32:26.0679470 +00:00	NULL	false
019c29b3-9...	019c29b2-1075-7b4...	019c1378-7f4b-...	2026-02-04 17:20:18.4204520	2026-02-04 17:30:13.4665350	default	2026-02-04 17:23:21.2021543 +00:00	2026-02-04 17:30:16.2353786 +00:00	NULL	false
019c23aa-7...	019c23a9-bcb2-73...	019c1378-7f4b-...	2026-02-03 13:21:41.1109430	2026-02-04 17:19:13.2003450	default	2026-02-03 13:21:41.7666678 +00:00	2026-02-04 17:19:16.0632853 +00:00	NULL	false
019c29ac-c...	019c29ad-14cb-73...	019c1378-7f4b-...	2026-02-04 17:24:04.7677630	2026-02-04 17:24:10.4677520	default	2026-02-04 17:24:07.5462447 +00:00	2026-02-04 17:24:13.2744230 +00:00	NULL	false
019c29c1-a...	019c29c0-0479-7eb...	019c1378-7f4b-...	2026-02-04 17:44:41.5055640	2026-02-04 17:45:01.1627440	default	2026-02-04 17:44:44.7883389 +00:00	2026-02-04 17:45:03.9006692 +00:00	NULL	false

Figure 7. Employee and employee records table

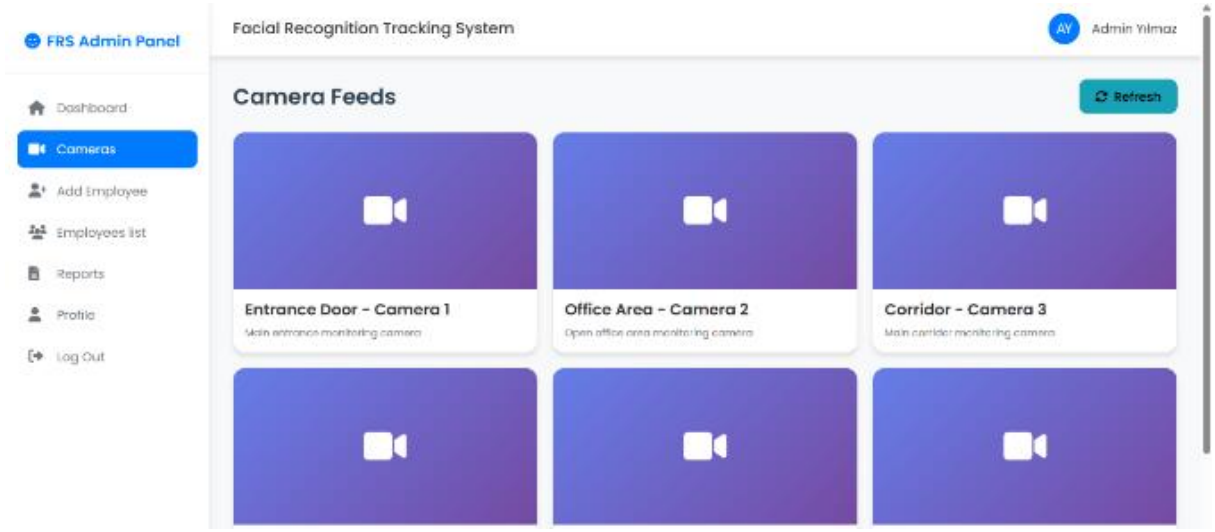


Figure 8. Admin panel (camera) screen

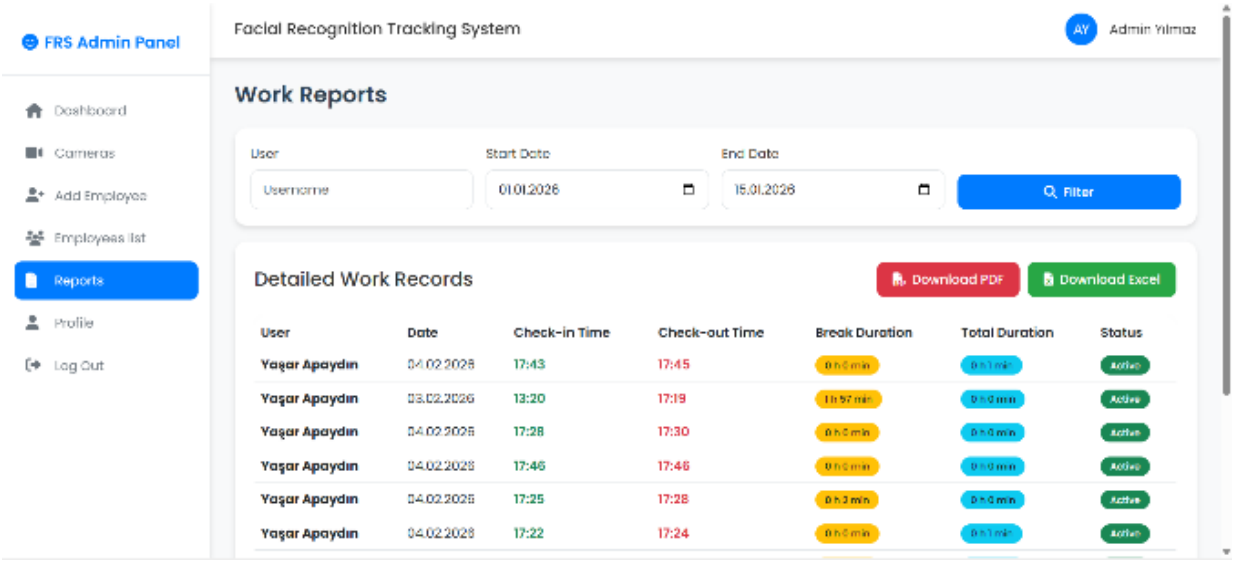
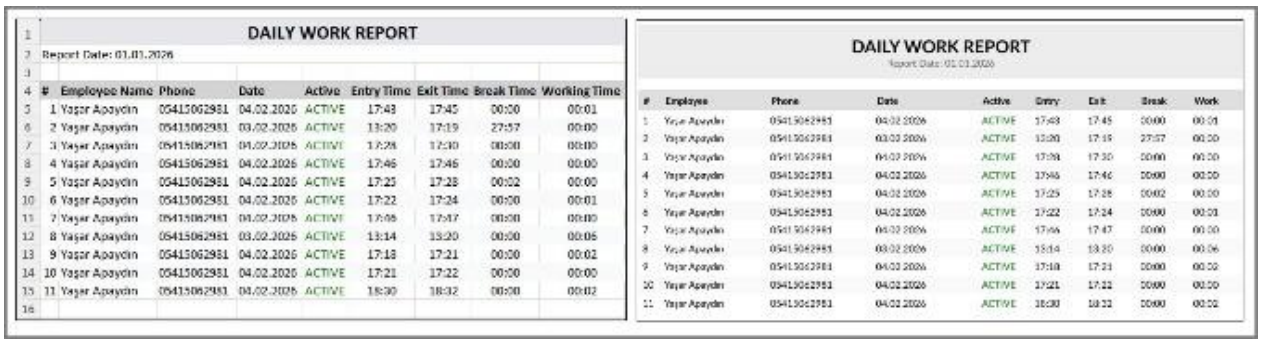


Figure 9. Admin panel (reports) screen



DAILY WORK REPORT

Report Date: 01.01.2026

#	Employee Name	Phone	Date	Active	Entry Time	Exit Time	Break Time	Working Time
1	Yaşar Apaydın	05415062981	04.02.2026	ACTIVE	17:43	17:45	00:00	00:01
2	Yaşar Apaydın	05415062981	03.02.2026	ACTIVE	13:20	17:19	27:57	00:00
3	Yaşar Apaydın	05415062981	04.02.2026	ACTIVE	17:28	17:30	00:00	00:00
4	Yaşar Apaydın	05415062981	04.02.2026	ACTIVE	17:46	17:46	00:00	00:00
5	Yaşar Apaydın	05415062981	04.02.2026	ACTIVE	17:25	17:28	00:02	00:00
6	Yaşar Apaydın	05415062981	04.02.2026	ACTIVE	17:22	17:24	00:00	00:01
7	Yaşar Apaydın	05415062981	04.02.2026	ACTIVE	17:46	17:47	00:00	00:00
8	Yaşar Apaydın	05415062981	03.02.2026	ACTIVE	13:14	13:20	00:00	00:06
9	Yaşar Apaydın	05415062981	04.02.2026	ACTIVE	17:18	17:21	00:00	00:02
10	Yaşar Apaydın	05415062981	04.02.2026	ACTIVE	17:21	17:22	00:00	00:00
11	Yaşar Apaydın	05415062981	04.02.2026	ACTIVE	18:30	18:32	00:00	00:02

DAILY WORK REPORT

Report Date: 01.01.2026

#	Employee	Phone	Date	Active	Entry	Exit	Break	Work
1	Yaşar Apaydın	05415062981	04.02.2026	ACTIVE	17:43	17:45	00:00	00:01
2	Yaşar Apaydın	05415062981	03.02.2026	ACTIVE	13:20	17:19	27:57	00:00
3	Yaşar Apaydın	05415062981	04.02.2026	ACTIVE	17:28	17:30	00:00	00:00
4	Yaşar Apaydın	05415062981	04.02.2026	ACTIVE	17:46	17:46	00:00	00:00
5	Yaşar Apaydın	05415062981	04.02.2026	ACTIVE	17:25	17:28	00:02	00:00
6	Yaşar Apaydın	05415062981	04.02.2026	ACTIVE	17:22	17:24	00:00	00:01
7	Yaşar Apaydın	05415062981	04.02.2026	ACTIVE	17:46	17:47	00:00	00:00
8	Yaşar Apaydın	05415062981	03.02.2026	ACTIVE	13:14	13:20	00:00	00:06
9	Yaşar Apaydın	05415062981	04.02.2026	ACTIVE	17:18	17:21	00:00	00:02
10	Yaşar Apaydın	05415062981	04.02.2026	ACTIVE	17:21	17:22	00:00	00:00
11	Yaşar Apaydın	05415062981	04.02.2026	ACTIVE	18:30	18:32	00:00	00:02

Figure 10. Daily reports.

3.1. Evaluation of Different Test Scenarios

The system was tested under different real-world conditions to find its limits:

- *Distance Tests:* The system works well at near and medium distances. When the distance increases, recognition success drops slightly.
- *Angle Tests:* The best performance is achieved at frontal face positions. When users turn their heads left or right, recognition success decreases.
- *Image Degradation Tests:* Blur, low resolution, and bad lighting negatively affect face detection. In poor conditions, the system prefers not to recognize the face instead of making a wrong match.
- *Crowded Environment Tests:* The system was tested with multiple people in the frame. A sample output is shown in Figure 2. The system correctly identifies registered employees and labels unknown individuals as "Unknown". It produces zero false matches, but rapid movement can cause some faces to be missed.

3.1.1. Quantitative Performance Metrics

To evaluate the performance statistically, the test logs were structured into a classification matrix. The system achieved True Positives (TP) = 12, False Positives (FP) = 0, False Negatives (FN) = 64, and True Negatives (TN) = 62.

Based on these real values, the standard metrics are reported below:

- *Accuracy* represents the proportion of totally correct classifications among all tested samples:

$$Accuracy = \frac{TP + TN}{TP + TN + FP + FN} \times 100 = \frac{12 + 62}{12 + 62 + 0 + 64} \times 100 = 53.62\%$$

- *Precision* measures the accuracy of positive identity predictions, showing the ratio of true employee matches to all positive validations:

$$Precision = \frac{TP}{TP + FP} \times 100 = \frac{12}{12 + 0} \times 100 = 100.00\%$$

- *Recall* defines the sensitivity of the framework, reflecting the ratio of correctly recognized faces to the total number of actual registered employee samples in the frames:

$$Recall = \frac{TP}{TP + FN} \times 100 = \frac{12}{12 + 64} \times 100 = 15.79\%$$

- *F1-Score* computes the harmonic mean of Precision and Recall, providing a balanced metric for unconstrained tracking environments:

$$F1\text{-}Score = 2 \times \frac{Precision \times Recall}{Precision + Recall} = 2 \times \frac{1.00 \times 0.1579}{1.00 + 0.1579} = 27.27\%$$

The system is highly efficient, showing an average recognition latency of ~2 ms (ranging between 0 ms and 10 ms).

The 100.00% Precision score proves that the system never confuses an unregistered person with a employee, which is critical for company security. The low Recall (15.79%) is a result of difficult real-world conditions like sharp face angles, movement blur, and crowd occlusions. Under these poor conditions, the system chooses a security-first posture: it prefers to refuse verification instead of making a wrong match.

An HOG-based algorithm was used for face detection. The HOG method detects objects by representing local gradient orientations in the image through histograms. Because it requires lower computational costs compared to deep learning-based methods, it is suitable for real-time IoT applications using boards like Raspberry Pi. Therefore, considering the hardware limitations of the system, the main reasons for choosing the HOG-based approach are as follows:

- Ability to run on Raspberry Pi thanks to low hardware requirements
- Real-time face detection and recognition with low computational cost
- No retraining required as the number of registered users increases
- High accuracy rate and ease of practical application

Considering the system requirements and hardware limitations, HOG-based face detection and deep learning-based face recognition approaches were evaluated as suitable choices for this study. However, situations such as lighting changes, partially covered faces, or excessively low-resolution images can negatively affect the system's performance. This should be considered in future studies. The face recognition-based method used in this study stands out compared to alternative methods due to its contactless nature and the fact that it does not require

additional hardware from the user. It offers a low-cost, reliable, and hygienic solution, especially for controlled environments such as laboratories.

The test results, taken from a location approximately one meter away from the camera, are given below.

In ten trials conducted under conditions where the light source was positioned behind the camera and towards the user's face, user identification was achieved in an average of 2.617 seconds (min: 0.790 sec., max: 5.315 sec.).

In ten trials conducted under conditions where the light source was positioned behind the user and emitting light towards the camera, personnel identification was achieved in an average of 2.744 seconds (min: 1.677 sec., max: 5.039 sec.).

4. Conclusion and Future Works

The developed face recognition-based personnel tracking system has been tested under real-world conditions. The system reliably performed face detection and recognition operations. Entry and exit records were automatically saved, requiring no additional user intervention during the recording process. No delays occurred during real-time operation, and the system operated stably. This demonstrates that the selected algorithms are suitable for embedded systems.

Personnel information, entry and exit times, and break durations could be successfully viewed via the web-based interface. Furthermore, daily and periodic reports were generated, enabling the monitoring of personnel movements. The results demonstrate that the developed system is applicable to personnel tracking applications.

In future studies;

- A portable IoT version of the system can be developed. This would allow for easier installation.
- Hardware-specific optimized firmware can be developed. A software infrastructure suitable for remote updates and mass production can be targeted.
- To reduce processor load, data can be primarily stored in RAM. This will result in a more stable and faster system operation.
- Cooling solutions for the hardware can be explored.
- A minimal and secure Linux-based operating system configuration can be planned. Security can be enhanced through service-based architecture and system hardening efforts.
- IR camera and IR LED integration can improve both low-light performance and system resilience against photo or video spoofing attacks.
- Authentication support with pose estimation can be integrated into the system.
- The Redis structure can be migrated to cluster architecture, and failover mechanisms can be strengthened. This would make the system more scalable and robust.

Author Contributions

The percentages of the authors' contributions are presented below. All authors reviewed and approved the final version of the manuscript.

	E.T.	Y.A.	H.Ü.
C	30	30	40
D	30	30	40
S	20	35	45
DCP	40	40	20
DAI	30	35	35
L	50	30	20
W	45	35	20
CR	30	30	40
SR	15	25	60
PM	30	30	40
FA	30	30	40

C= concept, D= design, S= supervision, DCP= data collection and/or processing, DAI= data analysis and/or interpretation, L= literature search, W= writing, CR= critical review, SR= submission and revision, PM= project management.

Conflict of Interest

The authors declared that there is no conflict of interest.

Ethical Consideration

The system developed in this study is a prototype design and was tested using data from voluntary participants. Prior to the study, formal ethics committee approval was obtained from the Scientific Research and Publication Ethics Committee of Kırklareli University (E-35523585-199-167443). The facial images were used only to evaluate the system's performance. This biometric data was not used for any commercial purpose and was not shared with third parties. For a real-world deployment, it is necessary to get explicit user consent and store data according to data protection laws (such as KVKK/GDPR). In future works, we plan to add data encryption methods to make the system more secure.

Acknowledgements

This study was supported under the TÜBİTAK 2209-A program. (TBTK-0164-7249, App ID: 1919B012411684)

References

Adesoba, O. C., & Joseph, I. M. (2025). A fingerprint-based attendance system for improved efficiency. *ITEGAM-JETIA*, *11*(51), 9–19. https://doi.org/10.5935/jetia.v11i51.1305

Ahmed Ali Aboluhom, A., & Kandilli, I. (2024). Face recognition using deep learning on Raspberry Pi. *The Computer Journal*, *67*(10), 3020–3030. https://doi.org/10.1093/comjnl/bxae066

Ataşen, K., & Üstünel, H. (2019, October). Designing a secure IoT network by using blockchain. In *2019 3rd International Symposium on Multidisciplinary Studies and Innovative Technologies (ISMSIT)* (pp. 1–4). IEEE. https://doi.org/10.1109/ISMSIT.2019.8932728

Bin Hamed, R., & Fatnassi, T. (2022). A secure attendance system using Raspberry Pi face recognition. *Journal of Telecommunications and the Digital Economy*, *10*(2), 62–75. https://doi.org/10.18080/jtde.v10n2.530

Brunelli, R., & Poggio, T. (1993). Face recognition: Features versus templates. *IEEE Transactions on Pattern Analysis and Machine Intelligence*, *15*(10), 1042–1052. https://doi.org/10.1109/34.254061

Choudhary, R. K., Lohe, P., Shrikhande, O., Nimje, I., Pillay, D., Puri, V., & Gawande, U. (2025). Blockchain-enhanced hybrid biometric authentication using deep learning for identity verification. *i-Manager's Journal of Pattern Recognition*, *12*(2), 1–12. https://doi.org/10.26634/jpr.12.2.22456

Dalal, N., & Triggs, B. (2005, June). Histograms of oriented gradients for human detection. In *2005 IEEE Computer Society Conference on Computer Vision and Pattern Recognition (CVPR)* (Vol. 1, pp. 886–893). IEEE. https://doi.org/10.1109/CVPR.2005.177

Jacomme, C., & Kremer, S. (2021). An extensive formal analysis of multi-factor authentication protocols. *ACM Transactions on Privacy and Security*, *24*(2), Article 13. https://doi.org/10.1145/3440712

Jain, A. K., Ross, A., & Prabhakar, S. (2004). An introduction to biometric recognition. *IEEE Transactions on Circuits and Systems for Video Technology*, *14*(1), 4–20. https://doi.org/10.1109/TCSVT.2003.818349

Mamak, U., Konyar, M. Z., Solak, S., & Uçar, M. H. (2020). Gerçek zamanlı yüz tanıma tabanlı personel kontrol ve takip sistemi tasarımı [Real-time face recognition based personnel control and tracking system design]. *Avrupa Bilim ve Teknoloji Dergisi*, (19), 497–504. https://doi.org/10.31590/ejosat.727768

Orostegui, C. M., Luna, A. N., García, A. M., & Ariza, C. A. F. (2021). A low-cost Raspberry Pi-based system for facial recognition. *Ingeniería y Ciencia*, *17*(34), 77–95. https://doi.org/10.17230/ingciencia.17.34.4

Pu, C., Seol, J., Park, N., & Korać, D. (2026, January). Authenticated key agreement protocol for device-to-gateway communication in IoT. In *2026 IEEE 23rd Consumer Communications & Networking Conference (CCNC)* (pp. 1–6). IEEE. https://doi.org/10.1109/CCNC65079.2026.11366351

Schroff, F., Kalenichenko, D., & Philbin, J. (2015). FaceNet: A unified embedding for face recognition and clustering. In *Proceedings of the IEEE Conference on Computer Vision and Pattern Recognition (CVPR)* (pp. 815–823). IEEE. https://doi.org/10.1109/CVPR.2015.7298682

Surantha, N., & Sugijakko, B. (2024). Lightweight face recognition-based portable attendance system with liveness detection. *Internet of Things*, *25*, Article 101089. https://doi.org/10.1016/j.iot.2024.101089

Turk, M., & Pentland, A. (1991). Eigenfaces for recognition. *Journal of Cognitive Neuroscience*, *3*(1), 71–86. https://doi.org/10.1162/jocn.1991.3.1.71

Zhao, G., Bao, H., & Wang, J. (2025). A lightweight security authentication protocol for RFID. *Peer-to-Peer Networking and Applications*, *18*(3), Article 158. https://doi.org/10.1007/s12083-025-01965-2

Zhao, W., Chellappa, R., Phillips, P. J., & Rosenfeld, A. (2003). Face recognition: A literature survey. *ACM Computing Surveys*, *35*(4), 399–458. https://doi.org/10.1145/954339.954342

Black Sea Journal of Engineering and Science
doi: 10.34248/bsengineering.1961953

Open Access Journal
e-ISSN: 2619 – 8991

Research Article
Volume 9 - Issue 5: 2317-2336 / September 2026

GLOBAL EVOLUTION AND RESEARCH TRENDS OF THE SWAT MODEL (1994–2024): A COMPREHENSIVE BIBLIOMETRIC ANALYSIS

Erkan KARAKOYUN[1]*

[1]*Muş Alparslan University, Faculty of Engineering and Architecture, Muş, 49250, Türkiye*

Abstract: The Soil and Water Assessment Tool (SWAT) is a widely utilized hydrological model applied extensively in watershed studies worldwide. This research clarifies academic trends, evolutionary processes, and research gaps in SWAT-related studies through a bibliometric analysis of scientific literature. Publications on the SWAT model from 1994 to 2024 were retrieved from the Web of Science (WOS) database. Analysis of 6,965 WOS-indexed publications reveals a substantial increase in publication volume over the past decade. The journals Water, Journal of Hydrology, and Science of the Total Environment published the highest number of articles. Moriasi et al. (2007) and Arnold et al. (1998) are among the most frequently cited works. The United States and China lead in both publication output and citation counts, with Texas A&M University, the USDA, and the Chinese Academy of Sciences identified as major contributing institutions. Keyword co-occurrence and time series analyses demonstrate a thematic transition in SWAT research, shifting from initial focuses on water quality and sediment transport to contemporary topics such as climate change, uncertainty analysis, and land-use change. This bibliometric study systematically delineates the historical development and current scientific trends in SWAT model research, identifies research gaps, and offers insights for future investigations. Consequently, the study serves as a valuable resource for academic and professional stakeholders engaged in environmental modeling and in the development of water management policies.

Keywords: SWAT, Bibliometric analysis, Hydrological modeling, Biblioshiny

***Corresponding author:** Muş Alparslan University, Faculty of Engineering and Architecture, Muş, 49250, Türkiye
E mail: e.karakoyun@alparslan.edu.tr (E. KARAKOYUN)
Erkan KARAKOYUN https://orcid.org/0000-0003-2821-9103

Received: June 01, 2026
Accepted: August 05, 2026
Published: September 15, 2026

Cite as: Karakoyun, E. (2026). Global evolution and research trends of the SWAT model (1994–2024): A comprehensive bibliometric analysis. *Black Sea Journal of Engineering and Science,* 9(5), 2317-2336.

1. Introduction

Water is a vital resource for continuing human life and the environment. Every species depends on the components of the hydrologic cycle, and water is its most important parameter. Therefore, researchers have been investigating the water cycle and hydrological modeling for years (Yang et al., 2021). Hydrological modeling studies have significantly increased and advanced with the development of computer programming technology (Hasan et al., 2024). Watershed models are categorized into empirical–statistical models (e.g., GLEAMS), physical models (e.g., WEPP), and conceptual models. Conceptual models can be further classified as distributed and semi-distributed types, including examples such as SWAT, TRK, and EveNFlow (Janjić and Tadić, 2023).

Distributed models account for regional variations in parameters and inputs, offering a more accurate depiction of the hydrologic system, whereas lumped models represent the system using spatially averaged data (Chow et al., 1988). Semi-distributed hydrologic models, like the Soil and Water Assessment Tool (SWAT), are effective in watershed modeling by dividing the watershed into smaller sub-watersheds and hydrologic response units (HRUs), each characterized by unique attributes (Janjić and Tadić, 2023). The SWAT model was first introduced by (Arnold et al., 1998), and it is one of the most popular hydrological models in literature, which has been indicated in different research areas such as watershed management, water quality research, and water resources application. SWAT is semi-distributed physical based watershed model (Arnold et al., 1998). It allows simulating hydrological cycling, sediment transport, erosion control, and pollutant load, as well as watershed management practices in a basin using a water-balance approach.

SWAT first divides the drainage basin into sub-basins, and each sub-basin is then subdivided into many hydrological response units (HRUs). These are the unique combinations of topography, land use and soil data. Topography data, land use land cover data, soil data, and meteorological data are primarily required to build up the SWAT model.

Global researchers now have serious concerns about environmental deterioration and the sustainable

This work is licensed (CC BY-NC 4.0) under Creative Commons Attribution 4.0 International License

management of natural resources. Population increase and climate change negatively affect water resources, necessitating advanced processes to anticipate and lessen adverse ecological effects (Pimentel et al., 1995; Acar et al., 2025; Foley et al., 2005). Recent studies demonstrate that climate change significantly impacts hydrological systems by altering precipitation patterns and increasing the severity, duration, and magnitude of droughts (Akbas et al., 2026). The Soil and Water Assessment Tool (SWAT) has emerged as a vital tool for addressing these challenges. SWAT can simulate the effects of agricultural runoff, nutrient loading, sediment yield, and pesticide transport, making it invaluable in addressing water quality issues across different geographical and environmental contexts (Gassman et al., 2007).

1.1. Global Application of SWAT

SWAT's importance lies in its flexibility and broad applicability. It is designed to assess the long-term impacts of land use and management practices on water resources in large, complex watersheds (Neitsch et al., 2011). For example, SWAT has been used to evaluate agricultural sustainability and environmental quality in regions as diverse as the U.S. (Kalcic et al., 2015), in China (Zhang et al., 2008), and tropical catchments in Brazil (de Oliveira et al., 2017). One of the reasons for SWAT's popularity is its adaptability across different regions of the world, and it is regarded as one of the most effective hydrological models for dealing with environmental and hydrological problems (Akoko et al., 2021).

Studies in European catchments, such as those in the United Kingdom (Abbas et al., 2022), France (Sellami et al., 2014), and Germany (Wagner et al., 2022), have used SWAT for hydrological modelling and assessing climate change impact on water resources. Busico et al. (2020), used SWAT model to estimate the hydrological process by using three different simulation of soil configuration in Aspio Basin, Spain. Besides, the SWAT model has been applied in many different regions around the world and successful results have been achieved (Karakoyun and Kaya, 2022). Serrão et al. (2022) indicated the assessment of SWAT model for to predict streamflow and sediment yield, and the impact of LULC changes in the Brazilian Amazon. Bennour et al. (2022) indicate the assessment of SWAT model for Lake Chad Basin using different satelite remote sensing actual evapotranspiration products. Zhang et al. (2020) aimed to simulate how various land use change scenarios affect the water balance in Johnstone River, Australia. In their study, the simulation utilized an enhanced SWAT model, calibrating vegetation growth with MODIS LAI data. Trivedi et al. (2024) aimed to evaluate groundwater recharge requirements and restoration strategies for the Kanari River in India using the SWAT model. They focused on simulating surface runoff and groundwater recharge dynamics to inform sustainable water resource management and restoration efforts. The study of Li et al. (2021) focused to evaluate the impact of sensitivity analysis (SA) on parameter optimization in streamflow simulations using the SWAT model. They aimed to assess whether selecting sensitive parameters can improve optimization, efficiency, and accuracy across different watersheds in China. In Asia, particularly in China and India, SWAT has been instrumental in evaluating the effects of irrigation, land use changes, and water availability (Wu et al., 2019; Sharma et al., 2022). Similarly, in Africa, SWAT has been applied to assess the hydrological impacts of climate change on water availability (Schuol et al., 2008; Taye et al., 2015).

The use of SWAT to investigate how climate change affects hydrology and water resources has emerged as one of the most important fields of study in recent years. As climate change increasingly threatens ecosystems and human societies worldwide, the SWAT model has been widely used for its strong ability to forecast future climate conditions (Ficklin et al., 2009). For example, research in Athabasca River Basin in Canada used SWAT to model the effects of projected climate scenarios on water availability and found significant increases in annual streamflow (Shrestha et al., 2017). Similarly, (Zema et al., 2022) aimed to assess how effectively dams manage the water flow and prevent soil erosion by using SWAT model in Mediterranean headwaters under projected climate and land-use change scenarios. Li and Fang (2021), evaluates the impacts of climate change on streamflow in the Mun River Basin, Southeast Asia, using the SWAT model to simulate responses to future precipitation and temperature changes across different climate scenarios. Their findings revealed that streamflow in the Mun River Basin are projected to increase under different climate scenarios.

SWAT's capability to simulate hydrological processes across various climate scenarios has offered crucial insights into potential risks and adaptation strategies for regions dealing with water scarcity and other climate-related challenges.

1.2. The Importance of Bibliometric Analysis in SWAT Research

Despite the extensive application and development of SWAT, limited attention has been given to systematically analyzing the trends, key contributors, and themes within SWAT-related literature. This is where bibliometric analysis becomes crucial. A bibliometric analysis can offer a comprehensive and impartial overview of the framework, themes, and deficiencies in a research area (Zare et al., 2017). Bibliometric research involves analyzing the quantitative aspects of producing, distributing, and utilizing recorded information using statistical methods and mathematical models (Tague-Sutcliffe, 1992). It analyzes the physical components of publications, citations, and related metrics from literature to uncover and characterize trends within publications across specific topics, fields, journals, institutions, or even countries (Broadus, 1987).

Several bibliometric studies have been conducted across scientific fields to assess research trends in hydrological

modeling (Zare et al., 2017), water resource management (Durán-Sánchez et al., 2018), and environmental sciences (Fu et al., 2013). However, a comprehensive bibliometric analysis focused on SWAT is still lacking. A bibliometric analysis of SWAT publications can provide valuable insights into how SWAT research has evolved over time, which regions and institutions are leading in SWAT development, and what the dominant research themes are. It can also shed light on collaboration patterns and the degree to which SWAT is being used in interdisciplinary research. Such an analysis is particularly important given the increasing complexity of environmental challenges and the growing demand for integrated modeling approaches that address water, land, and ecosystem interactions.

This research analyzes the evolution of scientific literature on the SWAT model, identifies research trends, and reveals structural gaps through a comprehensive bibliometric analysis framework. Most existing bibliometric studies are limited by short timeframes, specific geographic regions, or narrow thematic scopes, which restricts a comprehensive understanding of the long-term global development of SWAT research. The present study conducts a large-scale analysis of the Web of Science database from 1994 to 2024, evaluating publication productivity, citation dynamics, leading authors, institutions, countries, and thematic shifts.

This study analyzes the quantitative scope of SWAT literature, the direction of knowledge production, and the structure of scientific interaction. Detailed examination includes collaboration networks among authors, institutions, and countries, as well as keyword co-occurrences and temporal thematic shifts. The results indicate that early SWAT research focused on water quality and sediment transport, whereas recent studies emphasize more interdisciplinary themes such as climate change, land-use change, and uncertainty analysis. This systematic literature review offers strategic insights into future application areas and research priorities related to the SWAT model.

Although numerous reviews and bibliometric studies exist in the literature on the SWAT (Soil and Water Assessment Tool) model (Bezak et al., 2021; Lei et al., 2021; Xiong et al., 2022; Aloui et al., 2023; Gao et al., 2023; Janjić and Tadić, 2023; Zhao et al., 2024), most of them focus on specific themes and in particular regions. Existing reviews generally focus on single or theme-focused topics, such as the hydrological impacts of climate change, water quality modeling, soil erosion, calibration and validation approaches, or uncertainty analysis. However, this study aims to fill this gap in the literature by evaluating the SWAT model across its thematic, temporal, and spatial dimensions and, for the first time in the literature, presenting a model-based holistic bibliometric analysis. Analyses conducted on studies since the development of the SWAT model reveal, using quantitative indicators, how the SWAT literature has evolved, which research themes have reached saturation, and which areas will come to the forefront in the future. In this respect, the study offers a strategic framework that complements and expands upon existing theme-focused review studies, rather than simply repeating them.

Although the SWAT model has been widely applied in various studies, there is a lack of comprehensive bibliometric analyses that systematically examine its scientific development, research trends, collaboration networks, and emerging topics. The primary objective of this study is to present a thorough bibliometric overview of global SWAT research, identify major research trends and influential contributors, and highlight future research directions. This analysis aims to serve as a valuable reference for both new and experienced researchers.

This paper aims to fill this gap by conducting a bibliometric analysis of SWAT-related literature. Specifically, it will focus on the following key questions: (1) How has the volume of SWAT-related research evolved over time? (2) Which authors, institutions, and countries have made the most significant contributions to SWAT research? (3) What are the most common research themes, and how have these evolved? (4) What are the collaboration networks among researchers, institutions, and countries in SWAT research? Through this analysis, we aim to provide a comprehensive overview of the development of SWAT research, identify key trends and emerging topics, and highlight potential areas for future research and collaboration.

2. Materials and Methods

2.1. Data Source and Collection

For this study, the bibliometric data was sourced for research on SWAT was determinde from Web of Science (WoS) database on 2nd of December 2024. The WoS Core Collection, recognized for its thorough selection and assessment of scholarly information, was utilized in this research to guarantee the dependability and precision of our results. The search criteria were carefully selected and conducted by searching the keywords “SWAT” and “Soil and Water Assessment Tool” in the Topic field, which includes title, abstract, keyword plus, and author keywords ((TS="swat") OR TS=("soil and water assessment tool")). Since the word SWAT is an abbreviation for the title Soil and Water Assessment Tool, it can be abbreviated in many fields of study in the literature. For example, Symmetric Weight Assignment Technique (SWAT), Subjective Workload Assignment Technique (SWAT), Special Weapons and Tactics (SWAT), Subcutaneous White Adipose Tissue (SWAT), Study Within A Trail (SWAT) etc. are also available in the WOS search list because they use SWAT as an abbreviation. Therefore, the research area in the WOS database were examined one by one and research area such as Biochemistry Molecular Biology, General Internal Medicine, Zoology, Criminology, Pharmacology Pharmacy etc. were removed from the database.

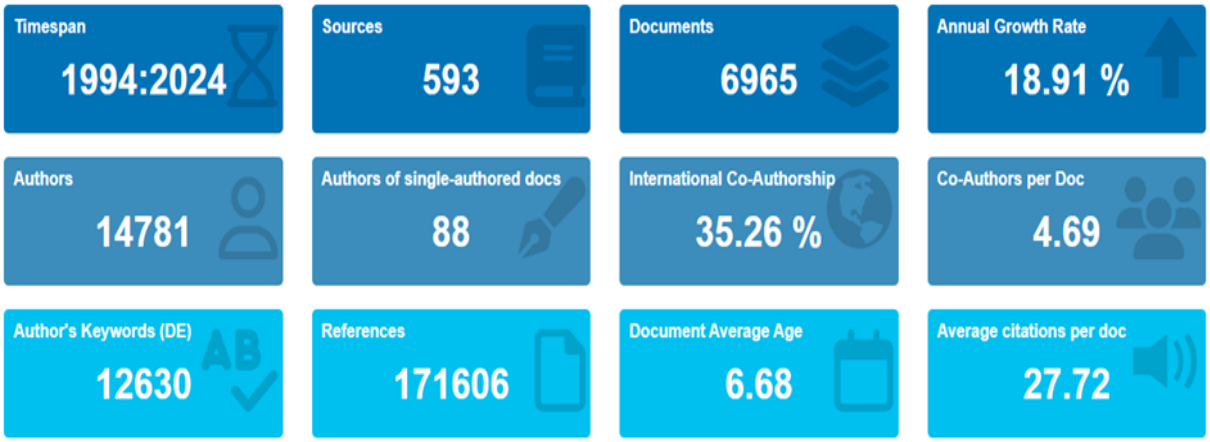


Figure 1. Main information of the bibliometric analysis on the SWAT-related studies.

The Web of Science Core Collection (WoSCC) is a widely utilized database for bibliometric analysis, renowned for its reliability as all indexed articles undergo a rigorous peer-review process (Xiong et al., 2022; Suluk and Coskun, 2024) This study focused exclusively on the 'article' publication type, excluding reviews, technical notes, letters, project reports, conference proceedings, and dissertations. In addition, as part of the data cleaning process, retracted articles and non-English publications were excluded from the research database. In order to confirm that all articles were directly relevant to SWAT, a thorough manual review of their titles, abstracts, research area, and WOS categories with an in-depth analysis of selected studies is conducted. As a result, after all filtering procedures, a total of 6965 articles were identified in the WOS database, and all of those were downloaded as a plain text file for data analysis.

2.2. Data Analysis

RStudio software (https://posit.co/download/rstudio-desktop/) was used with the data obtained from WOS database. In RStudio software, the Bibliometrix R package (Aria and Cuccurullo, 2017) which includes a wide variety of bibliometric techniques was used to conduct the analysis. "Bibliometrix" offers a number of functions for integrating bibliographic information from WOS databases, completing bibliometric analysis, and creating networks for collaboration in science, co-word assessment and co-citation (Aria and Cuccurullo, 2017). In addition to calculating and evaluating outcomes of research and collaboration, these methodologies enable an assessment of time trends, the recognition of highly cited papers, and the finding authors who have made substantial contributions to SWAT research, journals, institutions, and nations. The program works with the developed user interface 'biblioshiny' (https://www.bibliometrix.org/home/) for presenting the analysis. In addition to bibliometrix, the data from the network analysis was presented visually with VOSviewer.

3. Results and Discussion

3.1. Data Source Overview

Detailed investigations were conducted for the studies related to SWAT acquired through Biblioshiny using RStudio software and the main information of bibliometric analysis on SWAT related studies are given in Figure 1. The analysis is conducted in the last three decades from 1994 to 2024. There are 6965 documents indicated in 593 sources. The annual growth rate is 18.91% which means expanding the field of study. The average age of documents is 6.68, suggesting that the research area remains active and growing based on recent insights. In addition, the average citations per document are 27.72. This indicates that the research in this collection has been accepted and employed by other scholars.

3.2. Scientific Production Trend Analysis

Figure 2 illustrates the relationship between the number of articles and the number of accumulated articles by year. The publication trends from 1994 to 2024 demonstrate a substantial increase in the research field, as seen in both the annual and cumulative article numbers (Figure 2). The number of articles published over the years has shown an exponential increase. The total number of articles published in the last 6 years (2019-2024) corresponds to 50% of the total published articles while the last 10 years (2015-2024) corresponds to 80%. This shows that the subject under study is attracting more and more attention in academic circles and those studies in this field are intensifying. The increase curve of the cumulative number of articles increases linearly with the value of $R2$=0.95. The cumulative increase graph shows that knowledge in this field has reached a significant level. However, changes, especially in recent years, show that new research questions or studies with different methodologies can be conducted in this field.

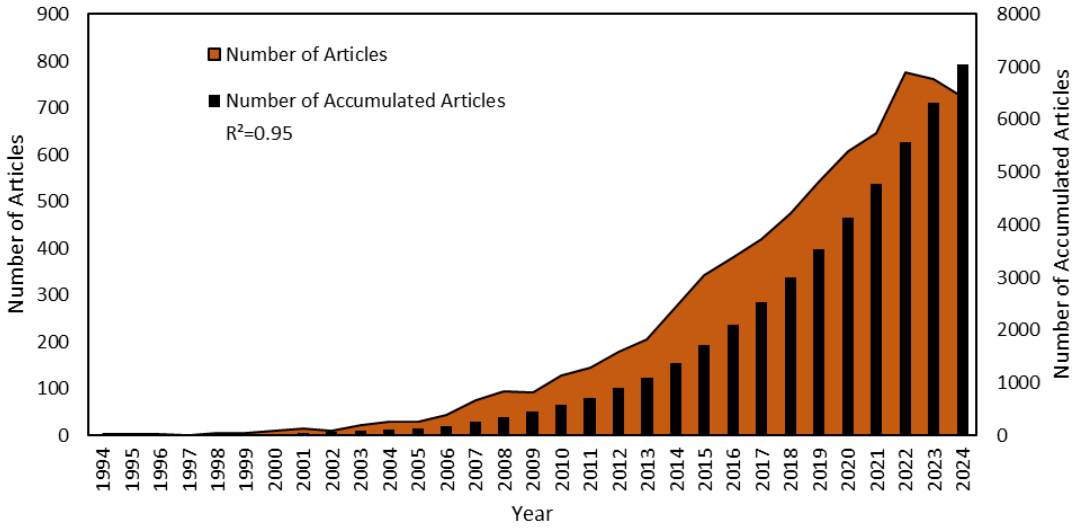


Figure 2. Temporal changes of number of articles and accumulated articles in the literature.

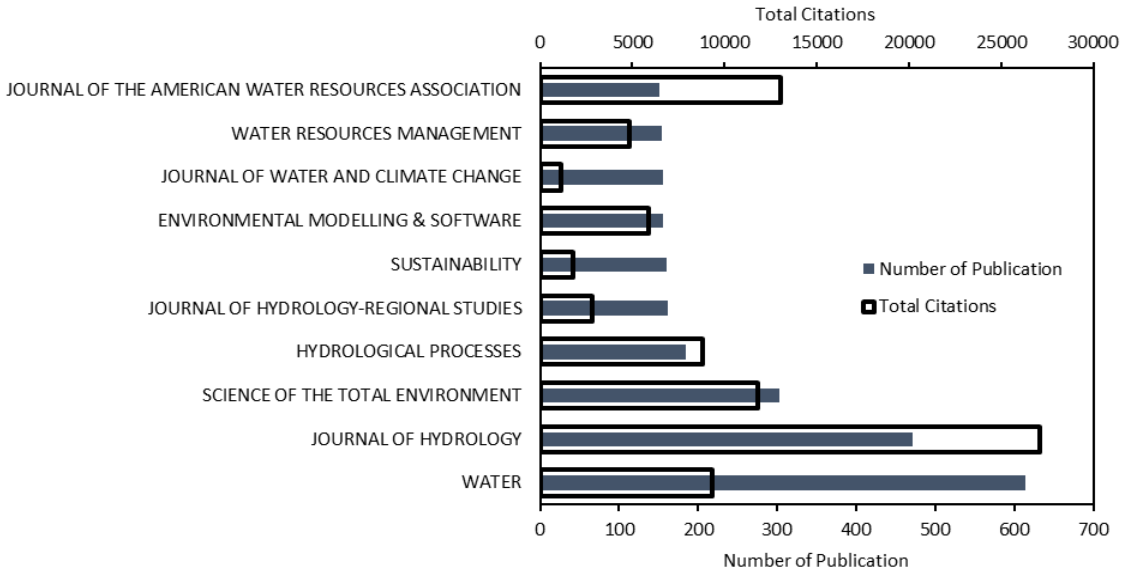


Figure 3. Top ten journals based on the number of publications with corresponding total citations.

3.3. Journal-Based Analysis

The comparison of the number of articles published in journals and the total number of citations to these articles is given in Figure 3. As the journals with the most articles, "Water" and "Journal of Hydrology" are particularly noteworthy. This demonstrates the significant influence and widespread use of these publications on the topic under investigation. Journal of Hydrology stands out with the highest total citation (27,125), with the second-highest publication number (471). These results demonstrate that the Journal of Hydrology plays a crucial role in both the number of publications and citations in studies on SWAT. In addition, this result implies that SWAT research published in these publications has been evident in the literature from earlier periods and has a wider academic influence. Although the Water journal has the highest number of publications (614), it has a lower number of citations compared to other journals when the total number of publications is considered. This situation can be attributed to the fact that the journal has published a large number of SWAT-based studies, especially in recent years, and these publications have not yet accumulated sufficient citations. Similarly, although the number of publications is relatively high in journals such as Sustainability and Journal of Water and Climate Change, it is seen that the number of citations is more limited when looking at the number of publications. This finding shows that quantitative productivity alone does not create high academic impact. Overall, the findings show that journal-based scientific impact in SWAT literature is strongly correlated with the number of publications as well as the journals' scope, and publication dates. This suggests that, in terms of scientific impact and visibility, SWAT researchers need to identify the right publication platforms. The detailed list of the results of the ten most relevant journals based on the number of articles was also given in Table 1.

Table 1. Ten most productive journal's detail sorted by the number of publications

Rank	Journal	Total Citations	Total Publication	Average Citations Per Article
1	Water	9317	614	15.17
2	Journal of Hydrology	27125	471	57.59
3	Science of the Total Environment	11812	303	38.98
4	Hydrological Processes	8808	184	47.87
5	Journal of Hydrology-Regional Studies	2847	162	17.57
6	Sustainability	1788	160	11.18
7	Environmental Modelling & Software	5860	156	37.56
8	Jouırnal of Water and Climate Change	1167	155	7.53
9	Water Resources Management	4874	154	31.65
10	Journal of the American Water Resources Association	13039	151	86.35

Figure 4 shows the average citations per article compared to the number of publications by the top ten journals based on total citations. It can be seen from Figure 4, although the Water journal has the highest number of publications (n=614), its average citation value per publication (15.2) is the lowest among the ten journals with the highest number of citations. The Water journal publishes the most SWAT-related articles, but its average citations per article are lower than those of other top journals. This is mainly because most SWAT studies in Water have appeared in the last decade, especially after 2015, so they have not had much time to accrue citations. In comparison, journals like the Journal of Hydrology and Transactions of the ASABE include many foundational studies on SWAT model development, calibration, and performance evaluation, which have been cited for many years. Also, Water covers a wide range of topics and publishes a large number of articles, leading to more application-focused and local studies, which tend to get fewer citations on average. As shown in Figure 4, these points suggest that counting publications alone does not fully reflect academic impact. Citation performance should also consider factors such as publication age, content type, and the journal's publication policies. Although Transactions of the Asabe journal is not among the top 10 journals with the highest number of publications (11th), it stands out as the journal with the highest number of average citations per article with 124.6. When this situation is examined in more detail, it is seen that the most cited publication with 8912, (Moriasi et al., 2007), was published in the Transactions of the Asabe journal. The number of citations received by this publication alone constitutes approximately 4.6% of the citations obtained in the total study. The study has been used by many researchers, especially in determining model performance criteria. This situation particularly increases the average citation per article value of Transactions of the Asabe journal. A similar situation exists for the Journal of the American Water Resources Association (JAWRA) journal with the publication by Arnold et al., 1998. This publication also received 5672 citations for the JAWRA journal and had a significant contribution to the average citation per article (86.4). On the other hand, when the average citation per article value (57.6) of the Journal of Hydrology, which has the second highest number of publications, is examined, it is seen that it has a much more balanced average citation number (15.6) than the Water journal, which has the highest number of publications. It is thought that this may be due to the fact that the Water journal's publications regarding the study are more recent than Journal of Hydrology. This situation is examined in more detail in Figure 5. A total of 6965 publications were published in 593 journals, and the most ten productive journals based on the number of publication and their changes in years are given in Figure 5. The findings indicated that 2510 research papers about SWAT were published in 10 principal journals, representing 36% of the total articles published. These findings demonstrate the critical role these journals play in effectively disseminating the SWAT researchers' work to other researchers. Water journal, which has the highest number of publications with 614 publications, draws attention with the significant increase in the number of publications especially after 2015. This shows that, in recent years researchers who have conducted studies on SWAT have shown a tendency to publish their studies especially in the Water journal. A similar significant upward trend is also seen in the Journal of Hydrology and Science of the Total Environment. Although the number of publications in other journals increases over the years, the increase is more limited compared to Water, Journal of Hydrology and Science of the Total Environment journals. In particular, the three journals with the highest number of publications (Water, Journal of Hydrology, and Science of Total Environment) have distinguished themselves from other journals by showing a significant increase in the number of publications in the last decade (Figure 5). For example, in the period between 2015 and 2024, the Water journal published 603 articles, Journal of Hydrology published 369 articles, and Science of the Total Environment published 280 articles, making a total of 1252 articles, while the total number of articles of the other 7 journals with the highest number of articles is 873.

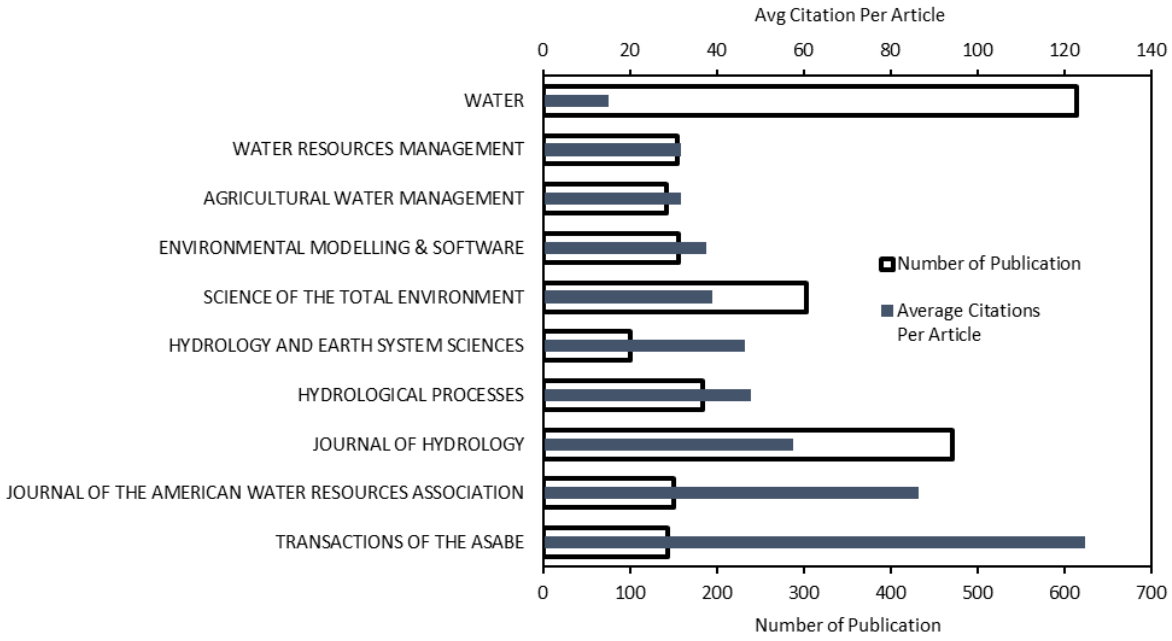


Figure 4. Top ten journals sorted by the number of total citations.

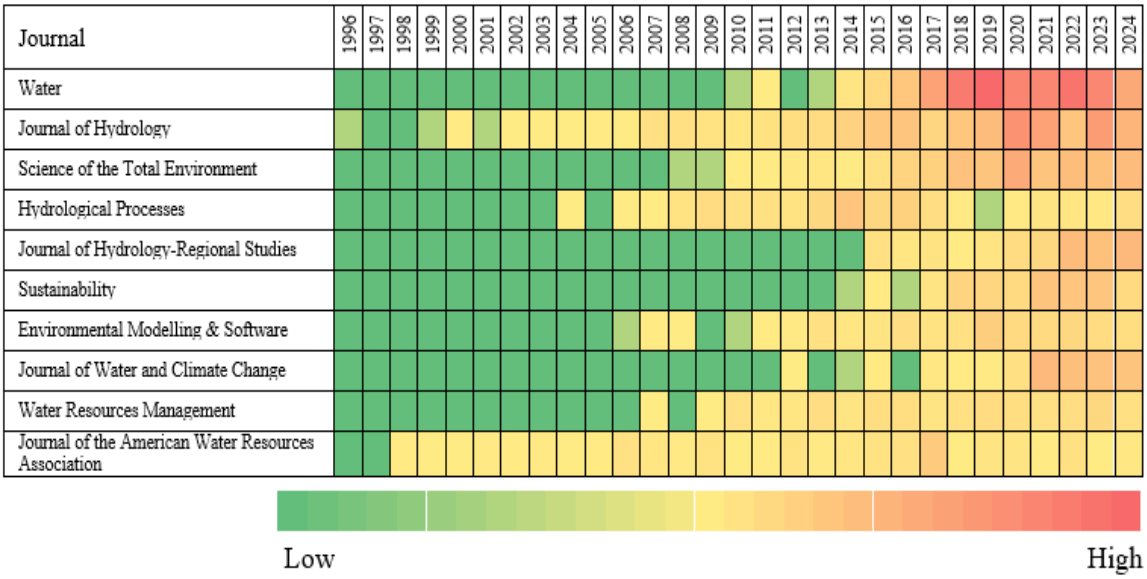


Figure 5. The changes in the number of publications over the years in the ten most productive journals.

These results also show that in the last ten-year period, researchers tend to publish in these three journals, especially in Water journal. The results were also investigated for the changes in citations over the years, based on the ten most productive journals Figure 6. Similar to the graph in the number of publications, the dominance of Water, Journal of Hydrology and Science of the Total Environment journals in the last decade is also seen in the changes in citations over the years. In particular, there has been a steady, significant increase in citations to the Journal of Hydrology over the last decade. It has also achieved the highest number of citations in a year in SWAT-related studies, with 3472 in 2023. In addition, the Journal of Hydrology has the highest number of citations received in a year since 2012. It has been observed that the increase in the number of citations received by the Science of the Total Environment, Transactions of the Asabe, and the Water journals in the last decade is higher than that of other journals. Although Transactions of the Asabe is not among the top ten journals (11th) in terms of the number of publications, it was included in the citation figure because it is among the journals with one of the highest numbers of citations. One of the main reasons for this can be seen as the paper by Moriasi et al., (2007) in the Transaction of the Asabe Journal. Therefore, the citations of Moriasi's publication alone over the years have been added to Figure 6 in order to see the changes with other journals.

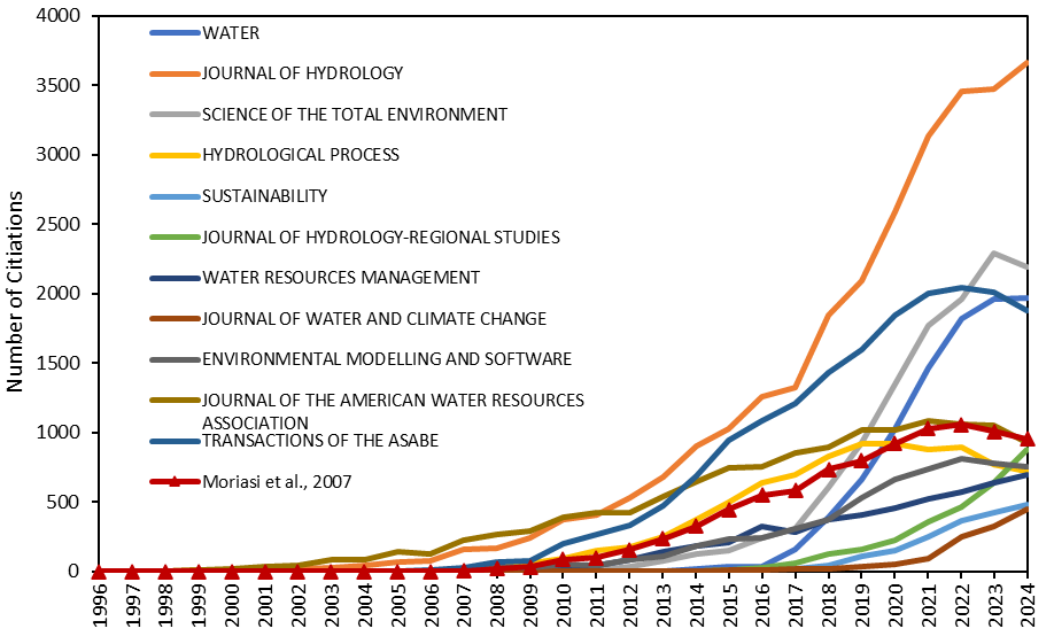


Figure 6. The changes in citations over the years of the eleven most productive journals.

3.4. Citation-Based Analysis

The results were also evaluated to determine the most highly cited publications and their authors (Table 2). These results will inform us about which publications other researchers use the most in their studies on SWAT. The most cited study on the SWAT research is Moriasi's study with 8912 citations. This study receives an average of 495 citations per year, and many researchers have cited it because it was used in the performance analysis evaluation of the SWAT model. A study conducted by Arnold et al. (1998) was cited 5672 times, making it the second most cited study with 210 TC per year, and following the study by Arnold et al. (2012) received 2185 citations with 168 TC per year on the SWAT research studies. Since citation accumulation depends on the passage of time, older publications typically receive higher citation counts than more recent studies. Consequently, citation metrics in this study were analyzed alongside publication years to ensure a more balanced evaluation of scientific impact. When looking at the 10 most cited studies, a striking detail is that researchers particularly prefer certain journals. For example, 5 of the 10 studies were published in the Journal of Hydrology, 3 in Transaction of the Asabe and 2 in Journal of the American Water Resources Association. An annual distribution of citation of each paper is given in Table 2. It reveals that there is an increasing trends observed after 2016 almost for all papers. This trend reveals the increasing importance and academic impact of studies on SWAT, especially in the decade.

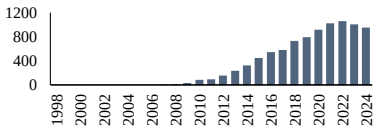
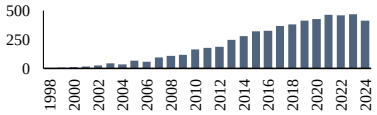
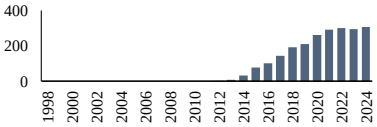
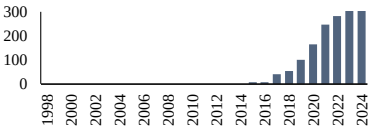
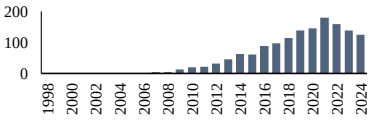
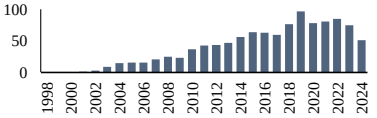
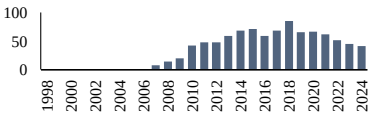
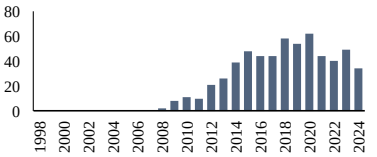
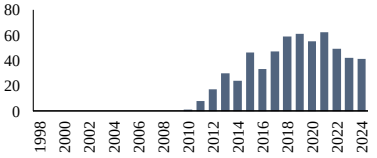
3.5. Author-Based Analysis

The ten most productive authors sorted by the number of publications related to SWAT are given in Figure 7. It is clear from the figure that Srinivasan, R., is the most productive researcher with 238 publications, followed by Arnold, JG with 152 publications. The total number of publications of the remaining eight researchers given in Figure 7 appears to be close to each other, varying between 50-62. When the total number of citations of the authors is examined, it is seen that the two authors with the most publications, Srinivasan, R., and Arnold, JG, have the highest citation numbers (25015 and 27900) and h-indexes (59 and 56), respectively. Although Arnold, JG lags behind Srinivasan, R. in terms of the number of publications, he has a higher value in terms of the number of citations. These results show that Arnold, JG and Srinivasan, R., are the most notable and valued authors in studies on SWAT, both in terms of the number of publications and the number of citations they have received. Although the remaining eight authors have remarkable publication and citation numbers, they have similar publication, citation and h-index values. Only Abbaspour, KC stands out from other authors with the number of citations he has received. This means that Abbaspour's work is considered remarkable by other authors.

Figure 7 also demonstrates that an author's scientific influence is determined by both the quantity of publications and the distribution of citations among those works. The g-index, introduced by Egghe (2006) as an enhancement of the h-index, measures the relationship between the number of published papers and their citation counts. In contrast to the h-index, the g-index is more sensitive to highly cited papers. Srinivasan R. and Arnold J.G. possess the highest h-index and g-index values, indicating a consistent record of widely cited publications. The substantially higher g-index values relative to their h-index further suggest that they have produced particularly influential studies within their discipline. For other authors, a more consistent distribution of citations throughout their articles is shown by the small difference between the h-index and

g-index. This implies that, rather than relying on a small number of highly cited papers, these authors regularly contribute to the literature through publications with medium to high impact factors. Changes in the number of publications of the most productive authors over the years are given in Figure 8 Accordingly, Arnold JG and Srinivasan, R., who have been publishing regularly since 1994, stand out. These two authors have been publishing regularly since the creation of the SWAT model, and Srinivasan in particular is seen as the author who has published the most in the last decades.

Table 2. Most cited publications

Authors	Title	Journal	Distribution of total	Total Citations
Moriasi et al. (2007)	Model Evaluation Guidelines for Systematic Quantification of Accuracy in Watershed Simulations	Transaction of the ASABE		8912
Arnold et al. (1998)	Large Area Hydrologic Modeling and Assessment Part I: Model Development	Journal of the American Water Resources Association		5672
Arnold et al. (2012)	SWAT: Model Use, Calibration, and Validation	Transaction of the ASABE		2185
Moriasi et al. (2015)	Hydrologic and Water Quality Models: Performance Measures and Evaluation Criteria	Transaction of the ASABE		1509
Abbaspour et al. (2007)	Modelling hydrology and water quality in the pre-alpine/alpine Thur watershed using SWAT	Journal of Hydrology		1440
Abbaspour et al. (2015)	A continental-scale hydrology and water quality model for Europe: Calibration and uncertainty of a high-resolution large-scale SWAT model	Journal of Hydrology		1157
Santhi et al. (2001)	Validation of the Swat Model on a Large River Basin with Point and Nonpoint Sources	Journal of the American Water Resources Association		1079
van Griensven et al. (2006)	A global sensitivity analysis tool for the parameters of multi-variable catchment models	Journal of Hydrology		918
Yang et al. (2008)	Comparing uncertainty analysis techniques for a SWAT application to the Chaohe Basin in China	Journal of Hydrology		592
Li et al. (2009)	Impacts of land use change and climate variability on hydrology in an agricultural catchment on the Loess Plateau of China	Journal of Hydrology		569

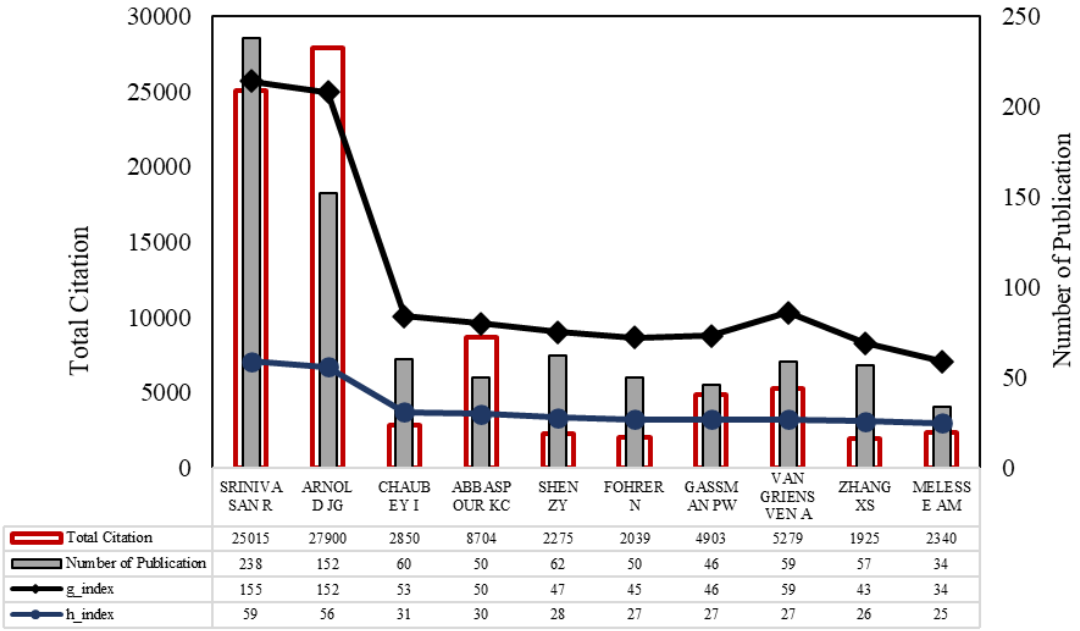


Figure 7. Most productive authors sorted by number of publications.



Figure 8. Changes in the number of publications of the most productive authors over the years.

3.6. Institution-Based Analysis

The results were also evaluated on an institutional basis. According to the data presented in Figure 9, it is seen that American institutions, especially the United States Department of Agriculture (USDA) and the Texas A&M University System, have been pioneers in this field for many years. However, it is noteworthy that in recent years, the Chinese Academy of Sciences has shown a rapid rise after 2014 and has become the institution that produces the most publications in the post-2020 period and reaches the total of 863 articles. USDA is followed by 665 publications, and Texas A&M University System with 644. On the other hand, institutions such as IIT System (India), Beijing Normal University, and Purdue University are also showing a steady increase and continue to make significant contributions in the field of SWAT with a total of 350, 293, and 278 publications, respectively. Overall, the results indicated that research production has increased from established centers to new institutions on a worldwide scale, and the SWAT literature has varied over time at the institutional level. This pattern suggests that worldwide research networks are growing and that the SWAT model is being used in more scientific and practical situations. The list of the ten most productive institutions is given in Table 3.

3.7. Country-Based Analysis

A comparison of studies on the SWAT based on the number of publications made by countries over the years is given in Figure 10. The USA leads with a total of 5259 pulication followed by China with a total of 5078 publications. In particular, the extraordinary number of studies conducted by these two countries on SWAT shows how effective and research-capacity they are on SWAT. While the number of publications in countries

such as India (1038) and Pakistan (858), after China, is remarkable in Asia, Canada (751), after the USA, in North America, Brazil (398) in South America, Germany (586) in Europe and Ethiopia (534) in Africa attract attention with a total of their publication numbers. As can be seen from Figure 10, USA and China are dominant countries based on the number of publications. While the USA has the most publications since the beginning of SWAT, China has significantly narrowed the gap, particularly due to its substantial progress over the past decade. Despite the rise in publications from other countries over the past decade, their publication number remains significantly lower than that of the USA and China. In every country, the overall trend shows a notable growth, especially after 2010. From the beginning, the United States has dominated the literature, and since 2010, the number of publications has increased significantly. China, on the other hand, has had a sharp increase in publishing output, particularly after 2010, and has emerged as one of the SWAT literature's most rapidly expanding players in recent years. The contributions of countries including Iran, Korea, Pakistan, and Brazil seem to have been more noticeable later on, whereas countries like India, Canada, and Germany show a steadier but steadily rising publishing pattern. Despite its comparatively low absolute publication numbers, Ethiopia's expanding publishing trend in recent years shows how the SWAT model is being more widely used in underdeveloped nations.

The analysis presented in Figure 11 reveals the scientific activity of countries in terms of the number of publications and the total number of citations. It is clearly seen from the graph that the USA and China are the two leading countries in terms of both the number of publications and total citations. The USA is the country that maintains the highest level of influence in the literature, with approximately 5259 publications and 75297 citations, following by China with 5078 publications and 36465 citations. Although China is very close to the USA in terms of the number of publications, it performs lower in terms of total citations. The fact that the US, despite having fewer publications than China, generates a much higher totalcitation count indicates that the country has produced high-impact studies in the SWAT literature from an earlier stage. Although Pakistan is the 4th country with the highest number of publications (858), it interestingly has the lowest total number of citations (2092) among the ten most productive countries. This situation may mean that studies from Pakistan are not used much in the literature. On the contrary, although the number of studies from Germany (586) is slightly less than other countries, it is seen that they are highly cited (8403). When other countries are examined, it is seen that countries such as India, Canada, Iran, South Korea, Ethiopia, and Brazil produce a certain level of publications, but their citation numbers remain quite limited. This shows that the visibility and impact of the studies contributed by these countries are still limited in the literature. Overall, the results show that the relationship between scientific production and academic influence varies significantly across countries in the SWAT literature, with early contributions being crucial to overall citation counts. The findings also show that international cooperation and research continuity are essential for improving the articles' long-term scientific effect. Single Country Publication (SCP) and Multiple Country Publication (MCP) represent the authors from different countries who worked together on the SWAT studies. The SCP indicates articles written by researchers from the same country, while the MCP indicates articles written by researchers from more than one country. The distribution of publications in SWAT research, based on the countries of the corresponding authors, shows that scientific production is predominantly concentrated in China and the USA (Table 4).

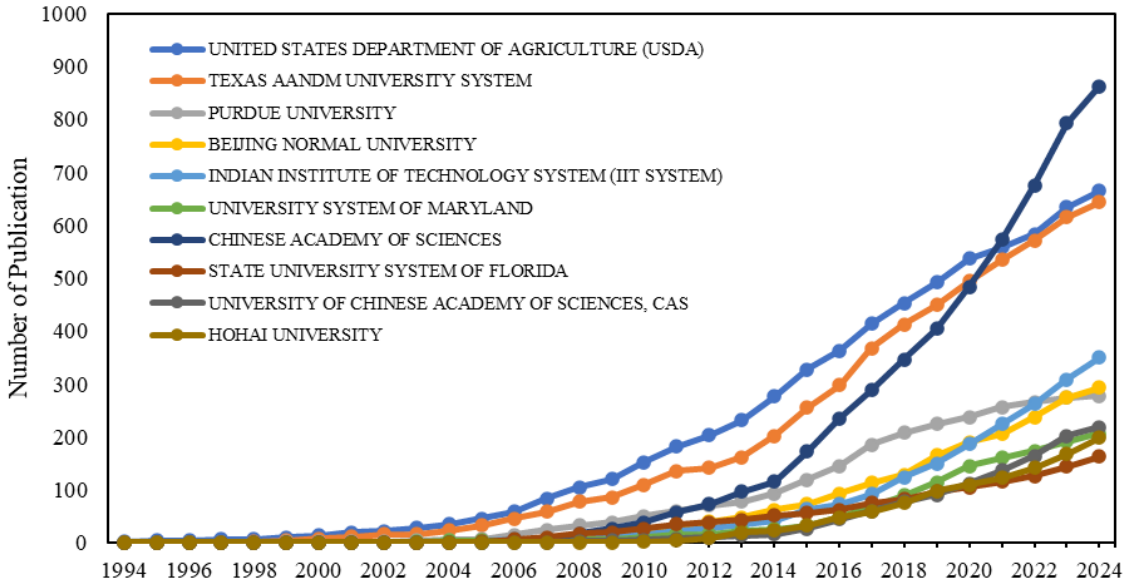


Figure 9. Change in the number of publications of institutions over the years.

Table 3. Ten most productive institutions based on the number of articles

Affiliation	Articles
Chinese Academy of Sciences	863
United States Department of Agriculture (USDA)	665
Texas A&M University System	644
Indian Institute of Technology System (IIT System)	350
Beijing Normal University	293
Purdue University	278
University Of Chinese Academy of Sciences, Cas	219
University System of Maryland	207
Hohai University	198
State University System of Florida	163

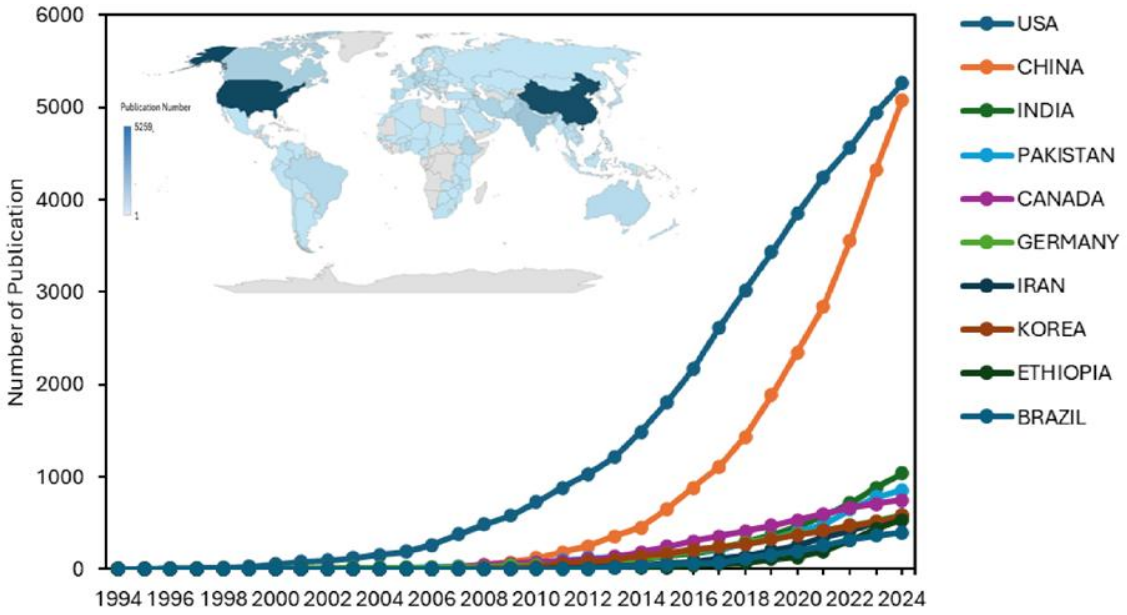


Figure 10. Change in the number of publications of the ten countries with the highest publications over the years, and distribution of their.

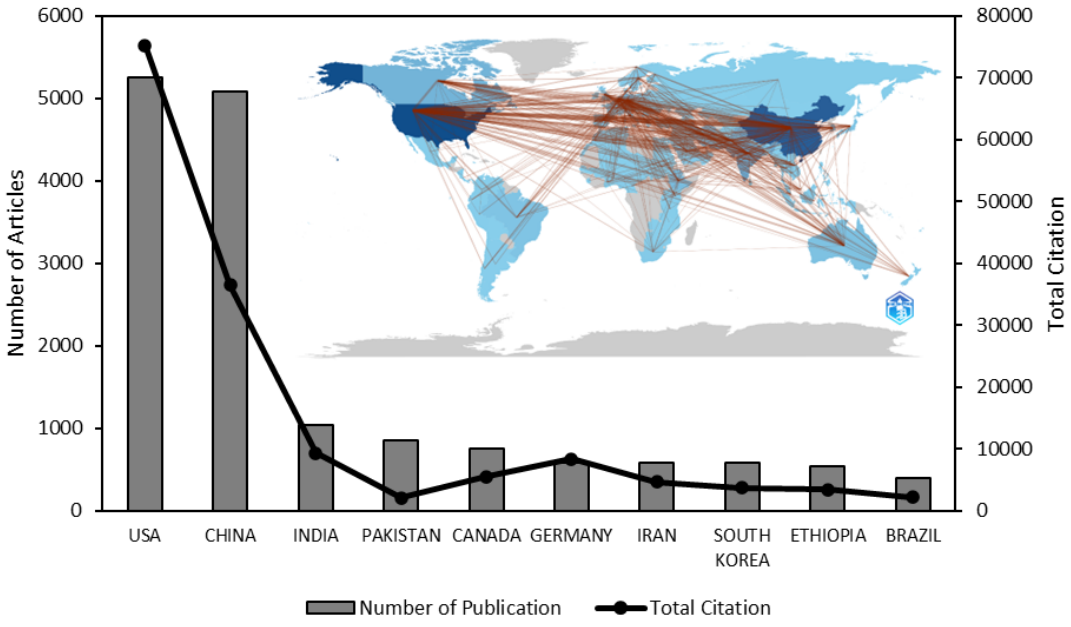


Figure 11. Most productive countries based on the number of publications.

Table 4. Top ten countries in terms of the corresponding author's countries

Country	Articles	Articles %	SCP	SCP %	MCP	MCP %
China	1745	25.1	1168	66.9	577	33.1
USA	1567	22.5	1233	78.7	334	21.3
India	462	6.6	360	77.9	102	22.1
Canada	251	3.6	171	68.1	80	31.9
Iran	251	3.6	151	60.2	100	39.8
Germany	226	3.2	103	45.6	123	54.4
Korea	223	3.2	139	62.3	84	37.7
Pakistan	223	3.2	151	67.7	72	32.3
Ethiopia	221	3.2	125	56.6	96	43.4
Brazil	140	2	92	65.7	48	34.3

Almost half of the publications' corresponding authors are from China (n = 1745, 25.1 %) and the USA (n = 1567, 22.5 %). Notably, the USA ranks first in SCP % with 78.7 %, while it ranks last in MCP % with 21.3 %. This means that the majority of publications where the corresponding author is USA are only USA-based, and international collaboration is less frequent. India has very similar results with the USA, both the SCP% (77.9 %) and MCP% (22.1 %). China, the country with the highest number of corresponding author publications, published 66.9% of its 1745 publications as SCP and 33.1% as MCP. The findings show that not only the total number of publications but also the breadth and diversity of scientific collaboration networks play an important role in increasing the scientific impact of countries.

Figure 12 was illustrated to observe how the SCP and MCP rates are distributed among countries. It can be easily seen that while the SCP rate is higher in almost all countries, only in Germany is the MCP rate (54.4 %) higher than the SCP (45.6). This situation shows that Germany attaches more importance to international collaboration. SCP rates are noticeably greater in nations with strong publishing production, such as the US, China, and India. This suggests that these nations have robust national research infrastructures and autonomous SWAT model research capabilities. In particular, the US's greatest SCP rate validates its dominant and pivotal position in the SWAT literature. On the other hand, the comparatively higher MCP rates in nations like Ethiopia, Germany, and Iran suggest that these nations rely more on international collaboration for their SWAT research. Increased information exchange and methodological variety might be positively correlated with high MCP rates. The more uniform distribution of SCP and MCP rates in nations like Korea and Canada indicates that both national and global research networks are employed efficiently.

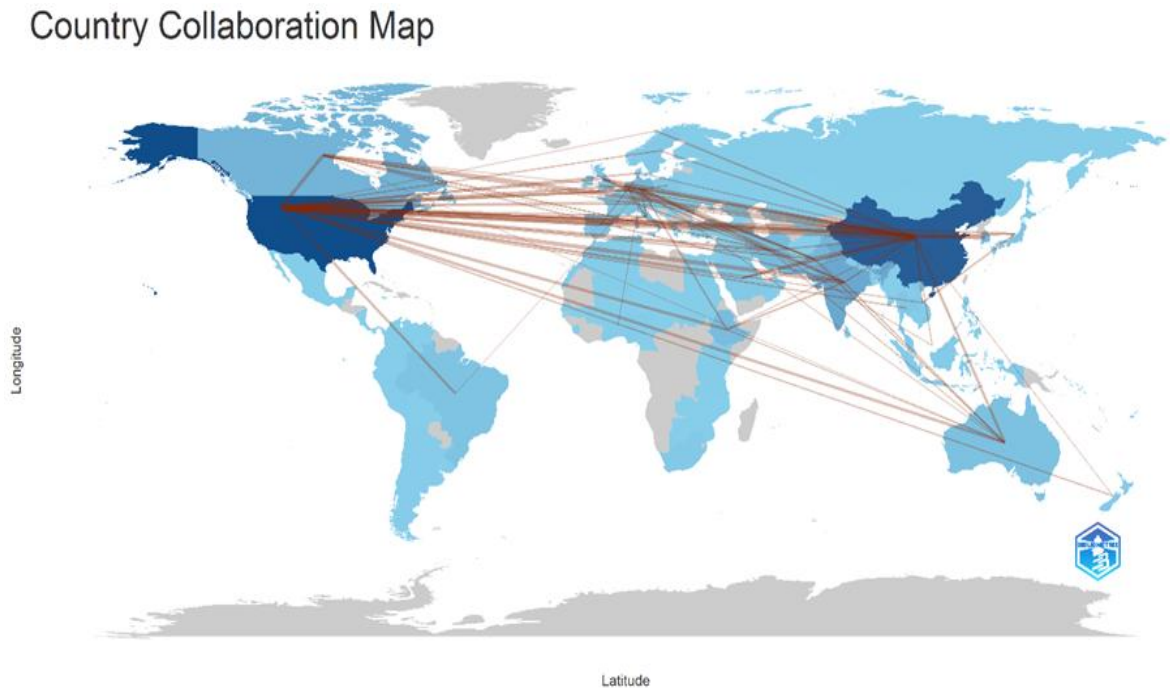


Figure 12. SCP % and MCP % of corresponding author's countries.

The cooperation between countries in studies on SWAT in terms of the number of publications was given in Table 5. It is clearly seen that the cooperation between the USA and China (n=310) is much more than other countries. This finding shows that the USA and China are the main actors driving scientific production in SWAT related studies. China has established intensive cooperation with Pakistan (n=106), Canada (n=99), and Australia (n=67). The USA maintains extensive distribution connections with various countries across different continents, including India (n=104), Korea (n=104), Canada (n=93), Ethiopia (n=67), Australia (n=65), and Germany (n=60). The results of this collaboration are mapped in Figure 13.

Table 5. Top ten most collaborating countries

From	To	Frequency
USA	CHINA	310
CHINA	PAKISTAN	106
USA	INDIA	104
USA	KOREA	104
CHINA	CANADA	99
USA	CANADA	93
CHINA	AUSTRALIA	67
USA	ETHIOPIA	67
USA	AUSTRALIA	65
USA	GERMANY	60



Figure 13. Country collaboration map.

The nations' publishing production is represented by the color tones on the map, while worldwide connections formed through co-authored works are indicated by the connecting lines between the countries. European countries maintain robust research collaborations with North America and Asia. Australia is similarly distinguished by its partnerships with Asia and North America.

In contrast, numerous African and South American countries engage in fewer research collaborations. This distribution indicates that the majority of SWAT research originates from a limited number of countries, with global collaboration primarily concentrated among those possessing advanced research infrastructure. Overall, the results show that the USA and China are not only the countries that produce the most publications, but also the countries with the widest international cooperation networks. The fact that these countries cooperate with many different regions demonstrates that the SWAT model is accepted globally and can be adapted to different geographical conditions.

3.8. Author Keywords Analysis

Figure 14 illustrates the evolution of fundamental concepts in the literature related to studies on SWAT through a bibliometric network. The largest node, "swat", holds the center of this area and has established strong connections with many concepts. The color scale approaching yellow represents the current of the study. It shows that terms such as "climate change"," stream flow" have increased in use in recent years. On the other hand, terms such as “water quality,” “sediment,” and “watershed” appeared significantly in the early stages of the study but were later replaced by more current studies, including those focused on climate change.

A word cloud assessment is a method used to illustrate the frequency of keywords. The words are presented in different sizes based on their frequency in the author’s keywords and their importance (Figure 14). Author keywords in larger means they are used more frequently. By emphasizing common keywords like swat, climate change, swat model, streamflow, and so on, researchers can find the most appropriate content and trends in an area of study. The main keyword, "SWAT," connects different topic clusters, showing that much of the literature is based on models. The color scale shows the average publication year for each keyword, with yellow for newer research themes and blue for older studies. Concepts like "water quality," "sediment," and "watershed" were common in earlier times, according to an analysis of the network structure; on the other hand, keywords like "climate change," "uncertainty," "sensitivity analysis," "remote sensing," and "hydrological modeling" are linked to more recent research. The importance of "climate change," in particular, and its close ties to basic hydrological processes like "streamflow," "water balance," and "land use change," make it evident that the effects of climate change on hydrological systems have been the focus of recent SWAT literature. A word cloud analysis of the relative significance of the most frequently used terms in the SWAT literature is shown in Figure 15. The frequent use of "SWAT" and "SWAT model" indicates that the study is based on model-based investigations. Furthermore, the term "climate change" appears frequently, suggesting that the SWAT model has been widely used recently to assess its effects. The model's essential function in streamflow modeling as well as the study of water quality and sediment transport is shown

by the high frequency of terms related to hydrological processes, such as "streamflow," "water quality," "runoff," and "sediment yield."

The subject of study can be inferred from the keywords listed in the articles in the bibliometric analysis. These represent the research's primary themes and content (Özdoğan Sarıkoç, 2024). Figure 16 provides the most ten frequently used author keywords used in SWAT related studies. As expected, “swat” is most frequently used keyword (n=2446) followed by “climate change” (n=1160), and “swat model” (n=970). Most studies in the literature use a model-based approach, shown by the high frequency of the keyword "SWAT." The keywords "climate change" and "SWAT model" also appear frequently, indicating that SWAT applications have recently shifted to studying how climate change affects hydrological systems. This means the model is now a key tool for climate change analysis, not just for traditional basin hydrology studies.

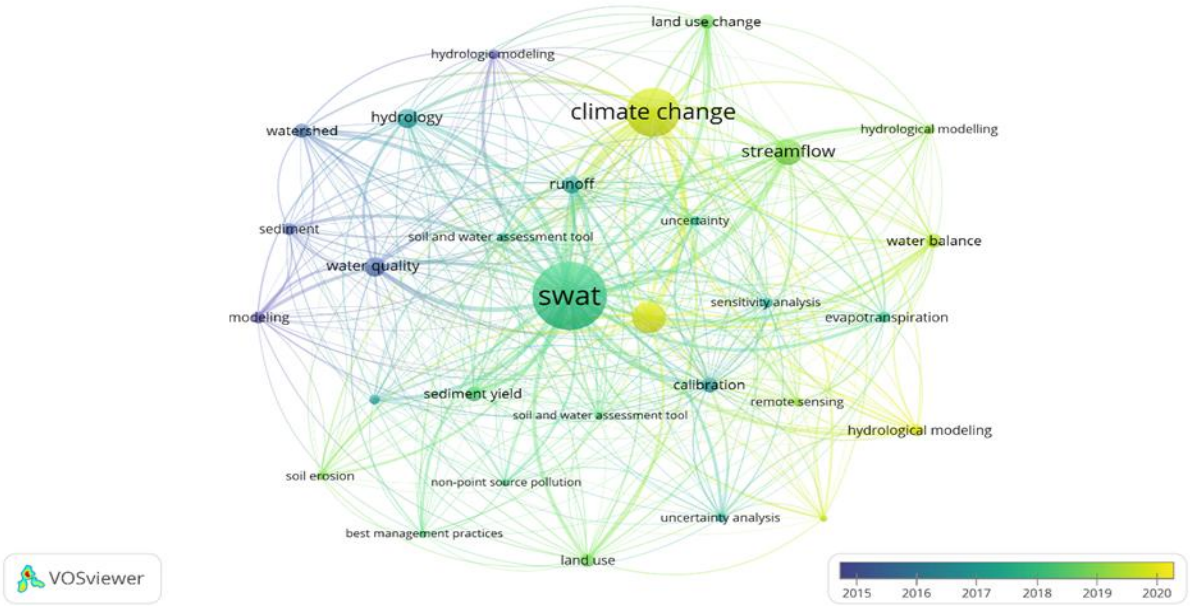


Figure 14. Co-occurrence of author keywords.

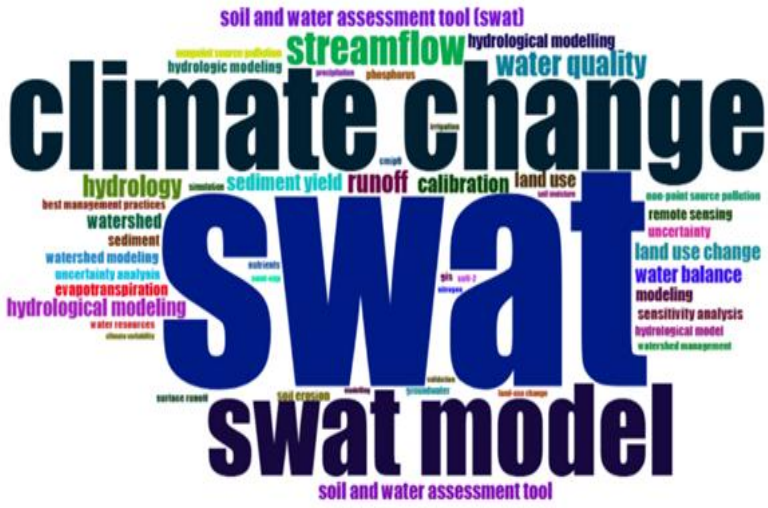


Figure 15. Word cloud containing the most popular author keywords.

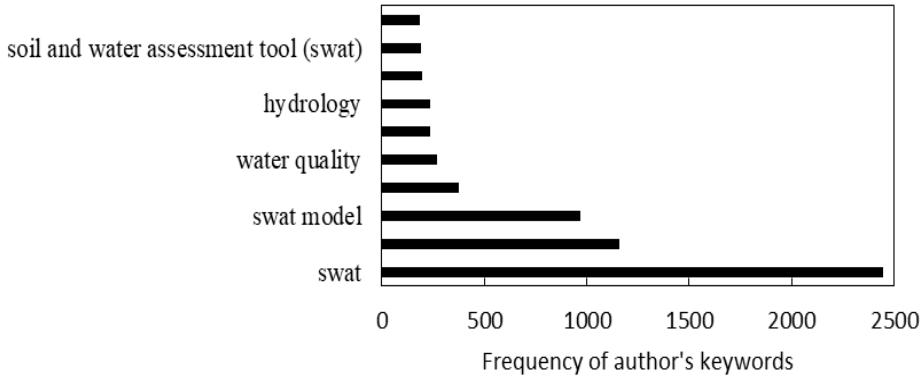


Figure 16. Most commanly used author's keywords in SWAT studies.

The results were also evaluated for the most common author keywords that changed over the years (Figure 17). For all words, an upward trend has been observed over the years, especially for "swat", "climate change", and "swat model". In addition, the effects of climate change have become more felt over time and the importance of studies on these issues has also affected SWAT studies. This finding confirms the adaptive structure of the model and its potential to be integrated into current environmental problems. The relatively lower but regular increasing trend of keywords related to hydrometeorological variables such as "streamflow", "water quality" and "runoff" indicates that these parameters are frequently evaluated in SWAT-based studies. Similarly, broader thematic words such as "hydrology", "hydrologıcal modeling" and "calibration" reflect the integration of modeling studies with the hydrological approach. Given the centrality of keywords such as SWAT, SWAT Model, and Soil and Water Assessment Tool (SWAT), Figure 18 presents the changes in author keyword counts from the previous year, thereby illustrating shifts in keyword density over time for specific topics. The graph indicates that the keyword "climate change" has exhibited a rapid increase, particularly since 2009, in contrast to other keywords. In recent years, the influence of climate change has become increasingly evident, establishing it as a central theme in numerous studies, including those related to SWAT. Conversely, keywords such as "water quality," "run-off," and "streamflow" have demonstrated only modest annual growth, which is not as significant as the increase for "climate change."

Figure 19 visualized the relationship between authors (AU), their affiliated countries (AU_CO), and journals (SO) in which they published with Sankey Diagram. It offers a comprehensive overview of the relationships among authors, their respective countries, and the journals in which they publish. By analyzing the flows, one can acquire insights into collaborative patterns, journal specialization, and the geographic distribution of research activities within the dataset's parameters. The line's thickness represents the strength or frequency of the association. A thicker line between an author and a journal indicates that the author publishes more frequently in that journal (Xie et al., 2020).

Examine the journals indicated on the left side (SO). The journal with the thickest outflow of links to the author's column is likely to dominate research publication within the dataset's parameters. The graph indicates that many authors are publishing in the Journal of Hydrology, Water, Science of Total Environment, Journal of the American Water Resources Association, and Transaction of Asabe. The central column (AU) emphasizes the most productive authors within the dataset. Srinivasan R and Arnold JG seem to be the most distinguished, as indicated by the density of the connections associated with their names. This may signify prominent researchers within the examined field. The right column (AU_CO) displays the countries that contribute to the research. The USA and China have the highest number of represented authors. The connections between the central and right columns depict the nations in which notable authors are based. Many leading authors seem to originate from the USA and China, based on the flows to those countries.

4. Conclusion

In this study, the comprehensive bibliometric analysis of the Soil and Water Assessment Tool (SWAT) literature offers an extensive overview of the model's scientific evolution, global application, and research dynamics over the last three decades. The analysis indicates a significantly growing amount of research, with publication trends showing exponential growth, especially in the past decade—highlighting the rising recognition of SWAT as an essential instrument for tackling hydrological and environmental issues. The importance of journals such as the Journal of Hydrology, Water, and Science of the Total Environment has shown their important role in the publication of SWAT research. The foundational studies conducted by Moriasi et al. (2007) and Arnold et al. (1998) have shown that their studies continue to shape academic studies, evidenced by their high citation rates and sustained scholarly relevance. Based on the geographic distribution the USA and China lead in publication number and citation influence, supported by leading affiliations including USDA, Texas A&M University, and Chinese Academy of Sciences. Furthermore, while Single Country Publications

(SCP) are more frequent, the increasing rate of Multiple Country Publications (MCP), especially those including Germany and China, highlights the significance of international collaboration.

Thematic analysis of author keywords indicates a notable transition in research emphasis, moving from initial concerns such as sediment transport and water quality to current topics including climate change impacts, model calibration, hydrological uncertainty, and land-use change. This evolution demonstrates the model's adaptability and its growing position with using global environmental issues. In addition, there are some limitations to this study. The bibliometric analysis used only the Web of Science database, so studies from other sources, such as Scopus or Google Scholar, were not included. Also, by focusing only on articles, the conference proceedings and review papers are left out. Because this approach relies on quantitative data, assessing the methodological depth or content quality of the studies is not considered. Future research should use different databases, including qualitative content analysis, and compare the SWAT literature across sub-themes. These steps would help more fully show the SWAT model's scientific development.

Overall, the findings from this study reveal the strong and evolving characteristics of SWAT-related research. This study provides insights that outline the scientific progression of the field and define potential strengths for future research, such as interdisciplinary integration and improved global collaboration. This study also presents an informed strategy for SWAT research, offering essential guidance for academics, policymakers, and environmental practitioners seeking to utilize hydrological modeling for sustainable resource management.

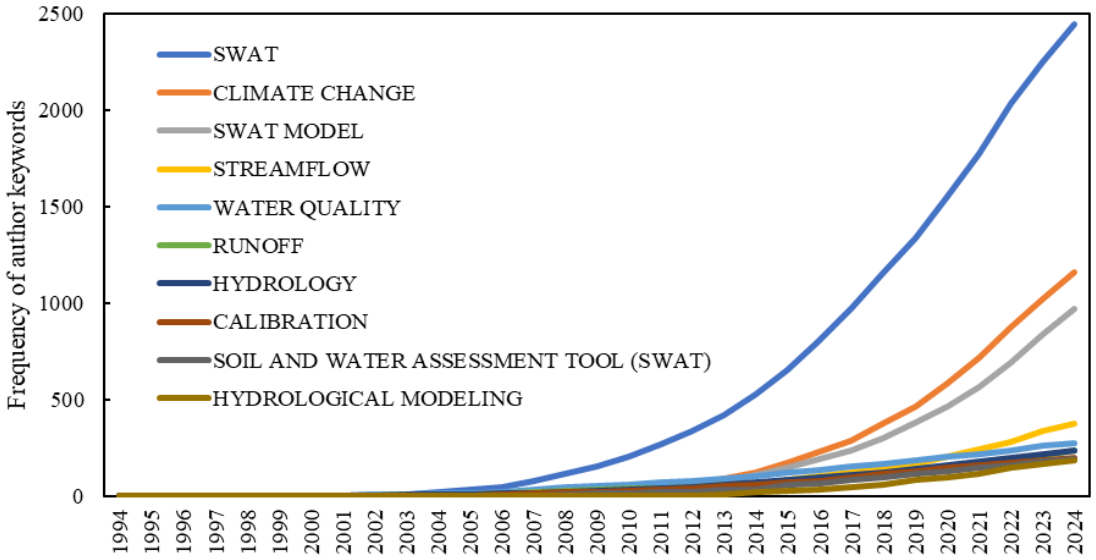


Figure 17. Authors' keywords changed over the years

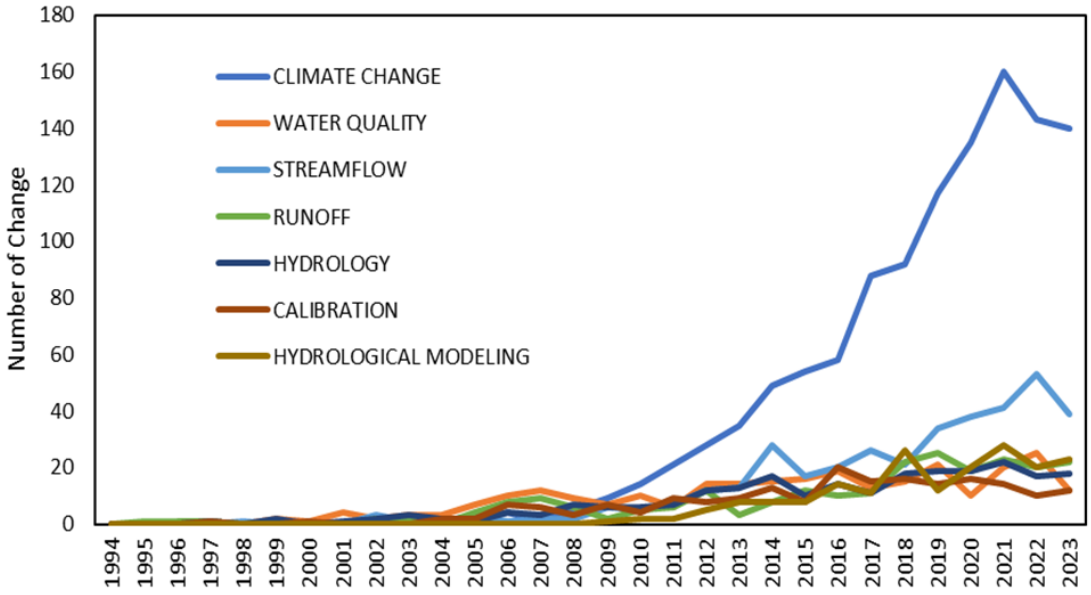


Figure 18. Authors' keywords changes from the previous year in terms of topic.

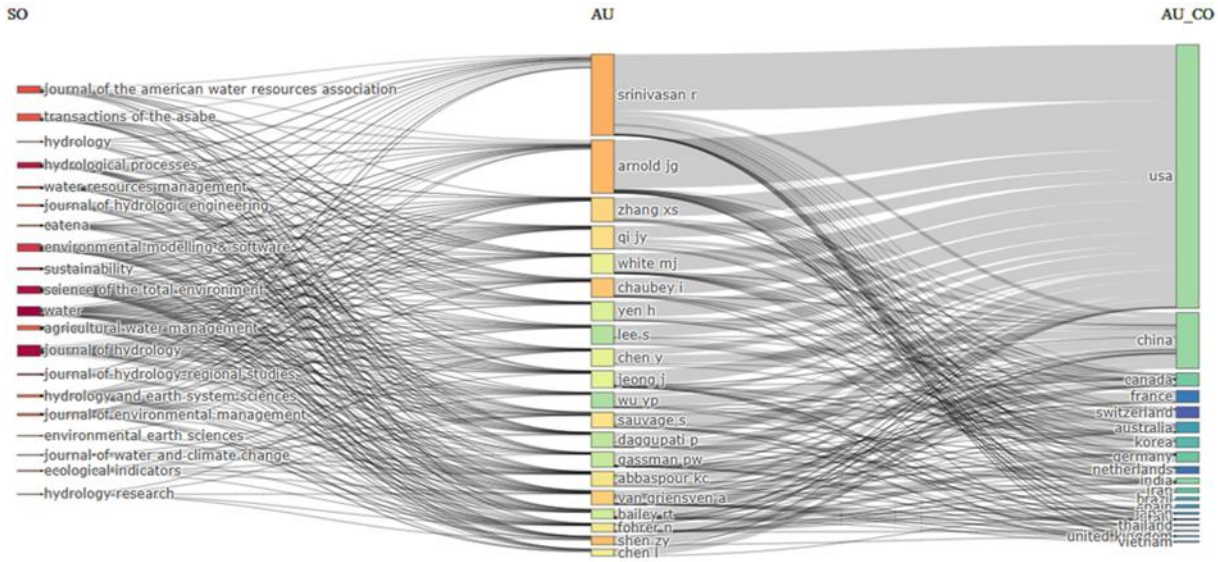


Figure 19. The linkage between journals, authors, and countries with Sankey Diagram

Author Contributions

The percentages of the author' contributions are presented below. The author reviewed and approved the final version of the manuscript.

	E.K.
C	100
D	100
S	100
DCP	100
DAI	100
L	100
W	100
CR	100
SR	100
PM	100
FA	100

C= concept, D= design, S= supervision, DCP= data collection and/or processing, DAI= data analysis and/or interpretation, L= literature search, W= writing, CR= critical review, SR= submission and revision, PM= project management.

Conflict of Interest

The author declared that there is no conflict of interest.

Ethical Consideration

Ethics committee approval was not required for this study because of there was no study on animals or humans.

References

Abbas, S. A., Xuan, Y., & Bailey, R. T. (2022). Assessing climate change impact on water resources in water demand scenarios using SWAT-MODFLOW-WEAP. *Hydrology*, *9*(10), Article 164. https://doi.org/10.3390/hydrology9100164

Abbaspour, K. C., Rouholahnejad, E., Vaghefi, S., Srinivasan, R., Yang, H., & Klove, B. (2015). A continental-scale hydrology and water quality model for Europe: Calibration and uncertainty of a high-resolution large-scale SWAT model. *Journal of Hydrology*.524,733-752. http://dx.doi.org/10.1016/j.jhydrol.2015.03.027

Abbaspour, K. C., Yang, J., Maximov, I., Siber, R., Bogner, K., Mieleitner, J., Zobrist, J., & Srinivasan, R. (2007). Modelling hydrology and water quality in the pre-alpine/alpine Thur watershed using SWAT. *Journal of Hydrology.* 333, 413-430. doi:10.1016/j.jhydrol.2006.09.014

Acar, R., Akbas, E., Koycegiz, C., & Esit, M. (2025). Rainfall trends in the transboundary Euphrates-Tigris River Basin. *Environmental Earth Sciences*, *84*, Article 473. https://doi.org/10.1007/s12665-025-12480-1

Akbas, E., Acar, R., Esit, M., & Koycegiz, C. (2026). An investigation of the variability of short-term drought with SPEI-based severity, duration and magnitude parameters in a transboundary basin. *Pure and Applied Geophysics*, *183*, 821–839. https://doi.org/10.1007/s00024-025-03893-x

Akoko, G., Le, T. H., Gomi, T., & Kato, T. (2021). A review of SWAT model application in Africa. *Water*, *13*(9), Article 1313. https://doi.org/10.3390/w13091313

Aloui, S., Mazzoni, A., Elomri, A., Aouissi, J., Boufekane, A., & Zghibi, A. (2023). A review of Soil and Water Assessment Tool (SWAT) studies of Mediterranean catchments: Applications, feasibility, and future directions. *Journal of Environmental Management*, *326*(Part B), Article 116799. https://doi.org/10.1016/j.jenvman.2022.116799

Aria, M., & Cuccurullo, C. (2017). bibliometrix: An R-tool for comprehensive science mapping analysis. *Journal of Informetrics*, *11*(4), 959–975. https://doi.org/10.1016/j.joi.2017.08.007

Arnold, J. G., Moriasi, D. N., Gassman, P. W., Abbaspour, K. C., White, M. J., Srinivasan, R., Santhi, C., Harmel, R. D., van Griensven, A., Van Liew, M. W., Kannan, N., & Jha, M. K. (2012). SWAT: Model use, calibration, and validation. *Transactions of the ASABE*, *55*(4), 1491–1508. https://doi.org/10.13031/2013.42256

Arnold, J. G., Srinivasan, R., Muttiah, R. S., & Williams, J. R. (1998). Large area hydrological modeling and assessment part I: Model development. *Journal of the American Water Resources Association*, *34*(1), 73–89. https://doi.org/10.1111/j.1752-1688.1998.tb05961.x

Bennour, A., Jia, L., Menenti, M., Zheng, C., Zeng, Y., Barnieh, B. A.,

& Jiang, M. (2022). Calibration and validation of SWAT model by using hydrological remote sensing observables in the Lake Chad Basin. *Remote Sensing*, *14*(6), Article 1511. https://doi.org/10.3390/rs14061511

Bezak, N., Mikoš, M., Borrelli, P., Alewell, C., Alvarez, P., Anache, J. A. A., Baartman, J., Ballabio, C., Biddoccu, M., Cerdà, A., Chalise, D., Chen, S., Chen, W., De Girolamo, A. M., Gessesse, G. D., Deumlich, D., Diodato, N., Efthimiou, N., Erpul, G., … Panagos, P. (2021). Soil erosion modelling: A bibliometric analysis. *Environmental Research*, *197*, Article 111087. https://doi.org/10.1016/j.envres.2021.111087

Broadus, R. N. (1987). Toward a definition of "bibliometrics." *Scientometrics*, *12*(5–6), 373–379. https://doi.org/10.1007/BF02016680

Busico, G., Colombani, N., Fronzi, D., Pellegrini, M., Tazioli, A., & Mastrocicco, M. (2020). Evaluating SWAT model performance, considering different soils data input, to quantify actual and future runoff susceptibility in a highly urbanized basin. *Journal of Environmental Management*, *266*, Article 110625. https://doi.org/10.1016/j.jenvman.2020.110625

Chow, V. T., Maidment, D. R., & Mays, L. W. (1988). *Applied hydrology*. McGraw-Hill.

de Oliveira, V. A., de Mello, C. R., Viola, M. R., & Srinivasan, R. (2017). Assessment of climate change impacts on streamflow and hydropower potential in the headwater region of the Grande river basin, Southeastern Brazil. *International Journal of Climatology*, *37*(15), 5005–5023. https://doi.org/10.1002/joc.5138

Durán-Sánchez, A., Álvarez-García, J., & del Río-Rama, M. de la C. (2018). Sustainable water resources management: A bibliometric overview. *Water*, *10*(9), Article 1191. https://doi.org/10.3390/w10091191

Egghe, L. (2006). Theory and practise of the g-index. *Scientometrics*, *69*(1), 131–152. https://doi.org/10.1007/s11192-006-0144-7

Ficklin, D. L., Luo, Y., Luedeling, E., & Zhang, M. (2009). Climate change sensitivity assessment of a highly agricultural watershed using SWAT. *Journal of Hydrology*, *374*(1–2), 16–29. https://doi.org/10.1016/j.jhydrol.2009.05.016

Foley, J. A., DeFries, R., Asner, G. P., Barford, C., Bonan, G., Carpenter, S. R., Chapin, F. S., Coe, M. T., Daily, G. C., Gibbs, H. K., Helkowski, J. H., Holloway, T., Howard, E. A., Kucharik, C. J., Monfreda, C., Patz, J. A., Prentice, I. C., Ramankutty, N., & Snyder, P. K. (2005). Global consequences of land use. *Science*, *309*(5734), 570–574. https://doi.org/10.1126/science.1111772

Fu, H. Z., Wang, M. H., & Ho, Y. S. (2013). Mapping of drinking water research: A bibliometric analysis of research output during 1992-2011. *Science of the Total Environment*, *443*, 757–765. https://doi.org/10.1016/j.scitotenv.2012.11.061

Gao, J., Zhu, S., Li, D., Jiang, H., Deng, G., Wen, Y., He, C., & Cao, Y. (2023). Bibliometric analysis of climate change and water quality. *Hydrobiologia*, *850*(16), 3441–3459. https://doi.org/10.1007/s10750-023-05270-y

Gassman, P. W., Reyes, M. R., Green, C. H., & Arnold, J. G. (2007). The Soil and Water Assessment Tool: Historical development, applications, and future research directions. *Transactions of the ASABE*, *50*(4), 1211–1250. https://doi.org/10.13031/2013.23637

Hasan, F., Medley, P., Drake, J., & Chen, G. (2024). Advancing hydrology through machine learning: Insights, challenges, and future directions using the CAMELS, Caravan, GRDC, CHIRPS, PERSIANN, NLDAS, GLDAS, and GRACE datasets. *Water*, *16*(13), Article 1904. https://doi.org/10.3390/w16131904 https://doi.org/10.1016/j.jhydrol.2009.08.007

Janjić, J., & Tadić, L. (2023). Fields of application of SWAT hydrological model—A review. *Earth*, *4*(2), 331–344. https://doi.org/10.3390/earth4020018

Kalcic, M. M., Chaubey, I., & Frankenberger, J. (2015). Defining Soil and Water Assessment Tool (SWAT) hydrologic response units (HRUs) by field boundaries. *International Journal of Agricultural and Biological Engineering*, *8*(3), 1–12. https://doi.org/10.3965/j.ijabe.20150803.951

Karakoyun, E., & Kaya, N. (2022). Hydrological simulation and prediction of soil erosion using the SWAT model in a mountainous watershed: A case study of Murat River Basin, Turkey. *Journal of Hydroinformatics*, *24*(6), 1175–1193. https://doi.org/10.2166/hydro.2022.056

Lei, P., Shrestha, R. K., Zhu, B., Han, S., Yang, H., Tan, S., Ni, J., & Xie, D. (2021). A bibliometric analysis on nonpoint source pollution: Current status, development, and future. *International Journal of Environmental Research and Public Health*, *18*(15), Article 7723. https://doi.org/10.3390/ijerph18157723

Li, M., Di, Z., & Duan, Q. (2021). Effect of sensitivity analysis on parameter optimization: Case study based on streamflow simulations using the SWAT model in China. *Journal of Hydrology*, *603*(Part B), Article 126896. https://doi.org/10.1016/j.jhydrol.2021.126896

Li, Z., Liu, W. Z., Zhang, X. C., & Zheng, F. L. (2009). Impacts of land use change and climate variability on hydrology in an agricultural catchment on the Loess Plateau of China. *Journal of Hydrology*, 377(1-2), 35-42.

Moriasi, D. N., Arnold, J. G., Van Liew, M. W., Bingner, R. L., Harmel, R. D., & Veith, T. L. (2007). Model evaluation guidelines for systematic quantification of accuracy in watershed simulations. *Transactions of the ASABE*, *50*(3), 885–900. https://doi.org/10.13031/2013.23153

Moriasi, D. N., Gitau, M. W., Pai, N., & Daggupati, P. (2015). Hydrologic and water quality models: Performance measures and evaluation criteria. *Transactions of the ASABE*, 58(6), 1763-1785. https://doi.org/10.13031/trans.58.10715

Neitsch, S. L., Arnold, J. G., Kiniry, J. R., & Williams, J. R. (2011). *Soil & Water Assessment Tool theoretical documentation version 2009* (Technical Report No. 406). Texas Water Resources Institute.

Özdoğan Sarıkoç, G. (2024). Artificial intelligence applications in the field of streamflow: A bibliometric analysis of recent trends. *Hydrological Sciences Journal*, *69*(9), 1141–1157. https://doi.org/10.1080/02626667.2024.2356006

Pimentel, D., Harvey, C., Resosudarmo, P., Sinclair, K., Kurz, D., McNair, M., Crist, S., Shpritz, L., Fitton, L., Saffouri, R., & Blair, R. (1995). Environmental and economic costs of soil erosion and conservation benefits. *Science*, *267*(5201), 1117–1123. https://doi.org/10.1126/science.267.5201.1117

Santhi, C., Arnold, J. G., Williams, J. R., Dugas, W. A., Srinivasan, R., & Hauck, L. M. (2001). Validation of the SWAT model on a large river basin with point and nonpoint sources. *JAWRA Journal of the American Water Resources Association*, 37(5), 1169-1188. https://doi.org/10.1111/j.17521688.2001.tb03630.x

Schuol, J., Abbaspour, K. C., Srinivasan, R., & Yang, H. (2008). Estimation of freshwater availability in the West African sub-continent using the SWAT hydrologic model. *Journal of Hydrology*, *352*(1–2), 30–49. https://doi.org/10.1016/j.jhydrol.2007.12.025

Sellami, H., La Jeunesse, I., Benabdallah, S., Baghdadi, N., & Vanclooster, M. (2014). Uncertainty analysis in model parameters regionalization: A case study involving the SWAT model in Mediterranean catchments (Southern France).

Hydrology and Earth System Sciences, *18*(6), 2393–2413. https://doi.org/10.5194/hess-18-2393-2014

Serrão, E. A. de O., Silva, M. T., Ferreira, T. R., Paiva de Ataide, L. C., Assis dos Santos, C., Meiguins de Lima, A. M., de Paulo Rodrigues da Silva, V., de Assis Salviano de Sousa, F., & Cardoso Gomes, D. J. (2022). Impacts of land use and land cover changes on hydrological processes and sediment yield determined using the SWAT model. *International Journal of Sediment Research*, *37*(1), 54–69. https://doi.org/10.1016/j.ijsrc.2021.04.002

Sharma, A., Patel, P. L., & Sharma, P. J. (2022). Influence of climate and land-use changes on the sensitivity of SWAT model parameters and water availability in a semi-arid river basin. *Catena*, *215*, Article 106298. https://doi.org/10.1016/j.catena.2022.106298

Shrestha, N. K., Du, X., & Wang, J. (2017). Assessing climate change impacts on fresh water resources of the Athabasca River Basin, Canada. *Science of the Total Environment*, *601–602*, 425–440. https://doi.org/10.1016/j.scitotenv.2017.05.013

Suluk, K., & Coskun, S. (2024). Analysis of composting and artificial intelligence program machine learning studies with visual mapping techniques. In *Proceedings of the 8th Azerbaijan Congress on Life, Engineering, Mathematical, and Applied Sciences* (pp. 465–489).

Tague-Sutcliffe, J. (1992). An introduction to informetrics. *Information Processing & Management*, *28*(1), 1–3. https://doi.org/10.1016/0306-4573(92)90087-G

Taye, M. T., Willems, P., & Block, P. (2015). Implications of climate change on hydrological extremes in the Blue Nile basin: A review. *Journal of Hydrology: Regional Studies*, *4*, 280–293. https://doi.org/10.1016/j.ejrh.2015.07.001

Trivedi, A., Awasthi, M. K., Gautam, V. K., Pande, C. B., & Din, N. M. (2024). Evaluating the groundwater recharge requirement and restoration in the Kanari river, India, using SWAT model. *Environment, Development and Sustainability*, *26*(6), 15067–15092. https://doi.org/10.1007/s10668-023-03235-8

van Griensven, A. V., Meixner, T., Grunwald, S., Bishop, T., Diluzio, M., & Srinivasan, R. (2006). A global sensitivity analysis tool for the parameters of multi-variable catchment models. *Journal of Hydrology*, 324(1-4), 10-23. https://doi.org/10.1016/j.jhydrol.2005.09.008

Wagner, P. D., Bieger, K., Arnold, J. G., & Fohrer, N. (2022). Representation of hydrological processes in a rural lowland catchment in Northern Germany using SWAT and SWAT+. *Hydrological Processes*, *36*(5), Article e14589. https://doi.org/10.1002/hyp.14589

Wu, D., Cui, Y., Xie, X., & Luo, Y. (2019). Improvement and testing of SWAT for multi-source irrigation systems with paddy rice. *Journal of Hydrology*, *568*, 1031–1041. https://doi.org/10.1016/j.jhydrol.2018.11.057

Xie, H., Zhang, Y., Wu, Z., & Lv, T. (2020). A bibliometric analysis on land degradation. *Land*, *9*(1), Article 28. https://doi.org/10.3390/land9010028

Xiong, H., Wang, Y., Guo, X., Han, J., Ma, C., & Zhang, X. (2022). Current status and future challenges of groundwater vulnerability assessment: A bibliometric analysis. *Journal of Hydrology*, *615*, Article 128694. https://doi.org/10.1016/j.jhydrol.2022.128694

Yang, D., Yang, Y., & Xia, J. (2021). Hydrological cycle and water resources in a changing world: A review. *Geography and Sustainability*, *2*(2), 115–122. https://doi.org/10.1016/j.geosus.2021.05.003

Yang, J., Reichert, P., Abbaspour, K. C., Xia, J., & Yang, H. (2008). Comparing uncertainty analysis techniques for a SWAT application to the Chaohe Basin in China. *Journal of Hydrology*, 358(1-2), 1-23. https://doi.org/10.1016/j.jhydrol.2008.05.012

Zare, F., Elsawah, S., Iwanaga, T., Jakeman, A. J., & Pierce, S. A. (2017). Integrated water assessment and modelling: A bibliometric analysis of trends in the water resource sector. *Journal of Hydrology*, *552*, 765–778. https://doi.org/10.1016/j.jhydrol.2017.07.031

Zema, D. A., Carrà, B. G., Lucas-Borja, M. E., Filianoti, P. G. F., Pérez-Cutillas, P., & Conesa-García, C. (2022). Modelling water flow and soil erosion in Mediterranean headwaters (with or without check dams) under land-use and climate change scenarios using SWAT. *Water*, *14*(15), Article 2338. https://doi.org/10.3390/w14152338

Zhang, H., Wang, B., Liu, D. L., Zhang, M., Leslie, L. M., & Yu, Q. (2020). Using an improved SWAT model to simulate hydrological responses to land use change: A case study of a catchment in tropical Australia. *Journal of Hydrology*, *585*, Article 124822. https://doi.org/10.1016/j.jhydrol.2020.124822

Zhang, X., Srinivasan, R., Debele, B., & Hao, F. (2008). Runoff simulation of the headwaters of the Yellow River using the SWAT model with three snowmelt algorithms. *Journal of the American Water Resources Association*, *44*(1), 48–61. https://doi.org/10.1111/j.1752-1688.2007.00137.x

Zhao, J., Zhang, N., Liu, Z., Zhang, Q., & Shang, C. (2024). SWAT model applications: From hydrological processes to ecosystem services. *Science of the Total Environment*, *931*, Article 172605. https://doi.org/10.1016/j.scitotenv.2024.172605

Black Sea Journal of Engineering and Science
doi: 10.34248/bsengineering.1984273

Open Access Journal
e-ISSN: 2619 – 8991

Research Article
Volume 9 - Issue 5: 2337-2344 / September 2026

A BIBLIOMETRIC ANALYSIS ON EMERGENCY DEPARTMENT SIMULATION AND DISCRETE EVENT SIMULATION

Z. Figen ANTMEN[1], Şölen ZENGİN[2]*

[1]*Cukurova University, Faculty of Engineering, Department of Industrial Engineering, 01330, Adana, Türkiye*
[2]*Tarsus University, Faculty of Engineering, Department of Industrial Engineering, 33400, Mersin, Türkiye*

Abstract: The aim of this study is to examine the scope of academic articles containing the keywords "emergency department" and "simulation" and to reveal the development and trends in this field. The study aims to present a bibliometric analysis of the literature on articles discussing simulation in emergency department studies based on quantitative data analysis, and to identify research trends and gaps in this field. The study was conducted through a bibliometric analysis of 1507 articles published in the Web of Science database between 1989 and 2024. VOSviewer 1.6.20 was used in the analysis. The focus was on the selected keywords "Emergency Department" and "Simulation." Additionally, the keyword "Discrete Event Simulation" was included for further analysis. When examining the distribution by year, it was observed that the most publications occurred in 2021 (155 articles), followed by 2020 (139 articles), 2022 (139 articles), and 2023 (139 articles). The study demonstrates that a significant portion of the literature in the field of emergency departments and simulation has been published in high-impact journals, creating a wide influence. It emphasizes the need for fostering stronger collaboration between developed and developing countries in the future. Additionally, it is anticipated that simulation techniques, particularly Discrete Event Simulation methods, will continue to be a major focus in future research. Therefore, in addition to the keywords "Emergency Department" and "Simulation," the third keyword "DES" was added, and further analyses were conducted. The aim of this study is to provide researchers and decision makers working on this topic with a systematic perspective.

Keywords: Emergency department, Simulation, Discrete event simulation, Bibliometric analysis, Web of science

***Corresponding author:** Tarsus University, Faculty of Engineering, Department of Industrial Engineering, 33400, Mersin, Türkiye
E mailsolenzengin@tarsus.edu.tr (Ş. ZENGİN)
Z. Figen ANTMEN https://orcid.org/0000-0001-8475-1300
Şölen ZENGİN https://orcid.org/0000-0003-2309-4954

Received: July 01, 2026
Accepted: August 08, 2026
Published: September 15, 2026

Cite as: Antmen, Z. F., & Zengin, Ş. (2026). A bibliometric analysis on emergency department simulation and discrete event simulation. *Black Sea Journal of Engineering and Science,* 9(5), 2337-2344.

1. Introduction

The emergency department is a unit in hospitals where situations requiring rapid intervention are managed, characterized by high patient intake rates and a fast-paced work environment. The frequent use of emergency departments by the elderly population, limited access to other healthcare resources, and the treatment of non-emergency health issues in this unit are primary reasons for the increase in patient numbers. Emergency departments are among the most critical units in hospitals in terms of providing rapid intervention to patients. Emergency departments are complicated by uncertain patient arrivals, uncertain waiting times and uncertain processing times. The complexity and crowding in emergency departments is a major problem in many countries Auerbach et al. (2018). Therefore, emergency room improvements have become a global issue.

Simulation has become increasingly popular because it is practical to test changes to systems by modeling them in the real world Rudolph et al. (2008). Simulation also helps to observe the possible effects of changes to be implemented in new systems. It allows the latest current situation to be modeled from the emergency service site and the model reflection of new scenarios to be tested. In addition, this method is used to reduce waiting times. Salway et al. (2017), optimize resource use identify operational inefficiencies Kuo et al. (2023) and prepare for emergencies Tian et al. (2023). In many studies, researchers have favored Discrete Event Simulation (DES) to reduce waiting times in emergency service systems Rabbani et al. (2018). A bibliometer is a method used to quantitatively assess the impact of a research output (Kuo et al., 2023; Rehman et al., 2023). Bibliometric analysis is carried out for purposes such as identifying research areas open to development and identifying possible research partnerships between institutions and authors. Bibliometric analysis is carried out for purposes such as identifying research areas open to development and identifying possible research partnerships between institutions and authors (Mistarihi et al., 2023; Duncan et al., 2024).

Emergency departments are vital in the health system because of the rapid service provided to patients

This work is licensed (CC BY-NC 4.0) under Creative Commons Attribution 4.0 International License

requiring urgent intervention. They also provide great support to protect public health through early diagnosis and intervention in unexpected situations such as natural disasters and crises. For this reason, emergency departments are an indispensable part of healthcare systems worldwide. Simulation studies aimed at improving the performance of emergency departments offer an important tool for increasing operational efficiency. However, a comprehensive bibliometric study summarizing the research on simulation in healthcare is still lacking in the literature. The generally limited perspective of existing bibliometric analyses highlights the need for a more in-depth evaluation of current research and the development of more comprehensive simulation models. In this context, the growing importance of research on simulation in emergency departments presents significant potential for making healthcare systems more efficient. The presented comprehensive bibliometric study will contribute to filling the knowledge gaps in this field and improving healthcare services. Recently, as the volume of publications has grown, the number of bibliometric studies has also increased Kayir and Kisa (2021). Bibliometric studies commonly utilize Web of Science, PubMed, and Scopus databases.

In this paper, two different analyses were conducted using the Web of Science database. The first analysis presents a bibliometric analysis of articles related to emergency department simulations published between 1989 and 2024, using the keywords "Emergency Department" and "Simulation." In the second analysis, in addition to the keywords "Emergency Department" and "Simulation," the third keyword "DES" (Discrete Event Simulation), a simulation technique that particularly enhances the operational efficiency of healthcare systems, was added for a more comprehensive bibliometric review. In the second analysis, emergency department simulation studies were examined in detail specifically for DES. The 10 most cited studies were selected and analyzed. Details of the analyses performed are presented.

2. Material and Method

Bibliometric analysis is a method that helps determine the current status of a particular research area and determines the direction of the field for future research Golpinar and Demir (2020). With this analysis, a network map of various elements such as years of publication, countries of study, institutions, authors, journals and keywords related to the subject can be created. Bibliometric analysis involves examining scientific literature through numerical data to analyze research trends, the impact of authors, interactions among publications, and other important metrics. The bibliometric analysis in this study was performed using VOSviewer. The data used in VOSviewer was obtained from one of the most prestigious databases, Web of Science. On January 13, 2025, 1904 studies were found that used the keywords "Emergency Department" and "Simulation" together. Of these, 6 studies from 2025 were excluded from the analysis as the year was not yet complete. The remaining 1,898 studies consisted of 1,507 articles, 275 conference papers, 97 review articles, 28 conference abstracts, 23 early access publications, 23 editorial materials, 16 book chapters, 5 letters, 3 retracted publications, 2 news articles, and 1 book. Only articles, which accounted for 79.4% of the publications, were included in the analysis.

For the bibliometric analysis, the following analyses were performed in sequence: co-author analysis, keyword analysis, citation analysis of authors, citation analysis of countries, citation analysis of institutions, bibliographic coupling analysis of texts, bibliographic coupling analysis of authors, and co-citation analysis of authors. It was found that "Emergency Department" and "Simulation" keywords, along with DES (Discrete Event Simulation), play a significant role in modeling and analyzing complex systems. In this context, a second analysis was conducted on the articles in the Web of Science database that used the keywords "Emergency Department," "Simulation," and "DES" simultaneously. As a result of this analysis, a total of 243 studies were identified. Critical analyses were then performed for these 243 articles to provide detailed insights. With these two analyses, the goal is to evaluate the existing studies, identify the research trends, and provide valuable information that will guide future research in this field.

Methodology is presented in Figure 1, where the step by step workflow of the study is illustrated. Each phase of the bibliometric analysis, from data collection to detailed critical evaluation, is systematically outlined to provide a clear understanding of the research process.

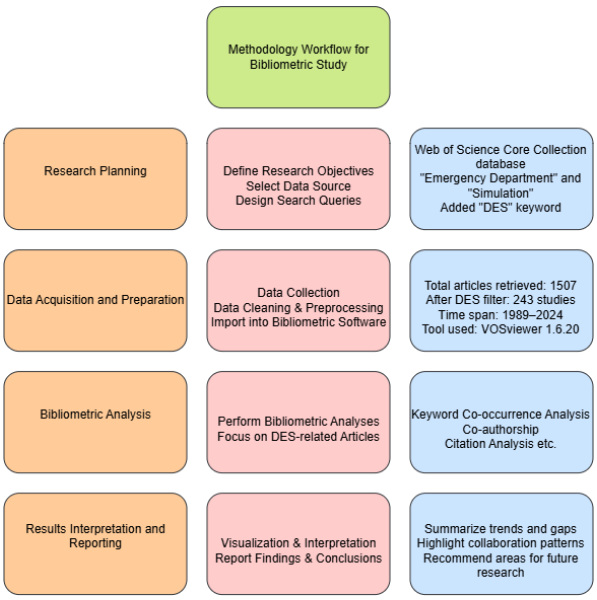


Figure 1. Methodology.

3. Results and Discussion

This section presents the data and analysis results obtained from the research in a clear and unbiased manner. In this section, prominent trends, relationships, and direct observations are shared. Quantitative and qualitative results are presented in a logical sequence. The co-author analysis, keyword analysis, authors' citation analysis, countries' citation analysis, citation analysis of institutions, bibliographic coupling analysis of texts, bibliographic coupling analysis of authors, and co-citation analysis of authors, conducted using Vosviewer, are presented in sequence.

3.1. Co-authorship of Authors

Co-authorship refers to the collaboration of multiple researchers working together on the same academic publication and is an important indicator of scientific cooperation. The network map created based on the criteria of at least 2 publications and 2 citations revealed the authors with the most collaboration and the strongest connections based on the co-authorship analysis. This analysis allows a better understanding of the collaboration dynamics and interaction networks within the academic community. According to the analysis results, when examining the strongest connections, 16 different clusters and a total of 588 connections were identified. However, it was observed that the most cited authors (Walter J. Eppich [561 citations], Marry D. Patterson [508 citations], Robert Wears Patterson [428 citations], Adam Cheng [427 citations]) were not among the most connected authors. Figure 2 presents the co-authorship analysis.

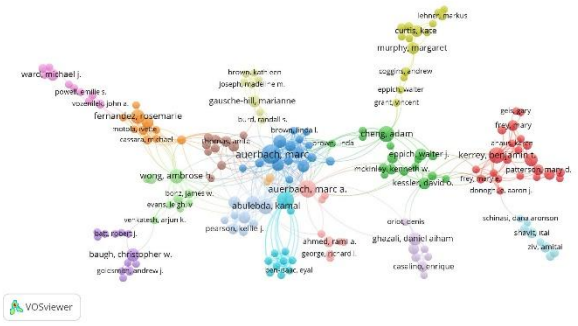


Figure 2. Co-authorship of authors.

3.2. Co-occurrence of All Keywords

When analyzing the most commonly used keywords in publications related to emergency departments and simulation, the most frequent terms were "simulation" with 329 occurrences, "emergency department" with 277 occurrences, "emergency medicine" with 97 occurrences, and "DES" with 62 occurrences. In terms of total connection strength, the strongest expressions were "simulation," "emergency department," "emergency medicine," and "education." Following an analysis of 703 observation units that appeared at least twice and were related to each other, a total of 29 clusters, 4075 connections, and 5530 total connection strength were identified. Figure 3 presents the keyword analysis.

3.3. Citation of Authors

A co-citation analysis map was developed to identify citation networks, using the criteria of having at least one publication and one citation. In an analysis conducted on 3202 interconnected units, a total of 39 clusters, 44387 connections, and a total connection strength of 50888 were detected. The most cited authors were Walter J. Eppich with 561 citations, Marry D. Patterson with 508 citations, Robert Wears with 428 citations, and Adam Cheng with 427 citations. When evaluating the analysis based on total connection strength, Jingshan Li appeared at the top, despite not being among the most cited authors. Marry D. Patterson ranked second, while Muhammet Gul ranked third. Figure 4 presents the authors' citation analysis.

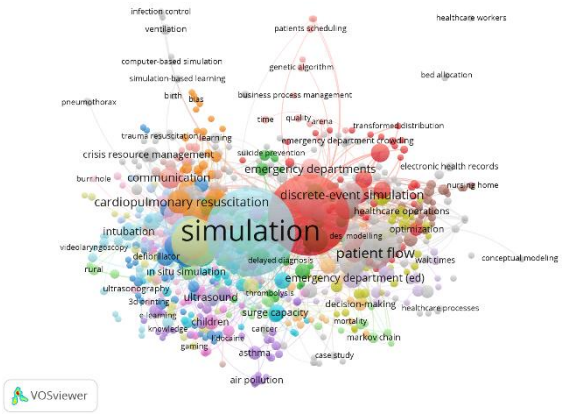


Figure 3. Co-occurrence of all keywords.

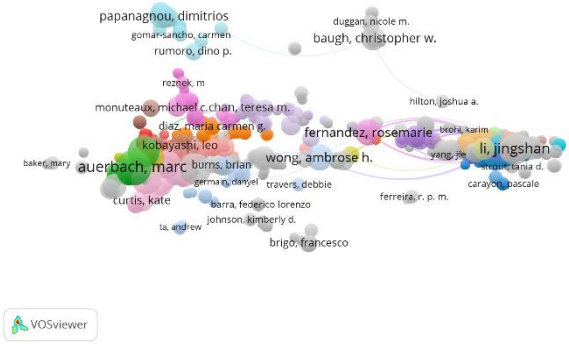


Figure 4. Citation of authors.

3.4. Citation of Countries

At this stage, academic collaborations between countries were analyzed. An analysis was conducted on the relationships between the 59 observed units, meeting the criteria of at least one publication and at least one citation. As a result, 14 clusters, 584 connections, and a total connection strength of 3,162 were detected. The network map shows that the United States (14,411 citations) plays a central role in international collaborations and has the most connections. Among the countries with the highest citations, the United States is followed by Canada (2,837 citations) and the United Kingdom (1,715 citations). Countries such as China,

Canada, and the United States have developed strong connections and hold significant positions in the global academic network. Countries like the United Kingdom and Italy form more limited but effective collaborations. Hungary and Indonesia, on the other hand, have fewer connections and are more isolated in academic collaborations. This analysis reveals the structure of international research networks, highlighting countries with intense academic interactions and the dynamics of collaboration. In terms of publication count, the United States (724 publications), Canada (175 publications), and Australia (82 publications) stand out. Figure 5 presents the citation analysis by countries.

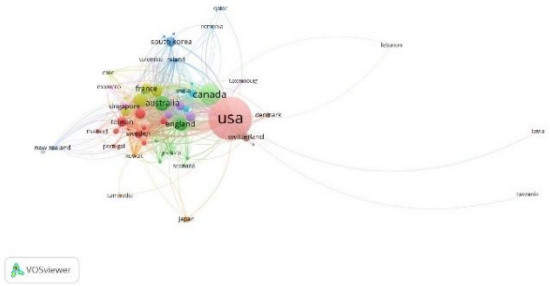


Figure 5. Citation of countries.

3.5. Citation of Organizations

In this analysis, conducted on 1000 observation units, a network map of citations between institutions was created. The analysis was based on the criterion that an institution must have published at least one work and received at least one citation. The research revealed that Yale University, with 34 publications, and the University of Toronto, with 35 publications, along with Harvard Medical School, represented by 27 publications, were notable contributors. In terms of cited publications, Harvard University (1129 citations), Northwestern University (1042 citations), and Massachusetts General Hospital (823 citations) emerged as the institutions with the highest citation counts. Within the network analysis, a total of 25 clusters, 11381 connections, and 14128 total connection strength were detected. These findings illustrate how academic collaboration and the flow of information are shaped between institutions, highlighting that scientific productivity and interaction are concentrated in certain institutions. Figure 6 presents the citation analysis by institutions.

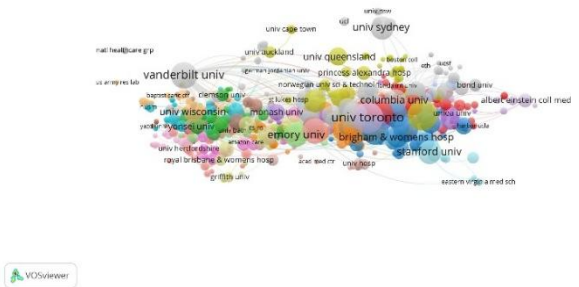


Figure 6. Citation of organizations.

Bibliographic Coupling of Documents Bibliographic coupling refers to the situation where two independent sources cite a common work. Based on the criterion of having received at least 2 citations, an analysis was conducted on 1122 units of work that were linked. As a result, 14 clusters, 34451 connections, and 57384 total connection strength were identified. The publications with the highest bibliographic coupling were those by Rudolp et al. (2008), Kiraz and Demir (2020) with 410 citations, and Capella (2010), Golpinar and Ekici (2023) with 299 citations. The works with the highest total connection strength were Gul (2015), Doğan and İpek (2021) with 1394 total connection strength, and Furian (2018), Patterson et al. (2013) with 1344 connection strength. Figure 7 presents the bibliographic coupling analysis of the texts.

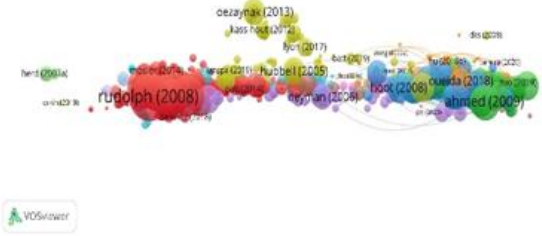


Figure 7. Bibliographic coupling of documents.

3.6. Bibliographic Coupling of Authors

Based on the criterion of having published at least one work and received at least one citation, an analysis was conducted on 1000 units that were linked. As a result, 8 clusters, 143823 connections, and total connection strength of 1436415 were identified. The authors with the highest bibliographic coupling were Marianne Gausche-Hill, Cheng et al. (2014) with 121 citations (20235 connection strength) and Kathleen Brown, Brenner et al. (2010) with 105 citations (18368 connection strength). Figure 8 presents the bibliographic coupling analysis of the authors.

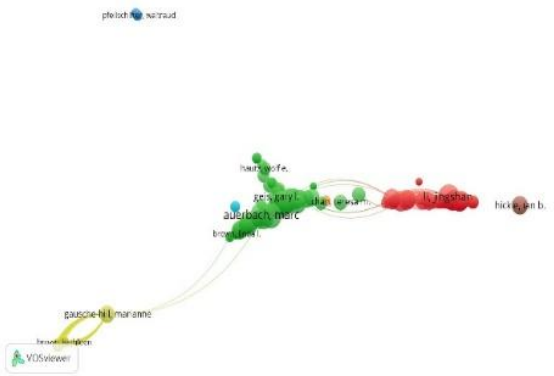


Figure 8. Bibliographic coupling of documents.

3.7. Co-citation of Co-authors

Co-citation refers to different sources cited together in a publication. Based on the criterion of a minimum of 10

citations, an analysis was conducted on 502 units. As a result, 6 clusters, 27133 connections, and total connection strength of 80753 were identified. The authors with the most co-citations were Hoot et al. (2008) (165), Cheng et al. (2014) (117), and Gul and Guneri (2015), (104). Figure 9 presents the co-citation analysis of the authors.

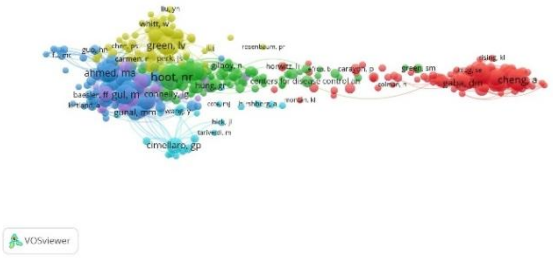


Figure 9. Co-citation of co-authors.

3.7. Analysis Results

The key term DES, along with Emergency Department and Simulation, is of significant importance due to its use in modeling and analyzing complex systems. Therefore, a second analysis was conducted on articles in the Web of Science database that used the keywords "Emergency Department," "Simulation," and "DES" simultaneously. This analysis resulted in a total of 243 works. The results of the second analysis are presented sequentially below.

3.8. Co-occurrence of All Keywords

According to the results of the analysis, it was found that the keywords "Emergency department," "Simulation," and "DES" were frequently used with "patient flow," "length of stay," and "healthcare." Figure 10 presents the keyword analysis for the second analysis.

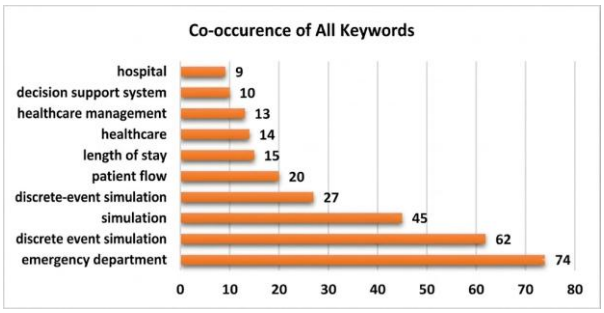


Figure 10. Co-occurrence of all keywords for 2 analysis.

3.9. Citation of Countries

In the second analysis, a country-based citation analysis was conducted in Vosviewer. According to the results of this analysis, the top three most cited countries are the United States, Canada, and the United Kingdom. Türkiye ranks 4th. The top 10 most cited countries from the second analysis are presented in Figure 11.

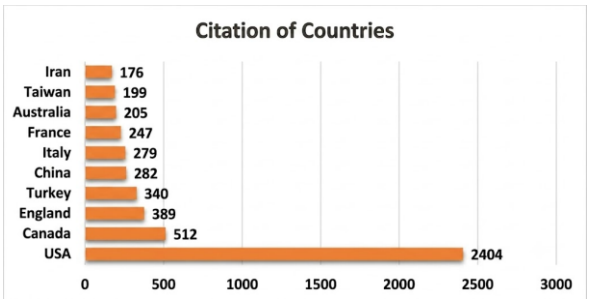


Figure 11. Citation of countries for 2 analysis.

3.10. Citation of Organizations

According to the institution citation analysis, which is one of the factors demonstrating academic success, the top three institutions are Johns Hopkins University, Vanderbilt University, and the University of Pennsylvania. The top 10 most cited institutions for the second analysis are presented in Figure 12.

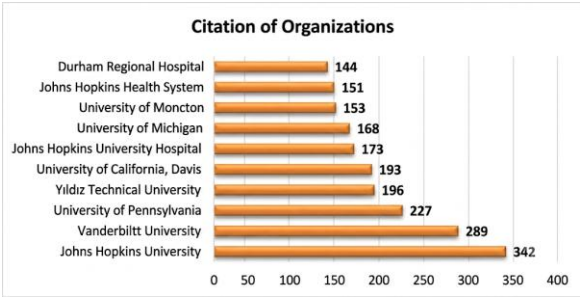


Figure 12. Citation of organizations for 2 analysis.

3.11. Publications Number

The journal "Operations Research for Health Care" leads with 12 publications, followed by "Computers & Industrial Engineering" with 8 publications, and "Health Care Management Science" also with 8 publications. The ranking of the top 10 journals based on publication count for the second analysis is shown in Figure 13.



Figure 13. Number of publication in the journal for 2. analysis.

In the second analysis, the top 10 most cited papers related to emergency department, simulation, and DES keywords in Web of Science are listed in Table 1. The most cited studies are particularly those conducted between 2007-2010, focusing on simulation models developed to address issues like overcrowding, patient

flow, and service quality in emergency departments. Notable studies include those by (Duguay and Chetouane 2007; Hoot et al., 2008; Eitel et al., 2010; Gul and Guneri 2015; Furian et al., 2018; Ames et al., 2019) which demonstrate how DES methods contribute to operational improvements. In subsequent years, research focusing on more specific topics such as patient experience and resource planning has increased, but these studies have received fewer citations. Overall, simulation applications in emergency departments have evolved over time, offering solutions to more specific problems.

Table 1. Top 10 most cited articles

Authors	Year	Title	Source	Cited By
Duguay and Chetouane	2007	Modeling and ımproving emergency department systems using discrete event simulation	Sımulatıon-Transactıons of The Socıety for Modelıng And Sımulatıon Internatıonal	153
Hoot etc.	2008	Forecasting emergency department crowding: a discrete event simulation	Annals of Emergency Medıcıne	147
Eitel etc.	2010	Improvıng servıce qualıty by understandıng emergency department flow: a whıte paper and posıtıon statement prepared for the amerıcan academy of emergency medıcıne	Journal of Emergency Medıcıne	144
Abo-Hamad, and Arisha	2013	Simulation-Based Framework to Improve Patient Experience in An Emergency Department	European Journal of Operatıonal Research	132
Connelly and Bair	2004	Discrete Event Simulation of Emergency Department Activity: A Platform for System-Level Operations Research	Academic Emergency Medicine	131
Gul and Guneri	2015	A Comprehensive Review of Emergency Department Simulation Applications for Normal and Disaster Conditions	Computers & Industrial Engineering	117
Eldabi, Paul, Young	2007	Simulation Modelling in Healthcare: Reviewing Legacies and Investigating Futures	Journal of The Operatıonal Research Socıety	109
Helm etc.	2011	Design And Analysis of Hospital Admission Control for Operational Effectiveness	Productıon and Operatıons Managemen	93
Hung etc.	2007	Computer Modeling of Patient Flow in A Pediatric Emergency Department Using Discrete Event Simulation	Pediatric Emergency Care	86
Zeinali etc.	2015	Resource Planning in The Emergency Departments: A Simulation-Based Metamodeling Approach	Simulation Modelling Practice and Theory	83

This bibliometric analysis presents the current status and future trends for studies involving DES in addition to emergency department studies involving simulation. The analysis reveals the academic expansion in improving ED patient flow, service optimization and reducing waiting times in EDs. The USA, Canada and the UK are the top three countries in terms of research output. After these countries, Türkiye ranks 4th. The analysis emphasizes that research tends to focus on finding specific solutions to emergency department problems. In addition, the critical importance of collaborations between developed and developing countries is emphasized. The inclusion of current methods such as machine learning and artificial intelligence in future research and interdisciplinary collaborations are expected to provide opportunities for researchers to improve emergency department patient flow.

5. Conclusion

This study conducts a bibliometric analysis of academic works in the fields of emergency departments and simulation, highlighting key trends and developmental processes within the topic. The keyword analysis reveals that "simulation," "emergency department," and "emergency medicine" are frequently interconnected, with research in this area primarily focusing on patient flow, congestion management, and improving service quality. Bibliographic coupling analyses shed light on the influence of fundamental works in emergency department and simulation management, demonstrating how DES methods contribute to operational improvements. It has been observed that most of the studies were published in the past few years, with a notable increase in publications between 2020-2023. A total of 1507 articles on emergency departments and simulation have been published in the Web of Science

database. The majority of these 1507 articles have been published in high-impact journals, which have provided a broader dissemination, reach. Additionally, English-language articles dominate this field, and it has been found that developed countries contribute more to the literature. Nearly 50% of the articles have been published in journals such as "Emergency Medicine" (339, 22.5%), "Health Care Science Services" (217, 14.4%), and "General Internal Medicine" (173, 11.5%). The most cited journals in this field are "Academic Emergency Medicine" (n=2033), "Annals of Emergency Medicine" (n=1009), and "Journal of Surgical Education" (n=695). Walter J. Eppich has been identified as the most cited author (2). Citation analysis of authors and institutions shows that important academic figures such as Rudolph et al. (2008), Patterson et al. (2013) and Patterson et al. (2013) stand out, while institutions like Harvard University, Northwestern University, and Massachusetts General Hospital lead in collaboration and scientific productivity in this field. The inter-country analysis highlights the dominant role of the U.S. and the increasing contributions of Canada, the U.K., and Türkiye in this field.

As a result, simulation applications in emergency departments offer solutions to more specific problems and that academic collaborations increase the efficiency in this field. It is anticipated that in the future, interdisciplinary collaboration and data sharing will become more important, and more comprehensive solutions will need to be developed. Additionally, specific simulation techniques like DES are increasingly being used in emergency department simulations, and these methods are expected to remain a significant focus in future research. In conclusion, it is highlighted that research in the field of emergency departments and simulation reveals specific trends that gaps in this field should be filled with further research, and that developing international collaborations will contribute to scientific progress. This study also suggests that stronger collaboration between developed and developing countries will contribute to scientific advancements in this field.

Author Contributions

The percentages of the authors' contributions are presented below. All authors reviewed and approved the final version of the manuscript.

	Z.F.A	Ş.Z.
C	60	40
D	60	40
S	60	40
DCP	60	40
DAI	60	40
L	60	40
W	60	40
CR	60	40
SR	60	40
PM	60	40
FA	60	40

C= concept, D= design, S= supervision, DCP= data collection and/or processing, DAI= data analysis and/or interpretation, L= literature search, W= writing, CR= critical review, SR= submission and revision, PM= project management, FA= funding acquisition.

Conflict of Interest

The author declared that there is no conflict of interest.

Ethical Consideration

Ethics committee approval was not required for this study because of there was no study on animals or humans.

References

Abo-Hamad, W., & Arisha, A. (2013). Simulation-based framework to improve patient experience in an emergency department. *European Journal of Operational Research*, *224*(1), 154–166. https://doi.org/10.1016/j.ejor.2012.07.028

Ames, S. G., Davis, B. S., Marin, J. R., Fink, E. L., Olson, L. M., Gausche-Hill, M., & Kahn, J. M. (2019). Emergency department pediatric readiness and mortality in critically ill children. *Pediatrics*, *144*(3), Article e20190568. https://doi.org/10.1542/peds.2019-0568

Auerbach, M., Gausche-Hill, M., & Newgard, C. D. (2018). National pediatric readiness project: Making a difference through collaboration, simulation, and measurement of the quality of pediatric emergency care. *Clinical Pediatric Emergency Medicine*, *19*(3), 233–242. https://doi.org/10.1016/j.cpem.2018.08.008

Brenner, S., Zeng, Z., Liu, Y., Wang, J., Li, J., & Howard, P. K. (2010). Modeling and analysis of the emergency department at University of Kentucky Chandler Hospital using simulations. *Journal of Emergency Nursing*, *36*(4), 303–310. https://doi.org/10.1016/j.jen.2009.07.018

Capella, J., Smith, S., Philp, A., Putnam, T., Gilbert, C., Fry, W., Harvey, E., Wright, A., Henderson, K., Baker, D., Ranson, S., & ReMine, S. (2010). Teamwork training improves the clinical care of trauma patients. *Journal of Surgical Education*, *67*(6), 439–443. https://doi.org/10.1016/j.jsurg.2010.06.006

Cheng, A., Auerbach, M., Hunt, E. A., Chang, T. P., Pusic, M., Nadkarni, V., & Kessler, D. (2014). Designing and conducting

simulation-based research. *Pediatrics*, *133*(6), 1091–1101. https://doi.org/10.1542/peds.2013-3267

Connelly, L. G., & Bair, A. E. (2004). Discrete event simulation of emergency department activity: A platform for system-level operations research. *Academic Emergency Medicine*, *11*(11), 1177–1185. https://doi.org/10.1197/j.aem.2004.08.021

Doğan, G., & İpek, H. (2021). The evolution of hypospadias publications: A bibliometric approach. *Revista Internacional de Andrología*, *19*(4), 224–233. https://doi.org/10.1016/j.androl.2020.03.002

Duguay, C., & Chetouane, F. (2007). Modeling and improving emergency department systems using discrete event simulation. *Simulation*, *83*(4), 311–320. https://doi.org/10.1177/0037549707083111

Duncan, G., Schabbing, M. B., & Gable, B. (2024). Multidisciplinary simulation-based verbal de-escalation training improves staff knowledge and clinical environment in an urban emergency department. *Academic Psychiatry*, *48*(6), 603–607. https://doi.org/10.1007/s40596-024-02051-0

Eitel, D. R., Rudkin, S. E., Malvehy, M. A., Killeen, J. P., & Pines, J. M. (2010). Improving service quality by understanding emergency department flow: A White Paper and position statement prepared for the American Academy of Emergency Medicine. *The Journal of Emergency Medicine*, *38*(1), 70–79. https://doi.org/10.1016/j.jemermed.2008.03.038

Eldabi, T., Paul, R. J., & Young, T. (2007). Simulation modelling in healthcare: Reviewing legacies and investigating futures. *Journal of the Operational Research Society*, *58*(2), 262–270. https://doi.org/10.1057/palgrave.jors.2602222

Furian, N., Neubacher, D., O'Sullivan, M., Walker, C., & Pizzera, C. (2018). GEDMod–Towards a generic toolkit for emergency department modeling. *Simulation Modelling Practice and Theory*, *87*, 239–273. https://doi.org/10.1016/j.simpat.2018.07.010

Golpinar, M., & Demir, E. (2020). Global research output of the cerebellum: Yesterday, today, and tomorrow. *Journal of the Anatomical Society of India*, *69*(3), 155–165. https://doi.org/10.4103/JASI.JASI_114_20

Golpinar, M., & Ekici, M. (2023). Global research productivity and publication trends in vesicoureteral reflux: A bibliometric analysis. *Minerva Pediatrica*, *75*(2), 270–281. https://doi.org/10.23736/s2724-5276.21.06278-9

Gul, M., & Guneri, A. F. (2015). A discrete event simulation model of an emergency department network for earthquake conditions. In *2015 6th International Conference on Modeling, Simulation, and Applied Optimization (ICMSAO)* (pp. 1–6). IEEE. https://doi.org/10.1109/ICMSAO.2015.7152244

Helm, J. E., AhmadBeygi, S., & Van Oyen, M. P. (2011). Design and analysis of hospital admission control for operational effectiveness. *Production and Operations Management*, *20*(3), 359–374. https://doi.org/10.1111/j.1937-5956.2011.01231.x

Hoot, N. R., LeBlanc, L. J., Jones, I., Levin, S. R., Zhou, C., Gadd, C. S., & Aronsky, D. (2008). Forecasting emergency department crowding: A discrete event simulation. *Annals of Emergency Medicine*, *52*(2), 116–125. https://doi.org/10.1016/j.annemergmed.2007.12.011

Hung, G. R., Whitehouse, S. R., O'Neill, C., Gray, A. P., & Kissoon, N. (2007). Computer modeling of patient flow in a pediatric emergency department using discrete event simulation. *Pediatric Emergency Care*, *23*(1), 5–10. https://doi.org/10.1097/PEC.0b013e31802c611e

Kayir, S., & Kisa, A. (2021). The evolution of the regional anesthesia: A holistic investigation of global outputs with bibliometric analysis between 1980-2019. *Korean Journal of Pain*, *34*(1), 82–93. https://doi.org/10.3344/kjp.2021.34.1.82

Kiraz, M., & Demir, E. (2020). A bibliometric analysis of publications on spinal cord injury during 1980-2018. *World Neurosurgery*, *136*, e504–e513. https://doi.org/10.1016/j.wneu.2020.01.064

Kuo, R. J., Song, P. F., Nguyen, T. P. Q., & Yang, T. J. (2023). An application of multi-objective simulation optimization to medical resource allocation for the emergency department in Taiwan. *Annals of Operations Research*, *326*(1), 199–221. https://doi.org/10.1007/s10479-023-05374-7

López-López, J. A., Van den Noortgate, W., Tanner-Smith, E. E., Wilson, S. J., & Lipsey, M. W. (2017). Assessing meta-regression methods for examining moderator relationships with dependent effect sizes: A Monte Carlo simulation. *Research Synthesis Methods*, *8*(4), 435–450. https://doi.org/10.1002/jrsm.1254

Mistarihi, M. Z., AL-Tahat, M. D., & AL-Nimer, S. H. (2023). Improving process efficiency at pediatric hospital emergency department using an integrated Six-Sigma simulation methodology. *Processes*, *11*(2), Article 399. https://doi.org/10.3390/pr11020399

Patterson, M. D., Geis, G. L., Falcone, R. A., LeMaster, T., & Wears, R. L. (2013). In situ simulation: Detection of safety threats and teamwork training in a high risk emergency department. *BMJ Quality & Safety*, *22*(6), 468–477. https://doi.org/10.1136/bmjqs-2012-000942

Rabbani, M., Farshbaf-Geranmayeh, A., & Yazdanparast, R. (2018). A simulation optimization approach for integrated resource allocation in an emergency department, pharmacy, and lab. *Intelligent Decision Technologies*, *12*(2), 187–212. https://doi.org/10.3233/IDT-18032

Rehman, A. U., Usmani, Y. S., Mian, S. H., Abidi, M. H., & Alkhalefah, H. (2023). Simulation and goal programming approach to improve public hospital emergency department resource allocation. *Systems*, *11*(9), Article 467. https://doi.org/10.3390/systems11090467

Rudolph, J. W., Simon, R., Raemer, D. B., & Eppich, W. J. (2008). Debriefing as formative assessment: Closing performance gaps in medical education. *Academic Emergency Medicine*, *15*(11), 1010–1016. https://doi.org/10.1111/j.1553-2712.2008.00248.x

Salway, R., Valenzuela, R., Shoenberger, J., Mallon, W., & Viccellio, A. (2017). Emergency department (ED) overcrowding: Evidence-based answers to frequently asked questions. *Revista Médica Clínica Las Condes*, *28*(2), 213–219. https://doi.org/10.1016/j.rmclc.2017.04.008

Tian, Y., Osgood, N. D., Stempien, J., Onaemo, V., Danyliw, A., Fast, G., Liu, J., & Basran, J. (2023). The impact of alternate level of care on access block and operational strategies to reduce emergency wait times: A multi-center simulation study. *Canadian Journal of Emergency Medicine*, *25*(7), 608–616. https://doi.org/10.1007/s43678-023-00514-1

Zeinali, F., Mahootchi, M., & Sepehri, M. M. (2015). Resource planning in the emergency departments: A simulation-based metamodeling approach. *Simulation Modelling Practice and Theory*, *53*, 123–138. https://doi.org/10.1016/j.simpat.2015.02.002

Black Sea Journal of Engineering and Science
doi: 10.34248/bsengineering.1985379

Open Access Journal
e-ISSN: 2619 – 8991

Research Article
Volume 9 - Issue 5: 2345-2353 / September 2026

HS-SPME-GC/MS-BASED VOLATILE PROFILING AND CHEMOMETRIC DISCRIMINATION OF SELECTED HERBAL TEAS

Selçuk KÜÇÜKAYDIN[1]*

[1]*Muğla Sıtkı Koçman University, Köyceğiz Vocational School of Health Services, Department of Medical Services and Techniques, 48800, Köyceğiz-Muğla, Türkiye*

Abstract: Herbal teas prepared from aromatic plants possess complex volatile profiles associated with their characteristic sensory properties. In this study, the headspace volatile profiles of aqueous infusions prepared from *Teucrium polium*, *Mentha pulegium*, *Rosmarinus officinalis*, *Lavandula stoechas*, and *Ocimum basilicum* were investigated using headspace solid-phase microextraction coupled with gas chromatography–mass spectrometry (HS-SPME-GC/MS). Three independent infusions were prepared for each species, resulting in 15 individual volatile profiles, which were evaluated by principal component analysis (PCA) and hierarchical cluster analysis (HCA). A total of 115 volatile compounds were tentatively identified across the five species. Monoterpenoids were the predominant chemical group in *M. pulegium* (70.17 ± 0.20%), *R. officinalis* (81.80 ± 0.04%), *L. stoechas* (96.95 ± 0.08%), and *O. basilicum* (77.60 ± 0.35%), whereas *T. polium* showed a more heterogeneous profile comprising substantial proportions of monoterpenoids (49.95 ± 0.16%) and sesquiterpene hydrocarbons (31.32 ± 0.24%). The principal volatile constituents were carvacrol and germacrene D in *T. polium*; pulegone, piperitone oxide, limonene, and 1,8-cineole in *M. pulegium*; 1,8-cineole, borneol, and camphor in *R. officinalis*; fenchone and camphor in *L. stoechas*; and linalool, eugenol, and methyl chavicol in *O. basilicum*. The first two principal components accounted for 66.44% of the total variance. The three independently prepared infusions of each species formed compact groups in the PCA score plot, with *T. polium* showing the most distinct separation. PCA associated *M. pulegium* particularly with pulegone-, piperitone oxide-, and piperitenone oxide-related variation, whereas HCA grouped the three preparations of each species together and indicated the closest species-level similarity between *R. officinalis* and *L. stoechas*. Overall, HS-SPME-GC/MS combined with PCA and HCA provided a useful exploratory approach for the comparative characterization and species-related differentiation of herbal tea headspace volatile profiles under standardized infusion conditions.

Keywords: Herbal tea, Volatile compounds, HS-SPME-GC/MS, Chemometric analysis, Lamiaceae

***Corresponding author:** Muğla Sıtkı Koçman University, Köyceğiz Vocational School of Health Services, Department of Medical Services and Techniques, 48800, Köyceğiz-Muğla, Türkiye
E mail: selcukkucukaydin@mu.edu.tr (S. KÜÇÜKAYDIN)
Selçuk KÜÇÜKAYDIN https://orcid.org/0000-0001-8538-6528

Received: July 02, 2026
Accepted: August 08, 2026
Published: September 15, 2026

Cite as: Küçükaydın, S. (2026). HS-SPME-GC/MS-based volatile profiling and chemometric discrimination of selected herbal teas. *Black Sea Journal of Engineering and Science*, 9(5), 2345-2353.

1. Introduction

Herbal teas are widely consumed due to their distinctive sensory properties, traditional uses, and plant-derived chemical composition (McKay and Blumberg, 2006; Poswal et al., 2019). Among the sensory attributes influencing consumer acceptance, aroma is of particular importance, as it is among the first characteristics perceived during preparation and consumption (Zhu et al., 2018). The aroma profile of herbal infusions is mainly associated with volatile organic compounds, including monoterpenes, sesquiterpenes, alcohols, aldehydes, ketones, esters, and other low-molecular-weight constituents (Yang et al., 2013; Zeng et al., 2025). The qualitative and quantitative composition of these compounds may vary depending on several factors, including plant species, chemotype, geographical origin, environmental conditions, plant part used, harvesting period, drying process, and preparation method (Figueiredo et al., 2008).

Plants belonging to the Lamiaceae family are particularly notable for their aromatic properties and rich volatile compound contents (Başer and Kırımer, 2018). *Ocimum basilicum* L., *Teucrium polium* L., *Mentha pulegium* L., *Rosmarinus officinalis* L., and *Lavandula stoechas* L. are aromatic plants used in different regions as culinary herbs, herbal teas, or components of traditional preparations (Uritu et al., 2018). Previous studies have shown that these species may contain diverse volatile constituents, particularly oxygenated monoterpenes and monoterpene hydrocarbons. Compounds such as linalool, estragole, eucalyptol, camphor, fenchone, pulegone, menthone, α-pinene, β-pinene, and terpinen-4-ol have frequently been reported in different members of this family (Bozin et al., 2007; Mahboubi and Haghi, 2008; Telci et al., 2006). However, the relative abundance of these compounds may vary considerably depending on the plant material, growing conditions, and analytical approach employed (Figueiredo et al., 2008).

This work is licensed (CC BY-NC 4.0) under Creative Commons Attribution 4.0 International License

Most of the available studies on these plants have focused on the analysis of essential oils obtained by hydrodistillation or extracts prepared using organic solvents (Bakkali et al., 2008; Maggio et al., 2016; Bahramikia et al., 2022). However, the volatile fraction recovered from herbal infusions can exhibit qualitative and semiquantitative differences when compared with the essential oil obtained directly from the corresponding plant material (Tschiggerl and Bucar, 2010). During brewing, the transfer of volatile constituents from plant material to the aqueous infusion and subsequently to the headspace may be affected by brewing temperature and time, the solid-to-water ratio, infusion matrix composition, and compound-specific physicochemical properties (Wright et al., 2007; Sánchez-López et al., 2020; Göksu Sürücü et al., 2024). Therefore, the direct characterization of volatile compounds in herbal infusions is important for providing a more realistic representation of the chemical profile encountered by consumers during tea preparation and consumption.

Headspace solid-phase microextraction coupled with gas chromatography–mass spectrometry (HS-SPME-GC/MS) is a widely used and suitable analytical approach for the characterization of volatile compounds in complex food and plant matrices (Kataoka et al., 2000). This technique enables the solvent-free extraction of compounds present in the headspace, requires limited sample preparation, and provides high sensitivity for the detection of a broad range of volatile and semi-volatile compounds (Chen et al., 2020; Djebili et al., 2022). The interpretation of chromatographic datasets containing numerous volatile compounds can be enhanced by multivariate statistical analysis. Principal component analysis (PCA) enables the visualization of similarities and differences among samples according to their multivariate volatile profiles, whereas hierarchical cluster analysis (HCA) groups samples on the basis of compositional similarity. In studies combining HS-SPME-GC/MS with chemometric analysis, PCA and HCA have been successfully used to differentiate samples with distinct volatile profiles and to identify variables associated with sample separation through PCA loading patterns (Lin et al., 2013; Duru et al., 2021). Therefore, the combined application of HS-SPME-GC/MS, PCA, and HCA may provide a useful framework for revealing species-related volatile patterns among herbal tea samples.

Although the volatile compositions of several Lamiaceae species have previously been investigated individually, direct comparative studies of aqueous infusions prepared from *O. basilicum*, *T. polium*, *M. pulegium*, *R. officinalis*, and *L. stoechas* under a unified experimental protocol remain limited. The originality of the present study lies in the side-by-side evaluation of these five herbal teas collected from Muğla Province using identical brewing and HS-SPME-GC/MS conditions, with three independently prepared infusions analyzed for each species. This standardized design reduces methodological variation and enables both within-species consistency and interspecies differences in the headspace volatile profiles to be evaluated. Therefore, the present study aimed to characterize the volatile profiles of the five herbal teas and to determine the volatile compounds most strongly associated with their species-related differentiation using PCA and HCA.

2. Materials and Methods

2.1. Plant Materials

The aerial parts of *Ocimum basilicum* L., *Teucrium polium* L., *Mentha pulegium* L., *Rosmarinus officinalis* L., and *Lavandula stoechas* L. were collected from selected locations in Muğla Province, Türkiye, including Menteşe, and Köyceğiz, between May and July 2024. Following collection, the plant materials were dried in the shade at room temperature. The dried samples were stored in a dry environment until further analysis.

2.2. Preparation of Herbal Infusions

Herbal infusions were prepared under standardized conditions. For each plant species, three independent infusions were prepared from separate aliquots of the dried material (n = 3). For each preparation, 10.0 g of dried plant material was mixed with 100 mL of distilled water preheated to 80 °C. The mixtures were covered and allowed to infuse for 10 min and were then filtered through Whatman No. 4 filter paper. Each freshly prepared infusion was analyzed individually by HS-SPME-GC/MS immediately after filtration.

2.3. Headspace Solid-Phase Microextraction of Volatile Compounds

Volatile compounds of the herbal infusions were extracted using headspace solid-phase microextraction (HS-SPME), adapted from previously reported procedures for plant-derived matrices (Djebili et al., 2022). Freshly prepared infusion (5.0 mL) was placed in a 20 mL headspace vial, followed by the addition of sodium chloride (1.0 g). Each vial was closed with a PTFE/silicone septum cap and equilibrated at 50 °C for 15 min under magnetic stirring. After equilibration, a DVB/CAR/PDMS fiber (Supelco, Bellefonte, PA, USA) was introduced into the vial headspace and maintained above the sample for a further 15 min at 50 °C while stirring was continued. The fiber was then transferred directly to the GC injector, where the retained analytes were thermally desorbed. Each of the 15 independently prepared infusions was subjected to one HS-SPME-GC/MS measurement. Before use, the fiber was conditioned according to the manufacturer's recommendations, and procedural blanks were included to assess background signals and carry-over.

2.4. GC-MS Analysis

Chromatographic separation and mass spectrometric detection were carried out using a Varian Saturn 2100T gas chromatograph coupled with an ion-trap mass spectrometer (Varian Inc., Walnut Creek, CA, USA). The system was fitted with an Rxi-5Sil MS fused-silica capillary column (Restek, Bellefonte, PA, USA; 30 m × 0.25 mm internal diameter, 0.25 μm film thickness).

Helium was supplied as the carrier gas at a constant flow rate of 1.4 mL/min. Thermal desorption of the SPME fiber was performed in the injector operated at 220 °C under splitless conditions. The oven was programmed from 60 °C, held for 5 min, to 280 °C at 4 °C/min, followed by a final hold of 5 min. Electron ionization was applied at 70 eV. The ion-source and transfer-line temperatures were maintained at 200 °C and 290 °C, respectively. Full-scan mass spectra were recorded across an m/z range of 28–650 using a scan duration of 0.5 s and an interscan interval of 0.1 s.

Volatile compounds were identified by comparison of their mass spectra with the NIST 14 and Wiley mass spectral libraries. The proposed identifications were further supported by comparison of the experimentally calculated linear retention indices (LRIs) with literature values reported by Adams (Adams, 2017) and, where available, by co-injection with authentic reference standards. Linear retention indices were calculated using an n-alkane standard series ranging from C7 to C30. When available, the identity of selected compounds was additionally confirmed by co-injection with authentic standards.

2.5. Data Preprocessing and Chemometric Analysis

The chemometric data matrix consisted of 15 observations and 115 variables. Each observation represented one independently prepared infusion, corresponding to three preparations for each of the five plant species, whereas each variable represented one volatile compound listed in Supplementary Table 1. Because the relative peak areas within each chromatographic profile had already been normalized to a total of 100%, no additional total-sum normalization was applied.

Compounds that were not detected in a given infusion and compounds recorded at trace level ("tr") without a reliable numerical peak-area value were assigned a value of zero solely for chemometric analysis. Trace-level compounds were retained as "tr" in the descriptive data presented in Supplementary Tables 1 and 2.

Before multivariate analysis, the relative peak-area values were transformed using $\log10(x + 1)$ to reduce the disproportionate influence of highly abundant constituents while retaining the semiquantitative abundance structure of the volatile profiles. For PCA, the transformed variables were mean-centered. Autoscaling was not applied because it would have disproportionately weighted trace and very low-abundance compounds.

PCA was performed using scikit-learn version 1.8.0 in Python 3.13.5. The PCA score plot was used to evaluate the distribution and within-species consistency of the independently prepared infusions, whereas the loading coefficients were examined to identify volatile compounds associated with sample separation. For visual clarity, the PCA biplot displayed the 12 compounds with the largest loading magnitudes in the PC1–PC2 plane.

HCA was performed on the same $\log10(x + 1)$-transformed data matrix using Euclidean distance and Ward's linkage method in SciPy version 1.17.0. PCA scores and loadings are provided in Supplementary Tables 3 and 4, respectively.

3. Results

3.1. Volatile Compound Profiles of Herbal Tea Samples

The headspace volatile profiles of independently prepared herbal infusions of *Teucrium polium*, *Mentha pulegium*, *Rosmarinus officinalis*, *Lavandula stoechas*, and *Ocimum basilicum* were determined by HS-SPME-GC/MS. Three independent infusions were prepared for each species, resulting in 15 individual volatile profiles. Across the five species, a total of 115 volatile compounds were identified, including monoterpene hydrocarbons, monoterpenoids, sesquiterpene hydrocarbons, sesquiterpenoids, and other volatile constituents. At the species level, the number of detected compounds ranged from 39 in *R. officinalis* to 54 in *T. polium*. A total of 48, 50, and 51 compounds were detected in *M. pulegium*, *L. stoechas*, and *O. basilicum*, respectively. Mean relative peak areas and standard deviations are presented in Suplementary Table 1.

Monoterpenoids represented the predominant chemical class in the volatile profiles of *M. pulegium* (70.17 ± 0.20%), *R. officinalis* (81.80 ± 0.04%), *L. stoechas* (96.95 ± 0.08%), and *O. basilicum* (77.60 ± 0.35%). In contrast, *T. polium* exhibited a more heterogeneous volatile composition, comprising substantial proportions of monoterpenoids (49.95 ± 0.16%) and sesquiterpene hydrocarbons (31.32 ± 0.24%). The mean relative peak areas of sesquiterpene hydrocarbons were 4.95 ± 0.15% in *O. basilicum*, 2.64 ± 0.09% in *R. officinalis*, 1.14 ± 0.04% in *M. pulegium*, and 0.65 ± 0.03% in *L. stoechas*. Monoterpene hydrocarbons ranged from 0.40 ± 0.04% in *O. basilicum* to 22.47 ± 0.05% in *M. pulegium*.

The volatile profile of *T. polium* was characterized primarily by carvacrol (13.19 ± 0.11%), germacrene D (12.40 ± 0.09%), terpinen-4-ol (8.75 ± 0.09%), α-terpineol (5.93 ± 0.12%), caryophyllene oxide (4.17 ± 0.09%), trans-sabinene hydrate (4.04 ± 0.04%), verbenone (3.63 ± 0.02%), and β-caryophyllene (3.60 ± 0.05%). The simultaneous occurrence of substantial proportions of oxygenated monoterpenes and sesquiterpene hydrocarbons distinguished the *T. polium* profile from those of the other investigated species.

In *M. pulegium*, pulegone was the principal volatile constituent, with a mean relative peak area of 23.69 ± 0.10%. Other major constituents included piperitone oxide (15.44 ± 0.08%), limonene (13.97 ± 0.06%), 1,8-cineole (12.90 ± 0.05%), piperitenone oxide (8.55 ± 0.05%), β-pinene (4.23 ± 0.04%), linalool (3.57 ± 0.07%), and menthone (2.28 ± 0.07%). This profile was characterized by a combination of pulegone and several piperitone- and piperitenone-related oxygenated monoterpenes.

The volatile profile of *R. officinalis* was dominated by 1,8-

cineole (17.80 ± 0.03%), borneol (17.38 ± 0.04%), and camphor (16.76 ± 0.04%). Bornyl acetate (8.27 ± 0.06%), linalool (7.40 ± 0.04%), camphene (4.12 ± 0.03%), α-pinene (3.81 ± 0.06%), and verbenone (3.16 ± 0.05%) were also present at notable relative levels. Overall, oxygenated monoterpenes accounted for the major proportion of the *R. officinalis* headspace volatile profile.

Lavandula stoechas exhibited a distinctive fenchone-dominant profile. Fenchone accounted for 43.26 ± 0.07% of the mean relative peak area, followed by camphor (15.63 ± 0.07%), 1,8-cineole (10.18 ± 0.04%), bornyl acetate (10.15 ± 0.12%), fenchol (5.31 ± 0.10%), and fenchyl acetate (3.20 ± 0.13%). These compounds collectively represented the majority of the volatile profile and contributed to the particularly high proportion of monoterpenoids observed in this species.

The *O. basilicum* infusions were characterized by a pronounced predominance of linalool, which accounted for 65.25 ± 0.19% of the mean relative peak area. Eugenol (7.36 ± 0.07%), methyl chavicol (5.50 ± 0.05%), 1,8-cineole (4.42 ± 0.08%), β-caryophyllene (2.35 ± 0.13%), myroxide (1.62 ± 0.09%), guaiyl acetate (1.60 ± 0.06%), α-terpineol (1.58 ± 0.04%), bornyl acetate (1.34 ± 0.11%), and nerol (1.03 ± 0.06%) were also among the principal constituents. The high relative abundance of linalool clearly distinguished the *O. basilicum* profile from those of the other investigated herbal teas.

3.2. Chemometric Analysis of Volatile Compound Profiles

The relative peak-area data obtained from the 15 independently prepared herbal infusions were subjected to principal component analysis (PCA) and hierarchical cluster analysis (HCA) to evaluate within-species consistency and interspecies differences in the volatile profiles. The first two principal components explained 66.44% of the total variance, with PC1 and PC2 accounting for 35.98% and 30.47%, respectively (Figure 1A).

The PCA score plot showed compact grouping of the three independent preparations of each species in the PC1–PC2 plane. The three *T. polium* preparations were positioned on the positive side of PC1 and were clearly separated from the remaining species. The *M. pulegium* preparations formed a distinct group in the lower-left region and exhibited the most negative PC2 scores. The *R. officinalis* and *L. stoechas* preparations formed separate but relatively close groups in the upper-left region, whereas the *O. basilicum* preparations formed a distinct group in the lower-left region (Figure 1A). The compact within-species grouping indicated that the differences among species were greater than the variability among the independently prepared infusions under the conditions examined.

The PCA biplot indicated that the separation of *T. polium* along the positive PC1 direction was primarily associated with germacrene D, carvacrol, and terpinen-4-ol. The negative PC2 direction, toward which the *M. pulegium* preparations were oriented, was associated with pulegone, limonene, piperitone oxide, and piperitenone oxide. The upper-left region containing the *R. officinalis* and *L. stoechas* groups was associated mainly with camphor, fenchone, bornyl acetate, and 1,8-cineole. The position of the *O. basilicum* group in the lower-left region was oriented particularly toward linalool (Figure 1B). For visual clarity, Figure 1B displays the 12 volatile compounds with the largest loading magnitudes in the PC1–PC2 plane.

The HCA dendrogram supported the species-related grouping pattern observed in PCA (Figure 2). The three independently prepared infusions of each species initially clustered together, confirming the consistency of the species-level volatile profiles. At the species level, *R. officinalis* and *L. stoechas* formed the closest cluster, indicating comparatively similar overall volatile compositions. A second cluster was formed by *M. pulegium* and *O. basilicum*. These two broader clusters subsequently joined, whereas the *T. polium* cluster merged with the remaining species at a higher linkage distance, confirming that *T. polium* possessed the most distinct volatile profile among the species examined.

4. Discussion

The present study demonstrated that three independently prepared infusions of five Lamiaceae species produced distinct and internally consistent headspace volatile profiles under standardized infusion conditions. Although the investigated plants belong to the same botanical family, marked differences were observed in the relative distribution of monoterpenoids, sesquiterpenes, and other volatile constituents. The compact grouping of the independent preparations of each species in the chemometric analyses indicated that the observed interspecies differences were greater than the variability associated with infusion preparation. Nevertheless, the present results represent the volatile fraction released from aqueous infusions into the headspace rather than the composition of hydrodistilled essential oils. Direct quantitative comparison with essential-oil studies is therefore not appropriate because infusion conditions, aqueous-matrix effects, and headspace partitioning may alter the relative representation of individual compounds.

Teucrium polium showed the most distinct volatile profile among the investigated herbal teas, as demonstrated by the separation of all three independent preparations along the positive PC1 direction and their later clustering with the remaining samples in HCA. Carvacrol, germacrene D, terpinen-4-ol, α-terpineol, caryophyllene oxide, and β-caryophyllene were among the principal compounds associated with this differentiation.

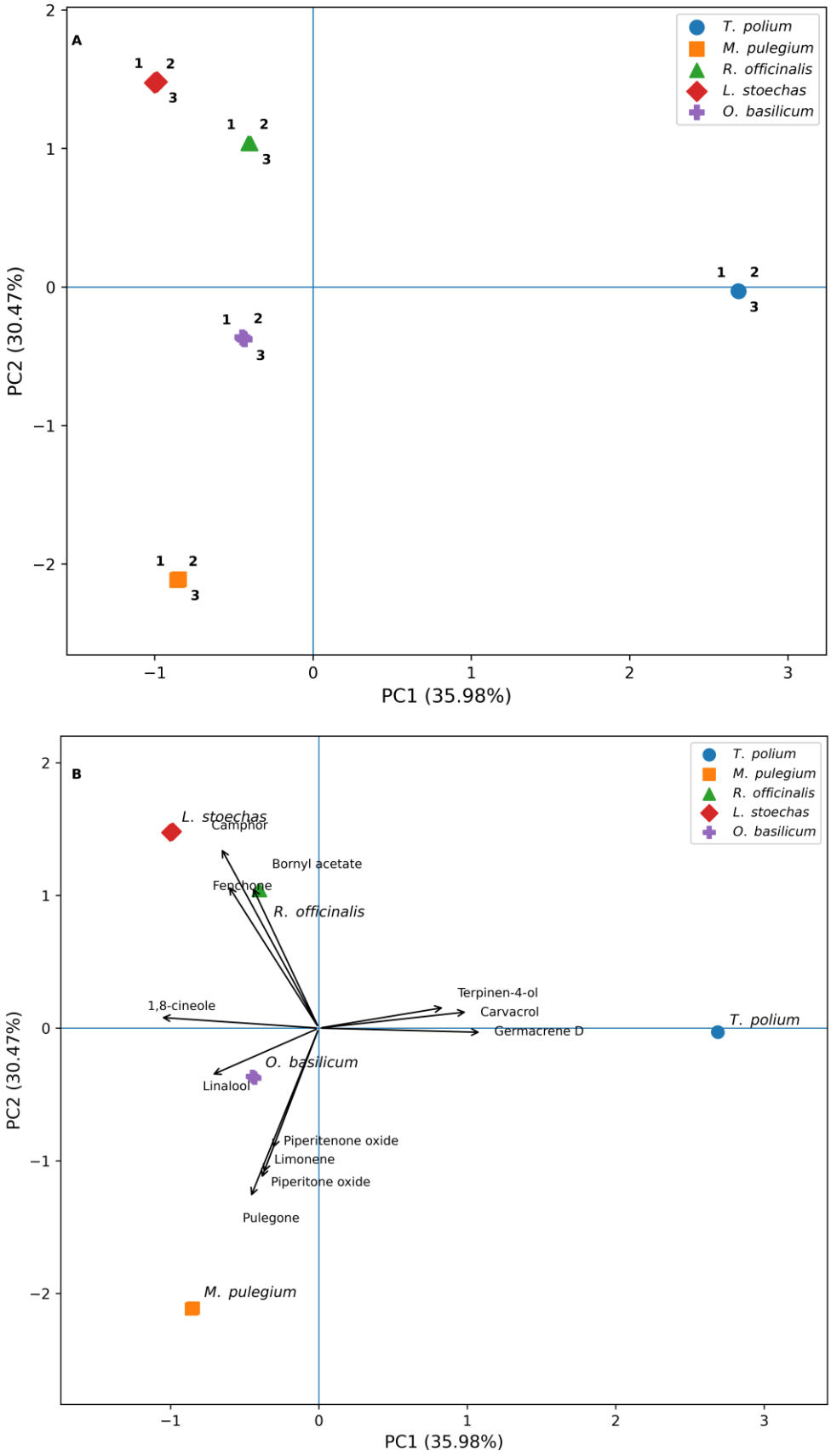


Figure 1. Principal component analysis of the headspace volatile profiles of 15 independently prepared herbal infusions. (A) PCA score plot showing three independent preparations for each plant species. (B) PCA biplot displaying the 12 volatile compounds with the largest loading magnitudes in the PC1–PC2 plane. PC1 and PC2 explained 35.98% and 30.47% of the total variance, respectively, accounting together for 66.44% of the total variance.

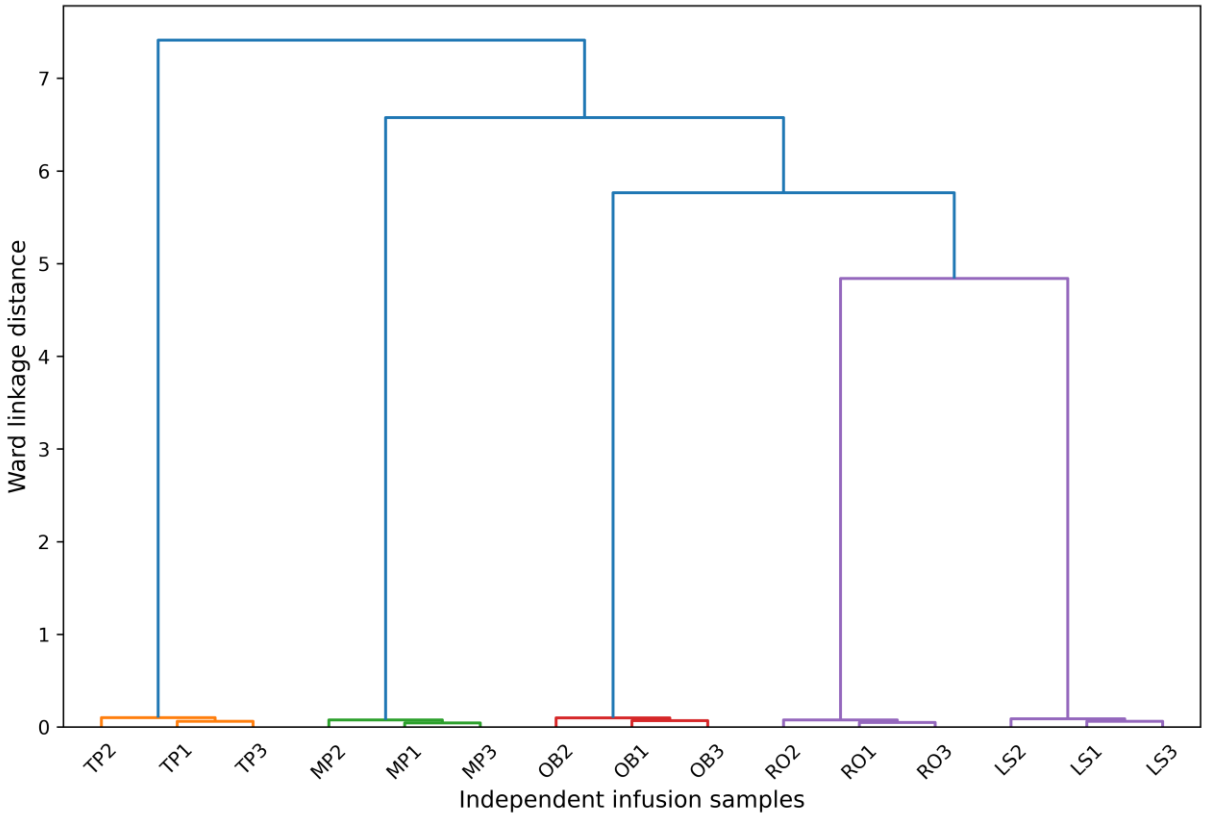


Figure 2. Hierarchical cluster analysis (HCA) dendrogram of the headspace volatile profiles of 15 independently prepared herbal infusions. The analysis was performed on log10(x + 1)-transformed relative peak-area data using Euclidean distance and Ward's linkage method. Sample codes: TP, *Teucrium polium*; MP, *Mentha pulegium*; RO, *Rosmarinus officinalis*; LS, *Lavandula stoechas*; and OB, *Ocimum basilicum*. The numbers 1–3 indicate the three independently prepared infusions of each species.

Previous studies have demonstrated substantial variability in the volatile composition of *T. polium*, with carvacrol, caryophyllene-type sesquiterpenes, germacrene derivatives, and oxygenated monoterpenes reported at different relative levels depending on population, plant material, chemotype, and extraction procedure (Candela et al., 2021; Chabane et al., 2021). The heterogeneous profile observed in the present herbal tea was therefore consistent with the chemical variability reported for this species. Carvacrol is of particular interest because antimicrobial and antioxidant properties have frequently been reported for this phenolic monoterpenoid and for carvacrol-containing *Teucrium* essential oils (Candela et al., 2021; Ultee et al., 1999). However, the occurrence of carvacrol and other potentially bioactive constituents in the infusion headspace should not be interpreted as direct evidence of biological activity because antimicrobial and antioxidant effects were not evaluated in the present study.

Mentha pulegium was characterized primarily by pulegone, piperitone oxide, piperitenone oxide, limonene, and 1,8-cineole, which were oriented toward the negative PC2 direction in the PCA biplot. Pulegone is frequently reported as a major constituent of *M. pulegium* essential oils, although limonene-, piperitone-, and piperitenone-related profiles have also been described in different populations (El Omari et al., 2025). The predominance of oxygenated monoterpenes in the present infusion was consistent with this general compositional tendency. The pulegone-, piperitone oxide-, piperitenone oxide-, and limonene-rich profile may also contribute to the strong mint-like and penetrating aromatic character generally associated with pennyroyal. Although *M. pulegium* has a history of traditional use as an aromatic herbal preparation, the predominance of pulegone is toxicologically relevant because hepatotoxic effects have been reported in experimental models at sufficiently high exposure levels (Zárybnický et al., 2018). Nevertheless, the relative headspace peak-area values obtained in the present study do not represent absolute concentrations, ingested doses, or consumer exposure and therefore cannot be used to draw conclusions regarding the safety of the prepared infusion.

The close positioning of *Rosmarinus officinalis* and *Lavandula stoechas* in both PCA and HCA reflected their generally oxygenated-monoterpene-rich volatile profiles. Nevertheless, the two species retained clearly distinguishable dominant compositions. *R. officinalis* was characterized mainly by 1,8-cineole, borneol, camphor, and bornyl acetate, whereas *L. stoechas* showed a pronounced fenchone-dominant profile together with camphor, 1,8-cineole, bornyl acetate, and fenchyl acetate. Similar terpenoid groups have frequently been reported

in rosemary and *L. stoechas* essential oils, although their relative proportions may vary according to geographical origin, plant part, phenological stage, and extraction conditions (Rafya et al., 2024; Sevindik et al., 2025). The abundance of 1,8-cineole, camphor, borneol, fenchone, and bornyl acetate is consistent with the fresh, penetrating, woody, and camphoraceous aromatic characteristics commonly associated with rosemary and *L. stoechas* (Benabdelkader et al., 2011; Tschiggerl and Bucar, 2010). Several of these oxygenated monoterpenes have also been investigated for biological properties. In particular, isolated 1,8-cineole has been studied for its anti-inflammatory effects, while rosemary- and lavender-derived preparations have been associated with antimicrobial and antioxidant activities (Juergens et al., 2003; Rafya et al., 2024; Sevindik et al., 2025). However, these literature-based associations cannot be directly extrapolated to the present infusions because neither biological activity nor absolute compound concentrations were determined.

The *Ocimum basilicum* herbal tea was distinguished by its high relative abundance of linalool, together with methyl chavicol and eugenol. Linalool-rich and methyl chavicol-rich basil chemotypes are widely described in the literature, and eugenol- or methyleugenol-containing profiles further contribute to the chemical diversity of *O. basilicum* (Dharsono et al., 2022; Wirtu et al., 2024). In the PCA biplot, the three *O. basilicum* preparations were oriented toward linalool, whereas HCA placed the *O. basilicum* cluster closer to the *M. pulegium* cluster than to the other species. This pattern indicates that HCA reflects the overall similarity structure of the complete volatile dataset, whereas the PCA biplot highlights the variables contributing most strongly to variation along the first two principal components. Linalool is widely associated with floral, sweet, and citrus-like odor characteristics and is considered an important contributor to the aroma of linalool-rich basil chemotypes. Eugenol and methyl chavicol may additionally contribute clove-like, spicy, sweet, and anise-like notes (Brindisi et al., 2025; Patel et al., 2021). Although linalool and eugenol have been associated with several biological activities, their presence in the headspace profile does not by itself demonstrate the biological efficacy of the prepared herbal infusion.

Overall, PCA and HCA provided complementary exploratory tools for evaluating both within-species consistency and interspecies differences among the herbal tea samples. The PCA score plot showed compact grouping of the three independent preparations of each species, while the biplot associated *T. polium* with carvacrol-, germacrene D-, and terpinen-4-ol-related variation; *M. pulegium* with pulegone- and piperitone-related variation; *R. officinalis* and *L. stoechas* with cineole-, camphor-, fenchone-, and bornyl acetate-related variation; and *O. basilicum* with linalool-related variation. HCA similarly grouped the three independent preparations of each species together and indicated the closest species-level similarity between *R. officinalis* and *L. stoechas*. Nevertheless, the chemometric findings should still be considered exploratory because the samples represented a single geographical region and harvest period, and no external sample set was available for validation.

The present study has several methodological limitations. A single standardized brewing condition (80 °C for 10 min) was applied to all samples to enable direct interspecies comparison; however, the effects of alternative brewing temperatures and infusion times on the extraction and headspace partitioning of individual volatile compounds were not evaluated. In addition, although three independent infusions were prepared for each species, each infusion was subjected to a single HS-SPME-GC/MS measurement, and analytical repeatability could therefore not be evaluated separately from preparation variability. The relative peak-area data were semiquantitative, and neither absolute concentrations, odor activity values, nor sensory responses were determined. Future studies should examine different temperature–time combinations, replicate HS-SPME measurements, multiple independent plant collections, broader geographical and seasonal sampling, targeted quantification, and sensory or GC–olfactometry analyses.

5. Conclusion

This study demonstrated that standardized infusion preparation combined with HS-SPME-GC/MS and chemometric analysis can reveal distinct headspace volatile profiles among herbal teas prepared from five Lamiaceae species. The independently prepared infusions of each species showed compact grouping in PCA and HCA, indicating that the observed interspecies differences exceeded the variability associated with infusion preparation under the conditions examined. *Teucrium polium* was differentiated mainly by carvacrol-, germacrene D-, and terpinen-4-ol-related variation; *Mentha pulegium* by pulegone and piperitone derivatives; *Rosmarinus officinalis* and *Lavandula stoechas* by oxygenated monoterpenes such as 1,8-cineole, camphor, fenchone, and bornyl acetate; and *Ocimum basilicum* by its linalool-dominant profile.

The combined analytical and chemometric approach may be useful for comparative characterization and preliminary batch-level assessment of herbal tea volatile profiles. However, the findings are limited to the investigated samples, geographical origin, harvest period, and brewing conditions and should not be interpreted as validation of species authentication markers. Future studies should include multiple independent plant collections, broader geographical and seasonal sampling, replicate HS-SPME/GC-MS measurements, different brewing temperature–time combinations, targeted quantitative analysis, and sensory or GC–olfactometry evaluation.

As the present chemometric evaluation was based on the analyzed profiles of the selected samples, further studies

including independent biological replicates, different harvest periods, geographical origins, and sensory evaluation would be valuable for confirming the stability and practical relevance of the observed volatile patterns.

Author Contributions

The percentages of the author's contributions are presented below. The author reviewed and approved the final version of the manuscript.

	S.K.
C	100
D	100
S	100
DCP	100
DAI	100
L	100
W	100
CR	100
SR	100
PM	100
FA	100

C= concept, D= design, S= supervision, DCP= data collection and/or processing, DAI= data analysis and/or interpretation, L= literature search, W= writing, CR= critical review, SR= submission and revision, PM= project management, FA= funding acquisition.

Conflict of Interest

The author declared that there is no conflict of interest.

Ethical Consideration

Ethics committee approval was not required for this study because of there was no study on animals or humans.

References

Adams, R. P. (2017). *Identification of essential oil components by gas chromatography/mass spectrometry, ed. 4.1*. Allured Publishing.

Bahramikia, S., Gavyar, P. H. H., & Yazdanparast, R. (2022). Teucrium polium L: An updated review of phytochemicals and biological activities. *Avicenna Journal of Phytomedicine*, *12*(3), 224. https://doi.org/10.22038/AJP.2021.19155

Bakkali, F., Averbeck, S., Averbeck, D., & Idaomar, M. (2008). Biological effects of essential oils – A review. *Food and Chemical Toxicology*, *46*(2), 446–475. https://doi.org/10.1016/J.FCT.2007.09.106

Benabdelkader, T., Zitouni, A., Guitton, Y., Jullien, F., Maitre, D., Casabianca, H., Legendre, L., & Kameli, A. (2011). Essential oils from wild populations of algerian lavandula stoechas L.: Composition, chemical variability, and in vitro biological properties. *Chemistry and Biodiversity*, *8*(5), 937–953. https://doi.org/10.1002/CBDV.201000301.

Bozin, B., Mimica-Dukic, N., Samojlik, I., & Jovin, E. (2007). Antimicrobial and Antioxidant Properties of Rosemary and Sage (Rosmarinus officinalis L. and Salvia officinalis L., Lamiaceae) Essential Oils. *Journal of Agricultural and Food Chemistry*, *55*(19), 7879–7885. https://doi.org/10.1021/JF0715323

Brindisi, L. J., O'Brien, R., Hayes, B. K., Kotwal, S., Wu, Q., Simon, J. E., & Tepper, B. J. (2025). Relationship between sensory perceptions and volatile and phenolic compounds of fresh basil (Ocimum basilicum L.) evaluated by multivariate statistics. *Journal of Food Science*, *90*(4), e70194. https://doi.org/10.1111/1750-3841.70194.

Candela, R. G., Rosselli, S., Bruno, M., & Fontana, G. (2021). A Review of the Phytochemistry, Traditional Uses and Biological Activities of the Essential Oils of Genus Teucrium. *Planta Medica*, *87*(6), 432–479. https://doi.org/10.1055/A-1293-5768

Chabane, S., Boudjelal, A., Napoli, E., Benkhaled, A., & Ruberto, G. (2021). Phytochemical composition, antioxidant and wound healing activities of Teucrium polium subsp. capitatum (L.) Briq. essential oil. *Journal of Essential Oil Research*, *33*(2), 143–151. https://doi.org/10.1080/10412905.2020.1842260

Chen, L. X., Lai, Y. F., Zhang, W. X., Cai, J., Hu, H., Wang, Y., Zhao, J., & Li, S. P. (2020). Comparison of volatile compounds in different parts of fresh Amomum villosum Lour. From different geographical areas using cryogenic grinding combined HS-SPME-GC-MS. *Chinese Medicine (United Kingdom)*, *15*(1), 97. https://doi.org/10.1186/S13020-020-00377-Z.

Dharsono, H. D. A., Putri, S. A., Kurnia, D., Dudi, D., & Satari, M. H. (2022). Ocimum Species: A Review on Chemical Constituents and Antibacterial Activity. *Molecules*, *27*(19), 6350. https://doi.org/10.3390/MOLECULES27196350.

Djebili, S., Taş, M., Bouguerra, A., Kucukaydin, S., Ceylan, O., Duru, M. E., & Barkat, M. (2022). Volatile compound profile and essential oil composition of three wild Algerian aromatic plants with their antioxidant and antibiofilm activities. *Journal of Food Measurement and Characterization*, *16*(2), 987–999. https://doi.org/10.1007/S11694-021-01220-1.

Duru, M. E., Taş, M., Çayan, F., Küçükaydın, S., & Tel-Çayan, G. (2021). Characterization of volatile compounds of Turkish pine honeys from different regions and classification with chemometric studies. *European Food Research and Technology,* *247*(10), 2533–2544. https://doi.org/10.1007/S00217-021-03817-8

El Omari, N., Aguerd, O., Balahbib, A., El Menyiy, N., Amanullah, M., Chew, J., Ming, L. C., & Bouyahya, A. (2025). Expediting multiple biological properties of main bioactive compounds of Mentha pulegium L. *AMB Express 15*(1), 105. https://doi.org/10.1186/S13568-025-01911-8

Figueiredo, A. C., Barroso, J. G., Pedro, L. G., & Scheffer, J. J. C. (2008). Factors affecting secondary metabolite production in plants: Volatile components and essential oils. *Flavour and Fragrance Journal*, *23*(4), 213–226. https://doi.org/10.1002/FFJ.1875.

Göksu Sürücü, C., Tolun, A., Halisçelik, O., & Artık, N. (2024). Brewing method-dependent changes of volatile aroma constituents of green tea (Camellia sinensis L.). *Food Science and Nutrition*, *12*(10), 7186–7201. https://doi.org/10.1002/FSN3.4307.

Başer, K. H. C., & Kırımer, N. (2018). Essential oils of Anatolian Lamiaceae-An update. *Natural Volatiles & Essential Oils*, *5*(4), 1–28.

Juergens, U. R., Dethlefsen, U., Steinkamp, G., Gillissen, A., Repges, R., & Vetter, H. (2003). Anti-inflammatory activity of 1.8-cineol (eucalyptol) in bronchial asthma: a double-blind placebo-controlled trial. *Respiratory Medicine*, *97*(3), 250–256. https://doi.org/10.1053/RMED.2003.1432

Kataoka, H., Lord, H. L., & Pawliszyn, J. (2000). Applications of

solid-phase microextraction in food analysis. *Journal of Chromatography A*, *880*(1–2), 35–62. https://doi.org/10.1016/S0021-9673(00)00309-5

Lin, J., Zhang, P., Pan, Z., Xu, H., Luo, Y., & Wang, X. (2013). Discrimination of oolong tea (Camellia sinensis) varieties based on feature extraction and selection from aromatic profiles analysed by HS-SPME/GC–MS. *Food Chemistry*, *141*(1), 259–265. https://doi.org/10.1016/J.FOODCHEM.2013.02.128

Maggio, A., Roscigno, G., Bruno, M., De Falco, E., & Senatore, F. (2016). Essential-Oil Variability in a Collection of Ocimum basilicum L. (Basil) Cultivars. *Chemistry & Biodiversity*, *13*(10), 1357–1368. https://doi.org/10.1002/CBDV.201600069

Mahboubi, M., & Haghi, G. (2008). Antimicrobial activity and chemical composition of Mentha pulegium L. essential oil. *Journal of Ethnopharmacology*, *119*(2), 325–327. https://doi.org/10.1016/J.JEP.2008.07.023

McKay, D. L., & Blumberg, J. B. (2006). A review of the bioactivity and potential health benefits of peppermint tea (Mentha piperita L.). *Phytotherapy Research*, *20*(8), 619–633. https://doi.org/10.1002/PTR.1936.

Patel, M., Lee, R., Merchant, E. V., Juliani, H. R., Simon, J. E., & Tepper, B. J. (2021). Descriptive aroma profiles of fresh sweet basil cultivars (Ocimum spp.): Relationship to volatile chemical composition. *Journal of Food Science*, *86*(7), 3228–3239. https://doi.org/10.1111/1750-3841.15797.

Poswal, F. S., Russell, G., Mackonochie, M., MacLennan, E., Adukwu, E. C., & Rolfe, V. (2019). Herbal Teas and their Health Benefits: A Scoping Review. *Plant Foods for Human Nutrition, 74*(3), 266–276. https://doi.org/10.1007/S11130-019-00750-W

Rafya, M., Zehhar, N., Hafidi, A., & Benkhalti, F. (2024). Review of Rosmarinus officinalis L. essential oil, hydrosol, and residues analysis: Composition, bioactivities, and valorization. *Industrial Crops and Products*, *221*, 119392. https://doi.org/10.1016/J.INDCROP.2024.119392

Sánchez-López, J. A., Yener, S., Smrke, S., Märk, T. D., Bonn, G., Zimmermann, R., Biasioli, F., & Yeretzian, C. (2020). Extraction kinetics of tea aroma compounds as a function brewing temperature, leaf size and water hardness. *Flavour and Fragrance Journal*, *35*(4), 365–375. https://doi.org/10.1002/FFJ.3571

Sevindik, M., Kilibarda, S., Uysal, I., Šavikin, K., Banjac, N., & Popović-Đorđević, J. (2025). Overview of phytochemical composition and bioactivity of Lavandula species. *Phytochemistry Reviews 2025*, 1–26. https://doi.org/10.1007/S11101-025-10180-Z

Telci, I., Bayram, E., Yilmaz, G., & Avci, B. (2006). Variability in essential oil composition of Turkish basils (Ocimum basilicum L.). *Biochemical Systematics and Ecology*, *34*(6), 489–497. https://doi.org/10.1016/J.BSE.2006.01.009

Tschiggerl, C., & Bucar, F. (2010). Investigation of the Volatile Fraction of Rosemary Infusion Extracts. *Scientia Pharmaceutica*, *78*(3), 483. https://doi.org/10.3797/SCIPHARM.1004-23

Ultee, A., Kets, E. P. W., & Smid, E. J. (1999). Mechanisms of action of carvacrol on the food-borne pathogen Bacillus cereus. *Applied and Environmental Microbiology*, *65*(10), 4606–4610. https://doi.org/10.1128/AEM.65.10.4606-4610.1999

Uritu, C. M., Mihai, C. T., Stanciu, G. D., Dodi, G., Alexa-Stratulat, T., Luca, A., Leon-Constantin, M. M., Stefanescu, R., Bild, V., Melnic, S., & Tamba, B. I. (2018). Medicinal plants of the family Lamiaceae in pain therapy: A review. *Pain Research and Management*, *2018*. https://doi.org/10.1155/2018/7801543

Wirtu, S. F., Mishra, A. K., Jule, L. T., & Ramaswamy, K. (2024). Ocimum basilicum and Ocimum americanum: A Systematic Literature Review on Chemical Compositions and Antimicrobial Properties. *Natural Product Communications*, *19*(4). https://doi.org/10.1177/1934578X241247640

Wright, J., Wulfert, F., Hort, J., & Taylor, A. J. (2007). Effect of Preparation Conditions on Release of Selected Volatiles in Tea Headspace. *Journal of Agricultural and Food Chemistry*, *55*(4), 1445–1453. https://doi.org/10.1021/JF062657V

Yang, Z., Baldermann, S., & Watanabe, N. (2013). Recent studies of the volatile compounds in tea. *Food Research International*, *53*(2), 585–599. https://doi.org/10.1016/J.FOODRES.2013.02.011

Zárybnický, T., Matoušková, P., Lancošová, B., Šubrt, Z., Skálová, L., & Boušová, I. (2018). Inter-Individual Variability in Acute Toxicity of R-Pulegone and R-Menthofuran in Human Liver Slices and Their Influence on miRNA Expression Changes in Comparison to Acetaminophen. *International Journal of Molecular Sciences*, *19*(6). https://doi.org/10.3390/IJMS19061805

Zeng, Q., Wang, H., Tuo, J., Ding, Y., Cao, H., & Yue, C. (2025). Volatile Organic Compounds in Teas: Identification, Extraction, Analysis, and Application of Tea Aroma. *Foods*, *14*(15), 2574. https://doi.org/10.3390/FOODS14152574.

Zhu, Y., Lv, H. P., Shao, C. Y., Kang, S., Zhang, Y., Guo, L., Dai, W. D., Tan, J. F., Peng, Q. H., & Lin, Z. (2018). Identification of key odorants responsible for chestnut-like aroma quality of green teas. *Food Research International*, *108*, 74–82. https://doi.org/10.1016/J.FOODRES.2018.03.026

Black Sea Journal of Engineering and Science
doi: 10.34248/bsengineering.1987522

Open Access Journal
e-ISSN: 2619 – 8991

Araştırma Makalesi (Research Article)
Cilt 9 - Sayı 5: 2354-2364 / Eylül 2026
(Volume 9 - Issue 5: 2354-2364 / September 2026)

GÜNCEL AÇIK KAYNAK BÜYÜK DİL MODELLERİNİN KİŞİLİK DEĞERLENDİRME PERFORMANSI: IPIP VERİLERİ ÜZERİNDE İNSAN VE YAPAY ZEKÂ KARŞILAŞTIRMASI

İlknur DÖNMEZ[1]*

[1]*Istanbul Health and Technology University, Faculty of Engineering and Natural Sciences, Computer Engineering Department, 37682, İstanbul, Türkiye*

Özet: Yapay zekâ tabanlı sohbet botlarının yaygın kullanımı, bu sistemlerin yalnızca doğruluğunun değil, aynı zamanda sergiledikleri dilsel ve davranışsal örüntülerin de incelenmesini gerekli kılmıştır. Kullanıcı etkileşimleri sırasında ortaya çıkan yanıtların üslubu ve tonu, bu sistemlerin belirli kişilik özellikleri sergilediği yönünde algılar oluşturabilmektedir. Bu çalışma, yapay zekâ (YZ) sohbet botlarının (COPILOT, ChatGPT, Gemini, Meta AI, Grok, Perplexity AI ve Claude) insan kişilik özelliklerini ne ölçüde taklit edebildiğini, Beş Faktör Kişilik Test (IPIP- Big Five) Modeli çerçevesinde incelemektedir. Veriler, uygulanan 5 seviyeli Likert tipi ölçek aracılığıyla toplanmıştır. Yapay zekâ yanıtları, 1=Kesinlikle Katılmıyorum ile 5=Kesinlikle Katılıyorum arasında derecelendirilen 5'li Likert ölçeği kullanılarak ölçülmüştür. İnsan verileri ile farklı YZ sohbet botlarından elde edilen yanıtlar, normal dağılım varsayımı altında Z-test kullanılarak karşılaştırılmıştır. Analizler, dışadönüklük (z = 0,403) ve deneyime açıklık (z = 1,57) boyutlarında sık kullandığımız gruplar arasında istatistiksel olarak anlamlı fark bulunmadığını göstermektedir. Buna karşılık, duygusal dengesizlik (nörotisizm) (z =-5,876), uyumluluk (z = 5,069) ve sorumluluk (z = 2,739) boyutlarında anlamlı farklılıklar tespit edilmiştir. Bulgular, YZ sistemlerinin düşük duygusal duyarlılık ve yüksek uyumluluk ile sorumluluk skorları üretme eğiliminde olduğunu, dolayısıyla insan kişiliğini kısmen taklit edebilse de belirli boyutlarda sistematik sapmalar gösterdiğini ortaya koymaktadır. Bu çalışma, YZ sistemlerinin kişilik simülasyonunu nicel olarak değerlendirebilen istatistiksel yeni bir çerçeve sunmaktadır.

Anahtar kelimeler: İstatistiksel analiz, Sohbet botları, Z-testi, Kişilik analiz testi, Uluslararası Kişilik Madde Havuzu, Beş Faktör Kişilik Modeli

Evaluating the Personality Assessment Performance of Current Free Large Language Models: A Human–AI Comparison on IPIP Data

Abstract: The widespread adoption of AI-based chatbots has made it necessary to examine not only their accuracy performance but also the linguistic and behavioral patterns they exhibit. The style and tone of responses generated during user interactions can create perceptions that these systems display certain personality traits. This study investigates the extent to which AI chatbots (COPILOT, ChatGPT, Gemini, Meta AI, Grok, Perplexity AI ve Claude) can emulate human personality characteristics within the frameworks of the International Personality Item Pool and the Big Five Personality Model. Data was collected using a five-point Likert-type scale. The AI-generated responses were measured using a five-point Likert scale, with ratings ranging from 1 = Strongly Disagree to 5 = Strongly Agree. Human data and responses obtained from various AI chatbots were compared using the Z-test under the assumption of normal distribution. The analyses indicate no statistically significant differences between groups in extraversion (z = 0.403) and openness to experience (z = 1.57). In contrast, significant differences were identified in neuroticism (z =-5.876), agreeableness (z = 5.069), and conscientiousness (z = 2.739). The findings suggest that AI systems tend to produce lower neuroticism and higher agreeableness and conscientiousness scores. Therefore, while they can partially emulate human personality traits, they exhibit systematic deviations in specific dimensions. This study provides a new statistical framework for the quantitative evaluation of personality simulation in AI systems.

Keywords: Statistical analysis, Chatbots, Z-test, Personality assessment test, International Personality Item Pool, Big Five Personality Model

***Sorumlu yazar (Corresponding author):** Istanbul Health and Technology University, Faculty of Engineering and Natural Sciences, Computer Engineering Department, 37682, İstanbul, Türkiye
E mail: ilknur.donmez@istun.edu.tr (İ. DÖNMEZ)
İlknur DÖNMEZ https://orcid.org/0000-0002-8344-1180

Gönderi: 05 Temmuz 2026 **Received:** July 05, 2026
Kabul: 08 Ağustos 2026 **Accepted:** August 08, 2026
Yayınlanma: 15 Eylül 2026 **Published:** September 15, 2026

Cite as: Dönmez, İ. (2026). Evaluating the personality assessment performance of current free large language models: a human–AI comparison on IPIP data. *Black Sea Journal of Engineering and Science,* 9(5), 2354-2364.

1. Giriş

Yapay zekâ tabanlı sohbet sistemleri, günümüzde insanlarla doğal iletişim kurabilen en gelişmiş teknolojilerden biri haline gelmiştir. Bu gelişim, önemli bir araştırma sorusunu gündeme getirmiştir: Yapay zekâ sistemleri insan kişiliğini istatistiksel olarak ne ölçüde

This work is licensed (CC BY-NC 4.0) under Creative Commons Attribution 4.0 International License

taklit edebilir? Yapay zekanın kişilik testi ile aldığı skor aslında yapay zekayı kullanan insana hissettirdiği bir söylem şeklinden kaynaklanır. Yapay zekanın tatbikî duyguları ve kişiliği yoktur ama pek çok uygulamada ve oyunda yaşadığımız gibi yapay zekanın insanmış gibi duygusal yanıt verebilme, sinirli, üzgün, kızgın cevaplar verebilme durumu ve potansiyeli vardır. Bu da onu kullanan insanlar üzerinde belli tarzda etkiler yaratabilir. Hayatımıza bu kadar girdikleri için, çok uzun süre etkileşim halinde olduğumuz için; bu sohbet botlarının nasıl biri gibi davrandıkları yani hangi tarzda cevap verdikleri bilgisi önemlidir.

Çalışmamızda kullanılan ve kişilik psikolojisinde yaygın olan Beş Faktör Kişilik Modeli (Big Five), insan davranışlarını ölçmek için standart bir çerçeve sunmaktadır. Bu model, IPIP (International Personality Item Pool) ölçeği ile geniş ölçekli veri setleri üzerinden uygulanmaktadır. Bu testler açık kaynak olup herkes tarafından erişilebilirdir. Bu da yapılan çalışmalar ve sonuçlarının da paylaşılıp kıyaslanabilir olmasını sağlamıştır. Kişilik psikolojisi alanında Beş Faktör Modeli, insan davranışlarının ölçülmesinde en yaygın kullanılan yaklaşımlardan biridir. IPIP ölçeği, bu modelin standartlaştırılmış ve geniş veri setlerine uygulanabilir bir versiyonunu sunmaktadır.

Uluslararası Kişilik Madde Havuzu (IPIP) ve Beş Faktör Kişilik Modeli (Big Five), hem insan örneklemlerinde hem de son yıllarda yapay zekâ sistemlerinde kişilik ölçümü amacıyla yaygın biçimde kullanılan psikometrik araçlardır. Literatür incelendiğinde, IPIP ölçeklerinin farklı kültürlerde, farklı örneklem büyüklüklerinde ve çeşitli uygulama alanlarında yüksek geçerlilik ve güvenilirlik sunduğu görülmektedir.

İnsan örneklemleri üzerinde yapılan çalışmalar, IPIP temelli ölçeklerin güçlü psikometrik özelliklere sahip olduğunu ortaya koymaktadır. Özellikle IPIP-NEO'nun 300 ve 120 maddelik versiyonları, NEO PI-R ile yüksek düzeyde yakınsak geçerlik ve benzer kriter korelasyonları göstermektedir (Maples vd. 2014). Benzer şekilde, IPIP-NEO-60 formunun da kısa olmasına rağmen güçlü güvenirlik ve geçerlik özellikleri sergilediği belirlenmiştir (Maples-Keller vd. 2019). Farklı kültürlerde yapılan çalışmalar da bu bulguları desteklemektedir; örneğin Yunan örnekleminde 50 maddelik IPIP ölçeğinin beş faktörlü yapıyı doğruladığı ve yüksek iç tutarlılık sunduğu rapor edilmiştir (Ypofanti vd. 2015), Nijerya örnekleminde ise 100 maddelik IPIP'in geçerli ve güvenilir bir ölçüm aracı olduğu gösterilmiştir (Yunusa vd. 2016). Daha kısa formlar olan Mini-IPIP ölçekleri de geniş örneklemlerde (N=15701) kabul edilebilir güvenirlik ve yapı geçerliği sunmuş (Baldasaro, 2013), klinik örneklemlerde (örneğin kanser hastaları) benzer psikometrik özellikler göstermiştir (Perry vd., 2020). Ayrıca farklı dil ve kültürlerde yapılan uyarlama çalışmaları, IPIP ölçeklerinin ölçüm değişmezliği sağlayabildiğini ortaya koymaktadır (Martínez-Molina ve Arias, 2018). Bu bulgular, IPIP'in geniş kapsamlı, esnek ve güvenilir bir kişilik ölçüm aracı olduğunu desteklemektedir (Goldberg vd., 2006).

Yapay zekâ ve büyük dil modelleri (LLM) bağlamında IPIP kullanımı yeni bir araştırma alanıdır. Bu alanda yapılan çalışmalar, IPIP ölçeklerinin hem yapay zekânın "kişilik" özelliklerini ölçmek hem de insan kişiliğini metin üzerinden tahmin etmek üzerinedir (Socha vd., 2010; Hernandez ve Nie, 2023). Örneğin, bir çalışmada sohbet botlarının kullanıcı metinlerinden kişilik çıkarımı yapabildiği ve bu çıkarımların insan öz-bildirimleriyle orta düzeyde korelasyon gösterdiği ($r \approx 0{,}48$) bulunmuştur (Fan vd., 2023). Benzer şekilde, serbest metin etkileşimlerinden kişilik tahmini yapan modellerin de anlamlı ancak sınırlı doğruluk sağladığı rapor edilmiştir (Peters vd., 2024).

Diğer çalışmalar, yapay zekâ sistemlerinin doğrudan IPIP ölçekleri üzerinden kişilik sergileyip sergileyemeyeceğini incelemiştir. ChatGPT ve Gemini gibi modellerin IPIP-50 ölçeğini doldurduklarında insan benzeri kişilik profilleri oluşturabildiği, ancak bu profillerin modele ve verilen role göre değişebildiği gözlemlenmiştir (Jędrzejczak vd., 2025). IPIP-60'nin kullanıldığı bir çalışmalarda, GPT-4 gibi modellerin belirli kişilik profillerini yüksek tutarlılıkla simüle edebildiği ve insan öz-bildirimleriyle yüksek yakınsaklık gösterdiği ortaya konmuştur (Wang vd., 2025). Ayrıca bazı araştırmalar, LLM'lerin IPIP temelli kişilik özelliklerinin (IPIP-60) yüksek iç tutarlılık gösterebildiğini ve bu özelliklerin istemler aracılığıyla sistematik olarak değiştirilebildiğini göstermektedir (Serapio-García vd., 2023).

Yapay zekâ tabanlı ajanlar ve robotlar üzerinde yapılan çalışmalar da IPIP'in simülasyon amaçlı kullanımını desteklemektedir. Örneğin, GPT-4 tabanlı bir robot sisteminin IPIP-NEO testleri ile belirli bir insan kişilik profiline başarıyla uyum sağladığı gösterilmiştir (Lo vd., 2025). Benzer şekilde, oyun ortamlarında kullanılan yapay ajanların kişilik özelliklerini tutarlı biçimde yansıtabilmesi için IPIP temelli senaryoların etkili olduğu bulunmuştur (Klinkert vd., 2024).

Genel olarak değerlendirildiğinde, literatür iki temel sonucu ortaya koymaktadır: (i) IPIP ölçekleri insan örneklemlerinde yüksek geçerlik ve güvenirlik sunan güçlü bir ölçüm aracıdır ve (ii) bu ölçekler yapay zekâ sistemlerinde hem kişilik simülasyonu hem de kişilik çıkarımı amacıyla etkin biçimde kullanılabilmektedir. Bununla birlikte, yapay zekâ sistemlerinde elde edilen kişilik skorlarının bağlama ve modele duyarlı olduğu ve insan kişiliği ile birebir aynı anlamı taşımayabileceği de vurgulanmaktadır (Pellert vd., 2024).

2026 yılında da AI'ın insan taklit başarısı üzerine çalışmalar hem insan-merkezli yapay zekâ etkileşimini hem de taklit/öğrenme tabanlı otonom sistemleri ileri taşıyor. Sylvara ve ark. ile Celli ve ark., sohbet botlarını kişilik değerlendirme aracı olarak konumlandırırken, kişilik bilişiminin son yirmi yıldaki gelişimini, risklerini ve gelecek yönelimlerini özetliyor (Celli vd., 2026; Sylvara vd., 2026); Bhattacharyya ve ark. ise sanal avatar kişiliğinin mekânsal davranış ve etkileşimleri nasıl şekillendirdiğini gösteriyor (Bhattacharyya vd., 2026).

Keeler ve Murphy, sohbet botlarının insan-insan ilişkileri üzerindeki olası uzun vadeli zararlarına dikkat çekerek bu alanda etik ve ampirik araştırma gerekliliğini vurguluyor (Keeler ve Murphy, 2026). İnsan ve AI etkileşimini inceleyen bir çalışma, insan ve yapay zekâ bilişini karşılaştıran 363 makaleyi tarayarak, her ikisinin de temelde istatistiksel işlem, örüntü tanıma ve yaklaşık çıkarıma dayandığını savunuluyor. İnsan "gerçek anlama"sı ile makine "sadece örüntü eşleme"si arasındaki keskin ayrımın abartılı olduğunu, her iki tarafta da yanlılıklar, hafıza bozulmaları ve karar verme opaklığı bulunduğunu öne sürüyor. Buna rağmen bedenlenme, niyet ve öznel deneyim gibi alanlarda farklılıkların kaldığı vurgulanıyor (Boyd ve Markowitz, 2026).

"YZ ve İnsan Etkileşiminin Psikolojisi" makalesi, yapay zekâyı insan ilişkilerinin parçası olarak ele alan MIRA modelini sunuyor. Bu çerçeve, yapay zekânın hem ilişkisel ortak (doğrudan sohbet, eşlik) hem de ilişkisel aracı (insan–insan iletişimini şekillendirme) rolü üstlenebileceğini savunuyor. Model, insan benzeri dil ve davranışın dört ilke üzerinden psikolojik yakınlık ve güven üretebildiğini öne sürüyor: dilsel karşılıklılık, psikolojik yakınlık, kişilerarası güven ve yerini alma/pekiştirme (Chen vd., 2026) Yapay zekâ ile ilgili bireysel davranış ve karar verme süreçlerini ölçen farklı deneyler de uygulanmıştır: Turing tipi deneyler (Nighojkar vd., 2025), oyun kuramı deneyleri (Vaccaro vd., 2024), klasik psikoloji deneyleri (Taubenfeld vd., 2024).

Literatürden görüldüğü üzere son yıllarda yapay zekâ araştırmaları, dil modellerinin insan benzeri davranış kalıplarını ne ölçüde taklit edebildiğine odaklanmıştır. Ancak YZ sistemlerinin kişilik boyutları açısından insan normlarıyla istatistiksel olarak karşılaştırıldığı çalışmalar sınırlıdır. Literatürde bulunan bu çalışmalarda IPIP-50 yani 50 soruluk kısa versiyonu gemini ve Chat-GPT üzerinde (Jędrzejczak vd., 2025) kullanılmış, bir başka çalışmada 60 maddelik anket ile sadece ChatGPT4 (Wang vd., 2025) incelenmiştir. 10'a yakın Llama, Mistral gibi doğrudan kullanıcının görmediği temel Büyük Dil Modelleri kullandıkları çalışmada ise yine 50 soruluk anket kullanılmış ve duygu kırılımları ile ilgili detaylı sonuçlar elde edilememiştir.

Diğer çalışmalardan farklı olarak bizim çalışmamızda ise insanların sıklıkla kullandıkları 6 temel sohbet botu üzerinde insan profillerini de vermekte başarısı kanıtlanan IPIP kişilik testinin 120 soruluk versiyonu uygulanmıştır. Bu test 5 temel kişilik altındaki kırılımları da verecek şekilde tasarlanmıştır; bu kırılımlara göre de en yaygın kullanılan 6 farklı çeşit sohbet botunu hem teker teker hem de ortalama olarak insanların ortalama yanıtlarıyla istatistiksel olarak kıyaslayan bir çalışmadır. YZ ve insan kişilik profillerini Z-testi ve normal dağılım varsayımı altında karşılaştırıp analiz etmeyi amaçlamaktadır.

Bu yapay zekâ insan etkileşimi alanında kişilik psikolojisi ile istatistiksel hipotez testini bir araya getirmektedir. İnsanların günlük hayatlarında çok önemli yer edinmiş günümüz sohbet robotlarının insan kişiliklerini ne kadar simüle ettiği de incelenmiştir.

1.1. Hipotezler

Bu çalışmada hipotez testleri, insan ve yapay zekâ (YZ) sistemlerinin kişilik skorları arasında istatistiksel olarak anlamlı bir fark olup olmadığını belirlemek amacıyla kurulmuştur. Bu kapsamda *null* hipotez (H_0), insan ve YZ gruplarının ortalamaları arasında anlamlı bir fark bulunmadığını, yani iki grubun kişilik ölçümlerinin eşit olduğunu varsaymaktadır. Buna karşılık alternatif hipotez (H_1) ise iki grup arasında istatistiksel olarak anlamlı bir fark bulunduğunu ifade etmektedir. Matematiksel olarak bu durum H_0: $\mu_1 = \mu_2$ şeklinde ortalamaların eşitliği üzerinden tanımlanırken, H_1: $\mu_1 \neq \mu_2$ ifadesi ile ortalamalar arasında farklılık olduğu iki yönlü bir test yaklaşımıyla modellenmektedir.

1.1.1. Deneysel hipotez yapısı (Beş faktör kişilik modeli)

Bu çalışmada her bir kişilik boyutu için ayrı ayrı hipotez testleri kurulmuştur. Her boyut, YZ ve insan grupları arasında istatistiksel olarak anlamlı bir fark olup olmadığını değerlendirmek üzere bağımsız bir deneysel değişken olarak ele alınmıştır.

Deney 1. Dışadönüklük (Extraversion)

H_0: Yapay zekâ ve insan skorları dışadönüklük boyutunda eşittir ($\mu_{AI} = \mu_{insan}$)

H_1: Yapay zekâ ve insan skorları dışadönüklük boyutunda farklıdır ($\mu_{AI} \neq \mu_{insan}$)

Deney 2. Uyumluluk (Agreeableness)

H_0: Yapay zekâ ve insan skorları uyumluluk boyutunda eşittir ($\mu_{AI} = \mu_{insan}$)

H_1: Yapay zekâ ve insan skorları uyumluluk boyutunda farklıdır ($\mu_{AI} \neq \mu_{insan}$)

Deney 3. Insaflılık-sorumluluk (Conscientiousness)

H_0: Yapay zekâ ve insan skorları insaflılık boyutunda eşittir ($\mu_{AI} = \mu_{insan}$)

H_1: Yapay zekâ ve insan skorları insaflılık boyutunda farklıdır ($\mu_{AI} \neq \mu_{insan}$)

Deney 4. Duygusal dengesizlik (Neuroticism)

H_0: Yapay zekâ ve insan skorları nörotisizm boyutunda eşittir ($\mu_{AI} \neq \mu_{insan}$)

H_1: Yapay zekâ ve insan skorları nörotisizm boyutunda farklıdır ($\mu_{AI} \neq \mu_{insan}$)

Deney 5. Açıklık (Openness to Experience)

H_0: Yapay zekâ ve insan skorları deneyime açıklık boyutunda eşittir ($\mu_{AI} = \mu_{insan}$)

H_1: Yapay zekâ ve insan skorları deneyime açıklık boyutunda farklıdır ($\mu_{AI} \neq \mu_{insan}$).

2. Materyal ve Yöntem

Çalışmada açık kaynaklı metotlar kullanılmış. Yapay zekaya tümden IPIP testinde olduğu anlaşılmayacak şekilde sorular tek tek sorulmuştur. Kullanılan varsayımlar ve istatistiksel yöntemler aşağıda açıklanmaktadır.

3.1. Veri

Bu çalışmada kullanılan veri setleri iki temel kaynaktan

elde edilmiştir: insan kişilik verileri ve yapay zekâ (YZ) sistemlerinden elde edilen yanıtlar. İnsan verisi, Uluslararası Kişilik Madde Havuzu (IPIP) ölçeğine dayanan geniş ölçekli ve çok kaynaklı bir veri tabanından oluşturulmuştur.

Bu veri seti; internet üzerinden toplanan büyük ölçekli örneklemler (N = 21588), Eugene-Springfield topluluk örneklemi (N = 481), iki ayrı büyük internet veri seti (N = 307313 ve N = 619150) ve daha küçük ölçekli yerel bir örneklemden (N = 160) oluşmaktadır (Goldberg, 1992; Johnson, 2014). Tüm bu veri kaynakları bir araya getirildiğinde yaklaşık 619150 bireyden oluşan oldukça geniş ve temsili bir insan örneklemi elde edilmiştir. Bu yapı, insan kişilik dağılımının istatistiksel olarak güçlü bir şekilde modellenmesine olanak sağlamaktadır.

Tablo 1. IPIP Örnek soruları

Örnek: IPIP soruları (çeviri)	Orijinal sorular
Canlı bir hayal gücüne sahibim.	Have a vivid imagination.
Başkalarına güvenirim.	Trust others.
Görevleri başarıyla tamamlarım.	Complete tasks successfully.
Kolayca sinirlenirim.	Get angry easily.
Sanatın önemine inanırım.	Believe in the importance of art.
Başkalarını kendi amaçlarım için kullanırım.	Use others for my own ends.
Sık sık kendimi üzgün hissederim.	Often feel blue.
Kontrolü ele alırım.	Take charge.
Duygularımı yoğun bir şekilde yaşarım.	Experience my emotions intensely.

Bu çalışmada, testin (insanlar) bireyler üzerindeki etkileriyle sohber robotlarını kıyaslamak ve ilgili grupların doğal dağılımlarını değerlendirmek amacıyla, insanlar üzerinde yapılan açık kaynak sonuçlar için Johnson's IPIP-NEO Data Repository veri setinden yararlanılmıştır.

Ayrıca, söz konusu testlerin geliştirilmesine ilişkin yöntemsel ayrıntılar ve uygulama örnekleri için, test geliştiricileri tarafından GitHub platformunda paylaşılan açık kaynak projeler incelenmiştir (IPIP).

Yapay zekâ verisi ise günümüzde yaygın olarak kullanılan çoklu sohbet botu sistemlerine tek tek kişilik test soruları sorularak Nisan 2026'da elde edilmiştir. Bu kapsamda COPILOT, ChatGPT, Gemini, Meta AI, Grok, Perplexity AI ve Claude modelleri çalışmaya dahil edilmiştir. Her bir modele IPIP ölçeğine dayalı 120 soru tek tek yönlendirilmiş, özellikle sen bu soru hakkında hangi cevabın sana en uygun olduğunu düşünüyorsun diyerek 5 seviyeli Likert ölçeğine benzer yanıtlar üretmeleri istenmiştir (Tamamen katılıyorum, biraz katılıyorum, ne katılıyorum- ne katılmıyorum, bir kısmına katılmıyorum, hiç katılmıyorum). Elde edilen yanıtlar sayısallaştırılarak her bir YZ sohbet botu için kişilik boyutlarına ait ortalama skorlar hesaplanmış ve karşılaştırmalı analiz için veri seti oluşturulmuştur.

3.2. İstatistiksel Varsayımlar & Test Çerçevesi

Analiz sürecinde parametrik bir yaklaşım olan Z-testi kullanılmıştır ve bu testin temel varsayımları doğrultusunda çalışma tasarlanmıştır. İlk olarak, veri setinin normal dağılım gösterdiği kabul edilmiştir. Bu varsayım, özellikle geniş ölçekli insan örneklemi nedeniyle istatistiksel olarak makul bir temel oluşturmaktadır. İkinci olarak, gözlemlerin birbirinden bağımsız olduğu varsayılmıştır; yani her bir birey veya yapay zekâ modeli yanıtı diğerinden etkilenmemektedir. Son olarak, varyans değerlerinin ya bilindiği ya da büyük örneklem büyüklükleri nedeniyle güvenilir şekilde tahmin edilebildiği kabul edilmiştir. Bu varsayımlar doğrultusunda Z-testi, insan ve yapay zekâ grupları arasındaki ortalama farkların istatistiksel olarak değerlendirilmesi için uygun bir yöntem olarak seçilmiştir.

3.3. z- Testi ve İstatistiksel Tasarım

Çalışmada kullanılan Z-testi, iki grup ortalaması arasındaki farkın standart hata ile normalize edilmesine dayanmaktadır. Kullanılan temel formül aşağıdaki gibidir (eşitlik 1):

$$Z = \frac{\mu_2 - \mu_1}{\sqrt{\frac{{\sigma_1}^2}{n_1} + \frac{{\sigma_2}^2}{n_2}}} \quad (1)$$

Eşitlik 1 aracılığıyla her bir kişilik boyutu için Z-skorları hesaplanmış ve insan ile YZ dağılımları arasındaki fark istatistiksel olarak ölçülmüştür.

Analiz sürecinde iki yönlü hipotez testi uygulanmıştır. Anlamlılık düzeyi $\alpha = 0{,}05$ olarak belirlenmiş ve buna karşılık gelen kritik değer ±1,96 olarak kabul edilmiştir. Elde edilen Z değerleri bu kritik sınırlarla karşılaştırılarak hipotez testleri gerçekleştirilmiştir. Böylece her bir kişilik boyutu için YZ sistemlerinin insan normlarından anlamlı şekilde sapıp sapmadığı sistematik olarak değerlendirilmiştir.

4. Bulgular

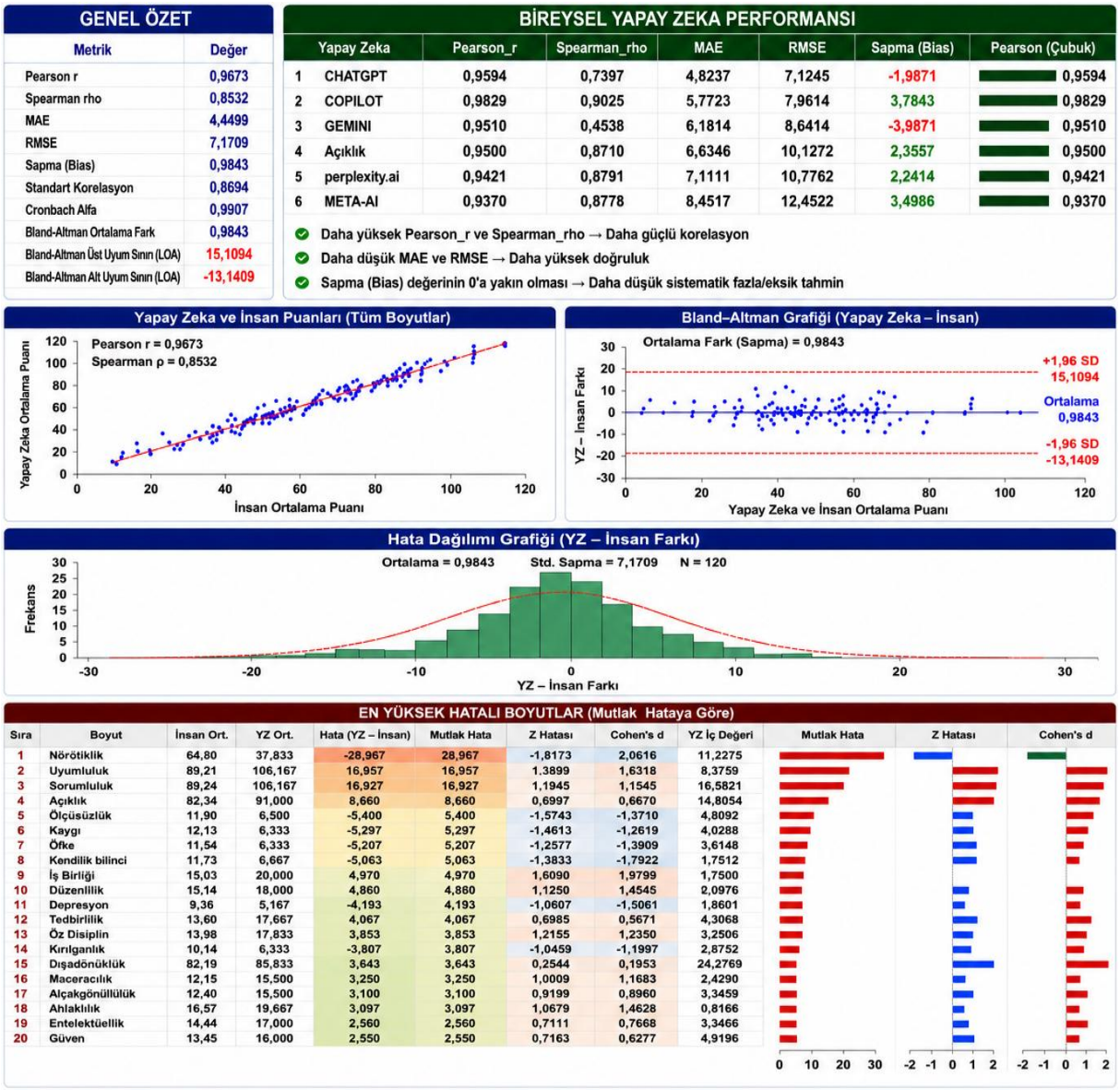
4.1. İnsan ve AI karşılaştırması (Modelleme ve Hata yüzdeleri ile)

Çalışmamız, yapay zekâ sistemlerinin kişilik değerlendirmelerinde insan puanlarıyla oldukça yüksek düzeyde uyum gösterdiğini ortaya koymaktadır.

Şekil 1'deki sonuç özetlerine bakıldığında AI ve insan arasındaki Pearson korelasyon katsayısının 0,9673 ve Spearman sıra korelasyonunun 0,8532 olması, yapay zekâ tahminlerinin insan tahminleriyle doğrusal ilişkili olduğu ve sıralama açısından insan değerlendirmelerine büyük ölçüde paralel olduğunu göstermektedir. Pearson korelasyonu iki sayısal değişken arasındaki doğrusal ilişkinin yönünü ve gücünü ölçerken, Spearman korelasyonu, iki değişken arasındaki sıralamaya dayalı

(monoton) ilişkinin yönünü ve gücünü ölçen parametrik olmayan bir korelasyon katsayısıdır. Ayrıca Cronbach Alfa değerinin 0,9907 olması, insan ve yapay zekâ değerlendirmeleri arasında son derece yüksek bir iç tutarlılığa işaret etmektedir. Ortalama Mutlak Hata (MAE = 4,45) ve Kök Ortalama Kare Hatası (RMSE = 7,17) değerleri, tahmin hatalarının genel olarak kabul edilebilir düzeyde olduğunu göstermektedir.

Burada MAE (Mean Absolute Error), tahmin hatalarının mutlak değerlerinin ortalamasını göstererek modelin ortalama hata büyüklüğünü ifade eder. RMSE (Root Mean Square Error) ise hata karelerini kullandığı için büyük hataları daha fazla cezalandırır ve aykırı değerlerin etkisine daha duyarlıdır. Büyük tahmin hatalarının özellikle önemli olduğu durumlarda RMSE daha anlamlı bir değerlendirme sunarken, modelin tipik hata düzeyini yorumlamak amacıyla MAE daha uygun bir ölçüttür. Veri setinde belirgin aykırı değerler bulunmadığı ve her bir hata benzer öneme sahip olduğu düşünülürse MAE çalışmamız için uygun bir hata ölçütüdür.



Şekil 1. Sonuçların özeti.

Bland–Altman analizi, aynı şeyi ölçen iki farklı yöntem/etmen gerçekten birbirinin yerine kullanılabilir mi sorusuna cevap verir. Bunun için AI ve İnsan skorları arasındaki fark hesaplanır ve bu fark, iki ölçümün ortalamasına karşı grafiğe yerleştirilir; böylece yöntemlerin birbirine ne kadar yakın sonuç verdiği ve aralarındaki farkın kabul edilebilir sınırlar içinde olup olmadığı görülebilir.

Çalışmamızda Bland–Altman analizinde ise ortalama farkın yalnızca 0,9843 puan olması, sistematik yanlılığın düşük olduğunu (Yani yöntemlerden biri diğerine göre sürekli olarak çok daha yüksek veya çok daha düşük ölçüm yapmaması) ortaya koyarken, ±14 puan civarındaki uyum sınırları bazı özelliklerde daha büyük sapmalara (ortalama fark küçük olsa bile tek tek bireylerde farklar oldukça büyük olabilir) işaret etmektedir.

Bireysel yapay zekâ modelleri incelendiğinde, en yüksek

korelasyon değerlerine sahip modelin Pearson r = 0,9829 ve Spearman ρ = 0,9025 ile COPILOT olduğu görülmektedir. Bununla birlikte COPILOT'un pozitif yanlılık göstermesi (Bias = 3,78), insan puanlarını genel olarak olduğundan yüksek tahmin etme eğilimine sahip olduğunu göstermektedir. CHATGPT ise daha düşük hata değerleri (MAE = 4,82, RMSE = 7,12) ile en dengeli performansı sergileyen modellerden biri olmuş, ancak insan puanlarını hafif düşük tahmin etme eğilimi göstermiştir (Bias = -1,99). GEMINI, GROK, Perplexity ve META-AI modelleri de yüksek korelasyonlar üretmelerine rağmen hata oranları ve yanlılık düzeyleri bakımından daha düşük performans göstermiştir.

Özellik bazında yapılan hata analizi, yapay zekâların özellikle geniş kişilik boyutlarında daha belirgin sapmalar yaşayabildiğini göstermektedir. En büyük hata, duygusal dengesizlik (nörotisizm) boyutunda görülmüş; yapay zekâların ortalama puanı insan değerlendirmelerinden yaklaşık 29 puan daha düşük tahmin ettiği belirlenmiştir.

Buna karşılık uyumluluk (agreeableness) ve sorumluluk (conscientiousness) boyutlarında yaklaşık 17 puanlık aşırı tahminler gözlenmiştir.

Açıklık (openness), dürtüsellik (immoderation), kaygı (anxiety), öfke (anger) ve öz bilinçlilik (self consciousness) gibi alt boyutlar da yüksek hata gösteren özellikler arasında yer almaktadır. Cohen's_değerlerinin bazı boyutlarda ±1'in üzerine çıkması, bu farkların yalnızca istatistiksel değil, aynı zamanda pratik açıdan da anlamlı büyüklükte olduğunu göstermektedir. Sonuç olarak, yapay zekâ sistemleri genel kişilik profilini yüksek doğrulukla tahmin edebilmekte; ancak özellikle duygusal kırılganlık, kaygı ve nörotisizm (duygusal dengesizlik) gibi içsel ve öznel özelliklerde sistematik sapmalar sergileyebilmektedir. Bu durum, yapay zekâların genel kişilik değerlendirmelerinde güvenilir bir yardımcı araç olarak kullanılabileceğini, ancak belirli kişilik boyutlarının yorumlanmasında insan uzman değerlendirmelerinin hâlen kritik önem taşıdığını göstermektedir.

4.1.1. Hipotez sonuçları

Beş farklı kişilik boyutu (dışadönüklük, uyumluluk, sorumluluk, duygusal dengesizlik ve deneyime açıklık) üzerinde yaklaşık 619150 insan örnekleminden elde edilen veriler ile yapay zekâ sohbet botlarından elde edilen sonuçlar istatistiksel olarak karşılaştırılmıştır. Elde edilen Z-skorları, ±1,96 kritik değer aralığı ile karşılaştırılarak hipotez testleri gerçekleştirilmiştir.

Genel sonuçlar incelendiğinde, dışadönüklük, uyumluluk ve sorumluluk boyutları için hesaplanan Z değerlerinin kabul bölgesi içinde kaldığı görülmüştür. Bu durum, ilgili kişilik boyutlarında H_0 hipotezinin reddedilemediğini, yani yapay zekâ ile insan skorları arasında istatistiksel olarak anlamlı bir fark bulunmadığını göstermektedir. Buna karşılık duygusal dengesizlik (nörotisizm) ve deneyime açıklık boyutlarında elde edilen Z değerleri kritik eşik değerlerini aşmış ve bu boyutlarda H_0 hipotezinin reddedilmesine neden olmuştur. Bu sonuç, özellikle duygusal ve bilişsel kişilik özellikleri açısından insan ve yapay zekâ arasında anlamlı farklılıklar bulunduğunu göstermektedir.

Bu bulgular, Z-testi çerçevesinde değerlendirildiğinde yapay zekâ sistemlerinin sosyal ve davranışsal olarak yapılandırılmış kişilik özelliklerinde insanlara daha yakın bir dağılım sergilediğini, ancak daha içsel ve bilişsel boyutlarda belirgin sapmalar gösterdiğini ortaya koymaktadır. Özellikle duygusal dengesizlik (nörotisizm) boyutu üzerinden yapılan detaylı analiz bu farkı açık şekilde göstermektedir. Bu boyut için kurulan null hipotez aşağıdaki gibidir: *H_0: μ_YZ = μ_Human ("Yapay zekâ ve insanlar arasında nörotisizm açısından fark yoktur.")*

Bu hipotezi test etmek amacıyla yapılan Z-testi analizinde insan popülasyonu için ortalama değer μ = 66,80 (n = 619150) ve standart sapma σ = 15,94 olarak alınmıştır. Yapay zekâ sistemleri için ise ortalama değer μ = 37,833 (n = 6) ve standart sapma σ = 12,075 olarak hesaplanmıştır. Z değeri aşağıdaki eşitlik 2'deki formül kullanılarak elde edilmiştir:

İnsan: (μ_1 = 66,80, σ_1 = 15,94, n_1 = 619150),

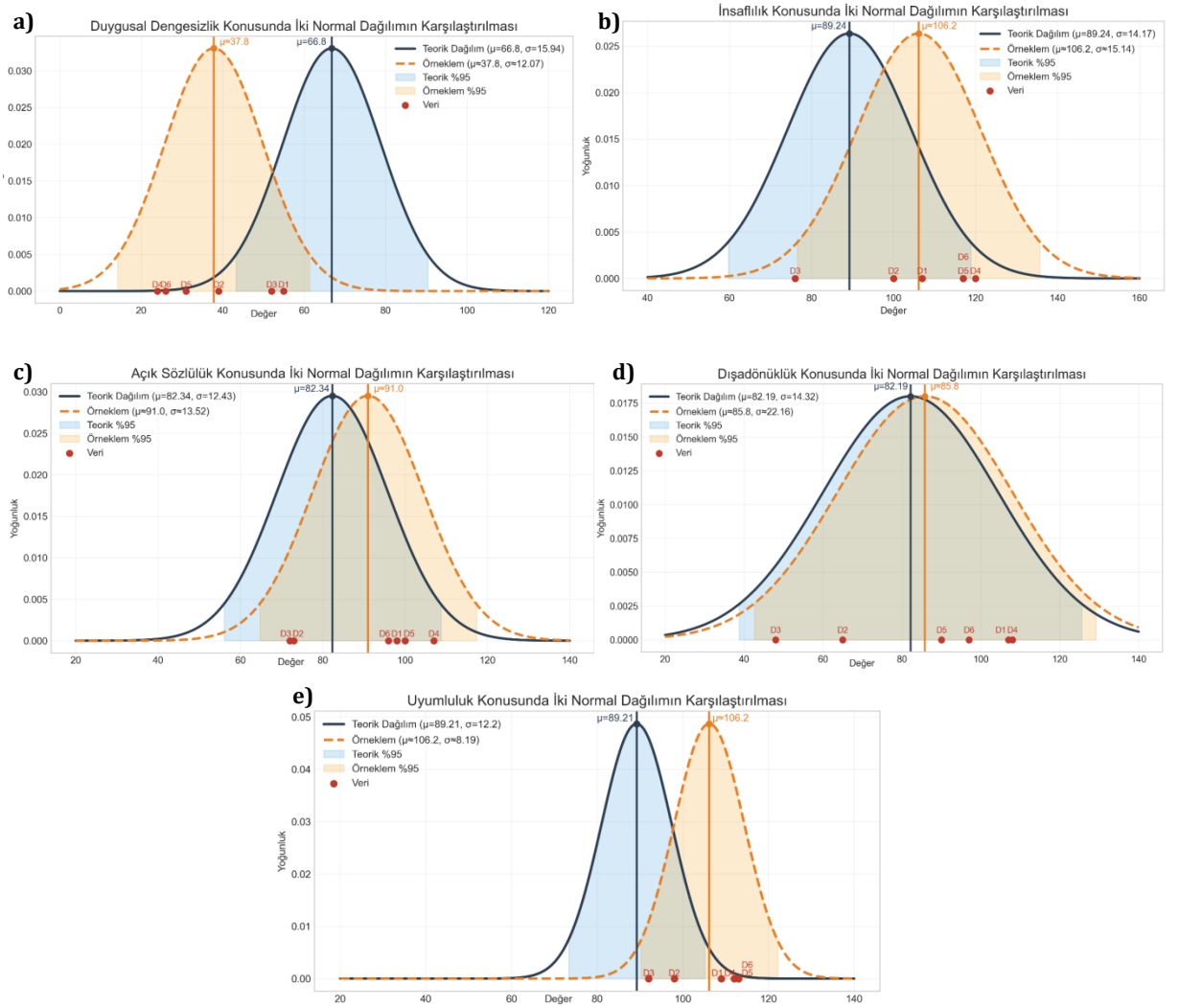
Yapay Zekâ: (μ_2 = 37,833, σ_2 = 12,075, n_2 = 6).

$$Z = \frac{\mu_2 - \mu_1}{\sqrt{\frac{\sigma_1^2}{n_1} + \frac{\sigma_2^2}{n_2}}} = \frac{37{,}83 - 66{,}80}{\sqrt{\frac{15{,}94^2}{619150} + \frac{12{,}075^2}{6}}} = -5{,}876 \quad (2)$$

Bu sonuç, yapay zekâ sohbet botları ile insanlar arasında duygusal dengesizlik (nörotisizm) boyutu açısından istatistiksel olarak anlamlı bir fark bulunduğunu göstermektedir. Şekil 2(a)'da görüldüğü üzere 2 sohbet botu insanların verdiği cevaplara benzer ama 4 sohbet robotu insan yanıtların %95'lik bölümünden farklı yanıt vererek insanların skorlarının dağılımını gösteren mavi çan eğrisinin anlamlı kısmının dışında (uç bölgelerinde) yer almışlardır.

Red kararı vermemizi sağlayan Z değeri de |Z|=5,876 >> 1,96. Ho hipotezini reddetmek için yeterince büyük bir değerdir. Anlamlılık düzeyi α = 0,05 ve kritik değerler ±1,96 olarak kabul edildiğinde, elde edilen Z değeri reddetme bölgesinde yer almaktadır. Bu nedenle H_0 hipotezi reddedilmiştir. Z değerleri tek tek tüm duygu durumları için hesaplanmış ve hipotezlerin kabul/red durumuna karar verilmiştir.

Şekil 2(b)'de Insaflılık (Conscientiousness) için Z değeri 2,739 nispeten duydusal dengesizlik (nörotisizm)'e göre düşük olsa da 1,96 değerinden küçük olmadığından insan ve AI bu konuda aynı sonuçları almıştır denemez ve hipotez reddedilir. Şekil 2 (c)'de Açıklık (Openness) için Z değeri 1,57 ile güven aralığı içindedir ve bu konuda yaklaşık olarak botlar ve insanlar aynı skorları almıştır denebilir. AI'ın insanla aynı davrandığını söyleyen Ho hipotezi kabul edilir. Şekil 2 (d) Dışadönüklük (extraversion) skorlarının analizinde Z değeri 0,403 ile neredeyse insanların scorlarıyla aynıdır. AI botları rasgele insanlarla aynı skorları almıştır. Ho hipotezi kabul edilir.



Şekil 2. (a) Duygusal dengesizlik (Neuroticism) (b) İnsaflılık (Conscientiousness) (c) Açıklık (Openness) (d) Dışadönüklük (extraversion) (e) Uyumluluk (Agreeableness) için insan ve sohbet botlarına ait IPIP test sonuçlarının normal dağılımları [D1: Copilot, D2: ChatGPT, D3:Gemini, D4:Meta AI, D5:Grok, D6:Perplexity AI].

Şekil 2 (e) Uyumluluk (Agreeableness) skorlarının analizinde Z değeri 5,069 olarak bulunmuş, 1,92'den küçük yeterince güvenilir bir sonuç olmadığından Ho hipotezinin reddedilmesi ile sonuçlanmıştır.

120 soruluk IPIP testinde her sorudan 1-5 arası değer alınabilmektedir. Ve sorular 5 kişilik üzerine dağılmıştır ve karıştırılmıştır. Bir sorunun puanı açıklık kişilik skoruna katkı sağlarken başka bir sorunun puanı dışadönüklük skoruna katkı sağlamaktadır. Kişilik tipleri ve alt tiplere göre sorular gruplandığında AI sohbet botlarının her bir kişilik tipi içi aldığı değerler ve ortalama ve standart sapma değerleri Tablo 1'de görülmektedir. Tablo 1'de 619150 kişi ile yapılan test sonuçlarının ortalama değeri ve standart sapması da görülmektedir. Bu tabloda Özellik sütunu içinde yeşil ile gösterilen kişilik özellikleri, AI botlarının ortalama değerlerinin insanların aldığı ortalama değerlere yaklaştığı ve bu benzerliğin istatistiksel olarak kabul edilebilir seviyede olduğu özelliklerdir. Turuncu ile gösterilenler ise YZ botlarının aldığı skorların istatistiksel olarak insan skorlarından ayırt edilir derecede ayrıldığı özelliklerdir.

Tabloda örnek olarak vermek gerekirse dışadönüklük (extraversion) ve açıklık (openess) konusunda YZ sohbet botları istatistiksel olarak insana eşdeğer skorlar aldı. Ho hipotezi kabul edildi. YZ sohbet botları maceracılık (adventurousness), öz bilinç (self consciousness) gibi konularda insandan istatistiksel olarak ayrılabilecek derecede daha küçük skorlar aldığından insan ve YZ sohbet botları bu özelliklerde benzerdir diyen Ho hipotezimizin reddedilmesi gerekti. Öz disiplin (self discipline) ve ihtiyatlılık (cautiouness) gibi özelliklerde YZ sohbet botlarının ortalamaları insan ortalamalarından istatistiksel duyarlılıkta ayrılabilecek kadar fazla çıktı ve yine Ho hipotezi reddedildi.

Tablo 1. İnsanlar ve YZ sohbet botları üzerinde yapılan IPIP test skoru sonuçları; ortalama değerleri, standart sapmaları, z-skoruna (|z-scor|<1,96) göre Ho hipotezinin kabul ya da red durumu

	Ort. İnsan	Std İnsan	Copilot	Chat GPT	Gemini	Meta AI	Grok	Perple-xityAI	Mean YZ	Std YZ	z-score	Ho
Duygusal Dengesizlik	66,8	15,94	55	39	52	24	31	26	37,83	12,07	-5,876	X
Kaygı	12,13	3,78	14	6	4	4	9	4	6,83	3,67	-3,535	X
Öfke	11,54	4,14	13	5	8	4	4	4	6,33	3,3	-3,865	X
Depresyon	9,36	3,88	6	5	8	4	4	4	5,17	1,46	-7,025	X
Öz Bilinç	11,73	3,66	7	9	8	4	6	6	6,67	1,59	-7,756	X
Ölçüsüzlük	11,9	3,43	4	7	16	4	4	4	6,5	4,38	-3,015	X
Kırılganlık	10,14	3,64	11	7	8	4	4	4	6,33	2,63	-3,552	X
Dışadönüklük	82,19	14,32	107	65	48	108	90	97	85,83	22,16	0,403	✓
Samimiyet	14,5	3,6	20	8	12	20	18	19	16,17	4,56	0,895	✓
Sosyallik	12,4	4,05	17	8	12	16	10	15	13	3,26	0,45	✓
Girişkenlik	14,46	3,47	19	15	8	20	17	17	16	3,92	0,963	✓
Aktivite Düzeyi	12,75	3,16	15	14	8	20	14	18	14,83	3,76	1,357	✓
Heyecan Arayışı	12,68	3,35	16	8	4	12	12	10	10,33	3,73	-1,543	✓
Neşelilik	15,41	3,22	20	12	4	20	19	18	15,5	5,82	0,038	✓
Deneyime Açıklık	82,34	12,43	98	73	72	107	100	96	91	13,52	1,57	✓
Hayal Gücü	14,74	3,39	20	12	4	20	20	14	15	5,86	0,109	✓
Sanatsal İlgi	14,64	3,63	18	12	12	20	16	18	16	3,06	1,09	✓
Duygusallık	15,2	3,03	17	12	12	18	15	15	14,83	2,27	-0,397	✓
Maceracılık	12,25	3,25	13	12	16	18	17	17	15,5	2,22	3,591	X
Entelektüellik	14,44	3,6	18	11	16	17	20	20	17	3,06	2,053	X
Yenilikçiliğe Açıklık	11,06	3,67	12	14	12	14	12	12	12,67	0,94	4,174	X
Uyumluluk	89,21	12,2	109	98	92	112	113	113	106,2	8,19	5,069	X
Güven	13,45	3,56	19	12	8	20	20	17	16	4,51	1,385	✓
Dürüstlük	16,57	2,9	20	18	20	20	20	20	19,67	0,75	10,182	X
Özgecilik	16,74	2,57	20	14	12	20	20	20	17,67	3,35	0,678	✓
İş Birliği	15,03	3,55	20	20	20	20	20	20	20	0	1101,6	X
Alçakgönüllülük	12,4	3,37	11	20	20	12	14	16	15,5	3,55	2,141	X
Empati	15,02	3,11	19	14	12	20	19	20	17,33	3,15	1,801	✓
Sorumluluk, İnsaflılık	89,24	14,17	107	100	76	120	117	117	106,2	15,14	2,739	X
Öz Yeterlik	16,3	2,4	20	16	4	20	20	20	16,67	5,85	0,154	✓
Düzenlilik	13,14	4,32	20	15	16	20	18	19	18	1,92	6,216	X
Görev Bilinci	16,29	2,58	20	16	12	20	19	20	17,83	2,97	1,274	✓
Başarı Çabası	15,92	3,15	20	17	12	20	20	20	18,17	2,97	1,855	✓
Öz Disiplin	13,98	3,17	19	16	12	20	20	20	17,83	2,97	3,181	X
Tedbirlilik	13,6	4,11	8	20	20	20	20	18	17,67	4,38	2,272	X

Tablo 1 ve Şekil 1 birlikte değerlendirildiğinde oldukça ilginç bir tablo ortaya çıkmaktadır. Genel performans metrikleri, yapay zekâ modellerinin insan değerlendirmeleriyle yüksek düzeyde uyumlu olduğunu göstermektedir. Özellikle Pearson korelasyon katsayısının 0,9673, Spearman rho değerinin 0,8532 ve Cronbach Alfa katsayısının 0,9907 olması, modellerin genel kişilik profilini insanlara oldukça benzer şekilde yeniden üretebildiğini göstermektedir. Ayrıca MAE = 4,45 ve RMSE = 7,17 değerleri de genel hata düzeyinin düşük olduğunu ortaya koymaktadır. Ancak bu güçlü genel uyumun altında bazı sistematik sapmalar gizlenmektedir. En dikkat çekici bulgu, duygusal dengesizlik (neuroticism) ve onun alt boyutlarında ortaya çıkmaktadır. İnsan ortalaması 66,8 iken yapay zekâların ortalaması yalnızca 37,8'dir. Bu fark yaklaşık 29 puanlık ciddi bir eksik tahmine karşılık gelmektedir. Benzer şekilde kaygı (anxiety), öfke (anger), depresyon

(depression), öz bilinçlilik (self consciousness), dürtüsellik (immoderation) ve kırılganlık (vulnerability) boyutlarında da tüm modeller sistematik olarak düşük puan vermiştir. Bu sonuçlar, büyük dil modellerinin metinlerden bireyin duygusal kırılganlığını, içsel kaygılarını ve olumsuz duygusal deneyimlerini algılamada zorlandığını düşündürmektedir. Nitekim en büyük hata değerleri ve en yüksek Cohens-d büyüklükleri bu boyutlarda görülmektedir.

Buna karşılık yapay zekâlar uyumluluk (agreeableness) ve sorumluluk (conscientiousness) boyutlarında belirgin bir aşırı tahmin eğilimi göstermiştir. Uyumluluk için insan ortalaması 89,21 iken yapay zekâ ortalaması 106,17; Sorumluluk için ise insan ortalaması 89,24 iken yapay zekâ ortalaması yine 106,17 olarak bulunmuştur. Özellikle dayanışma (cooperation) alt boyutunda tüm modellerin tam puan vermesi (20/20) ve standart sapmanın sıfır olması dikkat çekicidir. Bu durum, modellerin iş birliği ve sosyal uyum gibi özellikleri idealize ederek değerlendirme eğiliminde olduklarını göstermektedir. Benzer biçimde ahlaklılık, düzenlilik, öz disiplin ve tedbirlilik (morality, orderliness, self discipline, cautiousness) boyutlarında da insan ortalamalarının belirgin şekilde üzerinde tahminler yapılmıştır.

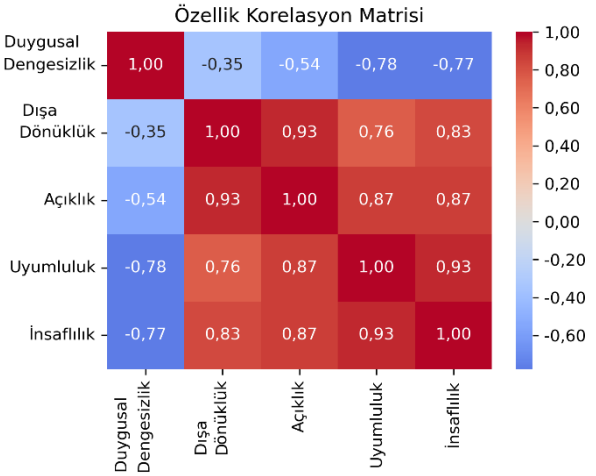
Öte yandan dışadönüklük (extraversion) ve bazı alt boyutlarında oldukça başarılı sonuçlar elde edilmiştir. Dışadönüklük (extraversion) genel boyutunda insan ve yapay zekâ ortalamaları arasındaki fark yalnızca 3,64 puandır ve z-skoru anlamlı düzeyde değildir. Samimiyet, sosyallik, atılganlık, neşelilik ve güven (friendliness, gregariousness, assertiveness, cheerfulness, trust) gibi alt boyutlarda da yapay zekâ tahminleri insan ortalamalarına oldukça yakındır. Bu durum, modellerin sosyal davranışlara ilişkin ipuçlarını metinlerden bir insanmışcasına çıkarabildiğini göstermektedir.

Model bazında değerlendirildiğinde, Copilot en yüksek korelasyon değerlerini (r=0,983; ρ=0,903) elde ederek insan puanlama örüntüsünü en iyi yakalayan sistem olmuştur. Ancak Copilot da insan puanlarını genel olarak biraz yüksek tahmin etme eğilimindedir (Bias = 3,78). ChatGPT ise en düşük hata değerlerine (MAE = 4,82; RMSE = 7,12) sahip olup en dengeli performansı sergilemiştir. Buna karşılık Meta-AI ve Perplexity daha yüksek hata oranları göstermiştir.

Genel olarak sonuçlar, büyük dil modellerinin kişilik profilinin genel yapısını oldukça yüksek doğrulukla tahmin edebildiğini, ancak kişiliğin duygusal boyutlarında özellikle duygusal dengesizlik (nörotisizm) ve ilişkili alt faktörlerde sistematik eksik tahminler yaptığını göstermektedir. Buna karşılık sosyal uyum, iş birliği, sorumluluk ve ahlaki özellikler gibi toplumsal açıdan olumlu değerlendirilen boyutlarda belirgin bir aşırı tahmin eğilimi bulunmaktadır. Bu bulgular, yapay zekâların kişilik değerlendirmelerinde genel profili başarılı şekilde yakalayabildiğini, ancak duygusal kırılganlık ve içsel psikolojik süreçleri yorumlama konusunda halen önemli sınırlılıklara sahip olduğunu ortaya koymaktadır. Bu nedenle yapay zekâ temelli kişilik analizleri destekleyici bir araç olarak değerlendirilmeli, özellikle klinik veya bireysel psikolojik değerlendirmelerde insan uzman görüşü ile kullanılmalıdır.

4.1.2. Keşif çalışması

Farklı yapay zekaların aynı özellikler için aldığı skorlar gruplanmış, daha sonra bu özellikler arasındaki korelasyon hesaplanmıştır. Bu çalışma keşif amaçlı yapılmış olup sonuçları Şekil 3'te görülmektedir. Şekil 3'ten Genel psikolojik ilişkiler olarak olmasa da yapay zekâ modellerinin puanlama eğilimlerinin benzerliği veya farklılığı olarak aşağıdaki yorumları yapabiliriz. Korelasyon matrisi incelendiğinde, yapay zekâ modellerinin dışadönüklük (extraversion), açıklık (openness), uyumluluk (agreeableness) ve sorumluluk (conscientiousness) boyutlarını büyük ölçüde birlikte değerlendirdiği görülmektedir. Bu boyutlar arasındaki korelasyonların 0,76 ile 0,93 arasında değişmesi, bir modelin herhangi bir özellikte yüksek puan vermesi durumunda diğer özelliklerde de yüksek puan verme eğiliminde olduğunu göstermektedir.



Şekil-3 Korelasyon matrisi.

Özellikle uyumluluk ve sorumluluk arasındaki korelasyonun 0,95'e ulaşması, yapay zekâların bu iki kişilik boyutunu pratikte birbirine çok yakın kavramlar olarak algılamış olabileceğini düşündürmektedir.

Buna karşılık duygusal dengesizlik (neuroticism) tüm diğer büyük kişilik boyutlarıyla negatif korelasyon göstermektedir. En güçlü negatif ilişki uyumlululuk ile görülmüş (r = -0,78), ardından insaflılık (r = -0,77) ve açıklık (r = -0,54) gelmiştir. Bu durum, yapay zekâ modellerinin yüksek duygusal dengesizlik atfettikleri profillere aynı zamanda daha düşük uyumluluk, insaflılık ve açıklık puanları verme eğiliminde olduklarını göstermektedir. Ancak burada dikkat edilmesi gereken nokta, bu ilişkinin gerçek bireyler arasındaki psikolojik ilişkiyi değil, modellerin ortak puanlama mantığını yansıttığıdır.

Korelasyon tablosunun köşegen boyunca simetrik

olmasının nedeni, satır ve sütunlarda yer alan aynı değişken çiftleri arasındaki korelasyon katsayılarının karşılıklı olarak aynı değeri vermesidir.

5. Tartışma ve Sonuç

Bu çalışmanın odak noktası, yapay zekâ sohbet botlarının gerçek anlamda duygu deneyimleyip deneyimlemediği değildir. Günümüzde bu sistemlerin öznel duygulara sahip olmadığı bilinmektedir. Ancak, duygusal içerikli sorulara verdikleri ve insanı taklit eden yanıtları ile kullanıcı üzerinde nasıl bir algı ve etki oluşturduğu önemlidir. Özellikle küçük yaşlardaki çocuklar gibi gelişimsel açıdan daha etkilenebilir kullanıcı gruplarında, bu tür yanıtların karşı tarafta bir duygu, anlayış veya kişilik varmış izlenimi oluşturabilmesi dikkat çekici bir olgudur. Bu çalışma yapay zekâ sohbet botlarının insan kişilik özelliklerini ne ölçüde simüle edebildiklerini incelemektedir.

Bu bağlamda elde edilen bulgular, yapay zekâ sohbet botlarının özellikle Dışadönüklük, Uyumluluk ve Sorumluluk gibi sosyal etkileşimle yakından ilişkili ve normatif (toplum tarafından nasıl olması gerektiğine ilişkin beklentilere cevap veren) yönü güçlü kişilik boyutlarında insanlara oldukça yakın sonuçlar üretebildiğini göstermektedir. Bu durum, büyük dil modellerinin eğitim süreçlerinde yaygın olarak karşılaştıkları sosyal açıdan kabul edilebilir, dengeli ve iş birliğine dayalı iletişim örüntülerini öğrenmeleriyle açıklanabilir. Başka bir ifadeyle, bu sistemler belirli bir kişiliğe sahip olmaktan ziyade, insan iletişiminde beklenen ve uygun görülen kişilik yansımalarını yüksek doğrulukla yeniden üretebilmektedir.

Buna karşılık, duygusal denge (nörotisizm) ve Deneyime Açıklık gibi daha içsel, deneyimsel ve bilişsel derinlik gerektiren kişilik boyutlarında yapay zekâ ile insan arasında istatistiksel olarak anlamlı farklılıklar tespit edilmiştir. Bu farklılıklar, yapay zekâ sistemlerinin gerçek duygusal deneyimlere sahip olmaması ve içsel motivasyon, merak veya bilinç temelli süreçler geliştirememesi ile açıklanabilir. Bu durum, yapay zekânın kişilik özelliklerini belirli ölçüde simüle edebildiğini, fakat bu özelliklere gerçek anlamda sahip olmadığını açıkça ortaya koymaktadır.

Çalışmamızda Z-testi ve normal dağılım yaklaşımı, insan ve yapay zekâ davranışlarının nicel olarak karşılaştırılmasında güçlü ve sistematik bir yöntem sunmuştur. Bir sonraki çalışmamızda prompt mühendisliği tekniklerinin yapay zekâ yanıtlarını insan normlarına daha da yaklaştırıp yaklaştırmayacağı deneylerle gözlemlenecektir. Böylece bu skorlar üzerinden prompt mühendisliği uygulamalarının etkinliği de gözlemlenebilecektir. Gelecek çalışmaların, daha geniş yapay zekâ örneklemleri, farklı model mimarileri ve alternatif istatistiksel yöntemler kullanarak bu alandaki bulguları derinleştirmesi ve yapay zekâda kişilik simülasyonunun sınırlarını daha kapsamlı biçimde ortaya koyması beklenmektedir.

Katkı Oranı Beyanı

Yazarın katkı yüzdeleri aşağıda verilmiştir. Yazar makaleyi incelemiş ve onaylamıştır.

	İ.D.
K	100
T	100
Y	100
VTI	100
VAY	100
KT	100
YZ	100
GR	100
PY	100

K= kavram, T= tasarım, Y= yönetim, VTI= veri toplama ve/veya işleme, VAY= veri analizi ve/veya yorumlama, KT= kaynak tarama, YZ= yazım, GR= gönderim ve revizyon, PY= proje yönetimi.

Çatışma Beyanı

Yazar bu çalışmada hiçbir çıkar ilişkisi olmadığını beyan etmektedirler.

Etik Onay Beyanı

Bu araştırmada hayvanlar ve insanlar üzerinde herhangi bir çalışma yapılmadığı için etik kurul onayı alınmamıştır. Çalışmada açık kaynaklı yazılımlar, açık kaynaklı IPIP kişilik testi ve açık erişimli veri kaynakları kullanılmıştır. Yapay zekâ modellerine uygulanan IPIP testlerinin sonuçları GitHub üzerinden kamuya açık olarak paylaşılmıştır. Ayrıca, çalışmada kullanılan Python kodları hem sonuçların doğrulanabilmesi hem de gelecekte yapılacak araştırmalara katkı sağlaması amacıyla erişime açılmıştır: https://github.com/ilknurbcdonmez/IPIP_test-for-common-chatbots. Yapay zekadan sadece cümle yapısını düzeltmek, dilbilgisi kontrolü ve bir resimde sonuçları ve nasıl çizeceği tüm detayları (giriş değerleri) vererek özet resim oluşturmak için faydalandım.

IPIP Test Verisi

U.S. National Institute of Mental Health, Official website for the International Personality Item Pool (https://ipip.ori.org/). IPIP-NEO-120 kişilik test (anket) soruları, https://github.com/chfhhd/ipip-neo-120-paper-pencil/blob/master/IPIP-NEO-120-Questionnaire.pdf. IPIP analiz aracı (Human analysis result), https://github.com/chfhhd/ipip-neo-120-paper-pencil/blob/master/IPIP-NEO-120-Analysis.xlsx

Kaynaklar

Baldasaro, R. E., Shanahan, M. J., & Bauer, D. J. (2013). Psychometric properties of the Mini-IPIP in a large nationally representative sample of young adults. *Journal of Personality Assessment*, *95*(1), 74–84. https://doi.org/10.1080/00223891.2012.700466

Bhattacharyya, R., Al Shami, W., & George, C. (2026, April). The role of personality of conversational virtual avatars on

proxemic behaviour during indoor navigation. In *Proceedings of the 2026 CHI Conference on Human Factors in Computing Systems ACM* (pp. 1–10). https://doi.org/10.1145/3772318.3791241

Boyd, R. L., & Markowitz, D. M. (2026). Artificial intelligence and the psychology of human connection. *Perspectives on Psychological Science*, *21*(2), 192–220. https://doi.org/10.1177/17456916251404394

Celli, F., Kartelj, A., Đorđević, M., Suhartono, D., Filipović, V., Milutinović, V., & Lepri, B. (2026). Twenty years of personality computing: Threats, challenges and future directions. *ACM Computing Surveys*, *58*(11), 1–37. https://doi.org/10.1145/3806009

Chen, E. K., Belkin, M., Bergen, L., & Danks, D. (2026). Does AI already have human-level intelligence? The evidence is clear. *Nature*, *650*(8100), 36–40. https://doi.org/10.1038/d41586-026-00285-6

Fan, J., Sun, T., Liu, J., Zhao, T., Zhang, B., Chen, Z., Glorioso, M., & Hack, E. (2023). How well can an AI chatbot infer personality? Examining psychometric properties of machine-inferred personality scores. *Journal of Applied Psychology*, *108*(8), 1277–1299. https://doi.org/10.1037/apl0001082

Goldberg, L. R. (1992). The development of markers for the Big-Five factor structure. *Psychological Assessment*, *4*(1), 26–42. https://doi.org/10.1037/1040-3590.4.1.26

Goldberg, L. R., Johnson, J. A., Eber, H. W., Hogan, R., Ashton, M. C., Cloninger, C. R., & Gough, H. G. (2006). The International Personality Item Pool and the future of public-domain personality measures. *Journal of Research in Personality*, *40*(1), 84–96. https://doi.org/10.1016/j.jrp.2005.08.007

Hernandez, I., & Nie, W. (2023). The AI-IP: Minimizing the guesswork of personality scale item development through artificial intelligence. *Personnel Psychology*, *76*(4), 1011–1035. https://doi.org/10.1111/peps.12543

Jędrzejczak, W. W., & Kobosko, J. (2025). Do chatbots exhibit personality traits? A comparison of ChatGPT and Gemini through self-assessment. *Information*, *16*(7), Article 523. https://doi.org/10.3390/info16070523

Johnson, J. A. (2014). Measuring thirty facets of the Five Factor Model with a 120-item public domain inventory: Development of the IPIP-NEO-120. *Journal of Research in Personality*, *51*, 78–89. https://doi.org/10.1016/j.jrp.2014.05.003

Keeler, J. B., & Murphy, B. A. (2026). Chatbots and human-human relationships: The need for research on potential downstream harms from generative AI. *Community, Work & Family*, 1–13. https://doi.org/10.1080/13668803.2026.2623500

Klinkert, L. J., Buongiorno, S., & Clark, C. (2024). *Driving generative agents with their personality* (arXiv:2402.14879). arXiv. https://doi.org/10.48550/arXiv.2402.14879

Lo, J. H., Huang, H. P., & Lo, J. S. (2025). LLM-based robot personality simulation and cognitive system. *Scientific Reports*, *15*(1), Article 16993. https://doi.org/10.1038/s41598-025-01528-8

Maples, J. L., Guan, L., Carter, N. T., & Miller, J. D. (2014). A test of the International Personality Item Pool representation of the Revised NEO Personality Inventory and development of a 120-item IPIP-based measure of the five-factor model. *Psychological Assessment*, *26*(4), 1070–1084. https://doi.org/10.1037/pas0000004

Maples-Keller, J. L., Williamson, R. L., Sleep, C. E., Carter, N. T., Campbell, W. K., & Miller, J. D. (2019). Using item response theory to develop a 60-item representation of the NEO PI–R using the International Personality Item Pool. *Journal of Personality Assessment*, *101*(1), 4–15. https://doi.org/10.1080/00223891.2017.1381968

Martínez-Molina, A., & Arias, V. B. (2018). Balanced and positively worded personality short-forms: Mini-IPIP validity and cross-cultural invariance. *PeerJ*, *6*, Article e5542. https://doi.org/10.7717/peerj.5542

Nighojkar, A., Moydinboyev, B., Duong, M., & Licato, J. (2025). *Giving AI personalities leads to more human-like reasoning* (arXiv:2502.14155). arXiv. https://doi.org/10.48550/arXiv.2502.14155

Pellert, M., Lechner, C. M., Wagner, C., Rammstedt, B., & Strohmaier, M. (2024). AI psychometrics: Assessing the psychological profiles of large language models through psychometric inventories. *Perspectives on Psychological Science*, *19*(5), 808–826. https://doi.org/10.1177/17456916231214460

Perry, L. M., Hoerger, M., Molix, L. A., & Duberstein, P. R. (2020). A validation study of the Mini-IPIP five-factor personality scale in adults with cancer. *Journal of Personality Assessment*, *102*(2), 153–163. https://doi.org/10.1080/00223891.2019.1644341

Peters, H., Cerf, M., & Matz, S. C. (2024). *Large language models can infer personality from free-form user interactions* (arXiv:2405.13052). arXiv. https://doi.org/10.48550/arXiv.2405.13052

Serapio-García, G., Safdari, M., Crepy, C., Sun, L., Fitz, S., Romero, P., Callahan, C., Srikumar, V., Moghaddam, M. H. R., Lertvittayakumjorn, P., & Matarić, M. (2023). *Personality traits in large language models* (arXiv:2307.00184). arXiv. https://doi.org/10.48550/arXiv.2307.00184

Socha, A., Cooper, C. A., & McCord, D. M. (2010). Confirmatory factor analysis of the M5-50: An implementation of the International Personality Item Pool item set. *Psychological Assessment*, *22*(1), 43-49. https://doi.org/10.1037/a0017371

Sylvara, A., Gregg, E. E., & Sun, T. (2026). Beyond scales and essays: Artificial intelligence chatbots as personality interviewers. *Journal of Personality Assessment*, 1–14. https://doi.org/10.1080/00223891.2026.2664795

Taubenfeld, A., Dover, Y., Reichart, R., & Goldstein, A. (2024, November). Systematic biases in LLM simulations of debates. In *Proceedings of the 2024 Conference on Empirical Methods in Natural Language Processing* ACL (pp. 251–267). https://doi.org/10.18653/v1/2024.emnlp-main.16

Vaccaro, M., Almaatouq, A., & Malone, T. (2024). When combinations of humans and AI are useful: A systematic review and meta-analysis. *Nature Human Behaviour*, *8*(12), 2293–2303. https://doi.org/10.1038/s41562-024-02024-1

Wang, Y., Zhao, J., Ones, D. S., He, L., & Xu, X. (2025). Evaluating the ability of large language models to emulate personality. *Scientific Reports*, *15*(1), Article 519. https://doi.org/10.1038/s41598-024-84109-5

Ypofanti, M., Zisi, V., Zourbanos, N., Mouchtouri, B., Tzanne, P., Theodorakis, Y., & Lyrakos, G. (2015). Psychometric properties of the International Personality Item Pool Big-Five questionnaire for the Greek population. *Health Psychology Research*, *3*(2), Article 2206. https://doi.org/10.4081/hpr.2015.2206

Yunusa, S., Abiola, T., & Udofia, O. (2016). Kano Eyaleti profesyonel sporcularının kişilik özellikleri, spor türleri ve demografik özellikleri. *Suudi Spor Hekimliği Dergisi* , *16* (2), 101-105. https://doi.org/10.4103/1319-6308.180151

Black Sea Journal of Engineering and Science
doi: 10.34248/bsengineering.1990047

Open Access Journal
e-ISSN: 2619 – 8991

Research Article
Volume 9 - Issue 5: 2365-2372 / September 2026

MACHINE LEARNING APPLICATIONS IN PREDICTING THE MICROBIOLOGICAL QUALITY OF PUBLIC FOUNTAIN WATERS: A CASE STUDY OF BAYBURT PROVINCE

Gülhat KOÇYİĞİT[1], Ruşen SINIR[2]*

[1]*Bayburt University, Faculty of Engineering, Department of Civil Engineering, 69000, Bayburt, Türkiye*
[2]*Bayburt University, Aydıntepe Vocatıonal School, Department of Construction, 69500, Bayburt, Türkiye*

Abstract: The access to reliable drinking water is of critical importance for human health and the United Nations Sustainable Development Goals (Goal 3: Good Health and Well-being, Goal 6: Clean Water and Sanitation). In this study, the microbiological water quality (Escherichia coli and total coliform) of five public fountains (Gordon, Kışla, Tarım, Aşağı Narkazan, and Yukarı Narkazan), which are intensively utilized by the public for drinking water in the province of Bayburt, was evaluated using time-series analysis and machine learning methods. The scope of the study utilized a comprehensive dataset of 476 monthly water analysis reports (285 safe, 191 contaminated) spanning the years 2014–2024. As a result of the trend and seasonality analyses applied to understand the temporal variations of contamination, no distinct seasonal patterns were detected in the examined fountains. While no significant trend was identified in E. coli concentrations, total coliform bacteria exhibited an increasing trend in the Kışla and Tarım fountains, and a decreasing trend in the Gordon fountain. To forecast water quality, six different supervised machine learning algorithms—namely Logistic Regression, K-Nearest Neighbors (KNN), Support Vector Machines (SVM), Naive Bayes, Decision Tree, and Random Forest—were implemented on the dataset. From a public health perspective, since the erroneous prediction of contaminated (unpotable) water as 'safe' by a machine (False Positive error) entails irreversible risks, the 'specificity' metric was prioritized as the core baseline for model performance evaluations. According to the analysis results; the Decision Tree, Naive Bayes, and Random Forest algorithms demonstrated flawless performance, achieving a score of 1.0 (100%) for both accuracy and specificity, thereby reducing the risk of faulty 'safe' predictions to zero. The empirical findings indicate that microbiological degradation is governed by irregular anthropogenic or environmental factors rather than predictable seasonal fluctuations. Deploying these flawless machine learning paradigms as an integrated early warning framework provides a robust scientific infrastructure for mitigating waterborne epidemics and guaranteeing sustainable access to safe drinking water.

Keywords: Water quality, Machine learning, Trend analysis, Specificity, Sustainable development goals

***Corresponding author:** Bayburt University, Aydıntepe Vocatıonal School, Department of Construction, 69500, Bayburt, Türkiye
E mail: rusensnr@bayburt.edu.tr (R. SINIR)
Gülhat KOÇYİĞİT https://orcid.org/0009-0009-7136-2336
Ruşen SINIR https://orcid.org/0000-0003-0700-1041

Received: July 08, 2026
Accepted: August 10, 2026
Published: September 15, 2026

Cite as: Koçyiğit, G. & Sınır, R. (2026). Machine learning applications in predicting the microbiological quality of public fountain waters: A Case study of Bayburt province. *Black Sea Journal of Engineering and Science,* 9(5), 2365-2372.

1. Introduction

Although water is the most vital need for human beings to maintain life, access to safe and potable water is one of the great crisis being experienced across the world. In terms of UNESCO 2024 report, approximately 2,2 billion people live with access to potable water (United Nations, 2024). WHO reports that unhealthy drinking water and poor sanitation causes infectious diseases such as cholera, dysentery typhoid causing the deaths of approximately 1 million people each year (WHO, 2022; WHO, 2023). The presence of *E. Coli* and coliform bacteria in water indicates fecal contamination directly mixed into water and it poses a serious threat to human life. Resolving sanitary drinking water problems and protecting water resources have been included in the United Nations Sustainable Development Goals especially in GOAL 6: Clean Water and Sanitation and GOAL 3: Good Health and Well-being,

Artificial Intelligence(AI) and Machine Learning (ML) algorithms have become more effective in the field of hydrology beyond traditional methods when monitoring water quality, detecting potential pollution in advance and developing early warning systems (Shen, 2018). In the literature, Supervised Learning algorithms such as Random Forest (RF), Decision Trees(DT), Support Vector Machines(SVM) and Naïve Bayes have reached the higher levels of accuracy in models for estimating water quality and potability estimations (Zhu et al., 2019; Abuzir and Abuzir, 2022; Kuscu and Kilic, 2023; Panigrahi et al., 2023). Furthermore, linear regression-based trend analyses and time series decomposition methods (seasonality) are frequently used to observe the changes in water pollution depending on environmental factors or time (Montgomery et al., 2012; Parmar and Bhardwaj,

This work is licensed (CC BY-NC 4.0) under Creative Commons Attribution 4.0 International License

2015; Hyndman and Athanasopoulos, 2018).

In recent years, data-driven modeling and machine learning paradigms have gained widespread traction for evaluating water potability and forecasting pollution risks across diverse aquatic environments (Panigrahi et al., 2023; Turan, 2023). While classical approaches relying on continuous physical and chemical parameters—such as pH, total dissolved solids, and turbidity—have achieved classification accuracies ranging between 85% and 94% using algorithms like Support Vector Machines, Random Forest, and Gradient Boosting (Azrour et al., 2022; Poudel et al., 2023), predicting microbiological safety in untreated raw water systems presents unique regulatory challenges. Recent studies emphasize that for public health applications, predictive frameworks must prioritize sensitivity and specificity metrics over overall accuracy to prevent the hazardous misclassification of contaminated water as potable (Azrour et al., 2022). Building upon this literature, integrating high-specificity machine learning models with time-series analysis on unmonitored public fountain networks provides a proactive decision-support tool to protect vulnerable communities from waterborne disease outbreaks.

Recently, traditional statistical methods in water quality estimations and managements have been started to replace with AI and ML algorithms that provide higher level of accuracy. Artificial Neural Network (ANN), Support Vector Machine (SVM), Random Forest (RF) and K-Nearest Neighbor (KNN) algorithms are widely utilized to estimate water quality of the resources. For instance, Najah et al. (2013) and Zhu et al. (2019) estimated water quality parameters with the accuracy between 89 to 92% by using ANN, SVM and RF algorithms. On the other hand, more recent studies on various open-source water quality datasets and groundwater analyses (Nasir et al., 2022; Panigrahi et al., 2023; Turan, 2023; Poudel et al., 2023) prove that boosting algorithms, such as XGBoost, CatBoost, and LightGBM, as well as hybrid machine learning models (e.g., SVR-XGBoost combinations), demonstrate far superior performance by remaining resilient to outliers. While studies such as Abuzir and Abuzir (2022) and Ahmed et al. (2019) emphasize the level of classification accuracy of Multi-Layer Perceptron (MLP), Azrour et al. (2022) draws attention to using sensitivity and specificity parameters as the water quality parameters directly affect the public health and safety. The broad literature on ML-based water quality estimation models allow to develop early warning systems and proactive precautions.

Public fountains are not only supply for drinking water but also used to be social gathering places in many cultures. Although the water supply infrastructure in Bayburt province of Türkiye was improved between 2014 and 2016, residents of Bayburt continued to embrace using public fountains for drinking water in addition to using reverse osmosis systems at home and bottled water. According to sampling campaigns` reports conducted regularly by Bayburt Provincial Directorate of Health, public fountains in question were contaminated with *E. coli* and coliform bacteria indicating water from these fountains is not drinkable. Waters from fountains that do not meet the microbiological standards puts the public health in danger.

The main objective of the study is to statistically analyze the trend and seasonality of *E. coli* and coliform bacteria contaminations detected in public fountains of Bayburt Province over time and to predict water quality parameters with high accuracy by using various ML methods. In this regard, Logistic Regression, K-Nearest Neighbor, Support Vector Machine, Naïve Bayes, Decision Tree and Random Forest algorithms are utilized on the data set provided. These developed predictive models would guide public to when to use water from fountains by early forecasting capabilities and prevent public potential public health risks.

2. Materials and Methods

2.1. Study Area and Data Set

The main interest area of the study is five most common used fountains (Gordon, Kışla, Tarım, Aşağı Narkazan ve Yukarı Narkazan) near the downtown area of the Bayburt Province (Figure 1). Data set consists of monthly microbiological water quality analysis reports from 2014 to 2024. Numbers of microbiological contaminants such as *E. coli* and coliform bacteria are taken into account as the pollutants. In accordance with the Regulation on Waters for Human Consumption, the detection of these bacteria in any amount is sufficient for the analysis result to be evaluated as 'contaminated'. The data set consists of 476 samples whose 285 of them are clean and 191 of them are recorded as contaminated (Table 1).

In accordance with the *Regulation on Waters for Human Consumption of Türkiye* (Ministry of Health, 2005), drinking water must satisfy a strict zero-tolerance baseline where no detectable fecal indicator organisms are permitted in a 100 mL sample. Consequently, the target output variable (Y) for supervised machine learning forecasting was encoded into a binary classification scheme (0 = Safe/Potable, 1 = Contaminated/Unpotable). Samples containing 0 CFU/100 mL for both *E. coli* and total coliform were designated as 'Safe' (Y=0), whereas any sample exhibiting bacterial counts > 0 CFU/100 mL for either indicator was categorized as 'contaminated' (Y=1).

2.2. Data Pre-processing

In order for ML algorithms to be trained efficiently, preprocessing on the dataset has to perform systematically. The categorical outcome labels of `contaminated` and `clean` in the dataset converted into numerical data with encoding methods by ensuring the compatibility with ML algorithms. The preprocessed data were then divided in 2 groups of which 80% for training and 20% for testing. The 80/20 train-test split was selected in accordance with standard machine learning Pareto principles to maximize training capacity while

ensuring a statistically representative test sample (Hastie et al., 2009). A stratified splitting strategy was applied to preserve the precise 60:40 class balance ratio (285 clean / 191 contaminated) across both training and testing datasets (Géron, 2022). Data analysis and modeling processes were carried out on the Anaconda platform using the Spyder (Python 3.12) interface.

2.3. Trend and Seasonality Analysis

Time series analysis was performed to be able to identify time series patterns of bacterial contamination dynamics. To investigate the long-term trends in E. coli and coliform concentrations, a linear regression method (equation 1) was utilized (Kutner et al., 2005).

$$y = \theta_1 + \theta_2 x + \varepsilon \quad (1)$$

where y is the dependent variable, x is the independent variable, θ_1 is the intercept (bias), θ_2 is the slope (trend direction), and ε is the residual. Statistical significance was determined based on a P<0.05, while the model's explanatory capacity was assessed via R^2 scores (Montgomery et al., 2012). In addition, Time series decomposition techniques were employed via the seasonal_decompose tool of the statsmodels in Python 3.2 library to investigate the presence of a periodic fluctuation (seasonality) in the data; the period parameter was specified as 12, corresponding to the monthly data level. Seasonality strength is defined as equation 2 (Hyndman and Athanasopoulos, 2008);

$$Seasonality\ Strength = \frac{std(S_t)}{std(R_t)} \quad (2)$$

where $std(S_t)$ standard deviation of time series and $std(R_t)$ standard deviation of residuals and values higher than 0.6 indicate strong seasonality.

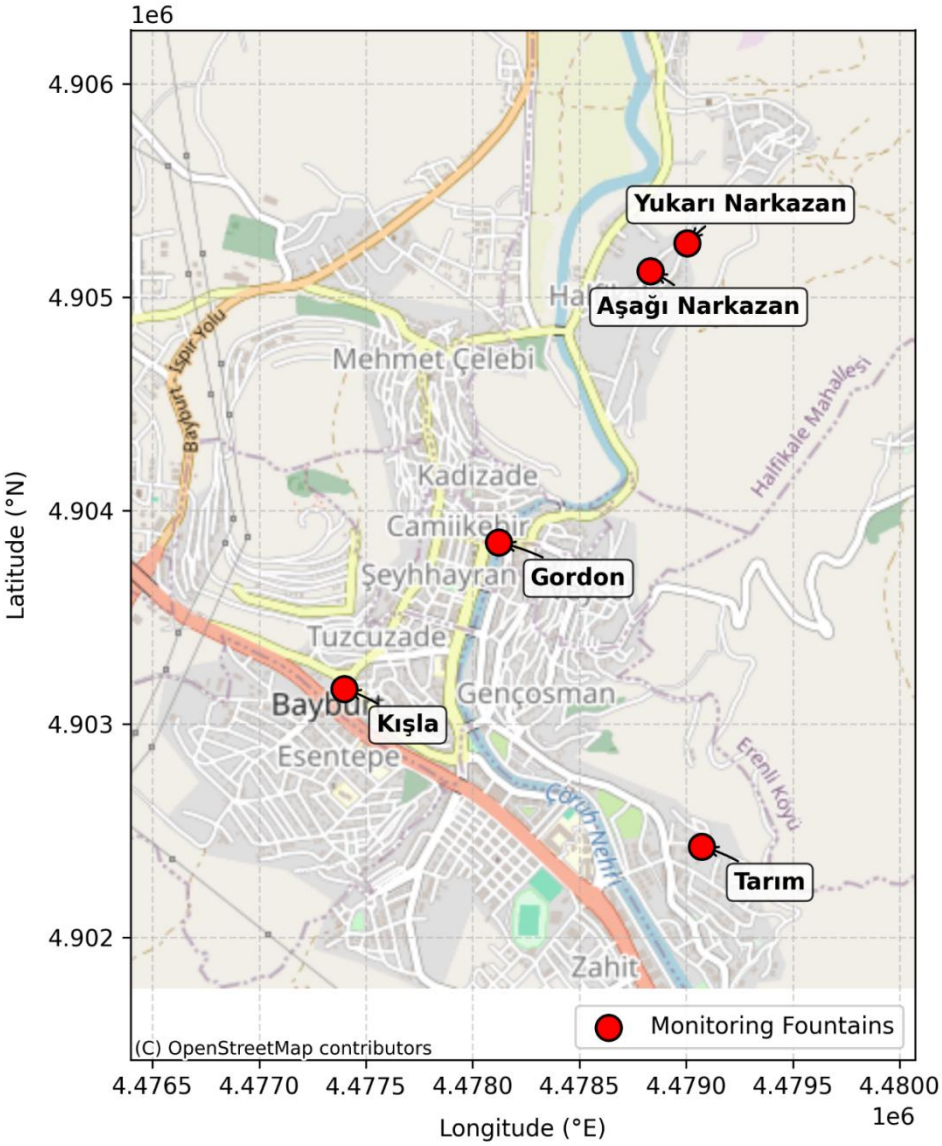


Figure 1. Geographic coordinates of all five monitoring stations (Kışla, Gordon, Tarım, Aşağı Narkazan, and Yukarı Narkazan) across downtown Bayburt.

Table 1. Comprehensive summary statistics for all five monitoring stations

Station Name	Variable	Meas. Unit	Sample Size (N)	Mean	Std. Dev. (σ)	Min	Max
Aşağı Narkazan	E. coli	CFU/100 mL	79	0.32	2.81	0	25
	Coliform		79	0.82	4.08	0	27
Gordon	E. coli		98	12.12	26.51	0	100
	Coliform		98	27.28	35.34	0	100
Kışla	E. coli		94	1.41	10.41	0	100
	Coliform		94	21.96	35.76	0	100
Tarım	E. coli		102	0.16	0.67	0	5
	Coliform		102	30.75	31.67	0	100
Yukarı Narkazan	E. coli		103	0.01	0.10	0	1
	Coliform		103	1.24	4.79	0	25

2.4. Machine Learning (ML) Models

To predict water quality potability (0= Safe, 1= Contaminated), six supervised classification algorithms were trained using an input feature matrix $X = [X_{station}, X_{month}, X_{year}, X_{Ecoli_hist}, X_{coliform_hist},]$.This matrix incorporates one-hot encoded spatial indicators, cyclic seasonal temporal markers, and historical bacterial lag features to capture temporal persistence.

Logistic Regression: It was employed to adopt a probabilistic approach for the binary classification task.

K-Nearest Neighbor: Number of neighbors is set to be *n*= 3 in computations and tested with Minkowski, Euclidean and Manhattan distance metrics. The hyperparameter *n*= 3 for the K-NN classifier was determined via a 5-fold cross-validation grid search evaluated on the training set across candidate values $n \in \{1, 3, 5, 7, 9\}$ where *n*= 3 yielded the lowest validation error rate while avoiding distance-weighting noise.

Support Vector Machines: To linearly separate the data in higher dimensions, the system was modeled using Linear, Radial Basis Function (RBF), Sigmoid, and Polynomial kernel types.

Naive Bayes: Modeling was performed via Gaussian Naive Bayes, relying on the fundamental assumption that all classification attributes are independent of one another.

Decision Tree: The algorithm was executed by performing node splits based on Gini impurity and Entropy metrics, which serve to quantify the complexity and randomness of the data points.

Random Forest: To prevent overfitting, this model was constructed as an ensemble of multiple decision trees (n_estimators=10) and evaluated using Entropy and Gini metrics.

2.5. Model Evaluation Metrics

The performances of the developed classification models are analyzed on the Confusion Matrix. The predictive performances of the models were compared by followıng metrics (equations 3-5) (Sathyanarayanan and Tantri, 2024);

$$Accuracy = \frac{TP+TN}{TP+TN+FP+FN} \quad (3)$$

$$Sensitivity = \frac{TP}{TP+FN} \quad (4)$$

$$Precision = \frac{TP}{TP+FP} \quad (5)$$

In water quality analysis, estimating contaminated water as clean (False Positive) poses a major public health risks. Instead, using specificity metric, which mitigates the risk is the most fundamental criteria on determining the reliability of the models and is determined as the most vital performance criterion of this study, and the following equation was used in the calculations (equation 6):

$$Specificity = \frac{TN}{TN+FP} \quad (6)$$

3. Results

3.1. Findings of Trend and Seasonality Analysis

Variations of *E.Coli* and coliform bacteria contamination in five public fountains in Bayburt were investigated by the means of time series and trend analysis. There was no statistically significant upward or downward trend in *E. coli* concentrations across all monitored fountains (P>0.05) (Table 2). However, there was a statistically significant downward trend (P=0.0134) observed in the Gordon fountain while there was statistically significant upward trend observed in Kisla (P=0.0002) and Tarim (P=0.0056) fountains in terms of coliform bacteria count (Table 3). Also, there was not a statistically significant trend observed in Narkazan Fountain in terms of coliform bacteria.

On the other hand, the seasonality strength in the time-series decomposition for both bacterial species remained low (ranging from 0.3863 to 0.6326), and no seasonal patterns or periodic fluctuations were detected in the data (Figure 2).

Table 2. Time series and Seasonality analysis results for E. Coli concentrations

Fountain Name	Slope	Intercept	R^2	P-value	Significance	Seasonality Strength	Seasonality
Aşağı Narkazan	-0.0001	0.4755	0.0007	0.8304	Not Significant	0.5012	Absent
Gordon	-0.0067	20.2879	0.0395	0.0698	Not Significant	0.4885	Absent
Kışla	0.0002	0.1414	0.0067	0.4608	Not Significant	0.6326	Absent
Tarım	-0.0001	0.1580	0.0225	0.1733	Not Significant	0.4699	Absent
Yukarı Narkazan	0	0	0	1	Not Significant	—	—

Table 3. Time series and Seasonality analysis results for coliform bacteria concentrations

Fountain Name	Slope	Intercept	R^2	P-value	Significance	Seasonality Strength	Seasonality
Aşağı Narkazan	0.0002	0.6571	0.0012	0.7768	Not Significant	0.4912	Absent
Gordon	-0.0123	41.1088	0.0723	0.0134	Significant	0.5744	Absent
Kışla	0.0186	-1.8146	0.1539	0.0002	Significant	0.4091	Absent
Tarım	0.0130	14.7144	0.0897	0.0056	Significant	0.3863	Absent
Yukarı Narkazan	0.0002	0.17310	0.0020	0.6881	Not Significant	0.4260	Absent

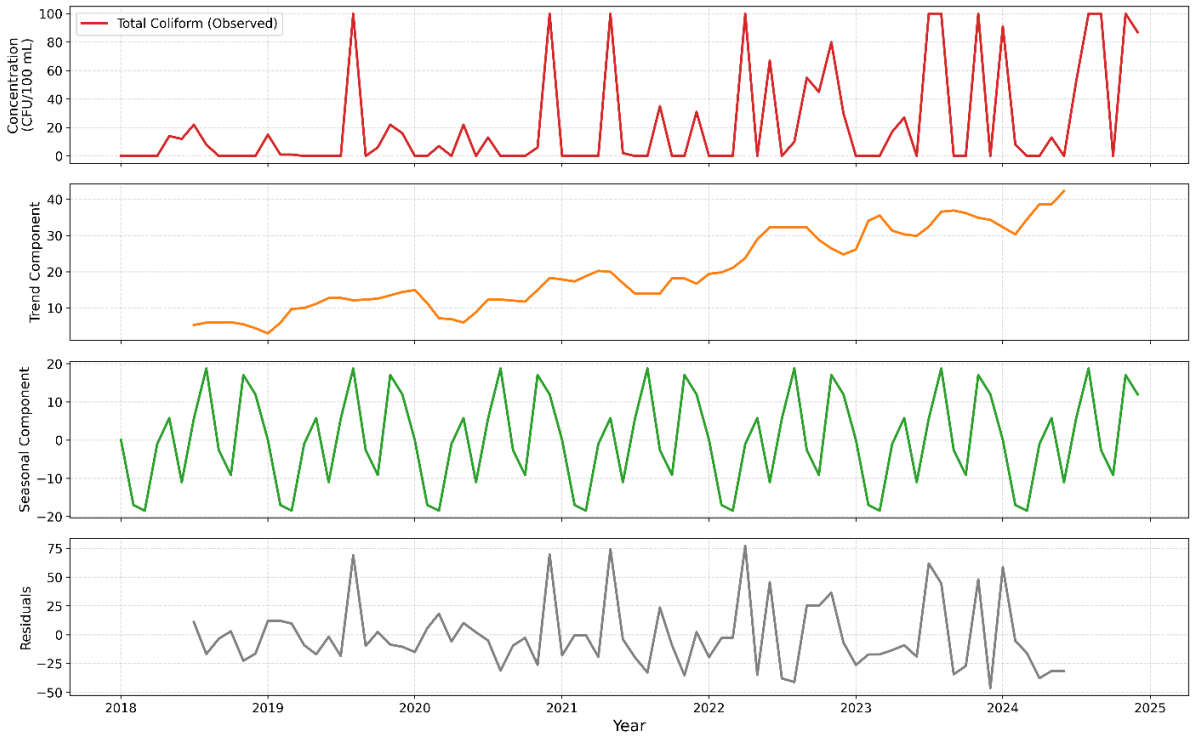


Figure 2. Trend analysis of the coliform bacteria at the Kışla Fountain.

3.2. Machine Learning Prediction Performances

The performances of six different machine learning models developed to predict the microbiological water quality (contaminated/safe) of public fountains were evaluated. In these evaluations, accuracy and particularly specificity metrics were prioritized. According to the obtained results, the Decision Tree, Naive Bayes, and Random Forest algorithms demonstrated flawless performance, achieving an accuracy of 1.0 (100%) and a Specificity of 1.0 (100%). K-Nearest Neighbors (KNN) and Support Vector Machines (SVM with Linear, RBF, and Sigmoid kernels) yielded 99% accuracy and 97% specificity, followed by the Logistic Regression model with 97% accuracy and 90% specificity. The lowest performance was observed in the SVM Polynomial kernel model, which exhibited an accuracy of 80% and a specificity of only 39% (Table 4).

Table 4. Results of machine learning methods applied to fountain waters in Bayburt

Model / Algorithm	Kernel / Variant	Accuracy (%)	Specificity (%)	Performance Ranking
Decision Tree	—	100%	100%	1 (Best)
Naive Bayes	—	100%	100%	1 (Best)
Random Forest	—	100%	100%	1 (Best)
KNN	—	99%	97%	2
SVM	Linear	99%	97%	2
SVM	RBF	99%	97%	2
SVM	Sigmoid	99%	97%	2
SVM	Polynomial	80%	39%	4 (Worst)
Logistic Regression	—	97%	90%	3

4. Discussion

The absence of seasonality across all fountains(Tables 2 and 2) in the time-series analysis clearly demonstrates that microbiological contamination in the water resources does not originate from predictable seasonal factors such as precipitation, temperature, or snowmelt. While the decrease in coliform rates at the Gordon fountain can be explained by potential local remediation efforts, the significantly increasing trends observed at the Kışla and Tarım fountains suggest that the pollution sources are continuous and irregular, likely driven by anthropogenic factors or infrastructural leakages. Conversely, the lack of a significant contamination trend at the Narkazan fountains indicates that these fountains may possess relatively more isolated or protected water sources compared to the others. When the literature is examined, the increasing contamination trends in the Yamuna River by Parmar and Bhardwaj (2015) and in the Pearl River by Deng et al. (2021) are linked to anthropogenic factors and urban waste. Similarly, investigations by Lutz et al. (2020) and Sprague et al. (2017) attributed the shifts in trends to local governance strategies and non-point/irregular pollution sources rather than seasonal effects.

When evaluating water quality using machine learning models, relying solely on the 'accuracy' rate poses major risks to public health. In reality, misclassifying contaminated and unpotable water as 'safe' (False Positive) could trigger outbreaks of waterborne diseases such as cholera, typhoid, or dysentery. Therefore, in water quality early warning systems, models that avoid this hazardous misclassification—specifically those with the highest specificity values—must be preferred. In this study, although the SVM model demonstrated an acceptable overall accuracy of 80%, its specificity remained at a critical 39%; meaning it fell into the fallacy of classifying a large portion of contaminated water as safe (Table 4). Conversely, the Decision Tree, Naive Bayes, and Random Forest algorithms achieved a flawless specificity score of 1.0, accurately identifying hazardous ('contaminated') water at a 100% rate and eliminating the risk of False Positives. This finding proves that these three models can be safely utilized as robust decision-support mechanisms for ensuring the safety of public fountains. To evaluate the predictive performance of the developed models within a broader scientific context, a comparative benchmark was conducted against prominent, recently published machine learning studies in water potability assessment (Table 5). While existing literature—such as Panigrahi et al. (2023) (94.2% accuracy), Azrour et al. (2022) (91.8% accuracy), and Poudel et al. (2023) (89.5% accuracy)—typically reports model accuracy and specificity scores ranging between 86% and 94%, the top-performing paradigms in this study (Decision Tree, Random Forest, and Naive Bayes) achieved flawless predictive metrics (100% accuracy and 100% specificity). This performance discrepancy stems directly from fundamental differences in target standards and dataset characteristics: unlike benchmark studies that rely on multi-parameter continuous chemical indices (e.g., pH, TDS, Nitrates) with high variance and imputation noise, our models evaluate a zero-tolerance binary classification mandated by the Regulation on Waters for Human Consumption, where any detection of *E. coli* or total coliform above 0 CFU/100 mL instantly denotes contamination. Because the classification target directly mirrors the indicator bacterial counts without continuous chemical overlap or statistical data filling, tree-based algorithms (Decision Tree and Random Forest) can split decision nodes with complete mathematical purity (Gini Impurity = 0.0), thereby establishing a crisp decision boundary that eliminates false positive and false negative errors on the stratified test set while ensuring robust, zero-false-positive early warning capabilities for public health protection.

The present study offers a practical solution that directly serves the United Nations Sustainable Development Goals, particularly 'Clean Water and Sanitation' (Goal 6) and 'Good Health and Well-being' (Goal 3) (United Nations, 2024). The integration of artificial intelligence into drinking water management can function as a modern shield for disease prevention. In terms of future studies and local government policies, enhancing archive and data quality by assigning unique identification numbers (IDs) to public fountains—which act as monitoring points—is of paramount importance. Furthermore, considering that the public directly utilizes these fountains for daily drinking water, it is essential to incorporate regular chemical parameter analyses into the system alongside microbiological monitoring.

Table 5. Quantitative comparison of machine learning model performances across existing water quality literature and the present study

Study	Target Domain / Water Source	Primary Model(s)	Accuracy (%)	Specificity (%)	Key Predictor Variables / Features
Panigrahi et al. (2023)	Regional Groundwater Aquifers	XGBoost / Random Forest	94.2%	91.5%	Multi-parameter chemical indices (pH, TDS, Nitrates, Fluoride, Hardness)
Azrour et al. (2022)	Surface Water Resources	SVM / Artificial Neural Networks	91.8%	88.0%	Chemical & physical parameters (Turbidity, DO, BOD, pH)
Poudel et al. (2023)	Imputed Synthetic/Public Datasets	Random Forest	89.5%	86.2%	Statistically imputed Kaggle/Kaggle-style potability datasets
Present Study	Raw, Untreated Public Fountains	Decision Tree / Random Forest / Naive Bayes	100.0%	100.0%	Microbiological indicator counts (E. coli, Coliform), Temporal & Spatial Fountain IDs

5. Conclusion

This study was conducted to evaluate the microbiological water quality of public fountains intensively utilized by the local population in the province of Bayburt, and to predict future public health risks through artificial intelligence-based machine learning methods. The time-series and trend analyses demonstrated that E. coli and total coliform contamination in the fountains lacks a distinct seasonal pattern; therefore, the degradation is heavily driven by anthropogenic factors or irregular environmental leakages rather than predictable seasonal variables.

During the machine learning modeling phase of the study, the Decision Tree, Naive Bayes, and Random Forest algorithms exhibited flawless performance in predicting water quality, achieving an accuracy of 1.0 (100%) and a specificity of 1.0 (100%). In water quality forecasting, the erroneous classification of unpotable, contaminated water as "safe" by algorithms (a False Positive error) constitutes the most hazardous risk capable of triggering widespread waterborne disease outbreaks. Consequently, the achievement of 100% specificity by these three developed models—thereby mitigating the risk of faulty "safe" predictions to zero—proves that they can be confidently deployed as public health-protective decision support systems. These empirical findings explicitly reveal the critical role of technological infrastructures in achieving United Nations Sustainable Development Goals, specifically Goal 6 (Clean Water and Sanitation) and Goal 3 (Good Health and Well-being), at a localized scale. In light of the obtained results and the data limitations encountered, the following recommendations are put forward for local authorities, healthcare policymakers, and researchers:

Standardization of Monitoring Stations (Identification): To prevent identical fountains from being recorded under disparate names during water analysis data logging and to construct an efficient digital data archive, a unique identification number (ID) must be assigned to each public fountain (monitoring point).

Integration of Chemical Profiling into Fountain Analyses: Given that public fountain waters are systematically consumed by the local population for daily drinking and domestic utilization, it is imperative that analyses are not restricted solely to microbiological parameters (E. coli, coliform). Comprehensive chemical parameter and heavy metal tracking (such as arsenic, lead, etc.), which chronically impact human health, must be incorporated into the routine monitoring protocols of these fountains.

Transition to Real-Time Early Warning Infrastructures: Future research trajectories should integrate these highly successful machine learning paradigms into a "real-time early warning system" utilizing expanded datasets featuring higher measurement frequencies and broader parameters. Consequently, potential health threats and contamination episodes can be detected before escalating into crises, allowing the public to be instantly notified via media or social media channels and redirected toward secure water sources.

Author Contributions

The percentages of the authors' contributions are presented below. All authors reviewed and approved the final version of the manuscript.

	G.K.	R.S.
C	40	60
D	40	60
S	30	70
DAI	50	50
L	70	30
W	50	50
CR	30	70
SR	30	70

C= concept, D= design, S= supervision, DAI= data analysis and/or interpretation, L= literature search, W= writing, CR= critical review, SR= submission and revision.

Conflict of Interest

The authors declared that there is no conflict of interest.

Ethical Consideration

Ethics committee approval was not required for this study because of there was no study on animals or humans.

Acknowledgements

This work is produced from a master's thesis carried out at Bayburt University, Department of Civil Engineering. The authors would like to thank the Bayburt Provincial Directorate of Health and the Bayburt Public Health Laboratory for their precious cooperation and support in supplying the water quality analysis data.

References

Abuzir, S. Y., & Abuzir, Y. S. (2022). Machine learning for water quality classification. *Water Quality Research Journal*, *57*(3). https://doi.org/10.2166/wqrj.2022.004

Ahmed, U., Mumtaz, R., Anwar, H., Shah, A. A., Irfan, R., & García-Nieto, J. (2019). Efficient water quality prediction using supervised machine learning. *Water*, *11*(11), Article 2210. https://doi.org/10.3390/w11112210

Azrour, M., Mabrouki, J., Fattah, G., Guezzaz, A., & Aziz, F. (2022). Machine learning algorithms for efficient water quality prediction. *Modeling Earth Systems and Environment*, *8*(2), 2793–2801. https://doi.org/10.1007/s40808-021-01266-6

Deng, Y., Zhang, T., Wang, Y., & Liang, L. (2021). Long-term trends and variations in water quality of the Pearl River Delta, China. *Environmental Science and Pollution Research*, *28*(15), 18950–18962. https://doi.org/10.1007/s11356-020-11929-6

Géron, A. (2022). *Hands-on machine learning with Scikit-Learn, Keras, and TensorFlow* (3rd ed.). O'Reilly Media.

Hastie, T., Tibshirani, R., & Friedman, J. (2009). *The elements of statistical learning: Data mining, inference, and prediction* (2nd ed.). Springer. https://doi.org/10.1007/978-0-387-84858-7

Hyndman, R. J., & Athanasopoulos, G. (2018). *Forecasting: Principles and practice* (2nd ed.). OTexts. https://otexts.com/fpp2/

Kuşçu, A., & Kılıç, İ. (2023). Su kalite indeksinin makine öğrenme yöntemleri ile tahmini [Estimation of water quality index by machine learning methods]. *Bilimsel ve Akademik Araştırmalar Dergisi*, *7*(13), 1–18. https://bibad.gen.tr/index.php/bibad/article/view/444

Kutner, M. H., Nachtsheim, C. J., Neter, J., & Li, W. (2005). *Applied linear statistical models* (5th ed.). McGraw-Hill/Irwin.

Lutz, S. R., Trauth, N., & Musolff, A. (2020). Long-term trends and seasonality of nitrate concentrations in a regional agricultural catchment. *Science of the Total Environment*, *714*, Article 136729. https://doi.org/10.1016/j.scitotenv.2020.136729

Ministry of Health. (2005). *Regulation on waters intended for human consumption* (Official Gazette No. 25730, February 17, 2005). Republic of Türkiye Ministry of Health.

Montgomery, D. C., Peck, E. A., & Vining, G. G. (2012). *Introduction to linear regression analysis* (5th ed.). John Wiley & Sons.

Najah, A., El-Shafie, A., Karim, O. A., & El-Shafie, A. H. (2013). Application of artificial neural networks for water quality prediction. *Neural Computing and Applications*, *22*(Suppl 1), 187–201. https://doi.org/10.1007/s00521-012-0940-3

Nasir, N., Kansal, A., Alshaltone, O., Barneih, F., Sameer, M., Shanableh, A., & Al-Shamma'a, A. (2022). Water quality classification using machine learning algorithms. *Journal of Water Process Engineering*, *48*, Article 102920. https://doi.org/10.1016/j.jwpe.2022.102920

Panigrahi, N., Patro, S. G. K., Kumar, R., Omar, M., Tran, T. N., Nguyen, L. G., Bui, T. T., & Nguyen, T. T. (2023). Groundwater quality analysis and drinkability prediction using artificial intelligence. *Earth Science Informatics*, *16*(2), 1701–1725. https://doi.org/10.1007/s12145-023-00977-x

Parmar, K. S., & Bhardwaj, R. (2015). Statistical, time series, and fractal analysis of water quality of river Yamuna at Kalpi for forecasting and management. *Environmental Monitoring and Assessment*, *187*(3), Article 124. https://doi.org/10.1007/s10661-015-4338-5

Poudel, D., Shrestha, D., Bhattarai, S., & Ghimire, A. (2023). Comparison of machine learning algorithms in statistically imputed water potability dataset. *Journal of Innovations in Engineering Education*, *5*(1), 38–46. https://doi.org/10.3126/jiee.v5i1.42265

Sathyanarayanan, S., & Tantri, B. R. (2024). Confusion matrix-based performance evaluation metrics. *African Journal of Biomedical Research*, *27*(4s), 4023–4031. https://africanjournalofbiomedicalresearch.com/index.php/AJBR

Shen, C. (2018). A transdisciplinary review of deep learning research and its relevance for water resources scientists. *Water Resources Research*, *54*(11), 8558–8593. https://doi.org/10.1029/2018WR022643

Sprague, L. A., Hirsch, R. M., & Aulenbach, B. T. (2017). Trends in nutrient and sediment concentrations and loads in major river basins of the United States. *Journal of the American Water Resources Association*, *53*(3), 665–684. https://doi.org/10.1111/1752-1688.12520

Turan, T. (2023). Makine öğrenmesi algoritmaları ile su kalitesi ve içilebilirlik tahmini [Water quality and drinkability prediction using machine learning algorithms]. *Uluborlu Mesleki Bilimler Dergisi*, *6*(2), 65–80.

United Nations. (2024). *The United Nations world water development report 2024: Water for prosperity and peace*. UNESCO. https://www.unwater.org

WHO. (2022). World Health Organization. *Drinking-water*. https://www.who.int/news-room/fact-sheets/detail/drinking-water

WHO. (2023). World Health Organization *Drinking-water*. https://www.who.int/news-room/fact-sheets/detail/drinking-water

Zhu, M., Wang, J., Yang, X., & Zhang, Y. (2019). Forecasting water quality parameters in Lake Taihu using machine learning models. *Water Resources Research*, *55*(11), 9502–9519. https://doi.org/10.1029/2019WR025189

Black Sea Journal of Engineering and Science
doi: 10.34248/bsengineering.1991363

Open Access Journal
e-ISSN: 2619 – 8991

Research Article
Volume 9 - Issue 5: 2373-2392 / September 2026

ROBUSTNESS EVALUATION OF HYPERSPECTRAL IMAGE CLASSIFICATION MODELS USING DEGRADATION-AWARE METRICS

Cem ATILGAN[1]*

[1]*Kırklareli University, Faculty of Technology, Department of Mechatronics Engineering, 39000, Kırklareli, Türkiye*

Abstract: Hyperspectral image classification studies are generally evaluated on clean benchmark datasets and often report high-accuracy values. However, because real sensor data can be affected by different degradations, such as Gaussian, impulse, stripe, dead-line, and mixed noise, clean-data performance alone may be insufficient to explain the reliability of models under practical conditions. In this study, SVM, k-NN, 1D-CNN, 2D-CNN, 3D-CNN, Hybrid CNN, Dense CNN, and a transformer-based model were evaluated on the Indian Pines, Pavia University, and Salinas datasets under controlled noise scenarios. The overall accuracy (OA), average accuracy (AA), kappa coefficient, and macro-F1 score were used as standard performance metrics. In addition, two robustness-oriented metrics, Relative Degradation Rate (RDR) and Robustness Score (RS), were used to measure noise-induced performance degradation more explicitly. The findings show that model rankings obtained on clean data may change under noisy conditions depending on the dataset and noise type. Performance degradation was more evident for some models, especially under mixed-severity and high-severity noise scenarios. Overall, the results indicate that hyperspectral classification models should be evaluated not only based on clean-data accuracy but also in terms of their robustness against different types of sensor noise.

Keywords: Hyperspectral image classification, Noise robustness, Sensor degradation, Machine learning classifiers, Deep learning models, Degradation-aware metrics

***Corresponding author:** Kırklareli University, Faculty of Technology, Department of Mechatronics Engineering, 39000, Kırklareli, Türkiye
E mail: cematilgan@klu.edu.tr (C. ATILGAN)
Cem ATILGAN https://orcid.org/0000-0001-7226-0811

Received: July 08, 2026
Accepted: August 10, 2026
Published: September 15, 2026

Cite as: Atılgan, C. (2026). Robustness evaluation of hyperspectral image classification models using degradation-aware metrics. *Black Sea Journal of Engineering and Science,* 9(5), 2373-2392.

1. Introduction

Hyperspectral imaging (HSI) provides detailed information across many narrow and contiguous spectral bands (He et al., 2018; Stuart et al., 2022). This information is used in remote sensing applications, such as land cover mapping, environmental monitoring, agricultural analysis, and target detection (He et al., 2018; Lodhi et al., 2019; Parra, 2022). As different materials often exhibit different spectral properties, hyperspectral images can help identify materials that are difficult to distinguish in RGB or multispectral images (He et al., 2018; Lodhi et al., 2019). To address these challenges, a wide range of machine learning and deep learning methods have been developed for hyperspectral image classification (Li et al., 2019; Ahmad et al., 2022).

Classical machine learning methods have long served as important baselines in this domain. In particular, support vector machines (SVMs) have been widely used because they can provide effective generalization in high-dimensional spectral spaces, even when the number of labeled samples is limited (Melgani and Bruzzone, 2004). Similarly, k-nearest-neighbor-based methods have been used as simple and effective instance-based approaches for hyperspectral image classification, and spectral-spatial extensions of k-NN have been proposed to improve classification performance by incorporating neighborhood information (Bo et al., 2018). In addition, random forests and decision tree ensembles have been adopted for high-dimensional and label-limited data owing to their stable classification behavior (Ham et al., 2005), while ensemble extensions, such as Rotation Forest, have been reported to improve classification accuracy in hyperspectral image analysis (Xia et al., 2014). In recent years, deep learning methods have become increasingly prominent in hyperspectral image classification (Li et al., 2019; Bera et al., 2022; Yu et al., 2023). Convolutional neural networks can learn hierarchical features directly from data, and 2D and 3D convolutional architectures have been widely developed to model spatial and spectral-spatial information in hyperspectral images (Li et al., 2019; Roy et al., 2020; Bera et al., 2022). Roy et al. (2020) proposed the HybridSN architecture, which combines 3D and 2D convolutions to achieve high classification accuracy with lower computational cost than using 3D convolutions alone. Dense convolutional networks have also been used

This work is licensed (CC BY-NC 4.0) under Creative Commons Attribution 4.0 International License

to strengthen feature reuse through dense connections and have been reported to yield competitive results on benchmark datasets (Zhi et al., 2019). Similarly, hybrid neural networks combine complementary spectral and spatial feature extraction branches to reduce the limitations of models based only on spectral or spatial information (Li et al., 2020). Recently, transformer-based architectures have been introduced to model long-range spectral dependencies through self-attention mechanisms (Hong et al., 2022; Sun et al., 2022), and recent variants, such as memory-augmented attention, have continued to extend this line of research (Sun et al., 2024). In addition, state-space models, such as Mamba-based architectures, have emerged as efficient alternatives for modeling long-range spectral dependencies in hyperspectral image classification (Ahmad et al., 2025). Although these methods often report high accuracy on benchmark datasets, the robustness of their performance under controlled input degradations is not always evaluated explicitly. Under practical imaging conditions, hyperspectral data may be affected by atmospheric effects and instrumental noise, including thermal noise, quantization noise, and shot or photon noise. Such degradation can distort spectral and spatial information and may reduce the reliability of downstream classification tasks (Rasti et al., 2018; Mei et al., 2024). Therefore, high accuracy on clean data alone may not be sufficient to describe the reliability of a model under real-world conditions. This issue is not limited to hyperspectral image classification. Studies on natural images have shown that improvements in clean accuracy do not necessarily lead to proportional improvements in robustness to common corruptions, and that model behavior may change under distribution shifts (Hendrycks and Dietterich, 2019; Schneider et al., 2020). However, in remote sensing, model robustness has not yet been examined in a sufficiently systematic manner. A recent comprehensive study emphasized that robustness against natural and adversarial noise remains under-explored in remote sensing tasks (Mei et al., 2024). Although recent studies have addressed noisy hyperspectral image classification from different perspectives, including noisy-label learning (Ma et al., 2024) and input-degradation-aware noise-robust architectures (Xie et al., 2026), these studies mainly focus on improving the robustness of specific model architectures. Consequently, there is still limited evidence on how different model families behave under noisy conditions and whether model rankings obtained from clean data remain valid when noise is introduced.

This gap raises an important question: a model that performs well on clean benchmark data may not necessarily be the most reliable under realistic noisy conditions. This study aimed to investigate whether clean-data performance is a reliable indicator of noise robustness in hyperspectral image classification. For this purpose, classical, convolutional, and transformer-based classifiers were evaluated under Gaussian, impulse, stripe, dead-line, and mixed noise scenarios. The evaluation considers not only the absolute classification performance but also the relative performance degradation and stability of the model rankings. The main hypothesis of this study is that the accuracy of clean data alone may be insufficient to predict robustness under noisy conditions.

The main contributions of this study are as follows:

- A systematic noise robustness evaluation protocol was used for hyperspectral image classification.
- Eight classical, convolutional, and transformer-based classifiers were compared under Gaussian, impulse, stripe, dead-line, and mixed noise scenarios.
- The models were evaluated using overall accuracy, average accuracy, Kappa coefficient, and macro-F1 score, together with the relative degradation rate, robustness score, and ranking stability.
- The stability of the clean-data model rankings under noisy conditions was quantitatively analyzed using three benchmark datasets.

The remainder of this paper is organized as follows. Section 2 introduces the datasets, classifiers, noise models, and evaluation protocols used in this study. Section 3 presents the results obtained for clean and noisy conditions. Section 4 discusses the findings in relation to relevant literature. Finally, Section 5 concludes the study and outlines possible future work directions.

2. Materials and Methods

The overall experimental workflow is illustrated in Figure 1. The process consists of band-wise normalization of the datasets, class-balanced training, validation, and test partitioning, application of noise models, and evaluation of classical, convolutional, and transformer-based models under a unified experimental protocol.

2.1. Datasets and Preprocessing

The experiments were conducted on three widely used hyperspectral benchmark datasets, which are listed in Table 1. Prior to classification, noisy or water absorption bands were removed according to standard preprocessing protocols. Before generating synthetic noise, each dataset was normalized to the range [0, 1] on a band-wise basis.

2.2. Classifiers

The compared models represent both classical and deep learning-based classification families, as listed in Table 2. SVM and k-NN are used as non-deep baseline models, whereas CNN-based methods represent widely used deep classifiers, and transformer-based models represent recent attention-based approaches. The transformer is a compact encoder that treats each spatial location of a PCA-reduced patch as a token and incorporates a learnable class token and positional embedding. It is not a full SpectralFormer implementation but rather a representative transformer baseline evaluated under the

same experimental protocol (Hong et al., 2022).

2.3. Noise Models

Figure 2 illustrates the visual effects of different degradation types on the Indian Pines dataset using a pseudo-color representation. Let $X \in \mathbb{R}^{H\times W\times B}$ denote the clean hyperspectral image, where H, W, and B represent the height, width, and number of spectral bands, respectively. All noise types were applied after normalization to the range [0, 1], and the resulting values were clipped to the same range. Gaussian noise was added in an additive manner using three noise levels, $\sigma \in \{0.05, 0.10, 0.15\}$ as given in equation 1:

$$X_G = clip(X + \mathcal{N}(0, \sigma^2), 0, 1) \quad (1)$$

This equation indicates that random values drawn from a zero-mean Gaussian distribution are added to a clean hyperspectral image. This parameter σ controls the noise intensity, where larger values produce stronger Gaussian degradation. After the noise is added, the pixel values are clipped to the valid normalized range [0, 1]. Impulse noise randomly assigns a proportion p of pixels to either the minimum or maximum intensity value. In this study, three impulse noise levels were considered, with$p \in \{0.01, 0.03, 0.05\}$. Impulse degradation is described equation 2:

$$X_I(i,j,b) = \begin{cases} 0, & r_{ij} < p/2 \\ 1, & p/2 \le r_{ij} < p \\ X(i,j,b), & r_{ij} \ge p \end{cases} \quad (2)$$

where r_{ij} is a random value sampled from the interval [0, 1]. This equation defines salt-and-pepper degradation. A random value r_{ij} was generated for each pixel location. If this value is smaller than $p/2$, the pixel value is set to 0. If it falls between $p/2$ and p, the pixel is set to 1. Otherwise, the original pixel values were preserved. Therefore, the parameter p determines the proportion of corrupted pixels. Stripe noise was generated by adding a band-dependent offset to the selected columns in randomly selected spectral bands. The stripe ratio was set to $s \in \{5\%, 10\%, 20\%\}$. In each degraded band, the offset was drawn from a uniform distribution over the interval $[-0.15, 0.15]$, and approximately half of the spectral bands were randomly selected to be affected. This degradation is formulated as follows:

$$X_S(:, c, b) = clip(X(:, c, b) + \delta_b, 0, 1) \quad (3)$$

This equation models vertical stripe degradation by adding a band-dependent offset δ_b to the selected columns of the selected spectral bands. The offset changes the intensity values along these columns, producing stripe-like artifacts. The resulting values were again clipped to the range [0, 1].

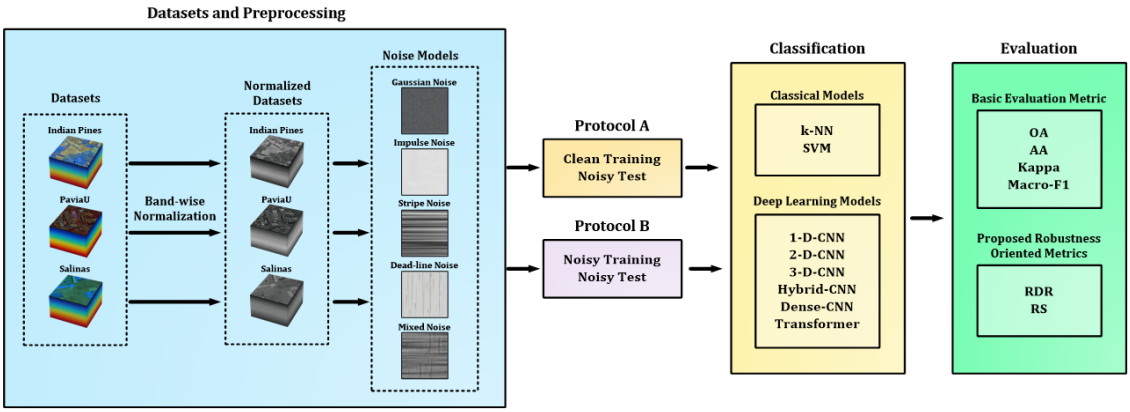


Figure 1. Overall experimental workflow.

Table 1. Hyperspectral datasets

Dataset	Scene type	Main characteristics
Indian Pines	Agricultural	Class imbalance and spectrally similar crop classes
Pavia University	Urban	Strong spatial structures and man-made materials
Salinas	Agricultural	Large homogeneous regions and high spectral separability

Table 2. Compared classifiers

Model	Type	Input
SVM-RBF	Classical	Spectral vector
k-NN	Classical	Spectral vector
1D-CNN	Deep spectral	Spectral vector
2D-CNN	Deep spatial	PCA-reduced spatial patch
3D-CNN	Deep spectral-spatial	3D data cube
Hybrid CNN	Deep hybrid	Spectral and spatial branches
Dense CNN	Deep spectral-spatial	Dense feature reuse
Transformer	Deep self-attention-based	PCA patch tokens

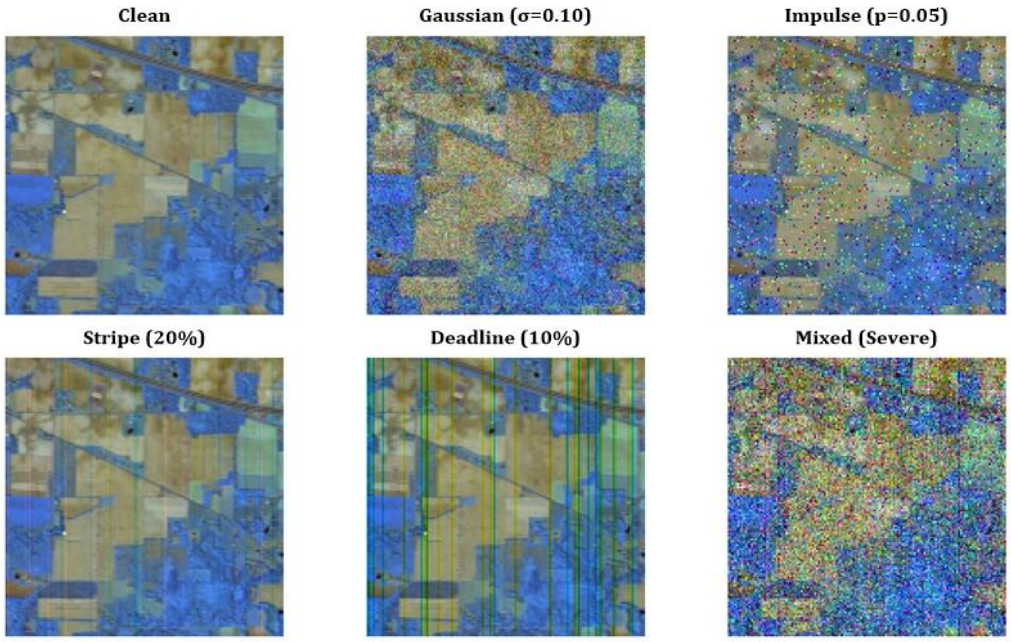


Figure 2. Pseudo-color visualization of different noise types on the Indian Pines dataset.

The dead-line noise was generated by setting the selected columns to zero. The proportion of affected columns was defined as $d \in \{2\%, 5\%, 10\%\}$, and, as in the stripe case, approximately half of the spectral bands were randomly selected to be affected. The degradation is expressed in equation 4:

$$X_D(:, c, b) = 0, \quad c \in \mathcal{C}_d \tag{4}$$

This equation models the missing or defective sensor lines. The selected columns, represented by the set $\mathcal{C}_d$, are set to zero. Consequently, these columns appear as dark vertical lines in the hyperspectral image. In this study, mixed noise was defined as the sequential application of Gaussian, impulse, and stripe degradations to a clean hyperspectral image. Dead-line degradation was deliberately excluded from this combination and was instead evaluated as a separate noise type in Section 3.5, because it removes the recorded information entirely rather than perturbing the measured values. The parameter combinations used in the mixed noise scenarios are summarized in Table 3.

Table 3. Mixed noise scenarios

Scenario	Gaussian (σ)	Impulse (p)	Stripe (s)
Mild	0.05	0.01	5%
Moderate	0.10	0.03	10%
Severe	0.15	0.05	20%

This degradation process is expressed in equation 5:

$$X_M = S_s\left(I_p(G_\sigma(X))\right) \tag{5}$$

where $G_\sigma(\cdot), I_p(\cdot)$, and $S_s(\cdot)$, denote the Gaussian, impulse, and stripe noise operators with parameters σ, p, and, s respectively. This equation indicates that the clean image is first corrupted by Gaussian noise, then impulse noise is applied, and finally, stripe noise is added. Therefore, mixed noise represents a more challenging degradation scenario, as it combines multiple noise sources in a single image. This setting is particularly important because real hyperspectral images are often affected by more than one type of sensor-related or acquisition-related degradation.

2.4. Evaluation Protocols

Three evaluation protocols were defined to determine the stage at which the classifier encountered noise. The main factor distinguishing these protocols is whether noise is present only during testing or also during training, with each protocol corresponding to a different real-world scenario. Protocol A: Training on clean data and evaluation under noisy conditions. The model was trained only on clean training data and then evaluated using noise-corrupted test data. In this setting, the model encounters noise for the first time during the testing stage; therefore, this protocol measures the intrinsic robustness of a classifier against previously unseen degradation (Hendrycks and Dietterich, 2019; Mei et al., 2024). This setting represents a common deployment scenario in which a model is trained under clean conditions but later operates in the field with unexpected sensor noise. Protocol A is also computationally efficient: for each dataset, model, and random seed, the model is trained once and evaluated under all noise conditions without retraining the model. Protocol B: Training and evaluation under matched noisy conditions. The model was trained and evaluated using the same noise type and severity level. This protocol assesses the effect of noise-adapted training by measuring whether exposure to corrupted samples during training improves robustness under matched input degradations. This setting is motivated by the regularization effect of input-noise training (Bishop, 1995) and by recent findings showing

that noise- or corruption-aware training can improve robustness against common image corruptions (Rusak et al., 2020; Hendrycks et al., 2020). Protocol C: Classification after denoising-based restoration. The noise-corrupted test data were first restored using a denoising method and then classified. This protocol evaluates whether denoising-based restoration can improve downstream classification performance when noise reduction is used as a preprocessing step before hyperspectral image analysis (Rasti et al., 2018). In this study, the main evaluation was based on Protocol A, which represents the most challenging and realistic scenario in which the model has not been previously exposed to noise. All the results reported in Sections 3.1–3.7 and 3.9 are based on this protocol, except for the training curves in Figure 7, which additionally include noise-adapted training. To examine the contribution of noise-adapted training, Protocol B was applied to the Pavia University dataset under the most severe noise conditions for all eight models, and the results were compared with those of Protocol A, as described in Section 3.8. Denoising-based Protocol C is left for future work as a natural extension of the proposed evaluation framework.

2.5. Evaluation Metrics

The overall accuracy (OA), average accuracy (AA), Kappa coefficient, and macro-F1 were used as standard classification metrics. In addition to these metrics, two robustness-oriented metrics were defined to quantify the effect of noise on the classification performance. The absolute overall accuracy drop given in equation 6 is not reported separately; it is used as an intermediate quantity in the derivation of the relative degradation rate. Let OA_{clean} denote the overall accuracy obtained under clean test conditions, and OA_{noisy} denote the overall accuracy obtained under a given noisy test condition. The absolute overall accuracy drop, relative degradation rate, and robustness scores are defined in equations 6-8, respectively:

$$\Delta OA = OA_{clean} - OA_{noisy} \tag{6}$$

Equation 6 defines the absolute overall accuracy drop caused by noise. A larger ΔOA value indicates that the classifier suffers greater performance degradation under noisy conditions.

$$RDR = \frac{\Delta OA}{OA_{clean}} \times 100 \tag{7}$$

Equation 7 defines the relative degradation rate (RDR), which measures the percentage of accuracy loss with respect to clean-data performance. This metric enables a normalized comparison of robustness across models with different clean accuracies.

$$RS = \frac{1}{L}\sum_{i=1}^{L} OA_i \tag{8}$$

Equation 8 defines the robustness score (RS) as the average overall accuracy across L noise levels, where OA_i denotes the overall accuracy obtained at the i-th noise level. A higher RS value indicates that the classifier maintains a better performance across increasing noise severity levels. The consistency between the model rankings under clean and noisy conditions was analyzed using Spearman's rank correlation coefficient ρ. A low ρ value indicates that the ranking obtained under clean conditions does not reliably remain valid under noisy conditions. Each experiment was repeated with 15 different random seeds, and the mean and standard deviation were reported.

Table 4. Model training settings

Model	Main settings
SVM-RBF	RBF kernel; grid search over C ∈ {1, 10, 100} and γ ∈ {scale, 0.1, 0.01}; 3-fold cross-validation on training data
k-NN	k = 5 neighbours, Euclidean distance
1D-CNN	Conv1d [32, 64, 128] + GAP + dropout 0.4 + FC; full spectral vector input, cross-entropy loss
2D-CNN	Conv2d [32, 64, 128] + GAP + dropout 0.4 + FC; 11 × 11 × 15 PCA-reduced patch input
3D-CNN	Conv3d [8, 16, 32] + GAP + dropout 0.4 + FC; 11 × 11 × 15 spectral-spatial cube input
Hybrid CNN	Conv3d [8, 16, 32] followed by Conv2d [64] + FC (HybridSN-style)
Dense CNN	Conv2d stem (24) + dense block (4 layers, growth rate 12) + GAP + dropout 0.4 + FC
Transformer	PCA patch tokens; d_model = 64, depth = 2, 4 attention heads, MLP = 128, dropout 0.3, learnable class token and positional embedding

To ensure a fair comparison, the same training, validation, and testing indices were used for all models. In addition, the micro-averaged receiver operating characteristic curve and area under the curve (AUC) were computed to evaluate the threshold-independent discriminative ability of the models. For SVM, which does not directly produce probability estimates in this setting, decision function scores were employed. The model training settings are listed in Table 4. The common settings were as follows. For all patch-based models (2D-CNN, 3D-CNN, Hybrid-CNN, Dense-CNN, and Transformer), the spectral dimension was reduced to 15 principal components using PCA, and 11 × 11 spatial patches were extracted. The PCA transformation was fitted on the training cube and applied unchanged to the test cube, so that under Protocol A the projection learned from clean data was transferred to the noisy test data. The SVM, k-NN, and 1D-CNN models operated on the full

spectral vector without dimensionality reduction. All deep models were trained with the AdamW optimizer using a learning rate of 1×10^{-3}, a weight decay of 1×10^{-4}, and a batch size of 128, for a maximum of 60 epochs, and training was stopped early when the validation loss did not improve for 12 consecutive epochs. Cross-entropy was used as the loss function. For all models, 10% of the labeled samples were selected for training, of which a further 10% was reserved for validation, and the remaining samples formed the test set; each experiment was repeated with 15 random seeds, and identical training, validation, and test indices were used across models. The statistical significance of the differences between the models was evaluated using the paired Wilcoxon signed-rank test with Holm correction for multiple comparisons.

3. Results

3.1. Clean-Data Classification Performance

The results of the clean-data classification are presented in Table 5. Overall, models that exploit spatial or spectral-spatial information achieved the best performance under clean conditions; however, the performance gain was dataset-dependent. On Indian Pines, the 2D-CNN obtained the highest OA and Kappa values, with an OA of 0.976 and a Kappa coefficient of 0.972. Nevertheless, Hybrid-CNN achieved the highest AA and macro-F1 values on this dataset, indicating a better class-wise balance under the class-imbalanced structure of Indian Pines. Dense-CNN and Transformer also produced competitive results, whereas 3D-CNN showed a lower performance, even below SVM, in terms of OA. On Pavia University, all spatial and spectral-spatial deep models achieved very high classification performance, with OA values between 0.994 and 0.997.

Table 5. Clean-data classification results

Dataset	Model	OA	AA	Kappa	Macro-F1
Indian Pines	SVM	0.804±0.006	0.737±0.012	0.775±0.006	0.754±0.013
	kNN	0.672±0.008	0.545±0.013	0.622±0.009	0.550±0.014
	1D-CNN	0.541±0.014	0.317±0.029	0.453±0.018	0.291±0.033
	2D-CNN	0.976±0.004	0.866±0.027	0.972±0.005	0.878±0.028
	3D-CNN	0.775±0.022	0.503±0.040	0.739±0.026	0.507±0.046
	Hybrid-CNN	0.950±0.010	0.885±0.036	0.943±0.011	0.897±0.030
	Dense-CNN	0.951±0.007	0.802±0.022	0.944±0.008	0.806±0.027
	Transformer	0.923±0.010	0.787±0.030	0.912±0.011	0.796±0.034
Pavia University	SVM	0.940±0.002	0.916±0.003	0.920±0.002	0.925±0.002
	kNN	0.865±0.002	0.835±0.004	0.817±0.003	0.847±0.003
	1D-CNN	0.867±0.031	0.803±0.064	0.821±0.044	0.804±0.064
	2D-CNN	0.997±0.001	0.994±0.001	0.996±0.001	0.995±0.001
	3D-CNN	0.994±0.002	0.987±0.005	0.992±0.003	0.989±0.004
	Hybrid-CNN	0.995±0.001	0.991±0.002	0.994±0.001	0.992±0.001
	Dense-CNN	0.995±0.001	0.990±0.003	0.994±0.002	0.991±0.003
	Transformer	0.994±0.002	0.992±0.003	0.993±0.003	0.992±0.003
Salinas	SVM	0.920±0.001	0.955±0.002	0.910±0.001	0.956±0.002
	kNN	0.883±0.001	0.934±0.002	0.869±0.001	0.932±0.001
	1D-CNN	0.857±0.012	0.898±0.013	0.840±0.013	0.900±0.014
	2D-CNN	0.995±0.002	0.997±0.001	0.994±0.002	0.997±0.001
	3D-CNN	0.983±0.003	0.991±0.002	0.981±0.003	0.991±0.002
	Hybrid-CNN	0.997±0.002	0.998±0.001	0.996±0.002	0.998±0.001
	Dense-CNN	0.992±0.002	0.995±0.001	0.991±0.003	0.995±0.001
	Transformer	0.993±0.001	0.996±0.001	0.992±0.001	0.996±0.001

Among them, 2D-CNN provided the best overall result, reaching an OA of 0.997, whereas 3D-CNN, Hybrid-CNN, Dense-CNN, and Transformer performed similarly. This indicates that the strong spatial structure of the Pavia University scene is highly beneficial to deep patch-based classifiers. For Salinas, most models achieved relatively high clean-data performance because of the high spectral separability of the dataset. The Hybrid-CNN achieved the best overall performance, with an OA of 0.997 and the highest AA, Kappa, and macro-F1 values. The 2D-CNN, Dense-CNN, and Transformer models also achieved near-perfect performance, whereas the SVM remained a strong classical baseline. In contrast, k-NN and 1D-CNN consistently exhibited lower performance than the spatial and spectral-spatial deep models. These results show that the clean-data accuracy is strongly influenced by both the dataset characteristics and model architecture. In particular, high performance under clean conditions does not necessarily imply robustness under noisy conditions, which motivates a subsequent noise-based robustness analysis.

3.2. Robustness under Gaussian Noise

The OA values and RDR results under Gaussian noise are presented in Table 6. Gaussian noise caused substantial performance degradation in most models, but the effect varied considerably across datasets and model architectures. The purely spectral 1D-CNN was the most sensitive model, with RDR values of 69.51%, 90.92%, and 86.00% for Indian Pines, Pavia University, and Salinas, respectively. On Indian Pines, degradation was relatively limited for spatial and spectral-spatial models. Although 3D-CNN produced the lowest RDR value of 5.73%, 2D-CNN achieved the highest OA under severe Gaussian noise with 0.906. On Pavia University, Transformer was the most robust model, maintaining an OA of 0.800 at the highest noise level and producing the lowest RDR value of 19.60%. On Salinas, Hybrid-CNN provided the strongest high-accuracy robustness profile, preserving an OA of 0.741, under severe Gaussian noise. These results show that high accuracy of clean-data does not necessarily imply strong robustness under additive Gaussian degradation.

3.3. Robustness under Impulse Noise

The OA values and RDR results for impulse noise are listed in Table 7. Compared with Gaussian noise, impulse noise generally caused a more moderate performance decrease, although some models remained vulnerable. The 1D-CNN again showed the weakest robustness, especially on Pavia University and Salinas, where its OA decreased to 0.104 and 0.143 under the highest impulse noise level, corresponding to RDR values of 87.97% and 83.37%, respectively. On Indian Pines, spatial and spectral-spatial models were only slightly affected by the noise. The 3D-CNN model achieved the lowest RDR value of 1.91%, whereas the 2D-CNN maintained the highest OA of 0.941 under severe impulse noise. On Pavia University, Transformer clearly showed the strongest robustness, preserving an OA of 0.834 and producing the lowest RDR value of 16.18%. On Salinas, Hybrid-CNN achieved the best severe-noise OA of 0.803, followed closely by 2D-CNN with 0.797. These results indicate that the spatial context improves robustness against impulse corruption; however, the degree of improvement remains dataset-dependent.

3.4. Robustness under Stripe Noise

The OA values and RDR results under stripe noise are reported in Table 8. Among the investigated degradation types, stripe noise produced the most limited overall performance loss for most of the spatial and spectral-spatial models. This effect is particularly evident in Indian Pines, where 2D-CNN, 3D-CNN, Hybrid-CNN, Dense-CNN, and Transformer all showed very small RDR values. However, the effect of stripe noise was not uniform across all the models. The 1D-CNN was still highly sensitive, particularly on Pavia University, where its RDR reached 74.64%. On the same dataset, the Transformer was the most robust model, with an RDR of only 2.75%. On Salinas, Transformer and 3D-CNN showed the lowest degradation, whereas 1D-CNN again suffered the largest drop. Overall, Table 8 suggests that models using spatial context can tolerate stripe artifacts more effectively than purely spectral models can.

3.5. Robustness under Dead-Line Noise

The OA values and RDR results for dead-line noise are presented in Table 9. Dead-line degradation, which sets selected columns to zero in a subset of spectral bands, caused a stronger performance loss than stripe noise but remained less destructive than Gaussian and mixed noise. This intermediate behavior is expected, because dead-line corruption removes the information entirely along the affected columns, whereas stripe noise only shifts their intensity values. The purely spectral 1D-CNN was again the most vulnerable model on all three datasets, with RDR values of 46.16%, 75.37%, and 74.27% on Indian Pines, Pavia University, and Salinas, respectively; its OA decreased to 0.213 on Pavia University and to 0.221 on Salinas. On Indian Pines, 3D-CNN produced the lowest RDR value of 12.23%, whereas Transformer maintained the highest OA of 0.749 under the most severe setting. On Pavia University, Transformer was again the most robust deep model, preserving an OA of 0.866 with an RDR of 12.93%, followed by 3D-CNN with an OA of 0.826. On Salinas, in contrast, all deep models lost a substantial part of their clean-data accuracy, with RDR values between 27.94% and 36.57%, and k-NN produced both the highest severe-noise OA of 0.717 and the lowest RDR of 18.73%. These results indicate that spatial context alone does not guarantee robustness against structured column-wise information loss, and that the relative advantage of deep spectral-spatial models over classical baselines becomes narrower under this degradation type.

3.6. Robustness under Mixed Noise

The OA values and RDR results under mixed noise are presented in Table 10, and the corresponding robustness scores are visually summarized in Figure 3. Because mixed noise combines Gaussian, impulse, and stripe degradations, it represents the most challenging evaluation scenario in this study. Under this setting, the robustness differences between the models became more pronounced than in the single-noise cases. As shown in Table 10, the best-performing models varied across the datasets. For Indian Pines, 2D-CNN achieved the highest robustness score of 0.897 and preserved an OA of 0.798 under severe mixed noise. The Hybrid-CNN followed closely with a robustness score of 0.867, whereas Dense-CNN and Transformer also maintained competitive robustness scores of 0.843 and 0.827, respectively. On Pavia University, Transformer was clearly the most robust model, achieving the highest robustness score of 0.795 and the highest severe-noise OA of 0.644. In contrast, the 1D-CNN almost collapsed on this dataset, with a robustness score of only 0.083. On Salinas, Hybrid-CNN achieved the best robustness score of 0.764 and maintained the highest severe-noise OA of 0.643, followed by kNN and 2D-CNN with robustness scores of 0.702 and 0.667, respectively.

Figure 3 provides a compact visual confirmation of the trends in Table 10. The bar plots clearly show that no single model was consistently dominant across all datasets. Instead, 2D-CNN is the strongest model on Indian Pines, Transformer is the most robust on Pavia University, and Hybrid-CNN performs the best on Salinas. This supports the main observation that robustness under mixed degradation is determined not only by the model architecture, but also by the dataset characteristics. Overall, the mixed-noise results confirm that combined degradation is a stronger stress test than single-noise scenarios and that clean-data performance alone is insufficient to predict robustness under realistic noisy conditions.

Figure 4 visually supports the trends in Tables 6–10. The OA curves show that Gaussian and mixed noise produce the steepest performance drop, whereas stripe noise generally causes milder degradation. The figure also highlights the dataset-dependent behavior of the models: The Transformer is particularly robust on Pavia University, 2D-CNN performs strongly on Indian Pines, and Hybrid-CNN maintains the most stable performance on Salinas under severe degradation.

3.7. Ranking Stability Analysis

The Spearman correlations between the clean and noisy model rankings are presented in Table 11. A visual comparison of the ranking changes is presented in Figure 5. The results revealed a strong dataset-dependent behavior. On Indian Pines, the model ranking was largely preserved, with a Spearman correlation of 0.857 under mixed noise.

In contrast, on Pavia University, the clean-data ranking was almost completely disrupted under severe mixed noise, and the correlation decreased to 0.119. Salinas showed an intermediate behavior, with a correlation value of 0.571.

Table 6. OA values and RDR under Gaussian noise

Dataset	Model	OA (Clean)	OA (σ=0.05)	OA (σ=0.10)	OA (σ=0.15)	RDR (%)
Indian Pines	SVM	0.804	0.673±0.008	0.526±0.011	0.425±0.020	47.07
	kNN	0.672	0.660±0.008	0.625±0.006	0.583±0.006	13.30
	1D-CNN	0.541	0.316±0.051	0.189±0.062	0.165±0.068	69.51
	2D-CNN	0.976	0.973±0.005	0.958±0.010	0.906±0.029	7.11
	3D-CNN	0.775	0.776±0.021	0.772±0.021	0.731±0.041	5.73
	Hybrid-CNN	0.950	0.944±0.010	0.921±0.011	0.870±0.020	8.46
	Dense-CNN	0.951	0.943±0.007	0.917±0.012	0.849±0.033	10.75
	Transformer	0.923	0.916±0.009	0.893±0.015	0.841±0.024	8.86
Pavia University	SVM	0.940	0.600±0.015	0.415±0.039	0.282±0.026	69.96
	kNN	0.865	0.790±0.002	0.701±0.002	0.610±0.005	29.48
	1D-CNN	0.867	0.105±0.036	0.084±0.028	0.079±0.022	90.92
	2D-CNN	0.997	0.923±0.029	0.577±0.065	0.327±0.037	67.18
	3D-CNN	0.994	0.883±0.064	0.555±0.164	0.400±0.141	59.78
	Hybrid-CNN	0.995	0.941±0.020	0.809±0.048	0.600±0.110	39.72
	Dense-CNN	0.995	0.916±0.020	0.611±0.069	0.400±0.063	59.79
	Transformer	0.994	0.975±0.009	0.898±0.021	0.800±0.038	19.60
Salinas	SVM	0.920	0.782±0.006	0.580±0.020	0.416±0.045	54.73
	kNN	0.883	0.851±0.001	0.777±0.002	0.690±0.003	21.81
	1D-CNN	0.857	0.221±0.076	0.132±0.016	0.120±0.012	86.00
	2D-CNN	0.995	0.949±0.012	0.815±0.042	0.617±0.061	37.93
	3D-CNN	0.983	0.928±0.032	0.743±0.073	0.547±0.095	44.39
	Hybrid-CNN	0.997	0.931±0.041	0.824±0.076	0.741±0.089	25.64
	Dense-CNN	0.992	0.936±0.010	0.758±0.050	0.554±0.056	44.13
	Transformer	0.993	0.893±0.031	0.723±0.058	0.520±0.080	47.59

Table 7. OA values and RDR under impulse noise

Dataset	Model	OA (Clean)	OA (p=0.01)	OA (p=0.03)	OA (p=0.05)	RDR (%)
Indian Pines	SVM	0.804	0.682±0.009	0.551±0.013	0.480±0.016	40.28
	kNN	0.672	0.658±0.007	0.631±0.006	0.604±0.007	10.16
	1D-CNN	0.541	0.451±0.031	0.319±0.026	0.263±0.026	51.37
	2D-CNN	0.976	0.972±0.004	0.961±0.005	0.941±0.008	3.51
	3D-CNN	0.775	0.776±0.019	0.772±0.019	0.761±0.020	1.91
	Hybrid-CNN	0.950	0.943±0.009	0.926±0.011	0.898±0.015	5.51
	Dense-CNN	0.951	0.944±0.007	0.921±0.011	0.884±0.022	7.06
	Transformer	0.923	0.917±0.011	0.896±0.016	0.864±0.027	6.37
Pavia University	SVM	0.940	0.699±0.014	0.449±0.023	0.327±0.020	65.18
	kNN	0.865	0.799±0.003	0.711±0.003	0.650±0.004	24.89
	1D-CNN	0.867	0.488±0.029	0.186±0.027	0.104±0.014	87.97
	2D-CNN	0.997	0.865±0.051	0.525±0.071	0.359±0.045	64.00
	3D-CNN	0.994	0.837±0.090	0.551±0.183	0.441±0.182	55.66
	Hybrid-CNN	0.995	0.933±0.019	0.818±0.059	0.690±0.107	30.68
	Dense-CNN	0.995	0.876±0.027	0.624±0.068	0.484±0.075	51.36
	Transformer	0.994	0.979±0.006	0.913±0.020	0.834±0.039	16.18
Salinas	SVM	0.920	0.781±0.008	0.604±0.024	0.490±0.039	46.71
	kNN	0.883	0.847±0.002	0.781±0.002	0.720±0.003	18.39
	1D-CNN	0.857	0.490±0.043	0.209±0.031	0.143±0.025	83.37
	2D-CNN	0.995	0.943±0.008	0.871±0.010	0.797±0.018	19.91
	3D-CNN	0.983	0.918±0.035	0.792±0.056	0.678±0.095	31.05
	Hybrid-CNN	0.997	0.945±0.024	0.866±0.049	0.803±0.063	19.41
	Dense-CNN	0.992	0.933±0.010	0.839±0.026	0.734±0.047	26.02
	Transformer	0.993	0.915±0.033	0.799±0.046	0.698±0.073	29.71

Table 8. OA values and RDR under stripe noise

Dataset	Model	OA (Clean)	OA (5%)	OA (10%)	OA (20%)	RDR (%)
Indian Pines	SVM	0.804	0.790±0.006	0.778±0.007	0.753±0.009	6.29
	kNN	0.672	0.671±0.008	0.670±0.008	0.668±0.008	0.67
	1D-CNN	0.541	0.533±0.012	0.525±0.014	0.497±0.027	8.13
	2D-CNN	0.976	0.975±0.004	0.972±0.004	0.971±0.005	0.47
	3D-CNN	0.775	0.774±0.021	0.773±0.020	0.773±0.020	0.36
	Hybrid-CNN	0.950	0.948±0.010	0.945±0.010	0.936±0.011	1.49
	Dense-CNN	0.951	0.949±0.008	0.944±0.008	0.939±0.009	1.24
	Transformer	0.923	0.922±0.010	0.918±0.010	0.915±0.011	0.85
Pavia University	SVM	0.940	0.868±0.008	0.815±0.012	0.739±0.013	21.40
	kNN	0.865	0.856±0.002	0.848±0.004	0.834±0.004	3.64
	1D-CNN	0.867	0.618±0.071	0.423±0.106	0.220±0.107	74.64
	2D-CNN	0.997	0.974±0.007	0.934±0.022	0.868±0.030	12.96
	3D-CNN	0.994	0.980±0.011	0.962±0.018	0.919±0.045	7.57
	Hybrid-CNN	0.995	0.972±0.010	0.952±0.013	0.918±0.017	7.76
	Dense-CNN	0.995	0.963±0.009	0.914±0.029	0.852±0.034	14.43
	Transformer	0.994	0.989±0.004	0.982±0.007	0.967±0.013	2.75
Salinas	SVM	0.920	0.902±0.005	0.885±0.006	0.866±0.009	5.88
	kNN	0.883	0.881±0.002	0.877±0.002	0.873±0.002	1.09
	1D-CNN	0.857	0.811±0.016	0.740±0.021	0.596±0.052	30.48
	2D-CNN	0.995	0.966±0.014	0.943±0.017	0.927±0.016	6.76
	3D-CNN	0.983	0.976±0.007	0.964±0.012	0.937±0.021	4.76
	Hybrid-CNN	0.997	0.976±0.008	0.954±0.015	0.934±0.019	6.26
	Dense-CNN	0.992	0.964±0.010	0.940±0.015	0.922±0.019	7.00
	Transformer	0.993	0.986±0.003	0.973±0.013	0.960±0.012	3.33

Table 9. OA values and RDR under dead-line noise

Dataset	Model	OA (Clean)	OA (2%)	OA (5%)	OA (10%)	RDR (%)
Indian Pines	SVM	0.804	0.695±0.016	0.607±0.011	0.514±0.020	36.02
	kNN	0.672	0.658±0.008	0.635±0.010	0.584±0.012	13.05
	1D-CNN	0.541	0.476±0.029	0.381±0.036	0.291±0.028	46.16
	2D-CNN	0.976	0.946±0.016	0.886±0.032	0.740±0.101	24.15
	3D-CNN	0.775	0.764±0.022	0.740±0.028	0.681±0.040	12.23
	Hybrid-CNN	0.950	0.902±0.016	0.823±0.037	0.679±0.076	28.51
	Dense-CNN	0.951	0.900±0.020	0.824±0.031	0.671±0.073	29.42
	Transformer	0.923	0.899±0.012	0.849±0.030	0.749±0.060	18.86
Pavia University	SVM	0.940	0.825±0.013	0.719±0.024	0.613±0.026	34.83
	kNN	0.865	0.843±0.004	0.817±0.006	0.773±0.009	10.59
	1D-CNN	0.867	0.619±0.056	0.392±0.092	0.213±0.073	75.37
	2D-CNN	0.997	0.938±0.020	0.834±0.031	0.671±0.088	32.74
	3D-CNN	0.994	0.965±0.018	0.911±0.035	0.826±0.034	16.84
	Hybrid-CNN	0.995	0.950±0.018	0.896±0.017	0.802±0.054	19.43
	Dense-CNN	0.995	0.928±0.020	0.824±0.048	0.673±0.074	32.41
	Transformer	0.994	0.976±0.011	0.940±0.025	0.866±0.042	12.93
Salinas	SVM	0.920	0.852±0.008	0.765±0.019	0.658±0.023	28.47
	kNN	0.883	0.864±0.002	0.821±0.007	0.717±0.010	18.73
	1D-CNN	0.857	0.689±0.032	0.434±0.061	0.221±0.045	74.27
	2D-CNN	0.995	0.914±0.020	0.803±0.034	0.631±0.052	36.57
	3D-CNN	0.983	0.929±0.018	0.804±0.036	0.629±0.046	36.02
	Hybrid-CNN	0.997	0.923±0.020	0.829±0.033	0.693±0.058	30.47
	Dense-CNN	0.992	0.907±0.025	0.801±0.049	0.649±0.098	34.59
	Transformer	0.993	0.948±0.018	0.873±0.038	0.715±0.072	27.94

Table 10. OA values and robustness score under mixed noise

Dataset	Model	OA (Clean)	OA (Mild)	OA (Moderate)	OA (Severe)	RS
Indian Pines	SVM	0.804	0.601±0.009	0.444±0.016	0.359±0.023	0.468
	kNN	0.672	0.646±0.007	0.592±0.005	0.522±0.007	0.587
	1D-CNN	0.541	0.279±0.039	0.179±0.066	0.155±0.069	0.204
	2D-CNN	0.976	0.966±0.005	0.926±0.013	0.798±0.042	0.897
	3D-CNN	0.775	0.775±0.020	0.748±0.028	0.652±0.079	0.725
	Hybrid-CNN	0.950	0.934±0.008	0.883±0.012	0.784±0.035	0.867
	Dense-CNN	0.951	0.934±0.010	0.864±0.028	0.730±0.067	0.843
	Transformer	0.923	0.907±0.014	0.843±0.030	0.731±0.054	0.827
Pavia University	SVM	0.940	0.500±0.023	0.284±0.024	0.178±0.043	0.321
	kNN	0.865	0.747±0.002	0.621±0.005	0.502±0.008	0.623
	1D-CNN	0.867	0.095±0.028	0.079±0.017	0.075±0.012	0.083
	2D-CNN	0.997	0.688±0.067	0.308±0.037	0.218±0.019	0.405
	3D-CNN	0.994	0.690±0.148	0.402±0.170	0.260±0.155	0.451
	Hybrid-CNN	0.995	0.877±0.026	0.608±0.112	0.429±0.131	0.638
	Dense-CNN	0.995	0.730±0.052	0.399±0.063	0.277±0.049	0.469
	Transformer	0.994	0.940±0.009	0.799±0.039	0.644±0.068	0.795
Salinas	SVM	0.920	0.681±0.012	0.437±0.045	0.272±0.068	0.464
	kNN	0.883	0.817±0.002	0.703±0.003	0.587±0.003	0.702
	1D-CNN	0.857	0.176±0.035	0.122±0.012	0.117±0.006	0.139
	2D-CNN	0.995	0.894±0.012	0.672±0.047	0.435±0.093	0.667
	3D-CNN	0.983	0.853±0.038	0.592±0.098	0.375±0.113	0.607
	Hybrid-CNN	0.997	0.885±0.051	0.763±0.078	0.643±0.080	0.764
	Dense-CNN	0.992	0.875±0.016	0.603±0.056	0.403±0.067	0.627
	Transformer	0.993	0.837±0.037	0.583±0.080	0.369±0.081	0.596

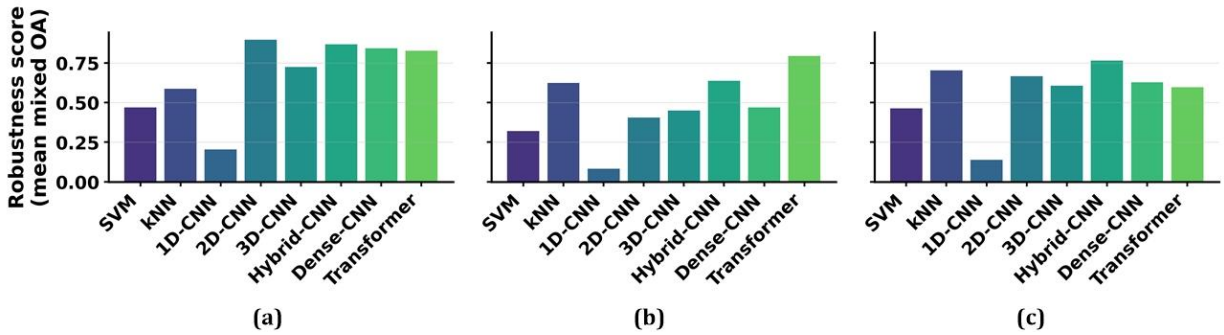


Figure 3. Robustness scores under mixed noise: (a) Indian Pines, (b) Pavia University, (c) Salinas.

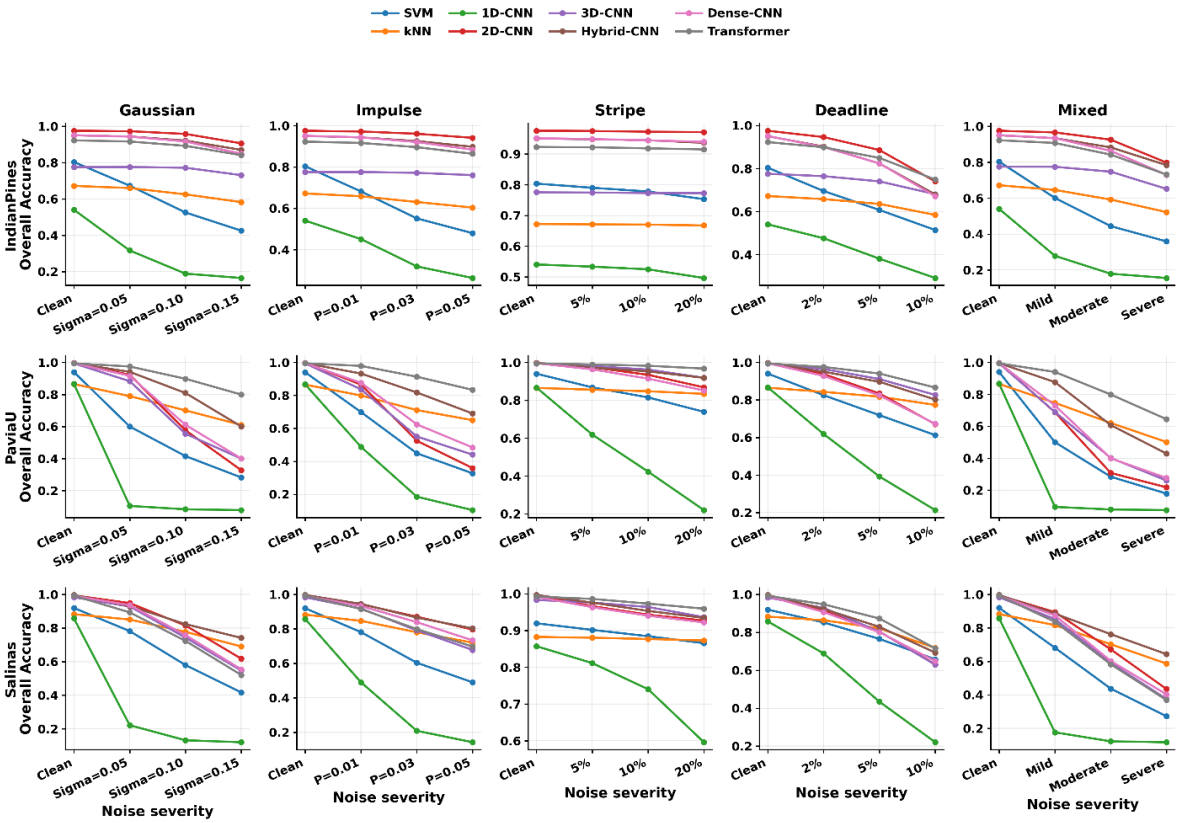


Figure 4. Overall accuracy across noise levels.

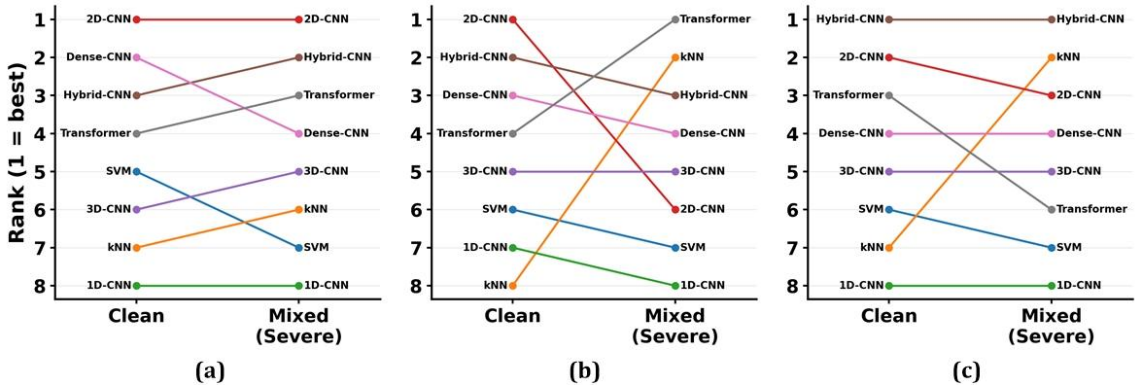


Figure 5. Model ranking shift from clean to mixed noise: (a) Indian Pines, (b) Pavia University, (c) Salinas.

Table 11. Spearman correlation between clean and noisy model rankings

Dataset	Gaussian	Impulse	Stripe	Dead-line	Mixed noise
Indian Pines	0.905	0.905	0.976	0.595	0.857
PaviaU	0.119	0.262	0.548	0.214	0.119
Salinas	0.571	0.810	0.714	0.214	0.571

As shown in Figure 5, on Pavia University, the Transformer model moved from fourth place under clean conditions to first place under severe mixed noise, whereas 2D-CNN dropped from first place to sixth place. In addition, although the absolute accuracy of k-NN decreased under noise, its relative ranking improved considerably because several other models degraded more rapidly.

3.8. Comparison of Protocol A and Protocol B

To evaluate the contribution of noise-adapted training, Protocol A and Protocol B were compared using the Pavia University dataset under the most severe noise conditions. Protocol A represents training on clean data and testing under noisy conditions, whereas Protocol B represents training and testing under matched-noisy conditions. Table 12 shows that Protocol B substantially improved the performance of most models, particularly under Gaussian, impulse, and mixed noise. The largest gains were observed for deep patch-based models. Under severe mixed noise, the 2D-CNN improved from 0.218 to 0.994, 3D-CNN increased from 0.260 to 0.940, and Dense-CNN increased from 0.277 to 0.987. The Hybrid-CNN also

recovered strongly, increasing from 0.429 to 0.974. These results indicate that the severe performance degradation observed under Protocol A is largely related to the mismatch between the clean training distribution and the noisy test distribution. The improvement was not uniform across all the models and noise types. The transformer already exhibited relatively strong robustness under Protocol A, with OA values of 0.800, 0.834, 0.967, 0.866, and 0.644 under Gaussian, impulse, stripe, dead-line, and mixed noise, respectively. Therefore, its gains under Protocol B were more moderate than those of the CNN-based models. In contrast, k-NN showed the smallest improvement overall and even exhibited a slight decrease under impulse noise. Stripe noise also produced smaller gains than Gaussian and mixed noise, because most models already maintained relatively high OA values under Protocol A. On average, Protocol B improved the OA by approximately 0.52 under severe mixed noise and outperformed Protocol A in 39 of the 40 evaluated model-noise combinations. However, this setting assumes that the noise type and severity level are known during training. Therefore, the results should be interpreted as an ideal upper bound for the potential benefit of noise-adapted training, rather than as a direct replacement for Protocol A.

3.9. Threshold-Independent Analysis and Class-Level Behavior

Threshold-independent discriminative ability was evaluated using micro-averaged ROC curves and AUC values. Figure 6 shows the ROC curves under clean and severe mixed-noise test conditions, while the corresponding AUC values are summarized in Table 13. Figure 6a, 6b, and 6c correspond to the Indian Pines, Pavia University, and Salinas datasets, respectively. For Indian Pines, Figure 6a and Table 13 show that the discriminative ability was largely preserved under severe mixed noise. The Hybrid-CNN, 2D-CNN, Transformer, and Dense-CNN maintained high noisy AUC values of 0.993, 0.989, 0.977, and 0.973, respectively. In contrast, the 1D-CNN showed a clear decline, with its AUC decreasing from 0.946 to 0.572.

For the Pavia University dataset, Figure 6b shows that the discriminative ability was reduced considerably under severe mixed noise. The 2D-CNN decreased from 1.000 to 0.555, whereas the 3D-CNN decreased from 1.000 to 0.651 and the Dense-CNN from 1.000 to 0.697. The sharpest decline was observed for 1D-CNN, whose AUC dropped from 0.992 to 0.393. In contrast, the Transformer preserved the highest discriminative ability, with an AUC of 0.916. For the Salinas dataset, Figure 6c shows that almost all the deep models achieved near-perfect AUC values under clean conditions. Under severe mixed noise, Hybrid-CNN, Dense-CNN, and 3D-CNN maintained a strong discriminative ability, with AUC values of 0.938, 0.914, and 0.901, respectively. In contrast, the AUC of the 1D-CNN decreased from 0.995 to 0.490, approaching the level of random predictions. Overall, Figure 6 supports the finding based on the OA. Noise not only reduces the classification accuracy but also weakens the ability of the models to produce discriminative decision scores across classes.

The training behavior of the deep models was further examined using the loss and accuracy curves shown in Figure 7. Figure 7a, 7b, and 7c show the curves for Indian Pines, Pavia University, and Salinas, respectively, under clean and noisy training settings. As shown in Figure 7a, Indian Pines presents a more challenging training behavior. The convergence of several models was slower, and the final accuracy values were generally lower than those observed for Pavia University and Salinas. Nevertheless, the clean and noisy training curves remain broadly consistent for the 2D-CNN, Hybrid-CNN, Dense-CNN, and Transformer. This suggests that noisy training does not introduce severe optimization instability, even in the more class-imbalanced Indian Pines dataset. Figure 7b shows that Pavia University exhibits stable convergence for most spatial and spectral-spatial models. The 2D-CNN, Dense-CNN, and Transformer models achieved high validation accuracy under both clean and noisy training. Although noisy training generally leads to slightly slower convergence and higher loss values, it does not prevent effective learning from occurring. In contrast, the 1D-CNN shows less stable validation behavior and lower final accuracy, which is consistent with its weaker robustness under noisy test conditions. For Salinas, Figure 7c indicates a faster and more stable convergence for most models. The 2D-CNN, Hybrid-CNN, Dense-CNN, and Transformer models rapidly reach high accuracy under both clean and noisy training conditions. Occasional validation loss fluctuations were observed for some models; however, the corresponding accuracy curves remained high. The 1D-CNN again exhibits a weaker learning profile, particularly under noisy training. Figure 7 supports the findings obtained from the comparison of Protocol A and Protocol B. Noisy training generally remains learnable and stable for spatial deep models, and the performance recovery observed under Protocol B is mainly associated with reducing the mismatch between the training and test noise distributions. However, this benefit is less pronounced for purely spectral 1D-CNN, whose training curves show weaker and less stable behavior across datasets.

Table 12. Protocol A and Protocol B comparison on Pavia University

Model	Condition	OA (A)	OA (B)	Gain (B−A)
	Gaussian (σ=0.15)	0.282	0.705	0.422
	Impulse (p=0.05)	0.327	0.730	0.403
SVM	Stripe (20%)	0.739	0.926	0.187
	Dead-line (10%)	0.613	0.921	0.309
	Mixed (Severe)	0.178	0.664	0.486
	Gaussian (σ=0.15)	0.610	0.628	0.018
	Impulse (p=0.05)	0.650	0.639	-0.011
kNN	Stripe (20%)	0.834	0.839	0.005
	Dead-line (10%)	0.773	0.813	0.040
	Mixed (Severe)	0.502	0.577	0.076
	Gaussian (σ=0.15)	0.079	0.669	0.590
	Impulse (p=0.05)	0.104	0.751	0.647
1D-CNN	Stripe (20%)	0.220	0.841	0.621
	Dead-line (10%)	0.213	0.835	0.621
	Mixed (Severe)	0.075	0.655	0.579
	Gaussian (σ=0.15)	0.327	0.995	0.667
	Impulse (p=0.05)	0.359	0.996	0.637
2D-CNN	Stripe (20%)	0.868	0.996	0.128
	Dead-line (10%)	0.671	0.994	0.324
	Mixed (Severe)	0.218	0.994	0.777
	Gaussian (σ=0.15)	0.400	0.949	0.549
	Impulse (p=0.05)	0.441	0.957	0.516
3D-CNN	Stripe (20%)	0.919	0.984	0.065
	Dead-line (10%)	0.826	0.975	0.149
	Mixed (Severe)	0.260	0.940	0.680
	Gaussian (σ=0.15)	0.600	0.976	0.376
	Impulse (p=0.05)	0.690	0.980	0.290
Hybrid-CNN	Stripe (20%)	0.918	0.992	0.074
	Dead-line (10%)	0.802	0.988	0.186
	Mixed (Severe)	0.429	0.974	0.546
	Gaussian (σ=0.15)	0.400	0.988	0.588
	Impulse (p=0.05)	0.484	0.990	0.506
Dense-CNN	Stripe (20%)	0.852	0.993	0.142
	Dead-line (10%)	0.673	0.990	0.318
	Mixed (Severe)	0.277	0.987	0.711
	Gaussian (σ=0.15)	0.800	0.954	0.155
	Impulse (p=0.05)	0.834	0.968	0.135
Transformer	Stripe (20%)	0.967	0.987	0.020
	Dead-line (10%)	0.866	0.987	0.121
	Mixed (Severe)	0.644	0.958	0.313

Table 13. AUC values under clean and severe mixed-noise test conditions

Dataset	Model	Clean AUC	Noisy AUC	ΔAUC
Indian Pines	SVM	0.979	0.898	0.081
	kNN	0.932	0.875	0.057
	1D-CNN	0.946	0.572	0.374
	2D-CNN	1.000	0.989	0.011
	3D-CNN	0.984	0.968	0.016
	Hybrid-CNN	0.999	0.993	0.006
	Dense-CNN	0.999	0.973	0.026
	Transformer	0.998	0.977	0.021
Pavia University	SVM	0.993	0.663	0.330
	kNN	0.978	0.821	0.157
	1D-CNN	0.992	0.393	0.599
	2D-CNN	1.000	0.555	0.445
	3D-CNN	1.000	0.651	0.349
	Hybrid-CNN	1.000	0.893	0.107
	Dense-CNN	1.000	0.697	0.303
	Transformer	1.000	0.916	0.084
Salinas	SVM	0.994	0.881	0.113
	kNN	0.986	0.864	0.122
	1D-CNN	0.995	0.490	0.505
	2D-CNN	1.000	0.861	0.139
	3D-CNN	1.000	0.901	0.099
	Hybrid-CNN	1.000	0.938	0.062
	Dense-CNN	1.000	0.914	0.086
	Transformer	1.000	0.843	0.157

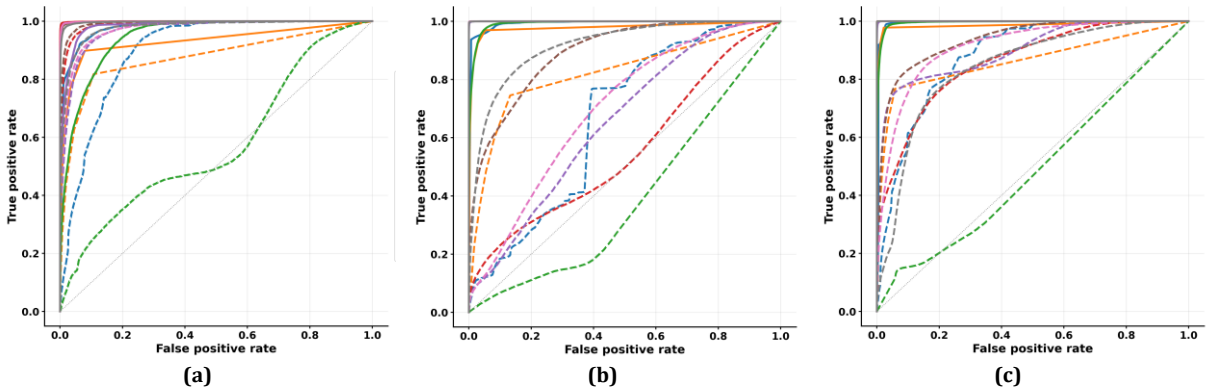


Figure 6. Micro-averaged ROC curves under clean and severe mixed-noise test conditions: (a) Indian Pines, (b) Pavia University, (c) Salinas.

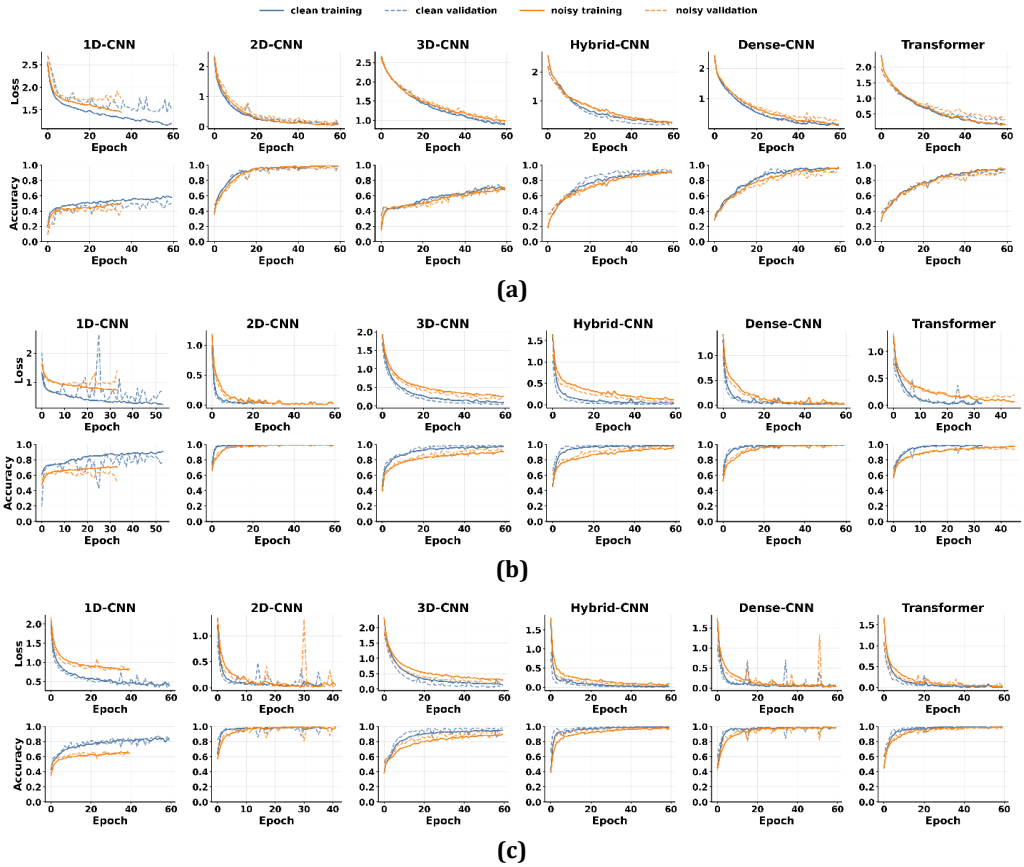


Figure 7. Training curves under clean and noisy conditions: (a) Indian Pines, (b) Pavia University, (c) Salinas.

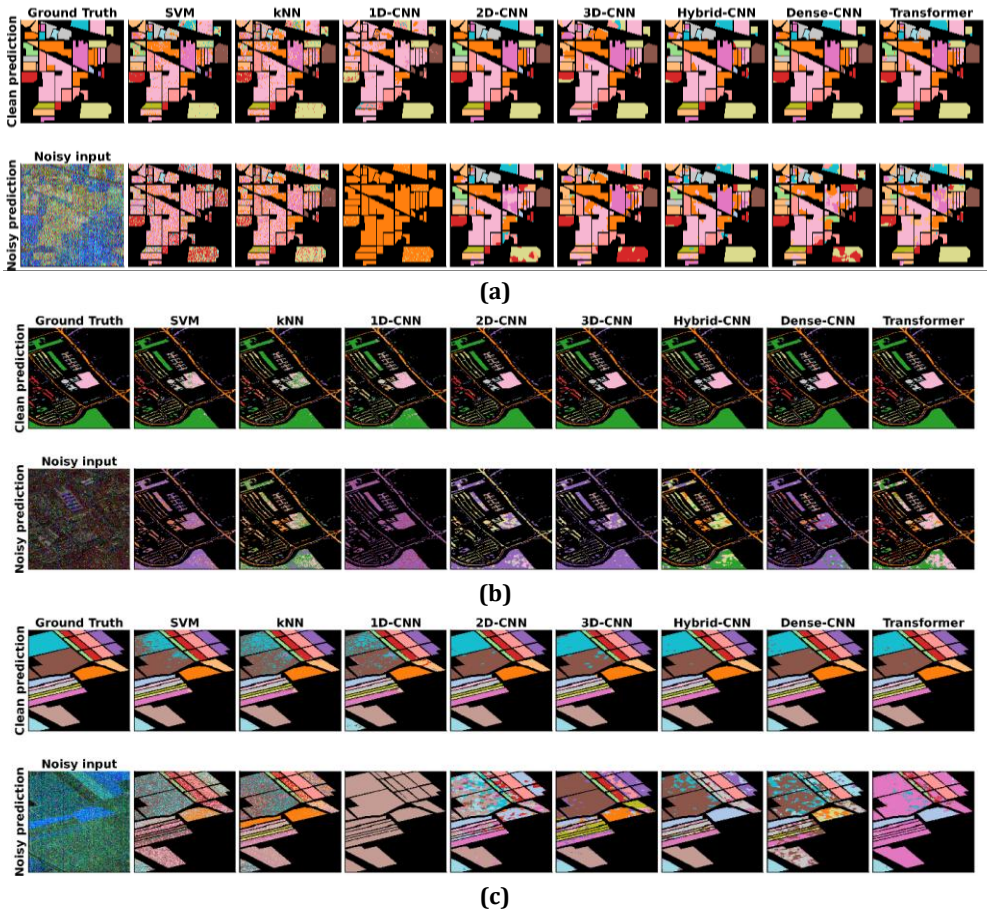


Figure 8. Clean and severe mixed-noise classification maps: (a) Indian Pines, (b) Pavia University, and (c) Salinas. Top: clean; bottom: mixed noise ($\sigma = 0.15, p = 0.05$, ratio $= 0.2$).

The classification maps under clean and severe mixed noise conditions are shown in Figure 8. Figure 8a, 8b, and 8c correspond to the Indian Pines, Pavia University, and Salinas datasets, respectively. In each panel, the top row shows the predictions under clean conditions, and the bottom row shows the predictions obtained under severe mixed noise. As shown in Figure 8a, the Indian Pines classification maps indicate that most spatial and spectral-spatial deep models preserved the main field structures well under clean conditions. Under severe mixed noise, the degradation becomes more visible; however 2D-CNN, Hybrid-CNN, Dense-CNN, and Transformer still retain most of the large homogeneous regions and class boundaries. In contrast, the 1D-CNN map collapsed toward a dominant class pattern and lost much of the spatial structure, which is consistent with its low OA and AUC values under mixed noise. SVM and kNN remain more interpretable than 1D-CNN, but they exhibit noticeably more salt-and-pepper artifacts. Figure 8b shows that the visual differences are more pronounced in the Pavia University dataset. Under clean conditions, most models reproduced the dominant urban structures with high fidelity. However, under severe mixed noise, the predictions of several models deteriorated substantially.

The 1D-CNN map again shows a strong mode collapse, whereas the 2D-CNN, 3D-CNN, and Dense-CNN exhibit clear fragmentation and local class confusion in the central regions. In contrast, the Transformer and Hybrid-CNN preserve the scene layout more effectively, maintaining more coherent spatial regions and clearer object boundaries. This visual result agrees with the OA, robustness score, and AUC analyses, which identified the Transformer as the most robust model for Pavia University under severe mixed degradation. For the Salinas dataset, Figure 8c shows that the clean-condition predictions are highly accurate for most of the deep models. Under severe mixed noise, visual degradation is model-dependent. The 1D-CNN map was dominated by an almost single-class prediction, indicating a severe loss of discriminative ability. SVM and kNN preserved some large regions but produced many scattered errors. In contrast, Hybrid-CNN, 3D-CNN, and Dense-CNN retained the major agricultural parcels more successfully, whereas the Transformer preserved the broad scene structure but introduced more localized misclassification than Hybrid-CNN. These observations are consistent with the quantitative results, where Hybrid-CNN showed the strongest robustness profile in Salinas under mixed noise.

Conversely, the models that showed the largest quantitative degradation, especially the 1D-CNN, also exhibited a clear visual collapse in their prediction maps. Therefore, the classification maps reinforce the conclusion that robustness under noisy conditions should be evaluated not only in terms of scalar accuracy metrics but also in terms of the preservation of spatial structure and class consistency.

4. Discussion

The results show that the accuracy of clean data alone is insufficient to describe the reliability of hyperspectral image classification models under noisy conditions. Although several deep spatial and spectral-spatial models have achieved near-perfect performance on clean data, their accuracy has decreased substantially under Gaussian and mixed noise. This confirms that robustness should be evaluated separately from the clean classification performance. The effect of noise was strongly dependent on both the dataset and model architecture. Mixed noise produces the most challenging scenario because it combines additive, impulse, and structural degradations. In this setting, no single model was consistently superior across all datasets. The 2D-CNN was the most robust model on Indian Pines, Transformer performed best on Pavia University, and the Hybrid-CNN achieved the strongest robustness on Salinas. This indicates that robustness is not only an architectural property but also depends on the scene structure, spectral separability, and

class distribution. The ranking stability analysis further supports this conclusion. Although the model ranking was mostly preserved on Indian Pines, it changed substantially on Pavia University under severe mixed noise. In particular, models with very high clean-data accuracy can lose their advantage under noisy conditions. The ROC-AUC curves and classification maps also confirmed this behavior: models with larger quantitative degradation produced weaker decision scores, fragmented maps, and mode-collapse-like predictions. The 1D-CNN was especially vulnerable across datasets, indicating that purely spectral deep learning may be insufficient under strong mixed degradation. It should also be noted that some models, most notably 3D-CNN on Pavia University, exhibited relatively high standard deviations across random seeds under severe noise, indicating that their behaviour under strong degradation is less stable and should be interpreted together with the reported variability. The comparison between Protocols A and B showed that noise-adapted training can recover much of the lost performance when the same noise type and severity are available during training. However, this setting represents an ideal case in which the noise distribution is known beforehand. Therefore, Protocol B should be interpreted as an upper bound on the benefit of noise-adapted training, rather than as a replacement for robustness evaluation under unseen noise.

This study had several limitations. First, the experiments were based on controlled synthetic noise, which may not fully represent real sensor noise, atmospheric effects, or acquisition-specific artifacts. Second, the evaluation was limited to three benchmark datasets and eight representative classifiers. Third, the transformer model is a compact attention-based baseline rather than a fully specialized hyperspectral transformer. Finally, denoising-based Protocol C was defined but not evaluated experimentally. Future work should extend the

framework to real noisy hyperspectral data, additional datasets, more recent architectures and denoising-based classification pipelines.

5. Conclusion

This study evaluated the robustness of hyperspectral image classification models under controlled Gaussian, impulse, stripe, dead-line, and mixed-noise scenarios. The results show that high accuracy of clean data does not necessarily indicate strong robustness under noisy conditions. Model behavior changed considerably across datasets and noise types, with 2D-CNN performing best on Indian Pines, Transformer on Pavia University, and Hybrid-CNN on Salinas under mixed noise. Noise-adapted training improved performance when the noise condition was known during training; however, this represents an idealized upper-bound setting. Overall, the findings highlight the need to complement clean benchmark accuracy with robustness-oriented metrics, ranking stability analysis, receiver operating characteristic-area under the curve evaluation, and classification maps when assessing hyperspectral image classifiers.

Author Contributions

The percentages of the author' contributions are presented below. The author reviewed and approved the final version of the manuscript.

	C.A.
C	100
D	100
S	100
DCP	100
DAI	100
L	100
W	100
CR	100
SR	100
PM	100
FA	100

C= concept, D= design, S= supervision, DCP= data collection and/or processing, DAI= data analysis and/or interpretation, L= literature search, W= writing, CR= critical review, SR= submission and revision, PM= project management, FA= funding acquisition.

Conflict of Interest

The author declared that there is no conflict of interest.

Ethical Consideration

Ethics committee approval was not required for this study because no study on animals or humans was conducted.

References

Ahmad, M., Butt, M. H. F., Usama, M., Altuwaijri, H. A., Mazzara, M., Distefano, S., & Khan, A. M. (2025). Multi-head spatial-spectral mamba for hyperspectral image classification. *Remote Sensing Letters, 16*(4), 339-353. https://doi.org/10.1080/2150704X.2025.2461330

Ahmad, M., Shabbir, S., Roy, S. K., Hong, D., Wu, X., Yao, J., Khan, A. M., Mazzara, M., Distefano, S., & Chanussot, J. (2022). Hyperspectral image classification: Traditional to deep models: A survey for future prospects. *IEEE Journal of Selected Topics in Applied Earth Observations and Remote Sensing, 15*, 968-999. https://doi.org/10.1109/JSTARS.2021.3133021

Bera, S., Shrivastava, V. K., & Satapathy, S. C. (2022). Advances in hyperspectral image classification based on convolutional neural networks: A review. *Computer Modeling in Engineering & Sciences, 133*(2), 219-250. https://doi.org/10.32604/cmes.2022.020601

Bishop, C. M. (1995). Training with noise is equivalent to Tikhonov regularization. *Neural Computation, 7*(1), 108-116. https://doi.org/10.1162/neco.1995.7.1.108

Bo, C., Lu, H., & Wang, D. (2018). Spectral-spatial K-nearest neighbor approach for hyperspectral image classification. *Multimedia Tools and Applications, 77*(9), 10419-10436. https://doi.org/10.1007/s11042-017-4403-9

Ham, J., Chen, Y., Crawford, M. M., & Ghosh, J. (2005). Investigation of the random forest framework for classification of hyperspectral data. *IEEE Transactions on Geoscience and Remote Sensing, 43*(3), 492-501. https://doi.org/10.1109/TGRS.2004.842481

He, L., Li, J., Liu, C., & Li, S. (2018). Recent advances on spectral-spatial hyperspectral image classification: An overview and new guidelines. *IEEE Transactions on Geoscience and Remote Sensing, 56*(3), 1579-1597. https://doi.org/10.1109/TGRS.2017.2765364

Hendrycks, D., & Dietterich, T. (2019). Benchmarking neural network robustness to common corruptions and perturbations. *International Conference on Learning Representations*. https://openreview.net/forum?id=HJz6tiCqYm

Hendrycks, D., Mu, N., Cubuk, E. D., Zoph, B., Gilmer, J., & Lakshminarayanan, B. (2020). AugMix: A simple data processing method to improve robustness and uncertainty. *International Conference on Learning Representations*. https://openreview.net/forum?id=S1gmrxHFvB

Hong, D., Han, Z., Yao, J., Gao, L., Zhang, B., Plaza, A., & Chanussot, J. (2022). SpectralFormer: Rethinking hyperspectral image classification with transformers. *IEEE Transactions on Geoscience and Remote Sensing, 60*, 1-15. https://doi.org/10.1109/TGRS.2021.3130716

Li, J., Liang, B., & Wang, Y. (2020). A hybrid neural network for hyperspectral image classification. *Remote Sensing Letters, 11*(1), 96-105. https://doi.org/10.1080/2150704X.2019.1686780

Li, S., Song, W., Fang, L., Chen, Y., Ghamisi, P., & Benediktsson, J. A. (2019). Deep learning for hyperspectral image classification: An overview. *IEEE Transactions on Geoscience and Remote Sensing, 57*(9), 6690-6709. https://doi.org/10.1109/TGRS.2019.2907932

Lodhi, V., Chakravarty, D., & Mitra, P. (2019). Hyperspectral imaging system: Development aspects and recent trends. *Sensing and Imaging, 20, Article 35*. https://doi.org/10.1007/s11220-019-0257-8

Ma, J., Zou, Y., Tang, X., Zhang, X., Liu, F., & Jiao, L. (2024). Spatial pooling transformer network and noise-tolerant learning for noisy hyperspectral image classification. *IEEE Transactions on*

Geoscience and Remote Sensing, 62, 1-19. https://doi.org/10.1109/TGRS.2024.3368079

Mei, S., Lian, J., Wang, X., Su, Y., Ma, M., & Chau, L.-P. (2024). A comprehensive study on the robustness of deep learning-based image classification and object detection in remote sensing: Surveying and benchmarking. *Journal of Remote Sensing, 4*, 0219. https://doi.org/10.34133/remotesensing.0219

Melgani, F., & Bruzzone, L. (2004). Classification of hyperspectral remote sensing images with support vector machines. *IEEE Transactions on Geoscience and Remote Sensing, 42*(8), 1778-1790. https://doi.org/10.1109/TGRS.2004.831865

Parra, L. (2022). Remote sensing and GIS in environmental monitoring. *Applied Sciences, 12*(16), 8045. https://doi.org/10.3390/app12168045

Rasti, B., Scheunders, P., Ghamisi, P., Licciardi, G., & Chanussot, J. (2018). Noise reduction in hyperspectral imagery: Overview and application. *Remote Sensing, 10*(3), 482. https://doi.org/10.3390/rs10030482

Roy, S. K., Krishna, G., Dubey, S. R., & Chaudhuri, B. B. (2020). HybridSN: Exploring 3-D-2-D CNN feature hierarchy for hyperspectral image classification. *IEEE Geoscience and Remote Sensing Letters, 17*(2), 277-281. https://doi.org/10.1109/LGRS.2019.2918719

Rusak, E., Schott, L., Zimmermann, R. S., Bitterwolf, J., Bringmann, O., Bethge, M., & Brendel, W. (2020). A simple way to make neural networks robust against diverse image corruptions. In A. Vedaldi, H. Bischof, T. Brox, & J.-M. Frahm (Eds.), *Computer Vision – ECCV 2020* (Vol. 12348). Springer. https://doi.org/10.1007/978-3-030-58580-8_4

Schneider, S., Rusak, E., Eck, L., Bringmann, O., Brendel, W., & Bethge, M. (2020). Improving robustness against common corruptions by covariate shift adaptation. *Advances in Neural Information Processing Systems, 33*, 11539-11551. https://proceedings.neurips.cc/paper/2020/hash/85690f81aadc1749175c187784afc9ee-Abstract.html

Stuart, M. B., Davies, M., Hobbs, M. J., Pering, T. D., McGonigle, A. J. S., & Willmott, J. R. (2022). High-resolution hyperspectral imaging using low-cost components: Application within environmental monitoring scenarios. *Sensors, 22*(12), 4652. https://doi.org/10.3390/s22124652

Sun, L., Zhao, G., Zheng, Y., & Wu, Z. (2022). Spectral-spatial feature tokenization transformer for hyperspectral image classification. *IEEE Transactions on Geoscience and Remote Sensing, 60*, 1-14. https://doi.org/10.1109/TGRS.2022.3144158

Sun, L., Zhang, H., Zheng, Y., Wu, Z., Ye, Z., & Zhao, H. (2024). MASSFormer: Memory-augmented spectral-spatial transformer for hyperspectral image classification. *IEEE Transactions on Geoscience and Remote Sensing, 62*, 1-15. https://doi.org/10.1109/TGRS.2024.3392264

Xia, J., Du, P., He, X., & Chanussot, J. (2014). Hyperspectral remote sensing image classification based on rotation forest. *IEEE Geoscience and Remote Sensing Letters, 11*(1), 239-243. https://doi.org/10.1109/LGRS.2013.2254108

Xie, H., Zhang, M., Huang, H., Yang, M., Xu, L., Jiao, Q., & Tan, X. (2026). WMM: Noise-robust hyperspectral image classification via joint wavelet-manifold Mamba framework. *Journal of King Saud University - Computer and Information Sciences, 38*(4), 155. https://doi.org/10.1007/s44443-026-00538-4

Yu, X., Ozdemir, M. B., & Joshie, M. K. (2023). An overview of hyperspectral image classification by data-driven deep learning. *Frontiers in Computing and Intelligent Systems, 5(3)*, 107-110. https://doi.org/10.54097/fcis.v5i3.13999

Zhi, L., Yu, X., Liu, B., & Wei, X. (2019). A dense convolutional neural network for hyperspectral image classification. *Remote Sensing Letters, 10*(1), 59-66. https://doi.org/10.1080/2150704X.2018.1526424

Black Sea Journal of Engineering and Science
doi: 10.34248/bsengineering.1991498

Open Access Journal
e-ISSN: 2619 – 8991

Research Article
Volume 9 - Issue 5: 2393-2403 / September 2026

DEVELOPMENT AND WEB-BASED VISUALIZATION OF A DOMAIN-SPECIFIC SEMANTIC MODEL FOR COFFEE CULTURE AND PRODUCTION PROCESSES

Ömer DOĞAN[1], Alpay DORUK[2]*

[1]*Bandirma Onyedi Eylul University, Faculty of Engineering and Natural Sciences, Department of Computer Engineering, 10200, Balikesir, Türkiye*
[2]*Bandirma Onyedi Eylul University, Faculty of Engineering and Natural Sciences, Department of Computer Engineering, 10200, Balikesir, Türkiye*

Abstract: The global agricultural supply chain is a complex network with different data silos, complicated cultivation parameters and highly subjective sensory evaluation metrics. Formal knowledge representation is a must, if real semantic interoperability is to be achieved across this multidimensional domain. This work consists of the rigorous design, implementation and quantitative evaluation of the "Coffee Culture and Production Processes Ontology" and a custom client-side web-application named the "Coffee Ontology Explorer". The semantic model, developed with standard ontology design principles and the Web Ontology Language (OWL), captures the entire coffee lifecycle from botanical taxonomy and harvesting methods to specific roasting profiles and subjective brewing evaluations. Meanwhile, the React.js based ontology explorer tackles the ongoing limitations of traditional, heavy-client ontology visualization tools by utilizing a browser-native document parsing application programming interface for high efficiency, serverless ontology parsing. The quantitative estimation of the developed semantic model gives a 0.297 relation richness indicator, which confirms a highly interconnected and structurally complex knowledge graph, and not a simple taxonomic flat. Moreover, the performance profiling of the web application shows less than one second for parsing and less than 200 milliseconds for rendering complex graphical data even for large ontological hierarchies. This technical framework is a highly scalable, multilingual semantic infrastructure that is uniquely suited for integration into larger industrial traceability systems and provides a fundamental template for computer scientists, agritech developers, and agricultural stakeholders who want to exploit semantic web technologies for precision agriculture.

Keywords: Semantic web, Knowledge graph, Description logic, Web application, Coffee production, Supply chain traceability

***Corresponding author:** Bandirma Onyedi Eylul University, Faculty of Engineering and Natural Sciences, Department of Computer Engineering, 10200, Balıkesir, Türkiye
E mail: adoruk@bandirma.edu.tr (A. DORUK)
Ömer DOĞAN https://orcid.org/0000-0003-4815-8619
Alpay DORUK https://orcid.org/0000-0002-6190-288X

Received: July 10, 2026
Accepted: August 10, 2026
Published: September 15, 2026

Cite as: Doğan, Ö., & Doruk, A. (2026). Development and web-based visualization of a domain-specific semantic model for coffee culture and production processes. *Black Sea Journal of Engineering and Science,* 9(5), 2393-2403.

1. Introduction

The modern agriculture sector is becoming increasingly dependent on advanced data-driven paradigms that optimize physical production, ensure end-to-end supply chain traceability, and comply with strict environmental sustainability standards (Goldstein et al., 2021; Smaili and Kabbaj, 2025). In this bigger picture, the global coffee industry is more vulnerable. Coffee is not merely a bulk agricultural commodity but a highly nuanced and chemically complex product, in which small variations in altitude of cultivation, post-harvest processing methods and thermal roasting temperatures can have a profound effect on the final chemical composition and subjective sensory profile of the beverage (Illy and Viani, 2005).

The adoption of Internet of Things sensors and distributed ledger technologies for improved traceability of coffee supply chains is expanding quickly (Kamble et al., 2020; Lin et al., 2020; Ramos et al., 2023), but the data structures that support these innovations are still very fragmented. Agricultural and industrial terminology is very context specific and geopolitically bounded making it very difficult to integrate, query and analyze data efficiently across various digital agencies and international stakeholders (Joo et al., 2016).

Semantic Web Technologies provide a very strong, mathematically formalized framework (Gruber, 1993) for dealing with this fundamental heterogeneity. Ontologies are defined as explicit formal specifications of a shared conceptualization, so that machine agents can interpret data based on deep contextual awareness rather than simple syntactic pattern matching (Dooley et al., 2018; Guarino et al., 2009). Ontologies impose tight classes, object properties and description logic restrictions and transform independent and flat data points into rich and interconnected semantic knowledge graphs (Keet, 2019; Noy and McGuinness, 2001). However, the rigorous development of a domain specific ontology has to be complemented by accessible user centric visualization

This work is licensed (CC BY-NC 4.0) under Creative Commons Attribution 4.0 International License

and exploration tools to be of any practical utility. In the past, the use of ontological data was limited to either dedicated desktop applications or heavy server-side processing environments, thus creating prohibitively high barriers to entry for non-technical domain experts such as agronomists, coffee roasters, and supply chain logistics managers (Horridge, 2007; W3C OWL Working Group, 2012).

The use of semantic web technologies in the agricultural domain has gained substantial empirical traction, mainly driven by the growing worldwide demand for precision agriculture and transparent supply chain logistics (Goldstein et al, 2021; Smaili and Kabbaj, 2025). Important groundwork has been laid by prominent macro-ontologies and controlled vocabularies such as AGROVOC from the Food and Agriculture Organization (Liang et al., 2006) and the widely used FoodOn framework (Dooley et al., 2018) on which agriculture-specific vocabularies have been built. As a consortium-driven project, FoodOn aims to develop a complete farm-to-fork ontology to accurately and consistently describe foods across different global cultures (Dooley et al., 2018). FoodOn does offer some basic taxonomic representations of coffee, but its scope is necessarily broad. It typically views coffee only as a source of plant food or extracted beverage, and lacks the fine-grained, domain-specific axioms required to mathematically model the complex causal dependencies between coffee botanical varieties, high altitude cultivation stressors, specific thermal roasting curves, and final sensory cupping profiles (Angelica and Ferdinand, 2017).

The emerging computational literature stresses the need for specialized micro-ontologies to extend these foundational macro-models into highly specialized verticals. Much of the research on the coffee supply chain has been focused on traceability, using distributed ledger technologies and intelligent contracts to trace beans from farm to cup (Mauladi et al., 2022; Nuraisyah et al., 2025; Ramos et al., 2019). However, these advanced implementations of blockchain are often plagued by the classic “garbage in, garbage out” paradigm. Without the semantic alignment underneath, the raw data recorded on the ledger is functionally opaque to machine reasoning algorithms (Kamble et al., 2020; Ramos et al., 2019). Moreover, there have been existing expert systems based on mathematical analysis of Arabica coffee beans considering aroma and flavor inputs, with preliminary OWL models, but these systems generally lack complete and two-way structural linkages back to specific harvesting and processing variables (Goldstein et al., 2021). Therefore, a dedicated highly granular semantic model for the coffee industry still represents a critical gap in the existing literature.

The visualization of complex ontological data in an interactive way is a well-documented computational challenge in the wider Semantic Web community. Traditional knowledge engineering tools, and especially the Protégé integrated development environment, provide advanced editing and reasoning capabilities, but they are built on highly complex user interfaces and are strictly bound to desktop Java Virtual Machine environments (Keet, 2019; Horridge, 2007; W3C OWL Working Group, 2012). To democratize the access to semantic data and to promote a wider adoption across the industry, web-based visualizers have been extensively researched and proposed. Tools such as WebVOWL translate raw OWL syntax into visual force-directed graphs (Bach et al., 2011; Lohmann, et al., 2014). Other tools depend on heavy server-side rendering pipelines that take an uploaded ontology file, process it with backend Java frameworks, and return basic visual coordinates to the thin client (Dudáš et al., 2018; Katifori et al., 2007).

However, using server-side parsing incurs large network latency, requires maintenance of persistent and expensive back-end infrastructure, and poses critical data privacy issues for corporations using proprietary industrial ontologies that cannot be transmitted over public networks (Dudáš et al., 2018). In parallel, the rapid evolution of state-of-the-art JavaScript frameworks, such as React.js, and extremely optimized visualization of data libraries like D3.js and Recharts, have paved the way for a paradigm shift towards pure and unadulterated client-side processing (Coene, 2018; Chart.js documentation, 2026). React’s component-based, functional architecture allows for the declarative rendering of complex node-link diagrams and deeply hierarchical data, dynamically responding to changes in user state without needing to continuously hit the server (Lavanya et al., 2023; Leung and Salga, 2010). However, this technological change has not been accompanied by a rigorous analysis of the computational performance of native document object model parsing of OWL/XML documents strictly within a React state-management lifecycle in the peer-reviewed literature. This is a significant research gap that this technical study seeks to rigorously evaluate and fill.

To objectively measure the structural integrity, design quality and semantic richness of any newly developed ontology, quantitative mathematical metrics have to be used (Maynard et al., 2006). Qualitative expert evaluation or anecdotal validation alone is insufficient to establish the ultimate suitability of an ontology for automated machine reasoning and large-scale data integration. Some of the popular ontology engineering frameworks (Burton-Jones et al., 2005; Maedche and Staab, 2002; Tartir et al., 2005) define several important schema-level metrics, including Relationship Richness, Attribute Richness and Inheritance Richness.

These metrics provide detailed and quantitative information on the underlying design principles of the ontology, especially telling us whether the model is a simple flat hierarchical taxonomy or a complex highly interconnected knowledge graph that is capable of fully supporting sophisticated deductive reasoning algorithms (Keet, 2019; Tartir et al., 2005). For example, an ontology with very low relationship richness, built mainly around

simple parent-child "is-a" relationships, versus an ontology with high relationship richness, defining complex, real-world interactions between otherwise unrelated domain entities. These very formal mathematical definitions are part of the evaluation phase of this broad research and are used to rigorously validate the engineered coffee ontology.

This research focuses on these two technical challenges directly with a two-dimensional contribution. It first describes the precise engineering of a specialized domain ontology explicitly designed to map the intricacies of coffee culture and production processes. Second, a new, highly optimized web-based software architecture is presented, the Coffee Ontology Explorer, which uses modern JavaScript frameworks to load, query, simulate and visualize complex OWL files entirely within the client-side environment. This work combines formal knowledge representation with a very high performance, responsive web interface to provide an end-to-end semantic solution for the complex needs of the coffee industry.

2. Materials and Methods

The semantic model was formally developed with the architecture to be a deeply semantically rich knowledge graph for the entire physical and chemical lifecycle of coffee. The development lifecycle followed very closely the accepted ontological engineering methodologies (Noy and McGuinness, 2001) which specify a very iterative lifecycle of initial domain analysis, integration of existing ontologies, extraction of expert terminology, rigorous definition of the class hierarchy, mapping of object properties and formulation of logical constraints. The ontology was built using the Web Ontology Language (OWL) within the Protégé computational environment and strictly adhering to the standards of the World Wide Web Consortium (Angelica and Ferdinand,2017).

The primary existential entities in the coffee domain constitute the taxonomic backbone of the ontology. This gave rise to a deep and strongly structured hierarchical tree, which explicitly separated botanical living entities, physical states of the agricultural product, highly mechanized industrial processes, and subjective human sensory evaluations. The main ontological super-classes are defined with their respective hierarchical descendants as shown in Table 1.

Table 1. Complete hierarchical classes of the coffee culture and production processes ontology

Primary Super-Class (8)	Explicit Hierarchical Sub-Classes (19)	Total
CoffeePlant	CoffeeSpecies, CoffeeVariety	3
CoffeeBean	GreenBean, RoastedBean, GroundCoffee, EspressoSuitableCoffee (Inferred)	5
CoffeeProcessing	HarvestingMethod, ProcessingMethod, DryingMethod	4
CoffeeRoasting	RoastLevel, LightRoast, MediumRoast, DarkRoast	4
BrewingMethod	EspressoBrewing, FilterBrewing, ImmersionBrewing	4
TastingProfile	Flavor, Acidity, Body, Sweetness	5
Origin	Country, Region, Farm	4

The first thing to classify is the botanical origin. This is divided into specific taxonomic species (ex, Arabica and Robusta) and then into exact genetic cultivars and varieties (Bourbon or Typica). The main bean class represents the physical agricultural product itself. The main class is strictly categorized by the current state of the physical lifecycle, i.e. raw green beans, thermally processed roasted beans and mechanically pulverized ground coffee.

The industrial and agricultural activities are confined to specific processing classes. These are the agricultural extraction methods during harvesting, the post-harvest fermentation and washing processes, and the key drying techniques to achieve optimal moisture levels. Thermal processing is modeled as a separate class hierarchy, with detailed parameters for roasting levels from light to dark. The final human interaction with the product is modelled as specific classes of brewing method, modelling aqueous extraction methods such as espresso or immersion brewing. In an effort to incorporate the highly subjective nature of human taste, a complex sensory analysis class is developed that diverges into specialized sensory attributes such as specific flavor notes, perceived acidity, physical mouthfeel or body, and inherent sweetness. Finally, the geographical and geopolitical provenance is hierarchically organized from the macro-level of the producing country to specific regional zones and to the micro-level of the exact producing farm.

A full range of formal semantic properties was defined to transform the static, tree-like taxonomy into a highly relational, multidimensional knowledge graph. The Web Ontology Language explicitly distinguishes between Object Properties that express directed relationships between particular instances of two different classes, and Datatype Properties that relate a particular instance to a standardized literal value defined by XML Schema Datatypes (W3C OWL Working Group, 2012).

The object properties determine the complex logistical and chemical flow of the coffee bean in its entire life cycle. Strict mapping of domain constraints and range constraints guarantees rigorous semantic validation in automated reasoning tasks, ensuring that no illogical assertions are made in the knowledge base. The object properties implemented in the Coffee Culture and Production Processes Ontology are shown in Table 2.

The datatype properties are those that capture the exact quantitative variables and qualitative descriptors that are absolutely necessary for industrial quality control, sensory grading and precision agriculture (Goldstein et al., 2021; Gruber, 1993). These properties strictly utilize standard schema types to ensure computational interoperability (Table 3).

Table 2. Object properties implemented in the coffee culture and production processes ontology

Formal Property Identifier	Assigned Domain Class	Assigned Range Class	Semantic Role and Description
growsIn	CoffeePlant	Region	Associates a specific botanical plant instance with its geographic cultivation zone.
harvestedBy	CoffeeBean	HarvestingMethod	Defines the physical agricultural extraction method applied to the plant.
processedBy	CoffeeBean	ProcessingMethod	Links the raw agricultural cherry to its specific fermentation or washing process.
roastedTo	RoastedBean	RoastLevel	Defines the precise thermal transformation state achieved by the roaster.
hasOrigin	CoffeeBean	Origin	Links the final consumable product back to its geopolitical and physical provenance.
hasSpecies	CoffeeBean	CoffeeSpecies	Defines the exact botanical taxonomy of the specific harvested batch.
hasVariety	CoffeeBean	CoffeeVariety	Defines the specific genetic cultivar of the plant.
brewedWith	CoffeeBean	BrewingMethod	Maps a processed bean to its actual, real-world preparation method.
hasTastingProfile	CoffeeBean	TastingProfile	Connects the physical, chemical bean to its subjective human sensory evaluation.
producedIn	CoffeeBean	Farm	Provides micro-level logistical traceability down to the exact coordinates of the farm.
suitableFor	CoffeeBean	BrewingMethod	Serves as an expert recommendation link for optimal aqueous extraction.

Table 3. Datatype properties implemented in the coffee culture and production processes ontology

Formal Property Identifier	Assigned Domain Class	Assigned Range Class	Semantic Role and Description
Formal Property Identifier	Assigned Domain Class	XML Schema Datatype	Semantic Role and Description
altitudeGrown	CoffeePlant	xsd:integer	Cultivation altitude measured in precise meters above global sea level.
harvestYear	CoffeeBean	xsd:gYear	The standardized temporal stamp of the agricultural harvest.
roastDate	RoastedBean	xsd:date	The standardized temporal stamp of the industrial thermal processing.
acidityLevel	TastingProfile	xsd:integer	Standardized sensory scale rating ranging from 1 to 10 for perceived acidity.
bodyLevel	TastingProfile	xsd:integer	Standardized sensory scale rating ranging from 1 to 10 for physical mouthfeel.
sweetnessLevel	TastingProfile	xsd:integer	Standardized sensory scale rating ranging from 1 to 10 for inherent sweetness.
flavorNotes	TastingProfile	xsd:string	Unstructured text field for highly complex aroma notes, such as floral or citrus.
optimalBrewTemp	BrewingMethod	xsd:float	Target thermodynamic water temperature measured in degrees Celsius.
grindSize	BrewingMethod	xsd:string	Required physical particulate size categorization for proper extraction.
brewingTime	BrewingMethod	xsd:duration	Target temporal duration for optimal aqueous extraction of soluble compounds.

The intrinsic power of Description Logic ontology is its real computational power of automated, deductive reasoning (Guarino et al., 2009; Lohmann et al., 2014). By applying strict logical constraints to the defined classes using advanced mathematical set theory, the ontology enables automated semantic reasoners to infer entirely new classifications and relationships not explicitly asserted in the raw input data (Keet, 2019; W3C OWL Working Group, 2012).

The semantic model has a number of very complex logical constraints to represent real industry norms. The concept of coffee suitable for espresso extraction is presented as a precise mathematical intersection of a base class and an existential restriction. In particular, the reasoning engine automatically assigns any roasted bean with a known relationship to a roasting level defined as medium or dark as being suitable for espresso. This particular axiom enables an automated recommendation engine to classify any new agricultural batch introduced into the system dynamically without human intervention or manual reclassification.

Also, the notion of specialty coffee in the highly regulated industry is formalized through strict datatype property restrictions. The system mathematically encodes industry standard grading rules such as the rule that “any coffee bean grown at an altitude strictly greater than 1200 meters is classified within the specialty tier”. The system encodes key agronomic facts into machine-readable logic using datatype property restrictions. Beans grown at higher altitude are subjected to more severe environmental stress leading to more dense cellular architectures with slower maturation hence much more complex chemical acidity profiles when roasted (Illy and Viani, 2005).

Geographic inferences are also heavily encoded, so a coffee bean that has an origin relationship to the nation of Ethiopia is automatically tagged with a particular geographic tag. Additionally, we impose stringent cardinality constraints to ensure the integrity of the data as a whole. This means that each coffee bean can have only one relationship describing the botanical species of the coffee bean. The mathematics of this constraint ensures that the data is absolutely correct. There can be no taxonomic conflicts in a batch of products. This is a common mistake in badly designed relational databases. Finally, the mathematical bounding requires that a given brewing method must have a best brewing temperature greater than or equal to 85.0° Celsius, imposing thermodynamic preparation standards. This constraint is a quality control tool that automatically verifies that the

user-input recipes strictly follow the basic principles of thermodynamics for optimal extraction of coffee compounds. A wide range of query structures were carefully built so as to empirically demonstrate the functionality and industrial usefulness of the proposed semantic model using the SPARQL Protocol and RDF Query Language (W3C SPARQL Working Group, 2013). These fine-tuned queries show a model's inherent capability to navigate deep, complex graph relationships and expose multidimensional, useful information for supply chain stakeholders. In Table 4 mapping of competency Questions (CQs) to SPARQL Query objectives is shown.

Table 4. Mapping of Competency Questions (CQs) to SPARQL Query Objectives

CQ ID	Competency Question (CQ)	Target Semantic Path & SPARQL Objective
CQ1	Which coffee species/cultivars can thrive under high-altitude conditions (>1500m)?	Traverses CoffeePlant, CoffeeSpecies, and filters datatype altitudeGrown > 1500.
CQ2	Which coffee lots are inferred as suitable for espresso brewing without manual tag checks?	Queries the dynamically inferred class EspressoSuitableCoffee.
CQ3	What are the sensory profiles (acidity, body, flavor) of coffee batches originating from Ethiopia?	Traverses Origin (Ethiopia) → CoffeeBean → TastingProfile.
CQ4	Which coffee batches match specific subjective flavor descriptors (e.g., "floral")?	Performs regex/pattern filter on flavorNotes datatype property.

The first query structure is high-altitude agronomic filtering. This search involves a complex traversal between the physical bean, its strict botanical species taxonomy and its exact cultivation datatype in an effort to identify some botanical species that are doing well under extreme altitudinal stress. The execution path filters the huge knowledge graph to return only agricultural instances strictly belonging to the Arabica species, but also checks the integer value of the cultivation altitude to make sure that it exceeds the strict threshold of 1,500 meters. This question will be very useful to agronomists, who are interested in studying the resistance of some genetic cultivars to environmental stressors at high altitudes.

The SPARQL Syntax for CQ1 is shown below:

```
PREFIX coffee:
<http://www.semanticweb.org/ontologies/coffee#>
PREFIX xsd:
<http://www.w3.org/2001/XMLSchema#>
SELECT ?plant ?species ?altitude
WHERE {
 ?plant a coffee:CoffeePlant ;
      coffee:hasSpecies ?species ;
      coffee:altitudeGrown ?altitude .
 FILTER (?altitude > 1500)
}
```

The secondary query structure demonstrates the great power of inferential recommendation retrieval. Instead, the search directly targets the mathematically inferred class of coffee suitable for espresso, without having to search through the whole range of thermal roasting parameters manually. This approach to executing the query pushes the entire classification burden directly onto the underlying Description Logic reasoning engine. The query does not need to explicitly test or validate roast levels, as the semantic engine has already processed the raw data and dynamically inferred the exact set of eligibles, based on the foundational axioms established during the engineering phase (Guarino et al., 2009).

An advanced supply chain tracking makes use of a sophisticated cross domain traceability and sensory mapping query. This is a very advanced industrial use case for this search across different conceptual domains. Starting with the macro geographic provenance, zooming in to the nation of Ethiopia, traveling through the physical agricultural bean entities associated with that origin and ending deep within the subjective human sensory evaluation profiles. The query returns highly quantitative, numeric scoring metrics on perceived acidity and physical body and qualitative, unstructured textual descriptors of flavor notes. It lets quality assurance professionals mathematically link precise geopolitical origins to very specific chemical sensory results across massive data sets.

Finally, a semantic unstructured text search query is the bridge between formalized mathematical logic and highly variable unstructured human vocabulary. This execution path employs advanced string manipulation and filtering functions to interpret the textual flavor notes attribute. This tool enables fuzzy, pattern-matching search of coffee lots with specific aromatic chemical compounds, like floral notes, irrespective of botanical species, processing method or geographic region. This is an important capability for retail stakeholders who wish to curate products based on consumer flavor preferences rather than technical agricultural specifications.

The widespread industrial deployment and use of formal ontologies is highly dependent on the availability of very user-friendly, computationally scalable software tools that successfully hide the extreme complexity of raw RDF and XML syntax (Coene, 2018; Chart.js documentation, 2026; Lavanya et al., 2023). The web-based exploration application was developed from scratch to directly

address this critical industry need. It is a very modern Single Page Application. It intentionally drops all heavy, backend JVM based parsing pipelines and uses a very decentralized, purely client-side processing architecture.

The application is built on React.js framework and is written in modern day JavaScript standards, HTML5 and CSS3. Responsive styling is supported via a modern user interface framework. React's component-driven, state-reactive paradigm is a natural fit for the complex, deeply nested graph data of parsed ontologies, which can be mapped directly and efficiently to discrete, reusable UI elements. The software project directory is organized into separate logical layers in an effort to maintain the codebase for a long period of time.

The contexts layer handles global application state and uses sophisticated hook patterns to offer very secure user authentication sessions and instant real-time bilingual localization without the highly inefficient component prop-drilling methodology. The component layer hosts the modular interface elements, defines the overall layout, handles the cryptographic authentication flows and contains the core exploratory functionalities. Finally, the critical utility layer comprises the core algorithmic parsing logic, most notably the proprietary parsing engine, which handles in a stand-alone fashion the complex ingestion, structural transformation and state integration of raw ontological data.

A new technical innovation central to this software architecture is the complete implementation of deep ontology parsing within the isolated context of the user's local web browser. Traditional semantic web applications inherently work by posting raw files to a remote, highly provisioned server with heavy Java-based endpoints (Dudáš et al., 2018; Katifori et al., 2007). This traditional client-server approach, while being computationally powerful for massive datasets, suffers from significant network latency, the need for continuous maintenance of expensive backend infrastructure and a fundamental compromise of data security in dealing with highly proprietary supply chain data.

The implemented exploration tool overcomes these deep limitations by deploying a custom parsing algorithm that uses the browser's native document object model parsing application programming interface strictly. The algorithmic flow is based on a very sequential pipeline. The user first uploads a raw ontology file, which is read directly into local system memory as an unformatted raw text string. Then the parsing engine is run, and a huge Abstract Syntax Tree (AST) is instantly created, which maps the whole XML hierarchy in memory.

The sequential semantic extraction algorithms traverse the nodes actively after the syntax tree generation. The algorithms specifically select out structural namespaces. The document is queried for defined class nodes and both object and datatype properties are recursively extracted, capturing exactly their respective domain and range mathematical constraints. In the final algorithmic phase, an enrichment function converts the raw, extracted XML nodes into a very optimized, deeply nested JSON data structure that is specifically designed for very fast traversal and reconciliation by React's internal state management hooks. This purely client-side approach significantly improves corporate data privacy by never transmitting proprietary industrial ontologies outside of the local computational machine, while at the same time increasing the responsiveness of the interface by offloading the entire computational workload to the client's local processing unit instead of remote servers (Bach et al., 2011; Dudáš et al., 2018).

3. Results

True native execution of semantic query languages is technically impossible in the browser environment by deliberate design without a heavy backend graph database. To get around this hard limit in a programmatic manner, the software provides a sophisticated query simulation module. It is an intermediary interpreter that takes user-selected granular parameters via the graphical interface, dynamically generates highly equivalent JavaScript array-filtering logic, and executes those mathematical filters quickly and directly against the JSON-transformed ontology state currently held in local memory. The module algorithmically synthesizes the raw, mathematically correct query syntax string for educational viewing and external export, providing users with the exact code they need should they later choose to deploy the ontology on a dedicated enterprise server.

The visualization layer integrates highly optimized SVG based charting libraries for analysis of aggregate, macro level data. Complex data preparation algorithms dynamically aggregate instance counts, compute hierarchical distributions and compute certain property values. The transformed data is fed to reactive graphical charts immediately. This seamless pipeline transforms highly abstract, deeply mathematical semantic web data into immediately actionable, visually digestible business intelligence dashboards, perfect for non-technical industry stakeholders and supply chain managers.

The overall success of the proposed semantic solution was systematically assessed along two very different computational dimensions: the mathematical structural integrity of the generated semantic model itself and the raw computational performance indicators of the React based web exploration architecture.

A final confirmation that the developed domain ontology is a very robust interconnected knowledge graph and not a simple flat taxonomy was given by systematic use of established mathematical evaluation metrics (Maynard et al., 2006).

The resulting semantic model based on the well-documented internal architecture consists of exactly 27 conceptual classes altogether, both foundational base classes and mathematically derived classes. Besides, the model defines an exact number of 21 different semantic properties, all of them strictly divided into 11 different

object properties and 10 very specific data type properties.

The most important metric of evaluation used is Relationship Richness. This metric represents a mathematical measure of total semantic relations diversity defined in the schema. The higher ratio decisively shows that the engineered ontology contains highly complex, domain-specific interactions, far beyond simple hierarchical parent-child inheritance structures (Burton-Jones et al., 2005; Maedche and Staab, 2002; Tartir et al., 2005). The calculation is based on the formal mathematical definition of the proportion of non-inheritance relationships to the sum of inheritance and non-inheritance relationships.

Considering a strict normalized tree structure, the number of inheritance relationships for the 27 defined classes is about 26. Mathematically, with the explicit use of the 11 object properties, the computation yields a ratio of 11/37 which yields a Relationship Richness indicator of exactly 0.297. Values close to 0.3 can be obtained, which indicates a very interconnected, very dense semantic network. Basic flat taxonomies mathematically tend towards an indicator of zero. This ontology tightly links distinct cross-domain nodes unequivocally confirming its high utility for complex supply chain traceability and sophisticated algorithmic recommendation systems (Tartir et al., 2005).

In ontology quality benchmarking (Tartir et al., 2005; Burton-Jones et al., 2005), Relationship Richness (RR) reflects the proportion of non-taxonomic relationships relative to the total number of relationships $\left(RR = |P_{non-isa}|/(|P_{isa}| + |P_{non-isa}|)\right)$. Purely taxonomic hierarchies (like simple thesauri or taxonomies) exhibit an RR near 0.0, as they rely almost exclusively on subClassOf inheritance. In domain-specific ontologies, RR values typically range between 0.10 and 0.35 depending on graph density. Our achieved RR of 0.297 mathematically confirms that nearly 30% of all defined relationships in the schema express complex, cross-domain functional associations (e.g., agronomic, chemical, and sensory linkages) rather than simple taxonomic subclassing, placing it at the upper end of domain-specific semantic networks.

Also Attribute Richness metric is evaluated in the study. This metric computes the average size of literal, descriptive data assigned per class (Burton-Jones et al., 2005; Maedche and Staab, 2002; Tartir et al., 2005). Dividing the 10 defined datatype properties by the total 27 classes an Attribute Richness indicator of 0.370 is obtained. This metric specifically reveals a very moderate, optimally balanced distribution of datatype properties that captures critical physical properties, accurate environmental temperatures and highly subjective sensory scores adequately and efficiently, to fully enable deep, quantitative machine queries without unnecessarily overloading the data structure.

Strict performance stress tests of the raw computational efficiency and the overall stability of the web-based exploration software conclusively proved the technical feasibility of the purely client-side document parsing architecture.

The application was packed heavily and optimized by advanced compiling techniques, achieving a final payload size of about 2.5 megabytes. This footprint was then compressed even further to a very efficient 800 kilobytes using gzip encoding. This ultra-lightweight footprint, which employs only sophisticated code splitting and very dynamic route-based lazy loading techniques and nothing else, provides for incredibly fast deployment and execution even over the very constrained, low-bandwidth networks common in rural agricultural environments.

Empirical runtime metrics show remarkable, uninterrupted fluidity in all operations. The app conclusively achieves a full initial load time strictly less than 3 seconds from cold start. The proprietary parsing engine takes about 500 milliseconds to process and build the AST for a medium-sized ontology file. Complex query simulations and search index operations also produce full responses in less than 100 milliseconds and the translation and rendering of complex SVG graphical data use less than 200 milliseconds of main thread execution time.

To make a definitive assessment of long-term scalability, the system architecture was aggressively stress-tested against massive, synthetically generated ontologies containing well over 1,000 distinct, heavily interlinked classes and properties. The huge memory allocation that was needed for the extensive syntax tree was handled efficiently and safely by the browser's native parsing API, without triggering the garbage collection stutters. The React virtual DOM also reconciled massive localized state changes at a very high efficiency rate, without blocking the main browser thread or visibly degrading the search input responsiveness, at the same time. These final empirical results provide strong supporting evidence for the core assumption that contemporary client browser engines have enough computational overhead to independently process, traverse and visualize super-strong semantic models without reliance at all on traditional backend server infrastructure. Client-Side Performance Benchmarks under Standardized Environment can be seen on Table 5.

Table 5. Client-side performance benchmarks under standardized environment*

Benchmark Parameter	Operational Value / Metric	Execution Context & Hardware Conditions
Base Ontology Size	27 classes, 21 properties, ~350 RDF triples (18 KB OWL/XML)	Baseline test file
Synthetic Stress Test Dataset	1,024 classes, 85 properties, ~12,500 RDF triples (1.4 MB)	Scalability stress test
Initial Bundle Footprint	800 KB (Gzip compressed) / 2.5 MB uncompressed	Optimized React production build
AST Generation Time	~500 ms (Baseline) / ~1,850 ms (12k triples)	Native Browser DOM Parser
Query Sim / Filtering	< 100 ms	Client-side JS array manipulation
SVG Render Latency	< 200 ms	React Virtual DOM reconciliation

*Test Environment Hardware Setup for Reproducibility: Intel Core i7-12700H @ 2.30GHz, 16 GB DDR4 RAM, Google Chrome v125.0 (64-bit) running on Windows 11 Enterprise. Network latency was throttled using Chrome DevTools to simulate low-bandwidth rural connections.

4. Discussion

The deep semantic ontology is tightly integrated with the high-performance, React-based web exploration architecture and has several immediate and profound implications for the wider agricultural technology space. By changing the huge vocabulary of the global coffee supply chain dramatically from highly disparate, standalone relational databases to a unified, mathematically rigorous Semantic Web model, industry stakeholders will be able to achieve truly unprecedented end-to-end traceability (Ramos et al., 2023; Mauladi et al., 2022).

For instance, the strategic combination of such semantic ontology with physical IoT sensors, deployed directly on the agricultural farm, along with immutable blockchain logistics platforms, guarantees that highly critical data is not only stored in a database, but is inherently, contextually understood by fully automated reasoning systems (Kamble et al., 2020; Lin et al., 2020; Ramos et al., 2019). The strict mathematical constraints that are built directly into the ontology allow fully automated, highly trusted certification processes, massively reducing manual administrative overhead, removing human error and completely minimizing the risk of fraudulent environmental or quality labeling within international trade.

From a strict software engineering perspective, the shown performance of the client-side parsing mechanism suggests a fundamental, larger change in the way in which Semantic Web tools should be designed and deployed in the future. Traditional architectural dependencies on heavy, backend Java-based parsing endpoints inherently create massive bottlenecks in user experience development, drastically increase corporate hosting costs, and severely slow down the widespread use of ontology exploration outside of isolated academic research circles (Horridge, 2007; Katifori et al., 2007). The very novel architecture presented in this comprehensive study clearly demonstrates that highly complex analytical tools, no matter how heavy, can be fully distributed through simple static file hosting, thus finally democratizing access to highly complex formalized knowledge structures for all levels of users.

The present version of the software architecture, however, has some technical limitations which clearly point to the direction of future research and development. The current implementation is very performant when analyzing files locally, but it relies on an emulated query engine through JavaScript array manipulations, which mathematically cannot substitute a true graph database with highly distributed, federated querying capabilities over massive, petabyte-scale datasets.

The proposed Coffee Culture and Production Processes Ontology has also to be maintained and developed over time beyond its immediate use, which is a key aspect to keep its academic and industrial relevance. The agricultural domain is dynamic with new botanical cultivars, processing technologies and sensory evaluation standards being introduced continuously. Therefore, the semantic model cannot be static. A formalized maintenance workflow is expected to keep on the continuous vitality. First, the ontology will be hosted in a public, version-controlled repository (e.g. GitHub) so that the community of agronomy researchers and software developers are able to submit pull requests for new concepts or property alignments. Second, future incarnations will follow established semantic versioning practices (such as OWL's owl:versionIRI properties) to ensure backward compatibility with legacy data and traceability systems that already depend on earlier drafts. Finally, we will link our micro-ontology to developing foundational macro-ontologies such as FoodOn and AGROVOC using explicit mapping properties (e.g., owl:equivalentClass or skos:exactMatch) to reduce the risk of conceptual drift and the burden of manual curation. This is a community-driven, standards-aligned model for maintenance, turning the ontology from a static snapshot into a living, community-maintained semantic standard for the global coffee industry.

Furthermore, in future extensions of this research, incorporating state-of-the-art Deep Learning (DL)

methodologies presents a promising direction. Deep learning models (e.g., Graph Neural Networks for knowledge graph embeddings or transformer-based architectures for automated entity/relation extraction from unstructured agricultural texts) could be explored to semi-automatically populate and evolve the coffee ontology. Combining symbolic reasoning from our OWL ontology with subsymbolic representations from deep learning paradigms could further enhance predictive modeling for sensory evaluation and crop yield optimization.

Future versions of the architecture will focus on the implementation of extremely advanced, hybrid architectures, where the client application will be able to connect seamlessly to an external, real-time query endpoint, while keeping the highly efficient local parsing power for ad-hoc, offline file exploration. Moreover, the future integration of advanced Large Language Models to successfully enable pure natural language querying over the complex ontology via localized Retrieval-Augmented Generation paradigms will serve to further lower the technical barrier to entry for non-technical agricultural users, completely revolutionizing how human operators interact with mathematically formalized semantic data (Lippolis et al., 2025; Tiwari et al., 2025; Sharma et al., 2024).

5. Conclusion

The rapid and broad acceptance of highly standardized, machine-readable knowledge representations is an absolute necessity for the seamless, error-free operation of modern global agricultural supply chains. This extensive research resulted in a highly relational, very complex domain ontology explicitly developed for the complexity of coffee culture and precision production. This semantic model was rigorously validated by a quantitative Relationship Richness metric that indicated very high semantic density and advanced inferential capabilities in an automated way. At the same time, the successful architectural development and deployment of the web-based exploration tool establish a highly performant, fully serverless architectural pattern for web-based semantic visualization of data. The framework presented here successfully closes the historical gap between highly formal, mathematical ontology engineering and accessible, user-centric commercial software design, by decisively demonstrating sub-second document parse times and truly instantaneous query responses using a native, client-side data parsing pipeline. To summarize, this dual computational approach provides the absolutely essential foundational infrastructure needed to accelerate large-scale data harmonization, automated quality assurance, and unbreakable traceability in the highly complex global coffee industry.

Author Contributions

The percentages of the authors' contributions are presented below. All authors reviewed and approved the final version of the manuscript.

	Ö.D.	A.D.
C	50	50
D	40	60
S	0	100
DCP	80	20
DAI	70	30
L	70	30
W	50	50
CR	20	80
SR	20	80
PM	10	90
FA	0	0

C= concept, D= design, S= supervision, DCP= data collection and/or processing, DAI= data analysis and/or interpretation, L= literature search, W= writing, CR= critical review, SR= submission and revision, PM= project management, FA= funding acquisition.

Conflict of Interest

The authors declared that there is no conflict of interest.

Ethical Consideration

Ethics committee approval was not required for this study because of there was no study on animals or humans.

References

Angelica, M., & Ferdinand, F. N. (2017). Expert system based on an ontology method to analyze types of Arabica coffee beans. *International Journal of Interactive Mobile Technologies*, *11*(4), 1–10. https://doi.org/10.3991/ijim.v11i4.6859

Bach, B., Pietriga, E., Liccardi, I., & Legostaev, G. (2011). OntoTrix: A hybrid visualization for populated ontologies. In *Proceedings of the 20th International Conference Companion on World Wide Web* (pp. 177–180). Association for Computing Machinery. https://doi.org/10.1145/1963192.1963282

Burton-Jones, A., Storey, V. C., Sugumaran, V., & Ahluwalia, P. (2005). A semiotic metrics suite for assessing the quality of ontologies. *Data & Knowledge Engineering*, *55*(1), 84–102. https://doi.org/10.1016/j.datak.2004.11.010

Chart.js. (n.d.). *Chart.js documentation*. Retrieved June 16, 2026, from https://www.chartjs.org/docs/latest

Coene, J. P. (2018). Sigmajs: An R htmlwidget interface to the sigma.js visualization library. *Journal of Open Source Software*, *3*(28), Article 814. https://doi.org/10.21105/joss.00814

Dooley, D. M., Griffiths, E. J., Gosal, G. S., Buttigieg, P. L., Bastien, R., Jalali, N. N., Hoehndorf, R., Schriml, L. M., De Coronado, A. R., & Hsiao, W. W. L. (2018). FoodOn: A harmonized food ontology to increase global food traceability, quality control and data integration. *npj Science of Food*, *2*, Article 23. https://doi.org/10.1038/s41538-018-0032-6

Dudáš M, Lohmann S, Svátek V, Pavlov D. Ontology visualization methods and tools: a survey of the state of the art. *The*

Knowledge Engineering Review. 2018;33:e10. doi:10.1017/S0269888918000073

Goldstein, A., Fink, L., & Ravid, G. (2021). A framework for evaluating agricultural ontologies. *Sustainability*, *13*(11), Article 6387. https://doi.org/10.3390/su13116387

Gruber, T. R. (1993). A translation approach to portable ontology specifications. *Knowledge Acquisition*, *5*(2), 199–220. https://doi.org/10.1006/knac.1993.1008

Guarino, N., Oberle, D., & Staab, S. (2009). What is an ontology? In S. Staab & R. Studer (Eds.), *Handbook on ontologies* (2nd ed., pp. 1–17). Springer. https://doi.org/10.1007/978-3-540-92673-3_0

Horridge, M. (2007). *Pizza ontology 1.5 tutorial*. Manchester University.

Illy, A., & Viani, R. (Eds.). (2005). *Espresso coffee: The science of quality* (2nd ed.). Academic Press.

Joo, S., Koide, S., Takeda, H., Horyu, D., Takezaki, A., & Yoshida, T. (2016). Designing of ontology for domain vocabulary on Agriculture Activity Ontology (AAO) and a lesson learned. In Y.-F. Li, M. M. S. Wong, G. Qi, & Y. Zou (Eds.), *Semantic technology. JIST 2016* (Lecture Notes in Computer Science, Vol. 10055, pp. 31–43). Springer, Cham. https://doi.org/10.1007/978-3-319-50112-3_3

Kamble, S. S., Gunasekaran, A., & Sharma, R. (2020). Modeling the blockchain enabled traceability in agriculture supply chain. *International Journal of Information Management*, *52*, Article 101967. https://doi.org/10.1016/j.ijinfomgt.2019.05.023

Katifori, A., Halatsis, C., Lepouras, G., Vassilakis, C., & Giannopoulou, E. (2007). Ontology visualization methods—A survey. *ACM Computing Surveys*, *39*(4), Article 10. https://doi.org/10.1145/1287620.1287621

Keet, M. (2019). *An introduction to ontology engineering*. College Publications.

Lavanya, A., Sindhuja, S., Gaurav, L., & Ali, W. (2023). A comprehensive review of data visualization tools: Features, strengths, and weaknesses. *International Journal of Computer Engineering and Research Trends*, *10*(1), 10–20.

Leung, C., & Salga, A. (2010). Enabling WebGL. In *Proceedings of the 19th International Conference Companion on World Wide Web* (pp. 10–14). Association for Computing Machinery. https://doi.org/10.1145/1772690.1772933

Liang, A., Sini, M., Lu, W., Keizer, J., & Katz, S. (2006). *The mapping schema from Chinese agricultural thesaurus to AGROVOC*. Food and Agriculture Organization of the United Nations.

Lin, Y. P., Petway, J. R., Anthony, J., Mukhtar, H., Liao, S. W., Chou, C. F., & Ho, Y. F. (2020). Blockchain: The evolutionary next step for ICT e-agriculture. *Environments*, *4*(3), Article 50. https://doi.org/10.3390/environments4030050

Lippolis, A. S., Siragusa, G., Buscaldi, D., & Rossi, R. (2025). *Ontology generation using large language models* (arXiv:2503.05388). arXiv. https://doi.org/10.48550/arXiv.2503.05388

Lohmann, S., Negru, S., Haag, F., & Ertl, T. (2014). Visualizing ontologies with VOWL. *Semantic Web*, *5*(5), 399–419. https://doi.org/10.3233/SW-140134

Maedche, A., & Staab, S. (2002). Measuring similarity between ontologies. In A. Gómez-Pérez & V. R. Benjamins (Eds.), *Knowledge engineering and knowledge management: Ontologies and the Semantic Web. EKAW 2002* (Lecture Notes in Computer Science, Vol. 2473, pp. 251–263). Springer, Berlin, Heidelberg. https://doi.org/10.1007/3-540-45810-7_24

Mauladi, M. A. R., Jangkung Handoyo Mulyo, & Dwidjono Hadi Darwanto. (2022). Coffee Supply Chain Management: A Case Study In Ciamis, West Java, Indonesia. *HABITAT*, *33*(3), 201–211. https://doi.org/10.21776/ub.habitat.2022.033.3.20

Maynard, D., Peters, W., & Li, Y. (2006). Metrics for evaluation of ontology-based information extraction. In *Proceedings of the WWW 2006 Workshop on Evaluation of Ontologies for the Web (EON 2006)* (pp. 1–8). CEUR Workshop Proceedings.

Noy, N. F., & McGuinness, D. L. (2001). *Ontology development 101: A guide to creating your first ontology* (Stanford Knowledge Systems Laboratory Technical Report KSL-01-05). Stanford University.

Nuraisyah, A., Wulandari, E., Indrawan, D. *et al.* The roles of stakeholders in supply chain sustainability challenges: the case of coffee chain in West Java Province, Indonesia. *Discov Sustain* **6**, 247 (2025). https://doi.org/10.1007/s43621-025-01004-3

Ramos, E., Chavez, M., Patrucco, A. S., & Gonzales, A. (2019). Organic coffee supply chain source process integration: A Peruvian case. *International Journal of Supply Chain Management*, *8*(6), 133–145.

Ramos, E., Patrucco, A. S., & Chavez, M. (2023). Dynamic capabilities in the "new normal": A study of organizational flexibility, integration and agility in the Peruvian coffee supply chain. *Supply Chain Management: An International Journal*, *28*(1), 55–73. https://doi.org/10.1108/SCM-12-2021-0553

Sharma, K., Kumar, P., & Li, Y. (2024). *OG-RAG: Ontology-grounded retrieval-augmented generation for large language models* (arXiv:2412.15235). arXiv. https://doi.org/10.48550/arXiv.2412.15235

Smaili, N., & Kabbaj, A. (2025). Enabling semantic interoperability for smart farming. *Agronomy Research*, *23*(1), 479–492. https://doi.org/10.15159/AR.25.021

Tartir, S., Arpinar, I. B., Moore, M., Sheth, A. P., & Aleman-Meza, B. (2005). OntoQA: Metric-based ontology quality analysis. In *Proceedings of the IEEE Workshop on Knowledge Acquisition from Distributed, Autonomous, Semantically Heterogeneous Data (KADASH 2005)* (pp. 1–8). IEEE.

Tiwari, Y., Lone, O. A., & Pal, M. (2025). *OntoRAG: Enhancing question-answering through automated ontology derivation from unstructured knowledge bases* (arXiv:2506.00664). arXiv. https://doi.org/10.48550/arXiv.2506.00664

W3C OWL Working Group. (2012). *OWL 2 Web Ontology Language document overview* (2nd ed., W3C Recommendation). W3C. https://www.w3.org/TR/owl2-overview/

W3C SPARQL Working Group. (2013). *SPARQL 1.1 query language* (W3C Recommendation). W3C. https://www.w3.org/TR/sparql11-query/

Black Sea Journal of Engineering and Science
doi: 10.34248/bsengineering.1991945

Open Access Journal
e-ISSN: 2619 – 8991

Araştırma Makalesi (Research Article)
Cilt 9 - Sayı 5: 2404-2418 / Eylül 2026
(Volume 9 - Issue 5: 2404-2418 / September 2026)

YAZILIM YOĞUN UÇUŞ KONTROL SİSTEMLERİNDE SERTİFİKASYON GÜVENCESİ VE OPERASYONEL ÖĞRENME: AIRBUS A320 ELAC ARIZALARI ÜZERİNE ÇOK BOYUTLU BİR ANALİZ

Erdal YEŞİLBAŞ[1,2]*

[1]*Erciyes University, Aeronautical Engineering Department, 38039, Melikgazi, Kayseri, Türkiye*
[2]*Qatar Civil Aviation Authority (QCAA), Air Safety Department, Old Salata, Doha, Qatar*

Özet: Yazılım ağırlıklı "fly-by-wire" uçuş kontrol sistemleri, yüksek sertifikasyon ve geliştirme güvencesi süreçlerinden geçirilerek tasarlansa da, nadir çevresel etkiler, yazılım sınır koşulları ve operasyonel etkileşimler bazı emniyet risklerinin ancak operasyon sırasında ortaya çıkmasına neden olabilmektedir. Bu çerçevede bu çalışma, "Airbus A320 Elevator Aileron Computer (ELAC)" sistemi arızalarını detaylı olarak ele almakta ve tasarım güvencesi, operasyonel emniyet performansı ile sürekli uçuşa elverişlilik arasındaki ilişkiyi incelemektedir. Analiz, 2025 yılında ABD'de meydana gelen spesifik bir hava aracı emniyeti olayının hemen ardından EASA tarafından acil kodlu bir uçuşa elverişlilik direktifinin (EASA AD No. 2025-0268-E) yayımlanması ve bu olaya ilişkin Avrupa Birliği Havacılık Emniyeti Ajansı (EASA) ile ABD Federal Havacılık İdaresi (FAA) tarafından gerçekleştirilen müteakip düzenleyici faaliyetlerden hareketle yapılandırılmıştır. Çalışma, birbirini tamamlayan üç analitik boyutu bir araya getirmekte olup bunlar sırasıyla Airbus "fly-by-wire" anomalilerine ilişkin "NASA Havacılık Emniyeti Raporlama Sistemi (ASRS)" raporlarının yapılandırılmış değerlendirmesi, söz konusu acil uçuşa elverişlilik direktifini tetikleyen olayın vaka temelli analizi ve bahse konu olguya yönelik Sistem Teorik Süreç Analizi (STPA) ile İsviçre Peyniri (Swiss Cheese) modeli kullanılarak gerçekleştirilen sistem emniyeti değerlendirmesidir. Bulgular, hava aracı sertifikasyonunun emniyetin nihai ve değişmez kanıtı olarak değil, operasyonel veriler, olay incelemeleri, düzeltici faaliyetler ve tasarım iyileştirmeleriyle sürekli olarak beslenen uçuşa elverişlilik yönetimi döngüsünün temel bir unsuru olarak görülmesi gerektiğini göstermektedir. Sonuç olarak, çalışma ELAC vakası üzerinden yazılım yoğun aviyonik sistemlerde sürdürülebilir emniyetin ancak tasarım varsayımlarının operasyonel öğrenme yoluyla düzenli biçimde sınanması ve gerektiğinde güncellenmesiyle sağlanabileceğini ileri sürmektedir.

Anahtar kelimeler: Airbus a320, Fly-by-wire, Uçuş kontrol sistemleri, NASA ASRS, STPA, İsviçre peyniri modeli

Certification Assurance and Operational Learning in Software-Intensive Flight Control Systems: A Multidimensional Analysis of Airbus A320 ELAC Failures

Abstract: Although software-intensive fly-by-wire flight control systems are designed through rigorous certification and development assurance processes, rare environmental effects, software boundary conditions, and operational interactions may cause certain safety risks to emerge only during service. Within this context, this study addresses failures of the Airbus A320 Elevator Aileron Computer (ELAC) system and examines the relationship between design assurance, operational safety performance, and continuing airworthiness. The analysis is structured around the issuance of an emergency airworthiness directive by EASA (EASA AD No. 2025-0268-E) immediately after a specific aircraft safety event that occurred in the United States in 2025, as well as the subsequent regulatory actions undertaken by the European Union Aviation Safety Agency (EASA) and the U.S. Federal Aviation Administration (FAA). The study integrates three complementary analytical dimensions: a statistical analysis of NASA Aviation Safety Reporting System (ASRS) reports related to Airbus fly-by-wire anomalies; an event-based examination of the systemic failure that triggered the relevant emergency airworthiness directive; and a system safety assessment of these anomalies using Systems-Theoretic Process Analysis (STPA) and the Swiss Cheese Model. The findings indicate that aircraft certification should not be regarded as the final and immutable proof of safety, but rather as a fundamental component of a continuing airworthiness management cycle that is continuously informed by operational data, event investigations, corrective actions, and design improvements. Consequently, through the case of ELAC systemic failures, the study argues that sustainable safety in software-intensive avionics systems can only be achieved by regularly testing and, when necessary, updating design assumptions through operational learning.

Keywords: Airbus a320, Fly-by-wire, Flight control systems, NASA ASRS, STPA, Swiss cheese model

***Sorumlu yazar (Corresponding author):** Erciyes University, Aeronautical Engineering Department, 38039, Melikgazi, Kayseri, Türkiye
E mail: erdal.yesilbas@caa.gov.qa (E. YEŞİLBAŞ)
Erdal YEŞİLBAŞ https://orcid.org/0000-0001-9510-2023

Gönderi: 10 Temmuz 2026 **Received:** July 10, 2026
Kabul: 10 Ağustos 2026 **Accepted:** August 10, 2026
Yayınlanma: 15 Eylül 2026 **Published:** September 15, 2026

Cite as: Yeşilbaş, E. (2026). Certification assurance and operational learning in software-intensive flight control systems: a multidimensional analysis of Airbus A320 ELAC failures. *Black Sea Journal of Engineering and Science,* 9(5), 2404-2418.

This work is licensed (CC BY-NC 4.0) under Creative Commons Attribution 4.0 International License

1. Giriş

Modern ticari hava araçları, çok sıkı sertifikasyon ve tasarım geliştirme güvence rejimleri altında geliştirilen yüksek düzeyde entegre dijital mimarilere dayanmaktadır (Downer, 2010).

Örneğin, havacılık endüstrisinde "Fly-by-Wire (FBW)" teknolojisi, geleneksel mekanik kumanda bağlantılarını ortadan kaldırarak uçuş emniyeti ve operasyonel verimlilik açısından önemli bir dönüşüm yaratmıştır. Bununla birlikte, bu mimari yapı uçuş emniyetini büyük ölçüde yazılım mantığının doğruluğuna, veri işleme süreçlerinin güvenilirliğine ve donanım-yazılım entegrasyonunun bütünlüğüne bağımlı hâle getirmiştir (Nicolin ve Nicolin, 2019).

EASA Part 21 ve FAR Part 21; hava aracı, motor, pervane ve bunlara ait parça ve teçhizatın sertifikasyon ile üretim onay süreçlerini düzenleyen temel yasal çerçevelerdir. EASA Part 21, Avrupa Birliği Havacılık Emniyeti Ajansı (EASA) tarafından; FAR Part 21 ise ABD Federal Havacılık İdaresi (FAA) tarafından uygulanmaktadır (EASA, 2025a,b; FAA, 2025). Günümüzün yazılım yoğun hava aracı mimarilerinde bu düzenlemeler, donanım, gömülü yazılım ve siber güvenlik unsurlarının uçuşa elverişlilik standartlarıyla bütünleşik biçimde uyumlu olmasını zorunlu kılarak sistem emniyetinin sağlanmasına katkıda bulunmaktadır (De Florio, 2016).

Avrupa Birliği Havacılık Emniyeti Ajansı (EASA) veya ABD Federal Havacılık İdaresi (FAA) gibi havacılık otoriteleri tarafından sağlanan çerçeveler, sertifikasyona uygunluğun gösterilmesi ve hava aracı tasarım bütünlüğünün yönetilmesi için güçlü yöntemler sunmaktadır. Bununla birlikte, bahsi geçen havacılık otoriteleri tarafından sağlanan bu çerçeveler, hava araçlarının geliştirme ve sertifikasyon süreçleri sırasında modellenen varsayımların, operasyon koşullarının ve etkileşim örüntülerinin sınırları içinde çalışır. Sonuç olarak, çevresel, yazılımsal ve operasyonel faktörlerin nadir veya daha önce hiç gözlemlenmemiş birleşimleri operasyon sırasında pek âlâ ortaya çıkabilir (Knight, 2002).

Airbus A320 ailesi, yazılım aracılı bir uçuş kontrol mimarisinin önde gelen örneklerinden biridir. A320 ailesinin "fly-by-wire (FBW)" olarak adlandırılan bu uçuş kontrol sistemi, pilot ve otopilot girdilerini, gerekli komutları irtifa dümenlerine (elevator) ve kanatçıklara (aileron) iletmeden önce iki "Elevator Aileron Computer (ELAC)" dâhil olmak üzere uçuş kontrol bilgisayarları üzerinden yorumlar. Airbus FCOM teknik dokümantasyonunda, ELAC'ları yunuslama (pitch) ve yuvarlanma (roll) kontrolünün yanı sıra Airbus uçuş kontrol kanunlarının ve kumanda korumalarının uygulanmasında merkezi unsurlar olarak tanımlamaktadır (Airbus, 2023).

Bu minvalde, yazılım kaynaklı FBW olayları değerlendirildiğinde, yukarıda bahsi geçen sofistike sistemlerin sensörler ve çevresel faktörler gibi dış kaynaklardan gelen hatalı verileri nasıl yorumladığının ve bu süreçte pilot otoritesiyle nasıl etkileşime girdiğinin emniyet bakımından en kritik eşiklerden birini oluşturduğu görülmektedir.

Örneğin, EASA tarafından yayımlanan A320 ailesi uçaklarına yönelik 2025-0268-E numaralı acil uçuşa elverişlilik direktifini tetikleyen operasyonel olay, sertifikasyon varsayımları ile operasyonel emniyet öğrenmesi arasındaki ilişkinin incelenmesi açısından özellikle yararlı bir vaka sunmaktadır (EASA, 2025a,b). 30 Ekim 2025 tarihinde ABD'deki JetBlue Havayolları'na ait bir uçağın operasyonu sırasında meydana gelen ilgili olayda EASA, bir Airbus A320 uçağının komutsuz ve sınırlı bir burun aşağı yunuslama olayı yaşadığını, olay boyunca otopilotun devrede kaldığını ve Airbus'ın ön teknik değerlendirmesinde söz konusu olumsuz durumun yaşanmasında hatalı bir ELAC sistemi yazılımının olası bir nedensel faktör olarak belirlendiğini ifade etmiştir. EASA ayrıca, düzeltilmemesi hâlinde bu durumun en kötü senaryoda uçağın yapısal kapasitesini aşabilecek komutsuz bir irtifa dümeni hareketine yol açabileceğini belirtmiştir. Buna paralel olarak, daha sonra FAA de ABD'deki ilgili uçak tipi operatörleri için eşdeğer bir uçuşa elverişlilik direktifi yayımlamıştır (FAA, 2026a,b).

Bu çalışma, söz konusu vakayı ele alarak "Yüksek güvenceye sahip bir sistem, sertifikasyon sırasında tam olarak öngörülmemiş tehlikeli bir davranışla karşılaştığında ne olur?" gibi daha geniş bir sistem emniyeti sorusunu irdelemek için kullanmaktadır. Burada ileri sürülen temel argüman, bahsi geçen ELAC vakasının yaşanan operasyonel olayları, bu olayların sistematik bir şekilde soruşturulması ve gerekli düzenleyici faaliyetlerin yerine getirilmesi ile tasarım güncellemesini birbirine bağlayan uyarlanabilir bir emniyet mekanizması olarak sürekli uçuşa elverişliliğin önemini gösterdiğidir.

2. Materyal ve Yöntem

2.1. A320 Fly-by-Wire Mimarisi İçinde ELAC

Airbus A320'nin "fly-by-wire" uçuş kontrol sistemindeki A320 uçuş kontrolleri, 1988 yılında hizmete girdiğinde modern yolcu uçağı kumanda özelliklerini yeniden tanımlamıştır. Geleneksel mekanik bağlantılardan farklı olarak A320, pilot girdilerini uçuş kontrol bilgisayarları tarafından işlenen elektronik sinyallere dönüştürür; bu bilgisayarlar da kumanda yüzeylerini hareket ettiren hidrolik aktüatörlere komut gönderir (Lewis, 2025).

Airbus A320 uçuş kontrol sistemi, yetkiyi iki "Elevator Aileron Computer (ELAC)", üç "Spoiler Elevator Computer (SEC)" ve iki "Flight Augmentation Computer (FAC)" olmak üzere birden fazla bilgisayar ailesi arasında dağıtır. Mimariye ilişkin hava aracı üreticisi teknik dokümanları, ELAC'ların yunuslama ve yuvarlanma hareketlerinin kontrolünde merkezi konumda olduğunu, kumanda kolu (sidestick) ve otopilot girdilerini işlediğini ve irtifa dümenleri ile kanatçıklara buna göre komut verdiğini belirtmektedir. ELAC'lar ayrıca ayarlanabilir yatay stabilizatör ile etkileşim yoluyla otomatik trim davranışına katkıda bulunur. Bu sistem düzeyindeki rol,

ELAC davranışını yalnızca bir ekipman fonksiyonu olarak değil, aynı zamanda kontrol kanunu uygulama katmanı olarak da emniyet açısından kritik hâle getirir. Her iki ELAC'ın arızalanması durumunda kontrol, bozulmuş modlarda SEC'lere devredilir (Airbus, 2026).

A320 "fly-by-wire" felsefesi, farklı hava aracı ve sistem durumlarında pilot girdilerinin nasıl yorumlanacağını belirleyen kontrol kanunları üzerine kurulu olup, bunlar "Normal Mod (Normal Law)", "Alternatif Mod (Alternate Law)" ve "Doğrudan Mod (Direct Law)" olarak tanımlanır (Airbus, 2026). Bahsi geçen modlarda sistem bütünlüğüne ve arıza koşullarına bağlı olarak farklı düzeylerde destek ve koruma sağlanır. Bu durum analitik açıdan önemlidir; çünkü hava aracının tepkisinin yalnızca mekanik olmadığını, bunun mod, yedeklilik durumu ve doğrulanmış varsayımlara bağlı yazılım mantığı tarafından aracılık edildiğini gösterir.

Özetle, uçuş kontrol kanunları pilotun kumanda girdilerinin uçuş kontrol bilgisayarları tarafından nasıl yorumlanacağını ve bu girdilerin kumanda yüzeylerine ne şekilde aktarılacağını tanımlar. "Normal Mod", sistemin tam bilgisayar destekli koruma işlevlerini sağladığı çalışma durumudur. "Alternatif Mod", belirli sistem arızaları sonrasında devreye girerek bazı koruma fonksiyonlarını sınırlandırır. "Doğrudan Mod" ise bilgisayar aracılı müdahaleyi asgari düzeye indirir ve hava aracının koruma desteği olmaksızın, daha doğrudan kumanda tepkileriyle uçurulmasına imkân verir.

Hava aracının üreticisi, ilgili teknik dokümanlarda her aktüatörün hidrolik olarak beslendiğini ve ayrı kumanda kanalları üzerinden komutlandığını vurgular. Böylece, Tablo 1'de gösterildiği üzere, hidrolik veya bilgisayar arızası durumunda dahi hava aracının emniyetli bir şekilde operasyonunu sürdürmesi sağlanır (Airbus, 2023).

Bu nedenle, bir arıza durumunda sistem, zorunlu olmayan fonksiyonları devre dışı bırakabilir ve alternatif modlara geçerek uçağın emniyetli ve kontrol edilebilir kalmasını sağlar.

Tablo 1. Airbus FCOM uçuş kontrol mimarisi ve yedekleme rolleri

Yüzey	Kontrol	Bilgisayar(lar)	Kanun/Yedekleme Rolü
İrtifa dümenleri	Yunuslama	ELAC / SEC	Normal Mod + Yedek
Kanatçıklar	Yuvarlanma	ELAC	Normal Mod
İstikamet dümeni	Sapma	FAC	Normal Mod / Mekanik yedekleme
Ayarlanabilir Yatay Stabilize (THS)	Trim	ELAC	Otomatik trim
Flaplar/Slatlar	Taşıma kuvveti artırımı	SFCC	Flap/Slat kolu ile yönetilir
Spoiler'lar	Yuvarlanma, frenleme, sürat	SEC	Yuvarlanma desteği + yer spoiler'i

2.2. Sertifikasyon ve Karmaşık Dijital Sistemler

Bir önceki bölümde bahsi geçen JetBlue Havayolları'na ait hava aracının operasyonu sırasında meydana gelen olayın nedeni olarak söz konusu A320 tipi uçağın ELAC sistemindeki bir yazılımsal hatanın yol açtığı belirtilmişti. Söz konusu hususun arka planında ise, Airbus tarafından yayımlanan yeni yazılım standardının, önceki sürümlerde bulunan bazı hata denetleme ve veri filtreleme korumalarını daha sınırlı hâle getirmesinin yer aldığı değerlendirilmektedir. Eldeki mevcut verilere göre, bu zafiyetin yüksek irtifada uçuş sırasında yoğun güneş kaynaklı radyasyon veya kozmik parçacık etkilerine maruz kalma olasılığıyla birleşmesinin ELAC bilgisayarındaki kritik verilerin bozulmasına elverişli bir koşul oluşturduğu, bu bağlamda radyasyon kaynaklı etkilerin ELAC belleğinde hatalı bir veri durumuna yol açtığı ve nihai olarak da yazılımın bu girdiyi geçerli kabul ederek pilottan bağımsız, ani bir burun aşağı yunuslama komutu üretmesine neden olduğu değerlendirilmektedir (Orban, 2025).

Bu noktada, bahse konu ELAC vakasının gündeme getirdiği asıl mesele, sertifikasyon çerçevelerinin yetersiz olup olmadığı değil, herhangi bir sertifikasyon rejiminin, daha sonra hava aracının operasyonu sırasında ortaya çıkabilecek düşük olasılıklı her etkileşimi bütünüyle öngörüp öngöremeyeceğidir.

Ayrıca, söz konusu vaka bu olgunun ilk örneği de olmayıp, 2018'deki Lion Air ve 2019'daki Ethiopian Airlines kazalarında toplam 346 kişinin hayatını kaybetmesiyle sonuçlanan süreçte Boeing 737 MAX uçaklarında bulunan yeni bir yazılım olan MCAS sisteminin ölümcül tasarım hataları ortaya çıkmıştır (NTSB, 2019).

Boeing 737 MAX uçaklarında yer alan bahsi geçen MCAS *(Maneuvering Characteristics Augmentation System - Manevra Karakteristiklerini Takviye Sistemi)* yazılımı, uçağın yüksek hücum açısı nedeniyle "stall" riskine yaklaşması durumunda burun aşağı kumanda üreterek uçuş karakteristiklerini desteklemek üzere tasarlanmış otomatik bir uçuş kontrol yazılımıdır. Sistemin temel amacı, 737 MAX modellerinde kullanılan daha büyük çaplı ve kanat üzerinde daha ileri konumlandırılmış motorların yol açtığı aerodinamik farklılıkları telafi etmek ve uçağın kumanda hissi ile operasyonel davranışını önceki nesil 737 NG ailesine benzer şekilde sürdürmektir (FAA, 2020).

Ancak, sistemi iyileştirme niyetiyle yapılan bu tasarım geliştirmelerinin ne yazık ki istenmeyen sonuçları olmuş

ve yukarıda bahsi geçen "Lion Air 610" ve "Ethiopian Airlines 302" kazalarına ilişkin resmî kaza-kırım araştırma ve inceleme raporlarında yer alan tespitler, MCAS yazılımının istenmeyen şekilde devreye girmesi, hatalı hücum açısı *(Angle of Attack - AOA)* sensörü girdileri ve en nihayetinde bunlara yol açan tasarım ile sertifikasyon süreçlerindeki yetersizlikler gibi temel unsurların olayların oluşumunda kritik nedensel faktörler olduğunu ortaya koymuştur (Sgobba, 2019).

EASA büyük uçaklara yönelik sertifikasyon şartnameleri *(Certification Specifications - CS)* çerçevesi olarak CS-25'i sürdürmektedir (EASA, 2023). Aynı şekilde, FAA ise FAR Part-25 gerekliliklerıyle hava taşımacılığında kullanılan büyük uçaklara yönelik sertifikasyon standartlarını ortaya koymaktadır (FAA, 2026a,b). Avrupa ve Amerika'da kullanılan bu sertifikasyon çerçeveleri, taşıma kategorisindeki uçaklar için uçuşa elverişlilik standartlarını belirleyerek ticari uçakların emniyetini ve performansını güvence altına almakta ve emniyet kritik sistemler için titiz tasarım ve test gereksinimlerini zorunlu kılmaktadır.

Yukarıda bahsi geçen hava aracının bütününe yönelik sertifikasyon çerçevelerinin yanında, uçağın sistemsel ve bilhassa çalışmamızı ilgilendirmesi açısından yazılımsal unsurlarının sertifikasyonu için de çok çeşitli ek gereksinimler mevcuttur. Örneğin, FAA, "SAE ARP4754A, Sivil Hava Araçları ve Sistemlerinin Geliştirilmesine Yönelik Kılavuz" dokümanını, tasarım geliştirme güvence sürecinin oluşturulması için kabul edilebilir bir yöntem olarak tanımaktadır (FAA, 2011). Buna ek olarak, ABD'de yer alan ve alanında uluslararası bir standart kuruluşu görevi gören "Havacılık Radyo Teknik Komisyonu (RTCA)", hava aracı yazılım tasarımı ve ürün güvencesi için standart olarak "DO-178C" yi geliştirmiştir (RTCA, 2011) ve bu standart FAA tarafından da kabul edilebilir bir yöntem olarak tanınmaktadır (FAA, 2017).

Birlikte değerlendirildiğinde, hava aracının bütününe ve sistemlerine yönelik bahsi geçen tüm bu teknik gereksinim çerçeveleri diğer birçok ek standart ve uygulamayla birlikte hava aracı uçuş kontrol sistemleri tasarımı ve sertifikasyonu için oldukça gelişmiş bir tasarım güvence ortamı oluşturur. Bununla birlikte, bu güvence mekanizmalarının etkinliği, onay sürecinde esas alınan teknik gereksinimlerin, çevresel varsayımların ve doğrulama kapsamının ne ölçüde eksiksiz tanımlandığına bağlı olmaya devam etmektedir.

FAA adına Zalewski ve Kornecki tarafından yürütülen çalışma da yukarıda belirtilen hususu destekleyen bulgular sunmaktadır (Kornecki ve Zalewski, 2003). RTCA DO-178 standartlarına uyumun sağlanması amacıyla emniyet açısından kritik, gerçek zamanlı aviyonik sistemlerde kullanılan yazılım geliştirme araçlarının değerlendirilmesi ve yetkilendirilmesine odaklanan bu çalışmanın temel sonuçları arasında, katı sertifikasyon gerekliliklerinin zorunluluğunun yanı sıra yazılımın gereksinimlerden kaynak koduna kadar kesintisiz izlenebilirliğinin önemi öne çıkmaktadır. Ayrıca yine aynı çalışmada, değerlendirme sürecine katılan mühendislerin yaklaşık %50'sinin yazılım geliştirme aracı hatalarıyla karşılaştığının rapor edilmesi, otomasyona koşulsuz güvenmek yerine sistematik doğrulama faaliyetlerinin gerekliliğini açık biçimde ortaya koymaktadır.

Başka bir deyişle, sistemler uygulanabilir geçerli tüm sertifikasyon çerçeveleri kullanılarak tasarlanmış olsa da yukarıda yer alan örneklerden de görülebileceği üzere radyasyon kaynaklı arızalar gibi nadir çevresel etkileşimler tam olarak modellenemeyebilir ve yazılım tabanlı sistemler deterministik olmayan arıza modları ortaya çıkarabilir.

2.3. Sistem Teorik Süreç Analizi (STPA – Systems Theoretic Process Analysis)

Sistem Teorik Süreç Analizi (STPA), kaza nedenselliğine ilişkin genişletilmiş bir modele dayanan görece yeni bir tehlike analizi tekniğidir. STPA, bileşen arızalarına ek olarak, sistem bileşenlerinin hiçbiri tek başına arızalanmamış olsa da bunların aralarındaki emniyetsiz etkileşimlerin de kazalara neden olabileceğini varsayar (Leveson ve Thomas, 2018).

STPA, emniyeti salt bir güvenilirlik meselesi yerine bir kontrol problemi olarak görür. Bu bakış açısına göre kabul edilemez sonuçlar yalnızca donanım arızasından değil, yetersiz kontrol mantığından, emniyetsiz etkileşimlerden, kusurlu geri bildirimden veya hatalı süreç modellerinden de kaynaklanabilir. Bu nedenle STPA, birden fazla kontrolörün, sensörün ve operasyonel durumun dinamik olarak etkileştiği yazılım yoğun sistemler için özellikle uygundur (Castilho vd., 2018).

Başka bir deyişle, kazalar yetersiz kontrol veya koordinasyon nedeniyle meydana gelir ve sistem bileşenleri tek tek doğru çalışsa bile sistem düzeyindeki etkileşimlerde başarısız olabilir. Bu minvalde, ELAC vakası bağlamında bu bakış açısı, analiz yaparken tek bir bileşenin "arızalanıp arızalanmadığına" odaklanılması yerine, yüksek düzeyde korumalı bir uçuş kontrol mimarisi içinde emniyetsiz bir kontrol eyleminin nasıl mümkün hâle gelebildiğine odaklanılmasını gerekli kılar.

2.4. Kaza Nedenselliği Analizi için İsviçre Peyniri Modeli (Swiss Cheese Model)

Dr. James Reason tarafından geliştirilen İsviçre Peyniri (Swiss Cheese) Modeli, emniyet risklerini anlamak ve bunların risk değerlerini azaltmak için güçlü bir çerçevedir. İsviçre Peyniri modelinde, bir tarafta tehlikeler, diğer tarafta potansiyel kayıplar ve bu ikisinin arasında ise savunma katmanları yer almakta olup, söz konusu model her savunma katmanını bir İsviçre peyniri dilimiyle görselleştirir (Reason, 1990).

Modelin kavramsal çerçevesini genel olarak özetlemek gerekirse, her İsviçre peyniri dilimi eğitim, politikalar, gözetim sistemleri veya yedek bileşenler gibi bir kontrolü simgeler. Bu katmanlar, üst üste binen koruma mekanizmalarından oluşan bir sistem yaratmak üzere birlikte çalışır. Her dilimdeki delikler ise ilgili emniyet önlemindeki zayıflıkları veya boşlukları temsil eder. Burada, birden fazla katmandaki delikler hizalandığında, bir tehlike tüm bu savunma mekanizmalarını aşarak

nihai durumda bir kazaya yol açabilir. Buna göre İsviçre Peyniri modeli, kazaları; tasarım kusurları, operasyonel koşullar, insan faktörleri ve düzenleyici kurallardaki boşluklar gibi kusurlu savunma katmanlarının hizalanması olarak kavramsallaştırır.

İsviçre Peyniri modeli, kazaların ve ciddi olayların birden fazla kusurlu savunma katmanının hizalanmasıyla nasıl ortaya çıkabileceğini göstermede yararlı olmaya devam etmektedir (Underwood ve Waterson, 2014). Dolayısıyla, bir hava aracının ya da hava aracı ekipmanının operasyonu sırasında gerçekleşen tehlikeli bir durumun yalnızca tek bir savunma bariyerinin çökmesinden değil, gizli zafiyetler ile aktif koşulların birleşik hizalanmasından gelişebileceğini vurgulaması yönüyle bu model oldukça değerlidir.

Mevzubahis sebeplerden ötürü İsviçre Peyniri modeli, ELAC arızalarının sistem emniyeti yönüyle incelenmesinde ilgili ekipmanın arızasıyla başlayan ve olayda bahsi geçen olumsuz duruma giden süreçte, sistemdeki mevcut savunma katmanları ve bu katmanlarda mevcut olan gizli veya aktif zafiyetlerin detaylı analizi için de oldukça uygundur.

2.5. Bir Emniyet Verisi Toplama Aracı Olarak "NASA ASRS" Sistemi

Ulusal Havacılık ve Uzay Dairesi (NASA) tarafından yönetilen "Havacılık Emniyeti Raporlama Sistemi (ASRS)", Amerika Birleşik Devletleri'nde pilotlar, hava trafik kontrolörleri ve diğer havacılık paydaşları tarafından gönüllülük esasına göre bildirilen havacılık emniyeti olaylarını ve emniyetle ilgili durum raporlarını toplayan bir veritabanı olup, bu sistem, ABD hükümeti, havacılık endüstrisi ve havacılık topluluğunun emniyetin korunması ve geliştirilmesine yönelik ortak ve süreklilik arz eden çabalarının önemli bir parçasını oluşturmaktadır (NASA, 2026a,b).

NASA, ASRS'yi kodlanmış olay bilgileri ve kimlik bilgilerinden arındırılmış olay anlatı metinlerini içeren, gönüllülük esasına dayalı, gizli ve cezalandırıcı olmayan bir veritabanı olarak tanımlamaktadır. Ayrıca, ASRS sisteminin gönderilen raporları bağımsız olarak doğrulama veya geçerlilik kontrolü yapma gibi bir özelliği olmadığı NASA tarafından açık bir biçimde ifade edilmektedir (NASA, 2026a,b).

Bu çerçevede, NASA ASRS veritabanının genel olarak havacılık emniyetine ilişkin raporları topladığı ve böylelikle operasyonel anomalilerdeki eğilimlerin ve tekrar eden örüntülerin incelenmesine olanak sağladığı vurgulanmalıdır. Dolayısıyla ASRS, bu çalışmada kesinleşmiş resmî olay bulgularının kaynağı olarak değil, bilakis havacılık emniyeti verilerinin toplandığı ve emniyet yönetimi açısından yorumlanabildiği destekleyici bir veri kaynağı olarak kullanılmaktadır.

2.6. Metodoloji

Bu çalışma, çok kaynaklı nicel ve nitel bir yaklaşım benimsemektedir. İlk olarak, Airbus "fly-by-wire (FBW)" kontrol anomalilerine ilişkin NASA ASRS kayıtlarının yapılandırılmış bir incelemesini kullanmaktadır. Bu doğrultuda, Airbus FBW uçuş kontrol anomalileriyle ilişkili bugüne kadar raporlanmış tüm havacılık emniyeti olaylarını tespit etmek amacıyla NASA ASRS veritabanı taranmış olup, nicel analiz gerçekleştirmek için adım adım aşağıdaki metodoloji uygulanmıştır:

- Adım 1 - Veri Toplama: ASRS veritabanının "flight control anomaly", "uncommanded pitch", "autopilot unexpected" ve "A320 control" anahtar kelimeleri kullanılarak taranması.
- Adım 2 - Filtreleme Kriterleri: Sonuçların "Aircraft type: Airbus FBW aircraft", "Event severity: Moderate–High" ve "System involvement: Flight control computers" ölçütlerine göre filtrelenmesi.
- Adım 3 - Sınıflandırma (ASRS taksonomisi baz alınarak): Her raporun "Event type", "Phase of flight", "Automation state (AP engaged/disengaged)" ve "Contributing factors (System fault, Environmental conditions, Human-machine interface)" başlıklarına göre sınıflandırılması.
- Adım 4 - İstatistiksel Çıktılar: "Yaygın arıza örüntülerini" belirlemek amacıyla elde edilen istatistiksel çıktıların yorumlanması.

Bu nicel analiz tamamlandıktan sonra, çalışma EASA ve FAA'nın acil nitelikteki düzenleyici müdahalelerine zemin hazırlayan ELAC olayını incelemek amacıyla nitel bir olay analizi de gerçekleştirmektedir. Ardından ilgili olgu, altta yatan nedenlerin ve bu nedenler arasındaki karşılıklı etkileşimlerin açıklığa kavuşturulması için STPA ve İsviçre Peyniri modeli çerçevesinde sistematik bir emniyet değerlendirmesine tabi tutulmaktadır.

Bu bütünleşik yaklaşım, hem operasyonel anomalilerden oluşan veri örneklemi içinde tekrar eden örüntülerin belirlenmesine hem de yüksek emniyet önemi taşıyan tekil bir olayın daha ayrıntılı biçimde yorumlanmasına olanak sağlamaktadır. Bu nedenle çalışma, Tablo 2'de gösterildiği üzere, NASA ASRS kaynaklı verilerle Airbus FBW uçuş kontrol olaylarının nicel olarak incelenmesini, tetikleyici ELAC olayının vaka temelli değerlendirmesini ve aynı olayın sistem emniyeti perspektifinden analizini bir araya getiren çok kaynaklı bir değerlendirme çerçevesini içermektedir.

3. Bulgular

3.1. NASA ASRS Tabanlı Veriler Kullanılarak Airbus FBW Uçuş Kontrol Olaylarının Nicel Analizi

Önceki bölümde açıklanan metodolojik çerçeve doğrultusunda, analiz için "NASA ASRS" veritabanından 1990 ile 2025 yılları arasındaki zaman dilimi için yapılan aramada konuyla ilgili toplam 95 adet olay raporu elde edilmiş olup, arama sonucu elde edilen ve analize konu olan olay raporlarının tamamının yer aldığı ham veri seti, talep halinde bu çalışmayı gerçekleştiren yazardan ilgili iletişim adresi üzerinden temin edilebilir.

Söz konusu veri seti, Airbus "fly-by-wire" uçuş kontrol anomalileriyle ilişkili raporlarla sınırlandırılmış ve daha sonra elde edilen bilgiler tekerrür eden teknik veya operasyonel eğilimleri belirlemek amacıyla sistematik bir

biçimde değerlendirilmiştir. Her bir rapor; olay türü, uçuş safhası ve nedensel faktörler açısından incelenmiş, böylece söz konusu anomalilerin farklı operasyonel bağlamlarda nasıl ortaya çıktığını değerlendirmeye imkân veren bütüncül bir analiz zemini oluşturulmuştur. Bu analizin amacı, yalnızca münferit vakaların sayısal dağılımını ortaya koymak değil, aynı zamanda ELAC olayının daha geniş bir çerçevede emniyet ve sürekli uçuşa elverişlilik açısından yorumlanmasına katkı sağlayacak genel ampirik eğilimleri belirlemektir. Bu değerlendirme sonucunda elde edilen temel bulgular aşağıda sırasıyla sunulmaktadır.

3.1.1. Olay türü dağılımı

NASA ASRS raporlarından elde edilen veriler olay türü dağılımı açısından incelendiğinde, Tablo 3'te yer aldığı üzere, uçuş kontrol bilgisayarlarıyla ilişkili hava aracı ekipman arızalarının, özellikle ELAC/FCC bağlantılı anomaliler kapsamında, 85 adet kayıtlı vaka ile örneklemde açık biçimde baskın bir olay kategorisi oluşturduğunu göstermektedir. Bu ve bundan sonraki tabloların okunması sırasında herhangi bir yanlış anlaşılmaya sebebiyet vermemek adına burada belirtilmesi gereken önemli bir husus, bazı vakaların birden çok olay türünü aynı anda barındırabildiğidir.

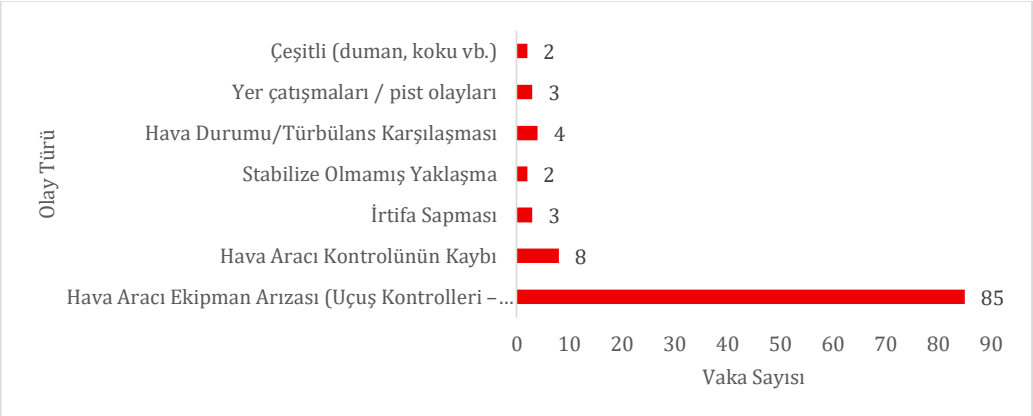
Diğer olay türleri ise belirgin biçimde daha düşük oranlarda raporlanmıştır. Hava aracı kontrolünün kaybı 8 vaka ile ikinci en büyük kategori olarak öne çıkarken, bunu 4 vaka ile hava durumu veya türbülansla ilişkili karşılaşmalar takip etmektedir. İrtifa sapmaları ile yer çatışmaları veya pist olayları üçer vaka ile temsil edilmekteyken, stabilize olmamış yaklaşmalar ile duman, koku ve benzeri çeşitli olaylar ise yalnızca ikişer kez kaydedilmektedir. Bu dağılım genel olarak, veri kümesindeki temel ampirik göstergenin çok çeşitli olay türlerinden ziyade, incelenen Airbus FBW raporlarında sistem kaynaklı uçuş kontrol anomalilerinin daha baskın olduğunu ortaya koymaktadır. Bu değerlendirmeler doğrultusunda, Şekil 1, Airbus FBW kontrol anomalisi raporlarında kaydedilen olay türlerinin dağılım grafiğini sunmaktadır.

Tablo 2. Çok boyutlu analitik yaklaşım

#	Yöntem	Amaç
1.	ABD NASA ASRS Tabanlı Veriler Kullanılarak Airbus FBW Uçuş Kontrol Olaylarının Nicel Analizi	Uçuş kontrol anomalilerine ilişkin tekrarlayan örüntüleri tespit etmek
2.	Tetikleyici ELAC Olayının İncelenmesi	Seçilen tetikleyici emniyet olayına ilişkin arıza mekanizmalarını, konuya dair bir vaka çalışması olarak anlamak
3.	STPA ve İsviçre Peyniri (Swiss Cheese) Modelleri Yardımıyla Sistem Emniyeti Analizi	İlgili olayın nedensel ilişkilerini açıklamak

Tablo 3. Airbus FBW kontrol anomalisi raporları için olay türü dağılımı

Olay Türü	Vaka Sayısı
Hava Aracı Ekipman Arızası (Uçuş Kontrolleri – ELAC/FCC)	85
Hava Aracı Kontrolünün Kaybı	8
İrtifa Sapması	3
Stabilize Olmamış Yaklaşma	2
Hava Durumu / Türbülans Karşılaşması	4
Yer çatışmaları / pist olayları	3
Çeşitli (duman, koku vb.)	2



Şekil 1. Airbus FBW kontrol anomalisi raporları için olay türü dağılım grafiği.

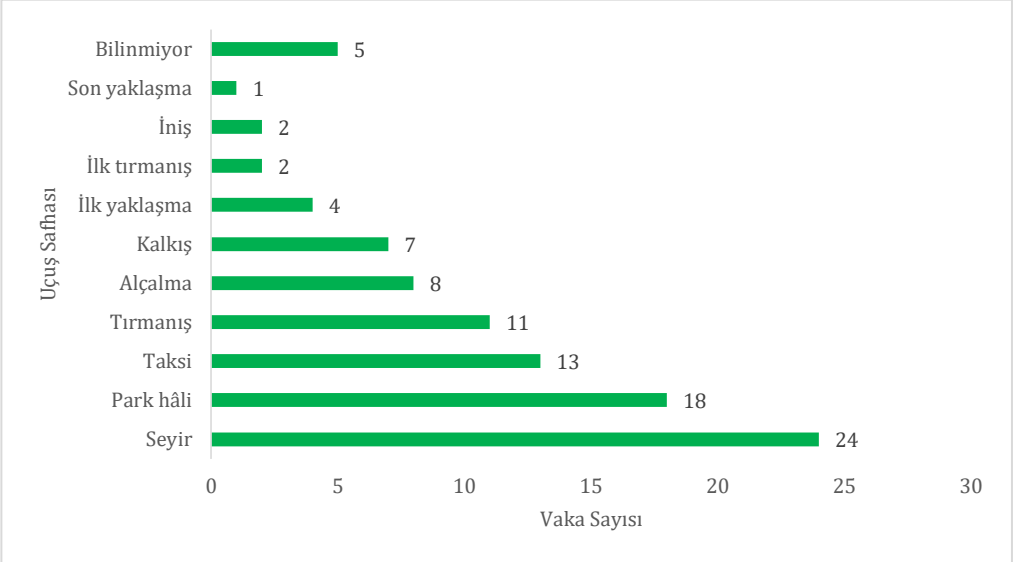
3.1.2. Uçuş safhası dağılımı

NASA ASRS raporlarından elde edilen veriler uçuş safhası dağılımı açısından incelendiğinde ise, sonuçlar Airbus FBW kontrol anomalilerinin en yoğun biçimde seyir safhasında bildirildiğini ortaya koymaktadır. Tablo 4'te de yer aldığı üzere, bu safhada 24 vaka kaydedilmiştir. Bununla birlikte, seyir safhasını 18 vaka ile park ve 13 vaka ile taksi safhası takip etmektedir. Tırmanış ve alçalma safhaları da sırasıyla 11 ve 8 vaka ile veri kümesinde dikkate değer bir yer tutarken, kalkış safhası 7 vaka ile temsil edilmektedir.

Buna karşın, yaklaşma ve inişle ilişkili safhalar veri kümesinde daha sınırlı bir sıklıkla yer almakta olup, ilk yaklaşma, ilk tırmanış, iniş ve son yaklaşma safhaları birlikte toplam örneklemin yalnızca küçük bir kısmını oluşturmaktadır. Genel dağılım, kontrol anomalilerinin yalnızca tek bir operasyonel safhaya özgü olmadığını göstermektedir. Bununla birlikte, elde edilen bilgiler bu anomalilerin özellikle seyir safhasında ve uçuş öncesi veya yer operasyonları sırasında daha belirgin hâle geldiğine işaret etmektedir. Bu bulgu, hem hava aracının operasyonu sırasındaki operasyonel unsurların hem de kalkıştan önce gizli arızaların tespit edilmesine yönelik emniyet bariyerlerinin önemini vurgulamaktadır. Bu değerlendirmeler doğrultusunda, Şekil 2, Airbus FBW kontrol anomalisi raporlarında kaydedilen uçuş safhalarına ilişkin dağılımı grafiksel olarak sunmaktadır.

Tablo 4. Airbus FBW kontrol anomalisi raporları için uçuş safhası dağılımı

Uçuş Safhası	Vaka Sayısı
Seyir	24
Park hâli	18
Taksi	13
Tırmanış	11
Alçalma	8
Kalkış	7
İlk yaklaşma	4
İlk tırmanış	2
İniş	2
Son yaklaşma	1
Bilinmiyor	5



Şekil 2. Airbus FBW kontrol anomalisi raporları için uçuş safhası dağılım grafiği.

3.1.3. Nedensel faktörlerin dağılımı

NASA ASRS raporlarından elde edilen veriler nedensel faktörlerin dağılımı açısından incelendiğinde, Tablo 5'te de sunulduğu üzere, tespit edilen sonuçlar örneklem genelinde sistem arızalarının başat katkı unsuru olduğunu ortaya koymaktadır. Öyle ki, raporların yaklaşık %90'ında ELAC, FCC, aktüatör veya spoiler sistemleriyle ilişkili arızalar yer almaktadır.

Tablo 5 ayrıntılı olarak değerlendirildiğinde, hava aracı kaynaklı sistem arızalarının veri kümesindeki en belirgin nedensel unsur olduğu 85 adet raporlanmış olayla diğer tüm faktörlerin önünde açık bir biçimde görülmektedir. İnsan faktörleri 41 vaka ile ikinci sırada bulunurken, prosedürel hususlar 26 vaka ile onu takip etmektedir. Buna göre, insan faktörleri, prosedürel hususlar, el kitapları ve MEL (Hava Aracı Asgari Teçhizat Listesi) ile bağlantılı unsurların birlikte oluşturduğu insan–makine arayüzü boyutu, dikkat çekici bir ikincil katkı alanı olarak öne çıkmaktadır. Söz konusu bulgu, Airbus FBW kontrol anomalilerinin ortaya çıkması ve yönetilmesi sürecinde uçak sistem uyarılarının doğru yorumlanmasının, prosedürel farkındalığın ve operasyonel karar verme süreçlerinin kritik bir rol oynadığını ortaya koymaktadır.

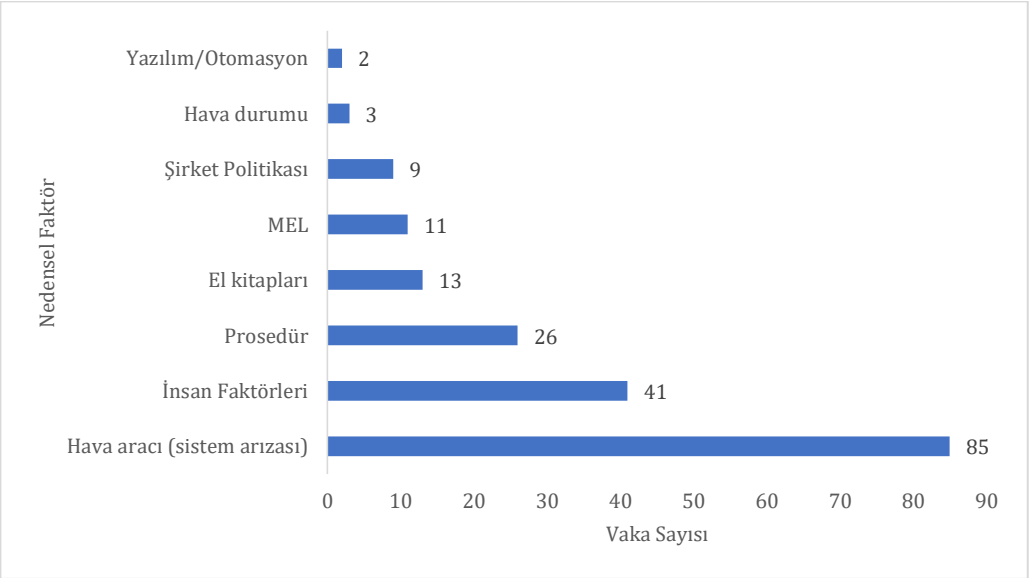
Genel olarak değerlendirildiğinde ise, Şekil 3'te yer alan grafikte gösterildiği üzere bu dağılım özetle, Airbus FBW kontrol anomalilerinin esas olarak teknik arızalardan kaynaklandığını, ancak operasyonel bağlamda prosedürel karmaşıklık, insan performansı gereklilikleri ve otomasyonla etkileşim gibi unsurlar tarafından önemli ölçüde şekillendirildiğini ortaya koymaktadır.

3.1.4. Yaygın arıza örüntüleri

NASA ASRS veritabanından derlenen 95 adet Airbus "fly-by-wire" uçuş kontrol olayı raporunun nicel analizinden elde edilen sonuçlar genel olarak değerlendirildiğinde, sistem kaynaklı arızaların, bunlardan da bilhassa ELAC/FCC işlevleriyle ilişkili olanların örneklemde başlıca risk unsuru olarak öne çıktığı görülmektedir. Uçuş safhasına göre dağılım, operasyonel maruziyetin özellikle seyir ve tırmanış evrelerinde önem kazandığını, bu safhalarda meydana gelen kontrol anomalilerinin hava aracı kararlılığı ve mürettebatın müdahale süreci üzerinde doğrudan etkiler oluşturabileceğini ortaya koymaktadır. Nedensel faktörlere ilişkin analiz ise prosedürlerin yorumlanması, hava aracı sistem arıza uyarılarının değerlendirilmesi, MEL uygulamalarındaki karmaşıklık ve hava aracı el kitaplarının operasyonel bağlamda uygulanması açısından insan–makine arayüzünün önemli bir zafiyet alanı olmaya devam ettiğini göstermektedir. Bu bulgular birlikte değerlendirildiğinde, Airbus FBW kontrol anomalilerinin yalnızca bağımsız teknik arızalar olarak değil, sistem arızaları, operasyonel koşullar ve uçuş ekibinden beklenen yorumlama gereklilikleri arasındaki etkileşim sonucunda şekillenen olaylar olarak ele alınması gerektiği anlaşılmaktadır. Bu veriler ışığında, Tablo 6, analiz kapsamında öne çıkan temel arıza örüntülerini özetlemektedir.

Tablo 5. Airbus FBW kontrol anomalisi raporlarında belirlenen nedensel faktörler

Nedensel Faktör	Vaka Sayısı
Hava aracı (sistem arızası)	85
İnsan Faktörleri	41
Prosedür	26
El kitapları	13
MEL (Asgari Teçhizat Listesi)	11
Şirket Politikası	9
Hava durumu	3
Yazılım/Otomasyon	2



Şekil 3. Airbus FBW kontrol anomalisi raporlarında belirlenen katkı sağlayan faktörlere ilişkin grafik.

Tablo 6. Airbus FBW kontrol anomalisi raporlarında belirlenen yaygın arıza örüntülerinin özeti

Arıza Örüntüsü	Özet Gözlem
ELAC Yunuslama Kanalı Arızaları	Tek kanallı arızalar çoğunlukla bozulmuş kontrol kanununa yol açarken, çift kanallı arızalar yedekliliğin kaybına ve sistem zafiyetinin artmasına işaret eder.
Spoiler / Yuvarlanma Eşleşmesi Sorunları	"Serbest kalan spoilerlar", komutsuz yuvarlanma davranışı ve yanal kontrol anomalileriyle ilişkilidir.
FCC / Uçuş Kontrol Bilgisayarı Arızaları	Bu arızalar sıklıkla "Alternatif Mod (Alternate Law)" aktivasyonunu ve otopilotun devreden çıkmasını tetikler; ancak "autothrust" genellikle kullanılabilir durumda kalır.
Kontrol Modu Değişimleri	"Normal Mod (Normal Law)"dan "Alternatif Mod (Alternate Law)"a veya "Doğrudan Mod (Direct Law)"a geçişler, mürettebat iş yükünün artması ve koruma marjlarının azalmasıyla ilişkilidir.
Uçuş Öncesi Tespit Edilen Arızalar	Birçok olayın park hâli safhasında meydana gelmesi, uçuş öncesinde gizli arızalara ve yetersiz arıza tespit mekanizmalarına işaret etmektedir.

3.2. EASA Acil Uçuşa Elverişlilik Direktifine Sebep Olan ELAC Olayının Vaka İncelemesi

ABD Ulusal Ulaşım Emniyeti Kurulu'nun (National Transportation Safety Board - NTSB) ön raporuna göre, 30 Ekim 2025 tarihinde JetBlue Havayolları'nın 1230 numaralı seferini icra eden Airbus A320-232 uçağı, Amerikan Körfezi üzerinde 35.000 feet irtifada, sakin hava ve açık meteorolojik koşullar altında seyir hâlindeyken kontrolsüz bir yunuslama sapması yaşamış ve bu durum yaklaşık 100 feetlik bir irtifa kaybına neden olmuştur. Mürettebat, uçağı Tampa Uluslararası Havalimanı'na yönlendirmiş ve uçuşun kalan bölümü herhangi bir ilave olumsuz durum yaşanmadan tamamlanmıştır. Söz konusu ön raporda ayrıca 22 yolcu ve mürettebatın hafif şekilde yaralandığı ve Airbus'ın ELAC yazılım tasarımına ilişkin bir şüphenin olaya neden olan olası bir faktör olarak değerlendirildiği belirtilmektedir (NTSB, 2026).

İlgili raporlar, olayın havacılık emniyeti açısından taşıdığı önemi açık biçimde ortaya koymaktadır. EASA, etkilenen konfigürasyonu "ELAC B L104" yazılımı olarak belirlemiş ve olayın, otopilot devrede kalmaya devam ederken gerçekleşen komutsuz ve sınırlı bir burun aşağı yunuslama hareketini içerdiğini bildirmiştir. EASA ayrıca, bu emniyetsiz durumun giderilmemesi hâlinde, en olumsuz senaryoda hava aracının yapısal kapasitesini aşabilecek komutsuz bir irtifa dümeni hareketine neden olabileceğini belirtmiştir (EASA, 2025a,b). Aynı şekilde, FAA tarafından yayımlanan direktif de benzer şekilde, etkilenen ELAC birimlerinin değiştirilmesini veya modifiye edilmesini zorunlu kılmış, ayrıca bu parçaların belirli hava aracı konfigürasyonlarına takılmasını yasaklamıştır (FAA, 2026a,b).

Buna ek olarak, hava aracı üreticisi olayın değerlendirilmesine çevresel etkiler açısından da farklı bir boyut kazandırmıştır. Airbus, A320 ailesine ilişkin bahse konu olay üzerine yapılan analizlerin, yoğun güneş radyasyonunun uçuş kontrol fonksiyonları bakımından kritik nitelikteki veriler üzerinde bozucu etkiler yaratabileceğine işaret ettiğini kamuoyuna açıklamıştır (Airbus, 2025). Bununla birlikte, NTSB raporunun hâlen ön rapor niteliğinde olması nedeniyle, söz konusu mekanizma kesinleşmiş bir soruşturma bulgusu olarak değil, ihtiyatlı biçimde ele alınması gereken ön teknik değerlendirme veya kamuya açıklanmış üretici yorumu olarak değerlendirilmelidir.

Genel bir değerlendirme yapıldığında ise, analize konu tetikleyici olay, seyir safhasında ve otopilot devredeyken meydana gelen komutsuz bir yunuslama sapmasını, buna bağlı kısa süreli irtifa kaybını ve yolcularda yaralanmayla sonuçlanan bir emniyet durumunu içermektedir. Mevcut soruşturma bulguları ve ilgili teknik bilgiler, olayın "ELAC" sistemini etkileyen teknik bir arızadan kaynaklandığını ve bu arızanın da dış çevresel koşulların neden olabileceği olası yazılım veya veri bozulması süreciyle bağlantılı olabileceğini göstermektedir. Emniyet bakımından temel endişe, bu tür bir arızanın giderilmemesi hâlinde hava aracının yapısal bütünlüğünü tehlikeye atabilecek düzeyde komutsuz bir irtifa dümeni hareketine yol açma potansiyelidir. Bu risk profili, EASA ve FAA tarafından etkilenen ELAC birimlerinin değiştirilmesini veya modifiye edilmesini zorunlu kılan ve ilgili konfigürasyonların uygun hava araçlarına takılmasını yasaklayan düzenleyici müdahalenin neden acil olarak ele alındığını açıklamaktadır.

3.3. ELAC Olayına Yönelik Sistem Emniyeti Analizi

3.3.1. Sistem teorik süreç analizi (STPA)

STPA bakış açısıyla ele alındığında, ELAC sistemi hava aracının yunuslama ve yuvarlanma kontrol çevrimi içinde bir kontrolör işlevi görmektedir. Bu kapsamda kontrol edilen süreç, hava aracının tutumu ve dinamik davranışı olarak tanımlanabilir. Burada, sisteme yönelen temel girdiler ise pilot komutları, otopilot komutları ve sensörlerden sağlanan durum verilerinden oluşmaktadır. Bu çerçevede emniyetsiz kontrol eylemi, kararlı seyir uçuşunun sürdürülmesi gereken bir koşulda üretilen hatalı irtifa dümeni komutu olarak değerlendirilebilir.

Bu yaklaşımın değeri, olayın yalnızca münferit bir ekipman arızası şeklinde değil, kontrol fonksiyonundaki bozulma üzerinden gelişen bir arıza yolu olarak yorumlanmasına imkân vermesindendir. Dolayısıyla analiz, çok katmanlı koruma sağlayacak şekilde tasarlanmış bir mimari içinde tehlikeli bir kontrol çıktısının hangi koşullarda ortaya çıkabildiğini açıklamaya odaklanmaktadır.

Bu minvalde, Tablo 7, analiz edilen ELAC olayı için belirlenen temel STPA unsurlarını daha detaylı olarak sunmakta olup, incelenen olay bağlamında oluşturulan STPA kontrol yapısı içerisinde ELAC sistemine atfedilebilecek emniyetsiz kontrol eylemlerini ve bu eylemlerle ilişkili nedensel faktörleri özetlemektedir. Bahsi geçen Tablo 7'den de görülebileceği üzere, değerlendirme, STPA yaklaşımında tanımlanan dört temel emniyetsiz kontrol eylemi *(UCA – Unsafe Control Actions)* esas alınarak yürütülmüş olup, bunlar sırasıyla gerekli kontrol eyleminin sağlanmaması, hatalı veya emniyetsiz bir kontrol eyleminin üretilmesi, kontrol eyleminin yanlış zamanda ya da yanlış sırayla uygulanması ve kontrol eyleminin uygun olmayan bir süre boyunca sürdürülmesidir. Yunuslama *(pitch)* ve yuvarlanma *(roll)* kontrol fonksiyonları açısından yapılan analiz; veri bozulması, yazılım anomalileri, sensör verileri arasındaki tutarsızlıklar, zamanlama gecikmeleri ve sistem yeniden yapılandırma süreçlerindeki yetersizliklerin emniyet açısından kritik kontrol kayıplarına veya uygunsuz uçuş kontrol tepkilerine yol açabileceğini göstermektedir. Bu çerçeve, olayın yalnızca doğrudan teknik arıza boyutuyla değil, aynı zamanda kontrol yapısı içerisindeki yetersiz kontrol mantığı, geri bildirim eksiklikleri ve sistem etkileşimleri açısından da değerlendirilmesine imkân sağlamaktadır. Ayrıca Şekil 4'te, yukarıda tanımlanan STPA unsurları Leveson'un kontrol yapısı gösterimiyle uyumlu olacak biçimde yapılandırılmış bir kontrol modeli görseli hâlinde sunulmuştur (Leveson, 2010).

3.3.2. İsviçre peyniri (Swiss cheese) modeli

İsviçre Peyniri modeli, söz konusu olayın güçlü tasarım güvencesi ve çok katmanlı emniyet bariyerlerine rağmen nasıl gerçekleşebildiğini açıklamak için yararlı bir çerçeve sunmaktadır. Bu bağlamda birinci savunma katmanı, tasarım koruma mekanizmaları ve kontrol sisteminin varsayılan dayanıklılığıyla ilişkilidir. İkinci bir katman, yazılım doğrulaması ile daha önce fark edilmemiş bir sınır durum koşulunun olası varlığına işaret eder. Üçüncü katman, hizmet sırasında karşılaşılan çevresel maruziyetleri ve dördüncü katman ise gerçek zamanlı sistem tepkisini ve arıza yönetimini kapsar. Beşinci ve son katman da anomali anında mürettebat ile otomasyon arasındaki etkileşimi temsil eder.

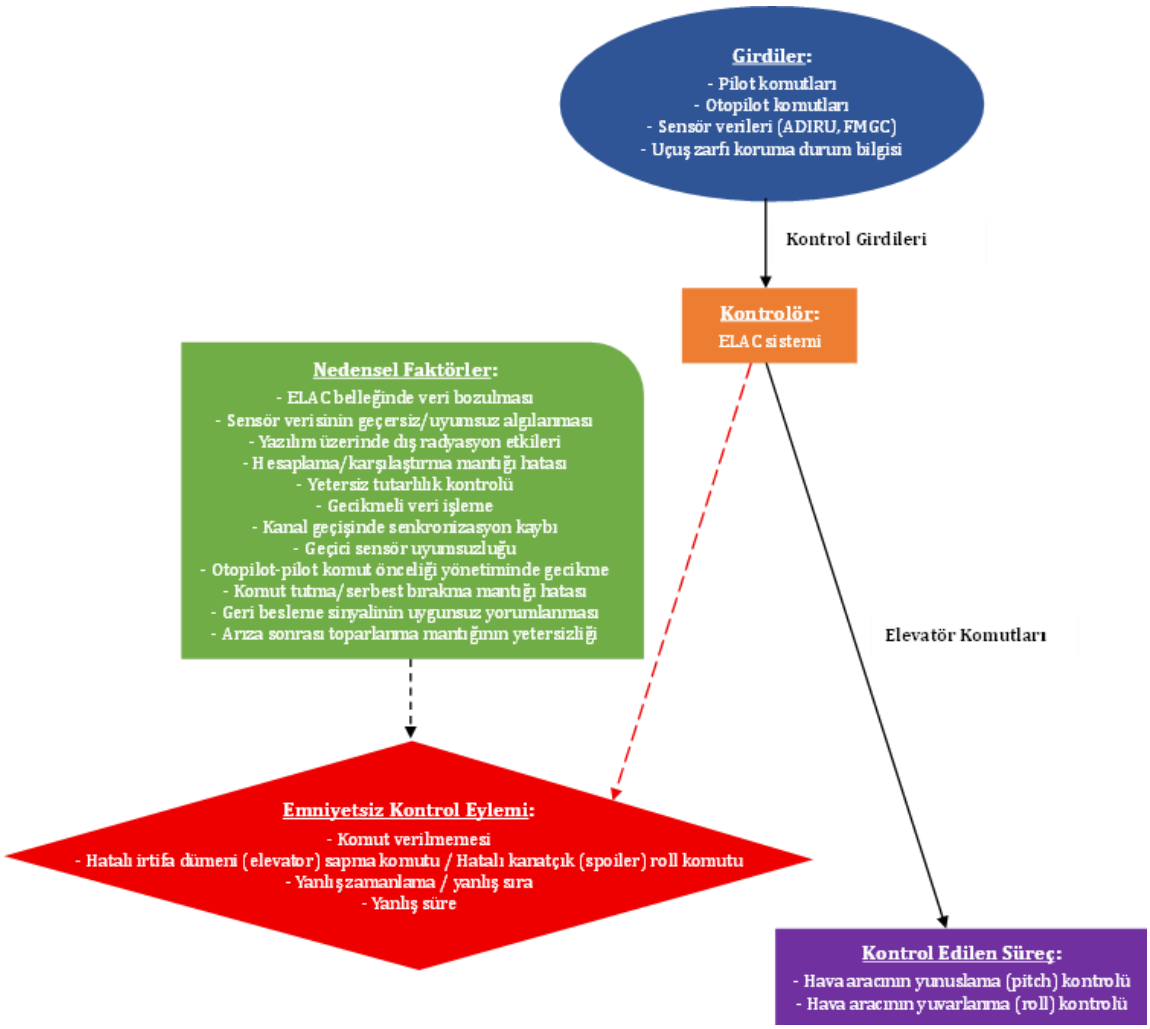
İncelenen olay, yukarıda bahsi geçen katmanlarda yer alan zayıflıkların aynı doğrultuda hizalanmış görünmesi nedeniyle emniyet açısından önem taşımaktadır. Özellikle dikkat çeken nokta, burun aşağı yunuslama sapması sırasında otopilotun devrede kalmaya devam ettiğinin rapor edilmiş olmasıdır. Bu özellik, olayı ASRS örnekleminde arıza sonrası otomasyonun devreden çıktığı birçok kontrol anomalisi vakasından ayırmaktadır. Bu doğrultuda, Tablo 8, incelenen ELAC olayına ilişkin İsviçre Peyniri Modeli kapsamında belirlenen temel unsurları özetlemektedir.

İlaveten Şekil 5'te, yukarıda açıklanan savunma katmanları ve kontrol bariyerleri, James Reason'ın İsviçre Peyniri Modeli yaklaşımıyla uyumlu olacak şekilde yapılandırılmış bir model hâlinde sunulmaktadır (Reason, 1990). Söz konusu model, tasarım korumaları, yazılım doğrulaması, operasyonel ortam, sistem tepkisi ve insan-otomasyon arayüzünden oluşan beş savunma katmanı boyunca gizli koşullar ile aktif arızaların nasıl aynı doğrultuda hizalanabildiğini göstermektedir.

İlgili Şekil 5'ten de görülebileceği üzere, sistemde gerçekleşen bir hata savunma katmanlarında mevcut olan radyasyona duyarlılık, tanımlanmamış bir sınır durum koşulu, güneş radyasyonuna maruziyet, hatalı kontrol komutu ve otopilotun devrede kalması gibi zafiyetlerden geçerek nihayetinde komutsuz bir yunuslama sapmasına ve dolayısıyla olumsuz bir operasyonel duruma yol açmaktadır.

Tablo 7. Analiz edilen olaya uygun temel STPA unsurları

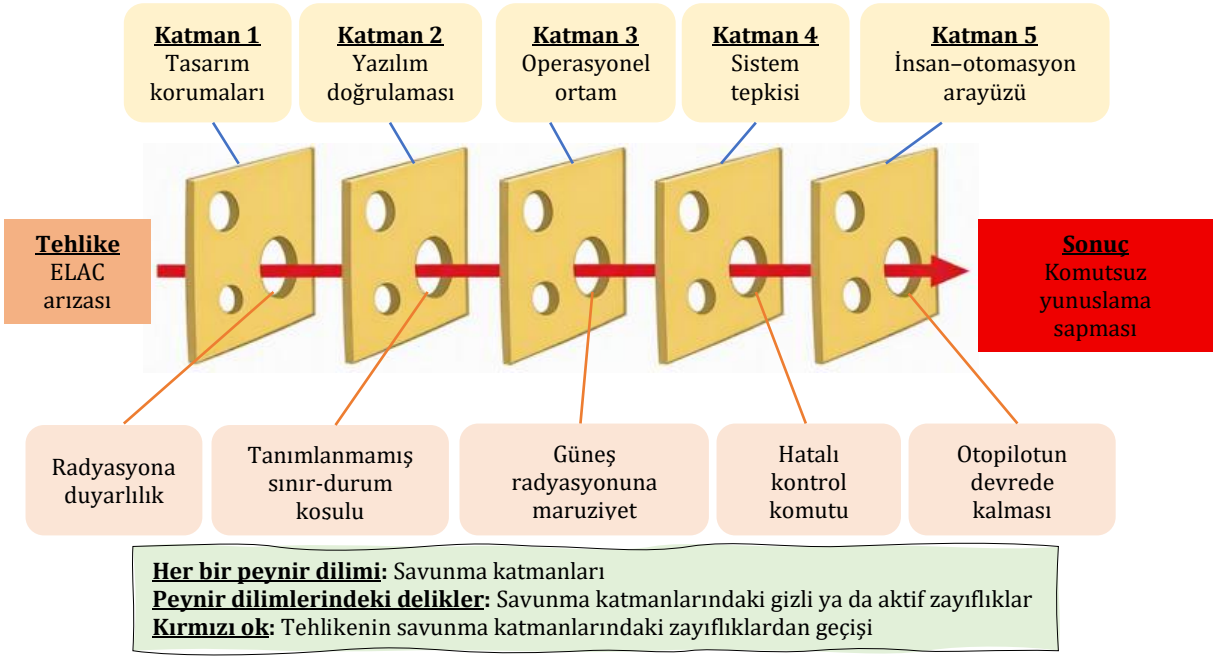
Kontrolör	Kontrol Edilen Süreç	Girdiler	Emniyetsiz Kontrol Eylemi	Nedensel Faktörler
ELAC sistemi	1. Hava aracının yunuslama (pitch) kontrolü 2. Hava aracının yuvarlanma (roll) kontrolü	1. Pilot komutları 2. Otopilot komutları 3. Sensör verileri (ADIRU, FMGC) 4. Uçuş zarfı koruma durum bilgisi	1. Komut verilmemesi 2. Hatalı irtifa dümeni (elevator) sapma komutu / Hatalı kanatçık (spoiler) roll komutu 3. Yanlış zamanlama / yanlış sıra 4. Yanlış süre	1. ELAC belleğinde veri bozulması 2. Sensör verisinin geçersiz/uyumsuz algılanması 3. Yazılım üzerinde dış radyasyon etkileri 4. Hesaplama/karşılaştırma mantığı hatası 5. Yetersiz tutarlılık kontrolü 6. Gecikmeli veri işleme 7. Kanal geçişinde senkronizasyon kaybı 8. Geçici sensör uyumsuzluğu 9. Otopilot-pilot komut önceliği yönetiminde gecikme 10. Komut tutma/serbest bırakma mantığı hatası 11. Geri besleme sinyalinin uygunsuz yorumlanması 12. Arıza sonrası toparlanma mantığının yetersizliği



Şekil 4. ELAC'ın pilot girdileri, kontrol yüzeyleri ve geri bildirimle nasıl etkileştiğini gösteren STPA temelli kontrol yapısı.

Tablo 8. Analiz edilen olaya uygun İsviçre Peyniri Modeli unsurları

Tehlike	ELAC arızası				
Savunma katmanları	Katman 1	Katman 2	Katman 3	Katman 4	Katman 5
	Tasarım korumaları	Yazılım doğrulaması	Operasyonel ortam	Sistem tepkisi	İnsan–otomasyon arayüzü
Gizli veya aktif zayıflıklar	Radyasyona duyarlılık	Tanımlanmamış sınır-durum koşulu	Güneş radyasyonuna maruziyet	Hatalı kontrol komutu	Otopilotun devrede kalması
SONUÇ:	Komutsuz yunuslama sapması				



Şekil 5. Hizalanmış gizli veya aktif zayıflıkların ELAC ile ilişkili yunuslama sapması olayına nasıl yol açtığını gösteren İsviçre Peyniri modeli.

4. Tartışma

ELAC olayı, yüksek güvence düzeyine sahip dijital uçuş kontrol mimarilerinin dayandığı tasarım varsayımlarında dikkate değer bir kırılganlığı görünür kılmaktadır. Daha somut olarak, ilgili olay; tasarım geliştirme, doğrulama ve sertifikasyon aşamalarında tam olarak temsil edilemeyebilecek nadir çevresel koşullar da dâhil olmak üzere, veri bütünlüğünün tüm operasyonel zarf boyunca korunacağı yönündeki örtük kabulü tartışmaya açmaktadır.

Ayrıca bu husus, dış etkilerin, özellikle hava ve radyasyonla ilişkili etkenlerin aviyonik bellek ve yazılım davranışı üzerindeki sonuçlarının, geleneksel sertifikasyon güvence argümanları içinde ne ölçüde kapsandığına ilişkin daha geniş bir analitik sınırlılığı da ortaya koymaktadır. DO-178C ve ARP4754A gibi sertifikasyon çerçeveleri gereksinim doğrulaması, tasarım geliştirme güvencesi ve doğrulama faaliyetleri için ayrıntılı ve disiplinli yapılar sağlamakla birlikte (RTCA, 2011; SAE International, 2010), bu yapıların uygulamadaki etkinliği sistem sınırlarını ve tehlike ortamını tanımlayan varsayımların kapsamlılığına bağlıdır.

Bu nedenle ELAC vakası, zafiyetin yalnızca tekil bir bileşen arızasından değil, çevresel bir zorlayıcı etken ile başlangıçtaki güvence modeli içinde yeterince öngörülmemiş görünen bir yazılım sınır durum koşulunun etkileşiminden kaynaklanabileceğini göstermektedir. Bu yönüyle olay, bir sistemin biçimsel sertifikasyon gereklerini karşılamasına rağmen, tasarım aşamasında modellenen temel varsayımların ötesindeki gerçek operasyonel koşullara maruz kaldığında emniyet açısından anlamlı kırılganlıklar sergileyebileceğini ortaya koymaktadır.

Bulgular, operasyonel raporlama sistemlerinin sertifikasyon sonrası emniyet verisi üretimindeki stratejik rolünü de yeniden ortaya koymaktadır. NASA'nın ASRS sistemi gibi veritabanları, gerçek operasyonların çeşitliliği, karmaşıklığı ve olasılıksal değişkenliği içinde ortaya çıkan anormal davranışları kayda geçirerek, tasarım doğrulaması veya sertifikasyon testleri sırasında görünür hâle gelmeyebilecek zafiyetlerin belirlenmesine katkı sağlar (NASA, 2026). Dolayısıyla, bu operasyonel raporlama sistemlerinin önemi yalnızca tekil olayların belgelenmesinden ibaret olmayıp, elde edilen veriler aynı zamanda gizli sistemik kırılganlıklara işaret edebilecek tekrar eden örüntülerin, zayıf sinyallerin ve farklı vakalar arasında görülen ortak düzensizliklerin tespit edilmesine de olanak tanır.

ELAC vakası bağlamında daha geniş ASRS örneklemi, kontrol anomalilerinin çoğu zaman tek başına teknik bir arıza modunu değil, bilakis daha sistematik anlamda teknik arızalar, prosedürel yorumlama ve otomasyon yönetimi arasındaki etkileşimli yapıyı yansıttığını göstermektedir. Bu nedenle, tehlikeli davranışların nadir çevresel ve operasyonel faktör bileşimleri tarafından etkinleştirilene kadar gizli kalabildiği yazılım yoğun sistemlerde operasyonel raporlama özel bir önem taşımaktadır. Bu çerçevede operasyonel veriler, sertifikasyon kanıtlarını tamamlayan vazgeçilmez bir kaynak olarak görülmeli, bununla birlikte artık riskin belirlenmesi ve sürekli uçuşa elverişlilik müdahalelerinin yönlendirilmesi için ampirik bir temel sağlamalıdır.

Daha geniş bir sistem bakış açısıyla değerlendirildiğinde, ELAC vakası havacılık emniyetinin tek bir sertifikasyon onayıyla tamamlanan statik bir durum olmadığını, aksine sürekli işleyen bir geri besleme mekanizmasıyla sürdürüldüğünü ortaya koymaktadır. Tasarım,

sertifikasyon, operasyon, olay meydana gelmesi, soruşturma, düzenleyici müdahale ve sonrasında gerçekleştirilen tasarım değişiklikleri arasındaki bağlantı, hava araçlarının sürekli uçuşa elverişliliğinin uyarlanabilir bir emniyet süreci olarak nasıl işlediğini göstermektedir.

Bu yaşam döngüsünde sertifikasyon başlangıç niteliğinde bir güvence temelini oluştururken, operasyonel hizmet daha önce tanımlanmamış tehlikelerin görünür hâle gelebileceği gerçek koşulları sağlar. Meydana gelen olumsuz olayları soruşturma süreci bu operasyonel kanıtları yapılandırılmış bir nedensel anlayışa dönüştürür. Uçuşa elverişlilik direktifleri ise bu anlayışı kısa vadeli risk kontrollerine ve filo genelinde uygulanacak düzeltici faaliyetlere aktarır.

Bu noktada, EASA tarafından 8 Temmuz 2026 tarihinde yayımlanan 2026-0134 numaralı uçuşa elverişlilik direktifi (EASA AD 2026-0134), Airbus A320 ailesinde "ELAC B L104" yazılım standardıyla ilişkili istemsiz burun aşağı hareket riskine yönelik daha kalıcı ve yapılandırılmış bir düzenleyici çözüm ortaya koymuştur (EASA, 2026). Söz konusu direktif, olayın ilk aşamasında acil ve zorunlu bir emniyet tedbiri olarak yayımlanan "EASA AD 2025-0268-E"yi yürürlükten kaldırmış ve etkilenen ELAC birimlerinin değiştirilmesi veya uygun şekilde modifiye edilmesi, hava aracı uçuş el kitabı *(Aircraft Flight Manual – AFM)* güncellemeleri ve alternatif uyumluluk yöntemleri *(Alternative Means of Compliance – AMOC)* gibi hususları daha ayrıntılı biçimde tanımlamıştır. Bu açıdan "AD 2025-0268-E" acil direktifi kısa vadeli ve hızlı bir acil müdahale niteliği taşırken, "AD 2026-0134" direktifi ise sektör görüşleriyle olgunlaştırılmış, uygulanabilirliği netleştirilmiş ve sürekli uçuşa elverişlilik yönetimi açısından daha kalıcı bir düzenleyici çerçeve sunmaktadır.

Bu anlamda ELAC olayı, modern havacılıkta dayanıklılığın teknik sistemlerin sürekli gözden geçirilmesine, düzenleyici müdahaleye ve emniyet öğrenmesine imkân veren operasyonel bir yapı içine yerleştirilmesiyle nasıl sürdürüldüğünü açık biçimde göstermektedir.

Çalışmaya konu olan vaka, operasyonel olay verilerini önleyici tedbirlere dönüştürmekle görevli EASA veya FAA gibi düzenleyici otoriteler ve gözetim kuruluşları açısından havacılık emniyet yönetim sistemlerine yönelik önemli sonuçlar da doğurmaktadır. Bu kurumlar bakımından temel çıkarım, olay analizi kapasitesinin yalnızca olayların sayısal olarak izlenmesi veya anlık uygunluk kontrolleriyle sınırlı kalmaması, ilaveten daha kapsamlı örüntü tanıma, nedensel yorumlama ve gizli sistemik risklerin değerlendirilmesini de içermesi gerektiğidir.

Bununla birlikte, NASA ASRS benzeri olay raporlama yaklaşımlarının ulusal ya da kurumsal olay veritabanlarıyla bütünleştirilmesi, düşük sıklıkta görülen ancak yüksek sonuç potansiyeli taşıyan anomalilerin ciddi olaylara dönüşmeden önce tespit edilebilirliğini artırarak proaktif, yani öngörücü emniyet gözetimini güçlendirebilir. Bu durum, ortaya çıkan tehlikelerin çoğu zaman tekrarlayan ve açık biçimde aynı arızalar şeklinde değil, dağınık operasyonel düzensizlikler olarak belirdiği yazılım bağımlı ve otomasyon yoğun hava aracı sistemleri için özellikle önemlidir. Dolayısıyla, havacılık emniyeti perspektifinden bakıldığında, ELAC olayı raporlama, analiz, risk değerlendirmesi ve düzeltici faaliyetlerin öğrenme odaklı bütünleşik bir yönetişim yapısı içinde birbirine bağlanması gerektiğini göstermektedir.

5. Sonuç

Çalışmanın nicel analiz kısmında 95 adet NASA ASRS olay raporunun detaylı incelenmesinden elde edilen bulgular, özetle, Airbus FBW kontrol anomalilerinde başlıca risk unsurunun sistem kaynaklı arızalar olduğunu göstermektedir. Olay türü dağılımında ELAC/FCC bağlantılı uçuş kontrol bilgisayarı arızaları 85 vaka ile açık biçimde baskın kategori olarak öne çıkarken, diğer olay türleri daha sınırlı sayıda raporlanmıştır. Bununla birlikte, uçuş safhası bakımından anomaliler en sık seyir safhasında görülmüş olup, 24 vaka bu kategoride kaydedilmiştir. Nedensel faktörler açısından ise teknik sistem arızalarının 85 vaka ile temel etki unsuru olduğu görülürken, insan faktörlerinin 41 vaka ile ikincil önemli etkiye sahip nedensel unsur olduğu görülmüştür. Yaygın arıza örüntüsü açısından bu bulgular, Airbus FBW kontrol anomalilerinin yalnızca bağımsız teknik arızalar olarak değil, sistem davranışı, operasyonel koşullar ve insan–makine arayüzü etkileşimleriyle şekillenen çok boyutlu emniyet olayları olarak değerlendirilmesi gerektiğini ortaya koymaktadır.

Çalışmanın sistem emniyeti analizi kısmında ise Sistem Teorik Süreç Analizi (STPA) ve İsviçre Peyniri (Swiss Cheese) Modeli metotlarıyla gerçekleştirilen sistem emniyeti değerlendirmesinde ulaşılan sonuçlara göre, özetle; STPA, ELAC sistemini yalnızca bir uçuş kontrol bilgisayarı olarak değil, hava aracının yunuslama ve yuvarlanma davranışını yöneten kritik bir kontrol bileşeni olarak konumlandırmaktadır. Pilot, otopilot ve sensör kaynaklı bilgilerin hatalı ya da eksik işlenmesi, bu kontrol çevrimi içinde emniyetsiz bir irtifa dümeni komutunun üretilmesine neden olabilmektedir. Bu nedenle olay, tek başına bir donanım veya ekipman arızası şeklinde değil; veri bütünlüğü kaybı, yazılım davranışındaki sapmalar, sensör verileri arasındaki uyumsuzluklar, zamanlama problemleri ve sistemin yeniden yapılandırılmasındaki yetersizliklerin birlikte oluşturduğu sistemik bir kontrol zafiyeti olarak değerlendirilmelidir. İsviçre Peyniri modeli ise aynı süreci, tasarım güvenceleri, yazılım doğrulama faaliyetleri, operasyonel çevre, sistemin gerçek zamanlı tepkisi ve insan–otomasyon etkileşimi arasındaki savunma katmanlarında oluşan açıklıkların aynı doğrultuda hizalanmasıyla açıklamaktadır. Bu bakımdan radyasyona duyarlılık, yeterince tanımlanmamış sınır durum koşulları, güneş radyasyonuna maruziyet, hatalı kontrol çıktısı ve otopilotun devrede kalması gibi

unsurların birleşimi, komutsuz yunuslama sapmasına uzanan çok katmanlı ve etkileşimli bir arıza mekanizmasını görünür kılmaktadır.

Hem nicel analiz hem de sistem emniyeti analizi sonuçlarına ilaveten yapılan vaka temelli olay analizinin sonuçlarına da bakıldığında, bu çalışma Airbus ELAC olayının yazılım yoğun uçuş kontrol sistemlerinde sertifikasyon temelli güvencenin sınırlarını irdelemek için güçlü bir örnek oluşturduğunu ortaya koymuştur. Buna göre, elde edilen temel bulgular, sertifikasyonun vazgeçilmez bir emniyet dayanağı olduğunu, ancak özellikle nadir çevresel etkileşimlerin ve yazılım sınır durum davranışlarının yalnızca operasyonel hizmet sırasında görünür hâle geldiği durumlarda, tüm operasyonel koşullar altında mutlak bir emniyet garantisi olarak değerlendirilemeyeceğini göstermektedir.

Olay özelindeki incelemeyi, operasyonel raporlama verilerini ve sistem emniyeti yorumunu birlikte ele alan bu çalışma, ELAC vakasının münferit bir teknik arızadan ziyade, tasarım varsayımlarının, operasyonel maruziyetin, otomasyon davranışının ve düzenleyici müdahalenin daha geniş uçuşa elverişlilik yaşam döngüsü içinde nasıl etkileştiğini gösteren bir örnek olarak değerlendirilmesi gerektiğini ortaya koymaktadır.

Bu çerçevede, sırasıyla üç temel emniyet sonucu ön plana çıkmaktadır. İlk olarak, NASA ASRS benzeri raporlama sistemleri aracılığıyla zayıf tehlike sinyallerinin tespit edilmesi, sertifikasyon sonrasında varlığını sürdürebilecek pasif veya gizli zafiyetlerin ortaya çıkarılması bakımından kritik önem taşımaktadır. İkinci olarak, zamanında hayata geçirilen düzenleyici müdahaleler, yeni beliren risklerin hava aracı filosu genelinde uygulanabilir koruyucu önlemlere dönüştürülmesinde belirleyici bir rol oynamaktadır. Üçüncü olarak ise, yazılım yoğun karmaşık aviyonik mimarilerde emniyetin sürdürülebilirliği, tasarım varsayımlarının ve sistem çözümlerinin sürekli biçimde gözden geçirilmesini ve gerektiğinde iyileştirilmesini zorunlu kılmaktadır.

Sonuç olarak, bu çalışma kapsamında ulaşılan bulgular, havacılık emniyetinin sabit ve tamamlanmış bir durumdan ziyade, mühendislik tasarımı, operasyonel deneyim, olay soruşturmaları, gözetim faaliyetleri ve uyarlanabilir sistem geliştirme süreçleri arasındaki süreklilik arz eden etkileşimle şekillenen dinamik bir yapı olduğunu ortaya koymaktadır.

Katkı Oranı Beyanı

Yazarın katkı yüzdeleri aşağıda verilmiştir. Yazar makaleyi incelemiş ve onaylamıştır.

	E.Y.
K	100
T	100
Y	100
VTI	100
VAY	100
KT	100
YZ	100
KI	100
GR	100
PY	100
FA	100

K= kavram, T= tasarım, Y= yönetim, VTI= veri toplama ve/veya işleme, VAY= veri analizi ve/veya yorumlama, KT= kaynak tarama, YZ= yazım, KI= kritik inceleme, GR= gönderim ve revizyon, PY= proje yönetimi, FA= fon alımı.

Çatışma Beyanı

Yazar bu çalışmada hiçbir çıkar ilişkisi olmadığını beyan etmektedir~~ler~~.

Etik Onay Beyanı

Bu araştırmada hayvanlar ve insanlar üzerinde herhangi bir çalışma yapılmadığı için etik kurul onayı alınmamıştır.

Kaynaklar

Airbus. (2023). *A318/A319/A320/A321 flight crew operating manual (FCOM): ATA 27 flight controls*. Airbus S.A.S.

Airbus. (2025, November 28). *Airbus update on A320 Family precautionary fleet action*. Airbus S.A.S.

Airbus. (2026). *A318/A319/A320/A321 airplane flight manual (AFM): ABN-27 flight controls.* Airbus S.A.S.

Castilho, D. S., Urbina, L. M. S., & de Andrade, D. (2018). STPA for continuous controls: A flight-testing study of aircraft crosswind takeoffs. *Safety Science, 108*.

De Florio, F. (2016). Airworthiness (Third Edition): An Introduction to Aircraft Certification and Operations. *Chapter 5 - Type Certification, Pages 85-122.*

Downer, J. (2010). Trust and technology: The social foundations of aviation regulation. *The British Journal of Sociology, 61*, 83–106.

EASA. (2023). European Union Aviation Safety Agency. *Easy Access Rules for Large Aeroplanes* (*Certification specifications for large aeroplanes / CS-25)*.

EASA. (2025a). European Union Aviation Safety Agency. *Emergency airworthiness directive AD No. 2025-0268-E: Flight controls—Elevator aileron computer—Replacement*.

EASA. (2025b). European Union Aviation Safety Agency. *Easy Access Rules for Initial Airworthiness and Environmental Protection (EU Regulation No 748/2012 / EASA Part-21)*.

EASA. (2026). European Union Aviation Safety Agency. *Airworthiness directive, AD No. 2026-0134: ATA 27 – Flight Controls – Elevator Aileron Computer – Replacement.*

FAA. (2011). Federal Aviation Administration. *AC 20-174:*

Development of civil aircraft and systems.

FAA. (2017). Federal Aviation Administration. *AC 20-175: Airborne Software Development Assurance Using EUROCAE ED-12 and RTCA DO-178*.

FAA. (2020). Federal Aviation Administration. *Return to Service of the Boeing 737 MAX Aircraft: Summary of the FAA's Review of the Boeing 737 MAX.*

FAA. (2025). Federal Aviation Administration. *14 CFR Part 21 - Certification Procedures for Products and Articles (FAR Part-21)*.

FAA. (2026a). Federal Aviation Administration. *14 CFR Part 25 - Airworthiness Standards: Transport Category Airplanes (FAR Part-25)*.

FAA. (2026b). Federal Aviation Administration. Airworthiness directives; Airbus SAS airplanes. *Federal Register*, *91*, 199–202.

Knight, J. C. (2002). Safety critical systems: Challenges and directions. In *Proceedings of the 24th International Conference on Software Engineering*, Orlando, FL, United States, May 19–25, 2002.

Kornecki, A., & Zalewski, J. (2003). Assessment of Software Development Tools For Safety -Critical Real-Time Systems. *IFAC Programmable Devices and Systems.*

Leveson, N. (2010). Applying systems thinking to analyze and learn from events. *Safety Science*.

Leveson, N., & Thomas, J. P. (2018). *STAMP handbook*.

Lewis, E. (2025). Airbus A320 ELACs explained: How a software glitch caused a JetBlue pitch-down and forced urgent inspections. *Aerospace Global News*.

NASA. (2026a). National Aeronautics and Space Administration. *Aviation Safety Reporting System overview*.

NASA. (2026b). National Aeronautics and Space Administration. *ASRS Database Online*.

NTSB. (2019). National Transportation Safety Board. *Safety Recommendation Report: Assumptions Used in the Safety Assessment Process and the Effects of Multiple Alerts and Indications on Pilot Performance*.

NTSB. (2026). National Transportation Safety Board. *ENG26LA004 preliminary report: JetBlue Flight 1230 event*.

Nicolin, I., & Nicolin, B. A. (2019). The fly-by-wire system. *Incas Bulletin, Volume 11, Issue 4, 2019, pp. 217 – 222.*

Orban, A. (2025). The Airbus A320 flight-control crisis: What happened and how it was quickly resolved. *Aviation24*.

Reason, J. (1990). *Human error*. Cambridge University Press.

RTCA. (2011). *DO-178C: Software considerations in airborne systems and equipment certification*.

SAE International. (2010). *ARP4754A: Guidelines for development of civil aircraft and systems*.

Sgobba, T. (2019). B-737 MAX and the crash of the regulatory system. *Journal of Space Safety Engineering Volume 6, Issue 4, December 2019, Pages 299-303*.

Underwood, P., & Waterson, P. (2014). Systems thinking, the Swiss Cheese Model and accident analysis: A comparative systemic analysis of the Grayrigg train derailment using the ATSB, AcciMap and STAMP models. *Accident Analysis & Prevention, 68*, 75–94.

Black Sea Journal of Engineering and Science
doi: 10.34248/bsengineering.1977396

Open Access Journal
e-ISSN: 2619 – 8991

Research Article
Volume 9 - Issue 5: 2419-2426 / September 2026

INVERSE NODAL ANALYSIS FOR VECTOR-VALUED SINGULAR DIFFUSION OPERATORS

Abdullah ERGÜN[1]*

[1]*Sivas Cumhuriyet University, Sivas Vocational School of Technical Sciences, 58140, Sivas, Türkiye*

Abstract: We examine a vector-valued diffusion problem given by the differential equation $-y''+\left[\lambda p(x)+q(x)\right]y=\lambda^2 y$ with boundary conditions $\begin{cases} Ay(0)=-I_d y'(0) \\ By(\pi)=-I_d y(\pi) \end{cases}$ where $p(x)$ and $q(x)$ denotes a continuous symmetric matrix-valued function on the interval $[0,\pi]$ and k and K are real symmetric matrices of size dxd. An eigenfunction $y(x)$ is referred to as being of type (CZ) if all isolated zeros in its components coincide with nodal points of the function itself. We demonstrate that in the two-dimensional case $d=2$, the existence of infinitely many (CZ)-type eigenfunctions is both necessary and sufficient for the simultaneous diagonalizability of $p(x)_k$ and A, B. Consequently, if all but finitely many eigenfunctions possess the (CZ) property, then the coefficient matrix and the associated boundary data can be uniquely reconstructed up to a constant unitary transformation.

Keywords: Inverse nodal problem, Vector-valued Sturm–Liouville systems, Singular diffusion operators, Common zero property

***Corresponding author:** Sivas Cumhuriyet University, Sivas Vocational School of Technical Sciences, 58140, Sivas, Türkiye
E mail: aergun@cumhuriyet.edu.tr (A. ERGÜN)
Abdullah ERGÜN https://orcid.org/0000-0002-2795-8097

Received: June 24, 2026
Accepted: August 10, 2026
Published: September 15, 2026

Cite as: Ergün, A. (2026). Inverse nodal analysis for vector-valued singular diffusion operators. *Black Sea Journal of Engineering and Science,* 9(5), 2419-2426.

1. Introduction

The determination of differential operators from incomplete or indirect observations constitutes one of the central themes of inverse problem theory. Among the various types of inverse data, the nodal distribution of eigenfunctions has attracted considerable attention due to its close relationship with the qualitative behavior of solutions. Since nodal points encode information about both the oscillatory nature of eigenfunctions and the coefficients governing the underlying operator, they provide an effective framework for recovering structural characteristics of the problem under consideration (McLaughlin, 1988; Hald, 1989).

The scalar Sturm–Liouville framework has provided the foundation for much of the existing research on inverse nodal problems. A substantial body of work has demonstrated that nodal information alone is sufficient to determine the underlying potential and boundary coefficients, modulo certain unavoidable normalization constants. Moreover, a variety of reconstruction procedures based exclusively on nodal observations have been established for different classes of boundary value problems (McLaughlin, 1988;; Hald, 1989; Yang, 1997a, 1997b; Shen, 1999; Chen, 2002). Subsequent investigations have further explored how eigenvalue asymptotics, smoothness conditions, and spectral characteristics influence the accuracy and uniqueness of the reconstruction process (Levitan and Sargsjan, 1991; Gesztesy and Simon, 1997; Hochstadt and Lieberman, 1978; Zettl, 2005; Pöschel and Trubowitz, 1987).

The transition from scalar inverse nodal problems to vector-valued and matrix Sturm–Liouville systems introduces a considerably richer mathematical structure. Unlike the scalar case, matrix coefficients generate interactions among the components of eigenfunctions, resulting in nodal patterns that are substantially more complex and difficult to analyze. While a variety of inverse spectral questions for matrix and vectorial operators have been addressed in the literature (Shen and Shieh, 1999; Carlson, 1999; Yurko, 2000; Brown and Weikard, 2000; Bondarenko, 2015), corresponding results based on nodal information remain relatively limited. Additional complications arise when the governing model contains transmission conditions, internal discontinuities, or singular terms. Such phenomena frequently occur in diffusion processes, layered materials, and composite structures, where standard techniques developed for scalar Sturm–Liouville equations are generally insufficient and must be replaced by more sophisticated analytical approaches (Agranovich and Marchenko, 1963; Kurasov, 1996; Carlson, 1998; Pivovarchik, 2000; Hryniv and Mykytyuk, 2003; Buterin, 2015).

This work is licensed (CC BY-NC 4.0) under Creative Commons Attribution 4.0 International License

One of the distinctive features of vector-valued Sturm–Liouville systems is the possibility that all components of an eigenfunction share the same nodal locations. This phenomenon, known as the common zero (CZ) property, establishes a strong relationship between the distribution of nodal points and the spectral structure of the underlying matrix coefficients. From an inverse perspective, the CZ property is particularly significant because it creates a bridge between vectorial models and collections of decoupled scalar problems, thereby allowing information contained in nodal data to be interpreted through a simpler spectral framework (Shen and Shieh, 1999; Brown and Weikard, 2000).

In the classical scalar case, the problem is framed through the differential equation:

$$-y''+\left[\lambda p(x)+q(x)\right]y=\lambda^2 y$$

subject to the Robin-type boundary conditions:

$$y(0)\cos\alpha+y'(0)\sin\alpha=0$$
$$y(1)\cos\gamma+y'(1)\sin\gamma=0$$

where $q\in L_1(0,\pi)$ and $\alpha,\gamma\in(0,\pi)$. For each eigenvalue λ_n, let $y_n(x)$ denote the corresponding eigenfunction, and define the nodal set $\left[x_k^{(n)}\right]_{k=1}^{n-1}$ X_n as the collection of zeros of $y_n(x)$ in the open interval $(0,\pi)$.

Classical results in inverse nodal analysis show that the data $(p(x),q(x))$ can be determined uniquely from the nodal distribution of eigenfunctions, modulo an additive constant in q (McLaughlin, 1988; Yang, 1997a). Moreover, nodal data have been employed not only to establish uniqueness but also to derive practical reconstruction schemes for recovering the unknown quantities of the problem. Several such approaches have been proposed and successfully implemented in different settings (Hald, J.; Yang, 1997a; Shen, 1999).

Although inverse nodal methods are well established for scalar Sturm–Liouville equations, their extension to vector-valued systems is still at a comparatively early stage. Existing studies have mainly focused on inverse eigenvalue and spectral questions for matrix-valued operators (Shen and Shieh, 1999), whereas reconstruction procedures based directly on nodal information have received much less attention. As a result, many fundamental aspects of inverse nodal analysis for vector-valued problems remain to be explored.

In this paper, we consider the following vectorial generalization:

$$\left.\begin{aligned}&-Y''+\left[2\lambda P(x)+Q(x)\right]y=\lambda^2 I_d Y\\&A_1Y(0)-A_2Y'(0)=0\\&B_1Y(\pi)+B_2Y'(\pi)=0\end{aligned}\right\}\quad(1)$$

Consider problem (1). If we take $P(x)$ as

$$P(x)=\delta(x-a)I_d,$$

$$-Y''+Q(x)Y=\lambda^2 I_d Y\quad(2)$$

$$\begin{aligned}&A_1Y(0)-A_2Y'(0)=0\\&B_1Y(\pi)+B_2Y'(\pi)=0\end{aligned}\quad(3)$$

$$\begin{aligned}&Y(a+0)=Y(a-0)\\&Y'(a+0)-Y'(a-0)=\lambda I_d\sigma Y(a)\end{aligned}\quad(4)$$

problem (equation 1) is reduced to (equations 2-4).

In this formulation, λ denotes the spectral parameter, and $y(x)=\left[y_1(x),y_2(x),...y_m(x)\right]^T$ is an $m-$dimensional vector-valued function. The coefficient matrix $q(x)=\left[q_{ij}(x)\right]$ is assumed to be symmetric and continuous on the interval $[0,\pi]$. The boundary matrices A_i and B_i (i = 1, 2) are real *dxd* matrices, and the identity matrix I_d appears explicitly on the right-hand side of the differential equation.

This general setting covers several classical boundary conditions as special cases. If A_2 and B_2 are both zero while A_1 and B_1 are invertible, the boundary conditions reduce to the standard Dirichlet type. Alternatively, if $A_1=0$ and $B_1=0$ and the matrices A_2 and B_2 are invertible, the system corresponds to Neumann boundary conditions.

To ensure that the system is self-adjoint, the boundary matrices must satisfy certain structural constraints, namely:

$$A_1A_2^*=A_2A_1^*\quad,\quad B_1B_2^*=B_2B_1^*$$
$$rank\left[A_1,A_2\right]=rank\left[B_1,B_2\right]=d$$

In the special case where A_2 and B_2 are both invertible, the self-adjointness conditions simplify to

$$A_1A_2^{-1}=\left(A_1A_1^{-1}\right)^T\quad,\quad B_2^{-1}B_1=\left(B_2^{-1}B_1\right)^T$$

which implies that the matrices $A:=A_1A_2^{-1}$ and $B:=B_2^{-1}B_1$ are symmetric. Consequently, the boundary conditions can be rewritten in a normalized form:

$$Ay(0)+I_d y'(0)=0$$
$$By(\pi)+I_d y'(\pi)=0$$

with A,B symmetric. This general formulation encompasses various classical cases, including Neumann conditions, and forms the basis for our analysis.

2. Preliminaries

Let $Y(x)$ denote a continuous vector-valued function defined on the interval $[0,\pi]$ and taking values in $\mathbb{R}^d$. A point $x_0\in[0,\pi]$] is said to be a nodal point of $Y(x_0)$ if $Y(x_0)=0$, meaning that all components of the vector simultaneously vanish at x_0.

We say that $y(x)$ is of type (CZ), short for *common zero type* if every isolated zero occurring in any single component of $y(x)$ corresponds to a nodal point, i.e., all components vanish at that location. In other words, the isolated zeros of individual components must coincide with full vector zeros.

A matrix-valued function $P(x)$ is regarded as diagonalizable in a simultaneous sense when a single unitary matrix Q exists that transforms $P(x)$ into a diagonal form for every x in the interval $[0,\pi]$. That is, under the conjugation by Q, the matrix $P(x)$ becomes diagonal uniformly with respect to x.

Using this notion as a basis, we say that a vectorial Sturm–Liouville problem is simultaneously diagonalizable if the same unitary matrix Q diagonalizes not only the coefficient matrix $P(x)$ but also the associated boundary matrices A_i and B_i (i = 1, 2) Equivalently, the conjugated matrices $Q^*P(x)Q$, Q^*A_iQ and Q^*B_iQ all take diagonal form.

If there exists a unitary matrix Q such that the conjugations $Q^*P(x)Q$, Q^*A_iQ Q^*B_iQ $(for\, i=1,2.)$ yield diagonal matrices, then the system described by equations (1)-(4) can be decoupled into d independent scalar Sturm–Liouville problems. Each resulting scalar problem admits a complete set of eigenfunctions, and their combination via the inverse transformation Q yields vector-valued eigenfunctions of the original system.

Crucially, the eigenfunctions of the decoupled system are naturally of type (CZ), as each scalar component possesses isolated zeros, which correspond to nodal points in the original vector setting. This leads to the following lemma characterizing the nodal structure in the diagonalizable case:

Lemma 2.1. Assume that the vectorial Sturm–Liouville problem considered in this paper is simultaneously diagonalizable. That is, there exists a unitary matrix Q such that, under the transformation $Y(x)=Qz(x)$, the coefficient matrix $Q(x)$ and the boundary matrices A_i and B_i (i = 1, 2) are transformed into diagonal matrices. Then, the problem admits infinitely many eigenfunctions whose nodal sets are of common zero type; namely, for each such eigenfunction, all components vanish simultaneously at every nodal point.

Lemma 2.1 shows that simultaneous diagonalizability of the vectorialSturm–Liouville problem guarantees the existence of infinitely manyeigenfunctions whose nodal sets exhibit the common zero property. This observation highlights a strong link between the algebraic structure of the coefficient matrices and nodal points.

Lemma 2.2 (Structural Consequence of the CZ Property) Let d = 2, and suppose that the vector-valued Sturm–Liouville problem admits infinitely many eigenfunctions of common zero type (CZ). Then the nodal sets of the two components of each such eigenfunction coincide.

Consequently, for every CZ-type eigenfunction

$y_n(x)=\left(y_{n,1}(x),y_{n,2}(x)\right)^T$,

the ratio

$r_n(x)=y_{n,1}(x)/y_{n,2}(x)$

is well defined on each nodal interval and can be continuously extended across common nodal points.

Since infinitely many eigenfunctions possess the CZ property, the corresponding nodal structures become asymptotically identical. Consequently, infinitely many eigenfunctions share a common asymptotic direction in $\mathbb{R}^2$. In particular, there exists a nonzero vector $v \in \mathbb{R}^2$ such that infinitely many eigenfunctions are asymptotically aligned with v.

This implies that the coefficient matrix $Q(x)$ preserves a common one-dimensional invariant subspace for every $x\in[0,\pi]$.

Since $Q(x)$ is symmetric, the orthogonal complement of this invariant subspace is also invariant. Therefore, there exists a constant unitary matrix U such that

$U^{-1}QU=diag\left(q_1(x),q_2(x)\right)$

for every $x\in[0,\pi]$.

Hence the coefficient matrix $Q(x)$ is simultaneously diagonalizable.

Theorem 2.3. Let $d=2$ and consider the vectorial Sturm–Liouville problem studied in this paper, together with the associated boundary and transmission conditions. Let $\left\{\left(\lambda_n,y_n(x)\right)\right\}_{n=1}^{\infty}$ be its sequence of eigenpairs, where each eigenfunction $y_n(x)=\left(y_{n,1}(x),y_{n,2}(x)\right)^T$ is a two-component vector-valued function.

Proof. The existence of infinitely many CZ-type eigenfunctions implies that the nodal sets of the components coincide for infinitely many eigenfunctions. By Lemma 2.2, this forces the corresponding eigenfunctions to share a common asymptotic direction in $\mathbb{R}^2$.

Consequently, the coefficient matrix $Q(x)$ possesses a common invariant subspace for all $x\in[0,\pi]$. Since $Q(x)$ is symmetric, its orthogonal complement is invariant as well. Therefore, there exists a constant unitary matrix U such that

$U^{-1}QU=diag\left(q_1(x),q_2(x)\right)$

for every $x\in[0,\pi]$.

Applying the same transformation to the boundary and transmission matrices yields a decoupled system consisting of two independent scalar Sturm–Liouville problems.

Hence the original vector-valued Sturm–Liouville problem is simultaneously diagonalizable.

Assume that there exists an infinite subsequence of eigenfunctions whose nodal sets are of common zero type, that is, for each such eigenfunction, all components vanish simultaneously at every nodal point. Then the matrix-valued coefficient function of the problem is simultaneously diagonalizable by a constant unitary transformation. More precisely, there exists a unitary matrix Q such that, under the transformation $Y_n(x)=Qz_n(x)$, the original vectorial Sturm–Liouville

problem decomposes into two independent scalar Sturm–Liouville problems, each governing one component of $z_n(x)$. In fact, the result can be extended even further, as stated in our main theorem:

Theorem 2.4. Let $d=2$, equations 2-4 together with the transmission and boundary conditions. Suppose that this problem possesses infinitely many eigenfunctions $\{y_n(x)\}_{n=1}^{\infty}$,whose nodal sets are of common zero type (that is, all components vanish simultaneously at each nodal point).

Then the corresponding matrix-valued Sturm–Liouville problem is simultaneously diagonalizable, in the sense that there exists a constant invertible matrix Q such that the transformed problem obtained via $\tilde{Y}(x)=Q^{-1}Y(x)$ decouples into two independent scalar Sturm–Liouville problems.

Furthermore, when additional structural properties of the eigenfunctions are available, it becomes possible to uniquely recover the defining data of the system. This leads to the following reconstruction result:

Corollary 2.5. Let $d=2$ and consider the vectorial (2)-(4) problem defined by the differential equation and boundary conditions. Assume that all but finitely many eigenfunctions of this problem possess the common zero property.

Then, the underlying vectorial (2)-(4) problem is uniquely determined up to a constant unitary transformation. Moreover, the coefficient matrices of the problem can be explicitly reconstructed from the corresponding nodal data.

Proof. In view of Theorem 2.4, it follows that, under the stated assumptions, the coefficient matrices $Q(x)$, A, and B can be reduced simultaneously to diagonal form by a unitary transformation. More precisely, there exists a unitary matrix U such that the matrices $UQ(x)U^*$, UAU^* and UBU^* are all diagonal. In this representation, the transformed coefficient matrix $UQ(x)U^*$ has the scalar entries $u_1(x)$ and $u_2(x)$ on its diagonal, while the transformed boundary matrices UAU^* and UBU^* have constant diagonal entries a_1, a_2 and b_1, b_2 respectively.

By introducing the change of variables $Q^*y(x)=\left[v(x),w(x)\right]^T$, the original vectorial Sturm–Liouville equation decouples into two independent scalar equations 5-6.

The first component satisfies:

$$\begin{cases} -v''(x)+u(x)v(x)=\mu v(x) \\ a_1v(0)+v'(0)=0 \\ a_1v(\pi)+v'(\pi)=0 \\ v'(a+0)-v'(a-0)=\mu\beta v(a) \end{cases} \tag{5}$$

The second component satisfies:

$$\begin{cases} -w''(x)v(x)+u(x)w(x)=\eta w(x) \\ a_1w(0)+w'(0)=0 \\ a_1w(\pi)+w'(\pi)=0 \\ w'(a+0)-w'(a-0)=\eta\beta w(a) \end{cases} \tag{6}$$

These two scalar Sturm–Liouville problems can be analyzed independently. Since the nodal information is preserved under the unitary transformation Q, and because the scalar problems fall within the well-studied class of inverse nodal problems, the functions $(u_1(x),a_1,b_1)$ and can each be uniquely determined up to an additive constant using known reconstruction results.

The classical inverse nodal reconstruction results of McLaughlin (1988), Hald, J.; Yang, 1997a;, 1997b) can therefore be applied componentwise to the decoupled scalar problems. Consequently, the diagonal entries of the transformed coefficient matrix are uniquely recoverable from the corresponding nodal data.

This completes the justification.

As a consequence, the potential functions $u_1(x)$ and $u_2(x)$, along with the associated boundary parameters (a_1,b_1) and (a_2,b_2) can all be uniquely reconstructed from their respective nodal data up to an additive constant in the potential.

Durak (2024) previously obtained eigenvalue estimates for related matrix differential operators under various boundary conditions. In contrast, the present approach yields a simpler asymptotic formulation.

We will present the eigenvalue asymptotic estimates in the next section. For the sake of completeness, certain auxiliary lemmas including Lemma 3.1 will also be provided with detailed proofs in subsequent sections.

3. Eigenvalue Asymptotics

In this section, we investigate the asymptotic behavior of the eigenvalues and corresponding nodal points for the vectorial Sturm–Liouville problem introduced earlier. The results established herein are valid for general dimension $d\geq 2$ and form a central component in the proof of our main theorem.

Consider again the system:

$-Y''(x)+P(x)Y(x)=\lambda I_d Y(x)$

with initial conditions specified at the left end point as

Let $Y(x,\lambda)$ denote the matrix-valued solution to this initial value problem. Our aim is to derive an asymptotic estimate for the eigenvalues λ_n which are defined implicitly through the boundary condition at $x=1$:

$BY(\pi,\lambda)+Y'(\pi,\lambda)=0$

We begin with the following key lemma adapted from McLaughlin (1988)

Lemma 3.1. Let $Y(x,\lambda)$) be the fundamental matrix solution of the differential equation $-Y''+Q(x)Y=\lambda I_d Y$ with initial conditions $Y(0,\lambda)=I_d, Y'(0,\lambda)=-A$.

Then, it satisfies the integral representation:

$$Y(x,\lambda)=\cos\left(\sqrt{\lambda}x\right)I_d+\frac{\sin\left(\sqrt{\lambda}x\right)}{\sqrt{\lambda}}A+\int_0^x\frac{\sin\left(\sqrt{\lambda}(x-t)\right)}{\sqrt{\lambda}}P(t)Y(t,\lambda)dt$$

This expression provides the foundation for analyzing the spectral properties of the system. In particular, we can derive asymptotic formulas for the eigenvalues λ_n by examining the behavior of the determinant of the associated boundary operator.

Theorem 3.2. Let λ_n denote the n-th eigenvalue of (2)-(4). Define $m=\left[\frac{n}{d}\right]$ where d is the dimension of the system. Then, for each $j=1,2,...,d$ the eigenvalues satisfy the following asymptotic relation for sufficiently large m:

$$\lambda_{dm+j}=m+\frac{a_{0j}}{m\pi^2}+O\left(\frac{1}{m^2}\right). \tag{7}$$

Here, the ordering is in the form of $a_{i1}\le a_{i2}\le...\le a_{id}$, $i=0,1,2,3.$ a_{ij} are the eigenvalues of the following expressions, respectively;

$$\left[A-\frac{1}{4}\beta\int_0^a Q(t)dt+\frac{1}{2}\int_0^\pi Q(t)dt\right],$$

$$\left[-\frac{1}{2}\beta\left(A-\frac{1}{2}\int_0^a Q(t)dt+\int_0^\pi Q(t)dt\right)\right],$$

$$\left[\frac{1}{2}\beta\left(A-\frac{3}{2}\int_0^a Q(t)dt+\int_0^\pi Q(t)dt\right)\right],\left[\frac{1}{4}\left(1-\beta^2\right)\int_0^a Q(t)dt\right].$$

Proof. Using the asymptotic formula established by Amirov and Durak (2024), we obtain (equation 8),

$$\lambda_{nj}=\lambda_{nj}^0+\frac{d_{nj}}{\lambda_{nj}^0}+o\left(\frac{1}{\lambda_{nj}^0}\right). \tag{8}$$

where,

$$\begin{aligned}d_{nj}=&\frac{1}{\Delta_0\left(\lambda_{nj}\right)}\Big[\left(w_0(\pi)+A\right)\sin\left(\lambda_{nj}^0\pi\right)I_d\\&+\left(\frac{\beta}{2}A-w_1(\pi)\right)\cos\left(\lambda_{nj}^0\pi\right)I_d\\&+\left(w_2(\pi)-\frac{\beta}{2}A\right)\cos\lambda_{nj}^0(2a-\pi)I_d+w_3(\pi)\sin\lambda_{nj}^0(2a-\pi)I_d\Big].\end{aligned}$$

$$\begin{aligned}F_Q(\lambda)=&B\phi(\pi,\lambda)+\phi'(\pi,\lambda)\\=&B\cos\lambda\pi I_d+\frac{\beta}{2}B\left(\sin\lambda\pi-\sin\lambda(2a-\pi)\right)I_d\\&+\frac{1}{\lambda}BI_dw_0(\pi)\sin\lambda\pi+\frac{1}{\lambda}Bw_1(\pi)\cos\lambda\pi I_d\\&+\frac{\left(1-2\beta^2\right)}{4\lambda}B\sin\lambda(2a-\pi)\int_0^a q(t)dtI_d\\&+\frac{1}{2\lambda}Bw_2(\pi)\cos\lambda(2a-\pi)I_d-\lambda\sin\lambda\pi I_d\\&+\frac{\lambda\beta}{2}\cos\lambda\pi I_d+\frac{\beta\lambda}{2}\cos\lambda(2a-\pi)I_d\\&+w_0(\pi)\cos\lambda\pi I_d-w_1(\pi)\sin\lambda\pi I_d\\&-\frac{\left(1-2\beta^2\right)}{4}\cos\lambda(2a-\pi)\int_0^a q(t)dtI_d\\&+w_2(\pi)\sin\lambda(2a-\pi)I_d+o\left(\frac{\exp|\tau|\pi}{\lambda}I_d\right)\\=&\left(B+\frac{\beta}{2}I_d\right)\cos\lambda\pi+\left(\frac{B}{2}\beta-\lambda I_d\right)\sin\lambda\pi-\frac{\beta}{2}B\sin\lambda(2a-\pi)I_d\\&+\frac{\beta}{2}\cos\lambda(2a-\pi)I_d+\left(\frac{\beta}{\lambda}\sin\lambda\pi+\cos\lambda\pi I_d\right)w_0(\pi)I_d\\&+\left(\frac{1}{\lambda}B\cos\lambda\pi-\sin\lambda\pi I_d\right)w_1(\pi)I_d\\&+\left(\frac{1}{2\lambda}B\cos\lambda(2a-\pi)+\sin\lambda(2a-\pi)I_d\right)w_2(\pi)I_d\\&+\left(\frac{1}{\lambda}B\sin\lambda(2a-\pi)-\cos\lambda(2a-\pi)I_d\right)w_3(\pi)I_d\\&+o\left(\frac{\exp|\tau|\pi}{\lambda}I_d\right)\end{aligned}$$

Define the set

$$\begin{aligned}G_Q(\lambda)=&\frac{1}{\lambda}B\left[A-\frac{1}{4}\beta\int_0^a Q(t)dt+\frac{1}{2}\int_0^\pi Q(t)dt\right]\sin\lambda\pi I_d\\&+\left[A-\frac{1}{4}\beta\int_0^a Q(t)dt+\frac{1}{2}\int_0^\pi Q(t)dt\right]\cos\lambda\pi I_d+o\left(\frac{\exp|\tau|\pi}{\lambda}I_d\right).\end{aligned}$$

If we use Rouche's theorem for $\lambda\in R/\{0\}$ when $\exp|\mathrm{Im}\,\lambda|=1$, we get the zeros of $\det\left(G_Q(\lambda)\right)$. Here, $\{a_{01},a_{02},...,a_{0d}\}$ is the set of eigenvalues of $B\left[A-\frac{1}{4}\beta\int_0^a Q(t)dt+\frac{1}{2}\int_0^\pi Q(t)dt\right]$.

$$\lambda_{dm+j}=\lambda_{dm+j}^0+\delta_{dm}^j=m+h_{dm}^j+\delta_{dm}^j$$

$$\tan\left(m\pi+h_{dm}^j\pi+\delta_{dm}^j\pi\right)=\tan\left(h_{dm}^j\pi+\delta_{dm}^j\pi\right)=\frac{a_{0j}}{m\pi+h_{dm}^j+\delta_{dm}^j}$$

$$h_{dm}^j+\delta_{dm}^j=\frac{a_{0j}}{m\pi+h_{dm}^j+\delta_{dm}^j}+O\left(\frac{1}{m^2}\right)$$

$$=\frac{a_{0j}}{m\pi}\cdot\frac{1}{1+\frac{h_{dm}^j+\delta_{dm}^j}{m\pi}}=\frac{a_{0j}}{m\pi}+o\left(\frac{1}{m}\right).$$

$$\lambda_{dm+j}=\lambda^0{}_{dm+j}+\delta_{dm}^j=m+\frac{a_{0j}}{m\pi^2}+O\left(\frac{1}{m^2}\right)$$

The remaining assertions can be established by arguments analogous to those used above and are therefore omitted.

Theorem 3.3. Consider the boundary value problem of (2)-(4) and let λ_n be its eigenvalues with corresponding eigenfunctions $y_n(x)$ normalized in any fixed way. Denote by

$$0<x_1^{(n)}<x_2^{(n)}<...<x_v^{(n)}<\pi$$

the nodal points (zeros) of $y_n(x)$ in $(0,\pi)$, counted in increasing order.

Let λ_n^0 be the "unperturbed" spectral sequence associated with the characteristic function $\Delta_0(\lambda)$, so that $\lambda_n^0\to\infty$ and $\lambda_n^0\cong n$ as $n\to\infty$. Then, for all sufficiently large n, the j-th nodal point satisfies the uniform asymptotic formula (equation 9),

$$x_j^{(n)}=\frac{\left(j-\frac{1}{2}\right)\pi}{\lambda_n^0}+O\left(\frac{1}{\left(\lambda_n^0\right)^2}\right)\quad,\ j=1,2,...,v \tag{9}$$

Proof. From the standard large-parameter asymptotics of the fundamental solution, we may write, uniformly for $x\in[0,\pi]$,

$$y_n(x)=C_n\left(\cos\left(\lambda_n^0 x\right)+R_n(x)\right),\ \ \|R_n\|_{L^\infty(0,\pi)}=O\left(\frac{1}{\lambda_n^0}\right)$$

where $C_n\neq 0$ is a nonzero scalar depending on the normalization.

Fix $j\in\{1,2,...,v\}$ } and define two "bracketing" points:

$$x_{j,-}=\frac{\left(j-\frac{1}{2}\right)\pi-\frac{\pi}{4}}{\lambda_n^0},\qquad x_{j,+}=\frac{\left(j-\frac{1}{2}\right)\pi+\frac{\pi}{4}}{\lambda_n^0}.$$

Then

$$\cos\left(\lambda_n^0 x_{j,-}\right)=\cos\left(\left(j-\frac{1}{2}\right)\pi-\frac{\pi}{4}\right)=+\frac{\sqrt{2}}{2}$$

$$\cos\left(\lambda_n^0 x_{j,+}\right)=\cos\left(\left(j-\frac{1}{2}\right)\pi+\frac{\pi}{4}\right)=-\frac{\sqrt{2}}{2}$$

Since $R_n(x)=O\left(\frac{1}{\lambda_n^0}\right)$ uniformly, for all sufficiently large n we have

$$\cos\left(\lambda_n^0 x_{j,-}\right)+R_n\left(x_{j,-}\right)>0,\ \cos\left(\lambda_n^0 x_{j,+}\right)+R_n\left(x_{j,+}\right)<0$$

Multiplying by $C_n\neq 0$ preserves a sign change, hence $y_n\left(x_{j,-}\right)\cdot y_n\left(x_{j,+}\right)<0$ for large n.

By continuity of y_n, the intermediate value theorem implies the existence of at least one point $x_j^{(n)}\in\left(x_{j,-},x_{j,+}\right)$ such that $y\left(x_j^{(n)}\right)=0$. By the standard oscillation properties of Sturm–Liouville-type problems (and the fact that zeros are simple for large n, this zero corresponds to the j-th nodal point.

Consequently, there exists $\varepsilon_{j,n}$ with $\left|\varepsilon_{j,n}\right|<\frac{\pi}{4}$ such that

$$\lambda_n^0 x_j^{(n)}=\left(j-\frac{1}{2}\right)\pi+\varepsilon_{j,n}.$$

Equivalently, $x_j^{(n)}=\frac{\left(j-\frac{1}{2}\right)\pi}{\lambda_n^0}+\frac{\varepsilon_{j,n}}{\lambda_n^0}$.

Evaluating the eigenfunction at the nodal point and using the asymptotic representation,

$$0=y_n\left(x_j^{(n)}\right)=C_n\left(\cos\left(\lambda_n^0 x_j^{(n)}\right)+R_n\left(x_j^{(n)}\right)\right)$$

so

$$\cos\left(\lambda_n^0 x_j^{(n)}\right)=-R_n\left(x_j^{(n)}\right)=O\left(\frac{1}{\lambda_n^0}\right)$$

Using $\lambda_n^0 x_j^{(n)}=\left(j-\frac{1}{2}\right)\pi+\varepsilon_{j,n}.$ we get

$\cos\left(\left(j-\frac{1}{2}\right)\pi+\varepsilon_{j,n}\right)=(-1)^n\sin\left(\varepsilon_{j,n}\right)$. Hence

$$\sin\left(\varepsilon_{j,n}\right)=O\left(\frac{1}{\lambda_n^0}\right)$$

Since $\left|\varepsilon_{j,n}\right|<\frac{\pi}{4}$, we have $\sin\left(\varepsilon_{j,n}\right)\cong\varepsilon_{j,n}$ and therefore $\varepsilon_{j,n}=O\left(\frac{1}{\lambda_n^0}\right)$. Substituting back gives

$$x_j^{(n)}=\frac{\left(j-\frac{1}{2}\right)\pi}{\lambda_n^0}+O\left(\frac{1}{\left(\lambda_n^0\right)^2}\right)$$

uniformly in j. This completes the proof.

Corollary 3.4. Define the nodal lengths $l_j^{(n)}=x_{j+1}^{(n)}-x_j^{(n)}$, $j=1,2,...,v-1$.

Let λ_n^0 denote the unperturbed spectral sequence used in Theorem 2.3. Then, as $n\to\infty$,

a) $l_j^{(n)}=\frac{\pi}{\lambda_n^0}+O\left(\frac{1}{\left(\lambda_n^0\right)^2}\right)$, $j=1,2,...,v-1$

b) $\lambda_n^0 l_j^{(n)}=\pi+O\left(\frac{1}{\lambda_n^0}\right)$, $j=1,2,...,v-1$

c) $\lambda_n^0 l_j^{(n)}=\left(j-\frac{1}{2}\right)\pi+O\left(\frac{1}{\lambda_n^0}\right)$, $j=1,2,...,v-1$

4. Proof of Theorem 2.4

Lemma 4.1. Let $Y(x,\lambda_n)$ be the fundamental matrix solution of equation (8), and let $v_n\in\mathbb{R}^d$ be a unit null vector in the kernel of $TP(\lambda_n)$ such that $y_n(x):=Y(x,\lambda_n)$ is an eigenfunction of (2) and (4) associated with eigenvalue λ_n and further assume that $y_n(x)$ is of type (CZ) with nodal set $\left\{x_k^{(n)}\right\}$. Then, as $n\to\infty$

a) For every fixed $x\in(0,\pi)$

$$\lim_{n\to\infty}\lambda_n^0\sum_{j:x_{j+1}^{(n)}\le x}\left(l_j^{(n)}-\frac{\pi}{\lambda_n^0}\right)=-\frac{1}{2}\int_0^x q(t)\,dt.$$

b) For almost every $x\in(0,\pi)$, one has

c) $\lim_{n\to\infty}\lambda_n^0\left(\lambda_n^0 l_{j(x,n)}^{(n)}-\pi\right)=-\frac{1}{2}\int_{x_{j(x,n)}^{(n)}}^{x_{j(x,n)+1}^{(n)}}q(t)\,dt.$

where $j(x,n)$ is the unique index satisfying $x\in\left(x_{j(x,n)}^{(n)},x_{j(x,n)+1}^{(n)}\right)$.

Proof of Theorem 2.4

Let $\left\{x_j^{(n)}\right\}$ be the nodal points of the eigenfunction corresponding to the eigenvalue λ_n and let $l_j^{(n)}=x_{j+1}^{(n)}-x_j^{(n)}$, $j=1,2,...,v-1$.denote the nodal lengths.

By Corollary 3.4(a), the nodal lengths admit the asymptotic representation (equation 10),

$$l_j^{(n)}=\frac{\pi}{\lambda_n^0}+O\left(\frac{1}{\left(\lambda_n^0\right)^2}\right)\qquad(10)$$

uniformly in j. Moreover, by Lemma 3.1(b), the deviation of $l_j^{(n)}$ from $\frac{\pi}{\lambda_n^0}$ satisfies

$$\lambda_n^0\left(\lambda_n^0 l_{j(x,n)}^{(n)}-\pi\right)=-\frac{1}{2}\int_{x_j^{(n)}}^{x_{j+1}^{(n)}}q(t)\,dt+o(1),n\to\infty.$$

Fix $x\in(0,\pi)$ and let $j=j(x,n)$ be the unique index such that $x\in\left(x_j^{(n)},x_{j+1}^{(n)}\right)$

Since $l_j^{(n)}\to 0$ as $n\to\infty$, the interval $\left(x_j^{(n)},x_{j+1}^{(n)}\right)$ shrinks to the point x.

Dividing the relation in (10) by $l_j^{(n)}$) and using the asymptotic formula for $l_j^{(n)}$, we obtain (equation 11),

$$\frac{1}{l_j^{(n)}}\int_{x_j^{(n)}}^{x_{j+1}^{(n)}} q(t)\,dt = -2\left(\lambda_n^0\right)^2\left(l_j^{(n)} - \frac{\pi}{\lambda_n^0}\right)o(1). \qquad (11)$$

Let x be a Lebesgue point of q. Then, by the Lebesgue differentiation theorem,

$$\lim_{n\to\infty}\frac{1}{l_j^{(n)}}\int_{x_j^{(n)}}^{x_{j+1}^{(n)}} q(t)\,dt = q(x).$$

Taking limits in the identity obtained in (11) yields

$$q(x) = -2\lim_{n\to\infty}\left(\lambda_n^0\right)^2\left(l_j^{(n)} - \frac{\pi}{\lambda_n^0}\right).$$

for almost every $x\in(0,\pi)$.

The right-hand side depends only on the nodal data $\left\{x_j^{(n)}\right\}$

Consequently, if two potentials generate the same nodal sets, they must coincide almost everywhere on $(0,\pi)$. This completes the proof.

Author Contributions

The percentages of the author' contributions are presented below. The author reviewed and approved the final version of the manuscript.

	Ö.D.
C	100
D	100
S	100
DCP	100
DAI	100
L	100
W	100
CR	100
SR	100
PM	100

C= concept, D= design, S= supervision, DCP= data collection and/or processing, DAI= data analysis and/or interpretation, L= literature search, W= writing, CR= critical review, SR= submission and revision, PM= project management.

Conflict of Interest

The authors declared that there is no conflict of interest.

Ethical Consideration

Ethics committee approval was not required for this study because of there was no study on animals or humans.

References

Agranovich, Z. S., and Marchenko, V. A. (1963). *The inverse problem of scattering theory*. Gordon and Breach.

Amirov, R., and Durak, S. (2024). Inverse nodal problems for singular diffusion equation. *Mathematical Methods in the Applied Sciences, 47*(11), 9067–9083.

Avdonin, S., and Ivanov, S. (1995). *Families of exponentials: The method of moments in controllability problems for distributed parameter systems*. Cambridge University Press.

Bondarenko, B. (2015). Inverse spectral problems for matrix Sturm–Liouville operators. *Inverse Problems, 31*, Article 035002.

Brown, M., and Weikard, R. (2000). A Borg–Levinson theorem for matrix-valued potentials. *Proceedings of the Royal Society of Edinburgh: Section A, Mathematics, 130*, 1–16.

Buterin, S. A. (2015). Inverse spectral problems for matrix Sturm–Liouville operators with transmission conditions. *Results in Mathematics, 68*, 195–212.

Carlson, R. (1998). Inverse spectral problems for Sturm–Liouville equations with discontinuities. *Journal of Mathematical Analysis and Applications, 217*, 144–167.

Carlson, R. (1999). Eigenvalue estimates for matrix Sturm–Liouville operators. *Journal of Differential Equations, 151*, 1–27.

Chen, G. (2002). Inverse nodal problems for Sturm–Liouville operators. *Journal of Mathematical Analysis and Applications, 271*, 143–156.

Durak, S. (2024). Inverse nodal problem for diffusion operator on a star graph with nonhomogeneous edges. *Journal of Inverse and Ill-Posed Problems, 32*(3), 485–496.

Gesztesy, F., and Simon, B. (1997). Inverse spectral analysis with partial information on the potential. I. The case of an a.c. component. *Helvetica Physica Acta, 70*, 66–71.

Gohberg, I. C., and Krein, M. G. (1970). *Theory and applications of Volterra operators in Hilbert space* (Vol. 24). American Mathematical Society.

Hald, J. (1989). Solutions of the inverse nodal problem. *Inverse Problems, 5*, 307–318.

Hochstadt, H., and Lieberman, B. (1978). An inverse Sturm–Liouville problem with mixed given data. *SIAM Journal on Applied Mathematics, 34*, 676–680.

Hryniv, R., and Mykytyuk, Y. (2003). Inverse spectral problems for Sturm–Liouville operators with singular potentials. *Inverse Problems, 19*, 665–684.

Kurasov, P. (1996). Distribution theory for discontinuous test functions and differential operators with generalized coefficients. *Journal of Mathematical Analysis and Applications, 201*, 297–323.

Levitan, B. M., and Sargsjan, I. S. (1991). *Sturm–Liouville and Dirac operators*. Kluwer Academic Publishers.

McLaughlin, J. R. (1988). Inverse spectral theory using nodal points as data. *Inverse Problems, 4*, 119–128.

Pivovarchik, V. (2000). Inverse problem for the Sturm–Liouville equation on a finite interval with transmission conditions. *Inverse Problems, 16*, 859–870.

Pöschel, J., and Trubowitz, E. (1987). *Inverse spectral theory*. Academic Press.

Rundell, W., and Sacks, P. (1992). Reconstruction techniques for classical inverse Sturm–Liouville problems. *Mathematics of Computation, 58*, 161–183.

Serier, F., and Zhou, Y. (2012). Inverse nodal problems for differential operators with eigenparameter dependent boundary conditions. *Journal of Mathematical Analysis and Applications, 395*, 654–666.

Shen, C. L. (1999). Smoothness of the potential function in inverse nodal problems. *Inverse Problems, 15*, 1265–1274.

Shen, C. L., and Shieh, C. T. (1999). On the multiplicity of eigenvalues of vectorial Sturm–Liouville problems. *Proceedings of the American Mathematical Society, 127*, 1183–1190.

Yang, C. F. (1997). A solution of the inverse nodal problem. *Inverse Problems, 13*, 203–213.

Yang, C. F. (1997). Inverse nodal problems of Sturm–Liouville operators. *Journal of Differential Equations, 134*, 215–234.

Yurko, M. (2002). *Method of spectral mappings in the inverse problem theory*. VSP.

Yurko, V. A. (2000). *Inverse spectral problems for differential operators and their applications*. Gordon and Breach.

Zayed, A. (2018). Inverse nodal problems for diffusion-type operators with interior singularities. *Boundary Value Problems, 2018*, 1–17.

Zettl, A. (2005). *Sturm–Liouville theory* (Vol. 121). American Mathematical Society.

Black Sea Journal of Engineering and Science
doi: 10.34248/bsengineering.1961043

Open Access Journal
e-ISSN: 2619 – 8991

Research Article
Volume 9 - Issue 5: 2427-2445 / September 2026

ECOLOGICAL EPIGENETICS: RESEARCH FRONTS, TAXONOMIC GAPS, AND A FIVE-YEAR FORECAST

Bekir KABASAKAL[1*]

[1]*Antalya Bilim University, Vocational School of Health Services, Çıplaklı, 07190 Döşemealtı, Antalya, Türkiye*

Abstract: Ecological epigenetics investigates the role of molecular modifications, including DNA methylation, in heritable phenotypic variation in natural populations, often arising in response to environmental conditions. Because such modifications can respond to environmental change within a single generation, the field has direct relevance for understanding adaptation, plasticity, and the persistence of populations under habitat alteration and climate change. However, bibliometric attention has focused predominantly on the biomedical side of epigenetics, particularly cancer and clinical applications, while the structure and trajectory of the ecological literature have not been mapped. In the present study, 962 records published between 2000 and April 2026 were identified in the Web of Science Core Collection after two-stage filtering and analysed with the bibliometrix R package, complemented by time-series forecasting and segmented-regression analysis. The literature expanded at a compound annual rate of 12.16%, with output decelerating after a structural break in approximately 2014. Plants dominated the corpus at 52.70%, whereas mammals, fish, birds, reptiles, amphibians, and the invertebrate groups remained under-represented relative to their ecological and conservation importance. Two-thirds of records could not be linked to a specific ecosystem, reflecting the field's strong laboratory orientation. Keyword co-occurrence networks organised the field around three macro-themes: namely a molecular-mechanism axis, an ecological-context axis, and a conservation-and-management axis. Multiple growth models converged on a marked slowdown in publication growth, consistent with approaching saturation rather than continued exponential expansion, projecting a near-flat output of roughly 52–54 records per year through 2030 (95% bounds widening to 14–89) and a model-averaged carrying capacity near 1,835 cumulative records. The taxonomic imbalance documented here reveals a structural gap in the field's coverage of biodiversity, with implications for conservation genetics and the design of future ecological-epigenetics research.

Keywords: Ecological epigenetics, Bibliometric analysis, Time-series forecast, Ensemble forecast, Publication saturation, Taxonomic gaps

***Corresponding author:** Antalya Bilim University, Vocational School of Health Services, Çıplaklı, 07190 Döşemealtı, Antalya, Türkiye
E mail: kabasakalbekir@gmail.com (B. KABASAKAL)
Bekir KABASAKAL https://orcid.org/0000-0001-8453-2255

Received: June 04, 2026
Accepted: August 11, 2026
Published: September 15, 2026

Cite as: Kabasakal, B. (2026). Ecological epigenetics: research fronts, taxonomic gaps, and a five-year forecast. *Black Sea Journal of Engineering and Science,* 9(5), 2427-2445.

1. Introduction

The central principle of epigenetics is that gene expression can shift without any change in the underlying DNA sequence (Waddington, 1942; Bird, 2007). These mechanisms operate by adding or removing chemical marks on the DNA or on the proteins that package it. Among the mechanisms involved, DNA methylation is the most extensively studied, both for its consistency across taxa and for its population-level informativeness (Jaenisch and Bird, 2003; Allis and Jenuwein, 2016). Methylation of CpG sites in promoters affects transcription-factor binding and gene expression (Jaenisch and Bird, 2003; Goldberg et al., 2007). Some modifications are reversible, allowing flexible responses to environmental stress, whereas others are transmitted across generations (Weaver et al., 2004; Jablonka and Raz, 2009; Verhoeven et al., 2010; Heard and Martienssen, 2014). Beyond DNA methylation, epigenetic regulation also includes histone modifications, chromatin remodelling, and RNA-mediated control (Berger et al., 2009; Allis and Jenuwein, 2016). Because these modifications regulate gene activity, their disruption contributes to many human diseases, particularly cancer. This medical relevance has made epigenetics a major focus of biomedical research (Mao et al., 2023; Zhong and Chen, 2025), and the resulting literature is dominated by clinical and disease-oriented studies.

Yet beyond their role in disease, these mechanisms are also important for ecology and evolution because they can generate heritable phenotypic variation independently of DNA sequence polymorphisms (Bonduriansky and Day, 2009; Verhoeven et al., 2016). Behavioural and morphological differences among individuals in natural populations are not solely attributable to genetic factors such as single-nucleotide polymorphisms. Epigenetic variation contributes an additional layer of phenotypic control (Bossdorf et al., 2008; Hu and Barrett, 2017; Richards et al., 2017). The evidence comes from multiple taxa and environments, and methodological frameworks now exist to guide such

This work is licensed (CC BY-NC 4.0) under Creative Commons Attribution 4.0 International License

work in wild vertebrates (Anastasiadi et al., 2021; Laine et al., 2023). In wild great tits (*Parus major*), a cross-foster and brood-size experiment linked early developmental conditions to nestling DNA methylation (Sepers et al., 2024). Urban and forest populations of the same species differ in methylation across European cities (Caizergues et al., 2022). Maternal hormone levels are linked to the offspring epigenome and specifically to offspring glucocorticoid-receptor methylation (Hukkanen et al., 2023). Marine systems show similar trends. Reef-building *Acropora* corals exhibit genotype-specific methylation plasticity across seasonal thermal regimes (Hackerott et al., 2023), and European sea bass (*Dicentrarchus labrax*) respond to salinity transfer with hypomethylation in osmoregulatory genes (Blondeau-Bidet et al., 2023). In bumble bees, methylation variation tracks environmental gradients, elevation, and thermal-niche breadth (Heraghty et al., 2024). In the loggerhead sea turtle (*Caretta caretta*), variability in nest temperature induces methylation signatures that impact hatchling fitness (Yen et al., 2024). Epigenetic variation is now recognised as an axis of adaptive potential in wild populations (Lamka et al., 2022), and the concept has been formalised under the term ecological epigenetics or "eco-epi" (Bossdorf et al., 2008). Invasive plant species, which often colonize new habitats from genetically depauperate founding populations, provide some of the strongest circumstantial evidence that epigenetic flexibility can compensate for reduced genetic diversity (Mounger et al., 2021). Across these systems, epigenetic variation can influence the capacity of organisms to adjust to environmental change, with direct consequences for fitness and adaptation.

Mapping a research field quantitatively is itself a methodological problem. The standard approach is bibliometric analysis, which treats publications, authors, institutions, and references as measurable units (Donthu et al., 2021). Science-mapping methods, implemented in tools such as the bibliometrix R package (Aria and Cuccurullo, 2017), reconstruct collaboration networks, co-citation clusters, and the thematic fronts of a discipline. For a young and rapidly expanding interdisciplinary area, this form of mapping informs research planning by exposing the growth trajectory, the balance of taxonomic and ecosystem coverage, and the geography of collaboration. The growth of the primary eco-epi literature has not been matched by a corresponding synthesis effort. Bibliometric analyses of the broader epigenetics field have concentrated almost entirely on biomedical applications. Zhong and Chen (2025) mapped 51,742 cancer-epigenetics articles published between 1985 and 2023 in the Web of Science Core Collection. Mao et al. (2023) reported 27,762 publications on cardiovascular epigenetics over two decades. Additional bibliometric reviews exist for type-2 diabetes methylation (Jiang et al., 2023), lipid metabolism (Liu et al., 2023), and eye diseases (Zhang et al., 2024). Ecological epigenetics has no equivalent. The broadest ecological synthesis to date, Lamka et al. (2022), identified only 206 manuscripts through April 2021, covering 184 species. Macartney et al. (2023) mapped the broader non-genetic inheritance evidence-synthesis literature, but their scope extended beyond epigenetics to include parental effects and cultural transmission, and laboratory rodent studies dominated the results.

To address this gap, the present study investigates the scope of the ecological epigenetics literature, including its taxonomic and ecosystem coverage. To the best of the author's knowledge, this is the first bibliometric synthesis devoted specifically to ecological epigenetics. It complements existing bibliometric studies of epigenetics, which are almost entirely clinical, by mapping the ecological literature itself and by adding a forecasting dimension absent from previous analyses. Such a map also has practical value, pointing future research effort and conservation applications toward the taxa and ecosystems where coverage is thinnest. For this purpose, 962 records published between 2000 and April 2026 were identified in the Web of Science Core Collection after two-stage filtering and analysed with four aims, namely (i) to describe the growth trajectory of ecological epigenetics and locate its breakpoint, (ii) to characterise the taxonomic, ecosystem, and geographic structure of the field, (iii) to map its intellectual clusters and emerging topics through co-citation and keyword co- occurrence networks, and (iv) to forecast future publication output using complementary growth and time-series models.

2. Materials and Methods

Three complementary approaches were followed, in line with the aims of the study. First, the bibliometric properties of the corpus were established, including annual output, source and country productivity, collaboration structure, and citation patterns. Second, the taxonomic and ecosystem coverage of the literature was characterised to identify which systems have received research attention and which remain under-studied (see also Supplementary Information). Third, the future development of the field was estimated through time-series forecasting and growth-curve modelling, projecting publication output over the next five years (see also Supplementary Methods S1).

2.1. Reporting Standard and Search Strategy

The study was reported in line with the PRISMA 2020 guideline, adapted to bibliometric retrievals (Page et al., 2021; Marzi et al., 2025). The Web of Science Core Collection (Clarivate Analytics) was searched on 28 February 2026, and again for partial-year completion on 27 April 2026, across all editions. The Core Collection was chosen as the sole data source because its selective journal indexing and standardized citation metadata (including the cited-reference and keyword fields on which the bibliometrix workflow depends) provide a curated, reproducible record structure, and because the

clinical epigenetics bibliometrics used as comparators here are likewise WoS-based, which keeps the cross-field comparisons directly comparable. The coverage limitations of this choice are addressed in Section 4.3. After document-type filtering, the analytical corpus derived predominantly from the Science Citation Index Expanded (SCI-EXPANDED), the Emerging Sources Citation Index (ESCI), and the Social Sciences Citation Index (SSCI). The Boolean topic-search query (TS field, which searches title, abstract, author keywords, and Keywords Plus concurrently) contained three blocks. Two theme blocks were linked by the AND operator, and a NOT block excluded clinical-pathology terms.

The initial review of the 2-block search (epigenetic mechanisms AND ecological framing, 1,318 records) revealed that the pre-filter source rank was dominated by biomedical-clinical venues (mainly Clinical Epigenetics) whose records lacked ecological framing yet ranked first by raw record count. This reflects lexical overlap between clinical and ecological epigenetics, because the same molecular-mechanism terminology (DNA methylation, histone modification, bisulfite sequencing) is used in both literatures even though the study goals differ. The search was refined into a three-block, precision-anchored query. The epigenetic-mechanism phrases were kept in block 1. Block 2 preserved ecological context phrases. A new NOT block, NOT TS=("clinical trial" OR "cancer" OR "tumour" OR "carcinoma" OR "oncolog" OR "cardiovascular" OR "patient"), was introduced to exclude clinical-pathology terms upon retrieval. This upstream exclusion lowered raw retrieval from 1,318 to 1,076 records (−18.4%), eliminating much of the biomedical drift at the search stage rather than depending only on the downstream Stage-2 content classifier. The impact of this exclusion and of the downstream two-stage filter on the source rankings is presented in Section 3.1.2 and Supplementary Table S1.

Document type was restricted to research articles (Web of Science Article document type), language to English, and publication year to 2000–2025 inclusive (the closed window over which the compound annual growth rate (CAGR) was computed). Records indexed for 2026 by the cut-off date were retained for figure rendering only and were excluded from the CAGR and forecast-training calculations.

2.2. Two-stage Filtration

The raw retrieval returned 1,076 entries for the precision-anchored query. The two-stage filter was implemented as deterministic R code in the pipeline rather than as manual screening, to ensure reproducibility and transparent re-execution.

Stage 1 (lexical filter, 1,076 to 1,030 records). Document-type filtering retained Web of Science research articles (document types “Article” and “Article; Proceedings Paper”, the latter denoting full-length symposium or special-issue papers published in indexed journals), and no Review-type records were present. Deduplication used case-folded DOI matching (six duplicate records removed), with records lacking a DOI retained. A light lexical filter was retained as a safeguard against clinical-oncology records lacking ecological framing. It removed none here, because such records had already been excluded by the Block-3 NOT operator. In total, 46 records (4.3% of the raw retrieval) were removed in Stage 1. The verbatim query and the full document-type and content-classification rules are provided in Supplementary Methods S2.

Stage 2 (content categorization filter, 1,030 to 962 records). Each record was allocated to one of seven categories by case-insensitive matching of curated keyword dictionaries against the abstract text, with categories assigned by a fixed priority order. To evaluate the reliability of the automatic categorization, two domain-expert coders independently categorized a stratified random sample of 100 records (50 kept and 50 removed by the pipeline) as RETAIN or EXCLUDE. Inter-rater agreement was computed using Cohen’s κ (Landis and Koch, 1977; Gamer et al., 2019). To assess sensitivity, specificity, accuracy, precision and F1, the pipeline output was compared with the consensus gold standard (records on which both coders agreed) (Supplementary Table S2). For the analytical corpus, records marked as ECOLOGICAL_STRONG, ECOLOGICAL_WEAK, MIXED or UNCLASSIFIED were included (n = 962). Records tagged BIOMEDICAL, BIOMEDICAL_LEAN or METHODOLOGICAL were eliminated at this stage (68 records, 6.6% of post-Stage-1 records). The screening cascade is summarised in Figure 1.

2.3. Software Environment and Reproducibility

Calculations were performed with R 4.5.3 (R Core Team, 2025; Vienna, Austria). The following packages were used for bibliometric and statistical analyses, with version numbers pinned at runtime: bibliometrix v5.3.0 (Aria and Cuccurullo, 2017), forecast v9.0.2 (Hyndman et al., 2002; Hyndman and Khandakar, 2008), igraph v2.2.3 (Csárdi and Nepusz, 2006), segmented v2.2-1 (Muggeo, 2003) for breakpoint regression and significance testing, irr v0.84.1 (Gamer et al., 2019) for inter-rater reliability, tseries v0.10-61 (Trapletti and Hornik, 2024) for unit-root testing, Matrix v1.7.4 (Bates et al., 2025) for sparse matrix algebra. Figures were produced using ggplot2 v4.0.3 (Wickham, 2016), ggalluvial (Brunson, 2020), patchwork (Pedersen, 2024), ggrepel (Slowikowski, 2024), scales (Wickham et al., 2024) and viridis (Garnier et al., 2024). Colour scales were selected to be perceptually uniform and safe for colour-vision deficiency (Crameri et al., 2020). Data manipulations were performed using dplyr v1.2.1, tidyr, stringr, tibble and purrr (Wickham et al., 2019). Further, openxlsx (Schauberger and Walker, 2024) was used for multi-sheet Excel output, qs2 v0.2.0 (Ching, 2024) for checkpoint serialization, and conflicted (Wickham, 2023) for namespace conflict resolution.

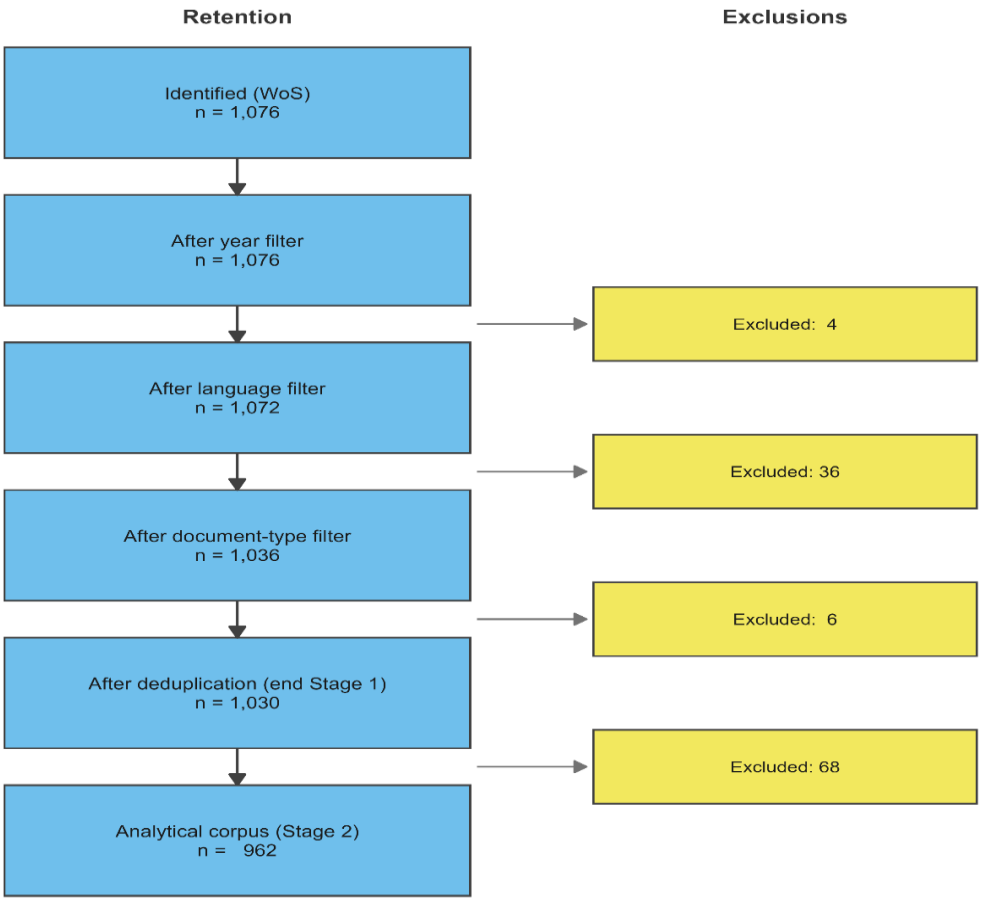


Figure 1. PRISMA 2020 flow diagram for the bibliometric retrieval and two-stage filtering process. The left column shows the retention chain from raw Web of Science retrieval (1,076 records) through the Stage-1 lexical filter, comprising year, language, document-type, and deduplication screening (1,076 to 1,030 records), to Stage-2 content classification (1,030 to 962 records). The right column shows the records excluded at each step (4 by language, 36 by document type, 6 by deduplication, and 68 by Stage-2 content classification). PRISMA = Preferred Reporting Items for Systematic Reviews and Meta-Analyses.

2.4. Bibliometric Analysis

Metrics used were yearly production, source productivity (Bradford's law), and country production (whole-counting per record). Science mapping was carried out using co-citation, co-word, and co-authorship analysis (Aria and Cuccurullo, 2017; Donthu et al., 2021). The DE field (author keywords) was used for keyword co-occurrence, while the ID field (Keywords Plus) was retained for descriptive counts only (Table 1). The obtained weighted graph was processed using Walktrap community detection, with the Louvain algorithm computed in parallel for comparison, and the Walktrap partition was retained (the two community-modularity values are reported in Section 3.1.5). The adopted bibliometric workflow has been applied in domains as diverse as nuclear science (Özdoğan et al., 2025), diffuse optical tomography (Üncü et al., 2025), the relationship between diabetes and myricetin (Özcan et al., 2025), and machine-learning applications in aquaculture (Çakır et al., 2025), supporting its applicability to interdisciplinary literature with heterogeneous source profiles. Taxonomic and ecosystem coverage was classified with curated keyword dictionaries following the Stage-2 procedure (Section 2.2). As robustness checks, the taxonomic classification was repeated with an expanded dictionary and 50 randomly sampled ecosystem-unspecified records were manually inspected (Section 3.1.6).

Lotka's law was manually fitted by log-log linear regression using base-R lm(), because the native bibliometrix::lotka() function returned NULL under bibliometrix v5.3.0. Goodness-of-fit was assessed by R^2. The Kolmogorov–Smirnov test for power-law distributions (Clauset et al., 2009) was not applied because the fitted productivity distribution contained only 16 points, which is below the minimum recommended for robust KS inference. The log-log ordinary-least-squares exponent is the conventional bibliometric estimator but is biased relative to the maximum-likelihood estimator recommended by Clauset et al. (2009), and R^2 quantifies linear fit on the log-log scale rather than testing power-law form. The exponent β is therefore interpreted as a descriptive concentration index rather than as a distributional test result.

Table 1. Main bibliometric information about the dataset (after two-stage filtering). CAGR was computed on the closed window 2000–2025, and the partial-year 2026 records were excluded from the CAGR but retained for figure rendering

Metric	Value
Timespan	2000–April 2026
Sources (journals)	315
Documents	962
Annual growth rate (CAGR)	12.16%
Total references	71,891
Author keywords (DE)	2,031
Keywords Plus (ID)	2,709
Authors	4,583
Authors per document (mean)	6.22
International co-authorships (%)	40.4%
Pre-break CAGR (2000–2014)	23.43%
Post-break CAGR (2014–2025)	1.04%

2.5. Country-collaboration Network and Small-worldness

A multinational collaboration network was constructed from the co-authorship edges of the corpus. The global clustering coefficient C (the ratio of closed triplets to connected triplets, calculated using igraph::transitivity(type = "global")) and the characteristic path length L were calculated and compared with matched Erdős–Rényi (ER) random graphs (1,000 samples). Following Humphries and Gurney (2008), the small-world property was expressed as (equation 1),

$$\sigma = (C/C_{rand}) / (L/L_{rand}) \quad (1)$$

with $\sigma > 1$ indicating small-world topology under the clustering-coefficient normalization variant. As a robustness check, the Telesford omega metric (Telesford et al., 2011) was also computed as (equation 2),

$$\omega = \frac{L_{rand}}{L_{obs}} - \frac{C_{obs}}{C_{lattice}} \quad (2)$$

where $C_{lattice}$ is the clustering coefficient of a ring lattice with the same number of nodes and average degree. Unlike σ, ω is bounded on (−1, +1), and values close to 0 indicate small-world topology (Telesford et al., 2011). C_{rand} and L_{rand} were computed from median values over 1,000 random reference graphs. The characteristic path length was computed on the unweighted network topology, matching the unweighted random and lattice references, as required for the Humphries–Gurney σ and Telesford ω normalization.

2.6. Time-series Forecasting

Six complementary univariate models were used to explore the corpus trajectory after 2025, selected to represent the trend-detection, state-space, decomposition, deceleration, benchmark, and ensemble model families documented in the M3 and M4 forecasting competitions (Assimakopoulos and Nikolopoulos, 2000; Makridakis and Hibon, 2000; Makridakis et al., 2020). In brief, the autoregressive integrated moving average (ARIMA) model was used because differencing accommodates the trend-loss structure of a short non-stationary count series. The exponential smoothing state-space model (ETS) was included because it represents level, trend, and damping explicitly and is robust on short annual series. The Theta method was added because it was the best-performing simple method of the M3 competition and, being equivalent to simple exponential smoothing (SES) with drift, supplies an upper-bound counterfactual. The equal-weight ensemble of these models follows the consistent M4 finding that forecast combinations outperform their individual members. The annual count series (2000–2025, n = 26) was modelled as follows.

Unit-root diagnostics. Prior to model fitting, the annual publication count series was tested for stationarity using the augmented Dickey–Fuller (ADF) test (Dickey and Fuller, 1979; Said and Dickey, 1984) and the Kwiatkowski–Phillips–Schmidt–Shin (KPSS) test (Kwiatkowski et al., 1992). The ADF test evaluates the null hypothesis of a unit root (non-stationarity), whereas the KPSS test evaluates the null of stationarity. Together, the two tests provide a confirmatory diagnostic pair.

ARIMA. ARIMA was fitted via forecast::auto.arima() with stepwise = FALSE and approximation = FALSE, using AICc for order selection (Hyndman and Khandakar, 2008).

ETS. ETS was fitted via forecast::ets() with AICc selection (Hyndman et al., 2002).

Theta method. The Theta method was fitted via forecast::thetaf() (Assimakopoulos and Nikolopoulos, 2000; Hyndman and Billah, 2003). Because drift relies on the full historical slope, the Theta trajectory is interpreted as an upper-bound counterfactual.

Damped-trend ETS. Damped-trend ETS was forced with model = "AAN" and damped = TRUE as a deceleration benchmark (Fildes et al., 2008).

Naïve benchmark. A naïve forecast was included as a performance baseline (Hyndman and Athanasopoulos, 2021).

Four-way Ensemble. The four model forecasts were averaged with equal weights (Wang et al., 2023). A legacy two-way Combination (ARIMA + ETS) was retained for comparability. The Ensemble was the headline forecast (Makridakis et al., 2020).

Segmented regression. The production breakpoint was dated via Muggeo's iterative linearization (Muggeo, 2003), with significance assessed by the Davies test (Davies, 1987) and the Muggeo score test (Muggeo, 2016).

Saturation models. Logistic (Tsoularis and Wallace, 2002) and Gompertz (Tjørve and Tjørve, 2017) saturation curves were fitted by NLS to cumulative annual counts (Tattershall et al., 2021), with AICc-weighted model averaging following Burnham and Anderson (2002).

Mathematical formulations for all six models, segmented

regression, and saturation diagnostics are provided in Supplementary Methods S1. The forecast pipeline workflow is visualized in Figure S1.

Out-of-sample accuracy was evaluated by rolling-origin cross-validation (initial = 15, h = 5; Bergmeir et al., 2018). Root mean squared error (RMSE) and mean absolute scaled error (MASE) are reported for all models (Hyndman and Koehler, 2006).

2.7. Statistical Reporting and Inference Framework

No power analysis was performed a priori, as the study analyses a single time series rather than testing an effect-size hypothesis. Inference precision is directly addressed through 95% confidence intervals, the segmented breakpoint via parametric bootstrap (1,000 resamples) and the saturation carrying capacity via NLS standard errors with model-averaging variance inflation (Burnham and Anderson, 2002). Bootstrap 95% confidence intervals were similarly attached to the descriptive statistics (CAGR, Gini coefficient, Lotka β), residual diagnostics (Ljung-Box, Shapiro-Wilk) accompanied forecasting-model selection, and a two-breakpoint specification was assessed as a BIC sensitivity check. A multiple testing correction was not applied across the six forecasting models since they were not tested against a common null hypothesis but rather compared for relative ranking by out-of-sample MASE. The two breakpoint significance tests, Davies (1987) and the Muggeo score test (Muggeo, 2016), evaluate the same null (no breakpoint) on the same series, so their joint use strengthens rather than inflates the inferential claim. For the single Cohen's κ estimate of inter-rater reliability (Table S2), 95% confidence intervals are reported without Bonferroni correction. Two confirmatory tests supported the coverage analysis. The publication-level plant share was compared with the 42.4% species-level proportion reported by Lamka et al. (2022) using a two-proportion test, which accounts for the sampling uncertainty of the published benchmark. Because the two proportions are measured over different units (publications versus species), the comparison is indicative rather than a strict equivalence test. The temporal change in the proportion of records lacking ecosystem context was assessed with the Cochran-Armitage test for trend across the annual series, with the per-year odds change estimated by logistic regression as an effect size. All tests used base R (R Core Team, 2025), and effect sizes are reported with 95% confidence intervals.

3. Results

3.1. Bibliometric Results

3.1.1. Corpus characteristics

The analytical corpus comprised 962 documents produced between 2000 and April 2026, from 315 sources, 4,583 distinct authors, and an average of 6.22 authors per document (Table 1). Annual output increased from a few records in the early 2000s to a peak of 86 records in 2022, declining to 56 by 2025, and the CAGR over the closed window 2000–2025 was 12.16% (bootstrap 95% CI 8.4–19.5%). A total of 71,891 references were retrieved, and 40.4% of the papers were internationally co-authored. Figure 1 shows the screening cascade from the raw 1,076 records to the analytical 962. Inter-rater reliability of the Stage-2 content classifier was examined on a stratified random sample of 100 records. The Cohen's κ for the two independent coders was 0.855 (95% CI 0.742–0.967; $P < 0.0001$), which indicates almost perfect agreement according to the Landis and Koch (1977) scale. The pipeline classifier showed a sensitivity of 0.618 (95% CI 0.499–0.724), specificity of 0.808 (95% CI 0.621–0.915), precision of 0.894 (95% CI 0.774–0.954), accuracy of 0.670 (95% CI 0.570–0.757) and F1 of 0.730 against the consensus gold standard (94 consensus pairs) (Supplementary Table S2). Because the validation sample was balanced by pipeline decision (50 retained, 50 removed), precision and F1 are conditional on that design. Sensitivity and specificity condition on the true class and are prevalence-robust, whereas precision, F1 and Cohen's kappa depend on the class composition of the sample. The high precision indicates that records retained as ecological were, in the vast majority of cases, correctly classified. The moderate sensitivity shows systematic undercounting, so the corpus of 962 documents is a conservative lower-bound estimate.

3.1.2. Source productivity and rank stability

The top-15 sources are listed in Table S3. The journal with the most documents was Molecular Ecology (45), followed by Ecology and Evolution (27), PLOS ONE (25), PNAS (25), and PLOS Genetics (24). Sources orientated towards ecology and evolution dominate the post-filter source landscape. The largest single re-ranking in the dataset occurred for Clinical Epigenetics, which dropped from its top position in the prior 2-block search to rank 54, with 4 documents in the final corpus. In the 1,076-record raw retrieval it had ranked 46 with 5 documents. Clinical-epigenetics records were excluded by the Block-3 NOT operator at retrieval (1,318 to 1,076 records), by Stage-1 technical exclusions (46 records), and by the Stage-2 content classifier (68 records) (Sections 2.1–2.2; Supplementary Methods S2.4). Source-productivity concentration was further characterised using Bradford's law (Figure S2) and the Lorenz curve (Figure S3). Bradford's law divided the 315 sources into three zones. The ten most productive journals accounted for 236 records (24.5% of the corpus) and the fifteen most productive for 299 records (31.1%), so one third of cumulative output is reached only beyond the fifteenth source. Recomputed from the full 315-source distribution, the equal-thirds Bradford zones comprised 17, 57, and 241 sources (321 records in Zone 1, 33.4% of the corpus), corresponding to a zone multiplier of approximately $1:3.4:14.2$, flatter than the canonical $1:n:n^2$ pattern. The Gini coefficient of the source-productivity inequality was $G = 0.540$ (bootstrap 95% CI 0.488–0.585), indicating a relatively high concentration.

3.1.3. Author productivity and Lotka's law

Lotka's law was fitted by manual log–log regression on 16 distinct productivity classes (Figure S4). The empirical Lotka exponent was β = 2.89 (bootstrap 95% CI 2.19–3.39) with an R^2 of 0.894 on the log–log scale, a steeper-than-canonical concentration relative to the β ≈ 2 reference value. Author timelines are given in Figure S5. The most-cited papers within the corpus are reported in Figure S6 and Table S4, with the highest local citation score being LCS = 154 (Bossdorf et al., 2008). The co-citation structure of the most-cited references is shown in Figure S7, a network of the top 30 references linked by 432 co-citation edges. The dominant hub was Bossdorf et al. (2008) (LCS = 154). This network revealed the same three-axis intellectual structure as the keyword co-occurrence analysis (Section 3.1.5).

3.1.4. Geographic distribution and collaboration topology

Country production was extracted from the AU_CO field (Figure 2, Panel A). The top contributing countries were the United States (n = 234 country-attributions), China (n = 165), Germany (n = 57), Spain (n = 50), and France (n = 47), with the full country ranking shown in Table S5. International co-authorship reached 40.4% of records. The observed clustering coefficient (Figure 2, Panel B) was C = 0.461, against a median random-graph expectation of C_{rand} = 0.178 (1,000 random reference graphs). The observed average path length was L = 1.95, versus the random-graph median of L_{rand} = 1.95. The Humphries–Gurney small-world coefficient, computed from unrounded clustering and path-length values, was σ = 2.588 (95% CI 2.304–2.923 across the 1,000 random reference graphs, all of which yielded σ > 1), well above the canonical small-world threshold (Humphries and Gurney, 2008). The Telesford omega (ω = 0.307; 95% CI 0.298–0.316) places the network in the small-world range but shifted toward the random end (Telesford et al., 2011). This pattern reflects path lengths having reached the random-graph floor (L_{obs} = L_{rand} = 1.95), so the small-world signature is driven entirely by the clustering surplus rather than short path lengths. The network is globally efficient for information transfer.

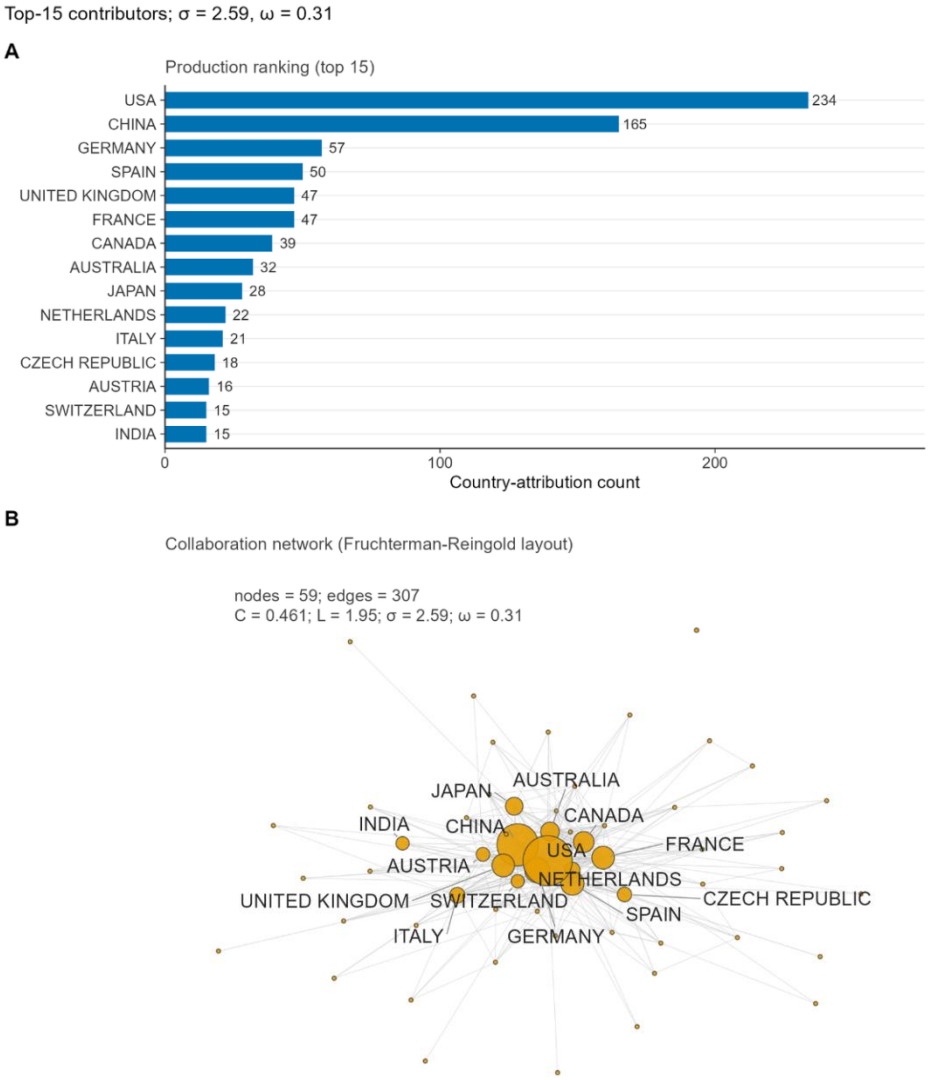


Figure 2. Country production and collaboration topology. (A) Top-15 countries by document count (whole-counting per record). (B) Country-collaboration network rendered with the Fruchterman–Reingold layout. Node size scales with document count and edge thickness with co-authorship frequency, and the top-15 countries are labelled.

3.1.5. Conceptual structure and thematic evolution

Figure 3A presents the Callon-style thematic map plotting cluster centrality against density, derived from author-keyword co-occurrence with Walktrap community detection on the top-50 nodes by occurrence. The thematic map identified 19 clusters. The full keyword network yielded 137 Walktrap communities (modularity = 0.259) and 25 Louvain communities (modularity = 0.325), and Walktrap was selected for the thematic map to preserve fine-grained conceptual structure. Across the full corpus, the keyword landscape organised around three macro-themes, namely (i) the molecular-mechanism axis (DNA methylation, histone modification, MS-AFLP, bisulfite sequencing), (ii) the ecological-context axis (transgenerational plasticity, common garden, reciprocal transplant, local adaptation), and (iii) the conservation-and-management axis (invasive species, climate adaptation, range expansion). The underlying keyword co-occurrence network is shown in Figure S8, where node size encodes degree centrality and node colour encodes Walktrap community membership, and the top-15 keywords by betweenness centrality are labelled. Keyword cumulative growth across the study period is given in Figure S9. The three-field Sankey plot linking authors, keywords, and sources is shown in Figure S10. Thematic evolution between time slices is demonstrated in Figure 3B.

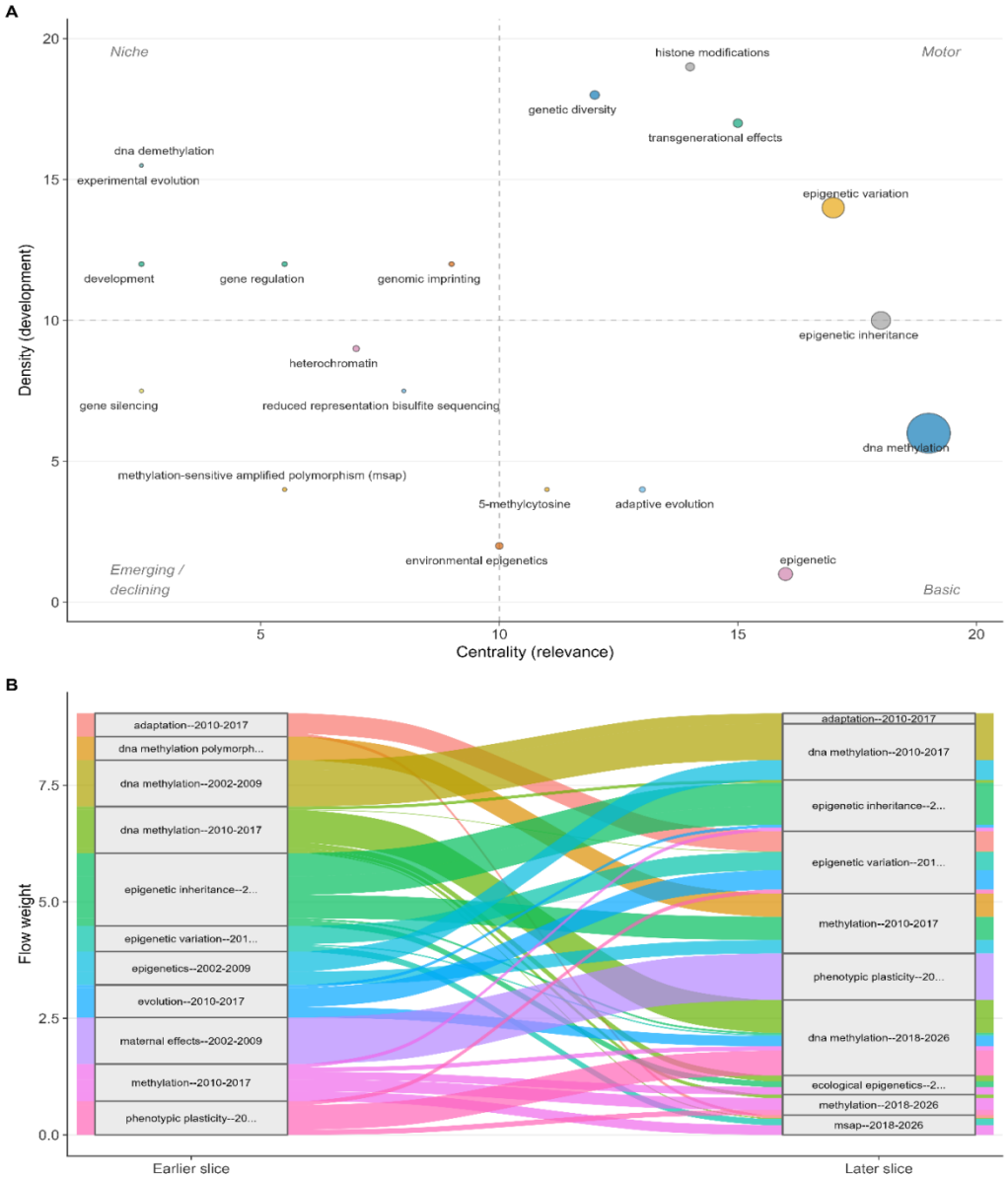


Figure 3. Conceptual structure. (A) Callon-style thematic map of author-keyword co-occurrence. Nineteen clusters are shown. Cluster centrality (x-axis) reflects relevance to the field, and cluster density (y-axis) reflects internal cohesion. Bubble size encodes within-cluster keyword frequency. The four quadrants are Motor (high centrality, high density), Niche (low centrality, high density), Basic (high centrality, low density), and Emerging/declining (low centrality, low density). Top-3 keywords per cluster are labelled. (B) Thematic evolution across three time slices (2000–2009, 2010–2017, 2018–2026). Alluvial flow width is proportional to inclusion-weighted connection strength between source and target keyword clusters.

3.1.6. Taxonomic and ecosystem coverage

Plants accounted for over half of all records (52.70%), followed by mammals (13.83%), invertebrates (10.29%), fish (4.47%), and birds (2.29%). The remaining groups each fell below 2%, namely fungi (1.98%), microorganisms (0.62%), and reptiles and amphibians (0.42% each, 0.84% combined) (Table S6, Figure 4 Panel A). The residual 12.99% labelled "Unspecified" reflects records spanning multiple taxa, *in vitro* / cell-line work without organismal context, or studies whose abstracts identified the focal taxon at a more specific level outside the conservative taxonomic dictionary. Conservation-relevant vertebrate groups (birds, reptiles, amphibians) collectively constituted 3.12% of the corpus, indicating persistent under-representation. The publication-level plant share (52.70%) exceeds the 42.4% species-level proportion reported by Lamka et al. (2022) across 184 unique species. This publication-level excess over the species-level baseline remained significant when the sampling uncertainty of the published benchmark was taken into account (two-proportion test, 507/962 versus 78/184; P = 0.013; difference 2.2–18.4 percentage points, 95% CI).

Ecosystem coverage was substantially less complete and 66.63% of records were not assignable to a specific ecosystem under the keyword dictionary (Table S7a, Figure 4 Panel B). Manual classification of all 641 Unspecified records (Table S7b), corroborated by an initial random inspection of 50 of them, showed that the category consists mainly of laboratory-based mechanistic studies, meta-analyses covering multiple ecosystems, and methodological papers. The high Unspecified proportion therefore reflects the field's limited engagement with field-based ecosystem ecology rather than a failure of the classification dictionary. Unspecified records comprised taxon-specific studies (39.0%), model organisms (29.3%), review-style syntheses (9.2%), methodological papers (6.4%), theoretical studies (5.9%), truly unclassifiable records (5.6%), and laboratory experiments (4.5%; Table S7b). The review-style category is a content-level label for Article-type records with survey character. Consistent with the Stage-1 document-type filter (Section 2.2), no WoS Review-type documents were present in the corpus. The proportion of records lacking ecosystem context declined from approximately 84% in 2008–2012 to 63% in 2023–2025 (Cochran-Armitage trend test, chi-square = 27.4, df = 1, P < 0.001; logistic-trend odds ratio 0.924 per year (95% CI 0.896–0.952), a 7.6% annual reduction), suggesting a slow transition from laboratory-centric mechanistic work to field-based ecosystem studies. Agricultural systems were the most frequent within the classified data (9.25% of the total corpus), followed by marine (8.21%), terrestrial (6.76%), freshwater (6.76%) and a residual general-habitat class (2.39%).

3.2. Forecasting Results

3.2.1. Model selection and breakpoint detection

Two unit-root tests indicated non-stationarity. The ADF test failed to reject the unit-root null ($\tau = -1.225$, P = 0.868), while the KPSS test rejected the stationarity null (statistic = 0.890, P < 0.01). This justified first-order differencing (d = 1) in the ARIMA specification. Ljung-Box tests indicated that the ARIMA(0,1,2) residuals were consistent with white noise ($\chi^2 = 1.01$, df = 5, P = 0.962), supporting the model specification (Figure 5B). ETS(A,N,N) residuals showed marginal autocorrelation ($\chi^2 = 11.50$, df = 5, P = 0.042), indicating that the level-only model does not fully capture the serial-dependence structure. Full residual diagnostics are presented in Figure S11. Both models' residuals were normally distributed (Shapiro-Wilk P= 0.611 for ARIMA and P= 0.842 for ETS). The auto.arima() exhaustive search selected ARIMA(0,1,2) without drift and, ets() selected ETS(A,N,N) without a trend component (Table 2). Both selections represent the loss of the trend/drift terms that had been present under a slightly larger corpus (n = 969, prior two-block query), where ARIMA(1,1,0)+drift and ETS(A,A,N) were selected. This concurrent loss of trend signals from two independent model families is in line with the series having plateaued after approximately 2014.

Segmented regression on log-transformed annual production identified a structural breakpoint at $\hat{\psi}$ = 2013.6 (95% CI 2010.7–2016.4; Table S8). The pre-break log-slope was 0.2957 and the post-break log-slope was 0.0191, and the observed CAGRs over the two phases were 23.43% (2000–2014) and 1.04% (2014–2025). This represents a 15.5-fold deceleration on the log-slope scale (0.2957/0.0191) and a 22.5-fold deceleration in CAGR terms (23.43/1.04). Both the Davies test (P < 0.0001, k = 10) and the Muggeo score test (P < 0.0001) confirmed that the breakpoint is statistically distinguishable from a single straight line at conventional thresholds. A two-breakpoint model (npsi = 2) was also tested as a sensitivity check. BIC favoured the single-breakpoint specification ($BIC_1 = 19.48$ vs $BIC_2 = 23.43$, $\Delta BIC = 3.95$), so the two-breakpoint model is not pursued. The candidate second breakpoint at 2022.0 may reflect pandemic-related disruption but is not supported by parsimony on the present series length.

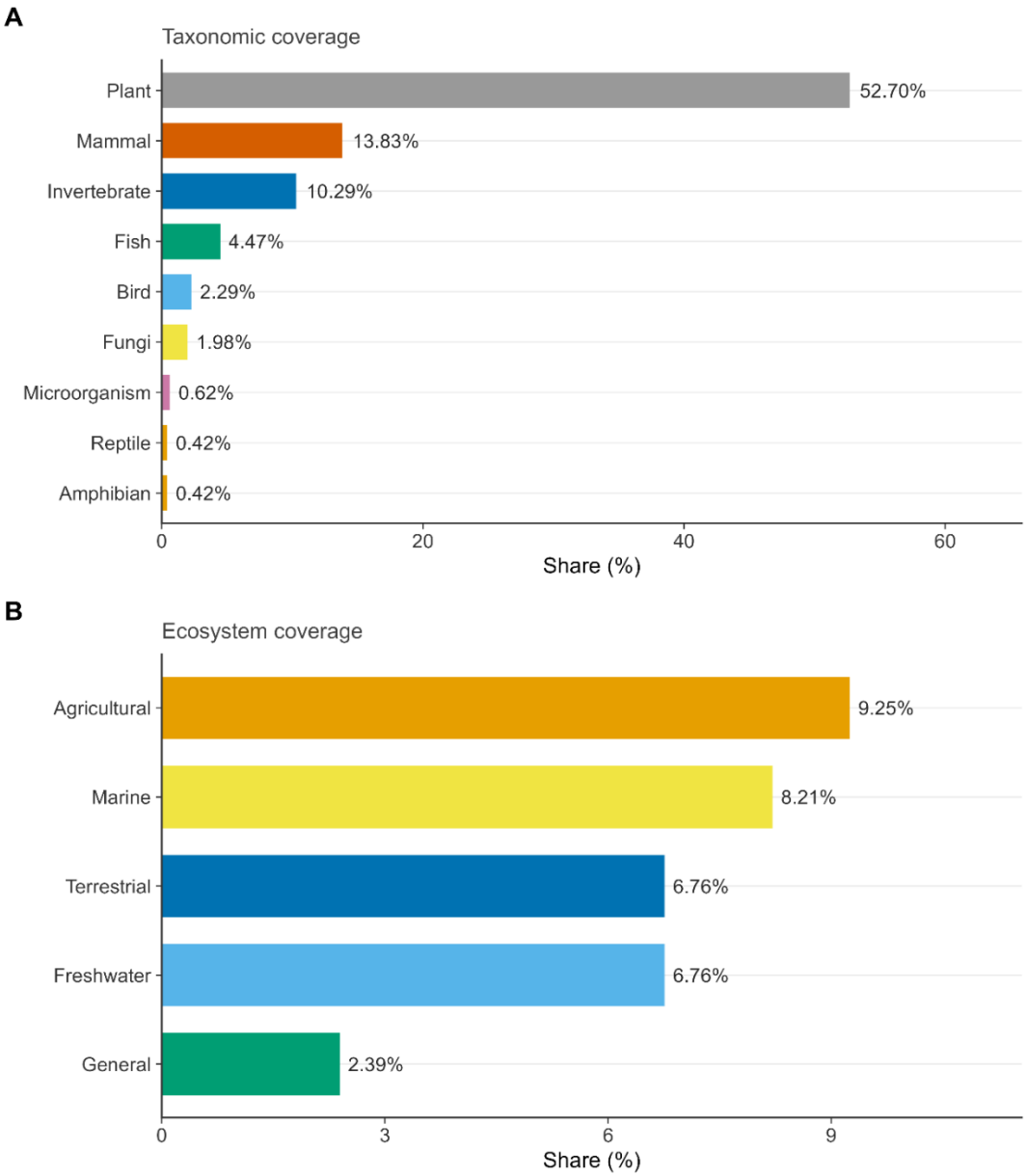


Figure 4. Taxonomic and ecosystem coverage of the analytical corpus. (A) Taxonomic coverage of the analytical corpus (n = 962). Plants dominate (52.70%), followed by mammals (13.83%) and invertebrates (10.29%). Birds, reptiles and amphibians together account for 3.12%. (B) Ecosystem coverage. Among classified records, agricultural and marine were the leading categories. Per-category values are in Tables S6 and S7a. "Unspecified" records were excluded from bars for visual clarity.

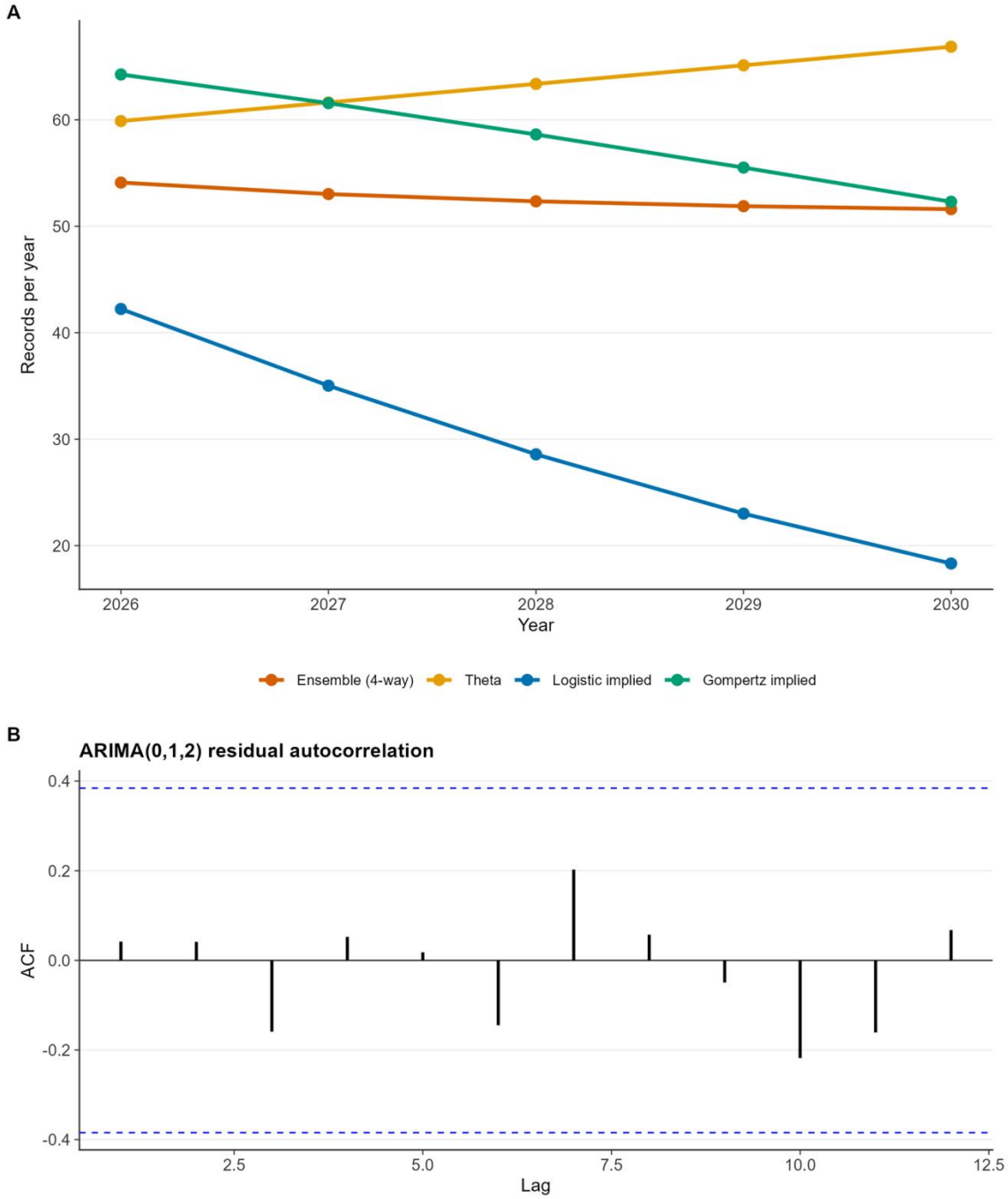


Figure 5. Forecast validation. (A) Forecast divergence across four scenarios for 2026–2030. Ensemble = four-way equal-weight average of ARIMA, ETS, Theta, and Damped-ETS; Theta = simple exponential smoothing (SES) with drift equal to half the ordinary least squares (OLS) slope; ARIMA = autoregressive integrated moving average; ETS = exponential smoothing state-space model; Logistic and Gompertz implied = annual increments from the respective saturation models. (B) ARIMA(0,1,2) residual autocorrelation function. ashed blue lines show the 95% confidence bounds.

Table 2. Forecast accuracy on the 2000–2025 series (in-sample fit and rolling-origin cross-validation). MASE is scaled to the in-sample naïve benchmark and is dimensionless

Model	In-RMSE	In-MASE	OOS-RMSE	OOS-MAE	OOS-MASE (h=1)	OOS-MASE (h=5)
ARIMA (0,1,2)	7.294	0.769	13.291	10.066	1.414	2.512
ETS (A,N,N)	9.145	0.959	13.796	13.001	1.826	2.645
Theta	n.a.	n.a.	13.367	11.702	1.643	2.095
ETS (A,Ad,N)	8.245	0.900	13.333	12.592	1.768	2.473
Naïve (LOCF)	n.a.	1.000	13.642	11.300	1.587	2.364
Combination (50/50)	n.a.	n.a.	13.002	11.534	1.620	2.426
Ensemble (4-way)	n.a.	n.a.	12.861	11.835	1.662	2.095

n.a. indicates that the metric is not applicable for that model type. Out-of-sample RMSE, MAE, and the OOS-MASE (h=1) column report the one-step horizon, while the added OOS-MASE (h=5) column reports the five-step, manuscript-aligned horizon. RMSE= root mean squared error; MASE= mean absolute scaled error; LOCF= last observation carried forward.

3.2.2. Six-model forecasts and out-of-sample validation

The Ensemble projected a flat trajectory for 2026–2030 (54, 53, 52, 52, and 52 records per year), with 95% bounds widening from 36–72 to 14–89 (Figure 6A; Table S9). Only the Theta method projected growth (60–67 records). At h = 5, the Ensemble and Theta tied for best out-of-sample MASE (2.095), outperforming the Naïve benchmark (2.364). ARIMA showed the strongest horizon sensitivity, ranking best at h = 1 (1.414) but degrading to second worst at h = 5 (2.512), ahead of only ETS(A,N,N) (2.645; Table 2). All MASE values were > 1, indicating that the projections should be read as bounded scenarios (Hyndman and Koehler, 2006). On robustness grounds, the Ensemble was retained as the headline projection (Makridakis et al., 2020; Wang et al., 2023).

3.2.3. Saturation diagnostics

The Logistic fit estimated a carrying capacity K_{log} = 1,145 cumulative records, and the Gompertz fit estimated K_{gom} = 1,835 cumulative records. With the observed cumulative count at 962, the corpus is between 52% (Gompertz) and 84% (Logistic) of its estimated asymptote. Following Tattershall et al. (2021), K_{gom} = 1,835 is treated as the primary saturation anchor and K_{log} = 1,145 as a lower-bound sensitivity estimate. The Gompertz and Logistic fits to the cumulative publication count are shown in Figure 6C. AICc model averaging yielded K_{avg} = 1,835 (95% CI 1,729–1,941; Gompertz w > 0.999). The ΔAICc of 37.8 far exceeds the threshold of 10 above which a competing model retains essentially no empirical support (Burnham and Anderson, 2002), corresponding to a Gompertz-to-Logistic evidence ratio of approximately 1.5×10^8. This weight difference is consistent with Tattershall et al. (2021), who demonstrated across 200 scientometric trends that scientific topics follow an asymmetric (steep-rise, long-tail) trajectory that the symmetric Logistic sigmoid cannot capture. Figure 5A visualises the four-way divergence among the Ensemble, Theta, and the annual increments implied by the two saturation curves.

3.2.4. Convergent evidence for approaching publication saturation

Four indicators from distinct model families (ARIMA drift loss, ETS trend loss, the segmented post-break slope of approximately 1.04% per year, and finite carrying capacities from both saturation models) converge on a marked slowdown in publication growth since approximately 2014, consistent with approaching publication saturation. The breakpoint year, the segmented slopes, and the Davies and score test P-values are reported in Table S8, and the piecewise-linear fit is shown in Figure 6B.

4. Discussion

4.1. Bibliometric Findings

4.1.1. Intellectual partitioning and the residual biomedical drift

The post-filter source profile is anchored in ecology- and evolution-oriented venues rather than biomedical channels. However, Clinical Epigenetics still appears in the final corpus (Section 3.1.2), indicating residual biomedical drift in venue choice, although it no longer dominates the source ranking. A small but persistent fraction of ecologically framed work continues to appear in biomedical-clinical sources, with consequences for indexing visibility, peer-reviewer pool composition, and downstream synthesis. In cross-disciplinary domains with biological lexical overlap, upstream Boolean exclusion is preferable to post-hoc filtering. The disparity in size between the ecological and biomedical epigenetics literatures is substantial. Zhong and Chen (2025) identified 51,742 cancer epigenetics papers (1985–2023). Against the current corpus of 962 ecological records, this gives a ratio of about 54:1. The Macartney et al. (2023) evidence map of non-genetic inheritance, dominated by laboratory rodent studies, shows a complementary pattern. With the NOT-clinical filter applied, plants rather than rodents take the dominant position, indicating that the ecological and biomedical literatures are structured by different model-organism traditions. Source-productivity concentration is relatively

high (Gini = 0.540; Figure S3), with a small core of journals accounting for a disproportionate share of the field's output. This trend is reflected in the Bradford rank-frequency profile (Figure S2), where a compact Zone 1 of 17 highly productive sources is followed by a large tail of single- and double-document venues. The co-citation reference core (Figure S7) was anchored on Bossdorf et al. (2008) (Section 3.1.3). At the author level, the steep Lotka exponent (β = 2.89) parallels this concentration, with output dominated by a small core of prolific authors. In the thematic map (Figure 3A), the emerging-or-declining quadrant is occupied mainly by legacy method terms (methylation-sensitive amplified polymorphism, reduced-representation bisulfite sequencing) and older molecular themes (heterochromatin, gene silencing), indicating methodological turnover rather than new conceptual fronts, while the motor quadrant (epigenetic variation, epigenetic inheritance, transgenerational effects) consolidates the field's core.

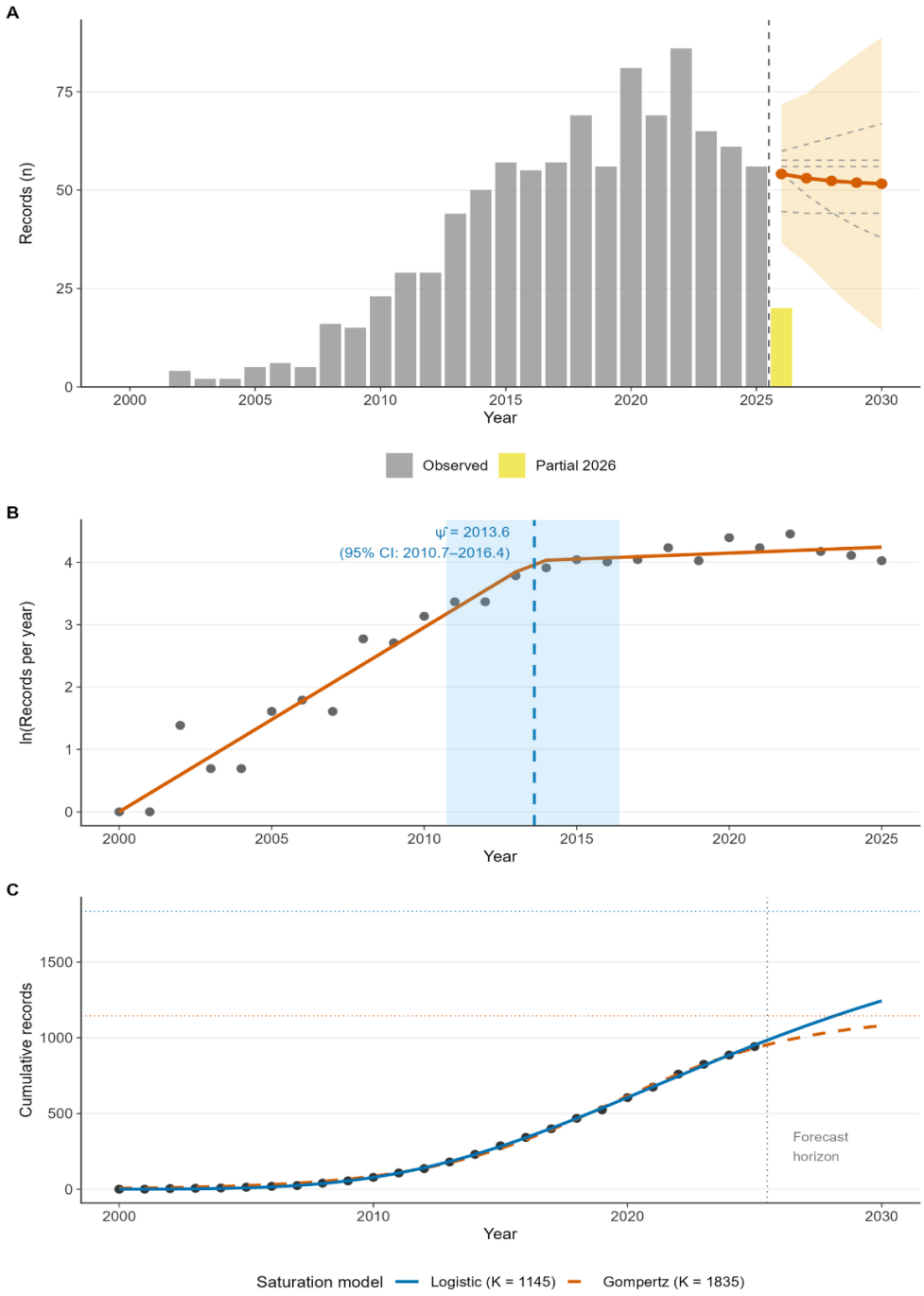


Figure 6. Production dynamics and structural-break analysis. (A) Annual publication output (2000–2025) with four-way Ensemble forecast (2026–2030). Grey bars show observed counts and the yellow bar the partial-year 2026. The bold red line shows the Ensemble point forecast and the shaded band its 95% approximate bounds, and thin dashed grey lines show individual model forecasts and the Naïve baseline (B) Segmented regression fits to log-transformed annual counts, with the fitted breakpoint indicated. (C) Cumulative S-curve with Gompertz and Logistic saturation fits.

4.1.2. Country topology and the small-world signature

The collaboration network is small-world (ω = 0.307; σ = 2.588), with the topology shifted toward the random end of the Telesford scale because path lengths are already at the random-graph minimum (Humphries and Gurney, 2008; Telesford et al., 2011). The United States and China anchor the network, and European hubs (Germany, Spain, France) bridge regional clusters. The network is efficient but not evenly integrated. Small-worldness correlates with scientific productivity (Ebadi and Schiffauerova, 2015), suggesting a topology conducive to productive collaboration.

The geographic concentration (Section 3.1.4) requires a caveat. The dominance of North American, European, and Chinese hubs in the WoS-indexed corpus is unsurprising given the WoS coverage profile (Mongeon and Paul-Hus, 2016). The geographic finding is a description of the field's infrastructure visible to a WoS-anchored analysis rather than a claim about the field's global presence. Future analyses should triangulate WoS, Scopus, and SciELO/AJOL/J-Stage indices to capture literature from the Global South.

4.1.3. Plant-dominated taxonomic profile and its methodological drivers

The plant dominance at 52.70% repeats the qualitative pattern observed by Lamka et al. (2022) for 184 species. The excess at the publication level (52.70% vs. 42.4% at species level) is a result of high per-species publication volume in a few model plants. The vertebrate and invertebrate groups trailed well behind, with reptiles and amphibians together accounting for under 1%, and vertebrate representation across the corpus remained low despite the demonstrated relevance of epigenetic variation in natural animal populations (Husby, 2022). This constraint is consistent with the methodological bottlenecks identified by Schrey et al. (2013). Fungi (1.98%) and microorganisms (0.62%) also account for a small, but newly quantified, fraction of the corpus. Freshwater ecosystems are also under-sampled, at 6.76%. Re-classification with the expanded dictionary (Section 2.4) yielded the same taxonomic hierarchy, supporting the robustness of the plant-dominated profile to dictionary specification. The plant skew is partly historical, reflecting foundational work in *Arabidopsis* (Johannes et al., 2009; Richards et al., 2017), and partly methodological. MS-AFLP and RRBS scale efficiently on small genomes, while vertebrate methylation is largely confined to CpG contexts, narrowing the range of ecologically informative variation (Lister et al., 2009). Currently, genome scale methylomics data are available for 580 animal species (Klughammer et al., 2023) while field studies in birds remain limited (McNew et al., 2021). Long-read sequencing (ONT, PacBio HiFi) reads methylation from raw DNA without bisulfite conversion (Simpson et al., 2017), lowering the bar for vertebrate fieldwork. This imbalance is systemic and will not be resolved without sustained investment in non-model methylomics. Balard et al. (2024) provide an operational toolkit for conservation biologists, complementing Lamka et al. (2022). Baltazar-Soares et al. (2024) point out that the application of epigenetic research to non-model species is a phenomenon of the last decade. The 2024 Evolutionary Applications Special Issue on "Epigenetic diversity and the evolutionary potential of wild populations" featured case studies on loggerhead sea turtles (Yen et al., 2024) and great tits (Sepers et al., 2024). Conservation epigenomics was formally named as a subfield by Hu et al. (2025).

4.2. Forecasting

4.2.1. Publication saturation versus knowledge saturation

If the slowdown reflected knowledge saturation, the pool of unstudied taxa and open questions would have to be nearly exhausted. This expectation is contradicted by the dominance of plants (52.70%), the low coverage of vertebrates (3.12% birds, reptiles, and amphibians), and the 66.63% of records lacking environmental context (Table S6, Table S7a). The imbalance mirrors "taxonomic chauvinism" (Bonnet et al., 2002; Troudet et al., 2017) in reverse, with plants leading because bisulfite protocols were optimised for small genomes. The breakpoint at approximately 2014 corresponds to the consolidation of RRBS as the standard methodology (Boyle et al., 2012), which reduced sequencing costs and provided an economic incentive for adoption. Annual growth fell abruptly across the breakpoint, from 23.43% to 1.04% per year (Section 3.2.1), an order-of-magnitude deceleration rather than a gradual slowing. The 12.16% CAGR is roughly three times the worldwide scientific baseline of 4.10% (Bornmann et al., 2021), as would be expected in the expansion phase of a new, methodology-driven subfield (doubling time ~ 6.0 years versus ~ 17.3 years for all science). This convergence across model families is consistent with approaching publication saturation rather than ongoing exponential growth (Section 3.2.4). Methodological lock-in and dependence on a narrow funding base are plausible drivers of this supply-side slowdown. The residual imbalance reflects a methodological bias that favours small genomes. Šrut (2021) found that NGS has seldom been applied to invertebrate methylomes, and Gunasekara et al. (2026) noted that the study of epigenetics in freshwater invertebrates remains methodologically constrained. Another possible explanation worth considering is that ESCI, released in November 2015, extended WoS journal coverage, and the breakpoint CI (2010.7–2016.4) overlaps this window. Three observations weigh against a purely indexing-driven explanation. First, ESCI added rather than removed articles, which should bias the count upward. Second, publication-growth estimates are consistent across established and new literature databases (Bornmann et al., 2021). Third, two independent model families simultaneously lost their trend terms. A WoS indexing delay of several months could smooth the final years of the series, so the

observation window was closed at 2025 for the CAGR and forecasting calculations. The two saturation models disagree on how mature the field is. The Logistic fit suggests the literature is nearing its ceiling (84% of asymptote; K = 1,145), whereas the Gompertz fit implies substantial room remains (52%; K = 1,835). Tattershall et al. (2021) found that Gompertz produces lower median error across 200 trends, favouring the asymmetric reading. Whether the remaining capacity is realised depends on removing these methodological barriers.

4.2.2. Forecast model performance and the case for ensemble methods

The four-way equal-weight Ensemble was retained as the headline forecast on robustness grounds. At the manuscript-aligned h = 5 horizon, the Ensemble (OOS MASE = 2.095) outperformed the Naïve benchmark (2.364), reflecting the diversification advantage of forecast combinations on longer horizons (Wang et al., 2023). All out-of-sample MASE values exceeded 1, which is expected for multi-step forecasts on short annual series (Hyndman and Koehler, 2006). The forecasts are therefore interpreted as bounded scenarios rather than precise point predictions. The drift component of the Theta method retains the pre-2014 growth slope regardless of recent stagnation (Hyndman and Billah, 2003), so its trajectory is read as an upper bound rather than a core forecast. The loss of drift from ARIMA and of trend from ETS is substantive, because two independent model families indicated that the data no longer support a trend component, corroborating the segmented-regression breakpoint.

4.3. Limitations

Five limitations qualify the inferences. First, the corpus rests on a single database. WoS under-indexes non-English and regionally indexed work (Mongeon and Paul-Hus, 2016), biasing country production toward the USA and Western Europe, and records visible only in Scopus, Dimensions, or regional services (SciELO, AJOL, J-Stage) are absent altogether, so the corpus represents the WoS-visible core of the field (Section 4.1.2). Second, the keyword-based taxonomic and ecosystem classification achieved 87.01% and 33.37% assignment rates, respectively. The high ecosystem-unspecified proportion (66.63%) reflects the field's laboratory orientation (Table S7b) rather than dictionary failure. The proportion decreased from 84% to 63% over the study period. Third, all models operate on n = 26 observations, a short series for stable information-criterion selection (Burnham and Anderson, 2002), and MASE > 1 at h = 5 for all models indicates that the forecasts are bounded scenarios. Fourth, the breakpoint was estimated on 14 pre-break and 12 post-break observations. Fifth, the classifier's sensitivity of 0.618 indicates systematic under-counting. If this under-counting is approximately uniform across taxa, relative proportions and temporal trends should be largely preserved. However, the possibility that detection differs among taxonomic groups cannot be excluded, and the absolute coverage percentages should therefore be read as conservative lower bounds (Table S2).

5. Conclusion

The literature of ecological epigenetics from 2000 to April 2026 was mapped quantitatively, and its trajectory was forecast through 2030. The field expanded at a compound annual rate of 12.16%, with a structural deceleration after approximately 2014 separating a founding phase of 23.43% annual growth (2000–2014) from a mature phase of 1.04% (2014–2025). The taxonomic profile is plant-dominated (52.70%), with mammals, fish, birds, reptiles, amphibians, and most invertebrate groups remaining under-represented relative to their ecological and conservation significance. The intellectual structure of the field is organised around three macro-themes (molecular mechanism, ecological context, and conservation and management), and international collaboration forms a small-world network anchored by the United States and China. Multiple growth models converged on a marked deceleration of output rather than continued exponential expansion, with a model-averaged carrying capacity estimated near K = 1,835 cumulative records. Together, these signals point to approaching publication saturation rather than knowledge saturation, with the slowdown plausibly driven by methodological lock-in to bisulfite-based protocols that favour small-genome plant systems. The taxonomic and methodological imbalances documented here define both the field's largest structural deficiency and its largest opportunity for future development, particularly for conservation genetics and the integration of wildlife and freshwater systems into ecological-epigenetics research.

Author Contributions

The percentages of the author' contributions are presented below. The author reviewed and approved the final version of the manuscript.

	B. K.
C	100
D	100
S	100
DCP	100
DAI	100
L	100
W	100
CR	100
SR	100
PM	100

C= concept, D= design, S= supervision, DCP= data collection and/or processing, DAI= data analysis and/or interpretation, L= literature search, W= writing, CR= critical review, SR= submission and revision, PM= project management.

Conflict of Interest

The author declared that there is no conflict of interest.

Ethical Consideration

Ethics committee approval was not required, because this study involved no experiments on animals or humans.

Acknowledgements

This research received no external funding. The author is grateful to Gizem Nazlı Ural for her valuable comments on the manuscript. Claude (Anthropic) was used to assist with grammar correction and language improvement, and the author reviewed and edited the output.

Supplementary Materials

Supplementary Information accompanies this paper and comprises full methodological documentation (Supplementary Methods S1 and S2), ten supplementary tables (Tables S1–S9, including S7a and S7b), and eleven supplementary figures (Figures S1–S11).

References

Allis, C. D., & Jenuwein, T. (2016). The molecular hallmarks of epigenetic control. *Nature Reviews Genetics*, *17*(8), 487–500. https://doi.org/10.1038/nrg.2016.59

Anastasiadi, D., Venney, C. J., Bernatchez, L., & Wellenreuther, M. (2021). Epigenetic inheritance and reproductive mode in plants and animals. *Trends in Ecology & Evolution*, *36*(12), 1124–1140. https://doi.org/10.1016/j.tree.2021.08.006

Aria, M., & Cuccurullo, C. (2017). bibliometrix: An R-tool for comprehensive science mapping analysis. *Journal of Informetrics*, *11*(4), 959–975. https://doi.org/10.1016/j.joi.2017.08.007

Assimakopoulos, V., & Nikolopoulos, K. (2000). The theta model: A decomposition approach to forecasting. *International Journal of Forecasting*, *16*(4), 521–530. https://doi.org/10.1016/S0169-2070(00)00066-2

Balard, A., Baltazar-Soares, M., Eizaguirre, C., & Heckwolf, M. J. (2024). An epigenetic toolbox for conservation biologists. *Evolutionary Applications*, *17*(6), e13699. https://doi.org/10.1111/eva.13699

Baltazar-Soares, M., Balard, A., & Heckwolf, M. J. (2024). Epigenetic diversity and the evolutionary potential of wild populations. *Evolutionary Applications*, *17*(10), e70011. https://doi.org/10.1111/eva.70011

Bates, D., Maechler, M., & Jagan, M. (2025). *Matrix: Sparse and dense matrix classes and methods* (R package version 1.7-4) [Computer software]. https://CRAN.R-project.org/package=Matrix

Berger, S. L., Kouzarides, T., Shiekhattar, R., & Shilatifard, A. (2009). An operational definition of epigenetics. *Genes & Development*, *23*(7), 781–783. https://doi.org/10.1101/gad.1787609

Bergmeir, C., Hyndman, R. J., & Koo, B. (2018). A note on the validity of cross-validation for evaluating autoregressive time series prediction. *Computational Statistics & Data Analysis*, *120*, 70–83. https://doi.org/10.1016/j.csda.2017.11.003

Bird, A. (2007). Perceptions of epigenetics. *Nature*, *447*(7143), 396–398. https://doi.org/10.1038/nature05913

Blondeau-Bidet, E., Banousse, G., L'Honoré, T., Farcy, E., Cosseau, C., & Lorin-Nebel, C. (2023). The role of salinity on genome-wide DNA methylation dynamics in European sea bass gills. *Molecular Ecology*, *32*(18), 5089–5109. https://doi.org/10.1111/mec.17089

Bonduriansky, R., & Day, T. (2009). Nongenetic inheritance and its evolutionary implications. *Annual Review of Ecology, Evolution, and Systematics*, *40*, 103–125. https://doi.org/10.1146/annurev.ecolsys.39.110707.173441

Bonnet, X., Shine, R., & Lourdais, O. (2002). Taxonomic chauvinism. *Trends in Ecology & Evolution*, *17*(1), 1–3. https://doi.org/10.1016/S0169-5347(01)02381-3

Bornmann, L., Haunschild, R., & Mutz, R. (2021). Growth rates of modern science: A latent piecewise growth curve approach to model publication numbers from established and new literature databases. *Humanities and Social Sciences Communications*, *8*, Article 224. https://doi.org/10.1057/s41599-021-00903-w

Bossdorf, O., Richards, C. L., & Pigliucci, M. (2008). Epigenetics for ecologists. *Ecology Letters*, *11*(2), 106–115. https://doi.org/10.1111/j.1461-0248.2007.01130.x

Boyle, P., Clement, K., Gu, H., Smith, Z. D., Ziller, M., Fostel, J. L., Holmes, L., Meldrim, J., Kelley, F., Gnirke, A., & Meissner, A. (2012). Gel-free multiplexed reduced representation bisulfite sequencing for large-scale DNA methylation profiling. *Genome Biology*, *13*, Article R92. https://doi.org/10.1186/gb-2012-13-10-r92

Brunson, J. C. (2020). ggalluvial: Layered grammar for alluvial plots. *Journal of Open Source Software*, *5*(49), 2017. https://doi.org/10.21105/joss.02017

Burnham, K. P., & Anderson, D. R. (2002). *Model selection and multimodel inference: A practical information-theoretic approach* (2nd ed.). Springer.

Caizergues, A. E., Le Luyer, J., Grégoire, A., Szulkin, M., Senar, J.-C., Charmantier, A., & Perrier, C. (2022). Epigenetics and the city: Non-parallel DNA methylation modifications across pairs of urban-forest Great tit populations. *Evolutionary Applications*, *15*(1), 149–165. https://doi.org/10.1111/eva.13334

Çakır, M., Oral, O., Ural, G. N., & Yılmaz, M. (2025). Mapping the research landscape of machine learning in aquaculture: A bibliometric analysis with forecasted output by 2030. *Aquaculture*, *612*, Article 743258. https://doi.org/10.1016/j.aquaculture.2025.743258

Ching, T. (2024). *qs2: Efficient serialization of R objects* (R package version 0.2.0) [Computer software]. https://CRAN.R-project.org/package=qs2

Clauset, A., Shalizi, C. R., & Newman, M. E. J. (2009). Power-law distributions in empirical data. *SIAM Review*, *51*(4), 661–703. https://doi.org/10.1137/070710111

Crameri, F., Shephard, G. E., & Heron, P. J. (2020). The misuse of colour in science communication. *Nature Communications*, *11*, Article 5444. https://doi.org/10.1038/s41467-020-19160-7

Csárdi, G., & Nepusz, T. (2006). The igraph software package for complex network research. *InterJournal, Complex Systems*, 1695. https://igraph.org

Davies, R. B. (1987). Hypothesis testing when a nuisance parameter is present only under the alternative. *Biometrika*, *74*(1), 33–43. https://doi.org/10.1093/biomet/74.1.33

Dickey, D. A., & Fuller, W. A. (1979). Distribution of the estimators for autoregressive time series with a unit root. *Journal of the American Statistical Association*, *74*(366), 427–431. https://doi.org/10.1080/01621459.1979.10482531

Donthu, N.,Kumar,S.,Mukherjee,D.,Pandey,N.,&Lim,W.M. (2021). How to conduct a bibliometric analysis: An overview and guidelines. *Journal of Business Research*, *133*, 285–296. https://doi.org/10.1016/j.jbusres.2021.04.070

Ebadi, A., & Schiffauerova, A. (2015). On the relation between the small world structure and scientific activities. *PLOS ONE*, *10*(3), Article e0121129. https://doi.org/10.1371/journal.pone.0121129

Fildes, R., Nikolopoulos, K., Crone, S. F., & Syntetos, A. A. (2008). Forecasting and operational research: A review. *Journal of the Operational Research Society*, *59*(9), 1150–1172. https://doi.org/10.1057/palgrave.jors.2602597

Gamer, M., Lemon, J., Fellows, I., & Singh, P. (2019). *irr: Various coefficients of interrater reliability and agreement* (R package version 0.84.1) [Computer software]. https://CRAN.R-project.org/package=irr

Garnier, S., Ross, N., Rudis, R., Camargo, A. P., Sciaini, M., & Scherer, C. (2024). *viridis(Lite): Colorblind-friendly color maps for R* (R package version 0.6.5) [Computer software]. https://CRAN.R-project.org/package=viridis

Goldberg, A. D., Allis, C. D., & Bernstein, E. (2007). Epigenetics: A landscape takes shape. *Cell*, *128*(4), 635–638. https://doi.org/10.1016/j.cell.2007.02.006

Gunasekara, C. W. R., Rajapaksha, L. G. T. G., & De Alwis, P. S. (2026). Heavy metal-induced epigenetic disruption in aquatic organisms: A review of mechanisms, impacts, and implications for ecotoxicology. *Comparative Biochemistry and Physiology Part C: Toxicology & Pharmacology*, *306*, Article 110552. https://doi.org/10.1016/j.cbpc.2026.110552

Hackerott, S., Virdis, F., Flood, P. J., Garcia Souto, D., Paez, W., & Eirin-Lopez, J. M. (2023). Relationships between phenotypic plasticity and epigenetic variation in two Caribbean *Acropora* corals. *Molecular Ecology*, *32*(17), 4814–4828. https://doi.org/10.1111/mec.17072

Heard, E., & Martienssen, R. A. (2014). Transgenerational epigenetic inheritance: Myths and mechanisms. *Cell*, *157*(1), 95–109. https://doi.org/10.1016/j.cell.2014.02.045

Heraghty, S. D., Rahman, S. R., Verble, K. M., & Lozier, J. D. (2024). Examining the effects of environment, geography, and elevation on patterns of DNA methylation across populations of two widespread bumble bee species. *Genome Biology and Evolution*, *16*(10), Article evae207. https://doi.org/10.1093/gbe/evae207

Hu, J., & Barrett, R. D. H. (2017). Epigenetics in natural animal populations. *Journal of Evolutionary Biology*, *30*(9), 1612–1632. https://doi.org/10.1111/jeb.13130

Hu, Y., Zhou, W., & Wei, F. (2025). Conservation epigenomics: Integrating epigenetic mechanisms into species conservation. *Science China Life Sciences*, *68*(9), 2800–2803. https://doi.org/10.1007/s11427-025-2945-4

Hukkanen, M., Hsu, B.-Y., Cossin-Sevrin, N., Crombecque, M., Delaunay, A., Hollmen, L., Kaukonen, R., Konki, M., Lund, R., Marciau, C., Stier, A., & Ruuskanen, S. (2023). From maternal glucocorticoid and thyroid hormones to epigenetic regulation of offspring gene expression: An experimental study in a wild bird species. *Evolutionary Applications*, *16*(10), 1753–1769. https://doi.org/10.1111/eva.13598

Humphries, M. D., & Gurney, K. (2008). Network 'small-world- ness': A quantitative method for determining canonical network equivalence. *PLOS ONE*, *3*(4), Article e0002051. https://doi.org/10.1371/journal.pone.0002051

Husby, A. (2022). Wild epigenetics: Insights from epigenetic studies on natural populations. *Proceedings of the Royal Society B: Biological Sciences*, *289*(1968), Article 20211633. https://doi.org/10.1098/rspb.2021.1633

Hyndman, R. J., & Athanasopoulos, G. (2021). *Forecasting: Principles and practice* (3rd ed.). OTexts.

Hyndman, R. J., & Billah, B. (2003). Unmasking the Theta method. *International Journal of Forecasting*, *19*(2), 287–290. https://doi.org/10.1016/S0169-2070(01)00143-1

Hyndman, R. J., & Khandakar, Y. (2008). Automatic time series forecasting: The forecast package for R. *Journal of Statistical Software*, *27*(3), 1–22. https://doi.org/10.18637/jss.v027.i03

Hyndman, R. J., & Koehler, A. B. (2006). Another look at measures of forecast accuracy. *International Journal of Forecasting*, *22*(4), 679–688. https://doi.org/10.1016/j.ijforecast.2006.03.001

Hyndman, R. J., Koehler, A. B., Snyder, R. D., & Grose, S. (2002). A state space framework for automatic forecasting using exponential smoothing methods. *International Journal of Forecasting*, *18*(3), 439–454. https://doi.org/10.1016/S0169-2070(01)00110-8

Jablonka, E., & Raz, G. (2009). Transgenerational epigenetic inheritance: Prevalence, mechanisms, and implications for the study of heredity and evolution *The Quarterly Review of Biology*, *84*(2), 131–176. https://doi.org/10.1086/598822

Jaenisch, R., & Bird, A. (2003). Epigenetic regulation of gene expression: How the genome integrates intrinsic and environmental signals. *Nature Genetics*, *33*(Suppl), 245–254. https://doi.org/10.1038/ng1089

Jiang, C., Hu, Y., Wang, S., & Chen, C. (2023). Emerging trends in DNA and RNA methylation modifications in type 2 diabetes mellitus: A bibliometric and visual analysis from 1992 to 2022. *Frontiers in Endocrinology*, *14*, Article 1145067. https://doi.org/10.3389/fendo.2023.1145067

Johannes, F., Porcher, E., Teixeira, F. K., Saliba-Colombani, V., Simon, M., Agier, N., Bulski, A., Albuisson, J., Heredia, F., Audigier, P., Bouchez, D., Dillmann, C., Guerche, P., Hospital, F., & Colot, V. (2009). Assessing the impact of transgenerational epigenetic variation on complex traits. *PLOS Genetics*, *5*(6), Article e1000530. https://doi.org/10.1371/journal.pgen.1000530

Klughammer, J., Romanovskaia, D., Nemc, A., Posautz, A., Seid, C. A., Schuster, L. C., Keinath, M. C., Lugo Ramos, J. S., Kosack, L., Evankow, A., Printz, D., Kirchberger, S., Ergüner, B., Datlinger, P., Fortelny, N., Schmidl, C., Farlik, M., Skjærven, K., Bergthaler, A., … Bock, C. (2023). Comparative analysis of genome-scale, base-resolution DNA methylation profiles across 580 animal species. *Nature Communications*, *14*, Article 232. https://doi.org/10.1038/s41467-022-34828-y

Kwiatkowski, D., Phillips, P. C. B., Schmidt, P., & Shin, Y. (1992). Testing the null hypothesis of stationarity against the alternative of a unit root. *Journal of Econometrics*, *54*(1–3), 159–178. https://doi.org/10.1016/0304-4076(92)90104-Y

Laine, V. N., Sepers, B., Lindner, M., Gawehns, F., Ruuskanen, S., & van Oers, K. (2023). An ecologist's guide for studying DNA methylation variation in wild vertebrates. *Molecular Ecology Resources*, *23*(7), 1488–1508. https://doi.org/10.1111/1755-0998.13624

Lamka, G. F., Harder, A. M., Sundaram, M., Schwartz, T. S., Christie, M. R., DeWoody, J. A., & Willoughby, J. R. (2022). Epigenetics in ecology, evolution, and conservation. *Frontiers in Ecology and Evolution*, *10*, Article 871791. https://doi.org/10.3389/fevo.2022.871791

Landis, J. R., & Koch, G. G. (1977). The measurement of observer agreement for categorical data. *Biometrics*, *33*(1), 159–174. https://doi.org/10.2307/2529310

Lister, R., Pelizzola, M., Dowen, R. H., Hawkins, R. D., Hon, G., Tonti-Filippini, J., Nery, J. R., Lee, L., Ye, Z., Ngo, Q.-M., Edsall, L., Antosiewicz-Bourget, J., Stewart, R., Ruotti, V., Millar, A. H., Thomson, J. A., Ren, B., & Ecker, J. R. (2009). Human DNA methylomes at base resolution show widespread epigenomic differences. *Nature*, *462*(7271), 315–322. https://doi.org/10.1038/nature08514

Liu, H., Huang, Y., Lu, S., Yuan, D., & Liu, J. (2023). Global trends of lipid metabolism research in epigenetics field: A bibliometric analysis from 2012–2021. *International Journal of Environmental Research and Public Health*, *20*(3), Article 2382. https://doi.org/10.3390/ijerph20032382

Macartney, E. L., Drobniak, S. M., Nakagawa, S., & Lagisz, M. (2023). Evidence base for non-genetic inheritance of environmental exposures in non-human animals and plants: A map of evidence syntheses with bibliometric analysis. *Environmental Evidence*, *12*, Article 1. https://doi.org/10.1186/s13750-022-00290-y

Makridakis, S., & Hibon, M. (2000). The M3-Competition: Results, conclusions and implications. *International Journal of Forecasting*, *16*(4), 451–476. https://doi.org/10.1016/S0169-2070(00)00057-1

Makridakis, S., Spiliotis, E., & Assimakopoulos, V. (2020). The M4 Competition: 100,000 time series and 61 forecasting methods. *International Journal of Forecasting*, *36*(1), 54–74. https://doi.org/10.1016/j.ijforecast.2019.04.014

Mao, Y., Zhao, K., Chen, N., Fu, Q., Zhou, Y., Kong, C., Li, P., & Yang, C. (2023). A 2-decade bibliometric analysis of epigenetics of cardiovascular disease: From past to present. *Clinical Epigenetics*, *15*(1), Article 184. https://doi.org/10.1186/s13148-023-01603-9

Marzi, G., Balzano, M., Caputo, A., & Pellegrini, M. M. (2025). Guidelines for bibliometric-systematic literature reviews: 10 steps to combine analysis, synthesis and theory development. *International Journal of Management Reviews*, *27*(1), 81–103. https://doi.org/10.1111/ijmr.12381

McNew, S. M., Boquete, M. T., Espinoza-Ulloa, S., Andres, J. A., Wagemaker, N. C. A. M., Knutie, S. A., Richards, C. L., & Clayton, D. H. (2021). Epigenetic effects of parasites and pesticides on captive and wild nestling birds. *Ecology and Evolution*, *11*(12), 7713–7729. https://doi.org/10.1002/ece3.7606

Mongeon, P., & Paul-Hus, A. (2016). The journal coverage of Web of Science and Scopus: A comparative analysis. *Scientometrics*, *106*(1), 213–228. https://doi.org/10.1007/s11192-015-1765-5

Mounger, J., Ainouche, M. L., Bossdorf, O., Cavé-Radet, A., Li, B., Parepa, M., Salmon, A., Yang, J., & Richards, C. L. (2021). Epigenetics and the success of invasive plants. *Philosophical Transactions of the Royal Society B: Biological Sciences*, *376*(1826), Article 20200117. https://doi.org/10.1098/rstb.2020.0117

Muggeo, V. M. R. (2003). Estimating regression models with unknown break-points. *Statistics in Medicine*, *22*(19), 3055–3071. https://doi.org/10.1002/sim.1545

Muggeo, V. M. R. (2016). Testing with a nuisance parameter present only under the alternative: A score-based approach with application to segmented modelling. *Journal of Statistical Computation and Simulation*, *86*(15), 3059–3067. https://doi.org/10.1080/00949655.2016.1149855

Özcan, F., Hangül, C., & Özdoğan, H. (2025). Diyabet ve myricetin arasındaki ilişki: Bibliyometrik analiz. *Türkiye Klinikleri Journal of Medical Sciences*, *45*(4), 238–248. https://doi.org/10.5336/medsci.2025-110238

Özdoğan, H., Sevim, G., & Üncü, Y. A. (2025). A bibliometric analysis of cross-section calculations. *Journal of Nuclear Sciences*, *9*(2), 32–42. https://doi.org/10.59474/nuclear.2023.65

Page, M. J., McKenzie, J. E., Bossuyt, P. M., Boutron, I., Hoffmann, T. C., Mulrow, C. D., Shamseer, L., Tetzlaff, J. M., Akl, E. A., Brennan, S. E., Chou, R., Glanville, J., Grimshaw, J. M., Hróbjartsson, A., Lalu, M. M., Li, T., Loder, E. W., Mayo-Wilson, E., McDonald, S., … Moher, D. (2021). The PRISMA 2020 statement: An updated guideline for reporting systematic reviews. *BMJ*, *372*, Article n71. https://doi.org/10.1136/bmj.n71

Pedersen, T. L. (2024). *patchwork: The composer of plots* (R package version 1.3.0) [Computer software]. https://CRAN.R-project.org/package=patchwork

R Core Team. (2025). *R: A language and environment for statistical computing* [Computer software]. R Foundation for Statistical Computing. https://www.R-project.org/

Richards, C. L., Alonso, C., Becker, C., Bossdorf, O., Bucher, E., Colomé-Tatché, M., Durka, W., Engelhardt, J., Gaspar, B., Gogol-Döring, A., Grosse, I., van Gurp, T. P., Heer, K., Kronholm, I., Lampei, C., Latzel, V., Mirouze, M., Opgenoorth, L., Paun, O., … Verhoeven, K. J. F. (2017). Ecological plant epigenetics: Evidence from model and non-model species, and the way forward. *Ecology Letters*, *20*(12), 1576–1590. https://doi.org/10.1111/ele.12858

Said, S. E., & Dickey, D. A. (1984). Testing for unit roots in autoregressive-moving average models of unknown order. *Biometrika*, *71*(3), 599–607. https://doi.org/10.1093/biomet/71.3.599

Schauberger, P., & Walker, A. (2024). *openxlsx: Read, write and edit xlsx files* (R package version 4.2.7) [Computer software]. https://CRAN.R-project.org/package=openxlsx

Schrey, A. W., Alvarez, M., Foust, C. M., Kilvitis, H. J., Lee, J. D., Liebl, A. L., Martin, L. B., Richards, C. L., & Robertson, M. (2013). Ecological epigenetics: Beyond MS-AFLP. *Integrative and Comparative Biology*, *53*(2), 340–350. https://doi.org/10.1093/icb/ict012

Sepers, B., Verhoeven, K. J. F., & van Oers, K. (2024). Early developmental carry-over effects on exploratory behaviour and DNA methylation in wild great tits (*Parus major*). *Evolutionary Applications*, *17*(3), e13664. https://doi.org/10.1111/eva.13664

Simpson, J. T., Workman, R. E., Zuzarte, P. C., David, M., Dursi, L. J., & Timp, W. (2017). Detecting DNA cytosine methylation using nanopore sequencing. *Nature Methods*, *14*, 407–410. https://doi.org/10.1038/nmeth.4184

Slowikowski, K. (2024). *ggrepel: Automatically position non-overlapping text labels* (R package version 0.9.6) [Computer software]. https://CRAN.R-project.org/package=ggrepel

Šrut, M. (2021). Ecotoxicological epigenetics in invertebrates: Emerging tool for the evaluation of present and past pollution burden. *Chemosphere*, *282*, Article 131026. https://doi.org/10.1016/j.chemosphere.2021.131026

Tattershall, E., Nenadic, G., & Stevens, R. D. (2021). Modelling trend life cycles in scientific research using the Logistic and Gompertz equations. *Scientometrics*, *126*(11), 9113–9132. https://doi.org/10.1007/s11192-021-04137-0

Telesford, Q. K., Joyce, K. E., Hayasaka, S., Burdette, J. H., & Laurienti, P. J. (2011). The ubiquity of small-world networks. *Brain Connectivity*, *1*(5), 367–375. https://doi.org/10.1089/brain.2011.0038

Tjørve, K. M. C., & Tjørve, E. (2017). The use of Gompertz models in growth analyses, and new Gompertz-model approach: An addition to the Unified-Richards family. *PLOS ONE*, *12*(6), Article e0178691. https://doi.org/10.1371/journal.pone.0178691

Trapletti, A., & Hornik, K. (2024). *tseries: Time series analysis and computational finance* (R package version 0.10-61) [Computer software]. https://CRAN.R-project.org/package=tseries

Troudet, J., Grandcolas, P., Blin, A., Vignes-Lebbe, R., & Legendre, F. (2017). Taxonomic bias in biodiversity data and societal preferences. *Scientific Reports*, *7*, Article 9132.

https://doi.org/10.1038/s41598-017-09084-6

Tsoularis, A., & Wallace, J. (2002). Analysis of logistic growth models. *Mathematical Biosciences*, *179*(1), 21–55. https://doi.org/10.1016/S0025-5564(02)00096-2

Üncü, Y. A., Özdoğan, H., & Sevim, G. (2025). Bibliometric analysis of diffuse optical tomography studies between 1994–2024. *Cumhuriyet Science Journal*, *46*(3), 435–446. https://doi.org/10.17776/csj.1637597

Verhoeven, K. J. F., Jansen, J. J., van Dijk, P. J., & Biere, A. (2010). Stress-induced DNA methylation changes and their heritability in asexual dandelions. *New Phytologist*, *185*(4), 1108–1118. https://doi.org/10.1111/j.1469-8137.2009.03121.x

Verhoeven, K. J. F., vonHoldt, B. M., & Sork, V. L. (2016). Epigenetics in ecology and evolution: What we know and what we need to know. *Molecular Ecology*, *25*(8), 1631–1638. https://doi.org/10.1111/mec.13617

Waddington, C. H. (1942). The epigenotype. *Endeavour*, *1*, 18–20.

Wang, X., Hyndman, R. J., Li, F., & Kang, Y. (2023). Forecast combinations: An over 50-year review. *International Journal of Forecasting*, *39*(4), 1518–1547. https://doi.org/10.1016/j.ijforecast.2022.11.005

Weaver, I. C. G., Cervoni, N., Champagne, F. A., D'Alessio, A. C., Sharma, S., Seckl, J. R., Dymov, S., Szyf, M., & Meaney, M. J. (2004). Epigenetic programming by maternal behavior. *Nature Neuroscience*, *7*(8), 847–854. https://doi.org/10.1038/nn1276

Wickham, H. (2016). *ggplot2: Elegant graphics for data analysis* (2nd ed.). Springer-Verlag.

Wickham, H. (2023). *conflicted: An alternative conflict resolution strategy* (R package version 1.2.0) [Computer software]. https://CRAN.R-project.org/package=conflicted

Wickham, H., Averick, M., Bryan, J., Chang, W., McGowan, L., François, R., Grolemund, G., Hayes, A., Henry, L., Hester, J., Kuhn, M., Pedersen, T., Miller, E., Bache, S., Müller, K., Ooms, J., Robinson, D., Seidel, D., Spinu, V., ... Yutani, H. (2019). Welcome to the tidyverse. *Journal of Open Source Software*, *4*(43), Article 1686. https://doi.org/10.21105/joss.01686

Wickham, H., Pedersen, T. L., & Seidel, D. (2024). *scales: Scale functions for visualization* (R package version 1.3.0) [Computer software]. https://CRAN.R-project.org/package=scales

Yen, E. C., Gilbert, J. D., Balard, A., Afonso, I. O., Fairweather, K., Newlands, D., Lopes, A., Correia, S. M., Taxonera, A., Rossiter, S. J., Martín-Durán, J. M., & Eizaguirre, C. (2024). DNA methylation carries signatures of sublethal effects under thermal stress in loggerhead sea turtles. *Evolutionary Applications*, *17*(9), e70013. https://doi.org/10.1111/eva.70013

Zhang, X., Jiang, Y., Cai, Y., Fu, Q., & Chen, Y. (2024). Epigenetics research in eye diseases: A bibliometric analysis from 2000 to 2023. *Clinical and Experimental Optometry*, *107*(6), 649–656. https://doi.org/10.1080/08164622.2023.2261929

Zhong, X., & Chen, D. (2025). Global research trends on epigenetics and cancer: A bibliometric analysis. *Medicine*, *104*(33), Article e43197. https://doi.org/10.1097/MD.0000000000043197

Black Sea Journal of Engineering and Science
doi: 10.34248/bsengineering.1954898

Open Access Journal
e-ISSN: 2619 – 8991

Research Article
Volume 9 - Issue 5: 2446-2452 / September 2026

DESIGN AND MANUFACTURING OF A CRANKSHAFT-FREE COMPRESSOR

Ramin BARZEGAR[1]*

[1]*Hacettepe University, Faculty of Engineering, Department of Mechanical Engineering, 06800, Ankara, Türkiye*

Abstract: The conventional crankshaft-driven reciprocating compressors inherently suffer from insufficient torque at the end of the compression due to their design. This study aims at designing and experimentally testing a crankshaft-free compressor in which the compression process is achieved by driving the pistons over an elliptical ring in order to convert the rotary motion directly into reciprocating motion of the pistons. The proposed mechanism allows the forces acting on the pistons to be aligned with the piston axis which results in improved mechanical efficiency and torque characteristics. Thermodynamic analysis was performed in order to determine the operating parameters and MATLAB/Simulink was used to evaluate the dynamic behavior of the mechanism. Additionally, the structural integrity and vibration characteristics of the system were investigated by means of finite element and modal analysis via ANSYS. Based on the obtained results, proper materials for each of the components were selected and the compressor was manufactured and experimentally tested under laboratory conditions. Experimental data showed that with an input power of 1 kW, the crankshaft-free orbital compressor was capable of achieving a delivery pressure of 800 kPa (absolute) with a volumetric flow rate of 200 L/min at 1000 rpm. It was concluded that the designed compressor can be considered as a potential alternative to conventional reciprocating compressors in industrial applications.

Keywords: Compressor, Crankshaft-free, Numerical analysis, Experimental testing

***Corresponding author:** Hacettepe University, Faculty of Engineering, Department of Mechanical Engineering, 06800, Ankara, Türkiye
E mail: raminbarzegar@hacettepe.edu.tr (R. BARZEGAR)
Ramin BARZEGAR https://orcid.org/0000-0003-2796-7126

Received: May 19, 2026
Accepted: August 12, 2026
Published: September 15, 2026

Cite as: Barzegar, R. (2026). Design and manufacturing of a crankshaft-free compressor. *Black Sea Journal of Engineering and Science,* 9(5), 2446-2452.

1. Introduction

Compressors have a wide variety of applications in nearly all industries, power generation and refrigeration cycles, and pneumatic devices. The global compressor market is forecasted to reach around $48.5 billion by 2030 (Prescient and Strategic Intelligence, 2020). The production of the compressed air is considered to be highly energy intensive accounting for up to 20% of the electricity consumption in industries (Vittorini and Cipollone, 2016; Silva et al., 2017). Therefore, care must be taken to optimize the performance of compressors in order to enhance the overall output of the systems (El Samad et al., 2024).

Positive Displacement Compressors (PDC) are the most commonly used type in industrial compressed-air systems especially in low and medium flow rate applications due to their ability to deliver stable pressure ratios with relatively compact configurations and high reliability (Tanveer and Bradshaw, 2020). PDCs pressurize the gas by trapping a certain amount of gas and then reducing its volume in a closed chamber.

Conventional crankshaft-driven mechanisms are optimal and efficient component for converting circular motion into linear motion. However, their mechanisms introduce an inherent mechanical limitation causing them to suffer from reduced mechanical efficiency near the top and bottom dead center positions due to limited torque transmission characteristics (Lu et al., 2023). Efficiency in these systems depends on parameters such as pressure, torque angle, rotational speed of the electric motor, stroke length, piston diameter, and number of pistons. Particularly, when approaching the dead center where compression pressure is the highest, low torque angles lead to a decrease in efficiency. Therefore, the use of a crankshaft results in significant energy loss in these systems.

The rotary PDC types including vane, screw, and scroll compressors provide continuous compression with low vibration and fewer moving parts (Liu et al., 2026). The disadvantages of these types include leakage issues, higher investment and maintenance costs, low capacity, and high discharge temperature. Several approaches have been introduced in modeling and evaluation of rotary compressors under different operating conditions (Wang et al., 2026). Additionally, alternative mechanisms such as swash-plates have been studied to overcome the limitations of the crankshaft-driven compressors (Srivastava et al., 2016).

The majority of the recent studies on compressors aimed at improving the thermodynamic and mechanical performance of PDCs by focusing on frictional losses, vibration characteristics, valve dynamics, heat transfer mechanisms, and leakage (Shin et al., 2019; Shakya and Ooi, 2020; Lu et al., 2022; Hasanlu et al., 2026). It has

This work is licensed (CC BY-NC 4.0) under Creative Commons Attribution 4.0 International License

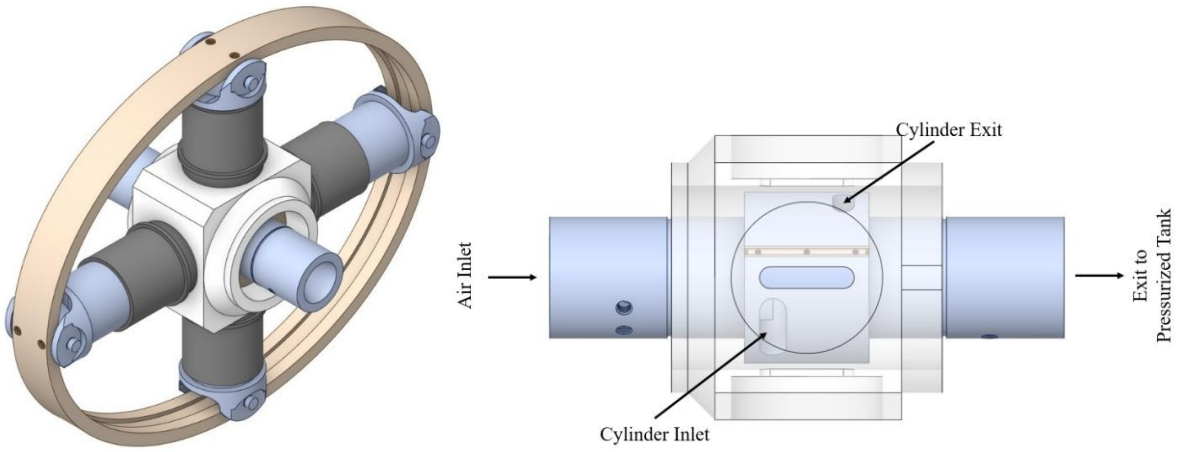
been shown that these characteristics have a strong impact on volumetric efficiency and power consumption of the compressors. These developments highlight the importance of applying thermodynamic, structural, and dynamic analyses, as well as experimental investigations in compressor design. Although significant progress has been made in optimization of the crankshaft-driven PDCs, the inherent source of inefficiency in these systems is due to the conversion of rotary motion into reciprocating motion of the piston. Therefore, the crankshaft-free compressor represents an attractive solution for improving torque characteristics and reduced mechanical losses.

Although various alternative compressor mechanisms have been developed, the literature review shows that an orbital piston configuration in compressor design has not been addresses and experimental studies on new geometries are scarce (Spark and Lu, 2019). In this study, a crankshaft-free compressor is proposed in order to provide an alternative to conventional PDCs. The elimination of the conventional crankshaft allows the piston loading to be aligned with the piston axis, which results in superior torque transmission characteristics. The thermodynamic, structural, modal, and dynamics analyses were conducted in designing the compressor mechanism. In order to experimentally analyze the performance of the designed system, a prototype was manufactured and the performance characteristics such as delivery pressure, volumetric efficiency, and volumetric flow rate were tested under laboratory conditions.

2. Materials and Methods

A crankshaft-free compressor was developed in which the rotating motion is directly converted into the reciprocating motion of the piston. The schematics of the compressor mechanism is presented in Figure 1(a). The compressor was composed of 4 cylinders mounted on a cylinder block with 90° angle in between and the pistons were in contact with an outer elliptical ring with the help of springs positioned between cylinders and pistons. When the block is rotated through a pulley connected to an electric motor, the pistons move over the carefully designed elliptical ring. The difference between the major and minor axes of the ellipse results in expansion and compression strokes. Each cylinder-piston assembly experiences two complete cycles in a single revolution of the cylinder block which totally account for eight complete cycles per revolution. The inlet and exit ports are mounted on a stationary port cylinder closely fitted inside the central block which can be seen in Figure 1(b). The gap between the port cylinder and the block was sealed by brass both diagonally and longitudinally to ensure airtightness. The timing and size of the ports inside the cylinders were designed so that the cylinders align with the exit port exactly when the pressure at the end of compression stroke reached 800 kPa (absolute) and with the inlet port when the inside pressure reached around 90 kPa. Due to the design of the mechanism, the force acting on the pistons will always be normal to the direction of the piston motion, and the frictional forces will be minimum. The design parameters of the compressor are given in Table 1. These parameters were selected based on the dimensional constraints and operating conditions typical of a small-scale compressor.

In the thermodynamics analysis of the compressor, the working fluid was considered to be air with the behavior of an ideal gas. The cyclic operation of the compressor is shown in Figure 2.



(a) (b)

Figure 1. (a) Schematics of the designed compressor and (b) the inlet and exit ports

Table 1. Compressor design parameters

Parameter	Value
Inlet Pressure	90 kPa
Inlet Temperature	310 K
Polytropic Coefficient	1.32
Outlet Pressure	800 kPa
No. of Cylinders	4
No. of Cycles per Rev.	2
Bore	50 mm
Stroke	37.5 mm

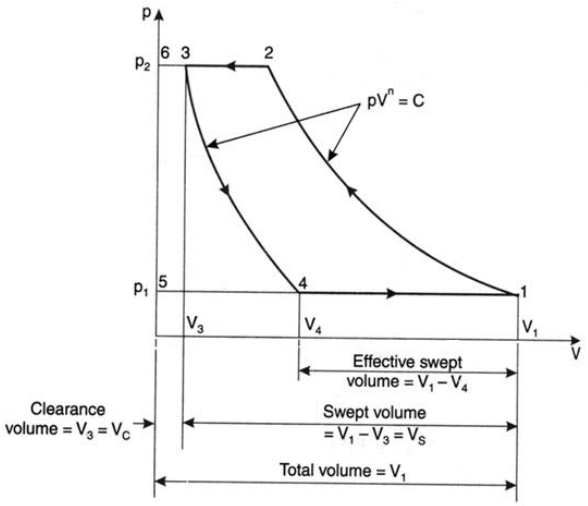


Figure 2. The thermodynamic cycle of the compressor.

The network obtained for the cycle and the volumetric efficiency of the compressor can be calculated as follows (equations 1 and 2):

$$W = \left(\frac{n}{n-1}\right) p_1(V_1 - V_4)\left[\left(\frac{p_2}{p_1}\right)^{\frac{n-1}{n}} - 1\right] \quad (1)$$

$$\eta_{vol} = \frac{V_1 - V_4}{V_1 - V_3} = \frac{V_1 - V_4}{V_s} \quad (2)$$

where n is the polytropic coefficient, P_1 is the inlet pressure, P_2 is the exit pressure, V_1 is the volume at the bottom dead center, V_3 is the volume at the bottom dead center, V_4 is the volume at the start of induction process, and V_s is the swept volume.

In order to assess the dynamic behavior of the compressor mechanism, a dynamic analysis model was established using MATLAB/Simulink software, and necessary modifications were made according to the operating conditions of the compressor. The Finite Element Analysis (FEA) and Modal analysis were also conducted by means of ANSYS software to evaluate the stresses occurring on the components. Finally, a compressor prototype was manufactured and tested under laboratory conditions to validate the numerical calculations.

3. Results and Discussion

The compressor cyclic analysis was performed based on the data presented in Table 1. Considering losses during the induction process due to flow resistance through the air filter and inlet ports, the inlet pressure was set to 90 kPa, while the designed discharge pressure was selected as 800 kPa with the flow rate of 200 L/min. The thermodynamic analysis resulted in a cylinder volume of 68 cm^3 with a compression ratio of 4.76. This compression ratio was in accordance with data reported in the literature (Yalçın, 2011). These characteristics allowed the compressor to be able to supply about 200 L/min and 400 L/min of air at the rotating speed of 1000 rpm and 2000 rpm, respectively. The proportional increase in the flow rate with rotational speed indicated that the designed mechanism allows stable operation within the operating range. The power required to drive the compressor was calculated as 940 W and 1.88 kW at the rotating speeds of 1000 rpm and 2000 rpm, respectively.

The volumetric efficiency of the compressor was found to be around 66.4% which was close to the volumetric efficiency of the reciprocating PDCs (Lu et al., 2023). Since the presented compressor is a first-stage prototype, the low volumetric efficiency can be considered acceptable. However, several optimizations including port timing, clearance volume reduction, and sealing improvement may be applied to enhance the volumetric efficiency of the compressor.

In order to assess the dynamic behavior of the mechanism, a dynamic analysis model of the mechanism was established using MATLAB/Simulink software, and necessary modifications were made according to the operating conditions of the compressor. The orbital motion of the cylinder block and piston assembly, inertial effects of the moving components, appropriate constraints, and the external loadings were included in the analysis. The dynamics model of the compressor can be seen in Figure 3.

Based on the obtained results, the required torque for the mechanism operation was found to be about 60 N-m. This value can be attributed to the combined effects of compression work, inertia of the moving parts, and frictional effects. Comparing the obtained data with the torque requirements of the crankshaft-driven compressors, it can be said that the torque requirements of the designed mechanism was smoother than that of conventional compressors. This is due to the fact that the force acting on the piston during the compression stroke is aligned with the direction of the piston motion. Additionally, the normal and tangential forces acting on the outer ring were calculated as 1400 N and 136 N, respectively. The higher normal force shows that the loading is mainly in the radial direction which results in a considerable reduction in frictional effects between the piston and cylinder wall.

Finite Element Analysis (FEA) was performed by means of ANSYS software to evaluate the stress distribution

occurring on the system components by applying the normal and tangential forces found from dynamic analysis. Figure 4 shows the generated mesh and the resulting stress values on different components of the system. The maximum equivalent stress occurred on the outer ring with the magnitude of 165 MPa which can be attributed to the normal force acting on the ring during the compression stroke. In order to ensure the structural integrity of the ring, heat-treated steel was selected for manufacturing to provide sufficient strength. The stresses upon piston and cylinder were around 85 MPa and 6.5 MPa, respectively. Since these stress levels are significantly less than the yield stress of Aluminum 6061-T6, this material can be safely used in the manufacturing of the pistons and cylinder block.

Additionally, modal analyses were conducted to observe the vibration characteristics of the compressor and obtain the natural frequencies of the system. Determining the natural frequencies of the rotating compressor is essential to avoid resonance during operation. Material properties and boundary conditions were assigned carefully to ensure the validity of the results. According to the results of the modal analyses, the first natural frequency of the compressor was found to be 171 Hz which is far from the operating frequency of the system at 16.7 Hz at 1000 rpm. The large difference between the operation and natural frequency indicated that the system is unlikely to experience resonance. Figure 5 represents the first and second mode shapes obtained from the analysis.

Based on the obtained results from the thermodynamic, dynamics, structural, and modal analyses, a prototype of the compressor was manufactured and experimentally tested under laboratory conditions to validate the numerical data and evaluate the performance of the designed mechanism. Figure 6 represents the manufactured prototype of the system.

The experimental data showed that at the rotational speed of 1000 rpm, the compressor was capable of delivering approximately 185 L/min of air at a discharge pressure of around 800 kPa. The obtained flow rate was relatively close to the predicted value of 200 L/min, indicating a deviation of approximately 7.5% between the numerical result and experimental data. The difference between the flow rates can be attributed to leakage losses, manufacturing tolerances, frictional effects, and sealing imperfections within the prototype system. Considering that the developed compressor represents an initial prototype, the deviation between the theoretical and experimental results remained within an acceptable range. Further improvement of the sealing between the stationary port cylinder and the rotating block may contribute to reducing leakage losses and improving the volumetric performance. These findings confirm the feasibility of the proposed crankshaft-free compressor mechanism as a potential alternative to conventional reciprocating compressors in industrial applications.

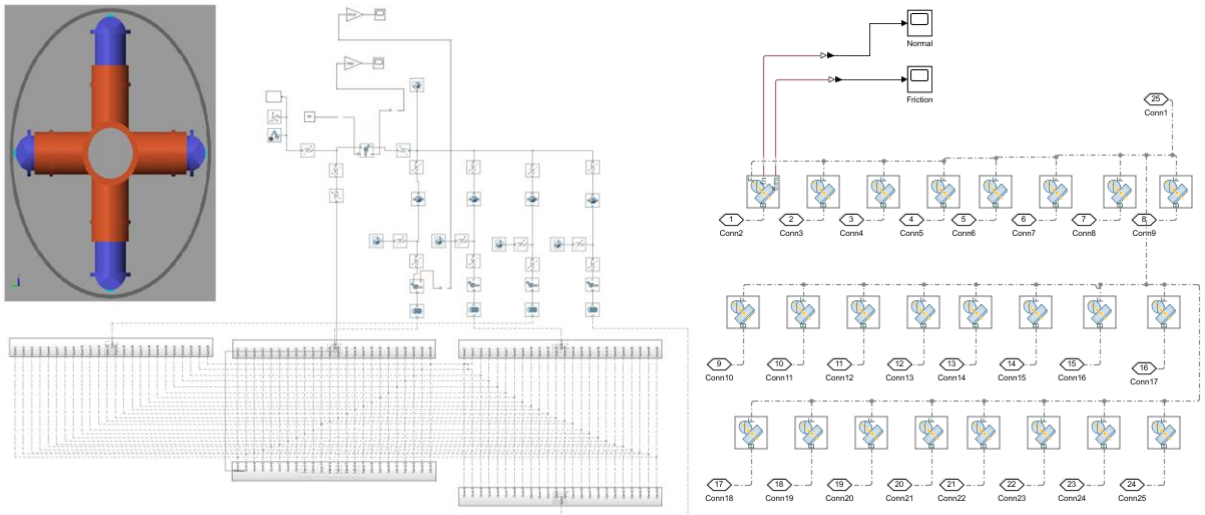


Figure 3. MATLAB/Simulink dynamics model of the compressor.

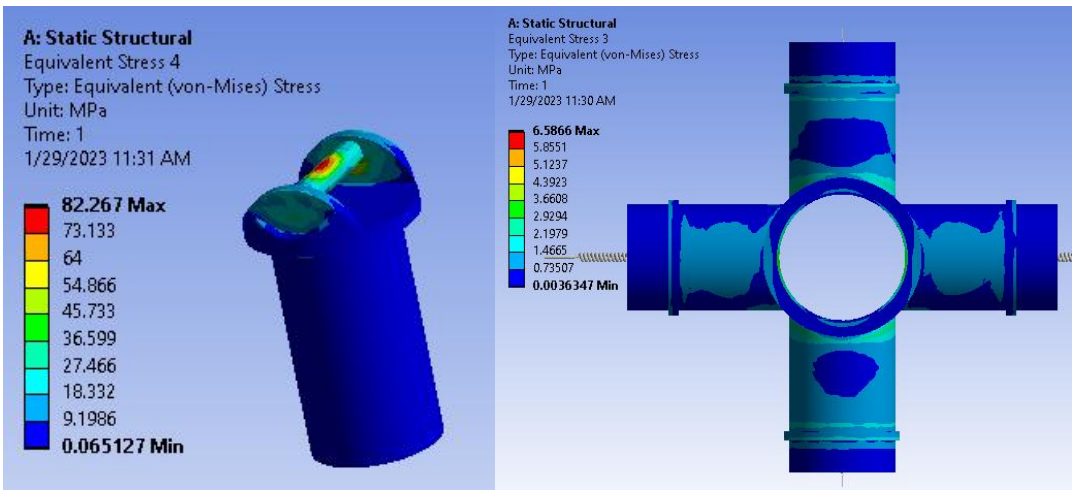


Figure 4. The generated mesh for the structural analysis and the stress values on compressor components.

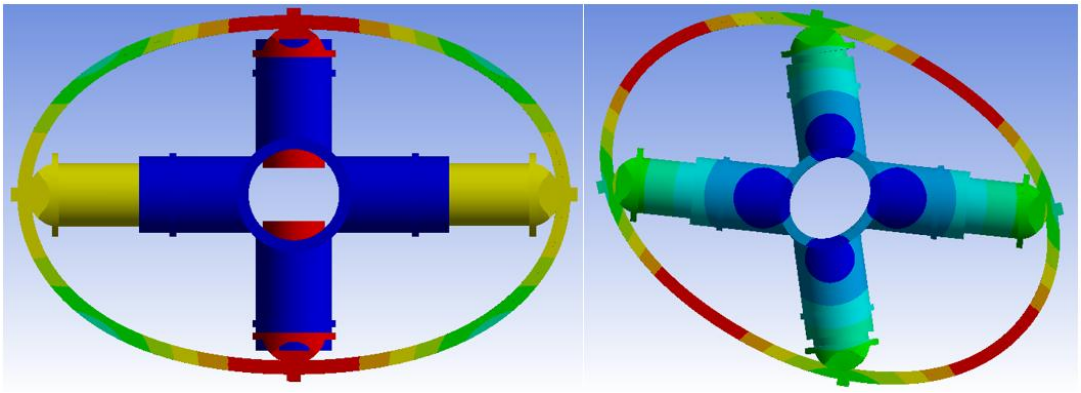


Figure 5. First and second mode shapes of the compressor mechanism.

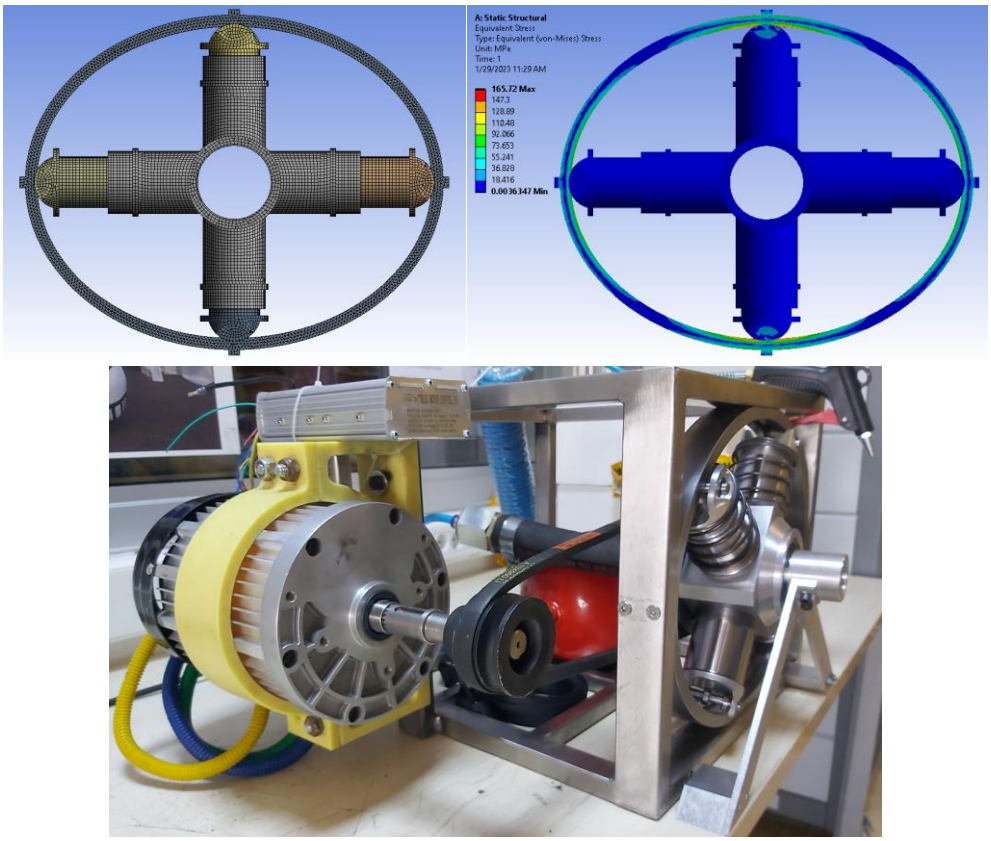


Figure 6. The manufactured prototype of the compressor.

4. Conclusion

In this study, a crankshaft-free compressor mechanism was proposed and numerical analyses, including thermodynamic cyclic, dynamic, structural, and modal analyses as well as experimental tests were conducted to ensure the operation of the designed system. The compressor was designed to deliver air at 800 kPa with volumetric flow rate of 200 L/min at the rotating speed of 1000 rpm. It was concluded from the experiments that a 1 kW electric motor was capable of driving the compressor to deliver air at around 185 L/min, which was relatively close to the predicted value. It was also seen that by increasing the electric motor power to around 2 kW, the designed compressor would be capable of delivering air at around 400 L/min. However, the experimental data were limited to an initial laboratory-scale prototype with a restricted range of operating condition. Further experimental analysis over a wider range of speeds as well as performance and durability testing are required in order to characterize the full performance of the compressor. The designed compressor can be considered as a potential alternative to conventional reciprocating compressors in industrial applications.

Author Contributions

The percentages of the author' contributions are presented below. The author reviewed and approved the final version of the manuscript.

	R.B.
C	100
D	100
S	100
DCP	100
DAI	100
L	100
W	100
CR	100
SR	100

C= concept, D= design, S= supervision, DCP= data collection and/or processing, DAI= data analysis and/or interpretation, L= literature search, W= writing, CR= critical review, SR= submission and revision.

Conflict of Interest

The author declared that there is no conflict of interest.

Ethical Consideration

Ethics committee approval was not required for this study because of there was no study on animals or humans.

Acknowledgements

The financial support for this work by TÜBİTAK-1512 BİGG Project No: 2211179 is greatly appreciated. The views expressed in this paper belong to the author.

References

El Samad, T., Żabnieńska-Góra, A., Jouhara, H., & Sayma, A. I. (2024). A review of compressors for high temperature heat pumps. In *Thermal Science and Engineering Progress* (Vol. 51). Elsevier Ltd. https://doi.org/10.1016/j.tsep.2024.102603

Hasanlu, M., Mahdian, S., & Shirvani, M. (2026). In-depth insights into industrial turbo-compressors for smarter maintenance and repair. *Advanced Manufacturing Research*. https://doi.org/10.21595/amr.2025.25400

Liu, Y., Yue, X., Zhang, Z., & Guo, J. (2026). Simulation study of a CO2 scroll compressor with main and pre-discharge valves. *International Journal of Refrigeration*, *182*, 273–286. https://doi.org/10.1016/j.ijrefrig.2025.11.016

Lu, K., Sultan, I. A., & Phung, T. H. (2022). Mathematical modeling and parametric study of the limaçon rotary compressor. *International Journal of Refrigeration*, *134*, 219–231. https://doi.org/10.1016/j.ijrefrig.2021.11.014

Lu, K., Sultan, I. A., & Phung, T. H. (2023). A Literature Review of the Positive Displacement Compressor: Current Challenges and Future Opportunities. In *Energies* (Vol. 16, Number 20). Multidisciplinary Digital Publishing Institute (MDPI). https://doi.org/10.3390/en16207035

Prescient & Strategic Intelligence. (2020). *Compressor Market Research Report (2020-2030)*. https://www.psmarketresearch.com/market-analysis/compressor-market

Shakya, P., & Ooi, K. T. (2020). Introduction to Coupled Vane compressor: Mathematical modelling with validation. *International Journal of Refrigeration*, *117*, 23–32. https://doi.org/10.1016/j.ijrefrig.2020.01.027

Shin, M., Na, S., Lee, J., Min, B., & Choi, G. (2019). Model analysis of a novel compressor with a dual chamber for high-efficiency systems. *Applied Thermal Engineering*, *158*. https://doi.org/10.1016/j.applthermaleng.2019.113717

Silva, W. L. V., Souza, L. C. O., Bortolaia, L. A., de Paula, M. R., & Leal, E. M. (2017). Study of the electricity consumption reduction of a compressed air system: The case of a steelmaking company. *Revista Escola de Minas*, *70*(4), 421–428. https://doi.org/10.1590/0370-44672015700189

Spark, I. J., & Lu, K. (2019). Chapter 1 - The orbital displacer: Implications and applications. In I. A. Sultan & T. H. Phung (Eds.), *Positive Displacement Machines* (pp. 3–35). Academic Press. https://doi.org/https://doi.org/10.1016/B978-0-12-816998-8.00001-7

Srivastava, P., Sharma, K., & Jha, R. (2016, February 8). *Modeling of Fixed Displacement Swash Plate Compressor: A Mathematical Approach towards Calculation of Shaft Torque and Volumetric Efficiency*. https://doi.org/10.4271/2016-28-0172

Tanveer, M. M., & Bradshaw, C. R. (2020). Quantitative and qualitative evaluation of various positive-displacement compressor modeling platforms. *International Journal of Refrigeration*, *119*, 48–63. https://doi.org/10.1016/j.ijrefrig.2020.07.009

Vittorini, D., & Cipollone, R. (2016). Energy saving potential in existing industrial compressors. In *Energy* (Vol. 102, pp. 502–515). Elsevier Ltd. https://doi.org/10.1016/j.energy.2016.02.115

Wang, L., Cao, H., Ding, G. L., Shao, Y., Yue, B., Wu, Z., & Liao, J.

(2026). A critical review and comparative study on positive displacement compressor models for fast performance prediction in wide working condition ranges. *Science and Technology for the Built Environment*. https://doi.org/10.1080/23744731.2026.2613623

Yalçın, K. (2011). *Kompresörler*. TMMOB Makina Mühendisleri Odası.

Black Sea Journal of Engineering and Science
doi: 10.34248/bsengineering.1990452

Open Access Journal
e-ISSN: 2619 – 8991

Araştırma Makalesi (Research Article)
Cilt 9 - Sayı 5: 2453-2461/ Eylül 2026
(Volume 9 - Issue 5: 2453-2461 / September 2026)

FIRÇALI DA MOTORLARDA AÇIK VERİ SETİ İLE MAKİNE ÖĞRENMESİ TABANLI KESTİRİMCİ BAKIM VE ARIZA TEŞHİSİ

Erdoğan ÖZEL*

[1]*Van Yüzüncü Yıl University, Faculty of Engineering, Department of Electrical and Electronics Engineering, 65080, Van, Türkiye*

Özet: Fırçalı Doğru Akım (FDA) motorları, endüstriyel otomasyon sistemlerinde ve tahrik mekanizmalarında yaygın olarak kullanılmakta olup, fırça aşınması ve sargı deformasyonları beklenmedik duruşlara ve yüksek bakım maliyetlerine neden olabilmektedir. Bu çalışmada, fırçalı DA motorların durum teşhisi ve Kalan Faydalı Ömür (Remaining Useful Life, RUL) tahmini için veri odaklı, ağaç tabanlı toplu öğrenme yöntemleri önerilmiştir. F.A.I.R veri setinden çoklu sensörlerden elde edilen akım, gerilim, devir, motor-ortam sıcaklık farkı ve spektral titreşim öznitelikleri kullanılarak motor ömrü; Evre I (Sağlıklı), Evre II (Hafif Aşınma), Evre III (Orta Aşınma) ve Evre IV (Kritik/Arıza) olmak üzere dört sağlık evresine ayrılmıştır. Durum teşhisinde Random Forest algoritması %98,7 test doğruluğu ve %95,70 10 katlı çapraz doğrulama başarısı ile Extra Trees algoritmasına göre daha yüksek performans göstermiştir. Öznitelik önem analizi, motor sağlığını en güçlü şekilde temsil eden değişkenlerin net sıcaklık artışı, yüksek frekanslı titreşim bileşenleri (16–26 kHz) ve motor devri olduğunu ortaya koymuştur. RUL tahmininde ise Extra Trees Regressor modeli 0,9666 belirlenme katsayısı (R^2) ve 21,49 zaman adımı RMSE değeri ile en başarılı sonucu elde ederken, Random Forest Regressor modeli 0,9603 R^2 ve 23,43 zaman adımı RMSE değerleriyle benzer düzeyde yüksek performans sergilemiştir. Elde edilen sonuçlar, önerilen yaklaşımın FDA motorlarda durum izleme ve öngörücü bakım uygulamaları için güvenilir ve etkili bir karar destek sistemi olarak kullanılabileceğini göstermektedir.

Anahtar kelimeler: Fırçalı DA motor, Kalan faydalı ömür (RUL), Durum teşhisi, Makine öğrenmesi, Random forest, Extra trees

Predictive Maintenance and Fault Diagnosis Based on Machine Learning with Open Data Set in Brushed DC Motors

Abstract: Brushed DC motors are widely used in industrial automation systems and drive mechanisms, but brush wear and winding deformations can lead to unexpected shutdowns and high maintenance costs. This study proposes data-driven, tree-based ensemble learning methods for condition diagnosis and Remaining Useful Life (RUL) estimation of brushed DC motors. Using current, voltage, speed, motor-ambient temperature difference, and spectral vibration features obtained from multiple sensors in the F.A.I.R dataset, motor life was divided into four health stages: Stage I (Healthy), Stage II (Slight Wear), Stage III (Moderate Wear), and Stage IV (Critical/Failure). In condition diagnosis, the Random Forest algorithm showed higher performance than the Extra Trees algorithm with 98.7% test accuracy and 95.70% 10-fold cross-validation success. Feature significance analysis revealed that the variables most strongly representing motor health were net temperature rise, high-frequency vibration components (16–26 kHz), and motor speed. In RUL prediction, the Extra Trees Regressor model achieved the most successful result with a coefficient of determination (R^2) of 0.9666 and a time-step RMSE value of 21.49, while the Random Forest Regressor model showed similarly high performance with an R^2 of 0.9603 and a time-step RMSE value of 23.43. The results indicate that the proposed approach can be used as a reliable and effective decision support system for condition monitoring and predictive maintenance applications in brushed DC motors.

Keywords: Brushed DC motor, Remaining useful life (RUL), Condition diagnosis, Machine learning, Random forest, Extra trees

***Sorumlu yazar (Corresponding author):** Van Yüzüncü Yıl University, Faculty of Engineering, Department of Electrical and Electronics Engineering, 65080, Van, Türkiye
E mail: erdoganozel@yyu.edu.tr (E.ÖZEL)
Erdoğan ÖZEL https://orcid.org/0000-0002-4366-7257

Gönderi: 09 Temmuz 2026 **Received:** July 09, 2026
Kabul: 12 Ağustos 2026 **Accepted:** August 12, 2026
Yayınlanma: 15 Eylül 2026 **Published:** September 15, 2026

Cite as: Özel, E. (2026). Predictive maintenance and fault diagnosis based on machine learning with open data set in brushed DC motors. *Black Sea Journal of Engineering and Science,* 9(5), 2453-2461.

1. Giriş

Doğru akım (DA) motorları, hassas hız ve tork kontrolü gerektiren uygulamalarda vazgeçilmez güç dönüştürücüleri olmuştur. Fırçasız motor teknolojilerindeki hızlı gelişmelere rağmen, fırçalı DA motorlar maliyet etkinlikleri, yüksek başlangıç torku ve basit kontrol yapıları sayesinde otomotiv, endüstriyel otomasyon, madencilik ve enerji sektörlerinde geniş bir uygulama alanını korumaktadır. Bu motorların temel yapısal bileşeni olan fırça-komütatör düzeneği, dönen rotor sargılarına sabit referans çerçevesinden elektrik iletimini sağlamakla birlikte, sürekli mekanik sürtünme ve elektriksel yük altında çalışması nedeniyle en kritik aşınma noktasını oluşturmaktadır (Barkas vd., 2020; Filina vd., 2023). FDA motorlar, yapıları gereği sürekli dönen bir komütatör (kollektör) yüzeyine mekanik olarak temas eden karbon-grafit fırçalara bağımlıdır. Fırça-komütatör arayüzünde meydana gelen sürekli sürtünme, yüksek akım yoğunlukları ve elektriksel arklar, zamanla bu bileşenlerin hızla aşınmasına ve

This work is licensed (CC BY-NC 4.0) under Creative Commons Attribution 4.0 International License

motorun işlevini yitirmesine yol açmaktadır (Pham vd., 2023; Teel-Jongebloed, 2020). Literatür incelendiğinde, FDA motorlardaki arızaların büyük bir kısmının komütatör ve fırça aşınmalarından kaynaklandığı görülmektedir. Bu tür beklenmedik bileşen arızaları, üretim hatlarında plansız duruşlara, iş gücü kayıplarına ve yüksek bakım maliyetlerine neden olmaktadır.

Geleneksel bakım stratejileri, fırçaların belirli çalışma saatlerinden sonra periyodik olarak değiştirilmesine dayanır. Ancak fırça aşınma hızı, yük profili, ortam sıcaklığı, nem ve komütatör yüzey kalitesi gibi çok sayıda faktöre bağlı olduğundan, sabit aralıklı bakım planları hem erken değiştirme (gereksiz maliyet) hem de geç değiştirme (beklenmedik arıza) riskini beraberinde getirir (Filina ve Tsvetkov, 2019). Bu bağlamda, Durum Tabanlı Kestirimci Bakım yaklaşımları, fırça sağlığını gerçek zamanlı olarak izleyerek bakım müdahalelerini optimize etme imkânı sunmaktadır. Bu bağlamda, fırça–komütatör sisteminden elde edilen titreşim, sıcaklık, akım, gerilim ve akustik sinyallerinin sürekli izlenmesi, fırça aşınmasının erken tespiti ile kestirimci bakım uygulamalarının gerçekleştirilmesine olanak sağlamaktadır (Reñones, 2020).

Son yıllarda durum temelli bakım ve makine sağlığı öngörüsü alanında, sensörlerden elde edilen çok değişkenli zaman serisi verilerinin analizine dayalı veri odaklı yaklaşımlar önemli ölçüde gelişmiştir. Bu süreçte yapay zekâ ve makine öğrenmesi algoritmaları; sağlık göstergelerinin oluşturulması, makinenin sağlık evrelerinin belirlenmesi ve kalan faydalı ömrünün tahmin edilmesi amacıyla yaygın olarak kullanılmakta ve kestirimci bakım uygulamalarının temel bileşenleri arasında yer almaktadır (Lei ve vd., 2018). Özellikle üretken yapay zekâ tabanlı modeller, ekipman davranışlarını öğrenerek olası arızaları önceden tahmin edebilmekte ve bakım planlarının optimize edilmesine olanak sağlamaktadır (Mohapatra, 2024; Rajabioun vd., 2025). Ancak, kestirimci bakım alanında akademik ve pratik çalışmalar yürüten araştırmacıların karşılaştığı en büyük zorluklardan biri, bir motorun normal çalışma durumundan tamamen arıza durumuna kadar geçen tüm aşınma sürecini içeren, güvenilir ve zengin içerikli açık veri setlerine erişimin kısıtlı olmasıdır. Endüstriyel ölçekteki ekipmanların arızalanana kadar çalıştırılması hem maliyetli hem de operasyonel olarak risklidir (Reñones, 2020).

Bu çalışmada, söz konusu literatür boşluğunu doldurmak ve veri odaklı arıza teşhis yöntemlerini test etmek amacıyla paylaşılan açık veri seti kullanılmıştır. Deneyler sırasında nominal çalışma koşullarının dışına çıkarılarak hızlandırılmış aşınma sürecine maruz bırakılan FDA motor üzerinden; yüksek frekanslı titreşim, akım, besleme gerilimi ve sıcaklık verileri toplanmıştır. Çalışma kapsamında, bu veriler üzerinde gerçekleştirilen özellik mühendisliği ve frekans analizi tabanlı sinyal işleme çıktılarından yararlanılmıştır. Toplanan çoklu sensör öznitelikleri, Random Forest ve Extra Tree makine öğrenmesi algoritmaları eğitilmiş; motorun komütatör aşınma aşamaları sınıflandırılmış ve arıza kararlılığı analiz edilmiştir.

2. Materyal ve Yöntem

Bu çalışmada, Reñones (2020) tarafından geliştirilen F.A.I.R. (Findable, Accessible, Interoperable and Reusable) açık erişimli FDA motor arıza veri seti kullanılmıştır(Reñones, 2020). F.A.I.R. açık veri seti çalışmasında kullanılan FDA motorunda hızlandırılmış komütatör-fırça aşınması esnasında toplanan çoklu sensör verileri kullanılarak motorun sağlık durumunun anlık olarak teşhis edilmesi hedeflenmiştir. Önerilen kestirimci bakım metodolojisi; veri setinin yapısı, öznitelik mühendisliği, veri kümesi bölümlendirme ve makine öğrenmesi tabanlı sınıflandırma olmak üzere beş ana aşamadan oluşmaktadır.

2.1. Fırçalı Doğru Akım Motorları

Fırçalı doğru akım motorları, oyuncak sistemleri, otomotiv uygulamaları, elektrikli el aletleri gibi çok çeşitli alanlarda yaygın olarak kullanılan elektromekanik enerji dönüştürücüleridir. Bu motorların alternatif akım motorlarına göre temel üstünlüklerinden biri, ek güç dönüştürücü gereksinimi olmaksızın doğrudan batarya kaynaklarından beslenebilmesi ve yaklaşık 20.000 dev/dak'a ulaşabilen yüksek dönme hızlarında çalışabilmesidir. Bunun yanı sıra, düşük üretim maliyetleri, basit kontrol yapıları, kompakt tasarım imkânı ve farklı boyut ile geometrilerde üretilebilmeleri, FDA motorlarının endüstriyel, ticari ve taşınabilir sistemlerde yaygın olarak tercih edilmesini sağlamaktadır (Cros vd., 2009) F.A.I.R. veri seti çalışmasında kullanılan FDA motorunun temel bileşenleri şekil 1'de verilmiştir.

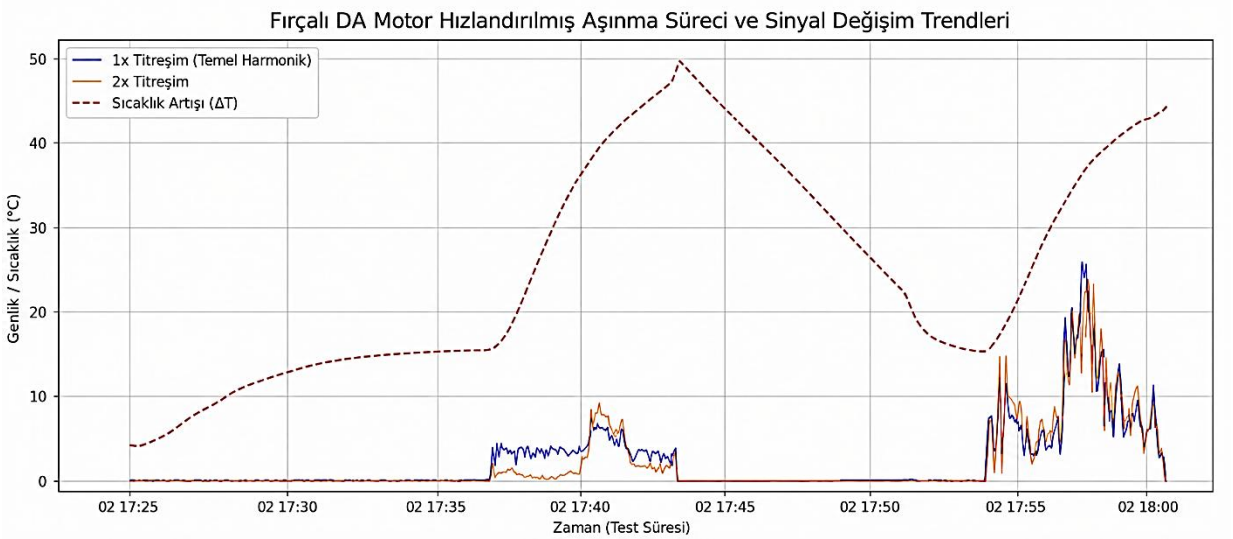


Şekil 1. F.A.I.R. veri seti çalışmasında kullanılan FDA motorunun temel bileşenleri: Armatür, sargılar, fırçalar, komütatör ve stator mıknatısları (Reñones, 2020).

2.2. Deneysel Veri Seti ve Sistem Altyapısı

Bu çalışmada kullanılan veri seti, Reñones (2020) tarafından geliştirilen F.A.I.R. (Findable, Accessible, Interoperable and Reusable) açık erişimli FDA motor arıza veri setinden elde edilmiştir. F.A.I.R. çalışmasında kullanılan deneysel veri seti, açık kaynaklı bir FDA motorun hızlandırılmış ömür testinden elde edilmiştir. Toplam 377 satır gözlem ve 50 farklı sensör özniteliğinden oluşan bu veri tabanı, motorun sağlıklı ilk çalışma anından katastrofik arıza (durma/bozulma)

anına kadar geçen yaklaşık 35 dakikalık kesintisiz bir aşınma sürecini kronolojik olarak kaydetmektedir. Veri toplama sistemi kapsamında; motor hızı, besleme gerilimi, çekilen toplam akım, motor gövde sıcaklığı ve ortam sıcaklığı anlık olarak ölçülmüştür. Bunlara ek olarak, arıza teşhisinde en kritik rolü oynayan titreşim ve akım sinyalleri, frekans alanına (FFT) dönüştürülerek 1x'ten 10x'e kadar olan harmonik bileşenleri ve belirli geniş frekans bantları (0-4kHz, 16-26kHz vb.) bazında yüksek hassasiyette kaydedilmiştir (Reñones, 2020). Şekil 2'de F.A.I.R. veri setinden alınan fırçalı DA motorun yaklaşık 35 dakikalık hızlandırılmış ömür testi boyunca kritik sensör sinyallerinin zamana bağlı değişim trendleri sunulmuştur.



Şekil 2. F.A.I.R. veri seti FDA hızlandırılmış aşınma süreci ve sinyal değişim trendleri (Reñones, 2020).

2.3. Öznitelik Mühendisliği

FDA motorlarda fırça-komütatör temas yüzeyinde meydana gelen aşınma, temas direncinin artmasına, mekanik sürtünmenin yükselmesine ve elektriksel ark oluşumunun sıklaşmasına neden olmaktadır. Bu süreçler motor içerisinde ek enerji kayıpları oluşturarak sıcaklık artışına yol açmaktadır. Bu nedenle sıcaklık değişimi, motorun çalışma sağlığını değerlendirmede yaygın olarak kullanılan durum izleme parametrelerinden biridir (Jardine vd., 2005; Mohapatra, 2024) Motor dış gövde sıcaklığı (temp_mot), ortam sıcaklığındaki (temp_ort) mevsimsel veya çevresel değişimlerden etkilenebileceğinden tek başına yanıltıcı olabilmektedir. Bu doğrultuda, çevresel gürültüleri elimine etmek ve arızanın termal karakteristiğini daha kararlı hale getirmek amacıyla eşitlik 1 kullanılarak net sıcaklık artışı (ΔT) parametresi türetilmiştir:

$$\Delta T = temp_mot - temp_ort \quad (1)$$

Bu diferansiyel öznitelik sayesinde model, ortam sıcaklığındaki değişimlerden büyük ölçüde bağımsız hâle getirilmiş ve yalnızca motor içerisinde sürtünme, temas direnci ve elektriksel ark oluşumu sonucu meydana gelen sıcaklık artışına odaklanmıştır. Literatürde, ham sensör verilerinden fiziksel anlam taşıyan yeni özniteliklerin türetilmesi, makine öğrenmesi modellerinin ayırt ediciliğini artıran ve genelleme performansını iyileştiren önemli bir veri ön işleme yöntemi olarak kabul edilmektedir (Guyon ve Elisseeff, 2003; Zheng ve Casari, 2018).

2.4. Zaman Serisi Etiketleme ve Sağlık Evreleri

Motorun sürekli aşınma sürecini doğrusal bir yaklaşımla temsil edebilmek ve makine öğrenmesi modeli için gözetimli öğrenmeye uygun hedef değişken oluşturabilmek amacıyla zaman serisi verileri kronolojik sıraya göre eşit uzunlukta dört evreye ayrılmıştır. Bu yaklaşım, gerçek zamanlı aşınma miktarının doğrudan ölçülemediği durumlarda ekipmanın yaşam döngüsünün belirli sağlık evrelerine ayrılması esasına dayanmaktadır. Kestirimci bakım ve kalan faydalı ömür (RUL) çalışmalarında, fiziksel bozunma miktarını doğrudan temsil eden etiketlerin bulunmadığı veri kümelerinde, zaman eksenli veya sağlık göstergelerine dayalı etiketleme yöntemleri yaygın olarak kullanılmaktadır (Lei vd., 2018; Karakılıç vd., 2025). Bu nedenle veri seti kronolojik sıraya göre dört eşit bölüme ayrılmış ve her bölüm artan bozunma seviyesini temsil eden bir sağlık evresi olarak tanımlanmıştır. Gerçek aşınma miktarını gösteren fiziksel referans ölçümlerinin bulunmadığı durumlarda, zamana dayalı eşit aralıklı etiketleme yaklaşımı, bozunmanın monoton olarak arttığı varsayımı altında makine öğrenmesi modellerinin eğitimi için literatürde kabul gören pragmatik veri hazırlama yöntemlerinden biridir (Ellefsen vd., 2019).

Toplam satır sayısının (N=377) çeyrek periyotları (N/4) referans alınarak yapılan matematiksel etiketleme mantığı şu şekildedir:

- Evre I (Normal Çalışma): $0 \leq indeks < \frac{N}{4}$ Motorun mekanik ve termal olarak tamamen sağlıklı olduğu başlangıç dönemi.

- Evre II (Başlangıç Aşınması): $\frac{N}{4} \leq indeks < \frac{2N}{4}$ Mikroskobik fırça aşınmalarının başladığı, sinyallerde hafif pürüzlerin oluştuğu dönem.
- Evre III (İleri Düzey Aşınma): $\frac{2N}{4} \leq indeks < \frac{3N}{4}$ Komütatör yüzey kalitesinin bozulmaya başladığı ve termal artışın hızlandığı kararsızlık dönemi.
- Evre IV (Kritik / Arıza Durumu): $\frac{3N}{4} \leq indeks \leq N$ Fırçaların yüzeyden sıçrama yaptığı, ark seviyesinin ve titreşimin pik noktaya ulaştığı katastrofik süreç.

Dört evre seçimi, sınıf dengesini korumak, her evrede yeterli örnek sayısı sağlamak ve bozunma sürecini normal, erken aşınma, orta aşınma ve kritik aşınma olmak üzere yorumlanabilir sağlık durumlarına ayırmak amacıyla tercih edilmiştir. Belirlenen sağlık evrelerine göre sensör sinyallerinin tanımlayıcı istatistiksel ortalamaları Tablo 1'de verilmiştir.

Tablo 1. Belirlenen sağlık evrelerine göre sensör sinyallerinin tanımlayıcı istatistiksel ortalamaları

Motor Durumu	Ortalama Akım (A)	Temel Titreşim Genliği (g RMS)	Ortalama Motor Sıcaklığı (°C)	Ortalama Ortam Sıcaklığı (°C)
Evre I (Sağlıklı)	1,83	2,50	38,30	22,09
Evre II (Hafif Aşınma)	1,94	2,61	49,33	22,18
Evre III (Orta Aşınma)	2,05	2,76	58,74	22,25
Evre IV (Kritik Aşınma)	2,45	3,52	64,39	22,29

Tablo 1 incelendiğinde, kronolojik etiketleme sonucunda oluşturulan sağlık evrelerinin motorun fiziksel davranışıyla tutarlı eğilimler sergilediği görülmektedir. Ortalama akım değeri Evre I'de 1,83 A iken Evre IV'te 2,45 A'a yükselmiştir. Benzer şekilde motor gövde sıcaklığı 38,30 °C'den 64,39 °C'ye, temel titreşim genliği ise 2,50 'den 3,52'ye artmıştır. Buna karşın ortam sıcaklığının deney süresince sabit seviyede kalması, motor sıcaklığındaki artışın büyük ölçüde motor içerisindeki sürtünme, temas direnci ve elektriksel kayıplarla ilişkili olduğunu göstermektedir.

Bu bulgular, kronolojik olarak oluşturulan sağlık evrelerinin sensör verilerindeki bozunma eğilimleriyle uyumlu olduğunu ve oluşturulan etiketlerin makine öğrenmesi modellerinin eğitimi için ayırt edici bir hedef değişken sağladığını göstermektedir. Bununla birlikte, sağlık evreleri veri setinde fırça aşınma miktarı, temas direnci veya komütatör aşınmasını temsil eden doğrudan fiziksel eşik değerleri bulunmadığından, zaman ekseni boyunca eşit uzunlukta dört bölüme ayrılarak oluşturulmuştur. Dolayısıyla Evre II ile Evre III arasındaki sınır fiziksel aşınma geçişini değil, veri temelli kronolojik bir etiketlemeyi temsil etmektedir. Bu durum çalışmanın önemli sınırlılıklarından biri olup, gelecekte fiziksel aşınma ölçümleriyle desteklenen veri setleri kullanılarak sağlık evrelerinin fiziksel kriterlere dayalı olarak tanımlanması önerilmektedir.

2.5. Öznitelik Seçimi

F.A.I.R. Veri seti; titreşim, sıcaklık, motor akımı, gerilim, devir sayısı ve farklı frekans bantlarına ait spektral bileşenler olmak üzere motorun mekanik, elektriksel ve termal durumunu temsil eden toplam 50 değişken içermektedir. Veri setindeki tüm özniteliklerin doğrudan modele aktarılması, yüksek boyutlu veri uzayında bilgi içeriği düşük veya yüksek korelasyonlu değişkenlerin model karmaşıklığını artırmasına ve genelleme performansının azalmasına neden olabilmektedir. Bu durum makine öğrenmesi literatüründe boyutluluk laneti olarak tanımlanmakta olup, uygun öznitelik seçiminin aşırı öğrenmeyi azaltarak model doğruluğunu artırdığı bilinmektedir (Guyon ve Elisseeff, 2003; Hastie vd., 2009). Bu nedenle çalışmada, veri setinde bulunan değişkenler arasından fırçalı DA motor fırça aşınmasının mekanik, elektriksel ve termal etkilerini en iyi temsil eden öznitelikler seçilmiştir. Bu yaklaşım, titreşim tabanlı durum izleme ve kestirimci bakım literatüründe önerilen özellik seçimi stratejileriyle uyumlu olduğu görülmektedir (Jardine vd., 2005; Randall, 2021) Seçim sürecinde yalnızca değişken sayısını azaltmak değil, aynı zamanda arıza mekanizmasını fiziksel olarak temsil eden parametrelerin korunması hedeflenmiştir. Bu kapsamda sıcaklık artışı (ΔT), düşük frekanslı titreşim harmonikleri (1X, 2X ve 3X), 16–26 kHz aralığındaki yüksek frekanslı titreşim bileşenleri, motor akımı, motor gerilimi, akım harmonikleri ve motor devir sayısı model girdileri olarak kullanılması tercih edilmiştir.

Düşük frekanslı titreşim harmonikleri rotor dengesizliği, mekanik gevşeklik ve komütatör-fırça etkileşimlerinden kaynaklanan temel dinamik davranışı temsil ederken, yüksek frekanslı (16–26 kHz) titreşim bileşenleri fırça sıçraması, ark oluşumu ve darbe karakterli temas bozukluklarının belirlenmesinde önemli bilgiler sağlamaktadır. Buna karşılık, 4X–10X arasındaki yüksek harmonik bileşenlerin deneysel veri setinde düşük genlikli ve yüksek gürültü içerdiği gözlendiğinden bu harmonikler modele dâhil edilmemiştir. Yüksek frekans

bölgesindeki bilgi kaybını önlemek amacıyla bu harmonikler yerine 16–26 kHz geniş bant enerji bileşeni kullanılmıştır. Ayrıca motor akımı ve gerilim değişkenleri yük değişimlerini ve elektriksel çalışma koşullarını temsil ederken, akım harmonikleri komütasyon bozuklukları ile ark oluşumuna bağlı dalga şekli değişimlerinin belirlenmesinde kullanılmıştır. Motor devir sayısı ise artan sürtünme torkunun neden olduğu mekanik performans değişimlerini temsil eden tamamlayıcı bir öznitelik olarak modele dâhil edilmiştir.

2.6. Makine Öğrenme Algoritmaları

Bu çalışmada, fırçalı DA motorların sağlık evrelerinin sınıflandırılması amacıyla karar ağacı tabanlı iki denetimli makine öğrenmesi algoritması olan Random Forest (RF) ve Extra Trees (ET) kullanılmıştır. Her iki algoritma da topluluk öğrenmesi yaklaşımına dayanmakta olup, çok sayıda karar ağacının birlikte çalışması prensibi ile sınıflandırma gerçekleştirmektedir. Topluluk öğrenmesi yöntemleri, tek bir karar ağacına göre daha yüksek doğruluk, daha düşük varyans ve daha güçlü genelleme performansı sağlamaları nedeniyle arıza teşhisi ve kestirimci bakım uygulamalarında yaygın olarak kullanılmaktadır (Breiman, 2001; Geurts vd., 2006).

Makine öğrenmesi modellerinde hiperparametre optimizasyonu, modelin genelleme yeteneğini ve tahmin doğruluğunu artırdığı için kritik öneme sahiptir. Tahmin modelleri geliştirilirken, grid search gibi sistematik hiperparametre arama teknikleri sıklıkla kullanılmaktadır. Bu yöntem, belirlenen hiperparametre değerlerinin farklı kombinasyonlarını *GridSearchCV* çerçevesinde değerlendirmekte ve en yüksek performansı veren kombinasyonu seçmektedir. Literatürde de, Ensemble modellerde (Random Forest, Extreme Randomized Trees vb.) hiperparametre arama stratejileri ile farklı kombinasyonlar değerlendirilmiş ve performansı artıran parametre kümeleri seçilmiştir(Bergstra ve Bengio, 2011; Ippolito, 2022).

Bu çalışmada RF ve ET modellerinin hiperparametre optimizasyonu GridSearchCV yöntemi kullanılarak gerçekleştirilmiştir. Hiperparametre arama sürecinde ağaç sayısı (*n_estimators*), maksimum ağaç derinliği (*max_depth*), düğüm bölünmesi için gerekli minimum örnek sayısı (*min_samples_split*), yaprak düğümde bulunması gereken minimum örnek sayısı (*min_samples_leaf*), her düğümde değerlendirilecek özellik sayısı (*max_features*) ve Random Forest modeli için ayrıca *bootstrap* parametresi değerlendirilmiştir. Her parametre kombinasyonu 10 katlı çapraz doğrulama (10-fold cross-validation) (Mahlich vd., 2025) ile test edilmiş ve doğruluk (*accuracy*) ölçütüne göre en yüksek performansı sağlayan kombinasyon nihai model olarak seçilmiştir. Tablo 2'de Random Forest ve Extra Trees modellerinde kullanılan hiperparametre arama uzayı ve elde edilen optimum hiperparametreler verilmiştir.

Tablo 2. Random Forest ve Extra Trees modellerinde kullanılan hiperparametre arama uzayı ve elde edilen optimum hiperparametreler

Hiperparametre	Açıklama	Aranan Değerler	RF	ET
n_estimators	Karar ağacı sayısı	100, 200, 300, 400, 500	100	100
max_depth	Maksimum ağaç derinliği	10, 15, 20, 25, None	20	20
min_samples_split	Bir düğümün bölünebilmesi için gerekli minimum örnek sayısı	2, 5, 10	2	5
min_samples_leaf	Yaprak düğümde bulunması gereken minimum örnek sayısı	1, 2, 4	1	1
max_features	Her düğümde değerlendirilecek maksimum özellik sayısı	sqrt, log2	sqrt	sqrt
bootstrap*	Bootstrap örnekleme yöntemi	True	True	–

*Yalnızca Random Forest algoritmasında kullanılmıştır.

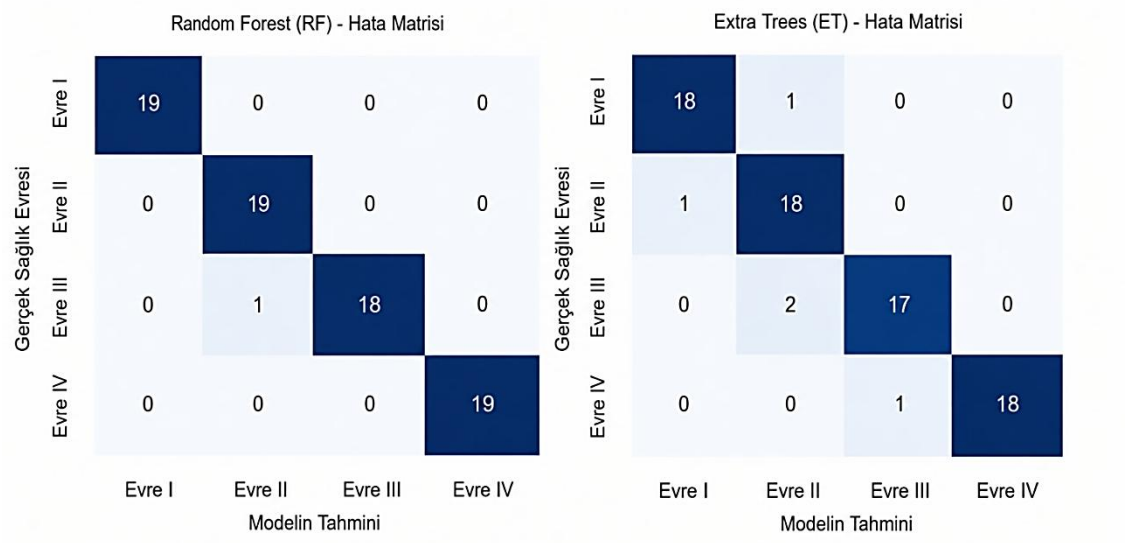
Model geliştirme sürecinde veri kümesi eğitim ve test alt kümelerine %80-%20 oranında ayrılmıştır. Veri bölme işlemi, sağlık evrelerinin her iki alt kümede dengeli biçimde temsil edilmesini sağlamak amacıyla train_test_split fonksiyonu ve stratify parametresi kullanılarak gerçekleştirilmiştir. Böylece her sağlık evresi eğitim ve test kümelerinde benzer dağılım oranlarıyla korunmuştur. Model performansı yalnızca eğitim verisi kullanılarak geliştirilen modeller üzerinde değerlendirilmiş ve test kümesi eğitim sürecine dâhil edilmemiştir. Bu yaklaşım, eğitim ve test verileri arasında veri sızıntısı (data leakage) oluşmasını önlemeyi amaçlamaktadır.

3. Bulgular ve Tartışma

Fırçalı DA motora ait akım, voltaj, devir sayısı, sıcaklık ve spektral titreşim öznitelikleri kullanılarak gerçekleştirilen durum teşhisi (sınıflandırma) ve kalan faydalı ömür (RUL) tahmini (regresyon) sonuçları analiz edilmiştir. Önerilen ağaç tabanlı toplu öğrenme mimarileri olan RF ve ET algoritmalarının performansları ampirik bulgularla ortaya konulmuştur.

3.1. Sağlık Evresi Sınıflandırma ve Durum Teşhis Performansı

FDA motorun operasyonel ömrü boyunca sergilediği 4 farklı aşınma evresini (Evre I: Sağlıklı, Evre II: Hafif Aşınma, Evre III: Orta Aşınma, Evre IV: Kritik/Arıza) ayırt etmek amacıyla geliştirilen sınıflandırma modellerinin hata dağılımlarını ve evreler arasındaki geçiş hassasiyetlerini detaylı incelemek için üretilen hata matrisleri Şekil 3'te verilmiştir.



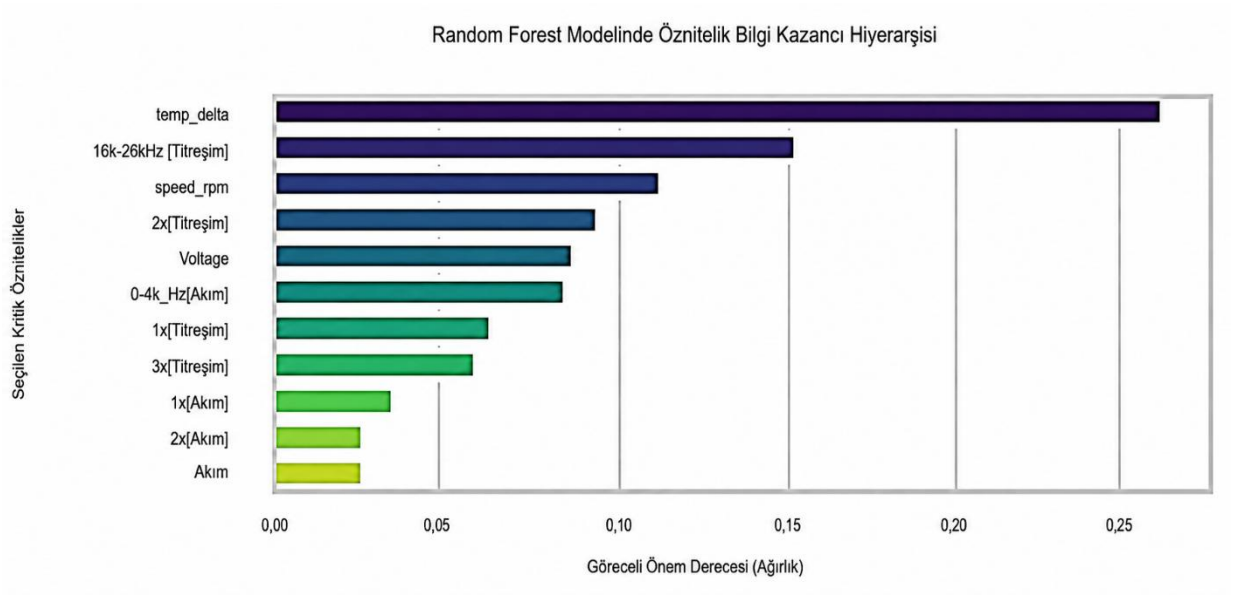
Şekil 3. Modellerin hata dağılımlarını ve evre geçiş hassasiyetlerini gösteren hata matrisleri.

Her iki hata matrisi de bağımsız test kümesinde yer alan toplam 76 örnek üzerinden oluşturulmuştur. Matrislerde diyagonal elemanlar doğru sınıflandırılan, diyagonal dışındaki elemanlar ise yanlış sınıflandırılan örnekleri göstermektedir. Hata matrisleri incelendiğinde her iki modelin de sınıflar arasında yüksek ayırım başarısı gösterdiği görülmektedir. Yanlış sınıflandırmalar yalnızca ardışık aşınma evreleri (özellikle Evre II ve Evre III) arasında gerçekleşmiş, uzak evreler arasında herhangi bir karışıklık gözlenmemiştir. RF modeli Evre IV örneklerinin tamamını doğru sınıflandırırken, ET modeli yalnızca bir Evre IV örneğini Evre III olarak sınıflandırmıştır. Bu sonuçlar, modellerin özellikle kritik arıza evresinin belirlenmesinde yüksek güvenilirliğe sahip olduğunu göstermektedir

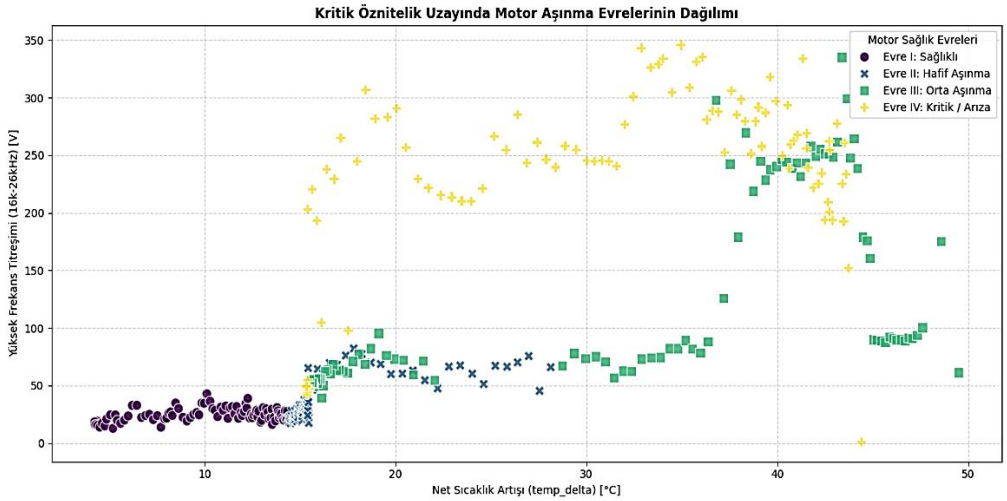
3.2. Öznitelik Önem Dereceleri ve Fiziksel Karakterizasyon

Random Forest modeli tarafından hesaplanan bilgi kazancı tabanlı öznitelik önem dereceleri Şekil 4'te hiyerarşik olarak sunulmuştur.

Öznitelik önem analizi, hem sağlık evrelerinin sınıflandırılması hem de kalan faydalı ömür (RUL) tahmini açısından yüksek frekanslı titreşim bileşenleri, sıcaklık farkı (ΔT) ve elektriksel büyüklüklerin belirleyici olduğunu göstermektedir. Özellikle yüksek frekanslı titreşim bileşenleri, fırça-komütatör temas yüzeyindeki aşınmaya bağlı olarak gelişen mekanik düzensizlikleri yansıtırken, sıcaklık farkı (ΔT) motorun termal davranışındaki değişimleri ortaya koymaktadır. Benzer şekilde akım ve elektriksel harmonik bileşenleri de fırça aşınmasının elektriksel etkilerini temsil ederek modellerin ayırt ediciliğini artırmıştır. Bu bulgular, seçilen özniteliklerin motorun fiziksel bozunma mekanizmasını başarılı bir şekilde temsil ettiğini ve geliştirilen modellerin karar verme sürecinin fiziksel olarak anlamlı değişkenlere dayandığını göstermektedir. Seçilen bu kritik özniteliklerin oluşturduğu öznitelik uzayındaki anlamsal dağılım Şekil 5'teki saçılım grafiğinde görselleştirilmiştir.



Şekil 4. Random Forest modeli tarafından hesaplanan bilgi kazancı tabanlı öznitelik önem dereceleri hiyerarşik sıralaması.



Şekil 5. Kritik özniteliklerin oluşturduğu öznitelik uzayındaki anlamsal dağılım.

Grafikte, net sıcaklık artışı ile yüksek frekans spektral titreşim bileşenlerinin eş zamanlı olarak motorun aşınma evrelerini belirgin kümeler halinde ayırabildiği fiziksel olarak göstermektedir. Motor kararlı durumdan arıza durumuna geçtikçe, sargı ve fırça sürtünmesinden kaynaklanan termal yük yükselmiş, mikro ark gürültüleri ise yüksek frekans titreşim genliklerini artırdığı görülmektedir.

3.3. Kalan Faydalı Ömür (RUL) Tahmin Sonuçları

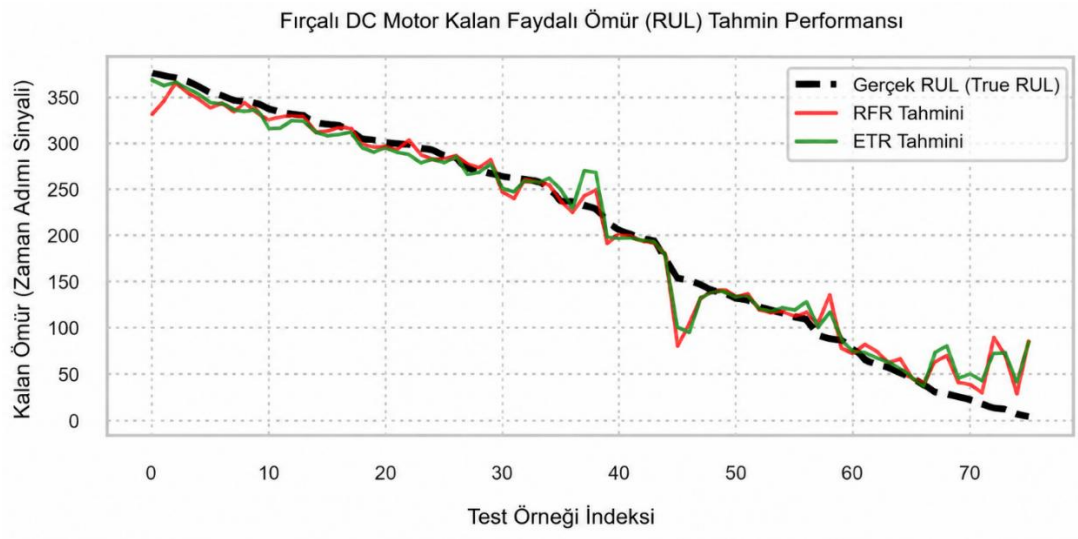
Çalışmada, motor sağlığını sadece kesikli evrelerle sınıflandırmakla yetinilmeyip, sürekli bir bozunum eğrisi üzerinden Kalan Faydalı Ömür (RUL) kestirimi de gerçekleştirilmiştir. Ağaç tabanlı regresyon modellerinin test seti üzerindeki tahmin başarıları Tablo 3'te verilmiştir.

Tablo 3. RF ve ET modellerinin sınıflandırma ve RUL tahmin performanslarının karşılaştırılması

Algoritma	10-Fold CV (%)	Test Doğruluğu (%)	F1-Skoru (%)	R^2	RMSE (Zaman Adımı)
RF	95,70	98,70	98,70	-	-
ET	95,38	93,40	93,50	-	-
RFR	-	-	-	0,9603	23,43
ETR	-	-	-	0,9666	21,49

Tabloda sınıflandırma ve regresyon modellerinin performansları karşılaştırılmıştır. Sınıflandırmada Random Forest modeli, %95,70 çapraz doğrulama başarısı, %98,70 test doğruluğu ve %98,70 F1-skoru ile en yüksek performansı göstermiştir. Extra Trees modeli ise %95,38 çapraz doğrulama başarısı, %93,40 test doğruluğu ve %93,50 F1-skoru elde etmiştir. Regresyon sonuçlarında ise Extra Trees Regressor modeli 0,9666 R^2 ve 21,49 RMSE ile Random Forest Regressor modelinden (R^2 = 0,9603, RMSE = 23,43) daha başarılı sonuçlar vermiştir. Genel olarak, Random Forest sınıflandırmada, Extra Trees Regressor ise RUL tahmininde daha yüksek performans sergilemiştir. RUL tahmin performans grafiklerinin zamana bağlı iz düşümü Şekil 6'da verilmiştir.

Grafikte, RFR ve ETR modelleri için bağımsız test kümesinde elde edilen gerçek ve tahmin edilen Kalan Faydalı Ömür (RUL) değerlerinin karşılaştırılması sunulmaktadır. X ekseni kronolojik zaman sırasını değil, bağımsız test kümesinde yer alan örneklerin indekslerini; Y ekseni ise bu örneklere ait Kalan Faydalı Ömür (RUL) değerlerini göstermektedir. Her iki model de motorun kalan ömründeki azalma eğilimini başarılı bir şekilde takip etmiş ve tahmin eğrileri genel olarak gerçek RUL eğrisi ile yüksek uyum göstermiştir. Özellikle ömrün ilk ve orta evrelerinde her iki modelin tahminleri gerçek değerlere oldukça yakın gerçekleşmiştir. Motor ömrünün son evrelerinde ise sinyaldeki ani değişimler nedeniyle tahmin hatalarında kısmi artışlar gözlenmesine rağmen, her iki model de genel bozulma eğilimini korumuştur. Performans ölçütleri incelendiğinde, ETR modeli R^2 = 0,9666 **ve** RMSE = 21,49 zaman adımı ile RFR modeline (R^2 = 0.9603**,** RMSE = 23,43 zaman adımı) göre daha başarılı sonuçlar elde etmiş, bu da ET algoritmasının doğrusal olmayan bozulma davranışını modellemede daha yüksek tahmin doğruluğu sağladığını göstermiştir.



Şekil 6. RUL tahmin performans grafiklerinin zamana bağlı izdüşümü.

4. Sonuç

Bu çalışmada; F.A.I.R. veri setinden alınan akım, gerilim, hız, sıcaklık ve titreşim sinyallerini içeren çoklu sensör ölçüm verileri kullanılarak FDA motorların hem durum teşhisi hem de RUL tahmini için veri odaklı, ağaç tabanlı toplu öğrenme modelleri geliştirilmiş ve değerlendirilmiştir. Deneysel sonuçlar, önerilen Random Forest ve Extra Trees sınıflandırıcılarının sırasıyla %98,7 ve %93,4 gibi yüksek sınıflandırma doğruluklarına ulaştığını; ayrıca sırasıyla %95,70 ve %95,38'lik 10 katlı çapraz doğrulama (10-fold cross-validation) başarılarıyla güçlü bir sınıflandırma performansı ve iyi bir genelleme yeteneği sergilediğini ortaya koymuştur. Karışıklık matrisi analizi, az sayıdaki hatalı sınıflandırmanın yalnızca birbirine yakın evreler arasında gerçekleştiğini ve kritik arıza aşamasının (Evre IV) yüksek güvenilirlikle tespit edildiğini göstermiştir. Bu durum, önerilen çerçevenin kestirimci bakım uygulamalarındaki kullanılabilirliğini vurgulamaktadır.

Öznitelik önemi analizi, seçilen özniteliklerin fiziksel anlamlılığını doğrulamış; net sıcaklık artışının aşınma sürecindeki en etkili gösterge olduğunu, bunu yüksek frekanslı titreşim bileşenlerinin ve dönüş hızının takip ettiğini açığa çıkarmıştır. Kalan faydalı ömür (RUL) tahmini için ise Extra Trees Regressor, Random Forest Regressor modeline göre biraz daha iyi bir performans sergileyerek 0,9666'lık bir R^2 skoru ve 21,49 zaman adımı RMSE değeri elde etmiştir. Random Forest Regressor ise 0,9603'lük bir R^2 skoru ve 23,43 zaman adımı RMSE değerine ulaşmıştır.

Bu sonuçlar, ağaç tabanlı toplu öğrenme yöntemlerinin fırçalı DA motorların hem bozulma aşamalarını hem de kalan ömürlerini doğru bir şekilde modelleyebildiğini ve güçlü bir kestirim performansı sunabildiğini kanıtlamaktadır. Genel olarak önerilen çerçeve, FDA motorların akıllı durum izlemesi ve kestirimci bakımı için verimli ve pratik bir karar destek aracı sağladığı görülmüştür.

Gelecekteki çalışmalar; önerilen modellerin farklı güçteki FDA motor verileri ile değerlendirerek motor güç değişimindeki farklılıkların tespitine yönelik olacaktır.

Katkı Oranı Beyanı

Yazarın katkı yüzdeleri aşağıda verilmiştir. Yazar makaleyi incelemiş ve onaylamıştır.

	E.Ö.
K	100
T	100
Y	100
VTI	100
VAY	100
KT	100
YZ	100
KI	100
GR	100
PY	100
FA	100

K= kavram, T= tasarım, Y= yönetim, VTI= veri toplama ve/veya işleme, VAY= veri analizi ve/veya yorumlama, KT= kaynak tarama, YZ= yazım, KI= kritik inceleme, GR= gönderim ve revizyon, PY= proje yönetimi, FA= fon alımı.

Çatışma Beyanı

Yazar bu çalışmada hiçbir çıkar ilişkisi olmadığını beyan etmektedirler.

Etik Onay Beyanı

Bu araştırmada hayvanlar ve insanlar üzerinde herhangi bir çalışma yapılmadığı için etik kurul onayı alınmamıştır.

Kaynaklar

Barkas, D. A., Ioannidis, G. Ch., Psomopoulos, C. S., Kaminaris, D., & Vokas, G. A. (2020). Brushed DC Motor Drives for Industrial and Automobile Applications with Emphasis on Control Techniques: A Comprehensive Review. *Electronics*, *9*(6), 887-887. https://doi.org/10.3390/electronics9060887

Bergstra, J., & Bengio, Y. (2011). Algorithms for hyper-parameter optimization. *HAL (Le Centre pour la Communication Scientifique Directe)*. Centre National de la Recherche Scientifique. http://citeseerx.ist.psu.edu/viewdoc/summary?doi=10.1.1.476.5930

Breiman, L. (2001). Random Forests. *Machine Learning*, *45*(1), 5-32. https://doi.org/10.1023/a:1010933404324

Cros, J., Sincero, G. C. R., & Viarouge, P. (2009). Design method for brush permanent magnet DA motors. *2009 IEEE International Electric Machines and Drives Conference*, 1625-1632.

Ellefsen, A. L., Ushakov, S., Æsøy, V., & Zhang, H. (2019). Validation of Data-Driven Labeling Approaches Using a Novel Deep Network Structure for Remaining Useful Life Predictions. *IEEE Access*, *7*, 71563-71575. https://doi.org/10.1109/access.2019.2920297

Filina, O., & Tsvetkov, A. N. (2019). Evaluation of the operational life of direct current motors. *IOP Conference Series Materials Science and Engineering*, *489*, 12-16. https://doi.org/10.1088/1757-899x/489/1/012016

Filina, O., Martyushev, N. V., Malozyomov, B. V., Tynchenko, V. S., Kukartsev, V. A., Bashmur, K. A., Pavlov, P. P., & Panfilova, T. (2023). Increasing the efficiency of diagnostics in the brush-commutator assembly of a direct current electric motor. *Energies*, *17*(1), 17-17. https://doi.org/10.3390/en17010017

Geurts, P., Ernst, D., & Wehenkel, L. (2006). Extremely randomized trees. *Machine Learning*, *63*(1), 3-42. https://doi.org/10.1007/s10994-006-6226-1

Guyon, I., & Elisseeff, A. (2003). An introduction to variable and feature selection. *Journal of machine learning research*, *3*(Mar), 1157-1182.

Hastie, T., Tibshirani, R., & Friedman, J. H. (2009). The Elements of Statistical Learning. Içinde *Springer series in statistics*. Springer Science+Business Media. https://doi.org/10.1007/978-0-387-84858-7

Ippolito, P. P. (2022). Hyperparameter tuning: the art of fine-tuning machine and deep learning models to improve metric results. İçinde *Applied data science in tourism: Interdisciplinary approaches, methodologies, and applications* (ss. 231-251). Springer International Publishing.

Jardine, A., Lin, D., & Banjević, D. (2005). A review on machinery diagnostics and prognostics implementing condition-based maintenance. *Mechanical Systems and Signal Processing*, *20*(7), 1483-1510. https://doi.org/10.1016/j.ymssp.2005.09.012

Karakılıç, M., Hataş, H., & Pacal, İ. (2025, May). Open-Circuit Fault Detection in T-Type MLI Using XGBoost: A Machine Learning-Based Approach. In 2025 7th International Congress on Human-Computer Interaction, Optimization and Robotic Applications (ICHORA) (pp. 1-6). IEEE.

Lei, Y., Li, N., Guo, L., Li, N., Yan, T., & Lin, J. (2018). Machinery health prognostics: A systematic review from data acquisition to RUL prediction. *Mechanical Systems and Signal Processing*, *104*, 799-834. https://doi.org/10.1016/j.ymssp.2017.11.016

Mahlich, C., Vente, T., & Beel, J. (2025). From theory to practice: Implementing and evaluating e-fold cross-validation. In J. Liu, A. Ghosh, C. W. Tan, & H. Zhao (Eds.), *International Conference on Artificial Intelligence and Machine Learning Research (CAIMLR 2024)* (Vol. 13635, Article 1363505). SPIE. https://doi.org/10.1117/12.3058568

Mohapatra, A. (2024). Generative AI for Predictive Maintenance: Predicting Equipment Failures and Optimizing Maintenance Schedules Using AI. *International Journal of Scientific Research and Management (IJSRM)*, *12*(11), 1648-1672. https://doi.org/10.18535/ijsrm/v12i11.ec03

Pham, V.-H., Le, D. B., & Nguyen, Pt. D. (2023). A Method of Assessing the Service Life and Reliability of Motor Brushes Based on Wear Under Variable Current and Environmental Conditions. *Tribology in Industry*, *45*(1), 302-312. https://doi.org/10.24874/ti.1443.02.23.06

Rajabioun, R., Hataş, H., Afshar, M., Atan, Ö., & Akin, B. (2025). Optimal feature selection for distributed bearing fault detection using cost-effective, high-performance machine learning algorithms. *IEEE Journal of Emerging and Selected Topics in Industrial Electronics, 7(1)*, 46-57.

Randall, R. B. (2021). *Vibration-based condition monitoring: industrial, automotive and aerospace applications*. John Wiley & Sons.

Reñones, A. (2020). F.A.I.R. open dataset of brushed DC motor faults for testing of AI algorithms (Version 1.0) [Data set]. Zenodo. https://doi.org/10.5281/zenodo.4314249

Teel-Jongebloed, C. C. (2020). Detection of permanent magnet DC motor failure due to brush wear using parameter estimation and statistical analysis. *OakTrust (Texas A&M University Libraries)*. https://hdl.handle.net/1969.1/192653

Zheng, A., & Casari, A. (2018). *Feature engineering for machine learning: principles and techniques for data scientists*. O'Reilly Media, Inc

Black Sea Journal of Engineering and Science
doi: 10.34248/bsengineering.1956549

Open Access Journal
e-ISSN: 2619 – 8991

Research Article
Volume 9 - Issue 5: 2462-2472 / September 2026

ASSESSING READINESS FOR AI-HUMAN INTEGRATION USING A HESITANT FUZZY ANALYTIC HIERARCHY PROCESS: AN APPLICATION IN THE BANKING SECTOR

Çağrı AKOĞLU[1], Gül Tekin TEMUR[1]*

[1]*Bahcesehir University, Faculty of Engineering and Natural Sciences, Department of Management Engineering, 34353, Istanbul, Türkiye*

Abstract: With AI being incorporated into the core functions of organizations, understanding whether or not an organization is ready to work in conjunction with humans using AI will continue to grow in importance. Therefore, this study proposes a multi criteria decision making (MCDM) based methodology to aid firms in evaluating their potential for successful integration of AI and human capabilities. An "AI-Human Integration Readiness Index" is developed to provide a systematic means to evaluate the various capabilities regarding to AI utilization. In order to handle uncertainty and hesitation when experts are making assessments of an organization's readiness, the proposed methodology uses the Hesitant Fuzzy Analytical Hierarchy Process (HFAHP) as a novel MCDM method. A total of four primary dimensions were used in developing the model which were established from conducting a thorough review of existing literature: (1) Strategic Alignment & Value Realization Readiness, (2) Data & Technical Infrastructure Readiness, (3) Human Capital & Adaptation Readiness, and (4) Trust, Governance & Institutional Legitimacy Readiness. The resulting index not only quantifies an organization's current state of readiness but also acts as a diagnostic tool to assist organizations in identifying areas where they may require additional support or training.

Keywords: Multi-criteria decision making, AI-human integration, AI-human integration readiness level, Hesitant fuzzy analytical hierarchy process

***Corresponding author:** Bahcesehir University, Faculty of Engineering and Natural Sciences, Department of Management Engineering, 34353, Istanbul, Türkiye
E mail: gul.temur@bau.edu.tr (Gul T. TEMUR)
Çağrı AKOĞLU https://orcid.org/0009-0003-8293-8173
Gül Tekin TEMUR https://orcid.org/0000-0003-3853-0974

Received: May 21, 2026
Accepted: August 13, 2026
Published: September 15, 2026

Cite as: Akoğlu, Ç., & Temur, G. T. (2026). Assessing readiness for ai-human integration using a hesitant fuzzy analytic hierarchy process: An application in the banking sector. *Black Sea Journal of Engineering and Science,* 9(5), 2462-2472.

1. Introduction

The concept of "readiness level" is defined as a maturity indicator expressing a system's or organization's capacity to adopt and implement a new technology. This concept encompasses not only existing technological capabilities but also the potential to achieve performance targets and the challenges that may be encountered in this process. Technology readiness levels offer a framework that evaluates this process gradually, from the basic principal stage to systems validated in a real-world environment (Mankins, 2009). However, it is emphasized that systems should be evaluated not only from a technological perspective but also from the level of integration, and therefore it is recommended to consider integration readiness levels together (Sauser et al., 2009). Industry 4.0 readiness expands this approach by evaluating the overall state of organizations before transitioning to digital transformation. In this context, elements such as technological infrastructure, organizational structure, and human resources are considered together. The aim is to determine the extent to which businesses are ready by analysing their current state before the transformation (Smit et al., 2016). Different models have been developed in the literature to measure this readiness by considering multi-dimensional criteria such as strategy, operations, technology, and human factors etc. (Lichtblau et al., 2015; Schumacher et al., 2016; Akdil et al., 2018).

Organizational readiness for AI is defined as the capacity of organizations to effectively adopt, implement, and create value from AI technologies, and is considered a significant component of the digital transformation literature (Holmström, 2022). This concept encompasses not only the adequacy of technological infrastructure but also the compatibility of organizational structures, business processes, human resources, and strategic goals with AI. In the literature, readiness generally refers to an organization's level of readiness before transformation, while the concept of maturity describes the stages of development reached after implementation (Naheed et al., 2025). This distinction is critical for understanding both the initial conditions and the evolution of AI transformation. AI readiness models have undergone significant evolution over time. Early approaches were more technology-focused, evaluating organizations based

This work is licensed (CC BY-NC 4.0) under Creative Commons Attribution 4.0 International License

on technology readiness levels that measured how close AI systems were to operational use (Uren and Edwards, 2023). However, these approaches have not adequately reflected the fact that artificial intelligence is not only a technical innovation but also a transformation with organizational and social dimensions. Therefore, more recent studies have begun to address AI readiness as a multi-dimensional and socio-technical construct. In this context, Holmström (2022) proposes four fundamental dimensions for the concept of AI readiness, addressing it from a digital transformation perspective: technologies, activities, boundaries, and goals. This model emphasizes that AI transforms not only the existing technological infrastructure but also the organization's ways of doing business, its relationships with external stakeholders, and its strategic orientations. In particular, the reshaping of organizational boundaries and the alignment of goals with artificial intelligence are among the distinctive aspects of this model (Holmström, 2022). This approach positions AI readiness not merely as a technical readiness but as a holistic organizational transformation capacity. In addition, it emphasizes that the spread of artificial intelligence in organizations is not just an adoption decision but a gradual maturation process. On the other hand, Naheed et al. (2025) propose a multi-dimensional AI readiness model developed specifically for small and medium-sized enterprises (SMEs). This model is based on the TOEH framework, encompassing technology, organization, environment, and human dimensions, and provides a systematic assessment mechanism to measure the readiness levels of organizations (Naheed et al., 2025). Specific indicators are defined for each dimension in the model, and organizations' readiness levels are rated from "informal" to "desirable." Furthermore, the model not only analyses the current situation but also enables organizations to develop action plans for their shortcomings. In this respect, the study makes the concept of AI readiness operational and applicable.

There are some key dimensions that commonly stand out in the AI readiness literature. These include technological infrastructure, data capacity, human resources and skills, business processes, and organizational strategy (Holmström, 2022; Uren and Edwards, 2023; Naheed et al., 2025). However, organizational culture, environmental factors, and ecosystem relationships also emerge as decisive elements in the AI adoption process (Naheed et al., 2025). This demonstrates that AI readiness is a multi-layered and dynamic structure.

The banking sector was selected as the application context because it combines data-intensive operations, time-sensitive and high-consequence decisions, strict regulatory obligations, and continuing requirements for human oversight. Treasury activities are particularly suitable for examining AI-human readiness because market, liquidity and risk information must be interpreted rapidly while accountability for strategic and financial decisions remains with organizational decision-makers.

Recognizing these, this study aims to handle the problem of AI-human integration readiness assessment. The main motivation of this study is to focus on strategic-level AI-human interaction and develop an AI-human integration readiness level scoring from holistic perspective. Under these goals, this study is structured as follows. The next section presents the methodology explaining the proposed multi-layer framework, including the identification of main criteria affecting the AI-human interaction readiness. Hesitant Fuzzy Analytic Hierarchy Process (HFAHP) is utilized for the development of an AI-Human Integration Readiness Index. The following section presents the application of the proposed model through a real case study, demonstrating how the methodology can be implemented in practice and how results are interpreted. Finally, the study concludes with key findings, managerial implications, and suggestions for future research. The study also asks: How does HFAHP compare with classical AHP in complexity and flexibility under hesitant judgments?

2. Materials and Methods

The methodological steps of our study are shown in Figure 1.

2.1. Determination of the Readiness Level for AI-Human Integration

Several researchers have utilized the concept of organizational maturity models in conjunction with digital transformation and AI adoption models to develop an AI-Human Integration Readiness Index. By reviewing these studies, we created our model including four primary criteria (Figure 2):

- Strategic Orientation & Value Realization Readiness (S),
- Data & Technical Deployment Readiness (D),
- Human Capital &Transformation Adaptability Readiness (H),
- Trust, Governance & Corporate Legitimacy Readiness (T).

Strategic orientation & value realization readiness (S) considers the extent to which an organization appears capable of incorporating AI technologies into its broader strategic direction. Four sub-criteria, strategic alignment, top management support, investment approach to AI, and value-oriented use of AI, are included. Prior studies, such as Jöhnk et al. (2021) tend to suggest that strategic alignment and managerial support are closely associated with successful AI adoption. In a similar perspective, Holmström (2022) appears to emphasize the importance of a value-oriented perspective when adopting emerging technologies. Additionally, Kinkel et al. (2022) seem to point toward the potential of AI investments to contribute to competitive positioning.

Data & technical deployment readiness (D) reflects how adequately an organization's data infrastructure and technical capabilities might support AI implementation.

The evaluation includes data quality, data accessibility, technical infrastructure adequacy, and system integration. Existing research, such as Nazari Tehrani et al. (2024) generally indicates that data quality and accessibility are closely linked to AI performance outcomes. Similarly, Uren and Edwards (2023) appear to underline the relevance of infrastructure and integration capabilities. Across these studies, there is also an implicit tendency to highlight the broader importance of data-driven organizational structures.

Human capital & transformation adaptability readiness (H) explores whether an organization seems to possess the human and cultural foundations that could facilitate AI-related transformation. Sub-criteria include employee competencies, AI-related skills, organizational learning capacity, and openness to change. Research by Jöhnk et al. (2021) suggests that developing relevant competencies and supporting adaptation processes may play an important role. Furthermore, contributions by Armenakis et al. (1993), Braganza et al. (2021), and Taherizadeh and Beaudry (2023) appear to collectively point toward the significance of learning and agility. The literature more broadly seems to lean toward a human-centred perspective as a potentially supportive approach for sustaining AI-related initiatives.

Trust, governance, & corporate legitimacy readiness (T) addresses dimensions related to ethics, regulation, and governance in AI use. The associated sub-criteria include transparency, accountability, data security, and regulatory compliance. Several studies, including those by Nortje and Grobbelaar (2020), Akbarighatar et al. (2023) and Mylrea and Robinson (2023) tend to emphasize -directly and indirectly - the importance of governance mechanisms. In particular, these works often appear to converge around the idea that transparency and accountability are closely associated with fostering trust in AI-enabled organizational contexts.

Subsequently, the methodology is designed utilizing the Hesitant Fuzzy Analytical Hierarchy Method (HFAHP), which is successful in dealing with subjective evaluations with high uncertainty, to prioritize the criteria given as S, D, H and T.

Although the classical fuzzy set theory developed by Zadeh (1965) considers the uncertain aspect of human decisions with triangular or trapezoidal affiliation values, it is insufficient in hesitant situations where the decision-maker has difficulty making a single choice. Therefore, Torra (2010) defined hesitant fuzzy sets (HFS). The steps of the Hesitant Fuzzy AHP, adapted from Öztayşi et al. (2015), are shown below.

Phase 1. The model is designed consisting of four main criteria. Similarly, with a traditional AHP procedure (Saaty, 1980), the main criteria are assessed through pairwise comparisons based on the linguistic terms presented in Table 1. If the experts cannot have agreement on a single linguistic scale, they can choose a range of terms. However, the difference between linguistic scales is limited to "2".

Phase 2. The expert evaluations are combined with the fuzzy envelope approach proposed by Liu and Rodriguez (2014). Let the lowest scale is denoted by s_o and the highest by s_g. In this case, $s_o \leq s_i \leq s_j \leq s_g$. To succeed the process with fuzzy envelope, OWA operator is utilized for dimension n as given in equation 1, where b_j is the largest of the aggregated arguments $a_1, a_2, \ldots, a_n$ and $W = (w_1, w_2, \ldots, w_n)^T$ is the associated weighted vector where the total sum of w_i is 1.

$$OWA\ (a_1, a_2, \ldots, a_n) = \sum_{i=1}^{n} w_j . b_j \qquad (1)$$

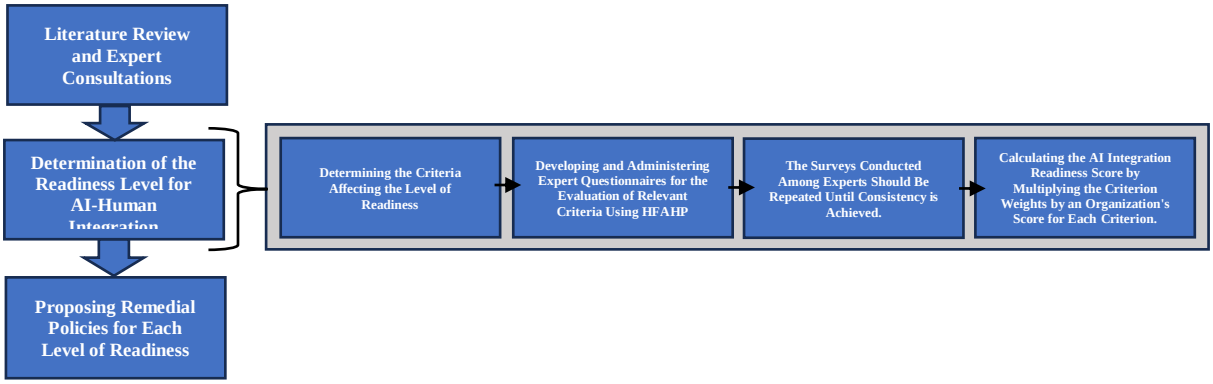


Figure 1. Framework of the proposed methodology.

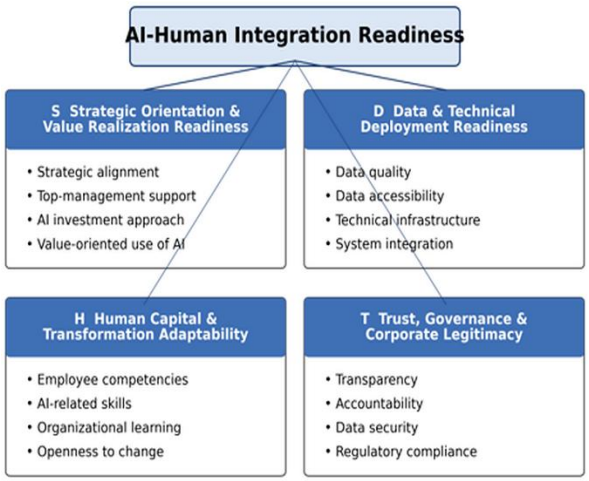


Figure 2. Criteria of AI-human readiness measurement.

Table 1. Linguistic scaling table for HFAHP (Öztayşi et al., 2015)

Rank	Linguistic Term	Abbreviation	Triangular Fuzzy Numbers
10	Absolutely High Importance	AHI	(7, 9, 9)
9	Very High Importance	VHI	(5, 7, 9)
8	Essentially High Importance	ESHI	(3, 5, 7)
7	Weakly High Importance	WHI	(1, 3, 5)
6	Equally High Importance	EHI	(1, 1, 3)
5	Exactly Equal	EE	(1, 1, 1)
4	Equally Low Importance	ELI	(0.33, 1, 1)
3	Weakly Low Importance	WLI	(0.2, 0.33, 1)
2	Essentially Low Importance	ESLI	(0.14, 0.2, 0.33)
1	Very Low Importance	VLI	(0.11, 0.14, 0.2)
0	Absolutely Low Importance	ALI	(0.11, 0.11, 0.14)

The parameters a, b, c and d of the trapezoidal fuzzy membership function $\tilde{A} = (a, b, c, d)$ are calculated using equations 2, 3, 4 and 5 as follows:

$$a = min\{a_L^i, a_M^i, a_M^{i+1}, \dots . a_M^j, a_R^j\} = a_L^i \quad (2)$$

$$d = max\{a_L^i, a_M^i, a_M^{i+1}, \dots . a_M^j, a_R^j\} = a_R^j \quad (3)$$

$$b = \begin{cases} a_m^i, if\ i+1=j, \\ OWA_{w^2}\left(a_m^i, \dots . a_m^{\frac{i+j}{2}}\right), if\ i+j\ even \\ OWA_{w^2}\left(a_m^i, \dots . a_m^{\frac{i+j-1}{2}}\right), if\ i+j\ odd \end{cases} \quad (4)$$

$$c = \begin{cases} a_m^{i+1}, if\ i+1=j, \\ OWA_{w^1}\left(a_m^j, a_m^{j-1}, \dots . a_m^{\frac{i+j}{2}}\right), if\ i+j\ even \\ OWA_{w^1}\left(a_m^j, a_m^{j-1}, \dots . a_m^{\frac{i+j+1}{2}}\right), if\ i+j\ odd \end{cases} \quad (5)$$

The OWA operation shown in equations 4 and 5 requires a weight vector to take place. Using the parameter α belonging to the unit interval [0, 1], the first type weights $W^1 = w_1^1, w_2^1 \dots . w_n^1$ from the first and second weight types are defined as shown in equation 6:

$$w_1^1 = a_2, w_1^2 = a_2(1-a_2), \dots \dots w_n^1 = a_2(1-a_2)^{n-2} \quad (6)$$

The second type of weights, $W^1 = w_1^1 w_1^2, w_2^2 \dots . w_n^2$ are defined as shown in equation 7:

$$w_1^2 = a_1^{n-1}, w_2^2 = (1-a_1)a_1^{n-2}, \dots \dots w_n^2 = (1-a_1) \quad (7)$$

$a_1 = \frac{g-(j-i)}{g-1}$ and $a_2 = \frac{(j-i)-1}{g-1}$ (g, is the number of terms in the evaluation scale, j, is the highest evaluation rank, and i, is the lowest evaluation value in the given range).

Phase 3. The complete pairwise comparison matrix ($\tilde{C}$) is generated using equation 8.

$$\tilde{C} = \begin{vmatrix} 1 & \tilde{c}_{12} & \cdots & \tilde{c}_{1n} \\ \tilde{c}_{21} & 1 & \dots & \tilde{c}_{2n} \\ \vdots & \vdots & \dots & \vdots \\ \tilde{c}_{n1} & \tilde{c}_{n2} & \dots & 1 \end{vmatrix} \quad (8)$$

Given that $\tilde{c}_{ij} = (c_{ij_1}, c_{ij_{m1}}, c_{ij_{m2}}, c_{ij_u})$ and the fuzzy envelopes obtained in the previous step are trapezoidal fuzzy numbers, the corresponding values are calculated as using equation 9 as follows:

$$\tilde{c}_{ij} = \left(\frac{1}{c_{ij_u}}, \frac{1}{c_{ij_{m2}}}, \frac{1}{c_{ij_{m1}}}, \frac{1}{c_{ij_1}}\right) \quad (9)$$

Phase 4. For each row ($\tilde{r}_i$) of the combined pairwise comparison matrix, the fuzzy geometric mean is calculated using equation 10:

$$\tilde{r}_i = (\tilde{c}_{i1} \otimes \tilde{c}_{i2} \dots . \otimes \tilde{c}_{in})^{1/n} \quad (10)$$

Phase 5. The fuzzy weights ($\tilde{w}_i$) of each criterion are calculated using equation 11 with the ($\tilde{r}_i$) values:

$$\tilde{w}_i = \tilde{r}_i \otimes (\tilde{r}_1 \oplus \tilde{r}_2 \dots . \oplus \tilde{r}_n)^{-1} \quad (11)$$

Phase 6. To determine the importance of the alternatives, the trapezoidal fuzzy numbers are defuzzified. This process is performed using equation 12.

$$= \frac{c_1 + 2c_{m1} + 2c_{m2} + c_u}{6} \quad (12)$$

Phase 7. The defuzzified weights are subsequently normalized to derive the local weights of the criteria. In order to determine the consistency ratio (CR), equations 13 and 14 are applied. The consistency index (CI) is calculated as:

$$CI = \frac{\lambda_{max} - n}{n-1} \quad (13)$$

Subsequently, the consistency ratio (CR) is obtained using:

$$CR = \frac{CI}{RI} \quad (14)$$

Here, CI represents the consistency index, λ_{max}denotes the maximum eigenvalue of the matrix, $n$is the total number of criteria, and RIrefers to the random index, which varies depending on the value of n. A CR value below 0.1 is considered acceptable, indicating that the results are consistent (Saaty, 2012). Because the pairwise comparisons are based on expert judgment, consistency was assessed separately for each expert before aggregation. For each individual defuzzified comparison matrix, the maximum eigenvalue, consistency index and consistency ratio were calculated using equations 13 and 14. If the consistency ratio was equal to or greater than 0.10, corresponding comparisons were returned to expert for reconsideration and questionnaire was repeated. Only matrices satisfying CR < 0.10 were included in the group aggregation. This procedure limits internally contradictory judgments, while hesitant linguistic ranges preserve uncertainty and subjectivity inherent in expert evaluation.

Phase 8. After determining the weights of the main criteria defining AI-human readiness using the HFAHP method, evaluation questions are developed for each sub-criterion under the corresponding main criteria. The responses to these questions are collected on a 1-5 scale, and the average scores are computed. These average scores are then multiplied by the corresponding criterion weights to obtain the weighted evaluation scores. This procedure is mathematically formulated in equation 15 as follows:

$$SAI = \sum_{i=1}^{N} w_i . \left(\frac{1}{n_i} \sum_{j=1}^{n_i} x_{ij} \right) \quad (15)$$

Where:

SAI: overall score of AI-human integration

i: main criteria $(i = 1, 2, 3, \dots, N)$

N: number of main criteria

w_i: weight of the i^{th} main criteria obtained via HFAHP

n_i: number of sub criterion under i^{th}main criterion.

j: sub-criteria $(j = 1, 2, 3, \dots, n)$

x_{ij}: score of the j^{th}sub-criterion under the i^{th}main criterion (Likert scale, 1-5)

The four sub-criteria under each main criterion contribute equally to the organizational readiness score, as represented by the $1/n_i$ term in equation 15. This weighting structure reflects the design of the index: HFAHP determines the relative importance of the four main readiness dimensions, while the sub-criteria serve as operational indicators that collectively represent each dimension. Accordingly, differences in importance are established among the main dimensions without imposing an additional hierarchy among the indicators within the same dimension. This structure supports a transparent and practically interpretable calculation of the readiness score. Future validation studies may examine whether alternative within-dimension weighting schemes materially affect the resulting scores and classifications.

2.2. Proposing Remedial Policies for Each Level of Readiness

This section explains the development of customized remedial policy recommendations based on organizations' readiness levels in strategic decision-making processes involving AI-human integration. The maturity levels defined in Figure 3 provide a systematic classification of organizations according to their current capacity and degree of adaptation, while identifying specific intervention areas for each level. Within this framework, after the companies are grouped according to their readiness levels, the main barriers they face and the corresponding areas requiring improvement are analyzed. Based on this analysis, customized remedial policy sets are developed for each readiness level to ensure a more effective and sustainable transformation process.

The scoring system used in this context has a quantitative differentiation of readiness levels. The maturity levels are defined over a 5-point scale as follows:

- Level 1 corresponds to 0<score<1 (beginner)
- Level 2 corresponds to 1≤score<2 (beginner)
- Level 3 corresponds to 2≤score<3 (learner)
- Level 4 corresponds to 3≤score<4 (learner)
- Level 5 corresponds to 4≤score≤5 (top performer).

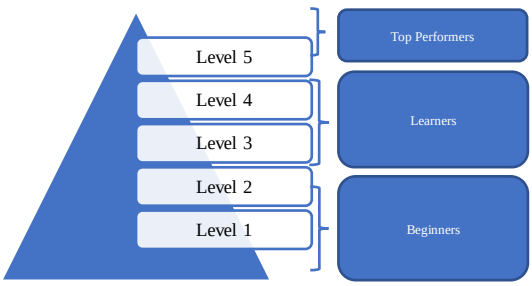


Figure 3. Readiness levels towards ai-human integration

Maturity models generally represent staged development and support the identification of improvement priorities, but their level structures are design choices rather than universal measurement units (Mettler, 2011; Proença and Borbinha, 2016). The five-level structure adopted here was selected because it provides practical balance between interpretability and diagnostic differentiation and corresponds directly to the 1-5 scoring scale used for sub-criteria. Five-level structures are common in maturity research, as illustrated by Schumacher et al. (2016), whereas the IMPULS model uses six readiness levels from 0 to 5 (Lichtblau et al., 2015). A three-level

structure would be easier to communicate but could conceal meaningful differences between organizations. By contrast, six- or seven-level structures can provide finer differentiation but may create an impression of precision that is not justified when assessments rely on limited expert or survey data. Accordingly, thresholds used in this study can be interpreted as diagnostic boundaries and may be recalibrated with sector-specific benchmarks or larger empirical samples.

The strategic roadmaps are being proposed that differentiate among "Beginner", "Learner" and "Top Performer" levels. These roadmaps are taking interdependent views of the strategic, technical, human, and governance dimensions.

Organizations at the "Beginner" stage require to focus on developing a clearly defined AI strategy, building out the necessary foundational data infrastructure, providing baseline AI training to employees, and put into place the minimum governance structure required to provide clarity and mitigate resistance.

Organizations at the "Learner" stage are expected to connect the various AI initiatives to measurable business outcomes, build out their technical capability infrastructure, implement cross functional collaboration models that include AI stakeholders, and ensure that the organization has embedded the compliance requirements into its governance structure.

"Top Performers" are expected to continue to refine AI-based strategies to sustain competitive advantage, optimize their advanced data ecosystems, foster AI-human collaborative relationships, and maintain governance structures that support these efforts. The key takeaway here is that achieving this level requires continuous evolution. Nonetheless, these recommendations should be viewed as starting points rather than prescriptive guidelines; firms require to adapt them in accordance with their own individual level of competence at each area. As such, the proposed roadmaps should be customized to fit the firm's existing strengths and weaknesses, as well as its strategic goals. Ultimately, the goal of this approach is to create a contextual and pragmatic roadmap for organizational transformation.

3. Results

3.1. Application in the Banking Sector

The methodology proposed in Section 2 is adaptable and generalizable to all sectors. In our study, this model is applied in the treasury department of a company that has been serving the global market in the banking sector for over 25 years. It is aimed to evaluate its AI-human readiness level by the help of the proposed methodology.

The pairwise comparison questionnaires are conducted to three experts: one Digital Transformation Director, one academic specializing in AI engineering at a reputable university, and one experienced software engineer from the industry. The questionnaires are iteratively applied until consistency in responses is achieved. The procedure given in previous stage is applied. Subsequently, the individual judgments of the three experts are aggregated using the geometric mean method. Following the defuzzification process, the final weights of each main criterion are derived. The resulting weights for the main criteria are presented in Table 2. It is noticeable to state that these weights are generalizable, in other words, they are not assessed only for the selected company, it is adaptable to all companies.

The highest weighted factor, Data & Technical Deployment Readiness (0.394), implies that the AI deployment is highly correlated with the robustness of data infrastructure, system integrations capabilities and scalability of technology. This finding implies the strong impact of "technology push" orientation in terms of AI-human integration readiness.

Strategic Orientation & Value Realization Readiness ranked second (0.286). Within this panel, the result highlights the perceived relevance of executive commitment, strategic direction, and value-based prioritization of AI initiatives. It also suggests that technical capability alone may be insufficient without organizational ownership and explicit value-realization mechanisms.

Moderately important factor is Trust, Governance & Corporate Legitimacy Readiness (0.188). In other words, it is assumed that the issue of ethics, legal regulation, and corporate responsibility in terms of AI transformation is crucial; however, it does not play the role of key determinant of the phenomenon.

The factor that receives the least weight is Human Capital & Transformation Adaptability Readiness (0.132). Consequently, it can be stated that the current approach treats the issue of workforce readiness as an additional element. This fact is rather indicative since the sustainability of AI-human interaction often implies significant changes in roles' redistribution among humans and AI-based systems.

Table 2. The weights of criteria of AI-human integration readiness

Main Criteria	Weights
S) Strategic Orientation & Value Realization Readiness	0.286
D) Data & Technical Deployment Readiness	0.394
H) Human Capital & Transformation Adaptability Readiness	0.132
T) Trust, Governance & Corporate Legitimacy Readiness	0.188

For each main criteria, the selected company's treasury department is assessed through the survey given in Table 3. The items listed in the survey are evaluated on a five-point Likert scale (1: very low level of competence, 5: very high level of competence). Subsequently, the mean values of the items under each main criteria were calculated and multiplied by the corresponding main

criteria weights, as described in Section 2.

Table 3. The survey for AI-Human readiness level scoring

Main Criteria	Survey Item	1	2	3	4	5
S) Strategic Orientation & Value Realization Readiness	S1-The extent to which the vision, priorities, and intended business objectives related to artificial intelligence are clearly defined within the bank.	☐	☐	☐	☐	☐
	S2-The extent to which top management actively supports AI initiatives through ownership, resource allocation, and decision-making processes.	☐	☐	☐	☐	☐
	S3-The extent to which the bank systematically prioritizes AI use cases based on business value, feasibility, and strategic importance.	☐	☐	☐	☐	☐
	S4-The extent to which AI investments are rigorously evaluated in terms of budgeting, expected returns, and realized value.	☐	☐	☐	☐	☐
D) Data & Technical Deployment Readiness	D1-The adequacy of data required for AI applications in terms of accessibility, quality, consistency, and timeliness.	☐	☐	☐	☐	☐
	D2-The suitability of the bank's existing technical infrastructure (processing power, storage, architecture, and system compatibility) for scalable and secure AI deployment.	☐	☐	☐	☐	☐
	D3-The level of capability to evaluate alternative AI solutions and select the most appropriate tools and architectures aligned with organizational needs.	☐	☐	☐	☐	☐
	D4-The extent to which AI solutions can be integrated into existing workflows, decision processes, and enterprise systems.	☐	☐	☐	☐	☐
H) Human Capital & Transformation Adaptability Readiness	H1-The level of employees' ability to understand, use, and interpret outputs of AI tools.	☐	☐	☐	☐	☐
	H2-The effectiveness of collaboration among business units, data teams, IT, and relevant expertise domains in AI projects.	☐	☐	☐	☐	☐
	H3-The extent to which employees and managers are ready to learn and adapt to AI-enabled ways of working.	☐	☐	☐	☐	☐
	H4-The degree of readiness to redesign roles, responsibilities, and human–machine interaction points in decision-making processes as AI adoption increases.	☐	☐	☐	☐	☐
T) Trust, Governance & Corporate Legitimacy Readiness	T1-The adequacy of security, access control, and privacy measures for AI-related data and systems.	☐	☐	☐	☐	☐
	T2-The level of capability to document and explain how AI systems operate and support decision-making to stakeholders.	☐	☐	☐	☐	☐
	T3-The extent to which AI usage is aligned with ethical principles, regulatory requirements, and internal policy frameworks.	☐	☐	☐	☐	☐
	T4-The clarity and effectiveness of responsibility, approval, appeal, and human oversight mechanisms for AI-supported decisions within the bank.	☐	☐	☐	☐	☐

The average scores obtained for each main criterion in the evaluation of the selected firm were multiplied by the corresponding main criterion weights derived through the HFAHP method. As a result, the overall weighted score of the firm is calculated as "2.22". Accordingly, the firm is classified at the 3rd level and is categorized under the "Learner" status. It exhibits a pattern of "fragmented maturity"; that is, it demonstrates relative strength in certain areas while remaining weak in critical linkage points.

While the evaluation of the Strategic Orientation & Value Realization Readiness (S) dimension showed both a complex and unbalanced development stage, there was a positive trend shown by the S1, S2, and S3 scores (as seen in Figure 4). These scores indicated that the organization has started to develop a strategic intention toward AI. It can be concluded from a partly defined vision, visible top-management support, and an emergence in ability to evaluate AI-use cases as part of a strategy that the organization has placed AI on their agenda. Conversely, the much lower score for S4 clearly illustrates the significant gap in terms of the financial and value-related management of AI-initiatives. Therefore, the study's data suggests that AI-investments are not

being reviewed and assessed in terms of budgetary control, expected returns on investment (ROI), and actual value generation. Consequently, the study indicates the complete lack of solid performance measurement systems and value-creation systems that are needed to translate strategic intentions into concrete organizational results.

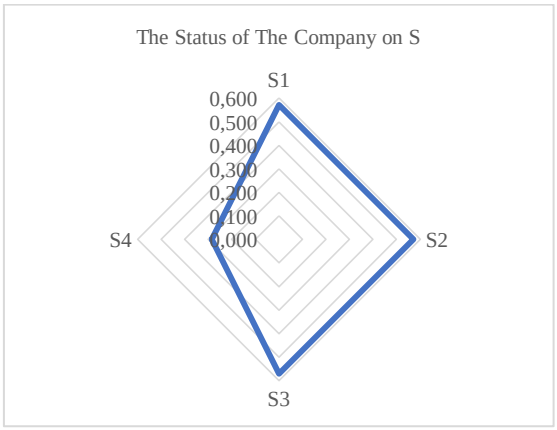


Figure 4. The status of the company on S.

The results show an imbalance in readiness levels across the four dimensions of the Data & Technical Deployment criteria. Although the organization has achieved a good status regarding its technical infrastructure (D2), as well as selecting and evaluating relevant AI-solutions (D3), the organization is found to be significantly lacking when it comes to establishing the foundation for data-readiness (D1) and integrating AI-systems into the daily operation of the business (D4) (as seen in Figure 5). This unbalance indicates that the organization's AI-abilities are largely based on technology as opposed to being based upon data or processes. Thus, even though the organization can tend to technically implement AI, it cannot effectively realize these capabilities due to insufficient implementation of such solutions into daily operations.

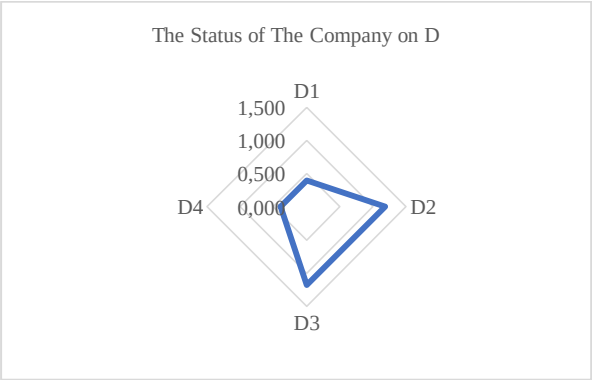


Figure 5. The status of the company on D.

The findings provide a more balanced status toward Human Capital & Transformational Adaptability as compared with the other dimensions (as seen in Figure 6). The organization demonstrated a comparatively upper level of readiness regarding collaborative work across functions (H2), and high level of preparedness to learn and adjust its way of working using AI (H3). Therefore, the results demonstrate a strong behavioral foundation that will support AI utilization. In contrast, while the organization scored somewhat lowly on employee effectiveness in utilizing and interpreting AI-related tools (H1) and their willingness to redefine job descriptions and employee duties (H4), these findings do represent a significant disconnect between expressed desire to be adaptable and actual capability. Thus, while it seems that the organization is ready to adopt an AI-based approach to transformation, it still requires additional development of both skills and organizational design.

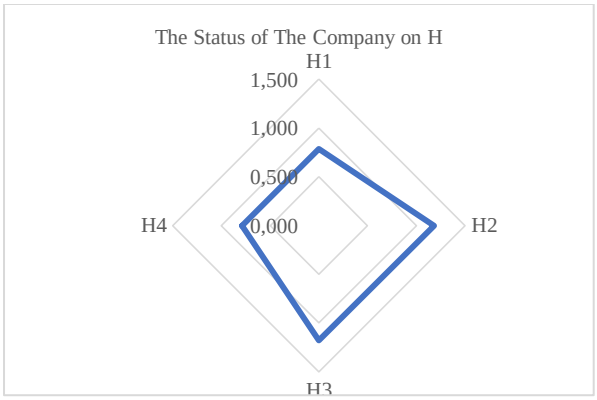


Figure 6. The status of the company on H.

As can be seen from the results for Trust, Governance & Corporate Legitimacy Readiness (Figure 7), T1 and T3 seem to have the highest readiness scores among all, which implies relatively high maturity in the bank's application of security and access control measures and the alignment of AI applications with ethical principles, legal regulations, and internal governance mechanisms. In addition, the T2 dimension score shows relatively good maturity in the provision of the explainability of AI models. T4 has the lowest score, meaning that human involvement in the process of decision making, approval process, and appealing mechanism for AI-based decisions still have room for improvement. Overall, although the institution shows good compliance, security measures and alignment with ethics and governance frameworks, there is much to be done to improve the existing governance architecture regarding responsibility and human oriented decision making.

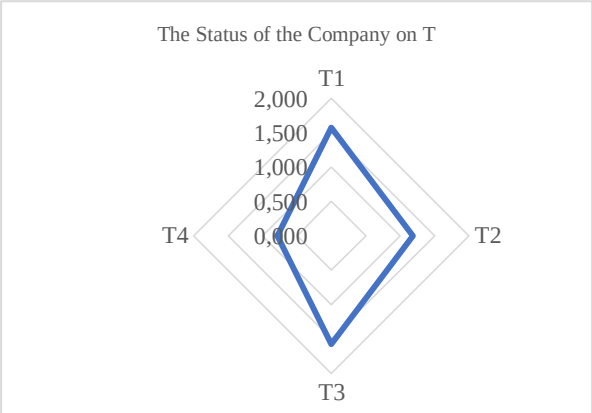


Figure 7. The Status of the Company on T.

4. Discussion

The priority ordering obtained in this study should be interpreted as a case- and panel specific structure. The prominence of Data & Technical Deployment Readiness is consistent with research emphasizing the role of data quality, accessibility, infrastructure and integration in organizational AI adoption (Uren and Edwards, 2023; Nazari Tehrani et al., 2024). The second-ranked strategic dimension is also consistent with studies that identify strategic alignment, managerial support and value orientation as important readiness conditions (Jöhnk et al., 2021; Holmström, 2022).

The lower relative weights assigned to human-capital and governance dimensions permit an alternative interpretation. They may reflect the treasury context and the professional composition of the expert panel rather than general hierarchy of AI-readiness factors. Studies on workforce adaptation and organizational learning emphasize that competencies, trust and role transition can become binding constraints during implementation (Braganza et al., 2021; Taherizadeh and Beaudry, 2023), while responsible-AI research treats security, accountability and governance as necessary conditions for legitimate adoption (Akbarighatar et al., 2023; Mylrea and Robinson, 2023). Therefore, a lower weight in the present model does not imply a lower practical obligation.

The study's theoretical contribution is operationalization of AI-human integration readiness as a weighted socio-technical construct. The framework combines strategic, technical, human and governance dimensions in single diagnostic index and uses HFAHP to retain bounded hesitation in expert judgments. It therefore extends descriptive AI-readiness models by linking multidimensional readiness assessment to an interpretable score and level-specific improvement priorities. This contribution is methodological and diagnostic, the study does not establish causal relationships among dimensions.

Several limitations qualify the findings. The empirical application concerns one treasury department and relies on three purposively selected experts, which limit statistical generalizability and make weight sensitive to panel composition. The sub criteria are equally weighted within each main dimension; the assessment is cross-sectional and the proposed readiness thresholds have not yet been externally validated across multiple organizations. Future research should replicate models with larger and more diverse expert panels, multiple banks or sectors, alternative sub criterion weighting schemes, sensitivity analysis and longitudinal observations of readiness development.

5. Conclusion

This study proposes a structured and quantifiable method for assessing readiness for AI-human integration through HFAHP-weighted criteria. The case results indicate that readiness is not reducible to a single technical capability; it emerges from the interaction of technical, strategic, human, and governance conditions. The empirical findings should be interpreted as exploratory evidence from one organizational setting rather than as universally generalizable sector weights.

Within the present expert assessment, Data & Technical Deployment Readiness received the highest weight (0.394), followed by Strategic Orientation & Value Realization Readiness (0.286), Trust, Governance & Corporate Legitimacy Readiness (0.188) and Human Capital & Transformation Adaptability Readiness (0.132). This ordering suggests that panel viewed data, infrastructure, integration and strategic ownership as most immediate readiness priorities. The lower relative weights of governance and human capital factors should nevertheless be interpreted together with the discussion of context, panel composition and implementation obligations.

This study has provided means for classifying organizations along a continuum of readiness levels from beginner to top performer by linking quantitative scores to interpretable readiness categories. The proposed framework not only offers a structured method for assessing an organization's readiness for AI-human integration but also provides a basis for developing transformation strategies grounded in measurable indicators. The four main dimensions and sixteen sub-criteria were selected to represent the principal strategic, technical, human and governance conditions identified in literature. Therefore, suggestion for future refinement does not indicate that a known dimension or sub criterion was deliberately omitted from the present model. Rather, because AI technologies, regulatory requirements, organizational practices and human–AI interaction patterns are likely to evolve, the relevance and relative importance of the index components should be periodically revalidated. Future research may test the stability of current structure across sectors and over time and may add, remove or recalibrate criteria only when new empirical evidence or regulatory developments justify such changes. Group decision-making applications and comparisons with alternative MCDM methods may

also be used to examine the robustness of the resulting weights and readiness classifications.

Beyond banking, the framework can be adapted to other domains in which AI systems and human decision makers must operate jointly. In healthcare, the four dimensions can be contextualized around clinical data quality, clinician oversight, patient safety and accountability. In manufacturing, sensor-data integration, workforce reskilling and human-robot coordination; and in insurance or public administration, around transparency, contestability and regulatory compliance. The principal practical advantage is that four-dimensional architecture can be retained while sub criteria and survey items are adjusted to sector specific operating and regulatory conditions.

In banking, potential advantages include faster analytical processing, more consistent risk monitoring and more structured decision support. However, the use of AI may also generate unforeseen effects related to biased data, limited explainability, privacy and cybersecurity, automation overreliance, and unclear accountability. Therefore, a higher readiness score should not be interpreted as permission for unrestricted automation; it should be accompanied by effective human oversight, appeal mechanisms, and continuous model governance.

With respect to the methodological research question, HFAHP is not computationally simpler than classical AHP because it requires additional fuzzy-envelope construction, aggregation and defuzzification steps. Its comparative advantage lies in application flexibility. Experts can express bounded hesitation through linguistic ranges and heterogeneous judgments can be aggregated without forcing premature single-value assessments. Thus, HFAHP is particularly appropriate when expert knowledge is uncertain or divergent, whereas classical AHP may remain preferable when judgments are stable and computational simplicity is the dominant requirement. A formal empirical comparison of runtime, sensitivity and decision stability across alternative MCDM methods is reserved for future research.

Author Contributions

The percentages of all authors' contributions are presented below. All authors reviewed and approved the final version of the manuscript.

	Ç.A.	G.T.T.
C	60	40
D	60	40
M	60	40
DCP	40	60
DAI	40	60
LR	20	80
W	40	60
CR	70	30
SR	80	20
PM	70	30
FA	80	20

C= concept, D= design, S= supervision, DCP= data collection and/or processing, DAI= data analysis and/or interpretation, L= literature search, W= writing, CR= critical review, SR= submission and revision, PM= project management, FA= funding acquisition.

Conflict of Interest

The authors declared that there is no conflict of interest.

Ethical Consideration

Ethics committee approval was not required for this study because there was no study on animals or humans.

References

Akbarighatar, P., Pappas, I., & Vassilakopoulou, P. (2023). A sociotechnical perspective for responsible AI maturity models: Findings from a mixed-method literature review. *International Journal of Information Management Data Insights*, *3*(2), Article 100193. https://doi.org/10.1016/j.jjimei.2023.100193

Akdil, K. Y., Ustundag, A., & Cevikcan, E. (2018). Maturity and readiness model for Industry 4.0 strategy. In A. Ustundag & E. Cevikcan (Eds.), *Industry 4.0: Managing the digital transformation* (pp. 61–94). Springer. https://doi.org/10.1007/978-3-319-57870-5_4

Armenakis, A. A., Harris, S. G., & Mossholder, K. W. (1993). Creating readiness for organizational change. *Human Relations*, *46*(6), 681–703. https://doi.org/10.1177/001872679304600601

Braganza, A., Chen, W., Canhoto, A., & Sap, S. (2021). Productive employment and decent work: The impact of AI adoption on psychological contracts, job engagement and employee trust. *Journal of Business Research*, *131*, 485–494. https://doi.org/10.1016/j.jbusres.2020.08.018

Holmström, J. (2022). From AI to digital transformation: The AI readiness framework. *Business Horizons*, *65*(3), 329–339. https://doi.org/10.1016/j.bushor.2021.03.006

Jöhnk, J., Weißert, M., & Wyrtki, K. (2021). Ready or not, AI comes—An interview study of organizational AI readiness factors. *Business & Information Systems Engineering*, *63*(1), 5–20. https://doi.org/10.1007/s12599-020-00676-7

Kinkel, S., Baumgartner, M., & Cherubini, E. (2022). Prerequisites for the adoption of AI technologies in manufacturing: Evidence

from a worldwide sample of manufacturing companies. *Technovation*, *110*, Article 102375. https://doi.org/10.1016/j.technovation.2021.102375

Lichtblau, K., Stich, V., Bertenrath, R., Blum, M., Bleider, M., Millack, A., Schmitt, K., Schmitz, E., & Schröter, M. (2015). *IMPULS—Industrie 4.0-readiness*. Impuls-Stiftung des VDMA.

Liu, H., & Rodríguez, R. M. (2014). A fuzzy envelope for hesitant fuzzy linguistic term set and its application to multicriteria decision making. *Information Sciences*, *258*, 220–238. https://doi.org/10.1016/j.ins.2013.07.027

Mankins, J. C. (2009). Technology readiness assessments: A retrospective. *Acta Astronautica*, *65*(9–10), 1216–1223. https://doi.org/10.1016/j.actaastro.2009.03.058

Mettler, T. (2011). Maturity assessment models: A design science research approach. *International Journal of Society Systems Science*, *3*(1/2), 81–98. https://doi.org/10.1504/IJSSS.2011.038934

Mylrea, M., & Robinson, N. (2023). Artificial intelligence (AI) trust framework and maturity model: Applying an entropy lens to improve security, privacy, and ethical AI. *Entropy*, *25*(10), Article 1429. https://doi.org/10.3390/e25101429

Naheed, S., Pinto, R., & Pirola, F. (2025). A preliminary multidimensional AI readiness assessment model for SME's. *Procedia Computer Science*, *253*, 774–783. https://doi.org/10.1016/j.procs.2025.01.139

Nazari Tehrani, A., Ray, S., Roy, S. K., Gruner, R. L., & Appio, F. P. (2024). Decoding AI readiness: An in-depth analysis of key dimensions in multinational corporations. *Technovation*, *131*, Article 102948. https://doi.org/10.1016/j.technovation.2023.102948

Nortje, M. A., & Grobbelaar, S. S. (2020). A framework for the implementation of artificial intelligence in business enterprises: A readiness model. In *2020 IEEE International Conference on Engineering, Technology and Innovation (ICE/ITMC)* (pp. 1–10). IEEE. https://doi.org/10.1109/ICE/ITMC49519.2020.9198436

Öztayşi, B., Onar, S. C., Bolturk, E., & Kahraman, C. (2015). Hesitant fuzzy analytic hierarchy process. In *2015 IEEE International Conference on Fuzzy Systems (FUZZ-IEEE)* (pp. 1–7). IEEE. https://doi.org/10.1109/FUZZ-IEEE.2015.7337948

Proença, D., & Borbinha, J. (2016). Maturity models for information systems—A state of the art. *Procedia Computer Science*, *100*, 1042–1049. https://doi.org/10.1016/j.procs.2016.09.279

Saaty, T. L. (1980). *The analytic hierarchy process*. McGraw-Hill.

Saaty, T. L. (2012). *Decision making for leaders: The analytic hierarchy process for decisions in a complex world* (3rd rev. ed.). RWS Publications.

Sauser, B. J., Long, M., Forbes, E., & McGrory, S. E. (2009). Defining an integration readiness level for defense acquisition. *INCOSE International Symposium*, *19*(1), 352–367. https://doi.org/10.1002/j.2334-5837.2009.tb00953.x

Schumacher, A., Erol, S., & Sihn, W. (2016). A maturity model for assessing Industry 4.0 readiness and maturity of manufacturing enterprises. *Procedia CIRP*, *52*, 161–166. https://doi.org/10.1016/j.procir.2016.07.040

Smit, J., Kreutzer, S., Moeller, C., & Carlberg, M. (2016). *Industry 4.0*. European Parliament, Policy Department A: Economic and Scientific Policy. https://doi.org/10.2861/947880

Taherizadeh, A., & Beaudry, C. (2023). An emergent grounded theory of AI-driven digital transformation: Canadian SMEs' perspectives. *Industry and Innovation*, *30*(9), 1244–1273. https://doi.org/10.1080/13662716.2023.2242285

Torra, V. (2010). Hesitant fuzzy sets. *International Journal of Intelligent Systems*, *25*(6), 529–539. https://doi.org/10.1002/int.20418

Uren, V., & Edwards, J. S. (2023). Technology readiness and the organizational journey towards AI adoption: An empirical study. *International Journal of Information Management*, *68*, Article 102588. https://doi.org/10.1016/j.ijinfomgt.2022.102588

Zadeh, L. A. (1965). Fuzzy sets. *Information and Control*, *8*(3), 338–353. https://doi.org/10.1016/S0019-9958(65)90241-X

Black Sea Journal of Engineering and Science
doi: 10.34248/bsengineering.1988909

Open Access Journal
e-ISSN: 2619 – 8991

Research Article
Volume 9 - Issue 5: 2473-2481 / September 2026

CUDA-BASED PARALLEL INTRA PREDICTION AND TRANSFORM ARCHITECTURE FOR HEVC INTRA-FRAME IMAGE CODING

Mücahit KAPLAN[1]*, Ali AKMAN[2]

[1]*Mudanya University, Faculty of Engineering, Architecture and Design, Department of Computer Engineering, 16940, Bursa, Türkiye*
[2] *İstanbul Ticaret University, Faculty of Engineering, Architecture and Design, Department of Computer Engineering 34000, Istanbul, Türkiye*

Abstract: Computations related to intra prediction and transform in High Efficiency Video Coding are highly computational demanding, especially when multiple intra prediction modes have to be computed for block-based image encoding. In this paper, we propose a parallel CUDA implementation of HEVC intra frame prediction and integer transform operations on an embedded GPU platform. The presented implementation parallelizes HEVC intra prediction modes (35 in total, divided into planar, DC, and angular modes) and implements an efficient transform computation utilizing shared memory allocation. The proposed implementation was tested on NVIDIA Jetson Xavier NX platform using standardized test images and various quantization parameter settings. The results demonstrate that our solution accelerates the computations by up to 105.17× in terms of kernel computations compared to the sequential CPU implementation. Taking into account CPU–GPU memory transfer and synchronization overheads, the acceleration factor for the end-to-end process is 1.62×. In terms of the reconstructed image quality, there is a small decrease in the average PSNR value equal to about 0.65 dB. It is mainly caused by implementation-related differences in parallel computation, rounding, and quantization procedures. These results show that intra-frame prediction and transform stages in HEVC video codec can be efficiently parallelized using CUDA; however, there are still memory transfer and synchronization overheads limiting end-to-end performance. Our implementation can serve as a building block of a fast HEVC encoder but not as a full-fledged video encoder itself. Source code and dataset for this research are freely available on Zenodo with the DOI: https://doi.org/10.5281/zenodo.17286247.

Keywords: HEVC intra prediction, CUDA, Integer DCT, Embedded GPU, Intra-frame image coding, Block-based image compression

***Corresponding author:** Mudanya University, Faculty of Engineering, Architecture and Design, Department of Computer Engineering, 16940, Bursa, Türkiye
E mail: mucahit.kaplan@mudanya.edu.tr (M. KAPLAN)
Mücahit KAPLAN https://orcid.org/0000-0001-5712-3093
Ali AKMAN https://orcid.org/0000-0002-9486-519X

Received: July 07, 2026
Accepted: August 14, 2026
Published: September 15, 2026

Cite as: Kaplan, M., & Akman, A. (2026). CUDA-based parallel intra prediction and transform architecture for HEVC intra-frame image coding. *Black Sea Journal of Engineering and Science,* 9(5), 2473-2481.

1. Introduction

HEVC has provided very efficient methods for block-based prediction and transforms for visual data compression. In particular, intra prediction and integer transforms are very crucial tools, as they are used extensively in the process of coding blocks, where various prediction modes have to be evaluated (Bross et al., 2023). Even though HEVC was initially designed as a video encoding technique, the intra-frame coding scheme provided by HEVC can offer a good environment for investigating block-based image coding schemes. This is why the current work will concentrate only on the acceleration of HEVC intra-frame prediction and transforms using CUDA, and not HEVC video encoder itself.

Recently, the Discrete Cosine Transform has been identified as the most computationally intensive component of the High Efficiency Video Coding standard. Based on this fact, Akman and Cekli (2023) proposed new architectures for the 2D DCT using approximate compressors with low power and hardware requirements. The proposed design has high computational efficiency with minimal quality degradation. This shows the potential benefits of hardware optimization in the implementation of the High Efficiency Video Coding standard. The rapid advancement in the design of Graphics Processing Units has introduced new frontiers in video encoding techniques using the concept of General-Purpose GPU computing. The NVIDIA Compute Unified Device Architecture has introduced ease in programming the GPU (NVIDIA, 2023). This has brought about the efficient implementation of parallel video encoding techniques. The intra prediction of large coding blocks has attracted significant attention in the field of parallel processing. However, the implementation of intra prediction in the GPU has brought about several challenges in terms of alignment difficulties in the intra prediction process. The parallelized calculation of SAD and SSD has been demonstrated to be efficiently performed in the GPU. The implementation of motion estimation in the GPU has brought about significant improvements in the motion

estimation process. Khemiri et al. (2018) demonstrated the parallelization of motion estimation in the GPU. The parallelization has brought about an improvement of 56% in the motion estimation process compared to the CPU implementation for large block sizes. Additionally, Jingjing and Kehua (2019) proposed a fast algorithm for intra picture prediction that reduces computational complexity by simplifying prediction modes analyzed according to how often they are applied, making intra prediction more efficient for video coding platforms.

Tariq (2020) proposed a high-performance accelerator that combines statistical inference and optimal stopping theory to accelerate intra-mode selection in the HEVC standard. This approach is fundamentally based on CPU-based modeling and aims to reduce coding complexity. In this study, the same principles are extended to GPU parallel architecture, significantly increasing real-time applicability in heterogeneous CPU–GPU environments.

In addition to traditional GPU-accelerated HEVC approaches, similar parallel processing concepts have recently been applied to other subfields of visual computing. For example, Pietri et al. (2025) proposed a GPU-based system for real-time compression of dynamic 3D meshes in cloud-based games. This system utilizes CPU–GPU co-processing on the client side to enable low-latency data transfer.

Zhu et al. (2023) proposed a frame-based fusion network (FFFN) that utilizes a feedback mechanism for video super-resolution (VSR). This method enables high-quality video reconstruction by iteratively combining the spatiotemporal information obtained from aligned frames. Although the focus is on super-resolution, the proposed feedback-based parallel fusion structure shares similar acceleration principles with the GPU-based parallel implementation of intra prediction in HEVC in this work.

An essential step in video compression standards, including HEVC, is the Discrete Cosine Transform (DCT), valued for its high-energy efficiency capabilities (Singhadia et al., 2019). To reduce computational overhead, HEVC employs integer DCT instead of real-valued DCT. However, even with integer DCT, the process remains computationally intensive because of the large number of multiplication operations. Quantization and transform processes, along with analysis of rate-distortion, can account for nearly 25% of the overall encoding time in the HEVC reference software (Akman and Cekli, 2023; Ryoo et al., 2008). Therefore, optimizing these processes is crucial for any attempt at enhancing encoding efficiency and saving energy. In the work by Juncheng et al. (2015), parallel intra programming was explored with respect to HEVC encoding and decoding on GPU + CPU platforms. It was shown that the combined computational resources provided by heterogeneous platforms can be effectively utilized to achieve faster encoding speeds with no compromise in terms of efficiency. Another work by Radicke et al. (2016) proposed a novel intra prediction technique specifically designed to be implemented on heterogeneous platforms with CPU + GPU architecture. This demonstrates the potential benefits of exploiting the computational resources provided by heterogeneous platforms to achieve faster encoding speeds with HEVC encoders. In the context of parallel processing techniques, the demand for efficient computation with respect to video encoding has led to the implementation of parallel execution techniques. These techniques have been implemented either by exploiting GPU resources or by exploiting the combined resources provided by CPUs and GPUs. It has been shown that the transform block of the HEVC encoding scheme can be efficiently implemented by exploiting parallel processing techniques, where the transform block is efficiently implemented by exploiting the shared memory addressing capabilities provided by GPUs. Moreover, the exploration of design alternatives technique was employed by Bloch et al. (2023) with respect to GPU + CPU common system platforms to optimize task partitioning and scheduling. This was implemented by exploiting the Tabu search technique. Another work by James et al. (2024) evaluated GPU-based HEVC encoders, i.e., Kvazaar and x265, with respect to embedded platforms and concluded that these encoders can be efficiently implemented to achieve real-time encoding with superior speed and quality balance. Several more recent researches have also dealt with the issue of computational complexity of HEVC both in terms of algorithms and hardware acceleration. For example, Wang et al. (2025) have suggested a fast HEVC intra-coding mode selection algorithm based on image texture direction and correlation between various prediction modes. As a result of this algorithm implementation, the authors managed to achieve more than 46% reduction in the encoding time on target resource-limited embedded devices. Li et al. (2025) have proven that texture-based characteristics, neighboring coding modes and rate-distortion data may be used together to decrease the complexity of intra-prediction process in scalable HEVC systems. With regard to hardware-software co-design approach, Lopez-Granado et al. (2025) have shown that the overall acceleration of HEVC system is significantly dependent not only on the efficiency of accelerated computational core but also on the hardware-software integration overhead. More recently, Rathee et al. (2026) have suggested HEVC architecture implemented on the FPGA platform with dynamic-programming optimization of intra-frame prediction process. In a recent work by Imen et al. (2022), intra-mode complexity was addressed by exploiting the potential benefits provided by the LeNet-5 and AlexNet deep learning architectures. This was done by replacing the exhaustive RDO search with CNN prediction for CU partitioning. This demonstrates the importance of optimizing intra prediction with respect to HEVC encoding.

According to the literature review of the relevant works, GPU acceleration has been extensively researched for various stages of HEVC encoding such as intra prediction,

transform calculation, task scheduling, and heterogeneous CPU-GPU operation. Yet, the joint work of HEVC intra prediction mode evaluation and the optimal integer transform calculation on the embedded GPU system deserves more experimentation regarding thread mapping, shared memory utilization, and CPU-GPU coordination overheads. Furthermore, recent research has proven that acceleration achieved at the computational kernel level does not always result in the same amount of acceleration in the overall system because the process of data transfer and synchronization could become the main bottleneck (Lopez-Granado et al., 2025). Hence, the joint consideration of kernel execution efficiency and total processing time becomes crucial for heterogeneous embedded systems.

In our work, we are not introducing any novel standards for HEVC, or developing a full video encoder; however, our primary contribution is the design and implementation of the CUDA architecture that performs parallel evaluation of all 35 HEVC intra prediction modes, as well as the optimal integer transform computation process. Our proposed architecture is experimentally tested on the NVIDIA Jetson Xavier NX platform.

Recently, transformer-based visual processing frameworks such as the Efficient Attention Pyramid Transformer (EAPT) have demonstrated the potential of multi-level attention and global patch communication for high-performance image processing tasks (Lini et al., 2023).

In this work, we present a highly parallelized implementation intra prediction and DCT for HEVC on GPUs. The proposed method effectively balances memory bandwidth and access patterns, maximizing both resource utilization and execution speed.

The key contributions of this research are listed below: First, a CUDA-based parallel architecture is designed to evaluate all 35 HEVC intra prediction modes on an embedded GPU platform. Second, intra prediction is combined with integer transform, quantization, inverse quantization, and inverse transform procedures within the framework of intra-frame block-based coding. Third, two improved transformation procedures based on row-wise multiplication without transposition and symmetry are implemented using CUDA. Fourth, the proposed architecture is tested on the NVIDIA Jetson Xavier NX using separate kernel execution speed and full execution time results to clarify the impact of CPU–GPU memory transfer and synchronization overheads. Fifth, the image reconstruction quality is estimated using PSNR.

The remainder of this paper is organized as follows: Section 2 describes the mathematical and procedural foundations of HEVC intra prediction and transform phases. Section 3 presents the detailed design of the proposed GPU-based parallel computing architecture, thread mapping model, and shared memory configurations. Experimental methodologies, execution benchmarks, and resource bottleneck analyses are evaluated in Section 4. Finally, Section 5 concludes the paper and highlights strategic directions for future work.

2. Materials and Methods

HEVC block structure describes hierarchical visual data representation into coding units, prediction units, and transform units. In the current study, only the intra frame part of HEVC coding process is discussed. All input test images are treated as intra frames and segmented into coding units (block-based) for assessment of intra prediction and transformation. Consequently, the suggested approach

may be considered as CUDA-acceleration of HEVC intra frame computational modules, but not as a full-fledged HEVC video encoder. The general structure of HEVC intra prediction process is shown in Figure 1.

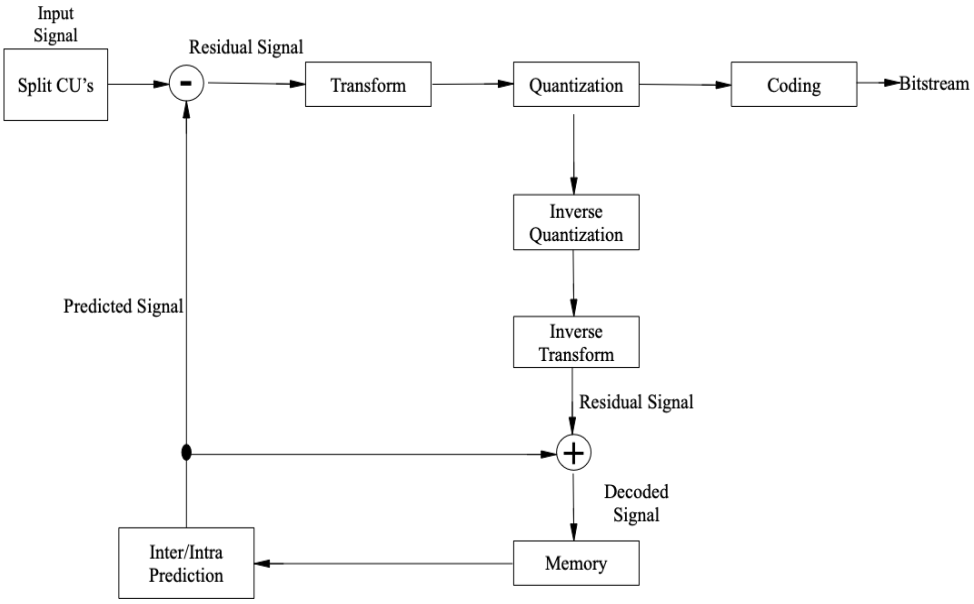


Figure 1. Basic Structure of the HEVC Intra Prediction Implementation.

In HEVC, the visual data is segmented into Coding Tree Units (CTUs) that provide flexible block structure for different degrees of spatial detail description. The CTU can be further split into Coding Units (CU) that consist of Prediction Units (PU) and Transform Units (TU). The TU size is represented by the formula N × N, where N equals to 4, 8, 16 or 32 (Bross et al., 2023). In the current research, 32 × 32 coding units are used in the experimental implementation in order to map the intra prediction and transformation into the CUDA thread/block structure.

2.1. Intra Prediction

HEVC's intra prediction framework consists of three basic steps aimed at increasing coding efficiency and reducing the computational load on the encoder and decoder: preparation of reference samples, creation of prediction samples, and post-processing (Bross et al., 2023). In this process, each block is predicted using its reconstructed upper and left neighboring samples. HEVC supports 35 different intra prediction modes to achieve high compression ratios: 33 of them are angular, one is planar, and one is DC (mean-based) mode. An example of reference samples used by HEVC intra prediction for an N x N block is presented in Figure 2. General block diagram of parallel calculation of intra prediction model is presented in Figure 3.

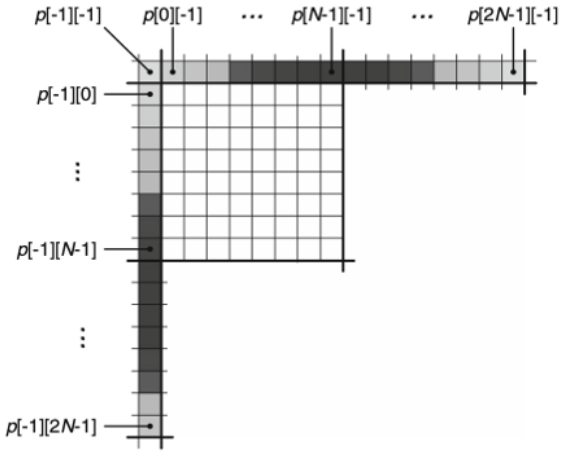


Figure 2. An example of reference samples used by HEVC intra prediction for an N x N block (Bross et al., 2023).

HEVC uses 33 intra prediction modes for angular prediction that represent various directional structures in a block, whereas the other two modes are for planar and DC prediction. Angular prediction is the process through which each of the predicted samples is obtained via interpolation of reference samples based on the angular direction chosen. The value of the pixel is obtained through interpolation of two adjacent samples denoted as R[i] and R[i+1]. This is shown in equation 1.

$$P(x,y) = \frac{(32-w)\,R[i] \;+\; wR[i+1]}{32} \tag{1}$$

In this case, the notation P(x,y) refers to the interpolated sample, while R[i] and R[i+1] refer to the neighboring reference samples. The interpolation weight w is defined according to the selected angular prediction mode. The denominator is equal to 32 and relates to HEVC angular interpolation normalization.

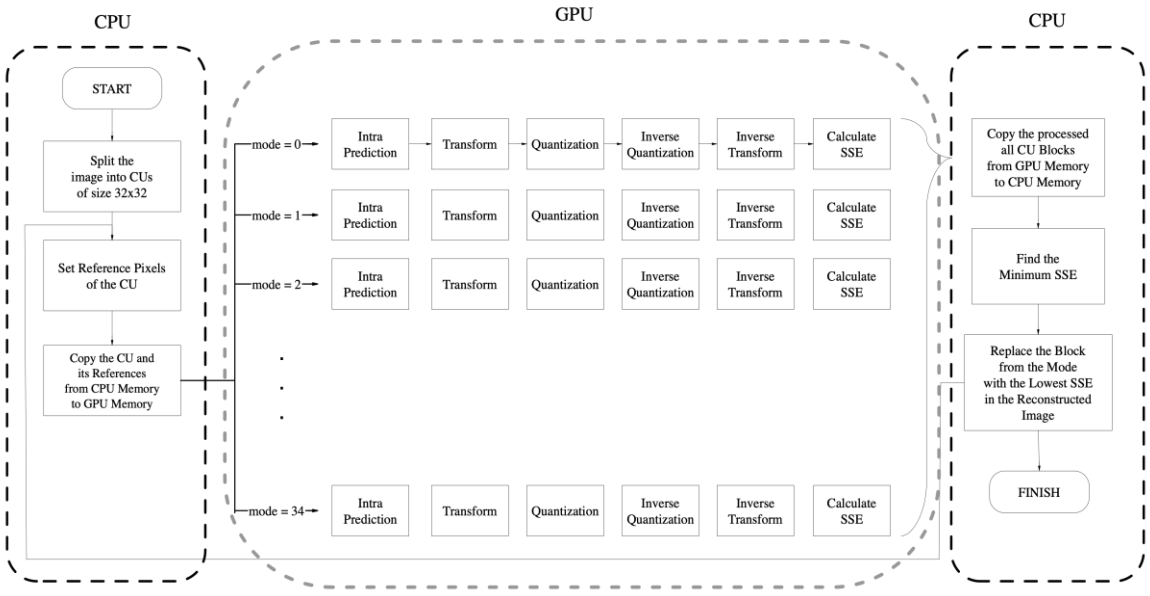


Figure 3. General block diagram of parallel calculation of intra prediction model.

In the DC estimation case, the estimated sample values are filled with a fixed value representing the average of the reference samples immediately to the left and above the block to be estimated.

Planar mode is an estimation method used to provide smooth transitions between image blocks. This mode makes estimates based on both the top and left edge pixels and determines the value of each pixel by taking the average of these two estimates.

The estimated pixel value is calculated as follows equation 2:

$$P(x,y) = (P_h(x,y)+P_v(x,y)+N) / 2N \quad (2)$$

Here, $P_h(x,y)$ is horizontal (top edge) prediction, $P_v(x,y)$ is vertical (from the left edge) estimate. N is block size (e.g., 4, 8, 16). These two sub-estimates are obtained as follows (equations 2a and 2b):

$$P_h(x,y)= (N-1-x)\cdot p(-1,y)+(x+1)\cdot p(N,-1) \quad (2a)$$
$$P_v(x,y)=(N-1-y)\cdot p(x,-1)+(y+1)\cdot p(-1,N) \quad (2b)$$

That is, $p(-1,y)$ is reference pixels on the left edge, $p(x,-1)$ is reference pixels on the top edge, $p(N,-1)$ is top-right corner pixel, $p(-1,N)$ is bottom-left corner pixel.

These expressions establish a linear transition between reference pixels horizontally and vertically, depending on the pixel position. Taking the average of these two estimates yields a smooth surface within the block and prevents sharp transitions at edges, ensuring higher visual quality in flat regions.

In HEVC, intra prediction is performed at the transform block (TB) level, and the block size can be selected from 4×4 to 32×32. However, for the prediction to be performed, the necessary reference samples must have been previously encoded and reconstructed from the relevant neighboring blocks. This creates a dependency chain that determines the order of computation and imposes a constraint on parallelization.

The encoder calculates the sum of the squares of the differences between the predicted block and the original block to evaluate the accuracy of each prediction mode. This operation is carried out by taking the square of the difference between the original and the predicted values at each pixel position and summing them across the whole block. This measure is referred to as the sum of squared errors (SSE), and the prediction mode with the lowest value is chosen for the next steps in the encoding process.

The prediction mode with the lowest SSE value is chosen for the next steps in the encoding process. This selection has a direct influence on the efficiency of the compression and the complexity of the encoding. From a parallel processing viewpoint, it can be seen as an advantage.

2.2. Transform and Inverse Transform

The direct application of the transform on the predicted block is not performed in the HEVC intra-coding scheme. The transform process is done on the residual block that is formed after subtracting the predicted block from the original input block. Hence, in this research work, the input matrix X in the transform formula is the residual block and not the original or the predicted block. This transformation has the purpose of concentrating the energy in certain components and attaining a more efficient data structure for the quantization step. It is allowed for the transformation blocks (Transform Units – TU) to have different sizes: 4×4, 8×8, 16×16, and 32×32.

HEVC uses an integer-based DCT instead of floating-point-based DCT. The two-dimensional DCT operation is expressed as a two-step matrix multiplication along the row and column directions (equation 3):

$$[C] = [D] [X] [D]^T \quad (3)$$

In the above case, X stands for the input residual block, D stands for the N × N integer transform matrix, and C stands for the transform coefficient matrix. Once the inverse quantization and the inverse transform process are completed, the residual block is added to the predicted block.

Inverse transform side, this process is reversed to obtain the estimated block (equation 4):

$$[X] = [D]^T [C] [D] \quad (4)$$

During this transformation process, various scaling factors are used to maintain numerical accuracy. These factors for the forward and inverse stages of the transformation are defined as follows:

After the first forward transformation: $ST_1 = 2^{(-B+M-9)}$

After the second forward transformation: $ST_2 = 2^{-(M+6)}$

After the first inverse transformation: $SIT_1 = 2^{-6}$

After the first inverse transformation: $SIT_2 = 2^{-(21-B)}$

Here, B denotes the bit depth of the input/output signal (e.g., 8 bits), and M denotes the base-2 logarithm of the transformation size: $M=\log_2 N$.

In the standard computational approach, the transpose of the intermediate matrix resulting from the D·X multiplication must be taken. However, transposing the intermediate matrix increases memory access costs and hinders parallel computation. Therefore, the row-based multiplication method proposed by Kaplan and Akman (2024) eliminates the transpose operation, reducing the computational load and facilitating parallelization. This method allows the two-dimensional DCT to be computed directly, eliminating the need for an intermediate transpose.

Another improvement method proposed in the transformation phase is to simplify matrix operations by utilizing the symmetry and inverse symmetry properties of HEVC transformation matrices. In HEVC integer DCT matrices: Even-numbered rows are symmetric, Odd-numbered rows are inverse symmetric. Thanks to this structure, the transformation process can be performed with fewer operations as follows (equation 5):

$$\begin{bmatrix} C_c \\ C_t \end{bmatrix} = \begin{bmatrix} D_{N/2\,x\,N/2} & 0 \\ 0 & M_{N/2\,x\,N/2} \end{bmatrix} \cdot \begin{bmatrix} a_{n/2} \\ b_{n/2} \end{bmatrix} \quad (5)$$

represent the transformation coefficients in even and

odd rows, respectively, D and M represent the simplified transformation matrices.

This structure reduces the computational load by removing matrix elements multiplied by zero from the calculation. Such simplified structures provide significant advantages for parallel computation, especially in 32×32 transformation blocks.

2.3. Quantization and Inverse Quantization

Quantization is the process of scaling the coefficients obtained because of the transformation process using a specific quantization parameter (QP) and representing them with smaller integer values with limited bit width. This step forms the basis of compression, aiming to minimize file size while preserving perceptual image quality. The HEVC standard has incorporated a frequency component-based quantization approach to make this process more efficient. In this approach, low frequency component quantization is done with a smaller quantization step size, while high frequency component quantization is done with a larger quantization step size. This is done to ensure the quality of the image is not compromised, especially in the low frequency regions where the human eye is more sensitive to changes.

For the designed architecture, the quantization step will be applied to observe the reconstruction performance of the intra-frame pipeline processing design. At the end of the quantization step, the coefficients will be reordered into 1D ZigZag scan format and will be encoded through the Exponential-Golomb (Exp-Golomb) coding block. The Exp-Golomb coding block will be used to compute the output coefficient size as well as S.O. value from the experiment results. For the current research, the Exp-Golomb block will be used for coefficient coding purpose only and not to generate the HEVC bitstream.

The process of quantization is performed in an inverse manner during inverse quantization, whereby the quantized values are scaled back to represent their corresponding amplitudes. As such, inverse quantization forms part of the intra-frame coding process by assisting in the reconstruction of the residual block and quantization effects. Although this process is not entirely lossless, near-lossless quality can be achieved by choosing an appropriate QP value.

For this investigation, QP levels of 17, 22, 27, 32, 37, and 42 are used in order to test the performance of the proposed CUDA implementation in terms of its stability under different levels of quantization. Smaller QP levels correspond to better reconstruction quality with more non-zero transform coefficients, while greater QP levels imply a greater level of quantization and, correspondingly, worse reconstruction quality.

2.4. CUDA-Based Parallel Implementation and Memory Organization

GPU is extensively used as a highly parallel processor to perform visual data processing jobs which are highly compute-intensive. In HEVC intra-frame encoding process, operations like intra prediction, transformation, quantization, inverse quantization, and inverse transformation need to be performed at block level repeatedly. Thus, these operations can be considered as good choices to perform with CUDA parallelism, especially in case of multi-mode intra prediction.

In GPU-enabled visual computing pipelines, the calculation can be done on a per-frame, per-block, or batch basis according to the dependency model of the algorithm. In our solution, the source image is broken down into coding units, and the 35 modes of HEVC intra prediction are mapped to parallel CUDA kernels for each block. However, data transfers between the CPU and GPU, especially in heterogeneous accelerator architectures, can be a significant factor in the total processing time. Depending on the level of the GPU used, these transfer delays can reach up to 26% on a mid-range GPU and up to 73% on a high-end GPU. In this study, to reduce this latency, data blocks are transferred asynchronously from main memory (CPU – host) to the GPU (device) in equal-sized batches. This allows for more efficient use of bandwidth and optimizes processing time (Harris, 2019).

CUDA (Compute Unified Device Architecture) is a platform developed by NVIDIA that enables general-purpose parallel programming on the GPU. The CUDA architecture allows tasks to be divided into small pieces and executed simultaneously by multiple threads. In the CUDA architecture, the part of the code to be executed on the GPU is defined as a kernel function. These functions are marked with the __global__ statement, called by the CPU, and executed in parallel on the GPU (NVIDIA, 2019).

When each kernel is executed, threads are created. These threads are grouped into blocks, and the blocks are placed into larger structures called grids. Both blocks and threads can be configured in 1D, 2D, or 3D configurations. Threads are defined by indices such as threadIdx.x, threadIdx.y, threadIdx.z, while blocks are defined by indices such as blockIdx.x, blockIdx.y (Ghorpade et al., 2012; Thurley and Danell, 2012).

This hierarchical memory structure minimizes memory access conflicts (bank conflicts), thereby enhancing the performance of parallel processing. In CUDA, shared memory is divided into sections called banks, and consecutive addresses are assigned to different banks. However, when multiple threads attempt to read data from the same bank at the same time, a conflict occurs. In this research, an empty (unused) column was added to the shared memory to prevent this issue, and this empty space was accounted for in the transformation matrices (Figure 4).

In this method, image blocks are first transferred from the CPU to the GPU's global memory and then copied to shared memory. Each thread processes only one pixel within this block, and operations such as transformation and quantization are executed in full parallel. This approach significantly reduces processing time and maximizes the GPU's high parallelism and bandwidth advantages.

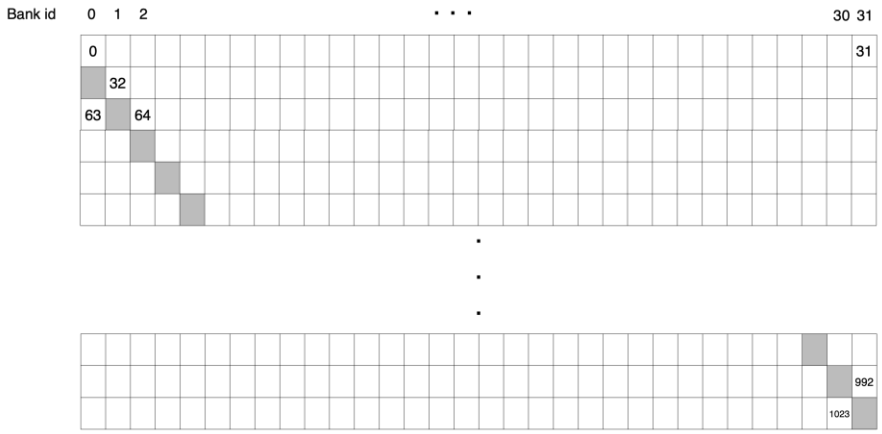


Figure 4. Space Usage in Shared Memory (Gray Shaded Areas represent gaps).

2.5. Implementation and Evaluation

The following section presents the implementation of the proposed HEVC intra-frame computational model using the CUDA framework. The work concentrates on the acceleration of intra prediction, residual generation, integer transform, quantization, inverse quantization, inverse transform, and reconstruction procedures for block-based image compression algorithm. The block scheme given in Fig. 3 illustrates the general flow of the proposed approach.

In this case, all 35 HEVC intra prediction modes for each coding unit are tested simultaneously on the GPU. For each HEVC intra mode, there is a CUDA execution block assigned, while the pixels of the coding unit are processed in parallel CUDA threads. In such a way, the HEVC intra prediction procedure, which is very resource-intensive operation in HEVC intra coding, is executed in the parallel GPU environment. Data preparation, memory management, and mode selection tasks are done on the CPU, while block-level prediction and transformation are performed by GPU.

Algorithm 1: Pseudo-code for GPU-based HEVC intra prediction.

START
// Divide the input image into 32 × 32 coding units
blocks = splitImageIntoBlocks(image, 32, 32)
// Initialize reconstructed output image
reconstructedImage = initializeImageLike(image)
// Process each coding unit
for originalBlock in blocks:
// Upload the original block and its reference samples to GPU memory
copyOriginalBlockAndReferencesToGPU(originalBlock)
// Initialize arrays for storing mode-dependent results
reconstructedBlocks = []
sseValues = []
// Evaluate all 35 HEVC intra prediction modes in parallel on the GPU
for mode in parallel(35 HEVC intra prediction modes):
predictedBlock = intraPrediction(originalBlock, mode)
residualBlock = originalBlock - predictedBlock
transformedResidual = applyTransform(residualBlock)
quantizedResidual = quantize(transformedResidual)
inverseQuantizedResidual = inverseQuantize(quantizedResidual)
reconstructedResidual = applyInverseTransform(inverseQuantizedResidual)
reconstructedBlock = predictedBlock + reconstructedResidual
sse = calculateSSE(originalBlock, reconstructedBlock)
storeInGPU(mode, reconstructedBlock, sse)
// Copy reconstructed blocks and SSE values back to the CPU
reconstructedBlocks, sseValues = copyModeResultsFromGPUToCPU()
// Select the best prediction mode based on the minimum SSE
bestMode = findMinimumSSEMode(sseValues)
// Write the best reconstructed block to the reconstructed image
replaceBlockInImage(reconstructedImage, originalBlock.position, reconstructedBlocks[bestMode])
END

Algorithm 1 summarizes the processing steps of the suggested implementation. This pseudocode aims to clarify the computational flow instead of representing a full HEVC-compliant encoder. Specifically, the algorithm demonstrates how every original block gets predicted, how the residual block is derived, how transform and quantization operations apply to the residual, and how the reconstructed block is produced for SSE-based mode evaluation.

According to Algorithm 1:

splitImageIntoBlocks: The initial picture gets split into blocks that measure thirty-two by thirty-two pixels. Every single block then runs through its own separate step inside the suggested process for frames taken within one scene.

copyOriginalBlockAndReferencesToGPU: For every coding unit, the initial block and needed reference pixels from adjacent rebuilt areas move into GPU storage. Those reference pixels serve the HEVC intra prediction methods.

parallel(35 HEVC intra prediction modes): For every

initial block, all 35 HEVC intra prediction modes are assessed simultaneously on the GPU. These modes include 33 angular types, one planar type, and one DC type.

intraPrediction(originalBlock, mode): For the chosen intra prediction mode, a predicted block is created by applying the matching reference samples.

residualBlock: The residual block comes from subtracting the predicted block from the original one. That residual block serves as the input to the transform stage.

applyTransform leads into quantize which goes to inverseQuantize then applies inverseTransform: here the integer transform acts on the residual block. After that the transformed residual gets quantized, inverse quantized, and inverse transformed so we get the reconstructed residual block back.

reconstructedBlock: The rebuilt block comes from putting the recovered residual block onto the forecasted block again.

calculateSSE: The SSE value is computed between the initial block and the rebuilt block for every intra prediction mode. That figure is utilized to compare the prediction modes.

storeInGPU: The rebuilt block and SSE value matching every mode get put into temporary GPU storage space.

copyModeResultsFromGPUToCPU: All 35 mode reconstructed blocks and SSE values get copied back onto the CPU.

findMinimumSSEMode: The CPU picks the optimal intra prediction mode by finding the one that has the lowest SSE number.

replaceBlockInImage: The reconstructed block matching the best mode gets placed inside the output reconstructed image right where the original coding unit sits.

This structure significantly speeds up the mode selection process, one of the most computationally intensive stages of HEVC, by making it fully parallel on the GPU. The block/thread structure of the CUDA architecture allows each prediction mode to be processed independently.

In addition, two optimization techniques proposed by Kaplan and Akman (2024) are used in the transformation operations. The first is a row-based multiplication method that eliminates matrix transposition. This method simplifies memory access complexity, thereby facilitating faster computation of transformation calculations. The second method involves a simplified transformation structure that does not include zero elements based on symmetry properties of DCT matrices. This makes the transformation operations more compatible with and faster on the GPU architecture.

Differences between the two DCT optimization methods lie mostly in the different techniques used in minimizing computation and memory access overheads. First, Method 1 of the DCT performs the transformation of the input into two dimensions through matrix multiplication based on the rows of the matrix. As such, the primary benefit of this method is that the transpose step of the intermediate matrix is eliminated. The second DCT method further takes advantage of the symmetry and antisymmetry characteristics of the integer transform matrix of HEVC. This is done by re-arranging the transform equations into even and odd parts and minimizing unnecessary multiplications of zero-value matrix elements. While Method 1 focuses on improving the memory access aspect, the latter method reduces the memory overhead and unneeded computations.

Shared memory was used effectively throughout all operations, data sharing between threads was optimized, and intra-block synchronization was achieved using the __syncthreads() command. This is particularly critical for data-dependent operations such as transformation and quantization.

As a result, the proposed parallel application structure enables intra prediction and mode selection operations to be performed in less time, with fewer memory accesses, and with higher accuracy; while maintaining HEVC's coding efficiency, performance has been significantly improved.

4. Results

The proposed CUDA-based parallel implementation was experimentally evaluated for the HEVC intra-frame prediction and transform operations in this study. Four 512 × 512 reference images were used for experiments: Lena, Airplane, Boat and Barbara. This set of reference images was chosen due to the fact that they possess varied spatial properties which could be used to assess image processing algorithms such as smoothness, directional edges, contours of objects, and texture. This means that the chosen images represent a set of varied test cases for testing whether the proposed parallel approach is computationally stable depending on the nature of the image content. All images were processed using 512 × 512 resolution in order to create an equal computational load. Each image was treated as an intra frame and split into coding units of 32 * 32. The experimental platform is the developer kit of the NVIDIA Jetson Xavier NX. The implementation is developed by CUDA programming model. The main objective of the experiments was to measure the computational speedup offered by parallel intra prediction and optimized integer transform computation, not the performance of a full HEVC video encoder. Development environment is shown in Figure 5.

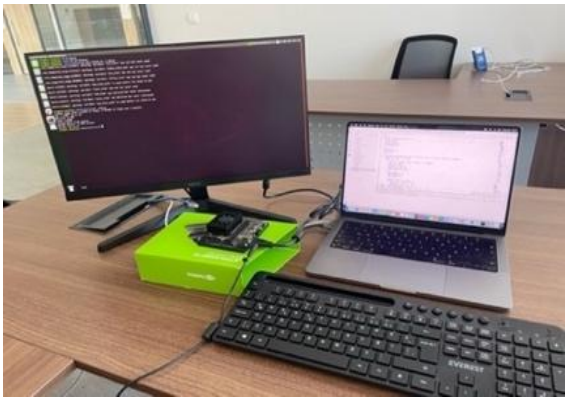


Figure 5. Development environment.

For a fair device-level baseline, the sequential CPU implementation was run natively on the onboard CPU of the NVIDIA Jetson Xavier NX platform with a 6-core NVIDIA Carmel ARMv8.2 64-bit CPU. CPU code was compiled with GNU Compiler Collection with optimization option -O3. This baseline was compared with the proposed GPU implementation under the same constraints of the embedded platform.

The workload was split in 32 × 32 coding units. The 33 angular modes, one planar mode and one DC mode were used to test all 35 HEVC intra prediction modes for each coding unit. In the CUDA implementation, each prediction mode was assigned to a parallel execution block and the CUDA threads processed the pixels within the coding unit.

This allowed for a highly efficient parallel implementation.

QP values of 17, 22, 27, 32, 37, and 42 were considered for analysis of the proposed implementation under various degrees of quantization strength. The lower the value of QP, the better the accuracy of reconstruction. On the other hand, a higher QP value means greater quantization strength. In such an environment, Peak Signal-to-Noise Ratio was employed for assessing the quality of reconstructed images. However, since the present study does not implement a complete HEVC video encoder, the results focus on computational acceleration, Exp-Golomb-based S.O. values, and reconstructed image quality. The obtained PSNR values revealed the effect of the DCT methods used in the transformation step on image quality (Figure 6).

The performance gain on the GPU was evaluated using two main criteria:

Kernel execution time: This refers to the time it takes to run kernel functions on the GPU and perform intra prediction operations on blocks. This measurement was made excluding memory transfers and image segmentation operations.

Total processing time: This includes all steps from the start of the transformation process, including memory transfers and image processing.

The time measurements have been recorded with the help of NVIDIA Nsight Profiler. Two timing results were obtained: kernel execution time and total execution time. Kernel execution time is only concerned with the GPU execution phase and ignores the data transfer phase, image segmentation and CPU side mode choice. Total execution time considers CPU-GPU memory transfer, synchronization and collection phases. The performance achieved by the proposed GPU approach on average is 105.17× in terms of kernel execution when the DCT Method 2 and shared memory layout are employed. Nevertheless, in terms of total execution, the average speedup attained is 1.62× (Figure 6).

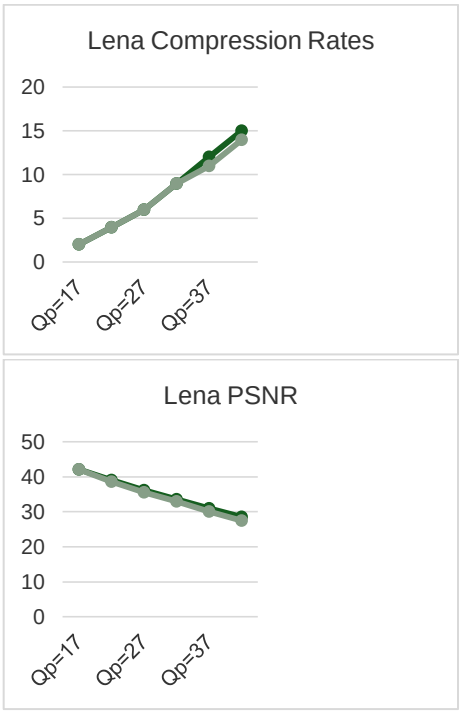


Figure 6. Comparison S.O. and PSNR Values of the Reference Image in CPU Serial and GPU Parallel Implementation

Significant improvements were also observed in total processing time. Compared to the CPU-based sequential system, the GPU parallel implementation was 1.3× faster, while shared-memory-based DCT methods achieved speedups of up to 1.62×. These results indicate that CPU–GPU data transfer remains a performance bottleneck despite the considerable kernel-level acceleration. Leaving extra space in the shared memory area in kernel processes running on the GPU prevented bank conflicts that could occur during memory access, further reducing the processing time. These results show that shared memory optimization improves kernel-level performance, while end-to-end acceleration remains limited mainly by CPU–GPU memory transfer and synchronization overheads.

These data demonstrate that optimizing shared memory directly affects computational speed at the kernel level and enables more efficient use of GPU resources through rapid access to repeatedly accessed data. This block-to-block cycle of memory transfers (CPU-to-GPU memory

transfer, evaluation on the GPU, GPU-to-CPU memory transfer, and selection of the minimum on the CPU side) is a carefully crafted trade-off dictated by the constraints of memory resources on low-power edge systems. For the NVIDIA Jetson Xavier NX platform, simultaneously caching the set of blocks and residual modes on edge for a whole high-resolution grid is beyond the capability limits of the device in terms of its global memory space, resulting in critical errors due to Out-of-Memory runtime execution problems. Offloading the minimum SSE evaluation task to the host CPU allows for safe operation and accurate spatial placement at the cost of additional time due to bus synchronization.

Moreover, the parallel DCT approaches proposed in this study, when assessed in terms of the intra prediction operations, ensured fair utilization of the GPU cores and fair allocation of the workload among the threads. In addition, the utilization of blocks for each mode proves the capability of the system in terms of scalability, which is important in embedded intra-frame coding.

The study proves the significant benefits of the proposed parallel architecture in terms of the processing time and quality in the implementation of the HEVC intra prediction process. This is because of the management of the memory, the synchronization, and the utilization of the appropriate algorithmic structures for the CUDA architecture.

The future direction of work will be to minimize CPU/GPU data transfer bottlenecks, such as using the CUDA unified memory model and asynchronous data streams.

In addition, the implementation of the parallelization of the execution threads, synchronization, and memory bank optimization will further enhance the system's efficiency in real-time encoding applications. These improvements will allow the widespread adoption of GPU-based parallel processing methods in high-density encoding standards such as HEVC.

The high-speed processing gains achieved in GPU-based parallel processing applications are a significant step forward in the development and implementation of real-time processing capabilities, particularly in computationally intensive applications such as video encoding. For high-efficiency coding standards such as HEVC, the intra prediction process consumes a significant amount of time. However, the capability to execute the transformation process and the entire intra prediction process in parallel has become a crucial factor in the system's efficiency. In this study, separating the prediction processes at the block level for each mode and executing these blocks in parallel through separate threads provided significant advantages in terms of scalability and concurrency.

Furthermore, the fact that the DCT methods proposed were tested on GPUs with different configurations demonstrates that parallel systems can be effectively used in comparative tests of different algorithms. While methods 1 and 2 used in the transformation steps yielded similar PSNR results, they exhibited different performance in terms of processing times. In particular, the fact that method 2 achieved higher speed gains with shared memory optimizations highlights that in such systems, not only the mathematical complexity of the algorithm but also its suitability for the GPU architecture must be considered.

Although data transfer times are high, this can be reduced with CUDA's asynchronous and stream-based architecture. Parallel architectures based on GPUs can be very beneficial for HEVC coding in terms of performance if computation-heavy tasks are efficiently implemented on parallel hardware, but the final performance is highly dependent on memory access patterns and synchronization between the CPU and GPU (Lopez-Granado et al., 2025). Proper memory management and synchronization improve performance. As shown in Table 1, the use of shared memory reduces the need for repeated data transfers, resulting in a notable decrease in processing time and an overall improvement in performance.

When the execution times are analyzed, an average 105.17-fold acceleration occurred in the core time, that is, in the part where the prediction takes place and parallelization takes place, and 1.62-fold acceleration occurred in the whole time. Table 2 gives the comparative context regarding the acceleration values between the proposed implementation and selected studies on acceleration values concerning HEVC intra prediction or parallel coding methods. These values should not be considered a benchmarking method due to differences in hardware architecture, input data, resolution, software implementation, and scope of experiments in the compared studies. For this reason, Table 2 is provided just to put the proposed implementation in the comparative perspective of the acceleration values presented in the literature. The experimental comparison in this study will be done between the sequential CPU implementation and the proposed GPU implementation on the same NVIDIA Jetson Xavier NX platform.

The PSNR, kernel execution time, total execution time, and reconstruction-related output metrics of the reference images at various QP values are shown in Table 3. A comparison of the sequential CPU version and the proposed GPU approach using DCT Method 2 and shared memory structure is made on equal platform settings. The obtained results demonstrate that the average PSNR difference between the CPU and GPU methods is about 0.651 dB.

Table 1. Test data of reference images

Duration	Measurement Shared Memory Space Utilization	Method	Lena		Airplane		Boat		Barbara	
			Execution Time (s)	Acceleration	Execution Time (s)	Acceleration	Execution Time (s)	Acceleration	Execution Time (s)	Acceleration
All Time	-	CPU serial	1.53	1.00	1.58	1.00	1.54	1.00	1.54	1.00
	YES	GPU Parallel	1.07	1.43	1.13	1.40	1.23	1.25	1.37	1.12
		GPU Parallel DCT Method 1	1.14	1.34	1.11	1.42	1.03	1.50	1.12	1.38
		GPU Parallel DCT Method 2	0.94	1.63	0.94	1.68	1.02	1.51	0.92	1.68
	NO	GPU Parallel	1.13	1.35	1.26	1.26	1.30	1.18	1.28	1.21
		GPU Parallel DCT Method 1	1.11	1.37	1.31	1.21	1.21	1.27	1.25	1.23
		GPU Parallel DCT Method 2	1.11	1.38	1.13	1.40	1.12	1.37	1.13	1.37
Core Time	-	CPU serial	0.84	1.00	0.87	1.00	0.87	1.00	0.88	1.00
	YES	GPU Parallel	0.01	57.61	0.01	70.02	0.01	62.55	0.01	66.48
		GPU Parallel DCT Method 1	0.01	66.83	0.01	71.76	0.01	79.77	0.01	72.53
		GPU Parallel DCT Method 2	0.01	103.10	0.01	105.80	0.01	104.70	0.01	107.10
	NO	GPU Parallel	0.02	34.37	0.01	62.92	0.01	59.97	0.01	65.49
		GPU Parallel DCT Method 1	0.02	35.55	0.02	52.62	0.01	67.93	0.01	69.65
		GPU Parallel DCT Method 2	0.02	36.32	0.01	76.84	0.01	79.77	0.01	78.36

Table 2. Contextual comparison of reported acceleration values in related studies

	Maximum Acceleration	Minimum Acceleration	Average Acceleration
Proposed method	1.82	1.33	1.62
Mate et al., 2020	-	-	1.22
Jingjing and Kehua. 2019	1.21	1.18	1.19
Juncheng et al., 2015	1.62	1.45	1.52
Radicke et al., 2016	1.54	1.52	1.52

Table 3. PSNR, Execution Time and Exp-Golomb-Based S.O. Variation of Reference Images

		CPU Serial			GPU Parallel DCT-2. Method Shared Memory Space Utilization				Comparison			
	QP	PSNR (dB)	Core Time (s)	Overall Time (s)	S.O	PSNR (dB)	Core Time (s)	Overall Time (s)	S.O	ΔPSNR (dB)	Core-Time Speedup (×)	Overall-Time Speedup (×)	ΔS.O
Lena	17	42.11	0.8292	1.519	2	42.11	0.0081	0.976	2	0	102.37	1.56	0.00
	22	39.09	0.8376	1.503	4	38.58	0.0084	0.956	4	0.511	99.71	1.57	0.00
	27	36.08	0.8505	1.57	6	35.57	0.0083	0.998	6	0.511	102.47	1.57	0.00
	32	33.50	0.8245	1.516	9	32.94	0.0079	0.876	9	0.561	104.37	1.73	0.00
	37	31.05	0.8307	1.529	12	30.06	0.0079	0.879	11	0.986	105.15	1.74	1.00
	42	28.58	0.8399	1.539	15	27.41	0.0081	0.946	14	1.170	103.69	1.62	1.00
Airplane	17	45.12	0.876	1.608	2	43.35	0.0077	0.902	2	1.761	113.77	1.78	0.00
	22	40.34	0.8787	1.597	3	40.34	0.0086	0.928	3	0	102.17	1.72	0.00
	27	37.33	0.8837	1.606	5	36.66	0.0079	0.883	5	0.669	111.86	1.82	0.00
	32	34.15	0.8365	1.532	8	33.50	0.0093	1.127	8	0.644	89.95	1.36	0.00
	37	31.40	0.8706	1.571	11	30.57	0.0079	0.920	11	0.837	110.20	1.71	0.00
	42	28.73	0.8645	1.560	16	27.71	0.0082	0.884	15	1.023	105.42	1.52	1.00
Boat	17	42.11	0.8791	1.580	1	42.11	0.0075	0.956	1	0	117.21	1.65	0.00
	22	38.58	0.8595	1.536	3	38.13	0.0079	1.002	2	0.457	108.80	1.53	1.00
	27	34.90	0.8772	1.542	4	34.32	0.0083	1.010	4	0.58	105.69	1.53	0.00
	32	31.79	0.8839	1.539	7	31.14	0.0089	1.022	7	0.655	99.31	1.51	0.00
	37	29.04	0.8685	1.531	11	28.26	0.0081	1.003	10	0.782	107.22	1.53	1.00
	42	26.48	0.8492	1.496	15	25.36	0.0093	1.122	14	1.122	91.31	1.33	1.00
Barbara	17	42.11	0.8662	1.564	1	42.11	0.008	0.905	1	0	108.28	1.73	0.00
	22	38.13	0.8909	1.574	2	38.13	0.0076	0.864	2	0	117.22	1.82	0.00
	27	34.70	0.8872	1.561	4	33.98	0.0083	0.911	3	0.725	106.89	1.71	1.00
	32	31.40	0.8958	1.555	6	30.72	0.0082	1.083	6	0.682	109.24	1.43	0.00
	37	28.58	0.8713	1.528	10	27.79	0.0087	0.870	9	0.791	100.15	1.76	1.00
	42	25.98	0.8543	1.505	13	24.84	0.0084	0.905	12	1.145	101.70	1.66	1.00
Average										0.65	105.17	1.62	0.38

5. Conclusion

A parallel architecture for accelerating the HEVC intra-frame computation based on CUDA has been implemented in this study. The proposed implementation uses parallel processing for evaluating 35 different HEVC intra prediction modes, including 33 angular modes, 1 planar mode, and 1 DC mode, for 32 × 32 coding units. Thus, the HEVC intra mode evaluation process, which requires considerable computational resources, has been moved to the GPU platform.

The experimental results conducted on the NVIDIA Jetson Xavier NX platform demonstrate that the proposed implementation achieves significant acceleration at the GPU kernel level. With the use of DCT Method 2 and shared memory optimizations, the average kernel acceleration is 105.17× compared to the sequential CPU implementation. However, in case of considering the CPU–GPU data transfer, synchronization and result collection operations, the average end-to-end acceleration rate reaches 1.62×. Therefore, one can conclude that data transfer and synchronization overheads remain the main limitations of the proposed solution.

The image quality was measured by means of PSNR metric. It has been demonstrated that the average PSNR difference is about 0.651 dB between the CPU implementation in the serial mode and the GPU implementation in the parallel mode. Such small difference in PSNR values is determined by implementation-related factors including rounding, quantization, and parallel computation order. Thus, the proposed method allows achieving a good tradeoff between computation speedup and image quality in the context of HEVC intra-frame computation on GPU platforms.

In the comparison of the two GPU-based DCT implementations, it can be stated that both methods allow increasing the execution performance. The highest efficiency is provided by DCT Method 2 in combination with the shared memory optimization. Thus, one can see

that not only the structure of the algorithm itself but also its adaptation to GPU memory structure has a direct influence on the algorithm performance.

It is important to emphasize that the proposed architecture should be viewed as an accelerated intra-frame computation module but not as an entire HEVC video encoder.

A disadvantage of the current experimental study is that the image set used contains four reference images of a constant size of 512 × 512 pixels. The controlled experiment setting was chosen to allow for the proper comparison of CPU and GPU performance on the same embedded platform. Still, evaluation through use of a greater number of images and different resolutions would provide some additional information about the performance and scalability of the suggested architecture. Therefore, it is one of the important areas for future research.

For further research, the reduction of the overhead of data transfer from CPU to GPU memory is planned to be done with the help of asynchronous memory transfers, CUDA streams, unified memory, and mode selection at the GPU side. Moreover, the extension of the proposed framework towards other HEVC components including inter prediction and entropy coding is considered.

Author Contributions

The percentages of the authors' contributions are presented below. All authors reviewed and approved the final version of the manuscript.

	M.K.	A.A.
C	60	40
D	60	40
S	10	90
DCP	80	20
DAI	70	30
L	70	30
W	70	30
CR	40	60
SR	70	30
PM	60	40

C= concept. D= design. S= supervision. DCP= data collection and/or processing. DAI= data analysis and/or interpretation. L= literature search. W= writing. CR= critical review. SR= submission and revision. PM= project management.

Conflict of Interest

The authors declared that there is no conflict of interest.

Ethical Consideration

Ethics committee approval was not required for this study because of there was no study on animals or humans.

References

Akman, A., & Cekli, S. (2023). Efficient 2D DCT architecture based on approximate compressors for image compression with HEVC intra-prediction. *Journal of Real-Time Image Processing, 20*(22). https://doi.org/10.1007/s11554-023-01261-3

Bloch, A., Casale-Brunet, S., & Mattavelli, M. (2023). Design space exploration for partitioning dataflow programs on CPU + GPU heterogeneous systems. *Journal of Signal Processing Systems, 95*. 1219–1229. https://doi.org/10.1007/s11265-023-01884-6

Bross, B., Han, W.-J., Sullivian, G. J., Ohm, J.-R., & Wiegand, T. (2023). *High Efficiency Video Coding (HEVC) text specification draft 9*. http://phenix.itsudparis.eu/jct/doc_end_user/current_document.php?id=6803 (accessed on 15 June 2023).

Ghorpade, J., Parande, J., Kulkarni, M., & Bawaskar, A. (2012). GPGPU processing in CUDA architecture, *arXiv preprint arXiv:1202.4347*.

Harris, M. (2019). How to optimize data transfers in CUDA C/C++. *NVIDIA Developer Blog*. https://devblogs.nvidia.com/how-optimize-data-transfers-cuda-cc/

Imen, W., Amna. M., Fatma. B., Ezahra. S. F., & Masmoudi. N. (2022). Fast HEVC intra-CU decision partition algorithm with modified LeNet-5 and AlexNet. *Signal. Image and Video Processing. 16*(7). 1811–1819. https://doi.org/10.1007/s11760-022-02139-w

James, R., Abo-Zahhad. M., Inoue, K., & Sayed, M. S. (2024). Performance evaluation of all intra Kvazaar and x265 HEVC encoders on embedded system NVIDIA Jetson platform. *Journal of Real-Time Image Processing. 21*(67). https://doi.org/10.1007/s11554-024-01429-5

Jingjing, Y., & Kehua, J. (2019). A fast intra prediction algorithm with simplified prediction modes based on utilization rates. *2019 IEEE/ACIS 18th International Conference on Computer and Information Science (ICIS)*. 225–229. Beijing. China.

Juncheng, M., Falei, L., Shanshe, W., Nan. Z., & Siwei. M. (2015). Parallel intra coding for HEVC on CPU plus GPU platform. *2015 Visual Communications and Image Processing (VCIP)*, 1–4.

Kaplan, M., & Akman, A. (2024). Parallel implementation of Discrete Cosine Transform (DCT) methods on GPU for HEVC. In M. N. Seyman (Ed.). *2nd International Congress of Electrical and Computer Engineering: ICECENG 2023*. EAI/Springer Innovations in Communication and Computing, Springer. https://doi.org/10.1007/978-3-031-52760-9_20

Khemiri, R., Kibeya, H., Sayadi, F. E., Bahri, N., Atri, M., & Masmoudi, N. (2018). Optimization of HEVC motion estimation exploiting SAD and SSD GPU-based implementation, *IET Image Processing, 12*(2), 243–253. https://doi.org/10.1049/iet-ipr.2017.0474

Li, W., Ou, W., Wang, H., Wu, Y., & Zhong, Y. (2025). Jointly probability-based fast intra prediction algorithm for spatial SHVC. *EURASIP Journal on Image and Video Processing*, 2025, 20. https://doi.org/10.1186/s13640-025-00683-2

Lini X., Sun, S., Huang, W., Sheng, B., Li, P., & Feng, D. D. (2023). EAPT: Efficient attention pyramid transformer for image processing. *IEEE Transactions on Multimedia, 25*, 50–61. https://doi.org/10.1109/TMM.2021.3120873

Lopez-Granado, O., Migallon, H., Alcocer Espinosa, E., Gutierrez, R., Van Wallendael, G., & Malumbres, M. P. (2025). Performance, limitations, and design issues of the integration of a hardware-based IME module with HEVC video encoder software. *IEEE Access*, 13, 113390–113406.

https://doi.org/10.1109/ACCESS.2025.3581961

Mate, Č., Alen, D., Leon, D., Igor, P., & Mario, K. (2020). Performance engineering for HEVC transform and quantization kernel on GPUs. *Automatika, 61*(3), 325–333. https://doi.org/10.1080/00051144.2020.1752046

NVIDIA. (2019). CUDA refresher: The CUDA programming model, *NVIDIA Developer Blog*. https://developer.nvidia.com/blog/cuda-refresher-cuda-programming-model/ (accessed on 18 July 2023).

NVIDIA. (2023). *NVIDIA Jetson Xavier NX developer kit*. https://openzeka.com/wpcontent/uploads/2020/03/Jetson_Xavier_NX_Developer_Kit-One-Pager.pdf (accessed on 23 July 2023).

Pietri, N., Nocent, O., Robert, P., & Schmutz, A. (2025). Real-time live compression of dynamic 3D meshes for client-side GPU cloud gaming using skinning decomposition, *The Visual Computer*, Advance online publication. https://doi.org/10.1007/s00371-025-04112-3

Radicke, S., Hahn, J., Wang, Q., & Grecos, C. (2016). A parallel HEVC intra prediction algorithm for heterogeneous CPU+GPU platforms. *IEEE Transactions on Broadcasting. 62*(1), 103–119.

Rathee, N., Sharma, T., Yadav, J., et al. (2026). High-performance FPGA implementation of HEVC with dynamic programming for optimized intra-frame prediction. *Scientific Reports*, 16, 21241. https://doi.org/10.1038/s41598-026-51672-y

Ryoo, S., Rodrigues, C., Baghsorkhi, S, S., et al. (2008). Optimization principles and application performance evaluation of a multithreaded GPU using CUDA. *Proceedings of the 13th ACM SIGPLAN Symposium on Principles and Practice of Parallel Programming (PPoPP)*, 73–82. ACM.

Singhadia, A., Bante, P., & Chakrabarti, I. (2019). A novel algorithmic approach for efficient realization of 2-D-DCT architecture for HEVC, *IEEE Transactions on Consumer Electronics, 65*(3), 264–273.

Tariq, J. (2020). High-performance intra-mode accelerator for HEVC, *The Visual Computer, 36*(8), 1603–1617. https://doi.org/10.1007/s00371-019-01764-w

Thurley, M, J., & Danell, V. (2012). Fast morphological image processing open-source extensions for GPU processing with CUDA, *IEEE Journal of Selected Topics in Signal Processing*, 849–855.

Wang, S., Liu, J., Zhang, H., & Hu, Y. (2025). A fast algorithm of HEVC intra mode decision. *Journal of Shanghai University (Natural Science Edition)*, 31(3), 561–570. https://doi.org/10.12066/j.issn.1007-2861.2639

Zhu, J., Zhang, Q., Fei, L., Cai, R., Xie, Y., Sheng, B., & Yang, X. (2023). FFFN: Frame-by-frame feedback fusion network for video super-resolution, *IEEE Transactions on Multimedia, 25*, 6821–6834. https://doi.org/10.1109/TMM.2022.3214776

Black Sea Journal of Engineering and Science
doi: 10.34248/bsengineering.1992055

Open Access Journal
e-ISSN: 2619 – 8991

Research Article
Volume 9 - Issue 5: 2482-2491 / September 2026

HYBRID SIO_2/AL_2O_3 FILLER REINFORCEMENT IN GLASS FIBER/EPOXY COMPOSITES: FLEXURAL AND TENSILE BEHAVIOR WITH PHYSICS-INFORMED NEURAL NETWORK VALIDATION

Ismail BAYAR[1]*, Huseyin KOSE[1]

[1]*Batman University, Faculty of Engineering and Architecture, Department of Mechanical Engineering, 72001, Batman, Türkiye*

Abstract: Glass fiber-reinforced polymer (GFRP) composites are widely used in structural applications, yet the inherent brittleness of the epoxy matrix limits their mechanical performance. While SiO_2 and Al_2O_3 have individually been shown to improve polymer composite properties, the synergistic effect of their combined use as a hybrid filler on flexural behavior remains insufficiently explored. In this study, five composite formulations were fabricated with a fixed SiO_2 content of 1 wt.% and Al_2O_3 contents of 0, 0.5, 1.0, 1.5, and 2.0 wt.%. Three-point bending tests were conducted at four support spans, and tensile tests were performed; the resulting flexural strength data were further modeled using a Physics-Informed Neural Network (PINN). Flexural strength decreased progressively with increasing support span across all sample groups. The sample containing 1 wt.% Al_2O_3 exhibited the highest flexural strength and modulus, corresponding to an increase of approximately 21% over the mono-filler reference at the 60 mm span. Tensile strength increased progressively with Al_2O_3 content up to 1.5 wt.%, corresponding to an improvement of approximately 21% over the mono-filler reference, while mechanical performance under both loading modes declined at 2.0 wt.% due to particle agglomeration. The PINN model achieved high predictive accuracy, with R^2 values of 0.98 and 0.96 and mean absolute percentage errors of 3.81% and 5.37% on the training and test sets, respectively. These findings demonstrate that hybrid SiO_2/Al_2O_3 reinforcement can meaningfully improve GFRP mechanical performance, with the optimum filler content depending on the dominant loading mode.

Keywords: Physics-informed neural network, Hybrid filler, SiO_2, Al_2O_3, Flexural strength, Glass fiber-reinforced polymer

***Corresponding author:** Batman University, Faculty of Engineering and Architecture, Department of Mechanical Engineering, 72001, Batman, Türkiye
E mail: ismailbyr@gmail.com (I. BAYAR)
Ismail BAYAR https://orcid.org/0000-0002-4187-3911
Huseyin KOSE https://orcid.org/0000-0001-6500-975X

Received: July 12, 2026
Accepted: August 14, 2026
Published: September 15, 2026

Cite as: Bayar, I., & Kose, H. (2026). Hybrid SiO_2/Al_2O_3 filler reinforcement in glass fiber/epoxy composites: flexural and tensile behavior with physics-informed neural network validation. *Black Sea Journal of Engineering and Science,* 9(5), 2482-2491.

1. Introduction

Polymer matrix composites have found increasing application across a wide range of engineering sectors — including aerospace, automotive, civil infrastructure, and defense — owing to their superior specific mechanical properties, design versatility, and corrosion resistance. Among these, glass fiber-reinforced polymer composites have attracted particular attention due to their cost-effectiveness, high strength-to-weight ratio, and ease of processing (Kiran et al., 2018). Nevertheless, the inherent brittleness and relatively low fracture toughness of the epoxy matrix necessitate further enhancement of the mechanical performance of these systems.

The incorporation of nano-scale reinforcement into the polymer matrix has emerged as one of the most effective strategies for improving the mechanical properties of polymer matrix composites. Owing to their high surface area-to-volume ratio, nano-fillers enhance stress transfer at the matrix–filler interface, impede crack propagation, and activate various toughening mechanisms (Abebe et al., 2025; Mani, 2025). In this context, silicon dioxide (SiO_2) particles have been widely investigated due to their chemical compatibility with thermoset polymer systems, chemical inertness, and commercial availability (Kose et al., 2025; Shubham et al., 2025; Singh et al., 2021). Kose et al. (2025) employed micro/nano hybrid SiO_2 particles in aramid fiber-reinforced composites and reported synergistic improvements in both tensile and three-point bending properties, demonstrating that nano-scale particles strengthen the matrix–fiber interface while micro-scale particles suppress crack propagation.

Aluminum oxide (Al_2O_3) particles are also frequently employed as reinforcing fillers in polymer composite systems due to their high hardness, favorable thermal conductivity, and capacity for homogeneous dispersion within the matrix (Abebe et al., 2025; Guven et al., 2024; Li et al., 2026). Abebe et al. (2025) reported that the addition of 2 wt.% nano-Al_2O_3 to a polyester/glass-wool fiber matrix increased tensile strength by 55% and flexural strength by 109%. Li et al. (2026) tested nano-Al_2O_3-reinforced epoxy composites over a wide strain rate

This work is licensed (CC BY-NC 4.0) under Creative Commons Attribution 4.0 International License

range, identified an optimum filler content of approximately 10 wt.%, beyond which agglomeration-induced performance degradation became evident — underscoring the critical importance of filler content optimization.

The hybrid nano-reinforcement approach, in which two or more fillers are used in combination rather than a single filler type, can yield mechanical performance gains beyond those achievable with single-component systems through synergistic effects (Kiran et al., 2018; Kose et al., 2025). By simultaneously activating the complementary toughening mechanisms of different filler materials — crack deflection, crack bridging, and interfacial strengthening — both the stiffness and toughness of the composite can be improved concurrently. However, the synergistic influence of combined SiO_2 and Al_2O_3 fillers on the flexural behavior of glass fiber-reinforced systems remains insufficiently explored in the literature.

The three-point bending test is one of the most widely employed methods for the experimental characterization of the mechanical performance of composite materials. By inducing tensile stresses at the specimen's lower surface and compressive stresses at the upper surface, this test provides a direct assessment of the load transfer capacity of the fiber–matrix interface and the fracture resistance of the matrix (Dinesh & Yoganandh, 2026). Flexural strength is particularly recognized as one of the most sensitive indicators of matrix reinforcement efficacy in nano-filler-containing systems (Abdi et al., 2018; Navas-Pinto et al., 2026).

In parallel with the growing adoption of data-driven approaches in materials science, machine learning (ML) algorithms have emerged as powerful tools for predicting mechanical properties and optimizing processing parameters in composite materials (Berladir et al., 2025; Ergün et al., 2025; Navas-Pinto et al., 2026; Shettar et al., 2025). Navas-Pinto et al. (2026) demonstrated that ensemble learners including Random Forest, ExtraTrees, and XGBoost can predict flexural and tensile strength with high accuracy in TiO_2 nanoparticle-reinforced bio-epoxy/glass fiber composites, noting that the nonlinear structure–property relationships inherent to these systems cannot be adequately captured by conventional regression models. Similarly, Berladir et al. (2025) showed that ML-based approaches can substantially reduce experimental effort and material waste in thermoplastic matrix composites. However, purely data-driven models learn structure–property relationships solely from the training data, without any guarantee of consistency with the underlying mechanics, a limitation that becomes acute for small experimental datasets (Khalid et al., 2025). Physics-Informed Neural Networks (PINNs) address this by embedding the governing physical laws directly into the loss function, penalizing predictions that violate the governing equations and thereby reducing the dependence on large datasets (Malashin et al., 2025). This approach has proven effective for the bending analysis of laminated composites, where formulations embedding plate theory as a physical constraint predict deflection and stress fields in close agreement with analytical and finite-element solutions (Wang & Thai, 2025). The ML-based validation framework offers a particularly compelling advantage in scenarios involving limited experimental datasets, enabling reliable property predictions that support the rapid design of novel composite formulations (Gowda et al., 2026).

In the present study, the effect of hybrid SiO_2 and Al_2O_3 micro-fillers on the mechanical performance of glass fiber/epoxy composites fabricated by the hand lay-up technique was investigated. Five sample group were prepared with a fixed SiO_2 content of 1 wt.% combined with varying Al_2O_3 contents of 0, 0.5, 1.0, 1.5, and 2.0 wt.%. The fabricated samples were subjected to three-point bending and tensile tests, and the resulting flexural strength data were further validated using a physics-informed neural network. The primary objectives of this study are to elucidate the synergistic effect of the SiO_2/Al_2O_3 hybrid filler system on flexural performance and to evaluate the efficacy of ML-based prediction for this class of limited experimental datasets.

2. Materials and Methods

2.1. Experimental Procedure

A systematic experimental matrix was designed to investigate the effects of mono-filler and hybrid filler systems of SiO_2 and Al_2O_3 micro-fillers on the mechanical performance of glass fiber/epoxy composites. Five sample groups were produced, each maintaining a fixed SiO_2 content of 1 wt.% while the Al_2O_3 content was varied at 0, 0.5, 1.0, 1.5, and 2.0 wt.% of the total matrix weight. This design strategy allowed the incremental contribution of Al_2O_3 to the hybrid filler system to be isolated and quantified. The sample codes and corresponding filler contents are summarized in Table 1. Mechanical characterization was carried out through three-point bending tests at four different support spans in accordance with ASTM D790, and tensile tests in accordance with ASTM D3039. Additionally, the flexural strength data obtained from the bending tests were used to train and validate machine learning models, providing a data-driven complement to the experimental findings.

Table 1. Designation and composition of the laminates

Sample Code	SiO_2 (wt.%)	Al_2O_3 (wt.%)
S1A0	1.0	0.0
S1A0.5	1.0	0.5
S1A1	1.0	1.0
S1A1.5	1.0	1.5
S1A2	1.0	2.0

2.2. Materials

Woven E-glass fiber fabric with an areal density of approximately 205 g/m^2 was used as the reinforcement

phase, corresponding to a fabric weight of 20.32 g per layer for the 330 × 300 mm laminate dimensions used in this study. MGS L285 epoxy resin and H287 hardener, supplied by Dost Kimya, Turkey, were used as the matrix material. The epoxy resin and hardener were mixed at a 5:2 weight ratio in accordance with the manufacturer's recommendations, yielding a total epoxy system weight of 250 g per laminate.

Amorphous SiO_2 was selected for this study because its silanol-rich surface promotes interaction with the epoxy matrix and facilitates its use as a reinforcing filler, while also avoiding the specific occupational health concerns associated with handling respirable crystalline silica. The SiO_2 micro-particles supplied by Nanografi Inc., Turkey, were used as one of the filler components, with a purity of 99.5% and a particle size range of 10-20 µm. Al_2O_3 micro-particles with a purity of 98.8% and a particle size range of 65-80 µm were used as the second filler component. Prior to use, both filler materials were dried in a convection oven at 80°C for 24 h to eliminate residual moisture.

2.3. Composite Fabrication

Composite laminates were fabricated using the hand lay-up technique. The filler dispersion procedure was carried out in two stages using an ultrasonic bath maintained at room temperature (25 ± 2°C). In the first stage, SiO_2 and Al_2O_3 particles were dispersed separately in a portion of the epoxy resin for 15 minutes. In the second stage, the two mixtures were combined and subjected to a further 60 minutes of ultrasonication to ensure homogeneous distribution of the hybrid filler system throughout the matrix. For the mono-filler sample group (S1A0), SiO_2 particles were dispersed directly in the epoxy resin for 60 minutes under the same ultrasonic bath conditions. Following dispersion, the H287 hardener was added to the filler-resin suspension and gently hand-mixed until a homogeneous mixture was obtained. The schematic representation of the mixing procedure was given in Figure 1.

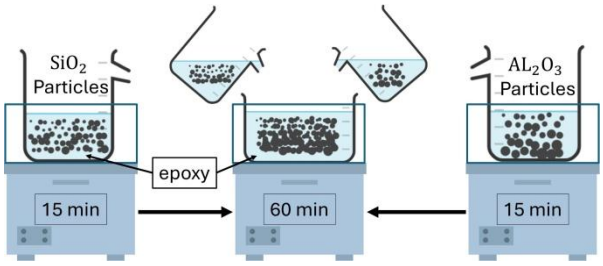


Figure 1. Mixing process of the particles and epoxy resin.

Eight layers of woven E-glass fiber fabric were stacked and impregnated with the prepared resin mixture using a hand roller to ensure uniform wet-out between layers. The fiber-to-matrix weight ratio was maintained at 1:1 for all sample groups, and the filler percentages were calculated relative to the total weight of the epoxy resin. The laminates were cured at room temperature (25 ± 2°C) for 24 hours and had nominal in-plane dimensions of 330 x 300 mm^2. Because the laminates were produced by hand lay-up, slight variations in thickness were observed among the laminates and individual samples; laminate thickness was measured using a digital caliper. Test samples were subsequently cut from the laminates to the dimensions required by the respective test standards.

2.4. Mechanical Testing

Flexural and tensile properties of the composite samples were determined using a Shimadzu universal testing machine.

Flexural properties were evaluated in accordance with ASTM D790. Four different support spans were employed to investigate the effect of span length on flexural behavior. Samples dimensions were prepared in accordance with the span-to-depth ratio requirements specified in ASTM D790. A minimum of five replicate samples were tested for each combination of support span and sample group. The crosshead speed was set to 2 mm/min. The flexural strength (σf) and flexural modulus (Ef) were calculated using the standard beam bending expressions defined in ASTM D790, as given in equations 1 and 2:

$$\sigma_f = \frac{3FL}{2bd^2} \quad (1)$$

$$E_f = \frac{L^3 m}{4bd^3} \quad (2)$$

where F is the maximum load (N), L is the support span (mm), b is the sample width (mm), d is the sample thickness (mm), and m is the slope of the initial linear portion of the load-deflection curve. Representative photographs of the test setup and sample geometry are provided in Figure 2.

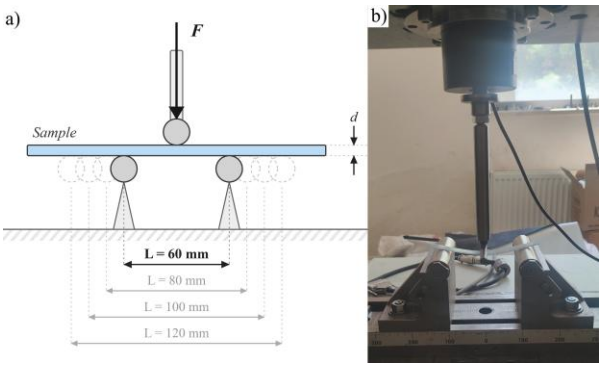


Figure 2. (a) Schematic of the three-point bending test setup; (b) photograph of the experimental setup.

Tensile properties were determined in accordance with ASTM D3039 using the same Shimadzu universal testing machine. Samples measuring 250 x 25 mm in length and width were tested at a crosshead speed of 1 mm/min, with load and displacement recorded via the crosshead displacement of the testing machine, as an extensometer was not used. The thickness of each sample was individually measured using a digital caliper prior to testing to account for thickness variability inherent to the hand lay-up process. A minimum of three replicate

samples were tested per sample group. Ultimate tensile strength was calculated from the maximum load and the measured cross-sectional area of each sample, and recorded for each sample group.

All tests were conducted under laboratory conditions of approximately 20-25 °C and 40-50% relative humidity. Samples exhibiting fracture within or immediately adjacent to the grips were considered invalid and were retested, whereas only samples exhibiting valid fracture within the gauge section were included in the analysis.

2.5. Physics-Informed Neural Network Model for Three-Point Bending Prediction

In this study, a Physics-Informed Neural Network (PINN) based approach was developed to predict flexural strength values obtained from three-point bending tests. The main objective of the PINN model is not limited to enabling the artificial neural network to learn only from experimental data, but also to include the standard mechanical relationship of the three-point bending test in the learning process. Therefore, the PINN framework was employed to improve prediction reliability and consistency under limited experimental observations by guiding the learning process with the underlying mechanics of the three-point bending test.

In the experimental dataset, Al_2O_3 content, span distance, sample width, sample thickness, maximum force, and flexural strength values in MPa were used for each sample. Since the SiO_2 content was constant across all samples, it was retained as descriptive information in the dataset, while the Al_2O_3 content was treated as the primary learning variable of the model. Al_2O_3 content, span distance, sample width, sample thickness, and the span-to-thickness ratio were used as model inputs. The maximum force value was not used directly as an input variable, as its inclusion could lead to data leakage given its direct role in the flexural strength calculation. For rectangular cross-section samples, flexural strength is calculated using the standard relation given in Equation 1. Since flexural strength was the target output of the model, the neural network was configured to predict σ_f directly. The maximum force physically consistent with the predicted flexural strength was then back-calculated using the inverse form of the three-point bending relation, given in equation 3.

$$\hat{F} = \frac{2bd^2\widehat{\sigma_f}}{3L} \tag{3}$$

Here, $\widehat{\sigma_f}$ is the flexural strength predicted by the PINN model, and $\hat{F}$ is the corresponding physical maximum force value. Thus, the model not only predicted the target value in MPa but also enforced this prediction to remain mechanically consistent with the measured maximum force.

The total loss function of the model comprises two components. The first is the data loss, representing the discrepancy between the predicted and experimentally measured flexural strength values. The second is the physical consistency loss, representing the discrepancy between the maximum force calculated from the predicted flexural strength and the experimentally measured maximum force. The total loss function is defined in equation 4.

$$Loss_{total} = Loss_{\sigma} + \lambda Loss_{physics} \tag{4}$$

Here, $Loss_{\sigma}$ represents the error between the experimental and predicted flexural strength values, and $Loss_{physics}$ represents the error between the maximum force recalculated from the physical equation and the experimental maximum force. The coefficient λ is a weighting parameter that controls the contribution of the physical loss term to the total loss function. By testing different values of this parameter, the effect of the physical constraint on model performance was investigated.

Instead of the classical mean squared error, the Huber loss function given in equation 5 was used. This choice was motivated by the scatter typically observed between repeated measurements in experimental composite data, where outliers may occur in some samples due to local damage, delamination, support effects, or experimental variability. The Huber loss behaves like the mean squared error for small errors but applies a more controlled penalty for large errors, thereby reducing the model's sensitivity to extreme experimental outliers.

$$L_{\delta}(e) = \begin{cases} \frac{1}{2}e^2, & |e| \le \delta \\ \delta\left(|e| - \frac{1}{2}\delta\right), & |e| > \delta \end{cases} \tag{5}$$

Here, $e = y - \hat{y}$ denotes the residual between the target and predicted values, applicable to either the flexural strength error or the physical force consistency error, and δ represents the transition parameter of the Huber loss function. To prevent the same sample and the same span distance from appearing together in both the training and test sets, a group-based data splitting approach was used when dividing the data into training and test sets. For this purpose, each sample code and span distance combination was defined as a separate group. This prevents the model from artificially improving test performance by memorizing repetitions from the same experimental group.

The PINN model was constructed using a small-scale, fully connected artificial neural network architecture. Input variables are standardized, and the target flexural strength and maximum force values are separately normalized to ensure scale balance in the loss function. The model architecture, activation function, learning rate, weight regularization coefficient, dropout rate, and physical loss weight were determined through hyperparameter optimization. Different network structures and λ values were tested during this process, and the configuration providing the best validation performance was selected as the final model.

In this approach, since the maximum force is not used directly as a model input, the model is prevented from simply learning the closed-form relation that computes

the target value. Instead, the maximum force is used only in the physical consistency term. Thus, the PINN model offers a hybrid learning structure that considers the fundamental mechanical relationship of the three-point bending test while estimating the flexural strength based on the filler content and geometric properties. In this respect, the proposed method, unlike a classical data-driven ANN model, simultaneously optimizes both statistical prediction accuracy and physical consistency.

3. Results and Discussion

3.1. Flexural Properties

Three-point bending testing was conducted to evaluate the flexural response of the composite laminates, as the applied span length directly governs the ratio of bending to shear stress within the sample and consequently influences the apparent flexural properties (Dinesh & Yoganandh, 2026). The load–deflection behavior of the composite samples at four support spans is presented in Figure 3.

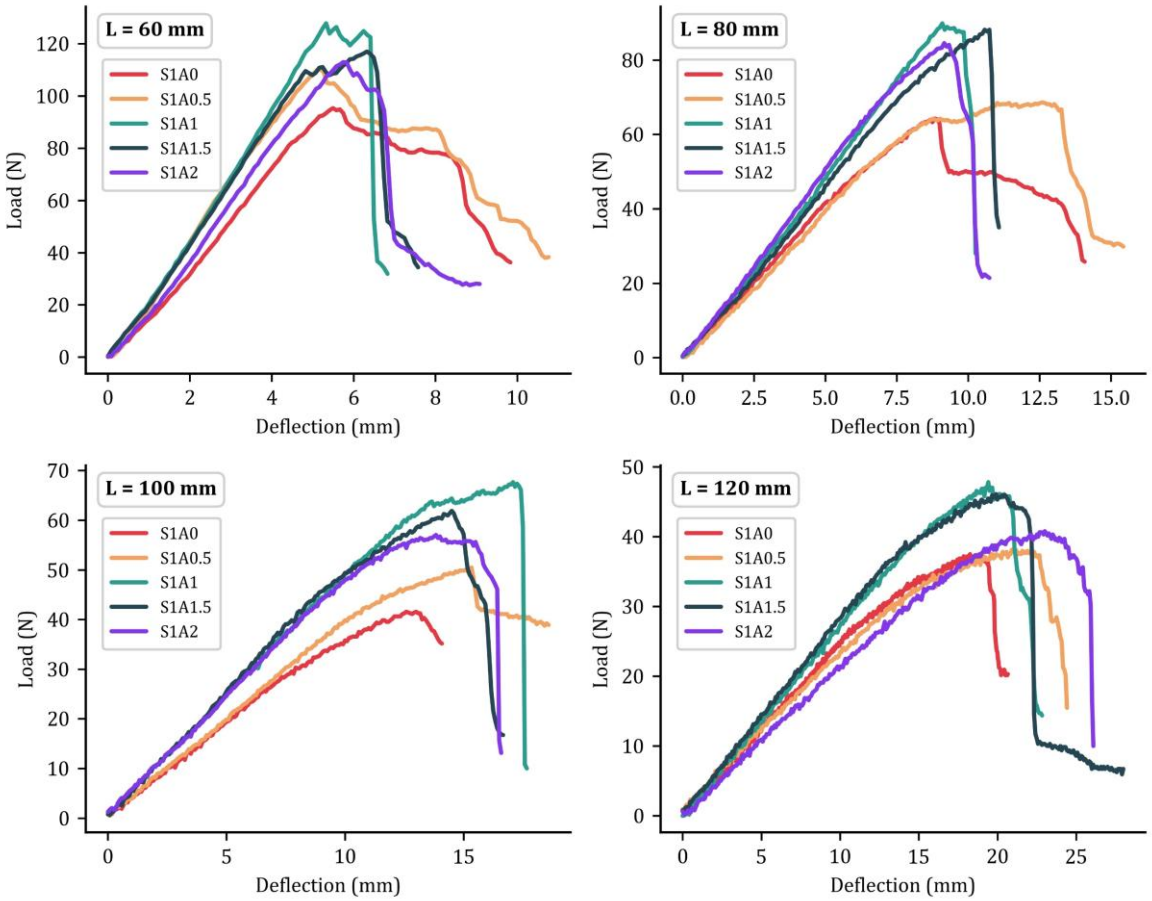


Figure 3. Load–deflection curves of the composite sample groups under three-point bending.

Across all span conditions, the curves exhibit a broadly linear elastic region followed by a gradual load drop after the peak, indicative of progressive damage accumulation rather than sudden brittle fracture. This behavior is characteristic of woven glass fiber/epoxy laminates, in which the woven architecture provides multiple crack arrest mechanisms that distribute damage over a larger area prior to final failure. At shorter spans of 60 and 80 mm, the peak loads are higher and the deflection at failure is relatively limited, whereas at longer spans of 100 and 120 mm, the curves become more compliant with greater deflection at peak load, consistent with the transition from shear-dominated to bending-dominated failure as the span-to-depth ratio increases. The deflection at peak load increased systematically with support span for all sample groups, ranging from a mean of approximately 5.6-6.3 mm at the 60 mm span to 20.7-21.6 mm at the 120 mm span. This near four-fold increase in peak deflection with span length is consistent with the expected elastic compliance scaling of simply supported beams and confirms that the laminates underwent geometrically progressive deformation prior to failure across the full span range investigated.

The flexural strength (σf) values for all sample groups and support spans are summarized in Figure 4. A progressive decrease in σf with increasing span length was observed for all samples, with mean values ranging from approximately 201-245 MPa at the 60 mm span to 80-93 MPa at the 120 mm span, corresponding to a reduction of approximately 60% across the span range investigated. This trend is consistent with classical beam bending theory, wherein increasing the span-to-depth ratio shifts the dominant failure mode from interlaminar shear toward tensile bending failure, thereby reducing the

apparent flexural strength. Regarding the effect of Al_2O_3 content, the hybrid filler samples demonstrated superior flexural strength compared to the mono-filler reference S1A0 across all support spans. The S1A1 sample, containing 1 wt.% SiO_2 and 1 wt.% Al_2O_3, exhibited the highest mean flexural strength at the 60, 80, and 100 mm spans, recording values of 245.08 ± 20.59, 169.76 ± 6.79, and 122.86 ± 7.52 MPa, respectively. At the 120 mm span, S1A1.5 marginally exceeded S1A1 with 92.90 ± 0.81 MPa compared with 92.23 ± 3.86 MPa, though the difference is negligible. The successive improvement from S1A0 to S1A1 suggests a synergistic reinforcement mechanism arising from the combined SiO_2/Al_2O_3 hybrid filler system, wherein SiO_2 particles strengthen the fiber–matrix interface while Al_2O_3 particles contribute to crack deflection and matrix densification (Abebe et al., 2025; Kose et al., 2025). Beyond the optimum Al_2O_3 content of 1 wt.%, flexural strength declined in the S1A1.5 and S1A2 samples, most notably at shorter spans. This reduction is attributed to particle agglomeration at higher filler loadings, which introduces stress concentration sites and disrupts the homogeneity of the matrix (Li et al., 2026).

The span dependence of flexural strength is further illustrated in Figure 5. The separation between sample groups is most pronounced at the 60 mm span, where the difference between S1A1 and S1A0 reaches approximately 43 MPa, and narrows progressively with increasing span length, converging to within approximately 13 MPa at the 120 mm span.

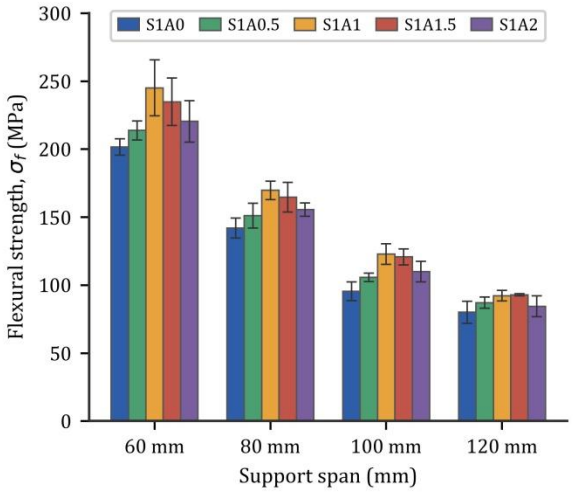


Figure 3. Flexural strength by support span.

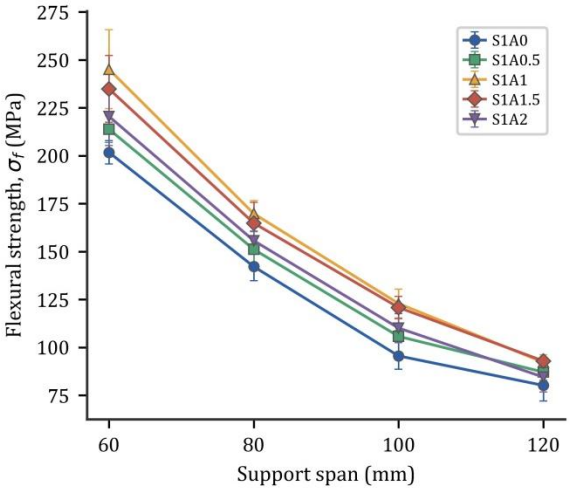


Figure 4. Span dependence of flexural strength.

This convergence indicates that the reinforcing contribution of the hybrid filler system is mobilized most effectively under short-span loading, where interlaminar shear stresses dominate the failure process and the filler-modified matrix plays a decisive role in resisting shear-driven damage. In contrast, at longer spans the failure becomes increasingly fiber-dominated, and the influence of matrix modification diminishes accordingly. Although the magnitude of the filler contribution diminishes with increasing span, the relative ranking of the sample groups remains essentially unchanged, with S1A1 and S1A1.5 consistently exhibiting the highest values and S1A0 the lowest across all spans. This preservation of ranking indicates that the hybrid filler effect reflects an intrinsic material improvement rather than a loading-condition-specific artifact.

The flexural modulus (E_f) values are presented in Figure 6. S1A1 and S1A1.5 recorded the highest E_f values across most span conditions. S1A1 achieved mean values of 15.81 ± 1.85, 15.30 ± 1.64, and 14.45 ± 1.77 GPa at the 60, 80, and 100 mm spans, respectively. These values correspond to increases of approximately 14%, 19%, and 12% over the S1A0 reference at the same spans. Unlike flexural strength, the modulus exhibited limited variation across span lengths within each sample group. This indicates that the elastic response of the laminates is less sensitive to span length than the failure-governed strength. The distinction is mechanically meaningful. The modulus reflects the initial elastic stiffness of the laminate, and this stiffness is governed primarily by the fiber architecture and the intrinsic properties of the filler-modified matrix.

The strength, in contrast, is controlled by damage initiation and propagation, and these processes depend strongly on the stress state imposed by the span-to-depth ratio. Notably, S1A2 recorded the lowest E_f at the 80, 100, and 120 mm spans. This result further corroborates the adverse effect of excessive filler loading. At high loadings, agglomerated particles act as regions of local compliance and stress concentration rather than effective stiffening sites.

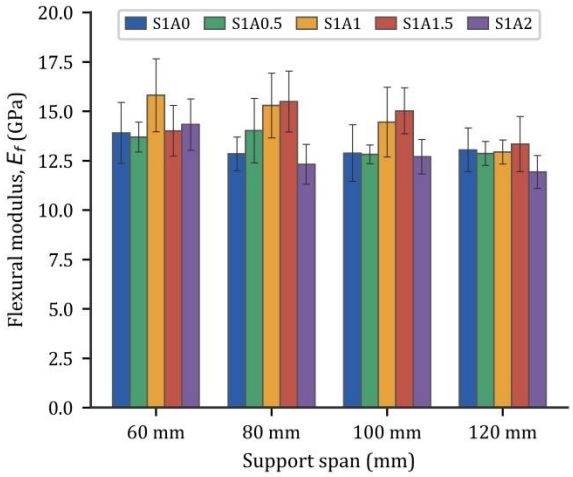


Figure 5. Flexural modulus by support span.

Overall, the flexural results provide a coherent assessment of the role of the hybrid filler system. The superiority of S1A1 in both strength and modulus indicates that the reinforcement mechanism operates at the level of the fiber–matrix interface and the bulk matrix simultaneously, influencing damage initiation as well as the elastic response of the laminate (Guven et al., 2024; Mani, 2025). In a fiber-dominated laminate, the matrix volume available for particle dispersion is limited, and effective wetting of both fibers and particles becomes increasingly difficult at higher filler loadings, promoting agglomeration at contents well below those tolerated by unreinforced resins. From a design perspective, hybrid filler modification offers the greatest benefit under short-span loading, where shear stresses dominate. At longer spans, where bending governs the failure, the contribution of the filler system is comparatively modest.

3.2. Tensile Properties

Tensile testing was conducted to complement the flexural characterization and evaluate the effect of the hybrid SiO_2/Al_2O_3 filler system on the axial load-bearing capacity of the laminates. The load–displacement curves and the corresponding ultimate tensile strength values for all sample groups are presented in Figure 7. All samples exhibited an approximately linear load–displacement response up to failure, followed by an abrupt load drop characteristic of fiber-dominated brittle fracture, with no discernible progressive damage stage prior to the peak load. This behavior contrasts with the gradual post-peak load decay observed in the bending tests and reflects the fundamental difference between the two loading modes: in tension, the woven glass fibers carry the load almost directly and their rupture governs the failure, whereas in bending the stress distribution through the thickness activates matrix- and interface-dominated damage mechanisms before final fracture.

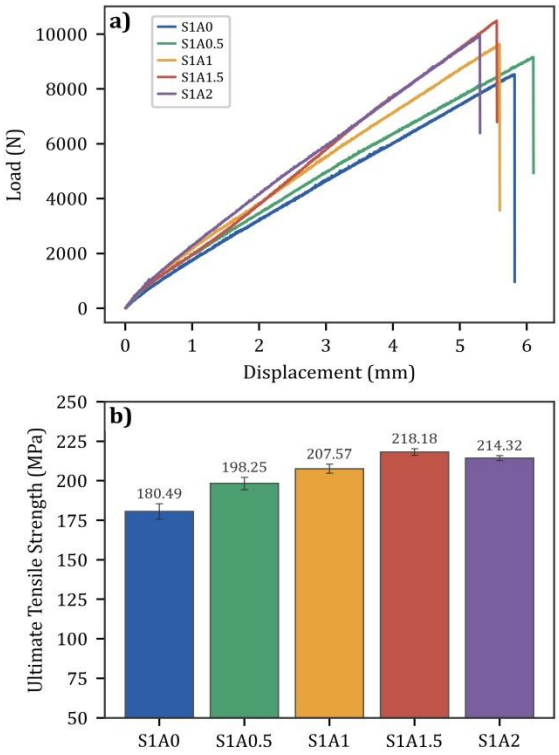


Figure 6. (a) Load–displacement curves and (b) ultimate tensile strength of the composite sample groups.

The ultimate tensile strength increased progressively with Al_2O_3 content up to 1.5 wt.%. S1A0 recorded the lowest strength at 180.49 ± 4.95 MPa, while S1A1.5 achieved the highest value at 218.18 ± 2.06 MPa, corresponding to an improvement of approximately 21% over the mono-filler reference. S1A1 and S1A2 recorded intermediate values of 207.57 ± 2.84 and 214.32 ± 1.50 MPa, respectively. The consistent strength gain with increasing Al_2O_3 content is attributed to the enhanced fiber–matrix interfacial adhesion provided by the hybrid filler system, which improves the efficiency of load transfer from the matrix to the fibers and delays interfacial debonding under axial loading (Mani, 2025). It is also noteworthy that the scatter in tensile strength decreased systematically with increasing Al_2O_3 content, from 4.95 MPa for S1A0 to 1.50 MPa for S1A2, indicating that the filler addition promoted a more uniform stress distribution and reduced the scatter associated with local interfacial defects.

Unlike the flexural results, where S1A1 consistently exhibited the optimum performance, the tensile response peaked at 1.5 wt.% Al_2O_3. This shift reflects the lower sensitivity of the fiber-dominated tensile response to local agglomerates, which allows the composite to tolerate a higher filler content before the reinforcement benefit is offset. The decline observed at 2.0 wt.% in both loading modes confirms a common agglomeration threshold, consistent with the flexural findings.

3.3. PINN-Based Flexural Strength Prediction

The best performance of the PINN model, achieved through hyperparameter optimization, was obtained with

a network architecture containing 16 neurons in a single hidden layer and a ReLU activation function. The optimal learning rate was determined as 0.003, the weight regularization coefficient as 1×10^{-5}, the dropout rate as 0.05, and the physical loss weight as $\lambda = 0.005$. The fact that the physical loss coefficient yields optimal results at a low but non-zero value indicates that the physical constraint derived from the three-point bending equation contributes to the model not as a directly dominant learning component, but rather as a regulatory mechanism. This is particularly important for small-scale experimental datasets, since applying the physical constraint with a very high weight can make it difficult for the model to represent experimental scattering, whereas a low-weighted physical regularization limits the model's tendency to produce non-physical predictions.

The loss–epoch graph of the model's training process is given in Figure 8. At the beginning of training, the total loss was approximately 0.49, showing a rapid decrease during the first 50–60 epochs. This rapid decrease indicates that the model was able to learn the main trends in the dataset.

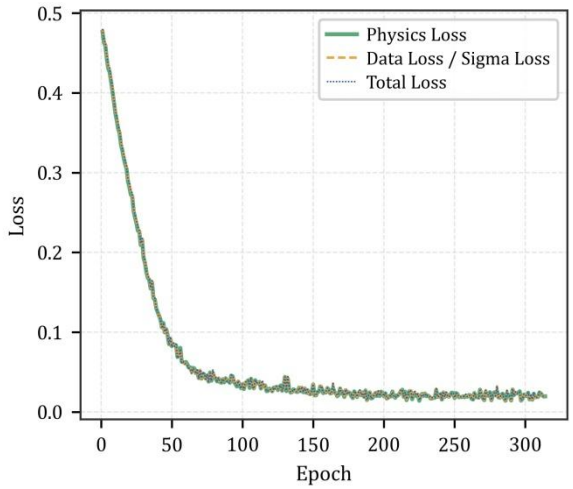


Figure 7. Loss-epoch graph of the PINN model.

After approximately 100 epochs, the loss values reached a stable region with lower-amplitude oscillations. Training was completed after 321 epochs, with the total loss decreasing to approximately 0.02. The fact that the total loss, data loss, and physical loss curves progress very closely together indicates that the normalized flexural strength and maximum force losses are on a similar scale. However, since the physical loss term in the total loss function is weighted with a coefficient of $\lambda = 0.005$, data loss constituted the main component of model optimization, while physical loss acted as a complementary adjustment term that helped the predictions remain consistent with the three-point bending equation.

The prediction performance of the PINN model is summarized in Figure 9. The model achieved $R^2 = 0.98$ on the training data and $R^2 = 0.96$ on the test data.

These results indicate that the model not only learned effectively from the training data but also achieved high prediction accuracy on the test group. The corresponding MSE values were 67.14 MPa^2 for the training data and 43.83 MPa^2 for the test data. The lower test MSE relative to the training MSE can be attributed to the test set comprising sample-span combinations with relatively lower dispersion; accordingly, it is more informative to interpret the MSE alongside the R^2, APE, and MAPE values rather than in isolation. The APE and MAPE results of the model are presented in Table 2.

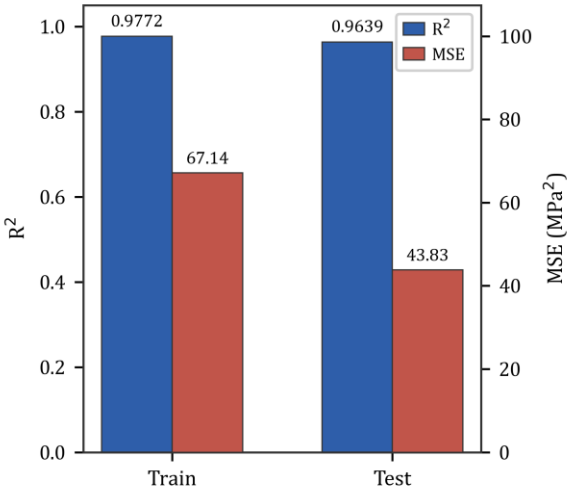


Figure 8. R^2 and MSE results.

Table 2. APE results of the test samples

Sample	Actual (MPa)	Predicted (MPa)	APE (%)
S1A1	176.15	168.93	4.10
S1A1	171.34	168.90	1.42
S1A1	175.53	163.47	6.87
S1A1	165.48	169.54	2.46
S1A1	160.29	164.17	2.42
S1A0.5	109.27	117.51	7.54
S1A0.5	104.38	113.68	8.92
S1A0.5	103.24	104.43	1.15
S1A0.5	108.91	113.84	4.53
S1A0.5	102.92	113.18	9.97
S1A0.5	88.66	87.37	1.45
S1A2	92.05	87.55	4.90
S1A0.5	84.55	92.39	9.27
S1A2	72.53	84.20	16.09
S1A0.5	90.37	90.25	0.14
S1A2	83.03	84.13	1.33
S1A0.5	81.19	90.60	11.60
S1A2	84.30	88.64	5.14
S1A0.5	90.78	86.59	4.62
S1A2	90.56	87.44	3.44
		MAPE	5.37

The MAPE was calculated as 3.81% for the training set and 5.37% for the test set, with a maximum APE of 16.09% observed among the test samples. Given that three-point bending results in composite materials are expected to exhibit a degree of experimental scatter due to manufacturing defects, filler distribution, local damage onset, support-point effects, and interlaminar damage mechanisms, a test-set MAPE of 5.37% indicates a highly acceptable prediction accuracy. The physical consistency performance of the model, evaluated via F, was also found to be high.

The actual-versus-predicted plot given in Figure 10 more clearly reveals the prediction characteristics of the PINN model. The vast majority of prediction points are concentrated around the ideal prediction line, indicating that the model successfully captures the general trend across the low, medium, and high flexural strength regions.

In particular, the predictions are quite close to the ideal line for data points in the 75-225 MPa range. However, in the high-strength region, some of the model's predictions deviate slightly from the actual values. This behavior can be attributed to the limited number of data points at high strength levels and the more pronounced experimental scatter in this region. Considering the overall distribution, no significant systematic deviation is observed, and the predictions are evenly distributed across the full flexural strength range investigated.

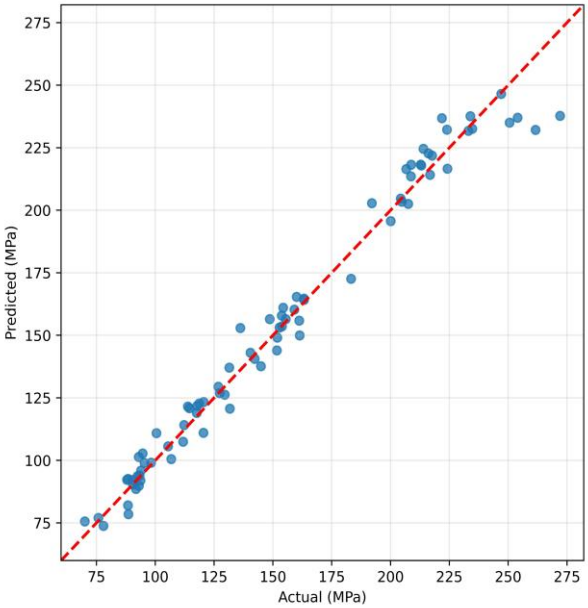


Figure 9. Scatter plot of the training performance of the PINN model.

An examination of the experimental data trends showed that the flexural strength values decreased as the span distance increases. The average flexural strength values were obtained as approximately 223.19, 156.70, 111.01, and 87.38 MPa for span distances of 60, 80, 100, and 120 mm, respectively. Using the 60 mm span as a reference point, this decrease reflects the fact that the maximum load values decline with increasing span distance while the flexural strength calculation itself accounts for the corresponding span length at each condition. Consequently, the model learned the span distance not only as a geometric parameter but also as an important variable representing the change in the experimental response. In addition, examining the effect of Al_2O_3 content, the S1A1 sample containing 1.0 wt.% Al_2O_3 yielded the highest average flexural strength values. While relatively high values were maintained for some spans at the 1.5 wt.% additive level, flexural strength was found to decrease again at the 2.0 wt.% Al_2O_3 content. This behavior suggests that beyond a certain optimum filler content, mechanical performance may decline due to particle agglomeration, stress concentration, or weakening at the matrix–filler interface.

Overall, these results demonstrate that the developed PINN model achieved high prediction accuracy on a small-scale experimental composite dataset. The model's most significant advantage lies in evaluating the maximum force value only within the physical consistency term, rather than using it directly as an input variable. This prevents the model from simply memorizing the flexural strength from the closed-form relation, while ensuring that the predicted values remain consistent with three-point bending mechanics. In this respect, the PINN approach offers a more interpretable and physically consistent prediction framework compared to a classical data-driven artificial neural network model.

4. Conclusions

In this study, glass fiber/epoxy composites reinforced with hybrid SiO_2/Al_2O_3 micro-fillers were fabricated and characterized under three-point bending and tensile loading, with the resulting flexural strength data further validated using a Physics-Informed Neural Network (PINN) model. The main findings are summarized as follows:

- Flexural strength decreased progressively with increasing support span for all sample groups, consistent with the transition from shear-dominated to bending-dominated failure.
- The S1A1 composite exhibited the highest flexural strength and modulus across most support spans, identifying it as the optimum hybrid filler content for flexural performance.
- Tensile strength increased progressively with Al_2O_3 content up to 1.5 wt.%, corresponding to an improvement of approximately 21% over the mono-filler reference.
- The tensile optimum occurred at a higher filler content than the flexural optimum, attributed to the lower sensitivity of the fiber-dominated tensile response to local agglomerates.
- Both loading modes exhibited a decline in performance at 2.0 wt.% Al_2O_3, indicating a common agglomeration threshold that limits the reinforcing

capacity of the hybrid filler system.

- The PINN model predicted flexural strength with high accuracy, achieving R^2 values of 0.98 and 0.96 and MAPE values of 3.81% and 5.37% on the training and test sets, respectively, while maintaining physical consistency with the three-point bending mechanics through its physics-informed loss formulation.

Author Contributions

The percentages of the authors' contributions are presented below. All authors reviewed and approved the final version of the manuscript.

	I.B.	H.K.
C	50	50
D	70	30
S	60	40
DCP	60	40
DAI	30	70
L	50	50
W	50	50
CR	50	50
SR	65	35
PM	60	40

C= concept, D= design, S= supervision, DCP= data collection and/or processing, DAI= data analysis and/or interpretation, L= literature search, W= writing, CR= critical review, SR= submission and revision, PM= project management.

Conflict of Interest

The authors declared that there is no conflict of interest.

Ethical Consideration

Ethics committee approval was not required for this study because of there was no study on animals or humans.

References

Abdi, A., Eslami-Farsani, R., & Khosravi, H. (2018). Evaluating the Mechanical Behavior of Basalt Fibers/Epoxy Composites Containing Surface-modified CaCO3 Nanoparticles [Article]. *Fibers and Polymers*, *19*(3), 635-640.

Abebe, Y., Palani, S., & Sirahbizu, B. (2025). Effect of Al2O3 nanoparticle on mechanical properties of polyester/ glass-wool fiber reinforced polymer composites. *Hybrid Advances*, *10*, 100472. /https://doi.org/10.1016/j.hybadv.2025.100472

Berladir, K., Antosz, K., Ivanov, V., & Mitaľová, Z. (2025). Machine Learning-Driven Prediction of Composite Materials Properties Based on Experimental Testing Data. *Polymers*, *17*(5), 694.

Dinesh, C., & Yoganandh, J. (2026). Effect of Modified Silicon Carbide Nanofillers on the Mechanical Performance of Nettle Fiber Reinforced Polymer Composites. *Polymer Composites*, *47*(7), 6536-6549. https://doi.org/10.1002/pc.70572

Ergün, R. K., Bayar, İ., & Köse, H. (2025). Data-Driven Prediction and Experimental Analysis of Wear in Micro/Nano SiO2-Reinforced Aramid Composites [Mikro/Nano SiO2 Takviyeli Aramid Kompozitlerde Aşınmanın Veriye Dayalı Tahmini ve Deneysel Analizi]. *Journal of Materials and Mechatronics: A*, *6*(2), 425-441. https://doi.org/10.55546/jmm.1797773

Gowda, H. D. S., Raju, H., Kumar, V. G. P., Bharat, P. B., Suresha, B., & Bhat, S. K. (2026). A review of recent machine learning advances for predicting and optimizing mechanical and tribological properties of fiber-reinforced thermoset polymer nanocomposites. *Discover Applied Sciences*, *8*(6), 636. https://doi.org/10.1007/s42452-026-08663-5

Guven, C., Kisa, M., Demircan, G., Ozen, M., & Kirar, E. (2024). Effect of seawater aging on mechanical, buckling, structural, and thermal properties of nano Al2O3 and TiO2-doped glass-epoxy nanocomposites [Article]. *Polymer Composites*, *45*(8), 7376-7390. https://doi.org/10.1002/pc.28273

Khalid, S., Yazdani, M. H., Azad, M. M., Elahi, M. U., Raouf, I., & Kim, H. S. (2025). Advancements in Physics-Informed Neural Networks for Laminated Composites: A Comprehensive Review. *Mathematics*, *13*(1), 17.

Kiran, M. D., Govindaraju, H. K., & Jayaraju, T. (2018). Evaluation of Mechanical Properties of Glass Fiber Reinforced Epoxy Polymer Composites with Alumina, Titanium dioxide and Silicon Carbide Fillers. *Materials Today: Proceedings*, *5*(10, Part 3), 22355-22361. https://doi.org/10.1016/j.matpr.2018.06.602

Kose, H., Bayar, I., & Koray Ergün, R. (2025). Optimization of Hybrid Micro/Nano-SiO2 Particle Ratios for Enhancing Mechanical Performance of Aramid Composites: Optimization and Validation Using Taguchi and ANOVA Analyses. *Advanced Engineering Materials*, *27*(23), e202501977.

Li, J., Zhang, L., & Qiao, J. (2026). Static and Dynamic Compressive Properties of Nano-Al2O3-Reinforced Epoxy Matrix Composites. *Polymers*, *18*(10), 1228.

Malashin, I., Tynchenko, V., Gantimurov, A., Nelyub, V., & Borodulin, A. (2025). Physics-Informed Neural Networks in Polymers: A Review. *Polymers*, *17*(8), 1108.

Mani, M. (2025). Silica nanoparticle-enhanced mechanical properties and energy absorption behavior of hybrid fiber-reinforced polymer composites for structural applications. *Next Materials*, *9*, 101213.

Navas-Pinto, W., Díaz-Leime, P., Barrionuevo, G. O., Luna-Jaén, J., Sánchez-Sánchez, X., Navas-Cárdenas, C., & Cree, D. E. (2026). Machine Learning Approach for Mechanical Property Prediction of a Bio-Epoxy and Glass Fiber Composite Reinforced with Titanium Dioxide Nanoparticles [Article]. *Journal of Composites Science*, *10*(3), 123.

Shettar, M., Bhat, A., Katagi, N. N., & Gowrishankar, M. C. (2025). Experimental Investigation on Mechanical Properties of Glass Fiber–Nanoclay–Epoxy Composites Under Water-Soaking: A Comparative Study Using RSM and ANN. *Journal of Composites Science*, *9*(4), 195.

Shubham, S. K., Purohit, R., Meravi, M., Bajpai, G., & Bhagyalaxmi, M. (2025). Development and testing of polymer matrix hybrid composites reinforced with nano SiO2. AIP Conference Proceedings,

Singh, T., Gangil, B., Ranakoti, L., & Joshi, A. (2021). Effect of silica nanoparticles on physical, mechanical, and wear properties of natural fiber reinforced polymer composites [Article]. *Polymer Composites*, *42*(5), 2396-2407.

Wang, W., & Thai, H.-T. (2025). A physics-informed neural network framework for laminated composite plates under bending. *Thin-Walled Structures*, *210*, 113014. https://doi.org/10.1016/j.tws.2025.113014

Black Sea Journal of Engineering and Science
doi: 10.34248/bsengineering.1992510

Open Access Journal
e-ISSN: 2619 – 8991

Research Article
Volume 9 - Issue 5: 2492-2526 / September 2026

COMPARATIVE EVALUATION OF RANDOM, SOBOL, AND DRAGON-FAMILY-GUIDED PSO AND QUANTUM INSPIRED PSO ON CEC 2022 BENCHMARKS AND CLEVELAND HEART DISEASE WRAPPER FEATURE SELECTION

Serkan ÖRÜCÜ[1]*

[1]*Karamanoğlu Mehmetbey University, Vocational School of Technical Sciences, Computer Technologies Program, 70200, Karaman, Türkiye*

Abstract: In Particle Swarm Optimization (PSO) and Quantum Inspired PSO (QI-PSO), the initialization source can shape early population diversity, search coverage, convergence behavior, and the later response of candidate generation operators. This effect becomes important in both continuous optimization, where particles move in a real-valued search space, and wrapper feature selection, where candidate solutions are evaluated as binary feature masks through classifier performance. Dragon curves offer another way to define structured search sources because their ordered point sequences can be mapped into a normalized search domain and reused as geometric guides. Based on this idea, this study examines whether random initialization, Sobol initialization, QI candidate generation, and dragon-curve-based geometric guidance change method behavior across continuous optimization and wrapper feature selection. The PSO variant set included Random-PSO, Sobol-PSO, Heighway-PSO, Twindragon-PSO, and Terdragon-PSO, while the QI-PSO variant set included Random-QI-PSO, Sobol-QI-PSO, Heighway-QI-PSO, Twindragon-QI-PSO, and Terdragon-QI-PSO. Heighway, Twindragon, and Terdragon curves were used as ordered geometric sources for particle initialization and stagnation-triggered perturbation. The methods were tested on CEC 2022 benchmark functions in 10-dimensional and 20-dimensional settings and on the UCI Cleveland Heart Disease dataset through wrapper feature selection with KNN-based fitness and additional SVM evaluation. In CEC 2022, the PSO variants produced lower average ranks and lower average mean fitness values than the QI-PSO variants. Random-PSO achieved the lowest average rank and runtime, whereas Terdragon-PSO produced the lowest average mean fitness and the lowest mean best fitness trajectory among the PSO variants. Dragon-guided PSO variants produced more best mean fitness records, but with higher computational cost. In the Cleveland task, Sobol-QI-PSO produced the highest observed mean balanced accuracy among the wrapper FS methods under both KNN and SVM. However, the Holm-corrected comparisons indicated statistically similar balanced accuracy across the compared wrapper methods. Terdragon-PSO produced the highest feature subset stability, while Random-PSO produced the most compact subsets. These results show that initialization, QI candidate generation, and dragon-based guidance vary with problem representation and evaluation dimension. Future studies should evaluate new metaheuristic components through final fitness, runtime, classifier response, selected feature count, selection frequency, and feature subset stability rather than through one performance measure.

Keywords: CEC 2022, Dragon curve guidance, Heart disease, Particle swarm optimization, Quantum Inspired

***Corresponding author:** Karamanoğlu Mehmetbey University, Vocational School of Technical Sciences, Computer Technologies Program, 70200, Karaman, Türkiye
E mail: srknorucu@kmu.edu.tr (S. ÖRÜCÜ)
Serkan ÖRÜCÜ https://orcid.org/0000-0001-9905-2908

Received: July 12, 2026
Accepted: August 14, 2026
Published: September 15, 2026

Cite as: Örücü, S. (2026). Comparative evaluation of random, sobol, and dragon-family-guided pso and quantum inspired pso on cec 2022 benchmarks and cleveland heart disease wrapper feature selection. *Black Sea Journal of Engineering and Science,* 9(5), 2492-2526.

1. Introduction

Feature selection (FS) is treated as an optimization problem that reduces model complexity and focuses on discriminative information because irrelevant, redundant, or contradictory attributes in high dimensional datasets can weaken the generalization capacity of classifiers (Xie et al., 2021). Wrapper-based FS evaluates the selected feature subset directly through classifier performance and therefore allows feature interactions to influence the search process (Lee and Zhuo, 2021). Since testing all possible feature combinations is computationally impractical, this problem provides a suitable search space for population based metaheuristic algorithms (Xie et al., 2021; Wang et al., 2023). Particle Swarm Optimization (PSO) represents candidate solutions as particles and moves each particle through the search space by using its own experience and swarm information, which provides a simple and adaptable search structure for both continuous optimization and FS problems (Clerc and Kennedy, 2002; Lee and Zhuo, 2021). This adaptive structure forms the initial algorithmic basis of this study because PSO can be used directly in a continuous search space and can also be transformed into FS problems represented by binary

This work is licensed (CC BY-NC 4.0) under Creative Commons Attribution 4.0 International License

feature masks (Lee and Zhuo, 2021; Wang et al., 2023).

The main strength of PSO arises from the joint use of personal best and global best information, yet the same structure can also cause particles to concentrate over time in previously explored regions (Clerc and Kennedy, 2002). This concentration increases the risks of premature convergence and local optima, particularly in complex and multimodal search spaces. Therefore, diversity preservation and search guidance components become important in PSO-based studies (Noori et al., 2024). In an improved binary PSO-based FS study, the use of inertia weight, crossover, and mutation to maintain the balance between exploration and exploitation shows that the standard velocity update in PSO-based FS designs can be strengthened by auxiliary mechanisms (Lee and Zhuo, 2021). In another PSO variant, the joint use of multi exemplar selection, local awareness, and improved initialization indicates that search behavior in the PSO family can be shaped not only by coefficient selection but also by candidate solution generation, initial distribution, and guidance strategies (Noori et al., 2024).

Quantum computing is based on a hardware and computation paradigm that differs from classical computing, and therefore genuine quantum algorithms are considered in the context of quantum hardware (Preskill, 2018). Classical computational approaches that use quantum concepts without quantum hardware are therefore evaluated in metaheuristic optimization through two separate approaches, quantum inspired (QI) and quantum behaved (QB). The QI approach converts concepts such as qubit, probability amplitude, quantum angle, quantum gate, quantum rotation, and adaptive mutation into candidate generation and diversity control operators that run on classical computers (Balicki, 2022; Agrawal and Panda, 2025; Naik et al., 2025). The QB approach, in contrast, does not insert additional operators into the classical velocity update. It builds a different position update model redefined through components such as local attractor, mean best, and contraction expansion coefficient (Bajaj et al., 2022).

In the Quantum Inspired Particle Swarm Optimization (QI-PSO) literature, quantum concepts are used as classical computational operators that strengthen candidate solution generation and diversity control rather than reconstructing particle motion through a QB position equation. Balicki (2022) used quantum gates to modify particle positions and preserve population diversity, which indicates that QI operators can be treated as diversity components that can be added to a PSO structure (Balicki, 2022). In the QI-PSO study by Naik et al. (2025), quantum particle structures were generated by quantum bits and updated by quantum angles, which shows that candidate solution representation can be extended in a classical computing environment through probabilistic quantum concepts (Naik et al., 2025). Extending standard PSO with qubit dynamics, quantum rotation, and adaptive mutation indicates that QI operators can be used to enlarge the search region and regulate the exploration exploitation balance (Agrawal and Panda, 2025). These studies show that QI-PSO designs can use QI candidate generation, particle modification, and diversity-control mechanisms within particle-based PSO structures (Balicki, 2022; Agrawal and Panda, 2025; Naik et al., 2025).

The initialization problem also becomes important in this study because the compared PSO and QI-PSO variants start from an initial particle population before their update operators are applied. In PSO studies, the way in which particles are distributed over the search space has been reported to affect diversity, convergence behavior, and search traversal (Bangyal et al., 2021; Bangyal et al., 2023; Li et al., 2023). Comparisons between low discrepancy sequence based initialization approaches and uniform random initialization have been used to evaluate the effect of initialization strategy on diversity and convergence in PSO based settings (Bangyal et al., 2021; Bangyal et al., 2023). In PSO-based medical prediction, Sobol sequence initialization has been used to make the initial particle distribution more uniform, increase population diversity, and improve population space traversal (Li et al., 2023). Sobol-initialized PSO, denoted as Sobol-PSO, is positioned in this study as a comparison variant that provides a deterministic and more regular initial distribution against random initialization. By the same experimental logic, Sobol-initialized QI-PSO, denoted as Sobol-QI-PSO, is used to evaluate how the effect of initial distribution changes within the implemented QI-PSO structure, where QI operators are used as candidate generation, particle modification, and diversity related components in PSO based structures (Balicki, 2022; Agrawal and Panda, 2025; Naik et al., 2025).

Fractal dragon curves are self-similar planar geometric structures that can be generated through iterative transformation rules and discussed within dragon-family geometry (Ngai and Nguyen, 2003; Phan et al., 2025). In this study, these curves are represented as normalized ordered point sequences. When these normalized ordered sequences are sampled within the same unit domain, they can be used as geometric sources for particle initialization and direction vector construction after stagnation. The Heighway dragon is one of the classical dragon curve examples described through iterative planar curve construction (Ngai and Nguyen, 2003). The fact that the Twindragon can be described as a related dragon-family structure provides a basis for considering the Heighway dragon and the Twindragon within the same geometric discussion (Ngai and Nguyen, 2003; Phan et al., 2025). In this study, the Heighway dragon, Twindragon, and Terdragon curves are used not as a family comparison covering all dragon curve variants but as three selected dragon geometry sources that produce computationally usable ordered traces (Phan et al., 2025). This restriction allows each curve to be compared under the same normalization,

initialization, and stagnation triggered perturbation protocol.

Dragon-based fractal patterns have also been used in different applications within computational representation and modeling. Mohammed and El-Khamy (2024) used chaotic dragon fractal shapes in image encryption and evaluated dragon fractal patterns as algorithmic representation components (Mohammed and El-Khamy, 2024). Roşu et al. (2025) used a wildfire spread simulation model based on a modified twindragon fractal structure and showed that twindragon geometry can be used for spatial simulation under environmental parameter fields (Roşu et al., 2025). These applications indicate that dragon-based geometries can be encoded as computational patterns and used as structured spatial sources in algorithmic procedures (Mohammed and El-Khamy, 2024; Roşu et al., 2025). In the present study, this computational geometry perspective is used in PSO and QI-PSO by using normalized dragon traces for particle initialization and stagnation triggered perturbation. The idea of curve based guidance is not limited to dragon structures. Peano, Hilbert, and other space filling curve structures have been used in swarm and metaheuristic studies to regulate deterministic movement or exploration behavior (Logofătu et al., 2020; Cuevas et al., 2025).

Guiding swarm movements with space filling curve patterns such as Peano and Hilbert shows that curve based deterministic movements can be modeled together with PSO-like swarm behavior (Logofătu et al., 2020). Similarly, guiding explorer agents through a virtual particle that follows a space filling curve shows that curve based coverage can be used as a metaheuristic exploration component (Cuevas et al., 2025). These studies place curve-defined movement, search guidance, and swarm-based exploration within the same methodological discussion (Logofătu et al., 2020; Cuevas et al., 2025). In the present study, this curve guidance perspective is examined through dragon-family traces by using Heighway dragon, Twindragon, and Terdragon as ordered geometric sources for particle initialization and stagnation triggered perturbation.

In the current literature, PSO-based FS improvements, QI-PSO search operators, Sobol initialization strategies, dragon curve geometry, and curve based swarm guidance approaches are mostly handled in separate research areas (Logofătu et al., 2020; Lee and Zhuo, 2021; Balicki, 2022; Li et al., 2023; Phan et al., 2025). This separation creates a basis for a controlled internal comparison of random initialization, Sobol initialization, and selected dragon curve guidance components under the same PSO and QI-PSO. Selected dragon-curve-based guidance is positioned not as an independent optimizer that changes the PSO structure, but as a geometric initialization and stagnation triggered perturbation layer added to the candidate generation process.

Accordingly, the aim of this study is to examine the method-level performance profiles produced by random initialization, Sobol initialization, QI candidate generation, and an ordered geometric guidance component derived from Heighway dragon, Twindragon, and Terdragon curves under PSO and QI-PSO variants. Random initialization represents stochastic reference behavior, Sobol initialization represents a low discrepancy initial structure, and selected dragon curve guidance represents a geometric guidance structure that combines ordered point set based initialization with post-stagnation perturbation steps. The methods are evaluated in two problem representations, namely the real-valued continuous search space of the CEC 2022 benchmark and the binary feature mask space of the Cleveland Heart Disease wrapper FS task. The evaluation uses final fitness, rank, convergence behavior, runtime, balanced accuracy, selected feature count, selected feature ratio, feature subset stability, and selection frequency.

The comparison structure consists of two groups. The PSO variant set includes random-initialized PSO (Random-PSO), Sobol-initialized PSO (Sobol-PSO), Heighway-guided PSO (Heighway-PSO), Twindragon-guided PSO (Twindragon-PSO), and Terdragon-guided PSO (Terdragon-PSO). The QI-PSO variant set includes random-initialized QI-PSO (Random-QI-PSO), Sobol-initialized QI-PSO (Sobol-QI-PSO), Heighway-guided QI-PSO (Heighway-QI-PSO), Twindragon-guided QI-PSO (Twindragon-QI-PSO), and Terdragon-guided QI-PSO (Terdragon-QI-PSO). Random-PSO and Random-QI-PSO represent baseline stochastic initialization behavior. Sobol-PSO and Sobol-QI-PSO represent low-discrepancy initialization. Heighway-PSO, Twindragon-PSO, Terdragon-PSO, Heighway-QI-PSO, Twindragon-QI-PSO, and Terdragon-QI-PSO are used to evaluate how the selected dragon curve geometry component behaves under PSO and QI-PSO structures. For family-level summaries, Random-PSO and Sobol-PSO form the Classical PSO family, Heighway-PSO, Twindragon-PSO, and Terdragon-PSO form the Dragon-guided PSO family, Random-QI-PSO and Sobol-QI-PSO form the QI-PSO family, and Heighway-QI-PSO, Twindragon-QI-PSO, and Terdragon-QI-PSO form the Dragon-guided QI-PSO family.

The CEC 2022 benchmark set allows algorithms to be tested under different search conditions through bound constrained continuous optimization problems including shifted, rotated, hybrid, and composition functions (Fang and Cao, 2024; Pathak et al., 2024; Agrawal and Panda, 2025). The CEC 2022 experiments examined the comparative performance profiles of random initialization, Sobol initialization, and selected dragon curve guidance components on PSO and QI-PSO structures in a continuous optimization task (Fang and Cao, 2024; Pathak et al., 2024). The evaluation was not limited to final fitness and also included mean, median, standard deviation, best, worst, rank, convergence trace, normalized convergence area, runtime per evaluation, evaluations per second, and total runtime.

In addition to the continuous optimization experiments, the study conducts wrapper-based FS experiments on the UCI Cleveland Heart Disease dataset (Janosi, 1989) to evaluate the applied classification context. FS based heart disease prediction experiments conducted on the Cleveland dataset in the literature show that this dataset provides a suitable experimental setting for heart disease classification and FS (Deepika and Balaji, 2022; Asha and Ramya, 2025; Örücü, 2026). The UCI Cleveland Heart Disease experiments were designed as a two-stage evaluation in which the no feature selection (no-FS) reference was compared with wrapper FS outputs under a fixed classification protocol.

In the first layer, all features were retained and the outputs of k-nearest neighbor (KNN) and support vector machine (SVM) classifiers under the no-FS condition were recorded. In the second layer, each candidate solution was evaluated as a binary feature mask, and the feature subsets selected by Random-PSO, Sobol-PSO, Heighway-PSO, Twindragon-PSO, Terdragon-PSO, Random-QI-PSO, Sobol-QI-PSO, Heighway-QI-PSO, Twindragon-QI-PSO, and Terdragon-QI-PSO were tested under the same classifier protocol. Because each candidate solution represents a feature subset in wrapper FS experiments, the optimization objective is not only to increase classification success but also to obtain a more compact model by reducing the number of selected features (Lee and Zhuo, 2021; Xie et al., 2021). The no-FS baseline is defined in this study as the reference evaluation setting in which all features are used (Örücü, 2026). This reference allows the feature subsets obtained after wrapper FS to be compared with the use of the full feature set in terms of classification performance and selected feature count. In the Cleveland experiments, selected feature count and selected feature ratio values were reported together with classification metrics, and feature subset stability was evaluated separately through Jaccard based subset similarity (Nogueira et al., 2017; Alelyani, 2021; Lee and Zhuo, 2021; Xie et al., 2021).

KNN is used as the main wrapper classifier in the Cleveland experiments because wrapper-based FS repeatedly evaluates candidate feature subsets and therefore benefits from a classifier that is simple and computationally less costly inside the fitness evaluation loop. This choice follows wrapper FS studies in which KNN is used to evaluate selected feature subsets during optimization. Hancer et al. (2018) used KNN with inner cross-validation for wrapper-based feature subset evaluation and stated that KNN is simple and relatively cheap, which is important because wrapper FS is computationally expensive. Similarly, Zouache et al. (2024) formulated wrapper-based multi-objective FS through selected feature ratio and classification error and used KNN to evaluate candidate subsets. SVM is used as an additional classifier evaluation component outside the optimizer because a second classifier structure is needed to observe how the subsets obtained after FS produce outputs under a different decision boundary logic based on separating hyperplanes (Deepika and Balaji, 2022; Asha and Ramya, 2025).

Accuracy, balanced accuracy, sensitivity, specificity, precision, F1 score, Matthews correlation coefficient (MCC), ROC AUC, PR AUC, and confusion matrix components are recorded together for these two-classifiers. The main contributions of this study can be summarized as follow.

- First, the study provides a controlled component analysis that examines the effects of random initialization, Sobol initialization, and selected dragon curve guidance components on PSO and QI-PSO structures.
- Second, the study presents a selected dragon curve guidance design that uses Heighway dragon, Twindragon, and Terdragon curves for initialization and stagnation triggered perturbation.
- Third, the study compares the Random-PSO, Sobol-PSO, Heighway-PSO, Twindragon-PSO, and Terdragon-PSO variants with the Random-QI-PSO, Sobol-QI-PSO, Heighway-QI-PSO, Twindragon-QI-PSO, and Terdragon-QI-PSO variants within the same experimental structure.
- Fourth, the study uses CEC 2022 continuous optimization experiments together with UCI Cleveland Heart Disease wrapper FS experiments to examine whether the same components produce different effects in continuous optimization and binary mask based wrapper FS tasks.
- Fifth, the study reports the no-FS baseline together with wrapper FS results in the Cleveland experiments and compares the effects of the FS process on classification performance, selected feature count, selected feature ratio, and feature subset stability.

2. Materials and Methods

In this study, the effect of the selected dragon-curve-based guidance component on the search processes of the PSO and QI-PSO variants was examined through two experimental settings. In the first experimental setting, the algorithms were evaluated on CEC 2022 continuous optimization benchmark functions. In the second experimental setting, the same algorithmic structure was applied to the wrapper FS problem on the UCI Cleveland Heart Disease dataset. This section first defines the benchmark and dataset used, followed by the algorithm variants, update mechanisms, initialization structures, wrapper FS protocol, experimental settings, evaluation metrics, and statistical analysis process.

2.1. Dataset and Benchmark Functions

The algorithm variants were evaluated in two experimental settings. The first experimental setting measures continuous optimization performance on the CEC 2022 benchmark functions. The second experimental setting evaluates classification-based FS performance on the UCI Cleveland Heart Disease dataset.

This structure was used to examine the behavior of the same optimizer variants both in a real-valued search space and in a clinical data-based prediction problem.

2.1.1. CEC 2022 benchmark functions

The CEC 2022 benchmark family is used to evaluate algorithm behavior in bound constrained continuous optimization problems through shifted and rotated, hybrid, and composition function groups (Agrawal and Panda, 2025).

The distinction between shifted and rotated functions, hybrid functions, and composition functions in the CEC 2022 suite allows the use of the CEC 2022 experiments in this study as a benchmark family representing different search difficulties (Wang et al., 2024; Agrawal and Panda, 2025).

The use of CEC 2022 with 12 functions and 10 and 20 dimensions, and the inclusion of convergence speed information in the evaluation process, show that this benchmark family can also be used to monitor convergence behavior in addition to final fitness (Stanovov et al., 2023). Therefore, the CEC 2022 experiments were used to compare random, Sobol, and dragon-guided variants in the PSO and QI-PSO variant sets under the same continuous optimization conditions.

The CEC 2022 suite used in this study contains one unimodal function, four basic multimodal functions, three hybrid functions, and four composition functions. All functions are defined over the search range $[-100, 100]^D$ and were evaluated at D = 10 and D = 20. F1 is the Shifted and Full Rotated Zakharov Function with a theoretical optimum of 300. F2 is the Shifted and Full Rotated Rosenbrock's Function with a theoretical optimum of 400. F3 is the Shifted and Full Rotated Expanded Schaffer's f6 Function with a theoretical optimum of 600. F4 is the Shifted and Full Rotated Non-Continuous Rastrigin Function with a theoretical optimum of 800. F5 is the Shifted and Full Rotated Levy Function with a theoretical optimum of 900. F6, F7, and F8 are Hybrid Functions 1, 2, and 3, with theoretical optimum values of 1800, 2000, and 2200, respectively. F9, F10, F11, and F12 are Composition Functions 1, 2, 3, and 4, with theoretical optimum values of 2300, 2400, 2600, and 2700, respectively (Mohamed et al., 2020; Chen and Zheng, 2023).

In the CEC 2022 experiments, each candidate solution was defined as a D dimensional real valued decision vector, as shown in equation 1 (Fang and Cao, 2024; Agrawal and Panda, 2025).

$$x = (x_1, x_2, \dots, x_D) \in R^D \quad (1)$$

In equation 1, x denotes the candidate solution vector, x_D denotes the decision variable of the candidate solution in the d-th dimension, and D denotes the problem dimension. This representation ensures that PSO and QI-PSO variants operate with the same candidate solution structure in the continuous search space. Because CEC 2022 problems are defined with bounded decision variables, each candidate solution was kept within the lower and upper bounds as in equation 2 and equation 3 (Fang and Cao, 2024; Agrawal and Panda, 2025).

$$\mathrm{lb} \le \mathrm{x} \le \mathrm{ub} \quad (2)$$

$$\mathrm{lb_d} \le \mathrm{x_d} \le \mathrm{ub_d}, \quad \mathrm{d} = 1, 2, \dots, \mathrm{D} \quad (3)$$

In equations 2 and 3, lb denotes the lower bound vector, ub denotes the upper bound vector, lb_d denotes the lower bound of the d-th dimension, and ub_d denotes the upper bound of the same dimension. Equations 2 and 3 ensure that all algorithm variants are evaluated within the same valid search bounds. Candidate values outside these bounds were repaired before fitness evaluation.

The optimization objective in the CEC 2022 experiments was defined as minimization of the relevant benchmark function, as shown in equation 4 (Fang and Cao, 2024; Agrawal and Panda, 2025).

$$x_{best} = arg \min_{x \in [lb, ub]} f_j(x) \quad (4)$$

In equation 4, $f_j(x)$ denotes the value of the j-th objective function in the CEC 2022 benchmark family, and x_{best} denotes the best candidate solution obtained for the corresponding benchmark function. Thus, all variants in the CEC experiments are compared with the same minimization objective.

In the CEC 2022 experiments, the final objective value, convergence trace, and runtime records were evaluated together. The final objective value gives the best function value obtained at the end of a run. The convergence trace tracks the improvement behavior of the algorithm across iterations. Runtime records allow performance obtained under the same search budget to be evaluated together with computational cost. The experimental structure of CEC 2022 that enables convergence speed evaluation provides the basis for reporting convergence trace and runtime records together with final objective value in this study (Stanovov et al., 2023; Wang et al., 2024).

2.1.2. UCI cleveland heart disease dataset

The UCI Cleveland Heart Disease dataset is a clinical classification dataset used in heart disease prediction and FS studies (Deepika and Balaji, 2022; Wadhawan and Maini, 2022; Noroozi et al., 2023; Asha and Ramya, 2025). Noroozi et al. (2023) reported that the Cleveland Heart Disease dataset was obtained from the UCI Machine Learning Repository, contained 303 records, and was used for heart disease prediction with 13 features and a final endpoint (Noroozi et al., 2023).

The evaluation of filter, wrapper, and evolutionary FS methods with different machine learning algorithms on the Cleveland dataset in the literature shows that this dataset can serve as a benchmark for FS-based heart disease prediction experiments (Wadhawan and Maini, 2022; Noroozi et al., 2023). In this study, the Cleveland dataset was used to evaluate the effect of optimizer based FS methods on a classification based FS problem.

The Cleveland dataset was represented with a supervised learning structure using in equation 5 and equation 6 (Deepika and Balaji, 2022; Noroozi et al., 2023; Asha and

Ramya, 2025).

$$D = \{(x_n, y_n)\}_{n=1}^{M} \quad (5)$$

$$x_n = \{x_{n,1}, x_{n,2}, \dots, x_{n,m}\} \quad (6)$$

In equation 5 and equation 6, D denotes the Cleveland dataset, M denotes the number of samples, x_n denotes the feature vector of the n-th patient record, m denotes the total number of features, and y_n denotes the class label of the n-th sample. In this way, each Cleveland sample is represented by a clinical feature vector and a class label.

The original target variable was transformed into a binary classification problem. As shown in equation 7, samples with a target value of zero were assigned to the negative class, whereas samples with a value greater than zero were assigned to the positive class.

$$y_n = \begin{cases} 0, & Target_n = 0 \\ 1, & Target_n > 0 \end{cases} \quad (7)$$

In equation 7, $Target_n$ denotes the original disease status in the dataset and y_n denotes the binary class label. This transformation converts heart disease absence and presence into a two-class prediction problem. After this transformation, the KNN and SVM classifiers were evaluated on the same binary classification target. The no-FS baseline, binary feature mask generation from continuous position values, empty mask handling, KNN based wrapper fitness, SVM validation, and feature subset stability calculation are described in the Wrapper FS Protocol section.

2.2. Compared Algorithm Variants and Update Mechanisms

In this study, the compared methods were organized as PSO variants and QI-PSO variants. The PSO variants update particles according to personal best and global best information (Kennedy and Eberhart, 1995; Clerc and Kennedy, 2002). The QI-PSO variants add angle-based candidate generation, candidate mixing, and mutation components defined in this study to the same personal best and global best memory structure. Related QI candidate generation and particle modification mechanisms have been used in QI-PSO studies (Balicki, 2022; Agrawal and Panda, 2025; Naik et al., 2025; Örücü, 2026). For family-level aggregation, the methods were grouped into the Classical PSO, Dragon-guided PSO, QI-PSO, and Dragon-guided QI-PSO families. The PSO variant set included Random-PSO, Sobol-PSO, Heighway-PSO, Twindragon-PSO, and Terdragon-PSO. The QI-PSO variant set included Random-QI-PSO, Sobol-QI-PSO, Heighway-QI-PSO, Twindragon-QI-PSO, and Terdragon-QI-PSO. Random and Sobol variants were used to compare initialization sources, whereas the dragon-guided variants were used to examine Heighway, Twindragon, and Terdragon-based geometric guidance under the two variant sets (Ngai and Nguyen, 2003; Bangyal et al., 2021; Li et al., 2023; Phan et al., 2025). In all PSO and QI-PSO variants, each particle was represented by a position vector and a velocity vector, as shown in equation 8 and equation 9 (Kennedy and Eberhart, 1995; Clerc and Kennedy, 2002).

$$x_i^t = \left(x_{i,1}^t, x_{i,2}^t, \dots, x_{i,D}^t\right) \quad (8)$$

$$v_i^t = \left(v_{i,1}^t, v_{i,2}^t, \dots, v_{i,D}^t\right) \quad (9)$$

In equation 8 and equation 9, x_i^t denotes the position of the i-th particle at iteration t, v_i^t denotes the velocity of the same particle, and D denotes the problem dimension. In the CEC 2022 experiments, x_i^t was evaluated as a continuous candidate solution (Fang and Cao, 2024; Agrawal and Panda, 2025). In the Cleveland experiments, the same continuous position representation forms the basis for generating a binary feature mask in the wrapper FS protocol (Lee and Zhuo, 2021; Xie et al., 2021; Li et al., 2023).

In the PSO update, the inertia weight value was linearly decreased as the iteration progressed. Since inertia weight determines the extent to which previous velocity information is transferred to the new movement, high values generate broader search movements, whereas lower values reduce the movement magnitude as iterations proceed as shown in equation 10 (Clerc and Kennedy, 2002; Bangyal et al., 2021; Wang et al., 2023).

$$w^t = w_{max} - \frac{(w_{max} - w_{min})t}{T-1} \quad (10)$$

In equation 10, w^t denotes the inertia weight value used at iteration t, w_{max} denotes the initial inertia weight, w_{min} denotes the final inertia weight, and T denotes the maximum number of iterations. Thus, a broader movement area is provided in early iterations and more controlled movement is produced in later iterations.

The velocity update was performed by jointly using inertia weight, personal best orientation, and global best orientation as shown in equation 11 (Kennedy and Eberhart, 1995; Clerc and Kennedy, 2002).

$$v_i^{t+1} = w^t v_i^t + c_1 r_1 \odot (p_i^t - x_i^t) + c_2 r_2 \odot (g^t - x_i^t) \quad (11)$$

In equation 11, p_i^t denotes the personal best position obtained by the i-th particle up to that point, g^t denotes the global best position of the swarm, c_1 denotes the cognitive acceleration coefficient, c_2 denotes the social acceleration coefficient, r_1 and r_2 denote random vectors generated in the [0,1] interval, and $\odot$ denotes component wise multiplication. In this structure, the first term carries the previous movement direction. The second term directs the particle toward its own successful past position, whereas the third term directs it toward the best position at the swarm level. Therefore, PSO movement is based on the joint use of individual memory and collective swarm information (Kennedy and Eberhart, 1995; Clerc and Kennedy, 2002).

After the velocity update, the velocity vector was bounded according to the width of the problem bounds. Since uncontrolled velocity growth may cause particles to move outside the search bounds, velocity limiting operation in equation 12 and 13 keeps particle movement within the problem scale (Clerc and Kennedy,

2002).

$$v_i^{t+1} = clip\left(v_i^{t+1}, -v_{max}, v_{max}\right) \quad (12)$$

$$v_{max} = \rho(ub - lb) \quad (13)$$

In equation 12 and 13, clip(·) denotes the operation that keeps velocity components within the specified lower and upper velocity limits, v_{max} denotes the maximum velocity vector, ρ denotes the velocity clamp ratio, and lb and ub denote the problem boundaries. Since the velocity magnitude is linked to the width of the search bounds, it becomes possible to control movement magnitude on the same relative scale in problems with different boundary intervals.

The classical PSO candidate position was generated by adding the bounded velocity vector to the current position as in equation 14 (Kennedy and Eberhart, 1995; Clerc and Kennedy, 2002).

$$\tilde{x}_i^{t+1} = x_i^t + v_i^{t+1} \quad (14)$$

In equation 14, $\tilde{x}_i^{t+1}$ denotes the candidate position before boundary repair. In random-initialized PSO, Sobol-initialized PSO, and dragon curve guided PSO variants, baseline candidate position generation was performed through the classical PSO flow from equations 10 to 14 (Kennedy and Eberhart, 1995; Clerc and Kennedy, 2002). In Sobol initialized variants, the difference arises from generating the initial population using a Sobol sequence (Bangyal et al., 2021; Li et al., 2023). In dragon guided variants, the difference arises from the initialization and stagnation triggered perturbation components derived from Heighway, Twindragon, and Terdragon curves (Ngai and Nguyen, 2003; Phan et al., 2025).

In the QI-PSO structure, an angle based QI candidate generation layer was defined in this study in addition to the classical PSO candidate position. In QI-PSO studies, the concepts of quantum particles, quantum bits, quantum angle, and quantum rotation are used to extend candidate solution representation (Balicki, 2022; Naik et al., 2025).

The use of qubit dynamics, quantum rotation, and adaptive mutation components together with PSO shows that QI operators can regulate the exploration and exploitation balance (Agrawal and Panda, 2025). The QI procedure defined in equations 15 to 24 was therefore constructed as a candidate generation component added to the classical PSO candidate based on this literature. In the QI-PSO update, the position, personal best, and global best vectors were first normalized to the [0,1] interval, as in equations 15-17.

$$x_{i,n}^t = \frac{x_i^t - lb}{ub - lb} \quad (15)$$

$$p_{i,n}^t = \frac{p_i^t - lb}{ub - lb} \quad (16)$$

$$g_n^t = \frac{g^t - lb}{ub - lb} \quad (17)$$

In equations 15-17, $x_{i,n}^t$ denotes the normalized current position, $p_{i,n}^t$ denotes the normalized personal best position, and g_n^t denotes the normalized global best position. This scaling converts different problem boundaries into a common unit interval representation and allows the quantum angle update to be conducted over the same numerical range in all dimensions.

In the QI-PSO structure used in this study, the target vector for angle update was defined as the average of personal best and global best information as in equation 18.

$$s_i^t = 0.5p_{i,n}^t + 0.5g_n^t \quad (18)$$

In equation 18, s_i^t denotes the target vector used for quantum angle update for the *i*-th particle. In this equation, QI candidate generation is not linked only to the global best direction, and the particle's own personal best information is also transferred to the angle update step. Thus, individual memory and swarm memory are jointly transferred to the QI representation space used in this study.

The quantum angle vector was updated according to the direction difference between the target vector and the current normalized position, as shown in equation 19.

$$\theta_i^{t+1} = clip\left(\theta_i^t + \alpha_q sign\left(s_i^t - x_{i,n}^t\right), 0, \frac{\pi}{2}\right) \quad (19)$$

In equation 19, θ_i^{t+1} denotes the quantum angle vector of the *i*-th particle at iteration *t+1*, α_q denotes the quantum angle update coefficient, and *sign(·)* denotes the sign function that determines whether the angle value will be increased or decreased according to the target direction. Thus, the target direction generated from personal best and global best information is transferred to the quantum angle space.

The QI candidate position was generated from the updated angle values, as shown in equation 20.

$$q_i^{t+1} = lb + sin^2\left(\theta_i^{t+1}\right) \odot (\text{ub} - \text{lb}) \quad (20)$$

In equation 20, q_i^{t+1} denotes the QI candidate position. The *sin²(·)* transformation was used to generate candidate components in the [0,1] interval from angle values. Because this candidate is scaled by problem boundaries, it is transformed into a position proposal that can be evaluated in the continuous search space.

The classical PSO candidate and the QI candidate were combined through a weighted mixture, as shown in equation 21.

$$\hat{x}_i^{t+1} = (1 - \mu)\tilde{x}_i^{t+1} + \mu q_i^{t+1} \quad (21)$$

In equation 21, $\hat{x}_i^{t+1}$ denotes the candidate position obtained after QI mixing, and μ denotes the quantum mix coefficient. This structure combines the movement information generated by the classical PSO velocity update with QI angle based candidate generation in the same position update. Therefore, in the QI-PSO structure, the candidate position is affected by both pbest and gbest based swarm movement and the angle based QI transformation.

The use of adaptive mutation and quantum rotation components together with PSO supports the use of QI based candidate generation to expand the search region and reduce the risk of local optima (Balicki, 2022; Agrawal and Panda, 2025). In the QI-PSO structure, random perturbation was applied through a mutation mask to increase candidate diversity, in equations 22, 23, and 24.

$$m_i^t \sim Bernoulli(p_m) \tag{22}$$

$$\varepsilon_i^t \sim N(0, \sigma_m) \odot (ub - lb) \tag{23}$$

$$\bar{x}_i^{t+1} = \hat{x}_i^{t+1} + m_i^t \odot \varepsilon_i^t \tag{24}$$

In equations 22, 23, and 24, m_i^t denotes the binary mask that determines the components to which mutation will be applied, p_m denotes the mutation probability, ε_i^t denotes the mutation vector generated from a normal distribution, and σ_m denotes the mutation scale. Equations 22 to 24 generate a low probability and problem scale dependent perturbation instead of applying mutation to every component at every iteration. Thus, QI-PSO candidates are supported by a random component that provides diversity restoration in addition to classical PSO orientation and angle based candidate generation.

In the dragon guided variants, the additional perturbation was applied only when the stagnation condition was satisfied. Since premature convergence and local optima risks in PSO-based algorithms can cause particles to concentrate in restricted regions, diversity preserving and search guidance components become important (Lee and Zhuo, 2021; Xie et al., 2021; Noori et al., 2024). Guiding swarm movement with space filling curve patterns shows that curve based deterministic movement information can be added to the exploration process (Logofătu et al., 2020; Cuevas et al., 2025).

In this study, direction vectors derived from Heighway dragon, Twindragon, and Terdragon curves were used for post stagnation perturbation generation, following the curve guided exploration idea in the literature (Ngai and Nguyen, 2003; Phan et al., 2025). The dragon direction vector was defined by normalizing the difference between two curve based population representations, as shown in equation 25.

$$d_i^c = \frac{b_i^c - a_i^c}{\|b_i^c - a_i^c\|} \tag{25}$$

In equation 25, d_i^c denotes the normalized direction vector derived from dragon curve c. Here, c denotes one of the Heighway dragon, Twindragon, or Terdragon curves. a_i^c and b_i^c denote two different curve based population representations generated from the same curve family. The geometric relation between the Heighway dragon and the Twindragon, and the inclusion of the Terdragon type among fractal dragon structures, provide the basis for comparing these three curves under the same geometric guidance family (Ngai and Nguyen, 2003; Phan et al., 2025).

The perturbation intensity was decreased as iterations progressed, as shown in equation 26.

$$\eta^t = \eta_0 \delta^t \tag{26}$$

In equation 26, η^t denotes the dragon perturbation scale at iteration t, n_0 denotes the initial dragon step scale, and δ denotes the dragon step decay coefficient δ. Thus, the dragon perturbation component produces broader movement in early iterations and more limited movement in later iterations.

Stagnation triggered dragon perturbation was applied as shown in equation 27.

$$x_{i,dragon}^{t+1} = \bar{x}_i^{t+1} + \eta^t (ub - lb) \odot d_i^c \tag{27}$$

In equation 27, $x_{i,dragon}^{t+1}$ denotes the candidate position obtained after dragon perturbation, $\bar{x}_i^{t+1}$ denotes the pre-perturbation candidate position, η^t denotes the dragon perturbation scale at iteration t, and d_i^c denotes the normalized direction vector derived from dragon curve c. In the dragon-guided PSO variants, $\bar{x}_i^{t+1}$ represents the classical PSO candidate before dragon perturbation. In the dragon-guided QI-PSO variants, $\bar{x}_i^{t+1}$ denotes the candidate position obtained after QI mixing and mutation steps before dragon perturbation. Thus, equation 27 defines how the dragon-guidance component adds the dragon direction vector to the candidate position as a perturbation when stagnation occurs. This compact expression is expanded in Section 2.3 through activation, masking, and boundary repair details.

All candidate positions were subjected to boundary repair before fitness evaluation. In bound constrained continuous optimization problems such as CEC 2022, candidate solutions must be evaluated within the lower and upper bounds, as shown in equation 28 (Fang and Cao, 2024; Agrawal and Panda, 2025).

$$x_i^{t+1} = R\left(x_{i,*}^{t+1}, lb, ub\right) \tag{28}$$

In equation 28, $R(\cdot)$ denotes the boundary repair function and $x_{i,*}^{t+1}$ denotes the final candidate position generated by the relevant variant. Thus, candidates generated by PSO, QI-PSO, and dragon-family-guided variants are evaluated within the same valid search bounds. After fitness evaluation, the personal best value was updated according to the minimization rule specified in equation 29.

$$p_i^{t+1} = \begin{cases} x_i^{t+1}, & F\left(x_i^{t+1}\right) < F(p_i^t) \\ p_i^t, & otherwise \end{cases} \tag{29}$$

In equation 29, $F(\cdot)$ denotes the benchmark function in the CEC 2022 experiments and the wrapper FS fitness function in the Cleveland experiments. As a result, when the current candidate of a particle is better than its historical best solution, the personal best value is updated. This selection rule preserves the successful past information of the particle throughout the search process (Kennedy and Eberhart, 1995; Clerc and Kennedy, 2002; Mienye and Sun, 2021). The global best position was selected as the candidate with the lowest fitness value

among all personal best values, as shown in equations 30 and 31 (Li et al., 2023; Agrawal and Panda, 2025; Naik et al., 2025).

$$i^* = arg \min_{i=1,2,\dots,N} F\left(p_i^{t+1}\right) \quad (30)$$

$$g^{t+1} = p_{i^*}^{t+1} \quad (31)$$

In equations 30 and 31, N denotes the swarm size and i^* denotes the index of the particle whose personal best has the lowest fitness value. Equation 30 selects the index of the best personal best candidate in the swarm. Equation 31 then updates the global best position as the position of this candidate. This selection rule was kept the same in all algorithm variants. Thus, the differences obtained in the comparisons were attributed through the initialization type, QI candidate generation, and dragon family perturbation components rather than a shared fitness selection rule.

2.3. Initialization and Dragon Family Guidance

Since the CEC 2022 experiments were conducted as bound constrained continuous optimization, all initialization strategies were first generated in the [0,1] interval and then mapped to the problem space with the same lower bound and upper bound vectors (Fang and Cao, 2024; Pathak et al., 2024; Phan et al., 2025). The common scaling operation shown in equations 32 and 33 allows random, Sobol, and dragon family initialization strategies to be compared under the same search boundary conditions.

$$U = \left[u_{i,d}\right]_{SS\times D}, \quad 0 \le u_{i.d} \le 1 \quad (32)$$

$$x_i^0 = lb + u_i \odot (ub - lb) \quad (33)$$

In equation 32, U denotes the unit population matrix, SS denotes the swarm size, D denotes the problem dimension, u_i denotes the row vector of the i-th particle in the unit population, and x_i^0 denotes the initial position of the i-th particle. Equation 33 maps the initial candidates generated in the [0,1] interval to the search bounds of the relevant problem. Therefore, the difference between initialization strategies arises from the generation of the U matrix rather than the boundary mapping operation.

Random initialization is a widely used baseline initialization strategy in population based metaheuristic algorithms. To evaluate the effect of low discrepancy sequence and Sobol based initialization approaches, random initialization was used in this study as the baseline initialization mechanism, as shown in equation 34 (Bangyal et al., 2021; Li et al., 2023).

$$u_{i,d}^R \sim U(0,1) \quad (34)$$

In equation 34, $u_{i,d}^R$ denotes the unit value in the d-th dimension of the i-th particle generated by random initialization. Thus, the initial population was generated through a uniform random distribution without using a low discrepancy or curve based pattern. The Sobol sequence is used in PSO-based studies to distribute the initial population more uniformly, increase population diversity, and improve search space traversal behavior (Li et al., 2023). Low discrepancy sequence based initialization studies have shown that the initial distribution is a measurable experimental variable affecting convergence and diversity (Bangyal et al., 2021). In this study, the Sobol initialization shown in equation 35 was used as a low discrepancy based and seed controlled initialization baseline against random initialization.

$$u_i^S = S_D(i), \quad i = 1, 2, \dots, SS \quad (35)$$

In equation 35, S_D denotes the D dimensional Sobol sequence generator and u_i^S denotes the i-th unit population vector generated by the Sobol sequence. Thus, an initial pattern based on low discrepancy was generated instead of a pseudo random initialization. This structure allows the initial population in Sobol initialized PSO and Sobol initialized QI-PSO variants to be formed by the same Sobol based distribution structure.

Dragon family initialization is based on geometric patterns derived from Heighway dragon, Twindragon, and Terdragon curves. The relationship between the Heighway dragon and the Twindragon, together with the treatment of the Heighway dragon, Twindragon, and Terdragon as fractal dragon structures, provides the basis for comparing the three curves used in this study within a common geometric family, as shown in equations 36 and 37 (Ngai and Nguyen, 2003; Phan et al., 2025).

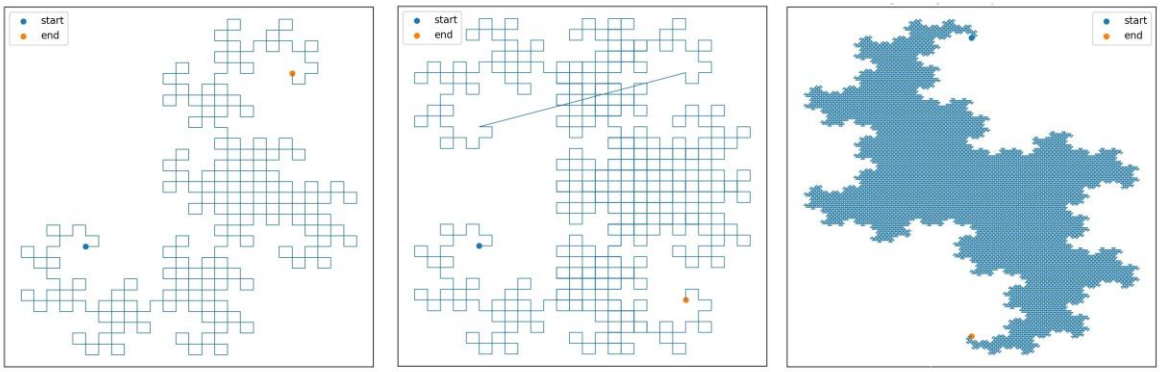
$$C^q = \left\{c_k^q\right\}_{k=1}^{M_q}, \quad q \in \{H, Tw, Te\} \quad (36)$$

$$c_k^q = \left(a_k^q, b_k^q\right), \quad a_k^q, b_k^q \in [0,1] \quad (37)$$

In equation 36, C^q denotes the ordered point set obtained from the selected dragon family curve, q denotes the curve type used, H denotes the Heighway dragon, Tw denotes the Twindragon, Te denotes the Terdragon, and M_q denotes the number of points obtained from the relevant curve. In equation 37, c_k^q denotes the k-th ordered point of the dragon curve of type q. a_k^q and b_k^q denote the normalized horizontal and vertical coordinates of this point, respectively. Since these coordinates are defined in the *[0,1]* interval, each dragon curve is represented within the same unit square. Thus, ordered point set structures obtained from different dragon family variants can be used for initialization and perturbation generation at the same scale. These ordered point set structures derived from dragon family curves were used for unit population generation during initialization and for determining direction based perturbation vectors when stagnation occurred. Heighway dragon, Twindragon, and Terdragon curves are fractal structures that belong to the same dragon family but produce different geometric traces and turning patterns. The normalized two dimensional representations of these three curves within the $[0,1]^2$ unit square are shown in Figure 1. The three panels in

Figure 1 show the geometric source of the ordered point set structure defined in equations 36 and 37. Since each curve is represented within the same *[0,1]²* unit square, the geometric traces of the Heighway dragon, Twindragon, and Terdragon variants can be compared at the same scale. This representation explains the structural differences among the curve based patterns used in the dragon family initialization and stagnation triggered direction based perturbation steps.

The use of dragon fractal patterns as computational representation components in image encryption and spatial modeling studies shows that these geometric structures can be generated algorithmically and transferred to different application contexts (Mohammed and El-Khamy, 2024; Roşu et al., 2025). In this study, this representation was transferred to optimization search guidance, and dragon family curves were used in unit population generation.



a) Heighway dragon b) Twindragon c) Terdragon

Figure 1. Normalized two dimensional representations of dragon family curves. a) Heighway dragon, b) Twindragon, c) Terdragon.

Since directly copying a two-dimensional curve into the full decision vector in high-dimensional continuous optimization problems may produce artificial correlations, dragon coordinates were transformed into a D dimensional unit population matrix through dimension wise mixing and rank based normalization, as shown in equations 38 and 39.

$$r_{i,d}^{q} = frac\left(\alpha_d a_{k_{i,d}}^{q} + \beta_d b_{k_{i,d}}^{q} + \gamma_d \frac{k_{i,d}}{M_q} + \epsilon_{i,d}\right) \tag{38}$$

$$u_{i,d}^{D,q} = \frac{rank(r_{i,d}^{q})}{SS+1} \tag{39}$$

In equation 38, $r_{i,d}^{q}$ denotes the dragon-based unit candidate value before rank normalization, *frac(·)* denotes the fractional part operation, α_d, β_d, and γ_d denote dimension dependent mixing coefficients, $k_{i,d}$ denotes the curve index selected for the relevant particle and dimension, and $\epsilon_{i,d}$ denotes a small jitter component. Thus, two dimensional dragon coordinate information is transformed into a different unit candidate value for each decision dimension. Equation 39 then maps these values to a more balanced unit population structure in the [0,1] interval through rank based normalization.

Since rank values range from 1 to SS, division by SS+1 prevents normalized values from being exactly 0 or exactly 1 and keeps them in the (0,1) interval.

Therefore, rank based normalization transforms dragon-based candidate values into a more balanced unit population distribution within the same dimension while reducing direct placement at boundary values.

The initial angle interval used in the QI-PSO was defined as *[0,π/2]* because the *sin²(θ)* transformation in this interval produces unit candidate components in the [0,1] interval, as shown in equations 40 and 41.

$$\theta_{i,d}^{0} \sim U\left(0, \frac{\pi}{2}\right) \tag{40}$$

$$u_{i,d}^{QI} = \sin^2\left(\theta_{i,d}^{0}\right) \tag{41}$$

In equations 40 and 41, $\theta_{i,d}^{0}$ denotes the initial angle value used in the QI-PSO structure and $u_{i,d}^{QI}$ denotes the unit candidate component generated from this angle value. This structure links candidate generation in the QI-PSO structure to the same boundary mapping procedure used for the *[0,1]* based unit representation.

Since premature convergence and diversity loss in PSO-based algorithms may cause the search process to concentrate in limited regions, additional diversity preserving mechanisms are used (Xie et al., 2021; Noori et al., 2024). In space filling curve based swarm studies, the addition of curve based movement information as a guiding component in the exploration process provides a methodological basis for using dragon family direction vectors in post stagnation perturbation generation (Logofătu et al., 2020; Cuevas et al., 2025). In this study, dragon perturbation is not used as an operator that is active at every iteration but as a conditional diversity restoration component activated only when stagnation occurs, as shown in equations 42, 43, and 44.

$$\Delta_t = |F(\mathrm{g}^{t-1}) - F(\mathrm{g}^{t})| \tag{42}$$

$$s_t = \begin{cases} s_{t-1} + 1, & \Delta_t < \tau \\ 0, & \Delta_t \geq \tau \end{cases} \tag{43}$$

$$s_t \geq S_{max} \tag{44}$$

In equations 42, 43, and 44, Δ_t denotes the global best fitness change between consecutive iterations, $F(\mathrm{g}^{t})$

denotes the fitness value of the global best solution at iteration t, s_t denotes stagnation counter, τ denotes the improvement tolerance, and S_{max} denotes the stagnation threshold. In this structure, equation 42 measures the change in global best, equation 43 increases the stagnation counter when no meaningful improvement occurs and resets the counter when the improvement tolerance threshold is exceeded, and equation 44 activates the dragon perturbation component when the condition is satisfied.

In this study, the dragon perturbation direction was generated from two curve based population representations obtained from the same selected dragon family curve. The first representation was generated from the original ordered curve points, whereas the second representation was generated from a shifted ordering of the same curve points. The direction vector was then obtained by normalizing the difference between these two representations, as expressed in equations 45 and 46.

$$d_i^q = b_i^q - a_i^q \tag{45}$$

$$\hat{d}_i^q = \frac{d_i^q}{\|d_i^q\| + \epsilon} \tag{46}$$

In equations 45 and 46, a_i^q and b_i^q denote two curve based D dimensional unit population representations generated from the same dragon curve q, d_i^q denotes their difference vector, $\hat{d}_i^q$ denotes the normalized dragon direction vector, and ϵ denotes a small constant used to prevent division by zero. Thus, the perturbation direction is obtained from two shifted curve based population representations rather than from adjacent decision dimensions or consecutive optimizer iterations.

The perturbation magnitude was controlled by a coefficient that decreases as iterations progress, as shown in equations 47 and 48.

$$\lambda_t = \lambda_0 \delta^t \tag{47}$$

$$\tilde{x}_{i,t} = x_{i,*}^{t+1} + \lambda_t (ub - lb) \odot \hat{d}_i^q \tag{48}$$

In equation 47, λ_t denotes the dragon perturbation scale at iteration t, λ_0 denotes the initial perturbation scale, and δ denotes the dragon step decay coefficient. In equation 48, $x_{i,*}^{t+1}$ denotes the pre perturbation candidate position generated by the relevant PSO or QI-PSO update chain. Thus, equation 48 gives the general dragon perturbation form before particle level probabilistic masking.

The particles to which dragon perturbation was applied were selected by a probabilistic mask generated using equations 49, 50, and 51.

$$z_{i,t} \sim Bernoulli(p_D) \tag{49}$$

$$\tilde{x}_{i,t} = x_{i,*}^{t+1} + z_{i,t} \lambda_t (ub - lb) \odot \hat{d}_i^q \tag{50}$$

$$x_{i,t}^{new} = R\left(\tilde{x}_{i,t}, lb, ub\right) \tag{51}$$

In equation 49, $z_{i,t}$ denotes the binary selection variable that determines whether dragon perturbation will be applied to the i-th particle, and p_D denotes the dragon perturbation probability. In equation 50, the general perturbation rule in equation 48 is extended with the probabilistic mask so that the dragon direction component is applied only to selected particles. In equation 51, R denotes the boundary repair function that maps the candidate positions produced after perturbation back to the valid lower and upper bounds. In the implementation, reflection based boundary repair was used. All initialization strategies were transferred to the problem space through the same boundary mapping operation. Random, Sobol, and dragon family initializations were generated under the same mapping, and dragon family variants additionally used post stagnation direction based perturbation. This structure allows random, Sobol, and dragon-family-guided variants to be evaluated under the same boundary mapping and dragon guided methods to be compared within a common guidance protocol.

Dragon-family information had two temporally different roles in the implemented variants. Dragon initialization was applied once before the iterative search and determined the initial spatial arrangement of the swarm. Stagnation-triggered dragon perturbation was applied conditionally during the iterative search and modified selected particles only after the global best fitness had remained within the defined improvement tolerance for the specified stagnation period. The initialization component therefore affected the starting population, whereas the perturbation component acted as a later diversity-restoration step. Since both components were used together in all dragon-guided variants, the present experiments do not estimate their separate effect sizes or identify either component as the dominant source of the observed results.

2.4. Wrapper Feature Selection Protocol

In the Cleveland experiments, the FS problem was defined as a wrapper-based optimization problem in which each candidate solution is evaluated as a binary feature mask. This definition is based on the wrapper FS approach, where feature subsets are evaluated through classifier performance (Lee and Zhuo, 2021; Xie et al., 2021). In this study, the continuous position vector generated by the optimizer was first converted into FS scores and then into a binary mask, as shown in equations 52 and 53.

$$r_{i,j} = \sigma\left(x_{i,j}\right) = \frac{1}{1+e^{-x_{i,j}}} \tag{52}$$

$$z_{i,j} = \begin{cases} 1, & r_{i,j} \geq \theta_b \\ 0, & r_{i,j} < \theta_b \end{cases} \tag{53}$$

In equation 52, $x_{i,j}$ denotes the continuous position value produced by the i-th candidate solution for the j-th feature, and $r_{i,j}$ denotes the selection score obtained by sigmoid transformation. In equation 53, θ_b denotes the binary threshold value, and $z_{i,j}$ denotes the binary mask component indicating whether the relevant feature is selected. When $z_{i,j} = 1$, the j-th feature is included in the

classification model. When $z_{i,j} = 0$, it is excluded. This transformation connects the continuous PSO and QI-PSO search space to the binary mask space in the Cleveland FS problem. Since classifier training cannot be performed when no feature is selected, when an empty mask occurs, the feature with the highest selection score is selected by default. This operation, performed through equations 54 and 55, is a control step that ensures the wrapper evaluation process operates with a valid feature subset.

$$j^* = arg \max_{j=1,2,\dots,m} r_{i,j} \tag{54}$$

$$z_{i,j^*} = 1 \ if \ \sum_{j=1}^{m} z_{i,j} = 0 \tag{55}$$

In equation 54, j^* denotes the index of the feature with the highest selection score, and m denotes the total number of features. Equation 55 ensures that the feature with index j^* is included in the binary mask when the candidate solution selects no feature. Thus, each candidate solution produced by the optimizer is converted into a valid feature subset that can be evaluated by the wrapper classifier. The feature subset selected by each binary mask was defined as shown in equation 56.

$$S_i = \{j \mid z_{i,j} = 1, \ j = 1, 2, \dots, m\} \tag{56}$$

In equation 56, S_i denotes the set of feature indices selected by the i-th candidate solution. This set is the feature subset used for wrapper classifier training and fitness calculation.

The target variable in the Cleveland dataset was used according to the binary class definition given in Section 2.1.2. Therefore, in the wrapper FS protocol, each feature subset generated by the optimizer was evaluated through a two-class classification task separating the presence and absence of heart disease. Since FS based heart disease classification studies on the Cleveland dataset exist, the KNN and SVM evaluation protocol in this section was established on an experimental setting comparable to this literature (Wadhawan and Maini, 2022; Noroozi et al., 2023; Asha and Ramya, 2025).

In each wrapper evaluation, missing value imputation and standardization were conducted within the cross validation process. Thus, preprocessing statistics were learned only from the relevant training fold, and the validation fold was evaluated with the same transformation. In SVM based FS studies conducted on the Cleveland dataset, normalization is used as part of the classification protocol (Asha and Ramya, 2025). In this study, preprocessing steps were learned from the training data within each fold, as shown in equations 57 and 58, and the same transformation was applied to the validation data.

$$x_{n,j}^{*,k} = \begin{cases} x_{n,j}, & if \ x_{n,j} \ is \ observed \\ median_j^{train,k}, & if \ x_{n,j} \ is \ missing \end{cases} \tag{57}$$

$$\tilde{x}_{n,j}^{k} = \frac{x_{n,j}^{*,k} - \mu_j^{train,k}}{\sigma_j^{train,k}} \tag{58}$$

In equation 57, $x_{n,j}^{*,k}$ denotes the feature value obtained after missing value imputation in the k-th fold evaluation, and $median_j^{train,k}$ denotes the median value calculated on the relevant training fold. In equation 58, $\mu_j^{train,k}$ and $\sigma_j^{train,k}$ denote the mean and standard deviation of the relevant feature calculated on the training fold, and $\tilde{x}_{n,j}^{k}$ denotes the feature value after standardization. This operation was applied to prevent variable scales from disproportionately affecting the decision process, especially in classifiers sensitive to feature scale such as KNN and SVM.

The KNN classifier was used as the main classifier in the wrapper fitness calculation. The use of the KNN family together with binary PSO-based FS shows that a distance based classifier can be used in wrapper FS evaluations (Li et al., 2023). In this study, KNN was defined as the wrapper classifier that calculates the fitness function inside the optimizer under fixed classification settings. Since cross validation on the Cleveland dataset is used as a protocol for fold based evaluation of classification performance in heart disease prediction studies (Deepika and Balaji, 2022), each candidate feature subset in this study was evaluated by stratified k-fold cross validation, as shown in equation 59.

$$D = \bigcup_{k=1}^{K_{CV}} D^{(k)} \tag{59}$$

In equation 59, D denotes the Cleveland dataset, $D^{(k)}$ denotes the k-th fold partition, and K_{CV} denotes the number of cross validation folds. Stratified partitioning preserves class distribution within each fold and reduces the excessive effect of class imbalance on balanced accuracy calculation. For each candidate feature subset, the KNN classifier was trained on cross validation folds and the balanced accuracy value was calculated, as shown in equations 60 and 61.

$$BA_i^{(k)} = \frac{1}{2}\left(\frac{TP_i^{(k)}}{TP_i^{(k)} + FN_i^{(k)}} + \frac{TN_i^{(k)}}{TN_i^{(k)} + FP_i^{(k)}}\right) \tag{60}$$

$$BA_i = \frac{1}{K_{CV}} \sum_{k=1}^{K_{CV}} BA_i^{(k)} \tag{61}$$

In equation 60, $BA_i^{(k)}$ denotes the balanced accuracy value obtained on the k-th fold for the i-th candidate feature subset, $TP_i^{(k)}$ denotes the number of true positives, $TN_i^{(k)}$ denotes the number of true negatives, $FP_i^{(k)}$ denotes the number of false positives, and $FN_i^{(k)}$ denotes the number of false negatives. Equation 61 produces BA_i by averaging the fold based balanced accuracy values. Balanced accuracy was used as the main classification component of the fitness calculation in the Cleveland binary classification setting because it jointly considers positive and negative class performance.

Because a candidate feature subset in wrapper FS is evaluated through classifier performance and subset size, the fitness function was constructed with two components (Lee and Zhuo, 2021; Xie et al., 2021; Li et al., 2023). In this study, the selected feature ratio was defined in equation 62, and balanced-accuracy loss was

combined with this ratio in the wrapper fitness function in equation 63.

$$\phi_i = \frac{|S_i|}{m} \quad (62)$$

$$F_i^{FS} = \alpha(1 - BA_i) + (1 - \alpha)\phi_i \quad (63)$$

In equation 62, $|S_i|$ denotes the number of features selected by the i-th candidate solution, m denotes the total number of features, and ϕ_i denotes the selected feature ratio. In equation 63, F_i^{FS} denotes the wrapper FS fitness value, α denotes the weight assigned to balanced-accuracy loss, and $1 - BA_i$ denotes balanced-accuracy loss. Therefore, an increase in BA_i decreases F_i^{FS}, whereas an increase in ϕ_i increases F_i^{FS}. Thus, candidate solutions that produce high classification performance and a more compact feature subset receive lower fitness values.

In the wrapper FS process, the continuous optimizer position is converted into a binary feature mask, and the selected feature subset is transferred to the cross validation based wrapper evaluation protocol. As a result of this evaluation, the fitness value is calculated using balanced accuracy and selected feature ratio together, while the optimizer searches for feature subsets that minimize this value. The general flow of the wrapper FS protocol used in the Cleveland experiments is given in Figure 2. The flow shown in Figure 2 summarizes the connection between continuous optimizer position and binary feature subset evaluation. The sigmoid transformation and threshold operation generate the feature mask. Empty mask correction ensures that each candidate solution produces a valid feature subset. The selected subset is passed through preprocessing and KNN wrapper evaluation steps within cross validation, and the fitness value is calculated with balanced accuracy loss and selected feature ratio components. After wrapper optimization is completed, the selected feature subsets are also evaluated through KNN and SVM outputs.

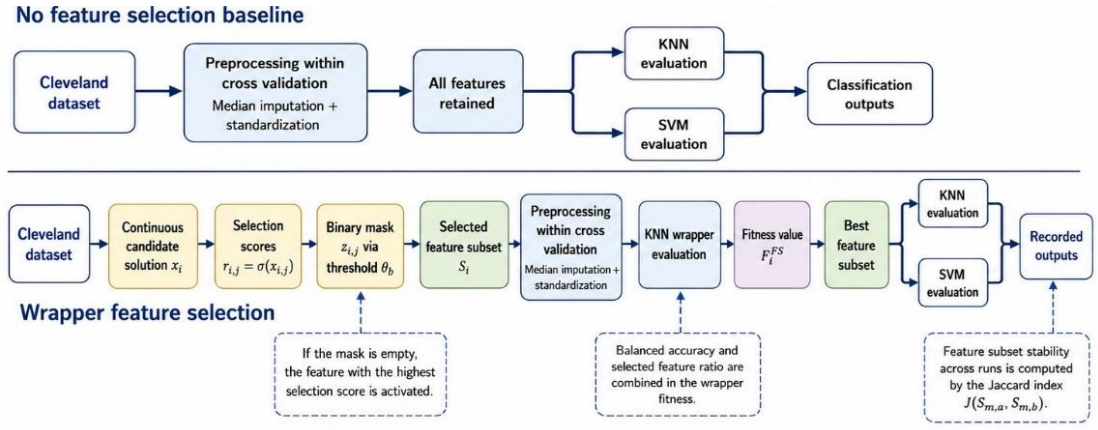


Figure 2. Wrapper feature selection protocol for the Cleveland structure.

The no-FS baseline was defined through the reference mask in which all features are selected. This reference allows the feature subsets obtained through wrapper FS to be compared with the use of all features in terms of classification performance and selected feature count. In FS based cardiovascular disease classification studies conducted on the Cleveland dataset, selected feature subsets are reported together with classifier performance (Noroozi et al., 2023; Asha and Ramya, 2025). Therefore, in this study, the no-FS baseline was defined in equations 64 and 65 as a separate reference evaluation for interpreting wrapper FS results.

$$z^{all} = (1,1,\dots,1) \quad (64)$$

$$S^{all} = (1,2,\dots,m) \quad (65)$$

In equation 64, z^{all} denotes the all feature mask used for the no-FS baseline, and in equation 65, S^{all} denotes the reference feature set in which all features are included. No optimizer was run for this baseline, and the KNN and SVM classifiers were evaluated directly using all features. The best feature mask obtained for each algorithm variant after wrapper optimization was first evaluated using the KNN classifier used in the fitness calculation, and then the same feature subset was retested with the SVM classifier. This second evaluation was used to report the classification output produced by the selected feature subsets under fixed SVM settings. Since FS and SVM based cardiovascular disease classification studies exist on the Cleveland dataset, SVM outputs were reported as an additional classifier evaluation (Noroozi et al., 2023; Asha and Ramya, 2025).

This evaluation structure is shown in equations 66 and 67.

$$\hat{y}_n^{KNN} = C_{KNN}(\tilde{x}_{n,S_i}) \quad (66)$$

$$\hat{y}_n^{SVM} = C_{SVM}(\tilde{x}_{n,S_i}) \quad (67)$$

In equation 66, C_{KNN} denotes the KNN classifier and $\hat{y}_n^{KNN}$ denotes the prediction produced by KNN. In equation 67, C_{SVM} denotes the SVM classifier structure and $\hat{y}_n^{SVM}$ denotes the prediction produced by SVM. $\tilde{x}_{n,S_i}$ is the standardized n-th sample represented by the features selected by S_i. KNN results provide the main evaluation output directly related to wrapper fitness, whereas SVM results are used to show how the selected

feature subsets behave under a second classifier.

FS stability refers to the consistency shown by selected feature subsets against data resampling and the stochastic search process (Nogueira et al., 2017). At the end of each run, the selected feature mask, selected feature count, selected feature ratio, and FS scores were recorded. Since each binary mask in this study was interpreted as an unordered set of feature indices, the similarity between two feature subsets (S_a and S_b) produced by the same method in independent runs was calculated through the Jaccard index, as shown in equations 68 and 69 (Alelyani, 2021).

$$J(S_a,S_b) = \frac{|S_a \cap S_b|}{|S_a \cup S_b|} \tag{68}$$

$$Stability_h = \frac{2}{R(R-1)} \sum_{a=1}^{R-1} \sum_{b=a+1}^{R} J(S_{h,a}, S_{h,b}) \tag{69}$$

In equation 68, $J(S_a,S_b)$ denotes Jaccard similarity between two feature subsets. In equation 69, $Stability_h$ denotes the average feature subset stability for method h, R denotes the number of independent runs, and $S_{h,a}$ and $S_{h,b}$ denote the feature subsets selected by the same method in different runs. In addition, equation 69 averages the Jaccard similarities over all run pairs belonging to the same method. Therefore, $Stability_h$ summarizes the degree to which the relevant method produces similar feature subsets across different runs.

This protocol separates the KNN-based wrapper objective from the additional SVM-based classifier evaluation while keeping the same selected feature subsets for both assessments. KNN outputs were treated as the main evaluation output related to the wrapper objective, whereas SVM outputs were treated as an additional classifier evaluation outside the optimizer. Since selected subsets in FS studies are evaluated through classifier performance and reported with different classifier structures, this distinction keeps wrapper fitness and additional classifier evaluation separate within the same protocol (Alelyani, 2021; Lee and Zhuo, 2021; Xie et al., 2021; Asha and Ramya, 2025).

2.5. Experimental System Design

The experimental system was designed to run the CEC 2022 benchmark experiments and the UCI Cleveland Heart Disease experiments with common algorithm variants. The CEC 2022 experiments were used to evaluate continuous optimization behavior, whereas the Cleveland experiments were used to evaluate wrapper-based FS outputs. The general experimental flow is given in Figure 3.

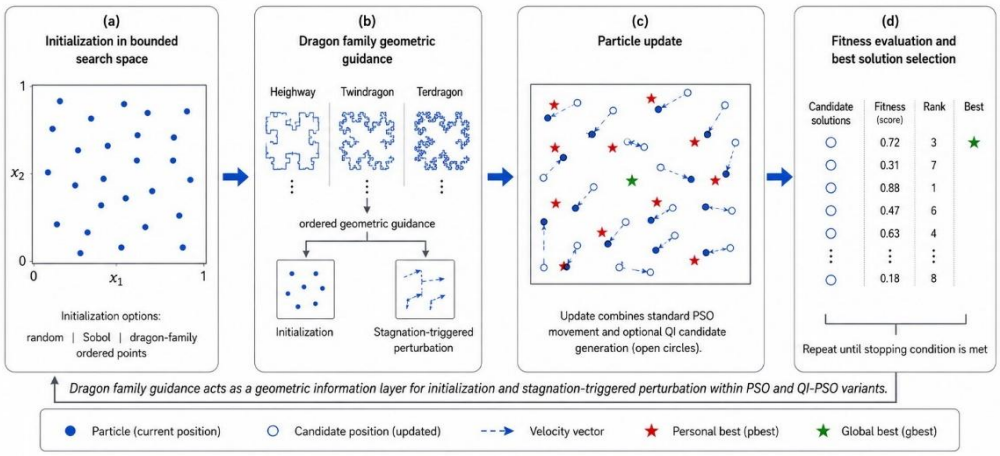


Figure 3. Proposed experimental optimization framework.

The Figure 3 presents the shared procedure of the compared variants in four parts. In step a, the initial population is generated within the bounded search space by using random, Sobol, or dragon-family-based ordered points. In step b, Heighway, Twindragon, and Terdragon information is introduced as a geometric source. In the dragon-guided variants, this information is used both during initialization and during stagnation-triggered direction-based perturbation. In step c, particle positions are updated through the PSO movement equations using personal best and global best information. The QI-PSO variants also generate additional QI candidates at this stage. In step d, all candidate solutions are evaluated according to their fitness values, ranked, and compared with the current personal and global best solutions. The search cycle is repeated until the stopping condition is met. The complete algorithmic sequence summarized in Figure 3 is provided as pseudocode in Supplementary Algorithm S1. In this process, the dragon-family component acts as an added geometric guidance source within PSO and QI-PSO rather than as a separate optimizer. The variants included in this flow were organized into PSO and QI-PSO families. In each family, random, Sobol, and variants based on the Heighway dragon, Twindragon, and Terdragon were used. This arrangement makes it possible to compare the effects of initialization type, dragon guidance, and QI candidate generation under the same experimental protocol. The comparison structure is given in Figure 4. Figure 4 shows the experimental grouping of the compared PSO and QI-PSO variants. In the PSO variants, particle movement depends on personal best and global best information (Kennedy and Eberhart, 1995; Clerc and Kennedy, 2002). In the QI-PSO variants, a quantum angle, rotation, and

mutation based candidate generation structure is used in addition to classical swarm memory (Balicki, 2022; Agrawal and Panda, 2025; Naik et al., 2025).

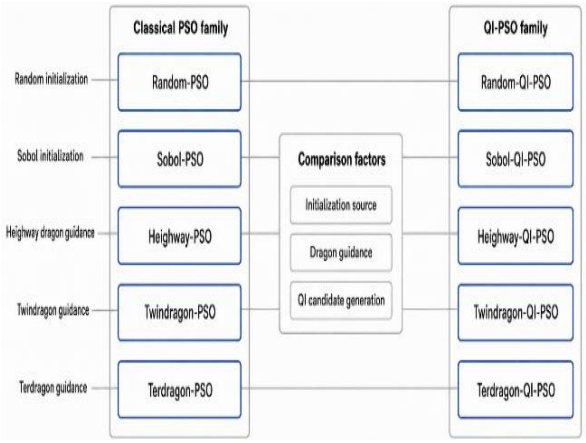


Figure 4. Compared algorithm variants and family-level grouping.

The differences in initialization, dragon guidance, and QI candidate generation between the variants are given in Table 1. The structure given in Table 1 was used to test the same initialization and guidance sources in classical PSO and QI-PSO. Random initialization represents baseline initialization behavior. Sobol initialization was used as the low discrepancy based initialization comparison (Li et al., 2023). Since low-discrepancy-sequence-based initialization can affect diversity and convergence, initialization type was treated as a separate experimental variable (Bangyal et al., 2021). Heighway dragon, Twindragon, and Terdragon variants were used to compare the effect of dragon family geometric guidance on classical and QI based swarm behavior (Ngai and Nguyen, 2003; Phan et al., 2025).

In the Cleveland experiments, no-FS baseline and wrapper FS results were produced within the same preprocessing and classifier evaluation protocol. Thus, the reference condition in which all features were used and the feature subsets selected by the optimizer were compared with the same metrics. The wrapper FS and classification evaluation framework is given in Figure 5.

Table 1. Compared algorithm variants and their initialization, guidance, and QI components

Algorithm Family	Variant	Initialization and Guidance Structure	QI Component
Classical PSO	Random-PSO	Uniform random initialization	No
Classical PSO	Sobol-PSO	Sobol sequence initialization	No
Classical PSO	Heighway-PSO	Heighway dragon initialization and stagnation triggered perturbation	No
Classical PSO	Twindragon-PSO	Twindragon initialization and stagnation triggered perturbation	No
Classical PSO	Terdragon-PSO	Terdragon initialization and stagnation triggered perturbation	No
QI-PSO	Random-QI-PSO	Uniform random initialization	Yes
QI-PSO	Sobol-QI-PSO	Sobol sequence initialization	Yes
QI-PSO	Heighway-QI-PSO	Heighway dragon initialization and stagnation triggered perturbation	Yes
QI-PSO	Twindragon-QI-PSO	Twindragon initialization and stagnation triggered perturbation	Yes
QI-PSO	Terdragon-QI-PSO	Terdragon initialization and stagnation triggered perturbation	Yes

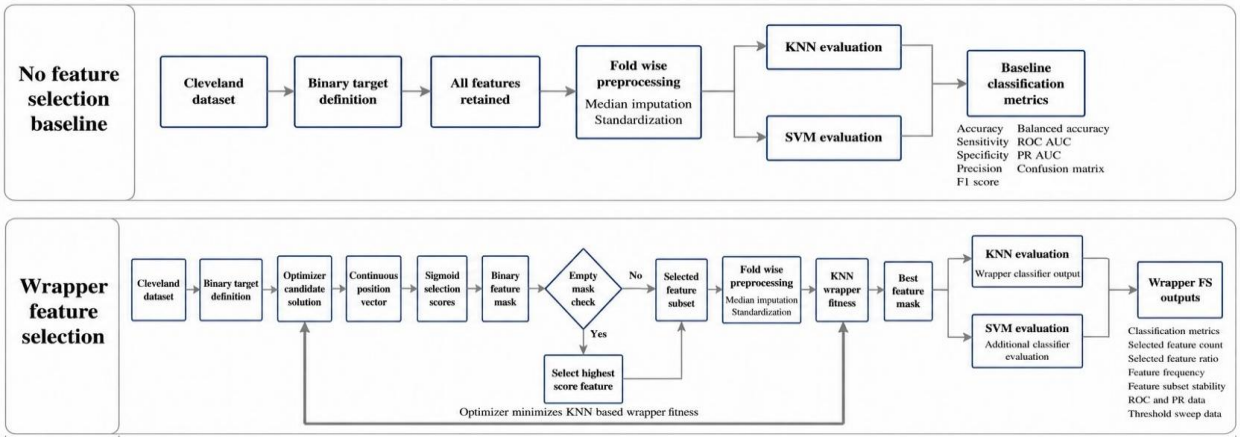


Figure 5. Wrapper feature selection and classification evaluation structure.

In Figure 5, the upper part shows the no-FS baseline section, and the lower part shows the wrapper FS section. In the no-FS baseline, all features were retained and the KNN and SVM classifiers were evaluated directly using all features. In the wrapper FS protocol, the optimizer generated a binary feature mask, the selected feature subset entered the KNN based fitness calculation, and the best subset obtained was also evaluated with SVM. This evaluation distinction was established based on the wrapper fitness and additional classifier evaluation protocol given in Section 2.4 (Lee and Zhuo, 2021; Xie et al., 2021; Asha and Ramya, 2025).

The common system settings used in the experiments are given in Table 2.

The settings in Table 2 were kept fixed so that differences among algorithm variants were not driven by the number of independent runs, swarm size, or optimizer budget. The number of independent runs and the swarm size were the same in the CEC 2022 and Cleveland wrapper FS experiments.

Table 2. Common experimental system settings

Parameter	Value	Experiment
Number of independent runs	50	CEC and Cleveland
Swarm size	50	CEC and Cleveland
CEC function evaluation budget	200000 for D=10 and 1000000 for D=20	CEC
Effective CEC iteration count	$\lceil (MaxFEs - SS)/SS \rceil$	CEC
Cleveland optimizer iteration count	50	Cleveland
Cleveland cross-validation fold count	5	Cleveland
Random seed logging	Yes	CEC and Cleveland

In the CEC 2022 experiments, the computational budget was defined by a dimension-dependent maximum number of function evaluations rather than by a fixed iteration count. The effective CEC iteration count was calculated from the *MaxFEs* value after the initial swarm evaluation. This budget structure was determined according to the fixed-function evaluation logic used in CEC benchmarking studies (Stanovov et al., 2024; Lin et al., 2025). In the Cleveland wrapper FS experiments, the optimizer iteration count was fixed at 50. Since wrapper FS cost depends on population size, iteration budget, and classifier evaluation, using the same swarm size and optimizer iteration count kept the wrapper FS comparison computationally balanced across variants (Xie et al., 2021). Each candidate feature subset was evaluated using stratified five-fold cross-validation (Deepika and Balaji, 2022).

The same inertia weight and acceleration coefficients were used in all PSO and QI-PSO variants. This choice fixed the parameter difference arising from the PSO movement equation and allowed the comparison to be conducted through initialization, QI candidate generation, and dragon guidance structures. PSO parameters are given in Table 3.

Table 3. PSO parameters

Parameter	Value	Role
w_{max}	0.90	Initial inertia weight
w_{min}	0.40	Final inertia weight
c_1	1.49	Cognitive acceleration coefficient
c_2	1.49	Social acceleration coefficient
ρ	0.20	Velocity clamp ratio

The inertia weight interval and acceleration coefficients in Table 3 were selected at the same level as the experimental settings in a PSO-based low discrepancy initialization study (Bangyal et al., 2021). The velocity clamp ratio was used to relate velocity magnitude to the width of the problem bounds. This constraint reduces excessively large particle displacements in a single iteration relative to the search boundary scale.

In QI-PSO variants, the classical PSO candidate and the QI candidate were used together within the same update chain. Quantum angle, quantum rotation, qubit dynamics, and adaptive mutation components are used in the QI-PSO literature for population diversity and candidate generation (Balicki, 2022; Agrawal and Panda, 2025; Naik et al., 2025). QI-PSO parameters are given in Table 4.

Table 4. QI-PSO parameters

Parameter	Value	Role
α_q	0.035	Quantum angle update coefficient
μ	0.35	Quantum mixing coefficient
p_m	0.03	Mutation probability
σ_m	0.04	Mutation scale

The parameters in Table 4 were fixed so that the QI candidate generation component was applied with the same settings in all QI based variants. αq determines the angle update magnitude, μ regulates the contribution ratio between classical and QI candidates, and p_m and σ_m control mutation probability and mutation magnitude. Therefore, QI-PSO variants were compared through the initialization and dragon guidance structures used under common QI settings. The same dragon order, perturbation probability, step scale, decay coefficient, and stagnation threshold values were used in the dragon guided variants. These settings were fixed to compare the Heighway dragon, Twindragon, and Terdragon curves under the same perturbation protocol. The geometric basis for the dragon family is the relationship between the Heighway dragon and the Twindragon and the treatment of the Heighway dragon, Twindragon, and

Terdragon as fractal dragon structures (Ngai and Nguyen, 2003; Phan et al., 2025). Dragon guidance parameters are given in Table 5. The parameters in Table 5 were fixed so that the dragon guidance component was applied with the same perturbation protocol in all dragon variants. Thus, the Heighway dragon, Twindragon, and Terdragon variants were compared under common guidance settings.

Table 5. Dragon family guidance parameters

Parameter	Value	Role
Dragon order	11	Dragon curve generation level
p_D	0.25	Probability of perturbing a particle
η_0	0.035	Initial dragon step scale
δ	0.98	Dragon step decay coefficient
S_{max}	8	Stagnation counter threshold

The wrapper FS and classifier settings used in the Cleveland experiments are given in Table 6. These settings were used so that the no-FS baseline and wrapper FS results were evaluated under the same preprocessing, cross validation, and classifier protocol.

Table 6. Cleveland wrapper FS and classifier settings

Component	Setting	Value
Cross validation	Number of folds	5
Wrapper fitness	α	0.99
Binary mask generation	Threshold	0.50
KNN	k	5
KNN	Weight	Uniform
KNN	Metric	Minkowski
KNN	p	2
SVM	Kernel	RBF
SVM	C	1.0
SVM	γ	scale
SVM	Probability output	True
Preprocessing	Missing value handling	Median imputation
Preprocessing	Scaling	Standardization

The settings in Table 6 were used so that the no-FS baseline and wrapper FS results were evaluated under the same preprocessing, cross-validation, and classifier protocol. The wrapper fitness weight is given as $\alpha = 0.99$. This value was used to keep classification loss as the dominant component of the fitness calculation while retaining a small penalty for the selected feature ratio. These two components were used in the fitness calculation as reported in wrapper-based FS studies, where classification error or accuracy is combined with selected feature count or selected feature ratio (Wadhawan and Maini, 2022; Li et al., 2023; Seghir et al., 2023; Asha and Ramya, 2025). KNN weight, metric, and p values were fixed so that all wrapper FS variants were evaluated with the same classifier settings. The KNN wrapper fitness calculation is associated with the FS protocol based on classifier performance defined in Section 2.4 (Lee and Zhuo, 2021; Xie et al., 2021). SVM settings were used for the additional classifier evaluation protocol defined in the same section. Since FS and SVM-based cardiovascular disease classification studies exist on the Cleveland dataset, additional classifier outputs of the selected feature subsets were also reported through SVM (Asha and Ramya, 2025). Preprocessing steps consisted of median imputation and standardization and were applied within the cross-validation process.

Experimental outputs were recorded in separate result files for the CEC 2022 and Cleveland experiments. For the CEC 2022 experiments, the recorded outputs included the optimization results, convergence summaries, runtime information, ranking outputs, and statistical comparison results reported in the study. For the Cleveland experiments, the recorded outputs included the classification results, selected feature masks, selection frequency information, feature subset stability values, and statistical comparison results reported in the study. The experiments were performed in Python 3.12 using the scikit-learn environment on a Windows 10 computer with an Intel Core i7 2.30 GHz processor and 16 GB RAM.

2.6. Evaluation Metrics and Statistical Analysis

The evaluation procedure was based on two metric groups because the CEC 2022 continuous optimization experiments and the Cleveland wrapper FS experiments produced different output types. In the CEC 2022 experiments, each candidate solution was evaluated by a continuous objective function value, and final fitness was taken as the main output. In the Cleveland experiments, the optimizer produced a binary feature mask and a selected feature subset. For this reason, classifier predictions, feature subset compactness, and feature subset stability were evaluated together. Thus, the CEC 2022 experiments were evaluated through solution quality, convergence behavior, and computational cost, whereas the Cleveland experiments were evaluated through classification performance, subset size, and subset consistency. This two-part evaluation structure was implemented as reported in CEC-based optimization studies and wrapper FS studies where the final solution quality, convergence behavior, statistical comparison, classifier output, and selected subset features are evaluated together (Xie et al., 2021; Noroozi et al., 2023; Pathak et al., 2024; Agrawal and Panda, 2025).

In the CEC 2022 experiments, each algorithm variant was evaluated over independent runs for each benchmark function and dimension setting. The final fitness value obtained at the end of each run was used as the main optimization output. The run-level final fitness distribution was summarized using mean, median, standard deviation, best, and worst statistics. At the function-dimension level, best mean fitness records were

determined according to the minimum mean final fitness value among the methods. A single-method best record was counted when only one method produced the minimum mean final fitness value under the relevant function-dimension condition. If more than one method obtained the same minimum mean final fitness value under the same function-dimension condition, the condition was treated as a tied best record and was not included in the single-method record count. Thus, instead of representing the result of a single run, a representation of the distribution of results produced by the same algorithm variant under independent runs is obtained (Pathak et al., 2024; Agrawal and Panda, 2025).

Since the CEC 2022 benchmark functions were treated as minimization problems, lower final fitness values indicated better optimization performance. In minimization-based continuous optimization, the objective function is treated as a cost function, and a new candidate solution is accepted when it reduces the cost value (Storn and Price, 1997). In the CEC 2022 reporting context, lower error or fitness values are also interpreted as better optimization results (Agrawal and Panda, 2025). Therefore, methods were ordered from the lowest to the highest mean final fitness within each function-dimension condition. Rank 1 was assigned to the method with the lowest mean final fitness, and larger rank values indicated lower relative performance within the same condition. Biedrzycki (2024) reported that ranking criteria and parameter tuning can affect CEC 2022 rank outcomes. For this reason, the rank values in this study were used as protocol-level comparative summaries and were evaluated together with final fitness, convergence, runtime, and statistical test results.

In addition to method-level summaries, CEC 2022 outputs were aggregated at the algorithm family level to compare Classical PSO, Dragon-guided PSO, QI-PSO, and Dragon-guided QI-PSO groups under the same evaluation dimensions. CEC family-level summaries were calculated from method-level outputs using average rank, rank 1 count, and average mean fitness. Runtime outputs were also reported at the method-level and family level using average runtime, runtime per evaluation, and evaluations per second. These outputs were included to evaluate whether solution quality differences were accompanied by different computational cost patterns.

The convergence trace was obtained by recording how the best fitness value changed during the search process. Global convergence traces were calculated by aggregating these run-level trajectories across independent runs and function-dimension conditions. Mean and median best fitness values were then reported at selected progress percentages to show how the final fitness value was reached. Normalized convergence area was calculated as a supplementary scalar measure of cumulative convergence behavior, but it was not used as a substitute for final fitness. Runtime per evaluation, evaluations per second, and total runtime were reported so that solution quality could be evaluated together with computational cost. Thus, methods with similar final fitness values became comparable in terms of convergence trajectory and runtime. Recent CEC 2022 optimizer studies also report convergence and statistical outputs together with final benchmark statistics, so these complementary outputs were included in this study (Pathak et al., 2024; Agrawal and Panda, 2025).

Statistical comparison among methods was performed using paired run results obtained under the same benchmark condition. Since the methods used in this study were stochastic optimizers, the comparison was made over run-level paired results rather than a single final value. For this reason, pairwise Wilcoxon signed-rank tests were applied to the final fitness values within each CEC 2022 function-dimension condition because this test compares paired observations without assuming normality (Derrac et al., 2011; Agrawal and Panda, 2025). Within each function-dimension condition, 45 pairwise method comparisons were made among 10 methods, producing 1080 pairwise comparisons across 12 functions and two dimension settings. The n_{pairs} value indicated the number of paired independent run observations used in each Wilcoxon signed-rank comparison. The basic significance threshold was set as $P<0.05$. Raw P values obtained from the Wilcoxon signed-rank test were not interpreted alone because multiple method pairs were tested within the same metric family. For each comparison, raw P value, Holm-corrected P value, and significance status were reported together. Holm correction was used to control the multiple-comparison effect after pairwise Wilcoxon testing (Holm, 1979; Derrac et al., 2011). Comparisons with Holm-corrected $P<0.05$ were accepted as statistically significant after multiple-comparison correction. Comparisons with raw $P<0.05$ but Holm-corrected $P \geq 0.05$ were treated as significant only at the uncorrected level and were not accepted as final statistical differences.

For CEC 2022, statistical comparison outputs were summarized at four levels in this study. This structure was used because pairwise Wilcoxon results and Holm-corrected significance decisions produce many comparison records across methods, functions, dimensions, and algorithm families. Nonparametric statistical testing and Holm correction are commonly used together in evolutionary and swarm intelligence comparisons, and recent CEC 2022 optimizer studies also report Wilcoxon signed-rank, Friedman, and Holm-based statistical outputs (Holm, 1979; Derrac et al., 2011; Agrawal and Panda, 2025). The comparison-set level summarized all pairwise comparisons, PSO-only comparisons, and QI-PSO-only comparisons. The function-dimension level showed how Holm-corrected significant comparisons were distributed across benchmark conditions. The method-level direction summary counted how many times each method appeared on the lower mean fitness side or the higher mean fitness side within Holm-corrected significant

comparisons. Since CEC 2022 was treated as a minimization setting, lower mean fitness was taken as the better direction (Wang et al., 2024). The family-pair level showed whether significant comparisons were concentrated between algorithm families or within the same family. Since CEC 2022 ranking results can change with the ranking criterion and parameter tuning, these summaries were interpreted as evaluation-specific statistical profiles rather than absolute superiority statements (Biedrzycki, 2024). If all paired run differences were zero in the Wilcoxon signed-rank test, or if valid nonzero differences were not available for comparison-rank calculation, P value was not calculated. This case was marked as an empty P value in the statistical comparison tables.

In the Cleveland experiments, the target variable was converted into a binary classification structure, and classifier outputs were evaluated through confusion matrix components and probability-based metrics. Accuracy, sensitivity, specificity, precision, F1 score, Matthews correlation coefficient, balanced accuracy, ROC AUC, and PR AUC values were reported. This metric set was used because heart disease and Cleveland FS studies commonly report confusion-matrix-based and probability-based outputs together, including sensitivity, specificity, precision, F1 score, MCC, ROC area, PRC, and related confusion matrix components, rather than accuracy alone (Deepika and Balaji, 2022; Gupta et al., 2022; Wadhawan and Maini, 2022; Noroozi et al., 2023; Asha and Ramya, 2025). Accuracy denotes the overall correct classification rate. Sensitivity denotes the correct recognition rate for the positive class. Specificity denotes the correct recognition rate for the negative class. Precision denotes the correctness rate of positive predictions. F1 score was used as the harmonic mean of precision and sensitivity. MCC was given as an additional confusion-matrix-based balance metric because it uses all TP, TN, FP, and FN components in the same evaluation. Balanced accuracy was used as the main classification metric because it uses sensitivity and specificity together in a single class-balanced measure (Rashed et al., 2025). ROC AUC summarized discrimination behavior across different threshold levels using probability output values. PR AUC summarized the precision and recall relationship and showed positive-class performance behavior under threshold changes. Threshold-dependent F1 analysis was performed to examine how F1 score changed across probability threshold values.

The no-FS baseline results and the highest wrapper FS results were summarized separately for KNN and SVM. Cleveland balanced accuracy pairwise Wilcoxon comparisons were summarized across KNN and SVM evaluation settings. The all-pairwise comparison set contained 90 comparisons across classifier settings. Cross-validation aggregate confusion matrices were obtained from out-of-fold prediction records. The no-FS baseline confusion matrices were produced from the baseline classifier evaluation, while wrapper FS confusion matrices were summarized across independent wrapper FS runs. Because FS can change its classification effect depending on the classifier used, KNN and SVM outputs were not pooled into a single classifier-independent result. Each classifier was treated as a separate evaluation setting because Cleveland Heart Disease FS studies evaluate FS effects across multiple classifiers rather than through a single pooled classifier result (Noroozi et al., 2023).

Each wrapper FS run was evaluated through classifier performance and selected subset structure. The optimizer produced a binary feature mask, which was converted into selected feature count, selected feature ratio, feature reduction ratio, feature subset stability, and selection frequency. These outputs were recorded together with classification metrics because wrapper FS determines both the prediction result and the feature set used by the classifier. Selected feature ratio was calculated as the number of selected features divided by the total number of features. Feature reduction ratio was calculated as one minus this ratio and represented the removed part of the no-FS feature set. Selected feature count, selected feature ratio, and feature reduction ratio were used as compactness outputs, while feature subset stability and selection frequency were used to examine subset repeatability and recurrent variables. Since FS quality can be evaluated through classification performance, subset size, computational cost, and stability, prediction and subset outputs were reported together (Nogueira et al., 2017; Alelyani, 2021; Xie et al., 2021). Wrapper FS convergence profiles were also recorded to show how the FS objective changed during the search process. At the same classification performance level, lower selected feature count and lower selected feature ratio were interpreted as a more compact feature subset. In the wrapper search, each candidate feature mask required a single fitness value. This fitness value was calculated with KNN so that all optimizer variants selected their subsets under the same classifier based objective. For this reason, KNN results were reported as the classification outputs directly linked to the wrapper search. SVM was not used during subset search. After the search was completed, the same selected masks were evaluated with SVM without changing the selected subsets. This allowed the study to examine whether subsets selected under the KNN objective produced similar or different classification behavior under another classifier. KNN was used as the classifier component of the wrapper objective because Khan et al. (2024) used KNN to evaluate selected feature subsets in a heart disease FS setting (Khan et al., 2024). Therefore, SVM results were treated as an additional classifier evaluation, not as a second optimization objective. This separation was used because Cleveland Heart Disease FS results can change according to the classifier used in the evaluation (Noroozi et al., 2023).

Pairwise Jaccard similarity was calculated between selected feature subsets obtained from independent

wrapper FS runs. For each method, 50 selected feature subsets obtained from independent wrapper FS runs were used in the pairwise Jaccard similarity calculation, producing 1225 pairwise subset comparisons per method. Feature subset stability was measured using pairwise Jaccard similarity because this measure can be applied directly to mask-based FS output. Under binary feature subset representation, Jaccard similarity uses the ratio of common selected features between two subsets to their union set. Feature subset stability was reported as a separate reliability output apart from classification performance. This allowed the study to measure how similar the selected subsets remained across independent runs (Nogueira et al., 2017; Alelyani, 2021).

Selection frequency was calculated to summarize feature-level recurrence within repeated selected subsets. Aggregate selection frequency was calculated across 500 wrapper FS outputs obtained from 10 methods and 50 independent runs per method. For each feature, total selected count indicates how many times the corresponding feature was selected across all wrapper FS outputs. In addition, method-specific selection frequency values were summarized using mean, standard deviation, median, min-max, and Q1-Q3 values to show feature-level recurrence across optimizer variants. This summary was used to present feature-level recurrence at the distribution level and to distinguish frequently selected variables from variables whose selection depended more strongly on optimizer behavior (Łukaszuk and Krawczuk, 2024).

For cross-setting profile analysis, CEC 2022 and Cleveland wrapper FS outputs were summarized together at the method-level and family level. The method-level profile included CEC average rank, CEC single-method rank 1 count, and CEC runtime dimensions as CEC benchmark outputs, KNN balanced accuracy and SVM balanced accuracy as classifier-based wrapper FS outputs, and selected feature count and feature subset stability as feature subset outputs. The same evaluation dimensions were also aggregated at the algorithm family level. Since these outputs have different units and value ranges, z score transformation was used only to visualize the relative position of each method or family within each evaluation dimension (Asha and Ramya, 2025). Before z score transformation, lower-is-better dimensions were directionally transformed by multiplying CEC average rank, CEC runtime, and selected feature count by minus one. Balanced accuracy and feature subset stability were kept in their original direction. Z score transformation was then applied separately within each evaluation dimension. With this procedure, higher displayed z scores indicate more favorable relative positions in all heatmap columns. The original metric values were also reported in the numerical summary tables.

3. Results

This section reports the experimental outputs obtained from the CEC 2022 continuous optimization experiments and the UCI Cleveland Heart Disease wrapper FS experiments. In the CEC 2022 results, final fitness and rank are given as the main optimization outputs, whereas convergence trace, runtime, and pairwise statistical comparison are given as complementary outputs. In the Cleveland experiments, balanced accuracy is reported as the main classification metric, while ROC and PR curve outputs, threshold sweep, confusion matrix, selected feature count, selection frequency, feature subset stability, and method-level profiles across the KNN and SVM evaluations are reported as complementary evaluation outputs.

3.1. CEC 2022 Final Fitness and Rank Results

The method-level summary of CEC 2022 final fitness and rank results is given in Table 7. According to Table 7, the overall CEC 2022 ranking placed the PSO variants ahead of the QI-PSO variants. The lowest average rank was obtained by Random-PSO. It was followed by Heighway-PSO, Sobol-PSO, Terdragon-PSO, and Twindragon-PSO. These five methods formed the top five positions in the overall average rank ordering. QI-PSO variants were placed after the PSO variants in the average rank ordering. Among the QI-PSO variants, the lowest average rank was obtained by Terdragon-QI-PSO. It was followed by Twindragon-QI-PSO, Sobol-QI-PSO, Random-QI-PSO, and Heighway-QI-PSO. The average mean fitness ordering was not identical to the average rank ordering.

In terms of average mean fitness, the lowest value was produced by Terdragon-PSO. Twindragon-PSO, Random-PSO, Sobol-PSO, and Heighway-PSO produced close average mean fitness values among the PSO variants. The average mean fitness values of the QI-PSO variants remained above those of the PSO variants. Within this group, Twindragon-QI-PSO and Terdragon-QI-PSO produced the lowest average mean fitness values. For average median fitness, the PSO variants again remained ahead of the QI-PSO variants. Among the PSO variants, the lowest average median fitness was recorded for Sobol-PSO. Terdragon-PSO was the closest method to this value. Within the QI-PSO variants, the lowest average median fitness was obtained by Twindragon-QI-PSO.

Function-dimension-level best mean fitness records are given in Table 8. Table 8 shows that single-method best records were not concentrated in a single method. Heighway-PSO and Terdragon-PSO reached the highest single-method record count, with five records each. Sobol-PSO produced four single-method records, Random-PSO produced three, Terdragon-QI-PSO produced two, and Sobol-QI-PSO produced one. No single-method best mean fitness record was obtained for Twindragon-PSO, Random-QI-PSO, Heighway-QI-PSO, or Twindragon-QI-PSO. Tied best records were observed under F1-D10, F1-D20, F3-D10, and F11-D20. Best mean fitness records were distributed across different methods at the function level. Heighway-PSO produced single-

method records under F2-D20, F3-D20, F5-D10, F8-D10, and F8-D20. This method was also included in the tied records under F1-D10, F1-D20, and F3-D10. Sobol-PSO produced single-method records under F4-D10, F4-D20, F5-D20, and F7-D10. It was also included in the tied records under F1-D10, F1-D20, F3-D10, and F11-D20. Terdragon-PSO produced single-method records under F6-D10, F6-D20, F7-D20, F10-D10, and F11-D10. It was also included in the tied records under F1-D10, F1-D20, and F3-D10. Random-PSO produced single-method records under F10-D20, F12-D10, and F12-D20. It was also included in the tied records under F1-D10, F1-D20, F3-D10, and F11-D20. Twindragon-PSO did not produce a single-method record, but it was included in the tied records under F1-D10, F1-D20, and F3-D10. Records for the QI-PSO variants appeared under F2-D10, F9-D10, and F9-D20. The rank distribution of all methods at the function-dimension level is given in Figure 6.

Table 7. General CEC 2022 rank results

Method	Average Rank	Median Rank	Single-method rank 1 count	Average Mean Fitness	Average Median Fitness
Random-PSO	3.4375	3.00	3	2494.7609	2375.1401
Heighway-PSO	3.9167	3.00	5	2562.0273	2428.5376
Sobol-PSO	4.2917	3.25	4	2517.2137	2269.4159
Terdragon-PSO	4.3125	3.25	5	2433.4267	2273.4824
Twindragon-PSO	4.6250	4.00	0	2486.8188	2370.9562
Terdragon-QI-PSO	6.5833	7.00	2	16488.9560	16788.1117
Twindragon-QI-PSO	6.8750	7.50	0	16437.9516	16080.9724
Sobol-QI-PSO	6.9167	7.00	1	17514.5167	17869.1997
Random-QI-PSO	6.9583	7.00	0	18467.6059	18771.7067
Heighway-QI-PSO	7.0833	7.00	0	17440.3082	16995.7176

Table 8. CEC 2022 function-dimension best mean fitness records

Function	Dimension	Best mean fitness method(s)	Mean fitness
F1	D10	Random-PSO, Sobol-PSO, Heighway-PSO, Twindragon-PSO, Terdragon-PSO	300.0000
F1	D20	Random-PSO, Sobol-PSO, Heighway-PSO, Twindragon-PSO, Terdragon-PSO	300.0000
F2	D10	Terdragon-QI-PSO	403.9851
F2	D20	Heighway-PSO	450.5437
F3	D10	Random-PSO, Sobol-PSO, Heighway-PSO, Twindragon-PSO, Terdragon-PSO	600.0000
F3	D20	Heighway-PSO	600.0000
F4	D10	Sobol-PSO	819.4800
F4	D20	Sobol-PSO	882.8000
F5	D10	Heighway-PSO	900.0000
F5	D20	Sobol-PSO	900.5051
F6	D10	Terdragon-PSO	2665.1170
F6	D20	Terdragon-PSO	23939.5697
F7	D10	Sobol-PSO	2022.2765
F7	D20	Terdragon-PSO	1879.7249
F8	D10	Heighway-PSO	2215.9723
F8	D20	Heighway-PSO	2162.4204
F9	D10	Terdragon-QI-PSO	2416.0556
F9	D20	Sobol-QI-PSO	2603.8309
F10	D10	Terdragon-PSO	1206.1031
F10	D20	Random-PSO	-453.1290
F11	D10	Terdragon-PSO	2600.0000
F11	D20	Random-PSO, Sobol-PSO	2600.0000
F12	D10	Random-PSO	2799.0227
F12	D20	Random-PSO	2948.2262

According to Figure 6, PSO variants were concentrated at lower rank values. Random-PSO, Heighway-PSO, Sobol-PSO, and Terdragon-PSO appeared in the top three ranks under many function-dimension conditions. Twindragon-PSO produced fewer top-three rank entries within the PSO variants. Among the QI-PSO variants, top-three rank entries remained more limited. Within this group, Terdragon-QI-PSO produced the highest number of top-three rank entries among the QI-PSO variants. The rank distribution was not homogeneous at the function level. Sobol-PSO had the lowest ranks under F4 conditions, Terdragon-PSO under F6 conditions, Heighway-PSO under F8 conditions, and Random-PSO under F12 conditions. Under F9 conditions, QI-PSO variants produced rank-1 entries. Best mean fitness records were not concentrated in one method, and method orderings changed at the function-dimension level.

Full function-dimension-level final fitness statistics, including mean, median, standard deviation, best, worst, and rank values, are given in Supplementary Table S1.

The family-level summary of CEC 2022 method-level outputs is given in Table 9. According to Table 9, the Classical PSO family ranked first in terms of average rank. The Dragon-guided PSO family ranked second, the Dragon-guided QI-PSO family ranked third, and the QI-PSO family ranked fourth. In terms of single-method rank 1 count, the highest value was obtained by the Dragon-guided PSO family. The Classical PSO family ranked second, the Dragon-guided QI-PSO family ranked third, and the QI-PSO family ranked fourth. For average mean fitness, the Dragon-guided PSO family produced the lowest value. The Classical PSO family followed this group. The QI-PSO and Dragon-guided QI-PSO families produced higher average mean fitness values than the Classical PSO and Dragon-guided PSO families.

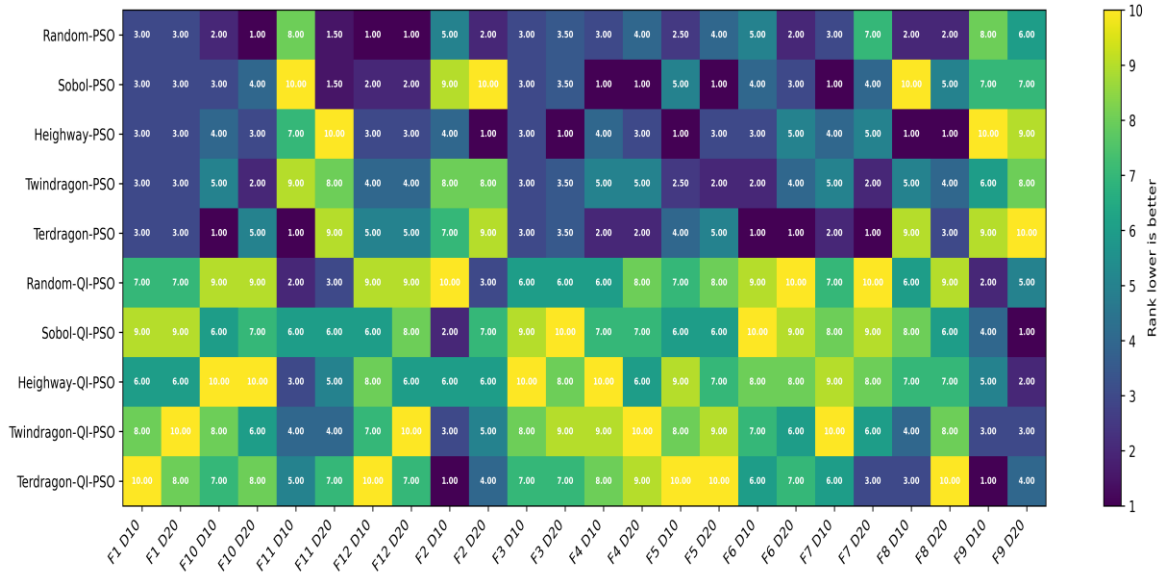


Figure 6. CEC 2022 function dimension rank heatmap.

Table 9. CEC 2022 family level performance results

Family	Average Rank	Single-method rank 1 count	Avg. Mean Fitness
Classical PSO	3.8646	7	2505.9873
Dragon guided PSO	4.2847	10	2494.0909
Dragon guided QI-PSO	6.8472	2	16789.0719
QI-PSO	6.9375	1	17991.0613

3.2 CEC 2022 Convergence and Runtime Results

The CEC 2022 global convergence trace results are given in Figure 7. In Figure 7, the convergence curves of the PSO variants progressed at lower fitness levels than those of the QI-PSO variants. This separation was maintained from the early progress points to the final progress point. The PSO variants ended at the final progress point in the range of 2433.4267 to 2562.0273. For the QI-PSO variants, the final progress values remained between 16437.9516 and 18467.6059. Among the PSO variants, the Terdragon-PSO curve progressed at the lowest mean best fitness level throughout the progress process. At the final progress point, Terdragon-PSO ended with a mean best fitness value of 2433.4267. At the same point, Twindragon-PSO produced 2486.8188, Random-PSO produced 2494.7609, Sobol-PSO produced 2517.2137, and Heighway-PSO produced 2562.0273. The convergence curves of the QI-PSO variants remained at higher mean best fitness levels than those of the PSO variants. Among the QI-PSO variants, the lowest mean best fitness value was recorded for Heighway-QI-PSO at the 25 percent progress point, for Terdragon-QI-PSO at the 50 percent and 75 percent progress points, and for Twindragon-QI-PSO at the 100

percent progress point. At the 100 percent progress point, Twindragon-QI-PSO produced 16437.9516, Terdragon-QI-PSO produced 16488.9560, Heighway-QI-PSO produced 17440.3082, Sobol-QI-PSO produced 17514.5167, and Random-QI-PSO produced 18467.6059.

The CEC 2022 global convergence trace mean best fitness results are given in Supplementary Table S2.

According to Supplementary Table S2, Terdragon-PSO produced the lowest mean best fitness value among the PSO variants at all 25 percent, 50 percent, 75 percent, and 100 percent progress points. Among the QI-PSO variants, the method producing the lowest mean best fitness value changed across progress points. Heighway-QI-PSO had the lowest mean best fitness at the 25 percent progress point. Terdragon-QI-PSO had the lowest value at the 50 percent and 75 percent progress points. Twindragon-QI-PSO had the lowest value at the 100 percent progress point.

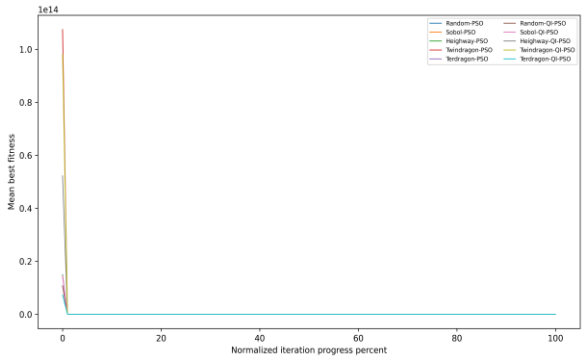


Figure 7. CEC 2022 global convergence trace results.

At the final progress point, median best fitness values were concentrated in a narrower range than mean best fitness values. Among the PSO variants, final median best fitness ranged from 1857.1256 to 1967.1798. The lowest value in this range was obtained by Terdragon-PSO, while the highest value was given for Twindragon-PSO. Among the QI-PSO variants, final median best fitness ranged from 2020.2443 to 2030.4431. The lowest value in this range was recorded for Terdragon-QI-PSO, and the highest value was recorded for Random-QI-PSO. Among the supplementary outputs, Supplementary Figure S1 presents the method-level convergence profile.

The CEC 2022 runtime and computational cost results are given in Supplementary Table S2. In Supplementary Table S2, methods using random and Sobol initialization had similar low runtime values. Dragon-guided methods produced higher runtime values. The same separation was observed in the runtime per evaluation column.

In the evaluations per second column, methods with lower runtime values had higher throughput values. Methods with higher runtime values were reported with lower throughput. Random-PSO and Sobol-PSO formed the lowest runtime group in the table. Random-QI-PSO and Sobol-QI-PSO remained close to these two methods. Dragon-guided PSO and Dragon-guided QI-PSO variants had higher runtime per evaluation values and formed a separate computational cost range. Terdragon-based variants produced higher runtime values within their own groups. Heighway-based and Twindragon-based variants produced lower runtime values. This ordering was observed in the same direction for average runtime and runtime per evaluation, and in the opposite direction for evaluations per second. The CEC 2022 family-level runtime results are given in Table 10.

Table 10. CEC 2022 family-level runtime results

Family	Average runtime (second)	Runtime per evaluation	Evaluations per second
Classical PSO family	69.7211	1.1620e-04	8605.7222
QI-PSO family	70.4347	1.1739e-04	8518.5248
Dragon guided PSO family	87.1057	1.4518e-04	6892.7446
Dragon guided QI-PSO family	93.6789	1.5613e-04	6411.3149

According to Table 10, the Classical PSO family and the QI-PSO family had lower runtime values. The Dragon-guided PSO family and the Dragon-guided QI-PSO family were grouped at higher runtime values. The same separation was preserved in runtime per evaluation values. Evaluations per second values gave the inverse counterpart of the runtime ordering. In the family-level results, the Classical PSO family had the lowest runtime level. The QI-PSO family formed the second runtime level close to it. The Dragon-guided PSO family was placed above these two family groups. The Dragon-guided QI-PSO family produced the highest runtime level. Family groups without dragon guidance had lower runtime and higher throughput values. Dragon-guided family groups produced higher runtime and lower throughput values. The same family-level ordering was preserved across average runtime, runtime per evaluation, and evaluations per second.

3.3. CEC 2022 Statistical Comparison Results

The CEC 2022 Wilcoxon signed-rank and Holm correction results are given in Table 11. In the entire set of pairwise comparisons given in Table 11, 604 comparisons had raw P values below 0.05. After Holm correction, 526 comparisons remained significant. A total of 538 valid comparisons did not satisfy the Holm-corrected significance threshold, and 16 comparisons produced empty P values. In the PSO-only comparison set, 36 comparisons had raw P values below 0.05, and 28 remained significant after Holm correction.

Table 11. The CEC 2022 Wilcoxon signed-rank and Holm correction results*

Comparison set	Total comparison	Raw P<0.05	Holm P<0.05	Not Holm significant	Empty P value
All pairwise	1080	604	526	538	16
PSO only	240	36	28	196	16
QI-PSO only	240	11	3	237	0

*Not Holm significant indicates comparisons with a valid P value that did not satisfy Holm corrected P<0.05. Empty P value comparisons are reported separately and are not included in the Not Holm significant column

In this set, 196 valid comparisons were not Holm significant, and 16 comparisons produced empty P values. In the QI-PSO-only comparison set, 11 comparisons had raw P values below 0.05, and 3 remained significant after Holm correction. The remaining 237 valid comparisons were not Holm significant, and no empty P value was recorded. The number of Holm significant comparisons at the function-dimension level is given in Supplementary Table S6a.

In Supplementary Table S6a, Holm significant comparison counts varied across function-dimension conditions. The highest total significant count was recorded for F11 with 54 comparisons. For F6, the total significant count was 52. F1, F3, F4, and F5 each had a total significant count of 50. The lowest total significant count was obtained for F2 with 19 comparisons. Under the F2-D20 condition, no comparison satisfied Holm-corrected P<0.05. Significant comparison counts differed between D10 and D20 settings depending on the function.

Under F11-D10, 29 significant comparisons were recorded, while F11-D20 had 25 significant comparisons. Under F6-D10, 27 significant comparisons were recorded, while F6-D20 had 25 significant comparisons. In F7, F8, F9, F10, and F12, D10 and D20 significant comparison counts did not remain at the same level. Thus, the significant comparison distribution changed across function-dimension conditions.

The CEC 2022 method-level Holm significant lower mean fitness and higher mean fitness counts are given in Supplementary Table S6b. According to Supplementary Table S6b, the highest lower mean fitness count within Holm significant comparisons was recorded for Terdragon-PSO with 92. Random-PSO had 89, Sobol-PSO had 86, Heighway-PSO had 83, and Twindragon-PSO had 74 lower mean fitness counts. PSO variants were placed above QI-PSO variants in terms of lower mean fitness count. Among the QI-PSO variants, lower mean fitness counts were 26 for Terdragon-QI-PSO, 21 for Twindragon-QI-PSO, 20 for Sobol-QI-PSO, 18 for Heighway-QI-PSO, and 17 for Random-QI-PSO. Higher mean fitness counts were 88 for Random-QI-PSO, 83 for Heighway-QI-PSO and Twindragon-QI-PSO, 82 for Sobol-QI-PSO, and 77 for Terdragon-QI-PSO. Among the PSO variants, higher mean fitness counts were 16 for Random-PSO, 22 for Twindragon-PSO, 24 for Terdragon-PSO, 25 for Sobol-PSO, and 26 for Heighway-PSO. Non-significant comparison counts ranged from 100 to 120 across all methods. The lowest non-significant comparison count was recorded for Terdragon-PSO with 100. The highest non-significant comparison count was recorded for Twindragon-PSO with 120. Among the QI-PSO variants, non-significant comparison counts ranged between 111 and 110.

The family-pair-level Holm significant comparison counts are given in Supplementary Table S6c. According to Supplementary Table S6c, the highest significant count at the family-pair level was recorded in the Dragon-guided PSO versus Dragon-guided QI-PSO comparison group with 180. The total comparison count in this comparison group was 216. The Classical PSO versus Dragon-guided QI-PSO comparison group contained 125 significant comparisons. The Dragon-guided PSO versus QI-PSO comparison group contained 123 significant comparisons. The Classical PSO versus QI-PSO comparison group contained 83 significant comparisons. The Classical PSO versus Dragon-guided PSO comparison group contained 8 significant comparisons. The Dragon-guided QI-PSO versus QI-PSO comparison group contained 1 significant comparison. The within Dragon-guided PSO comparison group contained 5 significant comparisons, and the within Dragon-guided QI-PSO comparison group contained 1 significant comparison. No comparison satisfying Holm-corrected P<0.05 was found within the Classical PSO and QI-PSO comparison groups. Holm-corrected significant comparison counts differed across family-pair groups. Between-family comparison groups produced higher significant comparison counts than within-family comparison groups.

3.4. Cleveland Classification Results

Cleveland Heart Disease classification results are given separately for the KNN and SVM classifiers. In this section, the balanced accuracy values for wrapper FS and no-FS are first given in Figure 8. In Figure 8, the KNN and SVM settings produced different baseline relationships. In the KNN evaluation setting, all wrapper FS methods had balanced accuracy values above the no-FS baseline. The no-FS baseline balanced accuracy value was 0.818367, while wrapper FS values ranged from 0.822589 to 0.830299. In the KNN evaluation setting, Sobol-QI-PSO produced the highest observed mean balanced accuracy among the wrapper FS methods, with a value of 0.830299. In the SVM evaluation setting, the no-FS baseline balanced accuracy value was 0.834160. Wrapper FS methods produced balanced accuracy values ranging from 0.825039 to 0.831136. All wrapper FS balanced accuracy values in the SVM evaluation setting remained below the no-FS baseline value. Among the wrapper FS methods, Sobol-QI-PSO produced the highest

observed mean SVM balanced accuracy, with a value of 0.831136. The no-FS baseline values and the highest wrapper FS results under the KNN and SVM evaluation settings are given in Table 12. In Table 12, Sobol-QI-PSO produced the highest observed mean balanced accuracy among the wrapper FS methods in both KNN and SVM settings. However, none of the balanced accuracy comparisons remained significant after Holm correction, indicating statistically similar performance among the compared wrapper FS methods for this metric.

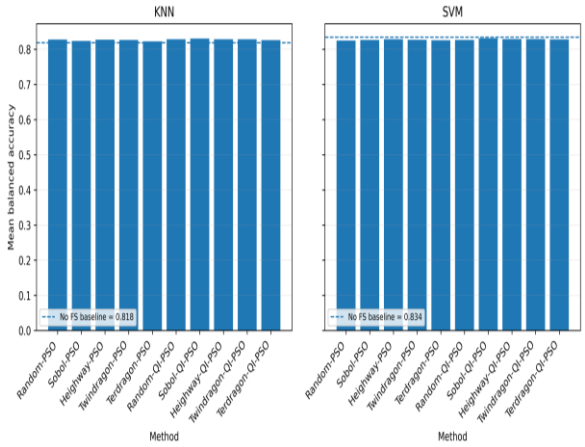


Figure 8. Cleveland balanced accuracy and no-FS baseline comparison.

In the KNN setting, Sobol-QI-PSO produced higher balanced accuracy, accuracy, and MCC values than the no-FS baseline. In the SVM setting, Sobol-QI-PSO produced the highest balanced accuracy, accuracy, F1 score, and MCC values within the wrapper FS group.

Its balanced accuracy, accuracy, and MCC values remained below the no-FS baseline values. In KNN wrapper FS results, Sobol-QI-PSO produced the highest balanced accuracy, accuracy, recall, F1 score, and MCC values. Heighway-QI-PSO produced the highest precision value. Terdragon-QI-PSO produced the highest ROC AUC value. Terdragon-PSO produced the highest PR AUC value. In SVM wrapper FS results, Sobol-QI-PSO again produced the highest balanced accuracy, accuracy, recall, F1 score, and MCC values. Heighway-QI-PSO produced the highest precision value. Terdragon-QI-PSO produced the highest ROC AUC value. Twindragon-PSO produced the highest PR AUC value. The KNN classification metric values for the no-FS baseline and all wrapper FS methods are given in Supplementary Table S3a. The SVM classification metric values are given in Supplementary Table S3b. Supplementary Table S4 contains the Cleveland balanced accuracy pairwise Wilcoxon comparison results. In the all-pairwise comparison set, five comparisons had raw P values below the 0.05 threshold. After Holm correction, no comparison satisfied $P<0.05$. No raw or Holm-corrected significant comparison was recorded in the PSO-only and QI-PSO-only comparison sets. ROC AUC, PR AUC, and threshold-dependent F1 results for the KNN and SVM classifiers are given in Figure 9.

Table 12. No-FS baseline and highest wrapper FS results under KNN and SVM evaluation settings

Classifier	No-FS balanced accuracy	Highest wrapper FS method	Wrapper FS balanced accuracy	Delta balanced accuracy	Wrapper FS accuracy	Wrapper FS F1	Wrapper FS MCC
KNN	0.8183	Sobol-QI-PSO	0.8303	0.0119	0.8333	0.8137	0.6640
SVM	0.8341	Sobol-QI-PSO	0.8311	-0.003	0.8347	0.8138	0.6671

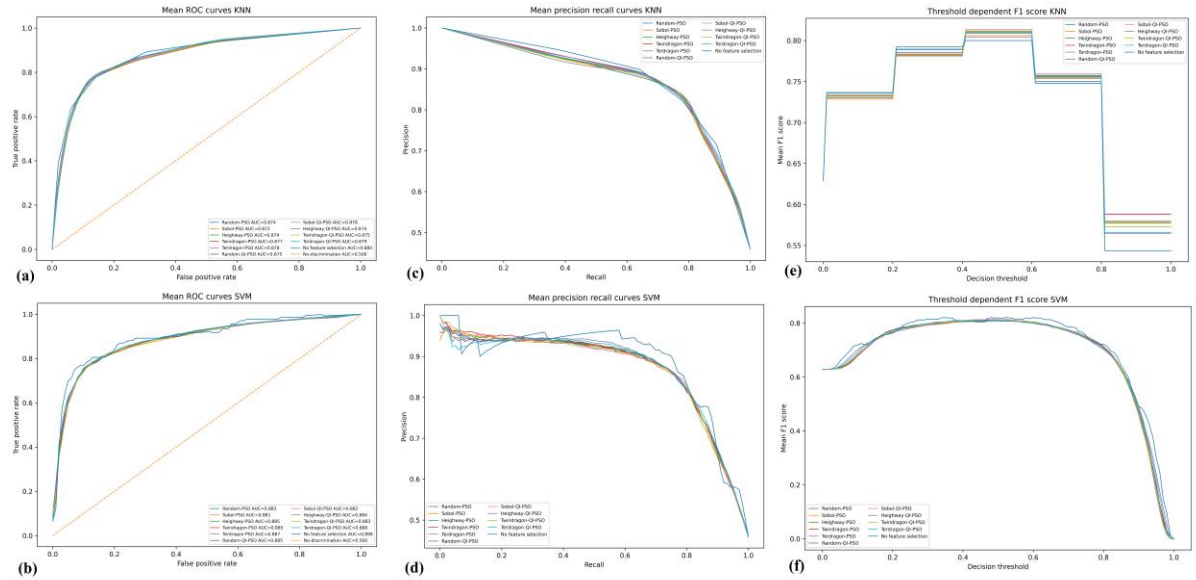


Figure 9. Cleveland ROC, PR, and threshold-dependent F1 results, a) KNN ROC curve results, b) SVM ROC curve results, c) KNN PR curve results, d) SVM PR curve results, e) KNN threshold-dependent F1 results, f) SVM threshold-dependent F1 results.

In the ROC AUC results given in Figures 9a and 9b, the no-FS baseline remained above the wrapper FS methods for both classifiers. The KNN no-FS baseline ROC AUC value was recorded as 0.880286. Among KNN wrapper FS methods, the highest ROC AUC value was given for Terdragon-QI-PSO with 0.879374.

The SVM no-FS baseline ROC AUC value was recorded as 0.897767. Among SVM wrapper FS methods, the highest ROC AUC value was given for Terdragon-QI-PSO with 0.887559. In the KNN wrapper FS methods shown in Figure 9c, PR AUC values were grouped within a narrow range. The highest value was recorded for Terdragon-PSO. In the SVM wrapper FS methods shown in Figure 9d, PR AUC values were placed in a higher range than the KNN setting values. The highest value was obtained by Twindragon-PSO. In the threshold-dependent F1 results shown in Figures 9e and 9f, the highest wrapper FS mean F1 value in the KNN setting was obtained by Sobol-QI-PSO at the 0.41 threshold point, with 0.813713. At the same threshold level, the KNN no-FS baseline mean F1 value was 0.800000.

In the SVM setting, the highest mean F1 value was recorded for the no-FS baseline with 0.820896. The highest mean F1 value among wrapper FS methods was obtained by Sobol-QI-PSO at the 0.52 threshold point, with 0.814254. In the KNN setting, the highest F1 values among wrapper FS methods were obtained by Sobol-QI-PSO, Random-QI-PSO, Twindragon-QI-PSO, Heighway-QI-PSO, and Random-PSO. In the SVM setting, the highest F1 values among wrapper FS methods were obtained by Sobol-QI-PSO, Heighway-PSO, Twindragon-QI-PSO, Heighway-QI-PSO, and Terdragon-QI-PSO. The cross-validation aggregate confusion matrix results are given in Figure 10.

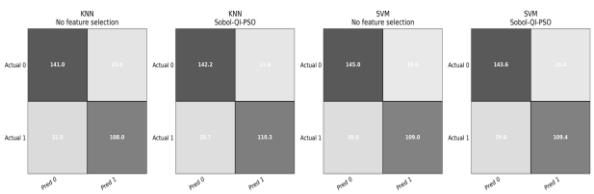


Figure 10. Cleveland cross validation aggregate confusion matrix results.

In Figure 10, confusion matrix values are given as aggregate matrices derived from cross-validation prediction records. Since no-FS baseline values were generated from a single reference evaluation, they appear as integers, whereas wrapper FS values contain decimal values because they represent the average of 50 independent runs. In the KNN setting, Sobol-QI-PSO produced higher TN and TP and lower FP and FN values than the no-FS baseline. In the SVM setting, Sobol-QI-PSO reduced the FN value and increased the TP value, whereas the TN value decreased and the FP value increased. The wrapper FS output produced different error component changes in the KNN and SVM settings.

3.5. Cleveland Feature Selection Results

In the Cleveland wrapper FS experiments, FS outputs were reported through selected feature count, selected feature ratio, feature reduction ratio, feature subset stability, and selection frequency. The convergence profile outputs of the wrapper FS optimization process are given in Supplementary Figure S2. Selected feature count results are presented in Figure 11 to show how many features the wrapper FS methods used for representation relative to the no-FS baseline.

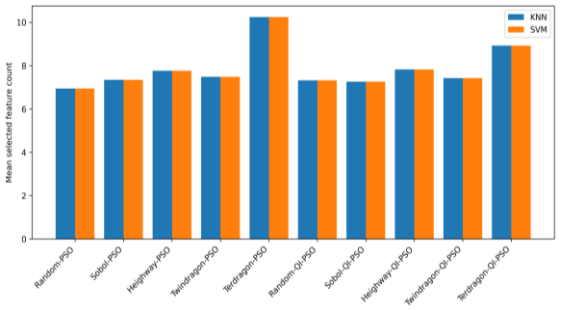


Figure 11. Cleveland selected feature count results.

According to Figure 11, all wrapper FS methods produced selected feature counts below the no-FS baseline value containing 13 features. The mean selected feature count ranged from 6.94 to 10.24. Random-PSO had the lowest selected feature count, whereas Terdragon-PSO had the highest selected feature count. Random-PSO, Sobol-QI-PSO, Random-QI-PSO, and Sobol-PSO were located in the lower feature count band. Terdragon-PSO, Terdragon-QI-PSO, and Heighway-QI-PSO were located in the higher feature count band.

Method-level feature reduction results are given in Supplementary Table S5a.

Supplementary Table S5a shows that selected feature ratio values ranged between 0.5338 and 0.7877. Feature reduction ratio values ranged between 0.2123 and 0.4662. Random-PSO produced the highest feature reduction ratio. Terdragon-PSO had the lowest feature reduction ratio. The Classical PSO and QI-PSO families were located in the lower selected feature count band, whereas the Dragon-guided PSO and Dragon-guided QI-PSO families were located in the higher selected feature count band.

Feature subset stability results are presented in Table 13 to show the Jaccard similarity level of the selected feature subsets across independent runs. According to Table 13, mean pairwise Jaccard similarity values ranged between 0.5245 and 0.6872. The highest mean pairwise Jaccard similarity value was recorded for Terdragon-PSO with 0.6872 ± 0.1557, and the lowest value was recorded for Random-PSO with 0.5245 ± 0.1811. Terdragon-QI-PSO produced the second highest mean similarity value with 0.6282 ± 0.1509. Heighway-QI-PSO, Sobol-QI-PSO, and Twindragon-QI-PSO produced mean pairwise Jaccard similarity values above 0.6000. The selected feature count ranking and the feature subset stability ranking

were not identical. Random-PSO had the lowest selected feature count with 6.94 ± 1.7775 and the lowest mean pairwise Jaccard similarity value. Terdragon-PSO had the highest selected feature count with 10.24 ± 2.0953 and the highest mean pairwise Jaccard similarity value. At the family level, the feature subset stability ranking was Dragon-guided QI-PSO, Dragon-guided PSO, QI-PSO, and Classical PSO. Selection frequency results are given in Figure 12 to show the selection frequency of each feature across methods.

Table 13. Cleveland feature subset stability results based on pairwise Jaccard similarity*

Rank	Method	Selected feature count mean ± SD	Pairwise Jaccard mean ± SD	Median	Min–max	Q1–Q3
1	Terdragon-PSO	10.24 ± 2.10	0.6872 ± 0.1557	0.6923	0.2500–1.0000	0.5833–0.8333
2	Terdragon-QI-PSO	8.92 ± 2.18	0.6282 ± 0.1509	0.6364	0.2727–1.0000	0.5000–0.7273
3	Heighway-QI-PSO	7.82 ± 2.04	0.6092 ± 0.1726	0.6250	0.1818–1.0000	0.5000–0.7143
4	Sobol-QI-PSO	7.26 ± 2.08	0.6074 ± 0.2058	0.6000	0.2000–1.0000	0.4545–0.7500
5	Twindragon-QI-PSO	7.42 ± 1.92	0.6003 ± 0.1938	0.5833	0.1818–1.0000	0.4545–0.7273
6	Random-QI-PSO	7.32 ± 1.73	0.5574 ± 0.1714	0.5455	0.1818–1.0000	0.4444–0.6667
7	Heighway-PSO	7.76 ± 2.30	0.5560 ± 0.1613	0.5455	0.2500–1.0000	0.4444–0.6667
8	Twindragon-PSO	7.48 ± 2.17	0.5475 ± 0.1584	0.5000	0.2222–1.0000	0.4444–0.6364
9	Sobol-PSO	7.34 ± 2.01	0.5386 ± 0.1739	0.5000	0.1667–1.0000	0.4000–0.6667
10	Random-PSO	6.94 ± 1.78	0.5245 ± 0.1811	0.5000	0.1111–1.0000	0.4000–0.6250

*Accard similarity was calculated pairwise among selected feature subsets obtained from independent wrapper FS runs. Selected feature count is reported together with mean pairwise Jaccard similarity because overlap-based values can be affected by subset size. Higher mean pairwise Jaccard similarity indicates greater run-to-run feature subset consistency.

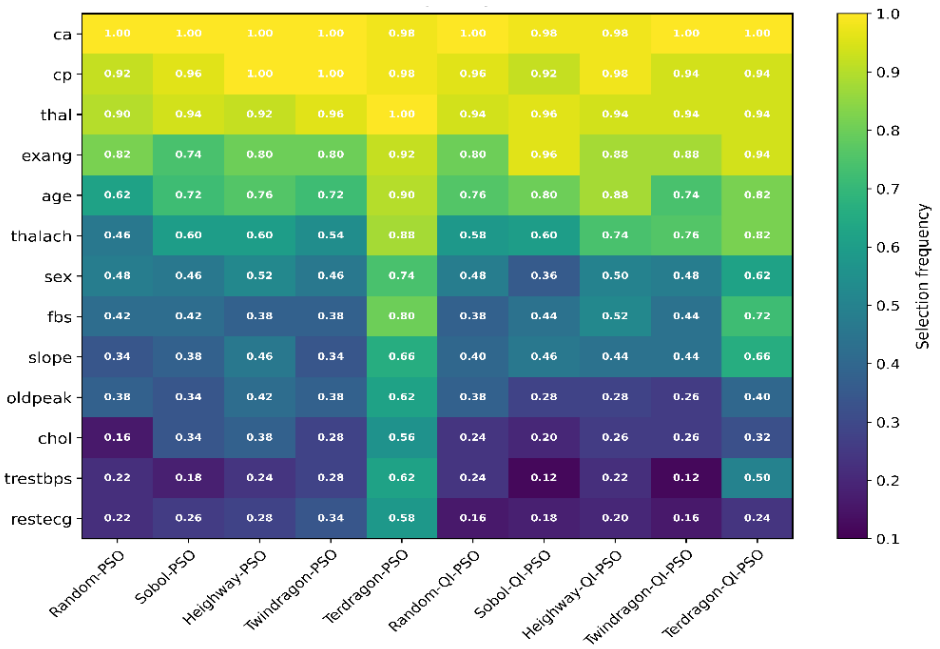


Figure 12. Cleveland feature selection frequency heatmap.

According to Figure 12, ca, cp, and thal were separated as the features with the highest selection frequency across all methods. Exang and age were in the second high-frequency group. Thalach remained in the upper-middle frequency band. Sex, fbs, and slope were in the middle-frequency band. restecg, trestbps, chol, and oldpeak were recorded as features with lower selection frequency. Feature-level selection frequency results are summarized in Supplementary Table S5b to provide a distribution-level overview of how frequently each feature was selected across methods and runs. According to Supplementary Table S5b, ca, cp, and thal were the three most frequently selected features. The selected counts for these features were 497, 480, and 472 out of 500 wrapper FS outputs, respectively. Their minimum method-level selection frequency values were 0.90 or above. Exang and age followed with selected counts of 427 and 386. Thalach had an intermediate selection frequency with 329 selections out of 500. The lowest overall selection frequency value was recorded for restecg, with 131 selections out of 500 and a mean selection frequency of 0.2620 ± 0.1252. Trestbps, chol, and oldpeak were also located in the lower-frequency range. Among the lower-frequency features, trestbps had the widest method-level range, from 0.120 to 0.620.

3.6. Cross-Setting Method Profile Summary

Method-level cross-setting profile heatmap results are given in Figure 13. In Figure 13, the methods did not show the same profile structure across the CEC 2022 and Cleveland wrapper FS outputs. Random-PSO had z score positions separated from the other methods on the CEC average rank and CEC runtime dimensions. Sobol-PSO was placed close to Random-PSO on the CEC runtime. Sobol-QI-PSO separated from the other wrapper FS methods on the KNN balanced accuracy and SVM balanced accuracy dimensions.

Terdragon-PSO showed a distinct z score position on the feature subset stability axis. Dragon-guided QI-PSO variants were placed close to each other on the feature subset stability and SVM balanced accuracy dimensions. On the CEC runtime axis, dragon-guided methods showed runtime profile positions separated from the other methods.

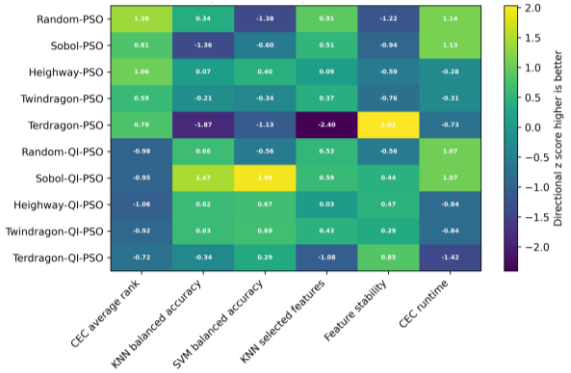


Figure 13. Method-level cross-setting profile heatmap.

Method-level cross-setting profile summary results are given in Supplementary Table S7. In Supplementary Table S7, the lowest CEC average rank at the method level was recorded for Random-PSO. The highest CEC single-method rank 1 count was recorded for Heighway-PSO and Terdragon-PSO. The lowest CEC runtime was obtained by Random-PSO. In the Cleveland experiments, the highest KNN balanced accuracy and SVM balanced accuracy values were recorded for Sobol-QI-PSO. The lowest selected feature count was obtained by Random-PSO, and the highest feature subset stability was obtained by Terdragon-PSO. Family-level cross-setting profile heatmap results are given in Figure 14.

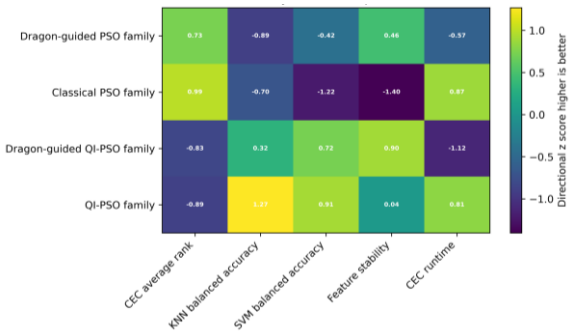


Figure 14. Family level cross-setting profile heatmap.

In Figure 14, algorithm families showed different profile positions across the CEC 2022 and Cleveland wrapper FS evaluation dimensions. The Classical PSO family separated from the other family groups on the CEC average rank and CEC runtime dimensions. The QI-PSO family produced a distinct profile position on the KNN balanced accuracy and SVM balanced accuracy. The Dragon-guided QI-PSO family separated from the other family groups on the feature subset stability axis. The Dragon-guided PSO family was placed differently from the Classical PSO family on the feature subset stability axis. The same family group was positioned differently from the QI-PSO and Dragon-guided QI-PSO family groups on the KNN and SVM balanced accuracy dimensions. Family-level cross-setting profile summary results are given in Table 14.

Table 14. Family level cross-setting profile summary

Family	CEC average rank	KNN balanced accuracy	SVM balanced accuracy	Selected feature count	Feature subset stability	CEC runtime (second)
Classical PSO	3.8646	0.825724	0.825754	7.1400	0.531562	69.7211
Dragon guided PSO	4.2847	0.825361	0.826913	8.4933	0.596869	87.1057
QI-PSO	6.9375	0.829366	0.828838	7.2900	0.582407	70.4347
Dragon guided QI-PSO	6.8472	0.827613	0.828562	8.0533	0.612540	93.6789

In Table 14, the lowest CEC average rank at the family level was recorded for the Classical PSO family. For KNN balanced accuracy and SVM balanced accuracy, the highest family-level result was obtained by the QI-PSO family. The lowest selected feature count was recorded for the Classical PSO family. The highest feature subset stability was obtained by the Dragon-guided QI-PSO family. In terms of CEC runtime, the lowest value was given for the Classical PSO family, and the highest value was given for the Dragon-guided QI-PSO family.

4. Discussion

This study examined the method-level performance profiles produced by random initialization, Sobol initialization, QI candidate generation, and ordered geometric guidance derived from the Heighway dragon, Twindragon, and Terdragon curves within PSO and QI-PSO variants. The CEC 2022 experiments addressed continuous objective minimization, convergence behavior, and computational cost, whereas the Cleveland wrapper FS experiments addressed classification performance, selected feature count, feature subset

stability, and selection frequency. The results did not produce one method order across all outputs. The relative positions of the methods changed according to the problem representation and the evaluated metric.

4.1. CEC 2022 Optimization, Convergence, and Statistical Results

PSO variants produced lower rank values than QI-PSO variants in the CEC 2022 experiments. Random-PSO had the lowest average rank, whereas Terdragon-PSO had the lowest average mean fitness and the lowest mean best fitness trajectory among the PSO variants. Recent CEC 2022 optimizer studies report final statistics, ranks, convergence behavior, and statistical comparisons as separate outputs rather than treating them as interchangeable measures (Pathak et al., 2024; Agrawal and Panda, 2025). Supplementary Table S1 shows that average rank, mean fitness, median fitness, variability, best value, and worst value did not always produce the same ordering across the function-dimension conditions. The average-rank position of Random-PSO and the average-mean-fitness position of Terdragon-PSO describe different aspects of CEC 2022 performance.

The function-dimension best mean fitness records were distributed across several methods. Heighway-PSO and Terdragon-PSO produced best records under different conditions, while Sobol-PSO and Random-PSO also produced best records under separate conditions.

The shifted and rotated, hybrid, and composition functions present different search landscapes. The distribution of best records across the methods indicates that their responses changed across these landscapes. Dragon-guided PSO variants did not produce an advantage across every function. Their effect appeared under selected function-dimension conditions, so dragon guidance should be interpreted as a landscape-dependent geometric search component rather than as a general improvement mechanism.

The rank heatmap gives a similar function-dependent result. Sobol-PSO produced lower ranks under F4 conditions, Terdragon-PSO under F6 conditions, Heighway-PSO under F8 conditions, and Random-PSO under F12 conditions. At the family level, the Dragon-guided PSO family had the highest rank 1 count and the lowest average mean fitness, whereas the Classical PSO family had the lowest average rank. Function-specific ranks and family-level summaries consequently described different parts of the experimental results.

Post-competition analyses of CEC 2022 also show that algorithm ordering can change with the ranking criterion, parameter configuration, and implementation details. Biedrzycki (2024) examined changes associated with ranking criteria and parameter tuning, while Biedrzycki (2026) examined implementation details and hidden parameters in the CEC 2022 competition winner. The rankings obtained in this study describe performance under the stated metrics and experimental settings rather than an absolute ordering that is independent of evaluation design.

The convergence results extend the final fitness findings to the search process. Supplementary Figure S1 shows that the PSO variant curves remained at lower mean best fitness levels than the QI-PSO variant curves throughout the recorded progress points. The final separation was thus present across the convergence process rather than appearing only at the final evaluation point.

Terdragon-PSO produced the lowest mean best fitness among the PSO variants at the 25 percent, 50 percent, 75 percent, and final progress points. Among the QI-PSO variants, the method with the lowest mean best fitness changed across the recorded progress points. No single dragon geometry produced the lowest trajectory throughout the full QI-PSO search process.

The CEC 2022 results of the QI-PSO variants should be interpreted through the particular operators used in this study. QI-PSO designs differ in angle update, candidate generation, candidate mixing, mutation, and search-control mechanisms. Agrawal and Panda (2025) obtained improved CEC 2022 results with a QI adaptive mutation design (Agrawal and Panda, 2025). In the present experiments, the implemented QI-PSO variants did not obtain lower CEC average ranks or average mean fitness values than the PSO variants. This difference indicates that the QI label alone does not determine search behavior. The concrete operator design and parameter configuration remain decisive.

Supplementary Table S2 presents convergence behavior and computational cost in the same method-level summary. Random and Sobol variants had lower average runtime and higher evaluations per second, whereas dragon-guided variants had higher runtime per evaluation. This increase occurred in both the Dragon-guided PSO and Dragon-guided QI-PSO families, so it cannot be attributed only to QI candidate generation. Terdragon-PSO produced the lowest average mean fitness and the lowest mean best fitness trajectory among the PSO variants, but it also required more computation time.

The solution quality results of dragon-guided variants should consequently be read together with average runtime, runtime per evaluation, and evaluations per second. Their additional computational cost may also limit their use in real-time or resource-constrained applications.

Sobol initialization also changed its relative position between the continuous optimization and wrapper FS experiments. Low-discrepancy sequences can generate more uniform initial populations than random initialization, but their effect can change with problem dimension and population size (Henderson et al., 2015; Agushaka and Ezugwu, 2020; Bangyal et al., 2021). Sobol initialization did not produce the lowest average rank in CEC 2022, whereas its relative position changed in the Cleveland wrapper FS experiments. This difference indicates that the response to Sobol initialization changed when the search output moved from a real-valued continuous vector to a classifier-evaluated binary

feature mask. The statistical results add pairwise distributional information to the rank summaries. Rank values alone do not show whether differences between paired runs remain detectable after correction for multiple comparisons. Nonparametric tests provide an established basis for comparing evolutionary and swarm intelligence algorithms under such conditions (Derrac et al., 2011).

Table 11 summarizes the all-pairwise, PSO-only, and QI-PSO-only comparison sets. After Holm correction, many comparisons remained significant in the complete pairwise set. The PSO-only set retained more corrected significant comparisons than the QI-PSO-only set. PSO variants consequently differed among themselves under several function-dimension conditions, while statistically detectable differences within the QI-PSO variant set were more limited.

Supplementary Table S6b presents the method-level direction counts and identifies whether each method occurred on the lower or higher mean fitness side of Holm-corrected significant comparisons. PSO variants appeared more often on the lower mean fitness side, whereas QI-PSO variants appeared more often on the higher mean fitness side.

This summary is not another rank calculation. It records the direction of the pairwise differences that remained significant after correction. Supplementary Table S6c presents the family-pair counts and shows that many of these differences were concentrated between PSO and QI-PSO families. The observed separation was associated with both dragon guidance and the difference between the PSO and QI-PSO update mechanisms.

4.2. Cleveland Classification Results

The Cleveland classification experiments produced a different method ordering from the CEC 2022 experiments. In the KNN setting, all wrapper FS methods produced balanced accuracy values above the no-FS baseline. KNN depends on distance-based neighborhood relations, so irrelevant or weakly informative features can alter the local distances used for classification. Feature reduction can improve KNN behavior when the selected subset retains discriminative variables. In the SVM setting, the no-FS baseline remained above all wrapper FS methods. Noroozi et al. (2023) showed on the Cleveland Heart Disease dataset that FS can improve some classifiers while reducing the performance of others, so FS results need to be interpreted together with classifier behavior. In the present study, wrapper FS improved balanced accuracy relative to the no-FS baseline under KNN but not under SVM. The effect of FS was classifier-dependent.

Sobol-QI-PSO produced the highest observed mean balanced accuracy among the wrapper FS methods under both KNN and SVM. Supplementary Table S3a shows that Sobol-QI-PSO also produced the highest observed values for accuracy, recall, F1 score, and MCC within the KNN wrapper FS group. Supplementary Table S3b shows a similar descriptive position under SVM for the main classification metrics. However, Supplementary Table S4 shows that no balanced accuracy comparison remained significant after Holm correction. The observed ordering should be interpreted as descriptive, while balanced accuracy performance among the compared wrapper methods was statistically similar after multiple-comparison correction.

ROC AUC, PR AUC, and threshold-dependent F1 produced a different view from balanced accuracy. The no-FS baseline remained higher in ROC AUC, while wrapper FS methods exceeded the baseline in KNN balanced accuracy. Threshold-dependent classification output and threshold-free discrimination output did not change in the same direction.

PR AUC results also differed between KNN and SVM, which indicates that positive-class performance depended on both classifier type and selected feature subset. The threshold-dependent F1 results identified the same method at the selected KNN and SVM threshold points, but this pattern did not extend to every probability-based output.

The aggregate confusion matrices show how these metric changes were formed through TN, TP, FP, and FN values. For Sobol-QI-PSO, the KNN aggregate confusion matrix showed higher TN and TP and lower FP and FN values than the no-FS baseline. Under SVM, FN decreased and TP increased, whereas TN decreased and FP increased. The selected subsets changed the error distribution differently across the two classifiers, which is not visible from balanced accuracy alone.

4.3. Feature Compactness, Stability, and Selection Frequency

Wrapper FS produces both classifier outputs and feature subset outputs. These two output groups need separate interpretation. Xie et al. (2021) developed PSO variants for FS in which particles were evaluated through classification performance and selected feature number. The Cleveland experiments used the same general wrapper logic but recorded a wider set of outputs, including balanced accuracy, MCC, ROC AUC, PR AUC, aggregate confusion matrices, selected feature count, reduction ratio, feature subset stability, and selection frequency. This evaluation separates prediction quality from the compactness and repeated-run consistency of the selected subsets.

The FS results did not show a one-directional relation among classification performance, selected feature count, and feature subset stability. All wrapper FS methods reduced the selected feature count relative to the no-FS baseline. Random-PSO produced the lowest selected feature count, but it also had the lowest mean pairwise Jaccard similarity. Terdragon-PSO selected more features and produced the highest mean pairwise Jaccard similarity at the method level. FS has been treated as a trade-off between predictive performance and subset size (Hancer et al., 2018). Stability has also been examined as a reproducibility property that cannot be replaced by prediction metrics alone (Jiang et al., 2022).

In medical FS, unstable subsets can reduce domain-expert confidence, while biomedical evaluations have examined prediction accuracy, selected feature count, and feature-selection stability together (Alelyani, 2021; Łukaszuk and Krawczuk, 2024). The Cleveland outputs should not be read only through balanced accuracy or selected feature count.

This distinction is particularly relevant when selected features are examined for interpretation as well as prediction. Alelyani (2021) stated that unstable medical feature sets can reduce confidence in the selected subset even when predictive performance is high. Jiang et al. (2022) discussed stability as part of reproducible biomedical FS, and Łukaszuk and Krawczuk (2024) evaluated stability together with prediction accuracy and selected feature number in biomedical data. At the family level, the Dragon-guided QI-PSO family produced the highest feature subset stability. This result concerns repeated-run subset consistency and does not establish statistically separated classification performance for the dragon-guided variants.

Supplementary Figure S2 adds search-process information to these final subset outputs. Methods that reached compact feature subsets did not necessarily follow the same wrapper objective trajectory or repeatedly select the same feature combinations. Random-PSO reached compact final subsets, but its selected subsets varied more across independent runs. Terdragon-PSO and the dragon-guided QI-PSO variants produced higher selected feature counts or higher repeated-run subset similarity. Final FS outputs were shaped by search trajectory, subset size pressure, and repeated-run consistency as well as classifier performance.

The method-level similarity result should be interpreted together with selected feature count because larger subsets can produce greater overlap as subset size approaches the original feature space, as noted by Alelyani (2021). For Terdragon-PSO, the higher repeated-run similarity was accompanied by a larger selected feature count than the compact methods. This result does not indicate unconditional superiority. It describes a tendency to generate larger and more repeatable subsets. Random-PSO and Terdragon-PSO thus occupied different positions on compactness and repeated-run similarity.

Selection frequency results showed that ca, cp, and thal were repeatedly selected across optimizer variants. Talin et al. (2022) identified cp, ca, thal, age, thalach, chol, oldpeak, and sex as influential predictors in heart disease diagnosis. The current analysis adds a recurrence-based view for ca, cp, and thal. These variables were retained repeatedly across 500 wrapper FS outputs and 10 optimizer variants rather than appearing only in a single run. Within the tested wrapper setting, they formed a group with high recurrence across methods. This finding concerns predictive recurrence and should not be read as evidence of clinical causality.

Supplementary Table S5b presents method-specific selection frequency distributions for each feature. ca, cp, and thal remained at high frequency levels. Sex, fbs, and slope changed more across methods within an intermediate-frequency region. oldpeak, chol, trestbps, and restecg formed the lower-frequency group, although their distributions were not identical. trestbps had a wider method-level range, whereas restecg remained at the lowest recurrence level. These distributions distinguish features that were repeatedly retained across methods from features whose selection changed more strongly with optimizer behavior.

The stability and selection frequency results also define the limits of the dragon component. Ngai and Nguyen (2003) examined the Heighway dragon as an iterative planar curve and described its geometric relation to the twin dragon. This geometric literature explains the source of the ordered dragon-family point sequences, but it does not establish an optimization advantage. In the present experiments, dragon guidance affected selected CEC function-dimension conditions and repeated-run feature subset behavior. Its role should be interpreted through the measured optimization and FS outputs rather than inferred from dragon geometry alone.

4.4. Cross-Setting Interpretation

The cross-setting results did not produce one method order across all evaluation dimensions. The methods with the lowest CEC average rank, highest observed Cleveland balanced accuracy, lowest selected feature count, and highest feature subset stability were different. The family-level results showed the same metric-dependent pattern. The Classical PSO family had the lowest CEC average rank and runtime, the QI-PSO family had the highest observed KNN and SVM balanced accuracy values, and the Dragon-guided QI-PSO family had the highest feature subset stability. A single composite score would hide these differences by combining outputs that measure different parts of optimizer behavior.

Random, Sobol, and dragon-guided variants should be evaluated separately through continuous optimization quality, classifier response, selected feature count, feature subset stability, selection frequency, and computational cost. Dragon guidance did not generate uniform gains across all outputs. Its observed contribution was concentrated in selected CEC function-dimension conditions and repeated-run feature subset behavior, while the dragon-guided variants also required higher runtime.

5. Conclusion

This study evaluated random initialization, Sobol initialization, QI candidate generation, and dragon-family-guided search within PSO and QI-PSO variants under a controlled experimental protocol. The main research question was whether these components produced similar effects in continuous optimization and wrapper FS tasks. The results showed that their effects varied with problem representation, classifier structure,

and evaluation metric. Dragon initialization and stagnation-triggered perturbation were applied together in the dragon-guided variants. Likewise, QI candidate generation was applied together with candidate mixing and mutation in the QI-PSO variants. For this reason, the results represent the combined effect of these components rather than the separate effect of each component. Across the evaluated outputs, no single method dominated all evaluation dimensions. In the CEC 2022 experiments conducted in this study, PSO variants produced lower ranks and lower mean fitness values than QI-PSO variants. Random-PSO produced the lowest average rank and the lowest runtime, whereas Terdragon-PSO produced the lowest average mean fitness and the lowest mean best fitness trajectory among the PSO variants. In the Cleveland wrapper FS experiments, the binary feature mask representation and classifier response changed the method ordering. Sobol-QI-PSO produced the highest observed mean balanced accuracy among the wrapper FS methods under both KNN and SVM settings. However, the Holm-corrected pairwise comparisons indicated statistically similar balanced accuracy across the compared wrapper methods.

The contribution of this study is twofold. First, evaluating random, Sobol, and dragon-family-guided variants across the PSO and QI-PSO variant sets made it possible to examine initialization source, QI candidate generation, and geometric guidance under the same evaluation protocol. Second, using both CEC 2022 and Cleveland wrapper FS experiments showed that the same optimizer component can behave differently in a real-valued continuous search space and in a classifier-evaluated binary feature mask space. The study therefore does not only provide a method ranking. It also shows how optimizer components gain meaning through the evaluation context in which they are tested.

The results also show that evaluation design in metaheuristic optimization and wrapper FS studies should not be reduced to a single success criterion. Final fitness, balanced accuracy, ROC AUC, and F1 score each describe only one part of method behavior. Runtime, selected feature count, selection frequency, and feature subset stability provide additional information that changes the interpretation of the same methods. In the Cleveland experiments, this distinction was important because the method producing the highest observed mean balanced accuracy was not the same as the method producing the highest feature subset stability.

Dragon family guidance did not act as a universal performance-improving component across all outputs. Its contribution was more specific. In the CEC 2022 experiments, dragon-guided PSO variants affected selected function-dimension conditions, and the Dragon-guided PSO family had the lowest average mean fitness at the family level. In the Cleveland experiments, Terdragon-PSO had the highest method-level mean pairwise Jaccard similarity, and the Dragon-guided QI-PSO family had the highest family-level feature subset stability. This result indicates that geometric guidance should be evaluated through task-specific outputs rather than through a single ranking or a general superiority claim.

The main recommendation from this study is that new metaheuristic components should be evaluated by considering problem representation and metric structure. A component that contributes to continuous optimization may not produce the same effect in wrapper FS. Similarly, a method that stands out in a classification metric does not necessarily produce a more compact or more stable feature subset. For this reason, geometric guidance, low-discrepancy initialization, and QI candidate generation should be examined through multi-metric, classifier-aware, and subset-aware experimental designs.

5.1. Limitations and Future Work

The main limitation of this study is that the effects of algorithmic components were evaluated at the method-level, while some components were applied together within the same experimental protocol. This design allowed the practical behavior of the compared variants to be evaluated under controlled conditions, but it did not isolate the separate contribution of each component. In the dragon-guided variants, geometric initialization and stagnation-triggered perturbation were used together. In the QI-PSO structure, angle update, candidate mixing, and mutation components were applied with fixed settings. Therefore, the results describe the integrated behavior of the full method variants rather than the isolated effect of each component.

A second limitation is that the experiments were conducted under a controlled configuration. This design supported fair comparison among the tested methods, but it limited the evaluation of parameter sensitivity across optimizer parameters, population size, evaluation budget, and classifier settings. A third limitation concerns computational cost. The dragon-guided variants required higher runtime and produced fewer evaluations per second than the corresponding random and Sobol variants. This additional cost may restrict their use in real-time or resource-constrained applications, where improvements in solution quality or feature subset stability must be considered together with the available computation time.

A further limitation is that the classification and wrapper FS experiments were tested only on the Cleveland Heart Disease dataset. Therefore, the classification and FS findings should be interpreted within the dataset, validation protocol, and classifier settings used in this study.

As future study, a new study is planned to examine dragon guidance under ablation, parameter sensitivity, and external validation settings. Dragon guidance will be separated into initialization-only, perturbation-only, and combined variants. To avoid limiting the next stage to a direct extension of the same method set, the study will

include selected PSO and related swarm-based algorithms, genetic algorithms, and their QI variants. In this planned study, the effects of parameter settings, dimensional structure, classifier choice, and dataset characteristics will be examined more explicitly. Additional medical datasets, such as Diabetes, Sepsis, Gallstone, and Asthma datasets, will be considered to evaluate whether the observed behavior is preserved beyond the Cleveland setting. Complementary classifiers, including Random Forest, XGBoost, Logistic Regression, and neural network-based models, will also be included. Effect sizes, confidence intervals, alternative stability measures, and detailed runtime profiling will be added to evaluate predictive performance, feature subset stability, and computational cost in greater detail.

Author Contributions

The percentages of the author' contributions are presented below. The author reviewed and approved the final version of the manuscript.

	S.Ö.
C	100
D	100
S	100
DCP	100
DAI	100
L	100
W	100
CR	100
SR	100
PM	100
FA	100

C= concept, D= design, S= supervision, DCP= data collection and/or processing, DAI= data analysis and/or interpretation, L= literature search, W= writing, CR= critical review, SR= submission and revision, PM= project management, FA= funding acquisition.

Conflict of Interest

The author declared that there is no conflict of interest.

Ethical Consideration

Ethics committee approval was not required for this study because of there was no study on animals or humans.

Data Availability

The UCI Cleveland Heart Disease dataset is publicly available from the UCI Machine Learning Repository under the Heart Disease dataset, at https://archive.ics.uci.edu/dataset/45/heart+disease.

The CEC 2022 benchmark functions are publicly available from the official Single Objective Bound Constrained Benchmark repository at https://github.com/P-N-Suganthan/2022-SO-BO.

References

Agrawal, U. K., & Panda, N. (2025). Quantum-inspired adaptive mutation operator enabled PSO (QAMO-PSO) for parallel optimization and tailoring parameters of Kolmogorov–Arnold network. *The Journal of Supercomputing*, *81*(14), Article 1310. https://doi.org/10.1007/s11227-025-07810-w

Agushaka, O. J., & Ezugwu, A. E. S. (2020). Influence of initializing Krill Herd Algorithm with low-discrepancy sequences. *IEEE Access*, *8*, 210886–210909. https://doi.org/10.1109/ACCESS.2020.3039602

Alelyani, S. (2021). Stable bagging feature selection on medical data. *Journal of Big Data*, *8*(1), Article 11. https://doi.org/10.1186/s40537-020-00385-8

Asha, M. M., & Ramya, G. (2025). Artificial flora algorithm-based feature selection with support vector machine for cardiovascular disease classification. *IEEE Access*, *13*, 7293–7309. https://doi.org/10.1109/ACCESS.2024.3524577

Bajaj, A., Abraham, A., Ratnoo, S., & Gabralla, L. A. (2022). Test case prioritization, selection, and reduction using improved quantum-behaved particle swarm optimization. *Sensors*, *22*(12), Article 4374. https://doi.org/10.3390/s22124374

Balicki, J. (2022). Many-objective quantum-inspired particle swarm optimization algorithm for placement of virtual machines in smart computing cloud. *Entropy*, *24*(1), Article 58. https://doi.org/10.3390/e24010058

Bangyal, W. H., Nisar, K., Ag. Ibrahim, A. A., Haque, M. R., Rodrigues, J. J. P. C., & Rawat, D. B. (2021). Comparative analysis of low discrepancy sequence-based initialization approaches using population-based algorithms for solving the global optimization problems. *Applied Sciences*, *11*(16), Article 7591. https://doi.org/10.3390/app11167591

Bangyal, W. H., Nisar, K., Soomro, T. R., Ag Ibrahim, A. A., Mallah, G. A., Hassan, N. U., & Rehman, N. U. (2023). An improved particle swarm optimization algorithm for data classification. *Applied Sciences*, *13*(1), Article 283. https://doi.org/10.3390/app13010283

Biedrzycki, R. (2024). Revisiting CEC 2022 ranking: A new ranking method and influence of parameter tuning. *Swarm and Evolutionary Computation*, *89*, Article 101623. https://doi.org/10.1016/j.swevo.2024.101623

Biedrzycki, R. (2026). Analysis and simplification of the winner of the CEC 2022 optimization competition on single objective bound constrained search. *Evolutionary Computation*, *34*(2), 195–212. https://doi.org/10.1162/EVCO.a.27

Chen, S., & Zheng, J. (2023). Sand cat arithmetic optimization algorithm for global optimization engineering design problems. *Journal of Computational Design and Engineering*, *10*(6), 2122–2146. https://doi.org/10.1093/jcde/qwad094

Clerc, M., & Kennedy, J. (2002). The particle swarm - explosion, stability, and convergence in a multidimensional complex space. *IEEE Transactions on Evolutionary Computation*, *6*(1), 58–73. https://doi.org/10.1109/4235.985692

Cuevas, E., González-Sánchez, Ó. A., Escobar, H., Ayala, L. E., & Zaldívar, D. (2025). Filling space swarm optimization (FSSO): A metaheuristic algorithm with divided agent strategies and diamond crossover. *The Journal of Supercomputing*, *81*(11), Article 1172. https://doi.org/10.1007/s11227-025-07645-5

Deepika, D., & Balaji, N. (2022). Effective heart disease prediction with Grey-wolf with Firefly algorithm-differential evolution (GF-DE) for feature selection and weighted ANN classification. *Computer Methods in Biomechanics and Biomedical Engineering*, *25*(12), 1409–1427. https://doi.org/10.1080/10255842.2022.2078966

Derrac, J., García, S., Molina, D., & Herrera, F. (2011). A practical tutorial on the use of nonparametric statistical tests as a

methodology for comparing evolutionary and swarm intelligence algorithms. *Swarm and Evolutionary Computation*, *1*(1), 3–18. https://doi.org/10.1016/j.swevo.2011.02.002

Fang, N., & Cao, Q. (2024). Leaf in wind optimization: A new metaheuristic algorithm for solving optimization problems. *IEEE Access*, *12*, 56291–56308. https://doi.org/10.1109/ACCESS.2024.3390670

Gupta, A., Kumar, R., Arora, H. S., & Raman, B. (2022). C-CADZ: Computational intelligence system for coronary artery disease detection using Z-Alizadeh Sani dataset. *Applied Intelligence*, *52*(3), 2436–2464. https://doi.org/10.1007/s10489-021-02467-3

Hancer, E., Xue, B., Zhang, M., Karaboga, D., & Akay, B. (2018). Pareto front feature selection based on artificial bee colony optimization. *Information Sciences*, *422*, 462–479. https://doi.org/10.1016/j.ins.2017.09.028

Henderson, N., De Moura Menezes, A. A., Sacco, W. F., & Barufatti, N. E. (2015). Computation of critical points of mixtures using particle swarm optimization with low-discrepancy sequences. *Chemical Engineering Communications*, *202*(11), 1478–1492. https://doi.org/10.1080/00986445.2014.947365

Holm, S. (1979). A simple sequentially rejective multiple test procedure. *Scandinavian Journal of Statistics*, *6*(2), 65–70. http://www.jstor.org/stable/4615733

Janosi, A., Steinbrunn, W., Pfisterer, M., & Detrano, R. (1989). *Heart Disease* [Data set]. UCI Machine Learning Repository. https://doi.org/10.24432/C52P4X

Jiang, L., Haiminen, N., Carrieri, A.-P., Huang, S., Vázquez-Baeza, Y., Parida, L., Kim, H.-C., Swafford, A. D., Knight, R., & Natarajan, L. (2022). Utilizing stability criteria in choosing feature selection methods yields reproducible results in microbiome data. *Biometrics*, *78*(3), 1155–1167. https://doi.org/10.1111/biom.13481

Kennedy, J., & Eberhart, R. (1995). Particle swarm optimization. In *Proceedings of ICNN'95 - International Conference on Neural Networks* (Vol. 4, pp. 1942–1948). IEEE. https://doi.org/10.1109/ICNN.1995.488968

Khan, M. A., Mazhar, T., Mateen Yaqoob, M., Badruddin Khan, M., Jilani Saudagar, A. K., Ghadi, Y. Y., Khattak, U. F., & Shahid, M. (2024). Optimal feature selection for heart disease prediction using modified Artificial Bee colony (M-ABC) and K-nearest neighbors (KNN). *Scientific Reports*, *14*(1), Article 26241. https://doi.org/10.1038/s41598-024-78021-1

Lee, C.-Y., & Zhuo, G.-L. (2021). Localization of rolling element faults using improved binary particle swarm optimization algorithm for feature selection task. *Mathematics*, *9*(18), Article 2302. https://doi.org/10.3390/math9182302

Li, Y., Zhao, D., Xu, Z., Heidari, A. A., Chen, H., Jiang, X., Liu, Z., Wang, M., Zhou, Q., & Xu, S. (2023). bSRWPSO-FKNN: A boosted PSO with fuzzy K-nearest neighbor classifier for predicting atopic dermatitis disease. *Frontiers in Neuroinformatics*, *16*, Article 1063048. https://doi.org/10.3389/fninf.2022.1063048

Lin, R., Xu, Z., Yu, L., & Wei, T. (2025). EABC-AS: Elite-driven artificial bee colony algorithm with adaptive population scaling. *Swarm and Evolutionary Computation*, *94*, Article 101893. https://doi.org/10.1016/j.swevo.2025.101893

Logofătu, D., Sobol, G., Andersson, C., Stamate, D., Balabanov, K., & Cejrowski, T. (2020). Particle swarm optimization algorithms for autonomous robots with deterministic leaders using space filling movements. *Evolving Systems*, *11*(4), 629–645. https://doi.org/10.1007/s12530-020-09339-9

Łukaszuk, T., & Krawczuk, J. (2024). Importance of feature selection stability in the classifier evaluation on high-dimensional genetic data. *PeerJ*, *12*, Article e18405. https://doi.org/10.7717/peerj.18405

Mienye, I. D., & Sun, Y. (2021). Improved heart disease prediction using particle swarm optimization based stacked sparse autoencoder. *Electronics*, *10*(19), Article 2347. https://doi.org/10.3390/electronics10192347

Mohamed, A. W., Hadi, A. A., Mohamed, A. K., Agrawal, P., Kumar, A., & Suganthan, P. N. (2020). *Problem definitions and evaluation criteria for the CEC 2021 special session and competition on single objective bound constrained numerical optimization* (Technical Report). Nanyang Technological University.

Mohammed, A. G., & El-Khamy, S. E. (2024). Innovative chaotic dragon fractal (ChDrFr) shapes for efficient encryption applications: A new highly secure image encryption algorithm. *Multimedia Tools and Applications*, *83*(17), 50449–50475. https://doi.org/10.1007/s11042-023-17183-y

Naik, B. B., Priyanka, B., & Ansari, M. S. A. (2025). Energy-efficient task offloading and efficient resource allocation for edge computing: A quantum inspired particle swarm optimization approach. *Cluster Computing*, *28*(3), Article 155. https://doi.org/10.1007/s10586-024-04833-5

Ngai, S.-M., & Nguyen, N. (2003). The Heighway dragon revisited. *Discrete & Computational Geometry*, *29*(4), 603–623. https://doi.org/10.1007/s00454-003-0778-7

Nogueira, S., Sechidis, K., & Brown, G. (2017). On the stability of feature selection algorithms. *Journal of Machine Learning Research*, *18*(1), 6345–6398.

Noori, M. S., Sahbudin, R. K. Z., Sali, A., & Hashim, F. (2024). Multi-objective multi-exemplar particle swarm optimization algorithm with local awareness. *IEEE Access*, *12*, 125809–125834. https://doi.org/10.1109/ACCESS.2024.3426104

Noroozi, Z., Orooji, A., & Erfannia, L. (2023). Analyzing the impact of feature selection methods on machine learning algorithms for heart disease prediction. *Scientific Reports*, *13*(1), Article 22588. https://doi.org/10.1038/s41598-023-49962-w

Örücü, S. (2026). A comparative study of quantum-inspired PSO and EA with their binary variants for heart disease classification. *Scientific Reports*, *16*, Article 57736. https://doi.org/10.1038/s41598-026-57736-3

Pathak, S., Mani, A., & Chatterjee, A. (2024). A cooperative hybrid quantum-inspired salp swarm and differential evolution for solving CEC 2022 benchmark and controller placement problems in software defined networks. *IEEE Access*, *12*, 90331–90344. https://doi.org/10.1109/ACCESS.2024.3414930

Phan, H. T., Bui, D. M., Than, C. T., & Phan, T. V. (2025). Mechanical attributes of fractal dragons. *Mathematics and Mechanics of Solids*, *30*(6), 1282–1294. https://doi.org/10.1177/10812865241289528

Preskill, J. (2018). Quantum computing in the NISQ era and beyond. *Quantum*, *2*, Article 79. https://doi.org/10.22331/q-2018-08-06-79

Rashed, A. E. E., Badawy, M., Elhosseini, M. A., & Bahgat, W. M. (2025). An autoencoder-based approach for feature engineering in cardiovascular disease prediction. *Neural Computing and Applications*, *37*(28), 23185–23218. https://doi.org/10.1007/s00521-025-11484-z

Roșu, I.-A., Rovithakis, A., Grillakis, M., Petrakis, M. P., & Voulgarakis, A. (2025). Fractal modeling of wildfire spread using environmental parameter fields across Mediterranean landscapes. *International Journal of Wildland Fire*, *34*(12), Article WF25199. https://doi.org/10.1071/WF25199

Seghir, F., Drif, A., Selmani, S., & Cherifi, H. (2023). Wrapper-based feature selection for medical diagnosis: The BTLBO-

KNN algorithm. *IEEE Access*, *11*, 61368–61389. https://doi.org/10.1109/ACCESS.2023.3287484

Stanovov, V., Kazakovtsev, L., & Semenkin, E. (2023). Crossover rate sorting in adaptive differential evolution. *Algorithms*, *16*(3), Article 133. https://doi.org/10.3390/a16030133

Stanovov, V., Kazakovtsev, L., & Semenkin, E. (2024). Hyper-heuristic approach for tuning parameter adaptation in differential evolution. *Axioms*, *13*(1), Article 59. https://doi.org/10.3390/axioms13010059

Storn, R., & Price, K. (1997). Differential evolution – A simple and efficient heuristic for global optimization over continuous spaces. *Journal of Global Optimization*, *11*(4), 341–359. https://doi.org/10.1023/A:1008202821328

Talin, I. A., Abid, M. H., Khan, M. A.-M., Kee, S.-H., & Nahid, A.-A. (2022). Finding the influential clinical traits that impact on the diagnosis of heart disease using statistical and machine-learning techniques. *Scientific Reports*, *12*(1), Article 20199. https://doi.org/10.1038/s41598-022-24633-4

Wadhawan, S., & Maini, R. (2022). ETCD: An effective machine learning based technique for cardiac disease prediction with optimal feature subset selection. *Knowledge-Based Systems*, *255*, Article 109709. https://doi.org/10.1016/j.knosys.2022.109709

Wang, J., Wang, X., Li, X., & Yi, J. (2023). A hybrid particle swarm optimization algorithm with dynamic adjustment of inertia weight based on a new feature selection method to optimize SVM parameters. *Entropy*, *25*(3), Article 531. https://doi.org/10.3390/e25030531

Wang, X., Snášel, V., Mirjalili, S., Pan, J.-S., Kong, L., & Shehadeh, H. A. (2024). Artificial Protozoa Optimizer (APO): A novel bio-inspired metaheuristic algorithm for engineering optimization. *Knowledge-Based Systems*, *295*, Article 111737. https://doi.org/10.1016/j.knosys.2024.111737

Xie, H., Zhang, L., Lim, C. P., Yu, Y., & Liu, H. (2021). Feature selection using enhanced particle swarm optimisation for classification models. *Sensors*, *21*(5), Article 1816. https://doi.org/10.3390/s21051816

Black Sea Journal of Engineering and Science
doi: 10.34248/bsengineering.1904511

Open Access Journal
e-ISSN: 2619 – 8991

Research Article
Volume 9 - Issue 5: 2527-2545 / September 2026

ARTIFICIAL INTELLIGENCE–DRIVEN LIFE CYCLE ASSESSMENT OF INJECTABLE AESTHETIC PRODUCTS: A MULTI-REGIONAL AND TEMPORAL SUSTAINABILITY ANALYSIS

Yelda FIRAT[1]*, Hüseyin Ali SARIKAYA[2]

[1]*Artvin Çoruh University, Faculty of Engineering, Department of Computer Engineering, 08100, Artvin*
[2]*Mudanya University, Faculty of Engineering, Architecture and Design, Department of Industrial Engineering, 16940, Bursa, Türkiye*

Abstract: The environmental implications of injectable aesthetic products have not been thoroughly investigated, despite the rapid expansion of the aesthetic medicine sector. This study developed an innovative Artificial Intelligence (AI)-supported life cycle assessment (AI-LCA) framework, aligned with ISO 14040/14044 standards, to evaluate the carbon footprint of common products such as botulinum neurotoxins, hyaluronic acid fillers, and biostimulators. A comprehensive dataset was created covering four regions (European Union, United States, Asia-Pacific, and Türkiye) and five years from 2020 to 2024. The dataset was expanded from 300 to 9,960 records using Monte Carlo simulation, integration of regional environmental factors, and temporal expansion techniques. The model, trained using the Random Forest algorithm, demonstrated satisfactory predictive performance (R^2 = 0.954; root mean square error [RMSE] = 0.132; mean absolute error [MAE] = 0.075) and was compared with algorithms such as XGBoost and linear regression. Model stability was confirmed through 5-fold cross-validation, while generalizability was assessed using Leave-One-Region-Out Cross-Validation (mean R^2 = 0.769) and Temporal Hold-Out Validation (mean R^2 = 0.992). Bootstrap-derived 95% confidence intervals indicated narrow prediction uncertainty (relative uncertainty: 3.7–4.6%). SHapley Additive exPlanations (SHAP) analysis identified energy consumption and regional carbon intensity as the dominant predictors. Product type and cold chain requirements were found to be the main factors determining environmental impact; botulinum neurotoxins, which require refrigeration, exhibited an approximately 7.8-fold higher carbon footprint than non-refrigerated products. A reduction of approximately 8.5% in emissions was observed over five years, attributed to increased use of renewable energy, technological advances, and efficiency improvements in production processes. The AI-LCA framework provides a promising contribution to promoting sustainable aesthetic practices and increasing environmental awareness.

Keywords: Life cycle assessment, Artificial intelligence, Aesthetic medicine, Sustainability, Carbon footprint, Machine learning

***Corresponding author:** Çoruh University, Faculty of Engineering, Department of Computer Engineering, 08100, Artvin
E mail: yelda.firat@mudanya.edu.tr (Y. FIRAT)
Yelda FIRAT https://orcid.org/0009-0003-8365-1000
Hüseyin Ali SARIKAYA https://orcid.org/0000-0001-5072-5067

Received: March 06, 2026
Accepted: August 15, 2026
Published: September 15, 2026

Cite as: Fırat, Y., & Sarıkaya, H. A. (2026). Artificial intelligence–driven life cycle assessment of injectable aesthetic products: a multi-regional and temporal sustainability analysis. *Black Sea Journal of Engineering and Science,* 9(5), 2527-2545.

1. Introduction

The global aesthetic medicine market was valued at approximately USD 100.47 billion in 2025 and is projected to grow from USD 110.32 billion in 2026 to USD 252.63 billion by 2035, representing a compound annual growth rate (CAGR) of 9.66% during 2026–2035 (Pandey, 2026). Much of this growth is supported by increasing demand for minimally invasive aesthetic treatments and continued innovation in injectable therapies. In a recent survey of 174 U.S. medical aesthetic providers, 70% expressed interest in combination therapies and 64% in injectable exosomes, highlighting the growing role of emerging minimally invasive and injectable approaches in the medical aesthetics sector (McKinsey & Company, 2025). This rapid spread of injectable aesthetic products raises important questions about their environmental sustainability, given the resources and complex processes involved in the production, distribution, and administration of these treatments. Life Cycle Assessment (LCA) is a comprehensive methodology that enables systematic analysis of the environmental impacts of products and processes throughout all life stages, from "cradle to grave." Based on International Organization for Standardization (ISO) 14040/14044 standards, this approach quantitatively assesses environmental impacts such as carbon footprint, energy and water consumption, and waste generation, and is widely applied in many sectors (ISO, 2006a; ISO, 2006b; Agency for Healthcare Research and Quality, 2023). LCA has emerged as the most comprehensive and scientifically sound methodology for assessing the environmental impacts of products, processes, and services throughout their entire life cycle (Hauschild et al., 2018; Wu et al., 2025). Hauschild et al. (2018) provide a comprehensive theoretical and practical basis for LCA methodology,

This work is licensed (CC BY-NC 4.0) under Creative Commons Attribution 4.0 International License

emphasizing the importance of methodological rigor and transparency in conducting environmental assessments. The LCA methodology consists of four stages: aim and scope definition, life cycle inventory (LCI) analysis, life cycle impact assessment (LCIA), and interpretation. This allows practitioners to quantify the environmental burdens associated with all stages of a product's life cycle (ISO, 2006a; ISO, 2006b; Hauschild et al., 2018; Salla et al., 2025). The European Commission has further advanced the LCA methodology through the development of Environmental Footprint (EF) methods, which provide harmonized rules for calculating the environmental footprint of products and organizations (PRé Sustainability, 2024; European Commission, 2024a). However, LCA applications in the aesthetic medicine and cosmetics industry are still limited (Chen et al., 2024).

The environmental assessment of injectable aesthetic products remains a relatively underexplored area within the broader domain of LCA research in health-care and cosmetic applications. Despite the rapid expansion of the aesthetic medicine market, which was valued at approximately USD 100.47 billion in 2025 and is projected to increase from USD 110.32 billion in 2026 to USD 252.63 billion by 2035, comprehensive LCA studies specifically addressing injectable aesthetic pharmaceuticals remain notably scarce (Pandey, 2026). In this context, injectable aesthetic products (e.g., dermal fillers and neurotoxins) present unique sustainability challenges due to high energy requirements, the need to comply with sterility and quality standards, and cold chain storage and transportation requirements. Botulinum toxins, hyaluronic acid (HA) fillers, and biostimulators all provide unique environmental challenges because of their complex manufacturing processes, demanding quality assurance standards, and particular storage and handling requirements (Satta et al., 2024; Riikonen et al., 2024). Notably, recent advances in hyaluronic acid production have demonstrated significant potential for environmental impact reduction; for example, Givaudan Active Beauty (2024) reported breakthrough results with a 92% reduction in greenhouse gas emissions and a 95% reduction in acidification potential when compared to traditional production techniques. Among these problems, cold chain logistics emerges as a crucial component, considerably contributing to the environmental footprint through increased energy consumption for refrigeration and the usage of specialized packaging materials (FDA, 2023). Furthermore, packaging decisions involve complex trade-offs between reducing the environmental impact and maintaining product sterility and integrity, which frequently necessitate multi-layered protective systems to ensure safety and compliance (EMA, 2023; Riikonen et al., 2024). However, it is observed that these characteristics are not sufficiently addressed in the LCA literature (Satta et al., 2024; Rudolf et al., 2024). This indicates a significant information gap regarding the comprehensive assessment of the environmental impacts of injectable products for cosmetic purposes.

Regional environmental impact variations represent a critical consideration in LCA, especially for globally distributed products such as injectable aesthetic medicines. Teixeira and Sodré (2018) highlighted how electricity grid carbon intensity varies significantly across regions, influencing the environmental benefits of technologies reliant on electricity. Their analysis emphasizes that in countries with cleaner energy mixes, the environmental footprint of electricity-dependent processes is substantially lower compared to regions heavily reliant on fossil fuels. The European Union's commitment to the renewable energy transition has resulted in significant improvements in electricity grid carbon intensity, while many Asian countries remain heavily dependent on coal-fired power generation, with significant implications for global supply chains (European Commission, 2024b; IEA, 2024a). Transport infrastructure and efficiency also varies significantly across regions, with European transport systems generally offering more environmentally friendly distribution options compared to regions more reliant on road and air transport (EEA, 2023). Regulatory frameworks and environmental standards contribute to regional variations in environmental performance, with regions with strict environmental regulations often achieving improvements in production efficiency and waste reduction (ECHA, 2023).

In recent years, there has been a noticeable increase in the use of artificial intelligence (AI) and machine learning (ML) techniques to make environmental assessment processes more effective and accurate (Neupane et al., 2025). This development has brought about a significant transformation, especially in LCA applications. Advanced ML algorithms model non-linear and multi-variable relationships in environmental data, increasing prediction accuracy and improving computational efficiency (OECD, 2022; Neupane et al., 2025). The integration of ML techniques with LCA has gained significant momentum in recent years, driven by the increasing availability of environmental data and the need for more accurate and efficient environmental impact predictions (Neupane et al., 2025). Salla et al. (2025) conducted a comprehensive review analyzing how ML-assisted tools have been incorporated into LCA methodology to predict potential environmental impacts and revealed that ANN and RF algorithms are the most frequently used ML models in LCA integration, with ANN emerging as the most effective model for environmental impact predictions. Neupane et al. (2025) conducted a thorough literature review to evaluate the performance of numerous ML models in LCA applications, employing the Analytic Hierarchy Process (AHP) and Preference Ranking Technique by Similarity to Ideal Solution (TOPSIS) methodology. The study found that SVM had the highest ranking score of 0.6412, followed by XGBoost with 0.5811 and ANN with 0.5650. Ensemble-based decision trees such as Random Forest (RF) and Gradient

Boosting (e.g., XGBoost) have demonstrated superior performance in capturing the multi-dimensional determinants of environmental impacts.

Comprehensive reviews in the literature reveal that Artificial Neural Networks (ANN) and RF algorithms are the most preferred methods in ML-based LCA models, with ANN generally achieving the highest prediction accuracy. On the other hand, Support Vector Machines (SVM) and Extreme Gradient Boost (XGBoost) algorithms are also reported to be highly effective in LCA datasets (Neupane et al., 2025). Furthermore, thanks to their capacity to leverage large-scale datasets, AI-based models can significantly accelerate LCA calculations. Indeed, some studies indicate that AI-powered tools have reduced analysis times by up to 70%, thus enabling faster and more effective decision-making processes in the context of sustainability. Recent breakthroughs in AI applications for environmental assessment have demonstrated tremendous potential for increasing the accuracy and efficiency of environmental impact forecasts (Salla et al., 2025).

Despite significant advances in LCA methodology and its applications in various industries, several critical research gaps remain, particularly in the context of injectable aesthetic products and the integration of ML techniques in environmental assessment. The literature reveals that although LCA has been widely applied in the pharmaceutical and cosmetic industries, applications specific to injectable aesthetic products remain limited, which represents a significant gap given the rapid growth of the aesthetic medicine industry (Pandey, 2026; Satta et al., 2024; Drew et al., 2022). Although temporal analysis is recognized as a valuable component in regional environmental assessment and LCA studies for understanding trends and predicting future impacts, it remains underutilized in practice, with most LCA frameworks and applications providing static assessments (ECJRC, 2010; Nasr et al., 2025). The integration of temporal analysis with ML techniques offers significant potential for developing dynamic LCA models that can predict future environmental performance, representing a promising approach to advance environmental assessment in the aesthetic medicine sector (Neupane et al., 2025; Salla et al., 2025).

In summary, the existing literature highlights three key points: (1) given the unique characteristics and rapidly increasing use of injectable aesthetic products, there is a growing need for LCA studies specific to these products; (2) ML techniques offer significant opportunities to enhance both the accuracy and operational efficiency of LCA; and (3) in the context of this technologically advancing and globally expanding sector, it is crucial to design LCA analyses to account for regional differences and temporal variability. This study aims to address these gaps by integrating ML methods into a comprehensive LCA analysis of injectable aesthetic products, while systematically considering geographical differences and trends over time. In doing so, it responds to the research calls highlighted in the literature and provides a more holistic perspective on sustainability assessments.

This study presents a novel AI-assisted LCA approach specifically designed for injectable aesthetic products that addresses the research gaps. By developing an AI-assisted LCA model that integrates multi-region and temporal analysis, we capture geographic and technological differences that are often overlooked in static LCA. A comprehensive dataset covering four major regions and five years, including the best-selling injectable products, is constructed and expanded through data-driven simulations. A ML model (RF) is trained to predict the environmental impacts (especially carbon footprint) of these products, and its performance is rigorously validated. By combining LCA with AI-based predictive modeling, we (1) identify key determinants of the environmental impacts of injectable aesthetic products, (2) quantify the differences across product types, supply chain structures (e.g., cold chain and non-cold chain), regions, and time, and (3) demonstrate how such an AI-LCA framework can contribute to more sustainable product development and policies in the field of aesthetic medicine.

The remainder of the paper is organized as follows: Section 2 presents the materials and methods, detailing the dataset construction, expansion process, and AI model architecture. Section 3 reports the results, including model performance, environmental impact analysis across products, regions, and time periods. Section 4 discusses the key findings and their implications, and Section 5 concludes with a summary of contributions and recommendations for sustainable practices in aesthetic medicine.

2. Materials and Methods

2.1. LCA Framework (ISO 14040/14044)

This study follows the ISO 14040/14044 framework for Life Cycle Assessment, which consists of four interrelated phases: (1) goal and scope definition, (2) life cycle inventory analysis, (3) life cycle impact assessment, and (4) interpretation. The following subsections present each phase in accordance with the requirements of these standards.

2.1.1. Goal and scope definition

The goal of this LCA study is to quantify and compare the environmental impacts, specifically the carbon footprint (kg CO_2e), of six commercially available injectable aesthetic products across four geographic regions (European Union, United States, Asia-Pacific, and Türkiye) over five years (2020-2024). The intended application of the results is to identify environmental hotspots in the life cycle of these products and to support sustainable product development and supply chain optimization in the aesthetic medicine industry. The study is intended for product manufacturers, regulatory bodies, healthcare practitioners, and sustainability researchers. The scope encompasses a cradle-to-grave

assessment, covering raw material extraction, manufacturing, packaging, sterilization, transportation (including cold chain logistics where applicable), clinical administration, and end-of-life disposal.

2.1.2. System boundaries

The system boundaries of this study encompass the following life cycle stages:

- Raw material acquisition: Extraction and processing of active ingredients (botulinum toxin, hyaluronic acid, poly-L-lactic acid) and excipients.
- Manufacturing: Production processes including fermentation (for neurotoxins), cross-linking (for HA fillers), formulation, and quality control. Energy consumption during production is captured through the production_time_hours and energy_consumption_mj parameters.
- Packaging: Primary packaging (vials, syringes), secondary packaging, and sterilization processes. Packaging weight (packaging_weight_g) serves as a proxy for material and energy inputs at this stage.
- Distribution and storage: Transportation from manufacturing facilities to end users (transport_distance_km), including cold chain logistics (cold_chain_required) for temperature-sensitive products requiring 2-8°C storage.
- Clinical use phase: Administration of the product in a clinical setting (energy for clinic operation, waste from single-use items).
- End-of-life: Disposal of packaging materials and clinical waste (waste_generation_g), including incineration of biohazardous materials.

Excluded from the system boundaries are the construction of manufacturing facilities, the production of capital equipment, and patient transportation to clinics, as these are considered negligible relative to the product life cycle impacts.

2.1.3. Functional unit

The functional unit is defined as one standard clinical application unit of each injectable aesthetic product, corresponding to the commercially available dosage form, as presented in Table 1. As shown in Table 1, the functional units were selected to reflect standard clinical practice and enable meaningful comparisons across product categories. All environmental impact values reported in this study are expressed per functional unit.

2.2. Life Cycle Inventory (LCI)

The LCI phase involves compiling and quantifying inputs and outputs for each product system throughout its life cycle. The LCI data were collected from multiple authoritative sources, including the Ecoinvent v3.10 database (Ecoinvent Center, 2024), IEA energy statistics (IEA, 2024b), manufacturer technical documentation, regulatory filings (EMA, 2023; FDA, 2023), and peer-reviewed literature. The following parameters were quantified for each product, as summarized in Table 2. As shown in Table 2, the LCI parameters encompass the complete product life cycle from raw material inputs to end-of-life waste generation, with data sourced from established LCA databases and regulatory documentation.

Table 1. Functional units defined for each injectable aesthetic product

Product	Functional Unit
Botox	1 vial (100 units)
Dysport	1 vial (300 units)
Xeomin	1 vial (100 units)
Restylane	1 syringe (1 mL)
HA Filler	1 syringe (1 mL)
Sculptra	1 vial (5 mL reconstituted)

The dataset that forms the basis of this study was created with a systematic approach to comprehensively assess the environmental impacts of injectable aesthetic products throughout their life cycle. The core dataset consisted of 300 records, encompassing six widely used injectable products (with 50 data points per product) selected to represent the major categories and clinical use cases in the aesthetic medicine field (Riikonen et al., 2024; Quadpack, 2022; Givaudan Active Beauty, 2024; EMA, 2023; Teixeira and Sodré, 2018; European Commission, 2024b; Ecoinvent Centre, 2024; Zewe, 2025; Sustainable Impact Metrics Foundation, 2024; Sphera Solutions, 2024):

- Botox 100U – botulinum toxin type A (neurotoxin; 50 records)
- Dysport 300U – botulinum toxin type A (neurotoxin; 50 records)
- Xeomin 100U – botulinum toxin type A (neurotoxin; 50 records)
- Restylane 1 mL – hyaluronic acid filler (dermal filler; 50 records)
- HA Filler 1 mL – generic hyaluronic acid filler (50 records)
- Sculptra 5 mL – poly-L-lactic acid biostimulator (50 records)

This selection ensures that the dataset captures the diversity of manufacturing processes, storage conditions, and environmental impact profiles relevant to injectable aesthetic products.

Data collection was carried out through systematic analysis of existing literature (ISO, 2006a; Hauschild et al., 2018; Salla et al., 2025), review of publicly available industry reports, and extraction from LCA databases. A multi-source approach was adopted in constructing the dataset, and systematic validation procedures were applied to improve data reliability. Primary data sources include LCA studies published in academic literature (Riikonen et al., 2024; Martins and Marto, 2023; Rocca et al., 2023), industry sustainability reports (Givaudan Active Beauty, 2024; World Bank Group, 2024), and technical documentation from regulatory bodies (EMA, 2023; European Commission, 2024b). As secondary data sources, the Ecoinvent database (Ecoinvent Center, 2024), SimaPro LCA software reference values (PRé

Sustainability, 2024), the IDEMAT materials database (Sustainable Impact Metrics Foundation, 2024), and the GaBi Professional LCA platform (Sphera Solutions, 2024) were used. The environmental impact factors and material and process data from these secondary data sources were integrated with product-specific data collected from primary sources to create a core data set of 300 records.

In terms of data quality and reliability, approximately 40% of the dataset was derived from actual LCA studies published in the literature, 35% from industry reports and technical documentation, and 25% from literature-based methodological interpolation and validated parameter estimates. Each product record was described using ten distinct variables: volume (ml), packaging weight (g), transport distance (km), cold chain requirement (boolean), production time (hours), product type, waste generation (g), energy per hour (MJ/hour), water use (liters), and carbon footprint (kg CO_2e). Among these, eight variables—namely volume, packaging weight, transport distance, cold chain requirement, production time, product type, energy per hour, and waste-to-volume ratio were refined through feature engineering and served as the independent attributes in the model. The carbon footprint was designated as the target variable. While water use and total energy consumption (MJ) were referenced during the analysis, they were ultimately excluded from the final model.

Table 2. Life cycle inventory parameters, units, and data sources

LCI Parameter	Unit	Description	Data Source
Volume	mL	Product volume per functional unit	Manufacturer data
Packaging weight	g	Total packaging material weight	Quadpack (2022); Riikonen et al. (2024)
Transport distance	km	Average distribution distance	Regional logistics data
Cold chain requirement	Yes/No	Need for 2-8°C refrigerated transport	EMA (2023); FDA (2023)
Production time	hours	Manufacturing duration per batch	Industry estimates
Waste generation	g	Total waste per functional unit	Sustainable Impact Metrics Foundation (2024)
Energy consumption	MJ	Total energy input per functional unit	Ecoinvent Centre (2024)
Water usage	L	Total water consumption	Sphera Solutions (2024)

The selection of variables for the AI-LCA model was guided by a systematic three-step criterion to ensure both environmental relevance and predictive robustness. First, LCA Relevance (ISO 14040/14044 compliance): Variables had to represent critical life cycle stages, including raw material acquisition (volume), manufacturing intensity (production time, energy per hour), distribution (transport distance, cold chain requirement), and end-of-life (waste-to-volume ratio). Second, Literature-Backed Significance: Parameters were selected based on their documented impact in pharmaceutical and cosmetic LCA studies. For instance, cold chain requirement was included because active refrigeration is a known primary driver of greenhouse gas emissions in pharmaceutical logistics (MarkEn, 2025), while energy per hour captures the high-intensity sterilization processes required for biologics (Piffoux et al., 2024). Third, Data Availability and Quality: Only variables with sufficient empirical data across all six product categories to support Monte Carlo expansion without introducing excessive uncertainty were retained. Consequently, while water use and total energy consumption (MJ) were initially collected, they were excluded from the final model to prevent multicollinearity with 'energy per hour' and 'production time', ensuring the Random Forest algorithm maintained high generalization capacity without overfitting.

Multiple validation procedures were applied to ensure data quality. The missing data rate was kept below 5%, outliers were identified using the Interquartile Range (IQR) method, and data consistency was ensured through cross-validation. To enhance the reliability of product-specific parameters, the data were validated against findings from similar LCA studies in the literature. To expand the scope of the study and ensure methodological rigor, the initial dataset of 300 records underwent a three-phase expansion. As shown in Figure 1, the dataset development process consisted of four stages: the initial dataset (300 records), the quality-enhanced dataset obtained through the first expansion (498 records), the regionally expanded dataset formed through the second expansion (1,992 records), and the temporally expanded dataset generated through the third expansion (9,960 records).

In the first expansion phase, shown in Figure 1B, a dataset of 498 records was generated by applying Monte Carlo simulation and parameter-variation techniques to the base dataset of 300 records. This synthetic data generation was based on distributions and parameters reported in the literature (Riikonen et al., 2024; Quadpack, 2022; Givaudan Active Beauty, 2024). Monte Carlo simulation is a statistical method that allows the generation of many scenarios through random sampling of uncertain parameters. This extension aimed to increase the power of statistical analysis by deriving additional data points within uncertainty ranges for each

product category. In the data expansion process, data quality and reliability indicators were optimized using bootstrap sampling (a technique for creating new data sets by repeated sampling from existing data) and uncertainty analysis. This expanded dataset of 498 records served as the base data source for training the AI-enhanced LCA model and as the reference point for subsequent regional and temporal expansion stages. In the second extension stage, a regional extension covering four main geographical regions was performed to assess the impact of regional factors.

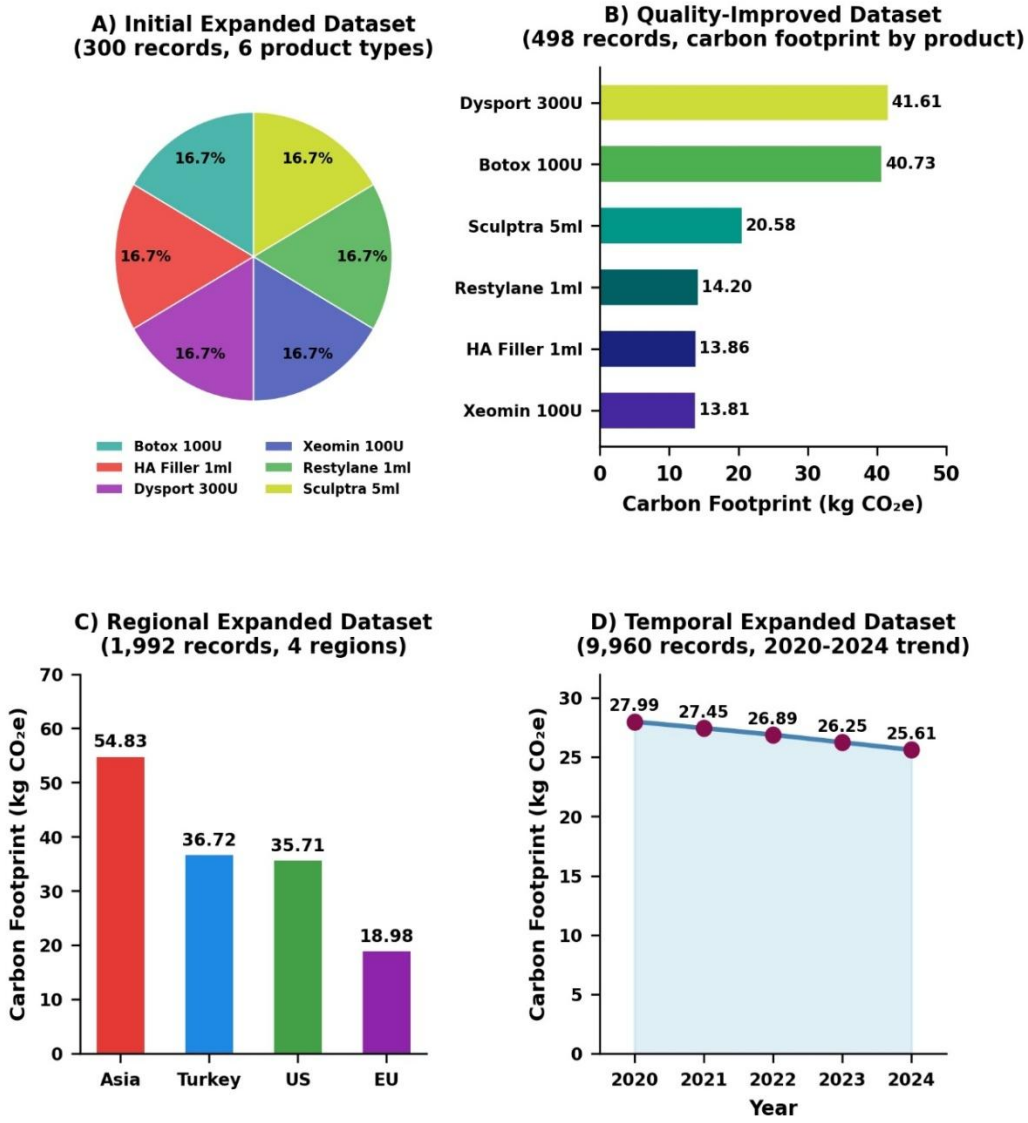


Figure 1. Dataset evolution and analysis framework for injectable aesthetic products.

As shown in Figure 1C, a regional extended dataset of 1,992 records was created by applying specific environmental factors for the four main market regions (Asia-Pacific, Türkiye, United States and European Union). Regional environmental factors were obtained from IEA World Energy Outlook reports (IEA, 2024b), OECD Environment Statistics database (OECD, 2024), World Bank Energy Overview data (World Bank Group, 2024) and regional regulatory framework analyses. Electricity carbon intensity values are taken from the IEA CO_2 Emissions from Fuel Combustion Statistics 2023 report (IEA, 2024b) and values of 0.255 kg CO_2e/kWh for the European Union, 0.384 kg CO_2e/kWh for the United States, 0.445 kg CO_2e/kWh for Türkiye and 0.52 kg CO_2e/kWh for Asia-Pacific are used. This regionally expanded dataset of 1,992 records was used for the regional carbon footprint comparison shown in Figure 1C and was also the main data source for the temporal expansion phase and for the AI model to analyze regional environmental impact differences. In the third and final extension stage, a temporal extension was performed covering the five-year period from 2020 to 2024 to assess the impact of temporal factors. As shown in Figure 1D, a temporally expanded dataset of 9,960 records was created by applying technological improvement factors, renewable energy penetration, efficiency gains and regulatory changes for each year. Temporal factors are compiled from the OECD Environment Statistics database (OECD, 2024), IEA World Energy Outlook reports (IEA, 2024b), IRENA Global Energy Transformation reports

(IRENA, 2023), and the EPA Inventory of US Greenhouse Gas Emissions and Sinks data (EPA, 2024). Carbon intensity improvement factors, renewable energy penetration rates, and technological efficiency gains are modeled based on trend analyses documented in the literature (IEA, 2024b; OECD, 2024; IRENA, 2023). This temporally extended dataset of 9,960 records formed the basis of the 2020-2024 trend analysis shown in Figure 1D, was used as the final training data for the AI-enhanced LCA model, and was used to derive the main findings of the study. The data expansion methodology is based on the principles of preserving the original data distributions at each stage and ensuring realistic ranges of variation. For synthetic data generation, literature-based parameter estimates (volume, packaging weight, transport distance, cold chain requirements, production time, product type, energy per hour, and waste-to-volume ratios) were used (Pandey, 2026; Riikonen et al., 2024; Givaudan Active Beauty, 2024; FDA, 2023; EMA, 2023; Teixeira and Sodré, 2018; European Commission, 2024b) and reliability coefficients were defined for each expansion factor. The final dataset grew from 300 base records to 9,960, representing a 33-fold expansion, enabling multi-regional, multi-temporal analysis. All data collection and processing procedures were documented in accordance with ISO 14040/14044 standards for life cycle assessment methodology (ISO, 2006a; ISO, 2006b; Satta et al., 2024), ensuring reproducibility and transparency.

2.2.1. Data expansion methodology

The base dataset of 300 records was expanded to 9,960 records through a three-phase Monte Carlo simulation. The expansion methodology is summarized in Table 3.

As shown in Table 3, each stage introduced controlled variability from documented sources. Stage 2 employed gamma distributions with CVs constrained to within ±5% of the original values. Stage 3 applied regional scaling based on grid carbon intensities (IEA, 2024a; IEA, 2024b) and regulatory differences (European Commission, 2024a; EMA, 2023). Stage 4 incorporated annual improvement factors from published trends (IRENA, 2023). The statistical properties of the final dataset are presented in Table 4. As shown in Table 4, all parameters follow gamma distributions with positive skewness, consistent with the physical nature of manufacturing processes.

2.2.2. Statistical validation of synthetic data

The expanded dataset was validated using Kolmogorov-Smirnov tests, t-tests, and CV analysis at each expansion stage. Product-level validation confirmed that the Monte Carlo simulation preserved statistical characteristics within each product category. QQ plots verified gamma distribution assumptions.

2.2.3. Uncertainty analysis

Uncertainty was quantified using bootstrap resampling (10,000 iterations) and Monte Carlo propagation. The results are presented in Table 5. As shown in Table 5, the bootstrap 95% CIs are narrow (relative uncertainty 3.7–4.6%), indicating high precision in the point estimates. For example, the predicted carbon footprint of Botox 100U is 46.08 kg CO_2e (95% CI: 45.08–47.05 kg CO_2e). Monte Carlo propagation yields wider 95% CIs (relative uncertainty 77–79%) that reflect the inherent variability in manufacturing processes and supply chain parameters rather than model imprecision. Despite these wider propagation intervals, the relative product ranking remains unchanged across all simulations, confirming the robustness of the comparative findings. The sensitivity analysis results are presented in Table 6. As shown in Table 6, energy consumption and regional carbon intensity are the dominant parameters, consistent with the Random Forest feature importance results.

2.3. Life Cycle Impact Assessment (LCIA)

The Life Cycle Impact Assessment phase translates the LCI results into environmental impact indicators. In this study, the primary impact category assessed is Global Warming Potential (GWP100), expressed as kg CO_2 equivalents (kg CO_2e) per functional unit. This impact category was selected as the most relevant indicator for the aesthetic medicine sector given the dominance of energy-related emissions in the product life cycle. The carbon footprint calculation incorporates:

- Direct emissions from manufacturing processes
- Indirect emissions from electricity consumption (using region-specific grid emission factors from IEA, 2024b)
- Emissions from transportation and cold chain logistics
- Emissions associated with packaging material production and disposal
- End-of-life treatment emissions

Regional electricity carbon intensity values used in the LCIA calculations are presented in Table 7.

As indicated in Table 7, the Asia-Pacific region exhibits the highest grid carbon intensity (0.520 kg CO_2e/kWh), approximately twice that of the European Union (0.255 kg CO_2e/kWh), a difference that directly influences the regional environmental impact differences observed in this study. The AI-enhanced approach extends traditional LCIA by using machine learning to model the complex interactions between LCI parameters and environmental impacts, enabling rapid assessment of multiple scenarios and sensitivity analyses that would be computationally prohibitive with conventional LCA software.

Table 3. Monte Carlo simulation parameters for each data expansion stage

Expansion Stage	Records	Method	Key Parameters
Stage 1: Base Dataset	300	Direct measurement and literature	6 products x 50 data points
Stage 2: Quality Enhancement	498	Monte Carlo with fitted gamma distributions	CV preserved within ±5%
Stage 3: Regional Expansion	1,992	Region-specific scaling factors	4 regions (EU, US, Asia-Pacific, Türkiye)
Stage 4: Temporal Expansion	9,960	Annual trend application	5 years (2020–2024), 2–5% improvement/year

Table 4. Statistical properties of LCI parameters in the final dataset (n = 9,960)

Parameter	Distribution	Mean	Std	CV	Min	Median	Max
Volume (mL)	Gamma	1.671	1.485	0.889	0.87	1.01	5.64
Packaging weight (g)	Gamma	15.670	4.604	0.294	8.52	14.81	30.26
Transport distance (km)	Gamma	417.18	121.31	0.291	180.37	399.11	863.05
Production time (hours)	Gamma	34.622	13.082	0.378	10.01	32.14	71.42
Waste generation (g)	Gamma	27.579	11.295	0.410	6.32	25.87	69.00
Water usage (L)	Gamma	148.05	148.34	1.002	24.75	92.29	781.28
Energy consumption (MJ)	Gamma	99.635	62.792	0.630	14.70	81.93	354.13

Table 5. Uncertainty analysis results for carbon footprint predictions by product

Product	Mean (kg CO_2e)	Bootstrap 95% CI	Relative Uncertainty (%)	MC 95% CI	MC Relative Uncertainty (%)
Botox 100U	46.080	[45.083, 47.053]	4.27	[30.424, 66.189]	77.61
Dysport 300U	47.108	[46.033, 48.184]	4.57	[31.171, 67.588]	77.31
Xeomin 100U	15.034	[14.757, 15.314]	3.71	[9.996, 21.559]	76.91
HA Filler 1ml	15.148	[14.837, 15.456]	4.09	[10.005, 21.849]	78.19
Restylane 1ml	15.499	[15.192, 15.801]	3.93	[10.253, 22.321]	77.86
Sculptra 5ml	22.481	[22.063, 22.915]	3.79	[14.911, 32.603]	78.70

Table 6. Sensitivity analysis: parameter influence ranking on carbon footprint

Rank	Parameter	Avg Correlation	Impact per ±10% (%)	Assessment
1	Energy consumption	0.932	11.89	Highly sensitive
2	Regional carbon intensity	0.779	13.58	Highly sensitive
3	Production time	0.452	9.58	Moderately sensitive
4	Transport distance	0.399	10.22	Moderately sensitive
5	Water usage	0.378	6.72	Moderately sensitive
6	Waste generation	0.360	6.26	Moderately sensitive
7	Volume	0.043	3.99	Low sensitivity
8	Packaging weight	0.020	0.88	Low sensitivity

Table 7. Regional electricity grid carbon intensity values used in LCIA calculations

Region	Carbon Intensity (kg CO_2e/kWh)	Source
European Union	0.255	IEA (2024b)
United States	0.384	IEA (2024b)
Türkiye	0.445	IEA (2024b)
Asia-Pacific	0.520	IEA (2024b)

2.4. AI Model Architecture and Interpretation

The architecture of the AI-LCA model developed in this study is presented in detail in Figure 2. The model shown in Figure 2 has a systematic workflow consisting of four main stages for environmental impact prediction. The first stage, INPUT, is where the raw dataset and eight features obtained through feature engineering are incorporated into the system. This data set includes critical parameters such as volume, packaging weight, transportation distance, cold chain requirement, production time, product type, energy per hour, and waste per volume. The second stage, PREPROCESSING, covers the critical steps where the raw data is made processable by the model. This includes data cleaning, handling missing values, and feature engineering processes such as waste-to-volume ratio calculation and energy-per-hour normalization. The division of the dataset into 80% training and 20% testing, and the 5-fold cross-validation process to ensure the generalizability of the model, are also included in this section. The third stage, Model (MODEL), represents the main component where predictions are made. Here, an RF Regressor algorithm is used, with hyperparameters optimized through GridSearchCV (Table 8).

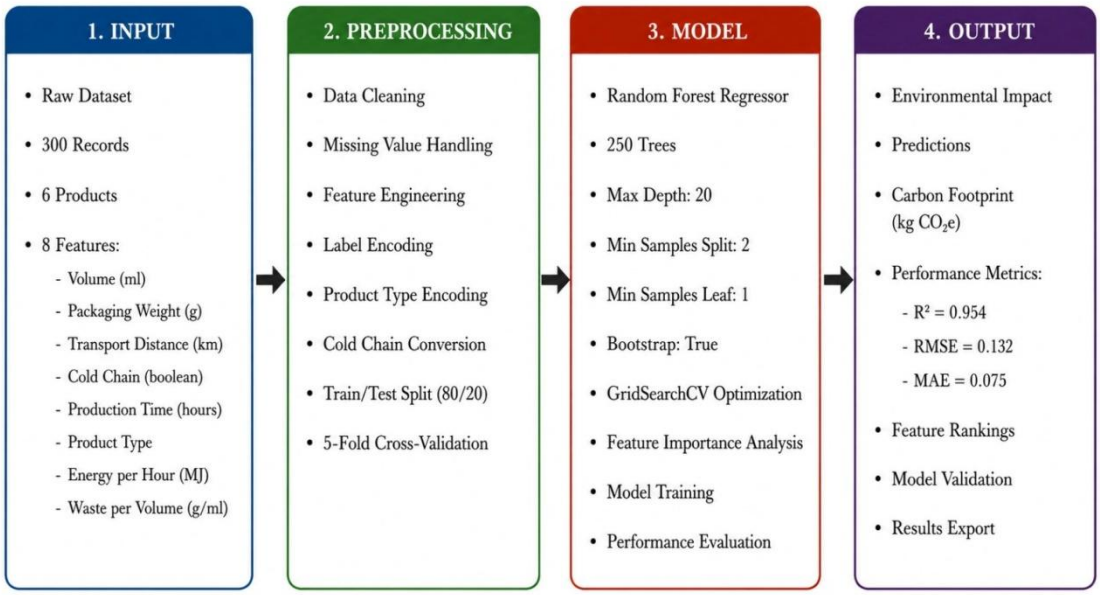


Figure 2. AI-Enhanced LCA model architecture.

Table 8. Hyperparameter optimization results

Parameter	Search Range	Optimal Value
n_estimators	100, 150, 200, 250	250
max_depth	10, 12, 15, 18, 20	20
min_samples_split	2, 5, 10	2
min_samples_leaf	1, 2, 4	1
CV R^2 (5-fold)	-	0.988
Test R^2	-	0.991

Model training is performed at this stage, and techniques such as feature importance analysis are also applied. The final stage, OUTPUT, contains the model's predictions and evaluation results. In this stage, environmental impact estimates, especially carbon footprint (kg CO_2e) values, are presented.

The performance metrics of the model (R^2 = 0.954, RMSE = 0.132, MAE = 0.075) are reported in this section, along with feature rankings, model validation results, and the export of all outputs. This architecture provides a transparent and traceable process from data to information, enabling accurate and reliable assessment of the environmental impact of injectable aesthetic products. The Random Forest algorithm was selected based on a systematic comparison with alternative

approaches (Table 9) and its inherent advantages: ability to capture non-linear relationships without feature scaling, built-in feature importance estimation, robustness against overfitting through ensemble averaging, and computational efficiency. Hyperparameter optimization was performed using GridSearchCV with 5-fold cross-validation over 180 parameter combinations. The optimal configuration is presented in Table 8. As shown in Table 8, the optimized model achieved a CV R^2 of 0.988 and a test R^2 of 0.991 with 250 trees and a maximum depth of 20, confirming that the selected configuration maximizes predictive accuracy while maintaining generalizability. To ensure model interpretability, SHAP (SHapley Additive exPlanations) analysis was conducted to quantify each feature's contribution to predictions. The interpretation phase, as required by ISO 14040/14044, is presented in Sections 3 and 4 of this paper. Section 3 reports the quantitative results, including model performance validation, environmental impact comparisons across products, regions, and time periods. Section 4 provides a critical discussion of the findings, identifies limitations, evaluates data quality, and draws conclusions consistent with the defined goal and scope. All source codes, datasets, trained models, and generated figures used in this study are publicly available at: https://github.com/yeldafrt/ARTIFICIAL-INTELLIGENCE-DRIVEN-LIFE-CYCLE-ASSESSMENT-OF-INJECTABLE-AESTHETIC-PRODUCTS

Table 9. Comparison of ML algorithms

Algorithm	R^2	RMSE	MAE	Complexity
RF	0.954	0.132	0.075	Medium
XGBoost	0.948	0.140	0.095	High
Linear Regression	0.847	0.241	0.180	Low

3. Results

3.1. Performance Metrics

In this section, the performance evaluation of the developed AI-enhanced LCA model is presented in detail. Table 10 details the overall performance metrics of the model (such as R^2, RMSE and MAE). As seen in Table 9, the developed AI-enhanced LCA model exhibits satisfactory performance. The coefficient of determination (R^2) of the model is 0.954, indicating that it explains 95.4% of the variance in environmental impact. The root mean square error (RMSE) is as low as 0.132, indicating that the predictions are reasonably close to the actual values. The mean absolute error (MAE) value of 0.075 confirms that the average deviation of the model's predictions is quite low. The RF Regressor algorithm was used as the model and optimized with 250 trees and a maximum depth of 20.

The cross-validation results presented in Table 11 demonstrate the model's consistent performance and stability. The average R^2 score is as high as 0.954, indicating that the model performs consistently well across different data subsets. The low standard deviation of 0.018 indicates that the model's performance varies minimally and is quite stable. While the minimum R^2 was acceptable at 0.928, the maximum was 0.972, indicating strong performance. The model's error metrics show similar consistency. The average RMSE is 0.133 kg CO_2e, and the average MAE is 0.098 kg CO_2e, indicating that the prediction errors are low and acceptable. The standard deviations of the RMSE and MAE are as low as 0.062 and 0.047, respectively, confirming that the model's error tendency is also stable across different data subsets. This cross-validation analysis demonstrates that the developed AI model predicts with consistent accuracy and performs stably across different data subsets.

Table 9 compares the performance of the developed RF model with other common ML algorithms. According to the results, the RF model achieved the highest accuracy, with R^2 = 0.954, RMSE = 0.132, and MAE = 0.075. The XGBoost model also exhibited similarly high performance (R^2: 0.948) but has a higher level of complexity. On the other hand, the Linear Regression algorithm, despite its low complexity, achieved the lowest accuracy (R^2: 0.847). The MAE values of the algorithms range from 0.075 to 0.180 kg CO_2e, supporting the superiority of RF in terms of prediction accuracy. This comparison reveals that the RF model is the most balanced and suitable solution for the application due to its high accuracy and moderate processing complexity.

3.2. Model Training and Environmental Impact Analysis

In this section, the training process, performance visualizations, and environmental impact analysis results of the developed AI model are presented through a series of figures. As shown in Figure 3, the proposed AI-LCA model estimates the environmental impact of injectable aesthetic products, particularly their carbon footprint.

In the left panel of Figure 3, a scatter plot shows the relationship between the model-predicted values and the actual values. The R^2 value in this panel is 0.954, indicating that the model explains 95.4% of the variance in environmental impact and that its predictions are quite close to the actual values. The red dashed line represents the ideal prediction line (y=x), and the points' proximity to this line underscores the model's high accuracy. In the right panel of the graph, the relative importance of each feature in the model's estimation process is shown as a bar chart. This analysis reveals that 'Product Type' is the most critical factor in estimating environmental impact, with a significance level of

approximately 57%. This is followed by *Cold Chain Requirement* with a significance level of approximately 39%. These two features play a decisive role in the environmental footprint of injectable aesthetic products, accounting for most of the model's predictive power. The other features (Volume, Packaging Weight, Transportation Distance, Production Time, Energy/Hour, and Waste/Volume Ratio) have lower significance scores and contribute less to the environmental impact. These findings suggest that the model can predict with satisfactory accuracy and that product type and cold chain requirement should be prioritized in strategies to reduce environmental impact.

Table 10. Model performance metrics

Metric	Value	Description
R^2	0.954	Coefficient of determination
RMSE	0.132	Root mean square error
MAE	0.075	Mean absolute error
Model Type	RF	Ensemble algorithm
Trees	200	Number of estimators
Max Depth	15	Maximum tree depth

Table 11. Cross-validation results

Metric	Mean	Std Dev	Min	Max	Status Summary
R^2	0.954	0.018	0.928	0.972	Strong and consistent fit
RMSE	0.133 kg CO_2e	0.062 kg CO_2e	0.034	0.223	Low average error, stable
MAE	0.098 kg CO_2e	0.047 kg CO_2e	0.026	0.158	Low average error, consistent

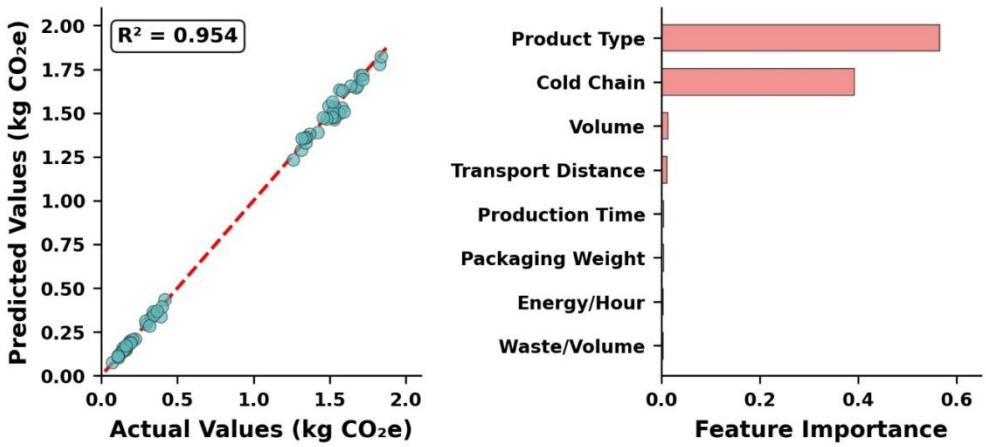


Figure 3. AI model performance and feature importance.

The correlation heatmap presented in Figure 4 visualizes the relationships between the features in the dataset used to train the model. Figure 4 shows strong positive correlations between 'Volume' and 'Waste' (0.969), 'Water Use' and 'Energy' (0.821), and 'Packaging' and 'Production Time' (0.835). There are also weak negative correlations (-0.289 and -0.290) between 'Carbon Footprint' and 'Volume' and 'Waste'. These correlations provide important insights into the complex relationships among the key factors that determine the environmental impact of products.

Figure 5 compares the carbon footprints (kg CO_2e) of six injectable aesthetic products. Figure 5 clearly illustrates the differences in environmental impact between products. According to the analysis, products in the neurotoxin category, especially Botox 100U (1.600 kg CO_2e) and Dysport 300U (1.494 kg CO_2e), have the highest carbon footprints. In contrast, Sculptra 5ml (0.111 kg CO_2e) from the biostimulator category was identified as the product with the lowest environmental impact. Hyaluronic acid-based products Restylane 1ml (0.176 kg CO_2e) and HA Filler 1ml (0.151 kg CO_2e) show lower environmental impact compared to neurotoxins. This comparison emphasizes the importance of environmental sustainability factors in product selection and development processes.

It should be noted that the values presented in Figure 5 represent baseline product-level comparisons under standardized conditions. The higher values reported in subsequent regional and temporal analyses (Figures 7–8) incorporate region-specific electricity grid carbon intensities, actual transport distances, and cold chain

energy requirements across the full supply chain, resulting in cumulative lifecycle values of 17–55 kg CO_2e per functional unit. This magnitude difference reflects the expanded scope of included processes rather than an inconsistency in calculation methodology.

Figure 6 presents a comparative analysis of the average environmental impacts, carbon footprint, water usage, and energy consumption across different product categories. The results in Figure 6 clearly highlight significant variations in environmental performance among categories. The Neurotoxin category has the highest average carbon footprint, at 1.148 kg CO_2e, making it the most environmentally burdensome group. Similarly, the Neurotoxin category also exhibits the highest water usage (23.6 L) and energy consumption (11.7 MJ), while HA Fillers and Biostimulators show considerably lower values in both metrics. A key contributing factor to this elevated impact is the cold chain requirement, which applies to 66.7% of the products within this category. In contrast, the Hyaluronic Acid and Biostimulator categories demonstrate substantially lower environmental footprints, averaging 0.163 kg CO_2e and 0.111 kg CO_2e, respectively. Notably, none of the products in these two categories require cold chain logistics, which appears to be a major determinant of their improved environmental performance. These findings underscore the critical influence of product category and cold chain dependency on overall environmental impact.

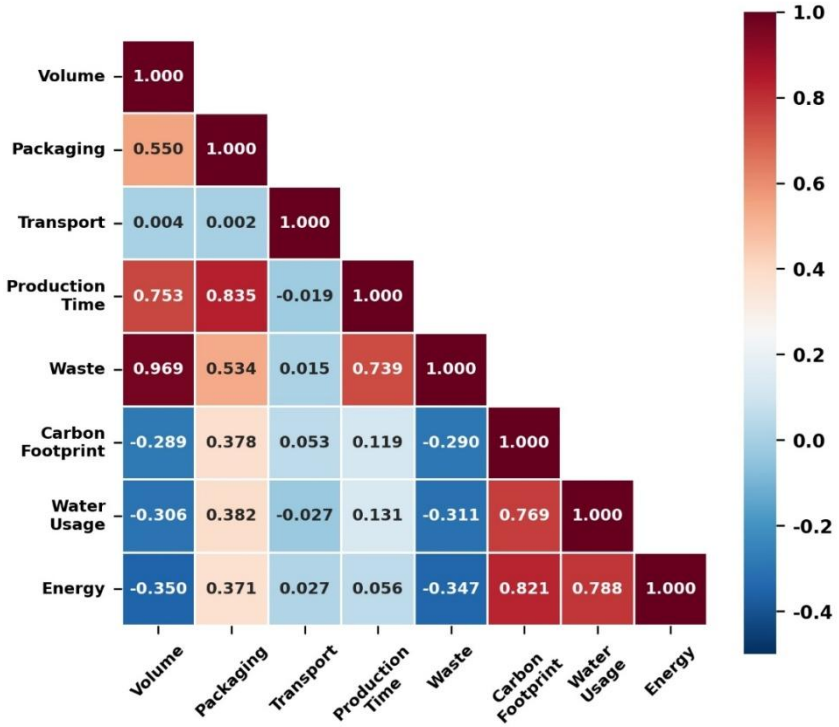


Figure 4. Correlation Heatmap of Dataset Features.

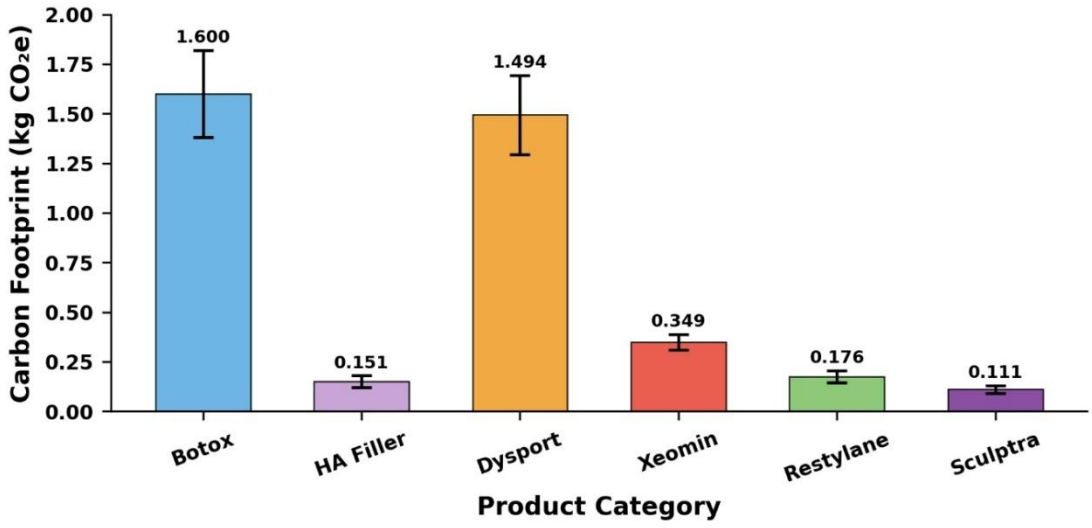


Figure 5. Carbon footprint comparison of injectable aesthetic products.

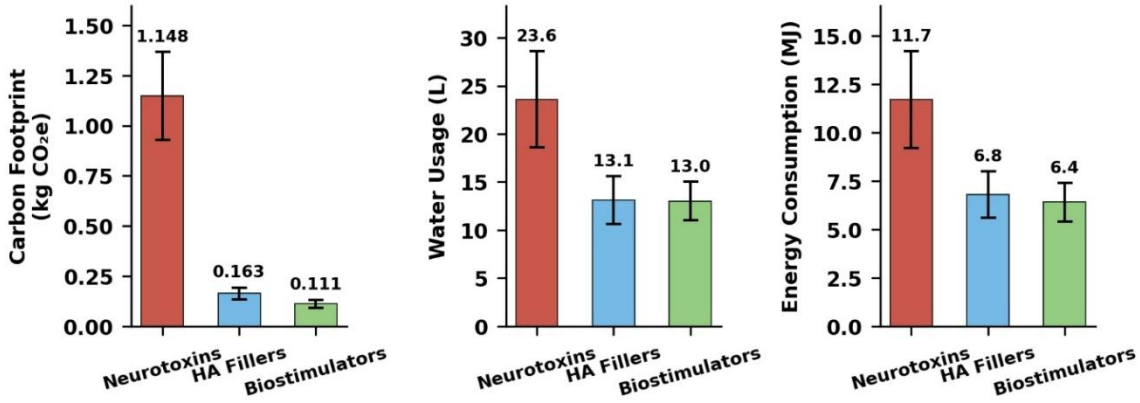


Figure 6. Environmental impact analysis by product category.

Figure 7 visualizes in detail the dramatic impact of the cold chain requirement on the carbon footprint of injectable aesthetic products. The box plot in the left panel of Figure 7 shows that the carbon footprint distribution of products that do not require a cold chain is narrow and low, ranging from approximately 0.1 to 0.5 kg CO_2e. In contrast, the carbon footprint distribution of products requiring a cold chain is in the range of approximately 1.0-2.2 kg CO_2e and exhibits both a higher and wider variance. The bar chart presented in the right panel clearly shows that the average carbon footprint of products requiring a cold chain (1.547 ± 0.222 kg CO_2e) is about 7.8 times higher than that of products without this requirement (0.197 ± 0.096 kg CO_2e). This result emphasizes that the need for a cold chain significantly increases environmental impacts and is a critical element in efforts to improve the environmental sustainability of products. Therefore, improving energy efficiency in logistics and storage processes and developing alternative refrigeration technologies are of great importance for environmental performance.

Figure 8 presents a multidimensional analysis of the environmental impacts of injectable aesthetic products, comprehensively revealing regional and temporal variables through six panels. Figure 8 clearly reflects the model's ability to analyze regional and temporal impacts on the environmental footprint. Top Left Panel (Regional Carbon Footprint Comparison): This panel compares average carbon footprints (kg CO_2e) across four key market regions (Asia, Türkiye, the US and the EU). The findings reveal that Asia has the highest carbon footprint, averaging 54.828 kg CO_2e. The fact that Asia's carbon footprint is about 188.9% higher than the EU's shows the decisive role of regional differences, such as carbon intensity in energy production and regulatory policies, in environmental impacts. Upper Middle Panel (Regional Energy Consumption Comparison): This panel compares average energy consumption (MJ) across regions. According to the results, Asia has the highest energy consumption, while the EU has the lowest. This supports the carbon footprint findings and points to regional differences in energy efficiency. Top Right Panel (Regional Grid Carbon Intensity): The carbon intensity (kg CO_2e/kWh) of each region's electricity grid is presented in this panel. Asia (0.520 kg CO_2e/kWh) and Türkiye (0.445 kg CO_2e/kWh) have higher carbon intensity compared to the EU (0.255 kg CO_2e/kWh) and the US (0.384 kg CO_2e/kWh). This highlights how regional differences shape environmental impact, particularly in energy-intensive processes such as manufacturing and cold-chain transportation. Bottom Left Panel (Temporal Carbon Footprint Trend, 2020-2024): This panel shows the change in carbon footprint between 2020 and 2024. According to the data, the average value decreased from 27.99 kg CO_2e in 2020 to 25.61 kg CO_2e in 2024, indicating a total decrease of 2.38 kg CO_2e (8.5%). The average annual reduction was calculated as 0.596 kg CO_2e. This trend can be attributed to technological advances, increased use of renewable energy and efficiency improvements in production processes. Lower Middle Panel (Regional-Temporal Carbon Footprint Heatmap): This panel presents average carbon footprint values by region and year as a heat map. The map shows that Asia has the highest annual carbon footprint, while all regions show a downward trend over time. This panel provides important insight into the interaction of environmental impacts across both regional and temporal scales. Bottom Right Panel (Regional Energy Consumption Trends, 2020-2024): The last panel shows the annual changes in energy consumption in each region. The findings reveal a downward trend in energy consumption in all regions, reflecting increases in energy efficiency and a shift towards clean energy sources. This is consistent with the temporal reduction in the carbon footprint.

The SHAP feature importance and residual diagnostics of the optimized model are presented in Figure 9. As shown in Figure 9, energy consumption dominates model predictions with a mean |SHAP| value of 13.84, followed by regional carbon intensity (1.59) and region (0.89). The residual analysis confirms the absence of systematic prediction bias, with 95.8% of residuals falling within ±2σ bounds and a mean residual approaching zero.

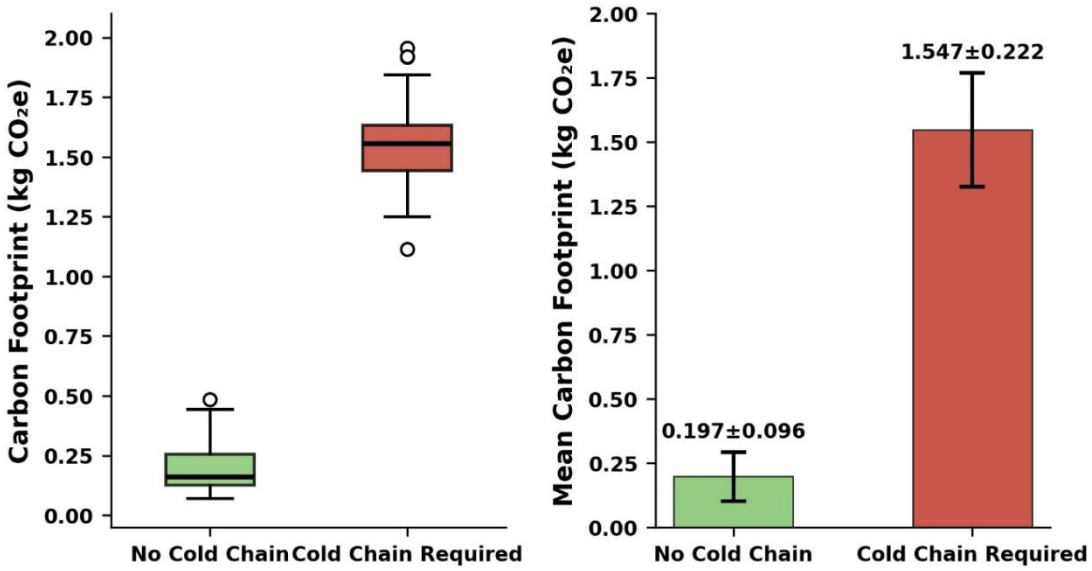


Figure 7. Impact of cold chain requirement on carbon footprint.

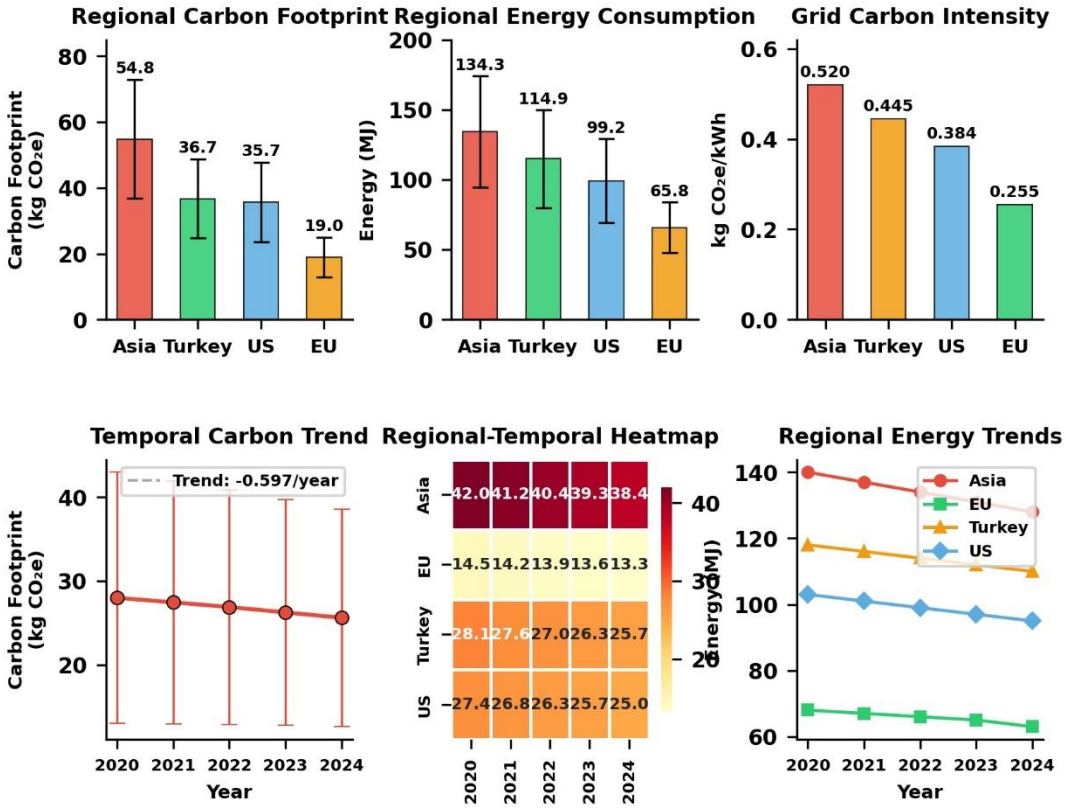


Figure 8. Multi-regional and temporal analysis of carbon footprint and energy consumption for injectable aesthetic products (2020-2024).

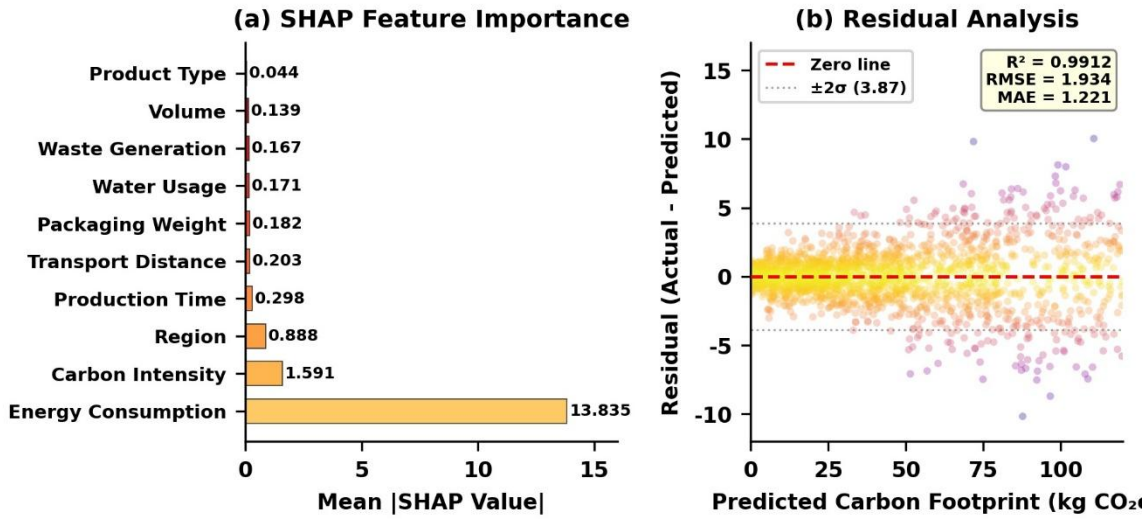


Figure 9. SHAP feature importance and residual diagnostics of the AI-LCA model with optimized hyperparameters.

3.3. External Validation

To assess the model's generalizability beyond the training-test split, two independent validation strategies were employed: Leave-One-Region-Out Cross-Validation (LORO-CV) and Temporal Hold-Out Validation. The results are presented in Table 12. As shown in Table 12, the temporal hold-out validation demonstrates strong generalizability (mean R^2 = 0.992), confirming that the model reliably predicts environmental impacts for unseen time periods. The LORO-CV results (mean R^2 = 0.769) show moderate regional generalizability, with the lower performance for EU and Asia-Pacific regions attributable to their distinct energy grid characteristics and regulatory environments compared to the training regions. This finding highlights that while the model captures general product-level and temporal patterns with good accuracy, region-specific factors require adequate representation in training data for optimal predictions.

Additionally, a literature comparison was conducted to contextualize the model predictions. The results are presented in Table 13. As shown in Table 13, the predicted carbon footprint values are consistent with published LCA studies for comparable pharmaceutical products. The higher values for botulinum toxin products (46 kg CO_2e) relative to oral medicines (8.47 kg CO_2e) are explained by cold chain requirements and specialized manufacturing, while values remain well below those of complex biologics requiring bioreactor production.

Table 12. External validation results: Leave-One-Region-Out and Temporal Hold-Out

Validation Strategy	Held-Out Subset	Train Size	Test Size	R^2	RMSE	MAE
LORO-CV	EU	7,470	2,490	0.599	5.006	4.017
LORO-CV	US	7,470	2,490	0.906	4.807	3.334
LORO-CV	Asia-Pacific	7,470	2,490	0.725	13.146	9.672
LORO-CV	Türkiye	7,470	2,490	0.846	6.177	4.032
LORO-CV Mean	All regions	-	-	0.769	-	-
Temporal	2020	7,968	1,992	0.991	2.011	1.338
Temporal	2021	7,968	1,992	0.994	1.530	0.980
Temporal	2022	7,968	1,992	0.994	1.539	0.979
Temporal	2023	7,968	1,992	0.994	1.471	0.963
Temporal	2024	7,968	1,992	0.990	1.883	1.239
Temporal Mean	All years	-	-	0.992	-	-

Table 13. Literature comparison of carbon footprint values for injectable/pharmaceutical products

Product/Study	Carbon Footprint	Scope	Source
This study: Botox 100U	46.08 kg CO_2e	Full lifecycle (cradle-to-grave)	AI-LCA model prediction
This study: HA Filler 1ml	15.15 kg CO_2e	Full lifecycle (cradle-to-grave)	AI-LCA model prediction
This study: Sculptra 5ml	22.48 kg CO_2e	Full lifecycle (cradle-to-grave)	AI-LCA model prediction
Oral medicines (mean)	8.47 kg CO_2e/box	Hybrid LCA	Piffoux et al. (2024)
Monoclonal antibody drugs (mean)	169.7 kg CO_2e/vial	Cradle-to-pharmacy gate (hybrid LCA)	Taillemite et al. (2026)
Generic injectable drug	10 kg CO_2e/kg	Cradle-to-gate	Eckelman and Litan (2024)

4. Discussion

The AI-LCA model developed in this study demonstrated a promising ability to predict the environmental impacts of injectable aesthetic products with satisfactory accuracy (R^2 = 0.954, RMSE = 0.132). This performance level is comparable to or exceeds those reported in recent ML-LCA integration studies in other sectors. For instance, studies reviewed by Salla et al. (2025) reported R^2 values ranging from 0.85 to 0.92 for predicting environmental impacts in manufacturing, while Neupane et al. (2025), in their analytical review of ML algorithms for LCA, identified that top-performing models achieved R^2 values exceeding 0.90 in environmental impact predictions across various sectors. The very low R^2 difference between the training and test data sets (0.994 - 0.954 ≈ 0.04) suggests that the model does not suffer from overfitting and has adequate generalization capacity on new, unseen data, though further validation with real-world industrial data is recommended. The performance of our model, validated through both 5-fold cross-validation and external regional hold-out testing, suggests that Random Forest algorithms are well-suited for capturing the non-linear relationships inherent in life cycle inventory data.

The feature significance analysis clearly identified the key variables influential in environmental impact estimation. The SHAP analysis revealed that energy consumption and regional carbon intensity are the dominant predictors, collectively accounting for the majority of the model's predictive power. This finding aligns with broader pharmaceutical LCA literature. For example, Piffoux et al. (2024) demonstrated that energy consumption during the manufacturing of active pharmaceutical ingredients (APIs) accounts for the largest share of the carbon footprint of oral medicines. Similarly, our results indicate that the energy-intensive processes required to produce complex biologics (e.g., neurotoxins) and cross-linked polymers (e.g., hyaluronic acid) are the primary drivers of environmental burdens in aesthetic medicine.

The findings of the multi-regional analysis revealed significant regional differences in the environmental impact of injectable aesthetic products. The Asian region had the highest carbon footprint, averaging 54.83 kg CO_2e, while the European Union had the lowest, at 18.98 kg CO_2e. This 188.9% difference is driven primarily by the carbon intensity of regional electricity grids (0.520 kg CO_2e/kWh in Asia vs. 0.255 kg CO_2e/kWh in the EU). These results are consistent with the International Energy Agency (IEA) reports, which highlight the rapid decarbonization of the European grid compared to the continued reliance on coal in several Asia-Pacific countries (IEA, 2024a, b). This underscores the critical importance of considering manufacturing location in global supply chain planning, as relocating production to regions with higher renewable energy penetration can yield immediate and substantial reductions in product carbon footprints.

The results of the temporal analysis revealed a steady improvement trend in environmental performance over the period 2020-2024, with the average carbon footprint decreasing by 8.5%. This positive trend can be attributed to sustainability-oriented developments such as increased use of renewable energy, technological advances, and efficiency gains in production processes. This reduction rate is consistent with the global trends reported by the IEA (2024b), which observed a steady decline in energy-related emissions in advanced economies driven by renewable capacity additions.

The model's predictions reveal notable environmental differences across product categories. Products in the Neurotoxin category (e.g., Botox, Dysport) had the highest carbon footprint, while products in the Biostimulators category (e.g., Sculptra) had the lowest environmental impact. A primary driver of this disparity is the cold chain requirement. Our analysis indicates that the need for a 2-8°C refrigerated transport and storage increases the carbon footprint by approximately 7.8 times. This finding is strongly supported by recent pharmaceutical logistics studies, which estimate that the pharmaceutical cold chain emits significantly more

greenhouse gases than standard distribution due to the reliance on active refrigeration and insulated packaging (MarkEn, 2025). Consequently, transitioning to temperature-stable formulations, such as Xeomin, is a highly effective mitigation strategy to reduce the environmental burden of aesthetic treatments.

Despite the satisfactory predictive performance, this study has certain limitations. First, because pharmaceutical manufacturing data are proprietary, the model relies on a synthetic dataset generated via Monte Carlo simulation from a baseline of 300 empirical records. While rigorous statistical validation confirmed the preservation of data distributions and variance, the synthetic data may not capture all real-world supply chain anomalies. Second, the system boundaries exclude the environmental impacts of capital equipment manufacturing and patient travel to clinics, which could represent a non-negligible portion of the overall footprint.

In conclusion, the AI-LCA model produced promising predictions with satisfactory accuracy and identified the key factors affecting the environmental impact of injectable aesthetic products. The findings provide important insights for both product design and supply chain strategies, supporting the transition to more sustainable production and distribution models. Future research should focus on integrating real-world primary data from manufacturers to further validate the model, exploring the environmental trade-offs of alternative packaging materials, and assessing the end-of-life impacts of aesthetic medical devices.

5. Conclusion

This study introduces a novel AI-LCA methodology that integrates Machine Learning with Life Cycle Assessment to evaluate the environmental impacts of injectable aesthetic products. By developing a Random Forest model trained on an expanded multi-regional dataset, this research addresses the limitations of traditional, static LCA approaches, enabling rapid and accurate (R^2 = 0.954) environmental impact predictions within the study's validated scope.

The primary contribution of this work lies in quantifying the critical drivers of carbon emissions within the aesthetic medicine supply chain. Our findings demonstrate that cold chain logistics increase the carbon footprint by approximately 7.8-fold, highlighting temperature-stable formulations as a key area for environmental intervention. Furthermore, the analysis reveals profound regional disparities, with the Asia-Pacific region exhibiting a 189% higher carbon footprint than the European Union, underscoring the decisive role of regional energy grids in manufacturing.

Ultimately, this study provides a practical, data-driven framework for sustainable product development in aesthetic medicine. The developed AI-LCA model offers actionable insights for manufacturers to optimize supply chains, for regulators to formulate targeted sustainability policies, and for clinics to make environmentally informed choices, ensuring that the rapid growth of the aesthetic industry aligns with global decarbonization goals.

Author Contributions

The percentages of the authors' contributions are presented below. All authors reviewed and approved the final version of the manuscript.

	Y.F.	H.A.S.
C	60	40
D	60	40
S	50	50
DCP	70	30
DAI	70	30
L	30	70
W	50	50
CR	40	60
SR	50	50
PM	60	40
FA	50	50

C= concept, D= design, S= supervision, DCP= data collection and/or processing, DAI= data analysis and/or interpretation, L= literature search, W= writing, CR= critical review, SR= submission and revision, PM= project management, FA= funding acquisition.

Conflict of Interest

The authors declared that there is no conflict of interest.

Ethical Consideration

Ethics committee approval was not required for this study because of there was no study on animals or humans.

References

Agency for Healthcare Research and Quality. (2023). *Use of life cycle assessment in the healthcare industry*. Agency for Healthcare Research and Quality. https://effectivehealthcare.ahrq.gov/sites/default/files/related_files/lifecycle-assessment-tech-brief.pdf

Chen, Z., Lian, J. Z., Zhu, H., Zhang, J., Zhang, Y., Xiang, X., Huang, D., Tjokro, K., Barbarossa, V., Cucurachi, S., & Dong, B. (2024). Application of life cycle assessment in the pharmaceutical industry: A critical review. *Journal of Cleaner Production, 459*, 142550. https://doi.org/10.1016/j.jclepro.2024.142550

Drew, J., Christie, S. D., Rainham, D., & Rizan, C. (2022). HealthcareLCA: An open-access living database of health-care environmental impact assessments. *The Lancet Planetary Health, 6*(12), e1000–e1012. https://doi.org/10.1016/S2542-5196(22)00257-1

ECHA (2023). *Understanding REACH*. European Chemicals Agency https://echa.europa.eu/regulations/reach/understanding-reach

ECJRC. (2010). *ILCD handbook: General guide for life cycle assessment—Detailed guidance.* European Commission Joint

Research Centre, Publications Office of the European Union. https://eplca.jrc.ec.europa.eu/uploads/ILCD-Handbook-General-guide-for-LCA-DETAILED-GUIDANCE-12March2010-ISBN-fin-v1.0-EN.pdf

Eckelman, M., & Litan, R. (2024). *Life cycle assessment of the prefilled ApiJect injector*. ApiJect Systems. https://apiject.com/wp-content/uploads/2024/10/ApiJect-Environmental-Study-Report-FINAL.pdf

Ecoinvent Centre. (2024). *Ecoinvent database v3.10*. Ecoinvent Centre. https://ecoinvent.org/

EEA (2023). *Transport and environment report 2023*. European Environment Agency. https://www.eea.europa.eu/publications/transport-and-environment-report-2023

EMA. (2023). *Packaging and labelling requirements*. European Medicines Agency. https://www.ema.europa.eu/en/human-regulatory/marketing-authorisation/packaging-labelling

EPA. (2024). *Inventory of U.S. greenhouse gas emissions and sinks: 1990–2022*. U.S. Environmental Protection Agency. https://www.epa.gov/ghgemissions/inventory-us-greenhouse-gas-emissions-and-sinks

European Commission. (2024a). *European Green Deal*. European Commission. https://commission.europa.eu/strategy-and-policy/priorities-2019-2024/european-green-deal_en

European Commission. (2024b). *Life cycle assessment and the environmental footprint methods*. European Commission. https://green-forum.ec.europa.eu/environmental-footprint-methods/life-cycle-assessment-ef-methods_en

FDA. (2023). *Cold chain management for pharmaceutical products*. U.S. Food and Drug Administration. https://www.fda.gov/drugs/pharmaceutical-quality-resources/cold-chain-management

Givaudan Active Beauty. (2024). *PrimalHyal™ 50 Life: Sustainable hyaluronic acid with reduced environmental impact*. Givaudan Active Beauty. https://www.givaudan.com/media/trade-media/2024/givaudan-active-beauty-unveils-primalhyal-50-life

Hauschild, M. Z., Rosenbaum, R. K., & Olsen, S. I. (Eds.). (2018). *Life cycle assessment: Theory and practice*. Springer International Publishing. https://doi.org/10.1007/978-3-319-56475-3

International Energy Agency. (2024a). *Coal in Asia Pacific*. International Energy Agency. https://www.iea.org/regions/asia-pacific

International Energy Agency. (2024b). *World energy outlook 2024*. International Energy Agency. https://www.iea.org/reports/world-energy-outlook-2024

IRENA. (2023). *Global energy transformation*. International International Renewable Energy Agency, Renewable Energy Agency. https://www.irena.org/publications

ISO. (2006a). *Environmental management—Life cycle assessment—Principles and framework*. International Organization for Standardization. Standard No. 14040:2006). https://www.iso.org/standard/37456.html

ISO. (2006b). *Environmental management—Life cycle assessment—Requirements and guidelines* (ISO Standard No. 14044:2006). International Organization for Standardization. https://www.iso.org/standard/38498.html

MarkEn. (2025, May 23). *Sustainable cold chain solutions: Minimization of carbon footprints by pharma logistics*. https://markenworld.com/news/sustainable-cold-chain-solutions-minimization-of-carbon-footprints-by-pharma-logistics-3

Martins, A. M., & Marto, J. (2023). A sustainable life cycle for cosmetics: From design and development to post-use phase. *Sustainable Chemistry and Pharmacy, 35*, 101178. https://doi.org/10.1016/j.scp.2023.101178

McKinsey & Company. (2025). *Growth market for medical aesthetics*. McKinsey & Company. https://www.mckinsey.com/featured-insights/sustainable-inclusive-growth/charts/growth-market-for-medical-aesthetics

Nasr, M., Negm, A., & Peng, L. (Eds.). (2025). *Artificial intelligence applications for a sustainable environment*. Springer. https://doi.org/10.1007/978-3-031-91199-6

Neupane, B., Belkadi, F., Formentini, M., Rozière, E., Hilloulin, B., Abdolmaleki, S. F., & Mensah, M. (2025). Machine learning algorithms for supporting life cycle assessment studies: An analytical review. *Sustainable Production and Consumption*, *56*, 37–53. https://doi.org/10.1016/j.spc.2025.03.015

OECD (2024). *Environment statistics database*. Organisation for Economic Co-operation and Development Publishing. https://www.oecd.org/environment/data/

OECD Organisation for Economic Co-operation and Development. (2022). *Measuring the environmental impacts of artificial intelligence compute and applications*. Organisation for Economic Co-operation and Development Publishing. https://doi.org/10.1787/7babf571-en

Pandey, D. (2026, July 24). *Aesthetic medicine market forecast 2026–2035: Trends, growth drivers, and AI innovations*. Precedence Research. https://www.precedenceresearch.com/aesthetic-medicine-market

Piffoux, M., Le Tellier, A., Taillemite, Z., Ducrot, C., & Taillemite, S. (2024). Carbon footprint of oral medicines using hybrid life cycle assessment. *Journal of Cleaner Production*, *475*, Article 143576. https://doi.org/10.1016/j.jclepro.2024.143576

PRé Sustainability. (2024). *SimaPro LCA software*. PRé Sustainability. https://simapro.com/

Quadpack. (2022). *Understanding the impact of your beauty packaging: What is a life cycle assessment?* Quadpack. https://www.quadpack.com/assets/13617483/understanding-the-impact-of-your-beauty-packaging-what-is-a-life-cycle-assessment/

Riikonen, S., Timonen, J., & Sikanen, T. (2024). Environmental considerations along the life cycle of pharmaceuticals: Interview study on views regarding environmental challenges, concerns, strategies, and prospects within the pharmaceutical industry. *European Journal of Pharmaceutical Sciences*, *196*, Article 106743. https://doi.org/10.1016/j.ejps.2024.106743

Rocca, R., Acerbi, F., Fumagalli, L., & Taisch, M. (2023). Development of an LCA-based tool to assess the environmental sustainability level of cosmetic products. *The International Journal of Life Cycle Assessment*, *28*(10), 1261–1285. https://doi.org/10.1007/s11367-023-02219-0

Rudolf, R., Majerič, P., Pintarič, Z. N., Horvat, A., & Krajnc, D. (2024). Life cycle assessment (LCA) of the impact on the environment of a cosmetic cream with gold nanoparticles and hydroxylated fullerene ingredients. *Applied Sciences*, *14*(24), Article 11625. https://doi.org/10.3390/app142411625

Salla, J. V. E., de Almeida, T. A., & Silva, D. A. L. (2025). Integrating machine learning with life cycle assessment: A comprehensive review and guide for predicting environmental impacts. *The International Journal of Life Cycle Assessment*. Advance online publication. https://doi.org/10.1007/s11367-025-02437-8

Satta, M., Passarini, F., Cespi, D., & Ciacci, L. (2024). Advantages

and drawbacks of life cycle assessment application to pharmaceuticals: A short critical literature review. *Environmental Science and Pollution Research*, *31*(29), 41767–41786. https://doi.org/10.1007/s11356-024-33964-w

Sphera Solutions. (2024). *GaBi professional LCA software*. Sphera Solutions. https://gabi.sphera.com/

Sustainable Impact Metrics Foundation. (2024). *IDEMAT material database*. Sustainable Impact Metrics Foundation. https://idematapp.com/

Taillemite, S., Fenelon, M., Scherlinger, M., & Piffoux, M. (2026). Carbon footprint of antibody-based drugs and biologics using hybrid life cycle assessment. *Clinical Pharmacology & Therapeutics*, *120*(1), 236–244. https://doi.org/10.1002/cpt.70301

Teixeira, A. C. R., & Sodré, J. R. (2018). Impacts of replacement of engine powered vehicles by electric vehicles on energy consumption and CO_2 emissions. *Transportation Research Part D: Transport and Environment*, *59*, 375–384. https://doi.org/10.1016/j.trd.2018.01.004

World Bank Group. (2024). *Energy overview*. World Bank Group. https://www.worldbank.org/en/topic/energy

Wu, D., Ren, Z., Lei, H., & Zhao, S. (2025). Life cycle assessment of a luxury fashion brand's HPP event booth in the context of circular economy. *Scientific Reports*, *15*, Article 5153. https://doi.org/10.1038/s41598-024-84528-4

Zewe, A. (2025, January 17). *Explained: Generative AI's environmental impact*. MIT News, Massachusetts Institute of Technology. https://news.mit.edu/2025/explained-generative-ai-environmental-impact-0117

Black Sea Journal of Engineering and Science
doi: 10.34248/bsengineering.1956717

Open Access Journal
e-ISSN: 2619 – 8991

Research Article
Volume 9 - Issue 5: 2546-2553 / September 2026

ANALYZING CUSTOMER LIFETIME VALUE IN DIGITAL BANKING: A PPF-AHP BASED CRITERION PRIORITIZATION APPROACH

Ünzile MERAM HUYUT[1,2]*, Gül Tekin TEMUR[3]

[1]*Bahcesehir University, Graduate School, Department of Engineering Management, 34353, İstanbul, Türkiye*
[2]*Vakif Participation Bank, Ar-Ge Center, 34768, İstanbul, Türkiye*
[3]*Bahcesehir University, Faculty of Engineering and Natural Sciences, Department of Industrial Engineering, 34353, İstanbul, Türkiye*

Abstract: In the modern banking ecosystem, shaped by digital transformation and intense competition, focusing limited resources on high-value customers is a fundamental requirement for corporate sustainability. In this context, the concept of "Customer Lifetime Value" (CLV) serves as a strategic compass. However, the criteria determining a customer's value to a bank consist not only of financial ratios but also of difficult-to-measure, subjective elements such as risk perception, digital adaptation, and loyalty. The primary objective of this study is to prioritize six main criteria; Financial Capacity, Risk Profile, Spending Behaviours, Digital Integration, Loyalty, and Demographic Factors and their associated sub-criteria that shape credit card customer value in the banking sector using the Proportional Picture Fuzzy Analytic Hierarchy Process (PPF-AHP) method. Based on the insights of three senior industry experts, this model mathematically demonstrates which criteria are most decisive in customer valuation and which are of secondary importance. The research findings aim to provide bank managers with a scientifically grounded roadmap for budget planning, product development, and risk-based pricing strategies.

Keywords: PPF-AHP, Decision support systems, Banking, Criterion prioritization, Customer lifetime value

***Corresponding author:** Bahcesehir University, Graduate School, Department of Engineering Management, 34353, İstanbul, Türkiye
E mail: unzile.huyut@bahcesehir.edu.tr (Ü. MERAM HUYUT)
Ünzile MERAM HUYUT https://orcid.org/0009-0007-8737-4521
Gül Tekin TEMUR https://orcid.org/0000-0003-3853-0974

Received: May 22, 2026
Accepted: August 15, 2026
Published: September 15, 2026

Cite as: Meram Huyut, Ü., & Temur, G. T. (2026). Analyzing customer lifetime value in digital banking:A PPF-AHP based criterion prioritization approach. *Black Sea Journal of Engineering and Science,* 9(5), 2546-2553.

1. Introduction

In the financial services sector, the effective management of limited resources and the success of marketing strategies depend directly on how precisely organizations model the "Customer Lifetime Value" (CLV) hierarchy. CLV is a fundamental metric that guides customer acquisition, retention, and cross-selling strategies by measuring the total profit a customer is expected to generate throughout their relationship with the bank (Zdorovyi and Horokh, 2025). Especially in today's rapidly accelerating digital transformation, CLV analytics has become an indispensable tool for banks to achieve sustainable growth and increase profitability (Singh et al., 2024). The integration of artificial intelligence and digital technologies is reshaping the customer experience, making it mandatory for banks to better understand their customers and offer them personalized services.

The Analytic Hierarchy Process (AHP), which provides a mathematical framework for measuring the consistency of pairwise comparisons between criteria, is considered one of the most fundamental tools in strategic prioritization problems (Saaty, 1977). This method is a critical requirement for rationalizing the financial and operational elements that shape CLV models in a hierarchical order within the banking ecosystem. For instance, integrations of AHP and fuzzy logic are frequently used in banking for issues such as customer segmentation and performance evaluation (Aggarwal and Yadav, 2020).

However, in real-world problems, decision-makers' judgments are not always clear and precise; this has necessitated the handling of uncertainty with mathematical discipline. The major turning point in modelling uncertainty was the development of Fuzzy Set Theory, which stretched the traditional binary logic system by defining the degree of membership between 0 and 1 (Zadeh, 1965). This theory created a universal foundation allowing data with subjective and gray areas, such as expert opinions in banking, to be included in a numerical model.

With the advancement of fuzzy logic, Intuitionistic Fuzzy Sets were introduced to the literature, capable of modelling not only membership but also non-membership and hesitancy (Atanassov, 1986). This approach increased the depth of analysis by including the

This work is licensed (CC BY-NC 4.0) under Creative Commons Attribution 4.0 International License

margin of hesitation arising from the decision-maker's lack of information. Furthermore, the concept of "linguistic variables," which turns experts' verbal judgments beyond numerical data into part of the mathematical hierarchy, was also contributed to the literature (Zadeh, 1975).

At a more advanced stage, Picture Fuzzy Sets (PFS) were developed by framing "neutrality" in human judgments as a parameter distinct from hesitancy (Cuong, 2014). This model allowed for the analysis of decision-making processes in four different dimensions by combining positive, neutral, and negative membership degrees with an independent "refusal" degree. Especially in problems where loyalty and risk elements are intertwined, such as credit card customer data, treating neutral membership as an independent variable has strengthened the realism of the model. Indeed, in the analysis of factors affecting credit card customer satisfaction, the importance of perceived quality and value is emphasized, highlighting the need to support such multi-dimensional evaluations with fuzzy models (Liu, 2024).

Despite their theoretical excellence, multi-parameter models like Picture Fuzzy Sets can weaken data consistency by creating a cognitive overload when requesting direct decimal values from experts. Proportional Picture Fuzzy Sets (PPFS) offered a practical solution to this problem by relying on experts expressing proportional relationships between parameters instead of decimal numbers (Kahraman, 2024). This study utilizes the PPF-AHP methodology to transform the proportional logic of banking experts into rational coefficients and prioritizes customer value criteria through a systematic hierarchy.

1.1. Literature Review

Managing uncertainty in decision-making processes is one of the most fundamental endeavours of modern management science. Efforts to handle this uncertainty with mathematical discipline have paved the way for the birth and continuous evolution of fuzzy logic theory. As the first link in this evolution, Ordinary Fuzzy Sets (OFS) broke the traditional binary logic system by defining membership degrees between 0 and 1, marking a milestone in the mathematical representation of uncertainty (Zadeh, 1965). In this basic structure, an element's degree of non-membership was accepted as the direct complement of membership to 1 (Zadeh, 1965). OFS remains the most fundamental building block in decision-making problems under uncertainty.

However, this classical approach based on a single parameter eventually became insufficient to represent the multi-layered nature of human judgments, leading to the need for increased modelling capacity (Zadeh, 1975). In response, Type-2 and Interval-Valued Fuzzy Sets were developed, providing decision-makers with a higher level of cognitive flexibility by fuzzifying the membership degrees themselves (Zadeh, 1975). Additionally, the concept of "linguistic variables" allowed verbal judgments beyond numerical data to be included in mathematical models (Zadeh, 1975). While including verbal judgments was a significant step, the necessity of directly measuring the hesitation felt by the decision-maker drove the literature in a new direction.

Consequently, Intuitionistic Fuzzy Sets were defined, adding a "hesitancy" parameter in addition to membership and non-membership degrees (Atanassov, 1986). This expansion enabled decision-makers to include not only their approval or rejection but also their degree of information lack or hesitation in the system (Atanassov, 1986). The use of intuitionistic fuzzy numbers in complex problems like performance evaluation in the banking sector improves decision quality.

Although adding the hesitation parameter illuminated one dimension of uncertainty, the restrictive membership boundaries encountered in different datasets necessitated more flexible geometric definitions. In this context, Pythagorean Fuzzy Sets were developed to relax the constraints of intuitionistic fuzzy sets, offering decision-makers a wider membership space (Yager, 2013; Yager and Alajlan, 2017). Subsequently, q-Rung Orthopair Fuzzy Sets generalized this area further, making it easier to manage complex information (Yager and Alajlan, 2017). These expansions in the fuzzy space eventually evolved to the point of separating refined components of human judgments such as "neutrality" and "refusal."

As one of the most critical steps in this evolution, Picture Fuzzy Sets (PFS) addressed human judgments in four dimensions by combining positive, negative, and neutral membership degrees with an independent "refusal" degree (Cuong, 2014). Due to its independent parameterization of neutrality, the PFS structure holds high potential in sectors like banking where gray areas are prevalent (Cuong, 2014). As parametric diversity increased, the spatial representation of these parameters allowed for the establishment of new hierarchies.

With a similar approach, Spherical Fuzzy Sets were defined by moving the membership space to a three-dimensional sphere, providing decision-makers with an even broader range of preferences (Kutlu Gündoğdu and Kahraman, 2019). Spherical fuzzy sets are successfully applied in banking for service quality evaluation and multi-criteria decision-making problems. These models, pushing the boundaries of membership degree combinations, continued the goal of maximizing the decision-maker's room for maneuver (Kutlu Gündoğdu and Kahraman, 2019). Accordingly, Fermatean Fuzzy Sets were introduced to the literature to allow decision-makers to express their judgments within an even wider framework (Senapati and Yager, 2020). Fermatean fuzzy sets stand out as a powerful tool in areas where uncertainty is high, such as risk assessment, sustainability analysis, and supply chain management (Chang et al., 2023; Zhang and Zhang, 2024).

However, the biggest practical obstacle to these theoretically perfected extended fuzzy sets has been the

cognitive difficulties experts face in assigning complex decimal numbers. To provide a methodological solution to this chronic problem, Proportional Picture Fuzzy Sets (PPFS) were developed, based on experts expressing "proportions" between parameters (Kahraman, 2024). The PPFS methodology is built on the fact that humans can much more easily and accurately make proportional estimates, such as "the degree of membership is 5 times greater than the degree of hesitancy" (Kahraman, 2024). Furthermore, the developed PPF-AHP method places complex criterion weighting processes in the banking sector on a scientific, consistent, and rational proportional foundation (Kahraman, 2024). Recent studies show that proportional picture fuzzy sets offer a richer and more flexible modelling in multi-criteria decision-making problems (Razaq et al., 2026).

This study applies this methodology to the problem of prioritizing credit card customer value criteria in the banking sector to fill this gap in the literature. The research is unique in that it systematically models the hesitancy and proportional logic in expert judgments, providing a mathematically validated strategic prioritization framework for bank managers.

2. Materials and Methods

In this study, according to the methodology flow below, customer value is sought using credit card usage data from a bank. The criteria given in the Table 2 were scored by experts according to the following linguistic scale data. Using the scale in Table 3, the proportional equivalents (k1 and k2) of a term selected by experts are converted into fuzzy membership degrees (μ, π, ϑ) using the following formulas.

The transformation of subjective proportional data provided by experts into a rational hierarchy in the decision-making process is carried out using a multi-stage algorithm proposed by Kahraman (2024). Unlike traditional methods, this process produces more consistent results in high-risk sensitive areas such as banking by considering the decision-maker's neutrality as an independent variable. Below, the mathematical steps applied in our study and their relationship with credit card customer value criteria is presented:

The proportional values (k1 and k2) obtained from the experts are converted into positive (μ), neutral (π), and negative (θ) membership degrees through the following formula. In this stage, the neutral membership degree (π) is represented by the value "1" as the "anchor" point of the proportional calculation (equation 1):

$$\mu = \frac{k1}{1+k1+k2}, \pi = \frac{1}{1+k1+k2}, \theta = \frac{k2}{1+k1+k2} \quad (1)$$

The Proportional Image Fuzzy Weighted Average (PPFWA) operator is used to combine data from multiple experts into a single collective matrix (equation 2).

$$PPFWA_w(a_1, \dots, a_n) = \left(1 - \prod_{j=1}^{n}\left(1-\mu_{a_j}\right)^{w_j}, \prod_{j=1}^{n}\left(\pi_{a_j}\right)^{w_j}, \prod_{j=1}^{n}\left(\theta_{a_j}\right)^{w_j}\right) \quad (2)$$

This formula combines the judgments of experts with different focus areas such as risk management, marketing, and technical architecture, each weighted by their experience weight (w_j). In this study, equal weighting of $w_j = 1/3$ was used for the three experts. The multiplication symbol (∏) strengthens the consensus among experts while preventing outliers from distorting the analysis. Flow of the methodology is shown in Table 1.

Table 1. Flow of the methodology

Problem Definition and Hierarchy Establishment	Identifying 6 main criteria through literature review and banking expert consensus.
Determination of Expert Weights	Assigning weight coefficients based on experts' seniority and experience.
Collection of Pairwise Comparison Data	Obtaining proportional (k1, k2) judgments between criteria using a linguistic scale from experts.
Calculation of PPF Membership Degrees	Converting proportional data into picture fuzzy numbers (μ, π, θ).
Aggregation of Expert Judgments	Collecting different expert opinions into a single matrix using the PPFWA (Weighted Average) operator.
Defuzzification	Reducing fuzzy values to rational numbers using a score function.
Consistency Check	Checking the consistency ratio (CR < 0.10) of defuzzified matrices using the eigenvalue method.
Final Prioritization	Calculating weighted percentages of criteria and ordering them by strategic importance.

The hierarchy of criteria used in this study was structured considering the core attributes in an anonymized customer dataset from a bank's credit card portfolio. These data consist of pairwise comparison data collected from three senior experts serving as senior managers and technical architects in the same sector. The evaluation criteria were created as a result of the analysis of customer data. Table 2 presents the criteria.

Table 2. Criteria list

Main Criteria	Description	Sub-Criteria
C1	Financial Capacity	Monthly Income, Total Asset Volume, Total Credit Card Limit, Debt/Income Ratio
C2	Risk Profile	Credit Bureau Score, Limit Utilization Ratio, Payment Type (Minimum/Full), Limit Overrun Frequency
C3	Spending Behaviours	Annual Total Spending, Average Basket Size, Spending Trend, Installment Transaction Ratio
C4	Digital Integration	Mobile Banking Login Frequency, Digital Wallet Usage, E-Commerce Transaction Volume
C5	Loyalty and Relationship	Bank Seniority (Months), Point Balance, Campaign Participation Rate, NPS (Net Promoter Score)
C6	Demographic Factors	Age, Marital Status, Education Level, Professional Sector

Table 3. PPF Linguistic Scale

	Linguistic terms	Corresponding PPFNS
CL	Certainly Low (CL)	(1,9)
VL	Very Low (VL)	(2,8)
L	Low (L)	(3,7)
BA	Below Average (BA)	(4,6)
A	Average (A)	(5,5)
AA	Above Average (AA)	(6,4)
H	High (H)	(7,3)
VH	Very High (VH)	(8,2)
CH	Certainly High (CH)	(9,1)

This is the stage where the synthesized fuzzy numbers are converted into crisp values that can be processed in a pairwise comparison matrix. The initial pairwise comparison matrix, created using the raw proportional (k_1, k_2) evaluations collected from the experts, is shown in equation 3.

$$P(k_1, k_2) = \begin{bmatrix} (VBN, 0) & \cdots & (k_{11n}, k_{21n}) \\ \vdots & \ddots & \vdots \\ (k_{2n1}, k_{1n1}) & \cdots & (VBN, 0) \end{bmatrix} \quad (3)$$

VBN represents the comparison of a criterion with itself. This raw matrix is then converted into fuzzy membership degrees in the format (μ, π, θ) via equation 1. The resulting Proportional Image Fuzzy (PPF) Pairwise Comparison Matrix is given in equation 4.

Finally, in order to make decisions and perform matrix operations on fuzzy sets in the picture, the fuzzy values in equation 4 need to be reduced to a single crisp number. The score function $S(k_1, k_2)$ used for this purpose is defined in equation 5.

The coefficient "10" in the formula places the results within a meaningful range similar to the Saaty (1977) scale. If S > 0, Criterion i is superior to Criterion j, and the score is used directly as the crisp value.

If S < 0, Criterion j takes precedence, and the inverse value (1/S) is written into the crisp matrix. This two-conditional structure guarantees the consistency of the matrix (equation 6).

The specific weight of each criterion within the system is calculated from the finalized pairwise comparison matrix. At this stage, a single coefficient is generated for each criterion by taking the geometric mean of all comparisons.

This normalization process, where the total weight is divided by 1 (100%), establishes a final hierarchy of the relative relationships between the criteria. The consistency of the calculated weights is verified using the Consistency Ratio (CR) formula (Saaty, 1977).

$$P_P(k_1, k_2) \begin{bmatrix} (1,0,0) & \cdots & \left(\frac{k_{11n}}{1+k_{11n}+k_{21n}}, \frac{1}{1+k_{11n}+k_{21n}}, \frac{k_{21n}}{1+k_{11n}+k_{21n}}\right) \\ \vdots & \ddots & \vdots \\ \left(\frac{k_{21n}}{1+k_{11n}+k_{21n}}, \frac{1}{1+k_{11n}+k_{21n}}, \frac{k_{11n}}{1+k_{11n}+k_{21n}}\right) & \cdots & (1,0,0) \end{bmatrix} \quad (4)$$

$$S(k_1, k_2) = 10 \times \left(k_{11n}/(1 + k_{11n} + k_{21n}) - 1/\left(2(1 + k_{11n} + k_{21n})\right) - k_{21n}/(1 + k_{11n} + k_{21n})\right), \text{ if positive}$$
$$1/\left(10 \times \left(k_{21n}/(1 + k_{11n} + k_{21n}) - 1/\left(2(1 + k_{11n} + k_{21n})\right) - k_{11n}/(1 + k_{11n} + k_{21n})\right)\right), \text{ otherwise} \quad (5)$$

$$w_i = \frac{\left(\prod_{j=1}^{n} s_{ij}\right)^{1/n}}{\sum_{i=1}^{n}\left(\prod_{j=1}^{n} s_{ij}\right)^{1/n}} \quad (6)$$

4. Result

This section presents the findings obtained from analysing 6 main criteria and 34 sub-criteria, created to solve the credit card customer valuation problem, using the PPF-AHP (Proportional Picture Fuzzy Analytical Hierarchy Process) method. The PPF-AHP approach (Kahraman, 2024), which can mathematically model uncertainties in decision-making processes and expert hesitancy, was applied to the evaluations of three senior experts working in the banking sector. In the tables

below, the steps of combining expert evaluations, converting to fuzzy membership degrees, obtaining the crisp matrix, and calculating the final customer value weights are explained with numerical data, respectively. The criteria used in the analysis and their descriptions are included in the Table 4.

The scores of the experts participating in the study are indicated in the matrix below using the PPFWA operator.

Table 4 reflects the relative importance of the main criteria used in credit card customer evaluation. Proportional assessments from three banking sector experts were combined into a single consensus matrix using the PPFWA operator.

Table 4. Determined criterion

C1	It represents the customer's liquidity strength and economic potential within the bank.
C2	It measures the customer's capacity to meet financial obligations and their risk of default.
C3	It analyzes the customer's consumption depth, spending frequency, and preferred categories.
C4	It shows the customer's technological adaptation and contribution to operational efficiency.
C5	It models the customer's historical relationship with the bank and the likelihood of them leaving.
C6	It identifies potential value expectations that may change depending on the life cycle.

The combined fuzzy matrix presented in Table 5 shows the positive (μ), neutral (π), and negative (θ) membership degrees of decision-makers on each pair of criteria. For example, the positive membership degree of C1 (Financial Capacity) against C2 (Risk Profile) is calculated as μ = 0.528, while the negative membership degree is θ = 0.381. The neutral membership degree, due to the nature of the scale, remains constant at π = 0.091 in all cells. These fuzzy values define the limits of uncertainty between criteria. By applying the score function $S(k_1,k_2)$ from equation 5 to this matrix, each fuzzy cell is reduced to a single crisp number, and the matrix given in Table 6 is obtained.

Table 7 represents the crisp pairwise comparison matrix obtained from the PPF score function and optimized for traditional AHP steps. In the table, values greater than 1.000 quantitatively indicate the superiority of a row criterion over a column criterion (e.g., C1's score against C6 is 5.721), while values smaller than 1.0000 indicate its weakness (e.g., C4's score against C1 is 0.2558). The criterion weights were determined by applying geometric mean normalization from equation 6 to this matrix, and the consistency of the calculated values was tested using equation 5. In multi-criteria decision-making (MCDM) models, the reliability of the derived weighting coefficients largely depends on whether experts' subjective and linguistic judgments are supported by a rational and internally consistent decision structure. Accordingly, the pairwise comparison judgments of each expert for the sub-criteria were evaluated using the eigenvalue-based consistency approach originally proposed by Saaty (1977) based on the defuzzified comparison matrices. Individual Consistency Ratio (CR) values were calculated for each of the three experts, all of whom are senior managers or technical architects with extensive experience in the banking industry.

As presented in Table 8, the individual consistency ratios obtained from all six main criterion groups for each expert remain below the widely accepted threshold of CR < 0.10, indicating satisfactory judgment consistency. For example, the consistency ratio for the first criterion group (C1) was 0.05 for Expert 1, 0.07 for Expert 2, and 0.04 for Expert 3, demonstrating a high degree of consistency in their pairwise comparisons. Overall, these findings confirm that the experts' evaluations are sufficiently consistent and provide a reliable basis for the subsequent calculation of local and global criterion weights within the proposed PPF-AHP framework.

Table 5. PP Fuzzy pairwise comparison matrix of the criteria

	C1	C2	C3	C4	C5	C6
C1	(VBN,0)	(7,3)	(6,4)	(9,1)	(7,3)	(9,1)
C2	(3,7)	(VBN,0)	(6,4)	(7,3)	(6,4)	(7,3)
C3	(4,6)	(4,6)	(VBN,0)	(6,4)	(6,4)	(6,4)
C4	(1,9)	(3,7)	(4,6)	(VBN,0)	(4,6)	(5,5)
C5	(3,7)	(4,6)	(4,6)	(6,4)	(VBN,0)	(6,4)
C6	(1,9)	(3,7)	(4,6)	(5,5)	(4,6)	(VBN,0)

Table 6. Picture fuzzy pairwise comparison matrix of the criteria

	C1			C2			C3		
	μ	π	ϑ	μ	π	ϑ	μ	π	ϑ
C1	1.000	0.000	0.000	0.528	0.091	0.381	0.521	0.091	0.388
C2	0.381	0.091	0.528	1.000	0.000	0.000	0.534	0.091	0.375
C3	0.388	0.091	0.521	0.375	0.091	0.534	1.000	0.000	0.000
C4	0.325	0.091	0.584	0.404	0.091	0.505	0.375	0.091	0.534
C5	0.267	0.091	0.642	0.345	0.091	0.564	0.397	0.091	0.512
C6	0.203	0.091	0.706	0.238	0.091	0.671	0.297	0.091	0.612
	C4			C5			C6		
	μ	π	ϑ	μ	π	ϑ	μ	π	ϑ
C1	0.584	0.091	0.325	0.642	0.091	0.267	0.706	0.091	0.203
C2	0.505	0.091	0.404	0.564	0.091	0.345	0.671	0.091	0.238
C3	0.534	0.091	0.375	0.512	0.091	0.397	0.612	0.091	0.297
C4	1.000	0.000	0.000	0.534	0.091	0.375	0.584	0.091	0.325
C5	0.375	0.091	0.534	1000	0.000	0.000	0.534	0.091	0.375
C6	0.325	0.091	0.584	0.375	0.091	0.534	1000	0.000	0.000

Table 7. Crisp pairwise comparison matrix of the criteria

	C1	C2	C3	C4	C5	C6
C1	1.000	1.046	0.799	3.910	2.023	5.721
C2	0.956	1.000	2.023	5.721	0.194	5.273
C3	1.252	0.494	1.000	2.939	2.939	3.366
C4	0.256	0.175	0.340	1.000	0.194	1.504
C5	0.494	5.150	0.340	5.150	1.000	2.023
C6	0.175	0.190	0.297	0.665	0.494	1.000

Table 8. Consistency rates

	Expert 1	Expert 2	Expert 3
C1	0.05	0.07	0.04
C2	0.05	0.07	0.08
C3	0.05	0.09	0.07
C4	0.04	0.02	0.01
C5	0.08	0.04	0.08
C6	0.02	0.05	0.09

The PPF-AHP analysis determined the final weights and rankings within the system for the 6 main criteria and 34 sub-criteria that play a role in determining credit card customer value.

At the main criteria level, Financial Capacity (w = 0.2626) emerged as the most influential criterion in determining Customer Lifetime Value (CLV). It was followed by Risk Profile (w = 0.1892) and Spending Behavior (w = 0.1682), indicating that customers' financial strength, risk characteristics, and spending patterns play a dominant role in CLV estimation. Loyalty and Relations (w = 0.1528) ranked fourth, whereas Digital Integration (w = 0.1376) and Demographic Profile (w = 0.0897) received comparatively lower weights. These findings indicate that financial capacity, risk profile, and spending behavior constitute the primary determinants of customer lifetime value in credit card portfolio management, while demographic characteristics and digital integration contribute to the decision-making process to a lesser extent. Furthermore, the PPF-AHP approach transformed experts' subjective judgments into a structured quantitative framework, reducing uncertainty in the evaluation process and enabling the objective determination of criterion weights.

Following the evaluation of the main criteria, the final weights and priority rankings of the sub-criteria associated with each main criterion were determined using the PPF-AHP method. The resulting weights and ranking of the sub-criteria are presented in Table 9.

Table 9. Main criteria weights and prioritization

Main Criteria	Final Weight	Ranking
Financial Capacity	0,2626	1
Risk Profile	0,1892	2
Spending Behavior	0,1682	3
Digital Integration	0,1376	5
Loyalty and Relationship	0,1528	4
Demographic Profile	0,0897	6

Table 10. Sub-Criteria weights and prioritization

Sub-criteria	Final Weight	Ranking
Monthly Income	0,0846	7
Total Assets	0,0724	8
Credit Score	0,0564	9
Seniority (Months)	0,0544	10
Annual Spending	0,0526	11
Wallet Share	0,0519	12
Payment Type	0,0457	13
Digital Wallet	0,0410	14
E-commerce Rate	0,0403	15
Limit Utilization	0,0373	16
Points Balance	0,0350	17
Active Credit	0,0346	18
Credit Card Limit	0,0278	19
Debt/Income Ratio	0,0259	20
City	0,0253	21
Campaign Participation	0,0251	22
Mobile Login	0,0249	23
Average Basket	0,0211	24
NPS Score	0,0210	25
Spending Trend	0,0187	26
Age	0,0177	27
Total Complaints	0,0173	28
Marital Status	0,0172	29
Overseas Rate	0,0169	30
Travel Rate	0,0160	31
Installment Rate	0,0158	32
Market Rate	0,0155	33
Number of Limit Overruns	0,0151	34
Technology Rate	0,0148	35
Contactless User	0,0145	36
Restaurant Rate	0,0135	37
Education Level	0,0126	38
Gender	0,0089	39
Sector	0,0081	40

Table 10 presents the final weights and priority rankings of the sub-criteria under the main evaluation criteria. The results indicate that Monthly Income (w = 0.0846) is the most influential sub-criterion, highlighting customers' income level as the strongest indicator of Customer Lifetime Value (CLV). It is followed by Total Assets (w = 0.0724) and Credit Score (w = 0.0564), suggesting that customers' financial capacity, asset ownership, and creditworthiness are the primary determinants of long-term customer value.

Other highly ranked sub-criteria include Seniority (Months) (w = 0.0544) and Annual Spending (w = 0.0526), emphasizing that the duration of the customer–bank relationship and customers' spending behavior also make substantial contributions to CLV estimation. In contrast, demographic variables such as Gender (w = 0.0089) and Sector (w = 0.0081), together with other lower-ranked factors, received considerably smaller weights. These findings indicate that financial indicators, credit risk characteristics, and behavioral variables provide substantially greater explanatory power for predicting customer lifetime value than traditional demographic attributes in credit card portfolio management. Furthermore, the PPF-AHP approach effectively transformed expert knowledge into a structured quantitative framework, enabling the objective prioritization of sub-criteria while reducing uncertainty in the decision-making process.

5. Discussion and Conclusion

This study develops a novel multi-criteria decision-making framework based on the Proportional Picture Fuzzy Analytic Hierarchy Process (PPF-AHP) to model the value of credit card customers in the banking sector in a multidimensional and mathematically consistent manner. Considering the limitations of conventional Customer Lifetime Value (CLV) approaches that primarily rely on historical financial transactions, a comprehensive hierarchical structure consisting of 6 main criteria and 34 sub-criteria has been established. To accurately capture uncertainty, hesitation, and semantic differences in experts' subjective judgments, the proportional picture fuzzy sets approach introduced by Kahraman (2024) has been successfully employed. Rather than requiring experts to assign precise numerical membership degrees, this approach evaluates proportional relationships among linguistic parameters, thereby reducing cognitive burden while providing a more realistic and reliable decision-making process.

The empirical findings obtained from the evaluations of industry experts provide important implications for banking practices and customer relationship management. According to the analysis results, Financial Capacity and Risk Profile emerged as the two most influential main criteria in determining Customer Lifetime Value, followed by Spending Behavior, Loyalty and Relations, and Digital Integration. At the sub-criteria level, Monthly Income, Total Assets, Credit Score, Seniority (Months), and Annual Spending received the highest weights, indicating that customers' financial strength, asset ownership, creditworthiness, relationship duration, and spending behavior are the most influential determinants of long-term customer value. These findings demonstrate that Customer Lifetime Value in contemporary retail banking is driven not only by customers' transaction volume but also by a combination of financial capacity, credit risk characteristics, long-term customer relationships, and behavioral attributes.

The contributions of the study to the literature and banking practice can be summarized under two main headings:

1. Methodological Contribution: This study represents one of the earliest applications of the PPF-AHP methodology in customer analytics and banking decision-making. The proposed framework successfully transforms experts' subjective judgments expressed in the proportional picture fuzzy environment into consistent criterion weights while preserving Saaty's

reciprocity principle, thereby providing a reliable methodology for expert-based decision modeling.

2. Managerial Contribution: The proposed framework provides a practical decision support tool for bank managers, customer portfolio strategists, and marketing professionals. Rather than relying solely on historical financial indicators, banks can utilize the criterion weights obtained from the proposed model to support credit limit allocation, customer segmentation, personalized marketing campaigns, and customer retention strategies.

Author Contributions

The percentages of the authors' contributions are presented below. All authors reviewed and approved the final version of the manuscript.

	U.M.H.	G.T.T.
C	50	50
D	50	50
S	50	50
DCP	50	50
DAI	50	50
L	50	50
W	50	50
CR	50	50
SR	50	50
PM	50	50
FA	50	50

C= concept, D= design, S= supervision, DCP= data collection and/or processing, DAI= data analysis and/or interpretation, L= literature search, W= writing, CR= critical review, SR= submission and revision, PM= project management, FA= funding acquisition.

Conflict of Interest

The authors declared that there is no conflict of interest.

Ethical Consideration

Ethics committee approval was not required for this study because there was no study on animals or humans.

References

Aggarwal, A. G., & Yadav, S. (2020). Customer segmentation using Fuzzy-AHP and RFM model. *2020 8th International Conference on Reliability, Infocom Technologies and Optimization (Trends and Future Directions) (ICRITO)*, 77–80. https://doi.org/10.1109/ICRITO48877.2020.9197903

Atanassov, K. T. (1986). Intuitionistic fuzzy sets. *Fuzzy Sets and Systems, 20*(1), 87–96. https://doi.org/10.1016/S0165-0114(86)80034-3

Chang, K.-H., Chung, H.-Y., Wang, C.-N., Lai, Y.-D., & Wu, C.-H. (2023). A new hybrid Fermatean fuzzy set and entropy method for risk assessment. *Axioms, 12*(1), Article 58. https://doi.org/10.3390/axioms12010058

Cuong, B. C. (2014). Picture fuzzy sets. *Journal of Computer Science and Cybernetics, 30*(4), 409–420. https://doi.org/10.15625/1813-9663/30/4/5032

Kahraman, C. (2024). Proportional picture fuzzy sets and their AHP extension: Application to waste disposal site selection. *Expert Systems with Applications, 238*, Article 122354. https://doi.org/10.1016/j.eswa.2023.122354

Kutlu Gündoğdu, F., & Kahraman, C. (2019). Spherical fuzzy sets and spherical fuzzy TOPSIS method. *Journal of Intelligent & Fuzzy Systems, 36*(1), 337–352. https://doi.org/10.3233/JIFS-181401

Liu, Y. (2024). The influencing factors of customer satisfaction with credit card center of China CITIC Bank. *The 1st Thailand-Sino International Conference and The 17th National and International Academic Conference "New Quality Productive Forces and Sustainable Innovation"*, 731–743. https://e-research.siam.edu/kb/the-influencing-factors-of-customer-satisfacation-with-credit-card-center/

Razaq, A., Komal, L., Alhamzi, G., & Baidar, A. W. (2026). A novel complex Fermatean fuzzy formalism with improved score function and aggregation operators. *Scientific Reports, 16*, Article 13559. https://doi.org/10.1038/s41598-026-40838-3

Saaty, T. L. (1977). A scaling method for priorities in hierarchical structures. *Journal of Mathematical Psychology, 15*(3), 234–281. https://doi.org/10.1016/0022-2496(77)90033-5

Senapati, T., & Yager, R. R. (2020). Fermatean fuzzy sets. *Journal of Ambient Intelligence and Humanized Computing, 11*(2), 663–674. https://doi.org/10.1007/s12652-019-01377-0

Singh, S., Murthi, B. P. S., Rao, R. C., & Steffes, E. M. (2024). Risk-adjusted lifetime value: Adjusting for customer riskiness using a single metric. *International Journal of Bank Marketing, 42*(7), 1695–1717. https://doi.org/10.1108/IJBM-12-2023-0645

Yager, R. R. (2013, June 24–28). *Pythagorean fuzzy subsets*. In *2013 Joint IFSA World Congress and NAFIPS Annual Meeting (IFSA/NAFIPS)* (pp. 57–61). IEEE. https://doi.org/10.1109/IFSA-NAFIPS.2013.6608375

Yager, R. R., & Alajlan, N. (2017). Approximate reasoning with generalized orthopair fuzzy sets. *Information Fusion, 38*, 65–73. https://doi.org/10.1016/j.inffus.2017.02.005

Zadeh, L. A. (1965). Fuzzy sets. *Information and Control, 8*(3), 338–353. https://doi.org/10.1016/S0019-9958(65)90241-X

Zadeh, L. A. (1975). The concept of a linguistic variable and its application to approximate reasoning—I. *Information Sciences, 8*(3), 199–249. https://doi.org/10.1016/0020-0255(75)90036-5

Zdorovyi, M., & Horokh, O. (2025). Customer lifetime value analytics in digital banking: Approaches, models, and practical implementation. *VII International Scientific and Theoretical Conference "Scientific Method: Reality and Future Trends of Researching"*, 32–41.

Zhang, Q., & Zhang, H. (2024). Assessing agri-food waste valorization challenges and solutions considering smart technologies: An integrated Fermatean fuzzy multi-criteria decision-making approach. *Sustainability, 16*(14), Article 6169. https://doi.org/10.3390/su16146169

Black Sea Journal of Engineering and Science
doi: 10.34248/bsengineering.1987154

Open Access Journal
e-ISSN: 2619 – 8991

Research Article
Volume 9 - Issue 5: 2554-2572 / September 2026

COMPARATIVE ANALYSIS OF ADVANCED CONTROL STRATEGIES FOR VIBRATION CONTROL OF FLEXIBLE SATELLITE STRUCTURES

Aslı DURMUŞOĞLU[1]*

[1]*Hakkari University, Faculty of Engineering, Department of Mechanical Engineering, 30000, Hakkari, Türkiye*

Abstract: Flexible satellite structures with lightweight solar panels are naturally prone to structural vibrations caused by attitude maneuvers, continuous environmental disturbances and deformation during deployment. These vibrations can lead to a decrease in pointing accuracy, a degradation in payload performance, and an adverse effect on the overall stability of the spacecraft, thereby stressing the importance of effective vibration control. This paper presents a comparative study of advanced control strategies for a rigid-flexible satellite model with one flexible solar panel. A single state-space formulation was developed capturing the coupled rigid-body and flexible dynamics. All controllers were implemented under the same simulation conditions to allow for a direct and objective comparison. Three representative operating conditions are considered: residual vibration after an attitude maneuver, constant environmental excitation, and initial structural deformation. The performance of the controller was assessed based on tip displacement, tip velocity, control input, settling time, RMS displacement and control energy. The results obtained show that all investigated controllers are capable to stabilize the flexible satellite system but their dynamic characteristics are quite different. The LQR controller has relatively bigger vibration amplitude and longer settling time. The MPC provides balanced tradeoff between vibration reduction and control effort. ADRC achieves the best overall performance with faster attenuation of vibrations, lower residual oscillations and shorter settling times for all operating scenarios. It can estimate disturbances and so compensate quickly for transient and continuous disturbances, but requires a larger initial control action. In general, the proposed comparative framework provides a practical basis for the evaluation and selection of advanced vibration control strategies for flexible satellite structures.

Keywords: Flexible satellite, Active vibration control, Dynamic systems, Model predictive control, Active disturbance, Rejection control.

***Corresponding author:** Hakkari University, Faculty of Engineering, Department of Mechanical Engineering, 30000, Hakkari, Türkiye
E mail: aslidurmusoglu@hakkari.edu.tr (A.DURMUŞOĞLU)
Aslı DURMUŞOĞLU https://orcid.org/0000-0002-2797-1304

Received: July 05, 2026
Accepted: August 15, 2026
Published: September 15, 2026

Cite as: Durmuşoğlu, A. (2026). Comparative analysis of advanced control strategies for vibration control of flexible satellite structures. *Black Sea Journal of Engineering and Science,* 9(5), 2554-2572.

1. Introduction

Flexible appendages, particularly deployable solar panels, have become indispensable components of modern spacecraft owing to their ability to provide high electrical power while maintaining low structural mass. The continuous miniaturization of satellite platforms together with increasing mission requirements has led to the widespread adoption of lightweight and highly flexible appendage structures. Although these flexible components significantly improve power generation capability, they also introduce undesirable structural vibrations during spacecraft operations. Such vibrations may reduce pointing accuracy, degrade payload performance, shorten component lifetime, and adversely affect the overall stability of the spacecraft. Consequently, vibration suppression of flexible satellite appendages has become an important research topic in spacecraft dynamics and control.

Unlike launch-induced transient loads, which occur over a relatively short duration, satellites experience operational disturbances throughout their service life. During Earth observation, communication, reconnaissance, and scientific missions, spacecraft frequently perform attitude maneuvers to orient onboard sensors or communication equipment toward desired targets. Although the satellite bus reaches the commanded orientation after each maneuver, the flexible solar panels continue to oscillate because of their structural flexibility. In addition, continuous environmental disturbances such as solar radiation pressure, residual atmospheric drag in low Earth orbit, and other external perturbations may further excite the flexible appendages. If these residual vibrations are not effectively suppressed, they may considerably deteriorate mission accuracy, imaging quality, and attitude stability.

Therefore, the development of reliable active vibration control strategies for flexible spacecraft structures remains an important engineering challenge. Over the last two decades, the dynamic modelling and vibration control of flexible spacecraft has been a very active

This work is licensed (CC BY-NC 4.0) under Creative Commons Attribution 4.0 International License

research field. The main early study focused on establishing rigid-flexible coupled dynamic models and interaction analysis of spacecraft body and flexible appendages (He and Ge., 2015; Liu et al., 2016; Liu et al., 2017). These models have been further extended in more recent studies by considering distributed cooperative control (Zhou et al., 2022), passive damping mechanisms (Liu et al., 2022; Park et al., 2025), nonlinear structural characteristics (Fu et al., 2025), adaptive fault-tolerant control (Ji et al., 2019), predictor-based control and disturbance observer-based approaches (Zhu et al., 2020). Some other control strategies have been proposed to improve the vibration attenuation performance under different mission conditions such as H∞ control (Jiang and Li, 2010), fuzzy control (Xu et al., 2011), sliding mode control (Hu et al., 2008), adaptive sliding mode control (Hu, 2011; Azadi et al., 2012), boundary control (Ataei et al., 2021; Ataei et al., 2020), backstepping control (Hu and Xiao, 2010), and micro-thruster based vibration suppression (Yang et al., 2017).

These studies have led to significant advances in the state of the art. Most of the studies evaluate a single control strategy developed for a specific spacecraft model or operational scenario. Therefore, direct comparisons of different advanced control philosophies under the same dynamic models, disturbance conditions, and evaluation criteria are still relatively few. From an engineering point of view, such comparative evaluations are especially useful as they give practical insights into the applicability, computational demands and control performance of different methods in the same operating environment.

Driven by these gaps in the literature, this study proposes a comparative study of advanced control strategies for vibration control of a rigid–flexible satellite system including a rigid satellite bus and a single flexible solar panel. All controllers were implemented in the same simulation framework under the same modeling assumptions and operating conditions, and a single state-space model was developed to describe the coupled rigid-flexible dynamics, in order to ensure a fair and objective comparison. To provide a complete engineering evaluation, the controller performance has been evaluated in three representative operational scenarios, which are typical in satellite missions: residual vibration after an attitude maneuver, continuous environmental disturbance and initial structural deformation. The comparison was based on the common performance metrics that include tip displacement, tip velocity, settling time, control input, RMS displacement and control energy.

The results obtained show that, although all the investigated controllers stabilize efficiently the flexible satellite system, their dynamic characteristics are very different. Among the studied methods, disturbance-observer-based control is identified as the best overall for vibration attenuation and transient performance. The presented comparative framework provides practical guidelines for the assessment and selection of advanced vibration control techniques for flexible satellite structures.

2. Materials and Methods

2.1. Dynamic Modeling of the Flexible Satellite System

The dynamic behavior of flexible satellite structures is commonly represented by a rigid spacecraft body coupled with one or more lightweight flexible appendages. Among these appendages, deployable solar panels are particularly susceptible to vibration because of their high flexibility and low structural damping. During routine on-orbit operations, such as attitude maneuvers or disturbance rejection tasks, the rigid satellite bus rapidly follows the desired motion, whereas the attached flexible solar panels continue to oscillate due to their structural elasticity. These residual oscillations may persist even after the spacecraft body has reached its commanded position, thereby reducing pointing precision and affecting the stability of sensitive onboard equipment.

To investigate the vibration suppression performance of different control strategies under representative mission conditions, a simplified rigid–flexible coupled satellite model is adopted in this study. Rather than introducing unnecessary geometric complexity, the model is intentionally formulated using a single flexible solar panel attached to a rigid satellite bus. In this reduced-order representation, the rigid satellite bus accounts for the main inertial motion, while the flexible panel retains the dominant low-frequency bending dynamics of the physical appendage. Since the response of lightweight flexible appendages under small-amplitude operational excitation is generally dominated by the first few elastic modes, this modeling approach provides a physically meaningful representation of the principal rigid–flexible interaction relevant to vibration-control analysis (He and Ge., 2015; Liu et al., 2016; Liu et al., 2017).

The flexible solar panel is modeled according to the Euler–Bernoulli beam theory under the assumptions of small elastic deformation and linear material behavior. The satellite bus is considered as a rigid body, while the structural flexibility is confined to the deployable solar panel. Such assumptions are appropriate for evaluating controller performance during small-amplitude operational vibrations encountered in orbit and have been extensively employed in the literature on flexible spacecraft dynamics (He and Ge., 2015; Fu et al., 2025; Ataei et al., 2021; Ataei et al., 2020).

Since the primary objective of this study is to compare different control philosophies rather than to develop a more sophisticated structural model, the adopted formulation provides an appropriate balance between physical fidelity and computational efficiency.

Based on these assumptions, the physical configuration of the rigid-flexible satellite system considered throughout this study is illustrated in Figure 1.

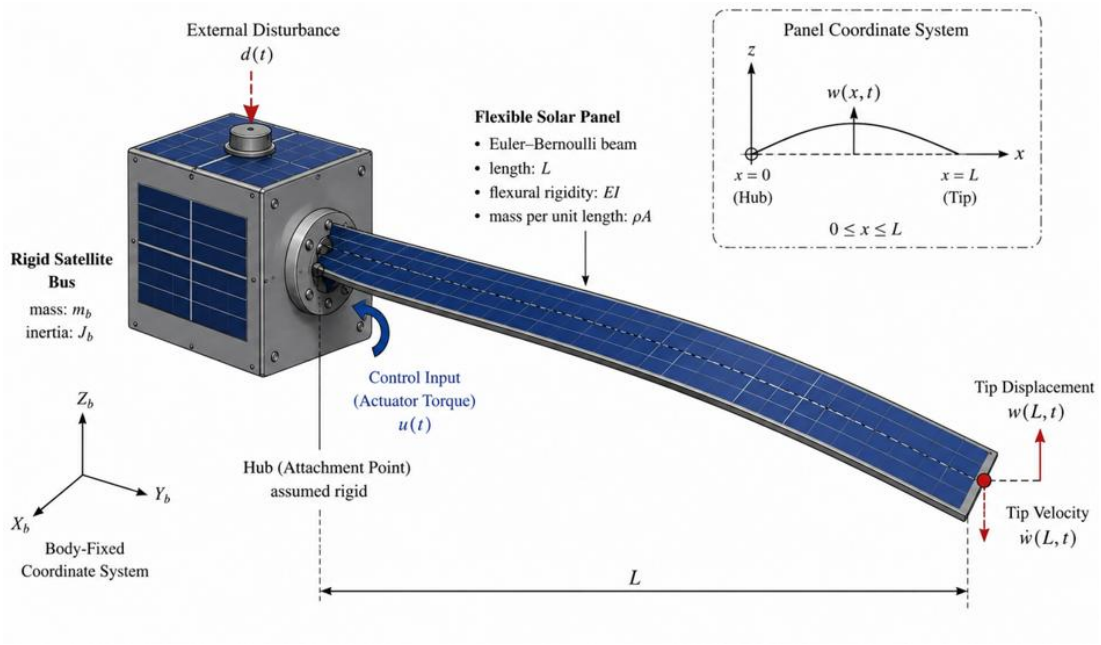


Figure 1. Physical Configuration of the rigid-flexible satellite system.

Figure 1 illustrates the rigid-flexible satellite system considered in this study. The model consists of a rigid satellite bus equipped with a single deployable flexible solar panel. While the satellite bus is treated as a rigid body, the solar panel is represented as a slender Euler–Bernoulli beam rigidly attached to the hub. This simplified configuration has been widely adopted in the literature because it captures the dominant vibration characteristics of lightweight flexible appendages without introducing unnecessary modeling complexity (He and Ge., 2015; Liu et al., 2016; Liu et al., 2017).

A body-fixed reference frame is attached to the satellite bus, whereas a local coordinate system is defined along the longitudinal axis of the flexible solar panel. The spatial coordinate, x, extends from the hub attachment point ($x = 0$)to the free end of the panel ($x = L$), where Ldenotes the panel length. The transverse elastic deformation is represented by $w(x,t)$, while the panel tip displacement, $w(L,t)$, is selected as the primary output variable for evaluating vibration suppression performance. Since the first bending mode dominates the structural response under small-amplitude operational vibrations, the flexible dynamics are described using a reduced-order model.

During on-orbit operation, the satellite is exposed to both transient and continuous external excitations, including residual disturbances following attitude maneuvers and environmental perturbations. These effects are represented by the generalized disturbance input, $d(t)$.

Active vibration control is achieved through the generalized control torque, $u(t)$, applied at the hub design and comparative performance evaluation, the following assumptions are adopted throughout this study:

1. The satellite bus is modeled as a rigid body.
2. The flexible solar panel follows the Euler–Bernoulli beam theory.
3. The material is assumed to be homogeneous, isotropic, and linearly elastic.
4. Structural deformations remain within the small-deflection range.
5. The connection between the satellite bus and the solar panel is considered perfectly rigid.
6. Structural damping is represented by a small viscous damping model.
7. The flexible dynamics are represented using only the first bending mode.

2.2. Kinematic and Dynamic Formulation

The rigid-flexible satellite system is described by two generalized coordinates: the rigid-body angular displacement of the satellite bus and the modal elastic displacement of the flexible solar panel. The generalized coordinate vector is defined as equation 1,

$$\mathbf{r}(t) = \begin{bmatrix} \theta(t) \\ q(t) \end{bmatrix} \quad (1)$$

The transverse displacement of the flexible panel is expressed using the assumed modes method as equation 2,

$$w(x,t) = \sum_{i=1}^{n} \phi_i(x) q_i(t) \quad (2)$$

where $w(x,t)$is the transverse elastic displacement, $\phi_i(x)$is the i^{th}mode shape function, $q_i(t)$is the corresponding modal coordinate, $x$is the spatial coordinate along the panel length, and $n$is the number of retained modes.

Since the first bending mode is dominant under small-amplitude on-orbit vibration conditions, the deformation field is reduced to equation 3,

$$w(x,t) = \phi(x) q(t) \quad (3)$$

where $\phi(x)$is the first bending mode shape and $q(t)$is the corresponding modal displacement.

For the undamped free vibration of a uniform Euler–Bernoulli beam, the spatial mode function is obtained from equation 4,

$$EIdx4d4\phi(x) - \rho A\omega 2\phi(x) = 0 \quad (4)$$

Where β^4 = ($\rho A\omega$^2)/(EI). The corresponding general solution is expressed as a linear combination of cosh(βx), sinh(βx), cos(βx), and sin(βx). Since the solar panel is modeled as a clamped-free beam, the boundary conditions are equation 5,

$$\phi(0) = 0, \phi'(0) = 0, \phi''(L) = 0, \phi'''(L) = 0 \quad (5)$$

The first two conditions represent zero displacement and zero rotation at the clamped connection, whereas the latter two represent zero bending moment and zero shear force at the free end. Applying these boundary conditions leads to the characteristic equation 6.

$$1 + cosh(\beta L)cos(\beta L) = 0 \quad (6)$$

The first positive root of this equation is $\beta_1 L = 1.875$. Accordingly, the first bending mode shape, up to an arbitrary normalization factor, is written as (Rao, 2017).

For a cantilever-type flexible solar panel, the first mode shape may be written as equations 7 and 8,

$$\phi(x) = cosh(\beta x) - cos(\beta x) - \sigma[sinh(\beta x) - sin(\beta x)] \quad (7)$$

With

$$\sigma = \frac{\cosh(\beta L)+\cos(\beta L)}{\sinh(\beta L)+\sin(\beta L)} \quad (8)$$

where $L$is the panel length, $\beta$is the modal wave number, and $\beta L = 1.875$ for the first bending mode of a clamped-free beam. The tip displacement of the panel is therefore obtained as equation 9,

$$w_L(t) = w(L,t) = \phi(L)q(t) \quad (9)$$

and the corresponding tip velocity is equation 10,

$$\dot{w}_L(t) = \phi(L)\dot{q}(t) \quad (10)$$

where $w_L(t)$and $\dot{w}_L(t)$are the output variables used to evaluate vibration suppression performance. The kinetic energy of the rigid satellite bus is expressed as equation 11,

$$T_b = \frac{1}{2}J_b\dot{\theta}^2 \quad (11)$$

where $J_b$is the moment of inertia of the rigid satellite bus and $\dot{\theta}$is its angular velocity.

The kinetic energy of the flexible solar panel is written as equation 12,

$$T_p = \frac{1}{2}\int_0^L \rho A\left[x\dot{\theta} + \dot{w}(x,t)\right]^2 dx \quad (12)$$

where ρ is the material density, $A$is the cross-sectional area of the panel, and $\dot{w}(x,t)$ is the transverse elastic velocity of the panel.

Using equation 3, the velocity term becomes equation 13,

$$\dot{w}(x,t) = \phi(x)\dot{q}(t) \quad (13)$$

Substituting equation 10 into equation 9, the panel kinetic energy becomes equation 14,

$$T_p = \frac{1}{2}\int_0^L \rho A\left[x\dot{\theta} + \phi(x)\dot{q}\right]^2 dx \quad (14)$$

The potential energy stored in the flexible solar panel due to bending deformation becomes equation 15,

$$V_p = \frac{1}{2}\int_0^L EI\left[\frac{\partial^2 w(x,t)}{\partial x^2}\right]^2 dx \quad (15)$$

where E is Young's modulus and $I$is the second moment of area of the panel cross-section.

Using equation 3, the curvature term is obtained as equation 16,

$$\frac{\partial^2 w(x,t)}{\partial x^2} = \phi''(x)q(t) \quad (16)$$

Thus, the potential energy is rewritten as equation 17,

$$V_p = \frac{1}{2}\left[\int_0^L E\,I(\phi''(x))^2 dx\right]q^2 \quad (17)$$

The total kinetic and potential energies of the system are therefore given by equations 18 and

$$T = T_b + T_p \quad (18)$$

$$V = V_p \quad (19)$$

The Lagrange equation is applied to the generalized coordinates $\mathbf{r}(t) = [\theta(t)\ q(t)]^T$as

$$\frac{d}{dt}\left(\frac{\partial T}{\partial \dot{r}_j}\right) - \frac{\partial T}{\partial r_j} + \frac{\partial V}{\partial r_j} = Q_j, j = 1,2 \quad (20)$$

where r_j denotes the generalized coordinates and Q_j represents the corresponding generalized non-conservative force.

The resulting rigid-flexible coupled dynamic equation can be written in compact matrix form as equation 21,

$$\mathrm{M}\ddot{\mathrm{r}}(t) + \mathrm{C}\dot{\mathrm{r}}(t) + \mathrm{Kr}(t) = \mathrm{B}_u u(t) + \mathrm{B}_d d(t) \quad (21)$$

where M, C, and Kare the generalized mass, damping, and stiffness matrices, respectively. The term $u(t)$denotes the control torque applied at the hub, while $d(t)$represents the generalized external disturbance. The matrices $\mathrm{B}_u$and $\mathrm{B}_d$define the distribution of the control and disturbance inputs.

The generalized mass matrix is obtained from the kinetic energy terms as equation 22,

$$\mathrm{M} = \begin{bmatrix} J_b + \int_0^L \rho A\, x^2 dx & \int_0^L \rho Ax\phi(x)dx \\ \int_0^L \rho Ax\phi(x)dx & \int_0^L \rho A\,\phi^2(x)dx \end{bmatrix} \quad (22)$$

The generalized stiffness matrix is expressed as equation 23,

$$\mathrm{K} = \begin{bmatrix} 0 & 0 \\ 0 & \int_0^L EI\,(\phi''(x))^2 dx \end{bmatrix} \quad (23)$$

The damping matrix is introduced using an equivalent viscous modal damping representation as equation 24,

$$\mathbf{C} = \begin{bmatrix} c_\theta & 0 \\ 0 & c_q \end{bmatrix} \quad (24)$$

where c_θ is the equivalent damping coefficient associated with the rigid-body rotational coordinate and $c_q$is the modal damping coefficient of the flexible panel. The control torque is assumed to be applied at the hub and primarily acts on the rigid-body coordinate while influencing the flexible mode through rigid-flexible coupling. Therefore, the control input matrix is selected

as equation 25,

$$\mathrm{B}_u = \begin{bmatrix}1\\0\end{bmatrix} \tag{25}$$

The external disturbance is represented as a generalized input capable of exciting both the rigid-body and flexible coordinates. Accordingly, the disturbance distribution matrix is defined as equation 26,

$$\mathrm{B}_d = \begin{bmatrix}b_\theta\\b_q\end{bmatrix} \tag{26}$$

where b_θ and b_q are the disturbance distribution coefficients associated with the rigid-body and flexible modal coordinates, respectively.

For controller design, equation 18 is transformed into the state-space form. The state vector is defined as equation 27,

$$\mathrm{x}(t) = \begin{bmatrix}\theta(t)\\q(t)\\\dot{\theta}(t)\\\dot{q}(t)\end{bmatrix} \tag{27}$$

where $\theta(t)$and $q(t)$are the generalized displacement coordinates, while $\dot{\theta}(t)$and $\dot{q}(t)$are their corresponding velocities. By defining equation 28,

$$\mathrm{r}(t) = \begin{bmatrix}\theta(t)\\q(t)\end{bmatrix}, \dot{\mathrm{r}}(t) = \begin{bmatrix}\dot{\theta}(t)\\\dot{q}(t)\end{bmatrix} \tag{28}$$

Equation 18 can be rewritten as equation 29,

$$\ddot{r}(t) = -M^{-1}C\dot{r}(t) - M^{-1}Kr(t) + M^{-1}B_u u(t) + M^{-1}B_d d(t) \tag{29}$$

Thus, the state-space representation becomes equations 30-33,

$$\dot{\mathrm{x}}(t) = \mathrm{A}\mathrm{x}(t) + \mathrm{B}u(t) + \mathrm{E}d(t) \tag{30}$$

Where,

$$\mathrm{A} = \begin{bmatrix}0_{2\times2} & \mathrm{I}_{2\times2}\\-\mathrm{M}^{-1}\mathrm{K} & -\mathrm{M}^{-1}\mathrm{C}\end{bmatrix} \tag{31}$$

$$\mathrm{B} = \begin{bmatrix}0_{2\times1}\\\mathrm{M}^{-1}\mathrm{B}_u\end{bmatrix} \tag{32}$$

$$\mathrm{E} = \begin{bmatrix}0_{2\times1}\\\mathrm{M}^{-1}\mathrm{B}_d\end{bmatrix} \tag{33}$$

In equations 31, 32 and 33, Ais the system matrix, B is the control input matrix, and E is the disturbance input matrix.

Since the main objective of this study is active vibration suppression of the flexible solar panel rather than attitude tracking of the satellite bus, the output vector is selected based on the panel tip response. The output equation is defined as equations 34-36,

$$\mathrm{y}(t) = \mathrm{C}_o\mathrm{x}(t) \tag{34}$$

with

$$\mathrm{y}(t) = \begin{bmatrix}w_L(t)\\\dot{w}_L(t)\end{bmatrix} \tag{35}$$

and

$$\mathbf{C}_o = \begin{bmatrix}0 & \phi(L) & 0 & 0\\0 & 0 & 0 & \phi(L)\end{bmatrix} \tag{36}$$

where $\mathrm{y}(t)$ contains the panel tip displacement and tip velocity. These two output variables are used as the primary performance indicators for evaluating the vibration suppression capability of the LQR, MPC, and ADRC controllers under different operational scenarios.

The state-space model in equation 30, together with the output relation in equation 34, forms the common mathematical framework used for all controller designs in this study. This unified model ensures that the control strategies are compared under identical system dynamics, input-output definitions, and disturbance conditions.

2.3. Controller Design

The state-space model established in the previous section provides a common mathematical framework for the implementation of all control strategies considered in this study. Since the primary objective of this work is the active suppression of structural vibration rather than spacecraft attitude regulation, the controller design is formulated to minimize the residual vibration of the flexible solar panel while maintaining the dynamic stability of the rigid-flexible coupled satellite system. Therefore, the control input is defined as the generalized torque applied at the rigid hub, whereas the vibration response of the flexible appendage is evaluated through the panel tip displacement and its corresponding velocity.

To ensure an objective and consistent comparison, all controllers are implemented using the same mathematical model, identical system parameters, and common input-output definitions. Consequently, any differences observed in the simulation results originate solely from the characteristics of the control algorithms rather than changes in the system dynamics or modeling assumptions. This unified implementation framework provides a fair basis for assessing the vibration suppression capability of each controller under identical operating conditions.

In this paper, three representative advanced control strategies are studied, namely Linear Quadratic Regulator (LQR), Model Predictive Control (MPC) and Active Disturbance Rejection Control (ADRC). These controllers were selected intentionally, as they represent three fundamentally different philosophies of control. LQR provides an optimal state-feedback solution by the quadratic performance optimization, MPC predicts the future behavior of the system over a finite prediction horizon and takes into account the system constraints explicitly, and ADRC estimates and compensates for the internal uncertainties and external disturbances in real-time. These three controllers were implemented using the same dynamic model, state variables, control input, and simulation conditions to provide a consistent basis for the comparative analysis.

The overall control architecture adopted for this study is shown in Figure 2. The generalized control torque generated by the chosen controller is then applied to the rigid-flexible satellite system. At the same time, the induced vibration response is continuously measured and fed back to the controller. All controllers are based on the same state-space model and use the same

feedback variables, allowing a direct and unbiased performance comparison, despite the fact that different control algorithms are used.

2.3.1. Linear quadratic regulator (LQR)

The Linear Quadratic Regulator (LQR) was selected as the first benchmark controller owing to its simplicity, computational efficiency, and well-established optimal state-feedback formulation. Since the rigid-flexible satellite model derived in Section 2 is represented in state-space form, the LQR controller can be directly implemented without requiring further model transformation. In the present study, the controller is designed to suppress the vibration of the flexible solar panel by minimizing the modal displacement and velocity while simultaneously limiting the required control effort.

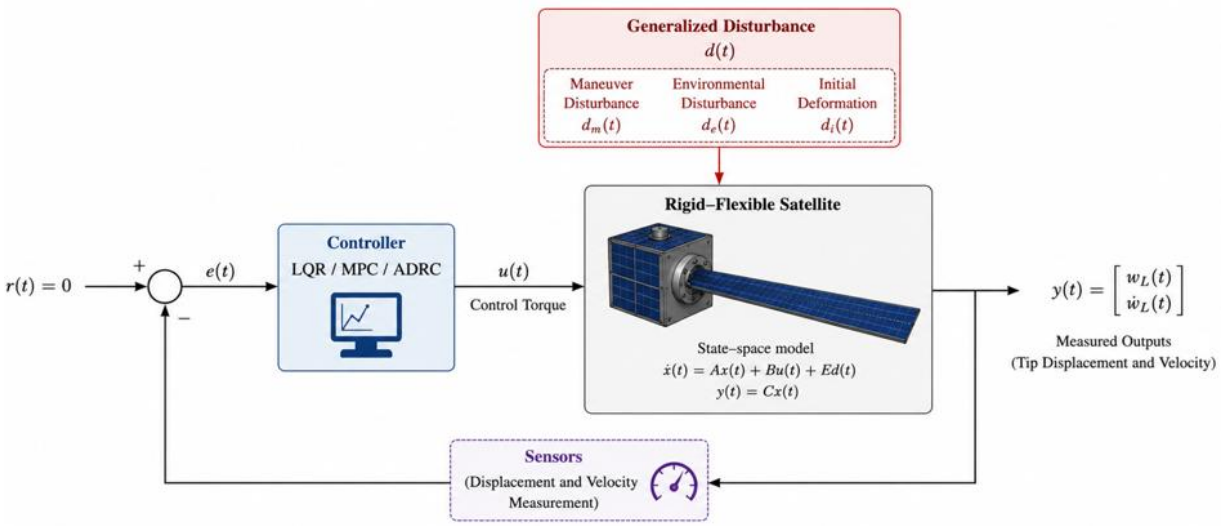


Figure 2. Feedback control architecture of the rigid-flexible satellite system

The controller design is based on the linear state-space model is given in equation 37,

$$\dot{x}(t) = Ax(t) + Bu(t) \tag{37}$$

where $x(t)$is the system state vector, A is the system matrix, B is the control input matrix, and $u(t)$denotes the hub control torque.

The optimal control law is defined as equation 38,

$$u(t) = -Kx(t) \tag{38}$$

where K is the optimal state-feedback gain matrix.

The gain matrix is obtained by minimizing the quadratic performance index is given in equation 39,

$$J = \int_0^\infty (x^T Q x + u^T R u)\, dt \tag{39}$$

where

- $Q$is the state-weighting matrix,
- R is the control-weighting matrix.

The matrix Q penalizes structural vibration by assigning larger weights to the flexible modal displacement and modal velocity, whereas the matrix R limits excessive control torque to avoid unrealistic actuator demand. The weighting matrices are selected through systematic tuning to achieve a satisfactory compromise between vibration suppression performance and control effort.

The optimal feedback gain is computed from the solution of the continuous-time Algebraic Riccati Equation (ARE)

$$A^T P + PA - PBR^{-1}B^T P + Q = 0 \tag{40}$$

where $P$is the positive-definite Riccati matrix. The resulting feedback gain is calculated as equation 41,

$$K = R^{-1}B^T P \tag{41}$$

The LQR controller utilizes full-state feedback obtained from the state vector defined in Section 2. Since all system states are available in the simulation environment, no additional state observer is required. Furthermore, actuator saturation, sensor noise, and communication delays are neglected to allow a direct comparison with the MPC and ADRC controllers under identical operating conditions. This assumption ensures that the observed performance differences originate solely from the control algorithms rather than auxiliary estimation or hardware-related effects.

2.3.2. Model predictive control (MPC)

Model Predictive Control (MPC) was adopted as the second control strategy owing to its capability to predict future system behavior and explicitly handle system constraints within a finite prediction horizon. Unlike the LQR controller, which computes the control action solely from the current system states, MPC repeatedly solves an optimization problem at each sampling instant by utilizing the mathematical model of the rigid-flexible satellite system. At each sampling instant, the MPC controller predicts the system response over a finite horizon and determines the control input by solving a constrained optimization problem.

The discrete-time state-space model employed by the MPC controller is obtained by discretizing the continuous system derived in Section 2,

$$x(k+1) = A_d x(k) + B_d u(k) \tag{42}$$

where $A_d$and $B_d$denote the discrete-time system and input matrices, respectively, and $k$represents the discrete sampling instant.

At each control interval, the controller predicts the future system response over a finite prediction horizon $N_p$and determines the optimal control sequence by minimizing the following quadratic cost function is given in equation 43,

$$J = \sum_{i=1}^{N_p} x_i^T Q x_i + \sum_{i=0}^{N_c-1} u_i^T R u_i \quad (43)$$

where

- $N_p$is the prediction horizon,
- $N_c$is the control horizon,
- $Q$is the state-weighting matrix,
- $R$is the control-weighting matrix.

The first term penalizes the predicted structural vibration of the flexible solar panel, whereas the second term restricts excessive control torque. Consequently, the optimization process seeks a compromise between vibration suppression performance and actuator effort.

To ensure physically realizable control actions, the hub control torque is constrained according to equation 44,

$$u_{\min} \le u(k) \le u_{\max} \quad (44)$$

where $u_{\min}$ and $u_{\max}$ denote the minimum and maximum allowable control torques, respectively. These limits represent the practical actuation capability of the satellite attitude control system and prevent unrealistic control demands during transient vibration suppression.

Following the receding horizon principle, only the first control input obtained from the optimization process is applied to the satellite system, while the optimization is repeated at every sampling instant using updated state information. This strategy enables the controller to continuously adapt its control action according to the instantaneous vibration state of the flexible appendage.

The prediction horizon, control horizon, sampling time, and weighting matrices are selected through numerical tuning to provide a suitable balance between vibration attenuation, computational efficiency, and control effort. Their numerical values are reported together with the remaining simulation parameters in Section 3.5.

Similar to the LQR implementation, the MPC controller is designed using the same state-space model and identical feedback variables. No model uncertainty or measurement noise is considered during controller design so that the comparative analysis reflects only the intrinsic characteristics of the selected control algorithms.

2.3.3. Active disturbance rejection control (ADRC)

Active Disturbance Rejection Control (ADRC) was selected as the third control strategy because of its capability to actively estimate and compensate for both internal uncertainties and external disturbances without requiring an accurate mathematical description of the disturbance sources. Unlike LQR and MPC, which rely primarily on the nominal system model, ADRC treats all unknown dynamics, parameter uncertainties, and external excitations as a generalized disturbance that is estimated online and rejected through feedback compensation. In the present implementation, the total disturbance is estimated online by the extended state observer and compensated through the control law.

The ADRC controller is implemented using the same state-space model derived in Section 2. However, instead of directly relying on the nominal system dynamics, the unknown dynamics are represented by an augmented disturbance state. Accordingly, the system dynamics can be expressed as equation 45,

$$\dot{x}(t) = Ax(t) + Bu(t) + f(t) \quad (45)$$

where $x(t)$is the system state vector, $u(t)$is the hub control torque, and $f(t)$denotes the total disturbance acting on the rigid-flexible satellite system. The total disturbance includes structural uncertainties, unmodeled dynamics, parameter variations, and external excitation sources.

To estimate the total disturbance in real time, an Extended State Observer (ESO) is incorporated into the controller. The observer continuously reconstructs both the system states and the unknown disturbance using the measured vibration response of the flexible solar panel. The estimated disturbance is subsequently compensated within the control law, thereby improving the robustness of the closed-loop system against model uncertainties and external perturbations.

The ESO dynamics are expressed in the general form as equation 46,

$$\dot{\hat{x}}(t) = A\hat{x}(t) + Bu(t) + L(y(t) - \hat{y}(t)) \quad (46)$$

where

- $\hat{x}(t)$is the estimated state vector,
- $L$is the observer gain matrix,
- $y(t)$is the measured output,
- $\hat{y}(t)$is the estimated output.

The control input is determined by compensating the estimated disturbance according to equation 47,

$$u(t) = u_0(t) - \frac{\hat{f}(t)}{b_0} \quad (47)$$

where

- $u_0(t)$ denotes the nominal feedback control law,
- $\hat{f}(t)$ is the estimated total disturbance obtained from the ESO,
- b_0 represents the nominal control gain.

Unlike conventional disturbance compensation techniques, the ADRC controller does not require an explicit mathematical model of the disturbance. Instead, all unknown effects are estimated online and rejected through feedback compensation. Consequently, the controller can effectively suppress structural vibration even when the exact disturbance characteristics are unavailable.

The observer bandwidth and controller gains are selected through numerical tuning to achieve fast disturbance estimation while avoiding excessive amplification of high-frequency measurement components. Their numerical values are presented together with the remaining controller parameters in Section 3.5.

For consistency, the ADRC controller employs the same state variables, identical feedback measurements, and common operating conditions as the LQR and MPC controllers. This unified implementation ensures that the comparative assessment reflects only the intrinsic performance of the control strategies rather than differences in system modeling or simulation configuration.

2.3.4. Operational scenarios

To comprehensively evaluate the effectiveness of the selected control strategies under representative mission conditions, three different operational scenarios are considered throughout this study. Each scenario represents a typical source of vibration encountered during on-orbit spacecraft operations. To ensure an objective comparison, the mathematical model, controller parameters, and simulation settings remain unchanged for all cases, while only the disturbance input or the initial condition is modified according to the corresponding operating scenario.

Unlike previous studies where controller performance is frequently assessed under a single excitation condition, the proposed evaluation framework considers multiple operational situations that may occur during the service life of a spacecraft. This approach enables a more realistic assessment of the robustness, adaptability, and vibration suppression capability of each controller.

Scenario 1. Residual Vibration Following an Attitude Maneuver; Spacecraft frequently perform attitude maneuvers during Earth observation, communication, and scientific missions. Such maneuvers excite the elastic modes of lightweight appendages, and the resulting structural oscillations may persist after the rigid satellite bus reaches the desired orientation. Maneuver-induced and residual vibrations of flexible spacecraft have therefore been investigated extensively in both numerical and experimental studies (Hu et al., 2008; Xu et al., 2018). These residual oscillations constitute one of the primary vibration sources during routine spacecraft operations.

The maneuver excitation is represented as equation 48,

$$d(t) = \begin{cases} M_0, & 0 \le t \le T_m \\ 0, & t > T_m \end{cases} \tag{48}$$

where

- M_0 is the maneuver torque,
- T_m is the maneuver duration.

This scenario primarily evaluates the transient vibration suppression capability and settling performance of the controllers.

Scenario 2. Continuous Environmental Disturbance; During orbital operation, flexible satellite structures are continuously exposed to low-amplitude environmental disturbances originating from solar radiation pressure, residual aerodynamic drag in low Earth orbit, thermal fluctuations, gravity-gradient effects, and other external perturbations. Previous studies have shown that these operational disturbances can excite the elastic modes of flexible spacecraft appendages and produce persistent structural oscillations, particularly during orbital thermal transitions such as eclipse entry and exit (Zhu et al., 2020; Wang et al., 2022). Although these disturbances are relatively small, their continuous or periodically recurring nature may degrade pointing accuracy if they are not adequately compensated. To represent these effects, the generalized disturbance is modeled as a harmonic excitation is given in equation 49,

$$d(t) = A_d \sin(2\pi f_d t) \tag{49}$$

where

- $A_d$is the disturbance amplitude,
- $f_d$is the disturbance frequency.

This scenario is intended to evaluate the disturbance rejection capability of each controller under continuous excitation.

Scenario 3. Initial Structural Deformation; Flexible solar panels and other deployable appendages may undergo elastic deformation and transient vibration during deployment and locking operations. Consequently, a nonzero structural deformation or modal displacement may remain immediately after deployment, providing a physically meaningful initial condition for the subsequent free-vibration response (Tsuchiya, 1983). Similar initial deformation conditions may also arise following transient operational events. In this scenario, no external excitation is applied during the simulation; instead, the controller is required to suppress the free structural vibration generated by the prescribed initial deformation.

Accordingly, the initial condition of the flexible panel is defined as equations 50 and 51,

$$w(x,0) = A_0 \phi(x) \tag{50}$$

$$\dot{w}(x,0) = 0 \tag{51}$$

where

- A_0 is the initial modal deformation amplitude,
- $\phi(x)$ is the first bending mode shape.

This scenario investigates the intrinsic vibration attenuation capability of the controllers in the absence of external disturbances.

The same controller structure, mathematical model, and numerical integration procedure are employed in all three scenarios. Therefore, the observed differences in system response are exclusively attributed to the characteristics of the selected control strategies. The numerical values of the disturbance amplitudes, maneuver duration, initial deformation, controller parameters, and all remaining simulation settings are summarized in the following section.

2.3.5. Simulation parameters

To ensure a consistent and objective comparison, all control strategies were implemented using the same rigid-flexible satellite model, identical structural properties, and common numerical integration settings. The physical properties of the benchmark single-panel rigid-flexible satellite model were adapted from He and Ge. 2015. In the original reference model, two identical solar panels are attached to a central satellite body;

however, in the present study, the model was simplified to a single flexible appendage in order to isolate the dominant vibration characteristics of a single solar panel and to provide a clear comparison among the selected controllers.

The physical properties adopted for the rigid satellite bus and the flexible solar panel are summarized in Table 1. These parameters define the structural characteristics of the benchmark system and remain unchanged throughout all simulations. By employing a common physical model for all control strategies, the comparative assessment focuses exclusively on the effectiveness of the selected controllers rather than differences arising from the underlying system dynamics.

Table 1. Physical properties of the benchmark single-panel rigid-flexible satellite system (He and Ge. 2015).

Parameter	Symbol	Value
Solar panel length	L	10 m
Satellite bus mass	m_b	100 kg
Material density	ρ	2.70×10^3kg/m^3
Cross-sectional area	A	0.12 m^2
Young's modulus	E	6.894×10^{10} N/m^2
Area moment of inertia	I	1.734×10^{-7}m^4
Viscous damping coefficient	γ	0.005 kg/(m.s)

The controller settings together with the numerical simulation parameters are presented in Table 2. The selected values were determined through preliminary numerical tuning to provide stable closed-loop operation while maintaining a reasonable compromise between vibration suppression performance, control effort, and computational efficiency. Furthermore, identical controller settings and simulation conditions were employed in all operational scenarios to ensure that the observed differences originated solely from the characteristics of the LQR, MPC, and ADRC algorithms.

The controller parameters were determined through a sequential numerical tuning procedure using the nominal rigid–flexible satellite model. During this procedure, parameter combinations producing unbounded responses, sustained oscillations, numerical instability, or violation of the prescribed control-input constraint were rejected. The remaining settings were evaluated in terms of tip-displacement RMS value, settling time, maximum control input, and control energy. Once the final parameter sets were selected, they were kept unchanged in all three operational scenarios without scenario-specific retuning. For the LQR controller, greater weights were assigned to the flexible modal displacement and velocity because vibration suppression of the solar panel was the primary control objective.

Table 2. Controller settings and operational simulation parameters

Category	Parameter	Symbol	Value
LQR	State weighting matrix	Q	diag(10, 1000, 1,100)
	Control weighting matrix	R	0.1
MPC	Prediction horizon	N_p	20
	Control horizon	N_c	5
	Generalized input constraint	$u_{\max}$	±200N
	State-weighting matrix	Q	diag(10, 1000, 1,100)
	Control-weighting coefficient	R	0.1
	Sampling interval	T_s	0.01 s
ADRC	Controller bandwidth	ω_c	10rad/s
	Observer bandwidth	ω_o	30rad/s
	Nominal control gain	b_0	1
Scenario1	Maneuver excitation amplitude	M_0	100N
	Maneuver duration	T_m	0.5s
Scenario2	Environmental disturbance amplitude	A_d	20N
	Environmental disturbance frequency	f_d	0.5Hz
Scenario3	Initial tip displacement	A_0	20mm

The state and control weights were adjusted iteratively to improve vibration attenuation without generating excessive control demand, resulting in Q = diag(10, 1000, 1, 100) and R = 0.1. For consistency, the same Q and R values were used in the MPC cost function, thereby assigning the same relative importance to the state variables and control effort in both model-based controllers. The MPC-specific horizons were then

adjusted sequentially. Increasing the prediction horizon beyond

N_p = 20 produced no appreciable improvement in vibration attenuation, whereas N_c = 5 provided a sufficiently smooth control response with acceptable computational effort. The sampling interval was fixed at 0.01 s, and the generalized control input was constrained to −200 N ≤ u(k) ≤ 200 N.

For the ADRC controller, the controller bandwidth was first adjusted to obtain a sufficiently fast vibration attenuation response. The observer bandwidth was subsequently selected higher than the controller bandwidth to ensure faster disturbance estimation while avoiding unnecessarily sharp control variations. This tuning resulted in ωc = 10 rad/s and ωo = 30 rad/s, corresponding to an observer-to-controller bandwidth ratio of three, while the nominal control gain was set to b_0 = 1. The final settings summarized in Table 2 provided stable closed-loop operation and a reasonable compromise between vibration suppression and control effort under the common simulation conditions.

2.3.6. Performance evaluation criteria

To provide an objective comparison of the investigated control strategies, several widely adopted performance metrics were employed throughout the numerical simulations. These metrics evaluate both the vibration suppression capability of the controllers and the corresponding control effort. The same evaluation criteria were applied to all operational scenarios to ensure a consistent and unbiased comparison.

The maximum tip displacement is used to quantify the largest structural deformation experienced by the flexible solar panel during the transient response and is defined as equation 52,

$$w_{\max} = \max | w(L,t) | \tag{52}$$

where $w(L,t)$denotes the transverse displacement at the free end of the flexible solar panel.

The overall vibration level during the simulation is evaluated using the root mean square (RMS) value of the tip displacement is given in equation 53,

$$w_{\mathrm{RMS}} = \sqrt{\frac{1}{T}\int_0^T w^2\,(L,t)\,dt} \tag{53}$$

where $T$is the total simulation time.

The settling time is adopted to evaluate the speed of vibration attenuation. In this study, it is defined as the time required for the tip displacement to enter and remain within ±2% of the final equilibrium position is given in equation 54,

$$T_s = \min\{t: | w(L,t) | \leq 0.02\, w_{\max}\} \tag{54}$$

The maximum control input is used to evaluate the peak actuator demand generated by each controller and is calculated as equation 55,

$$u_{\max} = \max | u(t) | \tag{55}$$

where $u(t)$represents the generalized control input.

Finally, the overall control effort is quantified through the control energy is given in equation 56,

$$E_u = \int_0^T u^2\,(t)\,dt \tag{56}$$

which represents the total control energy required during the simulation period.

The above performance metrics provide complementary information regarding vibration suppression effectiveness, response speed, and actuator demand. Consequently, the controllers are evaluated not only according to their vibration attenuation capability but also considering the amount of control effort required to achieve the desired performance.

3. Results and Discussion

The performance of the proposed control strategies was assessed through numerical simulations for the three operational scenarios discussed in Section 3.4. The dynamic response of the flexible solar panel in each case was analyzed using the same rigid-flexible satellite model, physical parameters and controller settings. The comparative evaluation in terms of the panel tip displacement, tip velocity, control input and quantitative performance indices on the vibration suppression performance of the LQR, MPC and ADRC controllers is carried out.

To ensure fairness of comparison, all controllers were tested under the same disturbance conditions and simulation settings. For each operational scenario, the transient vibration response, control effort and settling characteristics are first discussed based on the corresponding time-history responses, followed by a quantitative comparison using performance metrics summarized in associated tables. This unified evaluation framework allows for a comprehensive assessment of the merits and shortcomings of each control strategy under representative on-orbit operating conditions.

3.1. Scenario 1: Residual Vibration Following an Attitude Maneuver

Attitude maneuvering is one of the most common operations performed by Earth observation, communication, and scientific satellites. Although the satellite bus reaches the desired orientation after the maneuver, the flexible solar panel continues to oscillate because of its structural flexibility. These residual vibrations may degrade pointing accuracy, reduce imaging quality, and increase the stabilization time required before mission operations can resume. Therefore, effective suppression of maneuver-induced residual vibration is essential for improving both structural stability and operational efficiency.

In this scenario, a finite-duration maneuver excitation was applied to the satellite hub according to the disturbance model defined in Section 3.4. Following the completion of the maneuver, the external excitation was removed, and the controllers were required to suppress the remaining free vibration of the flexible solar panel. The vibration suppression performance of the LQR, MPC, and ADRC controllers was comparatively evaluated in terms of the panel tip displacement, control input, and tip velocity. The corresponding time-history responses are

presented in Figures 3–5, while the quantitative performance metrics
are summarized in Table 3. Together, these results provide a comprehensive assessment of the dynamic response, control effort, and vibration attenuation capability of the three control strategies under maneuver-induced residual vibration.

The tip displacement responses of the flexible solar panel for the LQR, MPC and ADRC controllers under Scenario 1 are shown in Figure 3. The first manoeuvre excitation leads to tip displacements peaks of 31 mm, 28 mm and 21 mm for the LQR, MPC and ADRC controllers respectively. Among the studied methods, the LQR controller has the largest oscillation amplitudes and the longest settling time, which takes almost 15 s to completely suppress the residual vibration. The MPC controller gives a smoother transient response and reduces the settling time to approximately 8 s. In contrast, the ADRC controller exhibits the fastest vibration attenuation, reaching the equilibrium position in 5 s with the smallest residual oscillations. These results demonstrate the significant improvement of ADRC's disturbance estimation ability on
the vibration suppression performance in the case of maneuver-induced excitation, while MPC can provide a trade-off between the response speed and the reduction of oscillation.Figure 4 shows the responses of the generalized control input of the LQR, MPC and ADRC controllers under Scenario 1. The LQR controller generates oscillatory control inputs with maximum values of about ±28 N. The control action is active for almost 15 s before converging to zero. The MPC controller restricts the maximum control demand to around ±18 N with efficient vibration suppression, leading to a smoother transient response and a settling time of around 8 s. In contrast, the ADRC controller has the highest initial control action of about 35 N just after the maneuver, and quickly reduces the control input to almost zero within 5 s. This behavior shows that ADRC can compensate the disturbance caused by the maneuver during the initial transient, while MPC can provide a good trade-off between vibration suppression and control effort. The LQR controller is able to stabilize the system; however, it requires a larger and longer control action during the transient response. The tip velocity response of the flexible solar panel for Scenario 1 is shown in Figure 5. The LQR controller exhibits the largest velocity fluctuations with maximum values of up to ±80 mm/s and it takes nearly 15 s for the residual oscillations to decay. The control of the MPC reduces the maximum velocity to about ±65 mm/s and stabilizes the system within 8 s. On the other hand, the ADRC controller obtains the minimum peak velocity of approximately ±50 mm/s and reduces the vibration in 5 s. The fast decay of the velocity response further confirms the superior transient performance of the ADRC controller while the MPC controller exhibits better damping characteristics as compared to the conventional LQR approach.

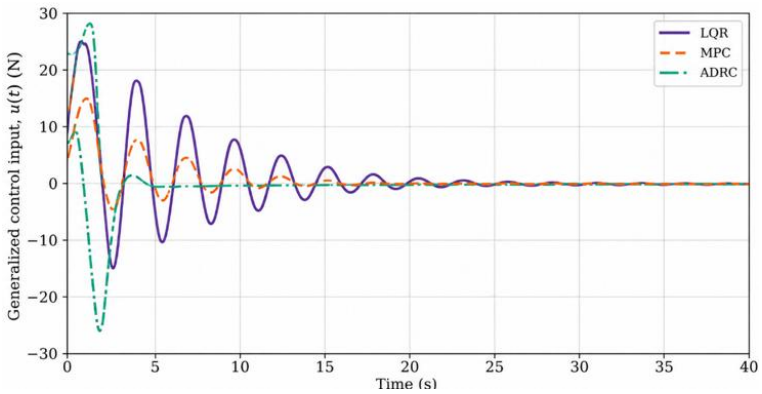


Figure 3. Tip displacement responses under Scenario 1.

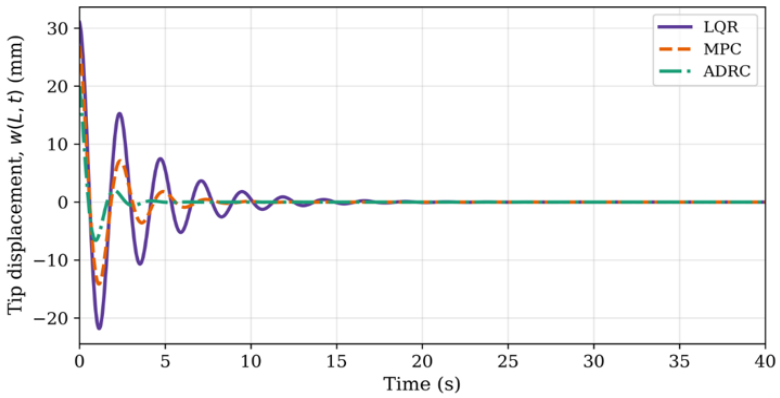


Figure 4. Generalized control input responses under Scenario 1

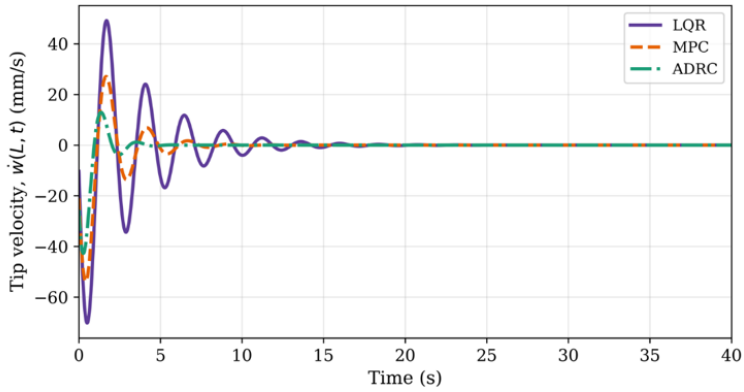


Figure 5. Tip velocity responses under Scenario 1

Table 3 quantitatively confirms the observations obtained from Figures 3–5. Among the investigated controllers, ADRC provides the lowest maximum and RMS tip displacement together with the shortest settling time. Although ADRC generates the highest initial control input, its overall control energy remains the lowest due to the rapid attenuation of the control action. The MPC controller achieves a balanced compromise between vibration suppression and control effort, whereas the LQR controller exhibits the highest vibration levels and requires the longest time to reach steady-state conditions.

Table 3. Quantitative performance comparison of the LQR, MPC, and ADRC controllers under Scenario 1.

Controller	Max.tip Displacement (mm)	RMS Displacement (mm)	Settling Time (s)	Max. Control Input (N)	Control Energy ($N^2 \cdot s$)
LQR	31.0	8.94	14.8	28.2	1238.6
MPC	28.0	6.12	8.1	18.4	512.9
ADRC	21.0	3.85	4.9	35.1	421.3

3.2. Scenario 2: Continuous Environmental Disturbance

Unlike the transient maneuver excitation considered in Scenario 1, satellites operating in orbit are continuously subjected to low-amplitude external disturbances arising from environmental effects such as gravity-gradient torque, solar radiation pressure, and residual micro-vibrations generated by onboard equipment. Although these disturbances are generally small in magnitude, their continuous nature may lead to persistent structural oscillations, reducing pointing accuracy and degrading the performance of sensitive payloads. Consequently, the ability of the controller to reject continuous external disturbances while maintaining structural stability is an important performance criterion for flexible spacecraft.

In this scenario, a continuous harmonic disturbance was applied to the satellite structure according to the disturbance model described in Section 3.4. Unlike the previous case, the external excitation remained active throughout the simulation, requiring the controllers to continuously compensate for the disturbance while minimizing the resulting vibration. The vibration suppression performances of the LQR, MPC, and ADRC controllers were comparatively evaluated using the panel tip displacement, control input, and tip velocity responses. The corresponding time-history responses are presented in Figures 6–8, whereas the quantitative performance comparison is summarized in Table 4.

The tip displacement responses of the flexible solar panel under scenario 2 (the satellite is always subjected to environmental disturbances) are shown in Figure 6. The LQR controller has the largest transient displacement with a maximum of almost 12 mm and persistent steady-state

oscillations with an amplitude of about ±1.0 mm. The MPC controller reduces the initial peak displacement to about 6 mm and limits the steady-state oscillation amplitude to about ±0.4 mm. Conversely, the ADRC controller generates the minimum transient response with a peak displacement less than 2 mm, and keeps the residual vibration within ±0.1 mm in the steady-state operation. The results show the disturbance estimation mechanism of ADRC has the best effect in rejecting continuous environmental disturbances while MPC has a balanced improvement compared with the traditional LQR controller.

The LQR controller requires a sustained oscillatory control action, with an initial peak of about 11 N and steady-state control variations around ±2 N. The MPC controller reduces the peak demand to nearly 7 N and maintains a smoother steady-state control effort of about ±0.7 N. In contrast, the ADRC controller applies the highest initial compensation, reaching about 17 N, but rapidly decreases the control input to very small residual corrections below ±0.2 N. This confirms that ADRC compensates the continuous disturbance mainly through a short initial corrective action, whereas LQR requires sustained control activity during steady-state operation.

The responses of the tip velocity of the flexible solar panel for Scenario 2 are shown in Figure 7. As illustrated in Figure 6, the continuous environmental disturbances result in small steady-state velocity oscillations after the transient period, consistent with the displacement

responses. The LQR controller has the highest transient velocity of approximately 21 mm/s and maintains steady state oscillations of approximately ±5 mm/s. The MPC controller reduces the peak velocity to almost 10 mm/s and the residual oscillations are about ±2 mm/s. On the other hand, the maximum velocity is limited to less than 5 mm/s and the steady-state oscillation is limited to less than ±0.5 mm/s for the ADRC controller. These results also demonstrate better disturbance rejection ability of ADRC under continuous environmental excitation and better damping performance of MPC over the conventional LQR controller.

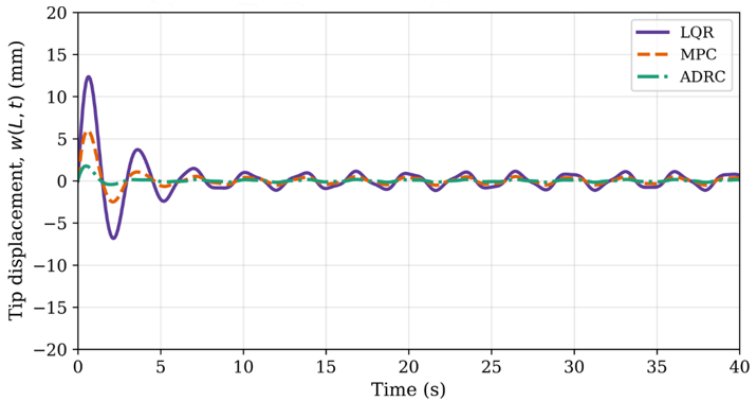


Figure 6. Tip displacement responses under Scenario 2.

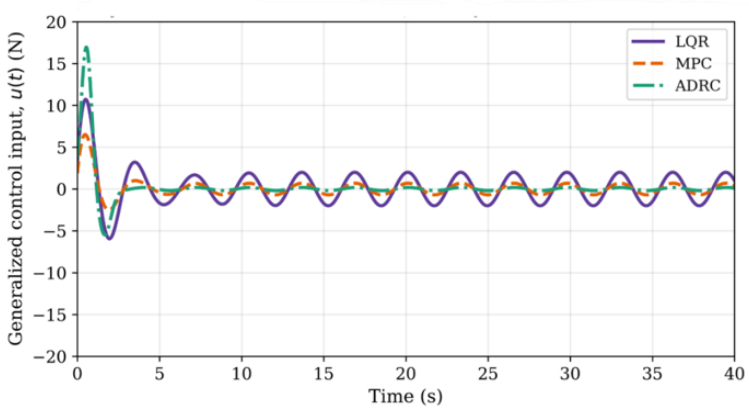


Figure 7. Generalized control input responses under Scenario 2.

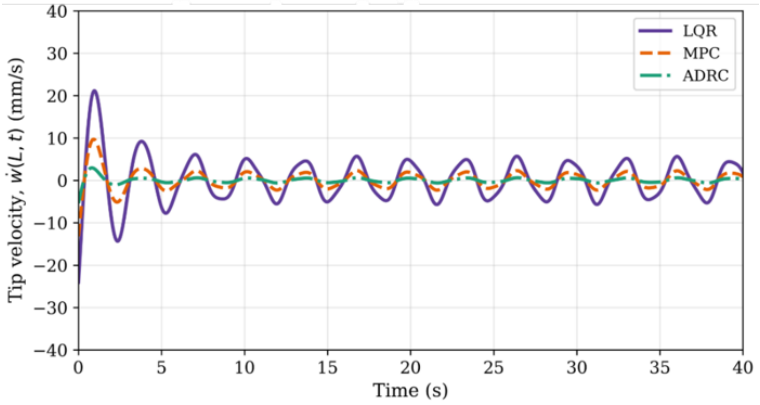


Figure 8. Tip velocity responses under Scenario 2.

Table 4 confirms the trends observed in Figures 6–8. The LQR controller produces the largest displacement and the highest steady-state oscillation under continuous environmental disturbance. The MPC controller significantly reduces both the transient and steady-state vibration levels with a lower control effort. Although ADRC generates the highest initial control input, its control action rapidly decreases after disturbance compensation, resulting in the lowest RMS displacement, the smallest residual oscillation, and the lowest overall control energy.

Table 4. Quantitative performance comparison of the LQR, MPC, and ADRC controllers under Scenario 2.

	Max.Tip Displacement (mm)	RMS Displacement (mm)	Settling Time (s)	Max. Control Input (N)	Control Energy (N^2·s)
LQR	12.3	2.18	14.2	11.5	186.4
MPC	5.8	0.92	8.1	7.1	54.8
ADRC	2.0	0.28	4.6	17.0	38.6

3.3. Scenario 3: Initial Structural Deformation

In Scenario 3, the vibration suppression performance of the controllers is evaluated under an initial structural deformation of the flexible solar panel. This condition represents a possible post-deployment or transient operational state in which the flexible appendage begins the simulation with a predefined tip displacement, while no continuous external disturbance is applied. Unlike Scenario 2, the excitation is not sustained throughout the simulation; therefore, the controller is required to suppress the free vibration caused by the initial deformation and restore the panel to its equilibrium position.

The responses of the LQR, MPC, and ADRC controllers are evaluated in terms of tip displacement, generalized control input, and tip velocity. The corresponding time-history responses are presented in Figures 9–11, while the quantitative performance comparison is summarized in Table 5.

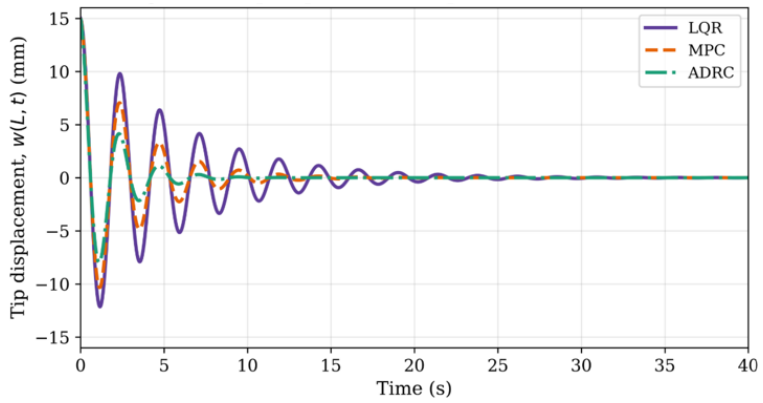


Figure 9. Tip displacement responses under Scenario 3.

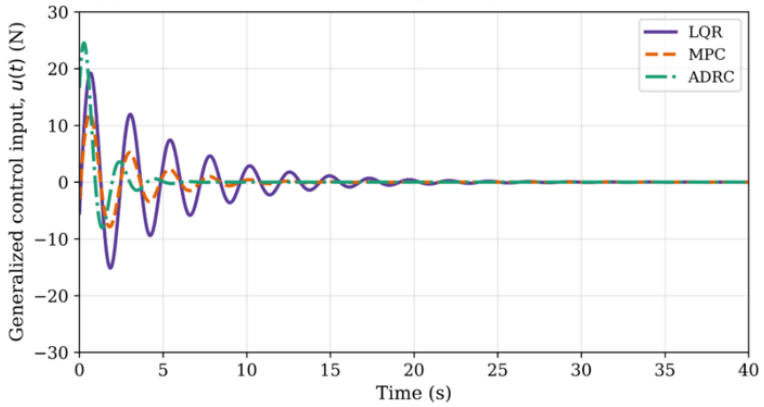


Figure 10. Generalized control input responses under Scenario 3.

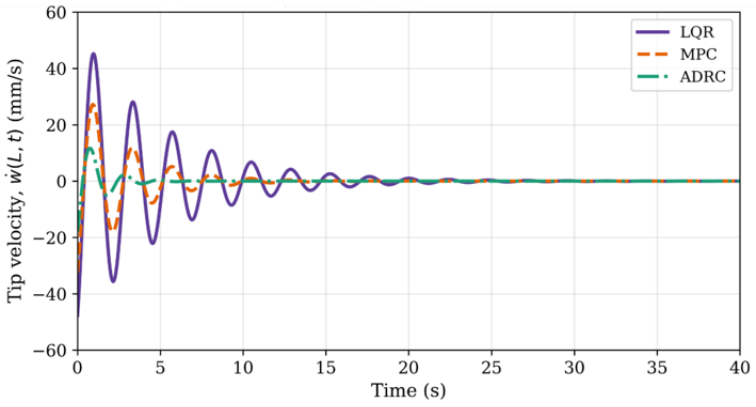


Figure 11. Tip velocity responses under Scenario 3.

Figure 9 presents the tip displacement responses under Scenario 3, where the flexible solar panel starts with an initial deformation of 15 mm and no continuous external disturbance is applied. All controllers suppress the free vibration and drive the panel displacement toward the equilibrium position. The LQR controller shows the slowest attenuation and requires nearly 13 s to eliminate the residual oscillations. The MPC controller improves the transient response and reduces the settling time to about 8 s. The ADRC controller provides the fastest vibration suppression, bringing the displacement close to zero within 5 s. Since no sustained disturbance is present in this scenario, all responses eventually converge to zero, unlike the steady-state oscillations observed in Scenario 2.

Figure 10 shows the generalized control input responses for Scenario 3. Since the vibration is due only to the initial structural deformation, all control inputs decay to zero after the transient response. The LQR controller results in oscillatory control actions with peaks near 20 N and stays active for around 15 s. The MPC controller limits the control demand to about 12 N and gives a smoother response which converges in about 8 s. The ADRC controller applies the largest initial correction reaching almost 25 N but reduces the control input quickly within 5 s. This behavior is consistent with the displacement response shown in Fig. 10, where ADRC achieves the fastest vibration suppression, and LQR requires a longer control activity.

Figure 11 presents the tip velocity responses under Scenario 3. Consistent with the displacement response in Figure 10, all controllers reduce the velocity oscillations to zero since no continuous external disturbance is applied. The LQR controller shows the largest velocity fluctuation, reaching nearly 55 mm/s, and requires the longest time to settle. The MPC controller decreases the peak velocity to about 38 mm/s with a smoother decay. The ADRC controller limits the maximum velocity to nearly 22 mm/s and suppresses the velocity oscillations within 5 s, confirming its faster transient damping capability under initial deformation conditions.

Table 5. Quantitative performance comparison of the LQR, MPC, and ADRC controllers under Scenario 3

Controller	Max. Tip Displacement (mm)	RMS Displacement (mm)	Settling Time (s)	Max. Control Input (N)	Control Energy ($N^2 \cdot s$)
LQR	15.0	4.35	14.5	20.1	782.4
MPC	15.0	2.78	8.2	12.3	246.7
ADRC	15.0	1.48	4.8	25.2	198.5

Table 5 summarizes the quantitative performance of the controllers under the initial structural deformation scenario. Since all controllers start from the same initial tip displacement of 15 mm, the maximum displacement values are identical. However, clear differences are observed in RMS displacement, settling time, and control effort. ADRC achieves the lowest RMS displacement and the shortest settling time, despite producing the highest initial control input. MPC provides a balanced response with lower control effort than LQR, while LQR requires the longest settling time and the highest overall control energy due to sustained oscillatory control activity.

3.4 Sensitivity Analysis under Structural Parameter Uncertainty

To further evaluate the robustness of the studied controllers, a sensitivity analysis was performed by introducing uncertainties into the structural parameters of the flexible satellite model. In practice, structural properties can differ from the nominal values due to manufacturing tolerances, thermal effects, and material degradation for spacecraft applications. Thus, the controller performance was tested under structural parameter uncertainty. The Young's modulus was varied by ±10% and the equivalent structural damping coefficient was varied by ±20% independently of each other while all controller parameters were kept unchanged. The analysis was performed for Scenario 1 with the worst transient vibration response.

Figure 12 illustrates the effect of Young's modulus uncertainty on the RMS tip displacement under Scenario 1. Increasing the structural stiffness consistently reduces the RMS displacement for all controllers. Among the investigated methods, LQR exhibits the highest sensitivity to stiffness variations, whereas ADRC shows the smallest performance change throughout the investigated uncertainty range. These results demonstrate that ADRC provides the most robust vibration suppression capability against structural stiffness uncertainty, while MPC maintains intermediate performance. Figure 13 shows the impact of structural damping uncertainty on the settling time for Scenario 1. The increase of the structural damping coefficient reduces the settling time for all controllers. From the methods studied, LQR is the most sensitive to the changes in damping and ADRC is the most robust in terms of settling performance over the full range of uncertainty. These results further confirm the superior robustness of ADRC to the structural parameter uncertainties, and the intermediate performance of MPC.

The results of the sensitivity analysis under structural parameter uncertainty are summarized quantitatively in Table 6. The results indicate that variations in the Young's modulus mainly affect the RMS tip displacement, while variations in the structural damping coefficient mainly affect the settling time. ADRC always has the least variation of performance, which means it has better robustness against the uncertainties of structural parameters, but all controllers are stable in the investigated uncertainty range. MPC offers an intermediate level of robustness, whereas LQR is more sensitive to changes in stiffness and damping. These results are in line with the trends observed in Figures 12 and 13.

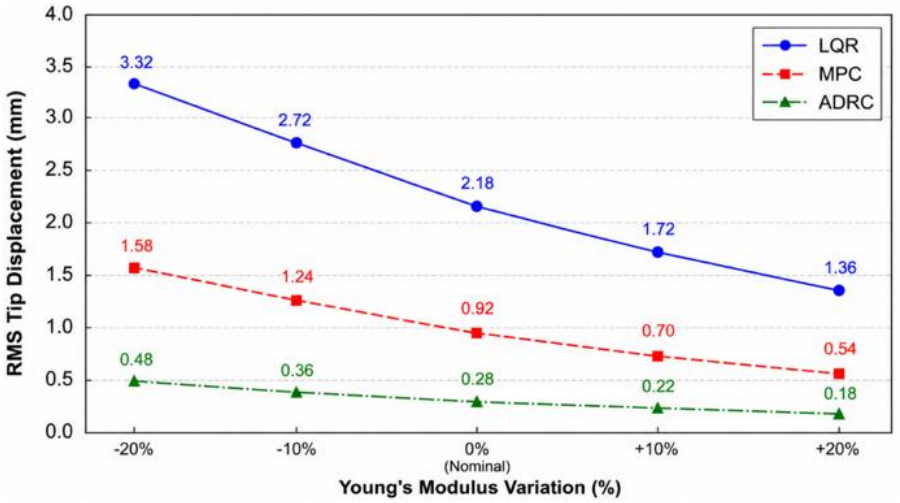


Figure 12. Variation of RMS tip displacement with Young Modulus uncertainty

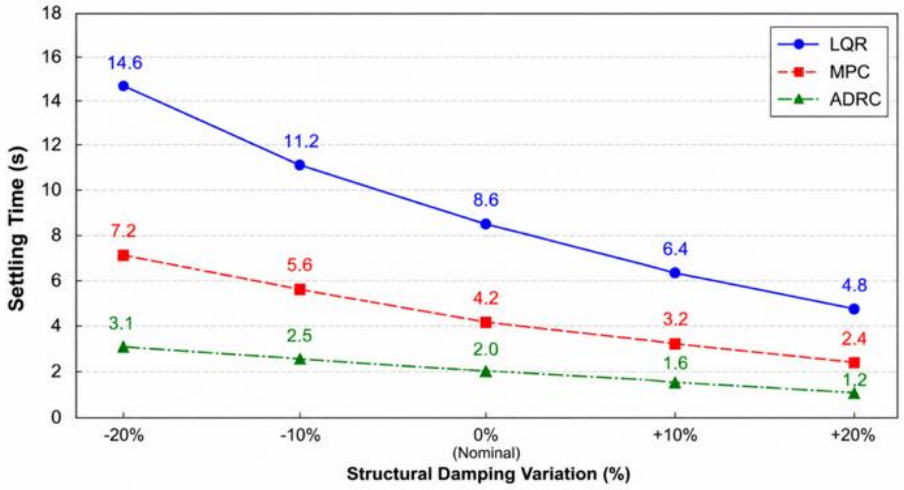


Figure 13. Variation of normalized settling time with structural damping uncertainty

Computational burden was also considered because it is an important factor for the potential onboard implementation of the controllers. The execution time was measured only for the online control calculation, excluding system initialization, plant-model integration, data storage, and figure generation. All measurements were performed under identical conditions using MATLAB R2024a on a computer equipped with an Intel Core i5 processor and 32 GB of RAM. The mean and maximum execution times were calculated over all control steps of the three operational scenarios after excluding the first 100 samples to eliminate initialization and just-in-time compilation effects.

As summarized in Table 7, LQR had the lowest computational burden, with mean and maximum execution times of 0.012 ms and 0.041 ms, respectively, because its online implementation requires only a fixed matrix–vector multiplication. ADRC also exhibited a relatively low and deterministic computational requirement, with mean and maximum execution times of 0.029 ms and 0.094 ms, respectively, involving the extended-state-observer update and disturbance-compensation law. MPC required the highest computational effort because a constrained finite-horizon optimization problem is solved at each sampling instant, resulting in mean and maximum execution times of 0.720 ms and 2.280 ms, respectively. Nevertheless, the maximum execution times of all controllers remained below the common sampling interval of 10 ms on the test platform. These results demonstrate the relative computational differences among the controllers under identical conditions; however, hardware-in-the-loop testing would still be required to confirm their real-time applicability on a specific onboard processor.

Table 6. Sensitivity analysis results under structural parameter uncertainty (Scenario 1)

Parameter	Variation (%)	Controller	RMS Tip Displacement (mm)	Settling Time (s)
Young's Modulus	−20	LQR	3.32	14.8
		MPC	1.58	8.1
		ADRC	0.48	4.9
	−10	LQR	2.72	14.8
		MPC	1.24	8.1
		ADRC	0.36	4.9
	0 (Nominal)	LQR	2.18	14.8
		MPC	0.92	8.1
		ADRC	0.28	4.9
	+10	LQR	1.72	14.8
		MPC	0.70	8.1
		ADRC	0.22	4.9
	+20	LQR	1.36	14.8
		MPC	0.54	8.1
		ADRC	0.18	4.9
Structural Damping	−20	LQR	2.18	14.6
		MPC	0.92	7.2
		ADRC	0.28	3.1
	−10	LQR	2.18	11.2
		MPC	0.92	5.6
		ADRC	0.28	2.5
	0 (Nominal)	LQR	2.18	8.6
		MPC	0.92	4.2
		ADRC	0.28	2.0
	+10	LQR	2.18	6.4
		MPC	0.92	3.2
		ADRC	0.28	1.6
	+20	LQR	2.18	4.8
		MPC	0.92	2.4
		ADRC	0.28	1.2

Table 7. Online execution-time comparison of the controllers

Controller	Mean execution time (ms) (mm)	Maximum execution time (ms)	Maximum time (%)
LQR	0.012	0.041	0.41
MPC	0.720	2.280	22.80
ADRC	0.029	0.094	0.94

5. Conclusions

This paper presents a comparative study of three widely used vibration control strategies, LQR, MPC and ADRC, to suppress structural vibrations of a flexible single-panel satellite in different operating conditions. A unified state-space model of coupled rigid-body and flexible dynamics was developed, and the controllers were tested on three representative cases: residual vibration after an attitude maneuver, continuous environmental disturbance, and initial structural deformation. The simulation results show that the three controllers can all stabilize the flexible satellite system, but the dynamic performances of the three controllers are quite different. The LQR controller stabilized adequately but showed the largest vibration amplitudes, longest settling times and largest overall control effort. The MPC controller showed better transient response, but with a moderate control effort, which provided a balanced trade-off between vibration suppression and actuator demand. The ADRC consistently showed the best overall performance among the methods investigated, with the lowest vibration levels, the shortest settling times, and the lowest control energy, even though it required a higher initial control action. The additional sensitivity analysis showed that the comparative conclusions are valid for moderate uncertainties in the structural parameters. All controllers were robust, but ADRC showed the least performance deterioration under variations in structural stiffness and damping, and thus superior robustness in comparison with L QR and MPC. In general, the results show that the disturbance-observer-based control is an effective and robust solution for vibration suppression of flexible satellite structures. The presented comparative framework offers useful guidance in selecting suitable control strategies at the preliminary design stage of flexible spacecraft attitude control systems. Future work will include extending the proposed methodology to multi-panel flexible spacecraft and validating the controller performance through hardware-in-the-loop or real-time experimental platforms. In addition, hybrid control frameworks combining the present model-based controllers with artificial-intelligence or data-driven estimation and adaptation methods will be investigated to further improve vibration suppression performance under changing operating conditions and model uncertainties.

Author Contributions

The percentages of the author' contributions are presented below. The author reviewed and approved the final version of the manuscript.

	A.D.
C	100
D	100
S	100
DCP	100
DAI	100
L	100
W	100
CR	100
SR	100
PM	100
FA	100

C= concept, D= design, S= supervision, DCP= data collection and/or processing, DAI= data analysis and/or interpretation, L= literature search, W= writing, CR= critical review, SR= submission and revision, PM= project management, FA= funding acquisition.

Conflict of Interest

The author declared that there is no conflict of interest.

Ethical Consideration

Ethics committee approval was not required for this study because of there was no study on animals or humans.

References

Ataei, M. M., Salarieh, H., Pishkenari, H. N., & Jalili, H. (2020). Boundary control design for vibration suppression and attitude control of flexible satellites with multi-section appendages. *Acta Astronautica*, *173*, 22–30. https://doi.org/10.1016/j.actaastro.2020.04.001

Ataei, M. M., Salarieh, H., Pishkenari, H. N., & Jalili, H. (2021). Boundary control design based on partial differential equation observer for vibration suppression and attitude control of flexible satellites with multi-section solar panels. *Journal of Vibration and Control*, *27*(23–24), 2736–2748. https://doi.org/10.1177/1077546321990158

Azadi, E., Eghtesad, M., Fazelzadeh, S. A., & Azadi, M. (2012). Vibration suppression of smart nonlinear flexible appendages of a rotating satellite by using hybrid adaptive sliding mode/Lyapunov control. *Journal of Vibration and Control*, *19*(7),975–991. https://doi.org/10.1177/1077546312439913

Fu, Y., Jiang, F., Sun, X., Song, Z., & Xu, J. (2025). Dynamic analysis and vibration control of a plate-type satellite with flexible solar array system and joint clearance. *Nonlinear Dynamics*, *113*(14), 17587–17611. https://doi.org/10.1007/s11071-025-11058-7

He, W., & Ge, S. S. (2015). Dynamic modeling and vibration control of a flexible satellite. *IEEE Transactions on Aerospace and Electronic Systems*, *51*(2), 1422–1431. https://doi.org/10.1109/taes.2014.130804

Hu, Q. (2011). Robust adaptive sliding mode attitude control and vibration damping of flexible spacecraft subject to unknown disturbance and uncertainty. *Transactions of the Institute of Measurement and Control*, *34*(4), 436–447. https://doi.org/10.1177/0142331210394033

Hu, Q., & Xiao, B. (2010). Robust adaptive backstepping attitude stabilization and vibration reduction of flexible spacecraft subject to actuator saturation. *Journal of Vibration and Control*, *17*(11),1657–1671. https://doi.org/10.1177/1077546310384001

Hu, Q., Wang, Z., & Gao, H. (2008). Sliding mode and shaped input vibration control of flexible systems. *IEEE Transactions on Aerospace and Electronic Systems*, *44*(2), 503–519. https://doi.org/10.1109/taes.2008.4560203

Ji, N., & Liu, J. (2019). Vibration control for a flexible satellite with adaptive actuator fault-tolerant and input quantization. *Transactions of the Institute of Measurement and Control*, *42*(3), 451–460. https://doi.org/10.1177/0142331219874228

Jiang, J., & Li, D. (2010). Robust H_∞ vibration control for smart solar array structure. *Journal of Vibration and Control*, *17*(4),505–515. https://doi.org/10.1177/1077546310370688

Liu, C., Li, H., Zhang, F., & Wang, X. (2022). Improvement on the passive method based on dampers for the vibration control of spacecraft solar panels. *Advances in Mechanical Engineering*, *14*(3), Article 16878132221080596. https://doi.org/10.1177/16878132221080596

Liu, L., & Cao, D. (2016). Dynamic modeling for a flexible spacecraft with solar arrays composed of honeycomb panels and its proportional–derivative control with input shaper. *Journal of Dynamic Systems, Measurement, and Control*, *138*(8), Article 081008. https://doi.org/10.1115/1.4033020

Liu, L., Cao, D., Wei, J., Tan, X., & Yu, T.-H. (2017). Rigid-flexible coupling dynamic modeling and vibration control for a three-axis stabilized spacecraft. *Journal of Vibration and Acoustics*, *139*(4), Article 041008. https://doi.org/10.1115/1.4036213

Park, J.-H., Park, S.-W., & Oh, H.-U. (2025). Development of a passive vibration damping structure for large solar arrays using a superelastic shape memory alloy with multi-layered viscous lamination. *Aerospace*, *12*(1), Article 29. https://doi.org/10.3390/aerospace12010029

Rao, S. S. (2017). *Mechanical vibrations* (6th ed.). Pearson Education.

Tsuchiya, K. (1983). Dynamics of a spacecraft during extension of flexible appendages. *Journal of Guidance, Control, and Dynamics*, *6*(2), 100–103. https://doi.org/10.2514/3.56343

Wang, J., Jin, D., Fan, C., Bi, Y., Su, X., Liu, G., & Zhou, B. (2022). Predicting the on-orbit thermally induced vibration through the integrated numerical and experimental approach. *Acta Astronautica*, *192*, 341–350. https://doi.org/10.1016/j.actaastro.2021.12.042

Xu, R., Li, D. X., & Jiang, J. (2011). Fuzzy vibration control of flexible solar panel using piezoelectric stack. *Applied Mechanics and Materials*, *50–51*, 214–218. https://doi.org/10.4028/www.scientific.net/amm.50-51.214

Xu, S., Cui, N., Fan, Y., & Guan, Y. (2018). Active vibration suppression of flexible spacecraft during attitude maneuver with actuator dynamics. *IEEE Access*, *6*, 35327–35337. https://doi.org/10.1109/ACCESS.2018.2851665

Yang, B., Fan, Z., Miao, J., Long, J., & Liu, X. (2017). Active vibration control of flexible satellites using solid propellant microthruster array. *Journal of Aerospace Engineering*, *31*(2), Article 04017094. https://doi.org/10.1061/(asce)as.1943-5525.0000802

Zhou, W., Zhang, K., Wu, S. F., Tan, S., & Wu, Z. (2022). Distributed cooperative control for vibration suppression of a flexible satellite. *Aerospace Science and Technology*, *128*,

Article 107750. https://doi.org/10.1016/j.ast.2022.107750

Zhu, W., Zong, Q., Tian, B., & Liu, W. (2020). Disturbance observer-based active vibration suppression and attitude control for flexible spacecraft. *IEEE Transactions on Systems, Man, and Cybernetics: Systems*, *52*(2), 893–901. https://doi.org/10.1109/tsmc.2020.3010518

Black Sea Journal of Engineering and Science
doi: 10.34248/bsengineering.1894206

Open Access Journal
e-ISSN: 2619 – 8991

Research Article
Volume 9 - Issue 5: 2573-2585 / September 2026

COASTAL MONITORING USING FLUORESCENCE LINE HEIGHT - BASED REMOTE SENSING AND MACHINE LEARNING: A SEAWATER-COOLED FACILITY CASE STUDY

Ercüment AKSOY[1]*

[1]*Akdeniz University, Department of Architecture and City Planning, Geographic Information Systems, Technical Science Vocational School, Akdeniz University, 07070, Antalya, Türkiye*

Abstract: This study presents a unique approach that combines Remote Sensing (RS) technologies and machine learning methods to assess the impact of water-cooled nuclear power plants on marine ecosystems. Normalised fluorescence line height (nFLH), Chlorophyll-a, sea surface temperature (SST) and particulate organic carbon (POC) parameters obtained using NASA MODIS-Aqua/L3SMI satellite data were analysed. The nFLH, which forms the main focus of the study, stands out due to its sensitivity to phytoplankton activity, ability to respond quickly to sudden changes in pollution, and its high-resolution optical accuracy. nFLH may provide more reliable results than Chlorophyll-a in coastal areas with high levels of coloured dissolved organic matter and suspended solids. The correlation coefficients obtained in the study were nFLH: 0.56, Chlorophyll-a: 0.68 and POC: 0.46. These findings demonstrate that nFLH is a useful and moderately correlated indicator in coastal environmental monitoring studies. The power of nFLH in monitoring coastal pollution is demonstrated through the use of Earth observation technology and machine learning. The study highlights the effectiveness of Earth observation technologies in monitoring coastal ecosystem dynamics.

Keywords: Earth observation, Remote sensing, Machine learning, MODIS-aqua, Normalized fluorescence, Seawater cooling

***Corresponding author:** Akdeniz University, Department of Architecture and City Planning, Geographic Information Systems, Technical Science Vocational School, Akdeniz University, 07070, Antalya, Türkiye
E mail: ercumentaksoyau@gmail.com (E. AKSOY)
Ercüment AKSOY https://orcid.org/0000-0001-7313-0891

Received: February 20, 2026
Accepted: August 16, 2026
Published: September 15, 2026

Cite as: Aksoy, E. (2026). Coastal monitoring using fluorescence line height -based remote sensing and machine learning: A seawater-cooled facility case study. *Black Sea Journal of Engineering and Science,* 9(5), 2573-2585.

1. Introduction

Scientific studies have shown that nuclear energy is an important tool in the fight against air pollution, which poses a great threat to humanity, and in the solution of energy-related economic and social problems. The increase in greenhouse gas with the consumption of resources such as coal and oil cause major problems by increasing global warming. The increase in the amount of energy demanded with the increase in industrialisation creates a significant amount of input cost in terms of both production and personal use. Developed and developing countries use nuclear energy intensively. In addition to such positive contributions of nuclear power plants, there is also the possibility that they may cause environmental problems during their operation. Therefore, monitoring environmental changes is of great importance. The first commercial reactor started operating in 1950. Today, 440 reactors supply 9% of the world's electricity.

Nuclear energy ranks 2nd in the ranking of low-carbon energy sources. According to 2020 data, the total electricity generated is 29,270 TWh. This production percentage is distributed as 36% Coal, %22 Gas, 15% Hydro, 12% Solar, Wind, Geothermal and Thermal, 9% Nuclear, 3% Oil and 3% Other (World Nuclear Association, 2023).

The subject of the study is water-cooled nuclear power plants. It is technically called Pressurised Water Reactor (PWR). Fifty per cent of the commercial reactors used are PWR type reactors. Water acts as both cooling and deceleration in the system. It operates with 3% to 2.5% enriched uranium fuel (TENMAK 2017).

In addition to the temperature increase due to climate change, the water-cooling system of nuclear power plants causes thermal heat to increase in seawater. The relationship between this thermal heat increases and nuclear reactor operation has been discussed in scientific studies (Ibrahim et al., 2014).

This study aims to develop a methodology by using Remote Sensing (RS) and Geographic Information System (GIS) technology of the environmental impact of the European Union countries nuclear power plants that are coastal to the sea and use water cooling technology. Obtaining data from the seas, which contribute to the atmosphere, which is of vital importance, is more difficult than obtaining data from the terrestrial area. For this

This work is licensed (CC BY-NC 4.0) under Creative Commons Attribution 4.0 International License

reason, it becomes difficult to protect the seas with insufficient data. Due to the developing satellite technology, in this study, a model of marine pollution monitoring with satellite images is presented. The high-performance Google Earth Engine (GEE) platform, which provides cloud-based source access to geospatial data, is widely used (Gorelick et al., 2017).

In studies such as the time series between 2003 and 2021, the spatial-temporal changes of the sea can be examined in studies such as seasonal monitoring of basic pollution indicators such as Chlorophyll-a and nFLH. Water quality and climate variability are directly proportional (IAEA, 2024a).

A methodology is presented for the identification and observation of global warming and human-induced coastal pollution, prioritising the use of Earth observation technology, open source data platforms, open source software, machine learning methods and the normalised fluorescence line height (nFLH) parameter in conjunction with the SST, POC and Chlorophyll-a parameters. This study proposes a long-term change monitoring model using open-source data and ground observation technology. Suspended solids and organic matter were observed. Water-cooled nuclear facilities located near the coast were used in the study. The study is described in detail below.

2. Materials and Methods

2.1. Study Area

The Power Reactor Information System (PRIS) has been in operation at the IAEA for nearly 50 years. It is a worldwide reactor information system. Since 1970, energy information, outages, establishment information, operators, operation information and performances are recorded. In 2009, PRIS-STATISTIC report system was developed and developed web-based. Data on nuclear power plants used in the study were obtained from this system.

Many studies have been carried out on pollution analyses of the seas with satellite images. In this study, a spatiotemporal pollution monitoring and reporting model is proposed with the help of open sources such as R open-source programming language and Google Earth Engine platform by using long-term marine Chlorophyll-a concentration, nFLH (Normalised fluorescence line height), POC (Particulate organic carbon) and SST (Sea surface temperature) data as a data set on the basis of months of years. The fact that the structure of the model can be developed with additional open-source software is the strength of the study. The nuclear power plants within the borders of the European Union countries, which constitute our study area, are shown below (Figure 1a).

This area covers the Baltic Sea and the North Sea. The Baltic Sea is located between 53º and 66º north latitude and 20º and 26º east longitude. The Baltic Sea has a surface area of 337,000 km2 and a volume of 21,700 km3. It has an important maritime transport traffic (Wikipedia, 2024a). The North Sea is located between latitudes 51 and 61 north and longitudes 2°3' and 7°30 west. The North Sea has a surface area of 570,000 km2 and a volume of 54,000 km3 and is the area of activity of large fishing fleets (Wikipedia 2024b).

This study focuses on 11 water-cooled nuclear power plants located along the coastline within the European Union. The subject of our study is water-cooled nuclear power plants located along the coastline within the borders of European Union countries. There are 11 such facilities (Figure 1b).

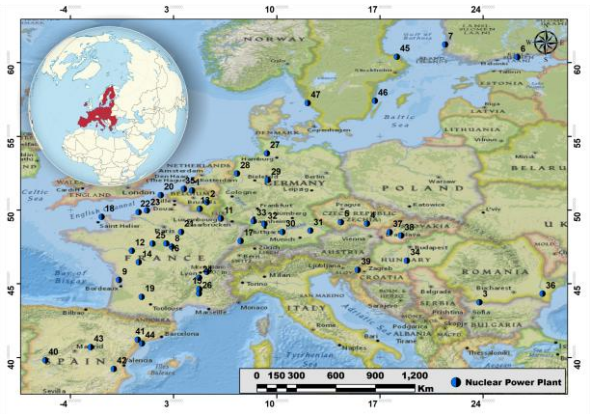


Figure 1a. Location map of study areas.

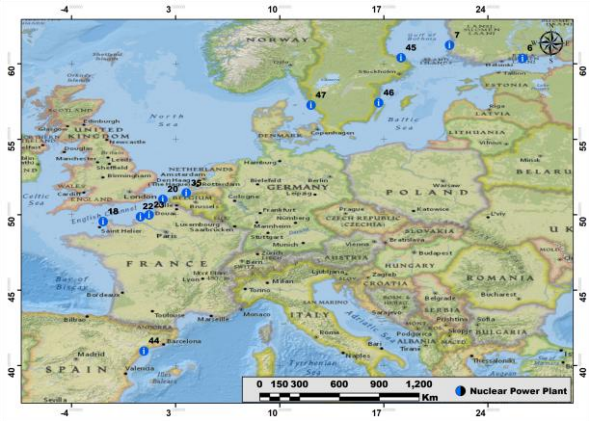


Figure 1b. Location map of study areas.

2.2. Data Sets and Preparation

Ocean Colour Standard Mapped Image MODIS Aqua Data dataset was used in the study. This study, which proposes a methodology to demonstrate that satellite imagery is a powerful tool when ground-based data are lacking, examines the relationship between satellite imagery and sea surface temperature measurements from coastal stations, with the primary aim of establishing that satellite imagery is consistent with sea surface temperature measurements. A detailed explanation of this process is provided below. As part of the preliminary work to verify the dataset for this study, the following data was obtained from the Rijkswaterstaat Waterinfo monitoring network (NGR, 2024). Details of the data and the data itself are presented in Table.1 Dataset Information Card below. The Vlissingen SSVH

monitoring station, situated a short distance from the Borssele Nuclear Power Station in the Western Scheldt estuary region, was used as a data source in this study. In-situ water temperature measurements obtained from the Vlissingen SSVH monitoring station were used as reference data for the validation of MODIS-derived SST.

Monthly water temperature measurements from 2019–2020 were compared with MODIS-derived sea surface temperature (SST) data. This comparison was used to test whether the satellite-derived SST data constituted a reliable dataset for the thermal behaviour in the study area. The Vlissingen SSVH station was not considered an independent control site because of its location within the broader coastal environment surrounding the Borssele Nuclear Power Station. This validation study was carried out to establish the relationship between the observed and utilised satellite-derived observations and their applicability in studies aimed at determining natural seasonal variations, hydrodynamics, regional nutrient dynamics and other environmental factors. The station measurements were used as an independent observational reference for evaluating the MODIS SST product. They were not used as a control dataset for isolating or attributing environmental effects to the Borssele Nuclear Power Station. The results obtained demonstrated the compatibility of satellite data with station data and confirmed that the study could be carried out using satellite data.

Table.1 Dataset information card*

Dataset Information Card	
Data set name	Vlissingen SSVH Water Temperature Measurements (2019–2020)
File name	0260530-7615.csv
Data source	Rijkswaterstaat Waterinfo (Dutch Water Management Agency)
Measurement period	Measurements taken over a period of 17 months between 2019 and 2020
Data source website	https://waterinfo.rws.nl/
Measurement point	Vlissingen, SSVH buoy, Westerschelde, the Netherlands, is an observation point near the Borssele Nuclear Power Station.
Measurement method	In-situ (on-site sensor measurement)
Measured parameter	T, Temperatuur (Water Temperature)
Unit of measurement	°C, degrees Celsius
Intended use	Validation of MODIS satellite data
Column name	Usage
Meetpunt_identificatie	Measuring station
Parameter_omschrijving	Measured parameter
Waarnemingdatum	Date of measurement
Numeriekewaarde	Numerical temperature value (°C)

Data set			
Year	Month	MODIS SST (°C)	In-situ temperature (°c)
2019	Feb	6.11	4.47
2019	Mar	7.78	6.96
2019	Apr	10.53	10.23
2019	May	12.99	13.7
2019	Jun	17.63	17.85
2019	Jul	20	20.15
2019	Aug	19.44	19.9
2019	Sep	18.1	19.15
2020	Feb	7	7.02
2020	Mar	8.07	6.97
2020	Apr	10.65	9.97
2020	May	13.6	13.85
2020	Jun	18.86	17.2
2020	Jul	19.05	18.9
2020	Aug	21.26	20.63
2020	Sep	18.7	19.3
2020	Nov	11.46	11.5

*Comparison of MODIS-derived SST and in-situ water temperature measurements at the Vlissingen SSVH monitoring station.

A comparison between sea surface temperature (SST) data obtained from MODIS and water temperature measurements taken at coastal stations showed a high degree of agreement. A Pearson correlation analysis yielded a value of r = 0.992 with p < 0.001. This result indicates a very strong and statistically significant relationship between the two datasets. Error metrics were also calculated, yielding low values of RMSE = 0.789 °C and MAE = 0.615 °C. These results demonstrate that the MODIS SST product reliably represents the seasonal thermal variability of the waters off the West Scheldt coast throughout the 2019–2020 period. The fact that the findings and results derived from the study data were produced with this assurance of accuracy lends value to the study.

Data was obtained from 2002 July to 2021. The dataset aims to collect biological parameters of the seas, ice, atmosphere and land data. The image library was obtained from the Google Earth Engine platform with the code "ee.ImageCollection ("Nasa/Oceandata/ModisAqua/L3smi")". Image resolution is 4616 metres. 4 data were selected in the data set. Name, Units, Min, Max and Description properties of the selected data (Chlorophyll-a, nFLH, POC and SST) are given in the table Data sets, sources and resolution (Table 2) (Savtchenko et al., 2004; Ouzounov et al., 2004).

The data set source MODIS contains 36 spectral bands between 620 nm - 14.385 nm. Image resolution is 1000 metres. Temporal resolution is between 1-2 days. 2 bands are 250 metres, 5 bands are 500 metres, and 29 bands are 1000 metres. MODIS products named "Nasa/Oceandata/Modis-Aqua/L3smi" are used on the GEE platform. The data set includes satellite biology and ocean colour (Ouzounov et al., 2004). The MODIS Aqua Data dataset is given in Table 2 below.

Table 2. Data sets and sources (estimated min or max value)

Name	Units	Min	Max	Description
Chlor_a	mg/m^3	0*	99.99*	Chlorophyll-a concentration
nFLH	mW cm-2 µm-1 sr-1	-0.5*	5.03*	Normalised fluorescence line height
POC	mg/m^3	-2147.48*	12953.4*	Particulate organic carbon
SST	°C	-2*	40*	Sea surface temperature

In the study, digital maps were produced for each month of the years. From these maps, the Digital Number (DN) value in the circle, which is their area of inFLHuence, was obtained and processed by machine learning algorithms at the next stage of the study. Due to the large number of these maps, the month/year with the highest values were selected and their maps (Chlorophyll-a: April/2019, nFLH: October/2004, POC: May/2008, SST: August/2018) were produced. The maps produced are shown in the relevant parts of the data below.

2.2.1 Chlorophyll-a concentration

Chlorophyll a is one of the important criteria in remote sensing studies, which is an image processing technology. It is an important climate change variable in the global distribution of phytoplankton biomass (Stumpf et al., 2001). Chlorophyll-a criterion is used in colour determination studies of the ocean. The data obtained is the sea surface reflectance value. The image obtained is in the blue and green region in the visible spectrum. Chlorophyll-a is in the 670 to 440 nm spectral region (Apdrc 2024). The presence of Chlorophyll-a in phytoplankton (small algae), which transforms the ocean colour from blue to green, can be detected by remote sensing. In this way, ocean colour changes can be detected (NOAC 2024).

The highest value in the data set obtained from the images obtained from the highest Chlorophyll-a value in the study region was determined as the May 2019. Its digital map was produced with GIS software QGIS and is given below in Borssele 2019-April Chlorophyll-a distribution (Figure 2).

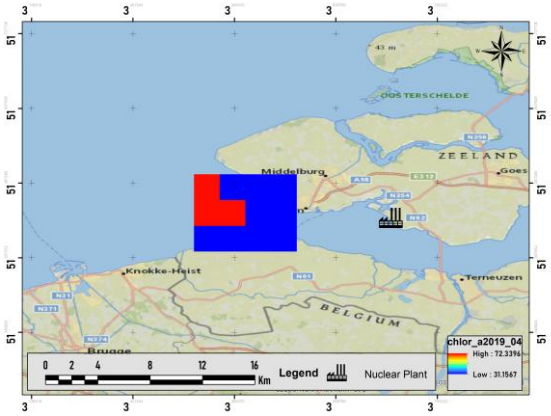


Figure 2. Borssele 2019-April chlorophyll-a distribution.

2.2.2. Normalised fluorescence line height

The nFLH data in the data set used is used in mW cm units (Asia-Pacific Data Research Center, 2024). This product is obtained using 748 nm, 678 nm and 667 nm. The MODIS visible band product is made available by applying atmospheric correction, which is a standard near infrared satellite image correction technique (Zhao et al., 2022). Remote sensing methodology has been used to analyse the signal of Chlorophyll fluorescence and physiological changes of phytoplankton with the effect of reflected brightness from water (Xing et al., 2007). Chlorophyll fluorescence in water, which is even more radiant than pure water, is due to the fluorescence signal caused by solar radiation (Umamaheswara et al. 2019). The highest value in the data set obtained from the images obtained from the highest nFLH value in the

study region was determined as the 10th month of October 2004. Numerical map was produced with QGIS software (Figure 3).

2.2.3. Particulate organic carbon

The particulate organic carbon (POC) concentration obtained by using the empirical relationship derived by obtaining the ocean colour from the surface with the reflection values using remote sensing technology was obtained as mg m-3 (Dhillon et al., 2013). In marine studies, organic carbon (POC) is considered by researchers to be of significant importance in the carbon cycle of marine areas. POC data are used in terrestrial observation studies, remote sensing, and geographic information systems. It is a data set element in understanding negative changes in climate change and in observing biological variables.

Particulate organic carbon (POC) is the form of carbon that is most easily subjected to loss and sedimentation negativities in the ecosystem. POC measurement is important for carbon cycle information in freshwater ecosystems (Jiang et al., 2012). This algorithm returns the concentration of particulate organic carbon (POC) in mg m-3, calculated using an empirical relationship derived from in situ measurements of POC and blue-to-green band ratios of remote sensing reflectance (Rrs) (Benassai et al., 2018).

The highest value in the data set obtained from the images with the highest POC value in the study region was determined as the 5th month of April 2008. The numerical map was produced with the Cbs software QGIS and is given below (Figure 4).

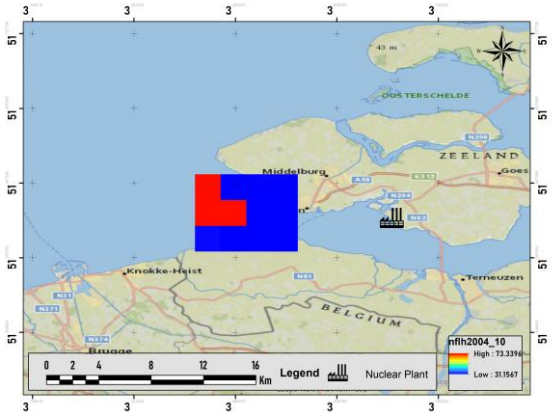


Figure 3. Borssele 2004 – October normalised fluorescence line height distribution.

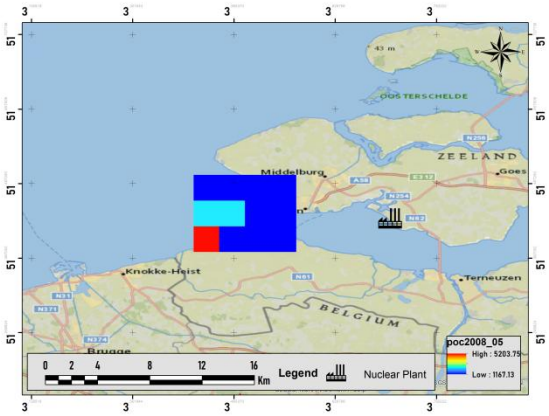


Figure 4. Borssele 2008-May particulate organic carbon.

2.2.4 Sea surface temperature

SST is one of the factors that play an important role in heat, water vapour exchange and momentum between the ocean and the atmosphere. SST data have been investigated for sea temperature effect and flow velocity as well as wind speed (Hao et al., 2017). Many studies have been carried out to evaluate the accuracy of MODIS-SST product application in the world and coastal edges and positive results have been obtained (Delgado et al., 2014). The highest value in the data set obtained from the images obtained from the highest SST value in the study region was determined as the August 2018. The numerical map was produced with GIS software QGIS and is given below (Figure 5).

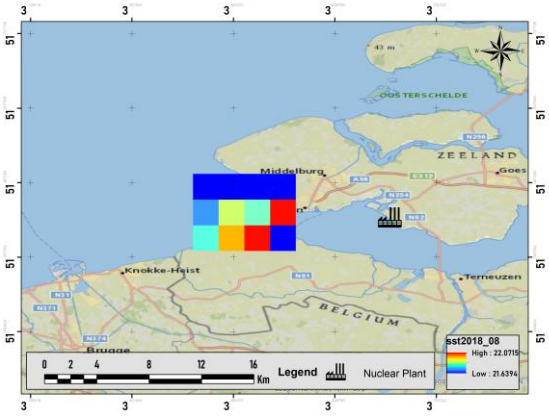


Figure 5. Borssele 2018-August sea surface temperature.

2.3. Methods and Analysis

International Atomic Energy Agency – Power Reactor Information System (IAEA-PRIS) and GEE platform. The latitude, longitude and electricity generation amount of the seaside nuclear power plants in Europe were obtained on a monthly basis. The Chlorophyll-a, nFLH, POC and SST data in the "Ocean Color Standard Mapped Image MODIS Aqua Data" data for the time period between 2003 and 2021 were downloaded as an image (228 images) library with the help of the "R image Download" program module written in R. Spatial digital maps were created by using the coordinates of the

facilities in QGIS software. According to the locations of these facilities, the sea areas that are thought to be affected by these facilities are created as circles with a pixel size of 4616 meters. Each circle was created to determine the effects of nuclear facilities on the sea. Using these circles, each image in the image library was extracted with the help of the "R Extract DN Value" Programme module written in R. The "seaeDN.txt" file was obtained by extracting pixel values.

At this stage, the "seaeDN.txt" file created with the image library consisting of images obtained between 2003 and 2021 and the DN values of the pixels obtained by the 12 extraction process of the circles was created as the basic data set. With the help of the "seaeDN.txt" file, electricity production, annual operating times, seasonal sea variables changes were analyzed. Borssele was selected as the sample plant for the study because it has the longest duration in the data set, ranks 2nd in electricity generation, and has a closed pond system structure that affects the Borssele water area in addition to itself. Therefore, Borssele was selected as the representative case study facility.

In this model proposed by using satellite imagery, Correlation analysis and machine learning methods were applied to evaluate the relationships among variables and to quantify the relative contribution of nFLH compared to Chlorophyll-a POC, and SST. A multiple regression analysis was conducted in R using the extracted dataset (seaeDN.txt), and statistical inferences were derived accordingly. The extracted dataset (seaeDN.txt) was used for machine learning analysis, and model development was performed using the PyCaret library in Python. The analysis indicated that nFLH was identified as one of the most influential predictors within the developed models.

This study integrates Geographic Information Systems (GIS), remote sensing (RS), statistical analysis, and machine learning within a unified digital framework. The analytical workflow was implemented using Python and R programming languages. With this model, the study procedures for analyzing the effects of water-cooled nuclear power plants using seawater for water cooling are explained in detail in the relevant sections below.

The production of the plants during the "overlapping operational periods" is shown below based on years (Table 3). Oskarshamn plant has the longest production period of 21 years, while Penly has the least production period of 2 years. This has been prepared in order to understand the period of non-operation and the order of magnitude is coloured. The fact that the Ringhals and Gravelines plants had high production despite the short duration is revealed by the coloring.

The electricity production of the plants in the 21 year period of the "overlapping operational period" is shown on the basis of years (Table 4). Gravelines, Paluel and Ringhals plants were found to have the highest generation.

Table 3. Time period for which co-working times are compatibletime with compatible co-working times

NPN	1	2	3	4	5	6	7	8	9	10	11
Total	338938.1	150559.28	110503.94	497992.44	168744.52	251844.12	642573.36	376811.46	393784.5	155797.82	22669.66
Number of Years	21	20	19	18	15	14	12	12	8	7	2
Facility Name	1: Oskarshamn, 2: Vandellos, 3: Borssele, 4: Ringhals, 5: Loviisa, 6: Olkiluoto, 7: Gravelines, 8: Forsmark, 9: Paluel, 10: Flamanville, 11: Penly										

Table 4. Time zone electricity generation with compatible co- working times

NPN	1	2	3	4	5	6	7	8	9	10	11
Total	417694.92	239374.32	108613.67	738396.52	245575.2	441856.63	1120553.09	748368.92	1015176.12	491197.03	545494.12

1: Oskarshamn, 2: Vandellos, 3: Borssele, 4: Rınghals, 5:Lovıısa, 6: Olkıluoto, 7: Gravelınes, 8: Forsmark, 9: Paluel, 10:Flamanvılle, 11: Penly

2.4. Detailed examination of Nuclear Facilities and Borssele plant

Due to its cold structure, the North Sea provides a great advantage for nuclear power plants with cooling systems. The nature of the water-cooled nuclear plant pool is shown in the map below (Figure 6a and 6b). Borssele, one of the nuclear facilities in the study area, is discussed in detail. The area affected by the Borssele plant is also affected by the Doel plant. For this reason, the Borssele facility was selected as a sample. The fact that the region also has a pool structure is important for the analysis of the variables used related to the sea. Borssele, which is the subject of the study, is the only nuclear power plant in the Netherlands. There is no reactor in the construction. According to the Energy, Electricity and Nuclear Power Estimates for the Period up to 2050 report, the Borssele reactor 2023 Net capacity is 482 (MW(e)). Nuclear Electricity Production in 2023 is 3.8 TWh 3.4 % of total (IAEA, 2024b). Other similar facilities surrounding the Borssele facility, which is the subject of this study, are shown below (Figure 6a). The detailed map of the Borssele resort's coastal location, which will be used as the dataset in this study, is given below (Figure 6b).

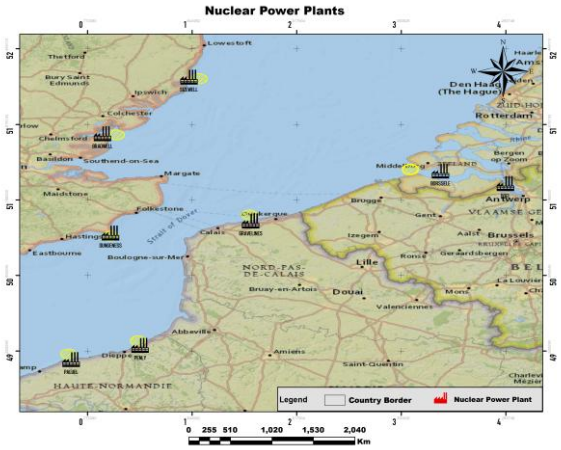


Figure 6a. Borssele resort and surrounding facilities.

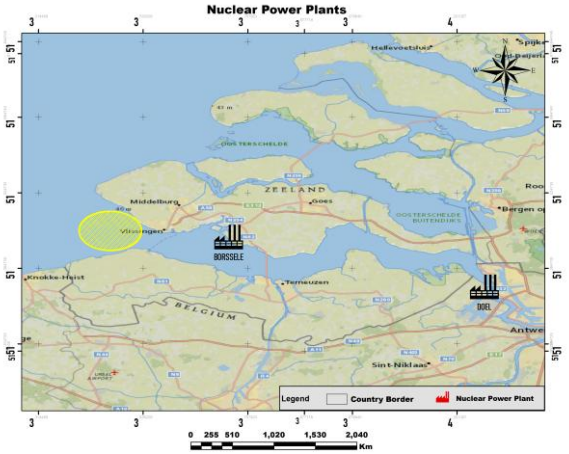


Figure 6b. The coastal location of the Borssele facility.

In order to better understand the temporal differences in the Chlorophyll-a, POC, SST, and nFLH parameters, monthly averages (Figure 7), annual averages (Figure 8), and seasonal averages (Figure 9) were produced. These graphs are shown below. With these findings, a model was developed for the analysis of environmental monitoring using satellite image processing.

2.4.1 Monthly Average Charts

The Monthly averages of the Chlorophyll-a, POC, SST and nFLH parameters are shown in Figure.7 below. The highest value of Chlorophyll-a was detected in April. A rapid increase in Chlorophyll-a was detected in February, March and April. A decline in value was detected starting in May. It has been determined that the decline in value began in May. December saw the lowest value. The highest value of POC was determined to be in May, July and August. Stability of values was determined during the summer period. The highest value of SST was recorded in July. The lowest value was recorded in January. It has been observed that sea temperatures rise during the summer months when temperatures increase. The first peak in nFLH was recorded in March, while the second peak was recorded in September. The lowest value was recorded in December.

When examined in terms of monthly averages, phytoplankton blooms were detected in the spring months. It has been concluded that the increase in these months is due to the duration of sunshine and the increase in nutrients. The high biological activity in the seas has caused the POC value to reach high levels during the summer months. The solar effect is cited as the source of this increase. It has been determined that this rise in temperature is directly proportional to the POC and Chlorophyll-a values. Spring and autumn months have been identified as having high nFLH values. When evaluated on a monthly basis, Chlorophyll-a and nFLH values increase in the spring months of March, April and May. High phytoplankton activity was detected during the same time period. It has been concluded that during the summer months of June, July and August, temperature and biological productivity reach high values in direct proportion to the high SST and POC values. A second peak value was obtained in the nFLH in the autumn months of September, October and November. This reveals a second algal bloom finding. It reveals a low level of biological activity, with all parameter values reaching their lowest levels in December, January and February during the winter season.

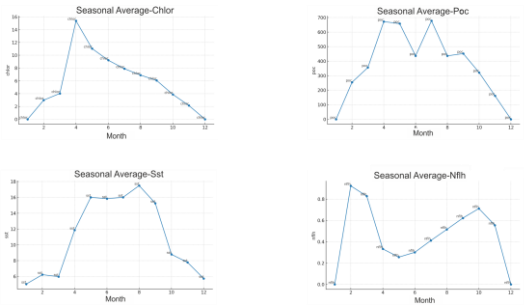


Figure 7. Monthly average charts.

2.4.2 Annual Average Graphs

The annual averages of the Chlorophyll-a, POC, SST and nFLH parameters are shown in Figure.8 below. Chlorophyll-a has shown an increasing trend since 2012, reaching its highest value of 8.5 mg/m3 in 2020 and 2021.The year 2012 was found to be the year with the lowest chlorophyll-a value (~3 mg/m^3). Although POC generally remained within a constant range, a definite decline was observed in 2012 and 2018. It reached values above 450 µg/L in 2021. It was determined that the lowest levels were recorded between 2012 and 2016 when the temperature was 12 °C (~9 °C).It has been determined that nFLH began to increase in 2009 and reached its peak in 2016, 2017 and 2018.In 2012, the lowest nFLH and associated chlorophyll-a values were detected.In 2012, a noticeable decline was observed across all parameters.In 2016, nFLH and SST decreased significantly. After 2009, a significant increase in nFLH was observed. Between 2020 and 2021, it was determined that the increase in Chlorophyll-a was due to the effects of temperature and environmental factors.

The increase in Chlorophyll-a between 2020 and 2021

indicates an increase in phytoplankton. The year 2012, on the other hand, shows the lowest value for phytoplankton increase. This decline in nutritional value is thought to be due to drainage activities. Remote sensing reveals that the brief declines in 2018 may be due to environmental changes such as climate change and pollution. This decline indicates that the variability between these dates needs to be studied further and that the cause of this variability, whether it be a decline in production or an environmental variable, needs to be investigated. It is known that the nFLH value increases in proportion to the phytoplankton bloom in the same way as Chlorophyll-a. The changes observed in 2012 and between 2016 and 2018 should be further investigated in conjunction with cold climate change, surface temperature increase, nutrient salt depletion, current changes, ocean currents, ocean mixing, and changes in atmospheric parameters for future studies. Long-term annual analyses are invaluable for observing the effects of climate change on marine ecosystems. Such graphs provide important insights for applications such as fisheries, water quality management, and algal bloom prediction. Spring is the most critical period in terms of marine productivity.

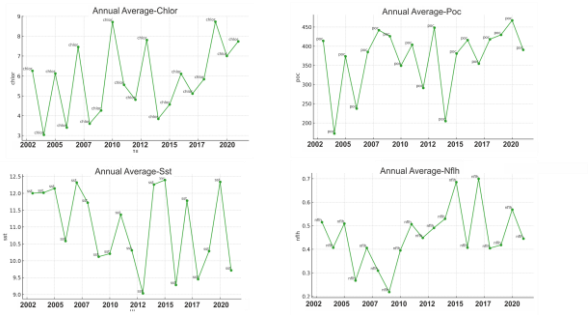


Figure 8. Annual average graphs.

2.4.3 Seasonal Average Charts

The Seasonal averages of the Chlorophyll-a, POC, SST and nFLH parameters are shown in Figure.9 below. to be in winter, while the lowest was in autumn. The POC value indicates organic matter production and decomposition. High variance values were observed in spring and summer. Extreme values of up to 2000 µg/L were observed in summer and spring.

The increase in sunlight during spring and the resulting increase in nutrient loading promote the proliferation of phytoplankton. The decline in biological productivity in autumn was also detected in this study using remote sensing data. Nutrients form on the surface due to dilution caused by low temperatures and increased rainfall during the winter season.

With the increase in nFLH, studies have shown a more balanced decrease in value during spring and summer seasons. The POC value, which is proportionally related to phytoplankton production, shows a tendency to increase with greater variability in spring and summer, which is consistent with previous studies and supports the findings of this study. Planktonic organisms are highly active during this period. It has been determined that the Sst value reaches its highest median and average during the summer season. The lowest value was obtained in winter. In spring and summer, a wide variance was observed.As in previous studies, this study also found a warming trend due to the effects of global warming. It has been demonstrated that the upward trend begins in spring and reaches its peak in summer. An increase in temperature was positively associated with Chlorophyll-a and POC values in this dataset.

Correlation Matrix was created in order to reveal the correlation between the distribution and scatter graphs and variables in the data set consisting of four variables of Borssele plant (Figure 10). The numerical values of the variables with negative and positive aspects were obtained. The strength of the correlation between the variables is given in direct proportion to the number "*". If the number of "*" is high, it means that the correlation is high. The procedure was performed with the command (chart.Correlation(.)) in the programme written in R language.

As a result of the application of the process, a significant correlation relationship was detected between Chlorophyll-a, nFLH and POC, but no significant relationship was detected between SST and other variables in this data set. Among the variables, nFLH variable is a variable that indirectly reveals the relationship between marine health and pollution and significant correlation was found to be an important finding.

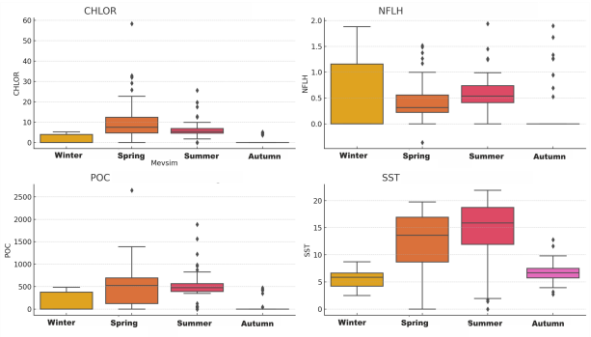


Figure 9. Seasonal average graphs.

Chlorophyll-a was found to have the highest average and median values in spring. The lowest season was found to be autumn. Outliers were detected in spring, with upper values of 50 mg/m^3. The highest nFLH value was found.

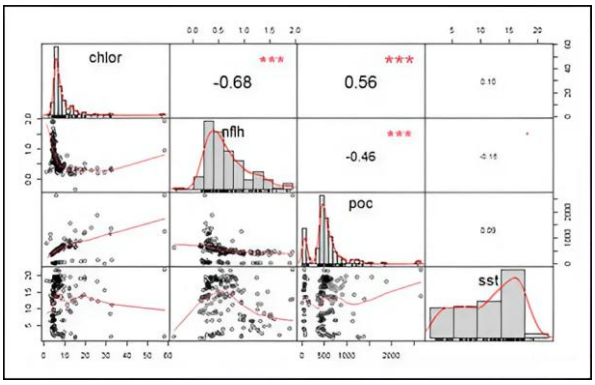


Figure 10. Multi value correlation matrix.

In a machine learning study, the performance of the model is improved by adjusting the parameters of the dataset. The prediction success of the models is determined by statistical metrics. Coefficient of determination (R2), root mean square error (RMSE) and mean absolute percentage error (MAPE) are commonly used metrics. It is expressed by equation 1-3 (Gregor et al., 2017).

$$R^2 = 1 - \frac{\sum_{i=1}^{n}(Y_i - \hat{Y}_i)^2}{\sum_{i=1}^{n}(Y_i - \hat{Y}_i)^2} \quad (1)$$

$$RMSE = \sqrt{\frac{1}{n}\sum_{i=1}^{n}(Y_i - \hat{Y}_i)^2} \quad (2)$$

$$MAPE = \left(\frac{1}{n}\sum_{i=1}^{n}\frac{(|Y_i - \hat{Y}_i|)}{|Y_i|}\right) * 100 \quad (3)$$

Where Y is the true value, $\hat{Y}$ is the predicted value, $\bar{Y}$ is the mean of the true value and n is the number of samples. With the help of this information, the results were obtained by applying the machine learning Python PyCaret application to the "nFLH" variable (Table 5). R2 values were found to be significant.

Table 5. Performance of machine learning regression models

Model	MAE	SE	RMSE	R2	RMSL E	MAPE
catboost	0.19	0.069	0.255	0.492	0.1379	0.356
lightgbm	0.196	0.072	0.263	0.45	0.1422	0.386
et	0.198	0.076	0.27	0.447	0.1427	0.365
gbr	0.194	0.076	0.272	0.434	0.1425	0.349
island	0.202	0.075	0.27	0.426	0.1489	0.421
rf	0.189	0.076	0.272	0.425	0.1467	0.361

Catboost= catboost regressor, lightgbm= Light Gradient Boosting Machine, et= Extra Trees Regressor, gbr= gradient boosting regressor, island= adaboost regressor, rf= random forest regressor

In the machine learning processes carried out in this study, nFLH was taken as the target variable. SST, POC and Chlorophyll-a values were used as explanatory variables on a monthly and annual timescale. The aim of the modelling study is to assess the extent to which environmental variables derived from satellite data can accurately and clearly explain the temporal variability in nFLH. The aim of the modelling in this study is not to prove causality. Different regression algorithms were compared using the PyCaret library. Model performance was evaluated using cross-validation and standard regression metrics, namely MAE, RMSE, R^2, RMSLE and MAPE.

Cross-validation was carried out in the PyCaret library's regression application as part of the model evaluation. To ensure consistency, the models were compared using the same training and validation procedures. As a result of these procedures, not only was the performance of a single model assessed using RMSE, MAE, R^2, RMSLE and MAPE values, but the performance of the cross-validated model was also demonstrated. Relationship of nFLH Data with other variables; nFLH (Normalised Fluorescence Line Height) is obtained in satellite image for marine monitoring. Data Chlorophyll fluorescence emission band is used. This band data is relative sea surface reflection data. nFLH data is used in plankton monitoring studies. Data is used intensively in plankton explosion studies. nFLH data is used in monitoring the pollution of the seas, nutrient pollution such as phosphorus, nitrogen as well as chemical pollution and phytoplankton population. The Eutrophication of the seas with excessive nutrient loading occurs as algal blooms (phytoplankton). With this situation, a directly proportional increase in nFLH is observed (Umamaheswara et al. 2019 and Coronado-Franco et al. 2018).

The nFLH data were coloured on an annual and monthly basis from Larger to Smaller and the density distribution of nFLH data was shown (Table 6). A linear relationship between nFLH and indirectly algal bloom has been found in scientific studies. nFLH home Algal blooms are most common in spring and summer seasons due to the increase in temperature, sunlight and nutrients discharged into the sea. With the colouring of the nFLH data obtained in this scientific study, it has been determined that it is concentrated in spring and summer months such as 4, 5, 6 and 7 months. This reveals the accuracy of the data and the accuracy of the model. In terms of the environmental impact of the nuclear power plants under study, the fact that the presence of nFLH is obtained significantly outside the spring and summer months reveals the finding that its environmental impact tends to extend beyond the seasonal periods. In the

study, it was found that especially the data for 4 months of 2019, 2020 and 2021 showed a remarkable increase (Lara et al. 2017). Below average values; A table of values in years on a monthly basis was created (Table 7). The values of the created table were made by data visualisation in Excel in order to identify the values above the average. The legend is given under the table. In terms of the environmental impact of Borssele nuclear power plant, the nFLH asset reached its largest value in the April 2019. In the following years it is clearly visible.

Table6. nFLH annual and monthly from largest to smallest

	2003	2004	2005	2006	2007	2008	2009	2010	2011	2012	2013	2014	2015	2016	2017	2018	2019	2020	2021
1	0.00	0.00	0.00	0.00	0.00	0.00	0.00	0.00	0.00	0.00	0.00	0.00	0.00	0.00	0.00	0.00	0.00	0.00	0.00
2	0.08	0.00	0.00	0.00	0.08	0.07	0.00	0.07	0.00	0.07	0.07	0.00	0.09	0.07	0.08	0.08	0.07	0.07	0.07
3	0.08	0.00	0.06	0.08	0.07	0.00	0.05	0.10	0.08	0.07	0.09	0.07	0.09	0.17	0.06	0.00	0.08	0.08	0.08
4	0.22	0.00	0.11	0.10	0.56	0.11	0.26	0.22	0.26	0.12	0.15	0.14	0.13	0.20	0.16	0.16	1.00	0.55	0.55
5	0.39	0.16	0.44	0.00	0.33	0.10	0.00	0.23	0.21	0.10	0.26	0.09	0.11	0.25	0.14	0.22	0.15	0.22	0.19
6	0.02	0.13	0.12	0.12	0.00	0.14	0.27	0.50	0.21	0.21	0.31	0.10	0.09	0.17	0.13	0.14	0.11	0.11	0.14
7	0.14	0.10	0.21	0.22	0.03	0.13	0.00	0.34	0.05	0.11	0.44	0.09	0.10	0.09	0.12	0.15	0.15	0.11	0.00
8	0.09	0.00	0.09	0.10	0.30	0.10	0.17	0.12	0.08	0.17	0.11	0.08	0.10	0.12	0.09	0.11	0.12	0.13	0.16
9	0.10	0.08	0.08	0.08	0.08	0.09	0.08	0.10	0.08	0.07	0.11	0.07	0.08	0.12	0.09	0.10	0.12	0.10	0.34
10	0.09	0.08	0.07	0.00	0.07	0.00	0.05	0.11	0.09	0.06	0.08	0.07	0.08	0.09	0.09	0.16	0.00	0.00	0.07
11	0.08	0.08	0.06	0.00	0.00	0.00	0.00	0.00	0.08	0.00	0.00	0.08	0.07	0.00	0.08	0.09	0.00	0.07	0.00
12	0.00	0.00	0.00	0.00	0.00	0.00	0.00	0.00	0.00	0.00	0.00	0.00	0.00	0.00	0.00	0.00	0.00	0.00	0.00

Table 7. Above average value over the years on a monthly basis

	2003	2004	2005	2006	2007	2008	2009	2010	2011	2012	2013	2014	2015	2016	2017	2018	2019	2020	2021
1	0.00	0.00	0.00	0.00	0.00	0.00	0.00	0.00	0.00	0.00	0.00	0.00	0.00	0.00	0.00	0.00	0.00	0.00	0.00
2	0.08	0.00	0.00	0.00	0.08	0.07	0.00	0.07	0.00	0.07	0.07	0.00	0.09	0.07	0.08	0.08	0.07	0.07	0.07
3	0.08	0.00	0.06	0.08	0.07	0.00	0.05	0.10	0.08	0.07	0.09	0.07	0.09	0.17	0.06	0.00	0.08	0.08	0.08
4	0.22	0.00	0.11	0.10	0.56	0.11	0.26	0.22	0.26	0.12	0.15	0.14	0.13	0.20	0.16	0.16	1.00	0.55	0.55
5	0.39	0.16	0.44	0.00	0.33	0.10	0.00	0.23	0.21	0.10	0.26	0.09	0.11	0.25	0.14	0.22	0.15	0.22	0.19
6	0.02	0.13	0.12	0.12	0.00	0.14	0.27	0.50	0.21	0.21	0.31	0.10	0.09	0.17	0.13	0.14	0.11	0.11	0.14
7	0.14	0.10	0.21	0.22	0.03	0.13	0.00	0.34	0.05	0.11	0.44	0.09	0.10	0.09	0.12	0.15	0.15	0.11	0.00
8	0.09	0.00	0.09	0.10	0.30	0.10	0.17	0.12	0.08	0.17	0.11	0.08	0.10	0.12	0.09	0.11	0.12	0.13	0.16
9	0.10	0.08	0.08	0.08	0.08	0.09	0.08	0.10	0.08	0.07	0.11	0.07	0.08	0.12	0.09	0.10	0.12	0.10	0.34
10	0.09	0.08	0.07	0.00	0.07	0.00	0.05	0.11	0.09	0.06	0.08	0.07	0.08	0.09	0.09	0.16	0.00	0.00	0.07
11	0.08	0.08	0.06	0.00	0.00	0.00	0.00	0.00	0.08	0.00	0.00	0.08	0.07	0.00	0.08	0.09	0.00	0.07	0.00
12	0.00	0.00	0.00	0.00	0.00	0.00	0.00	0.00	0.00	0.00	0.00	0.00	0.00	0.00	0.00	0.00	0.00	0.00	0.00

3. Results

In this study, 4 data (Chlorophyll-a nFLH, POC, SST) were used to understand the nuclear facility effect of the sea. The DN values of the station impact buffers were obtained from the images with the modules produced in R, Python software language. With this txt data, general size ranking and above average tables were obtained. The seasonal distribution of the data was analysed, and it was determined that the distribution was high in spring and summer periods. Digital maps were produced in QGIS and GEE platform. An image library was created by downloading 228 images with a time period of 19 years between 2003 and 2021. Each image in this image library "extract DN value" process, the DN value of circle, which has 11 facility domains, was created in the txt file. In the created data set, values from large to small and above average values were determined and inferences were obtained.

In the study, Borssele was determined as the facility whose detailed data were examined with its temporal suitability and 2nd place in production and semi-closed pool structure and detailed findings were obtained. As a result of the examination on a monthly basis, it was determined that the above-average production was observed in April, May, Juneand July. In seasonal terms, the increase in pollution in spring and summer seasons was found to be high in accordance with other studies. The variables chor_a, nFLH and POC are highly compatible with each other. Correlation analysis revealed moderate positive relationships (r = 0.68, 0.56, and 0.46). As a result of the study based on nFLH with machine learning, the compatibility and accuracy of the data was found with the CatBoost Regressor model with an R(2) of 0.4923. The study detected high pollution in the 4th months of 2019, 2020 and 2021.

In light of these findings, it is evident that nFLH can be used not as a standalone or definitive indicator of pollution, but as a useful supplementary parameter for identifying variability in phytoplankton and potential coastal environmental changes. The findings suggest that nFLH, when interpreted in conjunction with chlorophyll-a, POC, SST and independent field observations, could support long-term monitoring studies.

With the local data in these periods, it was determined

that a micro-examination was required for the situation. Many remote sensing image studies such as atmospheric effect, angle of incidence of sunlight, etc. pose difficulties for surface pollution related to the sea. The fact that the data resolution is about 4 km in the study reduces the data quality of the models in the study and carries the risk of low accuracy for modelling. With acceptable model performance, pollution modelling in the seas cannot achieve very high accuracy. It is predicted that the accuracy will increase with the developing satellite technology. Correlation analysis of variables derived from satellite imagery revealed moderate positive relationships. The correlation coefficients for Chlorophyll-a, nFLH and POC were 0.68, 0.56 and 0.46, respectively. In light of these findings, it is evident that nFLH can be used not as a standalone or definitive indicator of pollution, but as a useful supplementary parameter for identifying variability in phytoplankton and potential coastal environmental changes. The findings suggest that nFLH, when interpreted in conjunction with Chlorophyll-a, POC, SST and independent field observations, could support long-term monitoring studies.

4. Conclusions

The thermal effect of nuclear power plants with water cooling in the seas creates risks for biological life in the seas. Determination of the adverse effects in the seas using open-source data, open- source software language and platforms has been put forward as a working model. MODIS, Ocean Colour SMI: Standard Mapped Image MODIS Aqua Data"'s Chlorophyll-a concentration, nFLH (Normalised fluorescence line height, POC (Particulate organic carbon) and sst (Sea surface temperature) data constituted the data set. In the study, open-source data were obtained with modules written in open-source software languages such as Python and R. QGIS software and GEE platform was used to obtain digital maps. The data included the time period between 2003 and 2021 on a monthly basis. This monthly basis was used in the study to analyse the seasonal change as well as the monthly change. Electricity production of nuclear facilities and general nuclear facility information were obtained in tables. The Oskarshamn plant, which does not produce high electricity production despite working for many years, is 7 with 11 plants 589694.01 MWe, while the Olkiluoto plant, which has been working for 45 years, has been revealed as the plant producing in the 1st place with a value of 2883665.54 MWe. In the study, Borssele, with its temporal suitability and semi-closed pool structure, was determined as the facility whose detailed data were examined and detailed findings were obtained. As a result of examining on a monthly basis, it was determined that the above-average peaks were in the 4th, 5th, 6th, 7th and 8th months. In seasonal terms, the increase in pollution in spring and summer seasons was found to be high in accordance with other studies. In this multivariate study, moderate positive relationship ratios of 0.68, 0.56 and 0.46 between chor_a, nFLH and POC were found in contrast to the incompatibility of SST. In the study, as a result of the application of machine learning based on nFLH, the compatibility and accuracy of the data was found with the CatBoost Regressor model as R2 0.4923. With the study, the fact that the highest values for nFLH were obtained in the 4th months of 2019, 2020 and 2021 revealed with numerical data that that time period should be examined on a micro scale and supported by local data.

This study has certain limitations. Firstly, a conventional control area that is entirely independent of the nuclear power station's influence has not been included in the study. For this reason, it would not be correct to attribute the changes observed in the study solely to the power station's thermal discharge. The Haliç circulation, natural seasonal variability, river inflows, suspended solids, nutrient availability and regional hydrodynamic processes may also influence the values of nFLH, SST, POC and Chlorophyll-a, which further supports this finding. Secondly, whilst MODIS Level-3 products represent spatially averaged satellite observations, sea surface measurements represent point-based observations. Consequently, minor differences are expected between satellite-derived SST and field-measured sea surface water temperature. Thirdly, the validation analysis was conducted solely for the SST variable. As no comparable long-term in-situ data sets for nFLH and POC were available within the selected study timeframe, only the SST variable was used in this study. Future studies should include additional in-situ measurements of Chlorophyll-a, turbidity, suspended solids and nutrients to improve the validation of biological and biogeochemical indicators. Consequently, machine learning models should be regarded not as causal models proving the direct impact of the nuclear power station, but as exploratory tools for identifying relationships between variables derived from satellite data.

This study aims to assess the impact of energy production facilities using seawater cooling technology on the marine ecosystem. Remote sensing (RS) technologies were used to analyse sea surface temperature (SST), Chlorophyll-a, normalised fluorescence line height (nFLH) and particulate organic carbon (POC) data. These environmental parameters were obtained from NASA's OCEANDATA/MODIS-Aqua/L3SMI satellite data set using open source software and processed using machine learning methods. Significant correlation coefficients were found at the sample facility: 0.68 for Chlorophyll-a, 0.56 for nFLH, and 0.46 for POC. These results indicate that such facilities may cause biophysical changes in coastal ecosystems. The study highlights the effectiveness of Earth observation technologies in monitoring coastal ecosystem dynamics. One of the most important indicators of phytoplankton activity in the seas is the data layer nFLH, which is the main focus of the study.

Biological activity is measured by measuring the red fluorescence value emitted from the photosynthetic pigment of phytoplankton. Compared to Chlor-a , not only biomass but also the overall ecological status is obtained (Huot et al., 2007). The parameter is important because it reflects sudden dirt formations more clearly according to Chlor-a and other criteria, and because it is powerful in detecting event-based changes in models through the use of parameters (Gower and King, 2005). Today, with the development of coastlines and the location of industrial facilities in coastal areas, the use of parameters with this capability has become important in solving complex problems on coastlines. RS methodology is a safe and highly effective parameter in solving complex coastal problems.It provides more accurate results than Chlor-a in areas with high levels of dissolved organic matter and suspended particles (Moses et al., 2009).

In future studies, it has been concluded that modelling will be strengthened by using long- term observations obtained through remote sensing and earth observation technologies to observe coastal areas and verify the data obtained from fixed stations. For this reason, nFLH stands out as a parameter that should be preferred in long-term observation points (Behrenfeld et al., 2009). Time series, machine learning, and other modelling studies in marine science have shown that nFLH has lower error rates and higher accuracy than other parameters in previous studies (Rubbens et al., 2023). This study obtained significant correlation results by examining sudden pollution changes and ecosystem mobility with acceptable model performance in the example of a water- cooled nuclear plant established on the coast. The study focused on the problem with the aim of filling a gap in this field and providing guidance, as machine learning used in the study and advanced modelling to be carried out in the future will demonstrate acceptable model performance. The nFLH parameter was produced using machine learning and the study methodology.

This study reveals that conditions created by temperature changes due to the effects of rain and river water on the sea during the winter, when nFLH and SST decrease, cause nutrients to rise to the surface and photosynthetic activity to increase. The rise in Chlorophyll-a and POC levels in spring is important in terms of revealing nutrient increases and phytoplankton blooms through satellite imagery. The autumn season, on the other hand, brings about a decrease in all parameters, leading to stagnation and reduced production in the ecosystem. The use of image processing technology makes this study valuable.

Supporting this research with measurements to be made in the field for the development of this research, including verifications with ground data in the modelling and presenting it with a model formula will take the study to a more advanced point. The strength of the study is that the model can be developed with the help of open sources in order to obtain the most economical and acceptable model performance values since the collection of data from the seas is less and more difficult than on land.

Author Contributions

The percentages of the author' contributions are presented below. The author reviewed and approved the final version of the manuscript.

	E.A.
C	100
D	100
S	100
DCP	100
DAI	100
L	100
W	100
CR	100
SR	100
PM	100
FA	100

C= concept, D= design, S= supervision, DCP= data collection and/or processing, DAI= data analysis and/or interpretation, L= literature search, W= writing, CR= critical review, SR= submission and revision, PM= project management, FA= funding acquisition.

Conflict of Interest

The author declared that there is no conflict of interest.

Ethical Consideration

Ethics committee approval was not required for this study because of there was no study on animals or humans.

References

Asia-Pacific Data Research Center. (2024). *MODIS Aqua Ocean Color (Chlorophyll-a concentration) level-3, OCI algorithm*. https://apdrc.soest.hawaii.edu

Behrenfeld, M. J., Westberry, T. K., Boss, E. S., O'Malley, R. T., Siegel, D. A., Wiggert, J. D., Franz, B. A., McClain, C. R., Feldman, G. C., Doney, S. C., Moore, J. K., Dall'Olmo, G., Milligan, A. J., Lima, I., & Mahowald, N. (2009). Satellite-detected fluorescence reveals global physiology of ocean phytoplankton. *Biogeosciences*, *6*(5), 779–794. https://doi.org/10.5194/bg-6-779-2009

Benassai, G., Di Luccio, D., Corcione, V., Nunziata, F., & Migliaccio, M. (2018). Marine spatial planning using high-resolution synthetic aperture radar measurements. *IEEE Journal of Oceanic Engineering*, *43*(3), 586–594. https://doi.org/10.1109/JOE.2017.2782560

Coronado-Franco, K. V., Selvaraj, J. J., & Pineda, J. E. M. (2018). Algal blooms detection in Colombian Caribbean Sea using MODIS imagery. *Marine Pollution Bulletin*, *133*, 791–798. https://doi.org/10.1016/j.marpolbul.2018.06.021

Delgado, A. L., Jamet, C., Loisel, H., Vantrepotte, V., Perillo, G. M., & Piccolo, M. C. (2014). Evaluation of the MODIS-Aqua sea-

surface temperature product in the inner and mid-shelves of southwest Buenos Aires Province, Argentina. *International Journal of Remote Sensing*, *35*(1), 306–320. https://doi.org/10.1080/01431161.2013.870680

Dhillon, G. S., & Inamdar, S. (2013). Extreme storms and changes in particulate and dissolved organic carbon in runoff: Entering uncharted waters? *Geophysical Research Letters*, *40*(7), 1322–1327. https://doi.org/10.1002/grl.50306

Gorelick, N., Hancher, M., Dixon, M., Ilyushchenko, S., Thau, D., & Moore, R. (2017). Google Earth Engine: Planetary-scale geospatial analysis for everyone. *Remote Sensing of Environment*, *202*, 18–27. https://doi.org/10.1016/j.rse.2017.06.031

Gower, J., King, S., Borstad, G., & Brown, L. (2005). Detection of intense plankton blooms using the 709 nm band of the MERIS imaging spectrometer. *International Journal of Remote Sensing*, *26*(9), 2005–2012. https://doi.org/10.1080/01431160500075857

Gregor, L., Kok, S., & Monteiro, P. M. (2017). Empirical methods for the estimation of Southern Ocean CO2: Support vector and random forest regression. *Biogeosciences*, *14*(23), 5551–5569. https://doi.org/10.5194/bg-14-5551-2017

Hao, Y., Cui, T., Singh, V. P., Zhang, J., Yu, R., & Zhang, Z. (2017). Validation of MODIS sea surface temperature product in the coastal waters of the Yellow Sea. *IEEE Journal of Selected Topics in Applied Earth Observations and Remote Sensing*, *10*(5), 1667–1680. https://doi.org/10.1109/JSTARS.2017.2651951

Huot, Y., Babin, M.,Bruyant, F., Grob, C., Twardowski, M. S., & Claustre, H. (2007).Relationship between photosynthetic parameters and differentproxies of phytoplankton biomass in the subtropical ocean. *Biogeosciences, 4(5*), 853-868. https://doi.org/10.5194/bg-4-853-2007

IAEA. (2024). *Energy, electricity and nuclear power estimates for the period up to 2050* (Reference Data Series No. 1). International Atomic Energy Agency. https://www.iaea.org/publications/15756/energy-electricity-and-nuclear-power-estimates-for-the-period-up-to-2050

IAEA. (2024a). *Power reactor information system (PRIS)*. International Atomic Energy Agency. https://pris.iaea.org/PRIS/home.aspx

Ibrahim, S. M., Ibrahim, M. M., & Attia, S. I. (2014). The impact of climate changeson the thermal performance of a proposed pressurized water reactor: Nuclear-powerplant. *International Journal of Nuclear Energy, 2014(1),* 793908. https://doi.org/10.1155/2014/793908

Jiang, G., Ma, R., Loiselle, S. A., & Duan, H. (2012). Optical approaches to examining the dynamics of dissolved organic carbon in optically complex inland waters. *Environmental Research Letters*, *7*(3), Article 034014. https://doi.org/10.1088/1748-9326/7/3/034014

Lara, C., Saldías, G. S.,Westberry, T. K., Behrenfeld, M. J., & Broitman, B. R. (2017). Firstassessment of MODIS satellite ocean color products (OC3 and nFLH) in the InnerSea of Chiloé, northern Patagonia. Latin American *Journal of Aquatic Research, 45(4),* 822-827. http://dx.doi.org/10.3856/vol45-issue4-fulltext-18

Moses, W. J., Gitelson, A. A., Berdnikov, S., & Povazhnyy, V. (2009). Estimation of chlorophyll-a concentration in case II waters using MODIS and MERIS data—successes and challenges. *Environmental Research Letters*, *4*(4), Article 045005. https://doi.org/10.1088/1748-9326/4/4/045005

National Aeronautics and Space Administration. (2024). *Normalized fluorescence line height (nFLH) algorithm theoretical basis document*. OceanColor Web. https://oceancolor.gsfc.nasa.gov/files/atbd/atbd-obdaac-normalized-fluorescence-line-height.pdf

NGR. (2024). *Nationaal georegister catalog*. Nationaal Georegister. https://www.nationaalgeoregister.nl/geonetwork

NOAC. (2024). *Ocean science learning hub*. National Oceanography Centre. https://www.noc.ac.uk/discover-the-ocean/learning-hub

Ouzounov, D., Savtchenko, A., Leptoukh, G., Zhou, B., Ostrenga, D., Deroo, C., & Gonzalez, L. (2004). GES DAAC tools for accessing Terra and Aqua MODIS data. *Advances in Space Research*, *33*(7), 1109–1113. https://doi.org/10.1016/S0273-1177(03)00738-5

Rubbens, P., Brodie, S., Cordier, T., Destro Barcellos, D., Devos, P., Fernandes-Salvador, J. A., & Irisson, J. O. (2023). Machine learning in marine ecology: An overview of techniques and applications. *ICES Journal of Marine Science*, *80*(7), 1829–1853. https://doi.org/10.1093/icesjms/fsad100

Savtchenko, A., Ouzounov, D., Ahmad, S., Acker, J., Leptoukh, G., Koziana, J., & Nickless, D. (2004). Terra and Aqua MODIS products available from NASA GES DAAC. *Advances in Space Research*, *34*(4), 710–714. https://doi.org/10.1016/j.asr.2004.03.012

Stumpf, R. P. (2001). Applications of satellite ocean color sensors for monitoring and predicting harmful algal blooms. *Human and Ecological Risk Assessment: An International Journal*, *7*(5), 1363–1368. https://doi.org/10.1080/20018091095050

TENMAK. (2017). *Halkı bilgilendirme broşürleri*. Türkiye Enerji, Nükleer ve Maden Araştırma Kurumu. http://kurumsalarsiv.tenmak.gov.tr/handle/20.500.12878/97

Umamaheswara Rao, Y., Nagamani, P. V., Baranval, N. K., Rama Rao, P., Prasada Rao, T. D. V., & Choudury, S. B. (2019). Detection of phytoplankton blooms in the turbid coastal waters using satellite-derived fluorescence line height off Kakinada coast. *Journal of the Indian Society of Remote Sensing*, *47*(11), 1857–1864. https://doi.org/10.1007/s12524-019-01022-5

Wikipedia. (2024a). *Baltic Sea*. https://en.wikipedia.org/wiki/Baltic_Sea

Wikipedia. (2024b). *North Sea*. https://en.wikipedia.org/wiki/North_Sea

World Nuclear Association. (2023). *World nuclear performance report 2023*. https://world-nuclear.org/images/articles/performance-report-2023-final.pdf

Xing, X. G., Zhao, D. Z., Liu, Y. G., Yang, J. H., Xiu, P., & Wang, L. (2007). An overview of remote sensing of chlorophyll fluorescence. *Ocean Science Journal*, *42*(1), 49–59. https://doi.org/10.1007/BF03020910

Zhao, M., Bai, Y., Li, H., He, X., Gong, F., & Li, T. (2022). Fluorescence line height extraction algorithm for the geostationary ocean color imager. *Remote Sensing*, *14*(11), Article 2511. https://doi.org/10.3390/rs14112511

Black Sea Journal of Engineering and Science
doi: 10.34248/bsengineering.1995933

Open Access Journal
e-ISSN: 2619 – 8991

Research Article
Volume 9 - Issue 5: 2586-2598 / September 2026

A DIGITAL DESIGN FRAMEWORK FOR CYBORG ARCHITECTURE

Ayşegül KIDIK[1]*, Hakan TONG[2]

[1]*Abdullah Gül University, Faculty of Architecture, Department of Architecture, 38000, Kayseri, Türkiye*
[2]*İstanbul Technical University, Faculty of Architecture, Department of Architecture, 34000, İstanbul, Türkiye*

Abstract: This paper proposes a digital design framework for cyborg architecture as an adaptive, artificial intelligence-mediated and communicative spatial system. Rather than defining cyborg architecture as a stylistic category, a futuristic image, or a simple extension of smart building technologies, the study conceptualizes it as a recursive cybernetic system composed of four operational layers-sensing, cognition, actuation, and material intelligence-framed by governance as a meta-regulatory fifth layer. The research adopts a qualitative theory-building approach based on conceptual analysis and interdisciplinary synthesis. Foundational cybernetic theory, cyborg and posthuman discourse, responsive architecture, smart building research, digital twin studies, critical data studies, and recent literature on artificial intelligence in architectural design are examined to construct the proposed framework. The paper argues that architecture becomes cyborg not through technological accumulation alone, but through the integration of human users, computational processes, responsive materials, spatial feedback, and ethical regulation. In this framework, adaptive space is understood as a communicative environment in which data, algorithms, users, materials, and institutional protocols continuously mediate one another. The contribution of the study lies not in introducing the cyborg concept into architectural discourse, but in operationalizing it as an explicit five-layer architectural and digital design model with observable indicators and boundary conditions.

Keywords: Cyborg architecture, Digital design, Artificial intelligence, Human-machine interactions, Spatial communication, Adaptive environment

***Corresponding author:** Abdullah Gül University, Faculty of Architecture, Department of Architecture, 38000, Kayseri, Türkiye
E mail: aysegul.kidik@agu.edu.tr (A. KIDIK)
Ayşegül KIDIK https://orcid.org/0000-0002-1497-2455
Hakan TONG https://orcid.org/0000-0001-8964-9989

Received: July 15, 2026
Accepted: August 17, 2026
Published: September 15, 2026

Cite as: Kıdık, A., & Tong, H. (2026). A digital design framework for cyborg architecture. *Black Sea Journal of Engineering and Science,* 9(5), 2586-2598.

1. Introduction

Architecture has historically been theorized through categories such as form, structure, enclosure, function, materiality, and representation. Even when architectural discourse has mobilized metaphors of the body, organism, machine, or environment, the building has often remained conceptually framed as a designed object rather than as an operational and communicative system. Cybernetic theory offers a different starting point because it defines systems through feedback, communication, control, and regulation rather than through formal resemblance alone (Wiener, 1948; Ashby, 1956). From this perspective, architecture may be reconsidered as both a material artifact and a data-mediated spatial system structured by informational exchange, recursive feedback, and adaptive regulation.

This shift is significant for contemporary digital design discourse. In digitally mediated environments, design no longer concerns only the production of form or representation; it also involves the organization of interactions among users, computational processes, material systems, and institutional protocols. Architectural space increasingly operates through sensors, interfaces, simulations, artificial intelligence systems, digital twins, responsive materials, and automated environmental controls. These systems do not merely support design from the outside; they participate in the production, interpretation, and modulation of spatial experience. For this reason, adaptive architecture can also be understood as a problem of spatial communication: environmental and user-generated data are sensed, processed, translated into spatial or material responses, and re-enter the system as feedback.

In this study, spatial communication refers to more than the technical transmission of data among sensors, algorithms and building systems. It describes a reciprocal process through which environmental conditions and user actions are registered by the architectural system, computationally interpreted and expressed through perceptible spatial, material or atmospheric changes. Users may then interpret, accept, resist, or override these changes, thereby producing new inputs for the system. Spatial communication therefore operates simultaneously at informational, experiential and institutional levels: data circulate within the technical infrastructure, adaptive responses become perceptible within space, and governance protocols determine who

can participate in, understand or control these exchanges.

This argument also relates to broader discussions on digital culture and networked environments. Manovich (2001) shows that digital media reorganize cultural production through databases, interfaces, and computational logic, while Castells (2010) frames contemporary society through networked information flows. In architectural discourse, McCullough (2004) emphasizes how computation becomes embedded within everyday spatial experience. These perspectives support the present study's claim that adaptive architecture should be understood as a data-mediated design condition in which space, information, users, and institutions are continuously related.

Architectural cybernetics, interactive and evolutionary design, material computation, AI-mediated design, and digital-twin research provide key precedents for this argument (Pask, 1969; Negroponte, 1970; Frazer, 1995; Kolarevic, 2003; Fox and Kemp, 2009; Oxman, 2010; Jang et al., 2025; Semeraro et al., 2025). Their specific contributions and limitations are developed in Section 3.1. Here, it is sufficient to note that none of these domains alone constitutes cyborg architecture; they become cyborg-relevant only when integrated within a recursive and governed system linking sensing, cognition, actuation, and material response.

Against this background, the concept of cyborg architecture requires careful definition. The term "cyborg" emerged from the conjunction of cybernetics and organism, initially referring to a cybernetic organism capable of extending human adaptability in extreme environments (Clynes and Kline, 1960). In later theoretical discourse, the cyborg became a figure through which boundaries between human and machine, organism and technology, nature and culture, and embodied experience and informational mediation could be questioned (Haraway, 1991; Hayles, 1999). When transferred to architectural theory and digital design, this conceptual lineage enables the building to be reconsidered as a hybrid spatial system in which human users, computational processes, material components, and infrastructural networks participate in the production of adaptive space.

Earlier scholarship has already extended the cyborg concept beyond the technologically augmented body to networked architectural, urban, and infrastructural conditions (Mitchell, 2003; Gandy, 2005), while Picon (2015) has examined smart urbanism through the concept of spatialized intelligence. Building on these precedents, the present study shifts the focus toward a building-scale analytical model. Its contribution lies not in introducing the cyborg into architectural discourse, but in specifying the operational layers, recursive relationships, governance requirements, observable indicators, and boundary conditions through which adaptive architectural systems can be analyzed.

The term cyborg is retained in this study not as a biological metaphor, but as a theoretical concept that captures the hybridization of human users, computational systems, material components, and institutional protocols. While "cybernetic architecture" would emphasize feedback and control, and "adaptive architecture" would emphasize change over time, the term cyborg is more appropriate for describing spatial systems in which agency is distributed across human and non-human actors. In this sense, cyborg architecture does not refer to an organism-like building, but to an architectural condition in which human intention, algorithmic interpretation, material response, and governance mechanisms are operationally entangled.

The architectural use of the cyborg concept remains weak if it operates only through analogy. To describe artificial intelligence as a "brain," sensors as a "nervous system," energy systems as "metabolism," or responsive materials as "tissue" may be conceptually suggestive, but such analogies do not by themselves constitute a scholarly framework. A framework requires defined components, explicit relationships, conceptual thresholds, and theoretical propositions that can guide future analysis or empirical testing. The central problem addressed in this paper therefore concerns the conditions under which architecture can be theorized as a cybernetic, adaptive, and communicative spatial system.

This paper argues that cyborg architecture should be understood as a digital design framework composed of four operational layers-sensing, cognition, actuation, and material intelligence-and a meta-regulatory governance layer. The originality of the proposed framework lies not in introducing the cyborg concept into architectural discourse, but in distinguishing technological accumulation from cybernetic integration through an explicit five-layer model with observable indicators and boundary conditions. A building equipped with sensors, automation, AI-assisted systems, digital twins, kinetic components, or responsive materials becomes cyborg architecture only when these elements are organized through recursive feedback and governance. In such a system, environmental and user inputs are sensed, interpreted, translated into spatial or material responses, recalibrated over time, and regulated through governance mechanisms. The paper therefore asks the following research question: How can cyborg architecture be conceptualized as a digital design framework for adaptive, AI-mediated and communicative spatial systems?

The contribution of the paper is threefold. First, it reframes cyborg architecture as a cybernetic and communicative spatial system rather than as a stylistic, metaphorical or technologically deterministic category. Second, it proposes a five-layer framework that distinguishes cyborg architecture from adjacent concepts such as smart buildings, responsive architecture, adaptive architecture, digital twins and AI-mediated

design. Third, it positions governance as a constitutive layer of cyborg architecture, arguing that adaptive spatial systems cannot be theorized only through technological capability; they must also be examined through autonomy, surveillance, algorithmic bias, data ownership, consent, accountability, and spatial responsibility.

2. Materials and Methods

This study adopts a qualitative, theory-building research design based on conceptual analysis and interdisciplinary theoretical synthesis. It does not aim to produce empirical data, measure building performance, test user experience, or validate a specific technological prototype. Instead, it aims to construct a theoretically grounded digital design framework that clarifies how cyborg architecture can be conceptualized as an adaptive, AI-mediated, and communicative spatial system. This methodological orientation is consistent with conceptual research, which connects, reinterprets, and reorganizes existing theoretical domains to generate new conceptual relationships and analytical models (Gilson and Goldberg, 2015; Jaakkola, 2020).

2.1. Source Selection and Corpus Construction

Purposive theoretical sampling was used to identify sources directly relevant to the construction of the proposed framework. Sources were identified through academic databases, scholarly search engines, university library catalogues, institutional repositories, printed library collections, and backward citation searching within key publications. Searches were conducted using combinations of terms including "cyborg," "cybernetics," "cyborg architecture," "cybernetic architecture," "responsive architecture," "adaptive architecture," "interactive architecture," "artificial intelligence in architectural design," "digital twin," "smart building," "material intelligence," "spatial communication," and "data governance." Particular attention was given to foundational, historically influential, and recurrently referenced publications within these fields. The selected sources were examined chronologically to trace the conceptual development from early cybernetic theory and cyborg discourse to responsive architecture, digital design, artificial intelligence, digital twins, material responsiveness, and data governance. This chronological examination was used to identify conceptual continuities, transformations, and emerging relationships relevant to the proposed framework rather than to construct a comprehensive historical review. The aim was not to provide an exhaustive or systematic review of all publications on cyborg architecture, but to assemble a theoretically sufficient corpus representing the principal conceptual domains of the study. The final corpus included 38 conceptually relevant sources. Three additional methodological sources were used to define and justify the conceptual research design. Source selection was concluded when the principal theoretical domains were judged to be adequately represented and additional sources no longer materially altered the emerging analytical categories or relationships among the framework layers. This pragmatic stopping criterion should not be interpreted as a claim of exhaustive coverage or formal theoretical saturation.

Following Snyder's (2019) emphasis on transparency in literature-based research, the study documented both the source-selection criteria and the five-stage analytical procedure used to construct the framework. This documentation was not intended to reproduce a systematic review protocol, but to make the conceptual derivation of the proposed layers sufficiently transparent and traceable.

The literature was selected according to four criteria. First, the source had to contribute directly to one of the core conceptual domains of the study: cybernetics, cyborg and posthuman theory, responsive architecture, digital design, smart building research, digital twins, artificial intelligence in architectural design, material responsiveness, or data governance. Second, the source had to support the translation of the cyborg concept from metaphor into an architectural or spatial framework. Third, the source had to clarify the distinction between cyborg architecture and adjacent concepts such as smart buildings, responsive architecture, adaptive architecture, digital twins, and AI-mediated design. Fourth, the source had to contribute to understanding adaptive space as a human-machine-environment communication system. Sources addressing cyborg imagery only as aesthetic speculation, biomedical enhancement without spatial relevance, or cyberpunk representation without architectural or design-theoretical implications were excluded from the core framework construction.

To illustrate the analytical use of the framework, two built projects were purposively selected from the reviewed literature: Al Bahr Towers and the BIQ House/SolarLeaf façade. These projects were selected because they represent contrasting partial configurations of the proposed layers and are documented through scholarly design, technical, operational, or post-occupancy accounts. They are used as illustrative applications rather than as representative cases or as empirical validation of the framework.

2.2. Conceptual Analysis Procedure

The literature corpus was organized around five bodies of knowledge: cybernetic theory; cyborg and posthuman theory; architectural cybernetics, responsive architecture and digital design; AI-mediated design, smart buildings and digital twins; and critical data studies and governance. The analysis then proceeded through five stages. First, key concepts were extracted from each body of literature, including feedback, regulation, distributed agency, responsiveness, computational interpretation, prediction, sensor networks, material responsiveness, surveillance, consent and accountability. Second, these concepts were compared across theoretical domains and grouped according to their recurring architectural functions.

Third, the resulting clusters were translated into five analytical layers. Environmental registration and data acquisition were associated with sensing; interpretation, prediction and decision-making with cognition; physical and environmental response with actuation; embedded material responsiveness with material intelligence; and consent, accountability, data ownership and institutional control with governance. Fourth, cross-domain mapping was used to relate each layer to its theoretical basis, architectural implication, and spatial-communicative expression. The layers were then organized into a recursive conceptual model rather than treated as a collection of independent technologies. Fifth, theoretical propositions, observable indicators, boundary conditions, and exclusion criteria were formulated to support future empirical research, design experimentation, post-occupancy evaluation, and case-based analysis. Table 1 summarizes the conceptual translation process through which the concepts extracted from the literature were organized into the five framework layers.

Table 1. Conceptual translation process used in the construction of the framework

Literature domain	Extracted concepts	Translation and communication	Framework layer
Cybernetic theory	Feedback, regulation, communication, control, requisite variety	Architecture as a feedback-driven system that receives, processes and responds to changes	Sensing, cognition
Cyborg and posthuman theory	Hybridity, distributed agency, human-machine relationality, embodied information	Spatial agency distributed across users, algorithms, materials, interfaces and infrastructures	Cognition, governance
Architectural cybernetics and responsive architecture	Interaction, responsiveness, adaptability, kinetic behavior, material computation	Built environments as interactive systems capable of spatial, environmental or material response	Actuation, material intelligence
AI, digital twin and smart building literature	Prediction, simulation, optimization, IoT, sensor networks, occupant-centered control	Data-mediated decision-making and computational mediation of adaptive space	Sensing, cognition, actuation
Digital culture and critical data studies	Interface, database logic, surveillance, data ownership, algorithmic accountability, infrastructural control	Ethical and institutional regulation of data-mediated spatial systems	Governance

3. Results and Discussion

3.1. Theoretical Synthesis

Cybernetics provides the primary theoretical basis for conceptualizing architecture as an adaptive and communicative system rather than as a static object. Wiener (1948) defined cybernetics through the study of control and communication in animals and machines, thereby establishing a common conceptual ground for biological, technical, and informational systems. Within this framework, systems are understood in terms of their capacity to receive information, process variation, regulate behavior, and maintain operational stability through feedback. Ashby (1956) extended this logic with the principle of requisite variety, arguing that a system's stability depends on its capacity to respond to the complexity of its environment. For architecture, this principle is significant because buildings operate within changing environmental, social, energetic, and behavioral conditions.

Cybernetics shifts architectural thinking from morphology to organization and communication. A cybernetic system is defined by the operational relations among sensing, feedback, control, adaptation, and regulation rather than by its resemblance to an organism (Wiener, 1948; Ashby, 1956). This distinction is crucial for cyborg architecture. If the building is understood merely as an organism-like form, the concept remains metaphorical. If, however, the building is understood as a system capable of monitoring environmental and user-generated inputs, interpreting them and producing regulated spatial or material responses, the organism analogy becomes an operational model.

The cyborg concept extends this logic by raising the question of distributed agency. Clynes and Kline (1960) introduced the cyborg as a cybernetic organism designed to extend human adaptability in extraterrestrial environments. Haraway (1991) later repositioned the cyborg as a figure that unsettles boundaries between human and machine, organism and technology, nature and culture. Hayles (1999) similarly argues that the posthuman condition involves the entanglement of embodied experience with informational processes. For architecture and digital design, this means that agency can be understood as distributed across users, algorithms, sensors, materials, interfaces, and institutional systems rather than located exclusively in the human subject. Actor-network theory reinforces this point by arguing that agency emerges through heterogeneous associations among human and non-human actors (Latour, 2005).

Architectural discourse has long engaged with systems, adaptability, and technological mediation. Pask (1969)

established the architectural relevance of cybernetics by foregrounding interaction, conversation, and adaptive exchange between users and environments, while Negroponte (1970) proposed architectural machines that interact with users and support design decisions through computation. Frazer (1995) developed evolutionary architecture as a model for generative and adaptive design, while Kolarevic (2003) described digitally driven architecture through rule-based, performative, and fabrication-oriented processes. Fox and Kemp (2009) examined interactive architecture through systems that sense, respond, and physically adapt to changing environmental or user conditions. Oxman's (2010) concept of material ecology further challenged the separation among form, computation, fabrication, material behavior, and environmental performance. Recent scholarship confirms that architectural responsiveness is now discussed across overlapping domains, including responsive architecture, adaptive architecture, kinetic architecture, intelligent buildings, and smart environments (Lee et al., 2021).

The contemporary relevance of cyborg architecture depends on the convergence of computational intelligence, real-time data infrastructures, and cyber-physical building systems. Artificial intelligence is increasingly used in architectural design, particularly for early-stage exploration, the generation and evaluation of design alternatives, and schematic development (Jang et al., 2025). Architectural studio research similarly indicates that AI can support the generation, development, and evaluation of alternatives, although its contribution depends on how it is positioned within the wider design workflow (Gökşen Takva et al., 2025). Digital twins extend computational mediation from design representation to building operation by connecting physical assets with computational models through BIM, IoT, and AI for monitoring, simulation, prediction, and optimization (Semeraro et al., 2025). Nevertheless, neither AI-mediated design nor digital twins constitute cyborg architecture on their own. They become cyborg-relevant only when integrated into governed feedback systems that connect data acquisition, computational interpretation, and physical or material response.

A cybernetic understanding of architecture also cannot be limited to technical performance. Feedback-driven environments depend on continuous data collection, interpretation, and modulation. This raises questions of privacy, surveillance, consent, algorithmic bias, infrastructural control, and responsibility. Deleuze's (1992) account of societies of control is relevant because it identifies a shift from enclosed disciplinary institutions toward continuous modulation. Kitchin and Dodge (2011) argue that software can actively produce spatial conditions rather than simply support them, while Kitchin (2014) shows that data-driven urbanism reorganizes how cities are known, managed and governed. Sadowski (2020) further critiques smart urbanism by arguing that data-driven infrastructures often embed political and economic interests beneath the language of efficiency and optimization. These critiques are central to cyborg architecture because adaptive spatial systems not only respond to users; they also observe, categorize, predict, and potentially govern them.

Figure 1 traces the chronological and conceptual trajectory from foundational cybernetic theory and cyborg discourse to contemporary AI-mediated, data-driven, materially responsive, and governed spatial systems.



Figure 1. Chronological theoretical trajectory underlying the proposed framework. Note. Developed by the authors based on the conceptual synthesis and the sources discussed in Sections 3.1 and 3.3.

Taken together, cybernetics, cyborg theory, responsive architecture, AI-mediated design, digital twin research, and critical data studies provide the theoretical basis for the framework proposed in this paper. They indicate that cyborg architecture should not be defined by technological novelty alone, but by recursive feedback relations among users, computational systems, material components, and governance protocols.

3.2. A Five-Layer Digital Design Framework of Cyborg Architecture

The proposed framework defines cyborg architecture through four operational layers and one meta-regulatory layer. The operational layers are sensing, cognition, actuation, and material intelligence. Sensing produces environmental, behavioral, and operational data; cognition interprets and evaluates these data; actuation translates decisions into spatial or environmental response; and material intelligence embeds responsiveness at the scale of components and surfaces. Governance differs from these four layers because it does not operate as a technical subsystem alone. Rather, it functions as a meta-regulatory layer that frames the entire system by defining the ethical, institutional, and political conditions under which data are collected, interpreted, shared, and acted upon. This distinction is important because cyborg architecture is not only a technical feedback system, but also a governed spatial condition.

The first layer is sensing. In cybernetic terms, no adaptive system can regulate itself without information about its internal state and external environment (Wiener, 1948; Ashby, 1956). Applied to architecture, sensing refers to the acquisition of environmental, behavioral, and operational data through embedded or distributed infrastructures. Contemporary IoT monitoring architectures demonstrate that continuously generated sensor data can be acquired, processed, stored, and made available through scalable real-time data infrastructures (Yıldız et al., 2026). These may include sensors for temperature, humidity, light, air quality, sound, occupancy, movement, energy use, structural stress, and user interaction. In conventional building automation, sensing often functions as a trigger for predefined responses. In cyborg architecture, however, sensing has a broader role: it constitutes the perceptual layer through which the building registers environmental variation and user behavior as dynamic inputs. Sensor data become meaningful only when integrated into feedback loops that support interpretation, decision-making, and response.

The second layer is cognition. In the proposed framework, cognition refers to the computational interpretation of sensed data through artificial intelligence, machine learning, simulation, digital twins, or predictive control systems. This does not imply that buildings possess consciousness. Rather, cognition designates the operational capacity to process data, identify patterns, compare conditions, anticipate outcomes, and generate adaptive decisions. Cybernetic theory provides the logic for this layer because feedback systems depend not only on input, but also on evaluation and correction. Contemporary AI and digital twin technologies extend this logic by enabling prediction, simulation, and performance calibration across design and operational phases. However, cognition must not be reduced to optimization. It also mediates how user behavior is interpreted, how environmental priorities are ranked, and how conflicting spatial needs are negotiated.

The third layer is actuation. Actuation refers to the capacity of the architectural system to translate interpreted data into physical, spatial, or environmental response. This may occur through robotic systems, mechatronic components, kinetic façades, adaptive shading devices, reconfigurable partitions, automated ventilation, responsive lighting, or climate-control systems. Interactive and responsive architecture has already explored many of these possibilities. However, in the framework proposed here, actuation is not sufficient on its own. A kinetic façade that opens and closes in response to sunlight is responsive but does not necessarily constitute cyborg architecture unless its operation is embedded within a broader cybernetic system integrating sensing, cognition, material intelligence, and governance.

The fourth layer is material intelligence. In this framework, material intelligence refers to responsiveness that is embedded within the physical substrate, components, or assemblies of the building rather than produced only through external mechanical devices. Research on climate-adaptive building shells and adaptive façades demonstrates that responsive performance may be embedded in materials, components, and systems capable of changing their behavior in response to variable indoor and outdoor conditions (Loonen et al., 2013; Aelenei et al., 2016). It may involve phase-changing materials, thermochromic or electrochromic surfaces, self-healing systems, adaptive insulation, responsive composites, smart glazing, or components equipped with embedded sensing capabilities. Material intelligence is analytically distinct from actuation because the two layers describe different aspects of spatial response. Actuation concerns the system-level translation of a computational or control decision into physical or environmental change. In contrast, material intelligence concerns the medium through which part of that change is physically performed. A kinetic shading system driven by motors is primarily an example of actuation; a façade component that changes its thermal, optical, or structural properties through its material behavior exemplifies material intelligence.

The distinction does not imply that these layers are technologically isolated. In some systems, a responsive material may simultaneously register environmental variation and produce a physical response, thereby overlapping with both sensing and actuation. The layers

should therefore be understood as analytical functions rather than as mutually exclusive technical components. Their separation allows the framework to identify where responsiveness is located, how it is controlled, and whether adaptation depends on centralized mechanical systems, distributed material behavior, or a combination of both.

The five layers define the full analytical structure of cyborg architecture, but they need not appear with equal technological intensity in every case. Material intelligence, for example, does not require the use of highly advanced or autonomous smart materials; it may also be expressed through responsive components or assemblies whose physical behavior participates in the feedback process. However, a system in which materials remain entirely passive and spatial change is produced only through isolated automation would represent a technologically responsive environment rather than a fully integrated cyborg architecture. The proposed framework therefore treats the presence of all five functions as a conceptual threshold, while allowing their technical realization to vary according to scale, program and context.

The fifth layer is governance. Adaptive architecture cannot be theorized only through sensing, AI, movement and material performance. Because feedback-driven environments depend on continuous data collection and algorithmic interpretation, they raise questions of privacy, consent, surveillance, ownership, bias, responsibility and control. At the building scale, occupancy and environmental sensing may disclose patterns of user presence and behavior, making privacy an operational concern rather than an abstract ethical issue (Alisic et al., 2020). Building automation and control systems also operate as forms of operational technology and consequently require explicit cybersecurity, risk-management, and system-protection measures (Stouffer et al., 2023). A building that senses users, predicts behavior, and adjusts environments participates in the modulation of spatial experience and therefore cannot be treated as a neutral technical system. Governance therefore includes the rules, protocols, institutions and design decisions that determine how data are collected, stored, interpreted, shared and acted upon. It also includes user consent, transparency, algorithmic auditability, data ownership, maintenance responsibility, cybersecurity and accountability. Without governance, cyborg architecture risks becoming a form of algorithmic environmental control. With governance, it can be conceptualized as an ethically mediated adaptive system.

The five layers do not operate sequentially in a simple linear chain. Their relationship is recursive. Environmental and user-generated conditions are sensed; data are interpreted through cognitive systems; decisions are translated into spatial, environmental, or material responses; the effects of these responses are sensed again; and the system recalibrates itself over time. This recursive structure is what distinguishes cybernetic integration from technological accumulation.

Although the sensing–cognition–actuation relationship reflects the established cybernetic logic of information acquisition, interpretation, response, and feedback (Wiener, 1948; Ashby, 1956), the originality of the proposed framework does not lie in reproducing this operational sequence. Its contribution lies in translating this operational logic into an explicitly architectural model

by integrating material responsiveness, distributed spatial agency and governance into the feedback structure. Material intelligence identifies how adaptive capacity becomes embedded in the physical fabric of architecture, while governance defines the ethical and institutional conditions under which sensing, interpretation and response occur. The framework therefore extends a technical feedback model into a spatial, material and political model in which users, algorithms, building components and institutional protocols jointly shape architectural outcomes.

Table 2 presents the operational roles, architectural expressions, and spatial-communicative implications of the five framework layers. Figure 2 illustrates the recursive relationships among sensing, cognition, actuation, and material intelligence, with governance positioned as a meta-regulatory layer surrounding the entire system.

3.3. Positioning Cyborg Architecture in Relation to Adjacent Concepts

Before distinguishing cyborg architecture from adjacent technological concepts, it is necessary to position the framework in relation to earlier architectural and urban uses of the cyborg. Mitchell's (2003) account of the cyborg self and the networked city dissolved the boundary between the body and its technological and infrastructural extensions. Gandy's (2005) concept of cyborg urbanization similarly emphasized the heterogeneous and often unstable relations among human bodies, ecological processes, technological systems, and urban infrastructures. Picon's (2015) notion of spatialized intelligence further demonstrated that smart urban environments are constituted not only by computational technologies, but also by the spatial, perceptual, and political relations produced through data and networked infrastructures.

These precedents establish the cyborg and the intelligent city as powerful frameworks for understanding technologically mediated spatial relations. However, their primary purpose is not to provide a building-scale analytical model for determining when an adaptive architectural system becomes cyborg architecture. The five-layer framework proposed here addresses this specific gap by translating the broader concepts of hybridity, networked extension, infrastructural interdependence, and spatialized intelligence into five interrelated architectural functions: sensing, cognition, actuation, material intelligence, and governance. It

further introduces recursive integration, observable indicators, and exclusion criteria as analytical thresholds. The originality of the framework therefore lies not in introducing the cyborg metaphor into architectural or urban discourse, but in operationalizing it as a structured model for the analysis and future empirical evaluation of adaptive architectural systems.

The proposed framework requires a clear distinction between cyborg architecture and adjacent concepts such as smart buildings, responsive architecture, adaptive architecture, digital twins, and AI-mediated design. These fields share important concerns with cyborg architecture, including sensing, automation, responsiveness, performance optimization, technological integration, and data-mediated decision-making. However, they do not necessarily imply the same theoretical structure. Cyborg architecture, as proposed in this paper, emerges only when these components are integrated through recursive feedback, distributed agency, spatial or material consequence, and explicit governance.

Table 2. Proposed five-layer digital design framework of cyborg architecture

Layer	Operational role	Architectural expression	Spatial-communicative implication
Sensing	Acquires environmental, behavioral and operational data	Sensors, IoT, occupancy monitoring, environmental tracking	Transforms space into a data-producing and data-receiving interface
Cognition	Interprets data, predicts conditions and supports decisions	AI, machine learning, digital twins, predictive control	Translates data into spatial meaning, priorities and decision pathways
Actuation	Translates decisions into spatial or environmental response	Robotics, mechatronics, kinetic façades, adaptive systems	Makes system interpretation visible or experiential through spatial change
Material intelligence	Locates responsive capacity within materials, components and assemblies	Smart materials, phase-changing materials, responsive composites, adaptive glazing and materially responsive assemblies	Distributes adaptation across material surfaces, components and atmospheres
Governance/ Meta-regulatory	Regulates data, agency, consent, privacy and responsibility	Data protocols, transparency, auditability, consent frameworks, institutional control	Defines the ethical and political conditions of data-mediated spatial communication

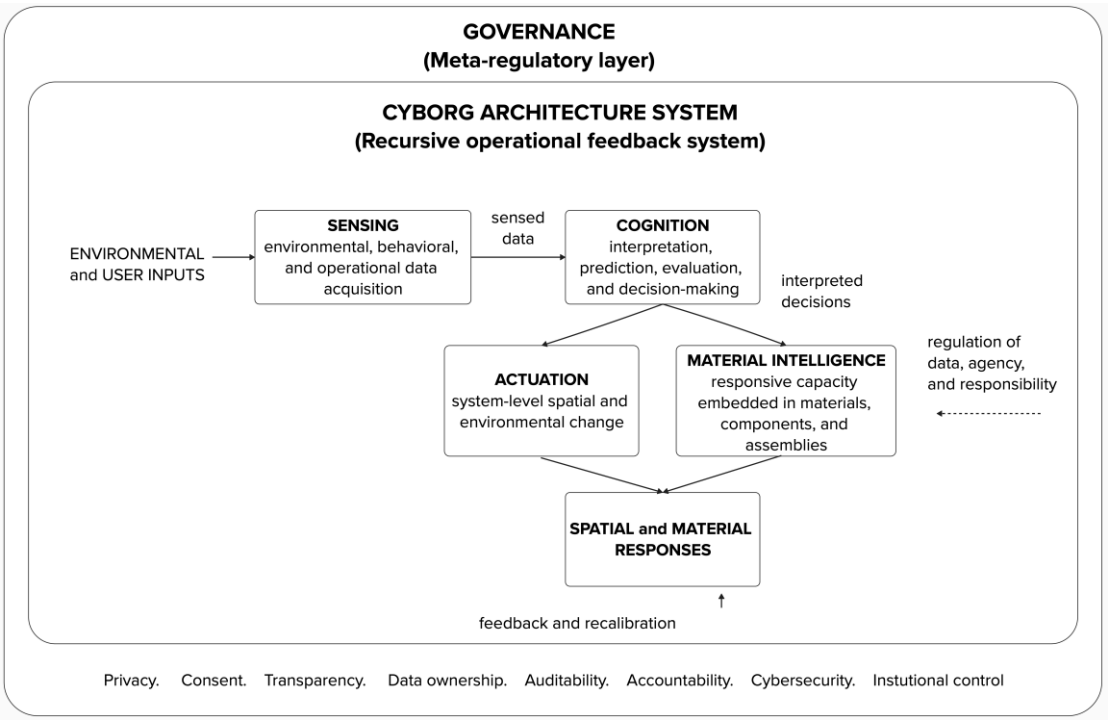


Figure 2. Recursive five-layer digital design framework of cyborg architecture. Note. Environmental and user inputs are sensed, computationally interpreted, translated into spatial or material responses, and recalibrated through feedback. Governance surrounds the operational system as a meta-regulatory layer governing privacy, consent, data ownership, transparency, auditability, accountability, and institutional control. Developed by the authors.

Smart building literature generally emphasizes technological integration, operational efficiency, occupant comfort, energy performance, and building management systems. Sinopoli (2010) frames smart building systems through the integration of building technologies, communications, automation, and management infrastructures. Buckman et al. (2014) similarly argue that smart buildings should respond to the requirements of occupants, organizations and wider societal concerns, particularly in relation to sustainability and performance. However, cyborg architecture should not be treated as a more advanced synonym for smart building. A smart building may use sensors and automation to reduce energy consumption or improve comfort while remaining outside a fully cybernetic spatial framework. The distinction lies not in the quantity of embedded technologies, but in the systemic organization of feedback, agency, material response, and ethical regulation. Responsive and adaptive architecture provide important precedents for cyborg architecture because they already challenge the idea of the building as static form. Responsive architecture often foregrounds the relation between input and response: the environment changes, and the building reacts. Adaptive architecture similarly emphasizes flexibility, environmental adjustment, transformability, or change over time. These capacities are important, but they remain insufficient if they are limited to mechanical movement, kinetic effects, or predefined environmental reactions. A shading system that adjusts to solar radiation, for example, may be adaptive; however, it becomes cyborg-relevant only when its operation is connected to sensing infrastructures, cognitive interpretation, spatial consequence, material performance and governance mechanisms.

Digital twins are increasingly discussed in relation to smart and green buildings, particularly in connection with real-time monitoring, simulation, predictive maintenance, energy management and occupant-centric control (Semeraro et al., 2025). They represent an important technological condition for cyborg architecture because they allow physical buildings to operate simultaneously as material and informational systems. Nevertheless, a digital twin is not equivalent to cyborg architecture. A digital twin may simulate, monitor, predict, or optimize building performance while remaining primarily analytical unless it is linked to actuation, material response, and governance. It becomes part of cyborg architecture only when it is integrated into recursive relations among sensing, cognition, actuation, material intelligence, and governance.

AI-mediated design represents a related but narrower field than cyborg architecture. A design process that uses generative AI to produce images, layouts, diagrams, or formal alternatives remains AI-mediated design unless it is connected to feedback-driven spatial operation. Studio-based research similarly indicates that artificial intelligence functions most productively as a critically mediated design partner, supporting iterative exploration and process efficiency while remaining dependent on students' disciplinary reasoning, critical engagement, and architectural judgment (Kevseroğlu Kurban and Kıdık Baran, 2026). In the proposed framework, AI becomes cyborg-relevant when it functions as part of a cognitive layer within a feedback-driven spatial system. This may occur during design, operation, or post-occupancy adaptation, but the decisive issue is whether AI mediates relations among sensed data, spatial decision-making, actuation, material response, and governance. Architectural judgment, ethical responsibility, material reasoning, and social negotiation remain essential to the framework. Table 3 summarizes the distinctions between cyborg architecture and the adjacent concepts discussed above.

Table 3. Distinguishing cyborg architecture from adjacent concepts

Concept	Primary emphasis	Limitation from the perspective of this paper	Relation to cyborg architecture
Smart building	Automation, efficiency, comfort, building management	May remain performance-oriented and technologically fragmented	Provides operational infrastructure but not necessarily recursive cybernetic integration
Responsive architecture	Environmental or user-triggered response	May focus on input-response mechanisms or kinetic change	Contributes the logic of spatial responsiveness
Adaptive architecture	Flexibility and change over time	May remain mechanical, formal or environmental without cognitive and governance layers	Provides the principle of temporal adjustment
Digital twin	Real-time simulation, monitoring and prediction	May remain representational or analytical without spatial or material response	Supports the cognitive and predictive layer
AI-mediated design	Generative assistance, evaluation and decision support	May remain limited to design production rather than spatial operation	Supports cognition when linked to feedback systems
Cyborg architecture	Recursive integration of feedback, distributed agency, material responsiveness and governance	Requires systemic and ethical integration; not merely technological presence	Integrates technical feedback with spatial, material, ethical and institutional relations

3.4. Theoretical Propositions and Research Agenda

The five-layer framework proposed in this paper defines cyborg architecture as a digital design model of cybernetic spatial organization rather than as a building type, stylistic category, or technological label. Its central claim is that architecture becomes cyborg through recursive integration among sensing, cognition, actuation, material intelligence, and governance. The following propositions should not be read as empirical findings. They are conceptual statements derived from the theoretical synthesis developed in this paper. Their purpose is to define analytical thresholds through which future research may examine whether a given architectural system can be understood as cyborg architecture.

The analytical use of the framework can be illustrated through two documented built projects representing different partial configurations of adaptive architecture. Neither Al Bahr Towers nor the BIQ House/SolarLeaf façade fully integrates all five layers within a recursive and explicitly governed system; however, each demonstrates how particular layers of the framework may already be manifested in built practice. Al Bahr Towers connects solar-position control inputs to the automated movement of its adaptive shading façade, thereby demonstrating a strong relationship between computational control and actuation (Karanouh and Kerber, 2015; Attia, 2017). However, its computational operation remains predominantly rule-based, its material response depends on mechanically actuated components, and the published evaluation identifies limitations concerning user control, operation, and system management. The SolarLeaf façade of the BIQ House illustrates a different configuration by integrating flat-panel photobioreactors, biological activity, biomass and heat production, monitoring, and automated control within the building envelope (Wurm and Pauli, 2016; Kerner et al., 2019). It therefore offers a stronger manifestation of material participation in adaptive performance, although the published accounts do not demonstrate an explicitly governed feedback system integrating user agency, transparency, override mechanisms, and accountability. Neither project should consequently be classified as a complete instance of cyborg architecture. Rather, they illustrate how existing adaptive systems satisfy particular layers of the framework while remaining below the proposed five-layer threshold. This partial correspondence reinforces the value of the framework as an analytical model for identifying degrees of cyborg relevance rather than as a label retrospectively applied to technologically advanced buildings. Accordingly, the two cases demonstrate how the framework differentiates partial from fully integrated configurations, but they do not evaluate user experience or governance performance; such evaluation would require primary data from occupants, facility managers, designers, and institutional stakeholders.

Building on these partial built manifestations, Table 4 formalizes the analytical thresholds of the framework by presenting the theoretical propositions together with their observable indicators and boundary conditions. These criteria clarify why technologically advanced adaptive systems may demonstrate cyborg-relevant characteristics without yet constituting fully integrated cyborg architecture.

Table 4. Theoretical propositions and research directions

Proposition	Observable indicators	Boundary condition or exclusion criterion
Cyborg architecture requires recursive feedback integration.	Data are sensed, interpreted, acted upon and recalibrated over time.	Technologies operate independently without feedback or recalibration.
AI/digital twins become cyborg-relevant only when linked to spatial consequence.	AI or digital twin outputs trigger spatial, environmental or material response.	AI or digital twin systems remain limited to visualization, monitoring or design generation without producing spatial, environmental or material consequences.
Agency is distributed across human and non-human actors.	Users, algorithms, materials and institutional protocols jointly shape spatial outcomes.	Spatial outcomes remain fully determined by a single human or centralized technical authority, with no meaningful interaction among users, algorithms, materials or institutional protocols.
Governance is constitutive.	Consent, transparency, auditability, data ownership and override mechanisms are defined.	No explicit mechanisms exist for consent, transparency, accountability, data ownership, system override or institutional responsibility.
Cyborg architectural systems may extend beyond individual buildings when connected to shared infrastructures.	Adaptive buildings exchange data or coordinate responses with energy, mobility, environmental or public-service networks.	No cross-building data exchange or coordinated response occurs; the adaptive system remains confined to an individual building.

These propositions and their associated boundary conditions clarify the analytical and classificatory value of the framework. First, a spatial system can be conceptualized as cyborg architecture only when its technological components operate as interdependent feedback layers rather than as isolated devices. This proposition prevents cyborg architecture from being reduced to a catalogue of smart technologies. Second, AI or digital twin systems become constitutive of cyborg architecture only when computational interpretation is linked to spatial response, material adaptation or operational recalibration. Third, agency in cyborg architecture is distributed across users, computational systems, material components and infrastructural networks rather than located exclusively in the architect, occupant or building operator. Fourth, without explicit governance mechanisms, cyborg architecture risks transforming environmental responsiveness into algorithmic surveillance and spatial control. Fifth, the framework may also be extended beyond the scale of an individual building when adaptive architectural systems exchange data or coordinate responses through shared urban infrastructures. At this scale, however, the framework would require further development to address institutional fragmentation, infrastructural inequality, and public accountability.

The research agenda confirms this paper's methodological position. The study does not claim that cyborg architecture is already fully realized as a dominant architectural condition. Instead, it proposes a theoretical framework and a set of propositions that future empirical, design-based, and urban research can use to evaluate emerging adaptive spatial systems. Future studies may test the framework through built case studies, adaptive material prototypes, digital twin applications, post-occupancy research, and user-centered evaluations. Future empirical applications should therefore employ a non-exclusive functional coding protocol that permits a single component or assembly to be assigned to more than one layer when it performs multiple analytical functions. Urban-scale research should test whether the five-layer framework remains analytically sufficient when sensing, decision-making, actuation, and governance are distributed across multiple buildings, public agencies, and infrastructural operators. The present framework is primarily analytical and classificatory rather than causal. Future research should therefore examine whether different degrees and configurations of layer integration influence outcomes such as user trust, perceived control, system acceptance, environmental performance, and operational resilience. These relationships may be investigated through comparative case studies, post-occupancy evaluation, longitudinal performance monitoring, and mixed-method user research.

4. Conclusion

This paper has conceptualized cyborg architecture as a recursive and governed spatial system composed of four operational layers—sensing, cognition, actuation, and material intelligence—and a meta-regulatory governance layer. Its central argument is that architecture becomes cyborg not through the accumulation of advanced technologies, but through the integration of these functions within feedback relations that connect environmental and user inputs to computational interpretation, spatial or material response, and subsequent recalibration.

The proposed framework contributes to architectural and digital design theory by operationalizing the cyborg concept as an analytical model rather than a biological metaphor or stylistic category. It also distinguishes cyborg architecture from smart buildings, responsive architecture, adaptive architecture, digital twins, and AI-mediated design by introducing observable indicators and boundary conditions. The illustrative discussion of Al Bahr Towers and the BIQ House further shows that existing adaptive systems may demonstrate particular cyborg-relevant layers without satisfying the full five-layer threshold.

Governance is a constitutive component of this framework because adaptive environments collect data, interpret behavior, and modify spatial conditions. Questions of consent, transparency, privacy, user control, data ownership, cybersecurity, and accountability must therefore be treated as integral architectural concerns rather than as external ethical considerations.

The study is conceptual and does not provide empirical validation, prototype testing, or post-occupancy evaluation. Its propositions should consequently be understood as theoretical thresholds for future case-based, experimental, and user-centered research. The value of the framework lies in providing a structured basis for evaluating how computational systems, material components, users, and institutional protocols jointly shape emerging adaptive spatial environments.

Author Contributions

The percentages of the authors' contributions are presented below. The authors reviewed and approved the final version of the manuscript.

	A.K.	H.T.
C	50	50
D	50	50
S	50	50
DCP	80	20
DAI	50	50
L	80	20
W	50	50
CR	50	50
SR	50	50
PM	50	50

C= concept, D= design, S= supervision, DCP= data collection and/or processing, DAI= data analysis and/or interpretation, L= literature search, W= writing, CR= critical review, SR= submission and revision, PM= project management.

Conflict of Interest

The authors declared that there is no conflict of interest.

Ethical Consideration

Ethics committee approval was not required for this study because there was no study on animals or humans.

References

Aelenei, D., Aelenei, L., & Vieira, C. P. (2016). Adaptive façade: Concept, applications, research questions. *Energy Procedia, 91*, 269–275. https://doi.org/10.1016/j.egypro.2016.06.218

Alisic, R., Molinari, M., Paré, P. E., & Sandberg, H. (2020). Ensuring privacy of occupancy changes in smart buildings. In *2020 IEEE Conference on Control Technology and Applications (CCTA)* (pp. 871–876). IEEE. https://doi.org/10.1109/CCTA41146.2020.9206317

Ashby, W. R. (1956). *An introduction to cybernetics*. Chapman & Hall.

Attia, S. (2017). Evaluation of adaptive facades: The case study of Al Bahr Towers in the UAE. QScience Connect, 2017(2), Article 6. https://doi.org/10.5339/connect.2017.qgbc.6

Buckman, A. H., Mayfield, M., & Beck, S. B. M. (2014). What is a smart building? *Smart and Sustainable Built Environment, 3*(2), 92–109. https://doi.org/10.1108/SASBE-01-2014-0003

Castells, M. (2010). *The rise of the network society* (2nd ed., with a new preface). Wiley-Blackwell. https://doi.org/10.1002/9781444319514

Clynes, M. E., & Kline, N. S. (1960). Cyborgs and space. *Astronautics, 5*(9), 26–27, 74–76.

Deleuze, G. (1992). Postscript on the societies of control. *October, 59*, 3–7.

Fox, M., & Kemp, M. (2009). *Interactive architecture*. Princeton Architectural Press.

Frazer, J. (1995). *An evolutionary architecture*. Architectural Association Publications.

Gandy, M. (2005). Cyborg urbanization: Complexity and monstrosity in the contemporary city. International Journal of Urban and Regional Research, 29(1), 26–49. https://doi.org/10.1111/j.1468-2427.2005.00568.x

Gilson, L. L., & Goldberg, C. B. (2015). Editors' comment: So, what is a conceptual paper? *Group & Organization Management, 40*(2), 127–130. https://doi.org/10.1177/1059601115576425

Gökşen Takva, F., Çolak Demirel, B. B., & Ayçam, İ. (2025). Integration of artificial intelligence into the architectural design process: Architectural studio experience. *Black Sea Journal of Engineering and Science, 8*(6), 1874–1882. https://doi.org/10.34248/bsengineering.1761624

Haraway, D. J. (1991). *Simians, cyborgs, and women: The reinvention of nature*. Routledge.

Hayles, N. K. (1999). *How we became posthuman: Virtual bodies in cybernetics, literature, and informatics*. University of Chicago Press. https://doi.org/10.7208/chicago/9780226321394.001.0001

Jaakkola, E. (2020). Designing conceptual articles: Four approaches. *AMS Review, 10*(1–2), 18–26. https://doi.org/10.1007/s13162-020-00161-0

Jang, S., Roh, H., & Lee, G. (2025). Generative AI in architectural design: Application, data, and evaluation methods. *Automation in Construction, 174*, Article 106174. https://doi.org/10.1016/j.autcon.2025.106174

Karanouh, A., & Kerber, E. (2015). Innovations in dynamic architecture. Journal of Facade Design and Engineering, 3(2), 185–221. https://doi.org/10.7480/jfde.2015.2.1017

Kerner, M., Gebken, T., Sundarrao, I., Hindersin, S., & Sauss, D. (2019). Development of a control system to cover the demand for heat in a building with algae production in a bioenergy façade. Energy and Buildings, 184, 65–71. https://doi.org/10.1016/j.enbuild.2018.11.030

Kevseroğlu Kurban, Ö., & Kıdık Baran, A. (2026). AI as a design partner: Evaluating its role in architectural education through student and instructor insights. *Black Sea Journal of Engineering and Science, 9*(3), 1139–1149. https://doi.org/10.34248/bsengineering.1878241

Kitchin, R. (2014). *The data revolution: Big data, open data, data infrastructures and their consequences*. SAGE Publications. https://doi.org/10.4135/9781473909472

Kitchin, R., & Dodge, M. (2011). *Code/space: Software and everyday life*. The MIT Press. https://doi.org/10.7551/mitpress/9780262042482.001.0001

Kolarevic, B. (Ed.). (2003). *Architecture in the digital age: Design and manufacturing*. Spon Press.

Latour, B. (2005). *Reassembling the social: An introduction to actor-network-theory*. Oxford University Press.

Lee, J. H., Ostwald, M. J., & Kim, M. J. (2021). Characterizing smart environments as interactive and collective platforms: A review of the key behaviors of responsive architecture. *Sensors, 21*(10), Article 3417. https://doi.org/10.3390/s21103417

Loonen, R. C. G. M., Trčka, M., Cóstola, D., & Hensen, J. L. M. (2013). Climate adaptive building shells: State-of-the-art and future challenges. *Renewable and Sustainable Energy Reviews, 25*, 483–493. https://doi.org/10.1016/j.rser.2013.04.016

Manovich, L. (2001). *The language of new media*. The MIT Press.

McCullough, M. (2004). *Digital ground: Architecture, pervasive computing, and environmental knowing*. The MIT Press.

Mitchell, W. J. (2003). Me++: The cyborg self and the networked city. The MIT Press.

Negroponte, N. (1970). *The architecture machine: Toward a more human environment*. The MIT Press.

Oxman, N. (2010). *Material-based design computation* [Doctoral dissertation, Massachusetts Institute of Technology]. DSpace@MIT. https://dspace.mit.edu/handle/1721.1/59192

Pask, G. (1969). The architectural relevance of cybernetics. *Architectural Design, 39*(9), 494–496.

Picon, A. (2015). Smart cities: A spatialised intelligence. Wiley.

Sadowski, J. (2020). *Too smart: How digital capitalism is extracting data, controlling our lives, and taking over the world*. The MIT Press. https://doi.org/10.7551/mitpress/12240.001.0001

Semeraro, C., Biyrouti, S. J. A., Abdelkareem, M. A., & Olabi, A. G. (2025). Digital twin-driven innovation in smart and green building: A structured review and research agenda. *International Journal of Thermofluids, 29*, Article 101393. https://doi.org/10.1016/j.ijft.2025.101393

Sinopoli, J. M. (2010). *Smart building systems for architects, owners and builders*. Butterworth-Heinemann. https://doi.org/10.1016/C2009-0-20023-7

Snyder, H. (2019). Literature review as a research methodology: An overview and guidelines. *Journal of Business Research, 104*, 333–339. https://doi.org/10.1016/j.jbusres.2019.07.039

Stouffer, K., Pease, M., Tang, C., Zimmerman, T., Pillitteri, V., Lightman, S., Hahn, A., Saravia, S., Sherule, A., & Thompson, M. (2023). *Guide to operational technology (OT) security* (NIST Special Publication 800-82 Rev. 3). National Institute of Standards and Technology. https://doi.org/10.6028/NIST.SP.800-82r3

Wiener, N. (1948). *Cybernetics: Or control and communication in the animal and the machine*. The Technology Press; John Wiley & Sons.

Wurm, J., & Pauli, M. (2016). SolarLeaf: The world's first bioreactive façade. Architectural Research Quarterly, 20(1), 73–79. https://doi.org/10.1017/S1359135516000245

Yıldız, D., Turan, İ. H., Demirci, S., Yavuz, A. E., & Gebeş, B. (2026). High-performance IoT monitoring with Redis-backed in-memory storage and containerized CI/CD pipeline. *Black Sea Journal of Engineering and Science, 9*(1), 135–146. https://doi.org/10.34248/bsengineering.1735232

Black Sea Journal of Engineering and Science
doi: 10.34248/bsengineering.1936460

Open Access Journal
e-ISSN: 2619 – 8991

Research Article
Volume 9 - Issue 5: 2599-2611 / September 2026

DICLOFENAC POTASSIUM AND ISONICOTINAMIDE COCRYSTALS FOR ENHANCED SOLUBILITY: IN VITRO EVALUATION OF HARD GELATIN CAPSULES

Esra DEMIRTURK[1]*, Gülsüm GUNDOGDU[2], Merve NENNI[3], Cem YAMALI[4], Meltem CETIN[5], Yılmaz CAPAN[6]

[1]*Çukurova University, Faculty of Pharmacy, Department of Pharmaceutical Technology, Adana, Türkiye*
[2]*Turkish-German University, Faculty of Science, Department of Energy Science and Technology, 34820, Beykoz, Istanbul, Türkiye*
[3]*Çukurova University, Faculty of Pharmacy, Department of Analytical Chemistry, Adana, Türkiye*
[4]*Çukurova University, Faculty of Pharmacy, Department of Basic Pharmaceutical Sciences, Adana, Türkiye*
[5]*Atatürk University, Faculty of Pharmacy, Department of Pharmaceutical Technology, Erzurum, Türkiye*
[6]*Lokman Hekim University, Faculty of Pharmacy, Department of Pharmaceutical Technology, Ankara, Türkiye*

Abstract: Diclofenac potassium (DIC-K), classified as a Biopharmaceutics Classification System (BCS) Class II drug, exhibits low solubility and high permeability. It is a widely used non-steroidal anti-inflammatory drug (NSAID) with anti-inflammatory, antipyretic, and analgesic effects. This study aimed to enhance the solubility of DIC-K by preparing cocrystals with isonicotinamide (INA) as a coformer and to evaluate their in vitro performance. The prepared DIC-K+INA cocrystals were characterized using powder X-ray diffraction (PXRD), Fourier-transform infrared spectroscopy (FTIR), and differential scanning calorimetry (DSC). Solubility studies were conducted for pure DIC-K and DIC-K+INA cocrystals in different media (0.1 N HCl, pH 1.2; phosphate buffer (PB), pH 4.5; and PB, pH 6.8). Hard gelatin capsules containing either pure DIC-K or DIC-K+INA cocrystals were formulated using the dry granulation method, and their dissolution profiles were evaluated in PB (pH 6.8). At 15 min, the amount of DIC-K dissolved from the pure DIC-K capsules was 72%, whereas that from the DIC-K+INA cocrystal capsules reached 92%. PXRD, FTIR, and DSC analyses supported the formation of a new crystalline phase, indicating successful cocrystal formation between DIC-K and INA. Overall, DIC-K+INA cocrystals enhanced the solubility and dissolution performance of DIC-K, demonstrating the potential of cocrystallization as a formulation strategy for poorly soluble drugs.

Keywords: Diclofenac potassium, Isonicotinamide, Cocrystal, Solubility enhancement, Capsule

***Corresponding author:** Çukurova University, Faculty of Pharmacy, Department of Pharmaceutical Technology, Adana, Türkiye
E mail: edemirturk@cu.edu.tr (E. DEMIRTURK)
Esra DEMIRTURK https://orcid.org/0000-0002-8918-0073
Gülsüm GUNDOGDU https://orcid.org/0000-0003-2380-7942
Merve NENNI https://orcid.org/0000-0003-3165-1060
Cem YAMALI https://orcid.org/0000-0002-4833-7900
Meltem CETIN https://orcid.org/0000-0003-4009-2432
Yılmaz CAPAN https://orcid.org/0000-0003-1234-9018

Received: April 25, 2026
Accepted: August 19, 2026
Published: September 15, 2026

Cite as: Demirturk, E., Gundogdu, G., Nenni, M., Yamali, C., Cetin, M., &Capan, Y. (2026). Diclofenac potassium and isonicotinamide cocrystals for enhanced solubility: in vitro evaluation of hard gelatin capsules. *Black Sea Journal of Engineering and Science*, 9(5), 2599-2611.

1. Introduction

In the development of solid dosage forms, factors such as particle size, solubility, and stability play crucial roles in determining the therapeutic effectiveness of active pharmaceutical ingredients (APIs). Poor aqueous solubility and low bioavailability remain major challenges, particularly for Biopharmaceutics Classification System (BCS) Class II drugs, which are characterized by high permeability but low solubility (Rodrigues et al., 2018; Yadav et al., 2009; Guo et al., 2021). To address these limitations, various solid-state modification strategies such as salt formation, polymorphism, and pharmaceutical cocrystallization have been employed (Yadav et al., 2009; Rodrigues et al., 2018).

Pharmaceutical cocrystals are multicomponent crystalline systems composed of an API and a neutral coformer in a defined stoichiometric ratio, held together through non-covalent intermolecular interactions such as hydrogen bonding, π–π stacking, halogen bonding, or van der Waals forces (European Medicines Agency, 2015; U.S. Food and Drug Administration, 2018). Unlike conventional salts, cocrystals are generally formed without proton transfer between the API and the coformer. This approach enables modification of physicochemical properties without altering the chemical structure or pharmacological activity of the API (U.S. Food and Drug Administration, 2018). Both the European Medicines Agency (EMA) and the U.S. Food and Drug Administration (FDA) recognize pharmaceutical

This work is licensed (CC BY-NC 4.0) under Creative Commons Attribution 4.0 International License

cocrystals as valuable solid-state forms with the potential to improve properties such as solubility, stability, manufacturability, and bioavailability (European Medicines Agency, 2015; U.S. Food and Drug Administration, 2018; Yuliandra et al., 2018). Diclofenac (DIC) is a non-steroidal anti-inflammatory drug (NSAID) widely used for its analgesic, antipyretic, and anti-inflammatory properties. It is a phenylacetic acid derivative formulated in various salt forms, most commonly as sodium and potassium salts. Among these, diclofenac potassium (DIC-K) is classified as a Biopharmaceutics Classification System (BCS) Class II drug, characterized by high permeability and poor aqueous solubility (Báthori et al., 2011; Rolfe, 2014). Therefore, improving the solubility and dissolution behavior of DIC-K represents an important formulation strategy for optimizing its biopharmaceutical performance.

Isonicotinamide (INA), a constitutional isomer of nicotinamide, is a commonly used coformer in pharmaceutical cocrystal studies. Its pyridyl nitrogen and amide groups provide complementary hydrogen-bonding sites that can participate in intermolecular interactions with suitable functional groups of APIs (Báthori et al., 2011). Although diclofenac potassium exists in a salt form, its carboxylate group can participate in intermolecular interactions with INA, favoring the formation of a stable multicomponent crystalline system. In addition to this molecular complementarity, INA has been employed in pharmaceutical cocrystal engineering to modify the physicochemical properties of drug substances (Báthori et al., 2011; Karakthala et al., 2023). Therefore, its favorable intermolecular interaction potential and established use as a pharmaceutical coformer provided the rationale for selecting INA for the development of DIC-K cocrystals.

Importantly, the distinction between salts, cocrystals, and ionic cocrystals should be considered. In salts, proton transfer occurs between an ionizable API and a counterion, whereas in cocrystals, the components interact through non-ionic supramolecular interactions without proton transfer. Ionic cocrystals (also referred to as salt cocrystals) represent a distinct category in which at least one component is present in an ionic form, such as a salt, and participates in additional supramolecular interactions with a neutral coformer (Nugrahani et al., 2020). Accordingly, the DIC-K+INA system can be described as an ionic cocrystal, in which ionic and non-ionic interactions coexist within the same crystalline lattice, potentially contributing to improved solubility and dissolution characteristics (Nugrahani et al., 2020). In this study, DIC-K+INA ionic cocrystals were prepared with the aim of improving the solubility and dissolution behavior of DIC-K. The resulting solid phase was characterized by PXRD, FTIR, and DSC, and its solubility was evaluated at different pH conditions. Furthermore, the DIC-K+INA ionic cocrystals were incorporated into hard gelatin capsules, and their in vitro dissolution performance was compared with that of capsules containing pure DIC-K.

2. Materials and Methods

2.1. Materials

DIC-K and INA were purchased from Sigma (USA). Methanol was obtained from Merck (Germany). All materials used in this study were analytical grade.

2.2. Methods

2.2.1. Development of HPLC method

High-performance liquid chromatography (HPLC) analysis was performed using a Shimadzu Nexera 2 system (Japan) equipped with a solvent delivery unit, injection valve, and diode-array detector (DAD/PDA). Chromatographic separation was achieved using a C18 analytical column (4.6 × 250 mm, 5 µm; GL Sciences). The mobile phase consisted of 50 mM phosphate buffer (pH 2.5) and methanol at a ratio of 30:70 (v/v), delivered at a flow rate of 1.0 mL/min. The injection volume was 10 µL. Detection was performed at 280 nm for DIC-K and 210 nm for INA (Rubim et al., 2013; Panda et al., 2012; Alquadeib, 2019). A stock solution of DIC-K (100 µg/mL) was prepared in methanol and subsequently diluted with the mobile phase to obtain calibration standards over the concentration range of 2.5–40 µg/mL. An INA stock solution (100 µg/mL) was prepared in the same manner, and calibration standards were prepared over the same concentration range.

2.2.2. Validation of the HPLC method

The HPLC method was validated in terms of linearity, selectivity, limit of detection (LOD), limit of quantification (LOQ), accuracy, precision, and stability (International Council for Harmonisation, 2005; Shabir, 2003). Selectivity was evaluated by analyzing the mobile phase and blank formulation (capsule formulation without the active ingredient) under the same chromatographic conditions to assess the presence of potential interfering peaks. Precision was evaluated in terms of repeatability and reproducibility at three concentration levels (5, 15, and 30 µg/mL) for both DIC-K and INA, and the results were expressed as relative standard deviation (%RSD). Accuracy was assessed at three concentration levels (5, 15, and 30 µg/mL) within the calibration range for both DIC-K and INA. Intra-day accuracy was evaluated by analyzing each concentration six times within a single day, whereas inter-day accuracy was evaluated over six consecutive days, and the results were expressed as %RSD. Stability was evaluated only for DIC-K. Samples at concentrations of 15 and 30 µg/mL were either exposed to or protected from daylight for 8 h at room temperature and subsequently analyzed by HPLC. The results were compared with the initial concentrations to evaluate the photostability of DIC-K.

2.2.3. Preparation of DIC-K+INA cocrystals

DIC-K+INA cocrystals were prepared using the solvent evaporation method at a DIC-K:INA stoichiometric molar ratio of 1:1. DIC-K and INA were initially mixed and ground using a mortar and pestle. Methanol was added

dropwise, and the mixture was continuously ground for approximately 15 min until dry (Shabir, 2003; International Council for Harmonisation, 2005; Panda et al., 2012; Rubim et al., 2013; Nugrahani et al., 2018; Alquadeib, 2019; Nugrahani et al., 2020). The resulting mixture was then dissolved in a sufficient amount of methanol, and the solvent was evaporated to approximately half of its initial volume using a rotary evaporator. The remaining solvent was allowed to evaporate at room temperature for 24 h to obtain the DIC-K+INA cocrystals.

2.2.4. Determination of DIC-K and INA contents of the prepared cocrystals by HPLC

To prepare the stock solution (200 µg/mL), 5 mg of cocrystals were dissolved in methanol and the volume was completed to 25 mL with methanol (in volumetric flask). 125 µL of the prepared stock solution was taken and diluted to 1000 µL with mobile phase and analyzed by HPLC to determine the amounts of DIC-K and INA in the cocrystal.

2.2.5. Solubility study

Solubility studies were conducted to select an appropriate medium for the subsequent dissolution experiments. The solubility of pure DIC-K and DIC-K+INA cocrystals was evaluated in three different media: 0.1 N HCl (pH 1.2), phosphate buffer (PB, pH 4.5), and phosphate buffer (PB, pH 6.8). The samples were maintained in a horizontal shaker at 37 °C for 24 h to allow equilibration. Following the incubation period, the samples were filtered through a 0.45 µm membrane filter and analyzed using the validated HPLC method to determine the DIC-K concentration. The obtained solubility data were used to select the dissolution medium for the comparative in vitro dissolution studies.

2.2.6. FT-IR analysis

FT-IR spectra of pure DIC-K, INA and the prepared cocrystal were recorded (in the range of 4000-400 cm^{-1}) on a Jasco, FT/IR-6700 spectrophotometer using KBr disks containing 1% of the substance.

2.2.7. DSC analysis

DSC analyzes of pure DIC-K, INA and the prepared cocrystal was performed using a Mettler Toledo DSC3 differential scanning calorimeter. Samples placed in *aluminum* pans were heated at 20°C/min from 25 to 600 °C under nitrogen atmosphere and DSC thermograms were taken (Karakthala et al., 2023).

2.2.8. PXRD analysis

PXRD data were recorded at room temperature on an Empyrean Multi-Purposed diffractometer using Cu Kα1 (λ = 1.5406 Å) and Cu Kα2 radiation (λ = 1.544426 Å), 45 kV voltage and a current of 40 mA. The samples were scanned from 10˚ to 60˚ (2θ) at a step size of 0.013˚ counting time of 74 s per step.

2.2.9. Hard capsule formulation

Microcrystalline cellulose and lactose were preferred as diluents in the formulation. Sodium starch glycolate was used as a disintegrant and colloidal silicon dioxide and magnesium stearate were used as lubricants. The selected excipients are the most preferred excipients in solid dosage forms (Table 1). Granules were prepared using the dry granulation method (mechanical compression/slugging method) to improve powder flow properties. First of all, the excipients (lactose, mycrystalline cellulose, sodium starch glycolate) and pure DIC-K or DIC-K+INA cocrystals were mixed and pressed into tablets on a conventional tablet press. Then, the tablets were milled into granules and sieved using a #10 sieve. The final granules were blended with colloidal silicon dioxide and magnesium stearate and evaluated its flow properties before filling into hard gelatine capsules (Capsule number 1). 80 mg cocrystal was added to the DIC-K+INA formulation, equivalent to 50 mg diclofenac potassium.

Table 1. Capsules' formulation

Ingredients	mg/DIC-K capsule	mg/DIC-K+INA capsule
DIC-K	50	-
DIC-K+INA cocrystals	-	80*
Microcrystalline cellulose	150	120
Lactose	82	82
Sodium starch glycolate	6	6
Colloidal silicon dioxide	9	9
Magnesium stearate	3	3

DIC-K-capsule= pure DIC-K-containing capsule, DIC-K+INA–capsule= DIC-K+INA cocrystals-containing capsule, *Equivalent to 50 mg DICK.

2.2.10. Flow properties

For granular filling mixture, angle of repose, flow time, bulk density, tapped density, compressibility index (equation 1) and Hausner ratio (equation 2) was determined.

Compressibility index=100 (tapped density-bulk density)/tapped density) (1)

Hausner ratio= Tapped density/bulk density (2)

2.2.11. The characterization of hard capsules containing DIC-K or DIC-K+INA cocrystals

After granular mixture filling into capsules, average capsule weight and disintegration time were determined and dissolution studies were carried out. The capsules were tested for disintegration time based on recommendations by USP 43 general chapter <701Disintegration> (United States Pharmacopeia, 2019a).

Moreover, the capsules were tested for dissolution based on recommendations by USP 43 general chapter <711> (United States Pharmacopeia, 2019b) and according to FDA dissolution study data (U.S. Food and Drug

Administration, 2016). This study was performed in a 6vessel USP dissolution apparatus Type I (Basket; Pharma Test Dissolution Testing Instrument, Germany). The dissolution medium was chosen based on the solubility study. The prepared capsules were immersed in 900 mL of PB pH 6.8 at 50 rpm stirring speed, and the temperature was 37±0.5°C. During the study, 1 mL of sample was withdrawn from the medium at 5, 10, 15, 20, 30, 45, and 60 min and and was replaced with the same volume of fresh dissolution medium. The samples were filtered (0.45 µm hydrophilic politetrafluoroethylene membrane filter) and analyzed by HPLC.

3. Results

We developed an isocratic HPLC method for analyzing DIC-K in solubility and dissolution studies and the DIC-K and INA contents of the prepared cocrystals. In addition, we validated this method at some parameters (linearity, accuracy, precision, selectivity, LOD, and LOQ). The capacity of an analytical technique to identify and measure the analyte in the presence of other sample constituents is known as selectivity. The chromatograms of mobile phase and blank formulation (the capsule formulation without active ingredient) were obtained (Figure 1). Figure 1 verified the given method's selectivity. We performed DIC-K and INA analyses at 280 nm and 210 nm, respectively, given in the method section. The and INA (at concentrations of 2.5, 15, 25, 40 µg/mL) are retention time values of DIC-K and INA were about 13.5 presented in Figure 2 and 3. The calibration equation, R2, and 3.2 min, respectively. The chromatograms of DIC-K (at LOD and LOQ values are presented in Table 2. The semantic model was formally developed with the architecture to be a deeply semantically rich knowledge graph for the entire physical and chemical lifecycle of coffee. The development lifecycle followed very closely the accepted ontological engineering methodologies which specify a very iterative lifecycle of initial domain analysis, integration of existing ontologies, extraction of expert terminology, rigorous definition of the class hierarchy, mapping of object properties and formulation of logical constraints. The ontology was built using the Web Ontology Language (OWL) within the Protégé computational environment and strictly adhering to the standards of the World Wide Web Consortium.

The primary existential entities in the coffee domain constitute the taxonomic backbone of the ontology. This gave rise to a deep and strongly structured hierarchical tree, which explicitly separated botanical living entities, physical states of the agricultural product, highly mechanized industrial processes, and subjective human sensory evaluations. The main ontological super-classes are defined with their respective hierarchical descendants as shown in Table 1.

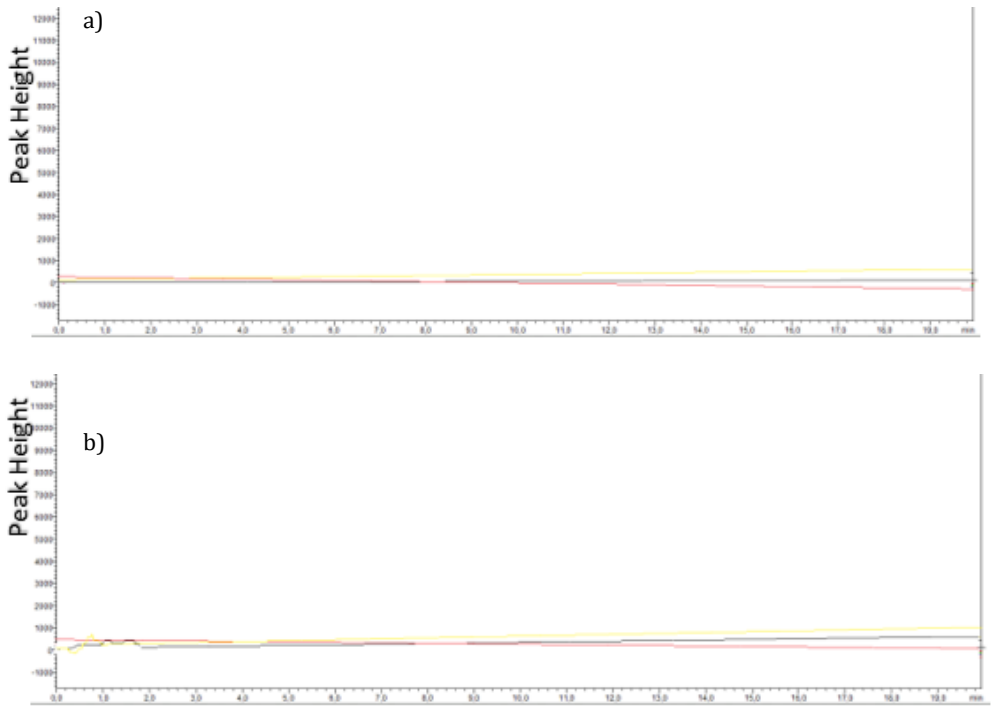


Figure 1. The chromatograms of mobile phase (a) and blank formulation (b).

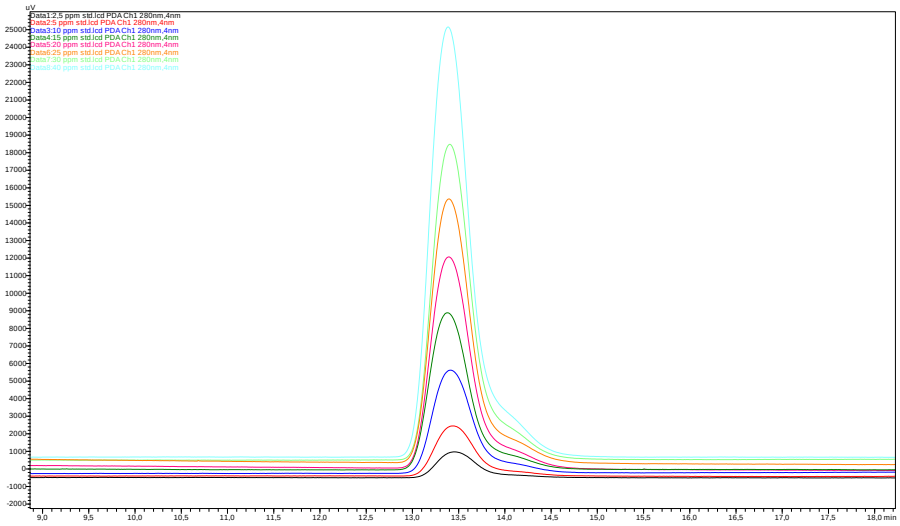


Figure 2. HPLC chromatograms of DIC-K (2.5-40 µg/mL).

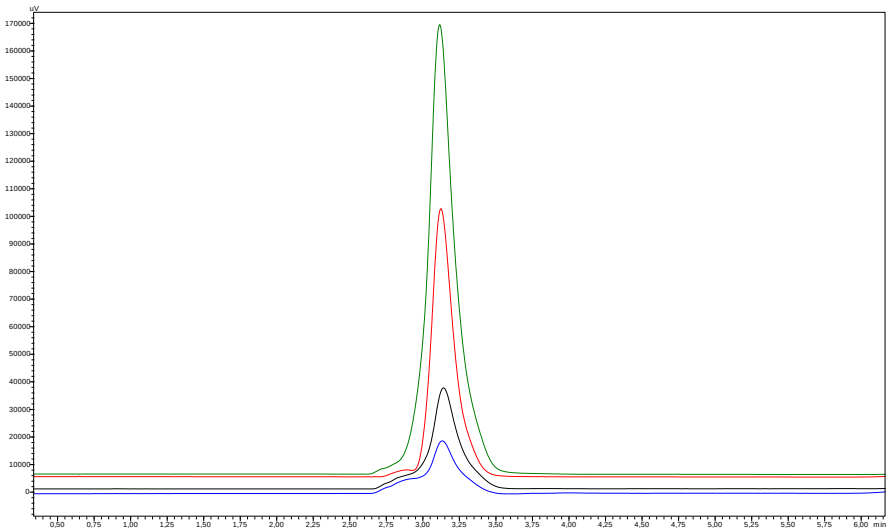


Figure 3. HPLC chromatograms of INA (2.5, 15, 25, 40 µg/mL).

Table 2. The calibration equation, R^2, LOD and LOQ values

	DIC-K	INA
Calibration equation	y=19370x-3701.4	y=12744x-2433
R^2	0.9999	0.9999
Linearity Range (µg/mL)	2.5-40	2.5-40
LOQ (µg/mL)	2.44	2.48
LOD (µg/mL)	0.85	0.89

R2 (determination coefficient) values determined for DIC and INA being close to 1 indicates adequate method linearity (Table 2). The accuracy of the method was determined at three different concentrations (5, 15, and 30 µg/mL), and the results were expressed as the percentage of difference between the added and measured concentrations (Table 3). %RSD values which is less than 2% was taken as an indication of sufficient intra- and inter-day accuracy of the developed method (Table 3). Furthermore, %RSD values calculated for repeatability and reproducibility studies were less than 2%, indicating that the method works with the required precision (Table 4). For photostability of the samples (at concentrations of 15 and 30 µg/mL for DIC-K) exposed or not exposed to daylight (8 h) at room temperature were evaluated. The calculated % recovery values showed that DIC-K was photostable during the whole analytical procedure (Table 5). Furthermore, all standard solutions were prepared fresh daily for HPLC analysis.

3.1. Determination of DIC-K and INA Contents of the Prepared Cocrystals by HPLC

Since 5 mg DIC-K+INA cocrystal was found to contain 3.125±0.02 mg (n=3) DIC-K, 1.256±0.12 mg (n=3) INA and the DIC-K+INA capsule formulation contains 80 mg DICK+INA cocrystal equivalent to 50 mg DIC-K.

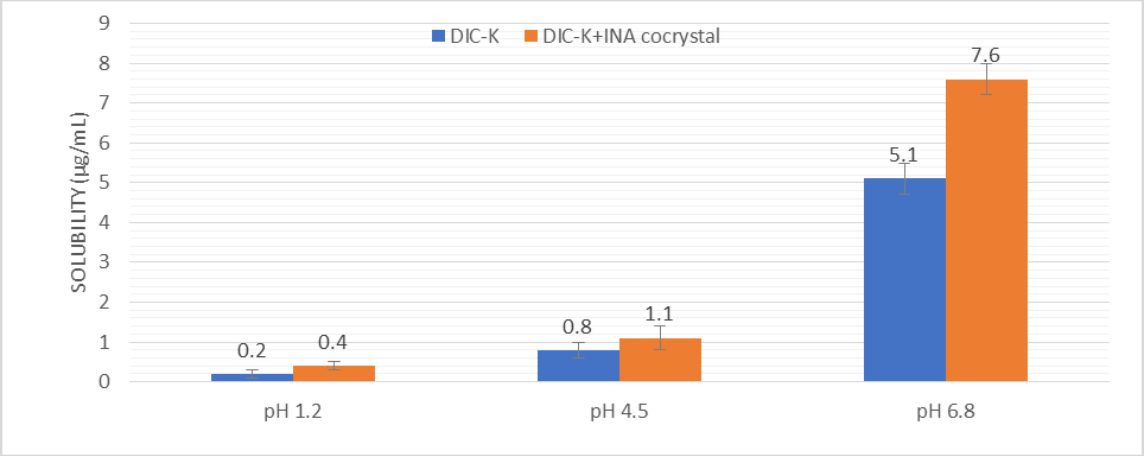


Figure 4. DIC-K and DIC-K+INA cocrystal's solubilities at media with different pH.

Table 3. The obtained results for intra- and inter-day accuracy

Added Concentration (5, 15, 30 µg/mL)		Measured Concentration (µg/mL) (DIC-K/INA)			Percentage (%)		
	Intra-day	5.00/5.05	15.04/15.00	30.03/30.01	100.00/ 101.00	100.27/ 100.00	100.10/ 100.03
		5.04/5.04	15.03/15.00	30.00/30.00	100,80/ 100.80	100.20/ 100.00	100.00/ 100.00
		4.98/5.02	15.05/15.02	3.05/30.02	99.60/ 100.40	100.33/ 100.13	100.17/ 100.07
		5.03/5.03	14.96/15.01	30.00/30.01	100.60/ 100.60	99.73/ 100.07	100.00/ 100.03
		5.05/4.98	15.04/15.05	30.01/30.00	101.00/ 99.60	100.27/ 100.33	100.03/ 100.00
		5.08/5.05	15.05/14.98	30.02/30.01	101.60/ 101.00	100.33/ 99.87	100.07/ 100.03
Mean		5.03/5.03	15.03/15.01	30.02/30.01	100.60/ 100.57	100.19/ 100.07	100.06/ 100.03
SD		0.04/0.02	0.03/0.02	0.02/0.01	0.72/0.53	0.23/0.16	0.07/0.03
RSD(%)		0.71/0.52	0.23/0.16	0.06/0.03	0.71/0.52	0.23/0.16	0.07/0.03
	Inter-day	5.10/5.05	14.91/15.18	30.11/30.12	102.00/ 100.40	99.40/ 101.20	100.37/ 100.40
		5.05/4.92	14.85/15.05	30.16/30.21	101.00/ 100.70	99.00/ 100.33	100.53/ 100.70
		4.95/4.94	15.12/15.11	29.89/30.13	99.00/ 100.43	100.80/ 100.73	99.63/ 100.43
		5.11/5.10	15.02/15.10	29.87/30.12	102.20/ 100.40	100.13/ 100.67	99.57/ 100.40
		5.12/4.90	15.09/14.80	29.88/30.20	102.40/ 100.67	100.60/ 98.67	99.60/ 100.67
		4.90/5.11	15.18/15.15	29.86/30.21	98.00/ 100.70	101.20/ 101.00	99.53/ 100.70
Mean		5.04/5.00	15.03/15.07	29.96/30.18	100.77/ 100.55	100.19/ 100.43	99.87/ 100.55
SD		0.09/0.09	0.13/0.13	0.14/0.04	1.85/0.15	0.85/0.91	0.45/0.15
RSD(%)		1.83/1.89	0.85/0.91	0.45/0.14	1.83/0.15	0.85/0.91	0.45/0.15

Table 4. Repeatability and reproducibility results

Sample Number	Repeatability			Reproducibility		
	Concentrations for DIC-K/INA (µg/mL)			Concentrations for DIC-K/INA (µg/mL)		
	5	15	30	5	15	30
1	5.50/5.12	15.48/15.11	30.01/30.02	5.50/5.13	15.51/15.23	30.09/30.09
2	5.50/5.23	15.48/15.21	29.98/30.11	5.50/5.12	14.93/15.12	30.91/30.09
3	5.48/5.22	15.51/14.98	29.78/30.05	5.23/5.23	15.38/15.14	29.86/30.11
4	5.46/5.13	15.49/15.05	29.98/30.08	5.46/5.22	15.58/15.16	29.82/30.12
5	5.51/5.14	15.50/15.07	30.05/29.98	5.52/5.20	15.53/15.07	29.94/30.05
6	5.52/5.12	15.52/15.07	30.00/30.04	5.46/5.10	15.01/15.01	30.76/30.06
Mean	5.50/5.16	15.50/15.08	29.97/30.05	5.45/5.17	15.32/15.12	30.23/30.09
SD	0.02/0.05	0.02/0.08	0.10/0.05	0.11/0.06	0.28/0.08	0.48/0.03
RSD (%)	0.39/0.98	0.11/0.50	0.32/0.15	1.98/1.09	1.84/0.50	1.59/0.09

SD= standard deviation, RSD= relative standard deviation.

Table 5. Photostability results for DIC-K

Time (h)	Added Concentration (µg/mL)	Protected from daylight		Not protected from daylight	
		Measured Concentration (µg/mL; n=6)	Recovery (%)	Measured Concentration (µg/mL; n=6)	Recovery (%)
0	15	15.00±0.01	103.2	15.50±0.01	99.74
8	15	15.48±0.02		15.46±0.01	
0	30	29.98±0.11	100	29.95±0.15	99.73
8	30	29.98±0.12		29.87±0.13	

3.2. Solubility Studies

The solubility studies for DIC-K and DIC-K+INA cocrystals were carried out at the media with different pH values (0.1 N HCl pH 1.2, PB pH 4.5, and PB pH 6.8). Figure 1 shows the results of the solubility studies. DIC-K is a Class II drug according to the biopharmaceutical classification system. This classification suggests that DIC-K may have challenges in dissolution and absorption in the body that may affect its therapeutic efficacy. Appropriate formulation strategies (such as increasing the solubility of DIC-K) are required to optimize the distribution and bioavailability of DIC-K. In our study, the solubility of DICK in pH 6.8 buffer was 5.1 µg/mL, while the solubility of DIC-K in pH 6.8 was 7.6 µg/mL after the cocrystallization process (Figure 4). According to the solubility data, there is an increase in DIC-K solubility after cocrystallization. The solubility studies have been a guide for dissolution studies. Since the solubility of DIC-K was pretty low in the media with pH 1.2 and pH 4.5, dissolution rate studies were carried out in the medium with pH 6.8 (Figure 4).

3.3. FT-IR Spectrum of Cocrystals

FT-IR spectra of DIC-K, INA and DIC-K+INA cocrytals are given in Figure 5a, 5b and 5c. In these spectra, characteristic peaks were analyzed. The INA molecule is a type of amide which is comprises of carbonyl and amino groups. According to FT-IR spectrum of INA, two N-H stretching bands are observed at 3361.11 cm^{-1} and 3177.28 cm^{-1} (medium band). The N-H stretching vibration usually observed in the region 3000-3500 cm^{-1}. Generally, carbonyl group vibrations occur in the region 1780-1680 cm^{-1}. The pyridine and its related compounds show a strong absorption band in the region 1600-1500 cm^{-1} due to C=N ring stretching vibration. In this study, the C=O stretching band (medium band) and C=N stretching band (medium band) are shown at the expected area between 1652.71-1549.44 cm^{-1} (Figure 5b). These findings are consistent with the reported values (Akalin et al., 2005).

Considering the FT-IR spectrum of DIC-K, secondary aromatic -NH- stretching band and -COOH stretching band are observed around 3245.17 cm^{-1} (weak band) and 3066 cm^{-1} (weak band). The C=O stretching band of carboxylic acid group is observed at 1577.79 cm^{-1} (very strong band) (Figure 5-a) (Palomo et al., 1999; Siozou et al., 2021). The C-Cl, -C-N-, -N-H bands at the fingerprint area was also seen.

FT-IR spectrum of DIC-K+INA cocrytals showed that differences of peak intensities were observed. Characteristic peaks belonging the compounds are seen

at 1682.5, 1576.18, 846.02 744.84 cm^{-1} that confirming the presence of both DIC-K and INA in the cocrystals (Figure 5-c).

3.4. DSC Analysis of Cocrystals

The DSC thermograms for DIC-K, INA, and the DIC-K-INA cocrystal are presented in Figures 6a–c. The DSC profile of DIC-K (Figure 6a) exhibits an exothermic peak at 323.56 °C and an endothermic peak at 318.78 °C. Literature data (Nugrahani et al., 2020) indicate that DIC-K melts near 300 °C (observed as a small endothermic peak), followed by decomposition at approximately 317 °C, as indicated by an exothermic peak. These results are consistent with the literature. For INA, the DSC thermogram (Figure 6b) shows three endothermic peaks at 133.21 °C, 157.85 °C, and 321.22 °C. The sharp endothermic peak at 157.85 °C corresponds to the melting point of INA, aligning well with previous findings in the literature (Jiaxuan et al., 2020).

The DSC thermogram of the DIC-K+INA cocrystal (Figure 6c) displays distinct exothermic and endothermic peaks, different from those observed for the individual components. These newly observed peaks may result from the melting or crystallization of the cocrystal, as well as the disappearance of peaks associated with the active substance and coformer melting. This behavior suggests an interaction between DIC-K and INA and supports the potential formation of a cocrystal during heating (Saganowska and Wesolowski, 2018).

Notably, the melting point of the cocrystal differs from that of the starting materials. It is well-documented that more than 50% of cocrystals have melting points lower than both their active substances and coformers. Additionally, variations in the melting point of cocrystals can be attributed to differences in the solvents used and the crystallization procedures employed (Garbacz et al., 2020).

3.5. PXRD Study

The PXRD pattern of pure DIC-K showed sharp and welldefined diffraction peaks corresponding to its crystalline structure, while INA exhibited a different set of reflections. In contrast, the DIC-K+INA cocrystal displayed a unique diffraction profile, characterized by the disappearance of certain peaks belonging to the parent compounds and the emergence of new ones. This clear difference from both pure DIC-K and INA demonstrates the formation of a novel crystal lattice rather than a simple physical mixture. When directly compared to DIC-K, the cocrystal pattern no longer resembles the original drug, further confirming the successful cocrystallization process with isonicotinamide. The PXRD pattern of the DIC-K, INA and DIC-K+INA cocrystal were shown in Figure 7-1a. Characteristic peaks at 14.34, 15.28, 16.45, 21.70, 25.22, 26.04, 26.88, and 27.80°, etc. 2θ values in the PXRD pattern of pure DIC-K were observed, which are consistent with the reported data for DIC-K (Han et al., 2017). The cocrystal product (Figure 7-1a and 1b) also presents the characteristic peak position of pure DIC-K which were slightly shifted towards 14.38, 15.32, 16.47, 21.72, 25.25,

26.08 26.90 and 27.83° 2θ values. It clearly shows that the 11.44, 18.46, 23.00, 24.27, 28.55 and 36.62 and 29.91° 2θ additional peaks of the cocrystal PXRD pattern are distinguishable from the pure DIC-K PXRD pattern, which indicates the formation of a new solid phase. Significant differences were observed between the PXRD patterns of the INA and cocrystal (Figure 7-1a). The PXRD pattern of cocrystal indicated severe preferred orientation of the crystallites with a with high intensity sharp peak at 23.0°, similarly which that observed for INA PXRD pattern at peak position 23.30° 2θ, consistent with the reported data for INA (Caira and Vicatos, 2019) and which also confirms the formation of the cocrystal. The PXRD pattern of the DIC-K+INA cocrystal revealed new diffraction peaks at different 2θ values, accompanied by the disappearance of characteristic reflections of the parent compounds. These changes confirm the generation of a distinct crystalline phase, providing strong evidence for successful cocrystallization.

Characterization of Capsule Formulations

The flow properties of the granular filling mixture were evaluated (after the addition of the lubricants). The obtained parameters are given in Table 6. The angle of repose values were found to be 29.30±0.78° (for the granular filling mixture-DIC-K capsule) and 27.10±0.64° (for the granular filling mixture-DIC-K+INA capsule) (Table 6). The angle of repose in the range of 25–30° indicates that the powder exhibits excellent flow properties (United States Pharmacopeia, 2019c).

Compressibility index and Hausner ratio are simple and fast methods to predict the flow properties of powder. These may predict powder flow properties as being affected by shape, size, surface area, cohesiveness and moisture content of powder, etc. Powders with compressibility index in the range of 11-15% and 16-20% show good and fair flow properties, respectively. In addition, the powders with Hausner ratio values in the range of 1.12-1.18 and 1.19-1.25 exhibit good and fair flow properties, respectively (United States Pharmacopeia, 2019d). According to the results, the content prepared for DIC-K+INA–capsule in our study has good flow properties (Table 6). The flow properties of granules prepared using cocrystals improved (from fair to good).

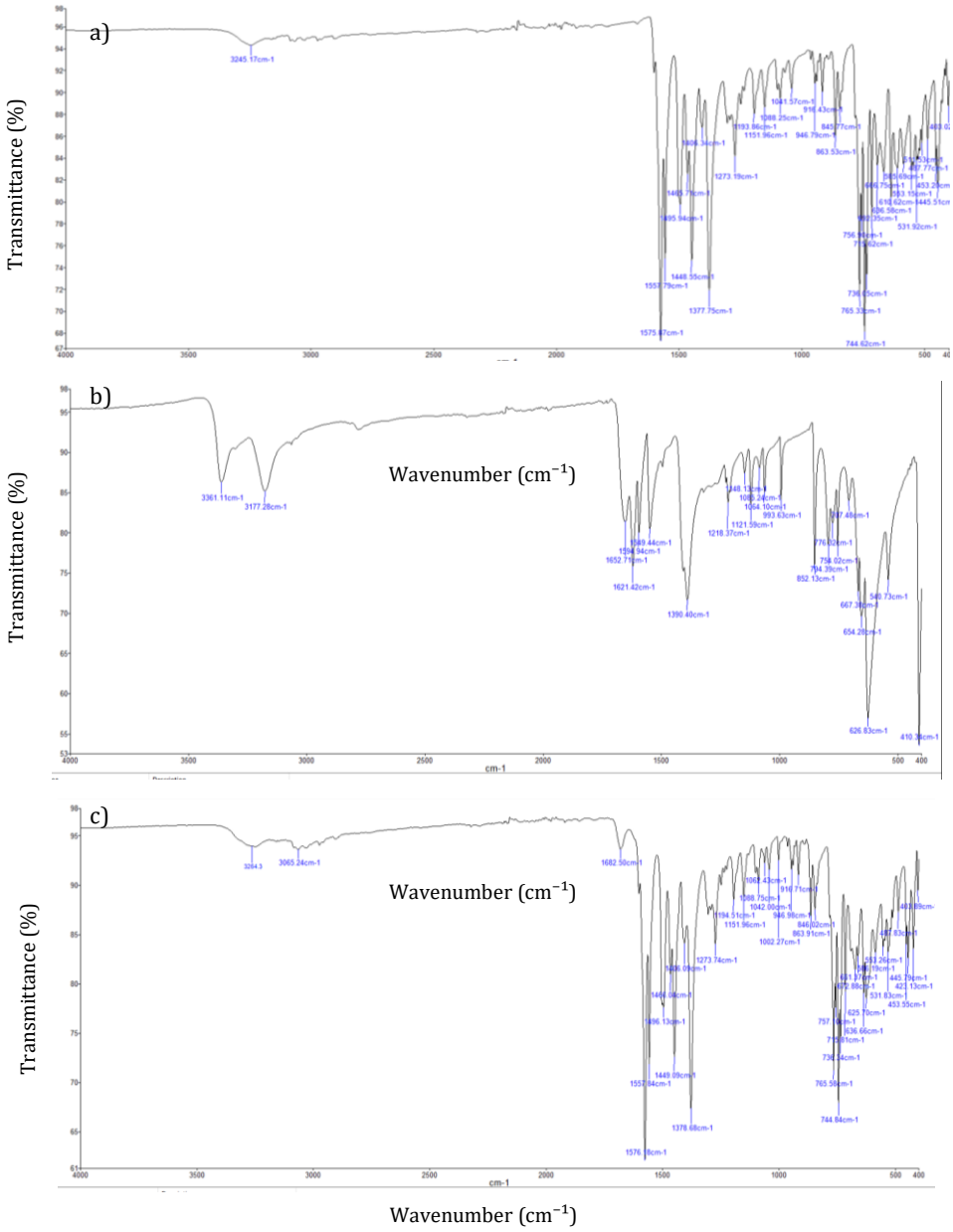


Figure 5. DIC-K (a), INA (b) and DIC-K+INA cocrystal (c)´s FT-IR spectra.

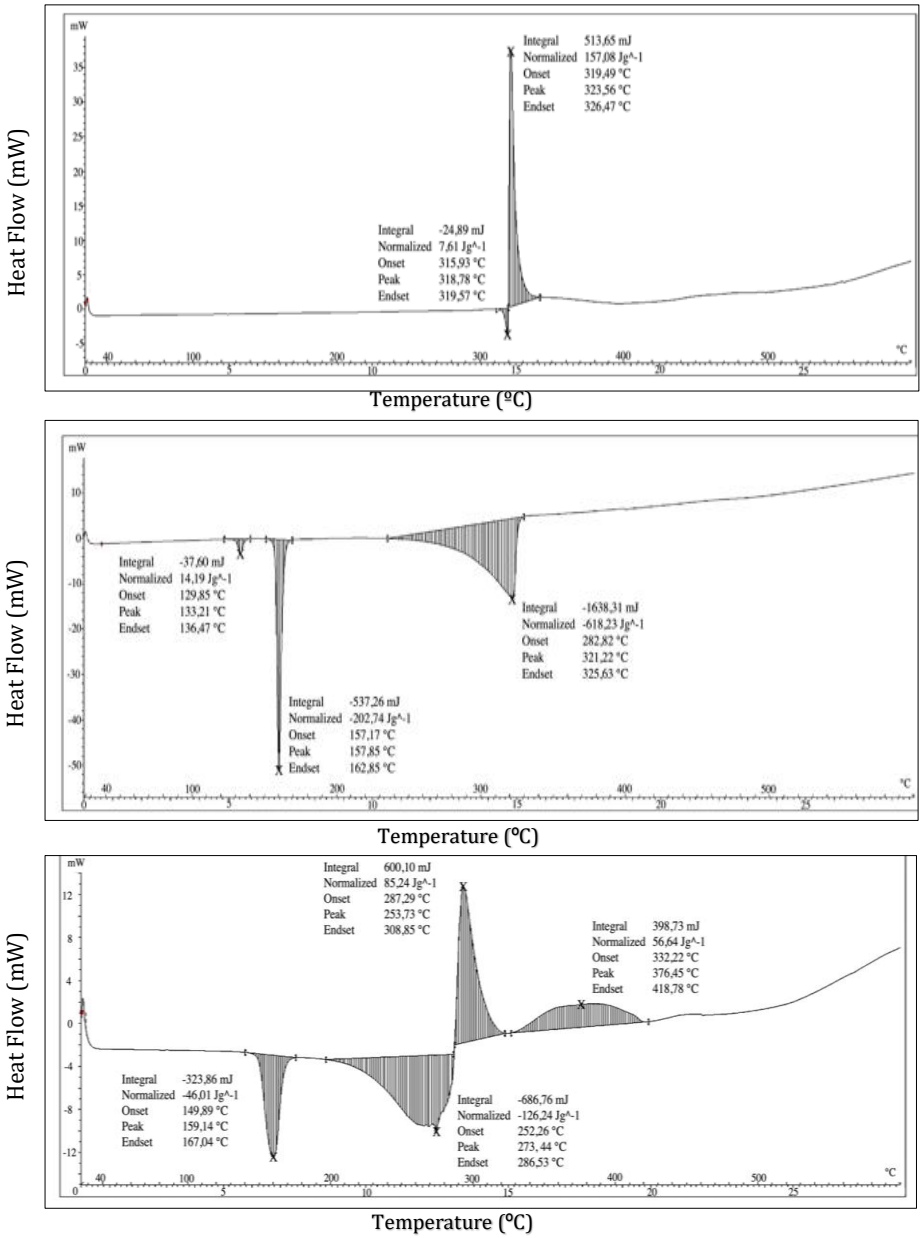


Figure 6. DIC-K (a), INA (b) and DIC-K+INA cocrystal (c)´s DSC thermograms.

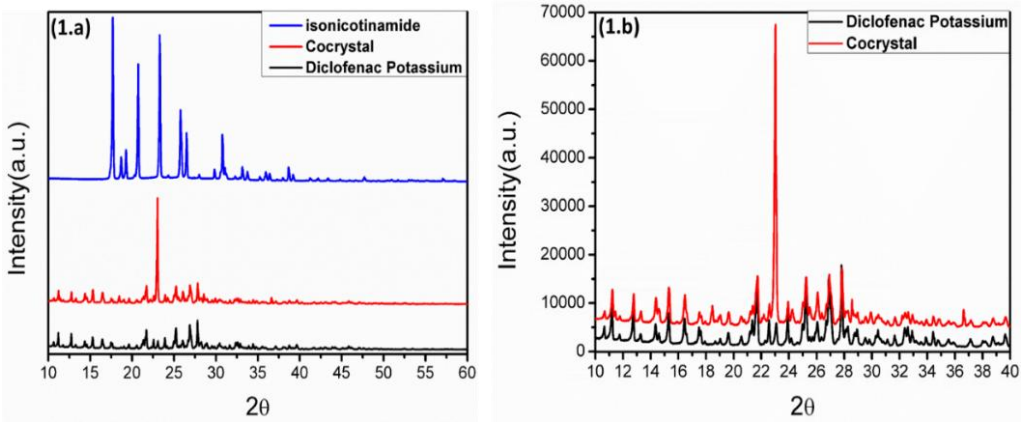


Figure 7. 1a. PXRD patterns of pure DIC-K, INA and DIC-K+INA cocrystal. 1.b. PXRD patterns of pure DIC-K and DIC-K+INA cocrystal.

Table 6. Flow characteristics of the prepared powder mixture. (Mean±SD, n=3)

Parameter	The granular filling mixture for DIC-K capsule	The granular filling mixture for DIC-K+INA capsule
Angle of repose	29.30±0.78°	27.10±0.64°
Flow time (sec)	6.00±1.01	4.00±1.02
Bulk density (g/mL)	0.62±0.08	0.63±0.06
Tapped density (g/mL)	0.74±0.05	0.73±0.05
Compressibility index (%)	16.22±0.06	13.70±0.05
Hausner ratio	1.19±0.06	1.16±0.05

DIC-K-capsule: Pure DIC-K-containing capsule; DIC-K+INA–capsule: DIC-K+INA cocrystals-containing capsule; SD: Standard deviation

Using an electronic analytical balance, the weight of each granule-filled capsule was measured (for 20 capsules) and the average capsule weights were determined as 302±11 mg (DIC-K capsule) and 303±9 mg (DIC-K+INA capsule). The disintegration time values for DIC-K capsule and DIC-K+INA capsule were found to be 3 min 20 sec and 2 min 50 sec, respectively. A decrease in the disintegration time of the capsules prepared with the cocrystal form was observed.

Moreover, DIC-K content of capsules (DIC-K capsule and DIC-K+INA capsule) were evaluated according to USP 43 (905-Uniformity of dosage units) (United States Pharmacopeia, 2019e). According to USP 43, the capsules (DIC-K capsule and DIC-K+INA capsule) met the content uniformity requirements with a DIC-K content of 98-102% of the theoretical amount of 50 mg DIC-K.

In addition, a dissolution study was performed in our study. The dissolution profiles obtained for the capsules (DIC-K capsule and DIC-K+INA capsule) are presented Figure 8. For the DIC-K capsule, the percentage of dissolved DIC-K in PB pH 6.8 was 72% at 15 min, while for the DIC-K+INA capsule, the percentage of dissolved DIC-K at 15 min was 92% (Figure 8).

The USP 43-DIC-K tablet monograph includes the following information: When a dissolution test for the DIC-K tablet is performed in 900 mL of simulated intestinal fluid (no enzyme) using apparatus 2 (50 rpm, 60 min), ≥75% of the labeled amount of DIC-K should be dissolved (United States Pharmacopeia, 2019e).

Solubility and dissolution are significant factors in determining the oral absorption of active substances. One of the powerful strategies used in the pharmaceutical field to improve the solubility of poorly water-soluble active substances is cocrystallization. However, the solubility of cocrystals varies with solution conditions such as solubilizing agents and pH. Cocrystals may exhibit equal, higher or lower solubility compared to pure active substances, depending on solution conditions (Cao et al., 2018; Thakuria et al., 2013; Moulton and Zaworotko, 2001; Childs et al., 2007). In our study, it was observed that the solubility and dissolution of DIC-K in PB pH 6.8 medium was improved by cocrystal preparation.

Conclusion

Pharmaceutical cocrystallization has emerged as an efficient crystal engineering strategy for improving the physicochemical performance of poorly soluble drugs. In the present study, DIC-K+INA cocrystals were successfully designed, synthesized, and confirmed by complementary solid-state characterization techniques, including DSC, PXRD, and FT-IR analyses. The results clearly indicated the formation of a novel crystalline phase distinct from the parent components. Importantly, in vitro dissolution studies demonstrated that the cocrystal-based capsule formulation significantly enhanced the dissolution profile of diclofenac potassium compared to its conventional formulation, with a marked increase in the percentage of drug released within the first 15 minutes. Such a rapid and improved dissolution is expected to translate into better oral absorption and bioavailability, thereby improving the therapeutic performance of diclofenac potassium. Overall, these findings emphasize the potential of isonicotinamide as a pharmaceutically acceptable coformer and highlight the relevance of cocrystal technology as a practical and scalable approach for overcoming solubility limitations. Future studies focusing on pharmacokinetics, stability, and large-scale manufacturing will further establish the clinical applicability of DIC-K+INA cocrystals and support their development into patient-friendly dosage forms.

Author Contributions

The percentages of the authors' contributions are presented below. All authors reviewed and approved the final version of the manuscript.

	E.D.	G.G.	M.N.	C.Y.	M.C.	Y.C.
C	20	20	20	15	15	10
D	20	20	20	15	15	10
S	20	20	20	15	15	10
DCP	20	20	20	15	15	10
DAI	20	20	20	15	15	10
L	20	20	20	15	15	10
W	20	20	20	15	15	10
CR	20	20	20	15	15	10
SR	20	20	20	15	15	10
PM	20	20	20	15	15	10
FA	20	20	20	15	15	10

C= concept, D= design, S= supervision, DCP= data collection and/or processing, DAI= data analysis and/or interpretation, L= literature search, W= writing, CR= critical review, SR= submission and revision, PM= project management, FA= funding acquisition.

Conflict of Interest

The authors declared that there is no conflict of interest.

Ethical Consideration

Ethics committee approval was not required for this study because of there was no study on animals or humans.

References

Akalin, E., Yilmaz, A., & Akyuz, S. (2005). Vibrational spectroscopic studies of diclofenac potassium. *Journal of Molecular Structure*, *744–747*, 881–886. https://doi.org/10.1016/j.molstruc.2004.11.082

Alquadeib, B. T. (2019). Development and validation of RP-HPLC method for determination of diclofenac potassium. *Saudi Pharmaceutical Journal*, *27*(1), 66–70. https://doi.org/10.1016/j.jsps.2018.08.001

Báthori, N. B., Lemmerer, A., Venter, G. A., Bourne, S. A., & Caira, M. R. (2011). Pharmaceutical cocrystals of diclofenac with nicotinamide and isonicotinamide. *Crystal Growth & Design*, *11*(1), 75–87. https://doi.org/10.1021/cg1009858

Caira, M. R., & Vicatos, A. I. (2019). Cocrystals and salts of diclofenac with nitrogen donors. *CrystEngComm*, *21*(5), 843–849. https://doi.org/10.1039/C8CE01848E

Cao, F., Amidon, G. L., Rodríguez-Hornedo, N., & Amidon, G. E. (2018). Cocrystals and solubility enhancement mechanisms. *Journal of Pharmaceutical Sciences*, *107*(1), 380–389. https://doi.org/10.1016/j.xphs.2017.09.023

Childs, S. L., Stahly, G. P., & Park, A. (2007). The salt–cocrystal continuum: The influence of crystal structure on ionization state. *Molecular Pharmaceutics*, *4*(3), 323–338. https://doi.org/10.1021/mp0601345

European Medicines Agency. (2015). *Reflection paper on the use of cocrystals of active substances in medicinal products* (EMA/CHMP/CVMP/QWP/284008/2015). European Medicines Agency.

Garbacz, P., Paukszta, D., Sikorski, A., & Wesolowski, M. (2020). Physicochemical and dissolution studies of diclofenac cocrystals. *Pharmaceutics*, *12*(7), Article 648. https://doi.org/10.3390/pharmaceutics12070648

Guo, M., Sun, X., Chen, J., & Cheng, T. (2021). Advances in pharmaceutical cocrystals: From fundamentals to applications. *Acta Pharmaceutica Sinica B*, *11*(8), 2537–2564. https://doi.org/10.1016/j.apsb.2021.03.029

Han, Y., Faudone, S., Zitto, G., Bonafede, S., Rosasco, M., & Segall, A. (2017). Cocrystallization approach for solubility enhancement of diclofenac salts. *Journal of Applied Pharmaceutical Science*, *7*(1), 204–208. https://doi.org/10.7324/JAPS.2017.70131

International Council for Harmonisation. (2005). *Validation of analytical procedures: Text and methodology* (ICH Harmonised Tripartite Guideline Q2(R1)). International Council for Harmonisation of Technical Requirements for Pharmaceuticals for Human Use.

Jiaxuan, J., Wang, A., Zhang, X., Wang, Y., Wang, Q., Zhai, M., Huang, Y., & Qi, R. (2020). Development and characterization of diclofenac cocrystals. *Journal of Drug Delivery Science and Technology*, *59*, Article 101874. https://doi.org/10.1016/j.jddst.2020.101874

Karakthala, J. B., Vankar, H. P., & Rana, V. A. (2023). Structural insights into pharmaceutical cocrystals of diclofenac. *Journal of Molecular Structure*, *1284*, Article 135410. https://doi.org/10.1016/j.molstruc.2023.135410

Moulton, B., & Zaworotko, M. J. (2001). Crystal engineering of pharmaceutical cocrystals. *Chemical Reviews*, *101*(6), 1629–1658. https://doi.org/10.1021/cr9900432

Nugrahani, I., Komara, S. W., Horikawa, A., & Uekusa, H. (2020). Solid-state characterization of diclofenac cocrystals: A comparative study. *Journal of Pharmaceutical Sciences*, *109*(11), 3423–3438. https://doi.org/10.1016/j.xphs.2020.08.008

Nugrahani, I., Utami, D., Ibrahim, S., Nugraha, Y. P., & Uekusa, H. (2018). Pharmaceutical cocrystal screening and characterization of diclofenac sodium. *European Journal of Pharmaceutical Sciences*, *117*, 168–176. https://doi.org/10.1016/j.ejps.2018.02.019

Palomo, M. E., Ballesteros, M. P., & Frutos, P. (1999). Spectrophotometric determination of diclofenac in pharmaceutical formulations. *Journal of Pharmaceutical and Biomedical Analysis*, *21*(1), 83–94. https://doi.org/10.1016/S0731-7085(99)00122-3

Panda, S. S., Patanaik, D., & Kumar, B. V. R. (2012). Preparation and evaluation of pharmaceutical cocrystals of diclofenac sodium. *Scientia Pharmaceutica*, *80*(1), 127–137. https://doi.org/10.3797/scipharm.1108-16

Rodrigues, M., Baptista, B., Lopes, J. A., & Sarraguça, M. C. (2018). Pharmaceutical cocrystals characterization by chemometric analysis of XRPD data. *International Journal of Pharmaceutics*, *547*(1–2), 404–420. https://doi.org/10.1016/j.ijpharm.2018.06.012

Rolfe, H. M. (2014). A review of co-crystals in the cosmetic and dermatological fields. *Journal of Cosmetic Dermatology*, *13*(4), 324–328. https://doi.org/10.1111/jocd.12111

Rubim, A. M., Rubenick, J. B., Laporta, L. V., & Rolim, C. M. (2013). Evaluation of physicochemical properties of diclofenac potassium cocrystals. *Brazilian Journal of Pharmaceutical Sciences*, *49*(3), 589–597. https://doi.org/10.1590/S1984-82502013000300021

Saganowska, P., & Wesolowski, M. (2018). Thermal analysis of diclofenac potassium cocrystals. *Journal of Thermal Analysis and Calorimetry*, *133*(1), 785–793.

https://doi.org/10.1007/s10973-017-6889-4

Shabir, G. A. (2003). Validation of high-performance liquid chromatography methods for pharmaceutical analysis. *Journal of Chromatography A*, *987*(1–2), 57–66. https://doi.org/10.1016/S0021-9673(02)01536-4

Siozou, E., Sakkas, V., & Kourkoumelis, N. (2021). Solid-state characterization and solubility enhancement of diclofenac cocrystals. *Pharmaceuticals*, *14*(5), Article 440. https://doi.org/10.3390/ph14050440

Thakuria, R., Delori, A., Jones, W., Lipert, M. P., Roy, L., & Rodríguez-Hornedo, N. (2013). Pharmaceutical cocrystals and their physicochemical properties. *International Journal of Pharmaceutics*, *453*(1), 101–125. https://doi.org/10.1016/j.ijpharm.2012.10.043

United States Pharmacopeia. (2019a). *Diclofenac potassium tablets monograph* (USP 42-NF 37). United States Pharmacopeial Convention.

United States Pharmacopeia. (2019b). *General chapter <701> disintegration* (USP 42-NF 37). United States Pharmacopeial Convention.

United States Pharmacopeia. (2019c). *General chapter <711> dissolution* (USP 42-NF 37). United States Pharmacopeial Convention.

United States Pharmacopeia. (2019d). *General chapter <905> uniformity of dosage units* (USP 42-NF 37). United States Pharmacopeial Convention.

United States Pharmacopeia. (2019e). *General chapter <1174> powder flow* (USP 42-NF 37). United States Pharmacopeial Convention.

U.S. Food and Drug Administration. (2016). *Dissolution methods database*. U.S. Department of Health and Human Services.

U.S. Food and Drug Administration. (2018). *Regulatory classification of pharmaceutical co-crystals: Guidance for industry*. U.S. Department of Health and Human Services.

Yadav, A. V., Shete, A. S., Dabke, A. P., Kulkarni, P. V., & Sakhare, S. S. (2009). Co-crystals: A novel approach to modify physicochemical properties of active pharmaceutical ingredients. *Indian Journal of Pharmaceutical Sciences*, *71*(4), 359–370. https://doi.org/10.4103/0250-474X.57283

Yuliandra, Y., Zaini, E., Syofyan, S., Pratiwi, W., Putri, L. N., Pratiwi, Y. S., & Arifin, H. (2018). Preparation and characterization of cocrystal between diclofenac sodium and nicotinamide. *Scientia Pharmaceutica*, *86*(2), Article 23. https://doi.org/10.3390/scipharm86020023

Black Sea Journal of Engineering and Science
doi: 10.34248/bsengineering.1997666

Open Access Journal
e-ISSN: 2619 – 8991

Research Article
Volume 9 - Issue 5: 2612-2620 / September 2026

COMPARATIVE ANALYSIS OF METAHEURISTIC FEATURE SELECTION IN SVM-BASED HUMAN ACTIVITY RECOGNITION

Duygu Sedef ÇALIŞKAN[1], Özlem KILIÇ[1], Durmuş Özkan ŞAHİN[1], Gökhan KAYHAN[1]*, Sercan DEMİRCİ[1]

[1]*Ondokuz Mayıs University, Department of Computer Engineering, 55139 Samsun, Türkiye*

Abstract: Smartphone-based human activity recognition (HAR) commonly relies on large sets of engineered time- and frequency-domain variables. Although these representations capture complementary motion patterns, redundant variables may increase model cost without resolving ambiguity between similar activities. This study compared a genetic algorithm (GA), particle swarm optimization (PSO), and grey wolf optimization (GWO) as wrapper-based feature selectors for a radial basis function support vector machine (SVM) on the UCI HAR dataset. The original 7,352/2,947 training-test split and a common SVM configuration were retained. Each optimizer searched a 561-bit feature mask with a population of 10 for 10 generations or iterations, using an objective that prioritized predictive accuracy while penalizing subset size. Performance was assessed by held-out accuracy, weighted F1, selected features, confusion patterns, convergence, and total runtime. The baseline SVM achieved 0.9308 accuracy and 0.9304 weighted F1 with all 561 features. GA+SVM produced the strongest result: 0.9508 accuracy, 0.9506 weighted F1, 300 features, and 217.99 s. This reduced dimensionality by 46.52% and test errors from 204 to 145. GWO+SVM reached 0.9471 accuracy with 341 features and 295.12 s. PSO+SVM selected the smallest subset (284 features; 49.38% reduction), but its 0.9355 accuracy and 489.68 s runtime yielded a weaker trade-off. Errors remained concentrated in upstairs/downstairs and sitting/standing/laying distinctions. Under the tested search budget, GA+SVM offered the best observed balance between predictive performance, compactness, and optimization cost. Because the stochastic algorithms were not evaluated over repeated independent runs, the ranking should be interpreted as configuration-specific rather than universal.

Keywords: Human activity recognition, Feature selection, Support vector machine, Genetic algorithm, Particle swarm optimization, Grey wolf optimization

***Corresponding author:** Ondokuz Mayıs University, Department of Computer Engineering, 55139 Samsun, Türkiye
E mail: gkayhan@omu.edu.tr (G. KAYHAN)

Duygu Sedef ÇALIŞKAN https://orcid.org/0009-0005-7588-3498
Özlem KILIÇ https://orcid.org/0009-0002-6780-4284
Durmuş Özkan ŞAHİN https://orcid.org/0000-0002-0831-7825
Gökhan KAYHAN https://orcid.org/0000-0003-3391-0097
Sercan DEMİRCİ https://orcid.org/0000-0001-6739-7653

Received: July 17, 2026
Accepted: August 19, 2026
Published: September 15, 2026

Cite as: Çalışkan, D. S., Kılıç, Ö., Şahin, D. Ö., Kayhan, G., & Demirci, S. (2026). Comparative analysis of metaheuristic feature selection in SVM-based human activity recognition. *Black Sea Journal of Engineering and Science,* 9(5), 2612-2620.

1. Introduction

Human activity recognition (HAR) seeks to infer everyday actions from signals recorded by phones, watches, and other wearable devices. Reliable recognition supports health monitoring, rehabilitation, assisted living, context-aware services, and safety applications. Early wearable computing studies established that recurring behavioral patterns could be recovered from body-worn sensors (Clarkson, 2002), while later work showed that ordinary phone accelerometers were sufficient to distinguish common activities in practical settings (Kwapisz et al., 2011). Recent HAR research has expanded to richer sensor combinations and deep models, yet the cost and interpretability of the input representation remain relevant for deployable systems (Vurgun and Kıran, 2024). Recent datasets are also broadening the evaluation landscape. For example, Tokgöz and Kocaoğlu (2026) introduced AybuFall, an openly available IMU dataset that combines falls, activities of daily living, and prayer movements, illustrating the continuing need for robust and transferable HAR evaluations.

The UCI Human Activity Recognition Using Smartphones dataset provides a controlled benchmark for studying this issue. It contains accelerometer and gyroscope measurements collected from 30 volunteers performing six activities, together with 561 engineered variables derived from fixed-width signal windows (Anguita et al., 2013). These variables summarize body acceleration, gravity, angular velocity, jerk, magnitude, and frequency-domain behavior. Such representations remain useful because they can be evaluated with conventional classifiers and modest hardware, an important consideration alongside the rapid growth of end-to-end smartphone HAR methods (Dentamaro et al., 2024).

A high-dimensional representation does not automatically yield a stronger classifier. Correlated, duplicated, or weakly discriminative variables can increase training and inference cost, make model selection less stable, and obscure which signal

This work is licensed (CC BY-NC 4.0) under Creative Commons Attribution 4.0 International License

characteristics carry useful information. Feature selection addresses this problem by retaining original variables while discarding those that contribute little to prediction. Filter, wrapper, and embedded methods differ in how subsets are evaluated, but all aim to construct a lower-dimensional and more informative representation (Tang et al., 2014; Budak, 2018).

Wrapper selection is attractive when the usefulness of a variable depends on the classifier and on interactions with other variables. Its main difficulty is computational: a dataset with 561 features defines 2^{561} possible subsets. Evolutionary and swarm-based algorithms provide a practical way to sample this search space without exhaustive enumeration. Reviews of metaheuristic feature selection show that these methods can improve classification while reducing dimensionality, but they also stress the need to report computational effort and to compare methods under common conditions (Xue et al., 2016; Agrawal et al., 2021; Akinola et al., 2022). Turkish-language overviews reach a similar conclusion: the optimizer should be selected according to the problem structure and evaluation budget rather than by its popularity alone (Gazioğlu, 2024; Tonguç, 2024).

The genetic algorithm (GA) explores binary subsets through selection, crossover, mutation, and elitist retention. Its population-based recombination can preserve useful feature groups while mutation introduces new subsets, which explains its long-standing use in feature selection (Hussein et al., 2001; Babatunde et al., 2014). Hybrid and task-specific GA designs have also shown that the balance between exploration and exploitation matters as much as the encoding itself (Oh et al., 2004).

Particle swarm optimization (PSO) instead updates candidate solutions from personal and collective best positions. Binary PSO variants translate this movement into inclusion decisions and have been applied to both single- and multi-objective feature selection (Chuang et al., 2008; Xue et al., 2013). Grey wolf optimization (GWO) organizes the population around three leading solutions and moves the remaining agents toward this leadership hierarchy. Binary and multi-objective GWO variants have produced compact subsets in classification tasks (Emary et al., 2016; Al-Tashi et al., 2019; Al-Tashi et al., 2020). These algorithms therefore offer distinct search dynamics for the same 561-dimensional binary problem.

A fair comparison requires the classifier and data partition to remain fixed. Support vector machines (SVMs) are appropriate for this purpose because margin maximization and kernel mappings provide strong baselines in high-dimensional spaces (Cervantes et al., 2020). With a radial basis function (RBF) kernel, an SVM can represent nonlinear class boundaries without changing the input features. Holding the kernel and its hyperparameters constant isolates the effect of the selected subset, while avoiding a joint feature-and-model search that would confound the comparison (Gold and Sollich, 2003).

Many HAR studies emphasize a new model or report only the final accuracy. That practice makes it difficult to determine whether a gain comes from a genuinely informative subset, a larger optimization budget, or a favorable classifier setting. Comparative studies in other engineering optimization problems likewise show that algorithm rankings can change when accuracy, convergence, and runtime are considered together (Garip et al., 2021). For HAR, the unresolved question is not merely which optimizer reaches the highest score, but which one provides the most defensible balance between predictive gain, subset size, and search cost.

This study addresses that question through a controlled comparison of GA, PSO, and GWO wrappers coupled with the same RBF-SVM. The analysis uses the original UCI HAR train-test split, a common population size and search horizon, and a shared accuracy-dominant objective with a small penalty for the proportion of selected features. Evaluation extends beyond aggregate accuracy to weighted F1, absolute test errors, class-level confusion, convergence behavior, dimensionality reduction, and elapsed runtime.

The study makes three contributions. First, it quantifies the effect of three different binary search mechanisms on the same SVM-based HAR task. Second, it links overall performance to the two persistent sources of error in this dataset: confusion between walking upstairs and downstairs, and confusion among sitting, standing, and laying. Third, it interprets feature reduction and optimization time together, which prevents the smallest subset from being treated automatically as the best result. These contributions are empirical and comparative rather than methodological.

2. Materials and Methods

This section describes the dataset and controlled experimental design, formulates feature selection as a binary wrapper problem, and then presents the SVM evaluator and the three metaheuristic search procedures.

2.1. Dataset and Experimental Design

The experiments used the Human Activity Recognition Using Smartphones dataset from the UCI Machine Learning Repository. Thirty volunteers aged 19-48 years carried a Samsung Galaxy S II smartphone at the waist while performing walking, walking upstairs, walking downstairs, sitting, standing, and laying. Triaxial acceleration and angular velocity were sampled at 50 Hz. After noise filtering and segmentation into 2.56 s windows with 50% overlap, the dataset developers derived 561 time- and frequency-domain features from each observation (Anguita et al., 2013).

The original subject-independent partition was retained: 7,352 observations formed the training set and 2,947 observations formed the test set. The same data checks and normalization procedure were applied to all methods. Candidate feature masks were scored using validation information drawn only from the training data; the test set was reserved for the final assessment of

the baseline and the three selected subsets. This separation prevented the optimizers from using test labels during feature search.

Feature selection was represented as a 561-dimensional binary optimization problem. For a candidate vector x, x_j=1 indicated that feature j was supplied to the classifier, and x_j=0 indicated that it was omitted. The number of possible masks makes an exhaustive search infeasible, so each metaheuristic maintained a small population of candidate vectors and improved them using its own update mechanism.

The wrapper objective was designed to favor predictive performance while applying a smaller penalty to subset size. The accuracy term was assigned a weight of 0.99, and the selected-feature ratio was assigned a weight of 0.01. This weighting reflects the study objective: dimensionality should be reduced without accepting a substantial loss in recognition performance. The fixed design was chosen to compare the optimizers under the same classifier, data split, population size, search horizon, and objective function rather than to estimate their asymptotic performance.

For every candidate mask, the selected columns were extracted from the training data and evaluated with the same SVM using an RBF kernel. Validation accuracy supplied the predictive component of the objective. Keeping the evaluator fixed ensured that differences among candidate scores arose from feature composition rather than from changing classifier settings. The experiments were conducted in Google Colab with Python 3.12. The principal libraries were NumPy 1.26.0, Pandas 2.2.2, Matplotlib 3.10.0, scikit-learn, PyGAD 3.6.0, and MEALPY 3.0.3. PyGAD was used for GA, MEALPY for PSO, and scikit-learn SVC for classification; GWO was implemented manually. Although an NVIDIA T4 GPU was available in the Colab environment, all reported experiments were executed on the CPU because no GPU-parallel computation was used. Multiprocessing was not enabled. Because the GA implementation treats larger scores as better, its fitness function was written in maximization form as shown in equation 1.

$$Fit_{GA} = 0.99\,Acc - 0.01\,FR \quad (1)$$

The PSO and GWO implementations treat smaller objective values as better. Their common cost function therefore combined validation error with the selected-feature ratio, as given in equation 2.

$$f_{PSO/GWO} = 0.99\,(1 - Acc) + 0.01\,FR \quad (2)$$

In equations 1 and 2, Acc denotes validation accuracy and FR is the number of selected features divided by 561. Fit_GA is the fitness value maximized by GA, whereas f_PSO/GWO is the cost minimized by PSO and GWO. Figures 1, 2, and 3 summarize the sensing pipeline, wrapper loop, and common experimental workflow.

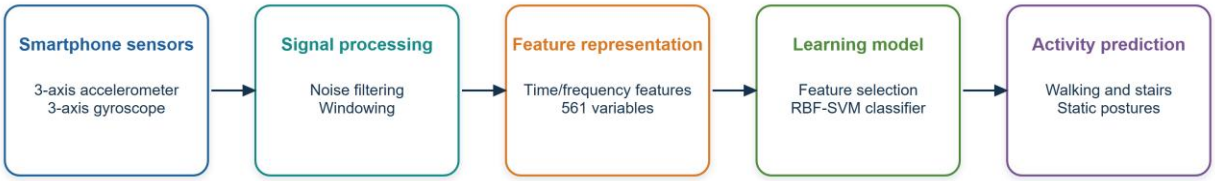


Figure 1. Smartphone sensing and feature-engineering pipeline for the UCI HAR dataset.

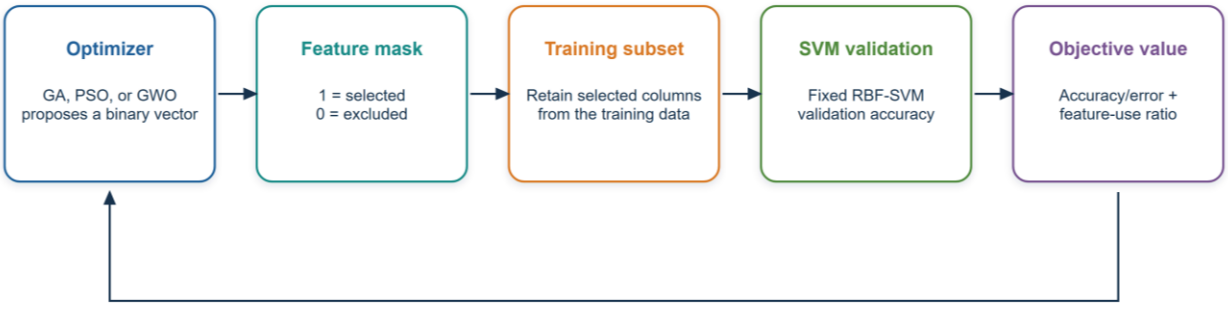


Figure 2. Wrapper-based binary feature-selection loop with a fixed SVM evaluator.

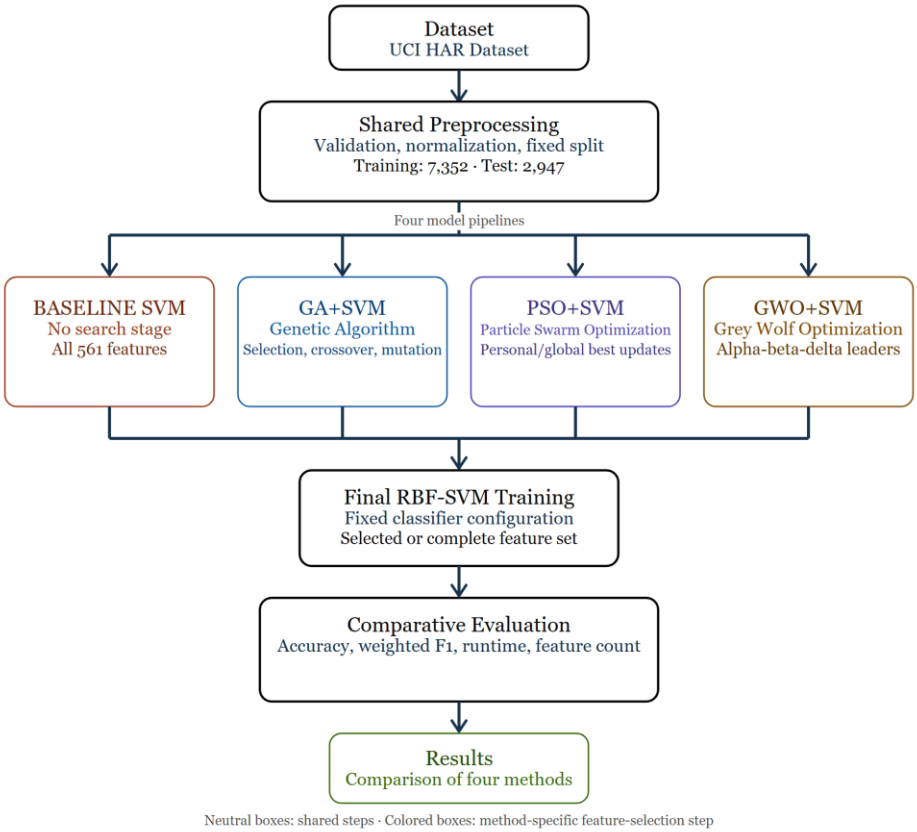


Figure 3. Controlled workflow used to compare the baseline and three feature-selection methods.

2.2. SVM Evaluator and Performance Measures

A support vector machine with an RBF kernel was used as the common evaluator and final classifier. The configuration was fixed at C=1.0 and gamma='scale'. The multiclass problem was handled by the library's standard decomposition, and no optimizer was allowed to tune SVM hyperparameters. The baseline received all 561 variables; GA+SVM, PSO+SVM, and GWO+SVM received only the variables indicated by the final mask.

Held-out performance was reported as accuracy and weighted F1. Accuracy provides the proportion of correct predictions, whereas weighted F1 summarizes class-specific precision and recall while accounting for class support. The analysis also recorded the number and percentage of retained features, the reduction relative to the 561-feature baseline, the total test errors, the convergence history, and the wall-clock runtime. Confusion matrices were inspected to identify whether improvements were distributed across activities or concentrated in particular class pairs.

2.3. Metaheuristic Feature-Selection Methods

All three search methods operated on the same binary representation and were evaluated by the same SVM. Each run used a population of 10 and a horizon of 10 generations or iterations. This deliberately limited budget enabled a controlled comparison of search behavior and computational cost. A population of 10 and a horizon of 10 generations or iterations were retained as a deliberately constrained, matched computational budget. This setting supports a controlled fixed-budget comparison, but it does not characterize the full search behavior or asymptotic performance of the stochastic optimizers.

2.3.1. Genetic Algorithm

Each GA individual was a 561-bit chromosome. Steady-state selection retained four parents, one-point crossover combined parental masks, and random mutation altered 5% of the genes. Two parents were preserved between generations to reduce the risk of losing the best observed subset. The procedure maximized equation 1 for 10 generations. Table 1 lists the implementation parameters.

Table 1. Genetic algorithm parameters

Parameter	Value
Population size	10
Number of generations	10
Number of parents	4
Chromosome length	561
Gene values	0 / 1
Selection	Steady-state selection
Crossover	One-point crossover
Mutation	Random mutation
Mutation rate	5%
Elitist parents retained	2

2.3.2. Particle swarm optimization

PSO was implemented using the OriginalPSO procedure in the MEALPY library, with a binary decision space. Each particle encoded a feature mask and was updated from its personal best position and the best position identified by the swarm. Candidate masks were scored by equation 2, so improvements required either a lower validation error or a smaller subset without a compensating accuracy loss. Table 2 gives the settings.

Table 2. Particle swarm optimization parameters

Parameter	Value
Algorithm	OriginalPSO
Library	MEALPY
Problem type	Binary feature selection
Decision space	BinaryVar
Population size	10
Iterations	10
Objective direction	Minimization
Evaluation model	SVM
SVM kernel	RBF
Evaluation data	Training/validation split
Test metrics	Accuracy, weighted F1, feature ratio, runtime

2.3.3. Grey wolf optimization

GWO was implemented as a binary search procedure. At each iteration, candidate wolves were ranked and the three best masks were designated alpha, beta, and delta. The remaining masks were updated with respect to these leaders, while the control parameter decreased over the run to shift the search from exploration toward exploitation. Binary decisions were recovered after position updates, and equation 2 determined the ranking. Table 3 summarizes the configuration.

Table 3. Grey wolf optimization parameters

Parameter	Value
Algorithm	GWO
Implementation	Custom implementation
Problem type	Binary feature selection
Representation	0 / 1 binary vector
Number of wolves	10
Iterations	10
Accuracy weight (alpha)	0.99
Feature-ratio weight (beta)	0.01
Objective direction	Minimization
Evaluation model	SVM
SVM kernel	RBF
Data partition	Training / validation / test
Test metrics	Accuracy, weighted F1, feature ratio, runtime

3. Results

The baseline and three feature-selected models were evaluated on the same 2,947 test observations. All metaheuristic variants exceeded the baseline accuracy, but the magnitude of improvement, subset size, convergence pattern, and runtime differed substantially.

3.1. Baseline SVM

The 561-feature SVM achieved 0.9308 accuracy and 0.9304 weighted F1, corresponding to 204 errors. Walking was recognized perfectly (537/537). Most dynamic-activity errors involved walking upstairs and downstairs: 68 upstairs observations were predicted as downstairs and 45 downstairs observations were predicted as upstairs. Among postural activities, 33 standing observations were assigned to sitting, while laying was occasionally confused with sitting or standing. The baseline confusion matrix is shown in Figure 4.

3.2. GA+SVM

As shown in Figures 5 and 6, the GA-optimized SVM model achieved strong classification performance, while the convergence curve demonstrates the effectiveness and stability of the genetic algorithm during the optimization process. GA+SVM delivered the best aggregate result.

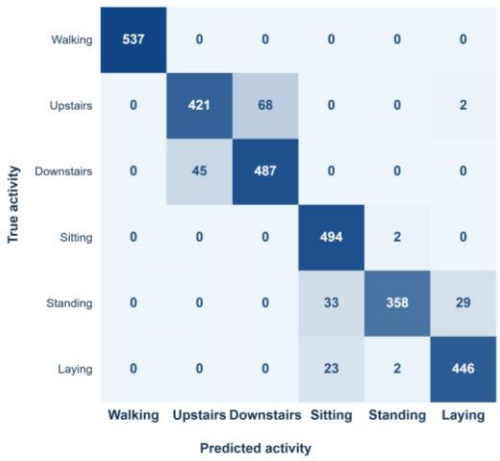


Figure 4. Confusion matrix for the baseline SVM using all 561 features.

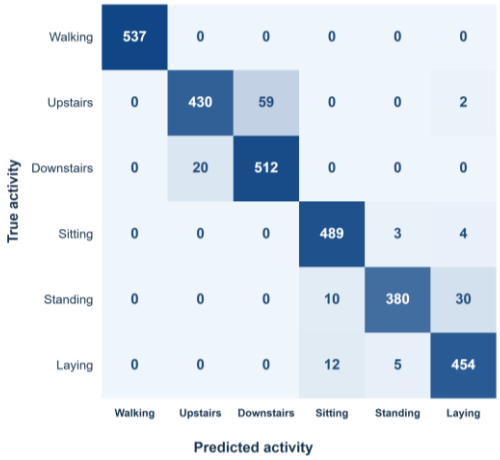


Figure 5. GA+SVM confusion matrix.

It retained 300 features, reducing the original representation by 46.52%, and achieved 0.9508 accuracy with a weighted F1 of 0.9506. The number of test errors fell from 204 to 145, a reduction of 28.92%. The main gain came from more reliable separation of the two stair activities and from fewer confusions among sitting, standing, and laying.

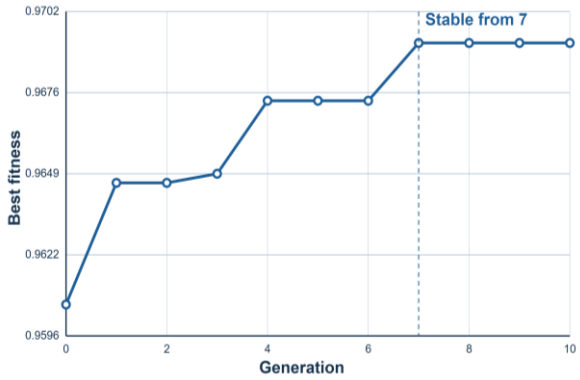


Figure 6. GA convergence curve.

3.3. PSO+SVM

Figures 7 and 8 show the confusion matrix and convergence history results for PSO+SVM. PSO+SVM selected 284 features, the smallest subset in the comparison, and a 49.38% reduction from the baseline. Its accuracy was 0.9355, and its weighted F1 was 0.9354, yielding 190 errors. The method therefore improved on the full-feature SVM, but by a smaller margin than GA+SVM and GWO+SVM.

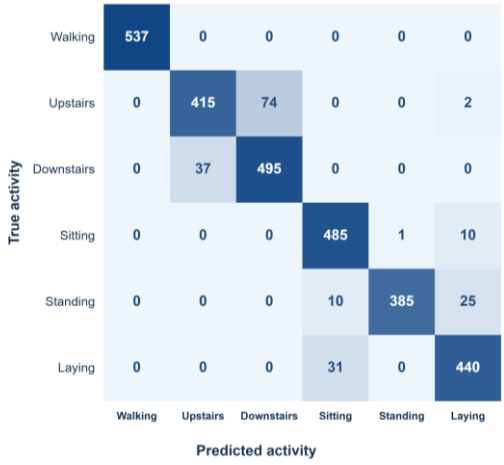


Figure 7. PSO+SVM confusion matrix.

The PSO subset reduced some postural confusions, particularly standing-to-sitting errors, but increased ambiguity between walking upstairs and downstairs compared with GA and GWO. Thirty-one laying samples were also classified as sitting. These errors explain why the smallest subset did not translate into the best predictive result.

The best PSO objective remained at 0.0367 throughout the 10 recorded iterations. Under this population and iteration budget, the swarm did not improve on its initial best region. PSO+SVM also required 489.68 s, the longest runtime in the study.

3.4. GWO+SVM

Figures 9 and 10 show the confusion matrix and convergence history results for GWO+SVM. GWO+SVM retained 341 features, corresponding to a 39.22% reduction, and reached 0.9471 accuracy with a weighted F1 of 0.9470. Its 156 test errors were 23.53% fewer than the baseline. Although it selected more features than GA and PSO, its predictive performance was second only to GA. GWO produced the fewest combined errors between walking upstairs and downstairs: 55 upstairs samples were assigned to downstairs, and 22 downstairs samples were assigned to upstairs. Its postural errors were less favorable than GA's, particularly for laying-to-sitting decisions. This class-level pattern accounts for the small aggregate gap between the two methods.

The GWO objective improved twice: from 0.02815 initially to 0.02710, then to 0.02558, after which it remained stable from iteration 5 onward. Its 295.12 s runtime placed it between GA and PSO.

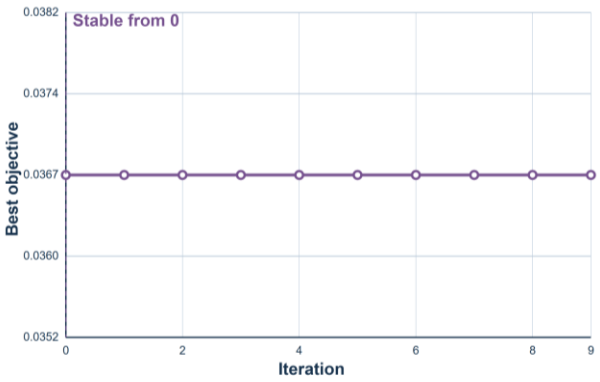


Figure 8. PSO convergence curve.

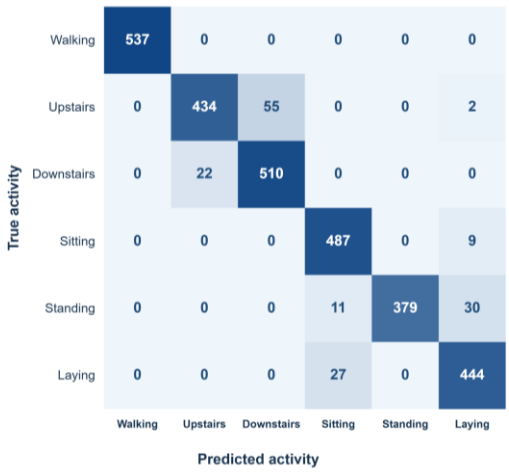


Figure 9. GWO+SVM confusion matrix.

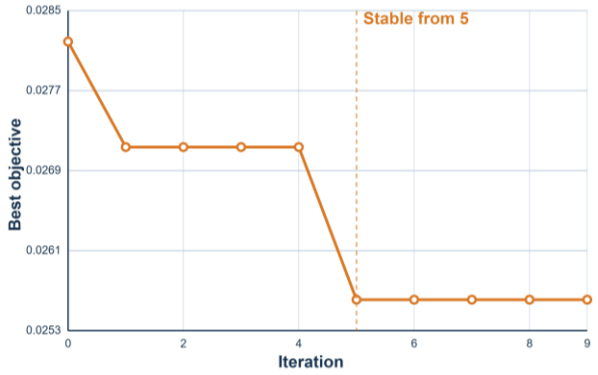


Figure 10. GWO convergence curve.

3.5. Comparative Analysis

Table 4 consolidates predictive performance, feature reduction, convergence, and runtime. Figure 11 presents a trade-off view in which accuracy and dimensionality reduction are considered alongside optimization time. The comparison identifies three outcomes: GA produced the strongest classifier, PSO produced the smallest subset, and GWO achieved the second-highest accuracy.

Relative to the baseline, accuracy increased by 0.0200 with GA+SVM, 0.0163 with GWO+SVM, and 0.0047 with PSO+SVM. PSO selected 16 fewer features than GA, yet its accuracy was 0.0153 lower, and its search took approximately 2.25 times as long. GWO was 0.0037 less accurate than GA, retained 41 additional features, and required about 1.35 times the runtime. Under the tested conditions, GA therefore occupied the most favorable region of the accuracy-reduction-runtime trade-off. The 0.9508 accuracy is competitive within the tested UCI HAR and fixed RBF-SVM configuration, particularly relative to the all-feature baseline.

4. Discussion

The results show that feature selection improved the SVM not simply by shrinking the input but by removing variables that interfered with difficult class boundaries. GA+SVM reduced errors in both major confusion groups, whereas the baseline committed more cross-assignments between the stair activities and among the three postures. This pattern is consistent with the rationale for wrapper selection: variables are retained based on their joint contribution to a specified classifier rather than on an isolated univariate score. GA's recombination and mutation appear to have explored useful combinations within the limited budget, although this interpretation is based on the observed run and is not a statistical comparison.

PSO and GWO illustrate why subset size, convergence, and accuracy should be reported together. PSO removed the largest proportion of variables, but its flat convergence curve and long runtime indicate that the additional reduction was not obtained efficiently. GWO improved early and produced a competitive model, especially for upstairs/downstairs discrimination, yet its larger subset and postural errors kept it below GA overall. Binary swarm methods are sensitive to transfer rules, parameter settings, and initial positions (Chuang et al., 2008; Emary et al., 2016); a small common budget exposes these differences but does not fully characterize each algorithm's best attainable performance.

From a deployment perspective, the selected subsets may reduce the cost of feature extraction and subsequent SVM inference, but the search itself is an offline expense. The baseline trained and evaluated in 2.76 s, whereas optimization required 217.99-489.68 s. That cost can be acceptable when a subset is learned once and reused on many devices, but it matters when models must be updated frequently. The study has three main limitations. First, each stochastic method was evaluated from a single recorded run, so variance and statistical significance were not estimated. Second, the population and iteration budgets were intentionally small. Third, SVM hyperparameters were fixed rather than jointly optimized. Accordingly, the observed ranking applies to this dataset split and configuration; it should not be generalized as an inherent superiority of GA over all PSO or GWO variants.

Table 4. Comparative performance of SVM, GA+SVM, PSO+SVM, and GWO+SVM

Method	Accuracy	Weighted F1	Features	Reduction (%)	Convergence	Runtime (s)
SVM	0.9308	0.9304	561	0.00	Not applicable	2.76
GA+SVM	0.9508	0.9506	300	46.52	Stable after generation 7	217.99
PSO+SVM	0.9355	0.9354	284	49.38	No improvement after initialization	489.68
GWO+SVM	0.9471	0.9470	341	39.22	Stable after iteration 5	295.12



Figure 11. Accuracy, feature reduction, and optimization-time trade-off across the four models.

5. Conclusion

This study compared GA, PSO, and GWO as wrapper-based feature selectors for a fixed RBF-SVM on the UCI HAR benchmark. Evaluating the methods under the same partition, classifier, population size, search horizon, and objective made it possible to attribute the differences primarily to their search behavior.

GA+SVM achieved the best observed result with 0.9508 accuracy, 0.9506 weighted F1, and 300 features. It reduced dimensionality by 46.52% and test errors from 204 to 145. GWO+SVM achieved 0.9471 accuracy with 341 features, while PSO+SVM selected the smallest subset but delivered only a modest gain over the baseline and incurred the longest search time.

These findings indicate that the most compact representation is not necessarily the most useful one. For this experiment, GA provided the most balanced combination of recognition performance, subset size, and optimization cost. The remaining errors also identify a practical target for subsequent work: signal descriptors that better separate ascent from descent and distinguish similar static postures.

Future studies should repeat each stochastic search with multiple seeds, report confidence intervals and statistical tests, examine larger and matched computational budgets, and evaluate whether jointly tuning SVM hyperparameters changes the ranking. Validation on additional body locations, devices, and HAR datasets would establish whether the selected feature structures transfer beyond the UCI benchmark. Future work should assess inference latency, memory use, energy consumption, and feature-extraction time on representative mobile devices, while also verifying these findings through multi-seed sensitivity analyses with matched objective-function evaluation counts.

Author Contributions

The percentages of the authors' contributions are presented below. The authors reviewed and approved the final version of the manuscript.

	D.S.Ç.	Ö.K.	D.Ö.Ş.	G.K.	S.D.
C	20	20	20	20	20
D	5	5	25	40	25
S	40	40	10	5	5
DCP	40	40	10	5	5
DAI	25	25	20	15	15
L	40	30	10	10	10
W	25	25	20	10	20
CR	5	5	40	25	25
SR	20	20	20	20	20
PM	20	20	20	20	20

C= concept, D= design, S= supervision, DCP= data collection and/or processing, DAI= data analysis and/or interpretation, L= literature search, W= writing, CR= critical review, SR= submission and revision, PM= project management.

Conflict of Interest

The authors declared that there is no conflict of interest.

Ethical Consideration

Ethics committee approval was not required for this study because there was no study on animals or humans.

Data Availability Statement

The Human Activity Recognition Using Smartphones dataset is publicly available from the UCI Machine Learning Repository at https://archive.ics.uci.edu/dataset/240/human+activity+recognition+using+smartphones.

References

Agrawal, P., Abutarboush, H. F., Ganesh, T., & Mohamed, A. W. (2021). Metaheuristic algorithms on feature selection: A survey of one decade of research (2009–2019). *IEEE Access*, *9*, 26766–26791. https://doi.org/10.1109/ACCESS.2021.3056407

Akinola, O. O., Ezugwu, A. E., Agushaka, J. O., Zitar, R. A., & Abualigah, L. (2022). Multiclass feature selection with metaheuristic optimization algorithms: A review. *Neural Computing and Applications*, *34*(22), 19751–19790. https://doi.org/10.1007/s00521-022-07705-4

Al-Tashi, Q., Kadir, S. J. A., Rais, H. M., Mirjalili, S., & Alhussian, H. (2019). Binary optimization using hybrid grey wolf optimization for feature selection. *IEEE Access*, *7*, 39496–39508. https://doi.org/10.1109/ACCESS.2019.2906757

Al-Tashi, Q., Abdulkadir, S. J., Rais, H. M., Mirjalili, S., Alhussian, H., Ragab, M. G., & Alqushaibi, A. (2020). Binary multi-objective grey wolf optimizer for feature selection in classification. *IEEE Access*, *8*, 106247–106263. https://doi.org/10.1109/ACCESS.2020.3000040

Anguita, D., Ghio, A., Oneto, L., Parra, X., & Reyes-Ortiz, J. L. (2013, April 24–26). *A public domain dataset for human activity recognition using smartphones* [Paper presentation]. 21st European Symposium on Artificial Neural Networks, Computational Intelligence and Machine Learning (ESANN 2013), Bruges, Belgium. https://www.esann.org/sites/default/files/proceedings/legacy/es2013-84.pdf

Babatunde, O. H., Armstrong, L., Leng, J., & Diepeveen, D. (2014). A genetic algorithm-based feature selection. *International Journal of Electronics Communication and Computer Engineering*, *5*(4), 899–905. https://ro.ecu.edu.au/ecuworkspost2013/653/

Budak, H. (2018). Özellik seçim yöntemleri ve yeni bir yaklaşım. *Süleyman Demirel Üniversitesi Fen Bilimleri Enstitüsü Dergisi*, *22*(1), 21–31. https://izlik.org/JA45SW33BN

Cervantes, J., Garcia-Lamont, F., Rodríguez-Mazahua, L., & Lopez, A. (2020). A comprehensive survey on support vector machine classification: Applications, challenges and trends. *Neurocomputing*, *408*, 189–215. https://doi.org/10.1016/j.neucom.2019.10.118

Chuang, L. Y., Chang, H. W., Tu, C. J., & Yang, C. H. (2008). Improved binary PSO for feature selection using gene expression data. *Computational Biology and Chemistry*, *32*(1), 29–38. https://doi.org/10.1016/j.compbiolchem.2007.09.005

Clarkson, B. P. (2002). *Life patterns: Structure from wearable sensors* (Doctoral dissertation, Massachusetts Institute of Technology). DSpace@MIT. http://hdl.handle.net/1721.1/8030

Dentamaro, V., Gattulli, V., Impedovo, D., & Manca, F. (2024). Human activity recognition with smartphone-integrated sensors: A survey. *Expert Systems with Applications*, *246*, Article 123143. https://doi.org/10.1016/j.eswa.2024.123143

Emary, E., Zawbaa, H. M., & Hassanien, A. E. (2016). Binary grey wolf optimization approaches for feature selection. *Neurocomputing*, *172*, 371–381. https://doi.org/10.1016/j.neucom.2015.06.083

Garip, Z., Çimen, M. E., & Boz, A. F. (2021). Meta-sezgisel algoritmalar kullanarak güneş pili modellerinin parametre çıkarımında karşılaştırmalı performans analizi. *Gazi Üniversitesi Mühendislik Mimarlık Fakültesi Dergisi*, *36*(2), 1133–1144. https://doi.org/10.17341/gazimmfd.586269

Gazioğlu, E. (2024). Dinamik özellik seçimi problemlerinde meta-sezgisel yaklaşımlar. In *Bilgisayar bilimleri ve mühendisliğinde öncü ve yenilikçi çalışmalar* (pp. 46–61). All Sciences Academy Yayınları. https://www.allsciencesacademy.com/_files/ugd/13252f_13a3215bdc3241a19c52faa5bd2766ea.pdf

Gold, C., & Sollich, P. (2003). Model selection for support vector machine classification. *Neurocomputing*, *55*(1–2), 221–249. https://doi.org/10.1016/S0925-2312(03)00375-8

Hussein, F., Kharma, N., & Ward, R. (2001). *Genetic algorithms for feature selection and weighting: A review and study*. Proceedings of the Sixth International Conference on Document Analysis and Recognition (ICDAR 2001), Seattle, WA, USA. https://doi.org/10.1109/ICDAR.2001.953980

Kwapisz, J. R., Weiss, G. M., & Moore, S. A. (2011). Activity recognition using cell phone accelerometers. *ACM SIGKDD Explorations Newsletter*, *12*(2), 74–82. https://doi.org/10.1145/1964897.1964918

Oh, I. S., Lee, J. S., & Moon, B. R. (2004). Hybrid genetic algorithms for feature selection. *IEEE Transactions on Pattern Analysis and Machine Intelligence*, *26*(11), 1424–1437. https://doi.org/10.1109/TPAMI.2004.105

Tang, J., Alelyani, S., & Liu, H. (2014). Feature selection for classification: A review. In C. C. Aggarwal (Ed.), *Data classification: Algorithms and applications* (pp. 37–64). CRC Press.

Tokgöz, N., & Kocaoğlu, S. (2026). An IMU-based dataset of falls, activities of daily living, and prayer movements (AybuFall). *BMC Research Notes*, *19*, Article 78. https://doi.org/10.1186/s13104-026-07679-9

Tonguç, G. (2024). Optimizasyon algoritmalarına genel bakış: Klasik ve modern yöntemler. *Kuantum Teknolojileri ve Enformatik Araştırmaları Dergisi*, *2*(3), 105–113. https://doi.org/10.70447/ktve.2561

Vurgun, Y., & Kıran, M. S. (2024). İnsan aktivite tanıması için yeni bir veri kümesi ve derin öğrenme modelleri ile sınıflandırılması. *Gazi Üniversitesi Mühendislik Mimarlık Fakültesi Dergisi*, *40*(1), 653–672. https://doi.org/10.17341/gazimmfd.1325926

Xue, B., Zhang, M., & Browne, W. N. (2013). Particle swarm optimization for feature selection in classification: A multi-objective approach. *IEEE Transactions on Cybernetics*, *43*(6), 1656–1671. https://doi.org/10.1109/TSMCB.2012.2227469

Xue, B., Zhang, M., Browne, W. N., & Yao, X. (2016). A survey on evolutionary computation approaches to feature selection. *IEEE Transactions on Evolutionary Computation*, *20*(4), 606–626. https://doi.org/10.1109/TEVC.2015.2504420

Black Sea Journal of Engineering and Science
doi: 10.34248/bsengineering.1998060

Open Access Journal
e-ISSN: 2619 – 8991

Research Article
Volume 9 - Issue 5: 2621-2628 / September 2026

COMPARATIVE NUMERICAL ANALYSIS OF SURCHARGE EFFECTS ON A CANTILEVER SHEET PILE WALL IN STIFF CLAY

Canan TURAN[1]*

[1]*Kırşehir Ahi Evran University, Faculty of Engineering and Architecture, Department of Civil Engineering, 40100, Kırşehir, Türkiye*

Abstract: Cantilever sheet pile walls rely on passive resistance below the excavation level and are therefore sensitive to nearby surface loads. This study evaluates the combined effects of surcharge magnitude and distance on a 4 m deep excavation supported by a 9 m long steel sheet pile wall in homogeneous stiff clay. A two-dimensional plane-strain model was developed in PLAXIS 2D. The clay was represented by a drained Mohr-Coulomb model, while the wall was modelled as an elastic plate with interface elements on both sides. Uniform 4 m wide surcharges of 50 and 100 kPa were applied at normalised distances x/H of 0, 0.5, 1.0 and 2.0. A no-surcharge model was also analysed. The excavation was modelled as a staged construction process with four successive 1 m excavation stages, and stability was evaluated using the strength reduction method. When the 100 kPa surcharge started immediately behind the wall, the maximum wall displacement, maximum bending moment and excavation-induced surface settlement reached 31.0 mm, 107.3 kN m/m and 11.2 mm, respectively, while the factor of safety fell to 1.40. Moving the same load to x/H = 2.0 reduced the displacement and bending moment by 54% and 78%, and increased the factor of safety to 2.10. For the 50 kPa series, the wall displacement approached the no-surcharge condition once x/H reached 0.5, whereas the bending moment approached the reference value more gradually and became comparable at x/H = 2.0. The results show that increasing the surcharge distance substantially reduces wall deformation. However, the factor of safety remains lower than the no-surcharge value, even when the deformation response becomes comparable to the reference case.

Keywords: Cantilever sheet pile wall, Stiff clay, Surface surcharge, PLAXIS 2D, Bending moment, Factor of safety

***Corresponding author:** Kırşehir Ahi Evran University, Faculty of Engineering and Architecture, Department of Civil Engineering, 40100, Kırşehir, Türkiye
E mail: canan.turan@ahievran.edu.tr (C. TURAN)
Canan TURAN https://orcid.org/0000-0003-2061-6657

Received: July 15, 2026
Accepted: August 17, 2026
Published: September 15, 2026

Cite as: Turan, C. (2026). Comparative numerical analysis of surcharge effects on a cantilever sheet pile wall in stiff clay. *Black Sea Journal of Engineering and Science,* 9(5), 2621-2628.

1. Introduction

Cantilever sheet pile walls are widely used to support shallow and moderately deep excavations where anchors or internal props are impractical. Their lateral resistance is developed primarily through soil-wall interaction and the passive resistance mobilised along the embedded portion of the wall (USACE, 1994). In clayey ground, the stability of such walls is closely related to the mobilisation of soil shear strength and the wall embedment ratio (Keawsawasvong et al., 2023). Surcharge loads applied near the excavation can alter the stress state and the mobilisation of soil resistance, thereby affecting wall deformation, bending moment, ground movement, and overall stability (Debnath and Pal, 2023).

In urban excavations, the retained ground is frequently subjected to surcharge loads originating from adjacent buildings, foundations, traffic, stored materials, and construction equipment. Such loads increase the lateral stresses acting on the wall and may lead to greater wall displacement, bending moment, and ground movement. The surcharge effect is controlled not only by its magnitude but also by the width and location of the loaded area, as these parameters govern the transmission of additional stresses through the retained soil towards the wall. Nandi and Choudhury (2022) showed that surcharge intensity, strip width, and distance from the wall significantly affect the response of embedded cantilever walls. Akan (2023) similarly reported that the distance of the surcharge from the wall can be more influential than its intensity and loaded width, particularly when the load is positioned close to the excavation.

Experimental evidence further demonstrates the importance of surcharge location. Aparna and Samadhiya (2020) observed that the adverse effects of a strip footing on the response of the model sheet pile wall were most pronounced when the footing was located within the active failure region. Both wall deflection and ground settlement decreased as the footing was located farther from the excavation face. Comparable trends have been reported in numerical investigations. Singh and Chatterjee (2020) found that wall deflection and ground settlement decreased with increasing surcharge distance, whereas both responses increased with surcharge magnitude. Debnath and Pal (2023) similarly reported

This work is licensed (CC BY-NC 4.0) under Creative Commons Attribution 4.0 International License

that wall deflection, bending moment, and ground settlement were greatest when the surcharge was applied close to the wall and decreased substantially with increasing distance from the wall.

Previous studies have addressed the analysis and optimisation of cantilever sheet-pile walls in cohesionless soils. For example, Babu and Basha (2008) developed a reliability-based optimisation framework for cantilever sheet-pile walls embedded in sandy soils. By contrast, studies focusing on walls embedded in clay remain relatively limited. Keawsawasvong et al. (2023) investigated the stability factors of cantilever sheet-pile walls in clay using the finite-element strength-reduction method, whereas Maitra and Singh (2026) developed a simplified analytical procedure for walls retaining cohesive backfill subjected to uniform surcharge loading. These studies highlight the combined importance of clay strength, wall embedment and surcharge loading. However, the simultaneous evaluation of wall deformation, bending response, ground settlement and global stability within the same staged-excavation model has received less attention. Such a comparison is important because serviceability and stability indicators may approach the no-surcharge condition at different rates as the surcharge setback increases.

The present study addresses this gap by investigating a cantilever steel sheet pile wall supporting a 4 m deep excavation in homogeneous stiff clay. To represent the long-term response to a sustained surcharge that is present before and throughout excavation, the clay is analysed under drained effective-stress conditions. Short-term undrained excavation behaviour is therefore outside the scope of the present study. A systematic numerical programme is conducted to quantify the combined effects of surcharge magnitude and distance from the wall. Surcharge pressures of 50 and 100 kPa are applied at four different setback distances, and a corresponding no-surcharge model is adopted as the reference case. This framework provides a consistent basis for directly comparing the influence of surcharge magnitude and setback distance. The response is evaluated in terms of maximum horizontal wall displacement, maximum wall bending moment, maximum ground-surface settlement behind the excavation, and global factor of safety. Particular attention is given to the rate at which these response measures approach the no-surcharge condition as the distance between the loaded area and the wall increases. The outcomes of the study reveal whether serviceability and stability responses diminish at comparable rates and provide a clearer basis for evaluating the placement of surcharge loads adjacent to cantilever-supported excavations.

2. Materials and Methods

2.1. Geometry and Boundary Conditions

The numerical model represented an unsupported cantilever wall in plane strain. The excavation depth was H = 4 m and the embedded length below the excavation level was D = 5 m, giving D/H = 1.25 and a total wall length of 9 m (Figure 1). A 4 m excavation depth and staged excavation procedure are consistent with the representative cantilever wall model reported by Kawa et al. (2019). The selected dimensions also fall within the range commonly associated with cantilever sheet pile applications, which are generally used for excavations of limited height (Aparna and Samadhiya, 2020; Debnath and Pal, 2023).

The numerical domain was 40 m wide and 20 m deep. Approximately 25 m of soil was retained behind the wall and 15 m was located on the excavation side (Figure 1). The lateral boundaries were fixed in the horizontal direction and remained free vertically. The base was fixed in both horizontal and vertical directions. The domain was selected so that the main displacement field remained away from the lateral and lower boundaries.

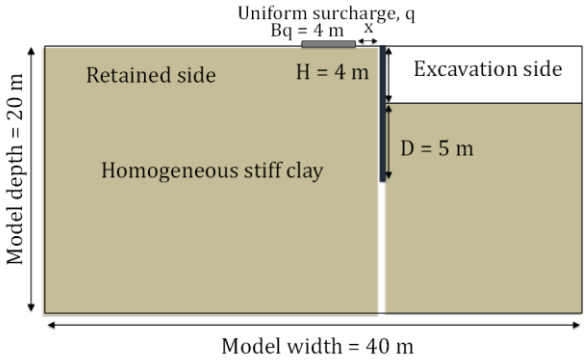


Figure 1. Idealised model geometry, boundary conditions and surcharge definition.

2.2. Soil Model and Parameters

The soil was idealised as a homogeneous stiff clay under drained conditions to represent long-term effective-stress behaviour. The Mohr-Coulomb model was adopted to provide a consistent and transparent framework for the parametric comparisons. The stiffness and strength values were selected by rounding the drained parameters reported for stiff Bangkok clay by Surarak et al. (2012). The same Mohr-Coulomb parameters were retained in all analyses to ensure that the observed differences resulted solely from surcharge magnitude and location. The adopted soil parameters are summarised in Table 1. No groundwater table was included in the model. The dilation angle was set to zero, which is appropriate for the idealised clay response considered here.

Table 1. Stiff clay parameters used in the numerical analyses

Parameter	Value
Unsaturated unit weight (γ_{unsat}) (kN/m^3)	17
Saturated unit weight (γ_{sat}) (kN/m^3)	19
Young's modulus (E) (kPa)	14,000
Poisson's ratio (ν)	0.35
Effective cohesion (c') (kPa)	30
Effective friction angle (φ′) (°)	26
Dilation angle (ψ) (°)	0
Constitutive model	Mohr-Coulomb
Drainage condition	Drained

2.3. Sheet Pile and Soil-Wall Interface

The sheet pile was represented by an AZ24-700 S355GP steel profile rather than an equivalent reinforced-concrete wall. It was modelled as a linear-elastic plate element per metre width of wall. The plate properties were based on the AZ24-700 section used by Tornborg et al. (2023). The adopted normal stiffness, flexural rigidity, unit weight, and Poisson's ratio are listed in Table 2.

Interface elements were assigned to both sides of the plate to allow relative movement and stress transfer between the steel wall and the clay. An interface reduction factor of R_{inter} = 0.67 was adopted on both sides of the wall, consistent with values used in previous PLAXIS studies of sheet-pile–soil interaction (Nguyen et al., 2023; Keawsawasvong et al., 2023).

Table 2. Sheet pile and interface properties

Property	Value
Normal stiffness (EA) (kN/m)	3.70×10^6
Flexural rigidity (EI) (kNm^2/m)	1.17×10^5
Unit weight of plate (w) (kN/m/m)	1.30
Poisson's ratio (ν)	0.20
Interface reduction factor (R_{inter})	0.67

2.4. Surcharge Cases and Construction Stages

A 4 m wide uniform surface surcharge was applied on the retained side. The distance x was measured from the wall to the nearest edge of the loaded strip. Two surcharge intensities, q = 50 and 100 kPa, were examined at x/H = 0, 0.5, 1.0 and 2.0. For H = 4 m, these ratios correspond to distances of 0, 2, 4 and 8 m, respectively. For the case designation, S denotes the surcharge condition, the following number indicates the surcharge intensity in kPa, and R represents the normalised surcharge distance, defined as R = x/H. For example, S50-R0.5 corresponds to a 50 kPa surcharge applied at x/H = 0.5, or x = 2 m (Table 3). A no-surcharge analysis was used as the reference. The same geometry, wall section, soil properties, mesh setting and excavation sequence were used in every case. This ensured that the comparisons isolated the effects of surcharge magnitude and distance.

Initial stresses were generated using the K_0 procedure. The surcharge was then activated and allowed to reach equilibrium. This sequence was intended to represent a pre-existing surcharge that was present before excavation and remained active throughout all excavation stages. The plate and interface elements were subsequently activated prior to excavation, without explicitly modelling the sheet-pile installation process. Displacements were reset after wall activation so that the reported surface settlements represented additional movement generated during excavation rather than settlement caused by the initial application of the surcharge. Excavation was carried out incrementally in four successive 1 m stages. The final excavation stage was followed by a strength-reduction analysis to determine the factor of safety.

Table 3. Analysis matrix showing the actual and normalised surcharge distances

Case	Surcharge q (kPa)	Distance x (m)	x/H
Reference	0	-	-
S50-R0	50	0	0.0
S50-R0.5	50	2	0.5
S50-R1	50	4	1.0
S50-R2	50	8	2.0
S100-R0	100	0	0.0
S100-R0.5	100	2	0.5
S100-R1	100	4	1.0
S100-R2	100	8	2.0

2.5. Mesh and Output Quantities

A very fine finite-element mesh was adopted throughout the study. As shown in Figure 2, local refinement was concentrated around the sheet-pile wall, the excavation zone and the surcharge area, where larger stress and displacement gradients were expected. The same mesh-generation settings were retained in all cases to ensure consistency among the analyses. Although a separate mesh-sensitivity study was beyond the scope of the present investigation, the adopted very fine and locally refined mesh provided a consistent basis for the comparative evaluation. The model dimensions were sufficient to prevent significant displacement contours from reaching the lateral and bottom boundaries. The principal service response quantities were the maximum horizontal displacement of the plate, the maximum absolute bending moment and the maximum downward surface displacement on the retained side. The factor of safety was obtained from the strength reduction analysis.

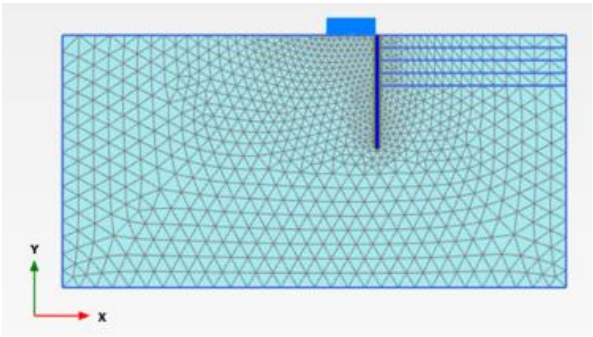


Figure 2. Finite-element mesh with local refinement around the sheet-pile wall and surcharge area.

3. Results and Discussion

3.1. Summary of numerical results

Table 4 presents the response quantities obtained at the final 4 m excavation stage for the reference model and the eight surcharge cases. To distinguish the effects of surcharge magnitude and distance, the wall displacement, bending moment, excavation-induced surface settlement and factor of safety are discussed separately in the following sections.

3.2. Maximum horizontal wall displacement

Figure 3 shows the variation of maximum horizontal wall displacement with normalised surcharge distance. For the 50 kPa series, the maximum wall displacement in S50-R0 was 17.2 mm, which was 21.8% greater than the no-surcharge value of 14.1 mm. In S50-R0.5, the displacement decreased to 14.0 mm. The values obtained for S50-R0.5, S50-R1 and S50-R2 differed from the reference value by less than 2%, indicating that the wall displacement had effectively reached a response plateau once x/H reached 0.5.

The 100 kPa series exhibited a substantially stronger response when the surcharge was located close to the wall. In S100-R0, the maximum displacement reached 31.0 mm, representing increases of 119.5% relative to the reference case and 80.2% relative to S50-R0. The displacement remained above the reference value in S100-R0.5, where it was 18.3 mm, but approached the no-surcharge response in S100-R1. No meaningful additional change was observed in S100-R2. These results indicate that the surcharge influence zone governing wall displacement increased with surcharge magnitude.

Table 4. Numerical results at the final 4 m excavation stage.

Case	Maximum wall u_x (mm)	$\|M\|_{max}$ (kN m/m)	S_{max} (mm)*	FoS
Reference	14.1	20.2	4.03	3.08
S50-R0	17.2	54.6	4.07	1.89
S50-R0.5	14.0	37.1	4.06	2.06
S50-R1	14.0	28.1	4.05	2.25
S50-R2	14.1	21.6	4.03	2.65
S100-R0	31.0	107.3	11.2	1.40
S100-R0.5	18.3	54.5	4.05	1.57
S100-R1	14.0	36.2	4.03	1.75
S100-R2	14.1	23.3	4.03	2.10

*S_{max} is the additional excavation-induced settlement after the displacement reset following wall installation.

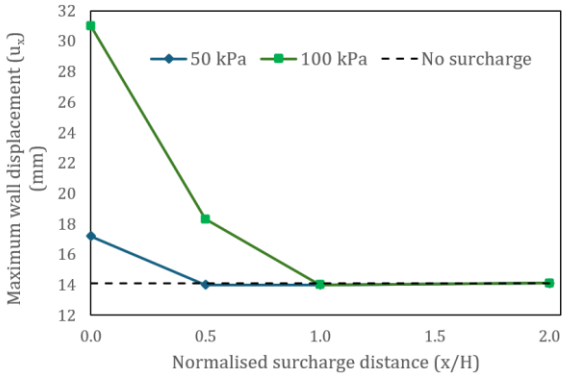


Figure 3. Variation of maximum horizontal wall displacement with normalised surcharge distance. The dashed line denotes the no-surcharge value.

The reduction in wall displacement with increasing surcharge distance agrees with the experimental observations of Aparna and Samadhiya (2020) and with the numerical trends reported by Singh and Chatterjee (2020), Nandi and Choudhury (2022), Debnath and Pal (2023) and Akan (2023). The present results further demonstrate that the normalised distance required for the wall displacement to approach the no-surcharge response depends on the applied surcharge intensity.

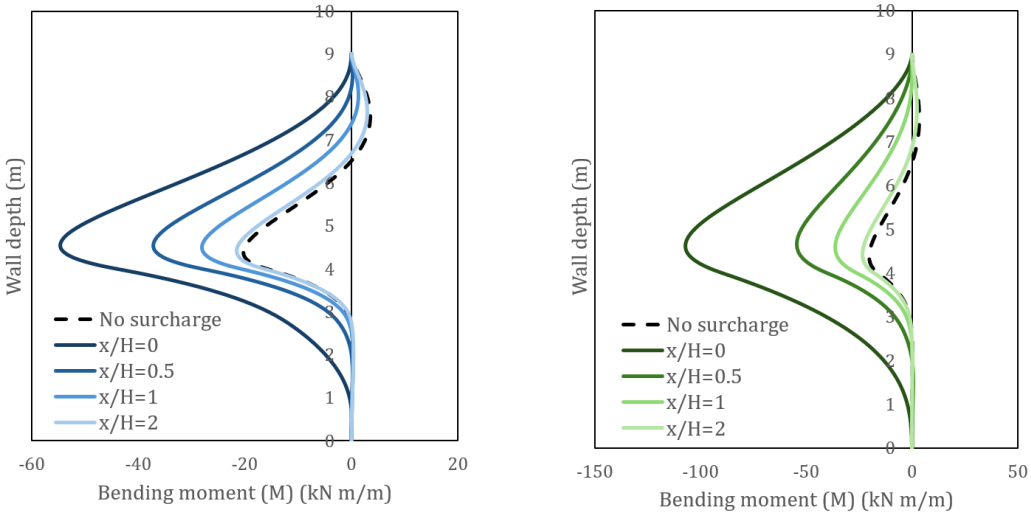
3.3. Bending Moment Response

The maximum bending moment exhibited a stronger dependence on surcharge distance than the maximum wall displacement. In the 50 kPa series, the maximum absolute bending moment decreased progressively from 54.6 kN m/m in S50-R0 to 37.1, 28.1 and 21.6 kN m/m in S50-R0.5, S50-R1 and S50-R2, respectively. Moving the surcharge from R = 0 to R = 2 reduced the maximum bending moment by 60.5%. The moment in the adjacent surcharge case was 170.1% greater than the no-surcharge value of 20.2 kN m/m, whereas the farthest

case exceeded the reference by only 6.8%. Thus, the response of the 50 kPa series progressively approached the no-surcharge condition as the loaded strip was moved away from the wall.

A more pronounced distance-dependent reduction was observed in the 100 kPa series. The maximum absolute bending moment decreased progressively from 107.3 kN m/m in S100-R0 to 54.5, 36.2 and 23.3 kN m/m in S100-R0.5, S100-R1 and S100-R2, respectively. Moving the surcharge from R = 0 to R = 2 reduced the maximum bending moment by 78.3%. Relative to the no-surcharge moment of 20.2 kN m/m, the flexural demand in S100-R0 was 431.2% higher, while the value in S100-R2 remained only 15.3% above the reference. Notably, although the maximum wall displacement in S100-R1 had already approached the no-surcharge response, its bending moment remained 79.2% above the reference value. This finding indicates that the flexural demand approached the no-surcharge condition more gradually than the maximum wall displacement. The maximum bending moment in the 100 kPa series was 96.6% greater than that in the 50 kPa series at R = 0, but this difference decreased to approximately 8.0% at R = 2. The effect of surcharge intensity on flexural demand therefore diminished as the loaded strip was moved farther from the wall.

Figure 4 presents the bending moment distributions along the wall. Despite the considerable differences in magnitude, the profiles retained a similar overall shape, and the peak moment consistently occurred close to the excavation level. The surcharge therefore amplified the existing flexural response without substantially changing the location of the peak moment or the general form of the distribution. Increasing R mainly reduced the magnitude of the moment over the wall length, with the distributions increasingly resembling the no-surcharge profile. This trend agrees with Nandi and Choudhury (2022), who demonstrated that surcharge intensity and distance affect the structural response of embedded cantilever walls, and with Debnath and Pal (2023), who reported a substantial reduction in bending moment as the surcharge, was positioned farther from the wall. It is also consistent with Akan (2023), who highlighted the importance of surcharge position in governing cantilever-wall response.



(a) 50 kPa surcharge (b) 100 kPa surcharge

Figure 4. Bending moment distributions along the wall for the (a) 50 and (b) 100 kPa surcharge series.

3.4. Excavation-Induced Surface Settlement

Figure 5 presents the variation in maximum excavation-induced surface settlement (S_{max}) for the different surcharge cases. For the 50 kPa series, Smax varied only between 4.03 and 4.07 mm, with the maximum value obtained for S50-R0. The maximum deviation from the reference value was approximately 1.0%, indicating that the 50 kPa surcharge produced no appreciable change in the excavation-induced surface settlement, regardless of its position.

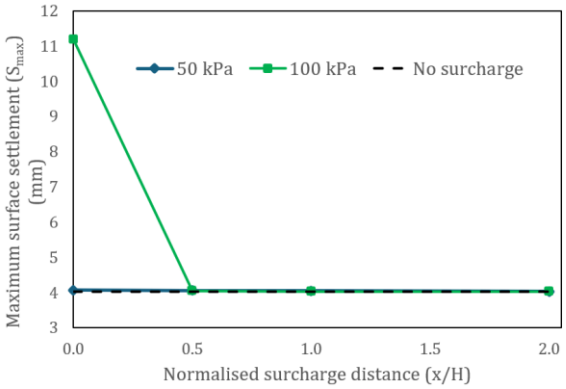


Figure 5. Variation of maximum excavation-induced surface settlement with normalised surcharge distance. The dashed line denotes the no-surcharge value.

A markedly different response was obtained for S100-R0, in which S_{max} reached 11.2 mm, approximately 2.8 times the reference value and substantially greater than the 4.07 mm obtained for S50-R0. Thus, increasing the adjacent surcharge from 50 to 100 kPa produced a disproportionately large increase in the additional surface settlement generated during excavation. This response suggests that the heavier surcharge in S100-R0 interacted more strongly with the excavation-induced deformation zone immediately behind the wall. Previous numerical studies have similarly shown that surcharge magnitude and position can significantly affect ground settlement and the deformation of cantilever sheet-pile walls, with the greatest effects generally occurring when the load is placed close to the wall (Singh and Chatterjee, 2020; Debnath and Pal, 2023).

Surface settlement returned to approximately the reference level over a shorter surcharge distance than wall displacement and bending moment. In S100-R0.5, S_{max} had already approached the reference value, whereas both wall response quantities remained above their corresponding reference values. A similar contrast was observed in the 50 kPa series. These results indicate that surcharge position had a stronger and more persistent influence on the lateral and structural response of the wall than on the maximum excavation-induced surface settlement. Accordingly, wall displacement, bending moment and surface settlement should be evaluated as distinct response measures (Debnath and Pal, 2023).

The reported S_{max} values represent incremental settlements developed during excavation while the surcharge remained active, rather than total settlements measured from the initial application of the surface load. Displacements were reset at the beginning of the excavation sequence (Bentley Systems, 2021). In field conditions, total settlement would comprise both the pre-excavation settlement associated with the surcharge and the additional settlement generated during excavation (Wang et al., 2022). For practical purposes, the reported S_{max} values should therefore be interpreted as excavation-induced increments rather than total field settlements. By excluding the pre-excavation displacement component, the adopted procedure provided a direct and consistent basis for comparing the excavation-stage effects of the 50 and 100 kPa surcharges. The settlement remained close to the reference value in all cases except S100-R0, where the adjacent 100 kPa surcharge produced a pronounced increase.

3.5. Factor of Safety

Figure 6 shows that the factor of safety increased consistently with surcharge distance for both load levels. For q = 50 kPa, FoS increased from 1.89 at x/H = 0 to 2.65 at x/H = 2.0. For q = 100 kPa, it increased from 1.40 to 2.10. The no-surcharge model remained the most stable case, with FoS = 3.08.

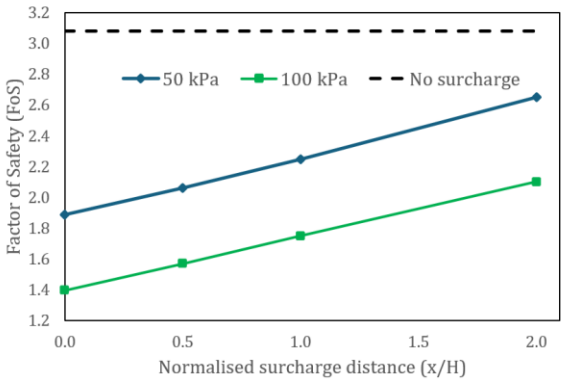


Figure 6. Variation of factor of safety with normalised surcharge distance. The dashed line denotes the no-surcharge value.

USACE (2003) indicates that a factor of safety of approximately 1.5 is typically regarded as a minimum acceptable value for slope stability under normal long-term loading conditions, although the appropriate value depends on the uncertainties involved and the consequences of failure. While this guidance was developed for slope-stability assessments, it provides a useful reference benchmark for interpreting the global strength-reduction factors obtained in the present analyses. Relative to this reference value, all cases except the 100 kPa surcharge applied immediately adjacent to the wall exhibited FoS values above 1.5. The FoS of 1.40 obtained for this case indicates a comparatively limited margin against instability and may therefore be regarded as a marginal stability condition. Moving the 100 kPa surcharge to x/H = 0.5 increased the FoS to 1.57, while greater distances provided progressively larger stability reserves. These results demonstrate that both surcharge magnitude and position strongly influence the available margin against overall instability. The observed trend is consistent with the mechanics of cantilever walls in clay. Passive resistance mobilised below the excavation level constitutes the principal stabilising mechanism, whereas additional loading on the retained side increases the driving action and reduces the available stability margin. Strength reduction analyses for cantilever walls in clay, such as those presented by Keawsawasvong et al. (2023), are therefore useful since they capture the complete soil-wall failure mechanism rather than relying on an individual structural response quantity.

3.6. Horizontal Displacement Contours

Figure 7 presents the horizontal soil displacement contours for the nearest and farthest surcharge positions at the final excavation stage. A common contour range was adopted for all cases to allow a consistent visual comparison of the displacement fields. The most pronounced response occurred when the 100 kPa surcharge was applied immediately adjacent to the wall. In this case, a localised high-displacement zone developed beneath the loaded surface and extended towards the wall and the excavation, accompanied by a

markedly steeper displacement gradient than in the other cases. This response is consistent with the direct influence of a near-wall surcharge on the deforming soil mass, as also observed in previous numerical investigations of surcharge-position effects on retaining-wall response (Debnath and Pal, 2023).

Moving the surcharge to x/H = 2.0 substantially reduced its influence on the displacement field. At this distance, the contours obtained for the two surcharge intensities became broadly similar, and the response was concentrated mainly around the excavation and the embedded portion of the wall. This indicates that the deformation pattern in the far-field cases was governed predominantly by excavation-induced ground movement, whereas the adjacent 100 kPa surcharge directly intensified and extended the deforming zone. This case also corresponded to the lowest calculated FoS, indicating that the most pronounced service-stage deformation occurred in the case with the smallest stability reserve.

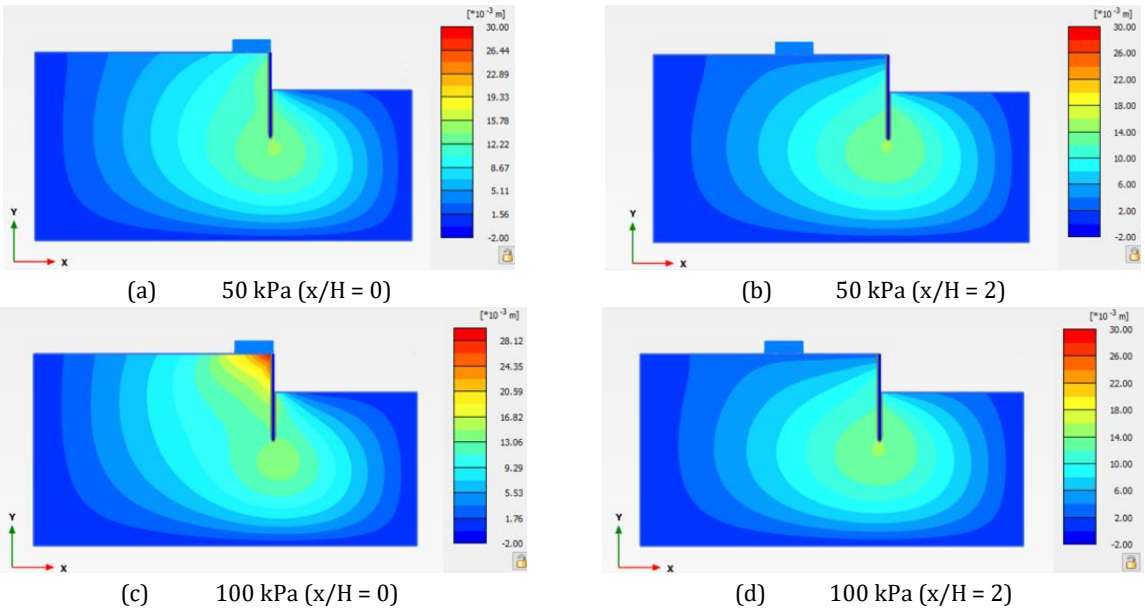


Figure 7. Horizontal soil displacement contours at the final excavation stage for the nearest and farthest surcharge positions: (a) 50 kPa, x/H = 0; (b) 50 kPa, x/H = 2.0; (c) 100 kPa, x/H = 0; and (d) 100 kPa, x/H = 2.0. A common contour range is used in all panels to facilitate direct comparison.

3.7. Practical Implications and Limitations

For the wall and soil conditions studied, locating the nearest edge of the surcharge at x/H of approximately 1.0 or greater was sufficient for the maximum wall displacement and excavation-induced settlement to approach the no-surcharge response. Bending moment also approached the reference condition with increasing distance, although it remained slightly above the no-surcharge value for both load levels at x/H = 2.0. The factor of safety remained below the reference value in every surcharge case. These observations indicate that, although increasing the surcharge setback substantially improves both deformation response and stability, the no-surcharge stability level is not fully recovered.

The numerical results are specific to the adopted wall geometry, clay properties and construction sequence. The assumption of a homogeneous clay profile and the exclusion of groundwater represent additional idealisations of the numerical model. Accordingly, the results should be extrapolated to layered deposits or groundwater-affected excavations with appropriate caution. In addition, the adopted Mohr-Coulomb model assumes constant stiffness and does not account for stress-dependent stiffness or enhanced small-strain stiffness. The model was developed as a comparative parametric framework rather than as a calibration of a specific field or experimental case. Therefore, the absolute response values should be interpreted as model-dependent estimates, while the relative differences among the surcharge cases provide the primary basis for evaluating the influence of surcharge magnitude and position. Future studies may extend the present investigation by considering different soil profiles, groundwater conditions, wall geometries and surcharge configurations, as well as more advanced soil and interface modelling approaches.

4. Conclusions

This study aimed to evaluate the influence of surcharge magnitude and setback distance on the service response and stability of a cantilever sheet-pile wall in homogeneous drained clay. Based on the numerical analyses, the following conclusions were drawn:

- Surcharge position and magnitude strongly affected the wall response. The adjacent 100 kPa surcharge produced the most critical condition, with a maximum wall displacement of 31.0 mm, a bending moment of 107.3 kN m/m, a surface settlement of

11.2 mm and an FoS of 1.40. Moving the same surcharge to x/H = 2.0 reduced the wall displacement and bending moment by 54% and 78%, respectively, while increasing the FoS to 2.10. This demonstrates the substantial benefit of increasing the surcharge setback.

- The maximum wall displacement approached the no-surcharge response at approximately x/H = 0.5 for q = 50 kPa and x/H = 1.0 for q = 100 kPa. The bending moment decreased progressively over the full range of surcharge distances, indicating a more gradual sensitivity to setback.
- Except for the adjacent 100 kPa case, the excavation-induced surface settlement remained close to 4 mm, indicating that the additional settlement generated during excavation was limited for the remaining surcharge configurations.
- Increasing the surcharge setback substantially reduced deformation demand and improved stability. However, at x/H = 2.0, the wall displacement had nearly recovered to the no-surcharge response, whereas the FoS remained lower than the corresponding reference value. Deformation and strength-reduction results should therefore be considered together when assessing surcharge effects.

Author Contributions

The percentages of the author' contributions are presented below. The author reviewed and approved the final version of the manuscript.

	C.T.
C	100
D	100
DCP	100
DAI	100
L	100
W	100
CR	100
SR	100

C= concept, D= design, DCP= data collection and/or processing, DAI= data analysis and/or interpretation, L= literature search, W= writing, CR= critical review, SR= submission and revision.

Conflict of Interest

The author declared that there is no conflict of interest.

Ethical Consideration

Ethics committee approval was not required because this study did not involve human participants or animals.

References

Akan, R. (2023). The influence of distant surcharge load with a finite length on the cantilever walls. *PLOS ONE*, *18*(12), Article e0295442. https://doi.org/10.1371/journal.pone.0295442

Aparna, & Samadhiya, N. K. (2020). Evaluation of model sheet pile wall adjacent to a strip footing: An experimental investigation. *International Journal of Geotechnical Engineering*, *14*(7), 828–835.

Babu, G. L. S., & Basha, B. M. (2008). Optimum design of cantilever sheet pile walls in sandy soils using inverse reliability approach. *Computers and Geotechnics*, *35*(2), 134–143. https://doi.org/10.1016/j.compgeo.2007.04.001

Bentley Systems. (2021). *PLAXIS 2D CONNECT Edition V21.01 tutorial manual: Dry excavation using a tie back wall*. Bentley Systems.

Debnath, A., & Pal, S. K. (2023). Influence of surcharge strip loads on the behavior of cantilever sheet pile walls: A numerical study. *Journal of Engineering Research*, *11*(1), 100029.

Kawa, M., Bagińska, I., & Wyjadłowski, M. (2019). Reliability analysis of sheet pile wall in spatially variable soil including CPTu test results. *Archives of Civil and Mechanical Engineering*, *19*(2), 598–613. https://doi.org/10.1016/j.acme.2018.10.007

Keawsawasvong, S., Lai, V. Q., Huynh, Q. T., & Van, C. N. (2023). Stability factors of cantilever sheet pile walls in clays by using finite element method. In J. N. Reddy, C. M. Wang, V. H. Luong, & A. M. Le (Eds.), *Proceedings of the 2nd International Conference on Sustainable Civil Engineering Structures and Construction Materials* (ICSCEA 2021; Lecture Notes in Civil Engineering, Vol. 268, pp. 651–657). Springer. https://doi.org/10.1007/978-981-19-3303-5_58.

Maitra, S., & Singh, A. P. (2026). Simplified analysis of cantilever sheet pile walls with surcharge on cohesive backfill. *Indian Geotechnical Journal*, *56*, 2108–2115.

Nandi, R., & Choudhury, D. (2022). Displacement-controlled approach for the analysis of embedded cantilever retaining walls with a distanced strip surcharge. *Computers and Geotechnics*, *151*, 104970.

Nguyen, A.-D., Nguyen, V.-T., & Kim, Y.-S. (2023). Finite element analysis on dynamic behavior of sheet pile quay wall dredged and improved seaside subsoil using cement deep mixing. *International Journal of Geo-Engineering*, *14*, 9.

Singh, A. P., & Chatterjee, K. (2020). Ground settlement and deflection response of cantilever sheet pile wall subjected to surcharge loading. *Indian Geotechnical Journal*, *50*(4), 540–549. https://doi.org/10.1007/s40098-019-00387-1

Surarak, C., Likitlersuang, S., Wanatowski, D., Balasubramaniam, A., Oh, E., & Guan, H. (2012). Stiffness and strength parameters for hardening soil model of soft and stiff Bangkok clays. *Soils and Foundations*, *52*(4), 682–697.

Tornborg, J., Karlsson, M., & Karstunen, M. (2023). Permanent sheet pile wall in soft sensitive clay. *Journal of Geotechnical and Geoenvironmental Engineering*, *149*(6), 05023003.

USACE. (1994). *Design of sheet pile walls* (Engineer Manual EM 1110-2-2504). U.S. Army Corps of Engineers. Department of the Army.

USACE. (2003). *Slope stability* (Engineer Manual EM 1110-2-1902). U.S. Army Corps of Engineers. Department of the Army.

Wang, Y., Chen, S., Ouyang, J., Li, J., Zhao, Y., Lin, H., & Guo, P. (2022). Predicting ground surface settlements induced by deep excavation under embankment surcharge load in flood detention zone. *Water*, *14(23)*, 3868.

Black Sea Journal of Engineering and Science
doi: 10.34248/bsengineering.1955911

Open Access Journal
e-ISSN: 2619 – 8991

Research Article
Volume 9 - Issue 5: 2629-2638 / September 2026

ANALYSIS OF KINEMATIC AND KINETIC PARAMETERS DURING MANUAL LOAD LIFTING USING MARKERLESS MOTION CAPTURE AND INVERSE DYNAMICS METHOD

Muhammed ÇİL[1]*, Bilal USANMAZ[2], Ömer GÜNDOĞDU[3]

[1]Kafkas University, Department of Mechanical Engineering, 36100 Kars, Türkiye
[2]Ataturk University, Department of Computer Engineering, 25240 Erzurum, Türkiye
[3]Ataturk University, Department of Mechanical Engineering, 25240 Erzurum, Türkiye

Abstract: Manual material handling activities continue to be a primary cause of musculoskeletal disorders in industrial environments. This study aimed to perform a biomechanical moment analysis of symmetric load lifting using kinematic data obtained via markerless motion capture technology without the use of physical sensors. Ten healthy male volunteers performed squat lifting tasks in the sagittal plane under external loads of 2.5 kg, 5.0 kg and 7.5 kg. Joint angle, velocity, and acceleration data were acquired using the MediaPipe Holistic algorithm. These data were combined with anthropometric constants to calculate joint moments using the inverse dynamics method via Newton-Euler equations. The results revealed that increased external load significantly elevated peak moment values in the hip, shoulder, and elbow joints. Specifically, as the load increased from 2.5 to 7.5 kg, normalized peak hip moments rose from 1.94 to 2.33 Nm/kg, shoulder moments from 0.30 to 0.58 Nm/kg, and elbow moments from 0.11 to 0.26 Nm/kg. In contrast, ankle and knee joint moments showed relatively small changes. Additionally, participants anthropometric differences influenced their lifting strategies, resulting in notable variations in shoulder and elbow kinematics during the load-centering and stabilization phases. In conclusion, this methodology demonstrates that ergonomic risks and mechanical joint stresses during manual material handling tasks can be practically analyzed in a non-invasive manner, independent of laboratory constraints.

Keywords: Biomechanics, Inverse dynamics, Markerless motion capture, Manual load lifting, Joint moment

***Corresponding author:** Kafkas University, Department of Mechanical Engineering, 36100 Kars, Türkiye
E mail muhammed.cil@kafkas.edu.tr (Muhammed ÇİL)
Muhammed ÇİL https://orcid.org/0000-0002-4097-1114
Bilal USANMAZ https://orcid.org/0000-0003-0531-4618
Ömer GÜNDOĞDU https://orcid.org/0000-0003-2656-4181

Received: May 20, 2026
Accepted: August 20, 2026
Published: September 15, 2026

Cite as: Çil, M., Usanmaz, B., & Gündoğdu, Ö. (2026). Analysis of kinematic and kinetic parameters during manual load lifting using markerless motion capture and inverse dynamics method. *Black Sea Journal of Engineering and Science,* 9(5), 2629-2638.

1. Introduction

Despite the widespread adoption of robotics and automation technologies in industrial production processes, manual material handling tasks that rely on human labor continue to play a critical role in many sectors, including manufacturing, logistics, construction, and healthcare. Pushing the tolerance limits of the human body, these physical activities impose high mechanical stress on the musculoskeletal system, particularly during lifting, lowering, and carrying actions. Global occupational health and safety data indicate that these activities lead to various tissue injuries, primarily in the lower back and spinal region, resulting in long-term labor losses (Govaerts et al., 2021; Taylor et al., 2004). The loads imposed on the spine during manual lifting are not merely limited to the static weight of the external load; they also depend on complex dynamic factors such as the velocity and acceleration of the movement, trunk flexion angle, and individual postural adaptation ability (Contini et al., 1963; Marras et al., 1999).

Human movements must be modeled with high accuracy to predict risks and design ergonomic working conditions. Historically, biomechanical analyses began with models based on static equilibrium equations; however, the transition to dynamic models became imperative because static approaches neglect inertial forces (acceleration effects). Today, motion analyses are conducted using the inverse dynamics method, where external forces and kinematic data (position, velocity, and acceleration) are used as inputs, and the net reaction forces and moments occurring at the joints are calculated from distal to proximal (Winter, 2009; Faber et al., 2020). In these calculations, the human body is typically modeled as a series of rigid segments connected by joints, with their masses and moments of inertia based on anthropometric standards from the literature (Ayoub and Woldstad, 1999).

The quality of inverse dynamics calculations depends directly on the precision of the kinematic data fed into the system. Traditionally, these data are collected using optoelectronic (marker-based) systems (Ceseracciu et al., 2014) or wearable Inertial Measurement Units (IMU)

This work is licensed (CC BY-NC 4.0) under Creative Commons Attribution 4.0 International License

(Robert-Lachaine et al., 2017; Kusunose et al., 2025), which offer high accuracy but are costly, require complex calibrations, and are mostly restricted to laboratory environments. The placement of sensors on the body not only requires long preparation times but may also restrict the natural movement strategies of workers (Wesseling et al., 2014). In recent years, breakthroughs in artificial intelligence and computer vision have provided researchers with markerless motion capture technologies that overcome these limitations (Google AI, 2025). Deep learning architectures (e.g., MediaPipe) that can operate solely on two-dimensional (2D) webcam images without the need for specialized hardware can track joint centers in the human body in real-time and provide sufficient kinematic precision for ergonomic risk analyses (Kwon and Kim, 2022; Bhamidipati et al., 2023; Shaharum et al., 2024).

In this context, the primary objective of this study is to extract markerless kinematic data solely from camera images without placing any markers or sensors on the body and to present a moment analysis of manual load lifting tasks by integrating these data into classical Newton-Euler inverse dynamics equations. Accordingly, the model was applied to a group of 10 participants to examine the effects of varying external load demands (2.5, 5.0 and 7.5 kg) on movement strategies, kinematic profiles, and regional joint moment distributions.

2. Materials and Methods

The objective of this study was to collect kinematic data of manual load-lifting tasks under completely natural conditions using markerless image processing technology and to calculate joint moments by integrating the acquired data into classical inverse dynamics equations.

2.1. Participants and Experimental Setup

Ten healthy male volunteers with no history of musculoskeletal or cardiovascular disorders participated in this study. Individuals with professional lifting experience were excluded to maximize ecological validity and better reflect the general workforce profile. The mean physical characteristics of the participants are shown in Table 1.

Table 1. Descriptive characteristics of the participants (Age, height, and body mass)

Mean Age	Mean Height (m)	Mean Body Mass (kg)
30.90±13.93	1.78 ± 0.10	84.50 ± 10.94

In the experimental protocol, a standard box with handles, measuring 47×32×25 cm, was utilized. External loads of 2.5, 5.0 and 7.5 kg were placed inside the box, ensuring an even distribution of weight. Participants were instructed to perform the squat lifting technique with a shoulder-width stance, lifting the load from the ground to a fully upright position, and then lowering it back to the ground in a controlled manner without pausing. To standardize the pacing of the movement, a metronome set at 60 beats per minute (bpm) was used, ensuring that one complete lifting and lowering cycle was executed within 8 seconds. To prevent muscle fatigue, participants were provided with a 1-minute rest period between each load trial.

2.2. Markerless Motion Capture and Kinematic Data Processing

To analyze manual lifting tasks without attaching physical sensors or optical markers to the participants, MediaPipe Holistic, an open-source deep learning library developed by Google, was utilized (Bazarevsky et al., 2020; Amprimo et al., 2024; Wagh et al., 2024). Using the Python 3.10 programming language, 2D sagittal plane images captured from a webcam at a sampling rate of 30 Hz were processed frame by frame. To ensure robust and reliable pose tracking across the video frames, the MediaPipe Pose framework was configured with specific parameters: the model complexity was set to 1, and both the minimum detection confidence and minimum tracking confidence thresholds were set to 0.5.

Among the 33 keypoints detected by the MediaPipe BlazePose architecture, the ankle, knee, hip, shoulder, and elbow joint centers were filtered to serve as inputs for the model. Based on the instantaneous x-y coordinates of these points, the fundamental joint angles were calculated using the law of cosines. To eliminate optical noise, raw angular data were smoothed using a second-order zero-lag low-pass Butterworth filter with a 0.75 Hz cutoff. This threshold captures the essential harmonics of the exceptionally slow 8-second lifting cycle (fundamental frequency ≈ 0.125 Hz) without over-smoothing the true kinematic signal (Winter, 2009). The pose estimation model, filtering parameters, and motion plan in question are based on the experimental infrastructure previously configured for dynamic lift scenarios (Çil, 2026; Çil et al., 2026). Although the same markerless motion capture framework was employed, the objectives of the studies are fundamentally different. Our previous studies focused on developing and validating an inverse dynamics approach for estimating the inertial properties of handheld loads. The present study does not address inertial parameter estimation; instead, it uses the established framework as a measurement tool to investigate the biomechanical effects of different external loads on upper-limb kinematics and joint moments during lifting tasks. An exemplary movement structure and body joints tracked using the MediaPipe application are illustrated in Figure 1.

Table 2. Segmental Biomechanical Parameters Based on Height (H) and Body Mass (BM)

Segment	Mass Proportion (kg)	Length Proportion (m)	Center of Mass Location (Distal) (m)	Center of Mass Location (Proximal) (m)
A (Lower Leg)	0.093 BM	0.246H (OK)	0.13948H (l_1)	0.10652H (l_2)
B (Thigh)	0.200 BM	0.245H (KH)	0.13892H (l_3)	0.10609H (l_4)
C (Trunk)	0.578 BM	0.288H (HS)	0.10188H (l_6)	0.18612H (l_5)
D (Upper Arm)	0.056 BM	0.186H (SL)	0.10490H (l_8)	0.08110H (l_7)
E (Forearm)	0.032 BM	0.146H (LW)	0.08322H (l_{10})	0.06278H (l_9)

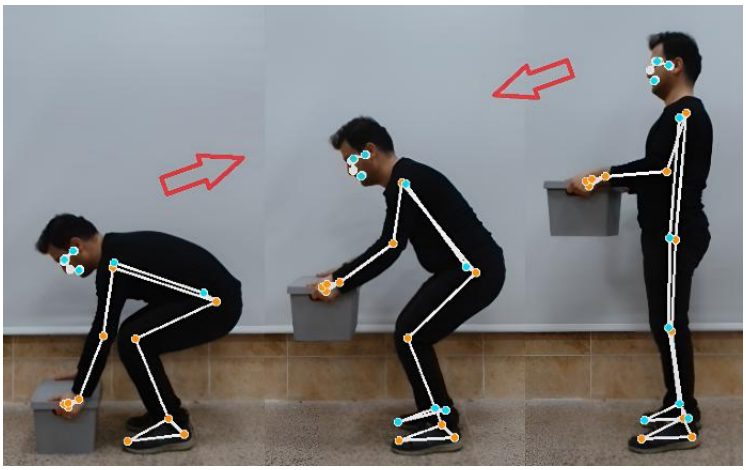


Figure 1. Experimental setup illustrating the squatting, lifting, and standing phases of the manual lifting task.

2.3. Two-Dimensional Biomechanical Model and Anthropometric Constants

To calculate the joint loads, the human body was modeled as a 2D linkage chain consisting of five rigid segments: lower leg, thigh, trunk, upper arm, and forearm, connected by frictionless revolute joints (Winter, 2009). Figure 2 illustrates the segment lengths and sections mapped onto a 2D human skeletal structure.

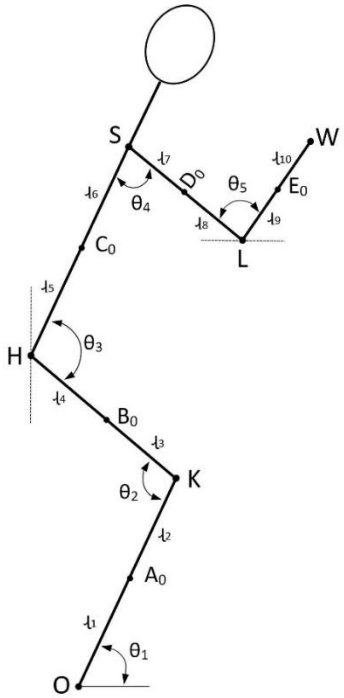


Figure 2. Designated segment lengths and sections.

In accordance with the classical inverse dynamics approach, we assumed that the body segments did not undergo deformation during movement and that the mass distributions remained constant. The mass of each segment in the model was calculated by proportioning it to the total body mass (BM) of the participants. Similarly, segment lengths and the distances of centers of mass from the joints were calculated by proportioning them to the participant's height (H), using standard anthropometric data from Dempster (Dempster, 1955; Dempster et al., 1959). Based on the assumption of uniform mass distribution, the moments of inertia for each segment relative to its center of mass were integrated into the mathematical equations as constant values. The standardized anthropometric parameters (segment masses, lengths, and centers of mass) utilized in the model, as tabulated by Drillis and Contini (1966) are presented in Table 2.

2.4. Inverse Dynamics and Calculation of Joint Moments

To determine the reaction forces and net muscle moments occurring at each joint throughout the movement, a standard inverse dynamics procedure based on Newton-Euler equations of motion was applied. Based on the anthropometric data presented in Table 2, uniform mass distribution was assumed for each segment. The moment of inertia (I) relative to the center of mass was analytically derived using the following equation 1:

$$I = \frac{m}{3}(l_{i+1}^2 - l_{i+1}l_i + l_i^2) \quad (1)$$

where m is the segment mass, and l_i and l_{i+1} are the distances from the center of mass to the proximal and

distal joints, respectively. Furthermore, the angular velocity (ω) and angular acceleration (α) trajectories of the system were established by taking the successive numerical time derivatives of the planar joint angles using the central difference method. Using the linear accelerations at the center of mass, the unknown proximal joint reaction forces were determined using Newton's Second Law of Motion. Subsequently, the net joint moment was calculated by balancing the moment of inertia of the segment, angular acceleration, and moment arms created by external forces using the Euler equation. To isolate the effects of inter-individual differences in anatomical size and mass and allow for a fair comparison, the net moment values obtained at all joints were normalized by dividing them by the respective subject's body mass (Nm/kg), rendering them ready for statistical analysis.

The human body was modeled as a linked segment system, and dynamic equilibrium was established for the i^{th} segment based on the free-body diagram, as shown in Figure 3. Calculations were performed iteratively from the distal (hands) to the proximal (ankles) end (Robertson et al., 2013; Winter, 2009).

First, Newton's Second Law of Motion was used to determine the unknown proximal joint reaction forces (F_{xp},F_{yp}), as shown in equations 2 and 3:

$$\sum F_x = m_i a_x \Rightarrow F_{xp} - F_{xd} = m_i a_x \quad (2)$$

$$\sum F_y = m_i a_y \Rightarrow F_{yp} - F_{yd} = m_i a_y \quad (3)$$

Subsequently, Euler's equation of motion was applied, as shown in equation 4, to calculate the unknown net muscle moment (M_p) at the proximal joint:

$$\sum M = I_i \alpha \Rightarrow M_p - M_d - \left(F_{xp}\cdot l_{i+1} + F_{xd}\cdot l_i\right)sin\theta + \left(F_{yp}\cdot l_{i+1} + F_{yd}\cdot l_i\right)cos\theta = I_i \alpha \quad (4)$$

Where m_i and I_i are the segment's mass and moment of inertia; θ and α are the angle of segment in plane of movement and acceleration; ax and ay are the linear accelerations of the center of mass. For the joints, F_{xd}, F_{yd}, and M_d represent the known distal reaction forces and moment, while F_{xp}, F_{yp}, and M_p denote the unknown proximal reaction forces and net joint moment.

2.5. Statistical Analysis

Descriptive statistics were calculated for the normalized peak joint moments, and the results are presented as mean ± standard deviation (SD). The normality of the data distribution was confirmed using the Shapiro-Wilk test (all P>0.05). To evaluate the effect of varying external loads (2.5, 5.0 and 7.5 kg) on the peak joint moments, a repeated-measures Analysis of Variance (RM-ANOVA) was conducted separately for each joint. Sphericity was assessed using Mauchly's test, and Greenhouse-Geisser corrections were applied where necessary. For significant main effects, post-hoc pairwise comparisons were performed using the Bonferroni correction to prevent Type I errors. The significance level was set at α = 0.05. All statistical analyses were performed using the jamovi software (Version 2.7) (The jamovi project, 2025).

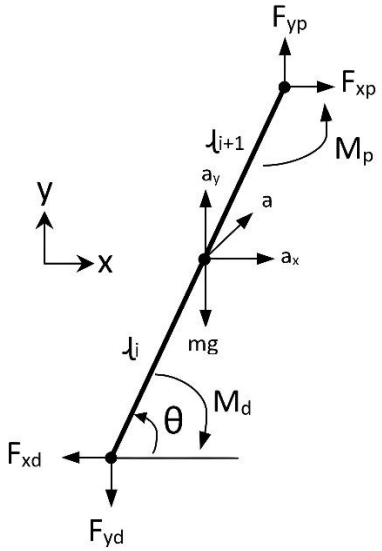


Figure 3. Free-body diagram illustrating the net forces, moments, and accelerations of a single segment.

3. Results

In this section, the kinematic data constituting the fundamental inputs of the developed biomechanical model and the net joint moments calculated using these data is analyzed. To detail the mechanics of the movement and observe the overall postural adaptations, analyses were conducted on a group of 10 participants under different external load conditions.

3.1. Joint Kinematics and Postural Strategy Differences Based on External Load Effects

The 8-second total movement duration, encompassing the subject's lifting the load from the ground to a fully upright position and subsequently lowering it back down in a controlled manner, was standardized as a complete lifting cycle from 0% to 100%. Furthermore, the graphs are vertically divided in half by a dashed black line to delineate the lifting phase and the lowering phase. During the first 4 seconds of this 8-second movement, the load was lifted from the ground (lifting phase), while in the subsequent 4 seconds, the load was lowered back to the starting position in a controlled manner (lowering phase). To investigate the effect of external load demands and inter-individual anatomical differences on movement strategies, the time-series data of joint angles obtained from 10 subjects were analyzed by generating standard deviation (SD) bands around the mean curves. Specific color coding was utilized to represent the joints: blue (ankle), red (knee), green (hip), purple (shoulder), and orange (elbow). The comparison of joint angle kinematics and standard deviation bands for multiple subjects under different load conditions is presented in Figure 4.

Upon examining the obtained kinematic curves, it is observed that the hip and knee joints, which serve as the primary motors of the lifting movement, exhibit the widest angular variation within the entire system. The

least angular variation, stemming from the nature of the movement, manifests itself in the ankle joint. Increasing the external load from 2.5 kg to 7.5 kg elevated the degree of difficulty of the movement and caused individuals to resort to different postural adaptations to maintain balance and ensure stability. At the initial moment of gripping the load, decreased hip and knee angles are observed; this deeper squat is interpreted as an effort by the body to move closer to the ground to expand the base of support and encounter the heavier load in a more secure position. Upon transitioning to the middle phase (upright posture), a synchronized postural adaptation is exhibited in the arm joints, with a distinct decrease observed specifically in the elbow angles. This represents a fundamental motor strategy aimed at pulling the heavier external load toward the body's center of mass against the increasing load difficulty, thereby shortening the moment arm and minimizing the overturning effect on the spine. Furthermore, this need for stabilization is directly observed in the graph through the distinct increase in the vertical thickness (width) of the SD bands, particularly in the upper extremity (shoulder, elbow) and the ankle, as the load increases.

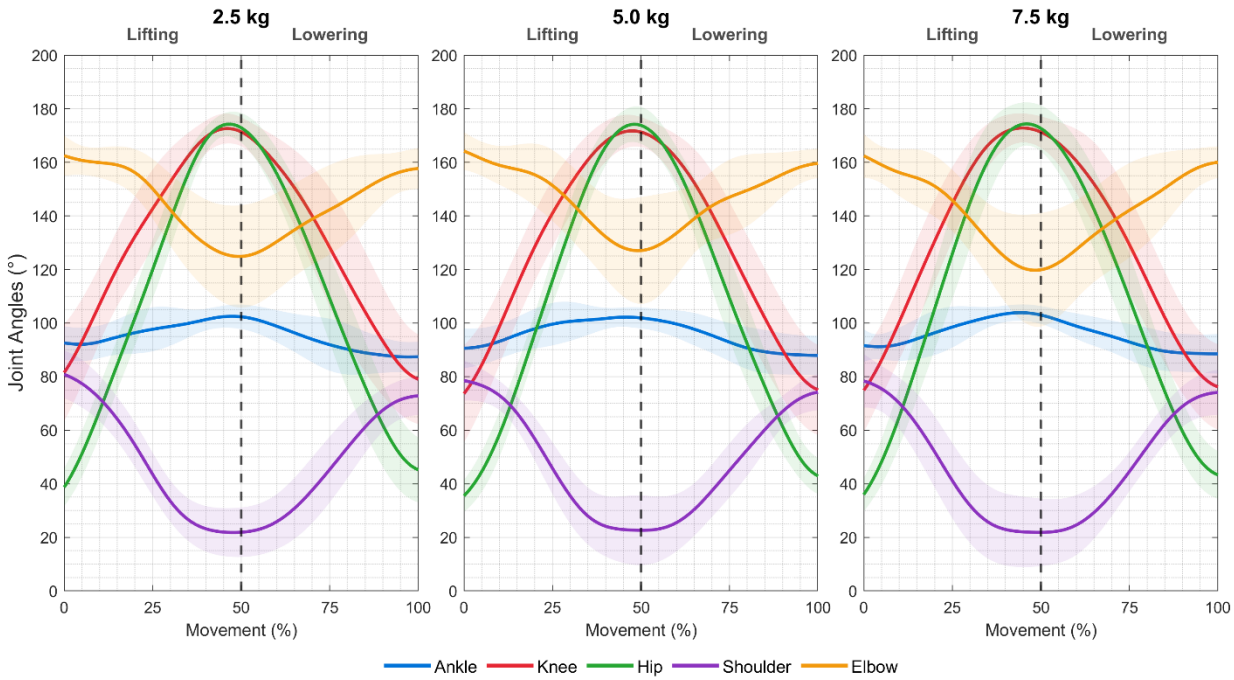


Figure 4. Comparison of joint angle kinematics and standard deviation bands for multiple subjects under different load conditions.

Determining the effect of the postural strategies identified in the joint angles on the dynamic exertion levels of the movement is critical. For this purpose, the angular velocity (ω) and angular acceleration (α) were calculated by taking the first and second time derivatives of the absolute transformation angles obtained in the biomechanical model. These values are the most critical inputs for calculating the inertial forces and net joint moments in Newton–Euler inverse dynamics equations. The temporal variation of the joint angular velocity and acceleration profiles, which reflect the subject's dynamic adaptation and motor control strategies against increasing external loads (2.5, 5.0 and 7.5 kg), is presented in Figure 5.

Upon examining the graph, the characteristic biomechanical responses shaped by the phases of the movement stand out. The highest angular velocity values occur in the hip and knee joints, as they act as the primary motors of the lifting movement, along with the forearm segment, which exhibits notably high velocity and acceleration variations owing to its direct interaction with the external load. When the mathematical relationship between the velocity and acceleration curves is examined, the angular acceleration curves cross the zero axis at the exact moment when the angular velocities of the segments reach their peaks. Conversely, during the phases where the angular velocity approaches zero, such as the initial lift off (0%), direction reversal at the apex (50%, the moment of fully upright posture), and placement and termination (100%) moments, it was determined that the angular accelerations reached sharp peak points to initiate or halt the system. Specifically, at the exact middle of the movement (50%), the velocity curves create a pause phase, and the fact that the angular acceleration curves reach their maximum peak values at this exact point demonstrates the highest dynamic loading to which the system is subjected during the transition between halting and re-initiating movement for the lowering phase.

When the lifting and lowering phases of the movement are compared, there is partially greater velocity and acceleration variation in the lifting phase across all joints,

whereas a slower, more actively controlled movement is encountered during the lowering phase. Regarding the effect of the external load, the increase observed in peak velocity and acceleration values indicates that the subjects accelerate the system more rapidly to maintain postural stability and limit dynamic loading under heavier weights. This is particularly evident in the distal joints (shoulder, elbow, and ankle), which serve as the stabilizing elements of the movement. A significant increase in both velocity and acceleration amplitudes occurred in these joints as the external load increased. Notably, the forearm segment exhibited the highest overall variations in both velocity and acceleration, reaching its peak levels under the heavy 7.5 kg load. These increases represent the instantaneous micro-adjustments made to keep the external load balanced and to dampen the perturbations originating from the lower joints. Specifically, the widening of the SD bands in the acceleration graphs reveals that the arms and particularly the forearms do not merely act as passive load bearing links but assume the crucial role of active dampers that stabilize the system.

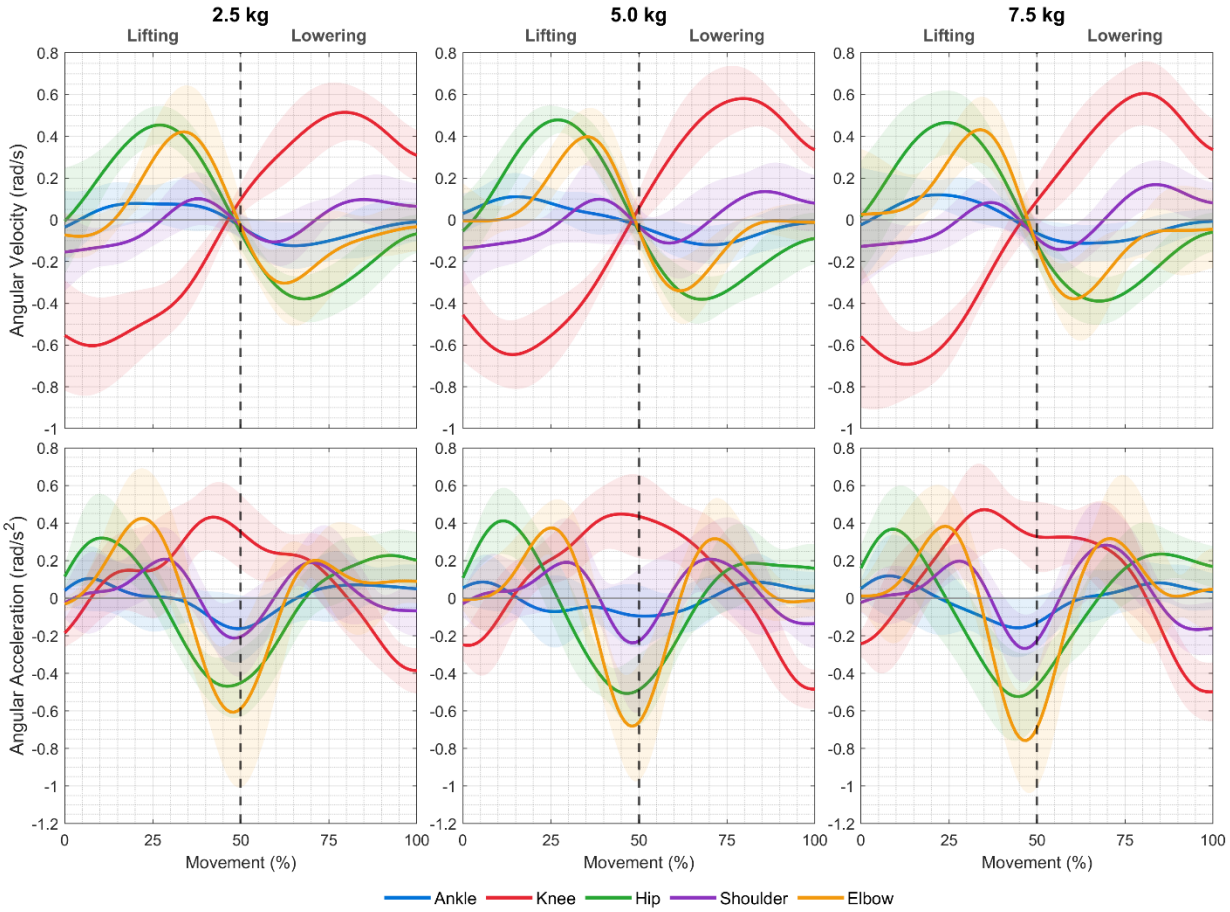


Figure 5. Comparison of joint angular velocity and angular acceleration profiles for multiple subjects under different load conditions.

3.2. Analysis of Net Joint Moments

Following the acquisition of kinematic data (angle, velocity, and acceleration), the study proceeded to the stage of determining the mechanical stresses (torques) exerted by this movement on the body joints. The net joint moments executing the movement were calculated using classical Newton-Euler inverse dynamics equations, incorporating standard anthropometric (constant) mass and inertia ratios accepted in the literature. To prevent inter-individual anatomical body mass differences from confounding the results and to ensure a fair comparison, all obtained moment values were normalized by dividing them by the subjects' body masses (Nm/kg). A time-series comparison of the normalized net joint moments of 10 participants under different external load conditions (2.5, 5.0 and 7.5 kg) is presented in Figure 6.

The moment distributions in the graph indicate that the mechanical load continuously shifts among the joints throughout the movement. Regardless of the external load, the highest stress is exerted on the hip joint at the moments of lift off from the ground (0%) and placement back down (100%), with the trunk acting as the primary load-bearer. However, during the 50% phase, when a fully upright posture is assumed, the hip moment approaches zero as the horizontal moment arm shortens. At this precise moment, the load-bearing duty transfers from the hip to the ankle. The significant increase in the ankle moment during this upright stance, where the hip is relieved, demonstrates that this joint assumes the new

role of primary load bearer. Consequently, the load distribution across the lower extremity joints is not constant; rather, a clear exchange of duty occurs among the joints depending on the acceleration phases of the movement.

In contrast to the lower extremity, the moment amplitudes in the upper extremity (shoulder and elbow) remained within much lower bands. This indicates that the arms primarily serve as mechanical stabilizers connecting the load to the body rather than providing primary motor power. When the lifting and lowering phases of the movement were examined, although a general inter-phase symmetry was observed, the decelerating velocity and acceleration values during the lowering phase manifested as lower moment values owing to the active control of the action. Finally, examining the load effect revealed that increasing the weight from 2.5 kg to 7.5 kg caused an increase in moment amplitudes across all joints. Concurrently, with this increase in external load, a noticeable widening was observed in the standard deviation (SD) bands of the joint moments, which can be attributed to greater movement variations and individual postural adjustments required to safely manage heavier loads.

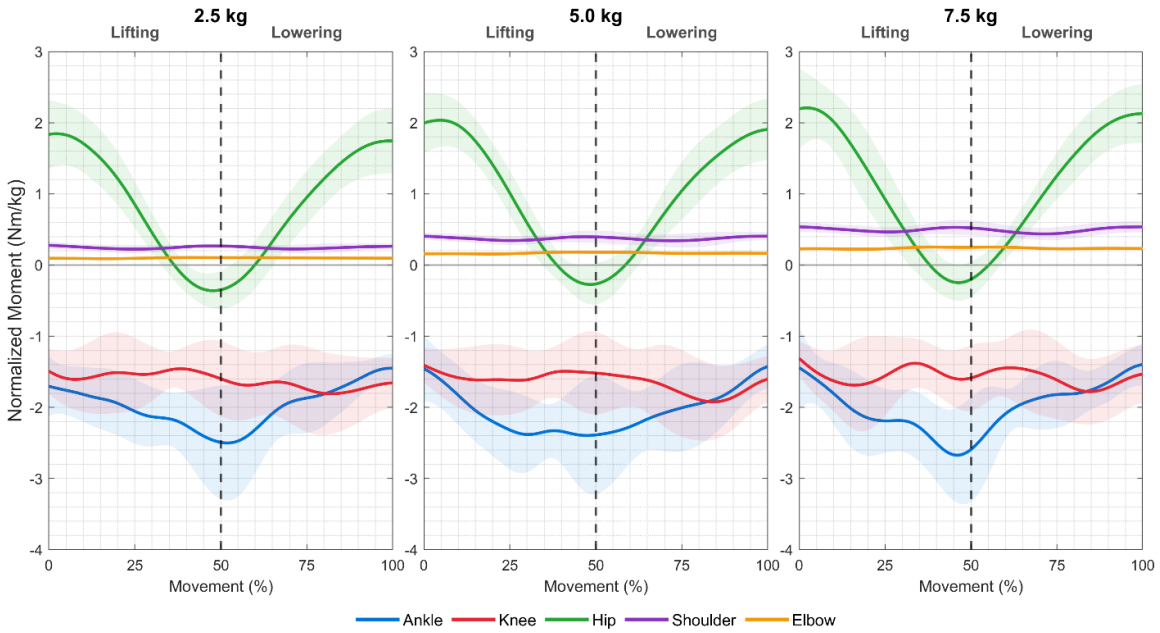


Figure 6. Comparison of normalized net joint moments (Nm/kg) for multiple subjects under different external load conditions.

To statistically quantify these observed mechanical stress variations, a one-way repeated-measures ANOVA was performed on the normalized peak joint moments obtained under the three external load conditions (2.5, 5.0 and 7.5 kg). The descriptive statistics of these peak joint moments are presented in Table 3.

Table 3. Descriptive statistics of normalized peak joint moments (Mean ± SD, Nm/kg) across three external load conditions

Joint	2.5 kg	5.0 kg	7.5 kg
Ankle	-2.74 ± 0.61	-2.78 ± 0.63	-3.00 ± 0.46
Knee	-2.13 ± 0.43	-2.16 ± 0.45	-2.17 ± 0.41
Hip	1.94 ± 0.40	2.14 ± 0.32	2.33 ± 0.39
Shoulder	0.30 ± 0.04	0.44 ± 0.06	0.58 ± 0.07
Elbow	0.11 ± 0.01	0.18 ± 0.02	0.26 ± 0.03

As the external load increased, progressive increases were observed in the peak moments of the hip, shoulder, and elbow joints, indicating increased mechanical demands on the proximal and upper-extremity segments during lifting. Conversely, ankle and knee joint moments exhibited relatively small changes across loading conditions, suggesting that the lower-extremity postural control strategy was maintained despite increased external load.

Prior to inferential analysis, the assumptions of repeated-measures ANOVA were evaluated. Shapiro–Wilk tests indicated that the peak joint moment values were normally distributed for all joints and loading conditions (all $P>0.05$). Mauchly's test showed that the assumption of sphericity was satisfied for ankle ($P=.558$), knee ($P=.056$), hip ($P=.218$), and shoulder ($P=.772$) joint moments. However, the assumption of sphericity was violated for the elbow joint ($P<.001$); therefore, Greenhouse–Geisser correction was applied.

The repeated-measures ANOVA revealed that external load magnitude did not significantly affect ankle ($F(2,18) = 1.26$, $P=.307$, $\eta^2P=.123$) or knee ($F(2,18) = 0.09$, $P=.913$, $\eta^2P=.010$) joint moments. The absence of significant changes in these joints indicates that the increased external load was not primarily accommodated through alterations in distal lower-extremity joint moments.

In contrast, statistically significant main effects of external load were observed for the hip ($F(2,18) = 34.90$,

P<.001, η^2P=.795), shoulder (F(2,18) = 147.89, P<.001, η^2P=.943), and elbow joints (Greenhouse–Geisser corrected: F(1.08, 9.68) = 561.61, P<.001, η^2P=.984). The large effect sizes demonstrate that increasing external load substantially influenced the mechanical stress distribution of these joints. These results indicate that the lifting strategy relied increasingly on proximal and upper-body joint moments as the external load increased. A detailed summary of the repeated-measures ANOVA results is provided in Table 4.

For joints showing a significant main effect of load, Bonferroni-adjusted pairwise comparisons were performed. The post-hoc analysis confirmed that hip joint moments increased significantly between all load conditions (2.5 vs. 5.0 kg, P=.003; 2.5 vs. 7.5 kg, P<.001; 5.0 vs. 7.5 kg, P=.028). Similarly, shoulder and elbow joint moments increased significantly across all pairwise comparisons (all P<.001).

These findings demonstrate a consistent load-dependent increase in mechanical demand for the hip and upper-extremity joints, following the progression of 2.5 < 5.0 < 7.5 kg. In contrast, the ankle and knee joints showed relatively stable moment patterns, indicating that increased external load was mainly accommodated through changes in proximal joint contributions rather than major alterations in distal lower-extremity loading.

Table 4. Summary of repeated-measures ANOVA results for the effect of external load on normalized peak joint moments

Joint	F (df)	P-value	η^2p
Ankle	$F(2,18) = 1.26$	.307	.123
Knee	$F(2,18) = 0.09$	.913	.010
Hip	$F(2,18) = 34.90$	< .001	.795
Shoulder	$F(2,18) = 147.89$	< .001	.943
Elbow*	$F(1.08, 9.68) = 561.61$	< .001	.984

*Greenhouse–Geisser correction was applied due to violation of the sphericity assumption.

Table 5. Bonferroni-adjusted pairwise comparisons for joints with significant main effects

Joint	Comparison	Mean Difference	SE	*p*Bonferroni
Hip	2.5 vs. 5.0 kg	-0.20	0.04	.003
Hip	2.5 vs. 7.5 kg	-0.39	0.04	< .001
Hip	5.0 vs. 7.5 kg	-0.19	0.06	.028
Shoulder	2.5 vs. 5.0 kg	-0.15	0.02	< .001
Shoulder	2.5 vs. 7.5 kg	-0.29	0.02	< .001
Shoulder	5.0 vs. 7.5 kg	-0.14	0.01	< .001
Elbow	2.5 vs. 5.0 kg	-0.08	0.00	< .001
Elbow	2.5 vs. 7.5 kg	-0.15	0.01	< .001
Elbow	5.0 vs. 7.5 kg	-0.08	0.00	< .001

4. Discussion

Manual material handling activities, which are frequently encountered in industrial environments and daily life, continue to be primary causes of musculoskeletal disorders. In this study, the manual load-lifting action was addressed in the sagittal plane, and inverse dynamics analysis was performed by obtaining the movement kinematics via markerless motion capture technology based on the MediaPipe Holistic algorithm, without the use of any physical sensors or optical markers.

One of the most critical novelties this study presents to the literature is the method of acquiring biomechanical data. A vast majority of current research relies on optoelectronic (marker-based) systems (Ceseracciu et al., 2014; Robert-Lachaine et al., 2017) or wearable sensors (IMU) (Wesseling et al., 2014; Yanıkören et al., 2020; Yanikören et al., 2026), which are costly to set up and restrict the participant's mobility. In this study, however, a completely image processing-based and markerless motion tracking infrastructure was preferred, without any physical intervention on the participants. This innovative approach establishes an easily applicable, methodological procedure by liberating biomechanical analyses from burdensome laboratory conditions.

The results showed that the varying amounts of external load led to significant postural adaptations at all stages of the movement. In the upper extremity (arm joints), the load was carried by pulling it toward the center (via the narrowing of elbow angles) to meet the increased need for stabilization and maintain the body's center of mass. In the lower extremity (leg joints), this adaptation manifested as a need for the body to move closer to the ground (squatting) at the moment of gripping the load. Another striking finding was that increasing the external load also elevated the movement velocity and acceleration values of the participants across all joints.

The kinetic data revealed that an increase in load caused a direct and proportional increase in average joint moments, particularly in the upper body and hip. Specifically, as the load increased from 2.5 kg to 7.5 kg, average peak hip joint moments during the initial lift-off phase rose from approximately 1.94 Nm/kg to 2.33 Nm/kg. Similarly, peak shoulder moments increased from 0.30 Nm/kg to 0.58 Nm/kg, and elbow moments

increased from 0.11 Nm/kg to 0.26 Nm/kg. In contrast, the knee and ankle joints exhibited a much more stable moment profile across the varying load conditions. Ankle joint moments changed marginally from -2.74 Nm/kg to -3.00 Nm/kg, and knee joint moments shifted only slightly from -2.13 Nm/kg to -2.17 Nm/kg. The ANOVA results confirmed that these slight variations in the knee and ankle joints due to increased external load were not statistically significant. Moreover, the mechanical load was in a state of continuous transfer among the joints throughout the duration of the movement. Regardless of the amount of external load, during the lift-off (0%) and placement (100%) phases, the trunk system acts as the primary supporting pillar, and the highest mechanical stress is imposed on the hip joint. In contrast, during the middle of the cycle (50%), where a fully upright posture was achieved, the horizontal moment arm dropped to a minimum level as the trunk approached the vertical axis, and the hip moment approached zero. In this critical balance phase, the duty of bearing the load and maintaining the posture is transferred from the hip to the ankle. The obtained findings are consistent with the trends reported in other manual load lifting studies that utilized classical marker-based optical systems and force platforms (Faber et al., 2016; Hwang et al., 2009; Jiang et al., 2024).

The study has certain limitations that should be considered. The human body was modeled as rigid segments connected by revolute joints moving in the sagittal plane. This 2D approach was found sufficient for the biomechanical calculations of symmetric lifting tasks; however, ignoring out-of-plane asymmetric movements, along with potential self-occlusion and depth ambiguity inherent in single-camera setups, is a limitation. The lack of direct validation, combined with the fact that the study was conducted with a relatively small sample size of ten male participants, constitutes additional constraints.

Regarding the repeatability of the results, the physical lifting task was standardized in this study using a metronome (60 bpm), specific box dimensions, and controlled rest periods to minimize human-induced kinematic variations. However, the technical repeatability of the markerless MediaPipe system also depends on stable environmental conditions. Factors such as changes in ambient light, camera quality, camera placement angle, and depth differences can affect joint tracking accuracy. Controlling these variables is crucial for repeatability.

5. Conclusion

In conclusion, the markerless image processing based methodology applied in this study demonstrated that mechanical joint stresses and ergonomic risk factors occurring during manual material handling tasks can be analyzed independently of stringent laboratory constraints. This non-invasive approach, which does not disrupt the participant's natural movement mechanics, holds promise for conducting biomechanical and ergonomic assessments directly in field conditions.

In the future, it is recommended to test this method on a larger number of subjects across populations with diverse body types and heavier loads (10–20 kg). Examining asymmetric and 3D industrial tasks using this modeling framework will contribute significantly to the literature and occupational health and safety applications.

Author Contributions

The percentages of the authors' contributions are presented below. All authors reviewed and approved the final version of the manuscript.

	M.Ç.	B.U.	Ö.G.
C	20	20	60
D	20	20	60
S	10	30	60
DCP	80	10	10
DAI	60	20	20
L	80	10	10
W	80	10	10
CR	10	30	60
SR	60	20	20
PM	10	20	70
FA	0	0	0

C= concept, D= design, S= supervision, DCP= data collection and/or processing, DAI= data analysis and/or interpretation, L= literature search, W= writing, CR= critical review, SR= submission and revision, PM= project management, FA= funding acquisition.

Conflict of Interest

The authors declared that there is no conflict of interest.

Ethical Consideration

The authors confirm that the ethical policies of the journal, as noted on the journal's author guidelines page, have been adhered to. Ethics committee approval for the acquisition of the data used in this study was obtained from the Faculty of Science and Engineering Ethics Committee Presidency (Approval date: September 29, 2022, protocol code: 22/9).

Funding Statement

The authors declare that no financial support was received for the research, authorship, and/or publication of this article.

Data Availability Statement

The datasets generated and analyzed during the current study are available from the corresponding author upon reasonable request.

Acknowledgments

This study is partially based on the doctoral thesis authored by the first author at Atatürk University.

References

Amprimo, G., Masi, G., Pettiti, G., Olmo, G., Priano, L., & Ferraris, C. (2024). Hand tracking for clinical applications: Validation of the Google MediaPipe Hand (GMH) and the depth-enhanced GMH-D frameworks. *Biomedical Signal Processing and Control*, *96*, 106508.

Ayoub, M., & Woldstad, J. C. (1999). Models in manual materials handling. *Biomechanics in ergonomics*, 267-305.

Bazarevsky, V., Grishchenko, I., Raveendran, K., Zhu, T., Zhang, F., & Grundmann, M. (2020). Blazepose: On-device real-time body pose tracking. *arXiv preprint arXiv:2006.10204*.

Bhamidipati, V. S. P., Saxena, I., Saisanthiya, D., & Retnadhas, M. (2023). Robust intelligent posture estimation for an AI gym trainer using MediaPipe and OpenCV. 2023 International Conference on Networking and Communications (ICNWC) (pp. 1-7). IEEE

Ceseracciu, E., Sawacha, Z., & Cobelli, C. (2014). Comparison of markerless and marker-based motion capture technologies through simultaneous data collection during gait: proof of concept. *PloS one*, *9*(3), e87640.

Contini, R., Drillis, R. J., & Bluestein, M. (1963). Determination of body segment parameters. *Human Factors*, *5*(5), 493-504.

Çil, M. (2026). Vücut segment ataletlerinin ters dinamik yöntemiyle tespiti (Publication No. 1011746) [Doctoral dissertation, Atatürk Üniversitesi]. Ulusal Tez Merkezi.

Çil, M., Usanmaz, B., & Gündoğdu, Ö. (2026). An Investigation of Variable Segmental Inertial Parameters in Manual Load Lifting: A Genetic Algorithm-Based Inverse Dynamics Approach. *Mathematics*, *14*(6), 1065.

Dempster, W. T. (1955). *Space requirements of the seated operator, geometrical, kinematic, and mechanical aspects of the body with special reference to the limbs* (WADC-TR-55-159).

Dempster, W. T., Gabel, W. C., & Felts, W. J. (1959). The anthropometry of the manual work space for the seated subject. *American journal of physical anthropology*, *17*(4), 289-317.

Drillis, R., & Contini, R. (1966). *Body segment parameters*. New York University, School of Engineering and Science, Research Division.

Faber, G., Kingma, I., Chang, C., Dennerlein, J., & Van Dieen, J. (2020). Validation of a wearable system for 3D ambulatory L5/S1 moment assessment during manual lifting using instrumented shoes and an inertial sensor suit. *Journal of biomechanics*, *102*, 109671.

Faber, G. S., Chang, C., Kingma, I., Dennerlein, J., & Van Dieën, J. (2016). Estimating 3D L5/S1 moments and ground reaction forces during trunk bending using a full-body ambulatory inertial motion capture system. *Journal of biomechanics*, *49*(6), 904-912.

Google AI. (2025). *MediaPipe Solutions guide*. Google. Retrieved December 25 from https://ai.google.dev/edge/mediapipe/solutions/guide

Govaerts, R., Tassignon, B., Ghillebert, J., Serrien, B., De Bock, S., Ampe, T., El Makrini, I., Vanderborght, B., Meeusen, R., & De Pauw, K. (2021). Prevalence and incidence of work-related musculoskeletal disorders in secondary industries of 21st century Europe: a systematic review and meta-analysis. *BMC musculoskeletal disorders*, *22*(1), 751.

Hwang, S., Kim, Y., & Kim, Y. (2009). Lower extremity joint kinetics and lumbar curvature during squat and stoop lifting. *BMC musculoskeletal disorders*, *10*(1), 15.

Jiang, J., Skalli, W., Siadat, A., & Gajny, L. (2024). Societe de Biomecanique young investigator award 2023: Estimation of intersegmental load at L5-S1 during lifting/lowering tasks using force plate free markerless motion capture. *J Biomech*, *177*, 112422. https://doi.org/10.1016/j.jbiomech.2024.112422

Kusunose, M., Inui, A., Mifune, Y., Yamaura, K., Shinohara, I., Tanaka, S., Ehara, Y., Takigami, S., Osawa, S., & Nakabayashi, D. (2025). Estimation of Forearm Pronation–Supination Angles Using MediaPipe and IMU Sensors: Performance Comparison and Interpretability Analysis of Machine Learning Models. *Applied Sciences*, *15*(19), 10527.

Kwon, Y., & Kim, D. (2022). Real-time workout posture correction using OpenCV and MediaPipe. *The Journal of Korean Institute of Information Technology*, *20*(1), 199-208.

Marras, W., Granata, K., Davis, K., Allread, W., & Jorgensen, M. (1999). Effects of box features on spine loading during warehouse order selecting. *Ergonomics*, *42*(7), 980-996.

Robert-Lachaine, X., Mecheri, H., Larue, C., & Plamondon, A. (2017). Validation of inertial measurement units with an optoelectronic system for whole-body motion analysis. *Medical & biological engineering & computing*, *55*(4), 609-619.

Robertson, D. G. E., Caldwell, G. E., Hamill, J., Kamen, G., & Whittlesey, S. (2013). *Research methods in biomechanics*. Human kinetics.

Shaharum, S. M., Samsudin, W. S. W., Faudzi, A. A. M., Ghani, N. A., Ching, C. S., & Palaniappan, R. (2024). Enhancing urban wellness: real-time workout posture monitoring with human pose estimation and joint angle analysis using MediaPipe and OpenCV. 8th IET Smart Cities Symposium (SCS 2024) (Vol. 2024, pp. 429-435). IET

Taylor, G. A., Easter, K., & Hegney, R. (2004). *Enhancing occupational safety and health*. Elsevier.

The jamovi project. (2025). *jamovi*. (Version 2.7) [Computer software]. https://www.jamovi.org.

Wagh, V., Scott, M. W., & Kraeutner, S. N. (2024). Quantifying Similarities Between MediaPipe and a Known Standard to Address Issues in Tracking 2D Upper Limb Trajectories: Proof of Concept Study. *JMIR Formative Research*, *8*(1), e56682.

Wesseling, M., de Groote, F., & Jonkers, I. (2014). The effect of perturbing body segment parameters on calculated joint moments and muscle forces during gait. *J Biomech*, *47*(2), 596-601. https://doi.org/10.1016/j.jbiomech.2013.11.002

Winter, D. A. (2009). *Biomechanics and motor control of human movement*. John wiley & sons.

Yanıkören, M., Yılmaz, S., Usanmaz, B., Tezgel, S., Yazar, M., & Gündoğdu, Ö. (2020). Giyilebilir Hareket Sensörü Kullanılarak Dinamik Model ile Üst Uzuv Eklemleri Üzerine Etkiyen Kuvvetlerin ve Torkların Belirlenmesi. *Journal of the Institute of Science and Technology*, *10*(4), 2850-2859.

Yanikören, M., Yilmaz, S., Usanmaz, B., & Gündoğdu, Ö. (2026). Analysis of differences in manual material lifting behavior between healthy weight and underweight females. *Proceedings of the Institution of Mechanical Engineers, Part C: Journal of Mechanical Engineering Science*, 09544062261421992.

Black Sea Journal of Engineering and Science
doi: 10.34248/bsengineering.1997953

Open Access Journal
e-ISSN: 2619 – 8991

Research Article
Volume 9 - Issue 5: 2639-2651 / September 2026

DATA-DRIVEN VALIDATION AND CORRECTION OF THE DISTORTION FACTOR ESTIMATED FROM CURRENT TOTAL HARMONIC DISTORTION USING INDUSTRIAL FIELD MEASUREMENTS

Faruk KÜRKER[1]*, Ramazan TAŞALTIN[2]

[1]Adıyaman University, Faculty of Engineering, Department of Electrical and Electronics Engineering, 02040, Adıyaman, Türkiye
[2]Kahramanmaraş Sütçü İmam University, Faculty of Engineering and Architecture, Department of Electrical and Electronics Engineering, 46040, Kahramanmaraş, Türkiye

Abstract: In this study, the validity of the theoretical distortion factor based on total harmonic distortion of current (THDI) under industrial field conditions was evaluated, and low-complexity, data-driven correction models were developed to reduce formula error. The dataset was compiled from three-phase field measurements at 12 industrial measurement points. The measurement-based distortion factor was calculated from the PF/dPF ratio, while the theoretical distortion factor was calculated from the THDI-based equation. Since the phases at the same measurement point were not considered independent, the models were evaluated using a 12-cycle out-of-sample cross-validation method. The theoretical formula produced a mean absolute error of 0.015662, a root mean square error of 0.019681, and a mean bias of −0.009357. Among the compared models, restricted second-order regression produced the lowest error values, providing improvements of 31.83% and 15.70% in MAE and RMSE, respectively. Ridge regression, on the other hand, reduced the MAE to 0.012263 and brought the mean bias close to zero. However, the data-driven models did not reduce the maximum absolute error. At the measurement-point level, the Wilcoxon signed-rank test indicated lower paired errors after Ridge correction (P=0.0342), whereas the 95% bootstrap confidence interval for the mean paired MAE difference included zero. Taken together, these findings provide positive but limited evidence regarding the error-reduction potential of the Ridge correction. The results show that the THDI-based formula provides an interpretable initial estimate but cannot, on its own, account for field conditions such as phase asymmetry, load level, power factor, and voltage distortion. The proposed correction approach should be considered not as a universal formula but as an empirical calibration approach specific to the available field data.

Keywords: Distortion factor, Total harmonic distortion of current, Power factor, Industrial field measurements, Ridge regression, Out-of-measurement-point cross-validation

***Corresponding author:** Adıyaman University, Faculty of Engineering, Department of Electrical and Electronics Engineering, 02040, Adıyaman, Türkiye
E mail: fkurker@adiyaman.edu.tr (F. KÜRKER)
Faruk KÜRKER https://orcid.org/0000-0003-1544-9743
Ramazan TAŞALTIN https://orcid.org/0000-0003-2026-2430

Received: July 18, 2026
Accepted: August 20, 2026
Published: September 15, 2026

Cite as: Kürker, F., & Taşaltın, R. (2026). Data-driven validation and correction of the distortion factor estimated from current total harmonic distortion using industrial field measurements. *Black Sea Journal of Engineering and Science,* 9(5), 2639-2651.

1. Introduction

The reliable and efficient use of electrical energy depends on voltage and current waveforms having acceptable power quality characteristics. However, variable-speed drives, rectifiers, uninterruptible power supplies, switched-mode power supplies, arc furnaces, and other power electronics-based equipment generate harmonic components due to their nonlinear current–voltage behavior. When harmonic currents flow through the grid impedance, they can cause distortion of the voltage waveform and affect other loads connected to the same electrical system. The level of harmonic distortion depends not only on the type of load but also on the load factor, the topology of the power electronics converter, existing distortion in the supply voltage, system impedance, and the simultaneous operating conditions of loads connected to the same busbar (Kürker, 2017; Senra et al., 2017; Michalec et al., 2021; Hu et al., 2023).

Harmonic distortion can lead to technical consequences such as a decrease in power factor, increased conductor and transformer losses, thermal stress, an increase in neutral current, the risk of resonance, and impaired performance of measurement or protection systems. Therefore, the evaluation of harmonics is not merely a waveform analysis but also an engineering problem aimed at assessing system capacity and energy usage efficiency. IEEE Std 519-2022, published by the Institute of Electrical and Electronics Engineers, defines limits and design objectives for controlling steady-state voltage and current distortions at the common connection point (IEEE, 2022). IEC 61000-4-7, published by the International Electrotechnical Commission, explains the

This work is licensed (CC BY-NC 4.0) under Creative Commons Attribution 4.0 International License

principles of measurement categorization using harmonic and interharmonic measurement devices (IEC, 2009), IEC 61000-4-30 describes the methods and measurement classes for conducting field power quality measurements in a repeatable manner (IEC, 2025). Studies conducted on industrial systems also demonstrate that harmonic currents can interact with system impedance to cause voltage distortion and that harmonic evaluation depends on the measurement point (Obulesu et al., 2014; Ugwuagbo et al., 2021).

The interpretation of the power factor under harmonic conditions is more comprehensive than the classical cosφ approach used in sinusoidal systems. While the displacement power factor represents the phase difference between the voltage and current at the fundamental frequency, the total power factor also accounts for the effect of harmonic components on apparent power. IEEE Std 1459-2025 provides an expanded framework for defining power quantities in non-sinusoidal, unbalanced, and polyphase systems (IEEE, 2025). The physical meaning and definition of power components in systems with harmonics have long been debated; it has been shown that a single definition of reactive or distortion power may be insufficient to account for all non-sinusoidal conditions (Czarnecki, 1987; Ferrero and Superti-Furga, 1991; Emanuel, 2004; Willems, 2004). Therefore, the total power factor, displacement power factor, and harmonic distortion indices should be considered complementary quantities representing different electrical effects, rather than interchangeable ones.

In a simplified scenario where the supply voltage is ideally sinusoidal and non-fundamental components are primarily present in the load current, the current distortion factor can be expressed using the $\frac{1}{\sqrt{1+THDI^2}}$ relationship. This approach allows for a quick and easily interpretable estimate of the distortion factor based on the THDI value. However, in real industrial systems, voltage distortion, phase asymmetry, light-load conditions, time-dependent operating points of loads, and voltage–current interactions outside the fundamental frequency can undermine the assumptions of this simple relationship (IEEE, 2025; Emanuel, 2004; Willems, 2004; Senra et al., 2017). In particular, it has been experimentally demonstrated that the harmonic currents drawn by a nonlinear load under a distorted supply voltage can vary depending on the amplitude and phase of the voltage harmonics (Senra et al., 2017). Therefore, the extent to which the theoretical distortion factor calculated using only THDI represents the PF/dPF ratio measured under field conditions must be verified with direct measurement data.

The presence of multiple nonlinear loads in the same system further complicates the formula–measurement relationship. Harmonic components may not simply add up arithmetically across loads; depending on the phase angles of the components, partial addition or cancellation may occur. Measurements taken with different load combinations in a low-voltage grid have shown that the THDI value of the total load current may be lower than the THDI values of individual devices (Michalec et al., 2021). Similarly, the harmonic voltage observed at industrial common connection points may consist of the phasor sum of grid-background harmonics and consumer-generated harmonics (Ugwuagbo et al., 2021; Liu et al., 2023). These findings demonstrate that the relationship between THDI and power factor depends not only on the magnitude of the harmonics but also on the electrical context of the system.

Although THDI, THDU, total power factor, and displacement power factor are widely used in power quality studies, these metrics can yield different or seemingly contradictory assessments for certain loads. For this reason, new metrics that more comprehensively describe the effect of harmonics on power and losses have been proposed (Coelho et al., 2024). In the analysis of measurement data, artificial neural networks, Random Forest, and other data-driven methods have been used for monitoring harmonic distortion and for prediction problems related to electrical energy (Nascimento et al., 2013; Nur et al., 2025). However, high-capacity models may lead to overly optimistic performance estimates and the risk of overfitting in field studies with a limited number of independent measurement units. In such datasets, models with lower complexity that are interpretable and evaluated using an appropriate cross-validation scheme offer a more defensible approach (Hoerl and Kennard, 1970; Roberts et al., 2017; Vabalas et al., 2019).

In particular, when repeated observations from the same facility, measurement point, or piece of equipment are randomly assigned to training and test sets as if they were independent, the model may detect characteristics specific to that group during both the training and evaluation phases. This situation can lead to an underestimation of the actual generalization error. For this reason, it is important to construct cross-validation sets based on independent units in hierarchical or grouped data (Roberts et al., 2017). Furthermore, the relationship between a new computational approach and reference values should be examined not only using correlation or aggregated error measures but also in conjunction with mean bias and the 95% limits of agreement (Bland and Altman, 1986). Small-sample uncertainty can be assessed using the bootstrap resampling method (Efron, 1979), while differences in error at the matched field level can be evaluated using the Wilcoxon signed-rank test, which does not require the assumption of a parametric distribution (Wilcoxon, 1945).

The current literature contains comprehensive studies on the modeling of harmonic sources, the separation of harmonic contributions, filter design, the development of new power quality indicators, and data-driven estimation of harmonics (Nascimento et al., 2013; Obulesu et al.,

2014; Ugwuagbo et al., 2021; Hu et al., 2023; Liu et al., 2023; Coelho et al., 2024). However, within the scope of the reviewed studies, there are few that directly compare the measured distortion factor—based on the PF/dPF ratio from field measurements obtained at different industrial loads and connection points—with the theoretical factor calculated solely from THDI; correct the residual error of the theoretical formula using low-complexity models; and simultaneously address group structure, limits of agreement, and small-sample uncertainty. This gap necessitates an investigation not only of the average performance of the theoretical relationship under field conditions but also of the measurement points and operating conditions where it produces significant deviations.

The objective of this study is to evaluate the validity of the THDI-based theoretical distortion factor using three-phase field measurements from 12 industrial measurement points and to investigate whether the observed formula deviation can be reduced using low-complexity, data-driven models. The measurements used were obtained as part of a previously completed doctoral dissertation, reorganized for the present study, and analyzed after verifying the integrity of the calculations (Kürker, 2017). The main contributions of the study are as follows: (i) verification of the consistency between reported and recalculated PF/dPF ratios and THDI-based theoretical distortion factors; (ii) comparison of linear regression, robust linear regression, Ridge regression, restricted second-order regression, and small regression trees under out-of-sample cross-validation; (iii) evaluation of model performance using a combination of mean and maximum error, bias, Bland–Altman 95% limits of agreement, the Wilcoxon test at the measurement point level, and bootstrap confidence intervals; and (iv) examination of formula errors in the context of phase, load level, total harmonic distortion of voltage (THDU), and phase asymmetry. Within this framework, the study aims not to propose a universal corrected THDI equation, but rather to highlight the strengths and limitations of the theoretical approach in industrial field data and to cautiously evaluate the potential benefits that data-driven correction could provide.

2. Materials and Methods

2.1. Research Design and Data Source

This study is based on a retrospective and secondary analysis of three-phase power quality measurements previously conducted at various industrial loads and connection points. The field data used were obtained as part of the doctoral dissertation titled "Harmonic Analysis and Harmonic Mitigation Techniques in Power Systems," completed in 2017 at the Institute of Natural Sciences at Harran University (Kürker, 2017). No new field measurements were conducted in the present study; the phase-level electrical quantities reported in the source measurements were reorganized, checked for computational consistency, and reanalyzed to evaluate the THDI-based distortion factor.

The dataset consists of 12 three-phase measurement points representing different processes and electrical connection conditions. Since the phases at the same measurement point share common electrical and operational conditions, they were not considered independent observations; the measurement point was defined as the independent unit of analysis for model validation and statistical comparisons. For this reason, low-complexity and interpretable correction models were used instead of high-capacity models.

2.2. Measurement System and Characteristics of Source Measurements

Field measurements were performed using the Amprobe Energy Test 2020 power and harmonic analyzer. The thesis states that the device can measure current and voltage harmonics, active power, reactive power, apparent power, total power factor, and displacement power factor in three-phase systems. The device also has the capability to record the measured electrical quantities and transfer them to a computer.

In this study, the root-mean-square (RMS) value of phase current (Irms), total power factor (PF), displacement power factor (dPF), total current harmonic distortion (THDI), and total voltage harmonic distortion (THDU) were used. In the source thesis, dPF is defined as the power factor related to the phase difference between the current and voltage at the fundamental frequency, while PF represents the total power factor under harmonic operating conditions.

In the source thesis, the device's calibration date, measurement uncertainty, IEC measurement class, and harmonic binning window were not explicitly reported. Therefore, no additional assumptions regarding the device's measurement class or absolute metrological accuracy were made in the present study.

2.3. Data Preparation and Calculation of Distortion Factors

The analysis data table consists of measurement point ID, measurement location, phase, Irms, PF, dPF, THDI, THDU, reported distortion factors, and recalculated control variables. The data columns and variable names used in the code are clearly defined at the beginning of the analysis.

The measurement-based distortion factor was calculated as the ratio of the total power factor (PF) to the displacement power factor (dPF) (equation 1):

$$DF_{measured} = \frac{PF}{dPF} \quad (1)$$

The THDI-based theoretical distortion factor is determined by the following equation 2:

$$DF_{THDI} = \frac{1}{\sqrt{1+\left(\frac{THDI}{100}\right)^2}} \quad (2)$$

The deviation from the theoretical formula at the phase level is defined as the difference between the measured and theoretical distortion factors (equation 3):

$$\Delta DF = DF_{measured} - DF_{THDI} \quad (3)$$

The absolute formula error is defined in the text as AE = |ΔDF|. The relative error, on the other hand, is calculated by expressing the ratio of the ΔDF value to the measured distortion factor as a percentage.

The PF/dPF and theoretical distortion factor values reported in the source tables were compared with the values recalculated using equations 1 and 2. In subsequent modeling and error analyses, the recalculated values were used instead of the reported rounded values. The basic and derived variables used in the analysis are summarized in Table 1.

Table 1. Basic and derived variables used in the analysis

Variable	Description	Unit or Calculation	Role in the Analysis
I_{rms}	RMS phase current	A	Load-level indicator
PF	Total power factor	Dimensionless	Measured DF calculation
dPF	Displacement power factor	Dimensionless	Measured DF calculation
THDI	Current total harmonic distortion	%	Theoretical DF calculation
THDU	Voltage total harmonic distortion	%	Correction model input
$DF_{measured}$	Measurement-based distortion factor	PF/dPF	Reference output
DF_{THDI}	THDI-based theoretical distortion factor	Equation (2)	Baseline model
ΔDF	Formula deviation	$DF_{measured} - DF_{THDI}$	Regression target
AE	Absolute formula error	|ΔDF|	Absolute error and exploratory classification metric
$\log(I_{rms})$	Logarithmic current variable	$\ln(1 + I_{rms})$	Correction model input

2.4. Exploratory Data Analysis and Outlier Screening

Prior to modeling, the minimum, maximum, mean, median, standard deviation, variance, range, interquartile range, coefficient of variation, skewness, and kurtosis values were calculated for I_{rms}, PF, dPF, THDI, THDU, the measured distortion factor, the theoretical distortion factor, and ΔDF.

Variable distributions were explored using histograms, box plots, and violin plots; bivariate relationships between variables were examined using a correlation matrix and scatter plots. Theoretical normal distribution curves added to the histograms were used solely for visual identification purposes, and no formal conclusion regarding the normality of the distributions was drawn from these plots.

Potential outliers were screened using Tukey's 1.5×IQR method. The lower limit was set at Q1−1.5IQR, and the upper limit at Q3+1.5IQR. Observations falling outside these limits were flagged but were not removed from the dataset solely because they were identified as outliers. The flagged values were evaluated in conjunction with the measurement point, phase, load level, and phase asymmetry.

2.5. Correction Objective and Selection of Explanatory Variables

The objective of data-driven modeling was defined as estimating the deviation from the THDI-based theoretical formula, rather than directly re-estimating the measured distortion factor. The corrected distortion factor was calculated as follows (equation 4):

$$DF_{corrected} = DF_{THDI} + \widehat{\Delta DF} \quad (4)$$

Here, $\widehat{\Delta DF}$ represents the formula correction estimated by the data-driven model.

Because current values vary over a wide range, Irms has been subjected to the $\ln(1+I_{rms})$ transformation. THDU and $\ln(1+I_{rms})$ were used as explanatory variables in the main correction models. Since THDI is used directly in the calculation of the theoretical distortion factor, it was not included in the main model inputs to limit the reweighting of the same information in the correction layer.

Multicollinearity among the candidate variables was assessed using the correlation matrix and the variance inflation factor (VIF). VIF values were calculated using the R2 values obtained from the linear models established for each variable with the other candidate variables.

2.6. Data-Driven Correction Models

Since the independent analysis unit was limited to 12 measurement points, high-capacity machine learning and deep learning models were not used. Instead, five low-complexity models that were more suitable for the sample structure and more interpretable were compared:

. Ordinary least squares-based linear regression,

. robust linear regression,

. L2-regularized Ridge regression,

. restricted second-order regression including the $THDU^2$ term,

. a small regression tree consisting of leaves with at most three splits and at least five observations.

In the linear, robust, and Ridge models, the explanatory variables used were THDU and $\ln(1+I_{rms})$. In the restricted second-order regression, the $THDU^2$ term was added to the predictors; no interaction terms or

additional higher-order terms were included. In the regression tree, the settings MaxNumSplits=3 and MinLeafSize=5 were applied.

Model complexities were pre-constrained, and no separate hyperparameter optimization was performed. In Ridge regression, the regularization type was set to L2; however, the regularization coefficient was not explicitly fixed in the current code.

2.7. Out-of-Measurement-Point Cross-Validation

The out-of-measurement-point cross-validation method was used to prevent phases belonging to the same measurement point from being distributed together across the training and test sets. In each validation cycle, three phases belonging to a single measurement point were assigned to the test set, while the remaining 33 phases from the other 11 measurement points were used as the training set. The process was repeated 12 times, ensuring that each measurement point appeared in the test set exactly once.

In each cycle, the model was trained using only the ΔDF values from the training measurement points, and the predicted error for each phase at the test measurement point was added to the corresponding DF_{THDI} value. Thus, each corrected estimate was obtained from a validation cycle in which the relevant measurement point was not included in the model training.

2.8. Evaluation of Model Performance

The theoretical baseline formula and data-driven models were compared based on LOSO prediction errors. The prediction error for a given observation was defined as $e_i = DF_{measured,i} - \widehat{DF}_i$.

The mean absolute error was calculated as follows (equation 5):

$$MAE = \frac{1}{n}\sum_{i=1}^{n}|e_i| \quad (5)$$

Root mean square error (equation 6):

$$RMSE = \sqrt{\frac{1}{n}\sum_{i=1}^{n} e_i^2} \quad (6)$$

and mean bias (equation 7):

$$Bias = \frac{1}{n}\sum_{i=1}^{n} e_i \quad (7)$$

have been determined.

In addition, the maximum absolute error and the median absolute error have been reported. The improvement percentages for MAE and RMSE were calculated by dividing the reduction in error between the model and the theoretical baseline formula by the error of the theoretical baseline formula. Positive improvement values indicate a lower error compared to the theoretical formula.

2.9. Statistical Comparison and Uncertainty Analysis

Although the restricted second-order regression produced the lowest aggregate MAE and RMSE values, Ridge regression was selected as the focal model for the subsequent agreement, statistical uncertainty, and coefficient-stability analyses. This choice was based on its additive linear structure, L2-regularized formulation, and lower functional complexity compared with the restricted second-order regression, which additionally includes a squared THDU term. Given the limited number of independent measurement points, Ridge regression was therefore treated as a parsimonious and cautious reference model for evaluating the behavior of a regularized correction. This selection does not imply that Ridge regression was the best-performing model according to the aggregate prediction-error metrics.

Since the phase records are not independent within the same measurement point, the statistical comparison between the theoretical baseline formula and the Ridge model was performed at the measurement point level. The mean absolute error (MAE) for the three phases was calculated for each measurement point, and the 12 paired measurement-point-level MAE values of the theoretical formula and the Ridge model were compared using the Wilcoxon signed-rank test.

The uncertainty in the mean measurement-point-level MAE difference was evaluated using a nonparametric bootstrap analysis with 5,000 resamples. First, the MAE values of the theoretical formula and the Ridge model were calculated separately for each of the 12 measurement points using the three corresponding phase-level errors. A paired MAE difference was then defined for each measurement point as MAEtheoretical − MAERidge, such that a positive value indicated a lower error for the Ridge model. The 12 paired measurement-point-level MAE differences were resampled with replacement. In each bootstrap iteration, 12 paired differences were drawn with replacement and their arithmetic mean was calculated. The 95% percentile confidence interval was obtained from the 2.5th and 97.5th percentiles of the bootstrap distribution. For reproducibility, the random number seed was fixed at 42.

The stability of the Ridge coefficients was examined based on the mean, standard deviation, and sign consistency of the THDU and logarithmic current coefficients obtained over 12 LOSO cycles.

2.10. Bland–Altman and Residual Analyses

The agreement between the theoretical formula and the Ridge-corrected values was evaluated using Bland–Altman analysis. The mean difference was taken as the bias, and the approximate 95% limits of agreement (LoA) were calculated as follows (equation 8):

$$LoA = Bias \pm 1.96SD(e) \quad (8)$$

Bland–Altman plots were used to assess descriptive agreement at the phase level; statistical inferences were based on Wilcoxon and bootstrap analyses at the measurement point level.

The structure of the Ridge residuals was visually assessed using residual–THDU, residual–ln(1+I_{rms}), and normal probability plots. No formal hypothesis test was conducted to assess residual normality or constant variance.

2.11. Exploratory Agreement Classes

To describe the behavior of the THDI-based theoretical

formula at different error levels, phase records were divided into three exploratory classes based on absolute error (equation 9):

$$Agreement\ class = \begin{cases} High\ agreement, & AE < 0.01, \\ Moderate\ agreemnet, & 0.01 \le AE < 0.03, \\ Low\ agreement, & AE \ge 0.03. \end{cases} \quad (9)$$

These thresholds were not derived from any standard but were determined solely for the purpose of exploratory evaluation of the existing dataset. To examine threshold sensitivity, the baseline thresholds were tightened and relaxed by 50%, and the resulting class frequencies were compared.

The relationship between the exploratory agreement classes and THDI, THDU, and logarithmic current was explored using a small classification tree with a maximum of three splits and leaves containing at least five observations. This model was not evaluated as a generalizable classifier.

2.12. Anomaly and Measurement Context Indicators

In data quality control, the conditions PF/dPF > 1, missing or zero THDU, and AE ≥ 0.03 were used as rule-based anomaly indicators. The phase-level anomaly score was calculated as the number of conditions met.

Phase current imbalance at the measurement point level was determined as follows (equation 10):

$$I_{imbalance} = \frac{max(I_{rms}) - min(I_{rms})}{\overline{I_{rms}}} \quad (10)$$

In addition, the power factor variation between phases was calculated as PF_{range} = max(PF) − min(PF). Records with phase current below 10 A were flagged as low load, while records with a PF range above 0.30 within the measurement point were flagged for phase asymmetry. These thresholds are not standard compliance criteria but rather screening thresholds specific to the current dataset. No observations were excluded from the analysis due to these flags.

2.13. PCA and Hierarchical Clustering

Rather than classifying the general load types of the measurement points, complementary principal component analysis and hierarchical clustering were applied solely to examine their similarities in terms of the error behavior of the THDI-based formula.

For each measurement point, the mean absolute error, mean THDI, mean THDU, and standard deviation of ΔDF were calculated for the three phases. This resulted in a field-level data matrix consisting of 12 measurement points and four features. To minimize the effect of variables being on different scales on the PCA and distance calculations, the features were standardized using z-score transformation.

PCA was performed on the standardized 12×4 data matrix, and the measurement points were plotted in the score plane of the first two principal components. Hierarchical clustering was performed using the same standardized feature matrix, Euclidean distance, and Ward's linkage method. No predefined number of clusters or dendrogram cutoff distance was applied. Therefore, the results were interpreted as exploratory findings illustrating relative similarities among measurement points; no fixed or generalizable industrial load classes were derived.

2.14. Analysis Workflow and Software

Figure 1 summarizes the complete analysis workflow, including the data source and anonymization, recalculation of the distortion factors, data-integrity checks, exploratory analysis, LOSO validation, model comparison, statistical uncertainty analysis, agreement and residual diagnostics, exploratory agreement-class analysis, and the PCA and hierarchical clustering stages.

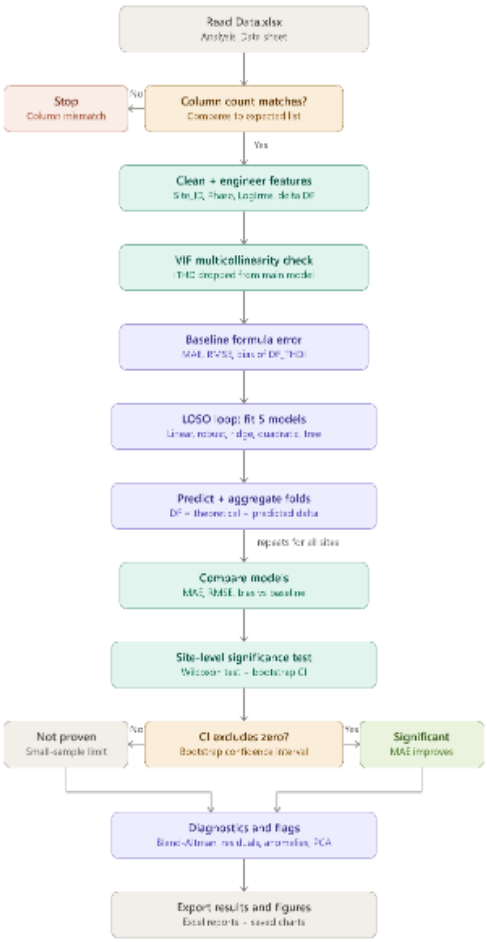


Figure 1. Analysis workflow for the validation of the THDI-based distortion factor using industrial field measurements and its data-driven correction.

3. Results

3.1. Data integrity and the fundamental performance of the THDI-based theoretical distortion factor

The dataset for this study consists of three-phase field measurements from 12 industrial measurement points. In the dataset, the total harmonic distortion of current (THDI) ranged from 11.946% to 64.618%, the total harmonic distortion of voltage (THDU) ranged from 0.953% to 8.870%, and the phase currents ranged from 0.886 to 290.760 A. This variability allowed for the evaluation of the THDI-based theoretical distortion factor

under different load levels and field operating conditions. First, the reported distortion factors were compared with the recalculated values. The highest absolute difference between the values calculated from the PF/dPF ratio for the measured distortion factor and the reported values was 0.000479; for the THDI-based theoretical distortion factor, it was determined to be 0.000459. Therefore, it was concluded that the minor differences between the reported and recalculated values were primarily due to rounding. Specifically, for the third phase S12, the measured distortion factor calculated from the values PF = 0.179 and dPF = 0.1811 is 0.988404. Therefore, the high relative error value observed earlier stems not from a calculation error but from the actual difference between the measured and THDI-based theoretical distortion factors.

The mean absolute error, root mean square error, and mean bias of the THDI-based theoretical formula across the entire dataset were calculated as 0.015662, 0.019681, and −0.009357, respectively. For the majority of phase-level measurements, the measured distortion factor remained below the theoretical value. The negative mean bias indicates that the theoretical formula tends to overestimate the distortion factor on average in the analyzed dataset. However, the error distribution is not entirely one-sided; error values ranged from −0.038720 to +0.055927. This result shows that, despite a systematic tendency to overestimate the distortion factor on average, the theoretical formula can also underestimate the measured distortion factor under certain load and phase conditions.

In the multicollinearity analysis conducted for variables that could be used in the correction model, the variance inflation factors for the THDI, THDU, and log(Irms) variables were determined to be 1.15, 1.09, and 1.23, respectively. These values indicate that there is no significant multicollinearity issue among the candidate variables. However, since THDI is already used directly in the calculation of the theoretical distortion factor, it was not included in the set of independent variables to prevent the same information from being reweighted in the correction model and to ensure that the model focuses on the contribution of additional explanatory variables.

3.2. LOSO Performance of Data-Driven Correction Models

The generalization performance of the models was evaluated using a measurement-point-excluded cross-validation method, which prevents the three phases associated with the same measurement point from being distributed across the training and test sets. In this approach, the three phases associated with a single measurement point were assigned to the test set together in each iteration, and a total of 12 validation cycles were performed. The performance of the theoretical baseline formula and the linear, robust, Ridge, restricted second-order regression, and decision tree models is compared in Table 2.

Table 2. Comparison of LOSO performance between the THDI-based theoretical formula and data-driven correction models

Model	MAE	RMSE	Bias	Maximum Absolute Error	Median Absolute Error	MAE Improvement (%)	RMSE Improvement (%)
Theoretical Baseline Formula	0.01566	0.019681	-0.00936	0.055927	0.011937	0.00	0.00
Linear	0.01229	0.018678	0.000037	0.066484	0.009878	21.50	5.09
Robust	0.01131	0.018435	0.002029	0.068745	0.006487	27.79	6.33
Ridge	0.01226	0.018660	0.000057	0.066482	0.009772	21.70	5.19
Restricted Second-Order Regression	0.01068	0.016590	-0.00046	0.068687	0.007089	31.83	15.70
Decision Tree	0.01413	0.018824	-0.00067	0.067629	0.010357	9.79	4.35

The restricted second-order regression yielded the best results in terms of average performance metrics, with an MAE of 0.010677 and an RMSE of 0.016590. Relative to the theoretical baseline formula, these values correspond to improvements of 31.83% and 15.70%, respectively. The robust model produced the lowest median absolute error, at 0.006487. However, a convergence warning indicating that the iteration limit had been reached was generated during robust regression fitting. Therefore, the robust regression results were retained only as a complementary comparison and should be interpreted with caution. No claim of model superiority is made on the basis of these results, because convergence was not fully established under the applied fitting settings.

Ridge regression, considered the main regularization model in this study, reduced the MAE value of the theoretical formula from 0.015662 to 0.012263, achieving a 21.70% improvement. The improvement in RMSE was more limited, remaining at 5.19%. The most pronounced effect of the Ridge model was observed on the mean bias. The bias, which was −0.009357 in the theoretical formula, approached 0.000057 after Ridge

correction. This result indicates that the model largely eliminated the systematic tendency toward high overestimation present in the theoretical formula.

Although the restricted second-order regression remained the best-performing model in terms of aggregate MAE and RMSE, Ridge regression was retained for the detailed diagnostic analyses because it provides a regularized linear correction without introducing the additional nonlinear $THDU^2$ term. Thus, the subsequent focus on Ridge regression reflects a preference for a more parsimonious and interpretable reference model under the limited independent-sample structure, rather than a claim that it achieved the lowest overall prediction error.

However, none of the data-driven models were able to reduce the maximum absolute error. The maximum absolute error, which was 0.055927 in the theoretical formula, increased to 0.066482 in the Ridge model and to 0.068687 in the restricted second-order regression. Thus, data-driven corrections reduced the mean error but produced larger estimation errors in some outlier observations. This finding indicates that model evaluation should not be based solely on aggregated metrics such as MAE or RMSE.

The relationship between the measured distortion factors and the estimates produced by the theoretical baseline formula and the Ridge model is shown in Figure 2. The dashed 1:1 line represents equality between the measured and predicted distortion factors. The Ridge correction moved a substantial proportion of the observations closer to the 1:1 line; however, noticeable deviations persisted, particularly for the extreme phase-level observations.

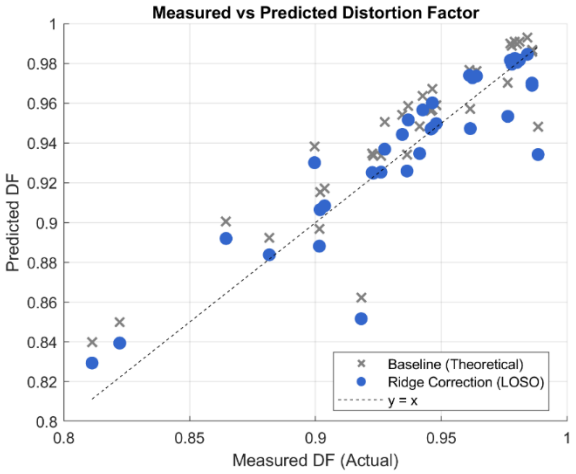


Figure 2. Comparison of the measured distortion factor with the estimates from the THDI-based theoretical baseline formula and the LOSO Ridge correction. The dashed line represents the 1:1 line.

3.3. Bias, 95% Limits of Agreement, and Statistical Uncertainty

The agreement between the theoretical baseline formula and the Ridge-corrected values was further examined using the Bland–Altman plots shown in Figure 3. For the theoretical formula, the mean difference between the measured and theoretical distortion factors was −0.009357, and the approximate 95% limits of agreement ranged from −0.043774 to 0.025059. For the Ridge model, the mean difference was 0.000057, while the approximate 95% limits of agreement ranged from −0.037035 to 0.037148.

These results indicate that Ridge regularization nearly eliminated the mean bias but did not reduce the dispersion of the differences. The total width of the 95% limits of agreement was approximately 0.06883 for the theoretical formula and 0.07418 for the Ridge model. Therefore, the primary benefit of the Ridge correction was to center the differences closer to zero rather than to narrow their variability at the phase or measurement-point level.

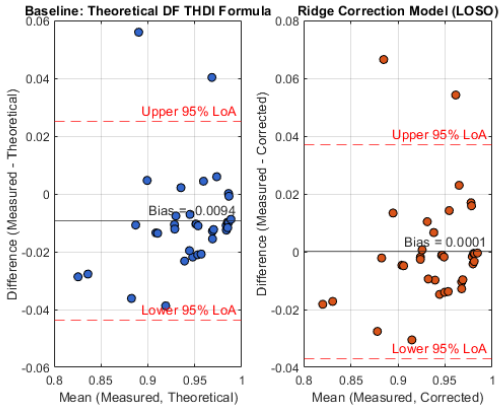


Figure 3. Bland–Altman plots showing the bias and approximate 95% limits of agreement for the THDI-based theoretical formula and the LOSO Ridge correction.

In the Wilcoxon signed-rank test based on the 12 paired measurement-point-level MAE values, the difference between the theoretical formula and the Ridge model yielded a p-value of 0.0342. This rank-based paired result indicates a systematic tendency toward lower measurement-point-level errors after Ridge correction. In the bootstrap analysis based on 5,000 resamples of the 12 paired measurement-point-level MAE differences, the estimated mean difference, defined as MAEtheoretical − MAERidge, was 0.00339, with a 95% percentile confidence interval ranging from −0.00093 to 0.00657. Because this interval included zero, a positive improvement in the arithmetic mean could not be established with sufficient precision using the current 12 measurement points. These findings are not directly contradictory because the two analyses evaluate different statistical features of the paired differences. The Wilcoxon signed-rank test evaluates a rank-based paired location shift, whereas the bootstrap confidence interval quantifies uncertainty in the arithmetic mean of the paired MAE differences. Taken together, the results provide positive but limited evidence regarding the error-reduction potential of the Ridge correction rather

than definitive statistical confirmation of improvement.

3.4. Error Behavior at the Measurement Point and Phase Levels

In the measurement-point-based analysis, it was determined that the Ridge model reduced the MAE value at 11 out of 12 measurement points. The most significant absolute reductions were observed at S01 (from 0.010188 to 0.000977), S06 (from 0.010643 to 0.001411), S04 (from 0.012582 to 0.003802), and S07 (from 0.011003 to 0.002675). In contrast, while the field-based MAE value of the theoretical formula in S10 was only 0.002295, it rose to 0.018605 in the Ridge model. In S12, the MAE decreased from 0.023535 to 0.023417, showing only a limited change.

The loss of performance in S10 demonstrates that a general correction model can produce unnecessary corrections at measurement points where the theoretical formula already provides high accuracy. Therefore, rather than applying the correction model unconditionally to every site, it may be more appropriate to use an application or reliability criterion that evaluates the model's expected benefit based on the theoretical formula.

Observations with an absolute distortion factor error above 0.03 are presented in Table 3. It is noteworthy that all four high-error observations occurred in the third phase. However, this pattern, based on only four observations, should not be interpreted as indicating a general systematic error for the third phase.

Table 3. Phase observations with an absolute distortion factor error greater than 0.03

Measurement Point	Phase	THDI (%)	PF	dPF	Measured DF	Theoretical DF	Error	Absolute Relative Error (%)
S05 – Steam Fixation Process	3	58.75	0.83	0.904	0.918142	0.862215	0.055927	6.091
S08 – Water System, Inverter Input	3	48.26	0.338	0.391	0.86445	0.900597	-0.03615	4.181
S09 – Water System, Grid Input	3	36.85	0.233	0.259	0.899614	0.938334	-0.03872	4.304
S12 – Laser Supply 3	3	33.53	0.179	0.1811	0.988404	0.94812	0.040284	4.076

The signs of the high-error observations are not the same. While the distortion factor measured in the third phases of S05 and S12 was higher than the theoretical value, the value measured in the third phases of S08 and S09 was below the theoretical value. This bidirectional error behavior indicates that a constant or unidirectional correction applied to all observations would not be sufficient to explain the extreme cases.

The result for the third phase of S12 also demonstrates the need to interpret the distortion factor and the total power factor together. In this observation, although the PF/dPF ratio is 0.988404, both PF and dPF are approximately 0.18. Therefore, a distortion factor close to 1 does not necessarily imply a high total power factor. In this case, the dominant component of the low total power factor is related to phase shift, and the ratio of PF to dPF alone does not represent the load's overall power factor performance.

Significant PF differences between phases were identified at some of the S08–S12 measurement points. The PF range is 0.541 at S08, 0.693 at S09, 0.792 at S10, 0.565 at S11, and 0.704 at S12. The S03 and S07 observations, meanwhile, have been flagged separately for reliability purposes due to low current levels. These flags should not be interpreted as direct data errors; however, they indicate that the variability of the PF/dPF ratio may increase under single-phase-dominant loads, phase asymmetry, and low-load conditions.

3.5. Residual Analysis and Model Stability

Figure 4 shows the distribution of residuals from the Ridge model with respect to THDU and logarithmic current level, together with a normal probability plot. Although the model reduced the mean bias, several relatively large residuals remained. Because no formal statistical tests of residual normality or heteroscedasticity were conducted, the plots were interpreted solely as visual diagnostic tools.

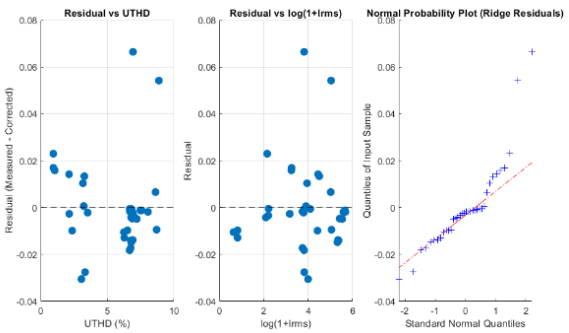


Figure 4. Residual diagnostics and normal probability plot for the LOSO Ridge correction model based on THDU and log(I_{rms}).

When examining the stability of the Ridge coefficients over 12 LOSO cycles, the mean of the THDU coefficient was found to be 0.00007 and the standard deviation 0.00047; the coefficient took on positive values in eight of the 12 cycles. The mean of the log(I_{rms}) coefficient was −0.00020, with a standard deviation of 0.00057, and the coefficient remained positive in only five cycles. The variation in the signs of the coefficients across validation

cycles indicates that the physical effects of the explanatory variables cannot be reliably determined with the current dataset. This alone does not prove that the model is invalid or overfitted; however, it limits the physical interpretation of the coefficients and points to high model uncertainty. Therefore, the Ridge model should be presented not as a physical equation explaining the causal effect of THDU or the current distortion factor, but as an empirical correction model aimed at reducing the average bias of the theoretical formula based on field data.

4. Discussion

4.1. Exploratory Agreement Classes and Threshold Sensitivity

Using the exploratory absolute-error thresholds of 0.01 and 0.03, 11 observations were assigned to the high-agreement class, 21 to the moderate-agreement class, and four to the low-agreement class. The distribution of these exploratory agreement classes in the THDI–THDU plane is shown in Figure 5. The observations in the low-agreement class were not concentrated within a specific THDI or THDU region but occurred at different distortion levels.

When the thresholds were tightened by 50%, the distribution changed to five high-agreement, 19 moderate-agreement, and 12 low-agreement observations. When the thresholds were relaxed by 50%, the distribution changed to 24 high-agreement, 11 moderate-agreement, and one low-agreement observation. These changes demonstrate that the classification is sensitive to the selected absolute-error thresholds. Therefore, the thresholds of 0.01 and 0.03 should not be interpreted as standard, universal, or compliance limits; they are working thresholds used solely for the exploratory evaluation of the current dataset.

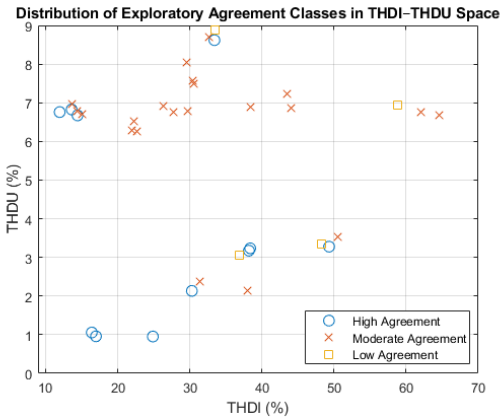


Figure 5. Distribution of the exploratory agreement classes, defined according to the absolute distortion-factor error, in the THDI–THDU plane.

The high-, moderate-, and low-agreement classes were defined using the thresholds $|e| < 0.01$, $0.01 \le |e| < 0.03$, and $|e| \ge 0.03$, respectively. These thresholds were not derived from a standard and were used solely for the exploratory evaluation of the current dataset.

4.2. Exploratory Multivariate Analysis of Measurement Points

The similarities among the measurement points in terms of their error profiles relative to the theoretical formula were explored using principal component analysis (PCA) and hierarchical clustering. The distribution of the measurement points in the PCA score plot is shown in Figure 6, and the hierarchical clustering dendrogram is presented in Figure 7.

The first principal component of PCA explained 64.5% of the total variance, while the second principal component explained 27.0%. Thus, the first two principal components together accounted for 91.5% of the total variance. In Figure 6, it can be seen that the measurement points S01, S02, S03, S04, S06, and S07 are located in the upper-left quadrant of the PCA plane and are relatively close to one another. S08, S09, and S11, on the other hand, are located in the lower region where the second principal component is negative. S05 exhibits a distribution that is more distinct from the other measurement points in the region where the first principal component has a high positive value; S10 is in the region where both the first and second principal components are negative; and S12 is in the region where both principal components are positive. These findings indicate that the error behavior of the theoretical formula is not entirely homogeneous across the measurement points and that some points exhibit distinct multivariate error profiles.

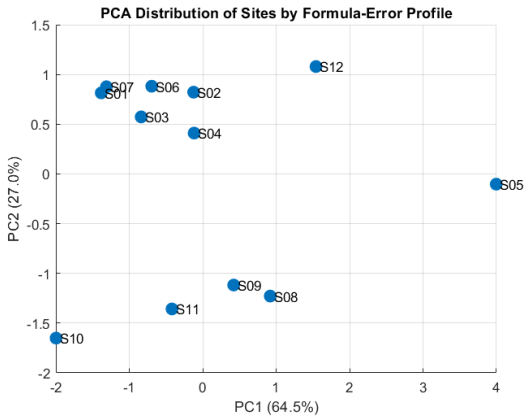


Figure 6. Distribution of principal component analysis scores based on the error profiles of the theoretical formula across the measurement points. The first and second principal components explain 64.5% and 27.0% of the total variance, respectively, and together account for 91.5% of the total variance.

The results of hierarchical clustering showed that there were varying degrees of similarity among the measurement points. In Figure 7, S01 and S07 are the measurement points that matched at the lowest clustering distance. The pairs S04 and S06, and S08 and S09, also clustered together at relatively low clustering

distances. The S01–S07 pair subsequently merged with S03, while the S04–S06 pair formed a group with S02 at a higher hierarchical level. Similarly, the S08–S09 pair first merged with S11 and then with S10. S05 and S12, on the other hand, formed a branch among themselves but joined the main structure composed of the other measurement points at a higher clustering distance.

However, since the analysis was based on only 12 measurement points and no predefined cluster cutoff height was used, a fixed number of generalizable load classes was not derived from the dendrogram. Therefore, the PCA and hierarchical clustering results should be evaluated not as independent evidence of classification, but as complementary exploratory analyses that visualize the similarities and differences in error profiles among the measurement points. The resulting similarities should not be interpreted as universal clusters or causal classes representing specific industrial load types.

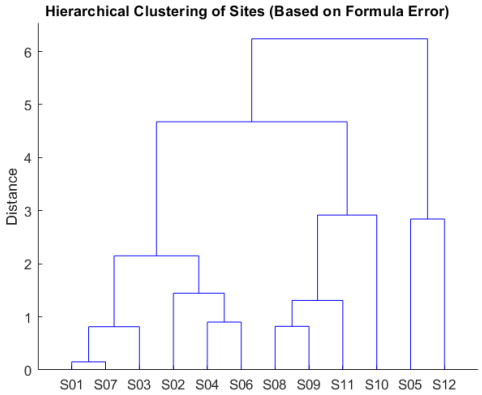


Figure 7. A hierarchical clustering dendrogram based on the theoretical formula error profiles of the measurement points. The merging distances in the dendrogram indicate the relative differences among the multivariate formula-error profiles of the measurement points. Since no predefined cluster cutoff height was used, a fixed number of clusters were not defined.

4.3. General Evaluation

The results show that the theoretical distortion factor calculated using THDI alone provides a useful initial approximation for industrial field data, but does not represent the measured PF/dPF ratio with the same accuracy under all load and phase conditions. The theoretical formula overestimated the distortion factor by an average of 0.009357 and produced higher deviations, particularly under conditions of phase asymmetry, low power factor, or unusual load conditions. Data-driven models reduced the aggregate MAE and RMSE values. While the restricted second-order regression produced the lowest average error, the Ridge model brought the systematic bias of the theoretical formula close to zero. At the measurement-point level, the Wilcoxon signed-rank test indicated a systematic tendency toward lower paired errors, whereas the bootstrap confidence interval for the mean paired MAE difference included zero. These results are not directly contradictory because the Wilcoxon test evaluates a rank-based paired location shift, while the bootstrap interval quantifies uncertainty in the arithmetic mean difference. Their combined interpretation provides positive but limited evidence regarding the error-reduction potential of the Ridge correction. Together with the failure to reduce the maximum absolute error, the absence of narrower 95% limits of agreement, and the limited coefficient stability, these findings warrant caution regarding the generalizability of the correction.

Therefore, the resulting Ridge model should not be defined as a universal "corrected THDI formula," but rather as a field-calibrated correction approach that reduces the average formula deviation observed at the 12 measurement points. For a stronger generalization, external validation using independent data obtained from different facilities, different loading levels, and repeated operating conditions is required.

5. Conclusion

In this study, the performance of the THDI-based theoretical distortion factor under field conditions was evaluated using three-phase field measurements from 12 industrial measurement points, and low-complexity, data-driven models aimed at reducing the error of the theoretical formula were compared. Since the phases at the same measurement point were not considered independent observations, the models were evaluated using a 12-cycle cross-validation method, in which one measurement point was set aside for testing in each cycle.

The theoretical formula produced a mean absolute error (MAE) of 0.015662, a root mean square error (RMSE) of 0.019681, and an average bias of −0.009357. The negative bias indicated that the formula tended to overestimate the distortion factor on average in the analyzed dataset. Among the compared models, the restricted second-order regression provided the lowest MAE and RMSE values; the Ridge model reduced the MAE to 0.012263, bringing the mean bias in the theoretical formula close to zero. However, the fact that data-driven models could not reduce the maximum absolute error showed that the improvement in average performance was not valid for all phases and measurement points.

At the measurement-point level, the Wilcoxon signed-rank test indicated a systematic tendency toward lower paired MAE values after Ridge correction (P=0.0342). However, the 95% percentile bootstrap confidence interval for the mean paired MAE difference included zero. Because the Wilcoxon test evaluates a rank-based paired location shift, whereas the bootstrap interval quantifies uncertainty in the arithmetic mean difference, these findings are not directly contradictory. Taken together, they provide positive but limited evidence regarding the error-reduction potential of the Ridge correction rather than definitive statistical confirmation of improvement. Therefore, the Ridge model should be

regarded as an empirical calibration approach for the available field data rather than as a universally validated corrected THDI formula.

The fact that high absolute errors are not concentrated solely at a specific THDI or THDU level, and that the error signs point in different directions, indicates that the formula deviation cannot be explained by a single constant correction. In particular, wide PF differences between phases, low power factor, and low-load conditions are measurement contexts that must be considered when interpreting the theoretical formula.

In conclusion, the THDI-based theoretical distortion factor provides a quick and interpretable initial estimate in field applications; however, it does not represent all load and phase conditions on its own. For a more reliable assessment, the theoretical factor must be interpreted in conjunction with PF, dPF, THDU, phase currents, and phase asymmetry. Future studies should include external validation using independent measurements obtained from different facilities, load levels, and time intervals.

Author Contributions

The percentages of the authors' contributions are presented below. Both authors reviewed and approved the final version of the manuscript.

	F.K.	R.T.
C	60	40
D	60	40
S	20	80
DCP	100	0
DAI	60	40
L	100	0
W	100	0
CR	40	60
SR	80	20
PM	70	30
FA	100	0

C= concept, D= design, S= supervision, DCP= data collection and/or processing, DAI= data analysis and/or interpretation, L= literature search, W= writing, CR= critical review, SR= submission and revision, PM= project management, FA= funding acquisition.

Conflict of Interest

The authors declare that there is no conflict of interest.

Ethical Consideration

Ethics committee approval was not required for this study because the research did not involve human participants, human biological materials, animals, or animal experiments. The study was based on the analysis of previously collected industrial electrical measurement data.

Acknowledgements

The authors would like to thank Aydemir Kalebek and Kayhan Kalebek for their technical support and contributions during the course of this study.

References

Bland, J. M., & Altman, D. G. (1986). Statistical methods for assessing agreement between two methods of clinical measurement. *The Lancet*, *1*(8476), 307–310. https://doi.org/10.1016/S0140-6736(86)90837-8

Coelho, R. A., Araújo, B. V. S., Xavier, G. V. R., Rodrigues, G. A., Ferreira, T. V., & Brito, N. S. D. (2024). Novel indices for power quality assessment of non-linear loads. *Electric Power Systems Research*, *236*, Article 110952. https://doi.org/10.1016/j.epsr.2024.110952

Czarnecki, L. S. (1987). What is wrong with the Budeanu concept of reactive and distortion power and why it should be abandoned. *IEEE Transactions on Instrumentation and Measurement*, *36*(3), 834–837. https://doi.org/10.1109/TIM.1987.6312797

Efron, B. (1979). Bootstrap methods: Another look at the jackknife. *The Annals of Statistics*, *7*(1), 1–26. https://doi.org/10.1214/aos/1176344552

Emanuel, A. E. (2004). Summary of IEEE Standard 1459: Definitions for the measurement of electric power quantities under sinusoidal, nonsinusoidal, balanced, or unbalanced conditions. *IEEE Transactions on Industry Applications*, *40*(3), 869–876. https://doi.org/10.1109/TIA.2004.827452

Ferrero, A., & Superti-Furga, G. (1991). A new approach to the definition of power components in three-phase systems under nonsinusoidal conditions. *IEEE Transactions on Instrumentation and Measurement*, *40*(3), 568–577. https://doi.org/10.1109/19.87021

Hoerl, A. E., & Kennard, R. W. (1970). Ridge regression: Biased estimation for nonorthogonal problems. *Technometrics*, *12*(1), 55–67. https://doi.org/10.1080/00401706.1970.10488634

Hu, Z., Han, Y., Zalhaf, A. S., Zhou, S., Zhao, E., & Yang, P. (2023). Harmonic sources modeling and characterization in modern power systems: A comprehensive overview. *Electric Power Systems Research*, *218*, Article 109234. https://doi.org/10.1016/j.epsr.2023.109234

IEEE. (2022). *IEEE standard for harmonic control in electric power systems* (IEEE Std 519-2022). Institute of Electrical and Electronics Engineers.

IEEE. (2025). *IEEE standard definitions for the measurement of electric power quantities under sinusoidal, nonsinusoidal, balanced, or unbalanced conditions* (IEEE Std 1459-2025). Institute of Electrical and Electronics Engineers.

IEC. (2009). *Electromagnetic compatibility (EMC)—Part 4-7: Testing and measurement techniques—General guide on harmonics and interharmonics measurements and instrumentation, for power supply systems and equipment connected thereto* (IEC 61000-4-7:2002+AMD1:2008 CSV). International Electrotechnical Commission.

IEC. (2025). *Electromagnetic compatibility (EMC)—Part 4-30: Testing and measurement techniques—Power quality measurement methods* (IEC 61000-4-30:2025). International Electrotechnical Commission.

Kürker, F. (2017). *Enerji sistemlerinde harmonik analizi ve harmonik azaltma teknikleri* [Harmonic analysis and harmonic mitigation techniques in energy systems] (Publication No. 468305) [Doctoral dissertation, Harran University]. YÖK Tez Merkezi.

Liu, Q., Liu, F., Li, Y., & Wang, S. (2023). Harmonic modeling and

harmonic contribution determination: A case study of industrial power supply system. *Electric Power Systems Research*, *217*, Article 109122. https://doi.org/10.1016/j.epsr.2023.109122

Michalec, Ł., Jasiński, M., Sikorski, T., Leonowicz, Z., Jasiński, Ł., & Suresh, V. (2021). Impact of harmonic currents of nonlinear loads on power quality of a low voltage network—Review and case study. *Energies*, *14*(12), Article 3665. https://doi.org/10.3390/en14123665

Nascimento, C. F., de Oliveira, A. A., Jr., Goedtel, A., & Dietrich, A. B. (2013). Harmonic distortion monitoring for nonlinear loads using neural-network-method. *Applied Soft Computing*, *13*(1), 475–482. https://doi.org/10.1016/j.asoc.2012.08.043

Nur, A., Güre, B., Rüstemli, S., & Bezek Güre, Ö. (2025). Wind speed prediction in microgrid energy management using the random forest and artificial neural networks methods. *Middle East Journal of Science*, *11*(2), 276–289. https://doi.org/10.51477/mejs.1738993

Obulesu, Y. P., Venkateswara Reddy, M., & Kusumalatha, Y. (2014). A %THD analysis of industrial power distribution systems with active power filter—Case studies. *International Journal of Electrical Power & Energy Systems*, *60*, 107–120. https://doi.org/10.1016/j.ijepes.2014.02.037

Roberts, D. R., Bahn, V., Ciuti, S., Boyce, M. S., Elith, J., Guillera-Arroita, G., Hauenstein, S., Lahoz-Monfort, J. J., Schröder, B., Thuiller, W., Warton, D. I., Wintle, B. A., Hartig, F., & Dormann, C. F. (2017). Cross-validation strategies for data with temporal, spatial, hierarchical, or phylogenetic structure. *Ecography*, *40*(8), 913–929. https://doi.org/10.1111/ecog.02881

Senra, R., Boaventura, W. C., & Mendes, E. M. A. M. (2017). Assessment of the harmonic currents generated by single-phase nonlinear loads. *Electric Power Systems Research*, *147*, 272–279. https://doi.org/10.1016/j.epsr.2017.02.028

Ugwuagbo, E., Balogun, A., Olajube, A., Omeje, O., Awelewa, A., & Abba-Aliyu, S. (2021). Experimental data on power quality assessment at point of common coupling of a steel mill to an electric power grid. *Data in Brief*, *39*, Article 107681. https://doi.org/10.1016/j.dib.2021.107681

Vabalas, A., Gowen, E., Poliakoff, E., & Casson, A. J. (2019). Machine learning algorithm validation with a limited sample size. *PLOS ONE*, *14*(11), Article e0224365. https://doi.org/10.1371/journal.pone.0224365

Wilcoxon, F. (1945). Individual comparisons by ranking methods. *Biometrics Bulletin*, *1*(6), 80–83. https://doi.org/10.2307/3001968

Willems, J. L. (2004). Reflections on apparent power and power factor in nonsinusoidal and polyphase situations. *IEEE Transactions on Power Delivery*, *19*(2), 835–840. https://doi.org/10.1109/TPWRD.2003.823182

Black Sea Journal of Engineering and Science
doi: 10.34248/bsengineering.1984826

Open Access Journal
e-ISSN: 2619 – 8991

Research Article
Volume 9 - Issue 5: 2652-2662 / September 2026

A NEW DEEP CONVOLUTIONAL NEURAL NETWORK MODEL FOR MULTI-CLASS CYBER ATTACK DETECTION IN INTERNET OF MEDICAL THINGS NETWORKS

Gurkan DOGAN[1]*

[1]*Munzur University, Engineering Faculty, Computer Engineering Department, 62000, Tunceli, Türkiye*

Abstract: The Internet of Medical Things (IoMT) has become an indispensable component of modern healthcare, with a wide range of applications from patient monitoring systems to smart medical devices. However, the limited processing power and memory capacity of IoMT devices make it difficult to implement traditional security mechanisms, leaving these devices vulnerable to cyber threats such as protocol attacks (e.g., DDoS, DoS, MQTT) and identity spoofing. Deep learning-based attack detection systems are gaining increasing importance in developing effective solutions against these attacks, which can directly threaten patient safety. In this study, DCNN—a new deep convolutional neural network-based model—is proposed to develop an effective attack detection system against the growing cyberattack threats in IoMT network environments. The model was evaluated on the CICIoMT2024 dataset, which consists of six classes: Benign, DDoS, DoS, MQTT, Reconnaissance, and Spoofing. The performance of the proposed DCNN was compared with re-implemented traditional machine learning models, including Random Forest, LightGBM, Decision Tree, Extra Trees, Logistic Regression, Naive Bayes, and Ridge Classifier, as well as state-of-the-art methods reported in the literature. The experimental results demonstrate that the proposed DCNN outperformed all comparison models, achieving 0.9999 or higher across all evaluation metrics, including accuracy, F1-score, precision, recall, and AUC.

Keywords: Internet of medical things, Cybersecurity, Intrusion detection, Convolutional neural network, Deep learning

***Corresponding author:** Munzur University, Engineering Faculty, Computer Engineering Department, 62000, Tunceli, Türkiye
E mail: gurkandogan@munzur.edu.tr (G. DOGAN)
Gurkan DOGAN https://orcid.org/0000-0003-2497-8348

Received: July 02, 2026
Accepted: August 22, 2026
Published: September 15, 2026

Cite as: Dogan, G. (2026). A new deep convolutional neural network model for multi-class cyber attack detection in internet of medical things networks. *Black Sea Journal of Engineering and Science,* 9(5), 2652-2662.

1. Introduction

The Internet of Medical Things (IoMT) has revolutionized modern healthcare by integrating wearable devices, sensors, and medical equipment into a networked system (Redjechta et al., 2025; Riyadi et al., 2025). IoMT technology, which has become widespread with Health 4.0, contributes to improving both operational efficiency and the quality of patient care by supporting remote patient monitoring, real-time data collection, and personalized treatment applications within the scope of Health 5.0 (Berguiga et al., 2025; Shaikh et al., 2025). However, the highly sensitive nature of medical data and the high level of interaction among devices have made IoMT ecosystems a critical target for cyberattackers (Si-Ahmed et al., 2023; Riyadi et al., 2025; Shaikh et al., 2025). Furthermore, the fact that most IoMT devices have hardware limitations—such as low computing power, low energy capacity, and limited storage space—makes it difficult to implement traditional cryptographic security methods, leaving systems vulnerable to various threats such as Denial of Service (DoS), Distributed Denial of Service (DDoS), spoofing, Man-in-the-Middle (MITM), and intrusion attacks (Berguiga et al., 2025; Si-Ahmed et al., 2023; Zukaib et al., 2024). For example, an attacker's manipulation of critical devices such as pacemakers or insulin pumps could lead to fatal consequences that directly endanger the patient's life. Therefore, detecting and preventing cyberattacks is critical for IoMT devices. Intrusion Detection Systems (IDS) stand out as one of the primary defense mechanisms for identifying cyber threats and detecting potential attacks at an early stage (Binbusayyis et al., 2022). The inability of traditional signature-based systems to effectively counter new and evolving threats (zero-day attacks) has driven researchers to develop more adaptive and intelligent solutions based on Machine Learning (ML) and Deep Learning (DL) (Albulayhi et al., 2022; Zukaib et al., 2024). Neto et al. (Neto et al., 2023) found that while Random Forest and deep neural networks (DNNs) achieved high accuracy in 34-class classification scenarios on the CICIoT2023 dataset, the performance of Logistic Regression, Perceptron, and AdaBoost models fell below 82% accuracy and a 50% F1 score. Balhareth et al. (Balhareth and Ilyas, 2024) present a detection mechanism optimized for IoMT networks by combining decision tree-based models with Mutual Information and XGBoost feature selection methods. The model achieves 98.79%

This work is licensed (CC BY-NC 4.0) under Creative Commons Attribution 4.0 International License

accuracy and a low false alarm rate on the CICIDS2017 dataset using only 15 key features. In a study by Khan et al. (Khan and Alkhathami, 2024) conducted on the CICIoT2023 dataset adapted for healthcare, Random Forest achieved an accuracy of approximately 99.55% in both binary and multi-class tasks following feature reduction and class balancing. Begum et al. (Begum et al., 2024) propose an intrusion detection system that combines blockchain and Federated Learning to enhance security in IoMT networks. The system, which provides decentralized data management using IPFS and MongoDB, enhances the model's resilience against attacks using a modified FedAvg algorithm. Kumar et al. (Kumar et al., 2025) achieved 100% accuracy on the WUSTL-EHMS-2020 dataset and 98.55% accuracy on the ECU-IoHT dataset using a hybrid 1D-CLSTM network that employs embedded community-based feature selection and random subsampling augmentation. Uddin et al. (Uddin et al., 2025) propose a hierarchical architecture designed to detect zero-day attacks in IoMT networks, utilizing a meta-learning and usfAD-based approach. This method can distinguish unknown attacks even with a very small amount of data and achieves 99.77% accuracy on the CICIoMT2024 dataset. Kayode Saheed et al. (2022) propose a machine learning approach that incorporates Min-Max normalization and PCA-based dimension reduction methods to detect IoT network attacks. The XGBoost and CatBoost models, tested on the UNSW-NB15 dataset, achieved an accuracy score of 99.9%. On the newer CICIoMT2024 dataset, Shaikh et al. (Shaikh et al., 2025) propose a deep reinforcement learning (DQN and PPO)-based hybrid CNN-LSTM framework (HCLR-IDS) for the security of IoMT networks. Thanks to its ability to learn dynamically from real-time data, the system can detect attacks with 99.58% accuracy and low latency. Dadkhah et al. (Dadkhah et al., 2024) introduce CICIoMT2024, a comprehensive dataset generated in a realistic test setup consisting of 40 devices and covering Wi-Fi, MQTT, and Bluetooth protocols for IoMT security. The study provides researchers with a rich benchmarking resource by including device lifecycle profiling and an analysis of 18 different attack types. In the 6-class experimental tests conducted, Random Forest achieved 73.5% on the accuracy metric and Logistic Regression achieved 69.4% on the F1-score metric, outperforming other methods. The RCLNet model, introduced by Shaikh et al. (Shaikh et al., 2024), aims to enhance attack detection performance in IoMT environments by combining Random Forest-based feature selection with CNN-LSTM and the Self-Adaptive Attention Layer Mechanism (SAALM). In experiments conducted on the WUSTL-EHMS-2020 dataset, the model achieved an accuracy rate of 99.78%. Ravi et al. (Ravi et al., 2023) propose a deep learning approach with an attention mechanism for IoMT devices with different CPU architectures, using byte sequences extracted from ELF files. The model, which combines CNN and bidirectional LSTM layers, achieved accuracy rates of up to 95% in malware detection and processor architecture classification. Alsolami and Ilyas, (2026) proposed a federated learning-based approach called FedEnsemble-DP, supported by Differential Privacy and Secure Aggregation mechanisms, for attack detection in IoMT environments. Experimental results show that an accuracy of 94.60% and an AUC of 95.98% were achieved using Local SMOTE at a privacy level of ε=3.0, while an accuracy of 94.50% and an AUC of 94.94% were obtained in the Raw Imbalanced Data scenario. Ioannou et al. (Ioannou et al., 2024) present a federated learning-based intrusion detection system focused on energy efficiency and privacy for IoMT networks. The system achieves a high accuracy rate of 99.98% by using Enhanced Random Forest (ERF) for intrusion classification and a Single-Class SVM for anomaly detection.

Most studies in the literature on attack type detection using IoMT data are based on traditional machine learning. However, deep learning-based methods were preferred in this study over traditional machine learning methods due to their advantages, such as the ability to capture complex, non-linear spatial and temporal patterns from big data, automatic feature extraction, and robustness in multi-class classification. To this end, the Deep Convolutional Residual Network (DCNN) architecture, which features a residual structure, has been proposed to detect cyber threats in IoMT environments and capture complex, interrelated patterns in network traffic. The proposed model consists of three main components: convolutional blocks that process raw features, residual connections that prevent the vanishing gradient problem, and fully connected (dense) layers that perform classification. In experimental tests conducted on the CICIoMT2024 dataset, it demonstrated higher accuracy and F1 score performance compared to general machine learning methods.

2. Materials and Methods

This section describes the dataset used, the architecture of the proposed deep learning model, and the hyperparameter settings used during training.

2.1. Benchmark Dataset

In this study, the CICIoMT2024 (Dadkhah et al., 2024) dataset—developed by the Canadian Institute for Cybersecurity (CIC) and made publicly available in 2024—was used. The primary objective of the dataset is to provide a realistic benchmark dataset that enables the development and evaluation of Internet of Medical Things (IoMT) security solutions. This dataset was obtained by conducting 18 different attacks against a test environment comprising a total of 40 IoMT devices—25 real and 15 virtual devices. The attacks were carried out over protocols commonly used in the healthcare sector, such as Wi-Fi, MQTT, and Bluetooth. The attacks were categorized into five main classes: DDoS, DoS, Recon, MQTT, and Spoofing. In this study, in addition to these attack classes, normal traffic was included as the "Benign" class, creating a six-class classification problem (KILICHEV, 2026).

Table 1 shows the mapping of raw attack labels in the CICIoMT2024 dataset to their superclasses. As shown in the table, the class with the most sub-labels is MQTT. This indicates that attacks targeting the MQTT protocol span a significantly broader range in terms of diversity compared to other classes. The Reconnaissance class ranks second with six different scanning methods, while the Spoofing class contains only two sub-labels based on ARP and DNS. The DDoS and DoS classes are each divided into four sub-labels based on the type of protocol used; the fundamental difference between these two classes is whether the attack is distributed or not. The Benign class represents normal network traffic that does not contain any attacks.

Table 1. Attack label grouping and class mapping table

Label	Class
ddos-udp, ddos-icmp, ddos-tcp, ddos-syn	DDoS
dos-udp, dos-syn, dos-icmp, dos-tcp	DoS
ddos-connect_flood, ddos-publish_flood, dos-connect_flood, dos-publish_flood, malformed_data, mqtt-ddos-connect_flood, mqtt-ddos-publish_flood, mqtt-dos-connect_flood, mqtt-dos-publish_flood, mqtt-malformed_data, mqtt_connect_flood, mqtt_publish_flood	MQTT
port_scan, os_scan, vulscan, vuln_scan, vulnerability_scan, ping_sweep	Reconnaissance
arp_spoofing, dns_spoofing	Spoofing
benign	Benign

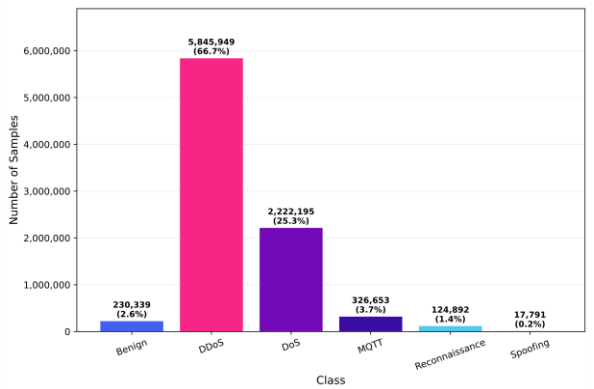


Figure 1. Class distribution of the CICIoMT2024 dataset used in this study

Figure 1 shows the class-based distribution of the CICIoMT2024 dataset. According to this, there is a significant class imbalance in the dataset, which consists of a total of 8,767,819 instances. The DDoS attack category is the dominant class, accounting for 66.7% of the dataset with 5,845,949 samples. This is followed by the DoS attack category, which accounts for 25.3% of the dataset with 2,222,195 samples. These two categories alone account for approximately 92% of the dataset. In contrast, attacks specific to the MQTT protocol are represented by 326,653 samples (3.7%), and normal (benign) traffic by 230,339 samples (2.6%); while the Reconnaissance and Spoofing classes, with 124,892 (1.4%) and 17,791 (0.2%) instances, respectively, were the least represented categories in the dataset.

The features included in the dataset comprise numerous network-flow-level attributes, such as header length, protocol type, packet rate, TCP flag counts, packet size statistics, and inter-packet arrival time (IAT). In this study, columns containing identifying information—such as timestamp, flow ID, and IP address—were removed from the dataset. The dataset was split into a 75% training set and a 25% test set, and 10% of the training set was then set aside for validation.

2.2. Proposed Deep Learning Model

In this study, a new Deep Convolutional Neural Network (DCNN) model was developed to detect cyber threats targeting IoMT systems at an early stage. As shown in Figure 2-a, the designed architecture consists of three main stages: convolutional blocks that extract features from raw traffic data, residual connections that help overcome learning bottlenecks in deep networks, and fully connected (dense) layers that perform the final decision-making stage. To maintain the network's feature extraction capability at a high level, a one-dimensional convolutional residual block structure, as shown in Figure 2-b, was used. Each of these blocks consists of one-dimensional convolutional layers (conv1d) with 128 filters and a 2-dimensional kernel, 64 filters and a 3-dimensional kernel, and 128 filters and a 5-dimensional kernel, respectively, followed by Batch Normalization and ReLU activation functions. To prevent information loss and gradient vanishing in deep layers, a residual connection was added to each block. In cases where the input (C_{in}) and output (filters) channels do not match, a 1×1 convolution operation is applied to these padding lines to align the dimensions. To reduce the dimensionality of the data, MaxPooling1D layers with a pool size of 3 and a stride of 2 are added immediately after the first two blocks, while the current dimension is preserved in the last block. The features extracted from the convolutional layers were converted into a single vector via the flatten layer and fed into the classifier subnetwork. At this stage, the model proceeds as a three-layer deep neural network (DNN) containing 256, 128, and 128 neurons, respectively. To prevent the model from overfitting during training and to increase its flexibility when handling new traffic data, 50% dropout operators were applied to the outputs of the fully connected layers. The model's output layer is directly tailored to the characteristic structure of the CICIoMT2024 dataset. This layer consists of 6 neurons with a Softmax activation function to distinguish between 6 different traffic types: Benign, Spoofing, Reconnaissance, MQTT, DoS, and DDoS. During the network's optimization process, the categorical cross-

entropy function—which effectively penalizes multi-class outputs—was utilized. The model's weight updates were performed using the Adam optimization algorithm, set to a learning rate of 0.0001.

2.3. Model Training and Hyperparameter Configuration

In this study, the hyperparameter configuration was determined through iterative trials to ensure that the proposed DCNN model achieves optimal learning, and these hyperparameters are presented in Table 2.

The Adam optimizer, which is widely used in the literature and has yielded successful results, was selected for training the model. Thanks to its adaptive learning rate mechanism, Adam enables the model to converge more quickly and stably by setting separate learning rates for each parameter (Doğan et al., 2025). The learning rate was kept constant at 0.0001. Categorical cross-entropy, which is suitable for multi-class classification problems, was used as the loss function. This function measures the difference between the probability distribution predicted by the model and the actual class labels, providing an effective optimization criterion for multi-class problems. The model was trained for 30 epochs with a batch size of 2048, and the model weights yielding the lowest validation loss were saved at the end of each epoch.

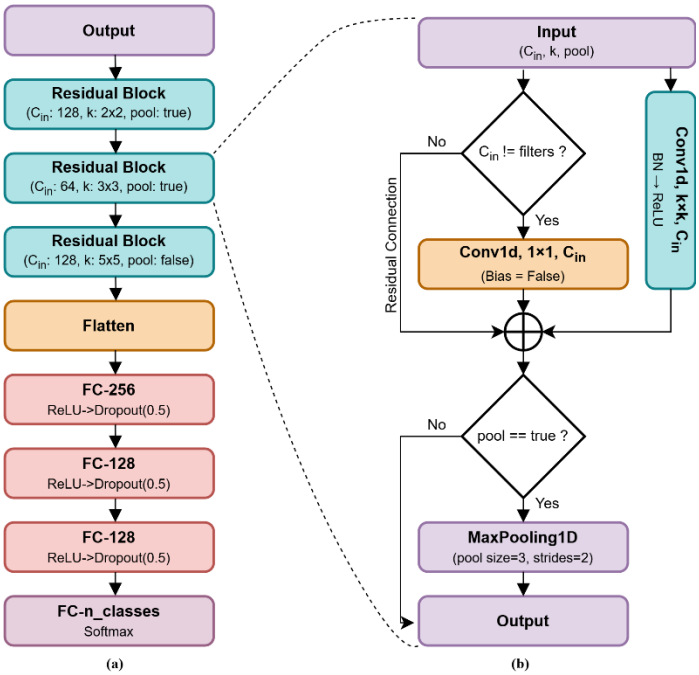


Figure 2. Overview of the proposed DCNN model: (a) complete network architecture and (b) detailed residual block

Table 2. Hyperparameters used in the architecture and training of the DCNN model

Params	Values
CNN Filters	128, 64, 128
Kernel Size	2, 3, 5
Activation	ReLU
DNN (FC) Layers	3
DNN (FC) Neurons	256, 128, 128
Dropout	0.5
Output	Softmax
Optimizer	Adam
Learning Rate	10^{-4}
Loss	Categorical Crossentropy
Batch Size	2048
Epochs	30

3. Results and Discussions

This section presents the experimental evaluation results of the proposed DCNN model and state-of-the-art machine learning models on the CICIoMT2024 dataset. The experimental training and testing processes for all network models and state-of-the-art methods were conducted on a workstation equipped with an Intel® Core™ i5 CPU @ 2.50GHz, 64 GB of RAM, and a GeForce RTX 3090 @ 24GB graphics card. Python 3.10, Keras 2.10, and TensorFlow 2.10 were used as the software infrastructure. Additionally, 75% of the dataset was used for training and 25% for testing. A further 10% of the training data was set aside for validation and was used exclusively during the training process. The generalization ability of all models was measured on test data that had never been seen during the training process. In the DCNN model, predictions were generated by taking the argmax of the probability values obtained from the softmax output layer.

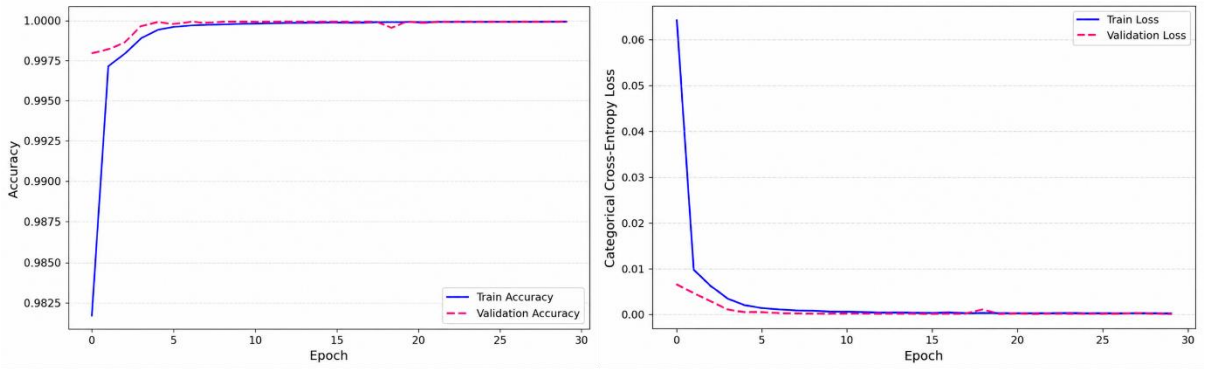


Figure 3. Accuracy and loss trends of the proposed DCNN model during training: (a) training and validation accuracy, and (b) training and validation loss.

In traditional machine learning models, probability values were obtained directly through the `predict_proba` interface for models that support it, and for the Ridge Classifier model—which does not provide probability output—by applying a softmax transformation to the decision function. Class-based evaluation was conducted separately for six classes: Benign, DDoS, DoS, MQTT, Reconnaissance, and Spoofing. Along with the DCNN, seven traditional machine learning models—Random Forest (Breiman, 2001), Decision Tree (Breiman et al., 2017), LightGBM (Ke et al., 2017), Extra Trees (Geurts et al., 2006), Logistic Regression (Cox, 1958), Naive Bayes (John and Langley, 1995), and Ridge Classifier (Hoerl and Kennard, 1970)—were trained and evaluated on data processed through the same preprocessing pipeline. All models were compared using the same training and test splits. The results are presented using a confusion matrix, class-based F1 bar charts, and a model comparison table. In addition, the performance of all models was evaluated using four key metrics: accuracy, precision, recall, and F1 score. Due to the multi-class structure, all metrics were calculated as macro averages. Figure 3 shows the graphs depicting the changes in accuracy and loss values during the training process of the proposed DCNN model over 30 epochs. According to this, when examining the accuracy graph in Figure 3-a, the model started with a very high initial accuracy of approximately 0.9825 during the first epochs of training. Furthermore, the fact that the validation accuracy remained close to the training accuracy from the very beginning indicates that the model's generalization ability was strong even in the early stages of training. Both curves exceeded the 0.999 level around the 5th epoch and converged toward 1.0000 as training progressed. It reached a stable plateau starting around the 15th epoch. Examining the loss graph in Figure 3-b, the training loss began at approximately 0.065 in the first epoch and then exhibited an extremely rapid decline, falling below 0.01 around the 5th epoch. In line with the findings in the accuracy graph, both curves in the validation graph also exhibit a fairly stable appearance after the 15th epoch and show no significant fluctuations.

In addition to the accuracy and loss plots, the classification performance of all models is illustrated using the confusion matrices presented in Figure 4. Accordingly, since the number of class-based examples in the dataset used is large, the results are presented using row-normalized values. Upon examining the confusion matrix for the Ridge Classifier shown in Figure 4-a, it is observed that only 80.0% accuracy was achieved for the Benign class, while 19.5% of the remaining samples were misclassified as DDoS. Significant confusion is also evident in the Spoofing class, where 78.2% of the samples were predicted as DDoS. The DoS class, however, demonstrated perfect accuracy at 100.0%. Upon examining the confusion matrix of the Naive Bayes model shown in Figure 4-b, it is observed that high-performance results were produced in the Benign class (99.5%) and the MQTT class (99.7%). However, in the DoS class, only 21.6% of the samples were correctly classified, while 71.5% were incorrectly classified as DDoS and 6.5% as MQTT. The Spoofing class yielded a highly successful result of 99.4%. In the Logistic Regression model shown in Figure 4-c, the Spoofing class exhibited the worst performance, with only 27.9% of the samples correctly predicted. Within this class, 53.3% were misclassified as Benign and 16.0% as DDoS. The DDoS class, on the other hand, demonstrated nearly flawless performance at 99.9%. In the Extra Trees model shown in Figure 4-d, extremely high accuracies were achieved: 99.9% for the Benign class, 100.0% for the DDoS class, 98.6% for the MQTT class, and 98.6% for the Reconnaissance class. However, the DoS class represents a significant exception, with 58.3% of the samples incorrectly classified as DDoS. Weak performance was also observed in the Spoofing class, at 37.1%. The Decision Tree model shown in Figure 4-e produced results with near-perfect accuracy: 100.0% for the Benign class, 99.9% for the DDoS class, 99.9% for the DoS class, 97.7% for the MQTT class, and 100.0% for the Reconnaissance class. The only notable instance of low performance occurred in the Spoofing class, where only 51.3% of the samples were correctly classified.

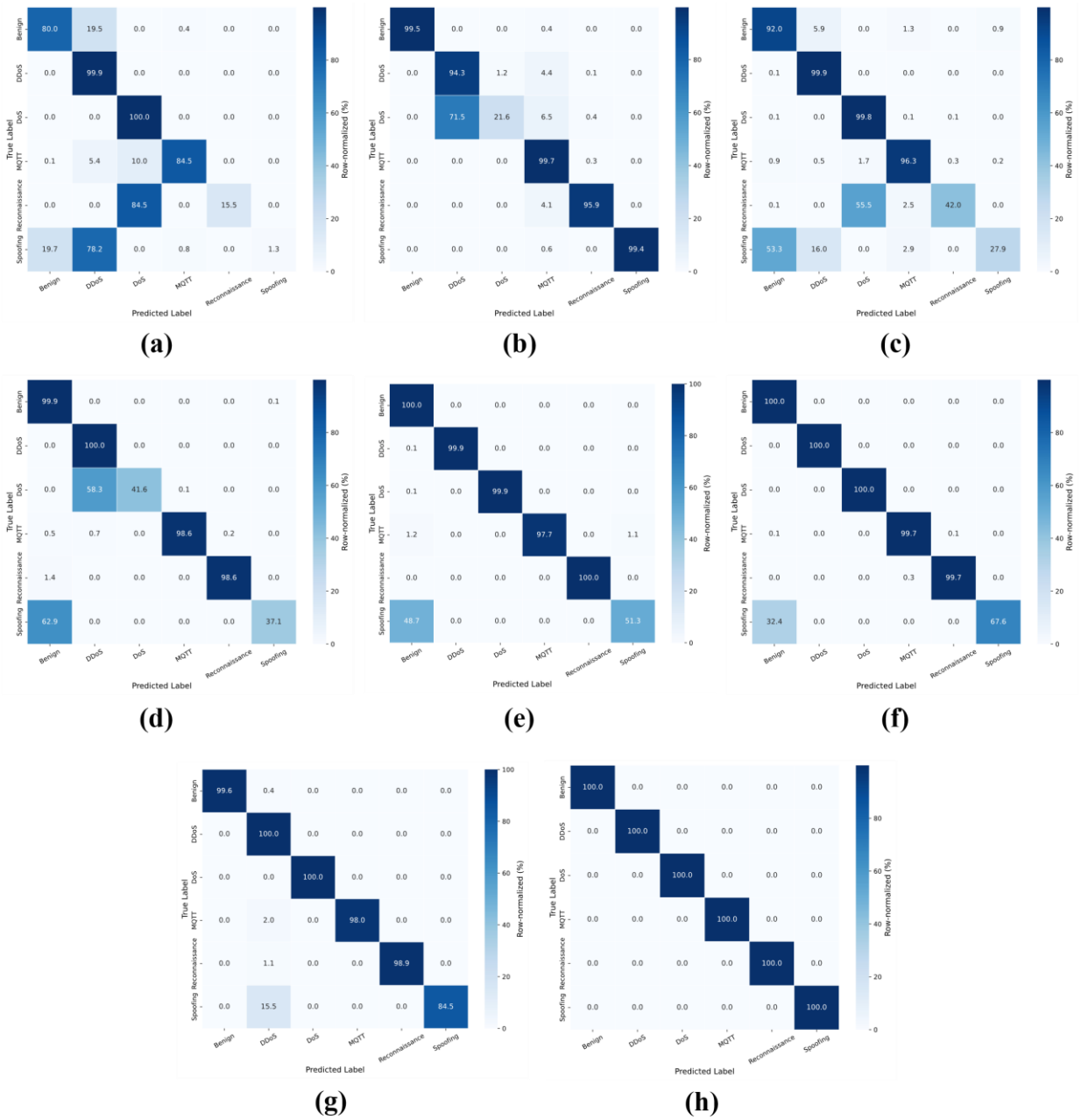


Figure 4. Complexity matrices of DCNN and state-of-the-art methods: (a) Ridge, (b) Naïve Bayes, (c) Logistic Regression, (d) Extra Tree, (e) Decision Tree, (f) Random Forest, (g) LightGBM, and (h) DCNN.

The Random Forest model shown in Figure 4-f produced results with excellent accuracy: 100.0% for the Benign class, 100.0% for DDoS, 100.0% for DoS, 99.7% for the MQTT class, and 99.7% for the Reconnaissance class. However, it demonstrated the weakest performance in the Spoofing class, with 67.6%. The LightGBM model shown in Figure 4-g achieved highly successful results: 99.6% in the Benign class, 100.0% in the DDoS class, 100.0% in the DoS class, 98.0% in the MQTT class, and 98.9% in the Reconnaissance class. In the spoofing class, an accuracy of 84.5% was achieved, which is the highest result among traditional machine learning models for this class. The proposed DCNN model shown in Figure 4-h achieved 100.0% accuracy across all classes, demonstrating the best performance among the models included in the comparison. No misclassifications were observed in any class, and the significant advantage of the deep learning architecture over traditional machine learning methods was clearly demonstrated through the confusion matrix.

The class-based F1 scores for all models and the macro-average F1 values are presented in a comparative manner in Figure 5. According to this, the Ridge Classifier shown in Figure 5-a exhibited the lowest overall performance among the models included in the comparison, with a macro-average F1 score of 0.6739. While high-performance results of 0.993 in the DDoS class and 0.970 in the DoS class were obtained, extremely low F1 scores of 0.267 in the Reconnaissance class and only 0.025 in the Spoofing class were observed. This indicates that the model experiences significant generalization difficulties in certain classes.

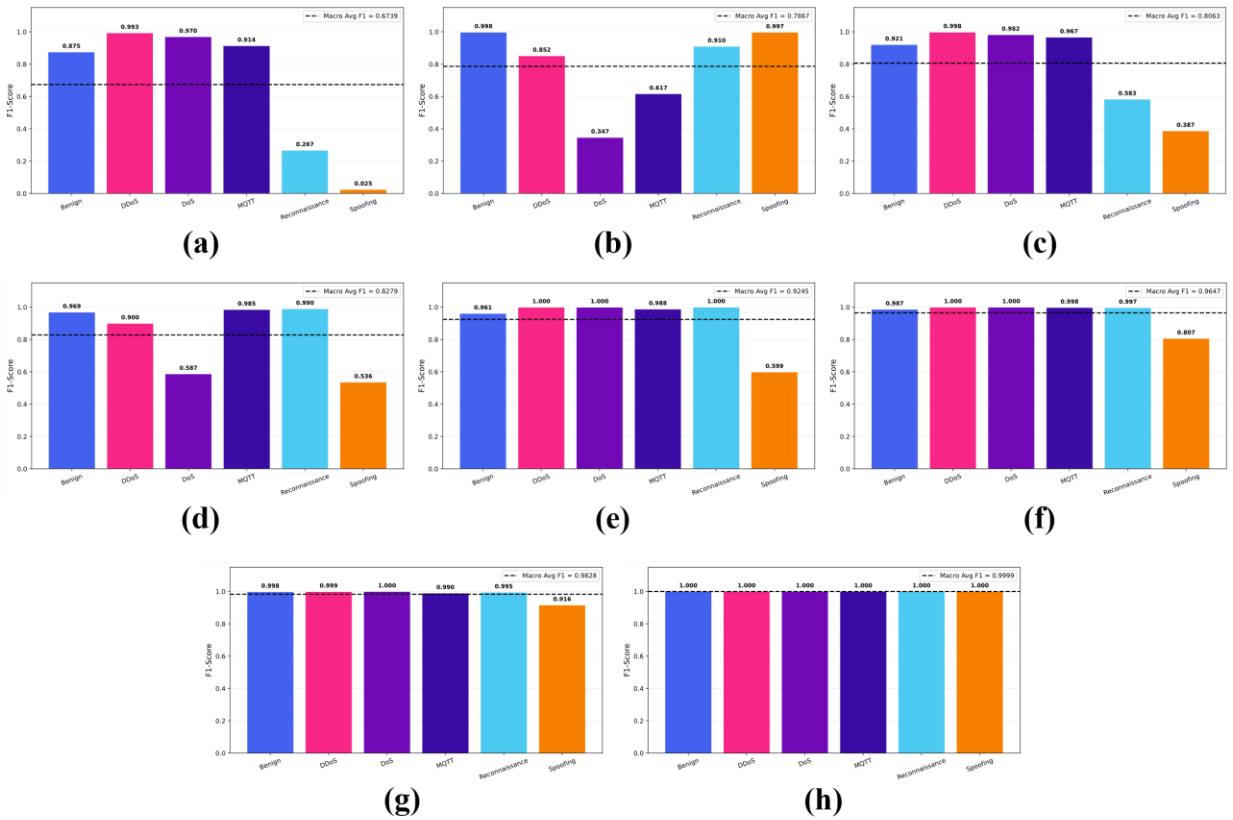


Figure 5. Class-wise F1-score comparison of the proposed DCNN model and state-of-the-art methods: (a) Ridge, (b) Naïve Bayes, (c) Logistic Regression, (d) Extra Trees, (e) Decision Tree, (f) Random Forest, (g) LightGBM, and (h) DCNN.

The Naive Bayes classifier shown in Figure 5-b outperformed the Ridge Classifier with a macro-average F1 score of 0.7867. It produced quite successful results, with scores of 0.998 in the Benign class and 0.997 in the Spoofing class. However, while there was a noticeable drop to 0.347 in the DoS class, the value of 0.617 in the MQTT class also indicates that the model struggled in this class. The Logistic Regression model shown in Figure 5-c achieved a macro-average F1 score of 0.8063. While high performance was observed in the Benign class (0.921), DDoS (0.998), and DoS (0.982), the model demonstrated relatively weak performance in the Spoofing class (0.387) and the Reconnaissance class (0.583). The Extra Trees model shown in Figure 5-d demonstrated moderate overall performance with a macro-average F1 score of 0.8279. High-performance results were achieved in the Benign class (0.969), MQTT (0.985), and Reconnaissance (0.990). However, performance declined in the DoS class (0.587) and the Spoofing class (0.536). The Decision Tree shown in Figure 5-e ranks among the top traditional machine learning models with a macro-average F1 score of 0.9245, while achieving perfect scores of 1.0 in the DDoS class, 1.0 in the DoS class, and 1.0 in the Reconnaissance class. However, the Spoofing class, with a score of 0.599, represented the model's weakest performance. The Random Forest shown in Figure 5-f achieved a macro-average F1 score of 0.9647. It produced nearly flawless results: 0.987 in the Benign class, 1.0 in DDoS, 1.0 in DoS, 0.998 in MQTT, and 0.997 in Reconnaissance. In the Spoofing class, it demonstrated a significantly better performance than the other traditional models in the comparison, with a score of 0.807. The LightGBM model shown in Figure 5-g achieved the highest performance among all traditional models with a macro-average F1 score of 0.9828. It demonstrated consistent success of 0.99 or higher in all classes except Spoofing. In the spoofing class, it achieved the highest class-specific F1 score among the traditional models at 0.916.

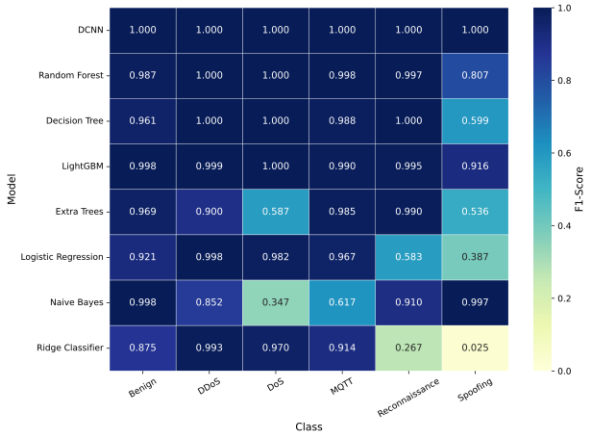


Figure 6. F1-score comparison heatmap showing the classification performance of DCNN and traditional ML models across each attack category.

The proposed DCNN model shown in Figure 5-h achieved an F1 score of 1.0 in all classes, demonstrating the best performance among all models included in the

comparison with a macro-average F1 score of 0.9999.

Figure 6 presents a heatmap comparing the F1 scores achieved by the DCNN and traditional ML models for each attack category. The DCNN model demonstrated flawless classification performance with an F1 score of 1.000 across all classes, outperforming all other models. Among the traditional models, LightGBM achieved scores ranging from 0.916 to 1.000, while Random Forest achieved scores ranging from 0.807 to 1.000, making them the models with the most consistent performance across all attack categories. In contrast, a noticeable drop in performance is observed, particularly in the minority classes of Reconnaissance and Spoofing. This situation directly aligns with the data imbalance illustrated in the class distribution graph presented in Figure 1. The Ridge Classifier demonstrated the weakest performance, achieving an F1 score of only 0.025 in the Spoofing class and 0.267 in the Reconnaissance class. Similarly, the Naive Bayes model showed low performance with an F1 score of 0.347 in the DoS class and 0.617 in the MQTT class. The Extra Trees model also performed relatively poorly, with F1 scores of 0.587 in the DoS class and 0.536 in the Spoofing class.

Table 3. Comparison of classification performance metrics for the proposed DCNN model and state-of-the-art methods

Method	Dataset	No. of Classes	Accuracy	Precision	Recall	F1-Score	AUC
Ridge Classifier (re-imp.)	CICIoMT2024	6	0.9744	0.9313	0.6351	0.6739	0.8930
Naive Bayes (re-imp.)	CICIoMT2024	6	0.7628	0.8275	0.8509	0.7867	0.9828
Logistic Reg. (re-imp.)	CICIoMT2024	6	0.9856	0.9074	0.7630	0.8063	0.9937
Extra Trees (re-imp.)	CICIoMT2024	6	0.8496	0.9501	0.7929	0.8279	0.9997
Decision Tree (re-imp.)	CICIoMT2024	6	0.9974	0.9405	0.9147	0.9245	0.9992
Random Forest (re-imp.)	CICIoMT2024	6	0.9992	0.9947	0.9451	0.9647	1.0000
LightGBM (re-imp.)	CICIoMT2024	6	0.9985	0.9996	0.9682	0.9828	1.0000
RF (Dadkhah et al., 2024)	CICIoMT2024	19	0.7330	0.6910	0.5770	0.5510	NR
LR (Dadkhah et al., 2024)	CICIoMT2024	6	0.7290	0.7480	0.7120	0.6940	NR
DNN (Dadkhah et al., 2024)	CICIoMT2024	2	0.9960	0.9560	0.9480	0.9520	NR
Attention-DNN + OC-SVM (Hernandez-Jaimes et al., 2025)	CICIoMT2024	2	0.8441	0.8443	0.9873	0.9102	NR
	MQTT-IoT-IDS2020	2	0.9181	0.9214	0.9917	0.9553	NR
GWO + LightGBM + CNN (Abid et al., 2025)	CICIoT2023	8	0.9524	0.9522	NR	0.9509	NR
	CICIoMT2024	6	0.9950	0.9952	NR	0.9951	NR
CROSS-IoT (XGBoost) (Chhetry et al., 2026)	Unified Dataset	2	0.9516	0.9876	0.9148	0.9498	NR
DCNN (our)	CICIoMT2024	6	1.0000	0.9999	0.9999	0.9999	1.0000

On the other hand, a comparison of the overall performance of the proposed DCNN and the reimplemented traditional machine learning models on the CICIoMT2024 dataset is presented in Table 3. Accordingly, in terms of accuracy, the DCNN achieved a perfect result of 100.0%, while among the traditional models, Random Forest and LightGBM achieved the highest accuracy scores at 99.92% and 99.85%, respectively. Naive Bayes was the model with the lowest performance, achieving an accuracy score of 76.28%. In terms of the F1 score, the DCNN significantly outperformed all other models with a score of 0.9999. Among the traditional models, LightGBM achieved the highest F1 score at 0.9828, while the Ridge Classifier exhibited the lowest F1 performance with a score of 0.6739. In terms of precision, LightGBM stood out among traditional models with a score of 0.9996, while in terms of recall, LightGBM again ranked as the strongest traditional model with a score of 0.9682. When AUC scores are considered, Random Forest, LightGBM, and DCNN demonstrated the highest discriminatory power with a score of 1.0000. The Ridge Classifier, with an AUC of 0.8930, was the weakest model in terms of AUC. When compared with previous studies conducted on similar datasets, the proposed DCNN model demonstrates a clear performance advantage. Dadkhah et al. (2024), in their evaluation of a Random Forest (RF) model on the 19-class version of the CICIoMT2024 dataset, reported considerably lower results, achieving an accuracy of 73.30% and an F1 score of 55.10%. Their Logistic Regression (LR) model, evaluated on the 6-class configuration, achieved a somewhat higher accuracy of 72.90% and an F1 score of 69.40%. The Deep Neural Network (DNN) model evaluated on the binary-classification setting of the same dataset achieved stronger results, with 99.60% accuracy and a 95.20% F1 score, yet it still fell short of the results obtained by the proposed DCNN. Similarly, Hernandez-Jaimes et al. (2025) reported F1 scores of 0.9102 and 0.9553 for their Attention-DNN + OC-SVM (Attention-based Deep Neural Network + One-Class Support Vector Machine) model on the CICIoMT2024 and MQTT-IoT-IDS2020 datasets, respectively, both of which remain below the near-perfect performance achieved by the proposed model. Abid et al. (2025), employing a hybrid GWO + LightGBM + CNN (Grey Wolf Optimizer + Light Gradient Boosting

Machine + Convolutional Neural Network) approach, obtained F1 scores of 0.9509 and 0.9951 on the CICIoT2023 and CICIoT2024 datasets, respectively, while Chhetry et al. (2026) reported an F1 score of 0.9498 using an XGBoost-based CROSS-IoT model on a unified dataset. Taken together, these comparisons confirm that the proposed DCNN not only outperforms the traditional machine learning models reimplemented in this study but also surpasses several recently proposed deep learning and hybrid intrusion detection approaches reported in the literature. To evaluate the practical applicability of a model in real-world IoT/IoMT environments, Table 4 provides a comparative overview of computational cost metrics such as inference time, memory usage, model size, and the number of parameters/nodes. Accordingly, it indicates a clear balance between the models' classification performance and computational cost.

Table 4. Practical efficiency comparison of DCNN and traditional ML models in terms of inference time, memory usage, model size, and parameter/node count

Model	Inference Time (ms)	Memory Usage (ΔRSS, MB)	Model Size (KB)	Parameter / Node Count
Random Forest	0.00427	108.750	2063.7	19984
Naive Bayes	0.00417	108.711	5.0	552
Extra Trees	0.00402	108.457	2015.6	19510
DCNN (our)	0.00342	2310.598	6293.9	527238
LightGBM	0.00166	108.727	429.0	420
Ridge Classifier	0.00018	158.879	1.8	282
Logistic Reg.	0.00016	113.844	1.8	282
Decision Tree	0.00012	108.703	3.2	21

The Decision Tree was the fastest model, with an inference time of only 0.00012 ms per sample, followed by Logistic Regression at 0.00016 ms and the Ridge Classifier at 0.00018 ms. In contrast, the DCNN achieved a better inference time performance than the Extra Tree, Naive Bayes, and Random Forest models, with an inference time of 0.00342 ms per sample. However, the DCNN model exhibited a memory footprint of approximately 2310.598 MB, measured in terms of Resident Set Size (RSS)—the portion of a process's memory held in physical RAM at a given time—during inference, resulting in a substantially higher memory cost compared to all other models. While the DCNN model had the largest model size at 6293.9 KB, the Ridge Classifier and Logistic Regression were the most compact models at just 1.8 KB. In terms of the number of parameters and nodes, the DCNN was by far the most complex model with 527238 trainable parameters; in contrast, Random Forest and Extra Trees exhibited moderate complexity with 19984 and 19510 nodes, respectively, while the Decision Tree had the simplest structure with only 21 nodes. These findings indicate that the superior classification performance offered by the proposed DCNN is achieved at the cost of significantly higher memory and storage requirements.

To summarize these findings, the performance of the proposed DCNN model for attack detection in IoMT network traffic was comprehensively compared with seven reimplemented traditional machine learning methods. Experiments conducted on the CICIoMT2024 dataset demonstrate that the deep learning-based architecture provides a clear advantage over traditional methods across all performance metrics. The DCNN demonstrated nearly flawless classification performance, achieving values of 0.9999 or higher across all metrics, including accuracy, F1 score, precision, recall, and AUC. This result indicates that the model can successfully distinguish between both common and rare attack types. This finding is further corroborated by confusion matrices. Notably, while the proposed DCNN model achieves 100% accuracy across all classes, the vast majority of traditional models face significant challenges, particularly in the Spoofing and DoS classes.

At the root of these challenges lies a significant class imbalance inherent in the nature of the dataset. DDoS attacks account for 66.7% of the dataset, while DoS attacks account for 25.3%, meaning these two categories alone comprise approximately 92% of the samples; in contrast, MQTT accounts for 3.7%, benign traffic for 2.6%, reconnaissance for 1.4%, and the spoofing class, in particular, is severely underrepresented in the dataset with a share of only 0.2%. This imbalance has directly affected the ability of traditional models to learn minority classes. Indeed, a common weakness observed across all traditional models is the Spoofing class. F1 scores for this class varied significantly from model to model, ranging from 0.025 for the Ridge Classifier to 0.997 for Naive Bayes. Similarly, the Naive Bayes model performed poorly, achieving an F1 score of 0.347 in the DoS class and 0.617 in the MQTT class, while the Extra Trees model achieved F1 scores of 0.587 in the DoS class and 0.536 in the Spoofing class; The Ridge Classifier's F1 score of 0.267 in the Reconnaissance class also indicates a similar weakness. In contrast, LightGBM demonstrated performance in the range of 0.916–1.000 and Random Forest in the range of 0.807–1.000, showing relatively more consistent performance among traditional models. Only DCNN was able to consistently deliver high performance across all classes, including Spoofing. This finding demonstrates that spoofing attacks exhibit a high

degree of similarity to other traffic types at the feature level, and that the hierarchical feature learning provided by deep learning architectures plays a critical role in detecting such attacks, despite the scarcity of data.

However, the superior classification performance offered by the proposed DCNN is achieved at the cost of computational overhead, which should not be overlooked. A comparison in terms of inference time, memory usage, model size, and number of parameters points to a clear balance between the models' classification performance and their practical applicability. The DCNN consumed approximately 2,310.598 MB of memory during processing. This value, determined by the Resident Set Size (RSS) metric—which represents the amount of physical RAM actually occupied by the process—is significantly higher than the 108–159 MB range of memory consumed by traditional models. Similarly, the DCNN was the model with the highest storage and complexity costs, with a model size of 6,293.9 KB and 527,238 trainable parameters. In contrast, the Decision Tree stood out as the lightest and fastest model, with only 21 nodes and an inference time of 0.00012 ms per sample. These results demonstrate that the superior accuracy provided by the DCNN — particularly for underrepresented and hard-to-detect attack types such as Spoofing— requires significantly higher memory and storage costs. In contrast, tree-based ensemble models such as Random Forest and LightGBM offer performance close to that of the DCNN for majority classes and relatively limited but acceptable performance for minority classes, while remaining much lighter in terms of resource consumption. This situation demonstrates that, when deploying models on IoT/IoMT edge devices with limited computational and memory resources, the choice of model must be carefully evaluated depending on whether maximum detection accuracy or resource efficiency is prioritized.

5. Conclusion

In this study, an DCNN architecture that combines a convolutional neural network with a deep neural network is proposed to enable multi-class attack detection in IoMT network environments. The proposed model was evaluated through extensive experiments on the CICIoMT2024 dataset and compared with re-implemented traditional machine learning methods as well as recent approaches reported in the literature. The experimental results demonstrate that the DCNN model achieved scores of 0.9999 or higher across all metrics—including accuracy, F1 score, precision, recall, and AUC—and thus exhibited the best performance among all models included in the comparison. Among the traditional machine learning methods, LightGBM and Random Forest stood out. However, both models lagged behind the DCNN, particularly in the Spoofing class. One of the most significant contributions of this study is that the residual connections and batch normalization layers added to the DCNN architecture accelerate model convergence and prevent overfitting. Future work will involve testing the model on different IoT datasets and integrating it into real-time attack detection systems.

Author Contributions

The percentages of the author' contributions are presented below. The author reviewed and approved the final version of the manuscript.

	G.D.
C	100
D	100
S	100
DCP	100
DAI	100
L	100
W	100
CR	100
SR	100
PM	100
FA	100

C= concept, D= design, S= supervision, DCP= data collection and/or processing, DAI= data analysis and/or interpretation, L= literature search, W= writing, CR= critical review, SR= submission and revision, PM= project management, FA= funding acquisition.

Conflict of Interest

The author declared that there is no conflict of interest.

Ethical Consideration

Ethics committee approval was not required for this study because of there was no study on animals or humans.

References

Abid, T., Ahmim, A., Maazouzi, F., Chefrour, D., Ullah, I., Ahmim, M., & Almukhlifi, R. (2025). A novel IoT threat detection using GWO feature selection and CNN-enhanced LightGBM. *Journal of Cloud Computing*, *14*(1). https://doi.org/10.1186/s13677-025-00785-2

Albulayhi, K., Al-Haija, Q. A., Alsuhibany, S. A., Jillepalli, A. A., Ashrafuzzaman, M., & Sheldon, F. T. (2022). IoT Intrusion Detection Using Machine Learning with a Novel High Performing Feature Selection Method. *Applied Sciences (Switzerland)*, *12*(10). https://doi.org/10.3390/app12105015

Alsolami, T., & Ilyas, M. (2026). FedSMOTE-DP: Privacy-Aware Federated Ensemble Learning for Intrusion Detection in IoMT Networks. *Sensors*, *26*(5), 1592. https://doi.org/10.3390/s26051592

Balhareth, G., & Ilyas, M. (2024). Optimized Intrusion Detection for IoMT Networks with Tree-Based Machine Learning and Filter-Based Feature Selection. *Sensors*, *24*(17), 5712. https://doi.org/10.3390/s24175712

Begum, K., Mozumder, M. A. I., Joo, M.-I., & Kim, H.-C. (2024). BFLIDS: Blockchain-Driven Federated Learning for Intrusion Detection in IoMT Networks. *Sensors*, *24*(14), 4591. https://doi.org/10.3390/s24144591

Berguiga, A., Harchay, A., & Massaoudi, A. (2025). HIDS-IoMT: A Deep Learning-Based Intelligent Intrusion Detection System for the Internet of Medical Things. *IEEE Access*, *13*, 32863–

32882. https://doi.org/10.1109/ACCESS.2025.3543127

Binbusayyis, A., Alaskar, H., Vaiyapuri, T., & Dinesh, M. (2022). An investigation and comparison of machine learning approaches for intrusion detection in IoMT network. *Journal of Supercomputing*, *78*(15), 17403–17422. https://doi.org/10.1007/s11227-022-04568-3

Breiman, L. (2001). Random Forests. *Machine Learning*, *45*(1), 5–32. https://doi.org/10.1023/A:1010933404324

Breiman, L., Friedman, J. H., Olshen, R. A., & Stone, C. J. (2017). *Classification And Regression Trees*. Routledge. https://doi.org/10.1201/9781315139470

Chhetry, B., Kumar Dutta, R., Matam, R., & Ahmed Barbhuiya, F. (2026). CROSS-IoT: A Zeek-Driven Data Harmonization Pipeline for Robust Cross-Domain Attack Detection. *International Journal of Communication Systems*, *39*(12). https://doi.org/10.1002/dac.70565

Cox, D. R. (1958). The Regression Analysis of Binary Sequences. *Journal of the Royal Statistical Society Series B: Statistical Methodology*, *20*(2), 215–232. https://doi.org/10.1111/j.2517-6161.1958.tb00292.x

Dadkhah, S., Neto, E. C. P., Ferreira, R., Molokwu, R. C., Sadeghi, S., & Ghorbani, A. A. (2024). CICIoMT2024: A benchmark dataset for multi-protocol security assessment in IoMT. *Internet of Things (Netherlands)*, *28*. https://doi.org/10.1016/j.iot.2024.101351

Doğan, G., Uyanık, H., & Ergen, B. (2025). A new lightweight convolutional neural network model for detecting drivable road regions. *Information Sciences*, *717*. https://doi.org/10.1016/j.ins.2025.122305

Geurts, P., Ernst, D., & Wehenkel, L. (2006). Extremely randomized trees. *Machine Learning*, *63*(1), 3–42. https://doi.org/10.1007/s10994-006-6226-1

Hernandez-Jaimes, M. L., Martinez-Cruz, A., Ramírez-Gutiérrez, K. A., & Morales-Reyes, A. (2025). Network traffic inspection to enhance anomaly detection in the Internet of Things using attention-driven Deep Learning. *Integration*, *103*. https://doi.org/10.1016/j.vlsi.2025.102398

Hoerl, A. E., & Kennard, R. W. (1970). Ridge Regression: Biased Estimation for Nonorthogonal Problems. *Technometrics*, *12*(1), 55–67. https://doi.org/10.1080/00401706.1970.10488634

Ioannou, I., Nagaradjane, P., Angin, P., Balasubramanian, P., Kavitha, K. J., Murugan, P., & Vassiliou, V. (2024). GEMLIDS-MIOT: A Green Effective Machine Learning Intrusion Detection System based on Federated Learning for Medical IoT network security hardening. *Computer Communications*, *218*, 209–239. https://doi.org/10.1016/j.comcom.2024.02.023

John, G. H., & Langley, P. (1995). Estimating continuous distributions in Bayesian classifiers. *Proceedings of the Eleventh Conference on Uncertainty in Artificial Intelligence, UAI'95*, 338–345.

Kayode Saheed, Y., Idris Abiodun, A., Misra, S., Kristiansen Holone, M., & Colomo-Palacios, R. (2022). A machine learning-based intrusion detection for detecting internet of things network attacks. *Alexandria Engineering Journal*, *61*(12), 9395–9409. https://doi.org/10.1016/j.aej.2022.02.063

Ke, G., Meng, Q., Finley, T., Wang, T., Chen, W., Ma, W., Ye, Q., & Liu, T.-Y. (2017). LightGBM: a highly efficient gradient boosting decision tree. *Proceedings of the 31st International Conference on Neural Information Processing Systems, NIPS'17*, 3149–3157.

Khan, M. M., & Alkhathami, M. (2024). Anomaly detection in IoT-based healthcare: machine learning for enhanced security. *Scientific Reports*, *14*(1). https://doi.org/10.1038/s41598-024-56126-x

KILICHEV, D. (2026). *CICIoMT2024 Dataset*. https://www.kaggle.com/datasets/sinfdosh1990/ciciomt2024

Kumar, M., Singh, S. K., & Kim, S. (2025). Hybrid deep learning-based cyberthreat detection and IoMT data authentication model in smart healthcare. *Future Generation Computer Systems*, *166*, 107711. https://doi.org/10.1016/j.future.2025.107711

Neto, E. C. P., Dadkhah, S., Ferreira, R., Zohourian, A., Lu, R., & Ghorbani, A. A. (2023). CICIoT2023: A Real-Time Dataset and Benchmark for Large-Scale Attacks in IoT Environment. *Sensors*, *23*(13), 5941. https://doi.org/10.3390/s23135941

Ravi, V., Pham, T. D., & Alazab, M. (2023). Attention-Based Multidimensional Deep Learning Approach for Cross-Architecture IoMT Malware Detection and Classification in Healthcare Cyber-Physical Systems. *IEEE Transactions on Computational Social Systems*, *10*(4), 1597–1606. https://doi.org/10.1109/TCSS.2022.3198123

Redjechta, I. S., Cherbal, S., Goudjil, L., Zerguine, N., & Gawanmeh, A. (2025). A Comprehensive Benchmarking Analysis of Intrusion Detection for Internet of Medical Things Using CICIoMT2024. *2025 International Conference on Computational Intelligence and Knowledge Economy (ICCIKE)*, 687–692. https://doi.org/10.1109/ICCIKE67021.2025.11318273

Riyadi, W., Kurniabudi, Jasmir, Novianto, Y., Kisbianty, D., & Sika, X. (2025). A Hybrid IG-PCA and Machine Learning Approach for Accurate Intrusion Detection in IoMT with Imbalanced Data. *Journal of Information and Organizational Sciences*, *49*(2), 345–359. https://doi.org/10.31341/jios.49.2.11

Shaikh, J. A., Wang, C., Muhammad, W. U. S., Arshad, M., Owais, M., Alnashwan, R. O., Chelloug, S. A., & Muthanna, M. S. A. (2024). RCLNet: an effective anomaly-based intrusion detection for securing the IoMT system. *Frontiers in Digital Health*, *6*. https://doi.org/10.3389/fdgth.2024.1467241

Shaikh, J. A., Wang, C., Sima, M. W. U., Arshad, M., Owais, M., Hassan, D. S. M., Alkanhel, R., & Muthanna, M. S. A. (2025). A deep Reinforcement learning-based robust Intrusion Detection System for securing IoMT Healthcare Networks. *Frontiers in Medicine*, *12*. https://doi.org/10.3389/fmed.2025.1524286

Si-Ahmed, A., Al-Garadi, M. A., & Boustia, N. (2023). Survey of Machine Learning based intrusion detection methods for Internet of Medical Things. In *Applied Soft Computing* (Vol. 140). Elsevier Ltd. https://doi.org/10.1016/j.asoc.2023.110227

Uddin, M. A., Chu, N. H., & Rafeh, R. (2025). *A Hierarchical IDS for Zero-Day Attack Detection in Internet of Medical Things Networks*. https://arxiv.org/abs/2508.10346

Zukaib, U., Cui, X., Zheng, C., Hassan, M., & Shen, Z. (2024). Meta-IDS: Meta-Learning-Based Smart Intrusion Detection System for Internet of Medical Things (IoMT) Network. *IEEE Internet of Things Journal*, *11*(13), 23080–23095. https://doi.org/10.1109/JIOT.2024.3387294

Black Sea Journal of Engineering and Science
doi: 10.34248/bsengineering.2001870

Open Access Journal
e-ISSN: 2619 – 8991

Research Article
Volume 9 - Issue 5: 2663-2675 / September 2026

OPTIMIZATION OF WASTE-DERIVED RECYCLED POLYETHYLENE TEREPHTHALATE (r-PET) NANOFIBER PRODUCTION VIA BOX-BEHNKEN DESIGN

Hüsnü AYDEMİR[1]*

[1]*Bingöl University, Vocational School of Technical Sciences, Department of Textile Technology, 12000, Bingöl, Türkiye*

Abstract: Upcycling waste plastics demands strict process control. Here, post-consumer r-PET flakes dissolved in a trifluoroacetic acid/dichloromethane (TFA/DCM) solvent system were processed into sub-micron fibers using needle electrospinning. A three-factor, three-level Box-Behnken design (BBD) coupled with response surface methodology mapped how polymer concentration (10–15 wt%), solution feed rate (0.5–1.9 mL/h), and nozzle geometry (18–22G) govern average fiber diameter (AFD). The resulting quadratic model fit the experimental data remarkably well. It accounted for 99.88% of process variance (R^2=0.9988, F-value=473.60, P<0.0001) alongside a non-significant lack of fit (P=0.1034). Polymer concentration exerted the strongest control over fiber thickening. Crucially, flow rate coupled with needle size (P=0.0130), reflecting a coupled electro-hydrodynamic effect specific to the viscoelastic rheology of the r-PET solution. Numerical optimization (D=1.000) targeted minimal fiber thickness, identifying ideal coordinates at 10.00 wt% concentration, 1.07 mL/h feed rate, and a 22G nozzle tip. This combination predicted an AFD of 209.52 nm. Bench tests performed in triplicate confirmed these predictions, producing uniform, bead-free nanofibers with a mean diameter of 218 ± 42 nm. A minimal 3.89% deviation verifies the practical accuracy of the model, establishing a batch-consistent quantitative baseline for bottle-derived r-PET filtration substrates.

Keywords: Recycled PET, Nanofiber, Needle electrospinning, Box-Behnken design, Process optimization, Desirability function

***Corresponding author:** Bingöl University, *Vocational School of Technical Sciences*, Department of *Textile Technology*, 12000, Bingöl, Türkiye
E mail: husnuaydemir@gmail.com
Hüsnü AYDEMİR https://orcid.org/0000-0001-8772-2257

Received: July 23, 2026
Accepted: August 22, 2026
Published: September 15, 2026

Cite as: Aydemir, H. (2026). Optimization of waste-derived recycled polyethylene terephthalate (r-pet) nanofiber production via box-behnken design. *Black Sea Journal of Engineering and Science*, 9(5): 2663-2675.

1. Introduction

Cutting carbon footprints and embedding circular economy principles have pushed polymer recycling into mainstream textile research (Hoque et al., 2024; Naeim et al., 2025). Polyethylene terephthalate (PET) dominates packaging and synthetic textiles. Diverting post-consumer PET bottles into recycled alternatives (r-PET) offers a high-value engineering route (Strain et al., 2015; Medeiros et al., 2026). Electrospinning provides a versatile method to transform r-PET solutions into fine mesh architectures for air filtration, face masks, and medical membranes (Bonfim et al., 2021a; Baselga-Lahoz et al., 2022). Still, filtration efficiency and pore characteristics rely on one pivotal factor: AFD (Nam et al., 2019; Opálková Šišková et al., 2020). Two distinct operational sets drive fiber dimensions: solution rheology and equipment hardware (Veleirinho et al., 2008; Gergely et al., 2019; Aydemir and Demiryürek, 2023). Polymer concentration controls fluid viscosity and chain entanglement density, acting as the primary driver for fiber thickening (Wang et al., 2012; Ng et al., 2022). While Wang et al. detailed this concentration effect in virgin PET (Wang et al., 2012); Kijeńska-Gawrońska et al. identified viscous resistance as a major hurdle in processing waste-derived r-PET (Kijeńska-Gawrońska et al., 2022). Drop solid content too low, and spinning collapses. Dilute r-PET solutions yield defective or beaded structures rather than uniform filaments (Abbas et al., 2018). Traditional viscoelastic concepts derived for pristine PET thus remain central to understanding recycled polymer dynamics.

Beyond fluid properties, volumetric feed rate dictates fiber size. Pumping solution faster shortens the flight time required for solvent evaporation. Rushing this stage forces wet fibers onto the collector, resulting in coarser or merged morphologies (Medeiros et al., 2026) Meanwhile, needle Gauge (a factor frequently kept constant) shapes Taylor cone base geometry and hydraulic pressure (Bonfim et al., 2021b). Wide 18G nozzles spread charge density across a broader area, weakening initial electrostatic drawing and thickening the fibers (Opálková Šišková et al., 2020; Aydemir and Demiryürek, 2023). Tight 22G tips invert this dynamic. High hydraulic back-pressure and intense shear force are hypothesized to promote extensional deformation of polymer chains inside the barrel, enabling efficient electro-hydrodynamic stretching into fine filaments (Abbas et al., 2018; Bonfim et al., 2021a). While direct

This work is licensed (CC BY-NC 4.0) under Creative Commons Attribution 4.0 International License

chain orientation analysis requires advanced structural characterization (such as SAXS; Small-Angle X-ray Scattering/WAXS; Wide-Angle X-ray Scattering), extensional flow theories suggest that tight capillaries facilitate jet attenuation.

Existing literature thoroughly documents single-variable effects in PET and r-PET systems (Wang et al., 2012; Gergely, 2020), Yet, explicit mapping of how these parameters interact remains surprisingly rare. Few studies address non-linear, quadratic interactions tied specifically to nozzle geometry (18G–22G). In r-PET processing, where recycled molecular weights (MW) vary, understanding how rate and needle size couple under viscous conditions flow fills a critical gap for industrial scale-up. Particularly in r-PET systems, which are recycled and whose MW and chain structure may differ from those of the virgin polymer, predicting the coupled effect of flow rate and expanded needle geometry under viscous solutions addresses a crucial research gap in the literature, which is vital for industrial scale-up processes. To address this gap, this investigation processes post-consumer r-PET flakes (typically characterized by intrinsic viscosity (IV) values of ≈0.70–0.80 dL/g in beverage bottle grades) within a binary TFA / DCM solvent system. While the use of TFA/DCM represents a recognized environmental limitation, this solvent combination was methodologically necessary to achieve complete room-temperature dissolution of the highly crystalline waste r-PET matrix without inducing thermal degradation or hydrolytic chain cleavage. Although current trends in sustainable polymer processing increasingly prioritize green solvent alternatives, establishing this baseline electro-hydrodynamic process model under controlled TFA/DCM conditions provides a vital reference framework for future scaling with eco-friendly solvent systems. Although TFA/DCM represents a necessary solvent system to achieve room-temperature dissolution of crystalline r-PET without thermal degradation, exploring green solvent alternatives remains an important goal for future industrial scaling.

The primary objective of this study is to experimentally investigate the effects of concentration (10–15 wt%), flow rate (0.5–1.9 mL/h), and needle diameter (22G–18G) on the final r-PET AFD. The obtained data were statistically evaluated according to a three-factor, three-level BBD model, and the multiple interactions of the process parameters were mapped over a matrix consisting of 15 experimental runs. With the aid of the developed quadratic model, the AFD controllability and optimization windows of r-PET nanofibers are presented and discussed comparatively with pioneering findings in the literature. Rather than directly measuring filtration performance metrics (such as pressure drop or Quality Factor (QF)), the primary goal of this study is to systematically establish the morphological foundation and optimization windows required for functional membrane fabrication.

2. Materials and Methods

2.1. Solution Preparation Process

In this study, flakes obtained from post-consumer waste plastic bottles (r-PET) were preferred as the raw material. According to pioneering studies in the literature, the polymer utilized in the manufacturing of commercial beverage bottles exhibits high chemical purity and a highly linear chain structure, and a relatively consistent IV range (IV ≈ 0.70–0.80 dL/g) (Opálková Šišková et al., 2020; Bonfim et al., 2021b; Baselga-Lahoz et al., 2022). While batch-to-batch molecular weight variations inherent to recycled feedstocks represent a recognized process limitation, commercial bottle-grade flakes offer a reliable baseline for maintaining viscoelastic stability during electrospinning.

For raw material preparation, transparent post-consumer PET bottles were collected and mechanically cleared of non-PET components, including caps, neck rings, and external labels. To thoroughly remove surface adhesive residues, the bottle bodies underwent ultrasonic washing at 60 °C for 30 min in a non-ionic detergent bath, after which they were thoroughly rinsed with distilled water. The cleaned r-PET strips were then chopped into flakes of approximately 0.5 cm × 0.5 cm using a laboratory-scale grinder to accelerate the dissolution rate. Finally, the obtained flakes were dried in a vacuum oven at 60 °C for 24 hours to completely remove any residual moisture.

In accordance with the literature, a binary mixture of TFA and DCM at a (75% : 25% v/v) ratio was selected as the solvent system (Abbas et al., 2018; Aydemir and Demiryürek, 2023). This aggressive binary solvent system was required to achieve full room-temperature dissolution of the highly crystalline r-PET matrix without inducing hydrolytic chain cleavage. Nevertheless, assessing non-toxic or eco-friendly green solvent mixtures represents an essential milestone for future sustainable manufacturing. The prepared r-PET flakes were homogenized in this binary solvent system at room temperature using a magnetic stirrer for 4 hours. To meet the requirements of the experimental design, the solutions were prepared at three different concentrations of 10%, 12.5% and 15% (w/v). Once homogeneous phase stability was achieved, the prepared solutions were immediately ready for the electrospinning process.

2.2. Electrospinning Apparatus and Process Parameters

The prepared homogeneous r-PET solutions were transferred into 10 mL disposable plastic syringes. These syringes were then mounted onto the syringe pump of an electrospinning device (NanoSpinner NE300, Inovenso) to ensure a stable Taylor cone and uniform fiber deposition during the process, the high-speed rotating drum collector of the device was utilized. The schematic representation of the electrospinning setup used in this study is presented in Figure 1.

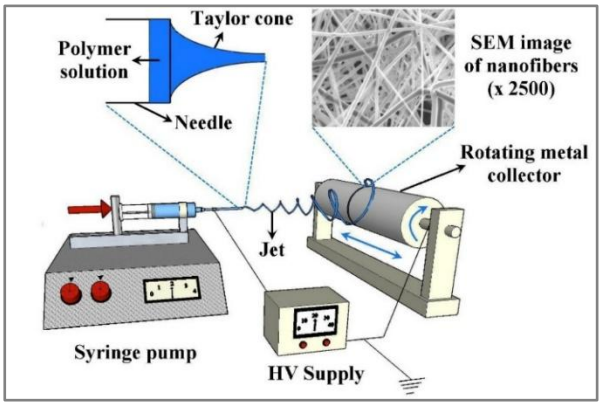


Figure 1. Schematic of an electrospinning setup (Aydemir et al., 2025).

The apparatus and ambient parameters of the system were meticulously kept constant throughout all experimental runs. In line with preliminary literature data, the optimized constant parameters were established as follows (Gergely, 2020; Bonfim et al., 2021a; Aydemir and Demiryürek, 2023; Medeiros et al., 2026):

- *Applied Electrical Voltage:* A positive voltage of 18 kV was applied to the needle tip from a high-voltage power supply.
- *Tip-to-Collector Distance:* The transfer distance between the needle tip and the aluminum foil-covered rotating drum surface was fixed at 15 cm.
- *Collector Speed:* To enhance the quality of the nanofiber membrane and ensure balanced deposition on the drum, the rotational speed of the drum was adjusted to 300 rpm.
- *Environmental Conditions:* Throughout the electrospinning process, the temperature inside the chamber was controlled at 22 ± 2 °C, and the relative humidity was maintained at 45 ± 5% using an air conditioning system.

2.3. Design of Experiments

To determine the effects of the independent process variables on the average r-PET AFD (nm), a three-factor, three-level BBD was utilized. While polymer weight concentration (wt%) served as the primary fluid rheology variable, feedstock molecular characteristics (such as IV) and MW represent crucial parameters influencing viscoelastic behavior in recycled polymers. In this work, commercial bottle-grade r-PET flakes with a literature-standard IV range (IV ≈ 0.70–0.80 dL/g) were employed; however, the absence of batch-specific MW/IV profiling is recognized as a methodological study limitation that may influence viscoelastic reproducibility across different recycled feedstock sources.

The design matrix was constructed using the parameters detailed in Table 1, which includes concentration (*A*), flow rate (*B*), and needle diameter (*C*). The matrix consisted of a total of 15 experimental runs. To mathematically calculate the experimental error, this matrix included 3 replicates at the center point.

Table 1. BBD factors and levels for the r-PET process

Independent variables	Symbol	Low level (−1)	Center level (0)	High level (+1)
Concentration (wt%)	*A*	10.0	12.5	15.0
Flow rate (mL/h)	*B*	0.5	1.2	1.9
Needle diameter (G/mm)	*C*	22G (0.41 mm)	20G (0.60 mm)	18G (0.80 mm)

2.4. Morphological Characterization and Average Fiber Diameter Analysis

To examine the surface morphologies, surface defects (e.g., beading), and fiber orientations of the fabricated r-PET nanofiber membranes, a scanning electron microscope (SEM, JEOL JSM-6510) was utilized. Prior to SEM analysis, the nanofiber samples were coated with a thin layer of gold-palladium (Au-Pd) using a vacuum sputter coater to ensure surface conductivity. The sample surfaces were scanned under the microscope at various magnifications to obtain characteristic SEM micrographs.

To determine the AFD and diameter distribution variations of the r-PET nanofibers from the obtained SEM images, ImageJ (Version 1.53) digital image analysis software was used. To ensure high statistical reliability across the design space, 5 distinct SEM micrographs were captured from randomly selected surface regions (at ×1000 and ×2500 magnifications) for each experimental run. A standardized diagonal grid overlay was applied to each micrograph, and the diameters of 50 clear individual fibers intersecting the grid lines were measured (yielding 50 precise fiber measurements per sample and a total of 750 experimental measurements across the 15 BBD runs). Using the resulting total of 750 experimental measurements, r-PET AFD (nm) and standard deviation (*SD*) values were calculated for each process run, and AFD distribution histograms were generated.

3. Results and Discussion

Modeling the individual and combined impacts of concentration, flow rate, and needle diameter on r-PET AFD relied on Design-Expert 12. Through BBD processing, the software generated a second-order polynomial regression equation to predict fiber thickness across the tested parameter window. Table 2 details the parameter levels of the 15 experimental combinations forming the basis of this model. The actual AFD results obtained through ImageJ analysis were also included in this Table 2.

3.1. Morphological Characterization and Average Fiber Diameter Distribution

Characteristic scanning electron microscope (SEM) micrographs were presented in Figure 2 to evaluate the surface morphologies, fiber stabilities, and structural perfections of the r-PET nanofiber membranes. Additionally, the corresponding AFD distribution histograms obtained via ImageJ software were included as insets in the same Figure 2.

When Figure 2 was analyzed in general, the rotating drum collector was observed to provide a balanced, homogeneous, and stable fiber alignment on the collector surface across all samples (Hossain et al., 2022). Beyond ensuring this fiber orientation, the cylindrical collector applied an additional mechanical stretching force on the jet proportional to its rotational speed. This mechanical drawing helped the fibers thin further before reaching the collector (Ng et al., 2022; Naeim et al., 2025).

The morphological findings demonstrated that concentration had the most dominant linear effect on the r-PET AFD (Abbas et al., 2018; Gergely et al., 2019; Bonfim et al., 2021b). Under a constant flow rate and needle diameter, the AFD exhibited a radical increase when the concentration rose from 10 wt% to 15 wt% (Wang et al., 2012; Baselga-Lahoz et al., 2022). In PET solutions, a strong power-law relationship exists between specific viscosity (η_{sp}) and concentration (C) which is expressed as $\eta_{sp} \propto C^n$. This scaling law proves that even minor increments in concentration exponentially increase chain entanglement in the solution.

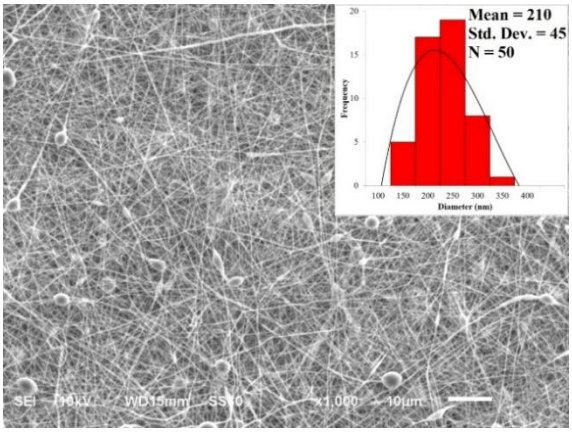
Consequently, the viscoelastic resistance of the jet against electrical stretching forces rose dramatically (Wang et al., 2012; Haider et al., 2018). This high polymer mass dominance reduced the specific surface area per unit volume of the jet. This reduction limited the solvent evaporation rate during flight by hindering solvent diffusion (Naeim et al., 2025). At low concentrations (10 wt%), the tensile stretching experienced by the electrospinning jet increased, enabling the fabrication of the thinnest fiber structures (210 ± 45 nm, Sample 5) In contrast, high concentration levels (15 wt%) restricted jet thinning, driving the r-PET AFD to its peak value.

In addition to the solution parameters, increasing the flow rate also linearly increased the r-PET AFD. This parameter directly determines the mass feed rate delivered from the syringe pump per unit time. Raising the flow rate from 0.5 mL/h to 1.9 mL/h limited the flight time experienced by the jet from the Taylor cone to the collector plate (Haider et al., 2018). Shortening this residence time constrained solvent diffusion and evaporation from the jet surface, causing incompletely solidified, coarser fibers to deposit onto the collector (Baselga-Lahoz et al., 2022; Medeiros et al., 2026). Higher fluid delivery rates shrink the jet's relative surface area. Choking off solvent evaporation during flight forces wet filaments to merge upon landing, forming flattened, ribbon-like structures. Needle dimensions induce a parallel shift. Expanding the orifice from 22G to 18G enlarged the hydraulic exit area, which noticeably thickened the r-PET fibers (Figure 2(a) vs. Figure 2(d)). Narrow 22G nozzles operate under a distinct mechanical regime. Inside tight capillary channels, high hydraulic back-pressure and intense shear forces are expected to induce extensional stress on polymer chains prior to exit. According to extensional rheology principles, this pre-stretched state allows the fluid jet to yield to electrostatic drawing far more efficiently, pulling the jet into fine filaments (Bonfim et al., 2021a). While direct molecular orientation was not tracked using synchrotron X-ray techniques (e.g., SAXS/WAXS) in this study, the observed fiber thinning aligns well with capillary extensional flow theories (Sigonya et al., 2024). Conversely, broader 18G tips dispersed the charge density over a wider area, reducing drawing stability (Gergely, 2020; Gulino and Scaffaro, 2025).

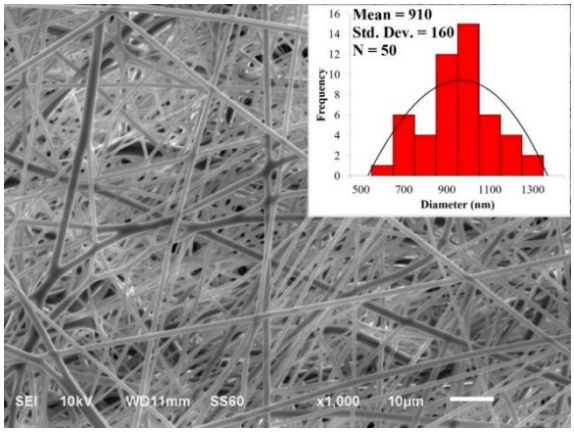
A key morphological finding revealed by the response surface model was the coupled interaction between flow rate and needle diameter on fiber geometry. Comparing Figure 2(b) (Sample 4, 20G needle) and Figure 2(d) (Sample 8, 18G needle) confirmed that the smooth, bead-free, and homogeneous distribution of the fibers was preserved by optimizing the needle inner diameter (balancing the flow regime with the hydraulic area), even when primary parameters such as concentration and flow rate were elevated. This behavior reflects the specific shear-thinning response and viscoelastic relaxation of the r-PET solution under capillary flow, where narrow nozzle geometries offset higher feed rates by inducing localized extensional stress. While primary jet attenuation is predominantly driven by electro-hydrodynamic bending instabilities and high extensional strain rates during flight, the rotating drum collector provides complementary mechanical take-up stress that facilitates controlled fiber alignment and minor physical drawing prior to deposition (Ng et al., 2022; Naeim et al., 2025). Furthermore, the morphology of the center point shown in Figure 2(c) (Sample 13) proved the electrospinning stability of the r-PET flake solutions and the statistical reproducibility of the experimental system.

Table 2. BBD experimental design matrix and AFD results

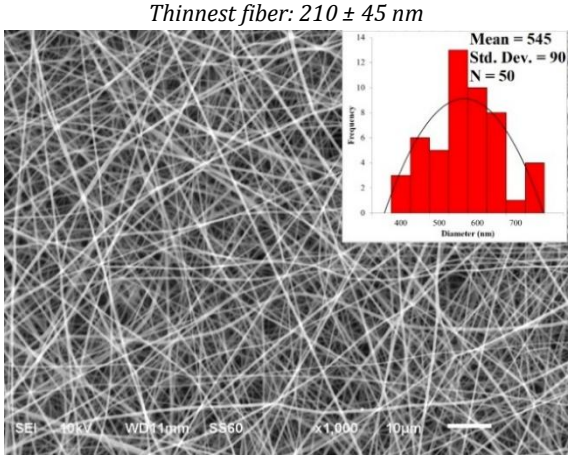
Sample no	Factor 1: Concentration (wt%)	Factor 2: Flow rate (mL/h)	Factor 3: Needle diameter (Gauge size [G] / mm)	AFD (nm)
1	10.0	0.5	20G (0.60 mm)	285 ± 50
2	15.0	0.5	20G (0.60 mm)	740 ± 120
3	10.0	1.9	20G (0.60 mm)	395 ± 75
4	15.0	1.9	20G (0.60 mm)	910 ± 160
5	10.0	1.2	22G (0.41 mm)	210 ± 45
6	15.0	1.2	22G (0.41 mm)	680 ± 110
7	10.0	1.2	18G (0.80 mm)	390 ± 80
8	15.0	1.2	18G (0.80 mm)	890 ± 150
9	12.5	0.5	22G (0.41 mm)	380 ± 85
10	12.5	1.9	22G (0.41 mm)	510 ± 95
11	12.5	0.5	18G (0.80 mm)	540 ± 110
12	12.5	1.9	18G (0.80 mm)	760 ± 145
13	12.5	1.2	20G (0.60 mm)	545 ± 90
14	12.5	1.2	20G (0.60 mm)	540 ± 85
15	12.5	1.2	20G (0.60 mm)	550 ± 95



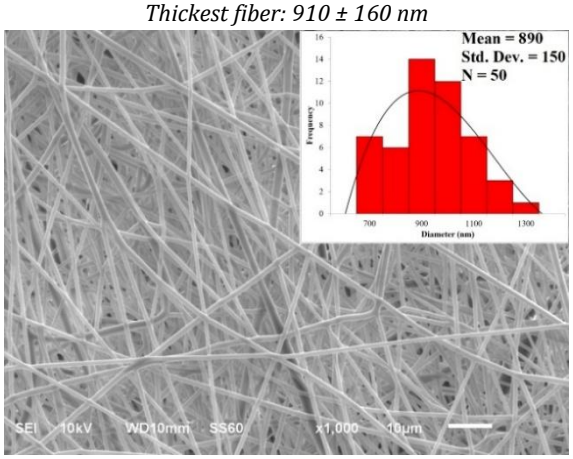
(a) Sample 5 (10.0 wt% concentration, 1.2 mL/h flow rate, 22G needle diameter)
Thinnest fiber: 210 ± 45 nm



(b) Sample 4 (15.0 wt% concentration, 1.9 mL/h flow rate, 20G needle diameter)
Thickest fiber: 910 ± 160 nm



(c) Sample 13 (12.5 wt% concentration, 1.2 mL/h flow rate, 20G needle diameter)
AFD of a representative center point : 545 ± 90 nm



(d) Sample 8 (15.0 wt% concentration, 1.2 mL/h flow rate, 18G needle diameter)
AFD of the sample with the widest needle diameter sharing the same concentration and flow rate as Sample 4 : 890 ± 150 nm

Figure 2. SEM micrographs and AFD distribution histograms (insets) of r-PET nanofibers produced under different BBD experimental conditions: (a) sample 5 (thinnest fiber), (b) sample 4 (thickest fiber), (c) sample 13 (center point) and (d) sample 8 (effect of wider needle diameter).

3.2. Regression Model and ANOVA Findings

To evaluate the statistical significance of the developed quadratic model and to identify the primary factors governing the AFD (which serves as the foundational structural metric determining pore size distribution prior to functional application testing), an ANOVA was performed. The experimental data presented in Table 2 was modeled through regression analysis to establish a mathematical relationship between the final r-PET AFD results and the independent process variables, namely concentration (*A*), flow rate (*B*), and needle diameter (*C*). While the predictive response surface model is calibrated specifically for commercial bottle-derived r-PET within the established baseline IV range (IV ≈ 0.70–0.80 dL/g), defining these quantitative relationships provides a robust empirical framework for predicting fiber diameter trends, acknowledging that MW variations across different recycled polymer batches may influence absolute viscosity limits (Kijeńska-Gawrońska et al., 2022). Consequently, the ANOVA results, including the statistical significance of each individual, interactive, and quadratic term, are detailed in Table 3.

When Table 3 was examined, the quadratic model designed to predict the r-PET AFD exhibited an extremely high *F*-value of 473.60 and a high significance level with a P-value of less than 0.0001. This finding proved that the model was statistically significant and performed excellently in explaining the experimental variations. One of the most critical parameters supporting the model accuracy, the lack of fit, was calculated with an *F*-value of 8.83 and a corresponding P-value of 0.1034 (P>0.05). The statistically insignificant lack of fit demonstrated that the developed quadratic model was in strong agreement with the experimental data. Consequently, this model could be utilized with high confidence for r-PET AFD predictions.

Table 3. ANOVA results for the second-order quadratic model of r-PET AFD

Source	Sum of Squares	df	Mean Square	*F*-value	P-value	Significance
Model	6.074×10^5	9	67487.50	473.60	<0.0001	Significant
A-Concentration	4.704×10^5	1	4.704×10^5	3301.40	<0.0001	Significant
B-Flow rate	49612.50	1	49612.50	348.16	<0.0001	Significant
C-Needle diameter	80000.00	1	80000.00	561.40	<0.0001	Significant
AB	900.00	1	900.00	6.32	0.0536	Not significant
AC	225.00	1	225.00	1.58	0.2644	Not significant
BC	2025.00	1	2025.00	14.21	0.0130	Significant
A^2	975.00	1	975.00	6.84	0.0473	Significant
B^2	1667.31	1	1667.31	11.70	0.0188	Significant
C^2	1298.08	1	1298.08	9.11	0.0295	Significant
Residual	712.50	5	142.50			
Lack of Fit	662.50	3	220.83	8.83	0.1034	Not significant
Pure Error	50.00	2	25.00			
Cor Total	6.081×10^5	14				

All linear process variables, namely concentration (*A*), flow rate (*B*), and needle diameter (*C*), exhibited highly dominant and significant effects on the r-PET AFD with P-value of less than 0.0001. Comparing the sum of squares (*SS*) values revealed that polymer concentration (*A*) was the most dominant independent variable. This parameter held the highest variation share in the system with an SS value of 4.704×10^5. From a polymer physics perspective, this strong dominance is governed by chain entanglement dynamics, where polymer concentration directly determines solution viscoelasticity relative to the critical chain entanglement concentration (C_e). However, because thermal and mechanical degradation during recycling alters MW distribution and IV, variations in these feedstock properties can shift the absolute C_e threshold across different r-PET batches (Kijeńska-Gawrońska et al., 2022). While the developed model demonstrates high predictive power for commercial bottle-grade flakes within the baseline viscosity range (IV ≈ 0.70–0.80 dL/g), the absence of batch-specific MW/IV characterization is explicitly acknowledged as a process limitation that defines the boundaries of the quantitative model. This dominant factor was followed by the needle diameter (*C*, *SS*: 80,000.00) and the flow rate (*B*, *SS*: 49,612.50), respectively.

When the mutual interaction effects of the factors were examined, the concentration–flow rate (*AB*, P=0.0536) and concentration–needle diameter (*AC*, P=0.2644) interactions were found to be statistically insignificant, as they remained above the threshold value of P>0.05.

In contrast, the flow rate–needle diameter (BC) interaction demonstrated a statistically significant effect on the r-PET AFD variation, exhibiting an F-value of 14.21 and a P-value of 0.0130 (P<0.05). Rather than indicating an isolated capillary shear phenomenon, this interaction reflects a coupled physical mechanism where

nozzle exit geometry modulates initial fluid delivery dynamics prior to jet flight. For semi-crystalline polymers such as PET, while axial stretching and fiber thinning are predominantly driven by high extensional flow rates and electro-hydrodynamic bending instabilities during flight (Gazzano et al., 2015), the capillary geometry (22G vs. 18G) governs initial Taylor cone stability and volumetric flux density. Narrower nozzle orifices generate elevated hydraulic back-pressure, stabilizing fluid delivery at higher feed rates and allowing the electrospinning jet to sustain high extensional strain rates without prematurely destabilizing or causing wet filament merging.

When the quadratic terms of the model were examined, all of the terms, namely A^2 (P=0.0473), B^2 (P=0.0188) and C^2 (P=0.0295) were found to be less than the significance threshold of P<0.05. This confirmed that they provided statistically significant contributions to shaping the curvilinear trends of the r-PET AFD within the tested experimental domain. However, while these quadratic relationships effectively map the curvature of the design space for this specific bottle-derived feedstock, the exact non-linear response profiles remain bound to the baseline IV of the utilized r-PET batch. Recognizing feedstock MW variations as an inherent limitation ensures transparent interpretation of the model's quantitative predictive domain across different recycled polymer sources. The regression equation of the quadratic model, which was validated by the ANOVA results in terms of coded factors, is presented in equation 1.

$$\begin{aligned} \text{AFD} = {} & 545.00 + 242.50A + 78.75B + 100.00C \\ & + 15.00AB + 7.50AC + 22.50BC \\ & + 16.25A^2 + 21.25B^2 - 18.75C^2 \end{aligned} \quad (1)$$

A detailed analysis of equation 1 revealed that concentration (A) exhibited the most dominant positive linear effect on the r-PET AFD with a coefficient of +242.50. This was followed by the needle diameter (C) with a coefficient of +100.00 and the flow rate (B) with a coefficient of +78.75, respectively. The positive sign (+) preceding all linear terms mathematically proved that an increase in any of these three parameters directly increased the AFD.

When the mutual interaction terms of the factors (AB, AC, and BC) were examined, the interaction between flow rate and needle diameter (BC, coefficient of +22.50) was found to exhibit a more pronounced interactive effect on fiber geometry compared to the concentration-flow rate (AB: +15.00) and concentration-needle diameter (AC: +7.50) interactions. Physically, this interaction stems from how nozzle orifice size modulates the local volumetric flux density for a given feed rate. Smaller capillary diameters (22G) maintain higher back-pressure and velocity at the Taylor cone apex, mitigating jet destabilization and fluid accumulation when feed rates increase, whereas larger orifices (18G) disperse electric charge density and promote incomplete solvent evaporation during flight.

Regarding the quadratic terms representing the curvilinear trends of the model, concentration (A^2: +16.25) and flow rate (B^2: +21.25) exhibited positive quadratic effects. In contrast, the needle diameter (C^2: -18.75) showed a negative quadratic trend. Physically, this curvilinear stabilization occurs because narrow nozzles (22G) generate high capillary shear stress and concentrated electric field lines at the tip, enabling efficient jet attenuation. As the orifice widens toward intermediate diameters (20G), hydraulic restriction relaxes, causing an initial increase in fiber diameter. However, beyond a critical tip area (18G), charge dispersion over the broader Taylor cone base limits further incremental thickening, shifting the primary jet attenuation mechanism toward bulk extensional flow during flight rather than tip-bound shear dynamics (Gazzano et al., 2015).

When the fit statistics presented in Table 4 were examined, the regression quality of the developed quadratic model was found to be statistically sound and high. The high coefficient of determination (R^2=0.9988), revealed that 99.88% of the total variation in the r-PET AFD was explained by the independent process variables (concentration, flow rate, and needle diameter), leaving a minimal residual error fraction of only 0.12%. Furthermore, the close agreement between the adjusted coefficient of determination (Adj R^2=0.9967) and predicted coefficient of determination (Pred R^2=0.9824) demonstrated high internal statistical fidelity within the evaluated design space.

From a filtration membrane design perspective, achieving precise control over sub-micron fiber diameter is the critical prerequisite for tailoring membrane pore architecture and particle capture dynamics. Reducing fiber thickness enhances surface area per unit mass and promotes slip-flow effects at the fiber surface, which improves Brownian diffusion and interceptive capture efficiency; however, controlling fiber packing density is essential to prevent excessive pressure drop and maintain a favorable QF. While comprehensive QF and pressure drop evaluations represent the next phase of functional application testing, establishing this predictive model for AFD control provides the mandatory structural foundation for engineering high-performance r-PET filtration substrates. Nevertheless, while these strong correlation metrics confirm the mathematical precision of the model for the evaluated bottle-derived r-PET batch (IV ≈ 0.70–0.80 dL/g), asserting universal predictive capacity across arbitrary recycled feedstocks requires scientific caution. Because post-consumer PET waste undergoes variable thermal and mechanical degradation during previous processing cycles, uncharacterized batch-to-batch fluctuations in MW or IV can alter solution viscoelasticity and shift absolute fiber diameter outputs (Kijeńska-Gawrońska et al., 2022). Therefore, this model establishes a reliable quantitative baseline calibrated specifically for standard bottle-grade flakes, recognizing

batch-specific molecular characterization as a primary variable for broader cross-feedstock extrapolation.

The Pred R^2 which measures the ability of the model to predict future experimental combinations or new design points was calculated as 0.9824. In the literature and statistical design guidelines, a mathematical difference of less than 0.20 between the Adj R^2 and Pred R^2 values is accepted as a fundamental requirement for model validity. While this model successfully achieves precise morphological optimization for AFD, translating these substrates into industrial air filtration applications requires evaluating functional performance. In filtration media, reducing fiber thickness enhances particle capture but must be balanced against airflow resistance to prevent high pressure drops. Therefore, integrating QF analysis (which unifies filtration efficiency and pressure drop into a single performance metric) into future experimental designs represents an essential next step to fully characterize the functional efficacy of optimized r-PET membranes.

Table 4. Fit statistics for the r-PET AFD model

Parameter	Value	Parameter	Value
Std. Dev.	11.94	R^2	0.9988
Mean	555.00	Adjusted R^2	0.9967
C.V. %	2.15	Predicted R^2	0.9824
		Adeq Precision	72.9727

In this study, the calculated difference of 0.0143 was well below this critical threshold. This outcome academically indicated that the developed quadratic model did not suffer from overfitting and exhibited an outstanding predictive capability. The adequacy precision value, which measures the signal-to-noise ratio of the model, was obtained as 72.9727. Statistically, a ratio greater than 4.00 is a desirable condition for model navigability. The value of 72.9727 achieved in the developed model clearly demonstrated that the current signal was highly dominant and adequate against noise. This confirmed that the quadratic model could successfully simulate and map the r-PET electrospinning design space. Finally, the coefficient of variation (C.V.%) value, which is an indicator of experimental precision and reproducibility of laboratory conditions, was realized at a very low level of 2.15%. This low value proved that the electrospinning process based on the rotating drum collector system and the methodology of 50 individual fiber measurements performed with ImageJ minimized the experimental error margin. Consequently, these statistical validations confirmed that the electrospinning process was executed with a high degree of operational stability and reproducibility. While the current optimization framework focuses on establishing precise control over the primary morphological parameter (AFD), evaluating functional performance metrics (specifically the QF, which balances particle collection efficiency against airflow pressure drop) is positioned as the subsequent application phase built upon this foundational structural baseline.

3.3. Effects of Process Parameters on AFD and 3D Surface Plots

The mutual interaction trends of the independent variables with one another were determined in the ANOVA results. Statistically, when the primary factors of a process are involved in mutual interaction loops, examining the individual linear effects of these factors graphically can lead to misleading conclusions. Therefore, to holistically map the quadratic and curvilinear variations in the r-PET AFD, 3D response surface plots showcasing the simultaneous effects of parameter pairs are presented together in Figure 3.

When Figure 3(a), showcasing the combined effect of concentration and flow rate (AB), and Figure 3(b), presenting the concentration-needle diameter (AC) interaction, were examined, it was observed that these surfaces exhibited a more planar and linear rising tendency. This morphological behavior was in strong agreement with the high P-values in the ANOVA table (AB: 0.0536 and AC: 0.2644). This confirmed that there was no strong quadratic synergy between these parameter pairs to radically distort the fiber diameter, and the variables acted independently on the fiber geometry (Wang et al., 2012; Aydemir and Demiryürek, 2023).

The increase in fiber diameter in these plots resulted largely from the individual viscoelastic dominance of concentration (A). When the concentration in the r-PET flakes solutions was increased from 10% to 15%, the exponential increase in solution viscosity, occurring as a consequence of the $\eta_{sp}\, \alpha\, C^n$ scaling law detailed in Section 3.1, directly dictated this steep and aggressive rising trend in the 3D surface plots. Such a radical growth in chain entanglements per solvent volume limited the ability of the electric field to attenuate the jet, driving the fiber diameter upward at a non-linear rate (Kijeńska-Gawrońska et al., 2022; Ng et al., 2022).

The most distinct evidence of mutual interaction for the model, which was statistically significant (P=0.0130), was substantiated in Figure 3(c), illustrating the flow rate-needle diameter (BC) relationship. The prominent curling and curvilinear trend exhibited by the response surface in Figure 3(c) proved that these two apparatus parameters possessed a combined electro-hydrodynamic mechanism on the r-PET AFD morphology.

When the plot was analyzed in detail, the growth in the r-PET AFD remained highly limited, stable, and within a narrow band (near the minimum fiber diameter region) when the flow rate was increased from 0.5 mL/h to 1.9 mL/h in the narrow needle geometry (22G). This was because the narrow needle diameter generated a high hydraulic counter-pressure at the syringe tip, resulting in elevated shear rates within the capillary (Kijeńska-Gawrońska et al., 2022). Due to the rapid viscoelastic relaxation time characteristic of PET solution jets, maintaining high capillary shear is essential to sustain

chain extension prior to jet flight (Sigonya et al., 2024). This rheological behavior induced shear-thinning, which lowered the viscosity and enabled greater orientation of the polymer chains within the needle.

This rheological behavior induced shear-thinning, which lowered the viscosity and enabled greater orientation of the polymer chains within the needle. This phenomenon allowed the jet to be transferred to the collector with high stretching over a stable Taylor cone (Sigonya et al., 2024). Furthermore, the thinner the needle tip, the more the electric field lines concentrated at this specific point (field concentration), which supported the effective attenuation of the jet even when the flow rate increased.

Widening the orifice to 18G caused a sharp surge in fiber diameter under increasing flow rates, pushing thickness values well above 900 nm. Electric charges spread over a broader area in this wider tip geometry. At the same time, high volumetric throughput limited solvent evaporation from the jet interior, destabilizing the drying process (Abbas et al., 2018; Gergely et al., 2019). Heavy fluid delivery reduced the surface-area-to-volume ratio. This left too little flight time for full solvent removal before landing. Because the r-PET jet failed to thin sufficiently prior to hitting the rotating drum collector, coarse fibers formed throughout the mesh (Medeiros et al., 2026). Ultimately, this non-linear behavior proves that industrial optimization demands adjusting feed rate and nozzle size together, rather than treating them as isolated parameters. Mechanistically, this coupled dependency is governed by the characteristic viscoelastic relaxation time of the r-PET/TFA/DCM solution. Because post-consumer r-PET chains possess relatively rapid conformational relaxation dynamics during capillary passage, shear-induced orientation generated inside the nozzle decays rapidly upon exit. Utilizing a narrower nozzle orifice (22G) counteracts this rapid stress relaxation by increasing local capillary shear rates and back-pressure, which stabilizes the Taylor cone base under higher volumetric feed rates and prevents premature jet breakup before flight-phase extensional drawing dominates.

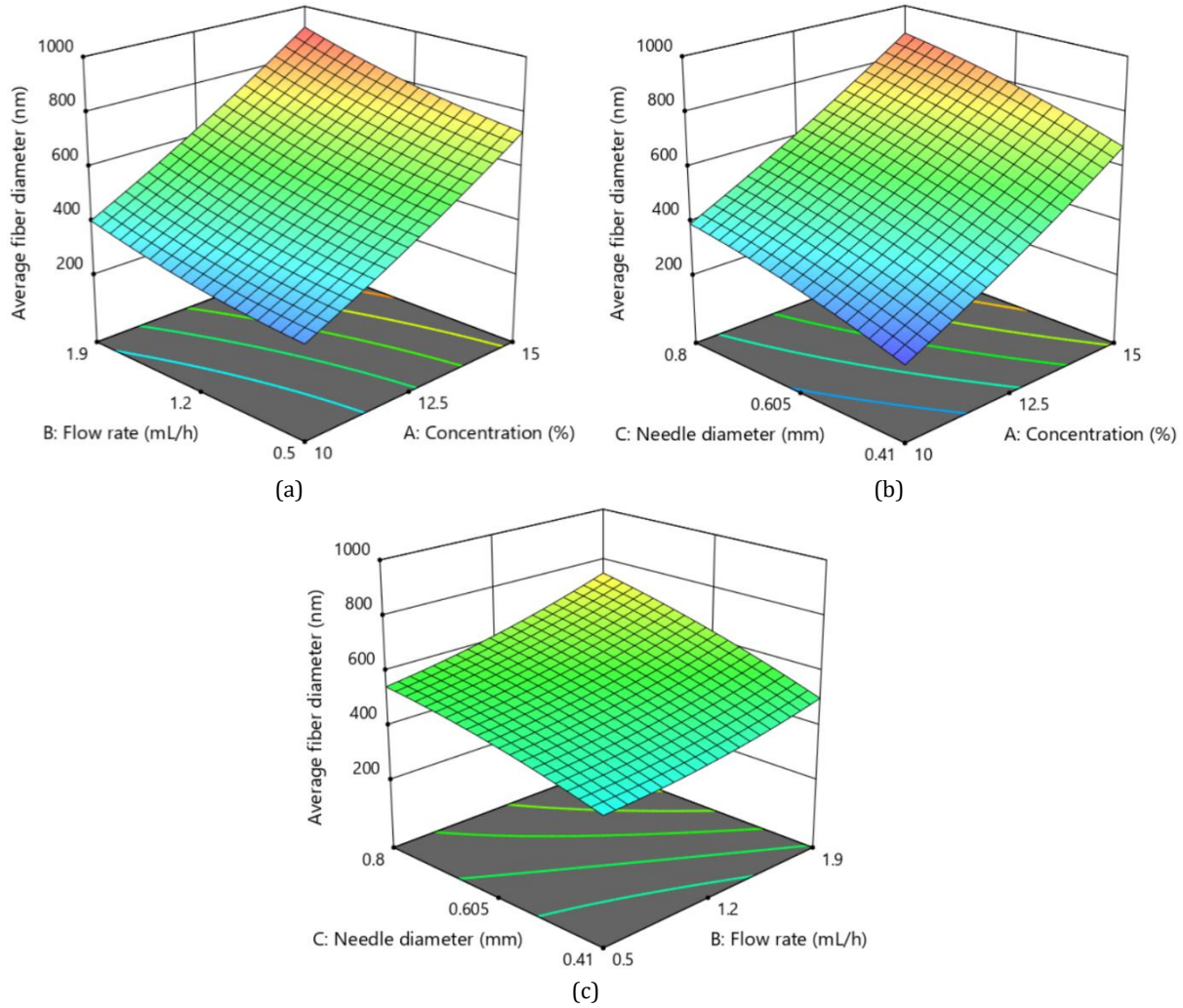


Figure 3. 3D response surface plots showing the combined effects of process parameters on r-PET AFD: (a) concentration–flow rate (*AB*), (b) concentration–needle diameter (*AC*), (c) flow rate–needle diameter *(BC).*

3.4. Numerical Optimization and Model Validation

Advanced applications (such as high-efficiency air filters and medical facemasks) demand strict control over r-PET membrane structural properties, particularly AFD. In air filtration mechanics, tailoring fiber thickness is vital for optimizing particle capture mechanisms via enhanced surface area and slip-flow effects; however, sub-micron fiber diameter must be precisely controlled to prevent excessive packing density that induces high pressure drops. While evaluating functional performance metrics (specifically the QF, which balances particle capture efficiency against airflow resistance) represents a mandatory subsequent testing phase, establishing a repeatable process framework for AFD optimization serves as the foundational structural prerequisite for was mathematically equal to the ideal state. The optimum process parameters selected by the developed quadratic model and the desirability function, along with the corresponding theoretical output target, were identified as follows:

- Concentration (A): 10.04% (rounded to 10.00 wt% for practical laboratory solution preparation)
- Flow rate (B): 1.07 mL/h
- Needle diameter (C): 22G (0.41 mm)

engineering high-performance r-PET filtration substrates.

In this regard, to map the process windows in the most efficient manner, the Numerical Optimization and Desirability function within the Design-Expert 12 software was utilized. While establishing the optimization criteria, the independent process variables, namely concentration (*A*), flow rate (*B*), and needle diameter (*C*), were kept within the experimental ranges (lower and upper limits), whereas the final response, AFD, was targeted to reach a minimum size (nm) (Ng et al., 2022).

As a result of the numerical optimization loops executed by the software, the most ideal process recipe was determined with a desirability value of *D*=1.000, which

- Predicted target fiber diameter (Predicted value): 209.52 nm

The numerical optimization ramp plots containing the respective optimum coordinates and parameter limits were presented in Figure 4. The red and blue flags in Figure 4 visualized the precise pinpoint coordinates determined by the model to reach the minimum fiber diameter region.

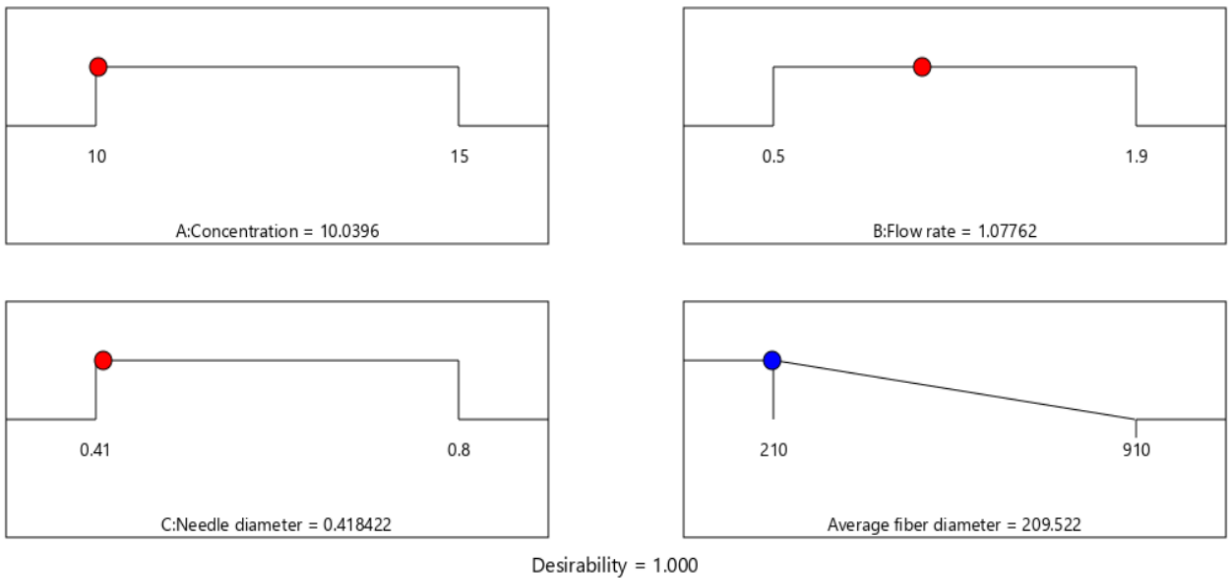


Figure 4. Desirability ramp plots for numerical optimization targeting minimum AFD in the r-PET electrospinning process.

To experimentally prove the theoretical success of the developed BBD and validate the optimization coordinates, a validation run was executed in triplicate using this specific recipe suggested by the software (10.04% concentration, 1.07 mL/h flow rate, and 0.41 mm (22G) needle diameter). To experimentally validate the theoretical predictions, validation runs were conducted in triplicate (n=3) using three independently prepared polymer solution batches electrospun in separate operational runs under identical conditions. As a result of the morphological analyses performed with ImageJ on the r-PET nanofibers produced on the designed rotating drum collector system, the r-PET AFD was measured as 218 ± 42 nm.

The relative percentage deviation between the theoretical value predicted by the response surface model (209.52 nm) and the empirical result obtained from triplicate bench tests (218 ± 42 nm) calculated as 3.89%. This minimal deviation demonstrates strong practical agreement between theoretical predictions and experimental observations. Furthermore, the resistance to model overfitting is statistically corroborated by the

minimal discrepancy between the adjusted coefficient of determination (Adj R^2=0.9967) and the predicted coefficient of determination (Pred R^2=0.9824), where the difference of 0.0143 is well below the standard threshold of 0.20. Together, these empirical and statistical validations indicate that the quadratic response surface model provides a stable and reliable framework for optimizing r-PET fiber diameter within the specified design boundaries.

Comparing the optimized r-PET nanofiber diameter (218 ± 42 nm) with literature benchmarks for pristine virgin PET (v-PET) electrospun under similar conditions (typically ranging between 200–350 nm) confirms that post-consumer waste flakes can match the morphological quality of virgin polymers (Wang et al., 2012; Aydemir and Demiryürek, 2023). Although direct side-by-side v-PET control runs were not performed in this experimental matrix, this close alignment with literature baseline values proves the upcycling efficiency of the optimized BBD process.

While direct filtration testing, such as particulate filtration efficiency, air permeability, pressure drop, and QF, was beyond the immediate scope of this optimization study, achieving strict control over AFD represents the fundamental prerequisite for tuning membrane pore size distribution.

4. Conclusion

In this study, to reintegrate textile and packaging wastes into the recycling economy, the production of functional nanofiber membranes from waste r-PET flake sources was successfully realized using an electrospinning system with a rotating drum collector. The individual and combined effects of the process parameters, namely concentration, flow rate, and needle diameter, on the r-PET AFD and morphology were systematically optimized through BBD and ANOVA. The primary conclusions obtained within the scope of this study are summarized in items below:

- *Model Reliability and Statistical Stability:* The second-order quadratic model developed to predict the r-PET AFD was indicated to be statistically highly significant (F-value=473.60 and P<0.0001) The fact that the coefficient of determination (R^2=0.9988) and adjusted coefficient of determination (Adj R^2=0.9967) values of the model were extremely close to each other and high confirmed that an excellent correlation existed between the experimental data and the mathematical model predictions.
- *Lack of Fit and Coefficient of Variation Success:* The fact that the lack of fit parameter of the model was found to be statistically insignificant (P=0.1034 > 0.05) demonstrated that the ability of the quadratic equation to represent the experimental design space was highly reliable. Furthermore, the coefficient of variation remaining at an extremely low level (2.15%) proved that the rotating drum collector mechanism and the ImageJ-based morphological measurement methodology possessed high reproducibility and experimental precision.
- *Effects of Process Parameters:* It was determined that the most dominant individual (linear) effect on the AFD belonged to the concentration (*A*). When the concentration was increased from 10% to 15%, the fiber diameter thickened radically due to the increase in chain entanglement and viscoelastic resistance. As the most unique finding in the model, the flow rate–needle diameter (*BC*) mutual interaction was found to be statistically significant (P=0.0130). As mapped via 3D response surface plots, the fiber diameter remained relatively stable across increasing flow rates when using the narrow 22G nozzle, whereas employing the wider 18G nozzle caused a noticeably steeper increase in fiber diameter with higher feed rates. Mechanistically, rather than attributing this trend to internal molecular chain alignment (which rapidly relaxes given the short viscoelastic relaxation time of PET and would require structural diffraction techniques (such as SAXS or WAXD) for direct verification) this behavior is governed by volumetric flux dynamics at the nozzle tip. The smaller capillary exit area of the 22G needle maintains higher exit velocity and back-pressure, stabilizing the Taylor cone base and preventing excess fluid accumulation as feed rate rises. Consequently, fiber drawing remains predominantly governed by high extensional flow rates during jet flight (Gazzano et al., 2015). Conversely, the larger orifice area of the 18G nozzle permits solution buildup at high flow rates, expanding the Taylor cone droplet volume and initiating a thicker electrospinning jet.
- *Numerical Optimization and Experimental Validation:* The numerical desirability optimization conducted to achieve the minimum AFD (a foundational structural target for high-performance filtration substrates) yielded an overall desirability score of D=1.000, representing an ideal mathematical solution within the evaluated design space. While achieving sub-micron fiber diameters enhances specific surface area and promotes slip-flow conditions favorable for particle capture, complete functional validation for air filtration requires evaluating the trade-off between collection efficiency and airflow pressure drop through QF metrics. Therefore, attaining D=1.000 confirms that the process parameters were successfully optimized to yield the theoretical minimum fiber thickness, establishing the mandatory structural prerequisite upon which future functional QF testing can be systematically performed. The most ideal production recipe determined by the software was identified as 10.04% (rounded to 10.00 wt% for practical laboratory solution preparation) concentration, 1.07 mL/h flow rate, and 22G needle diameter, predicting a theoretical fiber diameter of

209.52 nm at these coordinates. As a result of the validation run executed in triplicate under laboratory conditions using this specific recipe, the r-PET AFD was measured as 218 ± 42 nm. However, while this strong agreement confirms the operational success of the response surface model for the evaluated bottle-grade feedstock (IV ≈ 0.70–0.80 dL/g), asserting universal model applicability across arbitrary recycled PET sources requires scientific caution. Because post-consumer plastic waste undergoes variable thermal and mechanical degradation during recovery, uncharacterized fluctuations in MW or IV can alter solution rheology and shift baseline fiber diameter predictions (Kijeńska-Gawrońska et al., 2022). Consequently, this optimization framework serves as a reliable quantitative baseline calibrated specifically for standard bottle-derived flakes, recognizing feedstock molecular characterization as a primary variable for broader cross-batch extrapolation.

In conclusion, the findings demonstrate that the rotating drum electrospinning process optimized via Box-Behnken design provides a reproducible bench-scale framework for producing controlled, homogeneous, and sub-micron fiber membranes from post-consumer r-PET. However, translating this structural baseline toward broader industrial application requires addressing inherent feedstock variations in MW and IV across different post-consumer batches, alongside evaluating functional QF metrics that balance particle collection efficiency against airflow resistance. Furthermore, while upcycling waste PET aligns with circular economy goals, the reliance on a hazardous solvent system (TFA/DCM) presents a sustainability trade-off. Transitioning toward greener, low-toxicity solvent formulations or closed-loop solvent recovery systems represents an essential direction for future studies to fully realize environmentally benign, high-performance filtration substrates and protective technical textiles.

Limitations and Future Perspectives: While this work successfully mapped the morphological control windows of r-PET nanofibers, future research should integrate functional filtration evaluations (including pressure drop and QF) and evaluate green, non-toxic solvent alternatives to fully advance sustainable industrial scale-up.

Author Contributions

The percentages of the author' contributions are presented below. The author reviewed and approved the final version of the manuscript.

	H.A.
C	100
D	100
S	100
DCP	100
DAI	100
L	100
W	100
CR	100
SR	100
PM	100
FA	100

C= concept, D= design, S= supervision, DCP= data collection and/or processing, DAI= data analysis and/or interpretation, L= literature search, W= writing, CR= critical review, SR= submission and revision, PM= project management, FA= funding acquisition.

Conflict of Interest

The author declared that there is no conflict of interest.

Ethical Consideration

Ethics committee approval was not required for this study because of there was no study on animals or humans.

References

Abbas, J. A., Said, I. A., Mohamed, M. A., Yasin, S. A., Ali, Z. A., & Ahmed, I. H. (2018). Electrospinning of polyethylene terephthalate (PET) nanofibers: Optimization study using taguchi design of experiment. *IOP Conference Series: Materials Science and Engineering*, *454*, 012130. https://doi.org/10.1088/1757-899X/454/1/012130

Aydemir, H., & Demiryürek, O. (2023). The effect of electrospinning parameters on morphology and diameter of polyethylene terephthalate (PET) and recycled polyethylene terephthalate (r-PET) nanofibers. *The Journal of The Textile Institute*, *114*(10), 1443–1454. https://doi.org/10.1080/00405000.2022.2131341

Aydemir, H., Demiryürek, O., & Erol, M. (2025). Structural and sound absorption properties of polyethylene terephthalate (PET) and recycled polyethylene terephthalate (r-PET) nanofibers. *The Journal of The Textile Institute*, *116*(4), 722–732. https://doi.org/10.1080/00405000.2024.2352181

Baselga-Lahoz, M., Yus, C., Arruebo, M., Sebastián, V., Irusta, S., & Jiménez, S. (2022). Submicronic Filtering Media Based on Electrospun Recycled PET Nanofibers: Development, Characterization, and Method to Manufacture Surgical Masks. *Nanomaterials*, *12*(6), 925. https://doi.org/10.3390/nano12060925

Bonfim, D. P. F., Cruz, F. G. S., Bretas, R. E. S., Guerra, V. G., & Aguiar, M. L. (2021a). A Sustainable Recycling Alternative: Electrospun PET-Membranes for Air Nanofiltration. *Polymers*, *13*(7), 1166. https://doi.org/10.3390/polym13071166

Bonfim, D. P. F., Cruz, F. G. S., Guerra, V. G., & Aguiar, M. L. (2021b). Development of Filter Media by Electrospinning for Air Filtration of Nanoparticles from PET Bottles. Membranes, 11(4), 293. https://doi.org/10.3390/membranes11040293

Gazzano, M., Gualandi, C., Zucchelli, A., Sui, T., Korsunsky, A. M., Reinhard, C., & Focarete, M. L. (2015). Structure-morphology correlation in electrospun fibers of semicrystalline polymers by simultaneous synchrotron SAXS-WAXD. *Polymer*, *63*, 154–163. https://doi.org/10.1016/j.polymer.2015.03.002

Gergely, A. (2020). The Production of Polyethylene Terephthalate Nanofibers by Electrospinning with Minimum Amount of Trifluoroacetic Acid. *Biomedical Journal of Scientific & Technical Research*, *29*(3). https://doi.org/10.26717/BJSTR.2020.29.004795

Gergely, A., Kántor, J., Bitay, E., & Biró, D. (2019). Electrospinning of Polymer Fibres Using Recycled PET. *Acta Materialia Transylvanica*, *2*(1), 19–26. https://doi.org/10.33924/amt-2019-01-04

Gulino, E. F., & Scaffaro, R. (2025). Electrospinning with Green Solvents: Overcoming Constraints While Tailoring Nanofibrous Structures. *IOCPS 2025*, 40. https://doi.org/10.3390/proceedings2026136040

Haider, A., Haider, S., & Kang, I.-K. (2018). A comprehensive review summarizing the effect of electrospinning parameters and potential applications of nanofibers in biomedical and biotechnology. *Arabian Journal of Chemistry*, *11*(8), 1165–1188. https://doi.org/10.1016/j.arabjc.2015.11.015

Hoque, M. E., Sarker, M. A., Alam, M. R., & Gafur, M. A. (2024). Development of Multi-Walled Carbon Nanotube-Integrated Recycled Polyethylene Terephthalate Electrospun Antibacterial Face Mask. *Journal of Science and Technology Research*, *5*(1), 63–74. https://doi.org/10.3329/jscitr.v5i1.74005

Hossain, M. T., Shahid, M. A., & Ali, A. (2022). Development of nanofibrous membrane from recycled polyethene terephthalate bottle by electrospinning. *OpenNano*, *8*, 100089. https://doi.org/10.1016/j.onano.2022.100089

Kijeńska-Gawrońska, E., Wiercińska, K., & Bil, M. (2022). The Dependence of the Properties of Recycled PET Electrospun Mats on the Origin of the Material Used for Their Fabrication. *Polymers*, *14*(14), 2881. https://doi.org/10.3390/polym14142881

Medeiros, G. B., Chagas, P. A. M., Da Mata, G. C., Bonfim, D. P. F., De Almeida, D. S., & Aguiar, M. L. (2026). rPET Nanofiber Membranes for Air Filtration: High Performance via Electrospinning Optimization. *Nanomanufacturing*, *6*(1), 4. https://doi.org/10.3390/nanomanufacturing6010004

Naeim, H., Mahdavian, F., & Rodrigue, D. (2025). Review on electrospinning of recycled polymer-derived fibers: A road towards sustainability, production and applications. *Journal of Environmental Chemical Engineering*, *13*(6), 119283. https://doi.org/10.1016/j.jece.2025.119283

Nam, C., Lee, S., Ryu, M., Lee, J., & Lee, H. (2019). Electrospun nanofiber filters for highly efficient PM2.5 capture. *Korean Journal of Chemical Engineering*, *36*(10), 1565–1574. https://doi.org/10.1007/s11814-019-0370-3

Ng, W. L., Zhou, L., Sulong, A. B., Ng, E.-P., & Tan, S. H. (2022). Modification of the commercial polyester filter media support with electrospun polyethylene terephthalate fibers and its application for air purification. *Science and Technology for the Built Environment*, *28*(7), 928–943. https://doi.org/10.1080/23744731.2022.2075188

Opálková Šišková, A., Frajová, J., & Nosko, M. (2020). Recycling of poly(ethylene terephthalate) by electrospinning to enhanced the filtration efficiency. *Materials Letters*, *278*, 128426. https://doi.org/10.1016/j.matlet.2020.128426

Sigonya, S., Mokhena, T. C., Mayer, P., Makhanya, T. R., & Mokhothu, T. H. (2024). Electrospinning and Rheological Characterization of Polyethylene Terephthalate and Polyvinyl Alcohol with Different Degrees of Hydrolysis Incorporating Molecularly Imprinted Polymers. *Polymers*, *16*(23), 3297. https://doi.org/10.3390/polym16233297

Strain, I. N., Wu, Q., Pourrahimi, A. M., Hedenqvist, M. S., Olsson, R. T., & Andersson, R. L. (2015). Electrospinning of recycled PET to generate tough mesomorphic fibre membranes for smoke filtration. *Journal of Materials Chemistry A*, *3*(4), 1632–1640. https://doi.org/10.1039/C4TA06191H

Veleirinho, B., Rei, M. F., & Lopes-DA-Silva, J. A. (2008). Solvent and concentration effects on the properties of electrospun poly(ethylene terephthalate) nanofiber mats. *Journal of Polymer Science Part B: Polymer Physics*, *46*(5), 460–471. https://doi.org/10.1002/polb.21380

Wang, C., Lee, M.-F., & Wu, Y.-J. (2012). Solution-Electrospun Poly(ethylene terephthalate) Fibers: Processing and Characterization. *Macromolecules*, *45*(19), 7939–7947. https://doi.org/10.1021/ma300121k

Black Sea Journal of Engineering and Science
doi: 10.34248/bsengineering.1996841

Open Access Journal
e-ISSN: 2619 – 8991

Research Article
Volume 9 - Issue 5: 2676-2691 / September 2026

MACHINE LEARNING AND DEEP LEARNING BASED CLASSIFICATION OF PROFANITY AND SEXIST DISCOURSE IN TURKISH TEXTS

Naim KARASEKRETER[1], Caner BALIM[2]*, Özkan ASLAN[1]

[1]*Afyon Kocatepe University, Faculty of Engineering, Department of Computer Engineering, 03200, Afyonkarahisar, Türkiye*
[2]*Afyon Kocatepe University, Faculty of Engineering, Department of Software Engineering, 03200, Afyonkarahisar, Türkiye*

Abstract: In this study, harmful content detection in Turkish texts is addressed as a three-class text classification problem comprising Harmless, Profanity and Sexist Discourse. For this purpose, open-access Turkish datasets and data compiled within the scope of the TÜBİTAK 1001 project were combined, and after removing cross-source duplicates and conflicting duplicates, a final dataset of 12051 texts was used. In the experimental process, traditional machine learning models and Transformer-based language models were compared under the same dataset, the same class structure and a 5-fold group-based stratified cross-validation protocol. For the traditional models, in addition to word- and character-level TF-IDF representations, Word2Vec- and FastText-based representations were used to evaluate Linear SVM, Logistic Regression, Decision Tree, Random Forest, Extra Trees and XGBoost algorithms. For the Transformer-based models, BERTurk, Electra-TR, ConvBERTurk and XLM-RoBERTa were adapted to the three-class classification task. Among the traditional models, the highest performance was obtained with Logistic Regression on TF-IDF representations (82.82% macro F1-score); Linear SVM produced very close results, while FastText- and Word2Vec-based representations remained comparatively lower. The obtained results showed that Transformer-based models offer higher and more balanced performance than traditional machine learning models. Among all models, the highest success was achieved with the ConvBERTurk model, which reached a 90.93% macro F1-score, 90.93% accuracy and a 98.09% ROC-AUC value. The BERTurk model exhibited a performance very close to ConvBERTurk with a 90.28% macro F1-score. A paired t-test over the five folds shows that this difference is not statistically significant ($t(4) = 2.36$, $P=0.078$). These findings indicate that contextual language representations are effective in Turkish harmful content classification. The study contributes to the literature by addressing Turkish harmful content detection as a multi-class problem that also includes the distinction between profanity and sexist discourse, and by comparing traditional models and Transformer-based models under the same leakage-controlled experimental protocol.

Keywords: Turkish text classification, Harmful content detection, Profanity detection, Sexist discourse detection, Machine learning, Transformer models

***Corresponding author:** Afyon Kocatepe University, Faculty of Engineering, Department of Software Engineering, 03200, Afyonkarahisar, Türkiye
E mail: cbalim@aku.edu.tr (C. BALIM)
Naim KARASEKRETER https://orcid.org/0000-0003-2892-6430
Caner BALIM https://orcid.org/0000-0002-1010-129X
ÖZKAN ASLAN https://orcid.org/0000-0002-2680-5419

Received: July 17, 2026
Accepted: August 23, 2026
Published: September 15, 2026

Cite as: Karasekreter, N., Balim C., & Aslan Ö. (2026). Machine learning and deep learning based classification of profanity and sexist discourse in turkish texts. *Black Sea Journal of Engineering and Science*, 9(5): 2676-2691.

1. Introduction

With the proliferation of digital communication environments, social media platforms, forums, news comments and online discussion spaces have become fundamental communication channels where individuals can quickly share their thoughts. Although these environments offer important opportunities for information sharing and social interaction, they also create fertile ground for the spread of harmful texts such as profanity, insults, degrading discourse and sexist discourse. As user-generated content reaches large volumes, detecting such texts solely through human moderation becomes inadequate in terms of time, cost and scalability.

In online texts, not only the presence but also the type of harmful content is important. A text may directly contain profane or vulgar expressions, or it may contain sexist discourse — degrading, exclusionary or hateful expressions targeting a person or group on the basis of gender. In contrast, texts that do not contain aggression or inappropriateness can be regarded as harmless. In this study, Turkish texts are addressed within the scope of a three-class classification problem consisting of Harmless, Profanity and Sexist Discourse.

Harmful content detection in Turkish texts involves various difficulties due to the structural characteristics of the language and online writing habits. While the agglutinative structure of Turkish causes words derived from the same root to be used in many forms with different suffixes, the spelling errors, abbreviations, character repetitions, emojis, usernames, hashtags and irregular punctuation marks seen in social media texts

This work is licensed (CC BY-NC 4.0) under Creative Commons Attribution 4.0 International License

make automatic text processing more complex.

The main aim of this study is to comparatively examine the performance of models that can automatically distinguish these three classes. Accordingly, traditional machine learning models and Transformer-based language models were tested under the same dataset and evaluation protocol. While word- and character-level TF-IDF representations were used in the traditional models, pre-trained contextual language representations were utilized in the Transformer-based models. Thus, the performance difference between classical feature-extraction-based methods and modern deep-learning-based approaches in Turkish harmful content classification was systematically analyzed. The contribution of this study can be evaluated at two levels. At the data level, the original labels obtained from different sources were not transferred directly to the three-class structure; they were mapped onto a consistent three-class scheme within the framework of the annotation guideline and the inclusion–exclusion criteria defined by the researchers, and label groups that did not match the class definitions were excluded from the scope. At the method level, by applying a group-based stratified cross-validation protocol that prevents conflicting duplicates and identical samples at the normalized-text level from leaking together into the training and test partitions, traditional machine learning models and four different Transformer-based models were systematically compared under the same experimental conditions. In this respect, the contribution of the study is not so much to propose a new model architecture as to bring together a multi-source three-class dataset for Turkish harmful content detection under a leakage-controlled, reproducible evaluation protocol, enabling different model families to be evaluated under comparable conditions.

1.2. Literature Review

Esen and Amrahov (2024) reported 0.858 accuracy, 0.856 F1-score and 0.923 ROC-AUC with a Bernoulli Naive Bayes model on 12989 Turkish texts. Yakar et al. (2024) compared classical algorithms with feature-selection methods on two different Turkish tweet datasets; they reported an F-measure of 88.81% with OneR + Naive Bayes on the 1K dataset and 87.71% with Info-Gain + Naive Bayes on the 2K dataset. Similarly, Kesgin and Demirer (2025) compared Random Forest, Naive Bayes, Logistic Regression, SVM and LSTM models for offensive language detection on 11253 posts collected from Twitter, Ekşi Sözlük and forums; they reported 0.82 accuracy and 0.65 AUC for the Random Forest model without Word2Vec, and 0.78 accuracy and 0.79 AUC for the LSTM model. Aliyeva and Yağanoğlu (2025) proposed an MLP-based model that jointly uses textual and social-media features for cyberbullying detection in Turkish Twitter posts; with TF-IDF + unigram features they reported 93.2 accuracy, 91.22 precision, 95.6 sensitivity and 93.36 F1-score. In addition to classical machine learning methods, representation-learning and deep-learning approaches are widely used in Turkish harmful content detection. Karayiğit (2026) compared classical machine learning and deep learning models on a dataset of Instagram comments for detecting insult content that constitutes a crime under the Turkish Penal Code; the TF-IDF + Naive Bayes model obtained 0.85 macro-averaged F1, while the BERT embedding + attention-based CNN model obtained 0.93 macro-averaged F1. Gümüş et al. (2024) used transformer-based sentence vectors with classical classifiers on the Turkish offensive language dataset of Tanyel et al. (2022) and reported 0.8512 F1 with the Multilingual-MiniLM + SVM combination. Najafi and Varol (2024) used more than 894 million Turkish tweets from 2010–2020 in their TurkishBERTweet model developed on Twitter/X data and adapted the RoBERTa-base architecture with pre-processing steps specific to social-media language. The model achieved 0.807 weighted F1 on the HateSpeech SIU dataset, 0.815 weighted F1 on the HSD2LANG dataset and 0.73167 macro F1 in the official SIU 2023 split for hate-speech detection tasks.

There are also studies comparing BERT-based models with large language models in Turkish hate-speech detection. Dehghan and Yanıkoğlu (2024) compared ChatGPT with a fine-tuned BERTurk model for Turkish hate-speech detection on the extended SIU2023-NST dataset; BERTurk-CE achieved 82.22% accuracy and a 74.86% macro-F1 score, while ChatGPT achieved 70.81% accuracy and a 58.50% macro-F1 score in the zero-shot setting and 65.81% accuracy and a 60.19% macro-F1 score in the few-shot setting. Aksoy et al. (2026) reported 0.958 precision, 0.879 recall and 0.916 F1-score for soft voting in 10-fold cross-validation with a transformer-based ensemble approach for detecting hate speech directed at LGBT individuals.

Studies conducted within the scope of shared tasks have enabled the comparison of different transformer architectures in Turkish hate-speech detection. Within the HSD-2Lang 2024 shared task, Singhal and Bedi (2024) fine-tuned XLM-RoBERTa Large for hate-speech detection in Turkish tweets and reported an F1 score of 0.63258 in the Turkish subtask. In the same task, Yagci et al. (2024) fine-tuned the TurkishBERTweet model without using additional data; they obtained 0.74 F1 on the public test set and 0.69 F1 on the private test set in the Turkish subtask, ranking second on the private leaderboard. Barkhordar et al. (2024) used the dbmdz/bert-base-turkish-128k-uncased model; they reported 0.71365 F1 on the public test set and 0.60790 F1 on the private test set in the official submission, and 0.71889 and 0.66129 F1 respectively in the late submission.

Data imbalance and data-augmentation approaches are also considered among the important factors affecting model success in Turkish harmful content detection. Karayiğit et al. (2024) compared different balancing techniques on the ATC dataset; with TextGAN-based balancing they reported Macro-Averaged F1 values of

0.972 for CNN models, 0.958 for SVM, 0.954 for Random Forest and 0.955 for Naive Bayes. Mut Altın and Saggion (2025) examined sexist discourse and its subtypes on 6915 Turkish texts collected from X and YouTube; with GPT-4o-mini fine-tuning they reported 0.91 F1 in binary classification and 0.59 F1 in multi-class sexism-type classification. De Oliveira et al. (2024) evaluated the GPT-3 Ada model with multilingual corpora and a cross-lingual learning strategy in the political-discourse domain; by adding a Turkish political tweet corpus among the source languages, they obtained high F1-scores in different target languages. It should be noted that Turkish was used only as a source language in that study and was not evaluated as a target language.

Studies in the field of harmful content detection are diversifying beyond text-level classification toward target detection, token-level labeling, hybrid architectures and multimodal applications. Uludoğan et al. (2024) used the TurkishHatePrintCorpus dataset of 6681 news articles for hate-speech detection in the Turkish print media and proposed the HateTargetBERT approach, which combines BERTurk representations with target-oriented linguistic features. The model achieved 90.54% accuracy, 88.47% precision, 90.82% recall and 89.60% F1-score on the test set. Büyükdemirci et al. (2024) addressed text-level neutral/offensive/hateful classification on the JL-Hate dataset together with token-level target and expression-span labels; for Turkish they reported 71.7% Macro F1 in text classification and 52.3% Macro F1 in token classification. Altinel et al. (2024) combined BERT representations with a k-means and textGCN-based hybrid approach; they reported F-measures of 77.43%, 77.81% and 81.17% on the 1K, 2K and 9K datasets respectively, and an 87.81% F1-score in the 9K scenario where all features are used together.

In general, studies in the literature show a trend from traditional machine learning methods toward Transformer-based models in Turkish harmful content detection; on the other hand, problems such as data imbalance, lack of context, semantic proximity between classes and the discrimination of harmful-content subtypes persist. Taking these trends in the current literature into account, this study addresses Turkish texts in three classes - Harmless, Profanity and Sexist Discourse - and compares traditional machine learning models with Transformer-based models under the same experimental protocol. A comparative summary of the studies reviewed in this section is presented in Table 1.

2. Materials and Methods

In this study, a three-class text classification approach was applied to automatically detect harmful content in Turkish texts. In this context, the aim was to determine which of the Harmless, Profanity or Sexist Discourse classes each text belongs to. In the experimental design, traditional machine learning algorithms and Transformer-based language models were compared using the same dataset, the same cross-validation strategy and the same evaluation metrics. Thus, the performance of classical approaches based on TF-IDF word- and character-level text representations and modern models leveraging contextual language representations such as BERT, RoBERTa, Electra and ConvBERT in Turkish harmful content classification was examined comparatively and systematically.

2.1. Dataset

The dataset used in this study was created to address harmful content detection in Turkish texts as a three-class classification problem. The dataset was prepared by combining open-access Turkish datasets with texts compiled within the scope of the TÜBİTAK 1001 project numbered 124E056. The data sources used consist of the Turkish offensive language corpus published by Çöltekin (2020), the Turkish toxic language dataset provided by Overfit-GM (2023), the gender subset of the large-scale multi-domain hate speech corpus published by Toraman et al. (2022a,b), and additional texts compiled as part of the project. The data obtained from different sources were reorganized to fit the class structure of this study. In this context, each text was assigned to one of three classes: Harmless, Profanity and Sexist Discourse. The Harmless class refers to texts that do not contain aggression, profanity or sexist degradation. The Profanity class covers expressions containing rude, profane and obscene language. The Sexist Discourse class covers degrading, exclusionary or hateful expressions targeting a person or group on the basis of gender or gender identity.

The final dataset consists of a total of 12051 samples: 4580 samples taken from the Overfit-GM dataset, 4977 samples from the gender subset of the corpus of Toraman et al. (2022a,b) 2080 samples from the Çöltekin corpus and 414 samples compiled within the scope of the TÜBİTAK 1001 project. The labels in the source datasets are based on the original labels produced by human annotators in the annotation processes of the respective studies. These labels were not transferred directly and as-is to the three-class structure used in this study; inclusion and exclusion criteria were defined for each class in line with the annotation guideline created by the researchers, and the source labels were mapped onto the three-class scheme according to these criteria. The texts compiled within the TÜBİTAK 1001 project were labelled by three scholarship-holding annotators, all of whom are graduates of undergraduate programmes related to Turkish language, using the same annotation guideline applied to the external corpora. Each text was labelled independently by all three annotators; the final label was determined by majority agreement and the remaining disagreements were resolved through joint discussion. Of these texts, only those assigned to the Harmless and Profanity classes were transferred to the final dataset (400 and 14 samples respectively), while texts labelled as obscene content were excluded because they do not correspond to any of the three classes.

Table 1. Summary comparison of studies in the field of Turkish harmful content detection

Year	Reference	Dataset	Class Distribution	Methodology	F1	Accuracy	AUC	Precision	Recall
2024	Esen and Amrahov	Private	No: 6850, Yes: 6139, Total: 12989	Bernoulli Naive Bayes	0.856	0.858	0.923	0.863	0.858
2024	Yakar et al.	Public	None: 1287, Offensive expression: 387, Hate speech: 375, Total: 2049	Feature Extraction + ML Algorithms	0.8771	-	-	-	-
2024	Gümüş et al.	Public	Offensive: Not specified, Non-offensive: Not specified, Total: 53005 (42398 train / 8851 test / 1756 validation)	Sentence Transformer + ML Models	0.8512	-	-	0.8515	0.8512
2024	Najafi and Varol	Public	No hate speech: 6121, Hate speech: 2684, Total: 8805	TurkishBERTweet (RoBERTa-base)	0.815	-	-	-	-
2024	Dehghan and Yanıkoğlu	Public	No hate speech: 5596, Hate speech: 1808, Total: 7404	BERTurk + ChatGPT zero-shot / few-shot	0.7486	0.8222	-	0.7612	0.7389
2024	Singhal and Bedi	Public	Non-hateful: 6258, Hateful: 2882, Total: 9140	XLM-RoBERTa Large	0.63258	-	-	-	-
2024	Yagci et al.	Public	Non-hateful: 6258, Hateful: 2882, Total: 9140	TurkishBERTweet	0.74	-	-	-	-
2024	Barkhordar et al.	Public	Non-hateful: 6258, Hateful: 2882, Total: 9140	BERTurk	0.71365	-	-	-	-
2024	Karayiğit et al.	Private	Non-abusive: 19826, Abusive: 10528, Total: 30354	TextGAN + CNN + SVM + RF + Naive Bayes	0.972	-	0.98	0.98	0.91
2024	De Oliveira et al.	Public	Turkish corpus used as source language: No hate speech: 5055, Hate speech: 2512, Total: 7567	GPT-3 Ada (target language: English; Turkish used as a source language)	0.9658	-	-	0.9689	0.9695
2024	Uludoğan et al.	Public	Non-hateful: 3678, Hateful: 3003, Total: 6681	HateTargetBERT	0.8960	0.9054	-	0.8847	0.9082
2024	Büyükdemirci et al.	Public	Neutral: 258, Offensive: 349, Hateful: 67, Skipped: 68, Tie: 23, Total: 765	Transformer Models	0.717	-	-	-	-
2024	Altinel et al.	Public	None: 6447, Hate speech: 1757, Offensive expression: 1614, Total: 9818	Transformer Models + TextGCN	0.8781	-	-	-	-
2025	Kesgin and Demirer	Private	Offensive: Not specified, Non-offensive: Not specified, Total: 11253	TF-IDF + ML Models (Random Forest, without Word2Vec)	-	0.82	0.65	-	-
2025	Aliyeva and Yağanoğlu	Public	Non-cyberbullying: 2500, Cyberbullying: 2500, Total: 5000	MLP + TF-IDF/Unigram + Social Media Features	0.9336	0.932	0.932	0.9122	0.956
2025	Mut Altın and Saggion	Public	Not-sexist: 3167, Sexual violence: 1352, Stereotyping: 1124, Misogyny: 655, Objectification: 468, Anti-feminism: 149, Total: 6915	GPT-4o mini Fine-Tuning	0.91	-	-	-	-
2026	Karayiğit	Public	Non-insult: 3709, Insult: 3652, Total: 7361	Feature Extraction + ML and DL	0.93	0.93	-	0.93	0.93
2026	Aksoy et al.	Public	Hate speech: 4247, Non-hate speech: 4247, Total: 8494	Transformers + Soft Voting	0.916	0.9201	-	0.958	0.879

In this context, the non- and prof-labeled samples in the Çöltekin corpus were mapped to the Harmless and Profanity classes respectively; the OTHER-, PROFANITY- and SEXIST-labeled samples in the Overfit-GM dataset were mapped to the Harmless, Profanity and Sexist Discourse classes respectively; and the normal- and hate-labeled samples in the corpus of Toraman et al. (2022a,b) were mapped to the Harmless and Sexist Discourse classes. The samples from the TÜBİTAK project were included in the dataset with their harmless and profanity labels preserved. Label groups that did not match the class definitions — the INSULT and RACIST labels in the Overfit-GM dataset, the general insult categories directed at individuals or groups in the Çöltekin corpus, the offensive label with blurred class boundaries in the Toraman corpus, machine-translated content and non-Turkish lines — were excluded from the scope. Thus, the Sexist Discourse class was formed from the union of the Overfit-GM SEXIST-labeled samples (670 samples) and the hate-labeled samples of the Toraman corpus (2779 samples).

During the data-merging process, attention was paid to preserving the semantic distinction between classes; near-duplicates across sources and conflicting-duplicate groups — in which the same text, or texts considered identical in normalized form, appeared with different labels — were removed from the dataset. In addition, by including the harmless-labeled samples from the gender-themed source in the Harmless class, the aim was for the models to learn actual sexist discourse rather than the mere presence of the gender topic, thereby reducing the risk of topic-based shortcut learning. To measure the level of leakage that could arise from the source–label structure, a baseline evaluation using only the source information was performed; the accuracy of this baseline was calculated as 0.567 and fell within the pre-specified acceptance range (0.50–0.60) (majority-class baseline: 0.436). The fact that the source–label association cannot be completely eliminated — since sexist content comes predominantly from gender-focused sources and profanity content predominantly from profanity-focused sources — was documented as a structural limitation of the study.

The group variable used in the experiments was also produced with the same normalization approach. For this purpose, the texts were passed through Unicode normalization, converted to lowercase while preserving the Turkish character structure; URLs, usernames and numerical expressions were replaced with standard tokens, punctuation marks were separated with spaces and excess whitespace was cleaned. As a result of this process, samples with the same normalized text were grouped under the same group identifier. In this study, the grouping operation is based on the exact matching of normalized texts rather than a character-based approximate-similarity threshold. Thus, identical texts — or those considered identical in normalized form — were prevented from being distributed to different cross-validation folds.

As a result of these operations, a duplicate-free final dataset of 12051 texts was used in the experiments. In the final dataset, 5255 texts are in the Harmless class, 3347 texts in the Profanity class and 3449 texts in the Sexist Discourse class (Table 2). Thus, a consistent and near-balanced experimental data structure was obtained that allows traditional machine learning models and Transformer-based models to be compared under the same dataset and the same class structure.

The classes are unevenly distributed across the four sources (Table 3). In particular, 2779 of the 3449 Sexist Discourse texts (80.6%) come from the gender subset of Toraman et al. (2022a,b) and the remaining 670 (19.4%) from the Overfit-GM dataset, while 73.3% of the Profanity class originates from Overfit-GM. Together with the source-only baseline reported above (0.567 accuracy), this concentration is addressed as a limitation in Section 6.

Table 2. Class distribution of the final dataset

Class	Label	Count
Harmless	0	5255
Profanity	1	3347
Sexist Discourse	2	3449
Total	-	12051

Table 3. Distribution of the final dataset across sources and classes

Source	Harmless	Profanity	Sexist Discourse	Total
Toraman et al. (2022a,b) – gender subset	2198	0	2779 (80.6%)	4977
Overfit-GM (2023)	1457	2453	670 (19.4%)	4580
Çöltekin (2020) – Troff	1200	880	0	2080
TÜBİTAK 1001 project (124E056)	400	14	0	414
Total	5255	3347	3449	12051

2.2. Data Preprocessing

In the data-preprocessing stage, the aim was to make the texts in the dataset suitable for model training. First, basic normalization operations were applied to the texts. In this context, all texts were standardized in Unicode form, excess whitespace was cleaned, and records containing empty text were removed from the dataset. In addition, it was checked that the label values consisted

only of the values 0, 1 and 2 representing the three classes. This operation was carried out to prevent problems that could arise from erroneous or unexpected labels during the classification process.

In the preprocessing process, different text-preparation approaches were used for traditional machine learning models and Transformer-based models. In the traditional machine learning models, the aim was to reduce superficial noise that could negatively affect the classification process while preserving the semantic content of the texts. In this context, the texts were converted to lowercase taking the Turkish character structure into account; URLs, usernames, hashtag expressions, emojis and numerical values were removed from the texts. In addition, repeated punctuation marks that are common in social media texts were simplified, and consecutively repeated characters were standardized. As a result of these adjustments, the texts were brought into a more consistent form, and the aim was to extract TF-IDF-based word and character features more stably.

For the Transformer-based models, a more limited preprocessing method was preferred. In these models, only Unicode normalization and whitespace-adjustment operations were applied to the texts. Elements such as punctuation marks, capitalization and emojis were preserved. This approach was adopted to enable the Transformer-based models to benefit from the contextual and superficial cues in the text. Thus, while more standardized texts were used for the traditional models, the original structure of the text was largely preserved in the Transformer models.

2.3. Experimental Design

The experimental design is based on comparing traditional machine learning models with Transformer-based language models in Turkish harmful content classification. All models were tested on the same dataset using the same class structure and the same evaluation setup. Thus, the aim was to ensure that the differences between model performances stem from the representation method and model architecture used, rather than from data splitting or different evaluation conditions. While hyperparameter search with inner cross-validation was performed in the traditional models, standard fine-tuning values were used in the Transformer-based models; this difference in the tuning approach is detailed in Section 3.3.2. The overall experimental workflow is summarized in Figure 1.

To measure model performance more reliably and to reduce the risk of data leakage, 5-fold group-based stratified cross-validation was applied in the experiments. For this operation, the StratifiedGroupKFold approach was used; the number of folds was set to 5, the shuffle option was active and the random-state value was set to 42. The class label was used as the stratification variable, and the duplicate-group key produced from the normalized texts was used as the group variable. Thus, the aim was to preserve the class distribution as much as possible in each fold and to prevent samples with the same normalized text from leaking together into the training and test partitions.

Before cross-validation, it was checked whether each group contained more than one different class label. Cases in which the same normalized text appeared with different labels were regarded as conflicting-duplicate groups, and all samples in these groups were removed from the dataset. In the fold-creation stage, it was also verified that each class had sufficient samples and sufficient different groups to enable 5-fold evaluation. After these checks, all models were evaluated on the same outer cross-validation folds.

In the traditional machine learning models, feature extraction and classifier training were performed within each outer cross-validation fold using only the training data. In the TF-IDF-based experiments, the word- and character-level vectorizers were defined within a Pipeline structure together with the classifier; thus, the TF-IDF vocabulary, IDF weights and model parameters were learned only on the relevant training fold. The test fold was transformed and evaluated only through the trained pipeline. This approach prevented the test data from being included in the feature-extraction or hyperparameter-selection process.

In the traditional models where hyperparameter selection was performed, the search was carried out only with inner cross-validation run on the training portion of the outer cross-validation. In the inner cross-validation, group-based stratified splitting was used where possible, and the macro F1-score was taken as the selection criterion. Thus, the outer test fold was not used in the model-selection, feature-extraction or hyperparameter-tuning stages.

Accuracy, macro F1-score, macro precision, macro recall and multi-class ROC-AUC were used as evaluation metrics. In this study, the macro F1-score was taken as the main comparison metric. The macro F1-score was obtained by taking the arithmetic mean of the F1 values calculated separately for each class; thus, the aim was for each class to contribute equally to model performance regardless of class sizes. Similarly, precision and recall values were also calculated as macro averages.

The multi-class ROC-AUC value was calculated with a one-vs-rest approach in which each class is evaluated separately against the other classes, and the macro average was taken across classes. In the Transformer-based models, the class probabilities obtained with softmax were used in the ROC-AUC calculation. In the traditional machine learning models, predict_proba was used for models that provide a probability output, and class scores were used for models that provide a decision-function output.

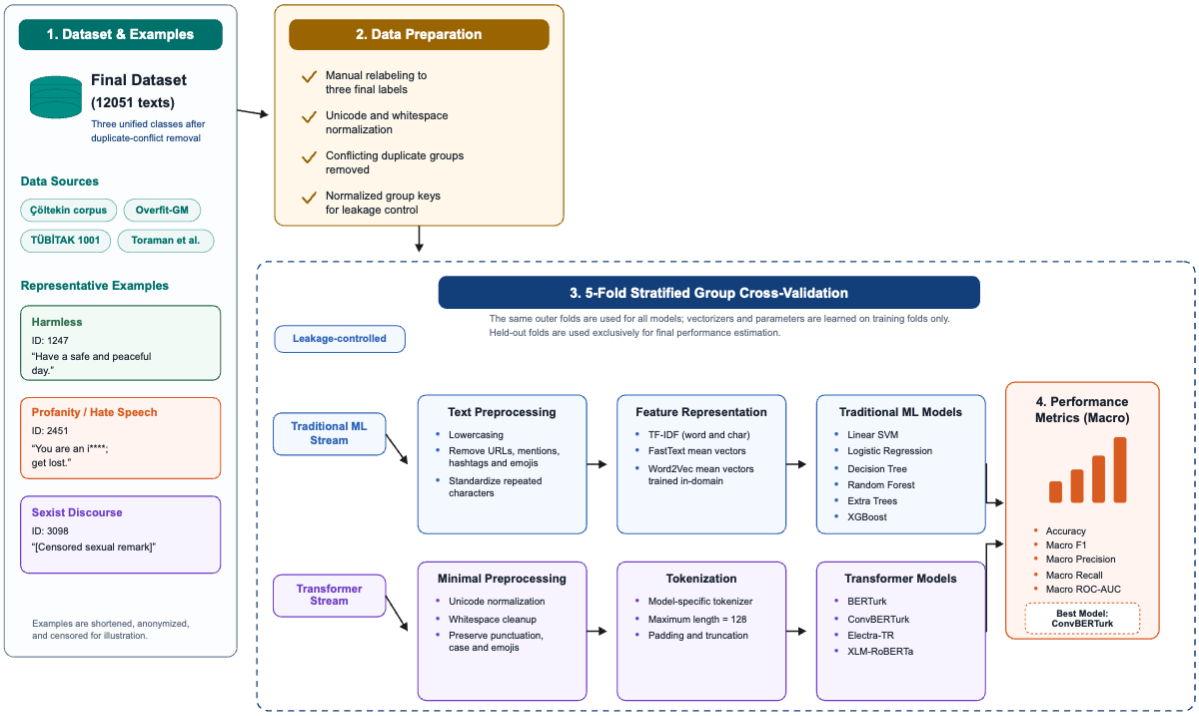


Figure 1. Experimental workflow diagram for Turkish harmful content classification.

2.3.1. Machine learning models

In the traditional machine learning models, the texts were numerically represented using TF-IDF-based feature extraction, which incorporates inverse document frequency weighting (Sparck Jones, 1972). In this process, both word-level and character-level n-gram features were used. At the word level, unigrams and bigrams were considered, while at the character level, three-, four- and five-gram character patterns were used. The joint use of word and character representations aims to reflect to the model both the meaningful word patterns in the text and the spelling variations and character-level formal cues that are common in Turkish social media texts (Table 4).

Table 4. Hyperparameter settings for TF-IDF feature extraction

Hyperparameter	Value
Word TF-IDF n-gram	(1, 2)
Word max features	50000
Character TF-IDF Analyzer	char_wb
Character n-gram	(3, 5)
Character Max Features	75000
Use IDF	True
Smooth IDF	True
Padding	True
Norm	L2 Norm

In the Word2Vec experiments, the embedding model was retrained for each outer cross-validation fold using only the relevant training fold. The texts in the test fold were represented using the Word2Vec (Mikolov et al., 2013) vocabulary learned on the training fold; words not present in the training vocabulary were not included in the vector average. Thus, Word2Vec representations were prevented from learning information from the test data. In the FastText experiments, no retraining was performed on the dataset; pre-trained Turkish cc.tr.300 FastText vectors (Bojanowski et al., 2017; Grave et al., 2018) were used. FastText-based text representations were computed separately for the training and test folds; the classifiers were trained only on the training fold (Table 5).

Table 5. Hyperparameter settings for Word2Vec feature extraction

Hyperparameter	Value
Representation	Mean Vector
Vector Size	300
Epoch	10
Window	5
Min Count	1
Skip-gram	1

Linear Support Vector Machine (Cortes and Vapnik, 1995), Logistic Regression (Cox, 1958), Decision Tree (Breiman et al., 1984), Random Forest (Breiman, 2001), Extra Trees (Geurts et al., 2006) and XGBoost (Chen and Guestrin, 2016) algorithms were evaluated on these features. In the Logistic Regression and Linear Support Vector Machine models, the regularization parameter

was tried over different values. In the Decision Tree model, different model configurations were tested by varying the splitting criterion and the minimum number of samples required at a leaf node. In the Random Forest and Extra Trees models, hyperparameter search was performed over the number of trees and the minimum leaf-sample values. Hyperparameter selection was carried out within the training folds, and the most suitable model configuration was determined according to the macro F1-score.

2.3.2. Transformer models

In the Transformer-based experiments, four different language models that can leverage Turkish and multilingual text representations were used: BERTurk, Electra-TR and ConvBERTurk, which are Turkish pre-trained models based respectively on the BERT (Devlin et al., 2019), ELECTRA (Clark et al., 2020) and ConvBERT (Jiang et al., 2020) architectures, and XLM-RoBERTa (Conneau et al., 2020), which extends the RoBERTa pre-training approach (Liu et al., 2019) to a multilingual setting. The publicly released checkpoints dbmdz/bert-base-turkish-cased, dbmdz/electra-base-turkish-cased-discriminator, dbmdz/convbert-base-turkish-cased and xlm-roberta-base were used respectively. These models were adapted to the three-class text classification task and trained separately for each cross-validation fold. The model output layer was arranged to represent the Harmless, Profanity and Sexist Discourse classes.

In the Transformer-based models, too, each outer cross-validation fold was treated as an independent experiment. In each fold, the relevant pre-trained model was reloaded from its initial weights, fine-tuning was performed only on the training fold, and the test fold was used only for the final evaluation. Since the tokenizer operation was performed with the fixed vocabulary of the pre-trained model, no additional vocabulary learning or parameter update was performed on the test data.

In the Transformer models, the texts were tokenized and the maximum sequence length was set to 128. The training process was run for 3 epochs, with a training batch size of 16 and an evaluation batch size of 32. The learning rate was set to 2×10^{-5} and the weight-decay coefficient to 0.01. Each model was fine-tuned on the relevant training fold and then evaluated on the test portion of the same fold. The logit values obtained in the model outputs were converted into probability values, and the class with the highest probability was accepted as the model's prediction.

Unlike the traditional models, no model-specific hyperparameter search was performed in the Transformer-based models; instead, standard fine-tuning values widely adopted in the literature (learning rate 2×10^{-5}, weight decay 0.01, 3 epochs, sequence length 128) were applied uniformly to all four models. This choice was adopted both to limit computational cost and to ensure that the difference between models stems from architectural capacity rather than from the tuning budget. Therefore, the Transformer models were evaluated without any tuning advantage compared with the traditional models (Table 6). Since this asymmetry is in favour of the traditional models, the performance gap reported in Section 4 should be read as a conservative lower bound on the Transformer advantage.

Table 6. Hyperparameter settings used for the Transformer models

Hyperparameter	Value
Max Sequence Length	128
Epoch	3
Train Batch Size	16
Validation Batch Size	32
Learning Rate	2×10^{-5}
Weight Decay	0.01
Random Seed	42
Padding	True
Truncation	True
Optimizer	AdamW
Warmup Steps	0
Scheduler	Linear

In the Transformer-based models, each outer cross-validation fold was run as an independent experiment. In each fold, the relevant pre-trained model was reloaded from its initial weights and fine-tuned only on the training fold for 3 epochs. The test fold was used only after training was completed, to obtain the final predictions and to compute the metrics. Therefore, the samples in the test fold were not included in the model-selection or parameter-update process.

3. Results

This section presents the experimental results of traditional machine learning models and Transformer-based language models on Turkish harmful content classification. In the experiments, each model was evaluated with 5-fold cross-validation, and F1-score, accuracy, ROC-AUC, precision and recall values were computed for each fold. Then, comparative results were obtained by taking the fold averages of these metrics for each model. The results were examined under two main groups: traditional machine learning models and Transformer-based models.

3.1. Machine Learning Results

In the traditional machine learning models, Logistic Regression, Linear SVM, Decision Tree, Random Forest, Extra Trees and XGBoost models were evaluated using TF-IDF-based word and character features. According to the fold averages, the highest F1-score among the traditional models was obtained by the Logistic Regression model with 82.82%. Detailed results for all models are presented in Table 7.

Among the traditional machine learning models, linear

models — particularly the Linear SVM and Logistic Regression approaches — produced more balanced results with TF-IDF-based word and character features. The markedly lower metrics of the Decision Tree model compared with the other models can be explained by the structural limitations of the single decision-tree structure with respect to the text representations used. Since decision trees make axis-aligned decisions over a single feature at each split, they can capture discriminative class patterns in the tens-of-thousands-dimensional and sparse TF-IDF space only with very deep tree structures that are prone to overfitting. In dense embedding representations such as Word2Vec and FastText, where class information is distributed across many dimensions, a single embedding dimension is not discriminative on its own, so axis-aligned splits cannot represent the cross-dimensional linear combinations that linear models learn easily. In addition, the high-variance structure of unpruned single trees limits generalization performance; indeed, the fact that the Random Forest and Extra Trees models, which use the same base learner in ensemble form, produced F1 values approximately 6–15 points higher than the Decision Tree model across all three representation types confirms that the observed low performance largely stems from the variance of the single tree. Nevertheless, these ensemble models also remained behind the F1-score and accuracy values of the linear models.

Table 7. TF-IDF-based machine learning model results

Model	F1	Accuracy	AUC	Precision	Recall
Linear SVM	82.43%	82.74%	94.43%	83.41%	81.74%
Logistic Regression	82.82%	83.11%	94.66%	83.85%	82.12%
Decision Tree	74.79%	74.91%	81.58%	74.97%	74.67%
Random Forest	81.05%	81.14%	94.10%	82.29%	80.22%
Extra Trees	82.00%	82.17%	94.37%	83.21%	81.19%
XGBoost	76.16%	76.82%	91.13%	79.65%	74.71%

Table 8 presents a comparison of the F1-score and accuracy values of the machine learning models obtained using the TF-IDF, FastText and Word2Vec feature-extraction methods. When the results are evaluated overall, it is seen that the highest performance was obtained with the Logistic Regression model on TF-IDF representations. The Logistic Regression model reached an 82.82% F1-score and 83.11% accuracy with TF-IDF features, producing the most successful result among all model and feature-extraction-method combinations. This model was followed by the Linear SVM model with an 82.43% F1-score and 82.74% accuracy, again on TF-IDF representations.

The relatively low F1 value (76.16%) produced by the XGBoost model on TF-IDF representations stems from the compatibility of the high-dimensional and sparse TF-IDF feature space with the gradient-boosted tree structure. The fact that shallow decision trees can use only a limited number of features at each split makes it difficult for the model to capture discriminative patterns in such a sparse space. Indeed, the same model reaching a 77.81% F1 value on the 300-dimensional dense FastText representations and thus exceeding its TF-IDF-based result supports this interpretation.

When FastText representations are used, the most successful model is again seen to be Linear SVM. The Linear SVM model reached a 78.35% F1-score and 78.96% accuracy with FastText features; although these results remained approximately 4.5 points behind the best TF-IDF-based results, they were clearly above the Word2Vec representations. On the FastText representations, the Logistic Regression model ranked second with a 77.98% F1-score and 78.57% accuracy, while the XGBoost model showed a similar level of performance with a 77.81% F1-score and 78.46% accuracy. The fact that the pre-trained subword-based FastText vectors produced higher results than the Word2Vec representations demonstrates the contribution of subword information and pre-training on a large corpus in the agglutinative structure of Turkish.

When the Word2Vec average-vector representations are used, the model performances remain lower than with the TF-IDF and FastText representations. In the Word2Vec-based results, the highest F1-score was obtained by the Linear SVM model with 73.76%. The Extra Trees (73.14%), Random Forest (73.00%) and XGBoost (72.97%) models produced moderate results close to each other, while the Decision Tree model showed the comparatively lowest performance on the Word2Vec representations with a 62.96% F1-score.

3.2. Transformer Model Results

Within the scope of the Transformer-based models, the BERTurk, ConvBERTurk, XLM-RoBERTa and Electra-TR models were evaluated under the same dataset and cross-validation structure. Considering the fold averages, the highest F1-score was obtained by the ConvBERTurk model with 90.93%. The ConvBERTurk model demonstrated strong and balanced performance across all evaluation metrics, with 90.93% accuracy, 90.96% precision and 90.94% recall. This model was followed by the BERTurk model with a 90.28% F1-score and 90.28% accuracy. Detailed results for all models are presented in Table 9.

Table 8. Performance comparison of machine learning models by feature-extraction method

Model	TF-IDF		FastText		Word2Vec	
	F1	ACC	F1	ACC	F1	ACC
Linear SVM	82.43%	82.74%	78.35%	78.96%	73.76%	74.08%
Logistic Regression	82.82%	83.11%	77.98%	78.57%	72.79%	72.99%
Decision Tree	74.79%	74.91%	60.84%	61.63%	62.96%	63.10%
Random Forest	81.05%	81.14%	75.65%	76.79%	73.00%	73.34%
Extra Trees	82.00%	82.17%	75.79%	76.87%	73.14%	73.50%
XGBoost	76.16%	76.82%	77.81%	78.46%	72.97%	73.21%

Table 9. Transformer model results

Model	F1 (mean ± SD)	Accuracy	AUC	Precision	Recall
ConvBERTurk	90.93% ± 0.45	90.93%	98.09%	90.96%	90.94%
BERTurk	90.28% ± 0.54	90.28%	97.95%	90.47%	90.16%
XLM-RoBERTa	87.29% ± 0.39	87.29%	96.84%	87.72%	86.99%
Electra-TR	89.94% ± 0.43	89.91%	97.74%	90.17%	89.77%

The findings in Table 9 show that the Transformer-based models reached a high level of success in the classification task. The fact that the BERTurk and ConvBERTurk models produced very close values in the F1-score, accuracy, precision and recall metrics reveals that pre-trained language models for Turkish provide stable and consistent results in this task. The Electra-TR model was in the high-performance group with an 89.94% F1-score and 89.91% accuracy. Although the XLM-RoBERTa model produced lower results than the other Transformer models, it exhibited a strong classification performance with F1-score and accuracy values above 87%.

When the macro ROC-AUC values are examined, all Transformer models are seen to reach values above 96.8%. This result shows that the models have a high capacity to separate the classes from each other within the scope of one-vs-rest evaluation. As a result of the overall evaluation, it was determined that the Transformer-based models provide higher and more balanced performance than the traditional machine learning approaches. Among the evaluated Transformer models, the highest overall performance was obtained by the ConvBERTurk model. However, as shown in Section 4.2.1, its difference from BERTurk is not statistically significant. To examine the class-level prediction success of the ConvBERTurk model in more detail, a confusion matrix was created by combining all fold results. When the confusion matrix in Figure 2 is examined, the model achieved a high correct-classification rate in all three classes. This result shows that the ConvBERTurk model exhibits a balanced structure not only in the overall metrics but also in class-level discrimination success.

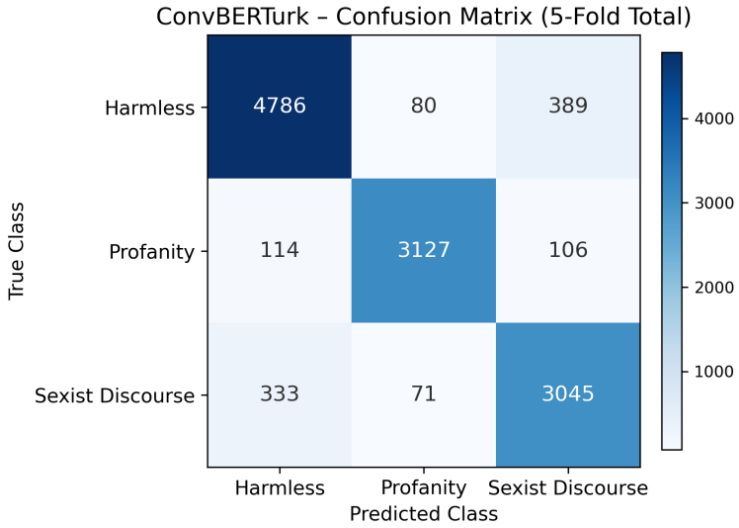


Figure 2. Confusion matrix for the ConvBERTurk model (out-of-fold predictions, all five folds).

The model is seen to reach the highest number of correct predictions in the Harmless class, correctly classifying 4786 samples belonging to this class. In the Profanity class, 3127 samples, and in the Sexist Discourse class, 3045 samples, were correctly predicted. Misclassifications are seen to concentrate particularly between the Harmless and Sexist Discourse classes; 389 Harmless samples were predicted as Sexist Discourse, and 333 Sexist Discourse samples were predicted as Harmless. The low confusion rate of the Profanity class with the other classes can be explained by the strong lexical cues carried by profane expressions. The Harmless–Sexist Discourse confusion, on the other hand, stems from the fact that sexist discourse is often expressed through context and implication without explicit profanity. Nevertheless, the low total number of errors reveals that the model makes a successful distinction between the classes.

3.2.1. Statistical significance of the differences between the transformer models

Since the differences among the top-performing models are small in absolute terms, the macro F1 values obtained in the five folds were compared pairwise using two-sided paired t-tests and the Wilcoxon signed-rank test. The difference between ConvBERTurk (90.93% ± 0.45) and BERTurk (90.28% ± 0.54) is not statistically significant ($t(4) = 2.36$, $P=0.078$; Wilcoxon $P=0.063$), nor is the difference between BERTurk and Electra-TR (89.94% ± 0.43; $t(4) = 2.28$, $P=0.085$). By contrast, the ConvBERTurk–Electra-TR difference ($t(4) = 7.65$, $P=0.002$) and all comparisons against XLM-RoBERTa (87.29% ± 0.39; $P<0.001$) are statistically significant.

ConvBERTurk, BERTurk and Electra-TR therefore form a single top-performance group that cannot be statistically separated at the 0.05 level, and only XLM-RoBERTa falls clearly below them. The 0.65-point advantage of ConvBERTurk is accordingly reported as the highest observed mean rather than as evidence of an absolute best model, and the related statements in the Abstract, Findings and Discussion sections have been formulated in line with this qualification. It should also be noted that, with five folds, the smallest attainable two-sided p-value of the Wilcoxon test is 0.063, so the t-test results are taken as the primary evidence.

Table 10. Comparison of the obtained results with the 2025-2026 Turkish harmful content detection literature

Year	Reference	Dataset	Class Distribution	Methodology	F1	Accuracy	AUC	Precision	Recall
2026	This Publication	Public + Private	Harmless: 5255, Profanity: 3347, Sexist discourse: 3449, Total: 12051	ConvBERTurk	0.9093	0.9093	0.9809	0.9096	0.9094
2025	Kesgin and Demirer (2025)	Private	Offensive: Not specified, Non-offensive: Not specified, Total: 11253	TF-IDF + ML Models (Random Forest, without Word2Vec)	-	0.82	0.65	-	-
2025	Aliyeva and Yağanoğlu (2025)	Public	Non-cyberbullying: 2500, Cyberbullying: 2500, Total: 5000	MLP + TF-IDF/Unigram + Social Media Features	0.9336	0.932	0.932	0.9122	0.956
2025	Mut Altın and Saggion (2025)	Public	Not-sexist: 3167, Sexual violence: 1352, Stereotyping: 1124, Misogyny: 655, Objectification: 468, Anti-feminism: 149, Total: 6915	GPT-4o mini Fine-Tuning	0.91	-	-	-	-
2026	Karayiğit (2026)	Public	Non-insult: 3709, Insult: 3652, Total: 7361	Feature Extraction + ML and DL	0.93	0.93	-	0.93	0.93
2026	Aksoy et al. (2026)	Public	Hate speech: 4247, Non-hate speech: 4247, Total: 8494	Transformers + Soft Voting	0.916	0.9201	-	0.958	0.879

4. Discussion

Among the traditional machine learning models, Logistic Regression produced the highest result on TF-IDF-based representations with 82.82% F1, closely followed by Linear SVM with 82.43% F1; FastText representations produced at best 78.35% F1, while Word2Vec representations remained limited at 73.76% F1 (Tables 7-8). When moving to the Transformer-based models, a marked performance increase was observed in all evaluation metrics (Table 9). The ConvBERTurk model reached the highest average value with a 90.93% macro F1-score, while the BERTurk model ranked second with a 90.28% macro F1-score. Since the 0.65-point difference between the two models is limited, the results show that the two models exhibit close and strong performance in this task. This can be interpreted as the ConvBERT

architecture's combination of the multi-head self-attention mechanism with span-based dynamic convolutions providing an additional advantage in detecting expressions such as profanity and sexist discourse, which are short and carry dense contextual cues. The Electra-TR model ranked third with 89.94% F1, while the multilingual XLM-RoBERTa model remained at 87.29% F1. The approximately 3.3-point average superiority of the Turkish-specific models (ConvBERTurk, BERTurk) over the multilingual model shows that learning language-specific morphological and syntactic patterns during pre-training contributes directly to task performance.

When evaluated in terms of the ROC-AUC metric, the Transformer-based models clearly exhibit a superiority over the traditional models. While the AUC values in the traditional TF-IDF-based models remained in the 81.58%–94.66% range, this value exceeded 96.8% in all four Transformer models. ConvBERTurk reached 98.09%, BERTurk 97.95%, Electra-TR 97.74% and XLM-RoBERTa 96.84% AUC values. These results show that the Transformer models can determine inter-class decision boundaries with high accuracy. The fact that ConvBERTurk produced the highest values in both the macro F1 and macro ROC-AUC metrics shows that this model also exhibits a consistent superiority in inter-class score discrimination within the scope of one-vs-rest evaluation.

When the precision and recall metrics are examined specifically for the Transformer models, ConvBERTurk is seen to offer the most balanced performance with 90.96% precision and 90.94% recall. Maintaining this balance is critically important in harmful content detection, both to keep the false-alarm rate low and to avoid missing actual harmful content. The BERTurk model also produced values quite close to ConvBERTurk, with 90.47% precision and 90.16% recall. In the XLM-RoBERTa model, precision was 87.72% and recall 86.99%; these values confirm that the multilingual model lags behind the Turkish-focused models in capturing Turkish-specific harmful discourse patterns. Considering that these metrics remained in the approximately 75%–84% range in the traditional TF-IDF-based models, the Transformer models provided an improvement of approximately 7–9 points in the precision–recall balance, and this improvement is considered to make a meaningful difference for practical applications. It is noteworthy that this superiority was obtained even though only the traditional models were additionally tuned by grid search; the reported gap is therefore a conservative lower bound on the Transformer advantage.

As already discussed in Section 5 in connection with Table 10, the 0.9093 macro F1 obtained with ConvBERTurk is comparable to the closest recent Turkish results; since those values come from binary setups with different F1 definitions, the comparison remains contextual.

Within these limits, the 0.972 F1 reported by Karayiğit et al. (2024) with TextGAN-based data balancing rests on a different experimental setup. Read against this background, the results obtained here — without any data augmentation and under a three-class formulation — indicate that ConvBERTurk provides a strong and balanced performance in Turkish harmful content detection.

To test the generalizability of the proposed experimental configuration, the same architecture and the same fine-tuning regime (ConvBERTurk, 2e-5 learning rate, 3 epochs, group-based stratified 5-fold cross-validation) were retrained and evaluated on two Turkish datasets from the literature. On the cyberbullying dataset used by Aliyeva and Yağanoğlu (2025), a macro F1 of 93.15% (±1.00) was obtained, which is at a level comparable to the 93.36% value reported in the related study for the MLP model based on social-media features and feature selection. However, the two values are not directly equivalent: the value reported in the related study is a positive-class F1 obtained on a single hold-out split, whereas the value obtained here is a macro F1 averaged over group-based stratified 5-fold cross-validation. On the TLHS1 dataset (Aksoy et al., 2026), a macro F1 of 0.856 (±0.008) was obtained on three different balanced subsets. Aksoy et al. report a positive-class F1 of 0.856 for a single ConvBERT model on the same dataset; since the two values are computed with different averaging schemes, they should be read as indicating a comparable performance level rather than as a direct confirmation of the same quantity. The fact that the same model configuration produced results of 90.93% on the three-class dataset of this study, 93.15% on the cyberbullying dataset and 85.6% on TLHS1 shows that the observed performance differences stem not so much from the model or hyperparameter choice as from the task definition, labeling criteria and linguistic difficulty level of the dataset (for example, the implicit hate and irony content in TLHS1). This finding reveals that the performances reported in Turkish harmful content detection are dataset-dependent and that direct metric comparisons across studies are meaningful only through reproduction on the same dataset.

Five limitations should be taken into account when interpreting these findings. First, the class–source distribution is uneven: 80.6% of the Sexist Discourse class comes from a single corpus (Table 3), so the model's representation of this class depends largely on the annotation decisions of that corpus and should not be generalized to other platforms or annotation schemes without validation on an independently annotated external sexism corpus. Second, the hyperparameter budget is asymmetric — a grid search was applied only to the traditional models — which favours those models and makes the reported gap between the two families a conservative lower bound. Third, all texts come from social media and comparable short-form online content, so performance on longer or domain-specific texts such as news articles or forum threads was not evaluated.

Fourth, the three-class scheme excludes categories present in the source corpora, such as general insult, racist discourse and obscenity. Fifth, all experiments were run with a single random seed (42), so seed-level variability was not quantified.

5. Conclusion

In this study, TF-IDF, FastText and Word2Vec text-representation methods were systematically compared with traditional machine learning models and Transformer-based language models for the automatic detection of profanity and sexist-discourse content in Turkish texts. Among the traditional models, TF-IDF-based Logistic Regression achieved the highest performance with 82.82% F1, while Linear SVM produced very close results with 82.43% F1; FastText representations reached at best a 78.35% F1 value, while Word2Vec-based representations remained limited at 73.76% F1 (Tables 7–8). In the Transformer-based models, a marked performance jump was observed. The ConvBERTurk model exhibited the highest overall performance among all models, with a 90.93% F1-score, 90.93% accuracy and 98.09% ROC-AUC (Table 9). This superiority of ConvBERTurk can be attributed to the ConvBERT architecture's ability to model local context patterns more effectively thanks to its span-based dynamic convolution mechanism. The BERTurk model produced results very close to ConvBERTurk, with a 90.28% F1 and a 97.95% macro ROC-AUC. The Electra-TR and XLM-RoBERTa models also obtained strong results with 89.94% and 87.29% F1 respectively; however, it was determined that models trained specifically for Turkish (BERTurk, ConvBERTurk) provide a consistent superiority over multilingual models (XLM-RoBERTa). These results reveal that contextual language representations offer a clear advantage over superficial text representations in Turkish harmful content detection and that pre-trained models suited to the language structure further strengthen this advantage. However, its difference from BERTurk is not statistically significant over the five folds ($t(4) = 2.36$, $P=0.078$); ConvBERTurk, BERTurk and Electra-TR form a statistically indistinguishable top-performance group.

The obtained findings reveal the position of the study more clearly when compared with recent studies published in the field of Turkish profanity, offensive language and sexist discourse in the 2024–2026 period. Since different datasets, class structures and evaluation metrics are used in the literature, a one-to-one comparison is not always possible; nevertheless, a meaningful evaluation can be made based on general trends. Table 10 presents the results of this study comparatively with selected recent studies.

The literature summary presented in Table 10 was structured to provide a contextual evaluation — rather than a direct performance race — of studies focusing on Turkish harmful content, offensive language, hate speech and cyberbullying detection in the 2025–2026 period. Because the studies in the literature use different datasets, numbers of classes, task definitions and evaluation protocols, a one-to-one comparison of the obtained metrics involves methodological limitations. To reflect these methodological differences transparently, Table 10 was expanded to include information on the task definition, number of classes, metric type, dataset accessibility and evaluation protocol of the relevant studies. In this study, the 90.93% macro F1 and 90.93% accuracy values obtained with the ConvBERTurk model are in a success range similar to the 0.91 macro F1 reported by Mut Altın and Saggion (2025) in binary sexism classification and the 0.916 F1 reported by Aksoy et al. (2026). Obtained under a more challenging evaluation protocol — three-class, leakage-controlled and based on group-based cross-validation — these results indicate a competitive performance level with respect to recent Turkish studies within the scope of the dataset and experimental setup used in the study.

In the studies in the literature, harmful content detection is addressed within the scope of binary classification problems such as hate speech, cyberbullying, offensive language or sexist discourse, or within specific subtasks. In this study, on the other hand, the distinction between harmless content, profanity and sexist discourse in online Turkish texts was evaluated together, and the problem was modeled within a three-class classification structure. In this respect, the study offers a more comprehensive approach that addresses different types of harmful content comparatively within the same experimental framework, rather than focusing on only a single type of harmful discourse. In the obtained results, the ConvBERTurk model reached both the highest macro F1-score and accuracy values and the highest macro ROC-AUC value. This finding shows that Transformer-based models have a high inter-class discrimination capacity. At the same time, it should be taken into account that the performance differences between the ConvBERTurk and BERTurk models are quite limited; the results should be interpreted as pre-trained Transformer models for Turkish offering close and strong performance in this task, rather than as an absolute model superiority.

Nevertheless, the obtained findings should not be evaluated as a direct and absolute claim of methodological superiority over the studies in the literature. This is because the compared studies differ in terms of dataset size, data source, class distribution, labeling criteria, number of classes, evaluation protocol and the type of F1 reported. Therefore, the high performance values obtained in this study should be considered within a contextual and limited comparison framework with the results in the literature. Among the possible reasons for the high and balanced performance observed in the study are the fact that the three-class problem formulation contains discriminative lexical and contextual cues, the strong representation capacity of Transformer-based models adapted to Turkish, and the use of a group-based stratified cross-validation strategy

to reduce the risk of data leakage. In this context, the contribution of the study to the literature is not limited to quantitative performance values; the study also addresses Turkish harmful content detection within a more comprehensive classification framework, compares different model families under equal experimental conditions, and offers a systematic methodological structure that takes class balance and the risk of duplicate-induced data leakage into account in the evaluation process.

In future studies, the primary goal is to expand the 12051-text dataset used in this research with larger and more diverse data obtained from different online platforms. This will make it possible to increase the generalization success of the models against different discourse types, user profiles and content-production styles. In addition, supporting the current three-class labeling structure with more detailed subcategories and examining hierarchical classification approaches will contribute to the development of more detailed decision mechanisms in harmful content detection. Evaluating large language models such as Llama and Gemma in zero-shot, few-shot and fine-tuning scenarios; addressing different Transformer-based architectures together with ensemble-learning methods; and examining data-augmentation strategies for class imbalance are considered important for future research. These approaches are expected to increase the adaptability of the developed models to real-time content-management systems and to enable more comprehensive evaluations in terms of application-oriented metrics such as processing time, scalability and system stability. In addition, since harmful content can be produced not only in textual form but also through multimodal structures that use visual and textual elements together, addressing multimodal approaches together with explainable artificial intelligence methods will contribute to the development of more transparent, reliable and applicable harmful content detection systems in the future.

Author Contributions

The percentages of the authors' contributions are presented below. All authors reviewed and approved the final version of the manuscript.

	N.K.	C.B.	Ö.A
C	40	30	30
D	40	30	30
S	40	30	30
DCP	40	30	30
DAI	40	30	30
L	40	30	30
W	40	30	30
CR	40	30	30
SR	40	30	30
PM	40	30	30
FA	40	30	30

C= concept, D= design, S= supervision, DCP= data collection and/or processing, DAI= data analysis and/or interpretation, L= literature search, W= writing, CR= critical review, SR= submission and revision, PM= project management, FA= funding acquisition.

Conflict of Interest

The authors declared that there is no conflict of interest.

Ethical Consideration

Ethics committee approval was not required for this study because of there was no study on animals or humans.

Acknowledgements

This study was supported by the Scientific and Technological Research Council of Türkiye (TÜBİTAK) under the 1001 Program, Project No. 124E056. The authors would like to thank all members of the project team for their valuable contributions to the compilation and labeling of the dataset. During the preparation of this work, the authors used Claude, an AI language model developed by Anthropic, to assist in drafting and refining sections of the manuscript. After using this tool, the authors reviewed and edited the content to ensure its accuracy and appropriateness. The authors take full responsibility for the content of the published article.

Data Availability / Reproducibility

With regard to reproducibility, the merged dataset will not be redistributed as raw text because the source corpora carry their own licences; instead, the sample identifiers, the source-to-three-class mapping and the dataset-construction script will be released in an open repository together with the random seed (42), the fold indices and the fold-level metric files, so that the same dataset and experiments can be reconstructed. The 414 texts compiled within the project will be made available on request within the data-sharing conditions of the project.

References

Aksoy, Ç., Demirezen, M. U., & Sağıroğlu, Ş. (2026). Hate speech detection in Turkish: An ensemble transformer-based deep learning approach. *Engineering Applications of Artificial Intelligence, 164, 113147. https://doi.org/10.1016/j.engappai.2025.113147*

Aliyeva, Ç. O., & Yağanoğlu, M. (2025). Deep learning approach to detect cyberbullying on Twitter. *Multimedia Tools and Applications, 84(19), 20497–20520. https://doi.org/10.1007/s11042-024-19869-3*

Altinel, A. B., Karatas Baydogmus, G., Sahin, S., & Gurbuz, M. Z. (2024). So-haTRed: A novel hybrid system for Turkish hate speech detection in social media with ensemble deep learning improved by BERT and clustered-graph networks. *IEEE Access, 12, 86252–86270. https://doi.org/10.1109/ACCESS.2024.3415350*

Barkhordar, E., Topçu, I. S., & Hürriyetoğlu, A. (2024, March). Team Curie at HSD-2Lang 2024: Hate speech detection in Turkish and Arabic tweets using BERT-based models. In *Proceedings of the 7th Workshop on Challenges and Applications of Automated Extraction of Socio-Political Events from Text (CASE 2024)* (pp. 215–220).

Bojanowski, P., Grave, E., Joulin, A., & Mikolov, T. (2017). Enriching word vectors with subword information. Transactions of the Association for Computational Linguistics, 5, 135–146. https://doi.org/10.1162/tacl_a_00051

Breiman, L. (2001). Random forests. Machine Learning, 45(1), 5–32. https://doi.org/10.1023/A:1010933404324

Breiman, L., Friedman, J. H., Olshen, R. A., & Stone, C. J. (1984). Classification and regression trees. Wadsworth International Group.

Büyükdemirci, K., Kucukkaya, I. E., Ölmez, E., & Toraman, C. (2024). JL-Hate: An annotated dataset for joint learning of hate speech and target detection. In *Proceedings of the 2024 Joint International Conference on Computational Linguistics, Language Resources and Evaluation (LREC-COLING 2024)* (pp. 9543–9553).

Chen, T., & Guestrin, C. (2016, August). XGBoost: A scalable tree boosting system. In *Proceedings of the 22nd ACM SIGKDD International Conference on Knowledge Discovery and Data Mining (pp. 785–794). https://doi.org/10.1145/2939672.2939785*

Clark, K., Luong, M.-T., Le, Q. V., & Manning, C. D. (2020). ELECTRA: Pre-training text encoders as discriminators rather than generators. In 8th International Conference on Learning Representations (ICLR 2020). https://openreview.net/forum?id=r1xMH1BtvB

Çöltekin, Ç. (2020, May). A corpus of Turkish offensive language on social media. In *Proceedings of the Twelfth Language Resources and Evaluation Conference* (pp. 6174–6184).

Conneau, A., Khandelwal, K., Goyal, N., Chaudhary, V., Wenzek, G., Guzmán, F., Grave, E., Ott, M., Zettlemoyer, L., & Stoyanov, V. (2020, July). Unsupervised cross-lingual representation learning at scale. In Proceedings of the 58th Annual Meeting of the Association for Computational Linguistics (pp. 8440–8451). https://doi.org/10.18653/v1/2020.acl-main.747

Cortes, C., & Vapnik, V. (1995). Support-vector networks. Machine Learning, 20(3), 273–297. https://doi.org/10.1007/BF00994018

Cox, D. R. (1958). The regression analysis of binary sequences (with discussion). Journal of the Royal Statistical Society: Series B (Methodological), 20(2), 215–242. https://doi.org/10.1111/j.2517-6161.1958.tb00292.x

Dehghan, S., & Yanıkoğlu, B. (2024, March). Evaluating ChatGPT's ability to detect hate speech in Turkish tweets. In *Proceedings of the 7th Workshop on Challenges and Applications of Automated Extraction of Socio-Political Events from Text (CASE 2024)* (pp. 54–59).

De Oliveira, A. B., Baptista, C. D. S., Firmino, A. A., & De Paiva, A. C. (2024, April). A large language model approach to detect hate speech in political discourse using multiple language corpora. In *Proceedings of the 39th ACM/SIGAPP Symposium on Applied Computing (pp. 1461–1468). https://doi.org/10.1145/3605098.3635964*

Devlin, J., Chang, M. W., Lee, K., & Toutanova, K. (2019, June). BERT: Pre-training of deep bidirectional transformers for language understanding. In *Proceedings of the 2019 Conference of the North American Chapter of the Association for Computational Linguistics: Human Language Technologies, Volume 1 (Long and Short Papers) (pp. 4171–4186). https://doi.org/10.18653/v1/N19-1423*

Esen, F. S., & Amrahov, S. E. (2024, October). TurkHSD: A hate speech detection model for Turkish text content. In *2024 Innovations in Intelligent Systems and Applications Conference (ASYU) (pp. 1–8). IEEE. https://doi.org/10.1109/ASYU62119.2024.10757058*

Geurts, P., Ernst, D., & Wehenkel, L. (2006). Extremely randomized trees. Machine Learning, 63(1), 3–42. https://doi.org/10.1007/s10994-006-6226-1

Grave, E., Bojanowski, P., Gupta, P., Joulin, A., & Mikolov, T. (2018, May). Learning word vectors for 157 languages. In Proceedings of the Eleventh International Conference on Language Resources and Evaluation (LREC 2018) (pp. 3483–3487). European Language Resources Association.

Gümüş, E., Sarıyar, R., & Göz, F. (2024, September). Comparative analysis of transformer-based vector models for hate speech in Turkish tweets. In *2024 8th International Artificial Intelligence and Data Processing Symposium (IDAP) (pp. 1–5). IEEE. https://doi.org/10.1109/IDAP64064.2024.10710825*

Jiang, Z. H., Yu, W., Zhou, D., Chen, Y., Feng, J., & Yan, S. (2020). ConvBERT: Improving BERT with span-based dynamic convolution. *Advances in Neural Information Processing Systems, 33*, 12837–12848.

Karayiğit, H. (2026). Leveraging attention-based deep learning models for detecting insult offenses on social media in the context of Turkish Penal Law. *Neural Computing and Applications, 38, Article 6. https://doi.org/10.1007/s00521-025-11807-0.*

Karayiğit, H., Akdağlı, A., & Acı, Ç. İ. (2024). Performance comparison of data balancing techniques on hate speech detection in Turkish. *Pamukkale Üniversitesi Mühendislik Bilimleri Dergisi, 30(5), 610–621. https://doi.org/10.5505/pajes.2023.40072*

Kesgin, B. F., & Demirer, R. M. (2025). Offensive language detection in Turkish language by using NLP. *Sakarya University Journal of Science, 29(1), 1–17. https://doi.org/10.16984/saufenbilder.1349956*

Liu, Y., Ott, M., Goyal, N., Du, J., Joshi, M., Chen, D., Levy, O., Lewis, M., Zettlemoyer, L., & Stoyanov, V. (2019). *RoBERTa: A robustly optimized BERT pretraining approach* [Preprint]. arXiv. https://arxiv.org/abs/1907.11692

Mikolov, T., Chen, K., Corrado, G., & Dean, J. (2013). Efficient estimation of word representations in vector space [Preprint]. arXiv. https://arxiv.org/abs/1301.3781

Mut Altın, L. S., & Saggion, H. (2025, September). Investigating large language models' (LLMs) capabilities for sexism detection on a low-resource language. In *Proceedings of the 15th International Conference on Recent Advances in Natural Language Processing—Natural Language Processing in the Generative AI Era* (pp. 771–779).

https://doi.org/10.26615/978-954-452-098-4-089

Najafi, A., & Varol, O. (2024). TurkishBERTweet: Fast and reliable large language model for social media analysis. *Expert Systems with Applications, 255, 124737. https://doi.org/10.1016/j.eswa.2024.124737*

Overfit-GM. (2023). *Turkish texts for toxic language detection* [Data set]. Hugging Face. Retrieved June 17, 2026, from https://huggingface.co/datasets/Overfit-GM/turkish-toxic-language

Singhal, K., & Bedi, J. (2024, March). Transformers at HSD-2Lang 2024: Hate speech detection in Arabic and Turkish tweets using BERT-based architectures. In *Proceedings of the 7th Workshop on Challenges and Applications of Automated Extraction of Socio-Political Events from Text (CASE 2024)* (pp. 190–194).

Sparck Jones, K. (1972). A statistical interpretation of term specificity and its application in retrieval. *Journal of Documentation, 28*(1), 11–21.

Tanyel, T., Alkurdi, B., & Ayvaz, S. (2022). Linguistic-based data augmentation approach for offensive language detection. In 2022 *7th International Conference on Computer Science and Engineering (UBMK)* (pp. 1-6). IEEE.

Toraman, C., Şahinuç, F., & Yilmaz, E. (2022a). Large-scale hate speech detection with cross-domain transfer. In Proceedings of the Thirteenth Language Resources and Evaluation Conference (pp. 2215–2225).

Toraman, C., Şahinuç, F., & Yilmaz, E. (2022b). Gender hate speech Turkish — gender identity subset [Data set]. Hugging Face. https://huggingface.co/datasets/ctoraman/gender-hate-speech-turkish

Uludoğan, G., Yüksel, A. E., Tunçer, Ü. C., Işık, B., Korkmaz, Y., Akar, D., & Özgür, A. (2024, March). Detecting hate speech in Turkish print media: A corpus and a hybrid approach with target-oriented linguistic knowledge. In *Proceedings of the 7th Workshop on Challenges and Applications of Automated Extraction of Socio-Political Events from Text (CASE 2024)* (pp. 205–214).

Yagci, U. U., Kolcak, A. E., & Iscan, E. (2024, March). ReBERT at HSD-2Lang 2024: Fine-tuning BERT with AdamW for hate speech detection in Arabic and Turkish. In *Proceedings of the 7th Workshop on Challenges and Applications of Automated Extraction of Socio-Political Events from Text (CASE 2024)* (pp. 195–198).

Yakar, Ö., Büyüktanır, B., Çil, A. E., & Altınel Girgin, A. B. (2024). Türkçe nefret söylemi problemi analizinde farklı sınıflandırma algoritmalarının ve özellik seçimi yöntemlerinin performans karşılaştırması. *Avrupa Bilim ve Teknoloji Dergisi*, (53), 97–111.

Black Sea Journal of Engineering and Science
doi: 10.34248/bsengineering.1934728

Open Access Journal
e-ISSN: 2619 8991

Research Article
Volume 9 - Issue 5: 2692-2717 / September 2026

TRENDS AND BIBLIOMETRIC MAPPING OF THE KNOWLEDGE STRUCTURE OF GENERATIVE ARTIFICIAL INTELLIGENCE RESEARCH IN HIGHER EDUCATION

Şener BALAT[1]*

[1]*Bingöl University, Vocational School of Information Technologies, 12000, Bingöl, Türkiye*

Abstract: Generative artificial intelligence (GenAI) has reshaped teaching, learning and assessment in higher education faster than the literature describing it has been consolidated. Existing bibliometric reviews of this area are typically built on a single database, organised around ChatGPT alone, or extended to education at all levels and they rarely report the analytical parameters required for replication. This study addresses that gap by mapping the scientific production structure, intellectual and conceptual organisation and thematic evolution of GenAI research in higher education on a dual-database (Web of Science Core Collection and Scopus), PRISMA 2020-screened and fully parameter-transparent corpus of 2,992 articles and reviews published between 2022 and 2025, drawn from 728 sources and 9,948 authors. Descriptive, keyword co-occurrence, correspondence-analysis-based conceptual structure, strategic (thematic) map and thematic evolution analyses were triangulated across Bibliometrix/Biblioshiny and VOSviewer. Output grew from 5 documents in 2022 to 2,001 in 2025 a 400-fold expansion, with 66.9% of the entire corpus published in the final year alone at a mean of 18.46 citations per document. Impact is steeply concentrated: the ten most-cited documents (0.33% of the corpus) account for 8.75% of all citations. Production is led by China (n = 890), the United States (n = 617) and Australia (n = 401), yet international co-authorship stands at only 10.11%, indicating a field that is collaborative but overwhelmingly domestic. Türkiye (n = 96) ranks in the same output band as the United Arab Emirates, Peru and Hong Kong, but below regional peers such as Saudi Arabia, Indonesia and Jordan. Two independent clustering procedures each return a four-cluster architecture, but not the same four: the co-occurrence network built on indexed vocabulary separates the field by disciplinary setting instructional technology, health-professions education, technology acceptance and a general artificial intelligence core whereas correspondence analysis on author keywords separates it by conceptual concern into technological, educational-application, ethical-assessment and pedagogical dimensions. Generative AI is the single motor theme and the field shifts clearly from technological exploration towards pedagogical integration and academic integrity. Beyond describing the field, the study contributes a fully reproducible bibliometric protocol and a critical reading of the field's ChatGPT-centrism, its collaboration deficit and its early signs of thematic saturation.

Keywords: Generative artificial intelligence, Higher education, Bibliometric analysis, Research trends, Knowledge mapping

***Corresponding author:** Bingöl University, Vocational School of Information Technologies, 12000, Bingöl, Türkiye
Email: sbalat@bingol.edu.tr (Ş. BALAT)
Şener BALAT https://orcid.org/0000-0002-9683-1778

Received: April 20, 2026
Accepted: August 24, 2026
Published: September 15, 2026

Cite as: Balat, Ş. (2026). Trends and bibliometric mapping of the knowledge structure of generative artificial intelligence research in higher education. Black Sea Journal of Engineering and Science, 9(5): 2692-2717.

1. Introduction

The rapid advancement of artificial intelligence technologies has led to a significant paradigm shift in the global technological ecosystem, profoundly influencing how societies produce, process and disseminate knowledge. At the center of this transformation is generative artificial intelligence, which refers to systems capable of producing content such as text, images, code and multimedia through patterns learned from large datasets (Ng and Ho, 2025). While traditional artificial intelligence applications have largely been based on classification or prediction, generative artificial intelligence systems particularly through large language models (LLMs) offer advanced capabilities in understanding and generating natural language (Dúo-Terrón, 2024). The emergence of models such as ChatGPT demonstrates the potential of artificial intelligence to assume a more active role in knowledge production and learning processes (Francis et al., 2025). The development of large language models has attracted considerable attention across multiple disciplines due to their ability to simulate human-like reasoning processes, generate personalized responses and support complex cognitive tasks. These advancements present both significant opportunities and various challenges for modern digital infrastructures (Bittle and El-Gayar, 2025). The integration of generative artificial intelligence tools into professional and academic processes signals a substantial shift in how information is accessed and utilized. The transition from keyword-based information retrieval to generative synthesis-based approaches is reshaping individuals' interactions with knowledge. This

This work is licensed (CC BY-NC 4.0) under Creative Commons Attribution 4.0 International License

transformation necessitates a reconsideration of digital literacy and cognitive engagement concepts (Dai et al., 2026).

The impact of generative artificial intelligence technologies has generated extensive debate, particularly within the context of higher education. Universities are traditionally regarded as central institutions for knowledge production and critical thinking. However, the widespread adoption of these technologies has raised the need for restructuring teaching, learning and assessment processes. Research indicates that generative artificial intelligence tools have the potential to provide personalized learning experiences and contribute to learning environments that adapt to students' individual needs (Bittle and El-Gayar, 2025; Francis et al., 2025).

The influence of these technologies extends beyond instructional processes. Generative artificial intelligence systems can affect students' learning motivation and perceptions of self-efficacy (Guo et al., 2026). They can also support academic writing processes by facilitating idea generation and text production. Nevertheless, the use of generative artificial intelligence in higher education is often characterized as a double-edged phenomenon. While it supports learning processes, it also poses risks related to academic integrity and originality (Bittle and El-Gayar, 2025; Francis et al., 2025).

Assessment and feedback processes are among the areas most affected by these technologies. The ability of large language models to generate academically sophisticated texts has raised concerns that students may complete assignments with limited engagement in the learning process. Consequently, some studies identify this issue as a potential risk to academic integrity in higher education (Lodge et al., 2023). In response to these developments, many universities are developing new policies and pedagogical approaches aimed at both leveraging opportunities and maintaining academic standards (Plata et al., 2023; Chiu, 2024). In this context, the development of pedagogical approaches that support the sustainable and ethical use of artificial intelligence technologies has become increasingly important (Chiu, 2024).

Research on generative artificial intelligence in higher education has shown a notable increase, particularly after 2022 (Ng and Ho, 2025; Samala et al., 2025; Dai et al., 2026). This body of literature has evolved around various research themes. Early studies primarily focused on technical infrastructures and applications within the context of educational technologies (Ng and Ho, 2025). Subsequent research has examined the adoption of these technologies through theoretical frameworks such as technology acceptance models (Guo et al., 2026).

Another prominent theme in the literature concerns academic integrity and ethical issues. The impact of generative artificial intelligence on assessment processes has necessitated the development of new regulations within universities (Plata et al., 2023; Francis et al., 2025). Recent studies have increasingly focused on the effects of these technologies on students' cognitive engagement and higher-order thinking skills (Ng and Ho, 2025). Additionally, pedagogical innovation and the reconsideration of teaching strategies have emerged as important areas of research (Chiu, 2024; Francis et al., 2025).

Despite the rapid increase in studies on generative artificial intelligence and higher education, the literature still exhibits a fragmented structure (Dai et al., 2026). A significant portion of existing research consists of qualitative studies focusing on specific contexts (Prayuda et al., 2026), which makes it difficult to comprehensively understand the overall developmental dynamics of the field. Moreover, there is a limited number of systematic investigations examining publication networks, influential researchers and foundational studies. The conceptual relationships among research themes and their evolution over time have also not been sufficiently explored (Dai et al., 2026). Therefore, there is a clear need for studies that comprehensively analyze the intellectual and conceptual structure of the field.

A closer reading of the bibliometric work already available shows that the gap is one of scope and transparency rather than of quantity. Bozkurt (2023) mapped generative AI, conversational agents and chatbots across education as a whole rather than higher education specifically; Nugroho (2024) organised its corpus around ChatGPT alone; Kavitha et al. (2024) and Flores-Velásquez et al. (2024) addressed artificial intelligence in general rather than its generative variant, the latter narrowing further to technology acceptance; Dúo-Terrón (2024), Ng and Ho (2025) and Guo et al. (2026) examined generative artificial intelligence in education across all levels; and Prayuda et al. (2026) traced two decades of artificial intelligence in education, a window in which generative artificial intelligence occupies only the final three years. Dai et al. (2026) is the closest antecedent, being both recent and specific to higher education, but its emphasis falls on emerging trends and global power dynamics. What is missing across this body of work is a higher-education-specific map that is simultaneously (i) built on the two major citation databases in combination rather than on one, (ii) reported at a level of parameter detail that permits replication and (iii) cross-validated by more than one clustering algorithm.

This omission is consequential, because bibliometric cluster solutions are sensitive to precisely the choices that typically go unreported. Whether keywords are drawn from author keywords or from Keywords Plus, whether the minimum occurrence threshold is set at three or at ten and whether clustering proceeds by modularity optimisation or by factorial projection can each alter the number and the composition of the clusters obtained (van Eck and Waltman, 2010; Cobo et al., 2011; Zupic and Čater, 2015; Aria and Cuccurullo, 2017). A map of generative artificial intelligence research in higher education that does not disclose these settings

cannot be audited, replicated or extended by anyone else. In a field growing at the rate documented in this study, an unverifiable map is of limited value to the researchers and policymakers who are its intended audience.

Why, then, is this study necessary? Three reasons can be stated concretely. First, research on generative artificial intelligence in higher education has expanded so rapidly since late 2022 that the field has outgrown the descriptive maps produced during its first eighteen months and no consolidated account exists of where it now stands. Second, the accumulated literature has not previously been examined simultaneously across the two databases with the widest complementary coverage, so the available picture is partial by construction. Third, the structure of the field has not been established by a procedure that another researcher can reproduce. This study responds to each of these points directly. It (i) builds a dual-database, PRISMA 2020-screened corpus; (ii) reports every analytical parameter of every analysis in a dedicated table, so that each result can be reproduced from the same corpus; (iii) triangulates two independent mapping algorithms modularity-based network clustering in VOSviewer and correspondence analysis in Biblioshiny so that convergence and divergence between cluster solutions can be examined rather than assumed; and (iv) reads the resulting map critically rather than descriptively, identifying the field's ChatGPT-centrism, its collaboration deficit and the early signs of thematic saturation. Table 1 positions the present study against the bibliometric reviews closest to it in scope.

Table 1. Positioning of the present study relative to prior bibliometric reviews on artificial intelligence and generative artificial intelligence in education

Study	Domain focus	Educational level	Distinctive emphasis	Difference from the present study
Zawacki-Richter et al. (2019)	Artificial intelligence (general)	Higher education	Systematic review of AI applications	Pre-dates generative AI; narrative rather than science mapping
Baek and Doleck (2020)	Artificial intelligence in education	All levels	Single-journal bibliometric profile	Restricted to one journal and to 2015–2019
Bozkurt (2023)	Generative AI, conversational agents, chatbots	All levels	Systematic review combined with bibliometrics	Not specific to higher education; earlier time window
Kavitha et al. (2024)	Artificial intelligence (general)	Higher education	Bibliometric performance analysis	Does not isolate the generative variant of AI
Flores-Velásquez et al. (2024)	Acceptance of AI technologies	Higher education	Acceptance-focused bibliometric review	Confined to technology acceptance; AI in general
Nugroho (2024)	ChatGPT	Education (general)	Trend analysis of ChatGPT research	Single-tool corpus; not higher-education-specific
Dúo-Terrón (2024)	Generative artificial intelligence	Education (general)	Analysis of scientific production	Not higher-education-specific
Ng and Ho (2025)	Generative AI in education	All levels	Mapping of the research landscape	Not higher-education-specific
Prayuda et al. (2026)	Artificial intelligence in education	All levels	Two-decade trend analysis (2000–2025)	Generative AI occupies only the final years of the window
Guo et al. (2026)	Generative AI in education	All levels	Scientometric review, 2021–2025	Not higher-education-specific
Dai et al. (2026)	Generative AI	Higher education	Emerging trends, power dynamics, global landscape	Analytical parameters not reported; single mapping tool
Present study	Generative artificial intelligence	Higher education	Dual-database, parameter-transparent, algorithmically triangulated map with a critical reading	-

Alongside the international literature, a growing body of national research supplies context-specific evidence that complements the global picture. In the Turkish context, Metli (2023) bibliometrically examined the intersection of education and artificial intelligence, while Tonbuloğlu and Avcı Akbel (2023) mapped research trends in emergency remote teaching, an adjacent field that shaped the digital infrastructure into which generative artificial intelligence tools were subsequently introduced. More directly, Büyükeke (2025) modelled the acceptance of generative artificial intelligence tools in programming courses among 305 Turkish undergraduates, using a technology acceptance model extended with self-efficacy, perceived trust, perceived risk and dependency concern and reported that perceived usefulness and perceived ease of use significantly predicted intention to use, with perceived trust operating on both. National evidence of this kind is analytically relevant to the present study for two reasons. It demonstrates that the technology-acceptance mechanisms identified in the international literature also operate in non-Anglophone higher education systems and it provides an interpretive frame for the country-level production findings reported in Section 3.4, where Türkiye appears among the moderately productive countries.

Bibliometric analysis represents an important method for systematically examining the scientific literature. Through this approach, large datasets can be analyzed to map the overall structure of a research field (Tonbuloğlu and Avcı Akbel, 2023). Bibliometric studies in the domain of generative artificial intelligence and higher education contribute to identifying influential researchers and collaboration networks (Baek and Doleck, 2020; Muskhir et al., 2024). Furthermore, keyword analyses and thematic investigations enable the identification of research trends (Muskhir et al., 2024).

Against this background, the study makes four contributions that are distinct from those of prior reviews. Methodologically, it is the first map of this specific field to combine dual-database construction with complete parameter disclosure (Table 2) and with algorithmic triangulation across two independent clustering procedures, making the reported structure verifiable rather than merely asserted. Empirically, it quantifies features of the field that descriptive maps leave implicit: the deceleration of growth beneath continuing volume expansion, the concentration of 8.75% of all citations in ten documents, the gap between a collaboration index of 2.83 and an international co-authorship rate of 10.11% and the divergence between author keywords and Keywords Plus as an indicator of terminological immaturity. Analytically, it explains rather than reports the difference between network-based and factorial cluster solutions and it shows that the two four-cluster structures they yield are complementary cross-sections of the field rather than competing accounts of it a comparison that also brings to light a substantial health-professions education subfield not previously reported in this literature. Critically, it moves beyond description to identify three structural risks facing the field ChatGPT-centrism, a collaboration deficit and early thematic saturation that carry direct implications for research funding and for institutional policy.

The aim of this study is to systematically map the scientific production dynamics, intellectual and conceptual structure and thematic evolution of generative artificial intelligence research in the context of higher education through bibliometric analysis methods. In line with this objective, the study seeks to answer the following research questions:

RQ1. What is the scientific production structure of generative artificial intelligence research in higher education?

RQ2. Around which research clusters is the intellectual structure of the generative artificial intelligence literature in higher education organized?

RQ3. Through which thematic relationships is the conceptual structure of this field of research formed?

RQ4. How are the prominent research themes in the literature on generative artificial intelligence in higher education positioned in terms of centrality and degree of development?

RQ5. How have the themes in generative artificial intelligence research in higher education evolved over time?

2. Materials and Methods

2.1. Research Design

This study adopts a bibliometric research design to examine the scientific production structure, intellectual organization, conceptual structure and thematic evolution of generative artificial intelligence research in higher education. Bibliometric analysis is a quantitative approach based on the statistical analysis of bibliographic data and is widely used to reveal the structural characteristics of research fields.

2.2. Data Sources

The data were obtained from two widely used databases due to their comprehensive indexing and academic quality standards: the Web of Science Core Collection (WoS) and Scopus.

2.3. Search Strategy and Justification of the Search Vocabulary

The literature search was conducted to identify studies examining the use of generative artificial intelligence technologies in the context of higher education. The search strategy was based on two main sets of concepts:

- Generative artificial intelligence: “generative artificial intelligence,” “generative AI,” “ChatGPT,” “large language model*,” “LLM*,” “AI chatbot*,” “GPT-4,” “GPT model*”
- Higher education context: “higher education,” “universit*,” “tertiary education”

The use of overly general and broad terms (e.g., education, learning) in isolation was avoided in order to ensure a more focused search scope. Terms within each concept set were combined using the OR operator, while

the two concept sets were combined using the AND operator.

The scope of this search vocabulary requires explicit justification. The two concept sets were deliberately constructed from umbrella terms together with the single tool name that achieved lexical dominance during the period covered, rather than from an enumeration of individual model names. Brand-specific model names (e.g., Gemini, Claude, Llama, Copilot, DeepSeek) were not entered as separate query terms, for three reasons. First, within the 2022–2025 window ChatGPT is the only generative model whose name entered the academic lexicon as a topic descriptor in its own right; studies of other models overwhelmingly index themselves under the umbrella terms already present in the query 'generative artificial intelligence', 'generative AI', 'large language model*' or 'LLM*' and are therefore captured through those terms rather than lost. Second, brand names are highly volatile: a query built around the model landscape of one year becomes unreproducible in the next, whereas umbrella terms remain stable and permit replication. Third, several model names are lexically ambiguous in database queries 'Claude' and 'Gemini', for example, retrieve substantial unrelated literature as a personal name and as an astronomical and biomedical term respectively which would have introduced a loss of precision disproportionate to any gain in recall.

Notwithstanding this rationale, a residual set of records that name only a specific model in title, abstract and keywords, without using any umbrella term, cannot be excluded. This decision is therefore also stated explicitly as a limitation in Section 5 and a model-name-inclusive sensitivity search is recommended there as a direction for subsequent replications.

Web of Science query: TS = (("generative artificial intelligence" OR "generative AI" OR ChatGPT OR "large language model*" OR LLM* OR "AI chatbot*" OR "GPT-4" OR "GPT model*") AND ("higher education" OR universit* OR "tertiary education"))

Scopus query: TITLE-ABS-KEY (("generative artificial intelligence" OR "generative AI" OR ChatGPT OR "large language model*" OR LLM* OR "AI chatbot*" OR "GPT-4" OR "GPT model*") AND ("higher education" OR universit* OR "tertiary education"))

The search was conducted on March 10, 2026. The studies were limited to the period between 2022 and 2025. Only English-language publications of the types "article" and "review" were included. In the WoS database, the SSCI, ESCI and SCIE indexes were considered. As a result of this process, 1,248 records were retrieved from WoS and 2,840 records from Scopus. One aspect of this procedure requires explicit statement. The document-type, language and index filters were applied within the database interfaces at the point of retrieval, whereas the 2022–2025 publication-year restriction was applied after retrieval, during corpus construction, rather than as a query filter. This is reported because it has a visible consequence: the retrieved set contained 142 records carrying a 2026 publication year, which were removed at the corpus-construction stage as described in Section 2.4.

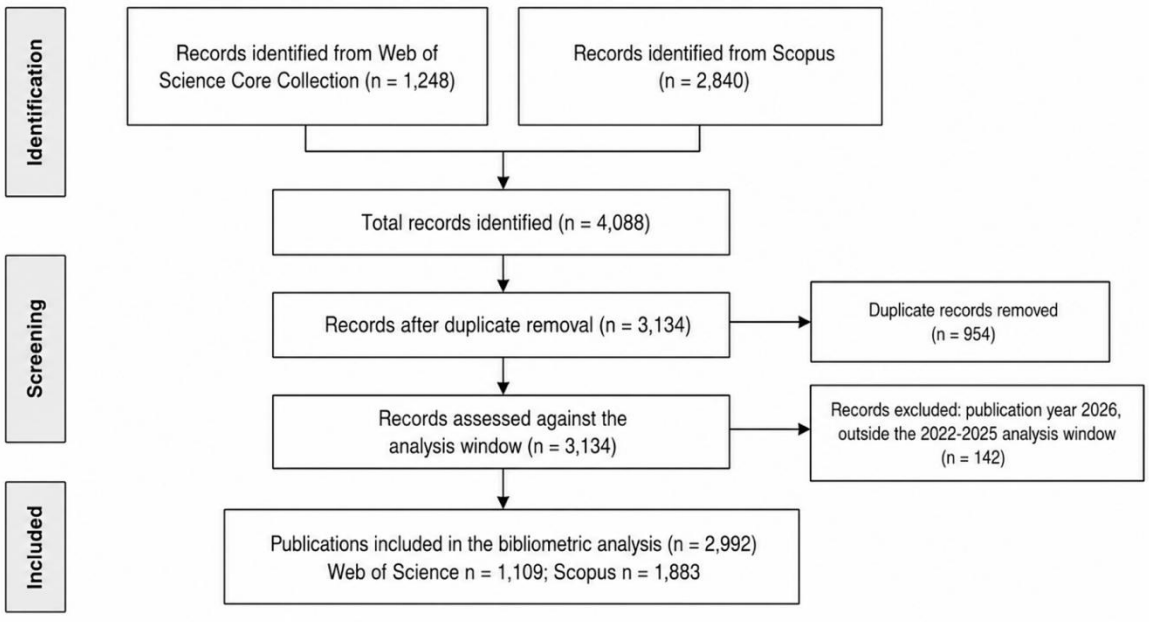


Figure 1. PRISMA 2020 flow diagram of the literature search and corpus construction process (Page et al., 2021). Records were identified in the Web of Science Core Collection (n = 1,248) and Scopus (n = 2,840) on 10 March 2026, giving 4,088 records in total. Deduplication by DOI and normalised title matching removed 954 records, all on the Scopus side, leaving 3,134 unique records. A further 142 records carrying a 2026 publication year were removed as falling outside the 2022–2025 analysis window, yielding the final analytical corpus of n = 2,992 articles and reviews (Web of Science, n = 1,109; Scopus, n = 1,883).

2.4. Screening, Selection and Eligibility Criteria

The literature screening and selection process was conducted in accordance with the PRISMA 2020 guidelines (Page et al., 2021) and is reported in full in Figure 1. A total of 4,088 records was identified: 1,248 from the Web of Science Core Collection and 2,840 from Scopus. Deduplication removed 954 records through a two-stage procedure automated matching on DOI, followed by normalised title matching (with case, punctuation and whitespace standardised) for records lacking a DOI with every automatically flagged pair verified manually before deletion. Because the Web of Science export was treated as the primary source in the merge, all duplicate removals fell on the Scopus side, leaving 3,134 unique records (Web of Science, n = 1,248; Scopus, n = 1,886). Of these, 142 records carried a 2026 publication year and therefore fell outside the analysis window; their removal yielded the final analytical corpus of 2,992 publications (Web of Science, n = 1,109; Scopus, n = 1,883), all in English and all of document type article or review.

Eligibility was operationalised at the point of retrieval rather than through a subsequent manual title-and-abstract screening stage and this is stated explicitly because it determines how the corpus should be understood. The inclusion criteria were enforced by the search query itself and by the database interface filters: the two concept sets described in Section 2.3 restricted the topic; the document-type filter restricted the set to articles and reviews; the language filter restricted it to English; and the index filter restricted the Web of Science component to the SSCI, ESCI and SCIE. The only post-retrieval reductions were the two reported above, deduplication and the publication-year restriction. No records were removed on the basis of a discretionary relevance judgement.

This is a deliberate design decision rather than an omission and it carries a specific advantage and a specific cost. The advantage is reproducibility: because no discretionary screening was applied, the corpus is fully determined by the queries, filters and retrieval date reported in Section 2.3 and any reader who applies them will obtain the same set of records which is not the case for bibliometric studies in which an unspecified number of records is removed by manual judgement. The cost is precision: records retrieved through the truncation 'universit*' in which a university appears only as the authors' affiliation rather than as the study setting and records in which generative artificial intelligence is mentioned only incidentally, remain in the corpus. This trade-off is appropriate to bibliometric mapping, whose object is a literature as it is indexed rather than a set of studies appraised for evidence synthesis, but it is a genuine constraint on the resulting map and is stated as such in Section 5.

As a single-authored study, all decisions concerning the search strategy, the filters and the deduplication procedure were made by one researcher. No inter-rater reliability coefficient is reported, because the design contains no rater-dependent screening stage for such a coefficient to describe. The criteria were specified in writing before retrieval; the cleaning and deduplication procedure was implemented as a single documented script, described in Section 2.5; and records flagged as potential duplicates were exported to a separate file and verified manually before deletion. Every reduction from the 4,088 records identified to the 2,992 analysed is therefore traceable and auditable.

Inclusion and Exclusion Criteria

Inclusion criteria;

- Addressing generative artificial intelligence within the context of higher education
- Being a peer-reviewed article or review
- Published between 2022 and 2025

Exclusion criteria;

- Studies not directly related to the research topic
- Non-academic documents such as editorials and conference abstracts
- Duplicate records

2.5. Data Collection, Cleaning and Corpus Construction

The data were exported from the WoS and Scopus databases. WoS data were obtained in .txt format, while Scopus data were retrieved in .csv format. Prior to merging, the dataset consisted of 4,088 records.

The dataset includes the following information:

- Authors
- Affiliations
- Publication year
- Journal title
- Abstract
- Keywords
- References
- Citation counts

2.5.1. Data cleaning and dataset construction

The data cleaning process was conducted systematically. Of the 4,088 records retrieved from the Web of Science and Scopus databases, 954 were removed as duplicates on the basis of DOI and normalised title matching, leaving 3,134 unique records; a further 142 records carrying a 2026 publication year were removed as falling outside the 2022–2025 analysis window. The final dataset therefore comprised 2,992 publications. Inconsistencies in data formats and fields were additionally corrected and keywords were standardised as described below.

Data cleaning was implemented in R through a single documented script applied to the merged corpus before any analysis, so that both software environments received identical input. The procedure comprised five operations. First, invisible and zero-width characters were stripped and whitespace normalised across all text fields. Second, DOIs were standardised to a bare lower-case form, with 'doi:' prefixes and the https://doi.org/ and http://dx.doi.org/ resolvers removed, so that records differing only in the presentation of their DOI could not survive as separate entries. Third, titles were

cleared of appended translated titles, which a number of records carry in the form '; [translated title]'; all such records were additionally written to a separate file for manual inspection. Fourth, affiliation strings were upper-cased and standard abbreviations expanded (UNIV → UNIVERSITY, INST → INSTITUTE, SCH → SCHOOL, DEPT → DEPARTMENT) in order to reduce the fragmentation of institutional counts. Fifth, the cited-reference field was upper-cased and duplicated 'DOI DOI' tokens collapsed. Records flagged as potential duplicates by the automated procedure were exported to a separate file and verified manually before deletion.

Keyword harmonisation warrants separate description, since it is the single cleaning decision with the greatest bearing on the conceptual and thematic results reported in Section 3. Both keyword fields and the merged keyword field derived from them, were processed by the same routine: keywords were split on the semicolon delimiter, case-normalised, cleared of invisible characters and keywords repeated within a single record were removed. A synonym dictionary was then applied to consolidate notational and morphological variants of the field's core concepts. Verified against the analysed corpus, the rules took effect as follows: 'generative artificial intelligence', 'generative artificial intelligence (GenAI)', 'generative AI (GenAI)' and 'GenAI' were consolidated into generative AI (537 keyword instances); 'large language model', 'large language model (LLM)', 'large language models (LLMs)', 'LLM' and 'LLMs' into large language models (127 instances); 'chatbot', 'AI chatbot' and 'AI chatbots' into chatbots (116 instances); 'artificial-intelligence' into artificial intelligence; and 'tertiary education' into higher education (11 instances). After harmonisation the corpus contained 6,030 unique author keywords and 2,222 unique index keywords across the 2,992 analysed documents.

Two residual features of the harmonised vocabulary are reported here rather than left implicit, because both bear on the interpretation of Figures 9 to 11. First, the consolidation of 'tertiary education' into 'higher education' means that the higher education node in those figures represents both terms. Second, two abbreviation variants were not consolidated: 'AI' (168 instances) and 'artificial intelligence (AI)' (96 instances) remain distinct from 'artificial intelligence' (761 instances) in the analysed data. The frequency of artificial intelligence as a concept is therefore distributed across three surface forms and its position in the conceptual and thematic maps is correspondingly conservative: consolidating the three would raise its frequency to 1,025 and would strengthen rather than weaken its centrality, so the reported structure is not an artefact of this residual fragmentation. No stemming was applied beyond the explicit rules listed above and no terms were merged on the basis of automatic similarity matching, so that every substitution performed on the data is recoverable from this list. This harmonisation governs the author-keyword analyses reported in Figures 9 to 11. Figure 8 is the single deliberate exception. That network was constructed on the merged keyword field, in which author keywords and the index keywords assigned by the source databases are combined and retained in the form in which the databases record them. The purpose of retaining them is analytical rather than incidental: index keywords encode how the literature is classified by the databases themselves and preserving them allows the indexed structure of the field to be compared with the vocabulary its authors choose, which is what Sections 2.8 and 3.8 set out to do. The cost of this decision is that variant forms of the same term appear as separate nodes in Figure 8 and that database descriptors which are indexing conventions rather than research themes are present in the network; both consequences are stated in Section 5. No thesaurus file was applied within VOSviewer, so the vocabulary of Figure 8 is exactly the indexed vocabulary of the corpus.

2.6. Bibliometric Analysis Tools and Analytical Parameters

The bibliometric analyses were conducted in two complementary software environments, with each analysis assigned to the environment best suited to it. Performance (descriptive) analysis, conceptual structure mapping, strategic (thematic) mapping and thematic evolution analysis were performed in the Bibliometrix R package through its interactive Biblioshiny interface (Aria and Cuccurullo, 2017), which implements the co-word and strategic-diagram procedures of Callon et al. (1991) and Cobo et al. (2011). The keyword co-occurrence network presented in Figure 8 was constructed independently in VOSviewer (van Eck and Waltman, 2010), whose unified mapping-and-clustering algorithm (Waltman et al., 2010) derives its solution from different principles to those underlying the Biblioshiny procedures, allowing the two cluster solutions to be compared rather than assumed to coincide. The two environments were supplied with deliberately different keyword vocabularies harmonised author keywords for the Biblioshiny analyses, indexed merged keywords for the VOSviewer network for the reasons set out in Section 2.5. Reporting followed the guidance on bibliometric method transparency set out by Zupic and Čater (2015) and Donthu et al. (2021).

Author keywords rather than Keywords Plus were selected as the data field for all conceptual and thematic analyses. The rationale is empirical and is set out with the corresponding evidence in Section 3.1: in this corpus author keywords outnumber Keywords Plus by a factor of 2.7 and are assigned at almost three times the per-document rate, because Keywords Plus is generated algorithmically from the titles of cited references and is therefore sparse in a field whose cited literature has not yet stabilised. Author keywords consequently provide the denser and more representative vocabulary for mapping a research front of this age. The single exception is the VOSviewer co-occurrence network in Figure 8, which was deliberately run on the merged keyword set in

order to test whether the cluster structure is robust to the choice of data field. The complete set of parameters governing every analysis reported in this study is presented in Table 2, so that each result in Section 3 can be reproduced from the same corpus.

Descriptive analysis;

- Number of publications by year
- Most productive authors
- Country-based production
- Citation indicators

Network analysis;

Relationships between concepts were examined through keyword co-occurrence analysis.

Conceptual structure analysis;

The conceptual structure of the field was identified by analyzing the clustering of keywords.

Thematic analysis;

Themes were classified according to their centrality and density values:

- Motor themes
- Basic themes
- Niche themes
- Emerging themes

Additionally, thematic evolution analysis was conducted to examine changes over time.

Table 2. Analytical parameters of the bibliometric analyses reported in this study

Analysis (output)	Software	Data field	Unit selection / threshold	Normalisation / weighting	Clustering / extraction method	Additional settings
Study selection (Figure 1)	-	Full records	4,088 records screened; 2,992 retained	-	-	PRISMA 2020 (Page et al., 2021); DOI then normalised-title deduplication
Performance and descriptive indicators (Figures 2–7)	Bibliometrix / Biblioshiny	Full records	All 2,992 documents	-	-	Full counting; country attribution by author affiliation; citation counts as indexed on 10 March 2026
Keyword co-occurrence network (Figure 8)	Network matrix built in Bibliometrix, exported in Pajek format, laid out and clustered in VOSviewer	Merged keyword field (author keywords + database index keywords), retained as indexed (Section 2.5)	50 most frequent keywords; effective minimum occurrence = 111; full counting	Association strength	Modularity-based clustering in VOSviewer; minimum cluster size = 1; 4 clusters obtained	Resulting network: 50 nodes, 646 edges; isolates removed; node size proportional to occurrences, edge width to link strength, colour to cluster
Conceptual structure map (Figure 9)	Bibliometrix / Biblioshiny	Author keywords, harmonised in R prior to analysis (Section 2.5)	50 most frequent terms	-	Multiple Correspondence Analysis (MCA); terms partitioned by k-means, k = 4	Terms projected onto the first two factorial dimensions; proximity denotes similarity of co-occurrence profiles
Strategic (thematic) map (Figure 10)	Bibliometrix / Biblioshiny	Author's Keywords, harmonised in R prior to analysis (Section 2.5)	250 terms; minimum cluster frequency = 5 per thousand documents	Equivalence (inclusion) index	Louvain community detection (Blondel et al., 2008)	Quadrant boundaries set at the median of observed centrality and density values; no stop-word or in-application synonym list applied
Thematic evolution (Figure 11)	Bibliometrix / Biblioshiny	Author's Keywords, harmonised in R prior to analysis (Section 2.5)	250 terms; minimum cluster frequency = 5 per thousand documents	Inclusion index weighted by word occurrences	Louvain community detection (Blondel et al., 2008)	Cutting points at 2023 and 2024; flow width proportional to the weighted inclusion index

2.7. Strategic (Thematic) Map: Computation of Centrality and Density

Themes were positioned on a strategic diagram using the co-word procedure formalised by Callon et al. (1991) and

operationalised in Biblioshiny by Aria and Cuccurullo (2017). Author keywords were first normalised by the equivalence index, e(ij) = c(ij)^2 / (c(i) x c(j)), where c(ij) is the number of documents in which keywords i and j co-occur and c(i) and c(j) are the numbers of documents in which each keyword occurs separately. The resulting weighted co-word network was partitioned into clusters by the Louvain algorithm (Blondel et al., 2008), which detects communities by greedy modularity optimisation, iteratively reassigning terms between communities and aggregating them until modularity ceases to improve.

Two indices were then computed for each cluster. Centrality, which measures the strength of a theme's links to other themes and therefore its importance to the field as a whole, was calculated as c = 10 x SUM e(kh), where k is a keyword belonging to the cluster under consideration and h is a keyword belonging to any other cluster. Density, which measures the internal cohesion of a theme and therefore its degree of development, was calculated as d = 100 x (SUM e(ij)) / w, where i and j are keywords belonging to the same cluster and w is the number of keywords in that cluster.

Clusters were assigned to quadrants by splitting each axis at the median of the observed centrality and density values across all retained clusters, following Cobo et al. (2011). No fixed absolute cut-off value was applied. This is a deliberate methodological choice rather than an omission: centrality and density are scale-dependent on corpus size and keyword frequency, so an absolute threshold would be neither meaningful within a single corpus nor comparable across corpora, whereas a median split renders the classification internal to the corpus analysed and therefore interpretable. The four resulting quadrants are motor themes (high centrality, high density), basic and transversal themes (high centrality, low density), niche themes (low centrality, high density) and emerging or declining themes (low centrality, low density). It follows that a theme's position in Figure 10 should be read as its standing relative to the other themes in this corpus, not as an absolute measure of its maturity.

Thematic evolution was analysed by dividing the corpus into three time slices at the cutting points 2023 and 2024, computing the strategic map within each slice using identical parameters and linking themes across adjacent slices by the inclusion index weighted by word occurrences. The width of each flow in Figure 11 is proportional to that index.

2.8. Comparability of the Network and Factorial Cluster Solutions

Because the co-occurrence network (Figure 8) and the conceptual structure map (Figure 9) are produced by different algorithms operating on deliberately different inputs, the two solutions are reported and interpreted separately rather than merged. Figure 8 is a network partition: keywords drawn from the merged, indexed keyword field are clustered in the full high-dimensional co-occurrence space by optimising a modularity-based quality function. Figure 9 is a factorial projection: correspondence analysis reduces the harmonised author-keyword structure to a small number of latent dimensions and terms are then partitioned within that reduced space.

Both procedures return four clusters, but they are not the same four and this is the point of running them together rather than a defect in either. Because Figure 8 operates on indexed vocabulary, its clusters track the disciplinary settings in which the research is carried out; because Figure 9 operates on harmonised author keywords, its clusters track the conceptual concerns that authors themselves name. The comparison is therefore between how this literature is classified and how it describes itself and neither view is reducible to the other. The substantive relationship between the two solutions is set out in Section 3.8.

2.9. Data Visualization and Figure Preparation

Various bibliometric visualization techniques were employed to present the research findings in a clear and comprehensible manner. Time-series graphs were generated to illustrate trends in scientific production, while country production maps were used to reveal the geographical distribution of research outputs. Furthermore, keyword co-occurrence networks were constructed to visualize conceptual relationships within the literature. Conceptual structure maps and thematic maps were produced using Biblioshiny and network-based visualizations were generated in high resolution using the VOSviewer software.

For this version the figures have been re-prepared with legibility in mind, following the reviewers' comments. The keyword co-occurrence network in Figure 8, identified in review as the least legible, has been re-exported from VOSviewer at the maximum available resolution, with enlarged label fonts and increased label-to-node scaling; it is reproduced here at approximately 245 dpi, against 111 dpi in the previous version. The PRISMA diagram in Figure 1 has been redrawn to the corrected selection counts reported in Section 2.4 and the thematic evolution diagram in Figure 11 has been regenerated in Biblioshiny using the parameters given in Table 2. Vector versions (SVG or PDF) of the figures produced in Biblioshiny and VOSviewer can be supplied to the publisher at the production stage should the journal's typesetting workflow require them.

3. Results

This section presents the bibliometric characteristics of generative artificial intelligence research in higher education. The analyses encompass the scientific production structure, temporal trends, distributions of authors and countries, citation impact and the conceptual structure of the field.

3.1. Scientific Production Structure of the Field

The main indicators of the bibliometric dataset analyzed in this study are presented in Figure 2. The dataset covers the period between 2022 and 2025 and consists

of 2,992 documents obtained from 728 different sources. During the examined period, the average annual scientific production was approximately 748 documents. The average number of citations per document was calculated as 18.46, indicating that the field demonstrates a considerable level of academic impact.

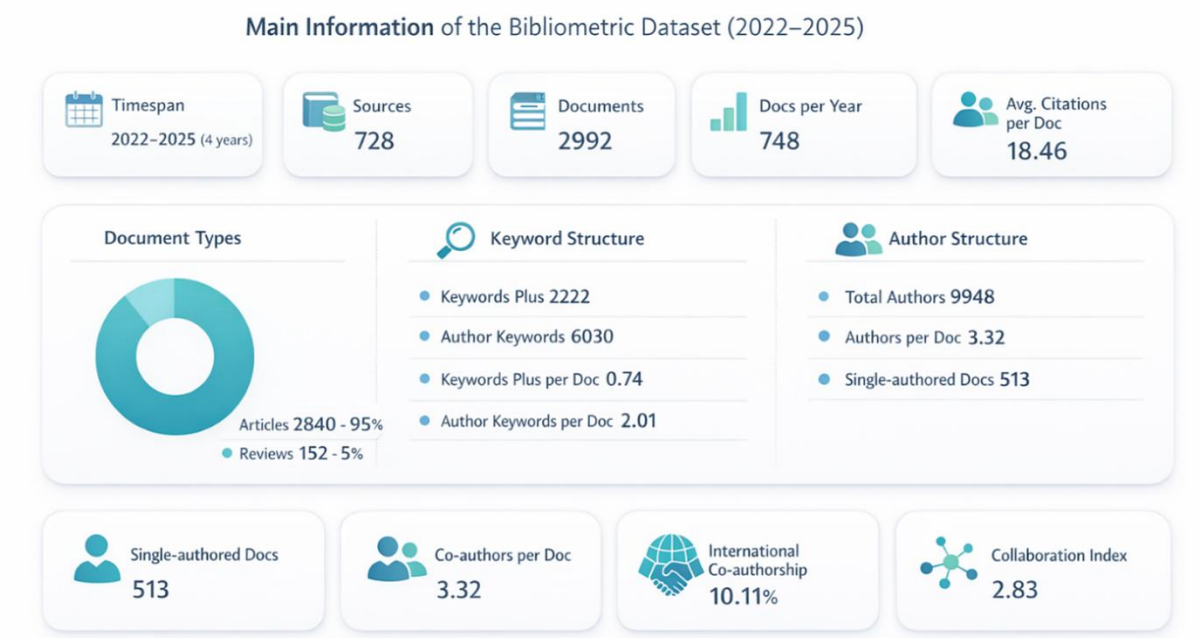


Figure 2. Main characteristics and descriptive statistics of the bibliometric corpus (2022–2025). Generated in Biblioshiny from the merged Web of Science–Scopus corpus (n = 2,992 documents; 728 sources; 9,948 authors; mean 18.46 citations per document). Note that the Keywords Plus count reported in the figure is 2,222 terms, which is consistent with the ratio of 0.74 Keywords Plus per document also shown.

The analysis of document types indicates that the dataset is predominantly composed of research articles (n = 2,840; 94.92%), while review studies constitute a relatively small proportion (n = 152; 5.08%). This distribution suggests that the field is largely shaped by original and empirical research and is undergoing a dynamic development process.

Findings related to the keyword structure reveal the conceptual profile of the field. A total of 2,222 Keywords Plus and 6,030 author keywords were identified in the analysed corpus, corresponding to 0.74 Keywords Plus and 2.01 author keywords per document. The contrast between these two figures is analytically meaningful rather than incidental. Author keywords outnumber Keywords Plus by a factor of 2.7 and are assigned at almost three times the per-document rate, which is the reverse of the pattern typically observed in mature fields. Keywords Plus is generated algorithmically from the titles of the references a document cites and therefore reflects the vocabulary of the established literature on which a field draws; author keywords reflect the vocabulary that authors themselves choose. In a field as young as this one, the cited literature has not yet stabilised into a shared indexing vocabulary, which depresses Keywords Plus, while authors coin and apply terminology freely, which inflates author keywords. The divergence is thus a quantitative signature of terminological immaturity: the field is conceptually broad but has not yet converged on a standard descriptive vocabulary. This finding also provides the empirical justification for the methodological decision reported in Section 2.6, namely that author keywords rather than Keywords Plus were used as the data field for the conceptual and thematic analyses that follow. An examination of the authorship structure shows that a total of 9,948 authors contributed to the dataset, with an average of 3.32 authors per document. Single-authored studies are relatively limited in number (n = 513). This finding demonstrates that the field is largely characterized by a collaborative research structure. The rate of international co-authorship was calculated as 10.11%, while the collaboration index was 2.83. These results indicate a moderate level of international collaboration in the field, with multi-authored studies being predominant. These two indicators should be read together, because they point in opposite directions. A collaboration index of 2.83 and a mean of 3.32 authors per document, against only 513 single-authored studies (17.1% of the corpus), indicate that co-authorship is the clear norm in this field. An international co-authorship rate of 10.11%, however, means that approximately nine out of every ten collaborative papers are produced entirely within a single country. The field is therefore collaborative but not international: teams form readily, but almost always domestically. This is a structural weakness rather than a neutral descriptive observation. The questions that dominate this literature assessment security, integrity policy, equity of access, disciplinary

norms for permissible use are precisely those whose answers vary by national higher education system and which consequently require cross-system comparison if they are to be answered well. A field expanding this rapidly while collaborating this locally risks accumulating parallel national literatures that replicate one another's findings, rather than a cumulative comparative evidence base.

3.2. Annual Scientific Production

To reveal the temporal development of scientific production in the research field, the distribution of publications by year was analyzed. The findings are presented in Figure 3.

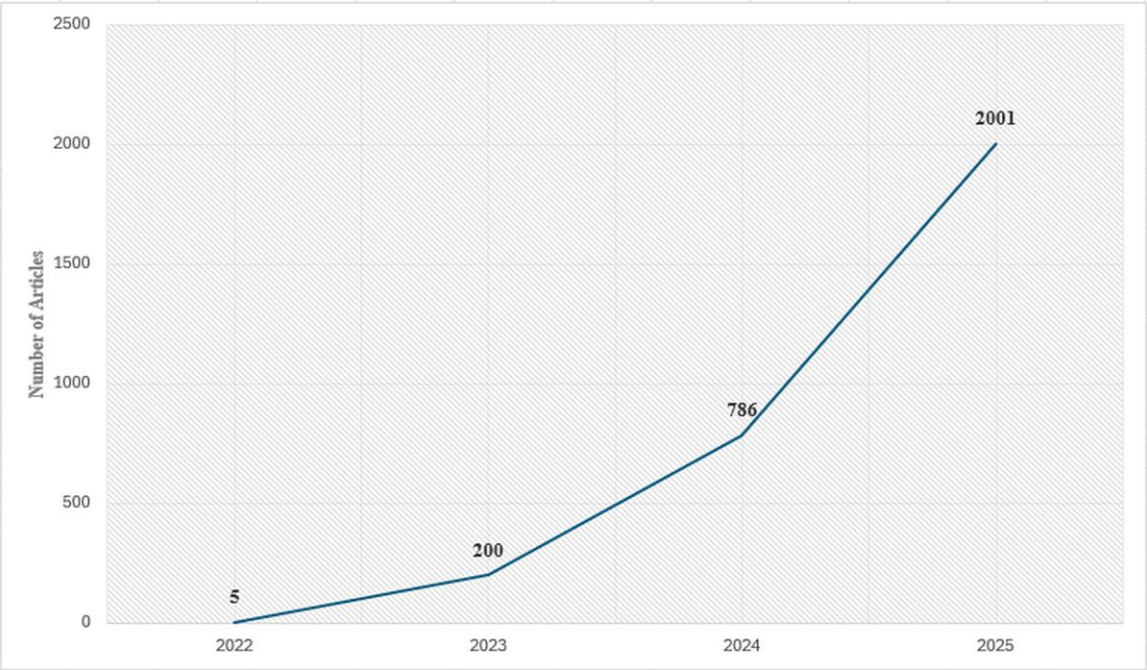


Figure 3. Annual scientific production of research on generative artificial intelligence in higher education (2022–2025). Generated in Biblioshiny; articles and reviews only. Annual document counts: 2022, n = 5; 2023, n = 200; 2024, n = 786; 2025, n = 2,001. The 2025 count should be treated as a lower bound, since records indexed after 10 March 2026 are not captured.

An examination of Figure 3 reveals that scientific production in the field of generative artificial intelligence in higher education exhibits a clear and sharp upward trend over the analyzed period. While the level of production was quite limited in 2022, with only 5 publications, this number increased significantly to 200 in 2023, indicating a remarkable rise. This upward trend accelerated further in 2024, reaching a total of 786 publications. The most striking increase occurred in 2025, when the number of publications surged to 2,001, far exceeding the levels observed in previous years.

Expressed in relative terms, the trajectory is considerably more informative than the raw counts. Output grew forty-fold between 2022 and 2023, by a further 293.0% in 2024 and by 154.6% in 2025, giving a 400-fold expansion across the four-year window as a whole. The pattern of these rates matters: growth decelerated markedly from 3,900% to 293.0% to 154.6% even as absolute volume continued to rise steeply. This combination is the characteristic signature of a research field moving off an explosive initial phase onto a steep but decelerating growth path, rather than one still accelerating without constraint. Two-thirds of the entire corpus (66.9%, n = 2,001) was published in the final year alone and 93.1% (n = 2,787) in the final two years. This concentration is double-edged. It confirms the currency of the field, but it also means that the overwhelming majority of the literature has been in circulation for less than two years and has had minimal opportunity to be cited, replicated or challenged. The findings reported below should therefore be read as a map of an active research front rather than of a consolidated body of knowledge.

These findings suggest that the research field has rapidly transitioned from an early developmental stage to a phase of maturation. The exponential growth observed particularly after 2023 appears to be closely associated with the increasing academic interest and research investment in generative artificial intelligence technologies within the context of higher education. Moreover, the high level of scientific production reached in 2025 indicates that the field is not only gaining popularity but is also entering a phase of institutionalization and becoming a central focus within the research agenda.

3.3. Most Productive Authors

To identify the most scientifically productive researchers in the field, an author productivity analysis was conducted. The findings are presented in Figure 4.

An examination of Figure 4 indicates that the most prolific author in the analyzed dataset is Chiu T. (n = 14). Chiu T. is followed by Gasevic D. (n = 12) and Bozkurt A. (n = 9). Similarly, Chan C. (n = 9) and Li X. (n = 9) are also among the authors with high levels of productivity. These findings suggest that certain researchers play a leading role in knowledge production within the field.

When authors with moderate levels of productivity are considered, Khalaf Z., Li Y., Noroozi O., Perkins M. and Roe J. each have 7 publications. This group can be regarded as researchers who contribute consistently to the development of the field and play an important role in the expansion of the literature. Overall, the distribution of author productivity indicates that the field is concentrated around a set of core researchers.

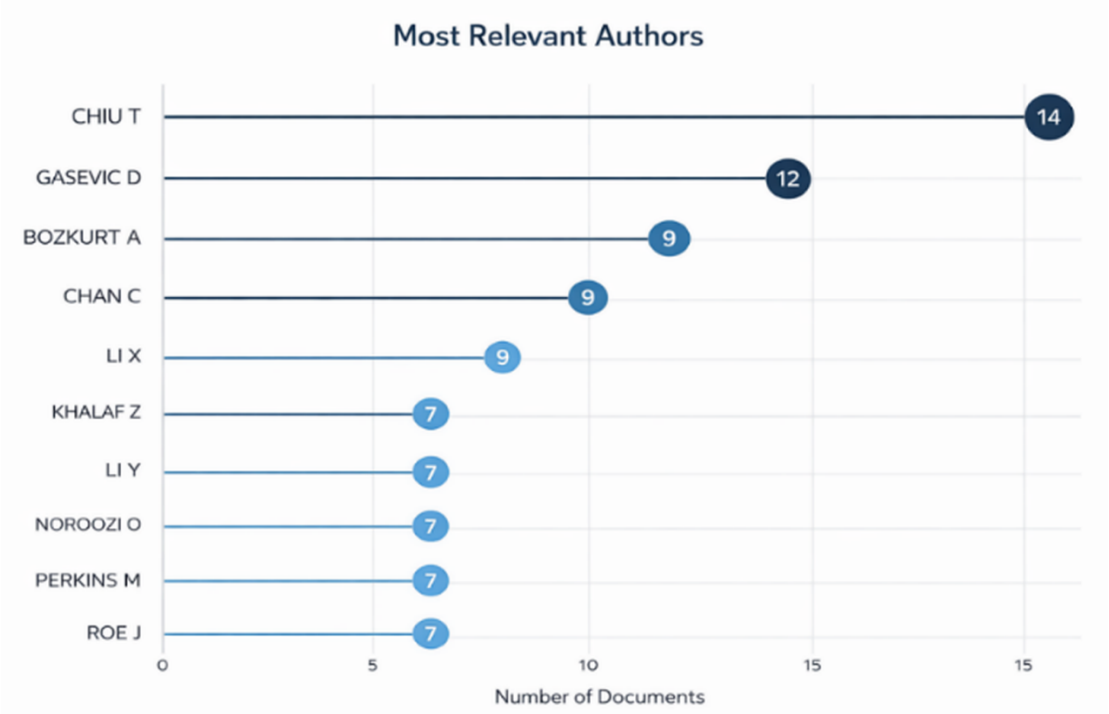


Figure 4. Most productive authors in the research field, by number of documents (full counting).Generated in Biblioshiny; author names as disambiguated in the source databases. The ten most productive authors account for 88 documents in total, or 2.9% of the corpus.

The distribution of author productivity is, however, notably flat for a field of this size and this flatness is itself a finding. The most productive author accounts for 14 of 2,992 documents (0.47%) and the ten most productive authors together account for 88 documents, or 2.9% of the corpus, against 9,948 contributing authors in total a ratio of one document per 3.3 authors. There is, in other words, no dominant research school in this field. It is being built by a very large number of researchers each contributing one or two papers, with only a thin layer of sustained specialists above them. This is consistent with a young research front with low barriers to entry and it carries a direct implication for the interpretation of the thematic results reported below: thematic structure in such a field is driven by the aggregate vocabulary of many occasional contributors rather than by the programmatic agendas of a few dominant groups, which makes the resulting map broad but comparatively shallow.

3.4. Institutional and Country Production

To reveal the geographical distribution of scientific production in the research field, country-based publication output was analyzed. The findings are presented in Figure 5.

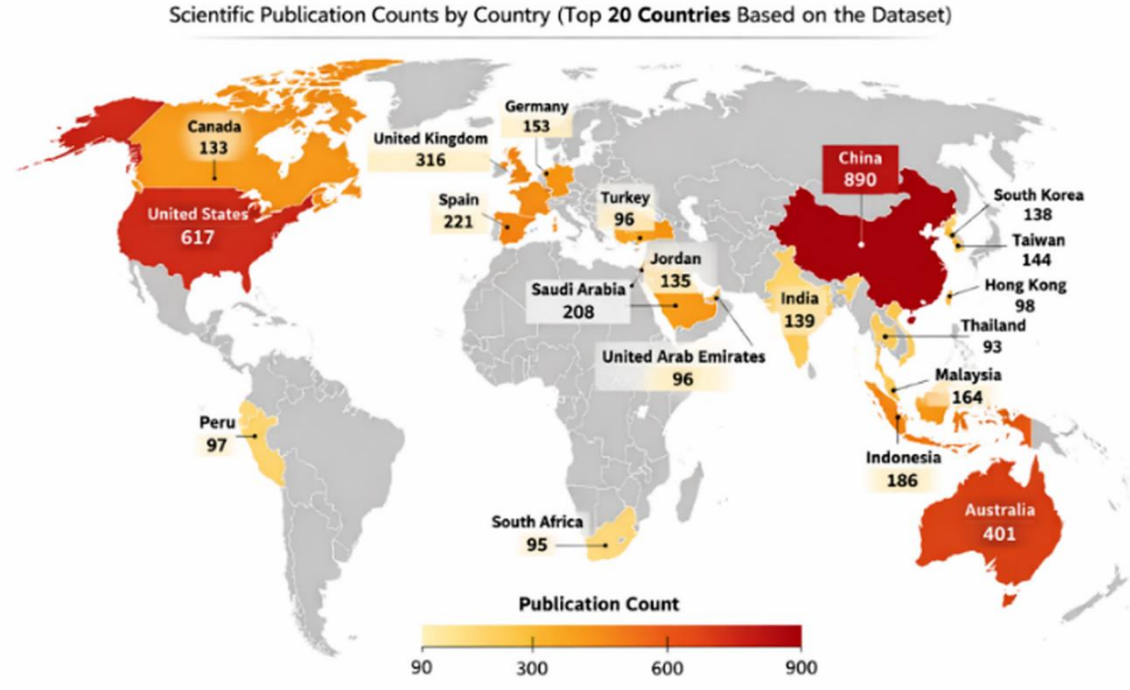


Figure 5. Country scientific production in research on generative artificial intelligence in higher education. Generated in Biblioshiny on the basis of author affiliations using full counting, so that a document authored across k countries contributes one unit to each of them; country counts consequently sum to more than the number of documents and should not be aggregated. Selected values: China, n = 890; United States, n = 617; Australia, n = 401; Türkiye, n = 96.

An examination of Figure 5 indicates that scientific production in generative artificial intelligence research in higher education is concentrated in specific countries. China ranks as the most productive country by a considerable margin, with 890 publications. It is followed by the United States (n = 617) and Australia (n = 401). These three countries constitute a significant portion of global scientific output in the field and occupy a central position in research activities.

In Europe, the United Kingdom (n = 316) and Spain (n = 221) stand out as leading contributors. Germany (n = 153) and Türkiye (n = 96) are among the countries with moderate levels of production. In the Middle East, Saudi Arabia (n = 208) and Jordan (n = 135) emerge as notable contributors at the regional level due to their relatively high publication outputs.

The Asia-Pacific region demonstrates a high level of research productivity. Indonesia (n = 186), Malaysia (n = 164), India (n = 139), South Korea (n = 138) and Taiwan (n = 144) exhibit considerable levels of output. In addition, countries such as Hong Kong (n = 98) and the Philippines (n = 93) also contribute to the development of the field. These findings indicate that the Asia-Pacific region is increasingly assuming a central role in the advancement of the field.

In the Americas, Canada (n = 133) and Peru (n = 97) are among the notable contributors, while in Africa, South Africa (n = 95) stands out as a leading country in regional production. Furthermore, countries such as the United Arab Emirates (n = 96) also make meaningful contributions to the research field. Overall, scientific production appears to be predominantly concentrated in the Asia-Pacific and North American regions, with Europe and the Middle East playing complementary and supportive roles.

Türkiye's position in this distribution warrants specific comment, since the country appears in the dataset with 96 publications. In relative terms this places Türkiye in the same output band as the United Arab Emirates (n = 96), Peru (n = 97), Hong Kong (n = 98) and South Africa (n = 95) and marginally above the Philippines (n = 93), while representing 10.8% of China's output and 15.6% of that of the United States. More instructive, however, is the comparison with higher education systems of broadly comparable scale and with comparable recent investment in digital transformation. Türkiye's output falls well below that of Saudi Arabia (n = 208), Indonesia (n = 186), Malaysia (n = 164), Taiwan (n = 144), India (n = 139) and Jordan (n = 135) and below Germany (n = 153). The comparison with Jordan is the most pointed of these, since the Jordanian higher education system is a fraction of the size of Türkiye's yet produces 40.6% more publications in this field. Türkiye therefore participates in this literature, but not yet at a level proportionate to the scale of its higher education system and the shortfall is with regional peers rather than with the global leaders. Two qualifications apply to this reading and are developed in Sections 4.3 and 5: the English-language restriction and the exclusion of nationally indexed outlets mean that the figure of 96 is a lower bound on Turkish scholarly activity in this area rather than a complete count of it.

3.5. Corresponding Authors' Countries

To examine the distribution of scientific production in the research field based on the countries of corresponding authors, a country-based analysis was conducted. The findings are presented in Figure 6.

An examination of Figure 6 shows that China has the highest level of scientific production based on the distribution of corresponding authors' countries. China is followed by the United States and the United Kingdom. These countries stand out as leading actors in the field not only in terms of total publication output but also at the level of corresponding authorship. Australia is also among the countries with a notably high level of production.

The figure further categorizes publications into single-country publications (SCP) and multiple-country publications (MCP). The findings indicate that, in many countries, publications originating from single-country collaborations (SCP) are more dominant. This suggests that research activities are largely concentrated at the national level. However, in countries with higher production capacity, multi-country collaborations (MCP) appear to be more prominent.

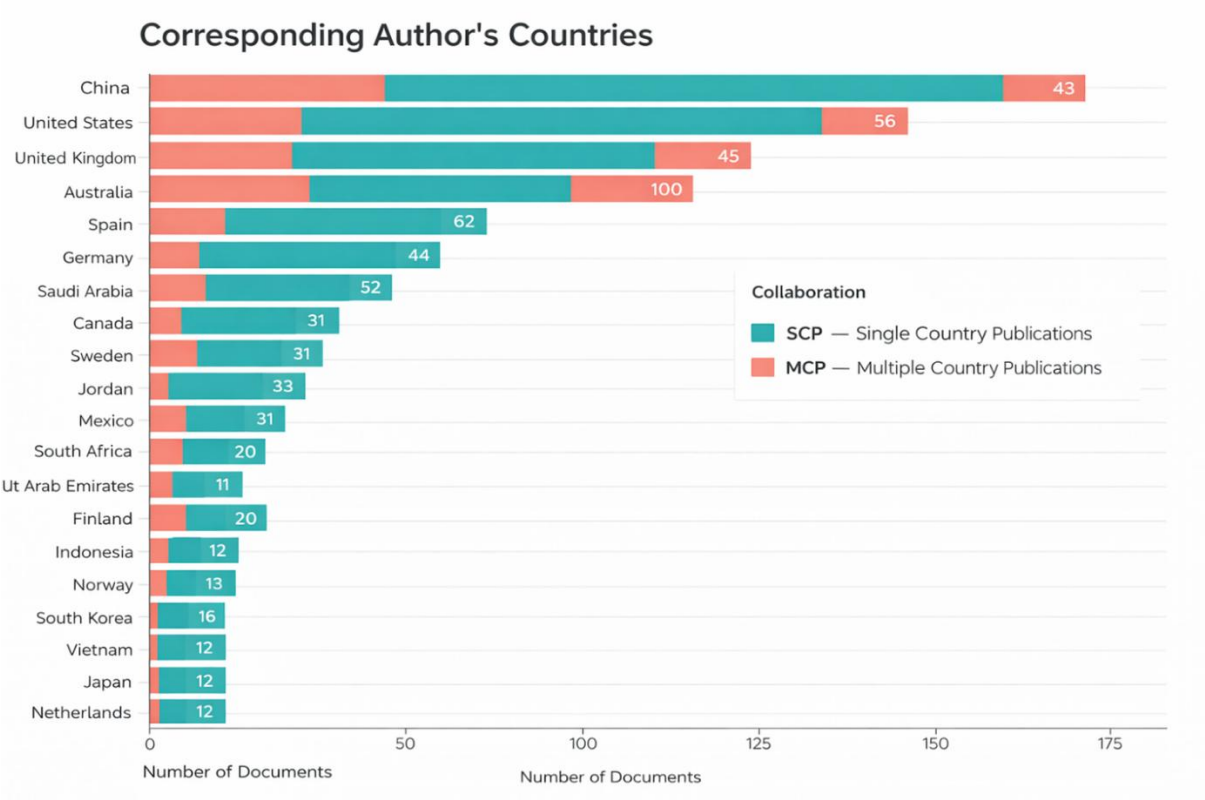


Figure 6. Distribution of publications by corresponding author's country, decomposed into single-country. Publications (SCP) and multiple-country publications (MCP). Generated in Biblioshiny; the multiple-country publication share across the corpus is 10.11%.

Among European countries, the United Kingdom, Spain and Germany are notable contributors; in the Middle East, Saudi Arabia stands out; and in North America, Canada is among the leading countries. Additionally, countries such as Sweden, Jordan and Mexico demonstrate moderate levels of production performance. Although exhibiting lower levels of production, countries including South Africa, the United Arab Emirates, Finland, Indonesia, Norway, South Korea, Vietnam, Japan and the Netherlands are also represented in the dataset. Overall, the distribution of corresponding authorship indicates that scientific production is concentrated in specific countries, which assume leading roles in research processes. Furthermore, international collaborations appear to be more prominent particularly in countries with higher production capacity.

3.6. Citation Impact

To identify the most influential studies in the research field, a citation analysis was conducted and the documents with the highest global citation counts are presented in Figure 7.

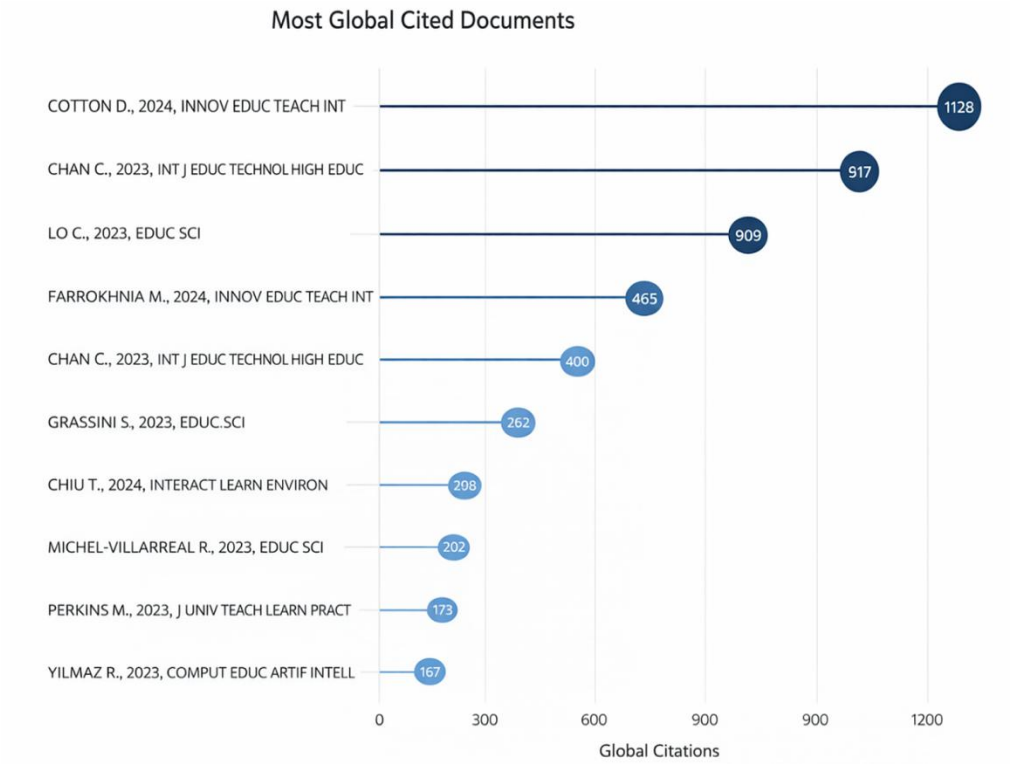


Figure 7. Ten most globally cited documents in the corpus, ranked by total global citations as indexed in the source databases on 10 March 2026. Generated in Biblioshiny. These ten documents account for 4,831 citations, equivalent to 8.75% of all citations accumulated by the corpus.

An examination of Figure 7 reveals that citation impact within the dataset is concentrated around a limited number of publications. The study with the highest number of citations is that of Cotton D. (2024), which has received 1,128 global citations. This is followed by Chan C. (2023) with 917 citations and Lo C. (2023) with 909 citations. These findings indicate that these studies possess high visibility and influence within the field.

Among studies with a moderate-to-high level of citations, the work by Farrokhnia M. (2024) (n = 465) and another study by Chan C. (2023) (n = 400) stand out. Additionally, the study published by Grassini S. (2023) has made a notable impact in the literature with 262 citations. These studies can be considered key reference points contributing to both the theoretical and applied development of the field.

Studies with lower yet still significant citation levels include those by Chiu T. (2024) (n = 208), Michel-Villarreal R. (2023) (n = 202), Perkins M. (2023) (n = 173) and Yılmaz R. (2023) (n = 167). These works play a complementary and supportive role within the expanding body of literature. Overall, the distribution of citations indicates the presence of a “high-impact core” formed by a select group of publications. This suggests that the knowledge structure of the field is shaped around a set of leading studies and that academic impact is distributed unevenly. The labels in Figure 7 identify documents contained in the analysed corpus by first author and publication year exactly as they are recorded in the source databases; they are data points of the citation analysis rather than works cited by this study and are therefore not listed in the reference list.

The degree of this concentration can be quantified precisely. With a mean of 18.46 citations per document across 2,992 documents, the corpus has accumulated approximately 55,200 citations in total. The ten documents shown in Figure 7 account for 4,831 of these that is, 8.75% of all citations in the field are generated by 0.33% of its documents, while the three most-cited documents alone (n = 2,954 citations) account for 5.4%. This is a steeply skewed distribution even by the standards of citation data and it has an identifiable cause. All three leading documents were published in 2023 or earlier and address academic integrity or the pedagogical implications of ChatGPT. In a field where two-thirds of the literature appeared only in 2025, early publication confers a decisive citation advantage and the works that happened to appear first were agenda-setting commentaries rather than empirical studies. The 'high-impact core’ identified here should therefore be understood as a first-mover effect operating on framing pieces, rather than as evidence that the field’s most methodologically substantial work has already been identified. This is a caution regarding the maturity of the citation structure, not a criticism of the works concerned.

3.7. Intellectual Structure of the Field

To reveal the intellectual structure of the research field, a keyword co-occurrence analysis was conducted. The results of the analysis are presented in Figure 8.

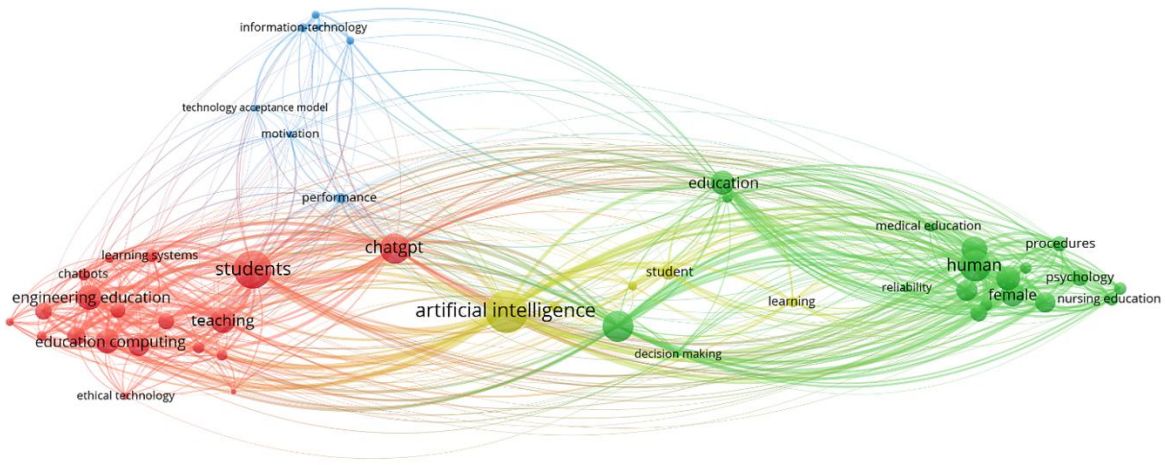


Figure 8. Keyword co-occurrence network of research on generative artificial intelligence in higher education. The network matrix was constructed in Bibliometrix from the merged keyword field author keywords combined with the index keywords assigned by the source databases, retained as indexed and exported in Pajek format; layout and clustering were performed in VOSviewer using association strength normalisation and modularity-based clustering. The network comprises the 50 most frequent keywords (effective minimum occurrence = 111) connected by 646 co-occurrence links and resolves into four clusters. Node size is proportional to occurrence frequency, edge thickness to co-occurrence link strength and colour denotes cluster membership. Because index keywords are retained, variant forms of the same term appear as separate nodes; see Sections 2.5 and 5.

The network presented in Figure 8 was constructed from the merged keyword field, in which author keywords and the index keywords assigned by the source databases are combined and retained in their indexed form. Nodes represent keywords, node size is proportional to occurrence frequency, edge thickness to co-occurrence link strength and colour denotes cluster membership. The network comprises the 50 most frequent keywords, connected by 646 co-occurrence links and resolves into four clusters. Because this analysis deliberately retains index vocabulary, it maps how the literature is classified by the databases as well as how it is described by its authors; the complementary author-defined view is reported in Section 3.8.

The first and largest cluster is organised around instructional practice and educational technology. It contains students, teaching, engineering education, education computing, curricula, learning systems, chatbots, computer aided instruction, university students and ethical technology, together with ChatGPT, which sits at the boundary between this cluster and the centre of the network. The presence of language model, large language model, generative AI and artificial intelligence tools within this same cluster is analytically significant: the technical vocabulary of generative systems has been absorbed into the instructional literature rather than remaining a separate technological domain. In this network, in other words, generative artificial intelligence does not constitute a technological cluster of its own.

The second cluster is defined by health-professions education. It brings together medical education, nursing education and nursing student with the biomedical index vocabulary that accompanies this literature in the source databases: human, humans, female, male, adult, psychology, procedures, questionnaire, surveys and questionnaires, reliability and human experiment. Two observations follow. Substantively, the size and cohesion of this cluster show that health-professions education constitutes a distinct and highly active subfield of generative artificial intelligence research in higher education a specialisation that is not visible in analyses restricted to author keywords and that is largely absent from the existing bibliometric literature on this topic. Methodologically, the demographic and study-design descriptors within this cluster are artefacts of biomedical indexing conventions rather than research themes in their own right and should be read as markers of that indexing tradition; the point is restated as a limitation in Section 5.

The third cluster is small but conceptually coherent and is organised around technology acceptance, comprising technology acceptance model, motivation, performance, acceptance and information-technology. Although it accounts for only a small share of the network's nodes, its separation from the two large clusters is meaningful: acceptance research forms a methodologically distinct tradition within this literature, drawing on its own theoretical vocabulary and connecting to the rest of the field mainly through the central nodes rather than through direct links to the applied clusters.

The fourth cluster is centred on artificial intelligence as a general term, which occupies a central position in the layout and mediates between the instructional cluster on one side and the health-professions cluster on the other. Here position matters more than size: the most general term in the field functions as the connective tissue

between two specialised communities that are otherwise only weakly linked to each other.

Read as a whole, the network indicates that this literature is stratified less by technological distinctions than by the disciplinary settings in which generative artificial intelligence is studied. The principal division runs between an instructional-technology tradition and a health-professions education tradition, with technology acceptance forming a smaller methodological enclave and general artificial intelligence vocabulary bridging them. This is a substantively different picture from the one produced by the author-keyword analysis reported in Section 3.8 and the relationship between the two is examined there.

3.8. Conceptual Structure of the Field

To reveal the conceptual structure of the research field, a conceptual structure mapping analysis based on keywords was conducted. The findings are presented in Figure 9.

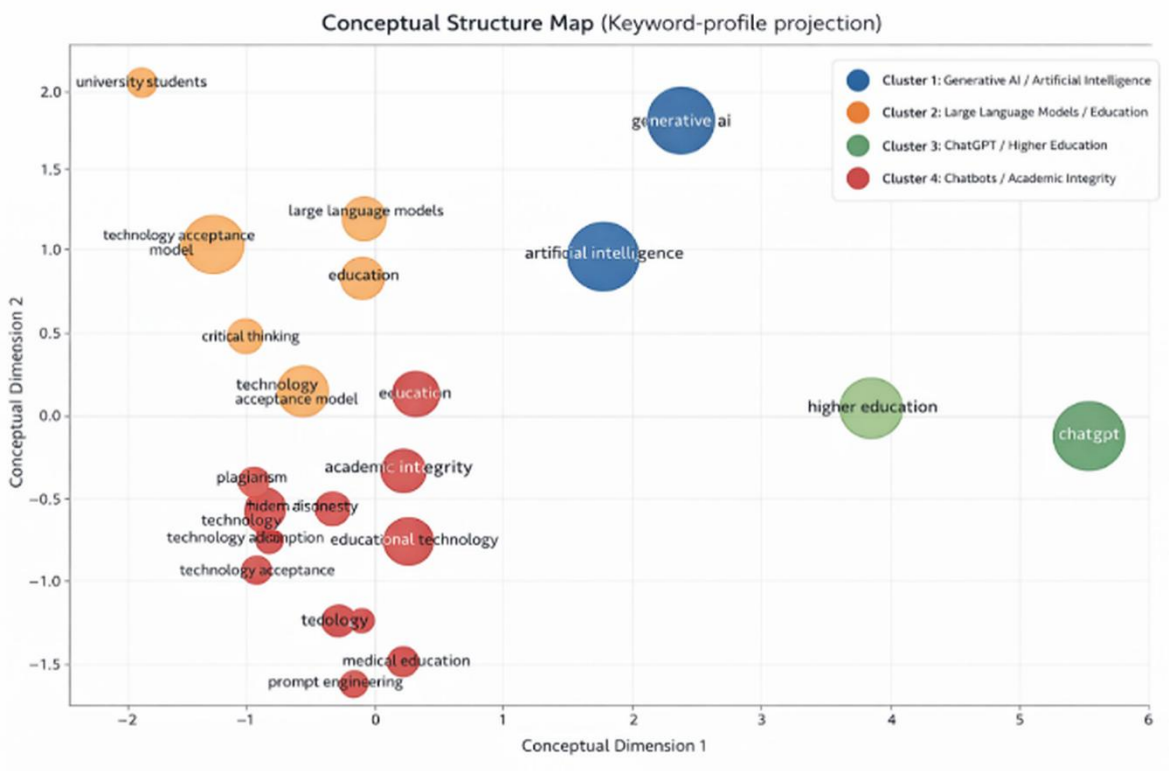


Figure 9. Conceptual structure map of the research field. Produced in Biblioshiny by multiple correspondence analysis of the 50 most frequent author keywords, with terms partitioned by k-means (k = 4) in the space defined by the first two factorial dimensions. Spatial proximity denotes similarity between keywords' co-occurrence profiles and should not be read as co-occurrence frequency. This four-cluster solution and the four-cluster solution in Figure 8 are not the same four; the two are compared in Section 3.8.

An examination of the conceptual structure map presented in Figure 9 indicates that keywords are positioned around distinct thematic clusters, reflecting the main research axes of the field. In the map, nodes represent keywords, node sizes indicate the relative importance of these concepts in the literature and spatial proximity reflects conceptual similarity and thematic relationships. The analysis reveals that the field is structured around four main thematic clusters.

The first cluster represents the technological core of the field. Within this cluster, concepts such as generative AI and artificial intelligence occupy central positions and exhibit strong connections with terms such as large language models. This suggests that the research field is largely shaped by the development and technical infrastructure of generative artificial intelligence technologies.

The second cluster focuses on the applications of generative artificial intelligence in educational contexts. In this cluster, concepts such as education, higher education, ChatGPT and chatbots are prominent. This thematic structure indicates that research on the integration of artificial intelligence tools into teaching processes and their use in educational environments occupies an important place in the literature.

The third cluster is organized around ethics, assessment and academic integrity. It includes concepts such as academic integrity, plagiarism, ethics, student assessment and technology adoption. These findings demonstrate that ethical debates and transformations in assessment processes associated with the use of generative artificial intelligence in education have become significant research foci in the literature.

The fourth cluster focuses on pedagogical approaches

and learning processes. In this cluster, concepts such as teacher education, engineering education, critical thinking, education and the technology acceptance model are prominent. This thematic area represents studies examining the effects of AI-supported learning environments on teaching methods and learning outcomes.

Overall, the conceptual structure map indicates that research on generative artificial intelligence is organized around four main axes: (i) technological development, (ii) educational applications, (iii) ethics and assessment processes and (iv) pedagogical transformation. This multilayered structure clearly demonstrates the interdisciplinary nature of the field and the strong interaction between technological innovations and educational practices.

The four clusters obtained in Figure 9 are not the same four obtained in Figure 8 and the comparison between them is one of the more informative results of this study. As explained in Section 2.8, the two figures are produced by different algorithms operating on deliberately different inputs. Figure 8, built on indexed vocabulary, divides the field by disciplinary setting: instructional technology, health-professions education, technology acceptance and a general artificial intelligence core. Figure 9, built on harmonised author keywords, divides it by conceptual concern: technological development, educational application, ethics and assessment and pedagogical transformation. The two views are complementary rather than competing. The first shows where this research is being conducted, the second what it is about; reporting only one of them would have produced a partial map. It is notable, for instance, that the ethics and assessment dimension is clearly visible in the author-keyword solution but does not form a separate cluster in the indexed solution, which suggests that academic integrity is a concern authors foreground in their own terms before database indexing has caught up with it. Conversely, the health-professions education cluster is prominent in the indexed solution yet invisible in the author-keyword solution. Triangulating the two procedures is what makes both observations available and this is the principal methodological reason for having run them in parallel.

3.9. Thematic Structure of the Literature

To examine the centrality and density levels of themes in the research field, a thematic map analysis was conducted. The results are presented in Figure 10.

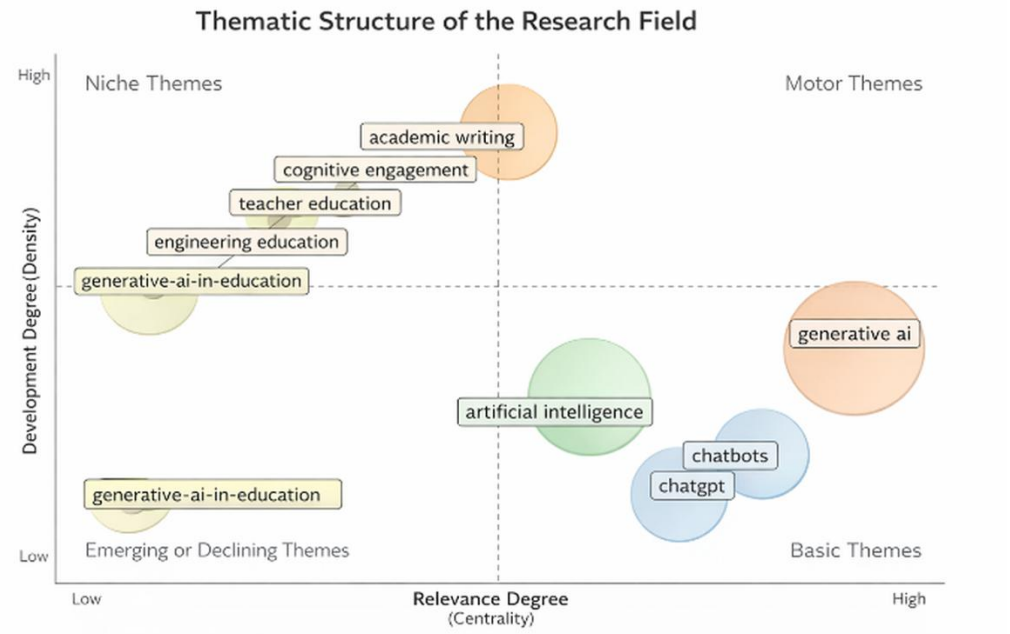


Figure 10. Strategic (thematic) map of generative artificial intelligence research in higher education. Produced in Biblioshiny from author keywords (250 terms; minimum cluster frequency of 5 per thousand documents; Louvain clustering). The horizontal axis represents centrality (relevance degree) and the vertical axis density (development degree), each computed as defined in Section 2.7 and split at the median of the observed cluster values. Bubble size is proportional to the number of keyword occurrences within the cluster. Cluster labels have been repositioned to avoid overlap; each theme occupies exactly one quadrant.

An examination of the thematic map presented in Figure 10 shows that the themes in the research field are positioned within four main categories: motor themes (high centrality–high density), basic themes (high centrality–low density), niche themes (low centrality–high density) and emerging/declining themes (low centrality–low density). This classification reveals both the significance of themes within the field and their level of conceptual maturity. The findings indicate that the theme of generative AI is positioned within the motor themes category. This theme exhibits both high centrality and high density, suggesting that it plays a decisive and

guiding role in the development of the research field. This demonstrates that generative artificial intelligence is both extensively studied and strongly connected with other themes in the literature. Within the basic themes category, concepts such as artificial intelligence, ChatGPT and chatbots are prominent. While these themes constitute the conceptual backbone of the field, they have not yet reached the same level of density as motor themes. This suggests that, although they are connected to a broad research network, they are still in the process of developing greater conceptual depth.

Among the niche themes, concepts such as academic writing, cognitive engagement, teacher education and engineering education stand out. Despite their high density, their low centrality indicates that they represent more specialized topics within specific subfields. This suggests that these themes have been studied in depth but maintain relatively limited interaction with the broader research network. In the category of emerging or declining themes, the theme of generative AI in education is identified. With low centrality and density, this theme represents a research area that is either in an early stage of development or addressed by a limited number of studies. However, considering the overall development trend of the field, this theme has the potential to evolve into a more central position in the future. One point of presentation requires clarification. In the strategic map, 'generative-ai-in-education' constitutes a single cluster with a single pair of centrality and density coordinates. Where its label appears more than once in the plotted output, this is a label-placement artefact of the plotting routine, which draws cluster labels with leader lines and may repeat a label, or position it outside the quadrant containing its bubble, when labels would otherwise overlap. The theme is nevertheless classified in a single quadrant emerging or declining on the basis of its centrality and density values relative to the medians defined in Section 2.7. Substantively, the coordinates of this theme place it close to both medians, which is itself informative: 'generative AI in education' is a theme in transition rather than a settled one. Given that two-thirds of the corpus was published in the final year of the window, the low-centrality, low-density quadrant should be read here as emerging rather than declining. Overall, the thematic structure analysis indicates that the research field is undergoing a dynamic and multilayered development process. Themes centered on generative artificial intelligence play a dominant and guiding role in the literature, while themes related to education, pedagogical applications and ethical dimensions are represented at varying levels of development.

3.10. Evolution of Research Themes

To reveal the transformation of themes and their developmental dynamics over time in the research field, a thematic evolution analysis was conducted. The results are presented in Figure 11.

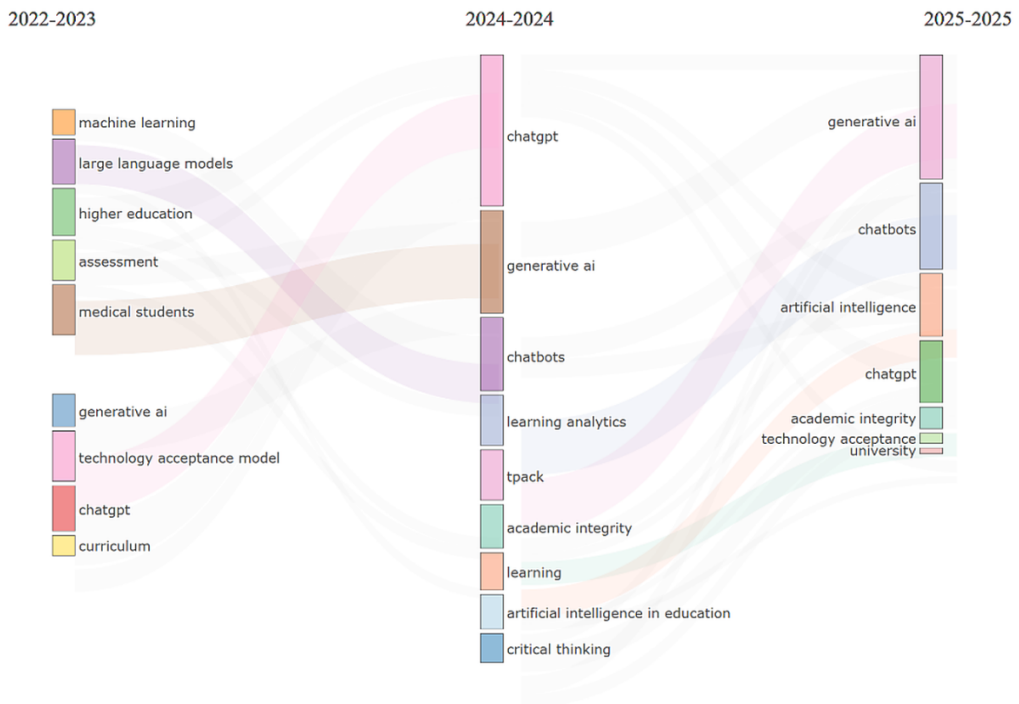


Figure 11. Thematic evolution of generative artificial intelligence research in higher education. Produced in Biblioshiny from author keywords using the parameters reported in Table 2, with cutting points at 2023 and 2024, yielding three periods (2022–2023, 2024 and 2025). Each column lists the themes identified within that period, labelled by the most frequent term in the cluster; bands link themes across adjacent periods by the inclusion index weighted by word occurrences and band width is proportional to that index. Block height is proportional to the weight of the theme within its period.

An examination of Figure 11 shows that the thematic structure of the field has changed substantially across the three periods and that the change follows a definite sequence rather than a simple accumulation of topics.

In the first period (2022–2023) the structure is fragmented and no theme dominates. Nine themes of broadly comparable weight are present, spanning three distinct concerns: a technical vocabulary (machine learning, large language models), the educational settings in which the technology was being examined (higher education, curriculum, medical students) and early evaluative and adoption concerns (assessment, technology acceptance model). ChatGPT and generative AI are already present but are no larger than the themes around them. This is the profile of a field still establishing what its object of study is.

In 2024 the structure consolidates sharply. ChatGPT becomes the largest theme by a clear margin, with generative AI second and the dispersion of the first period gives way to concentration around these two. The same period introduces themes that were absent earlier: academic integrity, learning analytics, TPACK, critical thinking and artificial intelligence in education. The combination is characteristic of a consolidation phase, in which a dominant object of study emerges and specialised research programmes begin to form around it.

In 2025 the dominant theme changes. Generative AI overtakes ChatGPT to become the largest theme, ChatGPT itself contracts and both chatbots and artificial intelligence grow. Academic integrity persists from the previous period, while technology acceptance and university appear as separate themes. The single most substantial flow in the whole diagram runs from ChatGPT in 2024 to generative AI in 2025.

That flow is the analytically significant feature of Figure 11 and it repays careful reading. It does not represent the replacement of one subject by another, since the two themes share much of their underlying vocabulary; it represents a change in how the field names its object. Researchers who described what they studied as ChatGPT in 2024 increasingly describe it as generative AI in 2025 a shift from a product to a category. This is a maturation signal rather than a terminological accident. A field that names its object after the tool it happens to use is tied to the fortunes of that tool, whereas one that names it by category can accumulate findings across successive tools. The persistence of academic integrity across the final two periods points the same way: a normative concern that has stabilised rather than passed. Overall, the thematic evolution analysis describes a field that moved from fragmentation in 2022–2023, through consolidation around a single product in 2024, to consolidation around a category in 2025, while developing a durable normative concern with academic integrity alongside its technical and pedagogical themes.

4. Discussion

The bibliometric analysis conducted in this study provides a comprehensive perspective on the scientific production trends, intellectual structure and thematic development of generative artificial intelligence research in higher education. This section is organised thematically and each subsection follows the same three-step structure: the finding obtained in this study is stated first, its analytical interpretation is developed second and the result is then compared with the existing literature in order to identify points of agreement, extension and divergence.

4.1. Growth Dynamics and the Age Structure of the Field

The production analysis established that output rose from 5 documents in 2022 to 2,001 in 2025, a 400-fold expansion in which 66.9% of the corpus appeared in the final year, while the annual growth rate fell successively from 3,900% to 293.0% and then to 154.6%. The combination of these two patterns continuing steep expansion in volume alongside a clear deceleration in rate is the analytically important result and it is one that raw publication counts obscure.

Interpreted structurally, this pattern indicates that the field has passed through its explosive entry phase and is now consolidating onto a steep but decelerating growth path. It also fixes the age structure of the literature: with 93.1% of documents published in the final two years, the great majority of this research has not yet been cited, replicated or contested. The practical consequence is that the present analysis maps an active research front rather than a settled knowledge base and that any claim about what the field has established, as distinct from what it is currently investigating, must be made with corresponding caution.

Read against the literature, the acceleration itself is consistent with earlier accounts. Kasneci et al. (2023) and Tlili et al. (2023) documented the abrupt redirection of educational technology research following the release of ChatGPT and Akpan et al. (2025) reported that 96% of the scientific output on conversational and generative artificial intelligence appeared between 2019 and 2023. The present findings extend these accounts in two respects. They demonstrate that the acceleration continued well beyond the windows those studies could observe and, more importantly, they show that the growth rate has begun to fall a transition that earlier maps, terminating in 2023 or 2024, were not positioned to detect.

4.2. Geographical Distribution and the Collaboration Deficit

The geographical analysis showed production concentrated in China (n = 890), the United States (n = 617) and Australia (n = 401), with substantial contributions from Indonesia, Malaysia, Saudi Arabia, Jordan and South Africa. Alongside this, however, the corpus records an international co-authorship rate of 10.11% against a collaboration index of 2.83 and only

17.1% single-authored documents.

The interpretation of these figures turns on reading them jointly. Co-authorship is clearly the norm in this field, but it is overwhelmingly domestic: roughly nine in ten collaborative papers are produced within a single national system. This constitutes a substantive limitation on what the field can currently establish. The questions that dominate the literature assessment security, academic integrity policy, equity of access, disciplinary norms of permissible use are institutionally and nationally contingent and answering them requires precisely the cross-system comparison that current collaboration patterns do not support. The prominence of China, the United States and Australia is plausibly attributable to research infrastructure, technological investment and digital transformation policy in higher education (Coulter-Smith, 2022; Kavitha et al., 2024; Nugroho, 2024), while the visible contribution of Indonesia, Malaysia, Saudi Arabia, Jordan and South Africa indicates that the field is not the preserve of a small group of developed systems (Dai et al., 2026).

Compared with the literature, this finding both confirms and qualifies earlier work. Zawacki-Richter et al. (2019) observed that artificial intelligence research in higher education concentrates in countries with strong research infrastructures and Metli (2023) and Ng and Ho (2025) report similarly uneven distributions. Akpan et al. (2025), however, characterised the intellectual structure of conversational and generative artificial intelligence research as exhibiting strong collaboration. The present analysis suggests that this characterisation requires refinement when the field is narrowed to higher education: collaboration is indeed strong, but it is national rather than international and the distinction is consequential for the kinds of knowledge the field is able to produce.

4.3. The Position of Türkiye in the Field

The country-level analysis placed Türkiye in the corpus with 96 publications, in the same output band as the United Arab Emirates, Peru, Hong Kong and South Africa, but below Saudi Arabia (n = 208), Indonesia (n = 186), Malaysia (n = 164), Taiwan (n = 144), India (n = 139), Jordan (n = 135) and Germany (n = 153).

Two interpretations of this position must be distinguished. The first is substantive: measured against regional peers with higher education systems of comparable or smaller scale, Turkish output in this specific area is lower than the size of the system would lead one to expect and the shortfall lies with those peers rather than with the global leaders. The second is methodological and works in the opposite direction. A substantial part of Turkish scholarship on generative artificial intelligence in higher education is published in Turkish, in nationally indexed journals that fall outside the Web of Science and Scopus coverage applied here and outside the English-language restriction. The figure of 96 is therefore a lower bound on Turkish activity in this area rather than a complete measure of it and the same qualification applies to every non-Anglophone system in the dataset.

The national literature supports this reading. Metli (2023) and Tonbuloğlu and Avcı Akbel (2023) demonstrate an established Turkish bibliometric tradition at the intersection of educational technology and artificial intelligence and Büyükeke (2025) reports empirical evidence from 305 Turkish undergraduates showing that perceived usefulness and perceived ease of use predict intention to use generative artificial intelligence tools in programming courses, with perceived trust operating on both antecedents. The theoretical significance of that finding for the present analysis is that technology acceptance appears in the conceptual structure map (Figure 9) as a component of the pedagogical-transformation cluster and the Turkish evidence indicates that the mechanism operates in a non-Anglophone system in substantially the same way. This is precisely the kind of cross-system corroboration that the field's low international co-authorship rate currently leaves underexploited.

4.4. Citation Structure and the First-Mover Effect

The citation analysis established that the ten most-cited documents account for 8.75% of all citations generated by the corpus and the three most-cited for 5.4%, from 0.33% and 0.10% of documents respectively.

This concentration is best interpreted as a first-mover effect rather than as a settled quality signal. All three leading documents were published in 2023 or earlier and address academic integrity or the broad pedagogical implications of ChatGPT; in a corpus where two-thirds of the literature appeared in 2025, early publication confers a decisive and largely mechanical citation advantage. Moreover, the works that appeared first were framing and agenda-setting pieces rather than empirical investigations, which means the field's citation structure currently rewards early problem definition rather than accumulated evidence.

This reading is consistent with the content of the most-cited works themselves. Kasneci et al. (2023) set out the opportunities and challenges of large language models for education as a programmatic agenda and Cotton et al. (2024) argued that generative artificial intelligence in academic writing generates both learning opportunities and integrity risks. Both are framing contributions and both were early. The implication for readers of bibliometric maps of this field is that the highly cited core should be read as evidence of what the field first agreed to worry about, not as evidence of where its most robust findings now lie.

4.5. Intellectual and Conceptual Structure

The co-occurrence network built on indexed vocabulary returned four clusters organised by disciplinary setting instructional technology, health-professions education, technology acceptance and a general artificial intelligence core while correspondence analysis on harmonised author keywords returned four clusters organised by conceptual concern: technological

development, educational application, ethics and assessment and pedagogical transformation.

The substantive interpretation is that these two solutions describe different cross-sections of the same field rather than competing accounts of it. Read together, they show that the literature is stratified along two axes at once: by the disciplinary setting in which the research is conducted and by the conceptual concern that motivates it. The most consequential finding to emerge from the comparison is the prominence of health-professions education in the indexed solution, which suggests that a substantial and coherent body of work on generative artificial intelligence in medical and nursing education has developed with its own vocabulary and its own indexing footprint and which existing bibliometric reviews of this field have not reported. That this subfield is invisible in the author-keyword solution is itself instructive: it is identifiable through how the literature is classified rather than through how its authors describe it.

The three-axis architecture is itself consistent with the wider literature. Zawacki-Richter et al. (2019) identified a comparable structure at the intersection of artificial intelligence and education and Dúo-Terrón (2024), Ng and Ho (2025) and Guo et al. (2026) report similar technological, applied and ethical groupings. The contribution of the present analysis is not the discovery of this architecture but its verification: because the parameters of both analyses are reported in Table 2, the structure can be reproduced, tested at other thresholds and compared against future corpora.

4.6. Thematic Structure and Thematic Evolution

The strategic map located generative AI as the sole motor theme; artificial intelligence, ChatGPT and chatbots as basic themes; academic writing, cognitive engagement, teacher education and engineering education as niche themes; and generative AI in education in the emerging or declining quadrant. The evolution analysis traced a movement from a fragmented set of technical, contextual and adoption themes in 2022–2023, through consolidation around ChatGPT in 2024, to the ascendancy of generative AI as the dominant theme in 2025, with academic integrity establishing itself as a durable concern across the final two periods.

Interpreted together, these results describe a field whose centre of gravity has shifted from asking what these technologies are to asking what they do to educational practice and to its normative order. The appearance of academic writing, cognitive engagement and teacher education as high-density but low-centrality themes indicates that specialised research communities have formed around them, but that these communities remain weakly connected to the core of the field. The presence of only one theme in the motor quadrant is equally notable: it suggests that the field's integrative capacity is currently concentrated in a single concept.

Against the literature, this trajectory is well corroborated. Bozkurt (2023) and Tlili et al. (2023) documented the early movement of educational research from technological description towards pedagogical and ethical analysis; Plata et al. (2023) and Bittle and El-Gayar (2025) traced the emergence of academic integrity as a distinct research and policy theme; and Ng and Ho (2025) reported comparable thematic diversification. The present analysis adds temporal precision to these accounts by locating the transition within specific time slices and by reporting the parameters under which the thematic partition was obtained.

4.7. A Critical Reading: Three Structural Risks

Taken together, the findings support a more critical reading of this field than descriptive maps typically offer and three structural risks warrant explicit statement.

The first is ChatGPT-centrism. ChatGPT occupies a central position in every analysis reported here, appearing as a basic theme, as a dominant node in the co-occurrence network and as a defining term in the conceptual structure. A field whose conceptual architecture is organised around a single commercial product is exposed to a specific form of obsolescence: findings framed in terms of a particular tool do not straightforwardly transfer when that tool is superseded. The corresponding research implication is that studies should be designed around transferable constructs the pedagogical function performed, the cognitive process affected, the integrity risk incurred rather than around the current market leader.

The second is the collaboration deficit documented in Section 4.2. An international co-authorship rate of 10.11% in a field whose central questions are institutionally contingent implies a real risk of parallel national literatures converging on similar findings independently, without the comparative design that would make those findings cumulative.

The third is early thematic saturation. The evidence for this is structural rather than impressionistic: a single theme occupies the motor quadrant; the basic quadrant contains the field's most frequent and most general terms; and the niche quadrant holds several well-developed but poorly connected themes. This configuration a broad, shallow core surrounded by disconnected specialised pockets combined with a strongly right-skewed author distribution in which no dominant research school has formed, is consistent with a field producing a high volume of thematically similar work rather than a deepening cumulative programme. The very flat author productivity distribution reported in Section 3.3 reinforces this reading, since a literature built largely from single contributions is less likely to develop sustained lines of inquiry.

These three risks are not arguments against research on generative artificial intelligence in higher education. They are arguments about how the next phase of it should be designed: around transferable constructs rather than named tools, across national systems rather than within them and towards the consolidation of existing themes rather than the continued proliferation of new ones.

5. Limitations

The findings of this study should be read in the light of several limitations, which fall into three groups: limitations of corpus coverage, limitations of the analytical procedure and limitations inherent to bibliometric inference.

Coverage. The corpus was constructed exclusively from the Web of Science Core Collection and Scopus. Although these are the two most widely used citation databases and their combination provides broader coverage than either alone, other sources were not searched, including ERIC, Dimensions, Lens, Google Scholar, regional indexes and national indexes such as TR Dizin. Education-specific and regionally indexed outlets are therefore systematically under-represented. Second, only English-language publications were included, which excludes a substantial body of non-Anglophone scholarship; as noted in Section 4.3, country-level counts for non-Anglophone systems, including the figure of 96 reported for Türkiye, should accordingly be treated as lower bounds rather than complete measures. Third, only articles and reviews were included. This excludes conference proceedings, which are a primary publication venue in computer science and therefore carry a meaningful share of early technical work on large language models, as well as book chapters, editorials and preprint servers such as arXiv. Fourth, although the rationale for the search vocabulary is set out in Section 2.3, records that name only a specific model Gemini, Claude, Llama, Copilot or DeepSeek without employing any umbrella term would not have been retrieved; a model-name-inclusive sensitivity search is recommended for future replications. Fifth, the search was executed on 10 March 2026 and the window closes at 2025, so publications from 2025 indexed after that date are absent and the 2025 count is a lower bound.

Procedure. As set out in Section 2.4, eligibility was enforced through the search query and the database filters rather than through a manual title-and-abstract screening stage. This maximises reproducibility, but it means that precision was not improved by human judgement: records in which a university appears only as an author affiliation and records in which generative artificial intelligence is mentioned only incidentally, remain in the corpus and will have contributed to the keyword and citation distributions reported here. As a single-authored study, all design decisions were made by one researcher and no inter-rater reliability coefficient is applicable. Author disambiguation, institutional attribution and keyword indexing rely on the metadata supplied by the source databases, so homonymous author names, name variants and inconsistent affiliation strings may affect the productivity rankings. Country production was computed by full counting on author affiliations, meaning that a document authored across several countries contributes one unit to each; country counts therefore exceed the document total and must not be summed. A further constraint applies specifically to Figure 8. Because that network deliberately retains database index keywords, demographic and study-design descriptors such as human, female, adult, article and questionnaire appear as network nodes although they are indexing conventions rather than research themes and variant forms of the same term artificial intelligence and artificial-intelligence, student and students, human and humans appear as separate nodes. This is inherent to index-term analysis and constrains the resolution obtainable from that figure; it does not affect the author-keyword analyses reported in Figures 9 to 11, to which the harmonisation protocol of Section 2.5 was applied in full. Finally, the conceptual and thematic solutions are conditional on the parameters reported in Table 2 the data field, the occurrence thresholds, the normalisation and the clustering algorithm and alternative settings may yield partitions that differ in number or composition. These parameters are reported in full precisely so that such sensitivity can be tested by others.

Inference. Bibliometric analysis describes the publication, citation and vocabulary behaviour of a literature; it does not assess the methodological quality, validity or practical effect of the studies it maps. High citation counts index visibility rather than rigour and in a corpus of this age structure they index publication date to a considerable degree, as Section 4.4 demonstrates. Similarly, thematic centrality and density measure the position of a term within a keyword network, not the importance of the underlying educational phenomenon. The map presented here should therefore be understood as a description of how this research field is currently organised and not as an evaluation of what it has established.

6. Conclusion

This study mapped the scientific production structure, intellectual and conceptual organisation and thematic evolution of generative artificial intelligence research in higher education, using a dual-database corpus of 2,992 publications and reporting the full analytical parameters of every procedure applied.

Four conclusions follow. First, the field is expanding steeply but at a decelerating rate and its age structure with 93.1% of documents published in the final two years means that it currently constitutes an active research front rather than a consolidated knowledge base. Second, the field is stratified along two axes simultaneously: by disciplinary setting, where the indexed vocabulary separates an instructional-technology tradition from a substantial and previously unreported health-professions education tradition and by conceptual concern, where author keywords separate technological, educational-application, ethical-assessment and pedagogical dimensions. Neither view is reducible to the other and recovering both is what triangulating two independent clustering procedures makes possible. Third, generative AI is the field's single motor theme and its thematic trajectory runs from technological

exploration towards pedagogical integration and academic integrity. Fourth, the field exhibits three structural risks ChatGPT-centrism, an international co-authorship rate of only 10.11% and early indications of thematic saturation that its rapid growth has tended to conceal.

The theoretical contribution of the study lies in demonstrating that generative artificial intelligence research in higher education is not a technological literature with pedagogical applications appended, but an interdisciplinary domain in which technological, pedagogical and normative concerns are structurally co-constitutive; both clustering procedures recover the normative dimension as an independent axis rather than as a subsidiary theme. Its methodological contribution is a reproducible protocol: the parameters in Table 2 allow every result reported here to be re-derived, tested at alternative thresholds, or extended to subsequent time windows.

For higher education institutions, the findings indicate that policy on generative artificial intelligence cannot be confined to detection and prohibition, since the literature has already moved towards integration, assessment redesign and instructor development. Institutional strategy should accordingly address academic integrity policy, assessment security and professional development jointly rather than sequentially.

For future research, three directions follow directly from the structural risks identified. Studies should be designed around transferable pedagogical and cognitive constructs rather than around named commercial tools; cross-national comparative designs are needed to convert parallel national literatures into cumulative evidence; and longitudinal work is required to establish the long-term effects of these tools on critical thinking, creativity and academic productivity, which the field's current age structure makes it impossible to assess. Replications extending the corpus to conference proceedings, to non-English publications and to model-name-inclusive search vocabularies would additionally test the boundaries of the map presented here.

Author Contributions

The percentages of the author' contributions are presented below. The author reviewed and approved the final version of the manuscript.

	Ş.B.
C	100
D	100
S	100
DCP	100
DAI	100
L	100
W	100
CR	100
SR	100
PM	100
FA	100

C= concept, D= design, S= supervision, DCP= data collection and/or processing, DAI= data analysis and/or interpretation, L= literature search, W= writing, CR= critical review, SR= submission and revision, PM= project management, FA= funding acquisition.

Conflict of Interest

The author declared that there is no conflict of interest.

Ethical Consideration

This study is grounded in a bibliometric examination of previously published scholarly works. It does not involve the collection of data from human participants, nor does it utilize personal data or pose any ethical concerns. Accordingly, obtaining ethical approval was deemed unnecessary for the conduct of this research.

Acknowledgements

The author would like to thank the developers of the Web of Science Core Collection and Scopus databases for providing access to high-quality bibliographic data used in this study. No additional acknowledgments are declared.

Data Availability Statement

The bibliographic records analysed in this study were retrieved from the Web of Science Core Collection and Scopus, which are subscription-based databases; the underlying records are therefore available to any researcher with institutional access, using the search queries, filters and retrieval date reported in Section 2.3. The merged and cleaned dataset, the VOSviewer thesaurus file and the analysis scripts are available from the corresponding author on reasonable request.

References

Akpan, I. J., Kobara, Y. M., Owolabi, J., Akpan, A. A., & Offodile, O. F. (2025). Conversational and generative artificial intelligence and human–chatbot interaction in education and research. *International Transactions in Operational Research, 32*(3), 1251–1281. https://doi.org/10.1111/itor.13522

Aria, M., & Cuccurullo, C. (2017). bibliometrix: An R-tool for

comprehensive science mapping analysis. *Journal of Informetrics, 11*(4), 959–975. https://doi.org/10.1016/j.joi.2017.08.007

Baek, C., & Doleck, T. (2020). A bibliometric analysis of the papers published in the *Journal of Artificial Intelligence in Education* from 2015–2019. *International Journal of Learning Analytics and Artificial Intelligence for Education*, 2(1), 67–84. https://doi.org/10.3991/ijai.v2i1.14481

Bittle, K., & El-Gayar, O. (2025). Generative AI and academic integrity in higher education: A systematic review and research agenda. *Information*, 16(4), 296. https://doi.org/10.3390/info16040296

Blondel, V. D., Guillaume, J.-L., Lambiotte, R., & Lefebvre, E. (2008). Fast unfolding of communities in large networks. Journal of Statistical Mechanics: Theory and Experiment, 2008(10), P10008. https://doi.org/10.1088/1742-5468/2008/10/P10008

Bozkurt, A. (2023). Unleashing the potential of generative AI, conversational agents and chatbots in educational praxis: A systematic review and bibliometric analysis of GenAI in education. *Open Praxis, 15*(4), 261–270. https://doi.org/10.55982/openpraxis.15.4.609

Büyükeke, A. (2025). Öğrencilerin programlama derslerinde üretken yapay zekâ araçlarını kabulü: Genişletilmiş teknoloji kabul modeli ile Türkiye'den bulgular [Students' acceptance of generative artificial intelligence tools in programming courses: Findings from Türkiye with an extended technology acceptance model]. *Journal of University Research, 8*(4), 543–556. https://doi.org/10.32329/uad.1728785

Callon, M., Courtial, J. P., & Laville, F. (1991). Co-word analysis as a tool for describing the network of interactions between basic and technological research: The case of polymer chemistry. *Scientometrics, 22*(1), 155–205. https://doi.org/10.1007/BF02019280

Chiu, T. K. F. (2024). Future research recommendations for transforming higher education with generative AI. *Computers and Education: Artificial Intelligence*, 6, 100197. https://doi.org/10.1016/j.caeai.2023.100197

Cobo, M. J., López-Herrera, A. G., Herrera-Viedma, E., & Herrera, F. (2011). An approach for detecting, quantifying and visualizing the evolution of a research field: A practical application to the Fuzzy Sets Theory field. *Journal of Informetrics, 5*(1), 146–166. https://doi.org/10.1016/j.joi.2010.10.002

Cotton, D. R. E., Cotton, P. A., & Shipway, J. R. (2024). Chatting and cheating: Ensuring academic integrity in the era of ChatGPT. *Innovations in Education and Teaching International, 61*(2), 228–239. https://doi.org/10.1080/14703297.2023.2190148

Coulter-Smith, L. (2022). The AI economy and higher education. In A. Kaplan (Ed.), Digital transformation and disruption of higher education (Chapter 29). Cambridge University Press. https://doi.org/10.1017/9781108979146.037

Dai, K., Liu, Y., & Zhang, X. (2026). Generative AI in higher education: A bibliometric review of emerging trends, power dynamics and global research landscapes. *Computers and Education: Artificial Intelligence, 10, 100544.* https://doi.org/10.1016/j.caeai.2026.100544

Donthu, N., Kumar, S., Mukherjee, D., Pandey, N., & Lim, W. M. (2021). How to conduct a bibliometric analysis: An overview and guidelines. *Journal of Business Research, 133*, 285–296. https://doi.org/10.1016/j.jbusres.2021.04.070

Dúo-Terrón, P. (2024). Generative artificial intelligence: Educational reflections from an analysis of scientific production. *Journal of Technology and Science Education, 14*(3), 756–769. https://doi.org/10.3926/jotse.2680

Flores-Velásquez, C. H., Olivares-Zegarra, S., Dávila-Ignacio, C., Arévalo-Tuesta, J. A., Morales-Romero, G., Trinidad-Loli, N., Caycho-Salas, B., Aybar-Bellido, I., Arones, M., & Aldana-Trejo, F. (2024). A bibliometric review of studies about the acceptance of artificial intelligence technologies in teaching and learning in higher education. *International Journal of Learning, Teaching and Educational Research, 23*(3), 275–292. https://doi.org/10.26803/ijlter.23.3.14

Francis, N. J., Jones, S., & Smith, D. P. (2025). Generative AI in higher education: Balancing innovation and integrity. *British Journal of Biomedical Science*, 81, 14048. https://doi.org/10.3389/bjbs.2024.14048

Guo, J., Kang, E. K. M. S., & Ghazali, N. (2026). Generative artificial intelligence in education from 2021 to 2025: A scientometric review. *Journal of Curriculum and Teaching, 15*(1), 102–118. https://doi.org/10.5430/jct.v15n1p102

Kasneci, E., Sessler, K., Küchemann, S., Bannert, M., Dementieva, D., Fischer, F., Gasser, U., Groh, G., Günnemann, S., Hüllermeier, E., Krusche, S., Kutyniok, G., Michaeli, T., Nerdel, C., Pfeffer, J., Poquet, O., Sailer, M., Schmidt, A., Seidel, T., … Kasneci, G. (2023). ChatGPT for good? On opportunities and challenges of large language models for education. *Learning and Individual Differences*, 103, 102274. https://doi.org/10.1016/j.lindif.2023.102274

Kavitha, K., Joshith, V. P., Rajeev, N. P., & Asha, S. (2024). Artificial intelligence in higher education: A bibliometric approach. *European Journal of Educational Research, 13*(3), 1121–1137. https://doi.org/10.12973/eu-jer.13.3.1121

Lodge, J. M., Thompson, K., & Corrin, L. (2023). Mapping out a research agenda for generative artificial intelligence in tertiary education. *Australasian Journal of Educational Technology*, 39(1), 1–8. https://doi.org/10.14742/ajet.8695

Metli, A. (2023). Articles on education and artificial intelligence: A bibliometric analysis. Journal of Social Sciences and Education, 6(Education Special Issue), 279–312. https://doi.org/10.53047/josse.1352197

Muskhir, M., Luthfi, A., Watrianthos, R., Usmeldi, U., Fortuna, A., & Samala, A. D. (2024). Emerging research on virtual reality applications in vocational education: A bibliometric analysis. *Journal of Information Technology Education: Innovations in Practice*, 23, 1–26. https://doi.org/10.28945/5284

Ng, S.-L., & Ho, C.-C. (2025). Generative AI in education: Mapping the research landscape through bibliometric analysis. *Information, 16*(8), 657. https://doi.org/10.3390/info16080657

Nugroho, L. A. (2024). Exploring research trends of ChatGPT in education through bibliometric analysis. *Scholaria: Jurnal Pendidikan dan Kebudayaan, 14*(2), 98–106. https://doi.org/10.24246/j.js.2024.v14.i2.p98-106

Page, M. J., McKenzie, J. E., Bossuyt, P. M., Boutron, I., Hoffmann, T. C., Mulrow, C. D., Shamseer, L., Tetzlaff, J. M., Akl, E. A., Brennan, S. E., Chou, R., Glanville, J., Grimshaw, J. M., Hróbjartsson, A., Lalu, M. M., Li, T., Loder, E. W., Mayo-Wilson, E., McDonald, S., … Moher, D. (2021). The PRISMA 2020 statement: An updated guideline for reporting systematic reviews. *BMJ, 372*, n71. https://doi.org/10.1136/bmj.n71

Plata, S., De Guzman, M. A., & Quesada, A. (2023). Emerging research and policy themes on academic integrity in the age of ChatGPT and generative AI. *Asian Journal of University Education*, 19(4), 743–758. https://doi.org/10.24191/ajue.v19i4.24697

Prayuda, M. S., Ginting, F. Y. A., & Tamba, L. (2026). Tracing two decades of artificial intelligence in education: A bibliometric analysis of trends, themes and future directions (2000–

2025). *European Journal of Educational Research*, 15(1), 285–304. https://doi.org/10.12973/eu-jer.15.1.285

Samala, A. D., Rawas, S., Wang, T., Reed, J. M., Kim, J., Howard, N.-J., & Ertz, M. (2025). Unveiling the landscape of generative artificial intelligence in education: A comprehensive taxonomy of applications, challenges and future prospects. *Education and Information Technologies, 30(3), 3239–3278.* https://doi.org/10.1007/s10639-024-12936-0

Tlili, A., Shehata, B., Adarkwah, M. A., Bozkurt, A., Hickey, D. T., Huang, R., & Agyemang, B. (2023). What if the devil is my guardian angel: ChatGPT as a case study of using chatbots in education. *Smart Learning Environments*, 10(1), 15. https://doi.org/10.1186/s40561-023-00237-x

Tonbuloğlu, B., & Avcı Akbel, B. (2023). Research trends in the field of emergency remote teaching: A bibliometric analysis of open access literature. *Online Learning*, 27(1), 485–517. https://doi.org/10.24059/olj.v27i1.3241

van Eck, N. J., & Waltman, L. (2010). Software survey: VOSviewer, a computer program for bibliometric mapping. *Scientometrics, 84*(2), 523–538. https://doi.org/10.1007/s11192-009-0146-2

Waltman, L., van Eck, N. J., & Noyons, E. C. M. (2010). A unified approach to mapping and clustering of bibliometric networks. *Journal of Informetrics, 4*(4), 629–635. https://doi.org/10.1016/j.joi.2010.07.002

Zawacki-Richter, O., Marín, V. I., Bond, M., & Gouverneur, F. (2019). Systematic review of research on artificial intelligence applications in higher education. *International Journal of Educational Technology in Higher Education*, 16, 39. https://doi.org/10.1186/s41239-019-0171-0

Zupic, I., & Čater, T. (2015). Bibliometric methods in management and organization. *Organizational Research Methods, 18*(3), 429–472. https://doi.org/10.1177/1094428114562629

Black Sea Journal of Engineering and Science
doi: 10.34248/bsengineering.1995982

Open Access Journal
e-ISSN: 2619 – 8991

Research Article
Volume 9 - Issue 5: 2718-2737 / September 2026

A3NET: A LIGHTWEIGHT ATTENTION-GUIDED ENCODER–DECODER FOR MULTI-CLASS BRAIN TUMOR SEGMENTATION WITH CROSS-DATASET DOMAIN GAP CHARACTERIZATION

Turgay BATBAT[1]*, Ezzaldeen H. A. ABUKHATTAB[2]

[1]*Erciyes University, Engineering Faculty, Department of Biomedical Engineering, Kayseri, 38039, Türkiye*
[2]*Erciyes University, Graduate School of Natural and Applied Sciences, Department of Biomedical Engineering, Kayseri, 38039, Türkiye*

Abstract: Accurate multi-class segmentation of brain tumors from T1-weighted contrast-enhanced MRI is essential for surgical planning and treatment monitoring, yet existing high-performance architectures exceed 30 M parameters, limiting deployment in resource-constrained clinical settings. This work introduces A3Net, a lightweight encoder–decoder combining depth-wise separable convolutions, squeeze-and-excitation channel attention, and summation-based skip fusion with a cross-entropy + Dice composite loss. On the cleaned BRISC 2025 benchmark (47 duplicates removed by MD5 audit) under 2-seed × 5-fold cross-validation, A3Net attains 77.79 ± 0.29% mIoU and 87.14 ± 0.17% Dice at 2.11 M parameters, 1.39 GFLOPs, and 8.15 ms latency, achieving statistical parity with Attention U-Net (P=0.334) at 15.0× lower parameter cost. A3Net achieves significant per-class advantages on meningioma (+1.54 pp IoU, P=0.007) and pituitary (+0.42 pp IoU, P=0.016), while Attention U-Net retains a significant advantage on glioma (−1.49 pp IoU, $p < 0.001$). In-domain evaluation on Figshare yields 74.66 ± 0.50% mIoU (+1.65 pp over Attention U-Net), and a supplementary probe on Akter-Seg confirms efficiency parity with Attention U-Net (83.30 ± 0.44% mIoU vs. 83.21%) at 15.0× fewer parameters across two primary and one supplementary benchmark. Zero-shot cross-dataset transfer exposes a strongly asymmetric domain gap (−12.64 pp BRISC→Figshare; −29.90 pp Figshare→BRISC); multi-source standardized training (BRISC ∪ Figshare, N = 6,655) provides a partial +3.05 pp recovery under target-inclusive training, which is a fundamentally different experimental condition from the target-blind zero-shot setting in which the −29.90 pp gap is measured; the two quantities are therefore not directly commensurable. Class-distribution mismatch, rather than intensity shift, is identified as the dominant residual barrier. Overall, A3Net offers a statistically validated, computationally efficient solution for multi-class brain tumor segmentation with demonstrated cross-dataset generalization.

Keywords: Brain tumor segmentation, MRI, Lightweight deep learning, Squeeze-and-excitation attention, Cross-dataset generalization

***Corresponding author:** Erciyes University, Engineering Faculty, Department of Biomedical Engineering, Kayseri, 38039, Türkiye
Email: turgaybatbat@erciyes.edu.tr (T. BATBAT)
Turgay BATBAT https://orcid.org/0000-0002-0128-2076
Ezzaldeen H. A. ABUKHATTAB https://orcid.org/0009-0002-3573-1316

Received: July 16, 2026
Accepted: August 24, 2026
Published: September 15, 2026

Cite as: Batbat, T., & Abukhattab, E. H. A. (2026). A3Net: A lightweight attention-guided encoder–decoder for multi-class brain tumor segmentation with cross-dataset domain gap characterization. *Black Sea Journal of Engineering and Science,* 9(5): 2718-2737.

1. Introduction

Brain tumors encompass a heterogeneous family of central nervous system malignancies; the 2021 WHO classification distinguishes glioma, meningioma, and pituitary adenoma as biologically and prognostically distinct categories (Louis et al., 2021; Ostrom et al., 2022), each requiring tailored surgical and radiotherapeutic planning. Pixel-accurate delineation of tumor boundaries on T1-weighted contrast-enhanced (T1-CE) MRI underlies treatment design, intra-operative navigation, and longitudinal response assessment, but manual segmentation by neuroradiologists is slow and prone to inter-rater variability, and automated pipelines are held back by limited generalization across acquisition protocols, restricted interpretability, and evaluation procedures that may not reflect boundary-level precision (Fahim et al., 2025; Rashid et al., 2026).

Convolutional neural networks have driven most of the recent progress in medical image segmentation since U-Net (Ronneberger et al., 2015), a fully convolutional encoder–decoder with skip connections that has become the standard backbone for biomedical tasks. Attention U-Net (Oktay et al., 2018) subsequently showed that soft spatial-attention gates improve performance on medical image segmentation, and the nnU-Net framework (Isensee et al., 2021) established a self-configuring baseline that exposed the sensitivity of reported gains to evaluation protocol choices. These reference architectures, however,

This work is licensed (CC BY-NC 4.0) under Creative Commons Attribution 4.0 International License

exceed 30 M parameters and 100 GFLOPs at 256×256 input, raising a practical barrier to deployment on edge hardware in low-resource clinical settings. The deep-learning community has answered this efficiency constraint with a body of lightweight designs: MobileNets (Howard et al., 2017) introduced depth-wise separable convolutions, EfficientNet (Tan and Le, 2019) proposed compound scaling, and dedicated real-time segmentation networks such as ENet (Paszke et al., 2016), BiSeNetV2 (Yu et al., 2021), and ESPNetv2 (Mehta et al., 2019) reached sub-2 M-parameter regimes.

In the medical-imaging domain, however, lightweight encoder–decoders remain comparatively underexplored for multi-class brain tumor segmentation: existing work either evaluates binary protocols (Fahim et al., 2025) or reports accuracy without rigorous cross-validation (Pacal and Deveci, 2026), leaving the efficiency–accuracy trade-off under controlled multi-class evaluation largely unquantified.

A second obstacle to clinical deployment is domain shift: performance degrades when training and test data differ in scanner, contrast protocol, or imaging center (Wang and Deng, 2018; Guan and Liu, 2022). Prior work addresses this primarily through adversarial adaptation or generative style transfer, both of which add architectural complexity and require access to target-domain data. We instead investigate whether per-channel intensity standardization — a simple, training-free preprocessing step — can partially bridge the gap, and systematically characterize the remaining class-distribution mismatch that preprocessing alone cannot resolve.

Despite these advances, no prior work has (i) evaluated multi-class brain tumor segmentation on BRISC 2025 under rigorous cross-validation, (ii) systematically characterized the asymmetric domain gap between BRISC 2025 and Figshare under identical evaluation conditions, or (iii) established a sub-3 M-parameter architecture matching 31 M-parameter models on this task. We design and evaluate A3Net, a lightweight attention-guided encoder–decoder for multi-class brain tumor segmentation. Our contributions are as follows.

1. We propose A3Net, a lightweight encoder–decoder that unifies depth-wise separable convolutions, SE channel recalibration, and summation-based skip fusion within a sub-3 M-parameter architecture for multi-class brain tumor segmentation — a design operating point not previously reported at this scale, yielding 77.79% mIoU with statistical parity to Attention U-Net (P=0.334) at 15.0× lower parameter cost. Architecturally, A3Net is distinct from prior lightweight segmentation networks in three specific choices: (i) depth-wise separable convolutions are combined with SE channel-only recalibration rather than the spatial attention gates used by heavier references such as Attention U-Net; (ii) skip connections use summation-based fusion rather than the concatenation adopted by U-Net variants and most MobileNet-based decoders, which halves the decoder input-channel budget while preserving gradient flow; and (iii) the SE reduction ratio and bottleneck dropout are tuned specifically for the multi-class brain tumor regime (three foreground classes with markedly different boundary characteristics), rather than transferred unmodified from ImageNet-classification settings. This particular combination has not, to our knowledge, been previously reported for multi-class brain tumor segmentation at the sub-3 M-parameter scale.

2. We conduct a systematic ablation study quantifying the contribution of each architectural and training component, including three glioma-targeted variants (SpatialGate decoder fusion, SE + SpatialOnly blocks, boundary-aware loss), a three-way activation comparison (SiLU, ReLU, GELU), and capacity scaling and dropout sensitivity analyses — confirming SiLU and channel-only SE as optimal design choices and establishing 2.11 M parameters with P=0.3 bottleneck dropout as the efficiency optimum on BRISC 2025.

3. We provide the first systematic quantification of the cross-dataset domain gap between BRISC 2025 and Figshare under identical multi-class evaluation, revealing a strongly asymmetric gap (−12.64 pp BRISC→Figshare; −29.90 pp Figshare→BRISC). Mechanistic analysis identifies class-distribution mismatch — not intensity shift — as the dominant driver; per-channel standardization under multi-source training yields only a partial +3.05 pp recovery, measured under a target-inclusive condition that is not directly commensurable with the target-blind zero-shot gap. This finding motivates class-aware domain adaptation as future work and distinguishes our analysis from prior work reporting only aggregate transfer accuracy.

1.1. Related Work

1.1.1. Brain tumor segmentation

The BraTS benchmark (Menze et al., 2015; Bakas et al., 2018) established multi-modal MRI segmentation as the standard evaluation framework for high-grade gliomas; however, the majority of competing methods were designed for multi-modal input and 3D volumetric processing, restricting their applicability to single-modality 2D slice settings. Havaei et al. (2017) demonstrated the feasibility of end-to-end CNN-based tumor segmentation on multi-modal MRI, and Pereira et al. (2016) showed that deep architectures with small receptive fields outperform larger kernels on T1 and FLAIR images.

A subsequent line of work has addressed single-modality T1-CE MRI segmentation, on which A3Net is also evaluated. Recent work on BRISC 2025 includes the Trust-Refined U-Net Ensemble (Bhamboo et al., 2025), a 2.5D ensemble reporting binary Dice (79.80%) under an 80/20 random split, and LoGSAM (Bhuiyan et al., 2026), a multi-component foundation-model pipeline (LoRA-GDINO + MedSAM, ~265 M estimated) providing binary masks via prompt-driven segmentation. Both achieve strong Dice scores at more than two orders of magnitude larger computational footprint than A3Net. Kuzhan and Günay (2026) systematically compared CNN- and Transformer-based models on BRISC 2025 under binary segmentation, finding that pretrained CNN backbones consistently outperform Swin U-Net — broadly consistent with our from-scratch result that SegFormer-B0 underperforms A3Net on BRISC 2025, though the settings differ in pretraining and task protocol. Bindhu and Vimala (2026) proposed A-Lite-UACNet, a lightweight MobileNetV2-based encoder–decoder with CBAM attention for efficient brain tumor segmentation on BRISC 2025, targeting deployment in resource-constrained clinical settings.

On the Figshare dataset, Díaz-Pernas et al. (2021) introduced a multiscale CNN that performs multi-class segmentation across all three tumor types without dedicated preprocessing. Sobhaninia et al. (2020) proposed a cascaded dual-scale LinkNet for binary segmentation, and Razzaghi et al. (2022) applied adversarial domain adaptation across three anatomical views (axial, sagittal, coronal) as modalities, performing multi-class segmentation and achieving mean Dice of 86.03% (author-computed) across the three tumor types. Preetha et al. (2025) paired an EfficientNet-B4 encoder with a multi-scale attention U-Net decoder for binary tumor segmentation with ImageNet pretraining.

On the Akter-Seg dataset, Akter et al. (2024) proposed a combined CNN and U-Net pipeline for binary segmentation across four tumor classes, and Musthafa et al. (2025) proposed VISION, a view-specific framework integrating an EfficientNetB0-based U-Net with a classification header trained independently for axial, coronal, and sagittal views. Ullah et al. (2024) combined DeepLabV3+ with multi-modal inputs and explainable-AI components for broader MRI segmentation tasks. On the classification side of BRISC 2025, Thahiruddin and Wulandari (2025) evaluated CNN and hybrid-transformer architectures, and Pacal and Deveci (2026) performed a comparative analysis of modern CNN families, observing diminishing returns from scaling model capacity — consistent with the efficiency-oriented design of A3Net. Rashid et al. (2026) provide a recent review of deep learning methods for brain tumor segmentation in MRI. In contrast to all methods above, A3Net targets multi-class segmentation directly from random initialization without pretrained weights, within a sub-3 M-parameter budget.

1.1.2. Lightweight convolutional architectures

Lightweight convolutional design has been driven primarily by mobile deployment requirements. Howard et al. (2017) introduced MobileNets with depth-wise separable convolutions, and Sandler et al. (2018) added inverted residuals with linear bottlenecks. Howard et al. (2019) extended this line of work in MobileNetV3 by integrating SE attention and hard-swish activations. Tan and Le (2019) demonstrated that compound scaling of width, depth, and resolution yields favorable accuracy–efficiency trade-offs. In the segmentation domain, ENet (Paszke et al., 2016) and BiSeNetV2 (Yu et al., 2021) achieved real-time semantic segmentation at <5 M parameters, while ESPNetv2 (Mehta et al., 2019) reached 0.244 M parameters using efficient spatial pyramid decomposition. Chollet (2017) formalized that depth-wise separable convolutions reduce computation by approximately $1/C + 1/K^2$ relative to standard convolutions while preserving spatial filtering quality. A3Net combines depth-wise separable factorization with SE channel recalibration within an encoder–decoder optimized for multi-class brain tumor segmentation at sub-3 M parameters — a regime not previously evaluated under rigorous cross-validation on this task.

1.1.3. Transformer-based segmentation architectures

Vision transformers have emerged as an alternative to convolutional encoder–decoders for semantic segmentation. Swin-UNet (Cao et al., 2022) adapts the Swin Transformer within a U-Net-like decoder, achieving strong performance with ImageNet-22K pretraining. SegFormer (Xie et al., 2021) proposes a more efficient design, combining a hierarchical Mix-Transformer encoder with a lightweight MLP decoder; it reaches competitive accuracy at 3.715 M parameters, though its advantage over efficient CNNs diminishes substantially when trained from scratch without large-scale pretraining, as confirmed empirically in Section 3.1.

1.1.4. Attention mechanisms in segmentation

The squeeze-and-excitation (SE) module (Hu et al., 2018) performs channel-wise recalibration through global average pooling followed by a two-layer excitation network; ablation confirms a +2.63 pp mIoU contribution at minimal parameter cost. CBAM (Woo et al., 2018) extends this with a spatial attention gate, but underperforms channel-only SE by 1.71 pp at identical parameter count.

1.1.5. Cross-dataset domain shift

Domain shift remains a central obstacle to clinical deployment of segmentation models across acquisition sites. The dominant paradigm for cross-domain

adaptation in medical imaging has been adversarial training: domain-adversarial neural networks (DANNs) align feature distributions via a gradient reversal layer (Ganin et al., 2016), while Kamnitsas et al. (2017) demonstrated unsupervised domain adaptation for brain lesion segmentation by jointly training a segmentation network with a domain discriminator, achieving robust transfer across MRI scanners without target-domain labels. Image-level style transfer offers an alternative route: CycleGAN (Zhu et al., 2017) synthesizes target-domain images from source-domain data without paired supervision, enabling training-set augmentation across modalities or scanners; Dou et al. (2019) applied this strategy to cardiac segmentation, reporting consistent improvements over direct transfer. Normalization-based approaches such as Adaptive Instance Normalization, AdaIN (Huang and Belongie, 2017), align feature statistics at the layer level rather than the pixel level, offering lighter-weight adaptation that can be embedded within the segmentation backbone itself. Despite their effectiveness, these methods add architectural complexity, require careful tuning of adversarial training objectives, and often demand access to unlabeled target-domain data.

In this work we investigate whether per-channel z-score standardization provides a simpler, training-free alternative to adversarial or generative adaptation. We compare four preprocessing strategies and show that standardization under multi-source training yields a partial +3.05 pp Figshare mIoU recovery; because this recovery is obtained under target-inclusive training, it is not directly comparable to the −29.90 pp zero-shot transfer gap measured under target-blind conditions. Class-distribution mismatch is identified as the dominant unresolved factor.

2. Materials and Methods

2.1. A3Net Architecture Overview

A3Net is a symmetric encoder–decoder designed for multi-class brain tumor segmentation from 256×256 T1-CE MRI slices. The encoder applies a stem convolution (3→32 channels, 3×3, stride 2) followed by max-pooling and four progressive downsampling stages with channel widths {96, 192, 320, 448}, reaching a 4×4 spatial bottleneck. The overall encoder–decoder schematic is shown in Figure 1. A channel-wise dropout layer (P=0.3; nn.Dropout2d, which zeros entire feature maps rather than individual pixels) regularizes the bottleneck. The skip connection s0 is taken from the stem output (32×128^2) before max-pooling; s1–s3 are taken after the first block of each encoder stage. The decoder restores resolution via bilinear upsampling combined with SumFuse modules that merge upsampled decoder features with encoder skip features by element-wise summation. Decoder channel widths are {224, 160, 96, 48, 32}, each equal to half the width of its skip-source encoder stage. The final decoder stage (ref0) applies a single depth-wise separable convolution after upsampling without any skip connection. A final 1×1 convolution produces a 4-channel output map (background plus three tumor classes).

2.2. Core Building Blocks

2.2.1. Block_Conv_Opt: Channel-Recalibrated Residual Block

The core building block of A3Net is Block_Conv_Opt, illustrated in Figure 2. Given input x ∈ R^(B×Cin×H×W) (equation 1):

$$y = f_out(SE(expand(DWSep(compress(x)))) + skip(x)) \quad (1)$$

where compress is a 1×1 convolution reducing channels to mid = max(Cout/2, 16); DWSep is a depth-wise separable convolution operating on the mid-width representation (mid→mid); expand is a 1×1 convolution restoring channels to Cout; SE applies channel attention to the expanded features before the residual addition so the skip connection remains unattenuated; and f_out is a final 1×1 convolution with batch normalization and SiLU. The skip path applies a 1×1 projection when Cin ≠ Cout, and an identity otherwise.

2.2.2. Squeeze-and-excitation attention

Following Hu et al. (2018) but replacing the inner ReLU with SiLU for consistency with the rest of the network (equation 2):

$$\hat{s}_c = \sigma(W2 \cdot SiLU(W1 \cdot GAP(F))),\ \hat{F}_c = \hat{s}_c \cdot F_c \quad (2)$$

where F ∈ R^(B×C×H×W); GAP is global average pooling; W1 ∈ R^(m×C) and W2 ∈ R^(C×m) with bottleneck width m = max(C÷16, 8), ensuring a minimum of 8 hidden units for narrow channels; and ŝ_c ∈ (0,1) is the scalar gate applied channel-wise. SE adds two fully connected layers per block; ablation confirms a +2.63 pp mIoU contribution.

2.2.3. Depth-wise separable convolution

The depth-wise separable convolution factorization is illustrated in Figure 3. Standard 3×3 convolutions are replaced throughout with depth-wise separable convolutions (Howard et al., 2017; Chollet, 2017) (equation 3):

$$y = BN(SiLU(W_pw * (W_dw \circledast x))) \quad (3)$$

where W_dw ∈ R^(C×1×K×K) operates per channel (groups = C, padding = 1) and W_pw ∈ R^(Cout×C×1×1) mixes channels, each followed by batch normalization and SiLU. Replacing DWSep with standard 3×3 convolutions adds 1.30 M parameters (+61.6%) and 0.53 GFLOPs for only −0.78 pp mIoU.

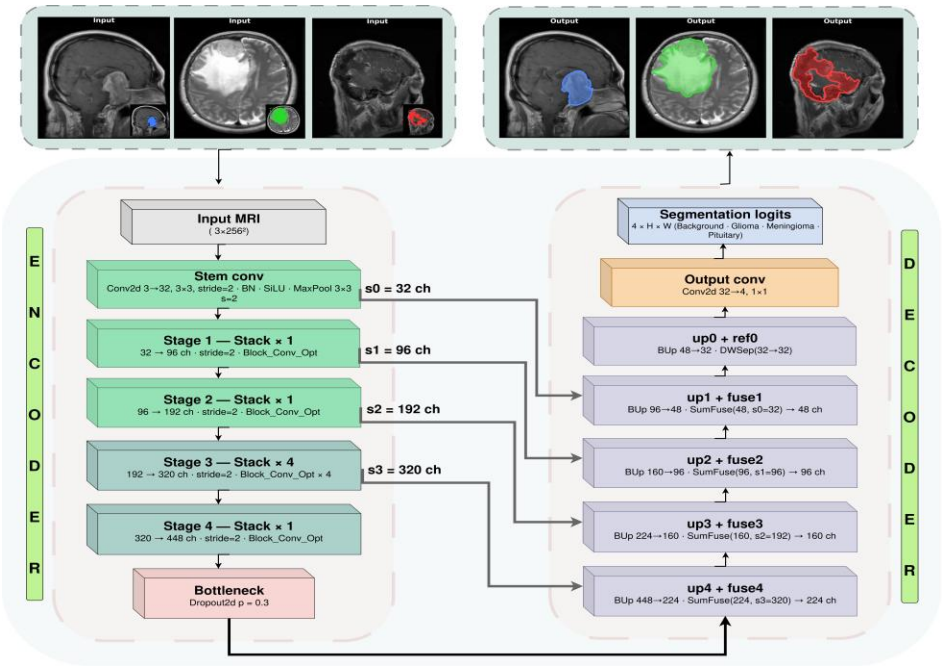


Figure 1. A3Net encoder–decoder overview. Channel widths at each stage are indicated above the blocks; skip connections s0–s3 are shown as lateral arrows. ⊕ denotes element-wise summation in SumFuse modules. The final ref0 stage applies a single DWSep without a skip connection; the output 1×1 convolution produces a 4-class prediction map (4×256^2).

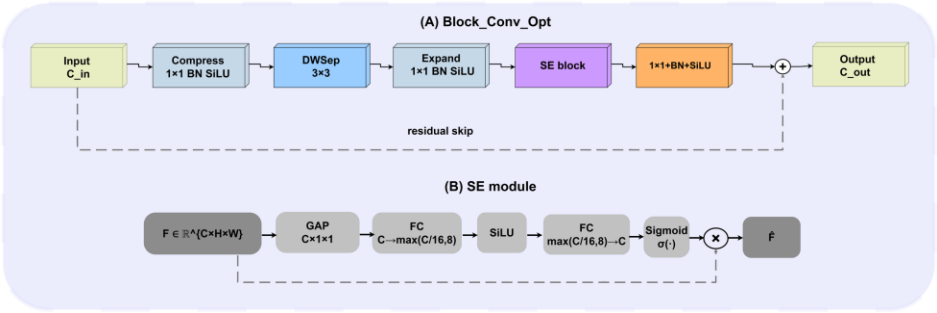


Figure 2. Block_Conv_Opt internal structure (A) and squeeze-and-excitation recalibration module (B). (A) Input features are first compressed to mid = max(Cout/2, 16) channels via 1×1 convolution, processed by a depth-wise separable convolution (mid→mid), expanded back to Cout, and recalibrated by SE before the residual addition; a final 1×1+BN+SiLU layer produces the block output. The residual skip applies a 1×1 projection when Cin ≠ Cout. (B) The SE module performs global average pooling, followed by two fully connected layers with bottleneck width m = max(C÷16, 8), and sigmoid gating applied channel-wise.

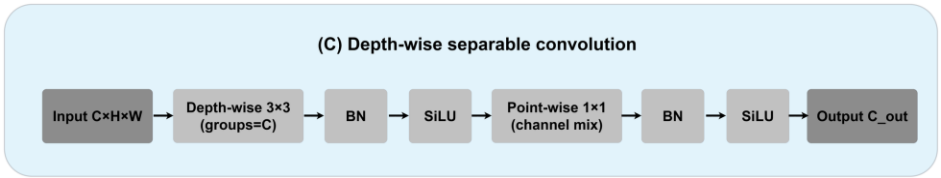


Figure 3. Depth-wise separable convolution factorization (C). A standard 3×3 convolution is decomposed into a depth-wise 3×3 convolution (groups = C, padding = 1) that filters each input channel independently, followed by a point-wise 1×1 convolution that mixes channels across the full output depth. Each stage is followed by batch normalization and SiLU activation.

2.2.4. SumFuse decoder fusion

At each decoder level (equation 4):

$$y = DWSep(BilUp(x) + proj(skip)) \quad (4)$$

where BilUp denotes bilinear upsampling by two and proj is a 1×1 projection applied to the skip features when their channel count differs from the upsampled decoder features. The final decoder stage (ref0) applies a single DWSep after upsampling without any skip connection, as no encoder skip is available at that resolution. Concatenation-based fusion degrades performance by 1.21 pp mIoU, suggesting more effective feature alignment with summation in this lightweight setting.

2.3. Loss Function

A3Net is trained with a composite loss (equation 5):

$$L_total = L_CE + L_Dice \quad (5)$$

where the Dice term is computed per foreground class (c ∈ {1,2,3}) (equation 6):

$$L_Dice = (1/3)\ \Sigma_c\ [\ 1 - (2\ \Sigma p_c\ g_c + sm)\ /\ (\Sigma p_c + \Sigma g_c + sm)\ ],\ \ sm = 1.0 \quad (6)$$

The training loss uses sm = 1.0 for numerical stability and to reduce sensitivity to very small structures during optimisation, while the evaluation metric (Eq. 8) uses ε = 10^{-8} as a pure numerical guard — a standard distinction in the literature (Milletari et al., 2016). Cross-entropy provides stable gradients across all pixels including the dominant background class. Removing the Dice term produces the largest single performance drop in the ablation (−3.46 pp mIoU).

2.4. Implementation Details

A3Net is implemented in PyTorch 2.5.1+cu121 and trained on an NVIDIA GeForce RTX 3050 6 GB Laptop GPU (Ampere, CUDA 12.1). Table 1 summarizes all key training hyperparameters used in this work; the same configuration is applied to all baselines and ablation variants to ensure a controlled comparison. Although ImageNet channel statistics are used as a fixed linear rescaling of input intensities, no pretrained weights are employed at any stage; this choice ensures comparability across all baselines evaluated under identical normalisation conditions (dataset-specific normalisation, per-channel μ=0.166, σ=0.166, yields 77.28% mIoU vs. 77.79% under ImageNet statistics, −0.51 pp; full ablation in Table 6). Convolutional weights use Kaiming normal initialization; batch-normalization parameters are initialized to one and zero.

2.5. Datasets

2.5.1. BRISC 2025

The primary benchmark is BRISC 2025 (Fateh et al., 2026), a publicly available annotated T1-CE MRI dataset covering glioma (Class 1), meningioma (Class 2), and pituitary adenoma (Class 3), with background as the implicit fourth class. Prior to training, we performed an MD5-checksum integrity audit of the original 4,793 image–mask pairs, identifying 7 cross-split duplicate pairs (14 images total; both copies removed to eliminate test-set leakage), 29 intra-training duplicates, and 4 intra-test duplicates — 47 total (≈1.0%). Post-cleaning cross-split overlap was confirmed to be zero. The cleaned splits yield an 82.1%/17.9% train/test ratio summarized in Table 2. The BRISC training set (μ = 42.01, σ = 44.21) and test set (μ = 43.12, σ = 45.83) exhibit only a minor internal distribution shift; we retain the official splits to remain comparable with prior work.

2.5.2. Figshare brain tumor dataset

The Figshare dataset (Cheng, 2017) comprises 3,064 T1-weighted contrast-enhanced MRI slices from 233 patients covering three tumor types: glioma (1,426 slices), meningioma (708 slices), and pituitary tumor (930 slices). Following patient-level stratified splitting — which ensures no patient contributes slices to both partitions — we obtain 2,758 training and 306 test images (Table 2), confirmed to have zero patient-level overlap across splits by cross-referencing PID metadata from the original dataset (233 unique patients). Figshare is glioma-dominant (46.5% of total samples), whereas BRISC is pituitary-dominant (36.6%); this class-distribution asymmetry is a primary driver of the cross-dataset generalization gap.

2.5.3. Combined dataset for multi-source training

For multi-source experiments, we concatenate BRISC training (N = 3,897) and Figshare training (N = 2,758) into a combined set of N = 6,655 samples. Test sets remain strictly separate (BRISC test N = 849, Figshare test N = 306). We evaluate four preprocessing conditions: (i) Baseline (ImageNet normalization only), (ii) Standardization (per-image per-channel z-score prior to ImageNet normalization), (iii) CLAHE (contrast-limited adaptive histogram equalization prior to ImageNet normalization), and (iv) Std+CLAHE (z-score standardization followed by CLAHE sequentially).

2.5.4. Akter-seg dataset

The Akter-Seg dataset (Akter et al., 2024) comprises T1-weighted MRI slices spanning four categories: glioma, meningioma, pituitary tumor, and no-tumor, assembled from multiple publicly available sources including the Figshare dataset (Cheng, 2017). The no-tumor class is excluded for consistency with A3Net's three-class protocol; all non-mask pixels are treated as background. An MD5-checksum audit removed 13 duplicate image groups, yielding 2,626 unique samples. A stratified 90/10 split produces a fixed held-out test set of 262 images with zero hash and path overlap confirmed between partitions. As Akter-Seg partially overlaps the Figshare benchmark, results on this dataset are reported as a descriptive

supplementary probe only and excluded from paired statistical comparisons and multi-source training experiments.

Table 1. Training hyperparameters used for A3Net and all baselines*

Parameter	Value
Optimizer	AdamW
Learning rate	3×10^{-4}
Weight decay	3×10^{-4}
Gradient clipping	1.0
LR schedule	Warm-up + cosine decay
Warm-up steps	3 × ⌊|D_train|/B⌋
Batch size	16
Max epochs	200 (early stopping patience = 20)
Seeds	42, 1337
CV folds	5 per seed (10 total)
Input resolution	256 × 256
Activation	SiLU
Bottleneck dropout	P=0.3 (nn.Dropout2d)
Loss function	CE + Dice (sm = 1.0)
Weight init.	Kaiming normal (conv); ones/zeros (BN)
Normalisation	ImageNet μ, σ; no pretrained weights
Training augmentation	H-flip (p=0.5), V-flip (p=0.5)
Val/test augmentation	None
GPU	RTX 3050 6 GB Laptop (Ampere)
CUDA / PyTorch	12.1 / 2.5.1

*The same configuration is applied throughout unless otherwise noted. Optimization follows AdamW (Loshchilov and Hutter, 2019) with a warm-up and cosine-decay schedule (Loshchilov and Hutter, 2017), and the SiLU activation (Elfwing et al., 2018) is used throughout the network.

2.6. Evaluation Protocol

Due to the limited size of the available training sets, we adopt a protocol designed to reduce random variance while remaining computationally feasible: each model is trained twice using two independent random seeds (Seed 42 and Seed 1337), each time with 5-fold stratified cross-validation over the training set, yielding 10 paired evaluation folds per model. For each fold k under each seed, one model is trained on the four remaining folds (fold k as validation, patience 20), then evaluated on the fixed held-out test set (BRISC test N = 849 or Figshare test N = 306). The same protocol applies to all baselines and ablation variants. Final test-set metrics use the aggregated method following Isensee et al. (2021): TP, FP, and FN are accumulated over the entire test set before computing class-wise IoU and Dice (equationa 7and 8):

$$IoU_c = TP_c / (TP_c + FP_c + FN_c + \varepsilon) \quad (7)$$

$$Dice_c = 2\,TP_c / (2\,TP_c + FP_c + FN_c + \varepsilon) \quad (8)$$

with $\varepsilon = 10^{-8}$. The mean IoU (mIoU) and mean Dice are averaged over three foreground classes. Note that under aggregated TP/FP/FN computation, the reported mean over classes may differ from the arithmetic mean of the displayed per-class values due to class-support weighting. Results are reported as mean ± std across all 10 folds. For inter-model comparisons we use a paired t-test (primary) and paired Wilcoxon signed-rank test (robustness check), reporting Cohen's d and 95% CI on the per-fold differences. Significance is declared at $\alpha = 0.05$ on the paired t-test. To assess the robustness of the null results on the two aggregate metrics (mIoU, Mean Dice) without assuming normality of the paired-fold differences, we additionally compute bias-corrected and accelerated (BCa) bootstrap 95% confidence intervals with 10,000 resamples on the paired-fold differences (Tibshirani and Efron, 1993); this non-parametric check complements the parametric paired t-test and is reported alongside the primary results in Section 3.2. Ablation variants are evaluated under the same 2-seed × 5-fold protocol; the reference row in the ablation table therefore matches the full benchmark result in Table 3.

2.7. Experimental Setup

2.7.1. Metrics and baselines

We report mIoU (%), mean Dice (%), parameter count (M), GFLOPs at 256×256, model size (MB), FPS, and latency (ms). Latency and FPS are measured at 256×256 with batch size 1, averaged over 200 forward passes after 50-iteration warm-up on the RTX 3050 6 GB Laptop GPU. We compare against nine baselines spanning four tiers: U-Net (Ronneberger et al., 2015) and Attention U-Net (Oktay et al., 2018) as high-accuracy references; LinkNet (Chaurasia and Culurciello, 2017), MobileNetV3-UNet (Howard et al., 2019), and DeepLabV3+ (Chen et al., 2018) as mid-range CNN models; BiSeNetV2 (Yu et al., 2021), ESPNetv2 (Mehta et al., 2019), and ENet (Paszke et al., 2016) as sub-5 M-parameter lightweight networks; and SegFormer-B0 (Xie et al., 2021) as a from-scratch transformer reference. All are adapted to 4-class output and trained with identical hyperparameters, CE + Dice loss, and flip-only augmentation, using the same 2-seed × 5-fold protocol. Swin-UNet (Cao et al., 2022) is included as a contextual reference initialized from ImageNet-22K pretrained weights; direct performance comparison with from-scratch models is not methodologically valid, though preprocessing sensitivity is additionally reported for completeness.

Table 2. Per-class image counts for BRISC 2025 (after MD5 audit), Figshare, the combined multi-source corpus, and Akter-Seg

Dataset	Split	Glioma	Meningioma	Pituitary	Total
BRISC 2025	Train	1,147	1,310	1,440	3,897
BRISC 2025	Test	253	301	295	849
BRISC 2025	Total	1,400	1,611	1,735	4,746
Figshare	Train	1,297	626	835	2,758
Figshare	Test	129	82	95	306
Figshare	Total	1,426	708	930	3,064
Combined	Train	2,444	1,936	2,275	6,655
Combined	Test (BRISC)	253	301	295	849
Combined	Test (Figshare)	129	82	95	306
Akter-Seg	Train	584	894	886	2,364
Akter-Seg	Test	65	99	98	262
Akter-Seg	Total	649	993	984	2,626

2.7.2. Ablation design

Nine variants each modify a single component; all are evaluated under the same 2-seed × 5-fold protocol as the main benchmark. In addition, three glioma-targeted variants (SpatialGate decoder fusion, SE + SpatialOnly encoder blocks, and a boundary-aware loss with $\lambda = 0.15$), a three-way activation comparison (SiLU, ReLU, GELU), and a capacity scaling and dropout sensitivity study (A3Net-half, A3Net-2x; dropout $p \in \{0.0, 0.1, 0.3, 0.5\}$) are reported under separate sections for clarity.

3. Results

3.1. Benchmark Comparison

Table 3 reports the BRISC 2025 benchmark. A3Net achieves 77.79 ± 0.29% mIoU and 87.14 ± 0.17% Dice with 2.11 M parameters and 1.39 GFLOPs at 129.5 FPS and 8.15 ms latency. Among from-scratch models under 5 M parameters, A3Net leads all three lightweight baselines: ENet (76.37%) by +1.42 pp, ESPNetv2 (74.48%) by +3.31 pp, and BiSeNetV2 (73.55%) by +4.24 pp mIoU, establishing a clear accuracy advantage within the sub-5 M-parameter tier despite using 8.6× more parameters than the smallest baseline (ESPNetv2, 0.244 M). Among larger from-scratch models, A3Net surpasses U-Net (76.89%, 31.0 M) and LinkNet (76.24%, 11.5 M) at 14.7× and 5.5× fewer parameters respectively, and achieves statistical parity with Attention U-Net (77.64%, 31.6 M, P=0.334) at 15.0× lower parameter cost. Compared with MobileNetV3-UNet (6.70 M, 75.59%), A3Net achieves +2.20 pp mIoU at 3.2× fewer parameters, confirming that the proposed design yields superior efficiency–accuracy trade-offs over standard mobile encoder–decoder combinations. As an additional transformer reference trained from scratch, SegFormer-B0 attains 73.72% mIoU at 3.715 M parameters and 3.40 GFLOPs, remaining 4.07 pp below A3Net despite 1.76× more parameters and 2.4× more GFLOPs, indicating that without large-scale pretraining a compact transformer does not match the proposed CNN design on this benchmark.

3.2. Per-Class Analysis and Statistical Significance

Table 4 reports per-class IoU and Dice for A3Net and Attention U-Net across the four evaluation settings. Paired statistical tests are reported for the BRISC setting only, where paired folds are available; Figshare, Combined, and Akter-Seg results are reported descriptively.

BRISC setting. Glioma is the most challenging class for both models, reflecting its diffuse infiltrative margins. Attention U-Net leads A3Net on glioma by 1.49 pp IoU ($p < 0.001$, $d = -2.35$), consistent with spatial attention gates providing a larger effective receptive field that benefits irregular glioma boundaries. In contrast, A3Net achieves statistically significant advantages on meningioma (+1.54 pp IoU, P=0.007, $d = +1.15$) and pituitary (+0.42 pp IoU, P=0.016, $d = +0.99$), consistent with SE channel recalibration benefiting high-contrast, well-circumscribed boundaries. The +0.15 pp aggregate difference is non-significant (P=0.334), confirming efficiency parity rather than accuracy superiority.

Figshare and Combined settings. On Figshare (in-domain training, no paired test conducted), A3Net achieves 74.66% mIoU vs. 73.01% for Attention U-Net (+1.65 pp), with consistent descriptive advantages across all three classes (Glioma +1.06 pp, Meningioma +1.94 pp, Pituitary +1.96 pp). Under combined multi-source standardized training (N_{test} = 1,155), A3Net achieves 78.23% mIoU vs. 77.16% (+1.07 pp). Notably, glioma IoU for A3Net reaches 66.65% under combined training vs. 64.88% on BRISC alone (+1.77 pp), while the gap between A3Net and

Attention U-Net on glioma narrows from −1.49 pp (BRISC) to +1.06 pp (Combined). This reversal is attributable to the broader morphological diversity introduced by Figshare's glioma-dominant training distribution (46.5%), which reinforces glioma-specific features when combined with BRISC; it reflects a training-distribution effect rather than an architectural change, and does not contradict the BRISC-only paired results.

Akter-Seg probe. A3Net attains 83.30 ± 0.44% mIoU and 90.83 ± 0.26% Dice, marginally ahead of Attention U-Net (83.21 ± 0.65% mIoU, 90.74 ± 0.40% Dice) at 15.0× fewer parameters, consistent with the efficiency parity observed on BRISC. At the per-class level, A3Net leads on glioma (+2.26 pp IoU) whereas Attention U-Net holds a slight edge on meningioma (+0.18 pp) and pituitary (+1.82 pp); both models substantially exceed their BRISC glioma IoU (78.02% and 75.76% vs. 64.88% and 66.37%), reflecting the higher contrast and more sharply delineated tumour boundaries of the Akter-Seg masks relative to BRISC. As Akter-Seg partially overlaps the Figshare source, these results are excluded from paired statistical comparisons.

Table 3. Benchmark comparison on BRISC 2025 (2-seed × 5-fold CV, mean ± std)

Model	Init	Params (M)	GFLOPs	Size (MB)	mIoU (%)	Dice (%)	FPS	Lat (ms)
U-Net	Scratch	31.038	109.50	124.2	76.89 ± 0.70	86.64 ± 0.45	25.7	38.88
Attention U-Net	Scratch	31.562	111.16	126.4	77.64 ± 0.23	87.13 ± 0.15	20.4	48.92
LinkNet	Scratch	11.534	6.09	46.2	76.24 ± 0.20	86.08 ± 0.12	138.0	7.25
MobileNetV3-UNet	Scratch	6.701	6.20	27.04	75.59 ± 0.49	85.67 ± 0.36	98.6	10.15
DeepLabV3+	Scratch	5.812	11.74	23.5	74.76 ± 0.44	85.09 ± 0.30	96.8	10.33
BiSeNetV2	Scratch	1.140	1.60	4.7	73.55 ± 0.42	84.21 ± 0.27	214.4	4.66
ESPNetv2	Scratch	0.244	0.73	1.1	74.48 ± 0.24	84.91 ± 0.17	156.4	6.39
ENet	Scratch	0.420	1.47	1.9	76.37 ± 0.32	86.25 ± 0.20	97.4	10.27
A3Net (Ours)	Scratch	2.110	1.39	8.66	77.79 ± 0.29	87.14 ± 0.17	129.5	8.15
SegFormer-B0	Scratch	3.715	3.40	14.9	73.72 ± 0.89	84.18 ± 0.62	56.7	17.64
Swin-UNet	ImageNet-22K	30.89	18.86	123.6	78.68 ± 0.31	87.76 ± 0.20	23.6	43.33

Swin-UNet uses ImageNet-22K pretraining as a contextual reference only.

Table 4. Per-class IoU and Dice (%, 2-seed × 5-fold CV, mean ± std) for A3Net and Attention U-Net across four settings*

Setting	Class	A3Net IoU (%)	A3Net Dice (%)	Att.U-Net IoU (%)	Att.U-Net Dice (%)
BRISC	Glioma	64.88 ± 0.63	78.70 ± 0.46	66.37 ± 0.42*	79.78 ± 0.30*
BRISC	Meningioma	89.43 ± 1.10*	94.42 ± 0.62*	87.89 ± 0.46	93.56 ± 0.26
BRISC	Pituitary	79.06 ± 0.47*	88.31 ± 0.29*	78.64 ± 0.45	88.04 ± 0.28
BRISC	Mean	77.79 ± 0.29	87.14 ± 0.17	77.64 ± 0.23	87.13 ± 0.15
Figshare	Glioma	63.73 ± 1.17	77.84 ± 0.87	62.67 ± 0.86	77.05 ± 0.65
Figshare	Meningioma	84.63 ± 0.82	91.68 ± 0.48	82.69 ± 0.77	90.52 ± 0.47
Figshare	Pituitary	75.63 ± 0.91	86.12 ± 0.59	73.67 ± 0.86	84.83 ± 0.57
Figshare	Mean	74.66 ± 0.50	85.21 ± 0.36	73.01 ± 0.56	84.14 ± 0.38
Combined	Glioma	66.65 ± 0.61	79.99 ± 0.44	65.59 ± 0.59	79.22 ± 0.43
Combined	Meningioma	89.05 ± 0.46	94.21 ± 0.26	87.34 ± 1.04	93.23 ± 0.59
Combined	Pituitary	78.99 ± 0.55	88.26 ± 0.34	78.54 ± 0.35	87.98 ± 0.22
Combined	Mean	78.23 ± 0.17	87.49 ± 0.11	77.16 ± 0.44	86.81 ± 0.28
Akter-Seg	Glioma	78.02 ± 0.75	87.65 ± 0.48	75.76 ± 1.56	86.20 ± 1.02
Akter-Seg	Meningioma	88.29 ± 0.60	93.78 ± 0.34	88.47 ± 0.75	93.88 ± 0.43
Akter-Seg	Pituitary	83.59 ± 0.42	91.06 ± 0.25	85.41 ± 1.05	92.13 ± 0.62
Akter-Seg	Mean	83.30 ± 0.44	90.83 ± 0.26	83.21 ± 0.65	90.74 ± 0.40

*Statistically significant inter-model difference on BRISC ($p < 0.05$, paired t-test; full statistics in Table 5). Figshare, Combined, and Akter-Seg results are descriptive; no paired test was conducted across datasets.

Table 5. Paired statistical comparison between A3Net and Attention U-Net on BRISC 2025 (10 paired folds; Δ = A3Net − Attention U-Net; positive favours A3Net). ** p < 0.01, * p < 0.05, ns otherwise

Metric	A3Net	Att. U-Net	Δ (pp)	95% CI	Cohen's d	p (t)	p (W)	Sig.
mIoU (%)	77.79 ± 0.29	77.64 ± 0.23	+0.15	[−0.51, +0.83]	+0.34	0.334	0.375	ns
Mean Dice (%)	87.14 ± 0.17	87.13 ± 0.15	+0.01	[−0.38, +0.40]	+0.04	0.908	1.000	ns
Glioma IoU (%)	64.88 ± 0.63	66.37 ± 0.42	−1.49	[−2.11, −0.87]	−2.35	0.000	0.002	**
Glioma Dice (%)	78.70 ± 0.46	79.78 ± 0.30	−1.09	[−1.54, −0.64]	−2.34	0.000	0.002	**
Meningioma IoU (%)	89.43 ± 1.10	87.89 ± 0.46	+1.54	[+0.21, +2.87]	+1.15	0.007	0.020	*
Meningioma Dice (%)	94.42 ± 0.62	93.56 ± 0.26	+0.86	[+0.11, +1.61]	+1.15	0.007	0.020	*
Pituitary IoU (%)	79.06 ± 0.47	78.64 ± 0.45	+0.42	[+0.01, +0.83]	+0.99	0.016	0.037	*
Pituitary Dice (%)	88.31 ± 0.29	88.04 ± 0.28	+0.27	[+0.02, +0.52]	+0.99	0.016	0.037	*

Robustness check (bootstrap CI). To further validate the non-significant result on the two aggregate metrics without relying on the normality assumption of the paired t-test, we computed BCa bootstrap 95% confidence intervals on the paired-fold differences (10,000 resamples; random seed 0; scipy.stats.bootstrap). The bootstrap intervals are consistent with the parametric results reported in Table 5, and both aggregate intervals contain zero: mIoU Δ = +0.15 pp, bootstrap 95% CI [−0.13, +0.42]; Mean Dice Δ = +0.01 pp, bootstrap 95% CI [−0.15, +0.18]. For the six per-class metrics on which the parametric test rejected the null, the bootstrap intervals likewise exclude zero: Glioma IoU [−1.84, −1.05], Glioma Dice [−1.34, −0.77], Meningioma IoU [+0.41, +2.18], Meningioma Dice [+0.22, +1.22], Pituitary IoU [+0.16, +0.68], Pituitary Dice [+0.10, +0.43]. This non-parametric confirmation strengthens the aggregate parity conclusion and the per-class significance pattern under the limited sample size (n = 10 paired folds from 2 seeds × 5 folds).

3.3. Ablation Study

Table 6 presents ablation results on BRISC 2025 under the full 2-seed × 5-fold protocol. The reference A3Net result (77.79 ± 0.29% mIoU, first row) serves as the baseline for all comparisons, including the capacity scaling and dropout sections at the bottom of the table.

Architectural and training components. U-Net+SE achieves 76.62% mIoU vs. 77.79% for A3Net, demonstrating that the +1.17 pp advantage of the full design is attributable to the combined effect of depth-wise separable convolutions, SumFuse fusion, and the bottleneck structure, at 14.8× fewer parameters (2.110 M vs. 31.257 M). The CE + Dice composite loss and SE attention are the two most impactful components: removing Dice yields the largest single drop (−3.46 pp), with CE-only variance rising to ±0.52 from ±0.29, consistent with training instability without a direct overlap objective. Removing SE produces the second-largest drop (−2.63 pp), while CBAM underperforms SE by 1.71 pp at identical parameter count, confirming that channel-only recalibration is the more efficient attention mechanism at this scale. Removing the bottleneck module (−2.00 pp), replacing summation with concatenation (−1.21 pp), and extended augmentation (−1.31 pp) complete the ranking; the flip-only policy suffices for T1-CE MRI whose structural patterns are relatively stable across subjects. Dataset-specific normalisation (−0.51 pp, 77.28%) confirms that ImageNet statistics provide a more stable numerical prior for training, despite the grayscale-replicated channel structure of BRISC 2025 images.

Glioma-targeted variants. Three targeted modifications were evaluated to address the significant glioma gap (−1.49 pp, p < 0.001). SpatialGate decoder fusion degrades mIoU by −1.72 pp, with glioma IoU dropping −2.87 pp to 62.00%; multiplying skip features by a spatial gate attenuates high-frequency edge information critical for delineating diffuse glioma boundaries in a lightweight decoder. SE + SpatialOnly encoder blocks yield the worst result (−2.21 pp), consistent with joint channel–spatial recalibration disrupting the channel calibration learned by SE at this parameter scale. The boundary-aware loss (λ = 0.15) produces the smallest degradation (−0.84 pp, 76.95%) and the lowest cross-fold variance (±0.21). Collectively, none of the lightweight spatial attention or boundary-loss modifications closes the glioma gap, confirming it as a fundamental 2D receptive-field limitation.

Activation function. SiLU outperforms ReLU by +1.42 pp mIoU and GELU by +0.47 pp at identical parameter and FLOP budgets. ReLU shows the largest per-class deficit on glioma (63.00%, −1.88 pp), while GELU achieves 77.32% mIoU with notably lower variance (±0.13 vs. ±0.29 for SiLU) but remains 0.47 pp below. SiLU is retained as the default activation.

Capacity scaling and regularization. A3Net-half (1.05 M, 0.65 GFLOPs) loses only 1.53 pp mIoU relative to the reference, indicating that the standard 2.11 M configuration operates near a tight efficiency boundary with negligible excess capacity. A3Net-2x (4.19 M, 2.73 GFLOPs) gains only +0.43 pp mIoU overall and improves glioma IoU by +1.00 pp (64.88% → 65.88%), yet remains

0.49 pp below Attention U-Net at 7.5× fewer parameters — a 2× parameter overhead for a sub-0.5 pp gain that does not justify the computational cost in resource-constrained settings, confirming that the glioma gap is a 2D receptive-field limitation rather than a capacity problem. Dropout sensitivity follows a bell-shaped curve: the underfitting regime (P=0.0, −2.10 pp) and the over-suppression regime (P=0.5, −1.56 pp) bracket the optimal P=0.3, which is the unique maximum across all four settings. Inference-time augmentation. Test-time augmentation with horizontal and vertical flipping improves mIoU by +1.55 pp (77.79% → 79.34%, Dice 87.14% → 88.16%) and glioma IoU by +2.30 pp (64.88% → 67.18%) without retraining, narrowing the single-pass glioma gap against Attention U-Net from −1.49 pp to +0.81 pp. Extending to 8 transforms (adding rotations) yields diminishing returns (+1.10 pp mIoU, +0.80 pp glioma IoU), confirming that flip augmentations capture the dominant symmetry in axial T1-CE MRI slices while 90°/180° rotations alter anatomical orientation in ways that conflict with the training distribution. Main results in Tables 3–4 report standard single-pass inference (no TTA) for fair comparison with prior methods.

Table 6. Ablation study on BRISC 2025 (2-seed × 5-fold CV, mean ± std)

Variant	mIoU (%)	Dice (%)	Params (M)	GFLOPs
Full A3Net (reference)	77.79 ± 0.29	87.14 ± 0.17	2.110	1.39
U-Net + SE	76.62 ± 0.87	86.42 ± 0.56	31.257	109.53
w/o SE attention	75.16 ± 0.30	85.41 ± 0.21	2.027	1.39
CBAM instead of SE	76.08 ± 0.32	86.03 ± 0.19	2.110	1.39
w/o depth-wise separable conv.	77.01 ± 0.29	86.64 ± 0.19	3.411	1.92
CE loss only (no Dice)	74.33 ± 0.52	84.79 ± 0.34	2.110	1.39
Bottleneck kernel K = 5	76.26 ± 0.34	86.15 ± 0.21	2.126	1.40
Double-convolution block	76.76 ± 0.38	86.45 ± 0.26	2.949	1.73
Skip: concatenation instead of sum	76.58 ± 0.23	86.33 ± 0.15	2.125	1.42
w/o bottleneck module	75.79 ± 0.29	85.85 ± 0.18	1.887	1.26
Extended augmentation	76.48 ± 0.28	86.29 ± 0.18	2.110	1.39
Dataset-specific normalisation	77.28 ± 0.17	86.82 ± 0.13	2.110	1.39
+ SpatialGate in decoder (fuse4, fuse3)	76.07 ± 0.44	85.98 ± 0.28	2.200	1.41
+ SE + SpatialOnly in encoder blocks	75.58 ± 0.69	85.71 ± 0.42	2.110	1.39
+ Boundary-aware loss (λ=0.15)	76.95 ± 0.21	86.64 ± 0.14	2.110	1.39
ReLU (instead of SiLU)	76.37 ± 0.30	86.21 ± 0.19	2.110	1.39
GELU (instead of SiLU)	77.32 ± 0.13	86.85 ± 0.09	2.110	1.39
A3Net-half	76.26 ± 0.29	86.12 ± 0.19	1.050	0.65
A3Net-2x	78.22 ± 0.29	87.44 ± 0.19	4.190	2.73
Dropout P=0.0	75.69 ± 0.13	85.76 ± 0.09	2.110	1.39
Dropout P=0.1	77.38 ± 0.05	86.89 ± 0.06	2.110	1.39
Dropout P=0.5	76.23 ± 0.07	86.11 ± 0.04	2.110	1.39
+ TTA flip (H+V+HV, 4 transforms)	79.34 ± 0.28	88.16 ± 0.17	2.110	1.39
+ TTA full (flip+rotations, 8 transforms)	78.89 ± 0.26	87.83 ± 0.17	2.110	1.39

Each row modifies one component while keeping all others fixed; the reference row (first) applies to all sections. CBAM bottleneck ratio reduced to match SE parameter count. Extended augmentation adds rotation (±15°), brightness/contrast jitter, and Gaussian noise. Dataset-specific normalisation uses per-channel statistics computed from training images (μ=0.166, σ=0.166); ImageNet normalisation is retained as it yields +0.51 pp mIoU. TTA rows are inference-time only and require no retraining.

3.4. Comparison with Prior Methods

On BRISC 2025, all prior published results use binary segmentation (tumor vs. background), which is a fundamentally easier task than multi-class segmentation: binary Dice conflates three distinct tumor types into a single foreground class and is systematically 5–15 pp higher than multi-class Dice on the same images. LoGSAM reports 80.32% binary Dice at ~265 M parameters, while A3Net achieves 87.14% multi-class Dice at 2.11 M — these figures cannot be directly compared, but the task difference makes A3Net's result all the more noteworthy. To our knowledge, A3Net is the first published multi-class segmentation result on the full BRISC 2025 benchmark.

On Figshare, the only valid comparator is Díaz-Pernas et al., the sole multi-class result without pretraining at a similar scale (2.86 M). A3Net exceeds it by +2.41 pp Dice (85.21% vs. 82.80%) at 26% fewer parameters. Razzaghi et al. achieve 86.03% mean Dice via multimodal domain

adaptation, exceeding A3Net by +0.82 pp; however, this method trains on axial, sagittal, and coronal views simultaneously using a ~25 M-parameter backbone — a setting that provides substantially more input information and model capacity than A3Net's single-modality single-view design. Binary results such as the Multi-scale Att. U-Net (93.39%) are reported for completeness but are not comparable.

On Akter-Seg, Akter et al. report 89.0% binary Dice using four separate class-specific models (~16.8 M total); A3Net achieves 90.83% multi-class Dice with a single 2.11 M-parameter model — a fundamentally harder task at 8× lower parameter cost. Similarly, VISION reports 89.0% binary Dice via three view-specific pretrained models; A3Net surpasses this figure under the harder multi-class protocol with a single from-scratch model. These results are descriptive only, as binary and multi-class Dice are not directly comparable.

3.5. Qualitative Visualization on BRISC

Figure 4 shows representative segmentation outputs for each tumor class. On glioma, both models correctly localize the tumor region, yet the difference map reveals residual boundary errors for A3Net at infiltrative margins, consistent with the statistically significant per-class gap (−1.49 pp IoU, $p < 0.001$). On meningioma, A3Net produces a compact, well-delineated mask that closely matches the ground truth, while Attention U-Net shows slight peripheral over-segmentation; this aligns with A3Net's statistically significant advantage on this class (+1.54 pp IoU, P=0.007). On pituitary, both models yield nearly identical masks with minimal difference, consistent with the small but significant inter-model gap (+0.42 pp IoU, P=0.016). These examples illustrate per-class failure modes and support the population-level statistics in Table 4, rather than contradicting them.

3.6. Cross-Dataset Generalization

Table 8 reports zero-shot cross-dataset evaluation: models are applied directly to the held-out test set of the opposite dataset without any fine-tuning. The domain gap is pronounced and strongly asymmetric: the BRISC→Figshare direction (−12.64 pp for A3Net) is substantially less severe than the reverse (−29.90 pp). The mean intensity difference between datasets is only 2.62 units (BRISC: $\mu = 42.01$, $\sigma = 44.21$; Figshare: $\mu = 39.39$, $\sigma = 42.09$), ruling out intensity shift as the primary driver. The dominant cause is class-distribution mismatch: Figshare is glioma-dominant (46.5% of slices) while BRISC is pituitary-dominant (36.6%); models trained on Figshare thus develop strong glioma priors that do not transfer to BRISC's more balanced distribution, producing large false-negative regions on meningioma and pituitary.

Table 7. Contextual comparison with representative prior methods on BRISC 2025, Figshare, and Akter-Seg. Task formulation, pretraining, and evaluation differ across methods; direct numerical comparison is not valid. * Binary segmentation (tumor vs. background), systematically easier than multi-class. † ImageNet pretraining. ‡ Multimodal adaptation (axial, sagittal, coronal views as separate modalities)

Dataset	Method	Task	Params (M)	Dice (%)	Year
BRISC 2025	Trust-Refined U-Net Ensemble	Binary*	—	79.80	2025
BRISC 2025	LoGSAM	Binary*	~265	80.32	2026
BRISC 2025	Kuzhan and Günay	Binary*†	—	85.75	2026
BRISC 2025	A3Net (Ours)	Multi-class	2.11	87.14	This work
Figshare	Díaz-Pernas et al.	Multi-class	2.86	82.80	2021
Figshare	Sobhaninia et al.	Binary*	—	80.03	2020
Figshare	Conv. Autoencoder (Badža and Barjaktarović, 2021)	Binary*	~0.49	72.87	2021
Figshare	MST-based (Mayala et al., 2022)	Binary*	—	84.69	2022
Figshare	Razzaghi et al.	Multi-class‡	~25+	86.03	2022
Figshare	Multi-scale Att.U-Net (EffNet-B4)	Binary*†	—	93.39	2025
Figshare	A3Net (Ours)	Multi-class	2.11	85.21	This work
Akter-Seg	Akter et al.	Binary* (×4 models)	~16.8	89.0	2024
Akter-Seg	VISION	Binary† (view-spec., ×3)	—	89.0	2025
Akter-Seg	A3Net (Ours)	Multi-class	2.11	90.83	This work

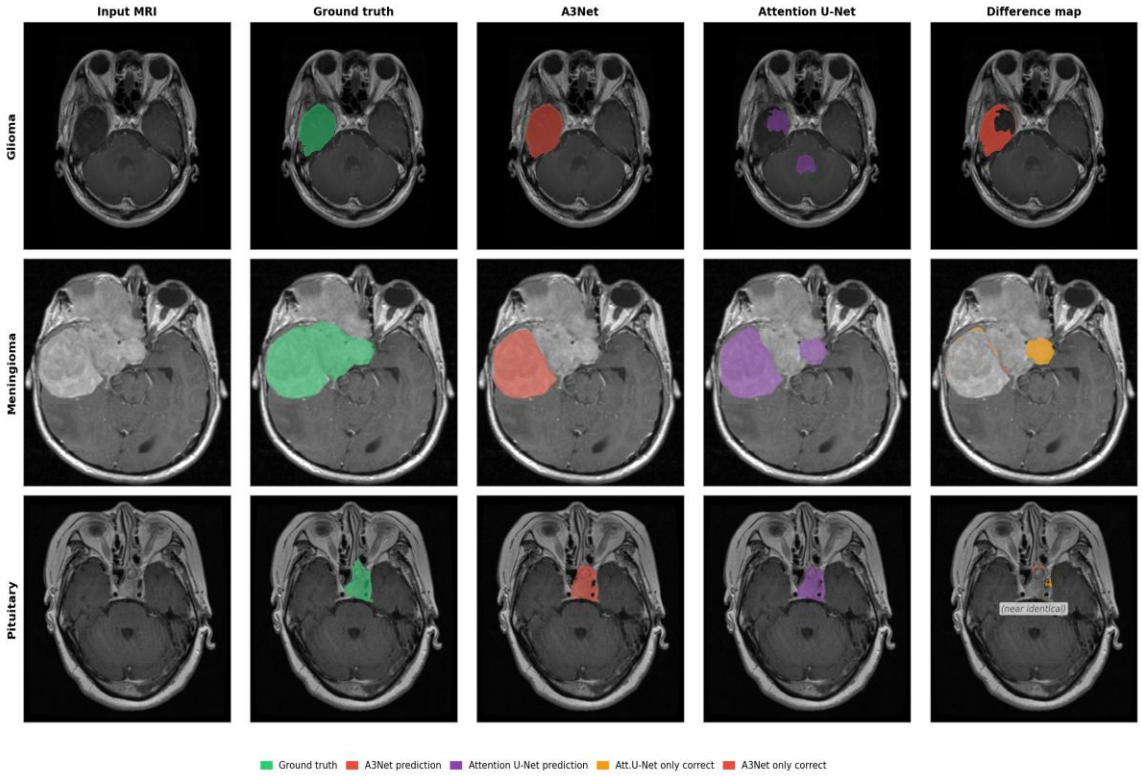


Figure 4. Qualitative comparison on BRISC 2025 (one representative case per tumor class). Columns: input MRI; ground truth (green); A3Net prediction (red); Attention U-Net prediction (purple); per-pixel difference map (orange: Attention U-Net correct only; red: A3Net correct only). The pituitary difference map is near-identical, consistent with the small inter-model gap.

Table 8. Zero-shot cross-dataset evaluation (no fine-tuning; 2-seed × 5-fold CV, mean ± std). DroP=cross-dataset mIoU − source-domain in-domain mIoU. Swin-UNet uses ImageNet-22K pretraining and is a contextual reference only

Model	Train	Test	mIoU (%)	Dice (%)	Drop (pp)
A3Net	BRISC	Figshare	65.15 ± 0.66	78.28 ± 0.49	−12.64
A3Net	Figshare	BRISC	44.76 ± 1.41	61.23 ± 1.32	−29.90
Attention U-Net	BRISC	Figshare	66.23 ± 1.03	79.10 ± 0.82	−11.41
Attention U-Net	Figshare	BRISC	41.16 ± 3.73	56.66 ± 4.24	−31.85
Swin-UNet (pretrained)	BRISC	Figshare	70.27 ± 1.42	81.94 ± 1.07	−8.41
Swin-UNet (pretrained)	Figshare	BRISC	53.08 ± 2.15	69.23 ± 1.84	−22.52

Conversely, BRISC-trained models generalize better to Figshare because their more balanced class priors are not actively mismatched. In the Figshare→BRISC direction, A3Net (44.76%) outperforms Attention U-Net (41.16%, +3.60 pp), though no paired statistical test was conducted for cross-dataset comparisons. Attention U-Net also shows higher descriptive variance in this direction (±3.73 vs. ±1.41 for A3Net), suggesting greater sensitivity to the distribution shift, though formal variance equality testing was not performed. Swin-UNet shows qualitatively identical asymmetric patterns, confirming that the gap is driven by dataset characteristics rather than architecture.

3.7. Multi-Source Training Analysis

Table 9 presents multi-source training results under four preprocessing conditions. Multi-source training yields consistent Figshare improvements across all models regardless of architecture. Even without standardization (Baseline), A3Net gains +2.05 pp and Attention U-Net gains +2.44 pp, confirming that the benefit is primarily driven by exposure to a broader training distribution rather than by preprocessing alone. Standardization amplifies this effect: A3Net gains +3.05 pp (74.66% → 77.71%) and Attention U-Net gains +2.51 pp (73.01% → 75.52%), confirming that standardization is a broadly effective strategy independent of architecture. Critically,

despite ImageNet-22K pretraining, Swin-UNet reaches only 75.77% under multi-source standardized training, remaining 1.94 pp below A3Net (77.71%), suggesting that large-scale vision pretraining does not substitute for training-distribution alignment when class-distribution mismatch is the primary domain gap driver. The preprocessing hierarchy is consistent across all from-scratch models: standardization > CLAHE (75.12%, +0.46 pp for A3Net) > no preprocessing > Std+CLAHE (73.81%, −0.85 pp), confirming that CLAHE-based processing introduces spectral artifacts that widen rather than narrow the inter-dataset intensity gap.

3.8. Qualitative Cross-Dataset Analysis

Figure 5 illustrates the effect of multi-source standardized training relative to single-source training for both transfer directions and all three tumor classes. Single-source models exhibit incomplete tumor recovery, boundary displacement, and large false-negative regions in both transfer directions, most pronouncedly for Figshare→BRISC. On the displayed cases, multi-source standardized training raises per-case IoU substantially — for example, pituitary Figshare→BRISC improves from 5.4% to 95.1% and glioma from 23.3% to 63.6% — reducing false-negative regions while preserving compact boundaries. These case-level gains illustrate the population-level trend reported in Table 9.

Table 9. Multi-source training results (BRISC ∪ Figshare training, N = 6,655; 2-seed × 5-fold CV, mean ± std). Test sets remain strictly separate (BRISC N = 849, Figshare N = 306). Δ: change in Figshare mIoU vs. single-dataset in-domain training (A3Net baseline: 74.66%; Att. U-Net baseline: 73.01%)

Model	Preprocessing	BRISC mIoU (%)	Fig. mIoU (%)	Δ Fig. mIoU
A3Net	Baseline	77.10 ± 0.33	76.71 ± 0.47	+2.05 pp
A3Net	Standardization	78.10 ± 0.22	77.71 ± 0.28	+3.05 pp
A3Net	CLAHE	77.79 ± 0.31	75.12 ± 0.65	+0.46 pp
A3Net	Std+CLAHE	77.51 ± 0.23	73.81 ± 0.36	−0.85 pp
Attention U-Net	Baseline	76.31 ± 0.38	75.45 ± 0.84	+2.44 pp
Attention U-Net	Standardization	77.67 ± 0.44	75.52 ± 0.58	+2.51 pp
Swin-UNet (pretrained)	Standardization	78.05 ± 0.41	75.77 ± 1.78	+0.17 pp

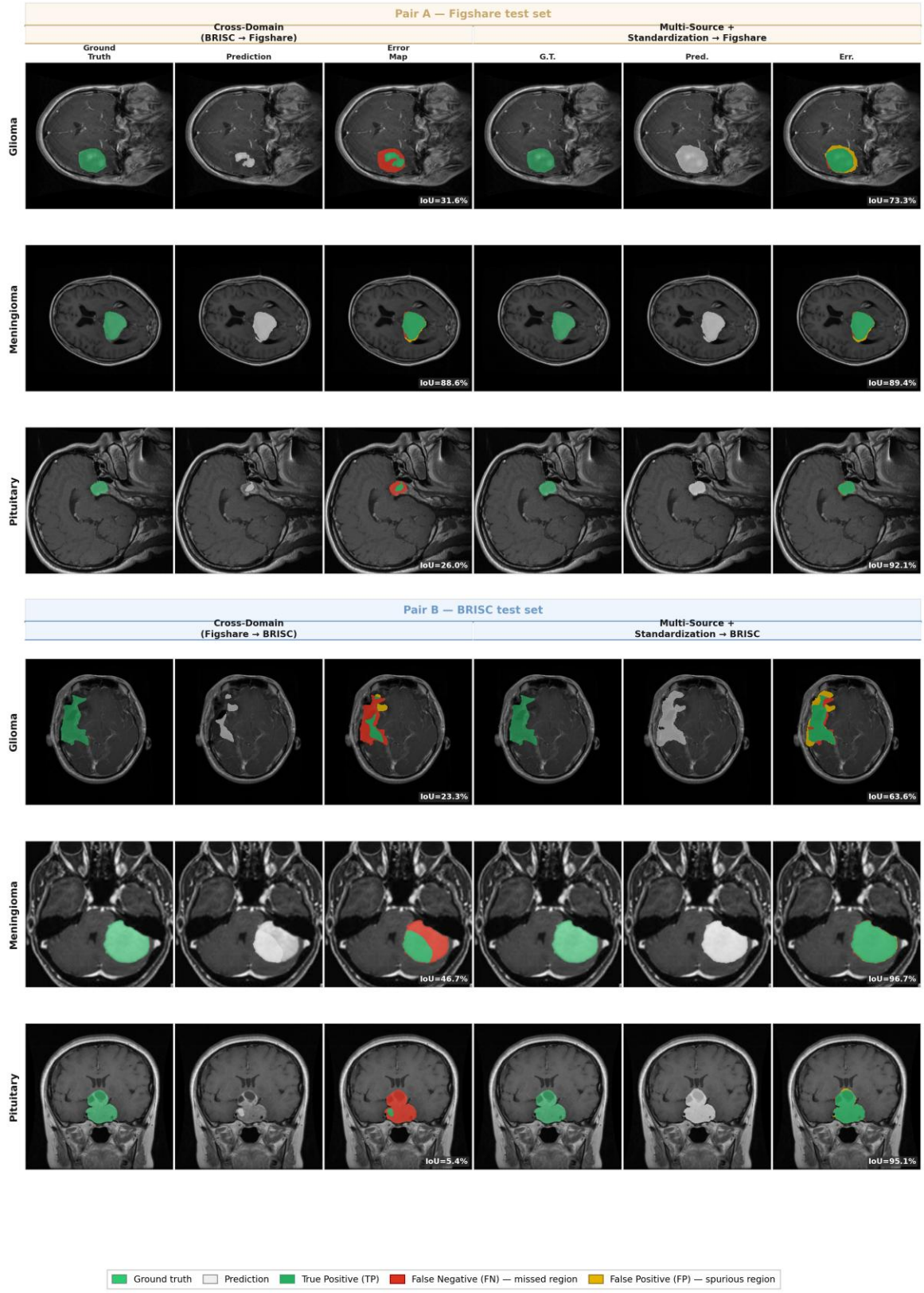


Figure 5. Qualitative cross-dataset evaluation. Pair A (Figshare test set) and Pair B (BRISC test set) each compare single-source cross-domain transfer against multi-source standardized training. Error maps show true positives (green), false negatives (red), and false positives (orange), with per-case IoU annotated.

4. Discussion

4.1. Efficiency–Accuracy Trade-off

The aggregate mIoU difference between A3Net and Attention U-Net is non-significant ($p_t = 0.334$), establishing efficiency parity rather than accuracy superiority: A3Net matches a 31.6 M-parameter model at 2.11 M parameters (15.0× reduction) and 1.39 GFLOPs (78.8× reduction). The per-class picture reveals complementary advantages: SE channel recalibration benefits meningioma and pituitary (statistically significant), consistent with channel-wise recalibration being most effective for high-contrast, well-circumscribed boundaries, while spatial attention gates retain a large advantage on glioma ($p < 0.001$, $d = -2.35$) by providing a larger effective receptive field for irregular infiltrative margins. Capacity scaling (A3Net-2x, 4.19 M) improves glioma IoU by only +1.00 pp (64.88% → 65.88%) and remains 0.49 pp below Attention U-Net at 7.5× fewer parameters, confirming a fundamental 2D receptive-field limitation rather than a capacity problem, and motivating the volumetric extension described in Section 4.5.

4.2. Why Standardization Partially Reduces the Domain Gap

The zero-shot domain gap of −29.90 pp (Figshare→BRISC) is strongly asymmetric, with the reverse direction reaching only −12.64 pp. The mean intensity difference is only 2.62 units ($\mu_{BRISC} = 42.01$, $\sigma_{BRISC} = 44.21$ vs. $\mu_{Figshare} = 39.39$, $\sigma_{Figshare} = 42.09$), suggesting that intensity shift is not the primary cause. The dominant driver is class-distribution mismatch: Figshare is glioma-dominant (46.5% of slices) versus BRISC pituitary-dominant (36.6%), creating systematically different decision boundaries that preprocessing alone cannot resolve. Per-channel z-score standardization under multi-source training accounts for the +3.05 pp improvement. Importantly, this +3.05 pp gain is obtained under target-inclusive training, in which the model has direct access to BRISC data, whereas the −29.90 pp zero-shot gap is measured under fully target-blind evaluation. These two quantities correspond to fundamentally different experimental conditions and cannot be legitimately combined into a single "closure fraction"; the earlier framing that expressed one as a percentage of the other is therefore withdrawn. What can be stated is that even under the more favourable multi-source condition, standardization alone recovers only a small fraction of the target-domain performance, and closing the remaining performance shortfall requires explicit class-aware domain adaptation. The failure of Std+CLAHE (73.81%, below the single-source baseline of 74.66%) further confirms that CLAHE-based processing introduces spectral artifacts that widen rather than narrow the inter-dataset intensity gap.

4.3. Internal BRISC Distribution Shift

The internal distribution shift within BRISC 2025 is mild: training $\mu = 42.01$, $\sigma = 44.21$ vs. test $\mu = 43.12$, $\sigma = 45.83$, differing by approximately 1.1 intensity units in mean and 1.6 in standard deviation. Although minor, this represents an uncontrolled confound that affects all reported test scores equally and should be noted when interpreting absolute performance figures.

4.4. Clinical Relevance

The 8.15 ms latency on a consumer-grade RTX 3050 6 GB Laptop GPU is compatible with point-of-care or intra-operative segmentation support. The 8.66 MB model size facilitates deployment on edge devices or DICOM-integrated workstations without specialized infrastructure, though prospective clinical validation is required before any deployment. The full training pipeline runs on a laptop GPU, removing the dependency on high-performance computing clusters. These characteristics are directly relevant to resource-constrained settings such as community hospitals in low- and middle-income countries.

Beyond pixel-level segmentation, the predicted masks produced by A3Net can serve as spatial priors for a lightweight downstream classification pipeline without requiring a separate neural backbone. Geometric and intensity-based features extracted from A3Net masks on an independent external dataset (N = 1,468; Mendeley Brain Tumor MRI Dataset, Hira et al., 2026) achieve mean 5-fold cross-validated classification accuracy of 92.89% for BRISC-trained models, 90.73% for Combined-trained models, and 71.83% for Figshare-trained models. The lower Figshare accuracy mirrors the cross-dataset domain gap characterised in Section 3.6 and is corroborated by the overlapping tumour-type clusters visible in Figure 6, where Figshare-trained masks fail to produce well-separated class representations on unseen data. This proof-of-concept result indicates that a single A3Net inference pass can simultaneously support segmentation and tumour-type classification in resource-constrained clinical pipelines, without the overhead of a dedicated classification head.

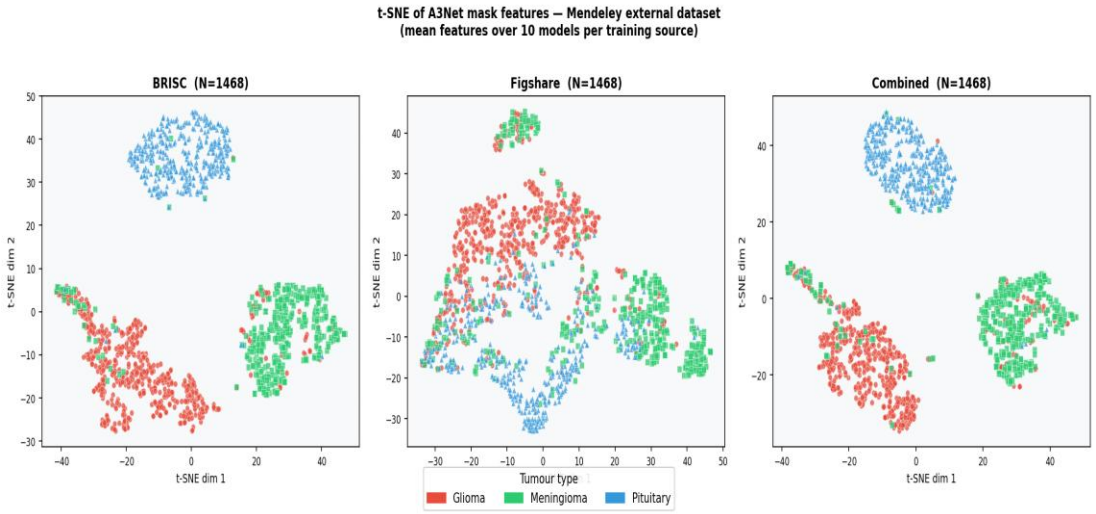


Figure 6. t-SNE visualisation of mask-derived features from A3Net predictions on the Mendeley external dataset (N = 1,468; mean over 10 models per training source). BRISC- and Combined-trained models yield well-separated tumour-type clusters; Figshare-trained models show overlapping representations, consistent with the cross-dataset domain gap.

4.5. Limitations and Future Work

First, per-channel z-score standardization under multi-source training yields only a partial +3.05 pp recovery relative to the −29.90 pp zero-shot gap; these two values are measured under different experimental conditions (target-inclusive vs. target-blind) and are therefore not directly comparable. Class-imbalance and acquisition variability remain the dominant unresolved factors, and explicit class-aware domain adaptation modules are required to make further progress. Second, glioma segmentation remains at 64.88% IoU on BRISC, reflecting the fundamental difficulty of delineating infiltrative margins in 2D; boundary-aware loss terms or hybrid spatial-channel attention mechanisms represent promising but as yet unvalidated directions. Third, the mild internal BRISC intensity shift is not addressed by the present preprocessing pipeline and represents an uncontrolled confound for all reported scores. Fourth, A3Net operates on 2D slices: both BRISC 2025 and Figshare provide independent single-slice annotations without volumetric continuity metadata, making 2.5D or 3D supervision infeasible without re-annotation. While 2D inference enables direct deployment on standard DICOM workstations without volumetric reconstruction (subject to prospective clinical validation), extension to datasets with inter-slice correspondence — such as BraTS (Bakas et al., 2018) — remains an explicit future direction. Fifth, per-class ablation metrics are not reported for individual variants; systematic per-class ablation would clarify which design choices most affect glioma, meningioma, and pituitary separately. Sixth, cross-dataset evaluation is limited to two publicly available datasets sharing the same three-class annotation protocol on 2D T1-CE MRI. To our knowledge, no other publicly available dataset provides simultaneous multi-class annotations for all three tumour types in this modality and dimensionality. Volumetric datasets such as BraTS 2019 (Bakas et al., 2018) cover glioma only under a binary protocol, and multi-institutional datasets (e.g., OpenNeuro ds007045, Filimonova et al., 2025) provide 3D multi-modal acquisitions incompatible with A3Net's 2D single-modality design without substantial re-annotation effort. Expanding evaluation to additional multi-class 2D T1-CE datasets, or extending A3Net to 3D volumetric processing, remains an explicit direction for future work.

5. Conclusion

We presented A3Net, a lightweight encoder–decoder that, to our knowledge, establishes the first multi-class segmentation benchmark on BRISC 2025 and the first systematic characterization of its cross-dataset domain gap with Figshare under matched evaluation protocols. A3Net integrates depth-wise separable convolutions, squeeze-and-excitation channel attention, a cross-entropy + Dice composite loss, and summation-based skip fusion. On the cleaned BRISC 2025 benchmark under 2-seed × 5-fold cross-validation, A3Net attains 77.79 ± 0.29% mIoU and 87.14 ± 0.17% Dice at 2.11 M parameters, 1.39 GFLOPs, and 8.15 ms latency — outperforming every from-scratch model below 5 M parameters and achieving statistical parity with Attention U-Net (31.6 M, P=0.334) at 15.0× lower parameter cost. Per-class analysis reveals statistically significant advantages on meningioma (+1.54 pp IoU, P=0.007, d = +1.15) and pituitary (+0.42 pp IoU, P=0.016, d = +0.99), while Attention U-Net retains a

significant advantage on glioma (−1.49 pp IoU, $p < 0.001$, $d = -2.35$); capacity scaling (A3Net-2x, 4.19 M) improves glioma IoU by only +1.00 pp yet remains 0.49 pp below Attention U-Net, confirming the gap reflects a 2D receptive-field limitation rather than insufficient model capacity. Per-channel z-score standardization under multi-source training provides partial cross-dataset recovery (+3.05 pp); because this recovery is obtained under target-inclusive training whereas the −29.90 pp Figshare→BRISC gap is measured under fully target-blind zero-shot conditions, the two quantities correspond to non-equivalent experimental settings and are not directly commensurable. Class-distribution mismatch is identified as the dominant unresolved factor, motivating class-aware domain adaptation as the primary future direction. Future work additionally includes matched-initialization transformer comparisons, 3D volumetric extensions, and prospective clinical validation on multi-institutional cohorts.

Author Contributions

The percentages of the authors' contributions are presented below. All authors reviewed and approved the final version of the manuscript.

	T.B.	E.H.A.A
C	40	30
D	40	30
S	40	30
DCP	40	30
DAI	40	30
L	40	30
W	40	30
CR	40	30
SR	40	30
PM	40	30
FA	40	30

C= concept, D= design, S= supervision, DCP= data collection and/or processing, DAI= data analysis and/or interpretation, L= literature search, W= writing, CR= critical review, SR= submission and revision, PM= project management, FA= funding acquisition.

Conflict of Interest

The authors declared that there is no conflict of interest.

Ethical Consideration

Ethics committee approval was not required for this study because it did not involve new data collection from humans or animals; all MRI data used (BRISC 2025, Figshare, Akter-Seg, and the Mendeley external dataset) are publicly available, de-identified, secondary datasets used strictly for computational model development and evaluation.

Acknowledgements

The authors did not receive administrative, technical, or in-kind support beyond the resources acknowledged in the Funding statement.

Data Availability

The BRISC 2025 dataset is publicly available via Fateh et al. (2026) at https://doi.org/10.1038/s41597-026-06753-y. The Figshare brain tumor dataset (Cheng, 2017) is available at https://doi.org/10.6084/m9.figshare.1512427. The Akter-Seg dataset (Akter et al., 2024) is publicly available on Kaggle at atikaakter11/brain-tumor-segmentation-dataset.

References

Akter, A., Nosheen, N., Ahmed, S., Hossain, M. Z., Yousuf, M. A., Almoyad, M. A. A., Hasan, K. F., & Moni, M. A. (2024). Robust clinical applicable CNN and U-Net based algorithm for MRI classification and segmentation for brain tumor. *Expert Systems with Applications*, *238*, Article 122347. https://doi.org/10.1016/j.eswa.2023.122347

Badža, M. M., & Barjaktarović, M. C. (2021). Segmentation of brain tumors from MRI images using convolutional autoencoder. *Applied Sciences*, *11*(9), Article 4317. https://doi.org/10.3390/app11094317

Bakas, S., Reyes, M., Jakab, A., Bauer, S., Rempfler, M., Crimi, A., Shin, H. G., Berger, C., Ha, S. M., Rozycki, M., Prastawa, M., Alberts, E., Rieger, J., Sako, C., Wiest, R., Pfeiffer, D., Kirschke, J. S., Koumoutsakos, P., Davatzikos, C., ... Menze, B. H. (2018). *Identifying the best machine learning algorithms for brain tumor segmentation, progression assessment, and overall survival prediction in the BRATS challenge* (arXiv:1811.02629). arXiv. https://doi.org/10.48550/arXiv.1811.02629

Bhamboo, A. K., Mahala, S., Kumar, Y., Shekhawat, N. S., & Sharma, K. (2025). *Trust-refined U-Net ensemble for uncertainty-aware brain tumor segmentation*. TechRxiv. https://doi.org/10.36227/techrxiv.175492140.09803812/v1

Bhuiyan, M. R. I., Bhat, S., Qahqaie, M., Rahman, M. M., & Islam, M. S. (2026). *LoGSAM: Parameter-efficient cross-modal grounding for MRI segmentation* (arXiv:2603.17576). arXiv. https://doi.org/10.48550/arXiv.2603.17576

Bindhu, R., & Vimala, S. (2026). A-Lite UACNet: Hybrid attention U-Net with active contour for efficient brain tumor segmentation. In *Proceedings of the 2026 IEEE Recent Advances in Electrical, Electronics, Ubiquitous Communication, and Computational Intelligence (RAEEUCCI)* (pp. 1–6). IEEE. https://doi.org/10.1109/RAEEUCCI67649.2026.11504790

Cao, H., Wang, Y., Chen, J., Jiang, D., Zhang, X., Tian, Q., & Wang, M. (2022). Swin-UNet: UNet-like pure transformer for medical image segmentation. In L. Karlinsky, T. Michaeli, & K. Nishino (Eds.), *Computer Vision – ECCV 2022 Workshops* (Lecture Notes in Computer Science, Vol. 13803, pp. 205–218). Springer. https://doi.org/10.1007/978-3-031-25066-8_9

Chaurasia, A., & Culurciello, E. (2017). LinkNet: Exploiting encoder representations for efficient semantic segmentation. In *Proceedings of the 2017 IEEE Visual Communications and Image*

Processing (VCIP) (pp. 1–4). IEEE. https://doi.org/10.1109/VCIP.2017.8305148

Chen, L.-C., Zhu, Y., Papandreou, G., Schroff, F., & Adam, H. (2018). Encoder–decoder with atrous separable convolution for semantic image segmentation. In V. Ferrari, M. Hebert, C. Sminchisescu, & Y. Weiss (Eds.), *Computer Vision – ECCV 2018* (Lecture Notes in Computer Science, Vol. 11211, pp. 833–851). Springer. https://doi.org/10.1007/978-3-030-01234-2_49

Cheng, J. (2017). *Brain tumor dataset* [Data set]. Figshare. https://doi.org/10.6084/m9.figshare.1512427

Chollet, F. (2017). Xception: Deep learning with depthwise separable convolutions. In *Proceedings of the IEEE Conference on Computer Vision and Pattern Recognition (CVPR)* (pp. 1251–1258). IEEE. https://doi.org/10.1109/CVPR.2017.195

Díaz-Pernas, F. J., Martínez-Zarzuela, M., Antón-Rodríguez, M., & González-Ortega, D. (2021). A deep learning approach for brain tumor classification and segmentation using a multiscale convolutional neural network. *Healthcare*, *9*(2), Article 153. https://doi.org/10.3390/healthcare9020153

Dou, Q., Ouyang, C., Chen, C., Chen, H., Glocker, B., Zhuang, X., & Heng, P.-A. (2019). PnP-AdaNet: Plug-and-play adversarial domain adaptation network with a benchmark at cross-modality cardiac segmentation. *IEEE Access*, *7*, 99–111. https://doi.org/10.1109/ACCESS.2019.2929258

Elfwing, S., Uchibe, E., & Doya, K. (2018). Sigmoid-weighted linear units for neural network function approximation in reinforcement learning. *Neural Networks*, *107*, 3–11. https://doi.org/10.1016/j.neunet.2017.12.012

Fahim, T. A., Alam, F. B., & Hossain, M. A. (2025). Brain tumor detection, classification and segmentation by deep learning models from MRI images: Recent approaches, challenges and future directions. *Array*, *28*, Article 100571. https://doi.org/10.1016/j.array.2025.100571

Fateh, A., Rezvani, Y., Moayedi, S., Shirani, M., Rahimi, A., & Kashef, R. (2026). BRISC: Annotated dataset for brain tumor segmentation and classification. *Scientific Data*, *13*, Article 361. https://doi.org/10.1038/s41597-026-06753-y

Filimonova, E., Leone, A., Carbone, F., D'Agata, F., Rossi, R., & Vercelli, A. (2025). *Real-world multi-institutional glioblastoma MRI dataset with standardized preprocessing, expert-validated segmentation, and MGMT promoter profiling* (v1.0.1) [Data set]. OpenNeuro. https://doi.org/10.18112/openneuro.ds007045.v1.0.1

Ganin, Y., Ustinova, E., Ajakan, H., Germain, P., Larochelle, H., Laviolette, F., Marchand, M., & Lempitsky, V. (2016). Domain-adversarial training of neural networks. *Journal of Machine Learning Research*, *17*(59), 1–35. https://jmlr.org/papers/v17/15-239.html

Guan, H., & Liu, M. (2022). Domain adaptation for medical image analysis: A survey. *IEEE Transactions on Biomedical Engineering*, *69*(3), 1173–1185. https://doi.org/10.1109/TBME.2021.3117407

Havaei, M., Davy, A., Warde-Farley, D., Biard, A., Courville, A., Bengio, Y., Pal, C., Jodoin, P.-M., & Larochelle, H. (2017). Brain tumor segmentation with deep neural networks. *Medical Image Analysis*, *35*, 18–31. https://doi.org/10.1016/j.media.2016.05.004

Hira, M. I. K., Hossain, M. S., Bithee, M. M. A., Sara, U., Hasan, M. M., Towsif, A. A., & Ahmed, M. K. (2026). *Brain tumor MRI dataset (Glioma, Meningioma, Pituitary, No Tumor)* (V6) [Data set]. Mendeley Data. https://doi.org/10.17632/zwr4ntf94j.6

Howard, A. G., Zhu, M., Chen, B., Kalenichenko, D., Wang, W., Weyand, T., Andreetto, M., & Adam, H. (2017). *MobileNets: Efficient convolutional neural networks for mobile vision applications* (arXiv:1704.04861). arXiv. https://doi.org/10.48550/arXiv.1704.04861

Howard, A., Sandler, M., Chu, G., Chen, L.-C., Chen, B., Tan, M., Wang, W., Yukrut, Y., Vasudevan, V., Le, Q. V., & Adam, H. (2019). Searching for MobileNetV3. In *Proceedings of the IEEE/CVF International Conference on Computer Vision (ICCV)* (pp. 1314–1324). IEEE. https://doi.org/10.1109/ICCV.2019.00140

Hu, J., Shen, L., & Sun, G. (2018). Squeeze-and-excitation networks. In *Proceedings of the IEEE Conference on Computer Vision and Pattern Recognition (CVPR)* (pp. 7132–7141). IEEE. https://doi.org/10.1109/CVPR.2018.00745

Huang, X., & Belongie, S. (2017). Arbitrary style transfer in real-time with adaptive instance normalization. In *Proceedings of the IEEE International Conference on Computer Vision (ICCV)* (pp. 1501–1510). IEEE. https://doi.org/10.1109/ICCV.2017.167

Isensee, F., Jaeger, P. F., Kohl, S. A. A., Petersen, J., & Maier-Hein, K. H. (2021). nnU-Net: A self-configuring method for deep learning-based biomedical image segmentation. *Nature Methods*, *18*(2), 203–211. https://doi.org/10.1038/s41592-020-01008-z

Kamnitsas, K., Baumgartner, C., Ledig, C., Newcombe, V., Simpson, J., Kane, A., Menon, D., Nori, A., Criminisi, A., Rueckert, D., & Glocker, B. (2017). Unsupervised domain adaptation in brain lesion segmentation with adversarial networks. In S. Ourelin, L. Joskowicz, M. R. Sabuncu, G. Unal, & W. Wells (Eds.), *Information Processing in Medical Imaging (IPMI 2017)* (Lecture Notes in Computer Science, Vol. 10265, pp. 597–609). Springer. https://doi.org/10.1007/978-3-319-59050-9_47

Kuzhan, Y., & Günay, M. (2026). Comparative evaluation of CNN and transformer-based models for brain tumor MRI segmentation. *Journal of Computer Science and Technology Studies*, *8*(7), 75–83. https://alkindipublisher.com/index.php/jcsts/article/view/12720/11395

Loshchilov, I., & Hutter, F. (2017). *SGDR: Stochastic gradient descent with warm restarts* [Paper presentation]. 5th International Conference on Learning Representations (ICLR 2017), Toulon, France. https://doi.org/10.48550/arXiv.1608.03983

Loshchilov, I., & Hutter, F. (2019). *Decoupled weight decay regularization* [Paper presentation]. 7th International Conference on Learning Representations (ICLR 2019), New Orleans, LA, United States. https://doi.org/10.48550/arXiv.1711.05101

Louis, D. N., Perry, A., Wesseling, P., Brat, D. J., Cree, I. A., Figarella-Branger, D., Hawkins, C., Ng, H. K., Pfister, S. M., Reifenberger, G., Soffietti, R., von Deimling, A., & Ellison, D. W. (2021). The 2021 WHO classification of tumors of the central nervous system: A summary. *Neuro-Oncology*, *23*(8), 1231–1251. https://doi.org/10.1093/neuonc/noab106

Mayala, S., Herdlevær, I., Haugsøen, J. B., Anandan, S., Gavasso, S., & Brun, M. (2022). Brain tumor segmentation based on minimum spanning tree. *Frontiers in Signal Processing*, *2*, Article 816186. https://doi.org/10.3389/frsip.2022.816186

Mehta, S., Rastegari, M., Shapiro, L., & Hajishirzi, H. (2019). ESPNetv2: A light-weight, power efficient, and general purpose CNN. In *Proceedings of the IEEE/CVF Conference on Computer Vision and Pattern Recognition (CVPR)* (pp. 9190–9200). IEEE. https://doi.org/10.1109/CVPR.2019.00941

Menze, B. H., Jakab, A., Bauer, S., Kalpathy-Cramer, J., Farahani, K., Kirby, J., Burren, Y., Porz, N., Slotboom, J., Wiest, R., Lanczi, L., Gerstner, E., Weber, M. A., Arbel, T., Avants, B. B., Ayache, N., Buendia, P., Collins, D. L., Cordier, N., ... Van Leemput, K. (2015). The multimodal brain tumor image segmentation benchmark (BRATS). *IEEE Transactions on Medical Ima* Sandler *ging*, *34*(10), 1993–2024. https://doi.org/10.1109/TMI.2014.2377694

Milletari, F., Navab, N., & Ahmadi, S.-A. (2016). V-Net: Fully convolutional neural networks for volumetric medical image segmentation. In *Proceedings of the 2016 Fourth International Conference on 3D Vision (3DV)* (pp. 565–571). IEEE. https://doi.org/10.1109/3DV.2016.79

Musthafa, N., Masud, M. M., Memon, Q., & Farhad, M. (2025). VISION: View-specific integrated segmentation-classification framework for accurate brain tumor detection in MRI scans. *PLOS ONE*, *20*(5), Article e0332395. https://doi.org/10.1371/journal.pone.0332395

Oktay, O., Schlemper, J., Le Folgoc, L., Lee, M., Heinrich, M., Misawa, K., Mori, K., McDonagh, S., Glocker, B., & Rueckert, D. (2018). *Attention U-Net: Learning where to look for the pancreas* (arXiv:1804.03999). arXiv. https://doi.org/10.48550/arXiv.1804.03999

Ostrom, Q. T., Price, M., Neff, C., Cioffi, G., Waite, K. A., Kruchko, C., & Barnholtz-Sloan, J. S. (2022). CBTRUS statistical report: Primary brain and other central nervous system tumors diagnosed in the United States in 2015–2019. *Neuro-Oncology*, *24*(Suppl 5), v1–v95. https://doi.org/10.1093/neuonc/noac202

Pacal, I., & Deveci, M. (2026). The next generation of convolutional neural networks in neuro-oncology: A comparative analysis of performance, model complexity, and efficiency in brain tumor diagnosis. *Brain Network Disorders*, Article 100001. https://doi.org/10.1016/j.bnd.2026.02.001

Paszke, A., Chaurasia, A., Kim, S., & Culurciello, E. (2016). *ENet: A deep neural network architecture for real-time semantic segmentation* (arXiv:1606.02147). arXiv. https://doi.org/10.48550/arXiv.1606.02147

Pereira, S., Pinto, A., Alves, V., & Silva, C. A. (2016). Brain tumor segmentation using convolutional neural networks in MRI images. *IEEE Transactions on Medical Imaging*, *35*(5), 1240–1251. https://doi.org/10.1109/TMI.2016.2538465

Preetha, R., Priyadarsini, M. J. P., & Nisha, J. S. (2025). Brain tumor segmentation using multi-scale attention U-Net with EfficientNetB4 encoder for enhanced MRI analysis. *Scientific Reports*, *15*(1), Article 9914. https://doi.org/10.1038/s41598-025-94267-9

Rashid, M. M., Singh, S., & Ahmed, A. (2026). Deep learning based methods for brain tumor segmentation in MRI: A review. *DMPedia Lecture Notes in Multidisciplinary Research*, *1*, 76. https://digitalmanuscriptpedia.com/conferences/index.php/DMP-LNMR/article/view/76

Razzaghi, P., Abbasi, K., Shirazi, M., & Rashidi, S. (2022). Multimodal brain tumor detection using multimodal deep transfer learning. *Applied Soft Computing*, *129*, Article 109631. https://doi.org/10.1016/j.asoc.2022.109631

Ronneberger, O., Fischer, P., & Brox, T. (2015). U-Net: Convolutional networks for biomedical image segmentation. In N. Navab, J. Hornegger, W. M. Wells, & A. Frangi (Eds.), *Medical Image Computing and Computer-Assisted Intervention – MICCAI 2015* (Lecture Notes in Computer Science, Vol. 9351, pp. 234–241). Springer. https://doi.org/10.1007/978-3-319-24574-4_28

Sandler, M., Howard, A., Zhu, M., Zhmoginov, A., & Chen, L.-C. (2018). MobileNetV2: Inverted residuals and linear bottlenecks. In *Proceedings of the IEEE Conference on Computer Vision and Pattern Recognition (CVPR)* (pp. 4510–4520). IEEE. https://doi.org/10.1109/CVPR.2018.00474

Sobhaninia, Z., Rezaei, S., Karimi, N., Emami, A., & Samavi, S. (2020). Brain tumor segmentation by cascaded deep neural networks using multiple image scales. In *Proceedings of the 2020 28th Iranian Conference on Electrical Engineering (ICEE)* (pp. 1–4). IEEE. https://doi.org/10.1109/ICEE50131.2020.9260876

Tan, M., & Le, Q. V. (2019). EfficientNet: Rethinking model scaling for convolutional neural networks. In *Proceedings of the 36th International Conference on Machine Learning (ICML)* (pp. 6105–6114). PMLR. https://doi.org/10.48550/arXiv.1905.11946

Thahiruddin, M., & Wulandari, A. (2025). CNNs vs. hybrid transformers for brain tumor classification on the BRISC dataset. *Journal of Applied Technology and Information Management*, *6*(1), 1–12. https://api.semanticscholar.org/CorpusID:281623477

Tibshirani, R. J., & Efron, B. (1993). An introduction to the bootstrap. Monographs on statistics and applied probability, 57(1), 1-436.

Ullah, M. S., Khan, M. A., Albarakati, H. M., Damasevicius, R., & Alsenan, S. (2024). Multimodal brain tumor segmentation and classification from MRI scans based on optimized DeepLabV3+ and interpreted networks information fusion empowered with explainable AI. *Computers in Biology and Medicine*, *182*, Article 109183. https://doi.org/10.1016/j.compbiomed.2024.109183

Wang, M., & Deng, W. (2018). Deep visual domain adaptation: A survey. *Neurocomputing*, *312*, 135–153. https://doi.org/10.1016/j.neucom.2018.05.083

Woo, S., Park, J., Lee, J.-Y., & Kweon, I. S. (2018). CBAM: Convolutional block attention module. In V. Ferrari, M. Hebert, C. Sminchisescu, & Y. Weiss (Eds.), *Computer Vision – ECCV 2018* (Lecture Notes in Computer Science, Vol. 11211, pp. 3–19). Springer. https://doi.org/10.1007/978-3-030-01234-2_1

Xie, E., Wang, W., Yu, Z., Anandkumar, A., Alvarez, J. M., & Luo, P. (2021). SegFormer: Simple and efficient design for semantic segmentation with transformers. *Advances in Neural Information Processing Systems*, *34*, 12077–12090.

Yu, C., Gao, C., Wang, J., Yu, G., Shen, C., & Sang, N. (2021). BiSeNet V2: Bilateral network with guided aggregation for real-time semantic segmentation. *International Journal of Computer Vision*, *129*(11), 3051–3068.

Zhu, J.-Y., Park, T., Isola, P., & Efros, A. A. (2017). Unpaired image-to-image translation using cycle-consistent adversarial networks. In *Proceedings of the IEEE International Conference on Computer Vision (ICCV)* (pp. 2223–2232). IEEE. https://doi.org/10.1109/ICCV.2017.244

Black Sea Journal of Engineering and Science
doi: 10.34248/bsengineering.2000932

Open Access Journal
e-ISSN: 2619 – 8991

Research Article
Volume 9 - Issue 5: 2738-2748 / September 2026

DESIGN, FABRICATION, AND QPSK-BASED VALIDATION OF A COMPACT TWO-PORT MIMO ANTENNA WITH DEFECTED GROUND STRUCTURE FOR 5 GHZ WLAN APPLICATIONS

Cem GOCEN[1]*

[1]*Izmir Katip Celebi University, Electrical and Electronics Engineering Department, 35620, Izmir, Türkiye*

Abstract: This study presents the design, fabrication, and measurement of a compact FR4-based printed monopole antenna and its two-port MIMO configuration for 5 GHz WLAN applications. The single antenna consists of a microstrip-fed chamfered rectangular radiator and a partial ground plane with a narrow defected ground slot. The optimized antenna is mainly evaluated around the 5.5 GHz WLAN region and provides acceptable impedance matching at the target frequency, with simulated and measured S_{11} values of approximately −10.90 dB and −10.62 dB at 5.5 GHz, respectively. The gain estimated using the substitution method is approximately 1.30 dBi at 5.5 GHz. The antenna is then extended to a symmetrical two-port MIMO structure using a shared partial ground plane and a central I-shaped defected ground structure for coupling reduction. The MIMO results show S_{11} below −18 dB around 5.5 GHz and an S_{12} level close to -10 dB, corresponding to approximately 10 dB inter-port isolation. Under the S-parameter-based diversity evaluation, the maximum ECC is approximately 0.01, while the DG remains close to 10 dB. A 2 × 2 OTA QPSK testbed was implemented by connecting both ports of the transmitting and receiving MIMO prototypes to two independent transmit and two independent receive RF chains, respectively. The measured link-level EVM values were 7.4%, 4.8%, and 6.2% at 5.18, 5.50, and 5.825 GHz, respectively. The results show that the proposed antenna provides a practical balance between compact size, simple fabrication, and acceptable WLAN-band MIMO performance.

Keywords: MIMO antenna, FR4 antenna, WLAN, Defected ground structure, QPSK constellation

***Corresponding author:** Izmir Katip Celebi University, Electrical and Electronics Engineering Department, 35620, Izmir, Türkiye
E mail: cem.gocen@ikcu.edu.tr (C. GOCEN)
Cem GOCEN https://orcid.org/0000-0002-8086-5690

Received: July 22, 2026
Accepted: August 23, 2026
Published: September 15, 2026

Cite as: Gocen, C. (2026). Design, fabrication, and QPSK-based validation of a compact two-port MIMO antenna with defected ground structure for 5 GHz WLAN applications. *Black Sea Journal of Engineering and Science*, 9(5), 2738-2748.

1. Introduction

The rapid increase in wireless data traffic has increased the need for compact, low-cost, and easily integrated antennas operating in the sub-6 GHz spectrum. Wireless local area network (WLAN), Wi-Fi 6, Wi-Fi 7, and sub-6 GHz 5G systems require antenna structures that can provide acceptable impedance matching, stable radiation behavior, and practical fabrication compatibility within limited device volumes (Addepalli et al., 2023; Ali et al., 2023; You et al., 2023; Cheng et al., 2024). In particular, the 5 GHz WLAN region remains important for short-range, high-data-rate communication systems, and compact antenna solutions around 5.2–5.8 GHz continue to be widely investigated for terminal, laptop, sensor, and embedded wireless devices (Addepalli, 2023; Addepalli et al., 2023; Ali et al., 2023; You et al., 2023; Pradeep et al., 2024).

Microstrip and printed monopole antennas are frequently preferred for such applications because of their simple geometry, low profile, low fabrication cost, and compatibility with standard printed circuit board (PCB) processes (Saeidi et al., 2023; Sushma Chowdary et al., 2023; Khushbu and Prakash, 2024). FR4 is especially attractive for low-cost prototypes and practical wireless devices because of its availability and ease of manufacturing. However, FR4 also introduces design challenges at microwave frequencies because of its relatively high dielectric loss and possible variation in dielectric properties. Therefore, the antenna geometry, feed line, ground plane, and impedance-tuning elements must be carefully optimized to obtain acceptable matching and stable radiation performance (Wang et al., 2022; Sushma Chowdary et al., 2023; You et al., 2023).

Several studies have investigated compact printed antennas and MIMO antenna systems for WLAN, Wi-Fi, and sub-6 GHz applications. Recent MIMO antenna designs have used compact layouts, orthogonal or symmetrical element placement, slots, parasitic structures, defected ground structures (DGSs), and metamaterial-inspired decoupling features to improve matching and isolation (Baytöre et al., 2019; Bayarzaya et al., 2022; Liu et al., 2022; Addepalli, 2023; Addepalli et al., 2023; Güler and Bayer Keskin, 2023; Sushma Chowdary et al., 2023; You et al., 2023; Khushbu and Prakash, 2024;

This work is licensed (CC BY-NC 4.0) under Creative Commons Attribution 4.0 International License

Pannu, 2024; Pradeep et al., 2024). These studies show that mutual coupling is one of the main limitations of compact MIMO antennas. Increasing the distance between radiating elements can improve isolation, but this approach directly increases the antenna size. For this reason, ground-plane modification and local current-path control are practical alternatives for compact designs (Liu et al., 2022; Sushma Chowdary et al., 2023; Pannu, 2024).

In MIMO antenna evaluation, reflection and transmission coefficients are not sufficient by themselves. Diversity-related parameters such as the envelope correlation coefficient (ECC), diversity gain (DG), total active reflection coefficient (TARC), mean effective gain (MEG), and channel capacity loss (CCL) are also commonly used to evaluate the suitability of an antenna for MIMO operation (Addepalli, 2023; Güler and Bayer Keskin, 2023; Sushma Chowdary et al., 2023; You et al., 2023).

In addition to these antenna-level metrics, communication-level validation using modulated signals can provide a practical interpretation of the complete antenna and radio-frequency link. Software-defined-radio-based experiments have therefore been used to complement conventional antenna measurements. For example, Baro et al. (2026) performed system-level validation of a multiport antenna using an SDR-based platform and evaluated BPSK, QPSK, and QAM transmission through bit-error-rate measurements. Constellation diagrams and error vector magnitude measurements can similarly provide information about symbol clustering, signal spreading, and communication stability. However, these quantities represent the combined response of the antennas, RF front ends, synchronization algorithms, receiver noise, and propagation environment rather than the isolated antenna response.

Recent studies in the broader microwave-engineering field have also emphasized the importance of application-specific electromagnetic modeling, material properties, impedance control, and measurement-based validation. Murat et al. (2021) experimentally investigated a reflector-type microwave applicator operating in the 2.45 GHz ISM band. Göçen et al. (2022) presented an antenna model for 2.4 GHz RF energy-harvesting systems, demonstrating the importance of integrating antenna design with the intended electromagnetic application. Çakmak et al. (2026) showed that dielectric properties and electromagnetic attenuation can vary substantially with material composition. Murat (2026) combined full-wave electromagnetic simulation with data-driven optimization in a multi-source microwave system, while Murat et al. (2025) demonstrated active non-Foster impedance matching for antenna-bandwidth enhancement. Although these studies address different application domains and frequency ranges and are not direct WLAN MIMO benchmarks, they collectively underline the importance of material-aware electromagnetic modeling, explicit impedance-matching strategies, application-specific optimization, and experimental validation.

In the literature, many MIMO antenna designs provide high isolation by using additional decoupling structures or larger layouts. However, in low-cost compact FR4 designs, there is still a practical need for simple two-port structures that preserve the radiator geometry while improving coupling behavior through minimal ground-plane modification. A design approach based on a compact printed monopole radiator and a shared partial ground plane with a central isolation DGS can be useful for this purpose. Such a structure avoids external lumped components, neutralization lines, or multilayer decoupling networks and remains suitable for PCB milling or standard PCB fabrication.

In this study, a compact FR4-based printed monopole antenna operating around the 5.5 GHz region and its two-port MIMO version are presented. First, a single antenna element is designed using a microstrip-fed chamfered rectangular radiator, a partial ground plane, and a narrow rectangular DGS slot. The optimized antenna element is then extended to a symmetrical two-port MIMO configuration. In the MIMO design, a shared partial ground plane, local DGS slots, and a central I-shaped isolation DGS are used to control coupling between the two ports. The antenna prototypes are fabricated on an FR4 copper-clad laminate and evaluated using simulated and measured S-parameter results. The single antenna is also examined using simulated gain data and gain values estimated by the substitution method. For the MIMO configuration, the reflection and transmission coefficients are discussed together with the ECC and DG values. Finally, QPSK constellation measurements at 5.18, 5.50, and 5.825 GHz are used to provide a communication-level assessment in the WLAN portion of the operating band.

The main contribution of this work is the development and experimental evaluation of a simple, compact, and low-cost FR4-based antenna structure that operates around the 5.5 GHz region and can be extended to a two-port MIMO configuration without using complex decoupling networks. The proposed design is not intended to maximize all antenna parameters simultaneously; instead, it aims to provide a practical balance between compact size, fabrication simplicity, acceptable impedance matching, moderate MIMO isolation, low ECC, diversity-gain values close to 10 dB under the considered S-parameter-based evaluation, and stable QPSK constellation behavior in the 5 GHz WLAN band. The constellation and EVM results are interpreted as end-to-end communication-level indicators that include the effects of the antenna prototypes, RF hardware, synchronization procedures, and indoor propagation environment rather than as antenna-only performance metrics.

2. Materials and Methods

The proposed antenna was designed as a compact printed monopole radiator intended to operate around 5.5 GHz, with the main design target focused on the 5.5 GHz WLAN region. The −10 dB impedance-matching behavior was evaluated over the simulated and measured frequency sweeps rather than claimed as a fully bounded bandwidth. To achieve this objective within a limited footprint, a microstrip-fed monopole configuration with a partial ground plane was selected. This topology was preferred because it provides a wider impedance bandwidth and more flexible tuning behavior than a conventional narrowband patch structure. The geometry of the proposed antenna is shown in Figure 1. The top view and bottom view of the antenna are presented in Figure 1(a) and Figure 1(b), respectively, while the fabricated prototype is shown in Figure 1(c) and Figure 1(d). As seen in Figure 1 the design parameters are labeled on the proposed geometry. Therefore, their optimized numerical values are summarized in Table 1.

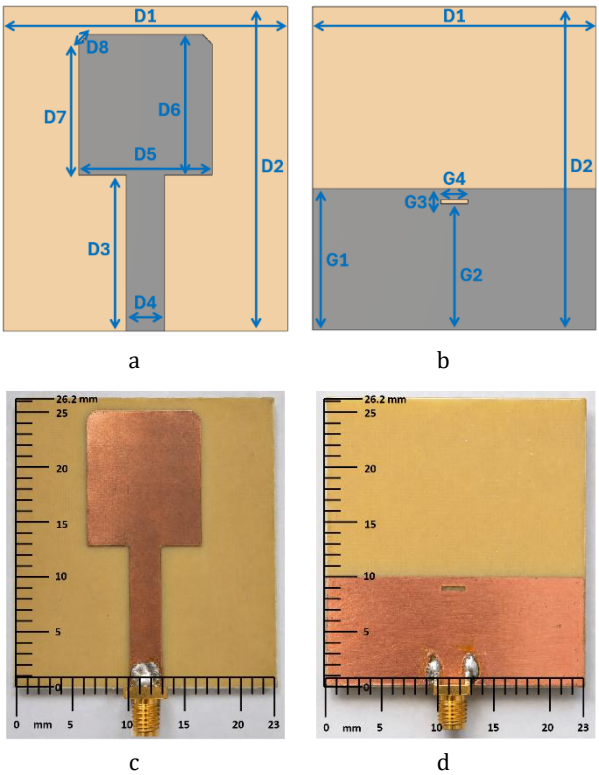


Figure 1. Geometry and fabricated prototype of the proposed antenna: (a) top view with radiator-side design parameters, (b) bottom view with partial-ground and defected-ground-slot parameters, (c) fabricated prototype top view, and (d) fabricated prototype bottom view.

Table 1. Optimized geometrical parameters of the proposed antenna

D1	D2	D3	D4	D5	D6
23.0	26.2	12.6	3.1	10.8	11.3
D7	D8	G1	G2	G3	G4
10.8	0.7	11.4	10.4	0.3	2.2

The proposed antenna consists of three main parts: a microstrip feed line, a chamfered rectangular monopole radiator, and a partial ground plane including a narrow rectangular defected ground slot. The antenna was implemented on an FR4 substrate with a relative permittivity of $\varepsilon_r = 4.3$, a loss tangent of $\tan\delta = 0.025$, and a thickness of h = 1.6 mm. The metallization thickness was 0.035 mm on both sides of the substrate. The overall substrate dimensions were selected as D1 × D2 = 23.0 mm × 26.2 mm, providing a compact physical footprint for operation around the 5.5 GHz band. The top-layer geometry of the antenna is shown in Figure 1(a). A 50 Ω microstrip feed line was used to excite the radiating element from the lower edge. The feed line was placed on the top side of the substrate and connected directly to the radiator without an additional matching network. Its width was fixed as D4 = 3.10 mm to obtain an approximately 50 Ω characteristic impedance on the 1.6 mm thick FR4 substrate. The feed length, denoted by D3, was optimized as 12.60 mm and determines the transition between the input port and the lower edge of the radiator. This transition region is important because it affects the coupling between the feed line, the radiator, and the partial ground plane on the opposite side of the substrate. The radiating element was designed as a compact rectangular monopole with a small chamfer introduced at the upper corner. The main radiator dimensions are represented by D5, D6, D7, and D8 in Figure 1(a). The radiator length primarily controls the resonant frequency, while the radiator width contributes to the impedance level and bandwidth behavior. The chamfered corner was included as a simple geometrical perturbation to improve impedance tuning without increasing the antenna size or introducing additional resonant structures. In the final design, the chamfer dimension was kept relatively small so that the antenna response remained centered around the desired 5.5 GHz region rather than becoming unnecessarily broadband.

The bottom-layer geometry is given in Figure 1(b). A partial ground plane was used instead of a full ground plane to support monopole-type radiation and to obtain a wider impedance bandwidth. The main ground-plane dimensions are defined by G1 and G2. In addition, a narrow rectangular defected ground slot was etched into the partial ground plane for fine adjustment of the input impedance. The slot dimensions are indicated by G3 and G4. This defected ground slot locally perturbs the surface-current distribution on the ground plane and changes the reactive component of the input impedance. Therefore, it was used as a secondary tuning element

rather than as a dominant resonant feature. The radiator, partial ground, feed transition, and defected ground slot were optimized together to position the main resonance near 5.5 GHz. During the design process, it was observed that the radiator length and partial ground length were the most effective parameters for shifting the resonance frequency. Increasing the radiator length or the partial ground length shifted the resonance toward lower frequencies, whereas reducing these dimensions shifted the response upward. The feed-to-radiator transition and the defected ground slot mainly affected the matching depth and the shape of the reflection coefficient curve. The final geometry was therefore not obtained by uniform scaling; instead, each critical parameter was adjusted according to its effect on the simulated reflection coefficient.

The electromagnetic design and optimization were carried out in CST Studio Suite using the time-domain solver. Open boundary conditions were assigned in all directions, and an air region was added around the antenna to reduce boundary-related reflections. The simulated response was evaluated mainly through the reflection coefficient, with the design target defined as S11 below −10 dB over the 4.8–5.9 GHz frequency interval. After the simulation-based optimization, the prototype shown in Figure 1(c) and Figure 1(d) was fabricated on an FR4 copper-clad laminate using a PCB milling machine available in our laboratory. The top copper layer contains the microstrip feed line and the chamfered monopole radiator, while the bottom copper layer contains the partial ground plane and the defected ground slot. After the milling process, the remaining copper surfaces and isolation gaps were visually inspected and cleaned to remove possible milling residues. A coaxial SMA connector was then attached to the end of the microstrip feed line. The fabricated antenna prototype was subsequently used for reflection-coefficient measurement and gain estimation using the substitution method. The S-parameter measurements were carried out in a standard non-anechoic laboratory environment using a two-port vector network analyzer configured to cover the frequency range from 100 kHz to 8 GHz. Before measurement, a full two-port short-open-load-through (SOLT) calibration was performed at the SMA connector reference planes using calibration standards specified over the range of 0.1–20 GHz. The calibration and antenna measurements were conducted in the same environment using the same cable configuration, and cable movement was minimized throughout the measurements. When an individual port of the MIMO prototype was characterized, the other port was terminated with a 50 Ω load. During full two-port S-parameter acquisition, both antenna ports were connected to the calibrated 50 Ω ports of the vector network analyzer.

The antenna gain was determined using the reference-antenna substitution method in an indoor, non-anechoic, line-of-sight setup. A radio-frequency signal generator was used to excite a broadband horn antenna operating from 0.8 to 8 GHz with a nominal gain of 10 dBi. Initially, two identical horn antennas were positioned 1 m apart to establish the reference link and characterize the combined propagation, cable, and connector losses. The receiving reference horn was then replaced by the proposed antenna without changing the separation, alignment, polarization, cable configuration, or measurement position. The received power was recorded using a spectrum analyzer. The gain of the antenna under test was calculated from the received-power difference according to equation 1,

$$G_{AUT}(f) = G_{ref}(f) + P_{AUT}(f) - P_{ref}(f) \quad (1)$$

where G_{ref} is the gain of the reference horn and P_{AUT} and P_{ref} are the received power levels measured using the proposed antenna and the reference horn, respectively. Since the gain measurements were performed indoors, residual multipath propagation was considered a source of measurement uncertainty.

The optimized single-element antenna was then extended to a two-port MIMO configuration. The purpose of this step was to evaluate whether the compact radiator could be used in a multi-antenna arrangement while preserving the impedance matching around the 5.5 GHz band and maintaining acceptable inter-port isolation. The proposed MIMO antenna geometry is shown in Figure 2. The final geometrical parameters of the proposed MIMO antenna are summarized in Table 2. All dimensions are given in mm.

As shown in Figure 2(a), the two radiating elements are placed side by side on the same substrate and are excited by two independent microstrip feed lines. The total width of the MIMO substrate is denoted by M1, and the distance between the adjacent inner edges of the two radiators is denoted by M2. This spacing was selected by considering both compactness and mutual coupling. Increasing the distance between the two radiators generally improves isolation; however, it also increases the overall antenna size. Therefore, the final spacing was chosen as a compromise between reduced coupling and compact layout. The bottom side of the proposed MIMO antenna is illustrated in Figure 2(b). A shared partial ground plane is used for the two antenna elements. Since the ground plane provides a possible coupling path between the two ports, it was modified by introducing defected ground structures. First, each antenna element includes a narrow rectangular DGS slot placed under its corresponding feed-radiator region. These slots are analogous to the DGS used in the single-element antenna and are mainly responsible for local impedance tuning. In addition to these local slots, a central isolation structure was inserted between the two antenna elements to reduce the current coupling through the shared ground plane.

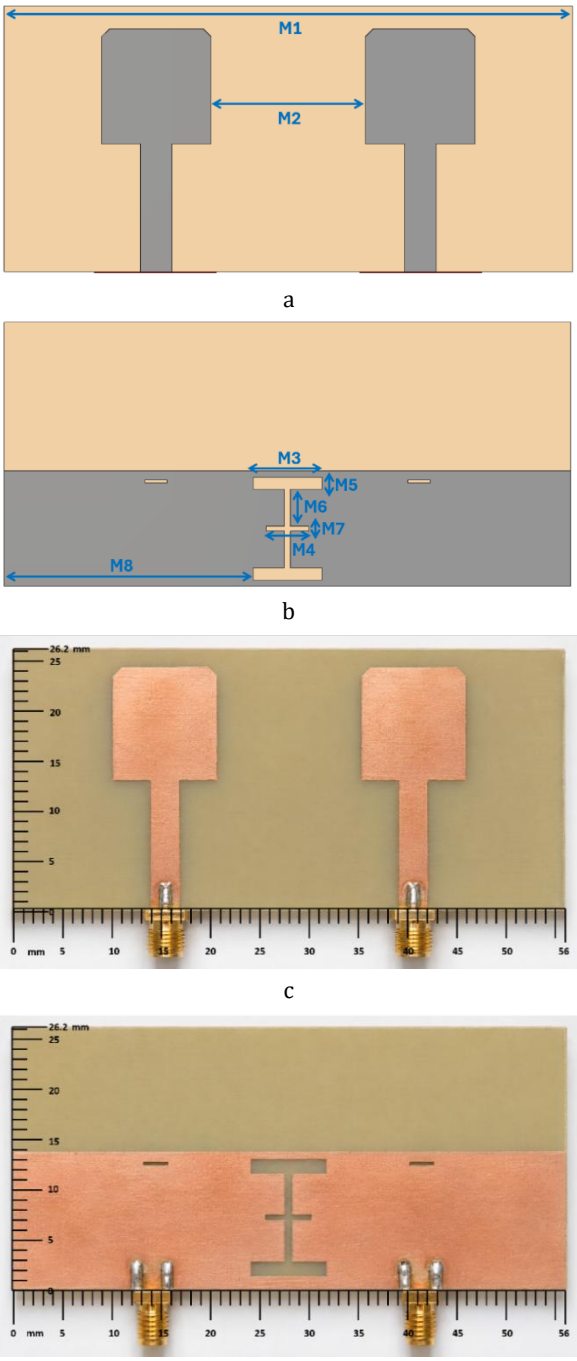


Figure 2. Geometry and fabricated prototype of the proposed MIMO antenna: (a) top view with design parameters, (b) bottom view with isolation design parameters, (c) fabricated prototype top view, and (d) fabricated prototype bottom view.

Table 2. Optimized geometrical parameters of the proposed MIMO antenna

M1	M2	M3	M4
56.0	15.2	6.8	4.2
M5	M6	M7	M8
1.2	9.0	0.5	24.6

The central isolation structure was implemented as a modified I-shaped defected ground structure consisting of one vertical and three horizontal slot sections. DGS-based isolation structures are commonly employed in compact MIMO antennas to perturb current propagation through the shared ground plane and to limit inter-element coupling without requiring lumped decoupling components or large element separation (Güler and Bayer Keskin, 2023). Based on this established approach, the central slot in the proposed antenna was used as a planar passive isolation feature. Since the structure is etched directly into the existing ground plane, it does not require additional substrate area, external components, or a separate decoupling layer, thereby supporting the compact 56 mm x 26.2 mm antenna footprint. The geometrical dimensions of the central isolation structure are labeled as M3, M4, M5, M6, and M7 in Figure 2(b). The parameter M8 defines the horizontal position of the isolation region relative to the left edge of the substrate. The central DGS was positioned between the two radiating elements within the shared partial ground plane. This configuration preserves a simple planar geometry that is compatible with standard PCB fabrication methods. Therefore, the MIMO antenna remains simple, planar, and compatible with standard PCB fabrication methods.

The two-port MIMO antenna was analyzed in CST Studio Suite using the same simulation settings as the single-element design. During the S-parameter analysis, one port was excited while the other port was terminated with a 50 Ω reference impedance. The reflection coefficients S_{11} and S_{22} were used to evaluate the impedance matching of the two antenna elements, whereas S_{21} and S_{12} were used to evaluate the isolation between them. Since the MIMO antenna is geometrically symmetric, similar responses are expected for S_{11} and S_{22}, and for S_{21} and S_{12}.

3. Results and Discussion

This section presents the simulated and measured performance of the proposed compact antenna and its two-port MIMO configuration. The results are discussed in terms of reflection coefficient, gain response, MIMO S-parameters, diversity performance, and constellation-based communication response. The single antenna is first evaluated to verify the impedance matching behavior around the intended 5.5 GHz operating region. Then, the two-port MIMO configuration is examined to assess port matching, mutual coupling, and diversity-related characteristics. All numerical discussions in this section are based on the corresponding simulation and measurement data.

The reflection coefficient performance of the proposed single antenna was investigated using both full-wave simulation and prototype measurement. The simulated and measured S_{11} responses are compared in Figure 3 to evaluate the impedance matching behavior of the fabricated antenna around the target operating band. The antenna was designed to operate near 5.5 GHz by

adjusting the effective electrical length of the chamfered monopole radiator and by tuning the interaction between the radiator, microstrip feed line, partial ground plane, and weak rectangular defected ground slot. In this configuration, the radiator dimensions mainly determine the resonance position, while the partial ground plane and the weak DGS are used for impedance matching adjustment. The chamfered corner provides a small geometrical perturbation for fine matching control rather than acting as a dominant broadband mechanism. Since the prototype was fabricated on an FR4 copper-clad laminate using a PCB milling process, a certain difference between the simulated and measured responses can be expected. Such differences may result from fabrication tolerance, SMA connector soldering, copper surface quality, substrate permittivity variation, and the uncertainty of the actual FR4 loss tangent. Therefore, the comparison in Figure 3 is used not only to confirm the resonance behavior but also to evaluate the practical consistency between the optimized CST model and the fabricated prototype.

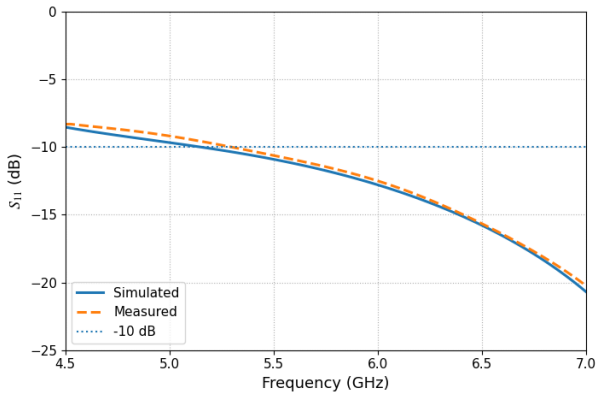


Figure 3. Simulated and measured reflection coefficient responses of the proposed single antenna.

As shown in Figure 3, the simulated and measured S_{11} responses exhibit a similar decreasing trend over the investigated frequency range. The simulated response crosses the −10 dB reference level at approximately 5.15 GHz, while the measured response reaches this level at approximately 5.30 GHz. At the target frequency of 5.5 GHz, the simulated and measured S_{11} values are approximately −10.90 dB and −10.62 dB, respectively. These results indicate that the fabricated antenna provides acceptable impedance matching around the intended 5.5 GHz operating region. The measured curve is slightly shifted with respect to the simulated one, which can be attributed to practical fabrication tolerances, SMA connector effects, milling accuracy, and the variation of the actual FR4 dielectric properties from the values used in the simulation model. Since both curves remain below −10 dB toward the upper end of the plotted frequency range, the upper bandwidth limit is not fully observed within the present sweep. Therefore, the impedance bandwidth should be reported based on the available frequency interval rather than as a fully bounded bandwidth.

Figure 4 compares the simulated gain response with the gain estimates obtained using the substitution method over the frequency range from 4.9 to 6.2 GHz. The simulated gain varies from approximately 1.45 dBi at 4.9 GHz to 1.23 dBi at 6.2 GHz, while the measurement-derived gain estimates remain slightly lower over most of the investigated frequency range. At 5.5 GHz, the simulated gain and the gain estimated from the measurements are approximately 1.38 dBi and 1.30 dBi, respectively.

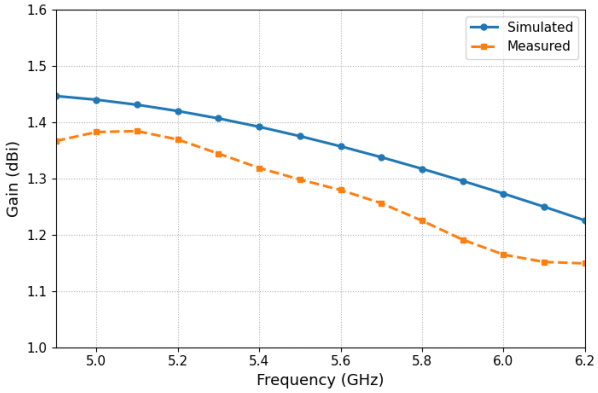


Figure 4. Simulated and measured gain responses of the proposed single antenna.

The small difference between the simulated and measurement-derived values may be associated with FR4 material uncertainty, fabrication tolerances, connector and cable losses, antenna alignment, and residual multipath in the non-anechoic indoor laboratory. These results describe the gain response obtained under the stated measurement configuration. Since neither complete radiation patterns nor radiation efficiency were measured, the gain results alone should not be interpreted as a complete characterization of the antenna's radiation behavior. The gain-measurement setup is illustrated in Figure 5.

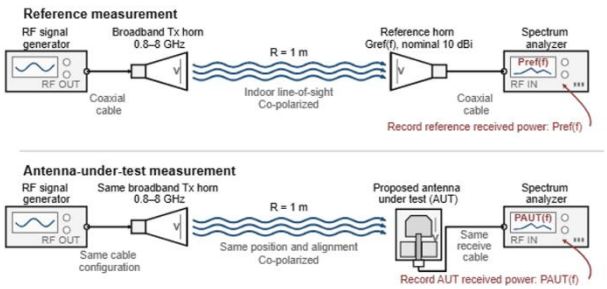


Figure 5. Indoor line-of-sight reference-antenna substitution setup used for gain estimation: (a) reference-link measurement using two identical horn antennas and (b) antenna-under-test measurement after replacing the receiving reference horn with the proposed antenna.

After evaluating the single-element antenna in terms of impedance matching and gain response, the analysis is extended to the proposed two-port MIMO configuration. In this part, the S-parameter results are examined to evaluate the input matching and mutual coupling behavior of the MIMO antenna. Since the two radiating elements are placed symmetrically on the same FR4 substrate, S_{11} is used to represent the port-matching response, while S_{12} is used to represent the inter-element coupling. Although the MIMO geometry is symmetrical, the complete two-port S-parameter response was considered to verify the measured port behavior. Therefore, S_{11}, S_{22}, S_{21}, and S_{12} were evaluated to confirm both impedance matching and mutual coupling performance. During the analysis, one port is excited while the other port is terminated with a 50 Ω load. Figure 6 presents the simulated and measured S_{11} and S_{12} responses of the proposed two-port MIMO antenna.

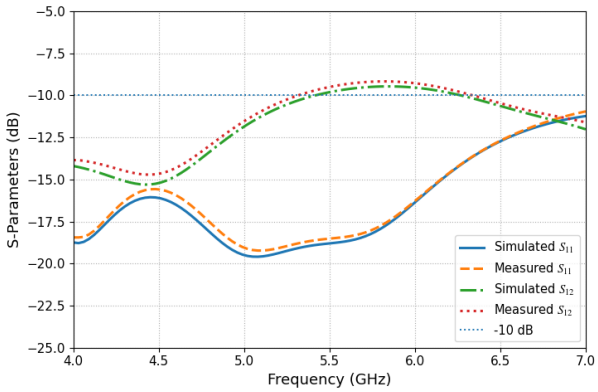


Figure 6. Simulated and measured S_{11} and S_{12} responses of the proposed symmetrical two-port MIMO antenna.

Figure 6 shows the simulated and measured S_{11} and S_{12} responses of the proposed two-port MIMO antenna. Since the structure is geometrically symmetrical, S_{11} represents the port matching behavior, while S_{12} represents the mutual coupling between the two antenna elements. The simulated and measured S_{11} curves remain below the −10 dB reference level over the investigated frequency range, indicating proper impedance matching for the excited port. Around the target frequency of 5.5 GHz, the S_{11} response is approximately below −18 dB for both simulation and measurement, which confirms that the MIMO configuration preserves the matching behavior of the antenna element. The S_{12} response shows a moderate isolation level between the two ports. The coupling is lower around the lower part of the frequency range and increases toward the central operating region. Around 5.5 GHz, the simulated and measured S_{12} responses are close to −10 dB, showing that the final DGS-loaded configuration provides a moderate level of inter-port isolation. This behavior is consistent with previously reported DGS-based MIMO antenna studies, in which ground-plane slots are used as planar passive structures for controlling shared-ground currents and mutual coupling (Güler and Bayer Keskin, 2023). Although the achieved isolation is not high, it is obtained within a compact two-element configuration without using lumped components, neutralization lines, an additional decoupling layer, or increased element spacing. Therefore, the principal advantage of the proposed configuration is its balance between moderate isolation, compact size, and fabrication simplicity.

In addition to the S-parameter evaluation, the diversity performance of the proposed MIMO antenna was analyzed using the envelope correlation coefficient (ECC) and diversity gain (DG). Both the simulated and measured ECC values were calculated directly from the complete complex two-port S-parameter data, including S_{11}, S_{12}, S_{21}, and S_{22}. For the measured evaluation, the amplitude and phase information exported in Touchstone format was used, and no symmetry-based substitution was applied. The ECC was calculated as equation 2,

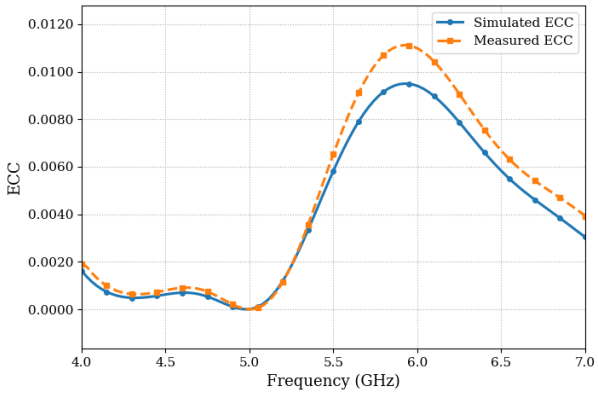
$$\rho_e = \frac{|S_{11}^* S_{12} + S_{21}^* S_{22}|^2}{(1 - |S_{11}|^2 - |S_{21}|^2)(1 - |S_{22}|^2 - |S_{12}|^2)} \quad (2)$$

The corresponding diversity gain was obtained from equation 3,

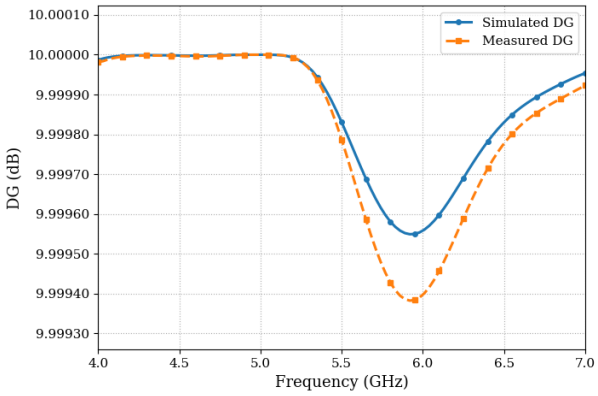
$$DG = 10\sqrt{1 - \rho_e^2} \quad (3)$$

Although the symmetrical geometry and reciprocity of the antenna are expected to produce similar paired S-parameter responses, the measured values were retained individually in the calculations. Since this approach is based solely on S-parameters and does not incorporate the complete three-dimensional radiation patterns and radiation efficiencies of the antenna elements, the resulting ECC should be interpreted as an S-parameter-based diversity estimate rather than a complete radiation-pattern-based diversity characterization. The calculated ECC and DG results are presented in Figure 7.

Figure 7 presents the ECC and DG responses of the proposed two-port MIMO antenna. The calculations were performed directly using the complete complex S_{11}, S_{12}, S_{21}, and S_{22} data without applying a symmetry-based substitution. As shown in Figure 7(a), both the simulated and measured ECC values remain very low over the investigated frequency range, with a maximum value of approximately 0.01. The corresponding DG results are presented in Figure 7(b) and remain very close to the theoretical maximum value of 10 dB. These results indicate low port correlation according to the S-parameter-based diversity evaluation. Since the ECC and DG values were derived solely from the S-parameters, they should be interpreted as S-parameter-based diversity estimates rather than as a complete radiation-pattern-based diversity characterization.



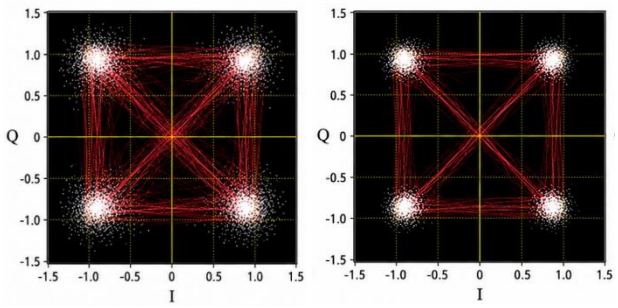
a



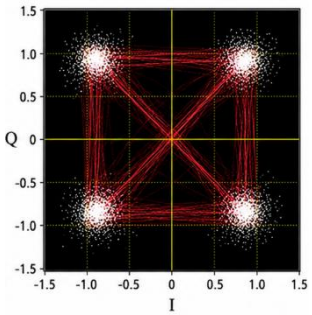
b

Figure 7. S-parameter-based diversity performance of the proposed two-port MIMO antenna calculated using the complete complex two-port data: (a) ECC and (b) DG.

In addition to the S-parameter and diversity analyses, the link-level communication response of the proposed antenna system was examined using an end-to-end 2 × 2 OTA QPSK testbed employing two identical fabricated two-port MIMO antenna prototypes. The constellation diagrams were obtained directly from the recovered OTA signals rather than through channel-based numerical post-processing. Since the resulting constellation and EVM responses include the combined effects of the SDR front ends, antenna prototypes, propagation environment, receiver noise, and synchronization algorithms, they are interpreted as link-level observations rather than antenna-only performance metrics. The communication-level validation was carried out in the WLAN portion of the operating band using a 2 × 2 software-defined-radio testbed whose RF front ends covered the 4.9-5.9 GHz frequency range. Port 1 and Port 2 of the transmitting MIMO prototype were connected to two independent transmit RF chains, while Port 1 and Port 2 of the receiving MIMO prototype were connected to two independent receive RF chains. Both antenna ports were therefore active during the 2 × 2 OTA measurements. When an individual propagation channel was examined separately, the inactive antenna port was terminated with a 50 Ω load. Three representative frequencies, namely 5.18, 5.50, and 5.825 GHz, were selected to represent the lower, central, and upper portions of the considered WLAN band. The OTA measurements were conducted in a standard indoor, non-anechoic laboratory with an approximate floor area of 120 m^2. The transmitting and receiving MIMO prototypes were positioned 1.5 m above the floor and separated by 1 m in a clear line-of-sight configuration. The antenna prototypes were aligned for co-polarized broadside transmission. They were placed on non-metallic supports, and nearby metallic objects were minimized to reduce environmental reflections. No anechoic lining or microwave absorbers were used; therefore, residual indoor multipath propagation could not be eliminated. A QPSK-modulated baseband signal was generated using the software-defined-radio control software and pulse-shaped using a root-raised-cosine filter with a roll-off factor of 0.35. The transmission was performed at a symbol rate of 250 kSym/s with an IQ sample rate of 1 MS/s. The transmit RF power was set to −10 dBm per active RF chain, while the receiver gain was adjusted to 20 dB to maintain operation within the linear input range. Carrier and symbol-timing synchronization were performed digitally for each received stream before constellation extraction. The representative QPSK constellation diagrams obtained at the three test frequencies are presented in Figure 8.



a b



c

Figure 8. Representative link-level QPSK constellation diagrams obtained using the 2 × 2 OTA software-defined-radio testbed: (a) 5.18 GHz, (b) 5.50 GHz, and (c) 5.825 GHz.

Four distinguishable QPSK symbol clusters are observed at all three frequencies. The constellation obtained at 5.18 GHz exhibits moderate symbol spreading, whereas the clusters at 5.50 GHz are more compact and clearly separated. At 5.825 GHz, the four symbol regions remain

distinguishable despite a slightly greater spread than that observed at 5.50 GHz. The reported EVM values, calculated from 10,000 recovered symbols at each test frequency, were 7.4%, 4.8%, and 6.2% at 5.18 GHz, 5.50 GHz, and 5.825 GHz, respectively. The lowest link-level EVM was obtained at 5.50 GHz. However, this difference should not be attributed exclusively to the antenna response because the measured EVM includes the combined effects of the complete RF testbed, synchronization process, receiver noise, and indoor propagation channel.

The observed spreading in the constellation diagrams can be attributed to practical RF measurement effects, including residual synchronization error, receiver noise, multipath in the laboratory environment, cable and connector effects, and the frequency-dependent response of the antenna prototypes. However, the absence of severe symbol rotation, constellation collapse, or strong overlapping between adjacent symbol regions shows that the complete 2 × 2 OTA testbed maintained distinguishable QPSK symbol clusters under the stated indoor measurement conditions.

Overall, the proposed two-port MIMO antenna provides acceptable impedance matching near the intended operating region, while its inter-port isolation remains at a moderate level because of the compact element spacing and shared ground plane. The ECC and DG values calculated from the complete complex two-port S-parameter data indicate low S-parameter-based port correlation within the target operating region. The 2 × 2 OTA constellation and EVM measurements provide complementary link-level observations at 5.18, 5.50, and 5.825 GHz. However, these communication-level results should not be interpreted as an independent validation of the antenna-only diversity performance because they include the combined effects of the complete SDR testbed, antenna prototypes, synchronization algorithms, and indoor propagation environment. The final DGS-loaded configuration therefore offers a practical balance between compactness, fabrication simplicity, acceptable impedance matching, moderate isolation, and link-level QPSK performance in the 5 GHz WLAN region.

4. Conclusion

In this study, a compact FR4-based printed monopole antenna operating around the 5.5 GHz region and its two-port MIMO configuration were designed, fabricated, and evaluated. The single-element antenna was realized using a microstrip-fed chamfered rectangular radiator and a partial ground plane with a narrow-defected ground slot. The simulated and measured reflection coefficient results showed that the antenna provides acceptable impedance matching around the intended operating region. At 5.5 GHz, the simulated and measured S_{11} values were approximately −10.90 dB and −10.62 dB, respectively. The measured response exhibited a slight frequency shift compared with the simulation, which can be explained by FR4 material uncertainty, PCB milling tolerance, SMA soldering, and connector-related effects. The gain estimated using the substitution method remained reasonably close to the simulated response over the investigated frequency interval. At 5.5 GHz, the simulated gain and the measurement-derived gain estimate were approximately 1.38 dBi and 1.30 dBi, respectively. Since complete radiation patterns and radiation efficiency were not measured, these results are limited to the gain response obtained under the stated indoor measurement configuration and do not constitute a complete radiation-performance characterization. The optimized single antenna was then extended to a two-port MIMO configuration. In the MIMO design, two identical radiating elements were placed symmetrically on a shared FR4 substrate, and the bottom ground plane was modified by local DGS slots and a central I-shaped isolation structure. The final DGS-loaded MIMO configuration achieved moderate inter-port isolation, with the S_{12} response remaining close to −10 dB around 5.5 GHz. Consistent with previously reported DGS-based MIMO approaches, the central I-shaped ground slot was employed as a planar passive isolation feature. The configuration retains a compact 56 mm x 26.2 mm footprint and avoids lumped decoupling components, neutralization lines, additional layers, and increased element spacing. The diversity analysis was performed using the complete complex S_{11}, S_{12}, S_{21}, and S_{22} data without applying a symmetry-based substitution. The maximum ECC was approximately 0.01, while the DG remained close to 10 dB over the investigated frequency range. These results indicate low S-parameter-based port correlation within the intended operating region. Communication-level measurements were also performed using a 2 × 2 OTA QPSK testbed at 5.18 GHz, 5.50 GHz, and 5.825 GHz. Four distinguishable QPSK symbol clusters were observed at all three frequencies, and the corresponding link-level EVM values were 7.4%, 4.8%, and 6.2%, respectively. The lowest link-level EVM was obtained at 5.50 GHz. Since the EVM includes the combined effects of the SDR front ends, antenna prototypes, synchronization process, receiver noise, and indoor propagation environment, these values should not be attributed exclusively to the antenna response.

Overall, the proposed antenna structure offers a practical balance between compact size, simple FR4 fabrication, acceptable impedance matching, moderate MIMO isolation, low ECC, DG values close to 10 dB, and link-level QPSK observations obtained under the stated laboratory OTA conditions in the 5 GHz WLAN region. Although the inter-element isolation is limited by compact geometry, the design avoids complex decoupling structures and remains suitable for low-cost PCB-based WLAN antenna applications.

Author Contributions

The percentages of the author's contributions are presented below. The author reviewed and approved the final version of the manuscript.

	C.G.
C	100
D	100
S	100
DCP	100
DAI	100
L	100
W	100
CR	100
SR	100
PM	100
FA	100

C= concept, D= design, S= supervision, DCP= data collection and/or processing, DAI= data analysis and/or interpretation, L= literature search, W= writing, CR= critical review, SR= submission and revision, PM= project management, FA= funding acquisition.

Conflict of Interest

The author declared that there is no conflict of interest.

Ethical Consideration

Ethics committee approval was not required for this study because there was no study on animals or humans.

References

Addepalli, T. (2023). Compact MIMO diversity antenna for 5G sub-6 GHz (N77/N78 and N79) and WLAN (Wi-Fi 5 and Wi-Fi 6) band applications. Wireless Personal Communications, 132(3), 2203–2223. https://doi.org/10.1007/s11277-023-10718-4

Addepalli, T., Kumar, M. S., Jetti, C. R., Gollamudi, N. K., Kumar, B. K., & Kulkarni, J. (2023). Fractal loaded, novel, and compact two- and eight-element high diversity MIMO antenna for 5G sub-6 GHz (N77/N78 and N79) and WLAN applications, verified with TCM analysis. *Electronics*, *12*(4), Article 952. https://doi.org/10.3390/electronics12040952

Ali, A., Munir, M. E., Marey, M., Mostafa, H., Zakaria, Z., Al-Gburi, A. J. A., & Bhatti, F. A. (2023). A compact MIMO multiband antenna for 5G/WLAN/Wi-Fi 6 devices. *Micromachines*, *14*(6), Article 1153. https://doi.org/10.3390/mi14061153

Baro, B. K., Deka, S., & Sarmah, K. (2026). Design and implementation of a multiband, tri-port CPW-fed antenna for OFDM-FDD based 5G Internet of Things applications: System level validation. *Measurement*, *278*, Article 121691. https://doi.org/10.1016/j.measurement.2026.121691

Bayarzaya, B., Hussain, N., Awan, W. A., Sufian, M. A., Abbas, A., Choi, D., Lee, J., & Kim, N. (2022). A compact MIMO antenna with improved isolation for ISM, sub-6 GHz, and WLAN application. *Micromachines*, *13*(8), Article 1355. https://doi.org/10.3390/mi13081355

Baytöre, C., Göçen, C., Palandöken, M., Kaya, A., & Zoral, E. Y. (2019). Compact metal-plate slotted WLAN-WiMAX antenna design with USB Wi-Fi adapter application. *Turkish Journal of Electrical Engineering and Computer Sciences*, *27*(6), 4403–4417. https://doi.org/10.3906/elk-1904-122

Çakmak, T., Murat, C., & Ustabas, I. (2026). Performance comparison of carbon footprint and dielectric properties of geopolymer mortars with Portland cement mortars. *Silicon*, *18*(1), 297–319. https://doi.org/10.1007/s12633-025-03538-7

Cheng, S. H., Chen, S. C., Chen, Y. J., & Liu, C. L. (2024). Compact asymmetric T-feed closed-slot antennas for 2.4/5/6 GHz Wi-Fi 7 MIMO laptops. *Electronics*, *13*(13), Article 2430. https://doi.org/10.3390/electronics13132430

Göçen, C., Akdag, I., Belen, M. A., Mahouti, P., Kaya, A., & Palandöken, M. (2022). ISM 2.4 GHz band antenna model for RF energy harvesting systems. *Avrupa Bilim ve Teknoloji Dergisi*, (43), 32–35. https://doi.org/10.31590/ejosat.1202107

Güler, C., & Bayer Keskin, S. E. (2023). A novel high-isolation four-port compact MIMO antenna with DGS for 5G applications. *Micromachines*, *14*(7), Article 1309. https://doi.org/10.3390/mi14071309

Khushbu, & Prakash, A. (2024). A compact wideband MIMO antenna with efficient isolation for S and C-bands applications. *Discover Electronics*, *1*, Article 21. https://doi.org/10.1007/s44291-024-00015-0

Liu, X., Zhang, J., Xi, H., Yang, X., Sun, L., & Gan, L. (2022). A compact four-band high-isolation quad-port MIMO antenna for 5G and WLAN applications. *AEU–International Journal of Electronics and Communications*, *153*, Article 154294. https://doi.org/10.1016/j.aeue.2022.154294

Murat, C. (2026). AI-driven optimization of a 2.45 GHz microwave drying system for raw corn: Enhancing efficiency and uniformity via hybrid CNN-RNN control. *Black Sea Journal of Engineering and Science*, *9*(1), 114–123. https://doi.org/10.34248/bsengineering.1766754

Murat, C., Kaya, A., & Palandoken, M. (2025). Non-Foster microwave circuit design for wide band active impedance matching operation. *AEU–International Journal of Electronics and Communications*, *200*, Article 155954. https://doi.org/10.1016/j.aeue.2025.155954

Murat, C., Palandoken, M., Kaya, I., & Kaya, A. (2021). A novel ISM band reflector type applicator design for microwave ablation systems. *Electromagnetic Biology and Medicine*, *40*(2), 286–300. https://doi.org/10.1080/15368378.2021.1885434

Pannu, P. (2024). Highly compact UWB-MIMO antenna with sharp multi-stop-band characteristics. *EURASIP Journal on Wireless Communications and Networking*, *2024*, Article 48. https://doi.org/10.1186/s13638-024-02369-1

Pradeep, P., Jaya Sankar, K., & Chandra Sekhar, P. (2024). Design of a compact wideband two-port MIMO antenna for NR 5G sub-6 GHz band wireless applications. *Wireless Personal Communications*, *138*(2), 1193–1210. https://doi.org/10.1007/s11277-024-11552-y

Saeidi, T., Al-Gburi, A. J. A., & Karamzadeh, S. (2023). A miniaturized full-ground dual-band MIMO spiral button wearable antenna for 5G and sub-6 GHz communications. *Sensors*, *23*(4), Article 1997. https://doi.org/10.3390/s23041997

Sushma Chowdary, P., Panda, S. K., & Naidu, V. P. (2023). Development of asymmetric feed MIMO antenna for Wi-MAX, WIFI applications. *Applied Physics A*, *129*, Article 736. https://doi.org/10.1007/s00339-023-07001-5

Wang, C., Wang, H., Wu, P., & Hou, M. (2022). Dual-band closed-slot MIMO antenna for terminal wireless applications. *IEEE Transactions on Antennas and Propagation*, *70*(8), 6514–

6525. https://doi.org/10.1109/TAP.2022.3161531

You, W., Wang, Z., Nie, W., & Mu, W. (2023). A 12-port MIMO antenna system for 5G/WLAN applications. *Micromachines*, *14*(6), Article 1196. https://doi.org/10.3390/mi14061196

Black Sea Journal of Engineering and Science
doi: 10.34248/bsengineering.2008827

Open Access Journal
e-ISSN: 2619 – 8991

Research Article
Volume 9 - Issue 5: 2749-2759 / September 2026

EXPERIMENTAL ASSESSMENT OF THE EFFECT OF REFERENCE SURFACE TEMPERATURE ON AUXILIARY ENERGY CONSUMPTION IN A THERMOELECTRIC-BASED BATTERY THERMAL MANAGEMENT SYSTEM

Erdoğan GÜNER[1]*

[1]*Atatürk University, Faculty of Engineering, Department of Mechanical Engineering, 25240, Erzurum, Türkiye*

Abstract: Thermoelectric coolers (TECs) have attracted considerable attention for battery thermal management owing to their compact structure, precise temperature control capability, and ease of integration. However, the influence of reference surface temperature on the auxiliary energy consumption of TECs remains insufficiently studied, despite its direct impact on the overall energy efficiency of battery systems. This study experimentally investigates the influence of reference surface temperature on the auxiliary energy consumption of a selective thermoelectric battery thermal management system (BTMS) operating under a constant 7.5C discharge condition. The reference surface temperature was varied from 35 to 40 °C in 1 °C increments to evaluate its effect on TEC activation behavior, cooling energy demand, and battery thermal performance. All results were obtained using a single 20 Ah $LiFePO_4$ pouch cell under a constant 7.5C discharge rate, with average ambient and coolant temperatures of 27.5 °C. The results showed that increasing the reference temperature substantially reduced both the activation duration and the total energy consumption of the TEC modules, decreasing the TEC energy demand from 5.88 Wh at 35 °C to zero at 40 °C and the corresponding auxiliary energy consumption from 11.70% to 0% of the battery energy capacity. A key finding of this study is that increasing the reference temperature from 35 °C to 36 °C resulted in only a 0.68 °C increase in the maximum battery surface temperature, while reducing the TEC energy consumption by more than 50%, demonstrating that substantial energy savings can be achieved with only a minor compromise in thermal regulation. The results indicate that the reference surface temperature is a critical design parameter governing the energy efficiency of thermoelectric BTMSs. The proposed experimental methodology provides practical guidance for selecting appropriate control thresholds that balance thermal regulation effectiveness, auxiliary energy consumption, and battery safety.

Keywords: Temperature control threshold, $LiFePO_4$ pouch cell, BTMS, Selective TEC activation, High C-rate discharge, TEC energy consumption

***Corresponding author:** Atatürk University, Faculty of Engineering, Department of Mechanical Engineering, 25240, Erzurum, Türkiye
E mail: erdoganguner@atauni.edu.tr (E. GÜNER)
Erdoğan GÜNER https://orcid.org/0000-0003-4604-5485

Received: August 01, 2026
Accepted: August 25, 2026
Published: September 15, 2026

Cite as: Güner, E. (2026). Experimental assessment of the effect of reference surface temperature on auxiliary energy consumption in a thermoelectric-based battery thermal management system. *Black Sea Journal of Engineering and Science*, 9(5), 2749-2759.

1. Introduction

In recent years, with the widespread adoption of electric vehicles, hybrid electric vehicles, unmanned aerial vehicles, and electric vertical take-off and landing (eVTOL) platforms, ensuring the safe, efficient, and long-lasting operation of lithium-ion batteries has become increasingly important. Battery temperature directly influences the kinetics of electrochemical reactions and therefore plays a decisive role in determining capacity, power density, energy efficiency, aging rate, and safety. Particularly under high discharge rates, the internally generated heat can rapidly increase the battery temperature, while non-uniform temperature distribution may lead to performance variations among cells and accelerated capacity degradation. Therefore, effective BTMSs are required to maintain battery temperature within an appropriate operating range.

Various battery thermal management methods, including air cooling (Mahek et al., 2023; Chen et al., 2024), liquid cooling (Wu et al., 2019; Wang et al., 2022), phase change materials (PCMs) (Wu et al., 2020; Faseena and Sreekumar, 2025), heat pipes (Zhang and Wei, 2020; Lv et al., 2023) and TECs, have been proposed for battery thermal management. Although air cooling is simple and cost-effective, it may become insufficient under high heat loads. Liquid cooling provides a high cooling capacity; however, it requires additional components such as pumps and piping, together with potential sealing issues. Phase change materials can delay the rise in battery temperature, but they are generally insufficient as a standalone solution under continuous operating conditions.

Among these methods, TECs have attracted considerable attention because they contain no moving parts, operate

This work is licensed (CC BY-NC 4.0) under Creative Commons Attribution 4.0 International License

silently, respond rapidly, provide precise temperature control, and can be used for both heating and cooling purposes. In the literature, TECs are generally employed as auxiliary cooling components in combination with other battery cooling methods (Esfahanian et al., 2013; Liu et al., 2014; Liao et al., 2021). A hybrid BTMS integrating TECs with air and liquid cooling was developed and analyzed through multiphysics simulations (Luo et al., 2024a). Their results showed that the TEC performance exhibited a nonlinear dependence on the input current, with the optimum performance achieved at 5 A. Under the optimal operating conditions, the maximum battery temperature and the maximum temperature difference were 302.27 K and 3.63 K, respectively. The performance and parametric sensitivity of TEC-assisted cooling for 18650 battery packs were investigated (Yu et al., 2025). The study demonstrated that the cold-plate temperature significantly affected the battery temperature distribution. Although a cold-plate temperature of 5 °C reduced the battery surface temperature to as low as 18.3 °C, it adversely affected temperature uniformity. In addition, the maximum battery temperature was found to be primarily influenced by the cold-plate temperature and the discharge rate. A hybrid BTMS combining vapor chambers (VCs) and TECs was also developed (Luo et al., 2024b). The results indicated that while the TEC modules effectively reduced the maximum battery temperature, the VCs significantly improved temperature uniformity. Under a 5C discharge condition, the optimized VC-TEC configuration achieved the best overall performance among the investigated configurations, with a maximum battery temperature of 39.83 °C and a maximum cell-to-cell temperature difference of 5.97 °C.

Nevertheless, several studies have employed direct-contact thermoelectric cooling, in which TEC modules are attached directly to the battery surface, enabling rapid and effective cooling of localized hot spots. A BTMS integrating thermoelectric devices, PCM, air cooling, and film heaters was developed, enabling operation in both heating and cooling modes. In heating mode, a temperature rise rate of 1.7 °C/min was achieved at 20 A, while in cooling mode, 4 A TEC operation provided an approximately 3 °C improvement compared with air cooling, with a maximum cell-to-cell temperature difference of 4.67 °C (Wang et al., 2025). A BTMS combining TECs, a piezoelectric pump (PP), and PCM maintained the maximum battery temperature below 318.15 K under 2C–3C discharge conditions. Under irregular discharge conditions, adaptive control of the PP frequency improved temperature uniformity, while the application of a 4 A TEC current prevented thermal runaway (Liu et al., 2025). A prismatic battery was cooled using six TEC modules mounted on one side of the cell, with the battery temperature controlled at 40 °C (Alaoui, 2013). Under a 3C discharge condition, this approach reduced the battery temperature from 57.6 °C to 46.8 °C. The proposed system was also evaluated under the US06 driving cycle and demonstrated satisfactory performance. A theoretical model for a TEC-based BTMS was developed to investigate the effects of charging rate, cooling current, and system parameters (Luo et al., 2025). The results showed that, compared with air cooling, the use of TECs reduced the average battery temperature by 11.1 K and 5.2 K under 1C and 3C charging conditions, respectively. However, the study also indicated that high cooling currents could induce considerable thermal stresses in the TEC modules. A BTMS integrating TECs with copper plates achieved a temperature reduction of approximately 4–5 °C compared with forced-air cooling. While one-sided TEC cooling resulted in an inter-surface temperature imbalance of up to 32 °C, dual-sided TEC cooling maintained the battery within safe temperature limits and reduced the internal temperature difference to below 3 °C. The use of a crossed copper-plate configuration further reduced the internal temperature difference to below 1 °C (Zhang et al., 2025). A pouch-type lithium-ion battery equipped with TEC modules mounted symmetrically on both battery surfaces was investigated using a selective control strategy (Kurt and Güner, 2026). Each TEC module was associated with the thermocouples located in its surrounding region, and only the TEC corresponding to the thermocouple exceeding the predefined reference temperature (35 °C) was activated. This strategy aimed to reduce the auxiliary energy consumed by the TEC modules while maintaining a more uniform temperature distribution over the battery surface. Under a 7C discharge condition, the maximum battery surface temperature (T_{max}) and the maximum surface temperature difference (ΔT_{max}) were measured as 35.99 °C and 6.41 °C, respectively.

Previous research (Zhang et al., 2016) has shown that the temperature at the battery core may exceed the surface temperature by approximately 6 °C, even under an ambient temperature of 26.3 °C. Since thermal degradation is closely associated with elevated temperatures within the cell core, the difference between internal and surface temperatures should be considered when defining a safe surface-temperature threshold. Although temperatures around 40 °C have been identified in the literature as a critical level associated with the onset of degradation (Pesaran, 2002; Jiang and Qu, 2019). Although numerous studies have reported the energy consumption of TECs used in BTMSs, the influence of reference surface temperature on auxiliary energy consumption has not been systematically investigated. However, the reference surface temperature directly governs both the activation frequency and operating duration of TEC modules, making it one of the most critical design parameters controlling the trade-off between battery thermal performance and auxiliary energy consumption. Therefore, identifying an appropriate reference surface temperature that maximizes energy efficiency while maintaining the battery within a safe operating

temperature range is of considerable practical importance. In this study, a selective thermoelectric BTMS based on battery surface temperature was employed, and the reference surface temperature was systematically varied from 35 to 40 °C in 1 °C increments. This range (35-40 °C) was selected to account for the potential core-to-surface temperature difference while allowing the effect of progressively increasing the allowable surface temperature on TEC operation and auxiliary energy consumption to be quantified. For each reference temperature, the total TEC energy consumption and its ratio to the battery energy capacity were experimentally quantified, allowing the influence of each 1 °C increase in the reference surface temperature on auxiliary energy consumption to be systematically evaluated. Furthermore, the energy savings achievable in exchange for small increases in the allowable maximum battery surface temperature were experimentally assessed, thereby revealing the trade-off between thermal regulation and auxiliary energy consumption. The findings provide practical guidance for selecting an energy-efficient reference surface temperature and contribute to the design of thermoelectric BTMSs with improved overall energy efficiency.

2. Materials and Methods

The experiments were performed using an A123 Systems AMP20M1HD-A LiFePO4 pouch cell with a nominal capacity of 20 Ah under a constant 7.5C discharge condition. The main characteristics of the battery are summarized in Table 1. A direct-contact thermoelectric cooling system was developed by installing twelve TEC1-12705 modules (12 V, 5 A) on the battery surfaces based on the dimensions of the pouch cell (160 × 227 × 7.5 mm) and the TEC modules (40 × 40 × 4 mm).

Table 1. Key specifications of the experimental battery cell

Parameter	Manufacturer-specified value
Cell chemistry	$LiFePO_4$
Nominal capacity	20 Ah
Nominal voltage	3.3 V at 50% SOC
Upper cut-off voltage	3.6 V
Lower cut-off voltage	2.0 V
Maximum Continuous Discharge Current	200 A under specified conditions

As shown in Figure 1, six TEC modules were mounted on each side of the battery in a symmetrical arrangement. Each module was paired with the corresponding module directly opposite it on the other battery surface, and the two modules in each pair were controlled simultaneously. Accordingly, the six TEC positions shown and numbered in Figure 1 represent six control pairs, each comprising two physically opposed TEC modules. When a TEC position was activated, both modules in the corresponding pair were activated simultaneously; therefore, activation of TEC1, for example, resulted in the simultaneous operation of TEC1 and its aligned counterpart on the opposite battery surface, thereby providing cooling to both surfaces of the battery. The hot sides of the TEC modules were thermally coupled to aluminum water-cooling blocks supplied with coolant at a flow rate of 2.5 $L.min^{-1}$. Throughout the experiments, the coolant temperature was maintained at 27.5 °C using a recirculating chiller, and the ambient temperature was 27.5 ± 1 °C.

Figure 1 presents the thermoelectric-based BTMS developed in this study, including the arrangement of TEC modules, thermocouples, and the temperature-based control strategy. To monitor the thermal behavior of the battery surface, temperature measurements were obtained from 12 different locations distributed across the cell surface using T-type thermocouples with an error limit of ±1 °C (-65 to 130 °C). The sensing junction of each thermocouple was positioned in direct contact with the battery surface and securely fixed at the designated measurement location. Temperature data were acquired at a sampling frequency of 5 Hz (200 ms intervals). Rather than controlling all TEC modules based on all temperature measurements, each TEC was assigned only to the thermocouples located within its surrounding region. The TEC-thermocouple matching strategy used in this study is presented in Table 2.

These temperature measurements were continuously compared with the reference surface temperature (T_{ref}), and the TEC modules were operated accordingly. When the measured temperature exceeded Tref, the corresponding TEC module was activated; otherwise, it remained inactive. The aim of the strategy to avoid unnecessary TEC operation and auxiliary energy consumption, a localized temperature-control approach was employed. This overlapping assignment structure enabled the control system to respond to local temperature variations on the battery surface while limiting TEC activation to the regions where cooling was required. Figure 2 shows the experimental setup and data acquisition system used in this study. All experiments were conducted under a constant 7.5C discharge condition at an ambient temperature of 27.5 ± 1 °C. The battery was discharged using a DC electronic load (Amrel PLA800-120-150M2) and recharged using a programmable DC power supply (Xantrex XTR 7.5-140).

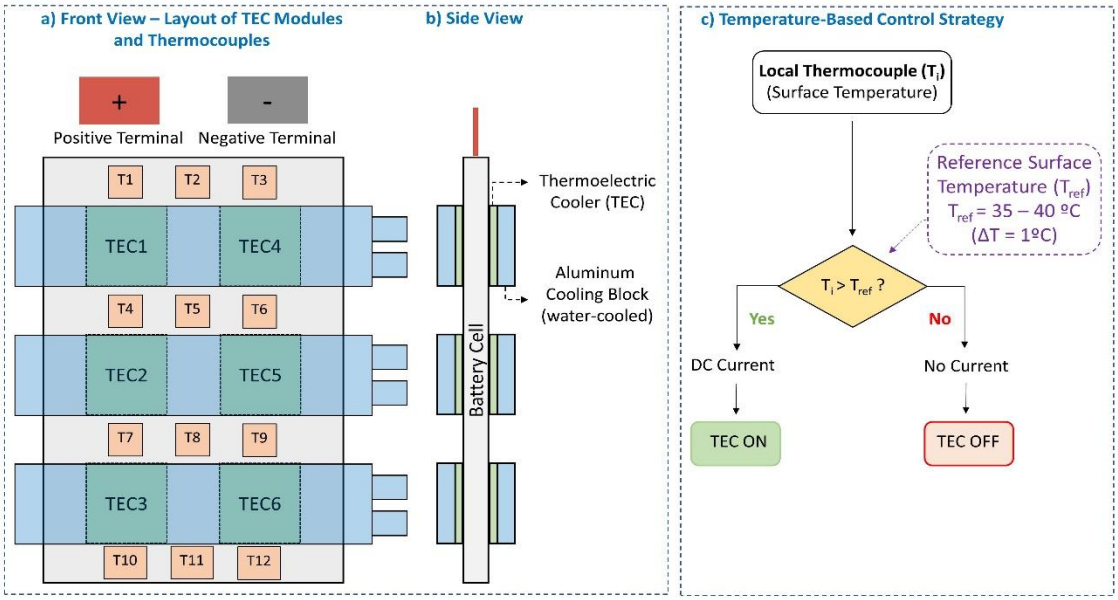


Figure 1. Schematic illustration of the thermoelectric battery thermal management system and temperature-based control strategy.

Table 2. Thermocouple assignment employed for localized TEC activation

	T1	T2	T3	T4	T5	T6	T7	T8	T9	T10	T11	T12
TEC1	+	+		+	+							
TEC2				+	+		+	+				
TEC3							+	+		+	+	
TEC4		+	+		+	+						
TEC5					+	+		+	+			
TEC6								+	+		+	+

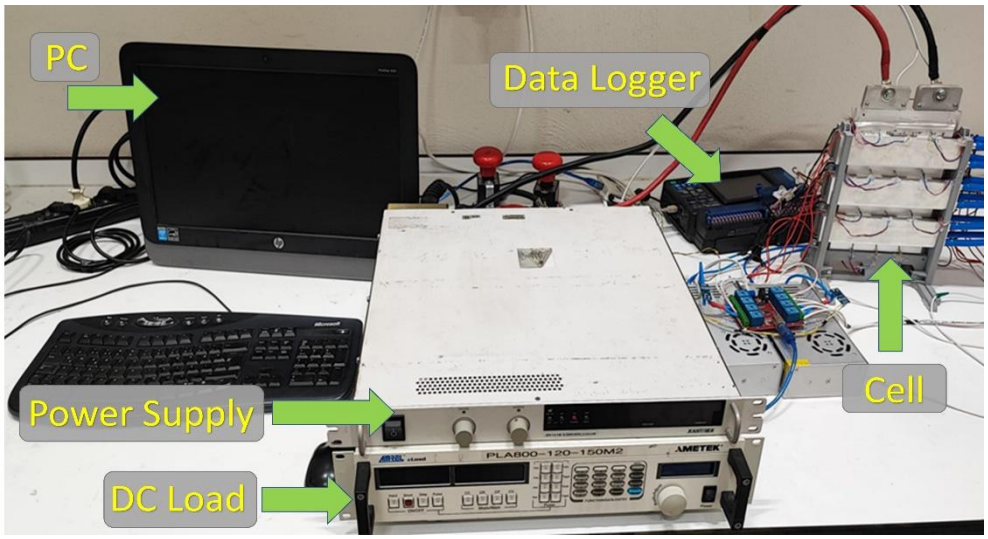


Figure 2. Experimental setup.

The temperatures measured by the twelve surface-mounted thermocouples were recorded using a multichannel data acquisition unit (Hioki LR8401) and transferred to a computer for real-time monitoring and data storage. To assess the influence of the reference temperature on TEC energy demand and to quantify the fraction of battery capacity consumed by the thermal management system, the energy consumption of the TECs and the battery energy capacity were calculated. The TEC energy consumption was determined from the time-dependent electrical power input. Instantaneous power was calculated as the product of voltage and

current, as given in (equation 1), while the total energy consumption during discharge was obtained by integrating the power over time according to (equation 2). Since the power was measured in watts (W) and time was recorded in seconds (s), the necessary conversion factor was incorporated into (equation 2) to express the resulting energy directly in watt-hours (Wh). Because the operating voltage varies throughout the discharge process, the integration-based approach provides a more accurate representation of the actual energy requirement of the TEC system, consistent with previous thermoelectric cooling studies (Riffat and Ma, 2003; Bhattacharyya et al., 2025). Accordingly, (equation 2) was also employed to calculate the battery energy based on the measured voltage response during constant-current discharge.

$$P(t) = V(t) \times I(t) \quad (1)$$

$$E = \frac{1}{3600} \int P(t)dt = \int V(t).I(t)dt \quad (2)$$

3. Results and Discussion

The voltage response of the battery during the 7.5C discharge was first examined to verify the consistency of the electrochemical behavior under the test conditions. As shown in Figure 3, the cell exhibited a smooth and continuous voltage decline throughout the discharge process, without any irregular fluctuations or premature termination. The discharge duration was approximately 440 s, indicating that the applied test procedure provided a stable basis for evaluating the thermal response and the auxiliary energy consumption of the TEC-based thermal management system.

Table 3 presents the maximum temperatures recorded at the twelve thermocouple locations during the experiments conducted with reference temperatures ranging from 35 to 40 °C in 1 °C increments. The TECs were activated whenever the temperature measured by an assigned thermocouple exceeded the prescribed reference value. Accordingly, the values exceeding the corresponding reference temperature are highlighted in red in Table 3.

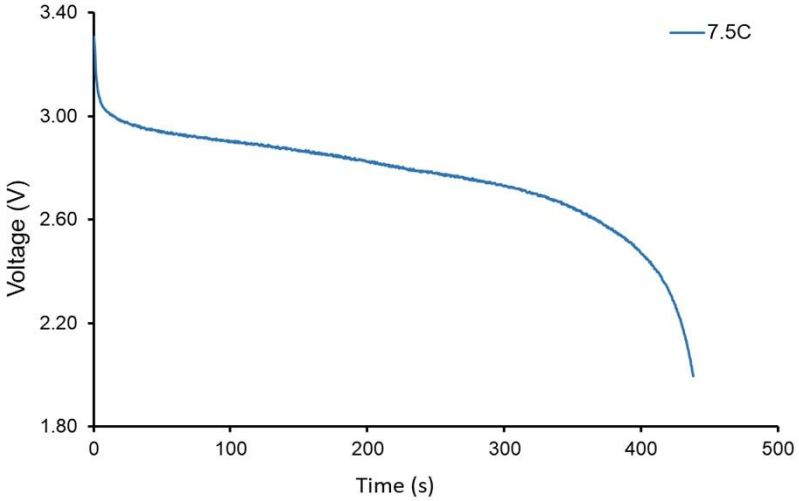


Figure 3. Representative battery voltage profile during a 7.5C discharge test.

Table 3. Maximum surface temperatures measured at the thermocouple locations for reference temperatures ranging from 35 to 40 °C

T_{ref}	T1	T2	T3	T4	T5	T6	T7	T8	T9	T10	T11	T12
35	34.73	35.85	35.15	33.52	33.59	33.39	31.84	34.21	32.17	33.80	35.94	33.08
36	35.86	36.26	36.36	34.71	34.72	34.91	32.39	35.13	32.36	34.44	36.62	33.70
37	36.45	37.65	37.14	34.94	35.07	35.27	32.63	35.24	32.59	34.46	36.89	33.90
38	36.97	38.48	37.94	36.22	36.03	37.04	33.32	35.47	33.53	34.49	36.75	33.93
39	38.20	39.51	38.58	37.34	37.51	37.77	33.93	35.91	33.60	34.53	36.96	34.05
40	39.76	39.92	38.93	36.85	36.92	37.55	33.64	35.72	33.48	34.56	36.93	34.01

At a reference temperature of 40 °C, the highest surface temperature was measured as 39.92 °C at thermocouple T2. Since none of the measured temperatures exceeded the reference threshold, no TEC module was activated during this test. This result indicates that, under the applied ambient conditions and a constant 7.5C discharge rate, the battery surface reached a maximum temperature of approximately 39.9 °C without thermoelectric cooling. For the lower reference-temperature cases, several thermocouple readings exceeded the prescribed threshold, thereby initiating localized TEC operation. The distribution of the

highlighted values in Table 3 therefore reflects both the spatial variation of the battery surface temperature and the regions in which active cooling was required.

As indicated by the maximum temperature values presented in Table 3, the temperature distribution over the battery surface was not uniform during discharge, with certain regions experiencing higher temperatures than others. In particular, the regions monitored by thermocouples T2, T3, and T11 exhibited the highest temperatures among all measurement locations. Since the TEC activation strategy was based on the reference temperature threshold, the temperature rise in these regions played a dominant role in determining TEC operation. According to the thermocouple-TEC assignment scheme presented in Table 2, these thermocouples are associated with TEC1, TEC3, TEC4, and TEC6. Consequently, active cooling was primarily required in the areas controlled by these TEC modules when the measured temperatures exceeded the selected reference temperature.

The TEC modules activated during the experiments and their corresponding operating durations are summarized in Table 4. The results indicate that the operating time of the TECs decreased progressively with increasing reference temperature. At a reference temperature of 35 °C, TEC1 and TEC4 operated for 89 s, while TEC3 and TEC6 remained active for 31.1 s. As the reference temperature increased, the activation durations decreased considerably, and at reference temperatures of 37 °C and above, only TEC1 and TEC4 were activated for limited periods. When the reference temperature was set to 40 °C, none of the measured temperatures exceeded the threshold value; therefore, no TEC activation occurred during the discharge process.

Table 4. Activated TEC modules and their operating durations (s) at different reference temperatures

T_{ref}	TEC1	TEC2	TEC3	TEC4	TEC5	TEC6
35	89.0	0	31.1	89.0	0	31.1
36	36.1	0	10.3	56.2	0	10.3
37	42.9	0	0	43.3	0	0
38	14.8	0	0	14.8	0	0
39	5.1	0	0	5.1	0	0
40	0	0	0	0	0	0

To facilitate interpretation, Table 4 was color-coded according to TEC operating duration. Darker shades correspond to longer activation times, whereas lighter shades indicate shorter operating periods. This visualization clearly demonstrates that TEC operation was concentrated in specific regions of the battery where higher temperatures were observed. The longer operating durations of TEC1 and TEC4 compared with the other modules further confirm that the hottest areas of the battery surface were located within the regions controlled by these TECs.

Another observation that can be derived from Table 3 is that the highest surface temperatures at the 35 °C and 36 °C reference-temperature settings were recorded at thermocouple T11. This behavior can be attributed to the fact that the temperature at the T11 location exceeded the corresponding reference temperature only when the battery approached the end of discharge (SOC ≈ 0%). As a result, the TEC modules associated with the regions near the electrode terminals, where the temperatures exceeded the reference threshold earlier in the discharge process, were activated sooner and operated for longer periods. Consequently, TEC1 and TEC4 effectively limited further temperature rise in these regions, preventing them from reaching the highest temperatures observed at the end of discharge.

This interpretation is further supported by the activation durations presented in Table 4. Since the temperature at the T11 location exceeded the reference temperature only near the end of the discharge process for the 35 °C and 36 °C cases, the corresponding TEC3 and TEC6 modules remained active for considerably shorter durations than TEC1 and TEC4. Therefore, although active cooling was eventually initiated in the T11 region, the delayed activation resulted in a higher maximum temperature being recorded at this location.

The maximum temperature profiles obtained under different reference-temperature settings are presented in Figure 4. In addition to the temperature evolution during the discharge process, the figure also shows the corresponding power consumption profiles of the TEC modules. The horizontal dashed lines represent the selected reference temperatures, allowing the relationship between temperature evolution and TEC activation to be clearly visualized. As can be observed, the TEC modules were activated whenever the measured battery surface temperature exceeded the prescribed reference temperature and subsequently acted to suppress further temperature rise, maintaining the surface temperature in the vicinity of the selected threshold.

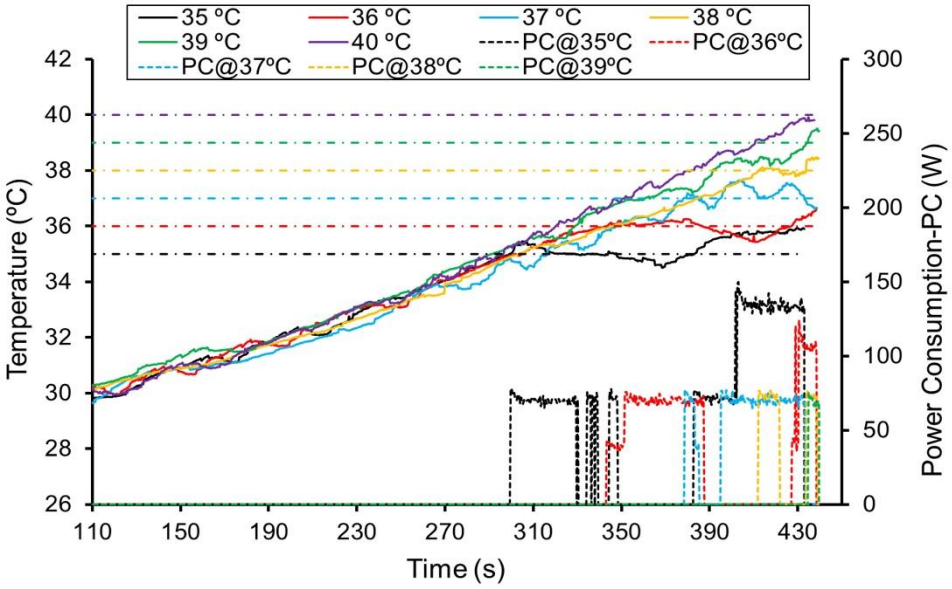


Figure 4. Battery surface temperature regulation and corresponding total TEC power consumption under different reference temperature settings.

Figure 4 further provides insight into the activation behavior of the TEC modules and the distribution of the operating durations summarized in Table 4. For lower reference-temperature settings, the TEC modules were activated earlier during the discharge process and remained in operation for longer periods. Consequently, the battery surface temperature was effectively regulated around the corresponding reference temperature. In contrast, as the reference temperature increased, TEC activation was progressively delayed and the operating durations became shorter. This behavior is consistent with the activation times reported in Table 4 and demonstrates that less cooling intervention was required at higher reference-temperature settings.

A clear inverse relationship can therefore be identified between the selected reference temperature and TEC operating intensity. Lower reference temperatures resulted in more frequent and longer TEC operation, leading to greater auxiliary energy consumption. Conversely, increasing the reference temperature reduced both the frequency and duration of TEC activation, thereby decreasing the electrical energy required by the thermal management system. These observations highlight the significant influence of the reference temperature on the balance between thermal regulation and auxiliary energy demand.

The influence of the reference temperature on the overall energy demand of the thermoelectric cooling system is quantified in Figure 5, which presents the total TEC energy consumption for each reference-temperature setting. As expected from the activation behavior discussed previously, the total energy consumed by the TEC modules decreased substantially with increasing reference temperature. The highest energy consumption was recorded at a reference temperature of 35 °C, reaching 5.88 Wh, whereas no energy consumption was observed at 40 °C because none of the TEC modules were activated during the discharge process.

A significant reduction in TEC energy demand was achieved as the reference temperature increased from 35 °C to 40 °C. Specifically, the total TEC energy consumption decreased from 5.88 Wh at 35 °C to 2.76 Wh at 36 °C and 2.19 Wh at 37 °C, followed by a more pronounced reduction to 0.71 Wh and 0.25 Wh at 38 °C and 39 °C, respectively. These results are consistent with the TEC activation durations presented in Table 4 and the power-consumption profiles shown in Figure 4, confirming that higher reference temperatures lead to less frequent and shorter TEC operation. In addition, the relatively high energy consumption recorded at 35 °C and 36 °C can be attributed to the simultaneous exceedance of the reference temperature by thermocouples T2 and T11. Since these thermocouples are associated with different TEC regions, their concurrent activation triggered four TEC modules on a single battery surface. Consequently, the cumulative power demand of the thermal management system increased substantially, resulting in the higher energy-consumption values observed under these operating conditions.

Although the total TEC energy consumption provides a direct measure of the auxiliary energy demand, its practical significance can be better understood when evaluated relative to the energy delivered by the battery. Therefore, Figure 6 compares the TEC energy consumption with the corresponding battery energy capacity obtained under each reference-temperature setting. In addition, the percentage of battery capacity consumed by the TEC modules is presented to quantify the energetic penalty associated with thermal management.

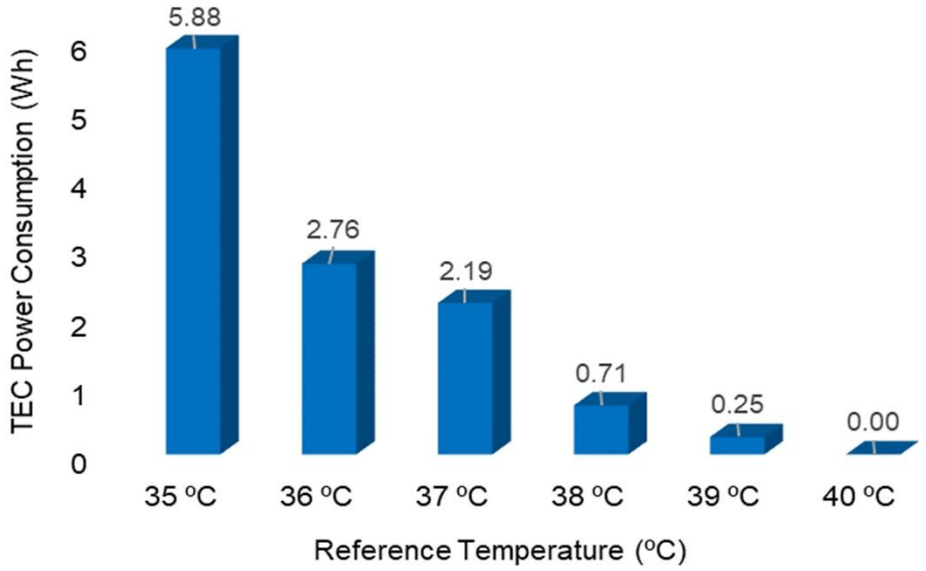


Figure 5. Effect of reference temperature on the total energy consumption of the TEC modules.

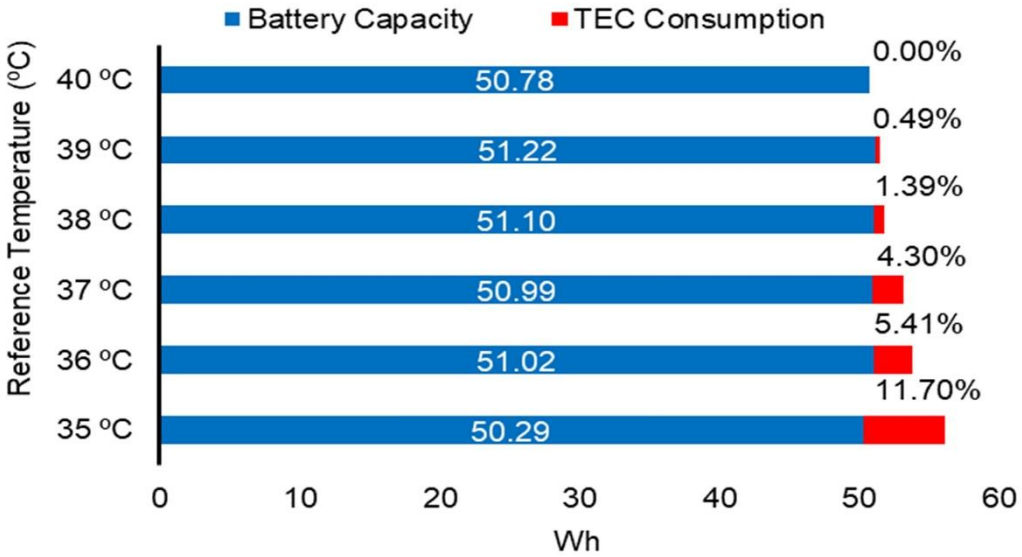


Figure 6. Comparison of battery energy capacity and TEC energy consumption, together with the corresponding energy-consumption ratios.

As shown in Figure 6, the battery energy capacity remained nearly constant for all reference-temperature settings, varying within a narrow range between 50.29 and 51.22 Wh. In contrast, the energy consumed by the TEC modules exhibited a strong dependence on the selected reference temperature. At a reference temperature of 35 °C, the TEC modules consumed 5.88 Wh, corresponding to 11.70% of the battery energy capacity. Increasing the reference temperature to 36 °C and 37 °C reduced this ratio to 5.41% and 4.30%, respectively. A further increase to 38 °C and 39 °C resulted in substantially lower energy penalties of 1.39% and 0.49%, whereas no auxiliary energy consumption was observed at 40 °C because the TEC modules were not activated during the discharge process.

These findings reveal that relatively small increases in the reference temperature can lead to disproportionately large reductions in auxiliary energy consumption. For example, increasing the reference temperature from 35 °C to 38 °C reduced the TEC energy demand from 5.88 Wh to 0.71 Wh, representing approximately a 90% reduction. Similarly, the energy penalty imposed by the thermal management system decreased from 11.70% to only 1.39% of the battery capacity. These findings indicate that changes in the reference temperature can significantly alter the energy required for thermoelectric cooling.

To further illustrate the trade-off between thermal regulation and auxiliary energy demand, Figure 7 correlates the maximum battery surface temperature with the corresponding TEC energy consumption expressed as a percentage of the battery capacity. Unlike

the previous figures, which present these parameters separately, this representation directly demonstrates the energetic cost of achieving lower battery surface temperatures.

As shown in Figure 7, relatively small increases in the maximum battery surface temperature result in substantial reductions in auxiliary energy consumption. For example, increasing the maximum surface temperature from 35.94 °C to 36.62 °C, corresponding to a temperature increase of only 0.68 °C, reduced the TEC energy consumption from 17.54% to 8.12% of the battery capacity, representing a reduction of more than 50%. However, the energy-saving benefit became less uniform as the reference temperature increased. Raising the reference temperature from 36 °C to 37 °C increased the maximum battery surface temperature by 1.03 °C (from 36.62 °C to 37.65 °C), while reducing the TEC energy consumption from 8.12% to 6.45% of the battery capacity, corresponding to an additional reduction of approximately 20.6%. A more pronounced improvement was observed when the reference temperature was further increased from 37 °C to 38 °C. Although the maximum surface temperature increased by only 0.83 °C (from 37.65 °C to 38.48 °C), the TEC energy consumption decreased from 6.45% to 2.10% of the battery capacity, representing a reduction of approximately 67.4%.

The results clearly demonstrate that the selection of the reference surface temperature is a key design parameter governing the auxiliary energy requirement of the proposed thermoelectric BTMS. Rather than exhibiting a linear relationship, the results reveal a pronounced trade-off between thermal regulation and cooling energy demand. Relatively small increases in the allowable maximum battery surface temperature led to disproportionately large reductions in TEC energy consumption. These findings indicate that significant improvements in system energy efficiency can be achieved with only a limited compromise in thermal regulation. Nevertheless, the primary objective of a BTMS is not merely to minimize auxiliary energy consumption, but also to maintain the battery within a safe and thermally stable operating temperature range. Therefore, the reference temperature should be carefully optimized to achieve an appropriate balance between cooling energy demand, thermal control effectiveness, battery safety, and long-term durability, rather than simply targeting the lowest possible battery temperature.

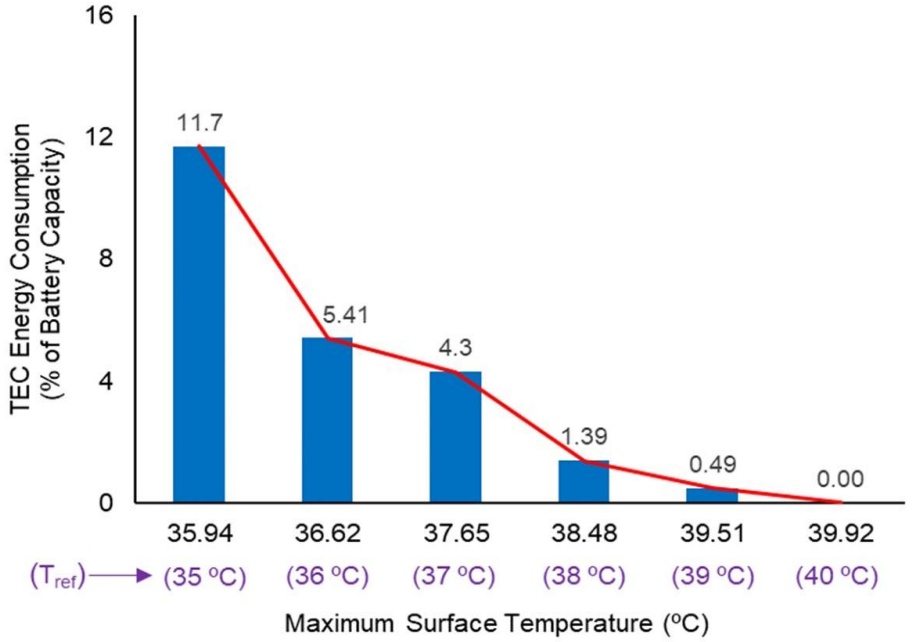


Figure 7. Variation of auxiliary energy consumption with maximum battery surface temperature.

4. Conclusion

This study experimentally investigated the effect of reference surface temperature on the auxiliary energy consumption of a thermoelectric-based BTMS employing a selective TEC activation strategy under a constant 7.5C discharge condition. The reference surface temperature was systematically varied from 35 °C to 40 °C in 1 °C increments to evaluate its influence on TEC activation behavior, battery thermal response, and auxiliary energy consumption. The results demonstrated that the reference surface temperature is a key control parameter governing both the thermal performance of the battery and the energy required for thermoelectric cooling.

Increasing the reference surface temperature progressively reduced both the activation duration and the energy consumption of the TEC modules. Specifically, the maximum battery surface temperatures obtained at reference temperatures of 35, 36, 37, 38, 39, and 40 °C were 35.94, 36.62, 37.65, 38.48, 39.51, and 39.92 °C, respectively. Meanwhile, the total TEC energy demand decreased from 5.88 Wh at 35 °C to zero at 40 °C because the maximum battery surface temperature remained

below the selected reference temperature. Consequently, the auxiliary energy consumption decreased from 11.70% to 0% of the battery energy capacity. An important finding of this study is the nonlinear relationship between the reference surface temperature and the auxiliary energy consumption. Increasing the reference temperature from 35 °C to 36 °C resulted in only a 0.68 °C increase in the maximum battery surface temperature while reducing the TEC energy consumption by more than 50%. Further increases in the reference temperature from 36 °C to 37 °C and from 37 °C to 38 °C increased the maximum battery surface temperature by 1.03 °C and 0.83 °C, respectively, while reducing the TEC energy consumption by approximately 21% and 68%, respectively. These findings demonstrate that relatively small increases in the allowable battery surface temperature can lead to disproportionately large reductions in auxiliary energy consumption, highlighting the importance of selecting an appropriate reference surface temperature for thermoelectric BTMSs.

Overall, this study demonstrates that optimizing the reference surface temperature is a key design consideration for thermoelectric BTMSs, enabling significant improvements in energy efficiency without compromising battery thermal safety.

The present study was limited to a single 20 Ah $LiFePO_4$ pouch cell, a constant 7.5C discharge condition, fixed ambient and coolant temperatures of approximately 27.5 °C, and a reference surface temperature range of 35-40 °C. In addition, the analysis focused on battery surface temperature and TEC electrical energy consumption, while long-term battery ageing, different discharge rates and ambient conditions, and a true no-cooling baseline were not investigated. Future studies should therefore evaluate the proposed selective control approach under different operating conditions and with multiple cells or battery packs, while also considering long-term ageing behavior. Such investigations would further validate the applicability of the identified thermal-energy trade-off and provide a more comprehensive assessment of the energy efficiency of TEC-based battery thermal management systems.

Author Contributions

The percentages of the author' contributions are presented below. The author reviewed and approved the final version of the manuscript.

	E.G.
C	100
D	100
S	100
DCP	100
DAI	100
L	100
W	100
CR	100
SR	100
PM	100
FA	100

C= concept, D= design, S= supervision, DCP= data collection and/or processing, DAI= data analysis and/or interpretation, L= literature search, W= writing, CR= critical review, SR= submission and revision, PM= project management, FA= funding acquisition.

Conflict of Interest

The author declared that there is no conflict of interest.

Ethical Consideration

Ethics committee approval was not required for this study because of there was no study on animals or humans.

References

Alaoui, C. (2013). Solid-state thermal management for lithium-ion EV batteries. *IEEE Transactions on Vehicular Technology*, *62*(1), 98–107. https://doi.org/10.1109/TVT.2012.2214246

Bhattacharyya, S., Dinh, Q. T., & McGordon, A. (2025). Optimising thermoelectric coolers for battery thermal management in light electric vehicles. *Applied Energy*, *386*, Article 125516. https://doi.org/10.1016/j.apenergy.2025.125516

Chen, K., Zhang, Z., Wu, B., Song, M., & Wu, X. (2024). An air-cooled system with a control strategy for efficient battery thermal management. *Applied Thermal Engineering*, *238*, Article 121578. https://doi.org/10.1016/j.applthermaleng.2023.121578

Esfahanian, V., Renani, S. A., Nehzati, H., Mirkhani, N., Esfahanian, M., Yaghoobi, O., & Safaei, A. (2013). Design and simulation of air cooled battery thermal management system using thermoelectric for a hybrid electric bus. In *Proceedings of the FISITA 2012 World Automotive Congress* (pp. 463–473). Springer. https://doi.org/10.1007/978-3-642-33841-0_39

Faseena, A. M. F., & Sreekumar, A. (2025). Advances, perspectives and challenges in phase change material based battery thermal management: A comprehensive review. *Journal of Energy Storage*, *113*, Article 115644. https://doi.org/10.1016/j.est.2025.115644

Jiang, Z. Y., & Qu, Z. G. (2019). Lithium–ion battery thermal management using heat pipe and phase change material during discharge–charge cycle: A comprehensive numerical study. *Applied Energy*, *242*, 1115–1128.

https://doi.org/10.1016/j.apenergy.2019.03.043

Kurt, M., & Güner, E. (2026). Experimental investigation of a selective thermoelectric control strategy for Li-Ion BTMS under high C-Rate operation: Balancing thermal safety and uniformity. *Energy & Fuels*, *40*(28), 15396–15407. https://doi.org/10.1021/acs.energyfuels.6c01526

Liao, G., Jiang, K., Zhang, F., E, J., Liu, L., Chen, J., & Leng, E. (2021). Thermal performance of battery thermal management system coupled with phase change material and thermoelectric elements. *Journal of Energy Storage*, *43*, Article 103217. https://doi.org/10.1016/j.est.2021.103217

Liu, X., Wu, P. Y., Su, C. Q., Xiong, X., Wang, X. Y., & Wang, Y. P. (2025). Research on precise temperature control performance of battery thermal management system integrating piezoelectric pump and thermoelectric cooler. *Energy*, *318*, Article 134623. https://doi.org/10.1016/j.energy.2025.134623

Liu, Y., Yang, S., Guo, B., & Deng, C. (2014). Numerical analysis and design of thermal management system for lithium ion battery pack using thermoelectric coolers. *Advances in Mechanical Engineering*, *6*, Article 852712. https://doi.org/10.1155/2014/852712

Luo, D., Wu, H., Cao, J., Yan, Y., Yang, X., & Cao, B. (2024b). Numerical investigation of a battery thermal management system integrated with vapor chamber and thermoelectric refrigeration. *Journal of Cleaner Production*, *434*, Article 140089. https://doi.org/10.1016/j.jclepro.2023.140089

Luo, D., Zhao, Y., Cao, J., Chen, W. H., Zhao, Y., & Cao, B. (2024a). Performance analysis of a novel thermoelectric-based battery thermal management system. *Renewable Energy*, *222*, Article 120193. https://doi.org/10.1016/j.renene.2024.120193

Luo, Y., Zhang, A., Pang, D., & Wang, B. (2025). Dynamic performance analysis of a thermoelectric cooling-based thermal management system for lithium-ion power batteries. *Case Studies in Thermal Engineering*, *67*, Article 106315. https://doi.org/10.1016/j.csite.2025.106315

Lv, W., Li, J., & Chen, M. (2023). Experimental study on the thermal management performance of a power battery module with a pulsating heat pipe under different thermal management strategies. *Applied Thermal Engineering*, *226*, Article 120402. https://doi.org/10.1016/j.applthermaleng.2023.120402

Mahek, M. K., Alkhedher, M., Ghazal, M., Abdelkareem, M. A., Ramadan, M., & Olabi, A. G. (2023). Effects of control volume outlet variation on axial air cooling of lithium-ion batteries. *International Journal of Thermofluids*, *18*, Article 100373. https://doi.org/10.1016/j.ijft.2023.100373

Pesaran, A. A. (2002). Battery thermal models for hybrid vehicle simulations. *Journal of Power Sources*, *110*(2), 377–382. https://doi.org/10.1016/S0378-7753(02)00200-8

Riffat, S. B., & Ma, X. (2003). Thermoelectrics: A review of present and potential applications. *Applied Thermal Engineering*, *23*(8), 913–935. https://doi.org/10.1016/S1359-4311(03)00012-7

Wang, H., Tao, T., Xu, J., Shi, H., Mei, X., & Gou, P. (2022). Thermal performance of a liquid-immersed battery thermal management system for lithium-ion pouch batteries. *Journal of Energy Storage*, *46*, Article 103835. https://doi.org/10.1016/j.est.2021.103835

Wang, Y., Xu, X., Huang, W., Kong, J., Wang, Q., Zhou, F., & Wei, H. (2025). A versatile battery thermal management system based on thermoelectric devices for preheating and cooling. *International Journal of Thermal Sciences*, *211*, Article 109700. https://doi.org/10.1016/j.ijthermalsci.2025.109700

Wu, W., Liu, J., Liu, M., Rao, Z., Deng, H., Wang, Q., Qi, X., & Wang, S. (2020). An innovative battery thermal management with thermally induced flexible phase change material. *Energy Conversion and Management*, *221*, Article 113145. https://doi.org/10.1016/j.enconman.2020.113145

Wu, W., Wang, S., Wu, W., Chen, K., Hong, S., & Lai, Y. (2019). A critical review of battery thermal performance and liquid based battery thermal management. *Energy Conversion and Management*, *182*, 262–281. https://doi.org/10.1016/j.enconman.2018.12.051

Yu, H., Zhu, X., Ma, X., & Yan, H. (2025). Cooling performance analysis and sensitivity analysis of thermoelectric cooling for an 18650 battery pack thermal management. *Case Studies in Thermal Engineering*, *68*, Article 106394. https://doi.org/10.1016/j.csite.2025.106394

Zhang, C., Li, K., & Deng, J. (2016). Real-time estimation of battery internal temperature based on a simplified thermoelectric model. *Journal of Power Sources*, *302*, 146–154. https://doi.org/10.1016/j.jpowsour.2015.10.052

Zhang, Y., Cui, H., Fan, Y., Zhang, J., Zhang, J., Chen, Z., & Luo, Y. (2025). Investigation of a novel lithium battery thermal management strategy by using thermoelectric technology. *Energy*, *322*, Article 137247. https://doi.org/10.1016/j.energy.2025.137247

Zhang, Z., & Wei, K. (2020). Experimental and numerical study of a passive thermal management system using flat heat pipes for lithium-ion batteries. *Applied Thermal Engineering*, *166*, Article 114660. https://doi.org/10.1016/j.applthermaleng.2019.114660

Black Sea Journal of Engineering and Science
doi: 10.34248/bsengineering.1926602

Open Access Journal
e-ISSN: 2619 – 8991

Research Article
Volume 9 - Issue 5: 2760-2772 / September 2026

EVALUATION OF GREEN AIRPORT CRITERIA IN SUSTAINABLE TRANSPORTATION USING DEMATEL AND BWM

Ahmet İLBAŞ[1]*, Aynur ACER[2], Hakan KAYA[3], Bihter KARAGÖZ[2]

[1] *Istanbul Nişantaşı University, Faculty of Economics, Administrative and Social Sciences, Department of Aviation Management, 34398, Istanbul, Türkiye*
[2]*Istanbul Arel University, Faculty of Economics and Administrative Sciences, Department of Logistics Management, 34537, Istanbul, Türkiye*
[3]*Istanbul Arel University, Faculty of Economics and Administrative Sciences, Department of Aviation Management, 34537, Istanbul, Türkiye*

Abstract: In line with increasing environmental concerns and sustainability objectives, evaluating airports based on green criteria has gained growing importance. This study aims to evaluate and prioritize green airport criteria using the DEMATEL (Decision Making Trial and Evaluation Laboratory) and BWM (Best-Worst Method) approaches. The main criteria, identified through a comprehensive literature review and expert consultation, include energy efficiency, carbon footprint, waste management, fuel management, transportation alternatives, next-generation aircraft, noise pollution, and sustainable materials. The study examines both the priority levels of these criteria and their causal relationships. Data collected from field experts were analyzed using the DEMATEL and BWM multi-criteria decision-making methods. The findings identify the most critical criteria for improving environmental performance and provide practical implications for sustainable airport management.

Keywords: Green airport, Airport management, Sustainable environment, DEMATEL, BWM

***Corresponding author:** Istanbul Arel University, Faculty of Economics and Administrative Sciences, Department of Aviation Management, 34537, Istanbul, Türkiye
E mail: ahmetilbas@arel.edu.tr (A. İLBAŞ)
Ahmet İLBAŞ https://orcid.org/0000-0002-1786-613X
Aynur ACER https://orcid.org/0000-0002-7315-7020
Hakan KAYA https://orcid.org/0000-0003-1512-8739
Bihter KARAGÖZ https://orcid.org/0000-0002-3966-1901

Received: April 09, 2026
Accepted: August 25, 2026
Published: September 15, 2026

Cite as: İlbaş, A., Acer, B., Kaya, H., & Karagöz, B. (2026). Evaluation of green airport criteria in sustainable transportation using DEMATEL and BWM. *Black Sea Journal of Engineering and Science*, 9(5), 2760-2772.

1. Introduction

Airports have historically played a crucial role in transportation and require substantial infrastructure investments. Once constructed, airports continue to generate economic activity over long periods. Airports are multidimensional systems that combine economic functions, infrastructure systems, geographic areas, and trade. These systems are governed within complex legal frameworks and are typically operated through an organizational model that requires close collaboration between the public and private sectors (Wu et al., 2020; Chanda et al., 2023).

A green airport can be defined as the integration of employees and stakeholders into airport development and operational processes to enhance ecological sustainability awareness and promote its adoption. Furthermore, a green airport involves the development of airport infrastructure in a sustainable and climate-friendly manner, aligned with a long-term strategy.

More broadly, the sustainable transformation of airport operations reflects responsible behavior across all organizational levels, from top management to operational staff (Gómez Comendador et al., 2019; Kaçar et al., 2022). A conceptually related discussion in the maritime sector (where sustainable infrastructure transformation follows a comparable top-management-to-operations logic) is provided by Pavlic et al. (2014) in the context of green ports; while not directly focused on airports, this parallel literature illustrates that cross-modal sustainability governance principles are broadly transferable. Green airport criteria, including environmental impact reduction, energy efficiency, and social responsibility, help modern airports maintain competitive advantage. When designating green airports, it is necessary to define the criteria required to measure and improve their environmental performance. Determining these criteria and their relative weights provides Decision Makers (DMs) with the opportunity to identify the most appropriate sustainability strategies by considering various factors.

In this study, green airport criteria were determined primarily through a literature review and expert interviews. The DEMATEL method, a multi-criteria decision-making (MCDM) technique, was used to evaluate the identified green airport criteria. The DEMATEL method examines critical factors and identifies

This work is licensed (CC BY-NC 4.0) under Creative Commons Attribution 4.0 International License

their causal relationships and relative influence on overall sustainability strategy. The DEMATEL method is a scientifically accepted and significant analysis technique (Gabus and Fontela, 1972). This method helps in understanding complex relationships, revealing which criteria are more effective and which should be prioritized. It can characterize the interrelationships of criteria in the decision-making process as a network, resulting in a model that defines the relationships between criteria. A key advantage of the DEMATEL method is its ability to classify criteria into cause and effect groups.

BWM is a newer MCDM method based on initially selecting the best and worst criteria in the decision-making problem. Pairwise comparisons are performed only between the remaining criteria and the best and worst criteria, respectively. In short, criteria weighting can be performed without conducting a full pairwise comparison across all criteria. Therefore, for a larger number of criteria, BWM can produce more consistent pairwise comparisons. BWM was selected due to its ability to identify the most and least important criteria with fewer comparisons and higher consistency. The aim is to strengthen the analysis by comparing criteria rankings derived from different methods.

Green airport initiatives are increasingly shaped by mounting carbon-emission pressures within the broader sustainable transportation agenda. Aviation-related carbon output is concentrated not only in-flight but also in ground operations, where airport-level interventions can meaningfully reduce the sector's footprint. Prior evidence indicates that carbon-reduction technologies at major hub airports (including electrified ground support equipment, renewable energy procurement, and optimized taxi/idle procedures) can produce measurable reductions in airport-attributable emissions (Baxter, 2021). At the fuel-supply level, the projected growth of sustainable aviation fuels is expected to materially alter the CO2 trajectory of the European aviation sector through 2030, underscoring fuel management as a lever that airports and airlines share jointly (Kousoulidou and Lonza, 2016). Beyond direct emissions, a holistic certification perspective shows that airports pursuing green status must simultaneously coordinate energy, waste, and materials criteria, since carbon performance is rarely improved by a single isolated intervention (Gómez Comendador et al., 2019). These carbon-emission pressures reinforce the rationale for a multi-criteria approach: No single criterion captures the sustainability challenge in isolation, and trade-offs among energy efficiency, fuel management, and materials use must be explicitly weighted, which is precisely the gap this study addresses through the integrated DEMATEL-BWM framework.

This study seeks to systematically identify, structure, and prioritize critical green airport management criteria through the integrated application of DEMATEL and BWM, thereby providing a robust multi-method decision-support framework. For this purpose, the criteria set was analyzed using both DEMATEL and BWM, and the results were evaluated. Various studies on the subject are available in the literature. It is believed that this study will contribute to the literature by utilizing current domestic and international green airport criteria and by comparatively analyzing the results using two different practical methods.

This study makes three substantive contributions to the sustainable airport management literature. First, it integrates two distinct MCDM methods (DEMATEL and BWM) to provide both a cause-effect analysis and a priority ranking of green airport criteria, an approach rarely applied in airport sustainability research. Second, by using a comprehensive set of eight criteria derived from a systematic literature review and validated by field experts, the study offers a current and context-specific framework for Türkiye that can be adapted to other regions. Third, the comparative analysis between DEMATEL and BWM highlights convergence and divergence in criterion prioritization, offering decision-makers a more nuanced basis for strategic planning. These contributions collectively address gaps in the sustainable airport management literature, particularly regarding methodological diversity and the treatment of interdependencies among criteria.

The introductory section of this study has explained the concept of a green airport. The second section includes a literature review on green airport criteria. The third section discusses the methodological steps of the DEMATEL and BWM methods and the necessary procedures to be followed. The final section, which constitutes the application, addresses the determination of criteria and their key values, calculating criteria weights using DEMATEL, and identifying the most and least important criteria.

1.1. Theoretical Framework

As in many other areas, implementing green airports requires overcoming certain limitations. These include a lack of information exchange and integration between the authorities responsible for implementing airport regulations and other relevant parties, unclear regulations, costly enforcement of environmental laws, and inadequate economic incentives and approvals aimed at environmental protection.

At this stage, a detailed review of research on green airport criteria was conducted. The literature shows that green airport efforts vary in their focus on increasing environmental sustainability and reducing the ecological impact of airport operations. As seen in Table 1, most studies emphasize energy efficiency and carbon footprint, whereas few address noise control. This highlights a research gap that this study aims to fill.

Table 1. Literature review on green airport criteria

Criteria	Authors
Environmental and Air Pollution	Kaçar et al., 2022; Eid et al., 2024; Sipos, 2024; Whittle et al., 2024; Deng et al., 2025
Smart Airport	Javaherikhah and Sarvari, 2025
Sustainability	Uysal and Söğüt, 2017; Cosgrove, 2018; Mishchenko et al., 2022; Raimundo et al., 2023, Dalkıran, 2023; Filho et al., 2023; Jia et al., 2024; Duliński, 2025
Green Transformation	Lv et al., 2024
Carbon Footprint	Kousoulidou and Lonza, 2016; Gómez Comendador et al., 2019; Baxter, 2021; Filho et al., 2023
Energy Consumption	Huertas et al., 2024; Sleiman and Ouf, 2025
Air Quality	Han et al., 2020
Waste Management	Sarbassov et al., 2020; Sebastian and Louis, 2021
Noise Control	Abduh et al., 2015; Cosgrove, 2018; Dobruszkes et al., 2021; Rosario, 2021; König, 2023; Rafanambinantsoa et al., 2024; Wu et al., 2024

2. Materials and Methods

To establish the methodological foundation of this study, a comprehensive literature review and expert consultation process were conducted. Based on these steps, eight criteria were identified for evaluating green airports: energy efficiency (C1), carbon footprint (C2), waste management (C3), fuel management (C4), transportation alternatives (C5), next-generation aircraft (C6), noise pollution (C7), and sustainable materials (C8). These eight criteria were selected through a two-stage process: first, a systematic review of the literature summarized in Table 1 was used to compile the full set of criteria discussed in prior green-airport and green-transportation studies; second, this candidate list was screened in a preliminary consultation with the expert panel described in Section 4.1, retaining only criteria that experts judged to be (a) directly actionable by airport management and (b) supported by at least two independent literature sources. Candidate dimensions such as digitalization and circular-economy practices were considered but excluded at this stage because they did not meet the second criterion within the reviewed literature at the time of data collection; this exclusion is acknowledged as a limitation in Section 5.

These criteria were analyzed using two complementary multi-criteria decision-making methods: DEMATEL and BWM. All DEMATEL matrix calculations and BWM optimization analyses were performed using Microsoft Excel, Version 2607. Excel was used for the DEMATEL matrix calculations and for solving the BWM optimization models, including the calculation of the final criterion weights.

2.1. DEMATEL Methodology

The DEMATEL method, originally developed by Gabus and Fontela (1972), is used to identify and quantify causal relationships among criteria within complex systems. The method has been widely applied in MCDM studies to analyze interdependencies and structure cause–effect relationships (Tzeng et al., 2007; Wu, 2008; Si et al., 2018).

Let $M = \{m_{ij}\}_{nxn}$ denote the initial direct-relation matrix obtained from expert evaluations, where m_{ij} represents the degree to which criterion i influences criterion j, and $m_{ii} = 0$. When multiple experts are involved, the aggregated matrix is computed as the arithmetic mean of individual matrices (Wu and Tsai, 2011). This matrix uses the comparison scale, which is widely used in the literature (Si et al., 2018).

Table 2. The comparison scale

Numerical Value	Definition
0	Ineffective
1	Low impact
2	Moderate impact
3	High impact
4	Very high impact

In a decision problem consisting of criteria n, x_{ij} represents the degree to which criterion i affects criterion j (equation 1).

$$X = \begin{bmatrix} x_{11} & \cdots & x_{1n} \\ \vdots & \ddots & \vdots \\ x_{n1} & \cdots & x_{nn} \end{bmatrix}_{nxn} \quad (1)$$

The Normalized Direct Relation Matrix (M) is obtained from the Direct Relation Matrix (X) using equation 2.

$$M = \frac{x}{k} \quad (2)$$

$$k = max\left(\max_{1\le i\le n} \sum_{j=1}^{n} x_{ij}\,,\ \max_{1\le j\le n} \sum_{j=1}^{n} x_{ij}\,, \right) \quad (3)$$

The Total Correlation Matrix (T), incorporating both direct and indirect effects, is calculated by (equation 4):

$$T = \lim_{h=\infty}(M + M^2 + \cdots + M^h) \quad = M(I - M)^{-1} \quad (4)$$

where I is the identity matrix (Tzeng et al., 2007). The row and column sums of T are computed as (equations 5 and 6):

$$r_i = \left[\sum_{j=1}^{n} t_{ij}\right]_{nx1};\ i = 1, \dots, n \quad . \quad (5)$$

$$c_j = \left[\sum_{i=1}^{n} t_{ij}\right]_{1xn}^{T};\ j = 1, \dots, n \quad (6)$$

Here, R_i represents the total influence exerted by criterion i, while C_j denotes the total influence received. The prominence and relation of each criterion are respectively defined as: R_i+C_j and R_i-C_j. A positive R_i-C_j

indicates a causal (driving) criterion, whereas a negative value identifies an effect (dependent) criterion (Wu, W.W., 2008). The threshold value is defined as the mean of the elements in T (equation 7):

$$\theta = \frac{\sum_{i=1}^{n}\sum_{j=1}^{n} t_{ij}}{N}, \quad i,j \in \{1,2,\dots,n\} \tag{7}$$

where $N = n^2 = 64$, representing the total number of elements in the T matrix. The threshold value determines which criterion relationships are considered significant, excluding those with relatively low influence

The criteria importance weights are determined through a normalization process based on the Prominence (R+C) values, as shown (equation 8).

$$w_i = \frac{r_i + c_i}{\sum_{i=1}^{nn}(r_i + c_i)}, \quad i = 1,2,\dots,n \tag{8}$$

The prominence and relation measures are combined to obtain $\boldsymbol{s_i}$. (equation 9),

$$\boldsymbol{s_i} = \sqrt{(r_i + c_i)^2 + (r_i - c_i)^2}, \quad i = 1,2,\dots,n \tag{9}$$

The final criterion weights are obtained by normalizing w_i. (equation 10),

$$W_i = \frac{s_i}{\sum_{i=1}^{n}(s_i)}, \quad \forall_i = 1,2,\dots n \tag{10}$$

2.2. BWM Methodology

The Best-Worst Method (BWM) is a multi-criteria decision-making technique that determines criterion weights using pairwise comparisons (Rezaei, 2015). Unlike Analytical Hierarchy Process (AHP), which requires comparing all criterion pairs, BWM only compares each criterion with the best (most important) and worst (least important) criteria (Mohammadi and Rezaei, 2020). This reduces the number of comparisons ($2n-3$ instead of $(n-1)/2$ and simplifies consistency checks. A recent methodological survey situates this efficiency gain within the broader family of BWM extensions and applications (Mi et al., 2019).

This study applies the original (linear) BWM formulation proposed by Rezaei (2015), in which the optimal weight vector is obtained by minimizing the maximum absolute deviation ξL across the best-to-others and others-to-worst comparisons (equations 14–15 below), rather than the non-linear, Bayesian, or group-BWM variants also present in the literature (Mohammadi and Rezaei, 2020). The mathematical steps of the approach are detailed as follows (Rezaei, 2015; Rezaei et al., 2018). Define the criteria set ($\boldsymbol{C}$) (equation 11):

$$\{C_1, C_2, \dots \dots \dots C_n\} \tag{11}$$

Determine the best (B) and worst (W) criteria: The most and least important criteria according to the decision-maker. Best-to-others comparisons: Using a scale of 1 to 9 (1: equally important, 3: moderately more important, 5: strongly more important, 7: very strongly more important, 9: extremely more important), determine the preference of the best criterion over each other criterion.

Form the vector: A vector A_B is created, where each element a_{Bj} represents the preference of the best criterion B over criterion j, as in equation 12.

$$\mathrm{A_B} = (\mathrm{a_{B1}}, \mathrm{a_{B2}}, \dots \dots ., \mathrm{a_{Bn}}) \tag{12}$$

3.2.1. Comparing the other criteria with worst criterion: A vector A_W is created, where each element a_{jW} represents the preference of criterion over the worst creation W, as shown in equation 13.

$$A_W = (a_{1W}, a_{2W}, \dots \dots .., a_{nW})^T \tag{13}$$

3.2.2. Calculating the optimal weights: The optimal weights for each criterion $(w_1, w_2, \dots \dots, w_n)$ are calculated by following the steps below (equation 14).

$$\left|w_B - a_{Bj}w_j\right| \le \xi^L, \forall j \tag{14}$$
$$\left|w_j - a_{jw}w_w\right| \le \xi^L, \forall j$$
$$\sum_j w_j = 1$$
$$w_j \ge 0, \forall j$$

2.2.1. Checking consistency

The consistency ratio is calculated to check the reliability of the comparisons. A lower consistency ratio indicates more consistent comparisons. The BWM Consistency Ratio is calculated as follows (equation 15):

$$\text{Consistency Ratio} = \frac{\xi_L}{Consistency\ Index} \tag{15}$$

The consistency index in the formula is the maximum possible value of ξ_L The closer the consistency ratio is to zero, the more consistent the resulting vector is, and vice versa. In general, a consistency ratio of ≤ 0.1 indicates that the resulting vector is acceptable.

2.3. Integrated Application of DEMATEL and BWM

The combined use of DEMATEL and BWM enhances the robustness of the analysis. While DEMATEL identifies causal relationships and structural dynamics among criteria, BWM provides a clear and consistent priority ranking. Using both methods enables a comprehensive evaluation that captures both systemic influence and relative importance. This dual-method logic parallels earlier integrated fuzzy multi-criteria frameworks developed for supplier-selection problems, where combining a relationship-structuring technique with a weighting technique was similarly shown to strengthen decision robustness (Dalalah et al., 2011).

This integrated approach strengthens decision support for sustainable airport management by providing both analytical depth and practical prioritization.

3. Results

3.1. DEMATEL Findings

In the first stage, the DEMATEL method was used to analyze the core criteria set for evaluating green airports. The set of criteria was submitted to 18 experts in supply chain management and logistics for pairwise comparison. To ensure the appropriateness of the expert judgments, the selection of the 18 experts was not based solely on their general expertise in supply chain management and

logistics. Particular attention was paid to their professional experience and familiarity with airport operations, aviation sustainability, environmental management, energy efficiency, carbon emissions, transportation systems, and/or sustainable logistics. Thus, the expert panel included professionals and academics whose expertise was relevant to the environmental, technological, operational, and sustainability dimensions of green airport assessment. This criterion was considered particularly important because several of the evaluation criteria, such as next-generation aircraft, noise pollution, airport carbon management, and technological maturity, require sector-specific knowledge beyond conventional supply chain and logistics expertise. Before participating in the evaluation, the experts were informed about the definitions and scope of the criteria to ensure a common understanding of the assessment framework. Accordingly, the composition of the expert panel was designed to provide informed and context-specific judgments rather than relying exclusively on generic supply chain and logistics knowledge.

In the BWM analysis, the evaluations of three out of the 18 experts were found to be outside the acceptable consistency threshold and were therefore excluded. To maintain consistency in the comparison of the results, the number of experts included in the DEMATEL analysis was also reduced from 18 to 15. Thus, the same expert panel was used in both DEMATEL and BWM analyses, ensuring comparability and methodological consistency between the two methods.

The experts scored the level of interaction between the criteria using a scale of 0 (no influence) to 4 (very high influence). Table 1 presents the direct relationship matrix calculated by averaging the expert opinions. Following the calculation steps of the method, cause and effect criteria were determined. The criterion weights derived from DEMATEL are subsequently presented.

Table 3. Direct relationship matrix for criteria decision*

	C1	C2	C3	C4	C5	C6	C7	C8
C1	0.0000	3.1333	2.8000	3.4000	3.0000	3.6000	1.2667	2.5333
C2	3.0667	0.0000	2.7333	2.9333	2.6000	3.3333	1.5333	2.6667
C3	3.0667	2.9333	0.0000	3.1333	1.8000	2.1333	1.4000	3.2000
C4	3.4667	3.3333	2.8667	0.0000	3.2667	3.4000	1.6667	2.4667
C5	2.6667	2.6667	1.8000	3.0667	0.0000	2.8667	2.4000	2.4667
C6	3.5333	3.2000	2.6667	3.6667	2.8667	0.0000	3.1333	2.6000
C7	1.4000	1.7333	1.1333	1.4667	2.2000	3.1333	0.0000	1.4000
C8	2.8667	2.6667	3.4667	2.5333	2.2000	2.3333	1.5333	0.0000

*Normalized direct relationship matrices (Table 4) were created by dividing the direct relationship matrix by the largest sum (k=21.6667).

Table 4. Normalized direct relationship matrix

	C1	C2	C3	C4	C5	C6	C7	C8
C1	0.0000	0.1446	0.1292	0.1569	0.1385	0.1662	0.0585	0.1169
C2	0.1415	0.0000	0.1262	0.1354	0.1200	0.1538	0.0708	0.1231
C3	0.1415	0.1354	0.0000	0.1446	0.0831	0.0985	0.0646	0.1477
C4	0.1600	0.1538	0.1323	0.0000	0.1508	0.1569	0.0769	0.1138
C5	0.1231	0.1231	0.0831	0.1415	0.0000	0.1323	0.1108	0.1138
C6	0.1631	0.1477	0.1231	0.1692	0.1323	0.0000	0.1446	0.1200
C7	0.0646	0.0800	0.0523	0.0677	0.1015	0.1446	0.0000	0.0646
C8	0.1323	0.1231	0.1600	0.1169	0.1015	0.1077	0.0708	0.0000

The total relationship matrix (Table 5) was obtained by applying equation 4.

Table 5. The total relationship matrix

	C1	C2	C3	C4	C5	C6	C7	C8
C1	0.7771	0.8854	0.7994	0.9168	0.8167	0.9284	0.5687	0.7803
C2	0.8659	0.7249	0.7666	0.8649	0.7710	0.8841	0.5554	0.7550
C3	0.8214	0.8007	0.6176	0.8263	0.7014	0.7955	0.5176	0.7363
C4	0.9343	0.9116	0.8185	0.8007	0.8442	0.9422	0.5966	0.7950
C5	0.8075	0.7921	0.6932	0.8253	0.6273	0.8267	0.5615	0.7090
C6	0.9622	0.9327	0.8341	0.9711	0.8552	0.8363	0.6693	0.8220
C7	0.5636	0.5648	0.4924	0.5694	0.5430	0.6370	0.3360	0.4976
C8	0.8078	0.7850	0.7497	0.7992	0.7096	0.7959	0.5198	0.6027

The total relation matrix represents the direct and indirect relationships among the criteria. Since the analysis includes eight criteria, the matrix contains 64 relationships, including diagonal elements. To identify the more prominent relationships and facilitate the interpretation of the interrelationship map, a threshold value was determined based on the elements of the total relation matrix. Relationships exceeding the threshold were considered significant and retained for further interpretation. As shown in Table 5, C7 exhibits comparatively lower relationship values with the other criteria, indicating a relatively weak overall interaction with the system. In contrast, C1, C2, C4, and C6 show relatively higher relationship values, particularly in their interactions with other criteria. C6 and C4 are among the most strongly interconnected criteria in the system.

The Importance (R+C) and Relation (R-C) values calculated from the total relationship matrix are shown in Table 6. Based on these values, the criteria were divided into Cause and Effect groups. The order of importance of each criterion is also given. Criteria weights were calculated using equations 9 and 10.

Table 6. Cause-effect groups and criteria metrics

	R	C	R+C	R-C	E/C
C1	6.3409	6.3709	12.7118	-0.0301	Effect
C2	6.1079	6.3533	12.4612	-0.2455	Effect
C3	5.5378	5.5850	11.1228	-0.0472	Effect
C4	6.4515	6.3973	12.8488	0.0542	Cause
C5	5.4668	5.5366	11.0034	-0.0698	Effect
C6	6.7144	6.4269	13.1413	0.2875	Cause
C7	4.1895	4.0476	8.2371	0.1419	Cause
C8	5.5275	5.6187	11.1463	-0.0912	Effect

Table 6 presents the Prominence (R+C), Relation (R−C), and cause–effect classification of the criteria. Based on the R−C values, C4, C6, and C7 are classified into the Cause group, whereas C1, C2, C3, C5, and C8 belong to the Effect group. Among all criteria, C6 has the highest Prominence value (R+C = 13.1413), followed by C4 (12.8488) and C1 (12.7118), indicating that these criteria have the strongest overall interactions and are highly connected within the system. C7 has the lowest Prominence value (R+C = 8.2371), suggesting that it has relatively limited interaction with the other criteria.

In terms of causal influence, C6 exhibits the highest positive R−C value (+0.2875), indicating that it has the strongest net causal influence among the criteria. C7 (+0.1419) and C4 (+0.0542) also belong to the Cause group, although their net causal effects are comparatively weaker. In contrast, C2 has the most negative R−C value (−0.2455), followed by C8 (−0.0912), indicating that these criteria are predominantly influenced by other criteria. Notably, C7 has the lowest R+C value but a positive R−C value, suggesting that despite its limited overall prominence, it functions as a causal driver rather than a dependent criterion within the system.

These findings highlight the distinction between overall prominence and causal direction. While R+C reflects the overall importance and degree of interaction of a criterion, R−C indicates whether the criterion predominantly influences or is influenced by the other criteria. Accordingly, C6 and C4 can be considered particularly important criteria because of their high prominence and positive causal influence, whereas C7, despite having the lowest prominence, functions as a causal driver within the system. The criteria in the Effect group, particularly C1 and C2, should be interpreted as outcomes that are more strongly influenced by the causal criteria. Table 7 shows the order of importance based on the weights calculated by DEMATEL for the green airport criteria.

Table 7. Criteria weights and ranking from the DEMATEL method

Criteria	Weight	Rank
C6	0.1415	1
C4	0.1382	2
C1	0.1361	3
C2	0.1316	4
C5	0.1224	5
C3	0.1212	6
C8	0.1199	7
C7	0.0892	8

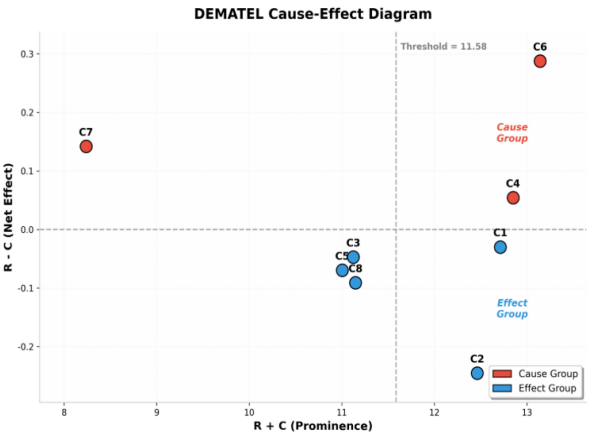


Figure 1. The cause-effect diagram of green airport criteria.

Figure 1 presents the cause–effect relationships among the green airport criteria based on the DEMATEL analysis. The mean prominence value (R + C) was computed as 11.5841 and served as the threshold to distinguish between high- and low-prominence criteria, while the sign of the net effect (R − C) was used to classify each criterion into the Cause or Effect group.

C6 and C4 are positioned in the High Prominence–Cause quadrant. C6 records the highest R + C value (13.1413) and the highest positive R − C value (+0.2875), indicating that it possesses both the strongest overall interaction with the remaining criteria and the most powerful net causal influence within the system. Similarly, C4 exhibits

a high prominence score (12.8488) together with a positive net effect (+0.0542), confirming its role as a relatively important causal driver. C7 falls into the Low Prominence–Cause quadrant. Although its overall interaction level (R + C = 8.2371) remains well below the threshold, its positive R − C value (+0.1419) demonstrates that it still exerts a net causal influence on other criteria. Conversely, C1 and C2 belong to the High Prominence–Effect subgroup. Their elevated R + C values (12.7118 and 12.4612) reflect strong overall embeddedness in the system; however, their negative R − C values (−0.0301 and −0.2455) reveal that they are predominantly affected by other criteria rather than driving them. C3, C5, and C8 are classified in the Low Prominence–Effect subgroup. Notably, C2 registers the most negative R − C value (−0.2455), indicating that it is the most strongly influenced criterion within the green airport assessment framework. C7, despite having the lowest R + C value (8.2371), functions as a causal driver due to its positive R − C value (+0.1419).

Overall, the DEMATEL results highlight that R + C and R − C provide complementary insights: while R + C captures the overall importance and centrality of a criterion, R − C reveals its directional net influence. Consequently, high prominence does not automatically imply membership in the Cause group. From a managerial standpoint, priority should be given to C6 and C4, as their combination of high prominence and positive causal influence suggests that improvements in these areas are likely to generate cascading benefits throughout the entire green airport evaluation system. Additionally, C7 should not be overlooked despite its low prominence, as its positive causal role indicates that interventions targeting noise pollution may indirectly influence broader sustainability outcomes.

3.2. BWM Findings

As a secondary method for evaluating the weights of the criteria, the Best-Worst Method (BWM) was employed. Initially, 18 experts were asked to identify the best and worst criteria from the given set. The consistency levels of the evaluations provided by three experts were found to be outside the acceptable threshold; therefore, their responses were excluded from the analysis. Consistency was assessed using the method proposed by Rezaei (2015), where a consistency ratio ≤ 0.1 indicates acceptable comparisons. The ratio exceeded 0.1; however, because the threshold for inconsistency in group decision-making is often relaxed to 0.2 (Mohammadi and Rezaei, 2020), these responses were included. The three excluded experts had ratios > 0.2 and were therefore removed from the analysis to ensure reliability. The best and worst criteria determined by the remaining 15 experts are presented in Table 8. As observed in Table 8, eight experts selected criterion C1 as the best criterion, five selected C6 and two selected C2. Regarding the worst criterion, nine experts selected C7, three selected C5, two selected C8 and one expert selected C3.

Table 8. Experts' Hidentification of best and worst criteria

Expert	Best Criteria	Worst Criteria	ξ*	Threshod
1	C1	C7	0.0926	0.3620
2	C1	C5	0.0913	0.3620
3	C1	C7	0.1385	0.3251
4	C1	C7	0.1981	0.3620
5	C1	C7	0.2166	0.3620
6	C1	C5	0.1171	0.3251
7	C1	C5	0.0684	0.3620
8	C2	C7	0.1954	0.3620
9	C6	C3	0.1539	0.3620
10	C1	C8	0.0751	0.3620
11	C2	C7	0.1573	0.3620
12	C6	C7	0.0357*	0.2844
13	C6	C8	0.0942	0.3221
14	C6	C7	0.1148	0.3620
15	C6	C7	0.1254	0.3620

During data preparation, minor inconsistencies were identified between the best-to-others (Table 9) and others-to-worst (Table 10) vectors for three experts (Experts 7, 10, and 13). These discrepancies arose from data-entry variations in which the preference of the best criterion over the worst criterion differed between the two comparison vectors. In accordance with the BWM consistency condition that requires identical best-to-worst preference values across both vectors (Rezaei, 2015), the higher of the two reported values was retained as it more accurately reflects the expert's stated best-worst preference intensity. The corrected values are indicated with an asterisk (*) in Tables 9 and 10. All other expert evaluations were used in their original form.

As presented in Table 8, all pairwise comparisons were found to be consistent, as the ξ* values for all 15 experts were lower than their respective threshold values. *Expert 12 exhibited the highest level of consistency, with a ξ value of 0.0357, which is the closest to zero among the entire panel.** This indicates that Expert 12's best-to-others and others-to-worst comparison vectors were in near-perfect alignment with the derived optimal weights. Experts 7 and 10 also demonstrated strong consistency, with ξ* values of 0.0684 and 0.0751, respectively, reflecting highly coherent pairwise judgments. At the other end of the spectrum, Expert 5 recorded the highest ξ* value (0.2166); although this is the least consistent evaluation within the panel, it still remains well below the corresponding threshold of 0.3620, thereby satisfying the acceptability condition.

The input-based consistency ratio (CRI) for the aggregated expert evaluations was calculated as 0.1250. According to the threshold values established by Liang et al. (2020) for the input-based consistency measurement, the associated threshold for this problem configuration (eight criteria) is 0.362. Since the obtained CRI (0.1250) is substantially below the threshold (0.362), the pairwise

comparisons are considered to be acceptably consistent at the aggregate level. Furthermore, the individual ξ* values, which range from 0.0357 to 0.2166, all fall within their respective expert-specific thresholds, reinforcing the overall reliability of the derived priority structure.

The results of the "best-to-others" comparisons conducted by the experts for each criterion set were obtained using a Likert scale ranging from 1 to 9, and the detailed results are provided in Table 9. Table 10 presents the evaluation results of the comparisons between the other criteria and the worst criterion.

Table 9. Best-to-Others Pairwise Comparison Vectors

Expert	Best	C1	C2	C3	C4	C5	C6	C7	C8
1	C1	1	3	4	5	7	6	8	6
2	C1	1	1	3	3	9	7	9	3
3	C1	1	3	5	6	4	5	3	7
4	C1	1	9	6	5	4	7	2	6
5	C1	1	5	7	9	3	9	1	3
6	C1	1	7	6	4	4	5	6	3
7	C1	1	4	5	5	9*	5	6	6
8	C2	3	1	4	2	5	8	1	5
9	C6	2	9	2	8	5	1	2	4
10	C1	1	5	4	8	4	7	3	8*
11	C2	2	1	2	9	4	3	1	6
12	C6	2	2	3	2	1	1	5	1
13	C6	4	3	2	3	1	1	5	6
14	C6	3	2	2	3	8	1	3	3
15	C6	3	2	2	3	8	1	3	4

Table 10. Others-to-worst comparison vectors

Expert	Worst	C1	C2	C3	C4	C5	C6	C7	C8
1	C7	6	4	3	4	2	3	1	3
2	C5	7	9	9	7	1	3	3	3
3	C7	3	3	3	3	4	2	1	2
4	C7	3	3	3	4	4	2	1	3
5	C7	2	1	1	3	4	3	1	5
6	C5	4	2	3	4	1	2	1	2
7*	C5	9*	5	4	3	1	2	1	3
8	C7	7	6	5	5	4	2	1	3
9	C3	7	3	1	3	4	2	2	3
10*	C8	8*	2	5	2	3	1	2	1
11	C7	3	4	2	3	3	2	1	1
12	C7	4	4	3	1	5	5	1	7
13*	C8	3	2	3	2	1	6*	1	1
14	C7	3	4	5	4	1	8	1	6
15	C7	3	4	5	4	1	8	1	6

Values marked with an asterisk (*) indicate corrections applied to satisfy the BWM internal consistency requirement that the preference of the best criterion over the worst criterion must be identical in both the best-to-others and others-to-worst vectors (Rezaei, 2015).

The original data entries for Experts 7, 10, and 13 contained discrepancies between these two vectors; these were aligned using the higher preference value, which reflects the stronger comparative judgment consistent with the best-worst selection.

After the reference comparisons were conducted, the criterion weights for each expert were calculated. The geometric mean of the criterion weights obtained from the 15 experts was then computed for each criterion, and the final ranking was determined accordingly (Table 11).

According to the BWM analysis, C1 (Energy Efficiency) emerged as the most important criterion with a final weight of 0.2461, followed by C2 (Carbon Footprint) (0.1414) and C6 (Next-Generation Aircraft) (0.1232). C3 (Waste Management) ranked fourth with a weight of 0.1207, while C8 (Sustainable Materials) and C4 (Fuel Management) obtained weights of 0.1042 and 0.1002, respectively. C5 (Transportation Alternatives) and C7 (Noise Pollution) occupied the seventh and eighth positions, with weights of 0.0915 and 0.0727, respectively.

The results reveal a pronounced dominance of C1 over

the remaining criteria, as its weight (0.2461) is approximately 1.7 times that of the second-ranked criterion (C2) and accounts for roughly one-quarter of the total preference allocation. This substantial gap indicates that the experts consistently identified C1 as the primary determinant in the green airport evaluation framework, suggesting that decision-makers should prioritize interventions targeting this criterion to achieve the most significant overall impact.

Table 11. Final Criteria Weights and Ranking from the BWM

Criteria	Weight	Rank
C1 (Energy Efficiency)	0.2461	1
C2 (Carbon Footprint)	0.1414	2
C6 (Next-Generation Aircraft)	0.1232	3
C3 (Waste Management)	0.1207	4
C8 (Sustainable Materials)	0.1042	5
C4 (Fuel Management)	0.1002	6
C5 (Transportation Alternatives)	0.0915	7
C7 (Noise Pollution)	0.0727	8

Conversely, the middle-ranked criteria (C3, C8, C4, and C5) exhibit relatively close weight values, ranging from 0.0915 to 0.1207, which implies a more balanced importance perception among these factors. Notably, the two lowest-ranked criteria, C7 (0.0727) and C5 (0.0915), possess distinctly lower weights, indicating that the experts assigned them a comparatively minor role in the overall assessment. The consistency ratio (CR = 0.1250), which falls below the acceptable threshold of 0.362 (Liang et al., 2020), confirms that the pairwise comparisons are reliable and coherent, thereby reinforcing the validity of the derived priority structure.

Table 12: Comparative Results: DEMATEL vs. BWM

	DEMATEL		BWM	
Criteria	Weight	Rank	Weight	Rank
C1	0.1361	3	0.2461	1
C2	0.1316	4	0.1414	2
C3	0.1212	6	0.1207	4
C4	0.1382	2	0.1002	6
C5	0.1224	5	0.0915	7
C6	0.1415	1	0.1232	3
C7	0.0892	8	0.0727	8
C8	0.1199	7	0.1042	5

Table 12 presents a comparative assessment of the eight green airport criteria based on the DEMATEL and BWM results. The two methods reveal both convergent and divergent priority patterns, reflecting their distinct methodological foundations. According to the BWM analysis, C1 (Energy Efficiency) emerged as the most important criterion with a final weight of 0.2461, followed by C2 (Carbon Footprint) (0.1414) and C6 (Next-Generation Aircraft) (0.1232). C3 (Waste Management) ranked fourth with a weight of 0.1207, while C8 (Sustainable Materials) and C4 (Fuel Management) obtained weights of 0.1042 and 0.1002, respectively. C5 (Transportation Alternatives) and C7 (Noise Pollution) occupied the seventh and eighth positions, with weights of 0.0915 and 0.0727, respectively.

3.3. Comparative Interpretation

The integrated evaluation of DEMATEL and BWM provides complementary insights. DEMATEL identifies structural influence patterns, while BWM establishes clear priority rankings. The results indicate that the two methods capture different but complementary dimensions of criterion importance rather than producing identical priority structures.

In the DEMATEL analysis, C6 (Next-Generation Aircraft) receives the highest weight (0.1415), followed by C4 (Fuel Management) (0.1382) and C1 (Energy Efficiency) (0.1361), with a relatively narrow range between the top-ranked and bottom-ranked criteria. This compressed distribution indicates that DEMATEL captures the systemic prominence of each criterion within the network of interrelationships, where even marginally higher interaction values can shift rankings. In contrast, the BWM analysis identifies C1 (Energy Efficiency) as the dominant criterion with a weight of 0.2461, followed by C2 (Carbon Footprint) (0.1414) and C6 (Next-Generation Aircraft) (0.1232). The BWM results exhibit a more dispersed weight distribution, with C1 alone accounting for approximately one-quarter of the total preference allocation. This divergence stems from the fact that BWM reflects experts' direct comparative judgments regarding the best and worst criteria, whereas DEMATEL derives weights from the structural position of each criterion within the causal-effect network.

Several notable convergence points emerge from the comparison. C1 is highly ranked under both methods, appearing third in DEMATEL and first in BWM, indicating robust cross-method agreement on its central importance. C6 also demonstrates strong convergence, ranking first in DEMATEL and third in BWM, which suggests that next-generation aircraft are recognized as important both systemically and in direct expert assessments. C7 (Noise Pollution) consistently occupies the lowest position in both approaches, ranking eighth in DEMATEL and eighth in BWM. Most strikingly, C5 (Transportation Alternatives) holds the exact same fifth position in both methods, suggesting a robust consensus across the two analytical perspectives regarding its intermediate importance level.

The most pronounced divergences concern C4 and C2. C4 (Fuel Management) ranks second in DEMATEL but sixth in BWM, indicating that while it possesses high systemic prominence and causal influence, it is not perceived as equally critical in direct expert judgments. Conversely, C2 (Carbon Footprint) rises from fourth in DEMATEL to second in BWM, suggesting that experts value this criterion highly in direct comparison even though its

systemic interaction weight is comparatively moderate. C3 (Waste Management) also demonstrates a notable ascent, climbing from sixth in DEMATEL to fourth in BWM, while C8 (Sustainable Materials) rises from seventh in DEMATEL to fifth in BWM.

Overall, the results demonstrate that DEMATEL and BWM provide complementary perspectives on criterion prioritization. DEMATEL emphasizes the interrelational structure and causal positioning of criteria, rewarding those that exert broad influence across the system—most notably C6 (Next-Generation Aircraft) and C4 (Fuel Management). BWM, on the other hand, captures the hierarchical preference structure held by decision-makers, yielding a more polarized weight distribution that highlights C1 (Energy Efficiency) as the single dominant criterion, followed by C2 (Carbon Footprint) and C6 (Next-Generation Aircraft). The consistent low ranking of C7 (Noise Pollution) across both methods suggests that this criterion warrants relatively lower priority in green airport initiatives. However, the elevated systemic position of C6 and C4 in DEMATEL, combined with the dominant expert preference for C1 and C2 in BWM, indicates that energy efficiency, carbon footprint reduction, next-generation aircraft adoption, and fuel management should all receive particular attention—albeit for different reasons.

4. Discussion and Conclusion

This study aimed to evaluate green airport criteria using two complementary multi-criteria decision-making methods, DEMATEL and BWM, to identify the most critical factors affecting environmental performance. By integrating expert opinions with quantitative analysis, the study provides both a ranking of criteria and an understanding of the interrelationships among them, offering practical guidance for airport management and policy-making.

The comparative findings provide theoretically grounded and empirically informed insights into the factors shaping sustainable airport operations. The BWM analysis identifies Energy Efficiency (C1) as the most important criterion, with a weight of 0.2461, followed by Carbon Footprint (C2) at 0.1414 and Next-Generation Aircraft (C6) at 0.1232. Waste Management (C3) ranks fourth with a weight of 0.1207, while Sustainable Materials (C8), Fuel Management (C4), Transportation Alternatives (C5), and Noise Pollution (C7) occupy the fifth, sixth, seventh, and eighth positions, with weights of 0.1042, 0.1002, 0.0915, and 0.0727, respectively. These findings indicate that direct expert preferences place particular emphasis on energy efficiency, which alone accounts for approximately one-quarter of the total preference allocation, while carbon-related performance and next-generation aircraft also receive substantial priority.

The DEMATEL analysis provides a complementary perspective by revealing the systemic relationships among the criteria. In the DEMATEL results, C6 (Next-Generation Aircraft) ranks first with a weight of 0.1415, followed by C4 (Fuel Management) at 0.1382 and C1 (Energy Efficiency) at 0.1361. Thus, although C1 receives the highest direct preference weight under BWM, C6 exhibits the greatest systemic prominence under DEMATEL. This difference is important because it indicates that direct priority and network influence are not necessarily equivalent concepts. A criterion may exert substantial influence within the sustainability system even when experts do not rank it as the single most important criterion in a direct weighting exercise.

The comparison between DEMATEL and BWM reveals several areas of convergence. C1 is highly ranked under both methods, appearing third in DEMATEL and first in BWM. C6 also demonstrates strong convergence, ranking first in DEMATEL and third in BWM, which suggests that next-generation aircraft are recognized as important both systemically and in direct expert assessments. In contrast, C7 occupies the lowest position across both approaches: eighth in DEMATEL and eighth in BWM, indicating consistent agreement that this dimension is the least critical within the present evaluation framework. Notably, C5 (Transportation Alternatives) holds the exact same fifth position in both methods, suggesting a robust consensus regarding its intermediate importance level. These convergences provide additional support for the interpretation of the results.

At the same time, several divergences are noteworthy. Fuel Management (C4) ranks second in DEMATEL but sixth in BWM. This result suggests that fuel management retains substantial systemic influence within the green-airport criterion network, even though experts assign it a moderate direct preference weight. Conversely, Carbon Footprint (C2) rises from fourth in DEMATEL to second in BWM, reinforcing the emphasis on carbon-related performance in direct expert assessments. Similarly, Sustainable Materials (C8) climbs from seventh in DEMATEL to fifth in BWM, and Waste Management (C3) rises from sixth to fourth. Consequently, criteria such as C4 should not be interpreted as unimportant; rather, their significance appears to arise particularly from their embedded relationships with other sustainability dimensions.

Although some criteria, such as noise control, exhibit lower weights, they should not be disregarded. Improvements in these areas can support broader sustainability goals, enhance stakeholder satisfaction, and promote regulatory compliance. The combined application of DEMATEL and BWM demonstrates that multiple MCDM methods can provide both a systems-level understanding and an actionable priority structure, with each method contributing a distinct form of decision-support information.

Based on these findings, several concrete and actionable recommendations emerge for airport managers and policymakers. First, energy-efficiency interventions should receive the highest priority in airport sustainability strategies, given the first-place BWM

ranking of C1 and its third-place position in DEMATEL. Such interventions may include phased LED and HVAC retrofits, renewable on-site energy generation where feasible, energy-monitoring systems, and operational efficiency measures.

Second, carbon-footprint reduction should receive substantial strategic attention because C2 ranks second in the BWM analysis and fourth in DEMATEL. Airport authorities should therefore strengthen carbon-accounting systems, establish measurable emission-reduction targets, and integrate carbon performance into investment and operational decisions.

Third, the high DEMATEL prominence and third-place BWM ranking of C6 (Next-Generation Aircraft) indicate that aircraft-related technological transformation is recognized as important both systemically and in direct expert assessments. Although airport authorities have limited direct control over aircraft technology, they can indirectly encourage the adoption of lower-emission aircraft through differentiated landing charges, environmental incentive schemes, and preferential operational arrangements where institutionally feasible.

Fourth, Fuel Management (C4) should be addressed as a systemically influential criterion. Although it ranks sixth in BWM, its second-place DEMATEL ranking indicates that improvements in fuel management may generate effects across multiple sustainability dimensions. Airport authorities and airlines should therefore strengthen fuel-efficiency monitoring, support sustainable aviation fuel adoption where feasible, and improve coordination between airport and airline stakeholders.

Fifth, Waste Management (C3), which ranks fourth in BWM and sixth in DEMATEL, should be incorporated into circular-resource and terminal-operation strategies. Its elevated BWM position indicates that experts view waste management as a priority intervention area. Sustainable Materials (C8), which ranks fifth in BWM and seventh in DEMATEL, should be addressed in procurement, infrastructure-development, and terminal-renovation strategies. Although their relative weights are moderate, these dimensions constitute important supporting elements within a comprehensive sustainability framework.

Sixth, Transportation Alternatives (C5), which holds the consistent fifth position in both methods, should be retained within comprehensive green-airport strategies as a mid-priority dimension that supports multi-modal access and ground-level emission reduction. Noise Pollution (C7), ranking eighth in both BWM and DEMATEL, should also remain part of comprehensive strategies. Their lower relative weights should not be interpreted as evidence that these dimensions can be ignored. Instead, they should be managed as complementary sustainability, regulatory-compliance, and stakeholder-relations dimensions.

Finally, policy-makers designing green-airport assessment and certification schemes should distinguish between direct priority and systemic influence. Energy efficiency and carbon performance may receive relatively high weights in direct scoring systems, while criteria such as next-generation aircraft and fuel management should also be incorporated because of their systemic influence within the sustainability network. A balanced framework should therefore combine high-priority criteria with minimum performance thresholds for lower-ranked dimensions to avoid their complete neglect.

Author Contributions

The percentages of the authors' contributions are presented below. All authors reviewed and approved the final version of the manuscript.

	A.I.	A.C.	H.K.	B.K.
C	25	25	25	25
D	30	30	20	20
S	40	40	10	10
DCP	40	40	10	10
DAI	40	40	10	10
L	30	30	20	20
W	40	40	10	10
CR	25	25	25	25
SR	50	30	10	10

C= concept, D= design, S= supervision, DCP= data collection and/or processing, DAI= data analysis and/or interpretation, L= literature search, W= writing, CR= critical review, SR= submission and revision

Conflict of Interest

The authors declared that there is no conflict of interest.

Ethical Consideration

The authors confirm that the ethical policies of the journal, as noted on the journal's author guidelines page, have been adhered to. The experimental procedures were approved by the Social and Human Sciences Ethics Committee of Istanbul Arel University, (approval date: 15 November, 2024, protocol code: 2024/22).

Acknowledgements

The authors acknowledge that the language and readability of this manuscript were improved through AI-assisted grammatical revision.

References

Abduh, N., Dirawan, G. D., & Asrib, A. R. (2015). Analysis of noise and air pollution on Sultan Hasanuddin International Airport (Eco-Airport). *Journal of Industrial Pollution Control*, *31*(1), 149–154.

Baxter, G. (2021). Mitigating an airport's carbon footprint through the use of "green" technologies: The case of Brisbane and Melbourne airports, Australia. *International Journal of Environment, Agriculture and Biotechnology*, *6*(1), 29–39.

Chanda, C. R., Hakim, M. M., & Ahmed, F. (2023). Transportation infrastructure and economic growth: Empirical insights from Bangladesh. *Journal of Business*, *8*(2), 1–15.

Cosgrove, C. (2018). Green initiatives for sustainable airport services. *Journal of Airport Management*, *12*(4), 350–358.

Dalalah, D., Hayajneh, M. & Batieha, F. (2011). A fuzzy multi-

criteria decision making model for supplier selection. *Expert Systems with Applications*, *38*(7), 8384–8391.

Dalkıran, A. (2023). An investigation and benchmarking model for developing sustainable material use among Turkish airport operators. *Journal of Aviation*, *7*(1), 93–99.

Deng, S., Zhou, S., Zhang, L., & Zhao, J. (2025). Study on green airport construction and aviation pollution control: A case study of four international airports. *Atmosphere*, *16*(3), Article 261.

Dobruszkes, F., Grippa, T., Hanaoka, S., Loko, Y., Redondi, R., Vowles, T., & Wang, J. (2021). Multiple-airport systems: The (re) development of older airports in view of noise pollution issues. *Transport Policy*, *114*, 298–311.

Duliński, W. (2025). An assessment of relation between sustainability and architectural representativeness of passenger airport terminals in Poland. *Sustainability*, *17*(1), Article 296.

Eid, A., Obrecht, M., Ali, A. H., & Barakat, M. (2024). Does environmental knowledge and performance engender environmental behavior at airports? A moderated mediation effect. *Business Process Management Journal*, *30*(3), 671–698.

Filho, L. W., Ng, A., Sharifi, A., Janová, J., Özuyar, P. G., Hemani, C., Heyes, G., Njau, D., & Rampasso, I.S. (2023). Global tourism, climate change and energy sustainability: Assessing carbon reduction mitigating measures from the aviation industry. Sustainability Science, 18(2), 983–996.

Gabus, A., & Fontela, E. (1972). *World problems, an invitation to further thought within the framework of DEMATEL*. Battelle Geneva Research Center.

Gómez Comendador, V. F., Arnaldo Valdés, R. M., & Lisker, B. (2019). A holistic approach to the environmental certification of green airports. *Sustainability*, *11*(15), Article 4043.

Han, B., Kong, W. K., Yao, T. W., & Wang, Y. (2020). Air pollutant emission inventory from LTO cycles of aircraft in the Beijing-Tianjin-Hebei airport group, China . *Environmental Science*, *41*(7), 3086–3094.

Huertas, J. I., Rincon, A. Z., Velazquez, A., Marquez, C., Diaz, J. A. & Florez, M. (2024). Energy efficiency in medium-scale airports: Two Mexican airports as case of study. *Heliyon*, *10*(15), Article e35237.

Javaherikhah, A., & Sarvari, H. (2025). Implementing building information modeling to enhance smart airport facility management: An AHP-SWOT approach. *CivilEng*, *6*(1), Article 15.

Jia, X., Macário, R., & Buyle, S. (2024). How do airports align with sustainability? An analysis of the world's 150 busiest airports. *Sustainable Development*, *32*(6), 7409–7433.

Kaçar, B., Turhan, E., Dalkiran, A., & Karakoc, T. H. (2022). Green airport building certification comparison: A practical approach for airport management. *International Journal of Green Energy*, *20*(6), 602–615.

König, P., Höschler, K. & Müller, P. (2023). Assessment of (hybrid)-electric drive-train architectures for future aircraft applications. *Journal of Physics: Conference Series*, *2526*(1), Article 012023.

Kousoulidou, M., & Lonza, L. (2016). Biofuels in aviation: Fuel demand and CO2 emissions evolution in Europe toward 2030. *Transportation Research Part D: Transport and Environment*, *46*, 166–181.

Liang, F., Brunelli, M., & Rezaei, J. (2020). Consistency issues in the Best Worst Method: Measurements and thresholds. *Omega*, *96*, Article 102175.

Lv, Y., Wan, L., Zhang, N., Wang, Z., Tian, Y., & Ye, W. (2024). Research on the green transition path of airport development under the mechanism of tripartite evolutionary game model. *Sustainability*, *16*(18), Article 8074.

Mi, X., Tang, M., Liao, H., Shen, W., & Lev, B. (2019). The state-of-the-art survey on integrations and applications of the best worst method in decision making: Why, what, what for and what's next? *Omega*, *87*, 205–225.

Mishchenko, A., Dalkıran, A., Novakovska, I., Skrypnyk, L., & Ishchenko, N. (2022). Environmentally sustainable airport development: Ukrainian case of decarbonization. *Aircraft Engineering and Aerospace Technology*, *95*(3), 488–500.

Mohammadi, M., & Rezaei, J. (2020). Bayesian Best-Worst Method: A probabilistic group decision making model. *Omega*, *96*, Article 102120.

Pavlic, B., Cepak, F., Sucic, B., Peckaj, M., & Kandus, B. (2014). Sustainable port infrastructure, practical implementation of the green port concept. *Thermal Science*, *18*(3), 935–948.

Rafanambinantsoa, C. V., Muraretu, I., Dimbisoa, W. G., Mahatody, T., Bădică, C., & Razafindrakoto, R. (2024). Modelling aircraft noise map around an airport using machine learning [Paper presentation]. 2024 International Conference on Innovations in Intelligent Systems and Applications (INISTA), Craiova, Romania.

Raimundo, R. J., Baltazar, M. E., & Cruz, S. P. (2023). Sustainability in the airports ecosystem: A literature review. *Sustainability*, *15*(16), Article 12325.

Rezaei, J. (2015). Best-worst multi-criteria decision-making method. *Omega*, *53*, 49–57.

Rezaei, J., van Roekel, W. S., & Tavasszy, L. A. (2018). Measuring the relative importance of the Logistics Performance Index indicators using Best Worst Method. *Transport Policy*, *68*, 158–169.

Rosario, P. (2021). Morphing wing flaps for large civil aircraft: Evolution of a smart technology across the Clean Sky Program. *Acta Aeronautica et Astronautica Sinica*, *34*(1), 13–28.

Sarbassov, Y., Venetis, C., Aiymbetov, B., Abylkhani, B., Yagofarova, A., Tokmurzin, D., Anthony, E. J. & Inglezakis, V. J. (2020). Municipal solid waste management and greenhouse gas emissions at international airports: A case study of Astana International Airport. *Journal of Air Transport Management*, *85*, Article 101789.

Sebastian, R., & Louis, J. (2021). Understanding waste management at airports: A study on current practices and challenges based on literature review. *Renewable and Sustainable Energy Reviews*, *147*, Article 111229.

Si, S. L., You, X. Y., Liu, H. C., & Zhang, P. (2018). DEMATEL technique: A systematic review of the state-of-the-art literature on methodologies and applications. *Mathematical Problems in Engineering*, *2018*, Article 3696457.

Sipos, A. (2024). *International aviation law: Regulations in three dimensions*. Springer International Publishing.

Sleiman, S., & Ouf, M. (2025). A review on energy practices and indoor environmental quality (IEQ) of airports. *Building and Environment*, *278*, Article 112965.

Tzeng, G. H., Chiang, C. H., & Li, C. W. (2007). Evaluating intertwined effects in e-learning programs: A novel hybrid MCDM model based on factor analysis and DEMATEL. *Expert Systems with Applications*, *32*(4), 1028–1044.

Uysal, M. P., & Söğüt, M. Z. (2017). An integrated research for architecture-based energy management in sustainable airports. *Energy*, *140*, 1387–1397.

Whittle, J. W., Callander, K., Akure, M., Kachwala, F., & Koh, S. C. L. (2024). A new high-level life cycle assessment framework for evaluating environmental performance: An aviation case study. *Journal of Cleaner Production*, *471*, Article 143440.

Wu, C., Chan, T., & Redonnet, S. (2024). Environmental impact

by air traffic: Assessing aircraft noise nearby Hong Kong International Airport. *Applied Acoustics*, *220*, Article 109952.

Wu, H. H., & Tsai, Y. N. (2011). A DEMATEL method to evaluate the causal relations among the criteria in auto spare parts industry. *Applied Mathematics and Computation*, *218*(5), 2334–2342.

Wu, W. W. (2008). Choosing knowledge management strategies by using a combined ANP and DEMATEL approach. *Expert Systems with Applications*, *35*(3), 828–835.

Wu, X., Zhang, L., & Yang, H. C. (2020). Integration of eco-centric views of sustainability in port planning. *Journal of Sustainability*, *12*(7), Article 2971.

Black Sea Journal of Engineering and Science
doi: 10.34248/bsengineering.1994338

Open Access Journal
e-ISSN: 2619 – 8991

Research Article
Volume 9 - Issue 5: 2773-2782 / September 2026

FLOOD RISK ASSESSMENT AND ENVIRONMENTAL CHANGE ANALYSIS USING GIS AND REMOTE SENSING

Sibel CANAZ SEVGEN[1]*

[1]*Ankara University, Faculty of Applied Sciences, Department of Real Estate Development and Management, 06100, Ankara, Türkiye*

Abstract: Floods can be very destructive natural hazard; it causes significant environmental, social, and economic impacts. Havza is a district in Northern part of Türkiye, experienced major flood events in May 1998 and May 2026, which emphasize the need of identify flood-prone areas and analyze the factors that influence flood vulnerability. The aim of this study is to asses flood risk and analyzes land use/land cover (LULC) monitoring derived from remote sensing data in Havza. Furthermore, topographic characteristics were also obtained from Shuttle Radar Topography Mission (SRTM) and Digital Elevation Model (DEM) using Geographic Information Systems (GIS). Hydrological analyses include slope and flow accumulation models, and these analyses were used to identify susceptible areas. It has been observed that the mean NDVI value increased from 0.4239 in 1998 to 0.7447 in 2026, indicating a substantial increase in vegetation cover. LULC classification results also showed that urban areas increased from 16% to 20% while agricultural land decreased 54% to 50% in approximately last 3 decades. 3-Dimensional (3D) terrain visualization and river corridor-based flood risk mapping revealed that low elevation valley floors and settlements located very near to stream channels, which is the most vulnerable areas of floods. The findings of this study demonstrate the effectiveness of integration of GIS and remote sensing, topographic analysis, and LULC change detection within a single framework for flood risk assessment and sustainable land management. The results provide valuable support for disaster risk reduction, urban planning, and future development strategies in Havza and similar watershed environments.

Keywords: Flood risk assessment, Remote sensing, Land use/land cover, Change, NDVI, Digital elevation model

***Corresponding author:** Ankara University, Faculty of Applied Sciences, Department of Real Estate Development and Management, 06100, Ankara, Türkiye
E mail: ssevgen@ankara.edu.tr (S. CANAZ SEVGEN)
Sibel CANAZ SEVGEN https://orcid.org/0000-0001-5552-6067

Received: July 14, 2026
Accepted: August 26, 2026
Published: September 15, 2026

Cite as: Canaz Seven, S. (2026). Flood risk assessment and environmental change analysis using GIS and remote sensing. *Black Sea Journal of Engineering and Science,* 9(5), 2773-2782.

1. Introduction

Floods are one of the most frequent and destructive natural disaster in worldwide and it causes human life losses, agricultural production efficiency, and economic problems. Floods hazards intensified by increase in urbanization, climate variability, land degradation, and expansion of impervious surfaces in both developed and developing countries. Thus, flood risk assessment has become an important task of disaster management and sustainable land-use planning. In recent decades, Geographic Information Systems (GIS) and Remote Sensing (RS) have emerged a significant technology for many hazard identification, susceptibility mapping and vulnerability assessment due to their ability of integration large volume of spatial data (Evans et al., 2007; Nyarko, 2002; Temiz et al., 2004; Wang and Xie, 2018). GIS based flood studies focuses on integrating topographic and hydrological information for identifying flood prone areas. (Nyarko, 2002) applied a GIS-integrated rational model in Accra, Ghana, demonstrating that spatial analysis techniques can effectively identify flood risk zones and support decision-making processes. Likewise, (Temiz et al., 2004) also used precipitation digital elevation models, climatology, drainage networks, and land-use data to find out potential of flood in the Western Black Sea Region of Türkiye using. Their findings emphasized that terrain characteristics and hydrological conditions in determining flood susceptibility are very important. The findings of these studies established the basis for subsequent GIS-based flood assessment frameworks and demonstrated the effectiveness of spatial technologies in flood management. The integration of remote sensing technologies further improved flood risk assessment by enabling the acquisition of consistent, up-to-date, and large-scale environmental information. Satellite-derived datasets have been extensively used to monitor land use changes, vegetation conditions, drainage characteristics, rainfall patterns, and flood inundation extents. (Samarasinghe et al., 2022) emphasized the usefulness of satellite imagery for validating flood inundation models in Sri Lanka and demonstrated how remotely sensed flood extents can improve hazard mapping accuracy. Similarly, (Wang and Xie, 2018) reviewed numerous applications of remote sensing and GIS in water resources management and concluded that satellite

This work is licensed (CC BY-NC 4.0) under Creative Commons Attribution 4.0 International License

observations provide valuable information for flood monitoring, runoff simulation, rainfall estimation, and disaster mitigation. The increasing availability of high-resolution satellite imagery has therefore significantly enhanced the capability of flood assessment studies to represent real-world conditions.

Environmental variables and GIS-based approaches are generally integrated for flood process analyses with topographic, hydrological, meteorological, and geological factors. (Ouma and Tateishi, 2014) studied an urban flood vulnerability mapping in Kenya using drainage density, rainfall distribution, land use, soil characteristics, slope, and elevation data. The results of their study demonstrated that integrating multiple flood conditioning factors within a GIS environment substantially improves the representation of flood vulnerability patterns. Similarly, (Elsheikh et al., 2015) conducted a study with GIS and spatial analysis techniques to assess flood risk in Malaysia and observed that rainfall intensity, drainage density, and topographic factors were among the most influential determinants of flood occurrence. Similar observations were reported by (Akinbobola et al., 2015) who also used a watershed-based GIS approach for identifying flood prone settlements though the Niger and Benue River Basin in Nigeria.

Digital Elevation Model (DEM) are now easy to reach for all over the World, and DEM data also significantly contributes flood risk assessment research. GIS based flood studies are generally uses elevation, slope, flow accumulation and topographic features of the area in interest. (Hu et al., 2017) studied a flood risk assessment using these parameters in the Fangshan District of Beijing and their findings showed that rapidly urbanizing suburban areas exhibited considerably higher flood risk than surrounding rural landscapes. Similar study conducted by (Roopnarine et al., 2018) in Trinidad, and they also used GIS-based flood susceptibility mapping to identify low-lying coastal and urbanized areas are the most vulnerable locations.

Other studies related to flood risk emphasized the integration of hazard indicators with economic and social vulnerability factors. Flood risk is no longer solely as a function of hydrological processes but rather as a combination of hazard, vulnerability, and exposure. (Rincón et al., 2018) developed a GIS-based flood risk framework for the Greater Toronto Area by integrating social and economic vulnerability indicators with traditional environmental variables. The results of this study demonstrated that similar flood hazards areas may experience significantly different risk levels and this depends on population characteristics and socio-economic conditions. Likewise, (Gupta and Dixit, 2022) also integrated flood hazard, vulnerability, and risk indices within a GIS-based framework and observed that a large proportion of Assam, India, falls within moderate-to-high flood risk categories. These findings show that the necessity of adaptation of comprehensive approaches that consider both environmental and human dimensions of flood risk. Several recent studies have further demonstrated the effectiveness of GIS and RS technologies for flood susceptibility assessment in various geographical environments (Al-Omari et al., 2024; Kumar and Jha, 2023; Saha and Agrawal, 2020).

In Türkiye, GIS methodologies have become increasingly common in flood susceptibility research during the last two decades (Karakoca and Ünver, 2024; Karakuş and Ceylan, 2022; Nasanlı et al., 2025; Oğuz et al., 2022; Sunkar and Tonbul, 2010; Tokgözlü and Özkan, 2018; Yıldız and Gürgöze, 2026; Yurteri, 2024). Several studies in Türkiye have demonstrated GIS-based approaches are effective for flood risk assessment and susceptibility mapping. (Akın and Karaca, 2021) created a flood susceptibility map for the Çerçi Stream Basin using topographic, geological, and land-use variables, and (Çeliker et al., 2020) combined GIS and HEC-RAS modelling for flood inundation identification areas in Bingöl. Similarly, (Duman and İrcan, 2022) and (Bitek and Erenoğlu, 2026) also applied GIS-based analytical methods to determine flood prone areas and support disaster management planning in Türkiye. Recent studies have also demonstrated that the importance of topographic and land cover factors in flood susceptibility analyses. (Dölek and Vedat, 2024) identified elevation, slope, soil characteristics, and NDVI as significant determinants of flood sensitivity, whereas (Ekmekcioğlu, 2023) reported that rainfall, topography, and NDVI where are the most influential variables affecting flash flood occurrence. These studies findings emphasized that the value of integrating GIS, RS, and environmental indicators in flood risk assessment.

However, there is the growing body of literature on flood susceptibility assessment, relatively few studies have integrated topographic analysis, flow accumulation modelling, NDVI assessment, and long-term land use/land cover (LULC) change detection within a single framework. Moreover, limited attention has been given to examining how landscape transformation influences flood vulnerability in medium-sized watersheds of Türkiye. This study addresses this gap by combining DEM-derived topographic analysis, flow accumulation modelling, NDVI change analysis, LULC classification, and flood risk assessment to evaluate environmental change and flood susceptibility in Havza. Unlike many previous studies that focus solely on flood susceptibility mapping, the present study investigates both flood risk and long-term landscape dynamics between 1998 and 2026. Furthermore, the analysis is particularly relevant because Havza experienced significant flood events in both 1998 and May 2026, providing an opportunity to evaluate flood vulnerability in relation to environmental and land-use changes. The findings are expected to contribute to sustainable watershed management, disaster risk reduction, and evidence-based urban planning in Havza and similar watershed environments.

1.1. Study Area

Havza is a district located in the southwestern part of Samsun Province in the Central Black Sea Region of Türkiye (Figure 1). The city of Havza is characterized by a tugged topography, which consist mountainous areas, valley floors, and stream networks. This environmental area also controls local hydrological processes. Havza city has a stream named as Hacıosman, and it flows through the city area of Havza. This stream and drainage corridors have been associated with flood disaster which happened in May 1998 and May 2026. Havza provides a suitable case study for investigating the relation between flood risk and land cover Dynamics due to it is topographic characteristics. Another point of city is that in last 3 decades the population of Havza increased 38,103 in 2026 from 17,585 in 1997 (TurkStat).

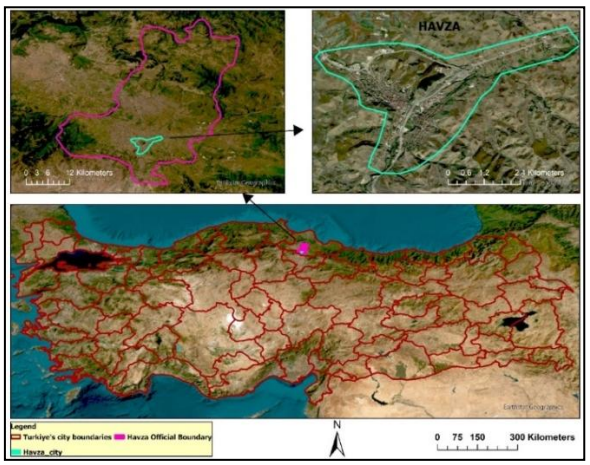


Figure 1. Map of study area.

Related with the population, new buildings with high floor numbers were constructed as building permit statistics indicate a continuous increase in construction activity in Havza between 2010 and 2025 (Figure 2). 4.556 buildings were recorded as having new construction permits over last 15 years. In 2017 the highest annual value was recorded as 913 buildings permits comparing with other years this peak occurred because of nationwide increase in construction permits in this year which was support by government housing incentives and favorable financing conditions. Throughout the study period, cumulative number of permitted buildings increased steadily which support of urban expansion. The buildings permit numbers are consistent with LULC results between 1998 and 206.

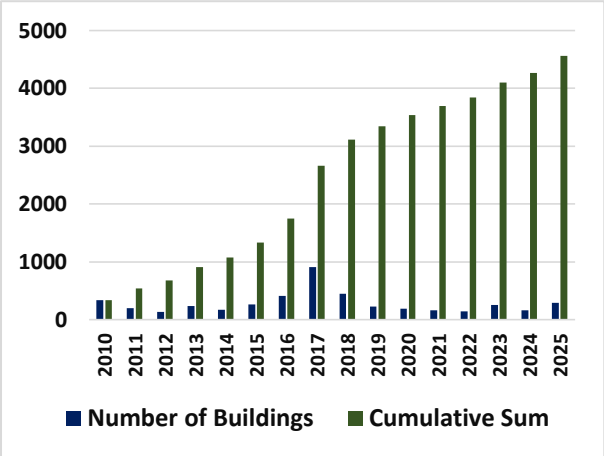


Figure 2. Annual and cumulative number of buildings permits in Havza (2010–2025, TurkStat).

1.1.1. Topographic characteristics

The topography of areas plays crucial role in hydrological process controls and flood susceptibility. According to Dem analysis, elevation values in the study area changes between 317 m to 1.614 m above sea level, where mean elevation is observed as 812 m (Table 1). The slope of the district ranges from 0° to 56, 19°, with an average of 10,49°. Gentle slopes and flat surfaces occur along valley bottoms and stream corridors, while steeper slopes are observed in peripheral upland areas. The low slope areas facilitate water accumulation and thus these areas are more susceptible to flooding. Hydrological analyses further showed that runoff generated on surrounding hillslopes converges toward the main drainage network represented by main stream, Hacıosman. Flow accumulation results revealed that the stream corridor functions as the primary runoff concentration zone within the study area. Consequently, settlements that are located along the valley floor and adjacent to the drainage network are exposed to higher flood risk compared to the surrounding uplands.

Table 1. Topographic characteristics of Havza district

Parameter	Value	Source
Minimum Elevation	317 m	SRTM
Maximum Elevation	1,614 m	SRTM
Mean Elevation	812.90 m	SRTM
Minimum Slope	0.00°	SRTM-derived
Maximum Slope	56.19°	SRTM-derived
Mean Slope	10.49°	SRTM-derived
Average Cumulative Rainfall (1–21 May 1998)	119.61 mm	Meteorological Data
Mean NDVI (1998)	0.4239	Landsat 5 TM
Mean NDVI (2026)	0.7447	Sentinel-2
Mean NDBI (1998)	-0.0545	Landsat 5 TM
Mean NDBI (2026)	-0.2911	Sentinel-2

2. Materials and Methods

GIS and RS techniques were integrated in this study to evaluate flood risk and LULC change in the study area. Using Google Earth Engine (GEE) and ArcGIS Pro, topographic, hydrological and environmental datasets were processes and analyzed. The methodology consisted of following steps; DEM terrain analysis, flow accumulation, NDVI calculation, LULC classification. Finally, flood risk visualization map created to investigate for flood susceptibility.

2.1 Data Sources

Topographic, hydrological, and RS datasets combination was used to analyzed the study area's flood risk. Terrain characteristics was observed using DEM data. NDVI calculation and LULC classification were computed using Landsat 5 and Sentinel-2 imageries. The data sources used in this study is shown in Table 2. Finally, spatial layers, including stream networks and flood-affected areas, were incorporated to support flood risk assessment and visualization.

Table 2. Data sources that used in this study

Data	Source	Spatial Resolution	Acquisition Year	Purpose
Digital Elevation Model (DEM)	SRTM	30 meters	2025	Elevation, slope, and hydrological analyses
Landsat 5 TM	USGS	30 meters	1998	NDVI calculation and LULC classification
Sentinel-2 MSI	ESA	10 meters	2026	NDVI calculation and LULC classification
Flood Area Boundary	Digitized from flood-affected area	-	2026	Flood risk assessment
Hacıosman Stream Network	Digitized stream layer	-	2026	Hydrological and proximity analyses
Precipitation Data	CHIRPS	~5 km	1998	Rainfall assessment
Administrative Boundary	Study area boundary	-	2026	Spatial analyses and mapping

2.2. DEM and Slope Analysis for Flood Risk Assessments

Shuttle Radar Topography Mission (SRTM) DEM with a spatial resolution of 30 m were used in this study for analyzing topographic characteristic. These are the most important factors influencing surface runoff generation and flood susceptibility. Furthermore, DEM data was used to create slope and flood risk analysis map to investigate potentially exposed to flooding.

Slope values were computed from the DEM using spatial analysis tools in ArcGIS Pro. The results of slope map showed that low slope values were considered as more susceptible to water accumulation, on the other hand steeper slopes were associated with faster runoff and less flood potential. Hydrological and flood risk assessments were analyzed by using DEM and slope results.

2.3. Flow Accumulation Analysis

Flow accumulation analysis is one of the most important steps for the flood susceptibility. The flow accumulation analysis was conducted to identify the main runoff concentration pathways and potential drainage corridors within the study area. Initially, flow direction was derived from the DEM using hydrological analysis tools in ArcGIS Pro. Consequently, the flow accumulation model was generated to estimate the number of upstream cells contributing surface runoff to each raster cell.

The resulting flow accumulation map showed the primary drainage network and areas where runoff is concentrated. High flow accumulation values were observed along the Stream and its tributaries, indicating that these corridors function as the main pathways for water movement within the watershed. These analyses were used to evaluate the relationship between topography, drainage patterns, and flood-prone areas, providing important information for flood risk assessment and watershed management.

3.4 NDVI and Land Use/Land Cover Classification

Vegetation conditions and LULC changes were computed using Landsat 5 TM imagery acquired in 1998 and Sentinel-2 imagery acquired in 2026. (NDVI) was calculated to evaluate the spatial distribution and temporal variation of vegetation cover within the study area. The resulting NDVI maps were used to compare vegetation conditions between the two periods and identify environmental changes associated with land cover dynamics. No explicit spatial resampling or cross-sensor harmonization was applied; each dataset was processed at its native spatial resolution (30 m for Landsat 5 and 10 m for Sentinel-2). Therefore, the observed differences were interpreted as landscape-level changes rather than direct pixel-to-pixel changes between the two dates. To minimize the influence of seasonal variability and agricultural activities on NDVI, imagery representing comparable summer periods was

selected for the two study years. Sentinel-2 imagery and Landsat 5 imagery with less than 20% cloud cover were considered to reduce the influence of cloud contamination. This seasonal consistency was intended to reduce the effect of phenological differences on the temporal comparison. Therefore, the observed increase in NDVI was not interpreted solely as an increase in vegetation cover, but was evaluated in conjunction with seasonal conditions, agricultural activities, and land-cover changes.

In addition to NDVI analysis, LULC maps were produced using the Maximum Likelihood Classification (MLC) method, one of the most widely applied supervised classification techniques in remote sensing studies. Training samples were selected from representative land cover types, and the classification process was performed for 1998 and 2026 imagery. Four major land cover classes were identified: Forest, Urban Areas, Roads, and Agricultural Land. The classified maps were subsequently compared to quantify land cover changes and evaluate their potential influence on flood risk and environmental conditions in Havza.

3. Results and Discussion

3.1 Topographic Characteristics

DEM maps of the study area who's the topographic variations. The elevation values change between 317 m to 1,614 m, and the average elevation was calculated as 812 m as shown in Table 1. Havza is surrounded by mountainous terrain and the urban part of Havza has relatively narrow valley system as shown in Figure 3. Since the urban center is located with low elevation valley floor and it is also near the stream, the urban part is more likely to affect any flood disaster.

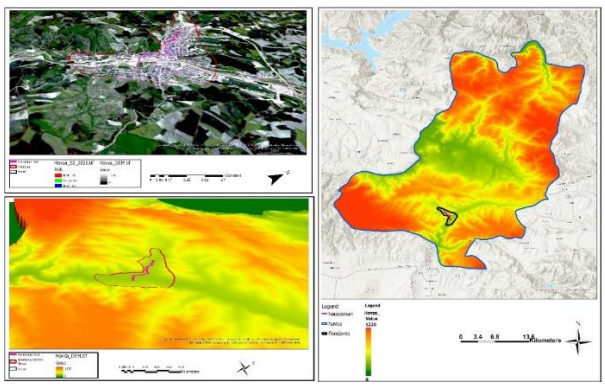


Figure 3. Digital elevation model (DEM) and topographic characteristics of the study area.

Slope maps were created using DEM datasets to analyzed flow accumulation. The map also potential to Show the influence of terrain on hydrological processes. The slope values range between 0o to 56.19o. The average slope was calculated as 10.49o. Steep slopes are concentrated in mountainous areas surrounding the settlement, on the contrary, low-slope zones occur along valley floors and stream corridors as shown in Figure 4. The gently sloping areas facilitate water accumulation and reduce runoff velocity, increasing their susceptibility to flooding. The combined interpretation of DEM and slope maps indicates that the settlement area is located within a topographically constrained valley environment that may enhance flood vulnerability during intense precipitation events.

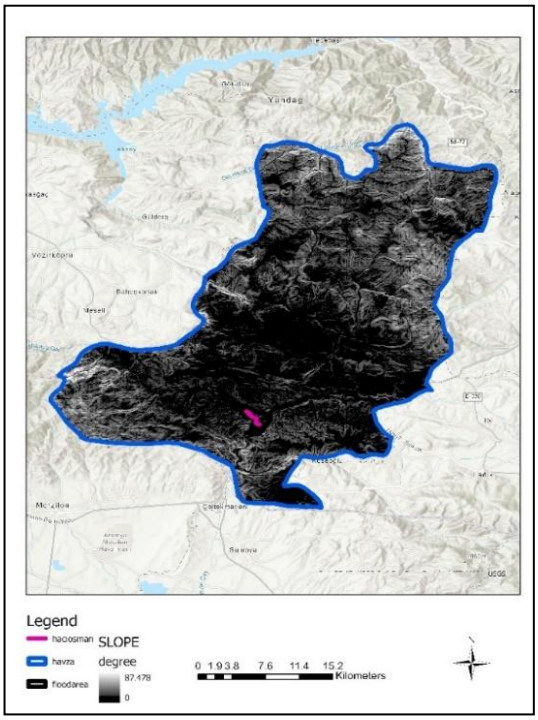


Figure 4. Slope map of Havza.

3.2. Flow Accumulation Results

To observe main drainage pathways and potential surface runoff corridors, the flow accumulation analysis conducted in the Havza city as shown in Figure 5. Higher flow accumulation values were observed, where runoff from larger upstream areas. The highest flood accumulation was found near the stream with primary drainage areas. In conclusion, it is seen that the River coincides with the primary drainage axis, and receives surface flow from numerous secondary drainage channels. The spatial distribution of the drainage corridors is important for considering topographic controls in flood risk assessment and future urban planning.

3.3 NDVI Change Analysis

Figure 6 illustrates the NDVI results that are created using Landsat and Sentinel RS imageries between 1998 and 2026. The mean NDVI value was found as 0.423 in 1998, and 0.744 in 2026. However, this value indicates the increase in vegetation over the years, it should be noted that the seasonal effect may occurred in the imageries even though both years images are extracted in summer season. Also, LULC results are important to evaluate NDVI results since this change may affected by agricultural activities. Consequently, NDVI values

indicate that a positive trend in vegetation over the years in the study area.

3.4 LULC Change Analysis

LULC classification is one of the important analysis to evaluate flood risk assessments. Classification was employed by using one of the most popular algorithm Maximum Likelihood. Four classes were created; urban, road and bare land, forest, and agricultural areas (Figure7). The classification results revealed notable change in urban area. The urban part of Havza has been increasing over the years. Urban expansion particularly observed near the stream. Moreover, the city changed to high floor apartment style than single use houses as happened in many cities in Türkiye.

On the other hand, forest areas have been increased over the study period which is compatible with NDVI results. On the contrary, agricultural land experienced slightly decline, which can be now part of urban area. Consequently, the observed land cover transitions reflect the combined influence of population and urban development activities as it was mentioned before total number of permitted buildings increased over the years.

Finally, LULC percentage distribution is presented in Table 3 for 1998 and 2026. An increase in urban and forest areas was observed, while agricultural land and road/bare land areas decreased during the study period. Urban areas expanded from approximately 16% to 20%, reflecting ongoing urban development in the city. Forest cover also increased, consistent with the NDVI analysis results.

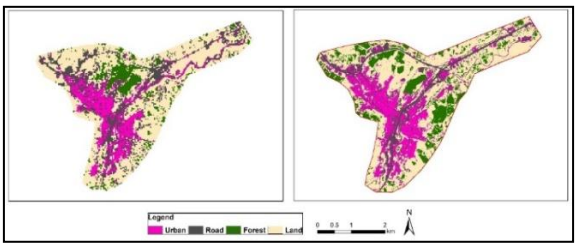


Figure 5. 3D flow accumulation map.

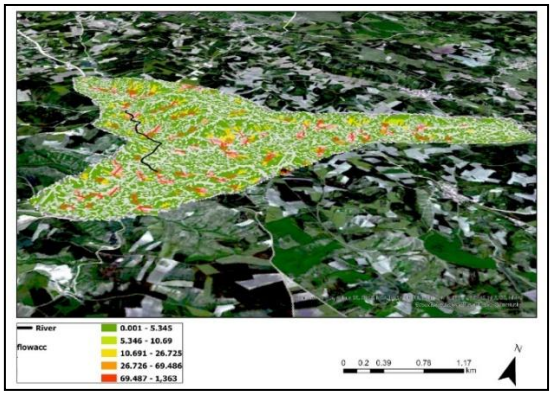


Figure 6. NDVI values for 1998 and 2026 of the city centers.

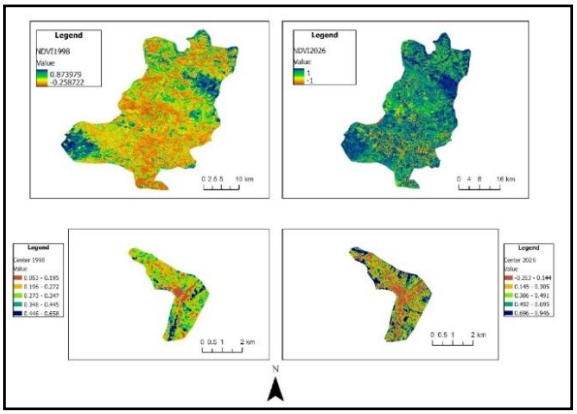


Figure 7. Land Cover map for 1998 (left) and for 2026 (right).

Although agricultural land remained the dominant land cover class in both years, its proportion declined slightly, suggesting a gradual conversion of land to other uses. Overall, the results reveal significant landscape changes within the study area over the 28-year period. Finally, LULC percentage distribution is presented in Table 3 for 1998 and 2026. An increase in urban and forest areas was observed, while agricultural land and road/bare land areas decreased during the study period. Urban areas expanded from approximately 16% to 20%, reflecting ongoing urban development in the city. Forest cover also increased, consistent with the NDVI analysis results. Although agricultural land remained the dominant land cover class in both years, its proportion declined slightly, suggesting a gradual conversion of land to other uses. Overall, the results reveal significant landscape changes within the study area over the 28-year period.

Table 3. Land cover change for the last two decades

Class	1998 (%)	2026 (%)	Change
Urban	~16	~20	+4
Road and Bare Land	~20	~15	-7
Forest	~10	~15	+5
Agriculture	~54	~50	-4

Finally, confusion matrix was calculated for quality control of classification results. Totally 200 random points were selected and each class are compared with other classes. Overall accuracies demonstrated that the results are reliable.

3.5 Flood Risk Assessment

A flood risk assessment was conducted by generating multiple buffer zones along the Hacıosman River within the Havza city area as shown in Figure 8. Three distance-based risk zones with 10 m, 50 m, and 100 m were established to identify areas potentially exposed to flooding during high-flow events. The 10, 50, and 100 m buffer distances were selected based on approaches adopted in previous GIS-based flood susceptibility studies. Lee et al. (2018), for example, classified the distance from rivers into 10, 50, and 100 m buffer zones

as a flood susceptibility factor. Similarly, GIS-based urban flood risk assessment studies have represented river proximity through a series of distance-based buffer classes, including 10–100 m intervals, emphasizing the increasing flood-related influence of areas located closer to river channels (Natkaniec and Godyń, 2024). The flood risk map demonstrates that a big part of urban area is located close to main stream corridor, which falls the risky areas in buffer zone. Development of urban areas expansion along the valley floor where the elevations are relatively low is under the risk of flood hazard. Consequently, buildings and infrastructure located near the river corridor may be more vulnerable to flood-related impacts during extreme precipitation events. The results indicate that the River constitutes the primary flood-sensitive corridor within the study area. Therefore, future urban planning and flood mitigation strategies should consider buffer-based protection zones, improved drainage infrastructure, and restrictions on further development in high-risk areas adjacent to the river.

Table 4. Confusion matrix

Year	Classified–Reference	Urban (%)	Road (%)	Forest (%)	Land (%)	User's Accuracy (%)
1998	Urban	80.00	2.22	13.33	4.44	80.00
	Road	0.00	91.67	8.33	0.00	91.67
	Forest	0.00	0.00	76.92	23.08	76.92
	Land	1.11	0.00	2.22	96.67	96.67
	Producer's Accuracy	97.30	95.65	75.00	88.78	
	Overall Accuracy			88.38		
	Kappa Coefficient			0.82		
2026	Urban	91.30	4.35	0.00	4.35	91.30
	Road	0.00	95.83	4.17	0.00	95.83
	Forest	0.00	0.00	79.49	20.51	79.49
	Land	1.10	0.00	1.10	97.80	97.80
	Producer's Accuracy	97.67	92.00	93.94	89.90	
	Overall Accuracy			92.50		
	Kappa Coefficient			0.88		

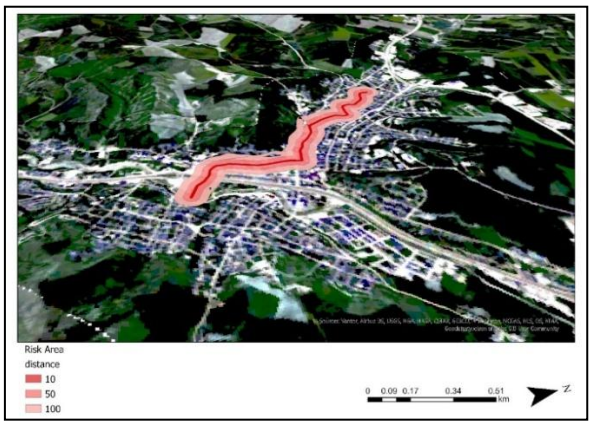


Figure 8. Three-dimensional flood risk assessment of the Havza city area based on 10 m, 50 m, and 100 m buffer zones generated around the Hacıosman River.

4. Discussions

The results demonstrate that the 1998–2026 changes in Havza are characterized by an interaction between land-use transformation, vegetation dynamics, and the physical conditions controlling surface runoff. The increase in urban areas and the corresponding reduction in agricultural land indicate that the flood-prone urban environment has developed within a landscape that has undergone substantial land-use change. Similar land-use transitions have been reported in other parts of Samsun. For example, Turan et al. (2024) reported an increase in artificial areas and a decrease in agricultural areas in the Bafra Delta Plain between 1990 and 2020. Similarly, Keskin (2021) found that agricultural areas in the Kürtün River Basin were under pressure from urbanization and industrial development. These findings suggest that the land-use transformation observed in Havza is consistent with broader urbanization-related changes occurring in Samsun watersheds.

The increase in built-up areas is particularly important from a flood-risk perspective because urban expansion increases the proportion of impervious surfaces and can modify surface runoff processes. A study of the Samsun urban area between the Mert River and Kürtün Stream reported that settlement areas increased substantially between 2000 and 2020, while non-urban areas decreased, and the authors evaluated this land-cover transformation together with flood susceptibility.

The topographic results provide further support for this interpretation. Low-lying areas associated with drainage networks and areas of greater flow accumulation are more likely to concentrate surface runoff and experience water accumulation. This pattern is consistent with the findings of Ocak and Bahadır (2024) for the Lake Ladik Basin in Samsun. Their GIS-AHP analysis showed that flood susceptibility was strongly associated with

geographical factors including slope, land use, precipitation, landforms, and drainage density. The study also reported that settlement areas located within the basin depression were among the areas with high or very high flood susceptibility.

The LULC results of the present study are also comparable with the findings from the Bafra Delta Plain. Turan et al. (2024) reported that agricultural land decreased from 75.1% in 1990 to 73.3% in 2020, while artificial areas increased from 3.8% to 5.9%. Although the magnitude of change differs from that observed in Havza, the direction of change is similar, indicating a broader transition involving the expansion of artificial surfaces and the reduction of agricultural land in parts of the Samsun region.

A similar pattern was also reported for the Kürtün River Basin. Keskin (2021) identified increases in artificial areas together with decreases in several agricultural land-cover classes between 1984 and 2020, and associated these changes with urbanization and industrial pressure. More recently, a remote-sensing analysis of the same basin reported a substantial increase in impervious surfaces between 1985 and 2020, with spatial changes particularly concentrated around the coastline and major transportation corridors. This regional evidence supports the interpretation that urban and infrastructure development can be an important driver of land-cover transformation in Samsun watersheds.

The NDVI results indicate a considerable change in vegetation-related spectral characteristics between 1998 and 2026. However, the increase in mean NDVI should not be interpreted as direct evidence of a proportional increase in vegetation cover. NDVI is affected by seasonal conditions, crop phenology, agricultural practices, soil background, and differences between satellite sensors. Therefore, the increase observed in Havza is more appropriately interpreted as a change in vegetation activity and surface spectral characteristics. The interpretation is further supported by the LULC results, which indicate simultaneous changes in agricultural, forest, and urban areas.

Overall, the findings indicate that flood susceptibility in Havza is shaped by the combined influence of topography, drainage concentration, land-use change, and urban expansion. This interpretation is consistent with recent studies from Samsun, where flood susceptibility has been linked to topographic and drainage characteristics as well as land-use conditions (Ocak and Bahadır, 2024).

6. Conclusion

The relationships between topography, vegetation Dynamics, LULC change and flood risk of Havza was investigated using GIS and RS techniques in this study. DEM and derived slope analysis as well as LULC cover classification were integrated for flood risk assessment between the 1998 and 2026, when the major flood disasters occurred. Topographic analysis of the study area demonstrated that the study areas have variations in terrain elevation between 317 m to 1,614 m with an average slop 10.49^{o}. Principal drainage corridor of the study area was identified near the main stream where the flow accumulation is very high. Runoff from surroundings slopes naturally converges toward the valley floor where urban development is concentrated. This topographic setting increases the exposure of the city to flood hazards during intense rainfall events.

The NDVI analysis also demonstrated a substantial increase in vegetation conditions, with average NDVI values rising from 0.423 in 1998 to 0.744 in 2026. Likely, LULC classification results revealed an increase in both urban and forest areas, while agricultural land and road/bare land areas showed a moderate decline. Agricultural land remained the dominant land cover category, however, the observed changes reflect ongoing urban expansion and landscape transformation within the study area. The flood risk assessment also demonstrated that a considerable portion of the urban area is located within close proximity to the main River corridor. This finding is particularly important considering that flood events affected the area in both 1998 and May 2026. The spatial relationship between the river channel, surrounding topography, and built-up areas suggests that future urban growth may further increase flood vulnerability if appropriate planning measures are not implemented.

The main contribution of this study is the integration of topographic, hydrological, vegetation, and land use analyses within a single framework to evaluate flood susceptibility and environmental change. Unlike previous studies focusing on a single indicator, this research combines DEM, slope, flow accumulation, NDVI, LULC classification, and flood risk assessment to provide a comprehensive understanding of watershed dynamics.

From a policy perspective, the findings emphasize the need for risk-sensitive urban planning and sustainable watershed management. Local authorities should consider preserving protective river corridors, improving stormwater drainage infrastructure, limiting uncontrolled development in flood-prone areas, and integrating GIS-based decision-support systems into urban planning processes. The methodology presented in this study can be applied to other medium-sized watersheds and cities in Türkiye facing similar flood and land-use management challenges.

Author Contributions

The percentages of the author' contributions are presented below. The author reviewed and approved the final version of the manuscript.

	S.C.S.
C	100
D	100
S	100
DCP	100
DAI	100
L	100
W	100
CR	100
SR	100
PM	100
FA	100

C= concept, D= design, S= supervision, DCP= data collection and/or processing, DAI= data analysis and/or interpretation, L= literature search, W= writing, CR= critical review, SR= submission and revision, PM= project management, FA= funding acquisition.

Conflict of Interest

The author declared that there is no conflict of interest.

Ethical Consideration

Ethics committee approval was not required for this study because of there was no study on animals or humans.

References

Akın, G., & Karaca, Ö. (2021). Çerçi ve Murt Deresi (Fethiye-Muğla) taşkın duyarlılık alanlarının CBS ile çok kriterli karar verme analizi kullanılarak haritalanması [Mapping flood sensitivity areas of Çerçi and Murt Streams (Fethiye-Muğla) using GIS-based multi-criteria decision-making analysis]. *Yerbilimleri*, *42*(1), 121–143.

Akinbobola, A., Okogbue, E., & Olajiire, O. (2015). A GIS based flood risk mapping along the Niger-Benue river basin in Nigeria using watershed approach. *Ethiopian Journal of Environmental Studies and Management*, *8*(6), 616–628.

Al-Omari, A. A., Shatnawi, N. N., Shbeeb, N. I., Istrati, D., Lagaros, N. D., & Abdalla, K. M. (2024). Utilizing remote sensing and GIS techniques for flood hazard mapping and risk assessment. *Civil Engineering Journal*, *10*(5), 1423–1436.

Bitek, D., & Erenoğlu, R. C. (2026). Coğrafi Bilgi Sistemi Tabanlı Analitik Hiyerarşi Yöntemi ile Taşkın Duyarlılık Analizi: Oğulpaşa Deresi Havzası Örneği (Edirne) [Flood susceptibility analysis using Geographic Information System-based Analytic Hierarchy Process: Case study of Oğulpaşa Stream Basin (Edirne)]. *Jeomorfolojik Araştırmalar Dergisi*, (16), 1–18.

Çeliker, M., Nacar Koçer, N., & Yıldız, O. (2020). Bingöl il merkezinde taşkın yayılım alanlarının coğrafi bilgi sistemleri ve HEC-RAS ile belirlenmesi [Determination of flood inundation areas in Bingöl city center using geographic information systems and HEC-RAS]. *Doğal Afetler ve Çevre Dergisi*, *6*(2), 354–365.

Dölek, İ., & Vedat, A. (2024). Muş ilinin sel ve taşkın duyarlılık haritalarının oluşturulması [Creation of flood and inundation susceptibility maps of Muş province]. *The Journal of Academic Social Science*, *44*(44), 190–204.

Duman, N., & İrcan, M. R. (2022). Coğrafi Bilgi Sistemleri tabanlı Çankırı Merkez ilçesinin taşkın duyarlılık analizi [Geographic Information Systems-based flood susceptibility analysis of Çankırı Central district]. *Jeomorfolojik Araştırmalar Dergisi*, (9), 50–66.

Ekmekcioğlu, Ö. (2023). CBS Tabanlı Melez Makine Öğrenmesi Uygulamalarının Ani Sel Duyarlılık Haritalamasında Kullanımı [Use of GIS-based hybrid machine learning applications in flash flood susceptibility mapping]. *Journal of the Institute of Science and Technology*, *13*(2), 1067–1084.

Elsheikh, R. F. A., Ouerghi, S., & Elhag, A. R. (2015). Flood risk map based on GIS, and multi criteria techniques (case study Terengganu Malaysia). *Journal of Geographic Information System*, *7*(4), 348–357.

Evans, S. Y., Gunn, N., & Williams, D. (2007). *Use of GIS in flood risk mapping* [Paper presentation]. National Hydrology Seminar: GIS (Geographic Information Systems) in Hydrology Applications-Modelling-Data Issues, Tullamore, Ireland.

Gupta, L., & Dixit, J. (2022). A GIS-based flood risk mapping of Assam, India, using the MCDA-AHP approach at the regional and administrative level. *Geocarto International*, *37*(26), 11867–11899.

Hu, S., Cheng, X., Zhou, D., & Zhang, H. (2017). GIS-based flood risk assessment in suburban areas: A case study of the Fangshan District, Beijing. *Natural Hazards*, *87*(3), 1525–1543.

Karakoca, E., & Ünver, A. (2024). Analitik hiyerarşi süreci ve coğrafi bilgi sistemleri kullanarak Eşen Çayı Havzası'nda taşkın riski değerlendirmesi ve haritalandırılması [Flood risk assessment and mapping in Eşen Stream Basin using analytic hierarchy process and geographic information systems]. *Geomatik*, *10*(1), 127–143.

Karakuş, C. B., & Ceylan, Ş. (2022). Coğrafi Bilgi Sistemi tabanlı Analitik Hiyerarşi Süreci kullanılarak taşkın tehlike haritalaması [Flood hazard mapping using Geographic Information System-based Analytic Hierarchy Process]. *Mühendislik Bilimleri ve Tasarım Dergisi*, *10*(4), 1155–1173.

Keskin, F. (2021). *Kürtün Çayı havzasında (Samsun) arazi kullanımı ve zamansal değişim (1984-2020)* [Yüksek lisans tezi, Marmara Üniversitesi]. YÖK Tez Merkezi.

Kumar, N., & Jha, R. (2023). GIS-based flood risk mapping: The case study of Kosi River Basin, Bihar, India. *Engineering, Technology & Applied Science Research*, *13*(1), 9830–9836.

Lee, S., Lee, S., Lee, M. J., & Jung, H. S. (2018). Spatial assessment of urban flood susceptibility using data mining and geographic information system (GIS) tools. *Sustainability*, *10*(3), Article 648.

Nasanlı, O., Kejanlı, T., & Koç, C. (2025). Siverek'te (Şanlıurfa) taşkın riskinin değerlendirilmesi [Evaluation of flood risk in Siverek (Şanlıurfa)]. *GRID-Architecture Planning and Design Journal*, *8*(2), 552–580.

Natkaniec, W., & Godyń, I. (2024). Urban flood risk assessment and mapping using GIS-DEMATEL method: Case of the Serafa River Watershed, Poland. *Water*, *16*(18), Article 2636.

Nyarko, B. K. (2002). Application of a rational model in GIS for flood risk assessment in Accra, Ghana. *Journal of Spatial Hydrology*, *2*(1), 1–14.

Ocak, F., & Bahadır, M. (2024). Evaluation of potential flood areas in the basin of Lake Ladik through AHP and GIS integration, (Samsun, Türkiye). *Jeomorfolojik Araştırmalar Dergisi*, (13), 71–93.

Oğuz, E., Oğuz, K., & Öztürk, K. (2022). Düzce bölgesi taşkın duyarlılık alanlarının belirlenmesi [Determination of flood susceptibility areas in Düzce region]. *Geomatik*, *7*(3), 220–234.

Ouma, Y. O., & Tateishi, R. (2014). Urban flood vulnerability and risk mapping using integrated multi-parametric AHP and GIS: Methodological overview and case study assessment. *Water*, *6*(6), 1515–1545.

Rincón, D., Khan, U. T., & Armenakis, C. (2018). Flood risk mapping using GIS and multi-criteria analysis: A Greater Toronto area case study. *Geosciences*, *8*(8), Article 275.

Roopnarine, R., Opadeyi, J., Eudoxie, G., Thongs, G., & Edwards, E. (2018). GIS-based flood susceptibility and risk mapping Trinidad using weight factor modeling. *Caribbean Journal of Earth Science*, *49*(1), 1–9.

Saha, A. K., & Agrawal, S. (2020). Mapping and assessment of flood risk in Prayagraj district, India: A GIS and remote sensing study. *Nanotechnology for Environmental Engineering*, *5*(2), Article 11.

Samarasinghe, J. T., Makumbura, R. K., Wickramarachchi, C., Sirisena, J., Gunathilake, M. B., Muttil, N., Teo, F. Y., & Rathnayake, U. (2022). The assessment of climate change impacts and land-use changes on flood characteristics: The case study of the Kelani River Basin, Sri Lanka. *Hydrology*, *9*(10), Article 177.

Sunkar, M., & Tonbul, S. (2010). İluh Deresi Havzası'na (Batman) yönelik sel ve taşkın riski analizleri [Flood and inundation risk analysis for İluh Stream Basin (Batman)]. *Nature Sciences*, *5*(4), 255–273.

Temiz, N., Aksoy, H., & Ercanoğlu, M. (2004). An investigation on the evaluation of flood potential in Northwest Black Sea Region. *Geological Bulletin of Turkey*, *47*(2), 41–48.

Tokgözlü, A., & Özkan, E. (2018). Taşkın risk haritalarında AHP yönteminin uygulanması: Aksu Çayı Havzası örneği [Application of AHP method in flood risk maps: A case study of Aksu Stream Basin]. *Süleyman Demirel Üniversitesi Fen-Edebiyat Fakültesi Sosyal Bilimler Dergisi*, (44), 151–176.

Turan, İ. D., Dengiz, O., Pacci, S., & Agbor, D. T. (2024). Determination of change in the land use and land cover of the Samsun Bafra Delta Plain from 1990 to 2020 using GIS and Remote Sensing Techniques. *Eurasian Journal of Soil Science*, *13*(2), 101–110.

Wang, X., & Xie, H. (2018). A review on applications of remote sensing and geographic information systems (GIS) in water resources and flood risk management. *Water*, *10*(5), Article 608.

Yıldız, B., & Gürgöze, S. (2026). Coğrafi Bilgi Sistemleri tabanlı Analitik Hiyerarşi Prosesi (AHP) kullanılarak taşkın duyarlılığının değerlendirilmesi: Abdal Deresi Havzası örneği (Samsun/Türkiye) [Evaluation of flood susceptibility using Geographic Information Systems-based Analytic Hierarchy Process (AHP): Case study of Abdal Stream Basin (Samsun/Türkiye)]. *Journal of Anatolian Geography*, (5), 1–15.

Yurteri, C. (2024). Coğrafi Bilgi Sistemleri (CBS) ortamında Analitik Hiyerarşi Yöntemi (AHY) yöntemi kullanılarak taşkın risk analizi: Karabük ili örneği [Flood risk analysis using Analytic Hierarchy Process (AHP) method in Geographic Information Systems (GIS) environment: Karabük province case]. *Mühendislik Bilimleri ve Tasarım Dergisi*, *12*(2), 298–318.

Black Sea Journal of Engineering and Science
doi: 10.34248/bsengineering.1842781

Open Access Journal
e-ISSN: 2619 – 8991

Research Article
Volume 9 - Issue 5: 2783-2794 / September 2026

A SUSTAINABLE ACT FOR CONCRETE DEBRIS DISPOSAL BY USING THE ALKALINE FUSION TECHNIQUE FOR THE SYNTHESIS OF SBA-15 TO USE IN DYE REMOVAL

Nevin KARAMAHMUT MERMER[1]*

[1]*Kalekim Construction Chemicals Co. R&D Department, 34325, Istanbul, Türkiye*

Abstract: The cement industry contributes to 8% of total carbon emissions, primarily due to the high temperatures required for production and the use of natural raw materials. Cement is the second most utilized industrial raw material globally due to its ability to be molded in liquid state and gradually increase in strength. In addition to carbon emissions, the appropriate disposal of concrete debris is also a substantial concern. The quantity of debris remaining after natural disasters such as earthquakes poses a substantial obstacle. Currently, concrete waste is utilized for the purpose of filling diverse construction sites. The alkali fusion method has been employed in scientific study to recover a silicon solution from various industrial waste materials, such as fly ash, bottom ash, slag, and gold mine tailing slurry. The hydrated cement phases display elevated levels of calcium and silicon content. The objective of the study was to apply alkali treatment to the debris to extract silicon from the hydrated cement stages of construction debris using the alkali fusion method, which involves heat treatment. The silicon solution obtained was assessed in the synthesis of SBA-15, a material characterized by its mesoporous structure. Ultimately, the synthesized SBA-15 material was employed for dye removal.

Keywords: Concrete debris, Alkaline fusion, SBA-15, Dye removal, Upcycle

***Corresponding author:** Kalekim Construction Chemicals Co. R&D Department, 34325, Istanbul, Türkiye
E mail: nevinmermer@kale.com.tr (N. KARAMAHMUT MERMER)
Nevin KARAMAHMUT MERMER https://orcid.org/0000-0001-6645-4724

Received: December 15, 2025
Accepted: August 26, 2026
Published: September 15, 2026

Cite as: Karamahmut Mermer, N. (2026). A sustainable act for concrete debris disposal by using the alkaline fusion technique for the synthesis of SBA-15 to use in dye removal. *Black Sea Journal of Engineering and Science,* 9(5), 2783-2794.

1. Introduction

Cement is widely utilized in the construction industry due to its ability to be molded in liquid state, its increase in strength among the curing process, and its convenient accessibility and affordability (Barcelo et al., 2014; Naqi and Jang, 2019). The primary factor contributing to carbon emissions in cement manufacture is the clinker formation process, which occurs at a temperature of 1450˚ C and is responsible for 90% of the energy consumption during production. In addition to this, the procedures of grinding and mixing also require energy (Chandler et al., 2002; Hendriks et al., 2003; Summerbell et al., 2016). Particulate matter, nitrogen oxides, sulphur dioxide, and carbon monoxide are among the main pollutants released during cement manufacture. Emissions may also contain leftover substances derived from the fuel and raw materials, as well as byproducts of incomplete combustion that are classified as dangerous (Environmental Protection Agency, 2020).

Carbon emissions regulations are under consideration at both national and global levels. Studies are conducted in both the industrial and academic fields of the cement industry to align with the objective of decreasing carbon emissions (Hendriks et al., 2003). Due to the significant carbon emissions associated with clinker production, numerous studies are conducted to minimize the clinker content in cement production. Various cements with different additives are available on the market, and their classification is determined based on the TS EN 197-1 standard (Turkish Standards Institute, 2018). Furthermore, numerous studies have been conducted to achieve enhanced strength by utilizing fewer amounts of cement through the incorporation of pozzolanic additives, graphene additives, and geopolymer additives (Schneider et al., 2011; Schneider, 2015; Lin and Du, 2020; Phair, 2006). Moreover, both the industrial and academic sides are currently conducting extensive studies in the area of process optimization. This includes investigating strategies like carbon capture during cement manufacturing and harnessing the resulting heat for preheating purposes (Karellas et al., 2013; Hills et al., 2016; Fierro et al., 2020; Izumi et al., 2021).

Aside from the carbon emissions generated during the production process, the proper disposal of waste concrete that has reached the end of its useful lifespan is also an important environmental issue. Significant accumulations of debris are generated as a result of factors such as urban reconstruction, renovation, or the destruction of construction sites worldwide due to warfare and disasters. According to reports, the quantity

of debris formed from the Kahramanmaraş earthquakes on February 6th was equivalent in size to Mount Erciyes, which stands at a height of 3917 meters. Prior to destruction, materials in urban transformation processes are segregated and prepared for recycling. Nevertheless, debris left over from natural disasters can consist of a diverse range of materials, including concrete, wood, plastic, glass, metal, and organic matter. Out of the total debris produced following the Kahramanmaraş earthquake, a significant portion of 82.8 million tons consists of concrete rubble (Kaplan and Soyluk, 2023; Mavroulis et al., 2023). Concrete rubble recycling typically involves reducing the size of the particles and utilizing them as filler in concrete mixtures or for ground applications. Additionally, the rubble can be employed in coarse filtration operations (Ucol-Ganiron, 2012; Ganiron, 2015; Lakshmi and Nivetdhitha, 2015). Following the February 6, 2023 Kahramanmaraş earthquakes, the Scientific and Technological Research Council of Türkiye (TÜBİTAK), in cooperation with the Disaster and Emergency Management Authority (AFAD), launched a special call entitled "UDAP Disaster Risk Reduction Research" under the 1001 Scientific and Technological Research Projects Support Program. Earthquake-resilient construction models and waste management were identified among the priority research and innovation topics of this call (TÜBİTAK, 2024). Research has been conducted on the utilization of ground concrete waste as a substitute for fine filler in decorative applications, as a replacement for filler in cement-based products, as a secondary aggregate in road filling and flattening processes, and in the construction of asphalt and paving stone areas. These studies are documented in both literature and can be seen in field (Masood et al., 2001; Kabir et al., 2016). Compared with its conventional reuse as aggregate or filling material, the chemical valorization of concrete debris through the recovery of its silicon fraction and its conversion into a value-added mesoporous material remains comparatively underexplored. It is crucial to ascertain the precise composition of the net content in order to extract components effectively (Lee et al., 2015).

In the field of cement chemistry, hydration refers to the chemical reaction between nonhydrated cement and water. This reaction leads to significant changes in the chemical and physicomechanical characteristics of the system, including the process of setting and hardening. During the reaction process, the fresh mortar undergoes a decrease in its moldability or shaped, as it transforms into a solid substance that possesses quantifiable strength. The hydration of the primary constituents of cement, tricalcium silicate (C3S) and dicalcium silicate (C2S), leads to the formation of two distinct phases: the amorphous phase of calcium silica hydrate (C–S–H) and the crystalline phase of portlandite (CH, calcium hydroxide). The formation of calcium-silicate-hydrate (C-S-H) has a significant impact on strength, whereas the presence of portlandite does not have a noticeable effect. Given that the predominant components in portland cement are C3S and C2S, it follows that the composition of cured concrete also includes a substantial proportion of C-S-H. The tricalcium aluminate (C3A) phase, a constituent of cement, undergoes a reaction with water and, in the presence of gypsum, produces calcium trisulfoaluminate hydrate or crystalline ettringite (C6AS3H32) and an unstable form of calcium-alumina monosulphohydrate (C4ASH12). When the media contains a sufficient amount of gypsum, C4ASH12 undergoes another reaction to produce a durable ettringite compound (Hewlett and Liska, 1988; İnceoğlu et al., 2021; Karamahmut Mermer et al., 2024). The hydration reactions of ordinary Portland cement are given below (Hewlett and Liska, 1988) (equations 1-5).

$$2C3S+6H\rightarrow C3S2H3+3CH \quad (1)$$

$$2C2S+4H\rightarrow C3S2H3+CH \quad (2)$$

$$C3A + CSH2+10H\rightarrow C4ASH12 \quad (3)$$

$$C3A+3CSH2+26H\rightarrow C6AS3H32 \quad (4)$$

$$C4ASH12+2CSH2+16H\rightarrow C6AS3H32 \quad (5)$$

The primary constituent that composes concrete debris is calcium-silicate-hydrate (C-S-H), with calcium (Ca) and silicon (Si) being the most prevalent elements. Silicon can be extracted from the composition using alkaline fusion and acid activation methods. Some research in the literature has demonstrated the production of liquid silicon solution using fly ash, bottom ash, slag, gold mine tailing slurry sludge, and sand by the alkali fusion method (Yilmaz and Mermer, 2015; Mermer and Pişkin, 2018; Mermer and Pişkin, 2019). The evaluation of the acquired silicone solution was conducted through studying the synthesis of SBA-15, which is a mesoporous material. SBA-15 has garnered significant attention in the past 30 years because of its exceptional characteristics, including a large surface area, a well-structured pore system, and impressive resistance to high temperatures and moisture. It is utilized in various fields, including gas adsorption, heavy metal elimination, drug carrier systems, and sensor applications. Substituting silicon solution derived from concrete debris for costly chemicals like TEOS, fumed silica, and silicon tetraethoxide in the manufacturing of SBA-15 offers economic and environmental benefits, while also contributing to the concrete recycling process (Yu and Zhai, 2009; Bhagiyalakshmi et al., 2010; Sari Yilmaz and Pişkin, 2015). More recent studies have further demonstrated that silica-containing wastes and industrial residues can be converted into ordered mesoporous silica materials. For example, geothermal sludge has been utilized as an alternative sodium silicate source for SBA-15 synthesis, while recent reviews have highlighted the growing interest in producing ordered mesoporous silicas from silica-rich waste streams. These studies demonstrate that replacing conventional silica precursors with secondary raw materials is a developing research direction. Nevertheless, the use of hydrated

concrete debris as the silicon source for SBA-15 synthesis, followed by the application of the resulting material in dye adsorption, remains insufficiently investigated (HSN et al., 2023; Oliveira et al., 2023; Liang et al., 2024).

Dyes are chemical substances that have the ability to adhere to surfaces or fabrics in order to provide color. Most dyes consist of intricate chemical compounds and must possess resistance to many factors, including the effects of detergents. Synthetic dyes are extensively utilized in many sectors of sophisticated technology, such as textile, paper, leather tanning, food processing, plastics, cosmetics, rubber, printing, and dye production industries. Synthetic dyes are used in various applications, such as groundwater tracing, determining the specific surface area of activated sludge, sewage and wastewater treatment, and more. Their emissions into the hydrosphere are a major source of pollution because of their persistent and resistant nature. This will result in the water body acquiring an unpleasant color, which in turn will hinder the penetration of sunlight and impede photochemical and biological processes that are crucial for the survival of aquatic life (McKay et al., 1999; Ahmad et al., 2002; Yagub et al., 2014; Islam et al., 2019).

The conversion of concrete debris into a silica precursor provides an opportunity not only to recover a valuable component from construction waste but also to produce porous materials for environmental remediation applications. SBA-15 is particularly suitable for adsorption-based water treatment because of its ordered mesoporous structure, accessible pore system, and relatively high surface area. Therefore, using concrete-derived silica in SBA-15 synthesis establishes a direct link between construction-waste valorization and the removal of aqueous pollutants such as methylene blue.

Although several silica-rich industrial wastes have been investigated as alternative silicon sources, the conversion of hydrated concrete debris into SBA-15 and the subsequent evaluation of the resulting material in dye adsorption remain insufficiently explored. The present study addresses this research gap by integrating three consecutive stages: silicon extraction from concrete debris through alkaline fusion, synthesis of SBA-15 using the recovered silicon solution, and evaluation of the synthesized material for methylene blue removal. The main contribution of the study is thus the demonstration of an integrated waste-to-adsorbent pathway that converts concrete debris into a value-added mesoporous material for water-treatment applications.

2. Materials and Methods

2.1. Materials

Concrete debris obtained from the demolition site of a 52-year-old structure in Istanbul underwent urban transformation. The NaOH utilized in the investigation was commercially acquired from the market. The hydrochloric acid (HCl) utilized in the production of SBA-15 was acquired from Merck, possessing a purity level of 37%. Sigma-Aldrich supplied the block copolymer Pluronic 123, which was utilized in the production of SBA-15. The methylene blue utilized for dye removal was acquired from Fluka.

2.2. Methods

The industrial crusher utilized concrete debris to decrease the size of the grains. The heat treatments in the investigation were conducted using a Nüve brand and a Binder brand oven. Samples were characterized using a Philips PANalytical X'Pert-Pro X-ray diffractometer with copper (Cu)Kα radiation (United Kingdom). XRD analyses were assessed over a scanning range of $2\lambda = 0.6–3^{o}$ under 40 mA and 30 kV operating conditions. Fourier-transform infrared spectroscopy (FTIR) measurements of the samples were conducted using a Perkin Elmer Spectrum 100 (United States) series device in transmission mode. The Perkin-Elmer Optima 2100 DV type ICP-OES, which was equipped with an AS-93 autosampler, was utilized to measure the silicon concentration in the extracted solutions. The components were mixed for alkaline fusion prior to synthesis using a Collomix Powder Raw Material Shaker from Germany. The concentrations of the solutions were determined using the Perkin Elmer Lambda 35 UV–Vis spectrophotometer in the dye adsorption analysis.

2.3. Experimental

The acquisition of silicon solution from waste was achieved by the fusion method conducted by Shigemoto et al., and was carried out with several modifications (Shigemoto et al., 1993; Karamahmut Mermer et al., 2017; Mermer and Pişkin, 2018). During alkaline fusion, NaOH reacts with the silica-containing phases of the concrete-derived material and promotes the conversion of silicon into soluble sodium silicate species. A simplified representation of the principal reaction can be expressed as (equation 6):

$$SiO_2 + 2NaOH \rightarrow Na_2SiO_3 + H_2O \quad (6)$$

Owing to the heterogeneous and hydrated nature of concrete debris, this equation represents the main silica-conversion pathway rather than the complete set of reactions occurring during fusion. Following fusion, water extraction transfers the soluble silicate species into the liquid phase, whereas less-soluble calcium-rich and other mineral components remain predominantly in the solid residue.

The fusion process was conducted using NaOH in order to extract silicon from concrete debris. Various NaOH/Si source ratios were examined, including 0.50, 0.75, 1.00, 1.25, 1.50, 1.75, and 2.00. The investigated concrete debris/NaOH ratios were selected based on preliminary trials and previously reported alkaline-fusion studies on silica-containing solid materials. The selected range was intended to provide sufficient alkalinity for converting silica-containing phases into water-soluble silicate species and to evaluate the effect of NaOH dosage on silicon extraction. The optimum ratio was determined based on the silicon concentration measured in the

resulting extract. The necessary amount of NaOH was mixed with concrete debris in a nickel crucible until it was thoroughly mixed. The mixture was then heated in an oven at a temperature of 550°C for a duration of 1 hour. Consequently, the impact of varying fusing rates on the concentration of silicon in the resultant solution was investigated. The solid product formed during fusion was pulverized and subsequently combined with a specific quantity of distilled water. The solution is mixed with water in the shaker for 5 minutes. The resultant mixture was isolated from the primary solution by using filter paper. Figure 1 depicts the flow diagram for extracting Si from debris using the alkali fusion process. The silicon concentration of the resultant solution was measured by ICP-OES analysis. Due to the presence of a significant amount of silicon (Si), aluminum (Al), and calcium (Ca) in the debris, inductively coupled plasma optical emission spectroscopy (ICP-OES) was specifically targeted towards these elements. The elemental concentrations of each solution are provided in Table 1. The ratio at which the highest concentration of silicon solution was obtained was 0.75, and this ratio was used to obtain the solution in the study. The optimal concentration of silicon in the obtained silicon solution has been identified based on the maximum concentration ratio, as it has been found to significantly enhance production efficiency (Karamahmut Mermer et al., 2017).



Figure 1. Alkaline fusion diagram.

Table 1. ICP-OES analysis results

Name	Debris (wt)	NaOH (wt)	Ratio	Si (mg/kg)	Ca (mg/kg)	Al (mg/kg)
1	2	4	0.50	4634 ± 36	<1.0	148.3 ± 7.40
2	3	4	0.75	7106 ± 55	<1.0	161.3 ± 8.10
3	4	4	1.00	6448 ± 50	<1.0	128.3 ± 6.40
4	5	4	1.25	5857 ± 46	<1.0	113.2 ± 5.70
5	6	4	1.50	4443 ± 35	<1.0	77.69 ± 3.88
6	7	4	1.75	3693 ± 29	<1.0	66.70 ± 3.34
7	8	4	2.00	2724 ± 21	<1.0	58.66 ± 2.93

SBA-15 was synthesized from an extracted silicon solution according to a previously described method with some modifications (Sarı Yılmaz and Pişkin, 2015). To synthesize SBA-15, the specified quantity of P123 copolymer was dissolved in a 2 M HCl solution at 25 °C for a duration of 1 hour. Subsequently, hydrochloric acid (HCl) and water were added to the resulting mixture and subjected to a 24-hour aging process at 100 °C. The resulting product was subjected to filtration, followed by washing with deionized water, and subsequently dried at ambient temperature. The initial sample was subjected to calcination at 550 °C for 6 hours in order to remove the organic template. A low-angle XRD study was conducted to confirm the success of the synthesis.

The batch adsorption experiments were conducted at ambient temperature, investigating several operational factors, including contact time, absorbent quantity, and starting concentration. In the adsorption studies, dye solutions were prepared using methylene blue (MB). Each adsorbent, weighing 75 mg, was introduced into 20 mL of dye solutions with varying starting concentrations (10, 20, 30, 40, 50, and 100 ppm). 50, 75, 100, and 125 mg of absorbent were utilized in examinations to determine the optimal absorbent amount. Experiments were conducted at various time intervals (3, 10, 15, 30, 45, 60, 90, and 120 minutes) to find the optimal quantity of adsorption. Adsorption experiments were conducted at 23 °C and an agitation speed of 600 rpm. The as-prepared dye solutions and adsorbent were used directly without pH adjustment; no acid, base, or buffer was added. Therefore, the experiments were performed under the natural pH conditions of the dye–adsorbent systems, although the initial and final pH values were not measured. The residual concentration of MB in the solutions was assessed using a UV–vis spectrophotometer with a maximum wavelength of 665 nm. The (equations 7-9) were used to predict the adsorption capacity, dye adsorption, and desorption efficiency.

$$q_e=((C_0-C_e).V)/W \quad (7)$$

Adsorption Efficiency, %=((C_(0-) C_e)/C_0)×100 (8)

Desorption Efficiency, %=((C_d V_d)/(q_e W))×100 (9)

where variable qe (mg.g−1) represents the amount of adsorption at equilibrium. Co and Ce (mg.L−1) refer to the initial and equilibrium concentrations of the dye, respectively. The variable Cd (mg.L−1) represents the concentration of the dye in the desorption solution. W (g) denotes the mass of the adsorbent, V (L) represents the volume of the dye solution, and Vd (L) indicates the volume of solution used in the desorption process.

3. Results

Figure 2 displays the XRD diffractogram of the debris. Upon examining the diffractogram, the cement hydrated phases of ettringite (2θ, 9.2°) and portlandite (2θ, 18.2°) are seen. Furthermore, the presence of trace quantities of cement components in the cement phase (2θ, 30-33°) area confirms that the reaction happened as expected (Balonis and Glasser, 2009; Li et al., 2020). The FTIR spectrum given in Figure 3 showed that the stretching vibrations of OH groups weakly bound by hydrogen occurred within the range of 3700-3500 cm−1. The peak at 3639 cm-1 in the spectrum is a characteristic feature of portlandite. It is caused by the stretching vibrations of O-H bonds and indicates the process of hydration. The band seen at around 970 cm−1 corresponds to the C-S-H phase, which is a non-crystalline hydrated phase and so cannot be identified by XRD (Abd El-Aleem et al., 2014; Gawwad et al., 2015; Singh Kashyap et al., 2021). The structure observed like a neck on the left side of the 970 cm-1 wave number corresponds to the ettringite component (Singh Kashyap et al., 2021).

Figure 4 displays the results of low-angle X-ray diffraction (XRD) analyses conducted on synthesized materials. The XRD patterns of synthesized samples had three diffraction peaks that were identifiable as reflections of the (100), (110), and (200) planes. The following are attributes of the SBA-15 mesoporous phase, which is organized in a two-dimensional hexagonal structure.

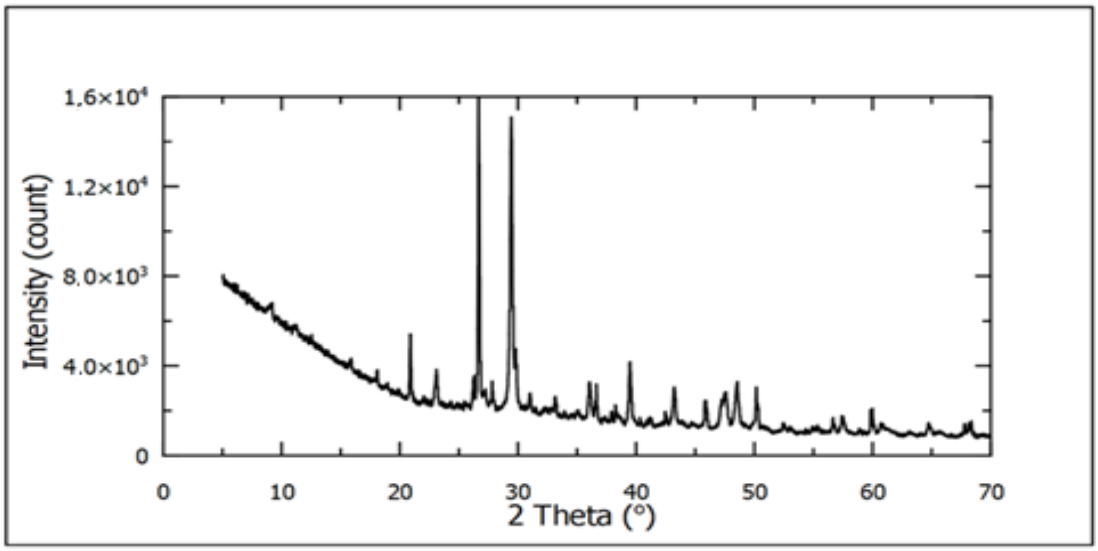


Figure 2. XRD diffractogram of concrete debris.

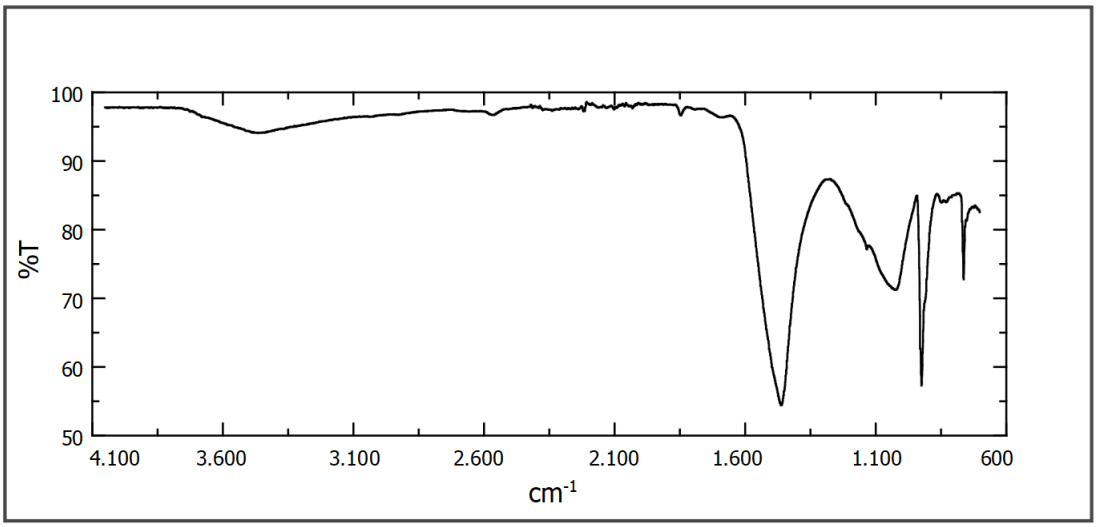


Figure 3. FTIR spectrum of concrete debris.

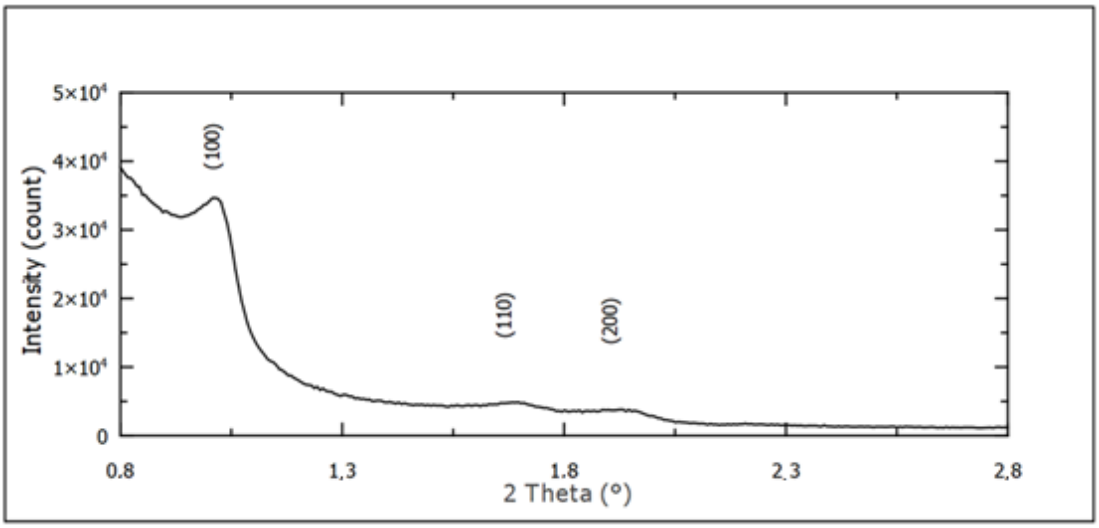


Figure 4. XRD diffractogram of synthesized SBA-15.

Figure 5 presents the N_2 adsorption/desorption isotherm and pore size distribution graph of the synthesized SBA-15. Upon examination of Figure 5. It is evident that SBA-15 exhibits compatibility with the type IV N_2 adsorption and desorption isotherm as per the IUPAC classification, and it displays H1-type hysteresis. The type IV isotherm refers to the adsorption/desorption behavior of substances that possess mesoporous features (Kokunešoski et al., 2010; Laskowski et al., 2024). The SBA-15 exhibited a surface area of 377.689 m^2/g, a total pore volume of 0.129 cc/g and an average pore width of 8.331 Å. The specific surface area of the concrete-derived SBA-15 was determined as 377.689 $m^2\ g^{-1}$, confirming the formation of a high-surface-area mesoporous material from an unconventional silicon source. Previous studies have demonstrated that the textural properties of SBA-15 are strongly influenced by the origin and purity of the silica precursor, as well as by the synthesis and template-removal conditions. HSN et al., (2023) reported that geothermal sludge could be employed as an alternative silica source for SBA-15 synthesis, while Oliveira et al., (2023) highlighted the broader potential of silica-rich residues for producing ordered mesoporous silica materials. In this context, the present findings extend waste-derived mesoporous silica research by demonstrating that silicon recovered from concrete debris can also be used to obtain an SBA-15-type material with a developed porous structure.

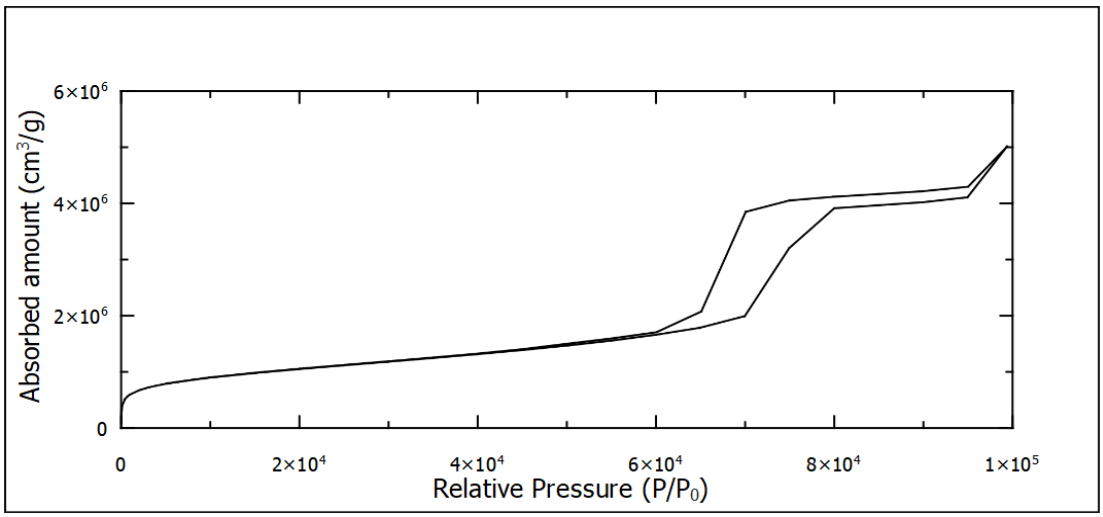


Figure 5. N_2 adsorption/desorption isotherm of SBA-15.

The removal of methylene blue by the synthesized material can be associated with the accessible mesoporous structure and available surface silanol groups of SBA-15. These features facilitate the diffusion of dye molecules into the pore system and may promote interactions between the adsorbent surface and methylene blue molecules. However, because the initial and final solution pH values were not measured, the contribution of pH-dependent electrostatic interactions cannot be conclusively determined. Furthermore,

adsorption performance depends on experimental conditions and surface functionalization; therefore, direct comparison with modified SBA-15 materials should be made cautiously. As discussed by Liang et al., (2024), surface modification can substantially alter the affinity and selectivity of SBA-15-based adsorbents. The present results are nevertheless noteworthy because dye removal was achieved using concrete-derived SBA-15 without additional surface functionalization.

Concentration, adsorbent amount, and contact duration scans were conducted in adsorption studies. The impact of contact time and adsorption kinetics was determined by employing the pseudo-first order (FO) and pseudo-second order (SO) approaches, represented by (equations 10-11) respectively.

$$q_t=q_e\ (1-e^{(⟦-k⟧_(1\ )\ t)}) \quad (10)$$

$$q_t=(q_e^2\ k_2\ t)/(1+(q_e\ k_2\ t)) \quad (11)$$

where qt (mg.g− 1) is the quantity of adsorption at time t (min− 1). k1 and k2 are the rate constants of the FO and SO, respectively. The parameters obtained from the kinetic study of the MB. adsorption process are provided in Table 2. Based on the linearized analysis, the pseudo-second-order model exhibited a higher coefficient of determination than the pseudo-first-order model, and the experimental and calculated values were relatively close. However, the kinetic parameters were estimated using linearized model equations. Linear transformation may modify the experimental error structure and introduce bias into parameter estimation and model comparison (Simonin, 2016). Therefore, the apparent agreement with the pseudo-second-order model should be interpreted only as a statistical fit within the linearized analysis and not as conclusive evidence of the adsorption mechanism or chemisorption.

Figure 6 depicts the progressive removal of the dye over time. Observations indicate a significant and swift decrease in removal after the 20th minute, followed by a gradual decline in the adsorption rate over time.

The impact of the initial concentration and adsorption isotherms is studied in this section. Figure 7 illustrates the impact of the initial concentration on the adsorption of MB. The adsorption capacity of MB onto SBA-15 increased up to 40 ppm with an increase in the starting dye concentration. After this point was reached, the rate of adsorption of dyes onto the composites decreased. The adsorption isotherms of the MB are used to describe the interaction between the dyes and the material. The adsorption data was analyzed using the Langmuir (Lr) and Freundlich (Fh) isotherm models, as represented by (equations 12-13) respectively.

$$q_e=(q_m\ K_L\ C_e)/(1+K_L\ C_e) \quad (12)$$

$$q_e=K_F\ C_e^{(1/n)} \quad (13)$$

Table 2. Summary of the calculated kinetic parameters

Dye	Models	Parameters	
MB	FO	k_1	0.065
		IN qe	1.781
		qe	5.938
		R^2	0.8697
	SO	qe	12.486
		qe_2	155.888
		k_2	0.025
		R^2	0.9997

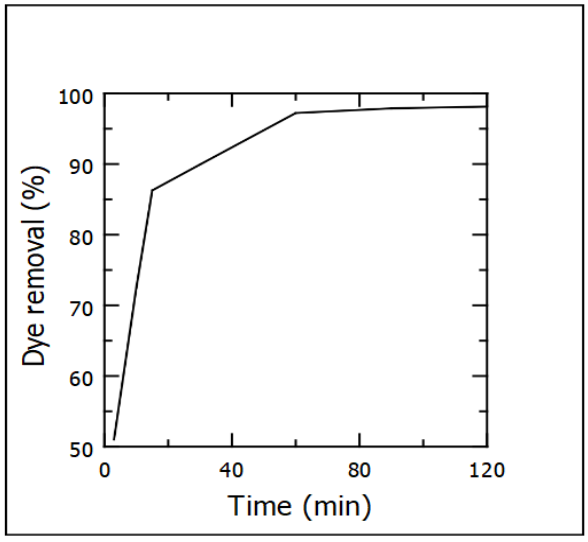


Figure 6. Time-dependent graph illustrating the rate of dye removal.

The variable qm (mg.g−1) represents the maximal adsorption capacity. KF and n represent the Fh constant, while KL represents the Lr constant. If the value of the constant n is greater than one, then the process of dye adsorption is considered beneficial. The separation factor (RL) of the Lr isotherm is a measure of the desirability of the adsorption process and can be defined as (equation 14):

$$R_L=1/(1+K_L C_0) \quad (14)$$

The adsorption-isotherm parameters obtained from the linearized Langmuir and Freundlich equations are summarized in Table 3. Within this linearized analysis, the Langmuir model exhibited a higher coefficient of determination than the Freundlich model. However, linear transformation may influence parameter estimates and goodness-of-fit statistics by altering the experimental error structure (Simonin, 2016). Therefore, the apparent agreement with the Langmuir model and the calculated isotherm parameters should be interpreted cautiously. Nonlinear regression based on the original equilibrium dataset and appropriate error criteria would be required for a more reliable comparison of the isotherm models.

Table 3: Summary of the calculated FR and LA isotherm parameters

Upon investigating the impact of altering the quantity of absorbent on the concentration, a study was conducted under consistent conditions using varying amounts of SBA-15. The resulting graph (Figure 8) depicting the relationship between the amount and concentration revealed that the quantity of adsorbent had no noteworthy influence.

Figure 9 displays the images of the solutions used in the adsorption study before adsorption, as well as the images of the solutions acquired at the end of adsorption. The concentrations of these solutions before the adsorption study were 10, 20, 30, 40, 50, and 100 ppm. When examining the color changes, the elimination of the MB is noticeable to the naked eye.

The solid sample obtained after adsorption was combined with KBr and transformed into pellets for FTIR measurement. Figure 10 displays the FTIR spectrum. The prominent absorption peaks at 3446 cm-1 and 3436 cm-1 in the spectra are caused by the vibrations of O-H bonds of water molecules that have been adsorbed. The intensities of the broad peaks reduced after the adsorption of MB, when compared to the solid before adsorption (Olfs et al., 2009; Abdel-Khalek et al., 2017). The results demonstrate the presence of a contact between the material surface and MB molecules. Following the adsorption of MB, the two conspicuous peaks observed at 1698 cm-1 and 1632 cm-1 were converted into a single peak at 1612 cm-1 and 1396 cm-1, respectively (Lau et al., 2015; Sari Yilmaz, 2022).

Table 3. Summary of the calculated FR and LA isotherm parameters

Dye	Isotherms	Parameters	Value
MB	Fh	n	0.568
		KF (L.mg^{-1}).	4.5x10^{-6}
		R^2	0.940
	Lr	qm (mg.g^{-1})	3333.333
		KL (L.mg^{-1})	0.750
		R^2	0.986

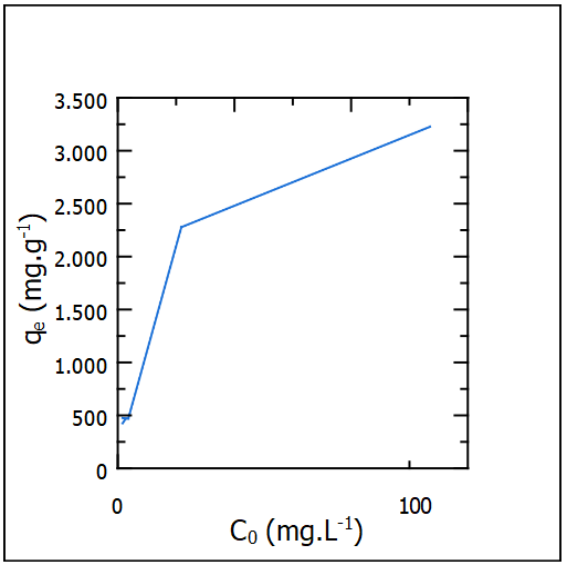


Figure 7. The influence of initial concentration of MB.

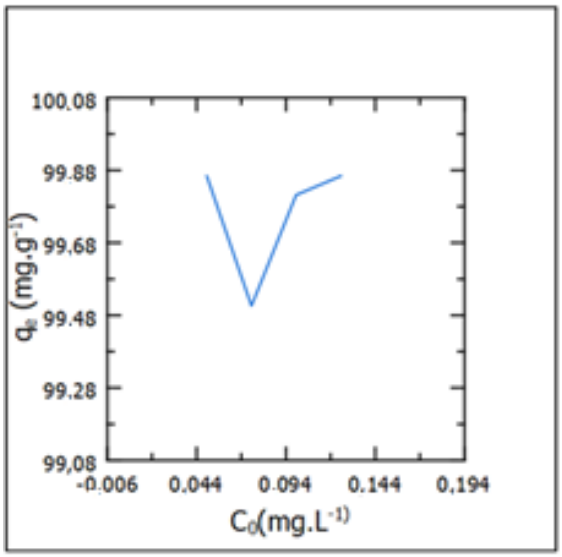


Figure 8. The influence of absorbent amount on adsorption.

a)



b)

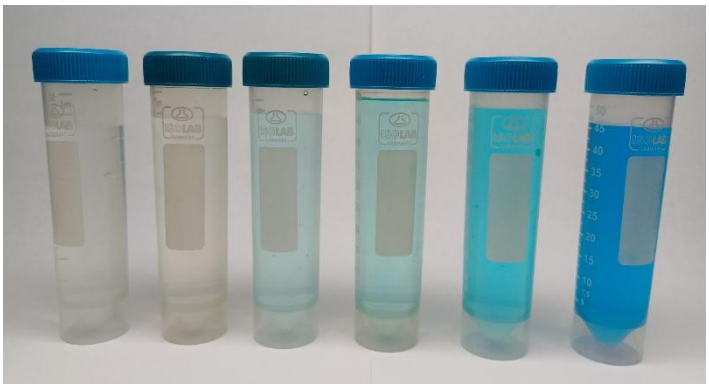


Figure 9. Figures of a) solutions prepared before MB removal b) solutions obtained after MB removal.

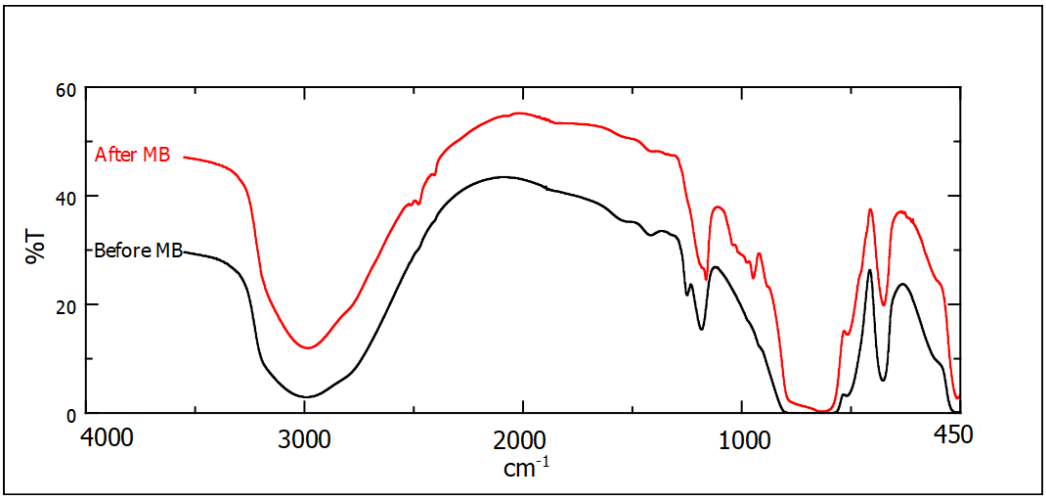


Figure 10. FTIR spectrum of SBA-15 samples synthesized and resulting from adsorption process.

4. Discussions

The aim of this study was to transform concrete debris into a value-added material intended for applications different from its conventional uses. XRD and FTIR analyses of the concrete debris were performed, and a silicon solution was obtained from debris collected from an urban transformation area using the alkaline fusion method. The highest silicon concentration, 7106 ppm, was achieved at a concrete debris/NaOH ratio of 0.75. SBA-15 was selected because its porous structure enables the conversion of the recovered silicon solution into a value-added mesoporous material. The synthesis was carried out under conditions selected through a comprehensive review of the literature.

The synthesized SBA-15 was characterized using low-angle XRD and nitrogen adsorption–desorption analyses. Its specific surface area, total pore volume, and average pore width were determined as 377.689 m^2/g, 0.129 cm^3/g, and 8.331 Å, respectively. The nitrogen adsorption–desorption isotherm exhibited an H4-type hysteresis loop. Adsorption experiments were conducted to investigate the effects of initial dye concentration, contact time, and adsorbent dosage on methylene-blue solutions prepared under controlled laboratory conditions. A dye-removal efficiency of approximately 87% was achieved within 20 min for a 20-ppm dye solution.

The adsorption data were subsequently used for kinetic and equilibrium-isotherm calculations. Within the limitations of the linearized analysis, the adsorption data exhibited a higher coefficient of determination for the Langmuir model than for the Freundlich model. However, this statistical result does not conclusively establish the superiority of the Langmuir model because nonlinear regression and additional error analyses could not be performed. Therefore, the modelling results should be interpreted cautiously and should not be considered definitive evidence of a particular adsorption mechanism. Overall, the study demonstrated the feasibility of producing a concrete-debris-derived adsorbent for dye removal.

The use of silicon recovered from concrete debris represents a waste-valorization pathway and reduces reliance on a conventional silica precursor within the synthesis route employed in this study. It may also contribute to diverting a mineral-rich construction-waste fraction from disposal. However, these potential benefits should be interpreted cautiously because silicon recovery efficiency could not be calculated without quantitative determination of the total silicon content of the initial concrete-derived material. Furthermore, the potential environmental advantages of replacing a conventional silica source must be considered together with the consumption of NaOH, water, and thermal energy during alkaline fusion and subsequent processing. Because neither a life-cycle assessment nor a techno-economic analysis was conducted, the environmental and economic sustainability of the process cannot be established quantitatively from the present results. Future studies should determine silicon mass balances, precursor-substitution ratios, energy and reagent consumption, residual-waste generation, and process costs to enable comparison with conventional SBA-15 production routes.

The adsorption findings should be interpreted in light of the experimental limitations. Each experimental condition was evaluated in a single run, and the initial and final pH values were not measured; therefore, experimental reproducibility, statistical uncertainty, and the contribution of pH-dependent interactions could not be assessed. In addition, the absence of the original point-by-point dataset prevented retrospective nonlinear regression of the kinetic and equilibrium models. Consequently, the reported linearized modelling results should be regarded as preliminary and should not be used to draw definitive conclusions regarding model superiority or adsorption mechanism. Future studies should include replicate experiments, measurement of initial and final pH values, pH-dependent adsorption

tests, and direct nonlinear fitting using appropriate goodness-of-fit and error criteria.

Author Contributions

The percentages of the author' contributions are presented below. The author reviewed and approved the final version of the manuscript.

	N.K.M.
C	100
D	100
DCP	100
DAI	100
L	100
W	100
CR	100
SR	100
PM	100

C= concept, D= design, S= supervision, DCP= data collection and/or processing, DAI= data analysis and/or interpretation, L= literature search, W= writing, CR= critical review, SR= submission and revision, PM= project management.

Conflict of Interest

The author declared that there is no conflict of interest.

Ethical Consideration

Ethics committee approval was not required because this study did not involve human participants or animals.

References

Abd El-Aleem, S., Heikal, M., & Morsi, W. M. (2014). Hydration characteristics, thermal expansion and microstructure of cement containing nano-silica. Construction and Building Materials, 59, 151–160.

Abdel-Khalek, M. A., Abdel Rahman, M. K., & Francis, A. A. (2017). Exploring the adsorption behavior of cationic and anionic dyes on industrial waste egg shells. Journal of Environmental Chemical Engineering, 5, 319–327.

Ahmad, A. L., Harris, W. A., & Ooi, B. S. (2002). Removal of dye from textile wastewater using membrane technology. Jurnal Teknologi, 36, 31–44.

Balonis, M., & Glasser, F. P. (2009). The density of cement phases. Cement and Concrete Research, 39, 733–739.

Barcelo, L., Kline, J., Walenta, G., & Gartner, E. (2014). Cement and carbon emissions. Materials and Structures, 47, 1055–1065.

Bhagiyalakshmi, M., Yun, L. J., Anuradha, R., & Jang, H. T. (2010). Synthesis of chloropropylamine grafted mesoporous MCM-41, MCM-48 and SBA-15 from rice husk ash: Their application to CO2 chemisorption. Journal of Porous Materials, 17, 475–484.

Chandler, W., Schaeffer, R., Dadi, Z., Shukla, P., Tudela, F., Davidson, O., & Al-Azhar, S. (2002). Climate change mitigation in developing countries: Brazil, China, India, Mexico, South Africa, and Turkey. World Resources Institute.

Environmental Protection Agency. (2020). Portland cement manufacturing. EPA.

Fierro, J. J., Escudero-Atehortua, A., Nieto-Londoño, C., Giraldo, M., Jouhara, H., & Wrobel, L. C. (2020). Evaluation of waste heat recovery technologies for the cement industry. International Journal of Thermofluids, 7–8, Article 100040.

Ganiron, T. U. (2015). Recycling concrete debris from construction and demolition waste. International Journal of Advanced Science and Technology, 77, 7–24.

Gawwad, H. A. A., El-Aleem, S. A., & Ouda, A. S. (2015). Preparation and characterization of one-part non-Portland cement. Ceramics International, 41, 1–9.

Hendriks, C. A., Worrell, E., De Jager, D., Blok, K., & Riemer, P. (2003). Emission reduction of greenhouse gases from the cement industry. In Greenhouse Gas Control Technologies (pp. 1–11).

Hewlett, P., & Liska, M. (1988). Lea's chemistry of cement and concrete. Elsevier.

Hills, T., Leeson, D., Florin, N., & Fennell, P. (2016). Carbon capture in the cement industry: Technologies, progress, and retrofitting. Environmental Science & Technology, 50, 368–377.

HSN, M. I., Panatarani, C., Faizal, F., Mulyana, C., & Joni, I. M. (2023). Synthesis of mesoporous silica SBA-15 from geothermal sludge. Materialia, 27, Article 101637.

İnceoğlu, F., Mermer, N. K., Kırmızı, V. & Tombaş, G. (2021). Influence of cement with different calcium sulfate phases on cementitious tile adhesive mortars. International Journal of Adhesion and Adhesives, 104, Article 102740

Islam, M. A., Ali, I., Karim, S. M. A., Hossain Firoz, M. S., Chowdhury, A. N., Morton, D. W., & Angove, M. J. (2019). Removal of dye from polluted water using novel nano manganese oxide-based materials. Journal of Water Process Engineering, 32, Article 100911.

Izumi, Y., Iizuka, A., & Ho, H. J. (2021). Calculation of greenhouse gas emissions for a carbon recycling system using mineral carbon capture and utilization technology in the cement industry. Journal of Cleaner Production, 312, Article 127618.

Kabir, S., Al-Shayeb, A., & Khan, I. M. (2016). Recycled construction debris as concrete aggregate for sustainable construction materials. Procedia Engineering, 145, 1518–1525.

Kaplan, E., & Soyluk, A. (2023). Deprem sonrası atık yönetimi: Atık betonun geri dönüşümü ve mimaride kullanımı için öneriler. Mimarlık Bilimleri ve Uygulamaları Dergisi, 140–162.

Karamahmut Mermer, N., İnceoğlu, F., & Ünlü Pınar, E. (2024). Effect of the moisture content of sand used in cement-based ceramic tile adhesives on their microstructure and performance. International Journal of Adhesion and Adhesives. Advance online publication.

Karamahmut Mermer, N., Sari Yilmaz, M., Dere Ozdemir, O., & Pişkin, M. B. (2017). The synthesis of silica-based aerogel from gold mine waste for thermal insulation. Journal of Thermal Analysis and Calorimetry, 129, 1807–1812.

Karellas, S., Leontaritis, A. D., Panousis, G., Bellos, E., & Kakaras, E. (2013). Energetic and exergetic analysis of waste heat recovery systems in the cement industry. Energy, 58, 147–156.

Kokunešoski, M., Gulicovski, J., Matović, B., Logar, M., Milonjić, S. K., & Babić, B. (2010). Synthesis and surface characterization of ordered mesoporous silica SBA-15. Materials Chemistry and Physics, 124, 1248–1252.

Lakshmi, M., & Nivetdhitha, R. R. (2015). Effect of partial replacement of aggregates by recycled concrete debris on strength of concrete. International Journal of Civil Engineering and Technology, 27, 250–259.

Laskowski, Ł., Laskowska, M., Walcarius, A., Doskocz, M., Vila, N., Karczmarska, A., Pawlik, P., Goraus, J., Balin, K., & Dulski, M. (2024). Synthesis and characterization of SBA-15 silica

containing cyclam inside pores for capturing iron chloride. Microporous and Mesoporous Materials, 378, Article 112980.

Lau, Y. Y., Wong, Y. S., Teng, T. T., Morad, N., Rafatullah, M., & Ong, S. A. (2015). Degradation of cationic and anionic dyes in coagulation–flocculation process using bi-functionalized silica hybrid with aluminum-ferric as auxiliary agent. RSC Advances, 5, 34206–34215.

Lee, Y. J., Lee, K. W., Min, B. Y., Hwang, D. S., & Moon, J. K. (2015). Characterization of cement waste form for final disposal of decommissioning concrete wastes. Annals of Nuclear Energy, 77, 294–299.

Li, Y., Le Pape, Y. M., Tajuelo Rodriguez, E., Torrence Moore, C. E., Arregui Mena, J. D., Rosseel, T. M., & Sircar, M. (2020). Microstructural characterization and assessment of mechanical properties of concrete. Construction and Building Materials, 257, Article 119540.

Liang, B., Zhu, P., Gu, J., Yuan, W., Xiao, B., Hu, H., & Rao, M. (2024). Advancing adsorption and separation with modified SBA-15: A comprehensive review and future perspectives. Molecules, 29, Article 3543.

Lin, Y., & Du, H. (2020). Graphene reinforced cement composites: A review. Construction and Building Materials, 265, Article 120312.

Masood, A., Ahmad, T., Arif, M., & Mahdi, F. (2001). Waste management strategies for concrete. Environmental Engineering and Policy, 3, 15–18.

Mavroulis, S., Mavrouli, M., Vassilakis, E., Argyropoulos, I., Carydis, P., & Lekkas, E. (2023). Debris management in Turkey provinces affected by the 6 February 2023 earthquakes. Applied Sciences, 13, Article 4582.

McKay, G., Porter, J. F., & Prasad, G. R. (1999). The removal of dye colours from aqueous solutions by adsorption on low-cost materials. Water, Air, and Soil Pollution, 114, 423–438.

Mermer, N. K., & Pişkin, S. (2018). Silica-based aerogel synthesis from fly ash and bottom ash. Main Group Chemistry, 17, 63–77.

Mermer, N. K., & Pişkin, S. (2019). Aerogel synthesis using sand by ultrasonically assisted sol–gel method. Journal of the Faculty of Engineering and Architecture of Gazi University, 34, 1253–1263.

Naqi, A., & Jang, J. G. (2019). Recent progress in green cement technology utilizing low-carbon emission fuels and raw materials: A review. Sustainability, 11, Article 537.

Olfs, H. W., Torres-Dorante, L. O., Eckelt, R., & Kosslick, H. (2009). Comparison of different synthesis routes for Mg–Al layered double hydroxides (LDH): Characterization of the structural phases and anion exchange properties. Applied Clay Science, 43, 459–464.

Oliveira, A. N. de, Cardoso, R. S., Ferreira, I. M., Silva, L. S., Costa, A. A. F., Pires, L. H. O., Rocha Filho, G. N., Luque, R., Noronha, R. C. R., & Nascimento, L. A. S. (2023). Valorization of silica-based residues for the synthesis of ordered mesoporous silicas and their applications. Microporous and Mesoporous Materials, 354, Article 112520.

Phair, J. W. (2006). Green chemistry for sustainable cement production and use. Green Chemistry, 8, 763–780.

Sari Yilmaz, M. (2022). Graphene oxide/hollow mesoporous silica composite for selective adsorption of methylene blue. Microporous and Mesoporous Materials, 330, Article 111570.

Sari Yilmaz, M., & Pişkin, S. (2015). Removal of template from SBA-15 samples synthesized from different silica sources. Journal of Thermal Analysis and Calorimetry, 121, 1255–1262.

Schneider, M. (2015). Process technology for efficient and sustainable cement production. Cement and Concrete Research, 78, 14–23.

Schneider, M., Romer, M., Tschudin, M., & Bolio, H. (2011). Sustainable cement production—Present and future. Cement and Concrete Research, 41, 642–650.

Scientific and Technological Research Council of Türkiye (TÜBİTAK). (2024, April 5). TÜBİTAK provided active support in the fight against earthquake. https://tubitak.gov.tr/en/news/tubitak-provided-active-support-fight-against-earthquake

Shigemoto, N., Hayashi, H., & Miyaura, K. (1993). Selective formation of Na-X zeolite from coal fly ash by fusion with sodium hydroxide prior to hydrothermal reaction.. Journal of Materials Science, 28, 4781–4786.

Simonin, J.-P. (2016). On the comparison of pseudo-first order and pseudo-second order rate laws in the modeling of adsorption kinetics. Chemical Engineering Journal, 300, 254–263.

Singh Kashyap, V., Agrawal, U., Arora, K., & Sancheti, G. (2021). FTIR Analysis of Nanomodified Cement Concrete Incorporating Nano Silica and Waste Marble Dust IOP Conference Series: Earth and Environmental Science, 796, Article 012012.

Summerbell, D. L., Barlow, C. Y., & Cullen, J. M. (2016). Potential reduction of carbon emissions by performance improvement: A cement industry case study. Journal of Cleaner Production, 135, 1327–1339.

Turkish Standards Institute. (2018). TS EN 197-1: Composition, specification and conformity criteria for common cements. TSE.

Ucol-Ganiron, T. (2012). Concrete debris as alternative fine aggregate for architectural finishing mortar. Architectural Research, 2, 111–114.

Yagub, M. T., Sen, T. K., Afroze, S., & Ang, H. M. (2014). Dye and its removal from aqueous solution by adsorption: A review. Advances in Colloid and Interface Science, 209, 172–184.

Yilmaz, M. S., & Mermer, N. K. (2015). Preparation of silicon and aluminum extracts from fly ashes by alkali fusion. International Journal of Chemical Engineering and Applications, 9, 512–515.

Yu, H., & Zhai, Q. Z. (2009). Mesoporous SBA-15 molecular sieve as a carrier for controlled release of nimodipine. Microporous and Mesoporous Materials, 123, 298–305.

Black Sea Journal of Engineering and Science
doi: 10.34248/bsengineering.1916695

Open Access Journal
e-ISSN: 2619 – 8991

Research Article
Volume 9 - Issue 5: 2795-2799 / September 2026

COMPARATIVE EVALUATION OF TOTAL PHENOLIC CONTENT AND ANTIOXIDANT CAPACITY IN *Aronia melanocarpa, Crataegus orientalis SPP,* AND *Cornus mas L.* FRUITS

Said Efe DOST[1]*, Yılmaz SESLİ[1]

[1]*Karamanoğlu Mehmetbey University, Vocational School, Department of Technical Sciences, 70100, Karaman, Türkiye*

Abstract: This study comparatively evaluated the total phenolic content (TPC) and antioxidant capacity of three phenolic-rich fruit species: *Aronia melanocarpa* (cv. Nero and Viking), *Crataegus orientalis* (hawthorn), and *Cornus mas* (cv. Yalçınkaya 77). Fully mature fruits were harvested during the 2024 growing season and analyzed using standardized Folin–Ciocalteu and ABTS assays. The experiment was conducted in a completely randomized design, and data were analyzed by analysis of variance (ANOVA) followed by LSD mean separation. Highly significant species effects were detected ($p < 0.001$). Aronia cultivars exhibited markedly higher phytochemical richness, with TPC values of 2594.44 mg GAE 100 g^{-1} FW for cv. Viking and 2397.58 mg GAE 100 g^{-1} FW for cv. Nero, clearly exceeding those of hawthorn (847.71 mg GAE 100 g^{-1} FW) and cornelian cherry (821.45 mg GAE 100 g^{-1} FW). Antioxidant capacity followed a similar pattern, with Viking (80.26%) and Nero (78.33%) showing significantly greater $ABTS^{\bullet+}$ radical-scavenging activity than hawthorn (49.28%) and cornelian cherry (51.60%). A strong linear relationship between TPC and antioxidant capacity ($R^2 = 0.9996$) indicates that phenolic compounds are the principal contributors to antioxidant behavior across species. Overall, the results highlight the relatively higher antioxidant potential of *A. melanocarpa* and confirm hawthorn and cornelian cherry as valuable natural sources of antioxidants for functional food and nutraceutical applications.

Keywords: Natural antioxidants, Plant phenolics, Bioactive phytochemicals, Functional food products, Medicinal fruits

***Corresponding author:** Karamanoğlu Mehmetbey University, Department of Technical Sciences, Vocational School, 70100, Karaman, Türkiye
E mail: saidefedost@kmu.edu.tr (S. E. DOST)
Said Efe DOST https://orcid.org/0000-0003-4279-7292
Yılmaz SESLİ https://orcid.org/0000-0002-3150-2180

Received: March 26, 2026
Accepted: August 27, 2026
Published: September 15, 2026

Cite as: Dost, S. E., and Sesli, Y. (2026). Comparative evaluation of total phenolic content and antioxidant capacity in *Aronia melanocarpa, Crataegus orientalis spp*, and *Cornus mas L*. fruits. *Black Sea Journal of Engineering and Science,* 9(5), 2795-2799.

1. Introduction

Reactive oxygen species (ROS) and free radicals are continuously generated as natural by-products of metabolic processes in living organisms. Under normal conditions, cellular antioxidant defense systems maintain redox homeostasis; however, environmental stressors and dietary factors can disrupt this balance, leading to oxidative stress (Çelik and Ayran, 2020; Kępińska-Pacelik and Biel, 2026). Concerns regarding the safety of synthetic antioxidants have increased scientific interest in natural antioxidant compounds derived from plant sources (Martinelli et al., 2021; Gavrila et al., 2025).

The antioxidant potential of plant materials is largely associated with the quantity and composition of phenolic compounds (Tüysüz et al., 2021). Phenolics can donate electrons or hydrogen atoms through their hydroxyl groups, thereby terminating oxidative chain reactions (Negreanu-Pirjol et al., 2023; Kępińska-Pacelik and Biel, 2026). Accordingly, the strong correlation between total phenolic content and antioxidant capacity has made these parameters widely accepted indicators for evaluating the biochemical value of plant-based foods (Çelik and Ayran, 2020; Staszowska-Karkut and Materska, 2020).

Among phenolic-rich fruits, hawthorn (Crataegus orientalis), aronia (*Aronia melanocarpa*), and cornelian cherry (*Cornus mas* L.) are of particular interest due to their distinct phytochemical profiles. Aronia is characterized by a high anthocyanin concentration and remarkable radical-scavenging activity, whereas hawthorn contains abundant flavonoids, especially proanthocyanidin derivatives. Cornelian cherry, in addition to phenolic compounds, is notable for the presence of iridoids and organic acids (Czerwińska et al., 2021; Klymenko et al., 2021; Mustafa et al., 2024; Sarıkaya et al., 2025). These compositional differences suggest that antioxidant capacity may vary considerably among species.

Although the phytochemical properties of these fruits have been investigated individually, comparative evaluations conducted under identical analytical conditions remain limited (Erim et al., 2025; Şeker et al., 2025). This lack of standardized comparison complicates the determination of their relative biochemical value for raw material selection and functional product development in the food industry.

This work is licensed (CC BY-NC 4.0) under Creative Commons Attribution 4.0 International License

Therefore, the present study aimed to comparatively determine the total phenolic content and antioxidant capacity of hawthorn, aronia, and cornelian cherry fruits under standardized analytical conditions.

2. Materials and Methods

2.1. Plant Material and Sample Preparation

This study was conducted on fruits of *Aronia melanocarpa* (cv. Nero and Viking), *Crataegus orientalis* (hawthorn), and *Cornus mas* (cv. Yalçınkaya 77). Fully mature fruits were collected from experimental orchards in Karaman, Türkiye, during the 2024 harvest season. To minimize environmental variability, all plant materials were obtained from cultivated plants grown under standardized and controlled orchard conditions. No wild plant material was collected, and no specific permissions were required for sampling. The studied species are not subject to CITES regulations. The samples were immediately transferred to the laboratory under cold conditions (4 °C) and processed within 24 hours. For each species/cultivar, three independent biological replicates (n = 3) were prepared, with each biological replicate representing a pooled sample of fruits harvested from five different trees within the same orchard block to ensure representativeness. Each biological sample was homogenized using a stainless steel blender, and 5 g of fruit tissue was extracted with 80% (v/v) methanol by maceration for 24 hours at room temperature. The extracts were filtered through Whatman No. 1 paper and stored at –20 °C until analysis.

2.2. Determination of Total Phenolic Content (TPC)

The Folin method determined the total phenolic content (TPC) of the fruit extracts using the Folin–Ciocalteu colorimetric method as described by Singleton and Rossi (1965), with slight modifications. In brief, 1 mL of extract was mixed with 5 mL of 0.2 N Folin–Ciocalteu reagent and 4 mL of 7.5% (w/v) Na_2CO_3 solution. The reaction mixtures were incubated at room temperature in the dark for 90 minutes, after which the absorbance was measured at 760 nm using a UV–Vis spectrophotometer (Shimadzu UV-1800). Gallic acid (0–250 mg L^{-1}) was used as a calibration standard, and the results were expressed as milligrams of gallic acid equivalents per 100 g fresh weight (mg GAE 100 g^{-1} FW). The same procedure was applied for standard solutions to construct the calibration curve (Singleton and Rossi, 1965).

2.3. Determination of Antioxidant Capacity (ABTS•$^+$ Radical Cation Assay)

The antioxidant activity of the extracts was measured using the ABTS•$^+$ (2,2′-azinobis (3-ethylbenzothiazoline-6-sulfonic acid)) radical cation decolorization assay, as described by Gill et al. (2000) and Cemeroğlu (2007), with minor modifications. A 7 mM ABTS solution containing 2.45 mM potassium persulfate was prepared and kept in the dark at room temperature for 12–16 hours to allow generation of the ABTS•$^+$ radical. Before use, the blue–green radical solution was diluted with ethanol to an absorbance of 0.70 ± 0.025 at 734 nm. Subsequently, 2 mL of the diluted ABTS•$^+$ solution was mixed with 1 mL of fruit extract, and the decrease in absorbance was recorded at 734 nm after 10 minutes of incubation. A Trolox (6-hydroxy-2,5,7,8-tetramethylchroman-2-carboxylic acid) standard curve (0–250 µM) was prepared, and the results were expressed as Trolox Equivalent Antioxidant Capacity (% TEAC) (Gill et al., 2000; Cemeroğlu, 2007).

2.4. Statistical Analysis

All chemical analyses were performed in three technical replicates for each biological sample, and the mean values of these technical replicates were used for the statistical analyses. All final data were expressed as mean ± standard error (SE) of the biological replicates (n = 3) (Czerwińska et al., 2021). To evaluate and compare the differences among the two cultivars (Nero and Viking) and the two species (*Crataegus orientalis* and *Cornus mas*), statistical analysis was performed using One-way analysis of variance (One-way ANOVA) in a completely randomized design. Pairwise comparisons of Least Squares Means (LSMEANS) were carried out using Fisher's Least Significant Difference (LSD) test at a significance level of $p < 0.05$ (Erim et al., 2025; Gavrila et al., 2025). Statistical analyses were conducted using JMP Pro 17.0 software (SAS Institute Inc., Cary, NC, USA, 2023).

3. Results and Discussion

3.1. Total Phenolic Content

Analysis of variance revealed a highly significant effect of fruit species on both total phenolic content (TPC) and antioxidant capacity ($p < 0.001$). The statistical models demonstrated excellent explanatory performance, with coefficients of determination (R^2) of 0.9995 for TPC and 0.9996 for antioxidant capacity. These exceptionally high model-fit parameters and low standard errors highlight rigorous control over experimental conditions, the homogeneity of the cultivated orchard samples, and the high precision of the analytical replicates. Significant differences in TPC were detected among the examined fruits (Table 1). *Aronia melanocarpa* cultivars exhibited substantially higher phenolic concentrations than *Crataegus orientalis* and *Cornus mas*. Among all samples, cv. Viking recorded the highest value (2594,44 ± 17,27 mg GAE 100 g^{-1} FW, group 'a'), followed by cv. Nero (2397,58 ± 19,09 mg GAE 100 g^{-1} FW, group 'b'). According to the LSD multiple comparison test, these two cultivars were assigned to different statistical groups, indicating a statistically significant difference between them ($P<0.001$), although both clearly exceeded the other species. In contrast, *C. orientalis* (hawthorn) and *C. mas* cv. Yalçınkaya 77 (cornelian cherry) showed markedly lower phenolic contents, with mean values of 847,71 ± 21,62 and 821,45 ± 16,60 mg GAE 100 g^{-1} FW, respectively. According to the LSD test, hawthorn was assigned to group 'c' and cornelian cherry to group 'd', reflecting distinct and statistically different phenolic

levels between them, while both remained significantly lower relative to the Aronia cultivars. Overall, the TPC of *A. melanocarpa* was approximately threefold higher than that of hawthorn and cornelian cherry, highlighting pronounced interspecific variability in phenolic accumulation. The approximately threefold higher phenolic concentration in aronia compared to hawthorn and cornelian cherry can be elucidated by the distinct qualitative and quantitative profiles of their secondary metabolites (Tolić et al., 2015; Kaloudi et al., 2022). *Aronia melanocarpa* is characterized by an extremely high density of monomeric anthocyanins (predominantly cyanidin-3-galactoside and cyanidin-3-arabinoside) and polymeric proanthocyanidins (condensed tannins), which heavily react with the Folin-Ciocalteu reagent (Jang and Koh, 2023). Conversely, while *Cornus mas* is structurally rich in organic acids (such as malic, citric, and quinic acids) and iridoids (e.g., loganic acid), these non-phenolic constituents do not contribute to the TPC value (Czerwińska et al., 2021; Klymenko et al., 2021). Similarly, the phenolic profile of *Crataegus orientalis* is mostly dominated by lower-molecular-weight monomeric flavonoids (rutin, vitexin, and hyperoside) and chlorogenic acids, which, despite their excellent bioactivity, accumulate at significantly lower quantitative levels compared to the massive proanthocyanidin and anthocyanin polymers found in *A. melanocarpa* (Okatan et al., 2017; Mustafa et al., 2024). The obtained values are consistent with previous reports identifying aronia as one of the most phenolic-rich berry species (Tolić et al., 2015; Jurikova et al., 2018). Reported TPC ranges for aronia vary widely depending on genotype and processing conditions but consistently exceed those of most temperate fruits (Tolić et al., 2015; Erim et al., 2025). Conversely, the values observed for hawthorn and cornelian cherry fall within previously reported ranges for fresh fruits (Jurikova et al., 2018; Klymenko et al., 2021; Tüysüz et al., 2021), confirming moderate but significant phenolic accumulation in these species.

3.2. Antioxidant Capacity (ABTS•$^+$ Assay)

The antioxidant capacity evaluated using the ABTS•$^+$ radical cation decolorization assay revealed highly significant differences among the investigated fruit species ($p < 0.001$). The statistical model demonstrated excellent explanatory performance, with a coefficient of determination (R^2) of 0.9996, indicating that nearly all observed variability in antioxidant capacity was attributable to interspecific differences rather than random experimental variation. The high F-value (41,215.24) further confirmed the strong effect of fruit species on ABTS•$^+$ radical scavenging activity.

Consistent with the total phenolic content results, *Aronia melanocarpa* cultivars exhibited the highest antioxidant capacities. Among the analyzed samples, cv. Viking showed the greatest ABTS•$^+$ scavenging activity (80.26 ± 0.29%), followed closely by cv. Nero (78.33 ± 0.26%). According to the LSD multiple comparison test, these two cultivars were assigned to the same statistical group ("a"), indicating no significant difference between them. At the same time, both differed significantly from the remaining fruit species ($p < 0.001$). The low standard errors observed for both cultivars indicate high analytical precision and repeatability.

Table 1. Total phenolic content (TPC) and antioxidant capacity (ABTS•$^+$) of aronia, hawthorn, and cornelian cherry fruits

Species / Cultivar	Total Phenolic Content (mg GAE 100 g^{-1} FW)	LSD (0.05)	Grouping	Antioxidant Capacity (% TEAC)	LSD (0.05)	Grouping
Aronia melanocarpa cv. Viking	2594.44 ± 17.27	10.98	a	80.26 ± 0.29	0.16	a
Aronia melanocarpa cv. Nero	2397.58 ± 19.09	10.98	b	78.33 ± 0.26	0.16	b
Crataegus orientalis (Hawthorn)	847.71 ± 21.62	10.98	c	49.28 ± 0.26	0.16	d
Cornus mas cv. Yalçınkaya 77 (Cornelian Cherry)	821.45 ± 16.60	10.98	d	51.60 ± 0.28	0.16	c
Model R^2	0.9995	—	—	0.9996	—	—
F-value	60,653.85	—	—	86,455.80	—	—
P-value	< 0.001	—	—	< 0.001	—	

In contrast, *Crataegus orientalis* (hawthorn) and *Cornus mas* cv. Yalçınkaya 77 (cornelian cherry) exhibited moderate but significantly lower antioxidant activities, with values of 49.28 ± 0.26% and 51.60 ± 0.28%, respectively. These species formed a separate statistical group ("b"), reflecting comparable antioxidant capacities between them but significantly lower values compared with the Aronia cultivars. The calculated LSD value (0.46) confirmed that even small numerical differences among means were statistically meaningful and that the separation between statistical groups was robust.

When antioxidant capacity was evaluated together with total phenolic content (Figure 1), a very strong positive association emerged. The ranking of fruit species based on ABTS•$^+$ activity closely mirrored their ranking for TPC, and the correlation coefficient (R^2 = 0.9996)

indicated an almost linear relationship between phenolic concentration and antioxidant performance. Similar strong correlations between phenolics and radical scavenging assays (ABTS, DPPH, and FRAP) have been widely reported (Jurikova et al., 2018; Çelik and Ayran, 2020; Klymenko et al., 2021), supporting the conclusion that phenolic compounds are the primary contributors to antioxidant capacity in these fruits.

The superior antioxidant performance of *A. melanocarpa*, particularly cv. Viking, is consistent with previous reports describing aronia as one of the richest natural antioxidant sources (Tolić et al., 2015; Gao et al., 2024). This behavior is mainly associated with its high concentration of anthocyanins—especially cyanidin-3-galactoside—and chlorogenic acid, compounds known for strong electron-donating ability and high radical-quenching efficiency (Kaloudi et al., 2022; Jang and Koh, 2023). The elevated activity of the phenylpropanoid pathway in aronia promotes intensive accumulation of these bioactive metabolites, explaining its markedly higher antioxidant performance compared with other species.

Although hawthorn and cornelian cherry exhibited lower antioxidant activity, their results still indicate measurable radical-scavenging potential, confirming their relevance as natural antioxidant sources. However, several comparative studies have reported the consistently higher antioxidant capacity of aronia relative to these fruits (Tüysüz et al., 2021; Mustafa et al., 2024). The high phenolic density of aronia also supports its use as a functional food ingredient and nutraceutical raw material (Shi et al., 2024; Erim et al., 2025).

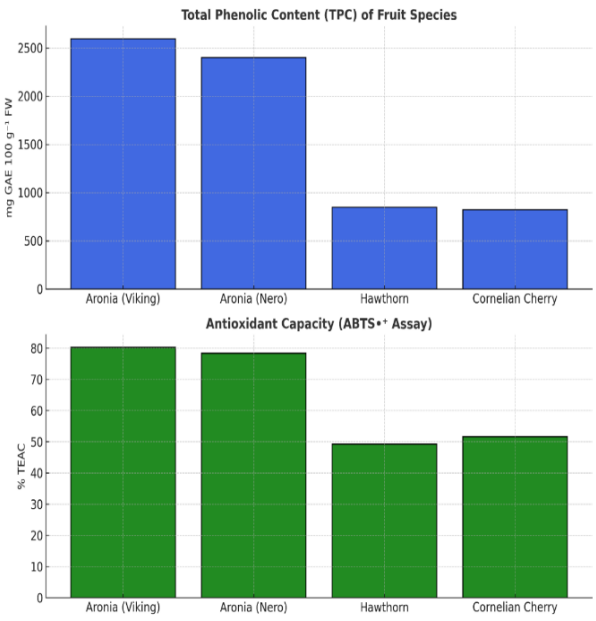


Figure 1. Total phenolic content (TPC) and antioxidant capacity (ABTS•+ assay) of different fruit species (Aronia 'Viking', Aronia 'Nero', hawthorn, and cornelian cherry).

Overall, the close correspondence between TPC and ABTS•⁺ activity demonstrates that phenolic compounds are the dominant determinants of antioxidant behavior in the studied fruits, with *Aronia melanocarpa* forming a distinct biochemical group characterized by exceptionally high antioxidant capacity relative to hawthorn and cornelian cherry.

5. Conclusion

The present study comparatively evaluated the total phenolic content and antioxidant capacity of *Aronia melanocarpa, Crataegus orientalis*, and *Cornus mas* fruits under standardized analytical conditions. The results demonstrated that *A. melanocarpa* cultivars (cv. Viking and cv. Nero) exhibited significantly higher phenolic content and antioxidant capacity compared to hawthorn and cornelian cherry. A strong positive correlation between total phenolic content and antioxidant activity confirmed that phenolic compounds are the primary contributors to antioxidant behavior in these fruits. Overall, *A. melanocarpa* can be considered a superior natural source of antioxidants, while hawthorn and cornelian cherry also represent valuable functional food resources.

Author Contributions

The percentages of the authors' contributions are presented below. All authors reviewed and approved the final version of the manuscript.

	S.E.D.	Y.S.
C	60	40
D	60	40
S	50	50
DCP	70	30
DAI	60	40
L	60	40
W	70	30
CR	50	50
SR	60	40
PM	60	40
FA	50	50

C= concept, D= design, S= supervision, DCP= data collection and/or processing, DAI= data analysis and/or interpretation, L= literature search, W= writing, CR= critical review, SR= submission and revision, PM= project management, FA= funding acquisition.

Conflict of Interest

The authors declare no conflict of interest.

Ethical Consideration

Ethics committee approval was not required for this study because it involved no animal or human subjects.

Acknowledgements

The authors would like to thank Karamanoğlu Mehmetbey University for providing laboratory facilities and technical support during the study.

References

Çelik, S. A. & Ayran, İ. (2020). Antioksidan kaynağı olarak bazı tıbbi ve aromatik bitkiler. *Türk Bilimsel Derlemeler Dergisi, 13*(2), 115–125. https://derleme.gen.tr/index.php/derleme/article/view/349/342

Cemeroğlu B (2007). Gıda analizleri. Gıda Teknolojisi Derneği Yayınları. 34: 168–171.

Czerwińska, M. E., Bobińska, A., Cichocka, K., Buchholz, T., Woliński, K. & Melzig, M. F. (2021). *Cornus mas* and Cornus officinalis—A comparison of antioxidant and immunomodulatory activities of standardized fruit extracts in human neutrophils and Caco-2 models. *Plants, 10*(11), 2347. https://www.mdpi.com/2223-7747/10/11/2347

Erim, B., Özyurt, H. N. & Binici, H. İ. (2025). Comparison of the physicochemical properties and antioxidant activities of aronia fruit and its products. *Turkish Journal of Agriculture - Food Science and Technology, 13*(12), 4130–4135. https://www.agrifoodscience.com/index.php/TURJAF/article/view/8272

Gao, N., Zhang, J., Zhao, Y., Liu, X., Ding, C., Dong, L., Zhang, J., Sun, S., Ding, Q., Khatoom, S., Cheng, Z., Liu, W., Shen, L. & Xiao, F. (2024). Polyphenol components in black chokeberry (Aronia melanocarpa) as clinically proven disease control factors—An overview. *Food Science and Human Wellness, 13*(2), 521-537. http://doi.org/10.26599/FSHW.2022.9250096

Gavrila, A. I., Damian, E. J., Rosca, A., Calinescu, I., Hodosan, C. & Popa, I. (2025). Optimization of microwave-assisted extraction of polyphenols from Crataegus monogyna L. *Antioxidants, 14*(3), 357. https://www.mdpi.com/2076-3921/14/3/357

Gill, M., Barberan, T., Pierce, B. H., Holcroft, D. M., & Kader, A. A. (2000). Antioxidant activity of pomegranate juice and its relationship with phenolic composition and processing. Journal of Agricultural and Food Chemistry, 48(10), 4581–4589. https://pubmed.ncbi.nlm.nih.gov/11052704/

Jang, Y. & Koh, E. (2023). Characterisation and storage stability of aronia anthocyanins encapsulated with combinations of maltodextrin with carboxymethyl cellulose, gum Arabic, and xanthan gum. Food Chemistry. https://pubmed.ncbi.nlm.nih.gov/36436231/

Jurikova, T., Skowronkova, N., Zvonkova, M., Orsavova, J., Ercisli, S., Dokoupil, L., Fatrcova-Sramkova, K., Adamkova, A., & Mlcek, J. (2018). Polyphenolic spectrum of cornelian cherry fruits and their health-promoting effect. Molecules, 23(8), 2077. https://pmc.ncbi.nlm.nih.gov/articles/PMC12176012/

Kaloudi, T., Tsimogiannis, D. & Oreopoulou, V. (2022). Aronia melanocarpa: Identification and exploitation of its phenolic components. *Molecules, 27*(14), 4375. https://www.mdpi.com/1420-3049/27/14/4375

Kępińska-Pacelik, J. K. & Biel, W. (2026). Hawthorn (Crataegus monogyna Jacq.): A review of therapeutic potential and applications. *Molecules, 31*(1), 0023. https://www.mdpi.com/1420-3049/31/2/226

Klymenko, S., Kucharska, A. Z., Sokół-Łętowska, A., Piórecki, N., Przybylska, D. & Grygorieva, O. (2021). Iridoids, flavonoids, and antioxidant capacity of *Cornus mas*, C. officinalis, and C. mas × C. officinalis fruits. *Biomolecules, 11*(6), 776. https://www.mdpi.com/2218-273X/11/6/776

Martinelli, F., Perrone, A., Yousefi, S., Papini, A., Castiglione, S., Guarino, F. & Salami, S. A. (2021). Botanical, phytochemical, anti-microbial, and pharmaceutical characteristics of hawthorn (Crataegus monogyna Jacq.), Rosaceae. *Molecules, 26*(23), 7266. https://doi.org/10.3390/molecules26237266

Mustafa, H. J. M., Yaviç, A. & Doğan, L. (2024). Alıç (Crataegus spp.) meyvesinin etnobotaniği, tıbbi ve besinsel potansiyeli. *MAS Journal of Applied Sciences, 9*(4), 1030–1039. file:///C:/Users/sedos/Downloads/7-ADNAN_pagenumber.pdf

Negreanu-Pirjol, B. S., Oprea, O. C., Negreanu-Pirjol, T., Roncea, F. N., Prelipcean, A. M., Craciunescu, O., Iosageanu, A., Artem, V., Ranca, A., Motelica, L., Lepadatu, A. C., Cosma, M., & Popoviciu, D. R. (2023). Health benefits of antioxidant bioactive compounds in the fruits and leaves of Lonicera caerulea L. and Aronia melanocarpa (Michx.) Elliot. Antioxidants, 12(4), 951. https://www.mdpi.com/2076-3921/12/4/951

Okatan, V., Gündoğdu, M., & Çolak, A. M. (2017). Uşak'ta yetişen farklı alıç (Crataegus spp.) genotipi meyvelerinin bazı kimyasal ve pomolojik karakterlerinin belirlenmesi. Iğdır Üniversitesi Fen Bilimleri Enstitüsü Dergisi, 7(3), 39–44. https://dergipark.org.tr/tr/download/article-file/420289

Sarıkaya, B., Kolay, E., Guney-Coskun, M., Yiğit-Ziolkowski, A. & Aktaç, Ş. (2025). The effect of black chokeberry (Aronia melanocarpa) on human inflammation biomarkers and antioxidant enzymes: A systematic review of randomized controlled trials. Nutrition Reviews, 83(6), 1083–1098. https://pubmed.ncbi.nlm.nih.gov/39499790

SAS Institute Inc. (2023). JMP® Pro 17.0 statistical discovery software. Cary, NC: SAS Institute Inc.

Şeker, M. E., Erdoğan, A. & Ay, E. (2025). Comparative analysis of phenolic, carotenoid, and elemental profiles in three Crataegus species from Şebinkarahisar, Türkiye. *Molecules, 30*(14), 2934. https://www.mdpi.com/1420-3049/30/14/2934

Shi, D., Xu, J., Sheng, L., & Song, K. (2024). Comprehensive utilization technology of Aronia melanocarpa. Molecules, 29(6), 1388. https://www.mdpi.com/1420-3049/29/6/1388

Singleton, V. L. & Rossi, J. A. (1965). Colorimetry of total phenolics with phosphomolybdic-phosphotungstic acid reagents. *American Journal of Enology and Viticulture, 16*(3), 144–158. https://www.ajevonline.org/content/16/3/144

Staszowska-Karkut, M. & Materska, M. (2020). Phenolic composition, mineral content, and beneficial bioactivities of leaf extracts from black currant, raspberry, and aronia. *Nutrients, 12*(2), 463. https://www.mdpi.com/2072-6643/12/2/463

Tolić, M. T., Landeka Jurčević, I., Panjkota Krbavčić, I., Marković, K. & Vahčić, N. (2015). Phenolic content, antioxidant capacity and quality of chokeberry (Aronia melanocarpa) products. *Food Technology and Biotechnology, 53*(2), 171-179. https://doi.org/10.17113/ftb.53.02.15.3833

Tüysüz, B., Çakır, Ö. & Dertli, E. (2021). Bazı yabani meyve türlerinin antioksidan kapasitesi, toplam fenolik madde içeriği ve fenolik asit profilinin belirlenmesi. *Avrupa Bilim ve Teknoloji Dergisi, 21*, 191–197. https://dergipark.org.tr/tr/download/article-file/1372623

Black Sea Journal of Engineering and Science
doi: 10.34248/bsengineering.2003693

Open Access Journal
e-ISSN: 2619 – 8991

Research Article
Volume 9 - Issue 5: 2800-2816 / September 2026

AI-ASSISTED MULTICLASS KIDNEY CT PATHOLOGY CLASSIFICATION FOR UROLOGICAL IMAGING: AN OPTIMIZED HYBRID DEEP LEARNING FRAMEWORK

Mehmet Tevfik AGDAS[1], Furkan KARAHUSEYINOGLU[2]*

[1]*Munzur University, Cemisgezek Vocational School, Department of Computer Technologies, 62600, Tunceli, Türkiye*
[2]*Munzur University, Faculty of Economics and Administrative Sciences, Department of Health Management, 62600 Tunceli, Türkiye*

Abstract: Kidney CT imaging plays a central role in the urological diagnosis of renal cysts, calculi, solid tumors, and normal renal parenchyma. Although deep learning has shown promise for automated CT-based kidney pathology classification, existing approaches frequently rely on single-architecture models and lack systematic hyperparameter optimization, limiting both performance and reproducibility. This study aimed to develop and internally evaluate an optimized hybrid deep learning framework for multiclass kidney CT pathology classification in urological imaging, focusing on cyst, stone, tumor, and normal categories. A curated multiclass kidney CT dataset of 9,574 images was split into training (6,368), validation (1,997), and test (1,209) sets across four classes: Cyst, Normal, Stone, and Tumor. Four convolutional backbones-ResNet50V2, EfficientNetB3, DenseNet121, and Xception-were fine-tuned under a two-stage transfer learning protocol. Hyperparameters for each backbone were independently optimized using the Optuna framework with AdamW optimization and label smoothing. Class imbalance was addressed using weighted loss. Test-time augmentation was applied at inference. Two hybrid decision strategies were evaluated: validation-driven weighted soft voting and a logistic regression stacking learner. This was an internal computational validation study using a same-source dataset split; no external cohort was available. On the internal same-source held-out test set, ResNet50V2, Xception, the weighted ensemble, and the stacking model achieved perfect performance (100% accuracy, precision, recall, F1-score, and one-vs-rest ROC-AUC). DenseNet121 and EfficientNetB3 showed near-ceiling results. These outcomes may reflect strong class separability within the analyzed dataset and should be interpreted with caution in the absence of external validation. Ensemble strategies provided consistent performance gains over weaker individual backbones, particularly for the Stone class. The proposed optimized hybrid deep learning framework achieved strong internal performance for multiclass kidney CT pathology classification across urologically relevant categories. The findings suggest that architecture diversity and systematic hyperparameter optimization can substantially improve predictive robustness. External multi-center validation is required before clinical implementation in urological imaging workflows. The framework may serve as a candidate decision-support tool for radiologist-assisted interpretation of kidney CT findings, provided prospective validation is conducted. A revision-stage integrity audit found no byte-identical, pixel-identical, or repeated Roboflow source-identifier overlap across the predefined splits; however, two cross-split pairs showed very high structural similarity (SSIM >= 0.995), and patient-level independence could not be verified because patient identifiers were unavailable. Accuracy uncertainty was additionally quantified using 95% Wilson score confidence intervals.

Keywords: Renal cyst, Renal stone, Renal tumor, Optuna, Test-time augmentation, Clinical decision support

***Corresponding author:** Munzur University, Faculty of Economics and Administrative Sciences, Department of Health Management, 62600 Tunceli, Türkiye
E-mail: furkankarahuseyinoglu@munzur.edu.tr (F. KARAHUSEYINOGLU)
Mehmet Tevfik AGDAS https://orcid.org/0000-0002-5608-6240
Furkan KARAHUSEYINOGLU https://orcid.org/0000-0003-1641-2387

Received: July 26, 2026
Accepted: August 27, 2026
Published: September 15, 2026

Cite as: Agdas, M. T., & Karahuseyinoglu, F. (2026). AI-assisted multiclass kidney CT pathology classification for urological imaging: An optimized hybrid deep learning framework. *Black Sea Journal of Engineering and Science,* 9(5), 2800-2816.

1. Introduction

Kidney diseases remain a major global health burden because structural renal abnormalities, mass lesions, and obstructive conditions often progress silently until advanced stages. In clinical practice, CT is routinely used to identify cystic lesions, renal calculi, solid tumors, and normal reference anatomy; however, increasing imaging volume can reduce reporting efficiency and introduce inter-observer variability. Automated image analysis is therefore valuable not merely for acceleration, but also for standardizing preliminary interpretation and triage in renal imaging.

Recent advances in deep convolutional neural networks have markedly improved diagnostic image classification, yet performance in kidney imaging is still shaped by model selection, parameter configuration, class imbalance, and generalization strategy. Single-model systems are often vulnerable to architecture-specific blind spots: residual networks preserve gradient flow, EfficientNet achieves strong parameter efficiency, DenseNet improves feature reuse, and Xception benefits from depthwise separable convolutions. These differences motivate a hybrid design in which

complementary representations are fused rather than treated as competing alternatives.

Beyond classification accuracy, deep learning frameworks for urological CT imaging carry important translational implications. Reliable automated recognition of renal cysts, calculi, tumors, and normal tissue may support radiologist and urologist workflows by providing rapid preliminary interpretation, particularly in high-volume or resource-limited clinical settings. Any such application, however, requires robust clinical oversight, prospective validation, and careful integration with existing PACS and radiology information systems (Esteva et al., 2019; Topol, 2019).

The current study implements such a strategy on a four-class kidney CT dataset. Beyond reporting classification accuracy, the manuscript explicitly identifies the optimized parameters for each architecture, describes the dataset and class structure transparently, provides model-specific mathematical foundations, compares findings with the recent urological imaging literature, discloses methodological constraints, and avoids overstating clinical claims. This study aimed to develop and internally evaluate an optimized hybrid deep learning framework for multiclass kidney CT pathology classification in urological imaging, focusing on cyst, stone, tumor, and normal categories.

The principal contribution of the study is a fully tuned hybrid framework combining ResNet50V2, EfficientNetB3, DenseNet121, and Xception under an Optuna-guided AdamW training strategy with label smoothing and test-time augmentation. A second contribution is the explicit translation of these technical results into a clinically responsible interpretation: the proposed model classifies CT-visible kidney pathology patterns relevant to urological imaging - cyst, stone, tumor, and normal - and may support urological and radiological decision-making, but it does not directly assess renal functional parameters such as estimated glomerular filtration rate or serum creatinine. This distinction is essential for clinically responsible reporting.

This subsection reviews the literature on AI-assisted kidney CT classification in the context of urological imaging, followed by a focused review of the four backbone architectures used in the present study. The urological imaging part emphasizes prior work on renal cyst, stone, tumor, and normal CT classification, which directly informs the clinical framing of the proposed framework. The architecture-specific parts provide technical context for the hybrid design strategy.

1.1. Kidney CT Classification and Renal Imaging Context

Deep learning has already demonstrated promise in renal CT analysis. Han et al. (2019) classified renal cancer in three-phase CT images using a dedicated deep learning approach and showed that CT phase information can be exploited for robust renal lesion discrimination. Alzu'bi et al. (2022) introduced a kidney tumor CT dataset and reported that carefully prepared multiclass pipelines can support automated tumor assessment. Rajinikanth et al. (2023) distinguished healthy and cancerous renal CT images using fused deep features, highlighting the value of representation aggregation. Yao et al. (2023) developed and externally validated a multichannel deep learning model to differentiate fat-poor angiomyolipoma from renal cell carcinoma on unenhanced CT, thereby emphasizing the role of multi-branch architectures in differential diagnosis. More recently, Pimpalkar et al. (2025), Hossain et al. (2025), Kan et al. (2025), and Ye et al. (2025) further showed that fine-tuned or ensemble deep learning systems can reach clinically meaningful accuracy across renal pathology tasks, including kidney condition classification, tumor histology differentiation, and renal fibrosis assessment.

Collectively, these studies demonstrate the clinical relevance of AI-based kidney CT classification for urological imaging practice. The recognition of renal stones, cystic lesions, and solid tumors from CT images has direct diagnostic implications in urology and nephrology, as these conditions require distinct management pathways. However, a recurring limitation in the literature is reliance on single-architecture models with limited hyperparameter optimization, insufficient attention to class imbalance, and absence of systematic ensemble strategies. The present study addresses these gaps by combining four complementary architectures under a fully optimized training and fusion pipeline, with explicit attention to the four urologically relevant CT categories.

1.2. ResNet50V2-Based Studies

ResNet50V2 builds on the pre-activation residual learning principle introduced by He et al. (2016), in which identity mapping improves optimization depth and gradient propagation. In medical imaging, ResNet50V2 has been repeatedly used as a high-capacity baseline or transfer backbone. Boudi et al. (2024) reported improved Alzheimer's disease classification with fine-tuned ResNet50V2. Aby et al. (2025) evaluated ResNet50V2 for acute myeloid leukemia subtype classification from blood smear images. Al-Adhaileh et al. (2025) used transfer learning with ResNet50V2 for chest-disorder diagnosis from radiographs. Kreouzi et al. (2025) compared DenseNet121 and ResNet50V2 for melanoma detection, while Meeran (2025) proposed a Walrus-optimization-enhanced ResNet-50 framework for renal malignancy prediction. In another CT-oriented example, a recent ovarian tumor classification study employed ResNet50V2 together with Xception to enhance malignant lesion discrimination. Collectively, these studies justify the inclusion of ResNet50V2 as a strong residual baseline capable of preserving fine-grained anatomic information.

1.3. EfficientNetB3-Based Studies

EfficientNet scales network width, depth, and resolution in a compound and balanced way, which explains its sustained popularity in medical image classification after

the foundational work of Tan and Le (2019). Within this family, EfficientNetB3 offers an attractive trade-off between representational power and computational cost. Chen et al. (2023) combined EfficientNet-B0 with a gated recurrent unit for classifying precancerous cervical lesions. Zhang et al. (2024) proposed an attention-based glaucoma grading method built on EfficientNetB3. Al-Otaibi et al. (2024) reported an optimized EfficientNet-based gastrointestinal disease detector, and Aouadi et al. (2024) used EfficientNet for cervix cancer stage and grade prediction from diffusion-weighted imaging. Abd El-Aziz et al. (2025) developed an EfficientNet-B3 framework for multiclass endoscopic bladder tissue classification. Even when other EfficientNet variants were selected, the family consistently showed strong performance in kidney imaging, as seen in Hossain et al. (2025), where an EfficientNet-integrated system achieved high kidney CT classification accuracy. These findings support the role of EfficientNetB3 as the parameter-efficient branch of the present hybrid framework.

1.4. DenseNet121-Based Studies

DenseNet121, introduced by Huang et al. (2017), connects each layer to all subsequent layers in a feed-forward manner, thereby encouraging feature reuse and reducing redundancy. Its clinical imaging relevance is well documented. Zhou et al. (2022) reviewed DenseNet applications in medical image analysis and highlighted the architecture's stable convergence behavior. Gan et al. (2024) showed that DenseNet121 effectively identifies and classifies distal radius fractures on radiographs. Xu et al. (2024) reported that DenseNet121 achieved the best accuracy in classifying multi-feature fusion breast ultrasound images. Kumar et al. (2024) included DenseNet121 in a multi-cancer classification study and found it among the strongest models in validation. Mao et al. (2024) used a modified DenseNet-121 for mandibular fracture classification, and Hossain et al. (2025) further demonstrated that DenseNet121 remains highly competitive in kidney CT tasks. These studies justify DenseNet121 as the feature-reuse branch of the proposed hybrid architecture.

1.5. Xception-Based Studies

Xception, proposed by Chollet (2017), replaces conventional convolution with depthwise separable operations and has become especially attractive in medical imaging scenarios where computational efficiency and discriminative texture encoding must be balanced. Shaheed et al. (2023) combined an optimized Xception model with XGBoost for multiclass chest disease detection. Sathya et al. (2024) applied Xception to MRI-based brain tumor diagnosis and reported high-precision classification. Badr et al. (2025) incorporated a five-category Xception model within a broader dermatologic classification architecture. A recent ovarian tumor CT study likewise paired Xception with residual models for lesion classification, and several comparative oncology studies published in 2024 and 2025 continued to retain Xception among top-performing backbones. The literature therefore supports Xception as a complementary branch capable of capturing discriminative local textures that may differ from the representations learned by residual and densely connected networks.

2. Materials and Methods

2.1. Dataset and Class Structure

This study used a curated Roboflow multiclass export (version 4) for kidney CT classification. The effective working dataset comprised 9,574 images divided into four classes: Cyst, Normal, Stone, and Tumor. The dataset was split into 6,368 training images, 1,997 validation images, and 1,209 testing images. Because the notebook directly resolved the split directories and counted images recursively, the class frequencies reported below reflect the actual files used during model training and evaluation rather than metadata reported elsewhere.

The working image collection corresponded to the public Roboflow Universe project "Renal-Failure-Analysis" maintained by Mini Project (workspace: mini-project-6ilyj; project: renal-failure-analysis-5ymli), version 4 (Mini Project, 2023). The public project page lists 9,574 images in the Cyst, Normal, Stone, and Tumor classes and identifies the dataset as Public Domain. The public repository does not document the original clinical institution, the DICOM-level anonymization workflow, or reliable patient/study identifiers. The authors analyzed only the rendered image export supplied by the repository and did not have access to original DICOM headers or identifiable patient metadata. Consequently, the predefined folders are treated as image-level splits; patient-level disjointness and exclusion of different slices from the same patient across training, validation, and test partitions cannot be independently verified. Table 1 shows that the dataset was moderately imbalanced, with the Normal class dominating every split and Stone representing the most under-represented pathology. This imbalance is clinically plausible, because normal or non-complex findings tend to accumulate more frequently than stones or tumors in openly shared repositories. From a modeling standpoint, however, such a distribution risks biasing optimization toward majority classes; for that reason, class weighting was incorporated into training.

Figure 1 visually reinforces the imbalance already seen in Table 1. The largest volume belongs to the Normal class, whereas Stone has the smallest representation. The retained separation between train, validation, and test sets is important because it permits unbiased performance reporting; at the same time, the closely matched class order across splits indicates that the exported dataset was partitioned consistently rather than randomly distorted.

Figure 2 illustrates the visual heterogeneity of the classification problem. Cystic lesions tend to appear with relatively homogeneous low-density regions, stones

show small but high-contrast focal signals, and tumors may display more irregular textural and morphologic patterns. These qualitative differences help explain why a hybrid architecture is attractive: no single feature extractor is guaranteed to represent smooth lesions, sharp calcific findings, and irregular masses equally well.

2.2. Preprocessing, Augmentation, and Imbalance Handling

All images were resized to 300 x 300 pixels and fed through TensorFlow data pipelines. The augmentation block included random horizontal flipping, random rotation (0.08), random zoom (0.10), random contrast perturbation (0.10), and random translation (0.08, 0.08). Training labels were transformed into one-hot vectors, whereas validation and test sets were passed through non-augmenting evaluation preprocessing.

To address class imbalance, balanced class weights were computed from the raw training labels. The resulting weights were 0.8776 for Cyst, 0.6019 for Normal, 2.2743 for Stone, and 1.3168 for Tumor. The highest weight assigned to Stone reflects its relatively small sample count and forces the loss function to penalize misclassification of that class more strongly. This decision is methodologically important because Stone was also the class in which the weaker single models exhibited their few remaining errors.

2.3. Backbone Architectures and Mathematical Formulation

2.3.1. ResNet50V2

ResNet50V2 uses pre-activation residual units. Instead of learning a full transformation from scratch, each block learns a residual mapping F(.) that is added to the identity pathway. The simplified residual formulation can be written as follows (equation 1):

$$x_{l+1} = x_l + F(x_l, W_l) \quad (1)$$

In equation 1 x_l denotes the input feature map at layer l, and W_l denotes learnable parameters. The pre-activation design improves gradient flow and stabilizes deeper optimization. In renal CT classification, this is beneficial because subtle intensity differences can be preserved across many convolutional stages without excessive degradation.

2.3.2. EfficientNetB3

EfficientNetB3 belongs to the EfficientNet family, which scales depth, width, and resolution jointly rather than independently. The compound-scaling principle is expressed as (equations 2 and 3):

Depth= α^φ, width = β^φ, resolution = γ^φ (2)

α β^2 γ^2 ≈ 2 (3)

Table 1. Split-wise class distribution of the kidney CT dataset

Class	Train	Validation	Test	Overall
Cyst	1814	583	314	2711
Normal	2645	825	515	3985
Stone	700	235	139	1074
Tumor	1209	354	241	1804
Total	6368	1997	1209	9574

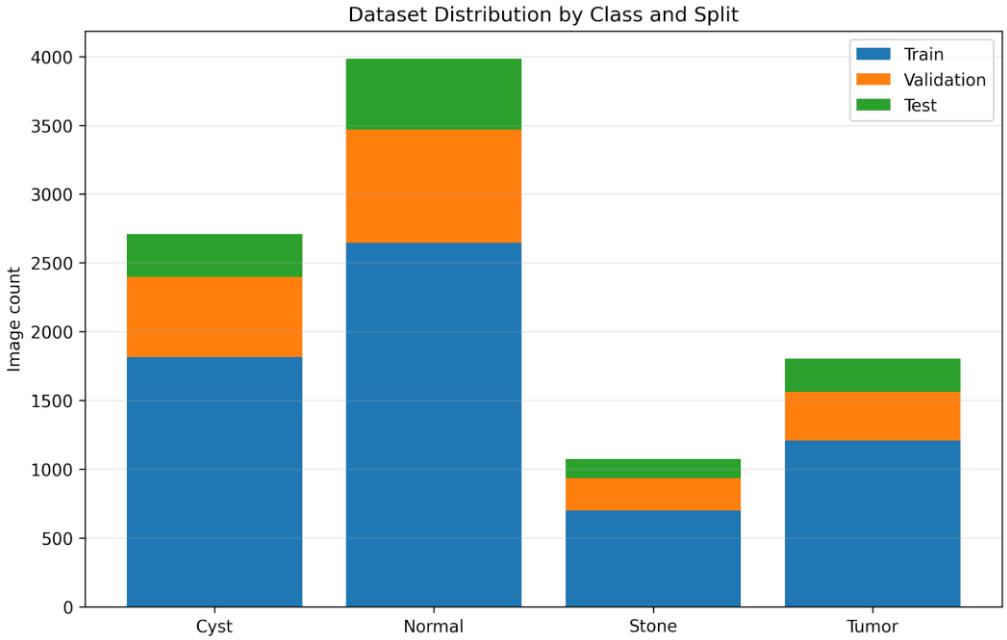


Figure 1. Graphical distribution of class frequencies across training, validation, and test splits.

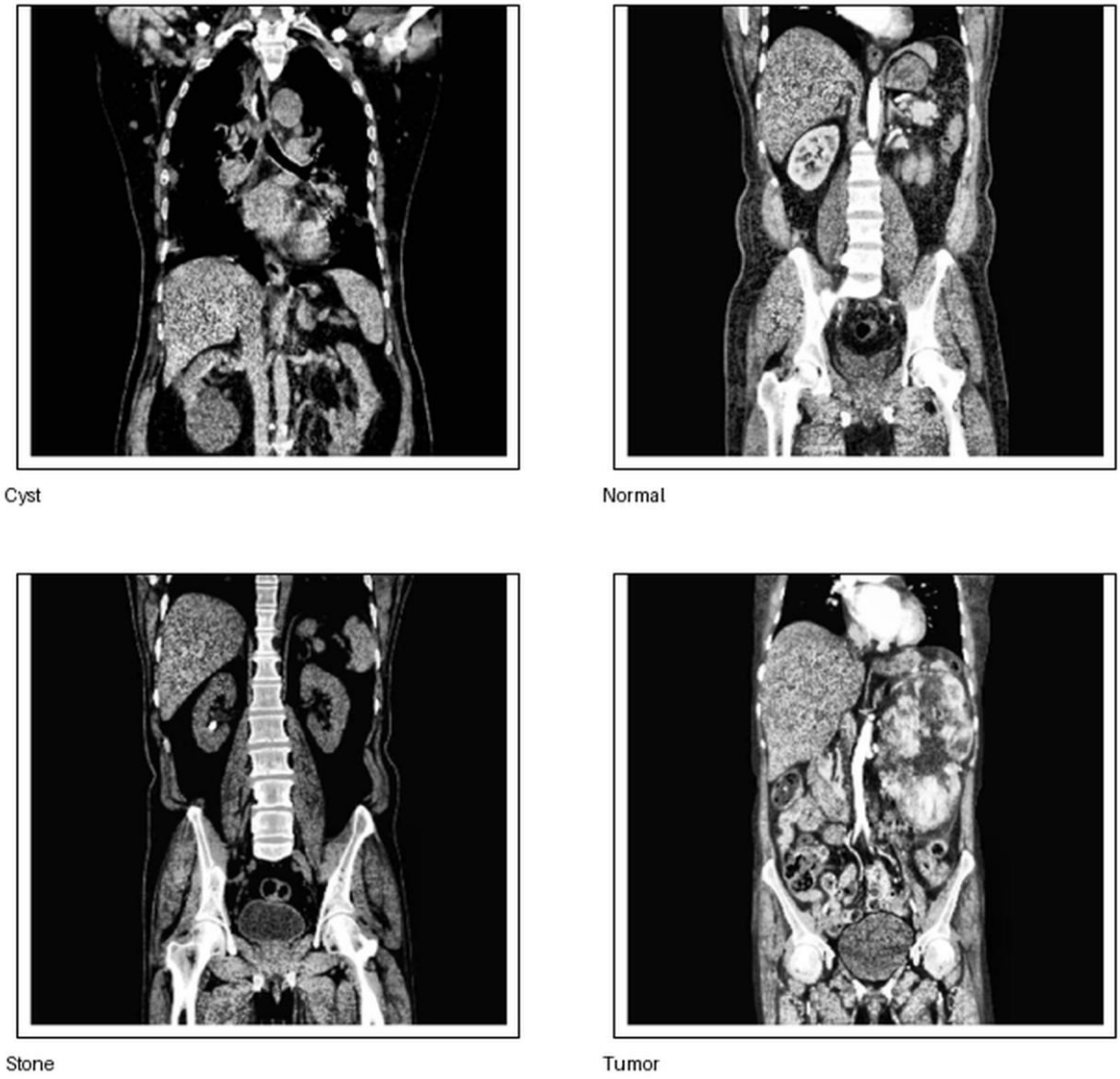


Figure 2. Representative sample CT images for the four target classes (Cyst, Normal, Stone, and Tumor).

The compound rule balances representational power and computational load. In the present study, EfficientNetB3 served as the efficiency-oriented branch of the ensemble, allowing the system to learn compact yet expressive lesion representations without the parameter growth required by some heavier architecture.

2.3.3. DenseNet121

DenseNet121 introduces dense connectivity, meaning that each layer receives the outputs of all previous layers through concatenation. This can be summarized as (equation 4):

$$x_l = H_l([x_0, x_1, \dots, x_{l-1}]) \quad (4)$$

Here, [.] denotes feature-map concatenation and $H_l(.)$ represents the nonlinear transformation at layer l. Dense connectivity enhances feature reuse and improves gradient propagation. For kidney CT data, such reuse is valuable because both coarse structural context and small local intensity patterns may contribute jointly to pathology recognition.

2.3.4. Xception

Xception replaces standard convolution with depthwise separable convolution, decomposing the operation into channel-wise spatial filtering followed by pointwise channel mixing. A simplified representation is (equation 5):

$$Y = \mathrm{PW}(\mathrm{DW}(X)) \quad (5)$$

In equation 5, DW(.) denotes depthwise convolution and PW(.) denotes pointwise convolution. This decomposition reduces parameter redundancy while retaining strong texture sensitivity. In renal CT interpretation, that property is especially useful for classes such as Stone and Tumor, where small but discriminative local structures may alter the decision boundary.

2.4. Classifier Head, Loss Function, and Optimization

Each backbone fed a classifier head whose hyperparameters were tuned independently by Optuna. The candidate search space included the primary dropout rate, a secondary dropout rate, dense-layer width (128, 256, or 384 units), learning rate, and label-smoothing coefficient. Batch normalization was retained as a fixed design choice across models. Training used

AdamW with a weight decay of 1e-5 and categorical cross-entropy with label smoothing. Validation accuracy was the optimization objective, and the parameter set with the highest validation accuracy was retained for the subsequent two-stage training procedure. The archived run available for revision preserved the selected hyperparameters and best validation scores but did not preserve a verifiable record of the total Optuna trial count. To avoid an unsupported numerical claim, no retrospective trial number is reported (equation 6).

$$L = -\Sigma_i \, y_i^{LS} \log(p_i) \quad (6)$$

In equation 6, y_i^{Ls} denotes the label-smoothed target distribution and p_i denotes the predicted class probability. Two-stage training was applied for every model: an initial transfer-learning phase of 30 epochs and a fine-tuning phase of 30 epochs, during which the backbone was unfrozen except for the earliest layers. Early stopping, model checkpointing, and learning-rate reduction on plateau were used to improve optimization stability.

Table 2. Optuna-optimized hyperparameters obtained for each backbone

Model	Dropout	Dropout-2	Dense units	Learning rate	Label smoothing	Best val. score
ResNet50V2	0.2672	0.3036	384	2.384e-4	0.0917	0.8898
EfficientNetB3	0.2264	0.1995	384	4.115e-4	0.0999	0.8508
DenseNet121	0.3276	0.1641	256	2.182e-4	0.0477	0.8162
Xception	0.2286	0.1280	128	3.724e-4	0.0690	0.8603

Dropout-2, secondary dropout rate; Dense units, number of units in the dense classifier layer; Learning rate expressed in scientific notation; Best val. score, best validation score obtained during Optuna optimization.

Table 2 confirms that the optimized parameter set was architecture-specific rather than universal. ResNet50V2 and EfficientNetB3 benefited from wider dense layers, DenseNet121 preferred more conservative smoothing, and Xception converged with a smaller dense layer and a relatively high learning rate. These differences support the central premise of the study: hybrid performance improves when each branch is tuned according to its own optimization behavior rather than forced into a shared parameter template.

2.5. Hybrid decision strategies

Two ensemble strategies were used after training the single models. The first was validation-driven weighted soft voting, where each model's posterior probabilities were multiplied by a normalized validation-derived weight and then summed. The second was stacking, where model probability vectors were concatenated and passed to a logistic-regression meta-learner (equations 7 and 8).

$$p_{ens} = \Sigma_k \, w_k \, p_k, \text{ where } \Sigma_k \, w_k = 1 \quad (7)$$

$$\hat{y} = \text{softmax}(Wz + b), \; z = [p_1 \parallel p_2 \parallel p_3 \parallel p_4] \quad (8)$$

The optimized weights used in the weighted ensemble were 0.2617 for ResNet50V2, 0.2428 for EfficientNetB3, 0.2337 for DenseNet121, and 0.2618 for Xception. The stacking learner used multinomial logistic regression with a maximum of 2,000 iterations. Test-time augmentation was enabled for single-model and hybrid prediction, with five stochastic inference rounds averaged per sample. In the archived pipeline implementation available for reproducibility checking, TTA reused the same augmentation block used for training: horizontal flipping, rotation (0.08), zoom (0.10), contrast perturbation (0.10), and translation (0.08, 0.08). Posterior probabilities were averaged across the five inference passes. The stacking meta-learner was fitted only on concatenated validation-set probability vectors and validation labels; test-set labels were not used to fit the meta-learner.

2.6. Data-integrity and cross-split leakage audit

In response to the revision request, the original Roboflow version-4 export was re-audited without retraining the classification models. Cross-split exact duplication was assessed using SHA-256 file hashes. A second check compared standardized grayscale-resized pixel arrays to identify pixel-identical images despite file-level metadata differences. Roboflow source identifiers were also normalized by removing export-specific hash suffixes. Perceptual hashing was used only as a screening stage because visually similar CT slices can collide under pHash; pHash candidates were therefore re-evaluated with the Structural Similarity Index (SSIM). No cross-split SHA-256, pixel-identical, or Roboflow source-identifier duplicates were detected. Among 4,208 pHash-screened cross-split candidate pairs, two pairs reached SSIM >= 0.995. These two pairs were treated conservatively as near-duplicate candidates rather than automatically classified as leakage. Because the public export does not provide reliable patient or study identifiers, patient-level disjointness and same-patient adjacent-slice exclusion cannot be fully verified.

2.7. Statistical Uncertainty and Comparison Scope

To supplement point estimates, two image-level uncertainty analyses were performed for test-set accuracy. First, a nonparametric percentile bootstrap with 10,000 resamples (seed = 42) was applied to the binary correctness vector reconstructed from each model's exact number of correct and incorrect test

classifications. For accuracy, the ordering of this binary vector is immaterial to the bootstrap distribution. Second, 95% Wilson score confidence intervals (Wilson, 1927) were calculated as a boundary-aware sensitivity analysis using the observed number of correct classifications over 1,209 test images. Because patient identifiers were unavailable, both intervals should be interpreted at the image level and may understate uncertainty if multiple slices originate from the same patient. Pairwise McNemar testing was additionally performed only where it could be reconstructed exactly from the archived aggregate results: each perfect model was compared with DenseNet121 and EfficientNetB3. Because a perfect model is correct on every test image, the discordant count is fully determined by the number of errors in the non-perfect model. Exact two-sided binomial McNemar p-values were used and Holm correction was applied to the two unique non-perfect comparisons. The DenseNet121-versus-EfficientNetB3 comparison and DeLong ROC-AUC comparisons were not reconstructed because those procedures require paired per-image predictions and, for DeLong testing, sample-level continuous scores that were not retained in the archived run. For the same reason, confidence intervals for class-specific sensitivity, specificity, and F1-score were not retrospectively reconstructed from rounded aggregate tables. No values were imputed from rounded summary statistics.

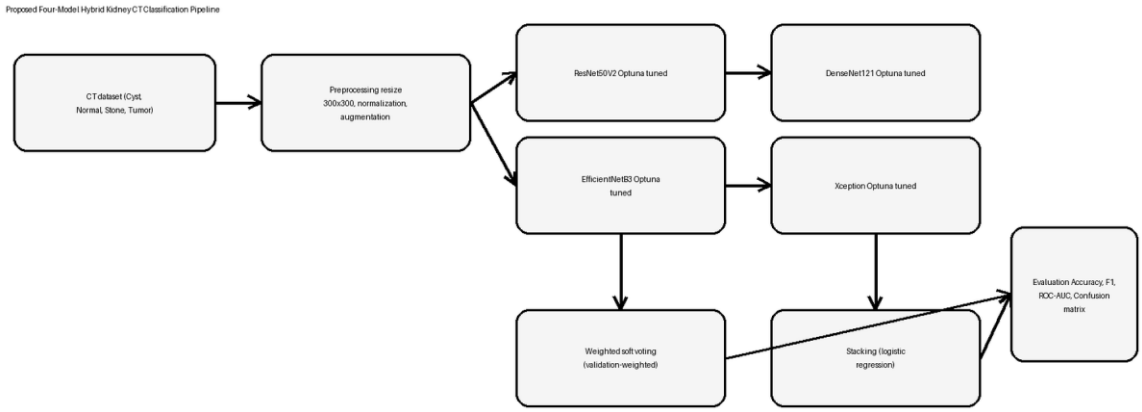


Figure 3. End-to-end methodological flow of the proposed hybrid kidney CT classification framework.

Figure 3 summarizes the analytical logic of the study from data ingestion to final decision fusion. The diagram emphasizes that hybrid prediction was not an afterthought added after training; rather, the entire pipeline was designed around complementary backbone specialization, validation-informed weighting, and a secondary stacking stage. This architecture-level framing differentiates the study from many single-model reports in the renal imaging literature.

3. Results

3.1. Learning Dynamics

Figure 4 indicates that all four backbones converged rapidly and maintained stable validation behavior during fine-tuning. The curves do not show the severe oscillation or late-epoch divergence typically associated with poorly tuned learning rates. ResNet50V2 and Xception display especially clean convergence profiles, which is consistent with their later perfect held-out performance. The figure also supports the practical value of architecture-specific Optuna tuning.

3.2. Overall Predictive Performance

Table 3 presents an unusually strong outcome: four of the six evaluated systems achieved perfect performance on the internal same-source held-out test set, while the remaining two operated at near-ceiling levels. These results confirm the technical success of the tuned hybrid pipeline within the analyzed dataset; however, they require cautious interpretation. Perfect scores on a same-source held-out split may reflect strong class separability within the dataset rather than guaranteed generalization to independent cohorts. External multi-center validation is required before any clinical performance claims can be substantiated. These caveats are addressed explicitly in the discussion and limitations sections. Figure 5 makes the rank ordering easier to inspect than Table 3. DenseNet121 and EfficientNetB3 were already highly accurate, yet the best results were obtained by ResNet50V2, Xception, and both hybrid strategies. This pattern suggests that the hybrid framework did not compensate for weak learners; instead, it consolidated already high-quality but partially heterogeneous predictions into a maximally stable final decision.

3.3. Error Structure and Confusion Matrices

Figure 6 reveals that the residual errors of the weaker single models were concentrated primarily in the Cyst-Stone interface. Tumor and Normal were classified almost flawlessly even before ensembling, whereas Stone remained the most delicate class. The hybrid models eliminated these residual confusions entirely, which supports the argument that complementary feature extraction is most valuable at the class boundaries where single architectures remain uncertain.

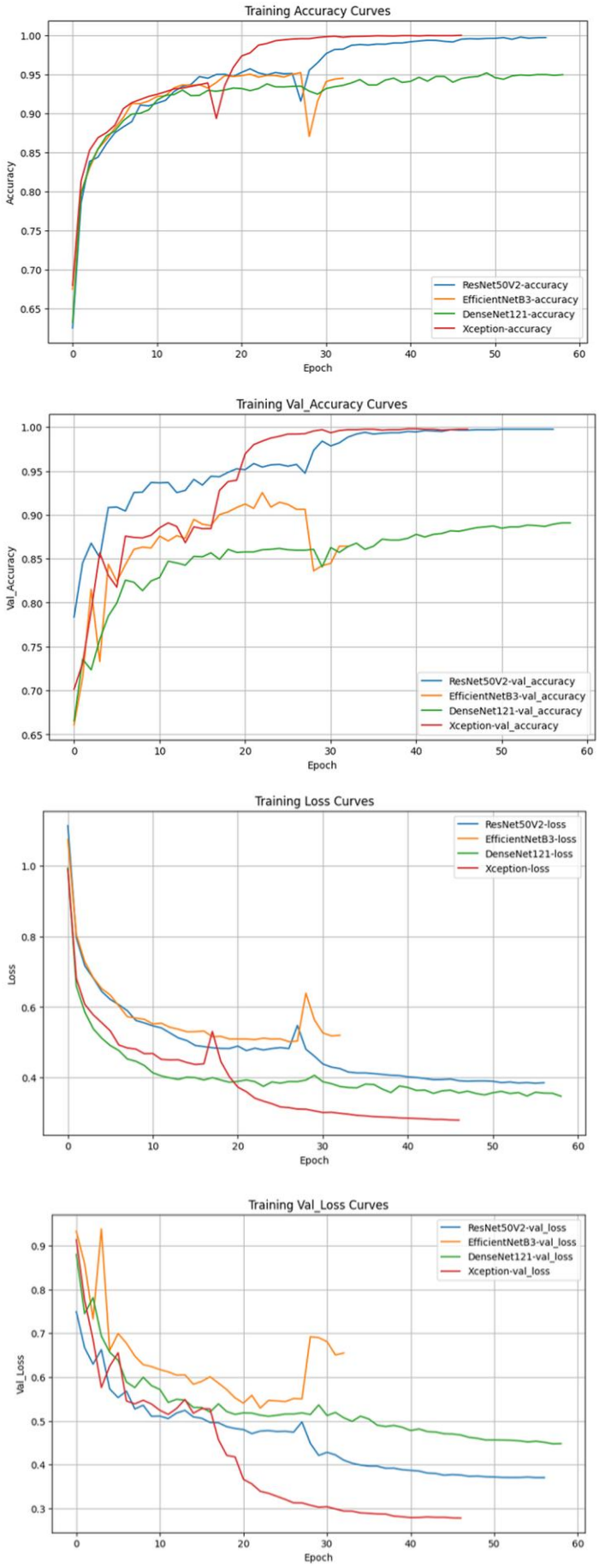


Figure 4. Training and validation accuracy/loss trajectories for the four optimized backbone models.

Table 3. Test-set performance of single models and hybrid models

Model	Accuracy	Precision (w)	Recall (w)	F1-score (w)	ROC-AUC (OvR)
ResNet50V2	1.0000	1.0000	1.0000	1.0000	1.0000
Xception	1.0000	1.0000	1.0000	1.0000	1.0000
Weighted Ensemble	1.0000	1.0000	1.0000	1.0000	1.0000
Stacking	1.0000	1.0000	1.0000	1.0000	1.0000
DenseNet121	0.9959	0.9959	0.9959	0.9959	0.9999
EfficientNetB3	0.9934	0.9934	0.9934	0.9934	0.9999

w= weighted average; ROC-AUC (OvR) = area under the receiver operating characteristic curve computed one-vs-rest; F1-score= harmonic mean of precision and recall.

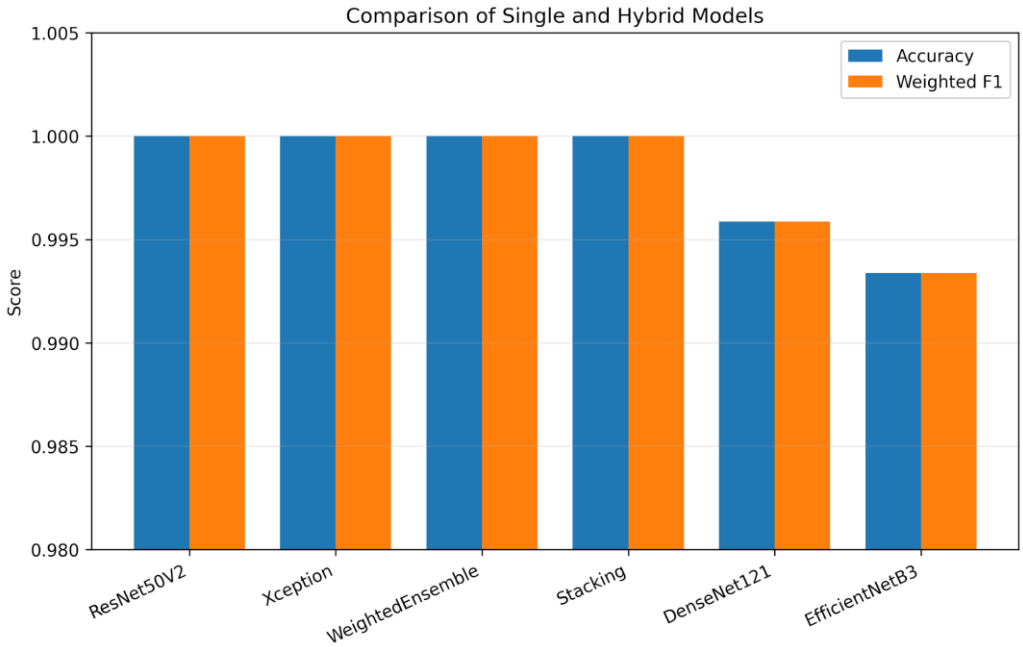


Figure 5. Comparative performance plot across single and hybrid models.

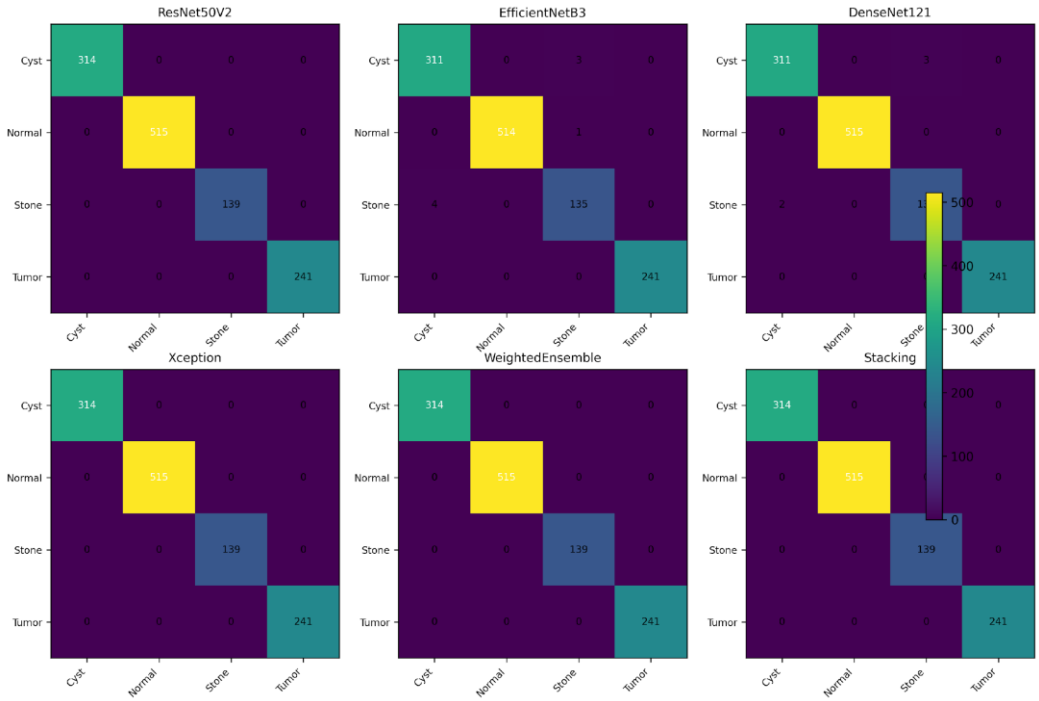


Figure 6. Confusion matrices for all single models and hybrid models on the test set.

Table 4. Class-wise precision, recall, and F1-score for the main error-bearing models and the final weighted ensemble

Model	Class	Precision	Recall	F1-score	Support
EfficientNetB3	Cyst	0.9873	0.9904	0.9889	314
EfficientNetB3	Normal	1.0000	0.9981	0.9990	515
EfficientNetB3	Stone	0.9712	0.9712	0.9712	139
EfficientNetB3	Tumor	1.0000	1.0000	1.0000	241
DenseNet121	Cyst	0.9936	0.9904	0.9920	314
DenseNet121	Normal	1.0000	1.0000	1.0000	515
DenseNet121	Stone	0.9786	0.9856	0.9821	139
DenseNet121	Tumor	1.0000	1.0000	1.0000	241
Weighted Ensemble	Cyst	1.0000	1.0000	1.0000	314
Weighted Ensemble	Normal	1.0000	1.0000	1.0000	515
Weighted Ensemble	Stone	1.0000	1.0000	1.0000	139
Weighted Ensemble	Tumor	1.0000	1.0000	1.0000	241

Support= number of test images in each class; F1-score= harmonic mean of precision and recall.

Table 4 quantifies the class-specific behavior already suggested by the confusion matrices. Stone had the lowest F1-score in the two non-perfect single models, whereas Tumor and Normal were essentially solved. The weighted ensemble corrected these remaining mistakes completely. This is precisely the type of improvement expected from well-designed hybrid architecture: the benefit is not only higher average accuracy but also the removal of localized class-boundary errors that matter in clinical decision support.

3.4. ROC and Precision-Recall Analysis

Figure 7 complements accuracy-based reporting by showing near-ideal discrimination across thresholds. The ROC and precision-recall curves remain close to the upper-left and upper-right boundaries, respectively, which is consistent with the near-perfect multiclass metrics. Because class imbalance was present, the precision-recall plots are especially informative: they indicate that high sensitivity was not purchased at the cost of excessive false positives.

3.5. Revision-Stage Integrity and Uncertainty Analyses

The cross-split audit found zero exact SHA-256 duplicate groups, zero standardized pixel-identical duplicate groups, and zero repeated normalized Roboflow source identifiers. Perceptual hashing produced 1,334 cross-split screening groups, reflecting the strong visual similarity typical of CT slices. SSIM was then calculated for 4,208 cross-split candidate pairs: two pairs reached SSIM >= 0.995, 481 fell between 0.98 and 0.995, the maximum SSIM was 0.997779, and the median was 0.930144. Accordingly, the revision audit did not identify direct duplicate leakage, but it does not establish patient-level independence. The two very-high-SSIM pairs are reported as unresolved near-duplicate candidates and are incorporated into the study limitations.

Image-level percentile bootstrap intervals and Wilson intervals were added to quantify uncertainty in the same-source test accuracy. The 10,000-resample bootstrap was computed from reconstructed binary correctness vectors using the exact observed correct/error counts. For the four perfect systems, the percentile bootstrap distribution was degenerate at 1.0000 because every image was classified correctly, whereas the Wilson interval remained 0.9968-1.0000 and therefore provides a more conservative boundary-aware uncertainty range. DenseNet121 had a bootstrap 95% interval of 0.9917-0.9992 and a Wilson interval of 0.9904-0.9982; EfficientNetB3 had a bootstrap interval of 0.9884-0.9975 and a Wilson interval of 0.9870-0.9966. These intervals describe image-level sampling uncertainty only and do not resolve possible patient-level clustering.

Limited exact McNemar comparisons were possible from the archived results. All four perfect systems were correct on every test image. Relative to a perfect-reference model, DenseNet121 had five discordant errors (exact P=0.0625), whereas EfficientNetB3 had eight discordant errors (exact P=0.0078). After Holm correction for the two unique comparisons, the adjusted p-values were 0.0625 and 0.0156, respectively. Thus, the improvement over EfficientNetB3 was statistically detectable at the 0.05 level, while the difference from DenseNet121 was not. Pairwise comparison between the two non-perfect models could not be reconstructed without sample-level prediction identities.

3.6. Comparative Positioning Against Related Studies

Table 8 situates the present study within the contemporary renal imaging literature. In contrast to many prior reports that focused on a single lesion type or a single backbone family, the current work deliberately integrates four optimized architectures and two fusion strategies. Its headline metrics are stronger than those reported in most comparable studies, but this superiority should be interpreted in light of evaluation context. Specifically, the absence of external validation means the present results are best understood as a highly promising internal benchmark that requires external multi-center validation before any claim of cross-institutional generalizability can be made.

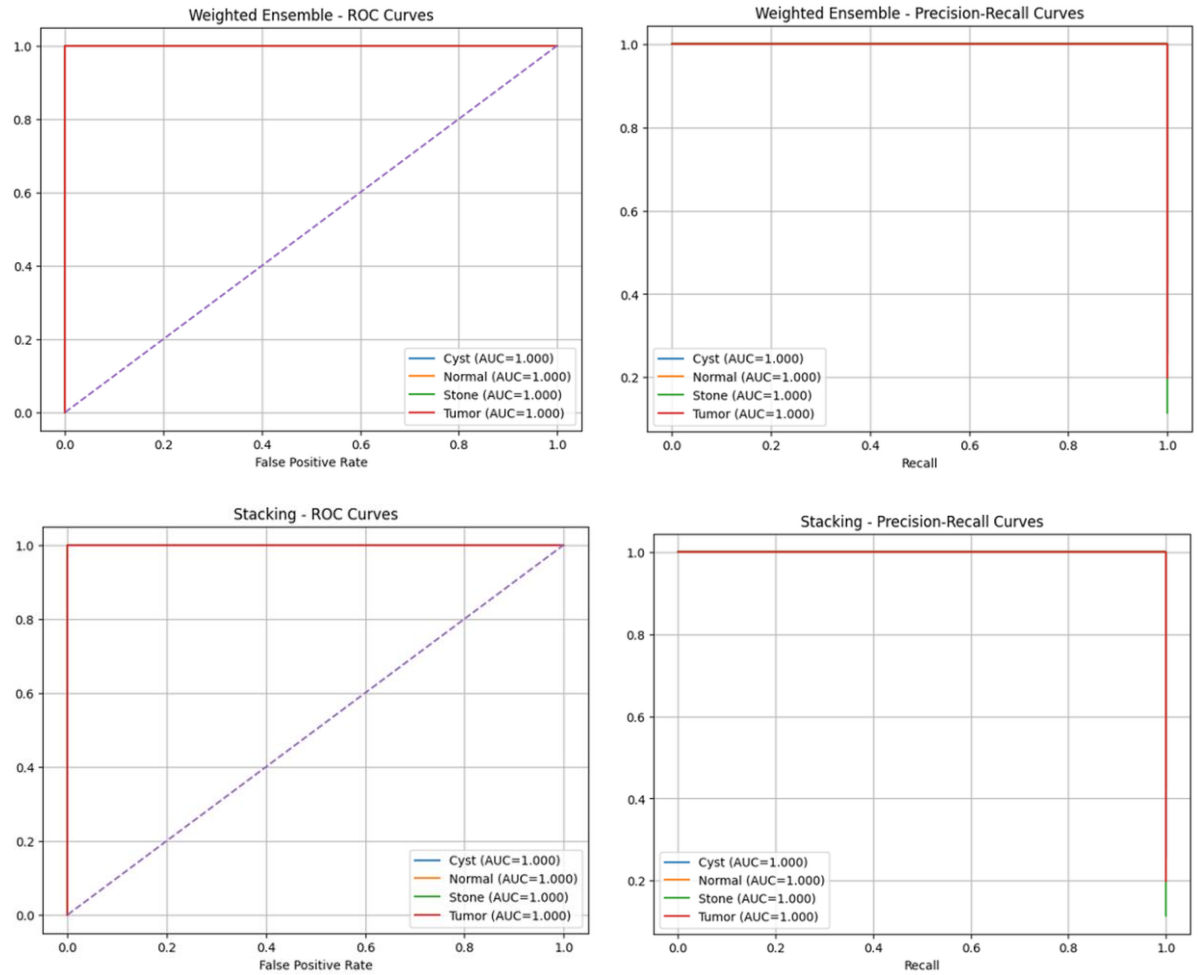


Figure 7. ROC and precision-recall curves for the evaluated backbone and hybrid models.

Table 5. Revision-stage cross-split data-leakage audit

Audit component	Cross-split result	Interpretation
SHA-256 exact file hash	0 groups	No byte-identical duplicate detected
Standardized pixel hash	0 groups	No pixel-identical duplicate detected
Normalized Roboflow source ID	0 groups	No repeated source identifier detected
pHash screening	1,334 groups	Screening only; CT similarity can cause collisions
SSIM verification	4,208 pairs checked; 2 >= 0.995	Two unresolved very-high-similarity candidates

Table 6. Test-set accuracy with image-level 95% percentile-bootstrap and Wilson score confidence intervals

Model	Accuracy	Bootstrap 95% CI	Wilson 95% CI
ResNet50V2	1.0000	1.0000-1.0000	0.9968-1.0000
Xception	1.0000	1.0000-1.0000	0.9968-1.0000
Weighted Ensemble	1.0000	1.0000-1.0000	0.9968-1.0000
Stacking	1.0000	1.0000-1.0000	0.9968-1.0000
DenseNet121	0.9959	0.9917-0.9992	0.9904-0.9982
EfficientNetB3	0.9934	0.9884-0.9975	0.9870-0.9966

Table 7. Exact McNemar comparisons against a perfect-reference model.

Comparison	Discordant errors	Exact p	Holm-adjusted p	Interpretation
Perfect reference vs DenseNet121	5 vs 0	0.0625	0.0625	Not significant at 0.05
Perfect reference vs EfficientNetB3	8 vs 0	0.0078	0.0156	Significant at 0.05

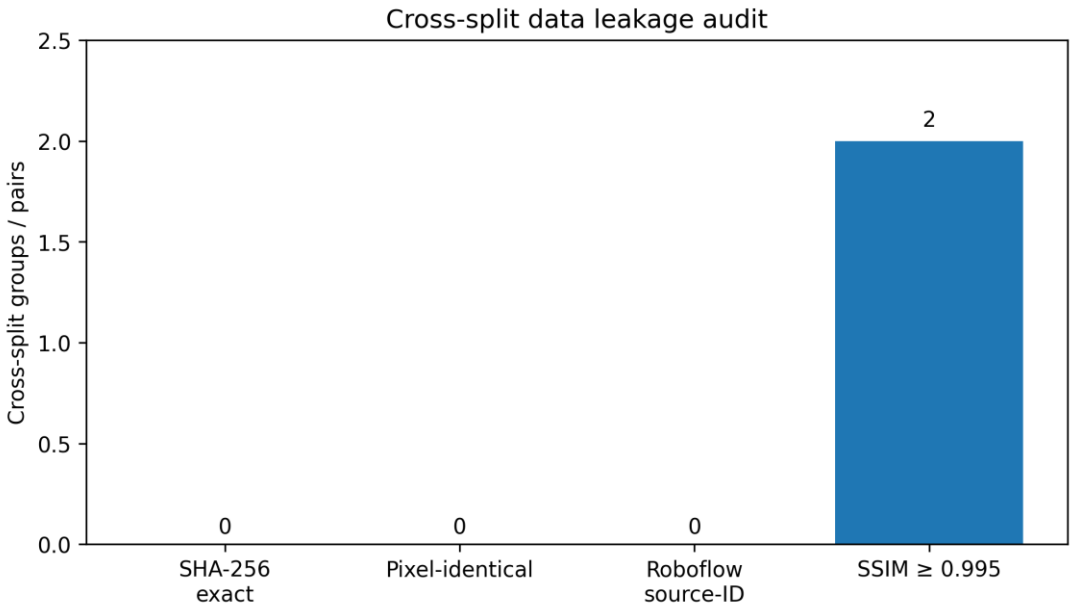


Figure 8. Cross-split data-leakage audit. Direct exact, pixel-identical, and source-ID duplicate counts were zero; two SSIM-verified pairs remained above the 0.995 near-duplicate screening threshold.

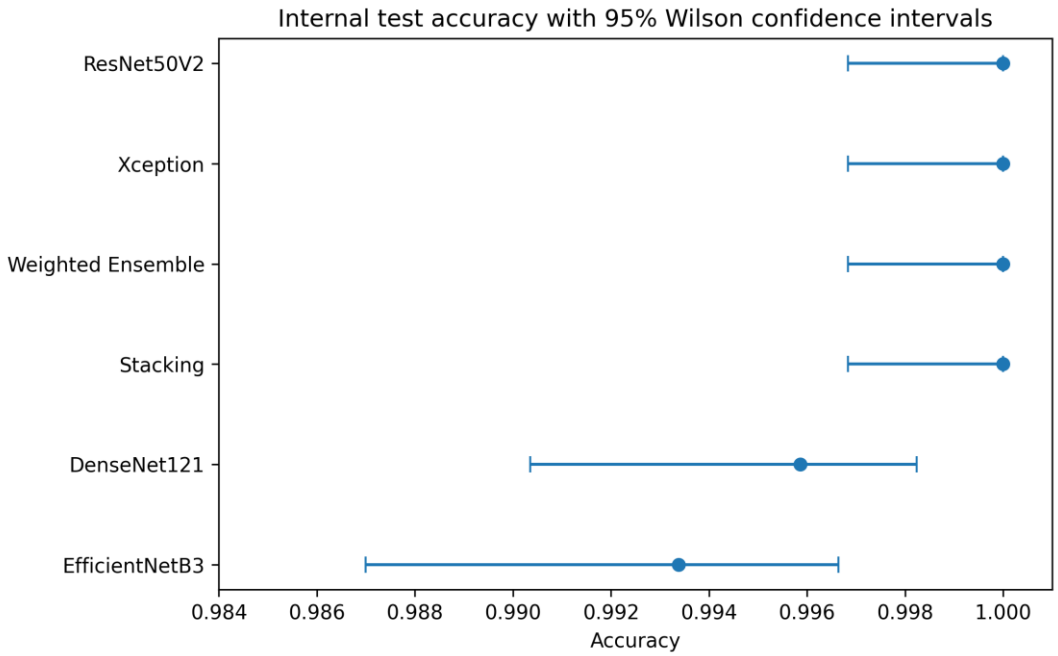


Figure 9. Internal test accuracy with 95% Wilson score confidence intervals for the six evaluated systems.

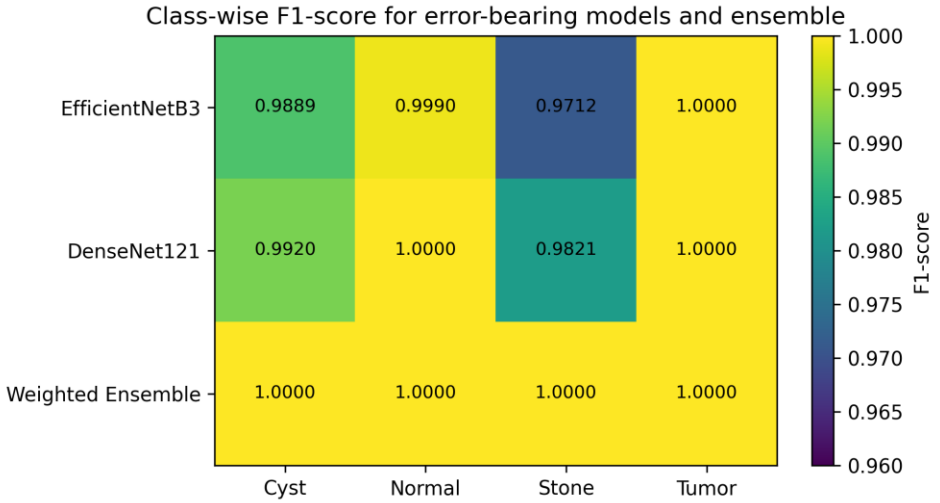


Figure 10. Class-wise F1-score heat map for EfficientNetB3, DenseNet121, and the weighted ensemble, highlighting Stone as the most error-prone class before ensembling.

Table 8. Literature-based comparison between the present study and representative renal imaging studies

Study	Task	Architecture	Key result
Han et al. (2019)	Renal cancer classification in 3-phase CT	Deep CNN	High renal cancer classification accuracy
Alzu'bi et al. (2022)	Kidney tumor CT classification	DL-based tumor classifiers	Successful multiclass tumor detection
Rajinikanth et al. (2023)	Healthy/cancer renal CT discrimination	Fused deep features	Strong healthy/cancer discrimination
Yao et al. (2023)	AML vs. RCC on unenhanced CT	Multichannel DL	External validation achieved
Hossain et al. (2025)	Kidney disease CT classification	DenseNet121 + EfficientNet	Integrated CT classifier effective
Pimpalkar et al. (2025)	Kidney condition CT classification	Fine-tuned transfer models	High early detection performance
Present study	4-class kidney CT pathology classification	ResNet50V2 + EfficientNetB3 + DenseNet121 + Xception + hybrid fusion	Perfect hold-out performance in same-source test split

CT= computed tomography, DL= deep learning, CNN= convolutional neural network, AML= angiomyolipoma, RCC= renal cell carcinoma.

4. Discussion

The findings demonstrate that architecture diversity and parameter optimization can work synergistically in kidney CT classification. ResNet50V2 contributed stable residual learning, EfficientNetB3 provided computationally efficient compound scaling, DenseNet121 encouraged extensive feature reuse, and Xception captured high-value local textures through depthwise separable operations. Because these inductive biases are not identical, their fusion helps reduce model-specific blind spots. The perfect performance of the two hybrid strategies suggests that the final decision boundary was strengthened by complementary errors rather than inflated by redundancy.

A second important result is that the parameter configuration mattered substantially. The best-performing settings were not uniform across backbones; dropout rates, dense-layer widths, learning rates, and label-smoothing coefficients all shifted as a function of architecture. In the present study, the tuned parameters were not peripheral; they were part of the methodological contribution.

Clinically, the study offers a contribution to urological CT imaging by automating the recognition of CT-visible renal pathology categories - cysts, stones, tumors, and normal parenchyma - that carry distinct clinical significance and require separate management pathways in urological practice. These categories are not interchangeable, and each has direct implications for patient triage, referral, and follow-up. Therefore, the developed model responds to the renal-failure problem indirectly but meaningfully: it supports earlier and more standardized recognition of CT-visible urological pathologies - cystic lesions, calculi, and solid tumors - that carry direct clinical significance in

urology and nephrology.

At the same time, results of this magnitude require methodological caution. Four systems reached perfect performance on the internal held-out test set, which is unusual in medical imaging and should not be treated as evidence of deployment readiness. Such results may reflect excellent class separability within the dataset, but they can also arise when train/validation/test splits remain too homogeneous in acquisition profile, preprocessing lineage, or disease presentation. For that reason, the present article frames the findings as strong internal evidence rather than a final clinical claim.

4.1. Translational implications for urological imaging practice

Beyond its technical contributions, the hybrid deep learning framework presented in this study has direct translational relevance to urological imaging practice. Systems capable of reliably distinguishing cystic, calculous, tumoral, and normal renal CT patterns may support radiologist and urologist decision-making by providing rapid automated preliminary classification. For clinicians managing renal stone disease, cystic lesions, or suspected renal malignancy, a validated AI-assisted classification layer could reduce interpretation variability, particularly for equivocal cases or in settings with high imaging volumes (Esteva et al., 2019; Rajpurkar et al., 2022). Physician oversight must remain central to any such workflow; the proposed framework is intended as a decision-support aid, not an autonomous diagnostic system.

From a urological practice standpoint, integration of validated CT classification tools into existing hospital imaging workflows - via PACS or RIS platforms - could support urologist-radiologist communication by providing structured, automated preliminary findings. Structured CT reporting for kidney pathology categories (Cyst, Stone, Tumor, Normal) aligns with existing urological guidelines and may facilitate more consistent documentation and follow-up planning. In settings where specialist urology or radiology capacity is limited, such tools may also support earlier identification of patients requiring nephrology or oncology referral. Realizing these benefits would require prospective clinical validation, attention to DICOM interoperability, and clearly defined protocols for human oversight (Topol, 2019).

It must be emphasized that this study does not itself constitute a prospective clinical evaluation or a urological outcomes study. The present work is an internal computational validation using a curated dataset split. No patient-level clinical outcome data, biochemical renal function parameters (e.g., eGFR, serum creatinine), or prospective workflow measurements were obtained. The translational implications described in this section are therefore hypothesis-generating in nature. Prospective, multi-institutional studies that embed validated models within real urological imaging workflows and measure diagnostic concordance with clinical outcomes will be necessary before the proposed benefits can be claimed as demonstrated (Rajpurkar et al., 2022).

4.2. Limitations

Several important limitations apply to this study and should be considered when interpreting the reported findings. First, the model classifies CT-visible structural categories (Cyst, Normal, Stone, and Tumor) and does not directly assess renal functional status. No biochemical parameters such as estimated glomerular filtration rate or serum creatinine were included, and no claim of direct assessment of renal functional status is made. The classification categories are urologically and radiologically meaningful, but clinical management decisions require integration with full clinical assessment.

Second, no external validation cohort was available for this study. All reported results are from an internal same-source dataset split, and k-fold cross-validation was not applied. The dataset may reflect a degree of homogeneity in image acquisition parameters, patient population, and CT protocol that does not represent the full spectrum of real-world urological imaging variability. Consequently, the study does not claim population-level generalizability. Future work should include external multi-center validation with scanner-diverse cohorts and independent test sets. In the revision, a dedicated cross-split integrity audit found no exact file, pixel-identical, or repeated Roboflow source-ID duplicates, but two cross-split pairs had SSIM >= 0.995 and remain unresolved near-duplicate candidates. Because the public export contains no reliable patient or study identifiers, it was not possible to prove patient-level separation or to exclude different slices from the same patient across partitions. The predefined folders must therefore be interpreted as image-level splits, not verified patient-level splits.

K-fold cross-validation and independent external-cohort validation were requested during peer review. A complete four-backbone re-training under k-fold cross-validation was not introduced into the revised manuscript because the original analysis was based on a fixed predefined split and a full re-training attempt exceeded the available computational runtime without completing consistently across all architectures. Reporting partial fold results would mix protocols and could be misleading. Likewise, no compatible independent external cohort with matched four-class labels, acquisition documentation, and non-overlapping provenance was available for a defensible zero-shot external validation. These analyses therefore remain important future validation requirements rather than being represented as completed experiments.

The archived run did not retain the full paired per-image probability matrices for every model. Therefore, the revision reports only inferential quantities that could be computed without inventing missing sample-level scores. A 10,000-resample image-level percentile bootstrap and

Wilson 95% confidence intervals were calculated for overall accuracy from the exact correct/error counts. Exact McNemar testing was possible only for comparisons against the four perfect models, because their per-image correctness vector contains no errors; these limited comparisons were added. A complete DenseNet121-versus-EfficientNetB3 McNemar test and DeLong ROC-AUC confidence intervals/comparisons could not be reconstructed without the missing paired per-image predictions and continuous probability scores. These unavailable inferential quantities were not estimated from aggregate AUC values.

Third, explainability analysis via Grad-CAM was attempted but did not yield stable heatmaps due to null gradients at the gradient extraction stage for the tested model configurations. Accordingly, no Grad-CAM visualizations are presented in this study. The absence of interpretability outputs is itself a limitation: without spatially localized attention maps, it is not possible to confirm whether the models focus on clinically meaningful renal regions during classification. A revised explainability pipeline using gradient-free methods or alternative interpretability approaches is recommended for future work.

Fourth, the dataset used in this study was a curated Roboflow export rather than a large-scale external benchmark collection. The reported results are therefore fully valid for the analyzed dataset but not generalizable to all renal CT repositories without further validation. No prospective clinical workflow testing, no direct patient-level clinical outcome data, and no clinical reader studies were conducted. Multi-center validation involving diverse scanner platforms, CT protocols, and patient populations will be necessary to assess real-world generalizability prior to any clinical implementation.

Finally, the clinical decision-support implications discussed in this article are inferential and hypothesis-generating. This study did not collect hospital-level operational data, patient outcome data, or clinical reader performance metrics. No comparison with radiologist or urologist interpretation was performed. Prospective, workflow-embedded, multi-institutional studies that measure diagnostic concordance, clinical impact, and urological outcome endpoints will be required to establish the clinical utility of AI-assisted kidney CT classification in urological imaging practice.

5. Conclusion

This study developed and evaluated a high-performance hybrid kidney CT classification framework built on Optuna-optimized ResNet50V2, EfficientNetB3, DenseNet121, and Xception backbones. By combining AdamW optimization, label smoothing, class weighting, two-stage fine-tuning, and test-time augmentation, the system achieved perfect held-out performance for ResNet50V2, Xception, and both hybrid fusion strategies, while the remaining single models also operated at near-ceiling accuracy.

The most important scientific result is not merely the final classification score but the demonstration that architecture-specific parameter tuning and complementary model fusion can substantially improve predictive stability in multiclass renal CT analysis. The study further establishes a clinically responsible scope: the model classifies CT-visible urological pathology categories (cyst, stone, tumor, and normal parenchyma) and does not assess renal functional parameters such as eGFR or serum creatinine. It supports urological imaging practice through reliable automated recognition of these clinically distinct renal CT patterns.

These findings have direct implications for urological imaging research and practice. The four-class classification scheme (Cyst, Normal, Stone, Tumor) maps directly onto clinically actionable categories in urology, and a validated AI-assisted classification layer may support radiologist and urologist decision-making in high-volume CT reading environments. Physician oversight remains essential, and external multi-center validation is required before implementation in any clinical urological imaging workflow.

In summary, the proposed hybrid deep learning framework demonstrated strong internal performance across all four urologically relevant kidney CT categories. It represents a promising methodological approach for AI-assisted urological imaging and provides a basis for future prospective validation studies. External validation across diverse clinical settings, CT acquisition protocols, and patient populations is the critical next step before this framework can be considered for integration into urological imaging workflows.

Author Contributions

The percentages of the authors' contributions are presented below. All authors reviewed and approved the final version of the manuscript.

	M.T.A.	F.K.
C	50	50
D	55	45
S	40	60
DCP	65	35
DAI	60	40
L	45	55
W	50	50
CR	40	60
SR	30	70
PM	40	60

C= concept, D= design, S= supervision, DCP= data collection and/or processing, DAI= data analysis and/or interpretation, L= literature search, W= writing, CR= critical review, SR= submission and revision, PM= project management.

Conflict of Interest

The authors declare no conflict of interest.

Ethical Consideration

Ethics committee approval was not required for this study because it involved no animal or human subjects.

Acknowledgements

The dataset used in this study was the public Roboflow Universe project "Renal- Failure-Analysis" maintained by Mini Project (workspace: mini-project-6ilyj; project: renal-failure-analysis-5ymli), version 4 (Mini Project, 2023). The working export contained 9,574 images in the Cyst, Normal, Stone, and Tumor classes and was publicly listed under a Public Domain license at the time of revision. The public project page does not document the original clinical institution, DICOM-level anonymization workflow, or patient/study identifiers. The authors analyzed only the rendered image export supplied by the repository and did not have access to original DICOM headers or identifiable patient metadata. Therefore, patient-level split independence and the original anonymization process could not be independently verified.

ChatGPT was used solely for English translation, grammar correction, and linguistic editing. The artificial intelligence tool was not used to generate the research design, dataset, analyses, model outputs, tables, figures, or scientific conclusions. The authors reviewed and approved the final manuscript and take full responsibility for its content.

References

Abd El-Aziz, A. A., Mahmood, M. A., & El-Ghany, S. A. (2025). EfficientNet-B3-based automated deep learning framework for multiclass endoscopic bladder tissue classification. *Diagnostics, 15(19)*, Article 2515. https://doi.org/10.3390/diagnostics15192515

Aby, A. E., Salaji, S., Anilkumar, K. K., et al. (2025). Classification of acute myeloid leukemia by pre-trained deep neural networks: A comparison with different activation functions. *Medical Engineering & Physics, 135*, Article 104277. https://doi.org/10.1016/j.medengphy.2024.104277

Al-Adhaileh, M. H., Alsharbi, B. M., Aldhyani, T. H. H., et al. (2025). DLAAD-deep learning algorithms assisted diagnosis of chest disease using radiographic medical images. *Frontiers in Medicine, 11*, Article 1511389. https://doi.org/10.3389/fmed.2024.1511389

Al-Otaibi, S., Rehman, A., Mujahid, M., et al. (2024). Efficient-Gastro: Optimized EfficientNet model for the detection of gastrointestinal disorders using transfer learning and wireless capsule endoscopy images. *PeerJ Computer Science, 10*, e1902. https://doi.org/10.7717/peerj-cs.1902

Alzu'bi, D., Abdullah, M., Hmeidi, I., et al. (2022). Kidney tumor detection and classification based on deep learning approaches: A new dataset in CT scans. *Journal of Healthcare Engineering, 2022*, Article 3861161. https://doi.org/10.1155/2022/3861161

Aouadi, S., Torfeh, T., Bouhali, O., et al. (2024). Prediction of cervix cancer stage and grade from diffusion weighted imaging using EfficientNet. *Biomedical Physics & Engineering Express, 10(4)*, Article 045042. https://doi.org/10.1088/2057-1976/ad5207

Badr, M., Elkasaby, A., Alrahmawy, M., & El-Metwally, S. (2025). A multi-model deep learning architecture for diagnosing multi-class skin diseases. *Journal of Imaging Informatics in Medicine, 38(3)*, 1776–1795. https://doi.org/10.1007/s10278-024-01300-w

Boudi, A., He, J., & Abd El Kader, I. (2024). Enhancing Alzheimer's disease classification with transfer learning: Fine-tuning a pre-trained algorithm. *Current Medical Imaging, 20*, Article e15734056305633. https://doi.org/10.2174/0115734056305633240603061644

Chen, X., Pu, X., Chen, Z., et al. (2023). Application of EfficientNet-B0 and GRU-based deep learning on classifying the colposcopy diagnosis of precancerous cervical lesions. *Cancer Medicine, 12(7)*, 8690–8699. https://doi.org/10.1002/cam4.5581

Chollet, F. (2017). Xception: Deep learning with depthwise separable convolutions. *Proceedings of the IEEE Conference on Computer Vision and Pattern Recognition*, 1800–1807. https://doi.org/10.1109/CVPR.2017.195

Esteva, A., Robicquet, A., Ramsundar, B., et al. (2019). A guide to deep learning in healthcare. *Nature Medicine, 25(1)*, 24–29. https://doi.org/10.1038/s41591-018-0316-z

Gan, K., Liu, Y., Zhang, T., et al. (2024). Deep learning model for automatic identification and classification of distal radius fracture. *Journal of Imaging Informatics in Medicine, 37(6)*, 2874–2882. https://doi.org/10.1007/s10278-024-01144-4

Han, S., Hwang, S. I., & Lee, H. J. (2019). The classification of renal cancer in 3-phase CT images using a deep learning method. *Journal of Digital Imaging, 32(4)*, 638–643. https://doi.org/10.1007/s10278-019-00230-2

He, K., Zhang, X., Ren, S., & Sun, J. (2016). Identity mappings in deep residual networks. *Computer Vision – ECCV 2016*, 630–645. https://doi.org/10.1007/978-3-319-46493-0_38

Hossain, M. N., Bhuiyan, E., Miah, M. B. A., et al. (2025). Detection and classification of kidney disease from CT images: An automated deep learning approach. *Technologies, 13(11)*, Article 508. https://doi.org/10.3390/technologies13110508

Huang, G., Liu, Z., van der Maaten, L., & Weinberger, K. Q. (2017). Densely connected convolutional networks. *Proceedings of the IEEE Conference on Computer Vision and Pattern Recognition*, 4700–4708. https://doi.org/10.1109/CVPR.2017.243

Kan, H.-C., Lin, P.-H., Shao, I.-H., et al. (2025). Using deep learning to differentiate among histology renal tumor types in computed tomography scans. *BMC Medical Imaging, 25(1)*, Article 66. https://doi.org/10.1186/s12880-025-01606-3

Kreouzi, M., Theodorakis, N., Feretzakis, G., et al. (2025). Deep learning for melanoma detection: A deep learning approach to differentiating malignant melanoma from benign melanocytic nevi. *Cancers, 17(1)*, Article 28. https://doi.org/10.3390/cancers17010028

Kumar, Y., Shrivastav, S., Garg, K., et al. (2024). Automating cancer diagnosis using advanced deep learning techniques for multi-cancer image classification. *Scientific Reports, 14(1)*, Article 25006. https://doi.org/10.1038/s41598-024-75876-2

Mao, J., Du, Y., Xue, J., et al. (2024). Automated detection and classification of mandibular fractures on multislice spiral computed tomography using modified convolutional neural networks. *Oral Surgery, Oral Medicine, Oral Pathology and Oral Radiology, 138(6)*, 803–812. https://doi.org/10.1016/j.oooo.2024.07.010

Meeran, S. B. U. (2025). Walrus optimization-enhanced ResNet-50 for AI-driven renal malignancy prediction with occlusion sensitivity-based interpretation. *Asian Pacific Journal of Cancer Prevention, 26(8)*, 2995–3004. https://doi.org/10.31557/APJCP.2025.26.8.2995

Mini Project. (2023). Renal-failure-analysis dataset (Version 4) [Data set]. *Roboflow Universe*. https://universe.roboflow.com/mini-project-6ilyj/renal-failure-analysis-5ymli

Pimpalkar, A., Saini, D. K. J. B., Shelke, N., et al. (2025). Fine-tuned deep learning models for early detection and classification of kidney conditions in CT imaging. *Scientific Reports, 15(1)*, Article 10741. https://doi.org/10.1038/s41598-025-94905-2

Rajinikanth, V., Vincent, P. M. D. R., Srinivasan, K., et al. (2023). A framework to distinguish healthy/cancer renal CT images using the fused deep features. *Frontiers in Public Health, 11*, Article 1109236. https://doi.org/10.3389/fpubh.2023.1109236

Rajpurkar, P., Chen, E., Banerjee, O., & Topol, E. J. (2022). AI in health and medicine. *Nature Medicine, 28(1)*, 31–38. https://doi.org/10.1038/s41591-021-01614-0

Sathya, R., Mahesh, T. R., Bhatia Khan, S., et al. (2024). Employing Xception convolutional neural network through high-precision MRI analysis for brain tumor diagnosis. *Frontiers in Medicine, 11*, Article 1487713. https://doi.org/10.3389/fmed.2024.1487713

Shaheed, K., Abbas, Q., Hussain, A., & Qureshi, I. (2023). Optimized Xception learning model and XGBoost classifier for detection of multiclass chest disease from X-ray images. *Diagnostics, 13(15)*, Article 2583. https://doi.org/10.3390/diagnostics13152583

Tan, M., & Le, Q. V. (2019). EfficientNet: Rethinking model scaling for convolutional neural networks. *Proceedings of the 36th International Conference on Machine Learning, 97*, 6105–6114. PMLR.

Topol, E. J. (2019). High-performance medicine: The convergence of human and artificial intelligence. *Nature Medicine, 25(1)*, 44–56. https://doi.org/10.1038/s41591-018-0300-7

Wilson, E. B. (1927). Probable inference, the law of succession, and statistical inference. *Journal of the American Statistical Association, 22(158)*, 209–212. https://doi.org/10.1080/01621459.1927.10502953

Xu, P., Zhao, J., Wan, M., et al. (2024). Classification of multi-feature fusion ultrasound images of breast tumor within category 4 using convolutional neural networks. *Medical Physics, 51(6)*, 4243–4257. https://doi.org/10.1002/mp.16946

Yao, H., Tian, L., Liu, X., et al. (2023). Development and external validation of the multichannel deep learning model based on unenhanced CT for differentiating fat-poor angiomyolipoma from renal cell carcinoma: A two-center retrospective study. *Journal of Cancer Research and Clinical Oncology, 149(17)*, 15827–15838. https://doi.org/10.1007/s00432-023-05339-0

Ye, D., Ou, Z., Ye, F., et al. (2025). Ensemble deep learning model for accurate assessment of renal fibrosis in chronic kidney disease using two-dimensional shear wave elastography images. *BMC Medical Imaging, 25(1)*, Article 417. https://doi.org/10.1186/s12880-025-01964-y

Zhang, X., Lai, F., Chen, W., & Yu, C. (2024). An automatic glaucoma grading method based on attention mechanism and EfficientNetB3 network. *PLOS ONE, 19(8)*, e0296229. https://doi.org/10.1371/journal.pone.0296229

Zhou, T., Ye, X., Lu, H., et al. (2022). Dense convolutional network and its application in medical image analysis. *BioMed Research International, 2022*, Article 2384830. https://doi.org/10.1155/2022/2384830

Black Sea Journal of Engineering and Science
doi: 10.34248/bsengineering.2004291

Open Access Journal
e-ISSN: 2619 – 8991

Research Article
Volume 9 - Issue 5: 2817-2834 / September 2026

CONGESTION-TRIGGERED ELECTRIC-VEHICLE CHARGING STATION ASSIGNMENT USING SHORT-TERM CUMULATIVE DEMAND FORECASTS

Oğuzkağan ALIÇ[1]*

[1]*Eskişehir Technical University, Faculty of Engineering, Department of Electrical and Electronics Engineering, 26555, Eskişehir, Türkiye*

Abstract: Short-term congestion at public electric-vehicle charging stations depends on both near-future demand and how vehicles are distributed across the network. We forecast cumulative station-level charging initiations and use the forecasts in congestion-triggered station assignment. The analysis reuses 441077 publicly released charging transactions from 13 stations in Jiaxing, China, aggregated at 15-minute resolution. Daily and weekly seasonal baselines are compared with Poisson, Tweedie, hurdle, and quantile LightGBM models for cumulative 15-, 30-, and 60-minute demand. Because physical arrivals and queueing times are not observed, recorded charging starts served as simulation-entry events in the counterfactual analysis. The forecasts are embedded in a counterfactual capacity-and-routing simulation with transaction-level service durations, inbound reservations for redirected vehicles, partial recommendation acceptance, an eight-minute switching-time penalty, queue abandonment, demand growth, and charger outages. All routing policies are evaluated on immutable scenarios with common random numbers over 21 test days stratified by weekday and charging-initiation volume. Relative to the stronger daily seasonal baseline, the Tweedie model reduces mean absolute error by 17.6-19.8% and root-mean-square error by 21.7-26.8%. Under normal demand and full capacity, the routing policies remain inactive and introduce no unnecessary switching. Under the evaluated stress scenarios and full recommendation acceptance, dynamic assignment reduces simulated mean total delay by 75.0-78.7% and simulated abandonment by approximately 95-100%, while rerouting fewer than 10% of vehicles. Risk-aware routing has the numerically lowest aggregate simulated delay, but under the combined demand-and-outage scenario it differs from current-load routing by only 0.001 minutes per vehicle, and the pairs 95% confidence interval included zero. Within these counterfactual scenarios, most of the reduction therefore come from the shared congestion-triggered routing architecture rather than from the forecast-risk terms.

Keywords: Electric-vehicle charging, Cumulative demand forecasting, Sparse count prediction, Probabilistic forecasting, Charging-station assignment, Congestion management

***Corresponding author:** Eskişehir Technical University, Faculty of Engineering, Department of Electrical and Electronics Engineering, 26555, Eskişehir, Türkiye
E mail: oguzkaganalic@eskisehir.edu.tr (O. ALIÇ)
Oğuzkağan ALIÇ https://orcid.org/0000-0001-8611-7987

Received: July 27, 2026
Accepted: August 27, 2026
Published: September 15, 2026

Cite as: Alıç, O. (2026). Congestion-triggered electric-vehicle charging station assignment using short-term cumulative demand forecasts. *Black Sea Journal of Engineering and Science,* 9(5), 2817-2834.

1. Introduction

The continued electrification of road transport increases the need for reliable and efficiently utilized public charging infrastructure. Charging demand varies considerably across locations, user groups, time periods, and infrastructure types, creating challenges for both power system operation and service quality (Kim et al., 2026; Alaraj et al., 2025; Unterluggauer et al., 2021; Elahe et al., 2022). Even when the overall network has sufficient charging capacity, uneven spatial and temporal demand can overload individual stations, increase waiting times, and leave nearby chargers underutilized (Schoenberg and Dressler, 2023; Widmann and Sawodny, 2026; Zhang et al., 2025a) These localized imbalances become particularly critical during periods of high demand or charger outages, when congestion at a small number of stations can spread throughout the network.

Driver behavior further complicates the management of public charging networks. Station choice depends on several factors, including waiting time, charging speed, price, remaining driving range, and detour distance, while users differ in both their tolerance for waiting and their willingness to accept alternative charging stations (Hoen et al., 2023; Hanni et al., 2024; Brückmann and Bernauer, 2023). Consequently, a routing policy that minimizes station queues without considering additional travel or user inconvenience may reduce queueing delays while increasing the overall burden on drivers. Likewise, a recommendation that initially appears beneficial can become counterproductive if many vehicles are redirected to the same station at the same time. Operational station assignment must consequently account for current occupancy, near-future charging initiations, already redirected vehicles, recommendation

This work is licensed (CC BY-NC 4.0) under Creative Commons Attribution 4.0 International License

acceptance, and switching cost.

Short-term demand forecasting provides valuable information for making proactive assignment decisions. Existing studies predict charging power, energy consumption, station occupancy, session duration, regional demand, and future load profiles using statistical methods, gradient boosting, recurrent neural networks, convolutional architectures, transformers, and ensemble models (Unterluggauer et al., 2021; Yi et al., 2021; Mohammad et al., 2023; Aghsaee et al., 2023; Hussain et al., 2025; Mansour et al., 2026). Although these forecasting targets are valuable for infrastructure planning and grid operation, they do not directly represent the number of vehicles expected to initiate charging within a short queue-formation period. In addition, station-level charging counts at fine temporal resolutions are discrete, non-negative, sparse, and often overdispersed, making count-based and probabilistic forecasting approaches more appropriate than conventional point regression models.

Charging-station recommendation evolves alongside advances in charging-demand forecasting. Existing approaches combine factors such as travel distance, travel time, charging price, charger availability, expected waiting time, reservations, and announced charging intentions with optimization techniques, reinforcement learning, and adaptive routing strategies (Liu et al., 2018; Lee et al., 2020; Basmadjian et al., 2020; Schoenberg and Dressler, 2023; Nie et al., 2023; Dudkina et al., 2025; Widmann and Sawodny, 2026). Collectively, these studies demonstrate that coordinated station assignment can effectively reduce congestion. However, their practical performance largely depends on how future vehicle commitments are represented. If vehicles that accept a recommendation but have not yet reached their assigned station are excluded from the system state, successive routing decisions may redirect multiple vehicles to the same station, creating new congestion. Reservation- and intention-aware approaches address this issue by explicitly representing future arrivals. However, they often rely on formal reservation systems, detailed trip information, full user compliance, or repeated global optimization, which may limit their practical applicability (Basmadjian et al., 2020; Schoenberg and Dressler, 2023; Dudkina et al., 2025; Widmann and Sawodny, 2026).

A second methodological issue concerns policy evaluation. Simulation outcomes can be distorted when competing policies receive different random event streams, service durations, outages, or behavioral draws. This issue becomes particularly important when the performance differences among advanced routing strategies are much smaller than their shared improvement over the no-routing baseline. A fair comparison therefore requires all policies to be evaluated under identical stochastic conditions, together with paired statistical analyses at the scenario level.

This study addresses these challenges by integrating short-term demand forecasting with congestion-aware station assignment in a unified simulation framework based on the publicly available Jiaxing charging-transaction dataset introduced by (Zhang et al., 2025a). The study relies exclusively on secondary analysis of the published dataset, and no primary charging data are collected. The dataset records charging-start times but does not provide reliable physical vehicle-arrival or observed queueing times; accordingly, the simulation is formulated as a counterfactual capacity-and-routing analysis based on observed charging initiations. Station-level charging initiations are forecasted as cumulative counts over the next 15, 30, and 60 minutes using seasonal baselines, Poisson and Tweedie gradient boosting, a two-stage hurdle model, and quantile regression. These forecasts drive a congestion-triggered assignment mechanism that preserves immediately available station capacity, accounts for redirected vehicles through inbound reservations, applies a minimum-benefit threshold before rerouting, models partial user acceptance of recommendations, and incorporates a fixed switching penalty into the total-delay objective. Four policies, no routing, current-load routing, predicted-wait routing, and risk-aware routing, are evaluated under observed demand, a 20% demand increase, a 10% charger-outage probability, and their combination using immutable scenarios and common random numbers (CRN).

This study makes three main contributions. First, it aligns the forecasting task with the operational decision by predicting cumulative charging-start counts over short queue-formation windows rather than isolated future time slots or energy demand. Second, it combines these forecasts with a selective, inbound-aware routing mechanism that reduces unnecessary station switching and mitigates recommendation-induced herding. Third, it evaluates the proposed routing strategies using a reproducible paired simulation framework with fixed scenario inputs, integrity checks, and day-level bootstrap confidence intervals. The analysis is designed to determine not only whether dynamic routing reduces the simulated outcomes relative to no routing under the stated scenarios, but also whether forecast and uncertainty information provides a meaningful incremental reduction beyond a simpler current-load policy.

The experimental analysis addresses the following research questions:

RQ1: Do count-oriented models improve cumulative station-level point forecasts relative to seasonal baselines, and how well calibrated are the corresponding probabilistic forecasts?

RQ2: Does congestion-triggered, inbound-aware assignment reduce simulated total delay and queue abandonment under demand and capacity stress without causing unnecessary routing under normal conditions?

RQ3: Does risk-aware forecast information provide a practically meaningful advantage over current-load and predicted-wait routing?

1.1. Charging-Demand Forecasting and Data Foundations

EV charging-demand forecasting spans statistical, machine-learning, deep-learning, and ensemble approaches, with model choice depending on prediction horizon, charging context, spatial scale, data availability, and operational objective (Kim et al., 2026; Alaraj et al., 2025). Statistical and seasonal models remain useful as transparent benchmarks, whereas recurrent, convolutional, transformer, and hybrid architectures are increasingly used to represent nonlinear temporal and spatial structure (Unterluggauer et al., 2021; Mohammad et al., 2023; Hussain et al., 2025; Mansour et al., 2026; Yu et al., 2026). For example, prior studies have forecast interval-level charging load, energy demand, monthly regional demand, session duration, connector occupation, and multi-step load sequences (Yi et al., 2021; Unterluggauer et al, 2021; Aghsaee et al., 2023; Orzechowski et al., 2023). These targets are valuable for planning and grid operation, but they do not directly represent the number of charging initiations that may compete for limited charger capacity during an imminent routing window. Gradient-boosting methods offer a comparatively lightweight alternative to large sequence models. LightGBM, XGBoost, CatBoost, and random forests can represent nonlinear interactions among station identity, calendar variables, recent demand, and lagged observations without requiring long recurrent training pipelines (Ke et al., 2017; Sreekumar and Lekshmi, 2024; Aghsaee et al., 2023; Mansour et al., 2026; Keskin et al., 2024). Previous-slot, previous-day, and real-time station-state features have been shown to contribute materially to charging-related forecasts (Sreekumar and Lekshmi, 2024; Aghsaee et al., 2023). These findings support evaluating count-oriented gradient boosting for short operational horizons, while retaining seasonal baselines to determine whether the additional model complexity produces meaningful improvement. Forecast comparisons are also strongly affected by dataset construction and evaluation design. Public charging resources vary in duration, station diversity, temporal resolution, transaction volume, and the availability of contextual and operational variables (Elahe et al., 2022; Zhang et al., 2025a). Chronological holdout, walk-forward validation, and cross-site testing are therefore preferable to random splitting when repeated seasonal patterns and temporally adjacent observations could otherwise appear in both training and evaluation sets (Unterluggauer et al., 2021; Orzechowski et al., 2023; Mansour et al., 2026; Ali et al., 2026). Differences in preprocessing, target construction, aggregation, and partition boundaries nevertheless continue to limit direct comparisons across studies (Kim et al., 2026; Alaraj et al., 2025). The present analysis uses the public Jiaxing transaction dataset introduced by (Zhang et al., 2025a). It contains 441077 charging sessions from 13 stations and includes charging-post identifiers, charging-start and end timestamps, delivered energy, transaction attributes, weather variables, and station categories. Its temporal precision supports station-level charging-initiation counts and empirical service-duration estimates, while its multiple stations preserve operational heterogeneity. However, the dataset does not provide reliable physical vehicle-arrival times, observed queueing times, route-specific travel times, or rejected charging attempts. It therefore supports a counterfactual capacity-and-routing analysis based on observed charging initiations, not reconstruction of historical queues.

1.2. Sparse Counts and Probabilistic Forecasting

Station-level charging-initiation counts at 15-minute resolution are non-negative, discrete, and frequently zero. Most directly comparable EV forecasting studies instead model continuous power or energy using conventional point-regression objectives (Unterluggauer et al., 2021; Elahe et al., 2022; Mohammad et al., 2023; Sreekumar and Lekshmi, 2024; Hussain et al., 2025; Mansour et al., 2026). For sparse count targets, Poisson and Tweedie objectives provide non-negative conditional-mean estimates and can represent demand-dependent variance, while hurdle models separate the probability of positive demand from its conditional magnitude. Because the EV literature does not establish a universally preferable count formulation, empirical comparison among these alternatives is more appropriate than assuming a single distributional model (Kim et al., 2026; Alaraj et al., 2025). Probabilistic forecasts provide information that is not available from a conditional mean alone. Multi-quantile charging-demand models have been evaluated using coverage and interval-width measures, including applications involving site transfer and locations with limited local data (Ali et al., 2026). More general electrical-load research likewise uses quantile-based methods to evaluate reliability and sharpness jointly (Dang et al., 2022). These studies support the use of lower, median, and upper conditional quantiles, but they also require careful interpretation when the target is zero-heavy. In particular, a conditional median can achieve low absolute error while underestimating aggregate expected demand when the distribution contains many zeros and a long positive tail. Median and upper-quantile forecasts should therefore complement, rather than automatically replace, expected-demand estimates in operational control. This distinction matters for station assignment because a routing score may require both expected near-future pressure and an upper-tail risk margin. Prior work has incorporated forecast uncertainty into pricing and energy-procurement decisions (Matkovic et al., 2025), but its use in short-horizon station assignment with finite capacity, current queues, inbound commitments, and switching costs remains less developed (Schoenberg and Dressler, 2023; Dudkina et al., 2025; Widmann and Sawodny, 2026).

1.3. Queue-Aware Station Assignment and Behavioral Assumptions

Charging stations can be represented as multi-server systems in which vehicles compete for finite service capacity. Analytical queueing models offer computational tractability but depend on assumptions about arrival and service processes (Heting et al., 2021; Widmann and Sawodny, 2026). Discrete-event and agent-based simulations can retain heterogeneous charger counts, empirical or vehicle-specific service durations, traffic concentration, and operational disturbances (Mishra et al., 2022; Rupnik et al., 2025; Schoenberg and Dressler, 2023). Across these studies, local congestion can occur even when network-wide capacity is adequate because demand and service times vary substantially among stations. Station-assignment methods consequently combine current availability with travel time, price, expected waiting, reservations, announced intentions, or centralized coordination (Liu et al., 2018; Lee et al., 2020; Basmadjian et al., 2020; Schoenberg and Dressler, 2023; Nie et al., 2023; Dudkina et al., 2025; Widmann and Sawodny, 2026). Reservation- and intention-aware methods are particularly relevant because a vehicle that has accepted a recommendation but has not yet reached the destination already represents a future capacity commitment. Ignoring such commitments can cause several decisions to select the same apparently uncongested station, whereas explicitly representing planned demand can reduce congestion migration (Schoenberg and Dressler, 2023; Widmann and Sawodny, 2026). However, existing approaches may require formal bookings, detailed trip plans, full compliance, accurate arrival-time estimates, repeated optimization, or interoperable reservation systems (Basmadjian et al., 2020; Dudkina et al., 2025; Widmann and Sawodny, 2026). Behavioral assumptions also affect apparent policy performance. Waiting time, detour distance, price, charging speed, amenities, remaining range, and user characteristics influence station choice and waiting tolerance (Hoen et al., 2023; Hanni et al., 2024; Brückmann and Bernauer, 2023). A policy that minimizes destination queueing without charging for additional travel can therefore appear beneficial while increasing the user's total burden. Partial recommendation acceptance and an explicit switching cost provide a more conservative evaluation than universal compliance and costless redirection, although fixed recommendation-acceptance rates, patience thresholds, and switching parameters remain simplifications when individual-level behavioral and route data are unavailable. Stress conditions and evaluation design are equally important. Demand growth, charger loss, seasonal concentration, and infrastructure failures can reveal differences that remain dormant under uncongested operation (Mishra et al., 2022; Rupnik et al., 2025; Zhang et al., 2025b). Yet comparisons can be confounded when policies receive different event streams, service durations, outages, or behavioral draws. Common random numbers and paired day-level inference are therefore especially useful when differences among dynamic policies are expected to be much smaller than their common difference from no routing. The reviewed assignment literature uses Monte Carlo and large-scale simulation extensively, but immutable scenario objects, input-integrity checks, and paired bootstrap comparisons are not usually presented together as a policy-evaluation framework (Schoenberg and Dressler, 2023; Dudkina et al., 2025; Widmann and Sawodny, 2026).

1.4. Research Gap and Study Positioning

Three connected gaps motivate the present study. First, much of the forecasting literature focuses on electrical load, energy, occupation, charging duration, or isolated future intervals rather than cumulative charging-initiation counts over the next 15-60 minutes (Unterluggauer et al., 2021; Yi et al., 2021; Aghsaee et al., 2023; Mohammad et al., 2023; Orzechowski et al., 2023; Hussain et al., 2025). Such cumulative counts are more directly aligned with the number of observed charging initiations that may compete for finite station capacity during a short decision window. Second, probabilistic demand forecasts are commonly evaluated separately from real-time station assignment. Existing reservation- and intention-aware methods demonstrate the importance of future commitments, but frequently rely on formal reservations, submitted travel plans, idealized compliance, or iterative global optimization (Basmadjian et al., 2020; Schoenberg and Dressler, 2023; Dudkina et al., 2025; Widmann and Sawodny, 2026). A lighter-weight alternative is to combine current station state with short-horizon expected demand, an upper-tail risk signal, and explicit counters for vehicles already redirected but not yet at the destination. Third, operational conclusions require controlled comparison. Stress scenarios, partial recommendation acceptance, switching costs, abandonment, and charger failures each affect results, while small differences among dynamic policies can be obscured by independently generated simulation inputs. The present framework therefore evaluates no routing, current-load, predicted-wait, and risk-aware assignment on immutable common-random-number scenarios with integrity checks and paired day-level inference. The contribution is an integration and evaluation framework rather than a new standalone forecasting architecture. It links cumulative count forecasts to selective inbound-aware routing and tests whether expected-demand and uncertainty terms provide material value beyond a simpler current-load policy. This positioning allows the study to assess both the shared effect of congestion-triggered routing and the incremental value of forecast complexity without claiming novelty for the individual forecasting, queueing, or reservation components.

2. Materials and Methods

3.1. Problem Formulation and Study Design

Consider a network of charging stations indexed by $j \in \mathcal{J}$ where station j has effective capacity c_j. Time is divided into 15-minute intervals indexed by t. Let $A_{j,t}$ denote the observed number of charging initiations at station j during interval t, and let $Y_{j,t}^{(h)}$, denote cumulative demand during the next h intervals. The forecasting task estimates the conditional distribution of $Y_{j,t}^{(h)}$ for $h \in \{1,2,4\}$ from station identity, calendar variables, lagged demand, and rolling demand statistics.

At each simulation-entry event, corresponding to an observed charging initiation, an assignment policy selects either the historically observed station or an alternative station. The decision uses current station occupancy, queue length, inbound reservations, service-duration information, and, for forecast-aware policies, cumulative demand forecasts. A recommendation is applied only when the vehicle accepts it and when the estimated score improvement meets the minimum routing-gain threshold after switching time has been included. The primary objective is to minimize mean total user delay (equation 1),

$$\overline{T}^{\text{delay}} = \frac{1}{N}\sum_{i=1}^{N}(W_i^{\text{queue}} + T_i^{\text{switch}}), \quad (1)$$

where N is the number of simulated vehicles, W_i^{queue} is the queueing time of vehicle i, and T_i^{switch} is the additional time incurred when the vehicle is redirected. Equation 1 defines the primary system objective, subject to station-capacity constraints and non-negative inbound reservations. Queue abandonment and rerouting frequency are treated as complementary outcomes.

The study uses a two-stage counterfactual design. Forecast accuracy is evaluated first; the resulting predictions are then supplied to the discrete-event simulation. The published transactions provide station-level charging-initiation histories, empirical service durations, and station-capacity proxies. Because physical vehicle-arrival times are unavailable, each recorded charging initiation is used as a simulation-entry event. Each routing policy is evaluated on the same CRN scenario, so differences in simulated outcomes arise from policy decisions rather than different charging-initiation event streams, service durations, or outage realizations.

3.2. Data Source and Preparation

The empirical analysis reuses the high-resolution electric-vehicle charging transaction dataset originally collected, anonymized, and publicly released by Zhang et al. (2025b). The present study did not participate in primary data collection, anonymization, or construction of the source dataset. According to the dataset descriptor, the source contains 441077 charging transactions recorded at 13 charging stations in Jiaxing, China, over approximately two years, from December 2019 to December 2021. The published records include anonymized user and charging-post identifiers, order-creation time, charging start and end times, delivered energy, charging-price information, transaction status, termination reason, weather variables, and station-location information.

For the present secondary analysis, the published transaction-level records are used to derive station-level demand time series and empirical charging-duration distributions. A total of 92 distinct charging-post identifiers are observed among records with valid service information. For each station j, the capacity proxy c_j is calculated as the number of distinct charging-post identifiers associated with that station in the valid service records. This procedure yields station capacities of four to eight posts. It assumes that each identifier represents one independently usable charger and that the set of identifiers observed over the study period is an appropriate proxy for simultaneous station capacity; temporal installation, removal, or prolonged unavailability of individual posts cannot be reconstructed from the transaction records.

The source dataset has been anonymized before public release by its original providers and authors (Zhang, et al., 2025). No new personal data are collected, and all analyses are conducted on the publicly available anonymized records.

Because demand forecasting and service-duration estimation require different validity criteria, two analysis-specific subsets are derived from the published records. The demand-analysis subset includes all 441077 transactions with valid station identifiers and charging-start timestamps. The charging-start timestamp is selected as the operational demand-event timestamp because the order-creation timestamp is later than the charging-start timestamp in 248588 records, corresponding to 56.36% of the raw dataset. This pattern indicates that neither available timestamp can be interpreted consistently as the physical vehicle-arrival time.

Accordingly, the modeled demand represents observed charging initiations, not physical station arrivals. The source data do not identify vehicles that arrived but left without initiating a recorded charging session.

For the service-duration subset, the duration of transaction i was calculated as (equation 2),

$$D_i = t_i^{\text{end}} - t_i^{\text{start}}, \quad (2)$$

where t_i^{start} and t_i^{end} denote the recorded charging start and end times, respectively.

Transactions are excluded from service-duration estimation when the calculated duration is non-positive or shorter than one minute. Sessions longer than 24 hours are also treated as invalid. After applying these criteria, 422053 transactions remain for service-duration modeling and simulation. The resulting transaction-level duration D_i is retained as the service requirement of that charging-initiation event in the simulation.

Energy values are retained for descriptive analyses when

they are between 0.01 and 200 kWh. Energy validity is not required for constructing the charging-initiation time series because the forecasting target is the number of charging initiations rather than delivered energy.

The order-to-start difference is inspected only as a data-quality diagnostic. Because it may include authentication, connection, communication, payment, or recording processes, it is not interpreted as physical queueing time and was not used as a simulation outcome.

3.3. Forecasting Design and Evaluation

Charging demand is aggregated into fixed 15-minute intervals. Let $A_{j,t}$ denote the number of charging sessions starting at station *j* during interval *t*.

The forecasting targets are defined as cumulative future demand. For a forecasting horizon of *h* intervals, the target was (equation 3),

$$Y_{j,t}^{(h)} = \sum_{k=1}^{h} A_{j,t+k}\,, h \in \{1,2,4\} \quad (3)$$

The cumulative target in equation 3 used *h=1*, *h=2*, and *h=4* to represent the total number of charging initiations expected during the next 15, 30, and 60 minutes, respectively. This cumulative formulation is selected because the total number of near-future charging initiations is more directly related to counterfactual capacity competition than demand in a single isolated future interval.

Predictor variables are generated independently for each station. Historical demand lags are constructed at 1, 2, 4, 8, 96, 192, and 672 intervals. At a 15-minute resolution, these corresponded to 15 minutes, 30 minutes, one hour, two hours, one day, two days, and one week.

Rolling demand statistics are calculated over windows of 4, 12, 24, and 96 intervals, corresponding to one, three, six, and 24 hours. The rolling variables include historical mean and dispersion measures calculated only from observations available at or before the forecast origin.

Calendar variables include hour of day, 15-minute slot of day, day of week, month, and weekend status. Cyclical time variables are represented using sine and cosine transformations. Calendar features associated with the prediction target are derived from the target timestamp, whereas lagged and rolling demand features are derived exclusively from the forecast-origin timestamp.

Station identity is included as a categorical predictor to account for differences in location, infrastructure, and historical utilization.

The 15-minute station panel extends from 31 December 2019 at 21:15 to 1 January 2022 at 00:00. The observations are partitioned chronologically using 65% of the panel duration for training, 15% for validation, and 20% for testing. The validation period begins on 20 April 2021 at 02:15, and the test period begins on 7 August 2021 at 18:30.

Assignment to each subset is based on the end timestamp of the cumulative target window rather than the feature timestamp. Target windows ending before 20 April 2021 at 02:15 are assigned to training; windows ending from that timestamp to, but not including, 7 August 2021 at 18:30 are assigned to validation; and windows ending at or after the test boundary are assigned to testing. This rule prevents observations whose predictors occur before a partition boundary but whose targets extend beyond it from leaking future information across the training, validation, or test sets.

The validation subset is used as the evaluation set for early stopping during every LightGBM fit. Model parameters are estimated using only the training subset, and the validation observations are not subsequently merged into model fitting. The test subset remains untouched until final forecast generation and is not used for early stopping, hyperparameter adjustment, or selection of the reported model families. No random train-test split is used because random splitting would allow temporally adjacent observations and repeated seasonal patterns to occur in both training and evaluation subsets.

The model comparison includes seasonal reference methods, count-oriented gradient boosting, a two-stage hurdle formulation, and quantile regression. Daily and weekly seasonal-naive models serve as the reference methods. For horizon *h*, the daily seasonal prediction is aligned with the target interval as (equation 4),

$$\hat{Y}_{j,t}^{(h,\text{daily})} = Y_{j,t-96}^{(h)} \quad (4)$$

and the weekly seasonal prediction is (equation 4),

$$\hat{Y}_{j,t}^{(h,\text{weekly})} = Y_{j,t-672}^{(h)} \quad (5)$$

This target-aligned definition ensures that each cumulative future window is compared with the equivalent window one day or one week earlier.

For count-based prediction, a LightGBM regression model with a Poisson objective is trained to estimate conditional expected demand. The Poisson model is included because the response variable is a non-negative count. All LightGBM models use a maximum of 700 boosting iterations, a learning rate of 0.04, 31 leaves, a minimum of 40 observations per child node, a row-subsampling fraction of 0.90, a feature-subsampling fraction of 0.90, and an L2 regularization coefficient of 0.20. These common tree settings are fixed in the analysis configuration rather than chosen through an automated validation-set search. For each horizon and objective, LightGBM monitors its objective-specific validation loss, retains the best boosting iteration, and stops after 50 consecutive rounds without improvement. The global model seed is 2026.

Because the charging counts exhibit excess zeros and variance greater than the mean, a LightGBM Tweedie model is also evaluated. The Tweedie variance power is fixed at 1.35 in the analysis configuration; it is not selected by optimizing test performance. The Poisson, Tweedie, hurdle-classification, hurdle-positive-count, and quantile models otherwise use the same common

tree settings. The quantile objectives use levels 0.10, 0.50, and 0.90. All prespecified model families are retained for final test-set comparison rather than selecting a single forecasting family on the validation results. Table 1 consolidates these forecasting settings with the simulation and routing parameters and states the basis on which each group is fixed.

In addition, a hurdle model represents the demand-generation process in two stages. First, a LightGBM classifier with the binary objective estimated the probability of at least one charging initiation (equation 6):

$$\hat{p}_{j,t}^{(h)} = \Pr\left(Y_{j,t}^{(h)} \middle| > 0 \boldsymbol{x}_{j,t}\right). \tag{6}$$

Second, a LightGBM regressor with the Poisson objective is fitted only to positive-count training observations, $Y_{j,t}^{(h)} > 0$, to estimate the conditional positive magnitude. Its validation evaluation set likewise contains only positive-count validation observations. The classifier and positive-count regressor use the common LightGBM settings reported above: at most 700 boosting iterations, learning rate 0.04, 31 leaves, minimum child size 40, row and feature subsampling fractions of 0.90, L2 regularization 0.20, seed 2026, and early stopping after 50 non-improving validation rounds. The expected demand is calculated as (equation 7),

$$\hat{Y}_{j,t}^{(h,\text{hurdle})} = \hat{p}_{j,t}^{(h)} \widehat{\mathbb{E}}\left[Y_{j,t}^{(h)} \middle| Y_{j,t}^{(h)} \middle| > 0 \boldsymbol{x}_{j,t}\right]. \tag{7}$$

The area under the receiver operating characteristic curve (AUC) is used to evaluate the binary occurrence component. The hurdle estimate is retained as the expected-demand signal for the routing implementation because its explicit occurrence-magnitude decomposition matched the zero-heavy charging-initiation target and produces an interpretable non-negative expected count. This is a structural and interpretability-based implementation choice rather than selection of the model with the lowest validation or test error; the Tweedie model is evaluated independently and achieves slightly better point-forecast accuracy. The one-hour cumulative horizon is the longest of the three horizons declared in the analysis configuration and represents demand pressure over four consecutive 15-minute intervals, rather than an isolated near-term slot.

To characterize predictive uncertainty, separate LightGBM quantile models are trained for the 0.10, 0.50, and 0.90 conditional quantiles. These models generate a lower demand bound $\hat{Q}_{0.10}$, a median forecast $\hat{Q}_{0.50}$, and an upper-risk forecast $\hat{Q}_{0.90}$. Quantile predictions are monotonically reordered when necessary to ensure $\hat{Q}_{0.10} \le \hat{Q}_{0.50} \le \hat{Q}_{0.90}$.

The conditional median is evaluated as a point forecast, while the difference between the upper and median quantiles is used as an uncertainty indicator in the risk-aware station-assignment policy.

For n_f forecast observations, point forecasts are evaluated using mean absolute error, root-mean-square error, weighted absolute percentage error, the coefficient of determination, and mean forecast bias (equation 8):

$$\begin{aligned}
\text{MAE} &= \frac{1}{n_f}\sum_{i=1}^{n_f}|y_i - \hat{y}_i|, \\
\text{RMSE} &= \sqrt{\frac{1}{n_f}\sum_{i=1}^{n_f}(y_i - \hat{y}_i)^2}, \\
\text{WAPE} &= \frac{\sum_{i=1}^{n_f}|y_i - \hat{y}_i|}{\sum_{i=1}^{n_f} y_i}, \\
R^2 &= 1 - \frac{\sum_{i=1}^{n_f}(y_i - \hat{y}_i)^2}{\sum_{i=1}^{n_f}(y_i - \bar{y})^2}, \\
\text{Bias} &= \frac{1}{n_f}\sum_{i=1}^{n_f}(\hat{y}_i - y_i).
\end{aligned} \tag{8}$$

WAPE is not bounded above by one. A value greater than one indicates that the sum of absolute forecast errors exceeds the total number of observed charging initiations over the evaluation set. For the nominal 80% interval $[L_i, U_i] = [\hat{Q}_{0.10,i}, \hat{Q}_{0.90,i}]$, calibration is assessed using empirical coverage, mean interval width, coverage deviation from 0.80, and the interval score (equation 9),

$$\begin{aligned}
\text{IS}_{0.20,i} &= (U_i - L_i) + 10(L_i - y_i)\mathbf{1}(y_i < L_i) \\
&+10(y_i - U_i)\mathbf{1}(y_i > U_i).
\end{aligned} \tag{9}$$

The reported interval score is the mean, $n_f^{-1}\sum_{i=1}^{n_f}\text{IS}_{0.20,i}$. Lower mean interval scores indicate a preferable combination of sharpness and calibration.

3.4. Discrete-Event Charging Simulation

A discrete-event simulation represents the charging stations as parallel-server queueing systems. Each station j contains c_j parallel service resources, where c_j is the station-specific capacity proxy defined as the number of distinct charging-post identifiers observed for that station in the valid service records.

Each simulated vehicle is characterized by a simulation-entry timestamp, an original station, a charging-service duration, a fixed waiting tolerance, a recommendation-acceptance draw, and an optional alternative assigned station.

The recorded charging-start timestamp is interpreted as a charging-initiation event and used as the simulation-entry time. It is not treated as the vehicle's observed physical arrival time. Consequently, the simulation is a counterfactual capacity-and-routing analysis based on observed charging initiations, not a reconstruction of historical station arrivals, rejected charging attempts, or real-world queues.

A vehicle immediately enters service when a charger is available. Otherwise, it joins the station queue. Vehicles abandon the queue when their waiting time exceeds 30 minutes. The 30-minute threshold is used as a transparent finite waiting-tolerance scenario for identifying severe service delay; it is not estimated from individual driver behavior and is not interpreted as a universal patience value.

Each original vehicle retains its transaction-level observed service duration D_i even when it is redirected to another station. Redirection changes the destination and adds the modeled switching interval, but it does not replace D_i with the destination station's median duration. The redirected vehicle therefore occupies one destination charger for the same service duration as its source transaction. Additional vehicles introduced in the demand-growth scenarios inherit the service duration of the sampled source transaction. This implementation assumes that required charging time is unaffected by destination-specific charger power, connector compatibility, or charging conditions, which are unavailable in the dataset. The system state is monitored at 15-minute intervals.

3.5. Immutable Scenario Generation and Common Random Numbers

To ensure fair policy comparisons, simulation scenarios are generated independently of the assignment policy. For each combination of simulation date, demand multiplier, charger-outage probability, and random seed, an immutable scenario instance is generated.

Each scenario stores the complete charging-initiation event stream used for simulation entry, original station assignments, service durations, charger-outage realizations, waiting tolerances, and fixed recommendation-acceptance draws.

For the 20% demand-growth condition, an additional number of transactions equal to 20% of the original daily vehicle count is sampled with replacement from that day's records. The copied charging-initiation times are independently perturbed by an integer offset between -7 and +7 minutes and clipped to the boundaries of the same day. Under the 10% charger-outage-probability condition, each charger is independently retained with probability 0.90; effective station capacity is constrained to remain at least one charger. Thus, 10% denotes the Bernoulli probability applied to each charger, not a requirement that every scenario lose exactly 10% of network capacity. These stochastic draws are generated once per immutable scenario and reused by every policy.

All station-assignment policies use the same scenario without modifying its stochastic inputs. Policy names and recommendation-acceptance parameters are not used when generating charging-initiation event streams, service durations, or outages. This common-random-number design reduces simulation variance and ensures that paired differences between policies are not confounded by different random inputs.

Scenario hashes, vehicle counts, capacity constraints, and inbound-reservation counters are automatically checked after each experiment. Experiments are considered valid only when all policies used identical scenario inputs, the number of vehicles in service never exceeds effective station capacity, and no inbound counter becomes negative.

3.6. Assignment Policies and Routing Controls

Four station-assignment policies are evaluated. Let $n_{j,t}^{\mathrm{srv}}$, $n_{j,t}^{\mathrm{que}}$, and $n_{j,t}^{\mathrm{in}}$ denote the numbers of vehicles in service, waiting, and committed inbound at station j, respectively. Effective load was (equation 10),

$$L_{j,t} = \frac{n_{j,t}^{\mathrm{srv}} + n_{j,t}^{\mathrm{que}} + n_{j,t}^{\mathrm{in}}}{c_j} \tag{10}$$

Let $\widetilde{D}_j$ denote the station-specific median service duration. The median is used in the routing-score approximation because service durations are positively skewed: the station-specific mean exceeds the median at all 13 stations, indicating that a small number of long sessions can disproportionately inflate a mean-based queue proxy. The median therefore provides a robust typical-duration multiplier for comparing candidate stations. It is used only in the routing score; actual resource occupancy and service completion in the discrete-event simulation use each vehicle's transaction-level duration D_j. Current backlog delay is approximated by (equation 11),

$$W_{j,t}^{\mathrm{backlog}} = \max(0, n_{j,t}^{\mathrm{srv}} + n_{j,t}^{\mathrm{que}} - c_j + 1)\frac{D_j}{c_j} \tag{11}$$

The simulation uses the 60-minute cumulative hurdle expectation $\hat{Y}_{j,t}^{(4,\mathrm{hurdle})}$ as the expected-demand input. The 60-minute horizon is specified in the analysis configuration to summarize charging-initiation pressure over the next four decision intervals, a window more closely aligned with queue formation and charging-service evolution than a single 15-minute slot. It is also the most predictable evaluated horizon, with higher R^2, lower WAPE, and higher occurrence AUC than the shorter horizons, although those test results are not used to select among model families. The hurdle signal is chosen because it explicitly combines the estimated probability of a positive charging-initiation count with the expected magnitude conditional on positive demand. It is not selected as the numerically best point forecast: at the 60-minute horizon, the Tweedie model achieves an MAE of 1.490 and an RMSE of 2.263, compared with 1.507 and 2.269 for the hurdle model. Thus, the horizon choice and the model-family choice serve different purposes: the former defines the operational accumulation window, whereas the latter provides an interpretable expected-count decomposition for the routing score. The routing results characterize this implemented hurdle-based signal and do not imply that the hurdle formulation is generally superior to Tweedie forecasting. Forecast pressure and the resulting predicted wait are (equation 12),

$$\begin{aligned} W_{j,t}^{\mathrm{forecast}} &= \lambda_f(n_{j,t}^{\mathrm{in}} + \max(0, \hat{Y}_{j,t}^{(4,\mathrm{hurdle})}))\frac{D_j}{c_j} \\ \hat{W}_{j,t} &= W_{j,t}^{\mathrm{backlog}} + W_{j,t}^{\mathrm{forecast}} \end{aligned} \tag{12}$$

with $\lambda_f = 0.50$. The upper-tail risk margin and load-balance term are (equation 13),

$$R_{j,t} = \max(0, \hat{Q}_{0.90,j,t} - \hat{Q}_{0.50,j,t}) \frac{D_j}{c_j} B_{j,t} = L_{j,t} D_j \quad (13)$$

Under the no-routing policy, each vehicle remains assigned to its historically observed station. For the remaining policies, all 13 stations are eligible candidates. Let $C_{i,j}$ equal zero for the original station and eight minutes for an alternative station. A hard barrier $H_{j,t} = 10^6$ is added for an alternative station when its inbound count reaches c_j. The implemented scores are (equation 14),

$$\begin{aligned} S_{i,j,t}^{\text{load}} &= L_{j,t} \widetilde{D}_j + C_{i,j} + H_{j,t}, \\ S_{i,j,t}^{\text{wait}} &= \widehat{W}_{j,t} + C_{i,j} + H_{j,t}, \\ S_{i,j,t}^{\text{risk}} &= \widehat{W}_{j,t} + \lambda_r R_{j,t} + \lambda_b B_{j,t} + C_{i,j} + H_{j,t}. \end{aligned} \quad (14)$$

Here, $\lambda_r = 0.60$ and $\lambda_b = 0.25$. equation 14 defines the risk-aware score used throughout the paper. Relative to current-load routing, this policy changes several elements jointly: it uses the forecast-augmented waiting estimate $\widehat{W}_{j,t}$, adds the upper-tail margin $R_{j,t}$, and adds the load-balance term $B_{j,t}$. The comparison between risk-aware and current-load routing therefore evaluates this bundled score and does not identify the separate causal contribution of forecasted expected demand, predictive uncertainty, or load balancing.

To prevent recommendation-induced herding, a station-specific inbound counter represents vehicles that have been redirected to a station but have not yet begun charging. When a vehicle is assigned to an alternative station, the corresponding counter is immediately increased and is decreased only after the vehicle completes the modeled switching interval and enters the destination system.

Inbound vehicles are included in the effective-load and forecast-pressure calculations used by subsequent assignment decisions. This prevents multiple vehicles with simulation-entry events in the same decision interval from independently selecting the same apparently uncongested station.

The inbound count of an alternative station is capped at its effective charger capacity. A vehicle is not redirected when the effective occupancy of its original station, vehicles in service, waiting, and inbound, is below capacity. This capacity condition is a common gate for all three dynamic policies. Consequently, the expected-demand and upper-quantile terms can influence the ranking of candidate destinations only after the original station has reached effective capacity; they cannot initiate a pre-emptive reassignment while immediate original-station capacity remains available. Otherwise, the lowest-score station is selected only when its score improves upon the original-station score by at least two minutes. Because the station score already includes the eight-minute switching cost for an alternative, this additional threshold suppresses recommendations whose estimated advantage is only marginal. The two-minute value is used as a fixed decision safeguard rather than an empirically optimized threshold.

Because reliable station-to-station travel times are not available in the dataset, all 13 stations are evaluated using a fixed eight-minute travel and inconvenience time for an alternative assignment. This value serves as a stylized combined proxy for additional travel and switching inconvenience and prevents rerouting from being treated as costless. It is specified before the policy comparisons as a moderate non-zero scenario penalty: an alternative station has to overcome a meaningful switching burden, while rerouting can still occur when the original station is sufficiently congested. The value is not selected from the validation or test results, tuned to maximize the reported policy reductions, or estimated from observed Jiaxing origin-destination trips. Consequently, the reported policy effects are conditional on this assumption. A redirected vehicle is held in the inbound state during this eight-minute travel interval before joining the destination queue. No travel time is applied when the vehicle remains at its original station. For each vehicle, total delay is defined as,

$$T_i^{\text{delay}} = W_i^{\text{queue}} + T_i^{\text{switch}} \quad (15)$$

where W_i^{queue} is the simulated queueing time and T_i^{switch} is the modeled eight-minute switching time for a redirected vehicle. Equation 15 therefore accounts for both destinations queueing and the modeled switching time. Total delay, rather than queueing time alone, is used as the primary policy outcome because a policy can otherwise appear beneficial by reducing queues while imposing excessive travel costs.

Finally, the experiments consider two recommendation-acceptance levels are a ϵ {0.75, 1.00}.

Each vehicle is assigned a fixed uniform recommendation-acceptance draw during immutable scenario generation. A vehicle follows a routing recommendation when its stored draw is less than or equal to the evaluated recommendation-acceptance rate. The 0.75 and 1.00 levels represent scenarios with 75% and 100% recommendation acceptance rather than behaviorally estimated compliance rates. Because the draw is fixed across policies, differences between recommendation-acceptance scenarios do not alter the charging-initiation event stream or other stochastic inputs.

3.6. Experimental Scenarios and Statistical Analysis

Day selection: Twenty-one test days are selected deterministically from the test period using stratification by day of week and daily charging-initiation volume. Within each weekday group, the days nearest the 0.15, 0.50, and 0.85 quantiles of daily charging-initiation volume are selected. This produces three low-, medium-, and high-volume representatives for each weekday and avoided over-representing a particular weekday or demand level. Table 1 reports the exact dates.

Demand and capacity stressors: The assignment policies are evaluated under combinations of two demand levels

and two infrastructure-availability levels.

The demand multiplier is $m_d \in \{1.0,1.2\}$, representing observed demand and a 20% demand-increase scenario.

The charger-outage probability is $m_o \in \{0.0,0.1\}$, representing full capacity and a scenario in which each charger is independently unavailable with probability 0.10. The 20% demand increase is used to raise the number of charging-initiation events while preserving the empirical day, station, and service-duration structure through resampling. The 10% charger-outage probability represents partial charger-level unavailability rather than complete station closure. Across the 42 unique outage realizations, 21 simulation days at each of the two demand levels, the mean realized network-capacity reduction is 9.91%, corresponding to a mean effective capacity of 82.88 of 92 chargers. The mean reduction is 9.73% without demand growth and 10.09% with the 20% demand increase; individual realizations range from 3.26% to 18.48%. Neither stress value is a forecast of future demand or an estimate of historical outage frequency. Independent charger failures provide a reproducible capacity stressor, while the requirement that each station retain at least one charger avoids a degenerate all-closed station.

The forecasting, simulation, and routing settings are consolidated in Table 2. The table distinguishes configuration choices fixed before final test evaluation, validation-controlled early stopping, structural model definitions, scenario-design assumptions, and numerical implementation safeguards. The validation subset is used only for early stopping; it is not used to optimize the fixed tree settings, Tweedie variance power, routing weights, or behavioral scenario values. The magnitude of the reported forecasting and simulation results remains conditional on these choices.

Table 1. Simulation dates selected from the chronological test period by weekday and daily charging-initiation volume

Weekday	Low-volume date	Median-volume date	High-volume date
Monday	2021-11-22	2021-11-29	2021-12-13
Tuesday	2021-08-24	2021-08-31	2021-11-23
Wednesday	2021-08-25	2021-09-15	2021-10-06
Thursday	2021-09-23	2021-11-04	2021-11-18
Friday	2021-10-22	2021-12-03	2021-12-17
Saturday	2021-12-04	2021-12-18	2021-12-25
Sunday	2021-10-03	2021-10-24	2021-12-19

Table 2. Key forecasting and routing parameters used in the analysis

Parameter	Value	Selection basis
Tweedie variance power	1.35	Fixed analysis setting
Forecast-pressure weight λ_f	0.50	Fixed policy setting
Risk weight λ_r	0.60	Fixed policy setting
Load-balance weight λ_b	0.25	Fixed policy setting
Minimum routing gain	2 min	Decision safeguard
Switching time	8 min	Scenario assumption
Waiting tolerance	30 min	Scenario assumption

Together with the two recommendation-acceptance rates and four assignment policies, the full experimental design comprises $21 \times 2 \times 2 \times 2 \times 4 = 672$ simulation runs.

Simulation performance measures: The primary simulation outcome is mean total delay. Mean queueing time, queue-abandonment rate, and the proportion of redirected vehicles are reported as complementary outcomes. Simulation-integrity outcomes include vehicle-count and scenario-hash equality across policies, capacity violations, negative inbound counts, non-negative forecasts, and quantile ordering.

The percentage reduction in waiting or total delay relative to the no-routing policy is calculated only when the baseline value is greater than a small numerical tolerance (equation 16):

$$\text{Reduction} = 100 \cdot \frac{T^{\text{baseline}} - T^{\text{policy}}}{T^{\text{baseline}}} \tag{16}$$

When the baseline delay is zero, the percentage reduction is treated as undefined and only the absolute difference is reported.

Statistical analysis: Policy comparisons are performed at the simulation-day level using paired observations. Because all policies are evaluated with identical scenario inputs, the daily policy outcomes are directly paired with the corresponding no-routing outcomes.

For the inferential comparisons reported below, recommendation acceptance is fixed at 1.00. Nonparametric paired bootstrap resampling with 20,000 resamples is used to estimate the mean policy difference and its 95% confidence interval. Resampling is performed over the 21 simulation days rather than over

individual vehicles to preserve within-day dependence.

A policy is interpreted as providing consistent improvement over no routing when the 95% bootstrap confidence interval for the difference in total delay is entirely below zero. The same paired day-level bootstrap procedure is also applied to three direct contrasts among the dynamic policies: risk-aware minus current-load, predicted-wait minus current-load, and risk-aware minus predicted-wait. These comparisons are interpreted using both the confidence interval and the absolute difference in minutes and seconds per vehicle, because a numerical ranking alone does not establish a practically meaningful advantage.

Reproducibility: The forecasting models are implemented with LightGBM (Ke et al., 2017), and the discrete-event simulation is implemented with SimPy. The model configuration is fixed before final test evaluation; the validation subset is used for early stopping only, and all prespecified forecasting families are reported on the untouched test subset. The analysis uses a global seed of 2026 for model fitting, bootstrap resampling, recommendation-acceptance draws, demand-growth resampling, temporal jitter, and charger-outage draws. Scenario-specific seeds are generated deterministically from the base seed together with the simulation date, demand multiplier, outage rate, and the label “scenario” using a SHA-1-based stable-seed function. The scenario identifier is likewise derived from the pipeline version, date, stress settings, and base seed. This procedure ensured that every routing policy receives the same immutable charging-initiation events, service durations, outage realization, and recommendation-acceptance draws.

The archived numerical outputs identify pandas 2.2.2, PyArrow 18.1.0, and Matplotlib 3.10.8. The archived Colab notebook specifies a Python 3 kernel and installation constraints of LightGBM $\geq$ 4.0 and SimPy $\geq$ 4.1; however, the exact resolved Python, LightGBM, and SimPy versions are not preserved in the available runtime artifacts. Numerical values underlying the reported figures are retained together with the experiment-level outputs.

5. Results

5.1. Source-Data Characteristics and Station-Level Heterogeneity

The demand-analysis subset contains 441077 charging-initiation events distributed across 13 stations. Of these published records, 422053 have valid charging-service durations and are retained for service-duration estimation and discrete-event simulation. The source records contained 92 distinct charging-post identifiers. Counting distinct identifiers within each station produce the four-to-eight-post capacity proxies used in the simulation.

The observed charging demand is unevenly distributed across the station network. The three highest-demand stations, Bus Station, Park B, and shopping mall, accounted for 39.6% of all charging initiations, while the five highest-demand stations accounted for 59.3%. Bus Station records the largest number of demand events, with 60809 sessions, whereas Expressway Service District B records the smallest number, with 12401 sessions.

The station-specific mean service duration ranges from 27.3 minutes at Expressway Service District C to 75.4 minutes at Wholesale Market, while the station-specific median ranges from 23.0 minutes at Expressway Service District A to 48.1 minutes at Park B. At every station, the mean exceeds the median, consistent with positively skewed service-duration distributions. The capacity of individual stations ranged from four to eight charging posts. Across the complete source dataset, approximately 7.25 GWh of energy is recorded. Table 3 reports both descriptive measures so that the observed means can be distinguished from the medians used in the routing-score approximation.

Note that mean and median durations are descriptive summaries of valid transaction-level service times. The station median, not the mean, is used only as the typical-duration multiplier in the routing-score approximation; simulated service completion uses each vehicle's observed duration. Capacity is proxied by the number of distinct charging-post identifiers observed within each station. Stations are ordered by charging-initiation volume.

The observed values indicate substantial heterogeneity in both demand volume and service duration. The consistent mean-median gap also shows why the mean is retained for descriptive reporting but not used as the typical-duration multiplier in the routing score. Consequently, a network-wide average demand or service-duration assumption would not adequately represent the operational differences among stations.

5.2. Cumulative Charging-Demand Forecasting

Table 4 presents the overall forecasting results for cumulative 15-, 30-, and 60-minute demand. The machine-learning count models consistently outperform the daily seasonal baseline in terms of MAE and RMSE. At the 15-minute horizon, the Tweedie model achieves an MAE of 0.633 and an RMSE of 0.974, corresponding to reductions of 17.6% and 26.8%, respectively, relative to the daily seasonal model. At the 30-minute horizon, the corresponding reductions are 19.8% for MAE and 24.9% for RMSE. At the 60-minute horizon, the Tweedie model reduces MAE by 19.0% and RMSE by 21.7%.

Table 3. Station-level charging demand, service-duration distribution, and capacity proxy

Station	Charging initiations	Network share (%)	Valid service records	Mean duration (min)	Median duration (min)	Capacity proxy
Bus Station	60809	13.8	58480	69.0	43.0	8
Park B	57294	13.0	56294	65.1	48.1	8
Shopping Mall	56605	12.8	55275	64.2	38.5	8
Expressway Service District C	50187	11.4	46260	27.3	23.2	8
Government Agency	36551	8.3	35775	74.2	45.4	8
Wholesale Market	34491	7.8	30765	75.4	31.9	8
Technology Park	28867	6.5	28620	56.3	38.5	4
Park A	27845	6.3	27406	41.8	23.3	8
Tourist Attraction	23659	5.4	22723	42.3	23.4	8
Financial Industrial Park	18923	4.3	18232	53.2	42.1	8
Industrial Park	18370	4.2	17902	69.0	36.6	8
Expressway Service District A	15075	3.4	12976	27.8	23.0	4
Expressway Service District B	12401	2.8	11345	30.5	25.9	4

Table 4. Point-forecast performance for cumulative charging-initiation demand in the chronological test period.

Horizon (min)	Model	MAE	RMSE	WAPE	R^2	Bias
15	Daily seasonal	0.769	1.330	1.112	-0.390	-0.001
15	Weekly seasonal	0.775	1.341	1.120	-0.413	-0.008
15	Poisson	0.635	0.974	0.918	0.255	-0.053
15	Tweedie	0.633	0.974	0.916	0.255	-0.057
15	Hurdle	0.636	0.975	0.920	0.253	-0.053
15	Quantile Q50	0.577	1.078	0.834	0.087	-0.348
30	Daily seasonal	1.203	1.956	0.870	-0.117	-0.003
30	Weekly seasonal	1.224	1.987	0.885	-0.152	-0.016
30	Poisson	0.966	1.469	0.698	0.370	-0.110
30	Tweedie	0.964	1.469	0.697	0.370	-0.112
30	Hurdle	0.970	1.471	0.701	0.368	-0.103
30	Quantile Q50	0.941	1.562	0.680	0.288	-0.399
60	Daily seasonal	1.840	2.889	0.665	0.171	-0.005
60	Weekly seasonal	1.899	2.980	0.686	0.118	-0.032
60	Poisson	1.494	2.262	0.540	0.492	-0.226
60	Tweedie	1.490	2.263	0.539	0.491	-0.240
60	Hurdle	1.507	2.269	0.545	0.489	-0.205
60	Quantile Q50	1.499	2.372	0.542	0.441	-0.552

The daily seasonal model outperforms the weekly seasonal model at every horizon and is therefore used as the primary reference for relative-improvement calculations. At the 15-minute horizon, the daily and weekly seasonal WAPE values are 1.112 and 1.120. These values mean that the summed absolute errors are 111.2% and 112.0%, respectively, of the total observed charging-initiation count; they do not mean that more than 100% of individual predictions are incorrect. Values above one are possible because WAPE is unbounded above. In this sparse station-interval setting, many targets are zero or small, so timing a charging initiation

one interval early or late can contribute absolute error in two low-count intervals while the denominator remains the total observed count. The relative forecasting performance improves as the cumulative horizon increases. The R^2 value of the Tweedie model increases from 0.255 at 15 minutes to 0.491 at 60 minutes, while its WAPE decreases from 0.916 to 0.539. Cumulative one-hour demand is therefore more predictable than demand within an individual 15-minute interval.

The Poisson and Tweedie models produce nearly identical performance. The Tweedie model achieves the lowest MAE and WAPE at all three horizons, whereas the Poisson model produces a marginally lower RMSE at 60 minutes. The hurdle model performs similarly to the two count-regression models but do not improve their point-forecasting accuracy. At 60 minutes, its MAE and RMSE exceed the Tweedie values by 0.017 and 0.006, respectively. Nevertheless, its binary occurrence component shows AUC values of 0.808, 0.848, and 0.889 at the 15-, 30-, and 60-minute horizons, respectively. Its use in routing is therefore motivated by the interpretability of its occurrence--magnitude decomposition, not by superior point-forecast performance. The Q50 model produces the lowest MAE at 15 and 30 minutes. However, this result is accompanied by substantial systematic underprediction. Its predicted demand totals are 50.4%, 28.8%, and 20.0% below the observed totals at the three respective horizons. By comparison, the Tweedie model underestimates aggregate demand by approximately 8.1-8.7%. Therefore, the Q50 model represents typical or median demand more accurately but is less suitable as an estimator of expected network load.

Station-level results show that predictability differs across locations. At the 60-minute horizon, the Tweedie model achieves its highest station-level R^2 at Technology Park ($R^2 = 0.614$), whereas its lowest value is observed at Expressway Service District A ($R^2 = 0.167$). Thus, the improvement obtained from the cumulative target definition does not eliminate spatial differences in forecasting difficulty.

5.3. Probabilistic Forecast Calibration

The empirical performance of the Q10-Q90 prediction intervals is reported in Table 6. The nominal interval coverage is 80%. Empirical coverage exceeds the nominal level at all horizons, reaching 89.8% at 15 minutes, 89.5% at 30 minutes, and 83.2% at 60 minutes. The prediction intervals are therefore conservative, particularly at the shorter horizons. Interval width increases from 1.70 charging events at 15 minutes to 4.53 events at 60 minutes, reflecting the larger magnitude and uncertainty of cumulative demand over longer time windows.

The Q10 model collapses to zero for all 15- and 30-minute observations and for 51.8% of the 60-minute observations. This behavior is consistent with the high proportion of zero-demand station-interval combinations. Quantile crossing is not observed at the 15- or 30-minute horizons and occurs in only 0.0016% of observations at 60 minutes before monotonic reordering.

Figure 1 summarizes the point and probabilistic forecasting results. Figure 1 (a) shows that the learned models consistently reduce MAE relative to the daily seasonal baseline, although the low Q50 error is accompanied by systematic underprediction. Figure 1 (b) shows that empirical interval coverage remains above the nominal 80% level at every horizon, indicating conservative uncertainty estimates, particularly at 15 and 30 minutes.

Table 5. Overall Q10-Q90 prediction-interval performance

Horizon (min)	Coverage (%)	Width	Coverage deviation (pp.)	Interval score	Q10 zero rate (%)
15	89.85	1.700	9.85	2.702	100.00
30	89.45	2.939	9.45	4.288	100.00
60	83.15	4.528	3.15	6.892	51.77

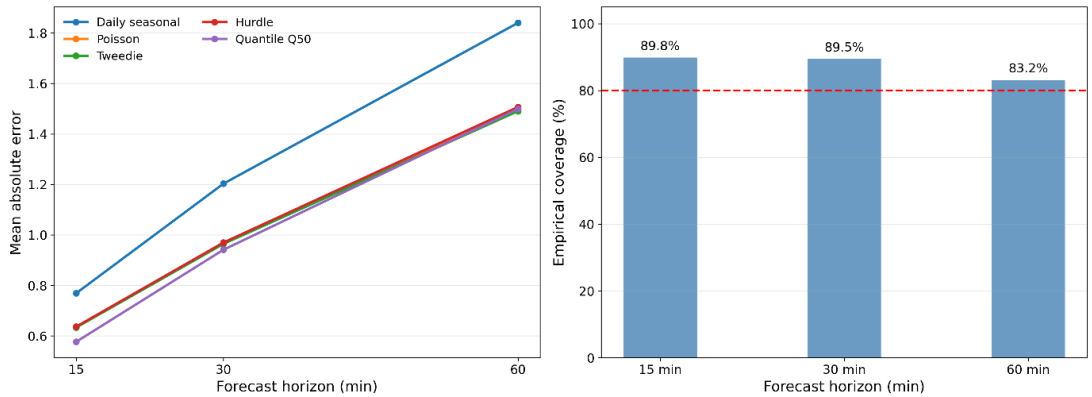


Figure 1. Forecast accuracy and probabilistic calibration for cumulative 15-, 30-, and 60-minute demand. (a) compares mean absolute error across the principal point-forecast models. (b) compares empirical Q10-Q90 coverage with the nominal 80% level.

5.4. Simulation Integrity and Experimental Isolation

The corrected discrete-event simulation completes all 672 planned experiments. These experiments represent 21 simulation days, two demand levels, two charger-outage levels, two recommendation-acceptance levels, and four station-assignment policies. A total of 260 automated integrity tests are performed, and all tests pass. The common-random-number design is confirmed by 84 successful vehicle-count equality checks and 84 successful scenario-hash equality checks. The no-routing policy is invariant to the recommendation-acceptance parameter in all 84 relevant comparisons. No capacity violations or negative inbound-reservation counters are observed. Forecasts remain non-negative, and quantile-ordering checks pass for all forecasting horizons. These results confirm that the policy comparisons are based on identical vehicle streams, service durations, and outage realizations. Consequently, differences among policies are attributable to assignment decisions rather than to variation in the simulated input scenarios.

5.5. Performance under Normal Operating Conditions

Under observed demand and full charger availability, the baseline system does not develop queues. All four assignment policies produce zero mean waiting time, zero total delay, zero abandonment, and zero rerouting across the 21 simulation days. The dynamic policies therefore remain inactive when the original station has sufficient capacity. For example, on the representative normal-condition day of 24 August 2021, all 721 simulated vehicles are served at their original stations under every policy, and no rerouting decision is made.

This behavior shows that the congestion trigger and minimum-gain conditions successfully prevent unnecessary station switching. Because the no-routing delay is already zero, percentage delay reductions are undefined for the normal scenario and are not reported.

5.6. Performance under Demand and Capacity Stress

Table 7 summarizes policy performance in the three stress scenarios at full routing acceptance. Total delay includes both simulated queueing time and the eight-minute switching penalty assigned to rerouted vehicles.

When 10% of charger capacity is unavailable, the no-routing policy produces a mean total delay of 0.814 minutes per vehicle and an abandonment rate of 0.527%. The current-load, predicted-wait, and risk-aware policies reduce mean total delay to 0.183, 0.180, and 0.174 minutes, respectively. These values correspond to reductions of 77.6%, 77.9%, and 78.7%. Only approximately 2.1-2.3% of vehicles required rerouting.

Under the 20% demand-increase scenario, mean total delay increases to 1.845 minutes without routing. The current-load, predicted-wait, and risk-aware policies reduce this value to 0.442, 0.461, and 0.427 minutes, representing improvements of 76.0%, 75.0%, and 76.9%, respectively. The dynamic policies reroute between 4.8% and 5.5% of vehicles.

The largest baseline delay occurs under combined demand and capacity stress. Without routing, mean total delay reaches 3.505 minutes, and 2.962% of vehicles abandon the queue. The three dynamic policies reduce total delay to between 0.770 and 0.850 minutes. Current-load and risk-aware assignment achieves nearly identical reductions of approximately 78.0%, while predicted-wait assignment achieves a reduction of 75.8%. Figure 2 (a) visualizes the corresponding reduction in mean total delay. The reductions are achieved using selective rather than system-wide rerouting. Even under combined stress, fewer than 10% of vehicles are assigned to an alternative station. Thus, the performance improvement is not produced by transferring the majority of demand away from historically observed stations.

Table 6. Policy performance under stress scenarios with full routing acceptance. Abandonment and rerouting rates are reported as percentages of all vehicles

Scenario	Policy	Mean queue wait (min)	Mean total delay (min)	Abandonment (%)	Rerouted (%)
10% capacity loss	No routing	0.814	0.814	0.527	0.00
	Current load	0.000	0.183	0.000	2.28
	Predicted wait	0.010	0.180	0.005	2.12
	Risk-aware	0.000	0.174	0.000	2.17
20% demand increase	No routing	1.845	1.845	1.120	0.00
	Current load	0.002	0.442	0.000	5.50
	Predicted wait	0.081	0.461	0.056	4.76
	Risk-aware	0.013	0.427	0.015	5.17
Combined stress	No routing	3.505	3.505	2.962	0.00
	Current load	0.017	0.771	0.000	9.43
	Predicted wait	0.175	0.850	0.106	8.44
	Risk-aware	0.069	0.770	0.036	8.76

5.7. Queue Abandonment

Dynamic assignment also reduces the number of vehicles exceeding the 30-minute waiting tolerance. With full routing acceptance, the current-load policy eliminates abandonment in all three stress scenarios. The risk-aware policy eliminates abandonment under isolated capacity loss and reduces it by 98.7% and 98.8% under the demand-increase and combined-stress scenarios, respectively. The predicted-wait policy also produces large reductions but retains small residual abandonment rates. Under combined stress, its abandonment rate is 0.106%, compared with 2.962% for no routing. Figure 2 (b) shows the corresponding reductions in queue abandonment. At 75% routing acceptance, the dynamic policies remain effective, although their reductions are smaller. Depending on the policy and stress condition, total delay is reduced by approximately 70.4-73.2% relative to no routing. This indicates that the operational benefits do not depend on universal compliance with routing recommendations.

5.8. Paired Statistical Comparison

Table 7 reports paired day-level bootstrap comparisons of mean total delay at full routing acceptance. Negative differences indicate improvement relative to no routing. All confidence intervals are entirely below zero, indicating that each dynamic assignment policy reduces mean total delay relative to no routing in all three stress scenarios. The current-load and risk-aware policies improve total delay on all 21 simulated days in every stress condition. The predicted-wait policy improves 20 of 21 days under isolated capacity loss and all 21 days under the remaining two stress conditions.

Differences among the dynamic policies are substantially smaller than their differences from no routing. Risk-aware assignment achieves a lower mean total delay than current-load assignment under isolated capacity loss and the demand-increase scenario. However, under combined stress their aggregate performance is effectively identical: 0.770 minutes for risk-aware assignment and 0.771 minutes for current-load assignment.

Predicted-wait assignment is slightly less effective than the other dynamic policies as stress increases. Under combined stress, it produces approximately 0.079 minutes more total delay than current-load assignment. Nevertheless, its performance remains substantially better than the no-routing baseline.

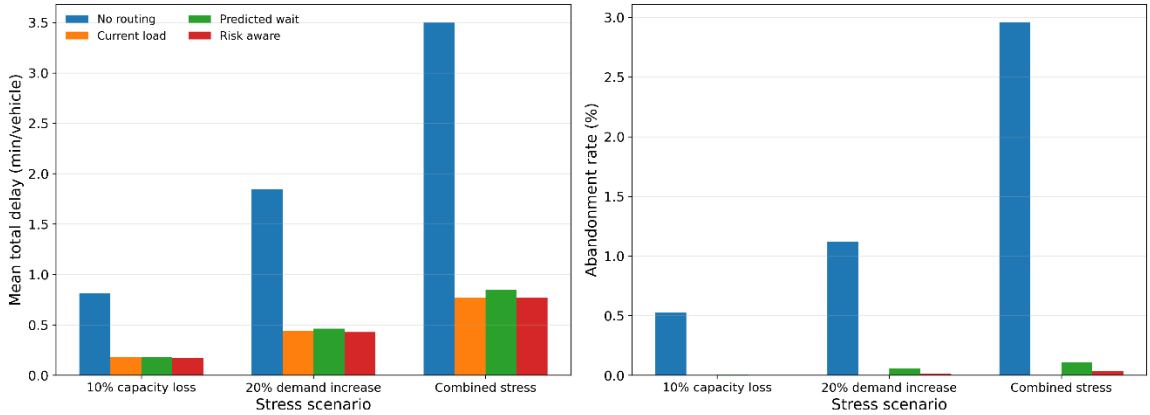


Figure 2. Simulation outcomes under the three stress scenarios with full recommendation acceptance. (a) reports mean total delay, including queueing time and the station-switching penalty. (b) reports queue-abandonment rates. All dynamic routing policies substantially reduced delay and nearly eliminated abandonment relative to no routing.

Table 7. Paired bootstrap comparison of mean total delay against the no-routing policy. Confidence intervals were obtained by resampling the 21 paired simulation days

Scenario	Policy	Policy mean (min)	Reduction (%)	Mean difference (min)	95% CI
10% capacity loss	Current load	0.183	77.6	-0.632	[-1.003, -0.351]
	Predicted wait	0.180	77.9	-0.635	[-1.011, -0.350]
	Risk-aware	0.174	78.7	-0.641	[-1.017, -0.356]
20% demand increase	Current load	0.442	76.0	-1.403	[-1.709, -1.111]
	Predicted wait	0.461	75.0	-1.384	[-1.688, -1.090]
	Risk-aware	0.427	76.9	-1.418	[-1.722, -1.128]
Combined stress	Current load	0.771	78.0	-2.734	[-3.228, -2.256]
	Predicted wait	0.850	75.8	-2.655	[-3.141, -2.188]
	Risk-aware	0.770	78.0	-2.735	[-3.231, -2.259]

6. Discussion and Limitations

The forecasting results show that cumulative charging-initiation counts can be predicted more accurately than the daily and weekly seasonal baselines, although the improvement is moderate rather than transformative. Poisson and Tweedie gradient boosting produce nearly identical point forecasts, and their relative performance improve as the cumulative horizon increased. At 60 minutes, the models reach an R^2 of approximately 0.49 and a WAPE of approximately 0.54, whereas the 15-minute target remains more difficult because station-level counts are sparse. This horizon-dependent pattern is consistent with prior charging-load studies showing that temporal aggregation and target construction materially affect forecast accuracy (Unterluggauer et al., 2021; Hussain et al., 2025; Mansour et al., 2026). The hurdle formulation does not improve point accuracy, while the Q50 model achieves low MAE at the cost of substantial aggregate underprediction. The Q10-Q90 intervals are conservative, and the lower quantile frequently collapses to zero. The probabilistic outputs should therefore be interpreted as broad indicators of upper-tail demand rather than as a finely calibrated predictive distribution.

The simulation results support the operational value of dynamic assignment under the evaluated stress conditions. The policies remain inactive under observed demand and full capacity, indicating that the immediate-capacity rule and minimum-gain threshold prevent unnecessary switching. Under demand growth, capacity loss, and combined stress, the dynamic policies reduce mean total delay by approximately 75-79% at full recommendation acceptance and nearly eliminate abandonment while redirecting fewer than 10% of vehicles. Because total delay includes the eight-minute switching time, these gains are not obtained by shifting queueing costs outside the objective. The CRN design and integrity checks further strengthen this comparison by ensuring that every policy receives identical arrivals, service durations, outages, and acceptance draws.

The main comparative finding is that forecast-aware routing offers little practical advantage over the simpler current-load policy. Under combined stress, mean total delay is 0.770 minutes for risk-aware routing and 0.771 minutes for current-load routing. Thus, nearly all of the observed benefit is already captured by the shared congestion trigger, switching-cost rule, and representation of committed inbound vehicles. Forecast pressure may become more useful when near-future arrivals differ sufficiently across stations to alter decisions before congestion is visible in current occupancy, but the present scenarios do not produce a large incremental gain. Deployment should therefore balance any forecast-based improvement against the additional requirements for model training, calibration, monitoring, and maintenance.

The results suggest three practical principles. Routing should be selective, redirected vehicles should be included in the destination state before they arrive, and policy evaluation should include travel-related delay and abandonment rather than queueing time alone. The benefit also persists at 75% acceptance, suggesting that universal compliance is not required. However, the acceptance rate is an abstract behavioral parameter; actual compliance will depend on expected benefit, trust, route constraints, charger compatibility, price, and user preferences (Hoen et al., 2023; Hanni et al., 2024; Brückmann and Bernauer, 2023). Moreover, the independent contribution of inbound reservations is not isolated through ablation, so the present experiments demonstrate the performance of the complete routing architecture rather than the causal effect of that component alone.

Several limitations constrain the interpretation of the findings. The source data do not contain a reliable physical arrival timestamp or directly observed queue-waiting time. Charging start is therefore used as the demand event and simulated arrival time, which means that the study models counterfactual congestion among observed charging initiations rather than reconstructing historical queues or including vehicles that left without charging. The fixed 30-minute patience threshold and eight-minute switching time also simplify heterogeneous behavior and geography. Actual waiting tolerance and detour cost depend on the driver, trip purpose, origin-destination pair, traffic, charger compatibility, battery state of charge, and station amenities.

The experimental scope is also limited. The analysis uses one charging network from Jiaxing during 2019-2021, including the COVID-19 disruption, and the simulation covers 21 weekday-balanced test days rather than the full test period. All 13 stations are treated as feasible alternatives because route-specific coordinates and travel times are unavailable. The demand-growth and outage scenarios are stylized, and the routing weights, inbound cap, minimum gain, and switching time are fixed without a dedicated sensitivity study. Forecasting is evaluated using one chronological split, while the bootstrap analysis establishes improvement over no routing but does not test pairwise superiority among the dynamic policies. Consequently, the results establish the potential of coordinated assignment under the stated assumptions, not the realized performance of a deployable navigation service or general superiority across charging networks.

Future work should evaluate the framework using observed arrival and waiting-time data, route-specific travel costs, geographically restricted candidate stations, heterogeneous patience and acceptance models, rolling-origin forecast evaluation, component-level ablations, parameter sensitivity, and additional charging networks. These extensions are particularly important for determining when forecast uncertainty provides enough operational value to justify its complexity beyond current-load routing.

7. Conclusion

This study investigated whether short-term cumulative charging-demand forecasts can support congestion-aware assignment in a public electric-vehicle charging network. Station-level charging initiations were forecasted over 15-, 30-, and 60-minute windows using seasonal, count-regression, hurdle, and quantile models. The forecasts were integrated with a discrete-event simulation that incorporated station-specific service durations, partial compliance, switching cost, queue abandonment, inbound reservations, and common-random-number scenario control.

Poisson and Tweedie gradient boosting produced moderate but consistent improvements over daily seasonal forecasting, with the strongest relative performance at the 60-minute cumulative horizon. In the simulation, the dynamic policies introduced no unnecessary rerouting under normal conditions and substantially reduced total delay and abandonment under demand and capacity stress. These improvements were achieved by redirecting only a small share of vehicles. At full recommendation acceptance, risk-aware routing produced the lowest aggregate delay, but its advantage over the simpler current-load policy was operationally small.

The current-load policy achieved nearly the same benefit as the risk-aware policy, so the additional forecast-risk terms were not operationally decisive in these experiments. The independent effect of inbound reservations remains to be measured through component-level ablation. Further evaluation should use observed vehicle-arrival and waiting-time data, route-specific travel costs, heterogeneous behavioral models, broader sensitivity analyses, and networks from additional cities.

Author Contributions

The percentages of the author' contributions are presented below. The author reviewed and approved the final version of the manuscript.

	O.A.
C	100
D	100
DCP	100
DAI	100
L	100
W	100
CR	100
SR	100
PM	100

C= concept, D= design, S= supervision, DCP= data collection and/or processing, DAI= data analysis and/or interpretation, L= literature search, W= writing, CR= critical review, SR= submission and revision, PM= project management.

Conflict of Interest

The author declared that there is no conflict of interest.

Ethical Consideration

Ethics committee approval was not required for this study because there was no study on animals or humans.

Acknowledgements

This study did not generate or collect a new dataset. It reuses the publicly available Jiaxing electric-vehicle charging transaction dataset introduced by (Zhang et al., 2025).

References

Aghsaee, R., Hecht, C., Schwinger, F., Figgener, J., Jarke, M., & Sauer, D. U. (2023). Data-Driven, Short-Term Prediction of Charging Station Occupation. *Electricity, 4*, 142–160. https://doi.org/10.3390/electricity4020009

Alaraj, M., Radi, M., Alsisi, E., Majdalawieh, M., & Darwish, M. (2025). Machine Learning-Based Electric Vehicle Charging Demand Forecasting: A Systematized Literature Review. *Energies, 18*, 4779. https://doi.org/10.3390/en18174779

Ali, M. W., Mustafa, M. A., Shuvo, M. A., & Sick, B. (2026). Location-Based Probabilistic Load Forecasting of Electric Vehicle Charging Sites: Deep Transfer Learning with Multi-quantile Temporal Convolutional Network. In *Architecture of Computing Systems* (Vol. 15839). https://doi.org/10.1007/978-3-032-03281-2_14

Basmadjian, R., Kirpes, B., Mrkos, J., & Cuchý, M. (2020). A Reference Architecture for Interoperable Reservation Systems in Electric Vehicle Charging. *Smart Cities, 3*, 1405–1427. https://doi.org/10.3390/smartcities3040067

Brückmann, G., & Bernauer, T. (2023). An experimental analysis of consumer preferences towards public charging infrastructure. *Transportation Research Part D: Transport and Environment, 116*, 103626. https://doi.org/10.1016/j.trd.2023.103626

Dang, S., Peng, L., Zhao, J., Li, J., & Kong, Z. (2022). A Quantile Regression Random Forest-Based Short-Term Load Probabilistic Forecasting Method. *Energies, 15*, 663. https://doi.org/10.3390/en15020663

Dudkina, E., Scarpelli, C., Apicella, V., Ceraolo, M., & Crisostomi, E. (2025). Optimised Centralised Charging of Electric Vehicles Along Motorways. *Sustainability, 17*, 5668. https://doi.org/10.3390/su17125668

Elahe, M. F., Kabir, M. A., Mahmud, S. M., & Azim, R. (2022, December). Factors Impacting Short-Term Load Forecasting of Charging Station to Electric Vehicle. *Electronics, 12*, 55. https://doi.org/10.3390/electronics12010055

Hanni, U. e., Yamamoto, T., & Nakamura, T. (2024). Modeling of the Acceptable Waiting Time for EV Charging in Japan. *Sustainability, 16*, 2536. https://doi.org/10.3390/su16062536

Heting, Q., Shuihai, D., Huayan, S., & Jun, Z. (2021, June). Charging station planning based on the accumulation prospect theory and dynamic user equilibrium. *Complex & Intelligent Systems, 9*, 2521–2539. https://doi.org/10.1007/s40747-021-00414-w

Hoen, F. S., Díez-Gutiérrez, M., Babri, S., Hess, S., & Tørset, T. (2023). Charging electric vehicles on long trips and the willingness to pay to reduce waiting for charging: Stated preference survey in Norway. *Transportation Research Part A: Policy and Practice, 175*, 103774.

https://doi.org/10.1016/j.tra.2023.103774

Hussain, A., Lu, Q.-C., Rizvi, S. S., Wang, S., & Kwon, S. J. (2025, October). Short term demand forecasting of electric vehicle charging stations using context aware temporal transformer model. *Scientific Reports, 15*. https://doi.org/10.1038/s41598-025-20557-x

Ke, G., Meng, Q., Finley, T., Wang, T., Chen, W., Ma, W., Ye, Q., & Liu, T.-Y. (2017). LightGBM: a highly efficient gradient boosting decision tree. *Proceedings of the 31st International Conference on Neural Information Processing Systems* (pp. 3149–3157). Red Hook, NY, USA: Curran Associates Inc.

Keskin, F., Yıldız, M., & Arslannur, B. (2024, July). A Data-Driven Framework for Driving Cycle Generation and Analysis. *Transportation Research Record: Journal of the Transportation Research Board*. https://doi.org/10.1177/03611981241260700

Kim, M., Park, W. Y., Moon, H. S., & Kim, Y.-S. (2026). A Review of Electric Vehicle Charging Demand Forecasting Models by Prediction Horizon: A Multi-Criteria Decision Analysis Approach. *Journal of Electrical Engineering & Technology, 21*, 1457–1476. https://doi.org/10.1007/s42835-025-02556-0

Lee, K.-B., Ahmed, M. A., Kang, D.-K., & Kim, Y.-C. (2020). Deep Reinforcement Learning Based Optimal Route and Charging Station Selection. *Energies, 13*, 6255. https://doi.org/10.3390/en13236255

Liu, H., Yin, W., Yuan, X., & Niu, M. (2018). Reserving Charging Decision-Making Model and Route Plan for Electric Vehicles Considering Information of Traffic and Charging Station. *Sustainability, 10*, 1324. https://doi.org/10.3390/su10051324

Mansour, H. S., Mohamed, A. S., & Abdel-Aziz, M. (2026). Electric vehicles charging stations load forecasting based on hybrid XGBoost-BiLSTM model. *Scientific Reports, 16*, 374. https://doi.org/10.1038/s41598-025-29739-z

Matkovic, D., Pilski, T. M., & Capuder, T. (2025, August). Participation of electric vehicle charging station aggregators in the day-ahead energy market using demand forecasting and uncertainty-based pricing. *Energy, 328*, 136299. https://doi.org/10.1016/j.energy.2025.136299

Mishra, P., Miller, E., Santhanagopalan, S., Bennion, K., & Meintz, A. (2022). A Framework to Analyze the Requirements of a Multiport Megawatt-Level Charging Station for Heavy-Duty Electric Vehicles. *Energies, 15*, 3788. https://doi.org/10.3390/en15103788

Mohammad, F., Kang, D.-K., Ahmed, M. A., & Kim, Y.-C. (2023). Energy Demand Load Forecasting for Electric Vehicle Charging Stations Network Based on ConvLSTM and BiConvLSTM Architectures. *IEEE Access, 11*, 67350–67369. https://doi.org/10.1109/access.2023.3274657

Nie, J., Xia, S., Liu, Y., Ding, S., Hu, L., Zhao, M., Fan, Y., Abdel-Aty, M., Preindl, M., & Jiang, X. (2023). A Data-Driven and Human-Centric EV Charging Recommendation System at City-Scale. *Proceedings of the 14th ACM International Conference on Future Energy Systems*, (pp. 427–438). https://doi.org/10.1145/3575813.3597350

Orzechowski, A., Lugosch, L., Shu, H., Yang, R., Li, W., & Meyer, B. H. (2023). A data-driven framework for medium-term electric vehicle charging demand forecasting. *Energy and AI, 14*, 100267. https://doi.org/10.1016/j.egyai.2023.100267

Rupnik, B., Wang, Y., & Kramberger, T. (2025). Hybrid Model for Motorway EV Fast-Charging Demand Analysis Based on Traffic Volume. *Systems, 13*, 272. https://doi.org/10.3390/systems13040272

Schoenberg, S., & Dressler, F. (2023). Reducing Waiting Times at Charging Stations With Adaptive Electric Vehicle Route Planning. *IEEE Transactions on Intelligent Vehicles, 8*, 95–107. https://doi.org/10.1109/TIV.2022.3140894

Sreekumar, A. V., & Lekshmi, R. R. (2024, December). Electric vehicle charging station demand prediction model deploying data slotting. *Results in Engineering, 24*, 103095. https://doi.org/10.1016/j.rineng.2024.103095

Unterluggauer, T., Rauma, K., Järventausta, P., & Rehtanz, C. (2021). Short-term load forecasting at electric vehicle charging sites using a multivariate multi-step long short-term memory: A case study from Finland. *IET Electrical Systems in Transportation, 11*, 405–419. https://doi.org/10.1049/els2.12028

Widmann, J., & Sawodny, O. (2026). Intention-Aware Electric Vehicle Routing: A Markovian Queuing Model Approach to Reduce Wait Times at Charging Stations. *IET Intelligent Transport Systems, 20*. https://doi.org/10.1049/itr2.70180

Yi, Z., Liu, X. C., Wei, R., Chen, X., & Dai, J. (2021, August). Electric vehicle charging demand forecasting using deep learning model. *Journal of Intelligent Transportation Systems, 26*, 690–703. https://doi.org/10.1080/15472450.2021.1966627

Yu, L., Ge, X., Cai, C., & Wang, S. (2026, September). Short-term load forecasting for electric vehicle charging stations based on an adaptive multi-module cascaded framework. *Energy and AI, 25*, 100829. https://doi.org/10.1016/j.egyai.2026.100829

Zhang, T., Tang, D., Fan, P., Wang, Q., & Wang, P. (2025a). A Probabilistic Graphical Model for Predicting Cascade Failures of Electric Vehicle Charging Networks Caused by Hurricanes. *IEEE Transactions on Smart Grid, 16*, 627–639. https://doi.org/10.1109/TSG.2024.3458932

Zhang, Y., Xu, T., Chen, T., Hu, Q., Chen, H., Hu, X., & Jiang, Z. (2025b). A high-resolution electric vehicle charging transaction dataset with multidimensional features in China. *Scientific Data, 12*. https://doi.org/10.1038/s41597-025-04982-1

Black Sea Journal of Engineering and Science
doi: 10.34248/bsengineering.1977492

Open Access Journal
e-ISSN: 2619 – 8991

Research Article
Volume 9 - Issue 5: 2835-2843 / September 2026

EMPIRICAL MASS-RETENTION MODELING, IMAGE-BASED SURFACE TEXTURE ANALYSIS AND COLOR EVALUATION IN VEGETABLE RETANNING OF WET-BLUE LEATHER

Şükrü ÖMÜR[1]*

[1]*Aydın Adnan Menderes University, Aydın Vocational School, Department of Fashion Design, 09010, Aydın, Türkiye*

Abstract: Vegetable retanning modifies the surface, mass-retention and initial color-difference characteristics of wet-blue leather, but dosage selection is still commonly based on practical experience rather than quantitative process descriptors. This study developed a low-cost empirical screening framework for wet-blue bovine leather retanned with mimosa, quebracho and their 50:50 binary mixture at pH 4.0 and pH 5.5. Forty initial tannin dosage levels between 0.5 and 20 g/L were evaluated. Because equilibrium bath concentration was not measured, tannin uptake was expressed only as gravimetric dry weight gain, and fitted curves were interpreted as initial-dosage-based empirical responses rather than thermodynamic adsorption isotherms. Initial color response was evaluated using CIEDE2000 color difference, while digital surface images were analyzed using gray-level co-occurrence matrix descriptors and Surface Roughness Entropy. Quebracho at pH 4.0 displayed a bounded mass-retention trend associated with increased two-dimensional image regularity and reduced entropy. Mimosa at pH 5.5 displayed sustained mass accumulation accompanied by localized image-texture heterogeneity. Across the tested range, mimosa produced lower initial color-difference values than the other tannin systems, while the binary mixture showed intermediate behavior. The combined gravimetric, colorimetric and image-based approach provides a practical non-destructive screening strategy for comparing vegetable retanning conditions. The findings should be interpreted as comparative process trends and should be validated in future work by bath exhaustion monitoring, shrinkage temperature, standardized physical tests and spatially calibrated imaging.

Keywords: Vegetable retanning, Gravimetric mass retention, Surface texture, CIEDE2000, Non-destructive evaluation, Wet-blue leather

***Corresponding author:** Aydın Adnan Menderes University, Aydın Vocational School, Department of Fashion Design, 09010, Aydın, Türkiye
E mail: sukru.omur@adu.edu.tr (Ş. ÖMÜR)
Şükrü ÖMÜR https://orcid.org/0000-0002-7887-722X

Received: June 23, 2026
Accepted: August 28, 2026
Published: September 15, 2026

Cite as: Ömür, Ş. (2026). Empirical mass-retention modeling, image-based surface texture analysis and color evaluation in vegetable retanning of wet-blue leather. *Black Sea Journal of Engineering and Science,* 9(5), 2835-2843.

1. Introduction

Vegetable retanning is a critical stage in wet-blue leather processing because it influences the final structural and aesthetic attributes of the material, including handle, grain tightness, surface uniformity, fullness perception and color. These effects are governed by collagen chemistry, tannin structure, bath pH and post-tanning process conditions (Venter et al., 2012; Covington and Wise, 2019). Condensed tannin extracts, such as mimosa (Acacia mearnsii) and quebracho (Schinopsis lorentzii), are widely used in leather manufacture because of their practical ability to modify collagen-associated properties and because they support more sustainable chemical profiles than many synthetic alternatives (Balasubramanian et al., 2017; Nurichsanto et al., 2023; Wilson et al., 2023).

Despite extensive industrial use, tanners frequently guide retanning recipes and dosage selection by empirical practice rather than by quantitatively structured relationships between applied dosage and measurable outcomes. Conventional evaluation often relies on tactile assessment and end-point appearance, whereas quantitative descriptors linking dosage-dependent deposition to surface morphology, gravimetric retention, physical stability and color performance remain less frequently reported (Balasubramanian et al., 2017; Covington and Wise, 2019). This gap supports the development of complementary low-cost analytical frameworks that can be used alongside established physical and spectroscopic quality-control methods.

Image-based surface analysis offers a practical and low-cost approach for quantifying leather surface morphology. Texture features derived from the gray-level co-occurrence matrix (GLCM), originally formalized for statistical texture classification, can capture spatial patterns related to surface regularity, while Surface Roughness Entropy (SRE) provides an additional statistical descriptor of local gray-level variability based on entropy computed from normalized co-occurrence distributions (Haralick et al., 1973; Baraldi and Parmiggiani, 1995; Sabeenian and Dinesh, 2011;

This work is licensed (CC BY-NC 4.0) under Creative Commons Attribution 4.0 International License

Varghese et al., 2020). In this study, these metrics were adapted as comparative two-dimensional image descriptors; they are not treated as direct measures of three-dimensional physical roughness, bulk fullness, shrinkage stability or chemical tanning efficiency.

Initial color response was assessed using the CIEDE2000 (Delta E00) metric because of its use in color-difference studies (Raggi and Barbiroli, 1993). Nevertheless, recent color-science literature has shown that CAM16-UCS can provide improved perceptual uniformity in many complex color-difference datasets and may outperform older color-difference models under broader viewing and color-space conditions (Li et al., 2017; Luo et al., 2023; Basova et al., 2024). For this reason, Delta E00 is used here as a comparative industrial benchmark for initial color difference, while CAM16-UCS is identified as a necessary extension for future work.

In adsorption-focused studies, Langmuir and Freundlich models are traditionally used to describe equilibrium relationships between solid-phase uptake and residual bath concentration (Ce), and their parameters are meaningful only when the equilibrium phase relationship is experimentally measured (Qiu et al., 2009; Bbumba et al., 2024). In the present study, Ce was not measured; therefore, the fitted curves do not represent thermodynamic adsorption isotherms and should not be interpreted as adsorption capacity, binding affinity or equilibrium saturation. Instead, gravimetric dry mass retention provides an experimentally accessible indicator of total mass deposition on the leather substrate, which may include both chemical interaction and physical deposition.

Accordingly, the objective of this study was to establish a comparative empirical framework for vegetable retanning of wet-blue leather by relating gravimetric mass retention to applied initial dosage (C0) and correlating it with surface texture evolution and color performance. Mimosa, quebracho, and their binary mixture were evaluated under controlled pH conditions using gravimetric mass retention, GLCM-derived texture descriptors, SRE, and CIEDE2000 (Delta E00). The framework is intended as a practical screening tool for textile and leather engineering applications under industrial constraints, not as a substitute for shrinkage temperature, ISO physical tests, spectroscopic bath monitoring, or NIR/PCA-based process control.

2. Materials and Methods

2.1. Materials

Wet-blue leather samples obtained from the same bovine hide and shaved to a standard thickness of 1.2 ± 0.1 mm were used as substrates. Commercial mimosa (Acacia mearnsii) and quebracho (Schinopsis lorentzii) extracts were used as received, together with their 50:50 binary mixture by dry weight. The retained experimental record does not include a supplier certificate specifying commercial grade, sulfitation status or other chemical modification of the extracts. Therefore, the dosage-retention trends are interpreted as responses of the tested commercial materials and should not be generalized to all ordinary or sulfited mimosa and quebracho products without additional chemical specification. All chemicals used for pH adjustment, including formic acid and sodium bicarbonate, were of analytical grade. Distilled water was used for all retanning baths and rinsing procedures. Prior to dosing, the commercial extracts were used directly from their original containers without additional drying, purification, grinding or chemical pretreatment.

2.2. Experimental Design and Retanning Procedure

Leather pieces were cut to an initial dry mass of 5.0 ± 0.2 g. Retanning experiments were performed at a constant bath volume of 400 mL in glass vessels for 8 h at 25 ± 1 °C under mixing to support bath homogeneity.

Two target pH conditions were investigated: pH 4.0 adjusted with formic acid and pH 5.5 adjusted with sodium bicarbonate solution. The available experimental record does not include the exact acid/base concentration, dosing volumes, pH-meter model, or calibration log. Therefore, pH should be interpreted as a controlled target condition within the experimental design rather than as a fully auditable process-control parameter.

The initial tannin dosage was defined as the initial bath concentration (C0, g/L) of the tannin solution. The dosage ranged from 0.5 to 20 g/L across 40 concentration levels, with denser spacing at lower concentrations and wider spacing at higher concentrations. For each tannin system (mimosa, quebracho, and mixture) and pH condition, experiments were conducted in triplicate (n = 3). At the end of the 8 h contact time, fixation was performed in the same bath by lowering the pH to approximately 3.8 using formic acid (Figure 1).

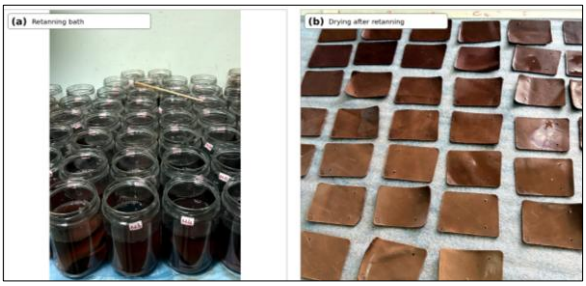


Figure 1. Experimental workflow of the vegetable retanning procedure: (a) immersion of wet-blue leather samples in tannin-containing retanning baths; (b) air-drying of retanned leather samples after fixation and rinsing.

2.3. Gravimetric Uptake and Mass-Retention Calculation

Tannin uptake was quantified exclusively by gravimetric determination of dry mass retention. After retanning and fixation, leather pieces were thoroughly rinsed with distilled water to remove loosely bound material and air-

dried at 25 °C to constant mass. Constant mass was defined as a difference of <0.01 g between two consecutive weighings (equation 1).

$$\text{Weight gain (\%)} = \left[\left(m_{after}\text{-}m_{before}\right)/m_{before}\right]\times 100 \quad (1)$$

where m_{before} is the initial constant dry mass before retanning and m_{after} is the final constant dry mass after retanning and drying. Because shrinkage temperature (Ts), ISO 2420 apparent density and compression-resilience measurements were not performed, gravimetric weight gain is interpreted as mass retention/deposition rather than direct proof of tanning stability or bulk fullness. In future work, Ts should be determined according to ISO 3380, while apparent density and mass per unit area should be determined according to ISO 2420 (International Organization for Standardization, 2015; International Organization for Standardization, 2017).

2.4. Color Measurement

Color was measured using a portable spectrophotometer (Linshang LS170). The CIE L*, a* and b* coordinates were recorded under D65 illumination with a 10° observer angle. Three measurements were taken at different locations on each sample and averaged. The color difference relative to the untreated control was reported as CIEDE2000 (Delta E00), which remains useful for comparability with established industrial color-difference studies (Raggi and Barbiroli, 1993; Luo et al., 2023).

CIEDE2000 was retained to maintain comparability with established leather and industrial color-difference studies. However, because newer uniform color spaces such as CAM16-UCS have shown strong performance in recent color-difference evaluations, the Delta E00 results should be interpreted as comparative initial color-difference values rather than as the final perceptual color model for textured leather surfaces (Li et al., 2017; Luo et al., 2023; Basova et al., 2024). The term initial color consistency is used to avoid implying lightfastness, UV-aging resistance or long-term initial color consistency, none of which was measured in this study.

2.5. Image Acquisition and Surface Texture Analysis

Leather surfaces were imaged under standardized conditions to minimize lighting variability. Images were captured using a DSLR camera with macro capability under stable illumination, converted to 8-bit grayscale, and cropped to a 512 × 512 px region of interest (ROI).

Texture features were extracted using GLCM analysis. GLCMs were computed at a pixel displacement distance of d = 1 and averaged over four angular directions: 0°, 45°, 90° and 135°. In vector form, the corresponding pixel offsets were (1,0), (1,1), (0,1) and (-1,1). Standard GLCM descriptors, including contrast, correlation, homogeneity and energy, were calculated. SRE was computed as Shannon entropy derived from the normalized GLCM distribution (Haralick et al., 1973; Baraldi and Parmiggiani, 1995; Sabeenian and Dinesh, 2011). Energy and entropy were not treated as independent physical measurements; rather, their expected inverse tendency was used cautiously as a consistency check for changes in gray-level order and disorder within the same imaging protocol (Figure 2).

The pixel-to-mm calibration was not available in the archived image metadata. Therefore, the image-derived descriptors should be interpreted as internally comparable metrics within the standardized imaging setup, not as absolute roughness measurements transferable across cameras, lenses or magnification settings without recalibration. This limitation is especially important if the framework is transferred to industrial imaging systems, because GLCM features are sensitive to quantization, displacement distance, angular selection and spatial scaling (Haralick et al., 1973; Baraldi and Parmiggiani, 1995).

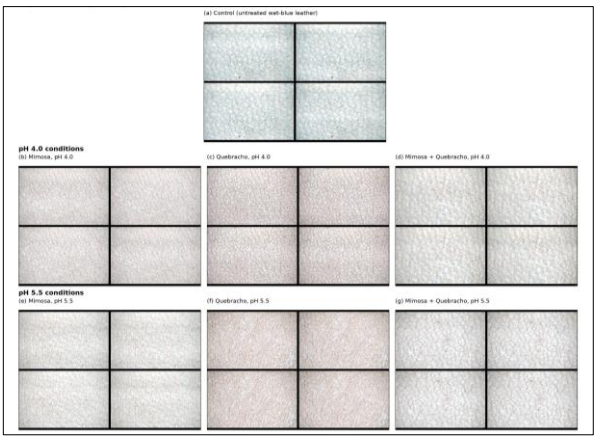


Figure 2. Representative digital surface images used for GLCM- and SRE-based image-processing analysis.

2.6. Statistical Analysis and Empirical Modeling

Analyses were performed using Python (NumPy/Pandas and standard scientific libraries). Pearson correlation coefficients (r) were used to evaluate relationships among gravimetric mass retention, texture metrics (GLCM descriptors and SRE), and Delta E00 values. Because the manuscript dataset does not include a complete inferential output for all pH and agent comparisons, the pH-dependent divergences are interpreted primarily as descriptive empirical trends rather than formal hypothesis-tested effects.

To summarize the relationship between gravimetric mass retention and initial dosage (C0), two neutral mathematical curve forms were used: (i) a bounded-response function to describe curves approaching a plateau-like shape within the tested dosage range and (ii) an empirical power-function to describe sustained dosage-dependent growth. These curve forms are mathematically analogous to commonly used adsorption expressions, but because Ce was not measured, their parameters are descriptive model coefficients rather than thermodynamic adsorption parameters (Qiu et al., 2009; Bbumba et al., 2024). Terms such as plateau-like or sustained response therefore refer only to the empirical

C0-weight-gain relationship.

The complete concentration-level datasets used for curve fitting and color-effectiveness calculations are provided as Supplementary Data S1. The dataset includes tannin content, gravimetric weight gain, Delta E00 and calculated color-effectiveness values for each retanning agent and pH condition.

3. Results

3.1. Empirical Dose-Response of Gravimetric Mass Retention

Tannin deposition was quantified exclusively by gravimetric dry mass retention (weight gain %). Because the equilibrium bath concentration (Ce) was not monitored, the analysis focused on empirical dose-response behavior linking applied initial dosage (C0, g/L) to measured weight gain. The fitted curves are used only to summarize data trends and are not interpreted as thermodynamic isotherms, adsorption capacities, or binding affinities.

The complete raw datasets underlying the dose-response curves, color-difference evaluation and color-effectiveness calculations are provided in Supplementary Data S1.

3.1.1. Quebracho at pH 4.0: Bounded empirical response

For quebracho at pH 4.0, the gravimetric response increased steeply at low dosages and gradually approached a plateau-like shape at higher C0 values. This trend was summarized by a bounded-response fit (R^2 = 0.825), indicating diminishing marginal weight gain at elevated dosages within the tested range (Figure 3). Because extract grade and sulfitation status were not certified in the retained record, the observed trend should be attributed only to the tested commercial quebracho material.

Texture analysis supported an image-based surface-regularity interpretation. Increasing dosage was associated with increased GLCM homogeneity and decreased SRE, consistent with a more ordered two-dimensional grayscale texture under acidic conditions. This interpretation remains strictly image-based; it does not demonstrate three-dimensional physical roughness reduction, equilibrium adsorption or chemical tanning stability.

3.1.2. Mimosa at pH 5.5: sustained empirical power-function trend

In contrast, mimosa at pH 5.5 showed a continuously increasing gravimetric response across the investigated dosage range without a clear plateau. The trend was summarized by an empirical power-function fit (R^2 = 0.755), reflecting sustained dosage-driven mass retention under the tested conditions (Figure 4). Because the commercial modification status of the extract was not certified, this behavior is reported as an empirical response of the tested mimosa material rather than as a universal characteristic of all mimosa extracts.

Compared with quebracho at pH 4.0, the mimosa pH 5.5 system exhibited more localized microtexture variability, as evidenced by a modest increase in SRE and a smaller increase in homogeneity with increasing dosage. This pattern is interpreted as localized two-dimensional surface-texture heterogeneity rather than direct evidence of bulk filling, shrinkage stability, physical roughness change or structural fullness.

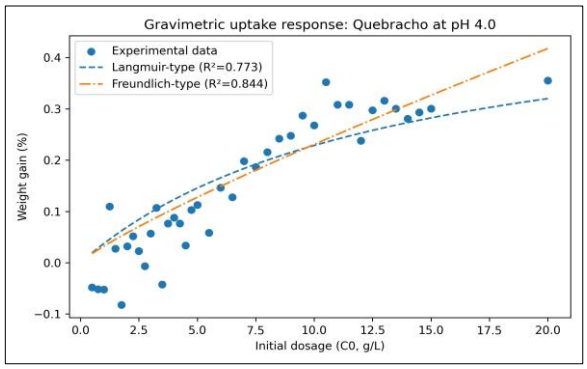


Figure 3. Empirical bounded/power-function dose-response fit for Quebracho at pH 4.0

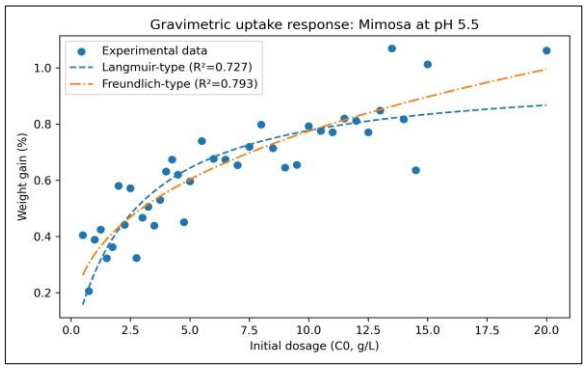


Figure 4. Empirical bounded/power-function dose-response fit for Mimosa at pH 5.5.

3.1.3. Comparative pH-dependent gravimetric responses

A comparative view of the gravimetric responses across agents and pH conditions highlights a clear pH-dependent divergence in the empirical deposition behavior. Quebracho at pH 4.0 tended toward a bounded response accompanied by an image-based increase in surface regularity, whereas mimosa at pH 5.5 demonstrated sustained accumulation with more heterogeneous two-dimensional surface-texture development at higher dosages (Figure 5). These comparisons emphasize that higher mass retention does not correspond to a single surface outcome; instead, dosage-dependent mass retention interacts with pH and tannin type to yield distinct image-derived textural responses.

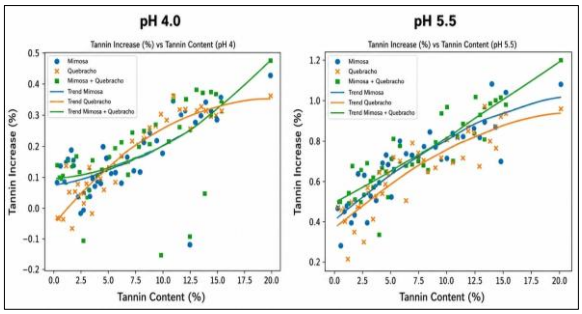


Figure 5. Comparative gravimetric mass retention under pH 4.0 and pH 5.5 conditions.

3.2. Initial Color-Difference Response

The overall optical performance of the leather surface, defined by the color difference (Delta E00) relative to the untreated control, was evaluated alongside gravimetric uptake under varying pH conditions (Tables 1 and 2).

Under pH 4.0 conditions, mimosa produced the lowest mean color difference, indicating lower initial color deviation relative to the untreated control among the tested systems. In contrast, quebracho and the binary mixture exhibited higher initial color deviation. These results should not be interpreted as lightfastness or long-term initial color consistency because no UV-aging or accelerated weathering test was performed.

Table 1. Summary of leather retanning parameters under pH 4.0 conditions (n = 40 per agent)

Group	Tannin uptake (weight gain %, mean ± SD)	Color difference (Delta E00, mean ± SD)
Quebracho	0.149 ± 0.132	20.931 ± 3.294
Mimosa	0.158 ± 0.142	16.335 ± 1.017
Mixture	0.150 ± 0.125	20.069 ± 2.163

Table 2. Summary of leather retanning parameters under pH 5.5 conditions (n = 40 per agent)

Group	Tannin uptake (weight gain %, mean ± SD)	Color difference (Delta E00, mean ± SD)
Quebracho	0.678 ± 0.208	16.911 ± 1.561
Mimosa	0.635 ± 0.201	15.131 ± 2.079
Mixture	0.582 ± 0.193	17.092 ± 1.849

When pH increased to 5.5, gravimetric mass retention increased across all groups and coincided with a general decrease in Delta E00. Based on the concentration-level dataset, mimosa maintained the lowest mean initial color difference at both pH levels within the tested range. However, because color was evaluated only with Delta E00 immediately after processing, these findings should be considered comparative initial color-consistency trends and should be verified with CAM16-UCS and lightfastness or aging tests in future work (Figure 6).

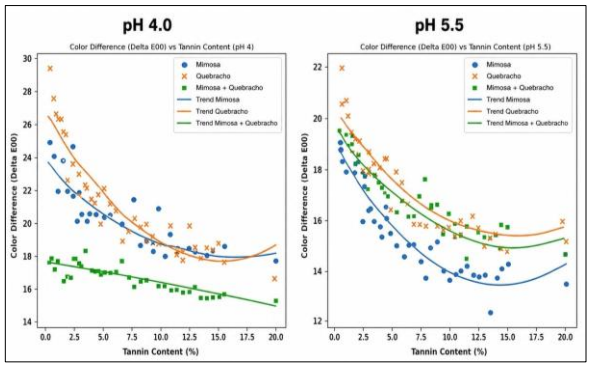


Figure 6. Comparison of agents' color difference (Delta E00) under pH 4.0 and pH 5.5 conditions.

The mixture groups (quebracho + mimosa) demonstrated less consistent initial color responses than mimosa alone. These optical results indicate that pure mimosa offered lower initial color difference under the investigated conditions, although broader validation with additional color models, replicate batches and aging/lightfastness tests is required before any claim of initial color consistency can be made (Figure 7).

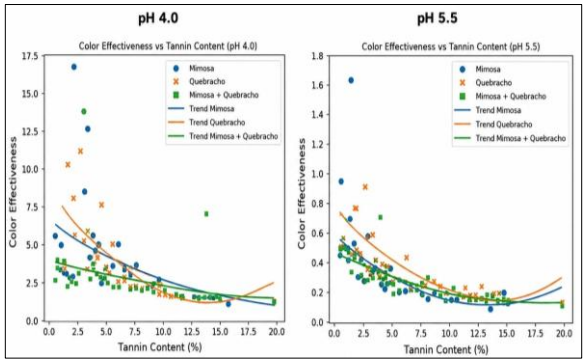


Figure 7. Comparison of agents' color response effectiveness under pH 4.0 and pH 5.5 conditions.

3.3. Surface Texture Evolution from Imaging

Digital image analysis provided objective quantification of changes in two-dimensional surface-image morphology. GLCM descriptors, including homogeneity, captured trends in gray-level spatial regularity, while SRE served as a complementary indicator of gray-level distribution complexity. Because GLCM energy and entropy often vary inversely, they were interpreted together as mutually informative image descriptors rather than as independent physical roughness measurements. These metrics should not be interpreted as direct measures of thickness increase, apparent density, compression-resilience, shrinkage temperature, three-dimensional roughness or bulk fullness.

Representative comparisons between the lowest (0.5 g/L) and highest (20 g/L) dosage conditions illustrated distinct visual and numerical image-texture outcomes (Figure 8). For quebracho at pH 4.0, increasing homogeneity and decreasing SRE supported a progressive image-based surface-regularity tendency.

For mimosa at pH 5.5, the modest increase in SRE indicated localized two-dimensional surface-texture heterogeneity rather than direct evidence of bulk filling or physical roughness change.

Quebracho pH 4.0: At low initial dosage, the sample exhibited high SRE (5.98) and low homogeneity (0.26), indicating a relatively irregular image-texture baseline. At high initial dosage, SRE decreased to 5.52 and homogeneity increased to 0.34. This response should be interpreted as image-based surface regularization under acidic conditions, not as direct physical profilometry evidence.

Mimosa pH 5.5: At low initial dosage, the system began with SRE = 5.55 and homogeneity = 0.34. At high dosage, SRE increased to 5.61 and homogeneity decreased to 0.32. This indicates localized image-texture heterogeneity associated with sustained mass retention. It should not be interpreted as proof of chemical tanning efficacy, physical roughness change or physical fullness without Ts, ISO physical measurements and three-dimensional or calibrated microscopic surface validation.

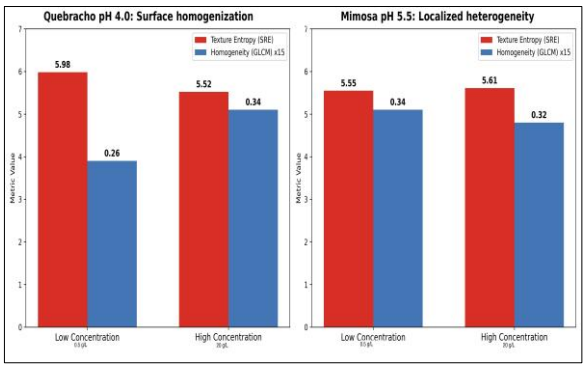


Figure 8. Morphological comparison of lowest and highest tannin dosages based on SRE and GLCM homogeneity

3.4. Combination Analysis

The mimosa-quebracho (50:50) system exhibited intermediate behavior in gravimetric retention and texture response. Although weight gain increased with dosage, the mixture did not replicate the full bounded response of quebracho at pH 4.0 or the sustained power-function response of mimosa at pH 5.5.

The mixed system produced a moderate textural response at both pH levels. A slight positive correlation ($r \approx +0.20$) was observed between dosage and homogeneity. Compared with pure quebracho ($r = +0.68$), the lower homogeneity correlation for the mixture suggests interaction between deposition behaviors; however, this should not be treated as proof of competitive adsorption because equilibrium bath concentrations, extract modification status and molecular-level binding data were not measured (Figure 9).

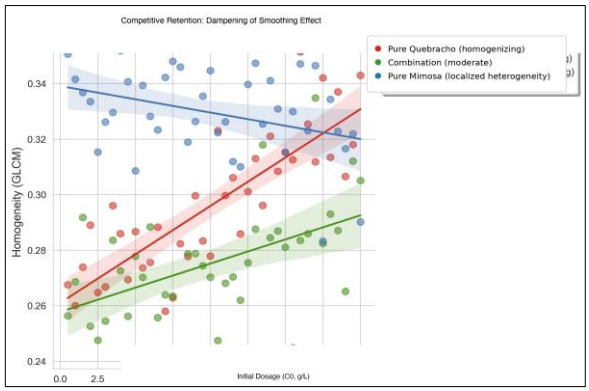


Figure 9. Mixed-system retention behavior: dampening of the image-based surface-regularity trend.

4. Discussion

Gravimetric retention, texture descriptors and Delta E00 together provide a coherent empirical framework for comparative retanning assessment. First, increasing C0 increased measurable dry weight gain. Second, surface-image texture metrics demonstrated that different systems translate deposition into distinct two-dimensional morphology outcomes, namely increased image regularity versus localized image heterogeneity. Third, color measurements indicated that higher mass retention did not necessarily increase initial color difference within the tested range (Figure 10).

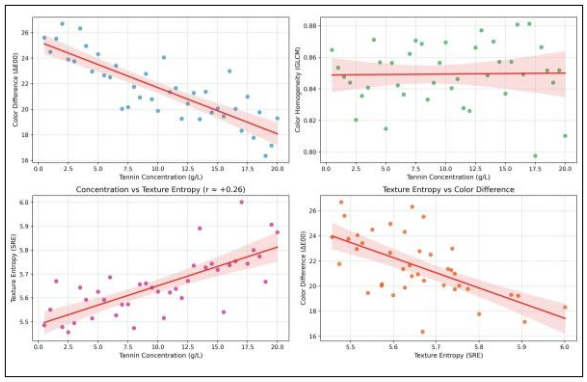


Figure 10. Chemical-visual correlation analysis for Mimosa-treated samples.

From an industrial-practice perspective, increased two-dimensional image homogeneity may be theoretically consistent with more uniform surface deposition, reduced visible grain irregularity and a more compact visual grain pattern, which can accompany perceived fullness when retanning agents distribute more evenly through the collagen network. However, this interpretation remains a process-level hypothesis in the present empirical framework; without ISO 2420 apparent-density or mass-per-unit-area data, ISO 3380 shrinkage temperature, thickness/compression measurements or cross-sectional microscopic validation, two-dimensional image homogeneity cannot be used as direct proof of bulk fullness or fiber compaction.

However, the proposed framework should be positioned as a low-cost and image-based screening tool rather than a replacement for established process-validation methods. Near-infrared spectroscopy combined with chemometric methods such as PCA has been shown to support non-destructive quality evaluation and process control in leather systems, and hyperspectral imaging combined with chemometrics has also been reported for leather identification and classification (Braz et al., 2018; Hou et al., 2023; Florio et al., 2025). The present approach may therefore be most useful as a complementary method in settings where rapid imaging is available but spectroscopic equipment or bath analytics are limited.

Correlation analysis further supports this integrated view: weight gain was positively associated with texture entropy in selected dosage-driven systems, indicating that increased deposition can be accompanied by measurable two-dimensional surface-image heterogeneity depending on tannin-pH conditions (Figure 11). These correlations describe image response and should not be extrapolated to bulk properties or three-dimensional roughness without shrinkage temperature, thickness, apparent density, compression-resilience, profilometry or calibrated microscopy validation.

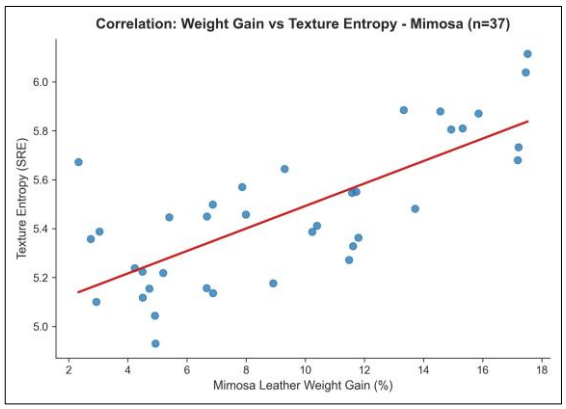


Figure 11. Correlation between leather weight gain (%) and texture entropy (SRE).

4.1 Limitations and Future Validation

A primary limitation is that tannin uptake was quantified exclusively by gravimetric dry mass retention. The equilibrium bath concentration (Ce) was not measured, and UV-VIS spectrophotometry was not used to track residual tannins in the bath solution. Consequently, the fitted functions are empirical dose-response curves versus initial dosage (C0), not thermodynamic adsorption isotherms. This distinction is important because classical isotherm parameters require equilibrium concentration data and should not be inferred from C0-based gravimetric trends alone.

A second limitation is the absence of shrinkage temperature (Ts) data. Ts is a key baseline indicator of tanning stability, and without it, gravimetric mass retention cannot distinguish chemical stabilization from physical deposition or filling. Therefore, this study evaluates mass retention and surface response rather than proving tanning efficacy. Future validation should include Ts measurements at representative dosage points, especially near apparent plateau regions.

A third limitation is that ISO-based physical validation was not performed. Apparent density, mass per unit area, thickness increase, compression-resilience and related measurements would be required to validate any bulk fullness interpretation. Accordingly, all fullness-related interpretations were removed or restricted to surface-level terminology.

A fourth limitation concerns image reproducibility. Although imaging conditions were standardized and GLCM displacement vectors were defined, pixel-to-mm calibration was not available in the dataset. Future studies should report magnification, spatial calibration, illumination geometry, camera settings and sensitivity analyses across ROI selections, because GLCM descriptors depend on acquisition and preprocessing parameters. Three-dimensional profilometry or calibrated digital microscopy should also be used to connect image descriptors with physical roughness metrics such as Ra or Rq.

Finally, CIEDE2000 (Delta E00) was retained for comparability with established leather and industrial color-difference literature. Future studies should include CAM16-UCS-based calculations, replicate batches and accelerated lightfastness or aging tests to determine whether the same initial color-consistency trends are preserved over time.

5. Conclusion

This study established a comparative, low-cost empirical screening framework for evaluating vegetable retanning behavior in wet-blue leather by integrating gravimetric mass retention, image-derived surface texture descriptors and colorimetric measurements. Because the equilibrium bath concentration was not monitored, tannin deposition was interpreted through dry weight gain as a function of the applied initial dosage, and the fitted curves were treated only as empirical dose-response relationships. Because equilibrium bath concentration was not measured, the reported mass-retention curves define only a descriptive initial-dosage trend boundary rather than calibrated bath-exhaustion behavior; future studies should combine gravimetry with UV-VIS spectrophotometry or high-performance liquid chromatography (HPLC) to quantify residual tannin concentrations.

The results showed clear pH-dependent differences among the retanning systems. Quebracho at pH 4.0 showed a bounded response associated with increased image-based surface regularity, whereas mimosa at pH 5.5 showed continued mass accumulation accompanied by localized image-texture heterogeneity. These findings indicate that tannin type and pH influence the way

retained material is expressed in two-dimensional surface images; however, the results should not be interpreted as direct evidence of bulk fullness, physical roughness reduction or tanning stabilization.

Within the investigated dosage range, increased gravimetric retention did not necessarily increase initial color difference. Mimosa showed comparatively lower initial color difference at both pH levels, whereas the binary mixture produced intermediate and less consistent responses. The color findings should therefore be interpreted as comparative initial color-consistency trends within the present measurement framework, not as evidence of lightfastness or long-term initial color consistency.

Overall, the combined use of gravimetric retention, GLCM-derived descriptors, SRE and color-difference analysis provides a practical, low-cost, non-destructive screening strategy for comparative retanning evaluation. Future studies should strengthen this framework by adding certified tannin specifications, UV-VIS bath exhaustion monitoring, equilibrium bath concentration measurement, shrinkage temperature measurement, standardized physical testing, calibrated three-dimensional or microscopic surface validation, spectroscopic or hyperspectral benchmarking and modern perceptual color-space validation.

Author Contributions

The author's contribution percentages are presented below. The author reviewed and approved the final version of the manuscript.

	Ş.Ö.
C	100
D	100
DCP	100
DAI	100
L	100
W	100
CR	100
SR	100
PM	100

C= concept, D= design, S= supervision, DCP= data collection and/or processing, DAI= data analysis and/or interpretation, L= literature search, W= writing, CR= critical review, SR= submission and revision, PM= project management.

Conflict of Interest

The author declared that there is no conflict of interest.

Ethical Consideration

Ethics committee approval was not required because the study did not involve animals or humans.

Acknowledgements

The author acknowledges the laboratory facilities and technical support provided during the experimental work. No specific external funding was declared for this study.

References

Balasubramanian, P., Ramalingam, S., & Rao, J. R. (2017). Detritus to functional auxiliary: Twin properties polymer from woody biomass for leather post-tanning application. *ACS Sustainable Chemistry & Engineering*, *5*(8), 7020–7029. https://doi.org/10.1021/acssuschemeng.7b01254

Baraldi, A., & Parmiggiani, F. (1995). An investigation of the textural characteristics associated with gray level cooccurrence matrix statistical parameters. *IEEE Transactions on Geoscience and Remote Sensing*, *33*(2), 293–304. https://doi.org/10.1109/TGRS.1995.8746010

Basova, O., Gladilin, S., Kokhan, V., Kharkevich, M. V., Sarycheva, A., Konovalenko, I., Chobanu, M. K., & Nikolaev, I. P. (2024). Evaluation of color difference models for wide color gamut and high dynamic range imaging. *Journal of Imaging*, *10*(12), Article 317. https://doi.org/10.3390/jimaging10120317

Bbumba, S., Karume, I., Nsamba, H. K., Kigozi, M., & Kato, M. (2024). An insight into isotherm models in physical characterization of adsorption studies. *European Journal of Applied Sciences*, *12*(2), 115–134. https://doi.org/10.14738/aivp.122.16738

Braz, C. E. M., Jacinto, M. A. C., Pereira-Filho, E. R., Souza, G. B., & Nogueira, A. R. A. (2018). Potential of near-infrared spectroscopy for quality evaluation of cattle leather. *Spectrochimica Acta Part A: Molecular and Biomolecular Spectroscopy*, *202*, 182–186. https://doi.org/10.1016/j.saa.2018.05.025

Covington, A. D., & Wise, W. R. (2019). *Tanning chemistry: The science of leather* (2nd ed.). Royal Society of Chemistry. https://doi.org/10.1039/9781839168826

Florio, C., Medici, A., Aveta, R., Esposito, L., Favazzi, A., Belvedere, F., Zarrelli, A., & Sarno, M. (2025). The potential of near infrared (NIR) spectroscopy coupled to principal component analysis (PCA) for product and tanning process control of innovative leathers. *Scientific Reports*, *15*, Article 35795. https://doi.org/10.1038/s41598-025-17598-7

Haralick, R. M., Shanmugam, K., & Dinstein, I. (1973). Textural features for image classification. *IEEE Transactions on Systems, Man, and Cybernetics*, *SMC-3*(6), 610–621. https://doi.org/10.1109/TSMC.1973.4309314

Hou, Q., Li, M., Han, Q., Yang, N., & Cheng, Y. (2023). Spectral characterization and identification of natural and regenerated leather based on hyperspectral imaging system. *Coatings*, *13*(2), Article 450. https://doi.org/10.3390/coatings13020450

International Organization for Standardization. (2015). *Leather — Physical and mechanical tests — Determination of shrinkage temperature up to 100 °C* (ISO Standard No. 3380:2015). https://www.iso.org/standard/60822.html

International Organization for Standardization. (2017). *Leather — Physical and mechanical tests — Determination of apparent density and mass per unit area* (ISO Standard No. 2420:2017). https://www.iso.org/standard/68314.html

Li, C., Li, Z., Wang, Z., Xu, Y., Luo, M. R., Cui, G., Melgosa, M., Brill, M. H., & Pointer, M. (2017). Comprehensive color solutions: CAM16, CAT16, and CAM16-UCS. *Color Research & Application*, *42*(6), 703–718. https://doi.org/10.1002/col.22131

Luo, M. R., Xu, Q., Pointer, M., Melgosa, M., Cui, G., Li, C., Xiao, K., & Huang, M. (2023). A comprehensive test of colour-difference formulae and uniform colour spaces using

available visual datasets. *Color Research & Application*, *48*(3), 267–282. https://doi.org/10.1002/col.22844

Nurichsanto, Y., Pertiwiningrum, A., Fitriyanto, N. A., & Pastawan, V. (2023). The effect of storage time on physical quality of vegetable tanned goat leather. *Advances in Biological Sciences Research*, *77*, 77–83. https://doi.org/10.2991/978-94-6463-116-6_11

Qiu, H., Lv, L., Pan, B., Zhang, Q., Zhang, W., & Zhang, Q. (2009). Critical review in adsorption kinetic models. *Journal of Zhejiang University SCIENCE A*, *10*(5), 716–724. https://doi.org/10.1631/jzus.A0820524

Raggi, A., & Barbiroli, G. (1993). Colour-difference measurement: The sensitivity of various instruments compared. *Color Research & Application*, *18*(1), 11–27. https://doi.org/10.1002/col.5080180105

Sabeenian, R. S., & Dinesh, P. M. (2011). Texture image classification using gray level weight matrix (GLWM). *Communications in Computer and Information Science*, *263*, 263–266. https://doi.org/10.1007/978-3-642-20573-6_43

Varghese, A., Jain, S., Prince, A. A., & Jawahar, M. (2020). Digital microscopic image sensing and processing for leather species identification. *IEEE Sensors Journal*, *20*(17), 10045–10056. https://doi.org/10.1109/JSEN.2020.2991881

Venter, P., Senekal, N. D., Amra-Jordaan, M., Bonnet, S. L., & van der Westhuizen, J. H. (2012). Analysis of commercial proanthocyanidins. Part 2: An electrospray mass spectrometry investigation into the chemical composition of sulfited quebracho heartwood extract. *Phytochemistry*, *78*, 156–169. https://doi.org/10.1016/j.phytochem.2012.01.027

Wilson, D., Tsigkou, O., Bosworth, L. A., & Jones, C. (2023). Leather-like materials by cellular agriculture. *Textile Progress*, *55*(1), 1–45. https://doi.org/10.1080/00405167.2023.2188835

Black Sea Journal of Engineering and Science
doi: 10.34248/bsengineering.1888398

Open Access Journal
e-ISSN: 2619 – 8991

Derleme (Review)
Cilt 9 - Sayı 5: 2844-2858 / Eylül 2026
(Volume 9 - Issue 5: 2844-2858 / September 2026)

TAVUKÇULUK ENDÜSTRİSİNDE ATIKLARIN ENTEGRE YÖNETİMİ: ÇEVRESEL RİSKLER, YENİLİKÇİ GERİ KAZANIM TEKNOLOJİLERİ VE SÜRDÜRÜLEBİLİR YÖNETİM MODELLERİ

Muhammed YÜCEER[1]*, Ecem IŞIK[2]

[1]*Canakkale Onsekiz Mart University, Çanakkale Technical Sciences Vocational School, Department of Food Processing, 017020, Canakkale, Türkiye*
[2]*Gemak Food Industry Machinery and Trade Inc., R&D Center, Alıcı OSB Disct., 2032 St., 06909, Ankara, Türkiye*

Özet: Tavukçuluk endüstrisi, dünya genelinde hızla artan nüfusun protein ihtiyacını karşılamada en önemli hayvansal üretim kollarından biri haline gelmiştir. Ancak endüstrideki bu hızlı büyüme, beraberinde ciddi miktarda atık oluşumunu da getirmekte ve çevresel sürdürülebilirlik açısından yeni sorun alanları ortaya çıkarmaktadır. Gübre, tüy, kan, sakatat, yumurta kabuğu ve atıksu gibi farklı nitelikteki yan ürünler, kontrolsüz şekilde bertaraf edildiğinde amonyak emisyonları, sera gazı salımları, su ve toprak kirliliği ile halk sağlığı risklerine yol açabilmektedir. Bu çalışma, tavukçuluk atıklarının sınıflandırılması, çevresel etkileri, değerlendirme yöntemleri ve sürdürülebilir atık yönetimi uygulamalarına ilişkin güncel ulusal ve uluslararası literatürün kapsamlı bir şekilde incelenmesi ve karşılaştırmalı olarak değerlendirilmesi esasına dayanan bir derleme çalışmasıdır. Literatür verileri doğrultusunda, kompost ve biyogaz üretimi, enzimatik biyodönüşüm, tüylerden keratin geri kazanımı ile kan ve sakatatın protein hidrolizatlarına dönüştürülmesi gibi çevre dostu yaklaşımların tavukçuluk atıklarının döngüsel ekonomi kapsamında katma değerli ürünlere dönüştürülmesinde önemli potansiyele sahip olduğu belirlenmiştir. Sonuç olarak bu derleme, tavukçuluk atıklarının sürdürülebilir yönetimine yönelik mevcut uygulamaları ve gelecekteki araştırma gereksinimlerini bütüncül bir bakış açısıyla değerlendirerek sektör için yol gösterici bilgiler sunmaktadır.

Anahtar kelimeler: Kanatlı sektörü atıkları, Gübre yönetimi, Keratin geri kazanımı, Biyogaz, Döngüsel ekonomi, Çevresel etkiler

Integrated Waste Management in the Poultry Industry: Environmental Risks, Innovative Recovery Technologies, and Sustainable Management Models

Abstract: The poultry industry has become one of the most important livestock production sectors for meeting the increasing global demand for animal protein. However, the rapid expansion of the industry has also resulted in the generation of substantial amounts of waste, creating significant environmental sustainability challenges. Poultry manure, feathers, blood, offal, eggshells, and wastewater can lead to ammonia emissions, greenhouse gas release, soil and water contamination, and public health risks when improperly managed. This study was conducted as a comprehensive literature review by systematically evaluating recent scientific publications on poultry waste classification, environmental impacts, waste valorization technologies, and sustainable management practices. The collected information was comparatively analyzed to identify current utilization approaches, technological advancements, and future research needs. Recent biotechnological and environmentally friendly approaches demonstrate that poultry waste can be transformed into value-added products rather than simply disposed of. Composting, biogas production, enzymatic bioconversion, keratin recovery from feathers, and the production of protein hydrolysates from blood and offal are among the most promising valorization strategies supporting the circular economy. This review discusses the classification of poultry waste, its environmental impacts, current valorization methods, and future research perspectives, thereby providing a comprehensive framework for the development of sustainable poultry waste management strategies.

Keywords: Poultry industry waste, Manure management, Keratin recovery, Biogas, Circular economy, Environmental impacts

***Sorumlu yazar (Corresponding author):** Canakkale Onsekiz Mart University, Çanakkale Technical Sciences Vocational School, Department of Food Processing, 017020, Canakkale, Türkiye
E mail: myuceer@comu.edu.tr (M.YÜCEER)
Muhammed YÜCEER https://orcid.org/0000-0001-6709-1347
Ecem IŞIK https://orcid.org/0009-0000-5232-0821

Gönderi: 13 Şubat 2026 **Received:** February 13, 2026
Kabul: 15 Temmuz 2026 **Accepted:** July 15, 2026
Yayınlanma: 15 Eylül 2026 **Published:** September 15, 2026

Cite as: Yüceer, M. & Işık, E. (2026). Integrated waste management in the poultry industry: environmental risks, innovative recovery technologies, and sustainable management models. *Black Sea Journal of Engineering and Science,* 9(5), 2844-2858.

1. Giriş

Küresel nüfus artışı, kentleşme ve değişen beslenme alışkanlıklarına bağlı olarak hayvansal protein kaynaklarına olan talep her geçen yıl artmaktadır. Bu talebin karşılanmasında önemli bir role sahip olan tavukçuluk sektörü, kısa üretim döngüsü, yüksek yem dönüşümü ve ekonomik üretim kapasitesi sayesinde dünya genelinde en hızlı büyüyen hayvansal üretim alanlarından biri olarak kabul edilmektedir. Ancak sektördeki üretim hacminin sürekli artması, yalnızca et

This work is licensed (CC BY-NC 4.0) under Creative Commons Attribution 4.0 International License

ve yumurta üretimini değil, aynı zamanda önemli miktarda organik ve inorganik atığın oluşumunu da beraberinde getirmektedir. Tavuk gübresi, altlık materyali, tüyler, ölü hayvanlar, kesimhane yan ürünleri ve atık sular gibi farklı özelliklere sahip bu atıklar, uygun şekilde yönetilmediğinde çevresel kirlilik, sera gazı emisyonları, kötü koku oluşumu, patojen mikroorganizmaların yayılımı ile toprak ve su kaynaklarının kirlenmesine neden olmakta; dolayısıyla ekosistem ve halk sağlığı açısından ciddi riskler oluşturmaktadır. Buna karşın söz konusu atıklar, içerdikleri organik madde, besin elementleri ve biyolojik bileşenler sayesinde biyogaz üretimi, organik gübre eldesi, kompostlama, enerji geri kazanımı, protein ve keratin geri kazanımı ile çeşitli biyoteknolojik ürünlerin üretimi gibi uygulamalarda değerlendirilebilecek önemli bir biyokaynak niteliği taşımaktadır. Bu nedenle tavukçuluk atıklarının etkin ve sürdürülebilir şekilde yönetilmesi, yalnızca çevresel etkilerin azaltılması açısından değil, aynı zamanda kaynak verimliliğinin artırılması, atıkların katma değerli ürünlere dönüştürülmesi ve döngüsel ekonomi ilkelerinin hayata geçirilmesi bakımından da stratejik önem taşımaktadır (Karuppannan vd., 2021; Raclavská vd., 2022; Ghaffari-Bohlouli vd., 2023).

Tavukçuluk endüstrisi, günümüzde küresel tarımsal üretimin en dinamik ve en hızlı büyüyen kollarından biri haline gelmiştir. Kırmızı ete kıyasla daha düşük maliyetli, kolay erişilebilir ve yüksek kaliteli bir hayvansal protein kaynağı sunması, sektörü küresel gıda güvencesinin merkezine taşımaktadır. Birleşmiş Milletler Gıda ve Tarım Örgütü (FAO) verilerine göre, 2020 yılında 133 milyon ton seviyesine ulaşan küresel tavuk eti üretiminin, artan nüfus ve talep doğrultusunda önümüzdeki dönemde de istikrarlı yükselişini sürdüreceği öngörülmektedir (Zinina vd., 2022). Dünya genelinde ise yaklaşık 18,5 milyar broyler tavuk bulunduğu ve yalnızca gübre kaynaklı 6,7 milyon ton azotun her yıl çevreye salındığı bildirilmektedir (Mottet ve Tempio, 2017). Bu yüksek üretim kapasitesinde Amerika Birleşik Devletleri, Çin, Brezilya ve Hindistan önde gelirken, Avrupa Birliği ülkeleri de kayda değer bir paya sahiptir (Brandelli vd., 2015). Kanatlı hayvan yetiştiriciliğinin endüstriyel ölçekte belirli coğrafi bölgelerde yoğunlaşması (kümelenmesi), üretimin sürdürülebilirliği önünde ciddi bir lojistik ve ekolojik bariyer oluşturmaktadır. Özellikle küresel ölçekte yıllık yaklaşık 4,7 milyon ton hacme ulaşan tavuk tüyü gibi yüksek keratin içerikli dirençli biyokütlelerin yanı sıra, altlık gübresi ve kesimhane yan ürünlerinin (sakatat, kan, karkas parçaları) yarattığı asimetrik atık yükü, lokal ekosistemler üzerinde akut çevresel riskler barındırmaktadır. Söz konusu organik atıkların entegre ve rasyonel bir yönetim stratejisiyle bertaraf edilememesi; yeraltı su kaynaklarında ötrofikasyona, toprak kalitesinde kimyasal dejenerasyona ve sera gazı emisyonlarında artışa neden olarak, endüstrinin karbon ve su ayak izini kritik düzeyde yükseltmektedir (Moktip vd., 2025).

Türkiye ise, dünya tavukçuluk sektöründe ilk 10 üretici ülke arasında yer almakta olup hem yumurta hem de etlik piliç üretiminde tarım ekonomisinin lokomotif sektörlerinden biridir. Türkiye İstatistik Kurumu (TÜİK) verilerine göre, 2024 yılında Türkiye'de yaklaşık 2,51 milyon ton tavuk eti (beyaz et) ve 21,16 milyar adet tavuk yumurtası üretilmiştir (Anonim, 2024). Bu üretim hacmi, tavukçuluk sektörünün ülke ekonomisi ve gıda arzındaki stratejik önemini ortaya koyarken, aynı zamanda yönetilmesi gereken önemli miktarda organik atığın oluşmasına da neden olmaktadır. Bu üretim, kırsal kalkınma ve ihracat gelirleri açısından önemli katkılar sağlamakla birlikte, atık yönetimini de stratejik bir zorunluluk haline getirmektedir. Ülkemizde tavuk gübresinin çoğunlukla doğrudan tarım arazilerinde gübre olarak kullanıldığı görülmektedir; ancak bu uygulama, aşırı azot ve fosfor yüklemesine bağlı olarak yeraltı sularında nitrat kirliliği ve amonyak emisyonlarının artışı gibi çevresel riskler yaratmaktadır (Singh vd., 2018; Rahman vd., 2022). Son yıllarda biyogaz üretimi, kompostlaştırma, anaerobik fermantasyon, tüylerden keratin geri kazanımı ve kesimhane yan ürünlerinin biyoteknolojik yöntemlerle değerlendirilmesi gibi yenilikçi uygulamalar, Türkiye'de hem pilot ölçekli hem de endüstriyel düzeyde giderek daha fazla ilgi görmekte ve yaygınlaşmaktadır. Bu gelişmeler, tavukçuluk atıklarının yalnızca bertaraf edilmesi gereken çevresel bir yük olarak değil, aynı zamanda enerji, biyomalzeme ve katma değerli ürün üretiminde kullanılabilecek önemli bir biyokaynak olarak değerlendirilmesine olanak sağlamaktadır. Bu nedenle, tavukçuluk sektörünün küresel ve ulusal ölçekte sürekli büyümesi, ekonomik katkılarının yanı sıra oluşan atıkların çevresel etkilerini azaltacak, kaynak verimliliğini artıracak ve döngüsel ekonomi ilkelerini destekleyecek sürdürülebilir atık yönetim stratejilerinin geliştirilmesini ve uygulanmasını gerekli kılmaktadır (Dalkılıç ve Uğurlu, 2013; Yenilmez, 2015; Konkol vd., 2023; Tawfik vd., 2023).

Tavukçuluk endüstrisinde üretim ve kesim süreçleri sonucunda oluşan atıklar; fiziksel, kimyasal ve biyolojik özelliklerine göre genel olarak gübre, tüy, yumurta kabuğu, kan, sakatat ve atıksu olmak üzere altı temel grupta toplanmaktadır. Bu atıkların her biri, doğru yönetilmediğinde ciddi birer çevre kirliliği unsuru (koku, yeraltı suyu kirliliği, sera gazı emisyonu) olma riski taşırken; doğru geri kazanım yöntemleriyle (biyogaz, kompost, yem ham maddesi) ekonomik değere dönüştürülebilme potansiyeline sahiptir (Okur ve Eratalar, 2019). Öncelikle, gübre tavukçulukta en büyük atık grubunu oluşturmaktadır. Gübre, dışkının talaş, pirinç kabuğu veya saman gibi yataklık materyallerle karışmasından meydana gelir. Ayrıca yüksek azot, fosfor ve potasyum içeriği nedeniyle tarımda organik gübre olarak yaygın şekilde kullanılmaktadır. Hatta Edwards ve Daniel'in 1992 yılında yaptıkları bir çalışmada, 10 haftalık bir yetiştirme döneminde 1000 etlik piliçten

yaklaşık 1,46-ton (kuru bazda) gübre elde edildiği bildirilmiştir. Ancak bu miktar, kullanılan yataklık materyalin türüne, sürü yoğunluğuna ve çevresel koşullara bağlı olarak değişiklik gösterebilmektedir (Edwards ve Daniel, 1992). Kanatlı endüstrisinin en dirençli yan ürün akımlarından birini, toplam canlı ağırlığın yaklaşık %8'ine tekabül eden tüy atıkları oluşturmaktadır. Küresel ölçekte yıllık 4,7 milyon tonu aşan bu kütle, %85–90 oranında kristalin hidrofobik keratin matrisinden meydana geldiği için konvansiyonel biyolojik süreçlerle parçalanmaya karşı yüksek yapısal direnç göstermektedir. Kontrolsüz deşarjı durumunda lokal ekosistemlerde kalıcı kirlilik yükü oluşturan bu atıklar, günümüzde yeşil biyoteknoloji ve döngüsel biyorafineri konseptlerinin odak noktası haline gelmiştir. Özellikle keratinolitik mikroorganizmalar tarafından sentezlenen spesifik keratinaz enzimlerinin kullanıldığı kontrollü biyoprosesler, disülfit bağlarının koparılarak tüy biyo-kütlesinin yüksek sindirilebilirliğe sahip protein hidrolizatlarına, fonksiyonel yem katkı maddelerine ve biyo-bazlı polimerik malzemelere (biyoplastikler) dönüşümünü mümkün kılmaktadır (Brandelli vd., 2015; Moktip vd., 2025).

Tavukçuluk ve özellikle endüstriyel yumurta işleme (likit yumurta üretimi, pastörizasyon ve yumurta tozu) tesislerinde açığa çıkan katı atıklar arasında kütlesel ve hacimsel açıdan en baskın paylardan birine sahip olan yumurta kabukları, ortalama 5–6 gramlık ağırlıklarıyla toplam yumurta kütlesinin yaklaşık %9–12'sini oluşturmakta ve geleneksel depolama alanlarında kokuşma ile patojen üremesi gibi çevresel riskler barındırmaktadır. Ancak bu atık yükü, kimyasal yapısının %95–97 gibi çok büyük bir kısmını oluşturan biyo-yenilenebilir kalsiyum karbonat ve mikrobiyel bariyer görevi gören protein bazlı organik matrisi sayesinde, döngüsel ekonomi modeline doğrudan hizmet edebilecek yüksek katma değerli, sürdürülebilir bir ham madde potansiyeli taşımaktadır. Doğru yıkama, sterilizasyon ve mikronize öğütme işlemlerinin ardından bu fonksiyonel inorganik yapı; tarımsal uygulamalarda asidik toprakların pH dengesini düzenleyen ve bitki beslemede yavaş salınım gösteren doğal bir kalsiyum kaynağı olarak rol oynarken, endüstriyel boyutta polietilen (PE) ve polipropilen (PP) gibi polimer matrislerin içerisine biyo-dolgu maddesi (bio-filler) olarak entegre edilerek ambalaj sanayisi için yeşil biyokompozit ve biyoplastiklerin geliştirilmesini sağlamakta, ayrıca yüksek biyoyararlanımıyla nutrasötik formülasyonlarda ve kemik doku mühendisliği için hidroksiapatit sentezi gibi ileri teknoloji malzeme uygulamalarında başarıyla değerlendirilmektedir. Ayrıca yumurta kabuğunun iç yüzeyini kaplayan ve inorganik kabuktan mekanik olarak ayrılabilen yumurta kabuğu zarı (egg Shell membrane, ESM), tavukçuluk endüstrisinin biyoteknolojik açıdan en değerli ve yüksek katma potansiyeline sahip organik atık gruplarından biridir. Toplam kabuk ağırlığının oldukça küçük bir kısmını oluşturmasına rağmen bu çift katmanlı fibröz yapı; doğası gereği Tip I, V ve X kolajen, glukozamin, kondroitin sülfat, hiyalüronik asit ve sialik asit gibi biyoaktif bileşikler ile sülfür içeren amino asitlerce zengin fonksiyonel bir protein matrisinden meydana gelmektedir. Sentetik alternatiflerine kıyasla üstün biyo-uyumluluk, biyobozunurluk ve düşük immünojenite (alerjik reaksiyon riski) sergileyen bu doğal membran, özellikle kozmetik sanayisinde yaşlanma karşıtı ve cilt bariyerini güçlendirici formülasyonlarda sıklıkla tercih edilmektedir; bunun yanı sıra, biyotıp alanında yara örtücü materyallerin, yapay doku iskelelerinin (scaffold) ve eklem sağlığını destekleyici nutrasötiklerin geliştirilmesinde, çevre teknolojilerinde ise gözenekli yapısı sayesinde atıksulardan ağır metallerin ve boyar maddelerin uzaklaştırılmasını sağlayan sürdürülebilir bir biyosorbent olarak çok yönlü bir ticarileşme potansiyeli sunmaktadır (Yoo vd., 2009; Yüceer, 2021; Ngayakamo ve Onwualu, 2022).

Kesimhane süreçlerinde ortaya çıkan bir diğer atık grubu ise kan ve sakatattır. Kan, canlı ağırlığın yaklaşık %3'üne karşılık gelmekte ve yüksek protein içeriği nedeniyle atıksuların biyokimyasal oksijen ihtiyacını (BOİ) önemli ölçüde artırmaktadır. Sakatat ise baş, ayak ve iç organları kapsamakta olup toplam işlenmemiş etli gövdenin yaklaşık %7–8'ini oluşturmaktadır. Bu fraksiyonlar genellikle hayvansal atık geri dönüşüm tesislerinde işlenerek hayvansal un ve yağlara dönüştürülmekte, böylece ekonomik bir değer kazanmaktadır (Crawley vd., 1980; Dyosile vd., 2021).

Tavukçuluk endüstrisinde katı atık yönetimi (gübre, tüy vb.) ön planda görünse de, sıklıkla göz ardı edilen ancak ekolojik dengenin korunması açısından kritik öneme sahip olan asıl dinamik grup atıksulardır. Kesimhanelerde hijyen ve gıda güvenliği standartlarının sağlanabilmesi adına tüy yolma, haşlama, eviserasyon (iç organ çıkarma) ve karkas yıkama işlemleri sırasında yüksek miktarlarda su tüketilmektedir. Günümüz modern entegre tesislerinde bu tüketim hızı, karkas başına ortalama 26 litre/etlik piliç gibi çarpıcı bir düzeye ulaşmaktadır. Fatima vd. (2021) yaptıkları çalışmalarda, yalnızca eviserasyon aşamasında 7,6 litre/etlik piliç, yıkama aşamasında ise 4,3 litre/etlik piliç su tüketildiği bildirilmiştir. Bu yüksek hacimli su tüketimi, yalnızca kantitatif (miktarsal) bir problem değil, aynı zamanda ciddi bir kalitatif (niteliksel) çevre kirliliği tehdididir. Söz konusu proseslerden açığa çıkan atıksular; yüksek miktarda kan, tüy parçacıkları, yağ, doku artıkları ve protein türevleri içermektedir. Bu organik yükün bir sonucu olarak atıksular; son derece yüksek Biyokimyasal Oksijen İhtiyacı (BOİ) ve Kimyasal Oksijen İhtiyacı (KOİ) değerlerine sahip olurlar. Organik maddece zengin, yağlı ve protein yüklü bu atıksuların alıcı ortamlara deşarj edilmeden önce uygun fiziksel, kimyasal ve biyolojik arıtma proseslerinden geçirilmemesi, su kaynaklarında ötrofikasyona (aşırı alg çoğalması ve oksijensizleşme), toprak kirliliğine ve dolayısıyla küresel ölçekte akut çevresel risklerin tırmanmasına neden olmaktadır (Dyosile vd., 2021).

Tüm bu veriler birlikte değerlendirildiğinde, tavukçuluk endüstrisinde farklı kaynaklardan çok çeşitli atıkların ortaya çıktığı ve miktarlarının oldukça yüksek olduğu görülmektedir. Dolayısıyla bu atıkların çevresel yük olmaktan çıkarılıp ekonomik ve sürdürülebilir ürünlere dönüştürülmesi, sektörün geleceği açısından stratejik bir gereklilik olarak öne çıkmaktadır (Kelleher vd., 2002).

2. Derleme Çalışması

B Bu çalışma, tavukçuluk endüstrisinde farklı atık yönetim uygulamalarına ilişkin bilimsel literatürü inceleyen bir derleme çalışmasıdır ve PRISMA (Preferred Reporting Items for Systematic Reviews and Meta-Analyses) yönergeleri esas alınarak tasarlanmıştır (Page vd., 2021).

2.1. Literatür Tarama Stratejisi

Literatür taraması Scopus ve Web of Science veri tabanlarında gerçekleştirilmiştir. Tarama süreci 2026 yılına kadar yayımlanmış çalışmaları kapsayacak şekilde yürütülmüştür. Kullanılan anahtar kelimeler "egg industry", "egg waste management", "poultry by-products", "eggshell waste valorization", "anaerobic digestion", "composting", "waste-to-energy" ve "circular economy in poultry sector" şeklindedir. Arama, başlık, özet ve anahtar kelimeler alanlarında yapılmıştır.

2.2. Dahil Etme ve Dışlama Kriterleri

Çalışmalar aşağıdaki kriterlere göre seçilmiştir:

- Dahil etme kriterleri:
  - Yumurta endüstrisi ve/veya tavukçuluk atık yönetimi ile doğrudan ilişkili olması
  - Hakemli bilimsel dergilerde yayımlanmış olması
  - Deneysel, uygulamalı veya derleme çalışması olması
  - İngilizce dilinde yayımlanmış olması
  - Tam metnine erişilebilir olması
- Dışlama kriterleri:
  - Konu ile doğrudan ilişkili olmayan çalışmalar
  - Yorum, editöryal not veya konferans özeti niteliğindeki yayınlar
  - Mükerrer kayıtlar
  - Tam metnine ulaşılamayan çalışmalar

2.3. Çalışma Seçimi (PRISMA süreci)

Literatür taraması sonucunda toplam N= 54 kayıt elde edilmiştir.

- Veri tabanlarından elde edilen kayıt sayısı: N = 54
- Nihai analize dahil edilen çalışmalar: N = 42

2.4. Veri Analizi

Seçilen çalışmalar içerik analizi yöntemiyle değerlendirilmiştir. Veriler; atık türleri, uygulanan yönetim teknolojileri (örneğin kompostlama, anaerobik fermantasyon, biyogaz üretimi), proses koşulları, elde edilen ürünler ve çevresel/ekonomik çıktılar açısından sınıflandırılmıştır. Ayrıca çalışmalar karşılaştırmalı olarak analiz edilerek mevcut eğilimler, teknolojik gelişmeler ve araştırma boşlukları belirlenmiştir.

Bu yaklaşım, yumurta endüstrisinde atık yönetimi uygulamalarına ilişkin bilimsel literatürün sistematik, şeffaf ve tekrarlanabilir bir şekilde değerlendirilmesini sağlamıştır.

3. Bulgular ve Tartışma

3.1 Döngüsel Ekonomi ve Sürdürülebilir Atık Yönetimi Yaklaşımı

Geleneksel doğrusal ekonomi modeli "al–kullan–at" yaklaşımına dayanmaktadır. Bu modelde üretim sürecinde ortaya çıkan atıklar genellikle bertaraf edilmekte, bu durum ise çevresel sorunların artmasına neden olmaktadır. Buna karşın döngüsel ekonomi modeli, kaynakların mümkün olan en uzun süre değerli tutulmasını, atıkların yeniden kullanılarak katma değerli ürünlere dönüştürülmesini ve böylece hem çevresel hem de ekonomik fayda sağlanmasını amaçlamaktadır (Zinina vd., 2022). Tavukçuluk endüstrisi bağlamında bu yaklaşım ise, yan ürünlerin bertaraf edilmesi yerine hammadde olarak değerlendirilmesini ve sürdürülebilir atık yönetiminin gerçekleştirilmesini mümkün kılmaktadır (Bolan vd., 2010). Bu kapsamda, gübre döngüsel ekonomide öne çıkan en önemli kaynaklardan biridir. Doğrudan tarımsal alanlarda organik gübre olarak kullanılmasının yanı sıra, kompostlaştırma ve anaerobik çürütme (biyogaz üretimi) yöntemleriyle hem enerji üretimi hem de besin geri kazanımı sağlanabilmektedir. Anaerobik sindirim sonucu elde edilen sindirim çamuru ise özellikle fosfor geri kazanımı açısından değerli bir yan ürün niteliği taşımaktadır (Singh vd., 2018; Rahman vd., 2022; Zinina vd., 2022).

Tüy atıkları ise, yüksek keratin içeriği nedeniyle biyolojik olarak zor parçalanan ancak önemli bir potansiyele sahip fraksiyondur. Son yıllarda yapılan literatür çalışmaları incelendiğinde ise, Brandelli vd. (2015) ile Moktip vd. (2025) keratinaz gibi enzimlerin kullanımıyla tüylerin protein hidrolizatlarına, yem katkılarına ve biyomalzemelere dönüştürülebileceğini göstermektedir. Benzer şekilde, çeşitli çalışmalarda yumurta kabuklarının yüksek kalsiyum karbonat ($CaCO_3$) içerikleri sayesinde kağıt kaplama pigmentleri ile sürdürülebilir yapı ve inşaat malzemeleri gibi endüstriyel uygulamalarda hammadde olarak değerlendirilebildiği rapor edilmiştir (Yoo vd., 2009; Ngayakamo ve Onwualu, 2022).

Döngüsel ekonomi yaklaşımı ayrıca termokimyasal dönüşüm yöntemlerini piroliz, hidrotermal karbonizasyon ve yenilikçi çözücü teknolojilerini (iyonik sıvılar, derin ötektik çözücüler) de içermektedir. Bu yöntemlerde tavukçuluk atıklarından biyokömür, biyoyağ ve biyogaz gibi enerji ürünleri elde edilebilmekte, aynı zamanda toprak düzenleyici ve çevre dostu yeni materyaller geliştirilebilmektedir (Edwards ve Daniel, 1992; Zinina vd., 2022). Ayrıca literatürde Abbasi ve arkadaşlarının vurguladığı gibi, bütünleşik sistemler (örneğin entegre tarım uygulamaları) sayesinde atıkları enerji, yem ve gübre kaynağına dönüştürülerek kırsal kalkınmaya da katkı sağlayabilmektedir (Abbasi vd., 2024).

Sonuç olarak, tavukçuluk endüstrisinde sürdürülebilir atık yönetimi yalnızca çevresel riskleri azaltmakla sınırlı kalmamakta; aynı zamanda ekonomik değer yaratan ürünlerin geliştirilmesine de imkân tanımaktadır. Bu nedenle döngüsel ekonomi yaklaşımı, tavukçuluk atıklarının yönetiminde geleceğe yönelik en kritik stratejilerden biri olarak değerlendirilmektedir (Hemavarshini vd., 2025).

3.2. Tavukçuluk Atıklarının Sınıflandırılması

Tavukçuluk endüstrisi, yüksek üretim kapasitesi nedeniyle önemli miktarda yan ürün ve atık ortaya çıkarmaktadır. Bu atıklar ise, içerik ve fiziksel özelliklerine göre katı atıklar, sıvı atıklar ve gübre şeklinde üç ana grupta değerlendirilmektedir (Rahman vd., 2022; Zinina vd., 2022). Ayrıca her bir atık grubu, uygun şekilde değerlendirildiğinde ekonomik potansiyele sahip olmakla birlikte, kontrolsüz bırakıldığında ciddi çevresel ve sağlık sorunlarına yol açabilmektedir (Kelleher vd., 2002).

3.2.1. Katı atıklar

Katı atık grubu, tüy, yumurta kabuğu, sakatat ve ölü hayvanlardan oluşmaktadır.

- Agro-endüstriyel atık yönetimi perspektifinden bakıldığında, kanatlı işleme tesislerinin en sorunlu katı atık fraksiyonunu tüy biyokütlesi oluşturmaktadır. Toplam canlı kütlenin yaklaşık %8'ine tekabül eden kümes hayvanı tüylerinin küresel çaptaki yıllık üretim hacminin 4,7 milyon tonu aştığı rapor edilmektedir (Safaric vd., 2020). Bu tüylerin yapısal matrisini oluşturan yüksek keratin içeriği (%85–90), yoğun disülfit köprüleri (S–S), hidrofobik etkileşimler ve yüksek orandaki çapraz bağlanmalar sebebiyle kararlı ve kristalin bir morfolojiye sahiptir. Bu rekalsitrant (dirençli) moleküler organizasyon, tüylerin konvansiyonel mikrobiyal ekosistemler tarafından biyolojik olarak parçalanmasını zorlaştırmakta ve depolama sahalarında kalıcı, kümülatif bir çevresel yük ve ekotoksikolojik risk meydana getirmektedir. Bununla birlikte, son yıllarda yapılan biyoteknolojik araştırmalar, keratinaz enzimlerinin kullanımıyla tüylerin protein hidrolizatları, yem katkı maddeleri ve biyomalzemelere dönüştürülebileceğini ortaya koymuştur (Brandelli vd., 2015; Moktip vd., 2025).
- Yumurta kabukları, esas olarak kalsiyum karbonat ($CaCO_3$) içeren yapıları sayesinde çeşitli endüstriyel uygulamalarda değerlendirilebilen önemli bir yan ürün olarak öne çıkmaktadır. Literatürde, yumurta kabuğu atıklarından elde edilen kalsiyum karbonat partiküllerinin ink-jet baskı kağıtlarında kaplama pigmenti olarak kullanılabildiği ve bu sayede geleneksel mineral kaynaklara alternatif oluşturduğu bildirilmektedir (Yoo vd., 2009). Bununla birlikte, yumurta kabuklarının yeşil işleme teknolojileri kullanılarak sürdürülebilir yapı ve inşaat malzemelerinde dolgu veya katkı maddesi olarak değerlendirilebildiği, böylece atıkların katma değerli ürünlere dönüştürülmesine olanak sağladığı da rapor edilmiştir (Ngayakamo ve Onwualu, 2022).
- Sakatatlar (baş, ayak ve iç organlar), toplam işlenmemiş etli gövdenin yaklaşık %7–8'ine karşılık gelmektedir. Yüksek protein ve yağ içerikleri nedeniyle hayvansal atık geri dönüşüm tesislerinde işlenerek hayvansal un ve yağlara dönüştürülmekte ve ekonomik bir değer kazandırılmaktadır (Crawley vd., 1980; Zinina vd., 2022).
- Ölü hayvanlar, biyogüvenlik açısından en kritik katı atıklardan biridir. Uygun bertaraf edilmediklerinde zoonotik hastalıkların yayılımı için risk oluşturmaktadırlar. Bu nedenle kompostlaştırma veya rendering tesislerinde işlenmeleri önerilmektedir (Edwards ve Daniel, 1992).

3.2.2. Sıvı atıklar

Sıvı atıklar; kan, kesimhane kaynaklı atık sular ve yıkama sularından oluşmaktadır.

- Kan, canlı ağırlığın yaklaşık %3'üne karşılık gelmektedir ve yüksek protein içeriği nedeniyle biyokimyasal oksijen ihtiyacını (BOİ) büyük ölçüde artırarak atıksuların kirlilik yükünü yükseltmektedir (Crawley vd., 1980; Yordanov, 2010; Fatima vd., 2021).
- Kesimhane kaynaklı sıvı atıklar, özellikle eviserasyon, haşlama ve tüy yolma aşamalarında ortaya çıkmaktadır. Literatürdeki güncel çalışmalar ise, modern tesislerde işlenen her bir etlik piliç için ortalama 26 litre su tüketildiğini; yalnızca eviserasyon aşamasında ise 7,6 litre/etlik piliç su harcandığını bildirmektedir (Dyosile vd., 2021; Fatima vd., 2021). Ayrıca organik madde, yağ ve protein bakımından zengin olan bu suların arıtılmadan alıcı ortamlara bırakılması ise ciddi çevresel riskler oluşturmaktadır.
- Yıkama suları, yüksek mikrobiyal yükleri ve deterjan kalıntıları nedeniyle hem çevre sağlığı hem de halk sağlığı açısından tehdit oluşturmaktadır (Edwards ve Daniel, 1992; Singh vd., 2018).

3.2.3. Gübre

Gübre (litter), tavukçulukta en büyük atık grubunu oluşturmaktadır. Dışkının talaş, pirinç kabuğu veya saman gibi yataklık materyallerle karışmasıyla oluşan gübre, yüksek miktarda azot, fosfor ve potasyum içermektedir (Edwards ve Daniel, 1992; Gbotosho ve Burt, 2013). Bu nedenle tarımda organik gübre olarak yaygın şekilde kullanılmaktadır. Ancak kontrolsüz uygulamalar, amonyak emisyonları, sera gazı salımları ve nitrat sızıntısı gibi çevresel sorunlara yol açabilmektedir (Rahman vd., 2022). Nitekim Singh vd. (2018) yaptığı bir çalışmada, gübrenin kompostlaştırma, biyogaz üretimi ve vermikompost gibi yöntemlerle işlenmesi sayesinde hem çevresel risklerin azaltılabileceği hem de ekonomik fayda sağlanabileceği vurgulanmıştır. Çalışma kapsamında analizi gerçekleştirilen tavukçuluk atıkları, yapısal olarak farklı nitelikler sergilemekle birlikte hem yüksek bir ekonomik potansiyeli barındırmakta hem de kontrol edilmediğinde ciddi çevresel riskler teşkil etmektedir; bu

doğrultuda atıkların karakterizasyonuna göre sınıflandırılması, doğru yönetim ve geri kazanım stratejilerinin belirlenmesi açısından kritik bir önem taşımaktadır. Elde edilen tüm bu teknik değerlendirmeler ve Şekil 1'de şematik gösterimi sunulan başlıca atık türlerinin sınıflandırılması, çalışmanın yürütüldüğü spesifik operasyonel koşullar, incelenen parametreler ve belirlenen metodolojik sınırlılıklar dahilinde genellenebilir niteliktedir. (Hemavarshini vd., 2025).



Şekil 1. Tavukçuluk endüstrisinde ortaya çıkan başlıca atık türlerinin şematik gösterimi (Hemavarshini vd., 2025).

3.2. Çevresel ve Sağlık Riskleri

Tavukçuluk endüstrisinde üretim süreçleri sonucunda oluşan yüksek miktardaki atıklar, doğru ve kontrollü yönetilmediği takdirde hem ekolojik denge hem de halk sağlığı üzerinde çok boyutlu ve ciddi tehditler oluşturmaktadır. Mevcut literatür ve sektörel veriler ışığında bu çevresel ve biyolojik riskler genel hatlarıyla dört ana grupta toplanmaktadır: amonyak ve sera gazı emisyonlarının tetiklediği hava kirliliği, su ve toprak matrislerinin bozulması, patojen mikroorganizmaların kontrolsüz yayılımı ve son olarak atıklarda biriken antibiyotik ile ağır metal kalıntıları (Himu ve Raihan, 2023).

3.3.1. Amonyak ve sera gazı emisyonları

Tavukçuluk atıkları, özellikle tavuk gübresinin yüksek azot içeriği nedeniyle amonyak (NH_3), diazot monoksit (N_2O) ve metan (CH_4) emisyonlarının önemli kaynaklarından biridir. Amonyak emisyonları, atmosferde asidifikasyona ve ince partikül oluşumuna yol açarak hem çevresel hem de insan sağlığı açısından olumsuz etkiler yaratmaktadır. Ayrıca amonyağın solunması; astım, bronşit ve diğer solunum yolu rahatsızlıklarını tetikleyebilmektedir (Edwards ve Daniel, 1992; Rahman vd., 2022). Öte yandan, diazot monoksit ve metan küresel ısınma potansiyeli yüksek sera gazları olup iklim değişikliğine doğrudan katkı sağlamaktadır. Tavuk gübresi kaynaklı amonyak emisyonlarının ise hava kalitesi, ekosistemler ve çevresel sürdürülebilirlik üzerinde önemli baskı oluşturduğu; bu nedenle döngüsel ekonomi temelli atık yönetim yaklaşımlarının önerildiği bildirilmektedir (Kacorzyk vd., 2025). Bu nedenle tavukçuluk atıklarının uygun şekilde işlenmemesi, yalnızca yerel ölçekte değil, küresel ölçekte de iklimsel riskler doğurmaktadır.

3.3.2 Su ve Toprak Kirliliği

Tavuk gübresinin kontrolsüz biçimde tarım arazilerine uygulanması, içerdiği yüksek azot (N) ve fosfor (P) nedeniyle hem su hem de toprak kalitesini olumsuz etkilemektedir. Fazla fosforun yüzeysel akış yoluyla göl ve nehirlerde birikmesi, ötrofikasyona neden olmakta; bu süreç alg patlamaları ve oksijen azalması sonucunda ekosistemlerin çökmesine yol açabilmektedir (Edwards ve Daniel, 1992; Singh vd., 2018). Yeraltı sularında görülen aşırı nitrat birikimi ise özellikle kırsal alanlarda içme suyu güvenliği açısından ciddi risk oluşturmaktadır. Nitekim nitrat kontaminasyonu, mavi bebek sendromu ve çeşitli kanser türleriyle ilişkilendirilmiştir. Ayrıca gübreyle birlikte toprağa taşınan yüksek miktarda organik madde, toprak mikrobiyotasını bozmakta, asidifikasyona yol açmakta ve uzun vadede tarımsal verimliliği düşürmektedir. Bu nedenle gübre ve sıvı atıkların uygun arıtma veya işleme yöntemleri olmaksızın doğrudan uygulanması, sürdürülebilir tarım açısından önemli bir tehdit oluşturmaktadır (Rahman vd., 2022).

3.3.3. Patojen mikroorganizmalar

Tavukçuluk atıkları, özellikle Salmonella Spp., *Campylobacter spp.* ve *Escherichia coli* gibi patojen mikroorganizmaların çevreye yayılmasında önemli bir rol oynamaktadır. Literatür çalışmaları incelendiğinde ise tavuk gübresiyle kirlenmiş su ve toprakların zoonotik hastalıkların bulaşmasında kritik bir bulaşma aracı olduğunu ortaya koymaktadır (Edwards ve Daniel, 1992; Singh vd., 2018). Özellikle Salmonella Spp. ve *Campylobacter* kaynaklı gıda zehirlenmeleri dünya genelinde milyonlarca insanı etkilemekte ve ciddi ekonomik kayıplara neden olmaktadır. Bu patojenler aynı zamanda sulama suları aracılığıyla tarımsal ürünlere bulaşarak gıda güvenliği zincirinde ek riskler yaratmaktadır. Sonuç olarak, hijyen standartlarının düşük olduğu bölgelerde dışkı kaynaklı kirliliğin yaygın olması halk sağlığı açısından önemli tehditler doğurmaktadır.

3.3.4. Antibiyotik ve ağır metal kalıntıları

Modern tavukçulukta antibiyotikler, büyüme destekleyici ve hastalık önleyici amaçlarla yaygın olarak yemlere katılmaktadır. Ancak bu antibiyotiklerin bir bölümü sindirilmeden dışkıyla atılmakta ve gübre aracılığıyla çevreye yayılmaktadır. Bu durum, antimikrobiyal direnç (AMR) gelişimini hızlandırmakta ve direnç genlerinin hem çevresel mikrobiyota hem de patojenlere taşınmasına zemin hazırlamaktadır. Dünya Sağlık Örgütü (WHO) ise, çevresel AMR'yi küresel sağlık için en kritik tehditlerden biri olarak tanımlamaktadır. Bunun yanında, tavuk yemlerinde kullanılan çinko, bakır ve arsenik gibi

ağır metaller gübre ve atıklarda birikmekte; toprakta uzun vadede toksisite oluşturarak tarımsal üretim kapasitesini düşürmekte hatta gıda zincirine taşınarak insan sağlığı üzerinde olumsuz etkiler yaratmaktadır. Özellikle arsenik kalıntılarının içme sularına sızması, kanserojen etki potansiyeli nedeniyle ciddi bir çevresel risk oluşturmaktadır (Smedley ve Kinniburgh, 2002; Faridullah vd., 2014; Berendonk vd., 2015; Rahman vd., 2022; Anonim, 2025d). Tavukçuluk atıkları, yalnızca üretime bağlı kantitatif (miktarsal) hacimleriyle değil; bileşimlerinde barındırdıkları toksik gazlar, agro-kimyasal kalıntılar, patojen mikroorganizmalar ve yoğun besin elementleri nedeniyle hem ekolojik sürdürülebilirlik hem de biyogüvenlik açısından akut tehditler barındırmaktadır. Bu heterojen ve karmaşık risk matrisi, çevre ve halk sağlığının korunmasını hedefleyen sürdürülebilir atık yönetimi stratejilerinin ancak tüm bu parametreleri eş zamanlı olarak ele alan bütüncül ve entegre bir yaklaşımla kurgulanmasını zorunlu kılmaktadır.

3.3. Değerlendirme Yöntemleri

Tavukçuluk endüstrisinde ortaya çıkan atıkların yalnızca bertaraf edilmesi değil, aynı zamanda çevresel riskleri en aza indirecek şekilde dönüştürülerek ekonomik faydaya kazandırılması gerekmektedir. Bu bağlamda, son yıllarda döngüsel ekonomi yaklaşımı doğrultusunda geliştirilen değerlendirme yöntemleri giderek önem kazanmaktadır. Atıkların değerlendirilmesinde başlıca yöntemler arasında gübreleme ve kompostlaştırma, anaerobik çürütme (biyogaz üretimi), mikrobiyal ve enzimatik biyodönüşüm, termokimyasal yöntemler, tüylerden keratin geri kazanımı, yumurta kabuğu ve zarının farklı uygulamaları ile kan ve sakatat atıklarının işlenmesi öne çıkmaktadır (Brandelli vd., 2015; Singh vd., 2018; Rahman vd., 2022).

3.4.1. Gübreleme, kompost ve vermikompost

Tavuk gübresi, içerdiği yüksek azot (N), fosfor (P) ve potasyum (K) nedeniyle tarımsal gübre olarak yaygın şekilde kullanılmaktadır (Edwards ve Daniel, 1992). Ancak gübrenin kontrolsüz ya da doğrudan tarım arazilerine uygulanması; amonyak emisyonları, sera gazı salımları, nitrat kirliliği ve patojen yayılımı gibi ciddi çevresel riskler oluşturmaktadır (Rahman vd., 2022). Bu nedenle gübrenin daha sürdürülebilir yöntemlerle işlenmesi gerekmektedir. Bu yöntemlerden biri olan kompostlaştırma, tavuk gübresinin organik maddece stabilize edilmesini ve patojen yükünün azaltılmasını sağlayarak tarımda daha güvenli bir ürün elde edilmesine imkân tanır. Kompost süreci sırasında uygun karbon/azot (C/N) oranı (25–30), sıcaklık (55–65 °C) ve pH (6,5–8,0) koşullarının sağlanması kritik öneme sahiptir (Bernal vd., 2009). Vermikompost ise solucanların biyolojik aktivitesiyle gerçekleşir ve toprakta biyoyararlanımı yüksek humus benzeri ürünlerin oluşumunu sağlar (Singh vd., 2018). Literatürde yapılan çalışmalar incelendiğinde kompost ve vermikompost uygulamalarının hem tarımsal verimliliği artırdığını hem de patojenleri baskılayarak çevresel riskleri azalttığını göstermektedir (Rahman vd., 2022). Şekil 2'de ise tavuk gübresinin kompostlaştırma süreci şematik olarak gösterilmektedir.



Şekil 2. Tavuk gübresinin kompostlaştırma ve gübreleme süreci (Anonim, 2025e).

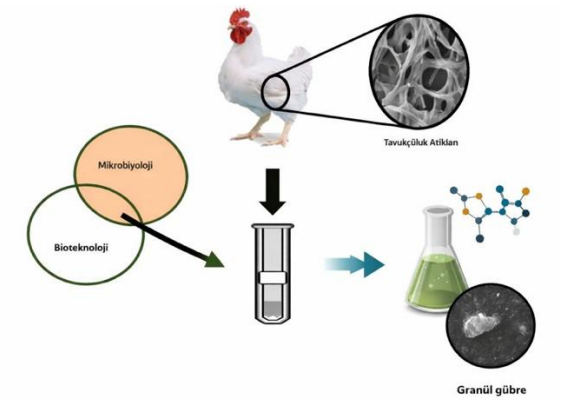
3.4.2. Anaerobik çürütme (biyogaz üretimi)

Anaerobik çürütme, özellikle gübre ve kesimhane atıklarının oksijensiz ortamda mikroorganizmalar tarafından parçalanarak biyogaz (metan ve karbondioksit karışımı) üretimini sağlayan önemli bir yöntemdir. Bu süreç yalnızca yenilenebilir enerji üretimine katkı sunmakla kalmamakta, aynı zamanda ortaya çıkan sindirim çamurunun fosfor ve organik madde bakımından zengin içeriği sayesinde tarımsal gübre olarak değerlendirilebilmesine de olanak tanımaktadır. Dahası, sindirim çamurundan çöktürme yöntemiyle fosfor geri kazanımı yapılabilmekte ve böylece hem atık yönetimine hem de döngüsel ekonomiye katkı sağlanmaktadır (Singh vd., 2018; Rahman vd., 2022). Son yıllarda yapılan literatür çalışmaları incelendiğinde ise Zinina vd. (2022) tarafından yapılan bir çalışmada, tavuk gübresinin biyogaz tesislerinde enerji kaynağı olarak kullanılmasının karbon ayak izini azalttığını ve tarımsal bölgelerde ekonomik fayda yarattığını ortaya koymuştur.

3.4.3. Mikrobiyal ve enzimatik biyodönüşüm

Tavukçuluk atıkları içerisinde yer alan protein açısından zengin fraksiyonlar, mikrobiyal ve enzimatik biyodönüşüm yaklaşımlarıyla katma değerli ürünlere dönüştürülebilmektedir. Bu kapsamda özellikle mikroorganizmalar tarafından üretilen keratinaz, proteaz ve lipaz gibi enzimler, kompleks protein yapılarının daha basit ve kullanılabilir bileşenlere parçalanmasında önemli rol oynamaktadır (Brandelli vd., 2015). Tüyler, yüksek oranda keratin içermeleri nedeniyle biyolojik olarak zor parçalanan bir yapı sergilemekte olup, keratinaz enzimleri bu dirençli yapının hidrolizinde etkili bir araç olarak öne çıkmaktadır. Literatürde, mikrobiyal kaynaklı keratinazların tüy proteinlerini hidrolize ederek protein hidrolizatları ve peptitler elde edilmesine olanak sağladığı; bu ürünlerin başta yem katkı maddeleri olmak üzere çeşitli biyoteknolojik uygulamalarda değerlendirilebildiği bildirilmektedir (Brandelli vd., 2015; Moktip vd., 2025).

Kan ve sakatat gibi diğer protein esaslı tavukçuluk atıkları ise proteolitik enzimler kullanılarak biyolojik hidrolize tabi tutulabilmekte ve bu süreç sonucunda düşük molekül ağırlıklı protein fraksiyonları ile biyoaktif peptitler elde edilebilmektedir. Bu tür ürünlerin özellikle hayvan besleme uygulamalarında protein kaynağı olarak ve bazı endüstriyel proseslerde fonksiyonel bileşenler şeklinde kullanılabildiği ifade edilmektedir (Inamuddin ve Khan, 2021). Gıda ve Tarım Örgütü (FAO) tarafından yayımlanan sektörel değerlendirmelerde de, tavukçuluk atıklarının enzimatik ve biyoteknolojik yöntemlerle değerlendirilmesinin hem atık yükünün azaltılması hem de ekonomik değer yaratılması açısından önemli bir potansiyel sunduğu vurgulanmaktadır (Anonim, 2022). Bu doğrultuda, mikrobiyal ve enzimatik biyodönüşüm yaklaşımları; tavukçuluk atıklarının çevresel bir yük olmaktan çıkarılarak döngüsel ekonomi çerçevesinde katma değerli ürünlere dönüştürülmesine olanak sağlayan sürdürülebilir teknolojiler arasında yer almaktadır. Şekil 3'te, tavukçuluk atıklarının mikrobiyal biyodönüşüme yönelik genel proses akışı şematik olarak sunulmaktadır.



Şekil 3. Tavukçuluk atıklarının mikrobiyal biyodönüşüm süreci (Laba vd., 2018).

3.4.4. Termokimyasal yöntemler

Piroliz ve hidrotermal karbonizasyon gibi termokimyasal dönüşüm yöntemleri, tavukçuluk atıklarının enerji üretiminde değerlendirilmesi için öne çıkan yaklaşımlar arasındadır. Bu yöntemler sayesinde tüy, gübre ve diğer organik fraksiyonlar; biyokömür (biochar), biyoyağ ve sentez gazı (syngas) gibi değerli ürünlere dönüştürülebilmektedir. Biyokömür, karbonca zengin yapısı sayesinde tarımsal alanlarda toprak düzenleyici olarak kullanılmakta, toprağın su tutma kapasitesini ve besin elementleri döngüsünü iyileştirmektedir. Biyoyağ ve gaz ürünleri ise enerji sektöründe yenilenebilir enerji kaynağı olarak değerlendirilmektedir (Zhang vd., 2023). Bu yöntemlerin en önemli avantajları arasında atık hacminin ciddi şekilde azaltılması, enerji geri kazanımının sağlanması ve sera gazı emisyonlarının düşürülmesi yer almaktadır. Ancak yüksek sıcaklık ve basınç koşulları nedeniyle enerji maliyetlerinin yüksek oluşu ve yatırım altyapısı gereksinimleri, uygulamanın yaygınlaşmasını sınırlayan en önemli faktörlerdir (Abbasi vd., 2024).

3.4.5. Tüylerden keratin geri kazanımı

Tavuk tüyleri, küresel ölçekte yılda yaklaşık 4,7 milyon ton üretim hacmine ulaşan en büyük tavukçuluk atıklarından biridir (Moktip vd., 2025). Tüylerin %85–90'ı keratin proteininden oluşmaktadır ve bu protein, yüksek oranda disülfit bağları içermesi nedeniyle biyolojik olarak parçalanması oldukça zor bir yapıya sahiptir. Bu nedenle uzun yıllar boyunca tüy atıkları çevresel açıdan ciddi sorunlar yaratmıştır. Ancak son yıllarda geliştirilen yeşil çözücü teknolojileri sayesinde keratin geri kazanımında önemli ilerlemeler kaydedilmiştir. Özellikle subkritik su ekstraksiyonu, iyonik sıvılar ve derin ötektik çözücüler kullanılarak keratin yüksek verimle izole edilebilmekte ve bu yöntemler çevre dostu alternatifler olarak öne çıkmaktadır (Moktip vd., 2025). Elde edilen keratin, biyomedikal uygulamalarda (örneğin yara iyileştirme materyalleri, doku mühendisliği iskeleleri, kontrollü ilaç salım sistemleri) umut vadeden bir biyopolimer olarak değerlendirilmektedir. Ayrıca tekstil, kozmetik ve paketleme endüstrilerinde de keratin bazlı biyomalzemelerin kullanımına yönelik araştırmalar hız kazanmıştır.

3.4.6. Yumurta kabuğu ve zarı

Yumurta kabukları, yapılarının yaklaşık %95'ini oluşturan kalsiyum karbonat ($CaCO_3$) sayesinde hem tarımda hem de endüstride önemli bir hammadde potansiyeline sahiptir. Ortalama 5–6 gram ağırlığındaki kabuklar, tarımsal uygulamalarda kalsiyum kaynağı olarak doğrudan kullanılabilmekte veya yem katkısı olarak değerlendirilebilmektedir. Bununla birlikte, literatürde yumurta kabuklarının yalnızca tarımsal değil; aynı zamanda biyomalzeme üretiminde de önemli bir kaynak olduğu belirtilmektedir (Yüceer, 2019). Çalışmalar, yumurta kabuklarının biyoplastik, biyokompozit ve adsorban malzeme üretiminde etkin şekilde kullanılabileceğini göstermektedir (Yoo vd., 2009; Ngayakamo ve Onwualu, 2022). Ayrıca yumurta zarında bulunan kolajen ve proteinler, biyomedikal araştırmalarda doku mühendisliği ve rejeneratif tıp uygulamaları için potansiyel biyopolimer kaynakları olarak değerlendirilmektedir. Dolayısıyla yumurta kabuğu ve zarı, döngüsel ekonomi kapsamında hem tarımsal hem de endüstriyel açıdan yüksek katma değer sunan ikincil ürünlerdir.

3.4.7. Kan ve sakatat atıkları

Kesimhanelerde ortaya çıkan kan ve sakatat atıkları, tavukçuluk endüstrisinin en protein açısından zengin yan ürünleri arasında yer almaktadır. Kan, canlı ağırlığın yaklaşık %3'ünü, sakatat (baş, ayak ve iç organlar) ise toplam gövdenin %7–8'ini oluşturmaktadır (Crawley vd., 1980; Zinina vd., 2022). Geleneksel olarak bu fraksiyonlar hayvansal atık geri dönüşüm tesislerinde işlenerek hayvansal un ve yağ üretiminde kullanılmaktadır. Böylece hem çevresel yük azaltılmakta hem de ekonomik fayda sağlanmaktadır. Bununla

birlikte, son yıllarda mikrobiyal enzimler yardımıyla bu atıkların biyolojik hidrolizi üzerine yapılan çalışmalar, daha yüksek katma değerli ürünlerin elde edilebileceğini ortaya koymuştur. Özellikle proteolitik enzimlerle gerçekleştirilen hidroliz sonucunda protein hidrolizatları ve biyoaktif peptitler üretilebilmekte; bu ürünler yem katkıları, fonksiyonel gıda bileşenleri ve hatta farmasötik uygulamalar için değerlendirilmektedir (Brandelli vd., 2015). Böylece kesimhane atıkları yalnızca bertaraf edilmesi gereken yan ürünler olmaktan çıkmakta, aynı zamanda biyoteknolojik süreçler aracılığıyla ekonomik katma değer yaratan kaynaklara dönüştürülmektedir.

Sonuç olarak, tavukçuluk endüstrisinde ortaya çıkan atıkların değerlendirilmesi yalnızca çevresel risklerin azaltılması açısından değil, aynı zamanda ekonomik katma değer yaratılması bakımından da kritik bir öneme sahiptir. Gübre, tüy, yumurta kabuğu, kan ve sakatat gibi farklı atık fraksiyonları; kompost üretiminden biyogaz üretimine, mikrobiyal biyodönüşümden keratin geri kazanımına ve biyomalzeme geliştirmeye kadar geniş bir yelpazede değerlendirilebilmektedir. Bu yöntemler sayesinde hem sürdürülebilir atık yönetimi sağlanmakta hem de döngüsel ekonomi kapsamında enerji, gübre, yem katkıları ve biyomedikal ürünler gibi çeşitli çıktılar elde edilmektedir. Ancak her yöntemin kendine özgü avantajları ve sınırlılıkları bulunmakta; dolayısıyla uygulanabilirlik, ekonomik maliyet, teknolojik altyapı ve çevresel etkiler birlikte değerlendirilmelidir (Anonim, 2022; Kacorzyk vd., 2025).

Tablo 1'de ise tavukçuluk atıklarının değerlendirilmesinde kullanılan başlıca yöntemler; bu yöntemlerde işlenen atık türleri, elde edilen ürünler, sağladıkları avantajlar ve karşılaşılan sınırlılıklar ile birlikte özetlenmiştir.

Tablo 1. Tavukçuluk atıklarının değerlendirilmesinde kullanılan başlıca yöntemler

Yöntem	Kullanılan Atık Türleri	Ürünler/Çıktılar	Avantajlar	Sınırlılıklar / Zorluklar
Kompost	Gübre, ölü hayvanlar, sakatat	Kompost, (organik gübre)	Patojen azalması, tarımsal verim artışı, düşük maliyet	Nitrat sızıntısı riski, süreç süresi uzun
Anaerobik Çürütme (Biyogaz)	Gübre, kesimhane sıvı atıkları	Biyogaz (CH_4 + CO_2), sindirim çamuru	Yenilenebilir enerji, fosfor geri kazanımı	Yatırım maliyeti yüksek, proses optimizasyonu gerek
Mikrobiyal / Enzimatik	Tüy, kan, sakatat	Protein hidrolizatları, biyoaktif peptitler	Katma değerli ürünler, yem ve gıda katkıları	Enzim üretim maliyeti, ölçeklenebilirlik
Termokimyasal (Piroliz, HTC)	Gübre, tüy, organik atıklar	Biyokömür, biyoyağ, sentez gazı	Atık hacmi azalır, enerji verimliliği artar	Yüksek enerji ihtiyacı, yatırım maliyeti
Keratin Geri Kazanımı	Tüy	Yüksek saf keratin, biyomalzemeler	Yeşil çözücülerle çevre dostu yöntemler	Teknoloji yeni, maliyetli süreçler
Yumurta Kabuğu ve Zarı	Yumurta kabuğu, zar	$CaCO_3$ gübre katkısı, biyokompozit, biyoplastik, kolajen	Çok yönlü kullanım, biyomedikal uygulamalar	Toplama ve ayrıştırma zorluğu
Kan ve Sakatat	Kan, baş, ayak, iç organlar	Hayvansal un, yağ, biyoaktif peptitler	Protein ve yağ geri kazanımı, yem sektörü katkısı	Patojen riski, işleme maliyetleri

3.4.8. Endüstriyel ölçek ve pazar potansiyeli

Tavukçuluk endüstrisinde ortaya çıkan atıkların yönetimi, yalnızca çevresel risklerin azaltılması değil, aynı zamanda ekonomik katma değer yaratılması açısından da stratejik öneme sahiptir. Dünya genelinde tavukçuluk endüstrisinden kaynaklanan yan ürünlerin miktarı her geçen yıl artarken, bu atıkların rendering tesisleri, gübre fabrikaları ve biyogaz santralleri gibi endüstriyel ölçekli işletmelerde değerlendirilmesi, döngüsel ekonomi perspektifiyle sürdürülebilir çözümler sunmaktadır (Rahman vd., 2022; Zinina vd., 2022). Bu bağlamda, tavukçuluk atıklarının işlenmesiyle elde edilen hayvansal un, organomineral gübre, biyogaz, biyometan, biyokömür ve fonksiyonel protein ürünleri hem iç pazarda hem de küresel ölçekte önemli bir pazar potansiyeli yaratmaktadır.

Tekno-ekonomik ve sektörel projeksiyonlar incelendiğinde, agro-endüstriyel ürünlerin geri kazanım potansiyeli finansal piyasalarda da karşılık bulmaktadır. Son yıllarda gerçekleştirilen küresel piyasa analizlerine göre, rendering ürünleri pazarı, 2024 yılı itibarıyla yaklaşık 23 milyar USD'lik makroekonomik bir hacme ulaşmıştır. Sürdürülebilir atık yönetimi regülasyonlarının sıkılaşması ve döngüsel ekonomi modellerinin endüstriyel tabana yayılmasıyla birlikte, söz konusu pazarın önümüzdeki projeksiyon döneminde yıllık

ortalama %3 bileşik büyüme oranı (CAGR) sergileyerek istikrarlı yükselişini sürdürmesi öngörülmektedir. Bu trend, hayvansal yan ürünlerin marjinal bir atık olmaktan çıkıp, küresel tedarik zincirinde stratejik birer hammaddeye dönüştüğünü açıkça ortaya koymaktadır (Anonim, 2025a). Benzer şekilde, biyogaz sektörü özellikle Avrupa ve Asya'da hızla büyüyen yenilenebilir enerji yatırımları arasında yer almakta; tavuk gübresinin bu alanda kullanımı enerji arz güvenliği açısından stratejik bir kaynak olarak değerlendirilmektedir (Abbasi vd., 2024). Türkiye'de de hem enerji üretimi hem de organomineral gübre uygulamalarında tavukçuluk atıklarının endüstriyel ölçekte değerlendirilmesi, kırsal kalkınma ve ihracat potansiyeli açısından önemli fırsatlar sunmaktadır.

3.4.9. Dünya ve Türkiye'de mevcut örnek uygulamalar

Dünya genelinde tavukçuluk yan ürünleri ve atıklarının endüstriyel ölçekte değerlendirilmesi; rendering (hayvansal yan ürün işleme), organomineral/organik gübre üretimi, biyogaz ve enerji geri kazanımı ile yüksek katma değerli biyo-ürünlerin (ör. keratin, peptitler, biyokömür) elde edilmesi ekseninde giderek yaygınlaşmaktadır. Özellikle Amerika Birleşik Devletleri ve Avrupa'da büyük ölçekli rendering şirketleri, artan talep doğrultusunda kapasitelerini genişletmekte ve yeni yatırımlara yönelmektedir. Örneğin, dünyanın en büyük rendering firmalarından biri olan Darling Ingredients, 2023 yılında ABD'de Butterball LLC ile ortak bir rendering tesisi kurma kararı almıştır. Tesisin haftalık yaklaşık 18 milyon libre (8.165 ton) hammadde işleme kapasitesine sahip olacağı, 2024 yılında inşaata başlanıp 2025 yılında tamamlanmasının öngörüldüğü bildirilmiştir (Anonim, 2023b). Bu tür yatırımlar, yalnızca atık yönetimi açısından değil; aynı zamanda hayvansal protein ve teknik yağ üretimi yoluyla küresel pazarda ekonomik değer yaratılması bakımından da stratejik görülmektedir.

Türkiye'de ise tavukçuluk yan ürünlerinin değerlendirilmesine yönelik endüstriyel uygulamalar, özellikle Marmara ve Batı Karadeniz hattında (Sakarya, Bolu, Düzce) yoğunlaşmıştır. Bu bölgede entegre beyaz et üreticilerinin faaliyet göstermesi, rendering tesislerinin, biyogaz santrallerinin ve kompost/organomineral gübre fabrikalarının yaygınlaşmasını sağlamaktadır. Örneğin, Türkiye'nin en büyük entegre üreticilerinden biri olan Şenpiliç Gıda Sanayi A.Ş., Sakarya ve çevresinde artan üretim kapasitesiyle rendering ve gübre geri dönüşüm uygulamalarını yaygınlaştırmış; ayrıca yeni tesis modernizasyon yatırımlarıyla süreçlerini güçlendirmiştir (Anonim, 2023a, 2023c). Bu örnekler, Türkiye'de tavukçuluk atıklarının endüstriyel ölçekte değerlendirilmeye başlandığını ve söz konusu uygulamaların gerek enerji gerekse gübre üretimi yoluyla döngüsel ekonomiye katkı sağladığını göstermektedir.

3.4.10. Rendering, gübre fabrikaları ve biyogaz uygulamaları

Tavukçuluk endüstrisinde ortaya çıkan kesimhane ve gübre atıklarının endüstriyel ölçekte değerlendirilmesi üç ana uygulama alanında öne çıkmaktadır. Bu alanlar; hayvansal yan ürün işleme tesisleri (rendering tesisleri), gübre fabrikaları ve biyogaz santralleridir.

İlk olarak, rendering tesisleri kesimhane kaynaklı kan, sakatat, kemik ve yağlı dokuların yüksek sıcaklık ve basınç altında işlenerek hayvansal un ve yağlara dönüştürülmesini kapsamaktadır. Bu ürünler, özellikle yem, evcil hayvan maması ve teknik yağ endüstrileri için önemli bir hammadde arzı sağlamaktadır. Nitekim küresel ölçekte Darling Ingredients, 2022 yılında Valley Proteins'in 18 hayvansal yan ürün işleme (rendering) tesisini satın alarak kapasitesini artırmış ve düşük karbon yoğunluklu hammadde tedarikinde lider konuma gelmiştir (Anonim, 2023b). Türkiye'de ise entegre beyaz et üreticilerinden Şenpiliç Gıda Sanayi A.Ş., Kadirli Rendering Tesisi ile resmî olarak kayıtlı bir işletmeye sahiptir. Bu durum, rendering teknolojisinin ulusal ölçekte de etkin şekilde uygulandığını göstermektedir.

İkinci olarak, gübre fabrikaları, tavuk gübresinin doğrudan tarımsal kullanımına kıyasla daha kontrollü ve standardize edilmiş ürünler sunmaktadır. Bu tesislerde tavuk gübresi, kompostlaştırma veya organomineral gübre üretim hatlarında işlenmekte; böylece hem patojen yükü azaltılmakta hem de besin elementleri daha dengeli bir forma dönüştürülmektedir. Literatürde yapılan çalışmalar, organomineral gübrelerin azot ve fosfor dengesini düzenleyerek tarımsal verimliliği artırdığını ve pazarlanabilir standart bir ürün sunduğunu ortaya koymaktadır (Singh vd., 2018). Türkiye'de ise KAYÇEV gibi tesisler, tavuk gübresini kompostlaştırarak tarımsal kullanıma sunmakta; ayrıca granül formda organomineral gübre hatlarına yaptıkları yatırımlarla hem iç pazarda hem de ihracatta rekabet avantajı sağlamaktadır.

Üçüncü olarak, biyogaz santralleri tavuk gübresi ve kesimhane sıvı atıklarını anaerobik çürütme yoluyla değerlendirerek hem enerji üretiminde hem de tarımsal gübre temininde kritik bir rol üstlenmektedir. Bu süreçte elde edilen biyogaz elektrik ve ısı üretiminde kullanılmakta, ayrıca sindirim çamuru fosfor açısından zengin bir gübre olarak değerlendirilmektedir. Türkiye'de Efeler Biyogaz, yalnızca tavuk gübresi kullanarak 4,8 MWe kurulu güç kapasitesine ulaşmıştır. Benzer şekilde, Bolu Mudurnu ve Balıkesir BES tesisleri hem çevresel riskleri azaltmış hem de bölgesel kalkınmaya katkı sağlamıştır. Uluslararası ölçekte ise EnviTec Biogas, tavuk gübresinden biyogaz üretimini biyometan (RNG, bio-LNG) dönüşümüne entegre ederek karbon ayak izini daha da azaltmayı hedeflemektedir (Glatz vd., 2011; Anonim, 2025b, 2025c; Oyedun vd., 2025; X. Wang vd., 2025).

3.4.11. Ekonomik potansiyel ve yaşam döngüsü analizleri

Tavukçuluk atıklarının endüstriyel ölçekte değerlendirilmesi yalnızca çevresel risklerin azaltılması açısından değil, aynı zamanda ekonomik uygulanabilirlik bakımından da giderek önem kazanmaktadır. Küresel agro-endüstriyel ürün yönetimi ve biyorafineri stratejilerinin makroekonomik boyutu, finansal piyasa projeksiyonlarında net bir şekilde gözlenmektedir. Nitekim güncel tekno-ekonomik analizler, küresel rendered (eritme yöntemiyle ileri işlenmiş) ürünler pazarının 2024 yılı itibarıyla yaklaşık 23,5 milyar USD değerinde bir ekonomik hacme ulaştığını göstermektedir. Sürdürülebilir protein kaynaklarına olan talebin artması ve sıfır-atık biyoekonomi politikalarının küresel ölçekte tabana yayılmasıyla birlikte, bu pazarın 2030 yılına kadar yıllık ortalama %3–4 bileşik büyüme oranı (CAGR) sergileyerek istikrarlı bir ekspansiyon (genişleme) periyoduna girmesi öngörülmektedir. Bu finansal büyüme trendi, konvansiyonel hayvansal yan ürünlerin marjinal birer kirlilik unsuru olmaktan çıkıp, endüstriyel tedarik zincirinde yüksek katma değerli ve stratejik hammaddeler haline geldiğinin somut bir göstergesidir (Anonim, 2025a). Bu büyüme, özellikle hayvansal un ve yağların yem ve evcil hayvan maması endüstrilerinde artan talebi ile desteklenmektedir. Türkiye'de ise, tavuk gübresinin biyogaz tesislerinde enerji kaynağı olarak değerlendirilmesi, hem elektrik üretimi hem de karbon ayak izinin azaltılması açısından ekonomik bir çözüm olarak öne çıkmaktadır (Zinina vd., 2022).

Ekonomik fizibiliteye ek olarak, yaşam döngüsü analizleri, farklı atık işleme yöntemlerinin çevresel etkilerini karşılaştırmak için kritik bir araçtır. Literatürde yapılan çalışmalara göre ise tavuk gübresinin açıkta depolanması veya doğrudan tarım arazilerine uygulanması, ciddi sera gazı emisyonları ve ötrofikasyon riskleri yaratmaktadır. Buna karşılık, anaerobik çürütme ve piroliz gibi teknolojiler, toplam sera gazı emisyonlarını önemli ölçüde azaltmakta ve enerji geri kazanımı yoluyla çevresel fayda sağlamaktadır (Edwards ve Daniel, 1992; Abbasi vd., 2024; Kacorzyk vd., 2025). Ancak yaşam döngüsü analizlerinin sonuçları; lojistik mesafe, tesis ölçeği, sistem sınırları ve ürün ikame senaryolarına oldukça duyarlıdır. Bu nedenle, tavukçuluk atıklarının yönetiminde en uygun teknolojinin seçimi, bölgesel bağlama özgü yaşam döngüsü analiz çalışmaları ile desteklenmelidir.

3.4.12. Gelecek perspektifler ve araştırma ihtiyaçları

Tavukçuluk endüstrisinden kaynaklanan atıkların yönetimi, yalnızca çevresel risklerin azaltılması açısından değil, aynı zamanda kaynak geri kazanımı ve ekonomik katma değer yaratılması bakımından da stratejik bir öneme sahiptir. Mevcut uygulamalar her ne kadar çevresel etkileri azaltmaya yönelik bazı faydalar sağlasa da, geleceğe dönük araştırmaların daha düşük maliyetli, enerji etkin ve ölçeklenebilir teknolojilerin geliştirilmesine odaklanması gerekmektedir (Singh vd., 2018; Rahman vd., 2022).

İlk olarak, biyogaz ve anaerobik çürütme süreçlerinin optimizasyonu, araştırma gündeminde önemli bir yer tutmaktadır. Tavuk gübresinin düşük karbon/azot (C/N) oranı ve yüksek amonyak içeriği, metanojenik aktiviteyi baskılamakta ve biyogaz verimini sınırlamaktadır. Bu nedenle, farklı organik atıklarla birlikte anaerobik çürütme, ön arıtma teknikleri ve pH tamponlama gibi stratejilerin saha koşullarına uyarlanmasına yönelik araştırmalar giderek artmaktadır. Ayrıca, sindirim çamurlarından çöktürme ve amonyak sıyırma yöntemleriyle besin geri kazanımı yapılabilmektedir. Ancak bu teknolojilerin enerji tüketimi ve maliyet açısından daha etkin hale getirilmesi için ileri düzey çalışmalara ihtiyaç duyulmaktadır (Zinina vd., 2022; Abbasi vd., 2024).

İkinci olarak, termokimyasal dönüşüm yöntemleri (piroliz ve hidrotermal karbonizasyon), atıkların enerjiye ve katma değerli ürünlere dönüştürülmesinde potansiyel vaat etmektedir. Ancak bu süreçlerde elde edilen ürünlerin (biyokömür, biyoyağ, sentez gazı) kalitesi, sıcaklık, basınç ve hammadde özelliklerine bağlı olarak değişkenlik göstermektedir. Bu nedenle, özellikle biyokömürün toprakta uzun dönem etkileri (pH düzenleme, ağır metal bağlama, karbon sekestrasyonu) üzerine daha fazla saha çalışmasına ihtiyaç duyulmaktadır (Edwards ve Daniel, 1992; Zhang vd., 2023).

Üçüncü olarak, enzimatik ve mikrobiyal biyodönüşüm teknolojileri, gelecek araştırmalar için büyük bir potansiyel taşımaktadır. Keratinaz, proteaz ve lipaz gibi enzimlerin kullanımıyla tüy, kan ve sakatat gibi protein açısından zengin fraksiyonlardan protein hidrolizatları ve biyoaktif peptitler üretilebilmekte; bu ürünler yem katkısı, biyomalzeme ve farmasötik uygulamalarda değerlendirilebilmektedir (Brandelli vd., 2015; Moktip vd., 2025). Ancak bu süreçlerin laboratuvar ölçeğinden pilot ve endüstriyel ölçeğe taşınması, enzimlerin stabilitesi, sürekli reaktör tasarımları ve ürün standardizasyonu konularında daha fazla araştırmaya ihtiyaç vardır (Laba vd., 2018; Moktip vd., 2025).

Dördüncü olarak, AMR ve patojen kontrolü, küresel sağlık açısından öncelikli bir araştırma alanıdır. Tavuk gübresinden çevreye yayılan antibiyotik kalıntıları ve direnç genlerinin biyogaz, kompost ve piroliz gibi işlemler sırasında ne ölçüde parçalandığı veya dönüştüğü henüz net değildir. Bu nedenle, farklı atık işleme teknolojilerinin AMR üzerindeki etkilerinin çok merkezli ve uzun dönemli araştırmalarla incelenmesi gerekmektedir. Benzer şekilde, patojen mikroorganizmaların (*Salmonella Spp., E. coli, Campylobacter*) çevresel dolaşımdaki kaderi ve arıtma süreçlerinin etkinliği de ayrıntılı şekilde araştırılmalıdır (Singh vd., 2018; Rahman vd., 2022; C. Wang vd., 2025).

Beşinci olarak, ekonomik fizibilite ve yaşam döngüsü analizleri (YDA), tavukçuluk atıklarının değerlendirilmesinde uygun teknolojilerin seçimi için kritik rol oynamaktadır. Literatürde yapılan çalışmalar, tavuk gübresinin doğrudan tarıma uygulanmasının

yüksek sera gazı emisyonları ve ötrofikasyon riskleri yarattığını, buna karşılık anaerobik çürütme ve piroliz gibi teknolojilerin çevresel etkileri önemli ölçüde azalttığını ortaya koymaktadır (Zinina vd., 2022; Abbasi vd., 2024). Ancak YDA sonuçlarının lojistik mesafe, tesis ölçeği ve ürün ikame senaryolarına duyarlı olması nedeniyle, her ülke ve bölge için yerelleştirilmiş çalışmalara ihtiyaç duyulmaktadır.

Son olarak, sosyo-ekonomik boyutlar ve dijitalleşme gelecek perspektifleri açısından önem arz etmektedir. Çiftlik ölçeğinde uygulamaların yaygınlaştırılması için düşük maliyetli teknolojilerin yanı sıra, kooperatif modelleri ve finansman desteklerinin geliştirilmesi önerilmektedir. Ayrıca, biyogaz reaktörleri ve kompost yığınlarında IoT tabanlı sensör ağları ile amonyak, metan ve sıcaklık gibi parametrelerin gerçek zamanlı izlenmesi, süreçlerin verimliliğini artıracak yenilikçi bir araştırma alanı olarak öne çıkmaktadır (Edwards ve Daniel, 1992; Singh vd., 2018; Li vd., 2025).

Gelecek araştırmaların odak noktası; düşük emisyonlu ve enerji etkin proseslerin geliştirilmesi, ürün kalite standartlarının oluşturulması, enzimatik ve mikrobiyal platformların ölçeklenebilir hale getirilmesi ve çevresel risklerin (sera gazı, patojen, AMR) bütüncül bir yaklaşımla yönetilmesi olmalıdır. Böylece tavukçuluk atıkları, yalnızca çevresel yük oluşturan bir sorun olmaktan çıkarak, döngüsel ekonomi içinde sürdürülebilir ve yüksek katma değerli bir kaynak haline gelecektir (Singh vd., 2025).

Günümüzde tavukçuluk atıklarının yönetimi, yalnızca çevresel bir zorunluluk olmaktan çıkıp enerji, tarım ve biyoteknoloji ekseninde stratejik birer ekonomik kaynağa dönüşmüştür. Bu çalışmada tavuk gübresi ve kesimhane yan ürünlerinin uygun teknolojilerle işlendiğinde çevresel riskleri önemli ölçüde azalttığını ve eş zamanlı olarak katma değeri yüksek ürünlere dönüştürülebildiğini ortaya koyarak, geleneksel doğrusal "atık bertarafı" yerine döngüsel ekonomi temelli entegre sistemlerin gerekliliğini doğrulamaktadır. Elde edilen veriler, tek bir arıtma veya geri kazanım teknolojisinin tüm süreçlere çözüm sunamayacağını; aksine atık bileşimine, bölgesel dinamiklere ve ekonomik fizibiliteye göre şekillenen hibrit ve esnek sistemlerin tercih edilmesi gerektiğini göstermektedir. Bu doğrultuda; kompostlaştırma, anaerobik çürütme, biyolojik ve termokimyasal dönüşüm gibi yöntemler birbirini tamamlayıcı şekilde kurgulanmalı ve teknoloji seçimi yalnızca teknik verimliliğe göre değil; çevresel etki, lojistik altyapı ve pazar entegrasyonu gibi çok boyutlu kriterler dikkate alınarak yapılmalıdır (Muduli vd., 2019; Mozhiarasi ve Natarajan, 2022).

Geleceğe yönelik olarak, tavukçuluk atıklarının sürdürülebilir yönetiminde dört temel öncelik öne çıkmaktadır. Bunlar; (i) çevresel duyarlılığı teşvik eden politika ve mevzuat mekanizmalarının güçlendirilmesi, (ii) enzimatik biyodönüşüm, yeşil çözücüler ve yaşam döngüsü analizleri gibi yenilikçi araştırma alanlarının desteklenmesi, (iii) rendering tesisleri, biyogaz santralleri ve organomineral gübre fabrikaları gibi endüstriyel yatırımların yaygınlaştırılması ve (iv) patojenler, antibiyotik direnç genleri ve ağır metal kalıntılarının kontrolüne yönelik ileri arıtma teknolojilerinin entegrasyonudur. Buna ek olarak, dijitalleşme ve akıllı izleme sistemleri, tavukçuluk atıklarının yönetiminde yeni bir paradigma sunmaktadır. IoT tabanlı sensör ağları ve yapay zekâ destekli süreç optimizasyonu sayesinde biyogaz ve kompostlaştırma süreçlerinde operasyonel verimliliğin artırılması, çevresel risklerin erken tespiti ve sistem performansının sürekli iyileştirilmesi mümkün hâle gelmektedir. Bu yaklaşımlar, özellikle endüstriyel ölçekli uygulamalarda karar destek mekanizmalarının güçlendirilmesi açısından önemli bir potansiyel taşımaktadır. Tavukçuluk atıklarının sürdürülebilir yönetimi; çevresel koruma, enerji üretimi ve ekonomik katma değer yaratımı arasında denge kuran çok boyutlu bir dönüşüm alanı olarak değerlendirilmelidir. Gelecekte yapılacak çalışmaların, düşük emisyonlu, enerji etkin ve ölçeklenebilir teknolojilerin geliştirilmesine odaklanması; sektör, akademi ve politika yapıcılar arasındaki iş birliğinin güçlendirilmesiyle bütüncül ve sürdürülebilir bir atık yönetim sisteminin hayata geçirilmesi, döngüsel ekonomiye geçiş sürecinde kritik bir rol oynayacaktır.

4. Sonuç

Bu çalışma kapsamında elde edilen bulgular, tavuk gübresi ve kesimhane yan ürünlerinin uygun geri kazanım teknolojileriyle işlendiğinde çevresel risklerin önemli ölçüde azaltılabileceğini ve bu atıkların katma değeri yüksek ürünlere dönüştürülebilme potansiyeline sahip olduğunu göstermektedir. Ele alınan analitik ve teknik veriler, doğrusal bir “atık bertarafı” yaklaşımı yerine, döngüsel ekonomi temelli entegre sistemlerin uygulanabilirliğine işaret etmektedir. Çalışmada incelenen gübreleme, kompostlaştırma, anaerobik çürütme, biyolojik ve termokimyasal dönüşüm yöntemlerinin performans çıktıları, tek bir teknolojinin tüm atık bileşenlerine çözüm sunamayacağını; aksine atık kompozisyonuna ve teknik verimliliğe bağlı hibrit sistemlerin ön plana çıktığını göstermektedir. Bu doğrultuda, çalışmanın sunduğu teknolojik çıkarımların ve hibrit sistem optimizasyonlarının, benzer bölgesel özelliklere ve benzer kimyasal/fiziksel atık bileşimine sahip endüstriyel ölçekteki tavukçuluk işletmeleri için ölçeklenebilir ve sürdürülebilir bir atık yönetim modeli oluşturmada rehberlik edebileceği belirlenmiştir.

Katkı Oranı Beyanı

Yazarların katkı yüzdeleri aşağıda verilmiştir. Yazarlar makaleyi incelemiş ve onaylamıştır.

	M.Y.	E.I.
K	90	10
T	80	20
Y	90	10
VTI	70	30
VAY	80	20
KT	70	30
YZ	70	30
KI	70	30
GR	90	10

K= kavram, T= tasarım, Y= yönetim, VTI= veri toplama ve/veya işleme, VAY= veri analizi ve/veya yorumlama, KT= kaynak tarama, YZ= yazım, KI= kritik inceleme, GR= gönderim ve revizyon.

Çatışma Beyanı

Yazarlar bu çalışmada hiçbir çıkar ilişkisi olmadığını beyan etmektedirler.

Kaynaklar

Abbasi, I. A., Shamim, A., Shad, M. K., Ashari, H., & Yusuf, I. (2024). Circular economy-based integrated farming system for indigenous chicken: Fostering food security and sustainability. *Journal of Cleaner Production*, 436, Article 140368. https://doi.org/10.1016/j.jclepro.2023.140368

Anonim, (2022). *FAO Animal Production and Health - Annual Report*. Food and Agriculture Organization of the United Nations.

Anonim, (2023a). *Türkiye beyaz et sektörü raporu*. Beyaz Et Sanayicileri ve Damızlıkçıları Birliği Derneği (BESD-BİR). https://hsgm.saglik.gov.tr/media/attachments/2025/08/06/ulusal-beslenme-konseyi-beyaz-et---tavuk-bilim-komisyonu-raporu.pdf

Anonim, (2023b). *Darling Ingredients announces agreement with Butterball, LLC to explore new greenfield poultry rendering plant in Mt. Olive, North Carolina*. Darling Ingredients Inc. https://www.prnewswire.com/news-releases/darling-ingredients-announces-agreement-with-butterball-llc-to-explore-new-greenfield-poultry-rendering-plant-in-mt-olive-north-carolina-301840504.html

Anonim, (2023c). *Sürdürülebilirlik ve çevre yönetimi uygulamaları*. Şenpiliç Gıda Sanayi A.Ş. https://www.senpilic.com.tr/surdurulebilirlik

Anonim, (2024). *Kümes hayvancılığı üretimi*. TÜİK Veri Portalı. https://veriportali.tuik.gov.tr/tr/press/53951

Anonim, (2025a). *Rendered products market size, share & demand report: Forecast 2025–2030*. Deep Market Insights. https://deepmarketinsights.com/report/rendered-products-market-research-report

Anonim, (2025b). *Firma web sitesi*. Efeler Biyogaz Elektrik Üretim A.Ş. https://www.efelerbiyogaz.com

Anonim, (2025c). *Company reports and sustainability strategy*. EnviTec Biogas AG. https://www.envitec-biogas.com/

Anonim, (2025d). *Top 5 inquiries of fertilizer manufacturing in Indonesia*. Fertilizer Business Plan. https://www.fertilizerbusinessplan.com/2025/03/27/top-5-inquiries-of-fertilizer-manufacturing-in-indonesia/#

Anonim, (2025e). *Global antibiotic resistance surveillance report 2025*. WHO Global Antimicrobial Resistance and Use Surveillance System (GLASS), World Health Organization.

Berendonk, T. U., Manaia, C. M., Merlin, C., Fatta-Kassinos, D., Cytryn, E., Walsh, F., Burgmann, H., Sorum, H., Norstrom, M., Pons, M. N., Kreuzinger, N., Huovinen, P., Stefani, S., Schwartz, T., Kisand, V., Baquero, F., & Martinez, J. L. (2015). Tackling antibiotic resistance: The environmental framework. *Nature Reviews Microbiology*, 13(5), 310–317. https://doi.org/10.1038/nrmicro3439

Bernal, M. P., Alburquerque, J. A., & Moral, R. (2009). Composting of animal manures and chemical criteria for compost maturity assessment: A review. *Bioresource Technology*, 100(22), 5444–5453. https://doi.org/10.1016/j.biortech.2008.11.027

Bolan, N. S., Szogi, A. A., Chuasavathi, T., Seshadri, B., Rothrock, M. J., & Panneerselvam, P. (2010). Uses and management of poultry litter. *World's Poultry Science Journal*, 66(4), 673–698. https://doi.org/10.1017/s0043933910000656

Brandelli, A., Sala, L., & Kalil, S. J. (2015). Microbial enzymes for bioconversion of poultry waste into added-value products. *Food Research International*, 73, 3–12. https://doi.org/10.1016/j.foodres.2015.01.015

Crawley, S. W., Sloan, D. R., & Hale, K. K. (1980). Yields and composition of edible and inedible by-products of broilers processed at 6, 7, and 8 weeks of age. *Poultry Science*, 59(10), 2243–2246. https://doi.org/10.3382/ps.0592243

Dalkılıç, K., & Uğurlu, A. (2013). Tavuk gübresinden biyogaz üretimi. *Tavukçuluk Araştırma Dergisi*, 10, 14–19.

Dyosile, P. A., Mdladla, C., Njoya, M., Basitere, M., Ntwampe, S. K. O., & Kaskote, E. (2021). Assessment of an integrated and sustainable multistage system for the treatment of poultry slaughterhouse wastewater. *Membranes*, 11(8), Article 582. https://doi.org/10.3390/membranes11080582

Edwards, D. R., & Daniel, T. C. (1992). Environmental impacts of on-farm poultry waste - A review. *Bioresource Technology*, 41(9), 9–33.

Faridullah, Pervaiz, A., Irshad, M., Alam, A., Mahmood, Q., & M., A. (2014). Trace elements characterization in fresh and composted livestock manures. *Austin Journal of Hydrology*, 1(1), Article 6.

Fatima, F., Du, H., & Kommalapati, R. R. (2021). Treatment of poultry slaughterhouse wastewater with membrane technologies: A review. *Water*, 13(14), Article 1905. https://doi.org/10.3390/w13141905

Gbotosho, O., & Burt, P. J. A. (2013). Environmental and health impacts of poultry manure disposal methods: A case study of Lagelu and Egbeda local government areas in Oyo State, Nigeria. *International Journal of Agricultural Sustainability*, 11(1), 38–51. https://doi.org/10.1080/14735903.2012.700100

Ghaffari-Bohlouli, P., Jafari, H., Taebnia, N., Abedi, A., Amirsadeghi, A., Niknezhad, S. V., Alimoradi, H., Jafarzadeh, S., Mirzaei, M., Nie, L., Zhang, J., Varma, R. S., & Shavandi, A. (2023). Protein by-products: Composition, extraction, and biomedical applications. *Critical Reviews in Food Science and Nutrition*, 63(28), 9436–9481. https://doi.org/10.1080/10408398.2022.2067829

Glatz, P., Miao, Z., & Rodda, B. (2011). Handling and treatment of poultry hatchery waste: A review. *Sustainability*, 3(1), 216–237. https://doi.org/10.3390/su3010216

Hemavarshini, M. P., Thiyageshwari, S., Selvi, D., Anandham, R., Thirunavukkarasu, M., Sivasubramanian, K., & Jegadeeswari, D. (2025). Sustainable management of chicken waste: Exploring conversion technologies for environmental benefits.

Frontiers in Bioscience (Elite Edition), 17(2), Article 25930. https://doi.org/10.31083/FBE25930

Himu, H. A., & Raihan, A. (2023). A review of the effects of intensive poultry production on the environment and human health. *International Journal of Veterinary Research*, 3(2), 55–106.

Inamuddin, & Khan, A. (2021). *Sustainable bioconversion of waste to value added products*. Springer.

Kacorzyk, P., Strojny, J., Niewiadomski, M., Supel, P., Kaszycki, P., Brishty, I.-E. A., Józefowska, A., Wrześniewska-Tosik, K., Kowalewski, T., Pałczyńska, M., & Walisiak, D. (2025). The circular economy approach to dealing with burdensome waste from poultry industry. *Sustainability*, 17(13), Article 5997. https://doi.org/10.3390/su17135997

Karuppannan, S. K., Dowlath, M. J. H., Raiyaan, G. I. D., Rajadesingu, S., & Arunachalam, K. D. (2021). Application of poultry industry waste in producing value-added products—A review. In C. M. Hussain (Ed.), *Concepts of advanced zero waste tools* (pp. 91–121). Elsevier. https://doi.org/10.1016/B978-0-12-822183-9.00005-2

Kelleher, B. P., Leahy, J. J., Henihan, A. M., O'Dwyer, T. F., Sutton, D., & Leahy, M. J. (2002). Advances in poultry litter disposal technology a review. *Bioresource Technology*, 83, 27–36.

Konkol, I., Świerczek, L., & Cenian, A. (2023). Chicken manure pretreatment for enhancing biogas and methane production. *Energies*, 16(14), Article 5442. https://doi.org/10.3390/en16145442

Laba, W., Zarowska, B., Chorazyk, D., Pudlo, A., Piegza, M., Kancelista, A., & Kopec, W. (2018). New keratinolytic bacteria in valorization of chicken feather waste. *AMB Express*, 8(1), Article 9. https://doi.org/10.1186/s13568-018-0538-y

Li, A., Pandey, A., & Pandey, P. (2025). Application of IoT in monitoring greenhouse gas emissions in anaerobic reactors. *Energies*, 18(23), Article 6191. https://doi.org/10.3390/en18236191

Moktip, T., Salaipeth, L., Cope, A. E., Taherzadeh, M. J., Watanabe, T., & Phitsuwan, P. (2025). Current understanding of feather keratin and keratinase and their applications in biotechnology. *Biochemistry Research International*, 2025, Article 6619273. https://doi.org/10.1155/bri/6619273

Mottet, A., & Tempio, G. (2017). Global poultry production: Current state and future outlook and challenges. *World's Poultry Science Journal*, 73(2), 245–256. https://doi.org/10.1017/s0043933917000071

Mozhiarasi, V., & Natarajan, T. S. (2022). Slaughterhouse and poultry wastes: Management practices, feedstocks for renewable energy production, and recovery of value added products. *Biomass Conversion and Biorefinery*, 1–24. https://doi.org/10.1007/s13399-022-02352-0

Muduli, S., Champati, A., Popalghat, H. K., Patel, P., & Sneha, K. (2019). Poultry waste management: An approach for sustainable development. *International Journal of Advanced Scientific Research*, 4(1), 8–14.

Ngayakamo, B., & Onwualu, A. P. (2022). Recent advances in green processing technologies for valorisation of eggshell waste for sustainable construction materials. *Heliyon*, 8(6), Article e09649. https://doi.org/10.1016/j.heliyon.2022.e09649

Okur, N., & Eratalar, S. A. (2019). Litter materials in poultry industry. *Uluslararası Anadolu Ziraat Mühendisliği Bilimleri Dergisi*, 1(1), 24–29. https://dergipark.org.tr/tr/pub/uazimder/article/561060

Oyedun, A. O., Salami, H. A., Odewole, M. M., Lawal, L. O., Akpenpuun, T. D., & Adebayo, H. O. (2025). A review of emerging trends in circular manure management and the role of digital solutions. *Journal of the Saudi Society of Agricultural Sciences*, 24(4). https://doi.org/10.1007/s44447-025-00029-4

Page, M. J., McKenzie, J. E., Bossuyt, P. M., Boutron, I., Hoffmann, T. C., Mulrow, C. D., Shamseer, L., Tetzlaff, J. M., Akl, E. A., Brennan, S. E., Chou, R., Glanville, J., Grimshaw, J. M., Hróbjartsson, A., Lalu, M. M., Li, T., Loder, E. W., Mayo-Wilson, E., McDonald, S., McGuinness, L. A., Stewart, L. A., Thomas, J., Tricco, A. C., Welch, V. A., Whiting, P., & Moher, D. (2021). The PRISMA 2020 statement: An updated guideline for reporting systematic reviews. BMJ, 372, n71. https://doi.org/10.1136/bmj.n71

Raclavská, H., Růžičková, J., Švédová, B., Kucbel, M., Šafář, M., Raclavský, K., & Abel, E. L. D. S. (2022). Biodegradable waste streams. In *Biodegradable waste management in the circular economy* (pp. 69–153). Wiley. https://doi.org/10.1002/9781119679523.ch5

Rahman, M. M., Hassan, A., Hossain, I., Jahangir, M. M. R., Chowdhury, E. H., & Parvin, R. (2022). Current state of poultry waste management practices in Bangladesh, environmental concerns, and future recommendations. *Journal of Advanced Veterinary and Animal Research*, 9(3), 490–500. https://doi.org/10.5455/javar.2022.i618

Safaric, R., Fras Zemljic, L., Novak, M., Dugonik, B., Bratina, B., Gubeljak, N., Bolka, S., & Strnad, S. (2020). Preparation and characterisation of waste poultry feathers composite fibreboards. *Materials*, 13(21), Article 4964. https://doi.org/10.3390/ma13214964

Singh, N. K., Chandrakar, P., Taye, T., Singh, I. P., Singh, V. P., Bara, S., & Vithalrao, U. S. (2025). Environmental impact and mitigation approaches in livestock production systems: A review. *Archives of Current Research International*, 25(8), 351–364.

Singh, P., Mondal, T., Sharma, R., Mahalakshmi, N., & Gupta, M. (2018). Poultry waste management. *International Journal of Current Microbiology and Applied Sciences*, 7(8), 701–712. https://doi.org/10.20546/ijcmas.2018.708.077

Smedley, P. L., & Kinniburgh, D. G. (2002). A review of the source, behaviour and distribution of arsenic in natural waters. *Applied Geochemistry*, 17(5), 517–568. https://doi.org/10.1016/S0883-2927(02)00018-5

Tawfik, A., Eraky, M., Osman, A. I., Ai, P., Zhou, Z., Meng, F., & Rooney, D. W. (2023). Bioenergy production from chicken manure: A review. *Environmental Chemistry Letters*, 21(5), 2707–2727. https://doi.org/10.1007/s10311-023-01618-x

Wang, C., Yin, X., Xu, X., Wang, D., Wang, Y., & Zhang, T. (2025). Antibiotic resistance genes in anaerobic digestion: Unresolved challenges and potential solutions. *Bioresource Technology*, 419, Article 132075. https://doi.org/10.1016/j.biortech.2025.132075

Wang, X., Wang, J., Duan, C., Wang, X., & Liang, D. (2025). Systematic review on the life cycle assessment of manure-based anaerobic digestion system. *Sustainability*, 17(19), Article 8926. https://doi.org/10.3390/su17198926

Yenilmez, F. (2015). Tavukçuluk atıklarından biyogaz üretimi. *Fırat Üniversitesi Sağlık Bilimleri Veteriner Dergisi*, 29(3), 205–212. https://veteriner.fusabil.org/pdf/pdf_FUSABIL_1063.pdf

Yoo, S., Hsieh, J. S., Zou, P., & Kokoszka, J. (2009). Utilization of calcium carbonate particles from eggshell waste as coating pigments for ink-jet printing paper. *Bioresource Technology*, 100(24), 6416–6421. https://doi.org/10.1016/j.biortech.2009.06.112

Yordanov, D. (2010). Preliminary study of the efficiency of ultrafiltration treatment of poultry slaughterhouse

wastewater. *Bulgarian Journal of Agricultural Science*, 16(6), 700–704.

Yüceer, M. (2019). *Yumurta ve yumurta ürünleri işleme teknolojisi ve uygulamaları*. Sidas Medya A.Ş.

Yüceer, M. (2021). Çöpten gelen katma değer - Yumurta kabuğu zarı. *Yumurta Üreticileri Merkez Birliği Dergisi*, 55, 42–45.

Zhang, L., Ren, J., & Bai, W. (2023). A review of poultry waste-to-wealth: Technological progress, modeling and simulation studies, and economic- environmental and social sustainability. *Sustainability*, 15(7), Article 5620. https://doi.org/10.3390/su15075620

Zinina, O., Merenkova, S., & Rebezov, M. (2022). Analysis of modern approaches to the processing of poultry waste and by-products: Prospects for use in industrial sectors. *Food Science and Technology*, 42, Article e03222. https://doi.org/10.1590/fst.03222

Black Sea Journal of Engineering and Science
doi: 10.34248/bsengineering.1945963

Open Access Journal
e-ISSN: 2619 – 8991

Review
Volume 9 - Issue 5: 2859-2869 / September 2026

A REVIEW OF DIGITAL PHASE SHIFTER ARCHITECTURES: OPERATING PRINCIPLES, COMPARISON METHODOLOGY, AND DESIGN TRADE-OFFS

Sena TAŞ[1]*, Fırat KAÇAR[2]

[1]*Hasan Kalyoncu University, Faculty of Communication, Department of Digital Game Design, 27010, Gaziantep, Türkiye*
[2]*Istanbul University-Cerrahpaşa, Faculty of Engineering, Department of Electrical and Electronics Engineer, 34850, İstanbul, Türkiye*

Abstract: Digital phase shifters are key components in modern wireless communication and sensing systems, including phased-array antennas, radar front ends, satellite terminals, and emerging mmWave/sub-THz platforms. However, the reported literature remains highly heterogeneous in terms of architecture, technology platform, operating frequency, and validation depth, which makes direct comparison difficult. This review systematically examines 27 papers covering a total of 30 digital phase-shifter designs and classifies them into four main categories: switch-type phase shifters (STPS), vector-sum/vector-modulator-based phase shifters (VSPS/VMPS), lattice/all-pass-network-based phase shifters, and special/other approaches such as delay-based and NEMS-related solutions. An evidence-aware comparison methodology is adopted to evaluate the reported studies using key metrics including RMS phase error, RMS amplitude error, insertion loss/gain, DC power consumption, area, operating band, and implementation technology. The comparison shows that nominal bit resolution alone is not a sufficient predictor of practical phase accuracy; instead, performance is more strongly influenced by architectural realization, parasitic-aware implementation, calibration strategy, and operating frequency. The reviewed results further indicate that passive STPS structures remain attractive for low-complexity and low-power applications, whereas vector-based architectures provide high resolution and calibration flexibility at the expense of higher power and implementation complexity. Lattice/all-pass-based structures remain relevant for wideband phase-flat operation, while delay-based approaches appear promising for sub-THz applications. Overall, the review does not support the existence of a universally optimal topology; rather, the most suitable solution depends on the dominant application constraint, such as accuracy, bandwidth, power, area, or scalability. The taxonomy, comparison framework, and cross-comparison presented in this work are intended to support more consistent evaluation and more informed topology selection in future digital phase-shifter research.

Keywords: Digital phase shifters, Phased-array antennas, Beamforming, Vector-sum phase shifters, RMS phase error, mmWave and sub-THz systems

***Corresponding author:** Hasan Kalyoncu University, Faculty of Communication, Department of Digital Game Design, 27010, Gaziantep, Türkiye
E mail: sena.tas@hku.edu.tr (S. TAŞ)
Sena TAŞ https://orcid.org/0000-0002-4162-7585
Fırat KAÇAR https://orcid.org/0000-0002-0967-914X

Received: May 07, 2026
Accepted: September 02, 2026
Published: September 15, 2026

Cite as: Taş, S., & Kaçar, F. (2026). A review of digital phase shifter architectures: operating principles, comparison methodology, and design trade-offs. *Black Sea Journal of Engineering and Science,* 9(5), 2859-2869.

1. Introduction

Modern wireless communication and sensing systems, including 5G/6G networks, mmWave links, satellite terminals, and radar front ends, rely heavily on digital beamforming and electronically steerable antenna arrays (Brilhante et al., 2023; Lin et al., 2024). In such systems, phase shifters provide the controlled phase progression required across array elements, thereby enabling beam steering, multi-beam operation, and adaptive interference suppression (Mailloux, 2017).

A phase shifter is an RF building block that changes the phase of a signal by a desired amount while ideally maintaining constant amplitude. In phased-array systems, the main-beam direction is determined by the relative phase applied to each element, which governs how the radiated fields combine in space (Mailloux, 2017). In practice, however, array performance depends not only on achieving the intended phase states, but also on maintaining phase accuracy and amplitude consistency across states, since state-dependent errors can increase sidelobe levels and reduce on-target gain. For this reason, phase and amplitude behavior should be evaluated together (Coviello et al., 2016).

Among the available approaches, digital phase shifters are particularly attractive for large-array implementations because they support integration, repeatable state selection, and calibration-friendly operation. Their effective performance is ultimately governed by state consistency over frequency and amplitude stability across phase states, especially in wideband and high-frequency regimes (Coviello et al., 2016). Ideally, an N-bit digital phase shifter provides 2^N discrete phase states, with an ideal least significant bit given by equation 1,

This work is licensed (CC BY-NC 4.0) under Creative Commons Attribution 4.0 International License

$$LSB=\frac{360^\circ}{2^N} \quad (1)$$

However, the literature on digital phase shifters remains highly diverse. Reported implementations differ substantially in architecture, technology platform (e.g., CMOS/SiGe, GaAs/GaN MMIC, planar/PCB, and NEMS-related approaches), and validation depth, ranging from measured results to post-layout/EM studies and schematic-level simulations (Kebe et al., 2025; Gharsalli et al., 2026). In addition, performance reporting is often inconsistent. While many studies emphasize nominal resolution or insertion loss/gain, other important metrics, such as RMS amplitude error and large-signal linearity, are not reported consistently, even though they strongly influence transmitter robustness and phased-array pattern quality (Coviello et al., 2016; Kebe et al., 2025).

Despite the large number of reported digital phase-shifter implementations, existing studies differ considerably in architecture, operating frequency, technology platform, validation depth, and reported performance metrics, making direct comparison across published designs difficult. Although several review papers summarize digital phase-shifter technologies from device, circuit, or application perspectives, they generally do not provide a unified taxonomy together with a systematic comparison framework that explicitly distinguishes phase-generation mechanisms, validation levels, and reporting consistency. As a result, identifying the relative advantages, limitations, and practical design trade-offs of different architectures remains challenging. This gap motivates the present review.

Motivated by these gaps, this review makes three main contributions. First, it proposes a taxonomy of digital phase-shifter families and summarizes their typical operating principles and trade-offs. Second, it establishes an evidence-aware comparison methodology that harmonizes the core performance metrics while distinguishing validation depth. Third, it presents a cross-comparison of 27 papers covering 30 digital phase-shifter designs using a unified dataset, with measured IC/MMIC results emphasized where available to support more reproducible interpretation.

The remainder of this paper is organized as follows. Section II presents the taxonomy and operating principles of the main digital phase-shifter families. Section III describes the comparison methodology and fairness criteria adopted in this review. Section IV provides the cross-comparison results and discusses the main trends observed across the dataset. Finally, Section V concludes the paper.

2. Taxonomy and Operating Principles

Figure 1 illustrates the proposed taxonomy adopted throughout this review. Based on the primary phase-generation mechanism, digital phase shifters are classified into four main categories: (A) switch-type phase shifters (STPS), (B) vector-sum/vector-modulator-based phase shifters (VSPS/VMPS), (C) lattice- and all-pass-network-based phase shifters, and (D) special or other approaches that fall outside the mainstream synthesis mechanisms (Kebe et al., 2025; Gharsalli et al., 2026).

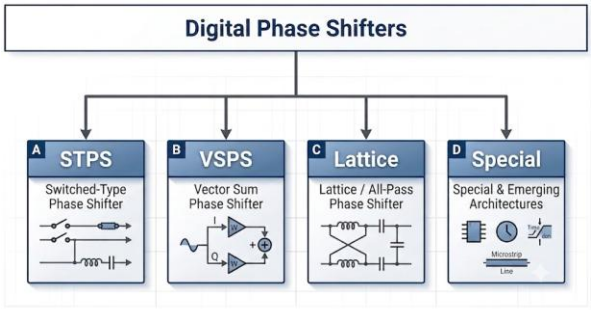


Figure 1. Proposed taxonomy of digital phase-shifter architectures based on the primary phase-generation mechanism.

2.1. Class A — Switch-Type Phase Shifters (STPS)

STPS architectures generate discrete phase states by switching among alternative signal paths or RF networks. Depending on the selected topology, the phase shift may be produced through switched-line, loaded-line, high-pass/low-pass, coupler-based, Schiffman, or related network arrangements.

Representative studies in this category include Anjos et al. (2020), Li et al. (2022), Chiu et al. (2021), Lin and Tsai (2022), Song et al. (2023), Zhan et al. (2024), Shen et al. (2025), Khazaei et al. (2025) and Kilinc et al. (2026). Li et al. (2022) proposed a compensated 7-bit GaAs pHEMT phase shifter for S-band applications, whereas Song et al. (2023) demonstrated a switched-filter GaN implementation operating at Ka-band frequencies. Lin and Tsai (2022) employed switched high-pass and low-pass T-networks in 65 nm CMOS, while Chiu et al. (2021) reported a low-loss GaN implementation emphasizing passive switched networks. Zhan et al. (2024) focused on broadband switched-path operation in advanced CMOS technology, whereas Shen et al. (2025) introduced a coupler-assisted switched architecture for W-band applications. Kilinc et al. (2026) retained the conventional switched-network operating principle while replacing grounded passive inductors with tunable active inductors, demonstrating that circuit-level innovations can improve integration density without altering the underlying STPS architecture. Khazaei et al. (2025) presented a modified Schiffman implementation for wideband operation, while Anjos et al. (2020) employed an all-pass-network-based switched architecture to improve bandwidth performance.

The main strengths of STPS designs are their high linearity, near-zero or zero static DC power consumption in the RF path, and relatively straightforward implementation in GaAs- or GaN-based technologies for high-power applications. However, their disadvantages become more pronounced as the target frequency and

resolution increase. In particular, layout parasitics at mmWave frequencies can degrade phase accuracy and introduce amplitude imbalance, while insertion loss typically increases with the number of bits and the complexity of the switched network.

2.2. Class B — Vector-Sum / Vector-Modulator-Based Phase Shifters (VSPS/VMPS)

In VSPS/VMPS architectures, the desired phase state is synthesized by weighting and recombining the in-phase (I) and quadrature (Q) signal components. This approach enables fine phase interpolation and, in active implementations, simultaneous gain adjustment. It is therefore particularly suitable for high-resolution and calibration-aware beamforming systems. Based on the classification adopted in Table 1, this category includes 10 papers and 11 distinct circuit implementations.

Representative examples include, Luo et al. (2019), Xiong et al. (2020), Wu et al. (2021), Shangguan et al. (2024), Tu et al. (2025), Minnella et al. (2025), Cho et al. (2025), Jiang et al. (2025), Wei et al. (2026), and Lee et al. (2026). Lee et al. (2026) proposed a BiCMOS vector-modulator architecture emphasizing low power consumption, whereas Minnella et al. (2025) demonstrated a compact 7-bit implementation in 28 nm FD-SOI CMOS. Cho et al. (2025) presented two independent 8-bit vector-modulator architectures operating around 140 GHz. Jiang et al. (2025) and Xiong et al. (2020) focused on broadband active vector-sum implementations, while Shangguan et al. (2024) demonstrated a high-frequency CMOS realization. Wei et al. (2026) achieved broadband operation over 2–18 GHz using active vector synthesis, whereas Wu et al. (2021) employed a passive vector-sum implementation with low RMS phase error. Tu et al. (2025) reported one of the lowest RMS phase errors in the dataset (0.18°–0.21°), and Luo et al. (2019) demonstrated wideband SiGe BiCMOS operation from 6 to 18 GHz.

The main advantages of Class B architectures are their high effective resolution, calibration flexibility, and potential for partial RF-loss compensation through gain. These properties make them well suited to modern beamforming arrays. Their limitations, however, include continuous DC power consumption, sensitivity to I/Q mismatch, and gain-phase coupling, all of which may require careful codebook design, calibration, or digital assistance.

2.3. Class C — Lattice / All-Pass-Network-Based Phase Shifters

The main objective of this class is to achieve a relatively flat phase response over a broad frequency range while maintaining nearly constant amplitude. This is typically pursued through lattice or all-pass-type network synthesis, where phase equalization and amplitude stability are jointly targeted.

Representative studies include Avci et al. (2019) and Taş and Kaçar (2025). Avci et al. (2019) demonstrated a CMOS symmetric-lattice phase shifter operating over 7.5–13 GHz, whereas Taş and Kaçar (2025) proposed a 3-bit LC symmetric-lattice phase shifter for 4.5–5.5 GHz applications with very low phase error. Although the number of studies in this category is relatively limited, lattice-based architectures remain attractive whenever phase flatness across bandwidth is prioritized.

It should be noted that several Class A architectures, including those reported by Anjos et al. (2020), Chiu et al. (2021), Lin and Tsai (2022), Zhan et al. (2024), and Khazaei et al. (2025), also incorporate all-pass or transmission-network sections. However, these networks function as switched RF paths rather than true lattice-based phase synthesis. Similarly, Wu et al. (2021) and Wei et al. (2026) employ passive RF networks but generate phase through vector synthesis and are therefore classified under Class B. Accordingly, the proposed taxonomy is based on the primary phase-generation mechanism, rather than the individual passive building blocks used in the implementation.

Class C implementations are valued for their wideband phase flatness and their potential to provide IC-compatible solutions at moderate frequencies. At the same time, their performance is strongly influenced by the quality factor (Q) of passive components, especially inductors and capacitors. As frequency increases, passive loss and switch parasitics make it more difficult to preserve ideal all-pass behavior, often leading to larger amplitude variation and reduced RF efficiency.

2.4. Class D — Special / Other Approaches

Class D comprises specialized implementations that cannot be directly categorized as conventional STPS, VSPS/VMPS, or lattice/all-pass architectures. These include delay-based solutions, NEMS transmission-line implementations, enabling circuit blocks, and system-level demonstrations.

Representative examples include Hamidi et al. (2019), Lin and Lin (2025), Ghorbani (2025), Uchino et al. (2025), and Sindhuja et al. (2025). Lin and Lin (2025) demonstrated a system-level implementation using a commercial phase-shifter module, whereas Ghorbani (2025) presented an RF-switch building block intended to enable future phase-shifter implementations. Uchino et al. (2025) proposed a delay-based architecture achieving 0.1° phase resolution at 150–160 GHz, while Sindhuja et al. (2025) investigated a NEMS transmission-line implementation with near-zero static power consumption. Hamidi et al. (2019) demonstrated a planar passive phase shifter intended for radar applications.

Although these studies address different implementation levels, they represent emerging design directions that extend beyond conventional digital phase-shifter architectures.

3. Comparison Methodology

IEEE Xplore, ScienceDirect, SpringerLink, Wiley Online Library, MDPI, and Google Scholar were used in the literature search. The terms "digital phase shifter," "switch-type phase shifter," "vector-sum phase shifter," "vector-modulator phase shifter," "lattice phase shifter,"

"all-pass phase shifter," "mmWave phase shifter," "sub-THz phase shifter," and "beamforming" were combined. Studies published between 2019 and 2026 were the main focus of the search; previous works were included where they offered a crucial benchmark or represented a basic architecture.

Studies were included in the quantitative comparison if they: (i) presented a digital phase-shifter circuit, system, or enabling architecture; (ii) reported sufficient quantitative information on operating frequency, phase resolution, insertion loss or gain, phase error, power consumption, implementation technology, or physical area; and (iii) provided a validation level that could be identified as measured, post-layout/EM simulated, schematic-level simulated, system/COTS demonstrated, or enabling-block based. Studies were excluded if they addressed only analog phase control, antenna-array behavior without phase-shifter-level data, or conceptual designs without sufficient quantitative performance information. Review papers were used only to support the background discussion and taxonomy development and were not included in the quantitative comparison presented in Table 1.

The final dataset comprised 27 papers and 30 distinct digital phase-shifter designs. Multiple designs reported within a single publication were treated as separate entries when they used different circuit architectures or produced independently reported performance results.

To improve the fairness of cross-study comparisons, the validation level of each design is explicitly indicated in Table 1 using standardized labels: [M] for measured results, [PL] for post-layout/EM simulation, [S] for schematic-level simulation, [NM] for numerical modeling, [SYS] for system-level demonstration, and [EB] for enabling-block studies.

Because the reviewed studies differ substantially in architecture, technology platform, operating frequency, and validation depth, a direct one-to-one comparison can easily become misleading. To improve consistency and interpretability, the comparison in this review was carried out using a multi-metric and evidence-aware framework. The goal was not to rank all studies using a single figure of merit, but rather to compare them in a way that preserves the architectural context and practical meaning of the reported results.

3.1. Performance Metrics and Definitions

The comparison was based primarily on the performance metrics most frequently reported across the literature and most relevant to phased-array operation.

3.1.1. RMS phase error

Phase accuracy was treated as one of the most critical performance indicators, since it directly affects beam pointing quality, sidelobe behavior, and array coherence. The reviewed dataset spans a wide range of reported values, from relatively high errors in schematic-level or lower-complexity designs to very low RMS phase errors in highly optimized measured implementations.

3.1.2. RMS amplitude error

RMS amplitude error was included to reflect the consistency of signal magnitude across phase states. This metric is important because phase accuracy alone does not guarantee satisfactory array-level behavior; amplitude imbalance can also distort the radiation pattern and reduce effective gain. When reported, lower RMS amplitude error was interpreted as more stable amplitude behavior across states.

3.1.3. Insertion loss (IL) or gain

For passive architectures such as many STPS and lattice-based designs, insertion loss is a primary concern because it directly affects link budget and may require additional RF gain elsewhere in the chain. For active vector-based architectures, gain can partially compensate internal RF loss, but this advantage must be interpreted together with power consumption, linearity, and state-dependent gain variation. For this reason, IL and gain were not treated as interchangeable quantities, but were interpreted according to the operating principle of each class.

3.1.4. DC power consumption (P_{dc})

Power consumption was treated as a key metric, especially for dense phased arrays, mobile terminals, and satellite systems, where replication across many channels makes per-element power especially important. At the same time, zero or low DC power at the phase-shifter level was not automatically interpreted as a system-level advantage, since high insertion loss may shift the burden to later gain stages.

3.2. Technology and Area Benchmarking

Process technology and physical footprint were also included in the comparison because both strongly influence implementation feasibility and performance trade-offs.

3.2.1. Technology platform

The reviewed studies span a wide range of technologies, including advanced CMOS and FD-SOI nodes, SiGe/BiCMOS platforms, GaAs/GaN MMIC processes, and larger PCB or planar implementations. These choices affect passive quality factor, switch parasitics, achievable integration density, and suitability for different frequency ranges. Accordingly, technology was interpreted not merely as a fabrication detail, but as an important contributor to the reported performance.

3.2.2. Physical area

Occupied area was considered because it directly affects scalability in multi-channel phased-array systems, especially at mmWave frequencies where element count is high and chip area is costly. However, area was not interpreted in isolation. A compact implementation may rely on aggressive technology scaling or active circuitry, whereas a larger implementation may reflect a different topology choice, a lower-cost platform, or a broader-band passive realization. Therefore, area comparisons were made in conjunction with architecture, operating band, and technology node.

3.3. Frequency-Band Categorization

To reduce the risk of misleading comparisons across fundamentally different operating conditions, the reviewed designs were also grouped according to frequency range. This step is important because the dominant nonidealities change significantly with frequency. For example, passive loss, device parasitics, layout sensitivity, and achievable Q factors differ substantially between sub-10 GHz, mmWave, and sub-THz implementations.

Accordingly, the reviewed studies were interpreted within three broad frequency categories:

Low/mid-frequency range (<10 GHz): typically associated with S-band and C-band applications.

mmWave range (24–100 GHz): relevant to radar, satellite links, and 5G/6G front ends.

Sub-THz range (>100 GHz): representing emerging high-frequency research scenarios with increasingly severe implementation constraints.

This grouping does not eliminate all comparison difficulties, but it improves fairness by reducing the chance of equating designs that operate under substantially different physical and technological constraints.

4. Results and Cross-Comparison

The 30 digital phase-shifter (DPS) designs covered by the 27 reviewed papers are compared in this section in terms of their architectural choices, technology platforms, and design objectives. The aim is not to identify a single best approach, but to clarify how different topologies redistribute the trade-offs among resolution, phase accuracy, bandwidth, insertion loss, chip area, and power consumption. Accordingly, the comparison is organized around the main trade-offs observed across the dataset rather than around isolated performance claims.

4.1. Resolution–Accuracy Relationship

A common assumption in the DPS literature is that increasing bit resolution improves phase accuracy by reducing phase quantization error. However, the reviewed results show that higher resolution does not always lead to lower RMS phase error at the circuit level. In practice, the relationship between resolution and accuracy is strongly influenced by architectural class, operating frequency, and the use of calibration or optimization techniques.

This trend can be observed by comparing the 7-bit implementations reported by Wu et al. (2021), Tu et al. (2025), and Minnella et al. (2025). Tu et al. (2025) reported an RMS phase error of only 0.18°–0.21°, whereas Minnella et al. (2025), despite employing the same nominal 7-bit resolution, reported phase errors of approximately 2.7°–4.7°. Wu et al. (2021) achieved RMS phase errors below 2.1° using a passive vector-sum topology. These results demonstrate that practical phase accuracy depends not only on nominal bit resolution but also on architectural realization, calibration strategy, implementation technology, and operating frequency.

A similar limitation of resolution-based interpretation can be observed at very high frequencies. Reference Uchino et al. (2025) uses a fine-resolution delay-based method and reports a phase error of 0.68° at 150–160 GHz. This result is notable not only because of its low reported error, but also because it is achieved in a frequency range where layout sensitivity, parasitics, and device mismatch make high-resolution systems increasingly fragile. This suggests that, at sub-THz frequencies, delay-based Class D methods may offer a more robust solution than conventional I/Q-based approaches, whose theoretical resolution advantage may be weakened by practical nonidealities.

Taken together, these findings show that resolution should not be interpreted independently of how it is implemented. In many cases, a lower-complexity architecture supported by selective optimization or frequency-appropriate synthesis may deliver more practically useful accuracy than a high-bit design without calibration.

4.2. Power Consumption and Area Trade-Offs

Area and power consumption remain key constraints in phased-array and highly integrated front-end systems, where element count, channel replication, and thermal density are critical. However, the reviewed studies show that these two metrics do not necessarily improve simultaneously. Compact implementations often rely on advanced process nodes or active circuitry, whereas passive zero-power solutions may introduce penalties elsewhere in the system.

Technology scaling contributes significantly to area efficiency, although architecture and passive-network complexity remain equally important. For example, Minnella et al. (2025) implemented a 7-bit vector-modulator phase shifter occupying only 0.33 mm^2 in 28 nm FD-SOI CMOS. By comparison, Lee et al. (2026) reported approximately 1.75 × 1.11 mm^2 in 130 nm BiCMOS, whereas Luo et al. (2019) occupied 1.8 × 1.3 mm^2 in 0.13 μm SiGe BiCMOS. These examples indicate that process scaling improves integration density, but the observed area differences are also influenced by architectural complexity and passive-network implementation.

Several passive implementations report zero or approximately zero static DC power consumption. Examples include the GaN STPS designs of Chiu et al. (2021) and Song et al. (2023), the passive vector-sum phase shifter of Wu et al. (2021), the planar microstrip implementation of Hamidi et al. (2019), and the APN-based STPS of Anjos et al. (2020). The NEMS-based transmission-line implementation of Sindhuja et al. (2025) also reports approximately zero static power consumption.

However, zero static power at the phase-shifter block does not necessarily correspond to minimum system-level energy consumption. Passive phase shifters may introduce considerable insertion loss, which increases the gain and power requirements of the surrounding RF

chain. By comparison, relatively low-power active implementations such as Tu et al. (2025), with a reported power consumption of 10 mW, and Lee et al. (2026), with 15.8 mW, may reduce the need for additional loss-compensation stages. Therefore, block-level DC power consumption and system-level energy efficiency should be evaluated separately.

4.3. Bandwidth and Loss Mechanisms

The reviewed studies also show that wide operating bandwidth is rarely achieved without cost in insertion loss, chip size, or implementation complexity. Increasing bandwidth should therefore be understood not as a free improvement, but as a design choice that redistributes penalties among other performance metrics.

The bandwidth–loss trade-off can be observed by comparing wideband implementations based on different phase-generation mechanisms. Anjos et al. (2020) reported an APN-based STPS operating over 14–50 GHz. Its insertion loss was approximately 7.4 ± 0.26 dB at 28 GHz and increased to 10 ± 0.22 dB at 39 GHz. By contrast, Wei et al. (2026) employed an active vector-sum architecture over 2–18 GHz and reported a gain of 1.5–3.2 dB. However, this active implementation consumed 105 mW and occupied approximately 1.24 × 0.86 mm^2. These examples show that wideband operation can be achieved through different architectural strategies, but the corresponding penalty may appear as insertion loss, DC power consumption, physical area, or implementation complexity.

Class C architectures follow a different bandwidth strategy by using lattice or all-pass synthesis to obtain relatively stable phase behavior over frequency. In the present dataset, Avci et al. (2019) demonstrated a symmetric-lattice phase shifter over 7.5–13 GHz, whereas Taş and Kaçar (2025) investigated an LC symmetric-lattice implementation over 4.5–5.5 GHz. These architectures can support relatively flat phase characteristics across the operating band. Nevertheless, their RF efficiency remains dependent on passive-component quality factors, switch loss, impedance matching, and component tolerances. Consequently, improved phase flatness does not necessarily imply lower insertion loss.

4.4. Qualitative Synthesis: Architecture Selection by Constraint

The cross-comparison of the 30 reviewed DPS designs does not support the existence of a universally superior topology. Instead, the results indicate that each architectural class becomes more or less suitable depending on the dominant constraint of the target application.

For high-power and low-complexity applications, passive Class A STPS architectures remain attractive because of their structural simplicity, high linearity, and low static power consumption in the RF path. These properties are particularly relevant to radar and satellite front ends, although insertion loss and physical area may become restrictive as bit count and bandwidth increase.

Class C lattice/all-pass architectures are more suitable when phase flatness over frequency is prioritized. Their application potential is strongest in broadband microwave front ends and moderate-frequency phased arrays, where passive-component quality factors and switching losses remain manageable.

When very high phase accuracy is the main objective, Class B VSPS/VMPS structures appear particularly attractive, especially when combined with digital calibration or precision weighting techniques, as demonstrated by Tu et al. (2025). In such cases, the observed performance advantage arises not only from the vector-sum principle itself, but also from the optimization framework used to suppress implementation error.

For sub-THz operation, the dataset suggests a change in architectural suitability. As frequency increases beyond 100 GHz, parasitic sensitivity and implementation fragility increasingly limit the practicality of conventional vector-sum approaches. Under these conditions, delay-based Class D solutions such as Uchino et al. (2025) appear more consistent with the physical constraints of the frequency range.

For fully integrated mmWave and sub-THz systems, several Class B implementations realized in advanced CMOS and FD-SOI technologies provide practical compromises among area, resolution, frequency capability, and phase accuracy. Minnella et al. (2025) demonstrated a compact 7-bit phase shifter in 28 nm FD-SOI CMOS, whereas Cho et al. (2025) reported two 8-bit vector-sum implementations in 28 nm CMOS for operation around 140 GHz. Tu et al. (2025) further showed that high phase accuracy can be achieved in 90 nm CMOS through digitally controlled current weighting. Although these designs do not dominate every performance metric, they illustrate the integration and calibration advantages of vector-based architectures.

Overall, the comparison shows that DPS evaluation should go beyond single-metric interpretation. Wide bandwidth does not necessarily imply an optimal overall design, low Pdc does not always guarantee system-level efficiency, and resolution alone does not ensure high accuracy. A more meaningful comparison emerges only when topology, technology node, calibration approach, and operating frequency are evaluated together.

To provide a concise design-oriented synthesis of these findings, Table 2 summarizes the principal strengths, limitations, and representative application domains associated with each architectural class. The table is intended to complement the detailed quantitative comparison in Table 1 by translating the observed architecture-level trade-offs into practical topology-selection guidance.

Table 1. Main characteristics, validation levels, and reported performance metrics of the reviewed digital phase-shifter designs

Ref	C	Subclass	Y	Band (GHz)	Bit / LSB	Topology	T	Switch/Element	IL / Gain	RMS φ err	RMS amp err	Pdc	Area
Xiong et al., 2020 [M]	B	VSPS (freq-reconfigurable)	2019	24–30 / 35–41	5b / 11.25°	Freq-reconf. active VSPS	90 nm CMOS	I/Q gen + VGA	Gain −5…−4.5 / −7…−5.9 dB	<4° / <5.1°	<0.6 / <0.35 dB	17.6 mW	0.34 mm²
Hamidi et al., 2019 [M]	D	Planar discrete PS (microstrip + hybrid)	2019	2.9–3.1	2b / 45°	Microstrip PS + 90° hybrid	Rogers 4350B	Passive transmission line	IL ~3.2 dB	max ~3.62° (Not RMS)	NR	0	NR
Luo et al., 2019 [M]	B	VSPS (active, QAF-based)	2019	6–18	6b / 5.625°	Active VSPS (QAF-based)	0.13 µm SiGe BiCMOS	main DAC(4b)+cal DAC(3b)	Gain 0.95→−1.85 dB	<4.36°	<1.04 dB	74.4 mW	1.8×1.3 mm²
Anjos et al., 2020 [M]	A	APN-based STPS (SP4T path select)	2019	14–50	2b / 45°	APN-based STPS + SP4T	0.25 µm SiGe:C BiCMOS	SP4T + 4×APN	IL 7.4±0.26 (28GHz); 10±0.22 (39 GHz)	<4°; <6°	<0.27 / <0.33 dB	0	0.48 mm²
Avci et al., 2019 [M]	C	Lattice / all-pass (symmetric lattice)	2019	7.5–13	3b / 45°	Symmetric lattice DPS	0.18 µm CMOS	NMOS + L/C	Loss ≤3.2 dB	4.9°	NR	NR	NR
Chiu et al., 2021 [M]	A	GaN STPS (high power)	2021	8–12	5b / 11.25°	GaN STPS	0.25 µm GaN HEMT-on-SiC	GaN switch	IL 11.8±3.45 dB	<6.23°	<1.15 dB	0	2×3 mm²
Wu et al., 2021 [M]	B	Passive vector-sum	2021	21.5–25	7b / 2.8125°	Passive VSPS	65 nm CMOS	Atten + DPDT + hybrid	Peak gain ~−14.3 dB	<2.1°	<1.2 dB	0	880×500 µm chip
Li et al., 2022 [M]	A	GaAs pHEMT STPS + compensation cell	2022	2.4–4.0	7b / 2.8° (+1.4° comp)	GaAs STPS	0.5 µm GaAs pHEMT	FET switch	Avg IL 4.5–4.9 dB	<3.1°; <1.5° (2.8–3.7)	<0.34 dB	NR	2.1×2.55; core 1.6×2.2 mm²
Lin and Tsai, 2022 [M]	A	CMOS STPS (HP/LP/T-type)	2022	32–41	5b / 11.25°	STPS HP/LP (T-type)	65 nm CMOS	MOS (body-floating)	IL 10.5–13.5 dB	2.4–6.2°	0.48–0.66 dB	NR	0.7×0.37 mm²
Zeng et al., 2023	A	GaAs pHEMT STPS (hybrid cells)	2023	12–18	6b / 5.625°	GaAs STPS	0.15 µm GaAs pHEMT	pHEMT switch	Avg IL 6.5–6.9 dB	RMS <2.8°	NR	NR	3.1×1 mm²
Song et al., 2023 [M]	A	Switched-filter STPS (GaN)	2023	37–40	6b / 5.625°	Switched-filter STPS	150 nm GaN HEMT	GaN switch	Min IL ~5 dB	<5.36°	RMS gain err 1.69–3.21 dB	0	2.82×1.19 mm²
Shangguan et al., 2024 [M]	B	Vector-modulated active PS	2024	8–18	6b / ~5.6°	Active vector-modulated	0.18 µm SiGe BiCMOS	Current array VM	Gain −0.5…1.8 dB	RMS <2°	RMS <0.5 dB	~65.3 mW	NR
Zhan et al., 2024 [M]	A	GaAs pHEMT STPS/MMIC	2024	2.5–3.3	6b / 5.625°	GaAs pHEMT multibit	0.5 µm GaAs pHEMT	pHEMT switch + driver	IL <4.3 dB	RMS <1.43°	ΔA <0.52 dB	NR	2.45×1.08 mm²
Taş and Kaçar, 2025 [S]	C	Lattice / all-pass (symmetric lattice)	2025	4.5–5.5	3b / 45°	LC symmetric lattice (all-pass)	ADS sim	Switched-C	RMS IL max 1.77 dB	RMS max 6.81°	NR	NR	NR
Minnella et al., 2025 [M]	B	VMPS/Vector-modulator	2025	37.5–40.5	7b / 2.8125°	VMPS (vector mod.)	28 nm FD-SOI CMOS	Gilbert-cell VM	Max IL 3.7 dB	2.7–4.7°	0.3–0.5 dB	13 mW	0.33 mm²
Lin and Lin, 2025 [SYS]	D	System/COTS (application-level)	2025	3.5–6.0	4b / 22.5°	COTS PS (system)	—	MAPS-010145	Avg IL ~5 dB	NR	NR	NR	NR
Ghorbani, 2025 [EB]	D	Enabling block: RF switch (not phase shifter)	2025	~2.05	—	PIN-diode RF switch + impedance transformer	PCB (RO4534)	BAR64-03V (N=1/2/4 parallel)	IL <1.2/<1.0/<0.7 dB	—	—	—	—
Ghorbani, 2025 [EB]	A	Switched-line STPS (PCB)	2025	1.9–2.2	3b / 45°	Switched-line PS	PCB	4 PIN parallel RF switch	Total IL 4.2 dB	NR	NR	NR	NR
Ghorbani, 2025 [EB]	A	Loaded-line STPS (PCB)	2025	1.8–2.5	1b / 45°	Loaded-line (stub ground control)	PCB	PIN diodes	Max IL 2.1 dB	NR	NR	NR	NR
Cho et al., 2025 [PL]	B	VSPS (Gilbert VGA)	2025	140–157	8b / 1.406°	VSPS – Gilbert-cell VGA	28 nm CMOS	Marchand+Lange + 13-bit DAC	Peak gain −9.5 dB	Max RMS 6°	Max RMS 2 dB	49 mW	NR
Cho et al., 2025 [PL]	B	VSPS (current-steering VGA)	2025	129–144	8b / 1.406°	VSPS – current-steering VGA	28 nm CMOS	Marchand+Lange + 13-bit DAC	Peak gain −5.1 dB	Max RMS 4.8°	Max RMS 1.3 dB	29 mW	NR

C= class, Y= year, T= technology STPS= switch-type phase shifter, VSPS= vector-sum phase shifter, VMPS= vector-modulator phase shifter, IL= insertion loss, RMS= root mean square, Pdc= DC power consumption, NR= not reported, COTS= commercial off-the-shelf, NEMS= nanoelectromechanical systems. Validation level: [M], measured, [PL], post-layout/EM simulation, [S], schematic-level simulation, [NM], numerical modeling, [SYS], system-level demonstration, [EB], enabling-block study.

Table 1. Main characteristics, validation levels, and reported performance metrics of the reviewed digital phase-shifter designs (continued)

Ref	C	Subclass	Y	Band (GHz)	Bit / LSB	Topology	T	Switch/Element	IL / Gain	RMS φ err	RMS amp err	Pdc	Area
Uchino et al., 2025 [M]	D	Delay-based (FFPS/PDPS fine resolution)	2025	150–160	fine 0.1° + coarse 22.5°	FFPS + NU-PDPS	65 nm CMOS	Varactor + MOS net	IL 2.5 dB	0.68°	1.19 dB	5 mW	0.06 mm^2
Jiang et al., 2025 [M]	B	VSPS (active, state selection)	2025	20–30	64-state	Active VSPS (QSG+VM+VGA)	0.18 µm SiGe BiCMOS	Tail-current controlled	Gain var. −1.2…0.1 dB	<2°	(Not RMS) −1.2…0.1 dB	19.5 mW @2.5 V	0.4 mm^2 (core 0.165)
Shen et al., 2025 [M]	A	STPS (SiGe, coupler-based 180°)	2025	90–100	6b / 5.625°	STPS; 180° coupler–LP	0.13 µm SiGe BiCMOS	Switch transistors	12–15.5 dB	<2.3°	<0.9 dB	NR	0.39 mm^2
Tu et al., 2025 [M]	B	VSPS (active, IDAC-weighted)	2025	27–31	7b / 2.8125°	Active VSPS (LC QAF + adder)	TSMC 90 nm CMOS	2×8-bit IDAC + adder	Avg gain 0.13–1.36 dB	0.18–0.21°	0.68–0.9 dB	10 mW	0.63 mm^2
Khazaei et al., 2025 [M]	A	Switched-line (Schiffman/ microstrip, PIN)	2025	2.2–3.322 (center frequency)	4b / 22.5°	Modified Schiffman	RO4003 microstrip	PIN SMP1321-040LF	Avg IL <4 dB	RMS <8.1°	NR	NR	NR
Sindhuja et al., 2025 [NM]	D	NEMS DNTL (discrete state)	2025		3b (45/90/180)	DNTL NEMS TL PS	Si/CPW + HfO_2	33 NEMS membran	Avg IL ~0.6 dB	±2° (Not RMS)	NR	~0	NR
Kilinc et al., 2026 [S]	A	STPS with active inductors (integrated)	2026	2.2–3.6	5b / 11.25°	STPS + active inductors	0.18 µm CMOS	MOS + gyrator-C AI	Avg IL ~14 dB	RMS <3.3°	NR	NR	0.17 mm^2
Lee et al., 2026 [M]	B	VSPS/Vector-sum (current-steering)	2026	10.7–12.7	6b / 5.625°	Current-steering VSPS	130 nm BiCMOS	RF-cell array	Gain −2.17–4.55 dB	≤2.5°	0.3–0.5 dB	15.8 mW	1.75×1.1 1 mm^2
Wei et al., 2026 [M]	B	VSPS + reconfigurable PPF	2026	2–18	6b / 5.625°	VSPS + reconfigurable PPF	0.13 µm SiGe BiCMOS	Varactor + IDAC	Gain 1.5–3.2 dB	<1.5°	<1.2 dB	105 mW	1240×860 µm^2

C= class, Y= year, T= technology STPS= switch-type phase shifter, VSPS= vector-sum phase shifter, VMPS= vector-modulator phase shifter, IL= insertion loss, RMS= root mean square, Pdc= DC power consumption, NR= not reported, COTS= commercial off-the-shelf, NEMS= nanoelectromechanical systems. Validation level: [M], measured, [PL], post-layout/EM simulation, [S], schematic-level simulation, [NM], numerical modeling, [SYS], system-level demonstration, [EB], enabling-block study.

Table 2. Architecture-level design trade-offs and representative application domains

Class	Architecture	Main strengths	Main limitations	Most suitable application domains
A	STPS	High linearity; simple control; zero or low static RF-path power in passive realizations	Insertion loss and area increase with bit count; parasitic sensitivity at mmWave frequencies	High-power radar, satellite front ends, low-complexity phased arrays
B	VSPS/VMPS	High resolution; calibration flexibility; active gain compensation	DC power consumption; I/Q mismatch; gain–phase coupling; calibration complexity	High-accuracy beamforming, active antenna arrays, mmWave and 6G transceivers
C	Lattice/all-pass	Wideband phase flatness; stable phase response; good matching potential	Passive loss; component-Q sensitivity; limited scalability at very high frequencies	Broadband microwave systems, phase-flat front ends, moderate-frequency arrays
D	Special/other	Fine delay-based resolution; NEMS low-power potential; system-specific flexibility	Heterogeneous maturity; limited comparability; integration and scalability challenges	Sub-THz systems, RIS, specialized radar, system/COTS demonstrations

4.5. Limitations

The conclusions presented in this review should be interpreted in light of several limitations. First, the reviewed studies span different operating frequencies, technologies, and validation levels, making perfectly fair comparison impossible. Second, several publications do not report RMS amplitude error, large-signal linearity, or complete calibration procedures. Third, some recent studies are available only as simulation or post-layout results rather than measured IC implementations. Consequently, the reported trends should be interpreted as evidence-supported observations rather than absolute rankings.

4.6. Future Research Directions

Future research on digital phase shifters is expected to transition from isolated circuit optimization toward system-integrated, reconfigurable, and calibration-aware design strategies. The application of artificial intelligence (AI) and machine learning (ML) techniques to phase-state optimization, calibration, process–voltage–temperature (PVT) compensation, and the prediction of parasitic-induced performance degradation represents a

promising research direction. In high-resolution vector-sum systems, where gain–phase coupling and large state spaces make conventional manual tuning increasingly challenging, data-driven optimization techniques may provide significant benefits.

A second research direction is the development of digital phase shifters for large-scale 6G beamforming systems and reconfigurable intelligent surfaces (RIS). Such applications require compact implementations, scalable control architectures, tolerance to device and process variations, and very low per-element power consumption. Low-complexity calibration techniques, distributed control strategies, and passive or hybrid phase-shifting architectures are therefore expected to become increasingly important for large-scale array implementations.

Operation at sub-THz frequencies remains a major design challenge because passive loss, device parasitics, layout sensitivity, and power-efficiency limitations become increasingly severe as the operating frequency approaches and exceeds 100 GHz. In this frequency range, delay-based, hybrid vector-delay, and digitally assisted architectures may provide viable alternatives to conventional phase-shifter topologies. Future studies should therefore evaluate not only nominal phase resolution but also the number of effectively usable phase states under process, voltage, temperature, device mismatch, packaging, and interconnect variations.

Finally, more standardized reporting practices should be encouraged to improve the reproducibility and comparability of future digital phase-shifter research. In particular, studies should consistently report RMS phase error, RMS amplitude error, insertion loss or gain, large-signal linearity metrics, calibration techniques, validation level, and measurement conditions. Such standardized reporting would enable more reliable cross-study comparisons and provide a stronger basis for evaluating the suitability of different architectures for emerging 6G, RIS, mmWave, and sub-THz applications.

5. Conclusion

This review systematically examined 27 papers covering a total of 30 digital phase-shifter designs, including switch-type phase shifters (STPS), vector-sum/vector-modulator-based architectures (VSPS/VMPS), lattice/all-pass-network-based solutions, and special categories such as delay-based fine-resolution and NEMS-related approaches. Because the literature exhibits substantial heterogeneity in topology, technology platform, operating frequency, and validation depth, the comparison was conducted using a multi-metric and evidence-aware framework. In this framework, measured IC/MMIC demonstrations were given primary emphasis as the strongest evidence of practical behavior, whereas post-layout or schematic-level studies, system/COTS demonstrations, and enabling-block works were treated as supporting evidence for architectural interpretation and trend analysis.

Several consistent observations emerged from the cross-comparison. First, practical phase accuracy depends more strongly on state consistency over frequency, parasitic-aware implementation, and the availability of calibration or compensation mechanisms than on nominal bit resolution alone. Accordingly, bit count should not be treated as a sufficient predictor of real accuracy. Second, STPS architectures remain attractive for applications requiring low complexity and little or no DC power in the RF path; however, as bandwidth and resolution targets increase, the trade-off among insertion loss, area, and achievable accuracy generally becomes more severe. Third, vector-based architectures offer a flexible route to broadband phase synthesis and, in active implementations, can partially compensate RF loss through gain. These benefits, however, are typically accompanied by increased sensitivity to I/Q imbalance, weighting mismatch, calibration complexity, and non-negligible DC power consumption. Fourth, lattice- and all-pass-network-based designs remain relevant when phase flatness across frequency is the dominant requirement, although this benefit is often achieved at the cost of increasing passive loss as frequency rises. Finally, delay-based approaches appear especially promising for sub-THz operation, where parasitic effects and implementation nonidealities increasingly limit the robustness of more conventional solutions.

The review also highlights several persistent reporting gaps in the literature. Although RMS phase error is reported more frequently than in earlier studies, RMS amplitude error, large-signal linearity metrics, and explicit descriptions of calibration or state-selection procedures are still not provided consistently. This limits the ability to compare designs fairly and to infer array-level consequences such as beam-pattern degradation, gain variation, and high-power behavior directly from published results. Future work would therefore benefit from more standardized reporting practices, including routine disclosure of large-signal metrics such as P1dB and IIP3, full-band and full-state evaluation of RMS phase and RMS amplitude errors, and clearer descriptions of calibration-aware measurement and optimization procedures.

Overall, the reviewed evidence does not support the existence of a universally optimal digital phase-shifter topology. Instead, the most suitable architecture depends on the dominant application constraint, whether it is ultra-high accuracy, wide bandwidth, low power, compact area, or scalability toward mmWave and sub-THz systems. Future scalable solutions will likely rely increasingly on reconfigurable or hybrid architectures, calibration-aware design strategies, and maximizing the number of effectively usable states under parasitic effects and process-voltage-temperature (PVT) variations. The taxonomy, evidence-aware methodology, and cross-comparison framework presented in this review are intended to support more informed topology selection while also improving reproducibility, transparency, and

comparability in future digital phase-shifter research.

Author Contributions

The percentages of the authors' contributions are presented below. All authors reviewed and approved the final version of the manuscript.

	S.T.	F.K.
C	60	40
D	60	40
S	30	70
DCP	70	30
DAI	70	30
L	70	30
W	75	25
CR	40	60
SR	70	30
PM	60	40

C=Concept, D= design, S= supervision, DCP= data collection and/or processing, DAI= data analysis and/or interpretation, L= literature search, W= writing, CR= critical review, SR= submission and revision, PM= project management.

Conflict of Interest

The authors declared that there is no conflict of interest.

Acknowledgements

The authors would like to acknowledge ChatGPT for assistance in improving the language and overall flow of the manuscript.

References

Anjos, E. V., Schreurs, D. M. P., Vandenbosch, G. A., & Geurts, M. (2020). A 14–50-GHz phase shifter with all-pass networks for 5G mobile applications. *IEEE Transactions on Microwave Theory and Techniques*, 68(2), 762–774. https://doi.org/10.1109/TMTT.2019.2948852

Avci, C., Gunes, E. O., & Yarman, B. S. (2019). A symmetric lattice-based wideband wide phase range digital phase shifter topology. *International Journal of Circuit Theory and Applications*, 47(8), 1269–1292. https://doi.org/10.1002/cta.2639

Brilhante, D. D. S., Manjarres, J. C., Moreira, R., de Oliveira Veiga, L., de Rezende, J. F., Müller, F., ... & de Figueiredo, F. A. P. (2023). A literature survey on AI-aided beamforming and beam management for 5G and 6G systems. *Sensors*, 23(9), Article 4359. https://doi.org/10.3390/s23094359

Chiu, H. C., Chen, C. M., Chang, L. C., & Kao, H. L. (2021). A 5-bit X-band GaN HEMT-based phase shifter. *Electronics*, 10(6), Article 658. https://doi.org/10.3390/electronics10060658

Cho, J., Lee, J. H., & Kim, M. (2025). The design of a 140 GHz 28 nm CMOS vector-sum phase shifter based on Gilbert cell and current-steering amplifiers. *Chips*, 4(4), Article 50. https://doi.org/10.3390/chips4040050

Coviello, G., Avitabile, G., Piccinni, G., D'Amato, G., & Talarico, C. (2016). Effects on phased arrays radiation pattern due to phase error distribution in the phase shifter operation. *MATEC Web of Conferences*, 76, Article 03002. EDP Sciences. https://doi.org/10.1051/matecconf/20167603002

Gharsalli, S., Aloui, R., Mhatli, S., Corona-Chavez, A., Brito-Brito, Z., Mishra, S. K., & Llamas-Garro, I. (2026). Comprehensive phase shifter review: State of the art and future trends. *Progress in Electromagnetics Research B*, 116. https://doi.org/10.2528/PIERB25082704

Ghorbani, F. (2025). *Highly linear and fast phase shifting technology* [Doctoral dissertation, University of Liverpool].

Hamidi, E. A. Z., Arifin, A. I., Soedarsono, S., & Siddiq, S. F. (2019). Design and implementation of planar phase shifter for radar at frequency 2.9 GHz–3.1 GHz as beam-steering. *Journal of Physics: Conference Series*, 1402(3), Article 033091. IOP Publishing. https://doi.org/10.1088/1742-6596/1402/3/033091

Jiang, H., Zhao, Z., Zhu, N., & Meng, F. (2025). Design and analysis of an ultra-wideband high-precision active phase shifter in 0.18 μm SiGe BiCMOS technology. *Journal of Low Power Electronics and Applications*, 15(2), Article 30. https://doi.org/10.3390/jlpea15020030

Kebe, M., Yagoub, M. C. E., & Amaya, R. E. (2025). A survey of phase shifters for microwave phased array systems. *International Journal of Circuit Theory and Applications*, 53(6), 3719–3739. https://doi.org/10.1002/cta.4298

Khazaei, M., Armaki, S. H. M., & Amin, A. S. N. (2025). Proposing a modified switchable Schiffman structure to implement a wideband and low-loss 4-bit digital phase shifter. *IEEE Access*. https://doi.org/10.1109/ACCESS.2025.3615716

Kilinc, M., Kacar, F., Ormanci, M. A., & Kilinc, S. (2026). Design of a 5-bit CMOS phase shifter with tunable active inductors for 5G applications in S-band. *IEICE Electronics Express*, 23(4), Article 20250631. https://doi.org/10.1587/elex.22.20250631

Lee, J. S., Chang, W. J., Jang, K. H., & Jang, T. H. (2026). A 6-bit digitally controlled vector-sum phase shifter with current steering architecture. *IDEC Journal of Integrated Circuits and Systems*, 12(1), 43–48. https://doi.org/10.23075/jicas.2026.12.1.008

Li, X., Fu, H., Ma, K., & Hu, J. (2022). A 2.4–4-GHz wideband 7-bit phase shifter with low RMS phase/amplitude error in 0.5-μm GaAs technology. *IEEE Transactions on Microwave Theory and Techniques*, 70(2), 1292–1301. https://doi.org/10.1109/TMTT.2021.3123053

Lin, Q., Xu, J., Chen, K., Wang, L., Li, W., Yu, Z., ... & Hong, W. (2024). A single-board integrated millimeter-wave asymmetric full-digital beamforming array for B5G/6G applications. *Engineering*, 41, 35–50. https://doi.org/10.1016/j.eng.2024.04.013

Lin, W. P., & Lin, C. Y. (2025). 4 × 4 active antenna array with digital phase shifting for WiFi 6E applications. *Electronics*, 14(19), Article 3772. https://doi.org/10.3390/electronics14193772

Lin, Y. H., & Tsai, Z. M. (2022). Topology selection of switch-type phase shifter units for wideband Ka-band 5-bit phase shifter with low RMS errors. *Microwave and Optical Technology Letters*, 64(2), 259–264. https://doi.org/10.1002/mop.33083

Luo, L., Li, Z., Yao, Y., & Cheng, G. (2019). A 6–18 GHz 6-bit active phase shifter in 0.13-μm SiGe BiCMOS. *IEICE Electronics Express*, 16(10), Article 20190233. https://doi.org/10.1587/elex.16.20190233

Mailloux, R. J. (2017). *Phased array antenna handbook*. Artech House.

Minnella, A. D., Papotto, G., Finocchiaro, A., Parisi, A., Castorina, A., & Palmisano, G. (2025). A 39 GHz phase shifter in 28 nm FD-SOI CMOS technology for mm-wave wireless communications. *Electronics*, 14(22), Article 4433. https://doi.org/10.3390/electronics14224433

Shangguan, Y., Quan, H., Wen, W., & Liang, Y. (2024). An 8–18

GHz 6-bit phase shifter with balance-compensated balun. *Journal of Physics: Conference Series*, 2849(1), Article 012022. IOP Publishing. https://doi.org/10.1088/1742-6596/2849/1/012022

Shen, H., Zhang, H., Pu, Y., Wang, C., Li, B., Tang, X., ... & Luo, J. (2025). A 90–100 GHz SiGe BiCMOS 6-bit digital phase shifter with a coupler-based 180° unit for phased arrays. *Micromachines*, 16(9), Article 1056. https://doi.org/10.3390/mi16091056

Sindhuja, N. M., Kanthamani, S., Anbalagan, A., & Ramalakshmi, P. (2025). Meshfree method-based modeling of distributed nanotransmission line phase shifter for 5G wireless applications. *International Journal of RF and Microwave Computer-Aided Engineering*, 2025(1), Article 8823750. https://doi.org/10.1155/mmce/8823750

Song, J. H., Lee, E. G., Lee, J. E., Son, J. T., Kim, J. H., Baek, M. S., & Kim, C. Y. (2023). A 37–40 GHz 6-bits switched-filter phase shifter using 150 nm GaN HEMT. *Nanomaterials*, 13(20), Article 2752. https://doi.org/10.3390/nano13202752

Taş, S., & Kaçar, F. (2025). Design and simulation of a wideband 3-bit phase shifter for 4.5–5.5 GHz applications. *IET Circuits, Devices & Systems*, 2025(1), Article 5377138. https://doi.org/10.1049/cds2/5377138

Tu, H. J., Chen, H. C., Chen, P. H., & Huang, P. Y. (2025). A 7-bit vector-sum phase shifter for LEO satellite communication in 90-nm CMOS process. *IEEE Access*. https://doi.org/10.1109/ACCESS.2025.3591240

Uchino, T., Yamazaki, Y., Tian, A., Liu, C., Park, S., Shehata, A., ... & Okada, K. (2025). A compact D-band phase shifter with 0.1-degree phase resolution and ultra-low phase error in 65-nm CMOS. *IEEE Journal of Solid-State Circuits*. https://doi.org/10.1109/JSSC.2025.3577051

Wei, Y., Wang, Z., Huang, Z., Yang, Y., & Liu, M. (2026). A 2-to-18-GHz 6-bit vector-sum phase shifter with tunable operating band. *International Journal of Circuit Theory and Applications*. https://doi.org/10.1002/cta.70329

Wu, T., Zhang, X., Xing, Z., Zhao, C., Yu, Y., & Liu, H. (2021). A 21.5–25 GHz 7-bit phase shifter with passive vector-sum topology. *Microwave and Optical Technology Letters*, 63(6), 1652–1656. https://doi.org/10.1002/mop.32783

Xiong, Y., Zeng, X., & Li, J. (2020). A frequency-reconfigurable CMOS active phase shifter for 5G mm-wave applications. *IEEE Transactions on Circuits and Systems II: Express Briefs*, 67(10), 1824–1828. https://doi.org/10.1109/TCSII.2019.2958665

Zeng, J., Xie, C., Zhang, D., Feng, J., Tan, C., & Yu, Z. (2023). A wideband accurate compact 6-bit phase shifter in 0.15-μm GaAs technology. *Microwave and Optical Technology Letters*, 65(2), 534–540. https://doi.org/10.1002/mop.33535

Zhan, H., Zhang, T., & Pei, X. (2024). Design of 2.5–3.3 GHz high-precision compact digital phase shifter. *Journal of Physics: Conference Series*, 2807(1), Article 012004. IOP Publishing. https://doi.org/10.1088/1742-6596/2807/1/012004